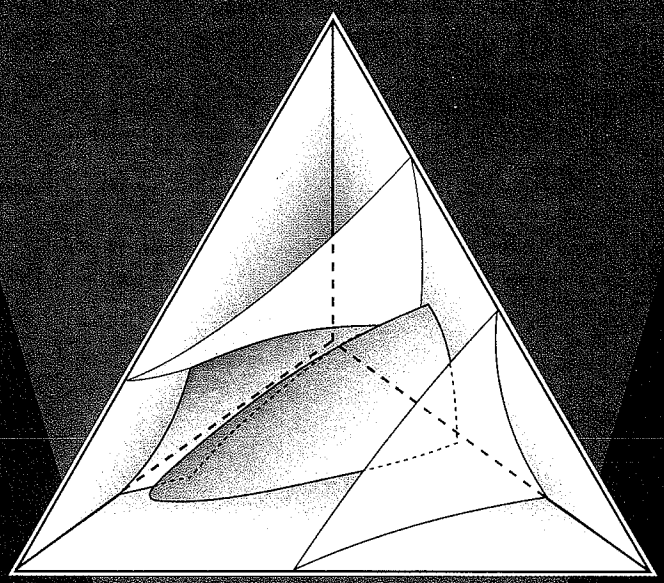
SLAG ATLAS



STAHLEISEN

SLAG ATLAS

2nd Edition

SLAG ATLAS

2nd Edition

Edited by

Verein Deutscher Eisenhüttenleute (VDEh)

VOEST ALPINE Industrieanlagenbau GmbH
CMP Marketing & Werkstoffforschung
Buch-Nr.: 101996
Standort: TSS-5
Eingang: 12.12.1995

Verlag Stahleisen GmbH

List of Authors:

M. Allibert
H. Gaye
J. Geiseler
D. Janke
B. J. Keene
D. Kirner
M. Kowalski
J. Lehmann
K. C. Mills
D. Neuschütz
R. Parra
C. Saint-Jours
P. J. Spencer
M. Susa
M. Tmar
E. Woermann

ECSC Research 7210-CF/107

This work is subject to copyright. All rights are reserved, whether the whole or part of the material is concerned, specifically those of translation, reprinting, re-use of illustrations, reproduction by photocopying machine or similar means, and storage in data banks.

© 1995 Verlag Stahleisen GmbH, D-Düsseldorf,
on behalf of the European Communities
Printed in Germany

ISBN 3-514-00457-9

Preface

In iron and steelmaking as well as in non-ferrous metal production and other refining technologies the use of slag is of essential importance. The refining reactions are controlled by metal/slag systems and nearly all process steps in iron and steel production, from hot metal production to special melting processes, as well as continuous casting, are closely related to the use of metallurgically effective slag. Knowledge of the properties of the slag used is needed to enable assessment of the various reactions and optimal process control.

As compared to metal melts, liquid slag display a greater variety of properties which can be varied over a wide range by changing compositions and temperatures. Complete and detailed information is needed to optimize the processes in iron and steelmaking; in particular, to optimize refining techniques in hot metal and in scrap-based steelmaking for lower contents of tramp elements and improved cleanness. In continuous casting processes the heat extraction, lubrication and surface quality have to be influenced in an optimal way by liquid casting slag.

The Committee on Metallurgical Fundamentals of the German Iron and Steel Institute (VDEh) therefore began already during the sixties with the compilation of slag data. The results were published in the first issue of the Slag Atlas, edited by VDEh with financial assistance of the European Coal and Steel Community (ECSC) in 1981.

But it was soon recognised that, without greater institutional efforts, a critical assessment of all data available was very difficult or even impossible due to incompleteness of the published data and because of the ever increasing amount of the data to be collected. Consequently, a critical selection was often not possible in the course of subsequent data compilation. Therefore in an international multi-partner research project of the ECSC (Project No. 7210-CF/107) a comprehensive review and evaluation of slag data was started in 1989 by co-working of VDEh, Max-Planck-Institut für Eisenforschung (MPI) and Lehrstuhl für Theoretische Hüttenkunde of RWTH Aachen in Germany, Institut de Recherches de la Sidérurgie Française (IRSID) and Institut National Polytechnique de Grenoble (INPG) in France as well as National Physical Laboratory (NPL) in the United Kingdom.

The research obtained significant results and improvements in the knowledge of slag properties. Furthermore, important data are now available on diffusion coefficients, heat conductivity, optical properties and sulphide and phosphate capacities. This information is particularly relevant due to the current efforts to reduce sulphur and phosphorous levels in steel, to control the kinetics of metal/slag reactions and the erosion of refractories and submerged entry nozzles, to precisely calculate thermal balance and heat transfer, and finally to contribute significantly to quality control in steel production.

The research project 7210-CF/107 was terminated with the production of a final report of over 2000 pages, presented in 15 volumes and compiled by the 6 partners. Due to the large amount of data reported, to the novel aspect of the work and to the active interest of researchers and production managers throughout the European steel industries, an action of valorization of the research results was desirable in order to adequately diffuse information to production, research and education establishments. So in the ECSC contract 7210-ZZ/608 the publication was prepared in this second issue of the Slag Atlas.

The editor is very grateful to all the authors listed up above for their comprehensive work and their engagement over many years. The editor thanks also Mrs. B. Schmitz and Dr.-Ing. J. A. Schmitz, Düsseldorf, for their excellent work in preparing this issue. Finally, special thanks are due to Dr. R. Tomellini, Brussels, for providing all the necessary support for publishing the results in this book.

We thank the European Commission for the financial assistance under the research promotion scheme by the ECSC.

Düsseldorf, September 1995

Verein Deutscher Eisenhüttenleute (VDEh)

Dr.-Ing. D. Springorum

Contents

Preface V

Explanation of frequently used symbols and abbreviations XVII

1 Structure of liquid slags 1
K. C. Mills

1.1 Introduction 2
1.2 Methods used to determine structure 2
1.2.1 X-ray, electron and neutron diffraction 2
1.2.2 Vibration spectroscopy 2
1.2.3 Nuclear magnetic resonance (NMR) 4
1.2.4 Electron spin resonance (ESR) 4
1.2.5 Mössbauer spectroscopy 4
1.2.6 X-ray absorption spectroscopy 4
1.2.7 X-ray emission spectroscopy 4
1.2.8 X-ray photon spectroscopy (XPS) or electron spectroscopy for chemical analyses (ESCA) 4
1.2.9 Chromatographic separation 4
1.2.10 Molar refractivity 5
1.3 The structure of slags containing silica and/or other complex-forming constituents 5
1.4 Appendix 6
1.5 References in Chapter 1 7

2 Basicity and optical basicities of slags 9
K. C. Mills

2.1 Basicity 10
2.2 Optical basicity 10
2.2.1 Introduction 10
2.2.2 Relation between optical basicity and partition of elements 11
2.2.2.1 Sulphur capacities 11
2.2.2.2 Phosphate capacities 12
2.2.2.3 Oxygen partition 13
2.2.2.4 Manganese partition 13
2.2.2.5 Vanadium partition 14
2.2.2.6 Water partition 14
2.2.3 Relation between optical basicity and the solubility of oxides in the slag 14
2.2.3.1 MgO solubility 14
2.2.3.2 K_2O solubility 14
2.2.4 Relation between optical basicity and thermodynamic properties 15
2.2.4.1 Activity coefficient of P_2O_5 15
2.2.4.2 Activity coefficient of FeO 16
2.2.4.3 Activity of CaO 16
2.2.4.4 Activity of Na_2O 16
2.2.5 Relation between optical basicity and structure and physical properties 16
2.2.5.1 Structure 16
2.2.5.2 Viscosity 17
2.2.5.3 Electrical conductivity 17
2.2.5.4 Thermal conductivity 18
2.2.5.5 Thermal expansion coefficient 18
2.2.6 Flux control in BOS process 18
2.3 Appendix 18
2.3.1 Methods used to obtain optical basicity values for oxides 18
2.3.1.1 Spectroscopic methods 18
2.3.1.2 Refractivity measurement 18
2.3.1.3 Curve fitting 18
2.3.1.4 Calculated values of Λ_{th} 18
2.4 References in Chapter 2 19

3 Phase diagrams 21
M. Kowalski, P. J. Spencer and D. Neuschütz

3.1 Introduction 22
3.1.1 Geometrical representation of phase equilibria 22
3.1.2 Methods of investigation of phase equilibria *(by E. Woermann)* 23
3.1.2.1 Starting materials 23
3.1.2.2 Crucible material 23
3.1.2.3 Quench-furnace 24
3.1.2.4 Redox reactions 24
3.1.2.5 Reaction time 24
3.1.2.6 Investigation of the run products 24
3.1.2.7 EMF-measurements 24
3.1.3 Thermodynamic models and databases for calculation of phase diagrams and thermodynamic properties of slags 25
3.1.3.1 Associated solution model 26
3.1.3.2 Cellular model 26
3.1.3.3 Modified quasi-chemical model 27
3.1.3.4 Sub-lattice model 27
3.1.4 Comments and selected calculated phase diagrams 27
3.2 Slag systems 30
3.2.1 Basic metal-nonmetal systems 30
Al-O 30; Ca-O 30; Co-O 31; Cr-O 31; Fe-O 32; K-O 33; Mg-O 34; Mn-O 34; Na-O 35; Ni-O 35; Si-O 36; Ti-O 36; V-O 37; Ca-F 37; Fe-S 38; Mn-S 38
3.2.2 Binary oxide systems 39
Al_2O_3-CaO 39; Al_2O_3-Cr_2O_3 39; Al_2O_3-FeO_x 40; Al_2O_3-K_2O 44; Al_2O_3-MgO 44; Al_2O_3-MnO_x 45; Al_2O_3-Na_2O 46; Al_2O_3-SiO_2 47; Al_2O_3-TiO_2 48; Al_2O_3-ZrO_2 49; B_2O_3-BaO 49; B_2O_3-CaO 50; B_2O_3-FeO_x 50; B_2O_3-K_2O 51; B_2O_3-MgO 52; B_2O_3-MnO_x 52; B_2O_3-Na_2O 53; B_2O_3-SiO_2 54; BaO-FeO_x 54; BaO-SiO_2 55; CaO-Cr_2O_3 56; CaO-FeO_x 57; CaO-MgO 61; CaO-MnO_x 61; CaO-P_2O_5 62; CaO-SiO_2 63; CaO-TiO_2 63; CaO-V_2O_5 64; Cr_2O_3-FeO_x 64; Cr_2O_3-MgO 68; CrO_x-SiO_2 68; FeO_x-K_2O 69; FeO_x-MgO 70; FeO_x-MnO_x 72; FeO_x-Na_2O 75; FeO_x-NiO 76; FeO_x-P_2O_5 77; FeO_x-SiO_2 79; FeO_x-SrO 81; FeO_x-TiO_2 81; FeO_x-ZrO_2 83; K_2O-P_2O_5 84; K_2O-SiO_2 85; K_2O-TiO_2 85;

Li_2O-SiO_2 86; MgO-MnO_x 86;
MgO-P_2O_5 88; MgO-SiO_2 88;
MgO-TiO_2 89; MnO_x-P_2O_5 89;
MnO_x-SiO_2 90; MnO_x-TiO_2 92;
Na_2O-P_2O_5 93; Na_2O-SiO_2 94;
Na_2O-TiO_2 94; P_2O_5-SiO_2 95;
PbO-SiO_2 95; SiO_2-SrO 96;
SiO_2-TiO_x 97; SiO_2-ZnO 98;
SiO_2-ZrO_2 98

3.2.3 Ternary oxide systems 99
Al_2O_3-B_2O_3-CaO 99; Al_2O_3-B_2O_3-SiO_2 99;
Al_2O_3-BaO-CaO 100; Al_2O_3-BaO-SiO_2 100;
Al_2O_3-CaO-Cr_2O_3 101; Al_2O_3-CaO-FeO_x 102;
Al_2O_3-CaO-K_2O 103; Al_2O_3-CaO-MgO 104;
Al_2O_3-CaO-Na_2O 104;Al_2O_3-CaO-SiO_2 105;
Al_2O_3-CaO-TiO_2 105; Al_2O_3-CaO-ZrO_2 106;
Al_2O_3-Cr_2O_3-FeO_x 107; Al_2O_3-Cr_2O_3-MgO 109;
Al_2O_3-FeO_x-MgO 110; Al_2O_3-FeO_x-MnO_x 110;
Al_2O_3-FeO_x-SiO_2 111; Al_2O_3-K_2O-SiO_2 112;
Al_2O_3-MgO-SiO_2 113; Al_2O_3-MgO-TiO_2 115;
Al_2O_3-MnO_x-SiO_2 116; Al_2O_3-Na_2O-SiO_2 117;
Al_2O_3-SiO_2-TiO_2 118; B_2O_3-CaO-FeO_x 118;
B_2O_3-CaO-SiO_2 119; BaO-SiO_2-TiO_2 120;
CaO-Cr_2O_3-SiO_2 120; CaO-FeO_x-MgO 121;
CaO-FeO_x-MnO_x 123; CaO-FeO_x-P_2O_5 124;
CaO-FeO_x-SiO_2 126; CaO-FeO_x-TiO_2 130;
CaO-K_2O-SiO_2 132; CaO-MgO-MnO_x 133;
CaO-MgO-P_2O_5 133; CaO-MgO-SiO_2 134;
CaO-MgO-TiO_2 135; CaO-MnO_x-P_2O_5 136;
CaO-MnO_x- SiO_2 136; CaO-Na_2O-P_2O_5 137;
CaO-Na_2O-SiO_2 138; CaO-P_2O_5-SiO_2 138;
CaO-SiO_2-TiO_2 140; Cr_2O_3-FeO_x-SiO_2 140;
Cr_2O_3-MgO-SiO_2 141; FeO_x-K_2O-SiO_2 142;
FeO_x-MgO-SiO_2 142; FeO_x-MgO-TiO_2 145;
FeO_x-MnO-P_2O_5 146; FeO_x-MnO_x-SiO_2 146;
FeO_x-MnO_x-TiO_2 147; FeO_x-Na_2O-SiO_2 148;
FeO_x-SiO_2-TiO_2 148; FeO_x-SiO_2-ZrO_2 149;
K_2O-Na_2O-P_2O_5 150; Li_2O-Na_2O-SiO_2 150;
MgO-MnO_x-SiO_2 151; MgO-P_2O_5-SiO_2 152;
MgO-SiO_2-TiO_2 153; MnO_x-Na_2O-SiO_2 153;
Na_2O-SiO_2-V_2O_5 154

3.2.4 Quaternary oxide systems 154
Al_2O_3-CaO-FeO_x-SiO_2 154;
Al_2O_3-CaO-MgO-SiO_2 156;
Al_2O_3-CaO-MnO_x-SiO_2 162;
Al_2O_3-CaO-Na_2O-SiO_2 163;
Al_2O_3-CaO-P_2O_5-SiO_2 166;
Al_2O_3-CaO-SiO_2-TiO_2 166;
B_2O_3-CaO-FeO_x-SiO_2 168;
CaO-FeO_x-MgO-SiO_2 169;
CaO-FeO_x-MgO-TiO_2 172;
CaO-FeO_x-MnO_x-P_2O_5 173;
CaO-FeO_x-MnO_x-SiO_2 173;
CaO-FeO_x-P_2O_5-SiO_2 174;
CaO-MgO-Na_2O-SiO_2 175;
CaO-MgO-P_2O_5-SiO_2 176;
CaO-MgO-SiO_2-TiO_2 178

3.2.5 Systems with five oxide components 181
Al_2O_3-CaO-Cr_2O_3-MgO-SiO_2 181;
Al_2O_3-CaO-MgO-MnO_x-SiO_2 183;
Al_2O_3-CaO-MgO-SiO_2-TiO_2 184;
CaO-FeO_x-MgO-SiO_2-TiO_2 186

3.2.6 Slag systems containing fluorine 186
Al_2O_3-CaF_2 186; BaO-CaF_2 187;
CaF_2-CaO 187; CaF_2-FeO_x 188;
CaF_2-MgO 188; CaF_2-NaF 189;
CaF_2-SiO_2 189; CaF_2-TiO_2 190;
AlF_3-CaF_2-NaF 190; Al_2O_3-CaF_2-CaO 191;
Al_2O_3-CaF_2-FeO_x 192; Al_2O_3-CaF_2-MgO 192;
Al_2O_3-CaF_2-SiO_2 192; Al_2O_3-CaF_2-TiO_2 193;
CaF_2-CaO-Cr_2O_3 193; CaF_2-CaO-FeO_x 193;
CaF_2-CaO-MgO 194; CaF_2-CaO-SiO_2 194;
CaF_2-CaO-TiO_2 195; CaF_2-FeO_x-SiO_2 195;
CaF_2-MgO-SiO_2 195; CaF_2-Na_2O-SiO_2 196;
CaF_2-SiO_2-TiO_2 196;
Al_2O_3-CaF_2-CaO-MgO 197;
Al_2O_3-CaF_2-CaO-SiO_2 198;
Al_2O_3-CaF_2-MgO-SiO_2 199;
CaF_2-CaO-FeO_x-SiO_2 199;
Al_2O_3-CaF_2-CaO-MgO-SiO_2 200

3.2.7 Slag systems containing sulphur 201
CaO-CaS 201; CaS-FeS 202;
CaS-MnS 202; Cu_2S-FeS 203;
Fe-O-S 203; FeS-MnS 204;
MnO-MnS 205; Al_2O_3-CaO-CaS 206;
Ca-Fe-O-S 206;
CaO-CaS-SiO_2 208; Fe-Mn-O-S 208;
FeO_x-FeS-SiO_2 209; Fe-Mn-O-S-Si 209

3.2.8 Other slag systems 210
CaC_2-CaF_2 210; CaF_2-CaO-CaS 211;
CaF_2-CaO-CaS-SiO_2 211
3.3 Figures and tables 212

4 Composition and structure of slags 215
J. Geiseler

4.1 Introduction 216
4.2 Blast furnace slags 216
4.3 Steelmaking slags 217
4.3.1 Phosphate slags 217
4.3.2 Lime-silicate slags 219
4.4 ESR slags 224
4.5 References in Chapter 4 224

5 Thermodynamic activity data for slag systems 225
M. Allibert, R. Parra, C. Saint-Jours and M. Tmar

5.1 Preliminary remarks on the activity data 226
5.2 Thermodynamic activity data 226

5.2.1 Binary systems 226
Al_2O_3-CaO 226; Al_2O_3-FeO 226;
Al_2O_3-MnO 226; Al_2O_3-SiO_2 227;
BaO-FeO 227; B_2O_3-MnO 227;
B_2O_3-Na_2O 227; B_2O_3-SiO_2 228;
CaF_2-CaO 228; CaF_2-FeO 228;
CaF_2-MgO 228; CaO-FeO 229;
CaO-SiO_2 229; FeO-P_2O_5 230;
FeO-SiO_2 230; FeO-SrO 230;
FeO-TiO_2 231; K_2O-SiO_2 231;
MgO-P_2O_5 231; MgO-SiO_2 232;

MnO-SiO_2 232; MnO-TiO_2 233;
Na_2O-P_2O_5 233; Na_2O-SiO_2 233

5.2.2 Ternary systems 234
Al_2O_3-CaF_2-CaO 234;
Al_2O_3-CaF_2-FeO 235;
Al_2O_3-CaF_2-MgO 236;
Al_2O_3-CaO-MgO 237;
Al_2O_3-CaO-SiO_2 237;
Al_2O_3-FeO-MnO 239;
Al_2O_3-MgO-SiO_2 240; Al_2O_3-Na_2O-SiO_2 241;
CaF_2-CaO-FeO 241; CaF_2-CaO-SiO_2 242;
CaO-FeO-Fe_2O_3 242; CaO-FeO-SiO_2 243;
CaO-MnO-SiO_2 244; CaO-Na_2O-SiO_2 245;
FeO-MgO-SiO_2 245; FeO-MnO-SiO_2 245;
FeO-MnO-TiO_2 247; FeO-Na_2O-SiO_2 248;
FeO-SiO_2-TiO_2 248; MgO-MnO-SiO_2 248;
MgO-Na_2O-SiO_2 248; MnO-SiO_2-TiO_2 249

5.2.3 Quaternary systems 249
Al_2O_3-CaF_2-CaO-SiO_2 249;
Al_2O_3-CaO-MgO-SiO_2 249;
Al_2O_3-CaO-MnO-SiO_2 250;
Al_2O_3-FeO-MnO-SiO_2 250;
CaF_2-CaO-FeO-SiO_2 250;
CaO-FeO-Fe_2O_3-SiO_2 251;
CaO-FeO-MgO-SiO_2 254

5.3 References in Chapter 5 254

6 Slag capacities 257
6.1 Sulphide capacities 258
H. Gaye and J. Lehmann

6.1.1 Sulphide and sulphate equilibria 258
6.1.2 Sulphide capacity 258
6.1.2.1 Sulphide capacity diagrams, preliminary remarks 258
6.1.2.2 Slag-metal sulphur partition diagrams, preliminary remarks 258
6.1.2.3 CaS saturation, preliminary remarks 259

6.1.3 Sulphide capacities calculated according to IRSID's slag model 259
Al_2O_3-CaO-SiO_2 259; Al_2O_3-MgO-SiO_2 260;
Al_2O_3-MnO-SiO_2 260; CaO-FeO-SiO_2 260;
CaO-MnO-SiO_2 260; FeO-MnO-SiO_2 260;
MgO-MnO-SiO_2 261

6.1.4 Sulphide capacities determined 261
6.1.4.1 CaF_2 bearing systems 261
6.1.4.2 Na_2O bearing systems 262
6.1.4.3 P_2O_5 bearing systems 263
6.1.4.4 TiO_2 bearing systems 263
6.1.5 Sulphur partition coefficients 265
6.1.6 CaS saturation diagrams 266
6.1.7 References in Chapter 6.1 267

6.2 Phosphate and phosphide capacities and phosphorus distribution 268
D. Kirner and D. Janke

6.2.1 Phosphate capacity 268
6.2.2 Phosphide capacity 268
6.2.3 Phosphorus distribution 269
6.2.4 Symbols used in the sections 6.2.5 and 6.2.6 269
6.2.5 Phosphate capacity and phosphorus distribution diagrams 269

6.2.5.1 Ternary systems 269
Al_2O_3-CaF_2-CaO 269;
Al_2O_3-CaO-FeO 270;
BaO-CaF_2-FeO 270;
CaF_2-FeO-MgO 270;
CaF_2-CaO-FeO 271;
CaO-FeO-P_2O_5 271;
CaO-FeO-SiO_2 272;
Na_2O-P_2O_5-SiO_2 273

6.2.5.2 Quaternary systems 273
BaF_2-BaO-Cr_2O_3-MgO 273;
CaO-FeO-MgO-SiO_2 273;
CaO-FeO-P_2O_5-SiO_2 275;
FeO-MgO-Na_2O-SiO_2 276

6.2.5.3 Systems with five and more components 276
Al_2O_3-CaF_2-CaO-Cr_2O_3-FeO-Li_2CO_3-MgO-SiO_2 276; Al_2O_3-CaF_2-CaO-FeO-MgO-MnO-P_2O_5-SiO_2 277;
Al_2O_3-CaO-FeO-MgO-P_2O_5-SiO_2 277;
B_2O_3-CaO-FeO-MgO-MnO-P_2O_5-SiO_2 277;
BaO-CaO-FeO-MgO-SiO_2 278;
CaF_2-CaO-FeO-MgO-SiO_2 278;
CaO-FeO-MgO-Na_2O-SiO_2 279;
CaO-FeO-MnO-P_2O_5-SiO_2 279;
FeO-MgO-MnO-Nb_2O_5-SiO_2 279

6.2.6 Phosphide capacity 280
6.2.7 References in Chapter 6.2 281

7 Solubility of gases in liquid slags 283
D. Kirner and D. Janke

7.1 Hydrogen 284

7.1.1 Binary systems 284
Al_2O_3-CaO 284; CaO-FeO_n 284;
CaO-SiO_2 284; MnO-SiO_2 285

7.1.2 Ternary systems 286
Al_2O_3-CaF_2-CaO 286;
Al_2O_3-CaO-SiO_2 286;
CaF_2-CaO-SiO_2 287; CaO-FeO-SiO_2 287;
CaO-Li_2O-SiO_2 289; CaO-MgO-SiO_2 289;
CaO-Na_2O-SiO_2 290; CaO-P_2O_5-SiO_2 290;
CaO-SiO_2-SrO 290; CaO-SiO_2-TiO_2 290;
FeO_n-Fe_2O_3-SiO_2 291

7.1.3 Quaternary systems 291
Al_2O_3-CaO-MgO-SiO_2 291;
CaF_2-CaO-FeO_n-SiO_2 291;
CaO-FeO-MgO-SiO_2 291

7.1.4 Industrial slags 292
7.1.4.1 Electric arc furnace slags 292
7.1.4.2 Synthetic slags 292

7.2 Nitrogen 294

7.2.1 Binary systems 294
Al_2O_3-CaO 294; CaF_2-CaO 298; CaO-SiO_2 299; Na_2O-SiO_2 300

7.2.2 Ternary systems 301
Al_2O_3-CaF_2-CaO 301; Al_2O_3-CaO-SiO_2 301; BaO-MgO-SiO_2 302; CaF_2-CaO-SiO_2 303; CaO-MgO-SiO_2 303

7.2.3 Quaternary systems and systems with more components 303
Al_2O_3-CaO-MgO-SiO_2 303; Al_2O_3-CaF_2-CaO-MgO-SiO_2 305; Al_2O_3-CaO-Fe_3O_4-FeS-MgO-MnO-SiO_2 306

7.2.4 Technological slags 307
7.2.4.1 Blast furnace slags 307
7.2.4.2 Electric arc furnace slags 307
7.3 Carbon dioxide 307

7.3.1 Binary systems 307
Al_2O_3-CaO 307; CaF_2-CaO 308; CaO-Fe_2O_3 308; Na_2O-P_2O_5 308; Na_2O-SiO_2 308

7.3.2 Ternary systems 309
$CaCl_2$-CaF_2-CaO 309; $CaCl_2$-CaO-SiO_2 309; CaO-Na_2O-SiO_2 310; Na_2O-P_2O_5-SiO_2 310

7.4 References in Chapter 7 310

8 Densities of molten slags 313
B. J. Keene and K. C. Mills

8.1 Definitions 314
8.2 Methods 314
8.2.1 Weighing method (pycnometry) 314
8.2.2 Buoyancy method (Archimedes Principle) 314
8.2.3 Volumetric method (dilatometer) 314
8.2.4 Pressure method 314
8.2.5 Droplet method 315
8.2.6 Suspension method 315
8.3 Densities 315

8.3.1 Pure substances 315
CaF_2 315; Fe_xO 315

8.3.2 Binary systems 316
Al_2O_3-CaF_2 316; Al_2O_3-CaO 317; Al_2O_3-Cr_2O_3 317; Al_2O_3-MgO 318; Al_2O_3-SiO_2 318; B_2O_3-CaO 318; CaF_2-CaO 319; CaF_2-Cr_2O_3 319; CaF_2-MgO 320; CaF_2-SiO_2 320; CaF_2-TiO_2 320; CaF_2-V_2O_5 321; CaF_2-ZrO_2 321; CaO-Fe_xO 321; CaO-P_2O_5 322; CaO-SiO_2 322; Fe_xO-SiO_2 323; MgO-SiO_2 324; MnO-SiO_2 324; Na_2O-P_2O_5 324; Na_2O-SiO_2 325

8.3.3 Ternary systems 325
Al_2O_3-B_2O_3-CaF_2 325; Al_2O_3-B_2O_3-CaO 326; Al_2O_3-CaF_2-CaO 326; Al_2O_3-CaF_2-MgO 327; Al_2O_3-CaF_2-Nb_2O_5 327; Al_2O_3-CaF_2-TiO_2 328; Al_2O_3-CaF_2-V_2O_5 328; Al_2O_3-CaO-Fe_2O_3 328; Al_2O_3-CaO-MgO 328; Al_2O_3-CaO-Na_2O 329; Al_2O_3-CaO-SiO_2 329; Al_2O_3-CaO-TiO_2 331; Al_2O_3-Fe_xO-SiO_2 331; Al_2O_3-MgO-SiO_2 332; Al_2O_3-Na_2O-SiO_2 332; Al_2O_3-SiO_2-TiO_2 333; CaF_2-CaO-SiO_2 333; CaO-CaS-SiO_2 334; CaO-Fe_xO-P_2O_5 334; CaO-Fe_xO-SiO_2 334; CaO-MgO-SiO_2 337; CaO-MnO-SiO_2 337; CaO-Na_2O-SiO_2 338; Fe_xO-MgO-SiO_2 338; Fe_xO-MnO-SiO_2 339; Fe_xO-Na_2O-SiO_2 339; MgO-Na_2O-SiO_2 339; MnO-Na_2O-SiO_2 339; MnO-P_2O_5-SiO_2 339

8.3.4 Quaternary systems 339
Al_2O_3-CaF_2-CaO-MgO 339; Al_2O_3-CaF_2-MgO-SiO_2 340; Al_2O_3-CaO-Fe_xO-SiO_2 340; Al_2O_3-CaO-MgO-SiO_2 340; Al_2O_3-CaO-MnO-SiO_2 341; Al_2O_3-CaO-Na_2O-SiO_2 342; Al_2O_3-Fe_xO-MgO-SiO_2 342; CaO-Fe_xO-MnO-SiO_2 343; Fe_xO-MgO-Na_2O-SiO_2 343

8.3.5 Effect of Fe_xO concentration 344
8.4 Appendix 345
8.4.1 Models to estimate some properties of slags 345
8.4.2 Model for estimating the density of slags 345
8.4.3 Alternative model for calculating the density of slags 345
8.5 References in Chapter 8 347

9 Viscosities of molten slags 349
K. C. Mills

9.1 Introduction 350
9.1.1 Temperature dependence of viscosity 350
9.2 Review of methods used to determine viscosities of slags 350
9.2.1 Capillary method 350
9.2.1.1 Applications 350
9.2.2 Falling body method 350
9.2.2.1 Applications 351
9.2.3 Concentric cylinder (rotation) method 351
9.2.4 Oscillating methods 351
9.2.4.1 Oscillating cylinder or plate 351
9.2.4.2 Oscillating vessel method 351
9.2.5 Industrial viscometers 352
9.2.6 Herty viscometer 352
9.2.7 Krabiell immersion viscometer 352
9.2.8 Inclined plane method 352
9.3 Experimental uncertainties in viscosity measurements 352
9.4 Models for estimating the viscosities of multi-component slags 352
9.4.1 Model due to Riboud et al. 353
9.4.2 Model due to Urbain et al. 353

9.5 Experimental data for viscosities 354

9.5.1 Pure components 354
Al_2O_3 354; B_2O_3 354; CaF_2 354;
CaO 355; FeO 355; P_2O_5 355; SiO_2 355

9.5.2 Binary systems 355
Al_2O_3-B_2O_3 355; Al_2O_3-CaF_2 355;
Al_2O_3-CaO 356; Al_2O_3-FeO 356;
Al_2O_3-Gd_2O_3 356; Al_2O_3-La_2O_3 356;
Al_2O_3-Nd_2O_3 356; Al_2O_3-SiO_2 356;
B_2O_3-SiO_2 357; CaF_2-CaO 357;
CaF_2-Cr_2O_3 357; CaF_2-Li_2O 357;
CaF_2-MgO 357; CaF_2-SiO_2 358;
CaF_2-TiO_2 358; CaF_2-V_2O_5 358;
CaO-FeO_2 358; CaO-P_2O_5 358;
CaO-SiO_2 359; FeO_x-SiO_2 359;
FeO_x-TiO_2 359; K_2O-SiO_2 360;
Li_2O-SiO_2 360; MgO-SiO_2 360;
MnO-SiO_2 360; MnO-TiO_2 360;
Na2O-P_2O_5 361; Na_2O-SiO_2 361

9.5.3 Ternary systems 362
Al_2O_3-CaF_2-CaO 362; Al_2O_3-CaF_2-Nb_2O_5 363;
Al_2O_3-CaF_2-SiO_2 363; Al_2O_3-CaF_2-TiO_2 363;
Al_2O_3-CaF_2-V_2O_5 363; Al_2O_3-CaF_2-Y_2O_3 363;
Al_2O_3-CaO-MgO 364; Al_2O_3-CaO-SiO_2 364;
Al_2O_3-CaO-TiO_2 365; Al_2O_3-CaO-ZrO_2 365;
Al_2O_3-FeO-SiO_2 365; Al_2O_3-K_2O-SiO_2 365;
Al_2O_3-MgO-SiO_2 366; Al_2O_3-MnO-SiO_2 366;
Al_2O_3-Na_2O-SiO_2 366; Al_2O_3-SiO_2-TiO_2 367;
Al_2O_3-SiO_2-ZnO 367; CaF_2-CaO-La_2O_3 367;
CaF_2-CaO-SiO_2 368; CaF_2-SiO_2-$(RE)_2O_3$ 369;
CaO-CaS-SiO_2 369; CaO-CoO-SiO_2 369;
CaO-Cr_2O_3-SiO_2 370; CaO-Fe_xO-SiO_2 370;
CaO-MgO-SiO_2 372; CaO-MnO-SiO_2 373;
CaO-Na_2O-SiO_2 373; CaO-NiO-SiO_2 373;
CaO-P_2O_5-SiO_2 374; CaO-SiO_2-TiO_2 374;
CaO-SiO_2-ZnO 374; CoO-Na_2O-SiO_2 374;
Fe_xO-MgO-SiO_2 374; Fe_xO-MnO-SiO_2 375;
Fe_xO-Na_2O-SiO_2 375; Fe_xO-SiO_2-TiO_2 375;
K_2O-SiO_2-TiO_2 375; Li_2O-SiO_2-TiO_2 375;
MgO-Na_2O-SiO_2 376; MgO-SiO_2-TiO_2 376;
MnO-Na_2O-SiO_2 376; MnO-SiO_2-TiO_2 376;
Na_2O-NiO-SiO_2 376; Na_2O-SiO_2-SrO 376;
Na_2O-SiO_2-TiO_2 376; Na_2O-SiO_2-ZnO 376

9.5.4 Quaternary systems 377
Al_2O_3-CaF_2-CaO-MgO 377;
Al_2O_3-CaF_2-CaO-MnO 377;
Al_2O_3-CaF_2-CaO-SiO_2 377;
Al_2O_3-CaF_2-CaO_2-TiO_2 379;
Al_2O_3-CaF_2-CaO-V_2O_5 379;
Al_2O_3-CaO-CaS-SiO_2 379;
Al_2O_3-CaO-Cr_2O_3-SiO_2 379;
Al_2O_3-CaO-Fe_xO-SiO_2 379;
Al_2O_3-CaO-MgO-SiO_2 381;
Al_2O_3-CaO-MnO-SiO_2 382;
Al_2O_3-CaO-Na_2O-SiO_2 382;
Al_2O_3-CaO-SiO_2-TiO_2 382;
Al_2O_3-Cr_2O_3-MgO-SiO_2 382;
CaO-Fe_xO-MgO-SiO_2 383;
CaO-Fe_xO-MnO-SiO_2 383;
CaO-MgO-MnO-SiO_2 383;
CaO-MnO-P_2O_5-SiO_2 383

9.5.5 Systems with five and more components 384
Al_2O_3-CaF_2-CaO-MgO-SiO_2 384;
Al_2O_3-CaO-CaS-MgO-MnO-SiO_2 384;
Al_2O_3-CaO-FeO-MgO-SiO_2 384;
Al_2O_3-CaO-MgO-MnO-SiO_2 385;
Al_2O_3-CaO-MgO-SiO_2-TiO_2 385

9.5.6 Iron and steelmaking slags 387
9.5.6.1 Blast furnace slags 387
9.5.6.1.1 Effect of Al_2O_3 and MgO 390
9.5.6.1.2 Effect of Ti_2O_3 and TiO_2 390
9.5.6.2 Mould fluxes (for continuous casting and bottom pouring) 391
9.5.6.3 Open-hearth slags 392
9.5.6.4 Oxygen steelmaking slags 393
9.5.6.5 ESR slags 396
9.6 Performance of Riboud and Urbain models in predicting viscosities of industrial slags 397
9.7 References in Chapter 9 397

10 Surface tension of slag systems 403
B. J. Keene

10.1 Definitions 404
10.1.1 Surface and interfacial tension 404
10.1.2 Contact angle, work of adhesion and spreading coefficient 405
10.2 Methods to determine surface and interfacial tension at high temperatures 406
10.2.1 Introduction 406
10.2.2 Maximum bubble pressure (MBP) and maximum drop pressure (MDP) 406
10.2.3 Sessile drop (SD) 408
10.2.4 Pendent drop (PD) 409
10.2.5 Drop weight (DW) 410
10.2.6 Detachment or maximum-pull methods 411
10.2.7 Levitating drop 412
10.3 Surface tension data 412

10.3.1 Pure components 412
Al_2O_3 413; B_2O_3 413; CaF_2 413;
Cr_2O_3 413; FeO, Fe_2O_3 413;
FeS 414; MnO 414;
Na_3AlF_6 414; SiO_2 414; TiO_2 414

10.3.2 Binary systems 415
Al_2O_3-CaF_2 415; Al_2O_3-CaO 415;
Al_2O_3-Cr_2O_3 416; Al_2O_3-MgO 416;
Al_2O_3-SiO_2 416; Al_2O_3-TiO_2 416;
Al_2O_3-ZrO_2 417; B_2O_3-CaO 417;
CaF_2-CaO 417; CaF_2-MgO 418;
CaF_2-SiO_2 418; CaF_2-TiO_2 418;
CaF_2-V_2O_5 418; CaO-Fe_xO 418;
CaO-P_2O_5 419; CaO-SiO_2 420;
CaO-V_2O_5 421; Fe_xO-MnO 421;
Fe_xO-P_2O_5 421; Fe_xO-SiO_2 421;
Fe_xO-TiO_2 422; K_2O-SiO_2 423;
Li_2O-SiO_2 423; MgO-SiO_2 423;
MnO-SiO_2 424; Na_2O-SiO_2 424

10.3.3 Ternary systems 424
Al_2O_3-B_2O_3-CaF_2 424;

Al_2O_3-B_2O_3-CaO 425;
Al_2O_3-CaF_2-CaO 425;
Al_2O_3-CaF_2-MgO 427;
Al_2O_3-CaF_2-TiO_2 428;
Al_2O_3-CaF_2-V_2O_5 428;
Al_2O_3-CaO-Cr_2O_3 428;
Al_2O_3-CaO-Fe_2O_3 428;
Al_2O_3-CaO-K_2O 429;
Al_2O_3-CaO-LiO_2 429;
Al_2O_3-CaO-MgO 429;
Al_2O_3-CaO-Na_2O 429;
Al_2O_3-CaO-SiO_2 430;
Al_2O_3-CaO-TiO_2 432;
Al_2O_3-CaO-V_2O_5 433;
Al_2O_3-Fe_xO-P_2O_5 433;
Al_2O_3-Fe_xO-SiO_2 434;
Al_2O_3-MgO-SiO_2 434;
Al_2O_3-MnO-SiO_2 435;
Al_2O_3-Na_2O-SiO_2 435;
Al_2O_3-SiO_2-TiO_2 435;
B_2O_3-CaO-K_2O 436;
B_2O_3-CaO-SiO_2 436;
CaF_2-CaO-SiO_2 437;
CaO-CaS-SiO_2 437;
CaO-Cr_2O_3-SiO_2 438;
CaO-Fe_xO-P_2O_5 438;
(CaO-P_2O_5)-FeO-Fe_2O_3 438;
CaO-Fe_xO-SiO_2 439;
CaO-MgO-SiO_2 440;
CaO-MnO-SiO_2 440;
CaO-Na_2O-SiO_2 441;
CaO-P_2O_5-SiO_2 441;
CaO-SiO_2-V_2O_5 441;
Fe_xO-MgO-SiO_2 442;
Fe_xO-MnO-SiO_2 443;
MgO-Na_2O-SiO_2 444

10.3.4 Quaternary systems 444
Al_2O_3-CaF_2-CaO-CaS 444;
Al_2O_3-CaF_2-CaO-MgO 444;
Al_2O_3-CaF_2-CaO-MnO 444;
Al_2O_3-CaF_2-CaO-SiO_2 445;
Al_2O_3-CaF_2-CaO-V_2O_5 446;
Al_2O_3-CaF_2-MgO-SiO_2 446;
Al_2O_3-CaO-Fe_xO-SiO_2 446;
Al_2O_3-CaO-MgO-SiO_2 447;
Al_2O_3-CaO-MnO-SiO_2 448;
Al_2O_3-CaO-Na_2O-SiO_2 449;
Al_2O_3-CaO-SiO_2-TiO_2 450;
Al_2O_3-FeO-Fe_2O_3-SiO_2 450;
Al_2O_3-Fe_xO-MgO-SiO_2 451;
CaO-CaS-MgO-SiO_2 451;
CaO-FeO-MgO-SiO_2 452;
CaO-MgO-Na_2O-SiO_2 453;
FeO-Fe_2O_3-MgO-SiO_2 454

10.3.5 Systems with five and more components 454
Al_2O_3-B_2O_3-CaO-MgO-SiO_2 454;
Al_2O_3-CaF_2-CaO-MgO-SiO_2 454;
Al_2O_3-CaF_2-CaO-Na_2O-SiO_2 456;
Al_2O_3-CaO-FeO-Fe_2O_3-SiO_2 456;
Al_2O_3-CaO-Fe_xO-MnO-SiO_2 456;
Al_2O_3-CaO-K_2O-MgO-SiO_2 457;
Al_2O_3-CaO-MgO-Na_3AlF_6-SiO_2 458;
Al_2O_3-CaO-MgO-Na_2O-SiO_2 458;
Al_2O_3-CaO-MgO-S-SiO_2 459;
Al_2O_3-CaO-MgO-SiO_2-TiO_2 459;
Al_2O_3-CaO-MgO-SiO_2-V_2O_5 460

10.4 References in Chapter 10 461

11 Interfacial tension between ferrous melts and molten slags 463
B. J. Keene

11.1 Importance of interfacial tension in metallurgical processes 464
11.1.1 Metal-slag refining processes 464
11.1.2 Removal of inclusions from molten metal 464
11.1.3 Filtration of metals 465
11.1.4 Assessment of the relative cleanness of refined alloys 465
11.2 Methods to determine interfacial tension 465
11.3 Electrocapillary phenomena 466
11.4 Data for interfacial tension and work of adhesion 467
11.4.1 Solid oxides 467

11.4.1.1 Various oxides 467; Al_2O_3 468; Cr_2O_3 469; SiO_2 470

11.4.2 Slags containing CaF_2 470
11.4.2.1 Pure CaF_2 470

11.4.2.2 Binary systems (containing CaF_2) 470
Al_2O_3 470; CaO 470; MgO 470; NaF 470; SiO_2 470; TiO_2 470; ZrO_2 470

11.4.2.3 Ternary systems (containing CaF_2) 474
Al_2O_3-CaO 474; CaO-SiO_2 477

11.4.2.4 Quaternary systems (containing CaF_2) 477
Al_2O_3-CaO-CaS 477; Al_2O_3-CaO-Cr_2O_3 478; Al_2O_3-CaO-SiO_2 478

11.4.2.5 Systems with five and more components (containing CaF_2) 479
Al_2O_3-B_2O_3-CaO-MgO-Na_3AlF_6-SiO_2 479;
Al_2O_3-CaC_2-CaO-MgO-SiO_2 480;
Al_2O_3-CaO-FeO-K_2O-MgO-MnO-SiO_2 480;
Al_2O_3-CaO-MgO-Na_2O-SiO_2 481;
Al_2O_3-CaO-MgO-SiO_2 481

11.4.3 Oxide slags 482

11.4.3.1 Binary systems 482
Al_2O_3-CaO 482; CaO-SiO_2 486; FeO-MnO 486; MnO-SiO_2 486

11.4.3.2 Ternary systems 487
Al_2O_3-CaO-FeO 487; Al_2O_3-CaO-SiO_2 487; Al_2O_3-MgO-SiO_2 492; Al_2O_3-MnO-SiO_2 492; Al_2O_3-MnO-TiO_2 492; CaO-FeO-SiO_2 493; CaO-MgO-SiO_2 493; CaO-MnO-SiO_2 494; FeO-MnO-SiO_2 496; MnO-P_2O_5-SiO_2 496; MnO-SiO_2-TiO_2 496; MnO-SiO_2-ZrO_2 496; MnO-SiO_2-(various oxides) 497

11.4.3.3 Quaternary systems 498
Al_2O_3-CaO-FeO-SiO_2 498;
Al_2O_3-CaO-MgO-SiO_2 499;
Al_2O_3-CaO-MnO-SiO_2 499;
Al_2O_3-CaO-Na_2O-SiO_2 500;
Al_2O_3-MnO-SiO_2-ZrO_2 500;
CaO-CaS-MnO-SiO_2 500;
CaO-MgO-MnO-SiO_2 501;
CaO-MnO-MnS-SiO_2 501

11.4.3.4 Systems with five and more components 502
Al_2O_3-CaO-Fe_xO-MgO-MnO-P_2O_5-SiO_2 502;
Al_2O_3-CaO-Fe_xO-MgO-MnO-SiO_2 502;
Al_2O_3-CaO-Fe_xO-MgO-SiO_2 503;
Al_2O_3-CaO-Fe_2O_3-MgO-SiO_2 504;
Al_2O_3-CaO-FeO-MnO-SiO_2 504;
Al_2O_3-CaO-Li_2O-MgO-SiO_2 505;
Al_2O_3-CaO-MgO-S-SiO_2 505;
Al_2O_3-CaO-MgO-SiO_2-TiO_2 506;
Al_2O_3-Fe_xO-MgO-MnO-SiO_2 506

11.4.3.5 Various complex slags 507
11.5 Electrocapillary data 509
11.6 References in Chapter 11 510

12 Contact angle and work of adhesion between ferrous melts and non-metallic solids 513
B. J. Keene

12.1 Introduction 514
12.2 Contact angle and work of adhesion 514
12.3 Factors affecting wettability and adhesion 515
12.3.1 Intermolecular bonding 515
12.3.2 Dispersion forces 515
12.3.3 Chemical forces 515
12.4 Surface topography 516
12.5 Temperature 517
12.6 Data 517
12.6.1 Carbides and graphite 517
Graphite 517; SiC 518; TiC 519;
TiC + WC 519

12.6.2 Nitrides 520
AlN 520; BN 520; Si_3N_4 520; TiN 520
12.6.3 Oxides 522

12.6.3.1 Pure oxides 522
Al_2O_3 522;
CaO 528;
Cr_2O_3 529;
HfO_2 529;
MgO 529;
Rare-earth oxides 530; SiO_2 530;
ThO_2 532; TiO_2 532; ZrO_2 532

12.6.3.2 Mixed oxides 532
12.6.4 Sulphides 534
12.6.5 Silicides 534
12.6.6 Additional data to section 12.6 534
12.7 Composition of ferrous melts 537
12.8 References in Chapter 12 538

13 Diffusion coefficients in molten slags 541
K. C. Mills

13.1 Introduction 542
13.2 Theory 542
13.2.1 Single component diffusion 542
13.2.1.1 Mean free path or statistical approach 542
13.2.1.2 Friction coefficient approach 542
13.2.1.3 Absolute rate theory approach 542
13.2.2 Multi-component diffusion 542
13.3 Experimental methods 542
13.3.1 Instantaneous plane source (IPS) 542
13.3.2 Capillary reservoir (CR) or Immersion method 543
13.3.3 Diffusion couple (DC) method 543
13.3.4 Electrochemical method 543
13.3.5 Molecular dynamics (MD) calculations 543
13.3.6 Experimental errors 543
13.4 Factors affecting diffusion coefficients 543
13.4.1 Temperature 543
13.4.2 Pressure 544
13.4.3 Slag composition 544
13.4.3.1 SiO_2 content 544
13.4.3.2 Moisture content 544
13.4.4 Radius and valency of diffusing species 544
13.4.4.1 Cations 544
13.4.4.2 Anions 544
13.5 Relationship of diffusivity with other properties 544
13.5.1 Viscosity 544
13.5.2 Electrical conductivity 546
13.6 Experimental data 546
13.6.1 Self diffusion coefficients in pure oxides 546
13.6.2 Self diffusion coefficients in molten slags 547
13.6.3 Impurity diffusion coefficients in molten slags 550
13.6.4 Chemical diffusion coefficients in molten slags 552
13.7 Appendix 555
13.7.1 Appendix 1 555
13.7.2 Appendix 2 555
13.8 References in Chapter 13 555

14 Electrical conductivities of molten slags .. 557
K. C. Mills

14.1 Introduction 558
14.1.1 Temperature dependence of electrical conductivity 558
14.1.2 Effects of double layer and of polarization resistance on conductivity 558
14.1.3 Experimental methods used to measure electrical conductivity 558
14.1.3.1 Capillary methods 558
14.1.3.2 Crucible cells 558
14.1.3.3 Central electrode cell 558
14.1.3.4 Two-electrode cell 558
14.1.3.5 Ring electrode cell 559
14.1.3.6 Four-electrode system 559
14.1.3.7 Measurement of resistance by ac bridges 559
14.1.3.8 Potentiometric techniques 559

14.1.3.9 Use of phase-shift devices 559
14.1.3.10 Other techniques of resistance measurement 559
14.1.4 Frequency dependency of conductivity and analysis of results 559
14.1.4.1 Circuits used for the representation of the measuring cell 559
14.1.4.2 Relationship between conductivity and frequency 559
14.2 Experimental date for specific electrical conductivity 560

14.2.1 Single components 560
Al_2O_3 560; CaF_2 560; FeO 560; Fe_2O_3 560; SiO_2 561

14.2.2 Binary systems 561
Al_2O_3-CaF_2 561; Al_2O_3-CaO 561; Al_2O_3-FeO 562; Al_2O_3-SiO_2 562; B_2O_3-CaF_2 562; CaF_2-CaO 562; CaF_2-FeO 562; CaF_2-La_2O_3 562; CaF_2-MgO 562; CaF_2-SiO_2 562; CaF_2-TiO_2 563; CaF_2-Y_2O_3 563; CaO-FeO 563; CaO-Fe_2O_3 563; CaO-SiO_2 564; FeO-MnO 564; Fe_2O_3-Na_2O 564; FeO_x-SiO_2 564; Fe_2O_3-SrO_2 565; FeO_x-TiO_2 565; K_2O-SiO_2 565; Li_2O-SiO_2 565; MgO-SiO_2 566; MnO-SiO_2 566; MnO-TiO_2 566; Na_2O-SiO_2 567; SiO_2-SrO 567

14.2.3 Ternary systems 567
Al_2O_3-CaF_2-CaO 567; Al_2O_3-CaO-MgO 568; Al_2O_3-CaO-SiO_2 568; Al_2O_3-CaO-TiO_2 569; Al_2O_3-CaO-ZrO_2 569; Al_2O_3-FeO_x-SiO_2 569; Al_2O_3-MgO-SiO_2 569; Al_2O_3-MnO-SiO_2 570; Al_2O_3-Na_2O-SiO_2 570; CaF_2-CaO-SiO_2 570; CaF_2-CaO-TiO_2 570; CaF_2-FeO-SiO_2 570; CaF_2-MgO-SiO_2 571; CaO-Cr_2O_3-SiO_2 571; CaO-FeO_x-SiO_2 571; CaO-MgO-SiO_2 571; CaO-MnO-SiO_2 572; CaO-Na_2O-SiO_2 572; CaO-P_2O_5-SiO_2 572; CaO-SiO_2-TiO_2 573; CaO-SiO_2-ZnO 574; FeO-MgO-SiO_2 575; FeO-MnO-SiO_2 575; FeO-MnO-TiO_2 575; FeO_x-Na_2O-SiO_2 575; Fe_2O_3-Na_2O-SiO_2 576; FeO-SiO_2-TiO_2 576; K_2O-MgO-SiO_2 576; K_2O-SiO_2-TiO_2 576; Li_2O-MgO-SiO_2 576; Li_2O-SiO_2-TiO_2 576; MgO-MnO-SiO_2 576; MgO-Na_2O-SiO_2 577; MgO-SiO_2-TiO_2 577; MnO-SiO_2-TiO_2 577; Na_2O-SiO_2-TiO_2 577; Na_2O-SiO_2-ZnO 577

14.2.4 Quaternary systems 578
Al_2O_3-CaF_2-CaO-MgO 578; Al_2O_3-CaF_2-CaO-SiO_2 578; Al_2O_3-CaF_2-CaO-TiO_2 579; Al_2O_3-CaF_2-MgO-SiO_2 579; Al_2O_3-CaO-Cr_2O_3-SiO_2 579; Al_2O_3-CaO-FeO_x-SiO_2 579; Al_2O_3-CaO-MgO-SiO_2 579; Al_2O_3-CaO-MnO-SiO_2 581; Al_2O_3-CaO-P_2O_5-SiO_2 582; Al_2O_3-CaO-SiO_2-TiO_2 582; Al_2O_3-CaO-SiO_2-V_2O_5 582; Al_2O_3-Cr_2O_3-MgO-SiO_2 583; Al_2O_3-Fe_2O_3-MgO-SiO_2 584; Al_2O_3-Fe_2O_3-Na_2O-SiO_2 584; Al_2O_3-Na_2O-SiO_2-TiO_2 584; CaF_2-CaO-MgO-SiO_2 584; CaO-FeO-MgO-SiO_2 584; CaO-Fe_2O_3-SiO_2-TiO_2 585; CaO-MgO-MnO-SiO_2 585; Fe_2O_3-Na_2O-SiO_2-TiO_2 585

14.2.5 Systems with five and more components 586
Al_2O_3-CaF_2-CaO-FeO-MgO-MnO-SiO_2 586; Al_2O_3-CaF_2-CaO-Fe_2O_3-MgO-SiO_2 586; Al_2O_3-CaF_2-CaO-MgO-SiO_2 586; Al_2O_3-CaO-Cr_2O_3-MgO-SiO_2 587; Al_2O_3-CaO-FeO-MgO-SiO_2 587; Al_2O_3-CaO-MgO-MnO-SiO_2 587; Al_2O_3-CaO-MgO-SiO_2-TiO_2 587
14.2.6 Blast furnace slags 587
14.2.7 BOS slags 588
14.2.8 Coal slags 588
14.2.9 ESR slags 588
14.3 References in Chapter 14 588

15 Thermal conductivities of slags 591
K. C. Mills and M. Susa

15.1 Introduction 592
15.1.1 Thermal conduction mechanisms 592
15.1.1.1 Lattice or "phonon" thermal conductivity 592
15.1.1.2 Radiation conductivity 592
15.1.1.3 Electronic conductivity 592
15.2 Experimental methods 592
15.2.1 Steady state techniques 593
15.2.1.1 Linear heat flow method 593
15.2.1.2 Radial heat flow (RHF) method 593
15.2.2 Non-steady state methods 593
15.2.2.1 Radial wave (RW) method 593
15.2.2.2 Modulated beam technique 593
15.2.3 Transient methods 593
15.2.3.1 Laser pulse (LP) method 593
15.2.3.2 Line source (LS) method 594
15.3 Factors affecting thermal conductivity 594
15.3.1 Solids 594
15.3.1.1 Crystallinity of sample 594
15.3.1.2 Porosity of sample 594
15.3.1.3 Glass transition temperature 594
15.3.2 Liquids 594
15.3.2.1 Degree of polymerisation of the sample 594
15.3.2.2 Relation to velocity of sound 594
15.4 Thermal conductivity data 595

15.4.1 Pure substances 595
CaF_2 595; SiO_2 595

15.4.2 Binary systems 595
Al_2O_3-CaO 595; Al_2O_3-MgO 595; Al_2O_3-SiO_2 595; CaO-Fe_2O_3 596; CaO-SiO_2 596; K_2O-SiO_2 596; MgO-SiO_2 596; Na_2O-SiO_2 596

15.4.3 Ternary systems 597
Al_2O_3-CaO-SiO_2 597; CaO-Fe_2O_3-SiO_2 597

15.4.4 Quaternary systems 598
Al_2O_3-CaF_2-CaO-SiO_2 598;
Al_2O_3-CaO-SiO_2-TiO_2 598

15.4.5 Continuous casting powders and slags 598
15.4.6 ESR slags 599
15.4.7 Rocks, Minerals 599
15.5 References in Chapter 15 599

16 Optical properties of slags: Data for refractive indices and absorption coefficients 601
M. Susa and K. C. Mills

16.1 Introduction 602
16.2 Refractive indices of slags 602
16.2.1 Introduction 602
16.2.2 Experimental methods 602
16.2.2.1 Immersion method (IM) 602
16.2.2.2 Brewster angle method (BR) 602
16.2.2.3 Pulfrich refractometer (PR) 602
16.2.2.4 Abbé refractometer (AR) 603
16.2.2.5 Minimum deviation method (MD) 603
16.2.2.6 Ellipsometry (EL) 603
16.2.3 Factors affecting refractive indices 603
16.2.3.1 Density 603
16.2.3.2 Composition 604
16.2.3.3 Wavelength 604
16.2.3.4 Temperature 604
16.3 Refractive index data 604

16.3.1 Pure substances 604
Al_2O_3 604; SiO_2 604

16.3.2 Binary systems 605
Al_2O_3-SiO_2 605; B_2O_3-SiO_2 605;
BaO-SiO_2 605; O-SiO_2 605;
Cs_2O-SiO_2 605; GeO_2-SiO_2 605;
K_2O-SiO_2 605; Li_2O-SiO_2 606;
MgO-SiO_2 606; Na_2O-SiO_2 606;
PbO-SiO_2 606; P_2O_5-SiO_2 606;
Rb_2O-SiO_2 606; SrO-SiO_2 606;
SiO_2-TiO_2 607

16.3.3 Ternary systems 607
Al_2O_3-CaO-SiO_2 607; Al_2O_3-FeO-SiO_2 607;
Al_2O_3-K_2O-SiO_2 607; Al_2O_3-MnO-SiO_2 607;
Al_2O_3-Na_2O-SiO_2 607; CaO-FeO-SiO_2 608;
CaO-MgO-SiO_2 608; CaO-Na_2O-SiO_2 608;
FeO-MgO-SiO_2 608; Fe_2O_3-K_2O-SiO_2 608;
Fe_2O_3-Na_2O-SiO_2 609; MnO-Na_2O-SiO_2 609

16.3.4 Quaternary systems 609
Al_2O_3-CaO-Fe_2O_3-SiO_2 609;
Al_2O_3-CaO-Na_2O-SiO_2 609

16.3.5 Continuous casting slags 609
16.4 Absorption coefficients of slags 610
16.4.1 Introduction 610
16.4.2 Experimental methods 610
16.4.2.1 Transmission methods 610
16.4.2.2 Reflectance measurements 610
16.4.3 Factors affecting absorption coefficients 610
16.4.3.1 Wavelength 610
16.4.3.2 Temperature 611
16.4.3.3 Transition metal oxides 611
16.4.3.4 Crystallinity 611
16.5 Absorption coefficient data 612

16.5.1 Pure substances 612
CaF_2 612; SiO_2 612

16.5.2 Binary systems 612
K_2O-SiO_2 612; Li_2O-SiO_2 612;
MgO-SiO_2 612; MnO-SiO_2 612;
Na_2O-SiO_2 612; PbO-SiO_2 613

16.5.3 Ternary systems 613
Al_2O_3-CaF_2-CaO 613;
Al_2O_3-CaO-SiO_2 613;
Fe_2O_3-Na_2O-SiO_2 613
16.5.4 Quaternary systems 614
Al_2O_3-CaO-FeO_x-SiO_2 614;
Al_2O_3-CaO-FeO_x-MgO-SiO_2 614

16.5.5 Coal slags 614
16.5.6 Continuous casting slags 615
16.5.7 Glasses 615
16.5.8 Minerals, Rocks 615
16.6 References in Chapter 16 615

Explanation of frequently used symbols and abbreviations

A	pre-exponential term in Arrhenius and Weymann equations
a	chemical activity
a	thermal diffusity
α	absorption (or extinction) coefficient
α	thermal expansion coefficient
B	activation energy term (= E/R) in Arrhenius and Weymann equations
B	basicity
B^{XS}	excess base
C	capacity
C	concentration
CHRP	chrono-potentiometry
CR	capillary reservoir method
CyV	cyclic voltametry
D	diffusivity coefficient
DC	diffusion couple
d	relative density
d	thickness of sample
E	activation energy
EMF	electromotive force
ESR	electro slag remelting
ESR	electro spin resonance
EXAFS	extended X-ray absorption fine structure
η	viscosity
F	Faraday constant
f	activity coefficient (Henry)
f	frequency
f	fugacity
G	Gibbs free energy
GE	gas exchange
γ	activity coefficient (Raoult)
γ	interfacial tension
γ	surface tension
H	enthalpy
ΔH^{mix}	enthalpy of mixing
IPS	instantaneous plane source method
IS	isomer shift
J	flux
K	equilibrium constant
k	Boltzmann constant
k	thermal conductivity
k_{eff}	effective thermal conductivity
k_{el}	electronic thermal conductivity
k_L	lattice (phonon) thermal conductivity
k_m	thermal conductivity of liquid at melting point
k_R	radiation (photon) conductivity
K, κ	electrical conductivity
κ	specific electrical conductivity
L	mean free path of phonons
LP	laser pulse method
LS	line source method
Λ	optical basicity
λ	mean free path
λ	thermal conductivity
MB	modulated beam method
MD	molecular dynamics calculation
m	mass
N	mole fraction (see also X, x)
NBO	non-bridging oxygen
NBO/Si	ratio of non-bridging oxygens per Si atom
NBO/T	number of non-bridging oxygen atoms per tetrahedrally coordinated atom, e.g. Al, Si, Ti etc.
NMR	nuclear magnetic resonance
n	number of atoms in a chemical compound
n	refractive index
ν	frequency
O^o	bridged oxygen
O^-	non-bridged oxygen
O^{2-}	free oxygen
O_2-P	oxygen permeation
O + R	oxidation and reduction
P	weight
PF	porous frit
p	pressure
p_i	partial pressure of i
Q	heat flux density
Q	number of bridging oxygen per tetrahedron
QS	quadrupole splitting
R	gas constant
R*	ratio of Al to cations
RA	residual activity
RDF	radial distribution function
RHF	radial heat flow method
RW	radial wave method
r	ionic radius
ρ	density
S	entropy
S	spreading coefficient
Si-O-Si	intertetrahedral angle of bridging oxygens with Si atoms
sc	supercooled melt
T	temperature
T	tetrahedral atom, e.g. Al, Si, in formulae
T_g	glass transition temperature
T_{liq}	liquidus temperature
TGA	thermogravimetric analysis
TMS	tri-methyl silyl derivates
T-O-T	intertetrahedral angle of bridging oyxgens with atoms such as Al, Si (denoted T)

TS	thin source
t	time
θ	contact angle between liquid metal and slag or solid non-metallic substrate
UV	ultra violet
V	volume
V	molar volume
v	average velocity of sound in the melt
W_A	work of adhesion
X, x	mole fraction (see also N)
XANES	X-ray near edge spectroscopy
y	distance (normal to the plane of diffusion)
z	electrical charge on cation, e.g. 2 for Ca^{2+}
%	mass % (unless otherwise stated)
IV	tetrahedral coordination of O around T atoms
VI	octohedral coordination of O around T atoms
{}	gas or vapour phase
[]	metal phase
()	slag phase

1

Structure of liquid slags

K. C. Mills

1.1 Introduction

The physico-chemical properties of metallurgical slags are controlled principally by their structures. Two theories have been put forward to account for the structure of liquid slags and their physico-chemical properties viz the molecular and the ionic theories.

The molecular theory assumes that a liquid slag is composed of individual oxides, fluorides etc. eg SiO_2, Al_2O_3, FeO, CaO, CaF_2 etc. and that these can combine to form $CaO.SiO_2$ etc. This proposition leads to use of the activity of a component eg SiO_2 which allows the effects of additions of say CaO to be characterised. However, electrical conductivity studies have shown that the conduction mechanism in liquid slags is predominantly ionic and that electronic conduction only becomes important in slags containing more than 70% FeO or MnO. Thus the molten slag must be ionic in nature. Herasymenko [1] first put forward the theory that liquid slags consisted of (I) cations, such as Ca^{2+}, Fe^{2+} etc., (II) anions such as O^{2-}, F^{2-}, S^{2-} and (III) anion complexes such as SiO_4^{4-}, PO_4^{3-}, AlO_3^{3-}.

Zachariasen [2] and Warren [4] showed that the principal feature of X-ray results was that SiO_4^{4-} tetrahedra which inter-connected to form 3-dimensional networks. Most of the earlier work on the structure was deduced from interpretations of data for physical properties and phase of equilibria. However, such deductions require a knowledge the mechanism by which the structure affects the particular physical property. In more recent years, spectroscopic techniques have been used to provide both an independent determination of slag structure and an insight into the mechanism responsible for the structure-property relationship. Much of the recent advances in the field of slag structure have come from geological laboratories involved in the study of the structures of magmas and natural minerals. Furthermore, several excellent reviews of the structures of silicate liquids have emanated from these same sources [5, 6] in recent years and are recommended to the reader who requires more detail than that given in this review.

1.2 Methods used to determine structure

Several methods have been used to determine the structures of slags, these can be classified into the following categories:

(a) physical property measurements,

(b) chromatographic separation of various polymeric units,

(c) X-ray and spectroscopic techniques,

(d) development of "structural" thermodynamic models,

(e) molecular dynamics (MD) calculations.

The structural information which can be derived from these techniques are given in **Tabs. 1.1** and **1.2.** A full description of the techniques lies outside the scope of this review; further details for the relevant physical property measurements are given in the relevant chapters of the Slag Atlas but brief details of the molar refractivity, chromatographic separation and the X-ray and spectroscopic techniques are given below. For a full description of the X-ray and spectroscopic methods the reader is referred to the reviews of Fleet [7] and Wong and Angell [8]. In spectroscopic studies it has become a common practice to compare the spectra of a melt (or quenched glass) with that obtained from its crystalline equivalent for which the structure is known (ie known bond lengths, and coordination eg whether a cation (eg Fe^{3+}) has tetrahedral (IV) or octohedral (VI) coordination). This process is usually referred to as "fingerprinting".

1.2.1 X-ray, electron and neutron diffraction

Diffraction techniques are the only methods which will provide an overall image of melt structures. RDF functions, shown in **Fig. 1.1** indicate the short- and intermediate-range order in the melt. The RDF's are a composite of the pairwise interactions for all atoms in the melt. Neutron diffraction has a distinct advantage over X-ray diffraction since scattering efficiencies are independent of atomic number.

1.2.2 Vibration spectroscopy

Vibration spectroscopy (Infra-red (IR), Ultra-violet (UV) and Raman have proved important tools in the determination of slag structures. Vibrational and rotational excitations in the sample are studied directly in the IR and microwave regions of the electromagnetic spectrum but in Raman these studies are transferred to the visible region where detection methods are well developed. It is for this reason that Raman spectroscopy has proved the most useful method to date for studying slag structure.

Molecular vibrations are classified into 3 modes viz symmetric stretching, asymmetric stretching and bending. Symmetric stretching leads to intense and partly polarised Raman lines whereas asymmetric bending leads to weak polarised lines. In crystalline materials the lattice vibrations are dominated by the silicate molecular units, and these produce well defined lines in the Raman spectrum **(Fig. 1.2).** However in melts (and quenched glasses) these are in the form of broad bands and must be deconvoluted **(Fig. 1.3).** Individual bands have been shown to be specific to certain anionic units eg SiO_2, $Si_2O_5^{2-}$ etc. and the concentrations of these species can be derived from areas under these peaks. More recently, Mysen [9] has suggested an alternative analytical treatment for the derivation of the concentrations of these anionic units which leads to values in closer agreement with those derived from NMR data.

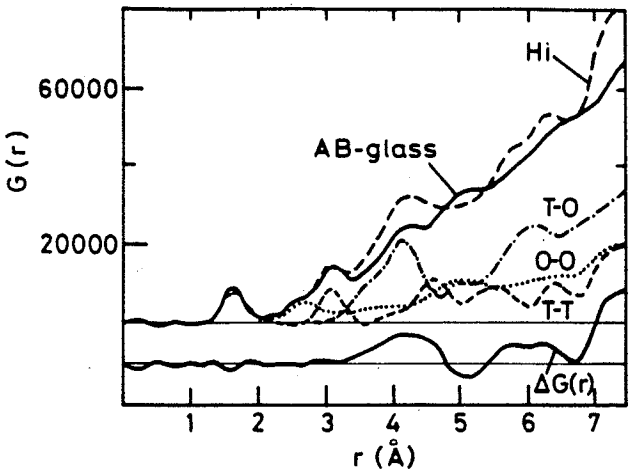


Fig. 1.1. Radial distribution function (G(r)) for NaAl Si_3O_8 quenched glass compared with contribution derived by pseudo crystalline model for T-O_n, O-O_n, ····, T-T_n; the lower curve ΔG(r) represents the difference between experimental and pseudo crystalline model

Tab. 1.1. Structural information obtained from X-ray and spectroscopic methods

Method	Measurement	Information obtained
X-ray, Neutron, Electron } Diffraction	RDF (Fingerprinting)	(I) Bond lengths eg (T(Si-O) (II) Co-ordination numbers (III) Intertetrahedral angles, T-O-T (IV) Overall intermediate structure (V) Local O co-ordination around large cations
Spectroscopy Infra-red (IR) Raman Ultra-violet (UV)		(I) Bond lengths (II) Bond angles (III) Identification and concentrations of various anionic units
NMR Spectroscopy	Chemical shift (Fingerprinting)	(I) Identification of and concentrations of different anionic units (II) Bond lengths (III) Bond angles
Mössbauer	Isomer shift (IS)	(I) Valence state (II) Co-ordination of environment eg identification and concentration of Fe^{3+} (IV) and Fe^{3+} (VI) sites
	Quadrupole splitting (QS)	(I) Distortion of oxygen polyhedron (II) Oxidation state eg Fe^{2+} or Fe^{3+} (III) Co-ordination eg Fe^{3+} (IV) or Fe^{3+} (VI)
X-ray Absorption Spectroscopy	EXAFS XANES (Fingerprinting)	(I) Bond length (II) Bond angles (III) Co-ordination of specific atoms eg Al in $NaAlO_2 + SiO_2$ or Ti^{4+} (IV) or Ti^{4+} (VI)
X-ray Emission Spectroscopy (ESCA or XPS) ESR Spectroscopy	K_α, K_β	(I) Co-ordination of specific elements eg Al, Fe in anionic units (II) Changes in valence state
Luminescence		(I) Co-ordination of Mn^{2+}, Fe^{3+}, Ti^{3+} or S (viz or S^{2-} or SO_4^{2-} in slag)
Spectroscopy		Separate peaks for Fe^{3+} (IV) and Fe^{3+} (VI) co-ordination

Tab. 1.2. Structural information obtained from various measurements

Method	Information provided
Chromatography	Distribution of chain lengths of various polymeric units
Density	Packing and co-ordination
Molar Volumes	
Molar refractivity	Concentration of O°, O^-, O^{2-}
Viscosity	(I) Activation energies, related to bond strength (II) The effect of different cations
Enthalpy of mixing, solution	(I) Measure of bond strength (II) Effect of different cations including ordering of structure
Electrical conductivity	Indication of ionic or electronic conduction
Liquidus phase equilibria (depression of freezing point)	Gives γ_{SiO_2}; $\gamma_{SiO_2} \rightarrow 1$ indicates increased ordering eg formation of Ti complexes
MD calculations	(I) Bond lengths (II) T-O-T angles (III) Co-ordination eg Al in $Na_2O + Al_2O_3 + SiO_2$ is (IV) even when $R^* > 1$
Structural thermodynamic models	Concentration of various anionic units present in the melt

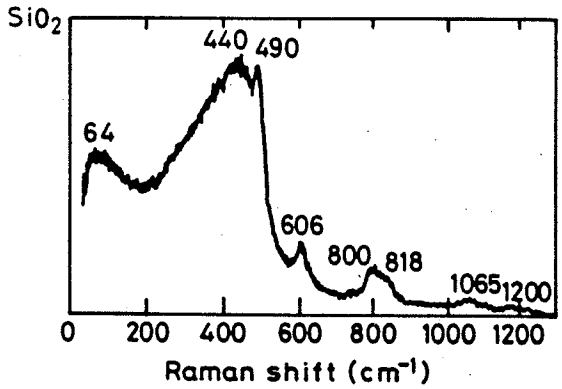


Fig. 1.2. Raman spectrum for vitreous SiO_2

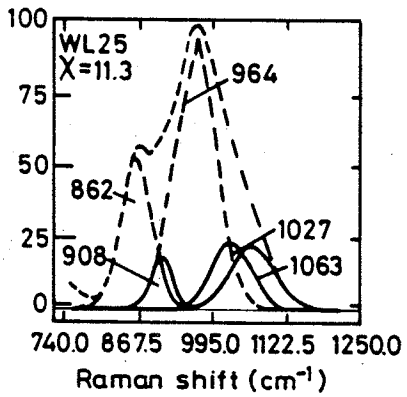


Fig. 1.3. Raman spectrum for a CaO + SiO_2 glass, showing deconvolution

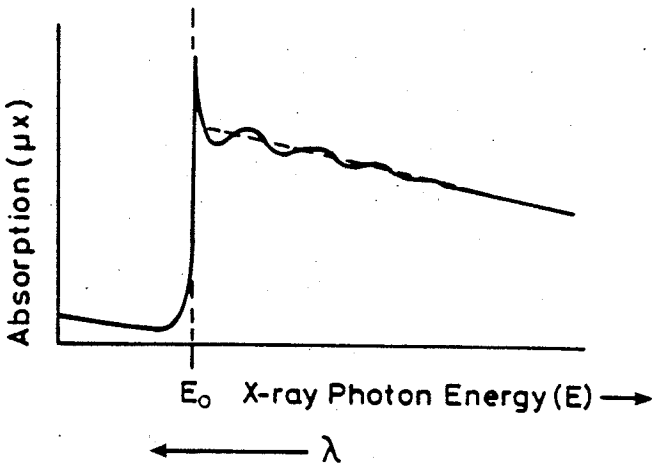


Fig. 1.4. Schematic representation of the fine structure in X-ray absorption profile; E is related to the wavelength, λ

1.2.3 Nuclear magnetic resonance (NMR)

When a specimen is placed in a magnetic field there is a change in the energy state of the molecule or atom. This change is dependent upon the magnetic field, the internal field of the sample, the chemical bond and the molecular motion. The outer electrons shield the nucleus and there is a minute change in the resonant energy, which results in a chemical shift in the NMR absorption peak; structural data can be derived from the chemical shifts.

1.2.4 Electron spin resonance (ESR)

ESR is based on the resonant absorption of long wavelength microwave radiation by electrons with unpaired spins. It has been used principally to determine the co-ordination of transition metals in the silicate network.

1.2.5 Mössbauer spectroscopy

Mössbauer (or nuclear resonance fluorescence) spectroscopy depends on the emission of γ-rays and their resonant absorption by atoms of the sample; this resonance is associated with allowable nuclear spin states. In practice, Mössbauer has been applied principally to slags containing Fe; the chemical isomer shift (IS) provides information on the valence state and the co-ordination environment of the atom (Fe) whereas the quadrupole splitting (QS) provides a measure of the distortion from cubic site symmetry. Mössbauer spectroscopy has proved particularly useful in differentiating between tetrahedral (IV) and octahedral (VI) co-ordination of Fe^{3+} in silicates.

1.2.6 X-ray absorption spectroscopy

X-ray absorption spectroscopy exists in two forms viz X-ray absorption near edge spectroscopy (XANES) and Extended X-ray absorption fine structure (EXAFS). The threshold energy (E_o) shown in **Fig. 1.4**, is associated with the energy required to eject a bound electron. XANES covers the range from E_o = 0 to 40 eV and EXAFS from 40 to 1000 eV. EXAFS provides a radial distribution function (RDF) and after Fourier transformation this yields information on bond lengths, bond angles (T-O-T) and coordination of specific atoms (cf RDF from diffraction which is a composite of all pairwise interactions). XANES tends to be more qualitative than EXAFS and is used particularly in the determination of the coordination geometry of the absorbing atom.

1.2.7 X-ray emission spectroscopy

The wavelength of X-ray lines vary slightly with the oxidation state of the atom and its coordination environment. The shifts in coordination geometry can be established from shifts in K_α and K_β lines after careful calibration with crystalline silicates of known structure ("fingerprinting").

1.2.8 X-ray photon spectroscopy (XPS) or electron spectroscopy for chemical analyses (ESCA)

This technique is based on the fact that when X-ray, UV radiation or a charged particle strike the sample, electrons are emitted and the energy levels of molecules or atoms can be derived from energy measurements.

1.2.9 Chromatographic separation

The concentrations of the various anionic emits (eg SiO_4^{4-}, $Si_2O_7^{6-}$, $Si_3O_{10}^{8-}$) in quenched glasses were determined [10 – 14] by addition of trimethylsilyl (TMS) derivatives to aqueous solutions of the glass; the volatile products are separated by gas chromotography and the concentrations of the various anions determined; crystalline materials were used as standards to calibrate the method. However te method is not always quantitative and internally consistent. Furthermore the results reported for the concentrations of the anionic species differed from values obtained by Raman spectroscopy, however, values reported by Pasishnik et al [14] were in essential agreement with concentrations obtained spectroscopically.

1.2.10 Molar refractivity

Ionic refractivity can be related to the size of the ionic radius but small, highly-charged cations hardly contribute to the molar refractivity. Iwamoto et al [15] determined the concentrations of non-bridging (O°) bridging (O^-) and free oxygens (O^{2-}) in quenched glasses with this technique.

1.3 The structure of slags containing silica and/or other complex-forming constituents

Virtually all metallurgical slags contain silica and/or other complex-forming components. The structure of silicate is therefore of special interest for understanding the structure and behaviour of slags.

Silicate slags are built up of Si cations which are surrounded by 4 oxygen anions arranged in the form of a tetrahedron. These SiO_4^{4-} tetrahedra are joined together in chains or rings by bridging oxygens (BO), (**Figs. 1.5** and **1.6**). Cations such as Na^+, Ca^{2+}, Mg^{2+}, Fe^{2+} tend to break these bonded oxygens and form non-bridging oxygens (NBO), O^-, and free oxygens, O^{2-}. The degree of depolymerisation of a silicate melt can be expressed by the ratio of (non-bridging oxygen atoms/number of tetrahedrally – coordinated atoms (eg Si)). This is usually denoted as the (NBO/T) ratio, and the physical properties, such as viscosity, thermal conductivity etc., are very dependent upon the (NBO/T) ratio.

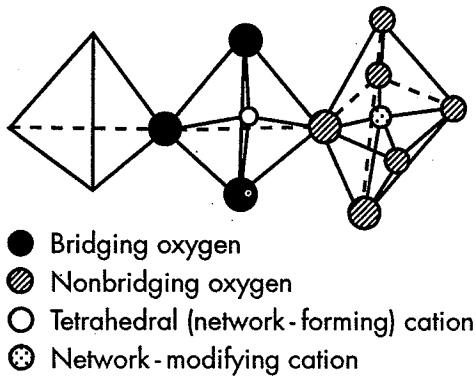


Fig. 1.5. Schematic representation of network of tetrahedra formed by Si etc. and oxygen atoms

The silicate melts contain various 3-dimensionally, interconnected anion units such as SiO_2, $Si_2O_5^{2-}$, $Si_2O_6^{4-}$, $Si_2O_7^{2-}$, SiO_4^{4-} which coexist in the melt (**Fig. 1.7**). The nature of the cation affects the proportion of these anionic units but not the overall degree of depolymerisation ie the (NBO/T) ratio; the more extreme units SiO_2 and SiO_4^{4-} are favoured by small cations of high valence eg Mg > Ca > Sr >Li > Na > K.

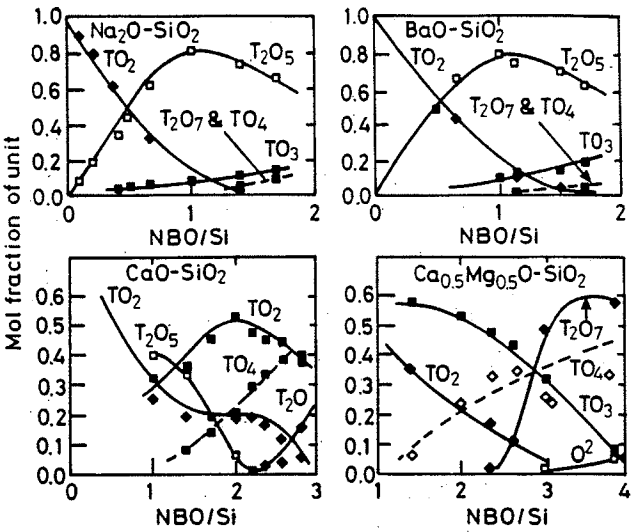


Fig. 1.7. Molar concentrations of various anionic units in binary SiO_2 + metallic oxides as a function of (NBO/Si) for the bulk composition (5)

Other cations such as Ti^{4+}, P^{5+}, Al^{3+} and Fe^{3+} also form tetrahedra and can be incorporated into the silicate network eg TiO_4^{4-}, PO_4^{3-}, AlO_4^{5-} and FeO_4^{5-}. However it is important that electrical charge-balance be maintained and cations are needed for charge-balancing ($Na^+AlO_4^{5-} = NaAlO_4^{4-}$). Divalent cations (eg Ca^{2+}) must charge-balance two AlO_4^{5-} tetrahedra and this requires some ordering of the melt; these duties are easier for larger cations (eg Ba^{2+}) than for small cations such as Mg^{2+} and this probably accounts for the cation effect mentioned above. There is evidence to suggest

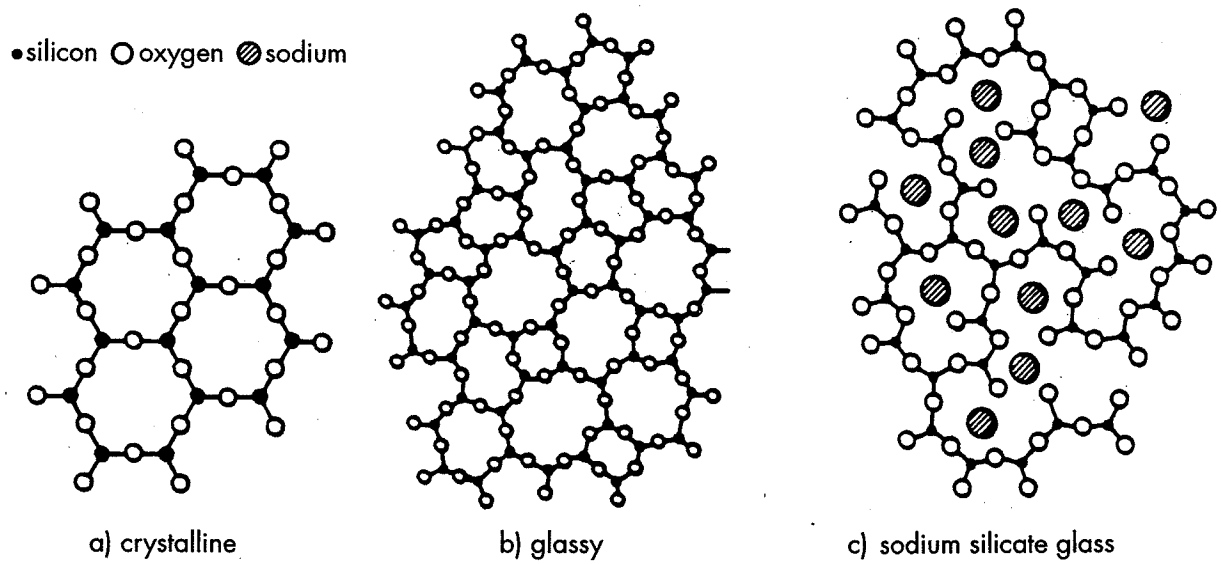


Fig. 1.6 a-c. Schematic representation in 2-dimensions of structure of (a) crystalline silica, (b) glassy silica and (c) sodium silicate glass

that cations involved in charge-balancing duties do not participate in network-breaking. Thus Al_2O_3 additions cause further polymerisation of the melt.

In slags containing iron oxides, Fe^{2+} ions tend to operate as network breakers but Fe^{3+} ions can function as both network formers and breakers. The tendency for network forming increases as the $(Fe^{3+}/Fe^{3+} + Fe^{2+})$ ratio increases and since this ratio tends to be low in steelmaking operations it can be assumed that Fe^{3+} ions usually tend to act as network breakers in steelmaking slags.

P_2O_5 forms PO_4^{3-} tetrahedra, although there is some tendency to form P-O-Si bonds, usually P_2O_5 tends to form phosphate complexes which result in increased polymerisation of the melt. Phosphate anions have a greater affinity for cations than silicate ions and this results in the creation of highly-polymerised silicate units eg SiO_2 in the melt.

In slags containing TiO_2, Ti^{4+} can act as both network breaker and former, however for the range 1 – 7 % TiO_2, which covers most steelmaking slags, TiO_2 operates as a network-former.

The addition of CaF_2 to acidic, polymerised, silicate melts results in the depolymerisation of the melt but in basic melts, it only acts as a diluent.

The physical properties of slags can be estimated from a knowledge of the structural characteristics such as the (NBO/T) ratio and the valency and size of the cations (see appendix).

Readers who wish more detailed information on the structures of slags containing silica and/or other complex-forming constituents are asked to refer to the original publications (see below and reviews [5, 6, 129]).

Slags containing	silica:	Ref. [16 – 64]
	alumina:	[65 – 87]
	iron oxide:	[88 – 94]
	titanium oxide:	[95 – 106]
	phosphorus oxide:	[107 – 111]
	fluorides:	[112 – 128]

1.4 Appendix

Calculation of (NBO/T)

The (NBO/T) ratio can be calculated in the following manner, a worked example is given below in **Tab. 1.3.**

1. Calculate mole fractions of various constituents eg X_{SiO_2}, $X_{Al_2O_3}$, X_{CaO}.

2. Since some molecules contain two cations eg Al_2O_3, P_2O_5, Fe_2O_3 multiply these mole fractions by 2 eg $2x_{Al_2O_3}$, $2x_{Na_2O}$

   Sum network formers (T)

   $$x_T = \sum x_{SiO_2} + 2x_{Al_2O_3} + f2x_{Fe_2O_3} + x_{TiO_2} + 2x_{P_2O_5}$$

3. Determine the fraction (f) of Fe^{3+} in (IV) coordination and that in VI coordination = (1 – f)

   In practice, f = 0 for most iron and steelmaking slags.

4. Determine total charge on network-breaking cations eg $\sum z_i x_i$

   $$y^{(1)}{}_{NB} = \sum 2(x_{CaO} + x_{MgO} + x_{FeO} + x_{MnO} + x_{Na_2O} + x_{K_2O}) + 6(1 - f)x_{Fe_2O_3}$$

5. Calculate $y^{(2)}{}_{NB}$ by allowing for the electrical charge balance of AlO_4^{4-}, FeO_4^{4-} (IV)

   $$y^{(2)}{}_{NB} = y^{(1)}{}_{NB} - 2X_{Al_2O_3} - 2fX_{Fe_2O_3}$$

6. (NBO/T) = $y^{(2)}{}_{NB}/x_T$

Tab. 1.3. Calculation of (NBO/T) for a blast furnace slag

Oxide	Mass %	x	x_T	$y^{(1)}{}_{NB}$	$y^{(2)}{}_{NB}$	(NBO/T)
SiO_2	36.1	0.3591	0.3591			
TiO_2	0.46	0.0034	0.0034			
Al_2O_3	13.1	0.0768	0.1536			
Fe_2O_3	–	–			– 0.1536	
P_2O_5	–	–				
CaO	40.9	0.4359		0.4359		
MgO	7.7	0.1142		0.1142		
FeO	0.40	0.0033		0.0033		
MnO	0.25	0.0021		0.0021		
Na_2O	0.20	0.0019		0.0019		
K_2O	0.50	0.0032		0.0032		
Σ			0.5161	1.1212		1.87
					+ 1.1212	
					0.9676	
(NBO/T) = 1.87						

1.5 References in Chapter 1

[1] Herasymenko, P.: Trans Faraday Soc., 34 (1938), 1245
[2] Zachariasen, W. H.: J. Amer. Chem. Soc., 54 (1932), 3841
[3] Warren, B. E.: Z. Kristall, 86 (1933), 349
[4] Warren, B. E.: Phys. Rev., 45 (1934), 657
[5] Mysen, B. O.: Earth Science Reviews, 27 (1990), 281 – 365
[6] Mysen, B. O.: Structure and properties of silicate melts. Publ. Elsevier, Amsterdam, 1988
[7] Fleet, M. E.: X-ray diffraction and spectroscopic studies on the structure of silicate glasses in short course in silicate melts. Edit. C. M. Scarfe; Mineralogical Soc., Canada, Ottawa, Ont., (1986), 1 – 35
[8] Wong, J.; Angell, C. A.: Glass structure by spectroscopy. Publ. Marcel Dekker Inc., New York, 1976
[9] Mysen, B. O.: J. Geophys. Res., 95 (1990), 15733
[10] Lentz, C. W.: Inorg. Chem., 3 (1964), 574
[11] Masson, C. R.: Proc. Royal Soc., A287 (1965), 201
[12] Gotz, J.; Masson, C. R.: J. Chem. Soc., (1970) A 1683
[13] Jeffes, J. H. E.: Proc. of 1st Intl. Conf. on Metall Slags and Fluxes, held Halifax, NS, 1980
[14] Pasishnik, S. V.; Ezikov, V. I.; Schkolnik, Y. S.; Bodrova, L. E.; Chuchmarev, S. K.; Pastukov, E. A.: Melts, 2 (1988), 221
[15] Iwamoto, N.; Makino, Y.: J. Non-Cryst. Solids, 34 (1979), 381
[16] Bell, R. J.; Dean, P.; Hibbins-Butler, D. C.: J. Phys. Chem. 3 (1970), 2111 – 2118
[17] Bell, R. J.; Dean, P.: Proc. of Intl. Conf. on Non-Crystalline solids. Edit R. W. Douglas and R. Ellis; Wiley Interscience, London (1972)
[18] Bell, R. J.; Hibbins-Butler, D. C.: J. Phys. Chem. 9 (1976), 2955 – 2959
[19] Mozzi, R. I.; Warren, B. E.: J. Appl. Cryst. 2 (1969), 149 – 192
[20] Konnert, J. H.; Karle, J.: Acta Cryst., A29 (1973), 702 – 710
[21] Vukevitch, M. R.: J. Non-Cryst. Solids, 11 (1972), 25 – 63
[22] Gaskell, P. H.; Tallant, I. D.: Phil. Mag., B42 (1980), 265 – 286
[23] Gaskell, P. H.; Mistry, A. B.: Phil. J., 39 (1979), 245 – 257
[24] Sharma, S. K.; Mammone, J. F.; Nicol, M. F.: Nature, 292 (1981), 140 – 141
[25] Newton, M. D.; Gibbs, G. V.: Phys. Chem. Mineral, 6 (1980), 221 – 246
[26] Chakoumakos, B. C.; Hill, R. J.; Gibbs, G. V.: Amer. Mineral, 66 (1981), 1237 – 1249
[27] Geisinger, K. I.; Gibbs, G. V.; Navrotsky, A.: Phys. Chem. Mineral, 11 (1985), 266 – 283
[28] Bockris, J. O'M.; MacKenzie, J. D.; Kitchener, J. A.: Trans. Farad. Soc., 51 (1954), 1734 – 1748
[29] Bockris, J. O'M.; Tomlinson, J. W.; White, J. L.: Trans. Farad. Soc., 52 (1956), 299 – 311
[30] Bockris, J. O'M.; Reddy, A. K. N.: Modern Electrochemistry. Publ. Plenum Press, New York, 1970
[31] Stebbins, J. F.; Carmichael, I. S. E.; Moret, L. K.: Contrib. Mineral Petrol, (1984), 131 – 148
[32] Ryerson, F. J.: Geochim Cosmochim Acta, 49 (1985), 637 – 651
[33] Toop, G. W.; Samis, C. S.: Trans AIME, 224 (1962), 878 – 887
[34] Masson, C. R.: Proc. Royal Soc., A287 (1965), 201
[35] Masson, C. R.: J. Amer. Ceram Soc., 51 (1968), 134 – 143
[36] Masson, C. R.: J. Non-Cryst. Solids, 1 (1977), 1 – 42
[37] Kapoor, G.; Frohberg, M. G.: Can. J. Chem, 48 (1970), 33
[38] Kapoor, G.; Mehrotra, G. M.; Frohberg, M. G.: Archiv f. d. Eisenhüttenw., 45 (1974), 213
[39] Gaye, H.; Welfringer, J.: Proc. of 2nd Intl. Symp. on Metallurgical Slags and Fluxes, held Lake Tahoe, Nev., 1984. Edit. H. A. Fine and D. R. Gaskell; publ. Metall Soc. AIME, Warrendale, Pa. (1984), 357 – 375
[40] Gaye, H.; Riboud, P. V.; Welfringer, J.: Proc. of 3rd Intl. Conf. on Metallurgical Slags and Fluxes, held Glasgow, June 1988. Publ. Inst. of Metals London (1989), 259 – 262
[41] Yokokawa, T.; Niwa, K.: Trans Jap. Inst. Metals, 10 (1969), 3
[42] Borgianni, C.; Granati, P.: Met. Trans B, 8B (1977) 147 and 10B (1979), 21
[43] Bottinga, Y.; Richet, P.: Earth Planet, Sci. Lett, 40 (1978), 382 – 400
[44] Burnham, C. W.: Geochim Cosmochim Acta, 39 (1975), 1077 – 1084
[45] Burnham, C. W.: Phys. Chem. Earth, 13 – 14 (1981), 191 – 227
[46] Burnham, C. W.; Nekvasil, H.: Amer. Mineral, 71, (1986), 239 – 263
[47] Soules, T. F.: J. Chem. Phys., 71 (1979), 4570 – 4578
[48] Matsui, Y.; Kawamura, K.: Nature, 285 (1980), 648 – 649
[49] Kubicki, J. D.; Lasaga, A. C.: Amer. Mineral, 73 (1988), 941 – 955
[50] Waseda, Y.; Toguri, J. M.: Met. Trans B, 8B, (1977), 563 – 568
[51] Iwamoto, N.; Umesaki, N.; Dohi, K.: J. Jap. Inst. Metals, 47 (1983), 382 – 389. See also Yogyo Kyokai-shi, 92 (1984), 201 – 209
[52] Waseda, Y.; Shiraishi, Y.; Toguri, J. M.: Trans. Jap. Inst. Metals, 21 (1980), 51 – 62
[53] Stebbins, J. F.: J. Non-Cryst. Solids, 106 (1988), 359 – 369
[54] Furukawa, T.; Fox, K. E.; White, W. B.: J. Chem. Phys., 15 (1981), 3226 – 3237
[55] Iguchi, Y.; Yonezawa, K.; Funaoka, Y.; Banya, S.; Nishina, Y.: Proc. 3rd Intl. Conf. on Metall Slags and Fluxes, Glasgow, June 1988. Publ. Inst. of Metals, London, 1989, 169 – 171
[56] Sharma, S. K.; Virgo, D.; Mysen, B. O.: Amer. Mineral, 64 (1979), 779 – 788
[57] Virgo, D.; Mysen, B. O.; Kushiro, I.: Science, 208 (1979), 1371 – 1373
[58] Pirou, B.; McMillan, P.: Amer. Mineral, 68 (1983), 426 – 443
[59] McMillan, P.: Amer. Mineral, 69 (1984), 645 – 659
[60] Mysen, B. O.; Virgo, D.; Seifert, F. A.: Rev. Geophys., 20 (1982), 353 – 383
[61] Dickinson, J. E.: Liquidus phase equilibria and melt structure. Short course in silicate melts. Edit C. M. Scarfe, Mineralogical Soc. Canada, Ottawa, Ont., (1986), 154 – 179
[62] Stebbins, J. F.: Nature, 330 (1987), 465 – 467
[63] Umesaki, N.; Iwamoto, N.; Takahashi, M.; Tatsumisago, M.; Minami, T.; Matsui, Y.: Trans. Iron Steel Inst. Japan, 28 (1988), 852 – 859
[64] Virgo, D.; Mysen, B. O.; Kushiro, I.: Science, 208 (1979), 1371 – 1373
[65] Dingwell, D. B.: Geochim Cosmochim Acta, 50 (1986), 1261 – 1265
[66] Schairer, J: F.; Bowen, N. L.: Amer. J. Sci., 245 (1955), 681 – 747
[67] Schairer, J. F.; Bowen, N. L.: Amer. J. Sci., 254 (1956), 129 – 195
[68] Navrotsky, A.; McMillan, P.; Coutoures, J. P.: Geochim Cosmochim Acta, 46 (1982), 2039 – 2049
[69] Roy, B. N.; Navrotsky, A.: J. Amer. Ceram. Soc., 67 (1984), 606 – 610
[70] Hervig, R. L.; Navrotsky, A.: Geochim Cosmochim Acta, 48 (1984), 513 – 522
[71] Frazer, D. G.; Rammensee, W.; Hardwick, A.: Geochim Cosmochim Acta, 49 (1985), 349 – 359
[72] Navrotsky, A.; Geisinger, K. L.; McMillan, P.; Gibbs, G. V.: Phys. Chem. Mineral, 11 (1985), 284 – 298
[73] Taylor, M.; Brown, G. E.: Geochim Cosmochim Acta, 43 (1979), 61 – 77 and 1467 – 1475
[74] Murdoch, J. B.; Stebbins, J. F.; Carmichael, I. S. E.: Amer. Mineral, 70 (1985), 332 – 343
[75] McMillan, P.; Piriou, B.; Navrotsky, A.: Geochim Cosmochim Acta, 46 (1982), 2021 – 2037
[76] Seifert, F. A.; Mysen, B. O.; Virgo, D.: Amer. Mineral, 67 (1982), 696 – 718
[77] Engelhardt, G.; Nofz, M.; Forkel, K.; Wishman, F. G.; Magi, M.; Samoson, A.; Lippmaa, E.: Phys. Chem. Glasses, 26 (1985), 157 – 165
[78] Kirkpatrick, R. J.; Oestrike, R.; Weiss, C. A.; Smith, K. A.; Oldfield, E.: Amer. Mineral, 71 (1986), 705 – 711
[79] Mysen, B. O.; Virgo, D.; Seifert, F. A.: Amer. Mineral, 69 (1985), 834 – 848
[80] Mysen, B. O.: Amer. Mineral, 75 (1990), 120 – 134
[81] Angell, C. A.; Cheeseman, P.; Tamaddon, S.: Science, 218 (1982), 885 – 887
[82] Ohtani, E.; Taulelle, F.; Angell, C. A.: Nature 314 (1985), 78 – 81
[83] Lacey, E. D.: Acta Cryst. 18 (1968), 141 – 150
[84] McKeown, D. A.; Galeener, F. L.; Brown, G. E.: J. Non-Cryst. Solids, 68 (1984), 361 – 378
[85] McKeown, D. A.; Waychunas, G. A.; Brown, G. E.: J. Non-Cryst. Solids, 74 (1985), 325 – 348 and 349
[86] Huang, C.; Behrman, E. C.: J. Non-Cryst. Solids, 128 (1991), 310 – 321
[87] Zirl, D. M.; Garofalini, S. H.: J. Amer. Ceram. Soc., 73 (1990), 2848 – 2856
[88] Fox, K. E.; Furukawa, Y.; White, W. B.: Phys. Chem. Glasses, 23 (1982), 169 – 178
[89] Cooney, T.; Sharma, S. K.; Urmos, J. P.: EOS, 68 (1987), 436
[90] Virgo, D.; Mysen, B. O.: Phys. Chem. Mineral, 12 (1985), 65 – 76
[91] Hollitt, M. J.; Cashion, J. D.; Brown, L. J.: Proc. 2nd Intl. Symp. on Metall Slags and Fluxes, held Lake Tahoe, Nev. (1984). Edit. H. A. Fine and D. R. Gaskell. Publ. Metall Soc. AIME, Warrendale, Pa. (1984), 961 – 972
[92] Brearly, M.: J. Geophys. Res., 95 (B10) (1990), 15703 – 15716
[93] Sugiyama, K.; Suh, I. K.; Waseda, Y.: Proc. of 3rd Intl. Conf. on Molten Slags and Fluxes, held Glasgow, June (1988). Publ. Inst. of Metals, London, 1989, 172 – 174
[94] Mysen, B. O.; Virgo, S. D.; Seifert, F. A.: Amer. Mineral, 69 (1985), 834 – 847
[95] Dickinson, J. E.; Hess, P. C.: Geochim Cosmochim Acta, 49 (1985), 2289 – 2296
[96] Sandstrom, D. R.; Lytle, F. W.; Wei, P.; Greegor, R. B.; Wong, J.; Schultz, P.: J. Non-Cryst. Solids, 41 (1980), 201 – 207
[97] Greegor, R. B.; Lytle, W. B.; Sandstrom, D. R.; Wong, J.; Schultz, P.: J. Non-Cryst. Solids, 55 (1983), 27 – 43
[98] Hanada, T.; Soga, N.: J. Non-Cryst. Solids, 38 (1980), 105 – 110
[99] Tobin, N. C.; Baak, T.: J. Opt. Soc. Amer., 58 (1968), 1459
[100] Chandrasekhar, H. R.; Chandresekhar, M.; Manghnani, M. H.: Solid State Commun, 31 (1979), 329 – 333
[101] Bihuniak, P. P.; Condrate, R. A.: J. Non-Cryst. Solids, 44 (1981), 331 – 344

[102] Dickinson, J. E.: Annual Meeting, Geol. Soc. Amer., Abstr. Prog., 16 (1984), 488
[103] Furukawa, T.; White, W. B.: Phys. Chem. Glasses, 20 (1979), 69 – 80
[104] Myson, B. O.; Seifert, F. A.; Virgo, D.: Amer. Mineral, 65 (1980), 867 – 884
[105] Wright, A. C.; Yarker, C. A.; Johnson, P. A. V.; Wedgewood, F. A.: in: Non-crystalline solids. Edit. G. H. Frischat, Trans Tech. Alfred University, NY, 118 – 123
[106] Iwamoto, N.; Hidaka, H.; Makino, Y.: J. Non-Cryst. Solids, 58 (1983), 131 – 141
[107] Visser, W.; van Groos, A. F.; Koster, A.: Amer. J. Sci., 279 (1979), 970 – 988
[108] Shibata, N.; Horigudhi, M.; Edahiro, T.: J. Non-Cryst. Solids, 45 (1981), 115 – 126
[109] Yang, W. H.; Kirkpatrick, R. J.; Turner, G.: J. Amer. Ceram. Soc., 69 (1986), C222 – C223
[110] Nelson, C.; Tallant, D. R.: Phys. Chem. Glasses, 25 (1984), 31 – 39
[111] Nelson, C.; Tallant, D. R.: Phys. Chem. Glasses, 26 (1985), 119 – 122
[112] Kozakevitch, P.: Rev. Met., 46 (1949), 572
[113] Bills, P.: J. Iron Steel Inst., 200 (1963), 133
[114] Baak, T.: Acta Chem Scand, 8 (1954), 1727
[115] Kumar, D.; Ward, R. G.; Williams, D. J.: Trans Faraday Soc., 61 (1966), 1850 – 1857
[116] Shiraishi, Y.; Saito, S.: J. Japan Inst. Metals, 29 (1965), 614
[117] Føland, T.: J. Amer. Ceram Soc., 41 (1958), 524
[118] Iwamoto, N.: Trans Jap. Weld. Res. Inst., 4 (1975), 91 – 99
[119] Ito, T.; Yanagase, Y.; Suginohara, Y.; Miyazaki, N.: J. Jap. Inst. Metals, 31 (1967), 290
[120] Mitchell, A.: Trans. Farad. Soc., 63 (1967), 1408
[121] Tsunawaki, Y.; Iwamoto, N.; Hattori, T.; Mitsuishi, A.: J. Non-Cryst. Solids, 44 (1981), 369 – 378
[122] Takusagawa, N.: J. Non-Cryst. Solids, 42 (1980), 35 – 40
[123] Iwamoto, N.; Makino, Y.: J. Non-Cryst. Solids, 46 (1981), 81 – 94
[124] Shinmei, M.; Imai, T.; Maekana, T.; Yokokawa, T.: Proc. 2nd Intl. Symp. on Metall Slags and Fluxes, held Lake Tahoe, Nev., 1984. Edit H. A. Fine and D. R. Gaskill. Publ. Metall Soc. AIME, Warrendale, Pa., 1984
[125] Dumas, P.; Corset, W.; Carvalho, Y.; Levy, Y.: J. Non-Cryst. Solids, 47 (1982), 239
[126] Mysen, B. O.; Virgo, D.: Phys. Chem. Mineral, 12 (1985), 77 – 85
[127] Mysen, B. O.; Virgo, D.: Contrib. Mineral Petrol, 91 (1985), 205 – 222
[128] Foley, S. F.; Taylor, W. R.; Green, D. A.: Contrib. Mineral Petrol, 93 (1986), 46 – 55
[129] Mills, K. C.: The structure of silicate melts. NPL Report DMM (A) 43 (1991). (Available National Physical Laboratory, Teddington, UK.)

2

Basicity and optical basicities of slags

K. C. Mills

2.1 Basicity

Reactions such as the desulphurisation and dephosphorisation of steel are dependent upon the activity of the free oxygen ($a_{O^{2-}}$) in the melt. However it is known that these refining reactions are improved with the use of more "basic" slags. Since, in practice, the activities of CaO, CaS etc. are difficult to measure for multicomponent slags, many attempts have been made to relate the desulphurising and dephosphorising power to the basicity of the slag. The simplest index of the basicity is the "V ratio" ie (% CaO/% SiO_2) and this has been used considerably by steelmakers but this ratio does not take into account MgO, Al_2O_3, FeO etc. which are frequently present in steelmaking slags. Consequently, several other indices of basicity have been used [1–13] and these are outlined in **Tab. 2.1.** The concept of excess base (B^{xs}) defined in equation (2.2), has also been used to determine the basicity of slags [14–16], where x represents the mole fraction and b values are constants related to the ion-oxygen attraction (see **Tab. 2.2**).

$$B^{xs} = \Sigma\, x_1 b_1 + x_2 b_2 + x_3 b_3 + ... \qquad (2.1)$$

The basicity has also been defined in terms of the solubility of gases such as O_2, N_2 or CO_2 in the slag [17, 18]. Wagner [19] proposed that the basicity could be expressed in terms of the carbonate capacity (B_{carb}) which is defined in equations (2.2) and (2.3) where $C^*_{CO_3^{2-}}$ denotes the value for a reference slag. The principal problem encountered with this index of basicity is the limited amount of data available for the carbonate capacities of slags.

$$B_{carb} = C_{CO_3^{2-}} / C^*_{CO_3^{2-}} \qquad (2.2)$$

$$C_{CO_3^{2-}} = \%_{CO_3^{2-}} / p_{CO_2} \qquad (2.3)$$

Attempts have also been made to define basicity in terms of various redox reactions eg Fe^{2+}/Fe^{3+}, Cr^{3+}/Cr^{6+}, Mn^{2+}/Mn^{3+} but there are also problems with this approach [17, 18].

Tab. 2.1. Typical examples of various indices used to express basicity

Index	Ref.
$\frac{\%\,(CaO)}{\%\,(SiO_2)}$	[2]
$\frac{x\,(CaO) + (MgO)}{x\,(SiO_2)}$	
$\frac{\%\,(CaO)}{\%\,(SiO_2) + \%\,(Al_2O_3)}$	[3]
$\frac{\%\,(CaO)}{\%\,(SiO_2) + \%\,(P_2O_5)}$	[4]
$\frac{x\,(MeO) - 3x\,(P_2O_5)}{x\,(SiO_2)}$	[5]
$\frac{\%\,CaO + 1.4\%\,MgO}{\%\,SiO_2 + 0.84\%\,P_2O_5}$	[6]
$\frac{x\,(MeO)}{x\,(SiO_2) + 2x\,(P_2O_5) + \frac{1}{2}x\,(Al_2O_3) + \frac{1}{2}x\,(Fe_2O_3)}$	[7]
$\frac{x(CaO) - 4x\,(P_2O_5)}{x\,(SiO_2)}$	[8]
$\%\,(CaO) - 1.86\%\,(SiO_2) - 1.19\%\,(P_2O_5)$	[9]
$x\,(MeO) - 2x\,(SiO_2) - 4x\,(P_2O_5) - 2x\,(Al_2O_3) - x\,(Fe_2O_3)$	[10]
$x\,(CaO) + \frac{2}{3}x\,(MgO)/x(SiO_2) + x\,(Al_2O_3)$	[11]
$x\,(CaO) + \frac{2}{3}x\,(MgO)/x(SiO_2) + x(Al_2O_3)$	[12]
$x\,(CaO) + 0.5x\,(MgO)/x(SiO_2) + 0.33x\,(Al_2O_3)$	[13]

Tab. 2.2.

Oxide	CaO	SiO_2	TiO_2	Al_2O_3	MnO	MgO	FeO
b_i	6.05	– 6.31	– 4.97	– 0.2	4.8	4.0	3.4

2.2 Optical Basicity

2.2.1 Introduction

Duffy and Ingram [20] noted that the shifts in frequency of the absorption band associated with the 6s – 6p transaction observed in the ultraviolet (UV) region of the spectrum can be related to the basicity of a glass or slag. These shifts in frequency were observed using tracer ions such as Tl^+, Pb^{2+} or Bi^{3+} with $d^{10}s^2$ configuration and have been attributed to changes in the electron donation resulting from the "nephelauxetic" effect. The frequency shift can be considered as a measure of the electron donor power and is usually expressed in terms of the optical basicity (Λ) defined in equations (2.4) to (2.6) where the subscript "free" refers to the probe ion eg Pb^{2+}.

$$\Lambda = \frac{\text{Electron donor power of slag}}{\text{Electron donor power of CaO}} \qquad (2.4)$$

$$\Lambda = (\nu_{free} - \nu_{slag}/\nu_{free} - \nu_{CaO}) \qquad (2.5)$$

$$\Lambda = (60700 - \nu_{slag})/31000 \qquad (2.6)$$

Experimental values obtained in this manner are given in **Tab. 2.3.** but Duffy and Ingram [21] showed that values of the optical basicities of the various oxides (denoted Λ_{th}) could be calculated from Pauling electronegativities. They also pointed out that values for the slag could be derived by use of equation (2.7) where n represents the number of oxygen atoms in the molecule eg 2 for SiO_2, 3 for Al_2O_3.

$$\Lambda = \frac{\Sigma x_1 n_1 \Lambda_{th1} + x_2 n_2 \Lambda_{th2} + x_3 n_3 \Lambda_{th3} + ...}{\Sigma x_1 n_1 + x_2 n_2 + x_3 n_3 + ...} \qquad (2.7)$$

Experimental values could not be obtained for slags containing transition metal oxides (eg FeO, MnO) since these absorbed strongly in the UV and consequently some workers [22, 23] used Pauling electronegativities to derive values of Λ_{th} for transition metal oxides, $\Lambda_{th}(FeO) = 0.51$, $\Lambda_{th}(Fe_2O_3) = 0.48$, $\Lambda(MnO) = 0.59$. However, other workers [24 – 28] have contested the use of these values and it would appear that sulphide capacities correlated better [24, 25] with the value $\Lambda_{th}(FeO) = 1.0$ whereas phosphorus capacities correlated better with $\Lambda_{th}(FeO)$ values of 0.51[30,

Tab. 2.3. Experimental and calculated values of the optical basicity

Oxide	Experimental values of Λ				Calculated values of Λ_{th}			Recommended Λ_{th}
	UV shift	PAS	Molar refractivity	Curve fitting	Pauling e.n.	Electron densities	en (ΔH°_{f298})	
Li_2O	1.00	(1.0 – 1.25)		1.3[c]	1.0	1.06		1.0[e]
Na_2O	1.15	(1.05 – 1.33)		1.25[c] 1.34[d]	1.15	1.11		1.15[e]
K_2O		(1.07 – 1.39)		1.14[c]	1.40	1.16		1.4[e]
Rb_2O						1.17		
Cs_2O						1.18		1.7[e]
BeO					0.605			
MgO	0.78				0.78	0.92		0.78[e]
CaO	1.0				1.0	1.0		1.0
SrO					1.10	1.04		1.1[e]
BaO	1.15				1.15	1.08		1.15[e]
B_2O_3	0.42				0.42	0.42		0.42[e]
Al_2O_3	0.605				0.60	0.66		0.605[e]
CO_2						0.40		
SiO_2	0.48					0.47		0.48[e]
GeO_2						0.58		
TiO_2				0.61[a], 0.55[b]	0.61	0.65		
VO_2				0.57[b]				
P_2O_5	0.40				0.40	0.38		0.40[e]
As_2O_3						0.72		
Sb_2O_3						0.84		
SO_3					0.33	0.29		
CrO								
MnO			0.97 ± 0.1	1.21[a]	0.59	0.95	0.87	1.0[e]
FeO			0.90 ± 0.1	1.03[a], 0.51[b]	0.51	0.94	0.82	1.0[e]
CoO					0.475	0.93		0.95[f]
NiO					0.475	0.92		0.95[f]
CuO					0.43	0.89		0.9[f]
ZnO	0.85		0.9 ± 0.07		0.55			0.9[f]
CdO					0.51			
PbO					0.48		1.1	1.15
Cr_2O_3			0.81 ± 0.1			0.77	0.70	0.8[f]
Fe_2O_3			0.80 ± 0.1	0.70	0.48	0.72	0.66	0.8[f]
CaF_2					0.43, 0.67			

[a] From sulphur capacity data [24]
[b] From phosphorus capacity data [30]
[c] From viscosity data [33]
[d] From activity data [34]
[e] Recommended [28]
[f] By comparison with other data

31]. Ingram[32] has suggested that Λ_{th} for transition metal oxides may adopt different values according to the reaction being studied. It should also be pointed out that departures from the rule shown in equation (2.7) have also been reported.

Other methods have been developed to measure [28, 35, 36] and calculate [36, 37] values of Λ_{th} for transition metal oxides and these are outlined in Appendix 2.4.; most of the Λ_{th} values support the higher values of Λ_{th} eg 1.0 for FeO and MnO (Tab. 2.3.). Recommended values [28] for Λ_{th} are given in the final column in Tab. 2.3. In this report the diagrams are those reported by the various authors where this has involved the use of Λ_{th} values significantly different from the recommended values, this fact is noted in the figure caption.

2.2.2 Relation between optical basicity and partition of elements

2.2.2.1 Sulphur capacities

The sulphur capacity C_s is usually defined by equation (2.8)

$$C_s = (\%S)\,(p_{O_2})^{0.5} / (p_{S_2})^{0.5} \qquad (2.8)$$

However it can also be expressed in the form of equation (2.9), the two capacities being linked by reaction (2.10)

$$C_s' = (\%S)[a_O] / [a_S] \qquad (2.9)$$

$$0.5\ S_2(g) + [O] = [S] + 0.5\ O_2(g) \qquad (2.10)$$

Sosinsky and Sommerville [25] derived the temperature dependence of C_S for slags with a range of optical basicities **(Fig. 2.1)** and which could be obtained using equation [2.11] where T is in K.

$$\log C_S = \left(\frac{22690 - 54640\,\Lambda}{T}\right) + 43.6\,\Lambda - 25.2 \qquad (2.11)$$

The temperature dependence of $\log (\%S)/[a_S]$ is given in equation (2.12)

$$\log(\%S)/[a_S] = \left(\frac{21920 - 54640\,\Lambda}{T}\right) + 43.6\,\Lambda - 23.9 - \log a_O \qquad (2.12)$$

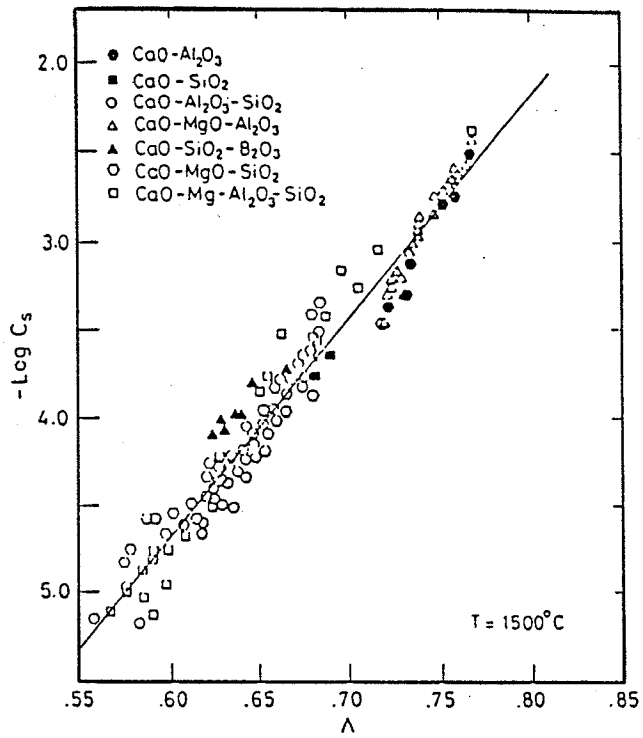


Fig. 2.1. Correlation of sulphur capacity (C_S) data at 1500 °C with optical basicity [24, 25]

Young [38] showed that equation (2.11) only applied to range where $\Lambda = 0.8$ **(Fig. 2.2)** which corresponds to the orthosilicate concentration ie (NBO/T) = 4 and reported the "best fit" relationships given in equations (2.13) and (2.14) for the two ranges

$$\Lambda < 0.8: \log C_S = -13.913 + 42.84\,\Lambda + 23.82\,\Lambda^2 - 11710\,T^{-1} - 0.02223\,(\%SiO_2)_{wt.} - 0.02275\,(\%Al_2O_3)_{wt.} \quad (2.13)$$

$$\Lambda \geq 0.8: \log C_S = -0.6261 + 0.4808\,\Lambda + 0.7917\,\Lambda^2 - 1697\,T^{-1} + \frac{2587\,\Lambda}{T} + 5.144 \times 10^{-4}\,(\%FeO)_{wt.} \quad (2.14)$$

2.2.2.2 Phosphate capacities

Various expressions have been used to express the phosphate capacities (C_P), the most useful being those associated with reactions (2.15) and (2.17), the associated phosphate capacities being denoted $C_P^{(1)}$ and $C_P^{(2)}$, which are defined by equations (2.16) and (2.18), respectively

$$0.5\,P_2(g) + 5/4\,O_2(g) + 1.5(O^{2-}) = (PO_4^{3-}) \quad (2.15)$$

$$C_P^{(1)} = \frac{(\%PO_4^{3-})}{p_{P_2}^{0.5}\,p_O^{1.25}} = \frac{K^{(1)}\,a_{(O^{2-})}^{1.5}}{f_{PO_4^{3-}}} \quad (2.16)$$

where $K^{(1)}$ is the equilibrium constant for reaction (2.16)

$$[P] + 2.5[O] = 0.5(P_2O_5) \quad (2.17)$$

$$C_P^{(2)} = \frac{(\%\,P)}{a_{[P]}\,a_{[O]}^{2.5}} = \frac{K^{(2)}\,(\%\,P)^{0.5}}{f_{(P_2O_5)}^{0.5}} \quad (2.18)$$

where $K^{(2)}$ is the equilibrium constant for reaction (2.17).

Gaskell [22] analysed phosphorus distribution data [39] and determined the relationship between optical basicity and the activity coefficient ratio ($\gamma_{M_3(PO_4)_2}/\gamma_{MO}$) for reaction (2.18) shown in **Fig. 2.3;** similar relationship were obtained for MgO and FeO.

$$3(M_2O) + 5[O]_{1\%} + 2[P]_{1\%} = 2M_3(PO_4)_2 \quad (2.18)$$

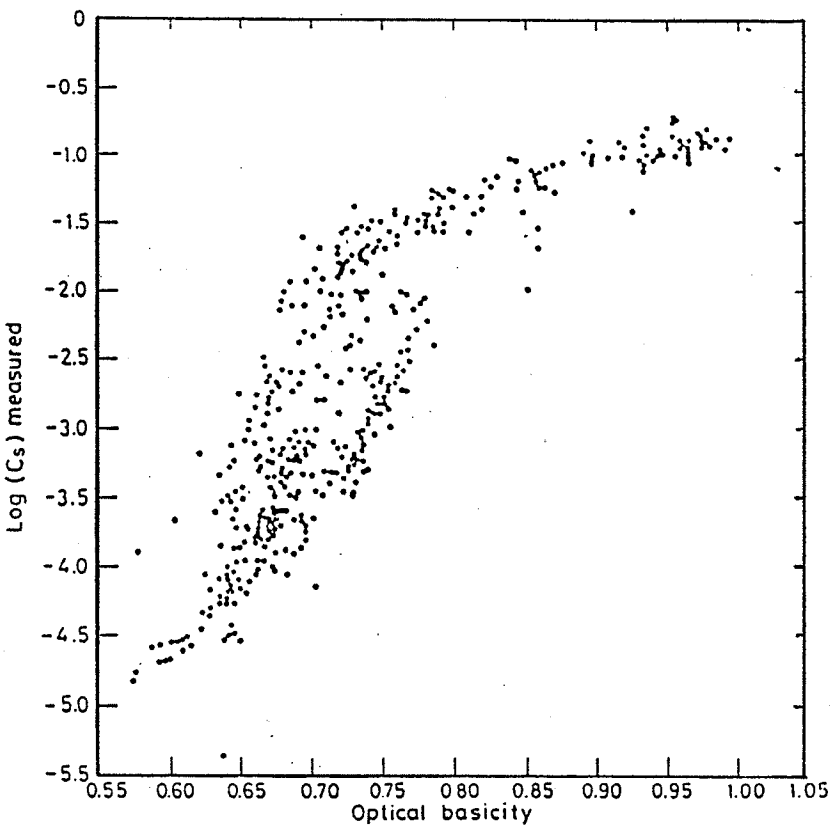


Fig. 2.2. The sulphur capacity (C_S) as a function of optical basicity [38]

Gaskell [22] derived data for the partition of phosphorus between the metal and slag phases and reported a linear correlation between the optical basicity and $\ln(x_{PO_4^{3-}}/[\%P]\,[\%O]^{2.5})$ which is shown in **Fig. 2.4** and equation (2.19)

$$\ln(x_{PO_4^{3-}}/[\%P]\,[O]^{2.5}) = -(558.9 + 2.175 \times 10^6 T^{-1} - 1.93 \times 10^9 T^{-2})\Lambda - 28.78 \quad (2.19)$$

Mori [23] showed that log $C_P^{(1)}$ at 1600°C could be correlated linearly with optical basicity[1] **(Fig. 2.5)** and equation (2.20)

[1] Values of $\Lambda(FeO) = 0.51$ and $\Lambda(Fe_2O_3) = 0.48$ were used in these calculations

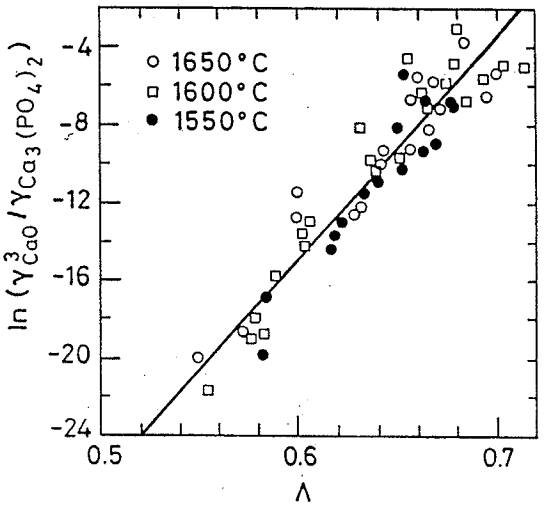


Fig. 2.3. The activity coefficient ratio ($\ln\gamma^3_{CaO}/\gamma_{Ca_3(PO_4)_2}$) as a function of optical basicity [22]; a value of Λ(FeO) = 0.51 was used in this study

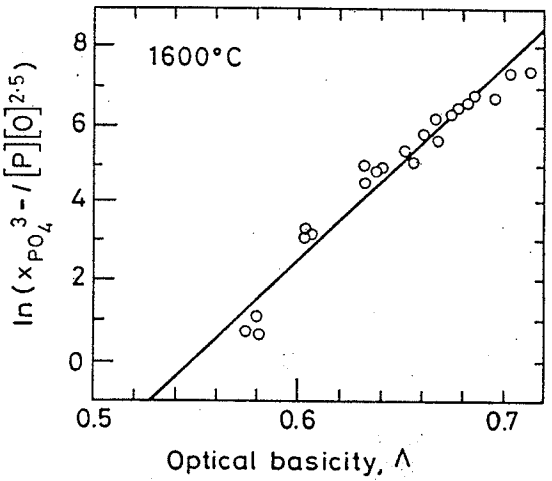


Fig. 2.4. The parameter ln ($x_{PO_4}^{3-}/[\%P][\%O]^{2.5}$) at 1600 °C as a function of the optical basicity [22]; (a value of Λ(FeO) = 0.51 was used in these calculations)

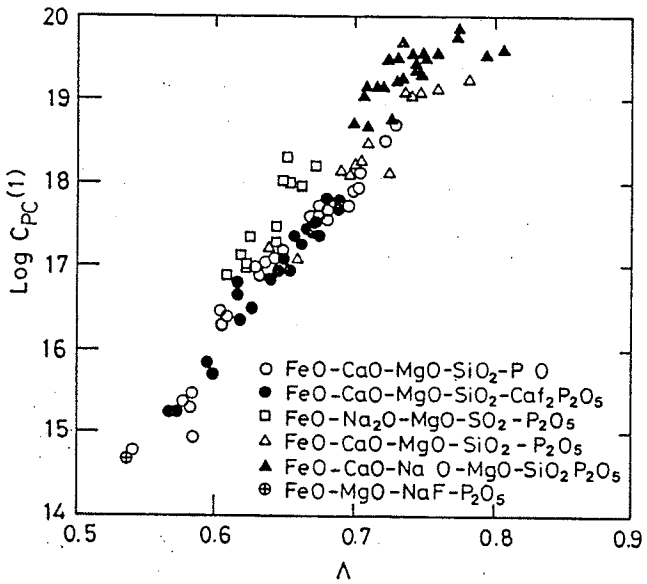


Fig. 2.5. Log $C_p^{(1)}$ as a function of optical basicity; a value of Λ(FeO) = 0.51 was used in these calculations [23]

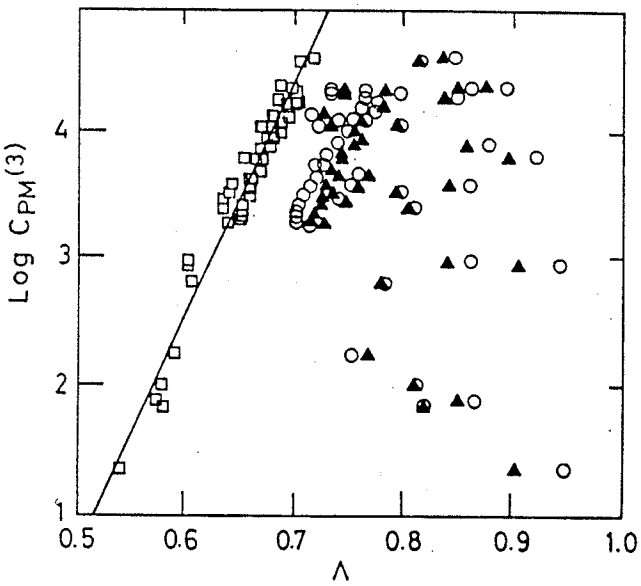


Fig. 2.6. Log $C_{PM}^{(3)}$ (for the monomer; M) as a function of the optical basicity using a value of Λ(FeO) of (I) 0.51 [29, 30],□; 1.03, [24, 25]○; 0.94; [26, 27] ▲

$$\log C_p^{(1)} = 17.55\,\Lambda + 5.72 \qquad (2.20)$$

Bergman [29, 30] showed the relationship between optical basicity and log $C_P^{(3)}$ (defined by equations 2.21 and 2.22) was more consistent than when a value of Λ(FeO) = 0.51 was used cf values of ca. 1.0 **(Fig. 2.6)**

$$[P] + 2.5[O] + 1.5(O^{2-}) = (PO_4^{3-}) \qquad (2.21)$$

$$C_P^{(3)} = \frac{(\%\,PO_4^{3-})}{[\%P]\,[\%O]^{2.5}} = \frac{C_p^{(1)}\,p_P^{0.5}\,p_{O_2}^{1.25}}{[\%P]\,[\%O]^{2.5}} \qquad (2.22)$$

Bergman [29, 30] analysed experimental data for phosphorus distribution [39, 40] in terms of monomer (PO_4^{3-}) and dimer ($P_2O_7^{4-}$) and showed that log $C_P^{(3)}$ for the monomer, (denoted as log $C_{P(M)}^{(3)}$) correlated linearly with the optical basicity (Fig. 2.6 and equation (2.23) where T is in K)

$$\log C_{PM}^{(3)} = 21.30\,\Lambda + 32912\,T^{-1} - 27.90 \qquad (2.23)$$

Young [38] preferred the use of Λ(FeO) = ca. 1.0 and established the empirical relationship given in equation (2.24) derived from a "best fit" of a large amount of data

$$\log C_P^{(2)} = -18.184 + 35.84\,\Lambda - 22.35\,\Lambda^2 + 22930\,T^{-1} - 0.0625(\%FeO) - 0.04256(\%MnO) + 0.359(\%P_2O_5)^{0.3} \qquad (2.24)$$

2.2.2.3 Oxygen partition

Bergman [29, 30] showed that oxygen distribution between metal and slag [39] could be expressed as a function of optical basicity (equation (2.25) and **Fig. 2.7**)

$$\log[\%O] = -1.907\,\Lambda - 6005\,T^{-1} + 3.57 \qquad (2.25)$$

2.2.2.4 Manganese partition

Kunisada and Iwai [41] showed that the Mn capacity, (defined in equation (2.26)) was a function of Λ **(Fig. 2.8** and equation 2.27))

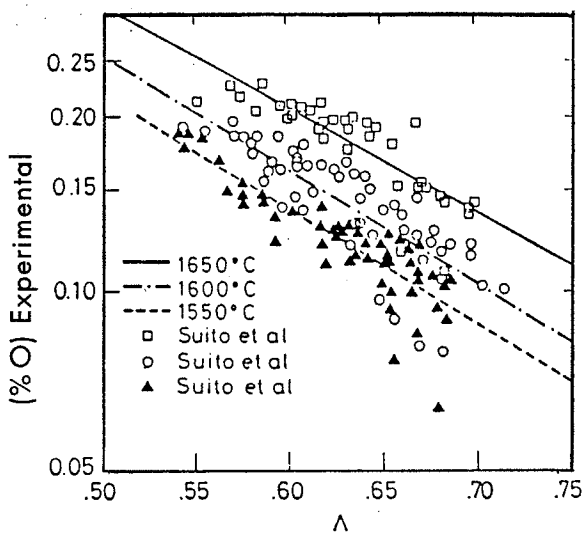


Fig. 2.7. The oxygen concentrations in the metal at various temperatures as a function of optical basicity [29]; a value of $\Lambda(FeO) = 0.51$ was used in these calculations

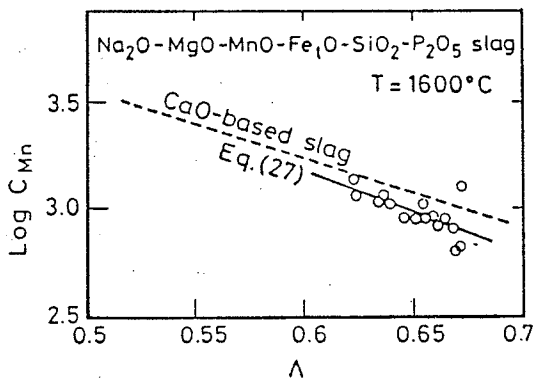


Fig. 2.8. The manganese capacity C_{Mn} as a function of optical basicity [41]; values of $\Lambda(FeO) = 0.51$ and $\Lambda Mn(O) = 0.59$ were used in these calculations

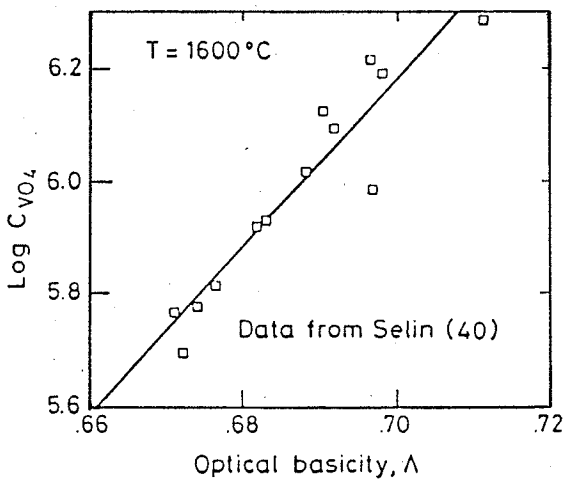


Fig. 2.9. The vanadium (V^{5+}) capacity $C_{VO_4^{3-}}$ as a function of optical basicity [31]; a value of $\Lambda(FeO) = 0.51$ was used in these calculations

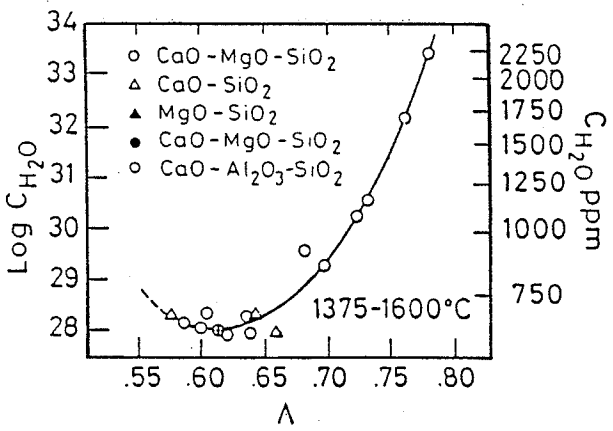


Fig. 2.10. Log C_{H_2O} as a function of optical basicity [42]

$$C_{Mn} = (\%Mn)/[a_{Mn}][a_o] \quad (2.26)$$

$$1600^{oC}: \log C_{Mn} = -3.77\,\Lambda + 5.44 \quad (2.27)$$

2.2.2.5 Vanadium partition

Bergman [31] found that the capacity of VO_4^{3-} (ie present as V^{5+}) which is defined in equation (2.28) was a linear function of the optical basicity (**Fig. 2.9** and equation (2.27))

$$C_{VO_4^{3-}} = (\%VO_4^{3-})/[\%V][\%O]^{2.5} \quad (2.28)$$

$$\log C_{VO_4^{3-}} = 14.92\,\Lambda - 4.26 \quad (2.29)$$

2.2.2.6 Water partition

Water in the slag, refractories or the atmosphere can result in hydrogen in the metal. The water capacity C_{H2O} (defined in equation (2.30), has been shown [42] to be function of optical basicity for slags containing CaO, MgO, Al_2O_3 and SiO_2 (**Fig. 2.10**) and equation (2.31)

$$C_{H_2O} = (\text{ppm } H_2O)/(p_{H_2O})^{0.5} \quad (2.30)$$

$$\log C_{H_2O} = 12.04 - 32.63\,\Lambda + 32.71\,\Lambda^2 - 6.62\,\Lambda^3 \quad (2.31)$$

2.2.3 Relation between optical basicity and the solubility of oxides in the slag

2.2.3.1 MgO solubility

Bergman [43] found the solubility of MgO (from the refractory), as defined by equations (2.32 – 2.34), was a linear function of optical basicity (**Fig. 2.11**)

$$MgO = (Mg^{2+}) + (O^{2-}) \quad (2.32)$$

$$K = a_{(Mg^{2+})}\, a_{(O^{2-})}/a_{MgO} \quad (2.33)$$

$$C_{Mg^{2+}} = (\%Mg^{2+})/a_{MgO} \quad (2.34)$$

2.2.3.2 K_2O solubility

Bergman [44] analysed data for the K_2O capacity (defined in equations (2.35 – 2.36)) and derived a linear correlation between $\%K_2O$ in the slag and the optical basicity (**Fig. 2.12,** equation 2.37, 2.38); however further analysis resulted

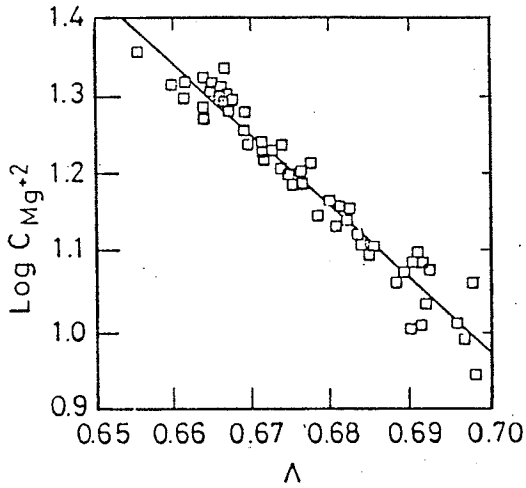


Fig. 2.11. Log C_{Mg}^{2+} as a function of optical basicity for steel-making slags [43]; a value of Λ(FeO) = 0.51 was used in these calculations

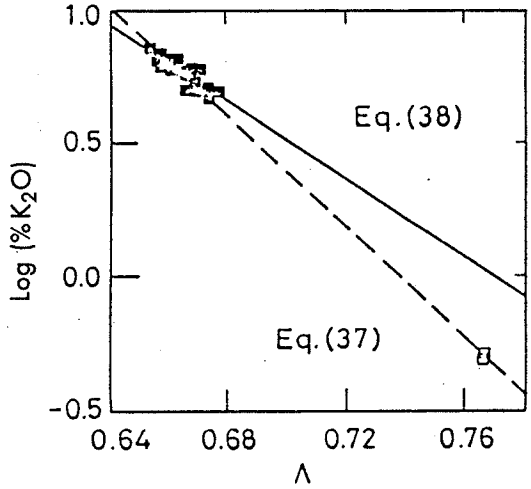


Fig. 2.12. Log (%K_2O) in the slag as a function of the optical basicity [44]; the relationship denoted by a solid line is preferred

in the preferred relationship given in equation (2.38).

$$K(g) + 0.25\ O_2 = (K^+) + 0.5(O^{2-}) \quad (2.35)$$

$$C_{K2O} = (\%K_2O)/p_K p_{O_2}^{0.25} \quad (2.36)$$

$$\log (\%K_2O) = -10.13\ \Lambda + 7.48 \quad (2.37)$$

$$\log (\%K_2O) = -7.12\ \Lambda + 5.49 \quad (2.38)$$

2.2.4 Relation between optical basicity and thermodynamic properties

2.2.4.1 Activity coefficient of P_2O_5

Mori [23] showed that log $\gamma_{P_2O_5}$ was a linear function of optical basicity (**Fig. 2.13** and equation 2.39))

$$\log \gamma_{P_2O_5} = 9.40 - 38.09\ \Lambda \quad (2.39)$$

Gaskell [22] found that values of log $\gamma_{P_2O_5}$ in slags containing Na_2O could be brought into line with the relationship obtained for slags containing CaO and BaO by use of a value Λ(Na_2O) = 1.34 (cf 1.15); a value of Λ(FeO) = 0.51 was used in these calculations.

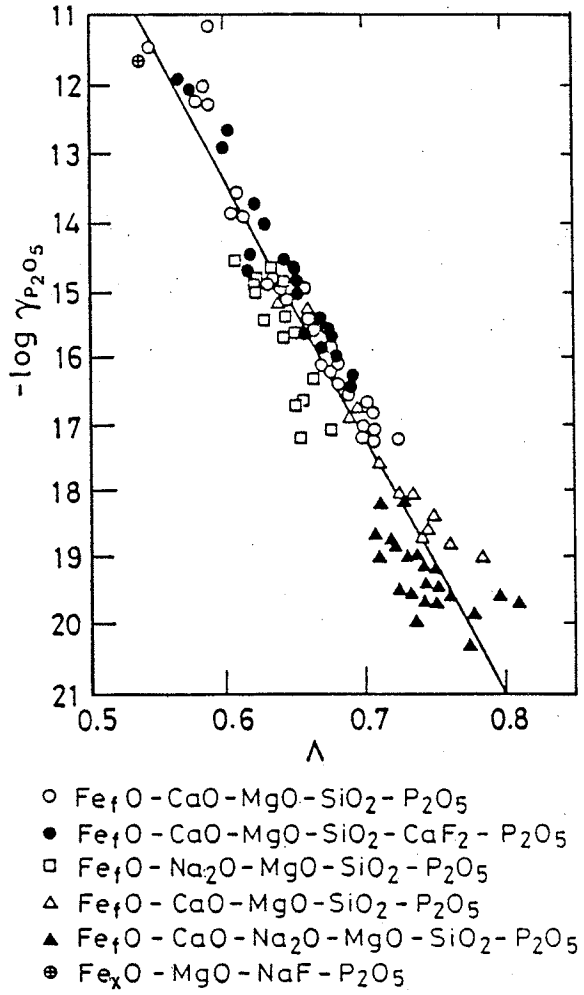


Fig. 2.13. Log $\gamma_{P_2O_5}$ as a function of optical basicity [23]; it was assumed all Fe present as FeO and Λ(FeO) = 0.51

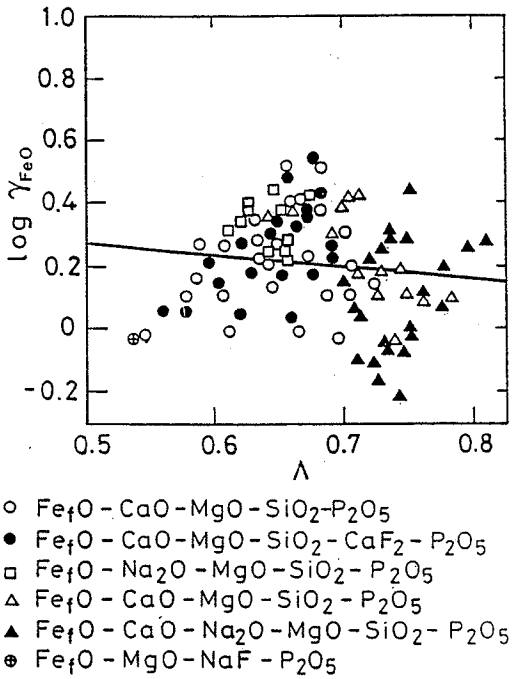


Fig. 2.14. Log γ_{FeO} as a function of optical basicity [23]; all Fe was assumed to be present as FeO and Λ(FeO) = 0.51 was used in these calculations

2.2.4.2 Activity coefficient of FeO

Mori [23] reported that the relationship between log γ_{FeO} and optical basicity showed a considerable degree of scatter **(Fig. 2.14)** which was attributed to variations in (Fe^{3+}/Fe^{2+}) ratios in the slag.

2.2.4.3 Activity of CaO

Gaskell [34] reported that log a_{CaO} was a linear function of the optical basicity for the $CaO + SiO_2$, $CaO + Al_2O_3$ and $CaO + Al_2O_3 + SiO_2$ systems (**Fig. 2.15** and equation (2.40)). The iso-a_{CaO} values in the ternary system were found [34] to be parallel to the iso-optical basicity curves **(Fig. 2.16)**.

$$\log a_{CaO} = 12.5\,\Lambda - 10 \qquad (2.40)$$

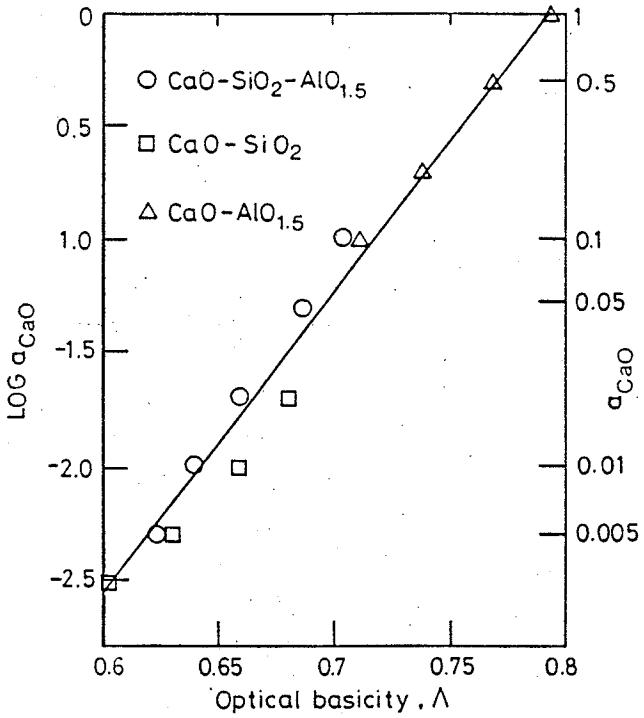


Fig. 2.15. Log a_{CaO} as a function of optical basicity [34]

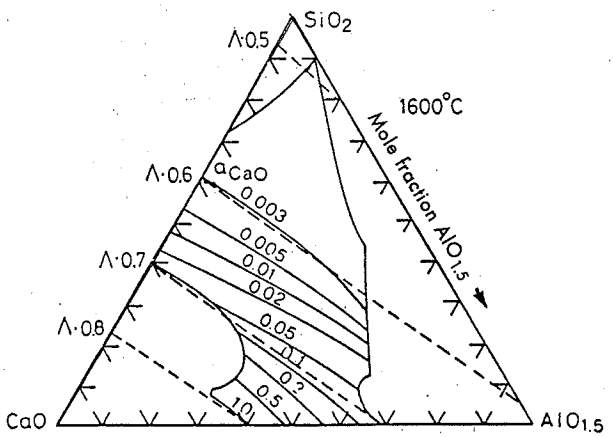


Fig. 2.16. Iso-a_{CaO} contours and iso-Λ lines in the system $CaO + AlO_{1.5} + SiO_2$ system at 1600 °C [34]

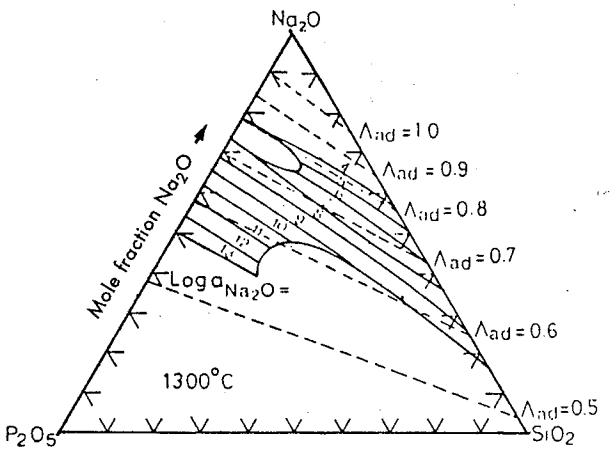


Fig. 2.17. Iso-a_{Na_2O} contours and iso-optical basicity in the system $Na_2O + SiO_2 + P_2O_5$ at 1300 °C [34]; a value of $\Lambda(Na_2O) = 1.34$ was used in these calculations, the use of $\Lambda(Na_2O) = 1.15$ would improve the degree of parallelism

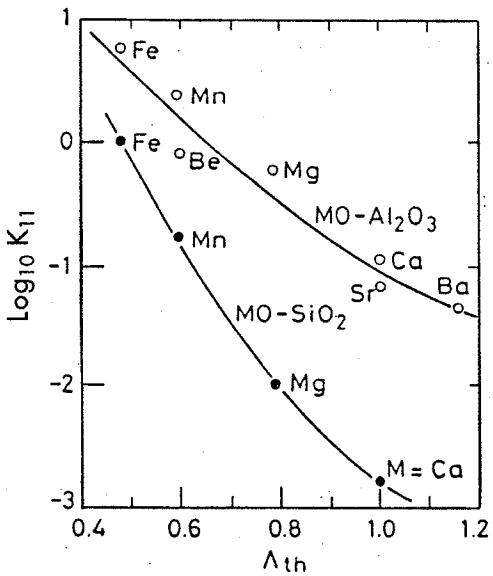


Fig. 2.18. Log K_{11} at 1600 °C as a function of the theoretical optical basicity, Λ_{th} for various metal oxides in the $MO-SiO_2$ and $MO-Al_2O_3$ systems [45]; values of 0.51 and 0.59, respectively, were adopted for Λ of FeO and MnO

2.2.4.4 Activity of Na_2O

Gaskell [34] pointed out that the iso-a_{CaO} contours showed a good degree of parallelism with the iso-optical basicity lines in the $Na_2O + P_2O_5 + SiO_2$ system (**Fig. 2.17**).

2.2.5 Relation between optical basicity and structure and physical properties

2.2.5.1 Structure

Masson [45] showed that the equilibrium constant (K_{11}) for the polymerisation reaction (equation (2.41)) was a linear function of the optical basicity of metal oxide (**Fig. 2.18**)

$$2SiO_4^{4-} = Si_2O_7^{6-} + O^{2-} \qquad (2.41)$$

The optical basicity provides a global measure of the concentrations of bridging (O°) non-bridging (O^-) and free oxy-

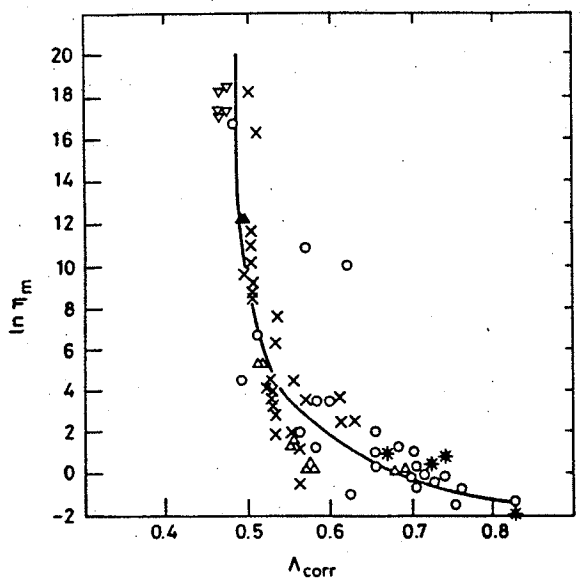


Fig. 2.19. The viscosities of silicates and alumino-silicates at the liquidus temperatures as a function of the optical basicity (Λ_{corr}) corrected for the concentration of 'network-breaking' metal oxides required to charge balance any Al_2O_3 present; ⊗, ●, silicates, X alumino-silicates ▲, $Al_2O_3 + SiO_2$ ▽ $BiO_3 + SiO_2$

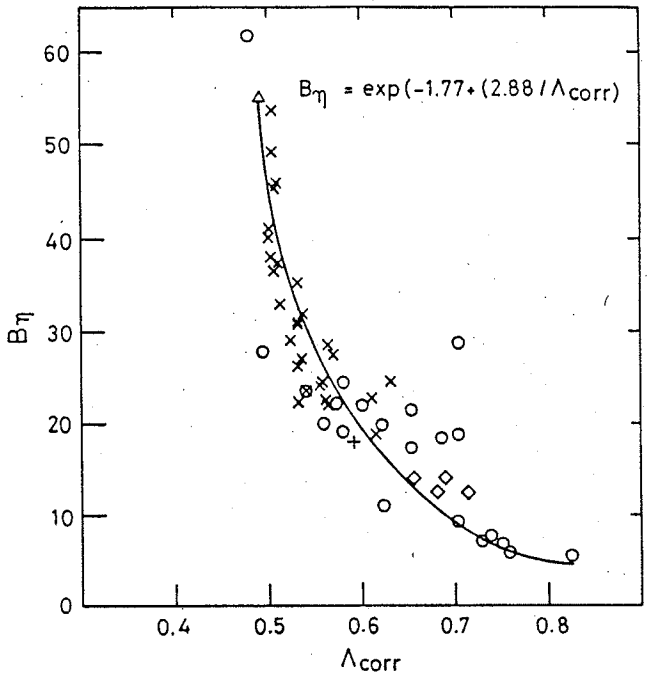


Fig. 2.20. The activation energy term for viscous flow (B_η) as a function of the corrected optical basicity, Λ_{corr} [46]; O, ● silicates; X, + alumino silicates; ▲, $Al_2O_3 + SiO_2$

gens (O^{2-}) in silicate and alumino-silicate melts and thus provides a measure of the depolymerisation of the melt[2]).

It has been pointed out [46] that when AlO_4^{5-} is incorporated into the SiO_4^{4-} structure, cations are required to provide electrical charge balance to the AlO_4^{5-} tetrahedra eg $Na^+AlO_4^{5-}$ and the cations involved are not available for network-breaking. Thus when comparing structurally-related properties of silicates with alumino-silicates it is necessary to correct the Λ for the concentration of cations required to charge balance the Al_2O_3 (and B_2O_3 and any Fe_2O_3 in octohedral positions). As an example for a slag containing $x(K_2O) = 0.1$ $x(CaO) = 0.2$ $x(Al_2O_3) = 0.2$ $x(SiO_2) = 0.5$ the corrected optical basicity (Λ_{corr}) would be calculated for the composition $x(CaO) = 0.1$, $x(Al_2O_3) = 0.2$ and $x(SiO_2) = 0.5$ since $x(M_xO) = 0.2$ would be required for charge balance and the oxides with largest Λ_{th} are used first for this duty.

2.2.5.2 Viscosity (η)

The viscosity of molten slags is related to the structure of the melt. The viscosities at the liquidus temperature (η_m) for a large number of silicate and alumino-silicates are plotted as a function of the optical basicity [46] in **Fig. 2.19**. The activation energy for viscous flow (E_η), given in equation (2.42) is considered to be the energy required to break the bonds in the slag to enable viscous flow to occur; the relationship with optical basicity (Λ_{corr}) is shown in **Fig. 2.20**. Viscosities can be calculated from equation (2.43)

$$\ln \eta = A_\eta - \frac{E_\eta}{RT} = A_\eta - \left(\frac{B_\eta}{T}\right) \qquad (2.42)$$

where T is the thermodynamic temperature (K).

$$\ln \eta = \frac{1}{(0.15 - 0.44\,\Lambda)} - \frac{1.77 + 2.88\,\Lambda^{-1}_{corr}}{T} \qquad (2.43)$$

[2]) similar to (NBO/Si) or (NBO/T)

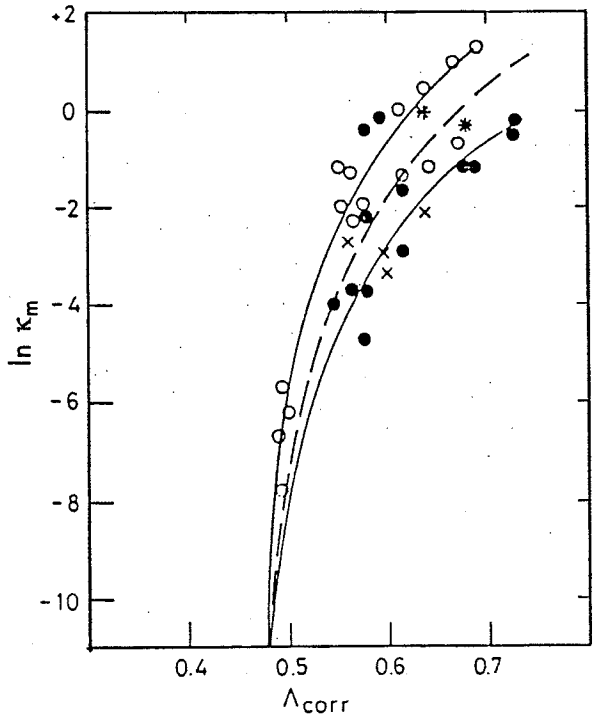


Fig. 2.21. Logarithm of the electrical conductivity at T_{liq} ($\ln \kappa_m$) as a function of the corrected optical basicity (Λ_{corr}) [46]; O, ● silicates, X alumino silicates

2.2.5.3 Electrical conductivity (κ)

The electrical conductivity of the melt at T_{liq} (κ_m) has been shown [46] to be a function of the corrected optical basicity (Λ_{corr}) as shown in **Fig. 2.21.**

2.2.5.4 Thermal conductivity (k)

The thermal conductivity of the melt at T_{liq} (k_m) has found to be [46] a function of the corrected optical basicity **(Fig. 2.22)**.

2.2.5.5 Thermal expansion coefficient

The thermal expansion coefficient (α) of the melt has been shown to be [46] a function of the corrected optical basicity (Λ_{corr}) **(Fig. 2.23)**.

2.2.6 Flux control in BOS process

Carey et al [47, 48] determined the lime and dolomite additions required to obtain target P contents of various steel grades by use of a mathematical model incorporating a target optical basicity value. This model was found to be superior to one based on the V ratio (ie (%CaO)/(%SiO_2)) and resulted in savings in CaO and dolomite additions.

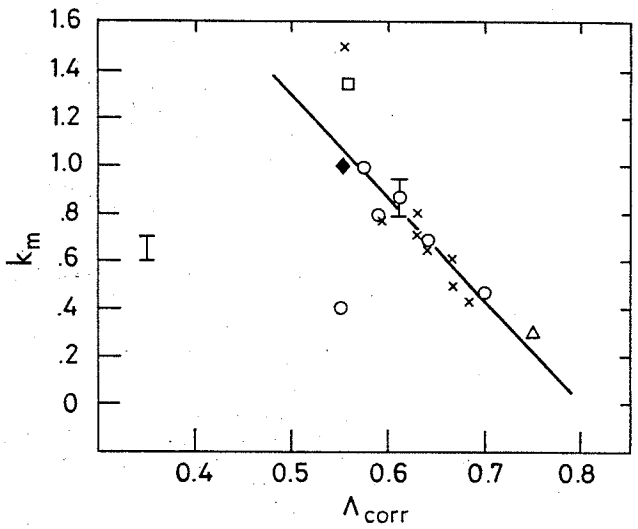


Fig. 2.22. The thermal conductivity at T_{liq} as a function of the corrected optical basicity [46]; O, silicate; X alumino-silicates

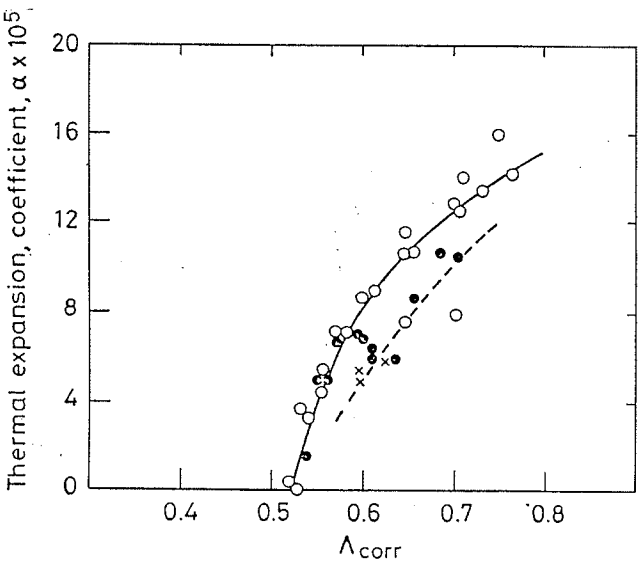


Fig. 2.23. The thermal expansion coefficient of the melt as a function of the corrected optical basicity [46]; O, silicates; X, alumino-silicates

2.3 Appendix

2.3.1 Methods used to obtain optical basicity values for oxides

2.3.1.1 Spectroscopic methods

The spectroscopic methods used to measure the optical basicity have been described in Section 2.2.1. Nakamura et al [35] used photoacoustic spectroscopy in an attempt to determine values of Λ for transition metal oxides. Values obtained for binary oxide glasses eg Na_2O-SiO_2 were in agreement with those derived by the conventional method.

Sumita et al [49] demonstrated that the Mössbauer isomer shift for Fe^{3+} is linearly related to optical basicity.

2.3.1.2 Refractivity measurement

Oxide ion refractivity $R_{O^{2-}}$ has been related to the optical basicity in the range 0.5 – 0.6 (equation 2.44)

$$\Lambda = 0.35\ R_{O^{2-}} - 0.81 \qquad (2.44)$$

It has been shown that it is more conveniant to relate Λ to electronic polarisability (α_m (in°A^3) than to the electronic molar refractivity (R_m (in cm^3)) since α and the refractive index (n) are related via equation (2.45) where ρ and M are the density and molecular weight of the oxide.

$$\alpha_m = \frac{0.397\ M}{\rho}\left(\frac{n^2-1}{n^2+2}\right) \qquad (2.45)$$

In practice, the electronic polarisability of the oxide ion $(\alpha_{O^{2-}})^{-1}$ can be derived by subtracting the cation polarisabilities from α_m and dividing by the number of oxygens in the formula eg 8 for $CaAl_2Si_2O_8$. A linear relation exists between $(\alpha_{O^{2-}})^{-1}$ and Λ (equation 2.46).

$$(1/\alpha_{O^{2-}}) = 1.0 - 0.6\ \Lambda \qquad (2.46)$$

Thus experimental values of the refractive index and density of glasses have been used [36] to derive sequentially α_m and $\alpha_{O^{2-}}$ for glasses containing transition metal oxides; these are given in Tab. 2.3. The method was checked by measuring Λ(ZnO) in this manner and comparing the value obtained with that obtained spectroscopically; there was good agreement between the values obtained.

2.3.1.3 Curve fitting

Values of optical basicity have been derived for individual oxides from "best fit" relationships for between Λ and various experimental properties eg sulphide capacities [24, 25], phosphate capacities [29, 31], thermodynamic properties [34].

2.3.1.4 Calculated values of Λ_{th}

Duffy and Ingram [36] showed that reliable values of optical basicity could be calculated from Pauling electronegativity values (X) using equation (2.47).

$$\Lambda_{th} = \frac{0.74}{(X - 0.26)} \qquad (2.47)$$

More recently, Duffy and Ingram [36] derived values for the electronegativity of oxygen (X_o) from values of the enthalpy of formation at 298 K (ΔH°_{f298}) for transition metal oxides. The calculation is outlined below:

1) $\Lambda X = \sqrt{[\Delta H^\circ_{f298}/23.06) + (n_o\,1.13)]/N}$

where n_o is the number of oxygen atoms per oxide molecule (eg 3 for Al_2O_3) and N is the number of bonds.

$\Delta H^o_{f298}(CaO) = 151.9$ kcal mol^{-1}, $n_o = 1$, $N = 2$ thus $\Delta X = 1.96$

$\Delta H^o_{f298}(Al_2O_3) = 399$ kcal mol^{-1}, $n_o = 3$, $N = 6$ thus $\Delta X = 3.31$

2) $X_o = X_M + \Delta X$ thus
$X_o(CaO) = X_{Ca} + \Delta X = 0.93 + 1.96 = 2.89$
$X_o(Al_2O_3) = X_{Al} + \Delta X = 1.45 + 1.86 = 3.31$

3) $X_o = 4.1 - (1.15/y_m)$

4) $\Lambda_{th} = (1/y_m)$.

2.4 References in Chapter 2

[1] Frohberg, M. G.; Kapoor, M. L.: Stahl und Eisen 91 (1971), 182
[2] Blum, L.: Stahl und Eisen 19 (1901), 1024/29
[3] Platz, B.: Stahl und Eisen 12 (1892), 218
[4] Flood, H.; Førland, D.: Acta Chem. Scand. 1 (1947), 592, 781 and 790
[5] Whiteley, J. H.: Proc. Cleveland Inst. Engrs. 59 (1922/23)
[6] Turkdogan, E. T.: Physical chemistry of oxygen steelmaking, thermochemistry and thermodynamics, Vol. II., Monroeville 1970
[7] Winkler, T. B.; Chipman, J.: Trans. Amer. Inst. min. metallurg. Engrs. 167 (1946), 111
[8] Darken, L. S.; Larsen, B. M.: Trans. Amer. Inst. min. metallurg. Engrs. 150 (1942), 87
[9] Herty, C. H.; Christopher, C. F.; Freemann, H.; Sandersen, J. F.: Mun. metallurg. Invest. Bull., No. 68, 1934, Stahl und Eisen 56 (1939), 165 – 168
[10] Grant, N. J.; Chipman, J.: Trans. Amer. Inst. min. metallurg. Engrs. 167 (1946), 134
[11] Hatch, G. G.; Chipman, J.: Trans. Amer. Inst. min. metallurg. Engrs. 185 (1949), 274
[12] Chipman, J.; Hatch, G.: Trans. Amer. Inst. min. metallurg. Engrs. 167 (1946), 134
[13] Kalyanram, M. R.; McFarlane, T. G.; Bell, H. B.: J. Iron Steel Inst. 195 (1960), 58 – 64
[14] Bodsworth, C.: Phys. Chem. of Iron and Steel Manufacture 1963, 428 – 434
[15] Elliott, J. F.; Gleiser, M.; Ramakrishna, V.: Thermochemistry for Steelmaking, Vol. 11, 600
[16] Brown, S. D.: PhD Thesis, University of Strathclyde (1977)
[17] Iwamoto, N.: Trans. Jap. Weld. Res. Inst. 3 (2) (1974), 89 – 98
[18] Iwamoto, N.: Trans. Jap. Weld. Res. Inst. 3 (2) (1978), 113 – 125
[19] Wagner, C.: Metall. Trans. 6B (1975) 405 – 409
[20] Duffy, J. A.; Ingram, M. D.: J. Non-Cryst. Solids, 21 (1976) 373
[21] Duffy, J. A.; Ingram, M. D.: J. Inorg. Nucl. Chem. 37 (1975), 1203 – 1206
[22] Gaskell, D. R.: Trans. ISI Japan, 22 (1982) 997 – 1000
[23] Mori, T.: Trans. Jap. Inst. of Metals 25 (11) (1984), 761 – 771
[24] Sommerville, E. D.; Sosinsky, J. J.: Proc. of the 2nd Intl. Conf. on Metall. Slags and fluxes, held Lake Tahoe, Nov. 1984. Edited by H. A. Fine and D. R. Gaskell. Publ. Met soc-AIME, Warrendale, Pa.
[25] Sosinsky, D. J.; Sommerville, I. D.: Metall. Trans, 17B (1986), 351
[26] Nakamura, T.; Ueda, Y.; Toguri, J. M.: J. Japan Inst. Metals 50 (1986), 456
[27] Nakamura, T.; Ueda, Y.; Toguri, J. M.: Proc. of 3rd Intl. Conf. on Metall. Slags and fluxes, held Strathclyde University, Glasgow 1988. Publ. Inst. of Metals, 146 – 149
[28] Duffy, J. A.; Ingram, M: D.: "Comments on the application of optical basicity to glass", submitted to J. Non-Cryst. Solids, 1991
[29] Bergman, A.; Gustafsson, A.: Steel Research 59 (1988), 281 – 288
[30] Bergman, A.; Gustafsson, A.: Proc. of 3rd Intl. Conf. on Metall. Slags and fluxes, held Strathclyde University, Glasgow, 1988. Publ. Inst. of Metals, 150 – 153
[31] Bergman, A.: Trans. ISI Japan 28 (1988), 945 – 951
[32] Ingram, M. D.: Proc. of 3rd Intl. Conf. on Metall. Slags and fluxes, held Strathclyde University Glasgow, 1988. Publ. Inst. of Metals, 166 – 168
[33] Shiraishi, Y.: Handbook of Physico-Chemical Properties at High Temperatures. Ed.: Y. Kawai and Y. Shiraishi. Publ. ISI Japan (1988), 121 – 144
[34] Gaskell, D. R.: Metall. Trans. B 20B (1989), 113 – 118
[35] Nakamura, R.; Ueda, Y.; Noguchi, F.: Proc. of 2nd Intl. Conf. of Metall. Slags and fluxes, held Lake Tahoe, 1984. Edit H. A. Fine and D. R. Gaskell. Publ. by Met. Soc. AIME, Warrendale, Pa., (1984) 1005 – 1013
[36] Duffy, J. A.; Ingram, M. D.: in EEC Report EUR 13176 EN: Use of the optical basicity concept for determining phosphorus and sulphur slag/metal partitions. Final Report contract – 7210 – CF 802, R. W. Young, (1991)
[37] Binks, J. H.; Duffy, J. A.: J. Solid State Chem. 87 (1990), 195 – 201
[38] Young, R. A.: EEC Report EUR 13176 EN (1991) (see ref. 36)
[39] Suito, H.; Inoue, R.; Takada, M.: Trans ISI Japan 21 (1981), 250 – 259
[40] Selin, R.: Doctoral Dissertation, Royal Inst. Tech., Stockholm, Sweden 1987
[41] Kunisada, K.; Iwai, H.: Trans. ISI Japan 27 (1987), 332 – 339
[42] Sosinsky, D. J.; Sommerville, I. D.; McLean, A.: Proc. Process Tech. Conf. ISS-AIME, 6 (1986), 697 – 703
[43] Bergman, A.: Steel Research, 60 (1989) 191 – 195
[44] Bergman, A.: Steel Research 60 (1989), 383 – 386
[45] Masson, C. A.: Proc. of 2nd Intl. Conf. on Metall. Slags and fluxes, held Lake Tahoe, Nev. (1984). Edited by H. A. Fine and D. R. Gaskell. Publ. Met. soc. AIME, Warrendale, Pa., (1984) 3 – 44
[46] Mills, K. C.: Trans. ISI Japan 33 (1993), 148 – 156
[47] Carey, C. L.; Serje, R. J.; Gregory, K.; Qinglin, H. E.: Proc. of 3rd Intl. Conf. on Metall. Slags and fluxes, held Strathclyde University, Glasgow (1988). Publ. Inst. of Metals (1988), 157 – 162
[48] He, Q. L.; Serge, R. J.; Carey, C. L.: Iron and Steelmaker (1991), 51 – 53
[49] Sumita, S.; Matsumoto, Y.; Morinaga, K.; Yanagase, T.: Trans. Japan. Inst. Metals 23 (7) (1982), 360 – 367

3

Phase diagrams

M. Kowalski, P. J. Spencer and D. Neuschütz

3.1 Introduction

Since the appearance of the first edition of *Slag Atlas* [1] a very large number of relevant papers and compilations on phase equilibria have been published. Among these are several new volumes of *Phase Equilibria Diagrams* [2], (*Phase Diagrams for Ceramists* up to 1992), or new international journals publishing evaluated phase diagram information, such as *Journal of Phase Equilibria*, *Journal of Alloy Phase Diagrams* and *CALPHAD*. The latter, which is concerned with the computer coupling of phase diagrams and thermochemistry, also reflects the progress which has been made during recent years in the modelling, assessment and calculation of phase diagrams and thermodynamic properties for systems of many different types. Phase equilibrium information of particular relevance for steel-making is contained in the proceedings of four successive *International Conferences on Metallurgical Slags and Fluxes* [3]. Despite these newer developments, the pioneer phase diagram studies carried out at the beginning of this century by researchers at the *Geophysical Laboratory of the Carnegie Institute in Washington* (see for instance [4-6]) continue to represent the classical standard in this field, and the results of this early work are often still valid.

In view of the very large number of available publications on phase diagrams, the task of collecting and evaluating the information they contain for the approximately 200 systems selected for inclusion in *Slag Atlas*, becomes daunting. Nevertheless, it is precisely because so much, often contradictory, information has been reported, that it is very important to provide users with quick access to a condensed and at least partially reviewed form of the most up-to-date phase diagram information available.

This second edition of *Slag Atlas* contains much work from the classical monograph *Phase Equilibria Among Oxides in Steelmaking* by Muan, Osborn [7], supplemented by information in *Phase Equilibria Diagrams* (Volumes 1-9, Annuals 91, 92 [2]), published by the American Ceramic Society, and in compilations by Berezhnoi [8], Toropov et al. [9] and Barzakovskii et al. [10]. In addition, relevant information on phase diagrams of CaF_2-containing systems has been extracted from the compilation by Mills, Keene [11]. The phase diagrams of binary metal-nonmetal systems are taken essentially from papers published in *Journal of Phase Equilibria* (earlier *Bulletin of Alloy Phase Diagrams*) and in the monograph by Kubaschewski [12]. The ternary systems with iron and sulphur are based on the compilation by Raghavan [13]. However, the major proportion of the most recent relevant papers has been found from a computer search based on *Chemical Abstracts*. The search was made up to June 1992. In addition, relevant journals publishing phase diagram information, such as *Journal of the American Ceramic Society*, *Metallurgical Transactions*, *Steel Research* (earlier *Archiv für Eisenhüttenwesen*), *Transactions of the Iron and Steel Institute of Japan* and *Izvestia Akademii Nauk SSSR*, have been searched through the last five years by hand.

The large number of publications relating to the most important slag systems, as well as the different manner of graphical representation of the results, makes a full survey of such systems impossible. In this compilation the figures are limited to those illustrating the phase equilibria in the temperature interval of interest in steel-making. For many systems of geological interest, the large number of studies of phase equilibria at high pressures has not been discussed in this compilation. References relating to glass-forming regions or metastable immiscibility in glass-forming systems are also generally excluded from this work. In many instances, supplementary information of interest for steel-making, but not used in this compilation is listed in the standard references.

Special effort has been made to present one, recommended phase diagram for each system. In many cases of binary systems, evaluation of all available information has enabled a revised phase diagram to be presented. For some systems, such recommended phase diagrams has been directly adopted from the literature. However, several cases remain where selection of a "correct" phase diagram from the contradictory information available is still impossible. For these, all relevant published results are presented. Since the number of publications concerning some slag systems is enormous, an attempt has been made to refer the user to the most important original papers as well as to the most recent compilations in which the systems are discussed in detail. If necessary, the critical aspects of the phase diagram presented are discussed briefly.

The general manner of graphical representation of phase equilibria used here is essentially that employed in the first edition of *Slag Atlas*. Wherever possible, the labelling of figures, the phase names and their stoichiometry, as well as the concentrations and temperatures of critical points, have been standardised. The melting points of slag components have been adjusted to the new International Temperature Scale ITS-90. To simplify the use of this compilation, the evaluated systems have been arranged such that systems containing the metal ions in different oxidation state, e.g. CaO-FeO_n, CaO-Fe_2O_3, CaO-FeO-Fe_2O_3 etc. have been placed together.

3.1.1 Geometrical representation of phase equilibria

There are many parameters, such as temperature, pressure, chemical potential, composition etc. which influence phase equilibria and which can be used to define the axes of a phase diagram. From a generalised Gibbs-Duhem equation results that all parameters influencing phase equilibria are either potentials (T-thermal potential, p-mechanical potential, μ-chemical potential) or conjugate extensive variables (N-number of moles, V-volume, S-entropy). Such a classification yields three possible types of two-dimensional representation of phase equilibria (Pelton, Schmalzried [14]):

1. the phase equilibria are plotted as a function of two potentials (e.g. pO_2 vs. T: predominance area diagram);
2. the phase equilibria are plotted as function of potential and as a function of the ratio of conjugate extensive variables (e.g. T vs. x_i and pO_2 vs. x_i diagrams);
3. the phase equilibria are plotted as function of two ratios of conjugate extensive variables (e.g. x_A vs. x_B isothermal diagrams for ternary A-B-C systems plotted usually in a Gibbs' triangle).

All possible phase diagrams within each category conform to the same topological rules. For instance, in the 1st category of phase diagrams (1-, 2- and 3-component systems) two-phase equilibria are represented by lines intersecting at points, indicating the condition for co-existence of three phases. In the 2nd category, two-phase equilibria are represented by an area and three-phase equilibria by straight lines. In the 3rd category of phase diagrams, equilibria between three phases are triangular areas. Figs. 3.5 and 3.7 illustrates respectively 1st and

2nd category type of phase diagrams for the Fe-O system. Such a classification should facilitate the use and interpretation of, for example, T vs. x and pO_2 vs. x diagrams, which belong in fact to the same topological category.
For the standard classification and interpretation of phase diagrams based on the phase transitions occurring in the system under consideration, the reader is referred to classical works by Rhines [15], (see also Massalski [16] and Pelton [17]).
Usually, the phase equilibria in oxide systems are presented as a function of temperature (T), partial pressure (p_i) of the system components and mole fraction (x_i). The full representation of phase equilibria using a simple two-dimensional diagram is possible only for a one-component system. For systems with more components it is nevertheless possible to use such a representation by fixing selected variables. However, a large number of binary systems in which the partial pressure of gas species is negligible can also be represented by a simple two-dimensional diagram. In all other cases, a T vs. x_i diagram is constructed by fixing the partial pressures in the gas phase at the equilibrium values over the relevant condensed phases. (these depend on the temperature and co-existing phase assemblages). A number of such diagrams (including oxygen isobars) for Cr-O, Fe-O, Mn-O and Ni-O systems are illustrated in Figs. 3.4, 3.6, 3.10 and 3.12 respectively. Unfortunately, no such diagrams are available for systems containing components with low boiling points. For this reason, some phase diagrams, for example those for systems with K_2O, Na_2O, P_2O_5 or CaF_2, must be considered incomplete.
As supplementary information to this compilation, the equilibrium vapour pressures of metals and pure metal oxides have been calculated using the THERDAS thermodynamic databank system [18]. The results are illustrated in Fig. 3.490.
Another possible method of producing a two-dimensional representation of a binary system taking into account the gas phase is to draw a set of isobaric or isothermal sections. By fixing two or more variables, a two-dimensional representation of a ternary or higher-order system is also possible. In this way isothermal sections, often drawn in the Gibbs' triangle, or composition sections (isopleths), are obtained. Through superposition of numerous isothermal sections, in particular those involving solid-liquid equilibria, the polythermal representation of liquidus and solidus surfaces also becomes possible. In the case of some systems containing metals of varying valency, isobars corresponding to the partial pressure of oxygen over condensed phases at, e.g. liquidus or solidus temperatures, are also drawn.
Further methods of graphical representation of phase equilibria include planar projection of different three-dimensional graphs, or different modes of projection (vertical, central or parallel) of multicomponent systems into two-dimensional diagrams. Although the first type of projection contains practically only qualitative information, it can be used to improve the clarity and comprehensibility of two-dimensional diagrams. The further projection methods make possible the two-dimensional representation of multicomponent systems, but the interpretation of the resulting diagrams is rather complex.
For further details on methods of illustrating phase equilibria in multicomponent systems, the user is refered to the first edition of *Slag Atlas* [1].

3.1.2 Methods of investigation of phase equilibria *(by E. Woermann)*

Each phase, and even more each multi-component multiphase system, is characterised by a unique set of physical properties. Thus it is impossible to devise a universal standard procedure for the investigation of phase diagrams. In each case definite decisions have to be made concerning the starting materials, the crucible material, the furnace atmosphere, the temperature treatment and the investigation of the run products.

3.1.2.1 Starting materials

For the attainment of equilibrium in the products an ideal homogeneity of the starting material is required. The first step is an accurate weighing of the available reagents. In some cases, however, it is not possible to handle the components directly. Alkalies are thus added not as an oxide, but in the form of some suitable alkali compound, e.g. an alkali silicate, which has to be prepared from the appropriate alkali carbonate and silica. Also it is almost impossible to weigh CaO accurately because of its rapid reaction with H_2O, even with atmospheric humidity. $CaCO_3$ is preferred, therefore, as a starting material, which is decarbonated in the sample during the first heating process > 900 °C. FeO cannot be weighed, since a corresponding stoichiometric compound does not exist. An appropriate mixture of Fe_2O_3 and metallic iron is preferred, which should, in a closed system, react according to: $Fe_2O_3 + Fe = 3FeO$. A detailed discussion of available reagents is given by Edgar [19].
For oxide systems it is common practice to homogenise accurately weighed proportions of high purity reagents under acetone in an agate mortar, or to mix the reagents with isopropanol in a ball mill. The dried powders may then be used for further investigations. Arbitrarily another step - the heating of the powder to some temperature below the solidus with a consequent second grinding in a ball mill - may be included. In SiO_2-rich silicate systems good results were obtained by heating the mixtures to temperatures well above their liquidus and cooling them rapidly to room temperature to form a silicate glass. A subsequent inspection of the refractive index of the glass helps to assess the degree of homogeneity attained, which is of exceptional importance in these systems in view of their sluggish reactions. Other methods have been developed, which are more tedious, but guarantee a high degree of homogeneity, such as sol-gel processes [20] or the hot petroleum method [21] which are both aimed at the conservation of the homogeneous distribution of the components dissolved in a dilute solution.

3.1.2.2 Crucible material

The majority of high temperature experiments require that the material to be investigated should be enclosed in a container. For an ideal crucible material it is required that it should be solid at the prevailing temperature and that it should not react with the sample. Only a few systems allow to select a truly ideal crucible material. It may either be a ceramic material, such as corundum, zirconia, mullite or silica glass, or a metallic material, mainly platin group elements or alloys. Oxide or silicate samples almost invariably tend to react with ceramic materials or vice versa. This introduces impurities into the sample. In some cases this may be neglected if the components introduced are also components of the system itself, (e.g. in a corundum crucible some additional Al_2O_3 is dissolved in a melt containing appreciable amounts of Al). The possible influence of an introduction of impurities into the system on the phase equilibria must be considered according to the circumstances. Platinum is employed in most routine investigations in the form of thin foils which are wrapped to small envelopes. It fails, however, in the investigation of iron bearing system, especially under reducing conditions, where

FeO partially dissociates to form Fe_2O_3 and Fe, while the latter in turn is alloying with Pt. The sample thus contains eventually less iron in a higher oxidation state than the starting mixture. In a temperature range up to 1150 °C a silver palladium alloy may be used, in order to diminish the loss of iron to the crucible [22]. In systems where a metal phase is stable, the same metal may be selected as crucible material. Thus pure iron is a suitable crucible material up to ~1530 °C for the investigation of iron metal bearing systems. Samples which are supposed to be exposed to sub-solidus temperatures only may be pressed into pellets or rods and suspended into the furnace on a thin wire, thus minimising any mutual contact.

3.1.2.3 Quench-furnace

Vertical tube furnaces are preferred for static quench processes. They consist of well insulated ceramic tubes, almost invariably alumina tubes, with a winding of a suitable resistance wire. For temperatures up to 1200 °C high temperature alloy wire, - such as Kanthal or Hoskins - gives satisfactory results. At higher temperatures platinum or an $Pt_{80}Rh_{20}$ alloy are often applied, although their life time and price are considerable obstacles. Molybdenum wire, instead, is a favourable candidate for high temperature applications. It is, however, restricted to temperature ranges <1850 °C because of the failure of the ceramic carriers. It is the required, however, that the heating element is protected against oxidation by a continuous H_2/N_2 gas flow. Detailed information for the construction of furnaces is given by Edgar [19]. As a rule small furnace dimensions, and also small sample dimensions are favourable for the attainment of constant temperature and reproducibility of the results.

3.1.2.4 Redox reactions

In oxide systems containing transition elements the oxidation state must be controlled. This can be done either in open or in closed systems.

In open systems a gas mixture with a controlled oxygen fugacity is passing continuously through the furnace until eventually an equilibrium between the oxygen potentials of the gas phase and the sample suspended in the furnace is attained. In an open system the redox state, e.g. the Fe^{2+}/Fe^{3+}–ratio in iron bearing systems, is thus adjusted to the preselected oxygen fugacity. The control of the oxygen fugacity in the gas phase is achieved by mixing pure gases, such as H_2/H_2O, or CO/CO_2 or H_2/CO_2, while the oxygen fugacity is calculated as a function of the mixing ratio and of temperature from thermodynamic data. The principles and methods are described by Muan [23], and in Ulmer [24]. Temperature–oxygen fugacity tables are compiled by Deines et al. [25]. The corresponding diagrams are shown in the Figs. 3.482 to 3.484.

In closed systems the composition of the starting mixture is fixed, while the oxygen fugacity is essentially unknown. The samples are welded in evacuated, gas tight containers, such as silica glass tubes or in metal capsules. Silica capsules, however, eventually tend to crack due to recrystallization at elevated temperatures. They may safely be applied only for about 3 days at 1100 °C, 1.5 days at 1200 °C or 0.8 days at 1300 °C. Metal capsules may be made from any metal which does not melt at the temperature of application and which does not interfere with the sample composition. Iron, e.g., is an ideal crucible material for all systems coexisting with metallic Fe at temperatures below ~1538 °C. At high temperatures and low oxygen fugacities molybdenum proved to be a suitable choice. After each run, however, the products should be carefully analysed for possible Mo–impurities. Since at elevated temperatures all metals behave as semipermeable membranes towards hydrogen, not only base metal but also noble metal capsules should be continuously flushes by a hydrogen and water free gas stream. Even "high purity" and "special purity" technical argon and nitrogen contain sufficiently high concentrations of impurities, mostly oxygen, to corrode a metal capsule and/or to reduce its contents due to hydrogen migration.

3.1.2.5 Reaction time

For each system a separate estimate of the time required for attainment of sample equilibrium is necessary. It is common to exceed this period considerably to order to acquire the equilibrium state in each and every run product without an undue risk. Even here, however, some exceptions have to be considered. Thus, e.g., the vapour pressures of alkalies at high temperatures result in their evaporation and in their corresponding degradation in the sample. This effect is reduced by short run duration.

The time required for equilibration varies in wide limits, depending sensitively on the temperature. Reactions in the solid state are, as a rule, very sluggish and it may be required to heat a sample several times, and for several days, with intermediate grindings, before a steady state is attained. Liquids generally react much faster, in the order of minutes or hours, but even here considerable differences occur between highly viscous, sluggish liquids, e.g. in silicate systems, and highly reactive liquids with low viscosities, e.g. in metal systems. Liquids act as transport media in samples containing both solids and a melt, thus enhancing all reactions and reducing the required time for attaining equilibrium. The rate of reaction during the heating, and also during the cooling process determines which method of further investigation may be applied. It may be either the *Static Methods*, in which the high temperature equilibria are "frozen in" by rapid cooling, for further investigation at room temperature, or the *Dynamic Methods* for investigation under prevailing conditions in fast reacting, "unquenchable" systems.

3.1.2.6 Investigation of the run products

In a quench process the samples are cooled "instantaneously" from the temperature of reaction in the furnace to room temperature by dropping them into water, or, if their phases react with water, in liquid nitrogen, or onto a large metal block in air, or by any other rapid cooling method. It is assumed that by this process the high temperature equilibrium state is maintained at room temperature. The quench method is most widely and successfully applied to the investigation of oxide and silicate systems.

The first inspection is always made under the microscope, either in polarised or in reflected light. The distribution of phases is indicative of probable equilibrium or of disequilibrium conditions in the sample. A distinction is also made between primary phases, i.e. phases that existed at the temperature of synthesis, or secondary phases, i.e. phases that formed during cooling. The most prominent under the secondary phases is a former liquid, which is now present as a solid, in SiO_2-rich samples as a glass or, where a glass could not be formed, in secondary crystalline phases, which can be distinguished from primary phases by the generally much finer grain size and intimate intergrowths. Most primary phases can be distinguished under the microscope, but often, e.g. in the case of solid solutions, their composition cannot immediately be verified. X-ray diffractometry may help to confirm the optical identification. It cannot, however, distinguish between primary and secondary crystalline phases. A most

powerful tool is the electron microprobe. Primary phases, solid solutions and secondary phases are analysed, while the resulting data points, preferably gained on grains of sufficient size in immediate neighbourhood of each other, immediately define tie lines, three phase triangles or multiphase polyhedra. Since the introduction of the microprobe phase equilibrium data are gained considerably faster and with an immense improvement in accuracy. Additional analytical methods, such as electron microscopy, can also be applied as need may arise.

Dynamic methods are successfully applied to the investigation of systems which preclude quenching processes due to their inherent rapid reactions, such as, e.g., metal systems. The differential thermal analysis (DTA) registers the temperature and enthalpy change of a sample on its intersection of a field boundary of the system during a heating or cooling process. Detailed discussions of the equipment and methods involved are found in Mackenzie [26]. In a scanning calorimeter (DSC) even the magnitude of the resulting heat effect may be determined. Thermogravimetric analyses (TG) provide information on weight changes, e.g. in dehydroxylation, decarbonation or redox reactions.

3.1.2.7 EMF-measurements

For a selected number of systems electrochemical measurements provided suitable data for the calculation of phase equilibria. Unfortunately only a limited number of ceramic materials comply with the required properties for suitable solid state electrolytes for EMF-measurements. They should be electronic insulators but preferably ion specific ion conductors, stable at high temperatures and chemically inert towards the sample to be investigated. Since, however, this set of requirements is rarely met by ceramic materials the application of EMF-measurements is rather limited. Also the data gained do not directly provide information on phase equilibria, but they form a reliable base for thermodynamic calculations of phase diagrams which are, as a rule, more precise than any direct determination. So far the widest application has been the measurement of oxygen potentials in redox reactions, employing stabilised zirconia, ZrO_2, as a solid state electrolyte. A concise discussion of the practical aspects of EMF-measurements is given by Sato [27]. Electrochemical cells for the measurement of sulphur potentials have also been applied successfully. Cation conducting solid state electrolytes, however, are rarely cation specific, but through special precautions is possible to arrive at meaningful results here too.

3.1.3 Thermodynamic models and databases for calculation of phase diagrams and thermodynamic properties of slags

During the past two decades important efforts have been made to develop thermodynamic models for application to multi-component oxide systems, especially those containing SiO_2. In association with these models, sets of self-consistent parameters have been developed which permit calculation both of the phase diagram and of the thermodynamic properties of the system concerned. The assessment procedure used helps in many cases to explain discrepancies among various sets of experimental data. An important consequence is that these thermodynamically consistent sets of parameters can be applied to practical problems using well tested methods of extrapolation or interpolation, thereby enabling costly and time-consuming experimental work to be considerably reduced.

For alloys, the above procedure has already been established as a working tool. Many systems have been consistently assessed and the data sets are being used in materials and process development. However, modelling of the thermodynamic properties of oxide systems is in a much earlier stage of development.

Generally, the Gibbs energy of any n-component phase can be described using the expression

$$G = G_o + G_{mix}$$

in which:

G_o is the Gibbs energy of a phase component (not necessarily identical with a system component),

G_{mix} is the Gibbs energy of mixing of the phase components and contains both ideal (G_{id}) and excess (G_{ex}) contributions.

Such model equations for the phases of a system must be integrated into a computer program, which by minimization of the Gibbs energy allows calculation of the properties of a single phase and an equilibrium state for a given condition. By carrying out a series of such equilibrium calculations in a given system, the corresponding phase diagram is produced.

At the present time, several thermodynamic databases and computer programs are available. The principal accessible metallurgical databases are: CSIRO, Australia [28, 29]; F*A*C*T, Canada [30, 31]; HSC, Finland [32]; MANLABS, U.S.A. [33]; MTDATA, U.K. [34, 35]; THERDAS, Germany [36]; THERMO-CALC, Sweden [37, 38]; THERMODATA, France [39]. For an extensive review of thermochemical databases, see Bale, Eriksson [40]. It must be noted, however, that the software developments are of great generality, whereas the databases, in particular those related to oxide systems, are still rather limited.

In many practical cases, the possibility of transfer or coupling of data between different databases is particularly important to allow full description of a particular system. To make this possible, the databases must use the same data for the pure elements and the same (or compatible) models must be used in assessing the thermodynamic properties of the phases of the system.

The numerical aspects of the assessment procedure (generation of a database) will not be discussed here. However, in order to understand the thermochemical implications, a brief discussion of the different models currently in use is given below. It must be noted that in an assessment all phases of a system are treated together. Data for a particular system obtained from different assessments cannot generally be combined in phase equilibrium calculations.

Of primary importance in the thermodynamic modelling of solution properties (G_{ex}) is a good understanding of the atomic structure of the phase under consideration. For crystalline phases, the sub-lattice model developed by Sundman, Ågren [41], which is based on the crystallographic structure of the materials concerned, has found wide acceptance. The structures of liquid "slags", however, are diverse and complex [42] and it is therefore difficult to develop a model which can be applied generally to a wide range of systems.

As indicated above, the Gibbs energy of a solution phase is described by two contributions, the first is obtained from the Gibbs energies of the pure phase components and the second from their properties of mixing. For metallic systems, the assumption of simple substitutional solution of the elementary

components of the melt with small deviations from ideality is in many cases a good physical picture. For liquid oxide systems, however, especially those containing SiO_2, the situation is far more complex. Attempts to use the same mathematical descriptions as those applied to alloys systems (Kaufman [43], Berman, Brown [44]) give rather unsatisfactory results. The silicate melts exhibit strong structural ordering in certain composition ranges, resulting in an enthalpy of mixing curve which exhibits a negative V-shaped peak and an m-shaped entropy of mixing curve with a minimum near the ordering composition. In binary silicate systems of the type M_iO-SiO_2, the ordering is observed at the composition X_{SiO2}=0.3333. By taking this structural phenomenon into account, it is possible to reduce the number of parameters which would be necessary to describe the thermodynamic properties of the system using a purely mathematical description.

Several structure-based models are currently in use. Among these, the associated solution, cellular, and modified quasichemical and sub-lattice models have been successfully applied to the assessment of numerous oxide systems.

In the associated solution model [45], the experimentally established "species" in the melt are chosen as the components of an ideal liquid phase. In order to make possible the modelling of miscibility gaps, polynomial excess terms expressing the concentration and temperature dependence of interactions between liquid species have to be introduced.

The cellular [46, 47] and modified quasichemical models [48] are based on the equilibrium reaction of bridged, non-bridged and free oxygen

$$O^o + O^{-2} = 2O^-.$$

In the cellular model, the reaction between M_iOM_i, SiOSi and $SiOM_i$ cells is considered, whereas in the modified quasichemical model, the M_i-M_i, Si-Si and Si-M_i cation pairs are chosen to represent the oxygen equilibria.

In the two ionic sub-lattice model of Hillert et al. [49], all liquid species are distributed between two sub-lattices, anionic and cationic, in a similar description to that used for crystalline phases.

A short review of all the above models is given below. It is important to note however, that only the associated solution and sub-lattice models are able to describe the continuous transition from metallic to oxidic liquid.

3.1.3.1 Associated solution model (Flood, Knapp [45])

In this model, the liquid phase is treated as an ideal solution formed from a set of associated species. In the same way as for a gas phase, the equilibrium state is calculated by a Gibbs energy minimization procedure for a given temperature and overall composition of the liquid. In their application of the model to the PbO-SiO_2 system Flood, Knapp [45] described the melt as consisting of the species Pb_2SiO_4 (SiO_4^{-4}), $PbSiO_3$ (SiO_3^{-2}) and $PbSi_2O_5$ ($Si_2O_5^{-2}$), in addition to the components PbO (O^{-2}) and SiO_2 (SiO_2). The resulting model of the liquid phase is in accord with experimental evidence for the anions present in silicate melts [42].

An assessment of the Fe-O-SiO_2 system by Björkman [50], based in part on earlier work by Goel et al. [51], utilised the associated species $Fe_3Si_2O_7$, $Fe_3Si_6O_{15}$ and Fe_2SiO_4 together with the components FeO, Fe_2O_3 and SiO_2, to describe the melt. A correct description of the ternary Fe-O-SiO_2 system was obtained [50] by simple combination of assessed data for the binary Fe-O and FeO-SiO_2 systems. Although the miscibility gap in the FeO-SiO_2 system was not taken into consideration (no repulsive interactions in the melt were introduced), the ability of the associated solution model to describe the transition from the pure metallic component to the oxide must be emphasized.

The model has been further applied to describe the melt in systems containing Al_2O_3, CaO, K_2O, MgO and SiO_2 (Hastie et al. [52, 53]). Acceptable agreement between calculated and experimental activity data for the components of the melts was reported, but no complete calculated phase diagrams were published.

In an assessment of the CaO-SiO_2 system by an Mey [54], only the associated specie Ca_2SiO_4, in addition to the components CaO and SiO_2, was chosen for the modelling of the liquid phase. A satisfactory description of phase equilibria and thermodynamic properties across the entire composition range was achieved by using additional excess terms to describe the interaction between associates in the liquid [54]. In particular, the excess terms allowed the miscibility gap to be reproduced. Similar non-ideal treatment of the melt has previously been applied by Goel et al. [51] to the system Fe-O-SiO_2.

Recently, non-ideal associated solution model has also been applied to description of liquid in the Cr-O and Ni-O systems [55] and will be extended on the quaternary system Cr-Fe-Ni-O. However, at the present time, the number of systems which have been assessed using the associated solution model is rather limited.

3.1.3.2 Cellular model (Kapoor, Frohberg [46, 56], *Gaye, Welfringer* [47, 57])

The formation of a silicate melt can be regarded as a change in the state of polarisation of oxygen ions according to the reaction $O^o + O^{-2} = 2O^-$. Furthermore, the state of polarisation of oxygen ions is influenced by the surrounding cations, so that the pure oxide can be represented as a symmetric M_iOM_i cell. An M_iO-SiO_2 melt can also be regarded as a mixture of symmetric M_iOM_i and SiOSi cells and asymmetric M_iOSi cells, whereby the energy of formation, W_{ij}, of an M_iOSi cell corresponds to the reaction between two M_iOM_i and SiOSi cells.

This approach can be extended to multicomponent systems [47], in which the liquid phase is assumed to consist of symmetric M_iOM_i and asymmetric M_iOM_j cells (as well as cells of the M_iOSi and SiOSi-type in systems containing silica). Analogous to the modelling of binary mixtures, the energy of formation, W_{ij}, of each asymmetric cell corresponds to the reaction between two symmetric M_iOM_i and M_jOM_j cells. With the assumption that the interactions between like cells can be neglected, and by application of "additivity rules" [47], all interactions can be reduced to just one E_{ij} parameter describing the "binary" interaction energy between symmetric and asymmetric cells. Thus, for the complete description of a multicomponent system, a set of W_{ij} (energy of formation) and E_{ij} (energy of interaction) binary parameters for all the constituent M_iO-M_jO binary systems is sufficient.

In order to obtain a satisfactory description of thermodynamic properties in systems with strong ordering effects (e.g. SiO_2-CaO, SiO_2-MgO, etc.), the introduction of a linear composition dependence of the W_{ij} and E_{ij} parameters is necessary.

Recently, this model has been extended to oxysulphide systems [57] so that the corresponding database now contains all combinations of the components Al_2O_3, CaO, CrO, Cr_2O_3, FeO, Fe_2O_3, MgO, MnO, SiO_2 and S, whereby for the latter, only sulphide capacities and sulphur partition coefficients can be calculated.

Although the accuracy of the calculated phase diagrams is not excellent, the agreement between calculated and experimen-

tal thermodynamic properties (especially component activities) is quite acceptable.
In a recent assessment of the $CaO-SiO_2$ system (Taylor, Dinsdale [58]) better agreement between the experimental and calculated phase diagram was obtained through the introduction of additional composition dependence of the W_{ij} and E_{ij} parameters.

3.1.3.3 Modified quasi-chemical model (Pelton, Blander [48])

The quasi-chemical theory [59], is a well-known approximation for solution phases with short-range order. If one considers a simple binary mixture of the two pure liquids, A and B, the theory focuses on the energy change for making some A-B bonds in the mixture at the expense of A-A and B-B bonds

$$A\text{-}A + B\text{-}B = 2A\text{-}B$$

In the general case, one can consider the energy change to be temperature dependent and represented by w-μT. If this energy change is zero, then the solution is an ideal mixture. As the energy change becomes negative, the formation of A-B pairs is favoured and the solution becomes more ordered (enthalpy of mixing curves exhibit a negative, V-shaped peak with a minimum at the equimolar AB composition). If w-μT becomes positive, A-A and B-B pairs are preferred and the solution shows a tendency to immiscibility.
When applied to molten silicates, the A-A, B-B and A-B bonds are formed between second-nearest-neighbour M_i and Si pairs. In real oxide systems, the ordering can occur at compositions different from equimolar, depending on the valencies of the cations. This is taken into account by use of equivalent mole fractions. In addition, the quasi-chemical theory is based on the assumption that pair bond energies are additive and independent of composition. However, in order to achieve a good agreement between calculated and experimental phase diagrams and thermodynamic data, a polynominal composition dependence of the w and μ parameters has been introduced.
Numerous binary and multicomponent systems containing different combinations of the components Al_2O_3, CaO, MgO, MnO, FeO, Na_2O, K_2O, TiO_2, Ti_2O_3 and ZrO_2 have been assessed using this model [60-66]. In particular, relatively complicated ternary systems with a strong tendency to ordering (e.g. Al_2O_3-CaO-SiO_2) or with a large miscibility gap (e.g. SiO_2-TiO_2-ZrO_2) have been successfully assessed. However, to obtain acceptable agreement between calculated and experimental phase diagrams, ternary interaction terms must be introduced [67].
Recently, this database has been extended to include sulphur [68], providing the possibility for calculation of the sulphur content of slags in multicomponent slag/metal/gas/solid equilibria.

3.1.3.4 Sub-lattice model (Hillert, Jansson, Sundman, Ågren [49])

The two-sub-lattice model for ionic solutions developed by Hillert et al. [49] is an extension of the general sublattice model [41], which has been applied successfully to the description of solid phases in many metallic systems. The sublattice description is related to the real crystallographic structure of the materials concerned. All atoms (ions) are distributed on sub-lattices, differing with respect to their co-ordination number and occupation (and charge). When applied to silicate melts, the liquid phase is assumed to consist of two sub-lattices, one for the cations, and one for the anions and neutral species.
In a recent evaluation of the $CaO-SiO_2$ system (Hillert et al. [69]) the liquid phase is represented by the formula $(Ca^{+2})_P(SiO_4^{-4},O^{-2},SiO_2^0)_Q$, where P and Q indicate the concentration and charge-dependent site number on each sublattice. The electro-neutral combination of cationic and anionic species results in phase components similar to those of the associated solution model.
At the present time, a number of metal-nonmetal systems (Al-O, Si-O, Fe-O) as well as some of the more important binary oxide systems ($CaO-SiO_2$, CaO-MgO, $MgO-SiO_2$ etc.) have been evaluated using this model [70-73]. The capability of this model to describe the continous transition from a metallic to an oxide melt is particularly emphasized.
In a very recent application of the two ionic sub-lattice model to the assessment of the Fe-O system (Sundman [74]), an excellent agreement between the calculated and experimental phase diagram and thermodynamic properties of the system was obtained. Using the evaluated set of model parameters, all relevant experimental data could be reproduced within the limits of experimental uncertainties. The calculated T vs. pO_2 diagram is reproduced in Figure 3.7.
The ability of this model to give good prediction and representation of behaviour in multicomponent systems has yet to be demonstrated.

3.1.4 Comments and selected calculated phase diagrams

At the present time, the greatest number of binary and multicomponent system evaluations have been carried out using the quasi-chemical and cellular models respectively. Moreover, the evaluated systems are described using only a small number of parameters. Taking into account the simplicity of these two models, the reproduction of phase diagrams and thermodynamic properties is remarkable. The slightly better results obtained using the quasichemical model can be explained by the fact that a smaller number of binary and no ternary interaction terms are used in the cellular model. However, the extension of both models to binary metallic and metal-nonmetal ranges is formally impossible.
Such a capability is provided by the sub-lattice model, which at the same time gives excellent agreement between calculated and experimental data. Although the physical background of this model is comprehensive and quite acceptable, the mathematics and notation used is rather complicated.
Simultaneous description of metallic and oxide melts is also possible using the associated solution model. However, the restricted number of assessed systems available limits considerably the application of this model to the solution of practical problems.
In the subsequent figs. (**Figs. 3.I, 3.II, 3.III and 3.IV**), comparison is made of the $CaO-SiO_2$ phase diagram, calculated using data evaluated by application of each of the models discussed above. The discrepancies between the different calculated diagrams relate mainly to the extension and form of the miscibility gap, the homogeneity range of the $3CaO.2SiO_2$ phase, and the stability limits of the $3CaO.SiO_2$ phase. If the critical temperature for the miscibility gap and the stability range of the $3CaO.SiO_2$ phase depend on the adopted experimental version of the phase diagram, then the form of the miscibility gap calculated using the associated solution or cellular model, as well as the extension of the homogeneity range of the $3CaO.2SiO_2$ phase, are essentially model-dependent. It should be noted, however, that a more complicated concentration dependence of the W_{ij} and E_{ij} parameters in the cellular model, and the application of higher-order ex-

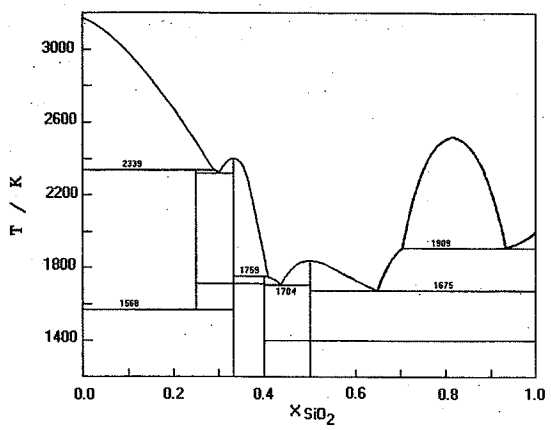


Fig. 3.I. CaO-SiO_2 phase diagram as assessed by an Mey [54] with the associated solution model (non ideal) for the liquid phase.

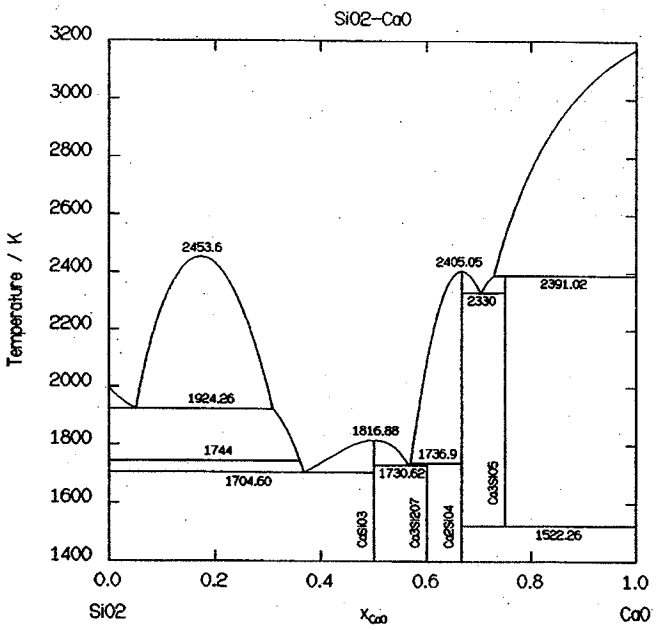


Fig. 3.II. CaO-SiO_2 phase diagram as assessed by Taylor, Dinsdale [58] with the cellular model for the liquid phase.

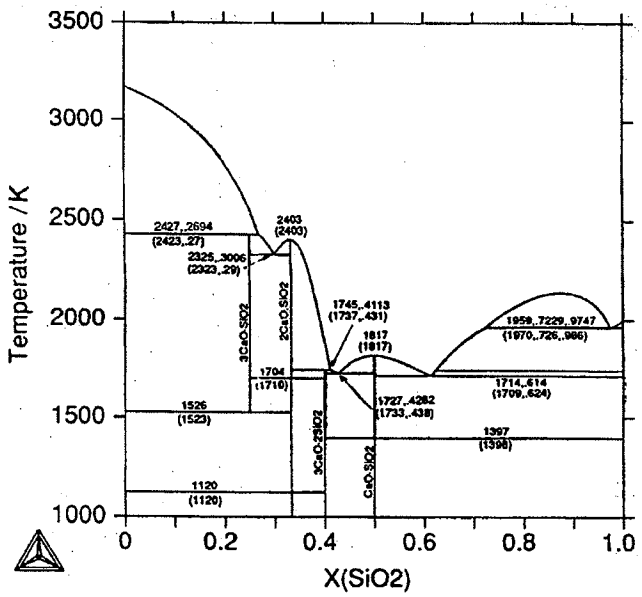


Fig. 3.IV. CaO-SiO_2 phase diagram as assessed by Hillert et al. [69, 75] with the sub-lattice model for the liquid phase.

cess terms in the associated solution model, could improve the thermodynamic description of the melt.

Although the phase equilibria predicted using the thermodynamic models have been experimentally confirmed for most of the CaO-SiO_2 system, there still remain a number of problems (e.g. the stability range of the 3CaO.SiO_2 phase) to be resolved through experimental measurements.

In conclusion, it can be stated that all of the models discussed here enable acceptable agreement between calculated and experimental data to be achieved. Thus, the main criterion in choosing between existing models and databases to resolve practical problems is perhaps the elements and systems they cover.

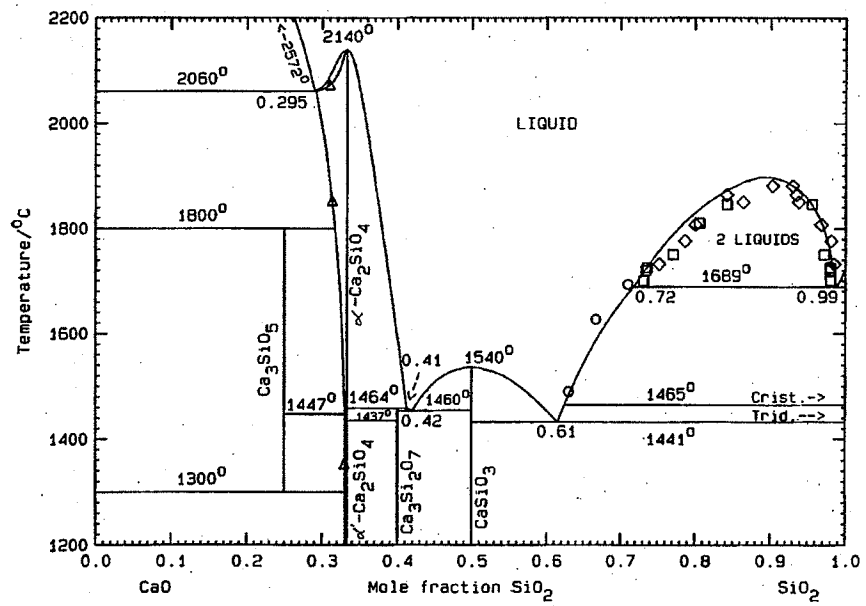


Fig. 3.III. CaO-SiO_2 phase diagram as assessed by Eriksson et al. [62] with the quasi-chemical model for the liquid phase.

References

[1] Slag Atlas, Ed.: Verein Deutscher Eisenhüttenleute, Düsseldorf, (1981)

[2] Phase Equilibria Diagrams (earlier Phase Diagrams for Ceramists), Ed.: American Ceramic Society, Westerville, Ohio, Vol.: I (1964), II (1969), III (1975), IV (1981), V(1983), VI (1987), VII (1989), VIII (1990), IX (1991), Annual 91 (1991) and Annual 92 (1992)

[3] Proceedings of International Conference on Metallurgical Slags and Fluxes, (1980), (1984), (1988), (1992)

[4] Bowen, N. L., J. Andersen: Am. J. Sci., 4-th Ser. 37 (1914), p. 487/501

[5] Rankin, G. A., F. E. Wright: Am. J. Sci., 4th Ser. 39 (1915), p. 1/79

[6] Rankin, G. A., E. H. Merwin: J. Am. Chem. Soc. 38 (1916), p. 568/88

[7] Muan, A., E. F. Osborn: Phase Equilibria Among Oxides in Steelmaking, Ed.: Addison-Wesley Publishing Company, Inc., Reading, Massachusetts, (1965)

[8] Berezhnoi, A. C.: Multicomponent Oxide Systems, Ed.: Naukovaya Dumka, Kiev, (1970)

[9] Toropov, N. A., W. P. Barzakovskii, W. W. Lapin, N. N. Kurtseva: Handbook of Phase Diagrams of Silicate Systems, Vol. I, Binary Systems, Ed.: Nauka, Leningrad, (1969)

[10] Barzakovskii, W. P., W. W. Lapin, A. I. Boykova, N. N. Kurtseva: Handbook of Phase Diagrams of Silicate Systems, Ternary Oxide Systems, Ed.: Nauka, (1974)

[11] Mills, K. C., B. J. Keene: Inter. Metals Rev., (1981) No. 1, p. 21/69

[12] Kubaschewski, O.: Iron - Binary Phase Diagrams, Ed.: Springer Verlag, Verlag Stahleisen mbh, Düsseldorf, (1982)

[13] Raghavan, V.: Phase Diagrams of Ternary Iron Alloys, Part 2, Ternary Systems Containing Iron and Sulphur, Ed.: The Indian Institute of Metals, Calcutta, (1988)

[14] Pelton, A. D., H. Schmalzried: Metall. Trans. 4 (1973), No. 5, p. 1395/404

[15] Rhines, F. N.: Phase Diagrams in Metallurgy, McGraw-Hill, (1956), p. 340

[16] Massalski, T. B.: Metall. Trans. B 20B (1989) No. 7, p. 445/73

[17] Pelton, A. D.: in Material Science and Technology, Vol. 5, Ed.: Hassen, P., Ed.: VCH Publishers Inc., (1991), p. 1/74

[18] THERDAS - Thermodynamic Databank System, Lehrstuhl für Theoretische Hüttenkunde, RWTH Aachen, Germany

[19] Edgar, A. D.: Experimental Petrology, Basic Principles and Techniques, Ed.: Clarendon Press, Oxford, (1973)

[20] Segal, D. L.: Chemical Synthesis of Advanced Ceramics, Ed.: Cambridge University Press, (1991)

[21] Reynen, P., H. Bastius, M. Faizullah, H. Kamtz: Ber. Dtsch. Keram. Ges. 54, (1977), p. 63/7

[22] Muan, A.: J. Am. Ceram. Soc.,.44 (1961) No. 6, p. 298

[23] Muan, A.: Am. J. Sci. 256 (1958), p. 171/207

[24] Nafziger, R. H., G. C. Ulmer, E. Woermann: in Research Techniques for High Pressure and High Temperature, Ed.: Ulmer, G.C., Springer Verlag, (1971), p. 9/42

[25] Deines, P., R. H. Nafziger, G. C. Ulmer, E. Woermann: Bull. Earth Mineral Sciences Experiment. Station, Pennsylvania State University, 88 (1974), p. 129

[26] Mackenzie, R.C.: Differential Thermal Analysis, Ed.: Academic Press Inc., Vol. I (1970), Vol. II (1972)

[27] Sato, M.: in Research Techniques for High Pressure and High Temperature, Ed.: Ulmer, G.C., Springer Verlag, (1971), p. 43/99

[28] Turnbull, A. G.: CALPHAD 7 (1983), p. 137

[29] Turnbull, A. G., M. W. Wadsley: The CSIRO-SGTE thermodata system (Version IV). CSIRO, Inst. of Energy and Earth Resources, Port Melbourne, Australia (1985)

[30] Thompson W. T., G. Eriksson, A. D. Pelton, C. W. Bale: Int. Symp. on Computer Software in Chemical & Extractive Metallurgy, Proc. Metall. Soc. of CIM, Montreal 1988, 11 (1988), p. 87

[31] Thompson W. T., A. D. Pelton, C. W. Bale: F*A*C*T Facility for the Analysis of Chemical Thermodynamics, guide to operations, McGill University Computing Centre, Montreal (1985)

[32] A. Roine: Int. Symp. on Computer Software in Chemical & Extractive Metallurgy, Proc. Metall. Soc. of CIM, Montreal 1988, 11 (1988), p. 15

[33] Kaufman, L., H. Bernstein: Computer Calculation of Phase Diagrams, Ed.: Acad. Press, New York (1970)

[34] Barry, T. I.; A. T. Dinsdale, R. H. Davies, J. Gisby, N. J. Pugh, S. M. Hodson, M. Lacy: MTDATA Handbook: Documentation for the NPL Metallurgical and Thermochemical Databank, National Physical Laboratory, Teddington, U.K. (1987)

[35] Dinsdale, A. T., S. M. Hodson, T. I. Barry, J. R. Taylor: Int. Symp. on Computer Software in Chemical & Extractive Metallurgy, Proc. Metall. Soc. of CIM, Montreal 1988, 11 (1988), p. 59

[36] Spencer, P. J., K. Hack: The Solution of Materials Problems using the Thermochemical Databank System THERDAS, Swiss Chem. 12 (1990) No. 10, p. 61/6

[37] Sundman, B., B. Jansson, J.-O. Andersson: CALPHAD 9 (1985), p. 153

[38] Sundman, B.: Int. Symp. on Computer Software in Chemical & Extractive Metallurgy, Proc. Metall. Soc. of CIM, Montreal 1988, 11 (1988), p. 75

[39] Cheynet, B.: Int. Symp. on Computer Software in Chemical & Extractive Metallurgy, Proc. Metall. Soc. of CIM, Montreal 1988, 11 (1988), p. 88

[40] Bale, C. W., G. Eriksson: Canad. Metall. Quart. 29 (1990) No. 2, p. 105/32

[41] Sundman, B., J. Ågren: J. Phys. Chem. Solids 42 (1981) p. 297/301

[42] Mills, K. C.: The structure of silicate melts, NPL Report DMM(A)43, Teddington, (1991)

[43] Kaufman, L.: CALPHAD 3 (1979) No. 1, p. 27/44

[44] Berman, R. G., T. H. Brown: Geochim. Cosmochim. Acta 48 (1984), p. 661/78

[45] Flood, H., W. J. Knapp: J. Am. Ceram. Soc. 46 (1963) No. 2, p. 61/5

[46] Kapoor M. L., M. G. Frohberg: Proc. Symp. Chemical Metallurgy of Iron and Steel, Sheffield, (1971), p.17/22

[47] Gaye H., J. Welfringer: Second International Symposium on Metallurgical Slags and Fluxes, Ed.: Fine, H. A., D. R. Gaskell, Lake Tahoe, 1984, Publ.: Metall. Soc. AIME, New York, (1984), p. 357/75

[48] Pelton, A D., M. Blander: Metall. Trans. 17B (1986), p. 805

[49] Hillert, M., B. Jansson, B. Sundman, J. Ågren: Metall. Trans. A 16A (1985), p. 261/6

[50] Björkman, B.: CALPHAD 9 (1985) No. 3, p. 271/82

[51] Goel, R. P., H. H. Kellogg, J. Larrain: Metall. Trans B. 11B (1980) No. 3, p. 107/17

[52] Hastie, J. W., D. W. Bonnell: High Temp. Sci. 19 (1985), p. 275

[53] Hastie, J. W., W. S. Horton, E. R. Plante, D. W. Bonnell: High Temp. - High Press. 14 (1982), p. 669/79

[54] an Mey, S.: PhD Thesis, RWTH Aachen, Germany, (1988), p. 118

[55] Kowalski, M., J. P. Spencer: submitted for publication in CALPHAD

[56] Kapoor M. L., G. M. Mehrotra, M. G. Frohberg: Proc. Aust. Inst. Mining Metall. (1975) No. 254, p. 11/7

[57] Gaye H., J. Lehmann, P. V. Riboud, J. Welfringer: Mém. Sci. Rev. Métall. (1989), p. 237/44

[58] Taylor, J. R., A. T., Dinsdale: CALPHAD 14 (1990) No. 1, p. 71/88

[59] Guggenheim E. A.: Proc. Roy. Soc. A148 (1935), p. 304

[60] Eriksson, G., A. D. Pelton: Metall. Trans. B 24B (1993), p. 795/805

[61] Eriksson, G., A. D. Pelton: Metall. Trans. B 24B (1993), p. 807/15

[62] Eriksson, G., P. Wu, A. D. Pelton: Canad. Metall. Q. 33 (1994) 13/21

[63] Wu, P., G. Eriksson, A. D. Pelton: J. Am. Ceram. Soc. 76 (1993) No. 8, p. 2059/64

[64] Wu, P., G. Eriksson, A. D. Pelton: J. Am. Ceram. Soc. 76 (1993) No. 8, p. 2065/75

[65] Wu, P., G. Eriksson, G., A. D. Pelton, M. Blander: Trans. Iron Steel Inst. Jpn. 33 (1993), p. 26/35

[66] Eriksson, G., P. Wu, A. D. Pelton: CALPHAD 17 (1993) No. 2. p. 189/207

[67] Wu, P.: PhD Thesis, Ecole Polytechnique, Montreal (1992)

[68] Pelton, A. D., G. Eriksson, A. Romero-Serrano: Metall. Trans. B 24B (1993), p. 817/25

[69] Hillert, M., B. Sundman, X. Wang: Metall. Trans. B 21B (1990) No. 2, p. 303/12

[70] Hillert, M., X. Wang: CALPHAD 13 (1989) No. 3, p. 253/66

[71] Hillert, M., X. Wang: CALPHAD 13 (1989) No. 3, p. 267/72

[72] Taylor, J. R., A. T. Dinsdale, M. Hillert, M. Selleby: CALPHAD 16 (1992) No. 2, p. 173/80

[73] Hillert, M., S. Jonsson: CALPHAD 13 (1992) No. 2, p. 193/8

[74] Sundman, B.: J. Phase Equilib. 12 (1991) No. 1, p. 127/40

[75] Hillert, M., B. Sundman, X. Wang, T. Barry: CALPHAD 15 (1991) No. 1, p. 53/58

3.2 Slag systems

3.2.1 Basic metal-nonmetal systems

Al-O

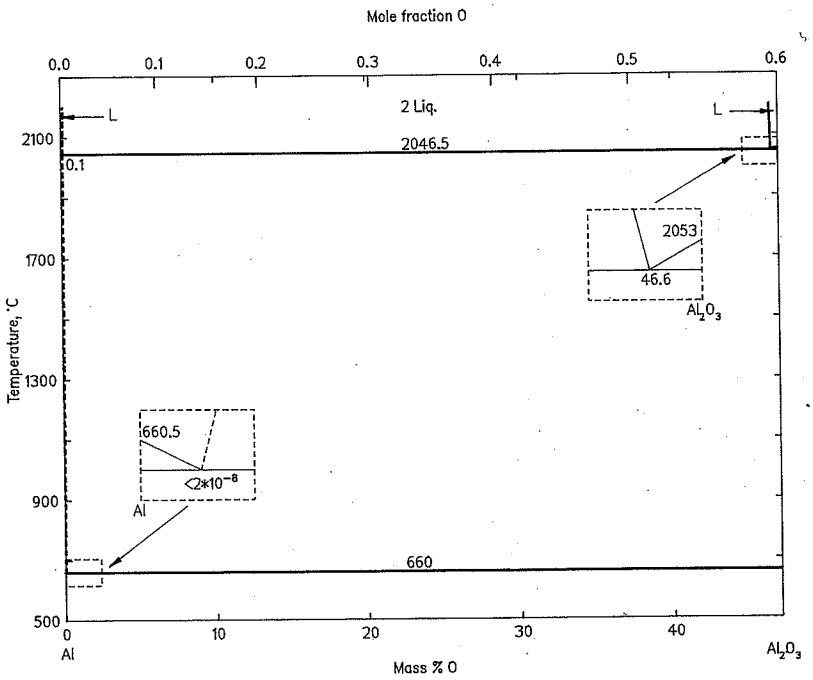


Fig. 3.1. Al-Al_2O_3 phase diagram as assessed by Wriedt [1], based mainly on the work of Gitlesen et al. [2] and Yanagida, Kröger [3]. For a theromdynamic assessment of the system and calculated version of the phase diagram see Taylor et al. [4]. The melting point of Al_2O_3 at 2053 °C, recommended by Schneider [5] (2054 °C on ITS-68) and commonly accepted in all compilations, has been adjusted to ITS-90.

References

[1] Wriedt, H. A.: Bull. Alloy Phase Diagrams 6 (1985) No. 6, p. 548/53
[2] Gitlesen, G., O. Herstad, K. Motzfeld: Selected Topics in High Temperature Chemistry, Forland, Ed.: Universitetsforlaget, Oslo, Norway (1966), p. 179/96
[3] Yanagida, H., F. A. Kröger: J. Am. Ceram. Soc. 51 (1968) No. 12, p. 700/6
[4] Taylor, J. R., A. T. Dinsdale, M. Hillert, M. Selleby: CALPHAD 16 (1992) No. 2, p. 173/80
[5] Schneider, S. J.: Pure Appl. Chem. 21 (1979), p. 117/22

Ca-O

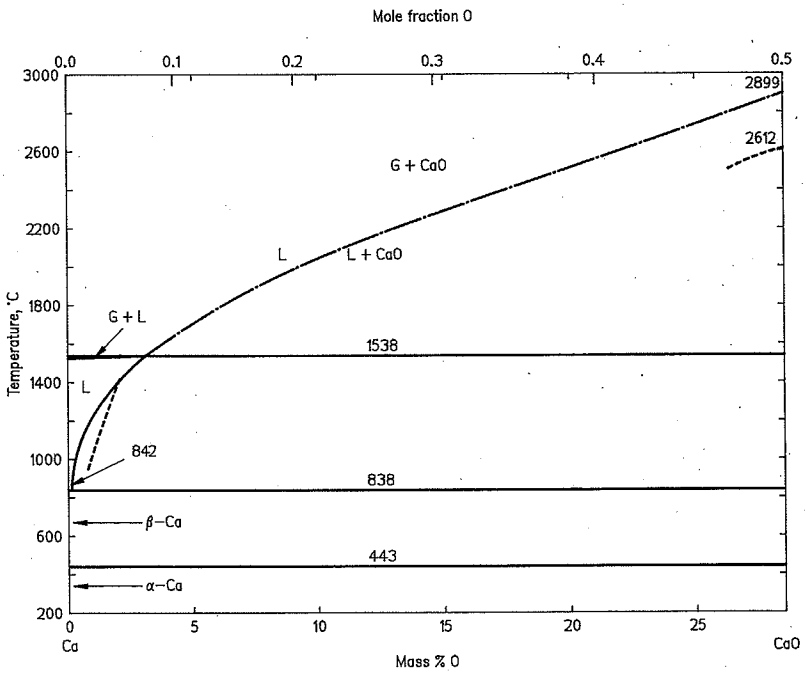


Fig. 3.2. Ca-CaO phase diagram at 1 atm total pressure, as calculated by Selleby et al. [1], according to experimental results reported by Bevan, Richardson [2]. The liquidus, when the gas phase is omitted, is shown with a dash-dot line. The solubility of CaO in liquid below the boiling point of CaO, reported recently by Fischbach [3], is shown in the figure with a dashed line. The melting point of CaO at 2612 °C (ITS-90) after Hlavac [4], is the "average" value from earlier measurements [5-11]. The tentative liquidus in the vicinity of the melting point of CaO is shown in the figure as a dashed line. Much higher values of the melting point of CaO, around 2900 °C, have been reported by Foex et al. [12-14] and recently by Yamada at al. [15]. This value is also accepted in the assessment by Selleby et al. [1]. In the present compilation the value proposed by Hlavac [4] has been adopted. In some cases, however, the calculated phase equilibria based on the higher value of the melting point of CaO are appended to the experimental diagrams. For the recent evaluation of experimental information, see Wriedt [16].

References

[1] Selleby, M., M. Hillert, B. Sundman: Report TRITA-MAC-0397, Royal Institute of Technology, Stockholm, (1989)
[2] Bevan, D. J. M., F. D. Richardson: Proc. Australian At. En. Symp. on the Peaceful Uses of At. En., 1958, Melbourne, University Press (1959), p. 586/7
[3] Fischbach, H.: Steel Res. 56 (1985) No. 7, p. 365/8
[4] Hlavac, J.: Pure Appl. Chem. 54 (1982) No. 3, p. 681/8
[5] Kanolt, C. W.: Z. Anorg. Chem. 85 (1914) No. 1, p. 1/19
[6] Schumacher, E. E.: J. Am. Chem. Soc. 48 (1926) No. 2, p. 396/405
[7] Olshansky, Ya. I.: Dokl. Akad. Nauk SSSR 59 (1948) No. 4, p. 1105/7
[8] Doman, R. C., J. B. Barr, R. N. McNally, A. M. Alper: J. Am. Ceram. Soc. 46 (1963) No. 7, p. 313/6
[9] Noguchi, T., M. Mizuno M., W. M. Conn: Solar Energy 11 (1967) No. 3-4, p. 145/52
[10] Panek, Z.: Silikaty /Praque/ 23 (1979) No. 2, p. 97/102
[11] Shevchenko, A. V., L. M. Lopato, V. S. Dvernyakov, V. V. Pasichnys: Dokl. Akad. Nauk SSSR, Ser. A 8 (1979), p. 682/5
[12] Foex, M.: Rev. Int. Hautes Tempér. et Réfract. 3 (1966), p. 309/26
[13] Foex, M., R. Delmas: C. R. Acad. Sci., Paris, Ser. C 265 (1967), p. 9/12
[14] Traverse, J. P., M. Foex: High Temp. - High Pressures 1 (1969), p. 409/27
[15] Yamada, T., M. Yoshimura, S. Somiya: J. Am. Ceram. Soc. 69 (1986) No. 10, p. C243/5
[16] Wriedt, H. A.: Bull. Alloy Phase Diagrams 6 (1985) No. 4, p. 337/42

Co-O

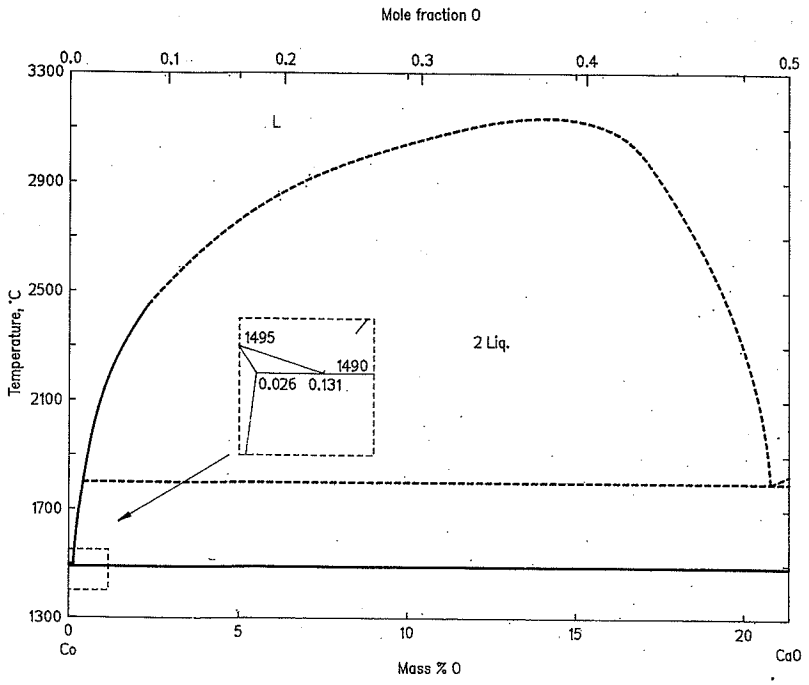


Fig. 3.3. Co-CoO phase diagram (schematic). The section shows the phase equilibria in the Co-rich portion of the system calculated by Jacob, Hajra [1] from their own experimental results and earlier investigations of this part of the system. For the phase equilibria in the vicinity of the melting point of CoO, see for instance, Coutures [2]. The numerous standard references are given in [1, 2]. The occurrence of a miscibility gap in the Co-O system at ambient pressures has been reported by Kato, Ringwood [3]. The dashed lines show the limits of liquid immiscibility at elevated pressures, as quoted in [3]. For equilibrium partial pressures of oxygen in the Co-CoO system, see Fischer, Pateisky [4], Jacobsson, Rosén [5], Schwab, Küstner [6] and O'Neill [7].

References

[1] Jacob, K. T., J. P. Hajra: Z. Metallkd. 76 (1985) No. 10, p. 709/13
[2] Coutures, J. P.: Rev. Int. Hautes Tempér. et Réfract. 16 (1979) No. 3, p. 211/24
[3] Kato, T, A. E. Ringwood: Phys. Chem. Minér. 16 (1989) No. 6, p. 524/38
[4] Fischer, W. A., G. Pateisky: Arch. Eisenhüttenwes. 41 (1970) No. 7, p. 661/73
[5] Jacobsson, E., E. Rosén: Scand. J. Metall. 10 (1981), p. 39/43
[6] Schwab, R. G., D. Küstner: Neues Jahr. Mineral., Abh. 140 (1981) No. 2, 111/42
[7] O'Neill, H. S. C.: Am. Mineral. 72 (1987) No. 3-4, p. 280/91

Cr-O

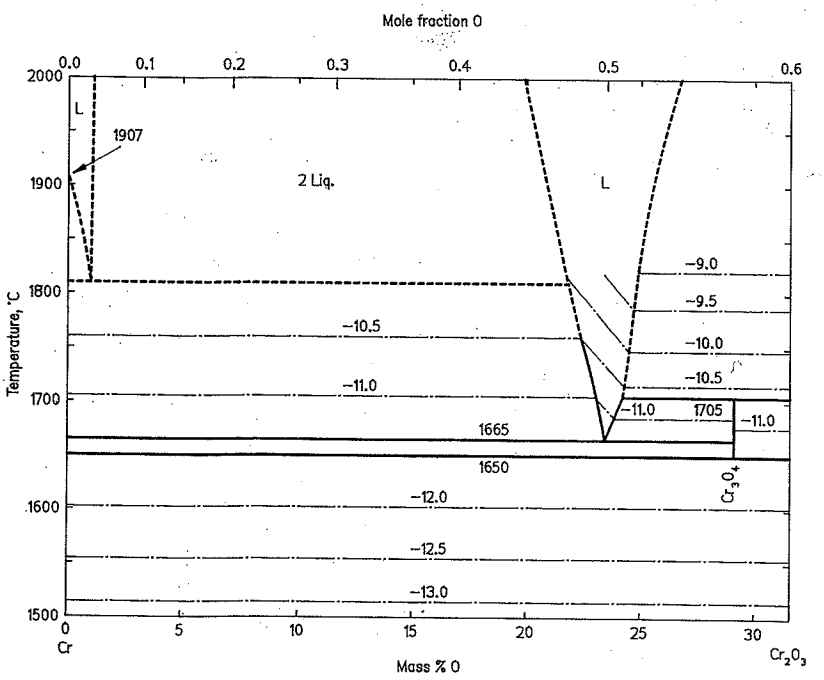


Fig. 3.4. Cr-Cr_2O_3 phase diagram with oxygen isobars (log pO_2, atm) after Toker et al. [1]. Thermodynamic information for the system is presented in the original paper by Toker et al. [1] and in the assessment made by Taylor, Dinsdale [2]. The melting point of Cr_2O_3 at 2333 °C after McNally at al. [3] and used in the assessment made by Taylor, Dinsdale [2] has been adjusted to ITS-90 (2330 °C on ITS-48). For the phase equilibria in the subsystem Cr_2O_3-CrO_3 and additional compounds containing chromium of higher valency, see for instance Abadir et al. [4] and Lerm et al. [5].

References

[1] Toker, N. Y., L. S. Darken, A. Muan: Metall. Trans. B 22B (1991) No. 4, p. 225/32
[2] Taylor, J. R., A. T. Dinsdale: Z. Metallkd. 81 (1990) No. 5, p. 354/65
[3] McNally, R. N., F. I. Peters, P. H. Ribbe: J. Am. Ceram. Soc. 44 (1961) No. 1, p. 491/3
[4] Abadir, M. F., A. M. Gadalla, Y. M. El-Agamawi: Trans. J. Br. Ceram. Soc. 75 (1976) No. 4, p. 74/6
[5] Lerm, A., G. Elbinger, P. Rosemann: Z. Anorg. Allg. Chem. 442 (1978) , p. 5/10

Fe-O

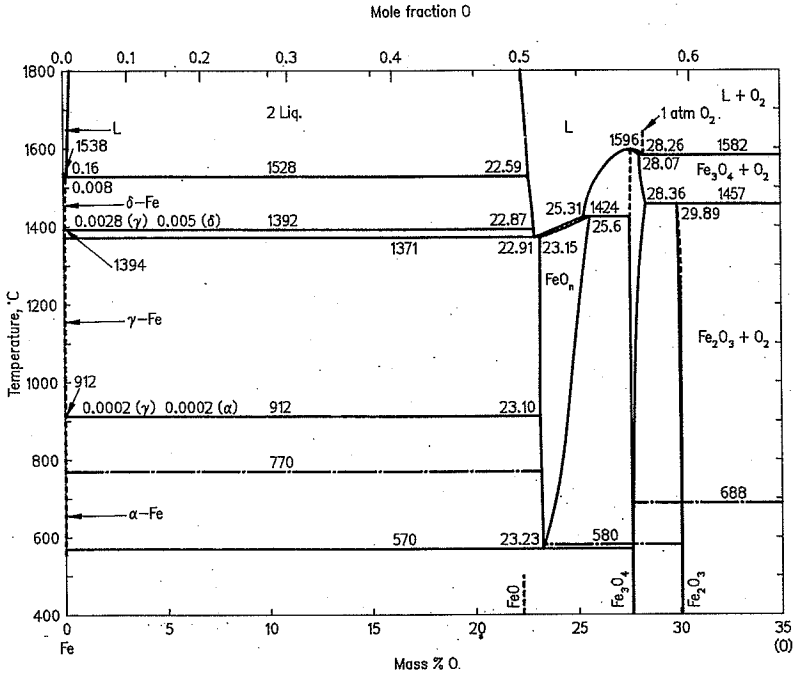


Fig. 3.5. Fe-O phase diagram (up to 35 mass % O) at 1 atm total pressure, as evaluated recently by Wriedt [1], based mainly on the version of the phase diagram reported by Darken, Gurry [2, 3]. After Ohtani, Ringwood [4], the miscibility gap persists up to approx. 2700 °C. For a previous evaluation of the system, see Spencer, Kubaschewski [5] and Kubaschewski [6]. Recently, a thermodynamic assessment and calculated phase diagram of the Fe-O system has been published by Sundman [7].

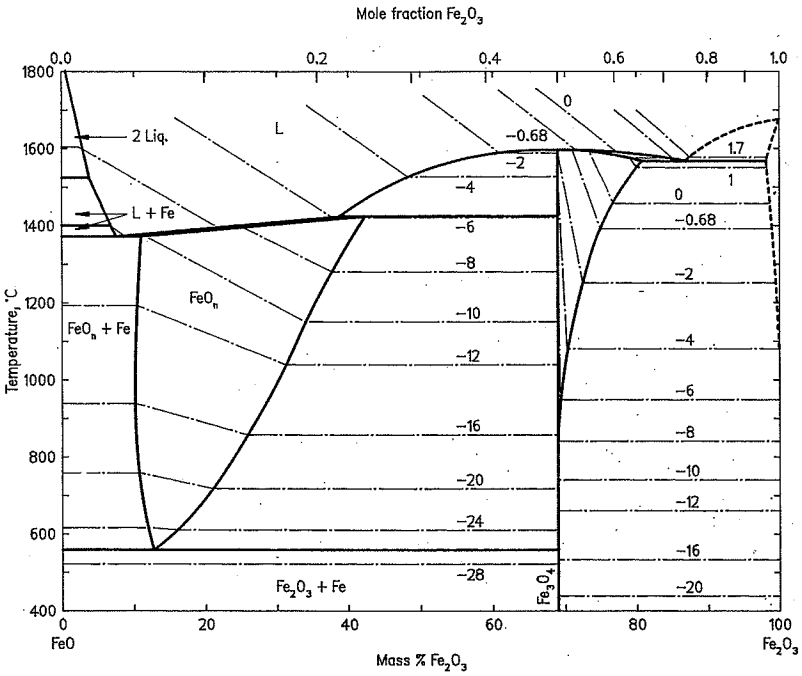
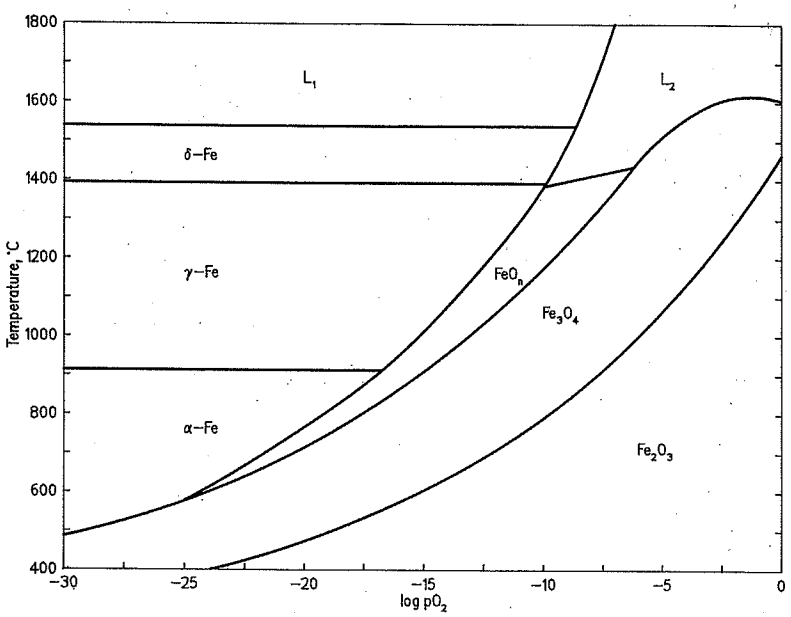


Fig. 3.6. FeO-Fe_2O_3 phase diagram with oxygen isobars (log pO_2, atm) after Muan, Osborn [8], based mainly on the previous works of Darken, Gurry [2, 3]. The oxygen isobars in the vicinity of the Fe_2O_3-Fe_3O_4 eutectic are as reported by Phillips, Muan [9].

Fig. 3.7. Temperature vs. log pO_2 phase diagram for the Fe-O system according to the thermodynamic assessment of the system by Sundman [7].

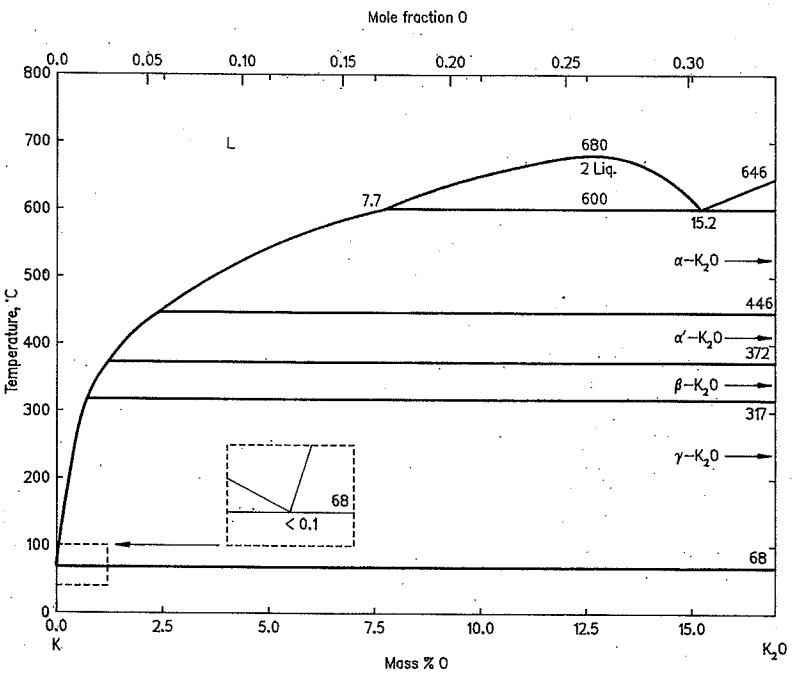


References

[1] Wriedt, H. A.: J. Phase Equilibria 12 (1991) No. 2, p. 170/200
[2] Darken, L. S., R. W. Gurry: J. Am. Chem. Soc. 67 (1945) No. 8, p. 1398/412
[3] Darken, L. S., R. W. Gurry: J. Am. Chem. Soc. 68 (1946) No. 5, p. 798/816
[4] Ohtani, E., A. E. Ringwood: Earth Planet. Sci. Lett. 71 (1984), p. 85/93
[5] Spencer, P. J., O. Kubaschewski: CALPHAD 2 (1978) No. 2, p. 147/67
[6] Kubaschewski, O.: Iron - Binary Phase Diagrams, Ed.: Springer-Verlag, Berlin, Heidelberg, New York, Verlag Stahleisen mbH, Düsseldorf, (1982)
[7] Sundman, B.: J. Phase Equilibria 12 (1991) No. 1, p. 127/40
[8] Muan, A., E. F. Osborn: Phase Equilibria Among Oxides in Steelmaking, Ed.: Addison-Wesley Publishing Company, Inc., Reading, Massachusetts (1965)
[9] Phillips B., A. Muan: J. Phys. Chem. 64 (1960) No. 10, p.1451/3

K-O

Fig. 3.8. Sub-system K-K_2O after Natola, Touzain [1] and Williams et al. [2].



References

[1] Natola, F., P. Touzain: Can. J. Chem. 48 (1970) No. 13, p. 1955/8
[2] Williams, D. D., J. A. Grand, R. R. Miller: J. Phys. Chem. 63 (1959) No. 1, p. 68/71

Mg-O

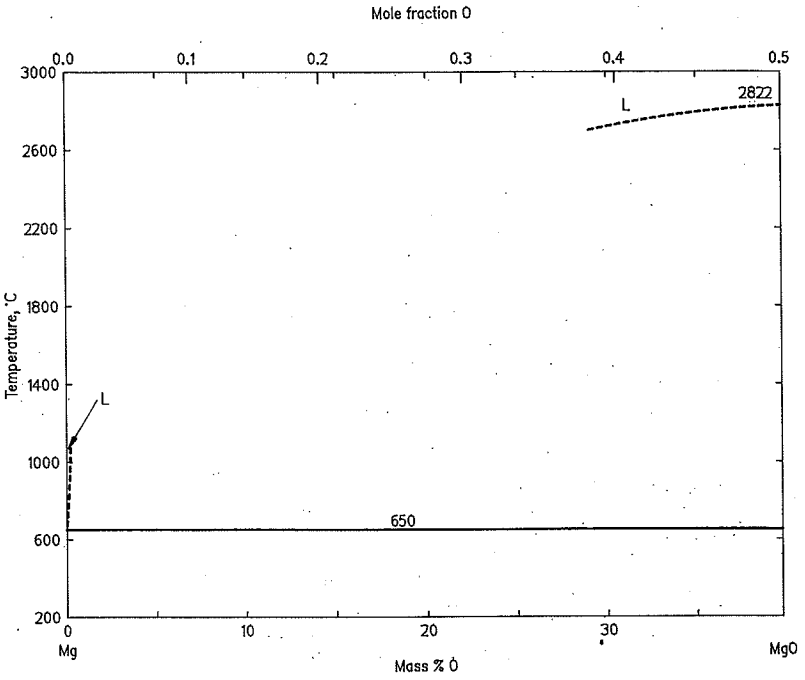


Fig. 3.9. Mg-MgO phase diagram as assessed by Wriedt [1]. After Kanolt [2], McNally et al. [3], Riley [4], and Panek [5], MgO melts at approx. 2800 °C. The melting point of 2822 °C (ITS-90) determined by Panek [5] has been adopted in this compilation. For a discussion of the melting point of MgO, see Hlavac [6], and for a recent thermodynamic assessment of the system and the calculated Mg-MgO phase diagram, see Hallstedt [7].

References

[1] Wriedt, H. A.: Bull. Alloy Phase Diagrams 8 (1987) No. 3, p. 227/33
[2] Kanolt, C. W.: Z. Anorg. Chem. 85 (1914) No. 1, p. 1/19
[3] McNally, R. N., F. I. Peters, P. H. Ribbe: J. Am. Ceram. Soc. 44 (1961) No. 1, p. 491/3
[4] Riley, B.: Rev. Int. Hautes Tempér. et Réfract. 3 (1966) No. 3, p. 327/36
[5] Panek, Z.: Silikaty /Praque/ 23 (1979) No. 2, p. 97/102
[6] Hlavac, J.: Pure Appl. Chem. 54 (1982) No. 3, p. 681/8
[7] Hallstedt, B.: CALPHAD 17 (1993) No. 3, p. 281/6

Mn-O

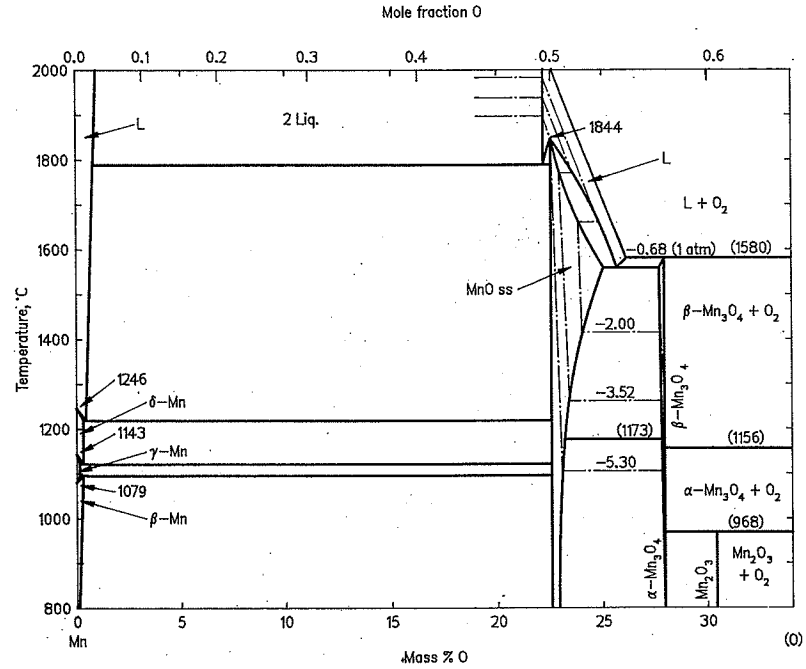


Fig. 3.10. Mn-O phase diagram (up to 35 mass % O) at 1 atm total pressure after Trömel et al. [1] based on their own investigations and earlier work by Hahn, Muan [2], Hed, Tannhauser [3], Schmahl, Hennings [4], and with the stoichiometry of the Mn_3O_4 phase as reported recently by Keller, Dieckmann [5]. The light dash-dot lines show the oxygen isobars (log pO_2, atm). The melting point of MnO (1844 °C on ITS-90) has been adopted from Schenck et al. [6]. The higher melting point of MnO (1875 °C) and incongruent decomposition to two liquids were reported by Oeters et al. [7]. According to Jacob [8], MnO melts congruently at 1830 °C (in vacuum). The decomposition temperature of Mn_3O_4 at 1580 °C was reported by Trömel at al. [1]. Previously, congruent melting of Mn_3O_4 has been reported by Hahn, Muan [2] and Hed, Tannhauser [3]. According to Schmahl, Hennings [4], that the congruent melting of Mn_3O_4 could be observed only at elevated pressures. For additional contributions to the Mn-O system, see also Schwerdtfeger, Muan [9], Shenouda, Aziz [10], Fix et al. [11], Huebner, Sato [12], Bransky, Tallan [13], Arabski, Carel [14], Schürmann, Bannenberg [15] and Keller, Dieckmann [16]. Recently, a thermodynamic assessment and calculated phase diagram of the Mn-O system has been published by Wang, Sundman [17].

References

[1] Trömel, G., W. Fix, K. Koch, F. Schaberg: Erzmetall 29 (1976) No. 5, p. 234/7
[2] Hahn, W. C., A. Muan: Am. J. Sci. 258 (1960) No. 1, p. 66/78
[3] Hed, A. Z., D. S. Tannhauser: J. Electrochem. Soc. 114 (1967) No. 4, p. 314/8
[4] Schmahl, N., D. F. K. Hennings: Arch. Eisenhüttenwes. 40 (1969) No. 5, p. 395/9
[5] Keller, M., R. Dieckmann: Ber. Bunsenges. Phys. Chem., 89 (1985), p. 1095/104
[6] Schenck, H., M. G. Frohberg, R. Nünninghoff: Arch. Eisenhüttenwes. 35 (1964) No. 4, p. 269/77
[7] Oeters, F., K. Koch, R. Scheel, U. Nölle: Arch. Eisenhüttenwes. 48 (1977) No. 9, p. 475/80
[8] Jacob, K. T.: Can. Metall. Q. 20 (1981) No. 1, p. 89/92
[9] Schwerdtfeger, K., A. Muan: Trans. Metall. Soc. AIME 238 (1967) No. 8, p. 1114/9
[10] Shenouda, F., S. Aziz: J. Appl. Chem. 17 (1967) No. 19, p. 258/62
[11] Fix, W., H. E. Wiemer, H. J. Tolkemit: Arch. Eisenhüttenwes. 40 (1969) No. 3, p. 215/21
[12] Huebner, J. S., M. Sato: Am. Mineral. 55 (1970) No. 5-6, p. 934/52
[13] Bransky, I.; N. M. Tallan: J. Electrochem. Soc. 118 (1971) No. 5, p. 788/93
[14] Arabski, J., C. Carel: Bull. Soc. Sci. Bretagne 55 (1983) No. 1-4, p. 121/6
[15] Schürmann, E., N. Bannenberg: Arch. Eisenhüttenwes. 55 (1984) No. 8, p. 349/58
[16] Keller, M., R. Dieckmann: Ber. Bunsenges. Phys. Chem., 89 (1985), p. 883/93
[17] Wang, M., B. Sundman: Metall. Trans. B 23B(1992) No. 12, p. 821/31

Na-O

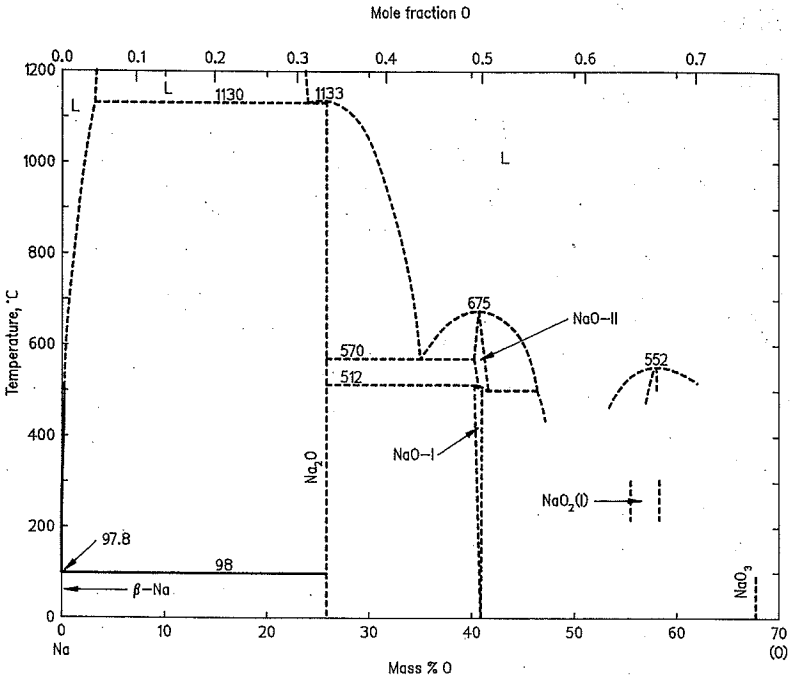


Fig. 3.11. Na-O phase diagram (up to 70 mass % O) as assessed by Wriedt [1]. The melting point of Na_2O after Bouaziz et al. [2], adopted in the assessment by Wriedt [1], is 1133 °C on the ITS-90. The polymorphic transformations of Na_2O at 750 and 970 °C reported by Bouaziz et al. [2] have not been confirmed in later studies. For a detailed discussion of the system and numerous standard references, see Wriedt [1].

References

[1] Wriedt, H. A.: Bull. Alloy Phase Diagrams 8 (1987) No. 3, p. 234/46

[2] Bouaziz, R., G. Papin, A.-P. Rollet: C. R. Acad. Sci., 262C (1966), p. 1051/4

Ni-O

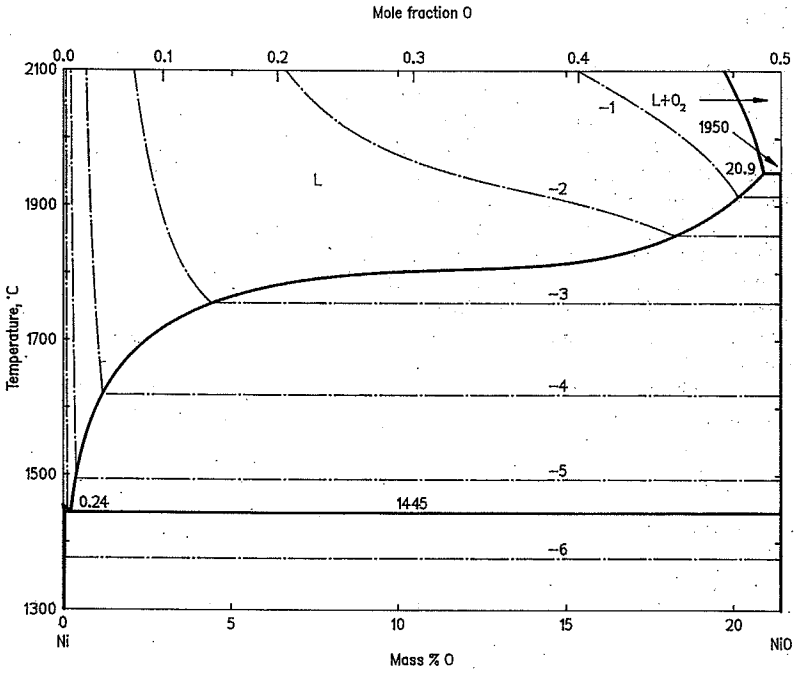


Fig. 3.12. Ni-NiO phase diagram with oxygen isobars (log pO_2, atm), as calculated by Kowalski, Spencer [1]. For experimental information concerning phase equilibria and thermodynamic of the system N-NiO, see the compilation by Neumann et al. [2] and also thermodynamic assessment by Taylor, Dinsdale [3]. The melting point of NiO after von Wartenberg et al. [4], when adjusted to ITS-90, is 1957 °C. From thermodynamic assessment of the system by Kowalski, Spencer [1] however, results an incongruent decomposition of NiO at 1950 °C. The restricted miscibility gap in the liquid has been modelled previously by Litvinov et al. [5] and recently by Taylor, Dinsdale [3].

References

[1] Kowalski, M, P. J. Spencer: submitted for publication in CALPHAD, (1994)

[2] Neumann, J. P., T. Zhong, Y. A. Chang: Bull. Alloy Phase Diagrams 5 (1984) No. 2, p. 141/4

[3] Taylor, J. R., A. T. Dinsdale: Z. Metallkd. 81 (1990) No. 5, p. 354/65

[4] von Wartenberg, H. V., H. J. Reusch, E. Saran E: Z. Anorg. Allg. Chem. 230 (1937) No. 3, p. 257/76

[5] Litvinov, S. L., T. S. Tsemekhman, B. P. Burylev, L V. Bochkova: Izv. Vyssh. Uchebn. Zaved., Tsvetn. Metall. (1982) No. 2, p. 30/4

Si-O

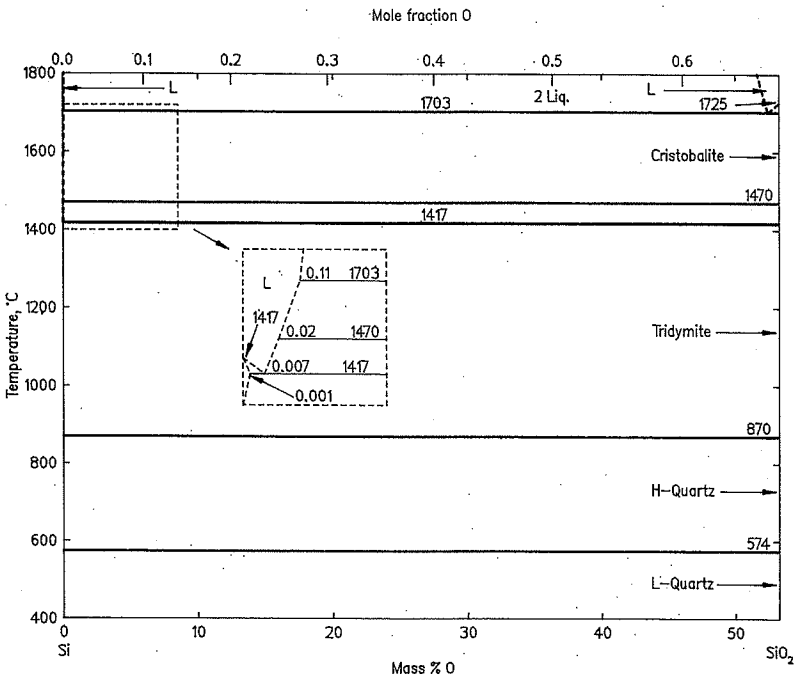


Fig. 3.13. Si-SiO_2 phase diagram as assessed by Wriedt [1], based mainly on the work of Johnson, Muan [2], with tridymite as the stable modification of pure SiO_2. The melting point of SiO_2 after Greig [3] (1713 °C on the Geophysical Temp. Scale), adjusted to ITS-90, is 1725 °C. A detailed discussion of the system, with numerous standard references, is given in the assessment by Wriedt [1]. For the recent thermodynamic assessment of the Si-O system and calculated phase diagram, see Hallstedt [4].

References

[1] Wriedt, H. A.: Bull. Alloy Phase Diagrams 11 (1990) No. 1, p. 43/61
[2] Johnson, R. E., A. Muan: J. Am. Ceram. Soc. 51 (1968) No. 8, p. 430/3
[3] Greig, J. W.: Am. J. Sci., 5-th Ser. 13 (1927) No. 73, p. 1/154
[4] Hallstedt, B.: CALPHAD 16 (1992) No. 1, p. 53/61

Ti-O

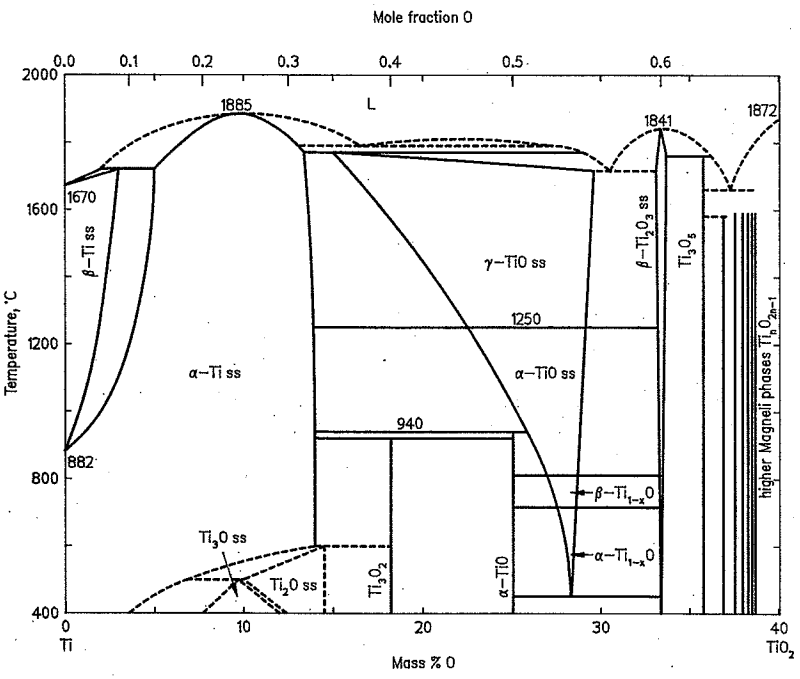


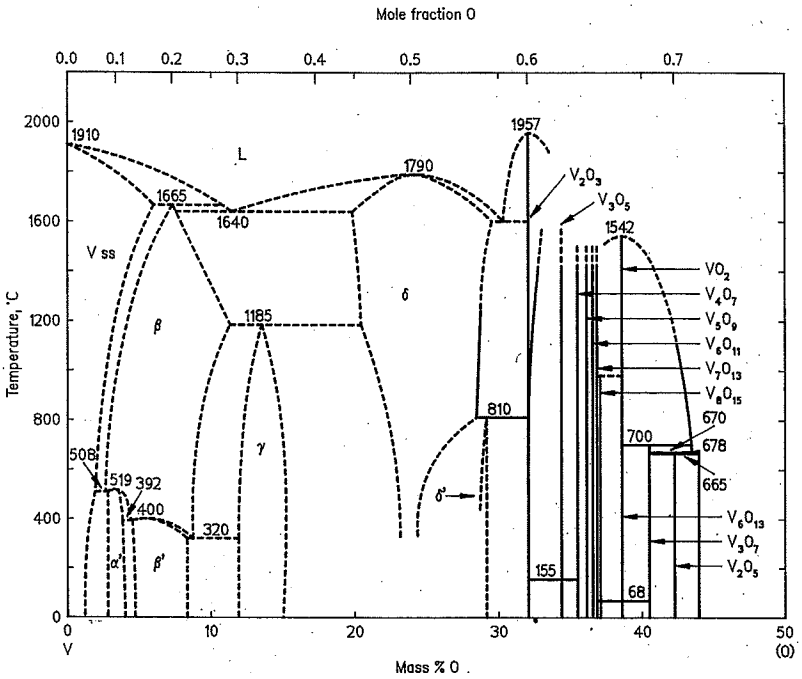
Fig. 3.14. Ti-TiO_2 phase diagram as assessed by Murray, Wriedt [1]. For a discussion of the system and numerous standard references, see 1). The melting points of TiO_2 and Ti_2O_3 adopted by Murray, Wriedt [1] after Brauer, Littke [2] and Wahlbeck, Gilles [3], when adjusted to ITS-90, are 1872 and 1841 °C, respectively. For recent thermodynamic assessments and calculated phase diagrams of the Ti-O and Ti_2O_3-TiO_2 system, see Pajunen, Kivalathi [4] and Eriksson, Pelton [5] respectively.

References

[1] Murray, J. L., H. A. Wriedt: Bull. Alloy Phase Diagrams 8 (1987) No. 2, p. 148/65
[2] Brauer, G., W. Littke: J. Inorg. Nucl. Chem. 16 (1960), p. 67/76
[3] Wahlbeck, P. G., P. W. Gilles: J. Am. Ceram. Soc. 49 (1966) No. 4, p. 180/3
[4] Pajunen, M., J. Kivalathi: Z. Metallkde. 83 (1992) No. 1, p.17/20
[5] Eriksson, G., A. D. Pelton: Metall. Trans. B 24B (1993), p. 795/805

V-O

Fig. 3.15. V-O phase diagram (up to 50 mass % O) at 1 atm total pressure as assessed by Wriedt [1]. For a discussion of the system and numerous standard references, see [1].

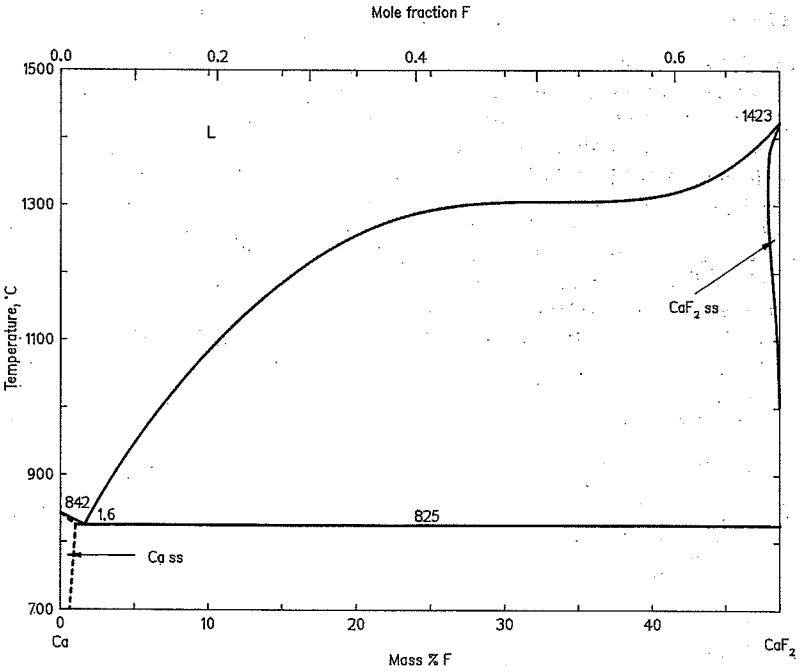


References

[1] Wriedt H. A.: Bull. Alloy Phase Diagrams 10 (1989) No. 3, p. 271/7

Ca-F

Fig. 3.16. Ca-CaF_2 phase diagram after Lichter, Bredig [1] and Dworkin, Bredig [2]. The small miscibility gap reported previously by Rogers et al. [3] is not confirmed. The melting point of CaF_2 at 1423 °C was determined by Kojima, Masson [4].



References

[1] Lichter, B. D., M. A. Bredig: J. Electrochem. Soc. 112 (1965) No. 5, p. 506/10

[2] Dworkin, A. S., M. A. Bredig: J. Phys. Chem. 75 (1971) No. 15, p. 2340/4

[3] Rogers, P. S., J. M. Tomlinson, F. D. Richardson: Proceedings of the International Symposium on the Physical Chemistry of Process Metallurgy, Pittsburgh 1959, Ed.: Interscience Publishers Inc. New York (1961), p. 909/25

[4] Kojima, H., C. R. Masson: Canad. J. Chem. 47 (1969), p. 4221/8

Fe-S

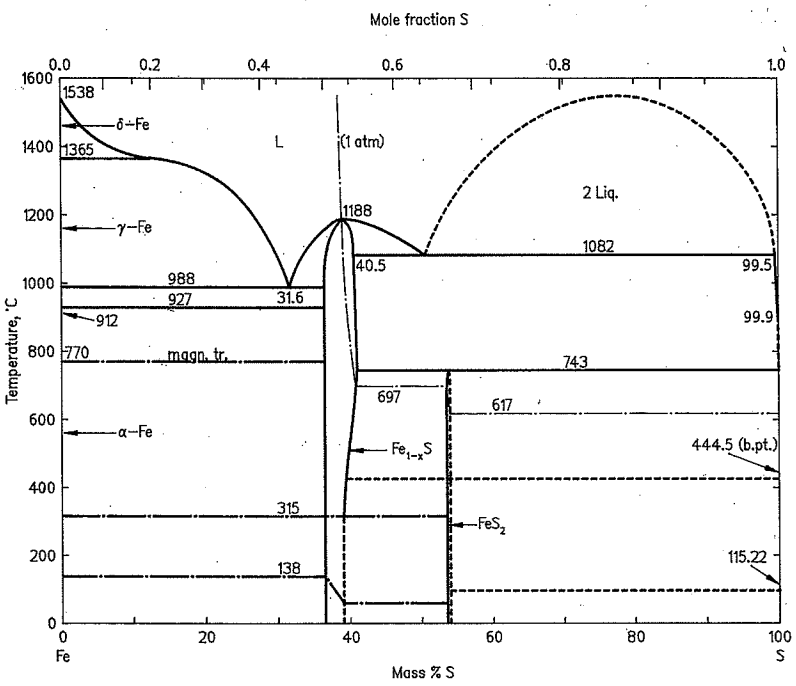


Fig. 3.17. Fe-S phase diagram as assessed by Kubaschewski [1], with miscibility gap calculated by Fernandez Guillermet et al. [2]. A thermodynamic assessment of the system has also been reported by Chuang et al. [3]. For numerous standard references, see original papers [1-3].

References

[1] Kubaschewski, O.: Iron-Binary Phase Diagrams, Ed.: Springer Verlag, Berlin, Heidelberg, New York, Verlag Stahleisen mbH, Düsseldorf (1982)

[2] Fernandez Guillermet, A., M. Hillert, B. Jansson, B. Sundman: Metall. Trans. B 12B (1982) No. 4, p. 745/54

[3] Chuang, Y. Y., K. C. Hsieh, Y. A. Chang: Metall. Trans. B 16B (1985) No. 6, p. 277/85

Mn-S

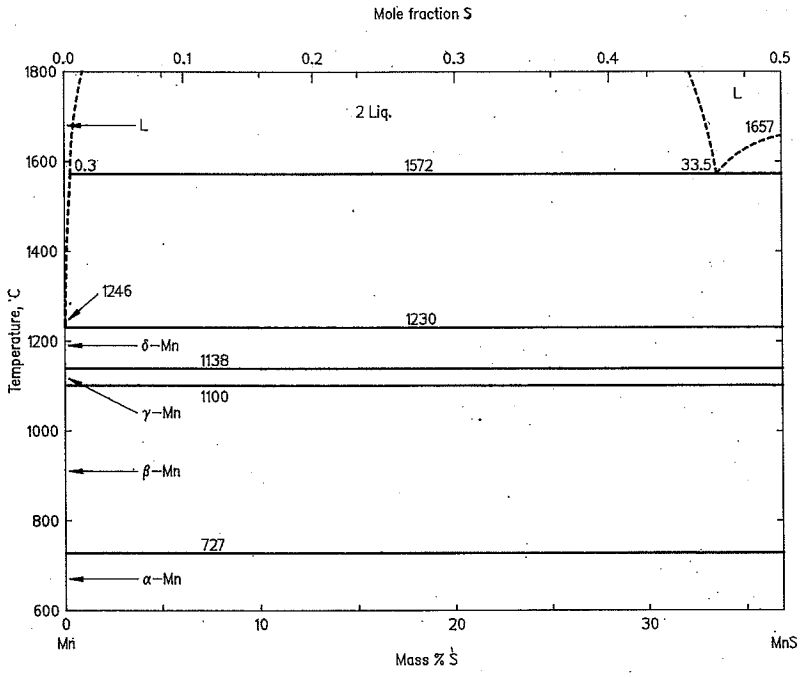


Fig. 3.18. Mn-MnS phase diagram after Vogel, Hotop [1] with revisions relating to the melting point of MnS and the monotectic temperature by Staffansson [2]. The melting point and transformation temperatures of pure Mn are adopted from Gokcen [3].

References

[1] Vogel, R., W. Hotop: Arch. Eisenhüttenwes. 11 (1937) No. 1, p. 41/54

[2] Staffansson, L.-I.: Metall. Trans. B 7B (1976) No. 3, p. 131/4

[3] Gokcen, N. A.: Bull. Alloy Phase Diagrams 10 (1989) No. 4, p. 313

3.2.2 Binary oxide systems

Al_2O_3-CaO

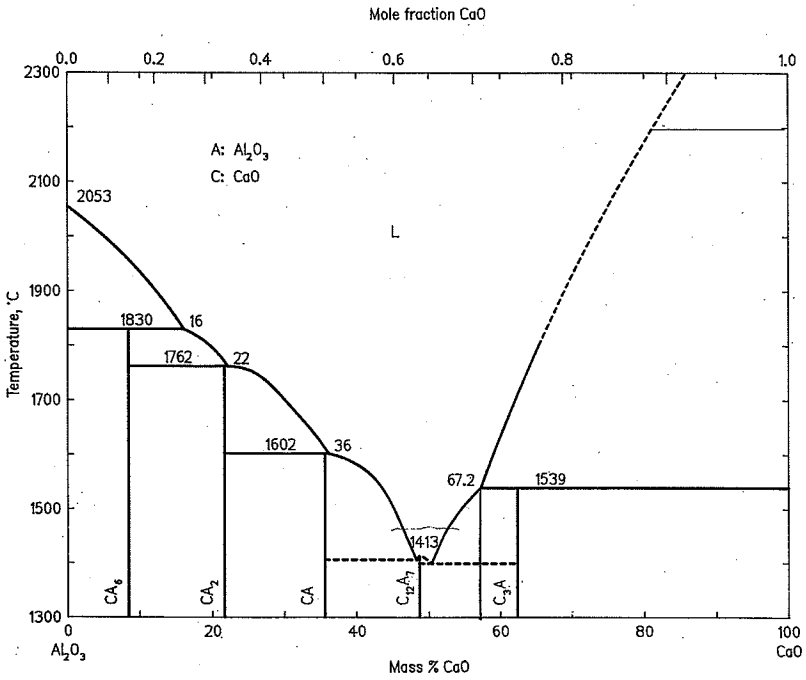


Fig. 3.19. Al_2O_3-CaO phase diagram after Nurse et al. [1, 2]. For similar versions of the system with incongruent melting of $CaO{\cdot}Al_2O_3$ and $CaO{\cdot}2Al_2O_3$, see also Imlach, Glasser [3] and Chatterjee, Zhmoidin [4]. In contrast, congruent melting of these compounds has been reported by Rankin, Wright [5], Rolin, Thanh [6], Rao [7] and accepted recently in the thermodynamic assessment of the system by Hallstedt [8]. The $12CaO{\cdot}7Al_2O_3$ phase reported previously by Nurse et al. [2] as stabilized by OH groups, has been definitely found by Jeevaratnam et al. [9], Imlach et al. [10], Cockayne, Lent [11] and Gladkiy at al. [12] to exist in the anhydrous state. According to Imlach et al. [10], the $12CaO{\cdot}7Al_2O_3$ phase is non-stoichiometric, with a small excess of oxygen, and the minimum oxygen partial pressure in the atmosphere leading to the formation of this phase is $10^{-7.3}$ atm (Gladkiy at al. [12]). The melting point of the $12CaO{\cdot}7Al_2O_3$ phase, 1413 °C, has been taken from Cockayne, Lent [11]. The liquidus relations in the vicinity of $12CaO{\cdot}7Al_2O_3$, as well as the location of both eutectics, have been drawn schematically in conformity with the $3CaO{\cdot}Al_2O_3$- and $CaO{\cdot}Al_2O_3$-liquidus determined by Nurse et al. [2]. For recent thermodynamic assessment of the system and calculated phase diagram, see also Eriksson, Pelton [13].

References

[1] Nurse, R. W., J. H. Welch, A. J. Majumdar: Trans. J. Br. Ceram. Soc. 64 (1965) No. 2, p. 409/18
[2] Nurse R. W., Welch J. H., Majumdar A. J.: Trans. J. Br. Ceram. Soc. 64 (1965) No. 6, p. 323/32
[3] Imlach, J. A., F. P. Glasser: Trans. J. Br. Ceram. Soc. 67 (1968) No. 12, p. 581/609
[4] Chatterjee, A. K., G. I. Zhmoidin: J. Mater. Sci. 7 (1972) No. 1, p. 93/7
[5] Rankin, G. A., F. E. Wright: Am. J. Sci., 4th Ser. 39 (1915), p. 1/79
[6] Rolin, M., P. H. Thanh: Rev. Int. Hautes Tempér. et Réfract. 2 (1965) No. 2, p. 175/85
[7] Rao, M. R.: J. Am. Ceram. Soc. 51 (1968) No. 1, p. 50/4
[8] Hallstedt, B.: J. Am. Ceram. Soc. 73 (1990) No. 1, p. 15/23
[9] Jeevaratnam, J., F. P. Glasser, L. S. D. Glasser: J. Am. Ceram. Soc. 47 (1964) No. 2, p. 105/6
[10] Imlach, J. A.: Cem. Concr. Res. 1 (1971), p. 57/61
[11] Cockayne, B., B. Lent: J. Cryst. Growth 46 (1979), p. 467/73
[12] Gladkiy, V. N., I. S., Kulikov, I. V., Ostrovskaya, A. A., Telegin: Izv. Akad. Nauk SSSR, Metal. (1980), p. 63/7
[13] Eriksson, G., A. D. Pelton: Metall. Trans. B 24B (1993), p. 807/15

Al_2O_3-Cr_2O_3

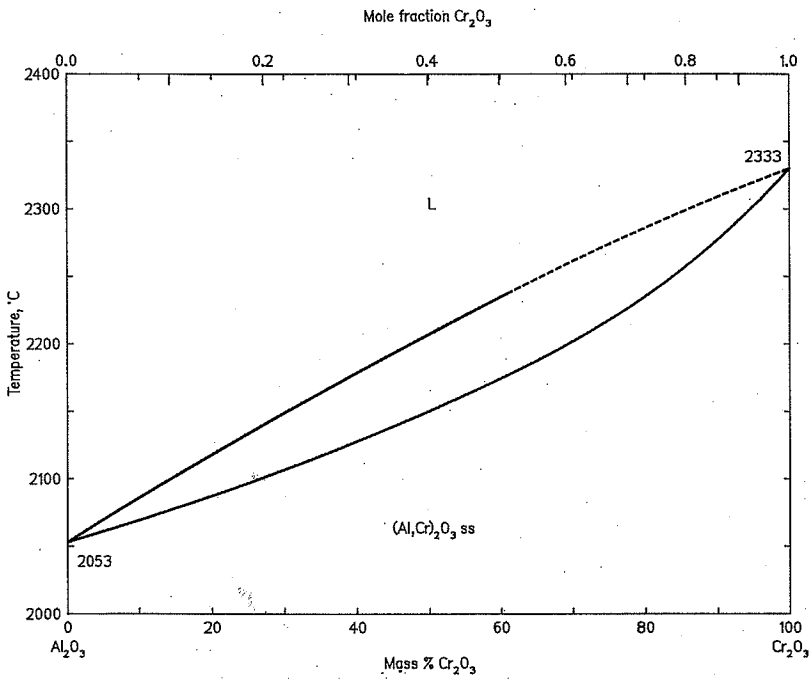
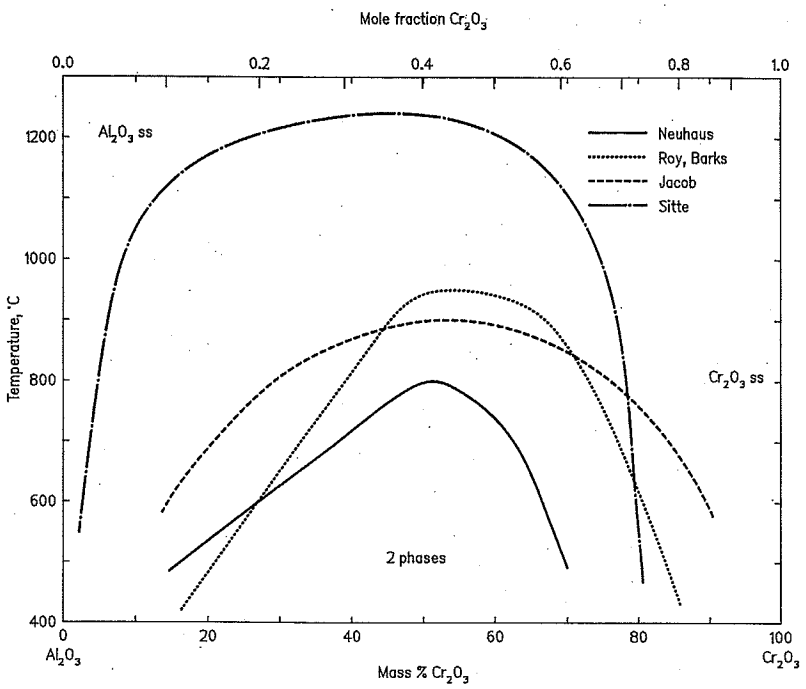


Fig. 3.20. Liquid-solid equilibria in the Al_2O_3-Cr_2O_3 system after Bunting [1].

Fig. 3.21. Miscibility gap in the Al_2O_3-Cr_2O_3 system after Roy, Barks [2] and Neuhaus [3] at elevated pressures and after Jacob [4] and Sitte [5] at normal pressure as derived from thermodynamic measurements. According to the thermodynamic analysis of the system made by Chatterjee et al. [6], the pressure-dependence of the critical temperature is very small (945 to 989 °C for pressures between 1 bar and 50 kbar). Liquidus temperatures in the ternary system Al_2O_3-Cr_2O_3-Cr have been reported by Schmitt et al. [7].



References

[1] Bunting, E. N.: J. Res. Nat. Bur. Stand., RP 317 6 (1931) No. 6, p. 947/9

[2] Roy, D. M., R. E. Barks: Nature /London/ 235 (1972) No. 58, p. 118/9

[3] Neuhaus, A.: The Physics and Chemistry of High Pressures, Ed.: Society of Chemical Industry, London, Gordon and Breach Inc., New York, (1963)

[4] Jacob, K. T.: J. Electrochem. Soc. 125 (1978) No. 2, p. 175/9

[5] Sitte, W.: Mater. Sci. Monogr. /React. Solids Pt. A/ 28A (1985), p. 451/6

[6] Chatterjee, N. D., H. Leistner, L Terhart, K. Abraham, R. Klaska: Am. Mineral. 67 (1982), p. 725/35

[7] Schmitt, T., G. Banik, B. Lux: Ber. Dtsch. Keram. Ges. 57 (1980) No. 4-5, p. 80/3

Al_2O_3-FeO_x

Fig. 3.22. Al_2O_3-FeO_n system in contact with iron, projected on the Al_2O_3-FeO section, after Fischer, Hoffmann [1]. See also Galakhov [2] for incongruent melting of $FeO{\cdot}Al_2O_3$. The solubility of $FeO{\cdot}Al_2O_3$ in the melt as determined by Rosenbach, Schmitz [3] is shown in the figure as a dash-dot line. Novokhatskii et al. [4] report the $FeO{\cdot}Al_2O_3$ phase to melt at 1820 °C, the eutectic between FeO_n and $FeO{\cdot}Al_2O_3$ to be located at 1310 °C and no mutual solubility to occur in the sub-system Al_2O_3-$FeO{\cdot}Al_2O_3$. For thermodynamic assessment of the system and calculated phase diagram, see Eriksson et al. [5].

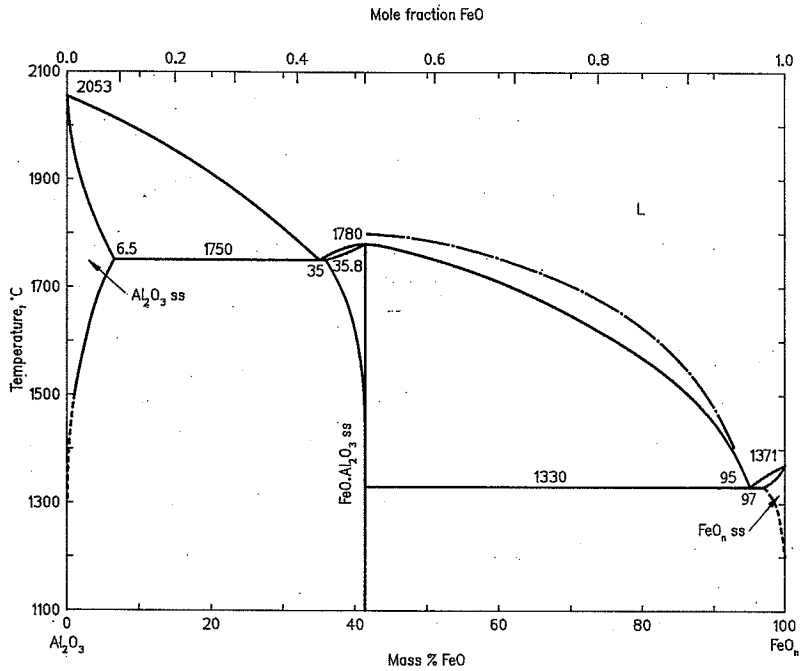


Fig. 3.23. Al_2O_3-FeO_x system in air after Muan, Gee [6], Muan [7] and Willshee, White [8] (phase relations above 1410 °C).

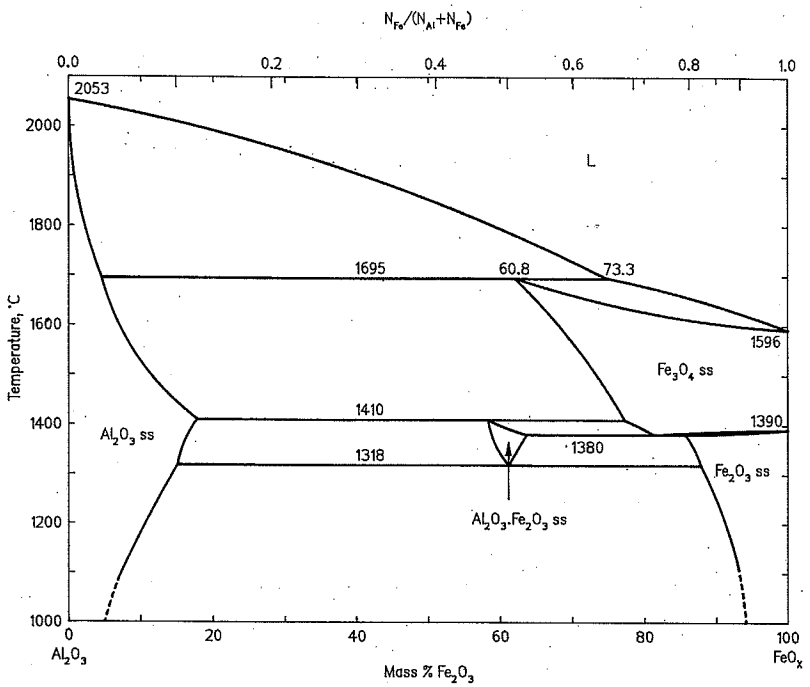
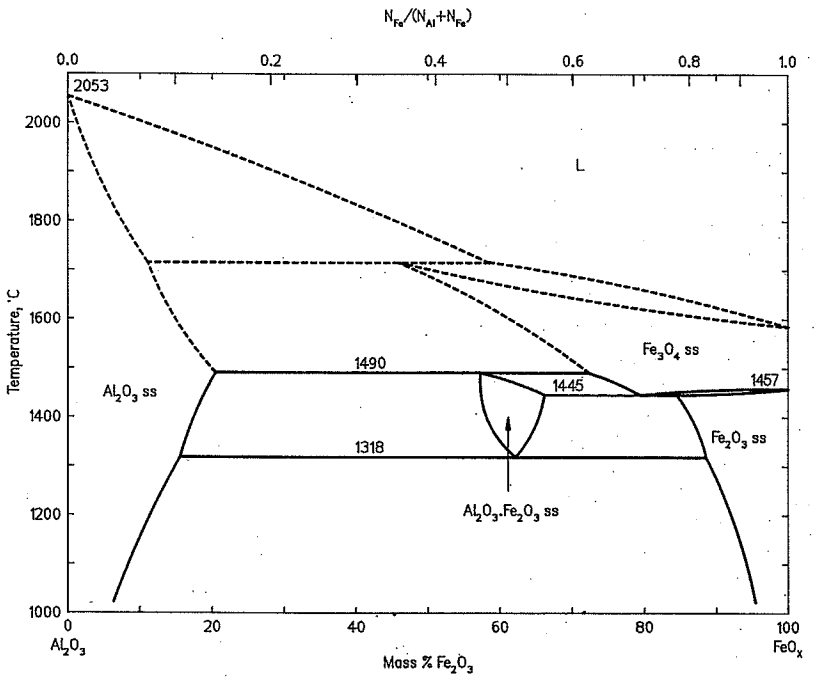


Fig. 3.24. Al_2O_3-FeO_x system at 1 atm O_2 pressure after Muan, Gee [6] and Muan [7].



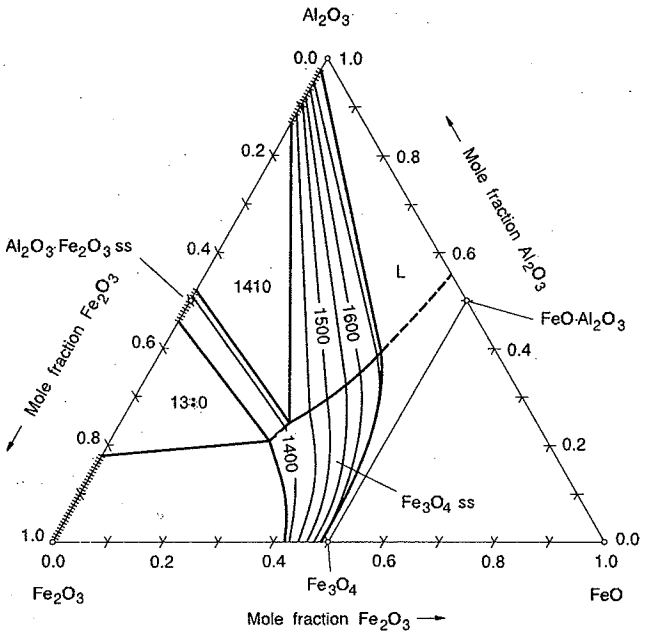


Fig. 3.25. Al_2O_3-FeO-Fe_2O_3 system in air after Willshee, White [8]. For isothermal sections between 900 and 1500 °C, see Richards, White [9], Atlas, Sumida [10] and Roiter [11].

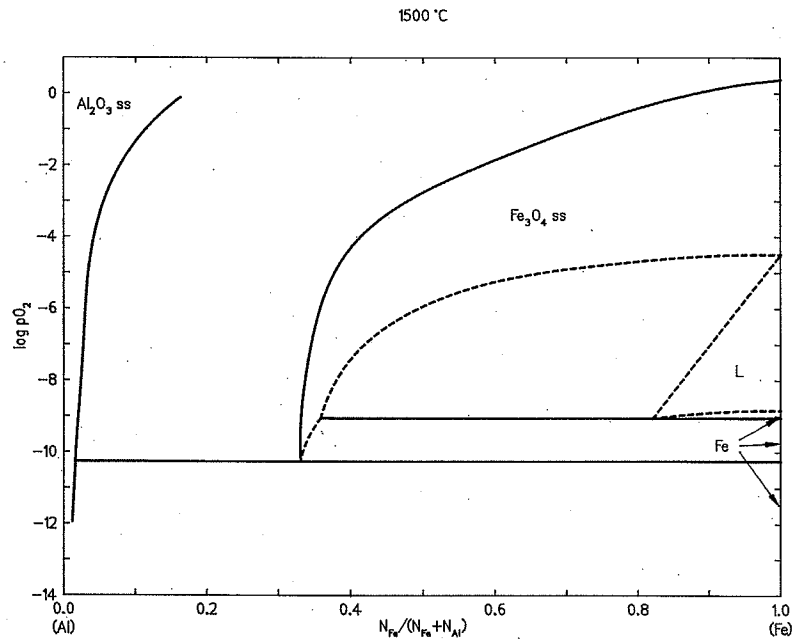


Fig. 3.26.

Fig. 3.27.

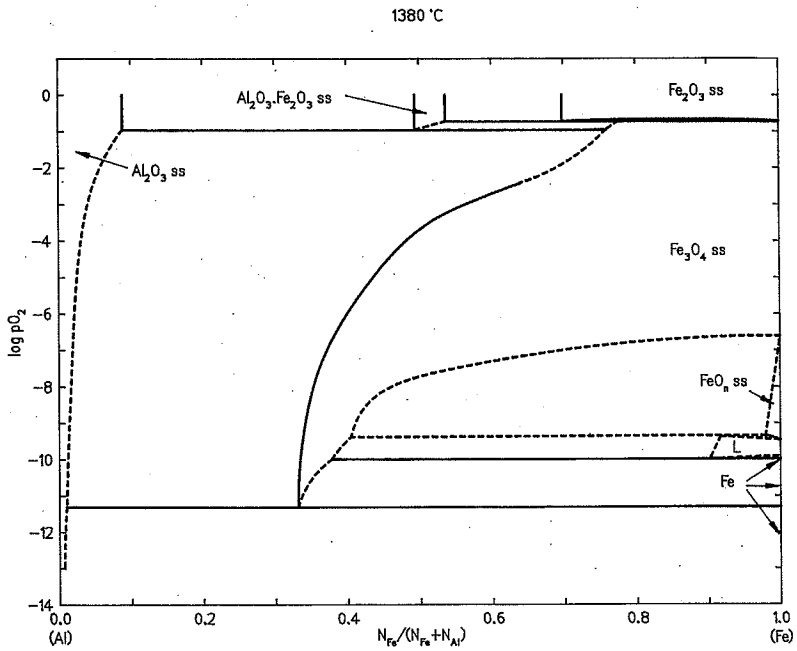
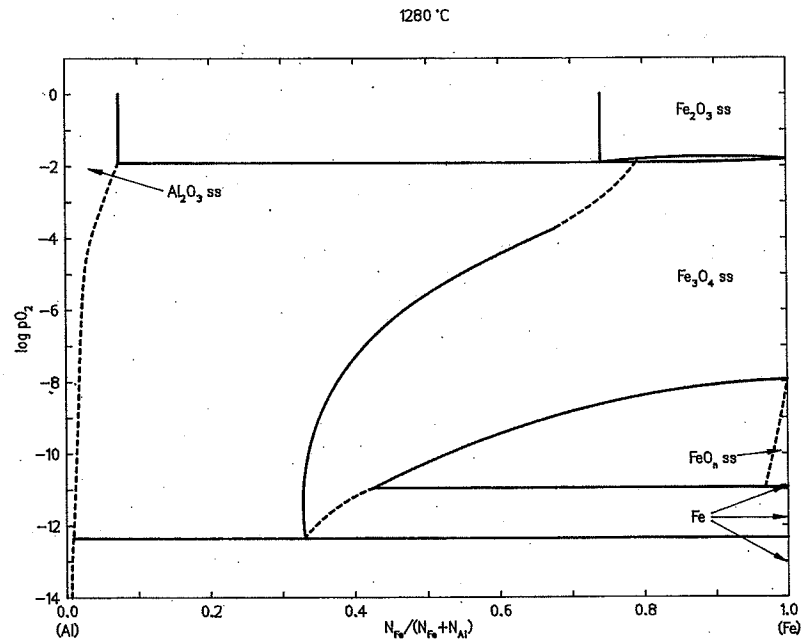


Fig. 3.28.



Figs. 3.26 to 3.28. Log pO_2 vs. $N_{Fe}/(N_{Al}+N_{Fe})$ phase diagrams for the system Al-Fe-O at 1500 °C, 1380 and 1280 °C after Meyers et al. [12] based on their own results and results by Fischer, Hoffmann [1], Muan, Gee [6], Atlas, Sumida [10] and Roiter [11].

For the Fe-rich region of the ternary system Al-Fe-O between 1500 and 1530 °C in air, see Elliot, Wright [13]; for the solubility of Al_2O_3 in Al-Fe-O melts, see Liang [14]. The thermodynamics of the system and deoxidation equilibria have been reported recently by Schürmann, Bannenberg [15].

References

[1] Fischer, W. A., A. Hoffmann: Arch. Eisenhüttenwes. 27 (1956) No. 5, p. 343/6

[2] Galakhov, F. Ya.: Izv. Akad. Nauk SSSR, Otdel. Khim. Nauk (1957) No. 5, p. 525/31

[3] Rosenbach, K., J. A. Schmitz: Arch. Eisenhüttenwes. 45 (1974) No. 12, p. 843/7

[4] Novokhatskii, I. A., B. V. Belov, A. V. Gorokh, A. A. Savinskaya: Zh. Fiz. Khim. 39 (1965) No. 11, p.2806

[5] Eriksson, G., P. Wu, A. D. Pelton: CALPHAD 17 (1993) No. 2. p. 189/207

[6] Muan, A., C. L. Gee: J. Am. Ceram. Soc. 39 (1956) No. 6, p. 207/214

[7] Muan, A.: Am. J. Sci. 256 (1958), p. 413/22

[8] Willshee, J. C., J. White: Trans. J. Br. Ceram. Soc. 67 (1968), p. 271/84

[9] Richards, R. G., J. White: Trans. J. Br. Ceram. Soc. 53 (1954), p. 233/70

[10] Atlas, L. M., W. K. Sumida: J. Am. Ceram. Soc. 41 (1958) No. 5, p. 150/60

[11] Roiter, B. D.: J. Am. Ceram. Soc. 47 (1974) No. 10, p. 509/11

[12] Meyers, C. E., T. O. Mason, W. T. Petuskey, J. W. Halloran, H. K. Bowen: J. Am. Ceram. Soc. 63 (1980) No. 11-12, p. 659/63

[13] Elliot, J. F., J. K. Wright: Can. Metall. Q. 11 (1972) No. 4, p. 573/584

[14] Liang, W. W.: Z. Metallkd. 73 (1982) No. 6, p. 369/75

[15] Schürmann, E., N. Bannenberg: Arch. Eisenhüttenwes. 55 (1984) No. 9, p. 409/14

Al_2O_3-K_2O

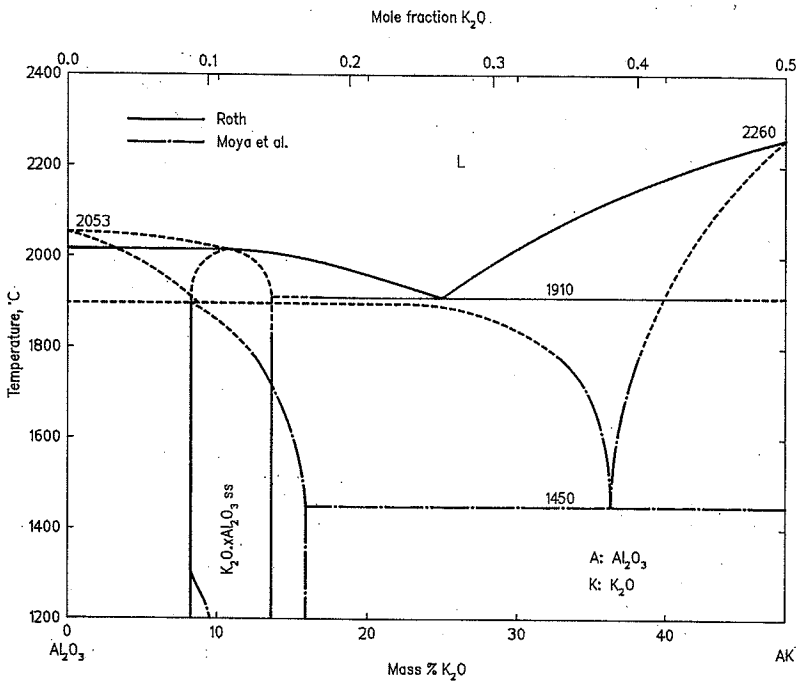


Fig. 3.29. Sub-system Al_2O_3-$Al_2O_3 \cdot K_2O$ after Roth [1, 2] and Moya et al. [3] with a much lower eutectic temperature (dash-dot lines). For thermodynamic assessment of the system and calculated phase diagram, see Eriksson et al. [4]. Thermodynamic of the system has also been discussed by Eliezer, Howald [5].

References

[1] Roth, R. S.: Adv. Chem. Ser., 186 /Solid State Chem.: Contemp. Overview/ (1980), p. 391/408
[2] Roth, R. S., J. R. Dennis, H. F. McMurdie: Phase Diagram for Ceramist, Vol. VI The American Ceramic Society, Westerville, Ohio, (1987)
[3] Moya, J. S., E. Criado, S. De Aza: J. Mater. Sci. 17 (1982) No. 8, p. 2213/17
[4] Eriksson, G., P. Wu, A. D. Pelton: CALPHAD 17 (1993) No. 2. p. 189/207
[5] Eliezer, I., R. A. Howald: High Temp. Sci. 10 (1978) No. 1, p. 1/16

Al_2O_3-MgO

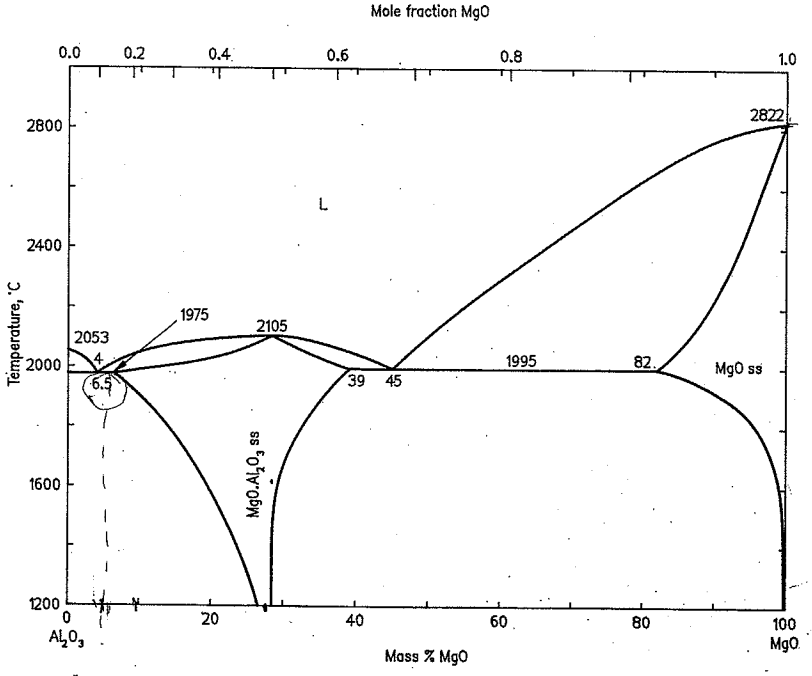


Fig. 3.30. Al_2O_3-MgO phase diagram based mainly on the results of Rankin, Merwin [1], Alper et al. [2] (sub-system MgO-$MgO \cdot Al_2O_3$) and Viechnicki at al. [3] (sub-system Al_2O_3-$MgO \cdot Al_2O_3$). Phase boundaries for the solid state have been re-investigated by Roy, Coble [4] and Ando, Momoda [5] (solubility of MgO in Al_2O_3), Stubican, Roy [6], Henriksen, Kingery [7] and Mori [8] (solubility of Al_2O_3 in MgO), Roy et al. [9], Shirasuka, Yamaguchi [10], Viertel, Seifert [11] and Panda, Raj [12] ($MgO \cdot Al_2O_3$ phase boundary). Particularly the solubility of Al_2O_3 in MgO determined by Alper et al. [2] was confirmed with minor changes in [6-8]. After Ando, Momoda [5] the maximum solubility of MgO in Al_2O_3 does not exceed 0.001 mass % MgO. A solubility of up to 6 mole % MgO in $MgO \cdot Al_2O_3$ at 1700 °C has been reported by Greskovich, Stubican [13]. The further Al_2O_3-rich solution phase ($13Al_2O_3 \cdot MgO$) with the α-Al_2O_3 structure has been discussed and reported to exist in the vicinity of the melting point of Al_2O_3 by and Lejus, Collongues [14] and Lejus [15]. Recently, thermodynamic evaluations of the system have been presented by Hallstedt, Hillert [16], Howald, Roy [17] Hallstedt [18] and Eriksson et al. [19]. In the last assessment made by Hallstedt [18], a minimum on the $MgO \cdot Al_2O_3$ liquidus curve instead of a eutectic between $MgO \cdot Al_2O_3$ and Al_2O_3, has been proposed.

References

[1] Rankin, G. A., E. H. Merwin: J. Am. Chem. Soc. 38 (1916), p. 568/88
[2] Alper, A. M., R. N. McNally, P. H. Ribbe, R. C. Doman: J. Am. Ceram. Soc. 45 (1962) No. 6, p. 263/8
[3] Viechnicki, D., F. Schmidt, J. W. McCauley: J. Am. Ceram. Soc. 57 (1974) No. 1, p. 47/8
[4] Roy, S. K., R. I. Coble: J.Am. Ceram. Soc. 51 (1968) No. 1, p. 1/6
[5] Ando, K., M. Momoda: Adv. Ceram. /Nonstoichiom. Comp./ 23 (1987), p. 137/47
[6] Stubican, V. S., R. Roy: J. Phys. Chem. Solids 26 (1965) No. 8, p. 1293/7
[7] Henriksen, A. F., W. D. Kingery: Ceramurgia Int. 5 (1979) No. 1, p. 11/17
[8] Mori, T.: Yogyo Kyokai Shi 90 (1982) No. 9, p. 551/2
[9] Roy, D. M., R. Roy, E. F. Osborn: Am. J. Sci. 251 (1953), p. 337/61
[10] Shirasuka, K., G. Yamaguchi: Yogyo Kyokai Shi. 82 (1974) No. 12, p. 650/3
[11] Viertel, H. U., F. Seifert: N. Jb. Mineral. Abh. 140 (1980) No. 1, p. 89/101
[12] Panda, P. C., R. Raj: J. Am. Ceram. Soc. 69 (1986) No. 5, p. 365/73
[13] Greskovich, C., V. S. Stubican: J. Am. Ceram. Soc. 51 (1968) No. 1, p. 42/6
[14] Lejus, A. M., R. Collongues: C. R. Acad. Sci., Ser. C 254 (1962) No. 1, p. 2780/1
[15] Lejus, A. M.: Rev. Int. Hautes Tempér. et Réfract. 1 (1964), p. 53/95
[16] Hallstedt, B., M. Hillert: CALPHAD 14 (1990) No. 1, p. 23/6
[17] Howald, R. A., N. B. Roy: CALPHAD 15 (1991) No. 2, p. 159/72
[18] Hallstedt, B.: Report TRITA-MAC-0399, Royal Institute of Technology, Stockholm, (1989)
[19] Eriksson, G., P. Wu, A. D. Pelton: CALPHAD 17 (1993) No. 2. p. 189/207

Al_2O_3-MnO_x

Fig. 3.31. Al_2O_3-MnO system in contact with metallic melts after Jacob [1]. A similar version of the system has been reported previously by Novokhatskii et al. [2]. After Fischer, Bardenheuer [3] the eutectic between $MnO{\cdot}Al_2O_3$ and MnO is located at 1580 °C. Earlier, a larger solubility of $MnO{\cdot}Al_2O_3$ in MnO-rich melts was reported by Oelsen, Heynert [4]. For thermodynamic assessment of the system and calculated phase diagram, see Eriksson et al. [5].

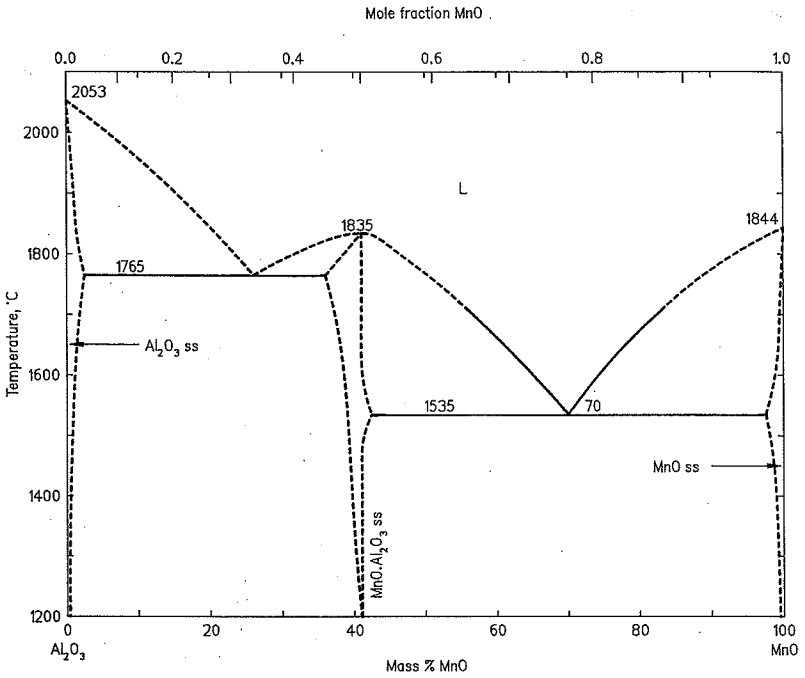
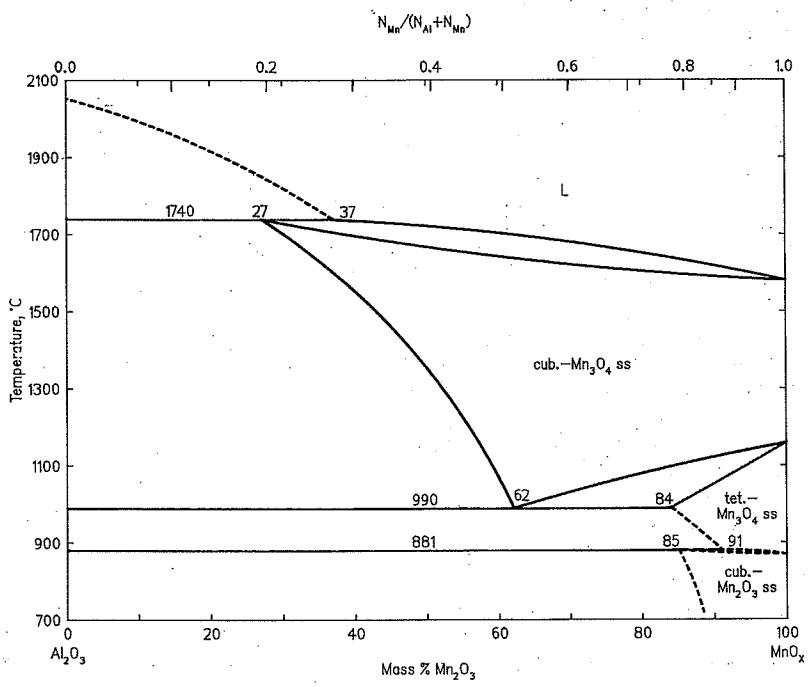


Fig. 3.32. Al_2O_3-MnO_x system in air after Ranganathan et al. [6].



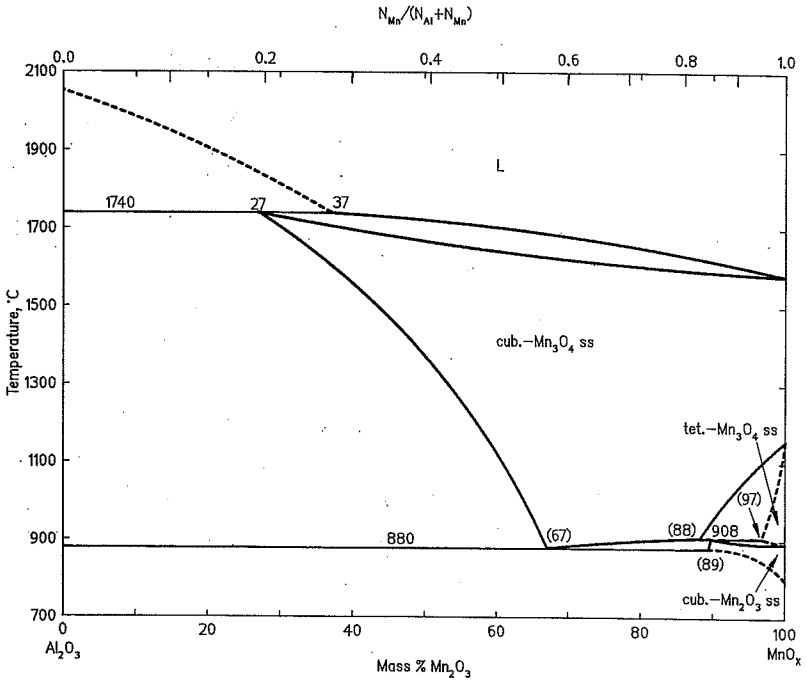


Fig. 3.33. Al_2O_3-MnO_x system in air after Dekker, Rieck [7].

An isothermal section through the ternary system Al-Mn-O at 930 °C has been reported by Hennings [8].

References

[1] Jacob, K. T.: Can. Metall. Q., 20 (1981) No. 1, p. 89/92
[2] Novokhatskii, I. A., A. A. Lenev, A. A. Savinskaya, A. V. Gorokh: Zh. Neorg. Khim. 11 (1966) No. 2, p. 231/2
[3] Fischer, W. A., P. W. Bardenheuer: Arch. Eisenhüttenwes. 39 (1968) No. 9, p. 637/43
[4] Oelsen, W., G. Heynert: Arch. Eisenhüttenwes. 26 (1955) No. 10, p. 567/75
[5] Eriksson, G., P. Wu, A. D. Pelton: CALPHAD 17 (1993) No. 2. p. 189/207
[6] Ranganathan, T., B. E. MacKean, A. Muan: J. Am. Ceram. Soc. 45 (1962) No. 6, p. 279/81
[7] Dekker, E. H. L. J., G. D. Rieck: Z. Anorg. Allg. Chem. 415 (1975) No. 1, p. 69/80
[8] Hennings, D. F. K.: Thesis, Saarbrücken (1967)

Al_2O_3-Na_2O

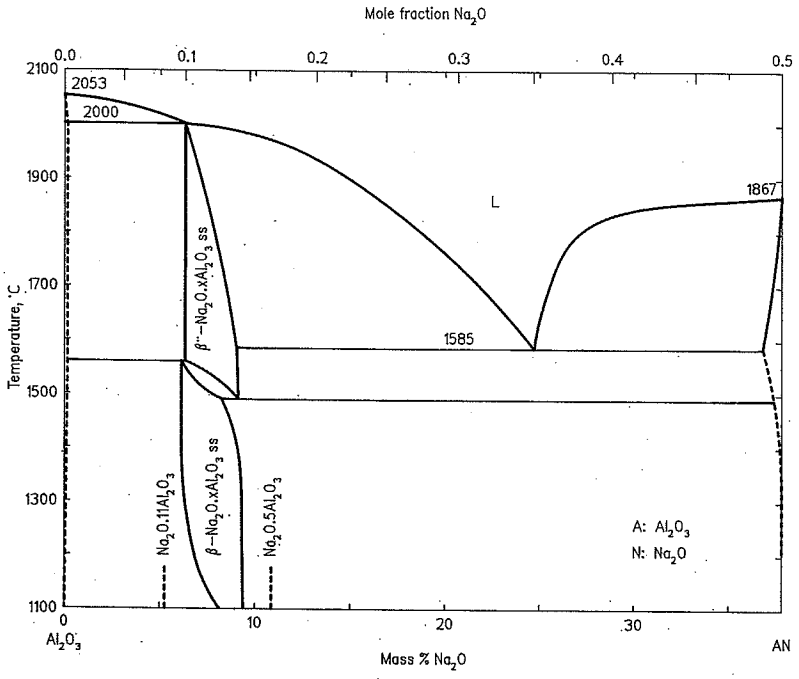


Fig. 3.34. Al_2O_3-Al_2O_3·Na_2O phase diagram.

The liquidus temperatures for the Na_2O·Al_2O_3- and for the Al_2O_3-rich regions of the system are taken from Weber, Venero [1] (quoted by Eliezer, Howald [2]) and from Rolin, Thanh [3] respectively. An estimated melting point of the Na_2O·Al_2O_3 phase, approx. 1850 °C, has been reported previously by Schairer, Bowen [4]. The version of the system with the ß- to ß"-Na_2O·xAl_2O_3 transformation located below the eutectic temperature is also supported by Ray, Subbarao [5]. Recently, the peritectic decomposition of ß" above 1680 °C has been reported by Aldén [6]. The phase equilibria involving the ß and ß" modifications, as well as the homogeneity ranges for both phases are drawn according to results reported by Scholder, Mansmann [7], Liebertz [8] and Le Cars et al. [9]. The maximum homogeneity range reported for the Na_2O·xAl_2O_3 solid solution extends from the Na_2O·5Al_2O_3 to the Na_2O·11Al_2O_3 composition [10]. As indicated by Le Cars et al. [9] and recently by Tomilov [11], the equilibrium state in the vicinity of the ß to ß" transformation seems to be very difficult to obtain because of the similar crystal structures of the two modifications and the disorder phenomena accompanying the transformation. A further metastable solid solution with the mullite structure, Na_2O·xAl_2O_3 (with x varying from 3 to 12), exists up to 1050 °C according to Elliot, Huggins [12]. The existence of this metastable solid solution has also been confirmed by Takahashi, Kuwabara [13, 14] and Plokhikh, Kaul [15]. For a previous evaluation and discussion of the Al_2O_3-Na_2O system, see DeVries, Roth [16]. Recently, the thermodynamics of the system was reviewed by Barsoum [17] and Eriksson et al. [18] and phase diagram has been calculated [18].

References

[1] Weber, N., A. F. Venero: 72nd Annual Meeting of the Am. Ceram. Soc., May 1970, Philadelphia, paper 5-JI-70, (1970)
[2] Eliezer, I., R. A. Howald: High Temp. Sci. 10 (1978) No. 1, p. 1/16
[3] Rolin, M., P. H. Thanh : Rev. Int. Hautes Tempér. et Réfract. 2 (1965) No. 2, p. 175/85
[4] Schairer, J. F., N. L. Bowen: Am. J. Sci. 254 (1956), p. 129/95
[5] Ray, K., E. C. Subbarao: Mater. Res. Bull. 10 (1975), p. 583/90
[6] Aldén, M.: Solid State Ionics 20 (1986) No. 1, p. 17/23
[7] Scholder, R., M. Mansmann: Z. Anorg. Allg. Chem. 321 (1963) No. 5-6, p. 246/61
[8] Liebertz, J.: Ber. Deut. Keram. Ges. 49 (1972) No. 9, p. 288/90
[9] Le Cars, Y., J. Théry, R. Collongues: C. R. Acad. Sci. 274C (1972) No. 1, p. 4/7
[10] Théry, J., D. Briancon: Rev. Int. Hautes Tempér. et Réfract. 1 (1964) No. 3, p. 221/7
[11] Tomilov, N. P.: Izv. Sib. Otdel. Akad. Nauk SSSR, Ser. Khim. Nauk (1986) No. 6, p. 92/8
[12] Elliot, A. G., R. A. Huggins: J. Am. Ceram. Soc. 58 (1975) No. 11-12, p. 497/500
[13] Takahashi, T., K. Kuwabara: J. Solid State Chem. 30/37 (1979) No. 3, p. 321/8
[14] Takahashi, T., K. Kuwabara: J. Appl. Electrochem. 10 (1980) No. 3, p. 291/7
[15] Plokhikh, A. A., A. R. Kaul : Izv. Akad. Nauk SSSR, Neorg. Mater. 21 (1985) No. 8, p. 1378/82
[16] DeVries, R. C., W. L. Roth : J. Am. Ceram. Soc. 52 (1969) No. 7, p. 364/9
[17] Barsoum, M.: J. Mater. Sci. 25 (1990) No. 10, p. 4393/400
[18] Eriksson, G., P. Wu, A. D. Pelton: CALPHAD 17 (1993) No. 2, p. 189/207

Al_2O_3-SiO_2

Fig. 3.35. Al_2O_3-SiO_2 phase diagram with incongruent melting of mullite ($3Al_2O_3 \cdot 2SiO_2$) according to Klug et al. [1] (full lines - recommended version of the phase diagram), Aksay, Pask [2] (dash-dot lines), and Shindo [3] (dashed lines). The version by Klug et al. [1] is also based on the previous results reported by Aramaki, Roy [4], Aksay, Pask [1] and Horibe, Kuwabara [5]. Earlier versions of the phase diagram with incongruent melting of mullite have been reported by Bowen, Greig [6], Shears, Archibald [7], Trömel et al. [8] and Welch [9]. As reported by Welch [9], Horibe, Kuwabara [5] and Shindo [3], the composition of liquid co-existing with mullite and Al_2O_3, in contrast to the phase diagram reported by Aksay, Pask [2], is rather close to the mullite composition.

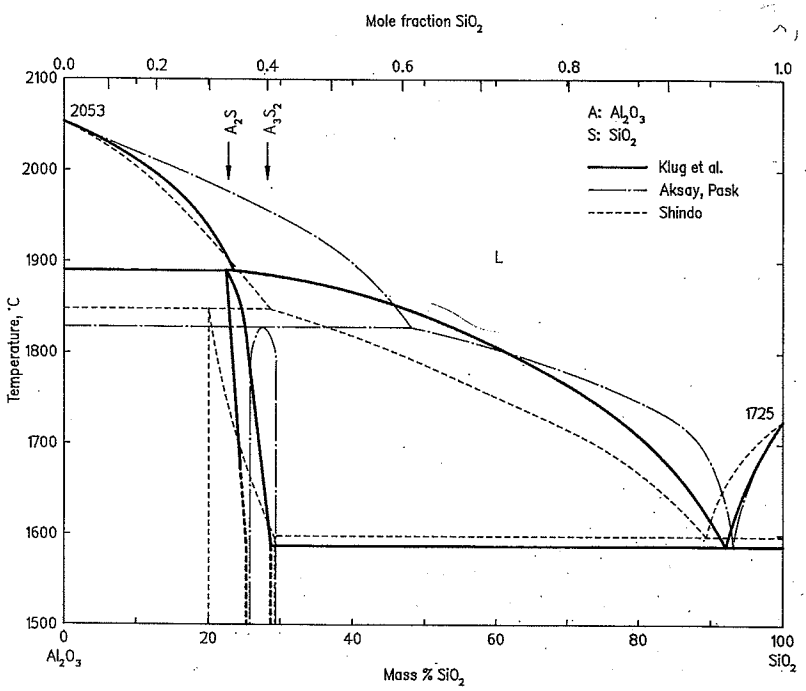
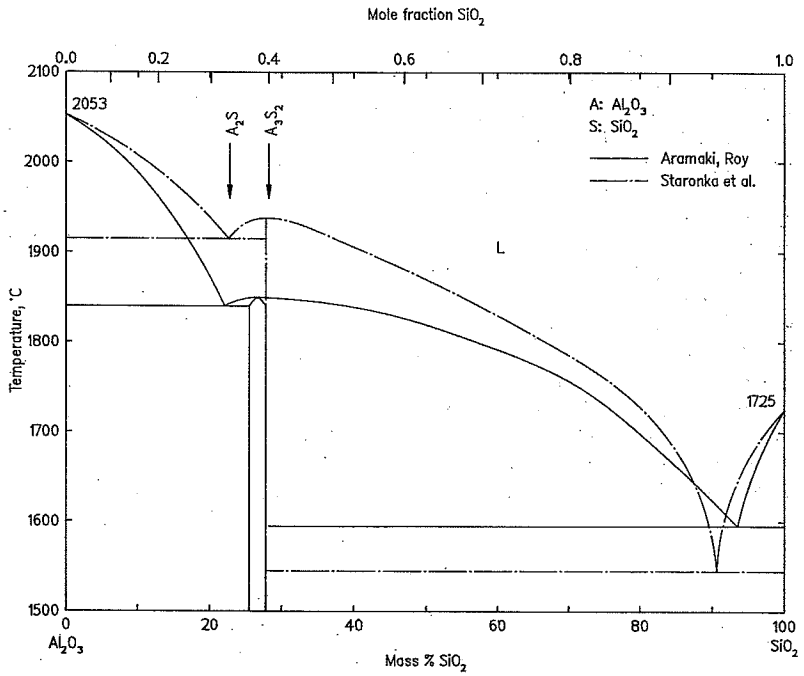


Fig. 3.36. Al_2O_3-SiO_2 phase diagram with congruent melting of mullite ($3Al_2O_3 \cdot SiO_2$) after Aramaki, Roy [4], as revised by Davis, Pask [10] and after Staronka et al. [11] (see also Toropov, Galakhov [12]). After Aksay, Pask [2] and Pask [13] the version of the system with incongruent melting of mullite represents the "stable" phase relations in this region of the system, and the version of the system with a congruent melting of mullite represents the "metastable" phase relations.



The limits of the mullite solid solution have been investigated by Kriven, Pask [14] and Okada, Otsuka [15]. For the metastable miscibility gap, see Risbud, Pask [16], Jantzen, Herman [17], McPherson [18], Jantzen et al. [19] and Averyanov, Areshev [20]. Recently, the different aspects of the phase equilibria in the Al_2O_3-SiO_2 system have been discussed extensively by Pask [21], Risbud [22], Roy [23] and Klug et al. [24]. For thermodynamic assessments of the system Al_2O_3-SiO_2 and Al-O-Si, see Eriksson, Pelton [25] and Hillert, Jonsson [26] respectively.

References

[1] Klug, F. J., S. Prochazka, R. H. Doremus: J. Am. Ceram. Soc. 70 (1987) No. 10, p. 750/9
[2] Aksay, I. A., J. A. Pask: Science 183 (1973) No. 4120, p. 69/71
[3] Shindo, I.: Ceram. Trans. 6 /Mullite Mullite Matrix Compos./ (1990), p. 103/13
[4] Aramaki, S., S. Roy: J. Am. Ceram. Soc. 45 (1962) No. 5, p. 229/42
[5] Horibe, T., S. Kuwabara: Bull. Chem. Soc. Jap. 40 (1967) No. 4, p. 972/82
[6] Bowen, N. L., J. W. Greig: J. Am. Ceram. Soc. 7 (1924) No. 4, p. 238/54
[7] Shears, E. C., W. A. Archibald: Iron Steel 27 (1954) No. 2, p. 61/6
[8] Trömel, G., K.-H. Obst, K. Konopicky, H. Bauer, I. Patzak: Ber. Dtsch. Keram. Ges. 34 (1957) No. 12, p. 397/402
[9] Welch, J. W.: Nature 186 (1960) No. 4724, p. 546/7
[10] Davies, R. F., J. A. Pask: J. Am. Ceram. Soc. 55 (1972) No. 10, p. 523/31
[11] Staronka, A., H. Pham, M. Rolin: Rev. Int. Hautes Tempér. et Réfract. 5 (1968) No. 2, p. 111/5
[12] Toropov, N. A., F. Ya. Galakhov: Izv. Akad. Nauk SSSR, Otdel. Khim. Nauk (1958) No. 1, p. 8/11
[13] Pask, J. A.: Mater. Sci. Monogr. 16 /Ceram. Powders/, (1983), p. 21/31
[14] Kriven, W. M., J. A. Pask: J. Am. Ceram. Soc. 66 (1983) No. 9, p. 649/54
[15] Okada, K., N. Otsuka: J. Am. Ceram. Soc. 70 (1987) No. 10, p. C245/7
[16] Risbud, S. H., J. A. Pask: J. Am. Ceram. Soc. 62 (1979) No. 3-4, p. 214/5
[17] Jantzen, C. M., H. Herman: J. Am. Ceram. Soc. 62 (1979) No. 3-4, p. 212/4
[18] McPherson, R.: J. Am. Ceram. Soc. 63 (1980) No. 1-2, p. 110/2
[19] Jantzen, C. M., D. Schwahn, J. Schelten, H. Herman: Phys. Chem. Glasses 22 (1981) No. 5, p. 122/37
[20] Averyanov, V. I., M. P. Areshev: Fiz. Khim. Stekla 15 (1989) No. 6, p. 846/53
[21] Pask, J. A.: Ceram. Trans. 6 /Mullite Mullite Matrix Compos./ (1990), p. 1/13
[22] Risbud, S. H.: Ceram. Trans., 6 /Mullite Mullite Matrix Compos./ (1990), p. 61/71
[23] Roy, R.: Ceram. Trans., 6 /Mullite Mullite Matrix Compos./ (1990), p. 45/50
[24] Klug, F. J., S. Prochazka, R. H. Doremus: Ceram. Trans., 6 /Mullite Mullite Matrix Compos./ (1990), p. 15/4
[25] Eriksson, G., A. D. Pelton: Metall. Trans. B 24B (1993), p. 807/15
[26] Hillert, M., S. Jonsson: CALPHAD 16 (1992) No. 2, p. 193/8

Al_2O_3-TiO_2

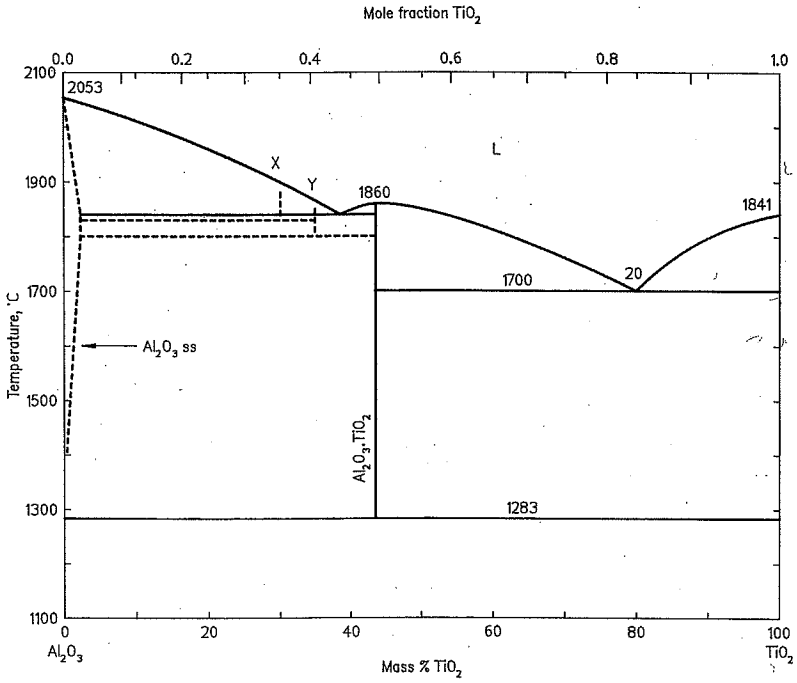


Fig. 3.37. Al_2O_3-TiO_2 phase diagram after Lang et al. [1], as revised by Goldberg [2], Lejus et al. [3], Azimov et al. [4] and Gulamova, Sarkisova [5]. In particular, the congruent melting of the Al_2O_3·TiO_2 phase and no confirmation of the high-temperature modification of Al_2O_3·TiO_2 have been found [2-4]. Additional phases of unspecified composition (X, Y: dashed lines in the figure) have been reported by Goldberg [2] and Lejus et al. [3] to exist above approx. 1800 °C. The complexity of the phase diagram in the vicinity of the melting point of Al_2O_3·TiO_2 has also been mentioned by Gulamova, Sarkisova [5]. The lower stability limit of Al_2O_3·TiO_2 was reported by Schreifels, Muan [6] to be 1286 °C. The solubility of TiO_2 in Al_2O_3 in air has been investigated by Winkler et al. [7] and Roy, Coble [8]. After Roy, Coble [8] the solubility of TiO_2 in Al_2O_3 ranges from approx. 0.9 mass % at 1400 °C to 2.3 mass % at 1700 °C.

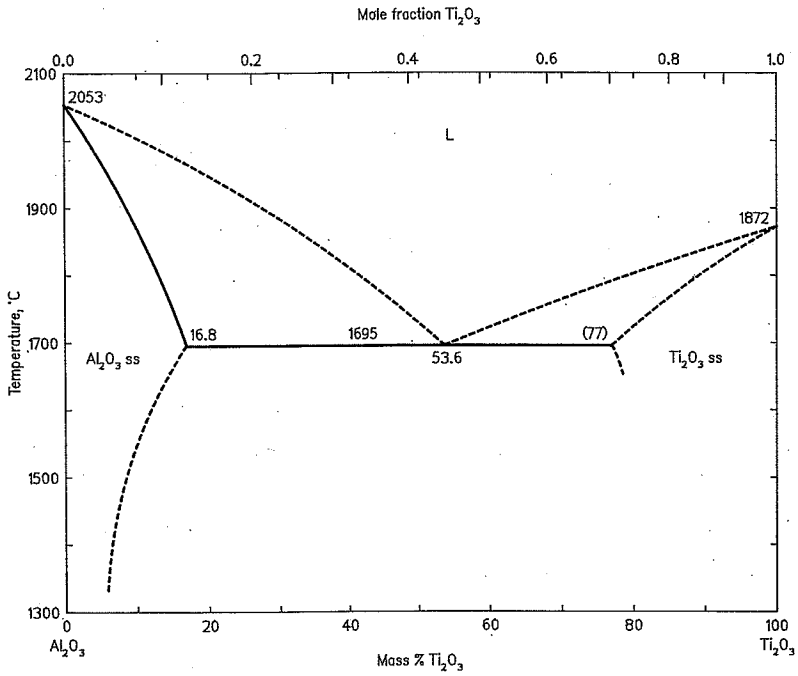


Fig. 3.38. Al_2O_3-Ti_2O_3 phase diagram after Belon, Forestier [9]. Previously, lower solubilities of Ti_2O_3 in Al_2O_3 were reported by McKee, Aleshin [10].

The phase equilibria in sub-solidus regions of the ternary systems Al-O-Ti and Al_2O_3-TiO_2-Ti_2O_3 have been reported by Glazova [11] and Monnereau et al. [12] respectively. The new ternary phase containing titanium of mixed valency, $Al_2Ti_7O_{15}$, found in [12] has been described by Remy et al. [13]. For the thermodynamics of the system, see Rahmel, Spencer [14].

References

[1] Lang, S. M., C. L. Fillmore, L. H. Maxwell: J. Res. Nat. Bur. Stand., RP 2316 48 (1952) No. 4, p. 298/312
[2] Goldberg, D.: Rev. Int. Hautes Tempér. et Réfract. 5 (1968) No. 3, p. 181/94
[3] Lejus, A.-M., D. Goldberg, A. Revcolevschi: C. R. Acad. Sci., Ser. C 263 (1966) No. 20, p. 1223/6
[4] Azimov, S. A., D. D. Gulamova, N. N. Melnik, M. K. Sarkisova, S. K. Suleimanov, L. M. Tsapenko: Izv. Akad. Nauk SSSR, Neorg. Mater. 20 (1984) No. 3, p. 469/71
[5] Gulamova, D. D., M. K. Sarkisova: Izv. Akad. Nauk SSSR, Neorg. Mater. 25 (1989) No. 5, p. 789/94
[6] Schreifels, W. A., A. Muan: Geochim. Cosmochim. Acta, Suppl., 6 /Proc. Lunar Sci. Conf., 6th/ (1975), p. 973/85
[7] Winkler, E. R., J. F. Sarver, I. B. Cutler: J. Am. Ceram. Soc. 49 (1966) No. 12, p. 634/7
[8] Roy, S. K., R. I. Coble: J. Am. Ceram. Soc. 51 (1968) No. 1, p. 1/6
[9] Belon, L., H. Forestier: C. R. Acad. Sci. 258 (1964) No. 17, p. 4282/4
[10] McKee, W. D., Jr., E. Aleshin: J. Am. Ceram. Soc. 46 (1963) No. 1, p. 54/8
[11] Glazova, V. V.: Dokl. Akad. Nauk SSSR 164 (1965) No. 3, p. 569/70
[12] Monnereau, O., F. Remy, A. Casalot: C. R. Acad. Sci., Ser. 2 301 (1985) No. 6, p. 375/8
[13] Remy, F., O. Monnerau, A. Casalot, F. Dahan, J. Galy: J. Solid State Chem. 76 (1988) No. 1, p. 167/77
[14] Rahmel, A., P. J. Spencer: Oxid. Metals 35 (1991) No. 1-2, p. 53/6

Al_2O_3-ZrO_2

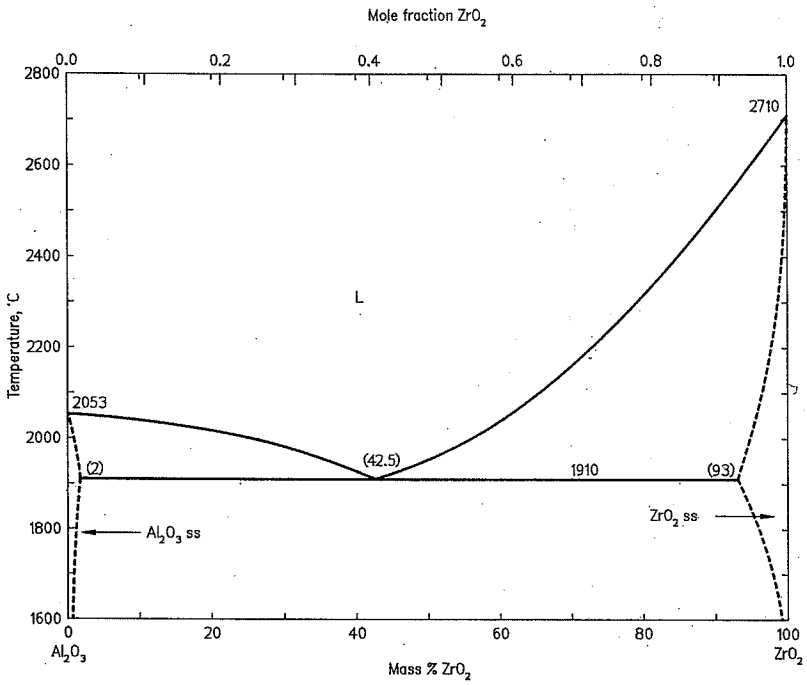


Fig. 3.39. Al_2O_3-ZrO_2 phase diagram after Alper et al. [1] with liquidus temperatures as revised recently for the entire temperature range by Fischer et al. [2]. The temperature and composition of the eutectic have also been reported by von Wartenberg et al. [3], Suzuki [4], von Krauth, Meyer [5], Schmid, Viechnicki [6], and recently by Volkova et al. [7], and vary from 1847 to 1920 °C and from 30 to 55 mass % ZrO_2 respectively. Recently, the existence of a metastable, cubic ZrO_2 solid solution containing up to 40 mole % Al_2O_3 has been reported by Yamaguchi et al. [8]. The solubility of Al_2O_3 in tetragonal- and monoclinic-ZrO_2 after Tananaev et al. [9] ranges up to 20 and 16 mole % Al_2O_3 respectively.

References

[1] Alper, A. M., R. C. Doman, R. N. McNally, H. C. Yeh: Use of phase diagrams in fusion- cast refractory materials research, Phase Diagrams, Volume 2,. Ed.: Academic, New York, (1970), p. 117/46

[2] Fischer, G. R., L. J. Manfredo, R. N. McNally, R. C. Doman: J. Mater. Sci. 16 (1981) No. 12, p. 3447/51

[3] von Wartenberg, H. V., H. Linde, R. Jung: Z. Anorg. Allg. Chem. 176 (1928), p. 349/62

[4] Suzuki, H., S. Kimura, H. Yamada, T. Yamauchi: J. Ceram. Assoc. Japan 69 (1961) No. 2, p. 52/9

[5] von Krauth, A., H. Meyer: Ber. Deut. Keram. Ges. 42 (1965) No. 3, p. 61/72

[6] Schmid, F., D. Viechnicki: J. Mater. Sci. 5 (1970), p. 470/3

[7] Volkova, I. Y., S. S. Semenov, A. E. Kravchik, S. S. Ordanyan, L. V. Kozlovskii: Izv. Akad. Nauk SSSR, Neorg. Mater. 23 (1987) No. 3, p. 448/51

[8] Yamaguchi, O., M. Shirai, M. Yoshinaka: J. Am. Ceram. Soc. 71 (1988) No. 12, p. C510/12

[9] Tananaev, I. V., M. S. Khodzhamberdiev, A. L. Salyn, E. N. Beresnev, V. I. Pakhomov, V. P. Orlovskii : Izv. Akad. Nauk SSSR, Neorg. Mater. 22 (1988) No. 11, p. 1925/7

B_2O_3-BaO

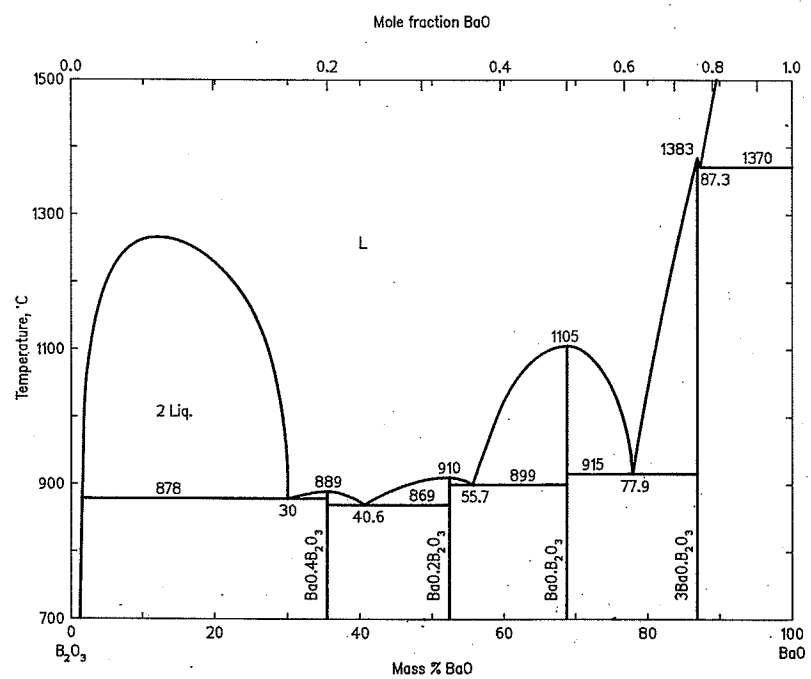


Fig. 3.40. B_2O_3-BaO phase diagram after Levin, McMurdie [1, 2] and Levin, Ugrinic [3] with miscibility gap as reported by Hageman, Oonk [4, 5]. The liquid immiscibility has also been investigated by Levin, Cleek [6], Clemens et al. [7], Ohta et al. [8] and Morinaga, Nakashia [9]. Values for T_c between 1180 and 1256 °C have been reported.

References

[1] Levin, E. M., H. F. McMurdie: J. Res. Nat. Bur. Stand., RP 1956 42 (1949) No. 2, p. 131/8

[2] Levin, E. M., H. F. McMurdie: J. Am. Ceram. Soc. 32 (1949) No. 3, p. 99/105

[3] Levin, E. M., G. M. Ugrinic: J. Res. Nat. Bur. Stand., RP 2430 51 (1953) No. 1, p. 37/56

[4] Hageman, V. B., H. A. J. Oonk: Phys. Chem. Glasses 20 (1979) No. 6, p. 126/9

[5] Hageman, V. B., H. A. J. Oonk: Phys. Chem. Glasses 28 (1987) No. 5, p. 183/7

[6] Levin, E. M., G. W. Cleek: J. Am. Ceram. Soc. 41 (1958) No. 5, p. 175/9

[7] Clemens, K., M. Yoshiyagawa, M. Tomozawa: J. Am. Ceram. Soc. 64 (1981) No. 6, p. C91/2

[8] Ohta, Y., K. Morinaga, T. Yanagase: Yogyo Kyokai Shi 90 (1982) No. 9, p. 511/6

[9] Morinaga, K., K. Nakashia: Yoyuen 29 (1986) No. 1, p. 49/60

B_2O_3-CaO

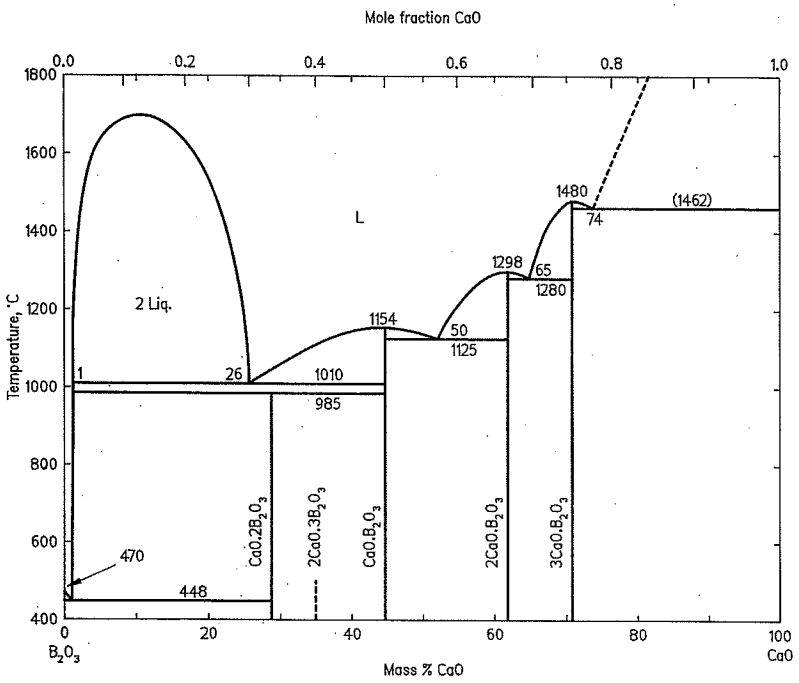


Fig. 3.41. B_2O_3-CaO phase diagram after Carlsson [1], as revised by Lawson, Glasser [2], and with miscibility gap after Hageman, Oonk [3]. The liquid immiscibility has also been investigated by Ohta et al. [4] and Morinaga, Nakashia [5]. An estimated value of T_c of 1515 °C has been reported. A further compound in the system, $2CaO{\cdot}3B_2O_3$, is reported by Hart, Brown [6] to form only under hydrothermal conditions.

References

[1] Carlsson, E. T.: J. Res. Nat. Bur. Stand., RP 510 9 (1932), p. 825/32

[2] Lawson, R. P., F. P. Glasser: Sci. Ceram. 14 (1988), p. 531/7

[3] Hageman, V. B. M., H. A. J. Oonk: Phys. Chem. Glasses 28 (1987) No. 5, p. 183/7

[4] Ohta, Y., K. Morinaga, T. Yanagase: Yogyo Kyokai Shi 90 (1982) No. 9, p. 511/6

[5] Morinaga, K., K. Nakashia: Yoyuen 29 (1986) No. 1, p. 49/60

[6] Hart, R. B., C. S. Brown: J. Inorg. Nucl. Chem. 24 (1962) No. 12, p. 1057/65

B_2O_3-FeO_x

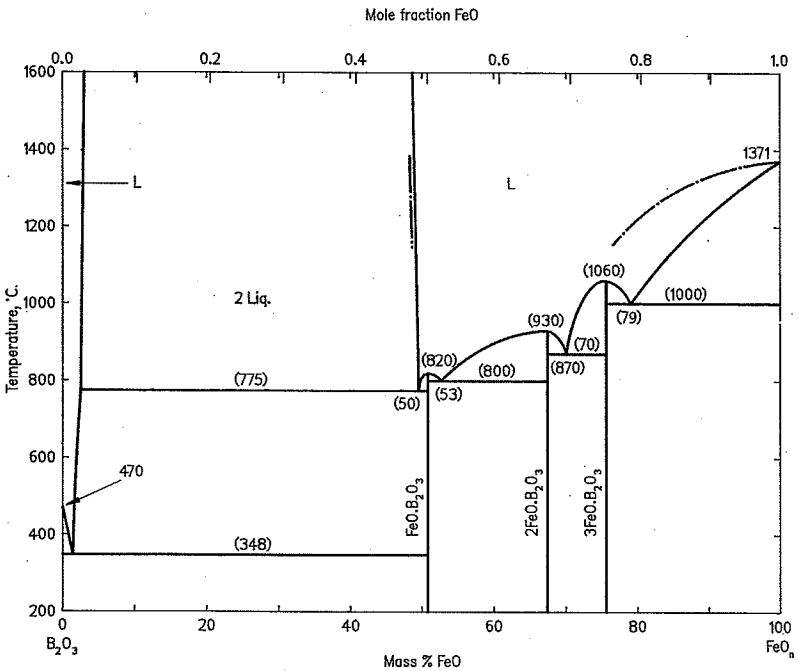
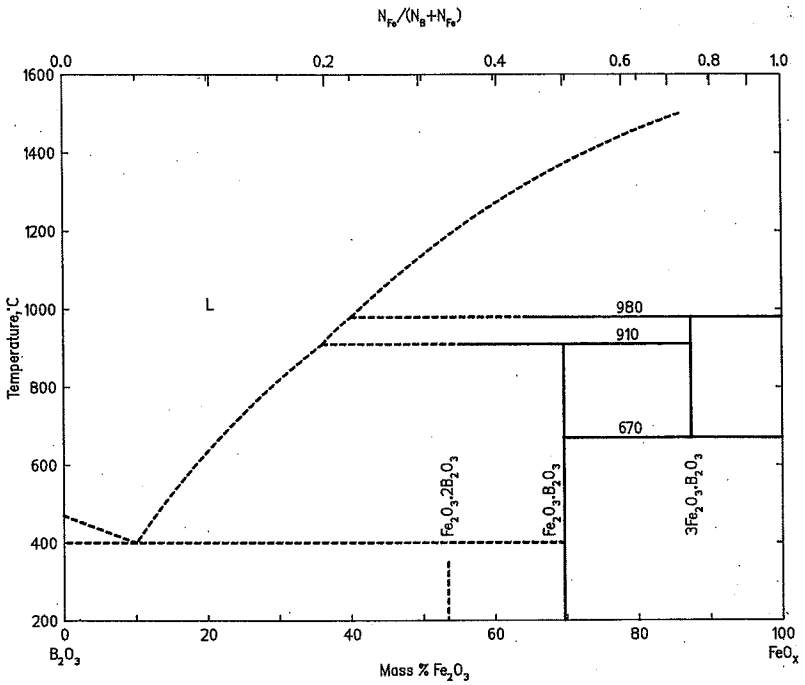


Fig. 3.42. B_2O_3-FeO_n system in contact with iron projected on the B_2O_3-FeO section after Koch et al. [1]. The dash-dot lines show the extension of the homogenous liquid between 1200 and 1400 °C as re-investigated recently by Fujiwara et al. [2].

Fig. 3.43. Tentative B_2O_3-FeO_x phase diagram in air based mainly on the results of Joubert et al. [3], Makram et al. [4], Zvereva et al. [5] (stability ranges of $B_2O_3 \cdot Fe_2O_3$ and $B_2O_3 \cdot 3Fe_2O_3$) and Selcuk [6] (solubility of Fe_2O_3 in melts). An additional phase, $2B_2O_3 \cdot Fe_2O_3$, melting incongruently at 910 °C, has been reported by Selcuk [6]. No evidence for liquid immiscibility in the B_2O_3-Fe_2O_3 system was found by Dimitriev et al. [7].



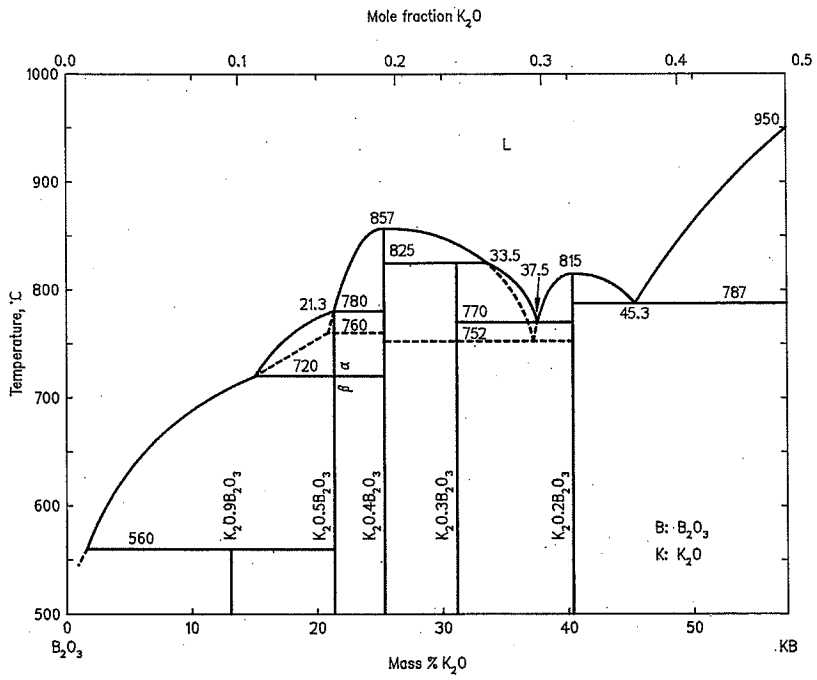
For an isothermal section through the system FeO-Fe_2O_3-B_2O_3 at 800 °C, containing the ternary phase $4FeO \cdot Fe_2O_3 \cdot B_2O_3$, see the original paper by Selcuk [6]. This section, however, is not consistent with the recommended binary edges B_2O_3-FeO and B_2O_3-Fe_2O_3. The phase equilibria in the sub-system B-Fe-FeO-B_2O_3 at 1600 and 1700 °C have been reported by Fujiwara et al. [2].

References

[1] Koch, K., J. Sittard, G. Trömel, H. Pöpperling: in Slag Atlas, (1981)
[2] Fujiwara, H., H. Moriya, M. Iwase: Iron Steelmaker 18 (1991) No. 1, p. 43/9
[3] Joubert, J. C., T. Shirk, W. B. White, R. Roy: Mater. Res. Bull. 3 (1968), p. 671/6
[4] Makram, H., L. Touron, J. J. Loriers: J. Cryst. Growth 13 (1972) No. 14, p. 585/7
[5] Zvereva, R. I., E. L. Duhovskaia, Y. L. Sapojnikov: Izv. Akad. Nauk SSSR, Neorg. Mater. 11 (1975) No. 2, p.282/4
[6] Selcuk, E.: Ironmaking Steelmaking 4 (1977) No. 2, p. 116/18
[7] Dimitriev, Y., E. Kashchieva, Y. Ivanova, S. Jambazov: J. Mater. Sci. 21 (1986), p. 3033/7

B_2O_3-K_2O

Fig. 3.44. B_2O_3-$K_2O \cdot B_2O_3$ phase diagram after Rollet [1, 2] and Tolédano [3] (B_2O_3-rich region of the system). The dashed lines show the metastable equilibria in the system. The metastable -$K_2O \cdot 5B_2O_3$ modification has been reported in 1,2) as crystallizing from $K_2O \cdot 5B_2O_3$ at 690 °C. Recently, similar invariant points in the sub-system B_2O_3-$B_2O_3 \cdot K_2O$ have been reported by Bergman, Mikhalkovich [5]. The existence of the compound $2K_2O \cdot B_2O_3$ reported earlier by Bergman, Vartbaronov [4] has not been confirmed in the more recent work of Bergman, Mikhalkovich [5].



References

[1] Rollet, A. P.: C. R. Acad. Sci. 200 (1935) No. 21, p. 1763/5
[2] Rollet, A. P.: C. R. Acad. Sci. 202 (1936) No. 22, p. 1863/5
[3] Tolédano, P.: Rev. Chim. Minér. 1 (1964) No. 3, p. 353/413
[4] Bergman, A. G., O. R. Vartbaronov: Zh. Neorg. Khim. 2 (1957) No. 3, p. 642/7
[5] Bergman, A. G., L. N. Mikhalkovich: Zh. Neorg. Khim. 15 (1970) No. 6, p. 1677

B_2O_3-MgO

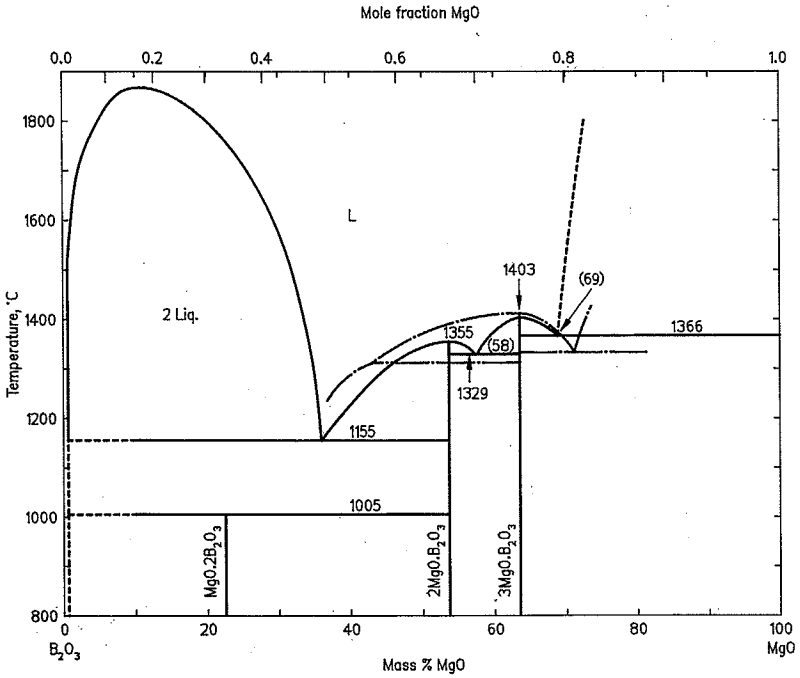


Fig. 3.45. B_2O_3-MgO phase diagram based mainly on the results due to Miyagawa et al. [1, 2] with the miscibility gap as determined recently by Hageman, Oonk [3]. Miyagawa at al. [1, 2] report the miscibility gap at the monotectic temperature to extend from approx. 1 to 23 mass % MgO. According to Ohta et al. [4] and Morinaga, Nakashia [5] the estimated value of the critical temperature for the liquid immiscibility is about 100 °C lower than the value reported by Hageman, Oonk [3]. Similar phase diagrams with congruently melting $2MgO{\cdot}B_2O_3$ and $3MgO{\cdot}B_2O_3$ have been reported earlier by Davis, Knight [6] and Toropov and Konovalov [7]. The phase equilibria according to Mutluer, Timucin [8], with incongruent melting of the $2MgO{\cdot}B_2O_3$ phase, are shown in the figure with dash-dot lines. The compound $MgO{\cdot}B_2O_3$ reported previously by Davis, Knight [6] and Toropov, Konovalov [7] is not confirmed in the earlier work due to Miyagawa et al. [1, 2] and Mutluer, Timucin [8] or in more recent investigations by Dell, Bray [9].

References

[1] Miyagawa, S., S. Hirano, S. Somiya: Bull. Tokyo Inst. Technolog. (1972) No. 108, p. 33/42

[2] Miyagawa, S., S. Hirano, S. Somiya: U.S.-Japan Seminar on Basic Science of Ceramics, Equilibria and Kinetics in Modern Ceramic Processing, May 1972, from Phase Diagrams for Ceramist, vol. IV, (1981)

[3] Hageman, V. B. M., H. A. J. Oonk: Phys. Chem. Glasses 28 (1987) No. 5, p. 183/7

[4] Ohta, Y., K. Morinaga, T. Yanagase: Yogyo Kyokai Shi 90 (1982) No. 9, p. 511/6

[5] Morinaga, K., K. Nakashia: Yoyuen 29 (1986) No. 1, p. 49/60

[6] Davis, H. M., M. A. Knight: J. Am. Ceram. Soc. 28 (1945) No. 4, p. 97/102

[7] Toropov, N. A., P. E. Konovalov: Zh. Fiz. Khim. 14 (1940) No. 8, p. 1103/10

[8] Mutluer, T., M. Timucin: J. Am. Ceram. Soc. 58 (1975) No. 5-6, p. 196/7

[9] Dell, W. J., P. J. Bray: Phys. Chem. Glasses 23 (1982) No. 4, p. 98/100

B_2O_3-MnO_x

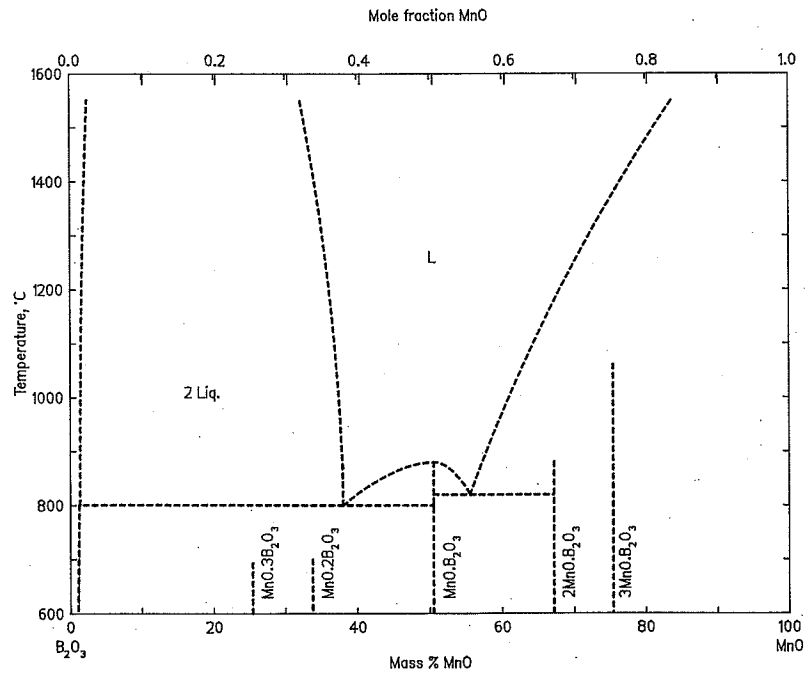


Fig. 3.46. Tentative B_2O_3-MnO phase diagram. The first version of the system with three congruently melting compounds, ie. $3B_2O_3{\cdot}MnO$, $2B_2O_3{\cdot}MnO$ and $B_2O_3{\cdot}MnO$ was reported by Mazzetti, de Carli [1]. Later a wide miscibility gap was found by Rao, Gaskell [2], who also questioned the existence of the $3B_2O_3{\cdot}MnO$ and $2B_2O_3{\cdot}MnO$ phases. Recently, Lavriv et al. [3] have reported the additional phases $B_2O_3{\cdot}2MnO$ and $B_2O_3{\cdot}3MnO$. The miscibility gap in the system has also been reported by Dimitriev et al. [4].
In the system B_2O_3-Mn_2O_3, Lavriv et al. [3] report the existence of the $Mn_2O_3{\cdot}B_2O_3$, $Mn_2O_3{\cdot}2B_2O_3$ and $Mn_2O_3{\cdot}3B_2O_3$ phases, which decompose at about 940 °C.

References

[1] Mazzetti, C., F. de Carli: Gazz. Chim. Ital. 56 (1926), p. 19/27

[2] Rao, B. K. P. D., D. R. Gaskell: Metall. Trans. B 12B (1981) No. 3, p. 469/77

[3] Lavriv, L. V., V. N. Pavlikov, E. S. Lugovskaya: Ukr. Khim. Zh. 56 (1990) No. 5, p. 455/8

[4] Dimitriev, Y., E. Kashchieva, Y. Ivanova, S. Jambazov: J. Mater. Sci. 21 (1986), p. 3033/7

B_2O_3-Na_2O

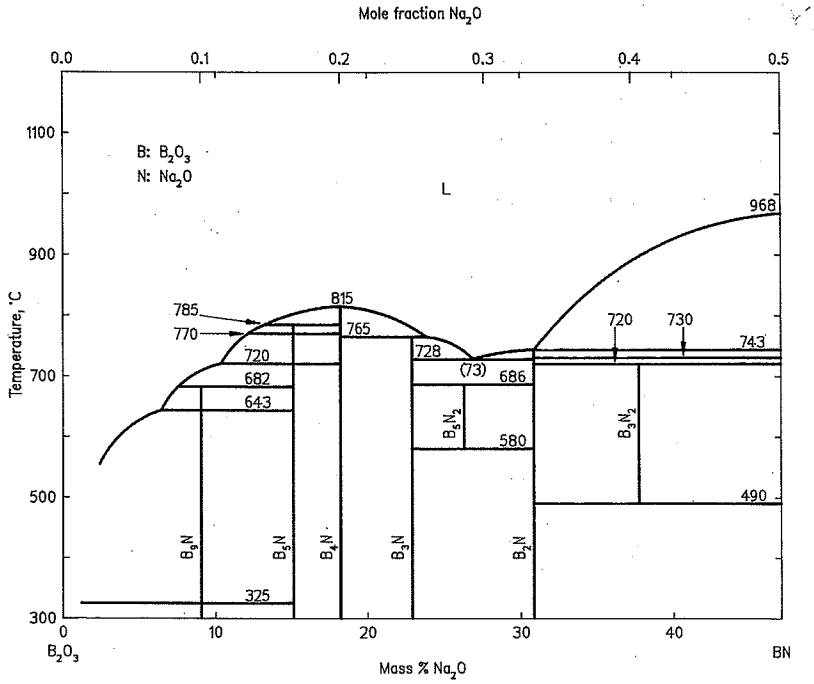


Fig. 3.47. Sub-system B_2O_3-$B_2O_3{\cdot}Na_2O$ after Milman, Bouaziz [1] (see also Morey, Merwin [2] and Mikhalkovich [3]). The sub-system $2B_2O_3{\cdot}Na_2O$-$B_2O_3{\cdot}Na_2O$ has also been investigated by Vartboronov, Bergman [4]. Two additional phases, $3B_2O_3{\cdot}2Na_2O$ and $5B_2O_3{\cdot}4Na_2O$, melting incongruently at 792 and 863 °C respectively, have been reported [4].

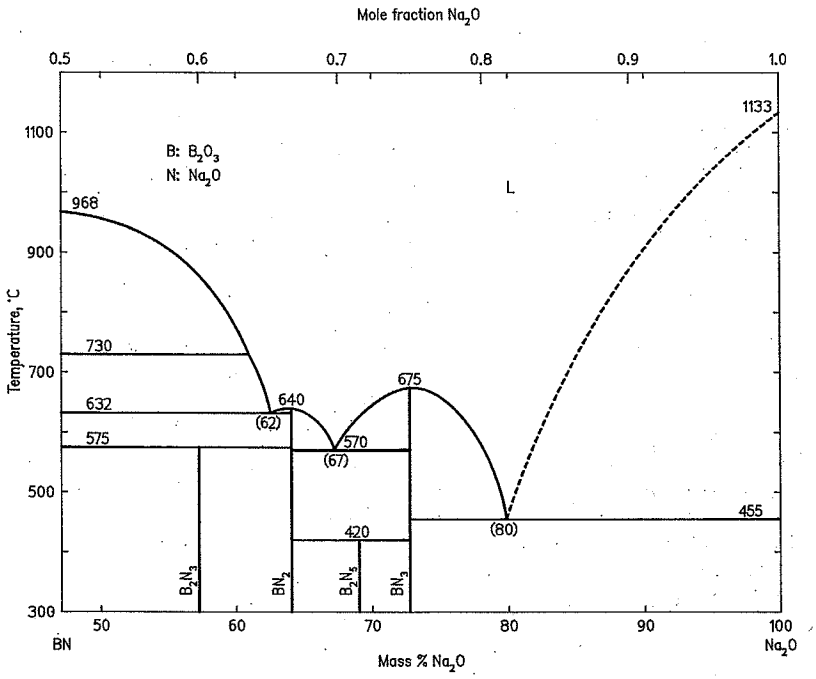


Fig. 3.48. Sub-system $B_2O_3{\cdot}Na_2O$-Na_2O after Milman, Bouaziz [1] (see also Morey, Merwin [2] and Mikhalkovich [3]).

References

[1] Milman, T., R. Bouaziz: Ann. Chim. /Paris/ (1968) No. 4, p. 311/21

[2] Morey, G. W., H. E. Merwin: J. Am. Chem. Soc. 58 (1936), p. 2248/54

[3] Mikhalkovich, L. N.: Zh. Neorg. Khim. 22 (1977) No. 3, p. 868/71

[4] Vartboronov, D. R., A. G. Bergman: Zh. Neorg. Khim. 13 (1968) No. 7, p. 1966/9

B_2O_3-SiO_2

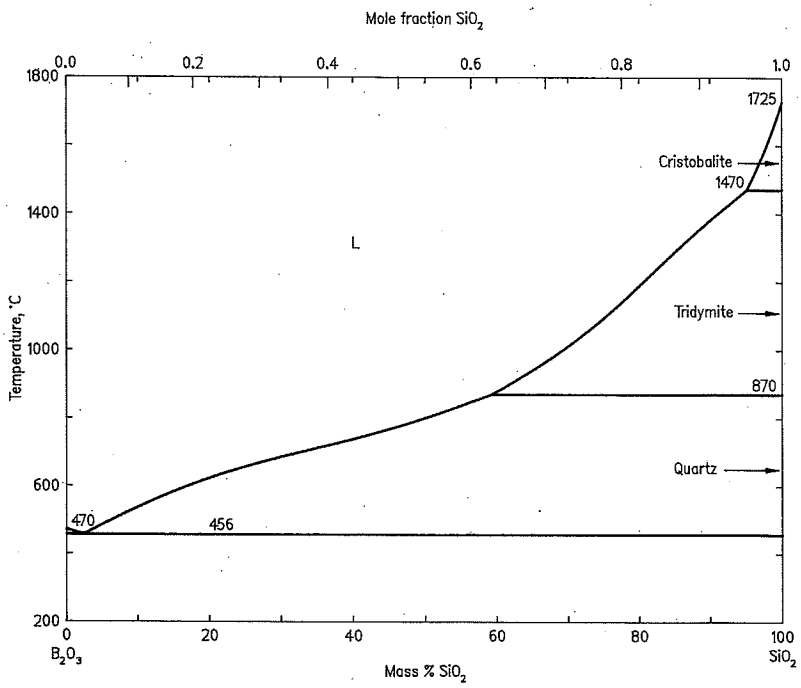


Fig. 3.49. B_2O_3-SiO_2 phase diagram after Rockett, Foster [1].

References

[1] Rockett, T. J., W. R. Foster: J. Am. Ceram. Soc. 48 (1965) No. 2, p. 75/80

BaO-FeO_x

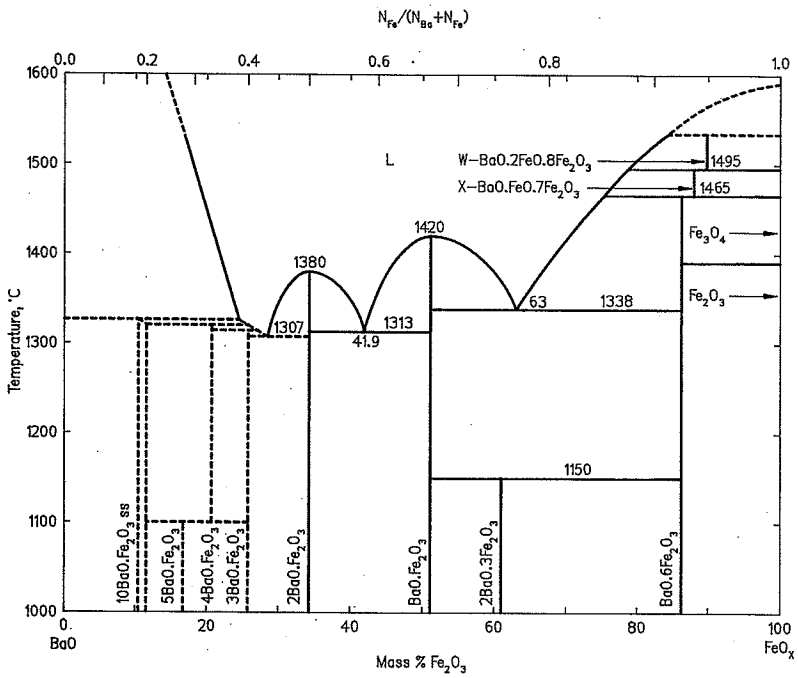


Fig. 3.50. BaO-Fe_2O_3 phase diagram in air based mainly on data by Batti [1] and Van Hook [2] for liquid-solid equilibria. For the sub-system 2BaO·Fe_2O_3-BaO·6Fe_2O_3, see also Goto, Takada [3]. The compound 2BaO·3Fe_2O_3 and its stability range are as reported by Sloccari [4]. The tentative phase equilibria in the BaO-rich region at sub-solidus temperatures (between 800 and 1150 °C) are as determined by Montorsi, Appendino [5]. The solid solution based on the 7BaO·2Fe_2O_3 composition, reported by Batti [1], has been replaced by two stoichiometric compounds 4BaO·Fe_2O_3 and 3BaO·Fe_2O_3. The lower stability limit for the 10BaO·Fe_2O_3 solid solution and for 3BaO·Fe_2O_3 in air has been located at 900 °C. For the sub-solidus relations in this part of the system in a neutral atmosphere and at 1 atm O_2 pressure, see the original paper by Montorsi, Appendino [5]. An alternative version of the sub-solidus relations in the BaO-rich region of the system has been reported by Pouillard et al. [6]. The 10BaO·Fe_2O_3 and 4BaO·Fe_2O_3 phases are not confirmed, and a solid solution based on the 3BaO·Fe_2O_3 composition has been found. For the liquidus surface with oxygen isobars in the Fe_2O_3-rich region of the BaO-FeO-Fe_2O_3 system, see Van Hook [2].

The stoichiometry of the 2BaO·Fe_2O_3 phase ($BaFeO_{3-x}$) with respect to oxygen contents, structure, and preparation condition has been investigated extensively by Mori [7, 8] and Negas, Roth [9]. For the polymorphism of BaO·Fe_2O_3, see Meriani [10].

References

[1] Batti, P.: Ann. Chim. /Rome/ 50 (1960), p. 1461/78
[2] Van Hook, H. J.: J. Am. Ceram. Soc. 47 (1964) No. 11, p. 579/81
[3] Goto, Y., T. Takada: J. Am. Ceram. Soc. 43 (1960) No. 3, p. 150/3
[4] Sloccari, G.: J. Am. Ceram. Soc. 56 (1973) No. 9, p. 489/90
[5] Montorsi, M., P. Appendino: Atti Accad. Sci. Torino, Cl. Fis. Mat. Nat. 113 (1979) No. 5-6, p. 479/90
[6] Pouillard, G., A. M. Shamsul, M. C. Trinel-Dufour, P. Perrot: J. Chem. Res., Synop. (1981) No. 5, p. 136/7
[7] Mori, S.: J. Am. Ceram. Soc. 48 (1965) No. 3, p. 165
[8] Mori, S.: J. Am. Ceram. Soc. 49 (1966) No. 11, p. 600/5
[9] Negas, T., R. S. Roth: J. Res. Nat. Bur. Stand., Sect. A 73 (1969) No. 4, p. 425/30
[10] Meriani, S.: Acta Cryst. B28 (1972), p. 1241/3

$BaO\text{-}SiO_2$

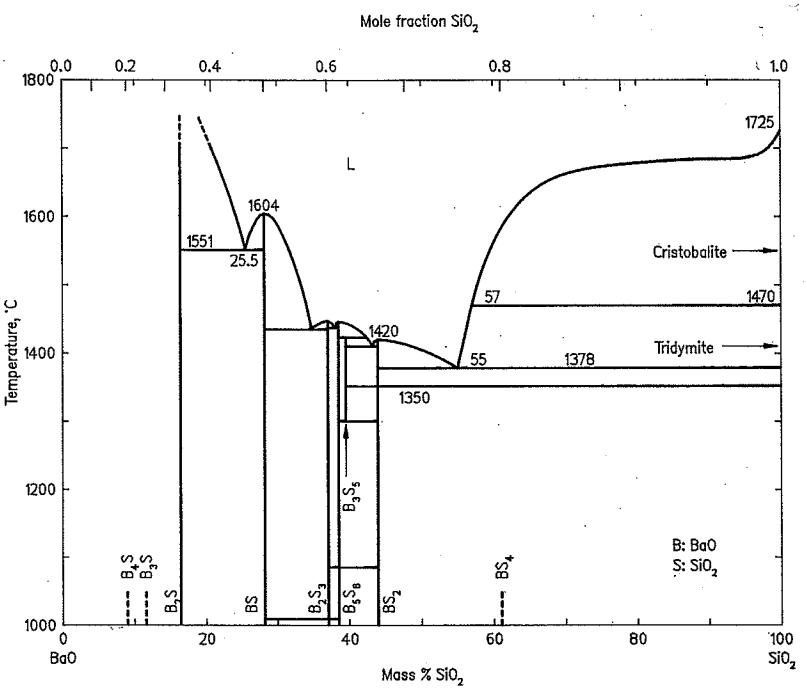


Fig. 3.51. $BaO\text{-}SiO_2$ phase diagram after Eskola [1], Greig [2], Roth, Levin [3], Oehlschlegel [4] and Oehlschlegel, Ohnmacht [5]. The additional compound $3BaO{\cdot}SiO_2$ has been reported by Glushkova [6], Brisi [7] and Eysel [8]. The other compounds existing in the system $BaO\text{-}SiO_2$, ie. $4BaO{\cdot}SiO_2$ and $BaO{\cdot}4SiO_2$ are as reported by Glushkova [6] and Yuan, Williams [9] (all of these phases are shown in the figure with dashed lines). The compound $4BaO{\cdot}7SiO_2$ found by Segnit, Stevens [10] is not confirmed in the later investigations by Oehlschlegel [4] and Oehlschlegel, Ohnmacht [5].

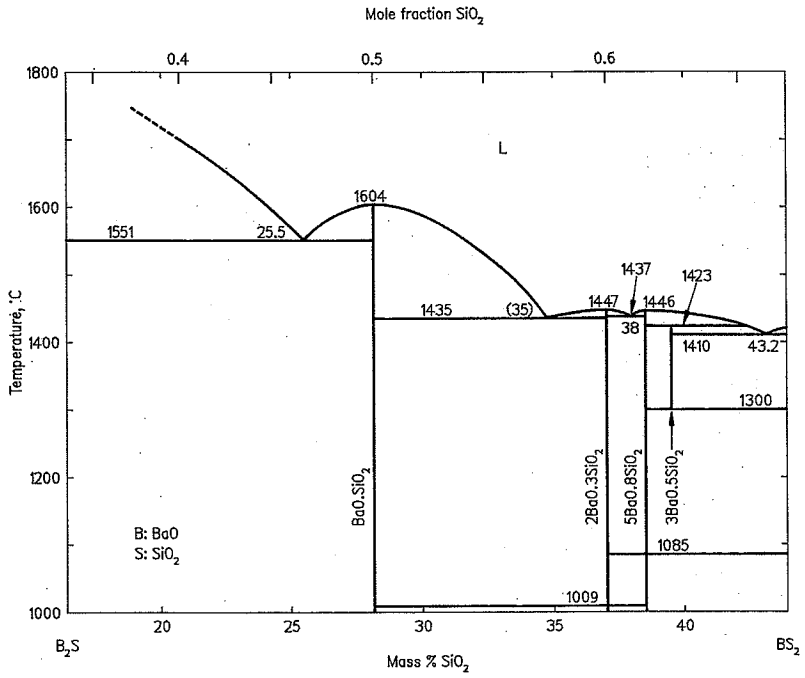


Fig. 3.52. Sub-system $2BaO{\cdot}SiO_2\text{-}BaO{\cdot}2SiO_2$ after Roth, Levin [3], Oehlschlegel [4], and Oehlschlegel, Ohnmacht [5].

References

[1] Eskola, P.: Am. J. Sci., 5-th Ser. 4 (1922) No. 23, p. 331/75
[2] Greig, J. W. : Am. J. Sci., 5-th Ser. 13 (1927) No. 73, p. 1/154
[3] Roth, R. S., E. M. Levin: J. Res. Nat. Bur. Stand., RP 2953 62 (1959) No. 5, p. 193/200
[4] Oehlschlegel, G.: Glastech. Ber. 44 (1971) No. 5, p. 194/204
[5] Oehlschlegel, G., W. Ohnmacht: Glastech. Ber. 48 (1975) No. 11, p. 232/6
[6] Glushkova, V. B.: Zh. Neorg. Khim. 2 (1957) No. 10, p. 2438/48
[7] Brisi, C.: Ind. Ital. Cemento 33 (1963) No. 6, p. 397/402
[8] Eysel, W.: Neues Jahr. Mineral., Monatsh. (1970) No. 12, p. 534/47
[9] Yuan, H., R. S. Williams: Chem. Mater. 2 (1990) No. 6, p. 695/700
[10] Segnit, E. R., T. J. Stevens: Naturwiss. 57 (1970) No. 5, p. 243/4

$CaO\text{-}Cr_2O_3$

Fig. 3.53. $CaO\text{-}Cr_2O_3$ phase diagram in a neutral atmosphere after results of von Wartenberg [1] as represented by Olshansky et al. [2] (sub-system $Cr_2O_3\text{-}CaO{\cdot}Cr_2O_3$) and Panek [3] (sub-system $CaO\text{-}Cr_2O_3{\cdot}CaO$). The temperature of the $\alpha\text{-}CaO{\cdot}Cr_2O_3$ ß-$CaO{\cdot}Cr_2O_3$ transformation in at 1645 °C as revised by Panek, Kanclir [4]. Panek, Kanclir [4] have reported the phases containing chromium at higher valency states (Fig. 3.54) to be stable also under reducing conditions. For their version of sub-solidus equilibria, see original paper [4]. An additional modification of $CaO{\cdot}Cr_2O_3$ stable below 1243 °C was reported by Kaiser et al. [5].

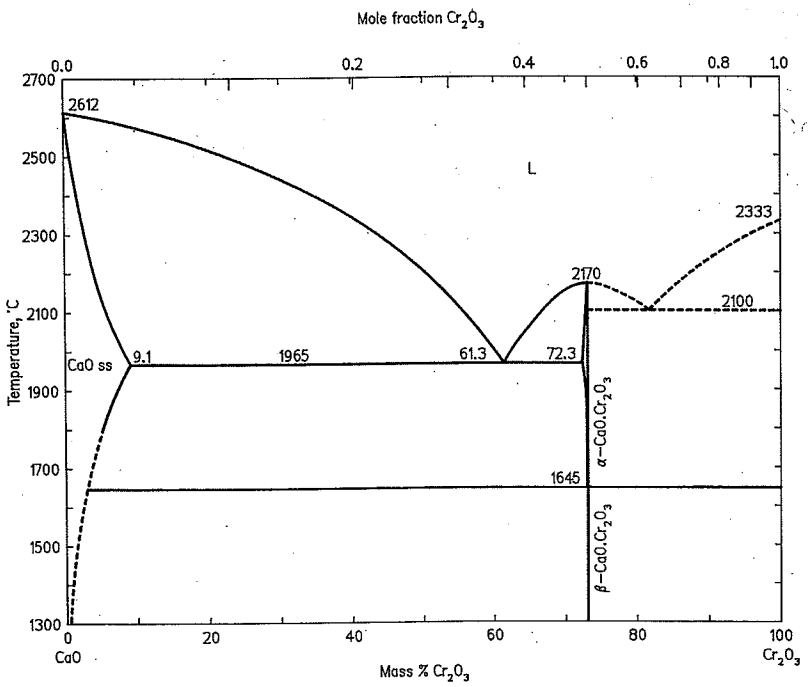


Fig. 3.54. $CaO\text{-}Cr_2O_3$ phase diagram in air, projected on the $CaO\text{-}Cr_2O_3$ section after Kaiser et al. [5]. For a similar version of the system, see also Panek [6]. The thermodynamic properties of compounds in the system have been reported by Havlica, Ambrúz [7] and recently by Jacob et al. [8].

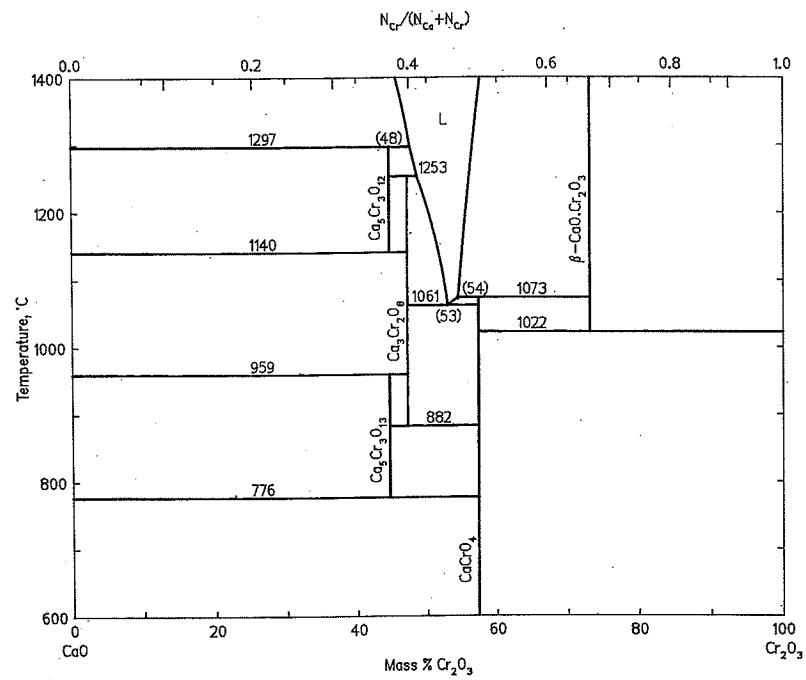
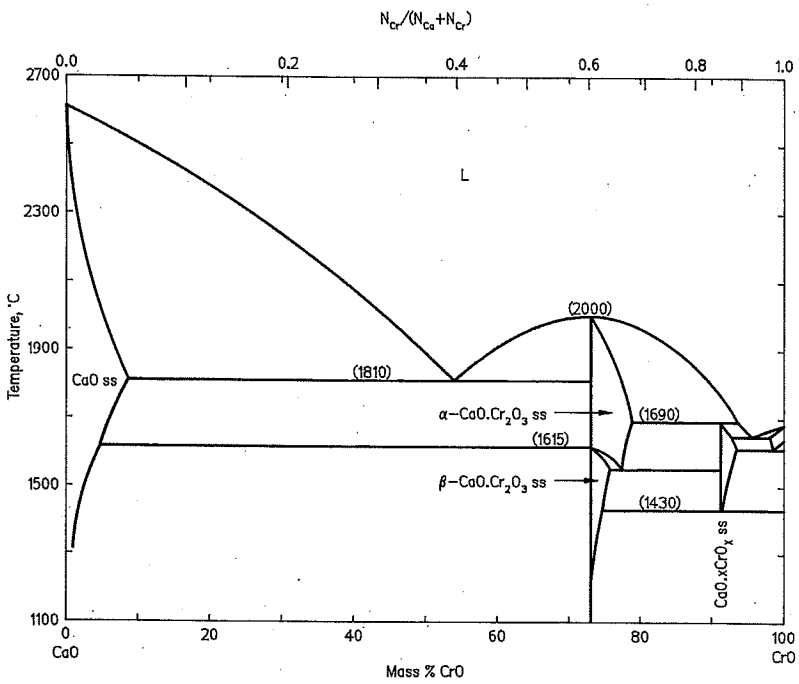


Fig. 3.55. CaO-CrO (CrO as hypothetical compound) system in contact with metallic chromium, as reported by Muan [9].



References

[1] von Wartenberg, H. V., H. J. Reusch, E. Saran: Z. Anorg. Allg. Chem. 230 (1937) No. 3, p. 257/76

[2] Olshansky, Ya. I., A. I. Tsvetkov, V. K. Shlepov: Dokl. Akad. Nauk SSSR 96 (1954) No. 5, p. 1007/9

[3] Panek, Z.: Silikaty 20 (1976) No. 1, p. 1/12

[4] Panek, Z., E. Kanclir: Silikaty 20 (1976) No. 2, p. 113/22

[5] Kaiser, A., B. Sommer, E. Woermann: J. Am. Ceram. Soc. 75 (1992) No. 6, p. 1463/71

[6] Panek, Z.: Silikaty 25 (1981) No. 2, p. 169/71

[7] Havlica, J., V. Ambrúz: Thermochim. Acta 93 (1985), p. 337/40

[8] Jacob, K. T., G. M. Male, K. P. Abraham: J. Electrochem. Soc 139 (1992) No. 2, p. 517/20

[9] Muan, A.: Proc. of International Conference on Applied Mineralogy, ICAM 81, Johannesburg, 1981 in: Spec. Publ. Geol. Soc. S. Afr. 7 (1983), p. 325/36

$CaO\text{-}FeO_x$

Fig. 3.56. CaO-FeO_n system in contact with iron, based mainly on the work of Allen, Snow [1] and Abbattista et al. [2] (versions of the phase diagram showing a minimum on the liquidus of the FeO_n solid solution) and the work of Obst, Stradtmann [3] and Schürmann, Kraume [4] (a compilation of their own and previously reported results). The phase equilibria involving the FeO_n solid solution are as reported by Abbattista et al. [2]. Numerous standard references are given in [2-4]. For the calculated phase diagram, see Hillert et al. [5]. The version of the phase diagram with a minimum on the liquidus of the FeO_n solid solution has been further supported by Johnson, Muan [6], Timucin, Morris [7], Lykasov, Kozheurova [8], Björkman [9] and recently by Bergman, Chengyi [10].

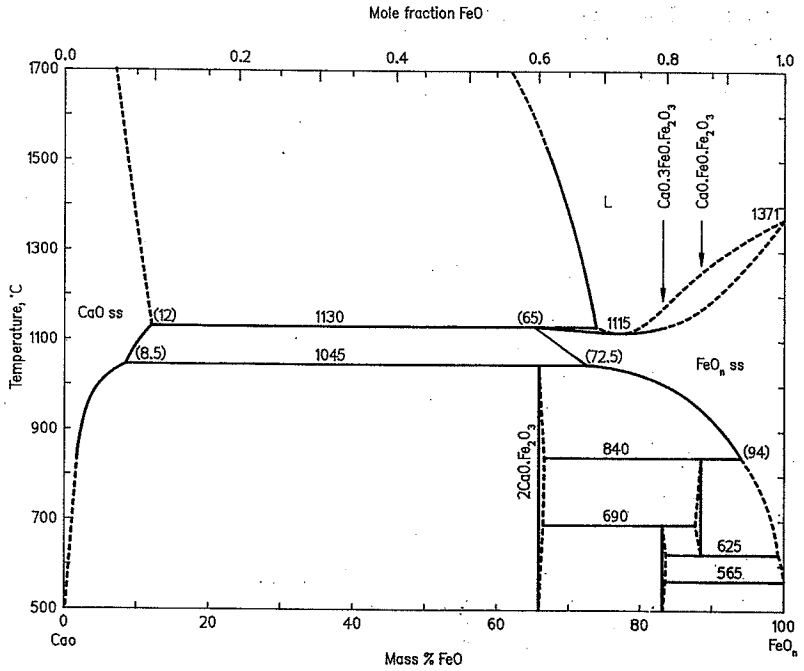


Fig. 3.57. CaO-FeO_x system in air according to Phillips, Muan [12]. The decomposition temperature of CaO·Fe_2O_3 was also re-investigated by Schürmann, Kraume [11] (dash-dot lines in the figure). For the composition of the liquid phase at liquidus temperatures, see original paper by Phillips, Muan [12] and also Fig. 3.59.

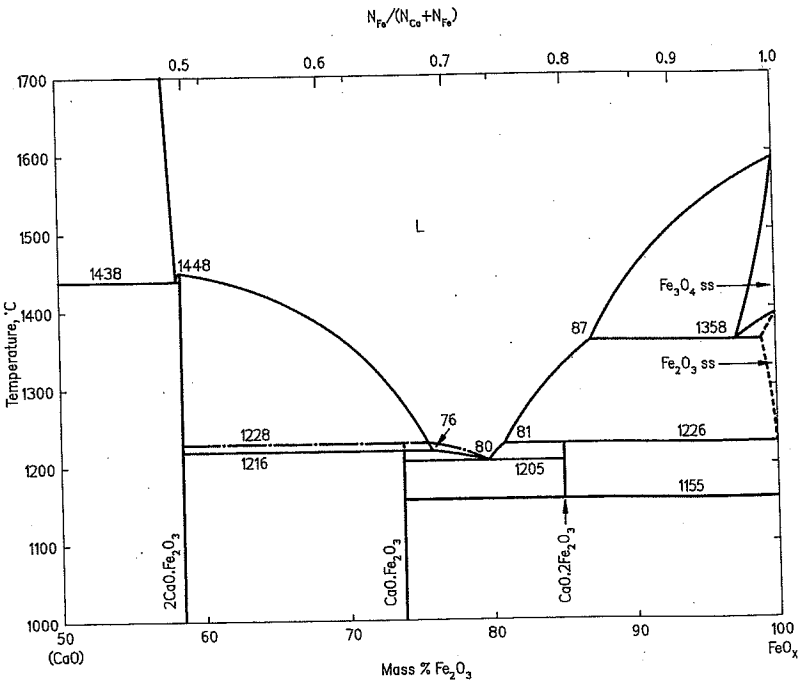
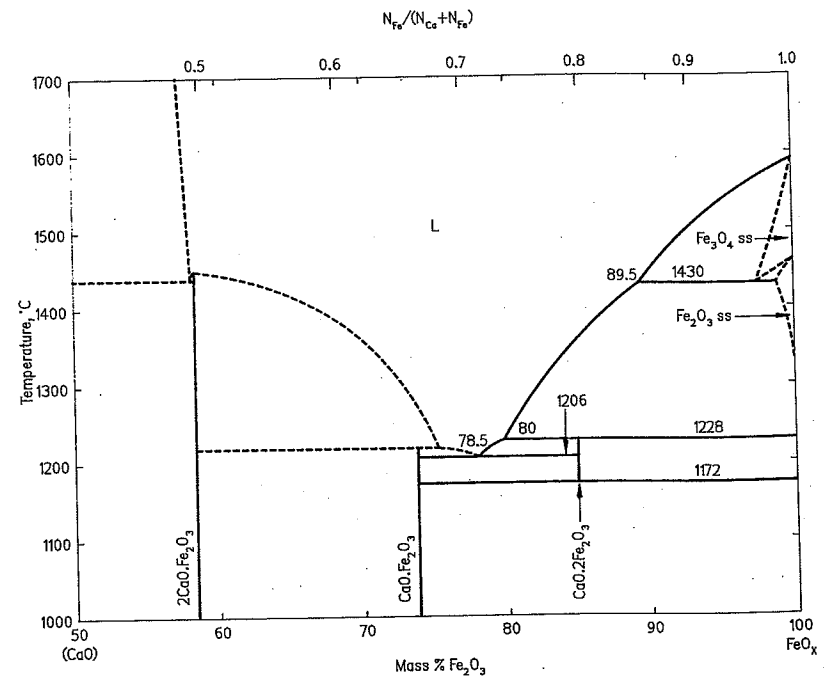


Fig. 3.58. CaO-FeO_x system at 1 atm O_2 pressure after Phillips, Muan [12]. For the composition of the liquid phase at liquidus temperatures, see original paper by Phillips, Muan [12] and also Fig. 3.59. For the system in an atmosphere consisting of CO_2 and H_2 in the ratio 1/9, see Riboud [13].



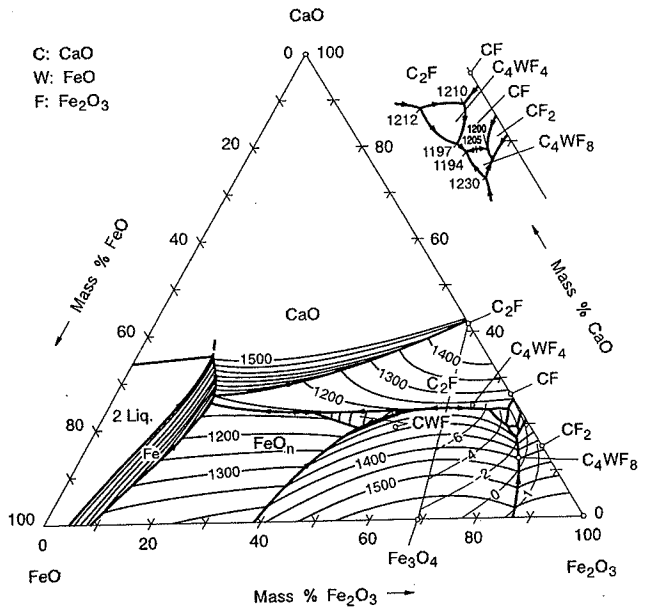


Fig. 3.59. Liquidus surface in the CaO-FeO-Fe_2O_3 system after Schürmann, Kraume [14] and Phillips, Muan [15] (Fe_2O_3-rich region of the system with log pO_2 isobars). Recently, the liquidus relations determined by Schürmann, Kraume [14] have been generally confirmed by Yazava et al. [16]. The CaO-FeO_n section with a eutectic between 2CaO·Fe_2O_3 and FeO_n is accepted here. For the liquidus isotherms above 1500 °C and the composition of the CaO solid solution co-existing with liquid, see Scheel [17].

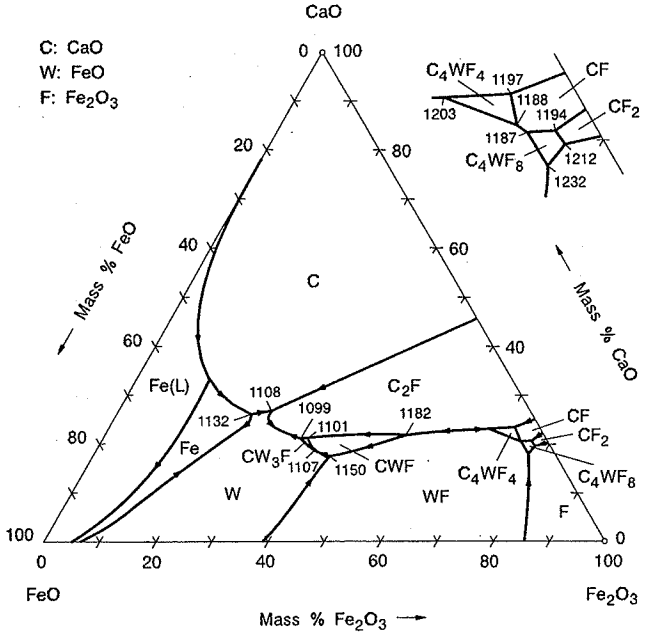


Fig. 3.60. Liquidus surface in the CaO-FeO-Fe_2O_3 system calculated by Hillert et al. [5]. The CaO-FeO_n section with a minimum on the liquidus of the FeO_n solid solution was used (see Fig. 3.56).

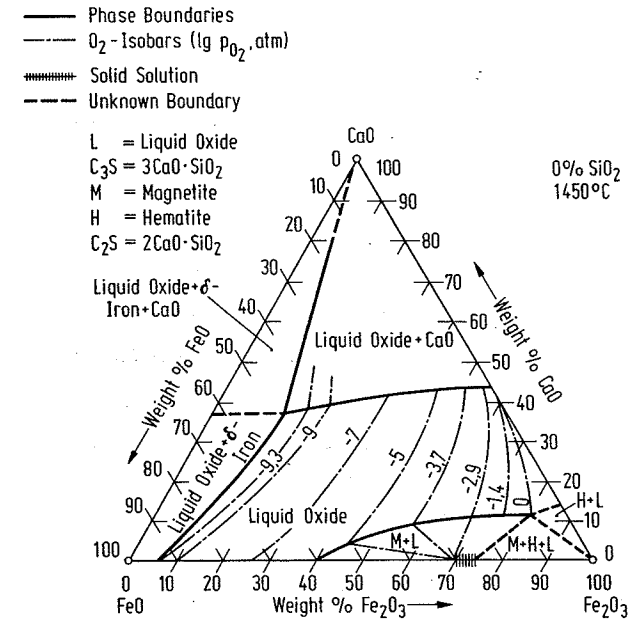


Fig. 3.61.

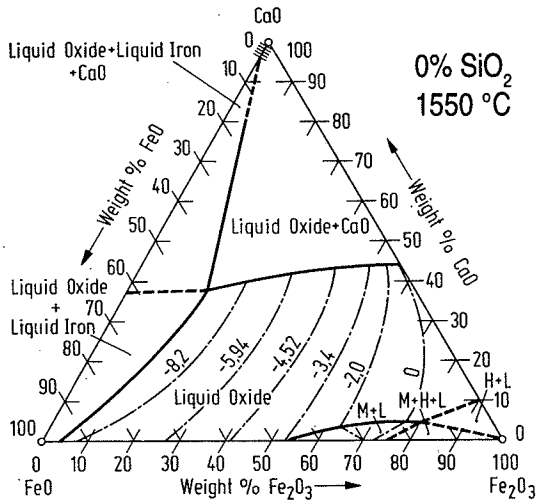


Fig. 3.62.

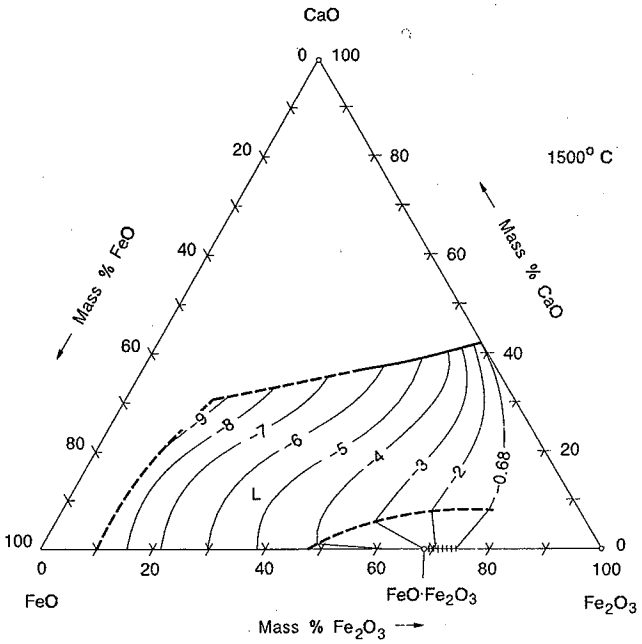


Fig. 3.63.

Figures 3.61 to 3.63. Isothermal sections through the system CaO-FeO-Fe_2O_3 with oxygen isobars (log pO_2, atm) at 1450 and 1550 °C after Timucin, Morris [18] and at 1500 °C after Hara et al. [19]. For the isothermal sections with oxygen isobars at 1200 and 1300 °C and for the isothermal section at 1600 °C, see Gurry, Darken [21] and Takeda et al. [22] respectively.

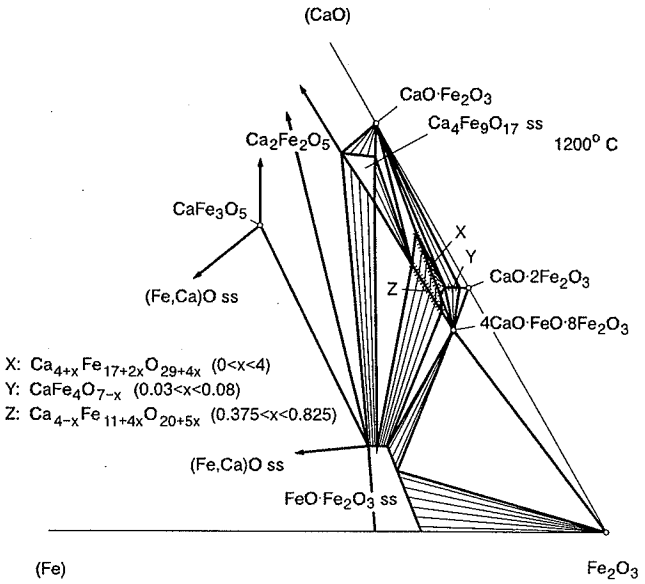


Fig. 3.64.

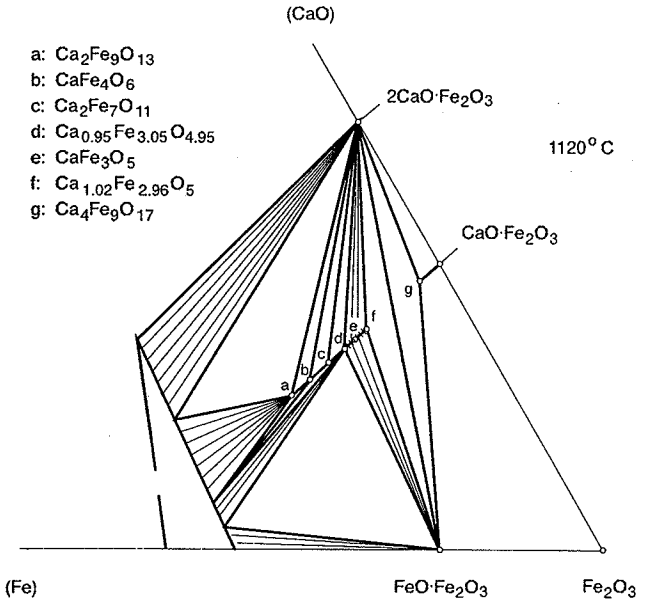


Fig. 3.65.

Figs. 3.64 and 3.65. Sub-solidus equilibria in the Fe_2O_3-rich region of the Fe-CaO-Fe_2O_3 system at 1200 °C after Millon et al. [23] and at 1120 °C after Malaman et al. [24]. The numerous ternary compounds reported and investigated previously, for instance by Asada et al. [25], Schürmann, Wurm [26] and Burdese et al. [27] have been re-investigated [23, 24]. In particular, a number of new non-stoichiometric solution phases covering the compositions of earlier-mentioned phases have been reported.

For the log pO_2 vs. $N_{Fe}/(N_{Fe}+N_{Ca})$ diagrams between 850 and 1050 °C, see Lykasov et al. [28, 29]. The oxygen potentials and phase equilibria in the ternary system Ca-Fe-O have also been investigated by Turkdogan [30]. Recently, the thermodynamics of the system and calculated phase equilibria in all ranges of composition and temperature have been reported by Hillert et al. [5].

References

[1] Allen, W. C., R. B. Snow: J. Am. Ceram. Soc. 38 (1955) No. 8, p. 264/80
[2] Abbattista, F., A. Burdese, M. Maja: Rev. Int. Hautes Tempér. et Réfract. 12 (1975) No. 4, p. 337/42
[3] Obst, K.-H., J. Stradtmann: Arch. Eisenhüttenwes. 40 (1969) No. 8, p. 615/7
[4] Schürmann, E., G. Kraume: Arch. Eisenhüttenwes. 47 (1976) No. 6, p. 327/31
[5] Hillert, M., M. Selleby, B. Sundman: Metall. Trans. A 21A (1990) No. 10, p. 2759/76
[6] Johnson, R. E., A. Muan: J. Am. Ceram. Soc. 48 (1965) No. 7, p. 359/64
[7] Timucin, M., A. E. Morris: Amer. Soc. Test. Mater., Spec. Tech. Publ., Volume Date 1969 (1970) No. 472, p. 25/31
[8] Lykasov, A. A., N. V. Kozheurova: Izv. Vyssh. Uchebn. Zaved., Chern. Metall. (1980) No. 4, p. 10/3
[9] Björkman, B.: Scand. J. Metall. 13 (1984) No. 4, p. 193/200
[10] Bergman, B., C. Chengyi: J. Am. Ceram. Soc. 71 (1988) No. 3, p. C121/5
[11] Schürmann, E., G. Kraume: Arch. Eisenhüttenwes. 47 (1976) No. 5, p. 267/9
[12] Phillips, B., A. Muan: J. Am. Ceram. Soc. 41 (1958) No. 11, p. 445/54
[13] Riboud, P.: Mém. Sci. Rev. Métall. 70 (1973) No. 11, p. 771/82
[14] Schürmann, E., G. Kraume: Arch. Eisenhüttenwes. 47 (1976) No. 7, p. 435/9
[15] Phillips, B., A. Muan: Trans. Metall. Soc. AIME 218 (1960) No. 12, p. 1112/8
[16] Yazava, A., Y. Takeda, Y. Waseda: Can. Metall. Q. 20 (1981) No. 2, p. 129/34
[17] Scheel, R.: Arch. Eisenhüttenwes. 45 (1974) No. 11, p. 751/6
[18] Timucin, M., A. E. Morris: Metall. Trans. 1 (1970) No. 11, p. 3193/201
[19] Hara, S., T. Araki, K. Ogino: Metall. Slags Fluxes, Int. Symp., Proc. 2nd (1984), p. 441/51 Ed.: Fine, H. A., D. R. Gaskell, Metall. Soc. AIME, Warrendale
[20] Larson, H., J. Chipman: Trans. Metall. Soc. AIME, J. Met. 197 (1953) No. 12, p. 1089/96
[21] Gurry, R. W., L. S. Darken: J. Am. Chem. Soc. 72 (1950) No. 9, p. 3906/10
[22] Takeda, Y., S. Nakazawa, A. Yazava: Can. Metall. Q. 19 (1980) No. 3, p. 297/305
[23] Millon, E., O. Evrard, A. Bonazebi, J. F. Brice, R. Gerardin: Mém. Sci. Rev. Métall. 83 (1986) No. 11, p. 583/93
[24] Malaman, B., H. Alebouyeh, F. Jeannot, A. Courtois, R. Gerardin, O. Evrard: Mat. Res. Bull. 16 (1981), p. 1139/48
[25] Asada, M., Y. Omori, K. Sanbongi: Trans. Iron Steel Inst. Jpn. 54 (1968) No. 1, p. 245/50
[26] Schürmann, E., P. Wurm: Arch. Eisenhüttenwes. 44 (1973) No. 9, p. 637/45
[27] Burdese, A., D. Firrao, C. Gianolio: Fiz. Khim. Okislov Met., Ed.: Balakirev, V. F., Nauka, Moscov, (1981), p. 82/8
[28] Lykasov, A. A., N. V. Kozheurova: Izv. Akad. Nauk SSSR, Neorg. Mater. 16 (1980) No. 6, p. 1079/82
[29] Lykasov, A. A., N. V. Kozheurova, G. I. Sergeev: Nauch. Tr. Mosk. In-t Stali i Splavov 148 (1983), p. 116/19
[30] Turkdogan, E. T.: Trans. Metall. Soc. AIME 221 (1961) No. 6, p. 546/53

CaO-MgO

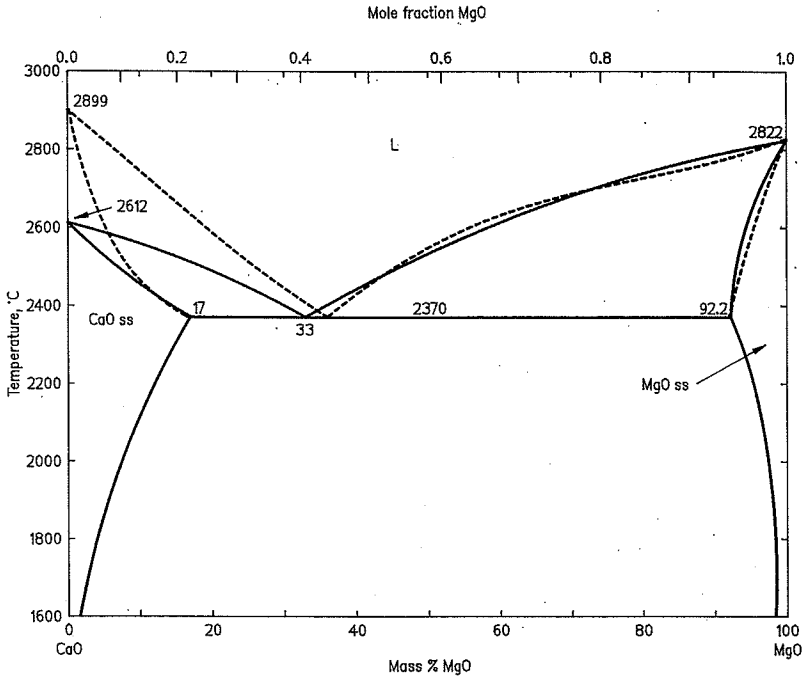


Fig. 3.66. CaO-MgO phase diagram after Doman et al. [1]. The solubility of CaO in MgO between 1100 and 1180 °C has later been re-investigated by Henney, Jones [2]. The mutual solubility at 1500 °C was also investigated by Shirasuka et al. [3]. The thermodynamics of the system and calculated phase equilibria in which the higher melting temperature of CaO is accepted have been reported by Hillert, Wang [4]. Their results are shown in the figure with dashed lines. For recent thermodynamic assessment and discussion of the system, see Jin, Du [5] Howald [6] and Wu at al. [7].

References

[1] Doman, R. C., J. B. Barr, R. N. McNally, A. M. Alper: J. Am. Ceram. Soc. 46 (1963) No. 7, p. 313/6

[2] Henney, J. W., J. W. S. Jones: Trans. J. Br. Ceram. Soc. 68 (1969), p. 201/3

[3] Shirasuka, K., G. Yamaguchi, M. Sekiya: Sekko To Sekkai (1975) No. 139, p. 223/6

[4] Hillert, M., X. Wang: CALPHAD 13 (1989) No. 3, p. 267/72

[5] Jin, Z., Y. Du: CALPHAD 16 (1992) No. 1, p. 33/36

[6] Howald, R. A.: CALPHAD 16 (1992) No. 1, p. 25/32

[7] Wu. P, G. Eriksson, A. D. Pelton: J. Am. Ceram. Soc. 76 (1993) No. 8, p. 2065/75

$CaO-MnO_x$

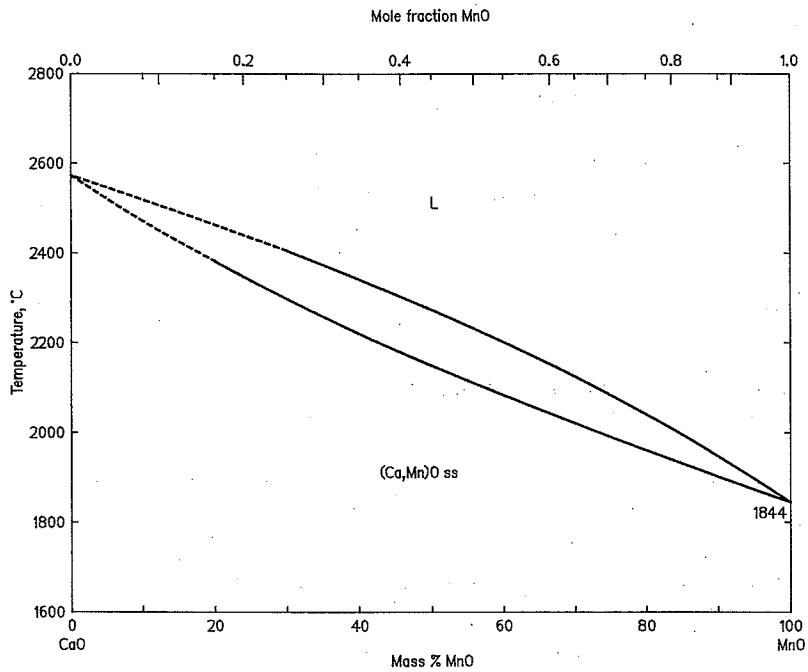
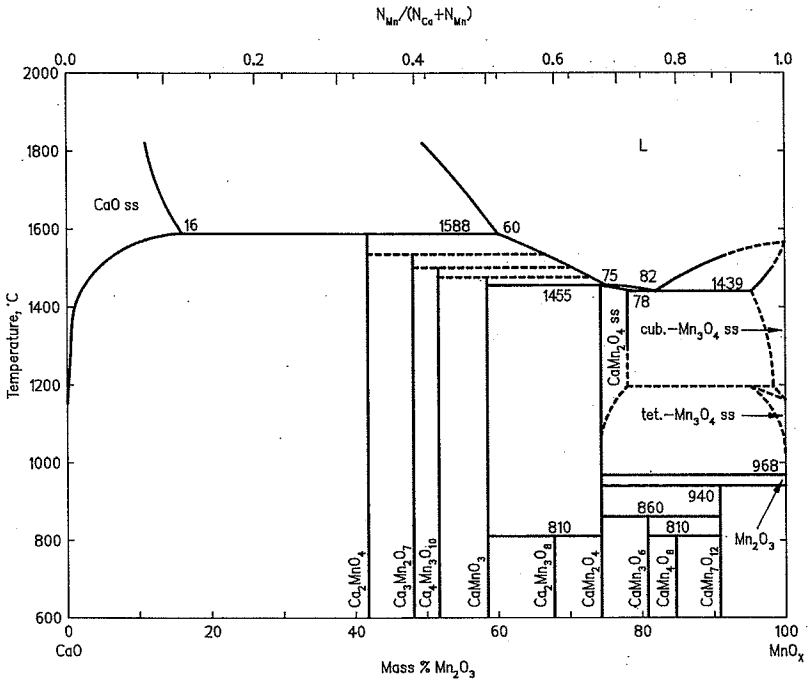


Fig. 3.67. CaO-MnO system under reducing conditions after Schenck et al. [1] (solidus as measured, liquidus as calculated). The miscibility gap in the (Ca,Mn)O solid solution below 1000 °C extends from 30 to 88 mass % MnO at 600 °C in a hydrogen atmosphere according to recent results of Pöppelmeier et al. [2].

Fig. 3.68. CaO-MnO_x system in air after Riboud, Muan [3] (liquid-solid equilibria) and Horowitz, Longo [4] (sub-solidus equilibria) projected on the CaO-Mn_2O_3 section. The sub-solidus relations after Horowitz, Longo [4] have been confirmed by Tanida, Kitamura [5] in the region of the perovskite-like phase $CaMnO_3$. The compounds in the system have also been investigated by Chrétien, Toussaint [6], Brisi, Lucco-Borlera [7], Bochu et al. [8] and Pavlotskii et al. [9]. For sub-solidus relations at 1 atm O_2 pressure, see original paper by Horowitz, Longo [4].



References

[1] Schenck, H., M. G. Frohberg, R. Nünninghoff: Arch. Eisenhüttenwes. 35 (1964) No. 4, p. 269/77

[2] Pöppelmeier, K. R., H. S. Horowitz, J. M. Longo: J. Less-Common Met. 116 (1986) No. 1, p. 219/27

[3] Riboud, P. V., A. Muan: J. Am. Ceram. Soc. 46 (1963) No. 1, p. 33/6

[4] Horowitz, H. S., J. M. Longo: Mater. Res. Bull. 13 (1978) No. 12, p. 1359/69

[5] Tanida, K., T. Kitamura: Tohoku Daigaku Senko Seiren Kenkyusho Iho 37 (1981) No. 1, p. 33/42

[6] Chrétien, A., H. Toussaint: C. R. Acad. Sci., Ser. C 251 (1960) No. 25, p. 2967/9

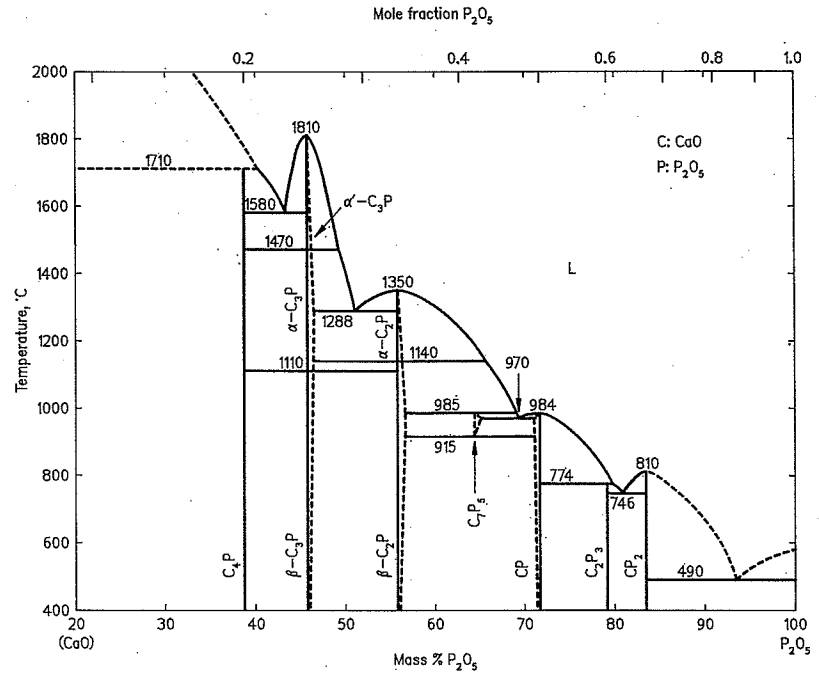
[7] Brisi, C., M. Lucco-Borlera: Inorg. Nucl. Chem. 27 (1965) No. 9, p. 2129/32

[8] Bochu, B., J. Chenevas, J. C. Joubert, M. Marezio: J. Solid State Chem. 11 (1974) No. 1, p. 88/93

[9] Pavlotskii, Y. V., M. V. Loginova, A. V. Polyanskii, I. T. Sheftel: Izv. Akad. Nauk SSSR, Neorg. Mater. 13 (1977) No. 3, p. 485/9

$CaO-P_2O_5$

Fig. 3.69. CaO-P_2O_5 phase diagram based mainly on the results of Trömel [1], Trömel, Fix [2] (sub-system CaO-$CaO{\cdot}P_2O_5$) and Hill et al. [3] (sub-system P_2O_5-$2CaO{\cdot}P_2O_5$). For the homogeneity ranges of compounds in the system (dashed lines), see Hill et al. [3], Welch, Gutt [4] and Terpstra et al. [5]. For polymorphism in $3CaO{\cdot}P_2O_5$, see also Nurse et al. [6, 7]. The CaO-P_2O_5 phase diagram has been discussed by Kreidler, Hummel [8].



References

[1] Trömel, G.: Stahl Eisen 63 (1943) No. 2, p. 21/30

[2] Trömel, G., W. Fix: Arch. Eisenhüttenwes. 32 (1961) No. 4, p. 209/12

[3] Hill, W. L., G. T. Faust, D. S. Reynolds: Am. J. Sci. 242 (1944) No. 9, p. 457/77

[4] Welch, J. H., W. Gutt: J. Chem. Soc. (1961) No. 10, p. 4442/4

[5] Terpstra, R. A., F. C. M. Driessens, H. G. Schaeken, R. M. H. Verbeeck: Z. Anorg. Allg. Chem. 507 (1983), p. 206/12

[6] Nurse, R. W., J. H. Welch, W. Gutt: Nature /London/ 182 (1958) No. 4644, p. 1230

[7] Nurse, R. W., J. H. Welch, W. Gutt: J. Chem. Soc. 63 (1959), p. 1077/83

[8] Kreidler, E. R., F. A. Hummel: Inorg. Chem. 6 (1967) No. 5, p. 884/91

$CaO\text{-}SiO_2$

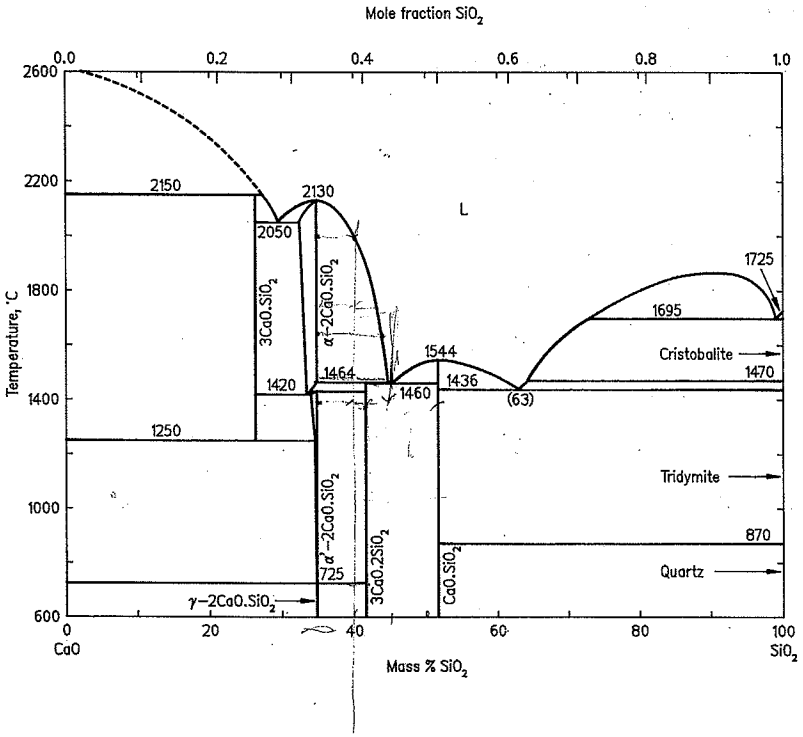


Fig. 3.70. $CaO\text{-}SiO_2$ phase diagram after Muan, Osborn [1], based mainly on the work of Rankin, Wright [2], and with revisions according to Tewhey, Hess [3] and Hageman et al. [4] (miscibility gap), Welch, Gutt [5], Gutt [6] and Gutt, Russell [7] (melting relations involving $3CaO{\cdot}SiO_2$) and Trömel et al. [8] (CaO excess in $2CaO{\cdot}SiO_2$). An alternative version of the system in the CaO-rich region, with the stability range of $3CaO{\cdot}SiO_2$ between 1300 and 1800 °C, was reported by Trömel et al. [8]. For the polymorphism in $2CaO{\cdot}SiO_2$, see also Foster [9] and Hanic et al. [10]. For thermodynamic assessments of the system and calculated phase diagrams, see an Mey [11], Taylor, Dinsdale [12], Eriksson et al. [13] and Hillert et al. [14, 15] (Figs. 3.I to 3.IV).

References

[1] Muan, A., E. F. Osborn: Phase Equilibria Among Oxides in Steelmaking, Ed.: Addison-Wesley Publishing Company, Inc., Reading Massachusetts, (1965)
[2] Rankin, G. A., F. E. Wright: Am. J. Sci., 4th Ser. 39 (1915), p. 1/79
[3] Tewhey, J. D., P. C. Hess: Phys. Chem. Glasses 20 (1979) No. 3, p. 41/53
[4] Hageman, V. B. M., G. J. K. Van den Berg, H. J. Janssen, H. A. J. Oonk: Phys. Chem. Glasses 27 (1986) No. 2, p. 100/6
[5] Welch, J. H., W. Gutt: J. Am. Ceram. Soc. 42 (1959) No. 1, p. 11/5
[6] Gutt, W.: Building Research Current Papers, CP90/68 (1968), 22 p.
[7] Gutt, W., A. D. Russell: J. Mater. Sci. 12 (1977) No. 9, p. 1869/78
[8] Trömel, G., W. Fix, R. Heinke: Tonind.-Ztg. 93 (1969) No. 1, p. 1/8
[9] Foster, W. R.: J. Am. Ceram. Soc. 51 (1968) No. 6, p. 353/4
[10] Hanic, F., I. Kaprálik, V. Figus, J. Stracelský: Trans. J. Br. Ceram. Soc. 82 (1983), p. 205/7
[11] an Mey, S.: PhD Thesis, RWTH Aachen, Germany, (1988), p. 118
[12] Taylor, J. R., A. T., Dinsdale: CALPHAD 14 (1990) No. 1, p. 71/88
[13] Eriksson, G., P. Wu, A. D. Pelton: Canad. Metall. Q. 33 (1994) 13/21
[14] Hillert, M., B. Sundman, X. Wang: Metall. Trans. B 21B (1990) No. 2, p. 303/12
[15] Hillert, M., B. Sundman, X. Wang, T. Barry: CALPHAD 15 (1991) No. 1, p. 53/58

$CaO\text{-}TiO_2$

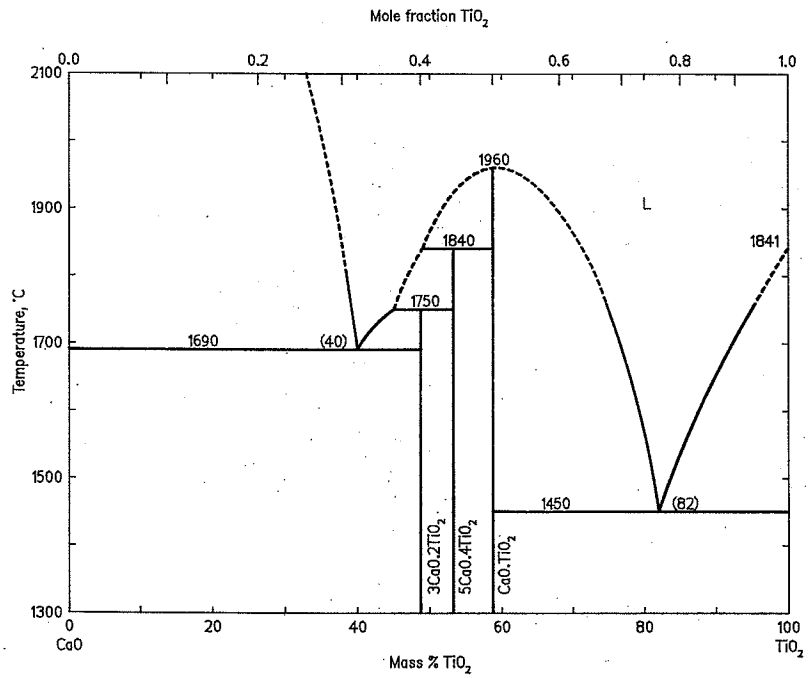


Fig. 3.71. $CaO\text{-}TiO_2$ phase diagram after Tulgar [1]. For earlier versions of the phase diagram, see DeVries et al. [2], Roth [3] and Jongejan, Wilkins [4]. An additional compound of composition $4CaO{\cdot}3TiO_2$ has been reported by Roth [3] and Jongejan, Wilkins [4]. After Imlach, Glasser [5], Kimura, Muan [6] and Shultz [7] only one solution phase, between the end-compositions $3CaO.2TiO_2$ and $4CaO.3TiO_2$, exists in this part of the system. For additional information about calcium titanates, see Reznitskii [8].

References

[1] Tulgar, H. E.: Istanbul Tek. Univ. Bul. 29 (1976) No. 1, p. 111/29
[2] DeVries, R. C., R. Roy, E. F. Osborn: J. Phys. Chem. 58 (1954) No. 12, p. 1069/73
[3] Roth, R. S.: J. Res. Nat. Bur. Stand., RP 2913 61 (1958) No. 5, p. 437/40
[4] Jongejan, A., A. L. Wilkins: J. Less-Common Metals 20 (1970) No. 4, p. 273/9
[5] Imlach, J. A., F. P. Glasser: Trans. J. Br. Ceram. Soc. 67 (1968) No. 12, p. 581/609
[6] Kimura, S., A. Muan: Am. Mineral. 56 (1971) No. 7-8, p. 1322/46
[7] Shultz, R. L.: J. Am. Ceram. Soc. 56 (1973) No. 1, p. 33/6
[8] Reznitskii, L. A.: Izv. Akad. Nauk SSSR, Neorg. Mater. 25 (1989) No. 2, p.346/8

$CaO\text{-}V_2O_5$

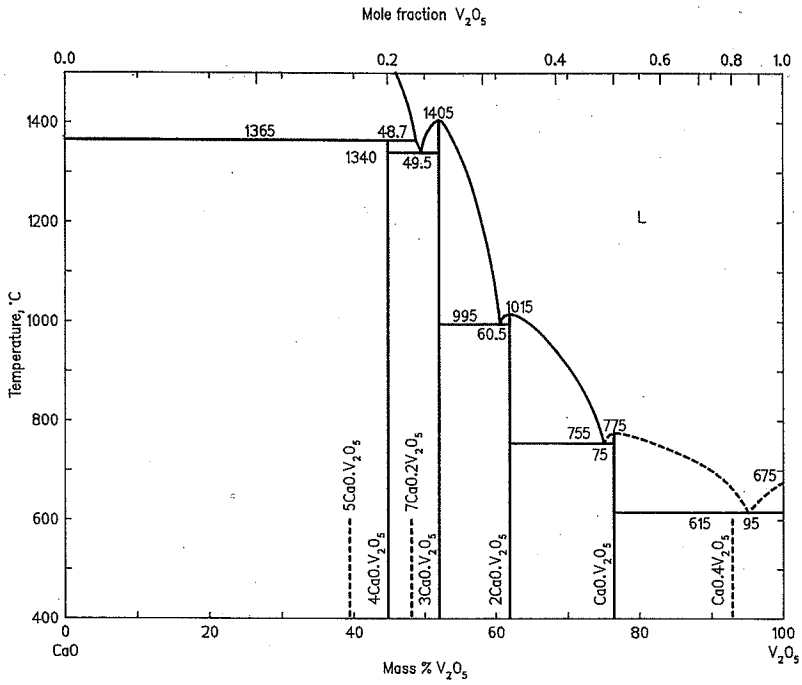


Fig. 3.72. $CaO\text{-}V_2O_5$ phase diagram in air after Yuan [1] with the V_2O_5-rich region of the system after Morozov [2] as revised by Fedorov et al. [3]. Contrary to the findings of Morozov [2], Yuan [1] report all compounds to melt congruently. For the $3CaO{\cdot}V_2O_5$ phase, this is in accord with previous work by Cox, Surek [4]. A polymorphic transformation of $3CaO{\cdot}V_2O_5$ slightly below its melting point has also been reported [4]. According to Bauer, Balz [5] the $4CaO{\cdot}V_2O_5$ phase melts at 1380 °C. The additional compounds $5CaO{\cdot}V_2O_5$ and $7CaO_2{\cdot}V_2O_5$ reported by Bouloux et al. [6], Fotiev, Makarov [7] and Parker, McCauley [8], are not confirmed by Yuan [1]. These phases, as well as a metastable $CaO{\cdot}4V_2O_5$ phase, melting incongruently at 645 °C and reported by Fedorov et al. [3], are shown in the figure with dashed lines.
The sub-system $V_2O_5\text{-}CaV_2O_5$ has been investigated by Volkov et al. [9]. A solution range of $Ca_xV_2O_5$, with x varying between 0.17 and 0.33 and with a congruent melting temperature of 724 °C has been reported. Phase equilibria in the sub-solidus region of the ternary systems $CaO\text{-}V_2O_5\text{-}V_2O$ and $CaO\text{-}V_2O\text{-}V_2O_3$ have been investigated by Bouloux et al. [6] and Slepukhin et al. [10] respectively. Additional compounds containing V(III) and V(IV) have been reported [6, 10]. The thermodynamics and phase equilibria in a portion of the ternary system Ca-O-V at 1000 °C have been reported by Panek et al. [11].

References

[1] Yuan, Y.: Steel Res. 62 (1991) No. 2, p. 60/5
[2] Morozov, A. N.: Metallurg 13 (1938) No. 12, p. 21/8
[3] Fedorov, P. I., N. P. Slotvinskii-Sidak, G. V. Vorobeva, V. K. Andreev: Izv. Vyssh. Uchebn. Zaved., Khim. Tekhnol. 14 (1971) No. 11, p. 1750/1
[4] Cox, C. D., T. Surek: J. Can. Ceram. Soc. 35 (1966), p. 45/7
[5] Bauer, V. H., W. Balz: Z. Anorg. Allg. Chem. 340 (1965) No. 5-6, p. 225/31
[6] Bouloux, J. C., J. Galy, P. Hagenmuller: Rev. Chim. Minér. 11 (1974) No. 1, p. 48/70
[7] Fotiev, A. A., V. A. Makarov: Zh. Neorg. Khim. 19 (1974) No. 4, p. 1116/8
[8] Parker, F. J., R. A. McCauley: J. Am. Ceram. Soc. 65 (1982) No. 7, p. 349/51
[9] Volkov, V. L., A. A Fotiev, L. L. Surat: Zh. Fiz. Khim. 49 (1975) No. 6, p. 1575/7
[10] Slepukhin, A. K., A. A. Fotiev, V. L. Volkov: Deposited Doc. VINITI 1336-75, (1975), 7 p.
[11] Panek, Z., K. Fitzner, T. Bold: Arch. Metall. 33 (1988) No. 1, p. 123/33

$Cr_2O_3\text{-}FeO_x$

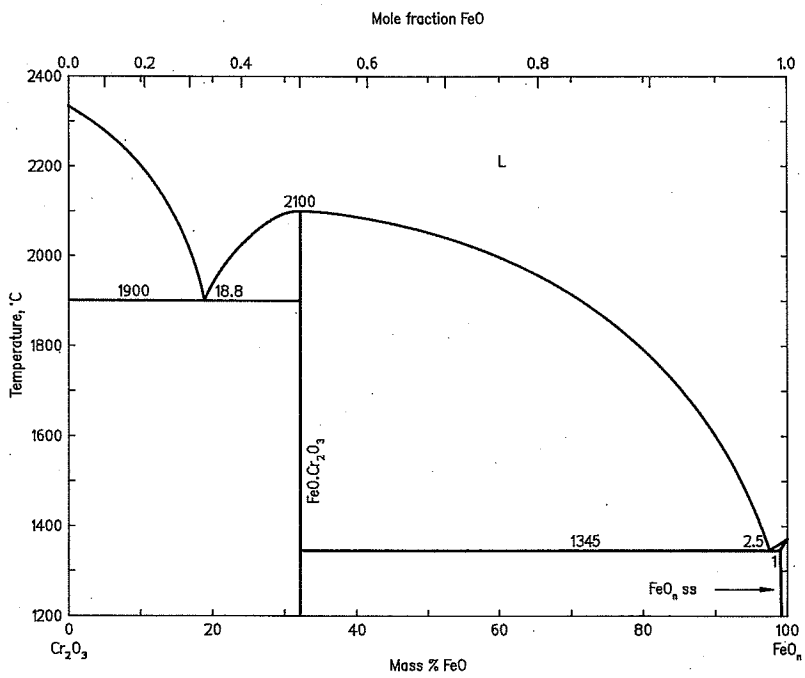


Fig. 3.73. $Cr_2O_3\text{-}FeO_n$ system under reducing conditions after Belov et al. [1] and Hoffmann [2].

Fig. 3.74. Cr_2O_3-FeO_n system in an atmosphere consisting of equal parts of CO_2 and H_2 (pO_2 approx. between 10^{-9} and 10^{-11} atm) after Riboud, Muan [3] projected on the Cr_2O_3-FeO section. The $FeO{\cdot}Cr_2O_3$ phase is stoichiometric with respect to oxygen content (oxygen to cation ratio=4/3). The apparent "FeO excess" in the $FeO{\cdot}(Cr,Fe)_2O_3$ solid solution results from the projection of phase equilibria on the Cr_2O_3-FeO section [3].

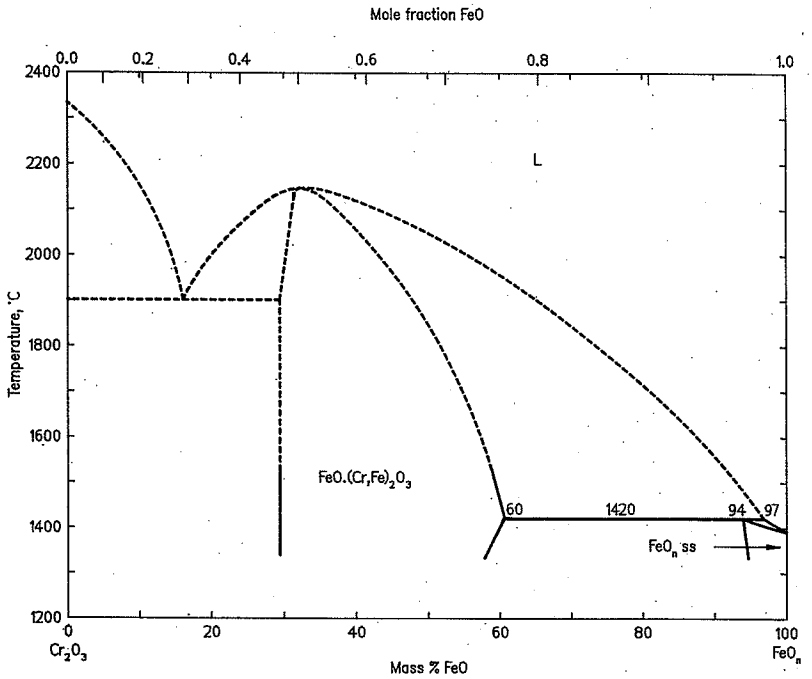
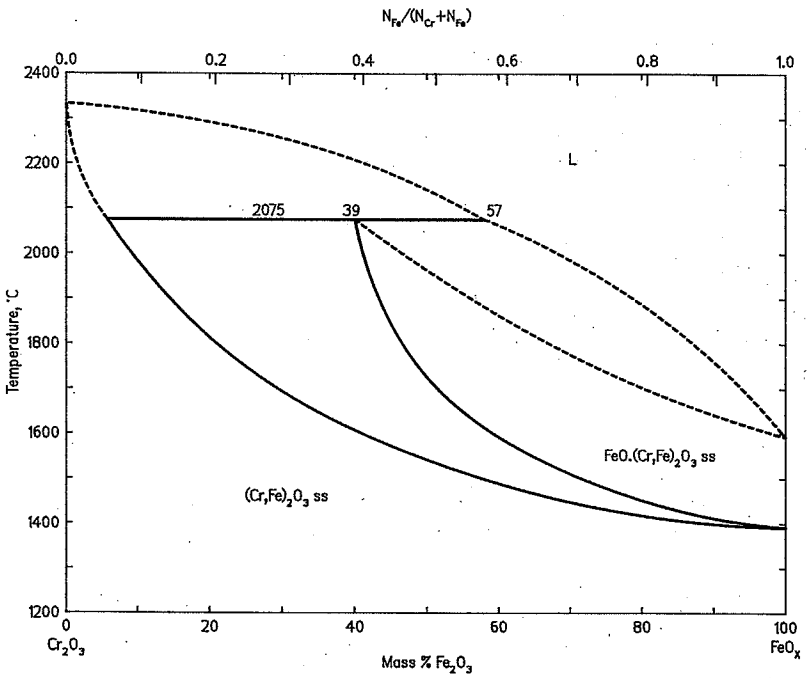


Fig. 3.75. Cr_2O_3-FeO_x system in air at 1 atm total pressure after Muan, Somiya [4] projected on the Cr_2O_3-Fe_2O_3 section.



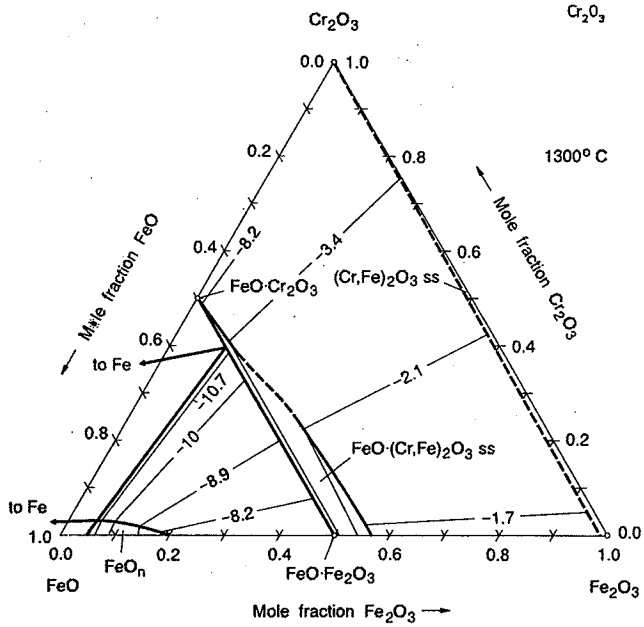


Fig. 3.76. Isothermal section through the ternary Cr_2O_3-FeO-Fe_2O_3 system at 1300 °C with oxygen isobars after Katsura, Muan [5].

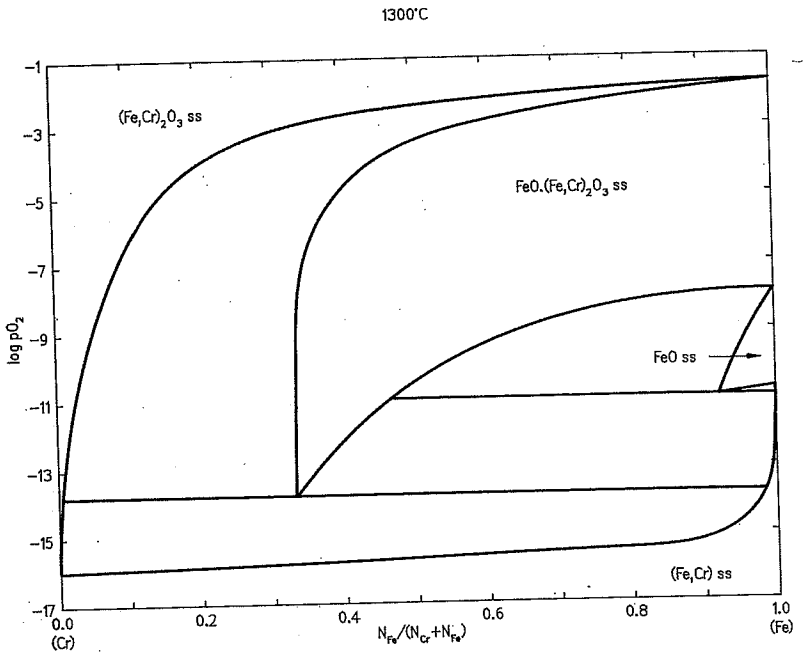


Fig. 3.77.

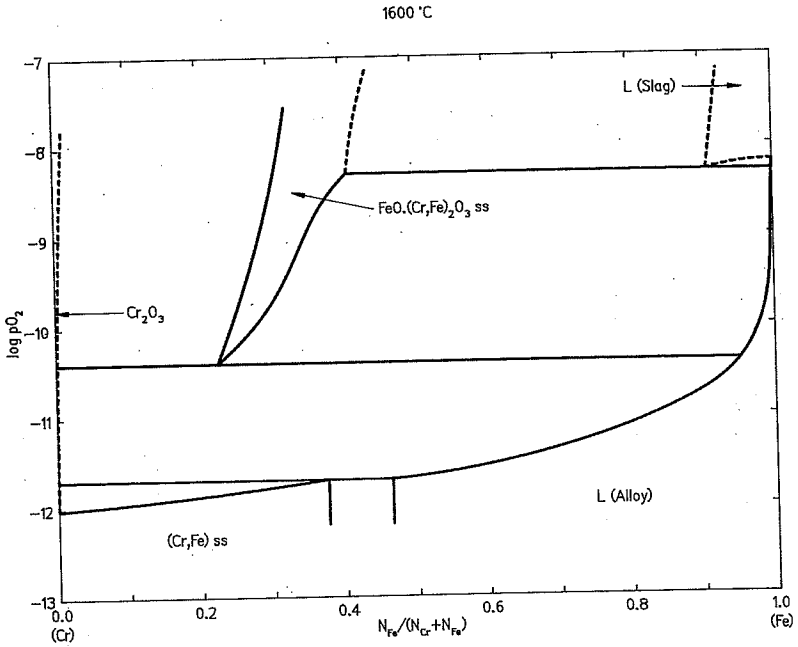
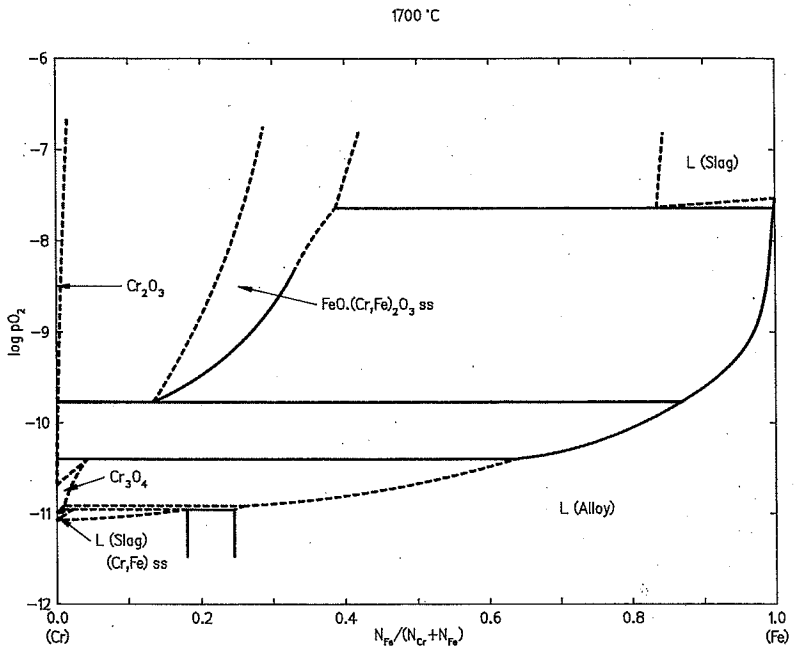


Fig. 3.78.

Fig. 3.79.



Figs. 3.77 to 3.79. Log pO_2 vs. $N_{Fe}/(N_{Cr}+N_{Fe})$ diagrams for the system Cr-Fe-O at 1300 °C calculated by Pelton et al. [6] according to experimental results by Katsura, Muan [5] and at 1600 and 1700 °C after Toker et al. [7].

The phase relations and equilibrium oxygen partial pressures between 850 and 1300 °C in the system Cr-Fe-O have also been extensively investigated by Seybolt [8], Snethlage, Klemm [9], Katsura et al. [10], Lykasov et al. [11] and Marhabi et al. [12]. For thermodynamic assessment of the complete system Cr-Fe-O, see Taylor, Dinsdale [13].

References

[1] Belov, B. F., I. A. Novokhatskii, L. N. Rusakov, A. V. Gorokh, A. A. Savinskaya: Zh. Fiz. Khim. 42 (1968) No. 7, p. 856/8

[2] Hoffmann, A.: Arch. Eisenhüttenwes. 36 (1965) No. 3, p. 155/62

[3] Riboud, P. V., A. Muan: Trans. Metall. Soc. AIME 230 (1964), p. 88/90

[4] Muan, A., S. Somiya: J. Am. Ceram. Soc. 43 (1960) No. 4, p. 204/9

[5] Katsura, T., A. Muan: Trans. Metall. Soc. AIME 230 (1964) No. 1, p. 77/84

[6] Pelton, A. D., H. Schmalzried, J. Sticher: J. Phys. Chem. Solids 40 (1979), p. 1103/22

[7] Toker N. Y., L. S. Darken, A. Muan: Metall. Trans. B 22B (1991) No. 12, p. 689/703

[8] Seybolt, A. U.: J. Elektrochem. Soc. 107 (1960) No. 3, p. 147/56

[9] Snethlage, R., D. D. Klemm: Neues Jahrb. Mineral., Abh. 125 (1975) No. 3, p. 227/42

[10] Katsura, T., M. Wakihara, S. Hara, T. Sugihara: J. Solid State Chem. 13 (1975) No. 1-2, p. 107/13

[11] Lykasov, A. A., G. G. Mikhailov, Y. S. Kuznetsov, V. I. Shishkov, E. L. Shakhin: Diffuz., Sorbtsiya Fazovye Prevrashch. Protsessakh Vosstanov. Met., Meeting Date 1978, Ed.: Ageev, N. V., Nauka, Moscov, (1981), p. 41/5

[12] Marhabi, L., M. C. Trinel-Dufour, P. Perrot, H. A. Lazouni, Z. Derriche: Ann. Chim. /Paris/ 12 (1987) No. 3, p. 223/35

[13] Taylor, J. R., A. T. Dinsdale: Z. Metallkde. 84 (1993) No. 5, p. 335/45

Cr_2O_3-MgO

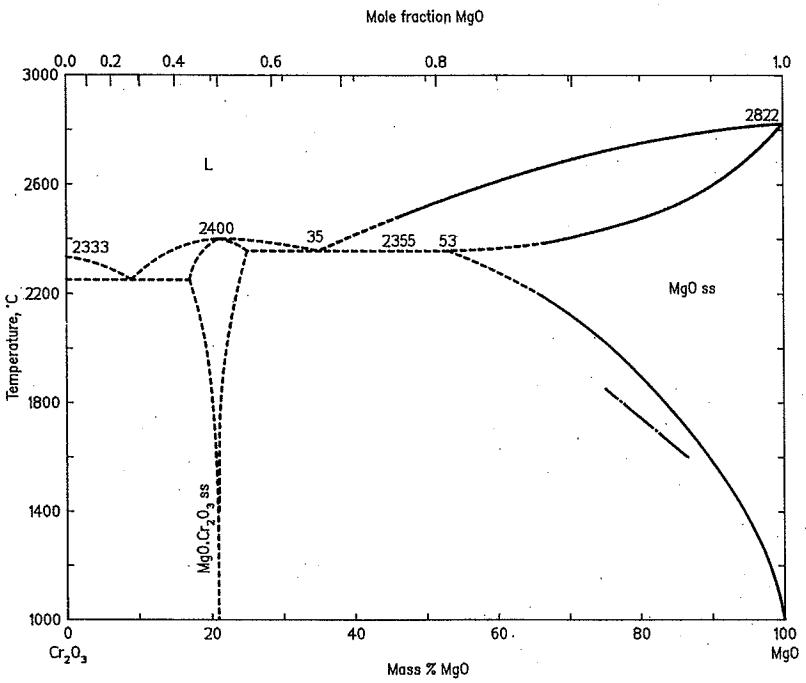


Fig. 3.80. Cr_2O_3-MgO phase diagram based mainly on the data of Alper et al. [1] (sub-system MgO-MgO·Cr_2O_3) and Wilde, Rees [2]. The solubility of Cr_2O_3 in MgO has been re-investigated by Greskovich, Stubican [3, 4], Ibrahim [5], Henriksen, Kingery [6], Dewendra et al. [7] and Woermann [8]. The greater solubility then reported by Alper et al. [1] was found in 3,4,5,7,8). The dash-dot line in the figure shows the solubility limit of Cr_2O_3 in MgO as determined recently by Woermann [8]. According to Warshaw, Keith [9] there is no mutual solubility in the sub-system Cr_2O_3-MgO·Cr_2O_3 at 1650 °C. Measurements by Somiya et al. [10] at 1400 °C show a few per cent solubility of MgO in Cr_2O_3 but no solubility of the system components in the MgO·Cr_2O_3 phase was observed. Recently, an additional metastable solution phase 2MgO·Cr_2O_3 has been reported by Titov et al. [11].

References

[1] Alper, A. M., R. N. McNally, R. C. Doman, F. G. Keihn: J. Am. Ceram. Soc. 47 (1964) No. 4, p. 30/3

[2] Wilde, W. T., J. Rees: Trans. J. Br. Ceram. Soc. 42 (1943) No. 7, p. 123/55

[3] Greskovich, C. D., V. S. Stubican: J. Phys. Chem. Solids 30 (1969), p. 909/17

[4] Greskovich, C. D., V. S. Stubican: J. Am. Ceram. Soc. 53 (1970) No. 5, p. 251/3

[5] Ibrahim, M.: Pakistan J. Sci., Ind. Res. 21 (1978) No. 3-4, p. 138/42

[6] Henriksen, A. F., W. D. Kingery: Ceramurgia Int. 5 (1979) No. 1, p. 11/17

[7] Dewendra, J. D., C. M. Wilson, N. H. Brett: Trans. J. Br. Ceram. Soc. 81 (1982) No. 6, p. 185/9

[8] Woermann, E.: private communication

[9] Warshaw, J., M. L. Keith: J. Am. Ceram. Soc. 37 (1954) No. 4, p. 161/6

[10] Somiya, S., S. Hirano, M. Ishizaka: Yogyo Kyokai Shi 85 (1977) No. 5, p. 201/9

[11] Titov, V. N., V. A. Ryabin, Y. A. Petrov, N. F. Seliverstov, T. N. Znitkova: Izv. Akad. Nauk SSSR, Neorg. Mat. 24 (1988) No. 11, p. 1934/5

CrO_x-SiO_2

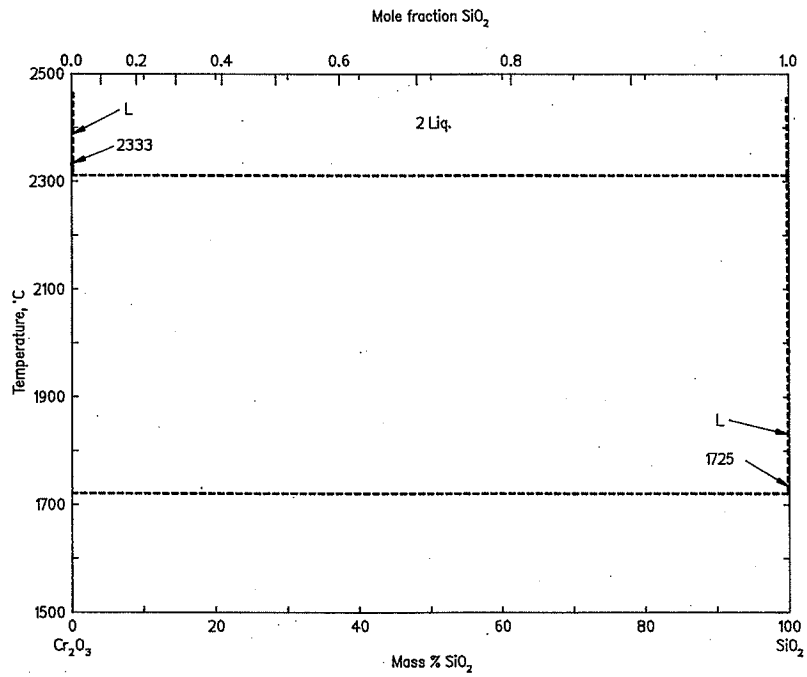
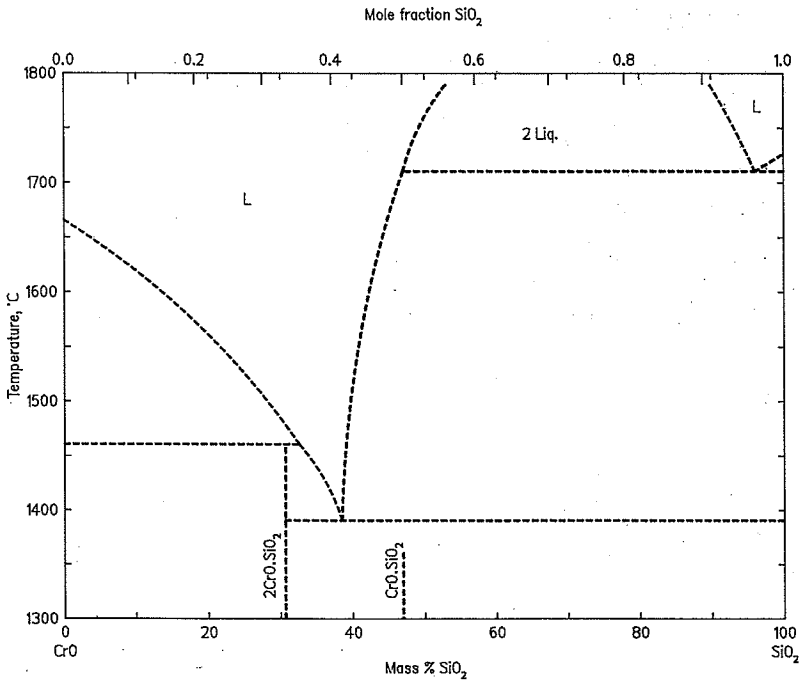


Fig. 3.81. Schematic representation of phase relations in the system Cr_2O_3-SiO_2 by Keith [1] according to comments by Bunting [2]. As reported by Bunting [2], the solubility of Cr_2O_3 in melts at about 2100 °C does not exceed 0.1 mass %. The phase equilibria in the system Cr_2O_3-SiO_2 have also been estimated by Glasser et al. [3]. A more restricted miscibility gap in the Cr_2O_3-rich region of the system was proposed.

Fig. 3.82. CrO-SiO_2 (CrO as hypothetical compound) phase diagram at low oxygen partial pressures (tentative) after Healy, Schottmiller [4]. The $2CrO{\cdot}SiO_2$ phase has also been confirmed and investigated by Cvetkov et al. [5]. Similar phase diagram features but without compound formation above 1300 °C, have been reported by Muan [6]. The additional compound $CrO{\cdot}SiO_2$ was also quoted in [6]. For the composition of the melts in the ternary system CrO-Cr_2O_3-SiO_2 between 1500 and 1750 °C, and for the isothermal section at 1700 °C, see original paper by Healy, Schottmiller [4].



References

[1] Keith, M. L.: J. Am. Ceram. Soc. 37 (1954) No. 10, p. 490/6

[2] Bunting, E. N.: J. Res. Nat. Bur. Stand., RP 203 5 (1930) No. 2, p. 325/7

[3] Glasser, F. P., I. Warshaw, R. Roy: Phys. Chem. Glasses 1 (1960) No. 2, p. 39/45

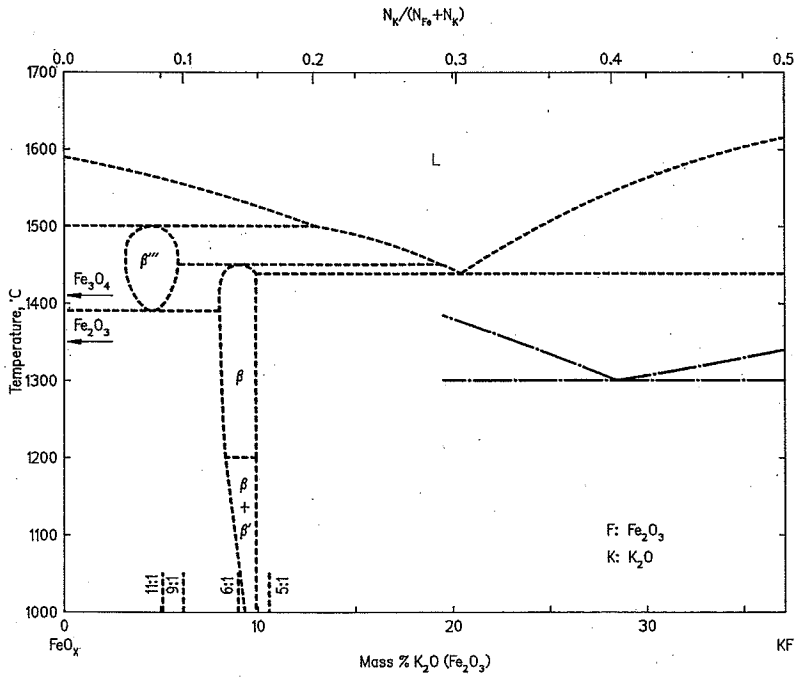
[4] Healy, G. W., J. C. Schottmiller: Trans. Metall. Soc. AIME 230 (1964) No. 3, p. 420/5

[5] Cvetkov, A. I., Z. P. Ershov, N. A. Matveeva: Izv. Akad. Nauk SSSR, Geol. Ser. (1964) No. 2, p. 3/14

[6] Muan, A.: Proc. of International Conference on Applied Mineralogy, ICAM 81, Johannesburg, (1981), in: Spec. Publ. Geol. Soc. S. Afr. 7 (1983), p. 325/36

FeO_x-K_2O

Fig. 3.83. Sub-system Fe_2O_3-$K_2O{\cdot}Fe_2O_3$ (tentative) according to Romanov et al. [1], Parker et al. [2] and Plante et al. [3]. After Takahashi et al. [4] the $K_2O{\cdot}Fe_2O_3$ phase melts at approx. 1340 °C and the eutectic is located at approx. 1300 °C (dash-dot lines in the figure). For the $K_2O{\cdot}xFe_2O_3$ solution phase (with x varying from 5 to 11), see Scholder, Mansmann [5], Dvoretskii et al. [7] and Belous et al. [6].



References

[1] Romanov, V. P., G. A. Candela, R. S. Roth, L. J. Swartzendruber: J. Appl. Phys. 507 (1979) No. 10, p. 6455/8

[2] Parker, H. S., R. S. Roth, C. D. Olson, E. R. Plante: Natl. Bur. Stand. (US) Int. Rep., NBSIR 78-1483 (1978), p. 84/100

[3] Plante, E. R., H. S. Parker, R. S. Roth, C. D. Olson: Natl. Bur. Stand. (US) Int. Rep., NBSIR 79-1767 (1979), p. 82/102

[4] Takahashi, T., K. Kuwabara, Y. Kase: Denki Kagaku Oyobi Kogyo Butsuri Kagaku 43 (1975) No. 5, p. 273/7

[5] Scholder, R., M. Mansmann: Z. Anorg. Allg. Chem. 321 (1963) No. 5-6, p. 246/61

[6] Belous, A. G., E. B. Novosadova, E. V. Pashkova: Ukr. Khim. Zh. 52 (1986) No. 9, p. 917/9

[7] Dvoretskii, N. V., E. G. Stepanov, T. N. Sudzilovskaya, G. R. Kotelnikov, V. V. Yun: Izv. Akad. Nauk SSSR, Neorg. Mater. 25 (1987) No. 2, p. 284/8

FeO_x-MgO

Fig. 3.84. FeO_n-MgO system in contact with iron Schenck, Pfaff [1] (solidus as determined experimentally and liquidus as calculated), projected on the FeO-MgO section. The liquidus temperatures for the FeO_n-rich region of the system determined experimentally by Scheel [2] are shown with dash-dot lines. Recently, the solubility of MgO in melts between 1550 and 1650 °C has been reported Shim, Ban-Ya [3] (dotted line in the figure).

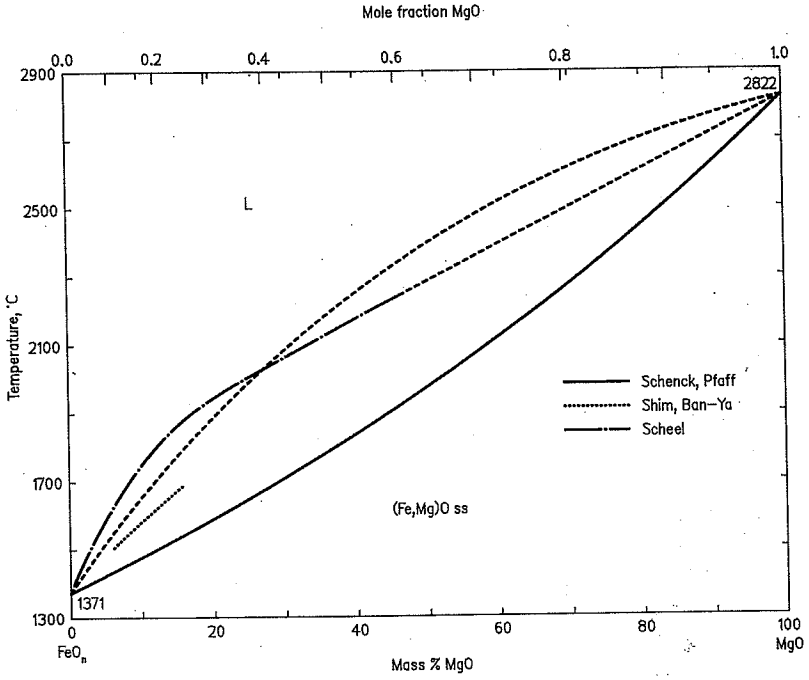
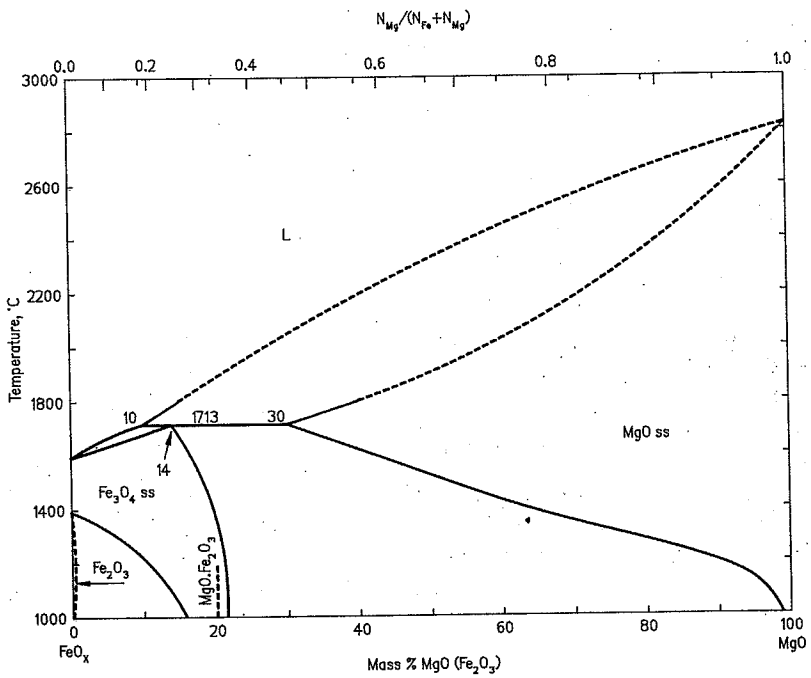


Fig. 3.85. FeO_x-MgO system in air after Phillips et al. [4] projected on the Fe_2O_3-MgO section. Similar phase diagrams have been reported by Willshee, White [5] and recently by Limbert et al. [6].



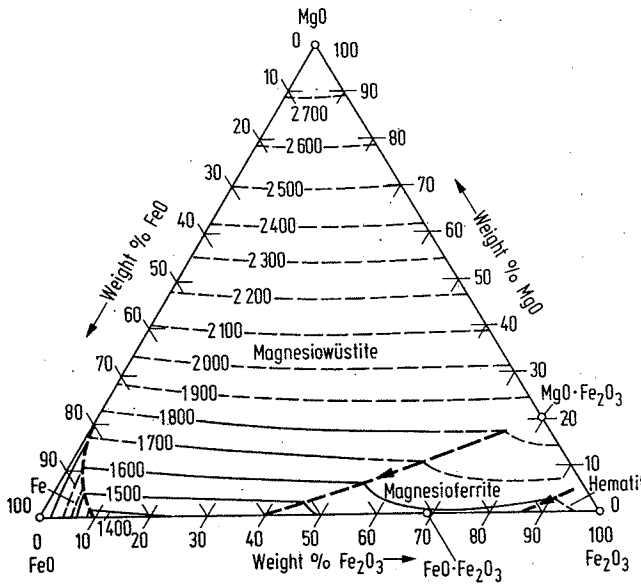


Fig. 3.86. Tentative liquidus surface in the system FeO-Fe_2O_3-MgO after Phillips, Muan [7]. For the isothermal sections between 1400 and 1800 °C, see original paper by Phillips, Muan [7].

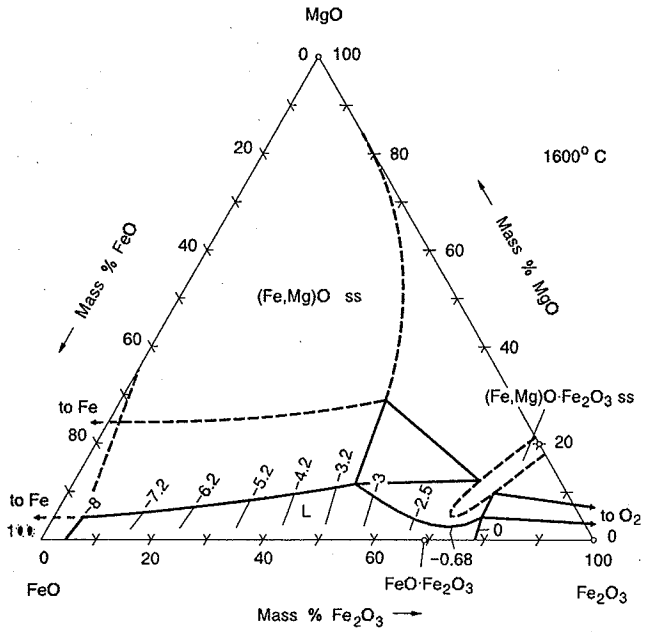


Fig. 3.87. Isothermal section through the FeO-Fe_2O_3-MgO system at 1600 °C with oxygen isobars over the liquid (log pO_2, atm) after Schürmann, Kolm [8].

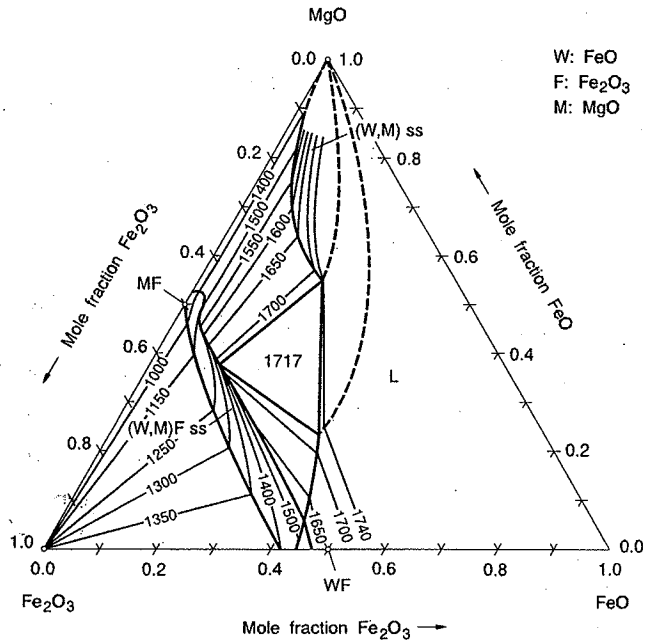


Fig. 3.88. Isobaric phase diagram for the system FeO-Fe_2O_3-MgO in air up to 1750 °C after Willshee, White [5], Richards, White [9] and Woodhouse, White [10].

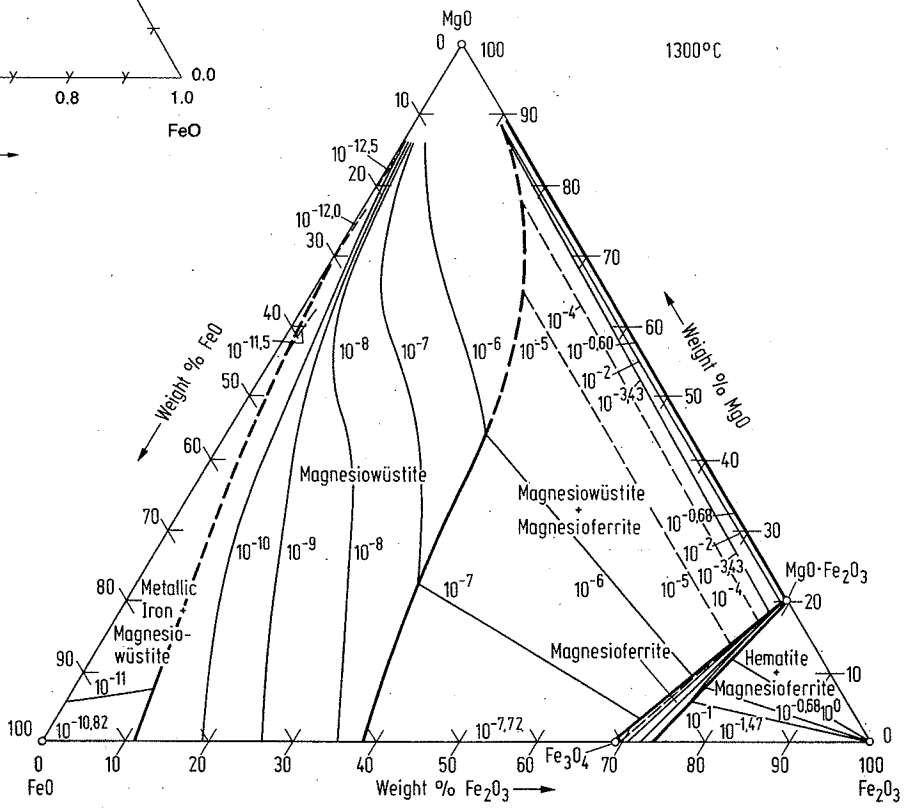
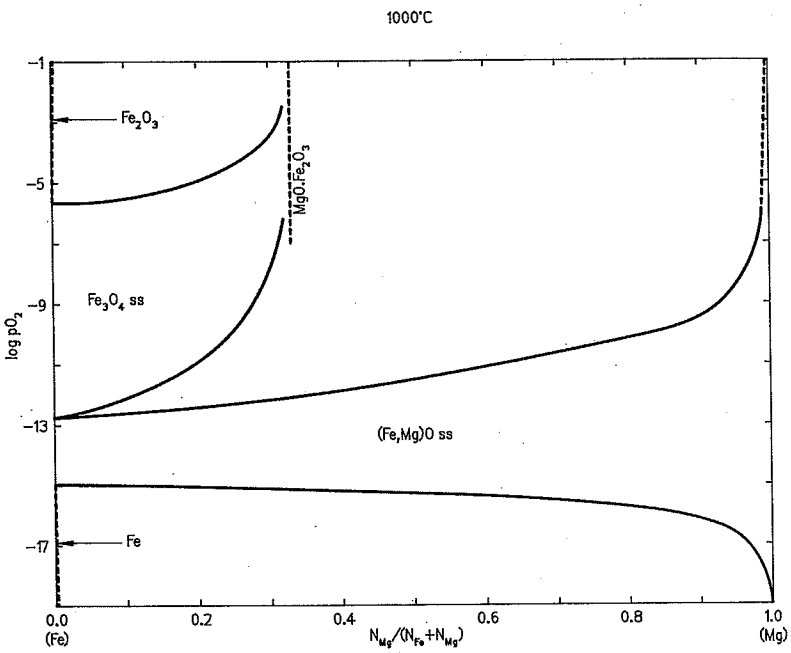


Fig. 3.89. Isothermal section through the system FeO-Fe_2O_3-MgO at 1300 °C with oxygen isobars after Speidel [11]. The phase equilibria and equilibrium oxygen partial pressures between 1000 and 1400 °C have also been investigated by Shishkov et al. [12], Saha, Biggar [13], Trinel-Dufour, Perrot [14], Paladino [15], Katsura, Kimura [16], Oleynikov et al. [17] and Reijnen [18].

Fig. 3.90. Log pO_2 vs. $N_{Mg}/(N_{Fe}+N_{Mg})$ diagram for the system Fe-Mg-O at 1000 °C after Trinel-Dufour, Perrot [14]. For the portion of the system at oxygen partial pressure between 10^{-11} and 10^{-16} atm, see also Lykasov et al. [19].



References

[1] Schenck, H., W. Pfaff: Arch. Eisenhüttenwes. 32 (1961) No. 11, p. 741/51
[2] Scheel, R.: Sprechsaal Keram., Glas, Baustoffe 108 (1975) No. 23-24, p. 685/6
[3] Shim, J.-D., S. Ban-Ya: Tetsu-to-Hagane 67 (1981) No. 10, p. 1735/44
[4] Phillips, B., S. Somiya, A. Muan: J. Am. Ceram. Soc. 44 (1961) No. 4, p. 167/9
[5] Willshee, J. C., J. White: Trans. J. Br. Ceram. Soc. 66 (1967) No. 11, p. 541/55
[6] Limbert, U., R. Fusenig, E. Woermann, M. Glaveris, H. Schweinsberg: Sprechsaal 117 (1984) No. 4, p. 314/22
[7] Phillips, B., A. Muan: J. Am. Ceram. Soc., 45 (1962) No. 12, p. 588/91
[8] Schürmann, E., I. Kolm: Steel Res. 59 (1988) No. 5, p. 185/91
[9] Richards, R. G., J. White: Trans. J. Br. Ceram. Soc. 53 (1954), p. 422/59
[10] Woodhouse, D., J. White: Trans. J. Br. Ceram. Soc. 54 (1955), p. 333/66
[11] Speidel, D. H.: J. Am. Ceram. Soc. 50 (1967) No. 5, p. 243/8
[12] Shishkov, V. I., A. A. Lykasov, A. F. Ilina: Zh. Fiz. Khim. 54 (1980) No. 3, p. 440/1
[13] Saha, P., G. M. Biggar: Indian J. Earth Sci. 1 (1974) No. 2, p. 131/40
[14] Trinel-Dufour, M. C., P. Perrot: Ann. Chim. /Paris/ 2 (1977) No. 6, p. 309/18
[15] Paladino, A. E.: J. Am. Ceram. Soc. 43 (1960) No. 4, p. 183/91
[16] Katsura, T., S. Kimura: Bull. Chem. Soc. Japan 38 (1965) No. 10, p. 1664/70
[17] Oleynikov, N. N., Y. G. Saksonov, Y. D. Tretyakov: Izv. Akad. Nauk SSSR, Neorg. Mater. 1 (1965) No. 2, p. 246/53
[18] Reijnen, P.: Philips Res. Rep. 23 (1968) No. 2, p. 151/88
[19] Lykasov, A. A., G. G. Mikhailov, Y. S. Kuznetsov, V. I. Shishkov, E. L. Shakhin: Diffuz., Sorbtsiya Fazovye Prevrashch. Protsesakh Vosstanov. Met., Meeting Date 1978, Ed.: Ageev, N. V., Nauka, Moscov, (1981), p. 41/5

FeO_x-MnO_x

Fig. 3.91. FeO_n-MnO system in contact with iron as calculated by Schürmann, Bannenberg [1] in agreement with experimental results by Fischer, Fleischer [2, 3], Fischer, Bardenheuer [4, 5] and Oeters et al. [6]. For the phase diagram showing also fields of metallic phases, see original papers Oeters et al. [6].

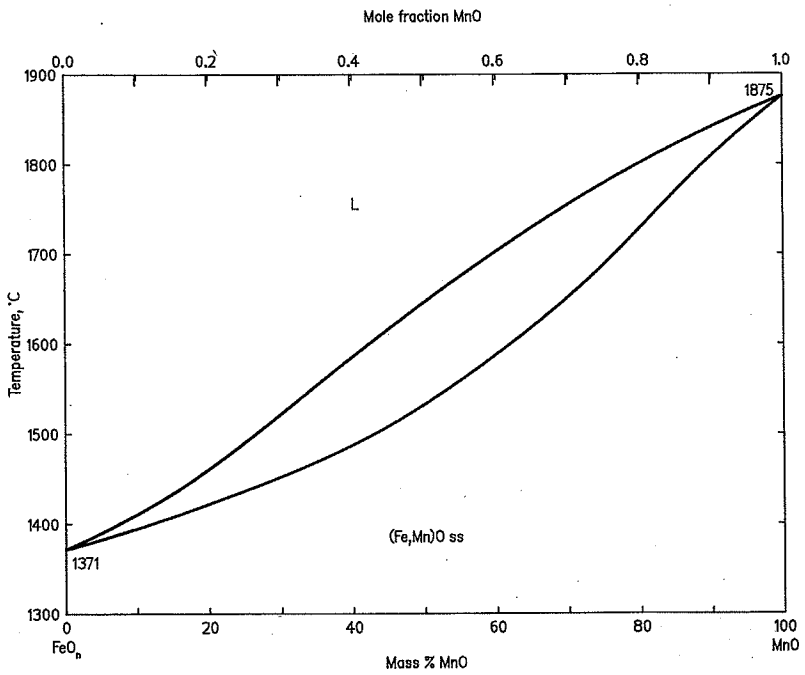


Fig. 3.92. FeO_x-MnO_x system in air projected on the Fe_2O_3-Mn_2O_3 section after Muan, Somiya [7]. The dash-dot lines show the phase boundaries in the FeO_x-rich region of the system as re-investigated by Bergstein, Kleinert [8].

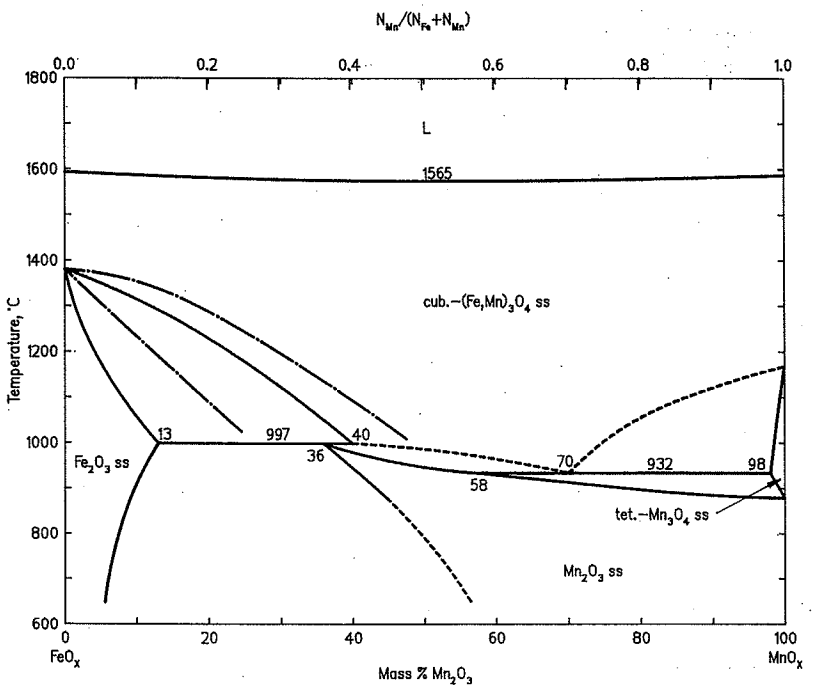
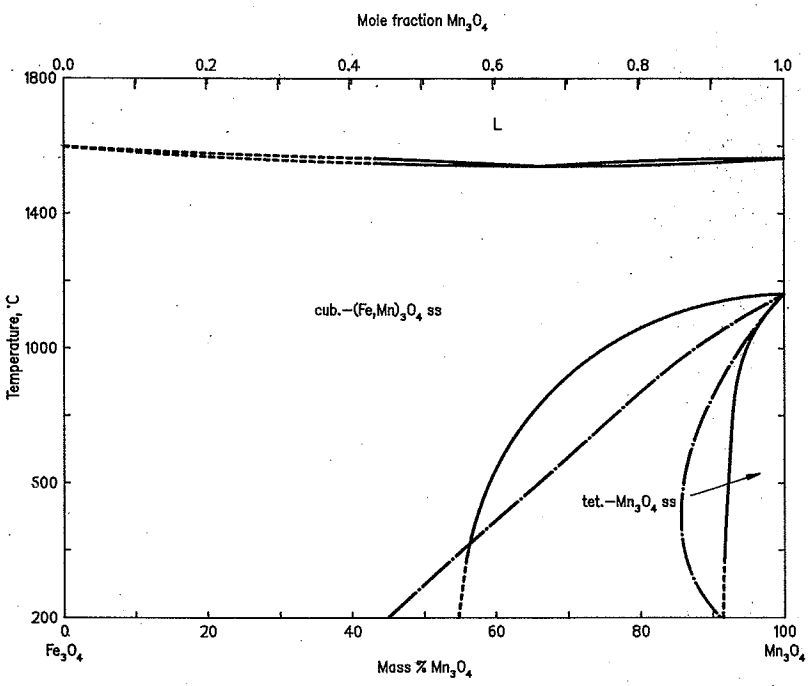


Fig. 3.93. Fe_3O_4-Mn_3O_4 system after Van Hook, Keith [9] with phase boundaries between cubic and tetragonal $(Fe,Mn)_3O_4$ solution phases as suggested by Holba et al. [10]. For cubic-tetragonal transformation, see also Brabers [11].



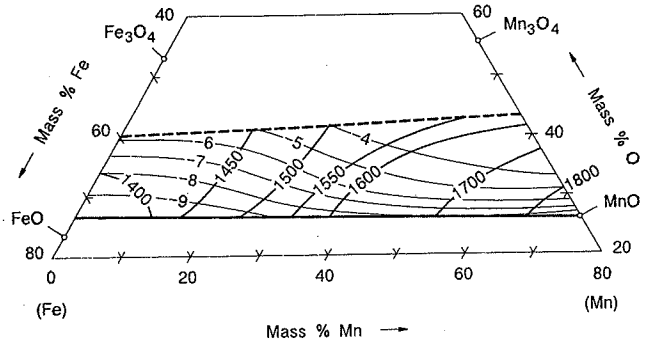


Fig. 3.94. Primary field of crystallization of (Fe, Mn)O with oxygen isobars in the ternary system Fe-Mn-O after Oeters et al. [6].

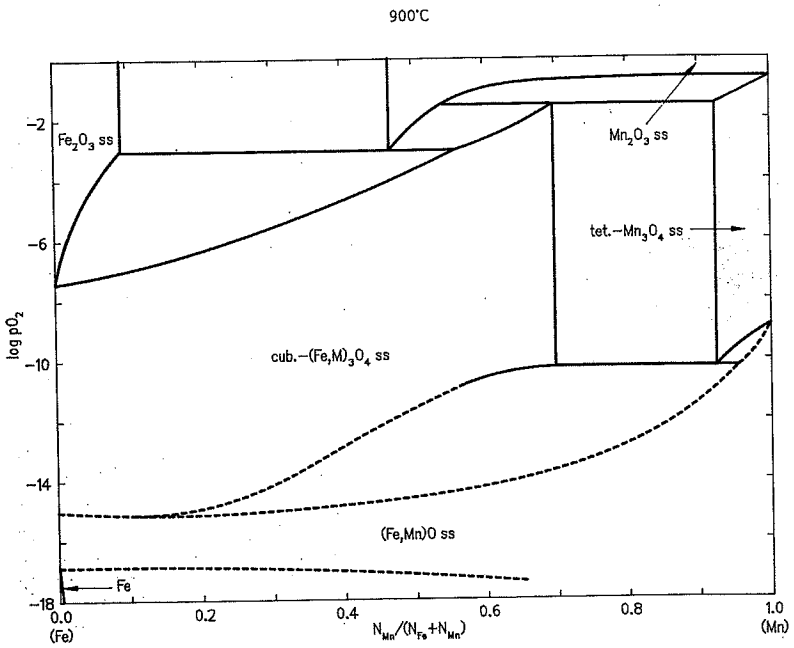


Fig. 3.95. Log pO_2 vs. $N_{Mn}/(N_{Fe}+N_{Mn})$ diagram for the system Fe-Mn-O at 900 °C calculated by Pelton et al. [12] based in part on original data by Muan, Somiya [7] and Van Hook, Keith [9]. For further diagrams between 700 and 1300 °C, see also Schwerdtfeger, Muan [13], Lykasov et al. [14] and Punge-Witteler [15].

The ternary system Fe-Mn-O has also been investigated by Gurry, Darken [16], Shafer [17], Büssem, Butler [18], Tretyakov et al. [19], Komarov et al. [20], Koch, Kaestle [21], Jacquemot, Gatellier [22], Mikhailov, Tanklevskaya [23], Terayama et al. [24], and Lykasov, Pavlovskaya [25].

References

[1] Schürmann, E., N. Bannenberg: Arch. Eisenhüttenwes. 55 (1984) No. 8, p. 349/58
[2] Fischer, W. A., H.-J. Fleischer: Arch. Eisenhüttenwes. 32 (1961) No. 1, p. 1/10
[3] Fischer, W. A., H.-J. Fleischer: Arch. Eisenhüttenwes. 36 (1965) No. 11, p. 791/8
[4] Fischer, W. A., P. W. Bardenheuer: Arch. Eisenhüttenwes. 39 (1968) No. 9, p. 637/43
[5] Fischer, W. A., P. W. Bardenheuer: Arch. Eisenhüttenwes. 39 (1968) No. 8, p. 559/70
[6] Oeters, F., K. Koch, R. Scheel, U. Nölle: Arch. Eisenhüttenwes. 48 (1977) No. 9, p. 475/80
[7] Muan, A., S. Somiya: Am. J. Sci. 260 (1962) No. 3, p. 230/40
[8] Bergstein, A., P. Kleinert: Collect. Czeh. Chem. Commun. 29 (1964) No. 10, p. 2549/51
[9] Van Hook, H. J., M. L. Keith: Am. Mineral. 43 (1958) No. 1/2, p. 63/83
[10] Holba, P., M. A. Khilla, S. Krupicaka: J. Phys. Chem. Solids 34 (1973) No. 3, p. 387/95
[11] Brabers, V. A. M.: J. Phys. Chem. Solids 32 (1971), p. 2181/91
[12] Pelton, A. D., H. Schmalzried, J. Sticher: Ber. Bunsenges. Phys. Chem. 83 (1979) No. 3, p. 241/52
[13] Schwerdtfeger, K., A. Muan: Trans. Metall. Soc. AIME 238 (1967) No. 8, p. 1114/9
[14] Lykasov, A. A., G. G. Mikhailov, Y. S. Kuznetsov, V. I. Shishkov, E. L. Shakhin: Diffuz., Sorbtsiya Fazovye Prevrashch. Protsessakh Vosstanov. Met., Meeting Date 1978, Ed.: Ageev, N. V., Nauka, Moscov, (1981), p. 41/5
[15] Punge-Witteler, B.: Z. Phys. Chem. /Munich/ 142 (1984) No. 2, p. 239/48
[16] Gurry, R. W., L. S. Darken: J. Am. Chem. Soc. 72 (1950) No. 9, p. 3906/10
[17] Shafer, M. W.: IBM J. Res. Develop. 2 (1958) No. 6, p. 193/9
[18] Büssem, W. R., S. R. Butler: J. Am. Ceram. Soc. 46 (1963) No. 9, p. 442/6
[19] Tretyakov, Y. D., Y. G. Saksonov, J. V. Gordeer: Izv. Akad. Nauk SSSR, Neorg. Mater. 1 (1965) No. 3, p. 413/8
[20] Komarov, V. F., N. N. Oleynikov, Y. G. Saksonov, Y. D. Tretyakov: Izv. Akad. Nauk SSSR, Neorg. Mater. 1 (1965) No. 3, p. 395/404
[21] Koch, K., G. Kaestle: Phys.-Chim. Sider., C.-R. Congr., Meeting Date 1978 (1979), p. 78/83
[22] Jacquemot, A.; C. Gatellier: Comm. Eur. Communities, EUR 6216, Pt. 1, Paper No. 4, p. 23
[23] Mikhailov, G. G., N. M. Tanklevskaya: Izv. Vyssh. Uchebn. Zaved., Chern. Met. (1981) No. 6, p. 5/9
[24] Terayama, K., M. Ikeda, M. Taniguchi: Trans. Jpn. Inst. Met. 24 (1983) No. 7, p. 514/17
[25] Lykasov, A. A., M. S. Pavlovskaya: Zh. Fiz. Khim. 62 (1988) No. 5, p. 1188/93

Fig. 3.96. FeO_n-Na_2O system under reducing condition after Dai et al. [1]. Below dash-dot line, metallic iron is present.

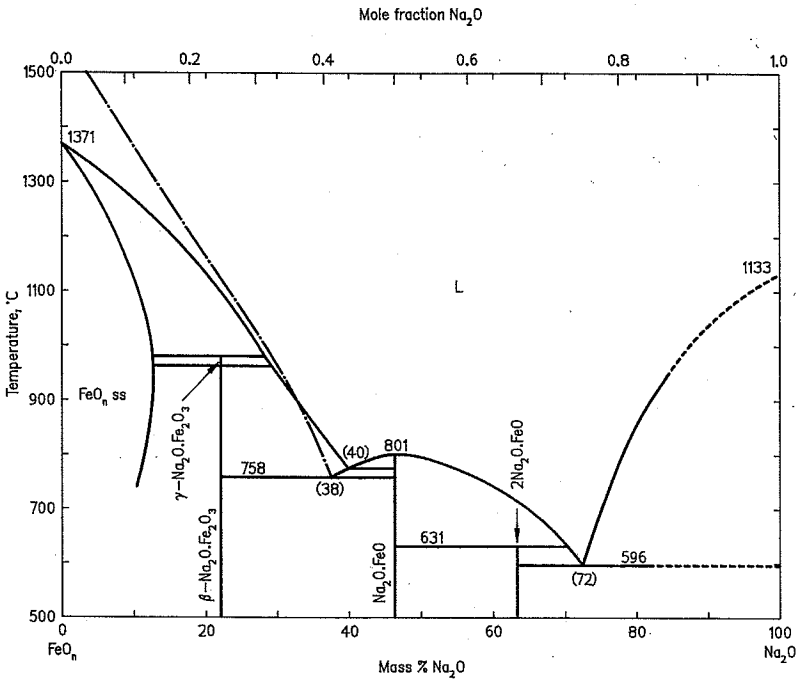
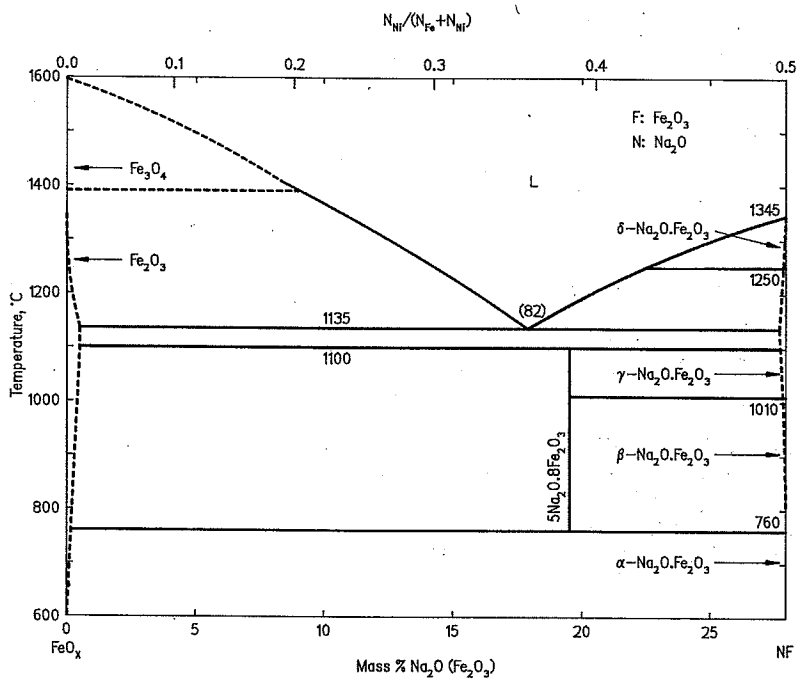
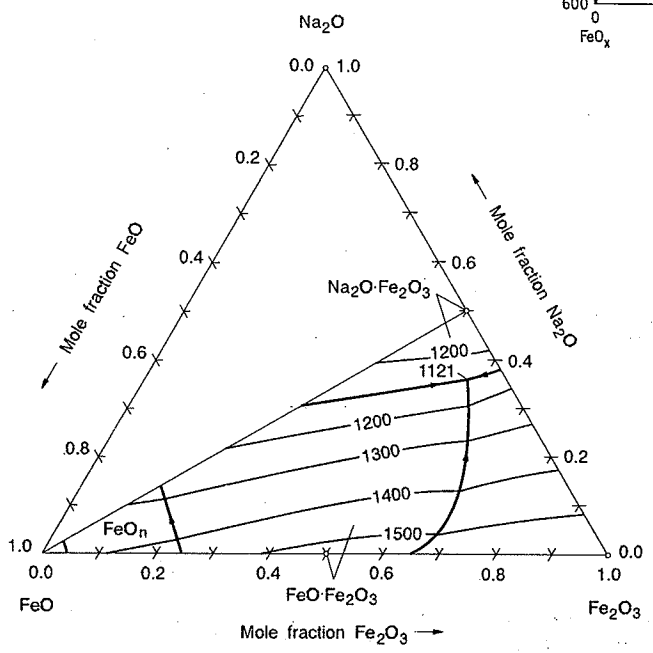


Fig. 3.97. Fe_2O_3-Na_2O-Fe_2O_3 phase diagram in air after Knick, Kohlmeyer [2] (liquid-solid equilibria) and Théry, Collongues [3] and Théry [4] (sub-solidus equilibria). The -Na_2O-Fe_2O_3 phase has been reported recently by Grey, Li [5] to exist above 1250 °C. For the stoichiometry of the $5Na_2O$-$8Fe_2O_3$ phase, see also Rooymans [6] and Scholder, Mansmann [7]. The extended metastable -Fe_2O_3 solid solution was reported by Théry [4] to exist up to 650 °C and 12 mass % Na_2O.





← **Fig. 3.98.** Liquidus surface in the sub-system FeO-Fe_2O_3-Na_2O after Dai et al. [8]. For the thermodynamics of the system and further isothermal and composition sections, see original paper by Dai et al. [1, 8].

References

[1] Dai, W., S. Seetharaman, L.-I. Staffansson: Scand. J. Metall. 13 (1984), p. 32/8

[2] Knick, R., E. J. Kohlmeyer: Z. Anorg. Allg. Chem. 244 (1940), p. 67/83

[3] Théry, J., R. Collongues: C. R. Acad. Sci., Ser. C 247 (1958) No. 22, p. 2003/6

[4] Théry, J.: Ann. Chim. /Paris/ 7 (1962), p. 207/38

[5] Grey, I. E., C. Li: J. Solid State Chem. 69 (1987), p. 116/25

[6] Rooymans, C. J. M.: J. Phys. Soc. Japan 17 (1962) No. 4, p. 722/3

[7] Scholder, R., M. Mansmann: Z. Anorg. Allg. Chem. 321 (1963) No. 5-6, p. 246/61

[8] Dai, W., S. Seetharaman, L.-I. Staffansson: Metall. Trans. B 15B (1984) No. 2, p. 319/27

FeO_x-NiO

Fig. 3.99. FeO_n-NiO system in contact with metallic alloys projected on the FeO-NiO section after Schenck et al. [1].

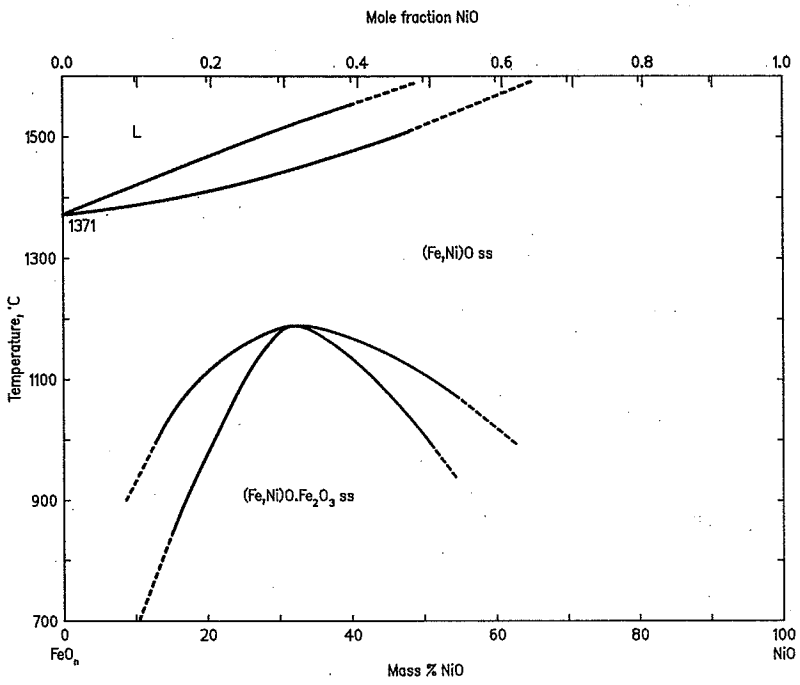
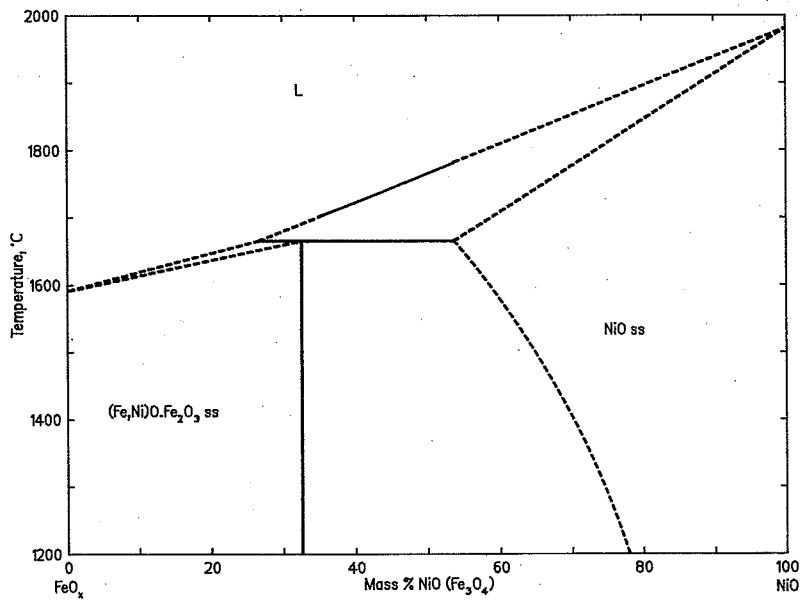


Fig. 3.100. Tentative FeO_x-NiO phase diagram in air according to Grutzeck, Muan [2].



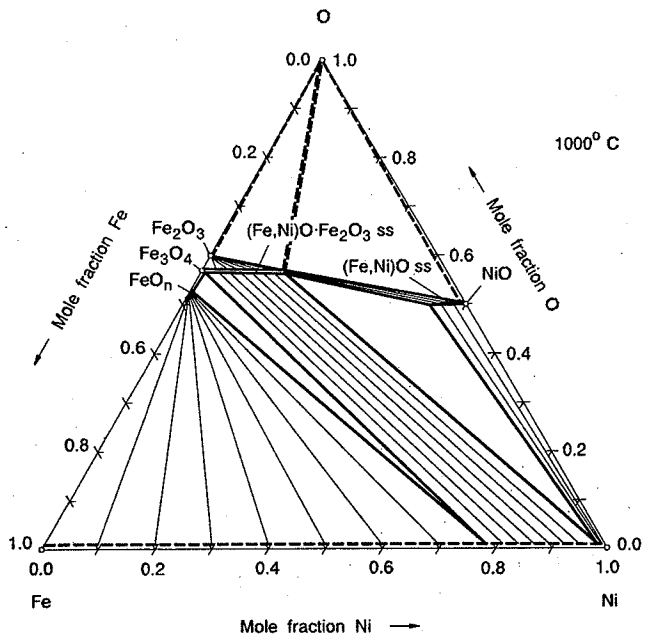
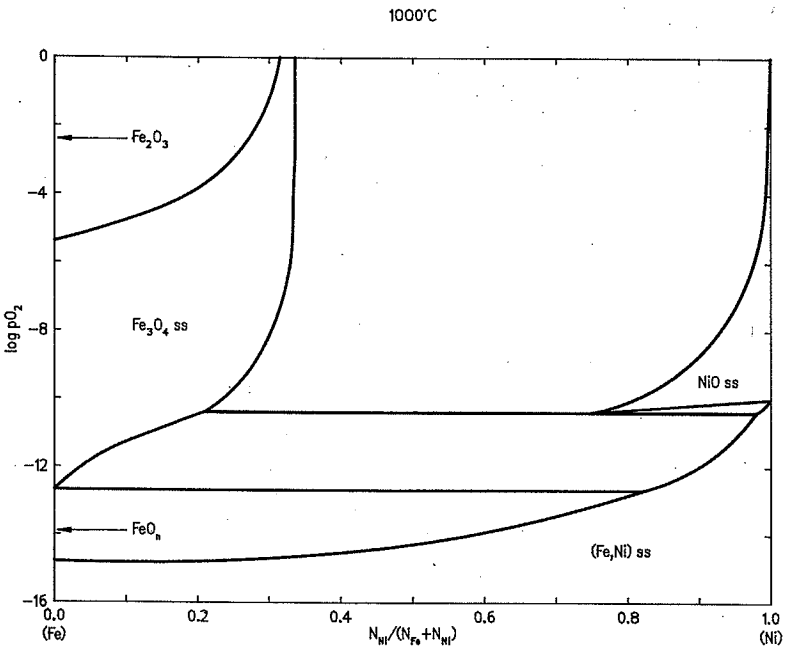


Fig. 3.101. Isothermal section through the ternary system Fe-Ni-O at 1000 °C, after Dalvi, Smeltzer [3].

Fig. 3.102. Log pO_2 vs. $N_{Ni}/(N_{Ni}+N_{Fe})$ diagram for the system Fe-Ni-O at 1000 °C computed by Pelton et al. [4] in agreement with experimental results by Davies, Smeltzer [5].



For additional contributions to the system Fe-Ni-O in the sub-solidus region, see Paladino [6], Shafer [7], O'Brayan et al. [8], Zacharias [9], Dalvi, Sridhar [10], Trinel-Dufour et al. [11-13] Shaw, Willis [14] and Lykasov et al. [15].

References

[1] Schenck, H., E. Steinmetz, R. Grundmann: Arch. Eisenhüttenwes. 39 (1968) No. 12, p. 895/901
[2] Grutzeck, M. W., A. Muan: J. Am. Ceram. Soc. 75 (1992) No. 6, p. 1342/50
[3] Dalvi, A. D., W. W. Smeltzer: J. Electrochem. Soc. 117 (1970) No. 11, p. 1431/6
[4] Pelton, A. D., H. Schmalzried, J. Sticher: J. Phys. Chem. Solids 40 (1979), p. 1103/22
[5] Davies, H., W. W. Smeltzer: J. Electrochem. Soc. 119 (1972) No. 19, p. 1362/8
[6] Paladino, A. E., Jr.: J. Am. Ceram. Soc. 42 (1959) No. 4, p. 168/75
[7] Shafer, M. W.: J. Phys. Chem. 65 (1961) No. 11, p. 2055/62
[8] O'Brayan, H. M., F. R. Monforte, R. Blair: J. Am. Ceram. Soc. 48 (1965) No. 11, p. 577/80
[9] Zacharias, H. J.: Phys. Status Solidi A 22 (1974) No. 1, p. K85/9
[10] Dalvi, A. D., R. Sridhar: Can. Metall. Q. 15 (1976) No. 4, p. 349/57
[11] Trinel-Dufour, M. C., G. Pouillard, P. Perrot: C. R. Acad. Sci., Ser. C 287 (1978) No. 11, p. 463/5
[12] Trinel-Dufour, M. C., G. Pouillard, P. Perrot: J. Chem. Res., Synop. (1979) No. 6, p. 191
[13] Trinel-Dufour, M. C., G. Pouillard, P. Perrot: J. Chem. Res., Synop. (1981) No. 3, p. 68
[14] Shaw, R. W., G. M. Willis: Can. Metall. Q. 20 (1981) No. 2, p. 153/61
[15] Lykasov, A. A., G. G. Mikhailov, Y. S. Kuznetsov, V. I. Shishkov, E. L. Shakhin: Diffuz., Sorbtsiya Fazovye Prevrashch. Protsessakh Vosstanov. Met., Meeting Date 1978, Ed.: Ageev, N. V., Nauka, Moscov, (1981), p. 41/5

FeO_x-P_2O_5

Fig. 3.103. The FeO_n-P_2O_5 system in contact with iron after Wentrup [1], Trömel, Schwerdtfeger [2] and Modaressi et al. [3] ($4FeO{\cdot}P_2O_5$ and $2FeO{\cdot}P_2O_5$ phases). An additional compound, $FeO{\cdot}P_2O_5$, was reported earlier by Wentrup [1]. The Fe-rich phosphate (10 mass % P_2O_5) reported by Trömel, Schwerdtfeger [2], is apparently a ternary phase $16FeO{\cdot}Fe_2O_3{\cdot}P_2O_3$ (9.78 mass % P_2O_5), as described by Modaressi et al. [3]. The dash-dot lines represent the ternary equilibria between solid alloys, molten alloys and oxide melts [2].

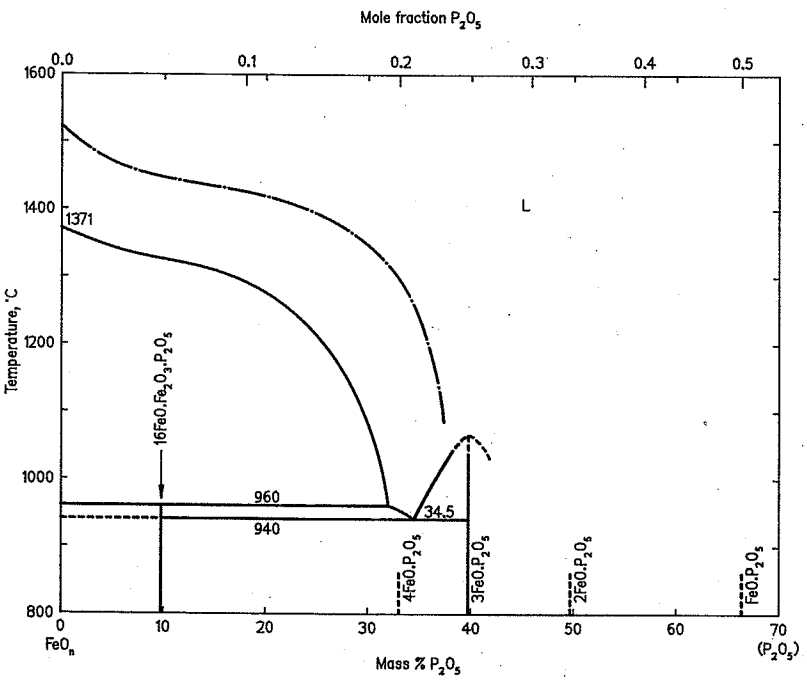
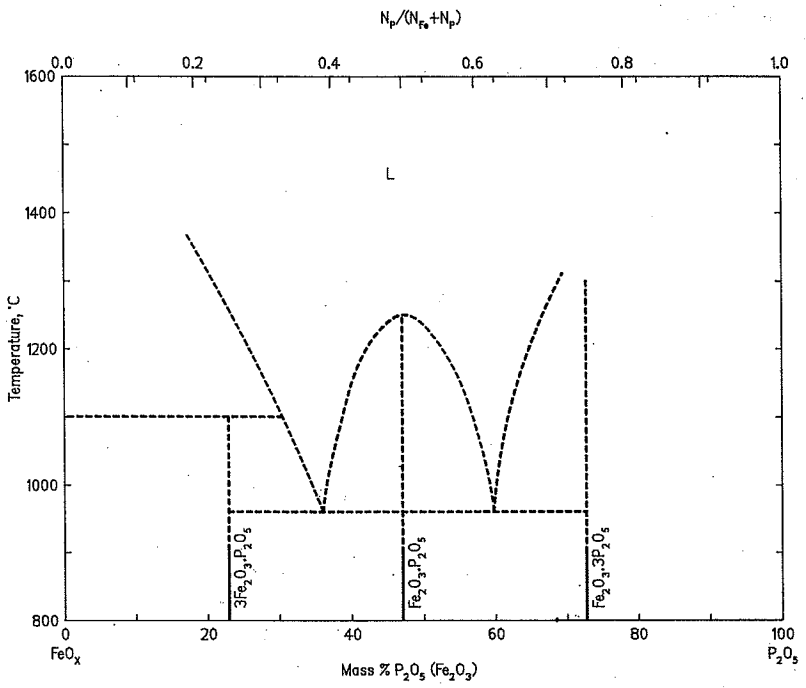


Fig. 3.104. Tentative phase equilibria in the Fe_2O_3-P_2O_5 system based on the work of Wentrup [1], Korinth, Royen [4] and Modaressi et al. [3]. As reported in [3, 4], the only stable binary compounds in this section are $3Fe_2O_3 \cdot P_2O_5$, $Fe_2O_3 \cdot P_2O_5$ and $Fe_2O_3 \cdot 3P_2O_5$. The $2Fe_2O_3 \cdot P_2O_5$ and $2Fe_2O_3 \cdot 3P_2O_5$ phases reported previously by Wentrup [1] have not been confirmed.



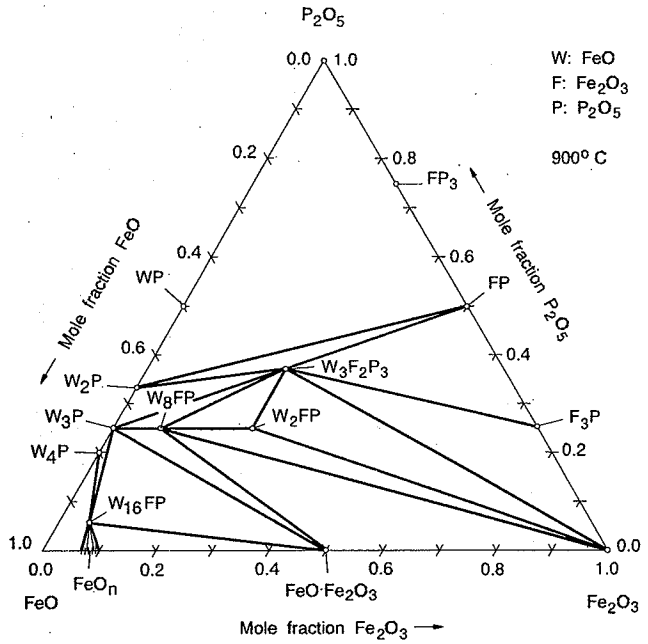


Fig. 3.105. Isothermal section through the FeO-Fe_2O_3-P_2O_5 system at 900 °C after Modaressi et al. [3]. Two ternary phases reported previously by Wentrup [1] have been reformulated. According to Gorgunov et al. [5], $3FeO \cdot 2Fe_2O_3 \cdot 3P_2O_5$ melts at 996 °C. For a discussion of the ternary system Fe-O-P, see Raghavan [6].

References

[1] Wentrup, H.: Arch. Eisenhüttenwes. 9 (1935) No. 1, p. 57/60

[2] Trömel, G., K. Schwerdtfeger: Arch. Eisenhüttenwes. 34 (1963) No. 1, p. 55/9

[3] Modaressi, A., J. C. Kaell, B. Malaman, R. Gerardin, C. Gleitzer: Mat. Res. Bull. 18 (1983) No. 1, p.101/9

[4] Korinth, J., P. Royen: Z. Anorg. Allg. Chem. 313 (1961) No. 3-4, p. 121/37

[5] Gorgunov, Y., B. Maksimov, Y. Kabalov, A. Ivachenko, O. Melnikov, N. Belov: Dokl. Akad. Nauk SSSR 254 (1980) No. 4, p. 873/7

[6] Raghavan, V.: Phase Diagrams of Ternary Iron Alloys, Part 2, Ternary Systems Containing Iron and Sulphur, The Indian Institute of Metals, Calcutta (1988)

FeO_x-SiO_2

Fig. 3.106. FeO_n-SiO_2 phase diagram in contact with iron, projected on the FeO-SiO_2 section and constructed according to results of Bowen, Schairer [1], Schuhmann, Ensio [2], Schenck, Wiesner [3] (solubility of SiO_2 in melt) and Babayan [4] (miscibility gap). Allen, Snow [5] report the eutectic between FeO_n and 2FeO·SiO_2 to be located at 21.5 mass % SiO_2. The Fe_2O_3 content in melts at liquidus temperatures after Bowen, Schairer [1] ranges from approx. 2 mass % Fe_2O_3 at 40 mass % SiO_2 to 12 mass % Fe_2O_3 in iron oxide melts.

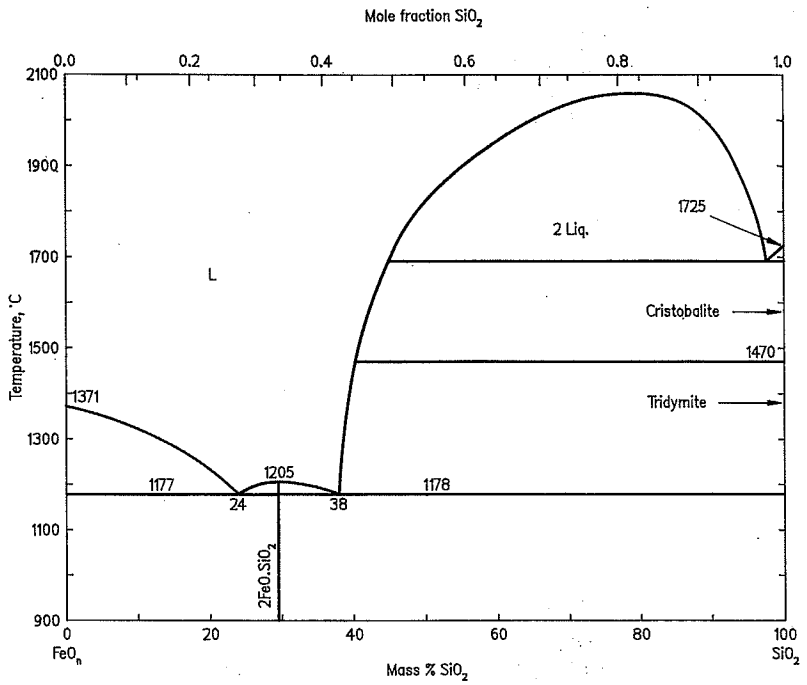
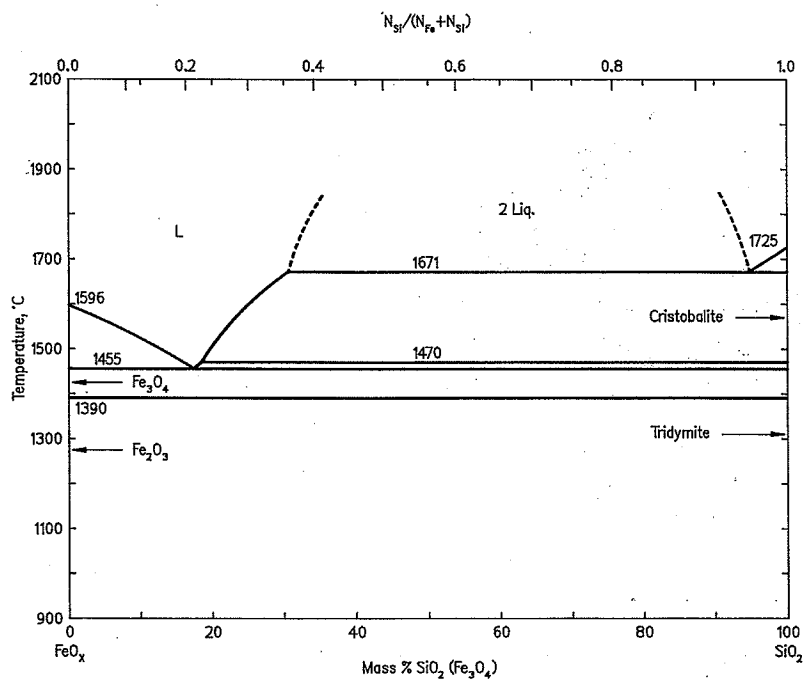


Fig. 3.107. FeO_x-SiO_2 system in air after Muan [6]. The phase equilibria have been projected on the Fe_3O_4-SiO_2 section. For the Fe_2O_3-SiO_2 tentative phase diagram at $pO_2 > 1$ atm, see Glasser et al. [7].



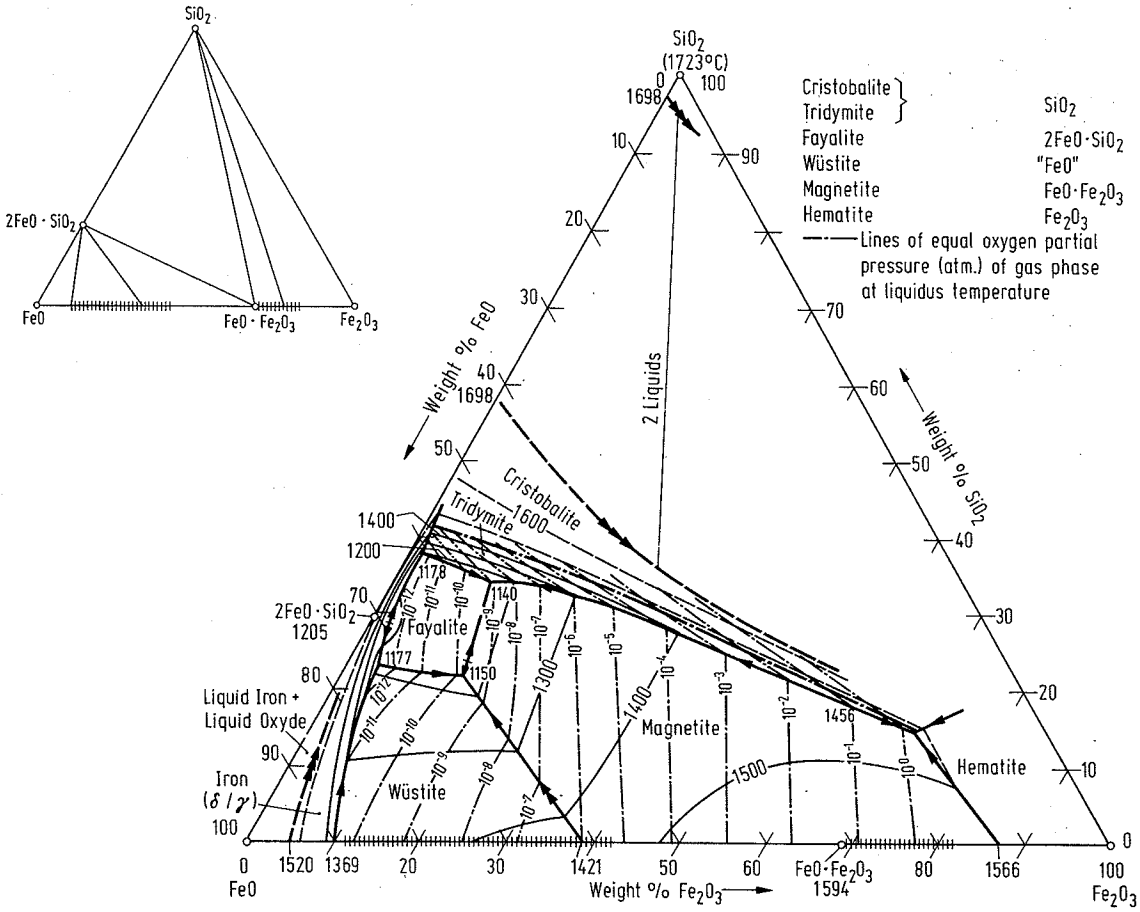


Fig. 3.108. Liquidus surface with oxygen isobars at liquidus temperatures in the system FeO-Fe_2O_3-SiO_2 after Muan, Osborn [8]. An earlier, similar version of the system has been reported by Schuhmann et al. [9] (see also Darken [10] and Gurry, Darken [11]). The section shows the compatibility relations in the FeO-Fe_2O_3-SiO_2 system.

The Fe-rich region of the ternary system Fe-O-Si between 1500 and 1538 °C has been reported by Elliot, Wright [12] and the isothermal section through the system Fe-Fe_2O_3-SiO_2 at 1200 °C by Schwerdtfeger, Muan [13].

References

[1] Bowen, N. L., J. F. Schairer: Am. J. Sci., 5th Ser. 24 (1932) No. 141, p. 177/213

[2] Schuhmann, R., Jr., P. J. Ensio: Trans. Metall. Soc. AIME, J. Metals. 3 (1951) No. 5, p. 401/11

[3] Schenck, H., G. Wiesner: Arch. Eisenhüttenwes. 27 (1956) No. 1, p. 1/12

[4] Babayan, S. A.: Arm. Khim. Zh. 28 (1975) No. 7, p. 533/9

[5] Allen, W. C., R. B. Snow: J. Am. Ceram. Soc. 38 (1955) No. 8, p. 264/80

[6] Muan, A.: Trans. Metall. Soc. AIME, J. Metals. 203 (1955) No. 9, p. 965/7

[7] Glasser, F. P., I. Warshaw, R. Roy: Phys. Chem. Glasses 1 (1960) No. 2, p. 39/45

[8] Muan, A., E. F. Osborn: Phase Equilibria Among Oxides in Steelmaking, Ed.: Addison-Wesley Publishing Company, Inc., Reading, Massachusetts (1965)

[9] Schuhmann, R. Jr., R. G. Powell, E. J. Michal: Trans. Metall. Soc. AIME, J. Metals 5 (1953) No. 9, p. 1097/104

[10] Darken, L. S.: J. Am. Chem. Soc. 70 (1948) No. 6, p. 2046/53

[11] Gurry, R. W., L. S. Darken: J. Am. Chem. Soc. 72 (1950) No. 9, p. 3906/10

[12] Elliot, J. F., J. K. Wright: Can. Metall. Q. 11 (1972) No. 4, p. 573/84

[13] Schwerdtfeger, K., A. Muan: Trans. Metall. Soc. AIME 236 (1966) No. 2, p. 201/11

FeO_x-SrO

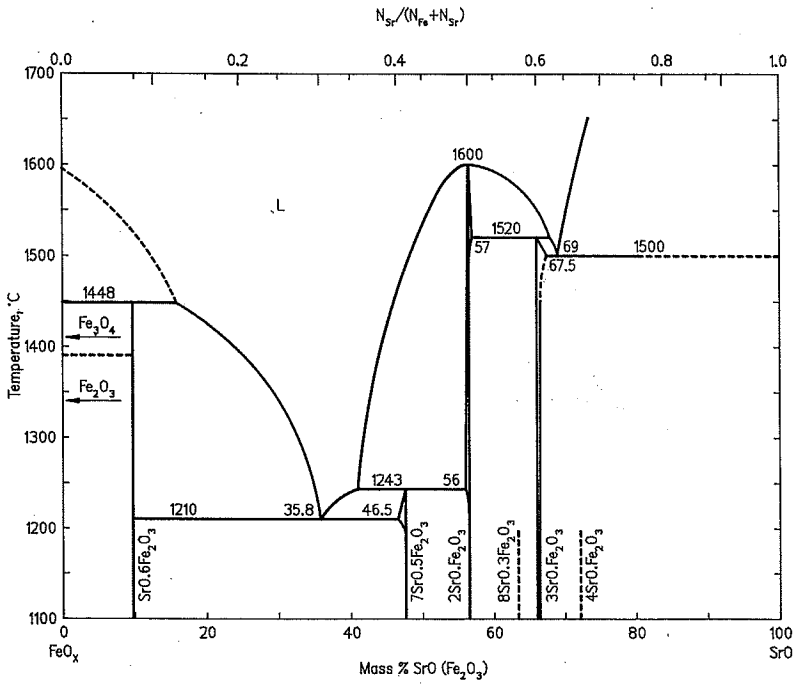


Fig. 3.109. FeO_x-SrO phase diagram after Batti [1]. Additional compounds with the formulas $Sr_4Fe_3O_{10-x}$, $Sr_3Fe_2O_{7-x}$, Sr_2FeO_{4-x} and $SrFeO_{3-x}$, containing an amount of Fe(IV) under 1 atm pO_2 and also at higher oxygen pressures, have been reported and described in numerous works due to Gallagher et al. [2-4], Brisi, Rolando [5] and Takeda et al. [6]. The homogeneity of the $SrO{\cdot}6Fe_2O_3$ phase at approx. 1150 °C after Akselrod et al. [7] ranges from 9.61 to 9.91 mass % SrO. The positions of additional compounds, but without any Fe(IV) content, are shown in the figure with dashed lines.

References

[1] Batti, P.: Ann. Chim. /Rome/ 52 (1962) No. 9-10, p. 941/61

[2] Gallagher, P. K., C. R. Kurkjian: Inorg. Chem. 4 (1965) No. 2, p. 214/9

[3] Gallagher, P. K.: Inorg. Chem. 5 (1965) No. 7, p. 965/70

[4] Gallagher, P. K., J. B. MacChesney, D. N. E. Buchanon: J. Chem. Phys. 45 (1966) No. 7, p. 2466/71

[5] Brisi, C., P. Rolando: Ann. Chim. /Rome/ 59 (1969), p. 385/99

[6] Takeda, Y., K. Kanno, T. Takada, O. Yamamoto, M. Takano, N. Nakayama, Y. Bando: J. Solid State Chem. 63 (1986) No. 2, p. 237/49

[7] Akselrod, N. L., M. G. Skovorodina, M. B. Vidrevich, E. V. Tkachenko, M. Y. Khodos: Izv. Akad. Nauk SSSR, Neorg. Mater. 22 (1986) No. 7, p. 1161/4

FeO_x-TiO_2

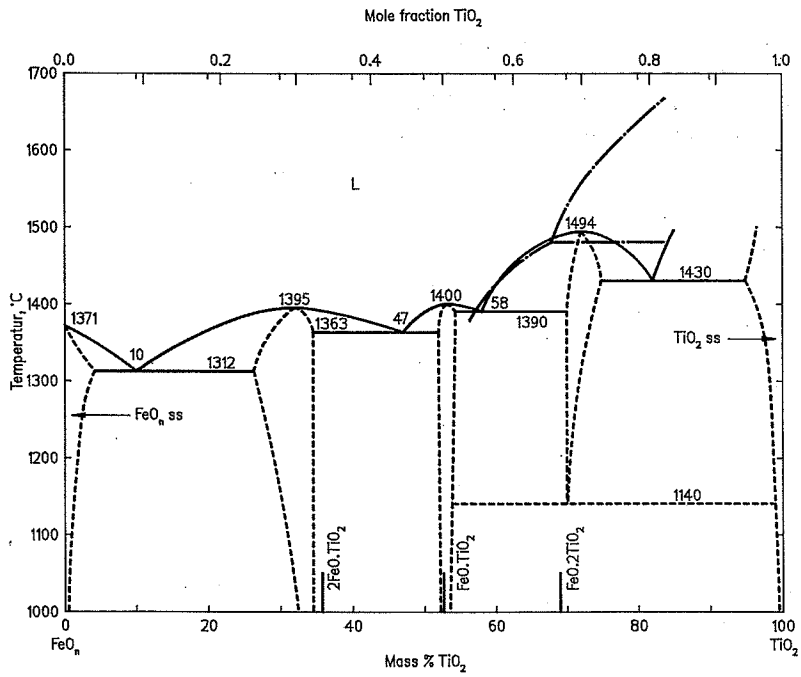
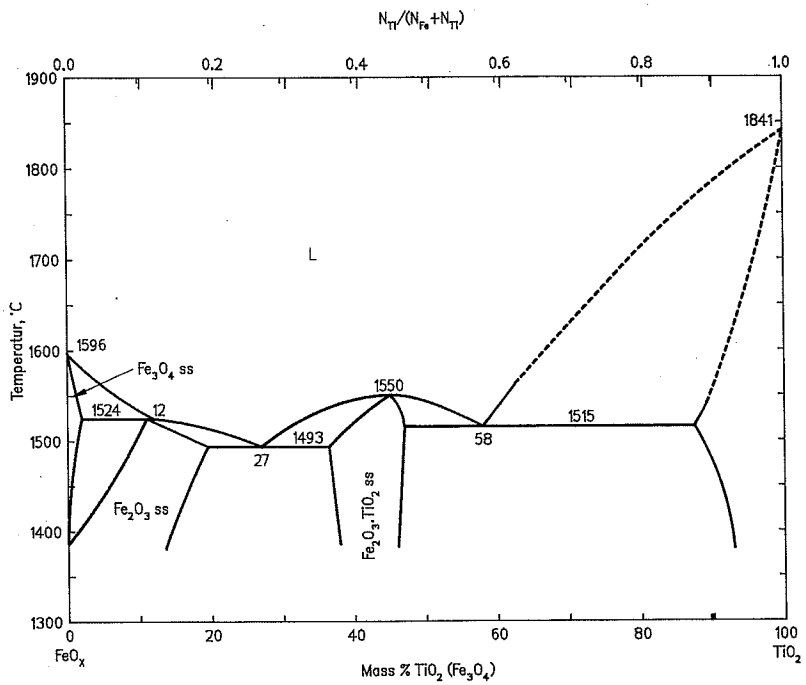


Fig. 3.110. FeO_n-TiO_2 system under reducing conditions after MacChesney, Muan [1] projected on the FeO-TiO_2 section. After Grau [2], and earlier Smith, Bell [3], the $FeO{\cdot}2TiO_2$ phase melts incongruently (dash-dot lines in the figure). The lower stability limit of the $FeO{\cdot}2TiO_2$ phase (1140 °C) is as reported by Lindsley [4]. For composition of iron titanium oxides in equilibrium with metallic iron at 1000, 11300 and 1300 °C, see also Simons, Woermann [5].

Fig. 3.111. FeO_x-TiO_2 system in air projected on the Fe_3O_4-TiO_2 section after MacChesney, Muan [6]. The composition of liquid and crystalline phases at liquidus temperatures is close to the Fe_3O_4-TiO_2 section [6].



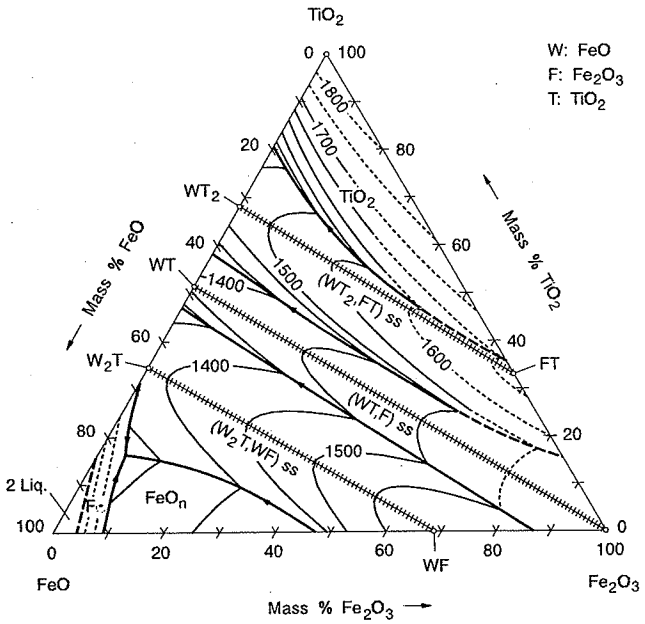


Fig. 3.112. Liquidus surface in the system FeO-Fe_2O_3-TiO_2 after Taylor [7]. The liquidus temperatures on the FeO-TiO_2 section are slightly higher than those reported by MacChesney, Muan [1].

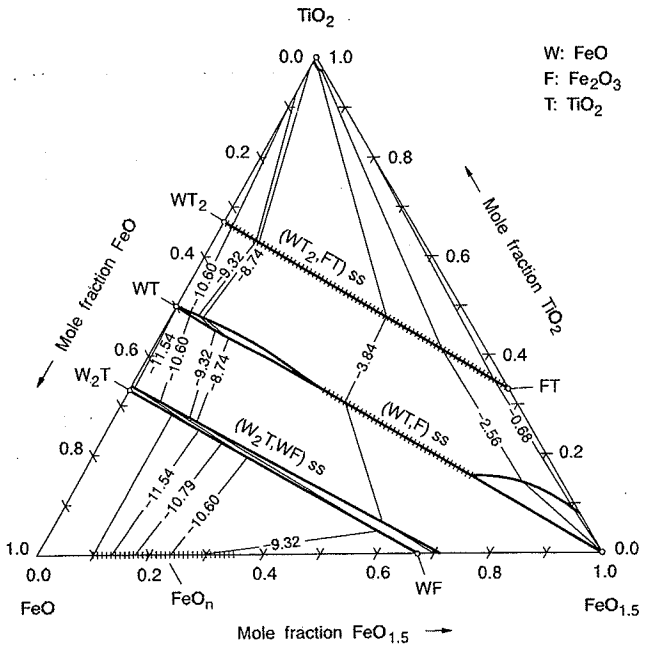


Fig. 3.113. Isothermal section through the system FeO-Fe_2O_3-TiO_2 at 1200 °C with oxygen isobars after Webster, Bright [8]. For a discussion of the ternary system, see also Lindsley [4].

Phase relations in the sub-solidus region of the ternary system Fe-O-Ti between 700 and 1220 °C have been investigated by Grey et al. [9, 10], Saha, Biggar [11], Shakhin et al. [12], Borowiec, Rosenqvist [13, 14] and Gupta et al. [15]. The sub-solidus equilibria in the Ti_3O_5-Fe_2O_3-TiO_2 and FeO-Fe_2O_3-2FeO-TiO_2 sections have been investigated by Grey, Merritt [16], Lindsley [17] and Prince [18]. The thermodynamics of the ternary system Fe-O-Ti and several log pO_2 vs. $N_{Ti}/(N_{Fe}+N_{Ti})$ diagrams between 1300 and 1600 °C have been reported by Sticher, Schmalzried [19]. For a recent thermodynamic assessment of the system FeO-TiO_2 and Fe-O-Ti, see Eriksson, Pelton [20, 21].

References

[1] MacChesney, J. B., A. Muan: Am. Mineral., 46 (1961), p. 572/83
[2] Grau, A. E.: Can. Metall. Q. 18 (1979) No. 3, p. 313/21
[3] Smith, I. C., H. B. Bell: Trans. Inst. Min. Metall. 79C (1970), p. C253/8
[4] Lindsley, D. H.: Short Course Notes - Mineral. Soc. Am., Ed.: Rumble D. III, 3 (1976) No. 11, p. L61/88
[5] Simons, B., E. Woermann: Contrib. Mineral. Petrol. 66 (1978), p. 81/9
[6] MacChesney, J. B., A. Muan: Am. Mineral. 44 (1959), p. 926/46
[7] Taylor, R. W.: J. Am. Ceram. Soc. 46 (1963) No. 6, p. 276/9
[8] Webster, A. H., N. F. H. Bright: J. Am. Ceram. Soc. 44 (1961) No. 3, p. 110/6
[9] Grey, I. E., A. F. Reid, D. G. Jones: Trans. Inst. Min. Metall., Sect. C 83 (1974) No. 6, p. C105/11
[10] Grey, I. E., C. Li, A. F. Reid: J. Solid State Chem. 11 (1974) No. 2, p. 120/7
[11] Saha, P., G. M. Biggar: Indian J. Earth Sci. 1 (1974) No. 1, p. 43/59
[12] Shakhin, E. L., G. G. Mikhailov, A. A. Lykasov, V. I. Shishkov: Zh. Fiz. Khim. 51 (1977) No. 10, p. 2519/23
[13] Borowiec, K., T. Rosenqvist: Scand. J. Metall. 10 (1981) No. 5, p. 217/24
[14] Borowiec, K., T. Rosenqvist: Scand. J. Metall. 14 (1985), p. 33/43
[15] Gupta, S. K., V. Rajakumar, P. Grieveson: Can. Metall. Q. 28 (1989) No. 4, p. 331/5
[16] Grey, I. E., R. R. Merritt: J. Solid State Chem. 37 (1981) No. 3, p. 284/93
[17] Lindsley, D. H.: Am. Mineral. 66 (1981) No. 7-8, p. 759/62
[18] Prince, G. D.: Am. Mineral. 66 (1981) No. 7-8, p. 751/8
[19] Sticher, J., H. Schmalzried: Arch. Eisenhüttenwes. 47 (1976) No. 5, p. 261/6
[20] Eriksson, G., A. D. Pelton: Metall. Trans. B 24B (1993), p. 795/805
[21] Eriksson, G., A. D. Pelton: submitted for publication in Ber. Bunsenges. Phys. Chem. (1994)

FeO_x-ZrO_2

Fig. 3.114. FeO_n-ZrO_2 phase diagram in contact with iron after Fischer, Hoffmann [1].

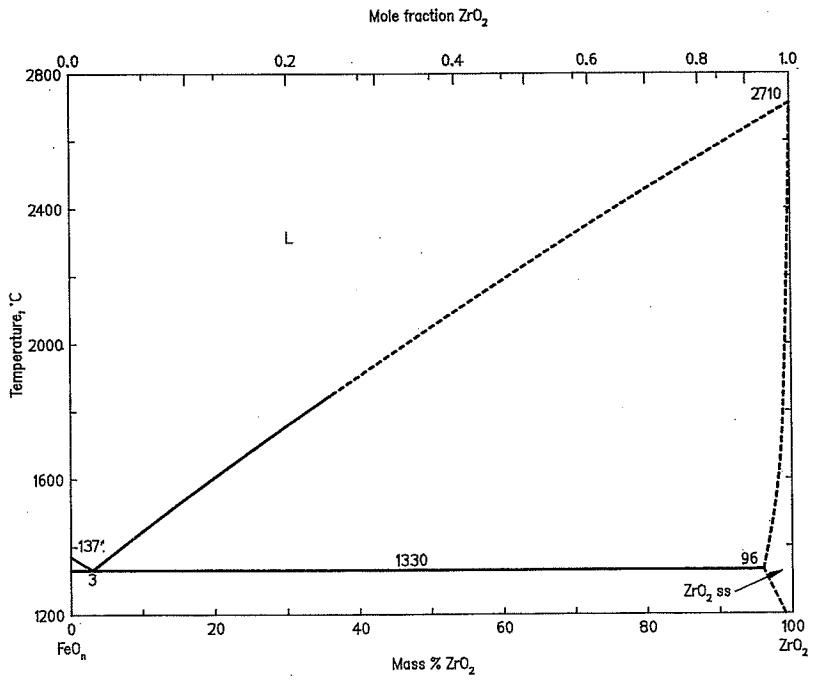
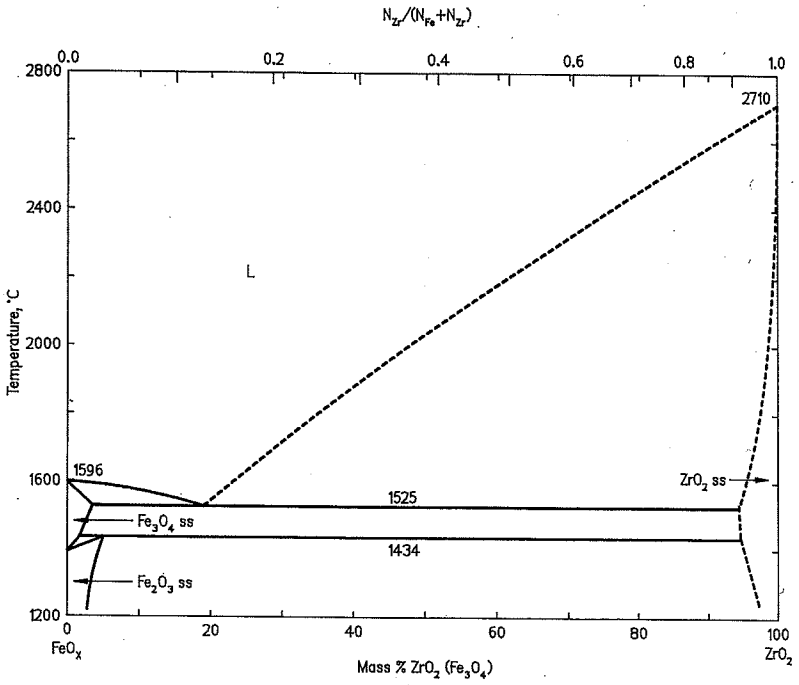


Fig. 3.115. FeO_x-ZrO_2 phase diagram in air after Jones et al. [2].



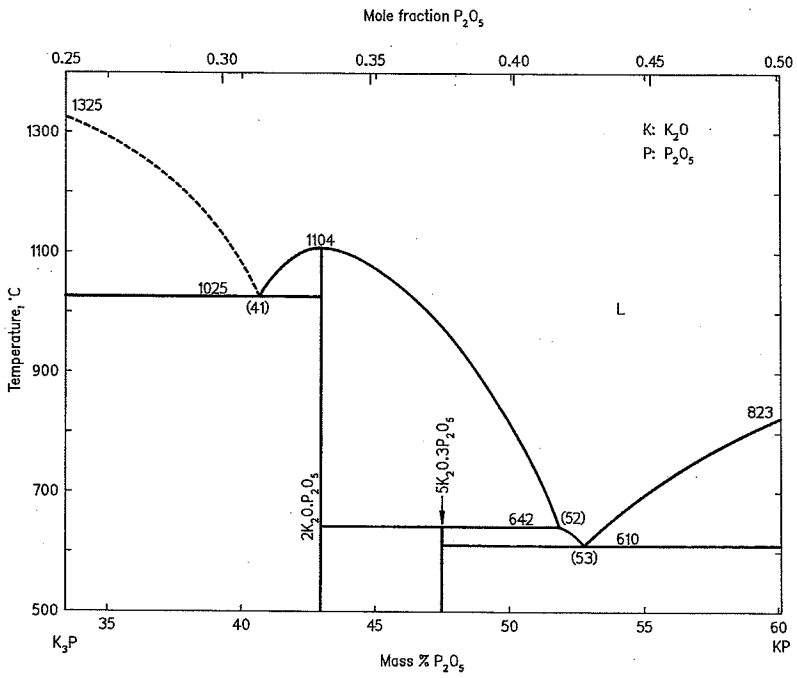
The solubility of Fe_2O_3 in monoclinic ZrO_2 up to 20 mol % has been reported by Collins, Ferguson [3]. The isothermal section through the ternary system FeO-Fe_2O_3-ZrO_2 at 1200 °C has been investigated by Katsura at al. [4]. The phase equilibria in the ternary system in air (up to 1300 °C) and at $pO_2=2\cdot10^{-3}$ atm (up to 1500 °C) have been reported by Kiminami [5, 6].

References

[1] Fischer, W. A., A. Hoffmann: Arch. Eisenhüttenwes. 28 (1957) No. 11, p. 739/43
[2] Jones, T. S., S. Kimura, A. Muan: J. Am. Ceram. Soc. 50 (1967) No. 3, p. 137/42
[3] Collins, J. F., I. F. Ferguson: J. Chem. Soc., (A) (1968) No. 1, p. 4/5
[4] Katsura, T., M. Wakihara, S. Hara, T. Sugihara: J. Solid State Chem. 13 (1975) No. 1-2, p. 107/13
[5] Kiminami, R. H. G. A.: Ceramica /Sao Paulo/ 33 (1987) No. 213, p. 207/9
[6] Kiminami, R. H. G. A.: Ceramica /Sao Paulo/, 34 (1988) No. 223, p. 121/3

K_2O-P_2O_5

Fig. 3.116. Sub-system $3K_2O{\cdot}P_2O_5$-$K_2O{\cdot}P_2O_5$ after Markina, Voskresenskaya [1]. Similar results have also been reported by Morey [2], Bergman, Sanzharova [3] and Znamierowska [4, 5]. According to measurements made by Znamierowska [5], the melting point of $3K_2O{\cdot}P_2O_5$ is 1620 °C. Recently, the position of the eutectic between $5K_2O{\cdot}3P_2O_5$ and $K_2O{\cdot}P_2O_5$ has been confirmed by Kaplun, Shishkin [6]. The numerous polymorphs of the potassium phosphates, not included in the figure, have been described in original papers by Markina, Voskresenskaya [1] and Znamierowska [4, 5].



References

[1] Markina, I. B., N. K. Voskresenskaya: Zh. Neorg. Khim. 14 (1969) No. 8, p. 1188/91
[2] Morey, G. W.: J. Am. Chem. Soc. 76 (1954) No. 18, p. 4724/32
[3] Bergman, A. G., Z. I. Sanzharova: Zh. Neorg. Khim. 14 (1969) No. 1, p. 297/8
[4] Znamierowska, T.: Pol. J. Chem. 52 (1978) No. 10, p. 1889/95
[5] Znamierowska, T.: Pol. J. Chem. 55 (1981) No. 4, p. 747/56
[6] Kaplun, A. B., A. V. Shishkin: Izv. Akad. Nauk SSSR, Neorg. Mater. 24 (1988) No. 6, p. 1051/2

K_2O-SiO_2

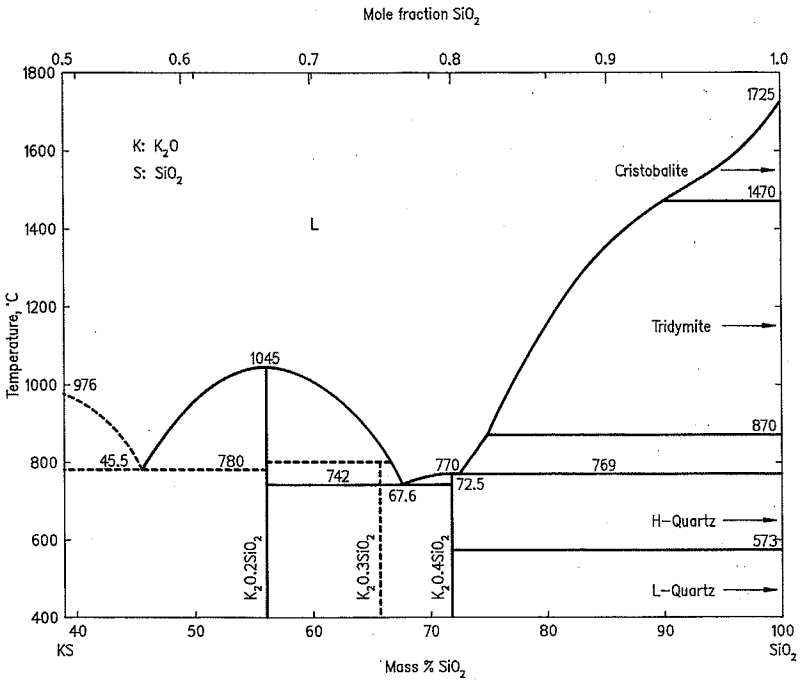


Fig. 3.117. Sub-system $K_2O{\cdot}SiO_2$-SiO_2 after Kracek [1] and Kracek et al. [2]. The additional compound $K_2O{\cdot}3SiO_2$, melting incongruently and reported by Eipeltauer, More [3] is indicated by a dashed line. For the phase equilibria in the SiO_2-rich region of the system, with tridymite as a solution phase and not as the polymorph of pure silica, see Wollast [4] and Holmquist [5]. For thermodynamic assessment of the system and calculated phase diagram, see Wu at al. [6].

References

[1] Kracek, F. C.: J. Am. Chem. Soc. 52 (1930), p. 1436/42

[2] Kracek, F. C., N. L. Bowen, G. W. Morey: J. Phys. Chem. 41 (1937) No. 9, p. 1183/93

[3] Eipeltauer, E., A. More: Radex Rundsch. (1960) No. 4, p. 230/8

[4] Wollast, R.: Silicates Ind. 26 (1961) No. 2, p. 89/92

[5] Holmquist, S. B.: J. Am. Ceram. Soc. 44 (1961) No. 2, p. 82/6

[6] Wu. P, G. Eriksson, A. D. Pelton: J. Am. Ceram. Soc. 76 (1993) No. 8, p. 2059/64

K_2O-TiO_2

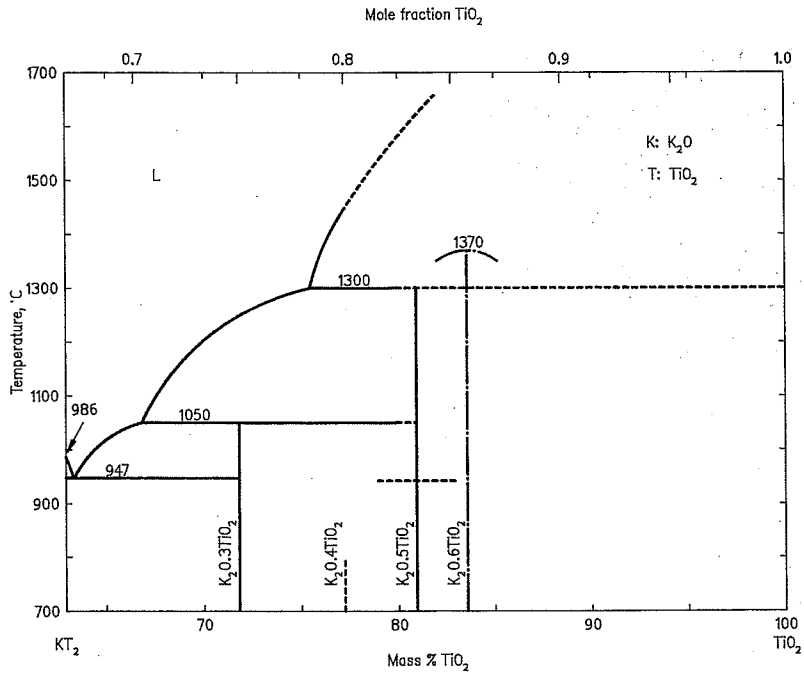


Fig. 3.118. Sub-system $K_2O{\cdot}2TiO_2$-TiO_2 after Schmitz-DuMont, Reckhard [1]. The additional system compound $K_2O{\cdot}6TiO_2$, melting congruently at 1370 °C has been investigated by Berry et al. [2] (dash-dot lines in the figure). The existence of the following compounds in the system K_2O-TiO_2 has also been reported by Keesmann [3], Marchand et al. [4], Mitsuhashi, Fujiki [5] and Kissel, Hoppe [6]: $3K_2O{\cdot}TiO_2$, $K_2O{\cdot}TiO_2$, $2K_2O{\cdot}3TiO_2$, $K_2O{\cdot}8TiO_2$ and non-stoichiometric K_xTiO_2 (potassium titanium bronze). For thermodynamic assessment of the system and calculated phase diagram, see Eriksson, Pelton [7].

References

[1] Schmitz-DuMont, O., H. Reckhard: Monatsh. Chem. 90 (1959) No. 2, p. 134/42

[2] Berry, K. L., V. D. Aftandilian, W. W. Gilbert, E. P. H. Meibohm, H. S. Young: J. Inorg. Nucl. Chem. 14 (1960) No. 3-4, p. 231/9

[3] Keesmann, I.: Z. Anorg. Allg. Chem. 346 (1966) No. 1-2, p. 30/43

[4] Marchand, R., L. Brohan, M. Tournoux: Mat. Res. Bull. 15 (1980) No. 8, p. 1129/33

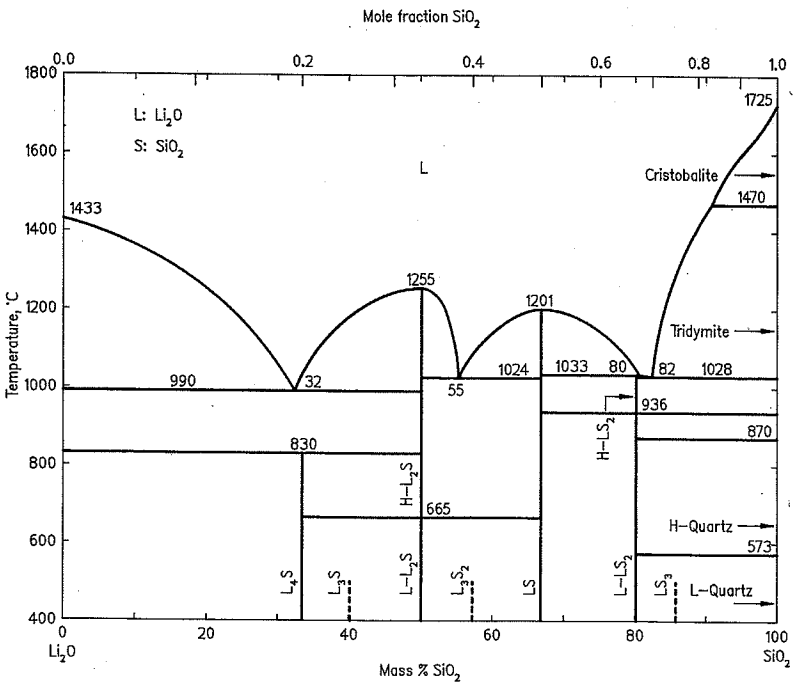
[5] Mitsuhashi, T., Y. Fujiki: Thermochim. Acta 88 (1985) No. 1, p. 177/84

[6] Kissel, J., R. Hoppe: J. Less-Common Met. 158 (1990) No. 2, p. 327/37

[7] Eriksson, G., A. D. Pelton: Metall. Trans. B 24B (1993), p. 795/805

Li_2O-SiO_2

Fig. 3.119. Li_2O-SiO_2 phase diagram after Kracek [1-3] (sub-system SiO_2-$2Li_2O{\cdot}SiO_2$) and Skokan et al. [4] (sub-system Li_2O-$2Li_2O{\cdot}SiO_2$). The compounds considered to be metastable are shown in the figure with dashed lines. For the SiO_2-rich part of the system with tridymite only stable as a binary solution phase, see Holmquist [4].



References

[1] Kracek, F. C.: J. Am. Chem. Soc. 52 (1930), p. 1436/42

[2] Kracek, F. C.: J. Phys. Chem. 34 (1930) No. 12, p. 2641/50

[3] Kracek, F. C.: J. Am. Chem. Soc. 61 (1939) No. 10, p. 2863/77

[4] Skokan, A., H. Wedemeyer, D. Vollath, E. Guenther: Proc. 14th Symp. on Fusion Technology, Avignon, Sept. 8-12, (1986), p. 1255/9

[5] Holmquist, S. B.: J. Am. Ceram. Soc. 44 (1961) No. 2, p. 82/6

MgO-MnO_x

Fig. 3.120. The system MgO-MnO at low oxygen partial pressure after Schenck et al. [1] (solidus measured, liquidus calculated).

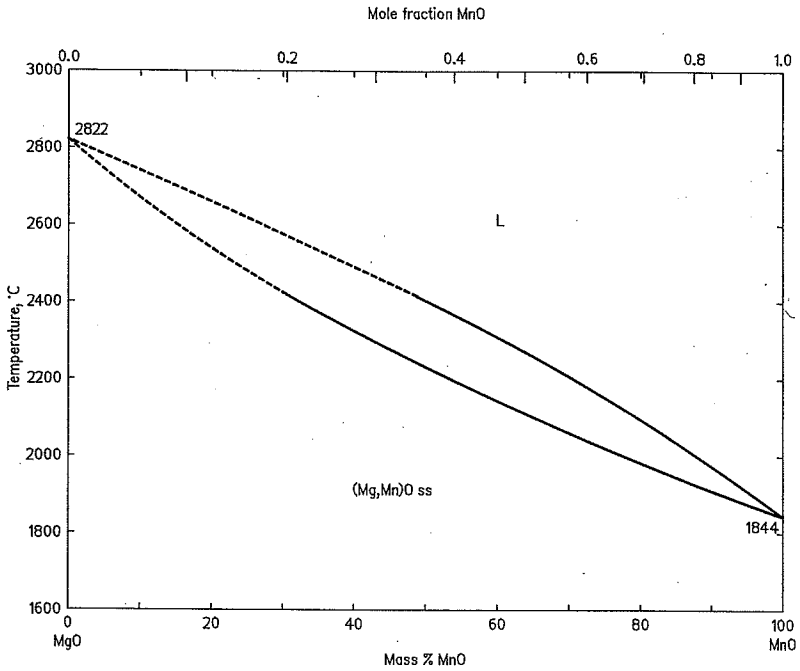


Fig. 3.121. The system $MgO\text{-}MnO_x$ in air, based mainly on the results of Riboud, Muan [2] (between 1300 and 1600 °C) and Barkhatov et al. [3, 4] and Golikov et al. [5] (between 800 and 1200 °C). The compound $6MgO{\cdot}MnO_2$ was reported and described by Kasper, Prener [6]. The overall manganese oxide content is recalculated to MnO.

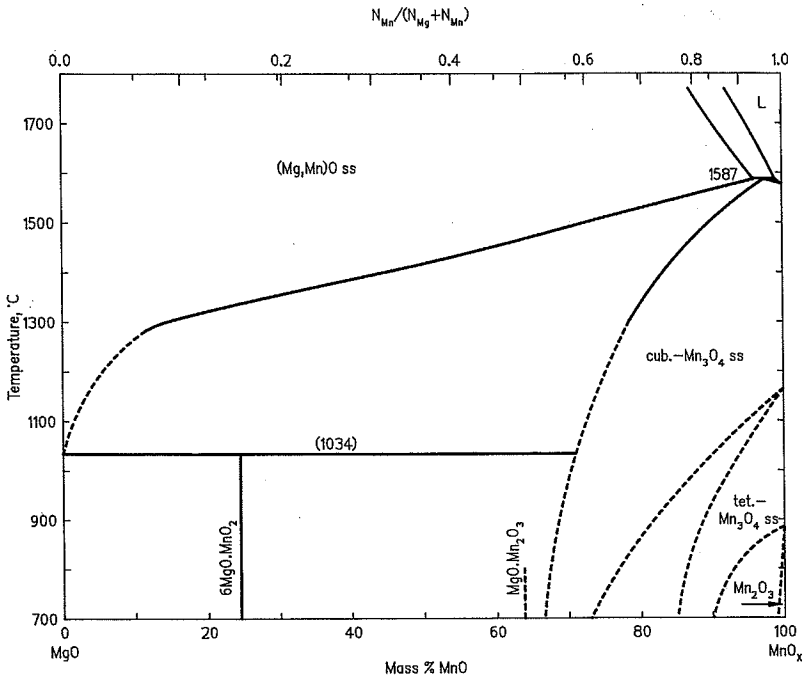
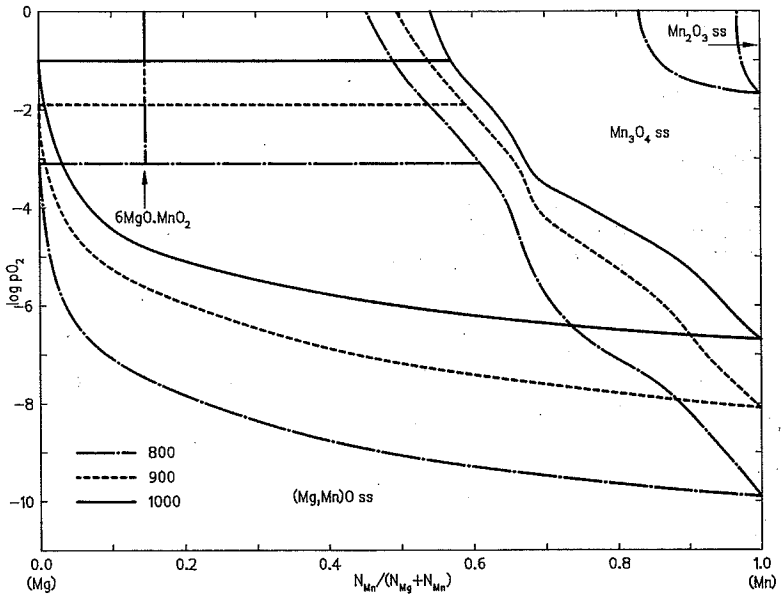
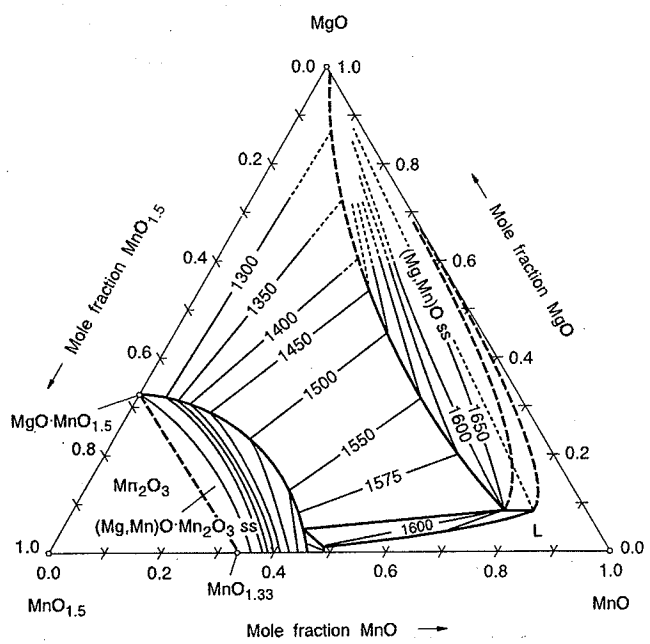


Fig. 3.122. Log pO_2 vs. $N_{Mn}/(N_{Mg}+N_{Mn})$ diagram for the system Mg-Mn-O at 800, 900 and 1000 °C after Golikov et al. [7].





← **Fig. 3.123.** Ternary system MgO-MnO-Mn_2O_3 in air after Oliveira, Brett [8].

References

[1] Schenck, H., M. G. Frohberg, R. Nünninghoff: Arch. Eisenhüttenwes. 35 (1964) No. 4, p. 269/77

[2] Riboud, P. V., A. Muan: J. Am. Ceram. Soc. 46 (1963) No. 1, p. 33/6

[3] Barkhatov, V. P., Yu. V. Golikov, A. G. Zalazinsky, V. F. Balakirev, G. I. Chufarov: Izv. Akad. Nauk SSSR 252 (1980) No. 2, p. 383

[4] Barkhatov, V. P., V. F. Balakirev, E. G. Kostitsyn: Fizikokhim. Metall. Margantsa 1983, Ed.: B. N. Laskorin (1983), p. 54/8

[5] Golikov, Yu. V, V. P. Barkhatov, V. F. Balakirev, V. I. Avdukov: High Temp.- High Pressures 21 (1989), p. 685/700

[6] Kasper, J. S., J. S. Prener: Acta Cryst. 7 (1954), p. 246/8

[7] Golikov, Yu. V., V. P. Barkhatov, V. F. Balakirev, G. I. Chufarov: Dokl. Akad. Nauk SSSR 262 (1982) No. 5, p. 1165/6

[8] Oliveira, V. A. G., N. H. Brett: J. Phys., Colloq., /C1/ 47 (1986), p. C1-453/9

$MgO\text{-}P_2O_5$

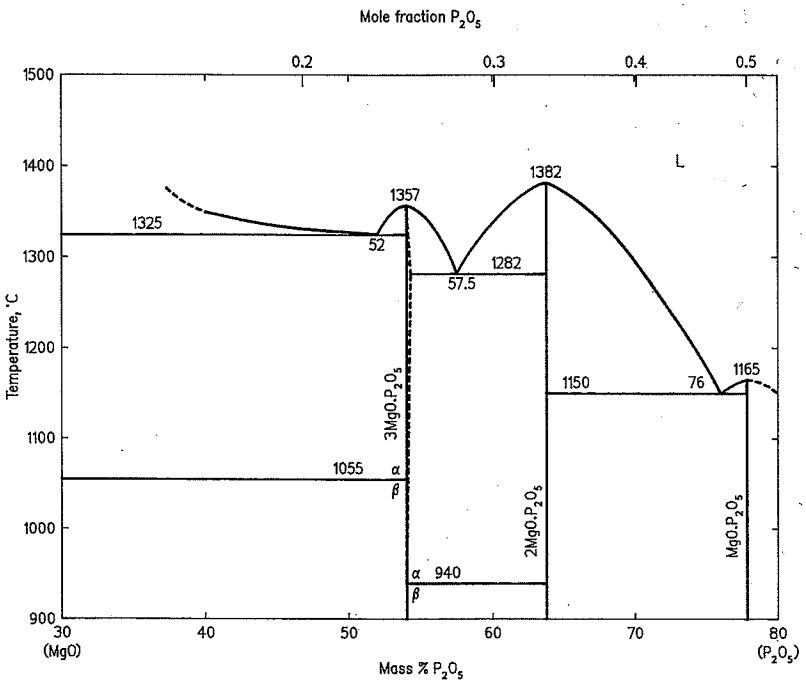


Fig. 3.124. $MgO\text{-}P_2O_5$ phase diagram after Berak [1]. The polymorphism in the $MgO{\cdot}P_2O_5$ phase reported by Berak [1] was not confirmed in the investigations made by Sarver et al. [2].

References

[1] Berak, J.: Roczniki Chem. 32 (1958), p. 17/22
[2] Sarver, J., M. Hoffman, F. Hummel: J. Electrochem. Soc. 108 (1961) No. 12, p. 1103/10

$MgO\text{-}SiO_2$

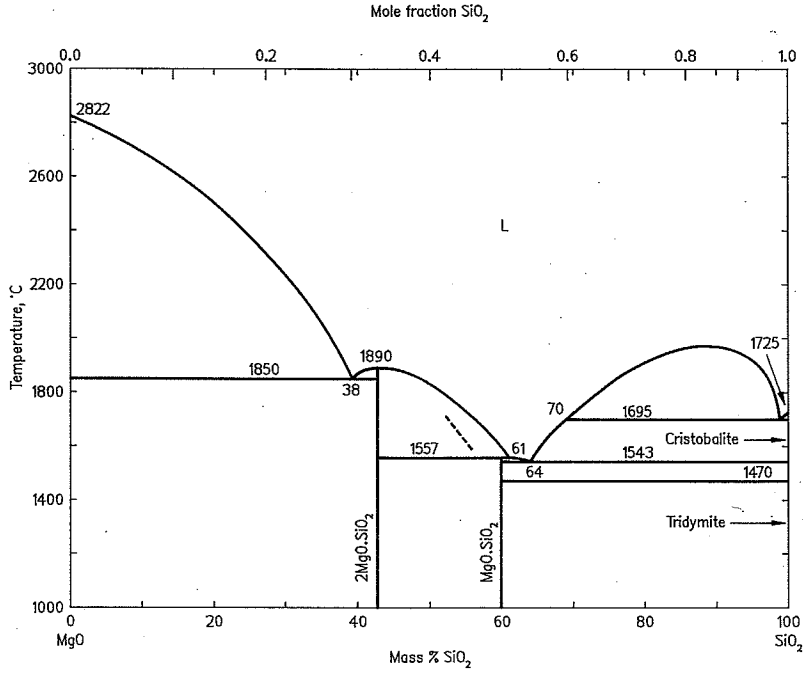


Fig. 3.125. $MgO\text{-}SiO_2$ phase diagram based mainly on the results of Bowen, Andersen [1], Smyth [2], Henriksen, Kingery [3], Henney, Jones [4] and Hageman, Oonk [5]. Contrary to previous results by Schlaudt, Roy [6], no solubility of SiO_2 in MgO was reported by Henney, Jones [4] and Henriksen, Kingery [3]. The polymorphism in $MgO{\cdot}SiO_2$ has been investigated by Foster [7], Atlas [8], Sarver, Hummel [9] and Smyth [2]. The miscibility gap in the system $MgO\text{-}SiO_2$ has been investigated by Greig [10], Olshansky [11] and recently by Hageman, Oonk [5]. The critical temperature reported by Hageman, Oonk [5], which is considerably below the previous reported values, has been adopted. The recent investigations of liquidus relations at 1600 and 1700 °C by Kambayashi, Kato [12, 13] (dashed line in the figure) suggest congruent melting of $MgO{\cdot}SiO_2$.

References

[1] Bowen, N. L., O. Anderson: Am. J. Sci., 4-th Ser. 37 (1914) No. 222, p. 487/501
[2] Smyth, J. R.: Am. Mineral. 59 (1974), p. 345/52
[3] Henriksen, A. F., W. D. Kingery: Ceramurgia Int. 5 (1979) No. 1, p. 11/17
[4] Henney, J. W., J. W. S. Jones: Trans. J. Br. Ceram. Soc. 68 (1969), p. 201/3
[5] Hageman, V. B., H. A. Oonk: Phys. Chem. Glasses 27 (1986) No. 5, p. 194/8
[6] Schlaudt, C. M., D. M. Roy: J. Am. Ceram. Soc. 48 (1965) No. 5, p. 248/51
[7] Foster, W. R.: J. Am. Ceram. Soc. 34 (1951) No. 9, p. 255/9
[8] Atlas, L.: J. Geol. 60 (1952), p. 125/47
[9] Sarver, J. F., F. A. Hummel: J. Am. Ceram. Soc. 45 (1962) No. 4, p. 152/6
[10] Greig, J. W. : Am. J. Sci., 5-th Ser. 13 (1927) No. 73, p. 1/154
[11] Olshansky, Ya. I.: Dokl. Akad. Nauk SSSR 76 (1951) No. 1, p. 94/6
[12] Kambayashi, S., E. Kato: J. Chem. Thermodyn. 15 (1983) No. 8, p. 701/7
[13] Kambayashi, S., E. Kato: J. Chem. Thermodyn. 16 (1984) No. 3, p. 241/8

$MgO\text{-}TiO_2$

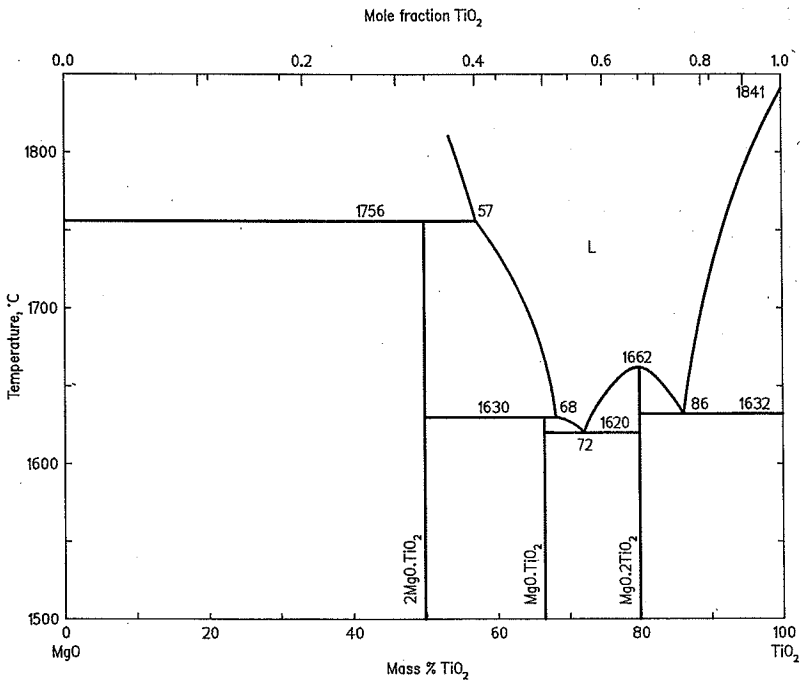


Fig. 3.126. $MgO\text{-}TiO_2$ phase diagram after Woermann et al. [1]. Similar versions of the phase diagram have been reported previously by Massazza, Sirchia [2], Rouf et al. [3] and recently by Shindo [5, 6]. The differences between temperatures of invariant points given in [1-3, 5, 6] range up to 50 degrees. The absence of mutual solubility between the compounds in the system has also been reported by Somiya et al. [4]. The titanium oxide excess in the $MgO{\cdot}TiO_2$ phase reported by Shindo [5, 6] was also found by Vasyutinskii [7] and Reznichenko et al. [8] in the sub-system $MgO{\cdot}TiO_2\text{-}Ti_2O_3$. The solubility of Ti_2O_3 in $MgO{\cdot}TiO_2$, as much as 33-35 mole% Ti_2O_3 at 1100 °C, has been reported by Reznichenko et al. [8]. The thermodynamics of the system and lower limits of stability for $2MgO{\cdot}TiO_2$ and $MgO{\cdot}2TiO_2$ at approx. 980 and 160 °C respectively, have been calculated by Wechsler, Navrotsky [9]. For thermodynamic assessment of the system and calculated phase diagram, see Eriksson, Pelton [10].

The sub-system $MgO{\cdot}TiO_2\text{-}Ti_2O_3$ has been investigated by Vasyutinskii [6] and characterised as a simple eutectic system with the eutectic composition close to the equimolar ratio of Ti_2O_3 and $MgO{\cdot}TiO_2$.

References

[1] Woermann, E., B. Brezny, A. Muan: Am. J. Sci. 267A (1969), p. 463/79

[2] Massazza, F., E. Sirchia: Chim. Ind. /Milano/ 40 (1958) No. 5, p. 376/80

[3] Rouf, M. A., A. H. Cooper, H. B. Bell: Trans. J. Br. Ceram. Soc. 68 (1969) No. 6, p. 263/7

[4] Somiya, S., S. Hirano, M. Ishizaka: Rep. Res. Lab. Eng. Mater., Tokyo Inst. Technol (1976) No. 1, p. 149/57

[5] Shindo, I.: J. Cryst. Growth 50 (1980) No. 4, p. 839/51

[6] Shindo, I.: Nippon Kessho Seicho Gakkaishi 8 (1981) No. 1, p. 1/18

[7] Vasyutinskii, N. A.: Izv. Akad. Nauk SSSR, Neorg. Mater. 13 (1977) No. 1, p. 177/8

[8] Reznichenko, V. A., M. S. Model, N. I. Talmud: Izv. Akad. Nauk SSSR, Neorg. Mater. 15 (1979) No. 9, p. 1694/5

[9] Wechsler, B., A. Navrotsky: J. Solid State Chem. 55 (1984) No. 2, p. 165/80

[10] Eriksson, G., A. D. Pelton: Metall. Trans. B 24B (1993), p. 795/805

$MnO_x\text{-}P_2O_5$

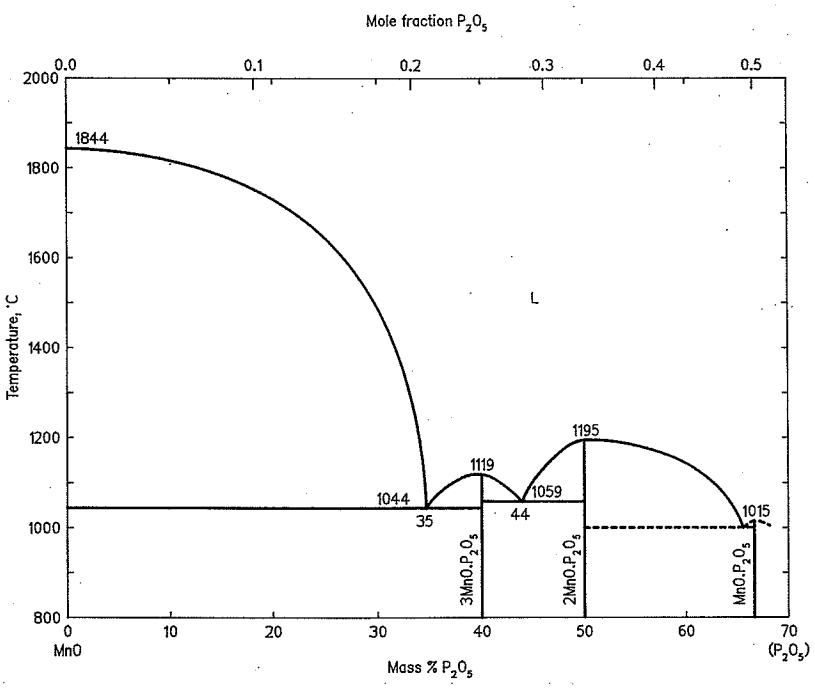
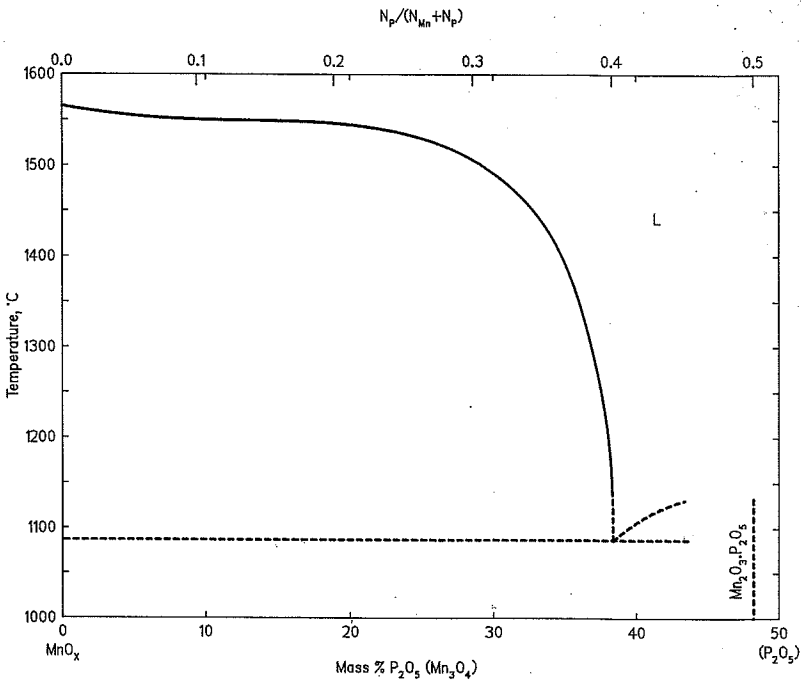


Fig. 3.127. $MnO\text{-}P_2O_5$ phase diagram in a neutral atmosphere after Pearson et al. [1], Fischer, Fleischer [2] and Konstant, Dimante [3]. The melting point of $MnO{\cdot}P_2O_5$ at 1015 °C has been reported by Bukhalova et al. [4, 5].

Fig. 3.128. MnO_x-P_2O_5 system in air after Fix et al. [6].



References

[1] Pearson, J., E. T. Turkdogan, E. M. Fenn: J. Iron Steel Inst. 176 (1954) No. 4, p. 441/4

[2] Fischer, W. A., H.-J. Fleischer: Arch. Eisenhüttenwes. 36 (1965) No. 11, p. 791/8

[3] Konstant, Z. A., A. I. Dimante: Izv. Akad. Nauk SSSR, Neorg. Mater. 13 (1977) No. 1, p. 99/103

[4] Bukhalova, I. G., I. G. Rabkina, I. V. Mardirosova: Zh. Neorg. Khim. 20 (1975) No. 3, p. 596/8

[5] Bukhalova, I. G., I. G. Rabkina, I. V. Mardirosova: Ukr. Khim. Zh. 41 (1975) No. 11, p. 1144/7

[6] Fix, W., H. E. Wiemer, H. J. Tolkemit: Arch. Eisenhüttenwes. 40 (1969) No. 3, p. 215/21

MnO_x-SiO_2

Fig. 3.129. MnO-SiO_2 system at low oxygen partial pressure (from $pO_2=10^{-10}$ at 1130 °C to $pO_2=10^{-6}$ atm at 1555 °C) after Glasser [1]. A similar version of the system in a helium atmosphere at 1 atm total pressure has been reported by Singelton et al. [2]. For thermodynamic assessment of the system and calculated phase diagram, see Eriksson et al. [3].

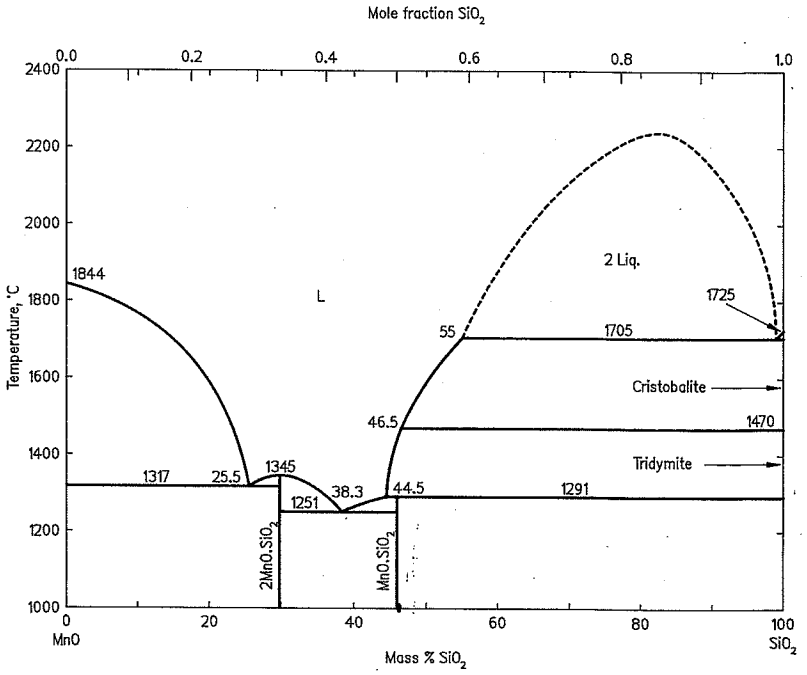
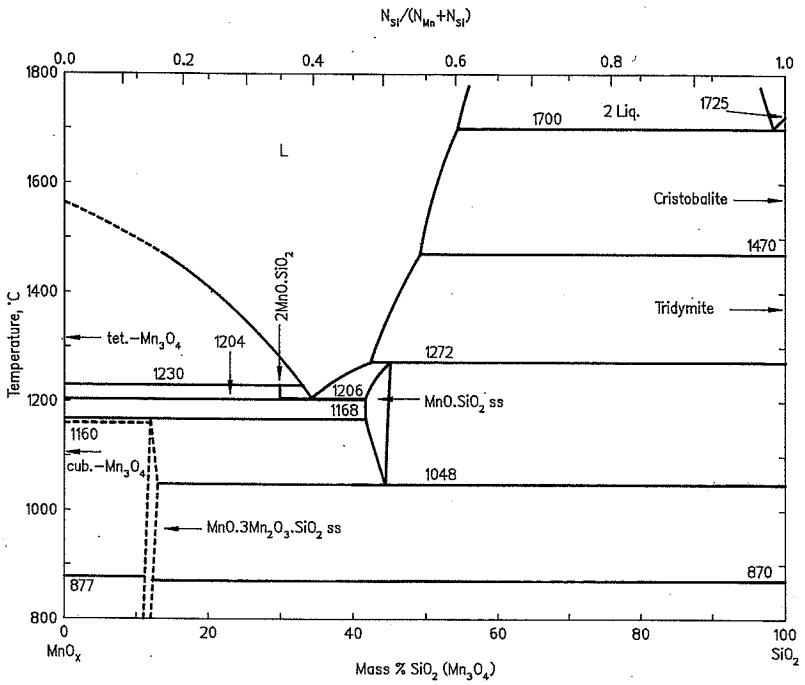


Fig. 3.130. MnO_x-SiO_2 system in air after Muan [4], revised in sub-solidus region by Abs-Wurmbach et al. [5]. For the true composition of liquid and crystalline phases at liquidus temperatures, see original paper [4]. Further sections at oxygen partial pressures of $10^{-1.1}$, $10^{-1.35}$ and $10^{-2.5}$ have been reported by Muan [6].



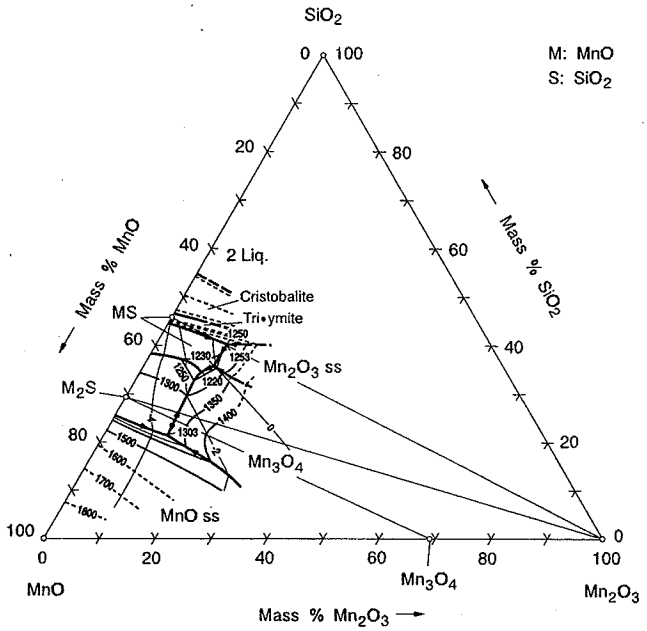


Fig. 3.131. Liquidus surface with oxygen isobars in the ternary system MnO-Mn_2O_3-SiO_2 after Morris, Muan [7].

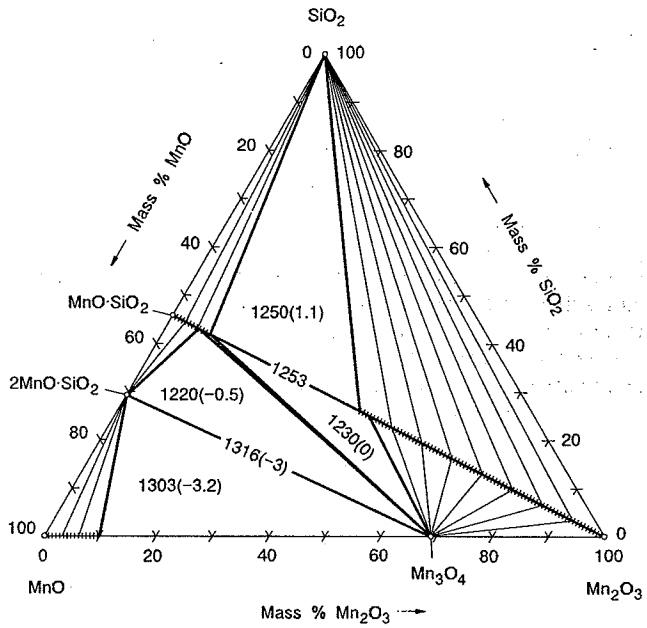


Fig. 3.132. Solidus surface in the ternary system MnO-Mn_2O_3-SiO_2 after Morris, Muan [7]. Oxygen equilibrium pressures (log pO_2, atm) are given in parenthesis.

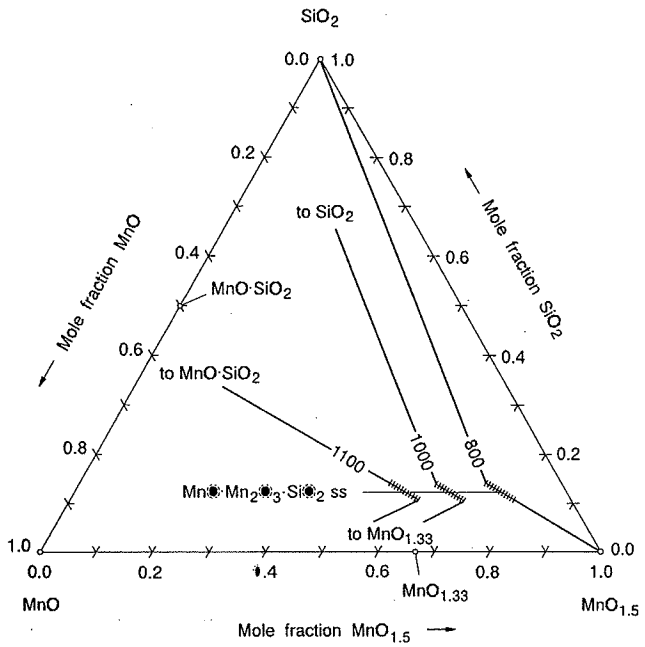


Fig. 3.133. Isothermal sections at 800, 1000 and 1100 °C through the ternary system MnO-Mn_2O_3-SiO_2 showing compatibility relations involving the $MnO{\cdot}3Mn_2O_3{\cdot}SiO_2$ solid solution (braunite) after Abs-Wurmbach [8].

References

[1] Glasser, F. P.: Am. J. Sci. 256 (1958) No. 6, p. 398/412
[2] Singelton, E. L., L. Carpenter, R. V. Lundquist: Rep. Invest. - U.S. Bur. Mines (1962) No. 5938, p. 1/31
[3] Eriksson, G., P. Wu, A. D. Pelton: Can. Metall. Q. 33 (1994), p. 13/21
[4] Muan, A.: Am. J. Sci. 257 (1959) No. 4, p. 297/315
[5] Abs-Wurmbach, I., T. Peters, K. Langer: Neues Jahrbuch Miner., Abh. 146 (1983) No. 3, p. 258/79
[6] Muan, A.: Am. Mineral. 44 (1959) No. 9-10, p. 946/61
[7] Morris, A. E., A. Muan: J. Metals 18 (1966) No. 8, p. 957/60
[8] Abs-Wurmbach, I.: Contrib. Mineral. Petrol. 71 (1980), p. 393/9

MnO_x-TiO_2

Fig. 3.134. MnO-TiO_2 system at low oxygen partial pressure after Leusmann [1]. The compound $2MnO{\cdot}TiO_2$ has been described previously by Grieve, White [2] as melting incongruently. For liquidus compositions at 1500 and 1550 °C, see also Martin, Bell [3] and Rao, Gaskell [4]. For thermodynamic assessment of the system and calculated phase diagram, see Eriksson, Pelton [5].

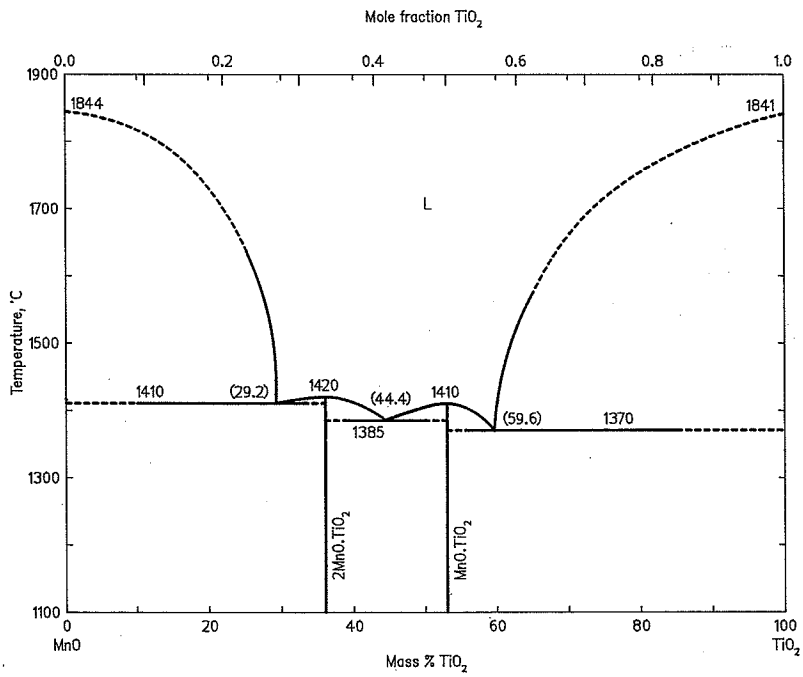
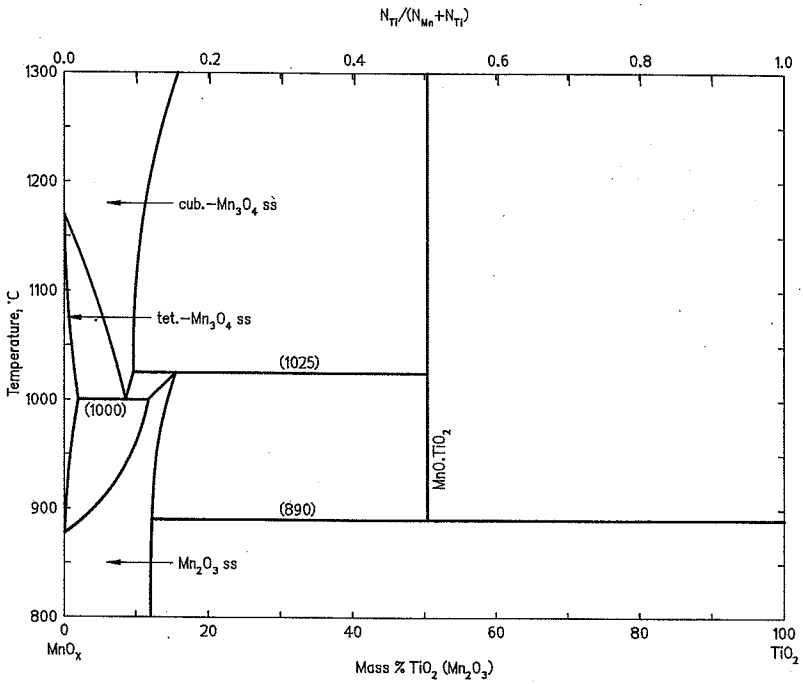


Fig. 3.135. Sub-solidus relations in the system Mn_2O_3-TiO_2 in air after Yankin et al. [6] and Chufarov et al. [7].



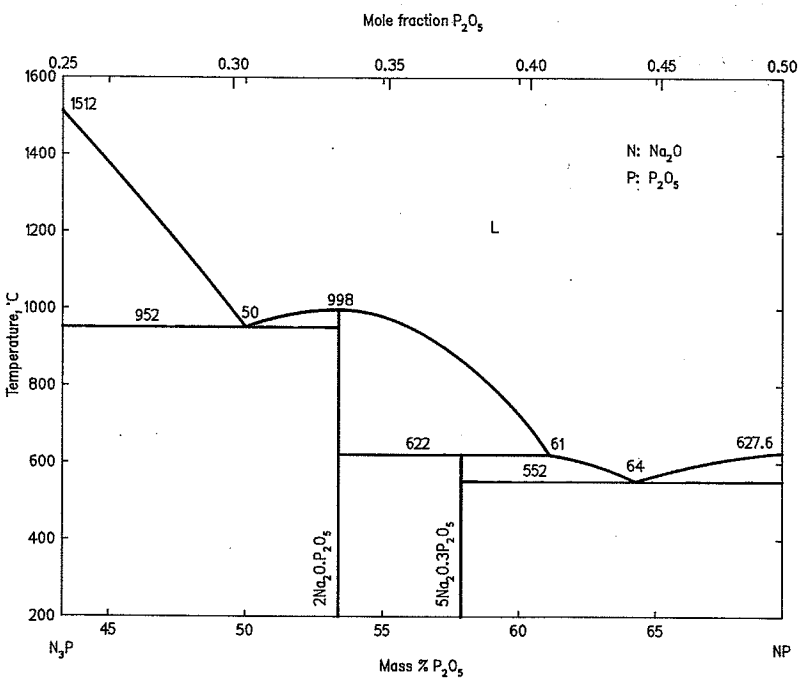
The phase relations in the ternary system Mn-O-Ti between 1100 and 1200 °C and under varying partial pressure of oxygen have been reported by Grey et al. [8], Leusmann [9] and Yankin at al. [10]. The mutual solubility between MnO and TiO has been investigated by Aivazov et al. [11, 12].

References

[1] Leusmann, D.: Neues Jahr. Mineral. Monatsh. (1979) No. 6, p. 262/6
[2] Grieve, J., J. White: J. Roy. Tech. Coll. (Glasgow) 4 (1940), p. 660/70
[3] Martin, E., H. B. Bell: Trans. Inst. Min. Metall., Sec. C. 83 (1974) No. 12, p. C193
[4] Rao, B. K. P. D., D. R. Gaskell: Metall. Trans. B 12B (1981) No. 3, p. 469/77
[5] Eriksson, G., A. D. Pelton: Metall. Trans. B 24B (1993), p. 795/805
[6] Yankin, A. M., V. F. Balakirev, G. I. Chufarov: Dokl. Akad. Nauk SSSR 269 (1983) No. 2, p. 417/8
[7] Chufarov, G. I., A. M. Yankin, V. P. Demin, Yu. V. Golikov, V. F. Balakirev: Zh. Fiz. Khim. 60 (1986) No. 4, p. 863/6
[8] Grey, I. E., C. Li, A. F. Reid: J. Solid State Chem. 17 (1976) No. 4, p. 343/52
[9] Leusmann, D.: Neues Jahr. Mineral. Monatsh. (1979) No. 12, p. 556/69
[10] Yankin, A. M., Yu. V. Golikov, V. F. Balakirev: High Temp. -High Pressures 20 (1988) No. 6, p. 687/92
[11] Aivazov, M. I., A. G. Sarkasyan, I. A. Domashnev, S. U. Gurov: Izv. Akad. Nauk SSSR, Neorg. Mater. 8 (1972) No. 7, p. 1218/20
[12] Aivazov, M. I., S. V. Gurov, A. G. Sarkisyan: Izv. Akad. Nauk SSSR, Neorg. Mater. 8 (1972) No. 5, p. 853/7

Na_2O-P_2O_5

Fig. 3.136. Sub-system $3Na_2O{\cdot}P_2O_5$-$Na_2O{\cdot}P_2O_5$ after Morey, Ingerson [1] and Osterheld, Bahr [2] (sub-system $2Na_2O{\cdot}P_2O_5$-$3Na_2O{\cdot}P_2O_5$). Similar phase diagrams have also been reported by Markina, Voskresenskaya [3], Bergman, Matrosova [4], Berak, Znamierowska [5] and Mikhalkovich [6]. For the numerous polymorphs of sodium phosphates, see original papers [5, 7].



References

[1] Morey, W., E. Ingerson: Am. J. Sci. 242 (1944) No. 1, p. 1/6
[2] Osterheld, R. K., E. W. Bahr: J. Inorg. Nucl. Chem. 32 (1970) No. 8, p. 2539/41
[3] Markina, I. B., N. K. Voskresenskaya: Russ. J. Inorg. Chem. 14 (1969) No. 8, p. 1188/91
[4] Bergman, A. G., V. A. Matrosova: Zh. Neorg. Khim. 14 (1969) No. 4, p. 1669/71
[5] Berak, J., T. Znamierowska: Ann. Soc. Chim. Polonorum /Rocz. Chem./ 46 (1972) No. 10, p. 1697/708
[6] Mikhalkovich, L. N.: Zh. Neorg. Khim. 22 (1977) No. 3, p. 868/71
[7] Ustyantsev, V. M., M. G. Tretnikova: Ogneupory (1976) No. 5, p. 53/7

Na_2O-SiO_2

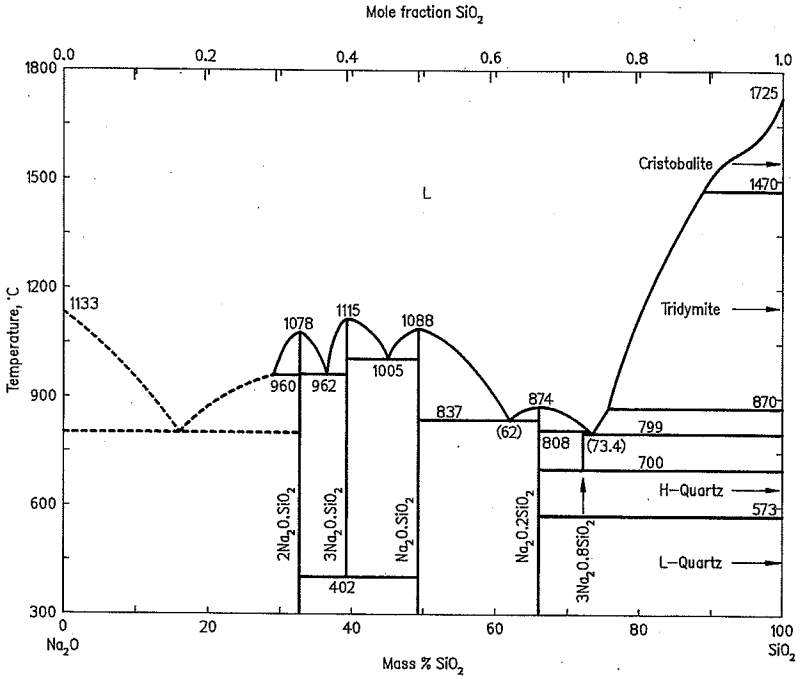


Fig. 3.137. Na_2O-SiO_2 phase diagram according to Kracek [1-3] (from 50 to 100 mass % SiO_2) and Willgallis [4], with the additional compound $3Na_2O{\cdot}8SiO_2$ found by Williamson, Glasser [5] and confirmed by Mogensen, Christensen [6]. The phase equilibria involving $3Na_2O{\cdot}8SiO_2$ have been drawn after Glasser, Marr [7] and Lee et al. [8]. The phase relations in the Na_2O-rich region of the system after D'Ans, Löffler [9] and Löffler [10]. For the SiO_2-rich part of the system with tridymite stable only as a binary solution phase, see Holmquist [11]. For thermodynamic assessment of the system and calculated phase diagram, see Wu et al. [12].

References

[1] Kracek, F. C.: J. Am. Chem. Soc. 52 (1930), p. 1436/42
[2] Kracek, F. C.: J. Phys. Chem. 34 (1930), p. 1583/98
[3] Kracek, F. C.: J. Am. Chem. Soc. 61 (1939) No. 10, p. 2863/77
[4] Willgallis, A.: Glastech. Ber. 42 (1969) No. 12, p. 506/9
[5] Williamson, J., F. P. Glasser: Science 148 (1965) No. 6, p. 1589/91
[6] Mogensen, G., N. H. Christensen: Phys. Chem. Glasses 22 (1981) No. 1, p. 17/22
[7] Glasser, F. P., J. Marr: J. Am. Ceram. Soc. 62 (1979) No. 1-2, p. 42/7
[8] Lee, F. C., J. Marr, R. P. Gunawardane, F. P., Glasser: Br. Ceram. Trans. J. 90 (1991) No. 1, p. 8/11
[9] D'Ans, J., J. Löffler: Z. Anorg. Allg. Chem. 191 (1930) No. 1, p. 1/35
[10] Löffler, J.: Glastech. Ber. 42 (1969) No. 3, p. 92/6
[11] Holmquist, S. B.: J. Am. Ceram. Soc. 44 (1961) No. 2, p. 82/6
[12] Wu. P, G. Eriksson, A. D. Pelton: J. Am. Ceram. Soc. 76 (1993) No. 8, p. 2059/64

Na_2O-TiO_2

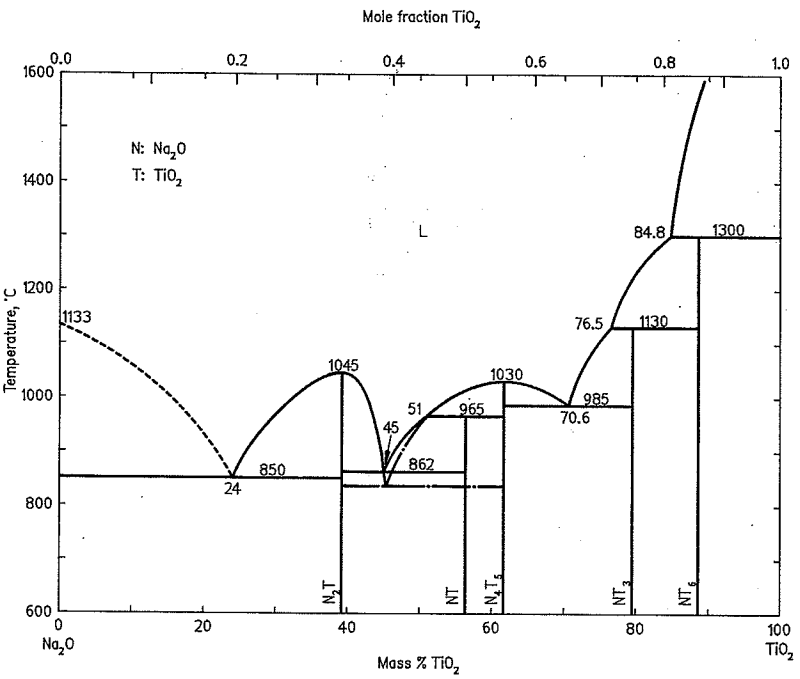


Fig. 3.138. Na_2O-TiO_2 phase diagram after Bouaziz, Mayer [1] and Gicquel al. [2] (dash-dot lines indicate the metastable phase equilibria). All phases reported in [1, 2] to exist in the system were recently confirmed by Bamberger, Begun [3]. The polymorphism in the $Na_2O{\cdot}TiO_2$ phase has been investigated by Hill et al. [4]. The additional system compound Na_xTiO_2 (sodium titanium bronze) with x varying between 0.129 and 0.25, containing Ti(III) has been investigated and discussed recently by Bamberger [5]. For thermodynamic assessment of the system and calculated phase diagram, see Eriksson, Pelton [6].

References

[1] Bouaziz, R., M. Mayer: C. R. Acad. Sci., Ser. C 272 (1971) No. 23, p. 1874/5
[2] Gicquel, C., M. Mayer, R. Bouaziz: C. R. Acad. Sci., Ser. C 275 (1972) No. 23, p. 1427/30
[3] Bamberger, C. E., G. M. Begun: J. Am. Ceram. Soc. 70 (1987) No. 3, p. C48/51
[4] Hill, W. A., A. R. Moon, G. Higginbotham: J. Am. Ceram. Soc. 68 (1985) No. 10, p. C266/7
[5] Bamberger, C. E.: J. Am. Ceram. Soc. 72 (1989) No. 3, p. 510/1
[6] Eriksson, G., A. D. Pelton: Metall. Trans. B 24B (1993), p. 795/805

P_2O_5-SiO_2

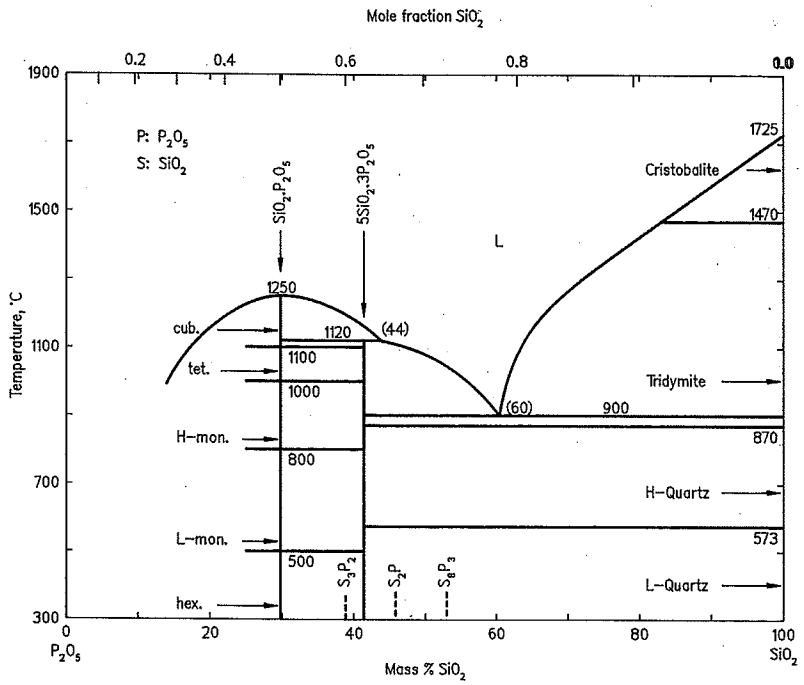


Fig. 3.139. P_2O_5-SiO_2 phase diagram according to Bondar, Malshikow [1] and Malshikow, Bondar [2]. The additional system compounds $2SiO_2 \cdot P_2O_5$ and $3SiO_2 \cdot 2P_2O_5$ have been reported by Tien, Hummel [3] and Robinson, McCartney [4]. Liebau et al. [5, 6] report a solution phase between the end-compositions $3SiO_2 \cdot 2P_2O_3$ and $8SiO_2 \cdot 3P_2O_5$. This range also includes the phases $5SiO_2 \cdot 3P_2O_5$ and $2SiO_2 \cdot P_2O_5$.

References

[1] Bondar, I. A., A. E. Malshikov: Dokl. Akad. Nauk SSSR 306 (1989) No. 1, p. 128/31
[2] Malshikov, A. E., I. A. Bondar: Zh. Neorg. Khim. 33 (1988) No. 1, p. 198/202
[3] Tien, T. Y., F. A. Hummel: J. Am. Ceram. Soc. 45 (1962) No. 9, p. 422/4
[4] Robinson, P., E. R. McCartney: J. Am. Ceram. Soc. 47 (1964) No. 11, p. 587/92
[5] Liebau, F., G. Bissert G., N. Köppen: Z. Anorg. Allg. Chem. 359 (1968) No. 3-4, p. 113/34
[6] Liebau, F., G. Bissert: Bull. Soc. Chim. France (1968), p. 1742/4

PbO-SiO_2

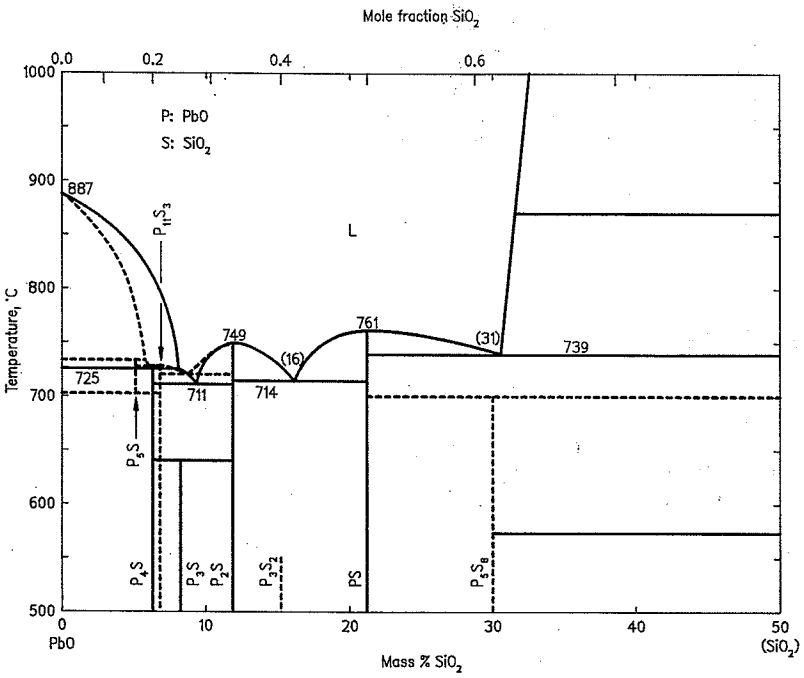
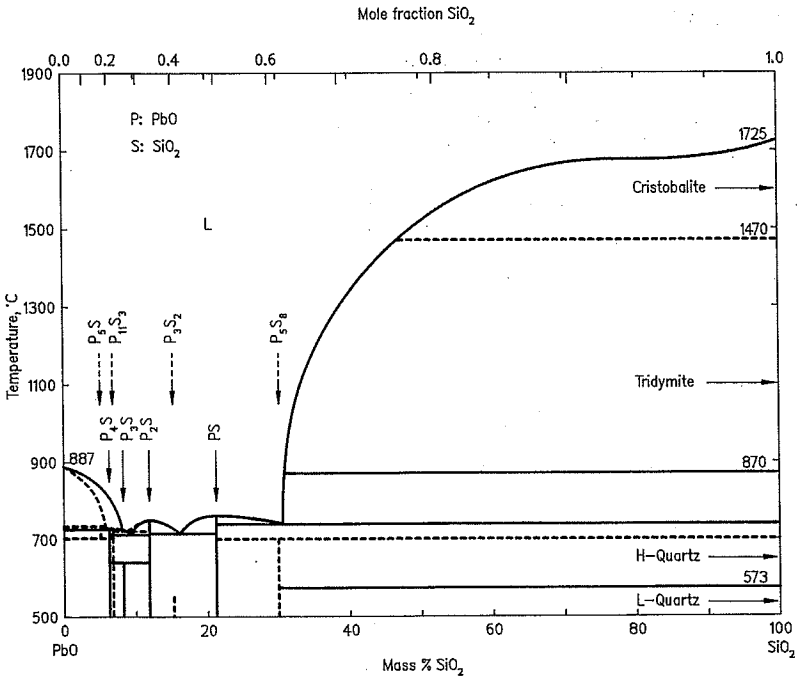


Fig. 3.140. PbO-SiO_2 phase diagram up to 50 mass % SiO_2 after Geller et al. [1] as revised by Smart, Glasser [2] and with the liquidus for the SiO_2-rich region of the system as reported by Calvert, Shaw [3]. Recently, the stoichiometry of both polymorphic modifications of the $4PbO \cdot SiO_2$ phase (the high-temperature form of $4PbO \cdot SiO_2$ stable between 720 and 725 °C, is not include in the figure) has been reformulated by Hirota, Hasegawa [4]. For the high- and low-temperature modifications respectively, the formulae $5PbO \cdot SiO_2$ and $11PbO \cdot 3SiO_2$ have been proposed. The compound $11PbO \cdot 3SiO_2$ has been found to melt congruently [4]. The phase relationships after Hirota, Hasegawa [4] are shown in the figure as dotted lines. The phase $3PbO \cdot 2SiO_2$, which melts incongruently at 710-715 °C, has been reported by Billhardt [5] and Kuxmann, Fischer [6]. For an alternative representation of sub-solidus equilibria and stability limits of compounds in the system, see Ott, McLaren [7]. The numerous polymorphs of lead silicates are not shown in the figure and are discussed in the original papers. For the influence of PbO on the polymorphism of SiO_2, see Negas, Sorell [8].

Fig. 3.141. PbO-SiO_2 phase diagram across the entire composition range. The SiO_2 liquidus is as reported by Calvert, Shaw [3].



References

[1] Geller, R. F., A. S. Creamer, E. N. Bunting: J. Res. Nat. Bur. Stand., RP 705 13 (1934) No. 2, p. 237/44

[2] Smart, R. M., F. P. Glasser: J. Am. Ceram. Soc. 57 (1974) No. 9, p. 378/82

[3] Calvert, P. D., R. R. Shaw: J. Am. Ceram. Soc. 53 (1970) No. 6, p. 350/2

[4] Hirota, K., Y. T. Hasegawa: Bull. Chem. Soc. Jap. 54 (1981) No. 3, p. 754/6

[5] Billhardt, H. W.: Glastech. Ber. 42 (1969) No. 12, p. 498/505

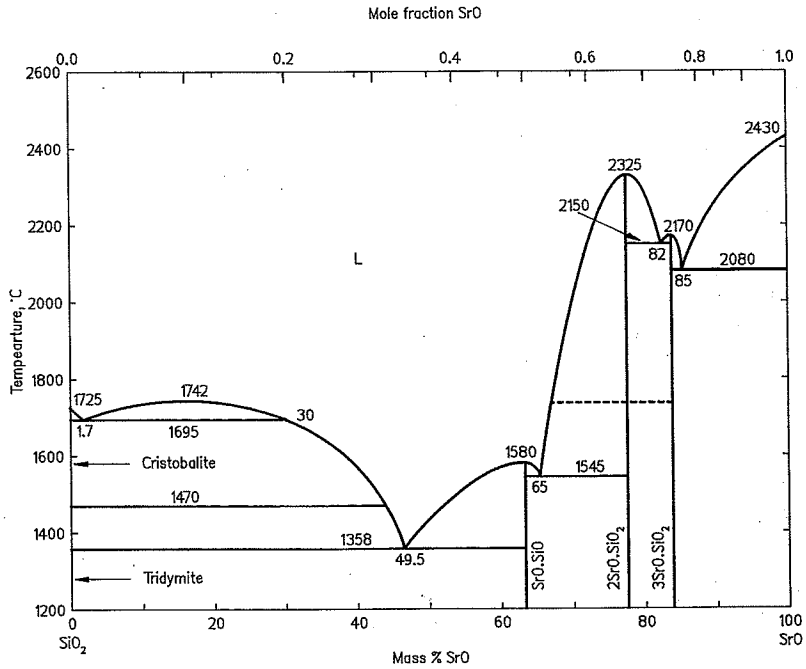
[6] Kuxmann, U., P. Fischer: Erzmetall 27 (1974) No. 11, p. 533/7

[7] Ott, W. R., M. G. McLaren: J. Am. Ceram. Soc. 53 (1970) No. 7, p. 374/5

[8] Negas, T., C. A. Sorell: J. Am. Ceram. Soc. 51 (1968) No. 11, p. 622/5

SiO_2-SrO

Fig. 3.142. SiO_2-SrO phase diagram constructed from obtained results by Eskola [1] (SiO_2-SrO·SiO_2 sub-system), Fields et al. [2] (SrO-SrO·SiO_2 sub-system) and Hageman, Oonk [3] (miscibility gap). A higher critical temperature for the miscibility gap was reported previously by Olshansky [4] (approx. 1900 °C).



References

[1] Eskola, P.: Am. J. Sci., 5-th Ser. 4 (1922) No. 23, p. 331/75

[2] Fields, J. M., Jr., P. S. Dear, J. J. Brown, Jr.: J. Am. Ceram. Soc. 55 (1972) No. 12, p. 585/8

[3] Hageman, V. B., H. A. Oonk: Phys. Chem. Glasses 27 (1986) No. 5, p. 194/8

[4] Olshansky, Ya. I.: Dokl. Akad. Nauk SSSR 76 (1951) No. 1, p. 94/6

SiO_2-TiO_x

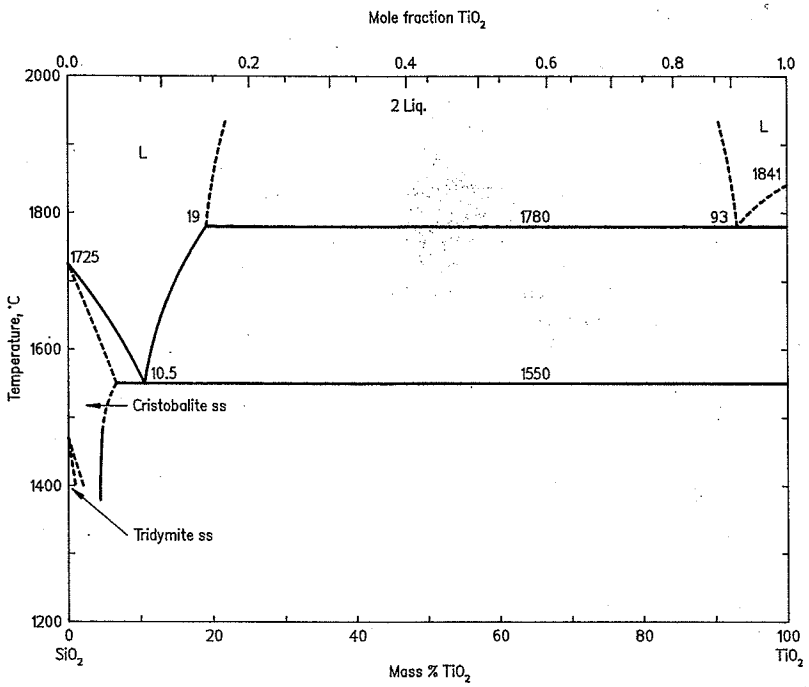


Fig. 3.143. SiO_2-TiO_2 phase diagram after DeVries et al. [1]. The recent results on the solubility of TiO_2 in SiO_2 reported by Kaneko et al. [2] and confirmed by Woermann [3] have been incorporated in the figure. The maximum solubility of TiO_2 in SiO_2 up to 10.8 mass % reported previously by Evans [4], is not confirmed [2, 3]. According to Massazza, Sirchia [5], the eutectic point is located at 12 mass % TiO_2.

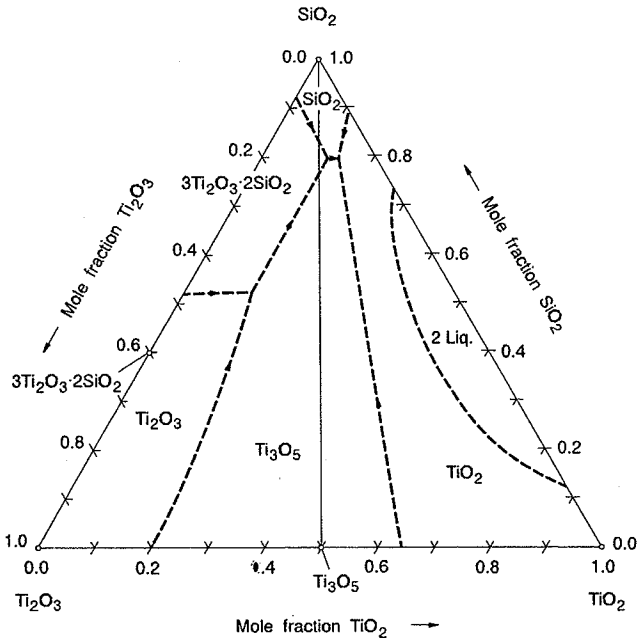


Fig. 3.144. Liquidus surface in the ternary system SiO_2-TiO_2-Ti_2O_3 after Roy et al. [6], as reproduced by Levin et al. [7]. For the present version of the binary edge Ti_2O_3-TiO_2, see Fig. 3.14.

The isothermal section at 1000 °C and the thermodynamics of the O-Si-Ti system have been reported recently by Rahmel, Spencer [8] and Do Vuong Hoahn et al. [9] respectively.

References

[1] DeVries, R. C., R. Roy R., E. F. Osborn: Trans. J. Br. Ceram. Soc. 53 (1954) No. 9, p. 525/40

[2] Kaneko, S., H. N. Tran, Y. Kubo, F. Imoto: Ceram. Int. 6 (1980) No. 3, p. 106/8

[3] Woermann, E.: private communication

[4] Evans, D. L.: J. Am. Ceram. Soc. 53 (1970) No. 7, p. 418/9

[5] Massazza, F., E. Sirchia: Chim. Ind. /Milano/ 40 (1958) No. 5, p. 376/80

[6] Roy, R., R. C. DeVries, D. E. Rase, M. W Shafer, E. F. Osborn: Pennsylvania State College, Quaterly Report on Contract No. DA36-039 sc-5594, Oct. 1 - Dec. 31 (1952)

[7] Levin, E. M., C. R. Robbins, H. F. McMurdie: Phase Diagram for Ceramist, Vol. I, The American Ceramic Society, 4055 N. High St., Columbus, Ohio 43214

[8] Rahmel, A, P. J. Spencer: Oxid. Metals 35 (1991) No. 1-2, p. 53/68

[9] Do Vuong Hoahn, G. Krabbes, R. Krauze: Z. Anorg. Allg. Chem. 558 (1988), p. 41/5

SiO_2-ZnO

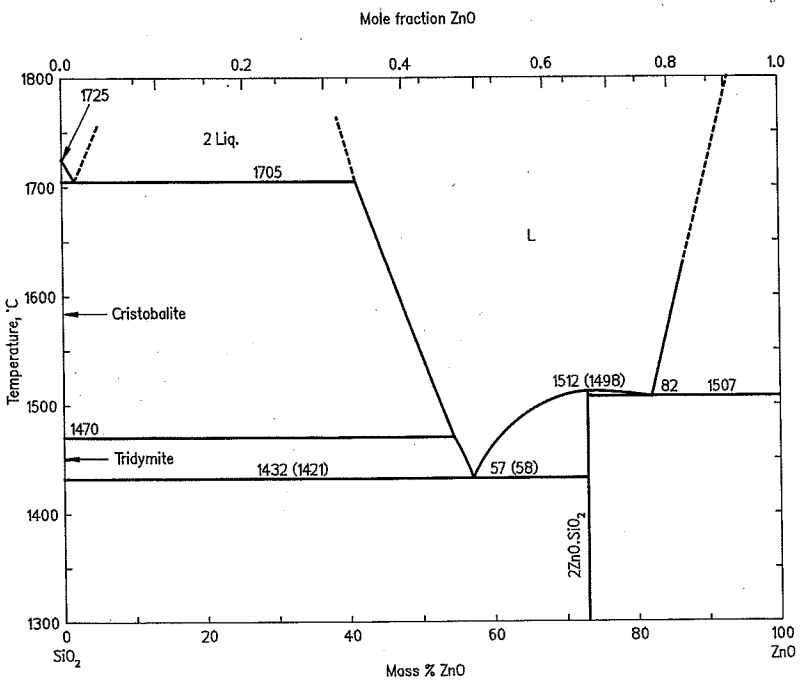


Fig. 3.145. The SiO_2-ZnO phase diagram after Bunting [1]. Some liquidus temperatures in the system have been re-investigated by Williamson, Glasser [2]. Their values for invariant points are given in the figure in parentheses. The absence of mutual solid solution in the sub-system SiO_2-$2ZnO{\cdot}SiO_2$ has been confirmed by Shevyakov et al. [4]. Two further phases in the system, ie. metastable solid solutions denoted ß-, and -$2ZnO{\cdot}SiO_2$, have been found by Williamson, Glasser [2, 3]. Recently, a thermodynamic assessment of the system SiO_2-ZnO has been presented by Björkman [5].

References

[1] Bunting, E.: J. Am. Ceram. Soc. 13 (1930) No. 1, p. 5/10

[2] Williamson, J., F. P. Glasser: Phys. Chem. Glasses 5 (1964) No. 2, 52/9

[3] Williamson, J., F. P. Glasser: Nature /London/ 201 (1964) No. 4916, p. 286/7

[4] Shevyakov, A. M., E. G. Semin, S. V. Fedorov, N. M. Korablev, V. P. Burkov, E. V. Komarov: Dokl. Akad. Nauk SSSR, Phys. Chem. 241 (1978) No. 3, p. 644/6

[5] Björkman, B.: Scand. J. Metall. 15 (1986) No. 4, p. 185/90

SiO_2-ZrO_2

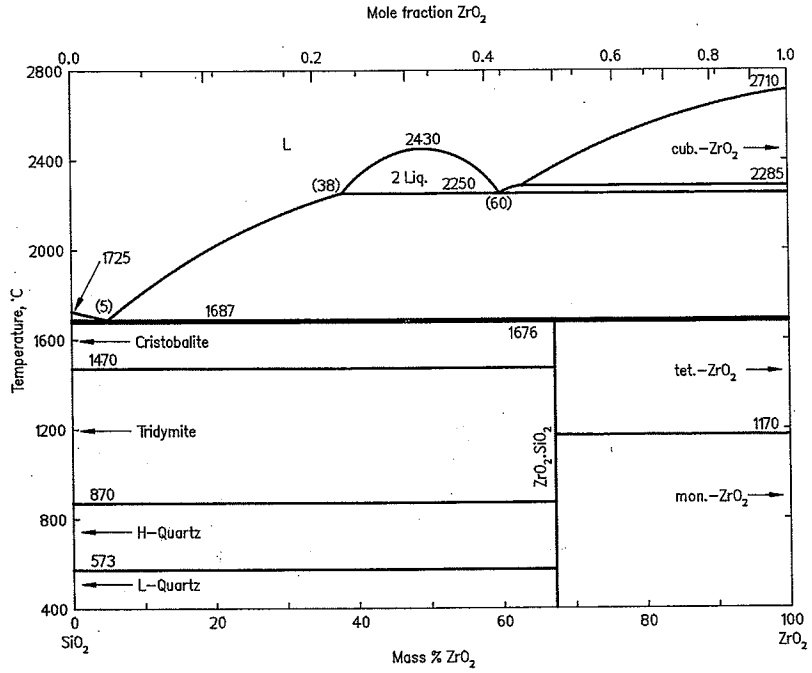


Fig. 3.146. The SiO_2-ZrO_2 phase diagram after Butterman, Foster [1], also incorporating previous results due to Curtis, Sowman [2] and Toropov, Galakhov [3]. The dissociation of $ZrO_2{\cdot}SiO_2$ in the solid state has also been also confirmed by Fischer at al. [4].

References

[1] Butterman, W. C., W. R. Foster: Am. Mineral. 52 (1967) No. 5-6, p. 880/5

[2] Curtis, C. E., H. G. Sowman: J. Am. Ceram. Soc. 36 (1953) No. 6, p. 190/8

[3] Toropov, N. A., F. Ya. Galakhov: Izv. Akad. Nauk SSSR, Otdel. Khim. Nauk (1956) No. 2, p. 158/61

[4] Fischer, W. A., D. Janke, M. Schulenburg: Arch. Eisenhüttenwes. 47 (1976) No. 10, p. 607/12

2.2.3 Ternary oxide systems

Al_2O_3-B_2O_3-CaO

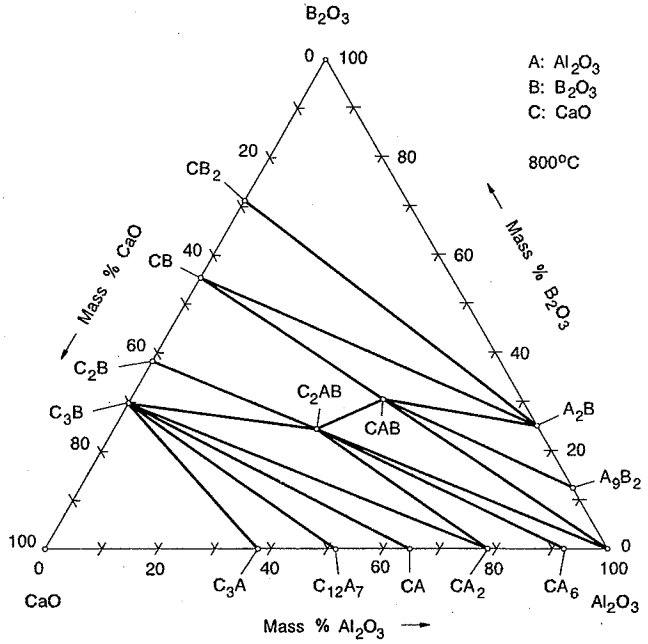


Fig. 3.147. Isothermal section through the system Al_2O_3-B_2O_3-CaO at 800 °C after Schäfer, Kuzel [1]. Two ternary compounds found by Schäfer, Kuzel [1] melt incongruently. The first, $CaO{\cdot}Al_2O_3{\cdot}B_2O_3$, melts at 1015 °C to form $9Al_2O_3{\cdot}2B_2O_3$ and liquid, the second, $2CaO{\cdot}Al_2O_3{\cdot}B_2O_3$, melts at 800 °C to form $CaO{\cdot}2Al_2O_3$ and liquid.

References

[1] Schäfer, U. L., H. I. Kuzel: Neues Jahr. Mineral. Monatssch. (1967) No. 4-5, p. 131/6

Al_2O_3-B_2O_3-SiO_2

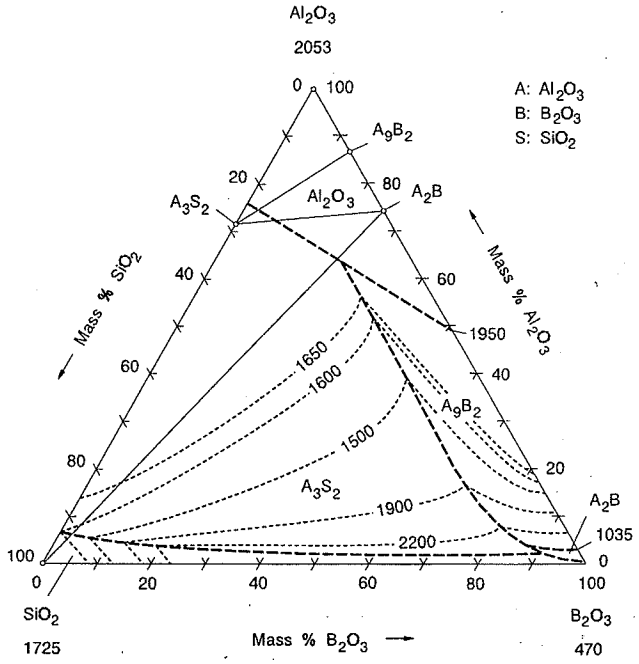


Fig. 3.148. Liquidus surface in the Al_2O_3-B_2O_3-SiO_2 system after Gielisse, Foster [1] as quoted by Hummel, Horn [2]. According to Nazarov, Akberdin [3] the coexistence of mullite with SiO_2 should be replaced by the line of coexistence of mullite with B_2O_3. The liquidus isotherms in the SiO_2-rich part of the system have been investigated by Dietzel, Scholze [4]. The unlimited solubility on the section $9Al_2O_3{\cdot}2B_2O_3$-$3Al_2O_3{\cdot}2SiO_2$ has been reported in [5].

References

[1] Gielisse, P. J., W. R. Foster: Quart. Progr. Rept. 931-8, The Ohio State Univ. Res. Fondation, (1961)
[2] Hummel, F. A., W. F. Horn: J. Aust. Ceram. Soc. 17 (1981) No. 1, p. 25/32
[3] Nazarov, B. K., A. A. Akberdin: Izv. Akad. Nauk SSSR, Met. (1986) No. 6, p. 61/3
[4] Dietzel, A., H. Scholze: Glastech. Ber. 28 (1955) No. 2, p. 47/53
[5] Levin, E. M., C. R. Robbins, H. F. McMurdie: Phase Diagram for Ceramist, Vol. I, The American Ceramic Society, (1964)

Al_2O_3-BaO-CaO

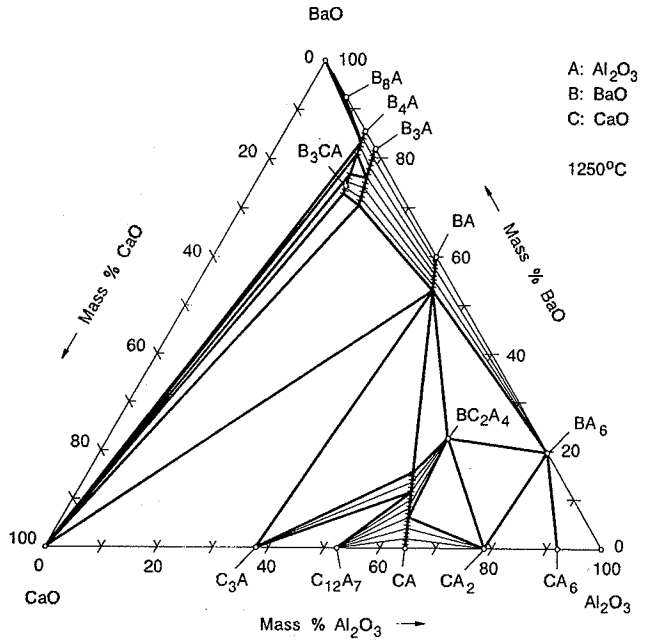


Fig. 3.149. Isothermal section through the system Al_2O_3-BaO-CaO at 1250 °C after Brisi, Montrosi [1] and Appendino [2] (sub-system BaO-CaO-3BaO·Al_2O_3).

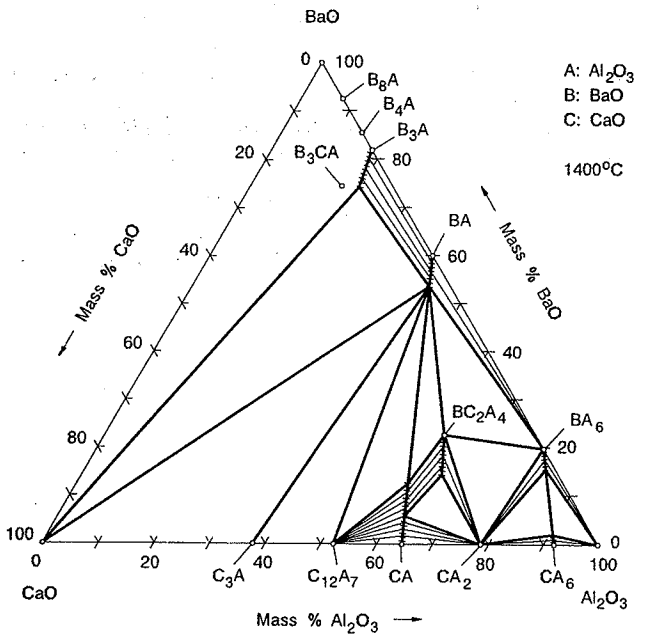


Fig. 3.150. Isothermal section through the system Al_2O_3-BaO-CaO at 1400 °C after Massazza [3] (BaO-rich region of the system was not investigated).

Mutual solubilities on the BaO·Al_2O_3-CaO·Al_2O_3 section have been investigated by Ito et al. [4]. According to Brisi, Montrosi [1] the BaO·2CaO·4Al_2O_3 phase is stable up to about 1450 °C. The ternary compound BaO·CaO·Al_2O_3 reported by Lapin [5] has not been confirmed by later investigations [1, 3].

References

[1] Brisi, C., M. A. Montrosi: Ann. Chim. /Rome/ 52 (1962), p. 785/94
[2] Appendino, P.: Ceramurgia 2 (1972) No. 1, p. 103/6
[3] Massazza, F.: Ann. Chim. /Rome/ 53 (1963), p. 1003/17
[4] Ito, S., K. Banno, K. Suzuki, M. Inagaki: Yogyo Kyokai Shi, 87 (1979) No. 7, p. 344/9
[5] Lapin, W. W.: Dokl. Akad. Nauk SSSR 96 (1954) No. 5, p. 1037/9

Al_2O_3-BaO-SiO_2

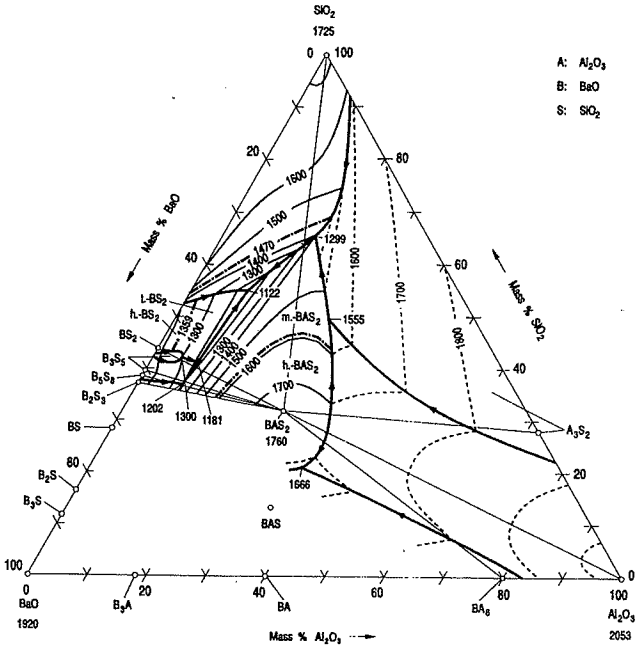


Fig. 3.151. Liquidus surface and sub-solidus relations in the Al_2O_3-BaO-SiO_2 system based mainly on the results of Semler, Foster [1], Lin, Foster [2], Oehlschlegel, Ohnmacht [3] and Woermann [4]. A solubility of SiO_2 in BaO·Al_2O_3·2SiO_2 in the SiO_2-BaO·Al_2O_3·2SiO_2 section of up to 4 mass % SiO_2 was reported by Corral, Verduch [5].

References

[1] Semler, C. E., W. R. Foster: J. Am. Ceram. Soc. 53 (1970), p. 595/8
[2] Lin, H. C., W. R. Foster: J. Am. Ceram. Soc. 53 (1970), p. 549/51
[3] Oehlschlegel, G., W. Ohnmacht: Glastech. Ber. 48 (1975) No. 11, p. 232/6
[4] Woermann, E.: private communication
[5] Corral, J. S. M., A. G. Verduch: Trans. J. Br. Ceram. Soc. 77 (1978) No. 2, p. 40/4

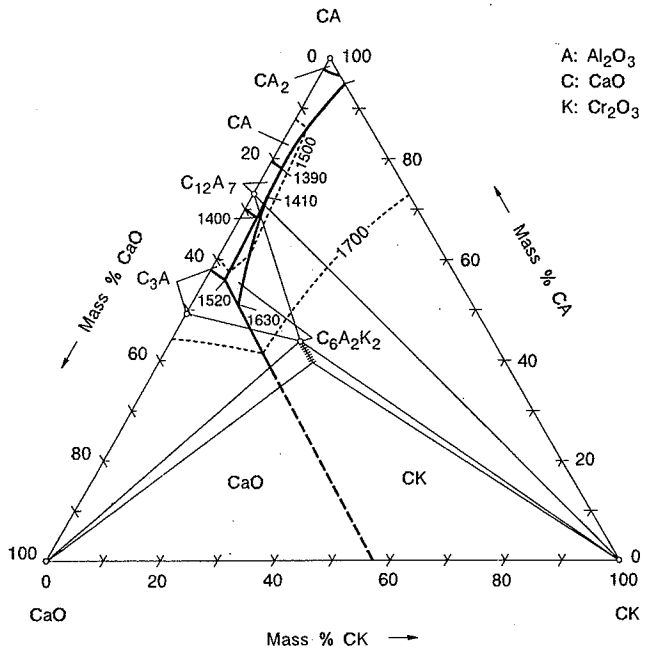


Fig. 3.152. Liquidus surface and compatibility relations at 1300 °C in the sub-system CaO-CaO·Al_2O_3-CaO·Cr_2O_3 under mildly reducing conditions after Kaiser et al. [1]. The liquidus temperatures in the CaO·Al_2O_3-CaO·$2Al_2O_3$-CaO·Cr_2O_3 sub-system have also been investigated by Melnik, Doronin [2].

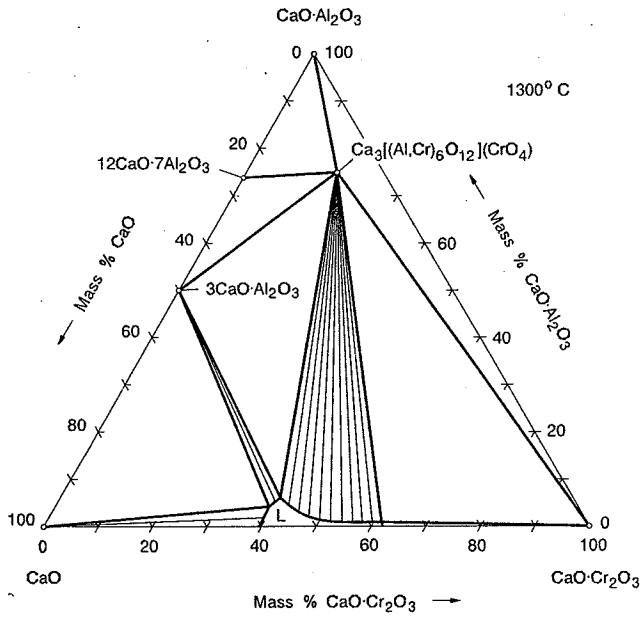


Fig. 3.153. Isothermal section through the sub-system CaO-CaO·Cr_2O_3-CaO·Al_2O_3 at 1300 °C in air after Kaiser [1]. The composition section CaO·Cr_2O_3-CaO·Al_2O_3 was reported earlier by Ford, Rees [3]. Previously, the $10CaO·8Al_2O_3·2Cr_2O_3·CrO_3$ and $4CaO·3Al_2O_3·CrO_3$ formulae were reported for the ternary phase in this system [3-5].

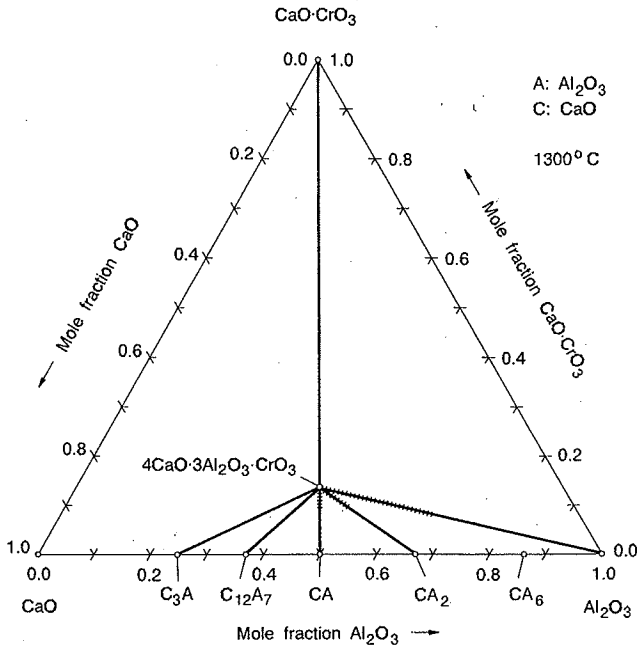


Fig. 3.154. Isothermal section through the system Al_2O_3-CaO-CrO_3 at 1300 °C in air after Peters, Hummel [6]

References

[1] Kaiser, A., B. Sommer, E. Woermann: J. Am. Ceram. Soc. 75 (1992) No. 6, p. 1463/71
[2] Melnik, M. T., E. V. Doronin: Ogneupory (1987) No. 1, p. 24/5
[3] Ford, W. B., W. J. Rees: Trans. J. Br. Ceram. Soc. 57 (1958) No. 5, p. 233/41
[4] Klyucharov, Ya. V., N. S. Gaenko: Izv. Akad. Nauk SSSR, Neorg. Mater. 12 (1976) No. 4, p. 670/3
[5] Mosalamy, F. H.: Tonind.-Ztg. 107 (1983) No. 11, p. 822/3
[6] Peters, D., A. F. Hummel: Cem. Concr. Res. 9 (1979) No. 2, p. 259/68

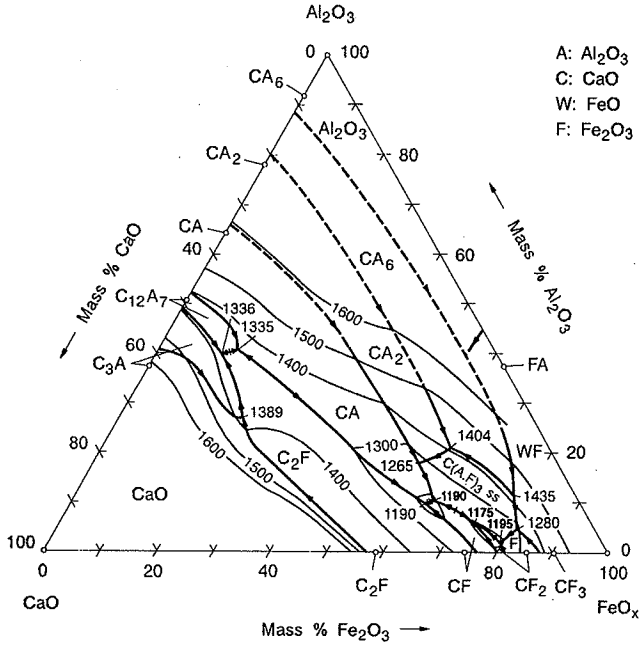


Fig. 3.155. Liquidus surface in the Al_2O_3-CaO-FeO_x system in air after Dayal, Glasser [1] and Lister, Glasser [2]. The figure also summarizes the results of earlier investigations of Brisi [3], Majumdar [4] and Schlaudt, Roy [5].

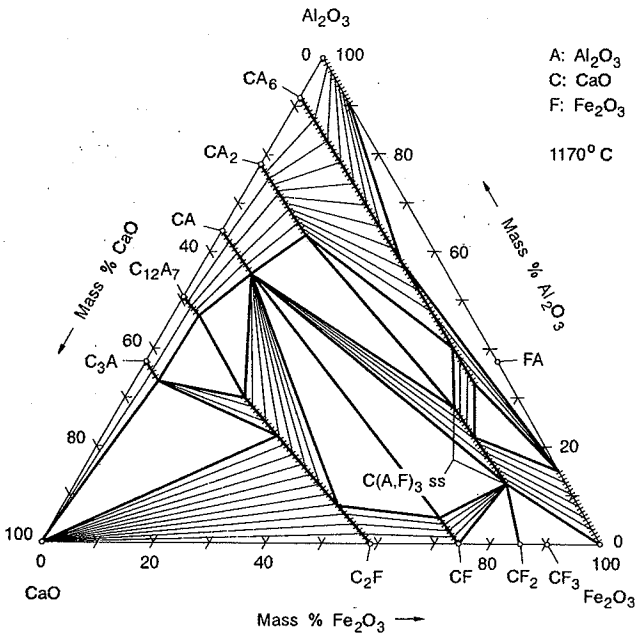


Fig. 3.156. Isothermal sections through the system Al_2O_3-CaO-FeO_x at 1170 °C in air after Dayal, Glasser [1].

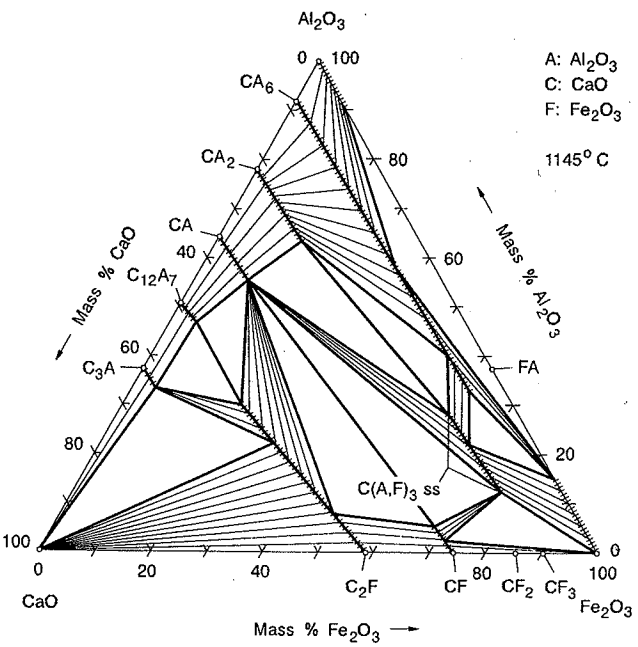


Fig. 3.157. Isothermal sections through the system Al_2O_3-CaO-FeO_x at 1145 °C in air after Dayal, Glasser [1]. For further isothermal sections at 1300 and 1330 °C, see original paper [1]. Some binary sections in the Al_2O_3-CaO-Fe_2O_3 system have also been investigated by Eremin et al. [6] and Eremin [7]. The phase equilibria determined by Dayal, Glasser [1] were generally confirmed. According to Malysheva [8], the ternary solution phase on the $CaO{\cdot}3Al_2O_3$-$CaO{\cdot}3Fe_2O_3$ section exists between approx. 1100 and 1260 °C within the following limits: 12-17 mass % CaO, 58-81 mass % Fe_2O_3 and 2-30 mass % Al_2O_3.

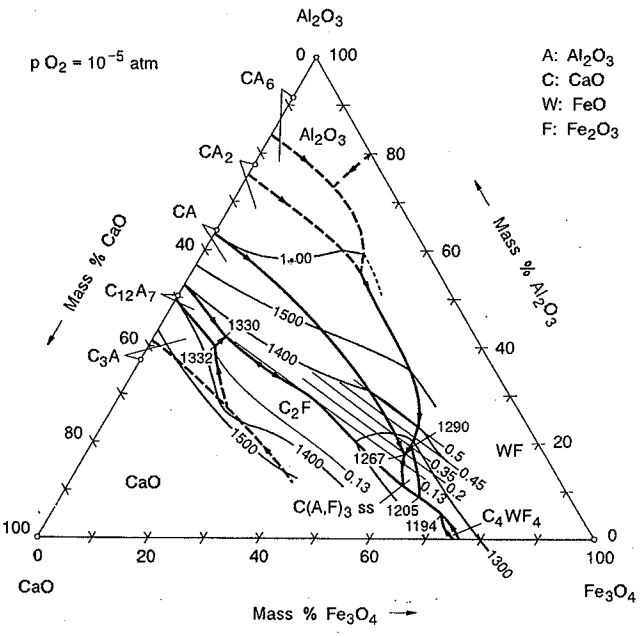


Fig. 3.158. Liquidus surfaces in the Al_2O_3-CaO-FeO_x system at $pO_2=10^{-5}$ atm after Imlach, Glasser [9]. The thin lines show the ratio Fe(III)/Fe(II) at liquidus temperatures.

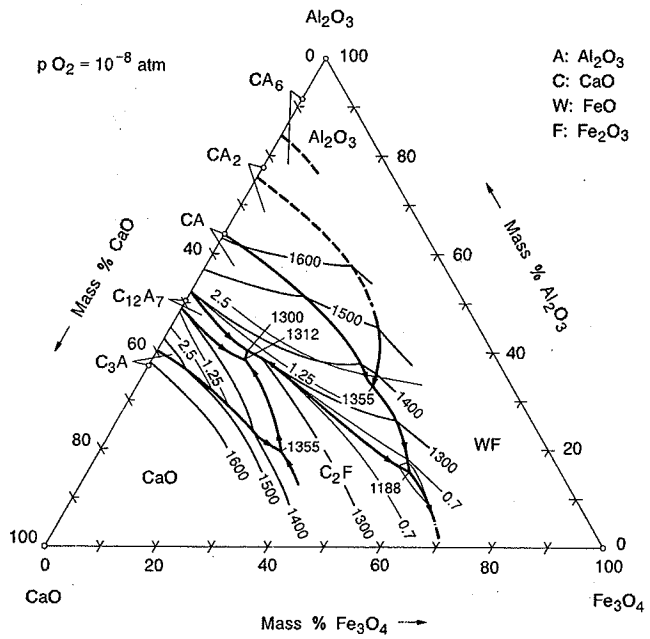


Fig. 3.159. Liquidus surfaces in the Al_2O_3-CaO-FeO_x system at $pO_2=10^{-8}$ atm after Imlach, Glasser [9]. The thin lines show the ratio Fe(III)/Fe(II) at liquidus temperatures. For the sub-solidus equilibria and the crystallisation path in the system Al_2O_3-CaO-FeO-Fe_2O_3, see original paper by Imlach, Glasser [9, 10].

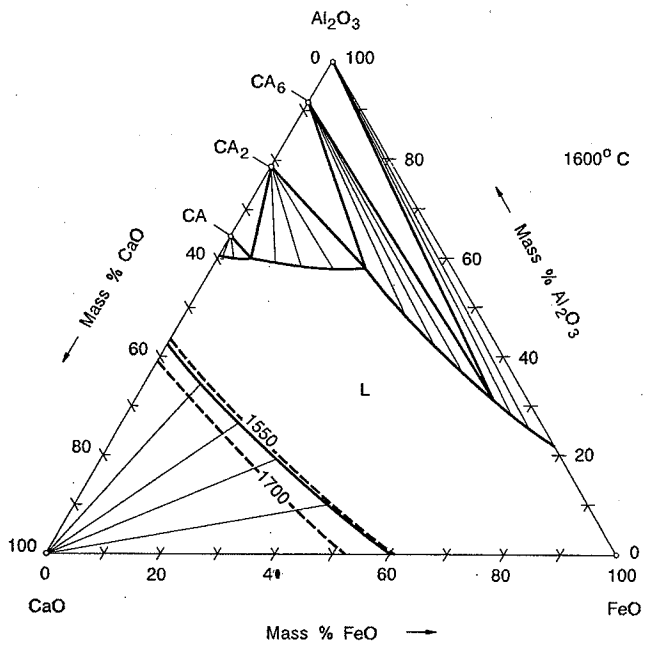


Fig. 3.160. Isothermal section through the Al_2O_3-CaO-FeO system in contact with metallic iron at 1600 °C after Wrampelmeyer et al. [11].

References

[1] Dayal, R. R., F. P. Glasser: Sci. Ceram., Volume Date 1965, 3 (1967), p. 191/214
[2] Lister, D. H., F. P. Glasser: Trans. J. Br. Ceram. Soc. 66 (1967) No. 7, p. 293/305
[3] Brisi, C.: Ann. Chim. /Rome/ 44 (1954), p. 500/11
[4] Majumdar, A. J.: Trans. J. Br. Ceram. Soc. 64 (1965) No. 2, p. 105/19
[5] Schlaudt, C. M., D. M. Roy: Nature /London/ 206 (1965) No. 4986, p. 819
[6] Eremin, N. I., O. I. Arakelyan, I. B. Firfarova: Izv. Akad. Nauk SSSR, Neorg. Mater. 10 (1974) No. 1, p. 106/11
[7] Eremin, N. I.: Izv. Akad. Nauk SSSR, Neorg. Mater. 10 (1974) No. 1, p. 103/5
[8] Malysheva, T. Y., I. V. Ostrovskaya, V. Y. Lyadova, M. S. Model, V. I. Ponomarev: Izv. Akad. Nauk SSSR, Met. (1976) No. 5, p. 78/86
[9] Imlach, J. A., F. P. Glasser: Trans. J. Br. Ceram. Soc. 70 (1971) No. 6, p. 227/34
[10] Imlach, J. A., F. P. Glasser: Trans. J. Br. Ceram. Soc. 72 (1973) No. 5, p. 221/8
[11] Wrampelmeyer, J.-C., S. Dimitrov, D. Janke: Steel Res. 60 (1989) No. 12, p. 539/49

Al_2O_3-CaO-K_2O

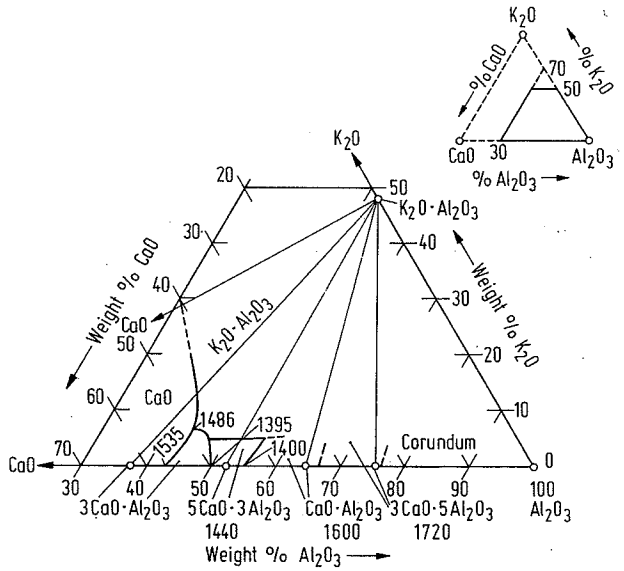


Fig. 3.161. Liquidus surface at the Al_2O_3-CaO edge of the Al_2O_3-CaO-K_2O system after Brownmiller [1].

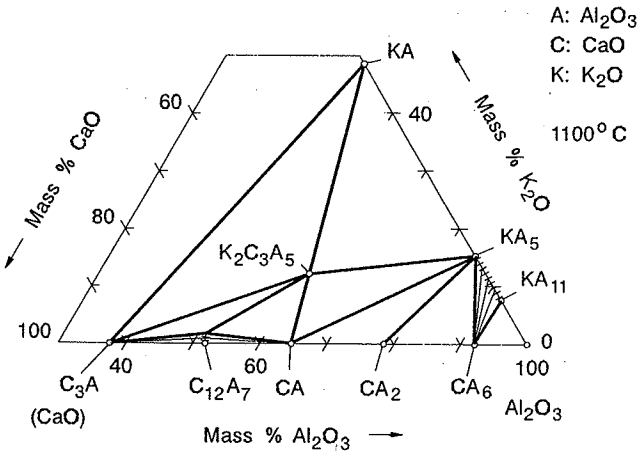


Fig. 3.162. Isothermal section through the Al_2O_3-CaO-K_2O system at 1100 °C as determined recently by van Hoek et al. [2].

References

[1] Brownmiller, L. T.: Am. J. Sci., 5th Ser. 29 (1935), p. 260/77
[2] van Hoek, J. A. M., F. J. J. van Loo, R. Metselaar: Mat. Sci. Monogr. 66B (1991), p. 581/90

Al_2O_3-CaO-MgO

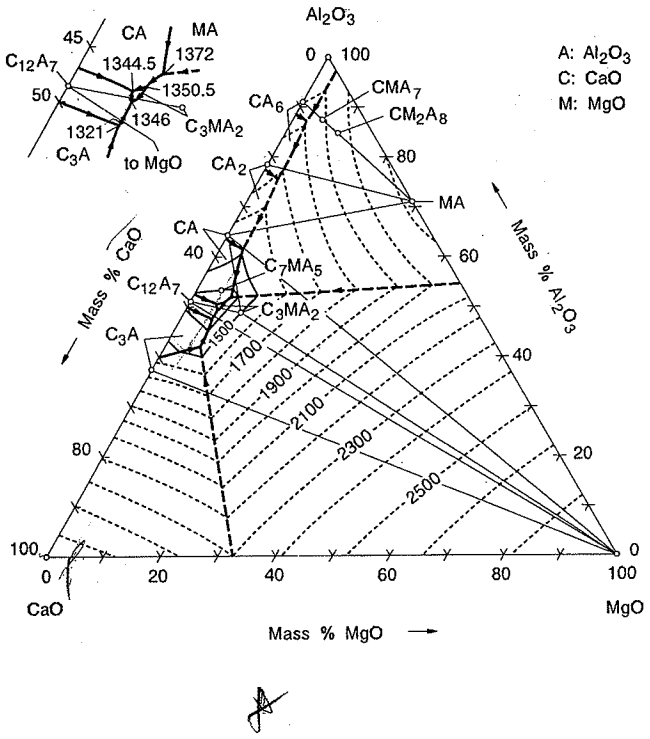


Fig. 3.163. Liquidus surface and sub-solidus equilibria in the Al_2O_3-CaO-MgO system based mainly on the work of Rankin, Merwin [1], Welch [2], Majumdar [3] (phase relations involving ternary compound), and Rao [4]. Liquidus temperatures for the sub-system $CaO{\cdot}Al_2O_3$-$MgO{\cdot}Al_2O_3$-MgO have also been investigated by Melnik et al. [5]. The existence of the $3CaO{\cdot}MgO{\cdot}2Al_2O_3$ phase was recently confirmed by Glasser, Marr [6]. An additional metastable compound, $7CaO{\cdot}MgO{\cdot}5Al_2O_3$, has been reported by Welch [2]. Recently, two further Al_2O_3-rich solution phases following the ideal chemical formulas $CaO{\cdot}MgO{\cdot}7Al_2O_3$ and $CaO{\cdot}2MgO{\cdot}8Al_2O_3$ has been found [7]. They melt incongruently at temperatures of 1850 to 1950 °C.

References

[1] Rankin, G. A., H. E. Merwin: J. Am. Chem. Soc. 38 (1916), p. 568/88
[2] Welch, J. H.: Nature /London/ 191 (1961) No. 4788, p. 559/60
[3] Majumdar, A. J.: Trans. J. Br. Ceram. Soc. 63 (1964), p. 347/64
[4] Rao, M. R.: J. Am. Ceram. Soc. 51 (1968) No. 1, p. 50/4
[5] Melnik, M. T., A. A. Kachura, N. V. Mokritskaya: Ogneupory (1989) No. 4, p. 27/8
[6] Glasser, F. P., J. Marr: Trans. J. Br. Ceram. Soc. 74 (1975) No. 4, p. 113/9
[7] Göbbels, M.: private communication

Al_2O_3-CaO-Na_2O

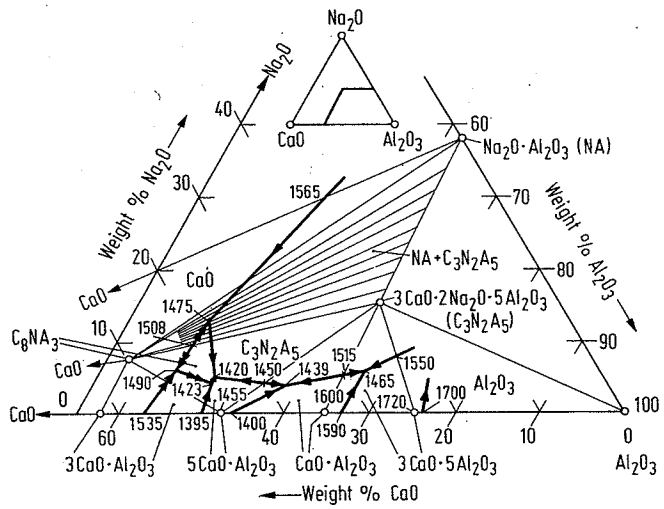


Fig. 3.164. Liquidus surface and compatibility relations in the Al_2O_3-CaO-Na_2O system after Brownmiller, Bogue [1].

References

[1] Brownmiller, L. T., R. H. Bogue: J. Res. Nat. Bur. Stand., RP 414, 8 (1932), p. 289/307
[2] Verweij, H., C. M. P. M. Saris: J. Am. Ceram. Soc. 69 (1986) No. 2, p. 94/8
[3] Zaldat, G. I., M. S. Kupriyanova, A. L. Tubolev: Izv. Akad. Nauk SSSR, Neorg. Mater. 21 (1985) No. 1, p. 51/3
[4] Fletcher, K. E., H. G. Midgley, A. E. Moore: Magaz. Concrete Res. 17 (1965) No. 53, p. 171/6

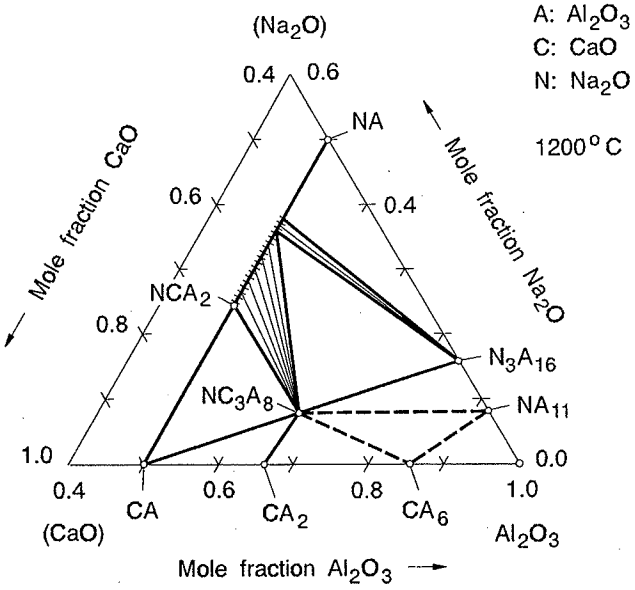


Fig. 3.165. Isothermal section through the system Al_2O_3-$CaO{\cdot}Al_2O_3$-$Na_2O{\cdot}Al_2O_3$ at 1200 °C after Verweij, Saris [2]. The phase relations in the Al_2O_3-rich region of the system (dashed lines) represent one possible version depending on the relative stability of the phases present [2]. According to Zaldat et al. [3], the phase $Na_2O{\cdot}3CaO{\cdot}8Al_2O_3$ reported by Verweij, Saris [2] has the composition $Na_2O{\cdot}4CaO{\cdot}10Al_2O_3$. For the isothermal section at 1397 °C, see original paper by Zaldat et al. [3]. The solubility of Na_2O in $3CaO{\cdot}Al_2O_3$ on the fictive section $3CaO{\cdot}Al_2O_3$-$3Na_2O{\cdot}Al_2O_3$ at 1350 °C and at compositions up to 9 mole % $3Na_2O{\cdot}Al_2O_3$, has been reported by Fletcher et al. [4].

Al_2O_3-CaO-SiO_2

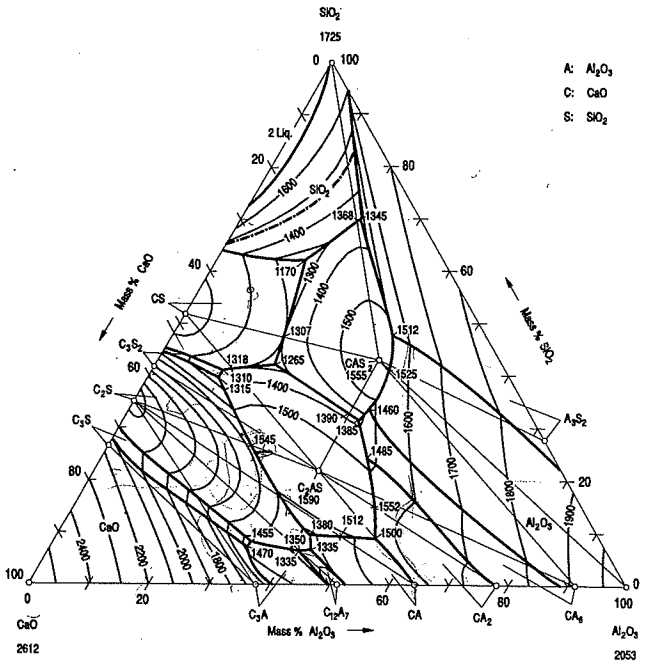


Fig. 3.166. Liquidus surface and sub-solidus equilibria in the Al_2O_3-CaO-SiO_2 system after Rankin, Wright [1], with later revisions due to Greig [2], Filonenko, Lavrov [3], Langenberg, Chipman [4], Aramaki, Roy [5] and Gentile, Foster [6]. The revisions of the $3CaO \cdot SiO_2$ primary field reported by Gutt, Russell [7], as well as the revision of the Al_2O_3- rich portion of the system due to Criado, De Aza [8] are also included in the figure. According to Longhi, Hays [9] the primary field of cristobalite on the $CaO \cdot Al_2O_3 \cdot 2SiO_2$-$SiO_2$ section ranges up to the eutectic between SiO_2 and $CaO \cdot Al_2O_3 \cdot 2SiO_2$. For thermodynamic assessment of the system Al_2O_3-CaO-SiO_2 and calculated phase equilibria, see Eriksson, Pelton [10].

References

[1] Rankin, G. A., F. E. Wright: Am. J. Sci., 4th Ser. 39 (1915), p. 1/79
[2] Greig, J. W. : Am. J. Sci., 5th Ser. 13 (1927) No. 73, p. 1/154
[3] Filonenko, N. E., I. V. Lavrov: Dokl. Akad. Nauk SSSR 66 (1949) No. 4, p. 673/6
[4] Langenberg, F. C., J. Chipman: J. Am. Ceram. Soc. 39 (1956) No. 10, p. 432/3
[5] Aramaki, S., S. Roy: J. Am. Ceram. Soc. 42 (1959) No. 12, p. 644/45
[6] Gentile, A. L., W. R. Foster: J. Am. Ceram. Soc. 46 (1963) No. 2, p. 74/6
[7] Gutt, W., A. D. Russell: J. Mater. Sci. 12 (1977) No. 9, p. 1869/78
[8] Criado, E., S. De Aza: Proc. 1st C.E.R.P., Ed.: Faenza Editrice (1976), p. 97/101
[9] Longhi, J., J. F. Hays: Am. J. Sci. 279 (1979) No. 7, p. 876/90
[10] Eriksson, G., A. D. Pelton: Metall. Trans. B 24B (1993), p. 807/15

Al_2O_3-CaO-TiO_2

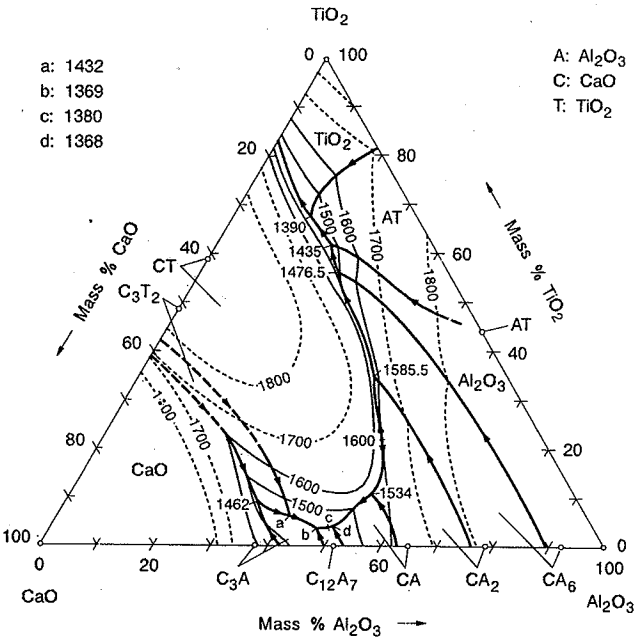


Fig. 3.167. Liquidus surface in the Al_2O_3-CaO-TiO_2 system after Imlach, Glasser [1].

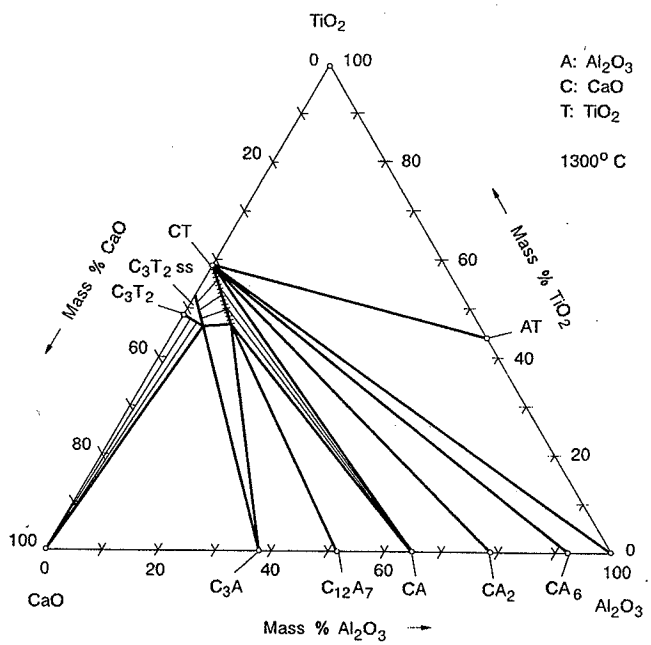


Fig. 3.168. Isothermal section through the Al_2O_3-CaO-TiO_2 system at 1300 °C after Imlach, Glasser [1]. For additional isothermal and composition sections, see original paper [1].

Al_2O_3-CaO-ZrO_2

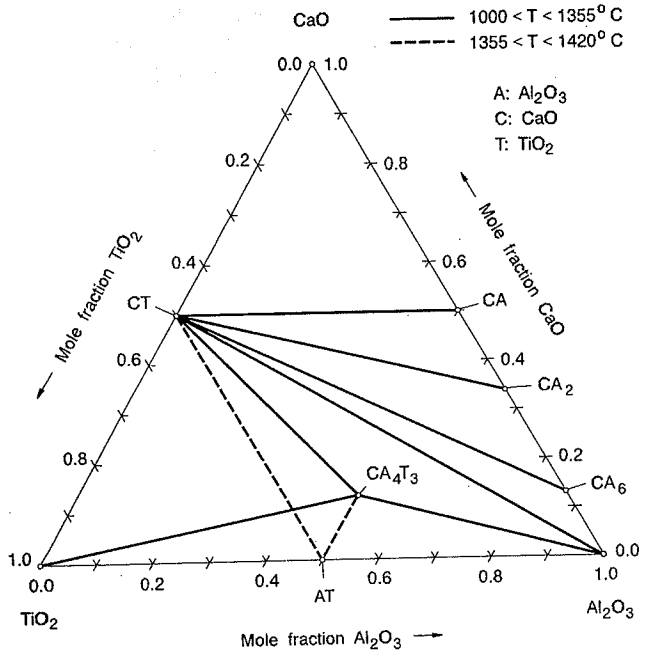


Fig. 3.169. Compatibility relations in the Al_2O_3-CaO-TiO_2 system between 1000 and 1420 °C after Morgan, Koutsoutis [2]. The melting behaviour of the $CaO{\cdot}4Al_2O_3{\cdot}3TiO_2$ phase was not reported [2]. The lower stability limit for the $Al_2O_3{\cdot}TiO_2$ phase at approx. 1355 °C [2] is much higher than the value selected for the Al_2O_3-TiO_2 phase diagram (Fig. 3.37) in this compilation. According to Imlach, Glasser [1], the liquid phase should already be present in the system above 1390 °C.

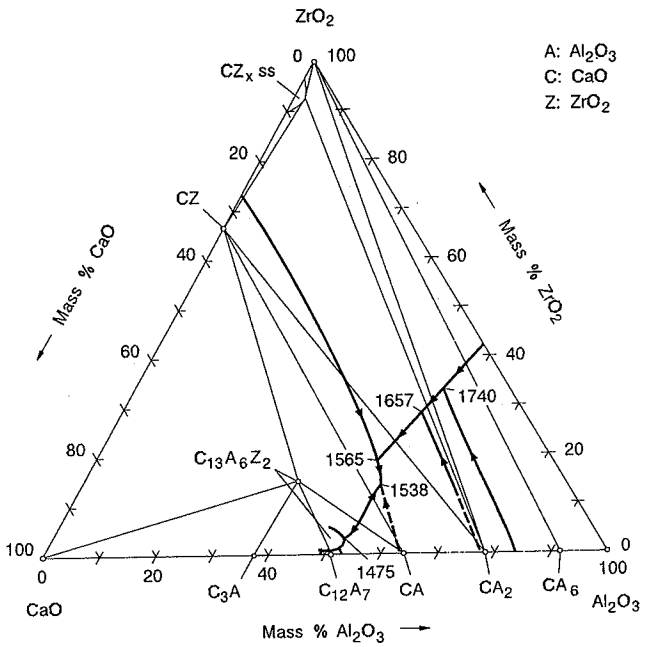


Fig. 3.170. Liquidus surface and compatibility relations in the Al_2O_3-CaO-ZrO_2 system after Monterous, White [1]. The only ternary compound, $13CaO{\cdot}6Al_2O_3{\cdot}2ZrO_2$, melts incongruently at 1540 °C to liquid and $CaO{\cdot}ZrO_2$ [1]. The compatibility relations involving the fluorite phase ($CaO{\cdot}xZrO_2$ solid solution) at 1380 °C is redrawn according to Muromura, Hinatsu [2]. The sub-solidus equilibria in [1,2] agree with previous results obtained by Berezhnoi, Kordyuk [3].

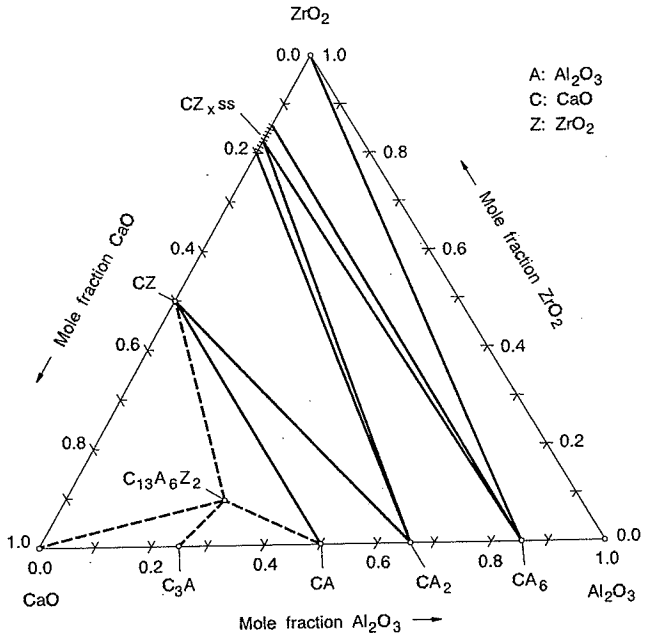


Fig. 3.171. Sub-solidus equilibria in the Al_2O_3-CaO-ZrO_2 system as determined by experiment and by calculation (dash-dot lines, 1327 °C) by Bannister [5, 6].

References

[1] Imlach, J. A., F. P. Glasser: Trans. J. Br. Ceram. Soc. 67 (1968) No. 12, p. 581/609
[2] Morgan, P. E. D., M. S. Koutsoutis: J. Mater. Sci. Lett. 4 (1985) No. 3, p. 321/3

References

[1] Monterous, E., J. White: Bol. Soc. Esp. Ceram. Y Vidrio 12 (1973) No. 4, p. 237
[2] Muromura, T., Y. Hinatsu: Mat. Res. Bull. 21 (1986) No. 1, p. 61/7
[3] Berezhnoi, A. S., R. A. Kordyuk: Dopov. Akad. Nauk Ukr. RSR. (1963) No. 10, p. 1344/7
[4] Liddle, J., N. H. Brett: Trans. J. Br. Ceram. Soc. 84 (1985) No. 4, p. 128/34
[5] Bannister, M. J.: Proc. - Aust. Ceram. Conf. 9 (1980), p. 46/51
[6] Bannister, M. J.: J. Aust. Ceram. Soc. 17 (1981) No. 1, p. 21/4

Al_2O_3-Cr_2O_3-FeO_x

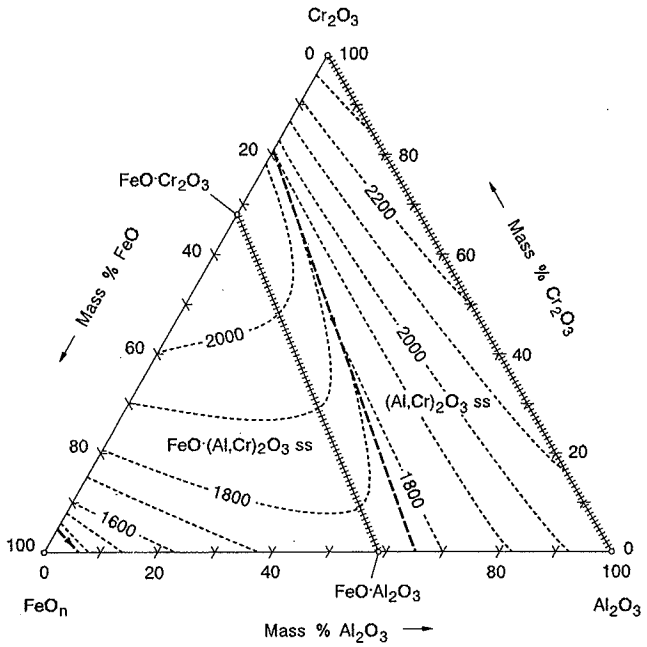


Fig. 3.172. Tentative liquidus surface in the Al_2O_3-Cr_2O_3-FeO_n system based mainly on the work of Rosenbach, Schmitz [1] and on the data for lower-order systems. For a tentative space representation of the system and isothermal sections, see original paper [1].

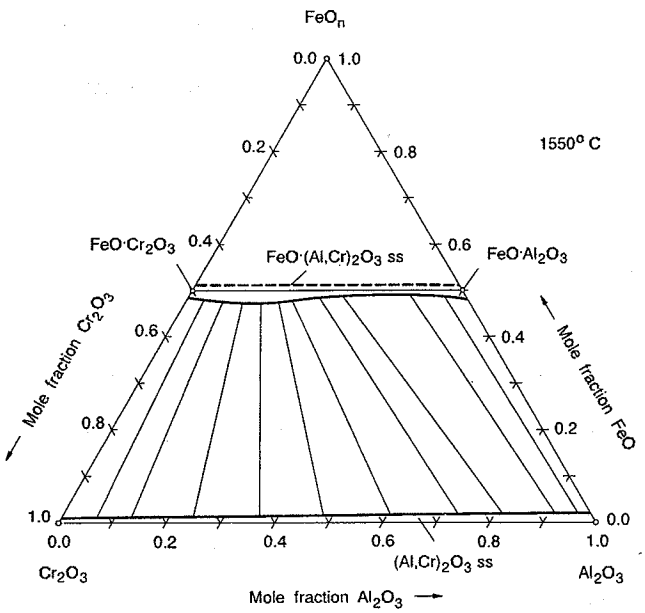


Fig. 3.173. Isothermal section through the system Al_2O_3-Cr_2O_3-FeO_n at 1550 °C and at low oxygen partial pressure ($7.61 \cdot 10^{-10}$ atm) showing tie-lines between $(Al,Cr)_2O_3$ and $FeO.(Al,Cr)_2O_3$ solid solutions after Jacob et al. [2]. For phase equilibria at 1100 °C, see Petric, Jacob [3].

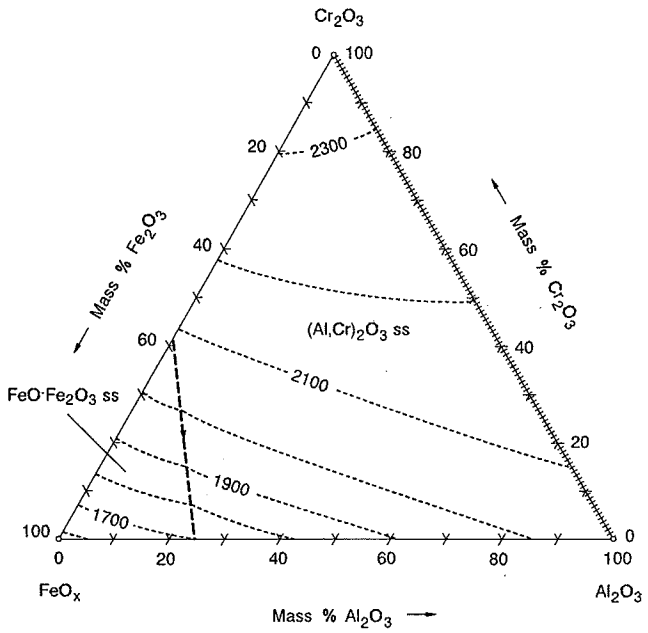


Fig. 3.174. Tentative liquidus surface in the system Al_2O_3-Cr_2O_3-FeO_x in air, based mainly on the work of Muan, Somiya [4] and lower-order systems.

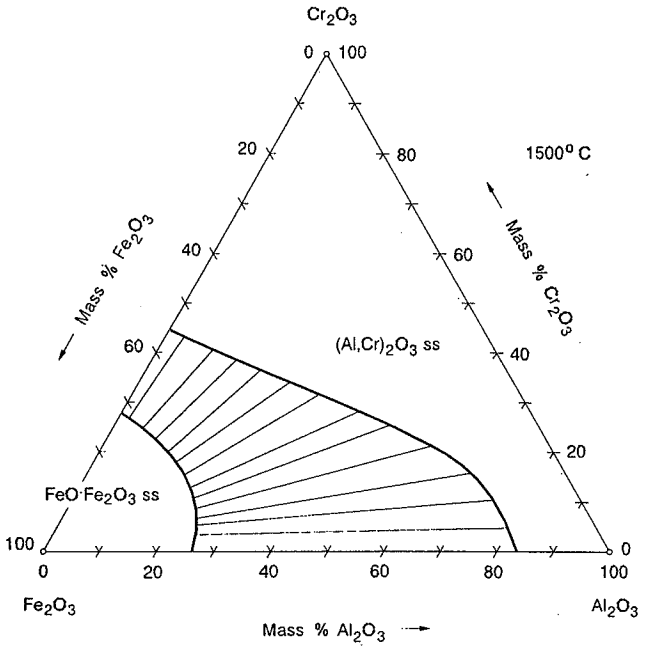


Fig. 3.175.

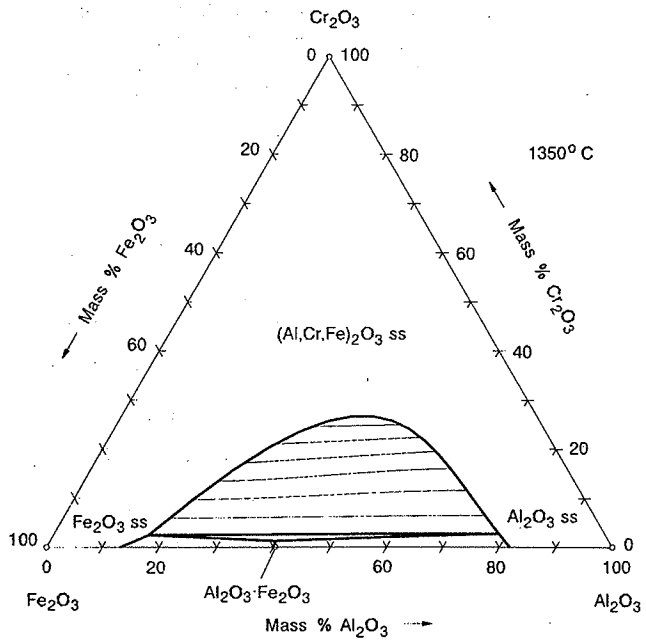


Fig. 3.176.

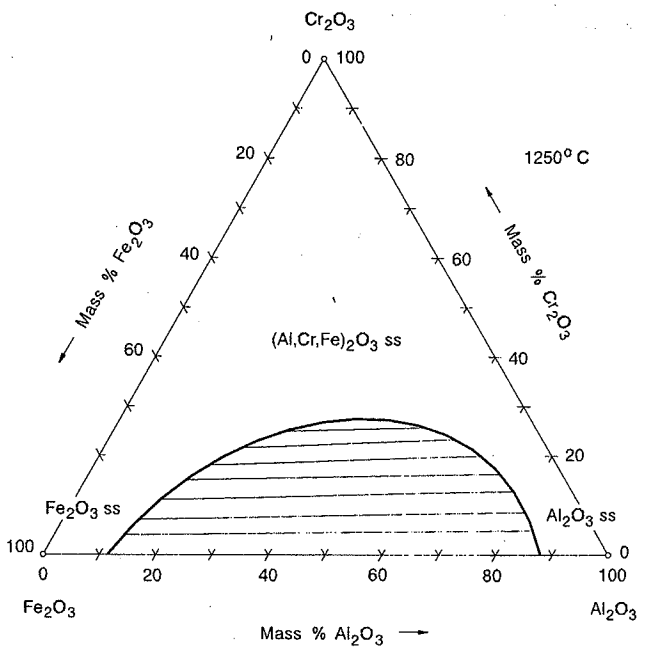


Fig. 3.177.

Figs. 3.175 to 3.177. Isothermal sections through the system Al_2O_3-Cr_2O_3-FeO_x in air at 1500, 1350 and 1250 °C after Muan, Somiya [4]. For further isothermal sections, a space representation of the system, and phase equilibria at 1 atm O_2 pressure, see original paper by Muan, Somiya [4].

The miscibility gap in the sub-system $FeO{\cdot}Fe_2O_3$-$FeO{\cdot}Al_2O_3$-$FeO{\cdot}Cr_2O_3$ between 500 and 1000 °C has been reported by Cremer [5]. For the system Al-Cr-Fe-O, see also Richards, White [6].

References

[1] Rosenbach, K., J. A. Schmitz: Arch. Eisenhüttenwes. 45 (1974) No. 12, p. 843/7

[2] Jacob, K. T., A. Petric, G. M. Kale, G. N. K. Iyengar: Ceram. Int. 13 (1987) No. 2, p. 123/9

[3] Petric, A., K. T. Jacob: Solid State Ionics 6 (1982) No. 1, p. 47/56

[4] Muan, A., S. Somiya: J. Am. Ceram. Soc. 42 (1959) No. 12, p. 603/13

[5] Cremer, V.: Neues Jahr. Mineral, Abh. 111 (1969) No. 2, p. 184/205

[6] Richards, R. G., J. White: Trans. J. Br. Ceram. Soc. 53 (1954), p. 422/59

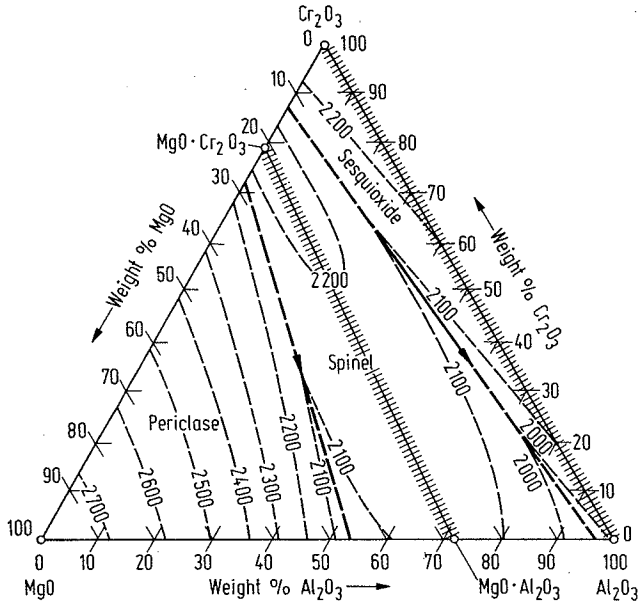


Fig. 3.178. Tentative liquidus surface in the system Al_2O_3-Cr_2O_3-MgO after Muan, Osborn [1] based in part on data of Wilde, Rees [2].

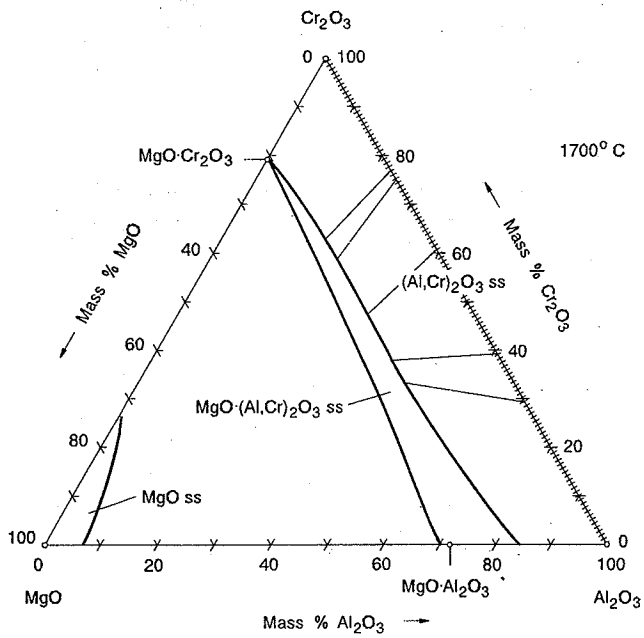


Fig. 3.179. Isothermal section through the system Al_2O_3-Cr_2O_3-MgO at 1700 °C after Greskovich, Stubican [3].

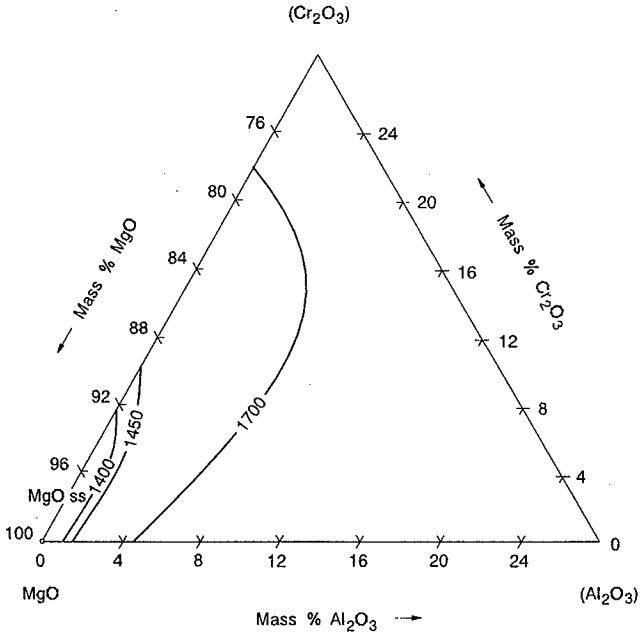


Fig. 3.180. Homogeneity range of the MgO solid solution in the system Al_2O_3-Cr_2O_3-MgO at 1400, 1450 and 1700 °C after Dewendra et al. [4]. Recently, the composition of the MgO solid solution between 1400 and 1700 °C has been reported by Butler, Sueli [5].

References

[1] Muan, A., E. F. Osborn: Phase Equilibria Among Oxides in Steelmaking, Ed.: Addison-Wesley Publishing Company, Inc., Reading, Massachusetts (1965)

[2] Wilde, W. T., J. Rees: Trans. J. Br. Ceram. Soc. 42 (1943) No. 7, p. 123/55

[3] Greskovich, C., V. S. Stubican: J. Am. Ceram. Soc. 51 (1968) No. 1, p. 42/6

[4] Dewendra, J. D., C. M. Wilson, N. H. Brett: Trans. J. Br. Ceram. Soc. 81 (1982) No. 6, p. 185/9

[5] Butler, B. C. M., E. E. Sueli: Trans. J. Br. Ceram. Soc. 87 (1988) No. 1, p. 14/6

Al_2O_3-FeO_x-MgO

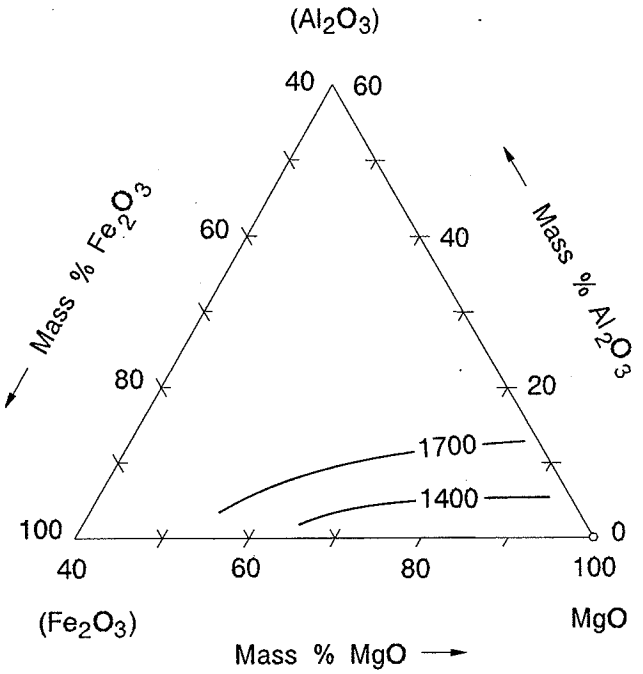


Fig. 3.181. Extension of the MgO solid solution in the system Al_2O_3-FeO_x-MgO at 1400 and 1700 °C after Butler, Sueli [1].

For additional studies concerning the solid phases, see Pismenskaya at al. [2] and Letyuk, Troneva [3]. The isothermal section through the system Al_2O_3-Fe_2O_3-MgO at 1400 °C was reported by Kwestroo [4].

References

[1] Butler, B. C. M., E. E. Sueli: Trans. J. Br. Ceram. Soc. 87 (1988) No. 1, p. 14/6
[2] Pismenskaya, G. M., V. F. Balakirev, G. P. Popov, G. I. Chufarov: Izv. Vyssh. Uchebn. Zaved., Chern. Met. 13 (1970) No. 8, p. 14/8
[3] Letyuk, L. M., N. M. Troneva: Izv. Akad. Nauk SSSR, Neorg. Mater. 9 (1973) No. 9, p. 1596/9
[4] Kwestroo, W.: J. Inorg. Nucl. Chem. 9 (1959), p. 65/70

Al_2O_3-FeO_x-MnO_x

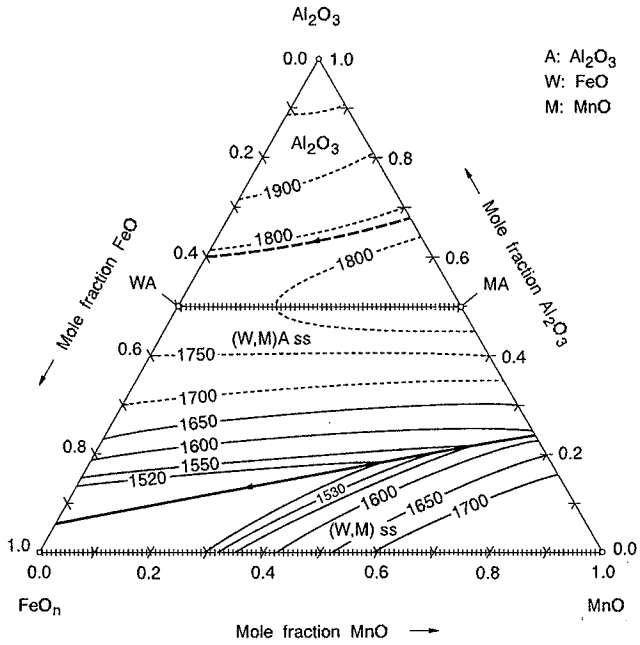


Fig. 3.182. Liquidus surface in the Al_2O_3-FeO_n-MnO system as drawn by Schürmann, Bannenberg [1], according to experimental results of Oelsen, Heynert [2] and Fischer, Bardenheuer [3]. The liquidus isotherms above 1600 °C are extrapolated from the binary systems.

The continuous spinel solid solution of the type $MnAl_xFe_{2-x}O_4$, with x changing from 0 to 2, has been investigated by Takenov et al. [4]. For additional information on deoxidation equilibria, see Ghosh [5], Pandit, Jacobs [6] and Schürmann, Bannenberg [1].

References

[1] Schürmann, E., N. Bannenberg: Arch. Eisenhüttenwes. 55 (1984) No. 10, p. 455/62
[2] Oelsen, W., G. Heynert: Arch. Eisenhüttenwes. 26 (1955) No. 10, p. 567/75
[3] Fischer, W. A., P. W. Bardenheuer: Arch. Eisenhüttenwes. 39 (1968) No. 9, p. 637/43
[4] Takenov, T. D., V. F. Balakirev, G. I. Chufarov: Izv. Akad. Nauk SSSR, Neorg. Mater. 1 (1965) No. 4, p. 587
[5] Ghosh, D. S.: Metal. ABM 37 (1981) No. 284, p. 397/402
[6] Pandit, S. S., K. T. Jacob: Steel Res. 58 (1987) No. 3, p. 105/10

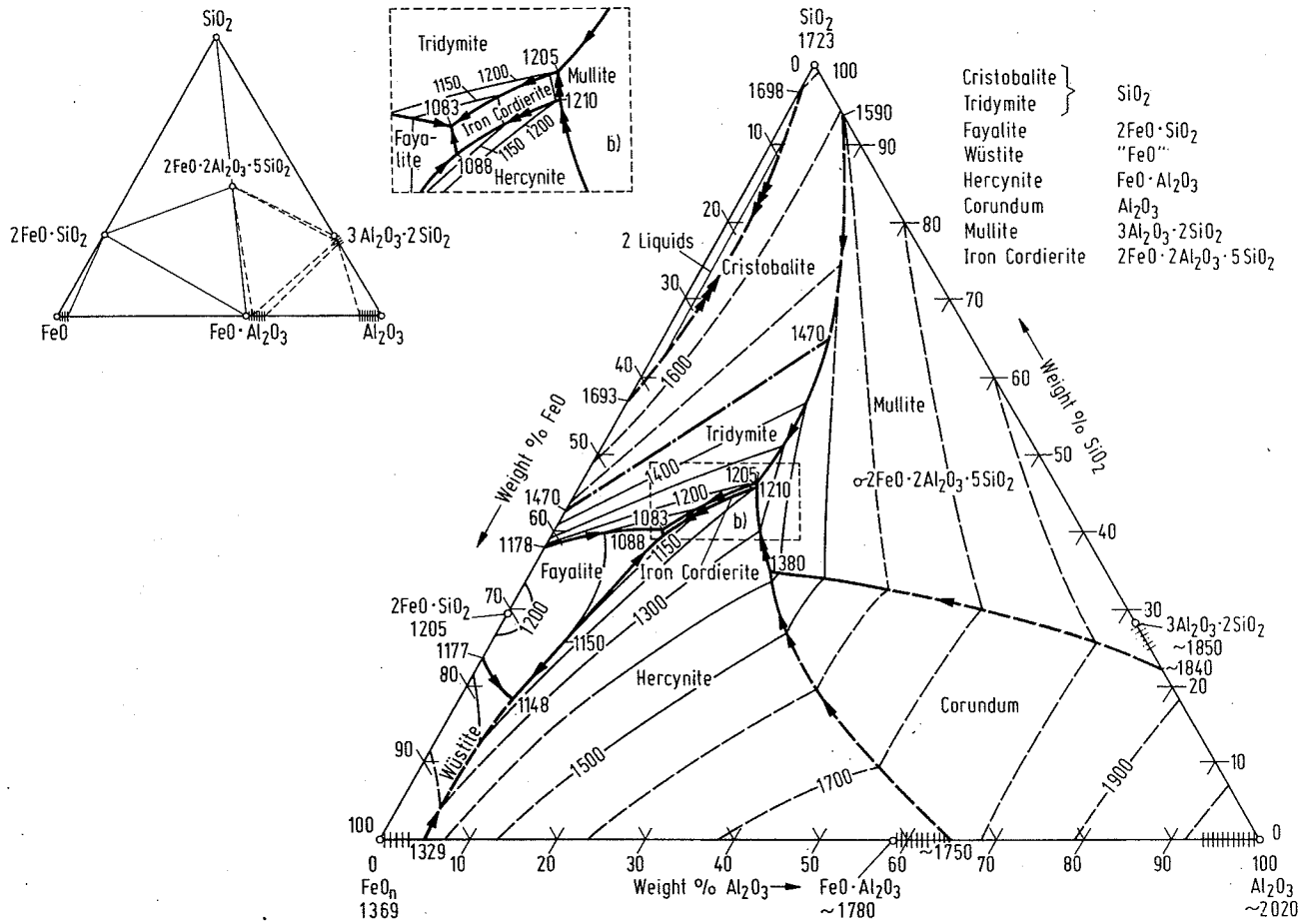


Fig. 3.183. Liquidus surfaces and compatibility relations in the system Al_2O_3-FeO_n-SiO_2 in contact with metallic iron after Schairer, Yagi [1] and Galakhov [2], as drawn by Muan, Osborn [3].

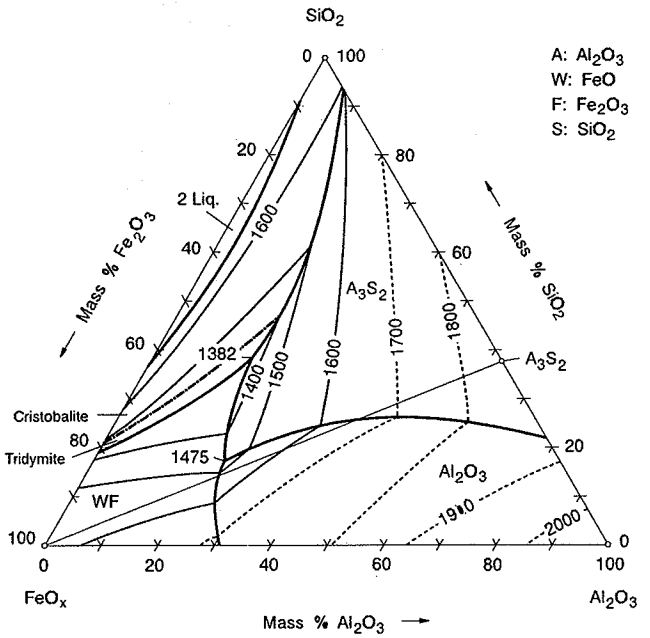


Fig. 3.184. Liquidus surface in the system Al_2O_3-FeO_x-SiO_2 in air after Muan [4], as revised by Idink, Woermann [5].

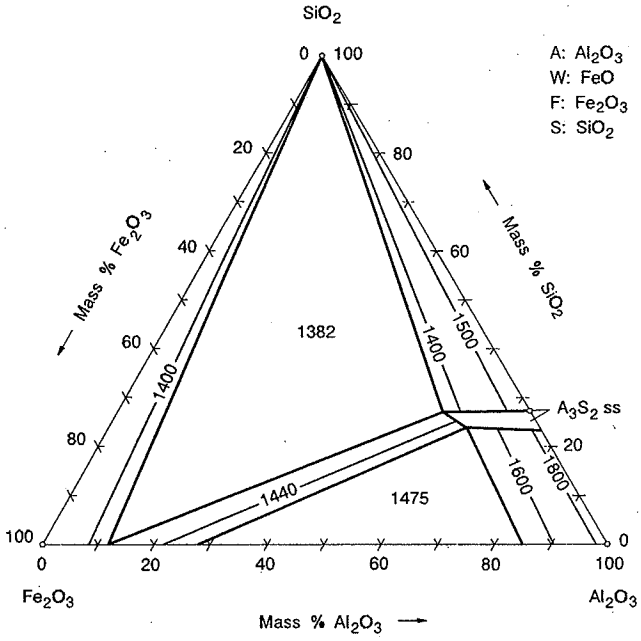


Fig. 3.185. Solidus surface in the system Al_2O_3-FeO_x-SiO_2 in air after Muan [4], as revised by Idink, Woermann [5].

For liquidus relations in the Al_2O_3-FeO_x-SiO_2 system at 1 atm O_2 pressure and for a space representation of liquidus relations in the system Al_2O_3-FeO-Fe_2O_3-SiO_2 system, see Muan [6]. For additional contributions to the system Al-Fe-Si-O, see also Mikhailov, Vilgelm [7] and Bagrova et al. [8].

References

[1] Schairer, J. F., K. Yagi: Am. J. Sci., Bowen Vol. (1952), p. 471/512
[2] Galakhov, F. Ya.: Izv. Akad. Nauk SSSR, Otdel. Khim. Nauk (1957) No. 5, p. 525/31
[3] Muan, A., E. F. Osborn: Phase Equilibria Among Oxides in Steelmaking, Ed.: Addison-Wesley Publishing Company, Inc., Reading, Massachusetts (1965)
[4] Muan, A.: J. Am. Ceram. Soc. 40 (1957) No. 4, p. 121/33
[5] Idink, H., E. Woermann: private communication
[6] Muan, A.: J. Am. Ceram. Soc. 40 (1957) No. 12, p. 420/31
[7] Mikhailov, G. G., E. M. Vilgelm: Izv. Vyssh. Uchebn. Zaved., Chern. Met. (1975) No. 3, p. 18/22
[8] Bagrova, T. A., A. D. Vaskevich, V. Y. Zaitsev, V. A. Kukoev: Izv. Akad. Nauk SSSR, Metal. (1986) No. 4, p. 31/6

Al_2O_3-K_2O-SiO_2

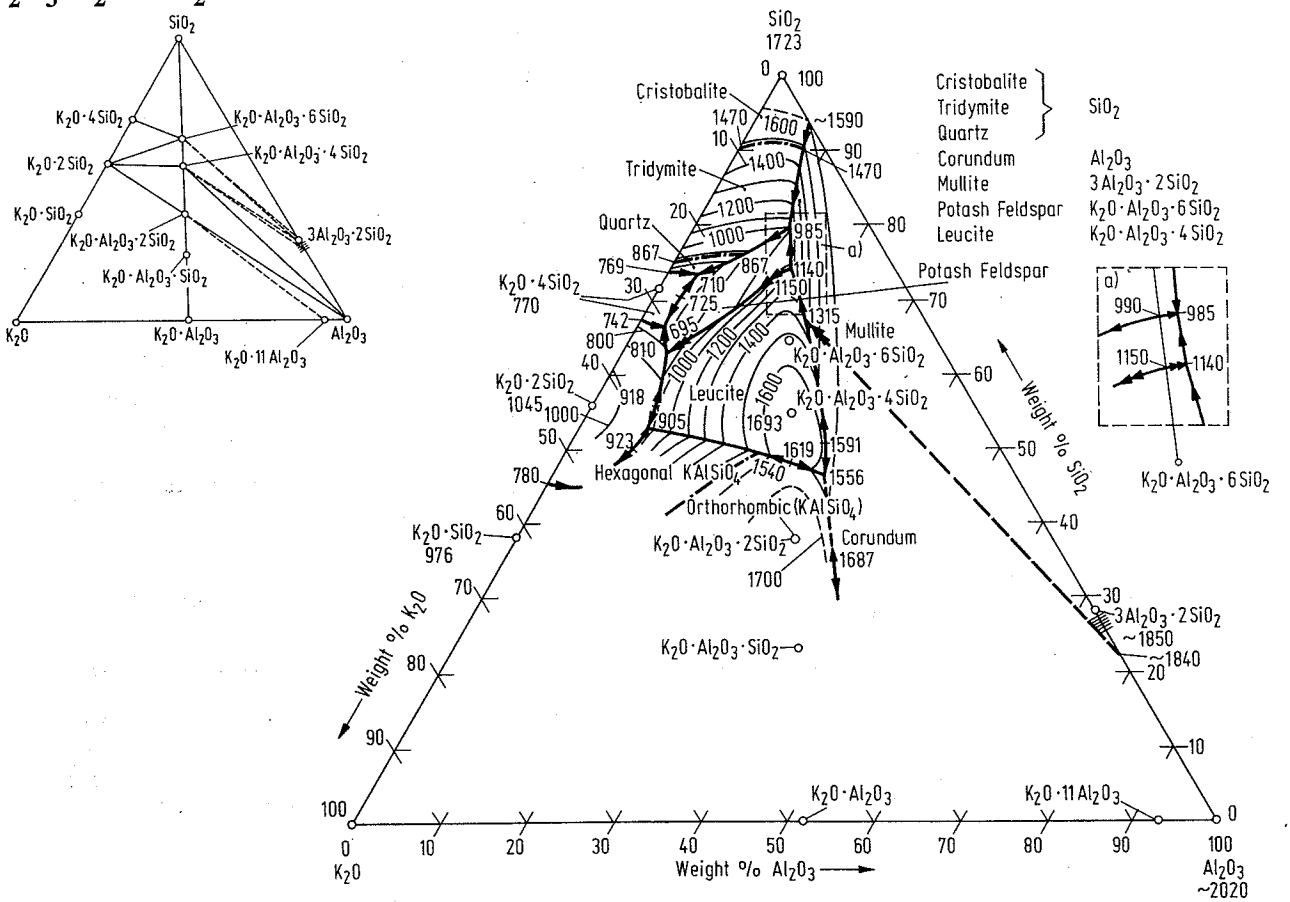


Fig. 3.186. Liquidus surface and sub-solidus equilibria in the SiO_2-rich portion of the Al_2O_3-K_2O-SiO_2 system after Schairer, Bowen [1, 2].

The composition section SiO_2-$K_2O{\cdot}Al_2O_3$ was investigated by Cook et al. [3] and Roth [4]. Contrary to results by Schairer, Bowen [1, 2], the compound $K_2O{\cdot}Al_2O_3{\cdot}2SiO_2$ is reported to melt incongruently. An additional solution phase has also been reported to exist on this section [3, 4].

References

[1] Schairer, J. F., N. L. Bowen: Am. J. Sci. 245 (1947) No. 4, p. 193/204
[2] Schairer, J. F., N. L. Bowen: Am. J. Sci. 253 (1955), p. 681/746
[3] Cook, L. P., R. S. Roth, H. S. Parker, T. Negas: Am. Mineral. 62 (1977) No. 11-12, p. 1180/90
[4] Roth, R. S.: Adv. Chem. Ser. 186 /Solid State Chem.: Contemp. Overview/ (1980), p. 391/408

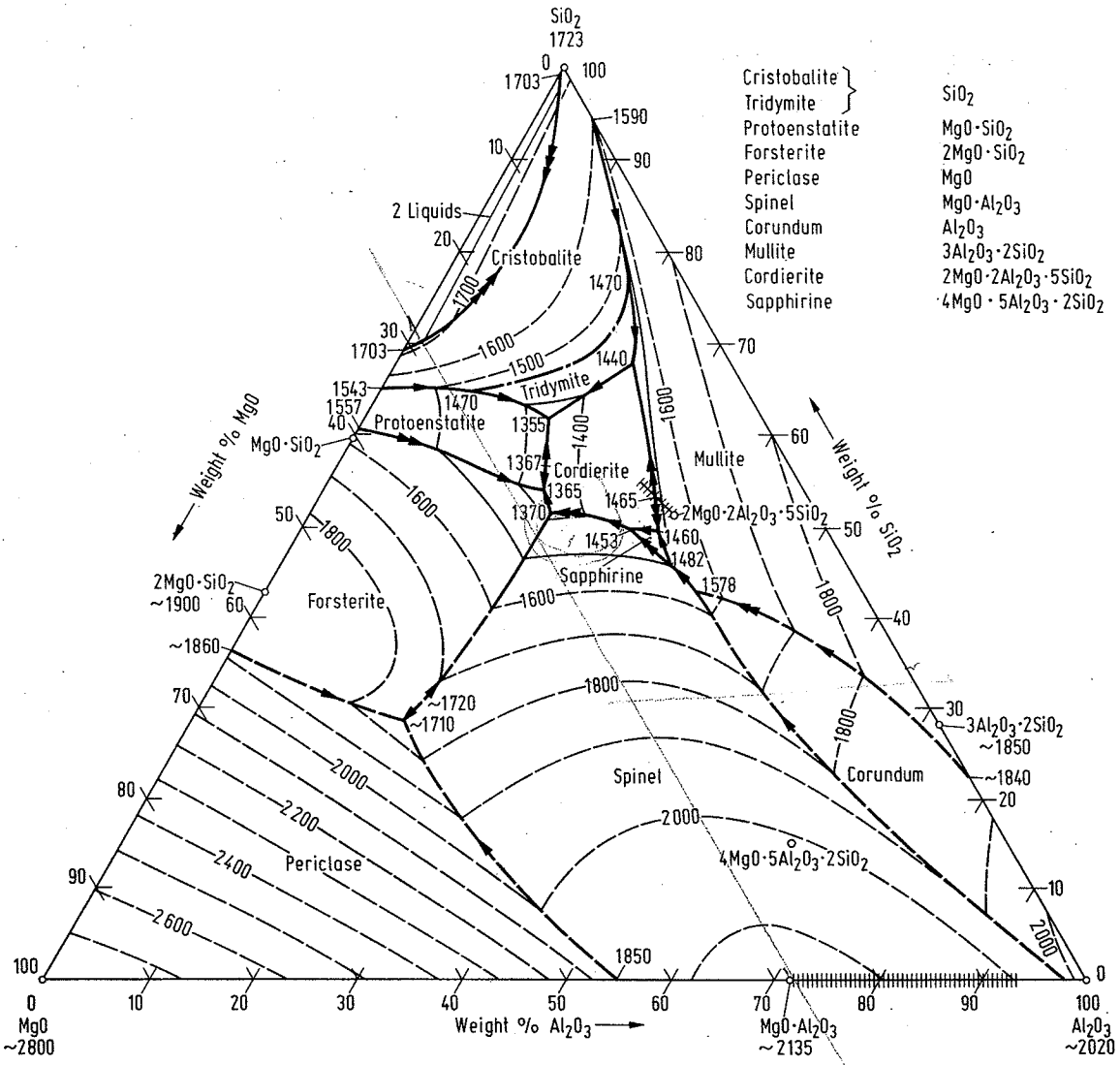


Fig. 3.187. Liquidus surface in the system Al_2O_3-MgO-SiO_2 after Osborn, Muan [1] based mainly on the work of Rankin, Merwin [2], Greig [3], Keith, Schairer [4], Foster [5, 6]. The invariant points bordering the primary fields of the $2MgO{\cdot}2Al_2O_3{\cdot}5SiO_2$ and $4MgO{\cdot}5Al_2O_3{\cdot}2SiO_2$ solution phases has been revised by Smart, Glasser [7].

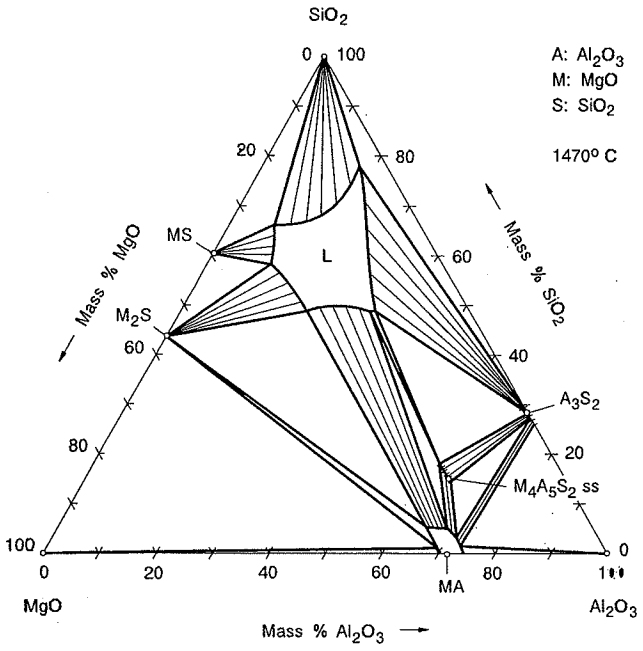


Fig. 3.188.

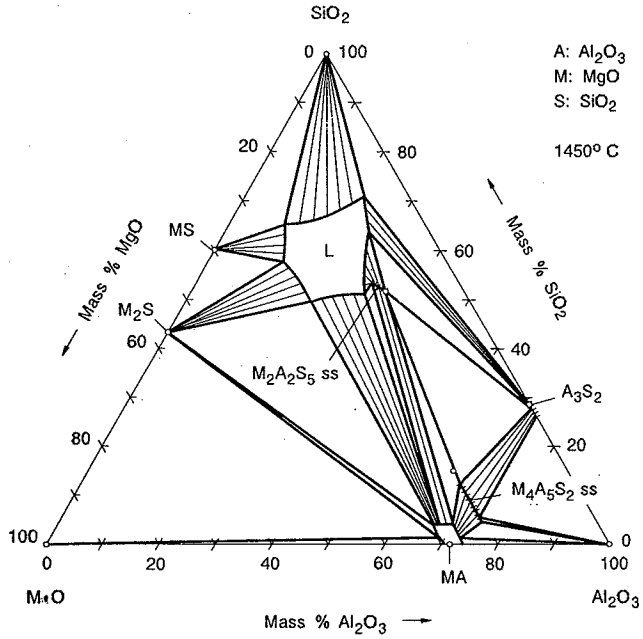


Fig. 3.189.

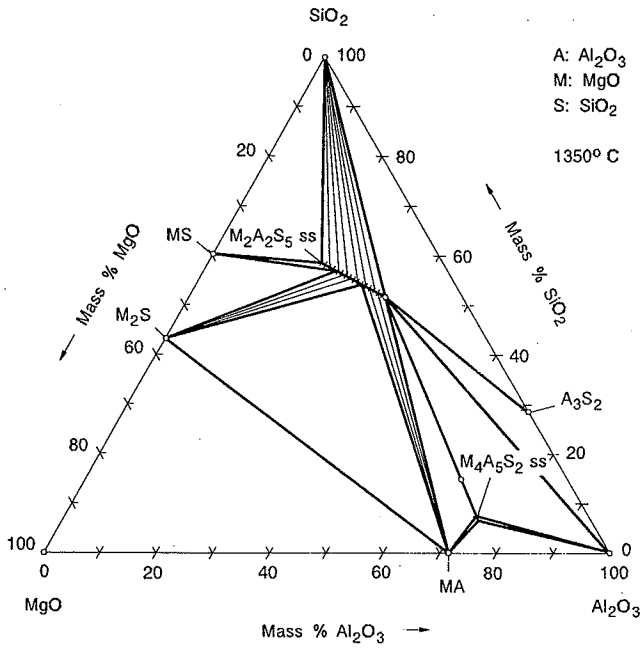


Fig. 3.190.

Figures 3.188 to 3.190. Isothermal section through the system Al_2O_3-MgO-SiO_2 at 1470, 1450 and 1350 °C after Smart, Glasser [8]. For further isothermal sections and composition sections, see original papers [8].

The extension of the $2MgO{\cdot}2Al_2O_3{\cdot}5SiO_2$-based solid solution has also been investigated by El Hage Maze [9] and Evans et al. [10]. The sub-solidus equilibria in the Al_2O_3-rich part of the system have been investigated previously by Foster [5, 6] and Schreyer, Schairer [11]. The coexistence of $MgO{\cdot}Al_2O_3$ and $3Al_2O_3{\cdot}2SiO_2$ as stable phase-assemblage at higher temperatures has also been reported. At lower temperatures (below 1350 °C), Smart, Glasser [8] report the assemblage $2MgO{\cdot}2Al_2O_3{\cdot}5SiO_2$ and Al_2O_3 to become more stable than $MgO{\cdot}Al_2O_3$ and $3Al_2O_3{\cdot}2SiO_2$. For the composition section $MgO{\cdot}Al_2O_3$-$2MgO{\cdot}SiO_2$, see Schlaudt, Roy [12].

References

[1] Osborn, E. F., A. Muan: Ceramic Fondation 1960 Publ. by Orton jr, Columbus/Ohio
[2] Rankin, A. G., H. E. Merwin: Am. J. Sci. 45 (1918) No. 268, p. 301/25
[3] Greig, J. W. : Am. J. Sci. 5th Ser., 13 (1927) No. 73, p. 1/154
[4] Keith, M. L., J. F. Schairer: J. Geol. 60 (1952) No. 2, p. 181/86
[5] Foster, W. R.: J. Am. Ceram. Soc. 33 (1950) No. 3, p. 73/84
[6] Foster, W. R.: J. Geol. 58 (1950) No. 2, p. 135/51
[7] Smart, R. M., F. P. Glasser: J. Mater. Sci. 11 (1976), p. 1459/64
[8] Smart, R. M., F. P. Glasser: Ceram. Int. 7 (1981) No. 3, p. 90/7
[9] El Hage Maze, S.: Bull. Soc. Fr. Ceram. 127 (1980), p. 63/5
[10] Evans, D. L., G. R. Fischer, J. E. Geiger, F. W. Martin: J. Am. Ceram. Soc. 63 (1980) No. 11-12, p. 629/34
[11] Schreyer, W., J. F. Schairer: J. Petrol. 2 (1961) No. 3, p. 324/406
[12] Schlaudt, C. M., D. M. Roy: J. Am. Ceram. Soc. 48 (1965) No. 5, p. 248/51

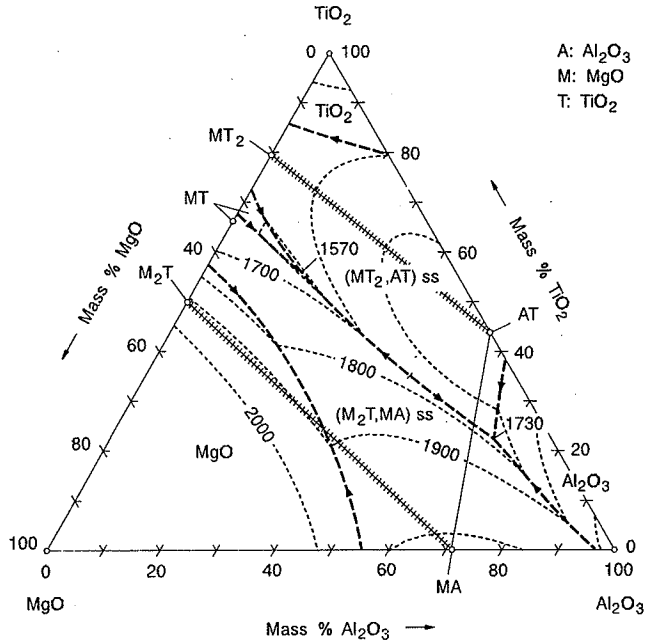


Fig. 3.191. Tentative liquidus surface in the Al_2O_3-MgO-TiO_2 system drawn according to results of Berezhnoi, Gulko [1] and adjusted to lower-order systems.

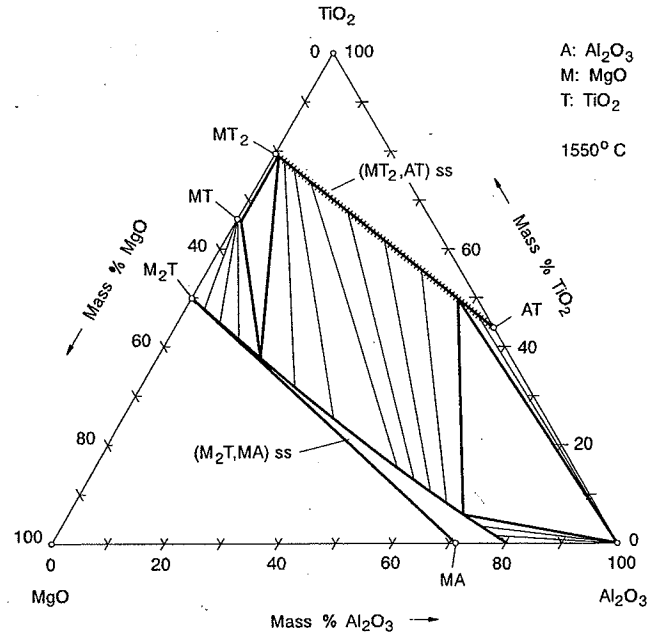


Fig. 3.192. Isothermal section at 1550 °C through the system Al_2O_3-MgO-TiO_2 after Boden, Glasser [2]. For further isothermal sections, see original paper [2]. The composition section $MgO{\cdot}Al_2O_3$-$2MgO{\cdot}TiO_2$ was investigated by Muan et al. [3].

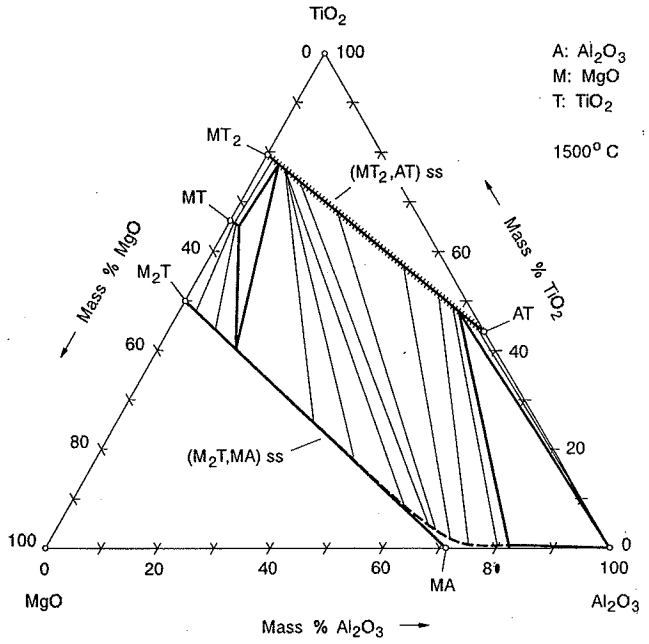


Fig. 3.193. Isothermal section through the system Al_2O_3-MgO-TiO_2 at 1500 °C according to Woermann [4].

The solubilities of MgO and TiO_2 in Al_2O_3 have been investigated by Roy, Coble [5].

References

[1] Berezhnoi, A. S., N. V. Gulko: Ukrain. Khim. Zhur. 21 (1955) No. 2, p. 158/66
[2] Boden, P., F. P. Glasser: Trans. J. Br. Ceram. Soc. 72 (1973) No. 5, p. 215/20
[3] Muan, A., J. Hauck, T. Löfall: Proc. Lunar. Sci. Conf. 3 (1972), p. 185/96
[4] Woermann, E.: private communication
[5] Roy, S. K., R. I. Coble: J. Am. Ceram. Soc. 51 (1968) No. 1, p. 1/6

Al_2O_3-MnO_x-SiO_2

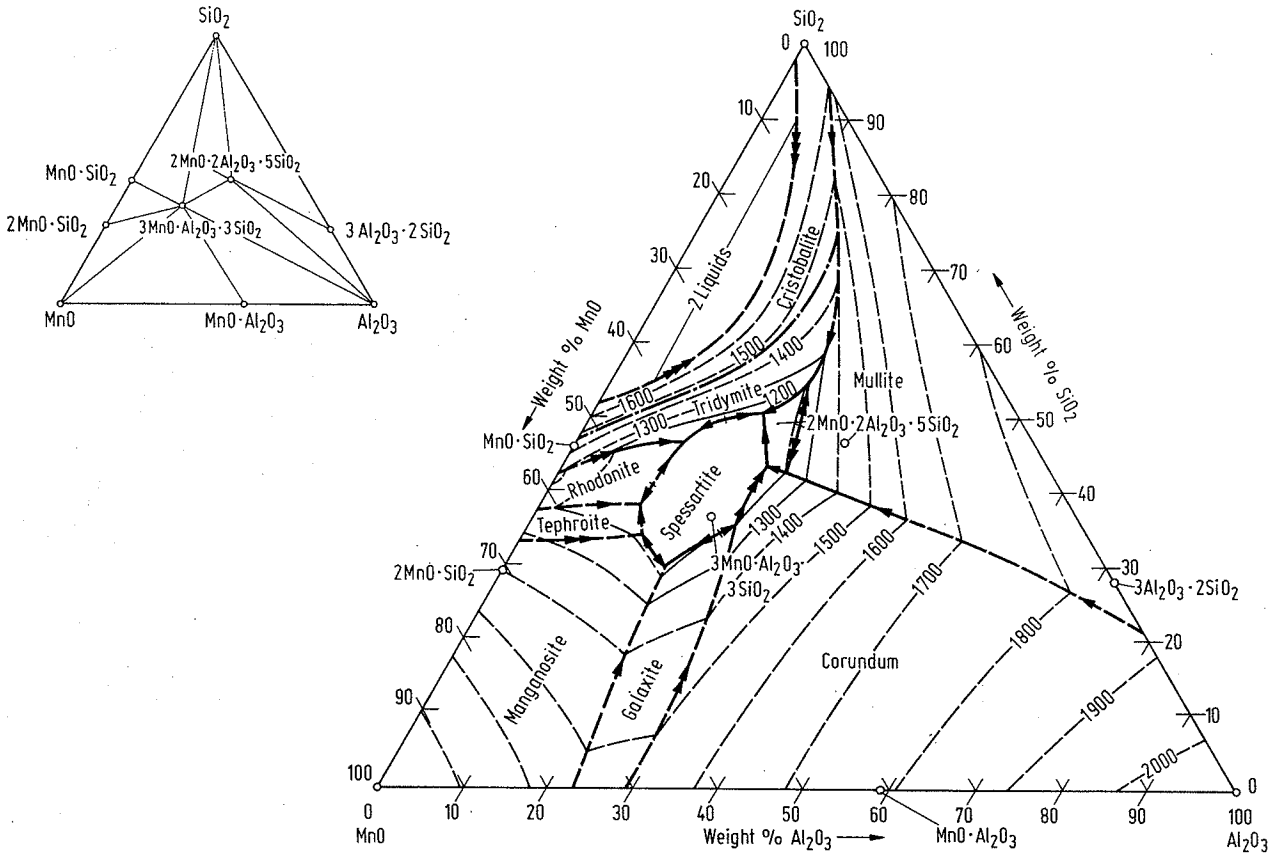


Fig. 3.194. Tentative liquidus surface and compatibility relations in the Al_2O_3-MnO-SiO_2 system under a neutral atmosphere after Osborn, Muan [1], according to experimental results of Snow [2] and Galakhov [3].

References

[1] Osborn, E. F., A. Muan: Ceramic Fondation 1960 Publ. by Orton jr, Columbus/Ohio
[2] Snow, R. B.: J. Am. Ceram. Soc. 26 (1943) No. 1, p. 11/20
[3] Galakhov, F. Ya.: Izv. Akad. Nauk SSSR, Otdel. Khim. Nauk (1957) No. 5, p. 525/31

Al_2O_3-Na_2O-SiO_2

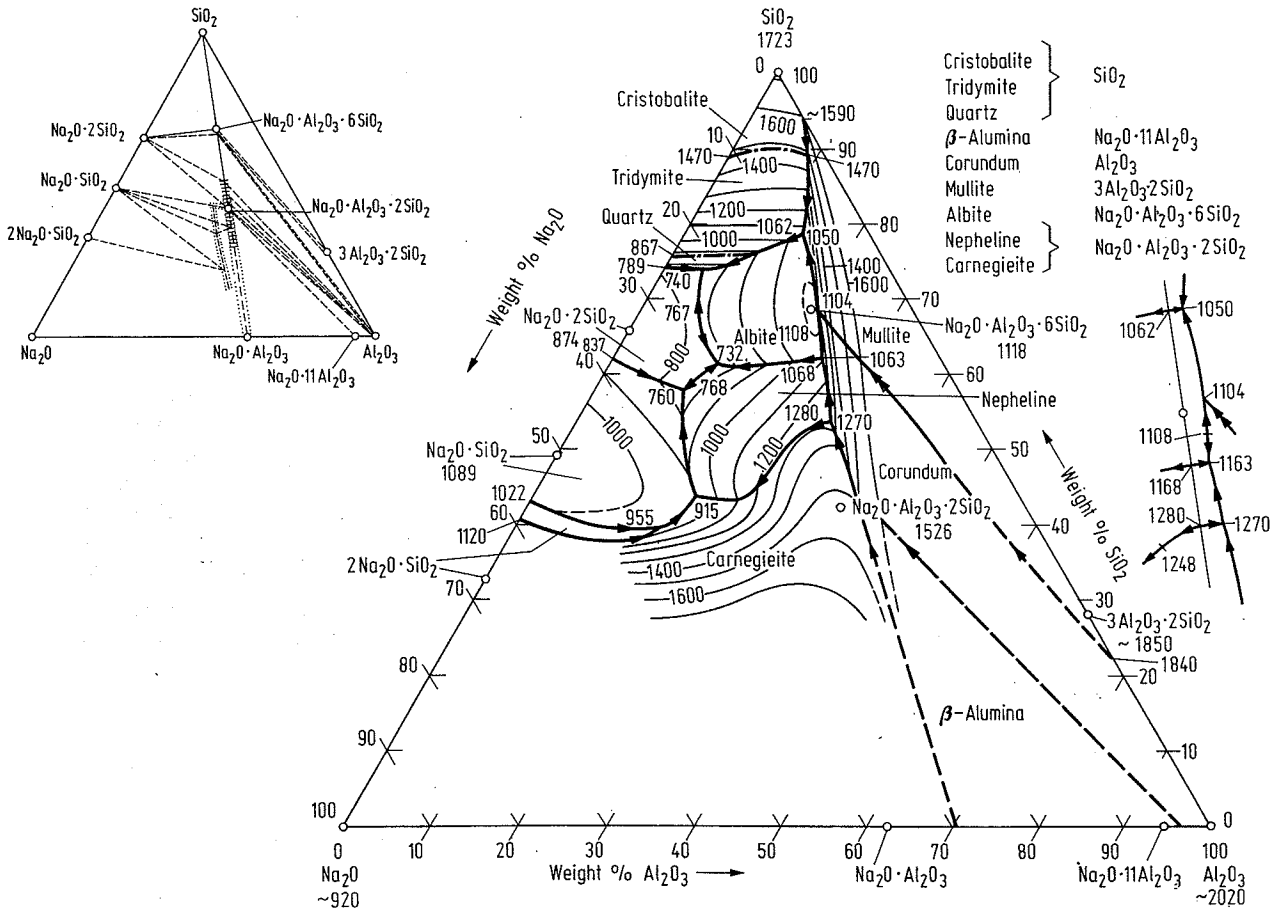
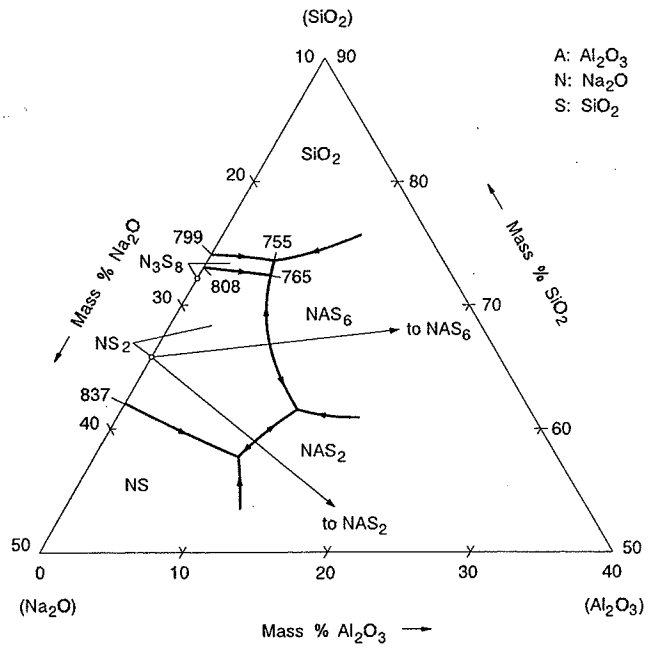


Fig. 3.195. Liquidus surface and compatibility relations in the Al_2O_3-Na_2O-SiO_2 system drawn by Osborn, Muan [1] according to experimental results of Bowen, Schairer [2, 3], De Pablo-Galan, Foster [4], and Galakhov [5].



← **Fig. 3.196.** Part of the liquidus surface in the Al_2O_3-Na_2O-SiO_2 system at the Na_2O-SiO_2 edge, as re-investigated by Moir, Glasser [6].

The solubility of Na_2O in mullite has been reported by Schneider [7] not to exceed 0.4 mass % Na_2O. The composition range for the $Na_2O{\cdot}Al_2O_3{\cdot}2SiO_2$-based solid solution at 1400 °C has been reinvestigated by Tyabotina, Yakovlev [8], who report the homogeneity range between the $Na_2O{\cdot}Al_2O_3{\cdot}2SiO_2$ and $Na_2O{\cdot}Al_2O_3{\cdot}(0.7)SiO_2$ compositions. Recently, the composition section SiO_2-$Na_2O{\cdot}Al_2O_3{\cdot}2SiO_2$ has been investigated by Badger, Hummel [9]. The results reported by Bowen, Schairer [2, 3] have been generally accepted.

References

[1] Osborn, E. F., A. Muan: Ceramic Fondation 1960 Publ. by Orton jr, Columbus/Ohio
[2] Schairer, J. F., N. L. Bowen: Am. J. Sci. 245 (1947) No. 4, p. 193/204
[3] Schairer, J. F., N. L. Bowen: Am. J. Sci. 254 (1956), p. 129/95
[4] De Pablo-Galan, L., W. F. Foster: J. Am. Ceram. Soc. 42 (1959) No. 10, p. 491/8
[5] Galakhov, F. Ya.: Izv. Akad. Nauk SSSR, Otdel. Khim. Nauk. (1959) No. 5, p. 770/3
[6] Moir, G. K., F. P. Glasser: Phys. Chem. Glasses 17 (1976) No. 3, p. 45/53
[7] Schneider, H.: J. Am. Ceram. Soc. 67 (1984) No. 7, p. C130/1
[8] Tyabotina, L. S., L. K. Yakovlev: Izv. Sib. Otdel. Akad. Nauk SSSR, Ser. Khim. Nauk (1979) No. 3, p. 133/7
[9] Badger, W. B., F. A. Hummel: J. Am. Ceram. Soc. 68 (1985) No. 2, p. C46/7

Al_2O_3-SiO_2-TiO_2

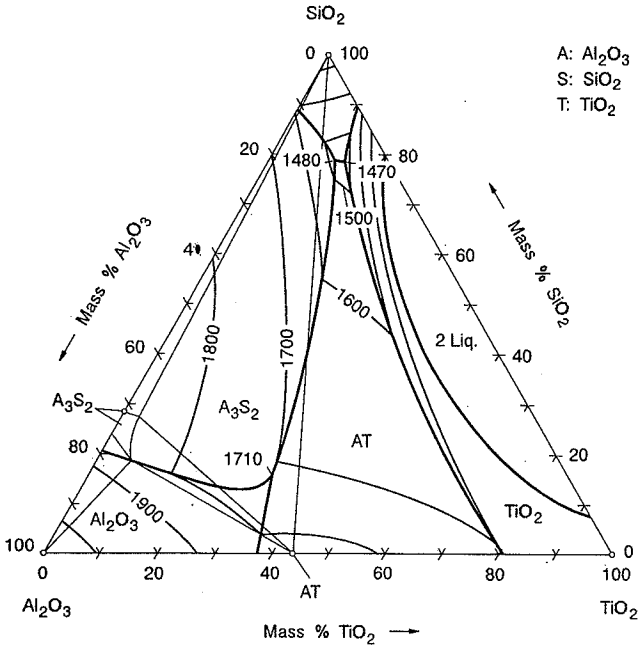


Fig. 3.197. Liquidus surface and phase relations at solidus temperatures in the Al_2O_3-SiO_2-TiO_2 system after Agamawi, White [1] Galakhov [2] and Green, White [3].

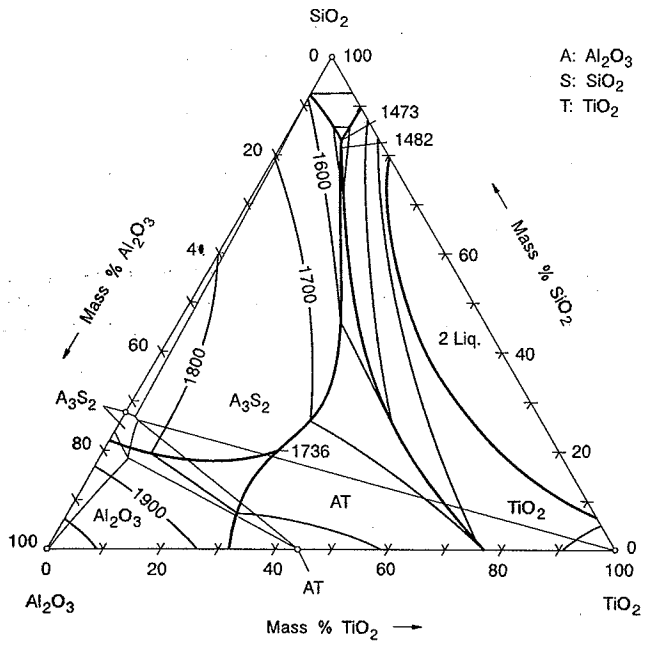


Fig. 3.198. Liquidus surface and phase relations at solidus temperatures in the Al_2O_3-SiO_2-TiO_2 system as revised recently by Woermann [4].

References

[1] Agamawi, Y. M., J. White: Trans. J. Br. Ceram. Soc. 51 (1952), p. 293/325

[2] Galakhov, F. Ya.: Izv. Akad. Nauk SSSR, Otdel. Khim. Nauk. (1958) No. 5, p. 529/34

[3] Green, C. R., J. White: Trans. J. Br. Ceram. Soc. 73 (1974) No. 5, p. 73/5

[4] Woermann, E.: private communication

B_2O_3-CaO-FeO_x

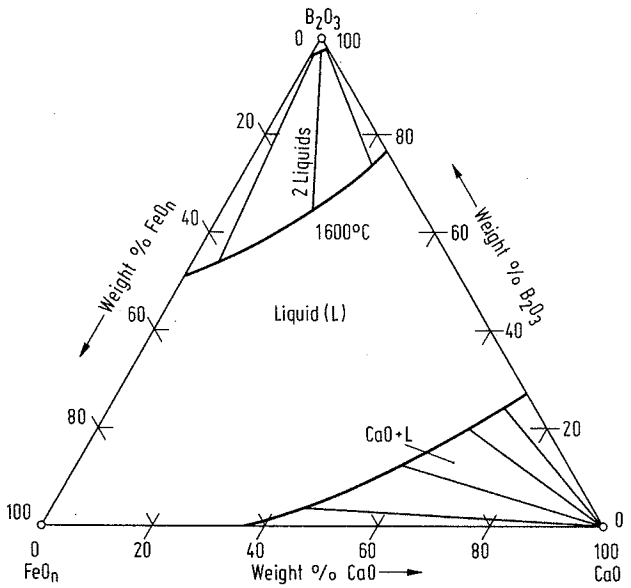


Fig. 3.199. Isothermal section through the system B_2O_3-CaO-FeO_n in contact with metallic iron at 1600 °C after Koch et al. [1].

References

[1] Koch, K., J. Sittard, G. Trömel, H. Pöpperling: in Slag Atlas (1981)

B_2O_3-CaO-SiO_2

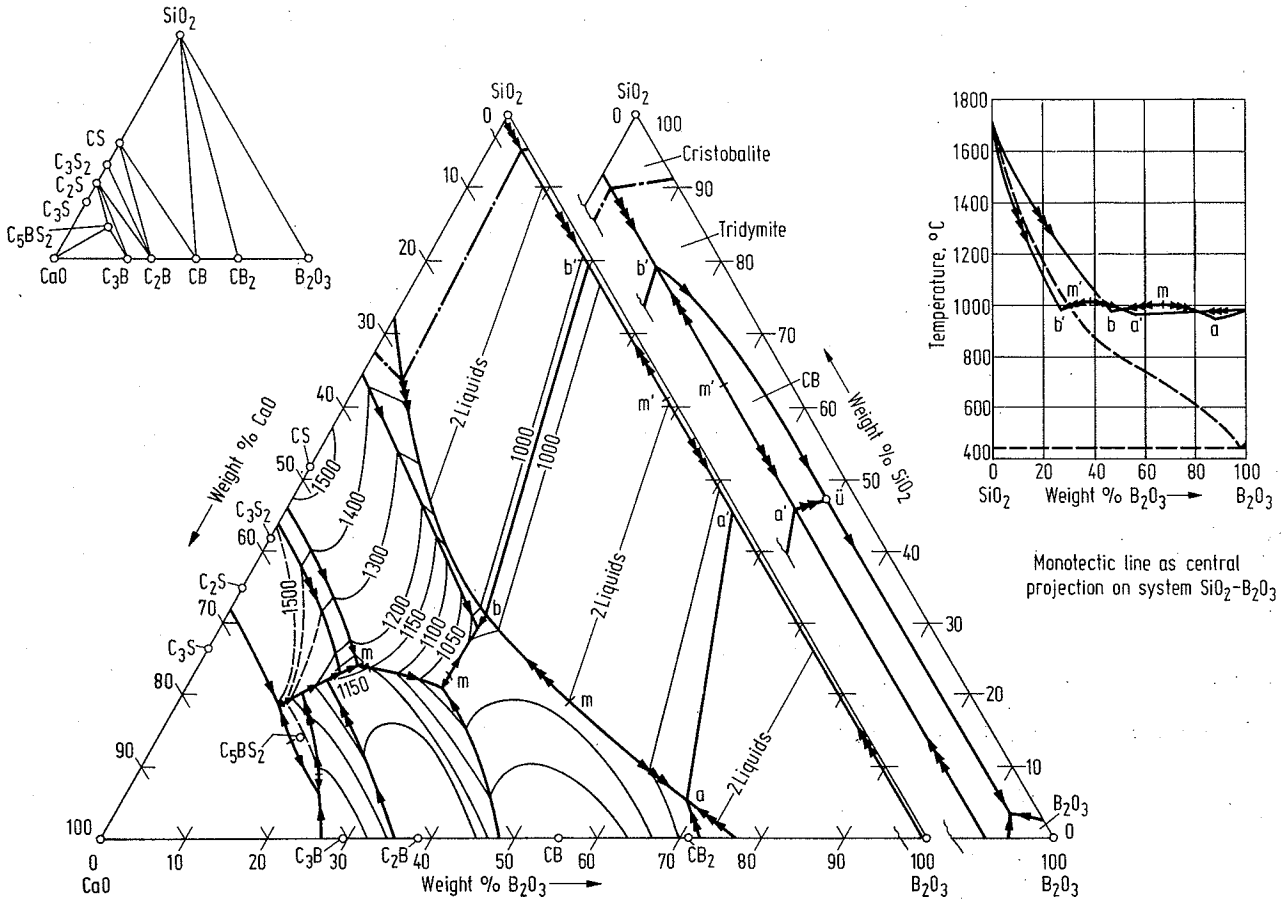


Fig. 3.200. Liquidus surface and compatibility relations in the B_2O_3-CaO-SiO_2 system as reported in Slag Atlas [1] after Flint, Wells [2] and Morey, Ingerson [3].

The sub-system $2CaO{\cdot}B_2O_3$-$2CaO{\cdot}SiO_2$ has been reinvestigated by Suzuki, Hira [4]. The compound $5CaO{\cdot}B_2O_3{\cdot}SiO_2$ reported previously by Flint, Wells [2] was not confirmed; instead, a new ternary compound $11CaO{\cdot}B_2O_3{\cdot}4SiO_2$ melting incongruently at 1440 °C, was reported [4]. The additional phase $B_2O_3{\cdot}CaO{\cdot}2SiO_2$, existing as the natural mineral (danburite), can be synthesised only hydrothermally [3]. For the calculated compatibility relations in the B_2O_3-CaO-SiO_2 system, see Tishura [5].

References

[1] Slag Atlas (1981)
[2] Flint, E. P., L. S. Wells: J. Res. Nat. Bur. Stand., RP 941, 17 (1936) No. 11, p. 727/52
[3] Morey, G. W., E. Ingerson: Am. Mineral. 22 (1937), p. 37/47
[4] Suzuki, K., I. Hira: Yogyo Kyokai Shi 78 (1970) No. 6, p. 189/95
[5] Tishura, T. A.: Ukr. Khim. Zh. 34 (1968) No. 5, p. 468/72

$BaO\text{-}SiO_2\text{-}TiO_2$

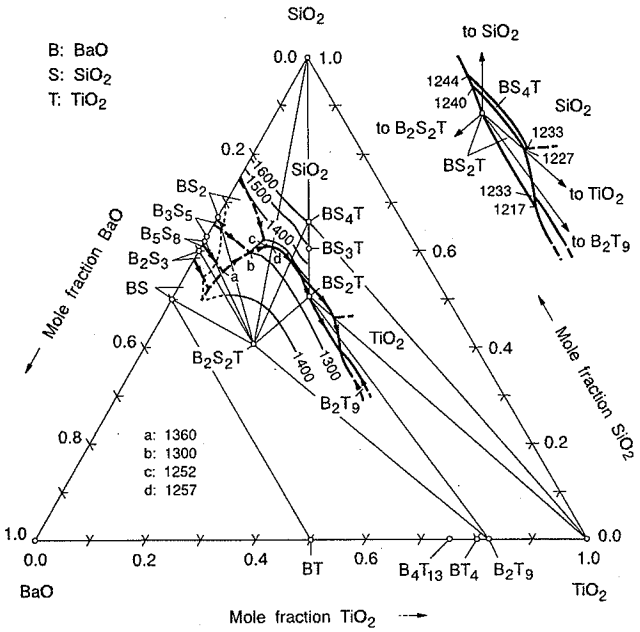


Fig. 3.201. Liquidus surface and sub-solidus equilibria in a portion of the $BaO\text{-}SiO_2\text{-}TiO_2$ system after Köppen, Dietzel [1, 2]. The section $BaO{\cdot}TiO_2\text{-}SiO_2$ and liquidus relations in the vicinity of the $BaO{\cdot}TiO_2\text{-}BaO{\cdot}SiO_2$ section have also been investigated by Rase, Roy [3] and Berberova et al. [4] respectively. The $BaO{\cdot}SiO_2{\cdot}TiO_2$ phase reported in [3, 4] was not confirmed in numerous investigations by Alfors et al. [5], Masse et al. [6], Robbins [7] and Belous et al. [8], instead, the stoichiometry $2BaO{\cdot}2SiO_2{\cdot}TiO_2$ was proposed. As reported by Belous et al. [8], the maximum solubility of TiO_2 in this phase at 1300 °C does not exceed 4 mole % TiO_2. The further compound $BaO{\cdot}TiO_2{\cdot}3SiO_2$ reported by Rase, Roy [3] and confirmed in succeeding works, exists only in the sub-solidus region of the system and decomposes at about 965 °C to $BaO{\cdot}TiO_2{\cdot}2SiO_2$ and $BaO{\cdot}TiO_2{\cdot}4SiO_2$ [3]. The liquidus temperatures in the glass-forming region of the system have also been measured by Cleek, Hamilton [9].

References

[1] Köppen, N., A. Dietzel: Naturwiss. 56 (1969) No. 9, p. 460/1
[2] Köppen, N., A. Dietzel: Glastech. Ber. 49 (1976) No. 9, p. 199/206
[3] Rase, D. E., R. Roy: J. Am. Ceram. Soc. 38 (1955) No. 11, p. 389/95
[4] Berberova, L. M., M. L. Sholokhovikh, N. N. Belyaev: Zh. Neorg. Khim. 16 (1971) No. 2, p. 539/43
[5] Alfors, J. T., M. C. Stinson, R. A. Matthews, A. Pabst: Am. Mineral. 50 (1965) No. 3-4, p. 314/40
[6] Masse, R., J. C. Grenier, A. Durif: Bull. Soc. Fr. Mineral. Cristallogr. (1967), p. 20/3
[7] Robbins, C. R.: J. Res. Nat. Bur. Stand. 74A (1970) No. 2, p. 229/32
[8] Belous, A. G., Z. Y. Makarova, O. A. Shakharov, V. P. Chalyi, I. Y. Gornikov: Ukr. Khim. Zh. 53 (1987) No. 9, p. 910/2
[9] Cleek, G. W., E. H. Hamilton: J. Res. Nat. Bur. Stand. 57 (1956) No. 6, p. 317/23

$CaO\text{-}Cr_2O_3\text{-}SiO_2$

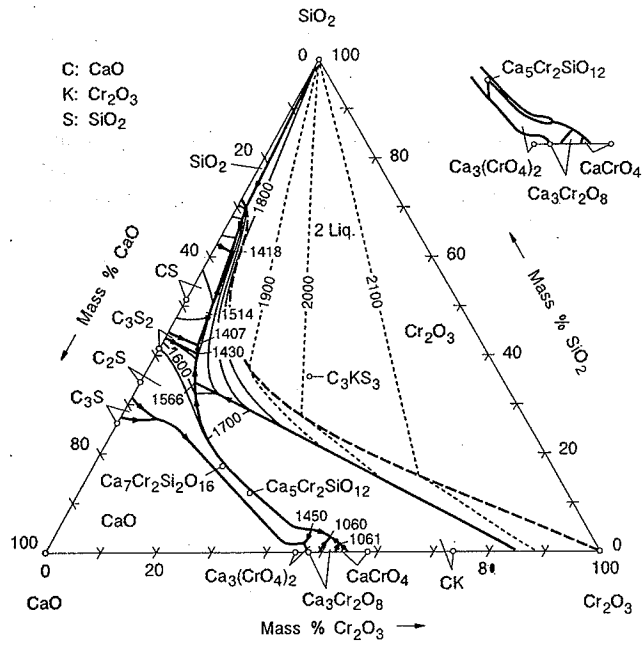


Fig. 3.202. Liquidus surface in the $CaO\text{-}Cr_2O_3\text{-}SiO_2$ system according to Glasser, Osborn [1] and de Villiers et al. [2] (the section shows alternative phase relations at the $CaO\text{-}Cr_2O_3$ edge). Lower eutectic temperatures along the eutectic in the vicinity of the $CaO{\cdot}SiO_2$ phase have been reported by Huckenholz [3].

References

[1] Glasser, E. P., E. F. Osborn: J. Am. Ceram. Soc. 41 (1958) No. 9, p. 358/67
[2] de Villiers, J. P. R., J. Mathias, A. Muan:Trans. Inst. Min. Metall., Sect. C 96 (1987) No. 6, p. C55/62

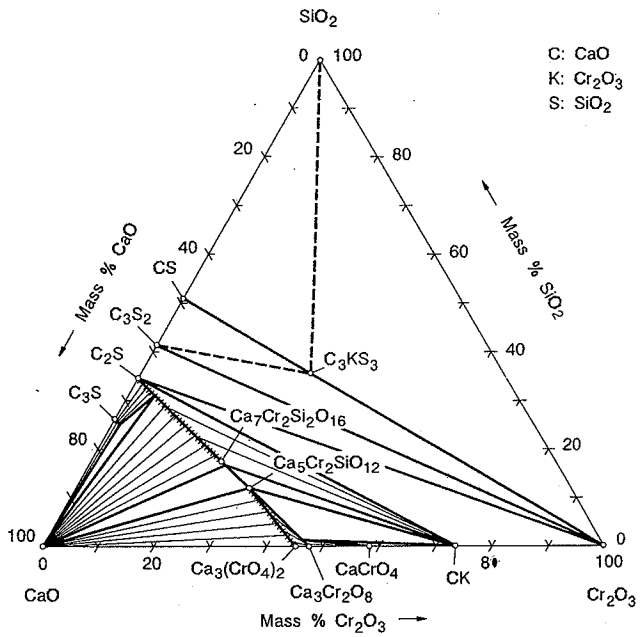


Fig. 3.203. Sub-solidus equilibria in the $CaO\text{-}Cr_2O_3\text{-}SiO_2$ system after Glasser, Osborn [1] and de Villiers et al. [2] with maximum homogeneity ranges of solution phases as reported by de Villiers et al. [2]. The dashed lines show the compatibility relations involving the $3CaO{\cdot}Cr_2O_3{\cdot}3SiO_2$ phase which decomposes above 1385 °C to $CaO{\cdot}SiO_2$ and Cr_2O_3 [3].

For the phase equilibria in the $CaO\text{-}CrO_x\text{-}SiO_2$ system under different levels of oxygen partial pressure, see de Villiers [4] and Nell, de Villiers [5].

[3] Huckenholz, H. G.: Neues Jahr. Mineral., Monatsh. (1975) No. 8, p. 337/60
[4] de Villiers, J. P. R.: J. Am. Ceram. Soc. 75 (1992) No. 6, p. 1333/41
[5] Nell, J., J. P. R. de Villiers: J. Am. Ceram. Soc. 76 (1993) No. 9, p. 2193/200

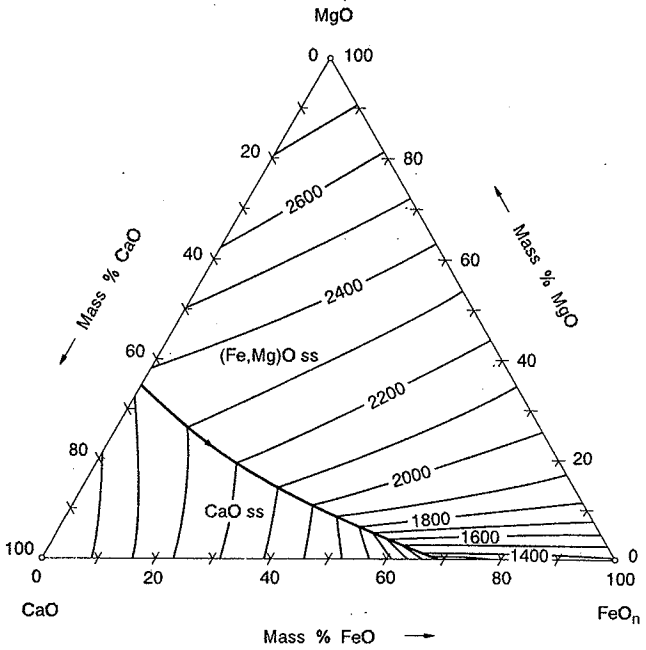


Fig. 3.204. Liquidus surface in the system CaO-FeO$_n$-MgO in contact with metallic iron projected on the CaO-FeO-MnO plane after Scheel [1]. For the phase equilibria between 1400 and 1650 °C, see also Trömel et al. [2] and Fischer, Spitzer [3].

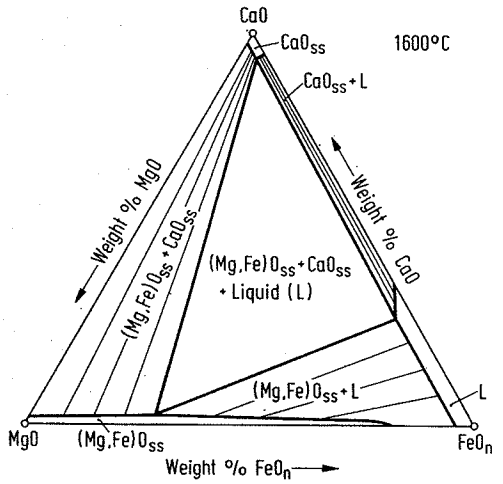


Fig. 3.205. Isothermal section at 1600 °C through the system CaO-FeO$_n$-MgO in contact with metallic iron projected on the CaO-FeO-MgO plane after Trömel et al. [4].

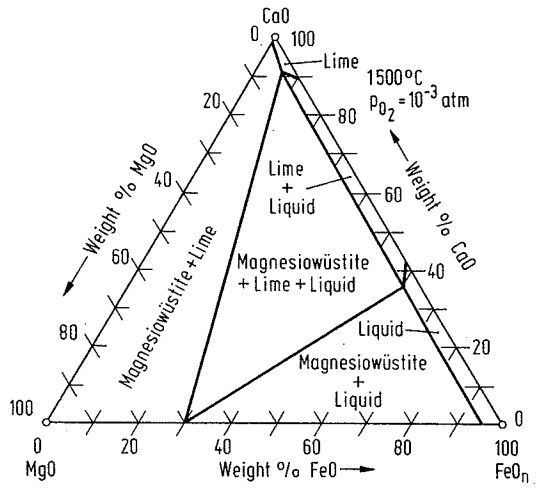


Fig. 3.206. Isothermal section at 1500 °C through the system CaO-FeO$_n$-MgO at oxygen partial pressure of 10^{-9} atm projected on the CaO-FeO-MgO plane after Johnson, Muan [5].

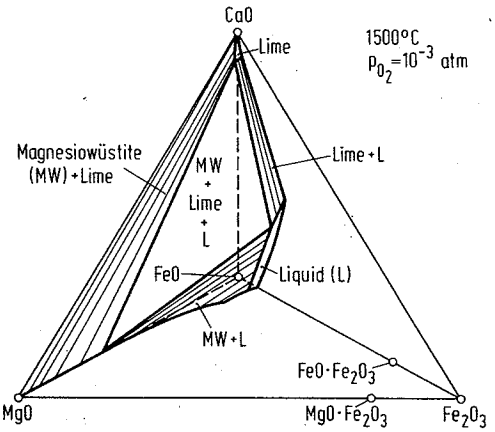


Fig. 3.207. Isothermal section at 1500 °C through the system CaO-FeO$_n$-MgO at oxygen partial pressure of 10^{-9} atm (space representation) after Johnson, Muan [5].

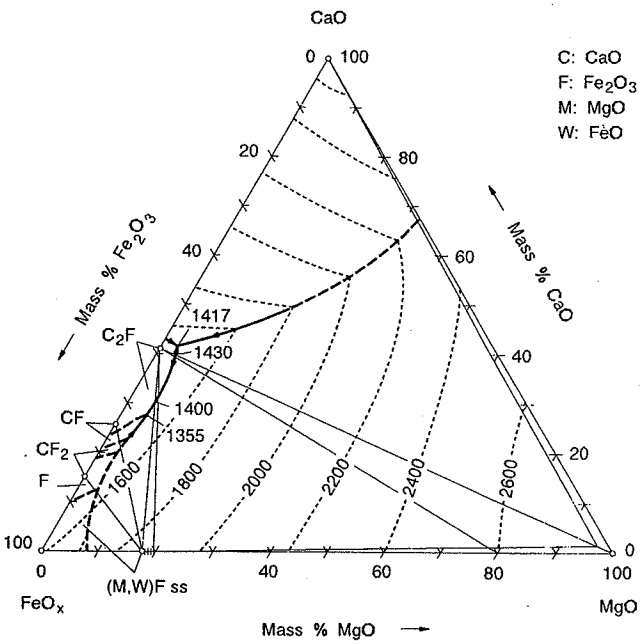


Fig. 3.208. Liquidus surface and compatibility relations in the system CaO-FeO$_x$-MgO in air, projected on the CaO-Fe$_2$O$_3$-MgO plane after Fusenig et al. [6].

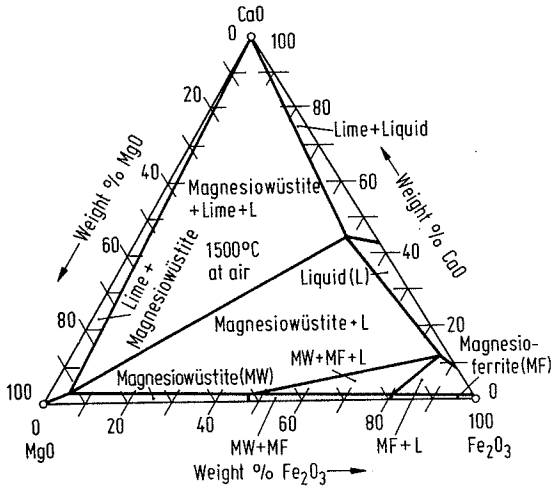


Fig. 3.209. Isothermal section at 1500 °C through the system CaO-FeO_x-MgO in air projected on the CaO-Fe_2O_3-MgO plane after Johnson, Muan [5].

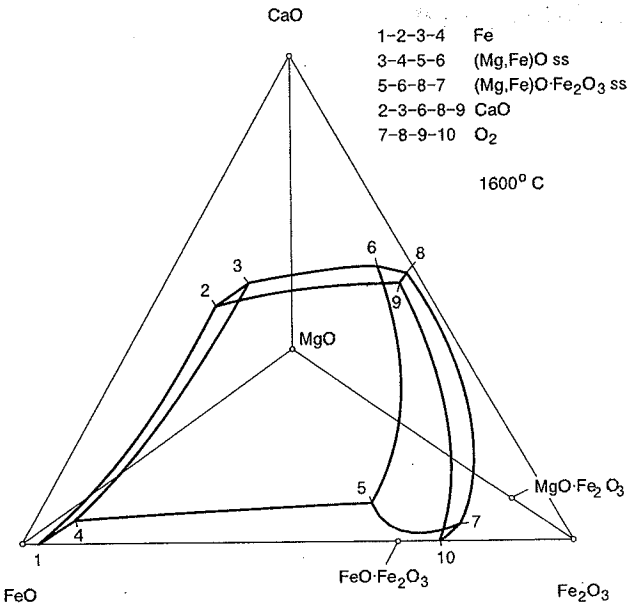


Fig. 3.211. Liquidus surface in the system CaO-FeO-Fe_2O_3-MgO at 1600 °C after Schürmann, Kolm [7].

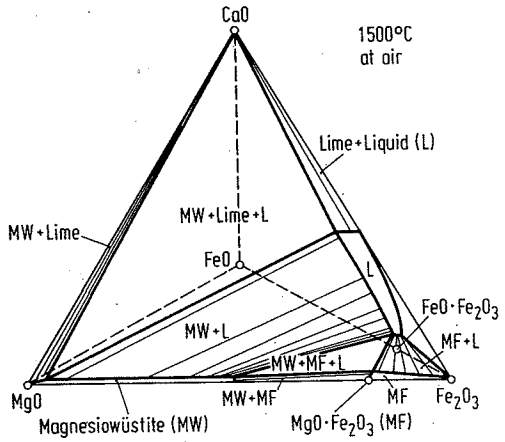


Fig. 3.210. Isothermal section at 1500 °C through the system CaO-FeO_x-MgO in air after (space representation) Johnson, Muan [5].

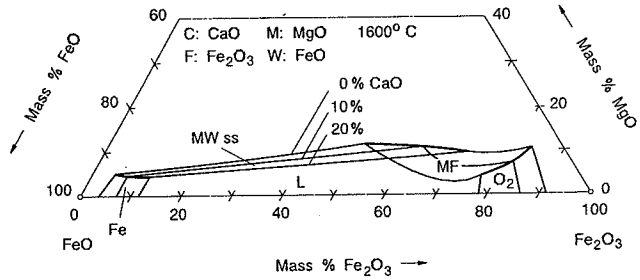


Fig. 3.212. The 1600 °C liquidus isotherms in the system CaO-FeO-Fe_2O_3-MgO at 0, 10 and 20 mass % CaO projected on the FeO-Fe_2O_3-MgO plane after Schürmann, Kolm [7].

References

[1] Scheel, R.: Sprechsaal Keram., Glas, Baustoffe 108 (1975) No. 23-24, p. 685/6

[2] Trömel, G., K.-H. Obst, E. Görl, J. Stradtmann: Tonind.-Ztg., Keram. Rundsch. 90 (1966) No. 5, p. 193/209

[3] Fischer, W. A., H. Spitzer: Arch. Eisenhüttenwes. 29 (1958) No. 10, p. 611/7

[4] Trömel, G., W. Fix, K. Kaup: Arch. Eisenhüttenwes. 38 (1967) No. 8, p. 595/605

[5] Johnson, R. E., A. Muan: J. Am. Ceram. Soc. 48 (1965) No. 7, p. 359/64

[6] Fusenig, R., U. Limbert, E. Woermann: Tonind.-Ztg. 108 (1984) No. 8, p. 515/23

[7] Schürmann, E., I. Kolm: Steel Res. 59 (1988) No. 5, p. 185/91

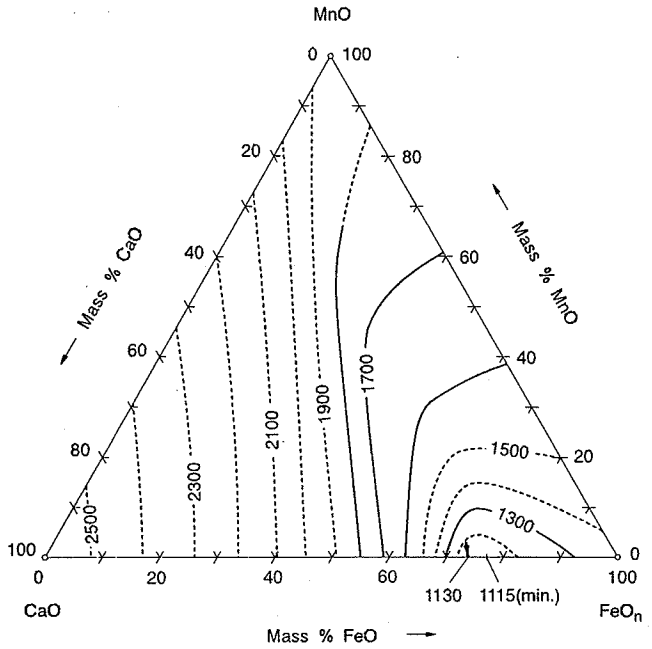


Fig. 3.213. Liquidus surface in the system CaO-FeO-MnO in contact with metallic iron according to Valla et al. [2] and Fischer, Fleischer [1].

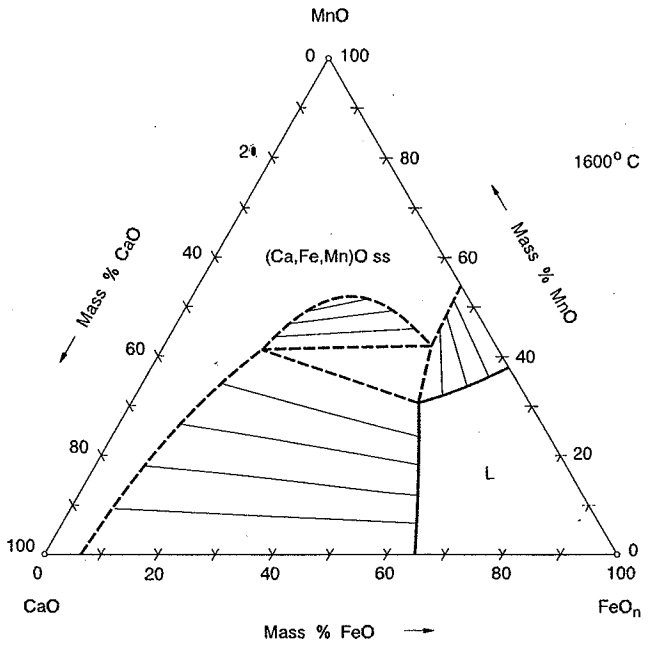


Fig. 3.215.

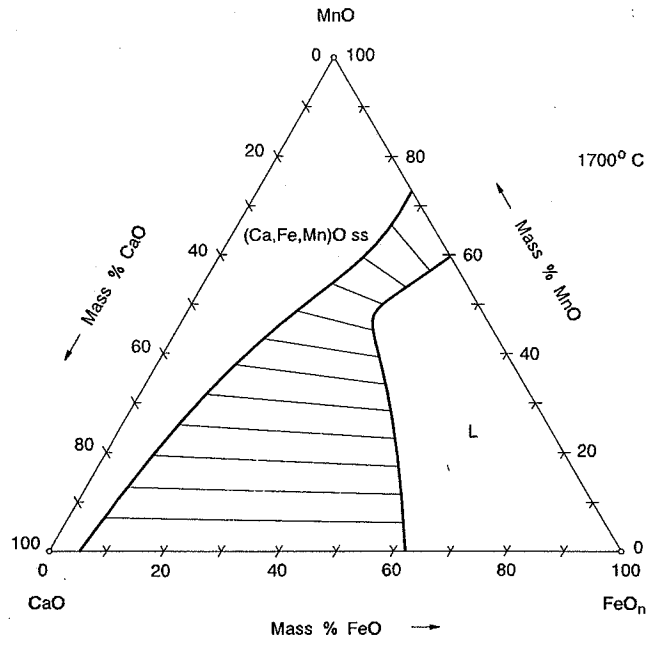


Fig. 3.214.

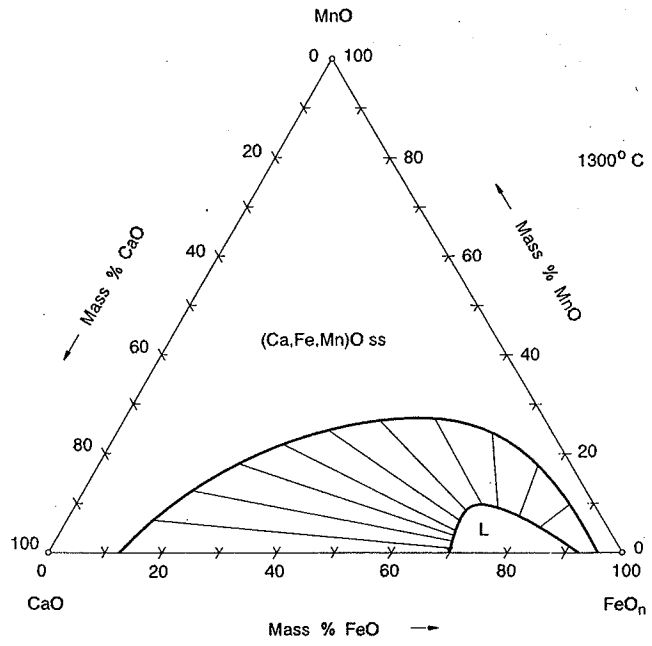


Fig. 3.216.

Figs. 3.214 to 3.217. Isothermal sections through the system CaO-FeO-MnO in contact with metallic iron at 1700, 1600 °C after Fischer, Fleischer [2], and at 1300 and 1150 °C after Valla et al. [1].

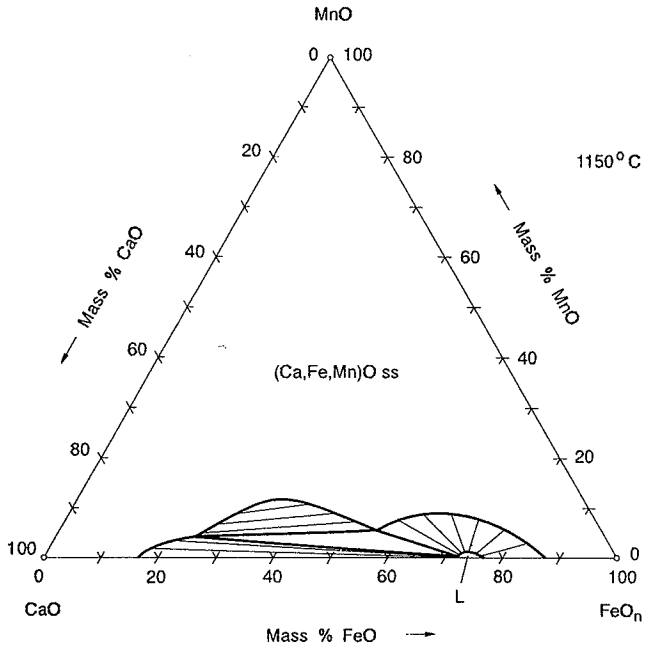


Fig. 3.217.

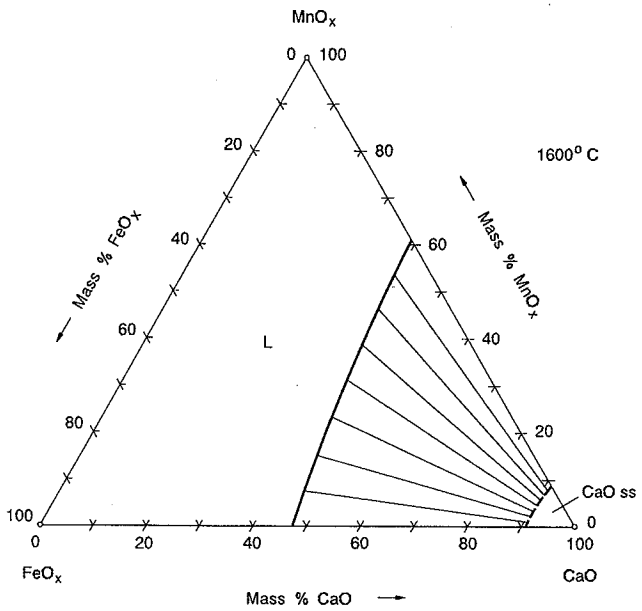


Fig. 3.218. Isothermal section through the system CaO-FeO_x-MnO_x at 1600 °C in air after Trömel et al. [3].

Figs. 3.214 to 3.217. Isothermal sections through the system CaO-FeO-MnO in contact with metallic iron at 1700, 1600 °C after Fischer, Fleischer [1], and at 1300 and 1150 °C after Valla et al. [2].

References

[1] Fischer, W. A., H.-J. Fleischer: Arch. Eisenhüttenwes. 32 (1961) No. 5, p. 305/13

[2] Valla, O., K. Grjotheim, A. Muan: Trans. Metall. Soc. AIME 242 (1968), p. 2389/92

[3] Trömel, G., W. Fix, H. E. Wiemer: Arch. Eisenhüttenwes. 40 (1969) No. 9, p. 673/9

$CaO\text{-}FeO_x\text{-}P_2O_5$

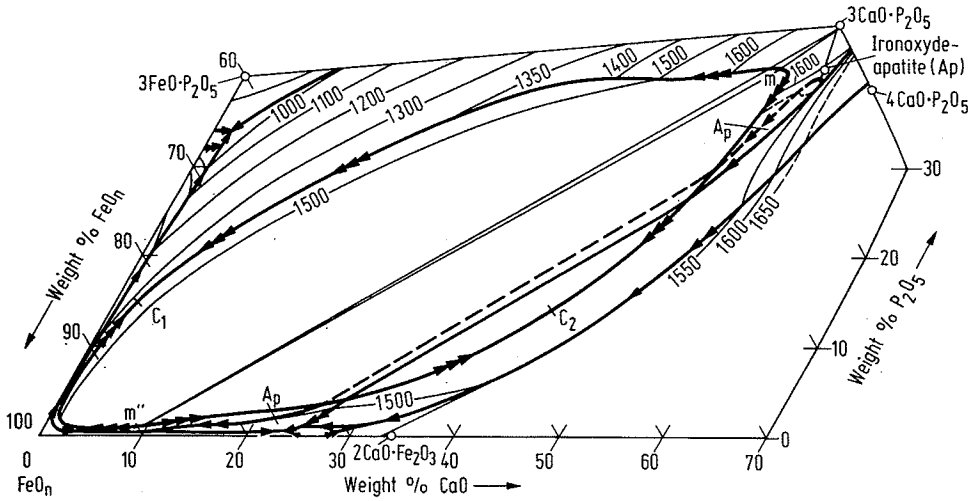


Fig. 3.219. Liquidus surface in the CaO-FeO-P_2O_5 system in contact with metallic iron after Trömel et al. [1].

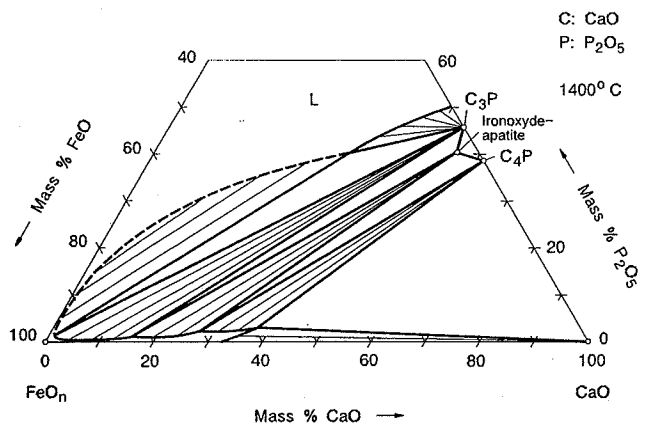


Fig. 3.220. Isothermal section through the system CaO-FeO-P_2O_5 at 1400 °C in contact with metallic iron after Trömel et al. [1]. For composition of iron oxide apatite, see also Fix, Bongers [2].

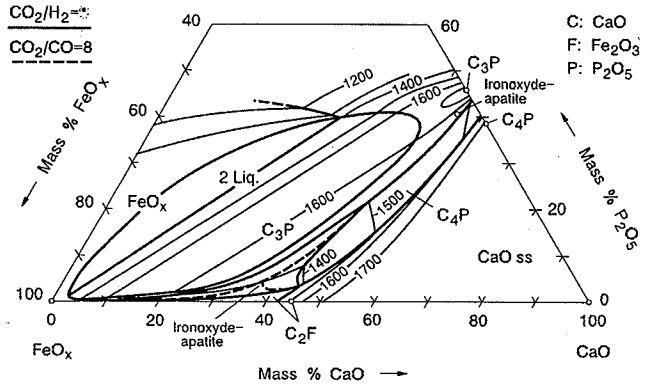


Fig. 3.221. Liquidus surface in the system CaO-FeO_x-P_2O_5 under a gas mixture consisting of CO_2 and H_2 with CO_2/H_2=9 (moist atmosphere) after Riboud [3]. The extension of the primary field of iron oxide apatite, under a gas mixture consisting of CO_2 and CO with CO_2/CO=8 (dry atmosphere) is shown with heavy dashed lines [3]. For isothermal sections at 1400 and 1500 °C, see original paper [3].

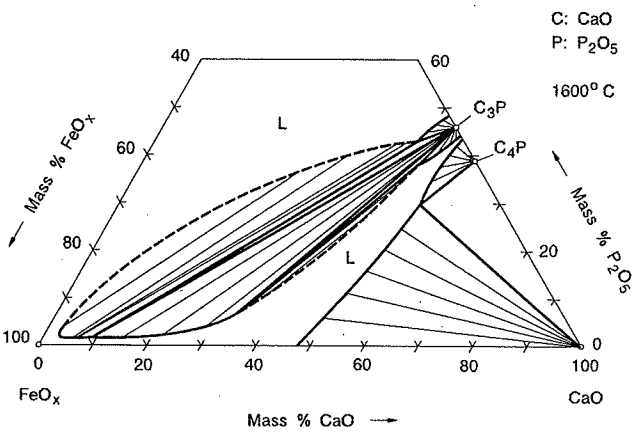


Fig. 3.222. Isothermal section through the system CaO-FeO_x-P_2O_5 at 1600 °C in air after Trömel et al. [4]. For isothermal section et 1400 °C and phase equilibria involving iron oxide apatite, see Riboud [5].

The phase equilibria in the system CaO-FeO-Fe_2O_3-P_2O_5 at 1600 °C have been reported by Trömel et al. [4] and Drewes, Olette [6].

References

[1] Trömel, G., W. Fix, U. Bongers: Arch. Eisenhüttenwes. 40 (1969) No. 10, p. 813/9
[2] Fix, W., U. Bongers: Microchem. Acta /Wien/, Suppl. III (1968), p. 155/63
[3] Riboud, P.: Mém. Sci. Rev. Métall. 70 (1973) No. 11, p. 771/82
[4] Trömel, G., W. Fix, H. E. Wiemer: Arch. Eisenhüttenwes. 40 (1969) No. 9, p. 673/9
[5] Riboud, P.: C. R. Acad. Sci., Ser. C 263 (1966) No. 18, p. 1054/7
[6] Drewes, E.-J., M. Olette: Arch. Eisenhüttenwes. 38 (1967) No. 3, p. 163/75

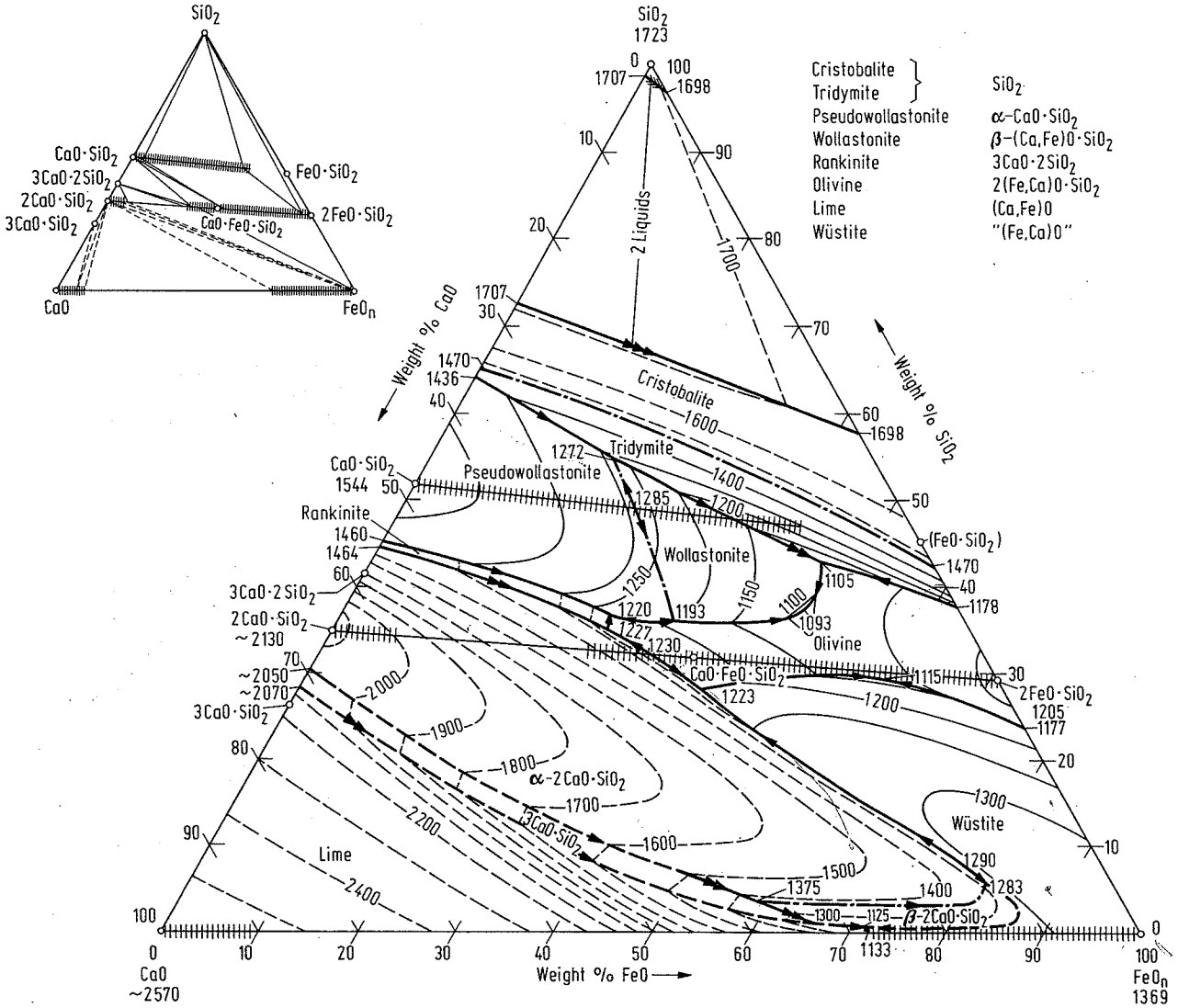


Fig. 3.223. Liquidus surface and the sub-solidus equilibria in the $CaO\text{-}FeO_n\text{-}SiO_2$ system as drawn by Osborn, Muan [1] according to experimental results by Bowen et al. [2], Allen, Snow [3], Schenck, Wiesner [4], and Bishop et al. [5]. For Fe_2O_3 contents in melts at liquidus temperatures, see original paper by Bowen et al. [2]. The composition of saturated liquid (between 1450 and 1650 °C) were also investigated by Trömel, Görl [6], Görl et al. [7], and Timucin, Morris [8].

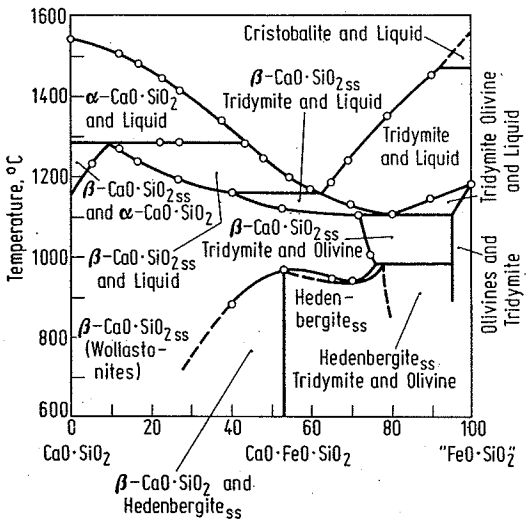


Fig. 3.224. Composition section $CaO\text{·}SiO_2\text{-}"FeO\text{·}SiO_2"$ after Bowen et al. [2].

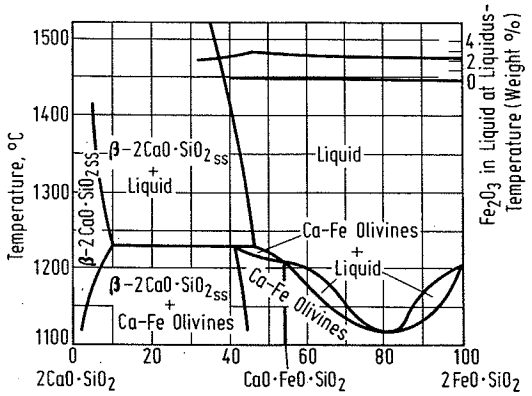


Fig. 3.225. Composition section $2CaO\text{·}SiO_2\text{-}2FeO\text{·}SiO_2$ after Bowen et al. [2]. For numerous isothermal sections, see original paper [2]. The sub-solidus relations determined by Bowen et al. [2] have been generally confirmed by Indyk, Bell [9].

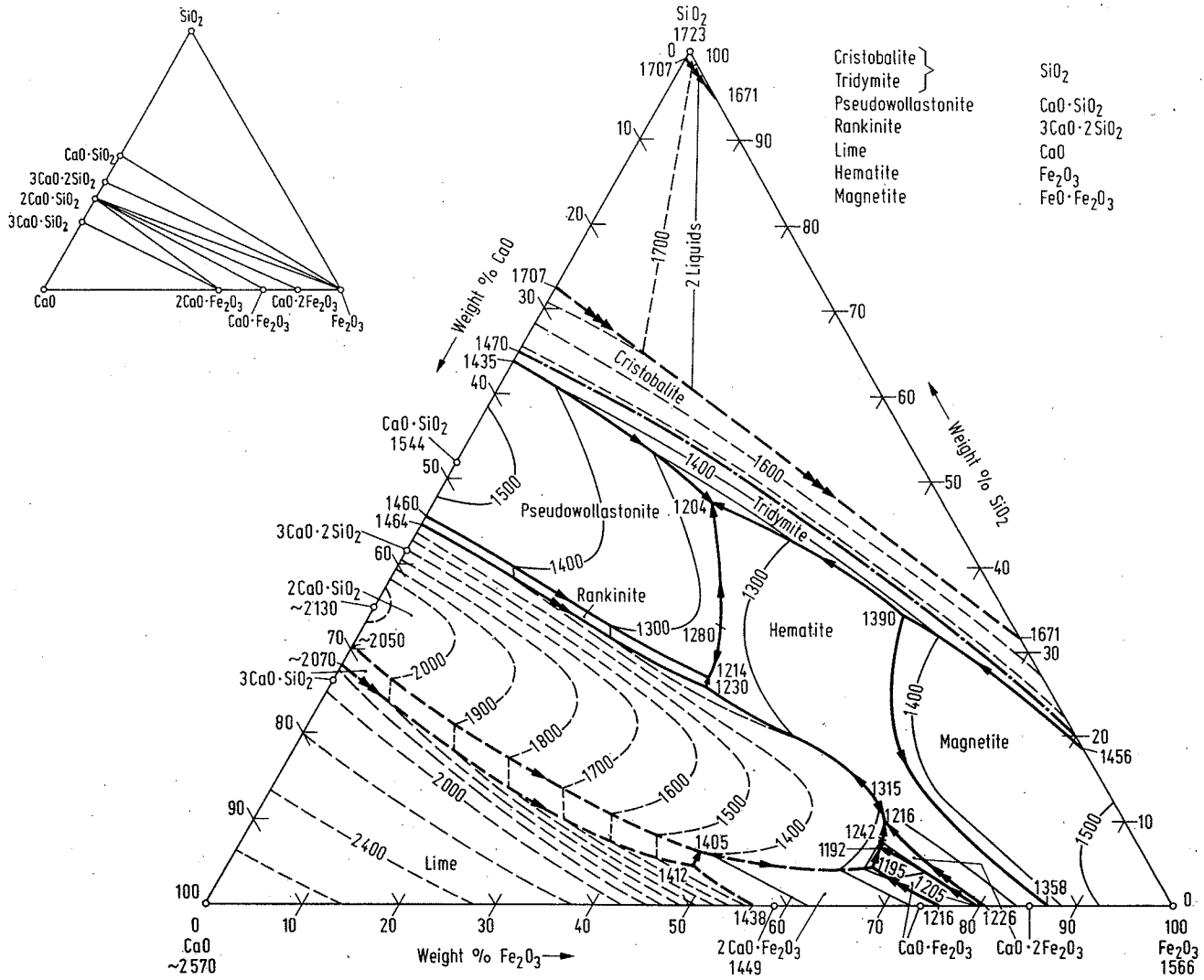


Fig. 3.226. Liquidus surface and sub-solidus equilibria (above lower stability limit of the $CaO{\cdot}2Fe_2O_3$ phase at 1155 °C) in the $CaO\text{-}FeO_x\text{-}SiO_2$ system in air after Phillips, Muan [10], based in part on the results of Budric [11].

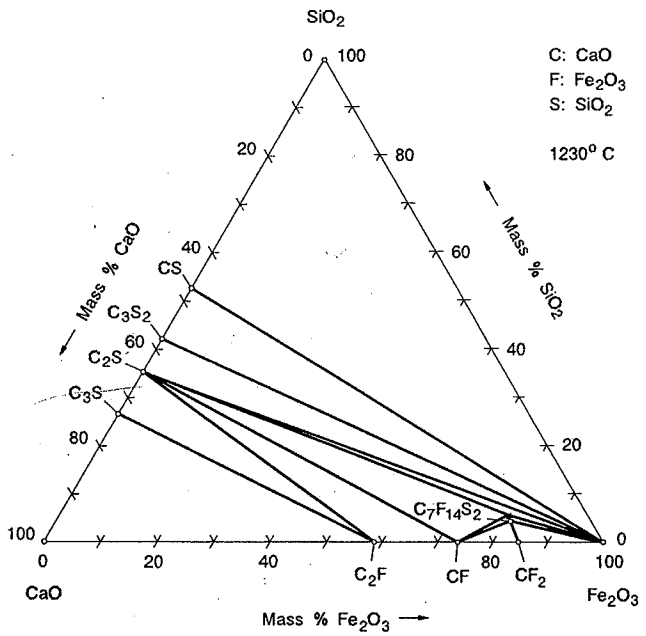


Fig. 3.227. Isothermal section through the $CaO\text{-}FeO_x\text{-}SiO_2$ system in air at 1230 °C, with the ternary compound $7CaO{\cdot}2SiO_2{\cdot}14Fe_2O_3$, as determined recently by Model et al. [12]. The reported temperature for this section is apparently higher than the solidus temperatures reported by Phillips, Muan [10] in this region of the system.

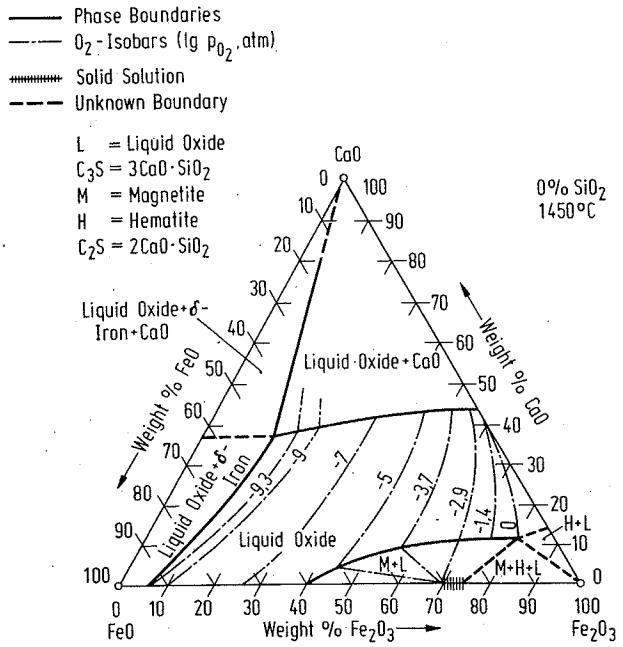


Fig. 3.228.

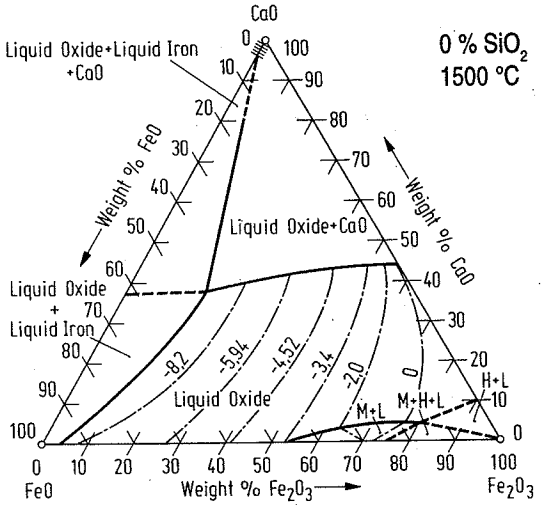


Fig. 3.229.

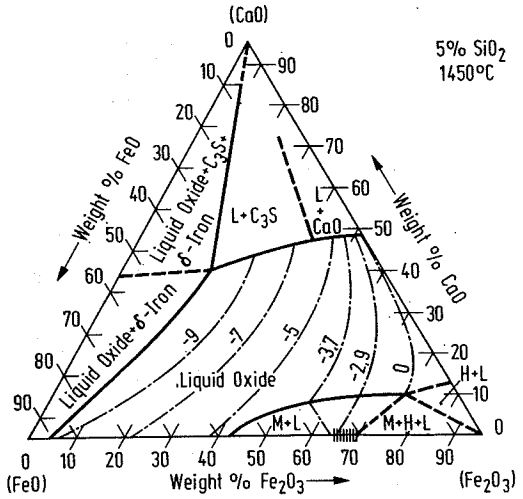


Fig. 3.230.

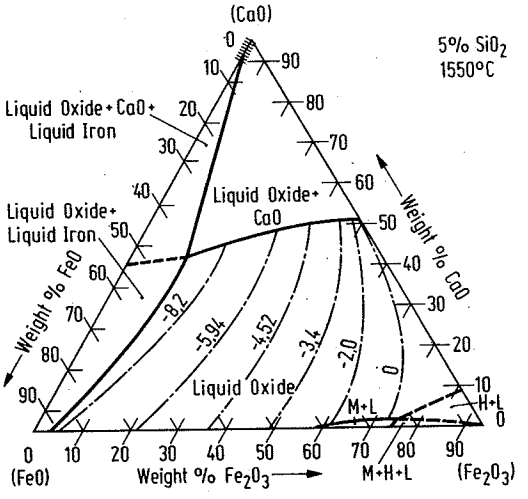


Fig. 3.231.

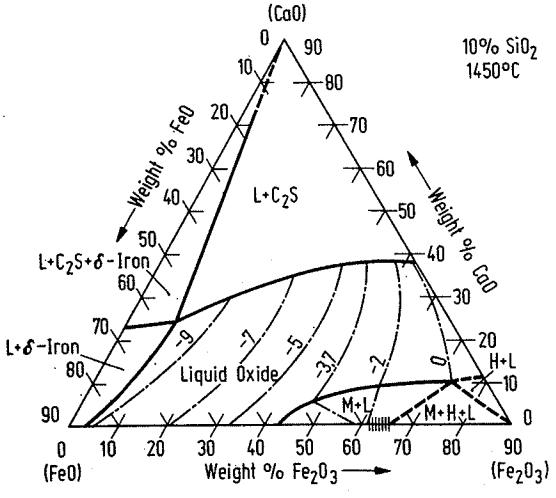


Fig. 3.232.

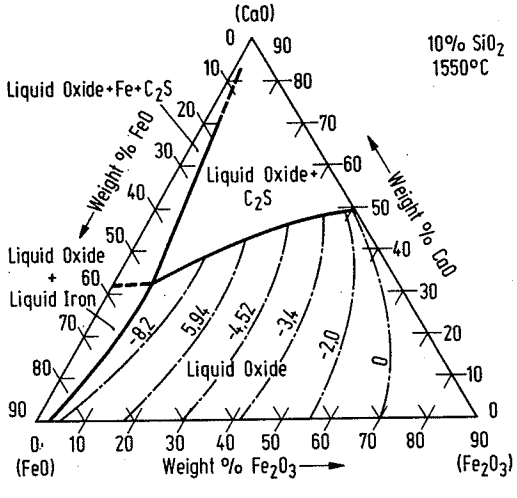


Fig. 3.233.

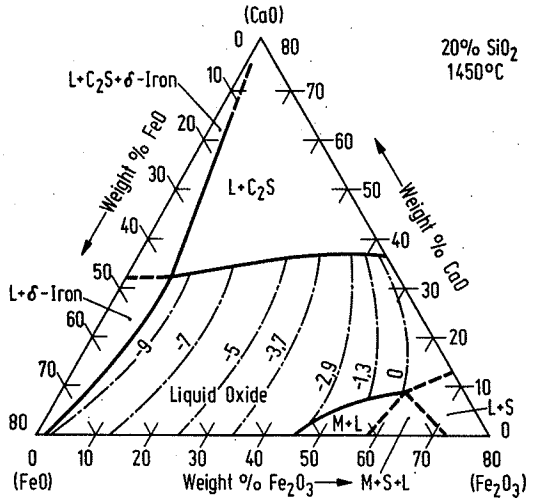


Fig. 3.234.

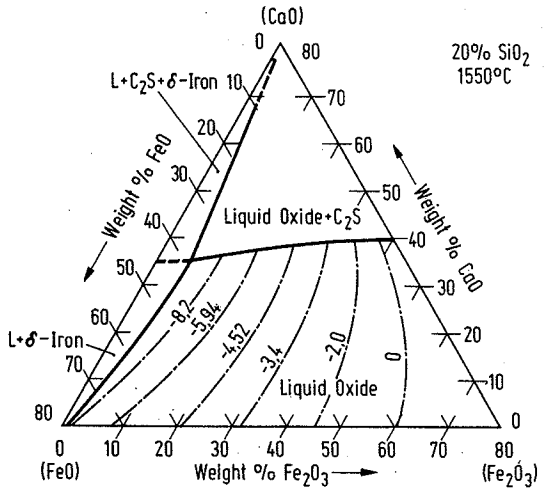


Fig. 3.235.

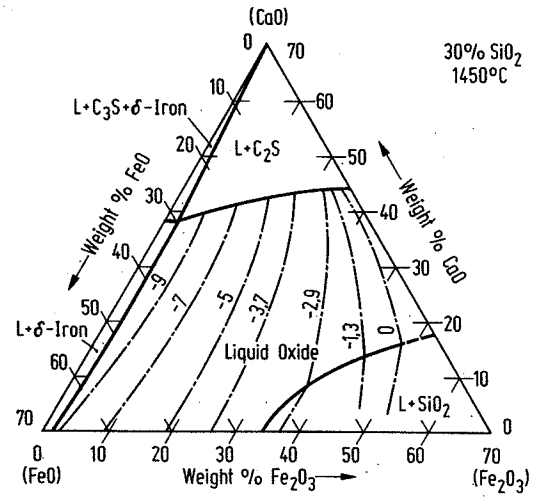


Fig. 3.236.

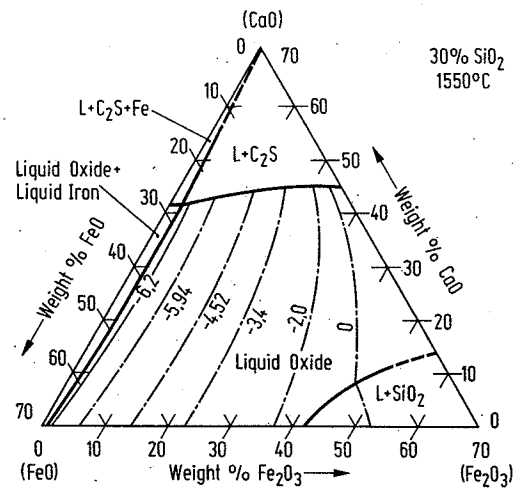


Fig. 3.237.

Figs. 3.228 to 3.237. Oxygen isobars (log pO_2, atm) over melts in the system CaO-FeO-Fe_2O_3-SiO_2 with SiO_2 levels between 0 and 30 mass % at 1450 and 1550 °C, as determined by Timucin, Morris [8].

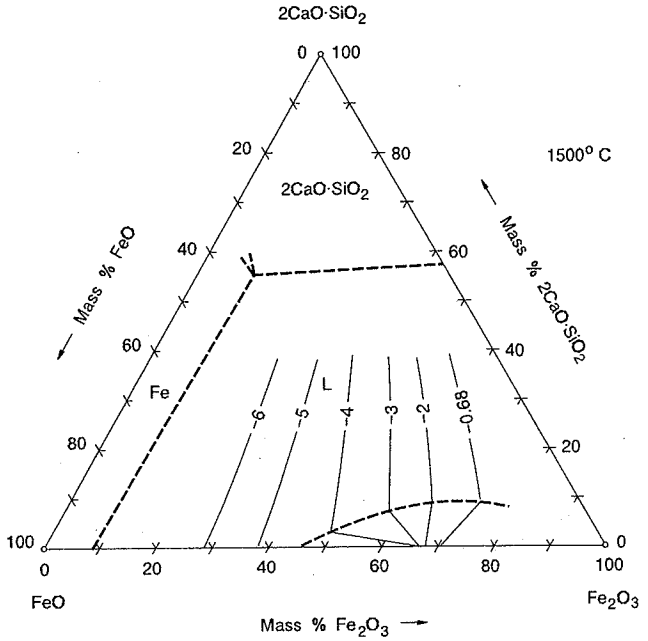


Fig. 3.238. Oxygen isobars in the sub-system FeO-Fe_2O_3-$2CaO{\cdot}SiO_2$ at 1500 °C after Hara et al. [13].

For the liquidus relations in the system CaO-FeO-Fe_2O_3-SiO_2 in the vicinity of the Fe_2O_3-$CaO{\cdot}SiO_2$ section in air, see Canha, Segadães [14]. The isothermal sections through the system CaO-FeO-Fe_2O_3-SiO_2 at 1300 and 1350 °C, and with 5, 10 and 15 mass % SiO_2 have been reported by Toguzov et al. [15]. The isothermal section at 1300 °C and at 10 and 20 mass % CaO have been reported by Yi et al. [16] and Zhang et al. [17]. For additional information, see also Vygen, Engell [18] and Schürmann, Winterfeld [19, 20]. For a thermodynamic assessment of the system Ca-Fe-O-Si, see Selleby [21].

References

[1] Osborn, E. F., A. Muan: Ceramic Fondation 1960, Publ. by Orton jr, Columbus/Ohio
[2] Bowen, N. L., J. F. Schairer, E. Posnjak: Am. J. Sci., 5th Ser. 26 (1933) No. 153, p. 193/284
[3] Allen, W. C., R. B. Snow: J. Am. Ceram. Soc. 38 (1955) No. 8, p. 264/80
[4] Schenck, H., G. Wiesner: Arch. Eisenhüttenwes. 27 (1956) No. 1, p. 1/12
[5] Bishop, H. L., Jr., N. J. Grant, J. Chipman: Trans. Metall. Soc. AIME 212 (1958) No. 4, p. 185/92
[6] Trömel, G., E. Görl: Arch. Eisenhüttenwes. 34 (1963) No. 8, p. 595/9
[7] Görl, E., F. Oeters, R. Scheel: Arch. Eisenhüttenwes. 37 (1966) No. 6, p. 441/51
[8] Timucin, M., A. E. Morris: Metall. Trans. 1 (1970) No. 11, p. 3193/201
[9] Indyk, B., H. B. Bell: J. Iron Steel Inst. 11 (1970), p. 1015/20
[10] Phillips, B., A. Muan: J. Am. Ceram. Soc. 42 (1959) No. 9, p. 413/23
[11] Burdic, M. D.: J. Res. Nat. Bur. Stand., RP 1340 25 (1940) No. 4, p. 475/88
[12] Model, M. S., T. Ya. Malysheva, V. Ya. Lyadova, N. V. Chugunova, E. V. Vlasova, G. K. Astakhova: Izv. Akad. Nauk SSSR, Met. (1987) No. 2, p. 3/9
[13] Hara, S., T. Araki, K. Ogino: Metall. Slags Fluxes, Int. Symp., Proc., 2nd (1984), p. 441/51 Edited by: Fine, H. Alan; Gaskell, David R. Metall. Soc. AIME: Warrendale, Pa.
[14] Canha, R. H., A. M. Segadães: J. Phys. Colloq. /C1/ 47 (1986) No. 2, p. C461/6
[15] Toguzov, M. Z., V. I. Yarygin, A. I.; Panchenko: Tsvetn. Met./Moscov/ (1987) No. 5, p. 26/8
[16] Yi, J., P. Zhang, D. Ye, X. Chen: Youse Jinshu 40 (1988) No. 1, p. 53/7
[17] Zhang, H., D. Ye, P. Zhang, X. Chen: Zhongnan Kuangye Xueyuan Xuebao 21 (1990) No. 4, p. 447/50
[18] Vygen, P., H.-J. Engell: Arch. Eisenhüttenwes. 40 (1969) No. 5, p. 359/65
[19] Schürmann, E., F. Winterfeld: Thyssenforschung 4 (1972) No. 3-4, p. 118/32
[20] Schürmann, E., F. Winterfeld: Stahl Eisen 93 (1973) No. 22, p. 1062/4
[21] Selleby, M.: Dissertation, Royal Institute of Technology, Stockholm, (1993)

CaO-FeO_x-TiO_2

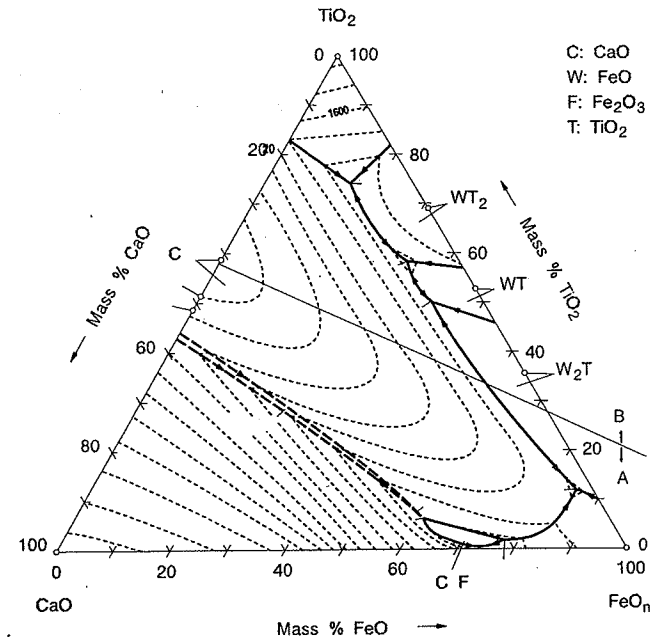


Fig. 3.239. Liquidus surface in the system CaO-FeO_n-TiO_2 under reducing conditions after Kimura, Muan [1]. The samples in region A were investigated in equilibrium with metallic iron, and those in region B at oxygen pressures corresponding to the equilibrium between FeO_n and metallic iron.

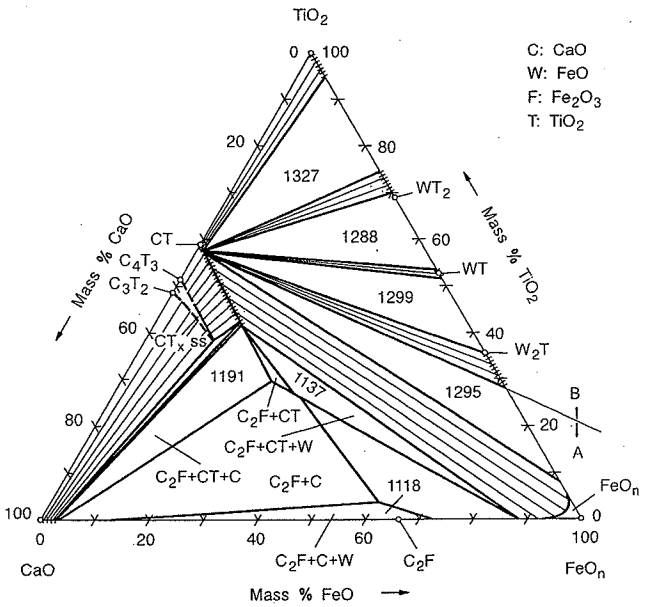


Fig. 3.240. Solidus surface in the system CaO-FeO_n-TiO_2 under reducing conditions after Kimura, Muan [1]. The samples in region A were investigated in equilibrium with metallic iron, and those in region B at oxygen pressures corresponding to the equilibrium between FeO_n and metallic iron.

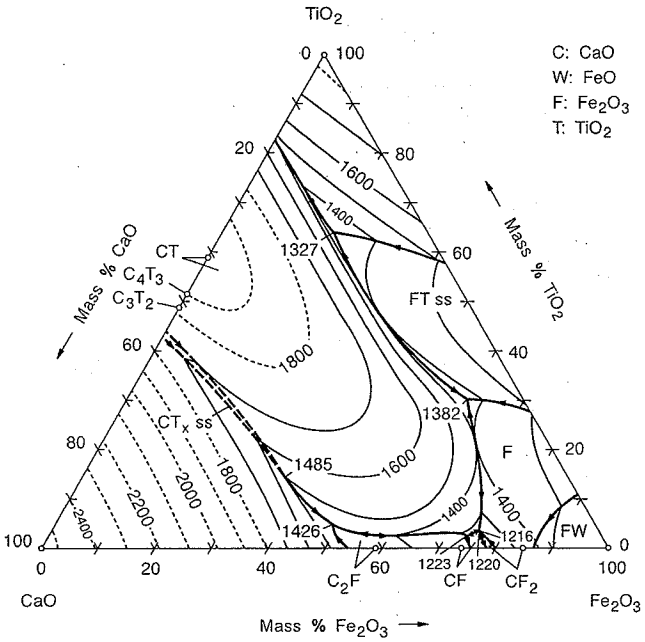


Fig. 3.241. Liquidus surface in the system CaO-FeO_x-TiO_2 in air after Kimura, Muan [2].

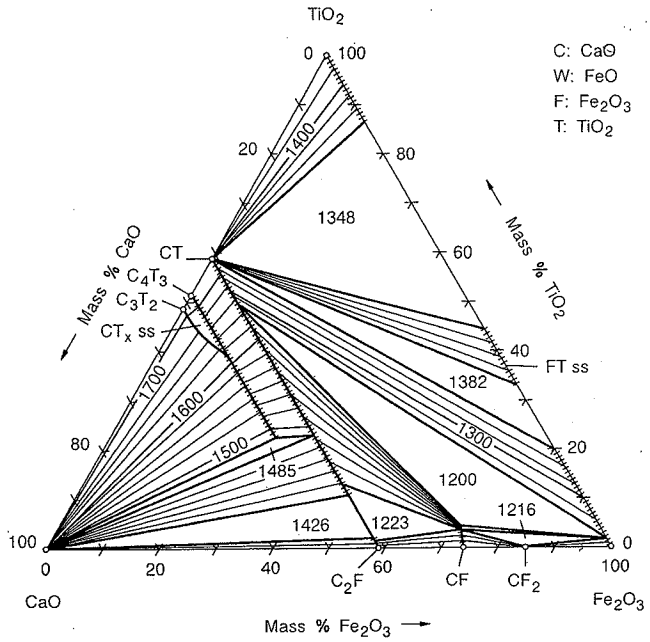


Fig. 3.242. Solidus surface in the system CaO-FeO_x-TiO_2 in air after Kimura, Muan [2].

The composition section $CaO{\cdot}TiO_2$-$2CaO{\cdot}Fe_2O_3$ has also been investigated by Panek et al. [3]. The eutectic temperature in this section (1350 °C) is considerably lower than that corresponding to the liquidus surface in the CaO-FeO_x-TiO_2 system as reported by Kimura, Muan [2].

References

[1] Kimura, S., A. Muan: Am. Mineral. 56 (1971) No. 7-8, p. 1347/58
[2] Kimura, S., A. Muan: Am. Mineral. 56 (1971) No. 7-8, p. 1322/46
[3] Panek, Z., E. Kanclir, J. Staron, M. Kozlovsky, S. Palco: Silikaty 20 (1976) No. 1, p. 13/22

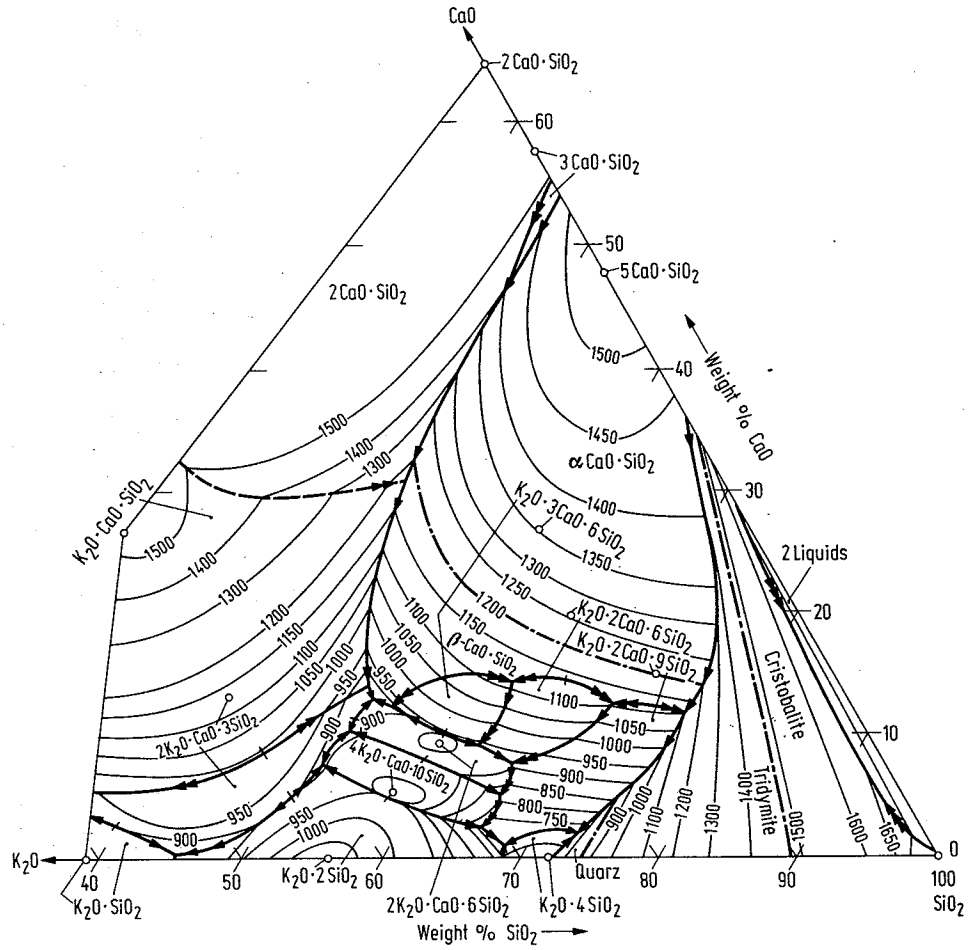


Fig. 3.243. Liquidus surface in a portion of the $CaO\text{-}K_2O\text{-}SiO_2$ system after Morey et al. [1, 2].

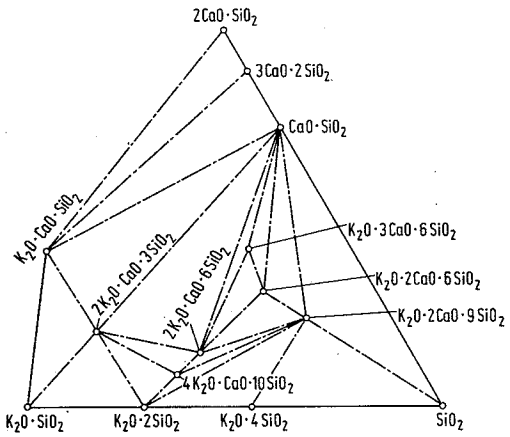


Fig. 3.244. Compatibility relations in a portion of the $CaO\text{-}K_2O\text{-}SiO_2$ system after Morey et al. [1, 2].

References

[1] Morey, G., F. C. Kracek, N. L. Bowen: J. Soc. Glass. Technol. 14 (1930) No. 54, p. 149/87
[2] Morey, G., F. C. Kracek, N. L. Bowen: J. Soc. Glass. Technol. 15 (1931) No. 57, p. 57/8

$CaO\text{-}MgO\text{-}MnO_x$

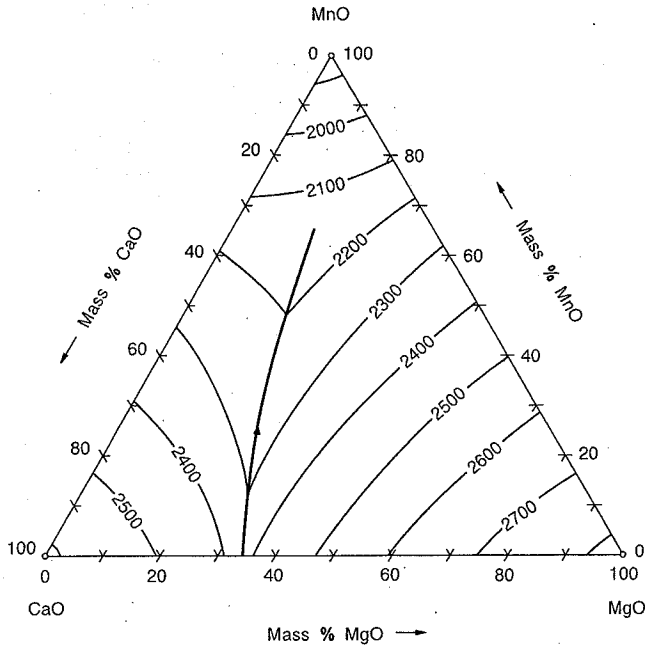


Fig. 3.245. Tentative liquidus surface in the CaO-MgO-MnO system according to Schenck et al. [1].

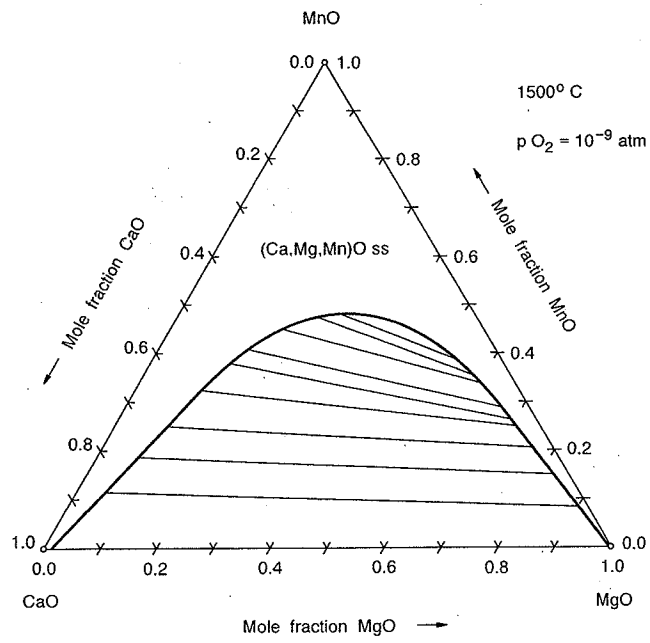


Fig. 3.246. Isothermal section through the system CaO-MgO-MnO at 1500 °C and at $pO_2=1\cdot10^{-9}$ atm, as determined experimentally by Woermann, Muan [2].

References

[1] Schenck, H., M. G. Frohberg, R. Nünninghoff: Arch. Eisenhüttenwes. 35 (1964) No. 4, p. 269/77

[2] Woermann, E., A. Muan: Mat. Res. Bull. 5 (1970) No. 10, p. 779/88

$CaO\text{-}MgO\text{-}P_2O_5$

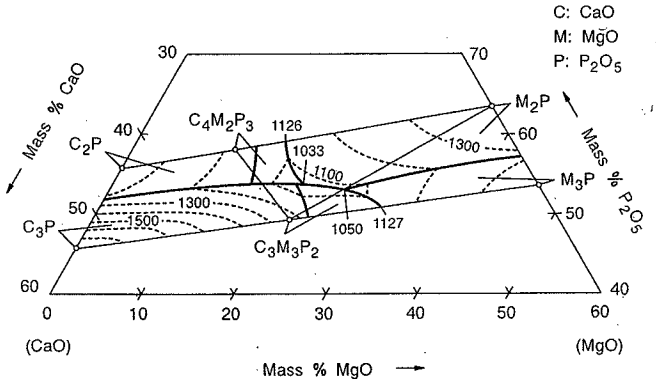


Fig. 3.247. Liquidus surface in the sub-system $3CaO\cdot P_2O_5$-$3MgO\cdot P_2O_5$-$2CaO\cdot P_2O_5$-$2MgO\cdot P_2O_5$ after Slawski [1, 2]. For the composition sections $3CaO\cdot P_2O_5$-$3MgO\cdot P_2O_5$ and $2CaO\cdot P_2O_5$-$2MgO\cdot P_2O_5$, see original papers by Slawski [1, 2] and also by Ando [3]. For all the compounds in the system, limited homogeneity ranges have been reported [1, 2].

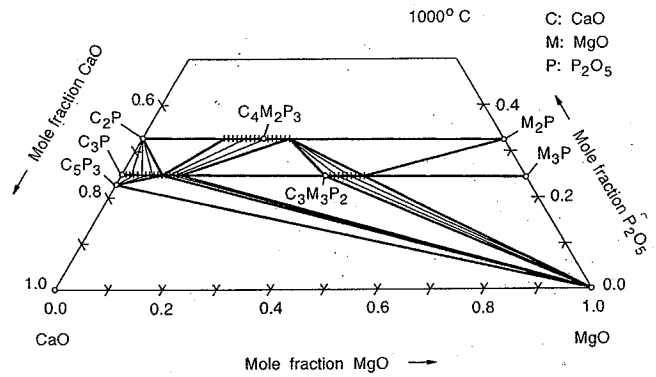


Fig. 3.248. Isothermal section through the system CaO-MgO-P_2O_5 at 1000 °C after Terpstra et al. [4]. The sub-solidus relations in the system have also been investigated by McCauley et al. [5]. For the ternary phase on the $2CaO\cdot P_2O_5$-$2MgO\cdot P_2O_5$ section, the composition $CaO\cdot MgO\cdot P_2O_5$ has been proposed. For a tentative isothermal section at 1600 °C, see Trömel et al. [6].

References

[1] Slawski, K.: Chem. Stosow., Ser. A. 10 (1966) No. 3, p. 305/18

[2] Slawski, K.: Chem. Stosow., Ser. A. 11 (1967) No. 3, p. 273/90

[3] Ando, J.: Bull. Chem. Soc. Jap. 31 (1958) No. 2, p. 201/5

[4] Terpstra, R. A., F. C. M. Driessens, R. M. H. Verbeeck: Z. Anorg. Allg. Chem. 515 (1984), p. 213/24

[5] McCauley, R. A., F. A. Hummel F. A., M. V. Hoffman: J. Electrochem. Soc. 118 (1971) No. 5, p. 755/9

[6] Trömel, G., W. Fix, K. Kaup: Arch. Eisenhüttenwes. 38 (1967) No. 8, p. 595/605

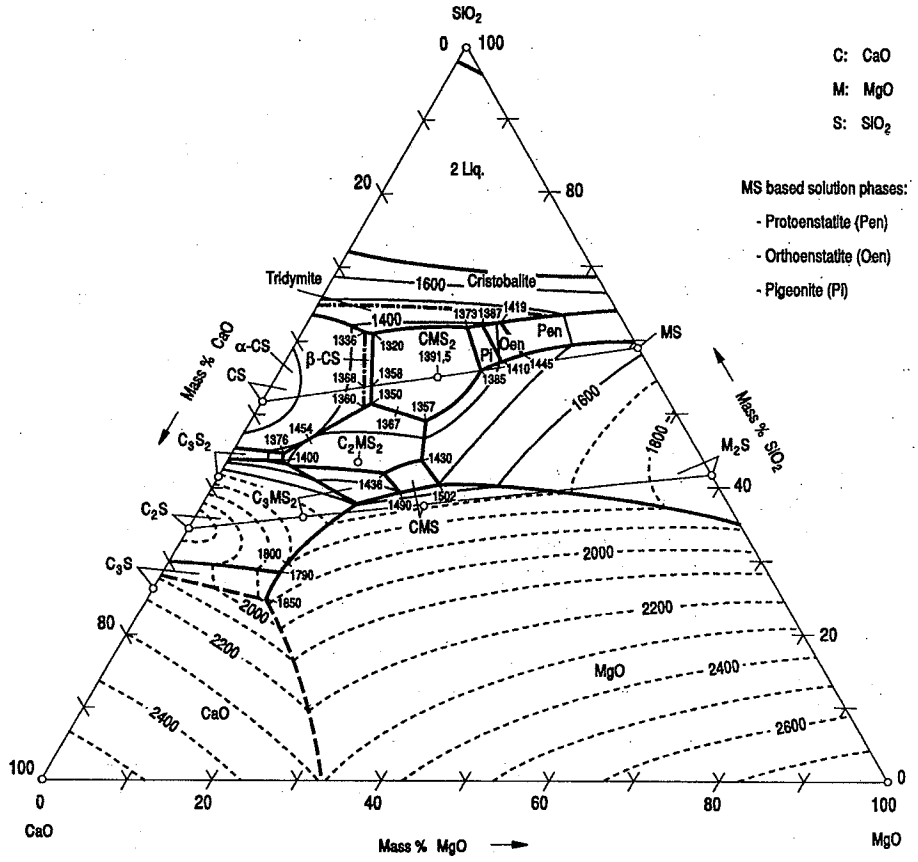


Fig. 3.249. Liquidus surface in the CaO-MgO-SiO_2 system as evaluated by Osborn, Muan [1]. Recent revisions concerning liquidus relations in the vicinity of the CaO·SiO_2-MgO·SiO_2 section reported by Kushiro [2], Longhi, Boudreau [3] and Liu, Presnall [4] are also incorporated in the figure.

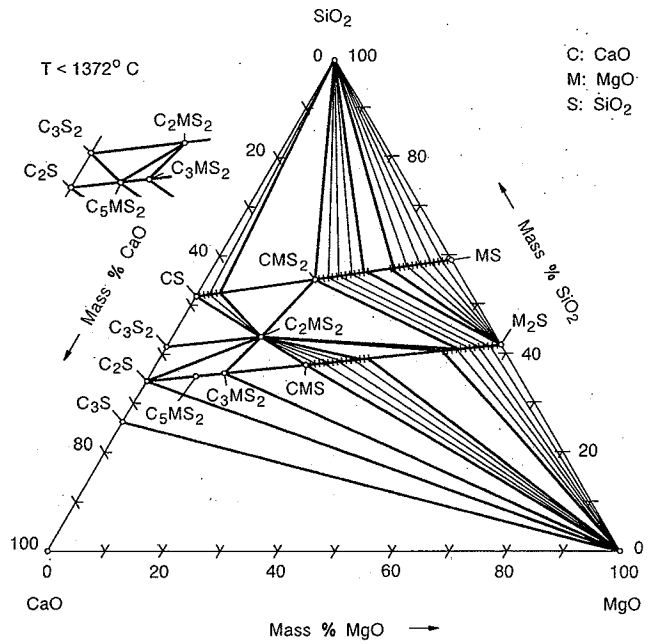


Fig. 3.250. Sub-solidus equilibria in the CaO-MgO-SiO_2 system as evaluated by Osborn, Muan [1]. Sub-solidus relations involving solution phases based on the MgO·SiO_2 composition (Fig. 3.251) are not included in the figure. The section shows the compatibility relations in the 2CaO·SiO_2-2MgO·SiO_2 section involving, below 1372 °C, the bredigite solution phase (the solid solution extends between the end-compositions 7CaO·MgO·4SiO_2 and 5CaO·MgO·3SiO_2) according to Lin, Foster [5]. For composition and stability range of bredigite, see also Gutt [6], Schlaudt, Roy [7] and Mosley, Glasser [8].

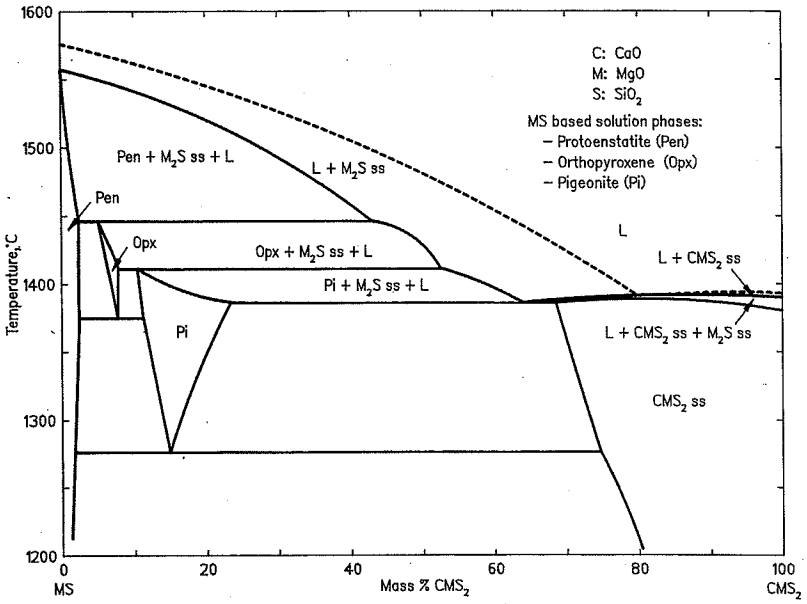


Fig. 3.251. Composition section $MgO{\cdot}SiO_2$-$CaO{\cdot}MgO{\cdot}2SiO_2$ according to results of Kushiro [2], Longhi, Boudreau [3] and Carlson [9].

References

[1] Osborn, E. F., A. Muan: Ceramic Foundation 1960, Publ. by Orton jr, Columbus/Ohio
[2] Kushiro, I.: Am. Mineral. 57 (1972) No. 7-8, p. 1260/71
[3] Longhi, J., A. E. Boudreau: Am. Mineral. 65 563-73 (1980)
[4] Liu, T. -C., D. C. Presnall: Am. Mineral. 74 (1989) No. 9-10, p. 1032/7
[5] Lin, H. C., W. R. Foster: J. Am. Ceram. Soc. 58 (1975) No. 1-2, p. 73
[6] Gutt, W.: Nature /London/ 207 (1965) No. 4993, p. 184/5
[7] Schlaudt, C. M., D. M. Roy: J. Am. Ceram. Soc. 49 (1966) No 8, p. 430/32
[8] Mosley, D., F. P. Glasser: J. Mat. Sci. 17(1982), p. 2736/40
[9] Carlson, W. D.: Am. Mineral. 73 (1988) No. 3-4, p. 232/41

CaO-MgO-TiO_2

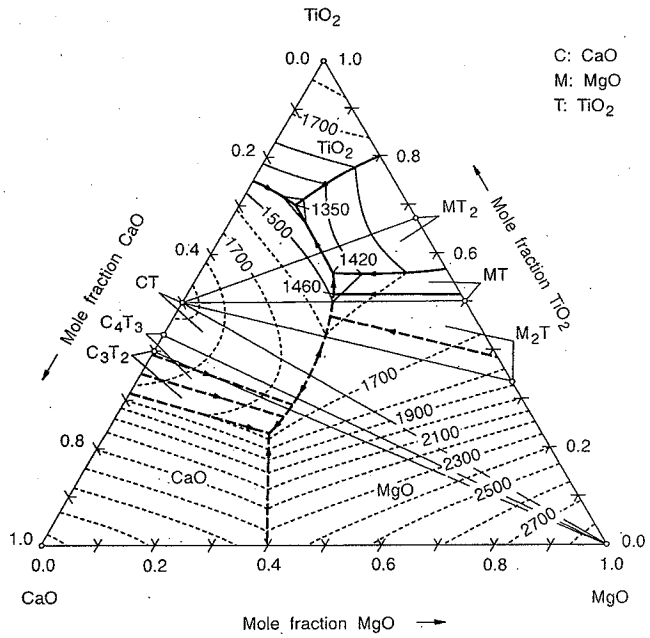


Fig. 3.252. Liquidus surface in the CaO-MgO-TiO_2 system according to results of Rouf et al. [1] (sub-system $CaO{\cdot}TiO_2$-$MgO{\cdot}TiO_2$-TiO_2).

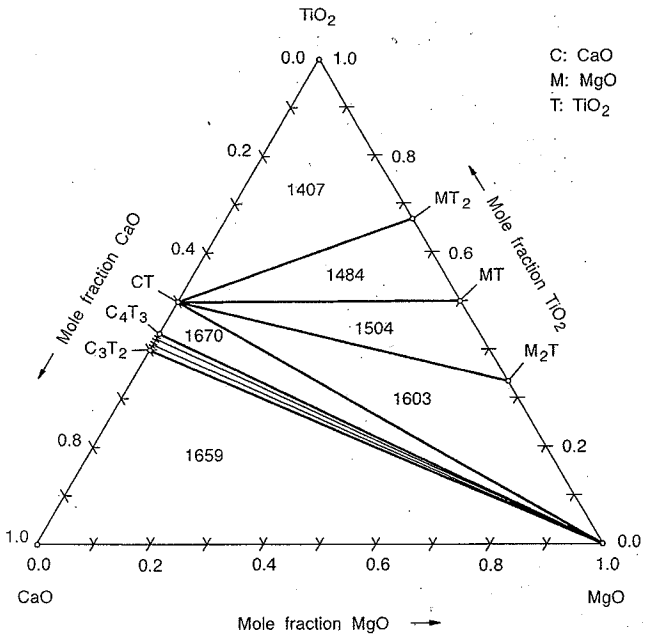


Fig. 3.253. Solidus surface in the system CaO-MgO-TiO_2 after Shultz [2]. The temperature of invariant points determined by Shultz [2] are approx. 50 degrees higher than those reported by Rouf et. al [1].

References

[1] Rouf, M. A., A. H. Cooper, H. B. Bell: Trans. J. Br. Ceram. Soc. 68 (1969) No. 6, p. 263/7
[2] Shultz, R. L.: J. Am. Ceram. Soc. 56 (1973) No. 1, p. 33/6

$CaO\text{-}MnO_x\text{-}P_2O_5$

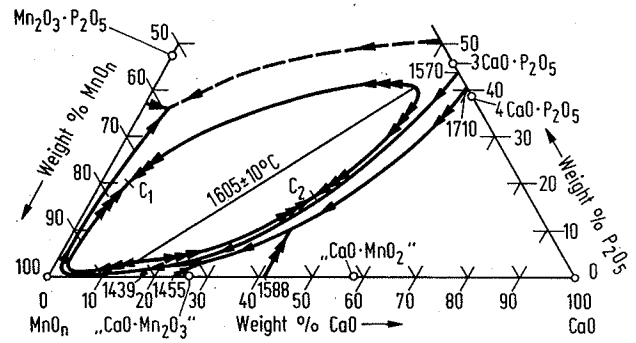


Fig. 3.254. Liquidus surface in the system $CaO\text{-}MnO_x\text{-}P_2O_5$ in air after Fix et al. [1]

References

[1] Fix, W., H. E. Wiemer, H. J. Tolkemit: Arch. Eisenhüttenwes. 40 (1969) No. 3, p. 215/21

$CaO\text{-}MnO_x\text{-}SiO_2$

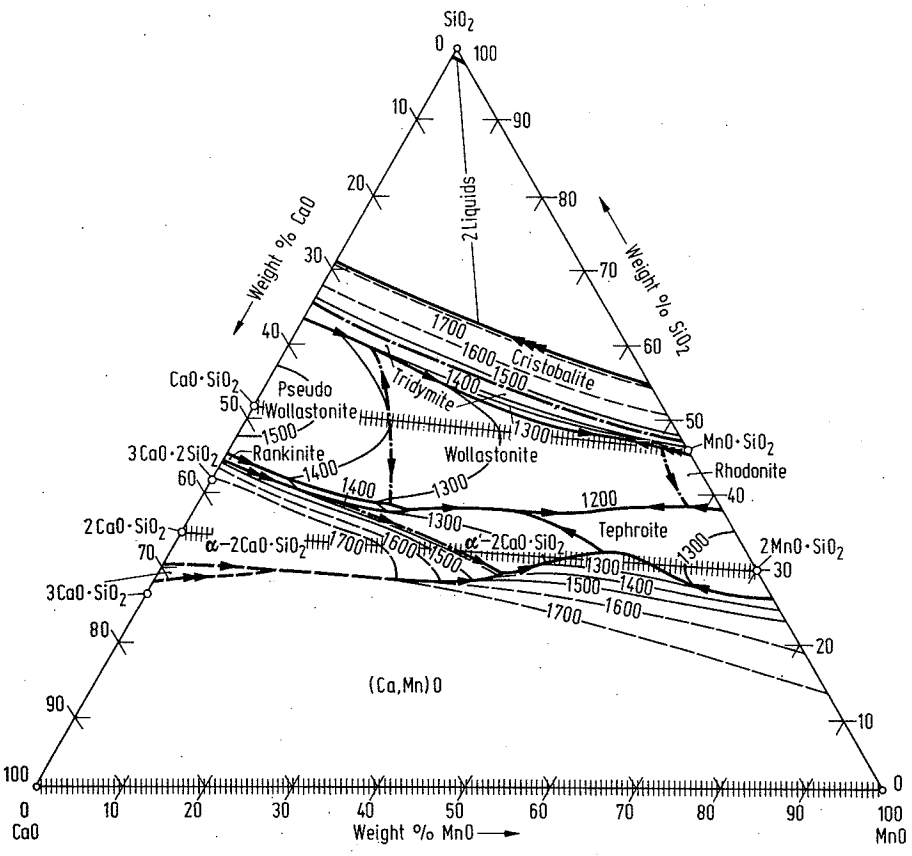


Fig. 3.255. Liquidus surface in the system $CaO\text{-}MnO\text{-}SiO_2$ at low oxygen partial pressure after Glasser [1, 2].

References

[1] Glasser, F. P.: Am. J. Sci. 259 (1961) No. 1, p. 46/59
[2] Glasser, F. P.: J. Am. Ceram. Soc. 45 (1962) No. 5, p. 242/9
[3] Mikirticheva, G. A., R. G. Grebenshchikov, S. K. Kuchaeva: Zh. Neorg. Khim. 30 (1985) No. 2, p. 487/91

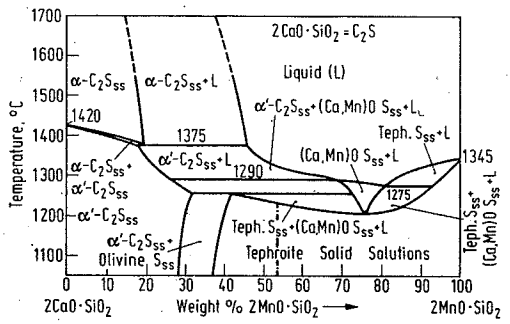


Fig. 3.256. Composition section $2CaO \cdot SiO_2\text{-}2MnO \cdot SiO_2$ after Glasser [1, 2].

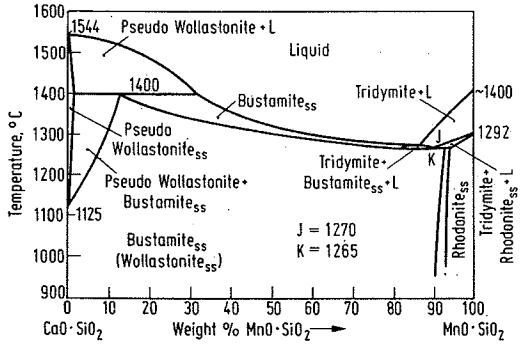


Fig. 3.257. Composition section $CaO \cdot SiO_2\text{-}MnO \cdot SiO_2$ after Glasser [1, 2]. Recently, a new ternary solution phase on the $CaO \cdot SiO_2\text{-}MnO \cdot SiO_2$ section was reported by Mikirticheva et al. [3].

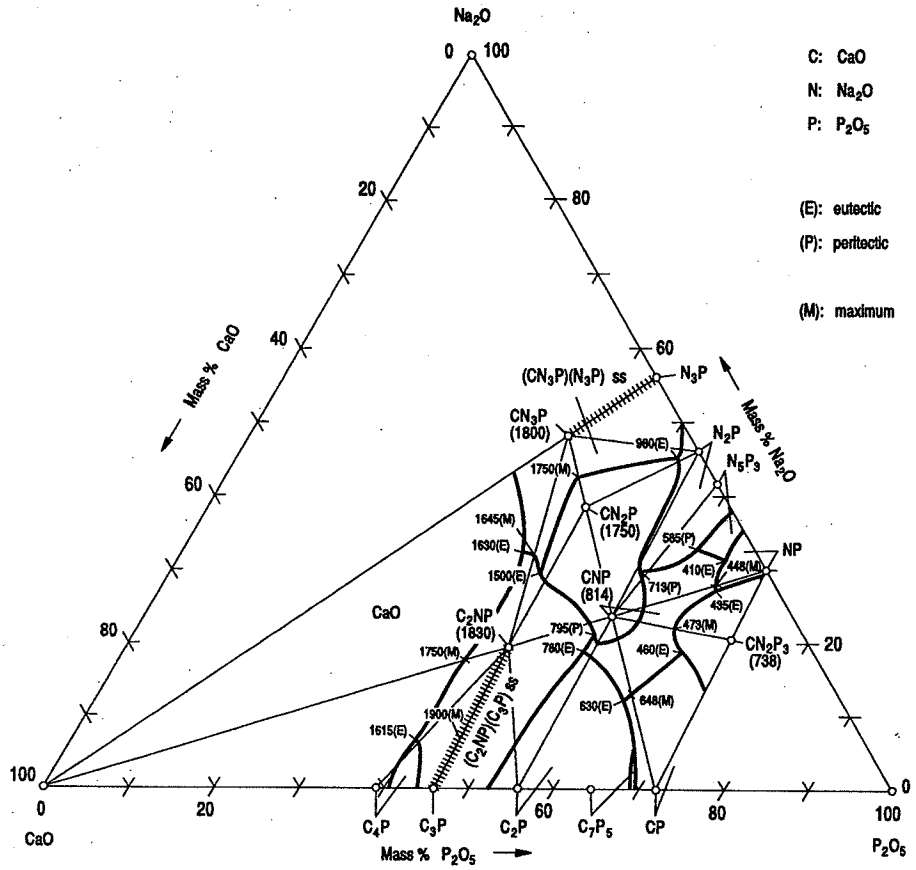


Fig. 3.258. Liquidus surface in part of the $CaO\text{-}Na_2O\text{-}P_2O_5$ system after Berak, Znamierowska [1-4]. For numerous binary sections showing, in particular, homogeneity ranges of solution phases and numerous polymorphs of compounds, see original papers [1-4]. A further incongruently melting compound, $2CaO{\cdot}Na_2O{\cdot}P_2O_5$ has been reported by Grenier et al. [5] to exist on the $CaO{\cdot}P_2O_5\text{-}Na_2O{\cdot}P_2O_5$ section. The composition section $3CaO{\cdot}P_2O_5\text{-}2CaO{\cdot}Na_2O{\cdot}P_2O_5$ has also been investigated by Ando, Matsuno [6] and Millet et al. [7, 8].

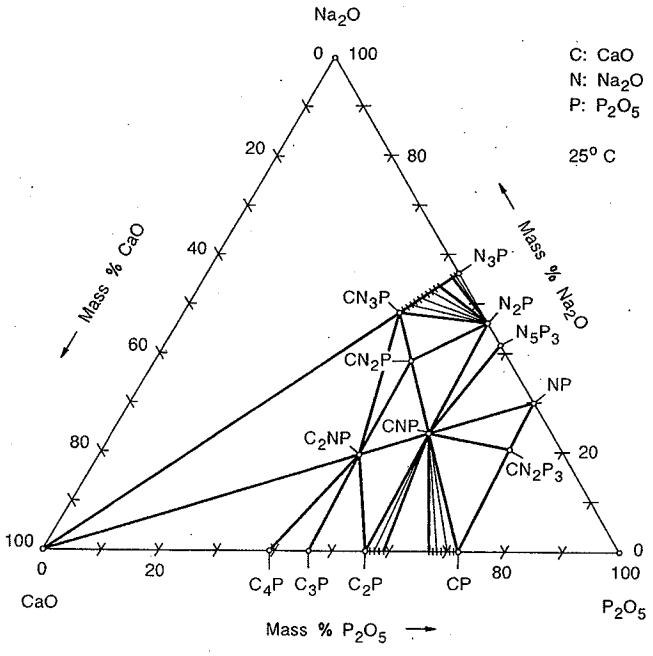


Fig. 3.259. Isothermal section through the $CaO\text{-}Na_2O\text{-}P_2O_5$ system at room temperature after Berak, Znamierowska [4]. For an alternative version of the sub-solidus equilibria, see Majling et al. [9].

References

[1] Berak, J., T. Znamierowska: Ann. Soc. Chim. Polonorum /Rocz. Chem./ 41 (1967) No. 12, p. 2065/9

[2] Berak, J., T. Znamierowska: Ann. Soc. Chim. Polonorum /Rocz. Chem./ 46 (1972) No. 10, p. 1697/708

[3] Berak, J., T. Znamierowska: Ann. Soc. Chim. Polonorum /Rocz. Chem./ 46 (1972) No. 11, p. 1921/9

[4] Berak, J., T. Znamierowska: Ann. Soc. Chim. Polonorum /Rocz. Chem./ 47 (1973), p. 1137/49

[5] Grenier, J. C., C. Martin, A. Durif: Bull. Soc. Fr. Mineral. Cristallogr. 93 (1970) No. 1, p. 52/5

[6] Ando, J., S. Matsuno: Bull. Chem. Soc. Jap. 41 (1968) No. 2, p. 342/7

[7] Millet, J. M., R. Sassoulas, A. Sebaoun: J. Therm. Anal. 28 (1983) No. 1, p. 131/46

[8] Millet, J. M., A. Sebaoun, G. Thomas: J. Therm. Anal. 29 (1984) No. 3, p. 445/63

[9] Majling, J., I. Kaprálik, D. Miklos: Silikaty /Prague/ 18 (1974) No. 2, p. 125/32

$CaO-Na_2O-SiO_2$

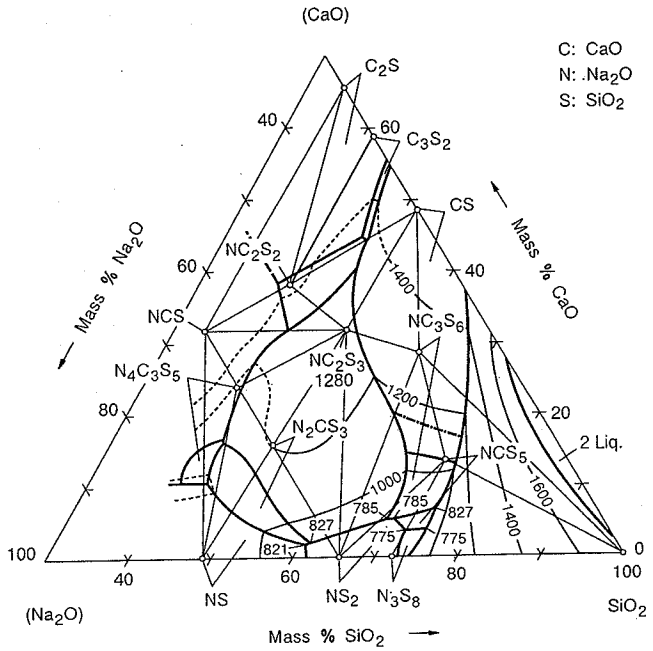


Fig. 3.260. Liquidus surface and sub-solidus relations in part of the $CaO-Na_2O-SiO_2$ system after Morey, Bowen [1], Morey [2], and Segnit [3], as revised by Shahid, Glasser [4, 5]. For the composition section $CaO{\cdot}SiO_2$-$Na_2O{\cdot}SiO_2$ showing homogeneity ranges of ternary phases, see Moir, Glasser [6].

References

[1] Morey, G. W., N. L. Bowen: J. Soc. Glass. Technol. 9 (1925) No. 35, p. 226/64
[2] Morey, G. W.: J. Am. Ceram. Soc. 13 (1930) No. 10, p. 683/13
[3] Segnit, E. R.: Am. J. Sci. 251 (1953) No. 8, p. 586/601
[4] Shahid, K. A., F. P. Glasser: J. Am. Ceram. Soc. 53 (1970) No. 7, p. 423
[5] Shahid, K. A., F. P. Glasser: Phys. Chem. Glasses 12 (1971) No. 2, p. 50/7
[6] Moir, G. K., F. P. Glasser: Trans. J. Br. Ceram. Soc. 73 (1974) No. 6, p. 199/206

$CaO-P_2O_5-SiO_2$

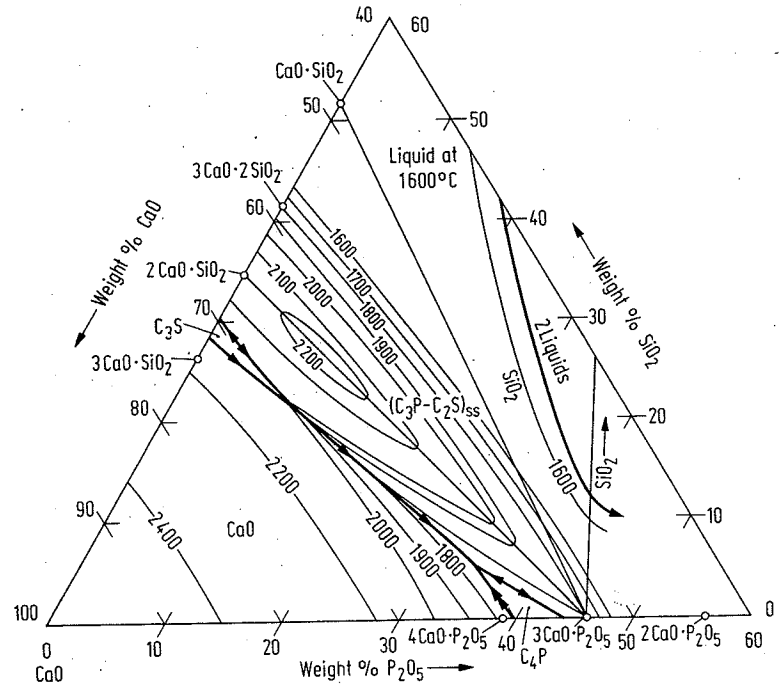


Fig. 3.261. Liquidus surface in the CaO-rich region of the $CaO-P_2O_5-SiO_2$ system after Drewes, Olette [1].

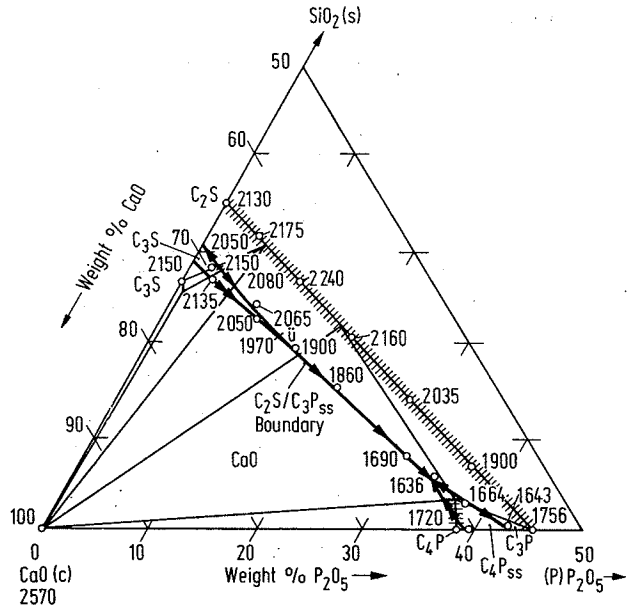


Fig. 3.262. Liquidus surface and compatibility relations in the CaO-rich region of the CaO-P_2O_5-SiO_2 system according to Gutt [2].

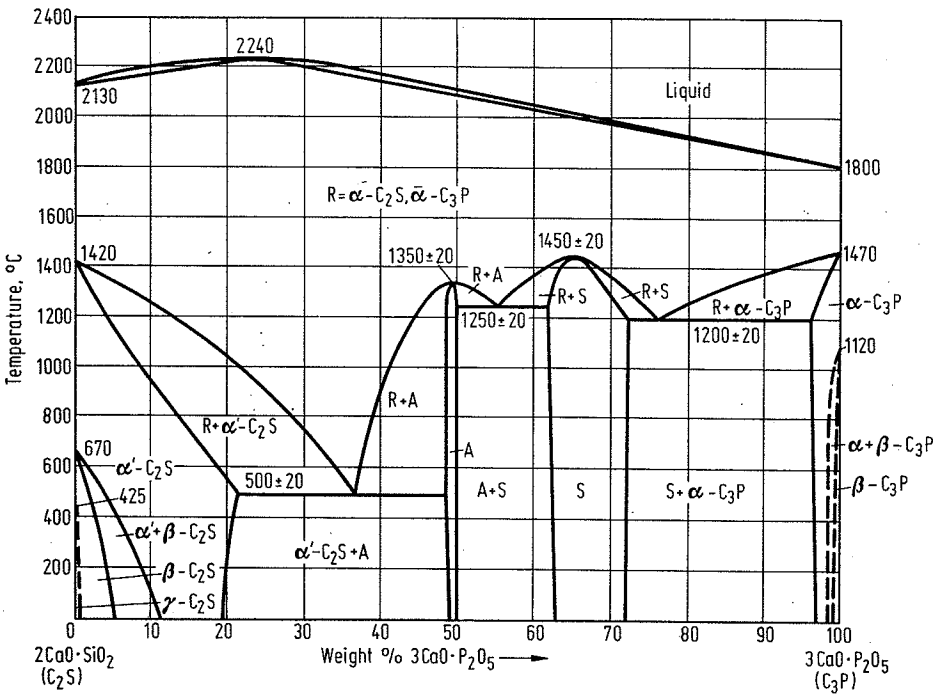


Fig. 3.263. Composition section $2CaO{\cdot}SiO_2$-$3CaO{\cdot}P_2O_5$ after Nurse et al. [3], as reinvestigated by Fix et al. [4].

For further contributions to the CaO-P_2O_5-SiO_2 system, see Koch, Fix [5] and Fix et al. [6].

References

[1] Drewes, E.-J., M. Olette: Arch. Eisenhüttenwes., 30 (1967) No. 3, p. 163/75
[2] Gutt, W.: Nature 197 (1963) No. 4863, p. 142/3
[3] Nurse, R. W., J. H. Welch, W. Gutt: J. Chem. Soc. 63 (1959), p. 1077/83
[4] Fix, W., H. Heymann, R. Heinke: J. Am. Ceram. Soc. 52 (1969) No. 6, p. 346/7
[5] Koch, K., W. Fix: Arch. Eisenhüttenwes. 41 (1970) No. 2, p. 111/8
[6] Fix W., G. Trömel, R. Heinke: Arch. Eisenhüttenwes. 40 (1969) No. 12, p. 979/84

$CaO\text{-}SiO_2\text{-}TiO_2$

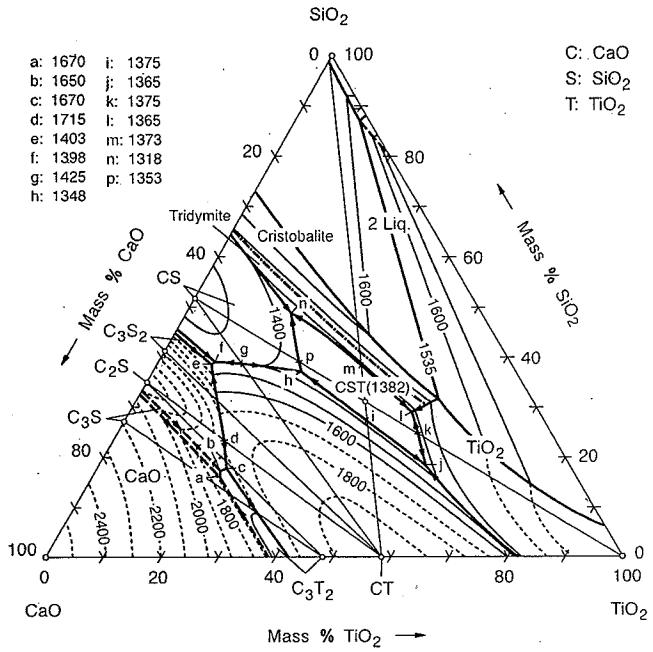


Fig. 3.264. Liquidus surface and compatibility relations in the $CaO\text{-}SiO_2\text{-}TiO_2$ system after DeVries et al. [1]. Similar phase relations on the binary section $CaO{\cdot}TiO_2\text{-}2CaO{\cdot}SiO_2$ have later been reported by Panek et al. [2].

$Cr_2O_3\text{-}FeO_x\text{-}SiO_2$

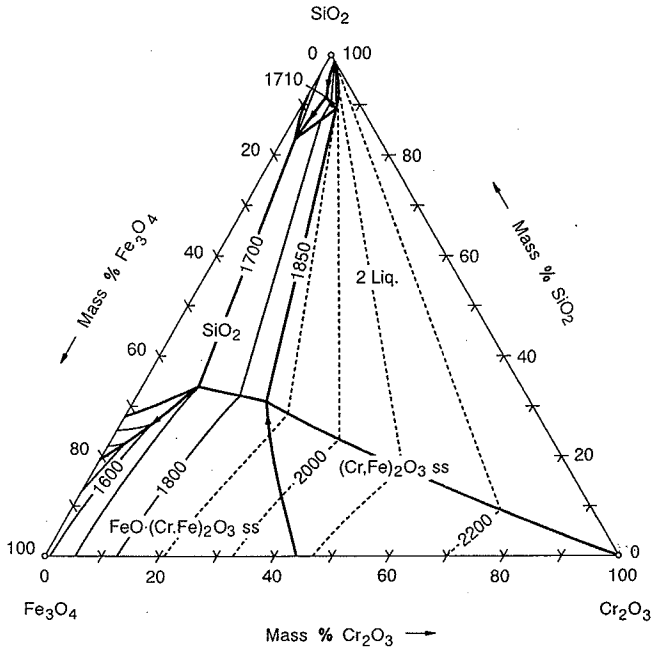


Fig. 3.266. Liquidus surface in the system $Cr_2O_3\text{-}FeO_x\text{-}SiO_2$ in air after Muan, Somiya [1]. For numerous isothermal sections between 1380 and 1860 °C, see original paper by Muan, Somiya [1].

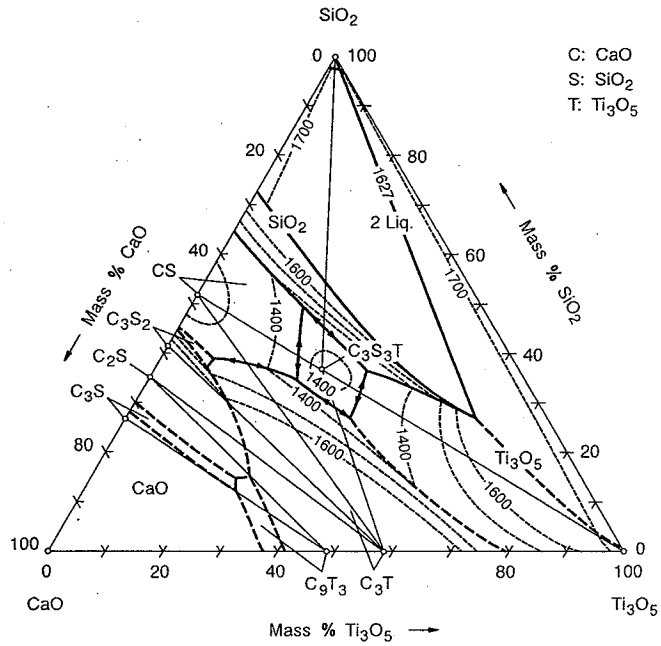


Fig. 3.265. Liquidus surface and compatibility relations in the $CaO\text{-}SiO_2\text{-}Ti_3O_5$ system as reported by Muan [3].

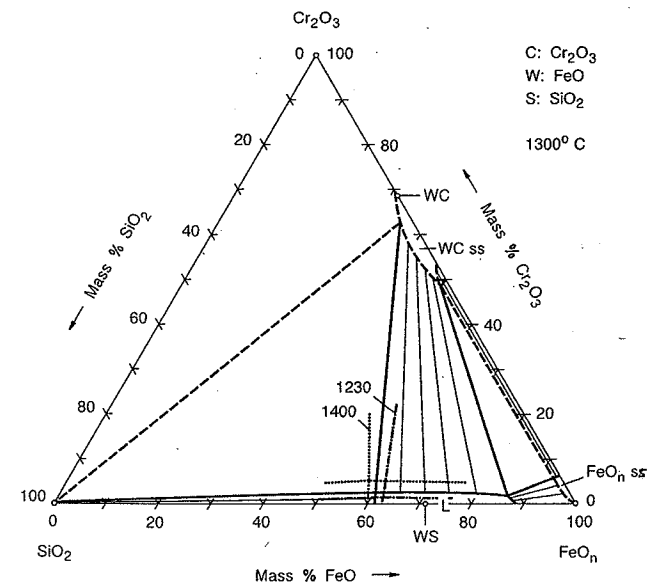


Fig. 3.267. Isothermal section through the system $Cr_2O_3\text{-}FeO_n$ss-SiO_2 in contact with metallic iron under a nitrogen atmosphere at 1300 °C after Eguchi et al. [2]. The regions of homogeneous liquid at 1230 and 1400 °C, as determined also by Eguchi et al. [2], are shown with dot and dash-dot lines respectively.

References

[1] DeVries, R. C., R. Roy, E. F. Osborn: J. Am. Ceram. Soc. 38 (1955) No. 5, p. 158/71

[2] Panek, Z., E. Kanclir, J. Staron, M. Kozlovsky, S. Palco: Silikaty 20 (1976) No. 1, p. 13/22

[3] Muan A.: Adv. Ceram. 3rd Meeting Date (1988), p. 25/44

References

[1] Muan, A., S. Somiya: J. Am. Ceram. Soc. 43 (1960) No. 10, p. 531/41

[2] Eguchi, M., R. Uchida, M. Chiba: Tohoku Daigaku Senko Seiren Kenkyusho Iho 33 (1977) No. 1, p. 24/30

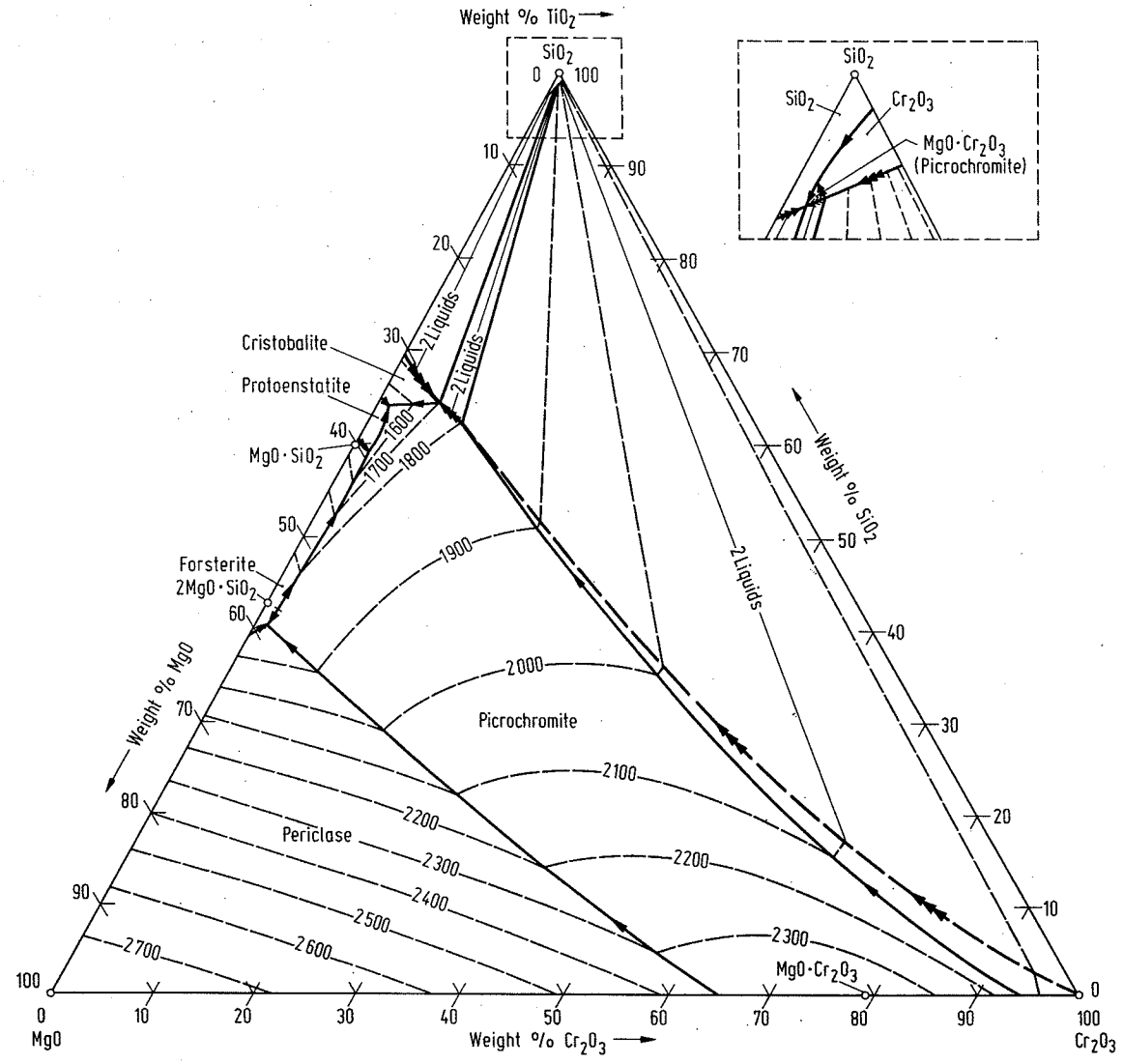


Fig. 3.268. Liquidus surface and sub-solidus equilibria in the system Cr_2O_3-MgO-SiO_2 in air (some of the runs were made in sealed cells) after Keith [1]. Compatibility relations determined by Keith [1] have also been confirmed by Ford, Rees [2]. According to Berezhnoi [3] the tie-line between SiO_2 and MgO·Cr_2O_3 should be replaced by a tie-line between Cr_2O_3 and MgO·SiO_2. The solubility of MgO·Cr_2O_3 in the melt at low oxygen partial pressure (pO_2=2.73·10^{-10} atm) and at 1600 °C has been investigated by Morita et al. [4, 5].

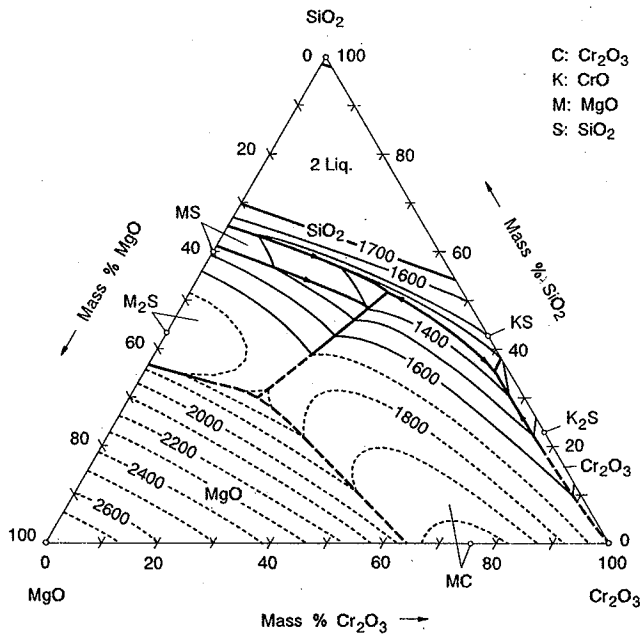


Fig. 3.269. Liquidus surface in the system Cr_2O_3-MgO-SiO_2 in contact with metallic chromium as reported by Muan [6] according to the results of Collins et al. [7].

References

[1] Keith, M. L.: J. Am. Ceram. Soc. 37 (1954) No. 10, p. 490/6
[2] Ford, W. B., W. J. Rees: Trans. J. Br. Ceram. Soc. 57 (1958) No. 5, p. 233/41
[3] Berezhnoi, A. C.: Multicomponent oxide systems, Ed.: Naukovaya Dumka, Kiev (1970), 490 p.
[4] Morita, K., A. Inoue, N. Takayama, N. Sano: Tetsu to Hagane 74 (1988) No. 6, p. 999/1005
[5] Morita, K., T. Shibuya, N. Sano: Tetsu to Hagane 74 (1988) No. 4, p. 632/9
[6] Muan A.: Adv. Ceram. 3rd Meeting Date (1988), p. 25/44
[7] Collins, H., Merkel, G., Muan, A.: in preparation

FeO_x-K_2O-SiO_2

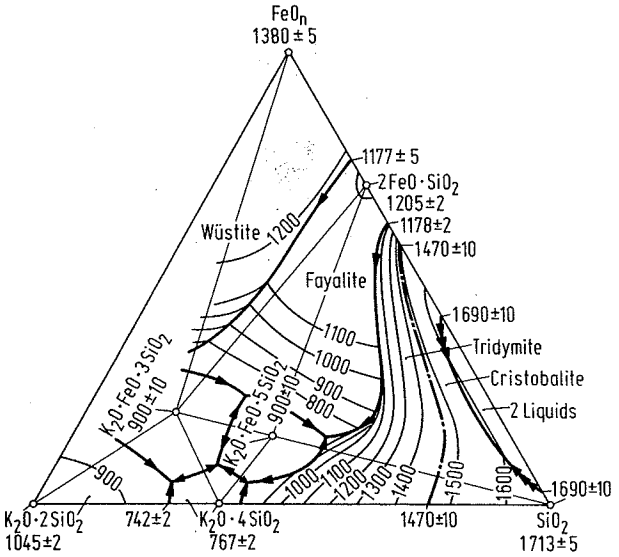


Fig. 3.270. Liquidus surface in the sub-system FeO_n-$K_2O{\cdot}2SiO_2$-SiO_2 in contact with metallic iron after Roedder [1].

For contributions to the system FeO_x-K_2O-SiO_2 system in air, see Roth [2], Bentzen [3], Protsyuk et al. [4] and Faust [5].

References

[1] Roedder, E.: Am. J. Sci. Bowen Vol.(1952), p. 435/56
[2] Roth, R. S.: Adv. Chem. Ser. 186/Solid State Chem.: Contemp. Overview/ (1980), p. 391/408
[3] Bentzen, J. J.: J. Am. Ceram. Soc. 66 (1983) No. 7, p. 475/78
[4] Protsyuk, A. P., G. A. Konechnyi, L. G. Latysheva: Izv. Akad. Nauk SSSR, Neorg. Mater. 15 (1979) No. 1, p. 173/4
[5] Faust, G. T.: Am. Mineral. 21 (1936) No. 12, p. 735/63

FeO_x-MgO-SiO_2

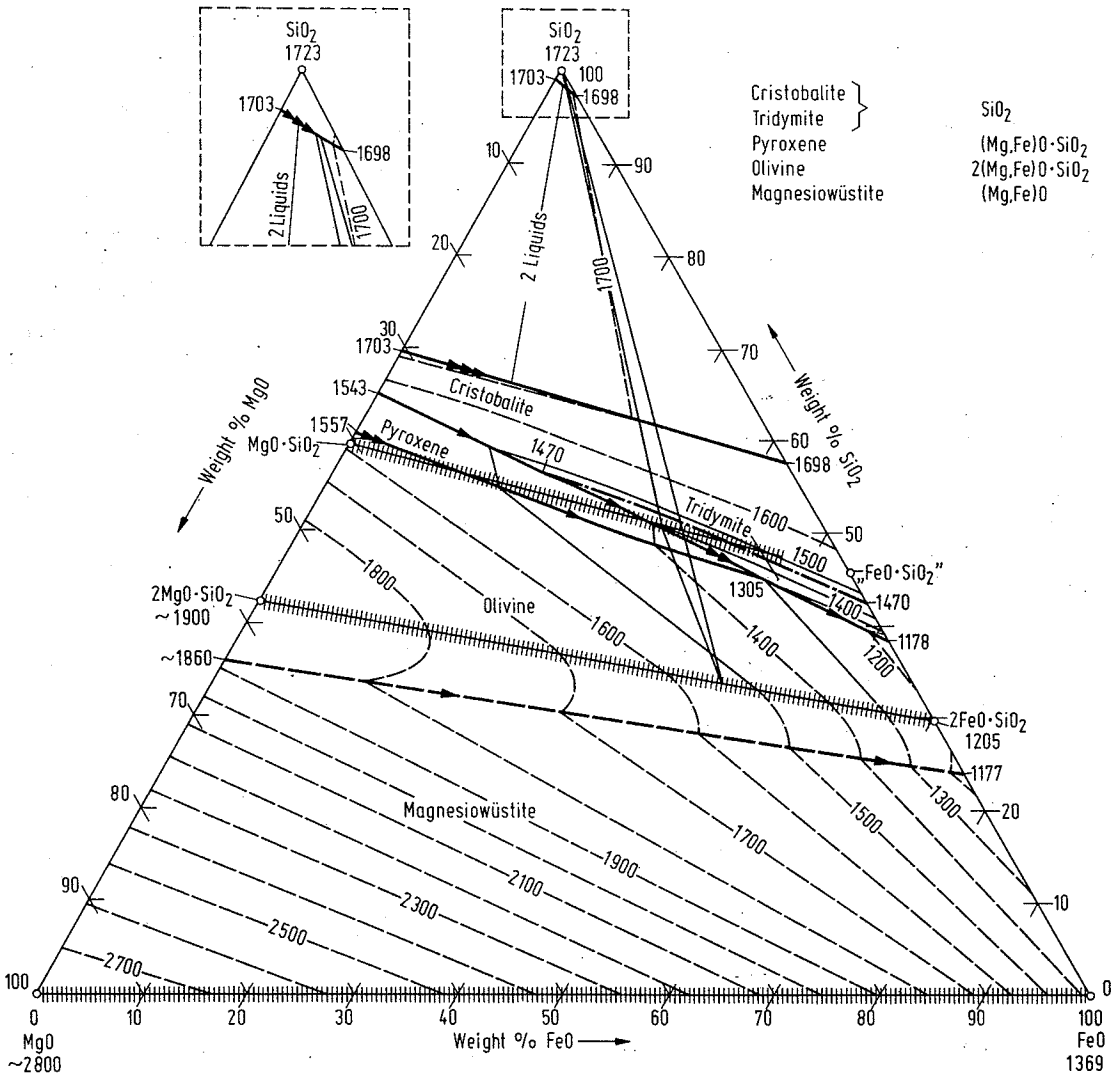


Fig. 3.271. Liquidus surface in the system FeO_n-MgO-SiO_2 after Bowen, Schairer [1]. Complete solid solubility on the $2FeO{\cdot}SiO_2$-$2MgO{\cdot}SiO_2$ section has been reported in [1]. For the composition section $FeO{\cdot}SiO_2$-$MgO{\cdot}SiO_2$, see Huebner, Turnock [2]. For a thermodynamic assessment of the system and calculated phase equilibria, see Wu et al. [3].

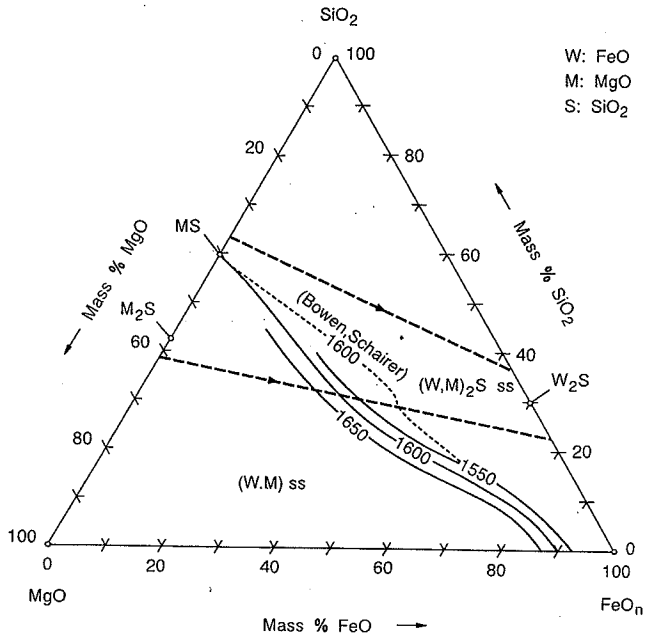


Fig. 3.272. Liquidus isotherms in the FeO_n-MgO-SiO_2 system in contact with metallic iron as determined by Shim, Ban-Ya [4].

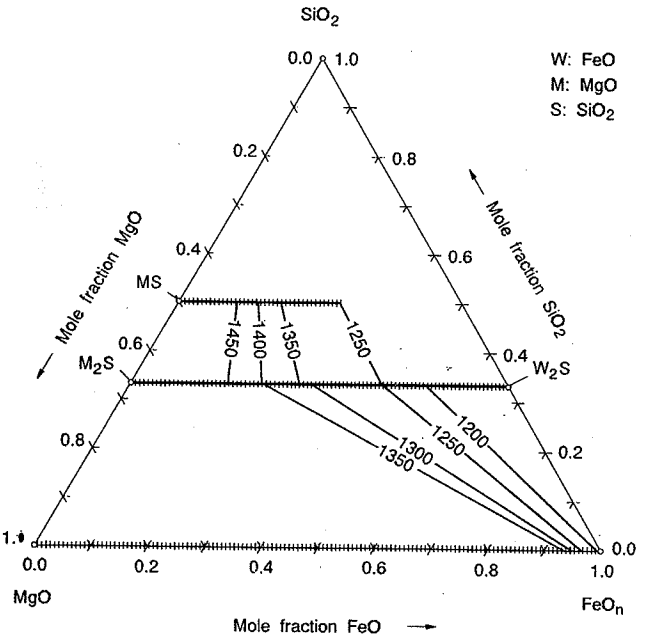


Fig. 3.273. Solidus surface in the FeO_n-MgO-SiO_2 system according to Nafziger, Muan [5].

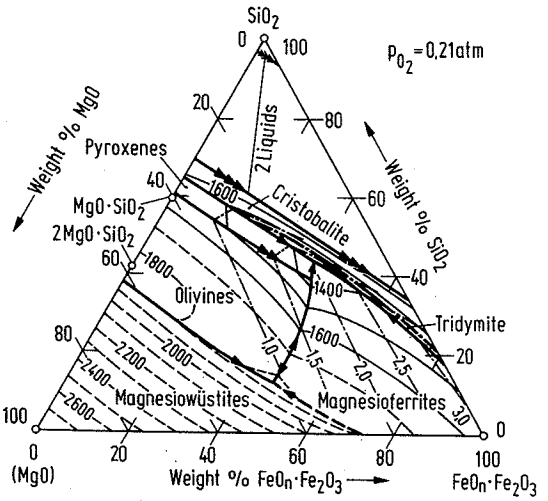


Fig. 3.274. Liquidus surfaces in the system FeO_x-MgO-SiO_2 in air projected on the FeO·Fe_2O_3-MgO-SiO_2 plane after Muan, Osborn [6]. The light dash-dot lines show the Fe_2O_3/FeO ratio in the liquid at liquidus temperatures.

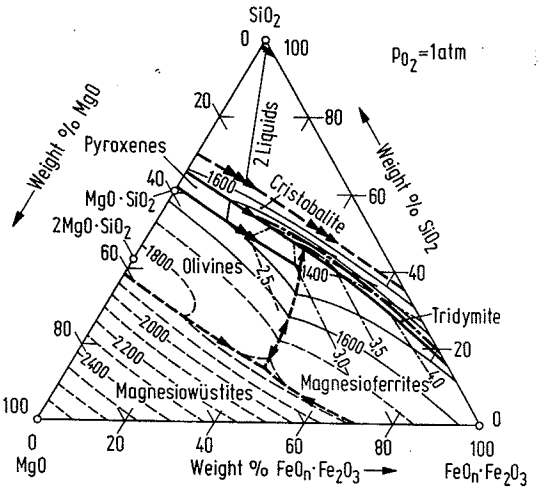


Fig. 3.275. Liquidus surfaces in the system FeO_x-MgO-SiO_2 at 1 atm O_2 pressure projected on the FeO·Fe_2O_3-MgO-SiO_2 plane after Muan, Osborn [6]. The light dash-dot lines show the Fe_2O_3/FeO ratio in the liquid at liquidus temperatures. For further figures showing phase relations at lower partial pressures of O_2, see [5].

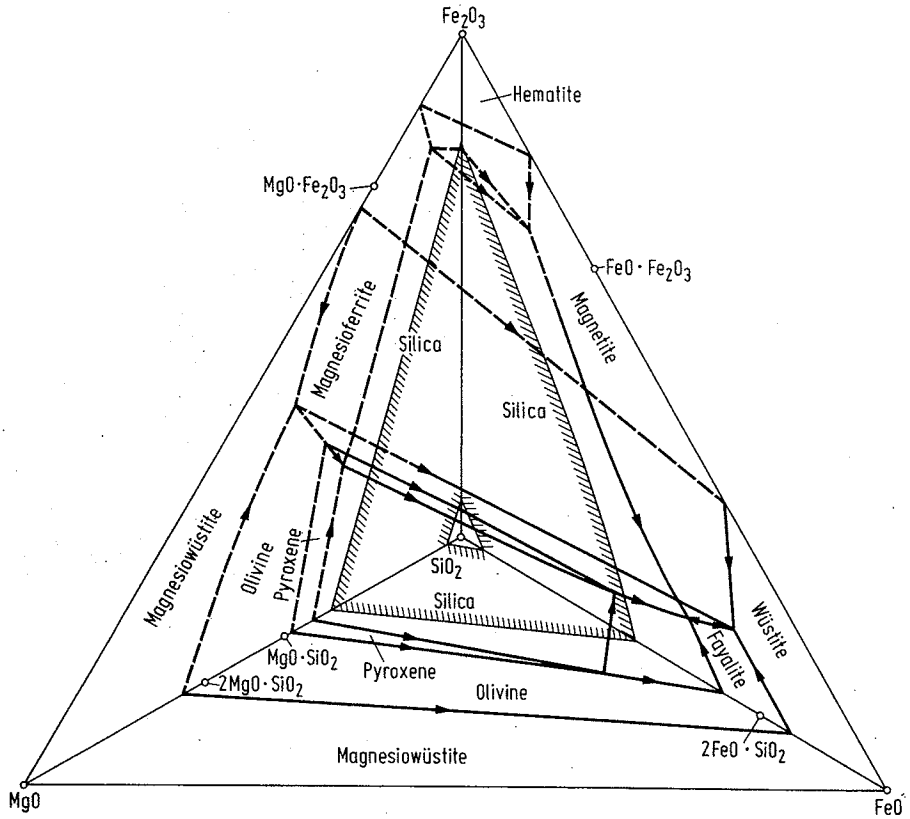


Fig. 3.276. Liquidus relations in the FeO-Fe_2O_3-MgO-SiO_2 system after Muan, Osborn [6]. For additional information, see also Speidel, Osborn [7].

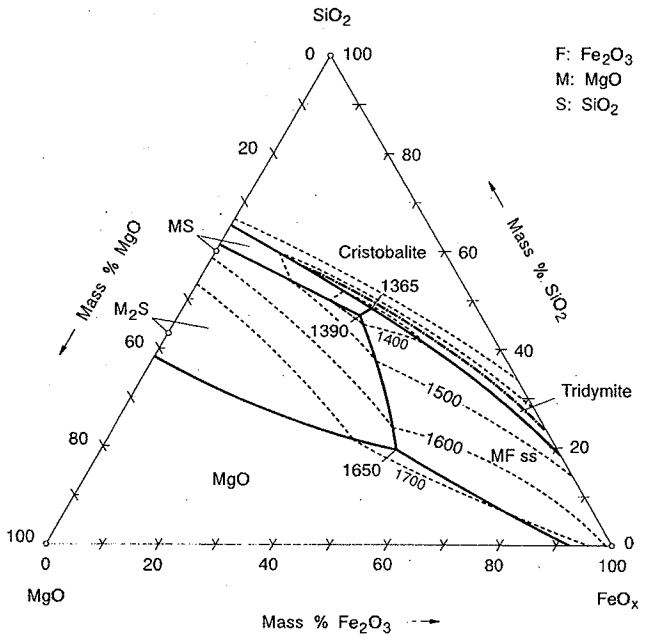


Fig. 3.277. Liquidus surface in the FeO_x-MgO-SiO_2 system in air projected on the Fe_2O_3-MgO-SiO_2 plane as revised by Correia, White [8].

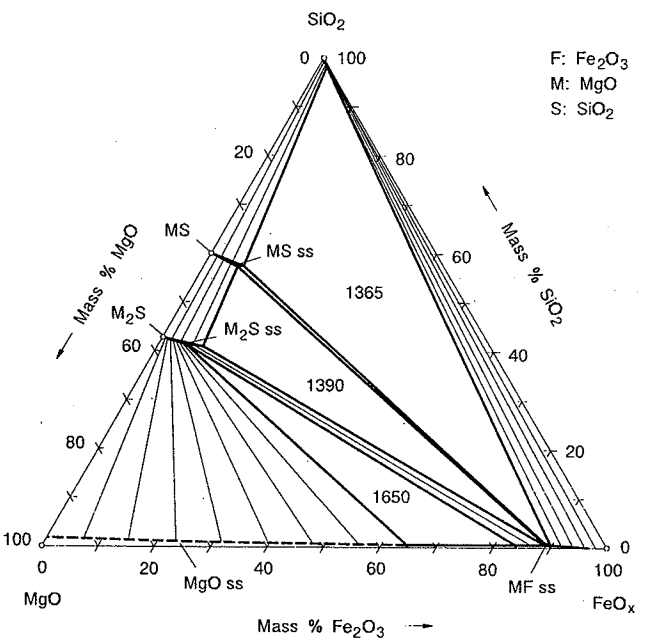


Fig. 3.278. Solidus surface in the FeO_x-MgO-SiO_2 system in air projected on the Fe_2O_3-MgO-SiO_2 plane after Correia, White [8]. For phase relations on the section $2MgO \cdot SiO_2$-$MgO \cdot Fe_2O_3$, see also Ambrúz et al. [9].

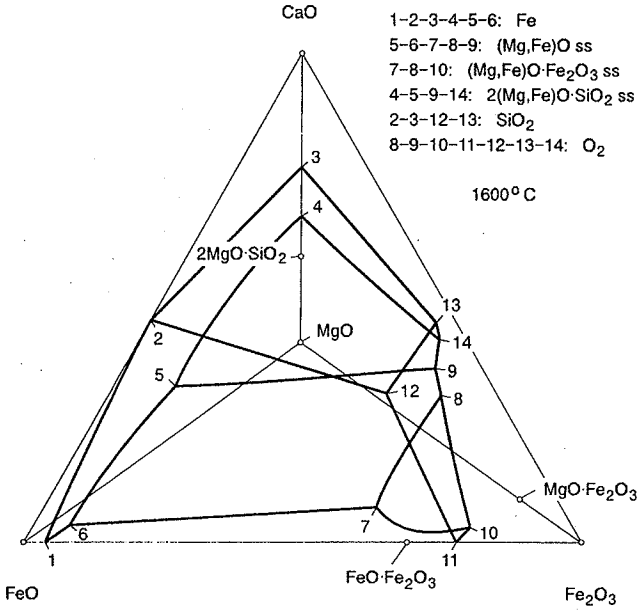


Fig. 3.279. Liquidus relations in the FeO-Fe_2O_3-MgO-SiO_2 system at 1600 °C after Schürmann, Kolm [10]

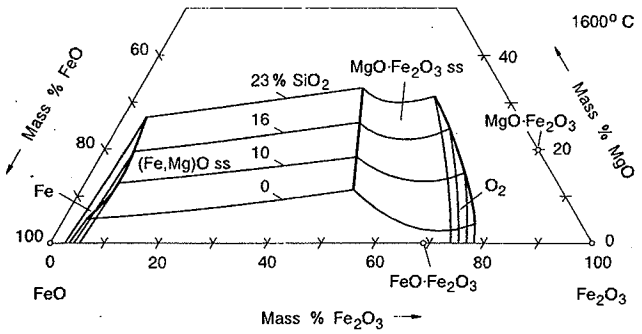


Fig. 3.280. Solubility limits of solid phases in homogeneous liquid in the FeO-Fe_2O_3-MgO-SiO_2 system at 1600 °C and at O, 10, 16 and 23 mass % SiO_2, projected on the FeO-Fe_2O_3-MgO plane after Schürmann, Kolm [10].

References

[1] Bowen, N. L., J. F. Schairer: Am. J. Sci. 5th Ser. 29 (1935) No. 170, p. 151/217

[2] Huebner, J. S., A. C. Turnock: Am. Mineral. 65 (1980) No. 3-4, p. 225/71

[3] Wu, P., G. Eriksson, G., A. D. Pelton, M. Blander: Trans. Iron Steel Inst. Jpn. 33 (1993), p. 26/35

[4] Shim, J.-D., S. Ban-Ya: Tetsu-to-Hagane 67 (1981) No. 10, p. 1735/44

[5] Nafziger, R. H., A. Muan: Am. Mineral. 52 (1967) No. 9-10, p. 1364/85

[6] Muan, A., E. F. Osborn: J. Am. Ceram. Soc. 39 (1956) No. 4, p. 121/40

[7] Speidel, D. H., E. F. Osborn: Am. Mineral. 52 (1967) No. 7-8, p. 1139-52

[8] Correia, R. N., J. White: Trans. J. Br. Ceram. Soc. 87 (1988) No. 6, p. 195/9

[9] Ambrúz, V., J. Havlica, E. Kanclir: Chem. Zvesti 35 (1981) No. 1, p. 51/5

[10] Schürmann, E., I. Kolm: Steel Res. 59 (1988) No. 5, p. 185/91

FeO_x-MgO-TiO_2

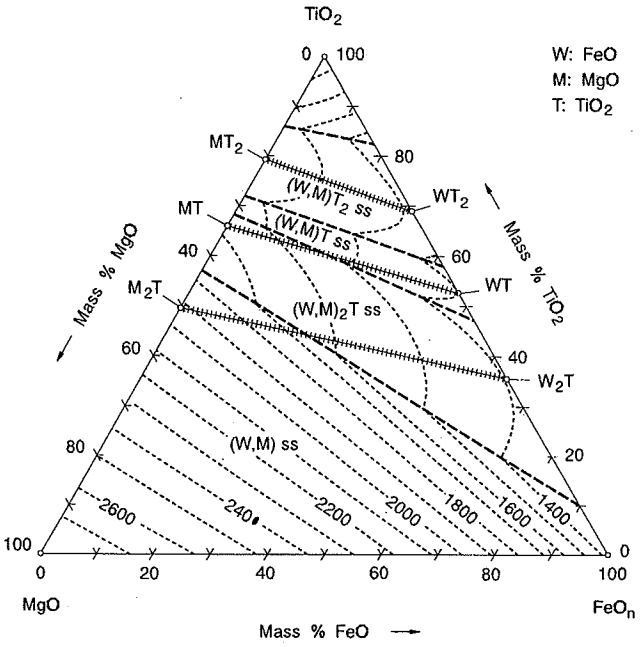


Fig. 3.281. Liquidus surface in the system FeO-MgO-TiO_2 at $pO_2=10^{-8}$ atm after Johnson et al. [1].

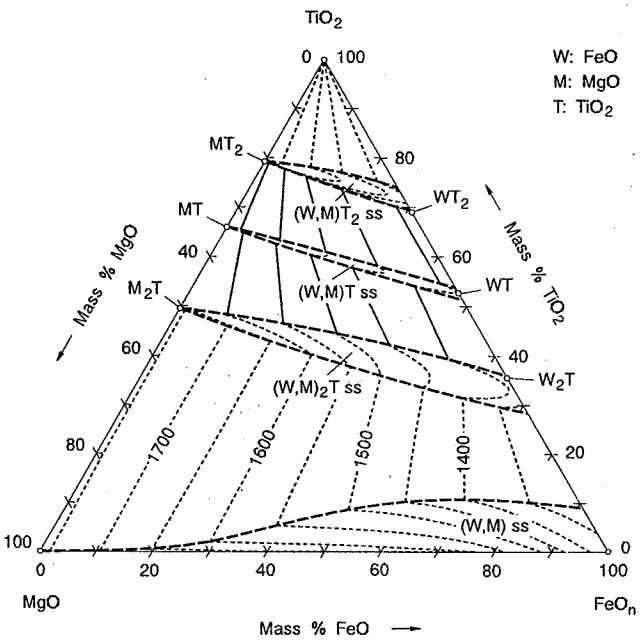


Fig. 3.282. Solidus surface in the system FeO_n-MgO-TiO_2 at $pO_2=10^{-8}$ atm after Johnson et al. [1].

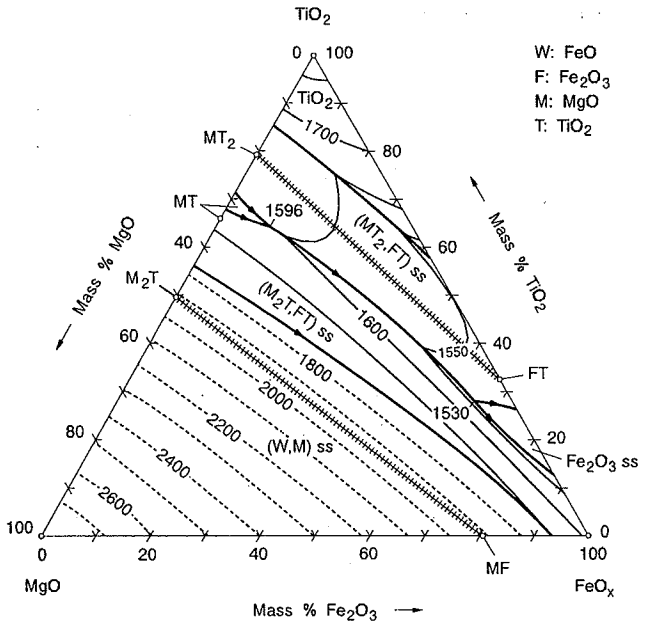


Fig. 3.283. Liquidus surface in the system FeO_x-MgO-TiO_2 in air after Woermann et al. [2].

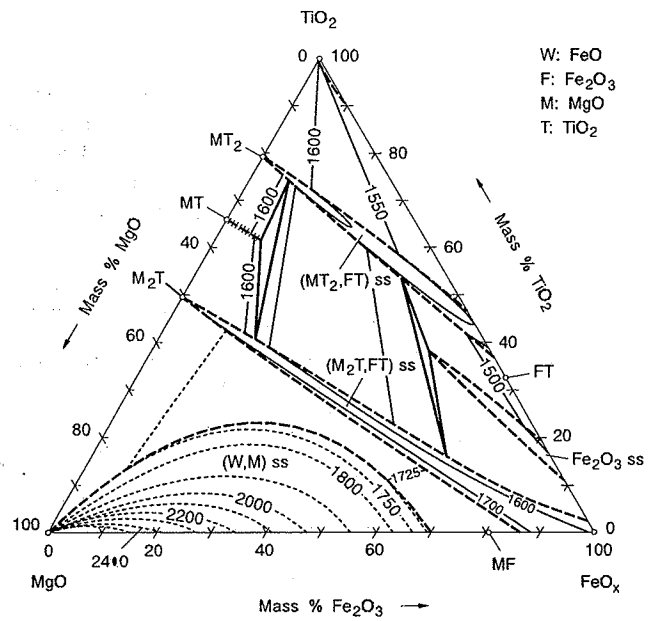


Fig. 3.284. Solidus surface in the system FeO_x-MgO-TiO_2 in air after Woermann et al. [2]

For the phase relations in the sub-solidus region of the system FeO-Fe_2O_3-MgO-TiO_2, see also Speidel [3] and Borowiec, Rosenqvist [4].

References

[1] Johnson, R. E., E. Woermann, A. Muan: Am. J. Sci. 271 (1971) No. 3, p. 278/92

[2] Woermann, E., B. Brezny, A. Muan: Am. J. Sci. 267A (1969), p. 463/79

[3] Speidel, D. H.: Am. J. Sci. 268 (1970) No. 4, p. 341/53

[4] Borowiec, K., T. Rosenqvist: Scand. J. Metall. 14 (1985), p. 33/43

FeO_x-MnO-P_2O_5

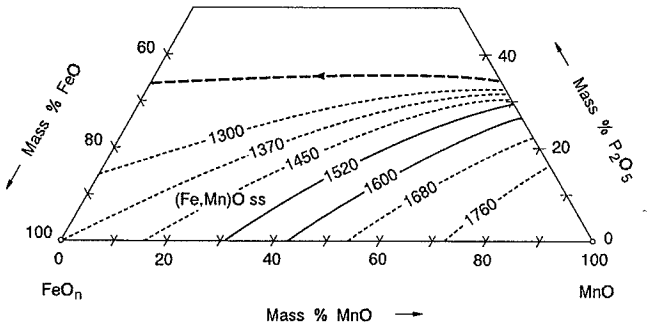


Fig. 3.285. The part of the liquidus surface in the system FeO_n-MnO-P_2O_5 in contact with metallic iron after Fischer, Fleischer [1].

References

[1] Fischer, W. A., H.-J. Fleischer: Arch. Eisenhüttenwes. 36 (1965) No. 11, p. 791/8

FeO_x-MnO_x-SiO_2

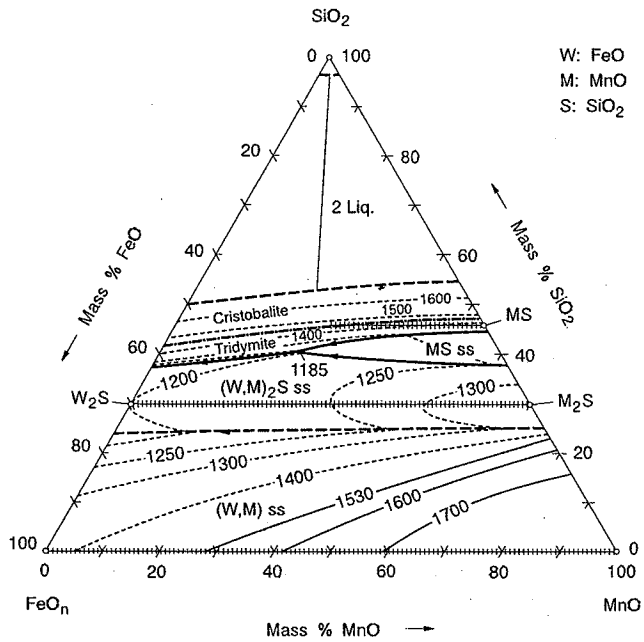


Fig. 3.286. Liquidus surface in the system FeO_n-MnO-SiO_2 in contact with metallic iron based mainly on the results of Riboud, Muan [1], Fischer, Bardenheuer [2] and Schenck, Wiesner [3].

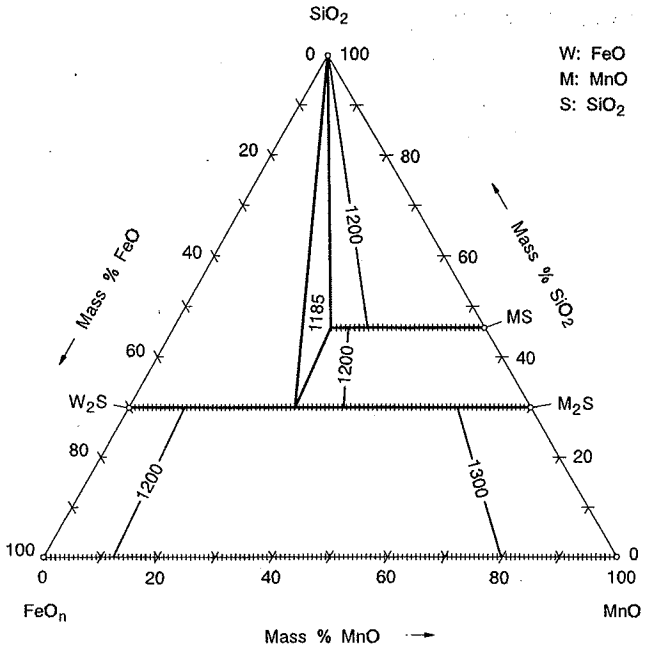


Fig. 3.287. Solidus surface in the system FeO-MnO-SiO_2 after Muan, Osborn [4]. For the 1150 °C isothermal section with oxygen isobars, see Schwerdtfeger, Muan [5].

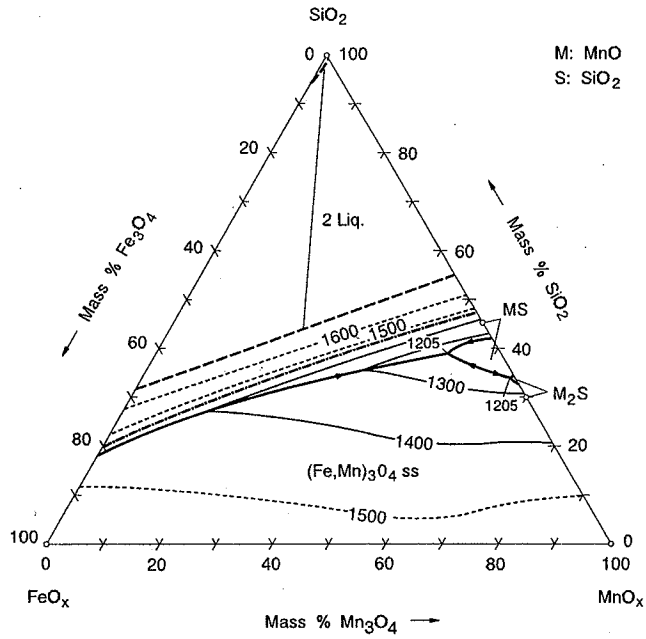


Fig. 3.288. Liquidus surface in the system FeO_x-MnO_x-SiO_2 in air, projected on the plane FeO·Fe_2O_3-MnO·Mn_2O_3-SiO_2 after Muan, Somiya [6].

For oxygen potential diagram at 1600 °C, see Cameron [7].

References

[1] Riboud, P. V., A. Muan: Trans. Metall. Soc. AIME 224 (1962), p. 27/33

[2] Fischer, W. A., P. W. Bardenheuer: Arch. Eisenhüttenwes. 39 (1968) No. 8, p. 559/70

[3] Schenck, H., G. Wiesner: Arch. Eisenhüttenwes. 27 (1956) No. 1, p. 1/12

[4] Muan, A., E. F. Osborn: Phase Equilibria Among Oxides in Steelmaking, Ed.: Addison- Wesley Publishing Company, Inc., Reading, Massachusetts, (1965)

[5] Schwerdtfeger, K., A. Muan: Trans. Metall. Soc. AIME 236 (1966) No. 2, p. 201/11

[6] Muan, A., S. Somiya: Am. Mineral. 46 (1961) No. 3-4, p. 364/78

[7] Cameron, D. I.: Trans. Metall. Soc. AIME 224 (1962) No. 12, p. 1285/7

FeO_x-MnO_x-TiO_2

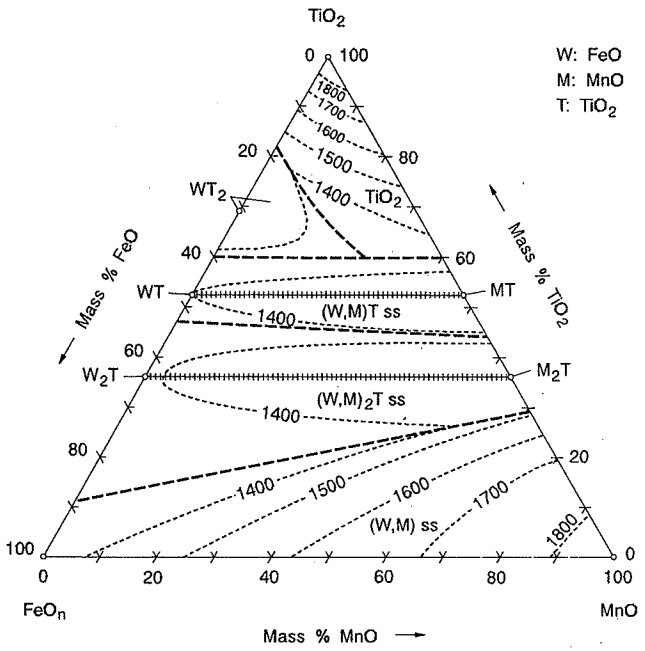


Fig. 3.289. Tentative liquidus surface in the FeO_n-MnO-TiO_2 system based on the results of Grieve, White [1] and adjusted to recommended version of lower-order systems.

Complete solubility between Fe_2TiO_4 and $MnFe_2O_4$ compositions between 1100 and 1300 °C under a controlled atmosphere has been reported by Shchepetkin et al. [2, 3]. For further studies of the phase equilibria in the sub-solidus region of the system, see Grey et al. [4] and Merritt [5, 6].

References

[1] Grieve, J., J. White: J. Roy. Tech. Coll. (Glasgow) 4 (1940), p. 660/70

[2] Shchepetkin, A. A., R. G. Zakharov, G. I. Chufarov: Izv. Akad. Nauk SSSR, Neorg. Mater. 5 (1969) No. 11, p. 1662/5

[3] Shchepetkin, A. A., V. I. Divinin, R. G. Zakharov, G. I. Chufarov: Izv. Akad. Nauk SSSR, Neorg. Mater. 6 (1970) No. 8, p. 1470/4

[4] Grey, I. E., A. F. Reid, D. G. Jones: Inst. Min. Metall., Trans., Sect. C 83 (1974) No. 6, p. C105/11

[5] Merritt, R. R.: J. Solid State Chem. 43 (1982) No. 3, p. 267/70

[6] Merritt, R. R.: J. Solid State Chem. 59 (1985) No. 2, p. 254/8

FeO_x-Na_2O-SiO_2

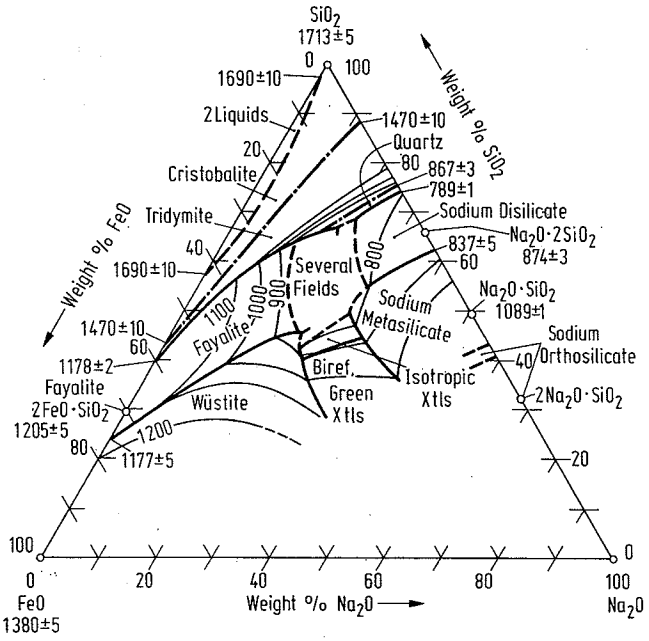


Fig. 3.290. Liquidus surface in the system FeO_n-Na_2O-SiO_2 according to preliminary results of Schairer et al. [1]. The composition of several ternary compounds was not specified. Previously, the compound $Na_2O{\cdot}FeO{\cdot}SiO_2$, melting incongruently at 976 °C, was reported by Carter, Ibrahim [2]. For the isothermal section at 1000 °C, see Hoge et al. [3].

The phase equilibria in the FeO_x-Na_2O-SiO_2 system in air have been investigated by Bowen et al. [4], Collins, Mulay [5], Bogacz et al. [6] and Grey, Li [7].

References

[1] Schairer, J. F., H. S. Yoder H. S., A. G. Keene: Carnegie Inst. Washington, Year Book 53 (1954), p. 123/5

[2] Carter, P. T., M. Ibrahim: J. Soc. Glass Technol. 36 (1952), p. 142/63

[3] Hoge, C. E., J. J. Brennah, J. A. Pask: J. Am. Ceram. Soc. 56 (1973) No. 2, p. 51/4

[4] Bowen, N. L., J. F. Schairer, H. W. Willems: Am. J. Sci., 5th Ser. 20 (1930) No. 120, p. 405/55

[5] Collins, D. W., L. N. Mulay: J. Am. Ceram. Soc. 53 (1970) No. 2, p. 74/6

[6] Bogacz, A., J. Gospos, J. Kalinowska, C. Mazanek: Pr. Nauk. Inst. Chem. Nieorg. Metal. Pierwiastkow Rzadkich Politech. Wroclaw. 27 (1975), p. 31/42

[7] Grey, I. E., C. Li: J. Solid State Chem. 69 (1987), p. 116/25

FeO_x-SiO_2-TiO_2

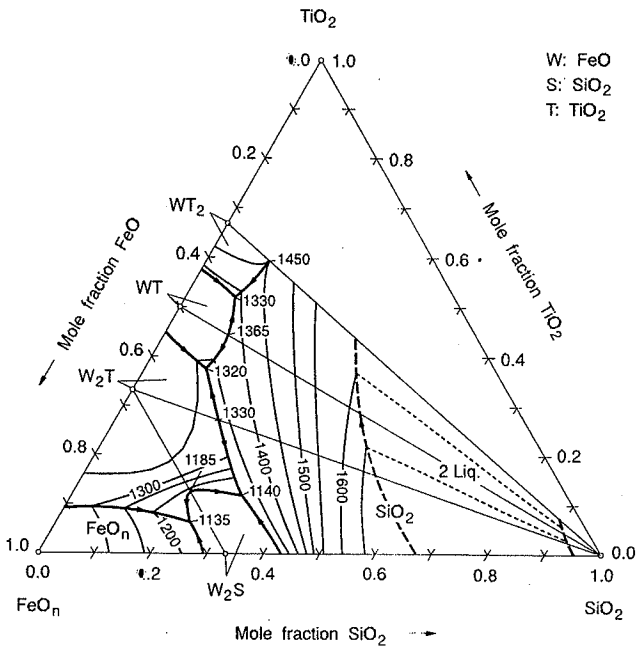


Fig. 3.291. Liquidus surface and sub-solidus equilibria in the system FeO_n-SiO_2-TiO_2 under reducing conditions after Ghita, Bell [1].

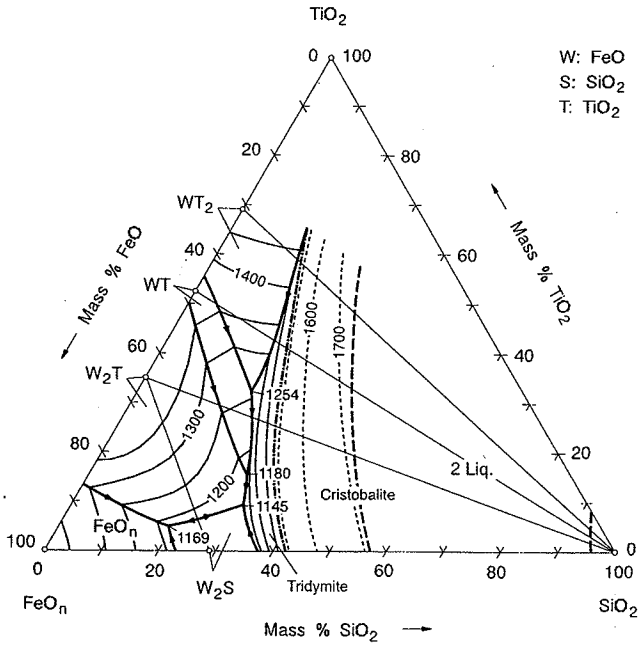


Fig. 3.292. Liquidus surface and sub-solidus equilibria in the system FeO_n-SiO_2-TiO_2 under reducing conditions according to Lamprecht, Woermann [2] and Woermann [3].

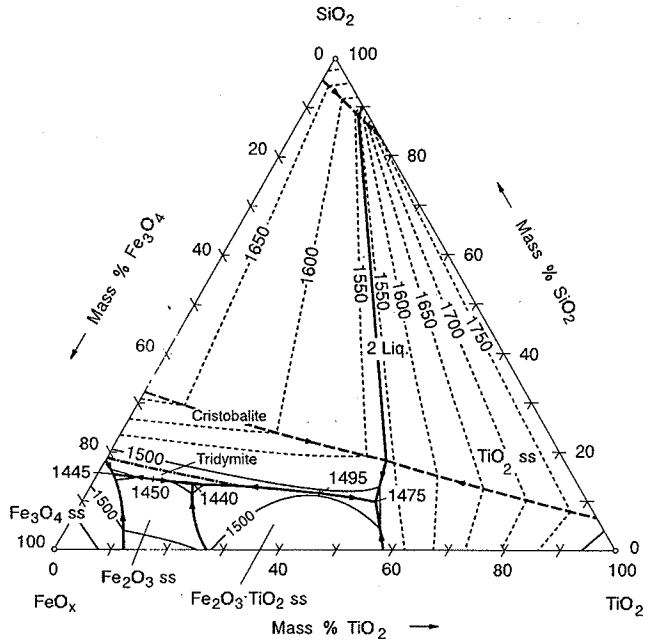


Fig. 3.293. Liquidus surface in the system FeO_x-SiO_2-TiO_2 in air projected on the Fe_3O_4-SiO_2-TiO_2 section after MacChesney, Muan [4].

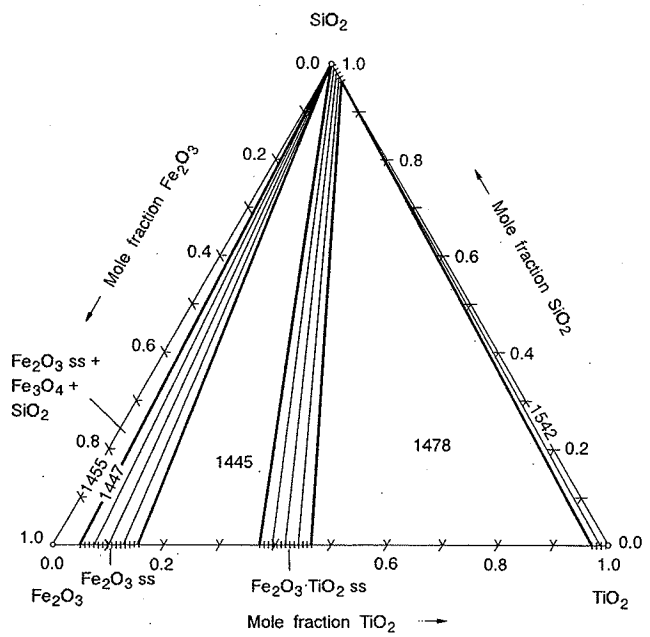


Fig. 3.294. Solidus surface in the system FeO_x-SiO_2-TiO_2 in air after Woermann [3].

For space representation of the liquidus relations in the system FeO-Fe_2O_3-SiO_2-TiO_2 in air in the vicinity of FeO·Fe_2O_3-SiO_2-TiO_2 sections, see original paper by MacChesney, Muan [4]. Recently, liquidus temperatures in the FeO_x-rich corner of the system for pO_2 pressures between $2 \cdot 10^{-2}$ and 10^{-6} atm have been reported by Ghita, Bell [5].

References

[1] Ghita, I., H. B. Bell: Can. Metall. Q. 21 (1982) No. 4, p. 347/51
[2] Lamprecht, A., E. Woermann: Naturwissenschaften 57 (1970) No. 1, p. 191
[3] Woermann, E.: private communication
[4] MacChesney, J. B., A. Muan: J. Am. Ceram. Soc. 43 (1960) No. 11, p. 586/91
[5] Ghita, I., H. B. Bell: Can. Metall. Q. 25 (1986) No. 1, p. 45/9

FeO_x-SiO_2-ZrO_2

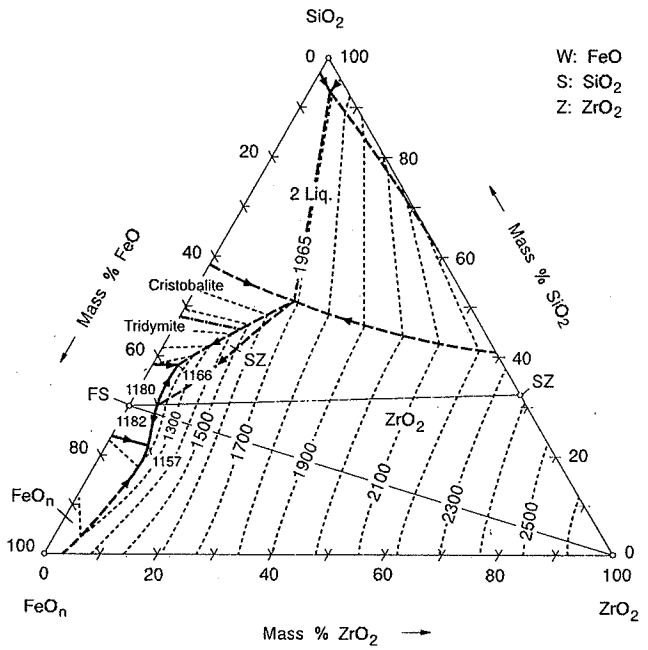


Fig. 3.295. Liquidus surface in the FeO_n-SiO_2-ZrO_2 system after Wells [1] as redrawn by Jones et al. [2].

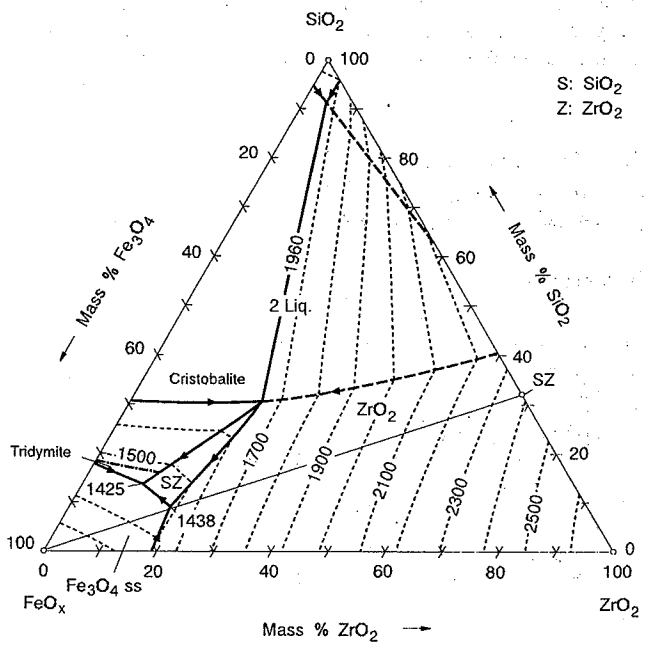


Fig. 3.296. Liquidus surface in the FeO_x-SiO_2-ZrO_2 system in air according to Jones et al. [2].

For space representation of liquidus relations, invariant points and crystallisation paths in the system FeO-Fe_2O_3-SiO_2-ZrO_2, see original paper by Jones et al. [2].

References

[1] Wells, R. G.: Ph.D. Dissertation, University of Michigan, Ann Arbor, Michigan, (1960)
[2] Jones, T. S., S. Kimura, A. Muan: J. Am. Ceram. Soc. 50 (1967) No. 3, p. 137/42

K_2O-Na_2O-P_2O_5

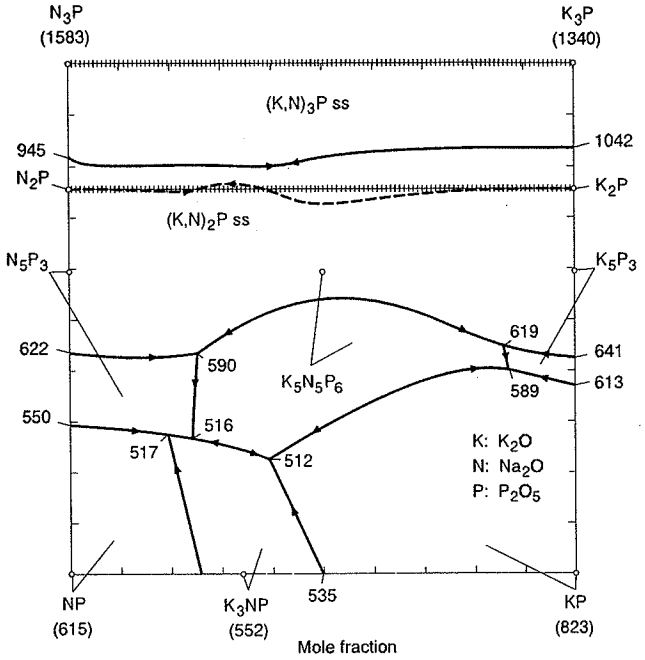


Fig. 3.297. Liquidus surface in the $K_2O{\cdot}P_2O_5$-$Na_2O{\cdot}P_2O_5$-$3K_2O{\cdot}P_2O_5$-$3Na_2O{\cdot}P_2O_5$ sub-system after Morey [1] and Morey et al. [2] as revised by Markina, Voskresenskaya [4] and Bukhalova, Mardirosova [3]. Complete solid solubility on the $2K_2O{\cdot}P_2O_5$-$2Na_2O{\cdot}P_2O_5$ section has been reported [1-3]. The dashed line shows the temperature maximum on the liquidus surface of the $2(K,Na)_2O{\cdot}P_2O_5$ solid solution (both end-members, ie. $2K_2O{\cdot}P_2O_5$ and $2Na_2O{\cdot}P_2O_5$ melt congruently). For the phase relations on the $K_2O{\cdot}P_2O_5$-$Na_2O{\cdot}P_2O_5$ section, see the original paper by Bukhalova, Mardirosova [3]. The compound $K_2O{\cdot}3Na_2O{\cdot}4P_2O_5$, which melts incongruently, has been reported previously by Morey et al. [2] to exist on the $K_2O{\cdot}P_2O_5$-$Na_2O{\cdot}P_2O_5$ section.

References

[1] Morey, G. W.: J. Am. Chem. Soc. 76 (1954) No. 18, p. 4724/32
[2] Morey, G. W., F. R. Boyd, Jr., J. L. England, W. T. Chen: J. Am. Chem. Soc. 77 (1955) No. 10, p. 5003/11
[3] Bukhalova, G. A., I. A. Mardirosova: Zh. Neorg. Khim. 11 (1966) No. 4, p. 495/8
[4] Markina, I. B., N. K. Voskresenskaya: Russ. J. Inorg. Chem. 14 (1969) No. 8, p. 1188/91

Li_2O-Na_2O-SiO_2

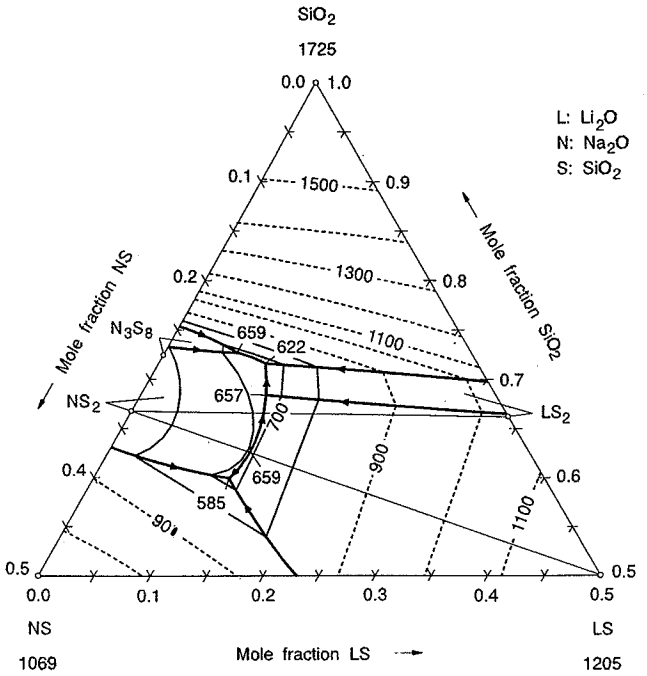


Fig. 3.298. Liquidus surface in the $Li_2O{\cdot}SiO_2$-$Na_2O{\cdot}SiO_2$-SiO_2 sub-system after West [1, 2].

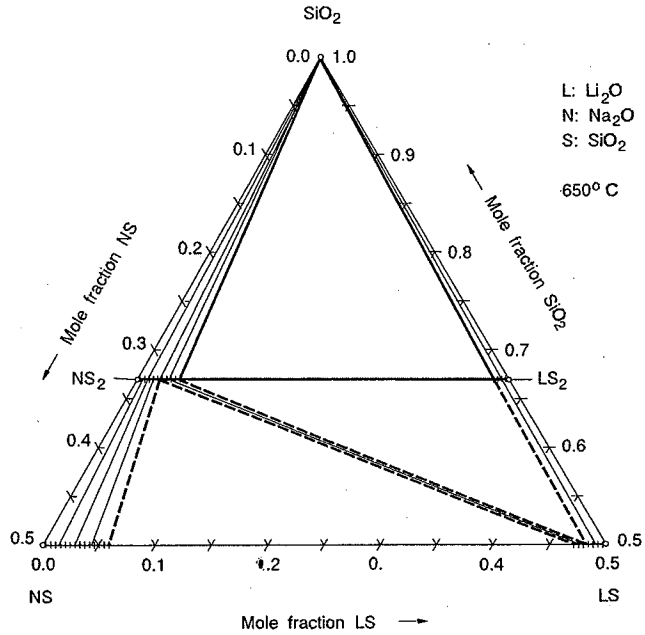


Fig. 3.299. Isothermal section through the sub-system $Li_2O{\cdot}SiO_2$-$Na_2O{\cdot}SiO_2$-SiO_2 at 620 °C after West [1, 2].

The compounds $Na_2O{\cdot}Li_2O{\cdot}2SiO_2$, $2Na_2O{\cdot}Li_2O{\cdot}3SiO_3$ $Na_2O{\cdot}2Li_2O{\cdot}3SiO_2$ and $Na_2O{\cdot}Li_2O{\cdot}2SiO_2$ reported earlier by Kracek [3] and Bergman et al. [4] to exist on the section $Na_2O{\cdot}SiO_2$-$Li_2O{\cdot}SiO_2$ have been identified by West [2] as an extended solution phase based on the end-members $Li_2O{\cdot}SiO_2$ and $Na_2O{\cdot}SiO_2$. For this section see original paper by West [1, 2].

References

[1] West, A. R.: J. Am. Ceram. Soc. 59 (1976) No. 3-4, p. 118/21
[2] West, A. R.: J. Am. Ceram. Soc. 59 (1976) No. 3-4, p. 124/7
[3] Kracek, F. C.: J. Am. Chem. Soc. 31 (1939) No. 10, p. 2863/77
[4] Bergman, A. G., A. K. Nesterova, N. A. Bychkova: Dokl. Akad. Nauk SSSR 101 (1955) No. 3, p. 483/6

$MgO\text{-}MnO_x\text{-}SiO_2$

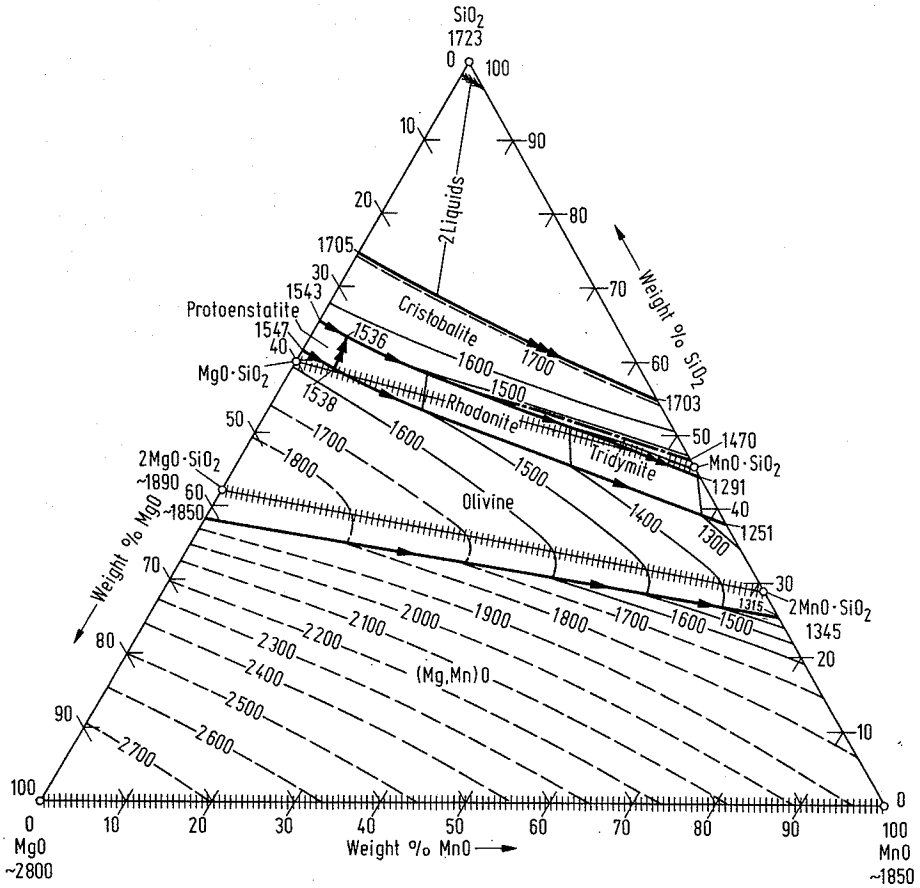


Fig. 3.300. Liquidus surface in the $MgO\text{-}MnO_x\text{-}SiO_2$ system in an atmosphere consisting of CO_2 and H_2 in the ratio 5:1 after Glasser, Osborn [1]. For the liquid-solid equilibria between 1533 and 1540 °C in the vicinity of the $MgO\text{-}SiO_2$ edge, see original paper.

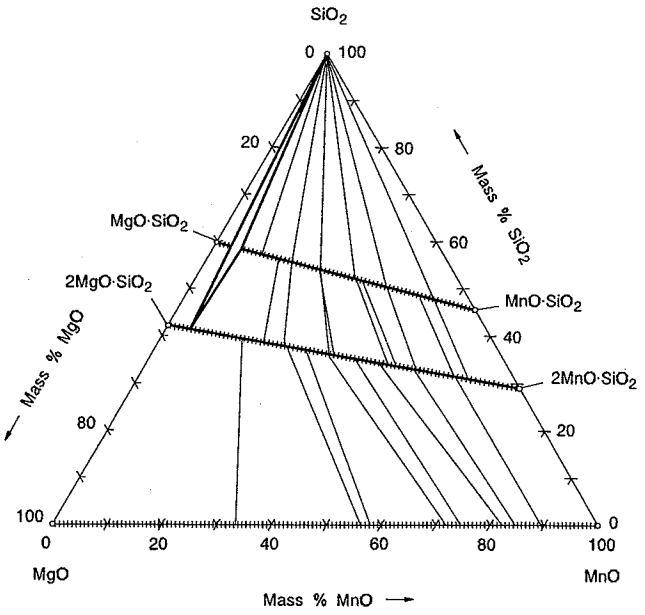


Fig. 3.301. Solidus surface in the $MgO\text{-}MnO_x\text{-}SiO_2$ system in an atmosphere consisting of CO_2 and H_2 in the ratio 5:1, (at oxygen partial pressure varying approx. from $pO_2=10^{-10}$ at 1130 °C to $pO_2=10^{-6}$ atm at 1555 °C) according to Glasser, Osborn [1], showing tie lines joining coexisting solution phases slightly below solidus temperatures.

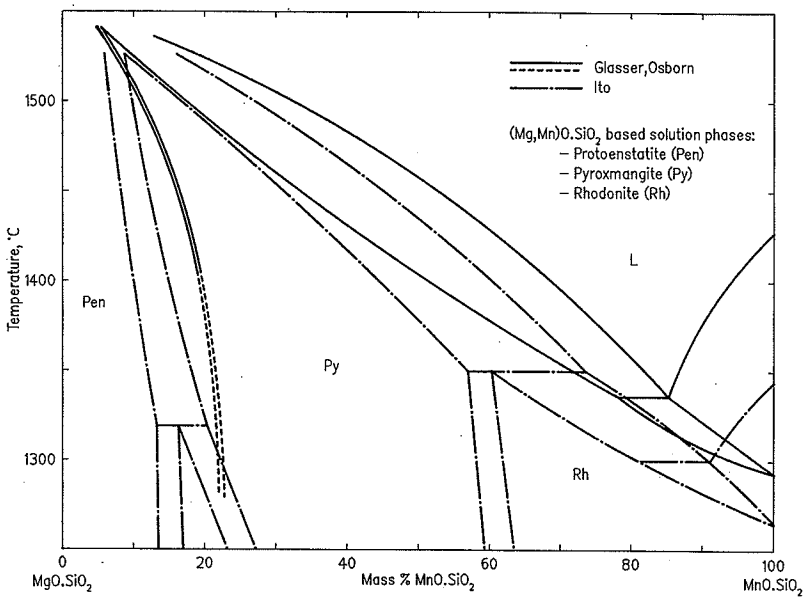


Fig. 3.302. Composition section $MgO{\cdot}SiO_2$-$MnO{\cdot}SiO_2$ after Glasser, Osborn [1] and Ito [2]. The dash-dot lines on the figure represent the results obtained by Ito [2] in air. In particular, an additional solution phase (pyroxmangite) between the $MnO{\cdot}SiO_2$-based solid solution (rhodonite) and the $MgO{\cdot}SiO_2$-based solid solution (protoenstatite) has been found [2]. Only a small amount of Mn_2O_3, due to atmospheric air, and not exceeding 1.5 mass % in the vicinity of the $MnO{\cdot}SiO_2$ composition, has been detected by Ito [2]. The other binary section $2MgO{\cdot}SiO_2$-$2MnO{\cdot}SiO_2$, is characterised by complete solid solution between the end members [1].

References

[1] Glasser, F. P., E. F. Osborn: J. Am. Ceram. Soc. 43 (1969) No. 3, p. 132/40

[2] Ito, J.: Am. Mineral. 57 (1972) No. 5-6, p. 865/76

MgO-P_2O_5-SiO_2

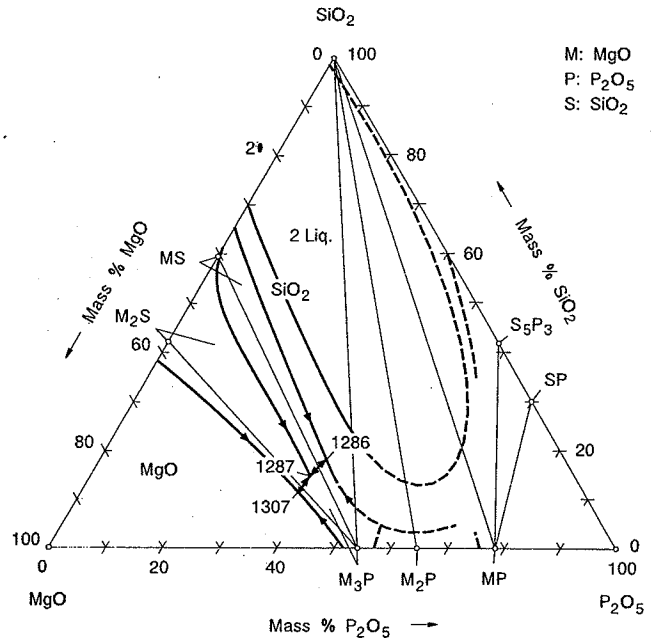


Fig. 3.303. Liquidus surface in the sub-system MgO-$3MgO{\cdot}P_2O_5$-SiO_2 according to Wojciechowska, Berak [1] and compatibility relations across the entire system as reported by Mihailescu [2].

References

1] Wojciechowska, J., J. Berak: Roczniki Chem. 33 (1959) No. 1-2, p. 21/8

[2] Mihailescu, I.: O. Mater. Constr. /Bucharest/ 17 (1987) No. 1, p. 41/3

$MgO-SiO_2-TiO_2$

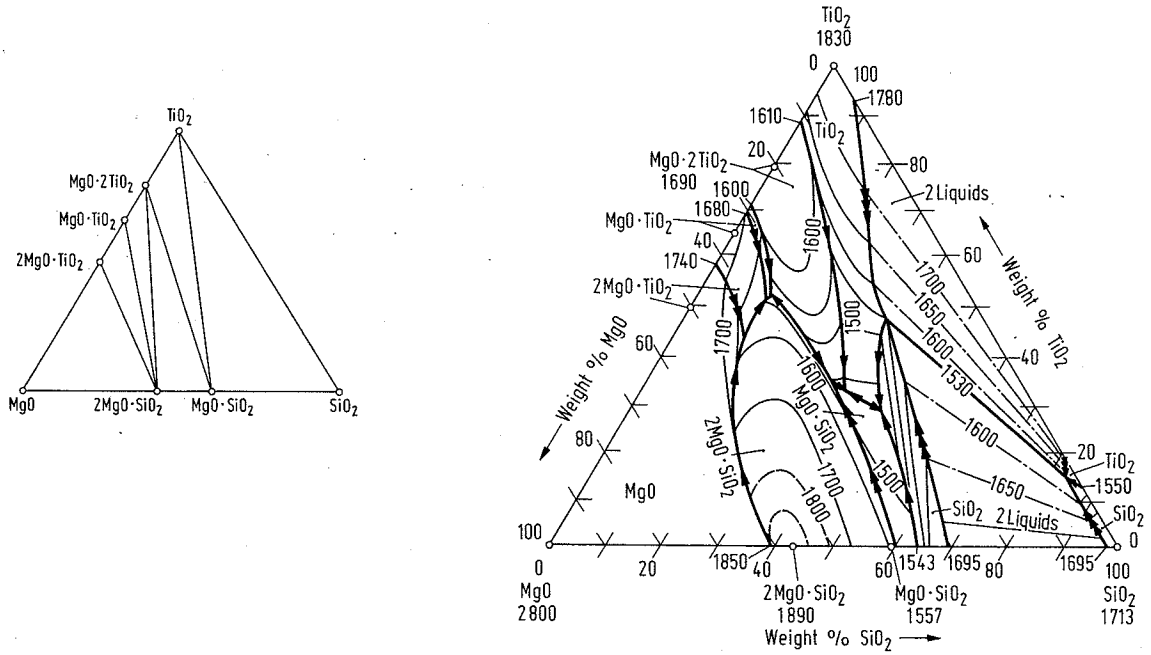


Fig. 3.304. Liquidus surface and sub-solidus equilibria in the $MgO-SiO_2-TiO_2$ system after Massazza, Sirchia [1]. For composition sections, confirming generally the results of Massazza, Sirchia [1], see also McGregor [2] and Panek et al. [3].

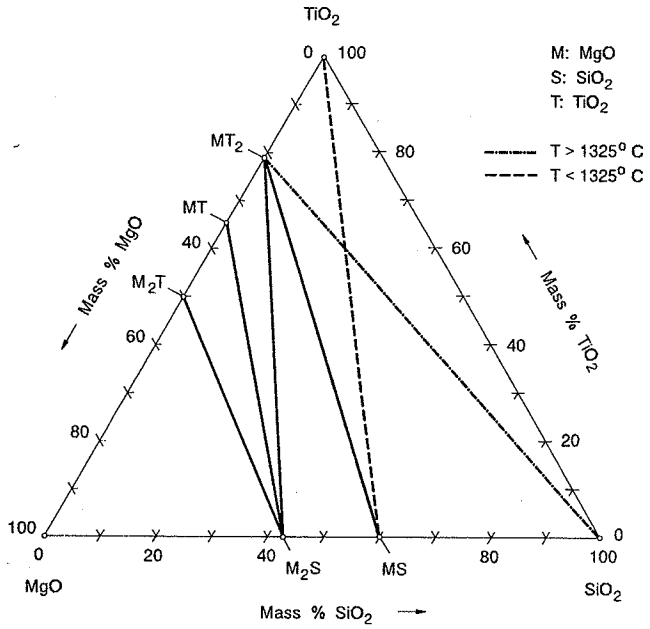


Fig. 3.305. Compatibility relations in the $MgO-SiO_2-TiO_2$ system after Woermann [4].

References

[1] Massazza, F., E. Sirchia: Chim. Ind., Milano 40 (1958) No. 6, p. 460/7
[2] McGregor, I. D.: Am. J. Sci. 267A (1969), p. 342/63
[3] Panek, Z., E. Kanclir, J. Staron, M. Kozlovsky, S. Palco: Silikaty 20 (1976) No. 1, p. 13/22
[4] Woermann, E.: private communication

$MnO_x-Na_2O-SiO_2$

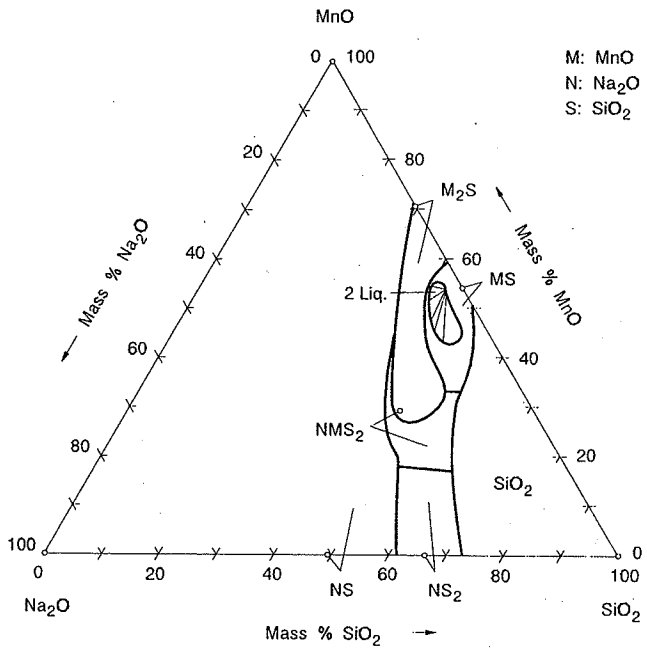


Fig. 3.306. Fields of primary crystallisation and two liquids region at 1200 °C in the SiO_2-rich region of the Na_2O-MnO-SiO_2 system after Hay et al. [1].

References

[1] Hay, R., P. T. Carter, S. K. Kabi: J. Soc. Glass Technol. 40 (1957), p. 429T/44T

Na_2O-SiO_2-V_2O_5

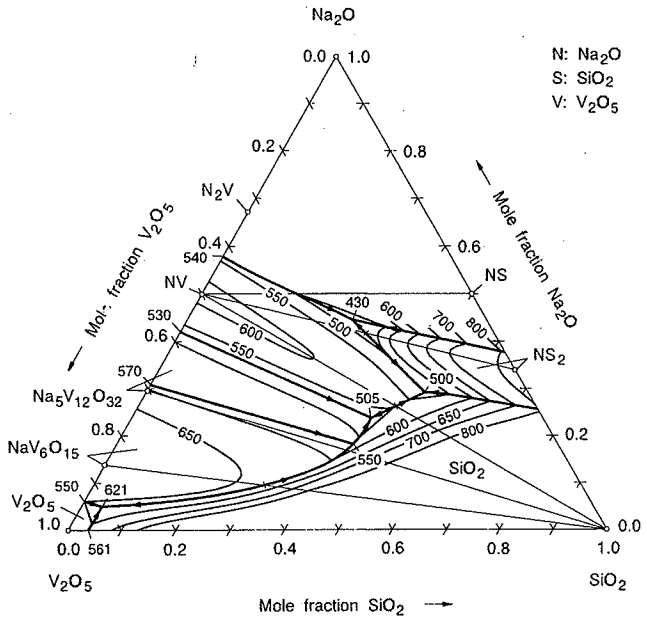


Fig. 3.307. Tentative liquidus surface and compatibility relations in the Na_2O-SiO_2-V_2O_5 system in air after Ingo et al. [1]. The composition section $Na_2O{\cdot}V_2O_5$-$Na_2O{\cdot}SiO_2$ has also been investigated by Fotiev et al. [2]. The possibility of existence of the $3Na_2O{\cdot}8SiO_2$ phase has not been excluded [1].

References

[1] Ingo, S., K. H. Karlsson, K. Heinanen: Scand. J. Metall. 10 (1981) No. 1, p. 45/6

[2] Fotiev, A. A., E. A. Buketov, N. Kh. Valikhanova, V. P. Malyshev: Zh. Prikl. Khim. /Leningrad/ 45 (1972) No. 11, p. 2381/5

2.2.4 Quaternary oxide systems

Al_2O_3-CaO-FeO_x-SiO_2

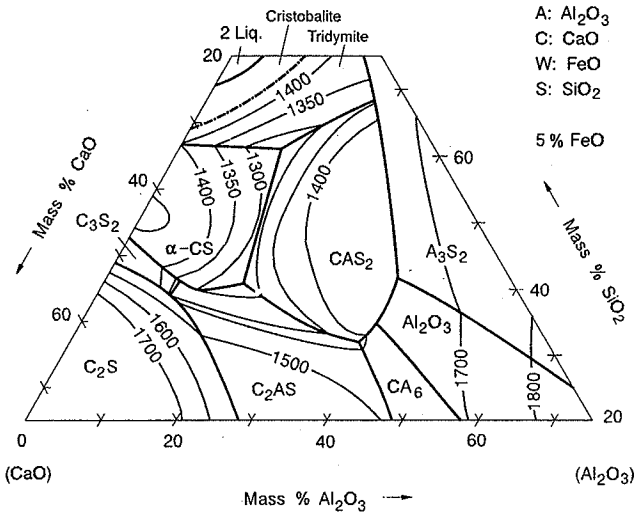


Fig. 3.308.

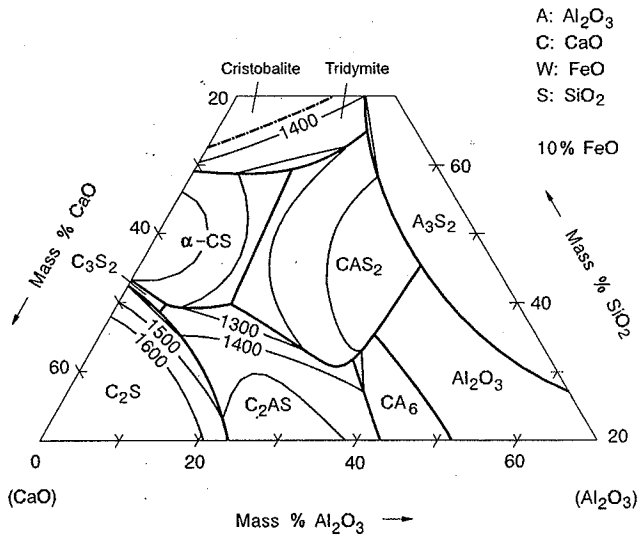


Fig. 3.309.

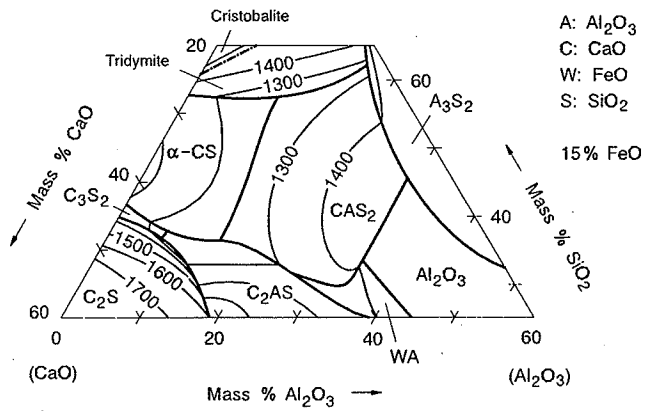


Fig. 3.310.

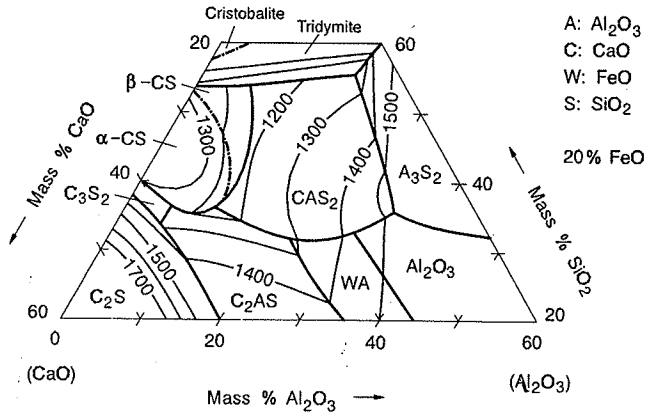


Fig. 3.311.

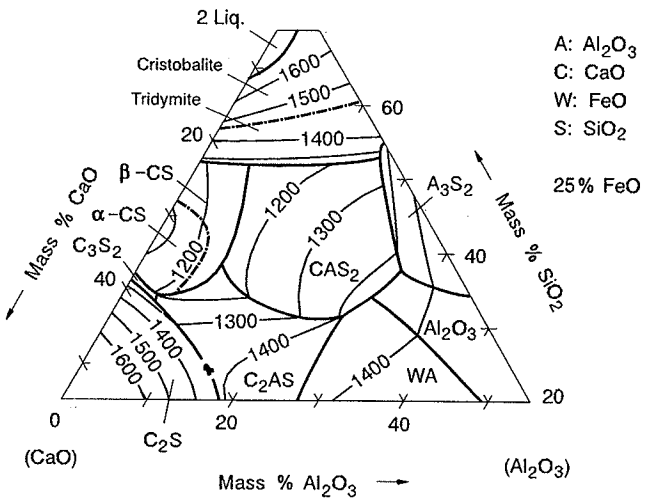


Fig. 3.312.

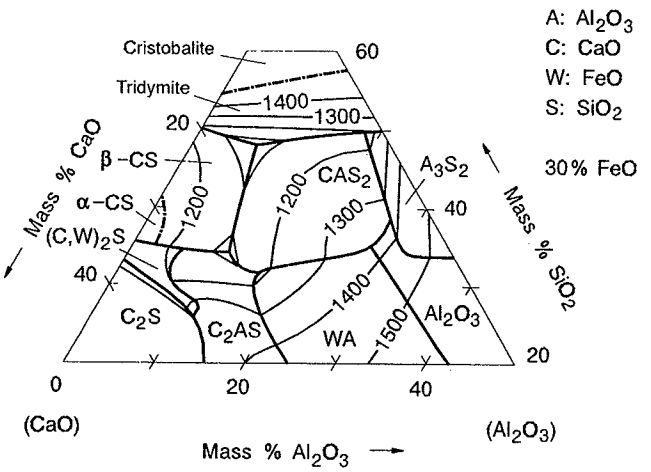


Fig. 3.313.

Figures 3.308 to 3.313. Tentative liquidus surfaces in the system Al_2O_3-CaO-FeO_x-SiO_2 with 5, 10, 15, 20, 25 and 30 mass % FeO (total iron oxide contents as re-calculated in equivalent FeO contents) after Kalmanovitch, Williamson [1] and Kalmanovitch et al. [2]. For the base system Al_2O_3-CaO-SiO_2, see Fig. 3.166.

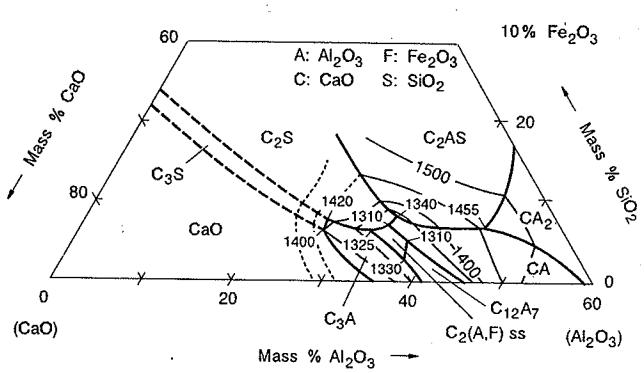


Fig. 3.314.

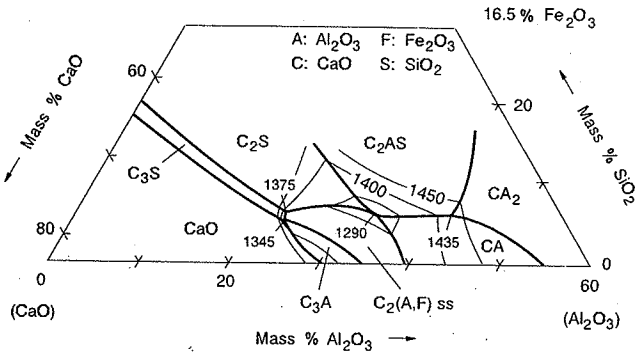


Fig. 3.315.

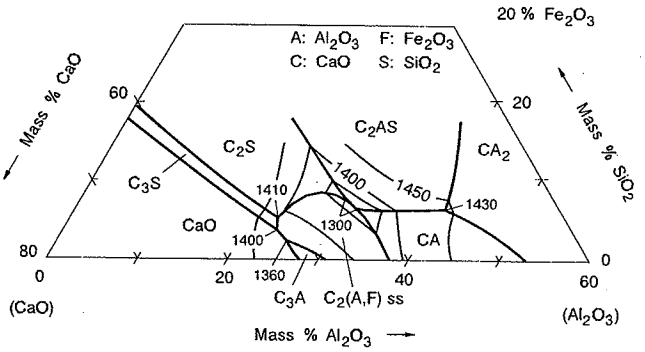


Fig. 3.316.

Figs. 3.314 to 3.316. Liquidus surface in the system Al_2O_3-CaO-FeO_x-SiO_2 in air with 10, 16,5 and 20 mass % Fe_2O_3 after Sorrentino, Glasser [3, 4]. For the space representation of the system, see original paper [3, 4].

Liquidus relations in numerous sub-systems of the Al_2O_3-CaO-FeO-SiO_2 system have been reported by Schairer [5] (SiO_2-CaO·Al_2O_3·2SiO_2-FeO, CaO·Al_2O_3·2SiO_2-Al_2O_3-FeO, CaO·SiO_2-CaO·Al_2O_3·2SiO_2-FeO, 2CaO·Al_2O_3·SiO_2-CaO·Al_2O_3·2SiO_2-FeO, CaO·SiO_2-2CaO·Al_2O_3·SiO_2-FeO) and Muan, Osborn [6] (2CaO·SiO_2-CaO·SiO_2-2CaO·Al_2O_3·SiO_2-FeO). Previously, some sub-systems of the Al_2O_3-CaO-FeO_x-SiO_2 system in air were investigated by Lea, Parker [7] and Swayze [8]. The phase relations in the sub-system FeO_x-SiO_2-CaO·Al_2O_3·2SiO_2 in air have been reported by Roeder, Osborn [9] and the sub-system Al_2O_3-Fe_2O_3-CaO·SiO_2 has been extensively investigated by Huckenholz et al. [10]. The central portion of the CaO-FeO_x-SiO_2 system at 5 mass % Al_2O_3 and at $pO_2=10^{-7}$ atm has been reported by Shigaki et al. [11]. The influence of Al_2O_3 on phase equilibria in the quaternary system has also been discussed by Yoon et al. [12]. For additional contributions concerning compounds in the Al_2O_3-CaO-FeO_x-SiO_2 system, see for instance Nurse, Midgley [13], Midgley [14], Ismatov et al. [15] and Model et al. [16].

References

[1] Kalmanovitch, D. P., J. Williamson: ACS Symp. Ser., 301/Miner. Matter Ash Coal/ (1986), p. 234/55
[2] Kalmanovitch, D. P., A. Sanyal, J. Williamson: J. Inst. Energy 59 (1986) No. 438, p. 20/3
[3] Sorrentino, F. P., F. P. Glasser: Trans. J. Br. Ceram. Soc. 74 (1975) No. 7, p. 253/6
[4] Sorrentino, F. P., F. P. Glasser: Trans. J. Br. Ceram. Soc. 75 (1976) No. 5, p. 95/103
[5] Schairer, J. S.: J. Am. Ceram. Soc. 25 (1942) No. 10, p. 241/74
[6] Muan, A., E. F. Osborn: Yearb. Am. Iron Steel Inst. (1951), p. 325/60
[7] Lea, F. M., T. W. Parker: Trans. Roy. Soc. /London/, Ser. A 234A (1934) No. 731, p. 1/42
[8] Swayze, M. A.: Am. J. Sci. 244 (1946) No. 1, p. 1/30
[9] Roeder, P. L., E. F. Osborn: Am. J. Sci. 264 (1966) No. 6, p. 428/480
[10] Huckenholz, H. G., W. Lindhuber, J. Springer: Neues Jahr. Mineral., Abh. 121 (1974) No. 2, p. 160/207
[11] Shigaki, I., M. Sawada, O. Tsuchiya, K. Yoshioka, T. Takahashi: Tetsu To Hagane 70 (1984) No. 16, p. 2208/15
[12] Yoon, S. J., Y. H. Cho, C. K. Yang: Taehan Kumsok Hakhoechi 26 (1988) No. 6, p. 552/60
[13] Nurse, R. W., H. G. Midgley: J. Iron Steel Inst. 174 (1953) No. 6, p. 121/31
[14] Midgley, H. G.: Trans. J. Br. Ceram. Soc. 66 (1967) No. 1, p. 1/13
[15] Ismatov, A. A., S. H. Azimov, B. M. Gulyamov, T. A. Ismatov: Izv. Akad. Nauk SSSR, Neorg. Mater. 22 (1986) No. 7, p. 1224/5
[16] Model, M. S., T. Y. Malysheva, V. Y. Lyadova, N. V. Chugunova, E. V. Vlasova, G. K. Astakhova: Izv. Akad. Nauk SSSR, Met. (1987) No. 2, p. 3/9

Al_2O_3-CaO-MgO-SiO_2

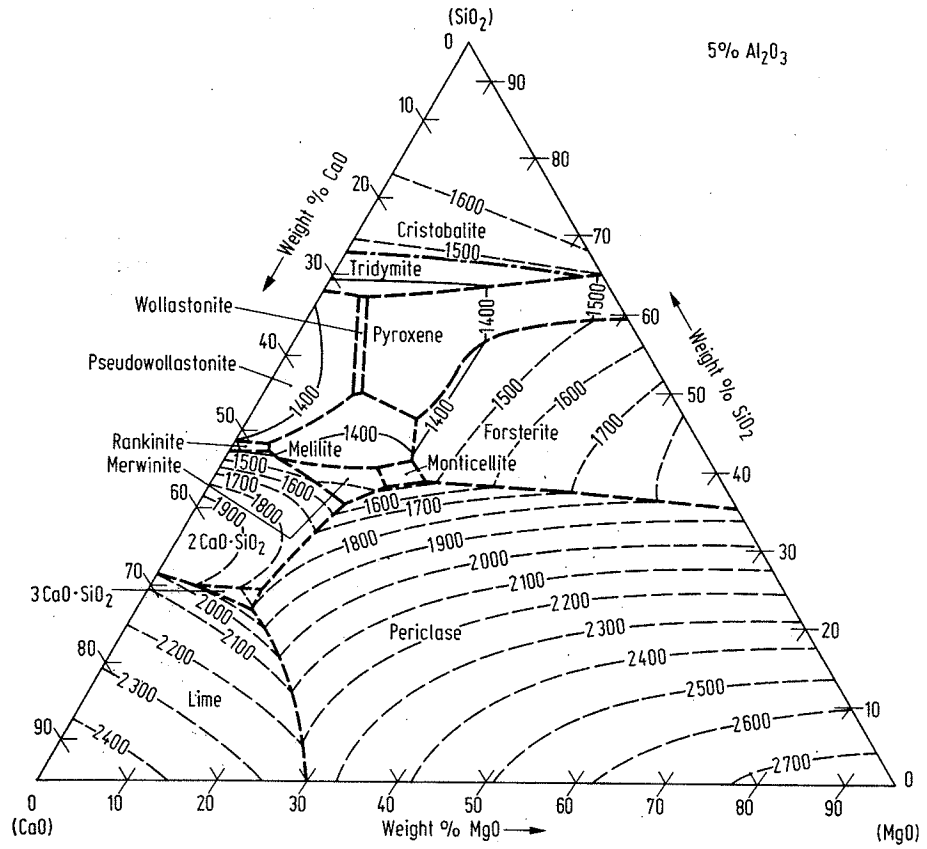


Fig. 3.317.

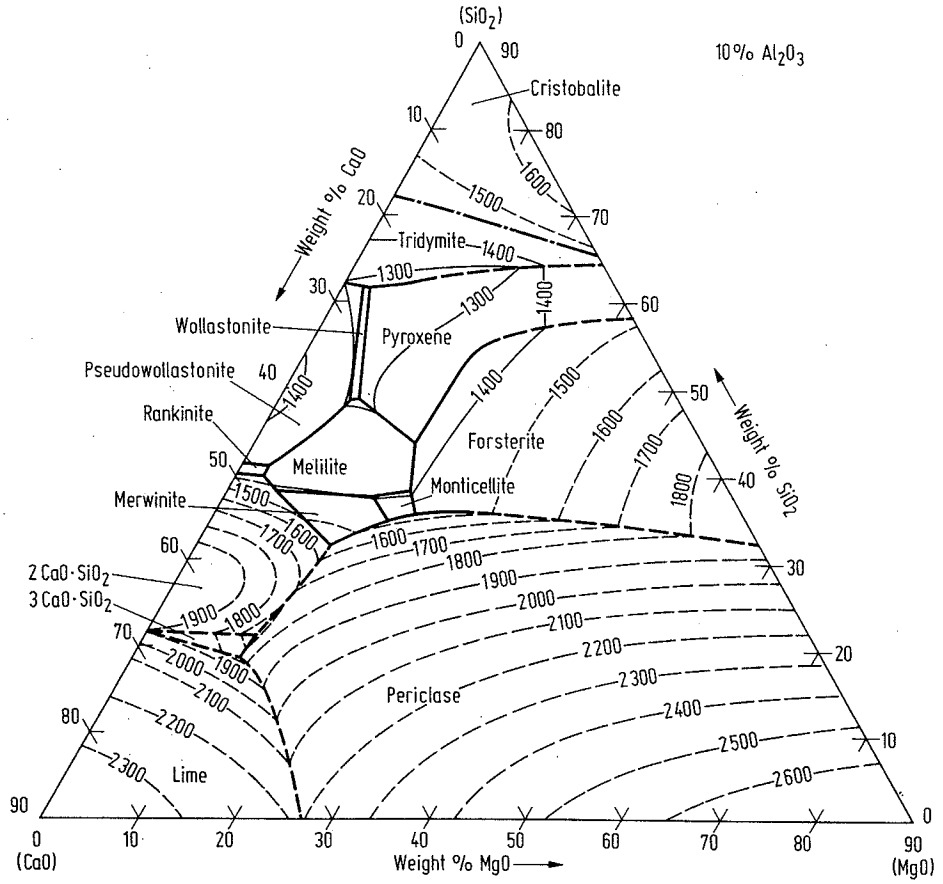


Fig. 3.318.

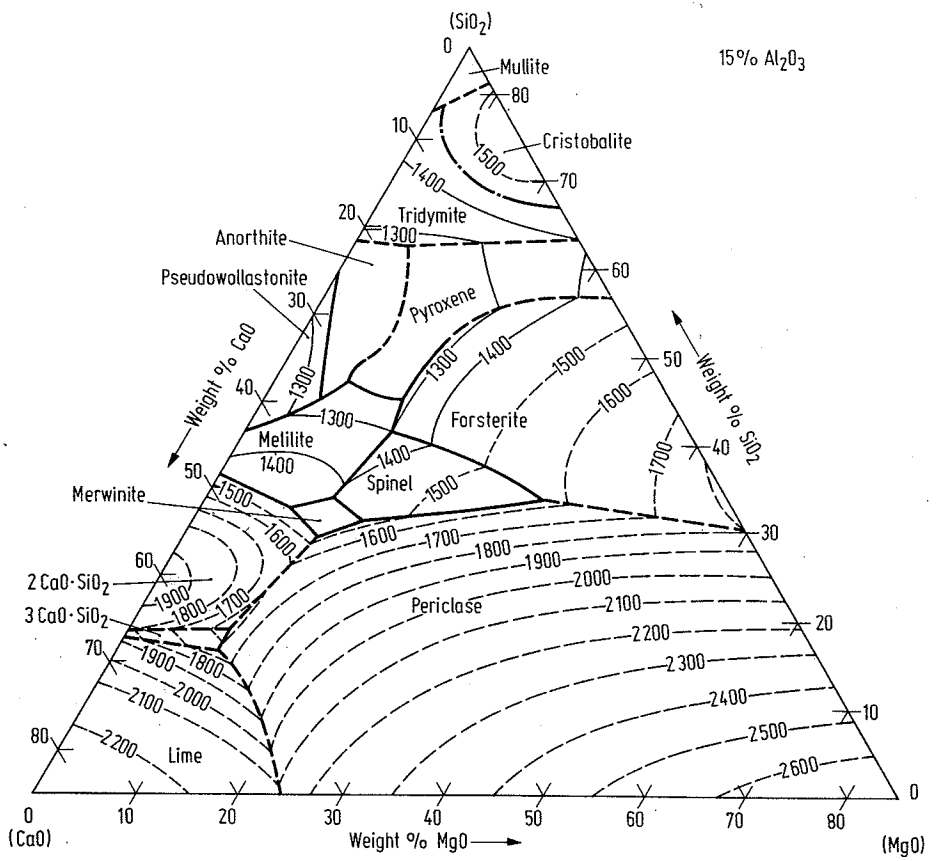


Fig. 3.319.

Figs. 3.317 to 3.323. Liquidus surface in the system Al_2O_3-CaO-MgO-SiO_2 with 5 to 35 mass % Al_2O_3 after Osborn et al. [1]. For the phase equilibria at solidus temperatures, see Osborn et al. [2]. For the base system CaO-MgO-SiO_2, see Fig. 3.249.

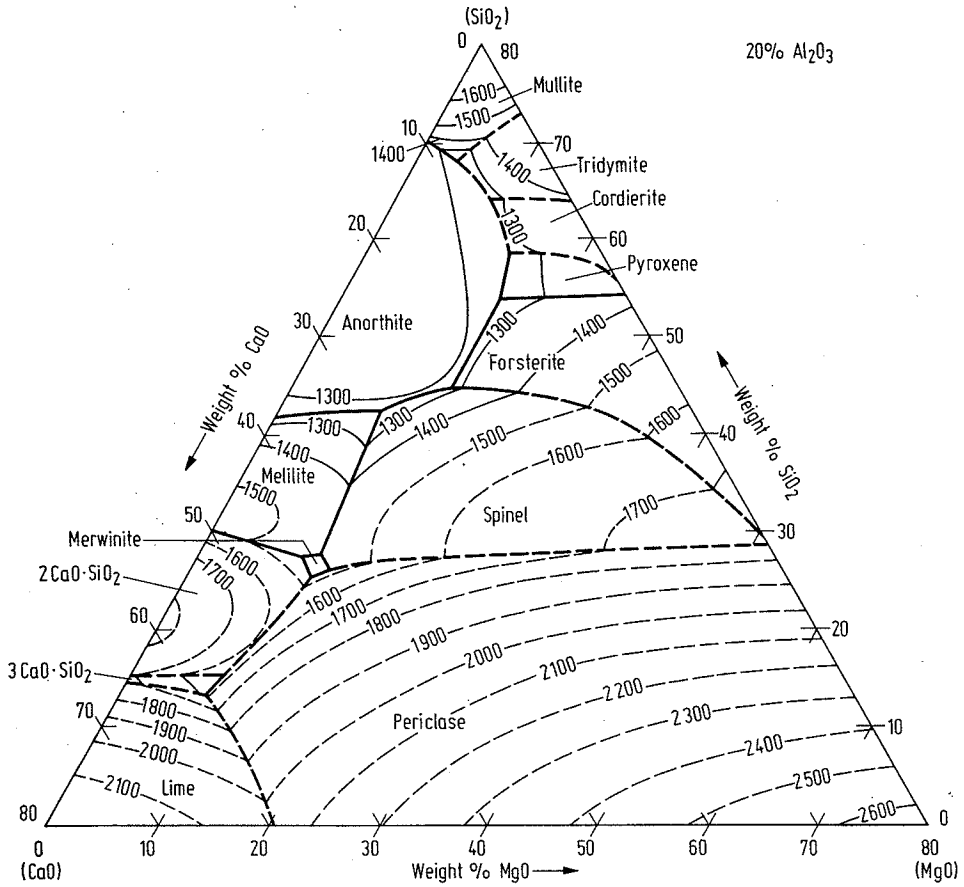


Fig. 3.320.

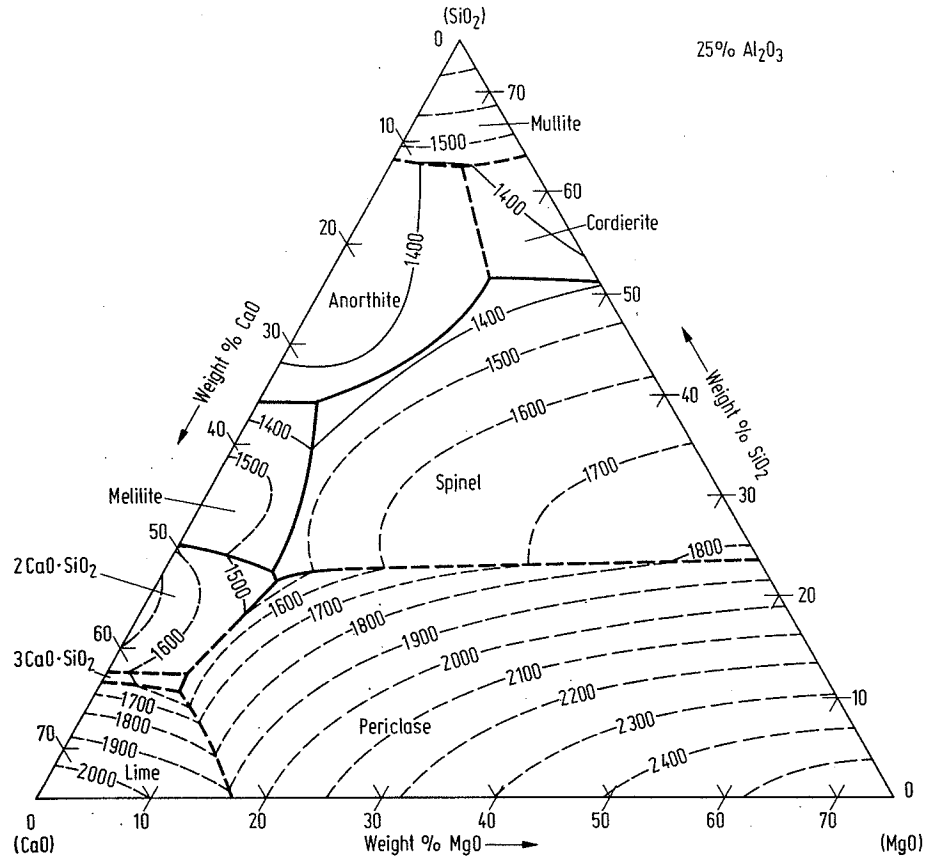


Fig. 3.321.

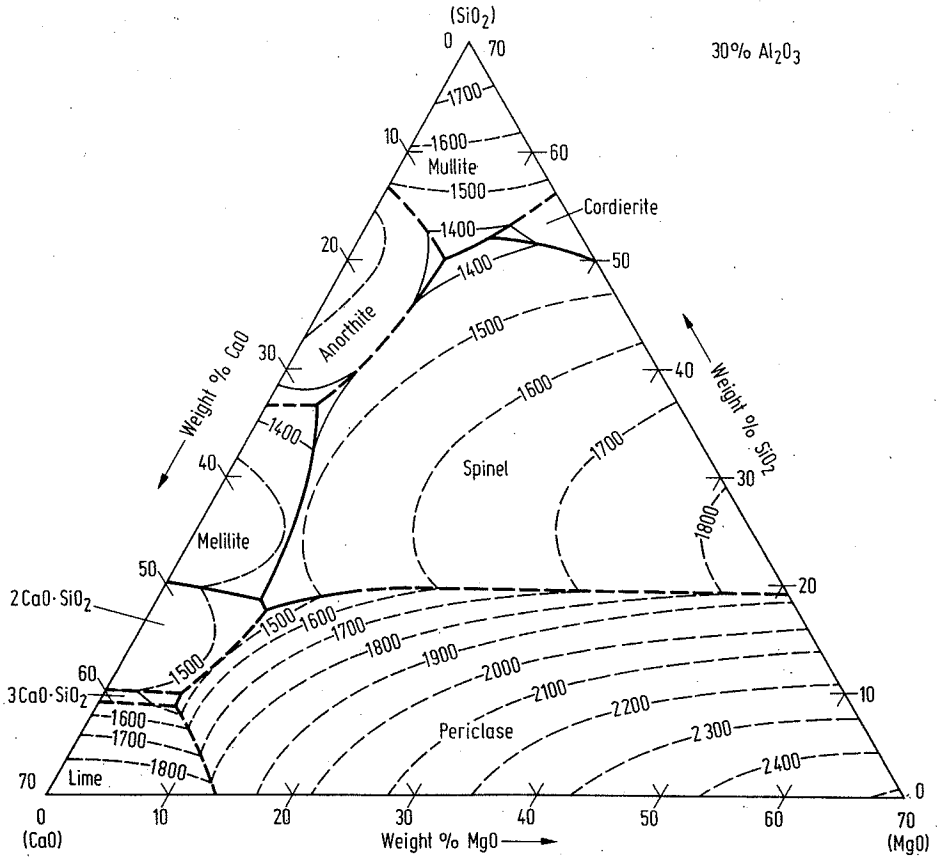


Fig. 3.322.

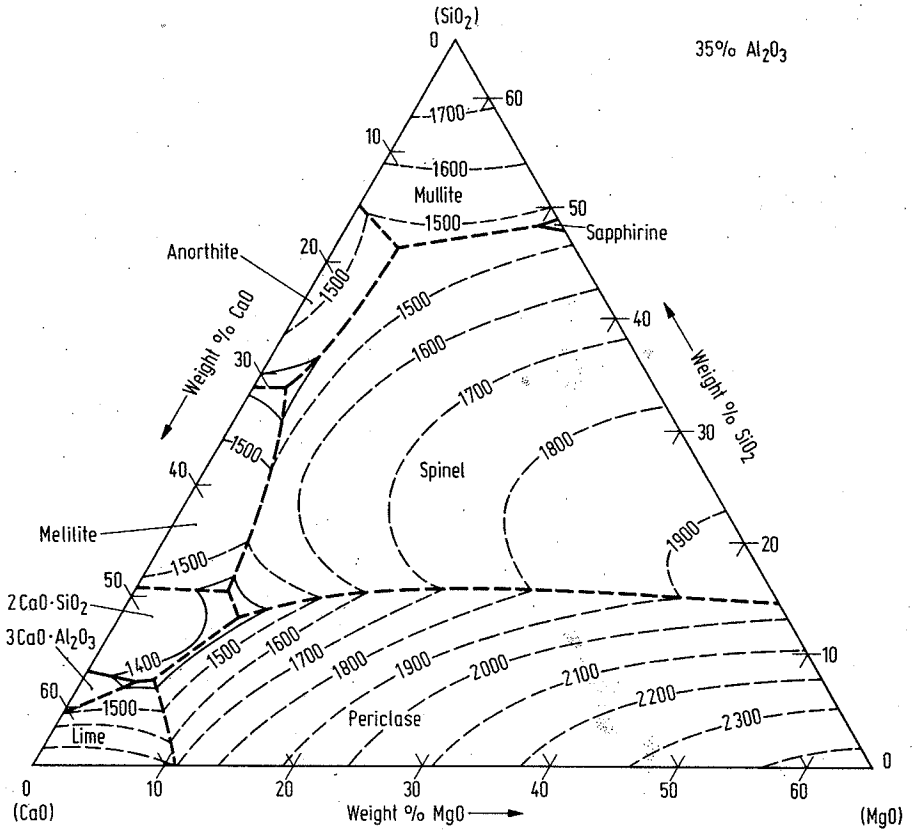


Fig. 3.323.

Figs. 3.317 to 3.323. Liquidus surface in the system Al_2O_3-CaO-MgO-SiO_2 with 5 to 35 mass % Al_2O_3 after Osborn et al. [1]. For the phase equilibria at solidus temperatures, see Osborn et al. [2]. For the base system CaO-MgO-SiO_2, see Fig. 3.249.

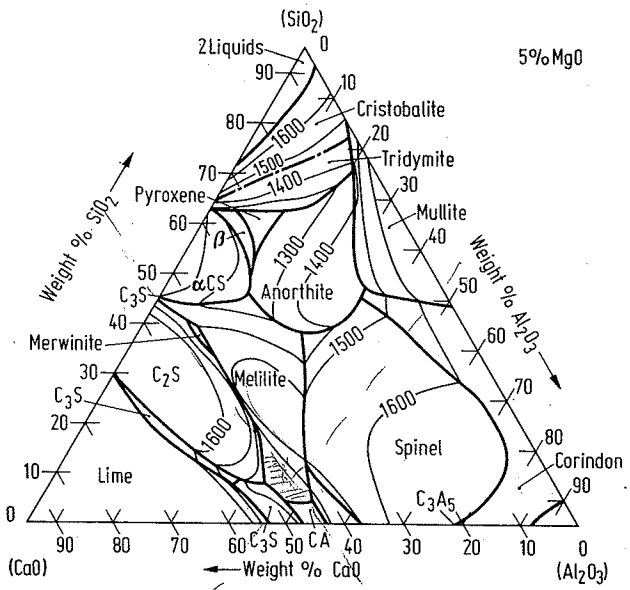


Fig. 3.324.

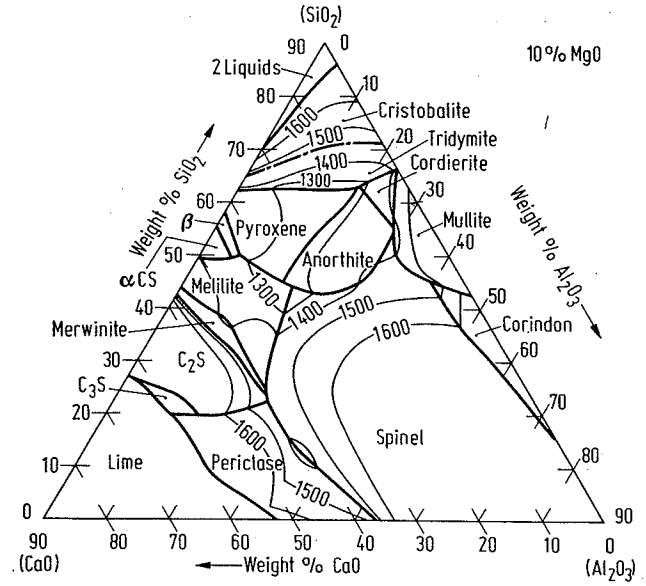


Fig. 3.325.

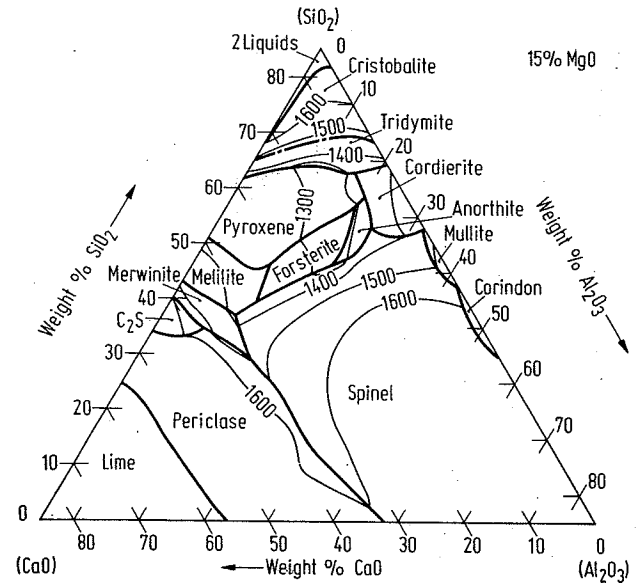


Fig. 3.326.

← **Figs. 3.324 to 3.326.** Liquidus surface in the system Al_2O_3-CaO-MgO-SiO_2 with 5, 10 and 15 mass % MgO after Cavalier, Sandreo-Dendon [3]. For the base system Al_2O_3-CaO-SiO_2, see Fig. 3.166.

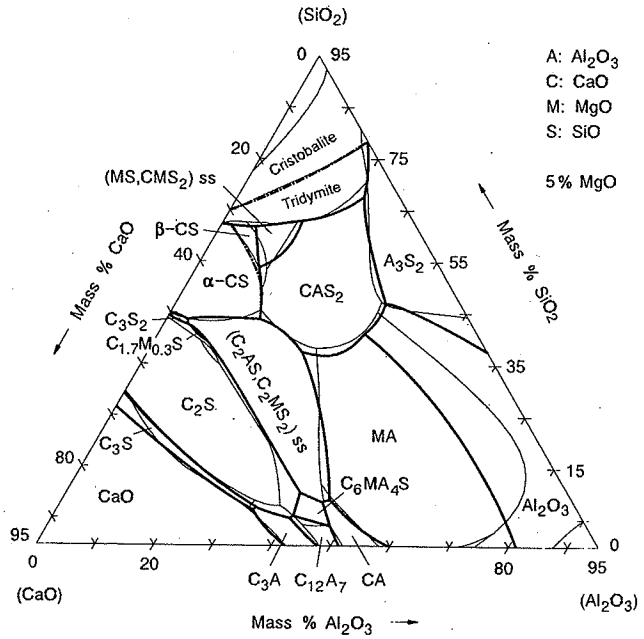


Fig. 3.327. Liquidus surface in the system Al_2O_3-CaO-MgO-SiO_2 with 5 mass % MgO after Gutt, Russel [4], as compared with phase boundaries determined previously in this plane by Cavalier, Sandreo-Dendon [3] (thin lines). For the base system Al_2O_3-CaO-SiO_2, see Fig. 3.166. Slightly different compositions of the quaternary phase, $6CaO.MgO.4Al_2O_3.SiO_2$, were reported by Glasser, Marr [5] and Kaprálik, Hanic [6]. An additional quaternary compound, $21CaO.7MgO.14Al_2O_3.SiO_2$, was reported in [5]. According to Kaprálik, Hanic [6] this is a metastable phase.

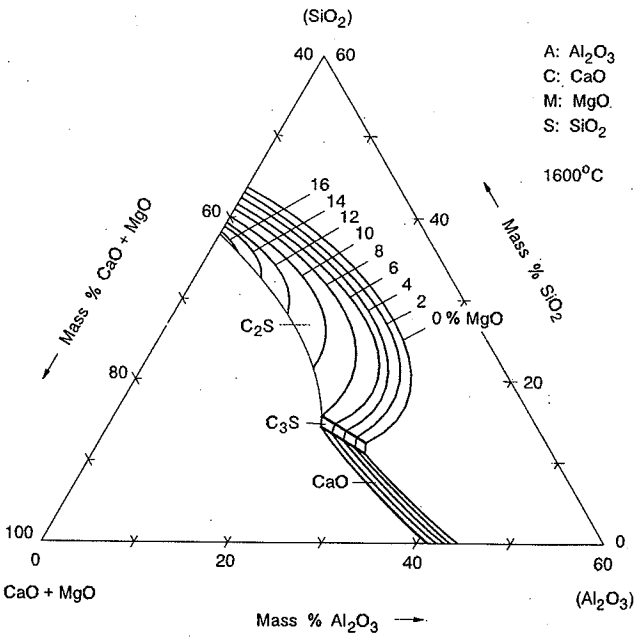


Fig. 3.328. Extension of primary fields of crystallisation (saturation lines) of CaO, $2CaO{\cdot}SiO_2$ and $3CaO{\cdot}SiO_2$ in the system Al_2O_3-CaO-MgO-SiO_2 at 1600 °C and for MgO contents up to 16 mass % after Koch et al. [7].

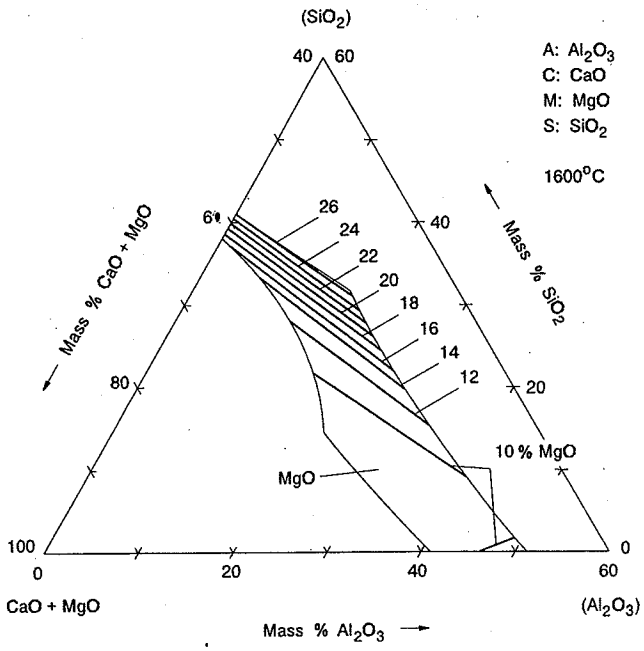


Fig. 3.329. Extension of primary fields of crystallisation (saturation lines) of MgO in the system Al_2O_3-CaO-MgO-SiO_2 at 1600 °C and for MgO contents up to 26 mass % after Koch et al. [7].

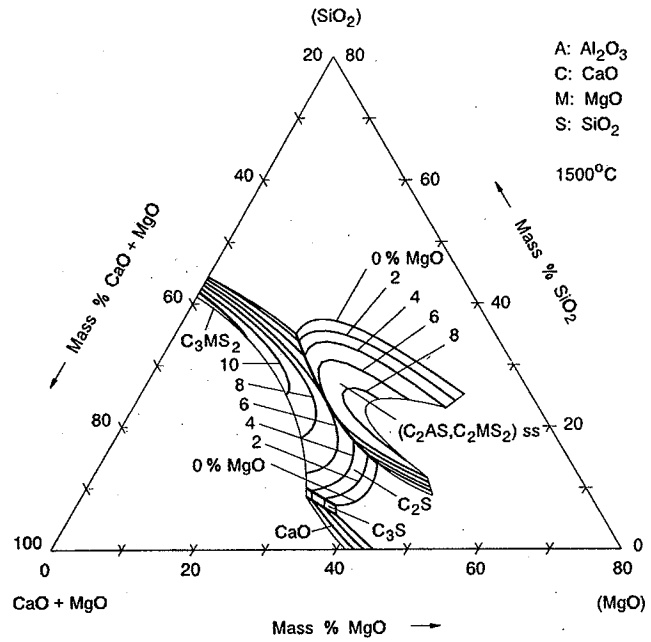


Fig. 3.330. Extension of primary fields of crystallisation (saturation lines) of CaO, $2CaO{\cdot}SiO_2$, $3CaO{\cdot}SiO_2$, $3CaO{\cdot}Al_2O_3$, $3CaO{\cdot}MgO{\cdot}2SiO_2$ and ($2CaO{\cdot}Al_2O_3{\cdot}SiO_2$, $2CaO{\cdot}MgO{\cdot}2SiO_2$) solution phase in the system Al_2O_3-CaO-MgO-SiO_2 at 1500 °C and for MgO contents up to 10 mass % after Koch et al. [7].

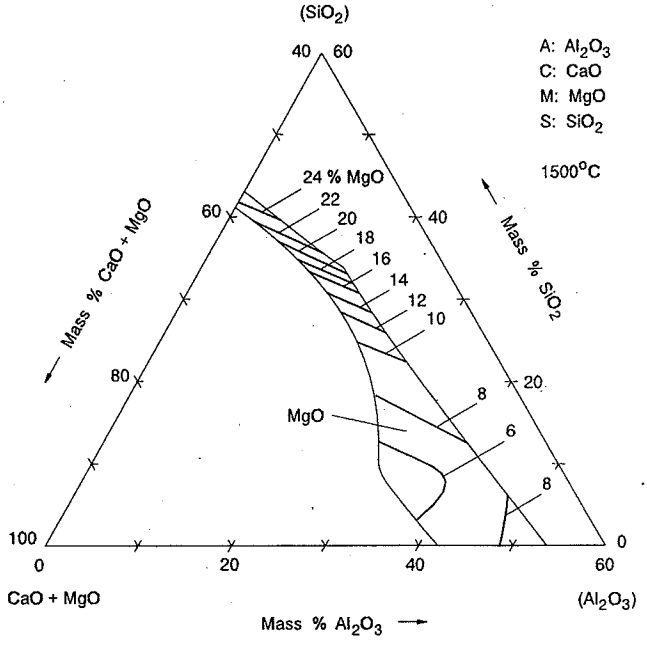


Fig. 3.331. Extension of primary fields of crystallisation (saturation lines) of MgO solution phase in the system Al_2O_3-CaO-MgO-SiO_2 at 1500 °C and for MgO contents up to 24 mass % after Koch et al. [7]. For space representation of liquidus relations at 1600 and 1500 °C and similar representation of the system at 1400 °C, see original paper by Koch et al. [7].

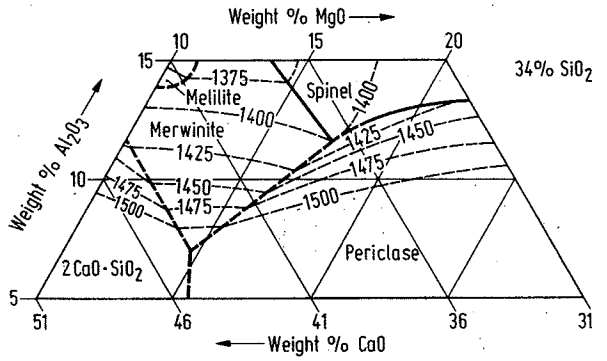


Fig. 3.332.

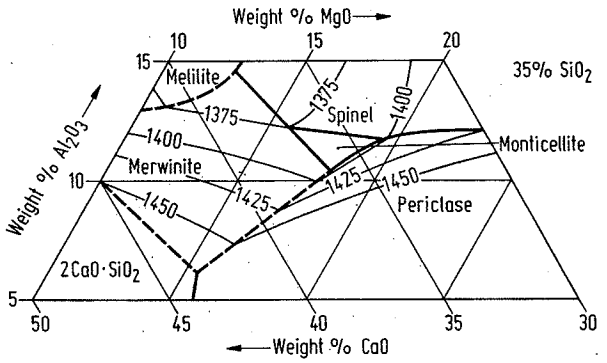


Fig. 3.333.

Figs. 3.332 to 3.335. Liquidus surface in the system Al_2O_3-CaO-MgO-SiO_2 with 34, 35, 36 and 37 mass % SiO_2 after Steyn, Watson [8]. For the liquidus relations at 38 mass % SiO_2, see original paper after Steyn, Watson [8]. For the base system Al_2O_3-CaO-MgO, see Fig. 3.163.

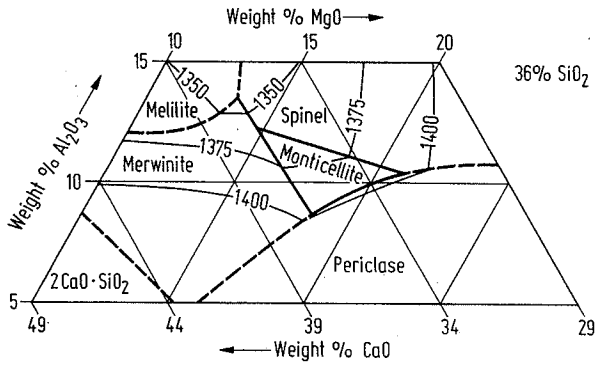


Fig. 3.334.

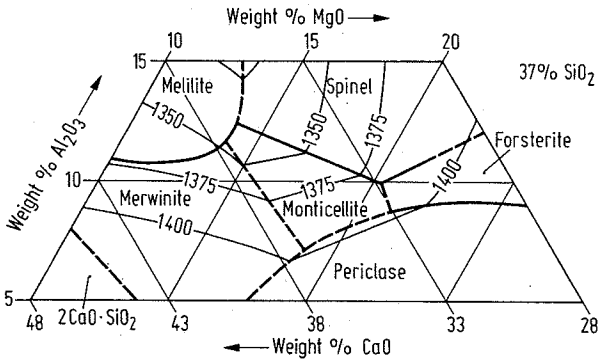


Fig. 3.335.

Figs. 3.332 to 3.335. Liquidus surface in the system Al_2O_3-CaO-MgO-SiO_2 with 34, 35, 36 and 37 mass % SiO_2 after Steyn, Watson [8]. For the liquidus relations at 38 mass % SiO_2, see original paper after Steyn, Watson [8]. For the base system Al_2O_3-CaO-MgO, see Fig. 3.163.

For the space representation of liquidus relations in the system Al_2O_3-CaO-MgO-SiO_2, based on the earlier works, see Koch et al. [9]. The phase equilibria involving the quaternary phase $6CaO{\cdot}MgO{\cdot}4Al_2O_3{\cdot}SiO_2$ and the ternary phase $5CaO{\cdot}MgO{\cdot}3SiO_2$ (bredigite) were investigated by Biggar [10]. For further contribution to the system Al_2O_3-CaO-MgO-SiO_2, see for instance, Gee, Osborn [11] (sub-system $2CaO{\cdot}MgO{\cdot}2SiO_2$-$2CaO{\cdot}Al_2O_3{\cdot}SiO_2$-$CaO{\cdot}MgO{\cdot}2SiO_2$-$CaO{\cdot}Al_2O_3{\cdot}2SiO_2$), Schairer, Yoder [12] (sub-system $MgO{\cdot}Al_2O_3$-$CaO{\cdot}Al_2O_3{\cdot}2SiO_2$-$2CaO{\cdot}MgO{\cdot}2SiO_2$-$CaO{\cdot}MgO{\cdot}2SiO_2$) or Yang et al. [13] (sub-system $CaO{\cdot}Al_2O_3{\cdot}2SiO_2$-$2CaO{\cdot}MgO{\cdot}2SiO_2$-$2MgO{\cdot}SiO_2$).

References

[1] Osborn, E. F., R. C. DeVries, K. H. Gee, H. M. Kraner: Trans. AIME, J. Metals 6 (1954) No. 1, p. 33/45
[2] Osborn, E. F., P. L. Roeder, G. C. Ulmer: Bull. Earth Miner. Sci, Exp. Sta. Pa. State Univ (1969) No. 85, p. 1/22.
[3] Cavalier, G, M. Sandreo-Dendon: Rev. Metall. 57 (1960) No. 12. p. 1143/57
[4] Gutt, W, A. D. Russell: J. Mater. Sci 12 (1977) No. 9, p. 1869/78
[5] Glasser, F. P., J. Marr: Trans. J. Br. Ceram. Soc. 74 (1975) No. 4, p. 113/9
[6] Kaprálik, I., F. Hanic: Trans. J. Br. Ceram. Soc. 79 (1980) No. 5, p. 128/33
[7] Koch, K., G. Trömel, G. Heinz: Arch. Eisenhüttenwes. 46 (1975) No. 3, p. 165/71
[8] Steyn J. G. D., M. D. Watson: J. Iron Steel Inst. 230 (1965) No. 5, p. 445/53
[9] Koch, K., G. Trömel, G. Heinz: Tonind.-Ztg. 99 (1975) No. 3, p. 57/62

Al_2O_3-CaO-MnO_x-SiO_2

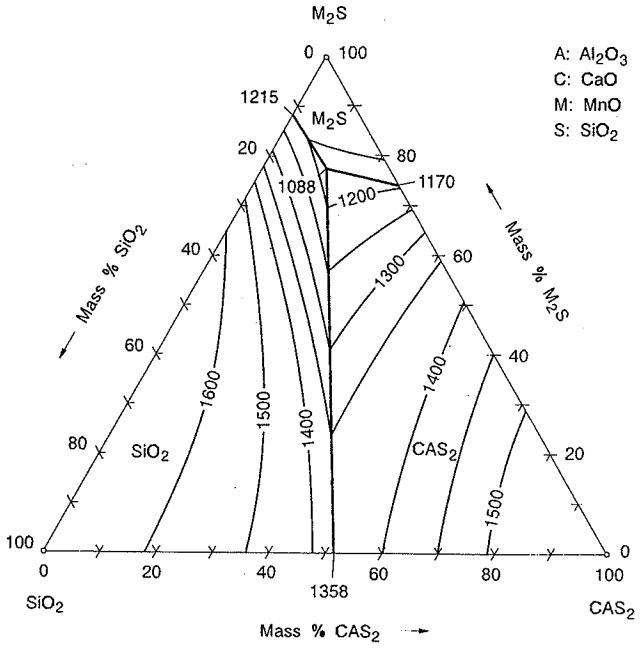


Fig. 3.336. Liquidus surface in the SiO_2-$2MnO{\cdot}SiO_2$-$CaO{\cdot}Al_2O_3{\cdot}2SiO_2$ sub-system after Baisanov et al. [1].

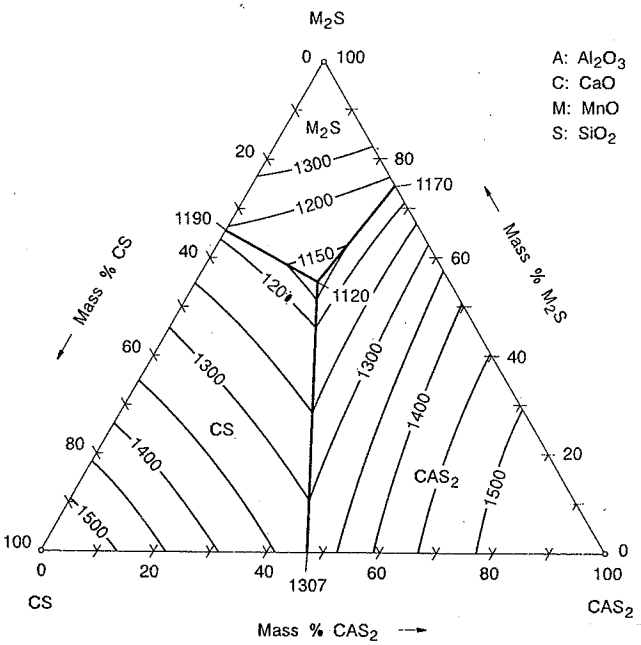


Fig. 3.337. Liquidus surface in the $CaO{\cdot}SiO_2$-$2MnO{\cdot}SiO_2$-$CaO{\cdot}Al_2O_3{\cdot}2SiO_2$ sub-system after Baisanov et al. [1].

[10] Biggar, G.: Cem. Concr. Res. 1 (1971), p. 493/513
[11] Gee, K. H., E. F. Osborn: Bull. Earth Miner. Sci., Exp. Sta, Pa. State Univ. (1969) No. 85, 23/51
[12] Schairer, J. F., H. S. Yoder, Jr.: Carnegie Inst. Washington, Year Book 68, (1970), p. 202/14
[13] Yang, H. Y., J. F. Salomon, W. R. Foster: Am. J, Sci. 272 (1972) No. 2, p. 161/88

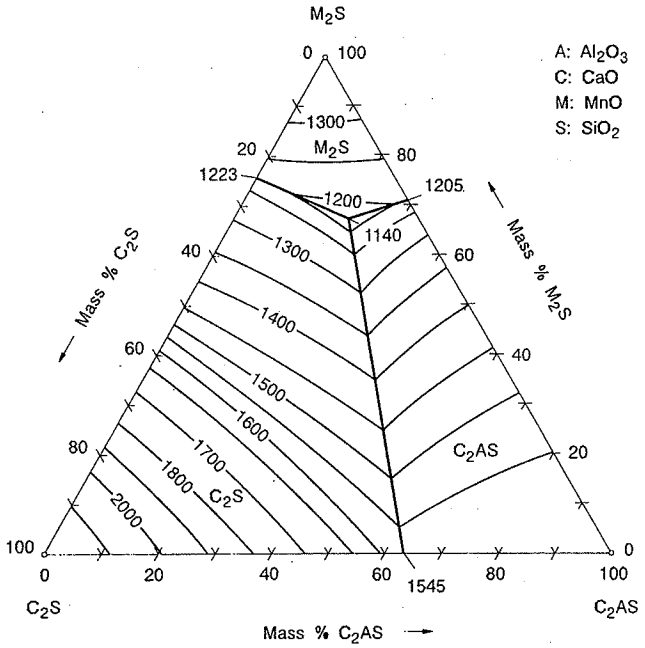


Fig. 3.338. Liquidus surface in the $2CaO{\cdot}SiO_2$-$2MnO{\cdot}SiO_2$-$2CaO{\cdot}Al_2O_3{\cdot}SiO_2$ sub-system after Baisanov et al. [1].

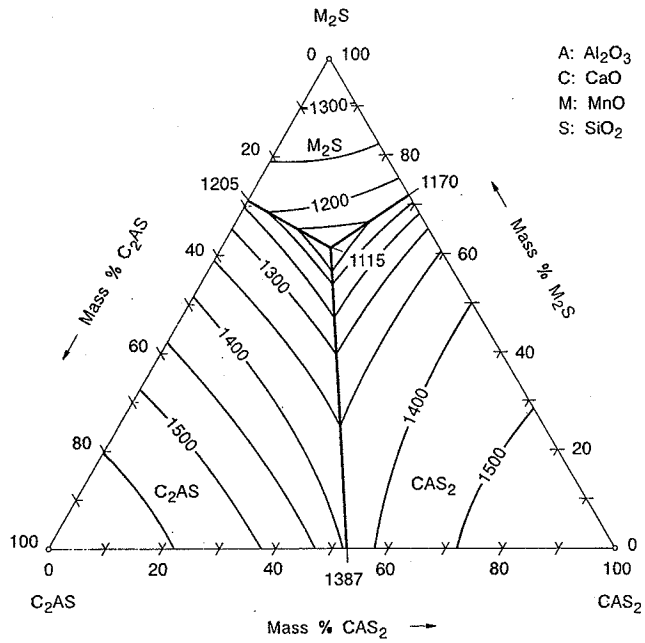


Fig. 3.339. Liquidus surface in the $2CaO{\cdot}Al_2O_3{\cdot}SiO_2$-$2MnO{\cdot}SiO_2$-$CaO{\cdot}Al_2O_3{\cdot}2SiO_2$ sub-system after Baisanov et al. [1].

For the sub-solidus equilibria in the Al_2O_3-CaO-MnO-SiO_2 system, see Takenov [2].

References

[1] Baisanov, S. O., T. D. Takenov, T. G. Gabdullin, E. A. Buketov: Fizikokhim. Metall. Margantsa, Ed.: Nauka, Moscov (1983), p. 58/62

[2] Takenov, T. D.: Kompleksn. Ispolz. Miner. Syrya (1987) No. 10, p. 55/9

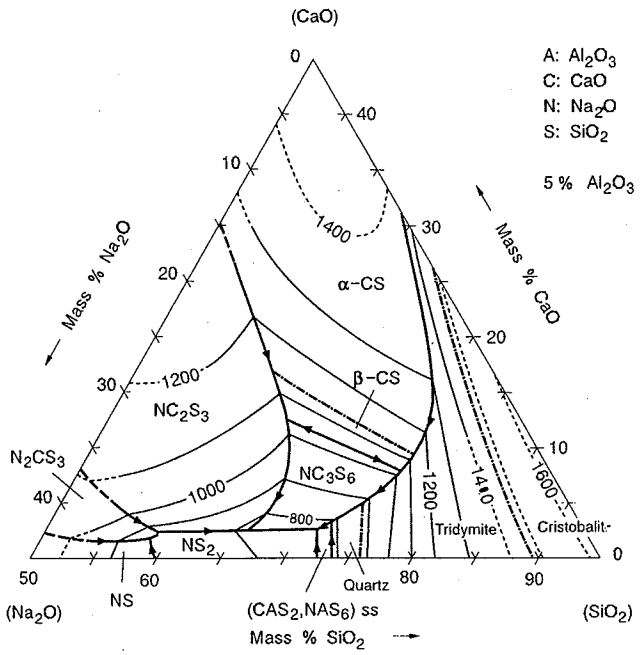


Fig. 3.340.

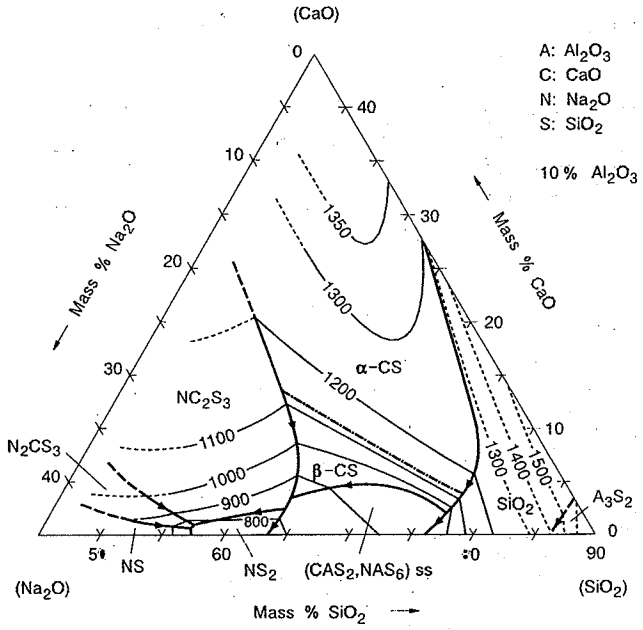


Fig. 3.341.

Figs. 3.340 to 3.342. Liquidus surface in the SiO_2-rich portion of the Al_2O_3-CaO-Na_2O-SiO_2 system at 5, 10 and 15 mass % Al_2O_3 after Moir, Glasser [1] (for the base system CaO-Na_2O-SiO_2, see Fig. 3.260). The liquidus relations in the SiO_2-rich portion of the Al_2O_3-CaO-Na_2O-SiO_2 system were also investigated by Preda, Burghelea [2]. For compatibility relations and crystallisation paths, see original paper by Moir, Glasser [1].

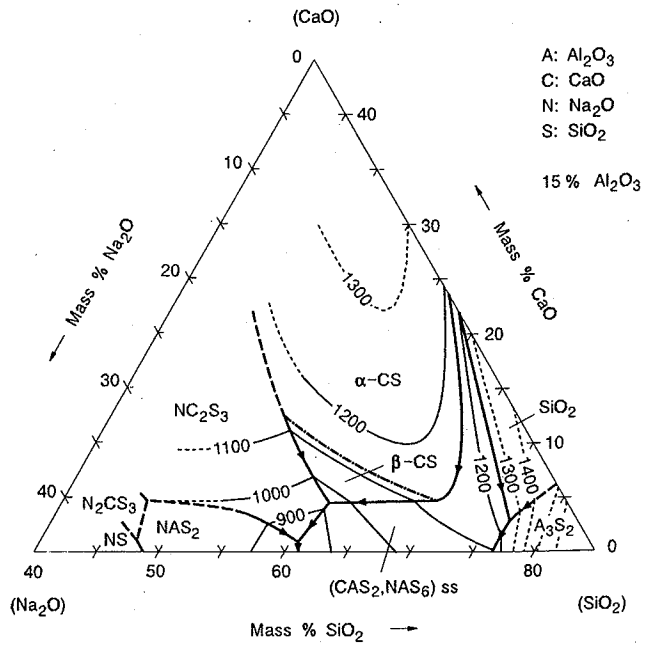


Fig. 3.342.

Figs. 3.340 to 3.342. Liquidus surface in the SiO_2-rich portion of the Al_2O_3-CaO-Na_2O-SiO_2 system at 5, 10 and 15 mass % Al_2O_3 after Moir, Glasser [1] (for the base system CaO-Na_2O-SiO_2, see Fig. 3.260). The liquidus relations in the SiO_2-rich portion of the Al_2O_3-CaO-Na_2O-SiO_2 system were also investigated by Preda, Burghelea [2]. For compatibility relations and crystallisation paths, see original paper by Moir, Glasser [1].

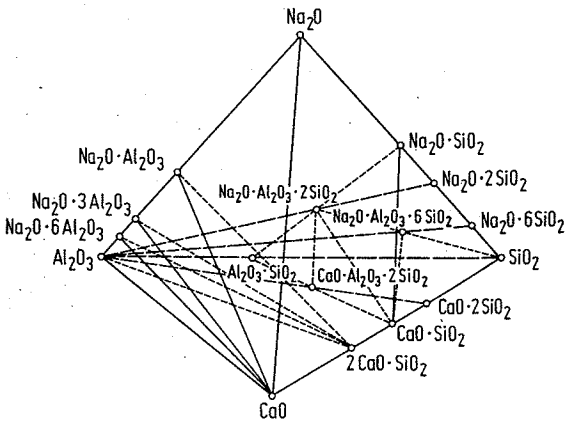


Fig. 3.343. Compatibility relation in the Al_2O_3-CaO-Na_2O-SiO_2 system after Greene, Bogue [3].

→ **Fig. 3.346.** Liquidus surface in the $CaO \cdot SiO_2$-$Na_2O \cdot Al_2O_3 \cdot 6SiO_2$-$Na_2O \cdot Al_2O_3 \cdot 2SiO_2$ sub-system after Foster [6].

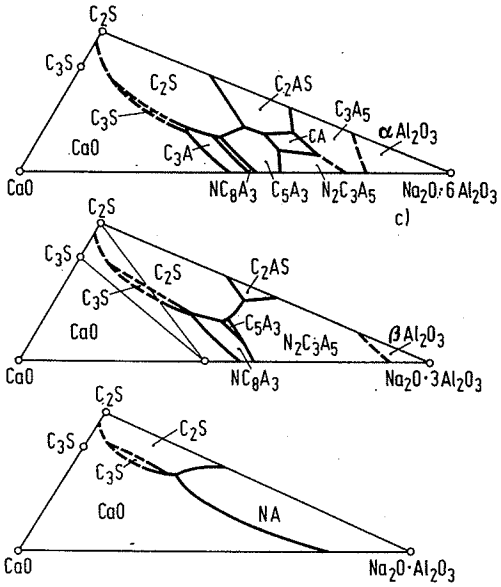


Fig. 3.344. Liquidus relations in the sub-systems CaO-$2CaO \cdot SiO_2$-$Na_2O \cdot 6Al_2O_3$, CaO-$2CaO \cdot SiO_2$-$Na_2O \cdot 3Al_2O_3$ and CaO-$2CaO \cdot SiO_2$-$Na_2O \cdot Al_2O_3$ Greene, Bogue [3]. For the base system Al_2O_3-CaO-SiO_2, see Fig. 3.166.

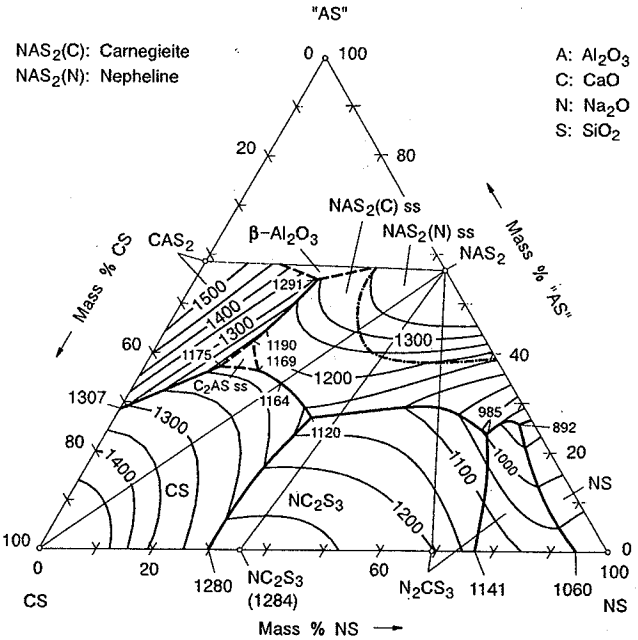
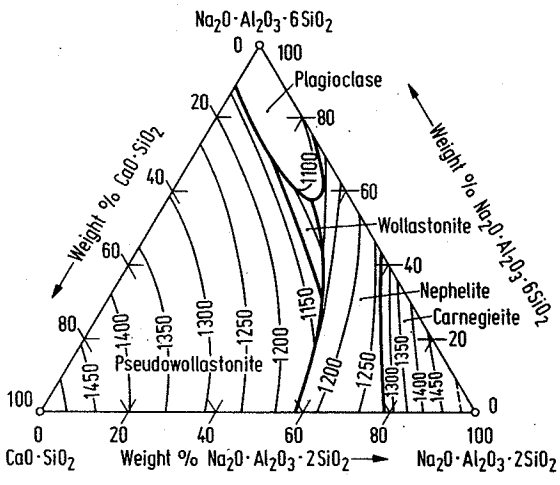


Fig. 3.345. Liquidus surface in the $CaO \cdot SiO_2$-$Na_2O \cdot SiO_2$-$CaO \cdot Al_2O_3 \cdot 2SiO_2$-$Na_2O \cdot Al_2O_3 \cdot 2SiO_2$ sub-system after Spivak [4] and Gummer [5].



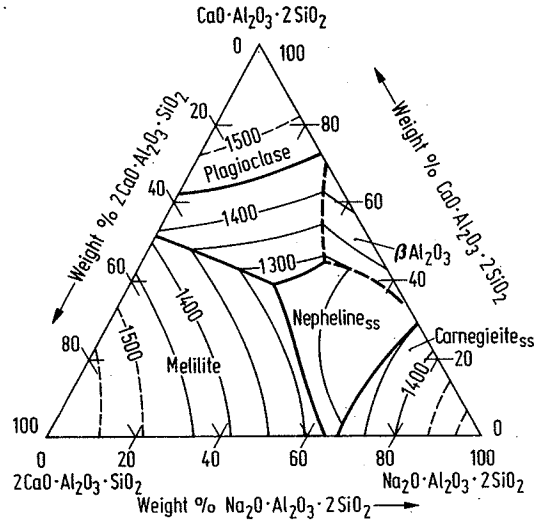


Fig. 3.347. Liquidus surface in the $2CaO{\cdot}Al_2O_3{\cdot}SiO_2$-$Na_2O{\cdot}Al_2O_3{\cdot}2SiO_2$-$2CaO{\cdot}Al_2O_3{\cdot}SiO_2$ sub-system after Goldsmith [7].

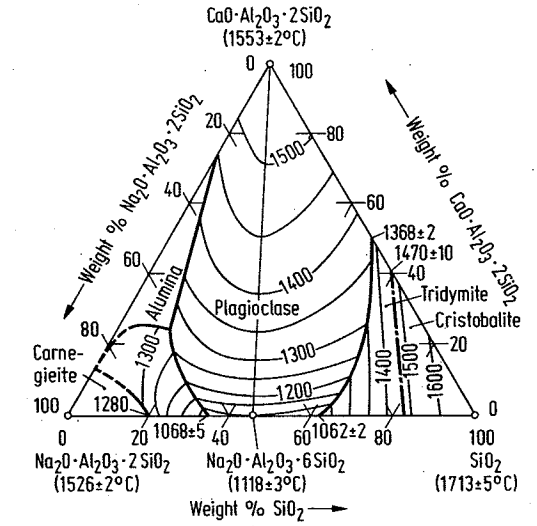


Fig. 3.348. Liquidus surface in the $Na_2O{\cdot}Al_2O_3{\cdot}2SiO_2$-$CaO{\cdot}Al_2O_3{\cdot}2SiO_2$-$SiO_2$ sub-system after Schairer [8].

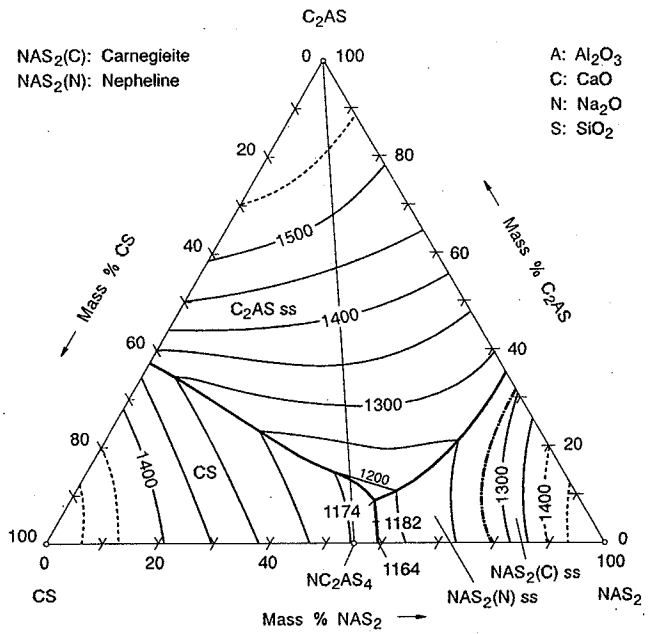


Fig. 3.349.

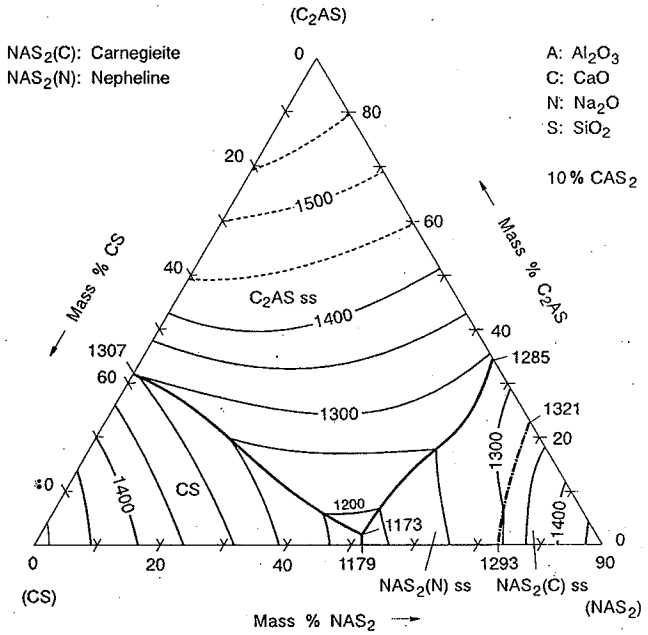


Fig. 3.350.

Figs. 3.349 and 3.350. Liquidus surface in the $CaO{\cdot}SiO_2$-$Na_2O{\cdot}Al_2O_3{\cdot}2SiO_2$-$2CaO{\cdot}Al_2O_3{\cdot}SiO_2$ sub-system with addition of O, (Juan [9], Schairer et al. [10]) and 10 mass % $CaO{\cdot}Al_2O_3{\cdot}2SiO_2$ (Yoder [11]).

The composition section $CaO{\cdot}Al_2O_3$-$Na_2O{\cdot}Al_2O_3{\cdot}2SiO_2$ has been investigated by Goldsmith [12]. For phase equilibria in the sub-systems containing the $3Al_2O_3{\cdot}2SiO_2$ phase (mullite), see Dinescu, Cerchez [13, 14] and Cerchez [15].

References

[1] Moir, G. K., F. P. Glasser: Phys. Chem. Glasses 17 (1976) No. 3, p. 45/53
[2] Preda, M., V. Burghelea: Mater. Constr. /Bucharest/ 11 (1981) No. 2, p. 91/4
[3] Greene, K. T., R. H. Bogue: J. Res. Nat. Bur. Stand., RP 1699 36 (1946) No. 2, p. 185/207
[4] Spivak, J.: J. Geol. 52 (1944), p. 24/52
[5] Gummer, W. K.: J. Geol. 51 (1943) No. 8, p. 503/30
[6] Foster, W. R.: J. Geol. 50 (1942), p. 152/73
[7] Goldsmith, J. R.: J. Geol. 55 (1947) No. 5, p. 381/404
[8] Schairer, J. F.: J. Am. Ceram. Soc. 40 (1957) No. 7, p. 215/35
[9] Juan, V. C.: J. Geol. 58 (1950) No. 1, p. 1/15
[10] Schairer, J. F., H. S. Yoder, Jr., C. E. Tilley: Carnegie Inst. Washington, Year Book 64 (1965), p. 95/100
[11] Yoder, H. S., Jr.: J. Geol. 60 (1952), p. 586/93
[12] Goldsmith, J. R.: Am. Mineral. 34 (1949) No. 7-8, p. 471/93
[13] Dinescu, R., M. Cerchez: Silicates Ind. 36 (1971) No. 6, p. 151/4
[14] Dinescu, R., M. Cerchez: Rev. Roum. Chim. 18 (1973) No. 1, p. 23/34
[15] Cerchez, M.: Ceram. Int. 13 (1987) No. 3, p. 189/96

Al_2O_3-CaO-P_2O_5-SiO_2

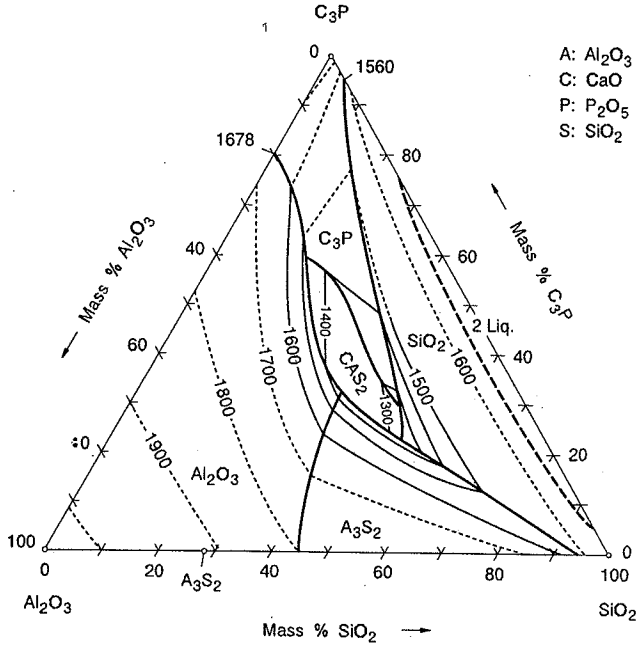


Fig. 3.351. Liquidus surface in the sub-system Al_2O_3-SiO_2-$3CaO{\cdot}P_2O_5$ after Pierre [1].

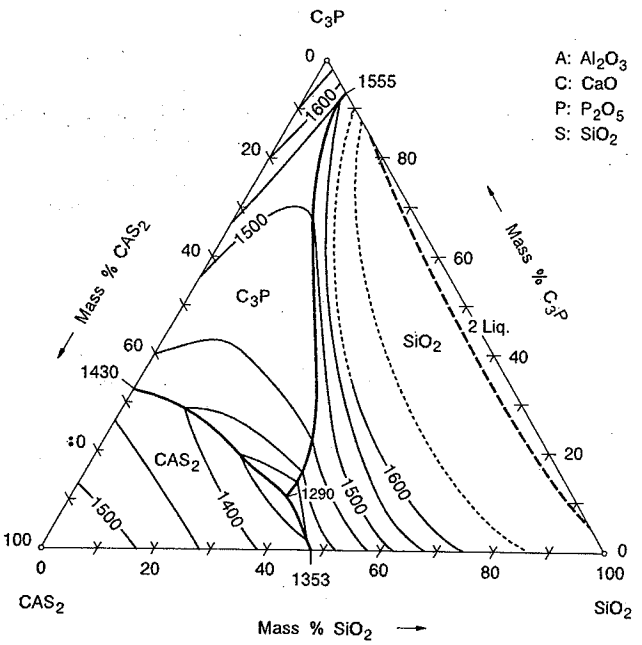


Fig. 3.352. Liquidus surface in the sub-system $CaO{\cdot}Al_2O_3{\cdot}2SiO_2$-$3CaO{\cdot}P_2O_5$-$SiO_2$ after Pierre [2].

The system Al_2O_3-CaO-P_2O_5-SiO_2 has been discussed by Takenov et al. [3]. The possibility of existence of quaternary phases has been mentioned.

Al_2O_3-CaO-SiO_2-TiO_2

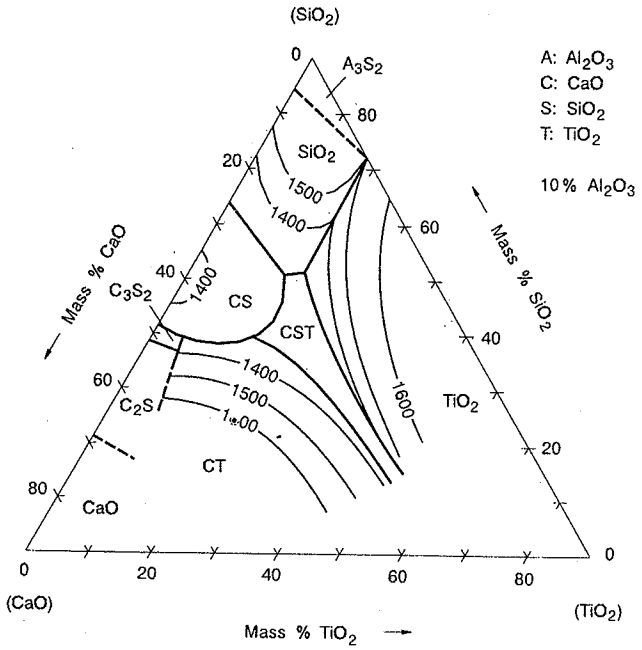


Fig. 3.353.

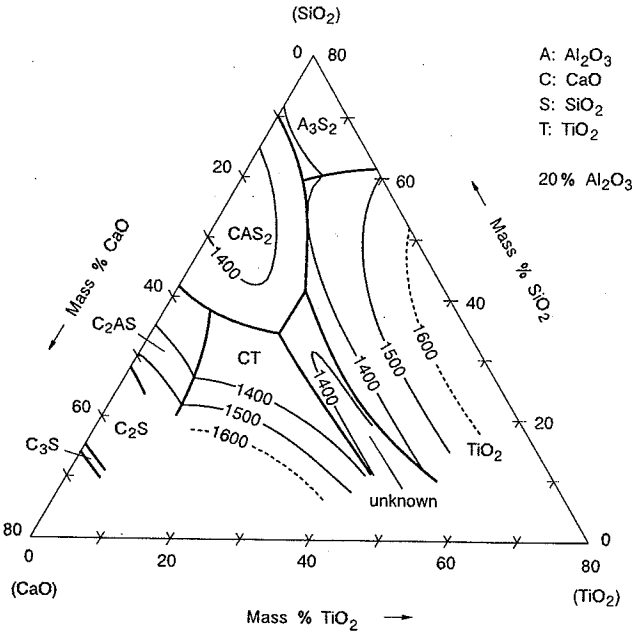


Fig. 3.354.

Figs. 3.353 and 3.354. Liquidus surface in the system Al_2O_3-CaO-SiO_2-TiO_2 at 10 and 20 mass % Al_2O_3 after Ohno, Roues [1]. For the base system CaO-SiO_2-TiO_2, see Fig. 3.264.

References

[1] Pierre, P. D. S. St.: J. Am. Ceram. Soc. 37 (1954) No. 6, p. 243/58
[2] Pierre, P. D. S. St.: J. Am. Ceram. Soc. 39 (1956) No. 4, p. 147/50
[3] Takenov, T. D., T. G. Gabdullin, M. Z. Tolymbekov: Deposited Doc. VINITI 1813-78 (1978), p. 12

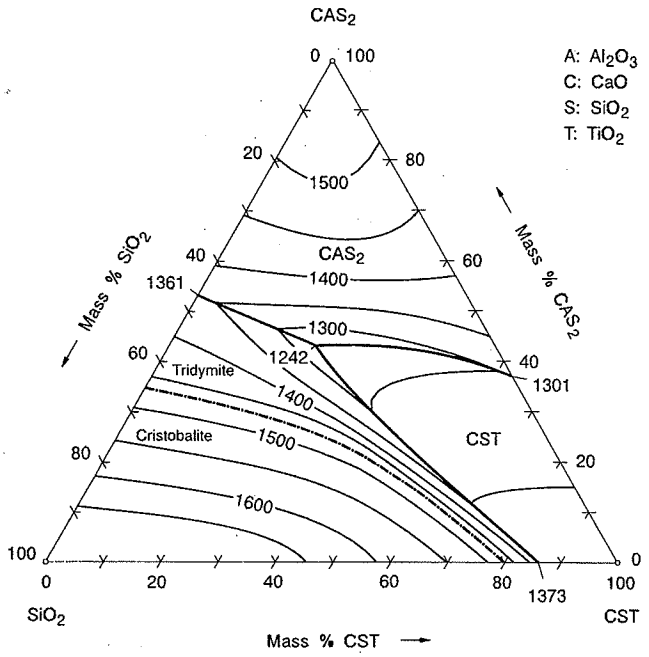


Fig. 3.355. Liquidus surface in the sub-system SiO_2-$CaO{\cdot}Al_2O_3{\cdot}2SiO_2$-$CaO{\cdot}SiO_2{\cdot}TiO_2$ after Agamawi, White [2].

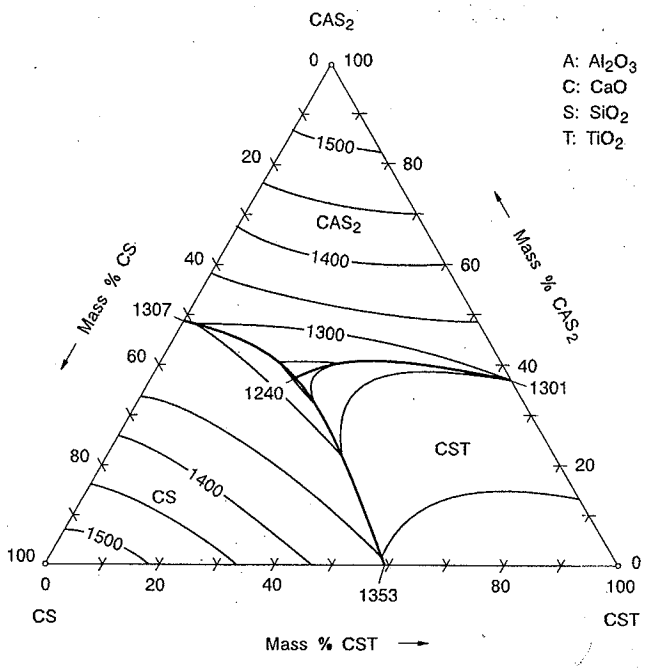


Fig. 3.356. Liquidus surface in the sub-system $CaO{\cdot}Al_2O_3{\cdot}2SiO_2$-$CaO{\cdot}SiO_2{\cdot}TiO_2$-$CaO{\cdot}SiO_2$ after Agamawi, White [3]. For the space representation of phase equilibria in the sub-system SiO_2-$CaO{\cdot}SiO_2$-$CaO{\cdot}Al_2O_3{\cdot}2SiO_2$-$CaO{\cdot}SiO_2{\cdot}TiO_2$, see original paper [3].

The Al_2O_3-rich region of the system Al_2O_3-CaO-SiO_2-TiO_2 was investigated by Jenkinson [4] and White [5].

References

[1] Ohno, K., M. H. Roues: Can. Metall. Q. 2 (1963) No. 3, p. 243/58
[2] Agamawi, Y. M., J. White: Trans. J. Br. Ceram. Soc. 52 (1953), p. 271/310
[3] Agamawi, Y. M., J. White: Trans. J. Br. Ceram. Soc. 53 (1954) No. 1, p. 1/38
[4] Jenkinson, D. A.: MSc Thesis, Sheffield University (1972)
[5] White, J.: Refract. J. (1977) Jan., p. 13/21

B_2O_3-CaO-FeO_x-SiO_2

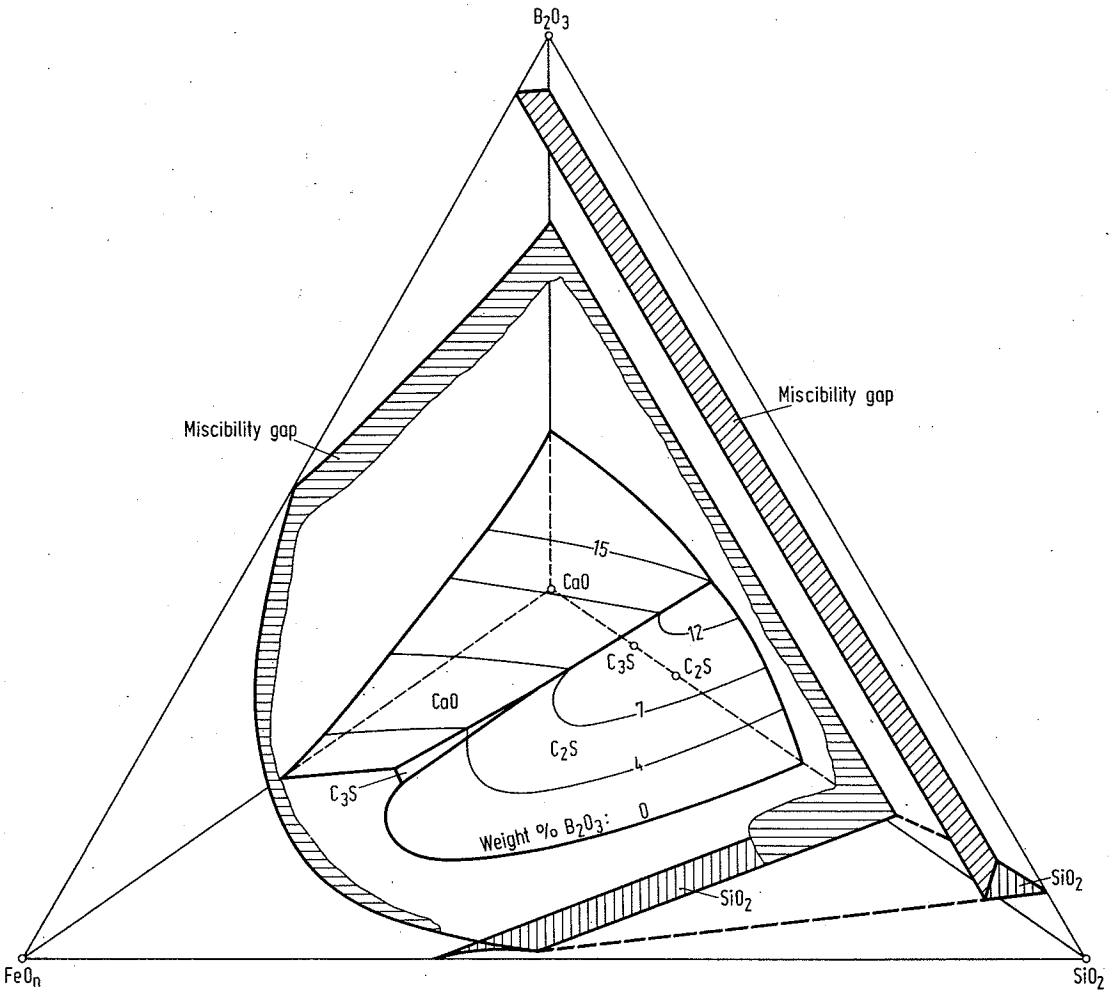


Fig. 3.357. Isothermal section through the system B_2O_3-CaO-FeO-SiO_2 in contact with metallic iron at 1600 °C after Koch et al. [1].

References

[1] Koch, K., J. Sittard, G. Trömel, H. Pöpperling: Slag Atlas (1981)

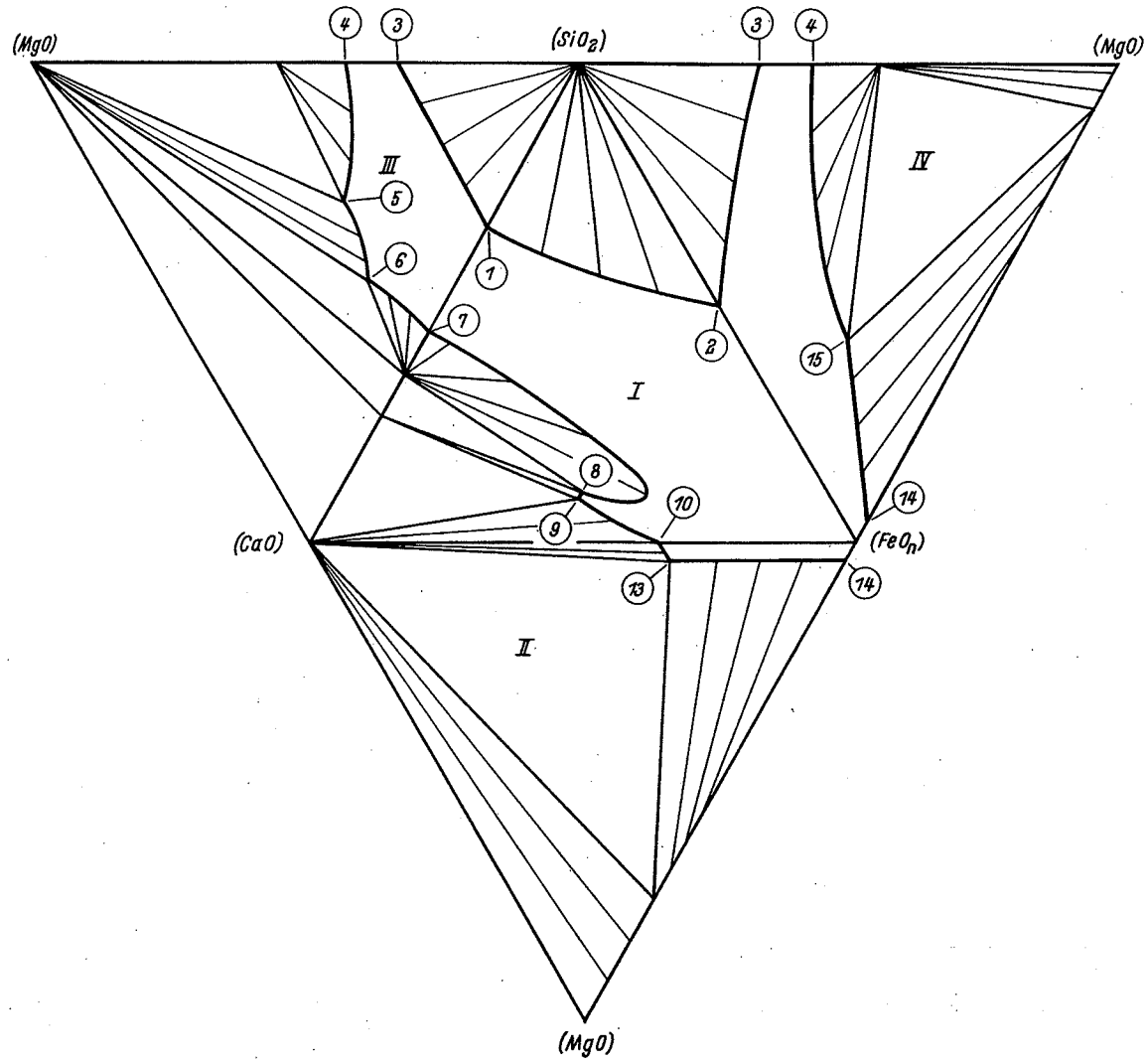


Fig. 3.358. Isothermal section through lower-order systems in contact with iron melt at 1600 °C after Trömel et al. [1].

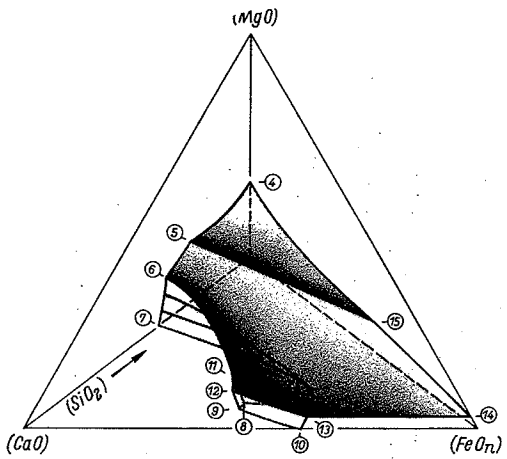
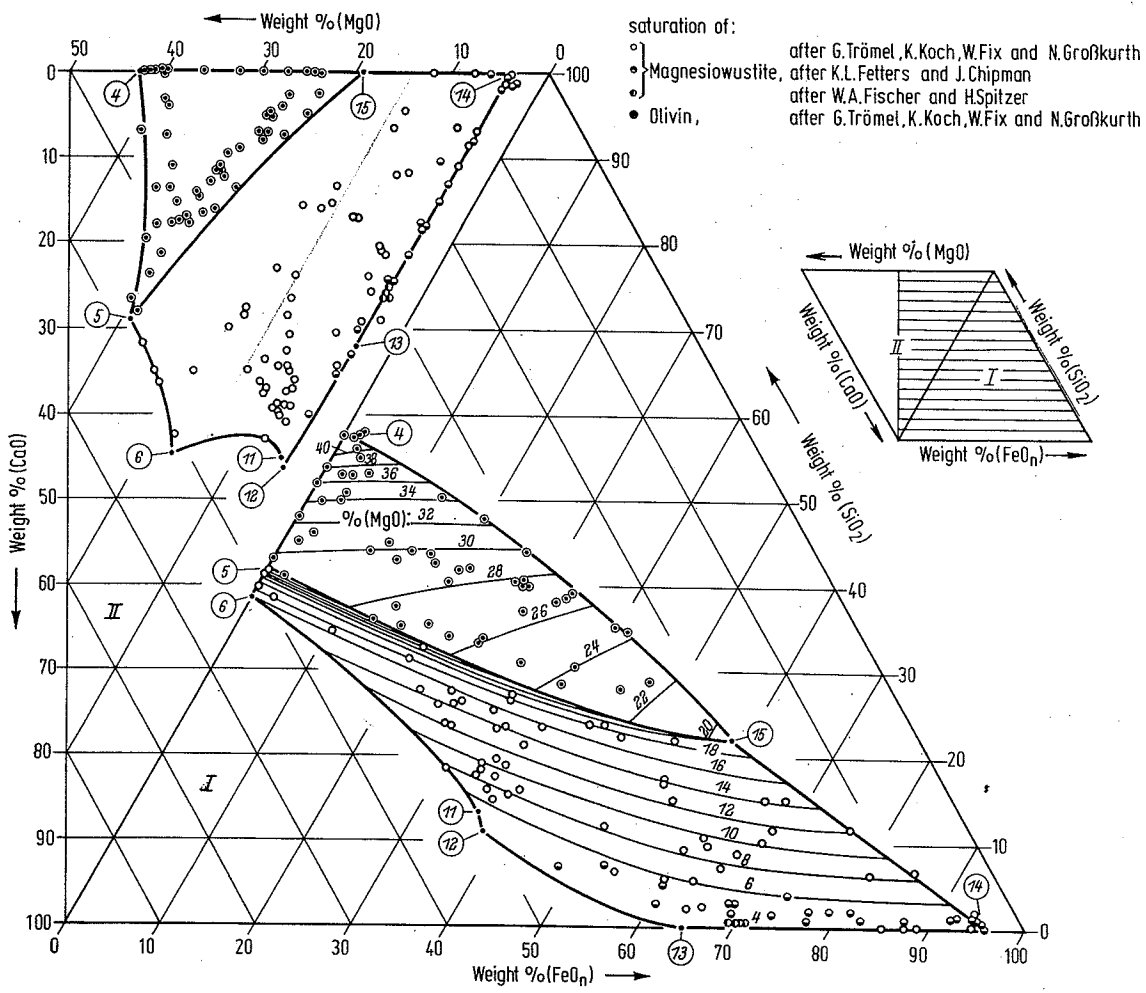


Fig. 3.359. Space representation of liquidus surfaces of CaO (9-10-13-12-9), (Fe,Mg)O (12-13-14-15-5-6-11-12), $2(Fe,Mg)\cdot SiO_2$ (5-15-4-5), $3CaO\cdot SiO_2$ (9-12-11-8-9) and $2CaO\cdot SiO_2$ (11-8-7-6-11) based solution phases in the system $CaO\text{-}FeO\text{-}MgO\text{-}SiO_2$ in contact with metallic iron at 1600 °C after Trömel et al. [1].



Number in figure	Composition of slags (weight %)				Sulfur distribution between slag and metal
	(FeO_n)	(CaO)	(SiO_2)	(MgO)	
4	0	0	57,0	43,0	0,1
5	0	29,5	41,5	29,0	0,2
6	0	44,0	38,5	17,5	0,4
7	0	56,0	44,0	0	0,5
8	45,0	44,5	10,5	0	10,0
9	45,0	46,0	9,0	0	11,0
10	64,0	36,0	0	0	14,5
11	36,0	46,0	13,0	5,0	6,0
12	38,0	47,0	11,0	4,0	7,0
13	63,0	33,0	0	4,0	13,0
14	96,0	0	0	4,0	4,0
15	58,0	0	22,0	19,0	1,5

Fig. 3.360. Extension of primary fields of crystallisation (saturation lines) of (Fe,Mg)O (11-12-13-14-15-5-6-11) and 2(Fe,Mg)·SiO_2 (5-15-4-5) based solution phases in the system CaO-FeO-MgO-SiO_2 in contact with metallic iron at 1600 °C after Trömel et al. [1] (parallel projection). The results of Fetters, Chipman [2] and Fischer, Spitzer [3] were also used to construct the figure. The table shows sulphur partition coefficients between slags and iron melts as determined in [1].

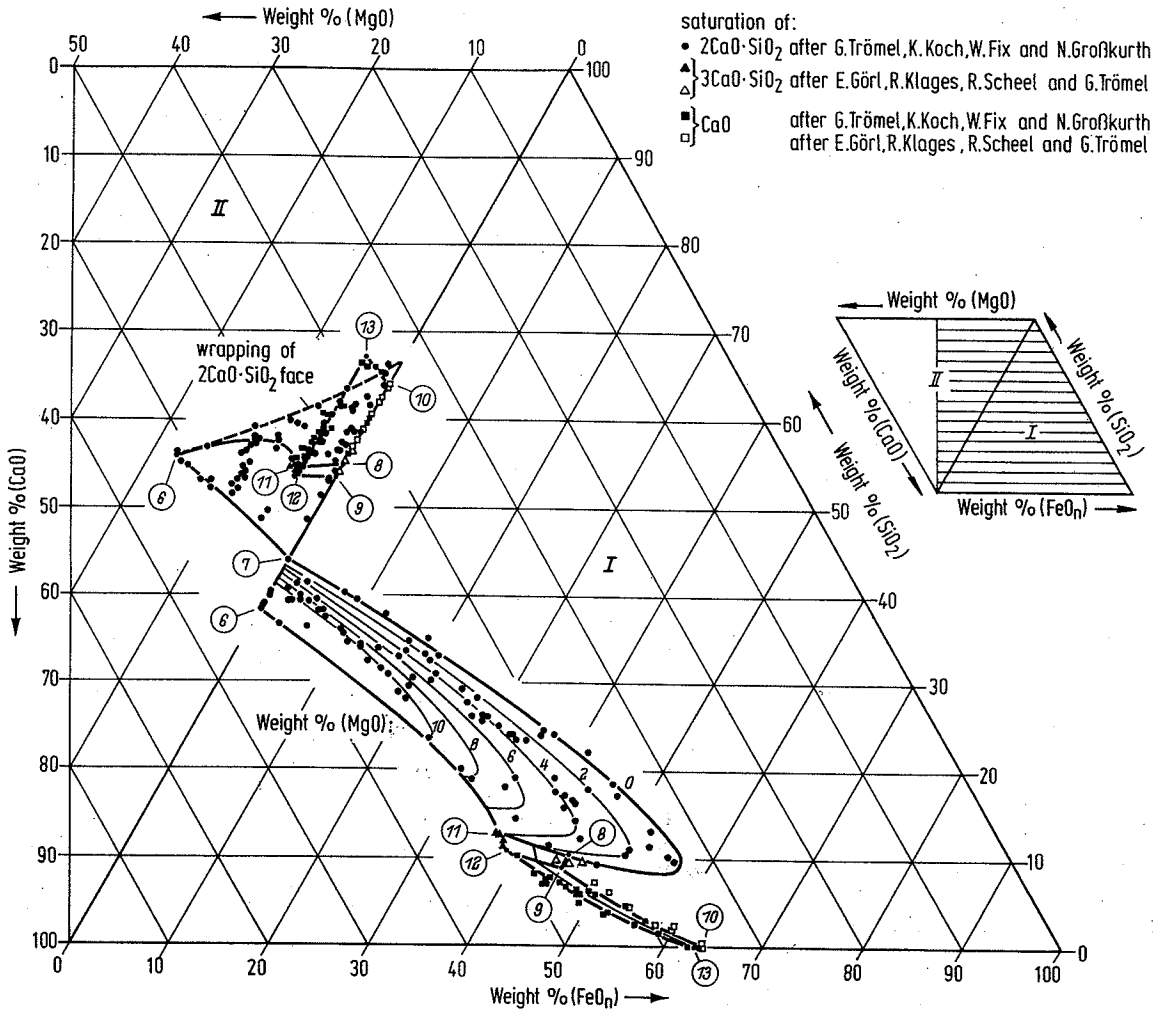


Fig. 3.361. Extension of primary fields of crystallisation (saturation lines) of CaO (10-9-12-13-10), $2CaO{\cdot}SiO_2$ (8-7-6-11-8) and $3CaO{\cdot}SiO_2$ (9-8-11-12-9) based solution phases in the system CaO-FeO-MgO-SiO_2 in contact with metallic iron at 1600 °C after Trömel et al. [1] (parallel projection). The results of Görl et al. [4] were also used to construct the figure.
For the liquidus relations in the system CaO-FeO-MgO-SiO_2 in contact with metallic iron at 1400 °C, see [5].

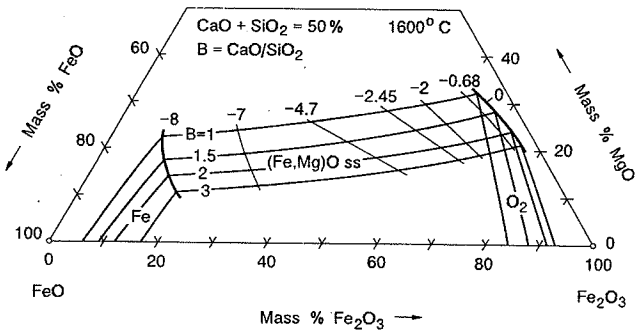


Fig. 3.362. Extension of primary fields of crystallisation (saturation lines) of (Fe,Mg)O in the system CaO-FeO-MgO-SiO_2 in contact with metallic iron at 1600 °C and at different CaO/SiO_2 ratios (B) after Schürmann, Kolm [6] (as projected on the FeO-Fe_2O_3-MgO plane). The thin lines show equilibrium partial pressures of oxygen (log pO_2, atm).

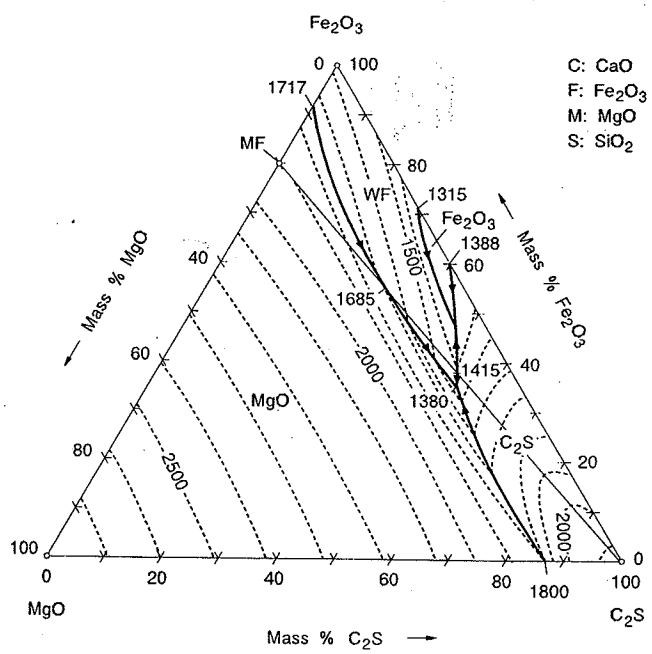


Fig. 3.363. Liquidus surface in the sub-system MgO-Fe_2O_3-$2CaO{\cdot}SiO_2$ after Fusenig et al. [7].

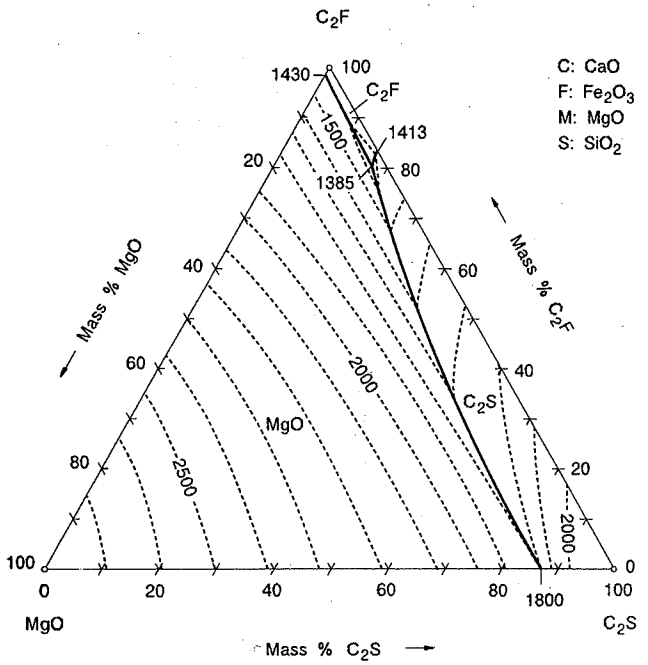


Fig. 3.364. Liquidus surface in the sub-system MgO-$2CaO{\cdot}SiO_2$-$2CaO{\cdot}Fe_2O_3$ after Fusenig et al. [7].

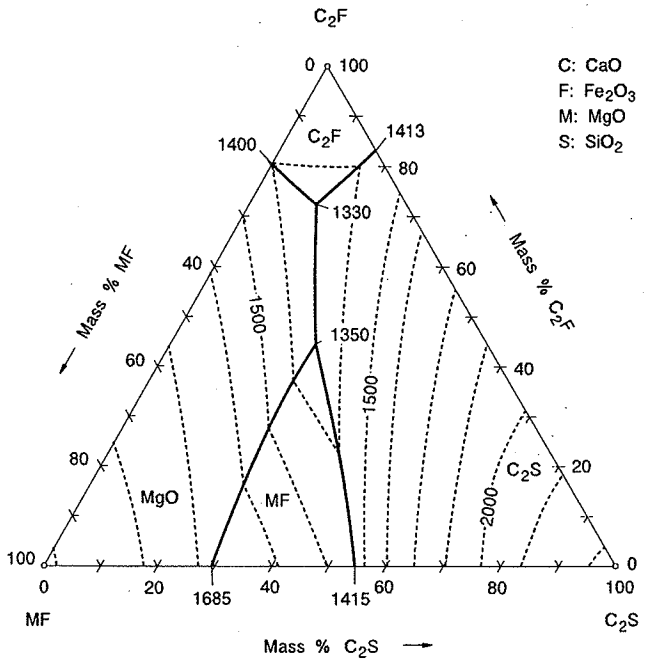


Fig. 3.365. Liquidus surface in the sub-system $2CaO{\cdot}SiO_2$-$2CaO{\cdot}Fe_2O_3$-$MgO{\cdot}Fe_2O_3$ after Fusenig et al. [7].

References

[1] Trömel, G., K. Koch, W. Fix, N. Großkurth: Arch. Eisenhüttenwes. 40 (1969) No. 12, p. 969/78
[2] Fetters, K. L., J. Chipman: Trans. Am. Inst. Min. Metal. Eng., Iron Steel Div. 140 (1940), p. 170/203
[3] Fischer, W. A., H. Spitzer: Arch. Eisenhüttenwes. 29 (1958) No. 10, p. 611/7
[4] Görl, E., R. Klages, R. Scheel, G. Trömel: Arch. Eisenhüttenwes. 40 (1969) No. 12, p. 659/67
[5] Knüppel, R., H. U. Helfmeier, F. Oeters: Arch. Eisenhüttenwes. 46 (1975) No. 9, p. 549/54
[6] Schürmann, E., I. Kolm: Steel Res. 59 (1988) No. 5, p. 185/91
[7] Fusenig, R., U. Limbert, E. Woermann: Tonind.-Ztg. 108 (1984) No. 8, p. 515/23
[8] Presnall, D. C.: Am. J. Sci. 264 (1966) No. 10, p. 753/809
[9] Nafziger, H. R.: Am. Mineral. 55 (1970) No. 11-12, p. 2042/52

For the sub-system FeO_x-$2MgO{\cdot}SiO_2$-$CaO{\cdot}MgO{\cdot}2SiO_2$ at different oxygen partial pressures, see Presnall [8]. The sub sub-system FeO_x-SiO_2-$CaO{\cdot}MgO{\cdot}2SiO_2$ under an atmosphere consisting of CO_2 and H_2 in ratio CO_2/H_2=50 was investigated by Nafziger [9].

CaO-FeO_x-MgO-TiO_2

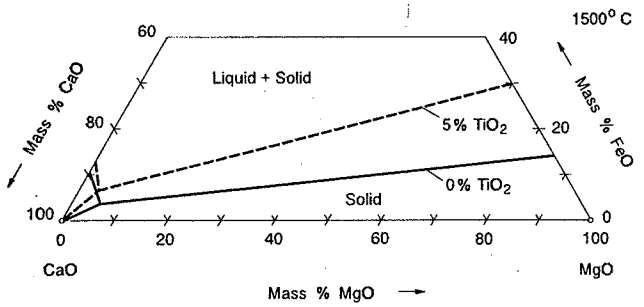


Fig. 3.366. Isothermal section through the system CaO-FeO-MgO-TiO_2 at 1500 °C and at 5 mass % TiO_2 under reducing conditions (10^{-9} atm O_2) after Schultz [1], compared with results by Johnson, Muan [2] for the base system CaO-FeO-MgO.

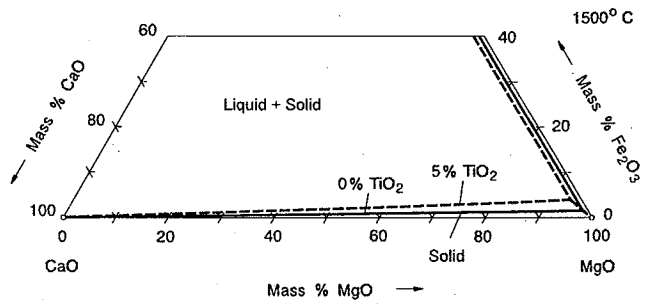


Fig. 3.367. Isothermal section through the system CaO-FeO_x-MgO-TiO_2 at 1500 °C and at 5 mass % TiO_2 in air after Schultz [1], compared with results by Johnson, Muan [2] for the base system CaO-FeO_x-MgO.

References

[1] Shultz, R. L.: J. Am. Ceram. Soc. 56 (1973) No. 1, p. 33/6
[2] Johnson, R. E., A. Muan: J. Am. Ceram. Soc. 48 (1965), p. 359/64

$CaO\text{-}FeO_x\text{-}MnO_x\text{-}P_2O_5$

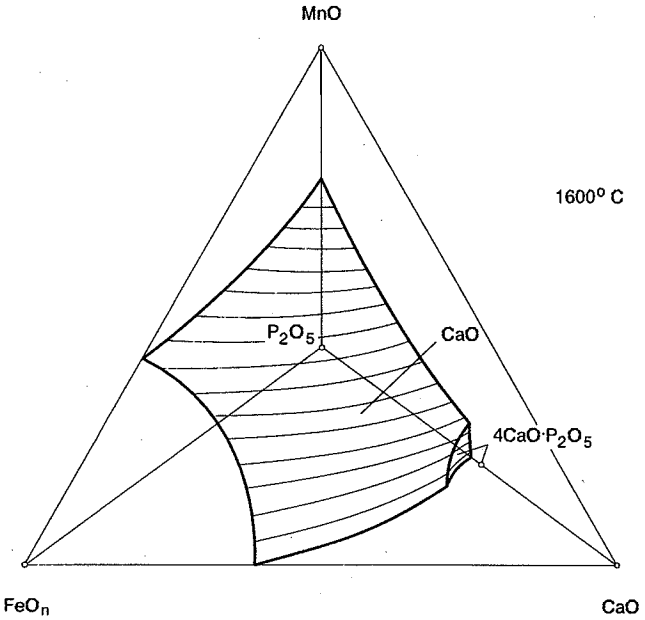


Fig. 3.368. Primary fields of crystallisation of CaO and $4CaO{\cdot}P_2O_5$ in the CaO-FeO-MnO-P_2O_5 system in contact with metallic iron at 1600 °C after Schürmann, Bannenberg [1] and Trömel, Fix [2].

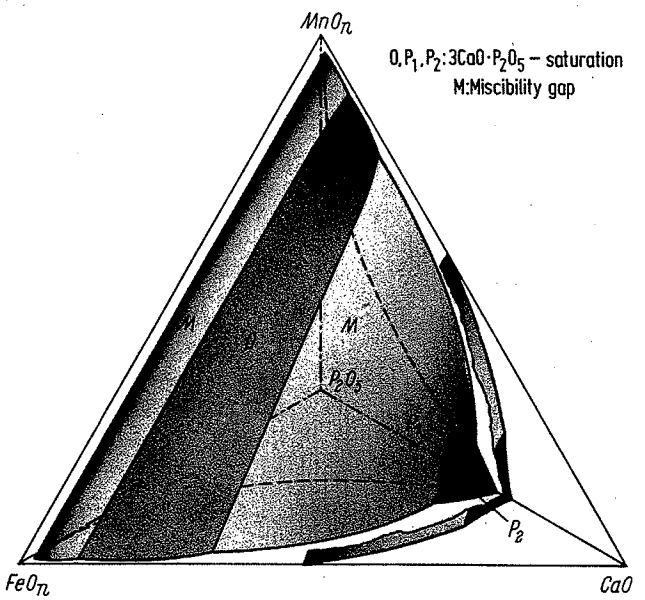


Fig. 3.369. Liquidus surfaces of the CaO, $4CaO{\cdot}P_2O_5$, $3CaO{\cdot}P_2O_3$ phases and the miscibility gap in the CaO-FeO_x-MnO_x-P_2O_5 system in air at 1600 °C after Trömel et al. [3]. For planar representation of the system (parallel projection), see original paper [3].

References

[1] Schürmann, E., N. Bannenberg: Arch. Eisenhüttenwes. 52 (1981) No. 10, p. 375/9

[2] Trömel, G., W. Fix: Arch. Eisenhüttenwes. 33 (1962) No. 11, p. 745/55

[3] Trömel, G., W. Fix, H. E. Wiemer: Arch. Eisenhüttenwes. 40 (1969) No. 9, p. 673/9

$CaO\text{-}FeO_x\text{-}MnO_x\text{-}SiO_2$

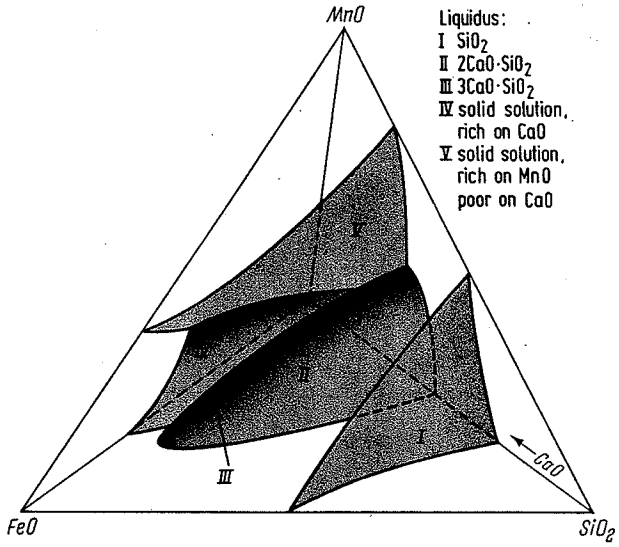


Fig. 3.370. Liquidus surface in the system CaO-FeO-MnO-SiO_2 in contact with metallic iron at 1600 °C after Görl et al. [1]. For the liquidus temperatures in the sub-system MnO-SiO_2-$2CaO{\cdot}Fe_2O_3$, see Sokolov et al. [2].

References

[1] Görl, E., R. Klages, R. Scheel, G. Trömel: Arch. Eisenhüttenwes. 40 (1969) No. 12, p. 959/67

[2] Sokolov, G. A., A. G. Sergeev, D. E. Matveev, E. M. Tonkikh: Fiz.-Khim. Osn. Protsessov Proizvod. Stali, Edited by: Ageev, N. V., Izd. Nauka: Moscov, USSR (1979), p. 146/50

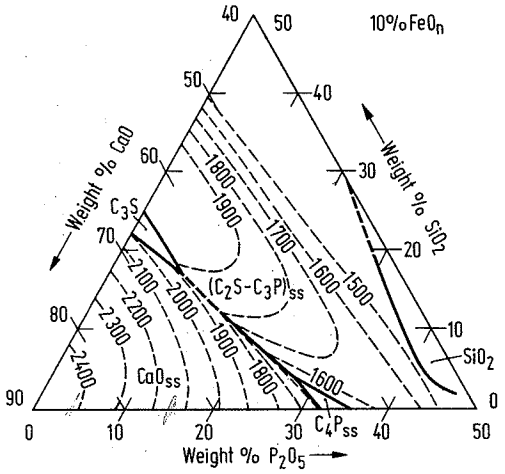


Fig. 3.371.

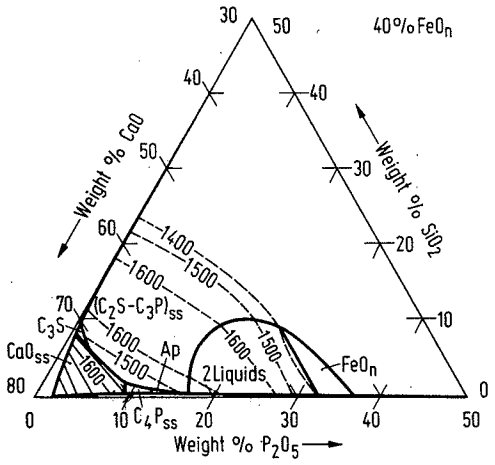


Fig. 3.374.

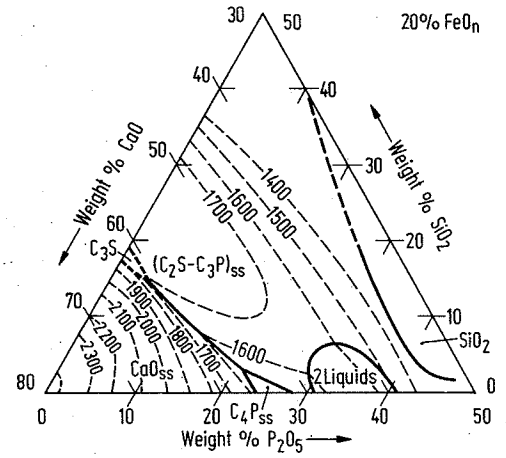


Fig. 3.372.

Figs. 3.371 to 3.374. Liquidus surface in the $CaO\text{-}FeO_x\text{-}P_2O_5\text{-}SiO_2$ system under an atmosphere consisting of CO_2 and H_2 in ratio CO_2/H_2=9, at 10, 20 30 and 40 mass % FeO (total iron oxide contents re-calculated as FeO) after Margot-Marette, Riboud [1-3] and Riboud, Margot-Marette [4]. For additional sections at 7.5, 15, 25 and 50 mass % FeO, see original paper 1-4). For the base system $CaO\text{-}P_2O_5\text{-}SiO_2$, see Fig. 3.261.

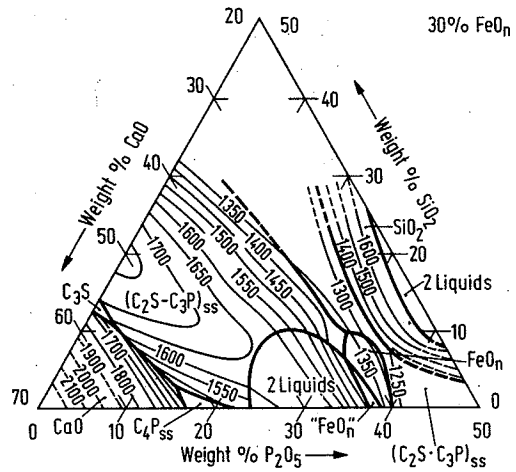


Fig. 3.373.

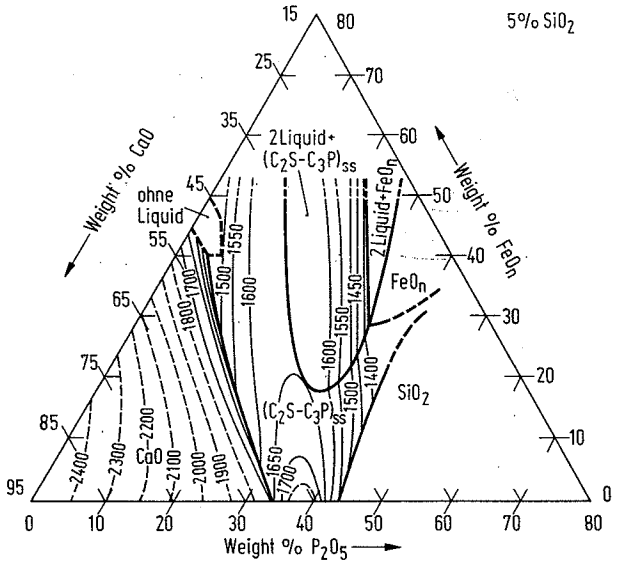


Fig. 3.375.

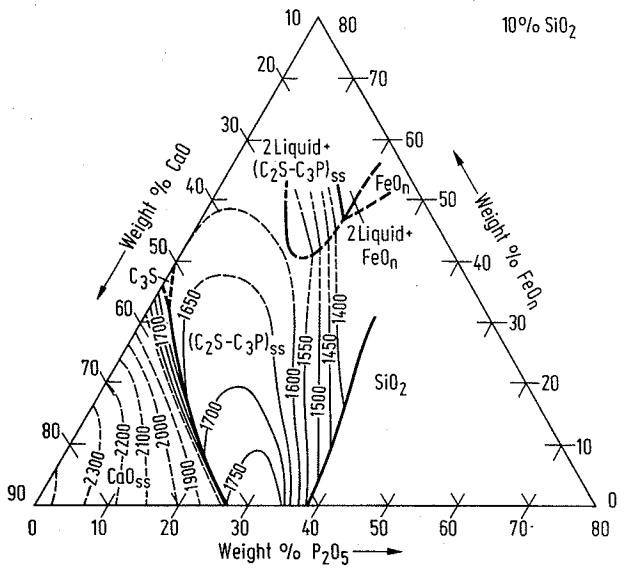


Fig. 3.376.

Figs. 3.375 and 3.376. Liquidus surface in the $CaO-FeO_x-P_2O_5-SiO_2$ system under an atmosphere consisting of CO_2 and H_2 in ratio $CO_2/H_2=9$, at 5 and 10 mass % SiO_2 after Margot-Marette, Riboud [1-3] and Riboud, Margot-Marette [4] (total iron oxide contents re-calculated as FeO). For the base system $CaO-FeO_x-P_2O_5$, see Fig. 3.219.

For the liquidus surface in the $CaO-FeO-P_2O_5-SiO_2$ system in contact with metallic iron at 10 mass % P_2O_5, see Werme, Lundh [5]. The phase equilibria in the system $CaO-FeO_n-P_2O_5-SiO_2$ in contact with metallic iron at 1600 °C have also been investigated by Trömel, Fritze [6], Drewes, Olette [7], Trömel et al. [8], Koch et al. [9] and Koch, Fix [10]. For the phase equilibria at 1400 °C, see Fix et al. [11]. The liquidus isotherms at 1350 and 1450 °C in the FeO_n-rich region of the system have been reported by Ito et al. [12]. For the compatibility relations in the sub-system $CaO-CaO{\cdot}Fe_2O_3-2CaO{\cdot}SiO_2-3CaO{\cdot}P_2O_5$, see Yang, Chang [13].

References

[1] Margot-Marette, H., P. V. Riboud: Mém. Sci. Rev. Métall. 63 (1966) No. 11, p. 959/67
[2] Margot-Marette, H., P. V. Riboud: Mém. Sci. Rev. Métall. 66 (1969) No. 7-8, p. 591/601
[3] Margot-Marette, H., P. V. Riboud: Mém. Sci. Rev. Métall. 69 (1972) No. 9, p. 593/604
[4] Riboud, P. V., H. Margot-Marette: Mém. Sci. Rev. Métall. 65 (1968) No. 7-8, p. 477/91
[5] Werme, A., P.-A. Lundh: Scand. J. Metall. 16 (1987) No. 1, p. 33/41
[6] Trömel, G., H. W. Fritze: Arch. Eisenhüttenwes. 28 (1957) No. 8, p. 489/95
[7] Drewes, E.-J., M. Olette: Arch. Eisenhüttenwes. 38 (1967) No. 3, p. 163/75
[8] Trömel, G., W. Fix, K. Koch: Arch. Eisenhüttenwes. 38 (1967) No. 3, p. 177/84
[9] Koch, K., W. Fix, G. Trömel: Arch. Eisenhüttenwes. 41 (1970) No. 3, p. 213/19
[10] Koch, K., W. Fix: Arch. Eisenhüttenwes. 41 (1970) No. 2, p. 111/8
[11] Fix, W., K. Koch, U. Bongers: Arch. Eisenhüttenwes. 46 (1975) No. 9, p. 555/9
[12] Ito, K., M. Yanagisawa, N. Sano: Tetsu-to-Hagane 68 (1982) No. 2, p. 342/4
[13] Yang, H.-Y, C.-L. Chang: Trans. J. Br. Ceram. Soc. 89 (1990), p. 159/63

$CaO-MgO-Na_2O-SiO_2$

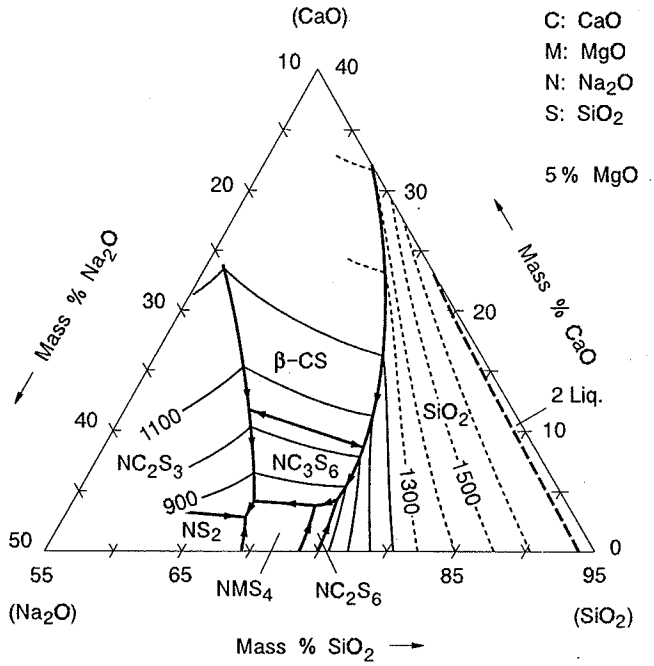


Fig. 3.377.

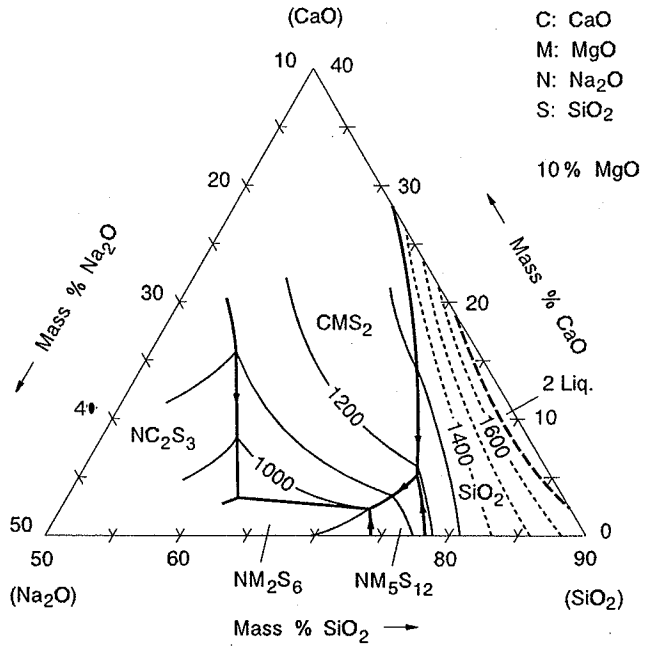


Fig. 3.378.

Figs. 3.377 and 3.378. Liquidus surface in the SiO_2-rich portion of the $CaO-MgO-Na_2O-SiO_2$ system with 5 and 10 mass % MgO after Shahid, Glasser [1]. For the base system $CaO-Na_2O-SiO_2$, see Fig. 3.260. For invariant points and crystallisation paths, see original paper [1].

References

[1] Shahid, K. A., F. P. Glasser: Phys. Chem. Glasses 13 (1972) No. 2, p. 27/42

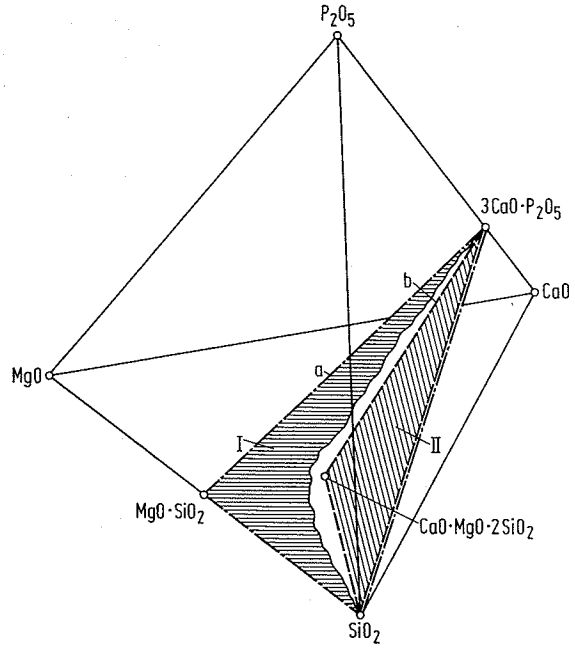


Fig. 3.379. Location of composition sections in the $CaO\text{-}MgO\text{-}P_2O_5\text{-}SiO_2$ tetrahedron.

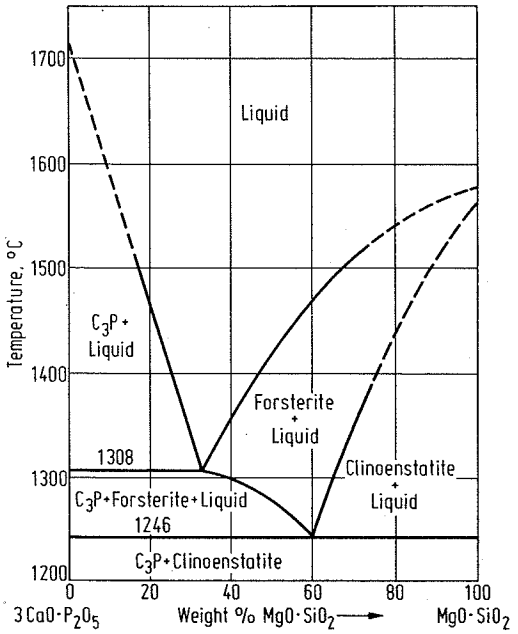


Fig. 3.381. Composition section $3CaO \cdot P_2O_5\text{-}MgO \cdot SiO_2$ (section a in Fig. 3.379) after Sata [1].

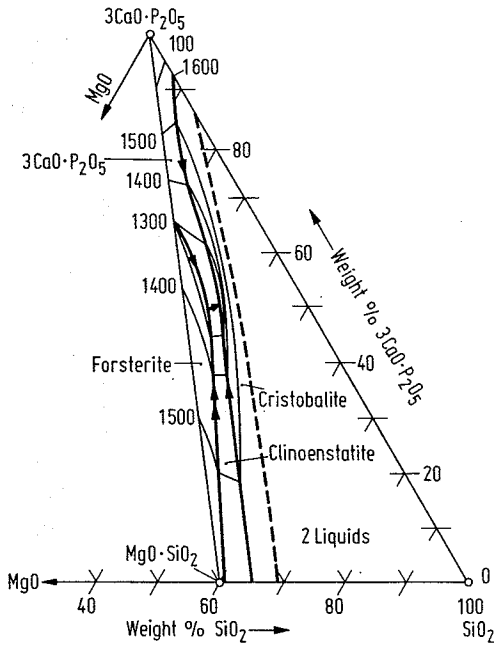


Fig. 3.380. Liquidus surface in the sub-system $MgO\text{-}3CaO \cdot P_2O_5\text{-}MgO \cdot SiO_2$ (section I in Fig. 3.379) after Sata [1].

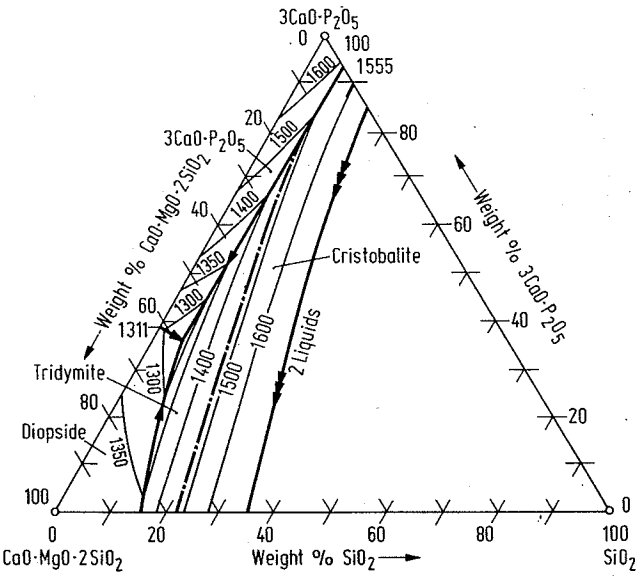


Fig. 3.382. Liquidus surface in the sub-system $SiO_2\text{-}3CaO \cdot P_2O_5\text{-}CaO \cdot MgO \cdot 2SiO_2$ (section II in Fig. 3.379) after Sata [2].

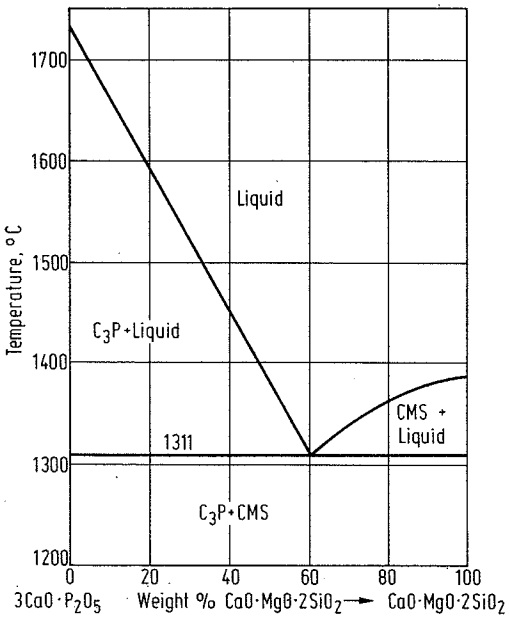


Fig. 3.383. Composition section $3CaO{\cdot}P_2O_5$-$CaO{\cdot}MgO{\cdot}2SiO_2$ (section b in Fig. 3.379) after Sata [2].

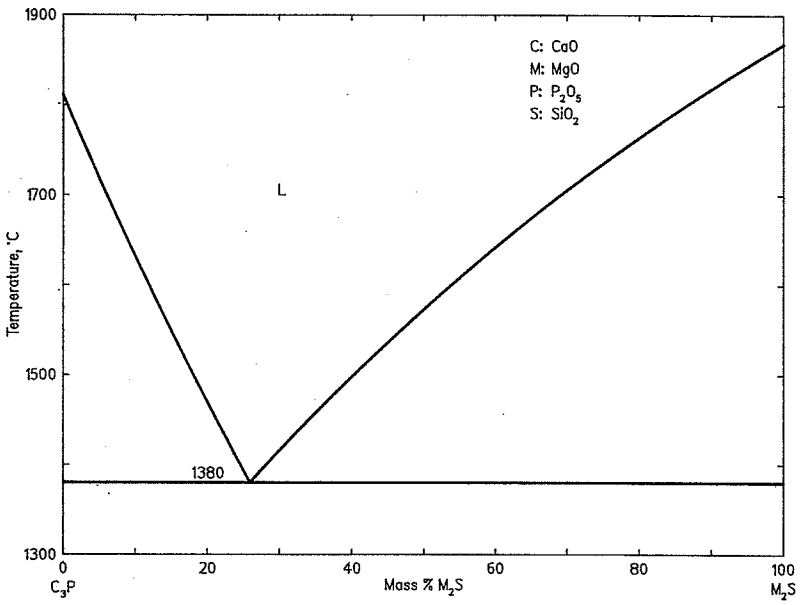


Fig. 3.384. Composition section $3CaO{\cdot}P_2O_5$-$2MgO{\cdot}SiO_2$ after Ustyantsev, Tretnikov [3].

References

[1] Sata, T.: Bull. Chem. Soc. Jap. 32 (1959) No. 4, p. 106/8
[2] Sata, T.: Bull. Chem. Soc. Jap. 31 (1958) No. 4, p. 408/12
[3] Ustyantsev, V. M., M. G. Tretnikov: Izv. Akad. Nauk SSSR, Neorg. Mater. 12 (1976) No. 10, p. 1894/6

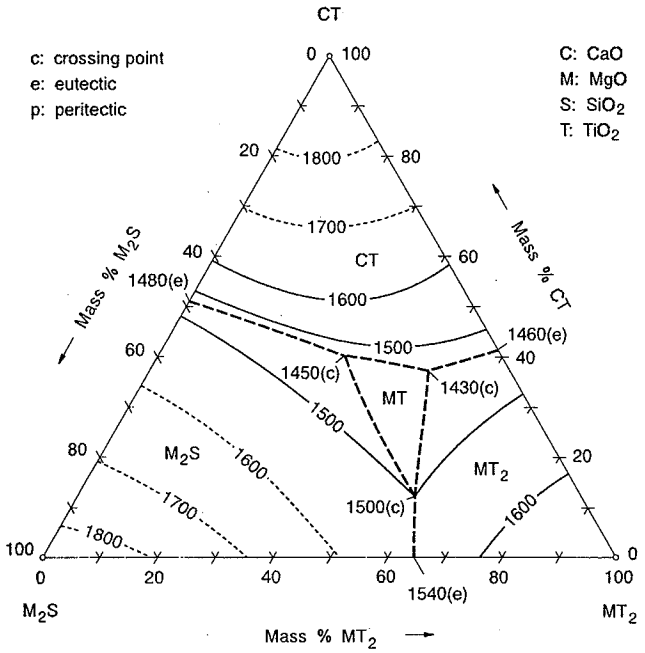


Fig. 3.385. Liquidus surface in the sub-system $CaO{\cdot}TiO_2$-$2MgO{\cdot}SiO_2$-$MgO{\cdot}2TiO_2$ after Bell et al. [1].

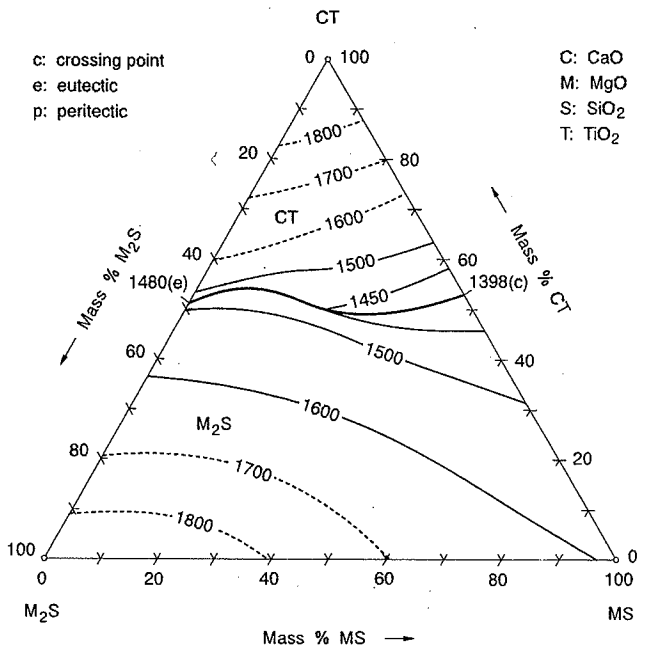


Fig. 3.387. Liquidus surface in the sub-system $CaO{\cdot}TiO_2$-$2MgO{\cdot}SiO_2$-$MgO{\cdot}SiO_2$ after Bell et al. [1].

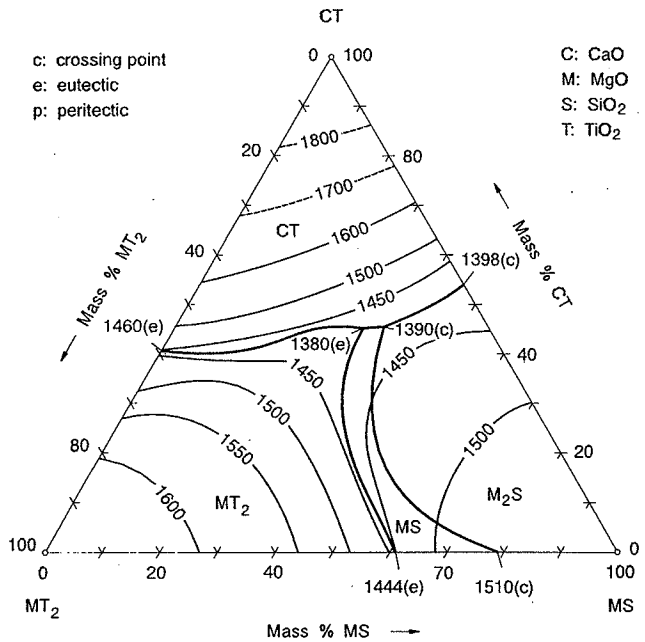


Fig. 3.386. Liquidus surface in the sub-system $CaO{\cdot}TiO_2$-$MgO{\cdot}SiO_2$-$MgO{\cdot}2TiO_2$ after Bell et al. [1].

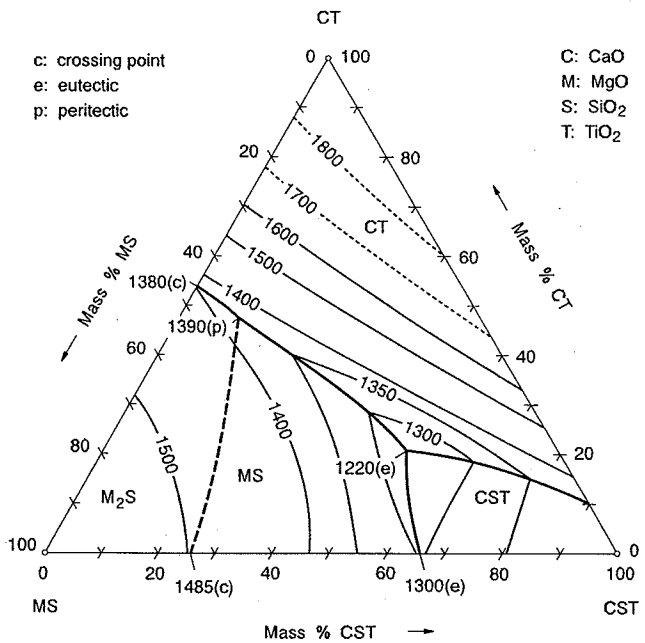


Fig. 3.388. Liquidus surface in the sub-system $CaO{\cdot}TiO_2$-$MgO{\cdot}SiO_2$-$CaO{\cdot}SiO_2{\cdot}TiO_2$ after Bell et al. [1]. For space representation of liquidus and compatibility relations in the sub-system $MgO\text{-}CaO{\cdot}TiO_2\text{-}SiO_2\text{-}TiO_2$, see Bell et al. [1].

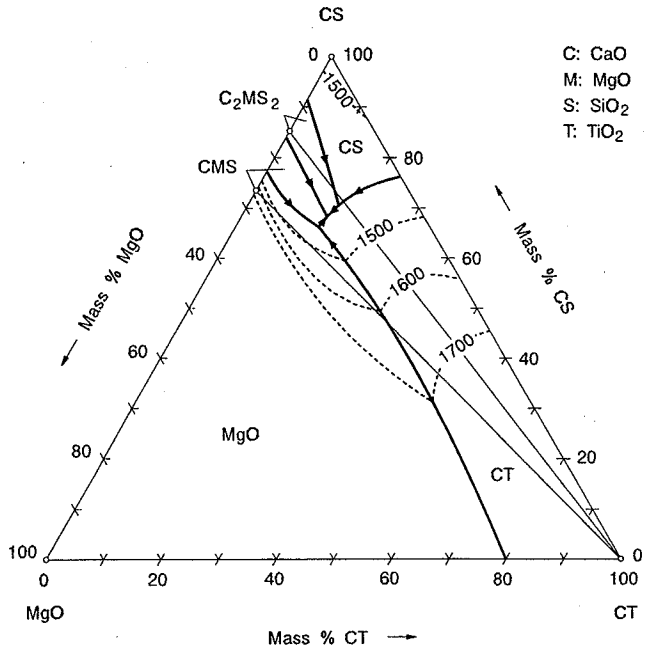


Fig. 3.389. Liquidus surface in the sub-system MgO-$CaO{\cdot}TiO_2$-$CaO{\cdot}SiO_2$ after Altunlu et al. [2, 3].

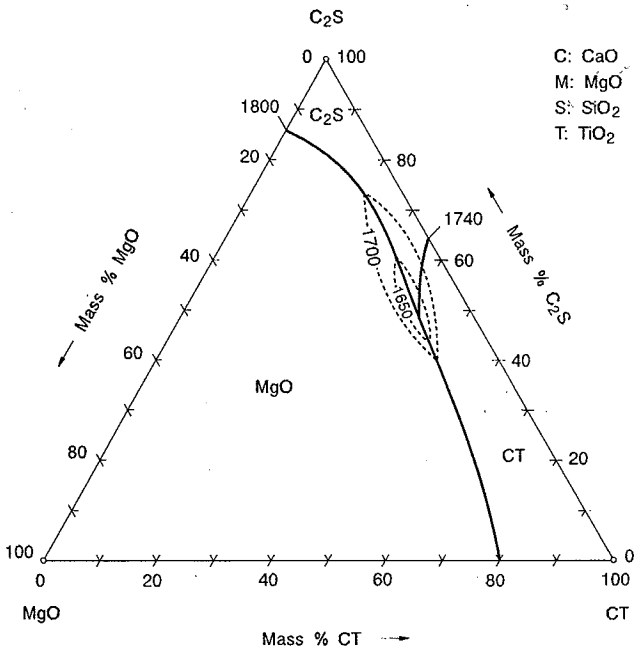


Fig. 3.390. Liquidus surface in the sub-system MgO-$CaO{\cdot}TiO_2$-$2CaO{\cdot}SiO_2$ after Altunlu et al. [2, 3].

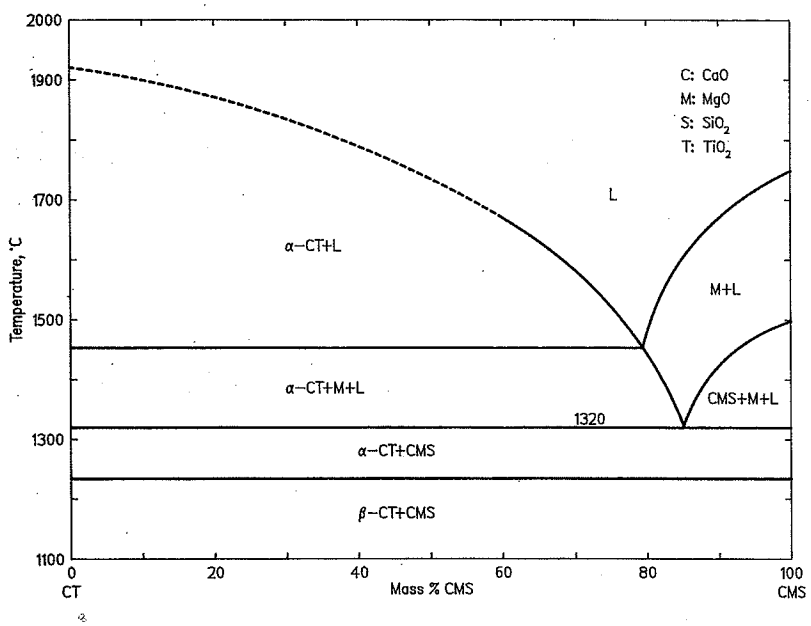


Fig. 3.391. Composition section $CaO{\cdot}TiO_2$-$CaO{\cdot}MgO{\cdot}SiO_2$ after Panek et al. [4].

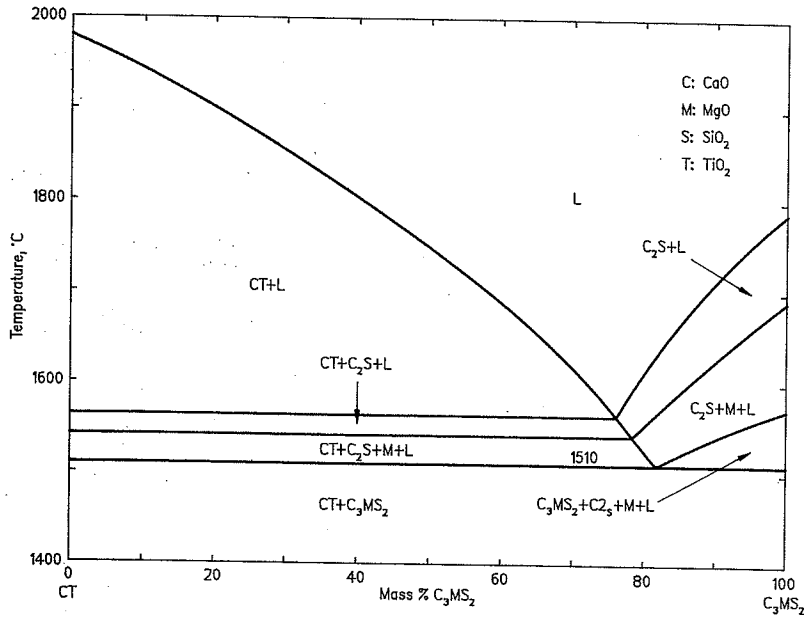


Fig. 3.392. Composition section $CaO{\cdot}TiO_2$-$3CaO{\cdot}MgO{\cdot}2SiO_2$ after Panek et al. [4].

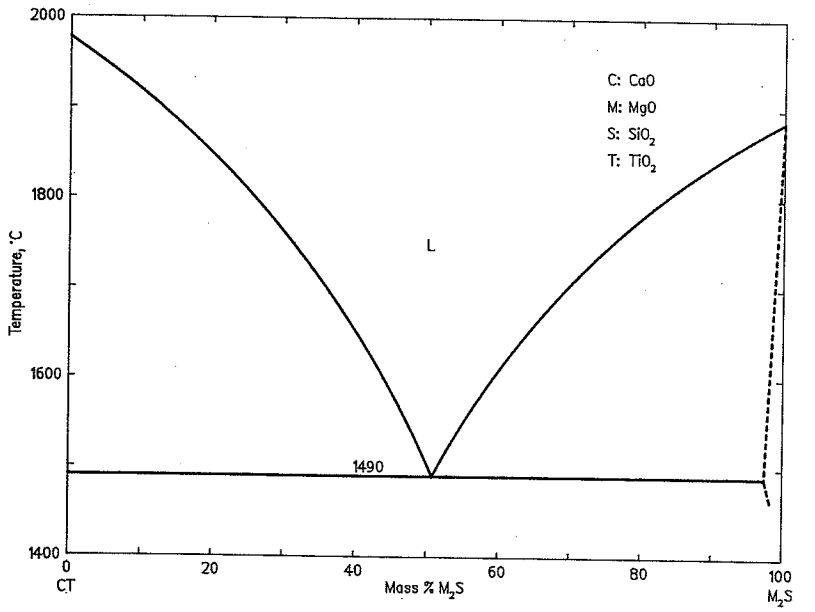


Fig. 3.393. Composition section $CaO{\cdot}TiO_2$-$2MgO{\cdot}SiO_2$ after Panek et al. [4].

References

[1] Bell, H. B., A. H. Cooper, Y. B. H. Mansor, R. J. Roxburgh: Spec. Publ. - Chem. Soc., /Proc. Conf.: High Temp. Chem. Inorg. Ceram. Mater./ 30 (1977), p. 41/50

[2] Altunlu, B., A. Z. Ogut, O. D. Toledo, N. H. Brett: Trans. J. Br. Ceram. Soc. 83 (1984) No. 3, p. 83/8

[3] Altunlu, B., A. Z. Ogut, O. D. Toledo, N. H. Brett: Trans. J. Br. Ceram. Soc. 83 (1984) No. 4, p. 115/9

[4] Panek, Z., E. Kanclir, J. Staron, M. Kozlovsky, S. Palco: Silikaty 20 (1976) No. 1, p. 13/22

3.2.5 Systems with five oxide components

Al_2O_3-CaO-Cr_2O_3-MgO-SiO_2

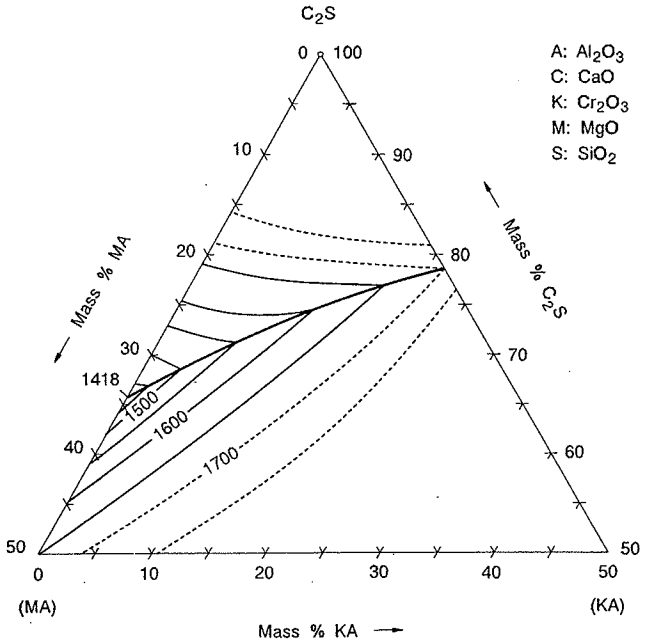


Fig. 3.394. Liquidus surface in the portion of the subsystem MgO·Al_2O_3-MgO·Cr_2O_3-2CaO·SiO_2 after El-Shahat, White [1].

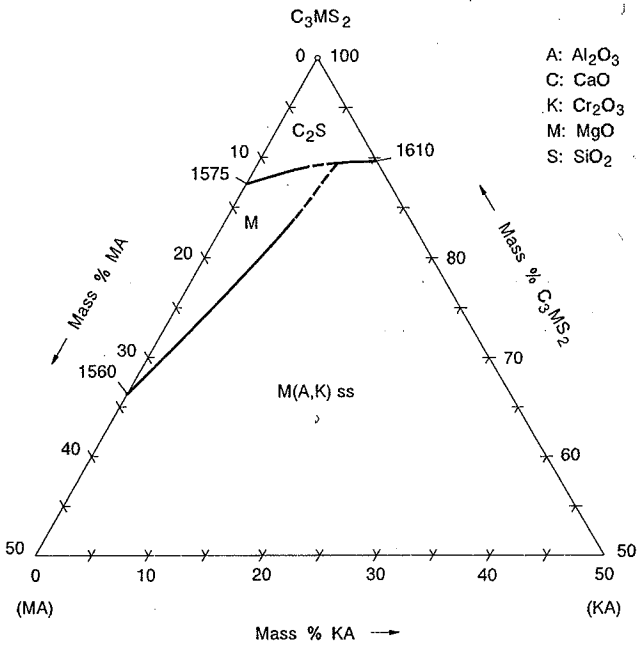


Fig. 3.396. Liquidus surface in the portion of the subsystem MgO·Al_2O_3-MgO·Cr_2O_3-3CaO·MgO·2SiO_2 after El-Shahat, White [3].

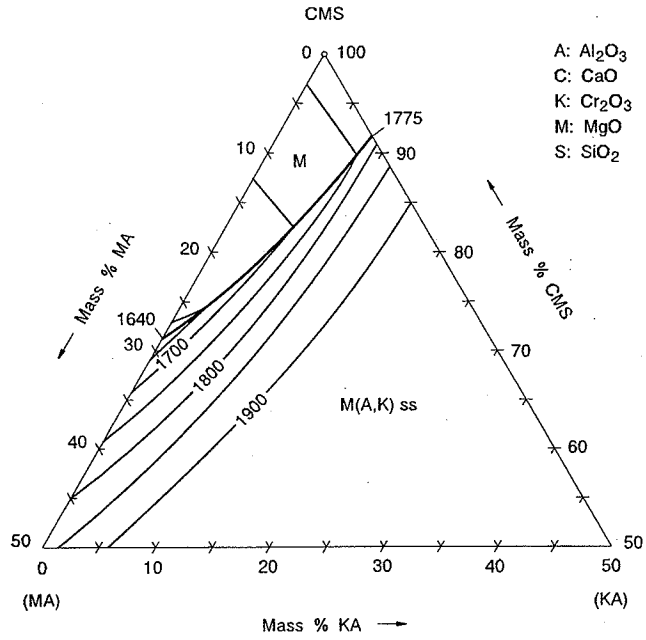


Fig. 3.395. Liquidus surface in the portion of the subsystem MgO·Al_2O_3-MgO·Cr_2O_3-CaO·MgO·SiO_2 after El-Shahat, White [2].

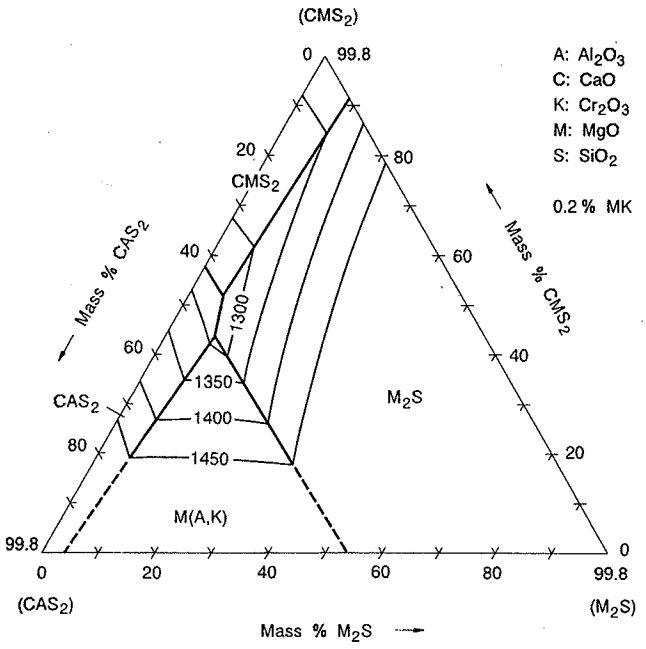


Fig. 3.397.

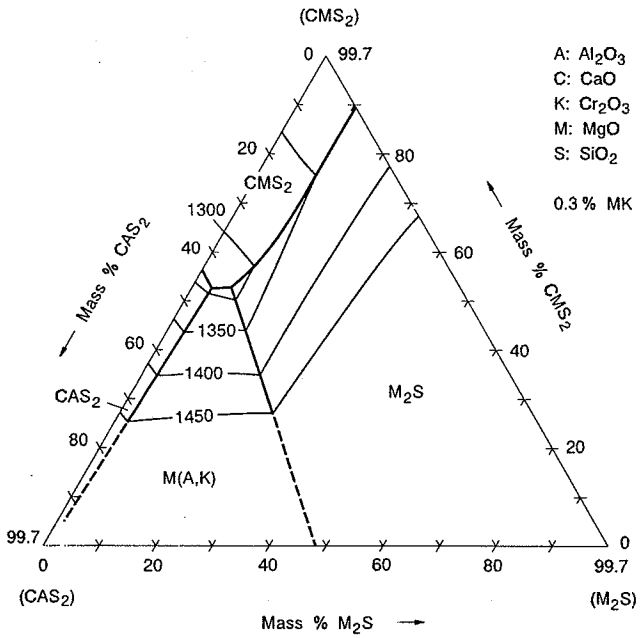


Fig. 3.398.

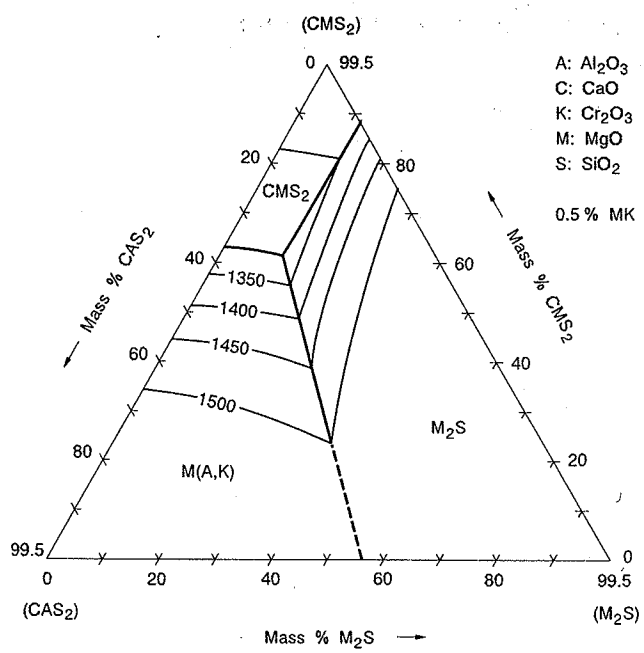


Fig. 3.399.

Figs. 3.397 to 3.399. Liquidus surface in the sub-system $CaO{\cdot}Al_2O_3{\cdot}2SiO_2$-$CaO{\cdot}MgO{\cdot}2SiO_2$-$MgO{\cdot}Cr_2O_3$-$2MgO{\cdot}SiO_2$ with 0.2, 0.3 and 0.5 mass % of $MgO{\cdot}Cr_2O_3$ after Onuma, Tohara [4].

For further contributions to the system Al_2O_3-CaO-Cr_2O_3-MgO-SiO_2, see also Berry et al. [5], Biggar [6], Baptista, White [7] and Segadães et al. [8].

References

[1] El-Shahat, R. M., J. White: Trans. J. Br. Ceram. Soc. 63 (1964) No. 6, p. 313/30

[2] El-Shahat, R. M., J. White: Trans. J. Br. Ceram. Soc. 65 (1966) No. 9, p. 497/519

[3] El-Shahat, R. M., J. White: Trans. J. Br. Ceram. Soc. 65 (1966) No. 6, p. 309/36

[4] Onuma, K., T. Tohara: Contrib. Mineral. Petrol. 84 (1983), p. 174/81

[5] Berry, T. F., W. C. Allen, R. B. Snow; J. Am. Ceram. Soc. 33 (1950) No. 4, p. 121/32

[6] Biggar, G. M.: Refract. J. 48 (1972) No. 1, p. 6/9

[7] Baptista, J. L., J. White: Trans. J. Br. Ceram. Soc. 78 (1979) No. 6, p. 122/9

[8] Segadães, A. M., N. H. Brett, J. White: Trans. J. Br. Ceram. Soc. 85 (1986), p. 194/200

Al_2O_3-CaO-MgO-MnO_x-SiO_2

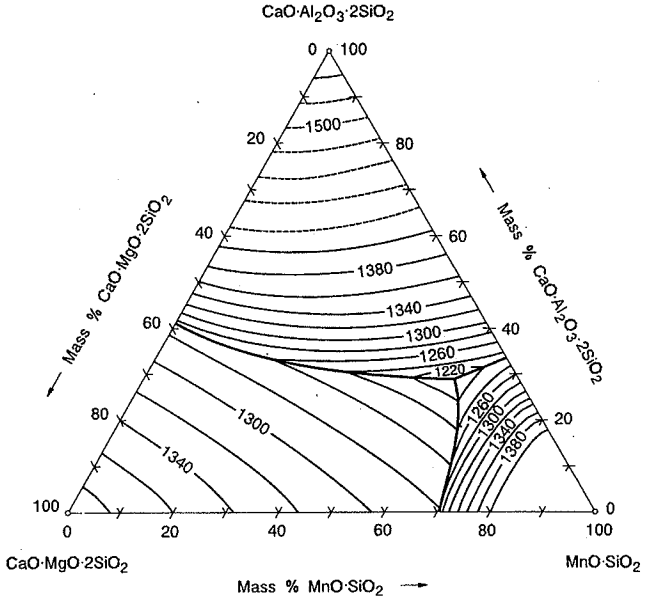


Fig. 3.400. Liquidus surface in the sub-system $CaO{\cdot}MgO{\cdot}2SiO_2$-$CaO{\cdot}Al_2O_3{\cdot}2SiO_2$-$MnO{\cdot}SiO_2$ after Bumpei Yoshiki [1].

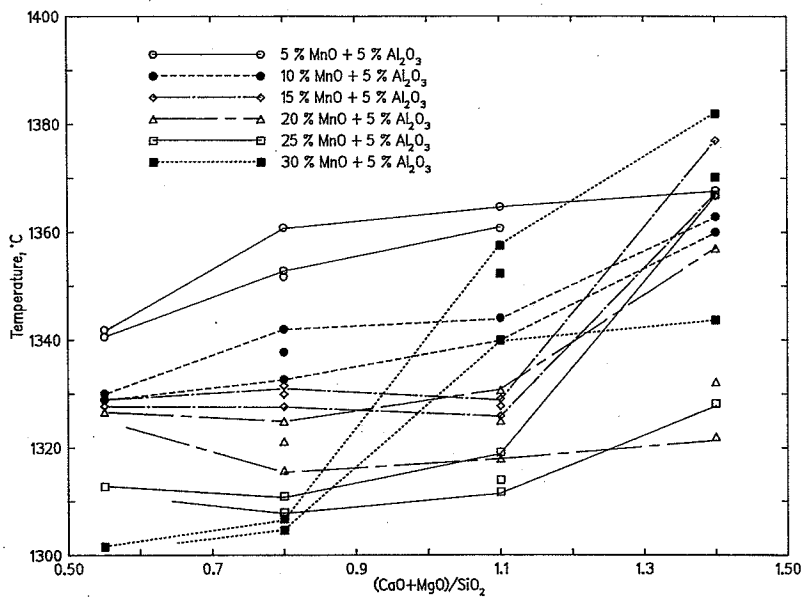


Fig. 3.401. Liquidus temperatures in the Al_2O_3-CaO-MgO-MnO-SiO_2 system as a function of the basicity ratio at various MnO contents and at 5 mass % Al_2O_3 after Eric et al. [2]. The concentrations of other slag components were as follow: CaO - 20 to 35, MgO - 5 to 15 and SiO_2 - 27 to 58 mass %.

References

[1] Bumpei Yoshiki: Glass Ind. 33 (1952) No. 7, p. 354/76

[2] Eric, R. H., A. A. Hejja, W. Stange: Miner. Eng. 4 (1991) No. 12, p. 1315/32

Al_2O_3-CaO-MgO-SiO_2-TiO_2

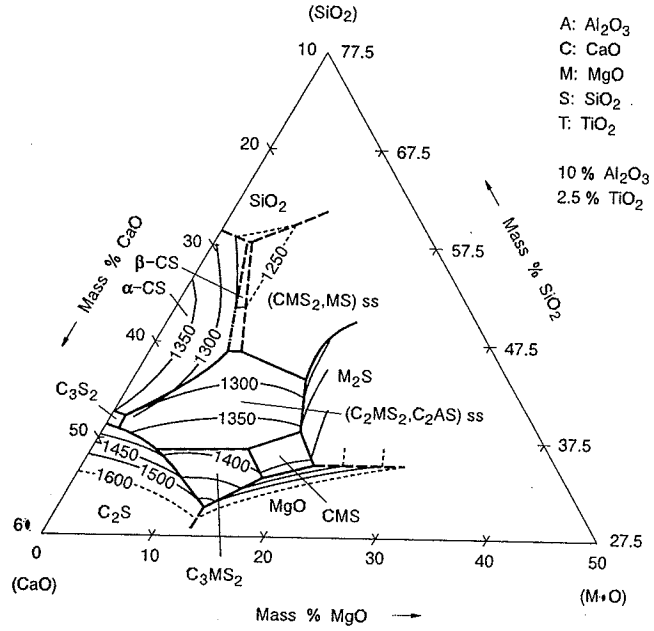


Fig. 3.402.

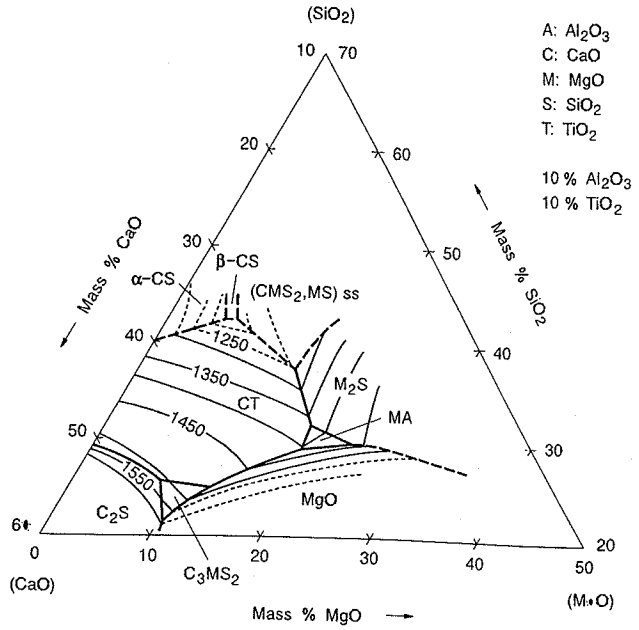


Fig. 3.404.

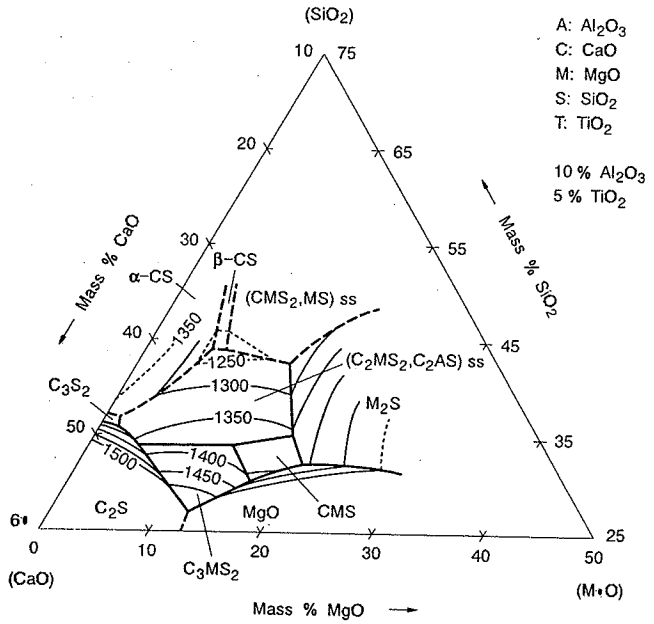


Fig. 3.403.

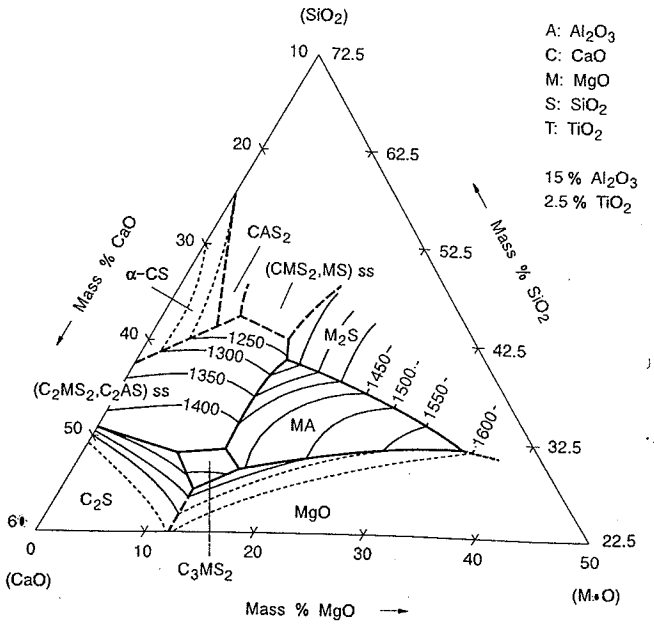


Fig. 3.405.

Figs. 3.402 to 3.405. Liquidus surfaces in the Al_2O_3-CaO-MgO-SiO_2-TiO_2 system with constant contents of Al_2O_3 and TiO_2 after Osborn, Gee [1]. For the base system CaO-MgO-SiO_2, see Fig. 3.249.

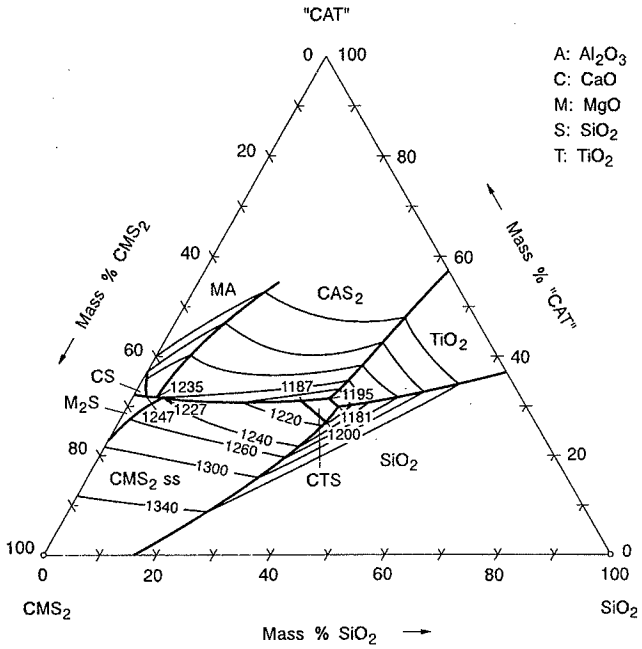


Fig. 3.406. Liquidus surface in the sub-system SiO_2-CaO·MgO·2SiO_2-"CaO·Al_2O_3·TiO_2" after Gupta et al. [2].

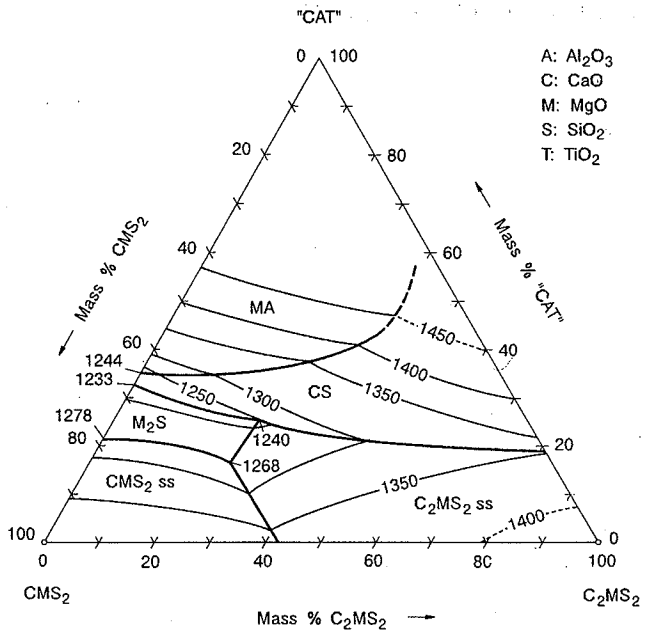


Fig. 3.408. Liquidus surface in the sub-system 2CaO·MgO·2SiO_2-CaO·MgO·2SiO_2-"CaO·Al_2O_3·TiO_2" after Onuma, Yagi [4] and Yagi, Onuma [5].

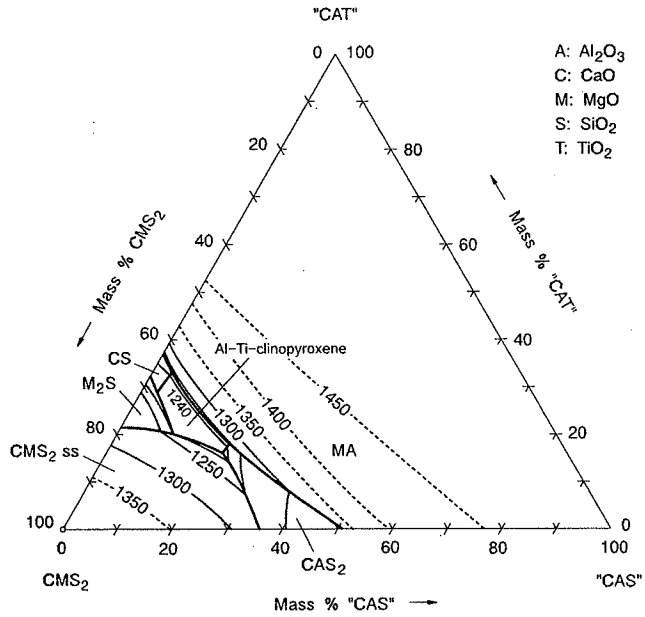


Fig. 3.407. Liquidus surface in the sub-system CaO·MgO·2SiO_2-"CaO·Al_2O_3·SiO_2"-"CaO·Al_2O_3·TiO_2" after Yang [3]. For the composition of the Al-Ti-clinopyroxene, see original paper [3].

For selected composition sections through the system Al_2O_3-CaO-MgO-SiO_2-TiO_2, see Jochens et al. [6] and McRae et al. [7].

References

[1] Osborn, E. F., K. H. Gee: Bull. Earth Miner. Sci. Exp. Sta., Pa. State Univ. (1969) No. 85, p. 57/80

[2] Gupta, A. K., K. Onuma, K. Yagi, E. G. Lidiak: Contrib. Mineral. Petrol. 41 (1973), p. 333/44

[3] Yang, H.-Y.: Proc. Geol. Soc. China (1975) No. 18, p. 48/58

[4] Onuma, K., K. Yagi: Mineral. Mag. 38 (1971) No. 296, p. 471/88

[5] Yagi, K., K. Onuma: Am. J. Sci., Schairer Vol 267A (1969), p. 509/49

[6] Jochens, P. R., G. Sommer, D. D. Howat: J. Iron Steel Inst. 207 (1969) Pt. 2, p. 187/92

[7] McRae, L. B., E. Pothas, P. R. Jochens, D. D. Howat: J. S. Afr. Inst. Mining Met. 69 (1969) No. 11, p. 577/94

$CaO\text{-}FeO_x\text{-}MgO\text{-}SiO_2\text{-}TiO_2$

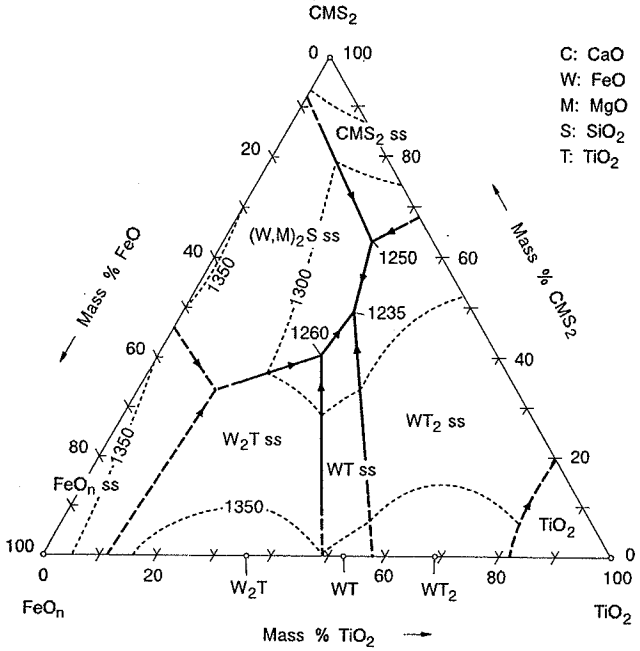


Fig. 3.409. Liquidus surface in the sub-system $FeO\text{-}TiO_2\text{-}CaO{\cdot}MgO{\cdot}2SiO_2$ in contact with metallic iron after Lipin, Muan [1].
For composition section $CaO{\cdot}MgO{\cdot}2SiO_2\text{-}CaO{\cdot}Fe_2O_3{\cdot}TiO_2$, see Huckenholz [2].

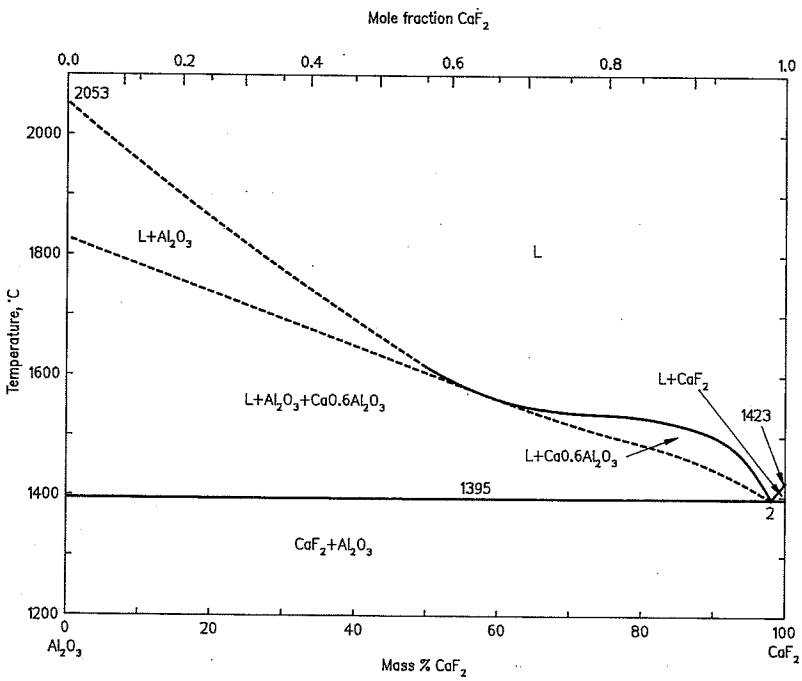
References

[1] Lipin, B. R., A. Muan: Geochim. Cosmochim. Acta, Suppl.: Proc. 6th Lunar Sci. Conf. 1 (1975), p. 945/58
[2] Huckenholz, H. G.: Am. J. Sci. 267A (1969), p. 209/32

3.2.6 Slag systems containing fluorine

$Al_2O_3\text{-}CaF_2$

Fig. 3.410. $Al_2O_3\text{-}CaF_2$ pseudo-binary system in a sealed cell after Chatterjee, Zhmoidin [1]. For similar phase diagrams, see also Povolotskii et al. [2] and Ries, Schwerdtfeger [3]. The thermodynamics of the system and calculated phase diagram were reported by Zaitsev et al. [4].



References

[1] Chatterjee, A. K., G. I. Zhmoidin: J. Mater. Sci. 7 (1972) No. 1, p. 93/7
[2] Povolotskii D. Ya., G. P. Vyatkin, Y. G. Ismailov: Sb. Nauch. Tr. Chelyabinsk. Politekhn. Inst. 166 (1975), p. 35/41
[3] Ries, R., K. Schwerdtfeger: Arch. Eisenhüttenwes. 51 (1980) No. 4, p. 123/9
[4] Zaitsev, A. I., N. V. Korolev, B. M. Mogutnov: High Temp. Sci., Volume Date 1988, 28 (1990), p. 351/77

$BaO\text{-}CaF_2$

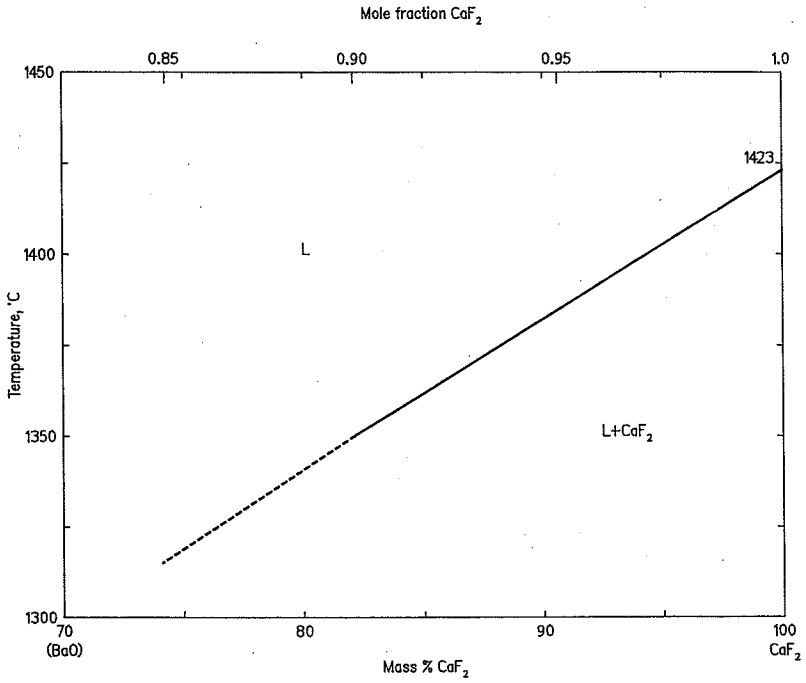


Fig. 3.411. The liquidus curve in the CaF_2-rich region of the $BaO\text{-}CaF_2$ system after Kojima, Masson [1].

References

[1] Kojima, H., C. R. Masson: Canad. J. Chem. 47 (1969), p. 4221/8

$CaF_2\text{-}CaO$

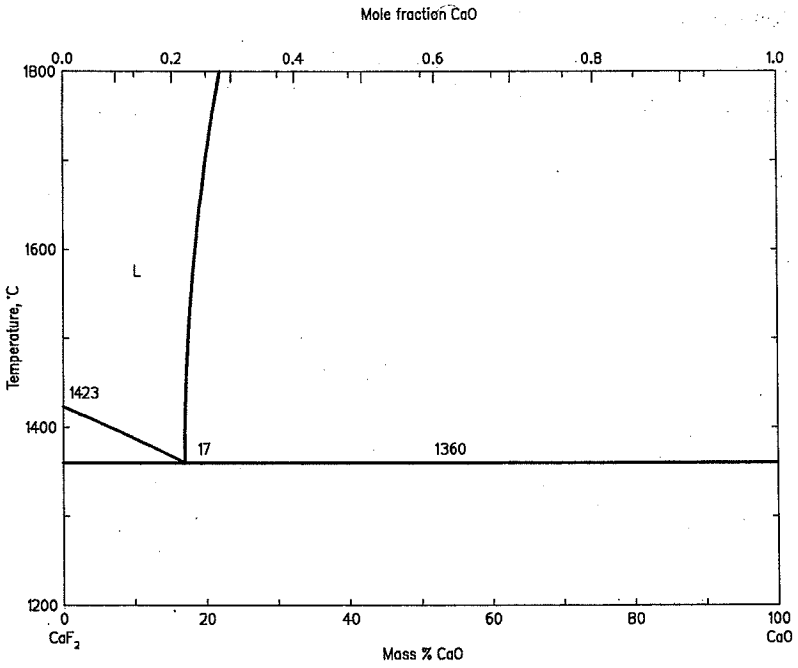


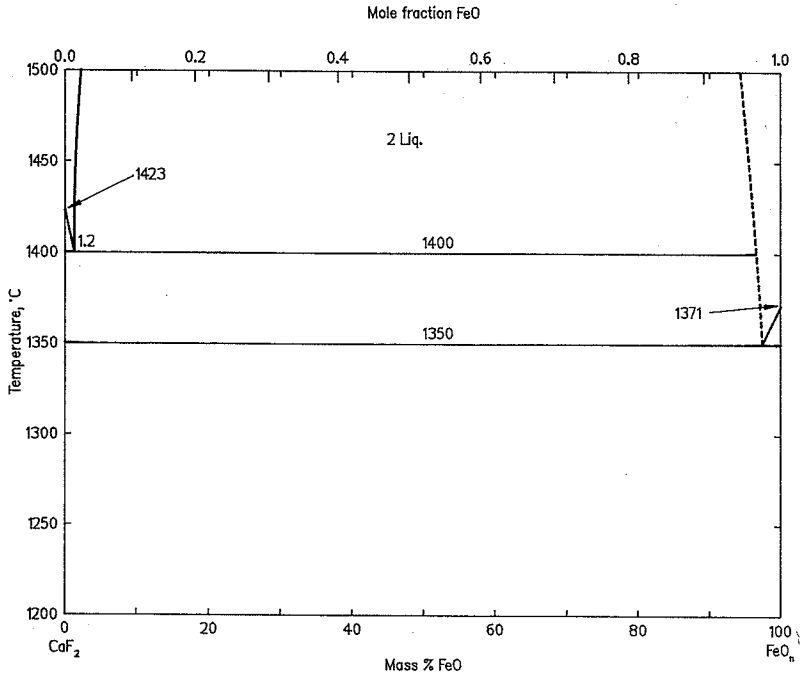
Fig. 3.412. $CaF_2\text{-}CaO$ phase diagram after Ries, Schwerdtfeger [1] (CaO-liquidus) and Kojima, Masson [2] (CaF_2-liquidus). Similar solubility of CaO in molten slags has been determined previously by Zhmoidin, Chatterjee [3].

References

[1] Ries, R., K. Schwerdtfeger: Arch. Eisenhüttenwes. 51 (1980) No. 4, p. 123/9
[2] Kojima, H., C. R. Masson: Canad. J. Chem. 47 (1969), p. 4221/8
[3] Zhmoidin, G. I., A. K. Chatterjee: Zavodskajy Laboratorija 38 (1972) p. 186/89

CaF_2-FeO_x

Fig. 3.413. CaF_2-FeO system in contact with metallic iron after Körber, Oelsen [1], Oelsen, Maetz [2] and Kay et al. [3] (extension of the miscibility gap in the CaF_2-rich region of the system between 1420 and 1500 °C). The solubility of FeO in CaF_2-rich melts at 1450 °C up to approx. 2 mass % FeO has been reported by Hawkins, Davies [4]. After Mitchel [5], the miscibility gap at 1500 °C range from 15 to 90 mass % FeO.



References

[1] Körber, F., W. Oelsen: Stahl Eisen 60 (1940) No. 42, p. 921/9

[2] Oelsen, W., H. Maetz: Mitt. Kaiser Wilhelm Inst. Eisenforsch.,Düsseldorf 23 (1941) No. 12, p. 195/207

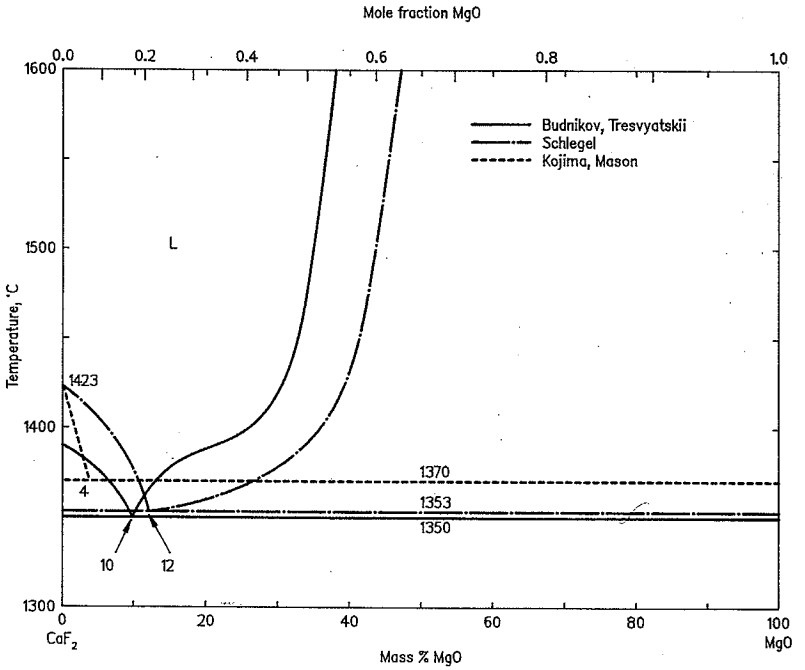
[3] Kay, D. A. R., A. Mitchel, M. Ram: J. Iron Steel Inst. 208 (1970) No. 2, p. 141/6

[4] Hawkins, R. J., M. W. Davies: J. Iron Steel Inst. 209 (1971) No. 3, p. 226/30

[5] Mitchel, A.: Can. Metall. Q. 20 (1981) No. 1, p. 101/12

CaF_2-MgO

Fig. 3.414. CaF_2-MgO phase diagrams after Budnikov, Tresvyatskii [1], Schlegel [2] and Kojima, Masson [3].



References

[1] Budnikov, P. P., S. G. Tresvyatskii: Ukrain. Khim. Zhur. 19 (1953), p. 552/5

[2] Schlegel, E.: Cercetari Metallurgice Bucureshi 9 (1967), p. 785/91

[3] Kojima, H., C. R. Masson: Canad. J. Chem. 47 (1969), p. 4221/8

CaF_2-NaF

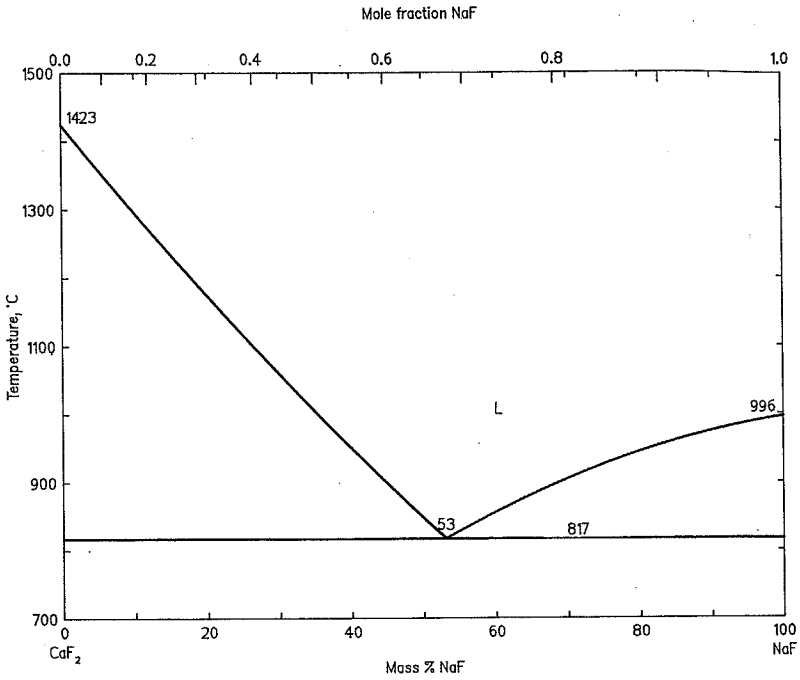


Fig. 3.415. CaF_2-NaF phase diagram calculated by Lin et al. [1] according to experimental results of Fedotieff, Iljinsky [2] and Silber, Ishaque [3].

References

[1] Lin, P. L., A. D. Pelton, M. L. Saboungi: Metall. Trans. B 13B (1982) No. 1, p. 61/9

[2] Fedotieff, P. P., W. P. Iljinsky: Z. Anorg. Allg. Chem. 129 (1923), p. 93/109

[3] Silber, P., M. Ishaque: C. R. Acad. Sci. 232 (1951), p. 1485/7

CaF_2-SiO_2

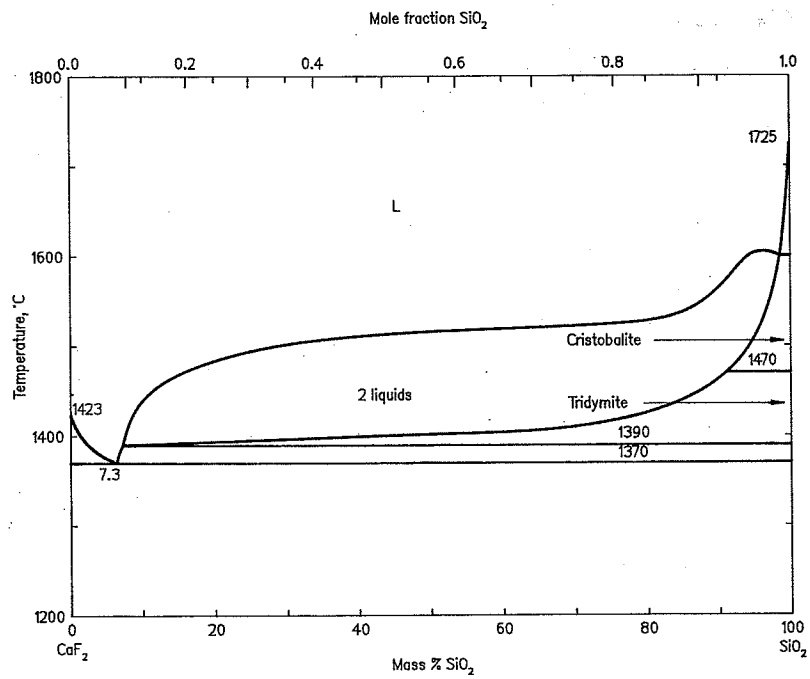


Fig. 3.416. CaF_2-SiO_2 phase diagram after Hillert [1]. The system CaF_2-SiO_2 has also been investigated by Putilin et al. [2], however, the final compositions of the investigated samples belong rather to the ternary system CaF_2-CaO-SiO_2.

References

[1] Hillert, L. H.: Acta Polytech. Scand., Chemistry Including Metallurgy, Series No. 90, (1970)

[2] Putilin, Y. M., A. D. Romanova, A. I. Milov: Ionnye Rasplavy (1976) No. 4 , p. 79/83

CaF_2-TiO_2

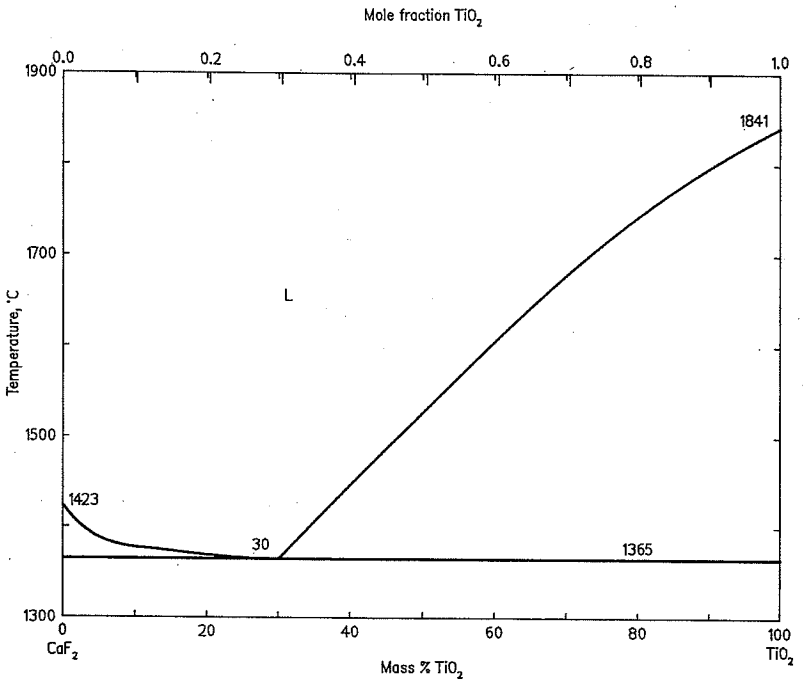


Fig. 3.417. CaF_2-TiO_2 phase diagram after Hillert [1].

References

[1] Hillert, L. H.: Acta Polytech. Scand., Chemistry Including Metallurgy, Series No. 90, (1970)

AlF_3-CaF_2-NaF

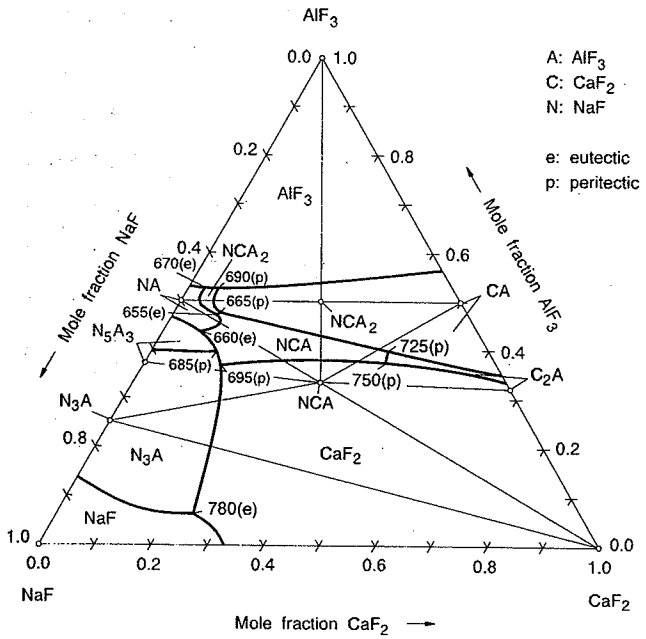


Fig. 3.418. Liquidus surface in the AlF_3-CaF_2-NaF system after Anufrieva et al. [1].

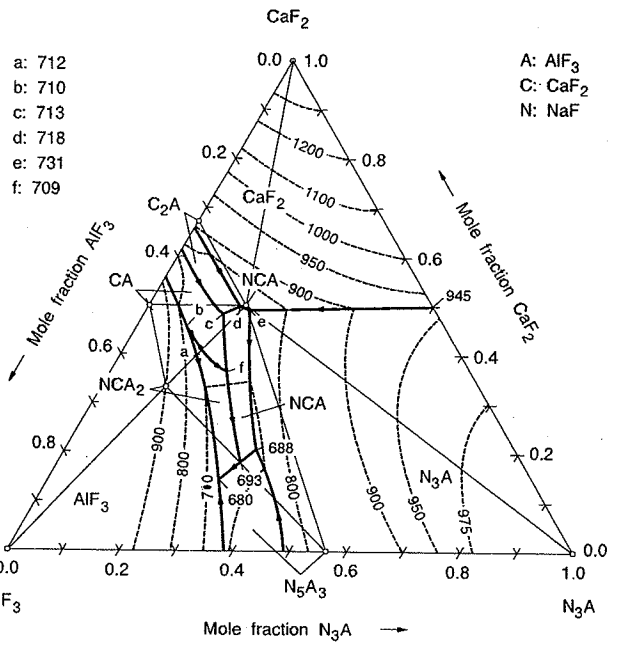


Fig. 3.419. Liquidus surface in the sub-system AlF_3-CaF_2-$3NaF{\cdot}AlF_3$ after Craig, Brown [2].

References

[1] Anufrieva, N. I., Z. N. Balashova, L. S. Baranova, V. N. Veretinskii: Tsvetn. Met. /Moscov/ 8 (1985), p. 66/71
[2] Craig, D. F., J. J. Brown, Jr.: J. Am. Ceram. Soc. 63 (1980) No. 5-6, p. 254/61

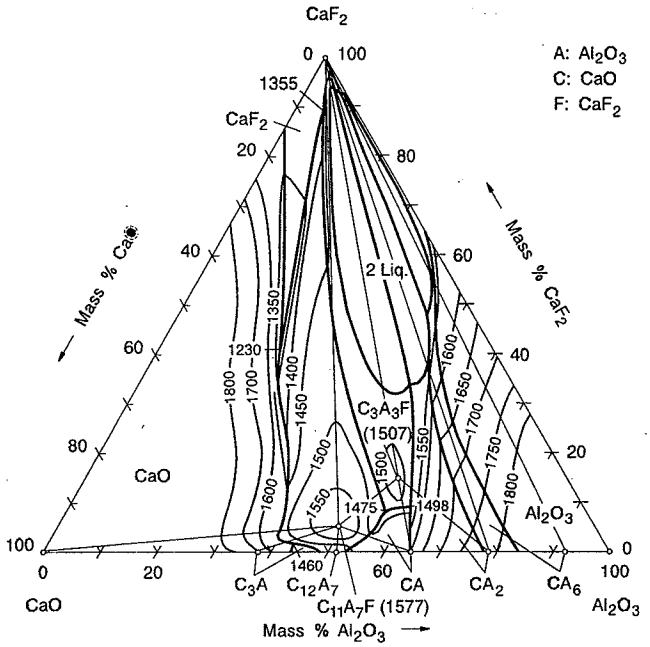


Fig. 3.420. Liquidus surface in the Al_2O_3-CaF_2-CaO system after Chatterjee, Zhmoidin [1] (sealed samples). For liquidus relations in numerous sub-systems, see also Chatterjee, Zhmoidin [2], Smirnov et al. [3] and Zhmoidin, Chatterjee [4].

The isothermal section through the system Al_2O_3-CaF_2-CaO at 1600 °C was reported by Ries, Schwerdtfeger [5]. The miscibility gap in the system has also been confirmed by Mitchell, Cameron [6] and Nakamura, Yanagase [7].

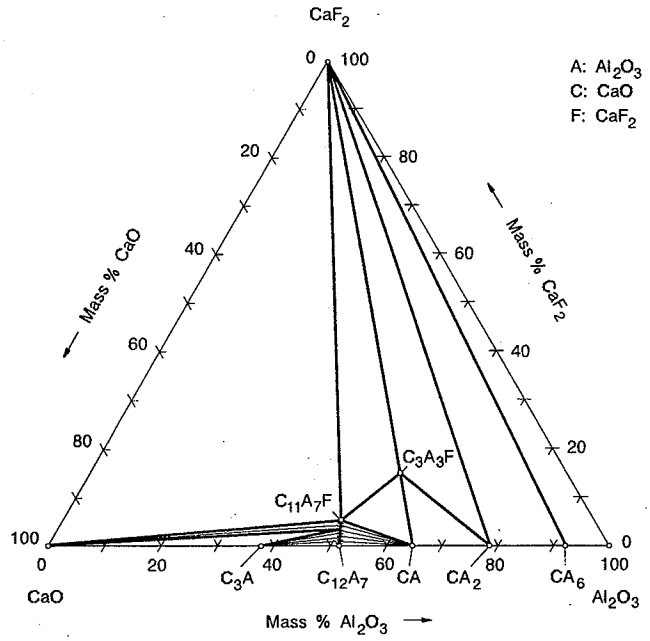


Fig. 3.421. Sub-solidus equilibria in the Al_2O_3-CaF_2-CaO system as determined by Brisi, Rolando [8] and confirmed by Chatterjee, Zhmoidin [1].

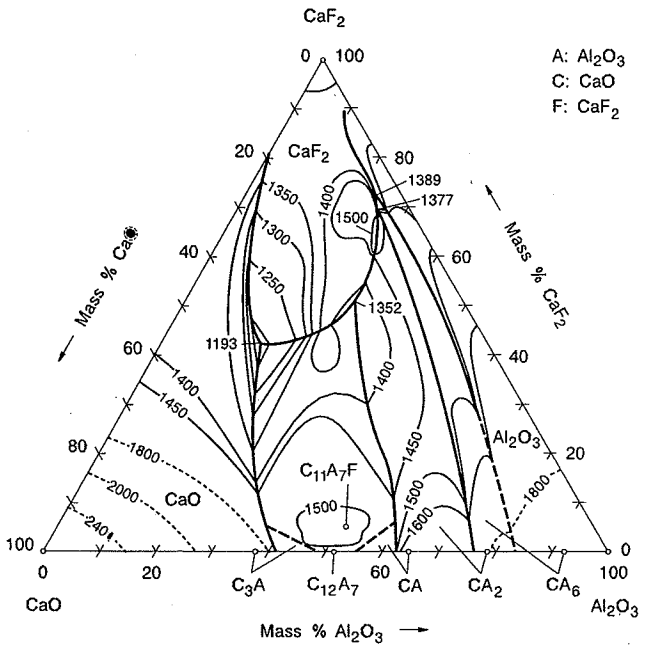


Fig. 3.422. Liquidus surface in the Al_2O_3-CaF_2-CaO system under 0.33 atm helium after Nafziger [9]. The sub-solidus equilibria after Brisi, Rolando [8] have also been confirmed.

Liquidus temperatures in the system under an argon atmosphere have been investigated by Povolotskii et al. [10]. For the thermodynamics of the system, see Zaitsev et al. [11, 12].

References

[1] Chatterjee, A. K., G. I. Zhmoidin: J. Mater. Sci. 7 (1972) No. 1, p. 93/7

[2] Chatterjee, A. K., G. I. Zhmoidin: Izv. Akad. Nauk SSSR, Neorg. Mater. 8 (1972) No. 5, p. 886/92

[3] Smirnov, G. S., A. K. Chatterjee, G. I. Zhmoidin: J. Mater. Sci. 8 (1973), p. 1278/82

[4] Zhmoidin, G. I., A. K. Chatterjee: Izv. Akad. Nauk SSSR, Neorg. Mater. 10 (1974) No. 10, p. 1846/51

[5] Ries, R., K. Schwerdtfeger: Arch. Eisenhüttenwes. 51 (1980) No. 4, p. 123/9

[6] Mitchell, A., J. Cameron: Metall. Trans. 2 (1971) No. 12, p. 3361/6

[7] Nakamura, T., T. Yanagase: J. Jpn. Inst. Met. 41 (1977) No. 2, p. 165/9

[8] Brisi, C., P. Rolando: Ann. Chim. /Rome/ 57 (1967) No. 11, p. 1304/15

[9] Nafziger, R. H.: High Temp. Sci. 5 (1973) No. 6, p. 414/22

[10] Povolotskii D. Ya., G. P. Vyatkin, Y. G. Ismailov: Sb. Nauch. Tr. Chelyabinsk. Politekhn. Inst. 166 (1975), p. 35/41

[11] Zaitsev, A. I., N. V. Korolev, B. M. Mogutnov: High Temp. Sci., Volume Date 1988, 28 (1990), p. 351/77

[12] Zaitsev, A. I., N. V. Korolev, B. M. Mogutnov: Zh. Fiz. Khim. 64 (1990) No. 6, p. 1494/504

Al_2O_3-CaF_2-FeO_x

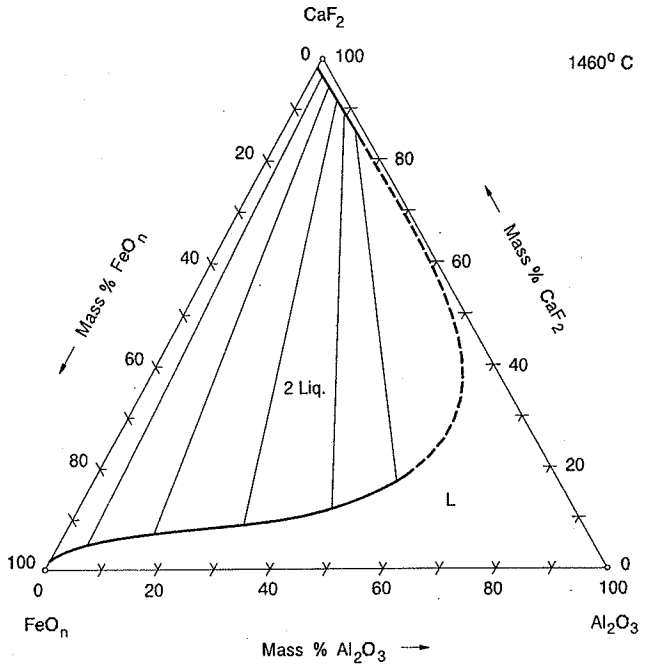


Fig. 3.423. Extension of the miscibility gap in the system Al_2O_3-CaF_2-FeO_n at 1460 °C after Ram [1], as quoted by Mills, Keene [2].

References

[1] Ram, M.: PhD thesis, University of Sheffield, (1967)
[2] Mills, K. C., B. J. Keene: Inter. Metals Rev. (1981) No. 1, p. 21/69

Al_2O_3-CaF_2-MgO

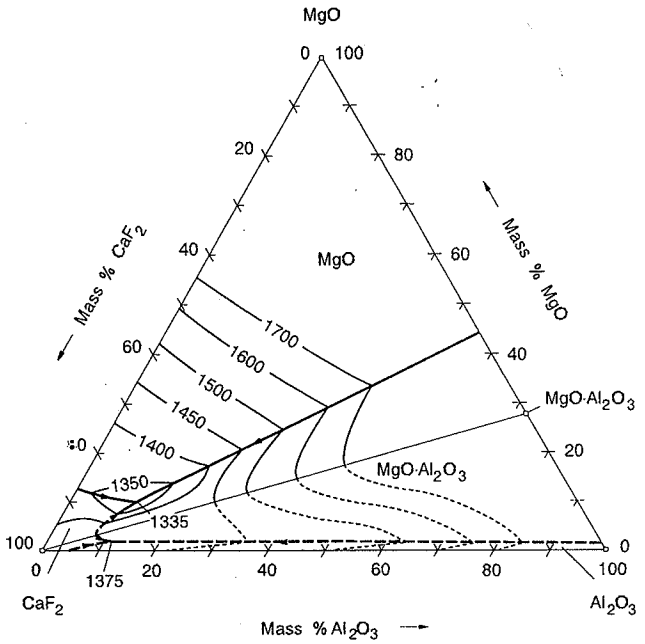


Fig. 3.424. Al_2O_3-CaF_2-MgO phase diagram in a neutral atmosphere after Povolotskii et al. [1]. Some liquidus temperatures for ternary compositions have also been reported by Keene, Quinn [2].

References

[1] Povolotskii, D. Ya., V. E. Roshchin, V. P. Gribanov, A. V. Rechkalova: Izv. Vyssh. Uchebn. Zaved., Chern. Metall. (1983) No. 4, p. 8/12
[2] Keene, B. J., T. J. Quinn: High Temp. - High Pressures 11 (1979), p. 693/702

Al_2O_3-CaF_2-SiO_2

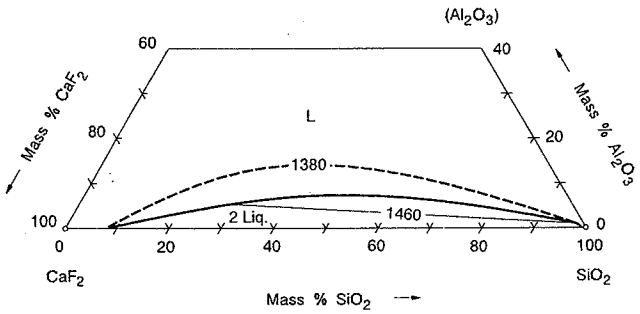


Fig. 3.425. Miscibility gap in the Al_2O_3-CaF_2-SiO_2 system after Hillert [1, 2] (1380 °C) and Yershova [3] (1460 °C). Some ternary compositions have also been investigated by Khokhlov et al. [4].

References

[1] Hillert, L. H.: Acta Chem. Scand. 19 (1965) No. 10, p. 2436/8
[2] Hillert, L. H: Acta Polytech. Scand., Chemistry Including Metallurgy, Series No. 90, (1970)
[3] Yershova, Z. P.: Geokhimiya (1957) No. 4, p. 350/8
[4] Khokhlov, B. G., L. E. Ugryumova, L. P. N, V. N. Solodehenko: Deposited Doc. VINITI (1983) No. 2368-83, p. 1/11

Al_2O_3-CaF_2-TiO_2

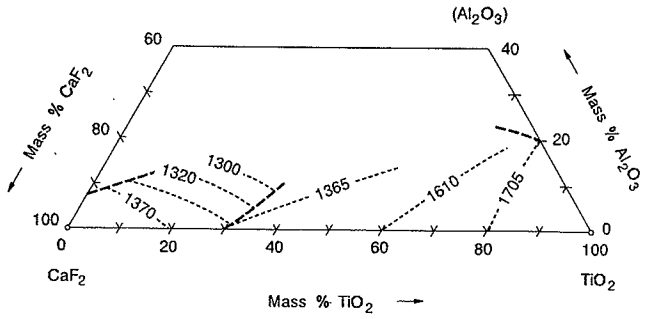


Fig. 3.426. Tentative liquidus surface in the Al_2O_3-CaF_2-TiO_2 system, as drawn by Mills, Keene [1] according to results by Hillert [2, 3].

References

[1] Mills, K. C., B. J. Keene: Inter. Metals Rev. (1981) No. 1, p. 21/69
[2] Hillert, L. H.: Acta Chem. Scand. 20 (1966) No. 1, p. 251/3
[3] Hillert, L. H.: Acta Polytech. Scand., Chemistry Including Metallurgy, Series No. 90, (1970)

CaF_2-CaO-Cr_2O_3

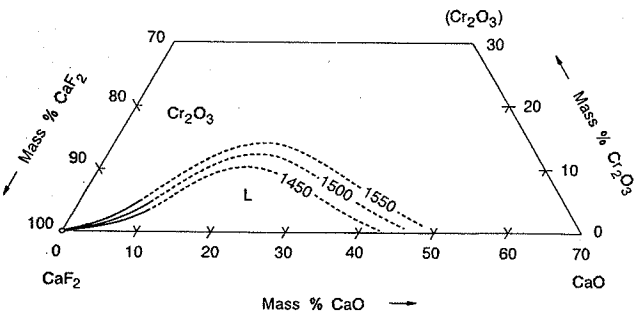


Fig. 3.427. Liquidus isotherms in the CaF_2-CaO-Cr_2O_3 system at low oxygen partial pressure (approx. 10^{-8} atm) after Mohanty, Kay [1]. Some liquidus temperatures in the CaF_2-rich region of the system have also been reported by Lobzhandize et al. [2].

References

[1] Mohanty, A. K., D. A. R. Kay: Metall. Trans. B 6B (1975) No. 1, p. 159/66
[2] Lobzhandize, R. B., A. F. Filippov, P. P. Evseev: Izv. Vyssh. Uchebn. Zaved., Chern. Met. (1970) No. 7, p. 57/60

CaF_2-CaO-FeO_x

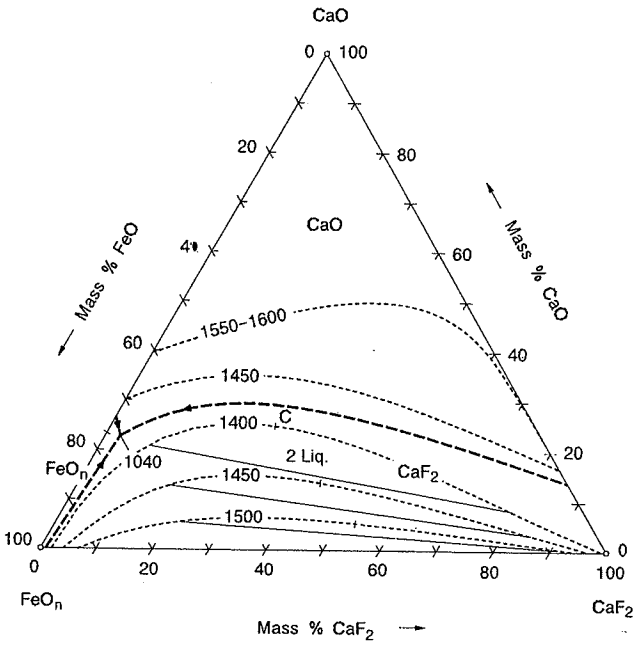


Fig. 3.428. Tentative liquidus surface in the CaF_2-CaO-FeO_n system in contact with metallic iron based on the results of Oelsen, Maetz [1], Hawkins, Davies [2], Mitchel [3], Shim et al. [4] (extention of the miscibility gap at 1450 and 1500 °C) and Wrampelmeyer et al. [5] (1550-1600 °C liquidus isotherm). For the isothermal section through the CaF_2-CaO-Fe_2O_3 system at 1000 °C, see Massazza et al. [6].

References

[1] Oelsen, W., H. Maetz: Mitt. Kaiser Wilhelm Inst. Eisenforsch., Düsseldorf 23 (1941) No. 12, p. 195/207
[2] Hawkins, R. J., M. W. Davies: J. Iron Steel Inst. 209 (1971) No. 3, p. 226/30
[3] Mitchel, A.: Can. Metall. Q. 20 (1981) No. 1, p. 101/12
[4] Shim, J. D., D. B. Hyun, E. C. Lee: Taehan Kumsok Hakhoechi 25 (1987) No 2., p. 125/30
[5] Wrampelmeyer, J.-C., S. Dimitrov, D. Janke: Steel Res. 61 (1990) No. 1, p. 1/7
[6] Massazza, F., M. Pezzuoli, C. Gilioli: Rev. Mater. Constr. Trav. Publics (1970) No. 633, p. 357/63

CaF_2-CaO-MgO

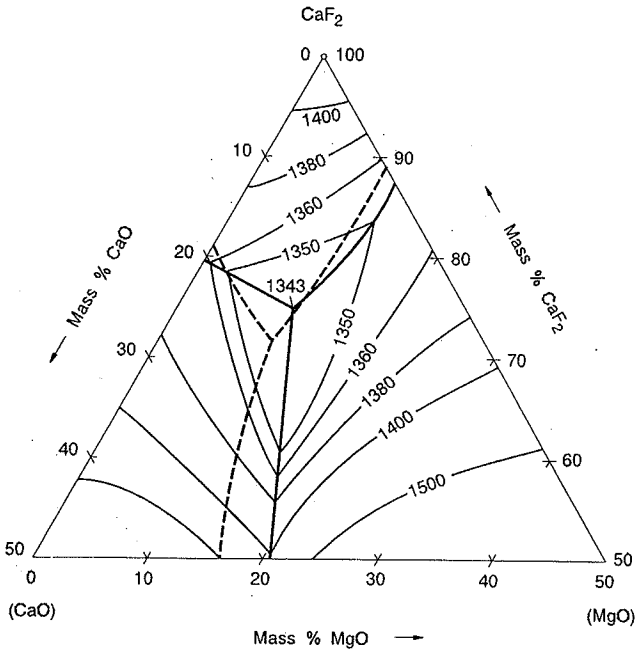


Fig. 3.429. Liquidus surface in the CaF_2-CaO-MgO system after Schlegel [1-3], as determined by DTA. The position of the ternary eutectic, determined by high-temperature microscopy [3], is shown in the figure with dashed lines.

References

[1] Schlegel, E.: Z. Chem. 5 (1965) No. 8, p. 316
[2] Schlegel, E.: Cercetari Metallurgice Bucureshi 9 (1967), p. 785/91
[3] Schlegel, E.: Silikattechnik 20 (1969) No. 3, p. 93/5

CaF_2-CaO-SiO_2

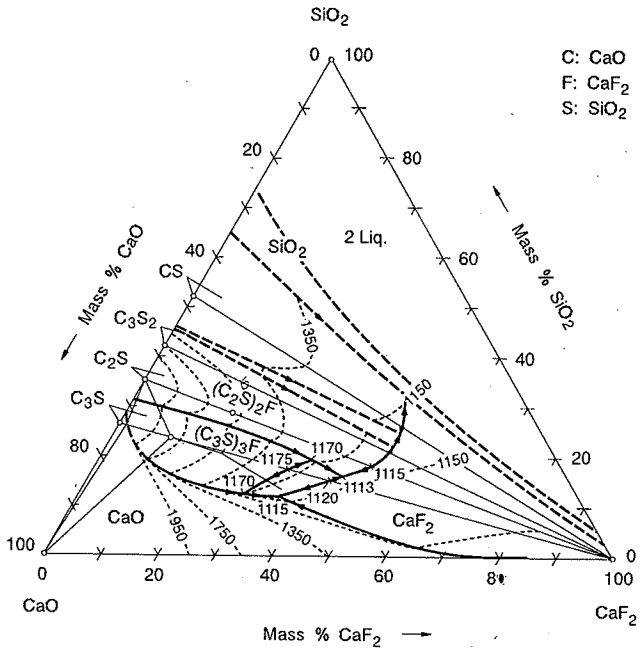


Fig. 3.430. Liquidus surface in the CaF_2-CaO-SiO_2 system according to Mukerji [1, 2], as revised by Gutt, Osborne [3-5]. The $3CaO{\cdot}2SiO_2{\cdot}CaF_2$ (cuspidine) and $4CaO{\cdot}2SiO_2{\cdot}CaF_2$ phases exist only below solidus temperatures. The $9CaO{\cdot}3SiO_2{\cdot}CaF_2$ phase is stable only in the narrow temperature range between 1100 and 1175 °C. An alternative location of the 1450 °C isotherm in the CaO-rich region of the system is proposed by Sommerville, Kay [6]. Liquidus isotherms in the CaF_2-rich region have been reported by Suito, Gaskell [7]. For further solution phases, with composition close to those reported by Gutt, Osborne [3-5], see Gilioli et al. [8], Pérez-Méndez et al. [9, 10] and Odler [11]. Recently, the 1300° isotherm in the CaO-rich region of the system was re-investigated by Selin et al. [12]. A lower solubility of CaO in the melt was reported [12].

References

[1] Mukerji, J.: Mém. Sci. Rev. Métall. 60 (1963) No. 11, p. 785/96
[2] Mukerji, J.: J. Am. Ceram. Soc. 48 (1965) No. 4, p. 210/3
[3] Gutt, W., G. J. Osborne: Trans. J. Br. Ceram. Soc. 65 (1966) No. 9, p. 521/35
[4] Gutt, W., G. J. Osborne: Trans. J. Br. Ceram. Soc. 67 (1968), p. 125/33
[5] Gutt, W., G. J. Osborne : Trans. J. Br. Ceram. Soc. 69 (1970), p. 125/9
[6] Sommerville, I. D., D. A. R. Kay: Metall. Trans. 2 (1971) No. 6, p. 1727/32
[7] Suito, H., D. R. Gaskell: Metall. Trans. B 7B (1976) No. 4, p. 567/75
[8] Gilioli, C., F. Massazza, M. Pezzuoli: Cem. Concr. Res. 9 (1979), p. 295/302
[9] Pérez-Méndez, M., R. A. Howie, F. P. Glasser: Cem. Concr. Res. 14 (1984), p. 57/63
[10] Pérez-Méndez, M., J. Fayos, R. A. Howie, J. A. Gard, F. P. Glasser: Cem. Concr. Res. 15 (1985), p. 600/4
[11] Odler, I., S. Abdul-Maula: J. Am. Ceram. Soc. 70 (1987) No. 1, p. 39/42
[12] Selin, R., Y. Dong, Q. A. Wu: Scand. J. Metall. 19 (1990), p. 98/109

CaF_2-CaO-TiO_2

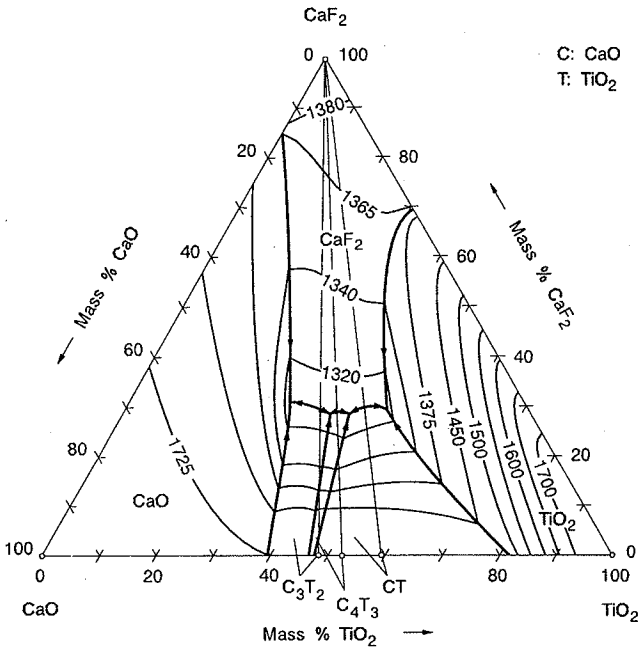


Fig. 3.431. Liquidus surface in the CaF_2-CaO-TiO_2 system after Hillert [1].

References

[1] Hillert, L. H.: Acta Polytech. Scand., Chemistry Including Metallurgy, Series No. 90, (1970)

CaF_2-MgO-SiO_2

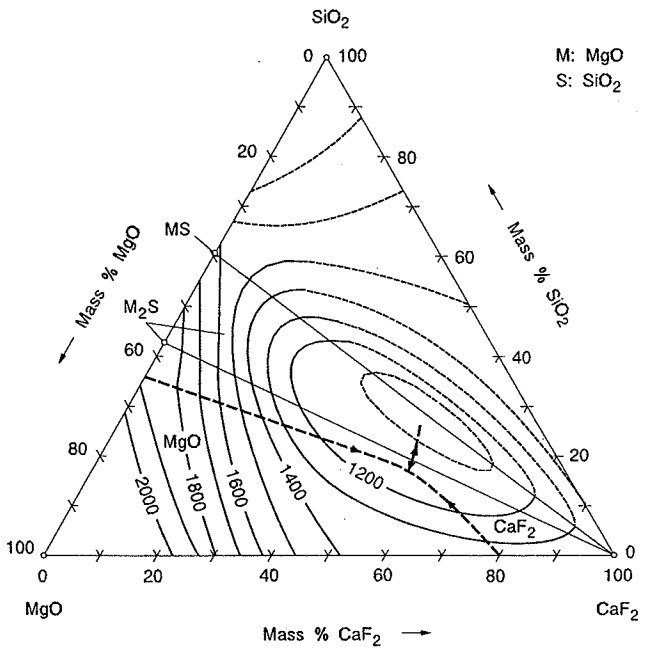


Fig. 3.433. Liquidus isotherms in the CaF_2-MgO-SiO_2 system as reported by Berezhnoi [1].

References

[1] Berezhnoi, A. S.: Dopov. Akad. Nauk Ukr. RSR (1951) No. 4, p. 248/52

CaF_2-FeO_x-SiO_2

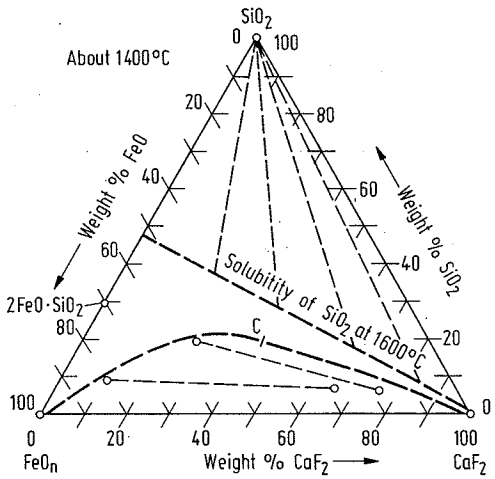


Fig. 3.432. Extension of the miscibility gap in the system CaF_2-FeO_n-SiO_2 in contact with metallic iron at 1400 °C and solubility of SiO_2 in the liquid at 1600 °C according to Oelsen, Maetz [1].

References

[1] Oelsen, W., H. Maetz: Mitt. Kaiser Wilhelm Inst. Eisenforsch., Düsseldorf 23 (1941) No. 12, p. 195/207

CaF_2-Na_2O-SiO_2

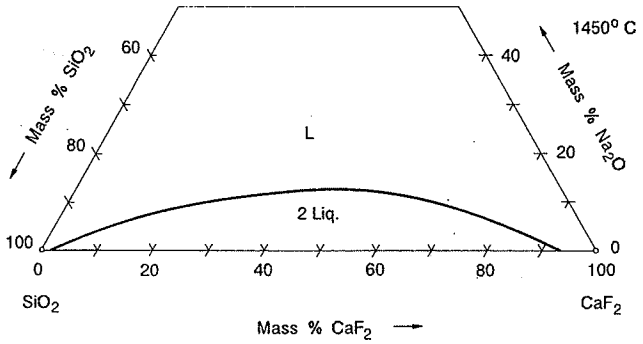


Fig. 3.434. Extention of the miscibility gap in the system CaF_2-Na_2O-SiO_2 at approx. 1450 °C after Yershova, Olshansky [1].

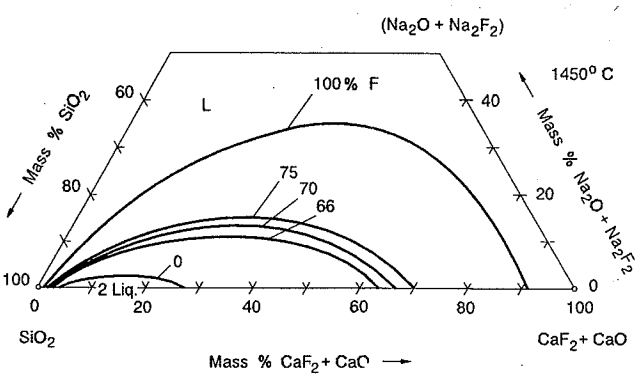


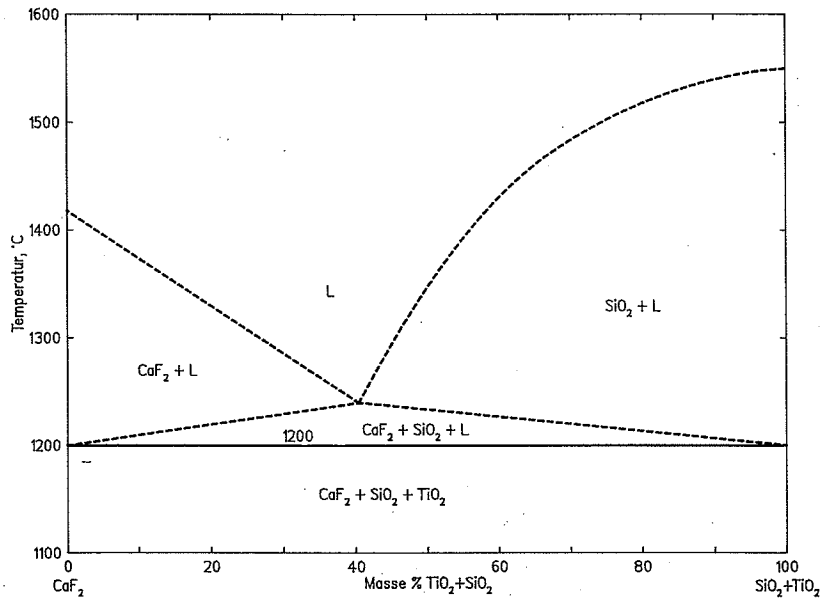
Fig. 3.435. Extension of the miscibility gap in the $CaF_2(CaO)$-$NaF(Na_2O)$-SiO_2 system at 0, 66, 75 and 100 mass % replacement of O^{-2} by F^- after Yershova, Olshansky [1].

References

[1] Yershova, Z. P., Ya. I. Olshansky: Geokhimiya (1958) No. 2, p. 189/202

CaF_2-SiO_2-TiO_2

Fig. 3.436. Composition section CaF_2-(10 mass % TiO_2 + 90 mass % SiO_2) (open cells) in the CaF_2-SiO_2-TiO_2 system after Hillert [1].



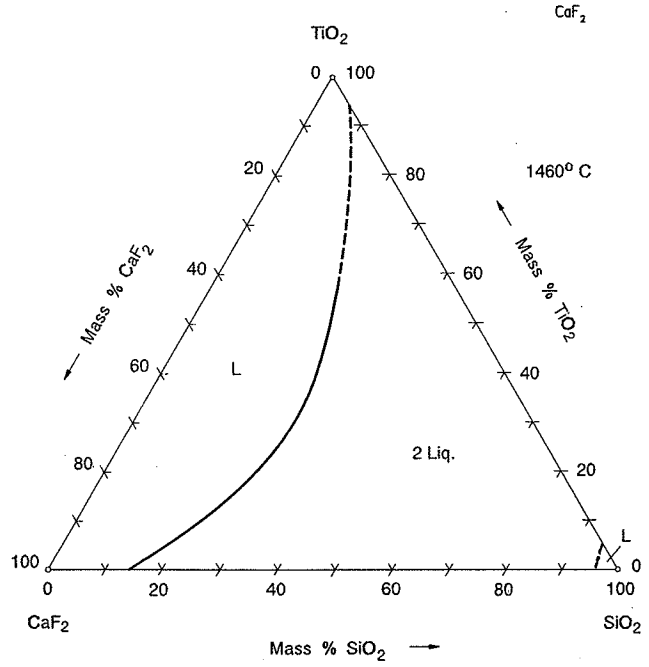


Fig. 3.437. Extension of the miscibility gap in the CaF_2-SiO_2-TiO_2 system at 1460 °C (sealed cell) after Hillert [1].

References

[1] Hillert, L. H.: Acta Polytech. Scand., Chemistry Including Metallurgy, Series No. 90, (1970)

Al_2O_3-CaF_2-CaO-MgO

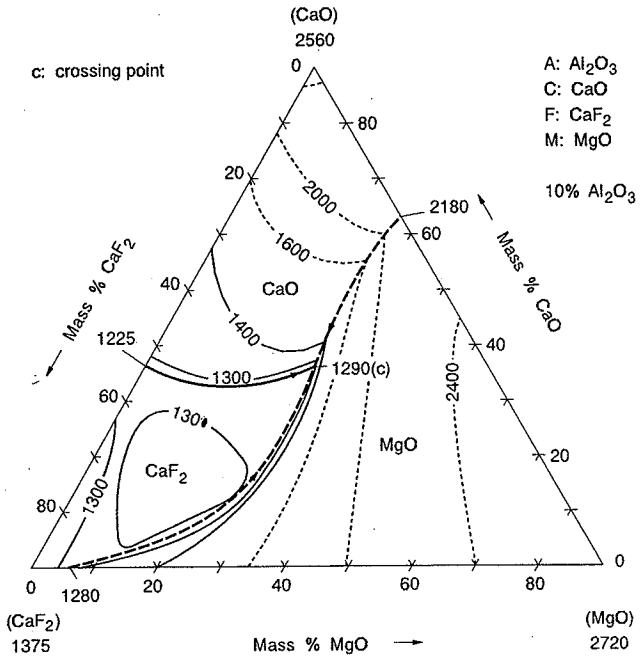


Fig. 3.438.

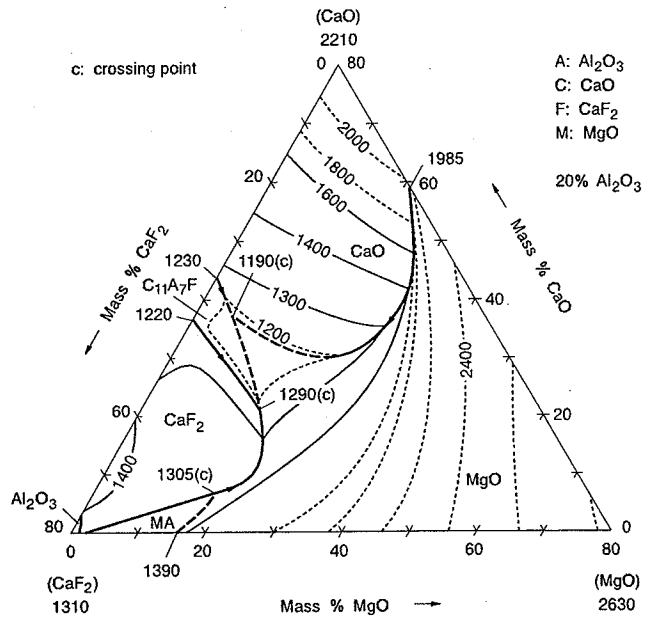


Fig. 3.439.

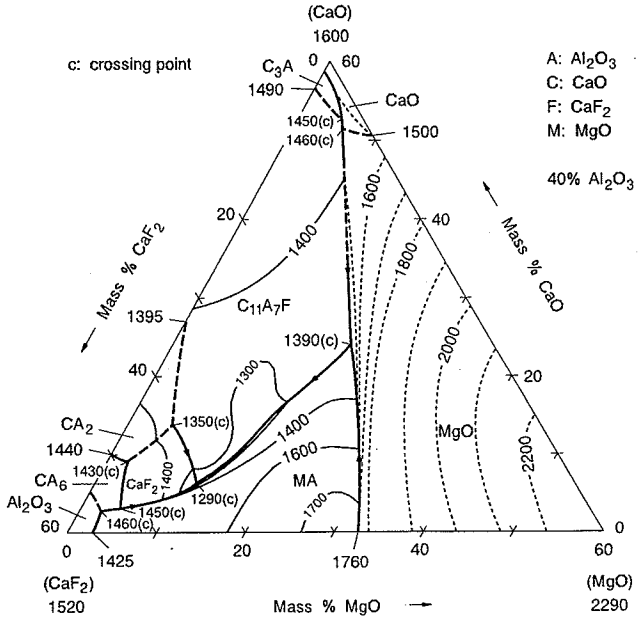


Fig. 3.440.

Figs. 3.438 to 3.440. Liquidus surface in the Al_2O_3-CaF_2-CaO-MgO system in an inert atmosphere with 10, 20 and 40 mass % Al_2O_3 after Nafziger [1]. For the base system CaF_2-CaO-MgO, see Fig. 3.429.

References

[1] Nafziger, R. H.: High Temp. Sci. 7 (1975) No. 3, p. 179/88

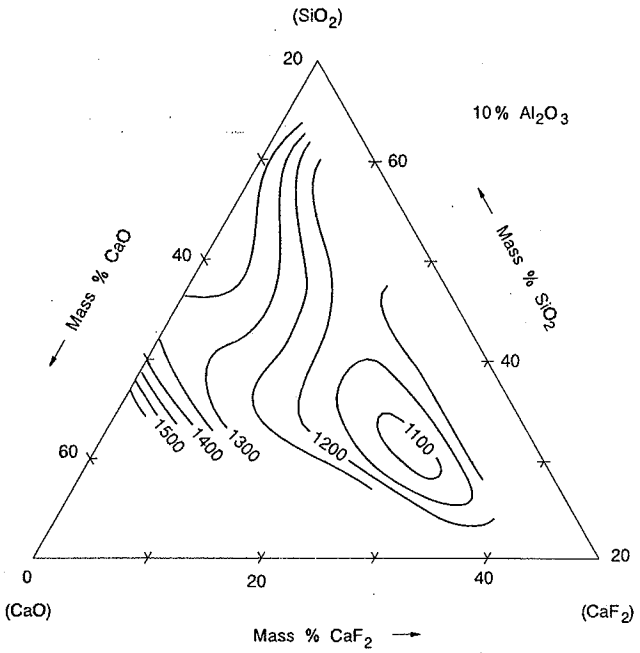


Fig. 3.441. Crystallisation temperatures in the Al_2O_3-CaF_2-CaO-SiO_2 system at 10 mass % Al_2O_3 after Akberdin et al. [1], as deduced from viscosity vs. temperature curves. Previously, the liquidus relations at 10 mass % Al_2O_3 were reported by Toropov, Bondar [2].

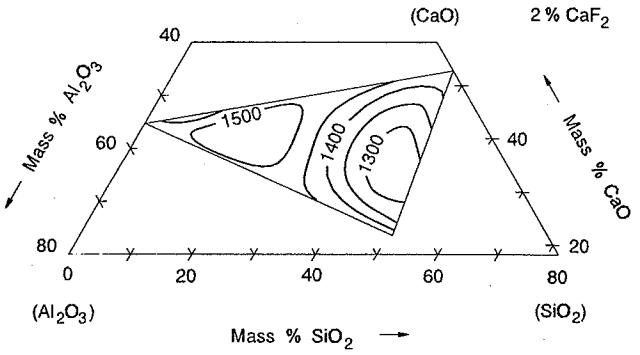


Fig. 3.442.

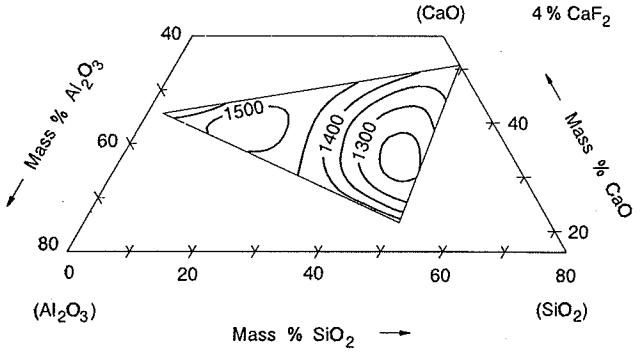


Fig. 3.443.

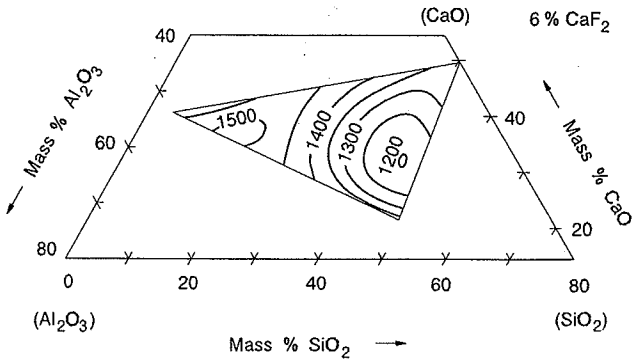


Fig. 3.444.

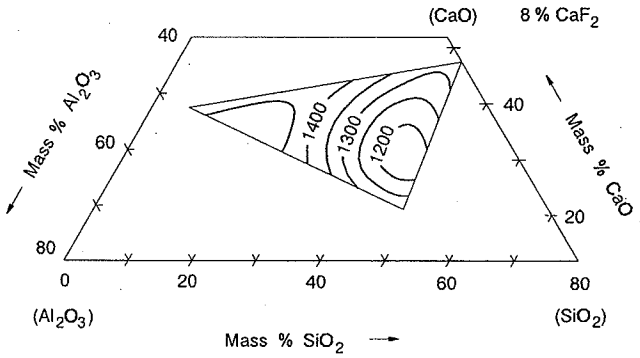


Fig. 3.445.

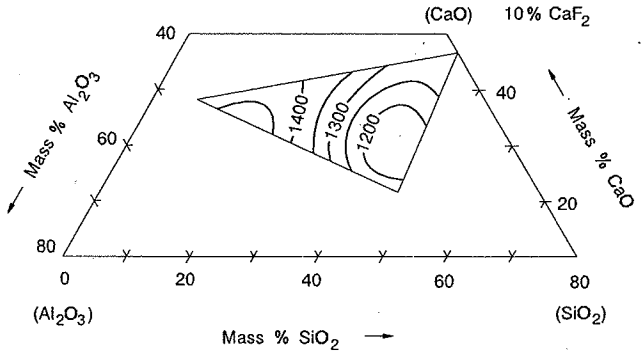


Fig. 3.446.

Figs. 3.442 to 3.446. Crystallisation temperatures in the Al_2O_3-CaF_2-CaO-SiO_2 system with 2, 4, 6, 8 and 10 mass % CaF_2 after Nadyrbekov et al. [3], as deduced from viscosity vs. temperature curves.

For compatibility relations in the system Al_2O_3-CaF_2-CaO-SiO_2, see also Snegirev et al. [5]. The composition section $3CaO{\cdot}SiO_2$-$12Ca(O,F){\cdot}7Al_2(O,F)_3$ has been investigated by Shame, Glasser [4].

References

[1] Akberdin, A. A., S. I. Galperin, V. A. Kim, E. I. Nikolai, G. M. Kireeva: Deposited Doc., VINITI 219-81 (1981), p. 14

[2] Toropov, N. A., I. A. Bondar: Izv. Akad. Nauk SSSR, Otdel. Khim. Nauk. (1959) No. 9, p. 1520/5

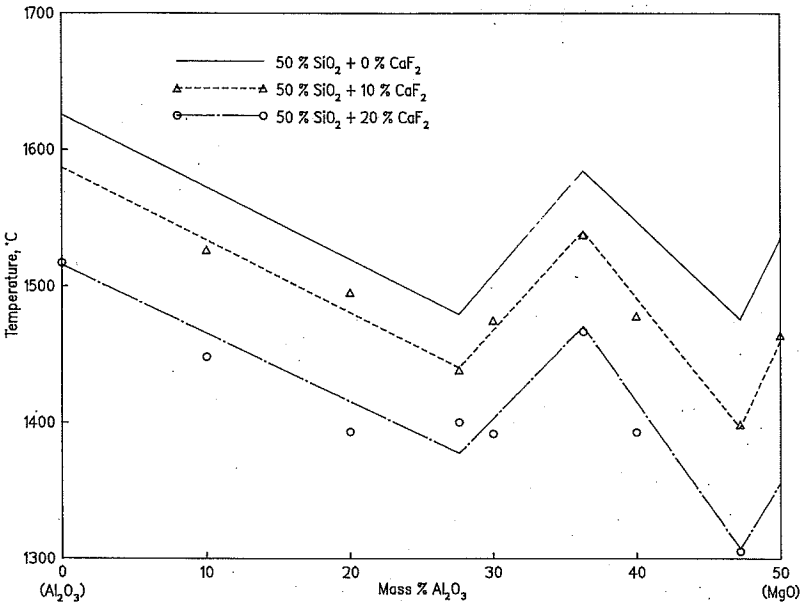
[3] Nadyrbekov, A. K., A. A. Akberdin, I. S. Kulikov, V. A. Kim: Deposited Doc., VINITI 3868-80 (1980), p. 26

[4] Shame, E. G., F. P. Glasser: Trans. J. Br. Ceram. Soc. 86 (1987), p. 13/7

[5] Snegirev, A. I., A. A. Fotiev, D. S. Rutman: Zh. Neorg. Khim. 32 (1987) No. 2, p. 253/5

Al_2O_3-CaF_2-MgO-SiO_2

Fig. 3.447. Influence of SiO_2 additions (10 and 20 mass % SiO_2) on the liquidus temperatures in the 50 mass % CaF_2 section of the system Al_2O_3-CaF_2-MgO after Povolotskii et al. [1]. For the liquidus relations in the base system Al_2O_3-CaF_2-MgO, see Fig. 3.424.
A quaternary compound of the composition $CaMg_{2.3}Si_{2.5}Al_{1.7}O_{10}F_2$, melting incongruently at approx. 1200 °C, has been reported by Lantukh et al. [2].



References

[1] Povolotskii, D. Ya., V. E. Roshchin, V. P. Gribanov, A V. Rechkalova: Izv. Vyssh. Uchebn. Zaved., Chern. Metall. (1983) No. 4, p. 8/12

[2] Lantukh, V. I., V. N. Pavlikov, E. S. Lugovskaya: Strukt. Svoistva Poroshk. Mater. Osn. Tugoplavkikh Met. Soedin., Ed.: Akad. Nauk Ukr. SSR, Inst. Probl. Materialoved., Kiev, (1984), p. 71/4

CaF_2-CaO-FeO_x-SiO_2

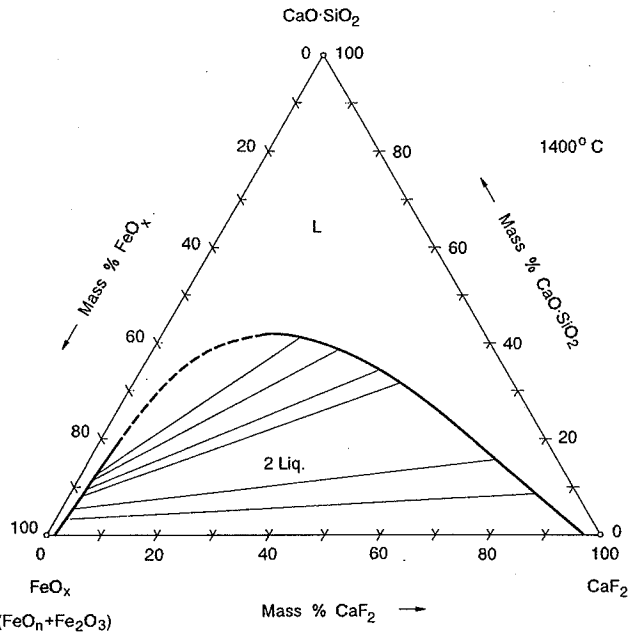


Fig. 3.448. Extension of the miscibility gap in the subsystem CaF_2-CaO·FeO-SiO_2 in contact with metallic iron at 1400 °C after Oelsen, Maetz [1].

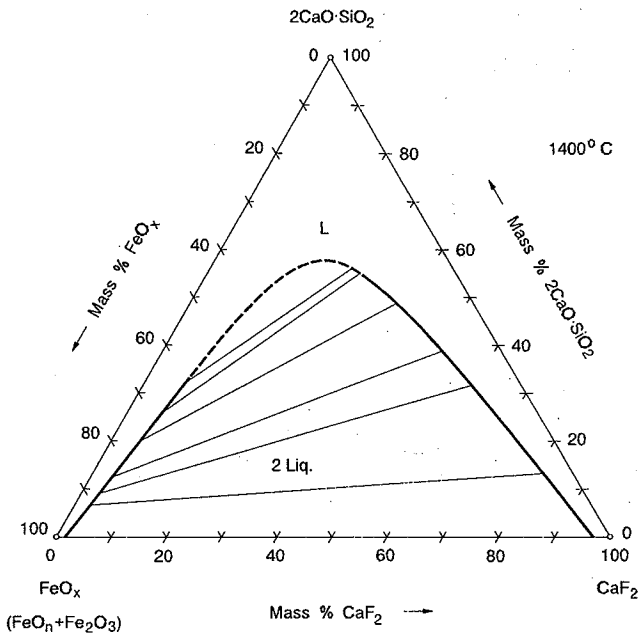


Fig. 3.449. Extension of the miscibility gap in the subsystem CaF_2-2CaO·FeO-SiO_2 in contact with metallic iron at 1400 °C after Oelsen, Maetz [1].

References

[1] Oelsen, W., H. Maetz: Mitt. Kaiser Wilhelm Inst. Eisenforsch., Düsseldorf 23 (1941), p. 195/207

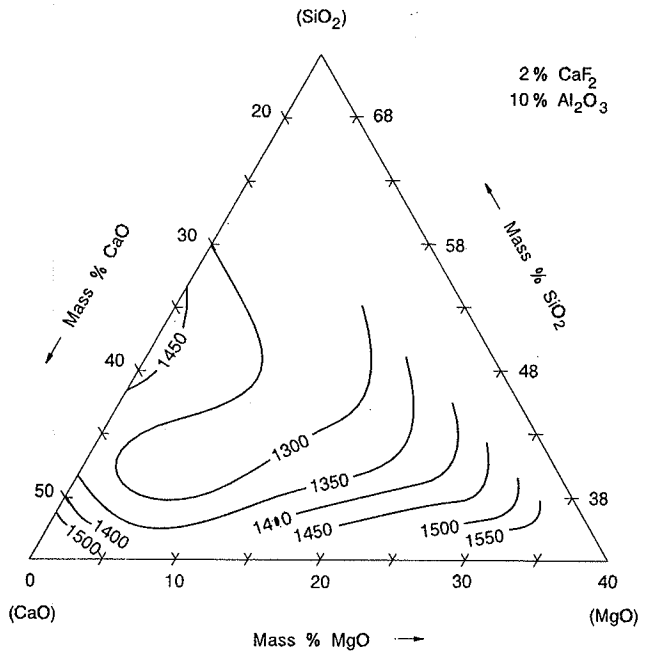


Fig. 3.450.

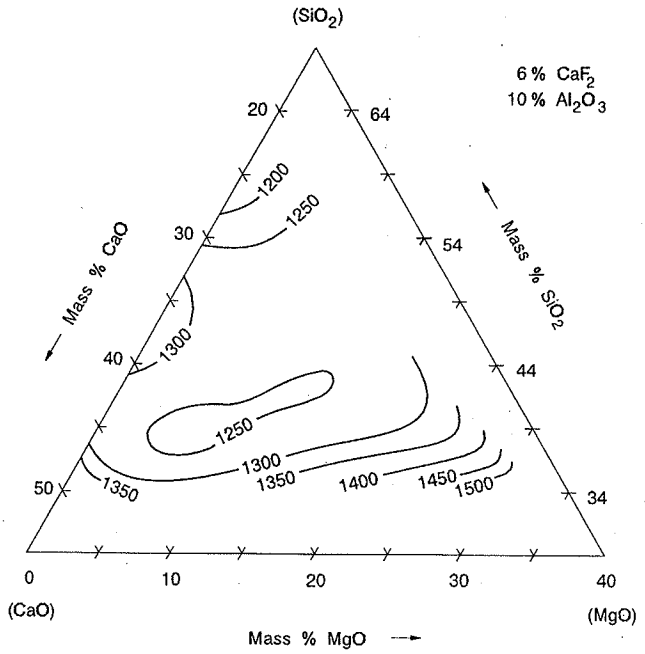


Fig. 3.452.

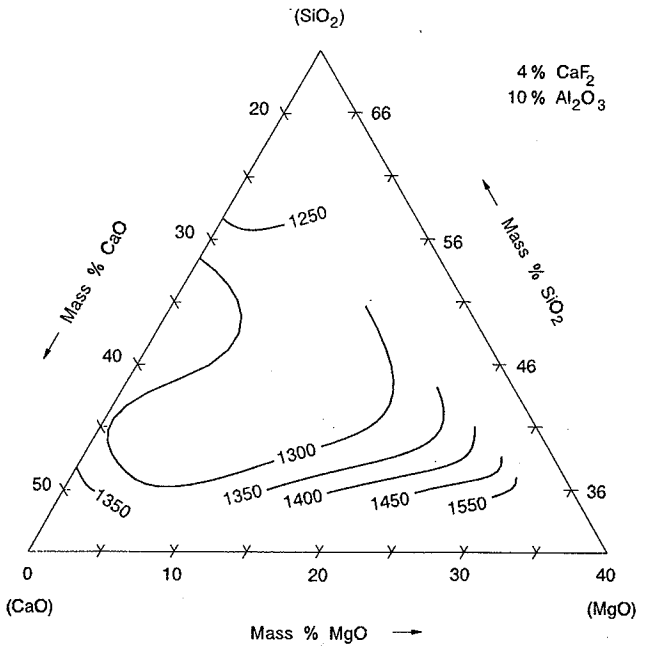


Fig. 3.451.

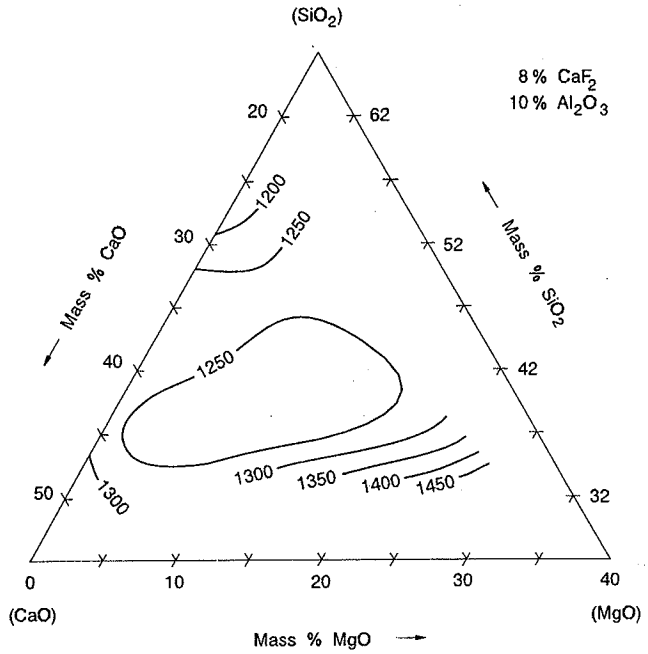


Fig. 3.453.

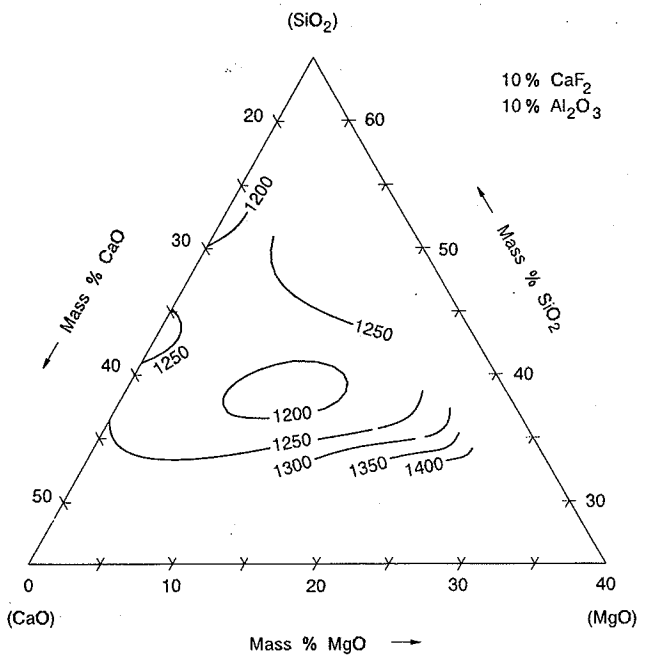


Fig. 3.454.

Figs. 3.450 to 3.454. Crystallisation temperatures in the Al_2O_3-CaF_2-CaO-MgO-SiO_2 system with 10 mass % Al_2O_3 and 2, 4, 6, 8 and 10 mass % CaF_2 after Akberdin et al. [1] as derived from viscosity vs. temperature curves.

References

[1] Akberdin, A. A., V. A. Kim, E. I. Nikolai: Deposited Doc. VINITI 1850-80 (1980), p. 26

3.2.7 Slag systems containing sulphur

CaO-CaS

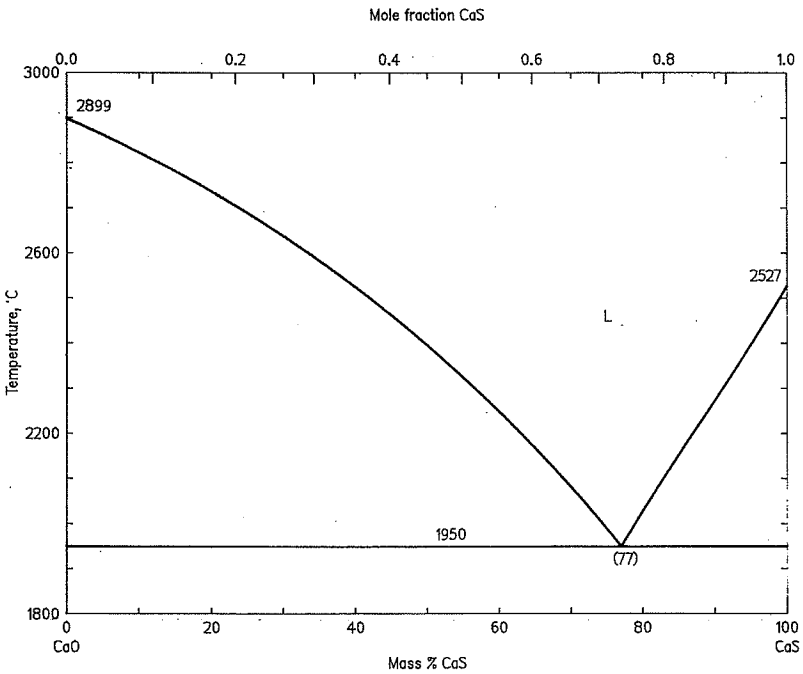


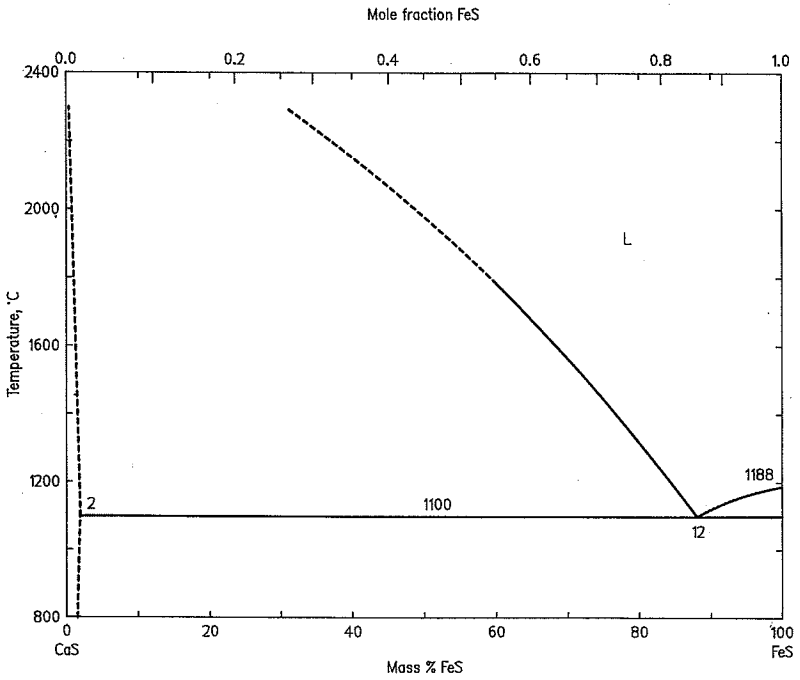
Fig. 3.455. CaO-CaS phase diagram calculated by Iha at al. [1] according to results of Koch, Trömel [2]. For additional contributions to the Ca-O-S system, see Fischer, Spitzer [3], Turkdogan et al. [4] and Kumar, Kay [5].

References

[1] Iha, A., V. O. Igiehorn, P. Grieveson: Scand. J. Metall. 20 (1991), p. 270/78
[2] Koch, K., G. Trömel, J. Laspeyres: Arch. Eisenhüttenwes. 48 (1977) No. 3, p. 133/8
[3] Fischer, W .A., H. Spitzer: Arch. Eisenhüttenwes. 29 (1958) No. 9, p. 535-42
[4] Turkdogan, E. T., B. B. Rice, J. V. Vinters: Metall. Trans. 5 (1974) No. 7, p. 1527/35
[5] Kumar, R. V., D. A. R. Kay: Metall. Trans. B 16B (1985) No. 6, p. 287/94

CaS-FeS

Fig. 3.456. CaS-FeS phase diagram after Vogel, Heumann [1] and Heumann [2]. The mutual solubility of the components has also been investigated by Skinner, Luce [3]. The results due to Heumann [2] were confirmed. For compilation of phase equilibria in the ternary Ca-Fe-S system, see Raghavan [4].



References

[1] Vogel, R., T. Heumann: Arch. Eisenhüttenwes. 15 (1941) No. 4, p. 195/9

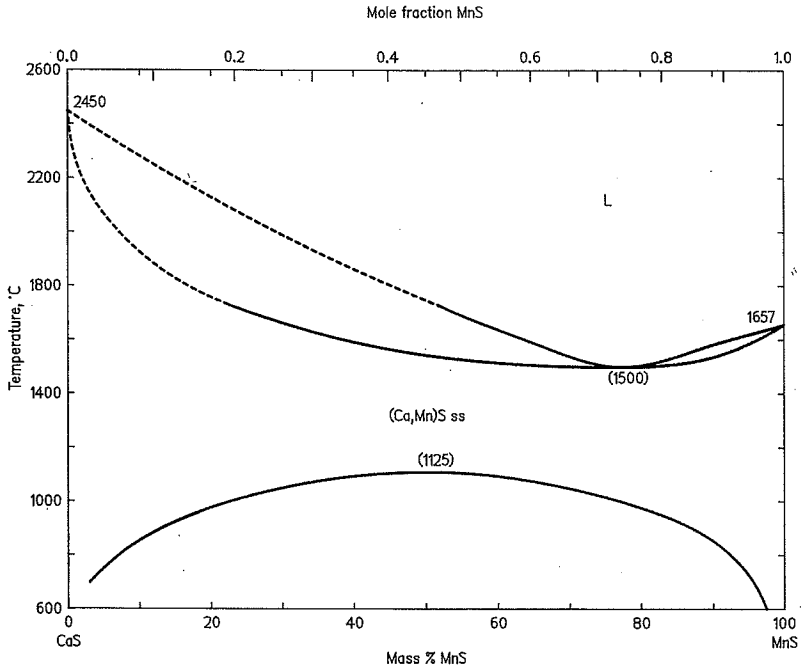
[2] Heumann, T.: Arch. Eisenhüttenwes. 15 (1942) No. 12, p. 557/8

[3] Skinner, B. J., F. D. Luce: Am. Mineral. 56 (1971), p. 1269/96

[4] Raghavan, V.: Phase Diagrams of Ternary Iron Alloys, Part 2: Ternary Systems Containing Iron and Sulphur, The Indian Institut of Metals, Calcutta, (1988)

CaS-MnS

Fig. 3.457. CaS-MnS phase diagram after Leung, van Vlack [1]. For mutual solubilities below 1000 °C, see also Skinner, Luce [2].



References

[1] Leung, C.-H., L. H. van Vlack: J. Am. Ceram. Soc. 62 (1979) No. 11-12, p. 613/6

[2] Skinner, B. J., F. D. Luce: Am. Mineral. 56 (1971), p. 1269/96

Cu_2S-FeS

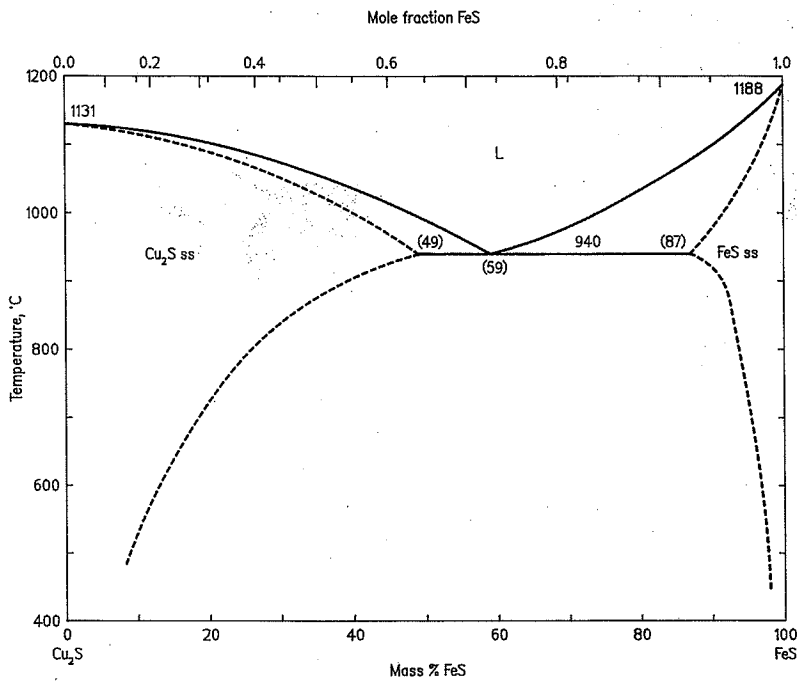


Fig. 3.458. Cu_2S-FeS phase diagram as reported by Chang et al. [1]. For the ternary Cu-Fe-S system and numerous standard references, see [1]. Recently, liquidus temperatures in the vicinity of the Cu_2S-FeS section in the Cu_2S-rich region of the system have been reinvestigated by Bystrov et al. [2]. The phase diagram reported in [1] was confirmed.

References

[1] Chang, Y. A., J. P. Neumann, U. V. Choudary: Phase Diagrams and Thermodynamic Properties of Copper-Sulphur-Metal Systems, INCRA Monograph VII, The International Copper Research Association, New York (1979), p. 58/88

[2] Bystrov, V. P., M. E. Aleksandrov, I. K. Almukhamedov: Tsvetn. Met. /N.Y./ 26 (1985) No. 10, p. 39/40

Fe-O-S

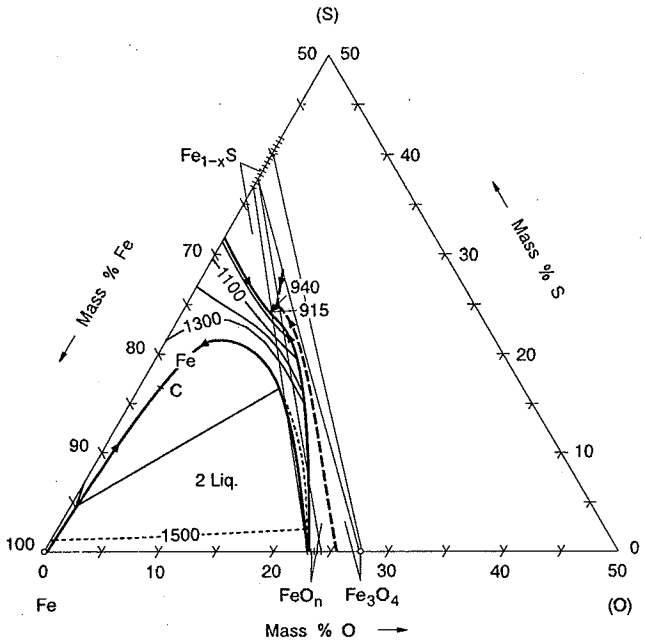
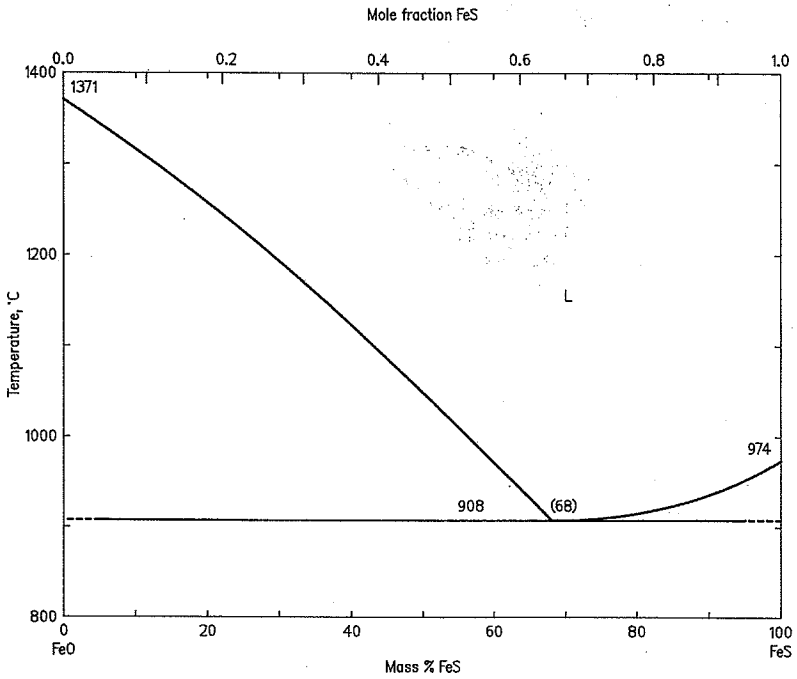


Fig. 3.459. Liquidus surfaces and compatibility relations at 900 °C in the Fe-rich region of the Fe-O-S system as assessed by Raghavan [1].

Fig. 3.460. FeO_n-$Fe_{1-x}S$ system in equilibrium with metallic iron according to Darken, Gurry [2]. This system is not a true binary. The melting temperatures of ternary mixtures are close to eutectic lines between binary eutectics (Fig. 3.459).



For a detailed discussion of the system Fe-O-S and numerous standard references, see [1]. Recently, thermodynamic and experimental information for the Fe-O-S system were reported and discussed by Hsieh, Chang [3] and Musbah, Chang [4].

References

[1] Raghavan, V.: Phase Diagrams of Ternary Iron Alloys, Part 2: Ternary Systems Containing Iron and Sulphur, The Indian Institut of Metals, Calcutta, (1988)

[2] Turkdogan, E. T., G. J. W. Kor, with Appendix by L. S. Darken, R. W. Gurry: Metall. Trans. 2 (1971) No. 6, p. 1561/70

[3] Hsieh, K., Y. A. Chang: Metall. Trans. B 17B (1986) No. 3, p. 133/46

[4] Musbah, O. A., Y. A. Chang: Oxid. Met. 30 (1988) No. 5-6, p. 329/43

FeS-MnS

Fig. 3.461. FeS-MnS system as reported by Raghavan [1].

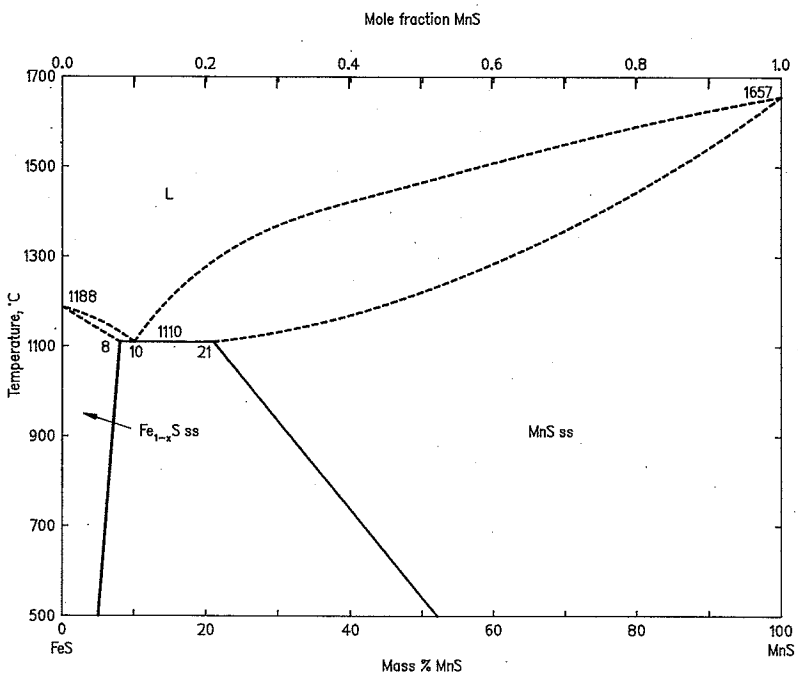
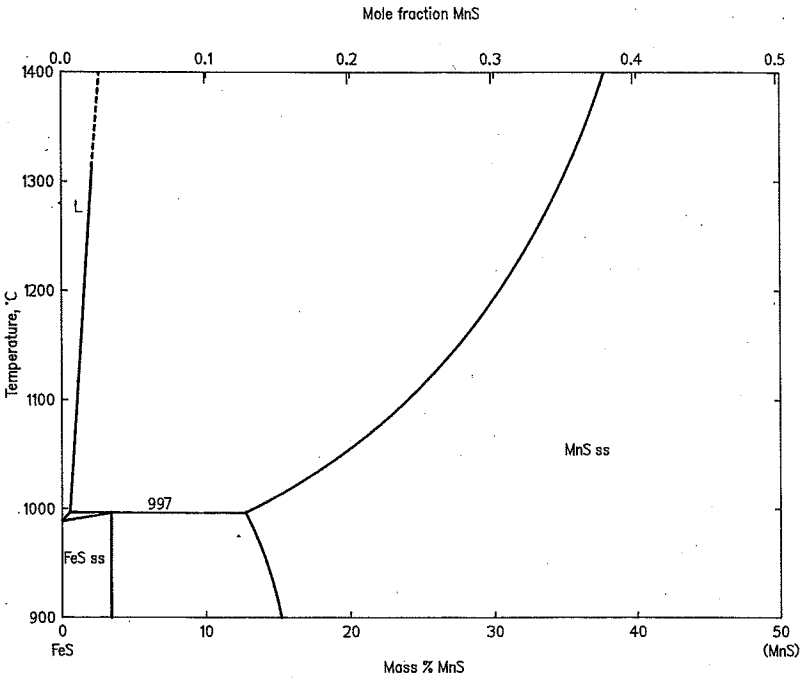


Fig. 3.462. FeS-MnS system in contact with metallic iron as reported by Raghavan [1].



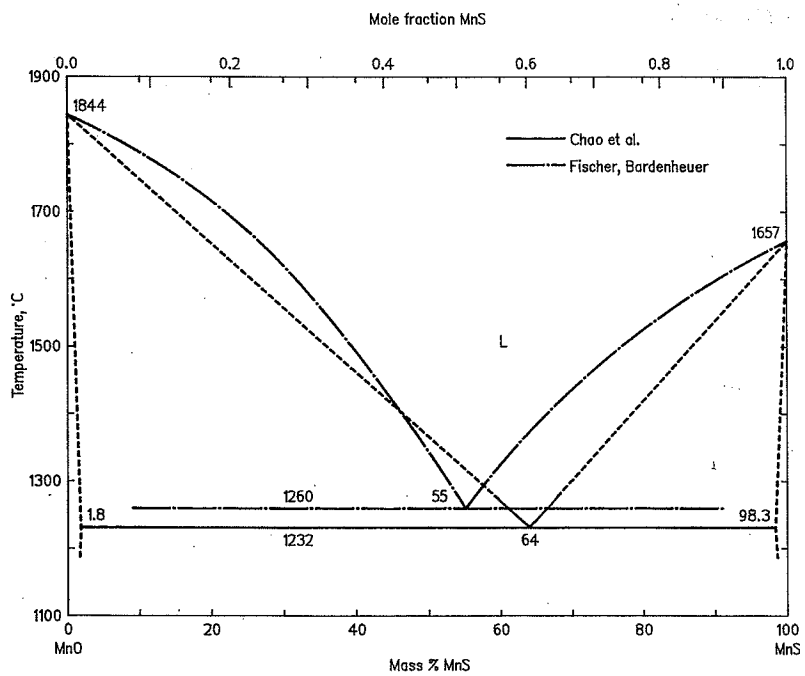
For a discussion of the Fe-Mn-S system and numerous standard references, see original paper.

References

[1] Raghavan, V.: Phase Diagrams of Ternary Iron Alloys, Part 2: Ternary Systems Containing Iron and Sulphur, The Indian Institut of Metals, Calcutta (1988)

MnO-MnS

Fig. 3.463. MnO-MnS phase diagram according to Fischer, Bardenheuer [1] (full lines) and Chao et al. [2] (dash-dot lines). For an earlier version of the phase diagram, see also Andrew et al. [3]. For additional contributions to the system Mn-O-S, see also Skeaff, Espelund [4] and Turkdogan et al. [5, 6].



References

[1] Fischer, W. A., P. W. Bardenheuer: Arch. Eisenhüttenwes. 41 (1970) No. 2, p. 119/24
[2] Chao, H. C., Y. E. Smith, L. H. Van Vlack: Trans. Metall. Soc. AIME 227 (1963) No. 6, p. 769/70
[3] Andrew, J. H., W. R. Maddocs, E. A. Fowler: J. Iron Steel Inst. 124 (1931) No. 2, p. 295/325
[4] Skeaff, J. M., A. W. Espelund: Can. Metall. Q. 12 (1973) No. 4, p. 445/54
[5] Turkdogan, E. T., G. J. W. Kor, with Appendix by L. S. Darken, R. W. Gurry: Metall. Trans. 2 (1971) No. 6, p. 1561/70
[6] Turkdogan, E. T., R. G. Olsson, J. V. Vinters: Metall. Trans., B 8B (1977) No. 1, p. 59/65

Al_2O_3-CaO-CaS

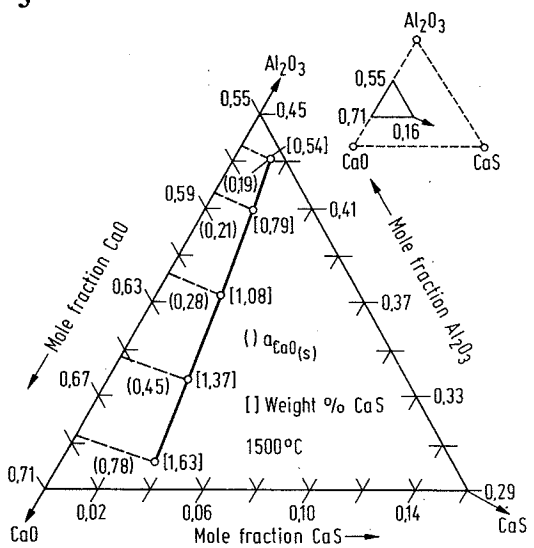


Fig. 3.464. 1500 °C isotherm on the primary field of crystallisation of CaS in the Al_2O_3-CaO-CaS system after Sharma, Richardson [1]. For additional contributions to the solubility of CaS in Al_2O_3-CaO slags, see Cameron et al. [2], Kor, Richardson [3] and Venkatadri [4].

References

[1] Sharma, R. A., F. D. Richardson: J. Iron Steel Inst. 198 (1961) No. 8, p. 386/90

[2] Cameron, J., T. B. Gibbons, J. Taylor: J. Iron Steel Inst. 204 (1966) No. 12, p. 1223/8

[3] Kor, G. J. W., F. D. Richardson: J. Iron Steel Inst. 206 (1968) No. 7, p. 700/4

[4] Venkatadri, A. S.: Trans. Indian Inst. Met. 36 (1983) No. 4-5, p. 389/94

Ca-Fe-O-S

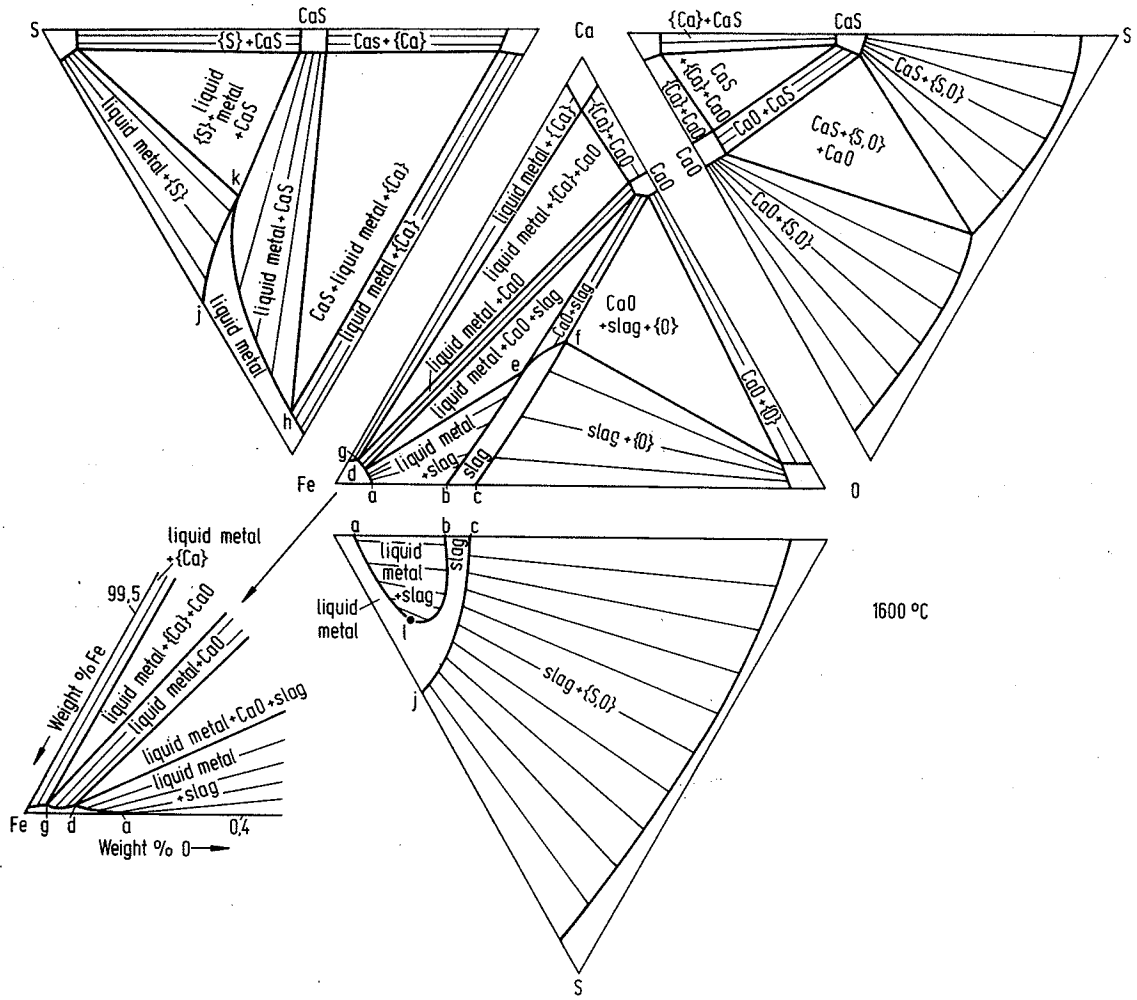


Fig. 3.465. Tentative phase relations at 1600 °C in the lower-order system of the system Ca-Fe-O-S according to Trömel et al. [1]. For 1400 °C isotherms, see original paper [1].

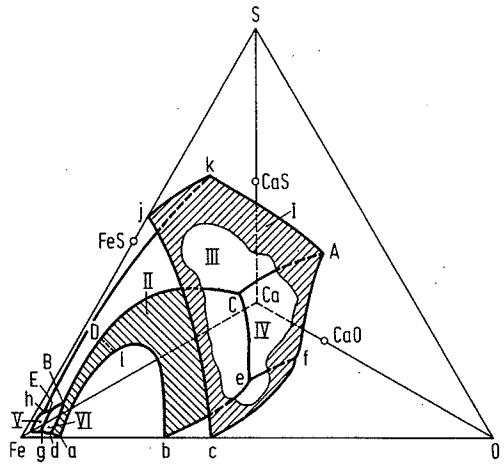


Fig. 3.466. Space representation of the Ca-Fe-O-S system at 1600 °C in contact with metallic iron after Trömel et al. [1]. For a detailed description of the phase equilibria along boundary surfaces within the quaternary system and a similar representation of the system at 1400 °C, see original paper [1].

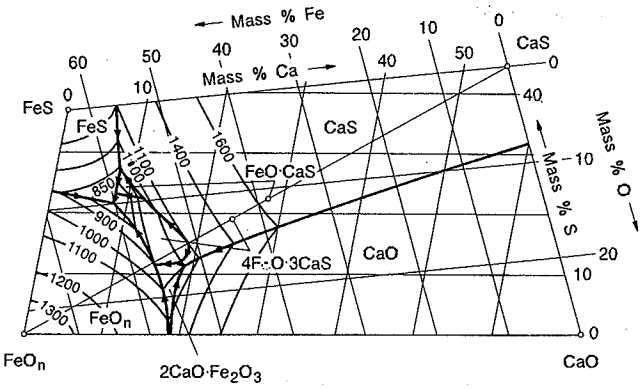
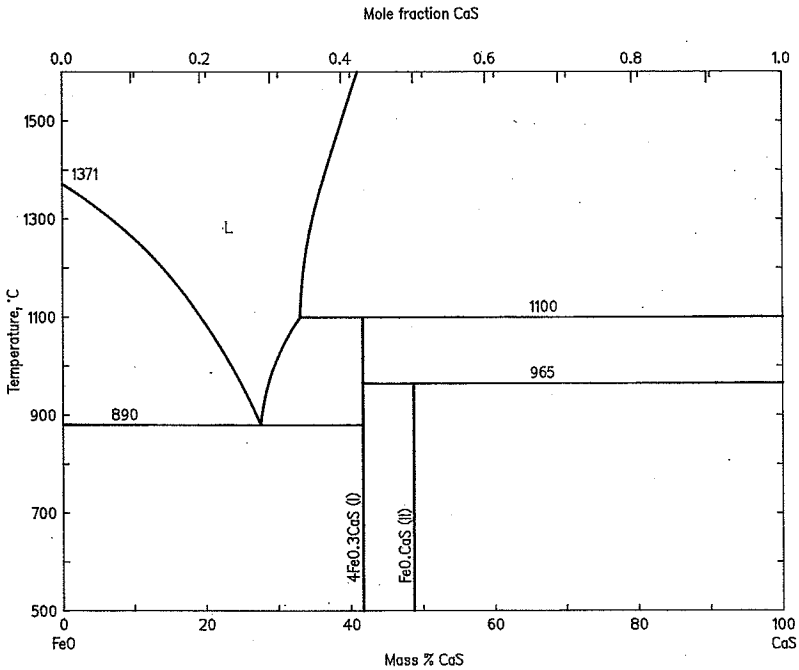


Fig. 3.467. Liquidus surface in the sub-system CaO-CaS-FeO_n-FeS in contact with metallic iron after Koch et al. [2]. For the oxysulfide phases I and II, the stoichiometries 4FeO·CaS ($Fe_4Ca_3S_3O_4$) and FeO.CaS (FeCaSO) have been reported. In further works [3-5] the stoichiometry of the oxysulfide phases has been revised. The formulae $2Fe_2O_3·3CaS$ ($Fe_4Ca_3S_3O_6$) for the oxysulfide I and $Fe_2O_3·2CaS$ ($Fe_2Ca_2S_2O_3$) for the oxysulfide II have been proposed. The influence of oxygen partial pressure on the formation of sulfur compounds in the Ca-Fe-O-S system has been discussed by Schürmann, Fischer [5]. The liquidus relations in the sub-system CaO-FeO_n-FeS in argon atmosphere were also investigated by Toguzov et al. [4].

Fig. 3.468. Sub-system FeO_n-CaS in contact with metallic iron after Koch et al. [2]. The phase equilibria on the composition section CaO-FeS were reported by Toguzov et al. [4]. For additional contributions to the system Ca-Fe-O-S, see also Mikhailov, Baibulenko [6], Grieveson, Turkdogan [7] and Iha et al. [8].



References

[1] Trömel, G., K. Koch, J. Geiseler: Arch. Eisenhüttenwes. 40 (1969) No. 2, p. 87/98

[2] Koch, K., G. Trömel, J. Laspeyres: Arch. Eisenhüttenwes. 48 (1977) No. 3, p. 133/8

[3] Kopalov, N. I., V. I. Yarygin, M. Z. Toguzov: Zh. Neorg. Khim. 25 (1980) No. 12, p. 3374/7

[4] Toguzov, M. Z., V. I. Yarygin, V. M. Fedotov, S. M. Minkevich, E. A. Sedchenko: Kompleksn. Ispolz. Miner. Syrya (1980) No. 4, p. 51/5

[5] Schürmann, E., H. Fischer: Steel Res. 58 (1987) No. 12, p. 531/7

[6] Mikhailov, G. G., E. P. Baibulenko: Izv. Vyssh. Uchebn. Zaved. Chern. Metall. (1981) No. 8, p. 1/4

[7] Grieveson, P., E. T. Turkdogan: Trans. Metall. Soc. AIME 224 (1962) No. 12, p. 1086/95

[8] Iha, A., V. O. Igiehorn, P. Grieveson: Scand. J. Metall. 20 (1991), p. 270/8

$CaO\text{-}CaS\text{-}SiO_2$

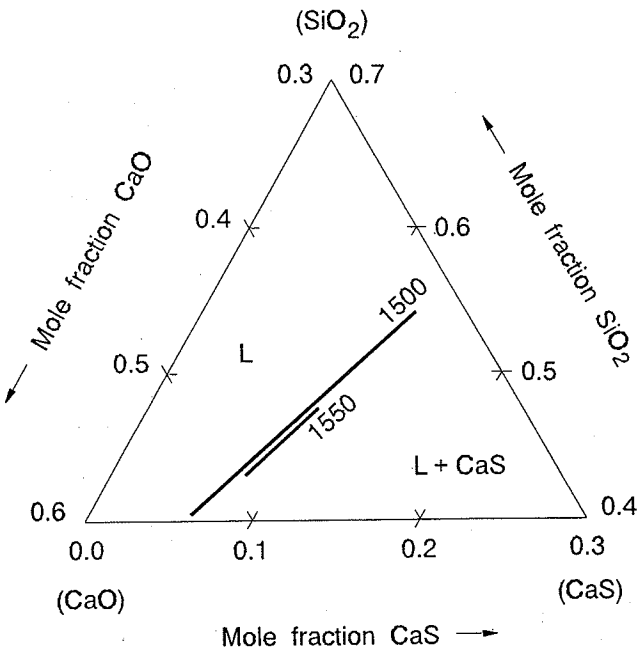


Fig. 3.469. 1500 and 1550 °C isotherms on the field of primary crystallisation of CaS in the system CaO-CaS-SiO_2 according to Sharma, Richardson [1].

References

[1] Sharma R. A., F. D. Richardson: J. Iron Steel Inst. (1962) No. 5, p. 373/9

Fe-Mn-O-S

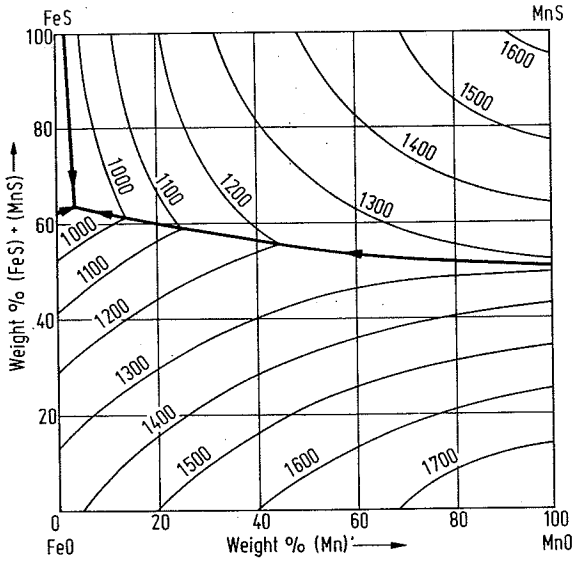


Fig. 3.470. Liquidus surface in the system FeO-FeS-MnO-MnS after Oelsen, Schürmann [1]. Liquidus relations in this system were reported previously by Wentrup [2] and Geißler, Kohlmeyer [3]. The location of invariant points was also determined by Turkdogan, Kor [4].

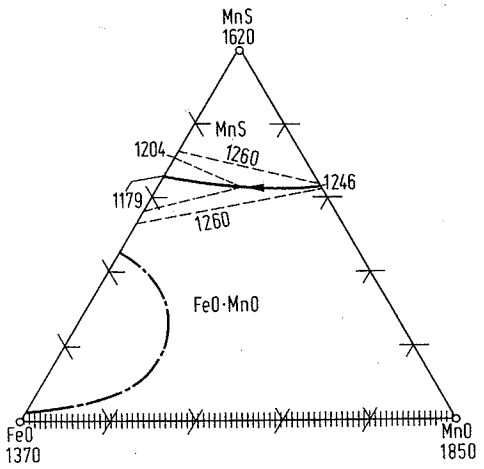


Fig. 3.471. Liquidus relations in the pseudo-ternary system FeO-MnO-MnS after Silverman [5]. As reported by Silverman [5], the crystallisation of compositions from the area limited by the dash-dot line finishes on the eutectic between the (Fe,Mn)O solid solution and FeS.

For additional contributions to the qaternary system Fe-Mn-O-S, see Fischer, Bardenheuer [6], Kor, Turkdogan [7] and Schürmann, Bannenberg [8].

References

[1] Oelsen, W., E. Schürmann: Hütte - Taschenbuch für Eisenhüttenleute, Berlin/Düsseldorf 1961.
[2] Wentrup, H.: Tech. Mitteilungen Krupp (1937) No. 5, p. 131/73
[3] Geißler, K., E. J. Kohlmeyer: Arch. Eisenhüttenwes. 29 (1958) No. 1, p. 57/63
[4] Turkdogan, E. T., G. J. W. Kor, with Appendix by L. S. Darken, R. W. Gurry: Metall. Trans. 2 (1971) No. 6, p. 1561/70
[5] Silverman, E. N.: Trans. Metall. Soc. AIME 221 (1961), p. 512/7
[6] Fischer, W. A., P. W. Bardenheuer: Arch. Eisenhüttenwes. 41 (1970) No. 2, p. 119/24
[7] Kor, G. J. W., E. T. Turkdogan: Metall. Trans. B 2B (1971) No. 6, p. 1571/8
[8] Schürmann, E., N. Bannenberg: Arch. Eisenhüttenwes. 55 (1984) No. 8, p. 349/58

FeO_x-FeS-SiO_2

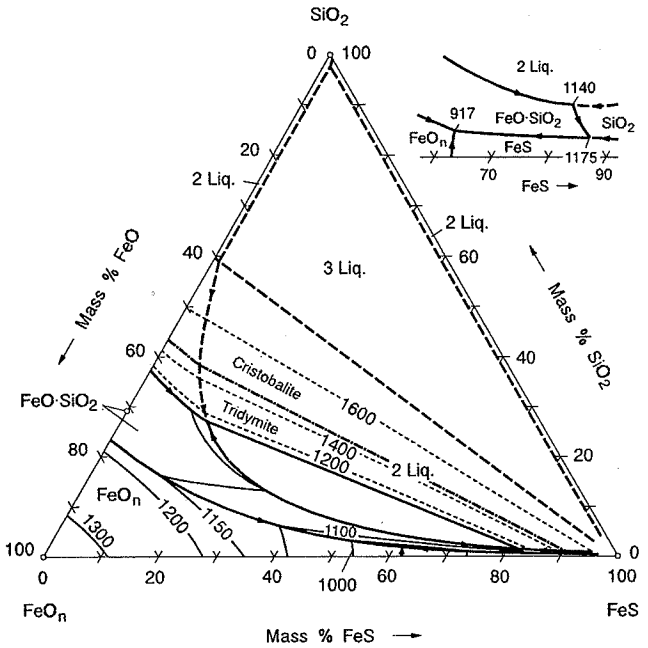


Fig. 3.472. Liquidus surface in the FeO-FeS-SiO_2 system in contact with metallic iron after Olshansky [1], and Yazava, Kameda [2], as revised by McLean [3]. The space representation of liquidus relations in the quaternary system FeO-Fe_3O_4-FeS-SiO_2 is reported in [3]. For additional contribution, see also Vogel [4] and Genevska et al. [5].

References

[1] Olshansky, Ya. I.: Dokl. Akad. Nauk SSSR 70 (1950) No. 2, p. 245/8
[2] Yazava, A., M. Kameda: Tech. Rep. Tohoku Univ. 18 (1953) No. 1, p. 40/58
[3] McLean, W. H.: Econ. Geol. 64 (1969), p. 865/84
[4] Vogel, R.: Arch. Eisenhüttenwes. 36 (1965) No. 7, p. 481/4
[5] Genevska, T., I. Grozdanov, P. Bakurdzhiev: Metalurgiya /Sofia/, (1973) No. 4, p. 17/9

Fe-Mn-O-S-Si

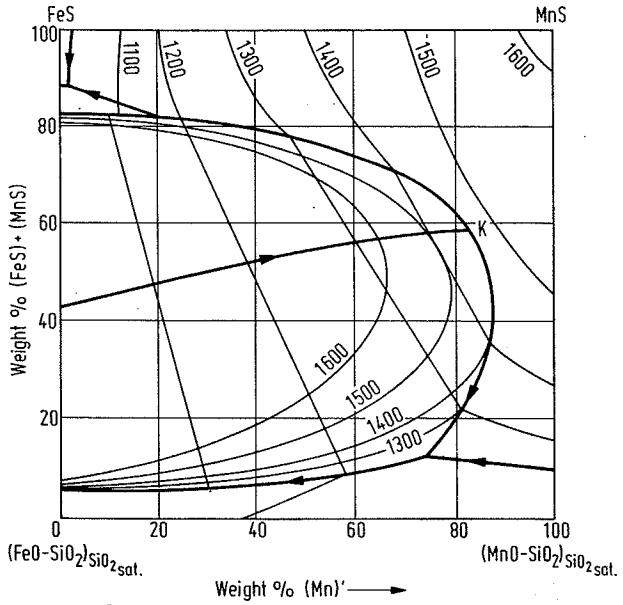


Fig. 3.473. Liquidus surface in the FeO-FeS-MnO-MnS-SiO_2 system after Oelsen, Schürmann [1] showing also isotherms on the miscibility gap surface and the location of critical temperatures. The binary compositions at the lower edge of the figure represent liquidus compositions in the SiO_2-rich region of the system.

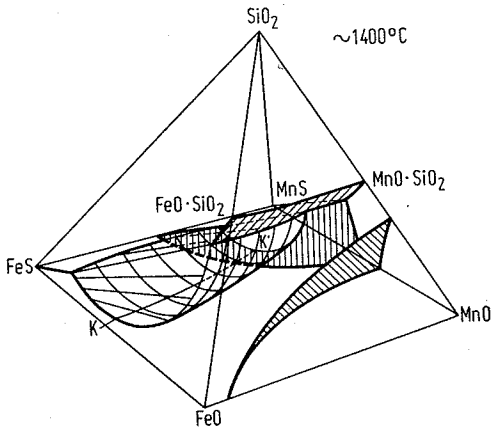


Fig. 3.474. Liquidus relations in the FeO-FeS-MnO-MnS-SiO_2 system at 1400 °C after Oelsen, Schürmann [1].

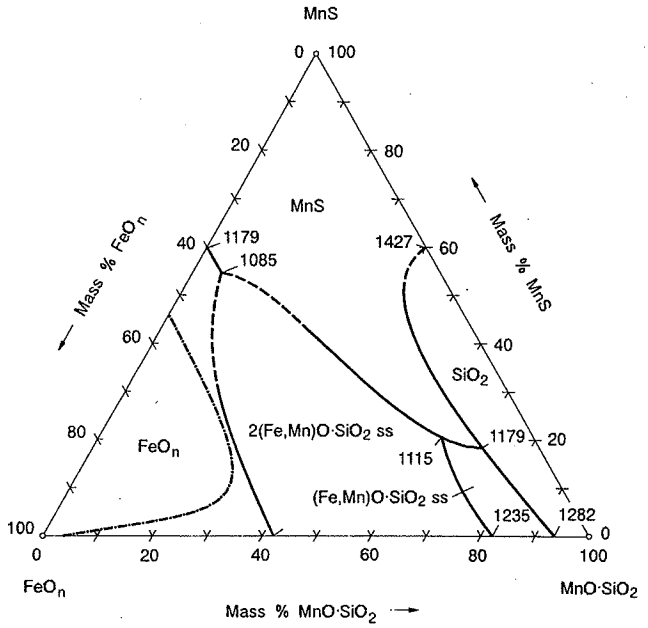


Fig. 3.475. Liquidus surface in the pseudo-ternary system FeO-MnO·SiO_2-MnS after Silverman [2]. Crystallisation of FeS was observed for starting compositions within the area delimited by the dash-dot lines.

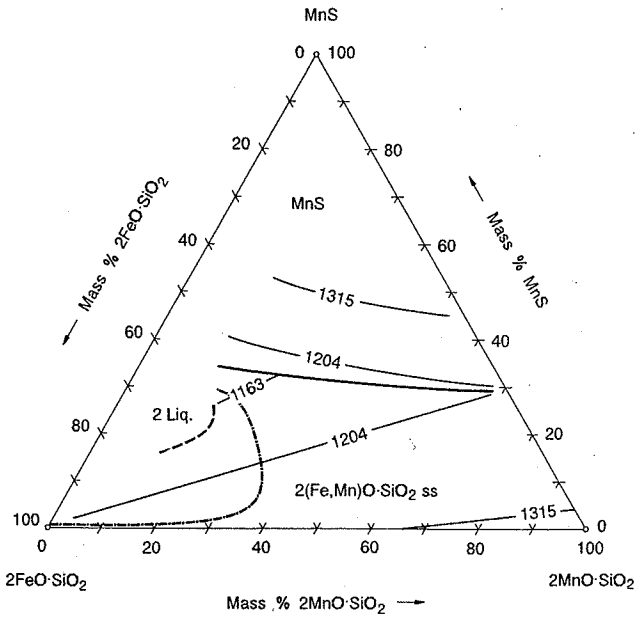


Fig. 3.476. Liquidus surface in the pseudo-ternary system FeO-2MnO·SiO_2-MnS after Silverman [2]. Crystallisation of FeS was observed for starting compositions within the area delimited by the dash-dot line. The dashed line denotes the limit of the miscibility gap.

References

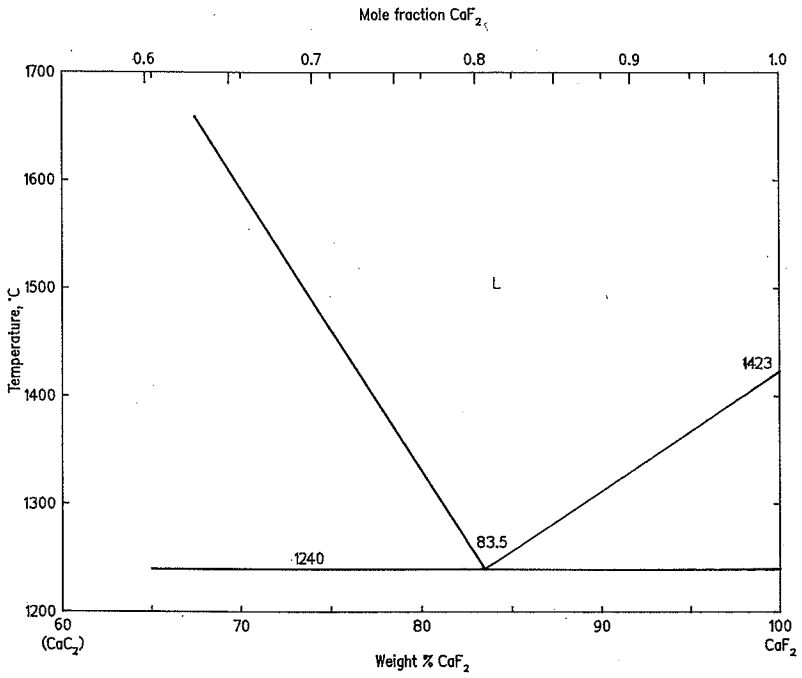
[1] Oelsen, W., E. Schürmann: Hütte - Taschenbuch für Eisenhüttenleute, 5th ed., Ed. Akademischer Verein, Berlin/Düsseldorf, 1961

[2] Silverman, E. N.: Trans. Metall. Soc. AIME 221 (1961), p. 512/7

3.2.8 Other slag systems

CaC_2-CaF_2

Fig. 3.477. CaC_2-CaF_2 phase diagram in the CaF_2-rich region of the system after Mitchell [1].



References

[1] Mitchell, A.: Trans. Metall. Soc. AIME 242 (1968) No. 12, p. 2507/11

CaF_2-CaO-CaS

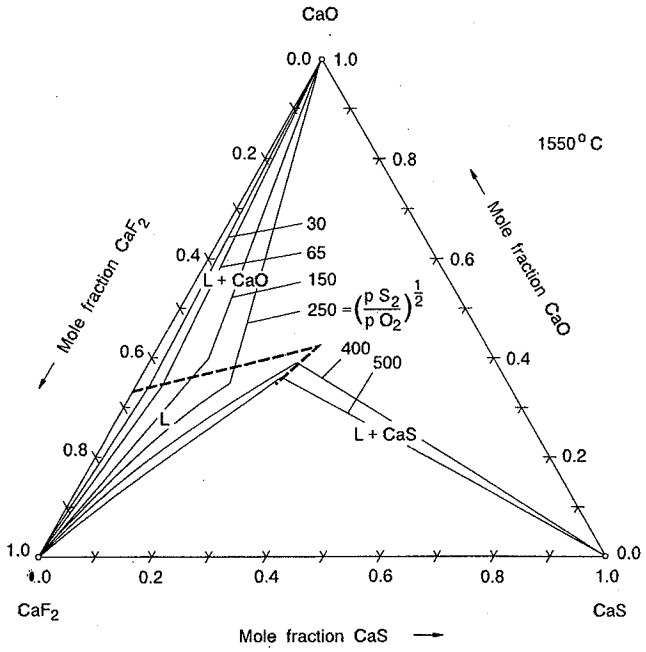


Fig. 3.478. Isothermal section through the system CaF_2-CaO-CaS at 1550 °C showing the composition of the CaO- or CaS-saturated liquid at different $(pS_2/pO_2)^{1/2}$ ratios after Hawkins et al. [1].

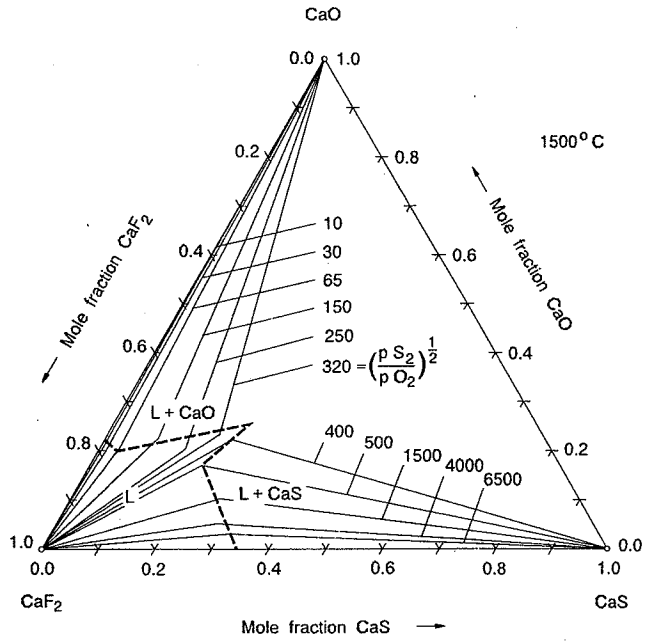


Fig. 3.479. Isothermal section through the system CaF_2-CaO-CaS at 1500 °C showing the composition of the CaO- or CaS-saturated liquid at different $(pS_2/pO_2)^{1/2}$ ratios after Hawkins et al. [1]

References

[1] Hawkins, R. J., G. S. Meherali, M. W. Davies: J. Iron Steel Inst. 209 (1971) No. 8, p. 646-57

CaF_2-CaO-CaS-SiO_2

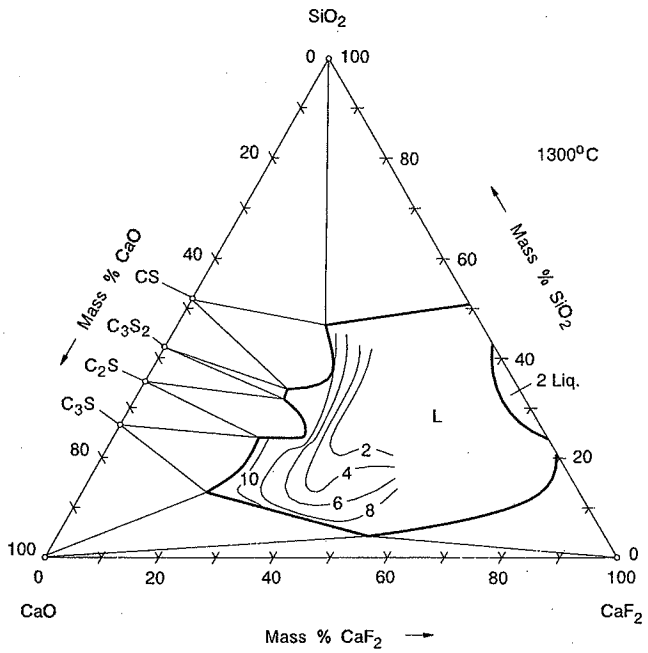


Fig. 3.480. Iso-solubility contours of CaS (in mass %) in CaF_2-CaO-SiO_2 melts at 1300 °C after Motohiro et al. [1].

References

[1] Motohiro, U., E. Sakurai, F. Tsukihashi, N. Sano: Steel Res. 60 (1989) No. 11, p. 496/502

3.3 Figures and tables

Fig. 3.481. Total vapour pressure (log p, atm) of gaseous phase over selected metallic (dashed curves) and oxide (solid curves) components as a function of temperature (calculated using the thermodynamic databank system THERDAS [1]).

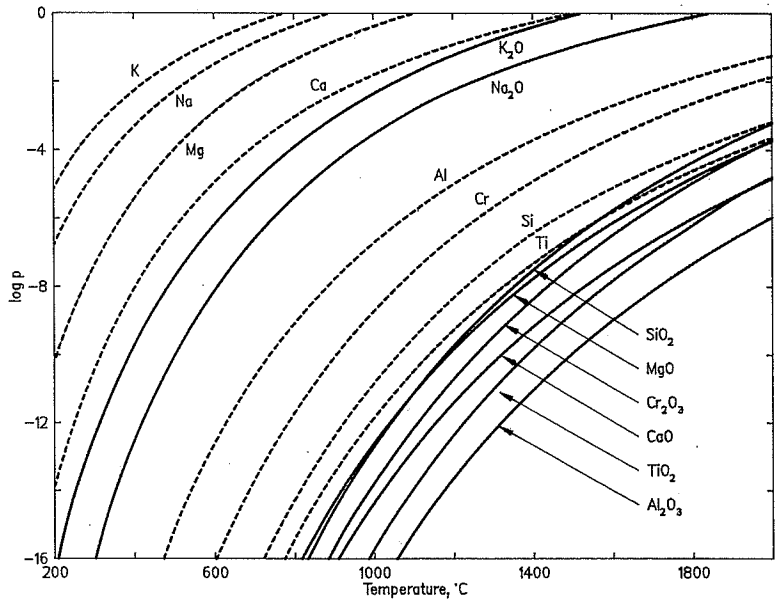


Fig. 3.482. Partial pressure of oxygen (log pO_2, atm) as a function of temperature and CO_2/CO ratios at a total pressure of 1 atm (calculated using the thermodynamic databank system THERDAS [1]).

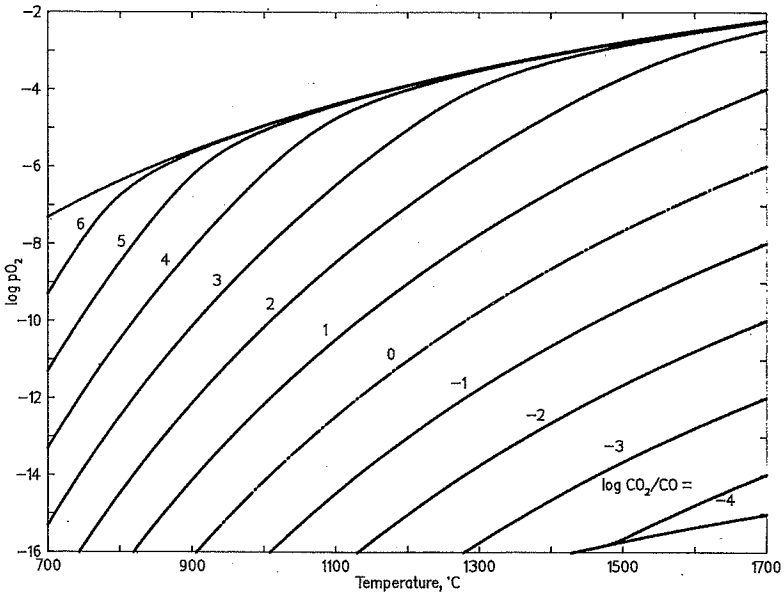


Fig. 3.483. Partial pressure of oxygen (log pO_2, atm) as a function of temperature and CO_2/H_2 ratios at a total pressure of 1 atm (calculated using the thermodynamic databank system THERDAS [1]).

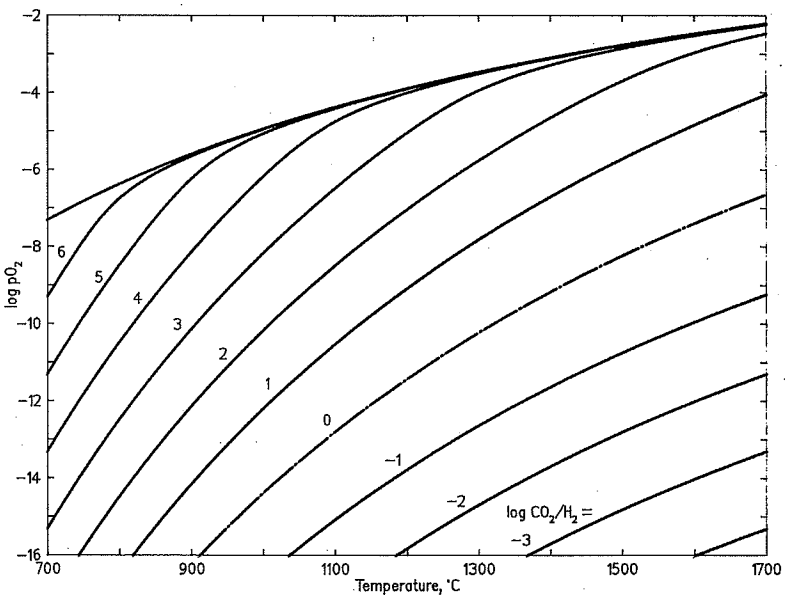
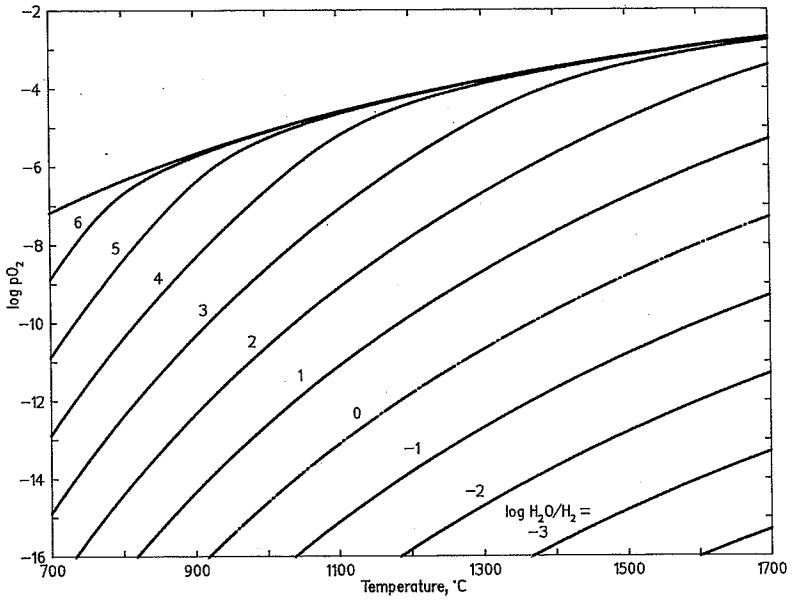


Fig. 3.484. Partial pressure of oxygen (log pO_2, atm) as a function of temperature and H_2O/H_2 ratios at a total pressure of 1 atm (calculated using the thermodynamic databank system THERDAS [1]).



Tab. 3.1. Melting points of selected slag components

Compound	Melting points/°C			References
	Original		IST-1990	
	Temp. Scale	Melting Point		
Al_2O_3	IPTS-68	2054	2053	2
B_2O_3	Geoph.	450	450	3, 4
CaF_2	(1969)	1423	1423	5
CaO	IPTS-68	2613	2612	6
	IPTS-68	2899	2898	7
CaS	(1958)	2525	2529	8
Cr_2O_3	IPTS-48	2330	2333	9
FeO_n	IPTS-27	1371	1371	10
Fe_3O_4	IPTS-27			
in O_2 at 1 atm	1583	1582	10	
in air at atm	1594	1593	10	
in O_2 at 0.00575 atm	1597	1596	10	
FeS	(1982)	1188	1188	11
MgO	IPTS-68	2823	2822	12
MnO	(1976)	1850	1849	13
MnS	IPTS-48	1655	1657	14
Na_2O	IPTS-48	1132	1133	15
NiO	IPTS-27	1960	1956	16, 17
SiO_2	Geoph.	1713	1725	18
TiO_2	IPTS-48	1839	1841	19, 20
Ti_2O_3	IPTS-48	1867	1869	19, 20
ZrO_2	(1977)	2710	2709	21, 22

Tab. 3.2. Differences between different temperature scales (Geophysical-1914, ITS-27, ITS-48, ITS-68 and ITS-90).

T/°C	t_{90}-t_{68}	t_{68}-t_{48}	t_{48}-t_{27}	t_{48}-$t_{Geoph.}$
100	-0.03	0.00	0.00	
200	-0.04	0.04	0.00	
300	-0.04	0.07	0.00	
400	-0.05	0.08	0.00	
500	-0.08	0.08	0.00	
600	-0.12	0.15	0.00	
700	0.20	0.39	0.24	
800	0.34	0.67	0.42	
900	-0.01	0.95	0.40	
1000	-0.19	1.24	0.20	0.3
1100	-0.26	1.50	-0.20	0.4
1200	-0.30	1.70	-0.60	0.6
1300	-0.35	1.80	-1.10	0.8
1400	-0.39	2.00	-1.70	1.0
1500	-0.44	2.20	-2.30	2.0
1600	-0.49	2.40	-3.00	3.7
1700	-0.54	2.60	-3.80	8.5
1800	-0.60	2.80	-4.60	18.0
1900	-0.66	3.00	-5.50	
2000	-0.72	3.20	-6.40	
2100	-0.79	3.50	-7.00	
2200	-0.85	3.70	-8.00	
2300	-0.93	4.00	-10.00	
2400	-1.00	4.20	-11.00	
2500	-1.07	4.50	-12.00	
2600	-1.15	4.80	-13.00	
2700	-1.24	5.00	-15.00	
2800	-1.32	5.30	-16.00	
2900	-1.41	5.60	-18.00	
3000	-1.50	5.90	-20.00	

References

[1] THERDAS - Thermodynamic Databank System, Lehrstuhl für Theoretische Hüttenkunde, RWTH Aachen, Germany
[2] Schneider, S. J.: Pure Appl. Chem., 21 (1979), p. 115
[3] Kracek, F. C., G. W. Morey, H. E. Merwin: Am. J. Sci., 5th Ser., 35 (1938), p. 143/71
[4] Schneider, S. J.: Nat. Bur. Stand., Monograph 68 (1963) No. 10, p. 1/31
[5] Kojima, H., C. R. Masson: Canad. J. Chem. 47 (1969), p. 4221/8
[6] Hlavac, J.: Pure Appl. Chem., 54 (1982) No. 3, p. 681/8
[7] Yamada, T., M. Yoshimura, S. Somiya: J. Am. Ceram. Soc. 69 (1968) No. 10, p. C243/5
[8] Juza, R., K. Bünzen: Z. Physik. Chem. /Frankfurt/, 17 (1958), p. 82/99
[9] McNally, R. N, F. I. Peters, P. H. Ribbe: J. Am. Ceram. Soc. 44 (1961) No. 1, p. 491/3
[10] Darken, L. S., R. W. Gurry: J. Am. Chem. Soc., 68 (1946) No. 5, p. 798/816
[11] Kubaschewski, O.: Iron - Binary Phase Diagrams, Ed.: Springer Verlag, Verlag Stahleisen mbH, Düsseldorf, (1982)
[12] Panek, Z.: Silikaty /Praque/ 23 (1979) No. 2, p. 97/102
[13] Trömel, G., W. Fix, K. Koch, F. Schaberg: Erzmetall, 29 (1976) No. 5, p. 234/7
[14] Staffansson, L.-I.: Metall. Trans. B, 7B (1976) No. 3, p. 131/4
[15] Bouaziz, R., G. Papin, A.-P. Rollet: C. R. Acad. Sci., Paris, 262C (1966), p. 1051/4
[16] Von Wartenberg, H. V., H. J. Reusch, E. Saran E: Z. Anorg. Allg. Chem., 230 (1937) No. 3, p. 257/76
[17] Neumann, J. P., T. Zhong, Y. A. Chang: Bull. Alloy Phase Diagrams, 5 (1984) No. 2, p. 141/4
[18] Greig, J. W. : Am. J. Sci., 5-th Ser., 13 (1927) No. 73, p. 1/154
[19] Wahlbeck, P. G., P. W. Gilles: J. Am. Ceram. Soc., 49 (1966) No. 4, p. 180/3
[20] Brauer, G., W. Littke: J. Inorg. Nucl. Chem., 16 (1960), p. 67/76
[21] Ackerman, R. J., S. P. Garg, E. G. Rauh: J. Am. Ceram. Soc., 60 (1977), p. 341/5
[22] Abriata, J. P., J. Garcés, R. Versaci: Bull. Alloy Phase Diagrams, 7 (1986) No. 2, p. 116/24

4

Composition and structure of slags

J. Geiseler

4.1 Introduction

An integral part of the hot metal and steel refining processes is the formation of slag. The slags are required to perform several functions. In metallurgical processes they must be formed in such a way that they operate as efficient media for metallurgical reactions. Individual slags are characterised by the conditions peculiar to each melting process. For example, in the case of the blast furnace process, it is first necessary to form a slag by the use of a variety of added components in such a way that the gangue and the coke ash can be separated as a liquid phase from the hot metal.

4.2 Blast furnace slags

For economic reasons, the location of iron and steel works in earlier times was closely associated with the availability of coking coal resources and ore deposits. Consequently, it was also possible to identify slag compositions which were typical to the ores smelted at each site. Given the possibilities of worldwide ore trading which exist nowadays, however, these differences have become virtually meaningless. In spite of the different burden compositions which occur, the same also applies today to the slags relating to Thomas (Basic Bessemer) hot metal and pig iron production for steelmaking, in which substantial variations also occurred in earlier times. Nowadays, the differences in the iron and manganese contents are negligible, while the substantial variations in phosphorus content and in temperature have remained. **Tab. 4.1** shows the average slag compositions of Germany's blast furnace plants.

Common to all these slags is the fact that they leave the metallurgical process as a homogeneous liquid phase and can be plotted on the basis of their characteristic constituents in the $CaO\text{-}SiO_2\text{-}Al_2O_3\text{-}(MgO)$ phase diagram. **Fig. 4.1** shows the average slag compositions from iron and steelmaking plants located in various geographical areas, using the conventional method of presentation on the basis of the $CaO\text{-}SiO_2\text{-}Al_2O_3$ and the $CaO\text{-}SiO_2\text{-}MgO$ systems [1, 2]. It is important to note within this context that the temperatures of the liquid slags lie above the solidus surfaces of the associated systems. Blast furnace slags can be processed from this condition into various products by applying a variety of cooling regimes [3].

1. A widely used method is to apply rapid cooling to the liquid blast furnace slag by employing copious amounts of water in complex granulation facilities. In this process, ≥ 90 % of the blast furnace slag solidifies as a vitreous product. This vitreous modification, known generally as "granulated blast furnace slag", possesses latent hydraulic properties. Cements can be manufactured from this product by adding alkaline (predominantly Portland cement clinker) or sulphate activators. The most important such products are Portland slag cement

Tab. 4.1. Average compositions of blast furnace slags

Blast furnace slags in West Germany	Mass %									kg slag/t hot metal	Temperature °C
	SiO_2	Al_2O_3	CaO	MgO	Fe_{total}	Mn_{total}	TiO_2	S_{total}	P_{total}		
Slags from high phosphorus hot metal	36.0	8.5	41.0	9.5	0.3	0.4	1.2	1.5	0.10	300	1400/1450
Slags from low phosphorus hot metal	37.0	10.5	40.0	9.5	0.2	0.3	1.0	1.5	0.01	250	1450/1500
MgO-rich slags from low phosphorus hot metal	38.5	8.0	35.5	13.5	0.2	0.2	0.9	1.5	0.01	230	1500

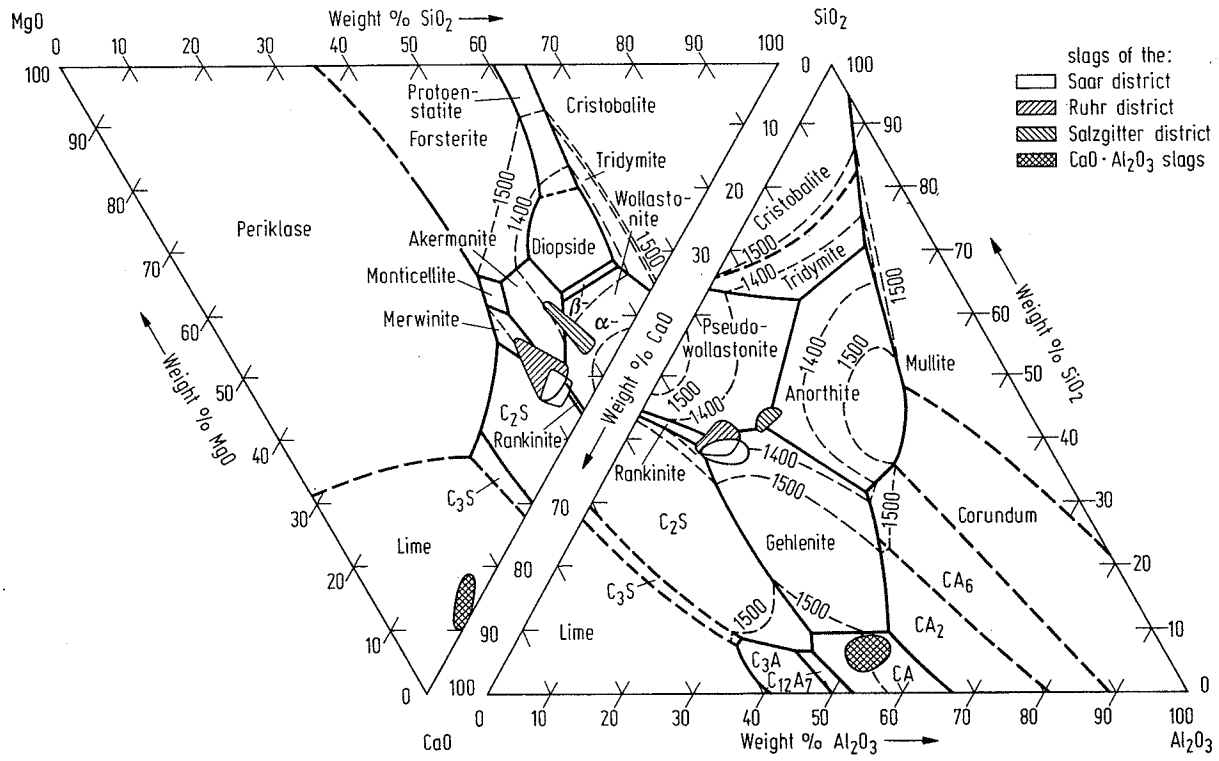


Fig. 4.1. Characteristic compositions of blast furnace slags of the systems $CaO\text{-}SiO_2\text{-}Al_2O_3$-and $CaO\text{-}SiO_2\text{-}MgO$ [1]

(6 to 35 % granulated blast furnace slag) and blast furnace slag cement (36 to 80 % granulated blast furnace slag). In addition, a cement containing 81 to 95 % granulated blast furnace slag has also been standardized within Europe (ENV 197). In earlier times aluminous cement was also manufactured from a blast furnace slag, the composition of which was deliberately adapted such that it lay within the range of the calcium aluminate group. Following slow cooling and crystalline solidification, this slag was finely ground and used as a refractory cement. For economic reasons, production in Germany has now ceased.

2. Using air or steam, liquid blast furnace slag can be atomized to produce a vitreous solidified product in the form of slag wool which can then be processed for the manufacture of high-temperature thermal, low-temperature thermal and sound insulation products.

3. With a little water added, blast furnace slag solidified from its liquid state can be expanded to produce a pumice-stone slag (foamed slag) which is used as a lightweight aggregate for concrete, as an insulant, and as a road construction material, particularly for the stabilization of soils with poor bearing resistance.

4. A product with similar properties is obtained in the so-called slag pelletizing process. The fines of the slag pellets which are produced are employed for the same applications as granulated blast furnace slag. The coarse fraction is employed in the same way as foamed slag (pumice-stone slag).

5. The most important product manufactured from blast furnace slag, aside from the granulate, is lump slag. This is produced by slowly cooling the liquid blast furnace slag in thin layers in air to enable crystalline solidification. Following the appropriate conditioning, this is then employed as an aggregate of concrete and as a mineral material in road construction. The good physical properties required for these applications, and particularly the strength of the product, are influenced by the mineral composition and the porosity of the slag as determined by composition and the solidification conditions [3-6].

The all so important primary crystallization of the mineral phases follows the conditions of the phase diagram. Within this context, **Fig. 4.2** shows the isothermal quaternary system $(CaO+MgO)\cdot SiO_2$-Al_2O_3 for 1500 °C [2]. The crystallization sequence can also be observed by stringing together further temperature diagrams. Examples are shown in **Figs. 4.3 a-d** in the form of various structures of blast furnace slag, the mineral content of which changes with increasing MgO content. **Fig. 4.4** shows a statistical analysis of the production and utilization of blast furnace slags during 1994 in Germany [7].

4.3 Steelmaking slags

4.3.1 Phosphate slags

Lime-phosphate slags are produced in the conversion of steel from hot metal with usually more than 0.5 % phosphorus. Their composition is essentially characterized by the components FeO_n, CaO, P_2O_5 and SiO_2. The contents of the individual components can vary within quite wide limits depending on the hot metal/pig iron used, the required steel quality and the resultant specific quantity of slag required. **Tab. 4.2** shows the average composition of slags from such processes, and **Fig. 4.5** shows their position in the phase diagram for FeO_n-CaO-P_2O_5-SiO_2 at 1600 °C [8, 9]. **Figs. 4.6 a-d** show a number of characterizing slag structures. The particular determinants in this respect are the precipitated mineral phases which characterize the con-

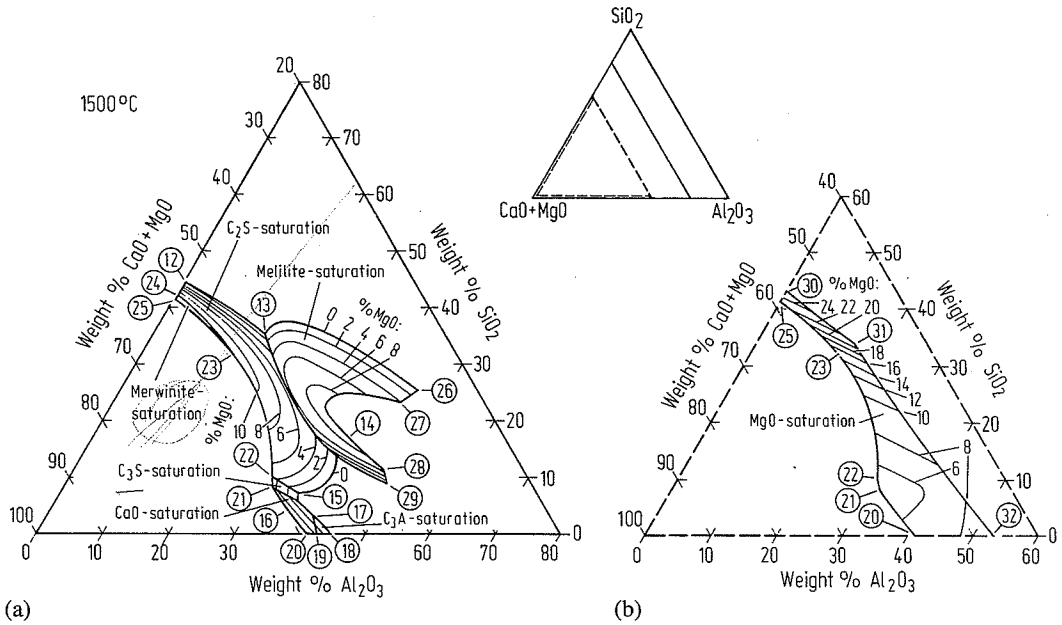


Fig. 4.2 a,b. Composition diagram (CaO + MgO)-SiO_2-Al_2O_3 at 1500 °C (after G. Heinz [2])

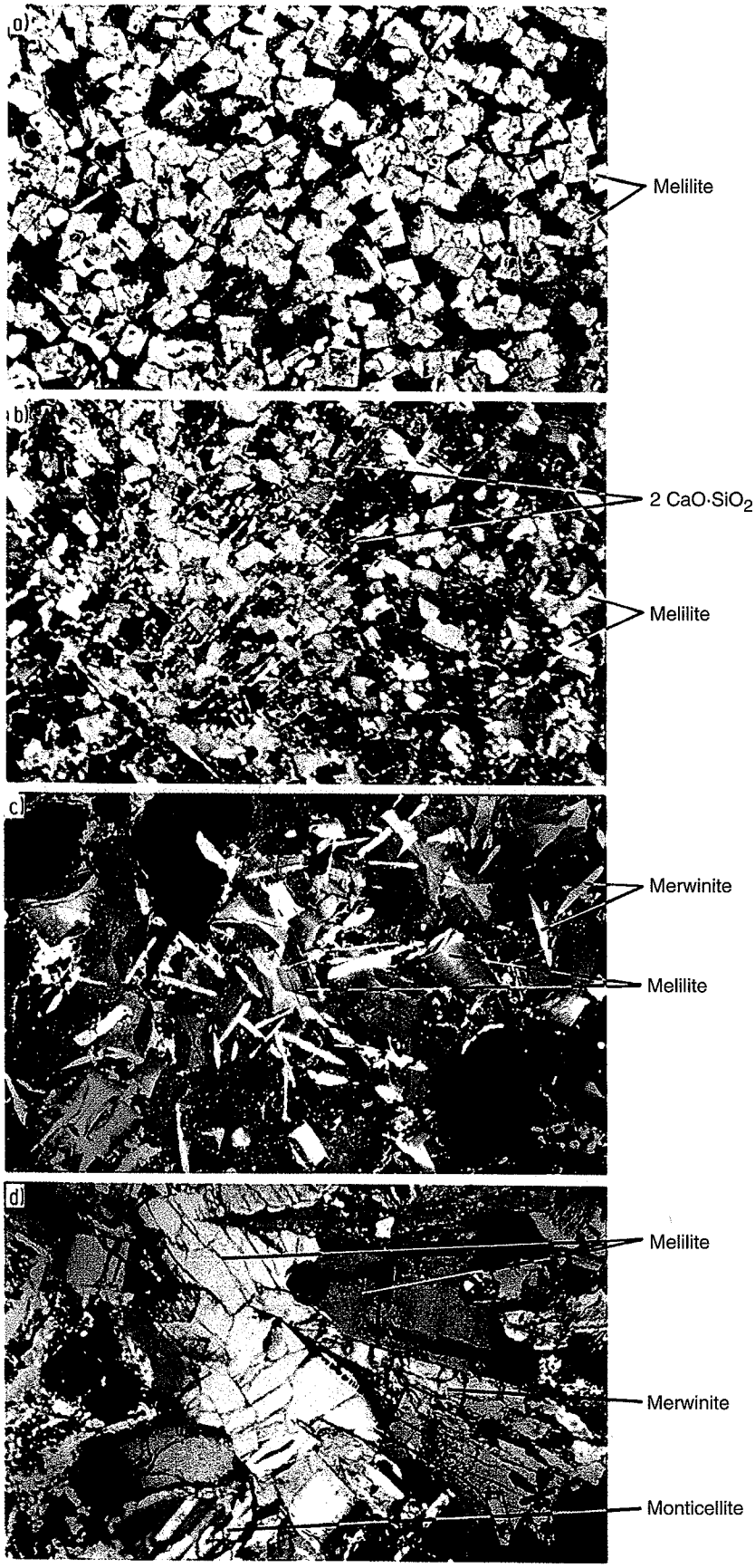


Fig. 4.3 a-d. Microstructure of blast furnace slags (crossed nicols except a)
(a) $CaO/SiO_2 = 1.25$; $Al_2O_3 = 14$ %; MgO = 4.5 %
(b) $CaO/SiO_2 = 1.25$; $Al_2O_3 = 14$ %; MgO = 4.5 %
(c) $CaO/SiO_2 = 1.28$; $Al_2O_3 = 12$ %; MgO = 6.0 %
(d) $CaO/SiO_2 = 1.39$; $Al_2O_3 = 11$ %; MgO = 9.9 %

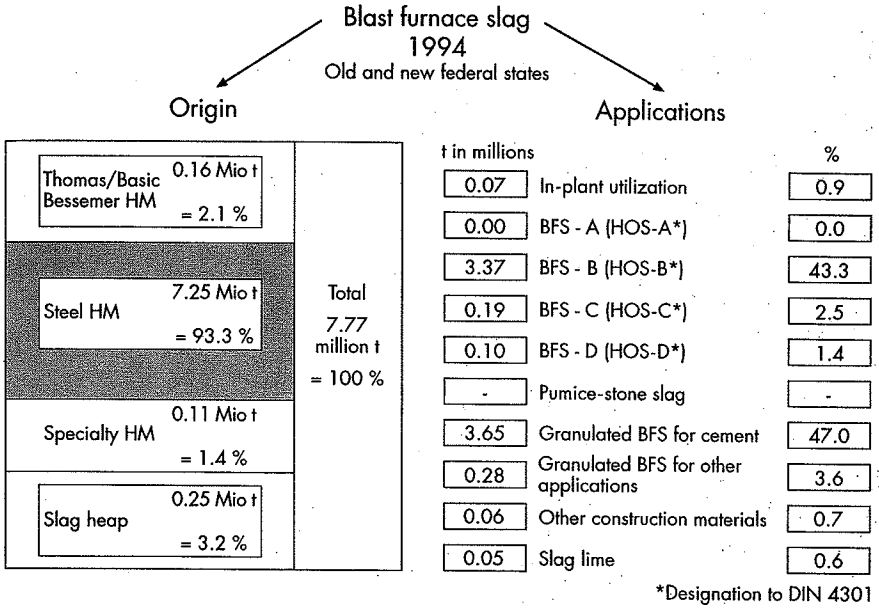


Fig. 4.4. Production and utilization of blast furnace slags in Germany

Tab. 4.2. Chemical compositions of converter specimens of calc-phosphate slags

Process	Mass %							
	Fe_{total}	Fe^{2+}	CaO	SiO_2	$P_2O_{5\,total}$	$P_2O_{5\,zitrsl.}$	MgO	MnO_n
Thomas	12.2	8.4	48.3	6.6	20.3	19.5	3.1	2.3
OBM/Q-BOP	15.6	6.1	49.3	5.9	14.7	13.3	7.6	1.9
LDAC-First slag	12.0	9.0	50.0	8.0	15.0	14.0	2.0	3.0
LDAC-Second slag	23.0	11.0	47.0	5.0	5.0	n. d.	2.0	3.0
zitrsl. = citric acid soluble								

dition of the slag; of these it is the silicophosphate solid solution which predominates, with a secondary role normally being played by tetracalcium phosphate. In addition, these slags may also be lime-saturated at the end of the blowing operation, depending on the metallurgical process conditions (**Figs. 4.6 b** and **d**).

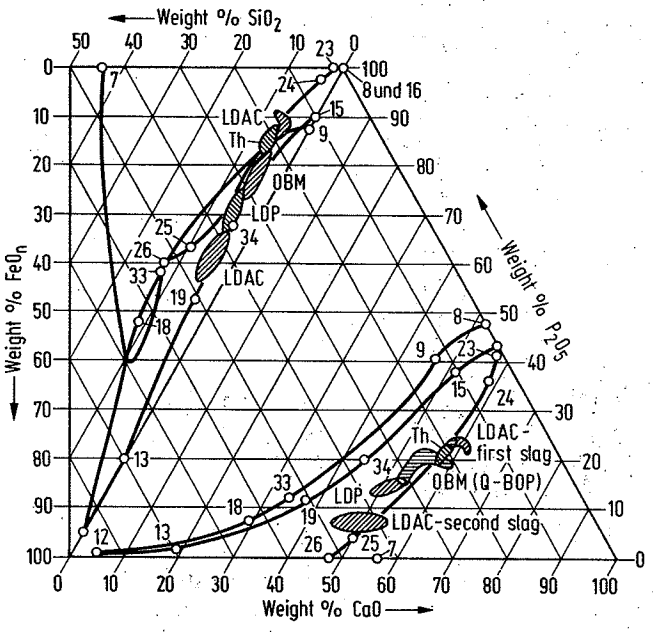


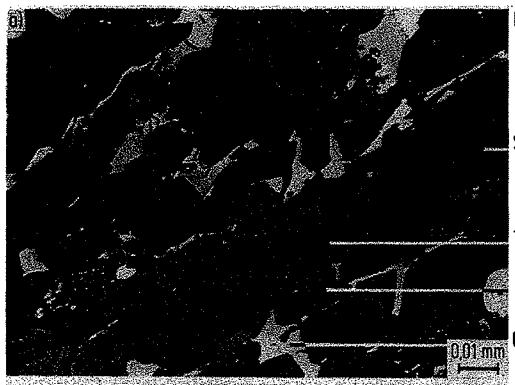
Fig. 4.5. Compositions of phosphate slags basic. LDP, OBM and LDAC steelmaking processes of the system CaO-FeO_n-P_2O_5-SiO_2 at 1600 °C (phase equilibria from refs. [5, 16])

Lime-phosphate slags were already being used in ground form back in 1880 as agricultural fertilizer under the name "Thomas phosphate" [10]. This phosphate is not water-soluble, and is only transformed into a plant nutrient by reaction and conversion processes which take place in the soil with the support of bacterial action. The nutrient value of the phosphate becomes accessible by virtue of the fact that a portion of the total phosphoric acid is soluble in citric acid. Silicophosphate and tetracalcium phosphate are readily soluble slag phases, and as such can be absorbed by plant life. The low-solubility phosphoric acid component is chemically bonded as iron oxide apatite [11-13], the precipitation of which can be prevented by applying sufficiently high siliconizing factors SiO_2/P_2O_5, or - where appropriate - by the addition of sand into the slag ladle [13-15]. **Figs. 4.7 a,b** show micrographs of lime-phosphate slags with varying siliconizing factors and correspondingly different phosphate solubilities.

4.3.2 Lime-silicate slags

Lime-silicate slags are formed in steelmaking processes employing low-phosphorus hot metal and/or scrap. Their melt equilibria and the phases of the refining slags which crystallize during cooling are approximately described in relation to the basic oxygen (BOF/LD), open-hearth (Siemens-Martin/SM) and electric arc furnace (EAF) processes by the conditions shown in the phase diagram FeO_n-CaO-SiO_2-(MnO_n, MgO) [16] (cf. phase diagrams in section 2.2).

Fig. 4.8 shows the slag conditions (slag path) occurring in the course of melt refining using the basic oxygen process [17-21]. Depending on the hot metal composition and steel analysis, deviations from this path are also possible. The first slag phase which forms consists of the oxides of the elements oxidized at the start of blowing, namely silicon, manganese and iron. The primary slag thus consists of iron-manganese silicates. This primary slag dissolves the added lime. At the same time, the proceeding decarburization reaction reduces the FeO content in the slag. As a result, the slag composition shifts towards the ternary region of the CaO-FeO_n-SiO_2-(MnO_n, MgO) system selected for illustration. Once virtually all the silicon has been slagged, the slag path changes direction, as a result of further lime dissolution and decarburization, towards the CaO corner of the system. The position of the final slags depends on the metallurgical conditions which have been applied and the desired steel analysis. Where the very low carbon contents which are common today are attained, more oxygen is available towards the end of the blowing process



Basic Bessemer slag, saturated with silicophosphate

Silicophosphate

Tetracalcium phosphate

Iron-oxide apatite

Calcium ferrite/calcio-wüstite

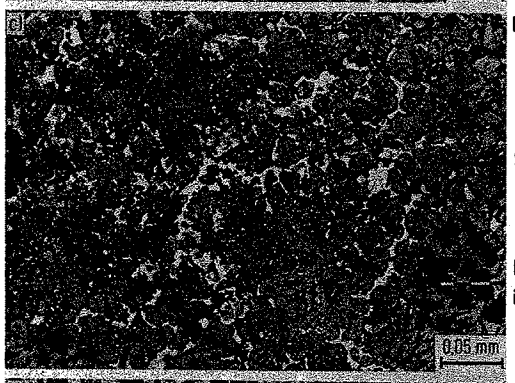


OBM-slag, saturated with solid solution between CaO and FeO

Solid solution between CaO and FeO

Silicophosphate, calcium ferrite/calcio-wüstite

Tetracalcium phosphate



Primary LDAC-slag, saturated with silicophosphate

Silicophosphate with

Residual lime, iron-oxide apatite, calcium ferrite/calcio-wüstite

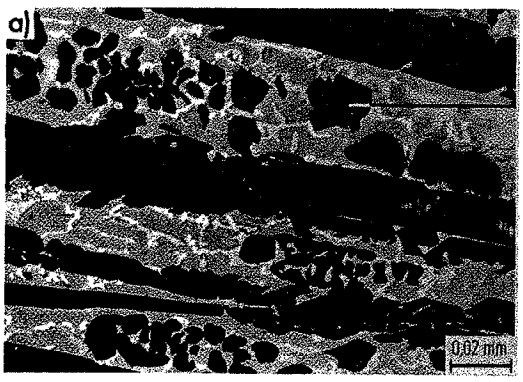


Secundary LDAC-slag, saturated with solid solution between CaO and FeO

Solid solution between CaO and FeO with

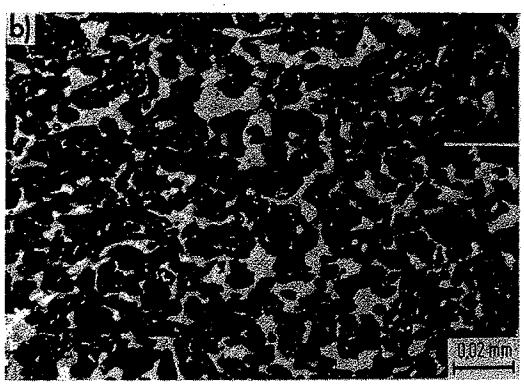
Silicophosphate, calcium ferrite / calcio-wüstite

Fig. 4.6 a-d. Microstructure of end-point slags from basic, OBM and LDAC processes (etched with ammonium citrate)



$SiO_2/P_2O_5 = 0.07$ (solubility: 71%)

Silicophosphate



$SiO_2/P_2O_5 = 0.34$ (solubility: 98.5%)

Silicophosphate

Fig. 4.7 a,b. Synthetic phosphate slags saturated with iron and lime solid solutions in the system $Fe\text{-}FeO_n\text{-}CaO\text{-}P_2O_5\text{-}SiO_2$ in order of increasing silica factor SiO_2/P_2O_5, etched with ammonium citrate

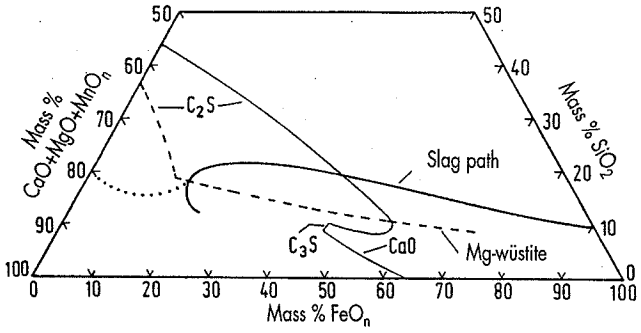


Fig. 4.8. Slag path in the manufacture of unalloyed and alloyed steels in the electric arc furnace
Saturation isotherm (1600 °C) for the system CaO-FeO$_n$-SiO$_2$
Saturation isotherm (1600 °C) for the system CaO-FeO$_n$-SiO$_2$-10 % MgO-10 % MnO$_n$

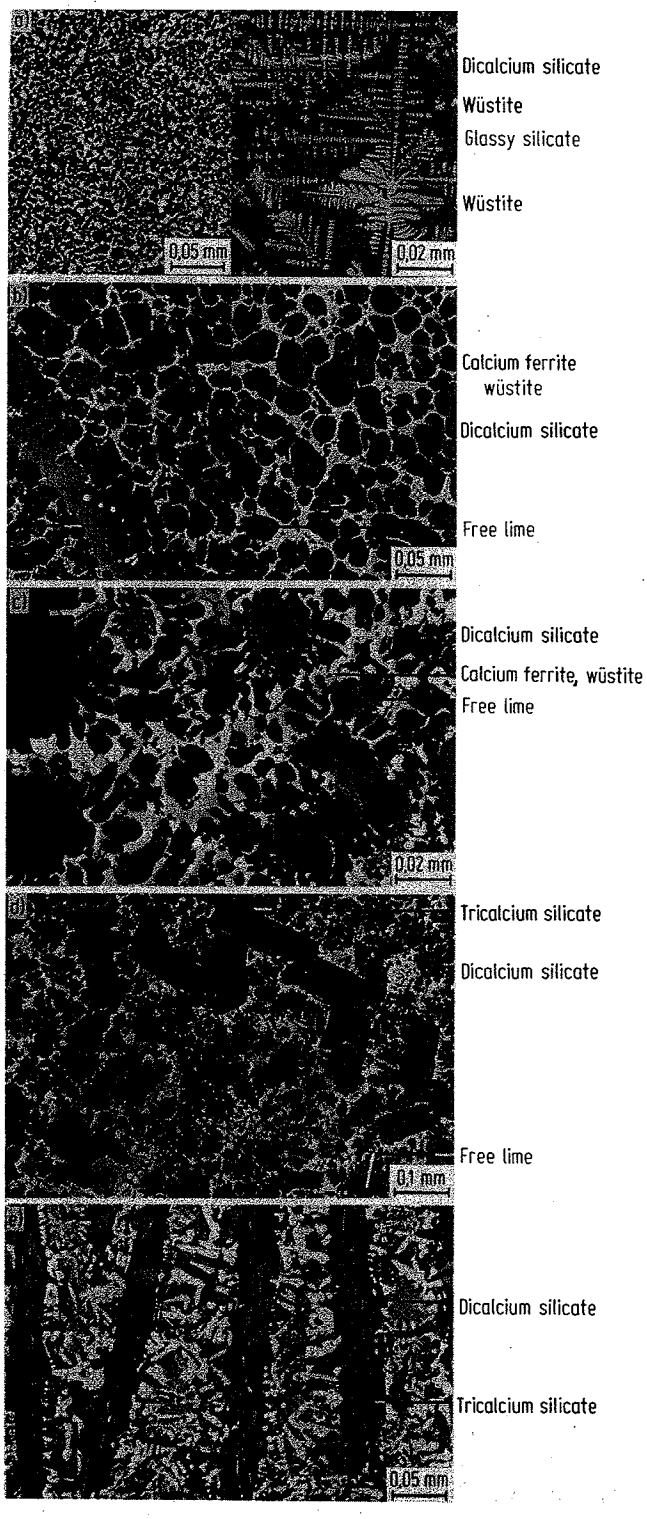


Fig. 4.9 a-e. Microstructure of LD slags
(a) after 10 % blowing time
(b) after 75 % blowing time
(c) to (e) end-point slags

than is necessary for decarburization, so that the FeO content rises again. Only in the case of caught (catch-carbon) heats is it possible to obtain a final slag of which the FeO content is at its lowest point along the slag path. With combined blowing, however, FeO contents are today achieved which are usually below 20 %.

Tab. 4.3 shows the typical compositions of final slags from the basic oxygen process. The mineral composition of these slags slowly cooled in air is characterized by precipitates of dicalcium silicate (C_2S), or more rarely of tricalcium silicate (C_3S)-dicalcium ferrite, and of wüstite in the form of calciowüstite and, at higher MgO contents, magnesiowüstite. **Figs. 4.9 a-e** show the microstructure of BOF slags characterizing the slag path and the final slag.

In order to achieve preset metallurgical objectives - and particularly sufficiently low phosphorus contents - the lime addition rates which are applied nowadays are such that the lime cannot be completely dissolved during the duration of a melt. As a result, undissolved lime, so-called free lime (CaO_{free}), remains in the tapped slags. In addition, lime precipitates during cooling from the solidified slag. The free lime can react with moisture or water and, as a result of the volume increase which occurs with hydration, adversely affects the constancy of volume of these slags. Constancy of volume is of decisive importance for slag utilization. Given sufficiently low contents of free lime (< 7 % CaO_{free}), slags may be considered for classified road construction and applications in water engineering (civil engineering hydraulics). BOF slag is highly regarded for such applications, due in particular to its high strength. However, the volume stability test is always more reliable as a means of evaluating constancy than selecting slags on the basis of their free-lime contents.

Slag-forming in the electric arc furnace and open-hearth furnace processes follows a pattern very similar to that observed in the basic oxygen process. Owing to the longer melting time, however, the MgO leached from the refractory lining materials also has to be taken into account. Consequently, the slag path is shown on the basis of the system FeO-CaO-SiO$_2$-MgO-MnO$_n$ (**Fig. 4.8** - dashed isotherms). Compared with the CaO-FeO$_n$-SiO$_2$ ternary system, the incorporation of MgO and MnO$_n$ pushes back

Tab. 4.3. Chemical composition of calc-silicate final slags of various processes in the production of unalloyed steels

Process	Mass %							
	Fe_{total}	Fe^{2+}	CaO_{total}	CaO_{free}	SiO_2	MgO	MnO_n	P_2O_5
Basic Oxygen Process Steel with < 0.1 % C	16.0	7.0	50.0	5.0	14.0	2.0	3.5	1.5
Open Hearth Process Steel with > 0.1 % C	14.0	10.0	45.0	5.0	13.0	9.0	7.0	1.5
and < 0.1 % C	20.0	14.0	41.4	<1.0	13.0	7.0	7.0	1.5
Electric Arc Furnace Process Steel with 0.1 % C	25.0	10.0	30.0	<1.0	15.0	5.0	5.0	<1.0

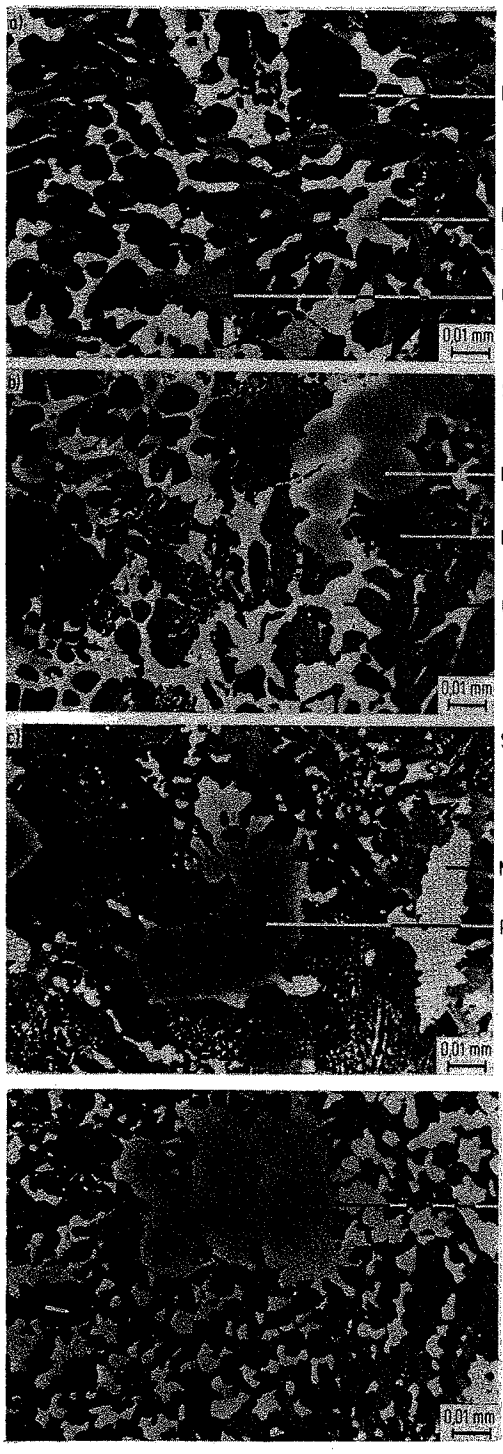


Fig. 4.10 a-d. Microstructures of OH end-point slags according to Tab. 4.3

the C_2S saturation region significantly towards the $CaO-SiO_2$ boundary system. As a result, magnesiowüstite saturation becomes predominant in the five-component system.

Examples for the chemical composition of the final slags of the open-hearth and electric arc furnace processes are indicated in **Tab. 4.3.** Following cooling, the phases dicalcium ferrite, magnesiowüstite and dicalcium silicate predominate in these final slags **(Figs. 4.10 a-d)**. Free lime is usually only present in concentrations which do not jeopardize volume stability. Instead, the non-dissolved MgO particles attain a greater importance as these may likewise undergo hydration when exposed to moisture [3, 22-25]. However, this hydration process occurs at a substantially slower rate than in the case of the free lime. Consequently, the constancy of volume of these slags can only be improved to a limited extent by weathering prior to their utilization. Volume stability must, therefore, be extensively ensured by metallurgical measures [23]. As in the case of the BOF slags, the applications for electric arc furnace and open-hearth furnace slags lie in classified road construction and water engineering. Owing to their high resistance to wear, EAF slags have proven particularly successful as mineral aggregates for the wearing course in road surfacing [3].

High-alloy stainless and heat-resistant stainless steels are today produced almost exclusively in the electric arc furnace with a downstream VOD (vacuum oxygen decarburization) or AOD (argon oxygen decarburization) treatment. The slag-forming process which occurs in the electric arc furnace can be represented by the phase diagram $CaO-FeO-SiO_2-MgO-MnO_n$.
While the slag path can initially be extensively described by the continuous line drawn in Fig. 4.8, the composition following the final reduction treatment of the slag is shifted to a point close to the boundary system $(CaO+MgO+MnO_n)-SiO_2$ (dotted line) [26].

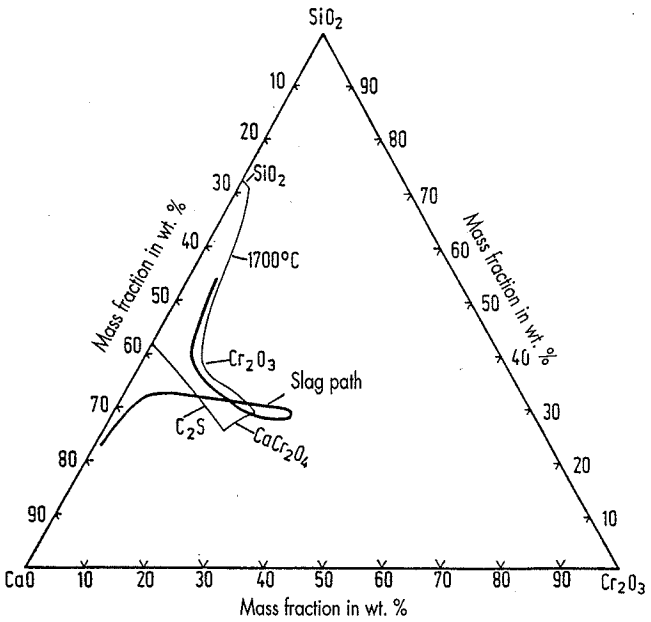


Fig. 4.11. Slag path in the manufacture of stainless and heat resistant steels

During the subsequent treatment of the melt tapped from the electric arc furnace in the VOD or AOD process, a slag initially forms from the iron slagged at the beginning of the process, and the oxides of the accompanying elements silicon and manganese [18]. This slag, which develops from the SiO_2 corner of the phase diagram relating to the CaO-Cr_2O_3-SiO_2 system (**Fig. 4.11**), reacts with lime. On attainment of low C contents, accelerated chromium oxidation occurs, so deflecting the slag path towards the Cr_2O_3 corner of this system. As soon as sufficiently low C contents have been achieved, the slag is reduced with FeSi. As a result, the slag composition shifts towards a point close to the CaO-SiO_2 boundary system.

Examples for the chemical composition of slags from the electric arc furnace and from the AOD converter are provided in **Tab. 4.4.** The mineral composition of the slag taken from the electric arc furnace is particularly characterized by dicalcium silicate precipitates. At lower basicities, melilite and merwinite precipitates occur. During cooling, the β - γ transformation can lead to these slags undergoing disintegration into a fine-grained fraction. This process can be extensively suppressed by accelerated cooling. As a result, a portion of the slag undergoes vitreous solidification. By comparison, the slag from the AOD converter exhibits a higher level of basicity. Generally, this slag disintegrates as a result of the β - γ transformation of the dicalcium silicate. Stabilization can be achieved by adding, for example, borate.

The range of applications of slags arising from the production of stainless and heat resistant steels has so far remained limited. Provided that the slags from the electric arc furnace do not undergo disintegration, they can be used following appropriate conditioning for pathway and playground construction, and also in earthworks engineering [28]. The disintegrated slags from the AOD converter are suitable, for example, for applications in earthworks engineering, as an undercourse for sett paving and in the production of impervious (barrier) layers for landfill sites and dykes [29].

Fig. 4.12 provides an overview of the production processes and applications of steelmaking slags in Germany for 1993.

Tab. 4.4. Chemical composition of the final slags formed in the electric arc furnace and AOD converter processes during the production of stainless and heat resistant steels

Process	Mass %					
	Fe_{total}	CaO_{total}	CaO_{free}	SiO_2	MgO	MnO_n
Electric Arc Furnace Process	1	45	≤10	30	7	2
AOD-converter process	2	50	≤10	20	4	1

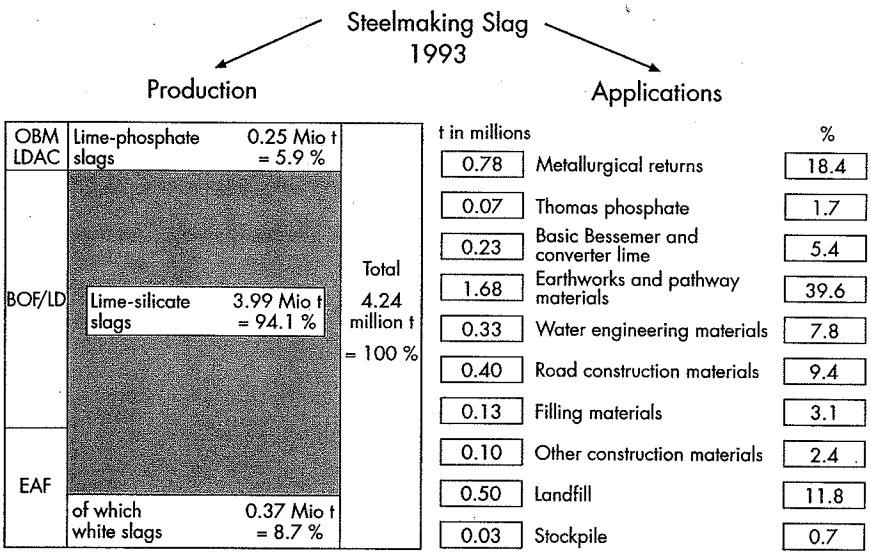


Fig. 4.12. Production and utilization of steelmaking slags in Germany

4.4 ESR slags

In the electro-slag refining (remelting) process, one or several consumable steel electrodes are immersed in a superheated, synthetically produced slag where they undergo drip-melting. The entire remelting process is performed in a water-cooled copper or steel mould in which the steel dripping through the slag collects and crystallizes into an ingot.

Tab. 4.5. Chemical composition of common ESR slags

Mass %						Remarks
CaF_2	CaO	MgO	TiO_2	Al_2O_3	SiO_2	
70				30		Good desulphurization, but some loss of Ti and Al
70	15			15		Same problem but better desulphurization
60	20			20		For steels without Ti and B, very good desulphurization
50			25	25		Reduced Ti loss but poor desulphurization
51	13	2	25		9	Starting slag

The slag bath, which acts as an ohmic resistor, converts electrical energy into heat. Provided that the process is properly controlled, the resultant ingots are free of internal defects and exhibit an extensively homogeneous structure, with the steel having been cleaned of unwanted impurities. The most important function in this remelting process is performed by the slag. Not only must it exhibit sufficient conductivity in the remelting temperature range, but also it must meet the following metallurgical requirements:

1. Good absorption capacity for inclusions of all types.
2. Undergo no reaction with the alloying elements of the steel.
3. Capable of reducing the sulphur content.

Tab. 4.5 shows some typical ESR slags and their associated applications [30-33].

4.5 References in Chapter 4

[1] Phase Diagrams for Ceramists: Americ. Ceram. Soc. 1956, 1964, 1969
[2] Heinz, G.: Totale Gleichgewichte zwischen kohlenstoffgesättigtem Eisen und schwefelhaltigen Hochofenschlacken aus Kalk, Kieselsäure, Tonerde und Magnesium. Dr. -Ing. Thesis, Technische Universität Clausthal 1973
[3] Geiseler, J.: Verwertung von Hochofen- und Stahlwerksschlacken. Schriftenreihe der Forschungsgemeinschaft Eisenhüttenschlacken, No. 1, 1 – 32
[4] Keil, F.: Hochofenschlacke. 2nd Ed., Verlag Stahleisen, Düsseldorf 1963
[5] v. Ende, H., K. Grebe, E. E. Hofmann: Stahl und Eisen 84 (1964), 1511 – 1521
[6] Fix, W., A. Moradoghli-Haftwani, K. Schwerdtfeger: Arch. Eisenhüttenwes. 46 (1975), 363 – 370
[7] Fachverband Eisenhüttenschlacken: Internal memorandum
[8] Trömel, G., W. Fix, K. Koch: Arch. Eisenhüttenwes. 38 (1967), 177 – 184
[9] Koch, K., W. Fix: Arch. Eisenhüttenwes. 41 (1970), 111 – 118
[10] Hoyermann, G.: Report on the meeting of the "Verein zur Beförderung des Gewerbefleisses". Stahl und Eisen 6 (1886) No. 1, 59 – 60
[11] Trömel, G., E. Görl, H.W. Fritze: Arch. Eisenhüttenwes. 36 (1965), 327 – 331
[12] Trömel, G., W. Fix, U. Bongers: Arch. Eisenhüttenwes. 40 (1969), 813 – 819
[13] Fix, W., K. Koch, U. Bongers: Arch. Eisenhüttenwes. 46 (1975), 555 – 559
[14] Dunkel, Th.: Stahl und Eisen 47 (1927), 1205 – 1207
[15] Obst, K.-H., J.J. Ueberhorst: Stahl und Eisen 81 (1961), 729 – 735
[16] Trömel, G., N. Grosskurth, K. Koch, W. Fix: Arch. Eisenhüttenwes. 41 (1970), 613 – 620
[17] Koch, K., J. Sittard, W. Domröse: Kalksilikatische Stahlwerksschlacken, Schlacken in der Metallurgie. Verlag Stahleisen, 191 – 206
[18] Geiseler, J., R. Baum, R. Heinke: Schlacken bei der Herstellung von Edelstählen. Schlacken in der Metallurgie. Verlag Stahleisen, 221 – 234
[19] Bardenheuer, F., H. v. Ende, P. Oberhäuser, E. Hoffmann: Arch. Eisenhüttenwes. 39 (1968), 571 – 576
[20] Münchberg, N., K.-H. Obst, G. Mahn, D. Nolle: Stahl und Eisen 101 (1981), 587
[21] Fix, W., K. Koch: Arch. Eisenhüttenwes. 39 (1968), 9 – 22
[22] Geiseler, J., R. Schlösser, R. Scheel, K. Koch, D. Janke: steel research 58 (1987), 210 – 214
[23] Geiseler, J., R. Schlösser: Kriterien zur Verwertung von Elektroofenschlacken. Preprints, 2nd European Electric Steelmaking Congress, Florence, 29 Sept. to 1 Oct. 1986
[24] Geiseler, J., R. Schlösser: Investigations concerning the structure and properties of steel slags. International conference on liquid slags and fluxes, Glasgow, 27 - 29.06.1988
[25] Forschungsgemeinschaft Eisenhüttenschlacken: Elektroofenschlacke - ein hochwertiger Mineralstoff für den Verkehrsbau, No. 3, Schriftenreihe der FEhS
[26] Geiseler, J., K. Grade, P. Valentin: Stahl und Eisen 103 (1983), 1013 – 1017
[27] Münchberg, W.: Stahl und Eisen 800 (1980), 1051 – 1055
[28] Landesumweltamt Nordrhein-Westfalen: Merkblatt für die Verwendung nicht güteüberwachter industrieller Reststoffe. Publication imminent
[29] Krass, K., H. Nendza, V. Stahlmann: Wasser und Boden 36 (1984), 158 – 163
[30] Holzgruber, W., E. Plöckinger: Stahl und Eisen 88 (1968), 638 – 648
[31] Latash, J. W.: Awtomat. Swarka (1958), 76 – 83
[32] Sickberth, A., G. Stolte: Elektrowärme international 28 (1970) No. 4, 185 – 191
[33] Duckworth, W. E., G. Hoyle: Electro-slag Refining. Chapman and Hall Ltd., London 1969

5

Thermodynamic activity data for slag systems

M. Allibert, R. Parra, C. Saint-Jours and M. Tmar

5.1 Preliminary remarks on the activity data

a) Standard states (or reference states) are the pure substances in their thermodynamic stable states at the given temperature unless otherwise stated.

b) Activity of standard state is unity unless otherwise stated.

c) A stable compound of the formula FeO does not exist. "FeO" as it is understood in this chapter is the liquid iron oxide in equilibrium with liquid or solid iron dependent on temperature, or wüstite in equilibrium with solid iron (see also Figs. 3.5. and 3.6., chapter 3).

d) In some figures the chemical compound alumina is given in the form $AlO_{1.5}$. In these cases the following correlations are valid:

$$Al_2O_3 = 2\,AlO_{1.5}$$
$$a_{Al_2O_3} = (a_{AlO_{1.5}})^2.$$

5.2 Thermodynamic activity data

5.2.1 Binary systems

Al_2O_3-CaO

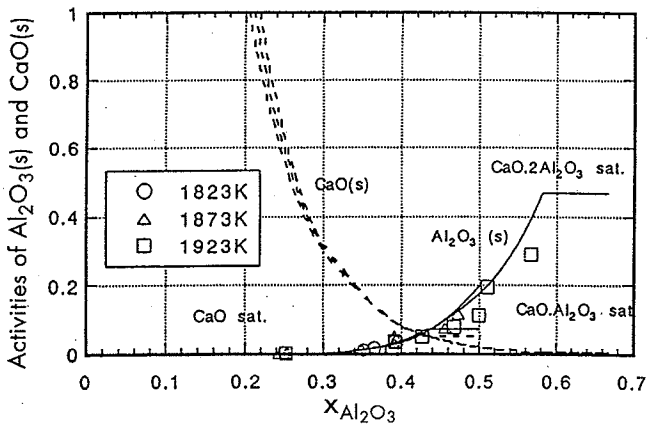


Fig. 5.1. Activities of Al_2O_3 and CaO in Al_2O_3-CaO slags, after Hino [1].
Reference states are the pure solids.

Al_2O_3-FeO

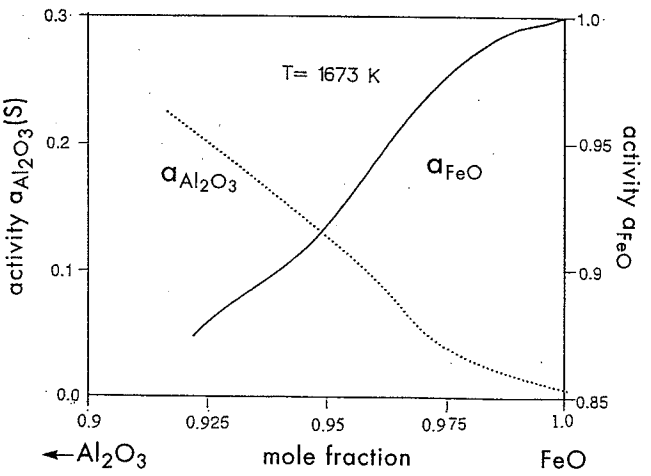


Fig. 5.2. Activity of Al_2O_3 and FeO at 1400 °C, after Ban-Ya et al. [2].
Activities are referred to pure solid Al_2O_3 or liquid FeO in equilibrium with solid iron.

Al_2O_3-MnO

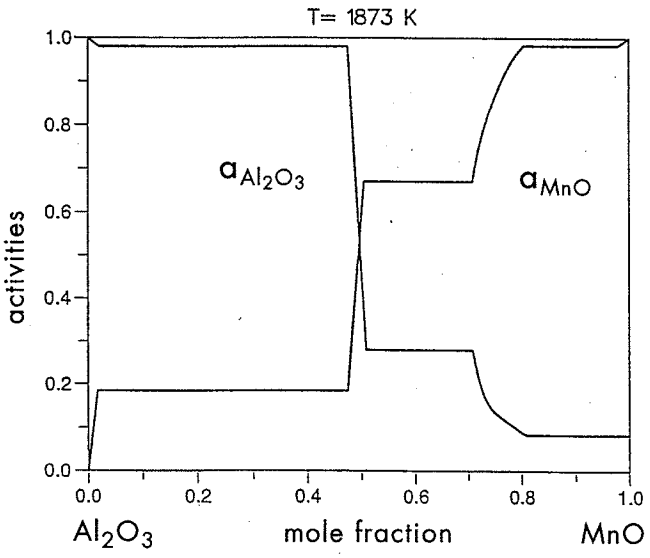


Fig. 5.3. Activity of Al_2O_3 and MnO at 1600 °C, after Jacob [3].
Activities are referred to pure solid Al_2O_3 or MnO

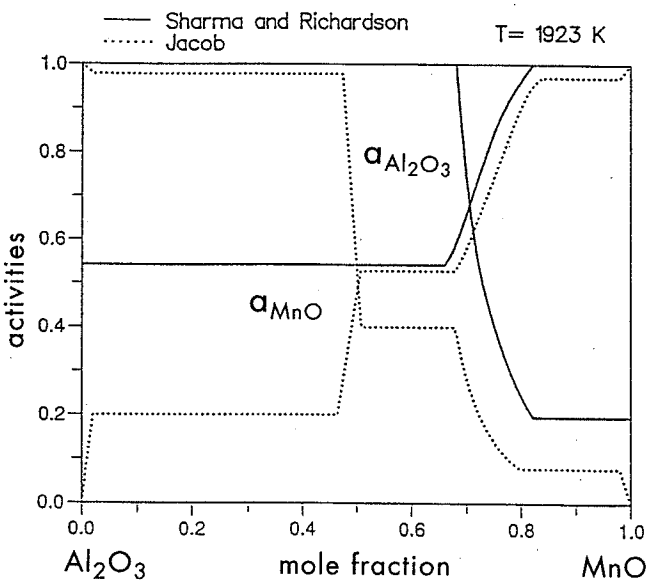


Fig. 5.4. Activity of Al_2O_3 and MnO at 1650 °C, after Sharma and Richardson [4], and Jacob [3].
Activities are referred to pure solid Al_2O_3 or MnO. The data by Jacob [3] are to be preferred.

Al_2O_3-SiO_2

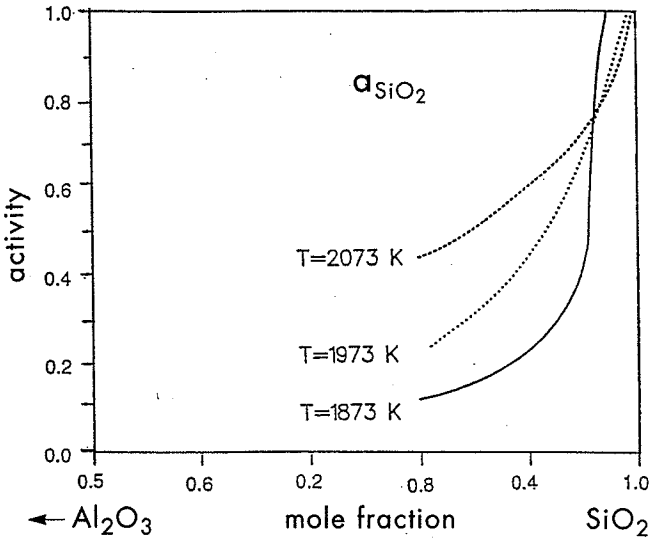


Fig. 5.5. Activity of SiO_2 at 1600, 1700 and 1800 °C, after Dhima et al. [5].
Activities are referred to pure solid SiO_2 at 1600 °C and to liquid SiO_2 at 1700 and 1800 °C.

B_2O_3-MnO

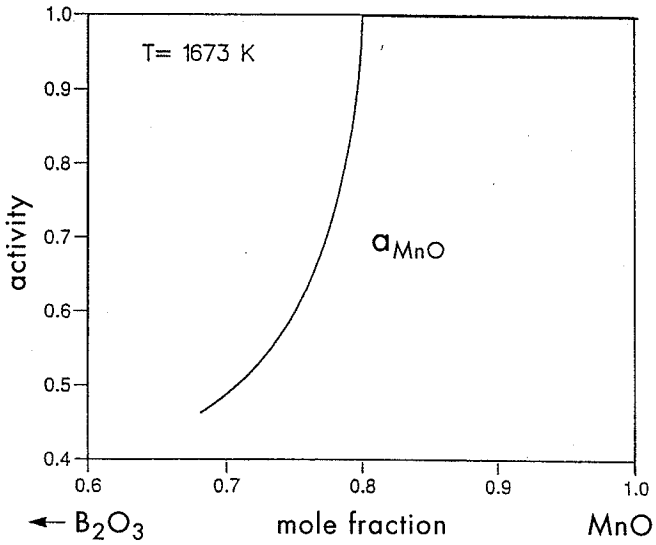


Fig. 5.7. Activity of MnO at 1400 °C, after Rao and Gaskell [7].
Activities are referred to pure solid MnO

BaO-FeO

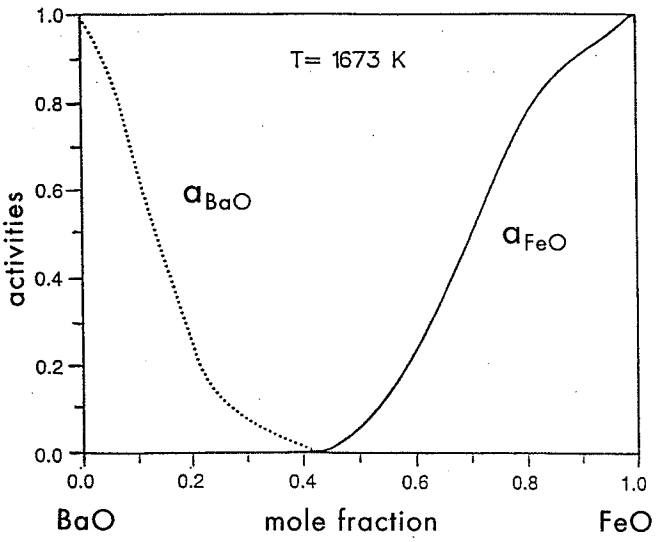


Fig. 5.6. Activity of BaO and FeO at 1400 °C, after Iwase et al. [6].
Activities are referred to pure super-cooled liquid BaO or pure liquid FeO in equilibrium with iron.

B_2O_3-Na_2O

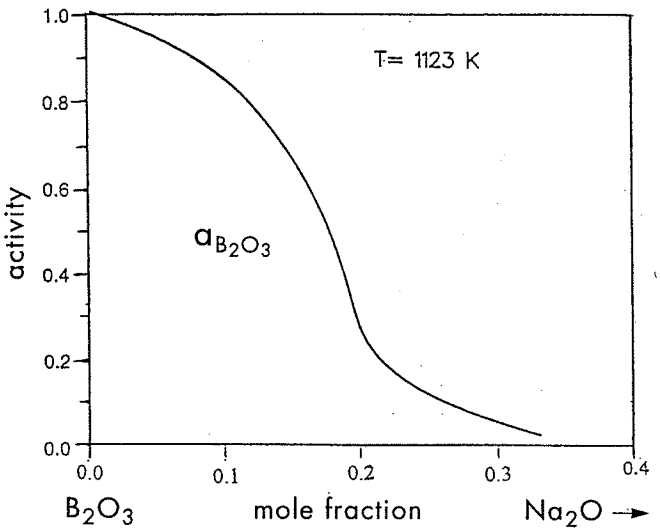


Fig. 5.8. Activity of B_2O_3 at 850 °C, after Itoh et al. [8], Sharma and Richardson [9], Chipman [10].
Activities are referred to pure liquid B_2O_3.

B_2O_3-SiO_2

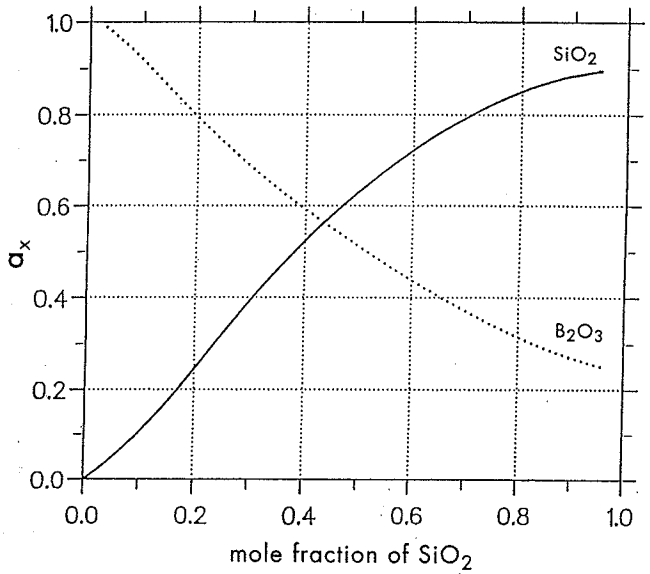


Fig. 5.9. Activity of B_2O_3 and SiO_2 in the B_2O_3-SiO_2 system at 1500 °C, after Chengtao and Chunlin [11]

CaF_2-FeO

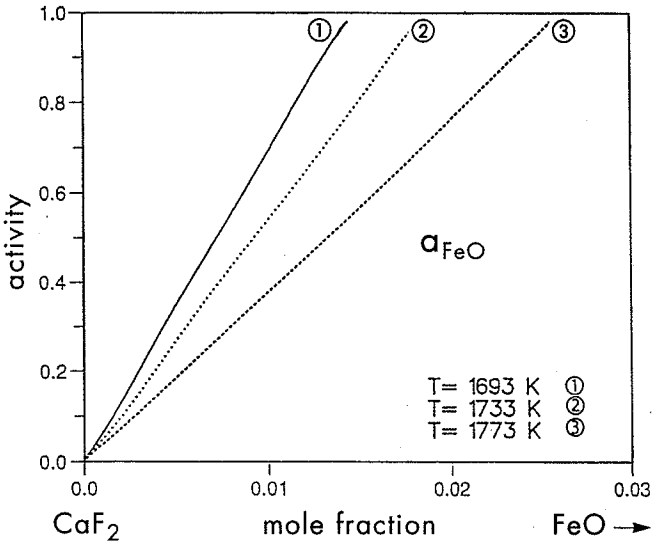


Fig. 5.11. Activity of FeO at 1420, 1460 and 1500 °C, after Kay et al. [14].
Activities are referred to pure liquid FeO in equilibrium with iron.

CaF_2-CaO

Tab. 5.1. Activity of CaO in CaF_2-CaO system at 1400 °C [12].

X_{CaO}	a_{CaO}
0.136	0.24
0.138	0.25
0.170	0.29
0.190	0.38

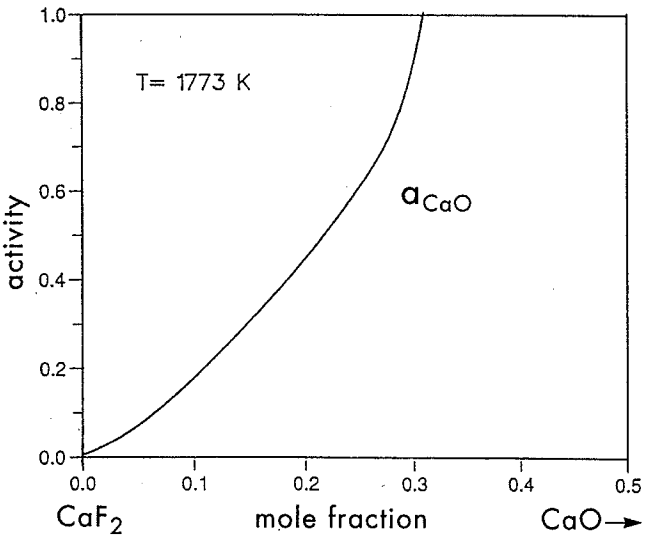


Fig. 5.10. Activity of CaO at 1500 °C, after Edmunds and Taylor [13].
Activities are referred to pure solid CaO.

CaF_2-MgO

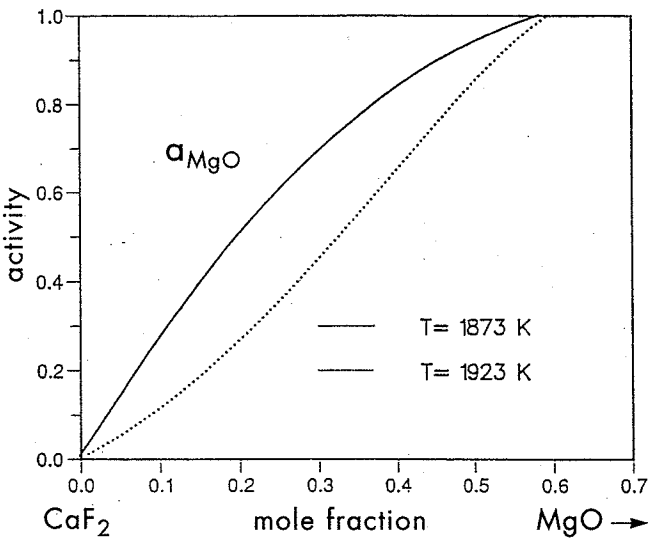


Fig. 5.12. Activity of MgO at 1600 and 1650 °C, after Chen et al. [15].
Activities are referred to pure solid MgO.

CaO-FeO

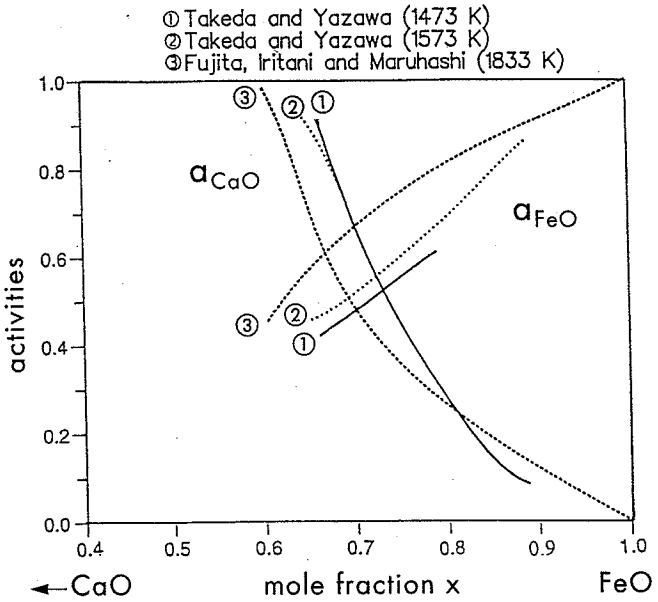


Fig. 5.13. Activity of CaO and FeO at 1200, 1300 and 1560 °C, after Takeda et al. [16] and Fujita et al. [17].
Activities are referred to pure solid CaO or pure liquid FeO in equilibrium with iron.

CaO-SiO_2

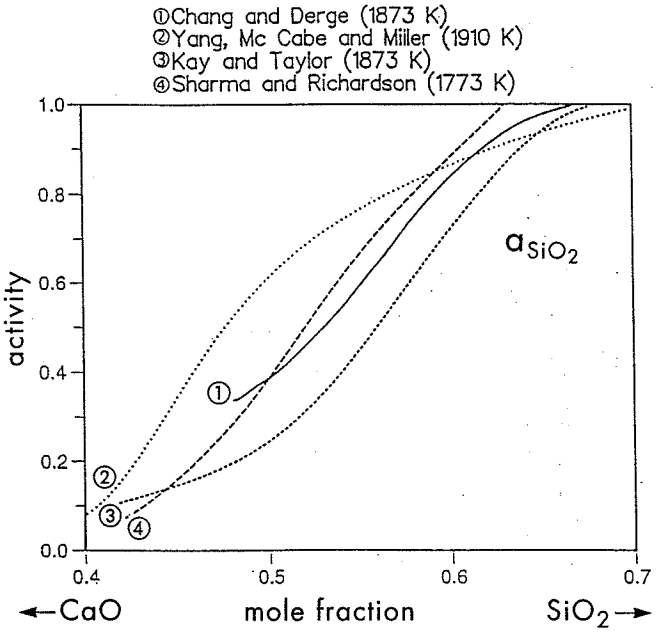


Fig. 5.15. Activity of SiO_2 at 1500, 1600 and 1637 °C, after Chang et al. [19], Yang et al. [20], Kay and Taylor [21], Sharma and Richardson [22].
Activities are referred to pure solid SiO_2.

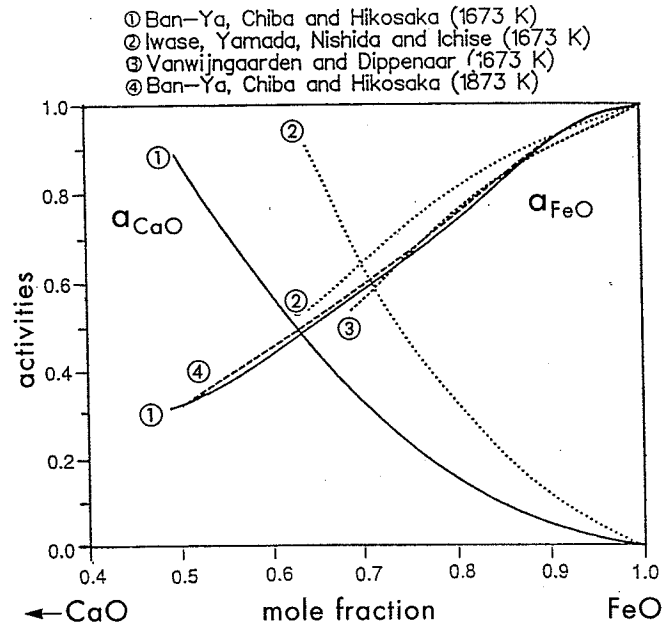


Fig. 5.14. Activity of CaO and FeO at 1400 and 1600 °C, after Ban-Ya et al. [2], Iwase et al. [6], Van Wijngaarden and Dippenaar [18].
Activities are referred to pure solid CaO or pure liquid FeO in equilibrium with iron.

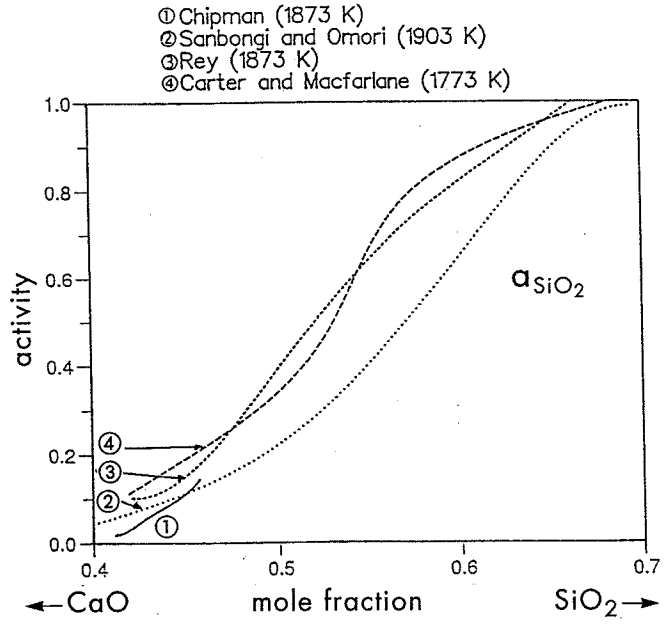


Fig. 5.16. Activity of SiO_2 at 1500, 1600 and 1630 °C, after Chipman [10], Sanbongi and Omori [23], Rey [24], and Carter and MacFarlane [25].
Activities are referred to pure solid SiO_2.

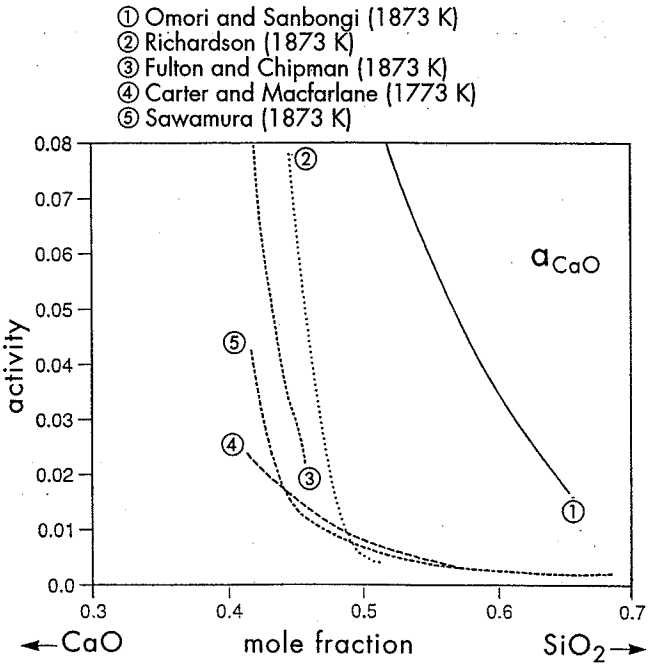


Fig. 5.17. Activity of CaO at 1550 and 1600 °C, after Omori et al. [26], Richardson [27], Fulton et al. [28], Carter and MacFarlane [25], and Sawamura [29].
Activities are referred to pure solid CaO.

$FeO\text{-}SiO_2$

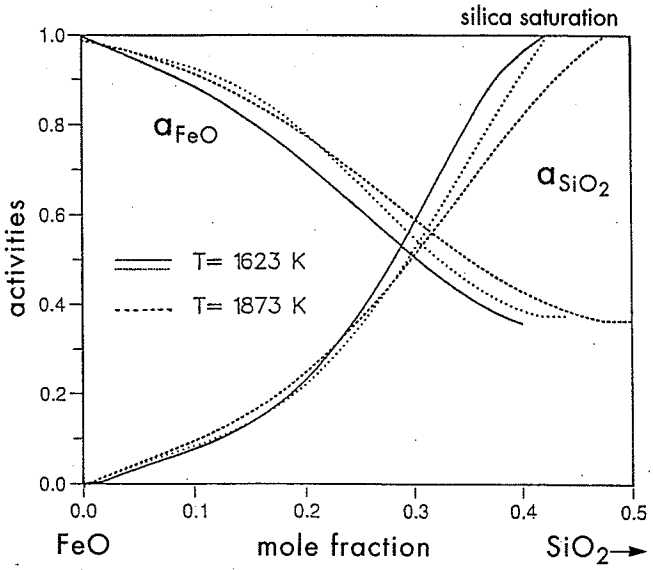


Fig. 5.19. Activity of FeO and SiO_2 at 1350 and 1600 °C, after various authors [31 to 36].
Activities are referred to pure liquid FeO in equilibrium with iron and solid SiO_2.

$FeO\text{-}P_2O_5$

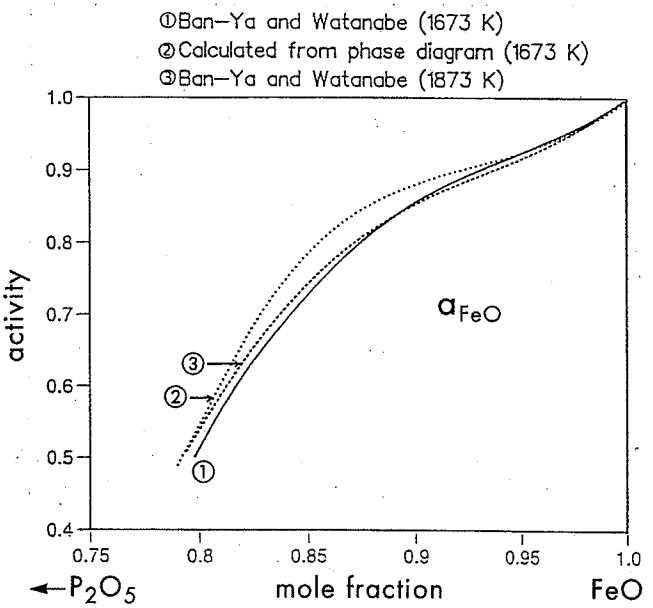


Fig. 5.18. Activity of FeO at 1400 and 1600 °C, after Ban-Ya et al. [30].
Activities are referred to pure liquid FeO in equilibrium with iron.

FeO-SrO

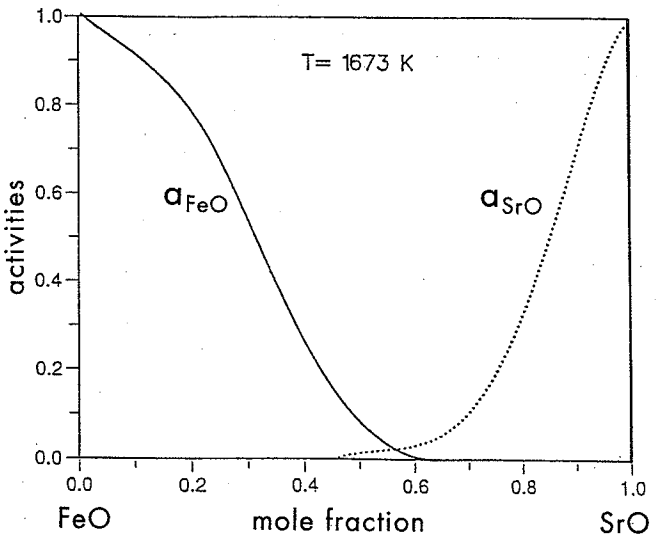


Fig. 5.20. Activity of FeO and SrO at 1400 °C, after Iwase et al. [6].
Activities are referred to pure liquid FeO in equilibrium with iron or pure super-cooled liquid SrO.

$FeO\text{-}TiO_2$

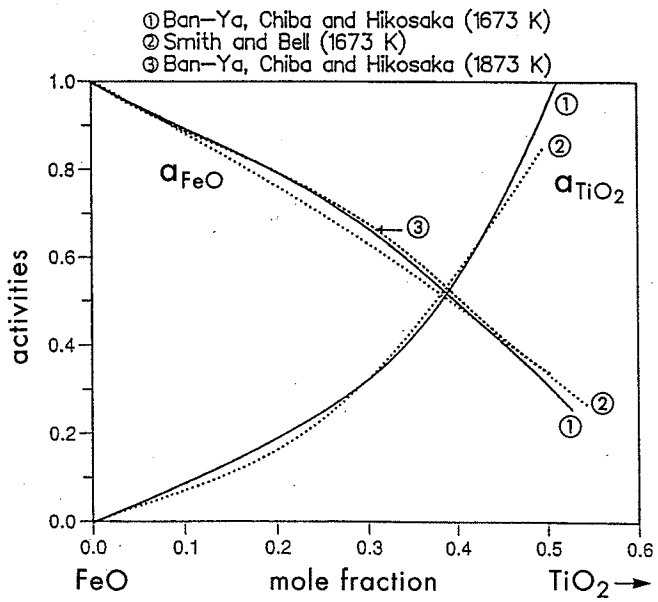


Fig. 5.21. Activity of FeO and TiO_2 at 1400 and 1600 °C, after Ba-Ya et al. [2], and Smith and Bell [37].
Activities are referred to pure liquid FeO in equilibrium with iron and solid TiO_2.

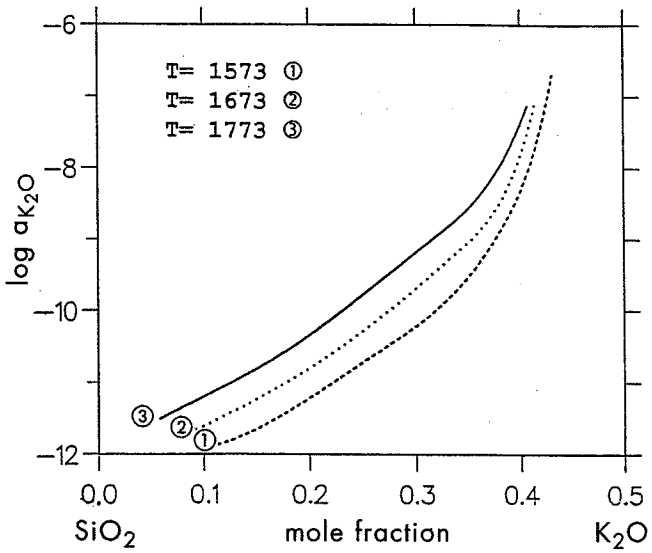


Fig. 5.23. Activity of K_2O at 1300, 1400 and 1500 °C in $K_2O\text{-}SiO_2$ slags.
Activities are referred to pure solide K_2O [38].

$K_2O\text{-}SiO_2$

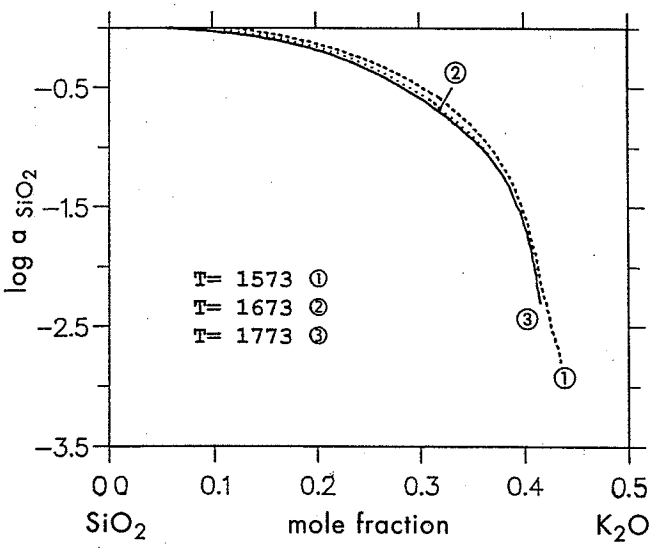


Fig. 5.22. Activity of SiO_2 at 1300, 1400 and 1500 °C in $K_2O\text{-}SiO_2$ slags.
Activities are referred to pure solide cristobalite [38].

$MgO\text{-}P_2O_5$

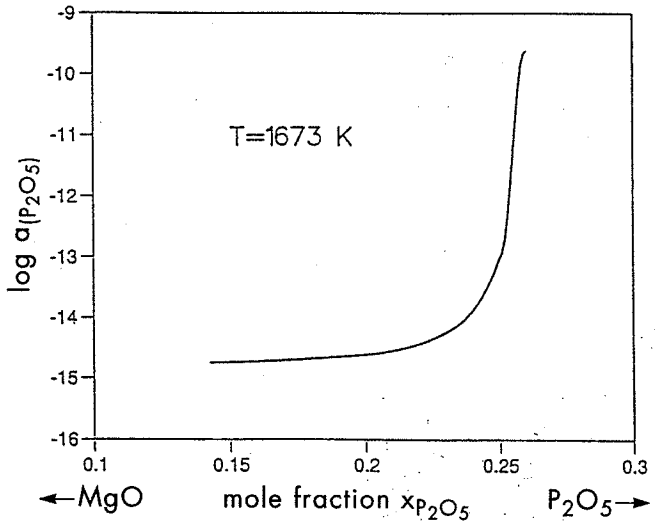


Fig. 5.24. Activity of P_2O_5 at 1400 °C, after Iwase et al. [39].
Activities are referred to pure liquid P_2O_5

$MgO\text{-}SiO_2$

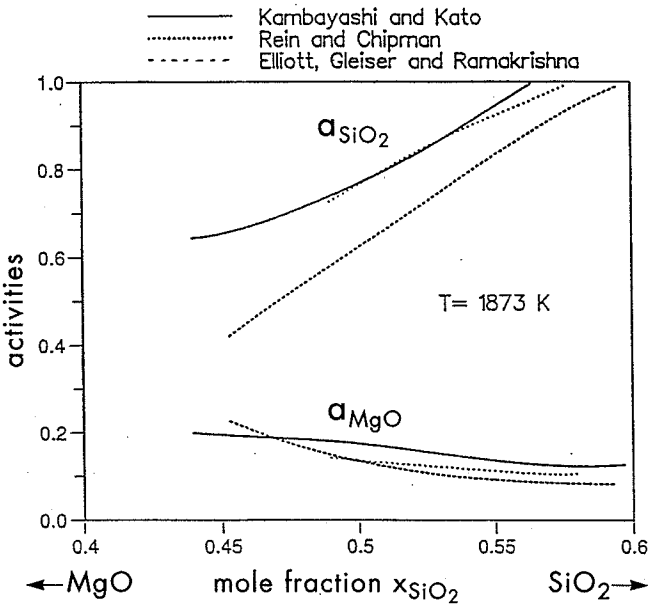


Fig. 5.25. Activity of MgO and SiO_2 at 1600 °C, after Kambayashi and Kato [40], Rein and Chipman [41], Elliott et al. [31].
Activities are referred to pure solids.

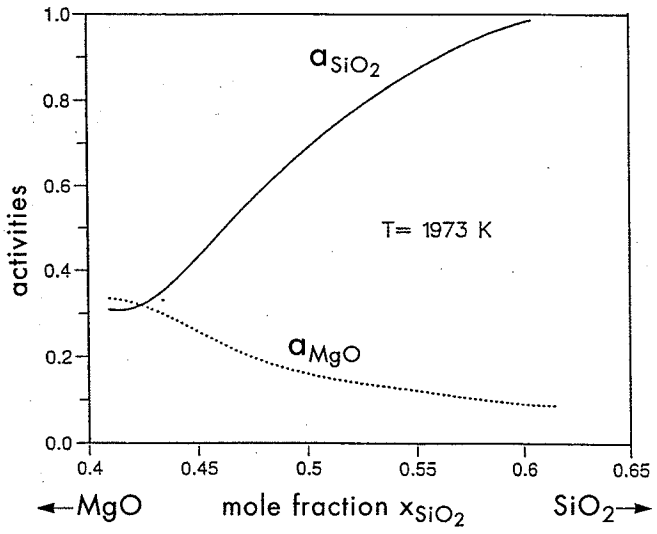


Fig. 5.26. Activity of MgO and SiO_2 at 1700 °C, after Kambayashi and Kato [40].
Activities are referred to pure solids.

$MnO\text{-}SiO_2$

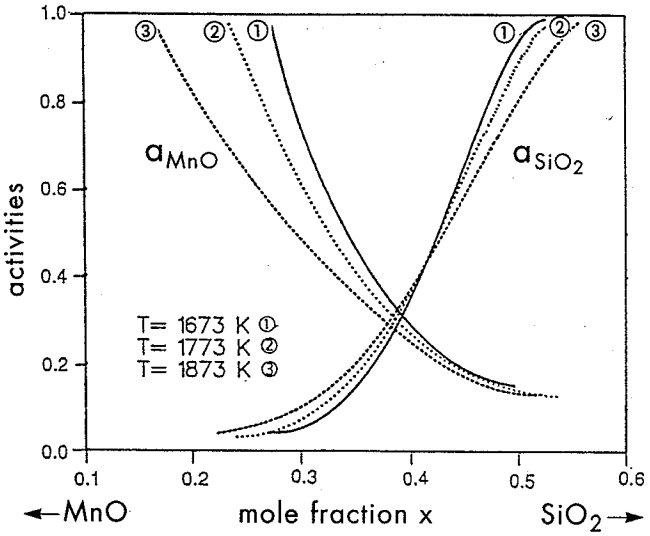


Fig. 5.27. Activity of MnO and SiO_2 at 1400, 1500 and 1600 °C, after Rao and Gaskell [42].
Activities are referred to pure solids.

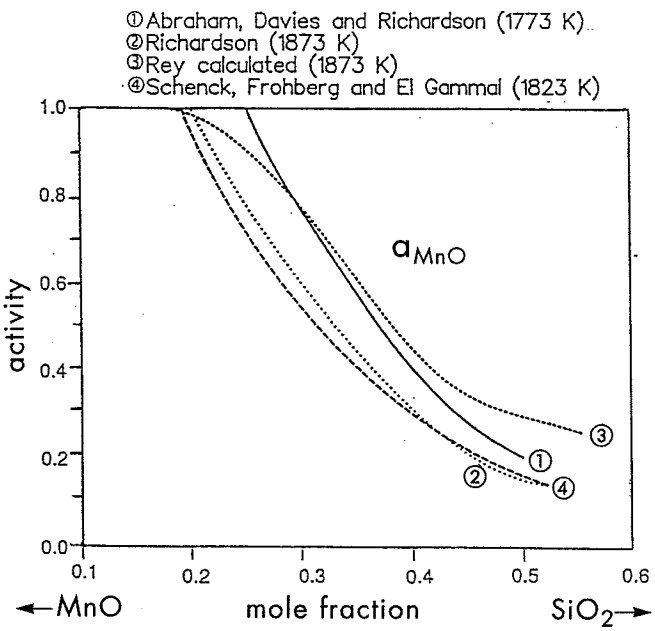


Fig. 5.28. Activity of MnO and SiO_2 at 1500, 1550 and 1600 °C, after Abraham et al. [43], Richardson [44], Rey [24] and Schenck et al. [45].
Activities are referred to pure solid.

$MnO\text{-}TiO_2$

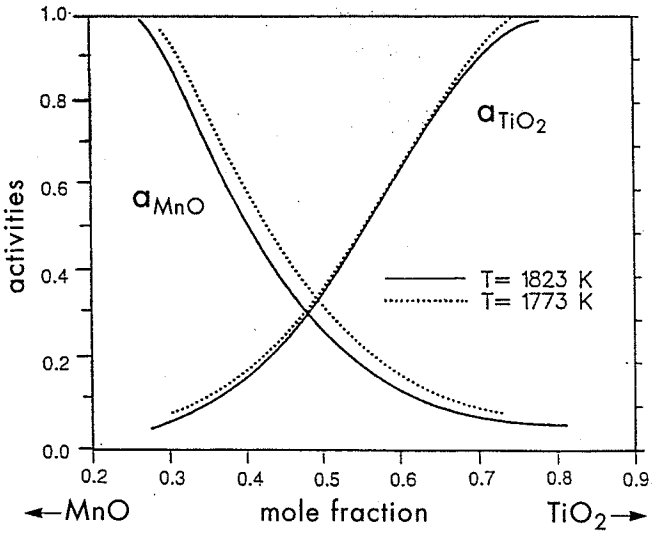


Fig. 5.29. Activity of MnO and TiO_2 at 1500 and 1550 °C, after Rao and Gaskell [7].
Activities are referred to pure solids.

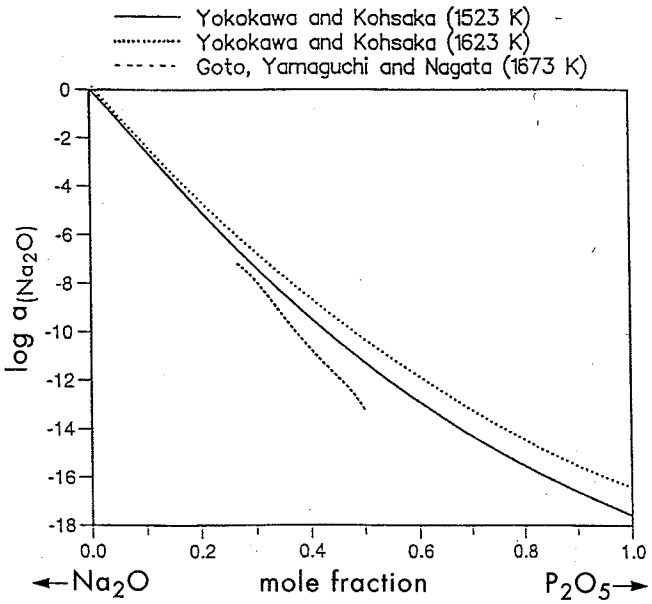


Fig. 5.31. Activity of Na_2O at 1250, 1350 and 1400 °C, after Yokokawa and Kohsaka [47] and Goto et al [46, 48].
Activities are referred to pure liquid Na_2O.

$Na_2O\text{-}P_2O_5$

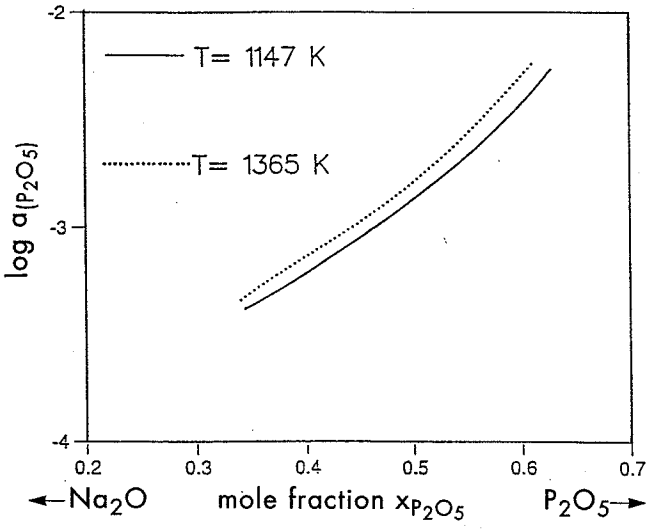


Fig. 5.30. Activity of P_2O_5 at 874 and 1092 °C, after Goto and Yamaguchi [46].
Activities are referred to pure solid P_2O_5.

$Na_2O\text{-}SiO_2$

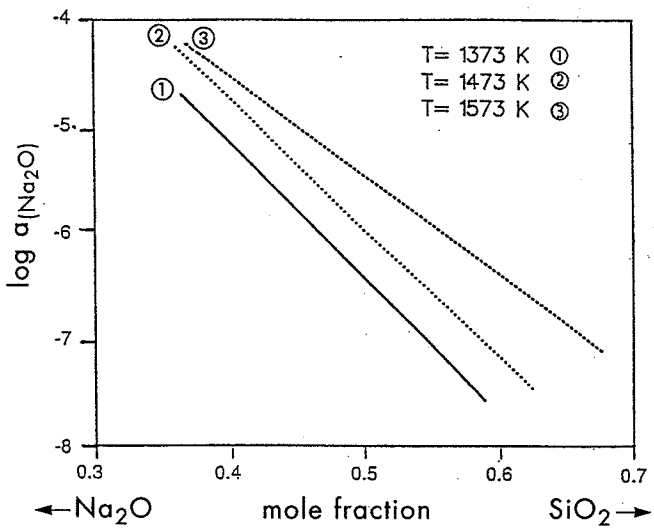


Fig. 5.32. Activity of Na_2O at 1100, 1200 and 1300 °C, after Tsukihashi and Sano [49].
Activities are referred to pure liquid Na_2O.

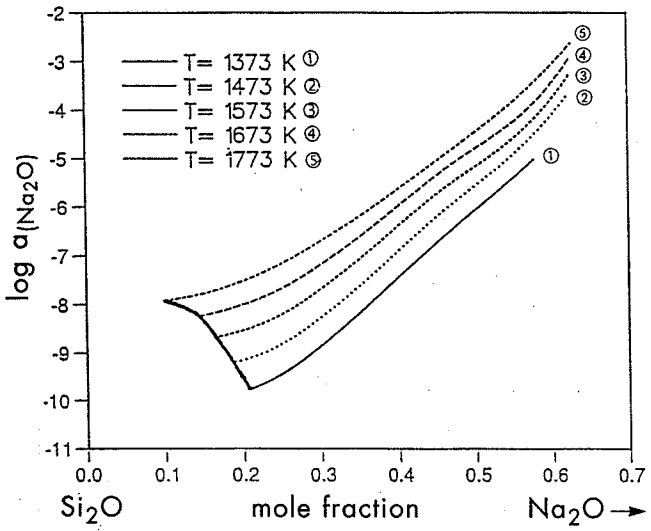


Fig. 5.33. Activity of Na_2O at 1100, 1200, 1300, 1400 and 1500 °C, after Goto and Yamaguchi [46].
Activities are referred to pure liquid Na_2O.

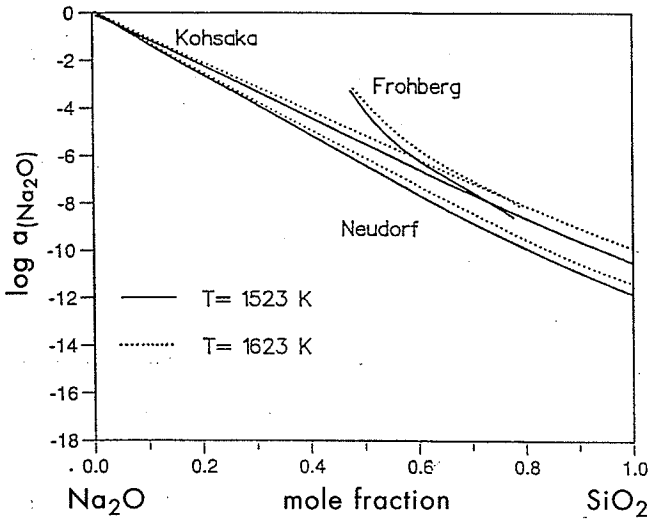


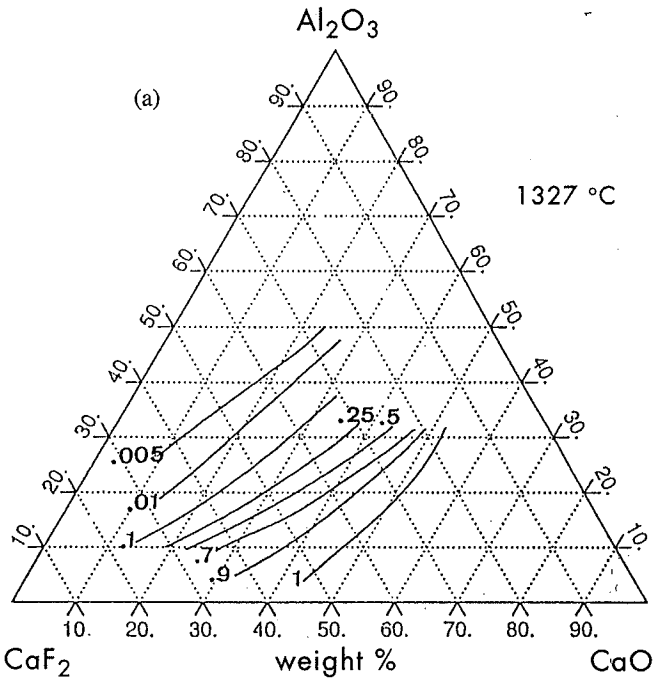
Fig. 5.34. Activity of Na_2O at 1250 and 1350 °C, after Kohsaka et al. [51], Frohberg et al. [52] and Neudorf and Gleiser [50].
Activities are referred to pure liquid Na_2O.

5.2.2 Ternary systems

Al_2O_3-CaF_2-CaO

Tab. 5.2. Activity of CaO in Al_2O_3-CaF_2-CaO system at 1400 °C, after Chattopadhyay and Mitchell [53].

X_{CaO}	a_{CaO}	$X_{CaO}/X_{Al_2O_3}$
0.403	0.05	3.05
0.470	0.09	3.14
0.520	0.09	3.08
0.560	0.10	3.10
0.220	0.08	3.90
0.380	0.17	4.99
0.410	0.18	6.27
0.320	0.22	7.02
0.260	0.24	7.67



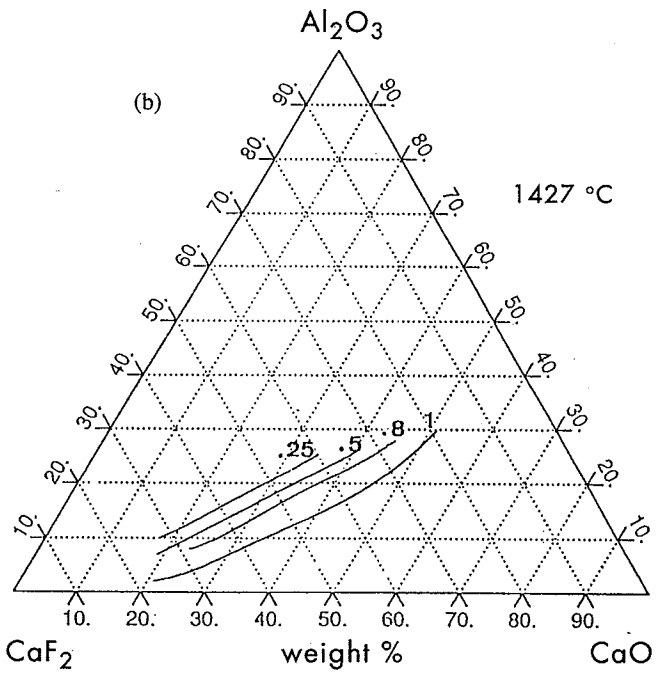
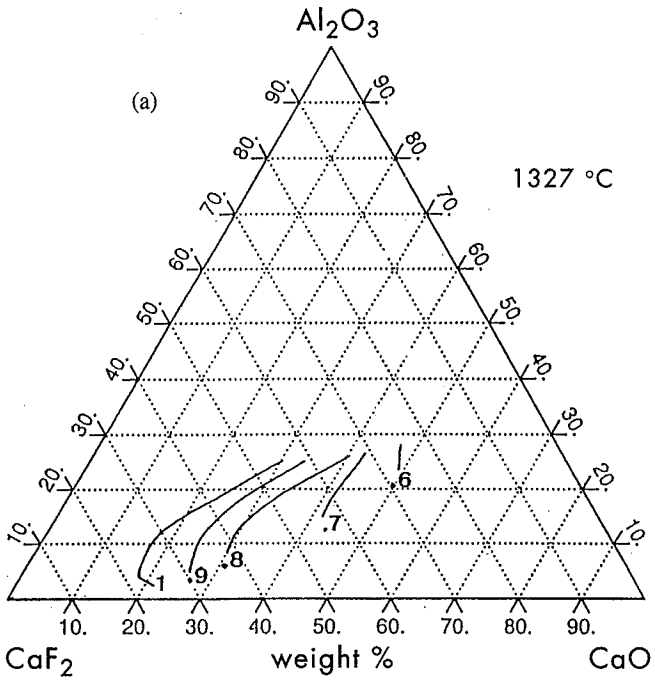


Fig. 5.35 a,b. a_{CaO} in Al_2O_3-CaF_2-CaO system at 1327 and 1427 °C, after Allibert, Chatillon [54].
Reference state: Two phase mixture saturated with solid CaO.



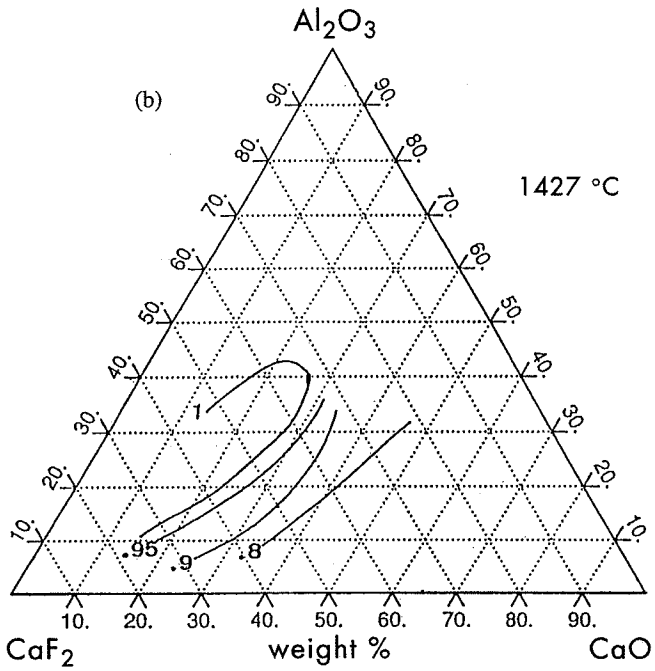


Fig. 5.36 a,b. a_{CaF_2} in Al_2O_3-CaF_2-CaO system at 1327 and 1427 °C, after Allibert and Chatillon [54].
Reference state: pure CaF_2.

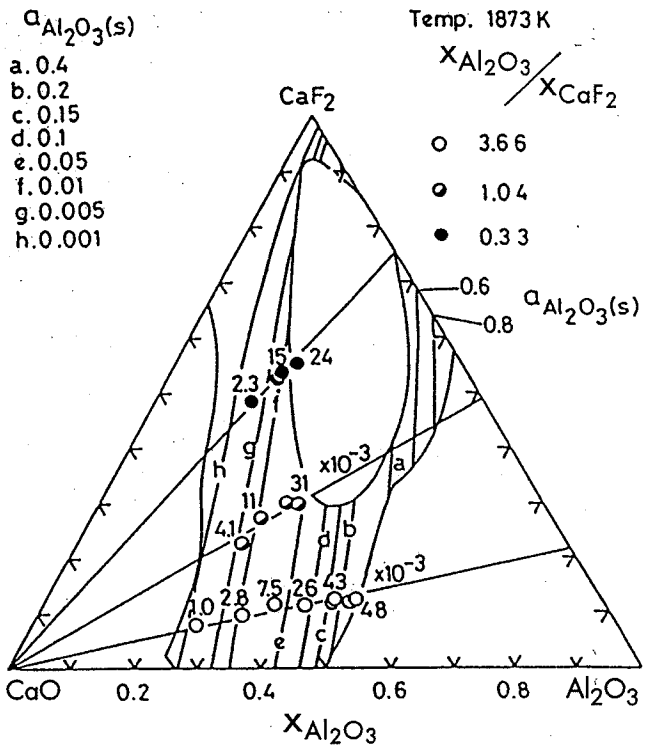


Fig. 5.37. Activity of Al_2O_3 in Al_2O_3-CaF_2-CaO slags at 1873 K, after Hino [1].
Reference state is pure solid alumina.

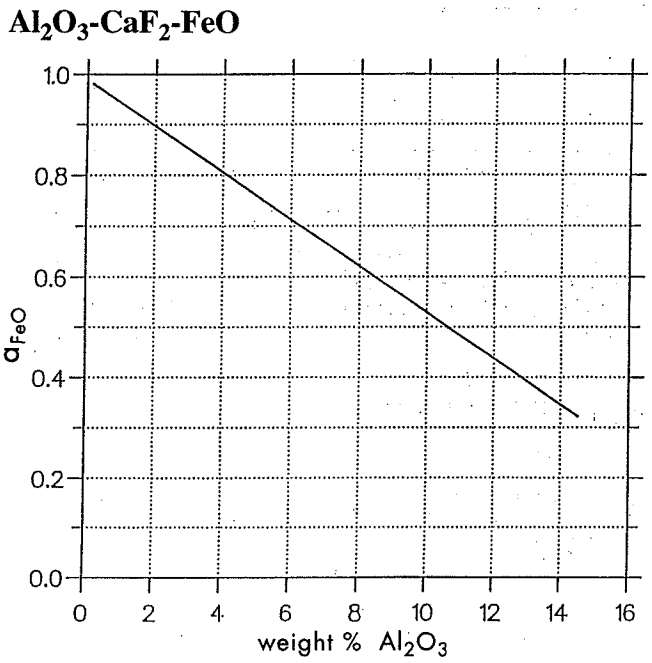
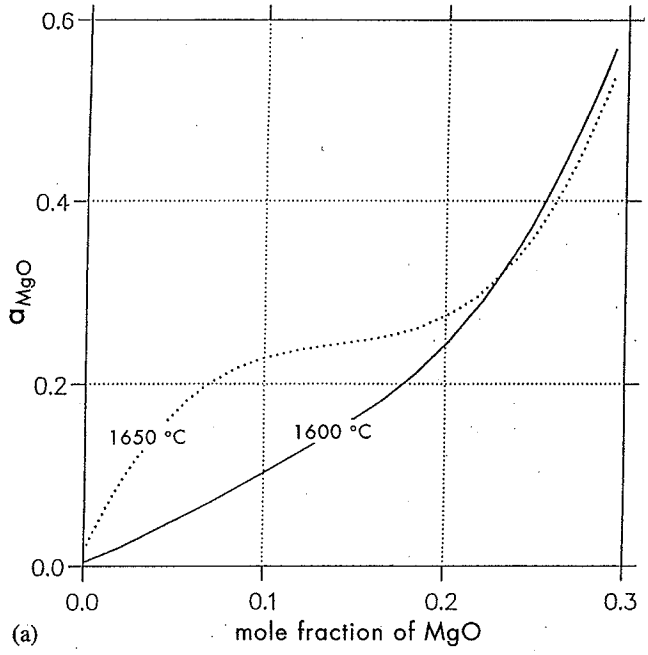


Fig. 5.38. Dependence of a_{FeO} on the alumina content at 1460 °C in Al_2O_3-CaF_2-FeO slags with 1.5 % FeO, after Ram [55]



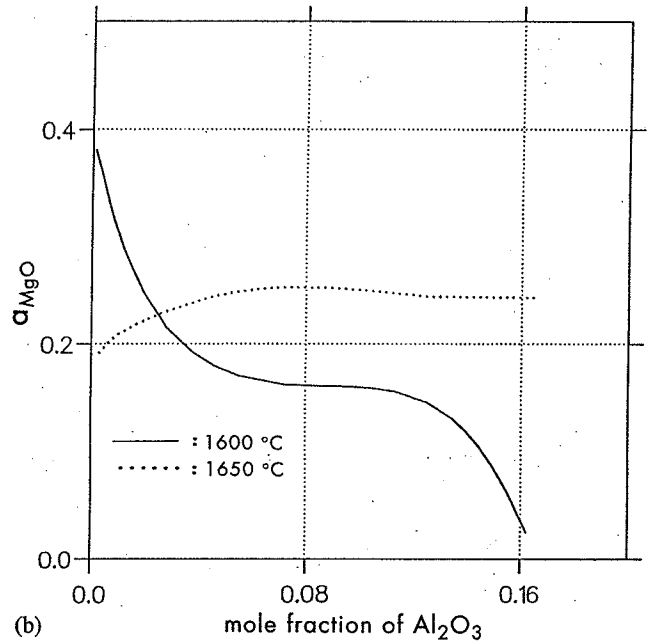
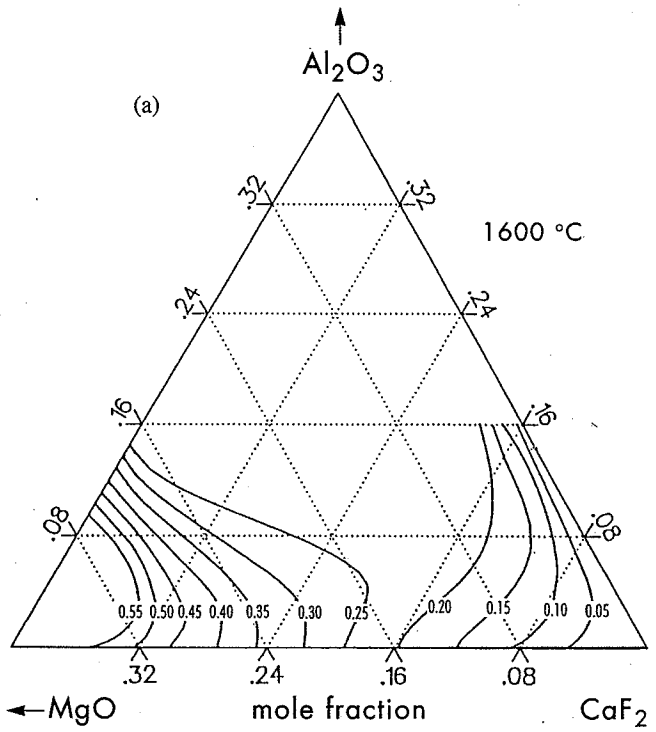


Fig. 5.39 a,b. Activity of MgO dependent on (a) the MgO content and (b) the Al_2O_3 content at 1600 and 1650 °C in the system Al_2O_3-CaF_2-MgO, after Chen and Zhao [15]. The mole fraction in (b) is 0.15.
Reference state is pure solid magnesia.



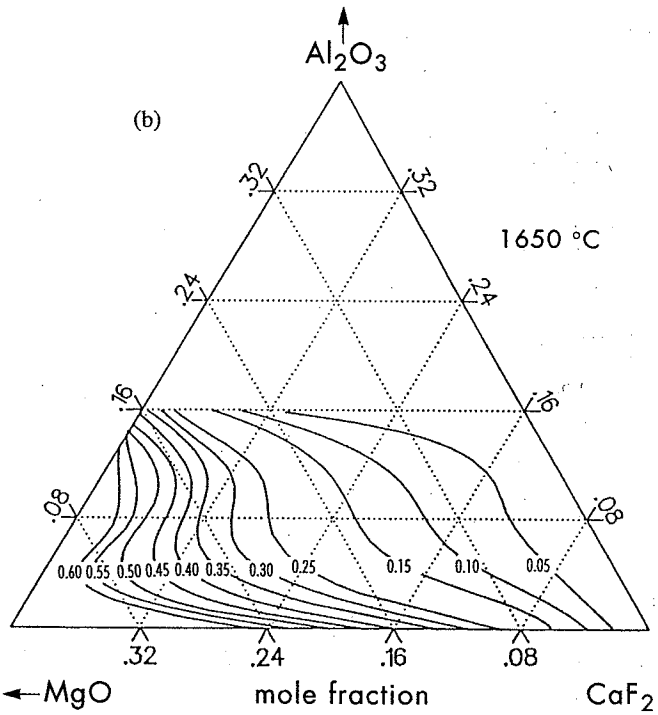


Fig. 5.40 a,b. Isoactivity diagram of MgO in the system Al_2O_3-CaF_2-MgO for the temperatures (a) 1600 and (b) 1650 °C, after Chen and Zhao [15].
Standard state is pure solid MgO.

Al_2O_3-CaO-MgO

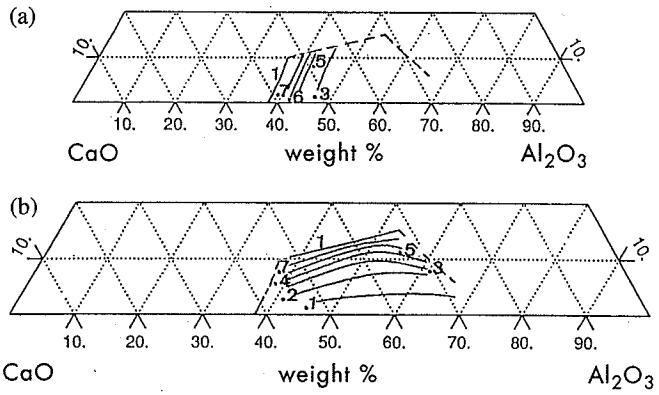


Fig. 5.41 a,b. Activity of (a) CaO and (b) MgO in the system Al_2O_3-CaO-MgO at 1687 °C, after Allibert et al. [56]. Standard states are pure solid CaO (a) and pure solid MgO (b).

Al_2O_3-CaO-SiO_2

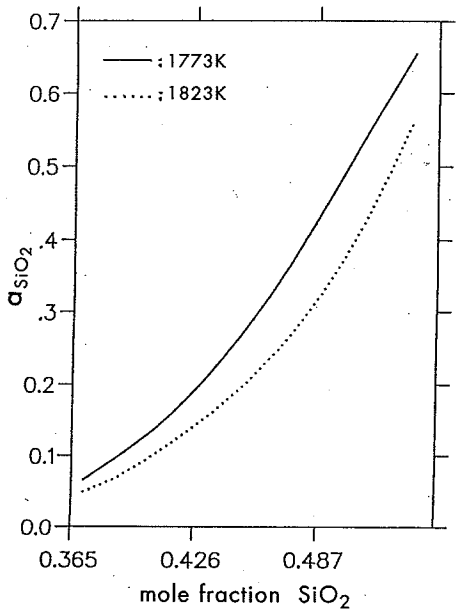
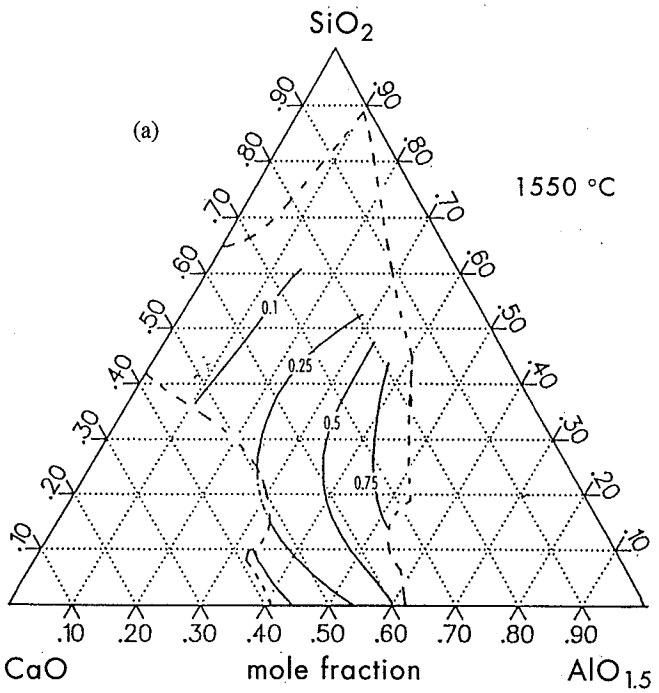


Fig. 5.42. Activity of silica in the CaO-SiO_2-10 % Al_2O_3 system at 1773 and 1823 K, after Kim et al. [57]



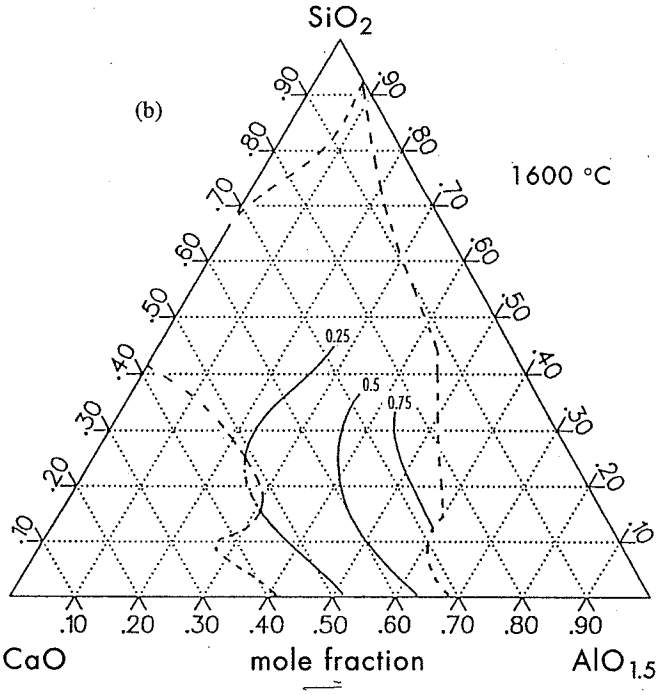
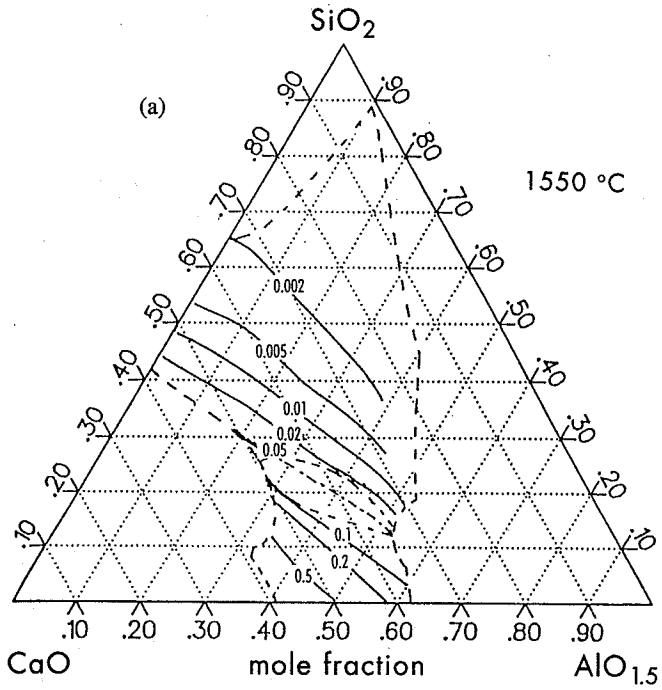
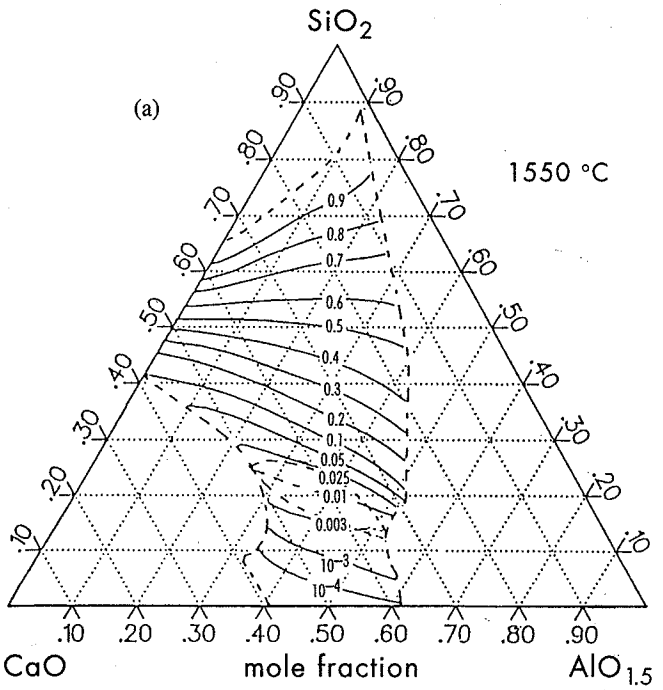


Fig. 5.43 a,b. Activities of $AlO_{1.5}$ in Al_2O_3-CaO-SiO_2 slags at (a) 1550 and (b) 1600 °C, after Rein and Chipman [41]. Standard state is pure solid $AlO_{1.5}$ with the relations $2\ AlO_{1.5} = Al_2O_3$ and $(a_{AlO_{1.5}})^2 = a_{Al_2O_3}$.





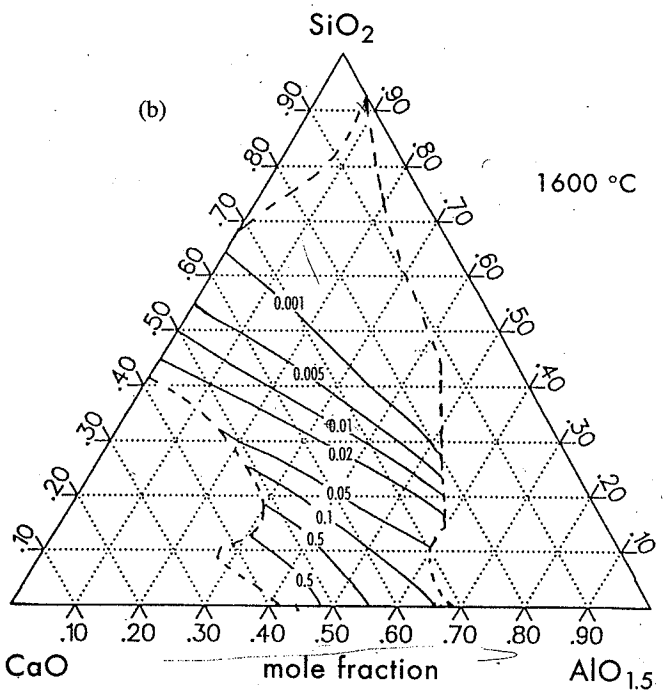


Fig. 5.44 a,b. Activities of CaO in Al_2O_3-CaO-SiO_2 slags at (a) 1550 and (b) 1600 °C, after Rein and Chipman [41]. Standard state in pure solid CaO.

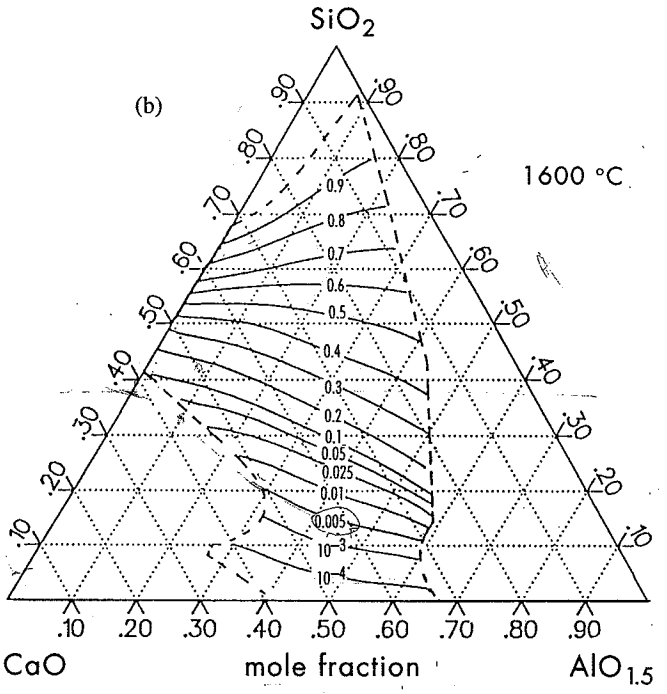
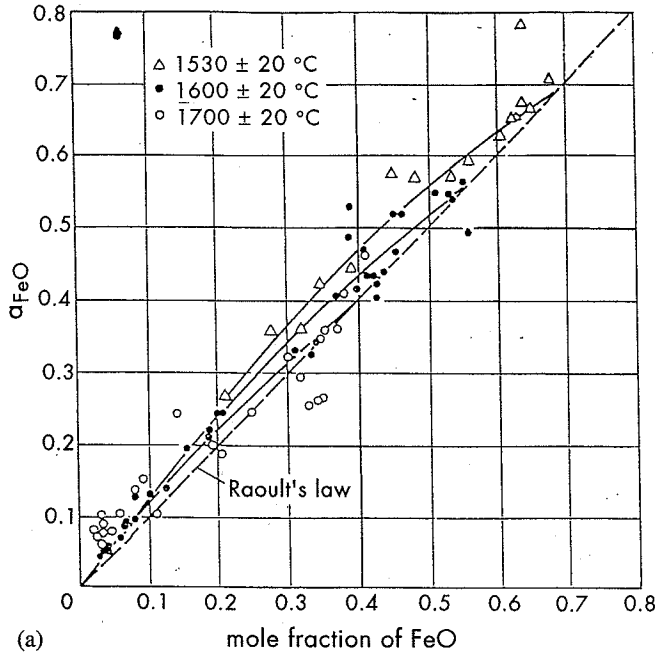


Fig. 5.45 a,b. Activities of SiO_2 in Al_2O_3-CaO-SiO_2 slags at (a) 1550 and (b) 1600 °C, after Rein and Chipman [41]. Standard state in pure solid silica.

Al_2O_3-FeO-MnO



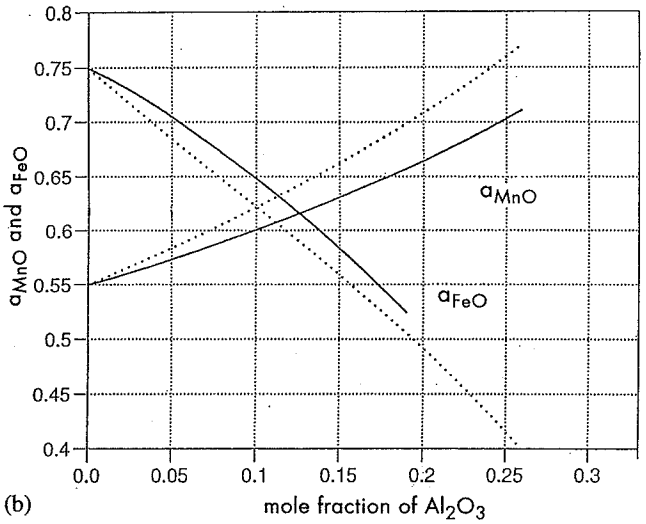


Fig. 5.46 a,b. Activities of FeO dependent (a) on FeO content at several temperatures and (b) of FeO and MnO dependent on alumina content at 1530 °C in Al_2O_3-FeO-MnO slags saturated with FeO-MnO solid solution, after Fischer and Bardenheuer [58]. The dotted curves in (b) represent Raoult's law. Standard states are liquid FeO in equilibrium with liquid iron and pure solid MnO.

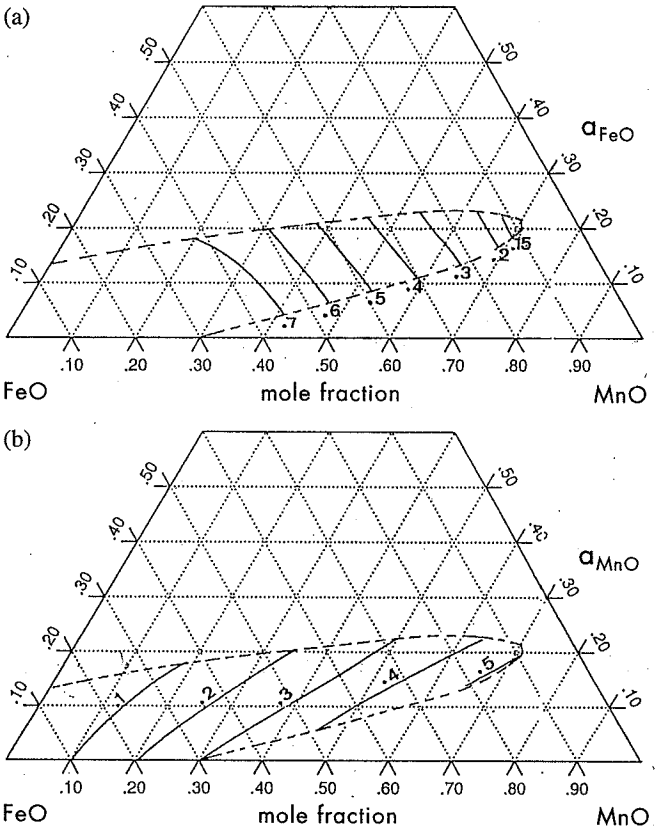
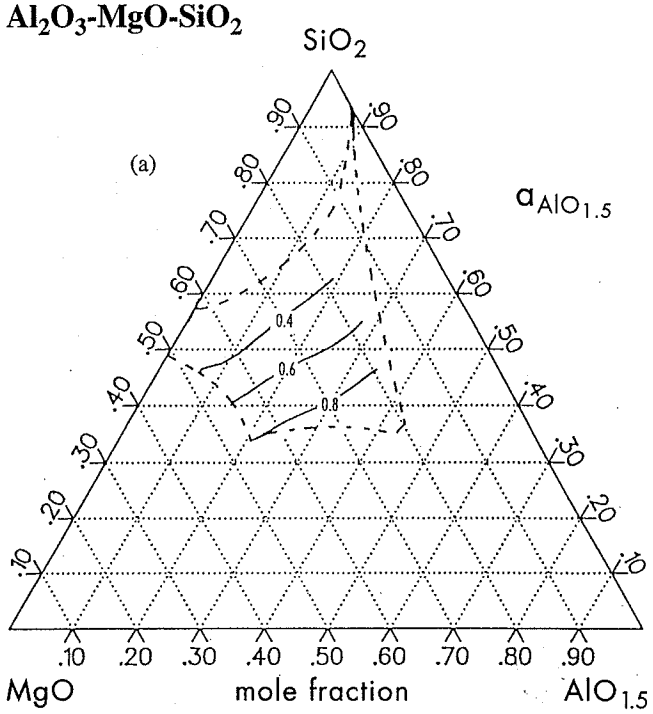
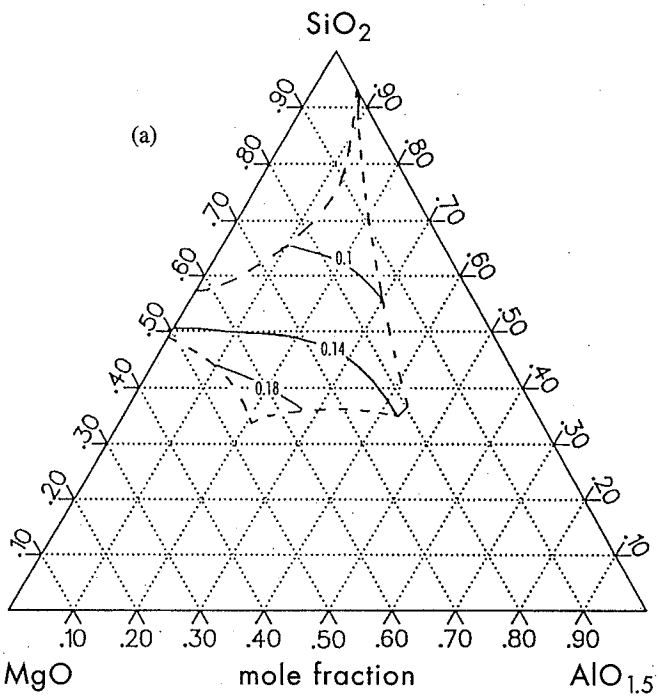
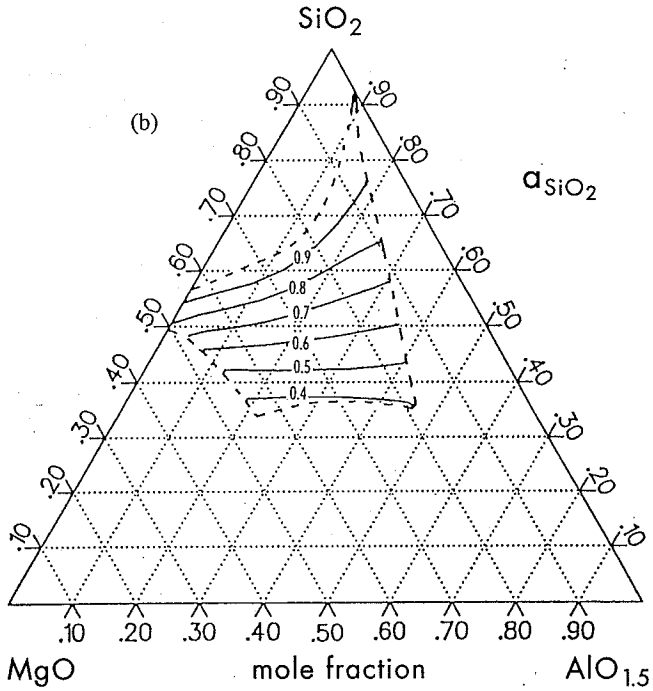


Fig. 5.47 a,b. Activities of (a) FeO and (b) MnO in Al_2O_3-FeO-MnO slags at 1550 °C, after Sommerville et al. [59].
- - - - phase limits
Reference states are the pure liquids.

Al_2O_3-MgO-SiO_2







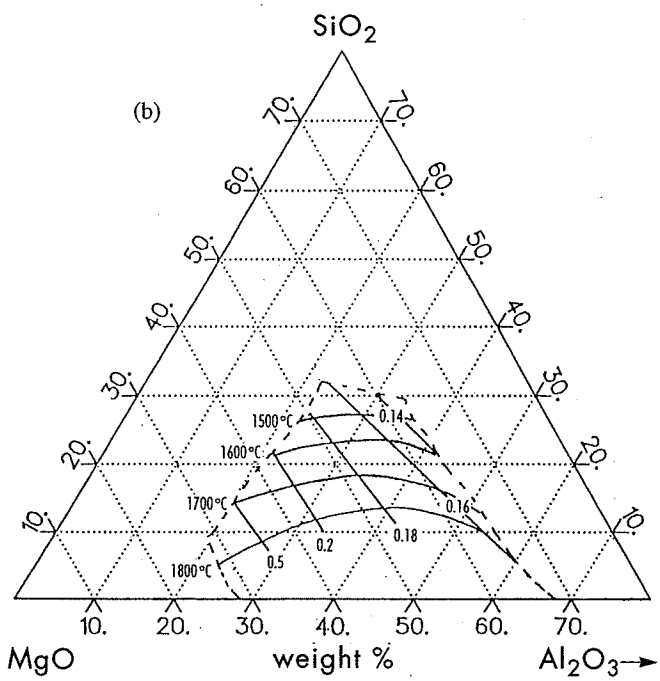


Fig. 5.48 a,b. Activities of (a) $AlO_{1.5}$ and (b) SiO_2 in the system Al_2O_3-MgO-SiO_2 at 1600 °C, after Rein and Chipman [41]. Standard states are pure solid $AlO_{1.5}$, with the relations $2\ AlO_{1.5} = Al_2O_3$ and $(a_{AlO_{1.5}})^2 = a_{Al_2O_3}$, and pure solid SiO_2.

Fig. 5.49 a,b. Activity of MgO in (a) Al_2O_3-MgO-SiO_2 slags at 1600 °C, after Rein and Chipman [41] and (b) on the liquidus surface in the spinel field of the same system, after Healy [60]. Reference state is pure solid MgO.

Al_2O_3-Na_2O-SiO_2

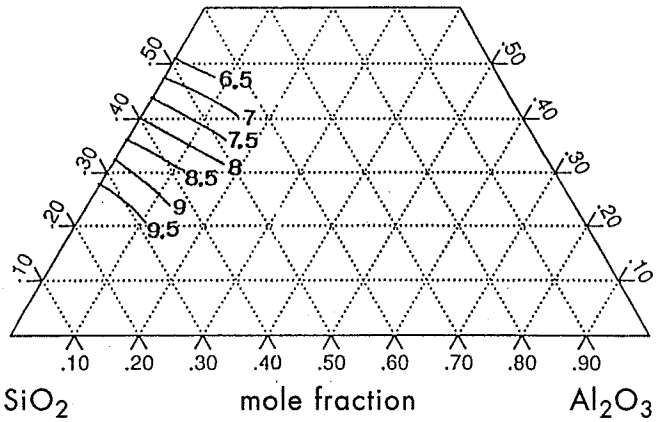
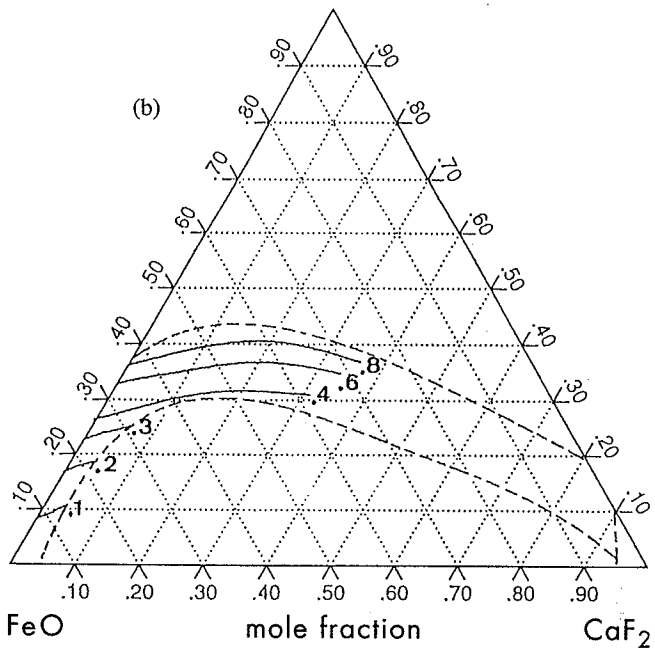
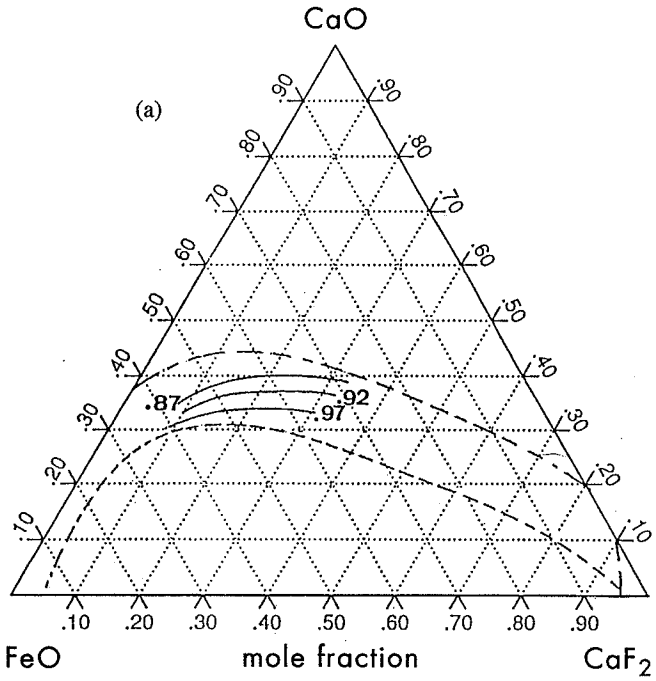


Fig. 5.50. Thermodynamic basicity pO = –log a_{Na_2O} at 1027 °C, after Itoh, Yokokaza [61].
Reference state: pure Na_2O at same temperature.



CaF_2-CaO-FeO



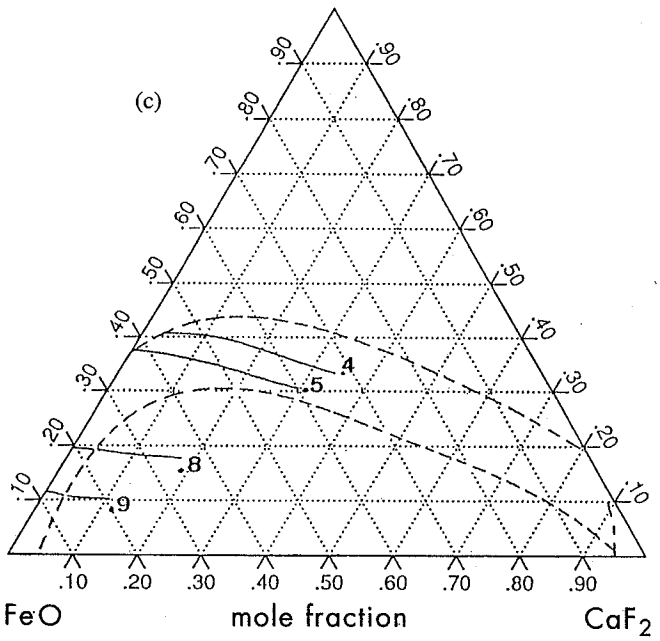


Fig. 5.51 a-c. Isoactivity curves for (a) CaF_2, (b) CaO and (c) FeO at 1400 °C in the system CaF_2-CaO-FeO, after Iwase et al. [62].
- - - - phase limits
Reference states are pure solid CaF_2, pure solid CaO and liquid FeO in equilibrium with solid iron.

CaF_2-CaO-SiO_2

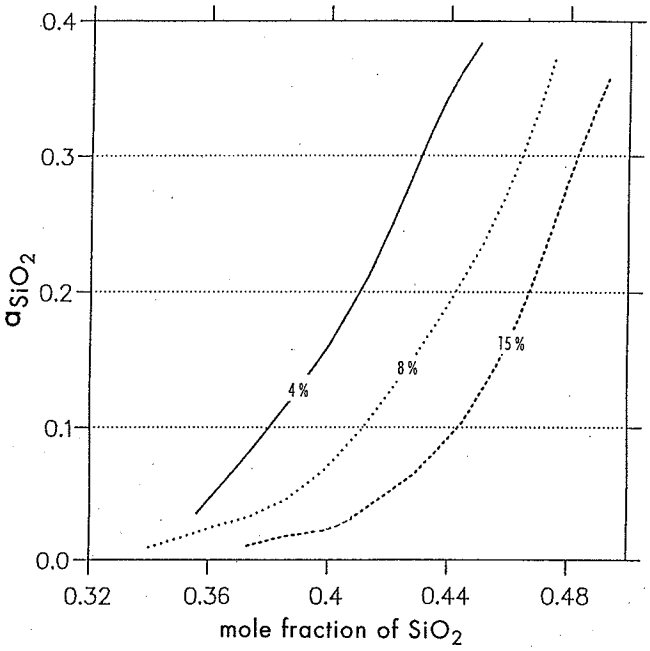
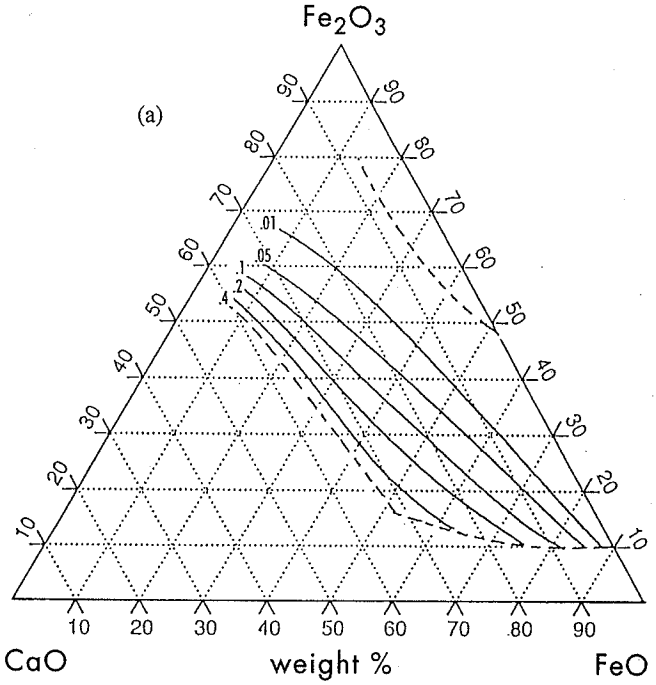


Fig. 5.52. The activity of SiO_2 as a function of SiO_2 in CaF_2-CaO-SiO_2 slags with 4 %, 8 % and 15 % CaF_2 at 1600 °C, after Gzielo, Iowsa and Budzik [63]

Tab. 5.3. Activity of CaO in CaF_2-CaO-SiO_2-system at 1400 °C, after Chattopaddhyay and Mitchell [53].

X_{CaO}	a_{CaO}	X_{CaO}/X_{SiO_2}
0.62	0.110	3.30
0.52	0.170	3.02
0.37	0.180	3.10
0.22	0.130	3.40
0.51	0.013	2.00
0.45	0.019	2.00
0.38	0.098	2.80
0.26	0.030	2.90

CaO-FeO-Fe_2O_3



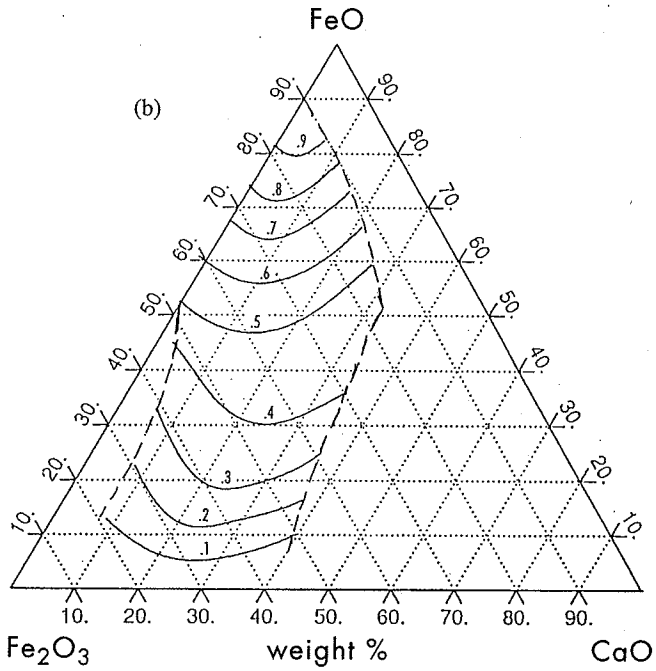
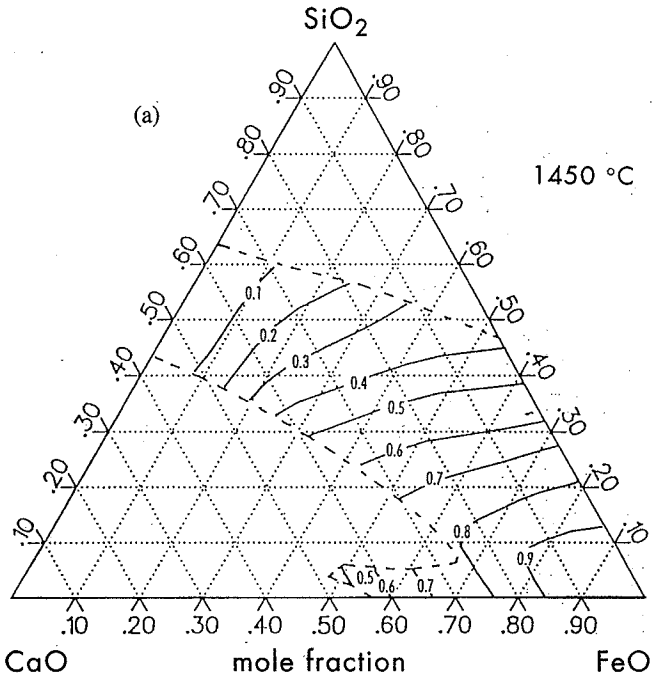
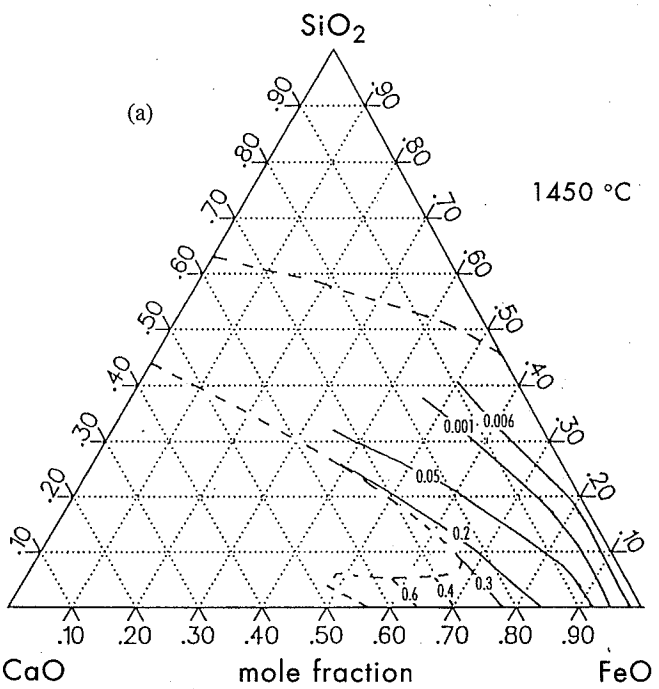


Fig. 5.53 a,b. Activities of (a) CaO and (b) FeO at 1500 °C in the system CaO-FeO-Fe_2O_3, after Hara et al. [64].
- - - - phase limits

CaO-FeO-SiO_2





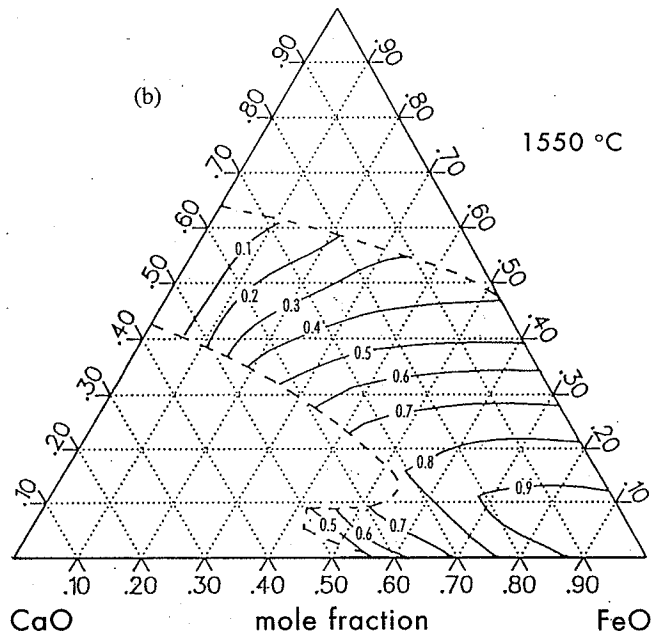


Fig. 5.54 a,b. Activity of FeO in the system CaO-FeO-SiO_2 at (a) 1450 and (b) 1550 °C, after Timucin and Morris [65].
- - - - phase limits

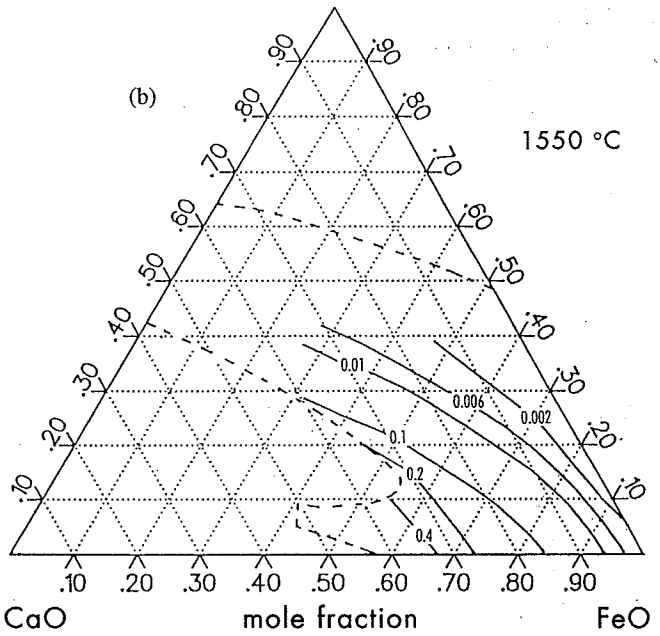
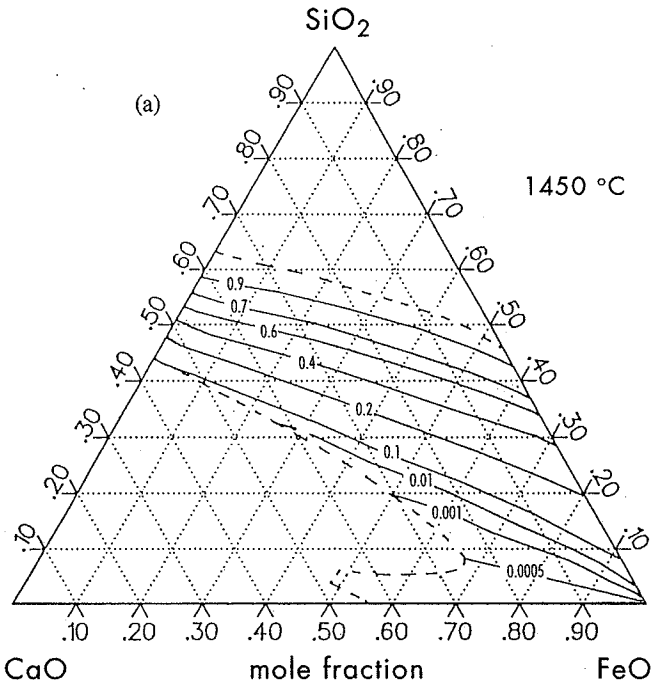


Fig. 5.55 a,b. Activity of CaO in the system CaO-FeO-SiO_2 at (a) 1450 and (b) 1550 °C, after Timucin and Morris [65].
- - - - phase limits



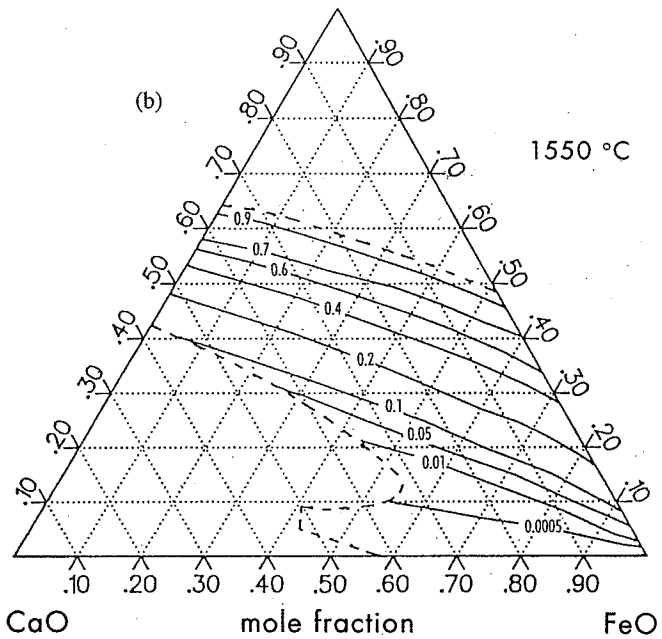


Fig. 5.56 a,b. Activity of SiO_2 in the system CaO-FeO-SiO_2 at (a) 1450 and (b) 1550 °C, after Timucin and Morris [65].
- - - - phase limits

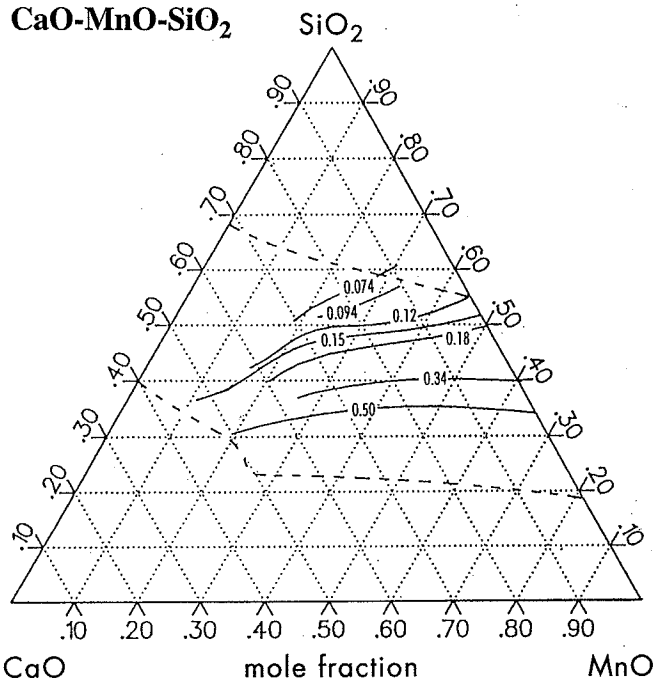
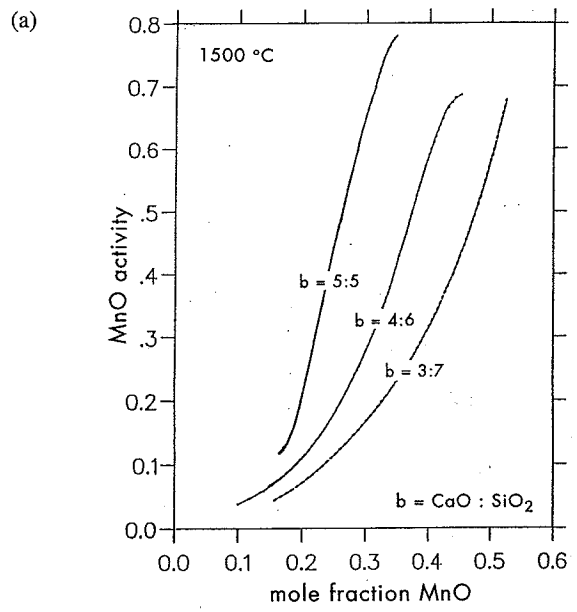


Fig. 5.57. Activity of MnO in the system CaO-MnO-SiO_2 at 1650 °C, after Abraham, Davies and Richardson [43]. Broken curves are probable liquidus.



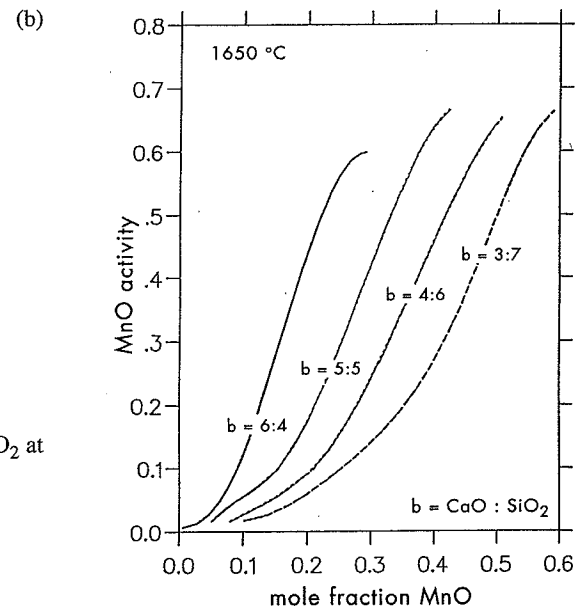
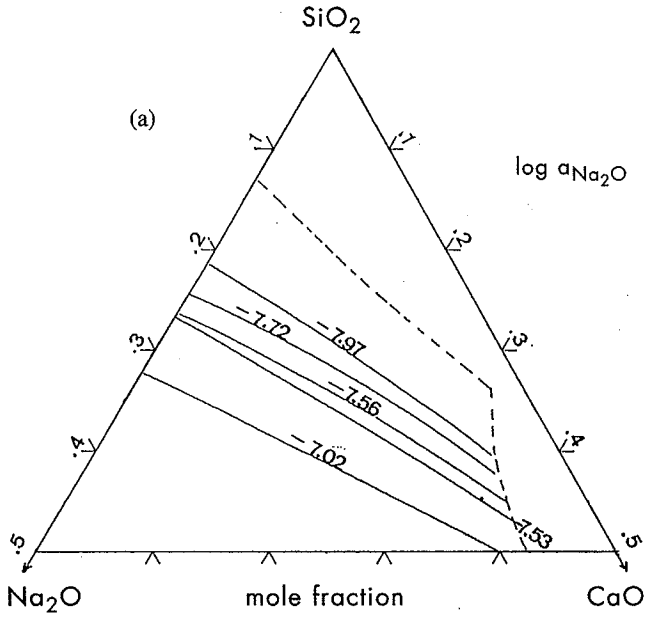


Fig. 5.58 a,b. Activity of MnO in the system CaO-MnO-SiO_2 at (a) 1500 and (b) 1650 °C and various basicities CaO : SiO_2, after Abraham, Davies and Richardson [43]. Reference state is pure solid MnO.

$CaO\text{-}Na_2O\text{-}SiO_2$



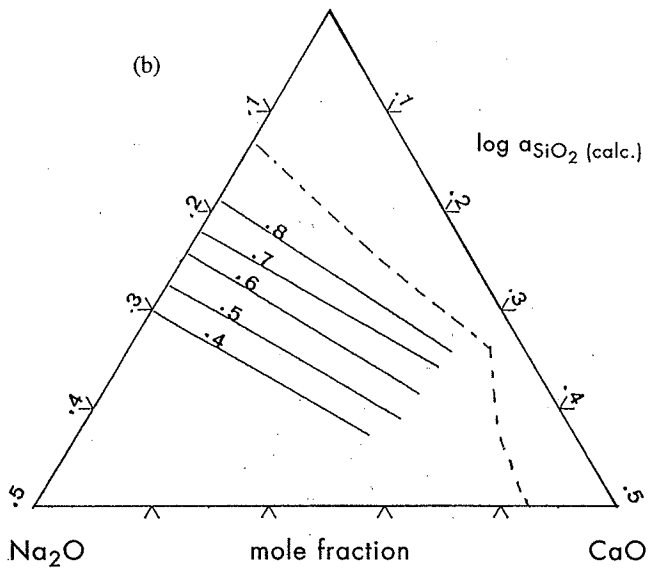


Fig. 5.59 a,b. Logarithmus of (a) a_{Na_2O} and (b) calculated activity of SiO_2 in the system $CaO\text{-}Na_2O\text{-}SiO_2$ at 1400 °C, after Rego, Sigworth and Philbrook [66].
- - - -phase limits

$FeO\text{-}MgO\text{-}SiO_2$

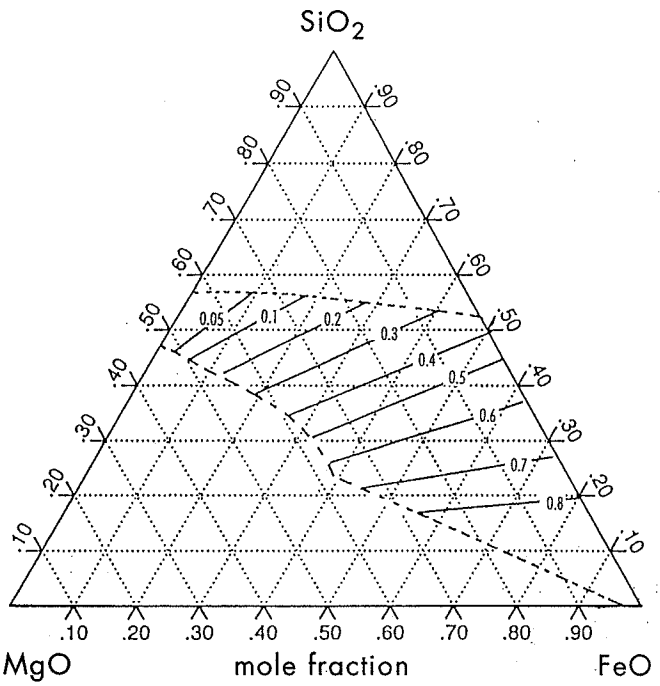


Fig. 5.60. Isoactivity curves for FeO in the FeO-MgO- SiO_2 system at 1600 °C, after Kojima, Inouye and Sano [67]

$FeO\text{-}MnO\text{-}SiO_2$

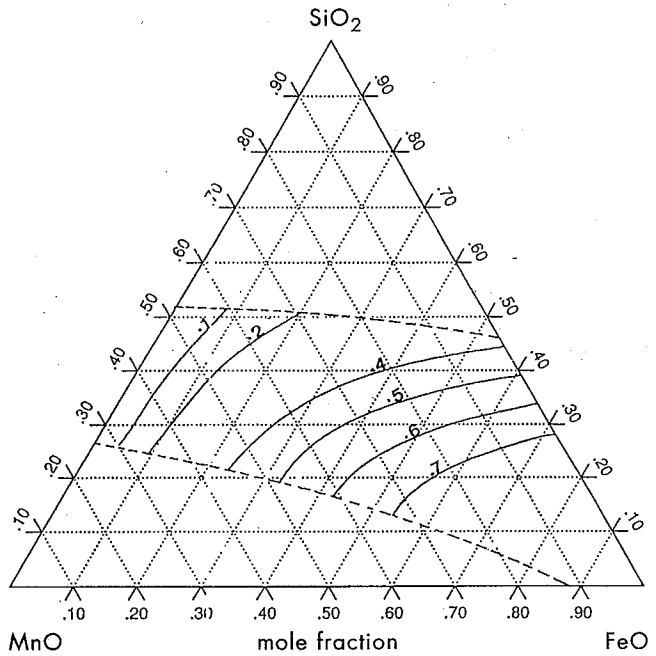
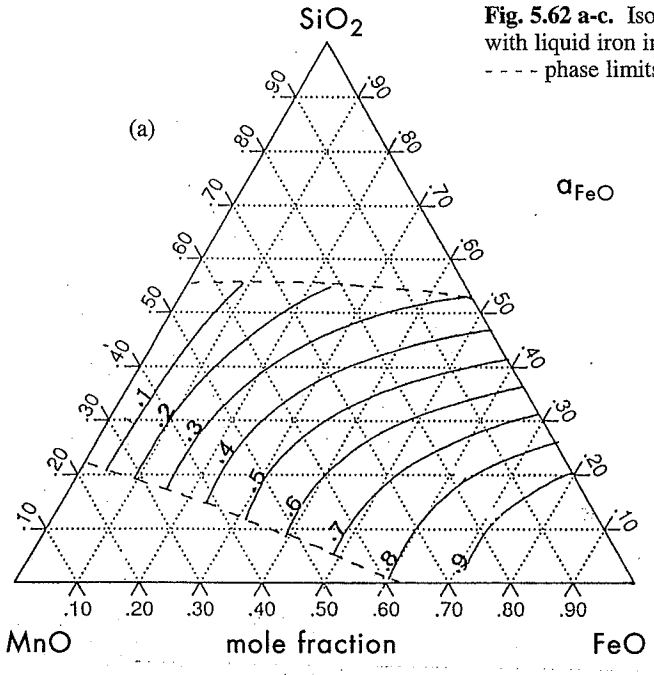
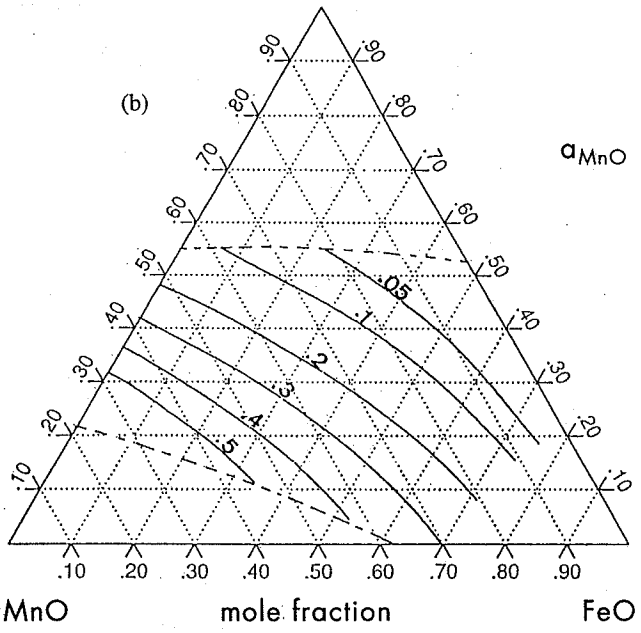


Fig. 5.61. Activity of $FeO\text{-}MnO\text{-}SiO_2$ slags in equilibrium with solid iron at 1450 °C, after Ban-Ya, Hino and Yuge [68].
- - - - phase limits





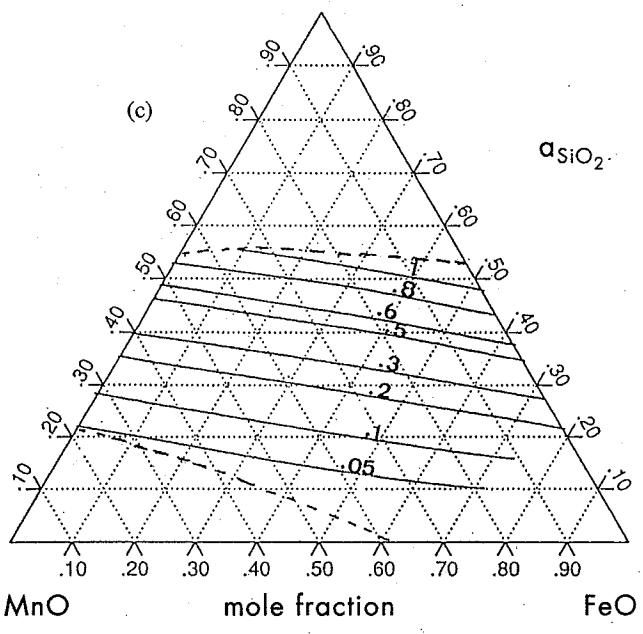
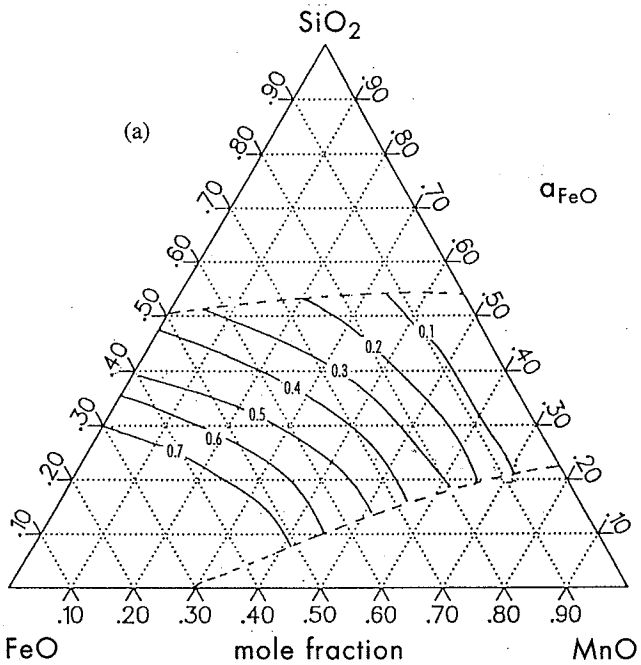


Fig. 5.62 a-c. Isoactivity curves of (a) FeO, (b) MnO and (c) SiO_2 in equilibrium with liquid iron in the system FeO-MnO- SiO_2, after Ban-Ya, Hino and Yuge [68].
- - - - phase limits



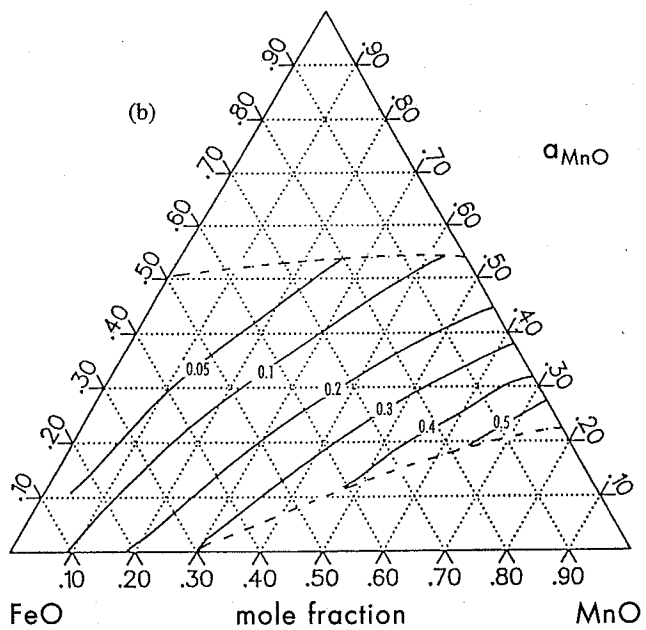
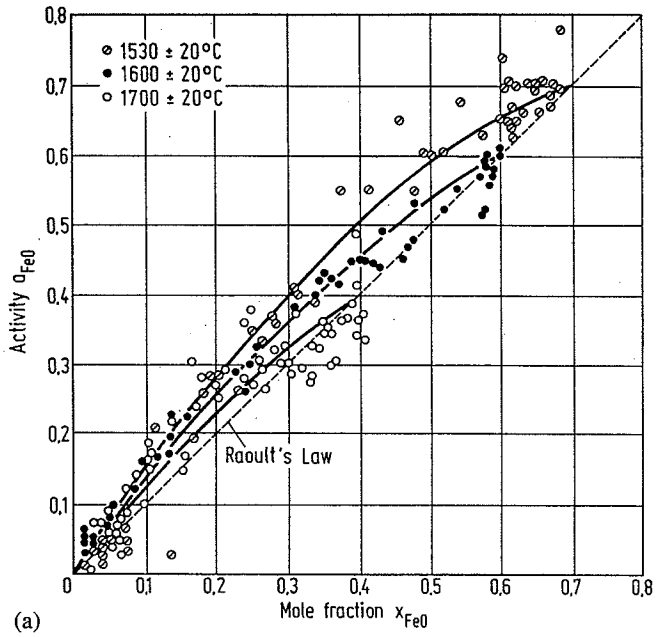
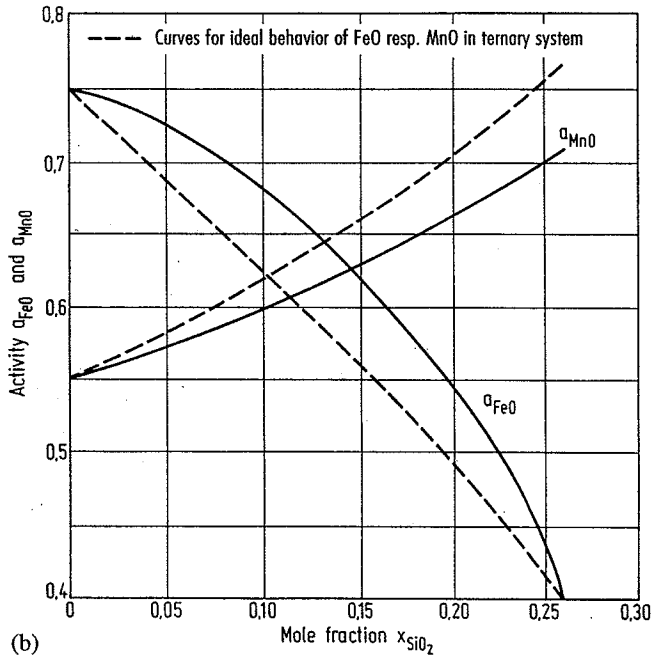


Fig. 5.63 a,b. Isoactivity curves of (a) FeO, (b) MnO in the system FeO-MnO-SiO_2 at 1550 °C, after Sommerville, Ivanchev and Bell [59].
- - - - phase limits

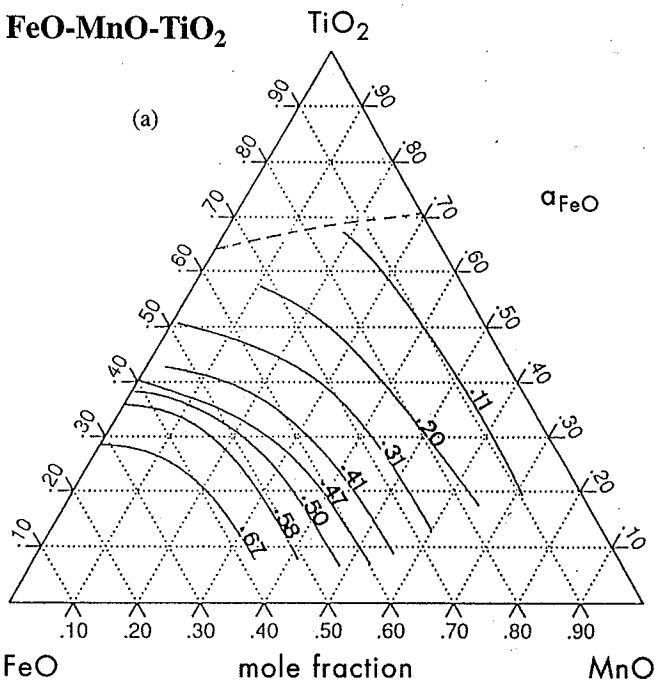


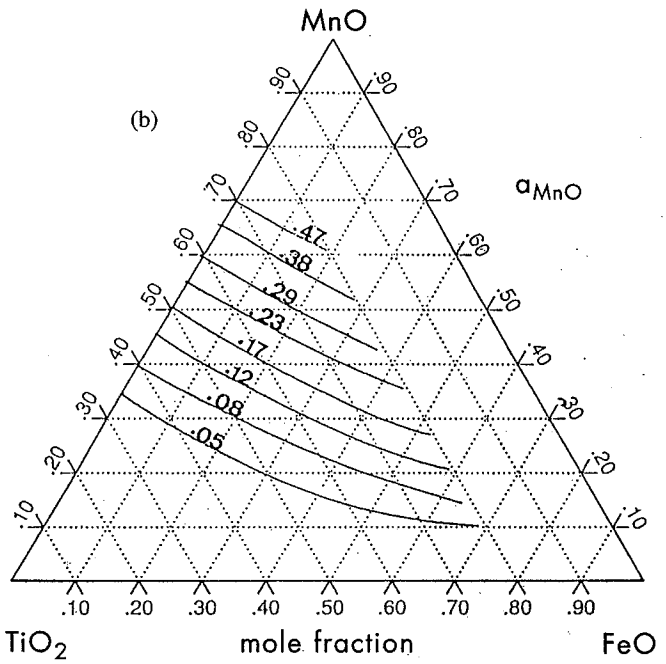
(a)



(b)

Fig. 5.64 a,b. Activity of (a) FeO dependent on FeO content at several temperatures and of (b) FeO and MnO dependent on silica content at 1530 °C in FeO-MnO-SiO_2 slags saturated with FeO-MnO solid solution, after Fischer and Bardenheuer [58]. Standard states are liquid FeO in equilibrium with liquid iron and pure solid MnO.





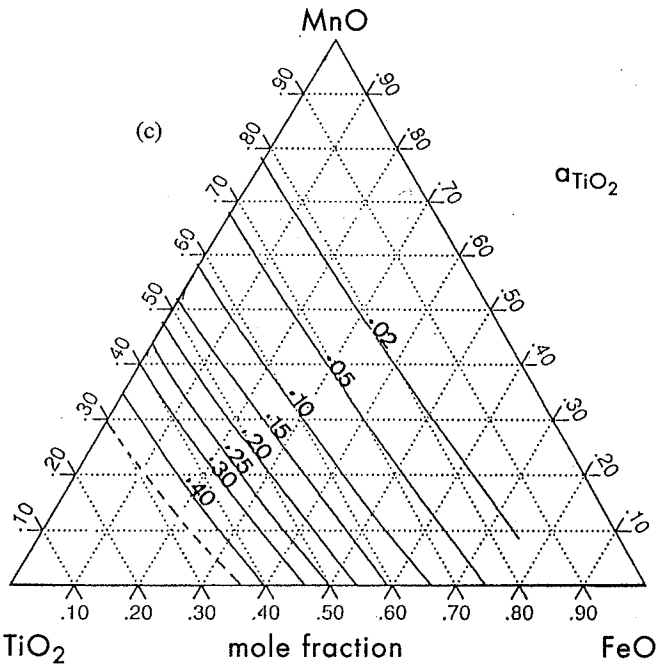


Fig. 5.65 a-c. Isoactivity curves of (a) FeO and (b) derived isoactivity curves of MnO and (c) TiO_2 in the system FeO-MnO-TiO_2 at 1475 °C, after Smith and Bell [69].
- - - - phase limits
Standard states are liquid pure FeO in equilibrium with solid iron and pure solid MnO and TiO_2.

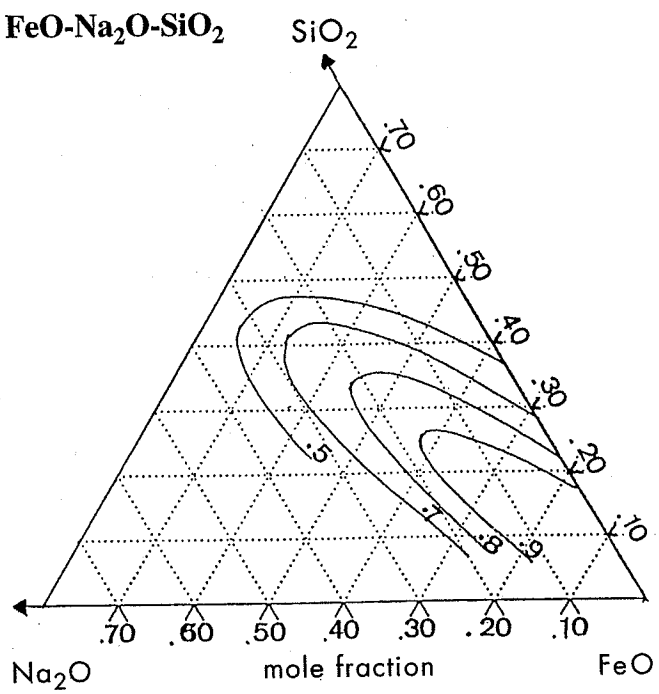


Fig. 5.66. Isoactivity lines of FeO in $FeO\text{-}Na_2O\text{-}SiO_2$ slags at 1400 °C, after Hyun et al. [70]

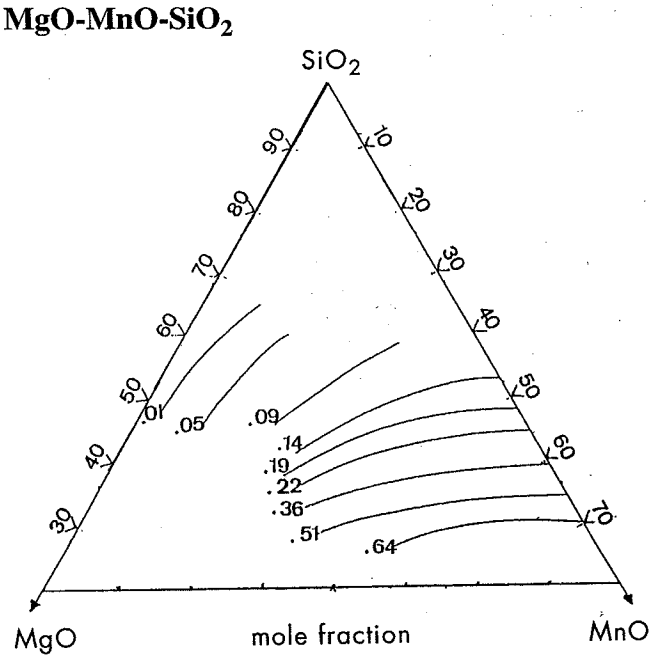


Fig. 5.68. Activities of MnO in $MgO\text{-}MnO\text{-}SiO_2$ melts at 1650 °C, after Mehta and Richardson [72]

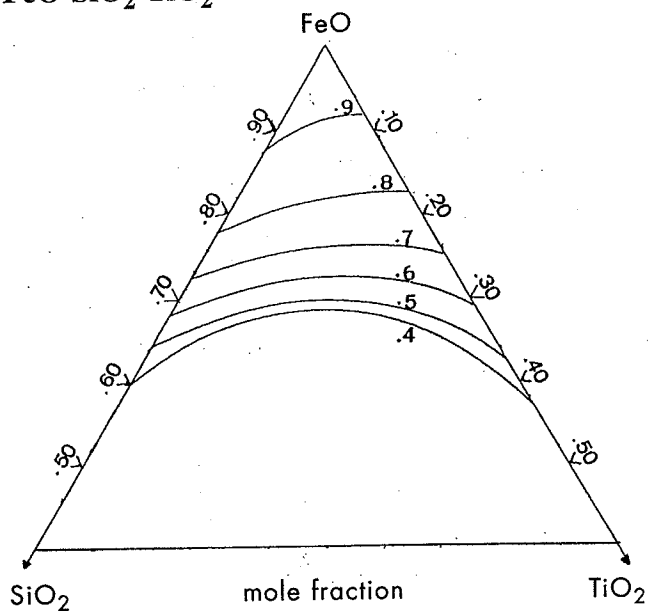


Fig. 5.67. FeO isoactivity curves in $FeO\text{-}SiO_2\text{-}TiO_2$ system at 1475 °C, after Sommerville and Bell [71]

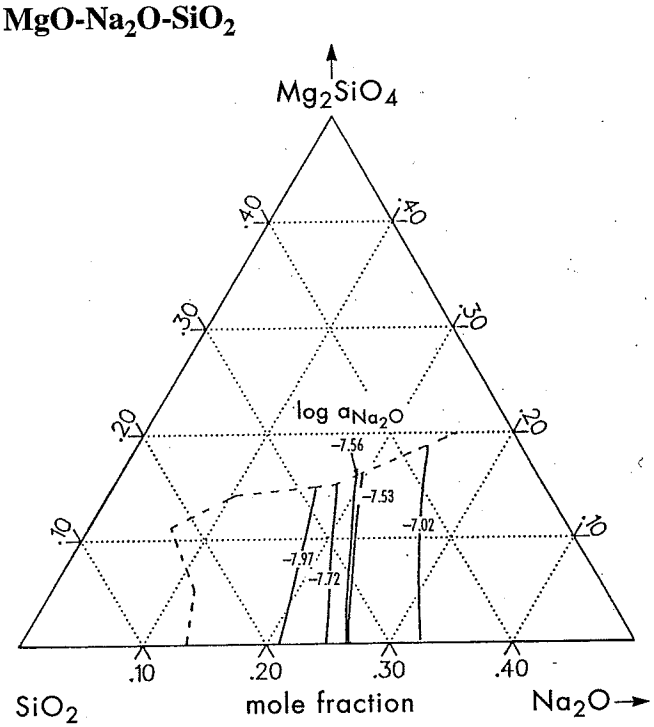


Fig. 5.69. Isoactivity data of Na_2O referred to liquid in the $MgO\text{-}Na_2O\text{-}SiO_2$ system at 1400 °C, after Rego, Sigworth and Philbrook [73]

$MnO\text{-}SiO_2\text{-}TiO_2$

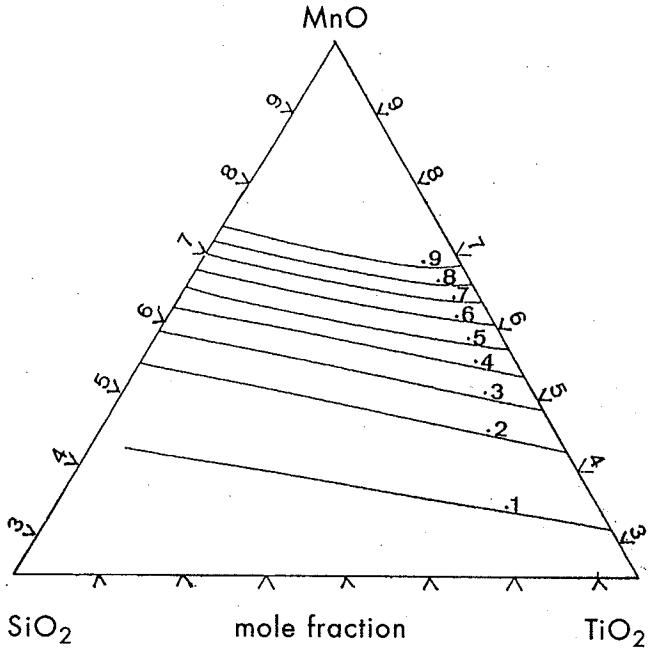


Fig. 5.70. Contours of Iso-a_{MnO} in melts in the system $MnO\text{-}SiO_2\text{-}TiO_2$ at 1500 °C, after Rao and Gaskell [74]

5.2.3 Quaternary systems

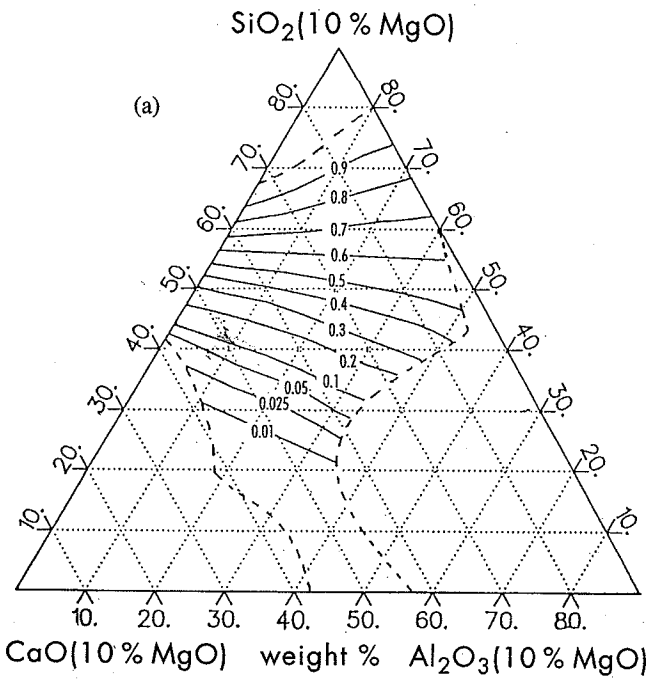
$Al_2O_3\text{-}CaF_2\text{-}CaO\text{-}SiO_2$

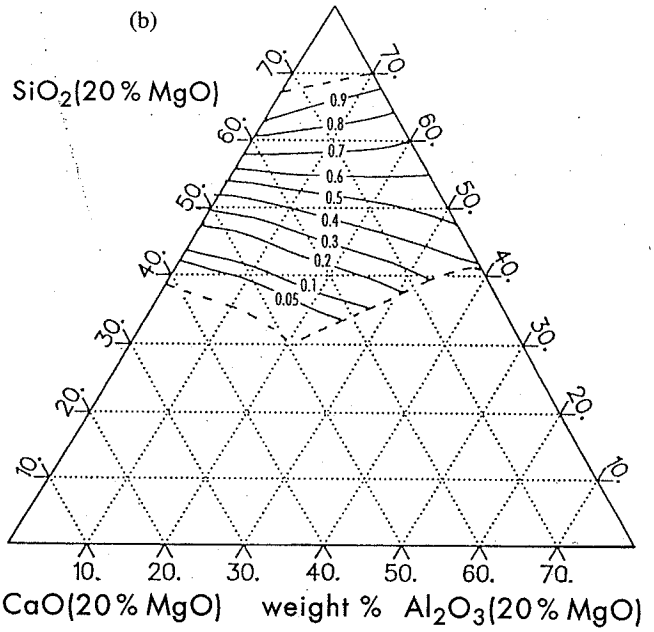
Tab. 5.4. Activity of SiO_2 in $Al_2O_3\text{-}CaF_2\text{-}CaO\text{-}SiO_2$ system at 1550 °C, after Gzielo and Iowsa [75].

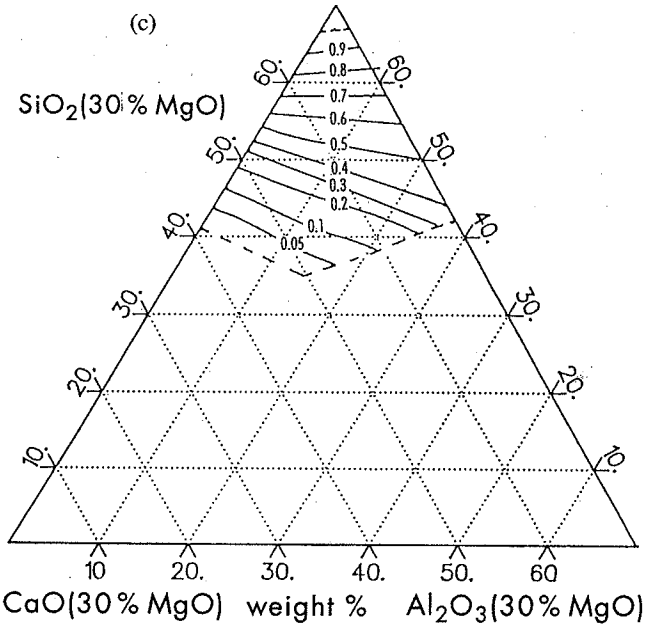
X_{CaO}	X_{SiO_2}	$X_{Al_2O_3}$	X_{CAF_2}	a_{SiO_2}
0.5005	0.3402	0.0949	0.0644	0.0142
0.4861	0.3624	0.0907	0.0608	0.0303
0.4575	0.3767	0.0982	0.0676	0.0407
0.4548	0.3898	0.0928	0.0626	0.0611
0.4341	0.4040	0.0937	0.0682	0.0866
0.4306	0.4156	0.0912	0.0626	0.1188
0.4012	0.4356	0.0945	0.0688	0.1792
0.3948	0.4488	0.0923	0.0641	0.2332
0.3673	0.4713	0.0953	0.0661	0.3393
0.3682	0.4765	0.0914	0.0639	0.3774
0.4081	0.3752	0.0946	0.1221	0.0117
0.3995	0.3802	0.0960	0.1243	0.0146
0.3930	0.3916	0.0926	0.1228	0.0233
0.3656	0.4119	0.0967	0.1258	0.0413
0.3642	0.4207	0.0927	0.1224	0.0584
0.3459	0.4359	0.0959	0.1223	0.0821
0.3254	0.4557	0.0942	0.1247	0.1494
0.3126	0.4688	0.0963	0.1223	0.2131
0.2968	0.4862	0.0951	0.1219	0.3204
0.2831	0.4980	0.0957	0.1232	0.3714

Fig. 5.71 a-c. Activity of SiO_2 at 1600 °C in the system $Al_2O_3\text{-}CaO\text{-}MgO\text{-}SiO_2$ with (a) 10 % MgO, (b) 20 % MgO and (c) 30 % MgO, after Rein and Chipman [41] ▶

$Al_2O_3\text{-}CaO\text{-}MgO\text{-}SiO_2$







Al_2O_3-CaO-MnO-SiO_2

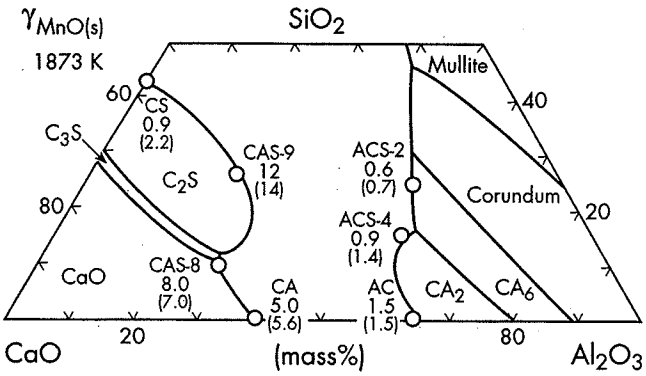


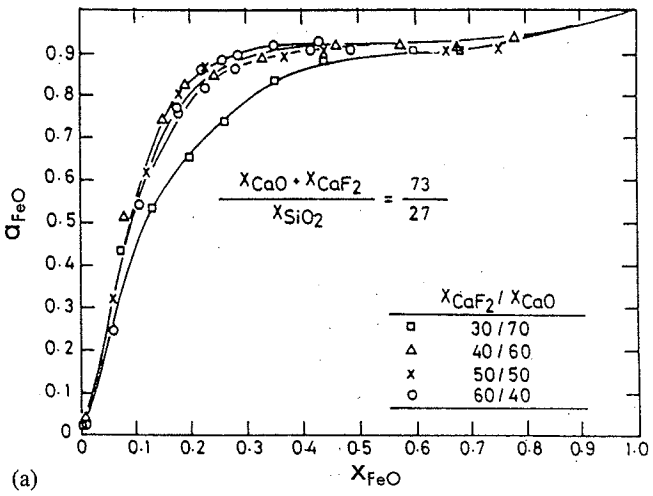
Fig. 5.72. Activity coefficient of $\gamma_{MnO(s)}$ in the system Al_2O_3-CaO-MnO-SiO_2 at 1600 °C, after Ohta [76]

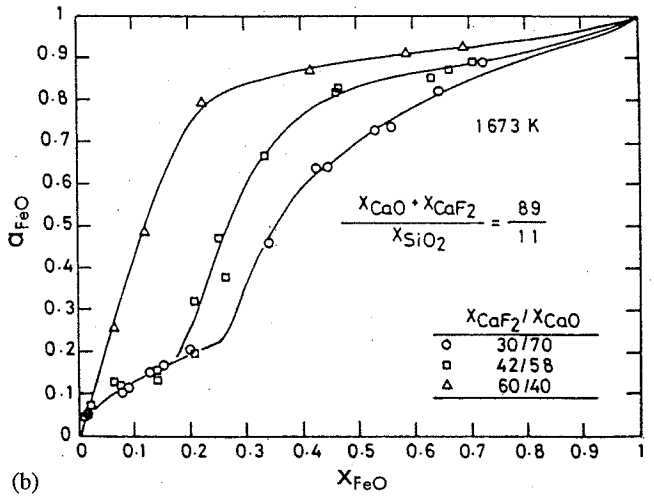
Al_2O_3-FeO-MnO-SiO_2

Tab. 5.5. Activity of FeO and MnO in the system Al_2O_3-FeO-MnO-SiO_2 at 1550 °C, after Sommerville, Ivanchev and Bell [59].

X_{MnO}	X_{SiO_2}	X_{FeO}	$X_{Al_2O_3}$	a_{FeO}	a_{MnO}
0.3410	0.1170	0.2910	0.2508	0.356	0.158
0.2640	0.1040	0.3760	0.2330	0.446	0.119
0.4150	0.1340	0.2136	0.2370	0.278	0.201
0.3100	0.1430	0.2930	0.2540	0.354	0.134
0.3670	0.1860	0.1970	0.2500	0.250	0.154
0.2720	0.1760	0.3070	0.2450	0.364	0.110
0.4890	0.1920	0.0677	0.2510	0.093	0.221
0.4330	0.2000	0.1170	0.2500	0.155	0.185
0.4890	0.2020	0.0660	0.2450	0.091	0.219
0.4130	0.2510	0.0739	0.2620	0.096	0.155
0.3760	0.2430	0.1220	0.2590	0.154	0.140
0.2930	0.2400	0.2000	0.2660	0.236	0.102
0.2210	0.2430	0.2750	0.2610	0.309	0.073
0.3750	0.2715	0.0864	0.2680	0.108	0.129
0.3455	0.2680	0.1248	0.2660	0.152	0.118
0.3055	0.2760	0.1597	0.2580	0.190	0.104
0.2610	0.2790	0.1922	0.2680	0.220	0.082
0.3935	0.2790	0.0606	0.2660	0.077	0.137
0.2590	0.2620	0.2040	0.2680	0.234	0.084
0.3840	0.1870	0.1940	0.2350	0.250	0.168
0.5480	0.1209	0.0955	0.2350	0.134	0.292

CaF_2-CaO-FeO-SiO_2





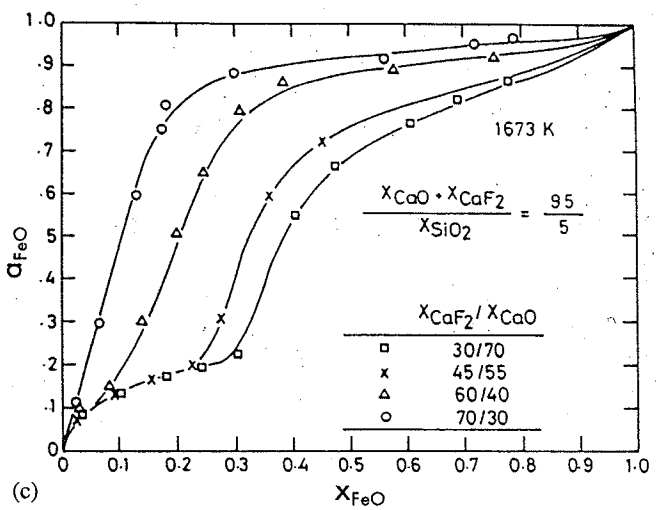


Fig. 5.73 a-c. Activity of FeO dependent on FeO content in the system CaF_2-CaO-FeO-SiO_2 at 1400 °C, after Iwase, Akizuki, Ichise and Tanaka [77].
Basicities $(X_{CaO} + X_{CaF_2})/X_{SiO_2}$ vary from (a) 73/27, (b) 89/11 to (c) 95/5 with different ratios X_{CaF_2}/X_{CaO}.
Standard state is pure liquid FeO in equilibrium with solid iron.
See also the paper by van Wijngaarden and Dippenaar [78].

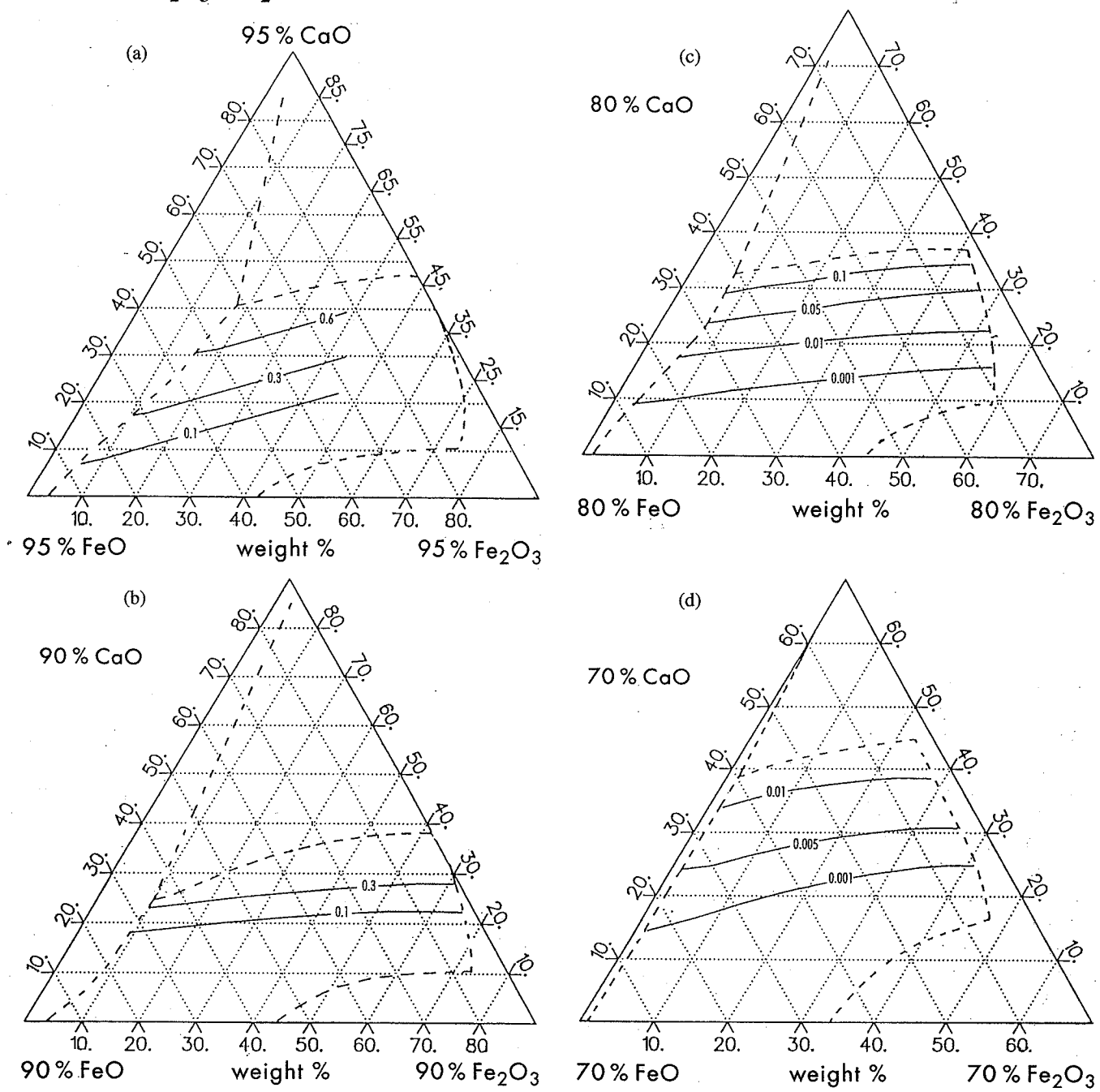


Fig. 5.74 a-d. Activity of CaO in the system $CaO\text{-}FeO\text{-}Fe_2O_3\text{-}SiO_2$ at 1450 °C with various SiO_2 contents: (a) 5 %, (b) 10 %, (c) 20 % and (d) 30 %, after Timucin and Morris [65]

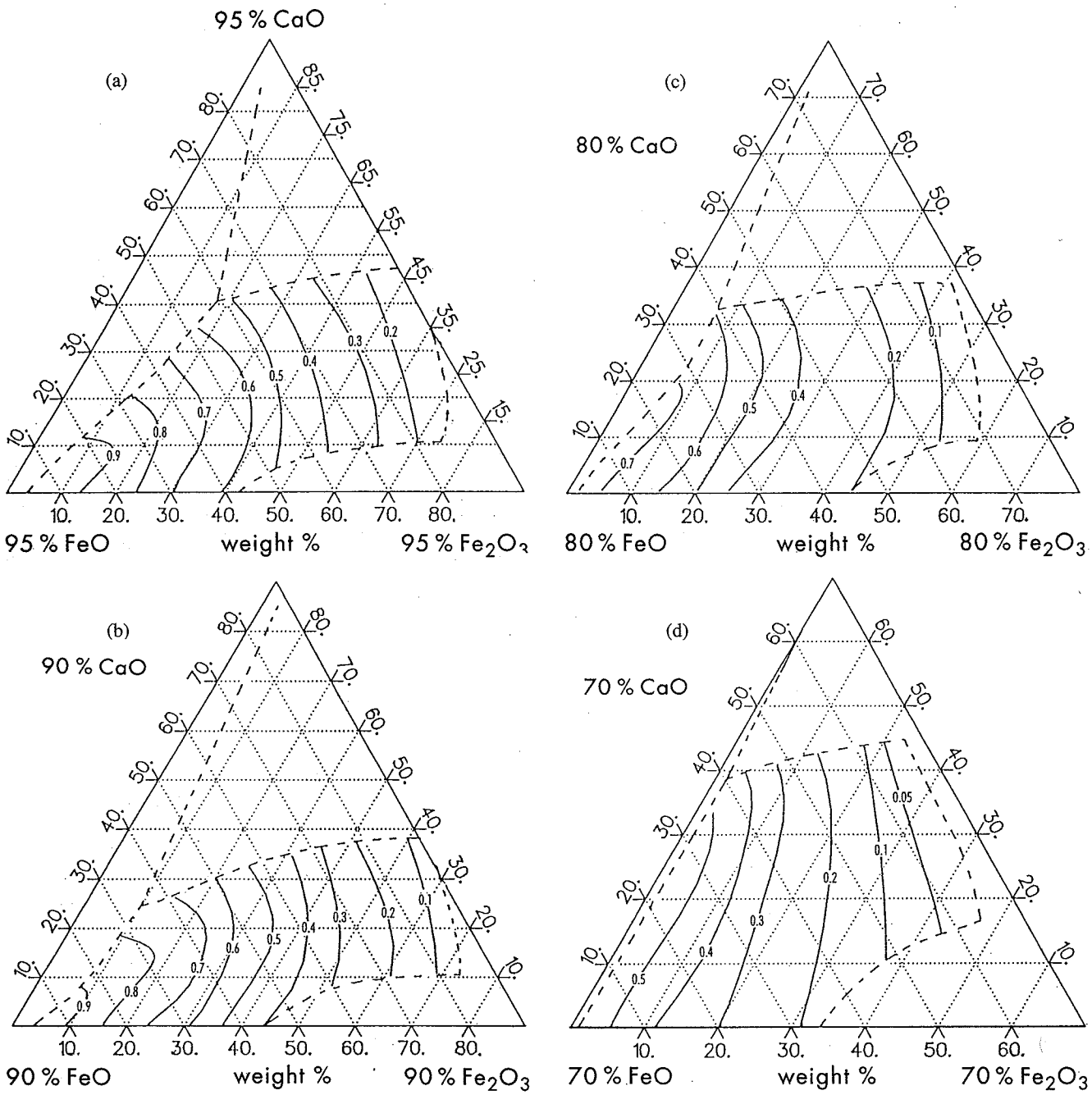


Fig. 5.75 a-d. Activity of FeO in the system CaO-FeO-Fe_2O_3-SiO_2 at 1450 °C with various SiO_2 contents: (a) 5 %, (b) 10 %, (c) 20 % and (d) 30 %, after Timucin and Morris [65]

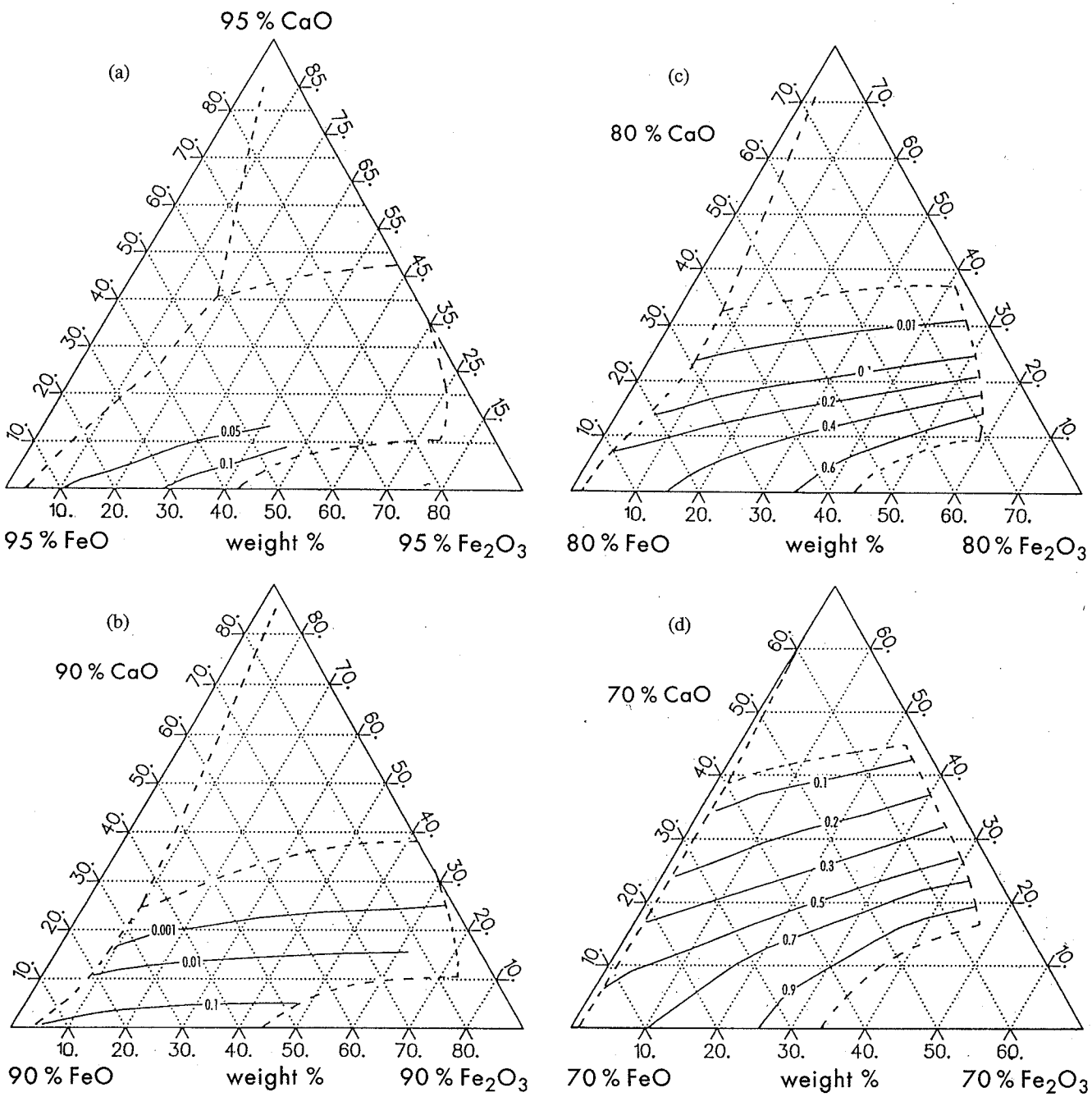


Fig. 5.76 a-d. Activity of SiO_2 in the system CaO-FeO-Fe_2O_3-SiO_2 at 1450 °C with different SiO_2 contents: (a) 5 %, (b) 10 %, (c) 20 % and (d) 30 %, after Timucin and Morris [65]

$CaO\text{-}FeO\text{-}MgO\text{-}SiO_2$

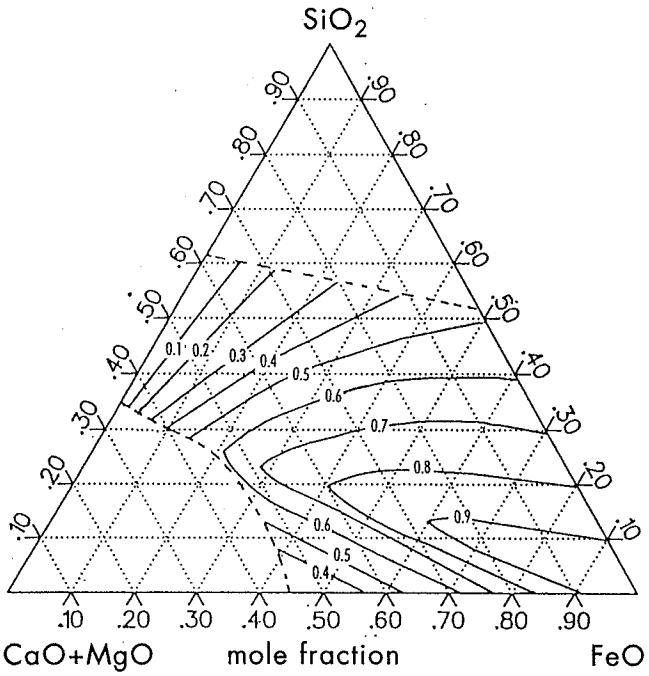


Fig. 5.77. Isoactivity lines of FeO in $CaO\text{-}FeO\text{-}MgO\text{-}SiO_2$ system at 1600 °C, after Taylor and Chipman [79]

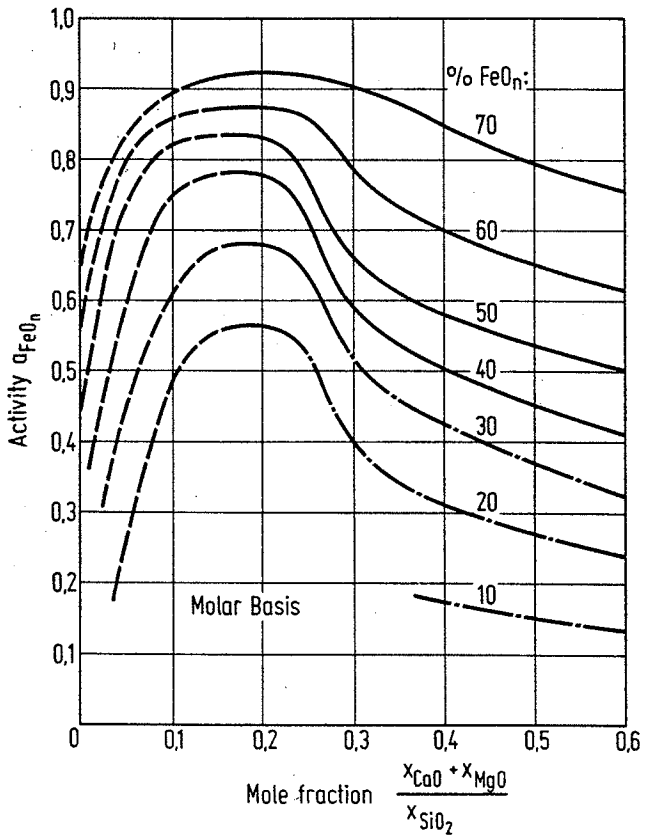


Fig. 5.78. Activity of FeO for various FeO contents dependent on the basicity $(X_{CaO} + X_{MgO})/X_{SiO_2}$ at 1600 °C in the system $CaO\text{-}FeO\text{-}MgO\text{-}SiO_2$, after Chipman and coworkers [80]

Tab. 5.6. Activity of MgO in $CaO\text{-}FeO\text{-}MgO\text{-}SiO_2$ system at 1600 °C, after Sbirzyanov [81]

X_{FeO}	X_{MgO}	X_{CaO}	X_{SiO_2}	a_{MgO}
0.1855	0.1107	0.4402	0.2606	0.0691
0.1355	0.1275	0.4347	0.3043	0.0657
0.1283	0.1411	0.4273	0.3033	0.0719
0.3081	0.1430	0.3174	0.2315	0.0732
0.3072	0.1394	0.3211	0.2322	0.0716
0.2625	0.1188	0.3757	0.2430	0.0671
0.7023	0.0733	0.1850	0.0394	0.0701
0.6104	0.0704	0.2882	0.0310	0.0789
0.4546	0.0698	0.3972	0.0784	0.0750
0.3640	0.2261	0.1522	0.2577	0.0663
0.3160	0.2790	0.1219	0.2830	0.0684
0.2371	0.2201	0.2622	0.2806	0.0805
0.8700	0.1065	0.0100	0.0135	0.0966
0.3234	0.1548	0.2839	0.2379	0.0704
0.3804	0.1165	0.3173	0.1858	0.0719
0.9134	0.0671	0.0013	0.0182	0.0576
0.9092	0.0689	0.0013	0.0206	0.0580
0.7273	0.0618	0.1883	0.0226	0.0653
0.6170	0.0597	0.3074	0.0159	0.0722
0.1208	0.1850	0.3803	0.3140	0.0803
0.3227	0.1701	0.2530	0.2542	0.0661
0.5746	0.1115	0.1638	0.1501	0.0552
0.4572	0.1342	0.1821	0.2264	0.0470
0.4782	0.1644	0.1447	0.2127	0.0567
0.6393	0.1978	0.0011	0.1618	0.0621
0.5639	0.2394	0.0011	0.1956	0.0629
0.9357	0.0563	0	0.0080	0.0526
0.9375	0.0559	0	0.0060	0.0528

5.3 References in Chapter 5

[1] Hino, M.: CAMP – ISIJ, vol. 7 (1994), 41
[2] Ban-Ya, S.; Chiba, A.; Hikosaka, A.: Tetsu-to-Hagane, 66 (10), (1980), 1484 – 1493
[3] Jacob, K. T.: Can. Metal. Quarterly, 20 (1), (1981), 89 – 92
[4] Sharma, R. A.; Richardson, F. D.: Trans. Met. Soc. AIME; 233, 1965, 1587 – 1592
[5] Dhima, A.; Stafa, B.; Allibert, M.: High Temp. Science, 21, 1986, 143 – 159
[6] Iwase, M.; Yamada, N.; Ichise, E.; Akizuki, H.: Arch. Eisenhüttenwes., 55 (9), (1984), 415 – 420
[7] Rao, B. K. D. P.; Gaskell, D. R.: Met. Trans. 12B, (1981), 469 – 477
[8] Itoh, H.; Sasahira, A.; Haekawa, T.; Yokokawa, T.: J. Chem. Soc. Faraday Trans. 1, 80, (1984), 473 – 487
[9] Sharma, R. A.; Richardson, F. D.: J. Iron Steel Inst., 200, (1962), 373 – 379
[10] Chipman, J.: Physical chemistry of process metallurgy, P. I. New York/London 1961, 27 – 64
[11] Chengtao, Z.; Chunlin, Ji: Journal of Northeast University of Technology, Vol. 11, 1990, 8 – 12
[12] Chattopadhyay, S.; Mitchell, A.: Metallurgical Transactions, Vol. 21B, 1991, 621 – 627
[13] Edmunds, D. M.; Taylor, J.: J. Iron Steel Inst., 210, (1972), 280 – 283
[14] Kay, D. A. R.; Mitchell, A.; Ram, M.: J. Iron Steel Inst., 208, (1970), 141 – 146
[15] Chen, C.; Zhao, W.: Acta Met. Sinica, 19 (1), 1983, A1 – A8
[16] Takeda, Y.; Yazawa, A.: Nippon Kogyokaishi, 96, (1980), 901 – 906
[17] Fujita, H.; Iritani, Y.; Maruhashi, S.: Tetsu-to-Hagane, 54, (1968), 359 – 370
[18] van Wijngaarden, M. J. U. T.; Dippenaar, R. J.: J. S. Afr. Inst. Min. Metall., 86 (11), 1986, 443 – 453
[19] Chang, L. C.; Derge, G.: Trans. Amer. Inst. Min. Metallurg. Engrs, 197, (1947), 60
[20] Yang, L.; Mac Cabe, L. C.; Miller, R.: Physical Chemistry of Steelmaking. Ed.: J. F. Elliott. New York/London 1958, 63
[21] Kay, D. A. R.; Taylor, J.: Trans. Faraday Soc., 56, (1960), 1372 – 1386
[22] Sharma, R. A.; Richardson, F. D.: J. Iron Steel Inst., 198, (1961), 386 – 390
[23] Sanbongi, K.; Omori, Y.: Physical Chemistry of metallic solutions and intermetallic compounds, II. London 1959

[24] Rey, M.: Physical Chemistry of process metallurgy. London (1948), 247
[25] Carter, P. T.; Macfarlane, T.: J. Iron Steel Inst., 185, (1957), 54 – 66
[26] Omori, Y.; Sanbongi, K.: J. Metals Inst. Japan, 25, (1961), 139 – 143
[27] Richardson, F. D.: Physical Chemistry of Metals. London (1953), 77 – 95
[28] Fulton, J. C.; Chipman, J.: Trans. Metallurg. Soc. AIME, 200, (1954), 1136 – 1146
[29] Sawamura, K.: Tetsu-to-Hagane Overseas, 2, (1962), 219 – 225
[30] Ban-Ya, S.; Watanabe, T.: Tetsu-to-Hagane, 63 (12), (1977), 27 – 36
[31] Elliott, J. F.; Gleiser, M.; Ramakrishna, V.: Thermochemistry for Steelmaking. Vol. II, Reading. Palo Alto/London, 1963, Mass
[32] Elliott, J. F.: J. Metals, 7, (1955), 485 – 488
[33] Schuhmann jr, R.; Ensio, P. J.: Trans. Metallurg. Soc. AIME, 191, (1951), 401 – 411
[34] Oeters, F.: Physikalische Chemie der Eisen- und Stahlerzeugung. Düsseldorf 1964, 159 – 162
[35] Turkdogan, E. T.; Pearson, J.: J. Iron Steel Inst., 173, (1953), 217 – 223
[36] Bodsworth, C.; Davidson, M.: Physical chemistry of process metallurgy, 1
[37] Smith, I. C.; Bell, H. B.: Trans. Inst. mining metall., sect. c, 79, (1970), 253 – 258
[38] Steiler, J. M.: Etude Thermodynamique des laitiers liquides du système K_2O-SiO_2, I.R.S.I.D.
[39] Iwase, M.; Akizuki, H.; Fujiwara, H.; Ichise, E.; Yamada, N.: Steel Research 58 (5), (1987), 215 – 219
[40] Kambayashi, S.; Kato, E.: J. Chem. Thermodynamics, 15, (1983), 701 – 707
[41] Rein, H. R.; Chipman, J.: Trans. Metallurg. SOC AIME, 233, (1965), 415 – 425
[42] Rao, B. K. D. P.; Gaskell, D. R.: Met. Trans. 12B, (1981), 311 – 317
[43] Abraham, K. P.; Davies, M. W.; Richardson, F. D.: J. Iron Steel Inst., 196, (1960), 82 – 89
[44] Richardson, F. D.: Physical Chemistry of Steelmaking. Ed.: J. F. Elliott. New York/London 1958, 68 – 76
[45] Schenck, H.; Frohberg, M. G.; El Gammal, T.: Arch. Eisenhüttenwes., 32, (1961), 509 – 511
[46] Goto, K. S.; Yamaguchi, S.: Rep. TKK-V (Helsinki Univ. Technol., inst. process. metall.) 1982, 17 – 42
[47] Yokokawa, T.; Kohsaka, S.: J. Chem. Engineering Data, 24, (1979), 167
[48] Goto, K. S.; Yamaguchi, S.: Metall. Slags Fluxes, 2nd Int. Symp., Proc., (1984), 467 – 480. Edited by Fine, H. A.; Gaskell, D. R. – Metall. Soc. AIME: Warrendale, Pa.
[49] Tsukihashi, F.; Sano, N.: Tetsu-to-Hagane, 71, (1985), 815 – 822
[50] Neudorf, D. A.; Gleiser, M.: Met. Trans., 11B, (1980), 607
[51] Kohsaka, S.; Sato, S.; Yokokawa, T.: J. Chem. Therm., 11, (1979); 547
[52] Frohberg, M.; Caune, G. E.; Kapoor, M. L.: Arch. Eisenhüttenwes., 44, (1973), 585
[53] Chattopadhyay, S.; Mitchell, A.: Metallurgical Transactions, Vol. 21B, 1991, 621 – 627
[54] Allibert, M.; Chatillon, C.: Can. Met. Q, 18 (1979), 349 – 354
[55] Ram, M.: Trans of the Indian Inst. of Metals. Vol. 32, No. 2 (1979)
[56] Allibert, M.; Chatillon, C.; Lourtau, R.: Rev. Int. Hautes Températures Réfractaires, Fr., 16 (1979), 33 – 37
[57] Kim, V. A.; Kulikov, I. S.; Akberdin, A. A.; Nikolai, E. I.: Russian Journal of Physical Chemistry, 57 (1) 1983, 43 – 46
[58] Fischer, W. A.; Bardenheuer, P. W.: Arch. Eisenhüttenw. Vol. 39 (1968), 637 – 643
[59] Sommerville, J. D.; Ivanchev, I.; Bell, H. B.: Proc. Int. Symp. Metall. Chem. Applications in Ferrous Metallurgy. The Iron and Steel Inst., Sheffield (1971), 23 – 25
[60] Healy, G. W.: ISS Trans. Vol. 9. (1988), 153 – 161
[61] Itoh, H.; Yokokawa, T.: Trans. Jap. Inst. Met., 25 (12) (1984), 879 – 884
[62] Iwase, N.; Ichise, E.; Yamada, N.: Trans. Iron and Steel Soc., AIME. Vol. 4 (1984), 47
[63] Gzielo, A.; Iowsa, Y. A.; Budzik, R.: Izvest. Vuz, Chern. Met., S, 1985, 41 – 45
[64] Hara, S.; Araki, T.; Ogino, K.: Metall. Slags Fluxes, 2nd Int. Symp. Proc. Met. Soc. AIME (1984), 441 – 451
[65] Timucin, M.; Morris, A. E.: Metallurg. Trans. Vol. 1 (1970), 3193 – 3201
[66] Rego, D. N.; Sigworth, G. K.; Philbrook, W. O.: Metallurg. Trans. B. Vol. 19 B (1988), 655
[67] Kojima, V. Y.; Inouye, M.; Sano, K.: Arch. Eisenhüttenw. Vol. 40 (1969); 337 – 340
[68] Ban-Ya, S.; Hino, M.; Yuge, N.: Iron and Steel Inst. Japan. Vol. 71 (1985), 853
[69] Smith, J. C.; Bell, H. B.: Trans. Inst. Min. Metall. Vol. 80 (1971), 655 – 659
[70] Hyun, D. B.; Shim, J. D.; Kim, S. N.; Lee, E. C.: J. of Korean Inst. Metals, 23 (3) (1985), 19 – 27
[71] Sommerville, J. D.; Bell, H. B.: Can. Metall. Q., 21 (1982), 145 – 155
[72] Mehta, S. R.; Richardson, F. D.: J. Iron Steel Inst. (1965), 524
[73] Rego, D. N.; Sigworth, G. K.; Philbrook, W. O.: Met. Trans., 20B, 1989, 757 – 758
[74] Rao, B. K. D. P.; Gaskell, D. R.: Metallurgical Trans. B, Vol. 12B (1981), 469
[75] Gzielo, A.; Jowsa, J.: Activity of SiO_2 in slags CaO-SiO_2-Al_2O_3-CaF_2. Archiwum Hutnictwa, 29 (2), 1984, 319 – 331
[76] Ohta, H.: CAMP – ISIJ. Vol. 7 (1994), 42
[77] Iwase, M.; Akizuki, H.; Ichise, E.; Tanaka, Y.:Steel Res. Vol. 57 (1986), 436 – 443
[78] van Wijngaarden, M. J. U. T., Dippenaar, R. J.: Iron Steelmaker, Trans ISS (1988), No. 2, 49 – 56
[79] Tylor, C. R.; Chipman, J.: Trans. Amer. Inst. Min. Metallurgy Engrs. Trans. AIME Vol. 154 (1943), 228 – 247
[80] Bishop jr., H. L.; Lander, H. N.; Grant, N. J.; Chipman, J.: J. Metals 8 (1956), 862 – 868
[81] Sbirzyanov, T. G.: Izvest. V.U.Z., Chern. Met., 1989, (7) 4 – 6

6

6.1 Sulphide capacities

H. Gaye and J. Lehmann

6.2 Phosphate and phosphide capacities in metallurgical slags

D. Kirner and D. Janke

6.1 Sulphide capacities

6.1.1 Sulphide and sulphate equilibria

Sulphur in slags can be present in the form of either sulphides or sulphates in accordance with the following expressions:

$$1/2S_2 + (O^{2-})_{slag} = 1/2O_2 + (S^{2-})_{slag}$$

$$1/2S_2 + 3/2O_2 + (O^{2-})_{slag} = (SO_4^{2-})_{slag}$$

$$K_1 = a_S^{2-}/a_O^{2-}.(P_{O_2}/P_{S_2})^{1/2}$$

$$K_2 = a_{SO_4}^{2-}/a_O^{2-}.P_{O_2}^{3/2}.P_{S_2}^{1/2}$$

Assuming that Henry's law is valid for a_S^{2-} and $a_{SO_4}^{2-}$, K_1 is a constant for oxygen pressure smaller than 10^{-6} atm and K_2 is a constant for $P_{O_2} > 10^{-5}$ atm [1]. It follows that where $P_{O_2} < 10^{-6}$ atm, the sulphur will be present in the slag as sulphide and where $P_{O_2} > 10^{-5}$ atm, conversely, in the form of sulphate **(Fig. 6.1).**

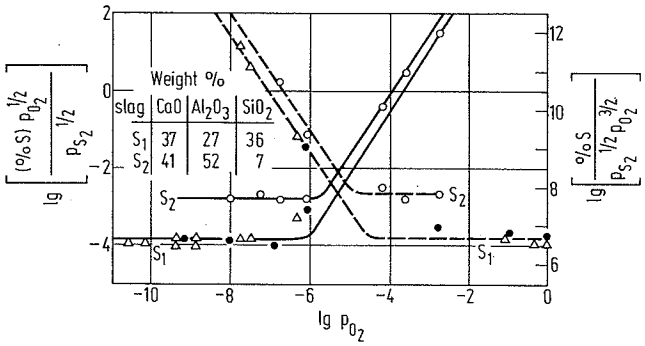


Fig. 6.1. Effect of oxygen partial pressure on the sulphide and sulphate capacity of Al_2O_3-CaO-SiO_2 slags at 1500 °C [3]

6.1.2 Sulphide capacity definitions

According to the preceding considerations, under metallurgical reducing conditions, the sulphur exchange between a slag and a gas phase can be represented by:

$$1/2S_2 + (O^{2-})_{slag} = 1/2O_2 + (S^{2-})_{slag}.$$

Therefore, Richardson and Fincham [1] proposed the following definition of the sulphide capacity, as a measurement of the capacity of a slag to hold sulphur:

$$C_S = (P_{O_2}/P_{S_2})^{1/2}.(\text{wt \%S}).$$

For the sake of commodity, in metallurgical applications, the gaseous reference states are often replaced by references to the 1 wt % dilute solution in the metal phase:

$$C_S' = (a_{[O]}/a_{[S]}) / (\text{wt \% S})$$

where $a_{[O]}$ and $a_{[S]}$ are respectively the activities of oxygen and sulphur in the metal phases expressed by using this reference. C_S' can be converted to C_S by the relationship:

$$C_S' = \exp(-2154/T+3.166).C_S.$$

6.1.2.1 Sulphide capacity diagrams, preliminary remarks

In order to facilitate the critical assessment of experimental data belonging to the system

$$Al_2O_3 - CaO - Cr_2O_3 - CrO - FeO - Fe_2O_3 - MgO - MnO - SiO_2 - S$$

the IRSID slag model [2, 3] has been used. In **Fig. 6.2** the C_S values calculated by the IRSID model are plotted against those experimental data used for the calibration of the IRSID model. In view of the experimental uncertainty which can even exceed 30%, the correlation is relatively good.

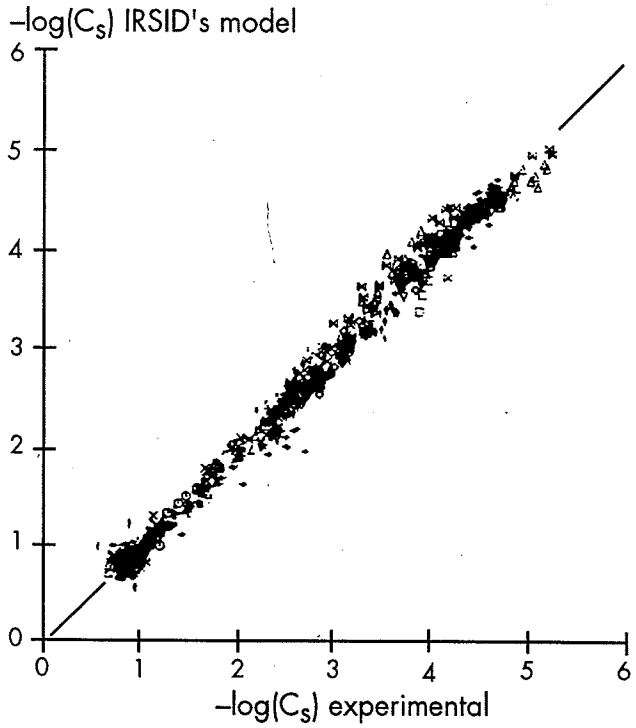


Fig. 6.2. Comparison between experimental values of sulphide capacity and values calculated with IRSID's model [2, 3]. System: Al_2O_3-CaO-FeO-Fe_2O_3-MgO-MnO-SiO_2-S

Because of its reliability, the IRSID slag model is also used for

- calculating interpolations and extrapolations and
- deriving slag/metal sulphur distribution coefficients.

Sulphide capacity data calculated according to the IRSID slag model are given in section 6.1.3. Where available, experimental points are plotted together with the calculated curves.

Slags containing CaF_2, Na_2O, P_2O_5 and TiO_2 are not yet described by the IRSID slag model. Sulphide capacity data belonging to these systems are given in section 6.1.4.

6.1.2.2 Slag-metal sulphur partition diagrams, preliminary remarks

The IRSID slag model has also been used to calculate the sulphur partition coefficient between slag and metal according to the following equation:

$$L_S = (\%\,S)_{slag} / [\%\,S]_{metal} = C_S'/ (f_{[S]} \cdot a_{[O]})$$

for the system

$Al_2O_3 - CaO - Cr_2O_3 - CrO - FeO - Fe_2O_3 - MgO - MnO - SiO_2 - S$.

In order to draw the iso-sulphur partition curves between slag and metal in oxide diagrams, the oxygen activity must be given or fixed by an oxide/deoxidizer equilibrium. The relevant oxide/deoxidizer couple for each diagram shown is given in the caption.

Iso-sulphur partition diagrams calculated according to the IRSID slag model for 1600 °C are compiled in section 6.1.5.

6.1.2.3 CaS saturation, preliminary remarks

Available experimental data on CaS saturation mainly concern the binaries Al_2O_3-CaO [4, 11, 12, 19] (Fig. 6.32) and CaO-SiO_2 [5, 46, 47, 48, 49] (Fig. 6.33). Data concerning the system CaO-SiO_2 are very scattered, while those belonging to the binary Al_2O_3-CaO are coherent.

The prediction of the CaS saturation by IRSID's model requires the calibration of an additional parameter, which is the value used by the model for CaS free enthalpy of fusion. This value is calculated in order to reproduce the experimental data on CaS saturation on the binary Al_2O_3-CaO (Fig. 6.32). The good fit obtained as well as the very satisfactory agreement between experimental and calculated values of the sulphide capacity (Fig. 6.2) allows the derivation of the CaS saturation in the ternary Al_2O_3-CaO-SiO_2 (Fig. 6.3.4).

CaS saturation has also been experimentally investigated in the CaF_2-CaO-SiO_2 system (Fig. 6.35) [45].

6.1.3 Sulphide capacities calculated according to IRSID's slag model

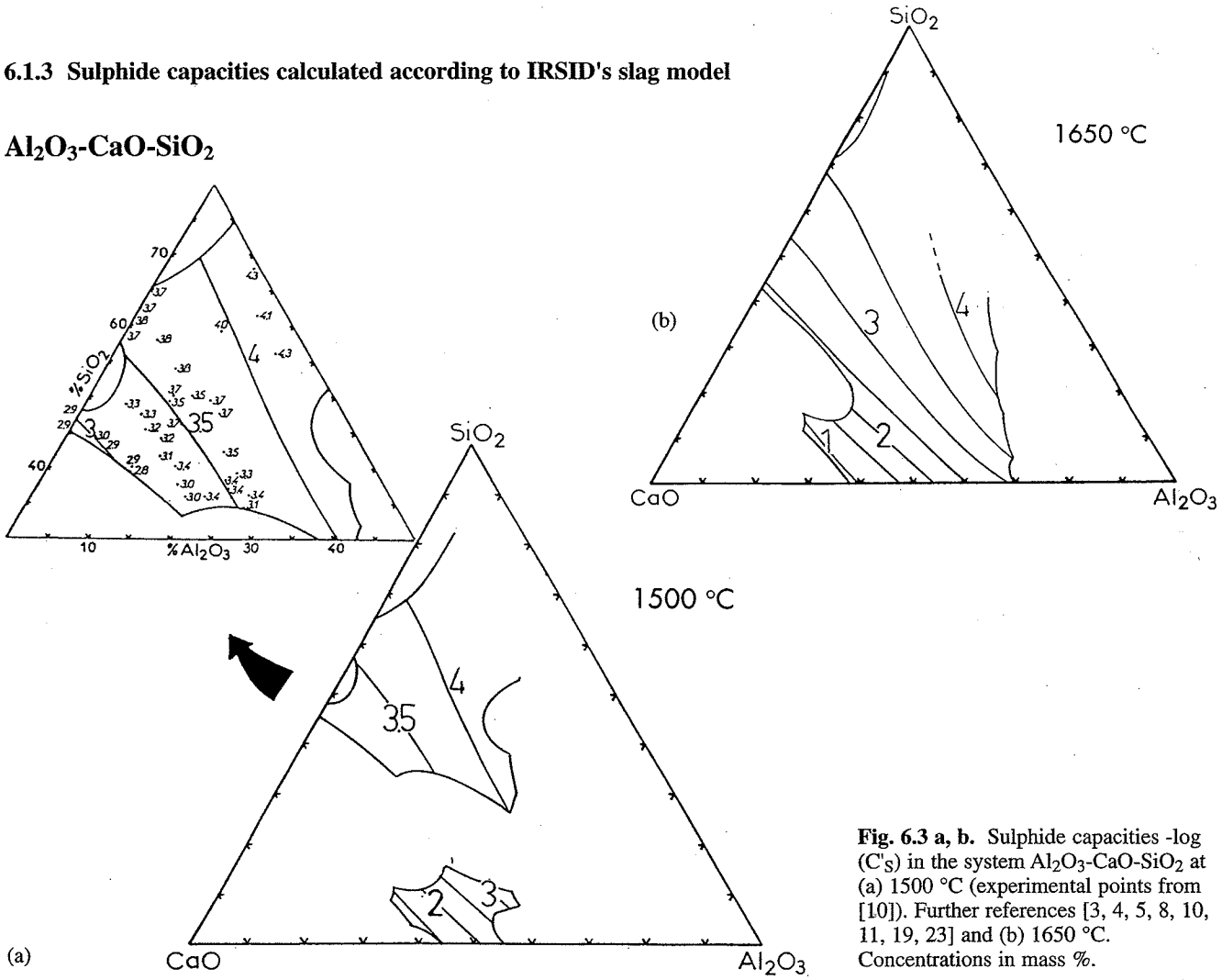


Fig. 6.3 a, b. Sulphide capacities -log (C'_S) in the system Al_2O_3-CaO-SiO_2 at (a) 1500 °C (experimental points from [10]). Further references [3, 4, 5, 8, 10, 11, 19, 23] and (b) 1650 °C. Concentrations in mass %.

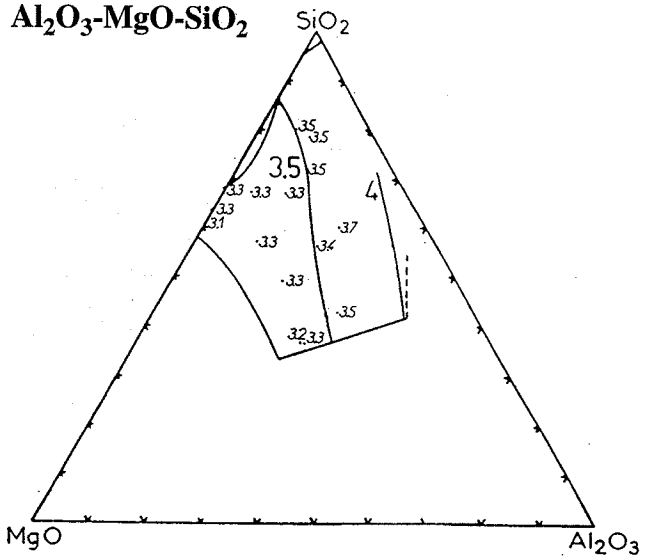
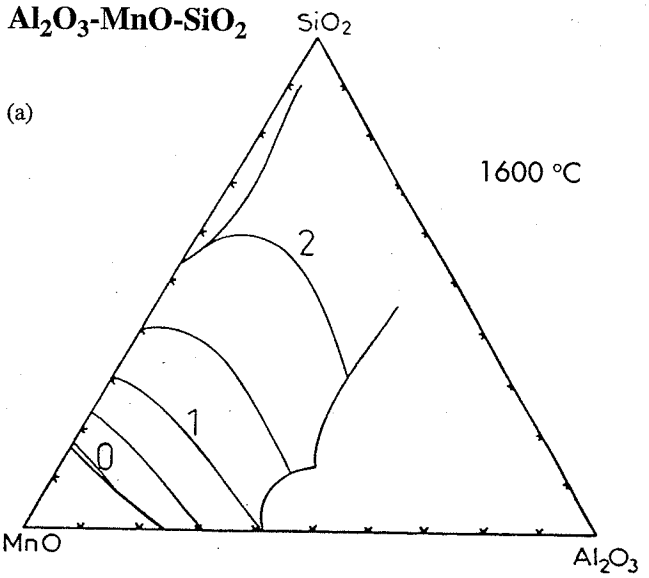


Fig. 6.4. Sulphide capacities -log (C'_S) in the system Al_2O_3-MgO-SiO_2 at 1650 °C (experimental points from [6]). Further reference [7]. Concentrations in mass %.



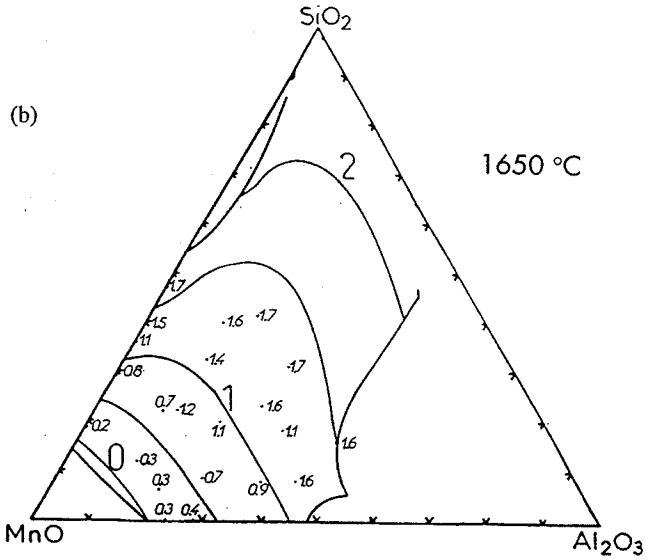


Fig. 6.5 a,b. Sulphide capacities -log (C'_S) in Al_2O_3-MnO-SiO_2 slags at (a) 1600 °C and (b) 1650 °C (experimental points from [6]). Further reference [9]. Concentrations in mass %.

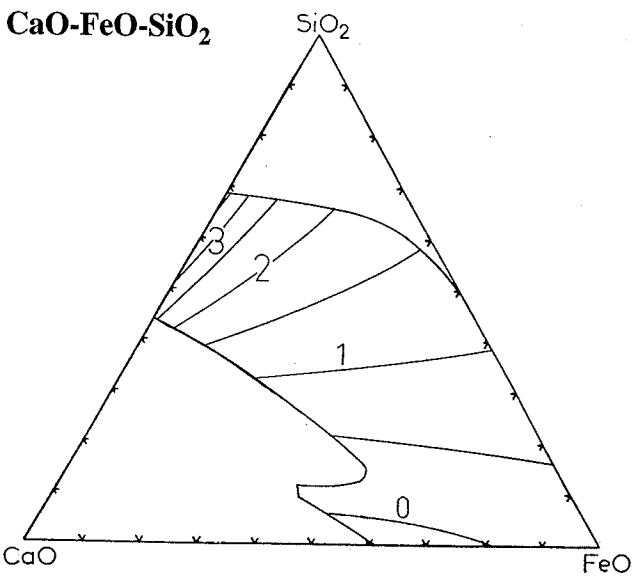


Fig. 6.6. Sulphide capacities -log (C'_S) in CaO-FeO-SiO_2 slags at 1600 °C. Concentrations in mass %.

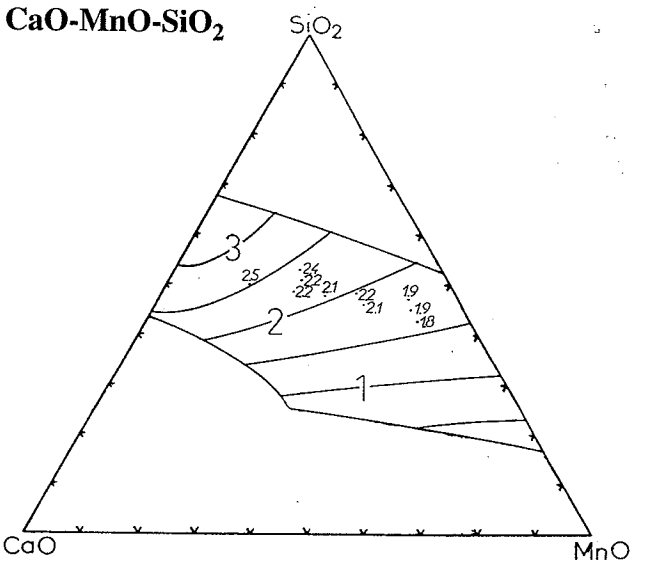


Fig. 6.7. Sulphide capacities -log (C'_S) in CaO-MnO-SiO_2 slags at 1600 °C (experimental points from [9]). Further reference [6]. Concentrations in mass %.

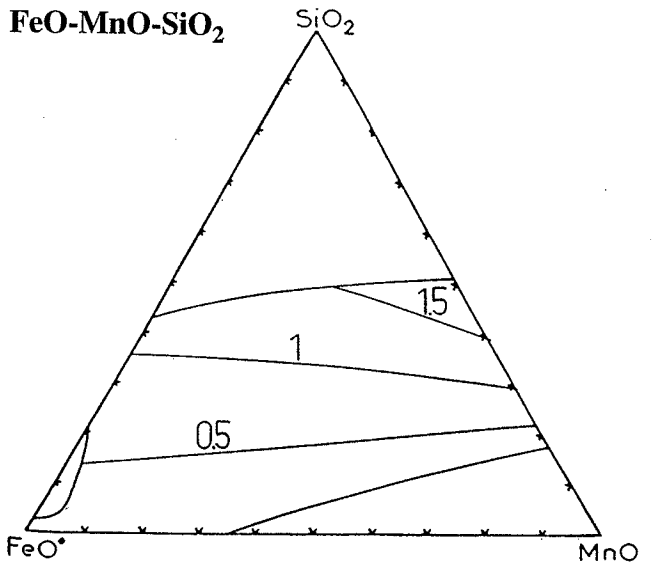


Fig. 6.8. Sulphide capacities -log (C'_S) in FeO-MnO-SiO_2 slags at 1550 °C. Concentrations in mass %.

MgO-MnO-SiO_2

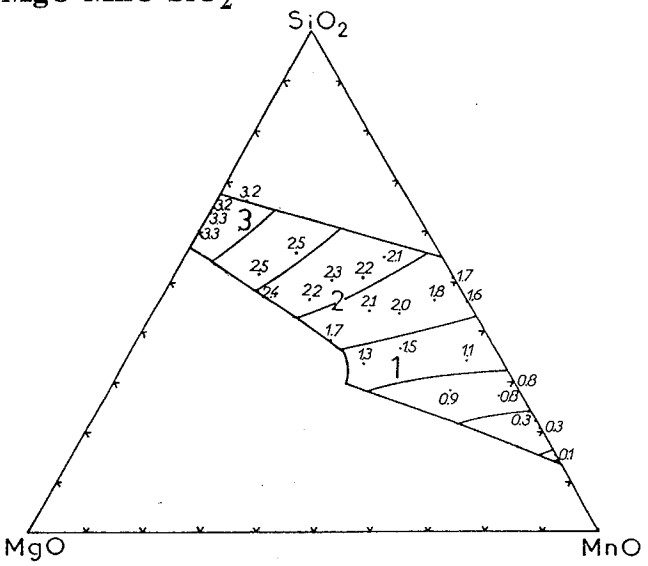


Fig. 6.9. Sulphide capacities -log (C'_S) in MgO-MnO-SiO_2 slags at 1650 °C (experimental points from [9]). Concentrations in mass %.

6.1.4 Sulphide capacities determined

6.1.4.1 CaF_2 bearing systems

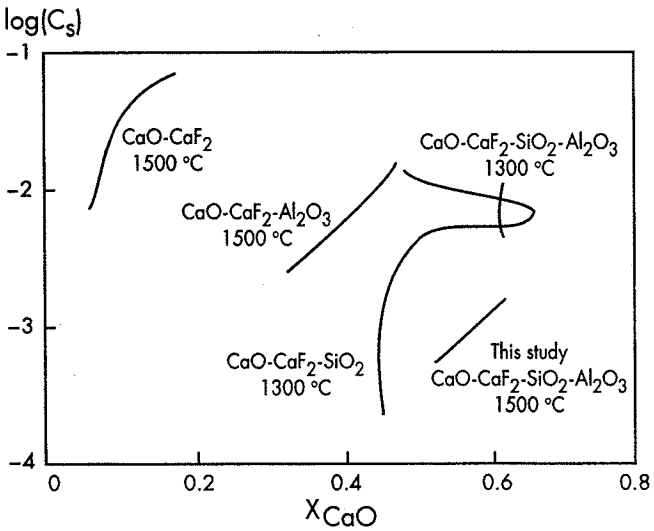


Fig. 6.10. Sulphide capacity as a function of the composition in various CaF_2-CaO based systems [31]: CaO-CaF_2 [32], CaO-CaF_2-Al_2O_3 [32], CaO-CaF_2-SiO_2 [33], CaO-CaF_2-SiO_2-Al_2O_3 [34]

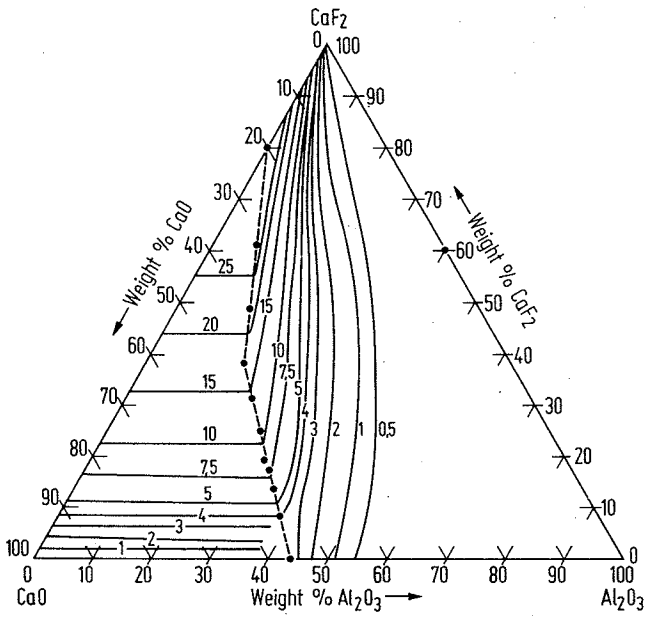


Fig. 6.11. Sulphide capacity values in the Al_2O_3-CaF_2-CaO system at 1500 °C [32]. The number on each curve indicate the capacity value times 10^3

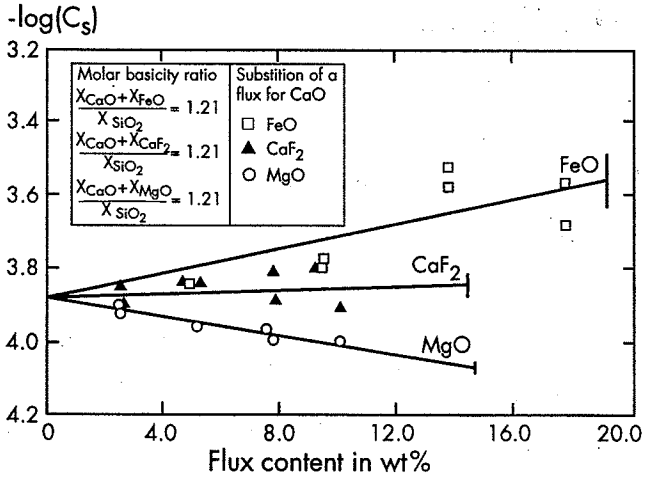


Fig. 6.12. Effect of CaF_2 (FeO and MgO) additions on the sulphide capacities in the binary CaO-SiO_2 at 1503 °C [40]

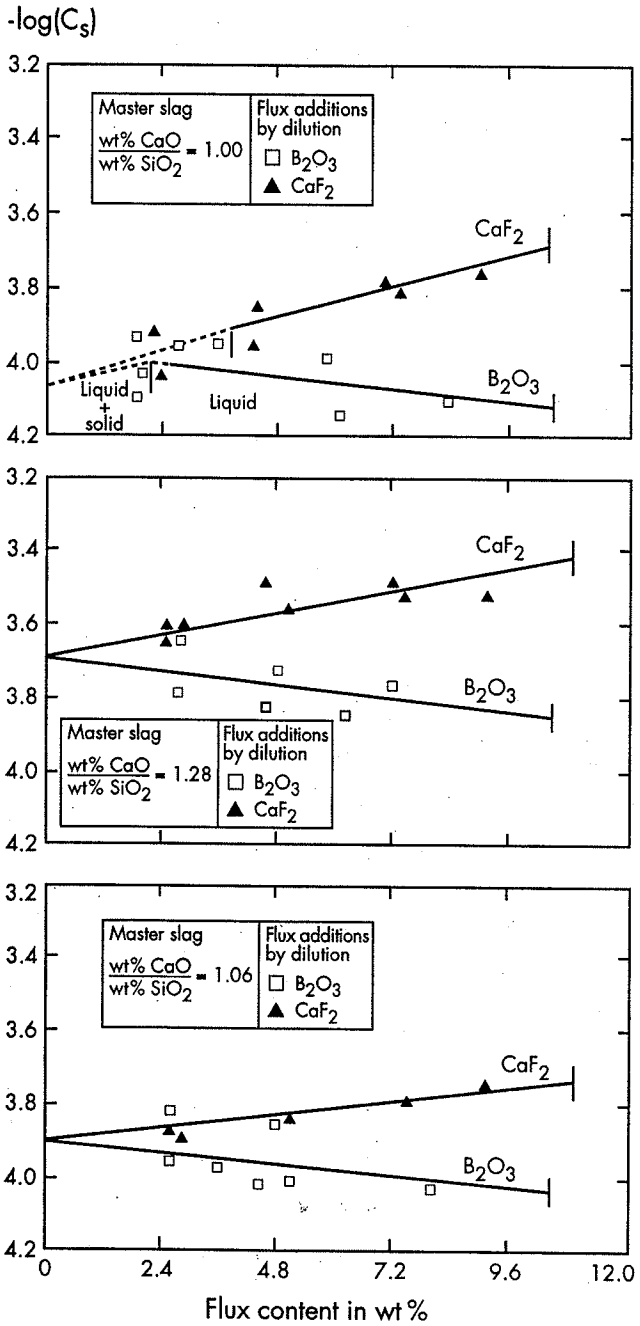


Fig. 6.13. Effect of CaF_2 (and B_2O_3) on the sulphide capacities in the binary CaO-SiO_2 at 1503 °C for various wt % CaO/wt % SiO_2 ratios [41]

6.1.4.2 Na_2O bearing systems

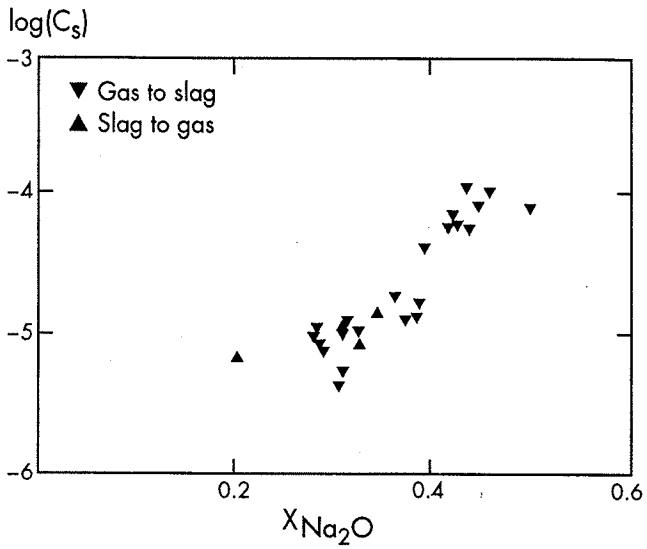


Fig. 6.14. Sulphide capacity values in the Na_2O-SiO_2 system at 1200 °C [37]

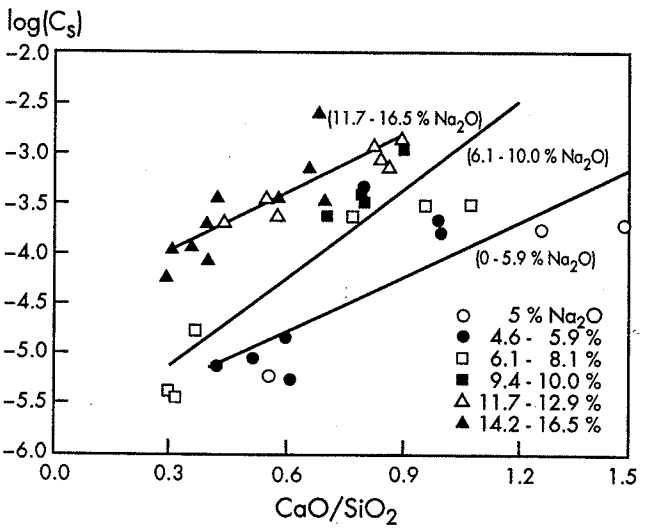


Fig. 6.15. Effect of Na_2O on sulphide capacity in the CaO-Na_2O-SiO_2 system at 1400 °C [38]

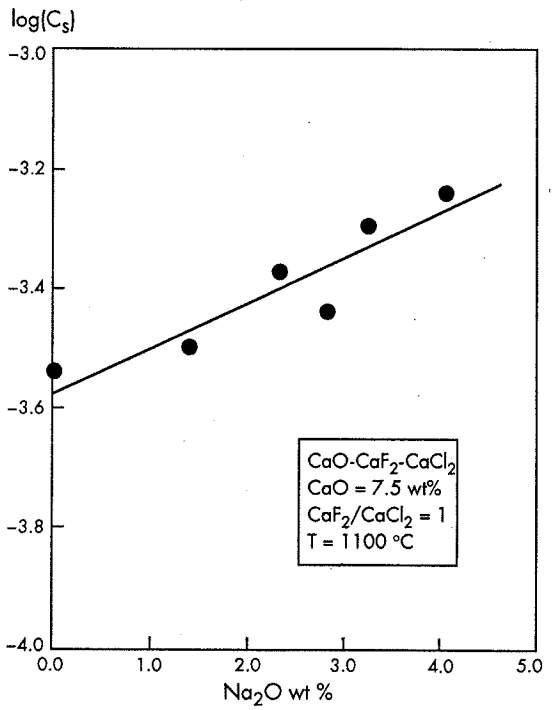


Fig. 6.16. Effect of small additions of Na_2O on the sulphide capacity in the $CaCl_2$-CaF_2-CaO system [36]

6.1.4.3 P_2O_5 bearing systems

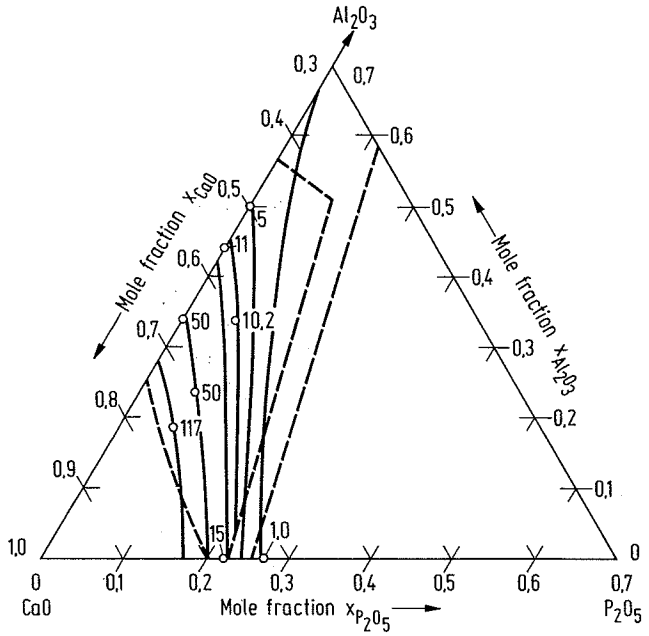


Fig. 6.17. Sulphide capacities $C_S.10^4$ in the system Al_2O_3-CaO-P_2O_5 at 1650 °C [7]

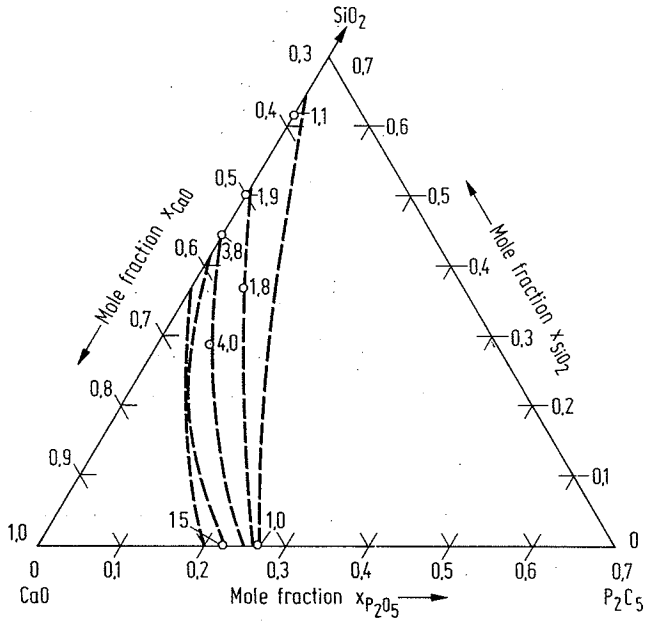


Fig. 6.18. Sulphide capacities $C_S.10^4$ in the system CaO-P_2O_5-SiO_2 at 1650 °C [7]

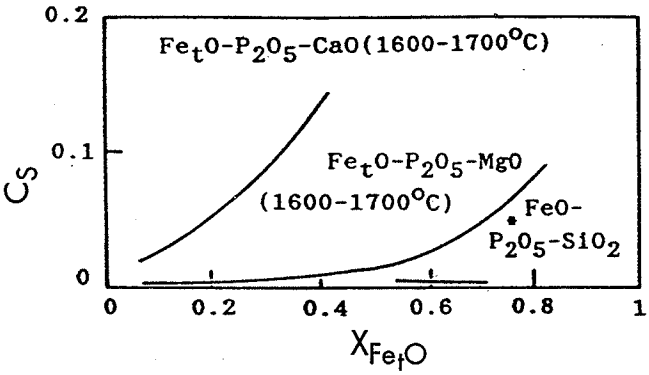


Fig. 6.19. Sulphide capacities C_S in CaO-FeO*-P_2O_5, FeO*-MgO-P_2O_5, FeO*-P_2O_5-SiO_2 slags at 1650 °C [44]
*(1400 - 1600 °C)

6.1.4.4 TiO_2 bearing systems

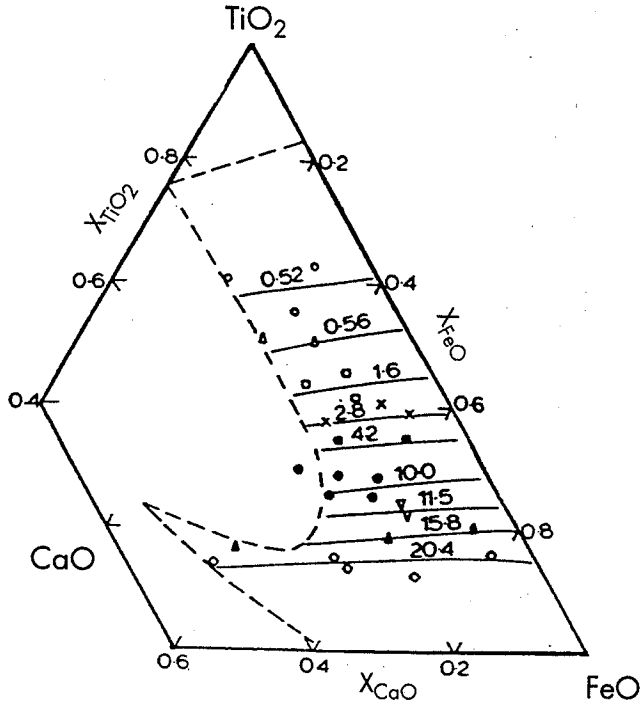


Fig. 6.20. Sulphide capacities $C_S.10^3$ in the system CaO-FeO-TiO_2 at 1500 °C ($P_{O_2} = 10^{-8}$ atm.) [42]

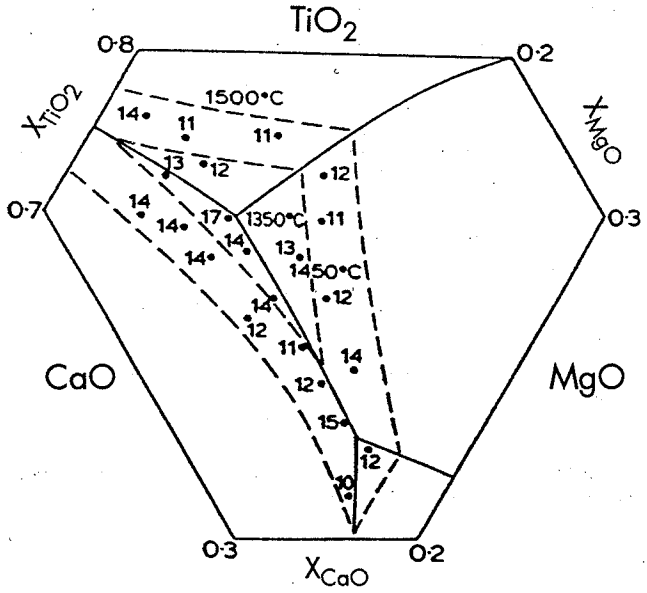


Fig. 6.21. Sulphide capacities $C_S.10^5$ in the system CaO-MgO-TiO_2 at 1500 °C ($P_{O_2} = 10^{-9}$ atm.) [43]

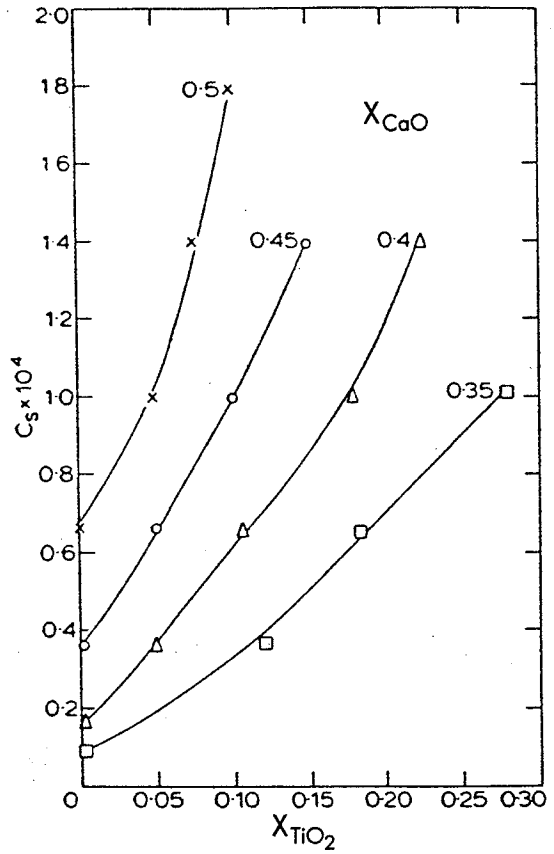


Fig. 6.22. Sulphide capacities C_S in the system $CaO\text{-}SiO_2\text{-}TiO_2$ at 1500 °C ($P_{O_2} = 10^{-9}$ atm.) [43]

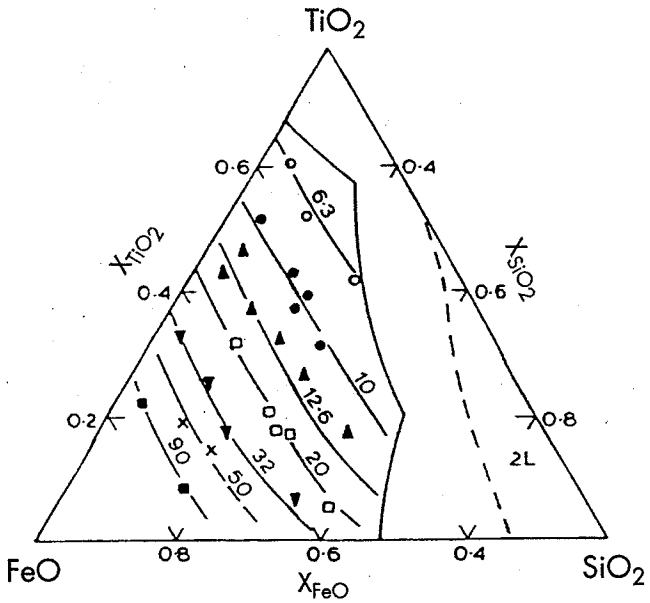


Fig. 6.23. Sulphide capacities $C_S.10^4$ in the system $FeO\text{-}SiO_2\text{-}TiO_2$ at 1500 °C ($P_{O_2} = 10^{-8}$ atm.) [42]

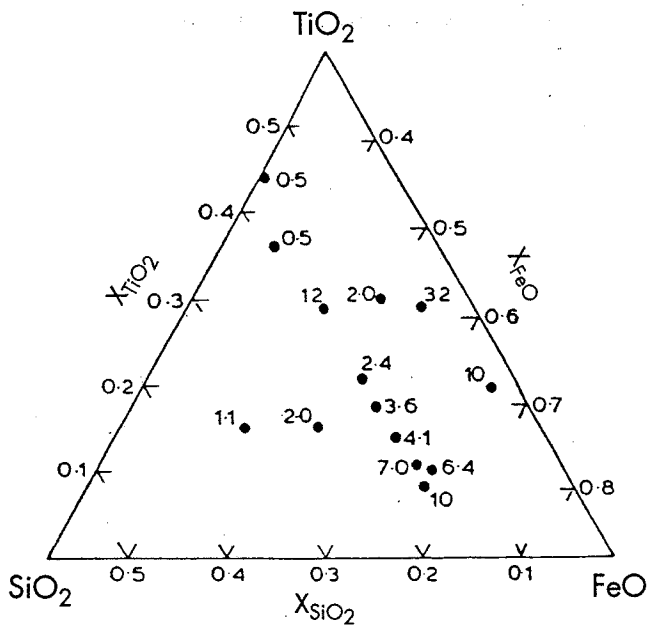


Fig. 6.24. Sulphide capacities $C_S.10^3$ in the system $CaO\text{-}FeO\text{-}SiO_2\text{-}TiO_2$ at 1500 °C and at 0.12 (±0.005) CaO mole fraction [42] ($P_{O_2} = 10^{-8}$ atm.)

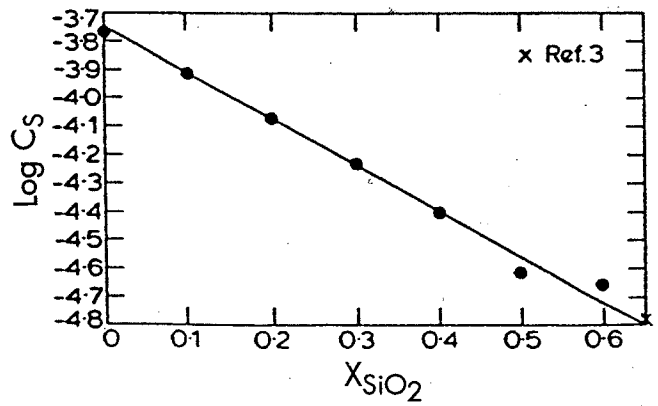


Fig. 6.25. Sulphide capacities C_S in the system $CaO\text{-}MgO\text{-}SiO_2\text{-}TiO_2$ at 1500 °C (at 0.20 CaO mole fraction and 0.15 MgO mole fraction and at $P_{O_2} = 10^{-9}$ atm.) [43]

6.1.5 Sulphur partition coefficients

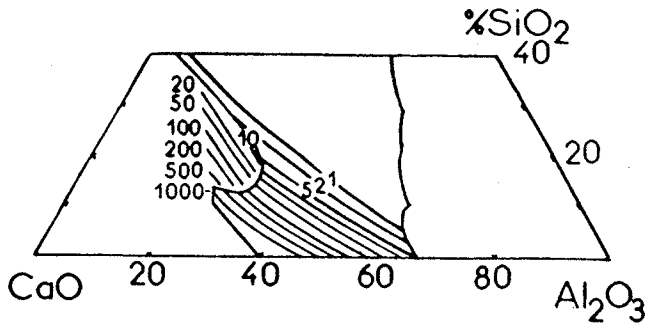


Fig. 6.26. Calculated sulphur partition coefficient between slag and metal in the system Al_2O_3-CaO-SiO_2. The oxygen activity is fixed by the equilibrium [Si]/SiO_2 with $a_{[Si]} = 0.4$

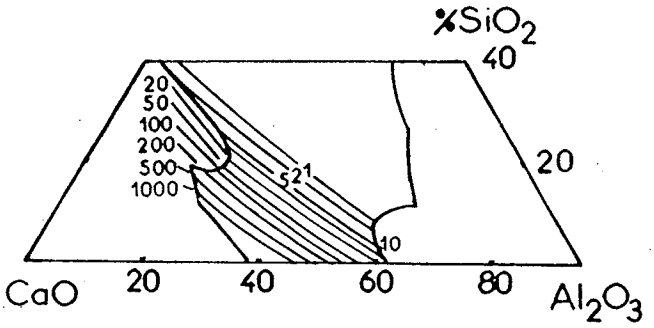


Fig. 6.27. Calculated sulphur partition coefficient between slag and metal at 1600 °C in the system Al_2O_3-CaO-SiO_2 with 5 % MgO. The oxygen activity is fixed by the equilibrium [Si]/SiO_2 with $a_{[Si]} = 0.4$

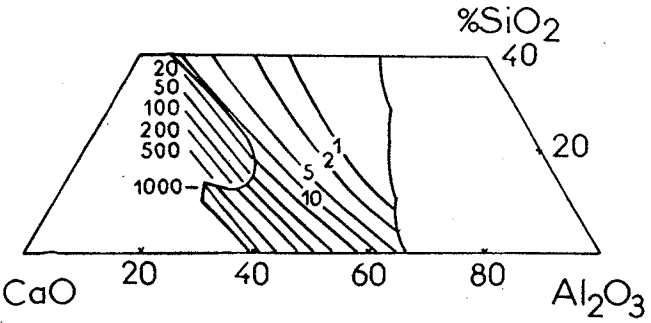


Fig. 6.28. Calculated sulphur partition coefficient between slag and metal at 1600 °C in the system Al_2O_3-CaO-SiO_2. The oxygen activity is fixed by the equilibrium [Al]/Al_2O_3 with $a_{[Al]} = 0.03$

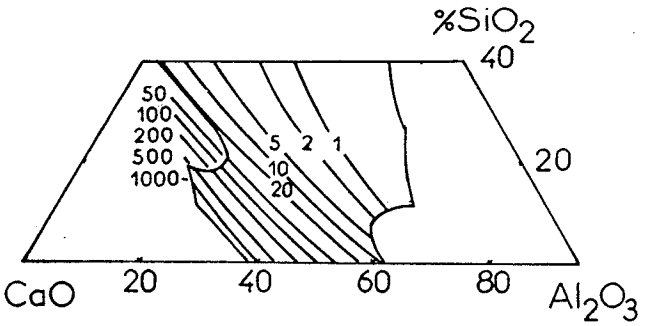


Fig. 6.29. Calculated sulphur partition coefficient between slag and metal at 1600 °C in the system Al_2O_3-CaO-SiO_2 with 5 % MgO. The oxygen activity is fixed by the equilibrium [Al]/Al_2O_3 with $a_{[Al]} = 0.03$

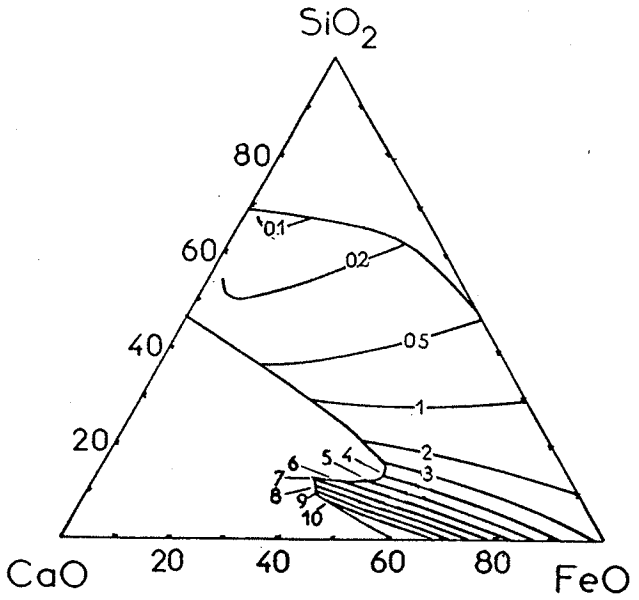


Fig. 6.30. Calculated sulphur partition coefficient between slag and metal at 1600 °C in the system CaO-FeO_n-SiO_2 in equilibrium with liquid iron

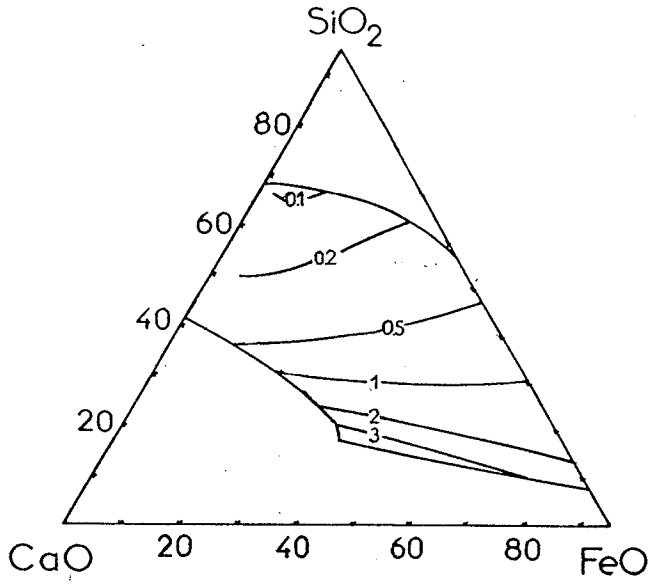


Fig. 6.31. Calculated sulphur partition coefficient between slag and metal at 1600 °C in the system CaO-FeO_n-SiO_2 with 5 % MgO in equilibrium with liquid iron

6.1.6 CaS saturation diagrams

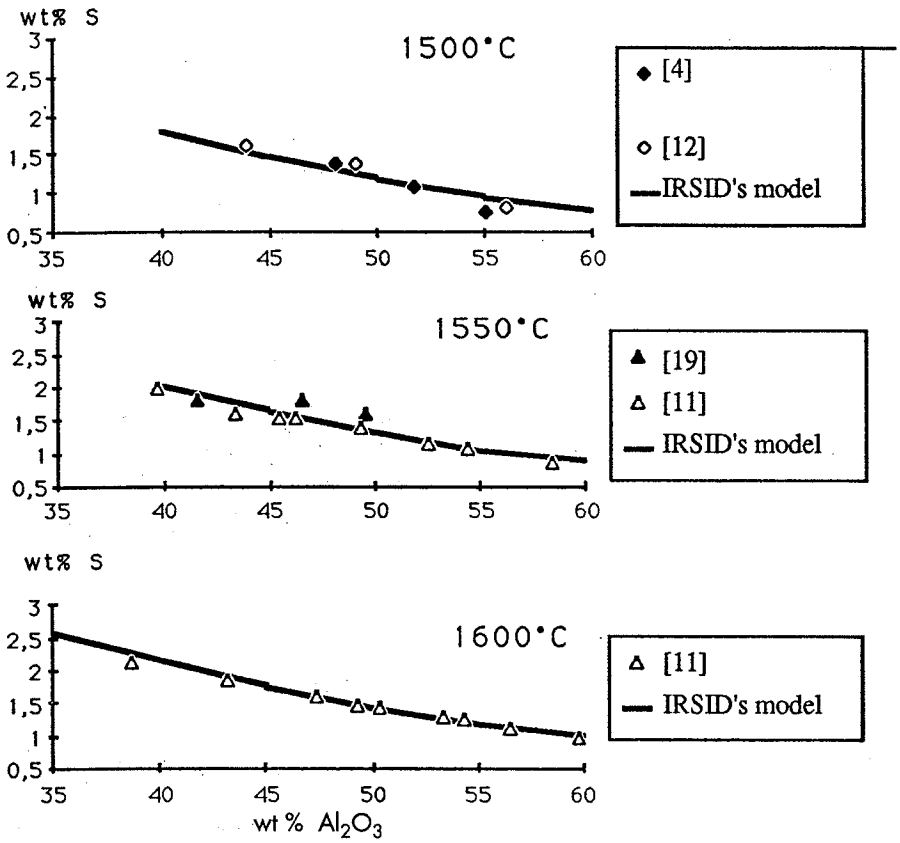


Fig. 6.32. Sulphur contents at CaS saturation on the binary Al_2O_3-CaO experimentally determined and calculated by IRSID's model

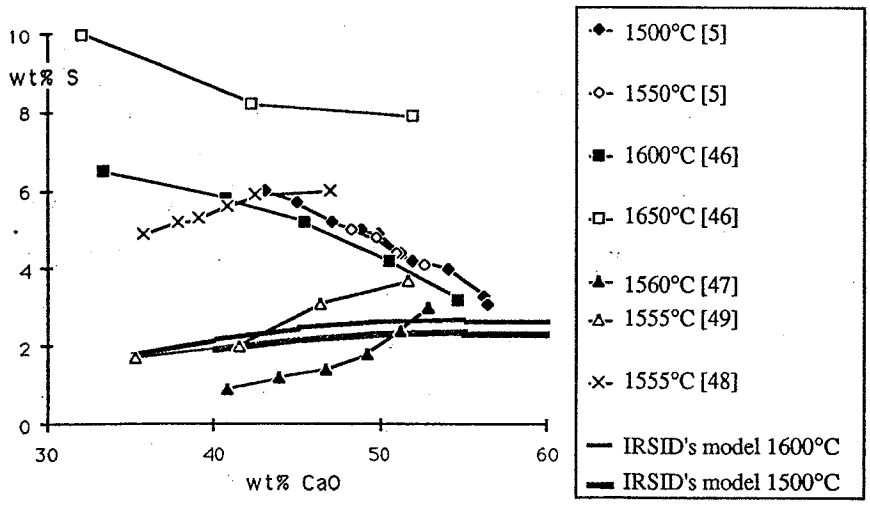


Fig. 6.33. Sulphur contents at CaS saturation on the binary CaO-SiO_2 experimentally determined and calculated by IRSID's model

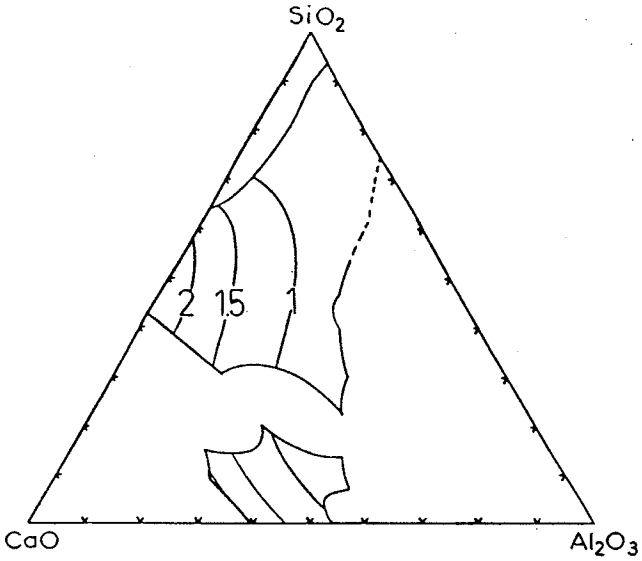


Fig. 6.34. Sulphur iso-content lines at saturation in CaS in the system Al_2O_3-CaO-SiO_2 at 1500 °C calculated by IRSID's model (in wt %)

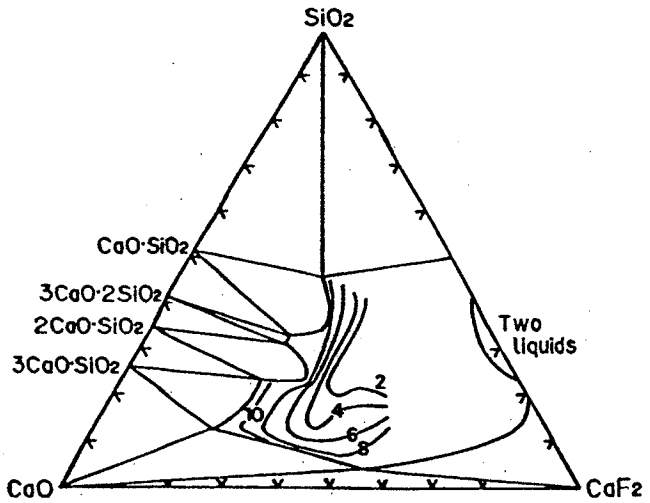


Fig. 6.35. CaS iso-solubility lines in the CaF_2-CaO-SiO_2 at 1300 °C [45] (in wt %)

6.1.7 References in Chapter 6.1

[1] Richardson, F. D.; Fincham, C. J. B.: Proc. Roy. Soc. (London) A 223 (1954), 40 – 62, and J. Iron Steel Inst. 178 (1954), 4 – 15
[2] Gaye, H.; Coulombet, D.: Comission des Communautés Européennes Rapport EUR 9428 FR
[3] Gaye, H.; Lehmann, J.: Riboud, P. V.: Welfringer, J. : Mém. Et. Sci. Rev. Mét. (1989), 237 – 244
[4] Sharma, R. A.; Richardson, F. D.: J. Iron and Steel Inst. 198 (1961), 386 – 390
[5] Sharma, R. A.; Richardson, F. D.: J. Iron and Steel Inst. 200 (1962), 373 – 379
[6] Sharma, R. A.; Richardson, F. D.: Trans. AIME 233 (1965), 1586 – 1592
[7] Abraham, K. P.; Richardson, F. D.: J. Iron and Steel Inst. 196 (1960), 313 – 317
[8] Carter, P. T.; MacFarlane, T. G.: J. Iron and Steel Inst. 185 (1957), 54 – 66
[9] Abraham, K. P.; Davies, M. W.; Richardson, F. D.: J. Iron and Steel Inst. 19 (1960), 82 – 89
[10] Kalyanram, M. R.; MacFarlane, T. G.; Bell, H. B.: J. Iron and Steel Inst. 195 (1960), 58 – 64
[11] Özturk, B., Turkdogan, E. T.: Met. Sci. 18 (1984), 299 – 309
[12] Kor, G. J. W.; Richardson, F. D.: J. Iron and Steel Inst. 206 (1968), 700 – 704
[13] Fetters, K. L.; Chipman, J.: Trans. AIME 145 (1941), 95 – 107
[14] Görl, E.; Oeters, F.; Scheel, R.: Archiv Eisenhüttenwes. 37 (1966), 441 – 451
[15] Fischer, W. A.; Spitzer, H.: Archiv Eisenhüttenwes. 29 (1958), 611 – 617
[16] Winkler, T. B.; Chipman, J.: Trans. AIME 167 (1946) 111 – 133
[17] Tsao, T.; Katayma, G.: Trans ISIJ 26 (1986), 717 – 723
[18] Venkatradi, A. S.; Bell, H. B.: J. Iron and Steel Inst. 207 (1969), 1110 – 1113
[19] Cameron, J.; Gibbons, T. B.; Taylor, J.: J. Iron and Steel Inst. 204 (1966), 1223 – 1228
[20] Grant, N. J.; Troili, O.; Chipman, J.: Trans. AIME 191 (1951) 672 – 673
[21] Grant, N. J.; Kalling, U.; Chipman, J.: Trans. AIME 191 (1951) 666 – 671
[22] Rocca, R.; Grant, N. J.; Chipman, J.: Trans. AIME 191 (1951) 319 – 326
[23] Taylor, J.; Stobo, J. J.: J. Iron and Steel Inst. 178 (1954), 360 – 367
[24] Grant, N. J.; Roberts; Chipman, J.: J. Metals 2 (1954), 145 – 149
[25] Katayama, H. G.; Tsao, T.; Matsushima, N.: Trans. ISIJ 28 (1988), 186 – 191
[26] Heinz, M.; Koch, K.; Janke, D.: Steel Res. 60 (1989), 246 – 254
[27] St. Pierre, G. R.; Chipman, J.: Trans. AIME 206 (1956), 1474 – 1483
[28] Shim, J. D.; Ban-Ya, S.: Tetsu-to-Hagane 68 (1982), 251 – 260
[29] Saint-Jours, C.: Thèse INP Grenoble (1988)
[30] Rachev, I. P.; Tsukihashi, F.; Sano, N.: Metall. Trans. B 22B (1991), 333 – 338
[31] Simeonov, S. R.; Ivanchev, I. N.; Hainadjiev, A. V.: ISIJ Intern. 31 (1991) No. 12, 1396 – 1399
[32] Kor, G. J.; Richardson, F. D.: Trans. AIME 245 (1969), 319 – 327
[33] Susaki, K.; Maeda, M.; Sano, N.: Metall. Trans. 21B (1990), 121 – 129
[34] Susaki, K.; Maeda, M.; Sano, N.: Metall. Trans. 21B (1990), 1081 – 1084
[35] Sakai, T.: CAMP-ISIJ 3 (1990), 932
[36] Simeonov, S.; Maeda, M.: CAMP-ISIJ 4 (1991), 943
[37] Rachev, I. P.; Tsukihashi, F.; Sano, N.: CAMP-ISIJ 4 (1991), 942
[38] Chan, A. H.; Fruehan, R. J.: Metall. Trans. 20B (1989), 71 – 76
[39] Chan, A. H.; Pak, J. J.; Fruehan, R. J.: 5th Int. Iron and Steel Congress, Process Technology Proc., Washington DC., Iron and Steel Society Inc., Warrendale, PA, 6 (1986), 467 – 473
[40] Bronson, A.; St. Pierre, G. R.: Metall. Trans. 12B (1981), 729 – 731
[41] Bronson, A.; St. Pierre, G. R.: Metall. Trans. 10B (1979), 375 – 380
[42] Ghita, I.; Bell, H. B.: Ironmaking and Steelmaking 9 (1982), 239 – 243
[43] Brown, S. D.; Roxburgh, R. J., Ghita, I.; Bell, H. B.: Ironmaking and Steelmaking 9 (1982), 163 – 167
[44] Nagabayashi, R.; Hino, M.; Ban-Ya, S.: Tetsu-to-Hagane 76 (1990), 183 – 190
(45] Uo, M.; Sakurai, E.; Tsukihashi, F.; Sano, N.: Steel Research 11 (1989), 496 – 502
[46] Sawamura, K.; Imaizumi, M.: Tetsu-to-Hagane 10 (1963), 1334 – 1336
[47] El Gammal, T.; Höhle, H. W.: Archiv. Eisenhüttenwes. 6 (1970), 523 – 528
[48] McCaffery, R. S.; Osterle, J. F.: Trans. AIME 63 (1923), 606
[49] Panov, A. S.; Kulikov, I. S.; Cylev, L. M.: Fiziko-chimiceskie osnovy proidzvodstva stali Moskva (1964), 100 – 106
[50] Drakaliysky, E.; Srinivasan, N. S.; Staffansson, L.-I.: Scand. J. Met. 20 (1991), 251 – 255
[51] Sosinsky, D. J.; Sommerville, I. D.: Met. Trans 17 B (1986), 331 – 337

6.2 Phosphate and phosphide capacities and phosphorus distribution

6.2.1 Phosphate capacity

The phosphate capacity C_P is derived from the dephosphorisation reaction of liquid iron with slag under oxidizing conditions. The reaction can either be described by the ionic slag model

$$\frac{1}{2}P_2\,(g) + \frac{5}{4}O_2\,(g) + \frac{3}{2}(O^{2-}) = (PO_4^{3-}) \qquad (6.1)$$

or by the molecular slag model

$$[P] + \frac{5}{2}[O] = \frac{1}{2}(P_2O_5). \qquad (6.2)$$

Phosphate capacity expressions are deduced from these dephosphorisation equations.

For the ionic slag model:

$$C_P\,(1) = \frac{\%(PO_4^{3-})}{p_{P_2}^{1/2} \cdot p_{O_2}^{5/4}} = \frac{K_{(1)}}{f(PO_4^{3-})} \cdot a^{3/2}(O^{2-})$$

and for the molecular slag model:

$$C_P\,(2) = \frac{\%(P)}{a_{[P]} \cdot a_{[O]}^{5/2}} = \frac{K_{(2)} \cdot \%(P)^{1/2}}{f_{(P_2O_5)}^{1/2}} \cdot \left(\frac{62}{142}\right)^{1/2}$$

Both of these C_P expressions are used in the diagrams compiled in section 6.2.5.

As far as the ionic slag model is concerned (6.1), the dissociation of the different slag components was assumed in the following way:

$Al_2O_3 + O^{2-} = 2\,AlO_2^-$

$B_2O_3 + 3\,O^{2-} = 2\,BO_3^{3-}$

$BaO = Ba^{2+} + O^{2-}$

$BaF_2 = Ba^{2+} + 2\,F^-$

$CaO = Ca^{2+} + O^{2-}$

$CaF_2 = Ca^{2+} + 2\,F^-$

$Cr_2O_3 + O^{2-} = 2\,CrO_2^-$

$FeO = Fe^{2+} + O^{2-}$

$Fe_2O_3 + O^{2-} = 2\,FeO_2^-$

$Li_2CO_3 = 2\,Li^+ + 2\,CO_3^{2-}$

$MgO = Mg^{2+} + O^{2-}$

$Nb_2O_5 + 3\,O^{2-} = 2\,NbO_4^{3-}$

$P_2O_5 + 3\,O^{2-} = 2\,PO_4^{3-}$

$SiO_2 + 2\,O^{2-} = SiO_4^{4-}$

$\%(PO_4^{3-})$ is calculated from (example for a slag containing CaO, FeO, Fe_2O_3, SiO_2, P_2O_5)

$$n_{O2-} = n_{CaO} + n_{FeO} - n_{Fe_2O_3} - 2\,n_{SiO_2} - 3\,n_{P_2O_5}$$

$$n_{FeO_2^-} = 2\,n_{Fe_2O_3}$$

$$n_{SiO_4^{4-}} = n_{SiO_2}$$

$$n_{PO_4^{3-}} = 2\,n_{P_2O_5}$$

$$\%(PO_4^{3-}) = \frac{n_{PO_4^{3-}}\,M_{PO_4^{3-}}}{\Sigma\, n_{anion}\,M_{anion}} \cdot 100$$

P_{O_2} is calculated from $\frac{1}{2}O_2 = [O]$

$$\Delta G^\circ = -28\,000 - 0.69\,T\ (cal) \qquad [11]$$

p_{P_2} is calculated from $\frac{1}{2}P_2 = [P]$

$$\Delta G^\circ = -157\,700 + 5.4\,T\ (J) \qquad [25]$$

$\log a_{[O]}$ and $\log a_{[P]}$ are calculated from

$$\log a_{[O]} = \log(\%\,[O]) + e_O^O\,(\%\,[O]) + \sum_j e_O^j([\%j]) + \sum_j r_O^j([\%j])^2$$

$$\log a_{[P]} = \log(\%[P]) + e_P^P\,(\%\,[P]) + \sum_j e_P^j([\%j]) \quad \Sigma r_P^j\,([\%j])^2$$

$a_{[O]}$ is calculated from [C] + [O] = CO(g)

$$\Delta G^\circ = -22\,200 - 38.34\,T\ (J) \qquad [25]$$

The activities were calculated based on the data given by Sigworth and Elliott for the interaction coefficients [11].

6.2.2 Phosphide capacity

Under reducing conditions phosphorus is supposed to be in the slag in the form of Ca_3P_2 according to the following equation:

$$3\,CaO + P_2(g) = (Ca_3P_2) + \frac{3}{2}O_2.$$

Phosphide capacity is defined for dephosphorization under reducing conditions.

$$\frac{1}{2}P_2(g) + \frac{3}{2}O^{2-} = p^{3-} + \frac{3}{4}O_2(g) \qquad (6.3)$$

Phosphide capacity:

$$C_{p^{3-}} = \frac{\%(P^{3-})\,p_{O_2}^{3/4}}{p_{P_2}^{1/2}} = \frac{K_{(3)}\,a_{O^{2-}}^{3/2}}{f_{P^{3-}}}$$

There are much less papers in literature for phosphide capacity than for phosphate capacity.

6.2.3 Phosphorus distribution

Phosphorus distribution can be represented with the following equations:

$$L_P = \frac{\%(P_2O_5)}{\%[P]} \tag{6.4}$$

$$L_P = \frac{\%(P)}{\%[P]} \tag{6.5}$$

From these possibilities equation (6.5) was chosen.

6.2.4 Symbols used in the sections 6.2.5 and 6.2.6

Phosphate capacity expressions:

$$C_P(1) = \frac{\%(PO_4^{3-})}{p_{P_2}^{1/2}\, p_{O_2}^{5/4}}$$

$$C_P(2) = \frac{\%(P)}{a_{[P]}\, a_{[O]}^{5/2}}$$

Phosphide capacity:

$$C_{P^{3-}} = \frac{\%(P^{3-})\, p_{O_2}^{3/4}}{p_{P_2}^{1/2}}$$

Phosphorus distribution:

$$L_P = \frac{\%(P)}{\%\,P}$$

P_i – partial pressure of component

%[i] – weight % of component i in metal

%(i) – weight % of component i in slag

a_i – activity of component i

f_i – Henry's activity coefficient

6.2.5 Phosphate capacity and phosphorus distribution diagrams

6.2.5.1 Ternary systems

Al_2O_3-CaF_2-CaO

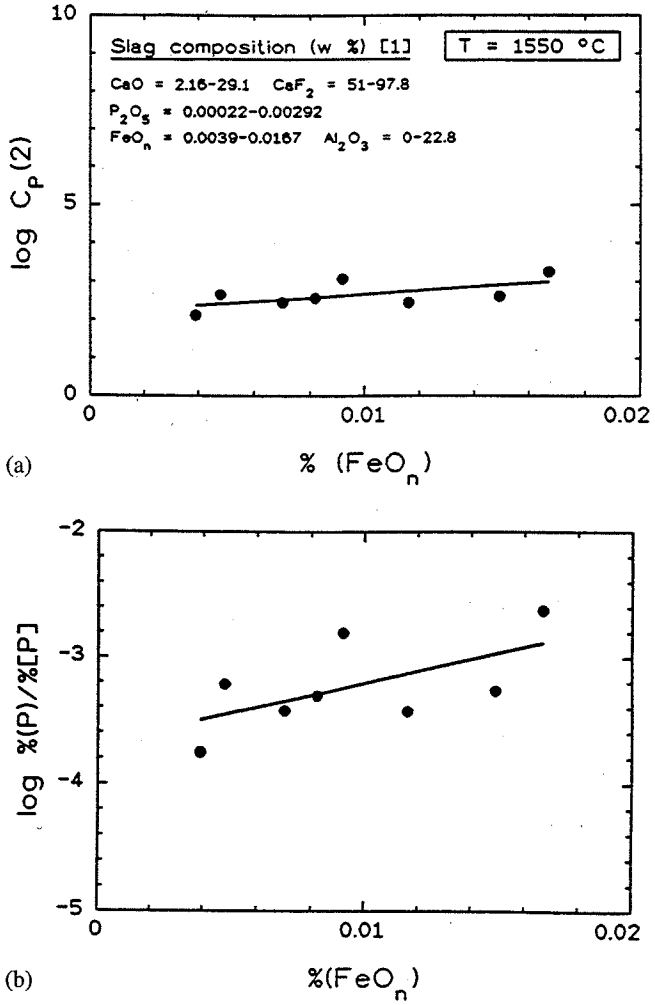
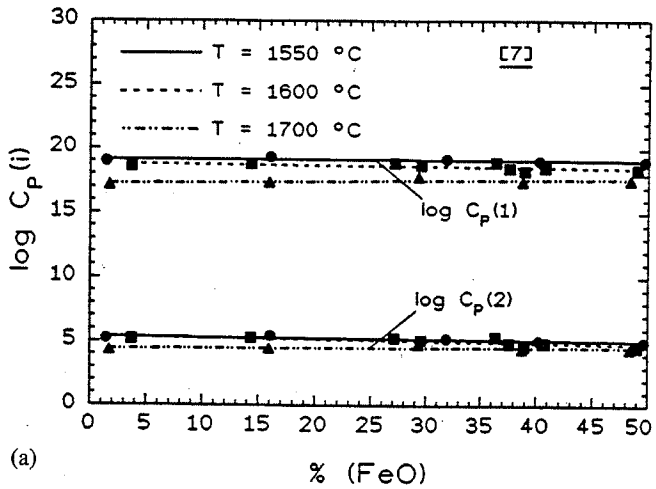
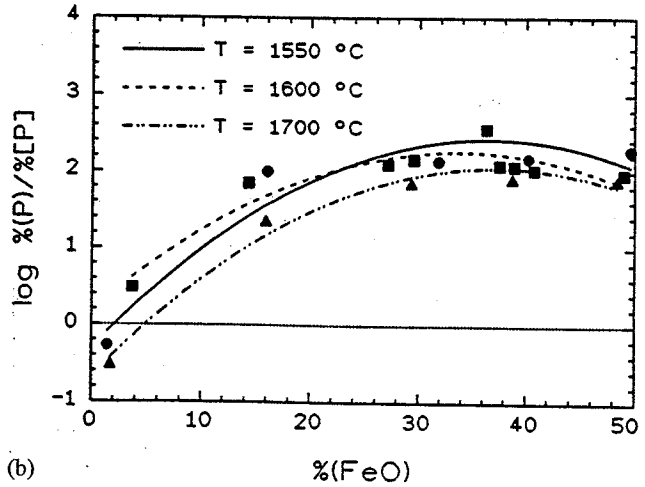


Fig. 6.36 a, b. Phosphate capacity (a) and phosphorus distribution (b) in the Al_2O_3-CaF_2-CaO system [1]

Al_2O_3-CaO-FeO



(a)



(b)

T_1 = 1550 °C — — log (P)/[P] (T_1) = 2
T_2 = 1600 °C ····· log (P)/[P] (T_2) = 2
T_3 = 1700 °C —— log (P)/[P] (T_3) = 2

(c)

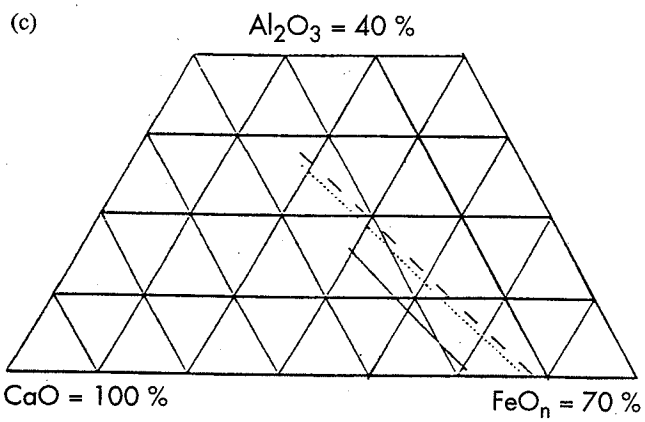
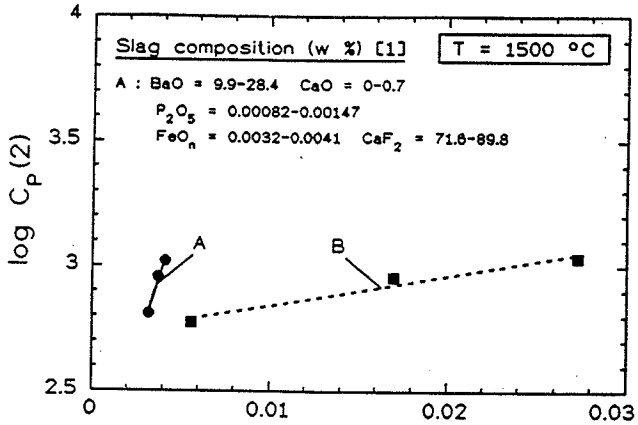


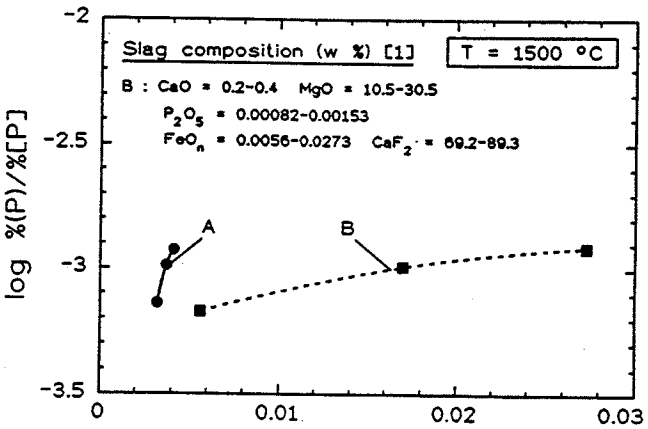
Fig. 6.37 a-c. Phosphate capacity (a) and phosphorus distribution (b, c) in the Al_2O_3-CaO-FeO_n system [7]

Slag compositions:	1550 °C	1600 °C	1700 °C
CaO:	41.3 - 57	38.5 - 55.4	47.5 - 60.5
Al_2O_3:	0 - 41.5	0 - 41.2	0 - 36.5
FeO:	1.43 - 49.62	3.7 - 49	1.71 - 48.37
Fe_2O_3:	0.09 - 7	0.4 - 21.1	0 - 4.1
P_2O_5:	0.058 - 0.41	0.19 - 1.25	0.035 - 0.38

$BaO-CaF_2$-FeO
CaF_2-FeO-MgO



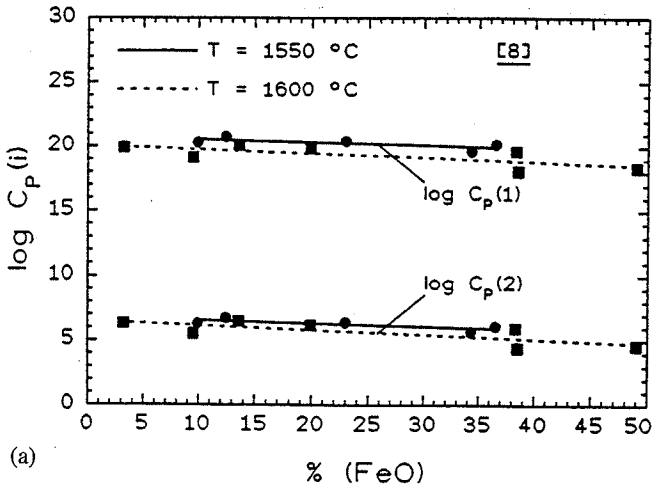
(a)

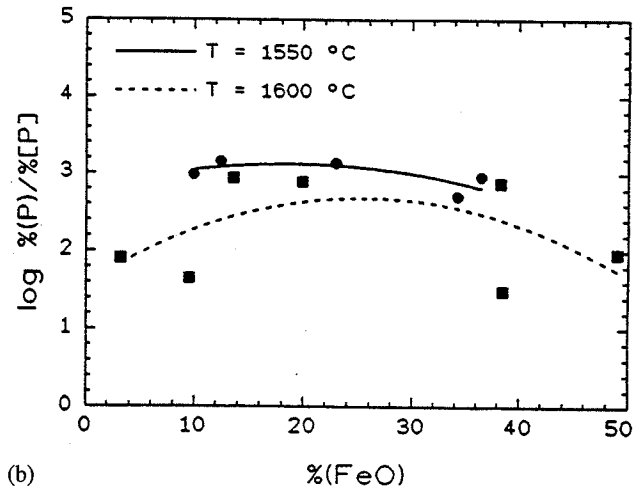


(b)

Fig. 6.38 a,b. Phosphate capacity (a) and phosphorus distribution (b) in the $BaO-CaF_2$-CaO and the CaF_2-CaO-MgO systems [1]

CaF_2-CaO-FeO





[8] T_1 = 1550 °C — log (P)/[P] (T_1) = 3
T_2 = 1600 °C -- log (P)/[P] (T_2) = 3

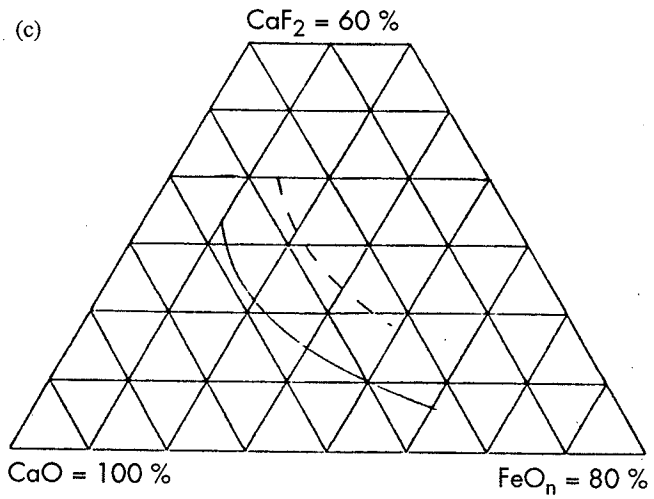
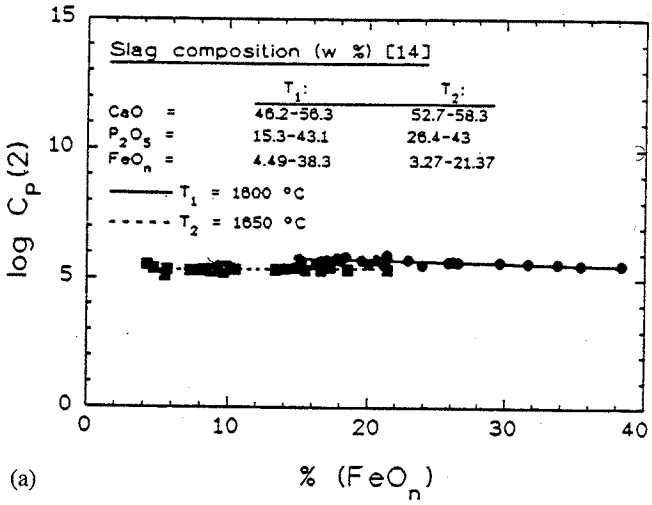
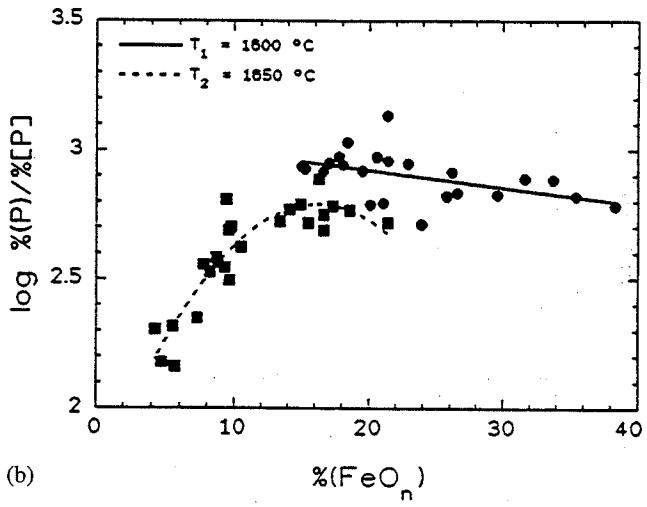


Fig. 6.39 a-c. Phosphate capacity (a) and phosphorus distribution (b, c) in the CaF_2-CaO-FeO_n system [8]

Slag compositions:	1550 °C	1600 °C
CaO:	41.6 - 57.4	42 - 47.6
CaF_2:	4.6 - 33	0 - 50.6
FeO:	9.9 - 36.49	3.2 - 49
Fe_2O_3:	0 - 16.73	0 - 6.2
P_2O_5:	0.44 - 0.83	0.3 - 0.86

CaO-FeO-P_2O_5





[14] T_1 = 1600 °C -·— log (P)/[P] (T_1) = 3
T_2 = 1650 °C --- log (P)/[P] (T_2) = 2
--- log (P)/[P] (T_2) = 3

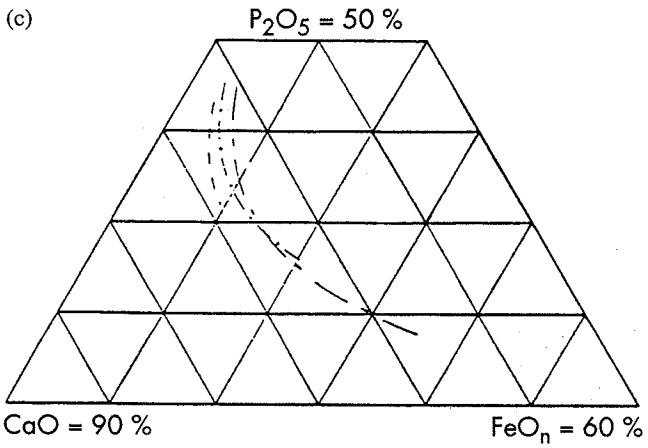
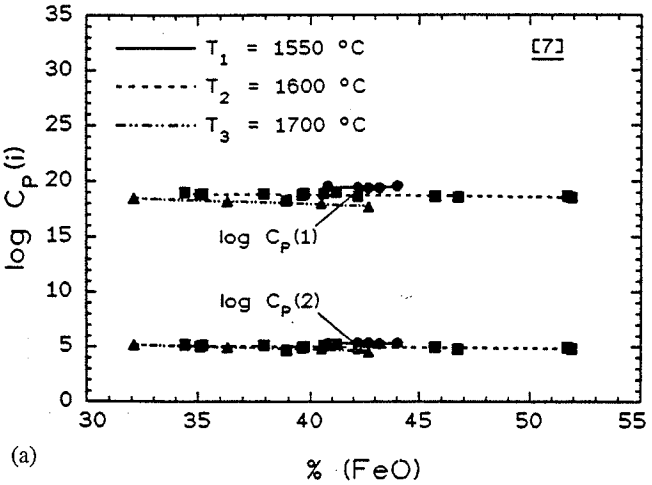
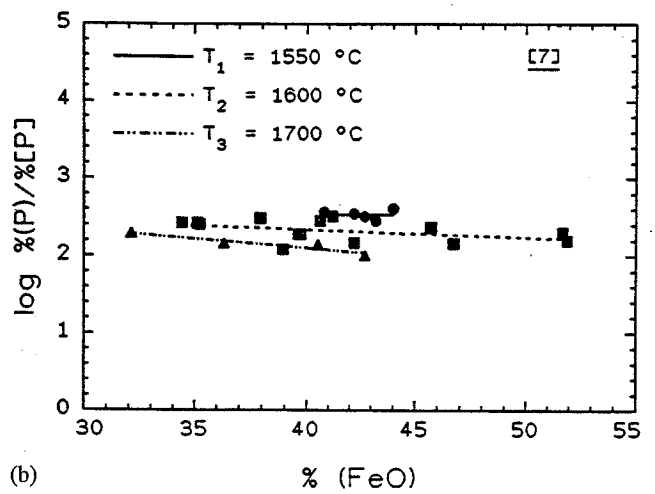


Fig. 6.40 a-c. Phosphate capacity (a) and phosphorus distribution (b, c) in the CaO-FeO_n-P_2O_5 system [14]



(a)



(b)

[7] T_1 = 1550 °C ---- log (P)/[P] (T_1) = 3
T_2 = 1600 °C – – – log (P)/[P] (T_2) = 2
T_3 = 1700 °C —— log (P)/[P] (T_3) = 2

(c)

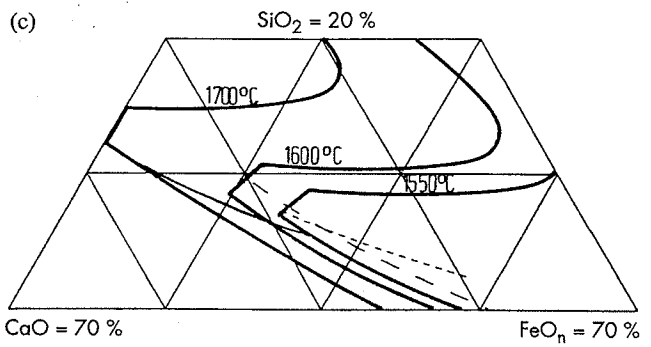
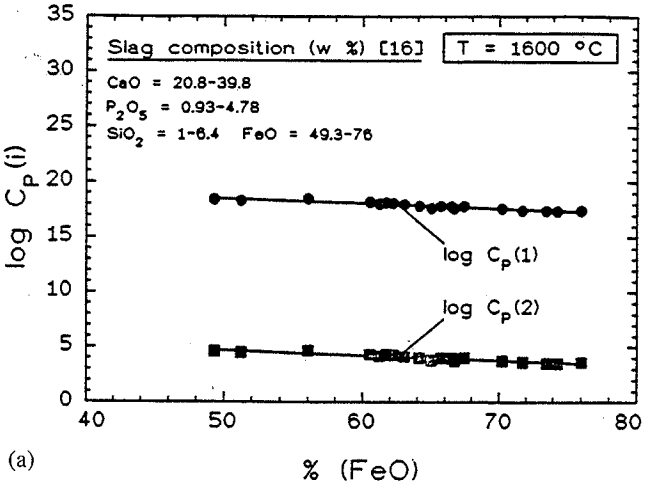
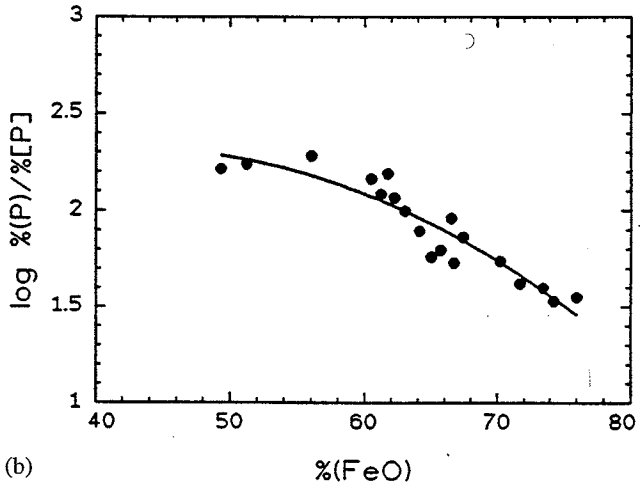


Fig. 6.41 a-c. Phosphate capacity (a) and phosphorus distribution (b, c) in the CaO-FeO_n-SiO_2 system [7]

Slag compositions:	1550 °C	1600 °C	1700 °C
CaO:	38.7 - 48.3	38.3 - 49.1	48 - 56
SiO_2:	2.29 - 7.8	0 - 9.3	4.4 - 11.3
FeO:	40.8 - 44	34.4 - 51.9	32.1 - 42.7
Fe_2O_3:	2 - 15.7	3.9 - 21.1	0 - 5.1
P_2O_5:	0.37 - 0.75	0.26 - 1.03	0.43 - 0.54



(a)



(b)

[16] T = 1600 °C – – – log (P)/[P] = 2

(c)

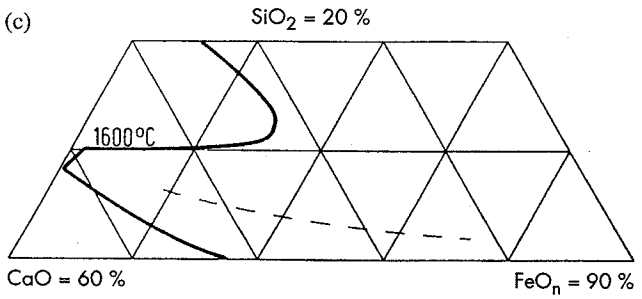


Fig. 6.42 a-c. Phosphate capacity (a) and phosphorus distribution (b, c) in the CaO-FeO_n-SiO_2 system [16]

Na_2O-P_2O_5-SiO_2

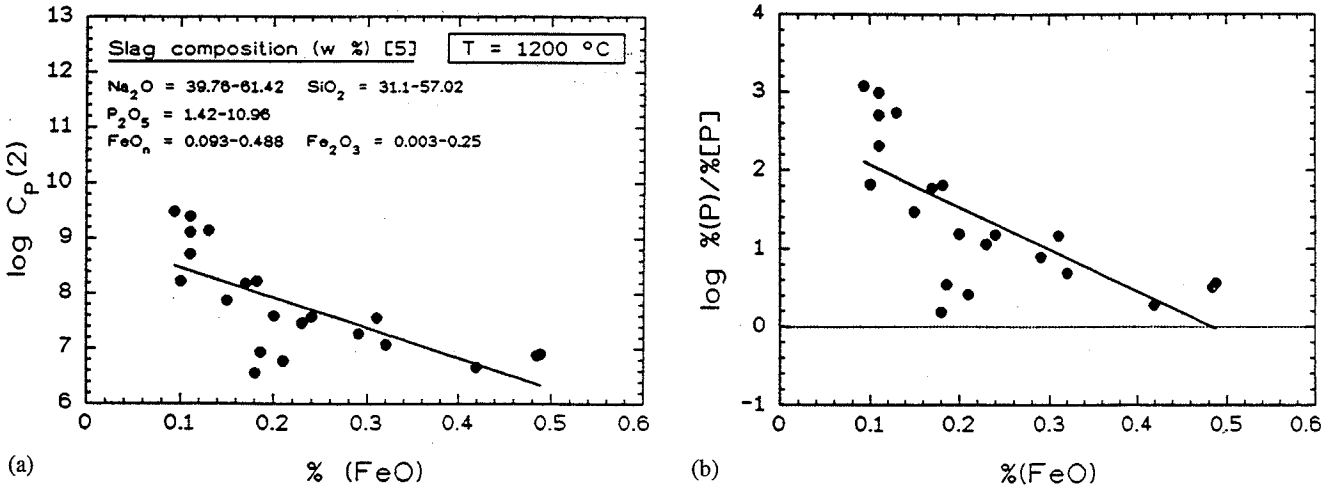


Fig. 6.43 a,b. Phosphate capacity (a) and phosphorus distribution (b) in the Na_2O-P_2O_5-SiO_2 system [5]

6.2.5.2 Quaternary systems

BaF_2-BaO-Cr_2O_3-MgO

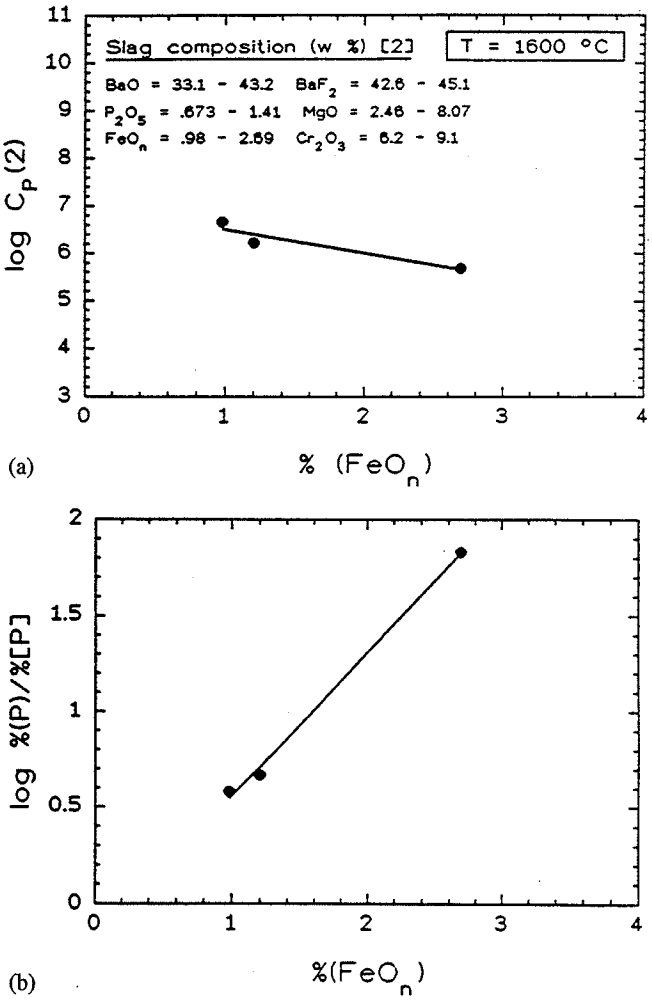


Fig. 6.44 a,b. Phosphate capacity (a) and phosphorus distribution (b) in the BaF_2-BaO-Cr_2O_3-MgO system [2]

CaO-FeO-MgO-SiO_2

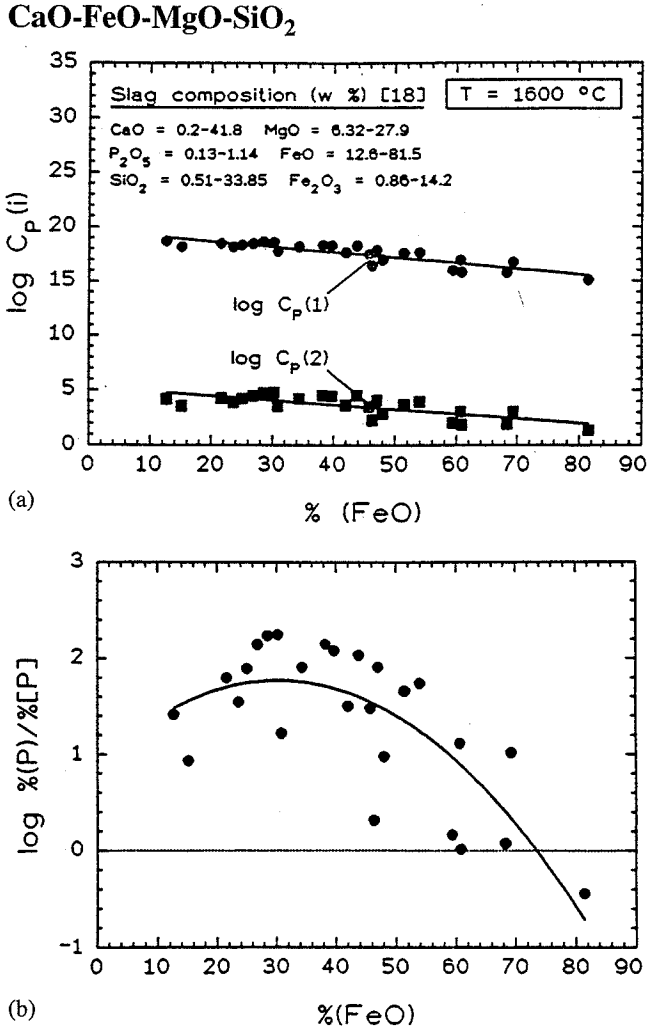


Fig. 6.45 a,b. Phosphate capacity (a) and phosphorus distribution (b) in the CaO-FeO_n-MgO-SiO_2 system [18]

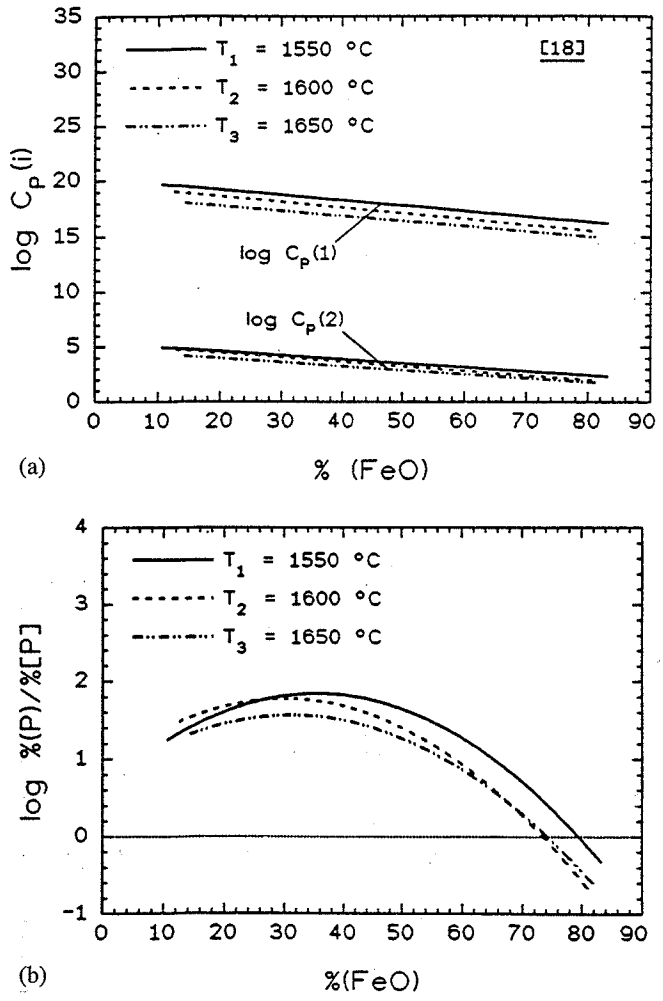


Fig. 6.46 a,b. Phosphate capacity (a) and phosphorus distribution (b) in the $CaO\text{-}FeO_n\text{-}MgO\text{-}SiO_2$ system [18]

Slag compositions:	1550 °C	1600 °C	1650 °C
CaO:	0.38 - 37.8	0.2 - 41.8	0.59 - 40.8
MgO:	5.41 - 21.4	6.32 - 27.9	5.85 - 29
SiO_2:	0.48 - 33.91	0.51 - 33.85	0.48 - 31.68
FeO:	10.6 - 83.2	12.6 - 81.5	14.3 - 81.9
Fe_2O_3:	0.6 - 10.6	0.86 - 14.2	1.19 - 11.9
P_2O_5:	0.149 - 0.963	0.13 - 1.14	0.118 - 0.927

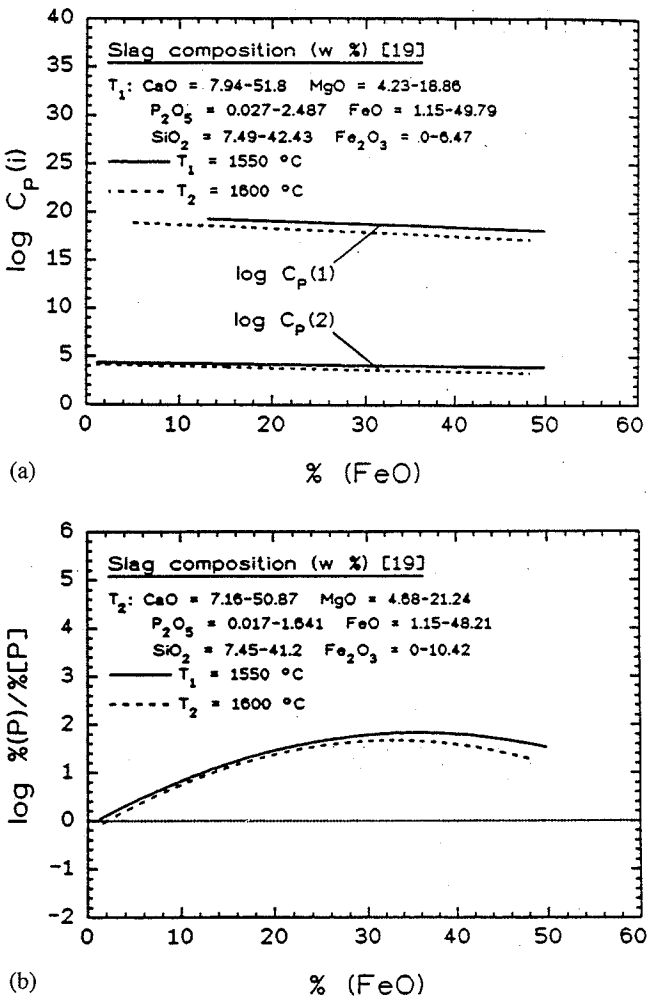


Fig. 6.47 a,b. Phosphate capacity (a) and phosphorus distribution (b) in the $CaO\text{-}FeO_n\text{-}MgO\text{-}SiO_2$ system [19]

$CaO\text{-}FeO\text{-}P_2O_5\text{-}SiO_2$

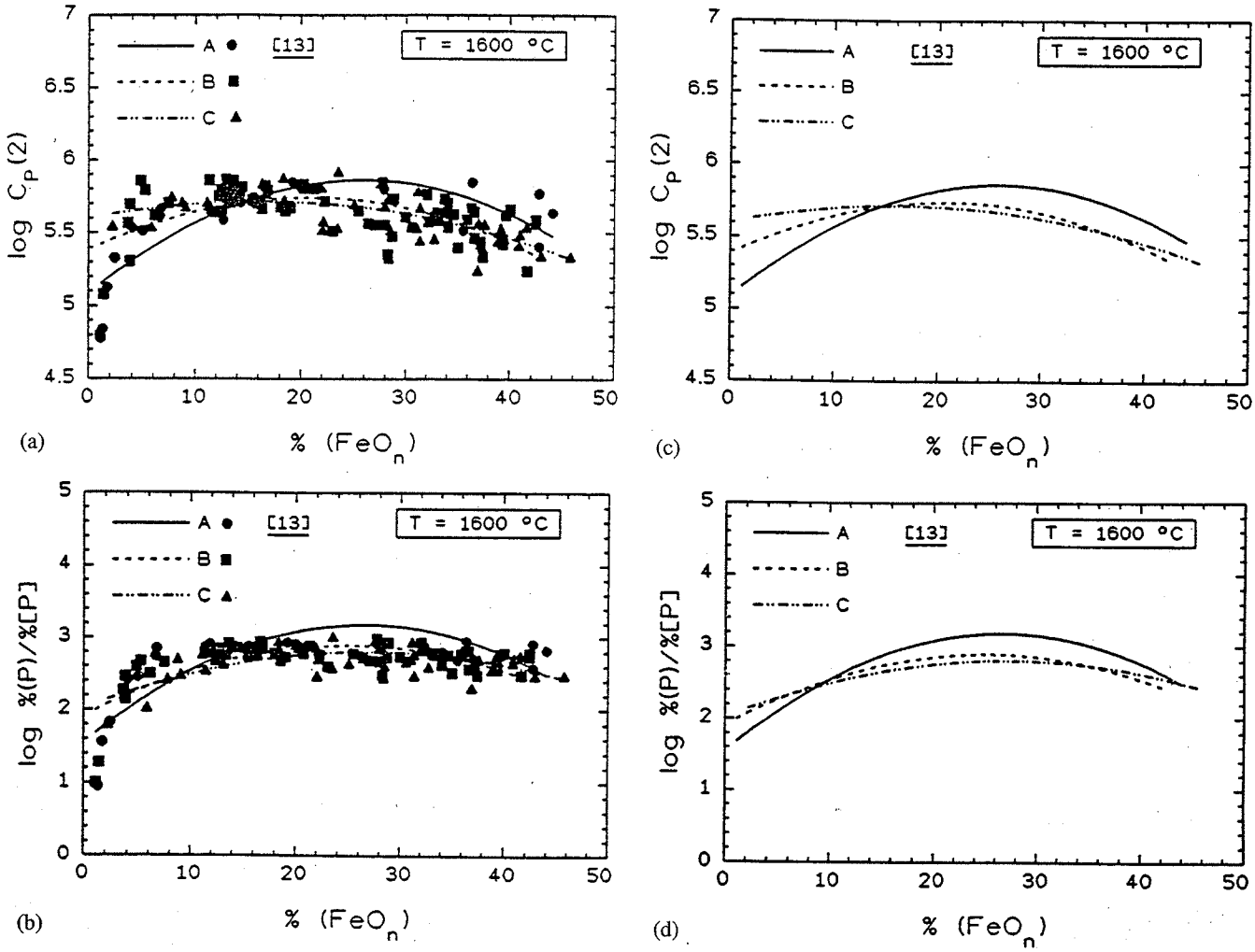


Fig. 6.48 a-d. Phosphate capacity (a, c) and phosphorus distribution (b, d) in the $CaO\text{-}FeO_n\text{-}P_2O_5$ (A), $CaO\text{-}FeO_n\text{-}P_2O_5\text{-}SiO_2$ (B) and $CaO\text{-}FeO_n\text{-}MnO\text{-}P_2O_5$ (C) systems [13]

Slag compositions:	A	B	C
CaO:	43.7 - 57.5	46.4 - 58.4	38.1 - 55.6
MnO:	-	-	0.75 - 15.4
SiO_2:	-	0.72 - 6.85	-
FeO_n:	1.1 - 44	1.1 - 42.4	2.2 - 45.7
P_2O_5:	10.8 - 42.2	6.3 - 40.5	7.7 - 40

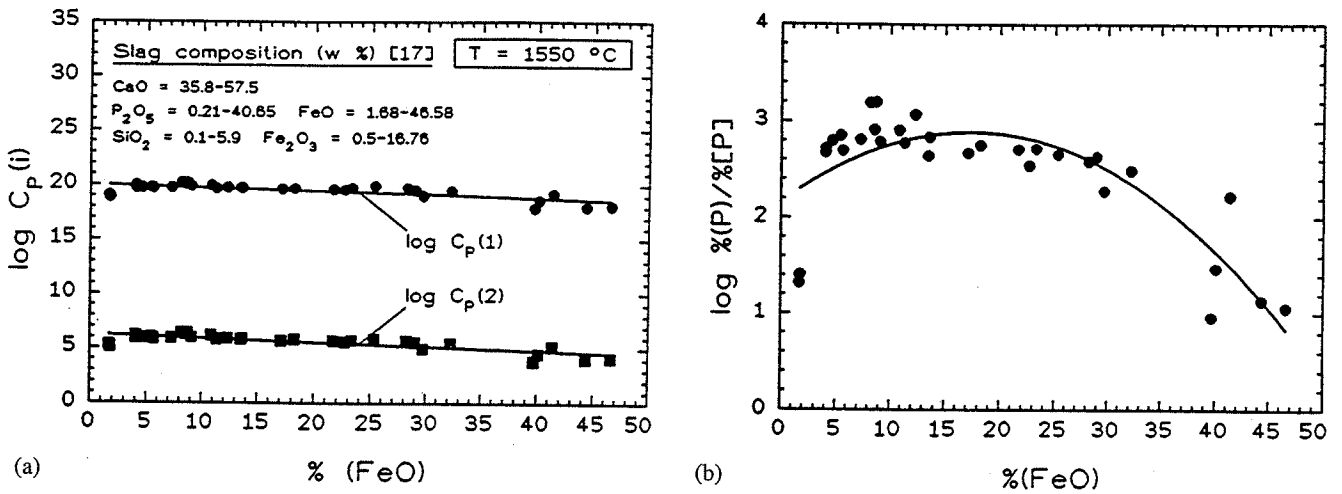


Fig. 6.49 a,b. Phosphate capacity (a) and phosphorus distribution (b) in the $CaO\text{-}FeO_n\text{-}P_2O_5\text{-}SiO_2$ system [17]

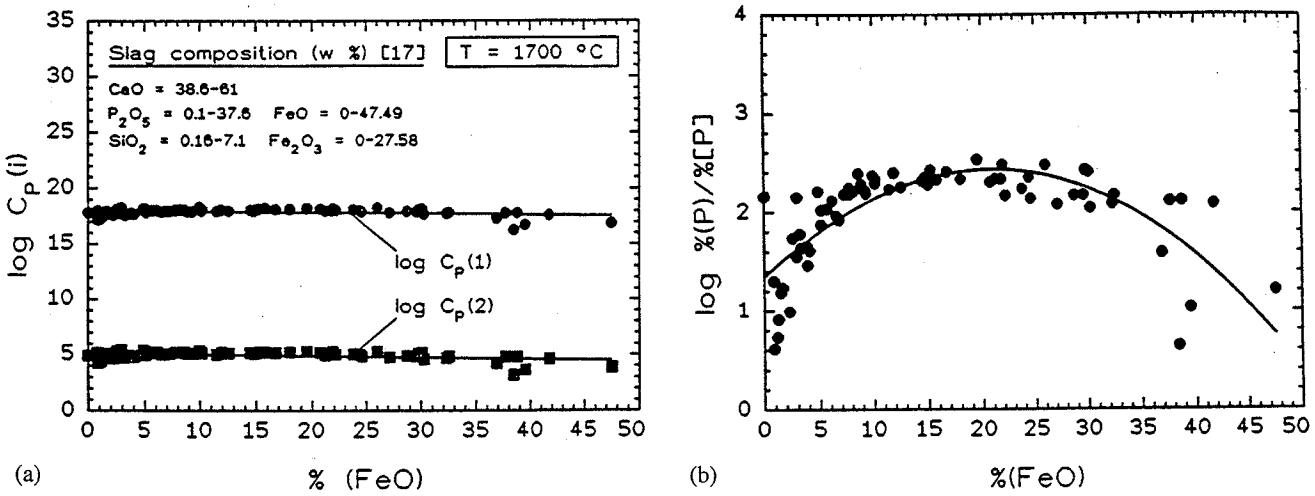


Fig. 6.50 a,b. Phosphate capacity (a) and phosphorus distribution (b) in the $CaO\text{-}FeO_n\text{-}P_2O_5\text{-}SiO_2$ system [17]

$FeO\text{-}MgO\text{-}Na_2O\text{-}SiO_2$

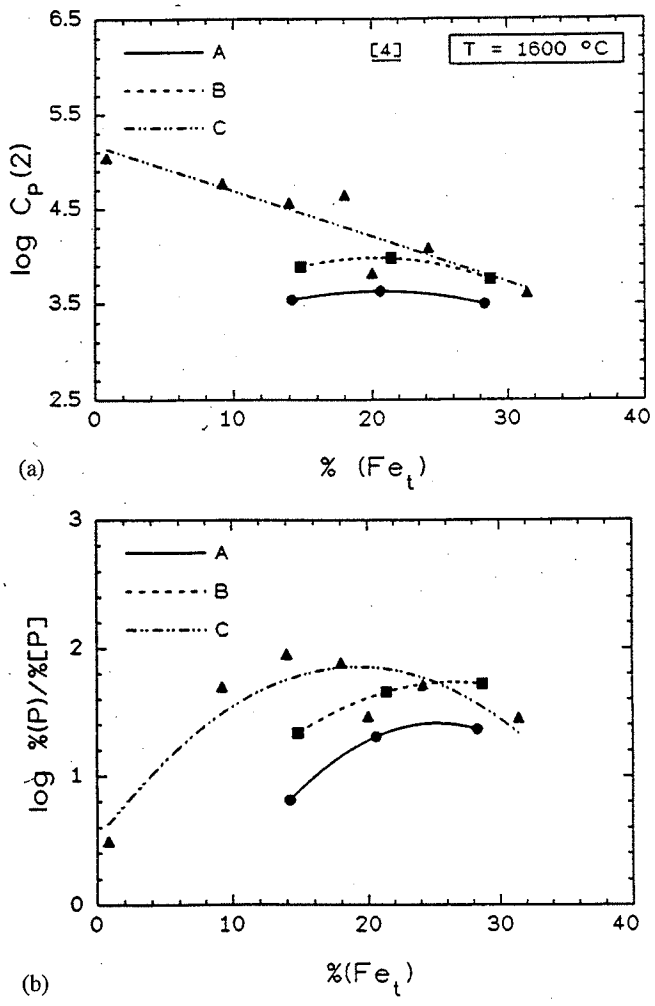


Fig. 6.51 a,b. Phosphate capacity (a) and phosphorus distribution (b) in the $FeO_n\text{-}MgO\text{-}Na_2O\text{-}SiO_2$ system [4]

Slag compositions:	A	B	C
MgO:	16.5 - 23.6	13.5 - 19.6	12.9 - 15.7
Na_2O:	13.2 - 16.9	17.0 - 21.3	19.8 - 36.3
SiO_2:	29.1 - 39.2	27.8 - 37.1	23.4 - 40.0
Fe_t:	14.2 - 28.3	14.8 - 28.7	0.8 - 31.4
P_2O_5:	0.83 - 1.23	1.14 - 1.45	0.43 - 3.11

6.2.5.3 Systems with five and more components

$Al_2O_3\text{-}CaF_2\text{-}CaO\text{-}Cr_2O_3\text{-}FeO\text{-}Li_2CO_3\text{-}MgO\text{-}SiO_2$

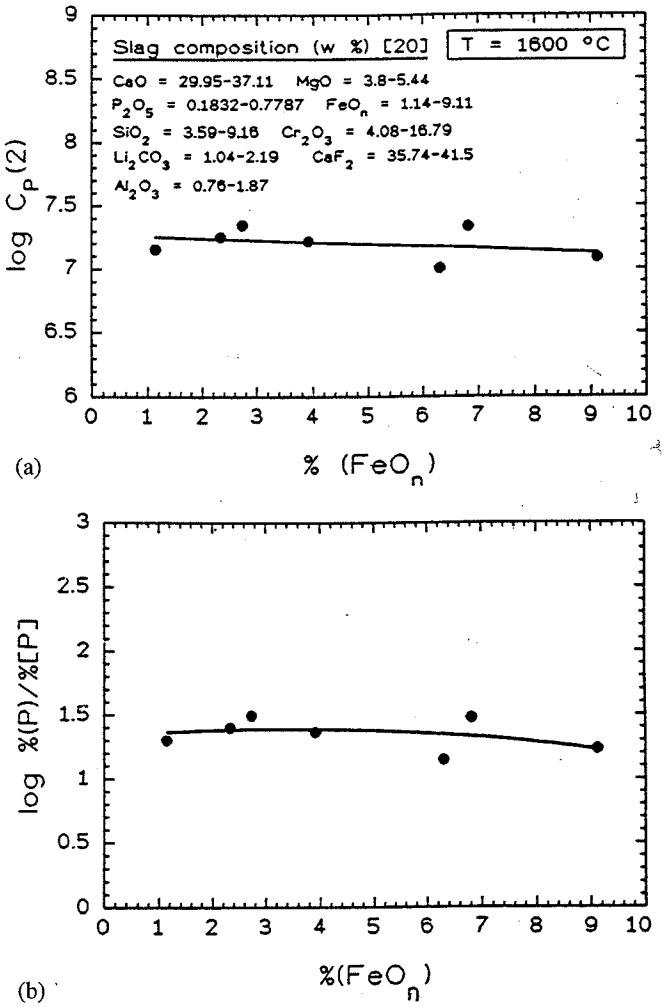


Fig. 6.52 a,b. Phosphate capacity (a) and phosphorus distribution (b) in the $Al_2O_3\text{-}CaF_2\text{-}CaO\text{-}Cr_2O_3\text{-}FeO_n\text{-}Li_2CO_3\text{-}MgO\text{-}SiO_2$ system [20]

Al_2O_3-CaF_2-CaO-FeO-MgO-MnO-P_2O_5-SiO_2

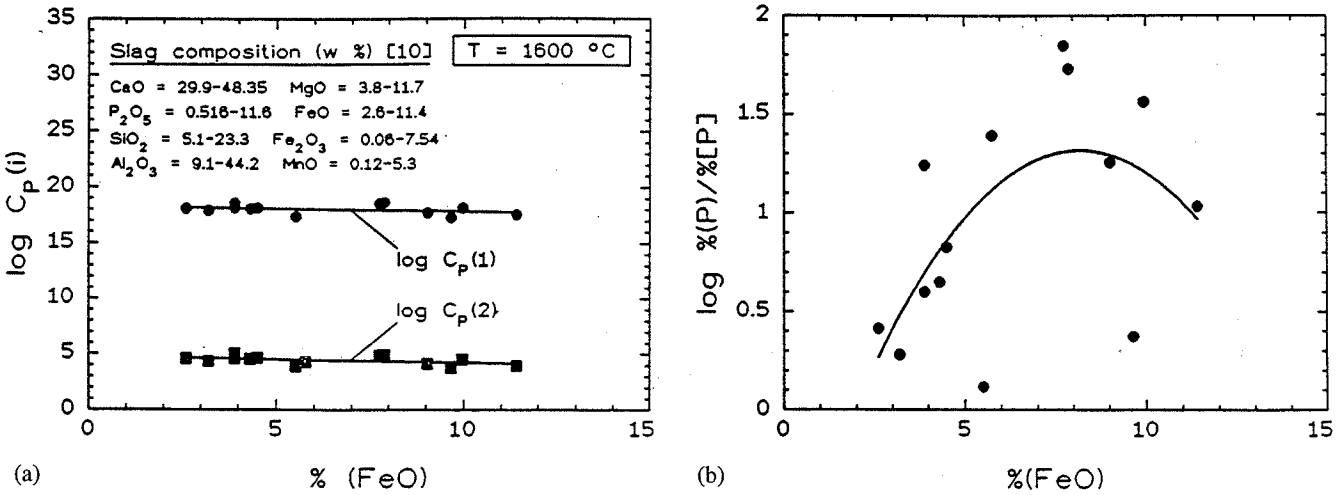


Fig. 6.53 a,b. Phosphate capacity (a) and phosphorus distribution (b) in the Al_2O_3-CaF_2-CaO-FeO_n-MgO-MnO-P_2O_5-SiO_2 system [10]

Al_2O_3-CaO-FeO-MgO-P_2O_5-SiO_2

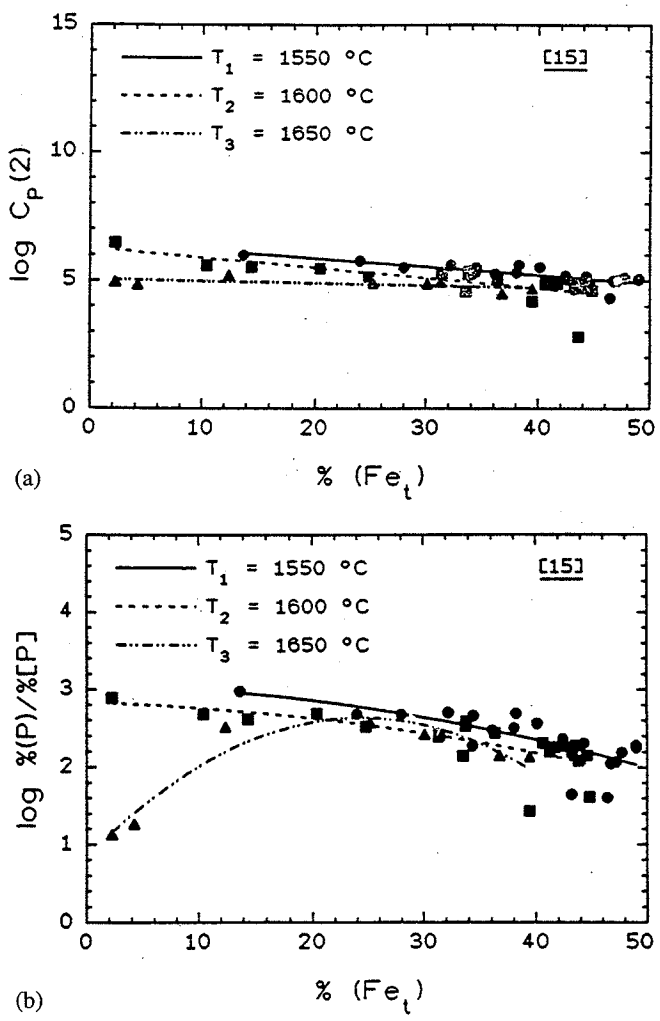


Fig. 6.54 a,b. Phosphate capacity (a) and phosphorus distribution (b) in the Al_2O_3-CaO-FeO_n-MgO-P_2O_5-SiO_2 system [15]

Slag compositions:	1550 °C	1600 °C	1650 °C
CaO:	26.8 - 46.6	32.7 - 57.7	41.8 - 59.3
MgO:	0 - 4.23	0 - 7.99	0 - 0.8
SiO_2:	0.46 - 4.87	0.61 - 5.33	0.69 - 2.71
Al_2O_3:	0 - 3.34	0 - 3.9	0 - 1.44
Fe_t:	13.7 - 49	2.22 - 44.8	2.21 - 39.4
P_2O_5:	0.28 - 15.3	0.25 - 37.6	5.34 - 35.3

B_2O_3-CaO-FeO-MgO-MnO-P_2O_5-SiO_2

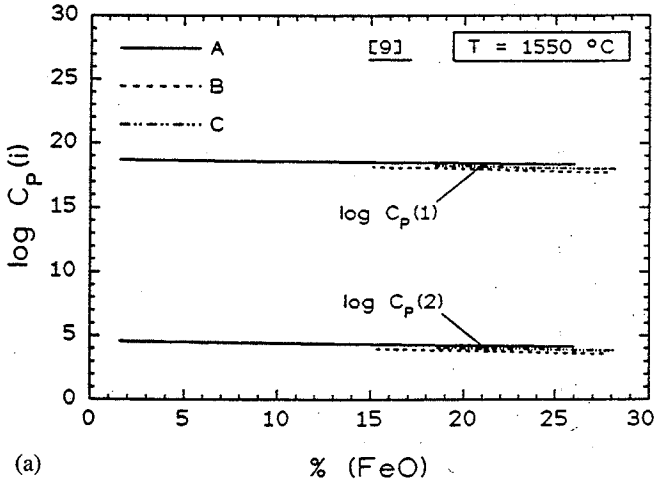


Fig. 6.55. Phosphate capacity in the CaO-FeO_n-MgO-P_2O_5-SiO_2 (A), B_2O_3-CaO-FeO_n-MgO-P_2O_5-SiO_2 (B) and CaO-FeO_n-MgO-MnO-P_2O_5-SiO_2 (C) systems [9]

Slag compositions:	A	B	C
CaO:	31.51 - 44.82	28.66 - 41.55	29.91 - 38.49
MgO:	5.94 - 13.3	8.8 - 14.12	7.05 - 10.54
MnO:	-	-	2.41 - 6.9
SiO_2:	14.45 - 28.92	17.01 - 23.04	14.14 - 2.79
B_2O_3:	-	3.09 - 3.49	-
FeO:	1.61 - 25.98	15.07 - 27.82	18.41 - 28.21
Fe_2O_3	2.4 - 24.32	4.4 - 6.98	7.07 - 12.17
P_2O_5:	4.78 - 9.76	4.3 - 5.44	3.83 - 4.95

$BaO\text{-}CaO\text{-}FeO\text{-}MgO\text{-}SiO_2$

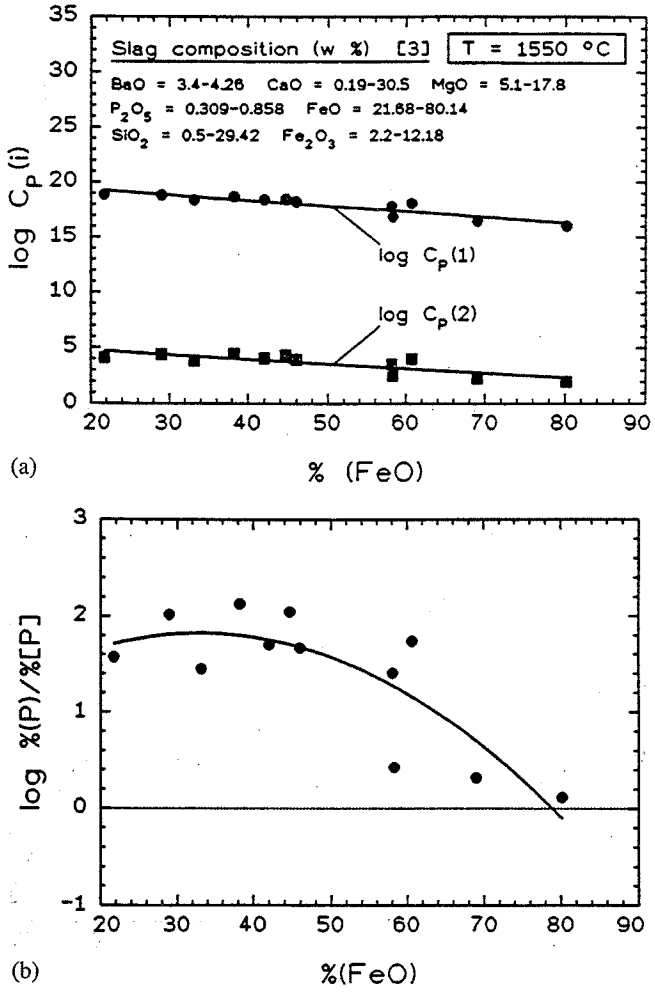


Fig. 6.56 a,b. Phosphate capacity (a) and phosphorus distribution (b) in the $BaO\text{-}CaO\text{-}FeO_n\text{-}MgO\text{-}SiO_2$ system [3]

$CaF_2\text{-}CaO\text{-}FeO\text{-}MgO\text{-}SiO_2$

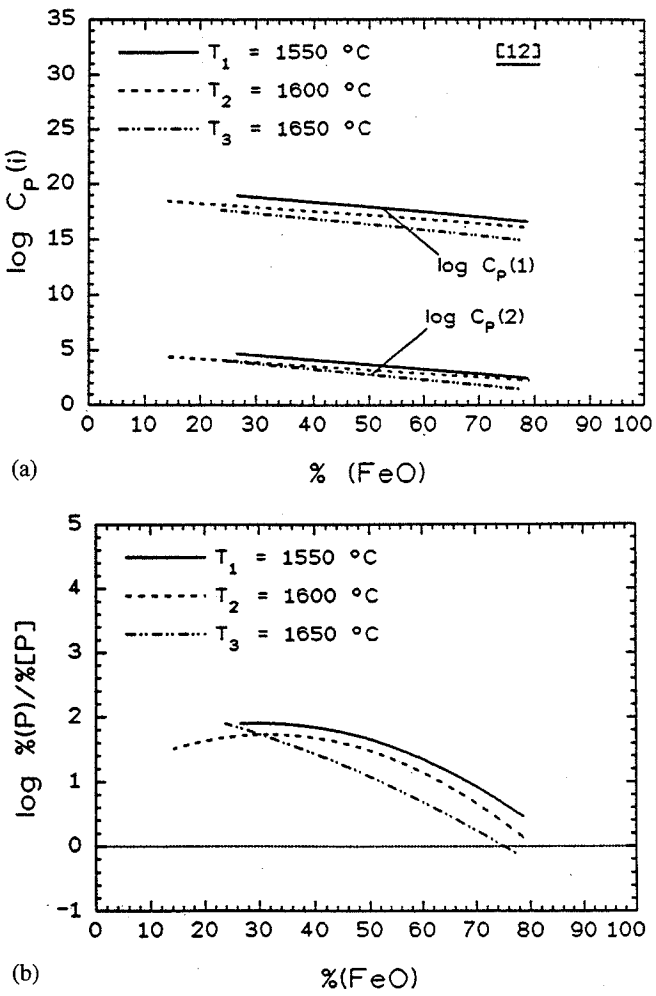


Fig. 6.57 a,b. Phosphate capacity (a) and phosphorus distribution (b) in the $CaF_2\text{-}CaO\text{-}FeO_n\text{-}MgO\text{-}SiO_2$ system [12]

Slag compositions:	1550 °C	1600 °C	1650 °C
CaO:	1.58 - 32.3	1.11 - 35.71	1.49 - 34.86
MgO:	6.06 - 21.65	8.14 - 26.67	8.97 - 25.3
SiO_2:	0.43 - 25.57	0.36 - 32.96	0.53 - 24.34
CaF_2:	1.12 - 3.87	1.04 - 3.66	1.44 - 3.14
FeO:	26.62 - 78.68	14.15 - 79.03	23.74 - 77.37
Fe_2O_3:	2.83 - 11.7	0.99 - 12.39	2.44 - 9.95
P_2O_5:	0.141 - 1.38	0.201 - 2.96	0.185 - 0.864

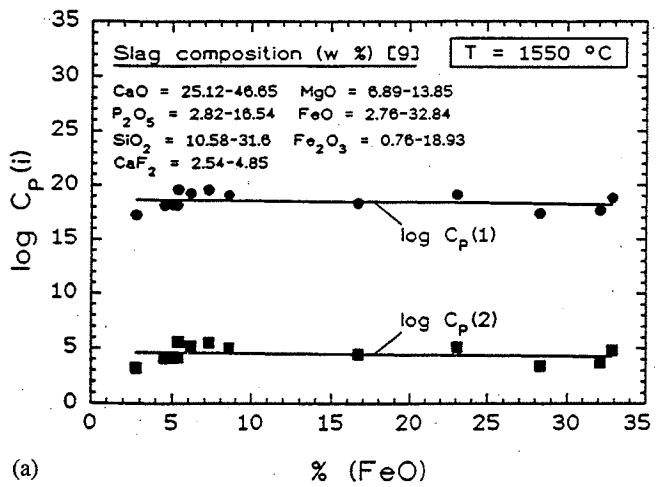


Fig. 6.58 a,b. Phosphate capacity (a) and phosphorus distribution (b) in the $CaF_2\text{-}CaO\text{-}FeO_n\text{-}MgO\text{-}SiO_2$ system [9]

$CaO-FeO-MgO-Na_2O-SiO_2$

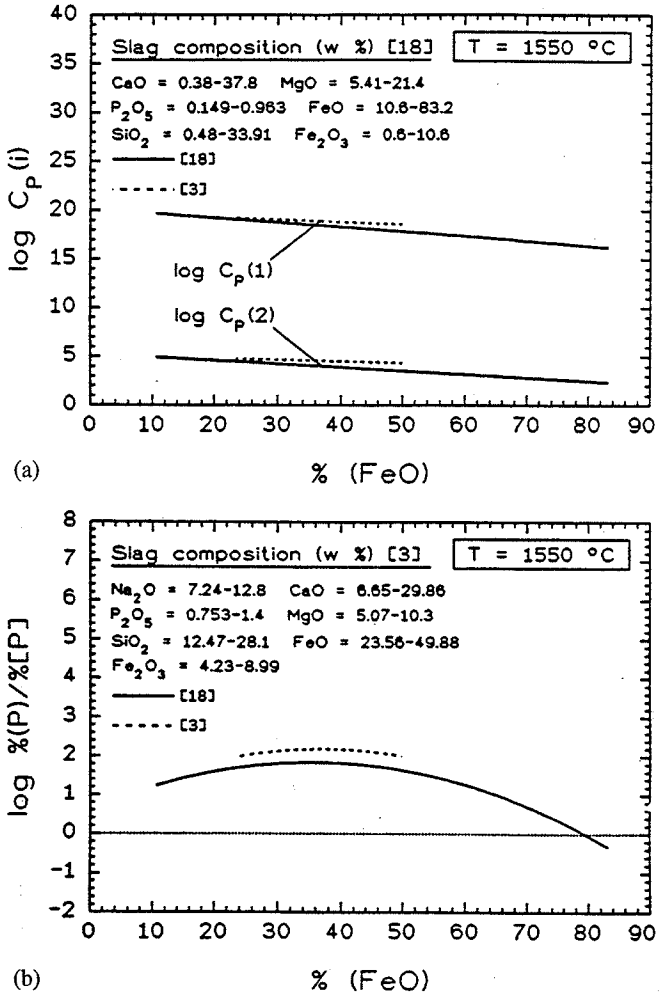


Fig. 6.59 a,b. Phosphate capacity (a) and phosphorus distribution (b) in the $CaO-FeO_n-MgO-SiO_2$ and $CaO-FeO_n-MgO-Na_2O-SiO_2$ system [3, 18]

$FeO-MgO-MnO-Nb_2O_5-SiO_2$

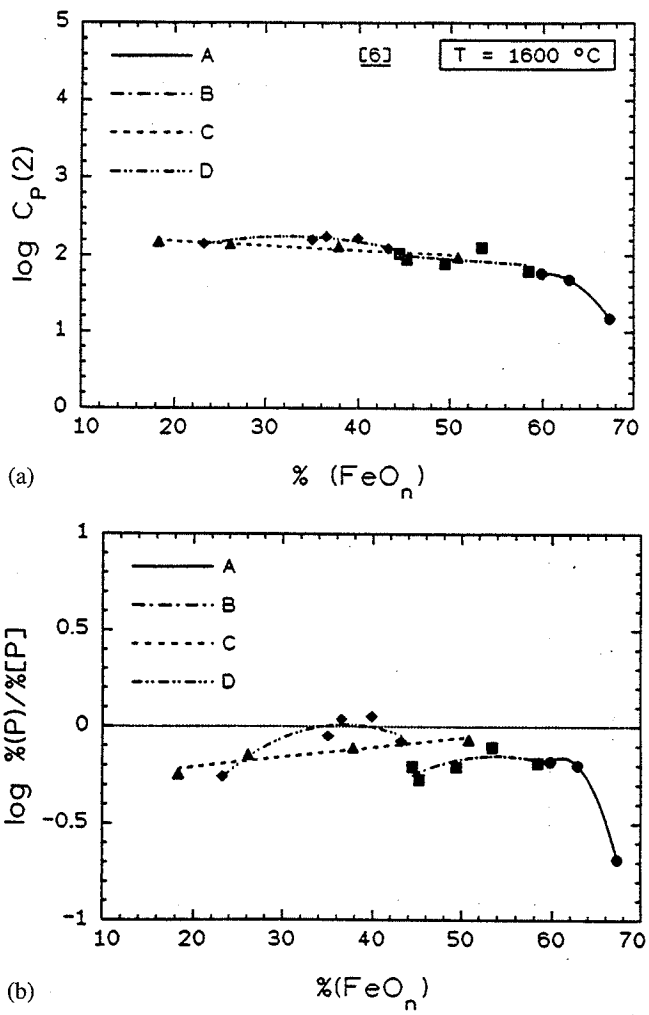


Fig. 6.61 a,b. Phosphate capacity (a) and phosphorus distribution (b) in the $FeO_n-MgO-Nb_2O_5-SiO_2$ (A, C) and $FeO_n-MgO-MnO-Nb_2O_5-SiO_2$ (B, D) systems [6]

Slag compositions:

	A	B	C	D
MgO:	19.7 - 20	19.8 - 23	23.4 - 36.7	22.5 - 37.6
MnO:	-	3.02 - 13.1	-	6.11 - 8.38
SiO_2:	1.83 - 2.67	2.22 - 6.81	10.05 - 32.95	14.15 - 26.3
Nb_2O_5:	14.9 - 32.04	15.02 - 33.47	19.28 - 26.63	14.65 - 32.04
FeO_n:	59.8 - 67.3	44.4 - 58.4	18.3 - 50.8	23.2 - 43.2
P_2O_5:	0.06 - 0.192	0.13 - 0.194	0.168 - 0.213	0.139 - 0.27

$CaO-FeO-MnO-P_2O_5-SiO_2$

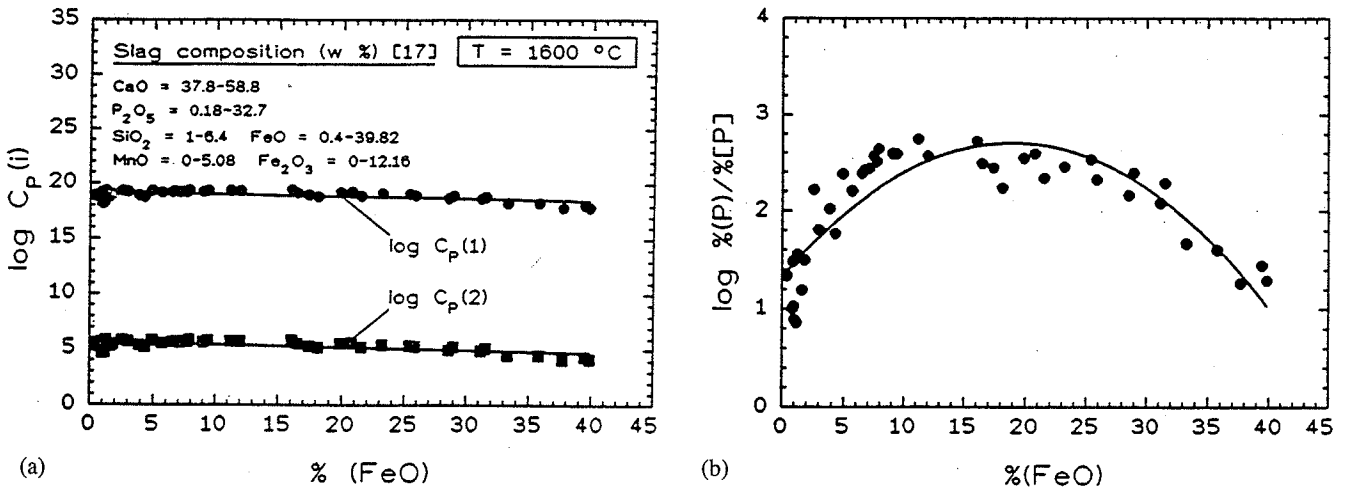


Fig. 6.60 a,b. Phosphate capacity (a) and phosphorus distribution (b) in the $CaO-FeO_n-MnO-P_2O_5-SiO_2$ system [17]

6.2.6 Phosphide capacity

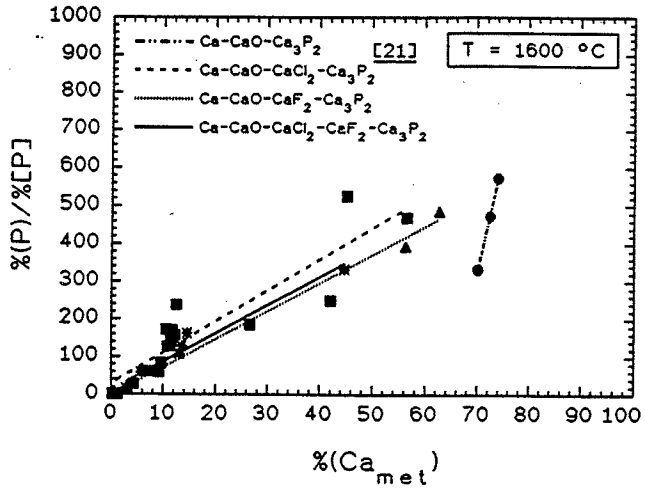


Fig. 6.62. Phosphorus distribution in the Ca-CaO, Ca-CaO-$CaCl_2$, Ca-CaO-CaF_2 and Ca-CaO-CaF_2-$CaCl_2$ systems, in 10 bar Ar [21]

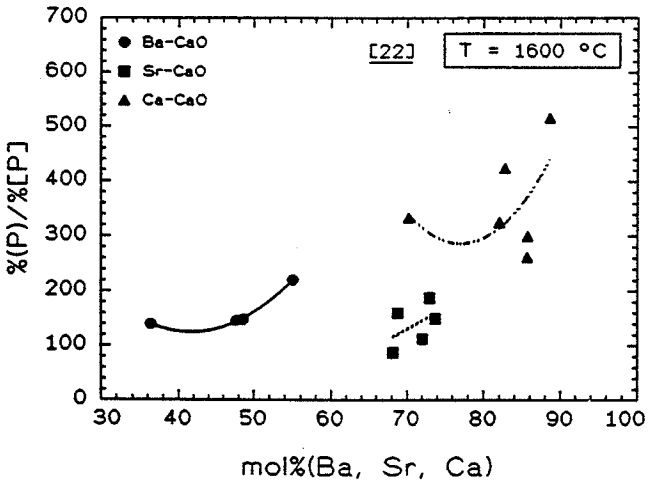


Fig. 6.63. Phosphorus distribution in the Ba-CaO, Ca-CaO and Sr-CaO systems, in 10 bar Ar [22]

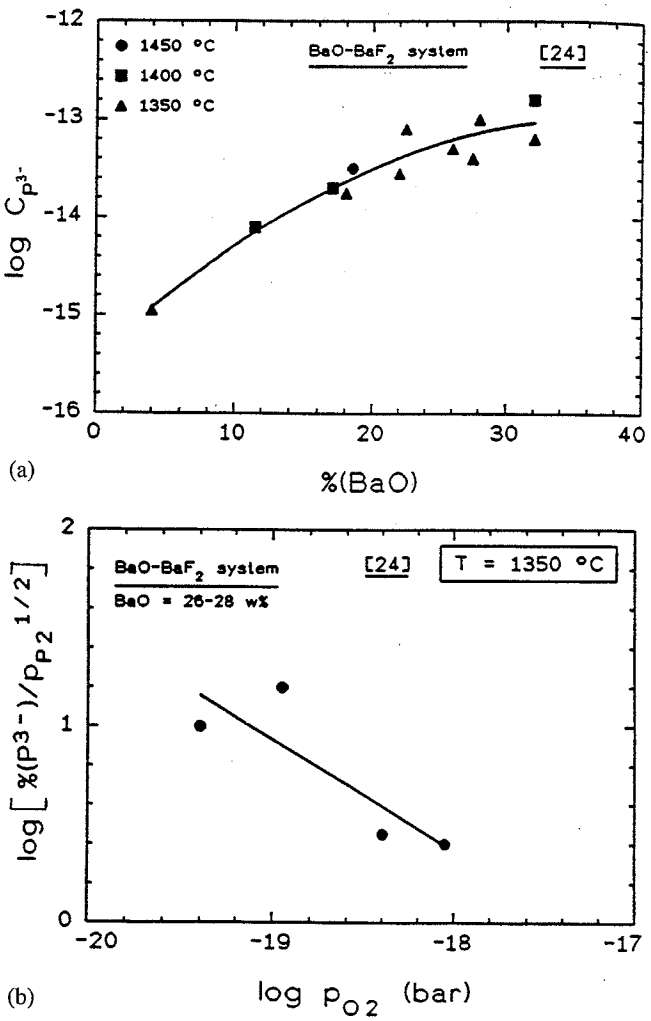
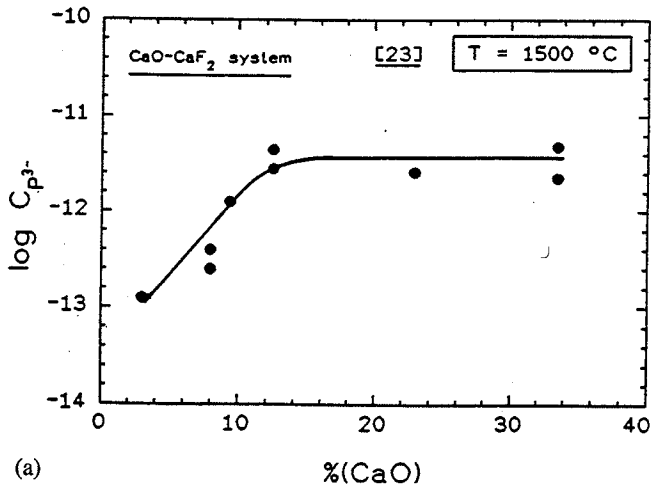


Fig. 6.65 a,b. Phosphide capacity (a) and phosphide content/ phosphorus partial pressure ratio (b) in the BaF_2-BaO system [24]



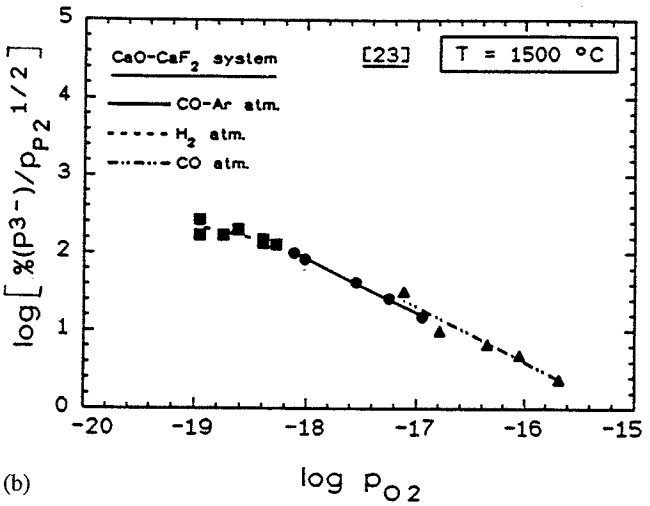


Fig. 6.64 a,b. Phosphide capacity (a) and phosphide/phosphorus partial pressure ratio (b) in the CaF_2-CaO system, for Ag-P alloy [23]

6.2.7 References in Chapter 6.2

[1] Inoue, R.; Suito, H.: Trans. ISIJ, Vol. 25, 1985, 118
[2] Inoue, R. et al.: Trans. ISIJ, Vol. 28, 1988, 179
[3] Suito, H.; Inoue, R.: Trans. ISIJ, Vol. 24, 1984, 47
[4] Kunisada, K.; Iwai, H.: Tetsu-to-Hagane, 1983, 1591
[5] Pak, J. J.; Fruehan, R. J.: Met. Trans. B, Vol. 17 B, 1986, 797
[6] Inoue, R. et al.: Trans. ISIJ, Vol. 27, 1987, 946
[7] Janke, D. et al.: Steel Res. (60), 1989, 539
[8] Janke, D. et al.: Steel Res. (61), 1990, 1
[9] Kor, G. J. W.: Met. Trans. B, Vol. 8B, 1977, 107
[10] Young, R. W.: ECSC Draft Final Report 7210. CF/802 (C6.1/87)
[11] Sigworth, G. K.; Elliott, J. F.: Metal Sci. 8, 1974, 298
[12] Suito, H.; Inoue, R.: Trans. ISIJ, Vol. 22, 1982, 869
[13] Trömel, G.; Fix, W.: Arch. Eisenhüttenwes. (33) 1962, 745
[14] Trömel, G. et al.: Arch. Eisenhüttenwes. (32) 1961, 353
[15] Fischer, W. A.; vom Ende, H.: Stahl u. Eisen (72) 1952, 1402
[16] Gaye, H.; Riboud, P.: IRSID, PCM 85-N. 8, Jan. 1985
[17] Knüppel, H.; Oeters, F.: Arch. Eisenhüttenwes. (81) 1961, 1437
[18] Suito, H. et al.: Trans. ISIJ, Vol. 21, 1981, 250
[19] Ting, T. et al.: Tetsu-to-Hagane, 1986, 225
[20] Maruhashi, S. et al.: Trans. ISIJ, Vol. 25, 1985, 963
[21] Köhler, M.: Dr.-Ing. Thesis, TU Clausthal, 1984
[22] Breitzmann, M.: Dr.-Ing. Thesis, TU Clausthal, 1987
[23] Tabuchi, S.; Sano, N.: Met. Trans. B, 15B, June 1984, 351
[24] Tabuchi, S.; Sano, N.: Tetsu-to-Hagane, 71, 6, 1985, 687
[25] Steelmaking Data Sourcebook, Gordon & Breach Sci. Publishers, 1988

7

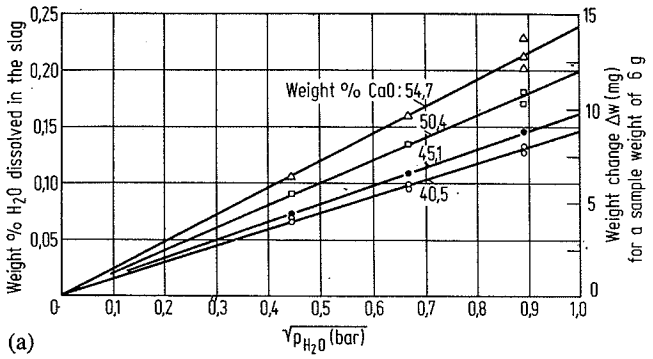
Solubility of gases in liquid slags

D. Kirner and D. Janke

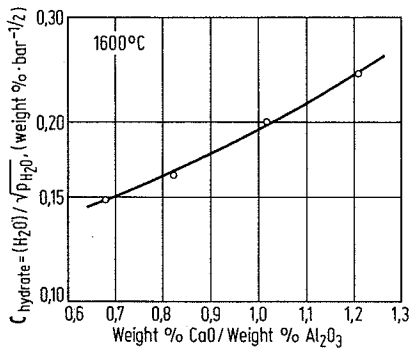
7.1 Hydrogen

7.1.1 Binary systems

Al_2O_3-CaO



(a)



(b)

Fig. 7.1 a,b. Influence of water vapour partial pressure (a) on H_2O content in Al_2O_3-CaO melts and (b) hydrate capacity for different CaO/Al_2O_3 ratios for 1600 °C and (Ar + H_2O) atmosphere. [Thermogravimetric measurements] [46]

CaO-FeO_n

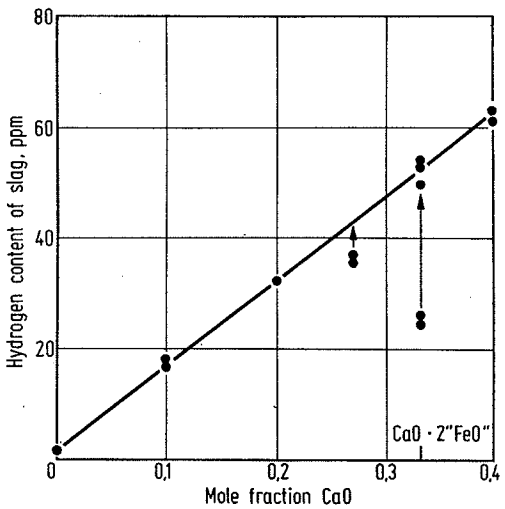


Fig. 7.2. Hydrogen solubility in CaO-FeO_n melts at 1600 °C and p_{H_2O} = 1.013 bar (Ar + p_{H_2O}) atmosphere with p_{H_2O} = 0.312 bar converted to p_{H_2O} = 1.013 bar [4]

CaO-SiO_2

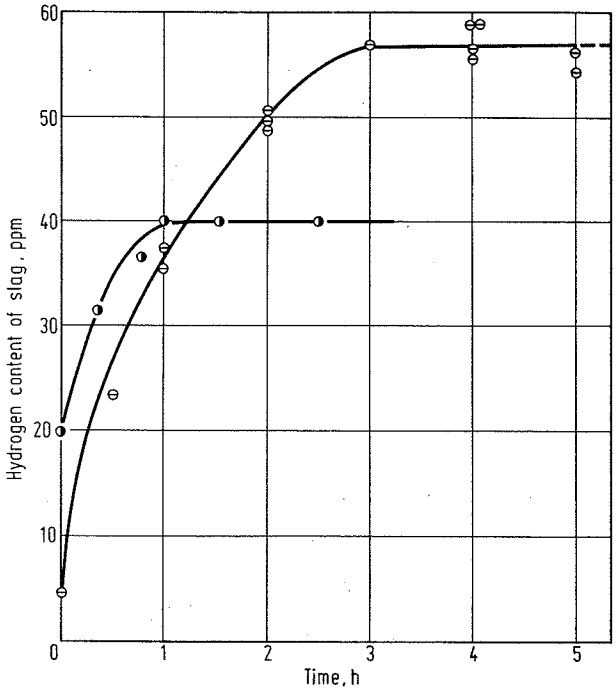


Fig. 7.3. Hydrogen content of CaO-SiO_2 slags in relation to reaction time at 1550 °C
⊖: Slag with 32.9 % CaO, 67.1 % SiO_2;
(H_2O + Ar) mixture surface applied: p_{H_2O} = 0.91 bar [1]
◑: Slag with 50 % CaO, 50 % SiO_2;
(H_2O + N_2) mixture surface applied: p_{H_2O} = 0.254 bar [2]

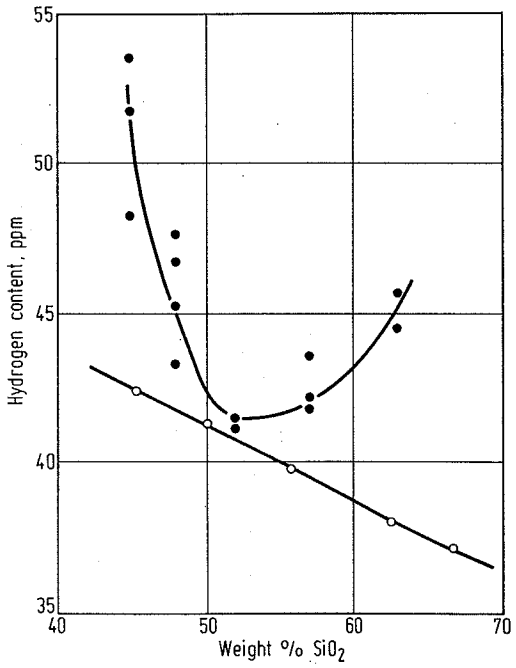


Fig. 7.4. Influence of SiO_2 content on hydrogen content in CaO-SiO_2 melts
● at 1600 °C; p_{H_2O} = 0.386 bar; (H_2O + Ar) atmosphere [3]
○ at 1550 °C; p_{H_2O} = 0.254 bar; (H_2O + N_2) atmosphere [2]

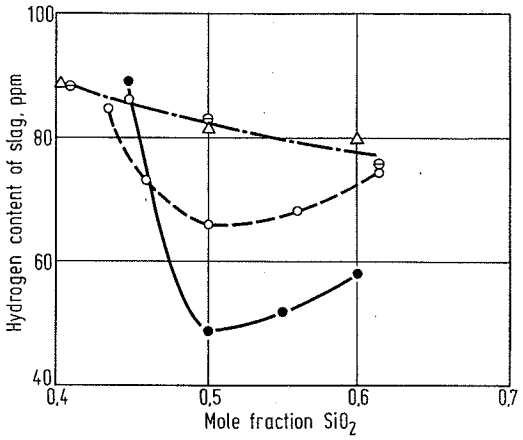


Fig. 7.5. Hydrogen solubility in CaO-SiO_2 melts at p_{H_2O} = 1.013 bar
● 1600 °C; (Ar + H_2O) atmosphere; p_{H_2O} = 0.312 bar, converted to 1.013 bar [4]
○ 1600 °C; (Ar + H_2O) atmosphere; p_{H_2O} = 0.386 bar, converted to 1.013 bar [3]
⊖ 1550 °C; (H_2 + N_2) atmosphere; p_{H_2O} = 1.013 bar [5]
△ 1550 °C; (H_2 + N_2) atmosphere; p_{H_2O} = 0.195 bar, converted to 1.013 bar [6]

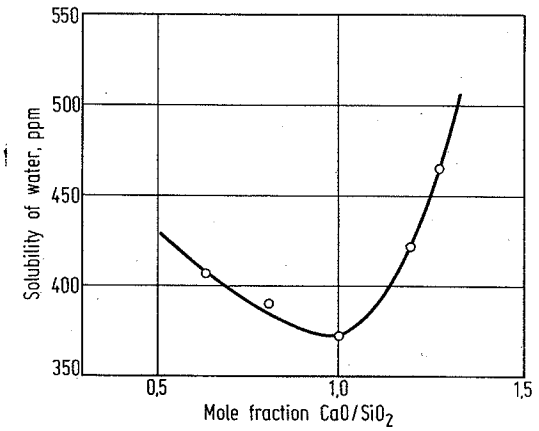


Fig. 7.6. Solubility of H_2O in CaO-SiO_2 melts at 1600 °C and p_{H_2O} = 0.385 bar in (H_2O + Ar) atmosphere [7]

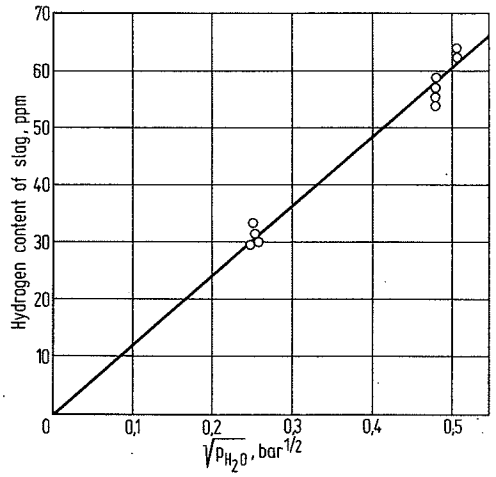


Fig. 7.7. Relationship between the hydrogen content in CaO-SiO_2 melts with 32.9 % CaO and 67.1 % SiO_2 and water vapour partial pressure at 1550 °C and (H_2O + Ar) atmosphere [1, 8]
(760 Torr = 1.013 bar)

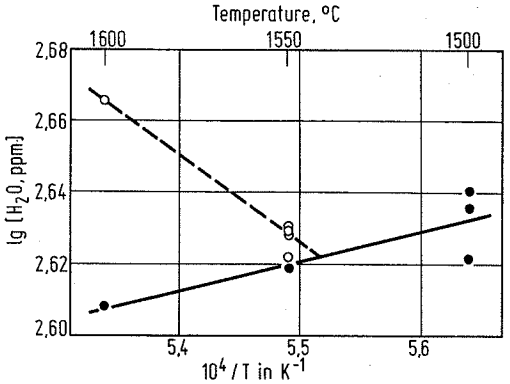


Fig. 7.8. Relationship between solubility of H_2O in CaO-SiO_2 melts and the temperature at p_{H_2O} = 0.386 bar in (H_2O + Ar) atmosphere [9]
● —— ●: mole fraction ratio x_{CaO}/x_{SiO_2} = 0.63
○ ------ ○: mole fraction ratio x_{CaO}/x_{SiO_2} = 1.26
Further literature references about hydrogen solubility in CaO-SiO_2 melts: [10, 11].

MnO-SiO_2

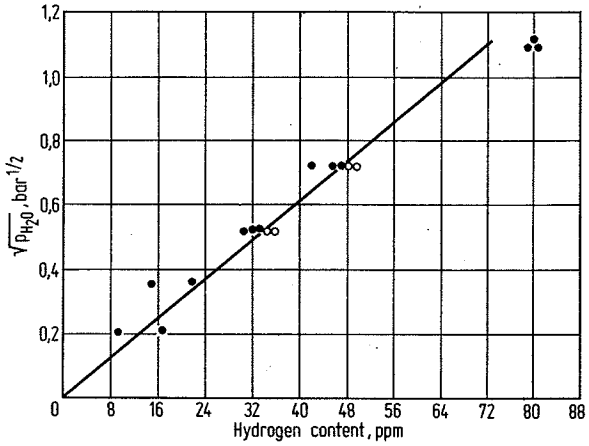


Fig. 7.9. Relationship between hydrogen solubility in MnO-SiO_2 melts with 62 % MnO and 38 % SiO_2 and water vapour partial pressure in (H_2O + N_2) atmosphere [5]
○ 1450 °C; ● 1350 °C (760 Torr = 1.013 bar)

7.1.2 Ternary systems

Al_2O_3-CaF_2-CaO

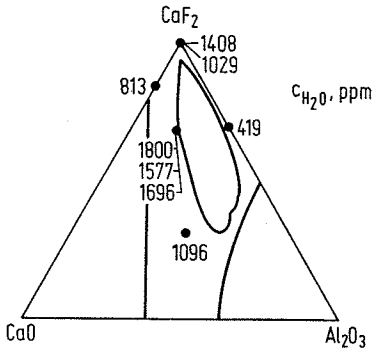


Fig. 7.10 a. Solubility of H_2O in Al_2O_3-CaF_2-CaO melts at 1550 °C and $p_{H_2O} = 88 \cdot 10^{-3}$ bar, $p_{HF} = 8.4 \cdot 10^{-3}$ bar [53]

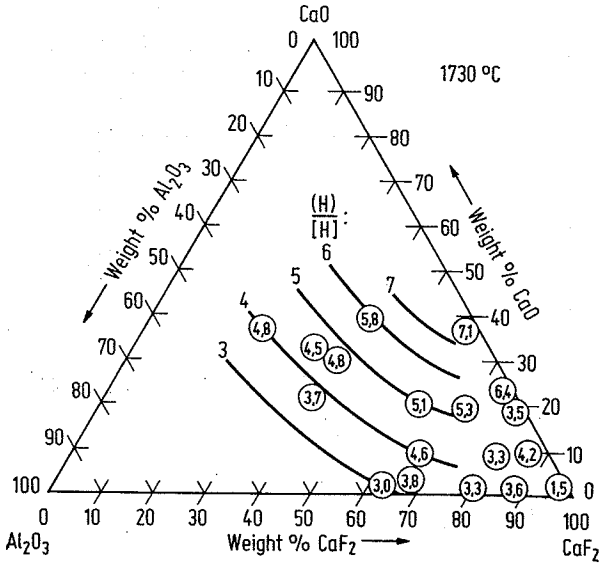


Fig. 7.10 b. Partition coefficient of hydrogen for slag and iron melt (Trials in a laboratory ESR plant) [53]

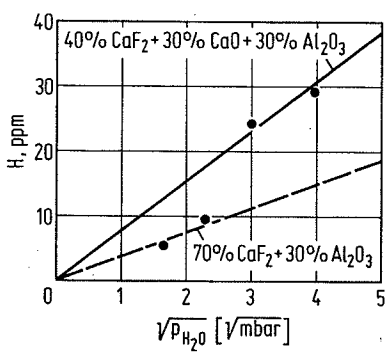


Fig. 7.10 c. Hydrogen content of an Al_2O_3-CaF_2-CaO melt in relation to water vapour partial pressure [53]

Al_2O_3-CaO-SiO_2

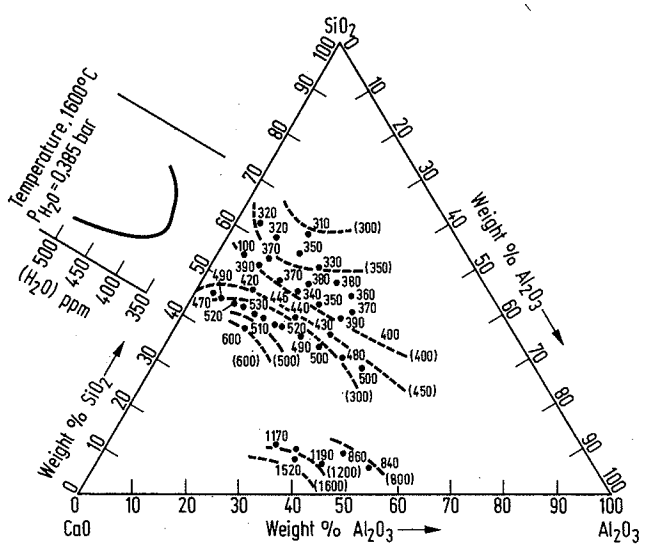


Fig. 7.11. Solubility of H_2O in Al_2O_3-CaO-SiO_2 melts at 1600 °C and $p_{H_2O} = 0.385$ bar in (Ar + H_2O) atmosphere [5]

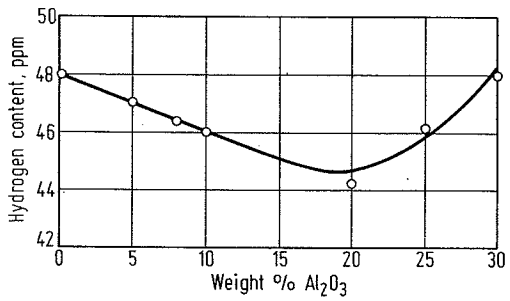


Fig. 7.12 a. Hydrogen solubility in Al_2O_3-CaO-SiO_2 melts with a ratio of CaO/SiO_2 = 0.59 at 1500 °C and $p_{H_2O} = 0.386$ bar in (Ar + H_2O) atmosphere [3]

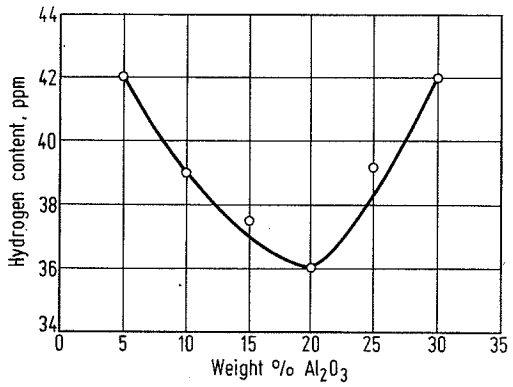


Fig. 7.12 b. Hydrogen solubility of Al_2O_3-CaO-SiO_2 melts for CaO-SiO_2 = 0.6 at 1550 °C and $p_{H_2O} = 0.254$ bar in (N_2 + H_2O) atmosphere [2]

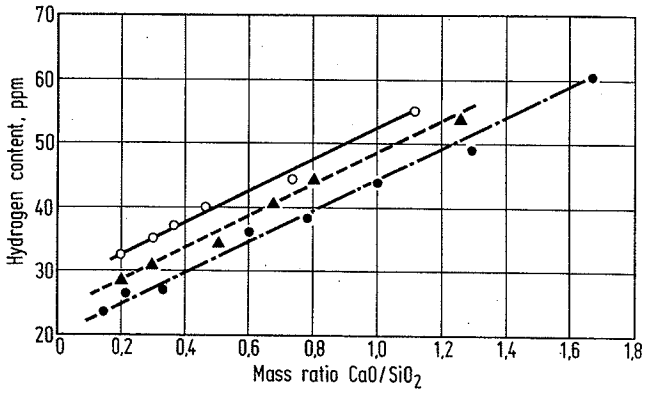


Fig. 7.13. Hydrogen solubility in Al_2O_3-CaO-SiO_2 melts in relationship to CaO/SiO_2 ratio at 1550 °C and p_{H_2O} = 0.254 bar in (N_2 + H_2O) atmosphere [2]
○: 5 % Al_2O_3 ▲: 10 %Al_2O_3 ●: 20 % Al_2O_3

CaF_2-CaO-SiO_2

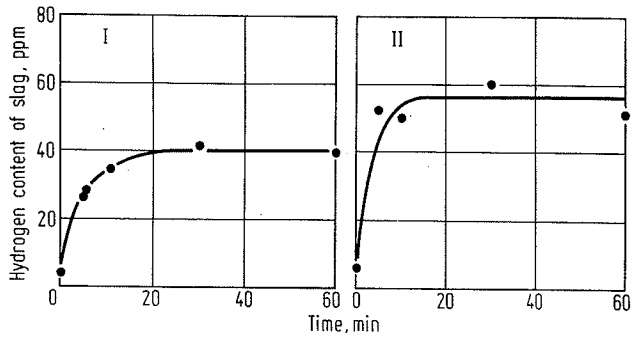


Fig. 7.16. Hydrogen saturation of CaF_2-CaO-SiO_2 melts at 1585 °C and p_{H_2O} = 0.455 bar in (Ar + H_2O) atmosphere [11]
Slag composition (mole ratios):
I: x_{CaF_2} = 0.159, x_{CaO} = 0.291, x_{SiO_2} = 0.551
II: x_{CaF_2} = 0.157, x_{CaO} = 0.416, x_{SiO_2} = 0.367

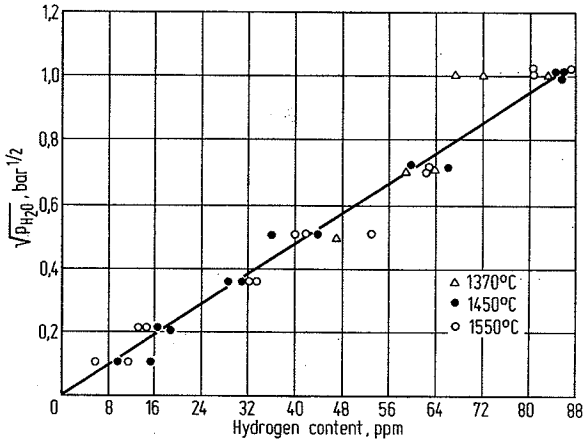


Fig. 7.14. Hydrogen solubility in Al_2O_3-CaO-SiO_2 melts in relationship to water vapour partial pressure at various temperatures in (N_2 + H_2O) atmosphere [5]
(Slag composition: 40 % CaO, 40 % SiO_2, 20 % Al_2O_3)

CaO-FeO-SiO_2

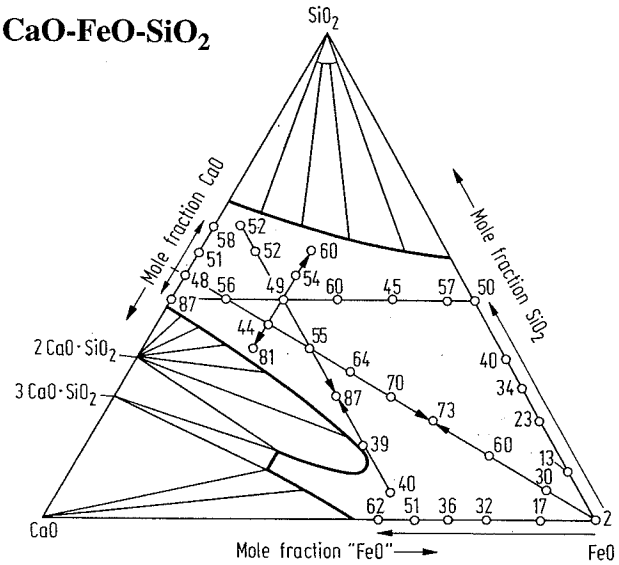


Fig. 7.17. Hydrogen solubility in CaO-FeO-SiO_2 melts at 1600 °C and 1.013 bar in (H_2O + Ar) atmosphere, converted from p_{H_2O} = 0.312 to 1.013 bar: hydrogen content in ppm [4]

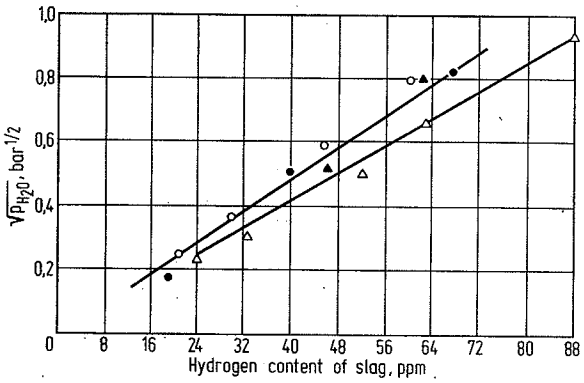


Fig. 7.15. Hydrogen solubility in Al_2O_3-CaO-SiO_2 melts in relation to water vapour pressure in (N_2 + H_2O) atmosphere [2].
Slag composition and temperature:
○: 40 % CaO, 40 % SiO_2, 20 % Al_2O_3; 1350 °C
●: 40 % CaO, 40 % SiO_2, 20 % Al_2O_3; 1450 °C
▲: 40 % CaO, 40 % SiO_2, 20 % Al_2O_3; 1550 °C
△: 57 % CaO, 27 % SiO_2, 16 % Al_2O_3; 1550 °C

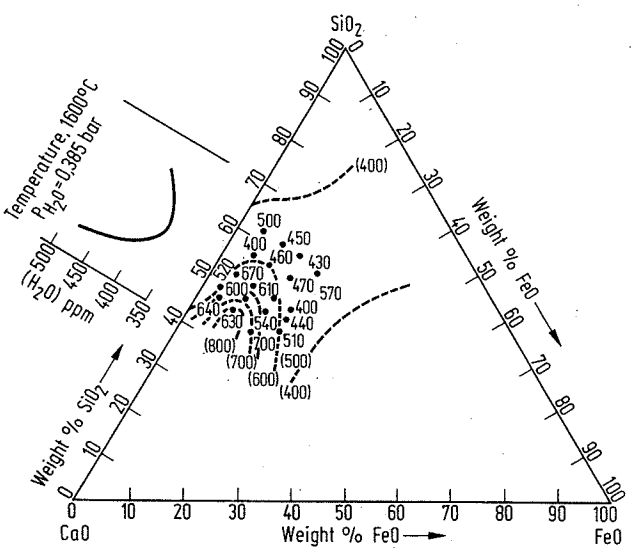


Fig. 7.18. Solubility of H_2O in CaO-FeO-SiO_2 melts at 1550 °C and p_{H_2O} = 0.385 bar in (H_2 + H_2O + Ar) atmosphere [9]
(760 mm Hg = 1.013 bar)

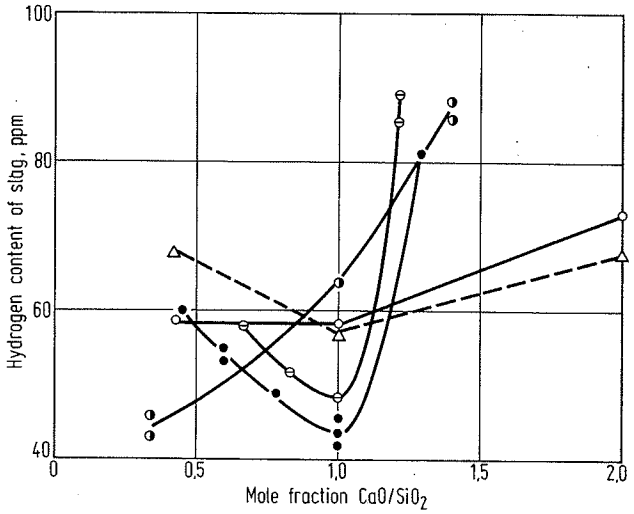


Fig. 7.19. Hydrogen solubility in $CaO\text{-}FeO\text{-}SiO_2$ melts in relation to CaO/SiO_2 ratios at 1.013 bar in $(Ar + H_2O)$ atmosphere [4, 8]
⊖: 0 % FeO, 1600 °C; p_{H_2O} = 0.312 converted to 1.013 bar [4]
●: 20 % FeO, 1600 °C; p_{H_2O} = 0.312 converted to 1.013 bar [4]
◑: 40 % FeO, 1600 °C; p_{H_2O} = 0.312 converted to 1.013 bar [4]
△: 24 % FeO, 1550 °C; p_{H_2O} = 0.101 converted to 1.013 bar [8]
○: 33 % FeO, 1550 °C; p_{H_2O} = 0.101 converted to 1.013 bar [8]

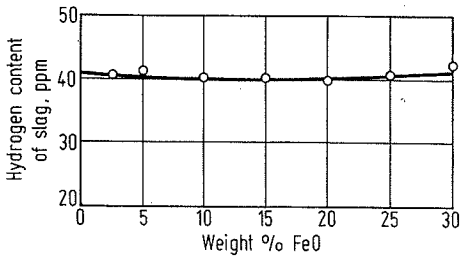


Fig. 7.21. Hydrogen solubility in $CaO\text{-}FeO\text{-}SiO_2$ melts at constant CaO/SiO_2 ratio 1, 1550 °C and p_{H_2O} = 0.253 bar in $(N_2 + H_2O)$ atmosphere [2]

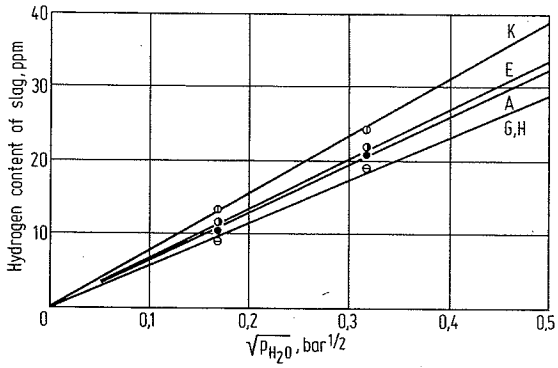


Fig. 7.22. Relationship between hydrogen content of $CaO\text{-}FeO\text{-}SiO_2$ slags and water vapour partial pressure at 1550 °C in $(Ar + H_2O)$ atmosphere [1, 8]
(760 Torr = 1.013 bar)
A: ●: x_{CaO} = 0.216; x_{FeO} = 0.264; x_{SiO_2} = 0.52
E: ◑: x_{CaO} = 0.52 ; x_{FeO} = 0.228; x_{SiO_2} = 0.251
G: ⊖: x_{CaO} = 0.188; x_{FeO} = 0.340; x_{SiO_2} = 0.472
H: ⊖: x_{CaO} = 0.266; x_{FeO} = 0.328; x_{SiO_2} = 0.406
K: ⦶: x_{CaO} = 0.467; x_{FeO} = 0.298; x_{SiO_2} = 0.235

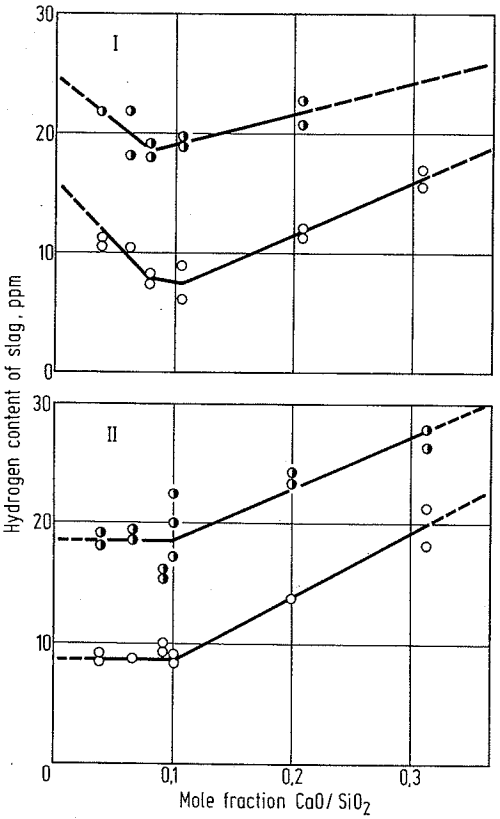


Fig. 7.20. Hydrogen solubility in $CaO\text{-}FeO\text{-}SiO_2$ melts in relation to mole ratio CaO/SiO_2 at 1550 °C in $(Ar + H_2O)$ atmosphere [1]
I: x_{FeO} = 0.24: p_{H_2O} = 0.101 bar
II: x_{FeO} = 0.33: p_{H_2O} = 0.028 bar

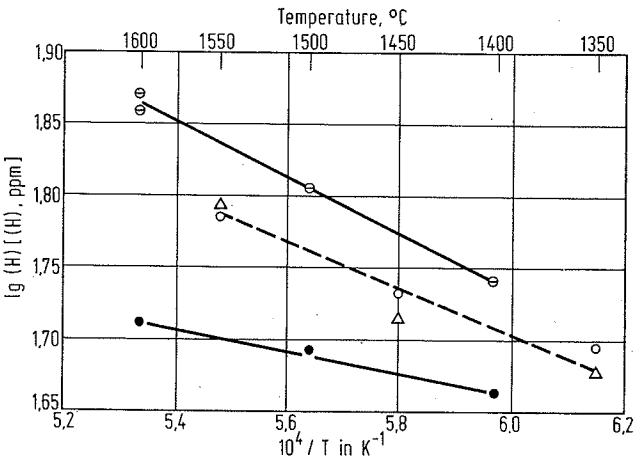


Fig. 7.23. Hydrogen solubility in $CaO\text{-}FeO\text{-}SiO_2$ slags in relation to temperature at p_{H_2O} = 1.013 bar in $(Ar + H_2O)$ atmosphere [8]
●: x_{CaO} = 0.35; x_{FeO} = 0.35; x_{SiO_2} = 0.30; p_{H_2O} = 0.312 bar converted to 1.013 bar
⊖: x_{CaO} = 0.20; x_{FeO} = 0.60; x_{SiO_2} = 0.20; p_{H_2O} = 0.312 bar converted to 1.013 bar
○: x_{CaO} = 0.387; x_{FeO} = 0.243; x_{SiO_2} = 0.37; p_{H_2O} = 0.101 bar converted to 1.013 bar
△: x_{CaO} = 0.334; x_{FeO} = 0.336; x_{SiO_2} = 0.33; p_{H_2O} = 0.101 bar converted to 1.013 bar

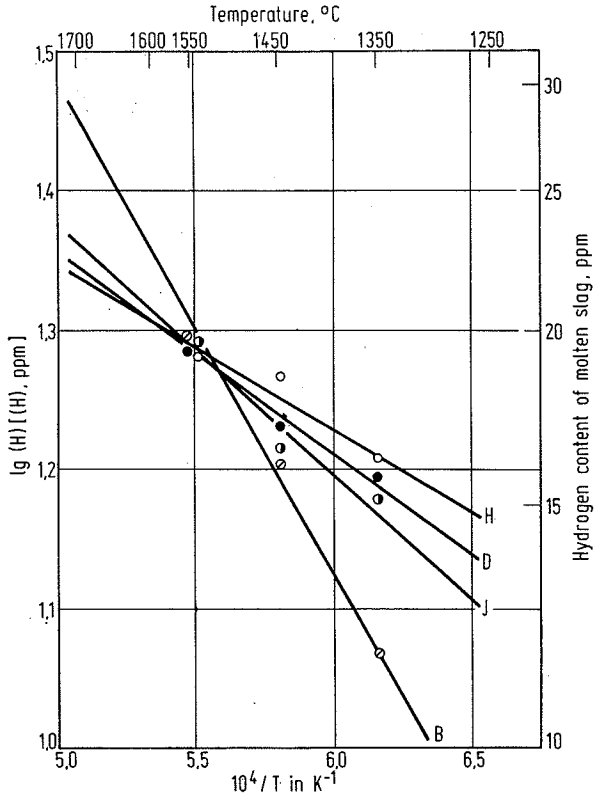


Fig. 7.24. Hydrogen solubility in $CaO\text{-}FeO\text{-}SiO_2$ slags in relation to temperature at $p_{H_2O} = 0.101$ bar in ($Ar + H_2O$) atmosphere [1]
B: ⊘: $x_{CaO} = 0.291$; $x_{FeO} = 0.245$; $x_{SiO_2} = 0.464$
D: ●: $x_{CaO} = 0.387$; $x_{FeO} = 0.243$; $x_{SiO_2} = 0.37$
H: ○: $x_{CaO} = 0.266$; $x_{FeO} = 0.328$; $x_{SiO_2} = 0.406$
J: ◑: $x_{CaO} = 0.334$; $x_{FeO} = 0.336$; $x_{SiO_2} = 0.33$

$CaO\text{-}Li_2O\text{-}SiO_2$

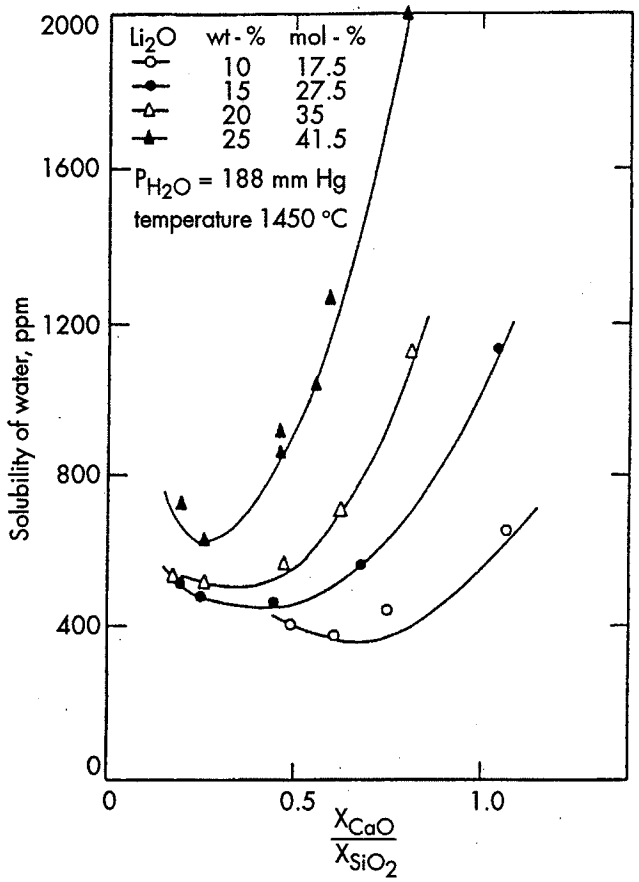


Fig. 7.25. Solubility of water in the $CaO\text{-}Li_2O\text{-}SiO_2$ system [54]

$CaO\text{-}MgO\text{-}SiO_2$

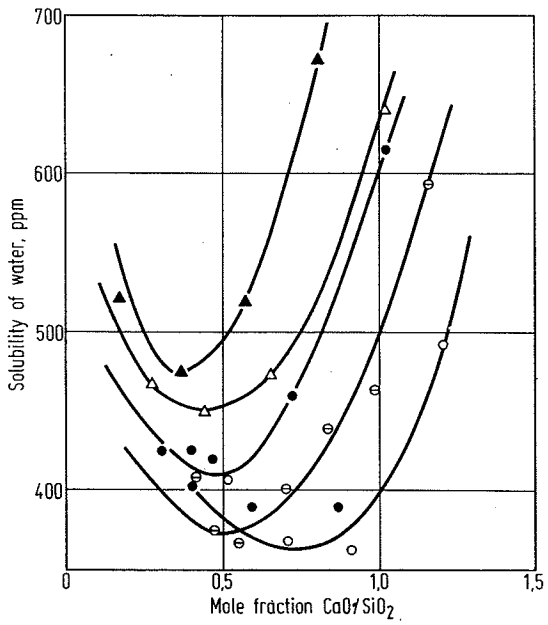


Fig. 7.26. Solubility of H_2O in $CaO\text{-}MgO\text{-}SiO_2$ melts at 1550 °C and $p_{H_2O} = 0.385$ bar in ($Ar + H_2O$) atmosphere [12]
Contents of MgO in weight %:
○——○: 5 % MgO
⊖——⊖: 10 % MgO
●——●: 15 % MgO
△——△: 20 % MgO
▲——▲: 25 % MgO

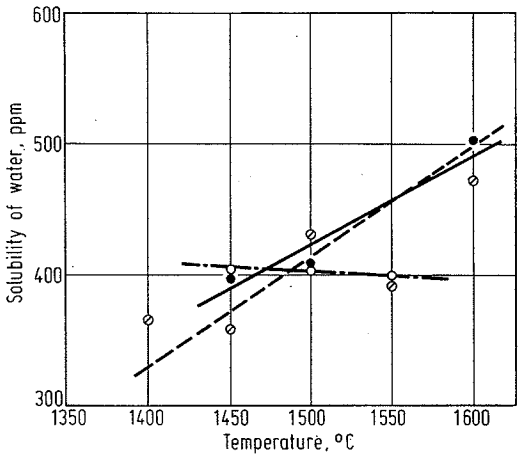


Fig. 7.27. Influence of temperature on solubility of H_2O in $CaO\text{-}MgO\text{-}SiO_2$ melts at p_{H_2O} = bar in ($Ar + H_2O$) atmosphere [12]

○- - - - -○ $\frac{X_{CaO}+X_{MgO}}{X_{SiO_2}}$ = 1.25
●————● = 1.0
○- - - - - -○ = 0.77

Tab. 7.1. Hydrogen content of a $CaO\text{-}MnO\text{-}SiO_2$ melt at 1400 °C and $p_{H_2O} = 0.027$ in (H_2O + air) atmosphere [10]

Slag composition weight %			Hydrogen content ppm
CaO	MnO	SiO_2	
35	30	35	27.5

$CaO\text{-}Na_2O\text{-}SiO_2$

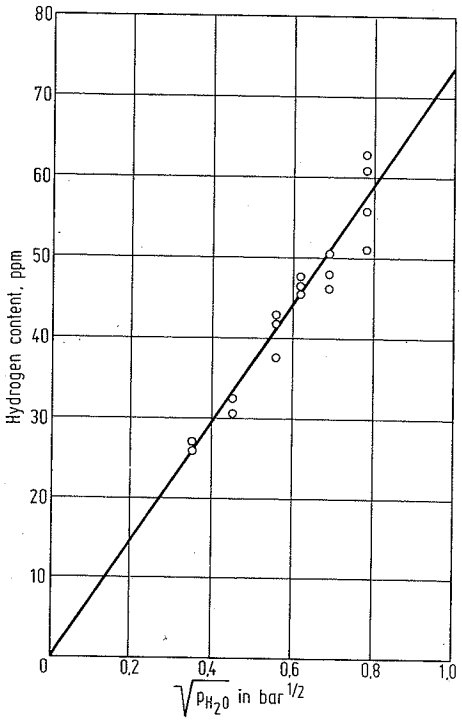


Fig. 7.28. Relationship between hydrogen content of a CaO-Na_2O-SiO_2 melt with 25 % CaO, 15 % Na_2O and 60 % SiO_2 and water vapour partial pressure in (Ar + H_2O) atmosphere at 1300 °C [3]

$CaO\text{-}P_2O_5\text{-}SiO_2$

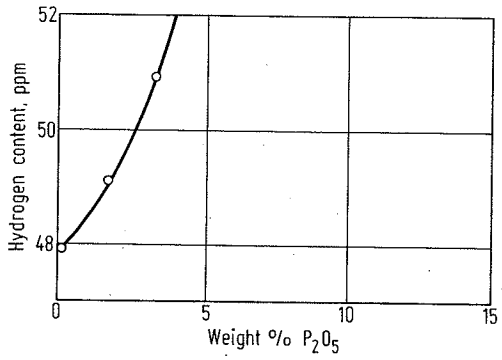


Fig. 7.29. Hydrogen solubility in a CaO-P_2O_5-SiO_2 melt with CaO/ SiO_2 ratio of 0.59 at 1500 °C and p_{H_2O} = 0.385 bar in (Ar + H_2O) atmosphere [3]

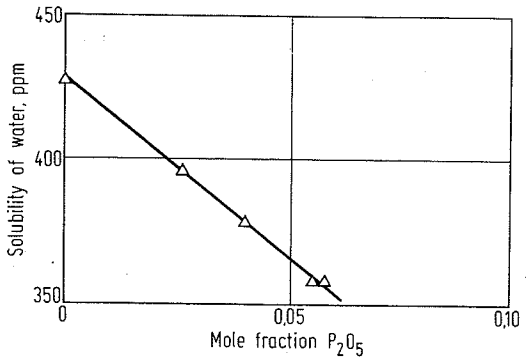


Fig. 7.30. Solubility of H_2O in CaO-P_2O_5-SiO_2 melt with mole fraction ratio x_{CaO}/x_{SiO_2} = 1.3 at 1550 °C and p_{H_2O} = 0.385 bar in (Ar + H_2O) atmosphere [9]

$CaO\text{-}SiO_2\text{-}SrO$

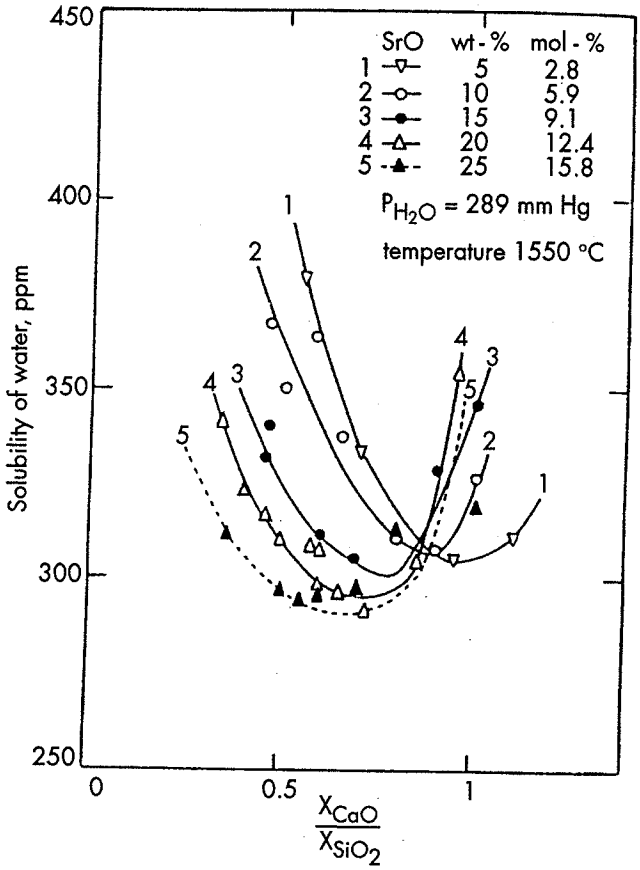


Fig. 7.31. Solubility of water in the CaO-SiO_2-SrO system [54]

$CaO\text{-}SiO_2\text{-}TiO_2$

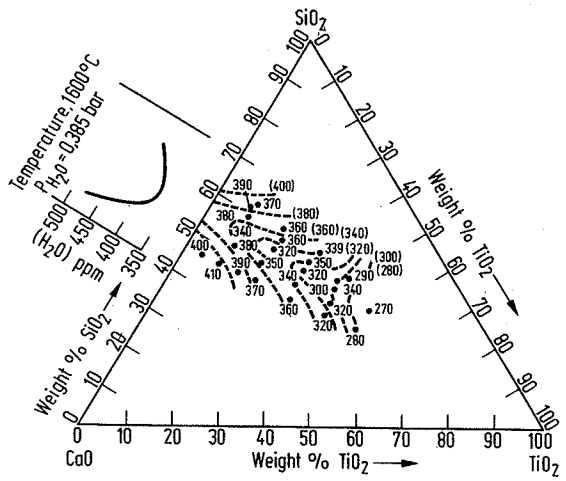


Fig. 7.32. Solubility of H_2O in CaO-SiO_2-TiO_2 melts at 1550 °C and p_{H_2O} = 0.385 bar in (Ar + H_2O) atmosphere [9] (content in ppm)

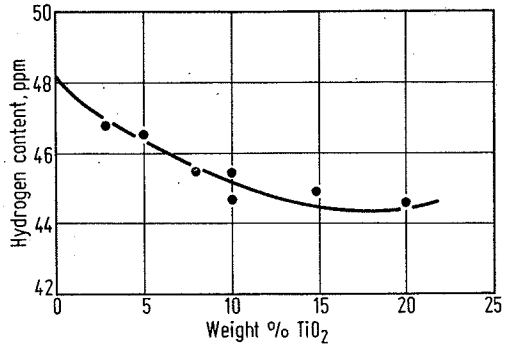


Fig. 7.33. Hydrogen solubility of $CaO\text{-}SiO_2\text{-}TiO_2$ melts at 1550 °C and p_{H_2O} = 0.385 bar in (Ar + H_2O) atmosphere at a weight ratio CaO/SiO_2 = 0.59 [3]

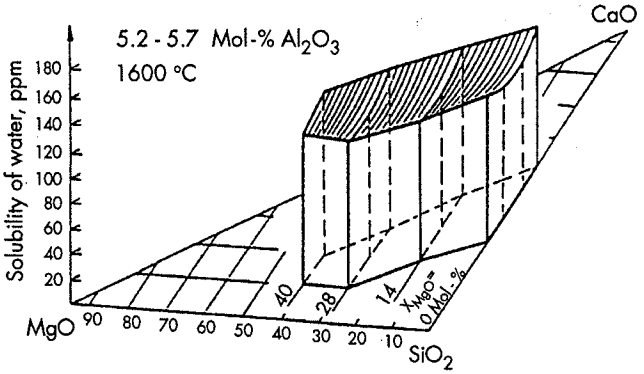


Fig. 7.35. Solubility of water in the Al_2O_3-CaO-MgO-SiO_2 system, p_{H_2O} = 21.95 mbar [55]

FeO_n-Fe_2O_3-SiO_2

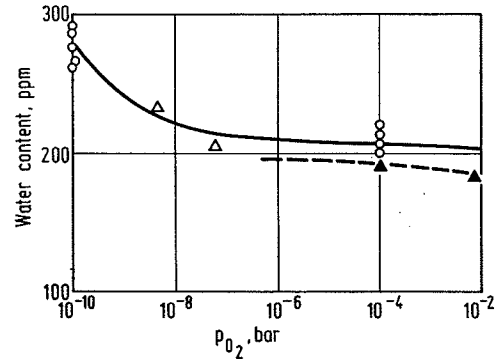


Fig. 7.34. Influence of oxygen partial pressure on the solubility of H_2O in a FeO_n-Fe_2O_3-SiO_2 system at 1500 °C and p_{H_2O} = 0.195 bar in (H_2 + H_2O + N_2) atmosphere [13]
——— { ○ mole fraction x_{SiO_2} = 0.40 to 0.41
——— { △ x_{SiO_2} = 0.375 to 0.380
– – – – ▲ x_{SiO_2} = 0.30 to 0.31

CaF_2-CaO-FeO_n-SiO_2

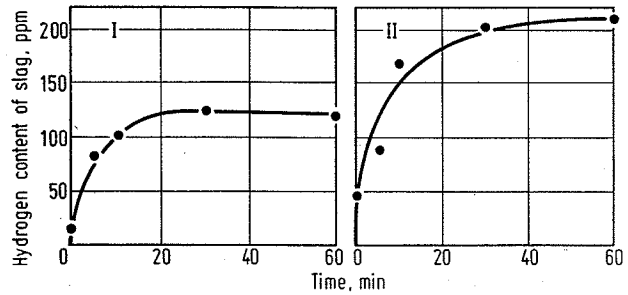


Fig. 7.36. Hydrogen solubility in two CaF_2-CaO-FeO_n-SiO_2 melts at 1585 °C and p_{H_2O} = 0.455 bar in (Ar + H_2O) atmosphere.
Compositions in mole percent:
I: 17.0 % CaF_2; 42.6 % CaO; 24.1 % FeO; 16.3 % SiO_2
II: 17.1 % CaF_2; 49.3 % CaO; 24.1 % FeO; 9.6 % SiO_2

7.1.3 Quaternary systems

Al_2O_3-CaO-MgO-SiO_2

Tab. 7.2. Solubility of H_2O in Al_2O_3-CaO-MgO-SiO_2 melts [14] (H_2 measured as H_2O)

No.	Slag composition % by weight				Temperature	H_2O concentration
	% Al_2O_3	% CaO	% MgO	% SiO_2	°C	ppm
1	42	53	2	3	1500	27.3
					1600	37.8
					1700	44.0
2	28	53	2	17	1600	27.8
3	42	41	2	15	1600	27.8

CaO-FeO-MgO-SiO_2

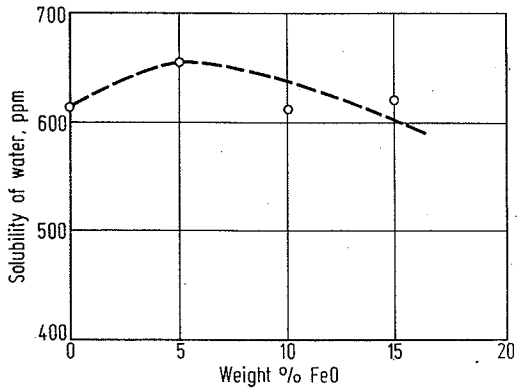


Fig. 7.37. Solubility of H_2O in CaO-FeO-MgO-SiO_2 melts in relation to FeO contents at 1550 °C and p_{H_2O} = 0.385 bar in (Ar + H_2O) atmosphere for $(x_{CaO} + x_{MgO})/x_{SiO_2}$ = 1.5 [12]

7.1.4 Industrial slags

7.1.4.1 Electric arc furnace slags

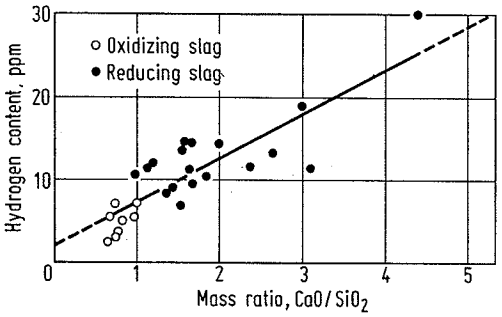


Fig. 7.38. Dependence of hydrogen content of an electric arc furnace slag on the basicity during the refining period on melting a steel with low carbon content [1, 8]

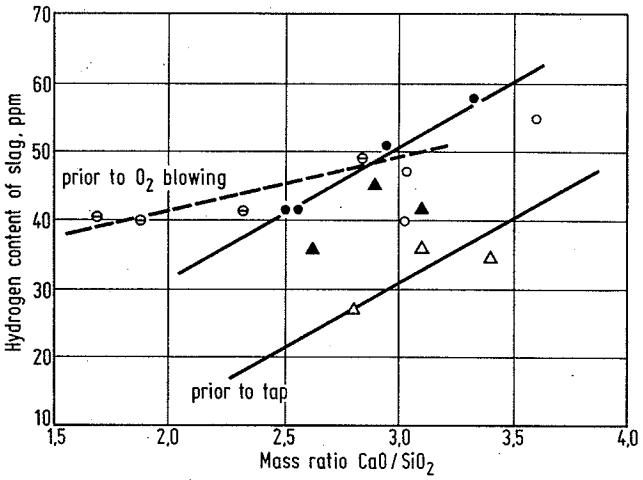


Fig. 7.39. Dependence of hydrogen contents of electric arc furnace slags on basicity [10]
○ p_{H_2O} = 0.028 to 0.031 bar, 1610 to 1650 °C
△ p_{H_2O} = 0.019 to 0.023 bar, 1610 to 1650 °C
● p_{H_2O} = 0.028 to 0.031 bar, 1570 to 1600 °C
▲ p_{H_2O} = 0.019 to 0.023 bar, 1570 to 1600 °C

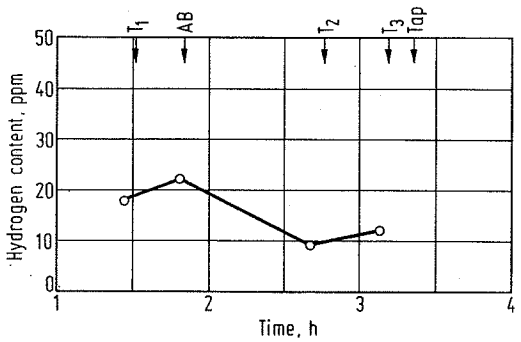


Fig. 7.40. Hydrogen contents of a basic electric arc furnace slag during oxidising phase [5]
T_1: 1575 °C,
T_2: 1570 °C, A: addition of burnt lime
T_3: 1600 °C, B: addition of ore

7.1.4.2 Synthetic slags

Tab. 7.3. Solubility of hydrogen in synthetic Al_2O_3-CaO-MgO-SiO_2 slags under reducing conditions at p_{H_2} = 1.013 bar [4]
Slag composition (weight %):
42 % Al_2O_3; 53 % CaO; 2 % MgO; 3 % SiO_2

Saturation conditions	Temperature °C	Hydrogen concentration ppm
graphite crucible	1600	74
	1700	131
MgO crucible	1600	0.9
	1700	50
MgO crucible; slag over a layer of 45 % ferrosilicon	1600	46
MgO crucible; slag over a layer of 75 % ferrosilicon	1600	60
MgO crucible; addition of 1 % Al to slag	1600	121
MgO crucible; addition of 2 % Al to slag	1600	146

Tab. 7.4. Variation of hydrogen content of slag and metal during treatment with synthetic slag in the ladle [15]. (Steel and slag molten separately; slag quantity 6 to 7 % of metal quantity, poured into ladle from a height of 4 m, temperature before tapping: about 1700 °C. Steel composition and slag composition (mass %))

	C	Si	Mn	Cr	Ni	others
A	0.32	1.05	0.95	0.95	0.2 max.	0.2 Cu, low S and P content
B	0.26	1.05	0.95	0.95	0.2 max.	0.2 Cu, low S and P content
C	1.02	0.25	0.3	1.5	0.3 max.	0.25 Cu max.
D	0.18	0.28	0.4	1.0	0.75	0.75 W, low S and P content
E	0.45	0.28	0.4	1.0	0.8	0.2 Mo, low S and P content

	Slag composition before treatment Slag composition after treatment									Concentrations in ppm			After treatment	
Steel	CaO	Al_2O_3	SiO_2	Fe_2O_3	TiO_2	MgO	Cr_2O_3	MnO	FeO	[H] before treatment	[H] after treatment	(H) before treatment	(H_2O)	(H_2O) + (H)
A	*52.80*	*40.77*	*2.20*	*0.11*	*0.03*	*0.81*	*0.07*	*0.07*	*0.21*	4.63	2.91	2.44	-	15.12
	50.07	37.76	6.78	0.09	0.61	3.57	0.07	0.07	0.35					
	51.66	*39.73*	*2.20*	*Sp*	*0.41*	*1.57*	*0.08*	*0.04*	*0.16*	4.25	3.21	6.03	8.59	28.05
	46.40	32.95	9.01	Sp	0.29	6.55	0.12	0.34	0.65					
	53.14	*40.02*	*1.70*		*0.60*	*1.80*	*0.06*	*0.05*	*0.21*	4.06	3.51	6.54	4.22	39.38
	48.16	36.14	6.30		0.30	6.11	0.06	0.28	0.57					
B	*49.38*	*40.61*	*2.94*		*0.41*	*3.27*	*0.07*	*0.02*	*0.29*	4.52	3.44	5.80	6.55	15.53
	46.75	37.42	6.58		0.33	4.97	0.06	0.18	0.68					
	49.56	*41.80*	*1.66*		*0.80*	*1.33*	*0.06*	*0.43*	*0.04*	5.89	2.07	3.03	4.04	15.80
	46.75	39.01	6.21		0.52	4.60	0.09	0.40	0.13					
	49.40	*41.40*	*3.02*	*Sp*	*0.40*	*3.40*	*0.04*	*0.02*	*0.30*	4.32	2.88	4.56	-	-
	-	-	-	-	-	-	-	-	-					
	53.61	*37.07*	*2.26*	*Sp*	*0.68*	*2.14*	*0.13*	*0.04*	*0.25*	4.41	4.27	6.00	2.79	11.60
	51.46	34.93	5.30	Sp	0.50	5.15	0.51	0.14	1.08					
C	*53.00*	*37.34*	*2.15*		*0.78*	*1.94*	*0.16*	*0.05*	*0.33*	4.80	4.67	5.37	3.08	7.56
	51.00	34.63	5.14		0.44	3.20	0.49	0.17	1.20					
	52.70	*38.40*	*2.08*		*0.80*	*2.11*	*0.14*	*0.03*	*0.30*	5.91	4.72	8.59	3.53	14.65
	51.50	35.70	6.10		0.54	3.21	0.45	0.12	1.05					
D	*52.97*	*39.00*	*2.20*		*0.63*	*2.54*	*0.04*	*0.03*	*0.48*	3.16	2.22	2.44	-	11.60
	47.90	37.17	6.23		0.54	5.58	0.27	0.37	1.03					
E	*51.70*	*41.80*	*2.15*	*0.11*	*0.86*	*1.70*	*0.05*	*0.08*	*0.30*	2.80	1.53	3.20	-	7.05
	50.95	37.50	6.90	0.08	0.40	3.60	0.06	0.15	0.32					
	52.00	*32.00*	*2.16*	*0.06*	*1.06*	*1.45*	*0.28*	*0.07*	*0.35*	3.96	3.60	7.56	-	17.20
	49.15	35.94	5.44	Sp	0.94	3.02	0.20	0.31	0.64					
C	*17.11*	*20.13*	*2.14*	*55.90***	*Sp*	*Sp*	*Sp*	-	*0.12*	5.26	2.40	12.65	-	10.61
	17.02	25.70	7.02	48.00	Sp	Sp	Sp	-	0.21					
E	*25.00*	*34.00*	*8.24*	*20.00*	*Sp*	*13.0*	*Sp*	*Sp*	*Sp*	5.66	1.35	17.67	-	5.55
	-	-	-	-	-	-	-	-	-					

Sp = traces, ** CaF_2
Further literature: [17-24]
Systems: Alkali or earthy alkali metals - silicic acid: [20-22]. Basic open hearth furnace slags: [1, 8, 15-19, 24]
Al_2O_3-CaF_2-CaO-FeO-MgO-SiO_2 [23]

7.2 Nitrogen

7.2.1 Binary systems

Al_2O_3-CaO

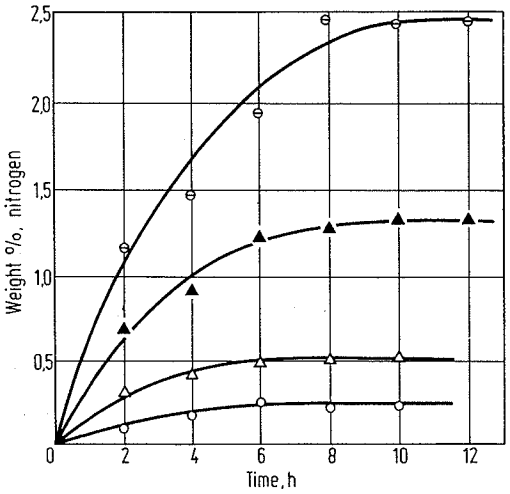


Fig. 7.41. Nitrogen contents of an Al_2O_3-CaO melt with 50 % CaO and 50 % Al_2O_3 (by weight) in relation to reaction time in (N_2 + CO) atmosphere at p_{N_2} = 0.93 bar and p_{CO} = 0.08 bar [25]
⊖ 1600 °C △ 1500 °C
▲ 1550 °C ○ 1460 °C

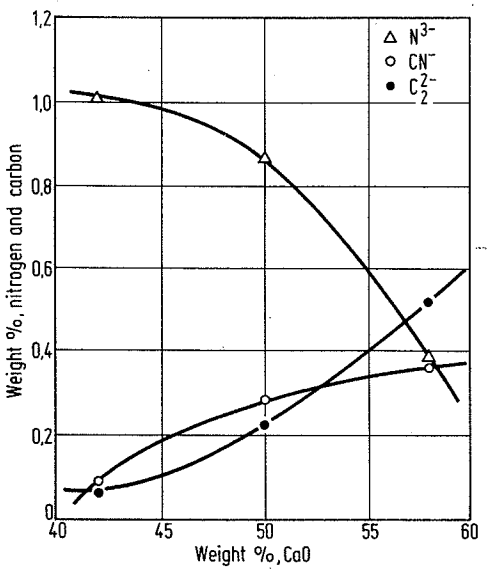


Fig. 7.43. Dependence of bonding forms of nitrogen and carbon on CaO content of an Al_2O_3 melt at 1550 °C, (N_2 + CO) atmosphere with p_{N_2} = 0.93 bar, p_{CO} = 0.08 bar in graphite crucible [27]

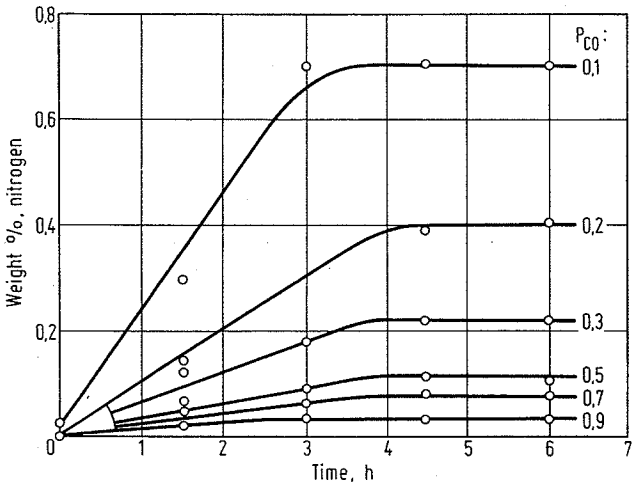


Fig. 7.42. Influence of CO partial pressure in bar on nitrogen solubility in Al_2O_3-CaO melts with 50 % CaO and 50 % Al_2O_3 (by weight) at 1550 °C. Mixture of (N_2 + CO) blown at 600 cm^3/m into graphite crucible [26]

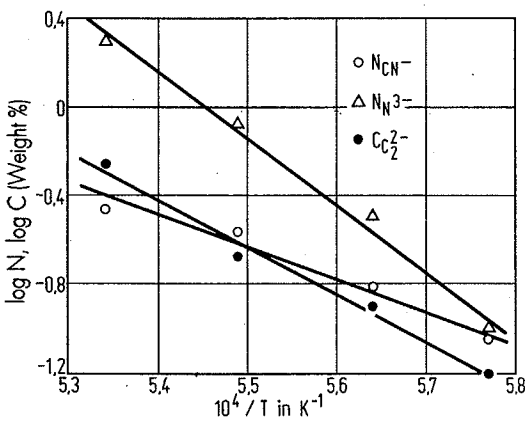


Fig. 7.44. Temperature dependence of bonding forms of nitrogen and carbon in an Al_2O_3-CaO melt with 50 % CaO, 50 % Al_2O_3 in (N_2 + CO) atmosphere at p_{N_2} = 0.93 bar and p_{CO} = 0.08 bar in graphite crucible [27]

Tab. 7.5. Equilibrium contents of total nitrogen, cyanide, and total carbon in Al_2O_3-CaO melts equilibrated with graphite and (N_2 + CO + Ar) mixtures at 1600 °C and 1 bar [47]

p_{N_2}, bar	p_{CO}, bar	p_{AR}, bar	Reaction Time, h	$(N)_{total}$, Wt Pct	(CN), Wt Pct	$(C)_{total}$, Wt Pct	Ca/Wt Pct Al*	$\frac{\text{Wt Pct CaO}}{\text{Wt Pct } Al_2O_3}$ ‡
Nominal Initial Composition: 40 Wt Pct CaO/60 Wt Pct Al_2O_3†								
0.05	0.50	0.45	30	0.054	0.015	0.062	0.936	0.693
0.05	0.50	0.45	100	0.065	0.016	0.065	0.907	0.672
0.10	0.50	0.40	30	0.068	0.024	0.062	0.936	0.694
0.25	0.50	0.25	30	0.13	0.032	0.064	0.936	0.696
0.50	0.50	0	30	0.15	0.041	0.075	0.936	0.696
0.05	0.20	0.75	100	0.16	0.018	0.11	0.907	0.674
0.05	0.20	0.75	54	0.18	0.019	0.10	0.907	0.675
0.05	0.40	0.55	54	0.080	0.013	0.068	0.907	0.673
0.05	0.65	0.30	30	0.039	0.014	0.040	0.936	0.694
0.05	0.95	0	30	0.023	0.013	0.030	0.936	0.693
0.10	0.20	0.70	100	0.33	0.025	0.16	0.907	0.679
Nominal Initial Composition: 45 Wt Pct CaO/55 Wt Al_2O_3†								
0.05	0.50	0.45	30	0.053	0.029	0.085	1.132	0.838
0.10	0.50	0.40	30	0.063	0.041	0.090	1.132	0.837
0.25	0.50	0.25	30	0.11	0.062	0.092	1.132	0.839
0.50	0.50	0	30	0.15	0.086	0.115	1.132	0.840
0.05	0.40	0.55	54	0.074	0.029	0.12	1.118	0.827
0.05	0.65	0.30	30	0.040	0.022	0.080	1.132	0.837
0.05	0.95	0	30	0.030	0.020	0.060	1.132	0.838
0.05	0.95	0	54	0.031	0.021	0.070	1.118	0.827
0.10	0.20	0.70	70	0.25	0.057	0.21	1.118	0.832
0.20	0.20	0.60	70	0.35	0.076	0.22	1.118	0.837
Nominal Initial Composition: 50 Wt Pct CaO/50 Wt Pct Al_2O_3								
0.05	0.50	0.45	30	0.052	0.052	0.19	1.345	0.990
			55	0.052	0.044	0.18	1.333	0.982
0.10	0.50	0.40	30	0.074	0.055	0.18	1.345	0.992
			55	0.074	0.049	0.17	1.333	0.984
0.25	0.50	0.25	30	0.12	0.093	0.20	1.345	0.993
			55	0.11	0.093	0.20	1.333	0.983
0.50	0.50	0	30	0.17	0.15	0.21	1.345	0.994
			55	0.16	0.13	0.20	1.333	0.985
0.05	0.95	0	30	0.030	0.031	0.090	1.345	0.994
			55	0.028	0.026	0.090	1.333	0.985
0.05	0.65	0.30	30	0.043	0.036	0.14	1.345	0.992
			55	0.043	0.038	0.13	1.333	0.984
0.05	0.40	0.55	30	0.063	0.049	0.20	1.345	0.990
			55	0.063	0.039	0.17	1.333	0.983
0.05	0.29	0.75	30	0.14	0.085	0.33	1.345	0.988
			55	0.14	0.070	0.29	1.333	0.982

* The Ca/Al ratios are round values. They are read from the curves representing the chemically analysed Ca/Al ratios as a function of time. For each master slag one single curve was drawn to represent all the experimental points (see Figs. 7.1 and 7.2).

† Two batches of master slag were prepared in the investigation of the 40 pct CaO/60 pct Al_2O_3 and 45 pct CaO/55 pct Al_2O_3 slags which had slightly different compositions. Hence, two different numerical values appear in the column for Ca/Al.

‡ Calculated

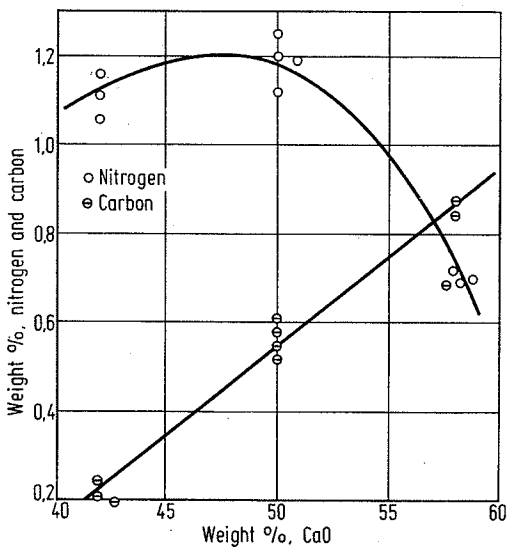


Fig. 7.45. Influence of CaO content on nitrogen and carbon content of Al_2O_3-CaO melts at 1550 °C in (N_2 + CO) atmosphere p_{N_2} = 0.093 bar, p_{CO} = 0.08 bar in graphite crucible [25]

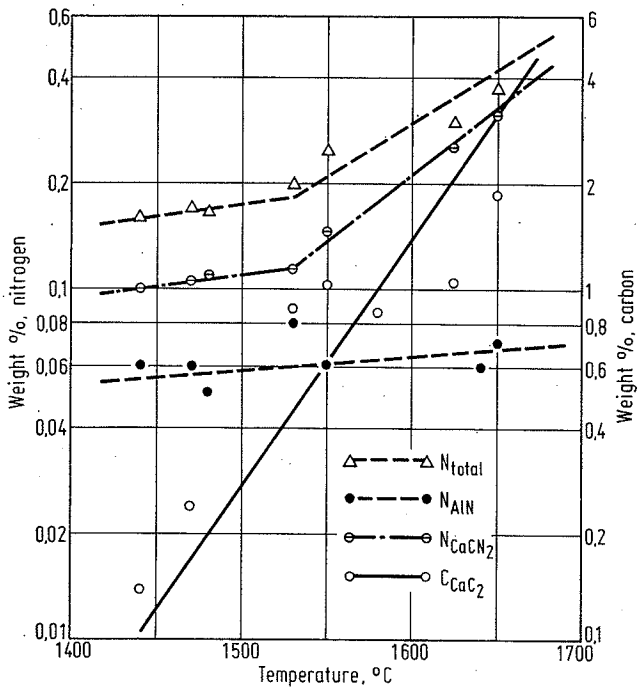


Fig. 7.46. Temperature dependence of different bonding forms of nitrogen and carbon in an Al_2O_3-CaO melt with 50 % CaO, 50 % Al_2O_3 (by weight) at p_{N_2} = 1.013 bar in graphite crucible after a reaction period of 30 min [28]

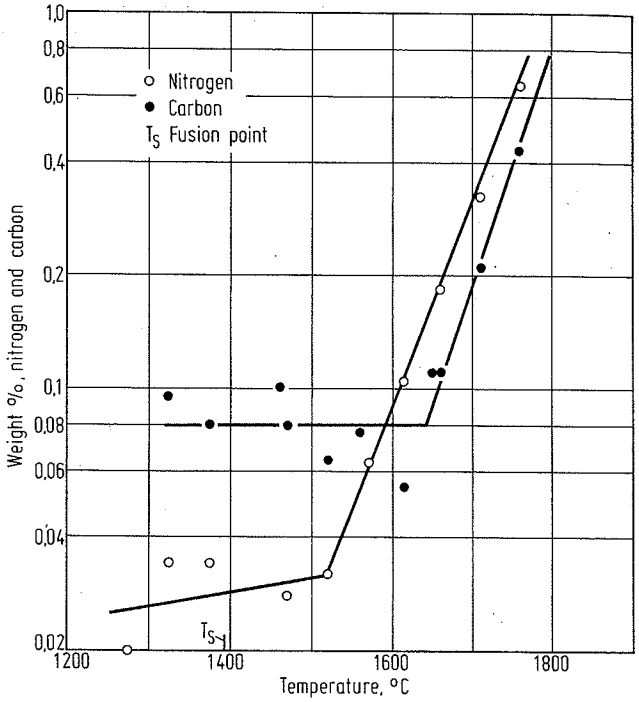


Fig. 7.48. Temperature dependence of carbon and nitrogen contents of an Al_2O_3-CaO melt with 50 % CaO, 50 % Al_2O_3 (by weight) at p_{N_2} = 1.013 bar in graphite crucible after reaction time of 30 min [28]

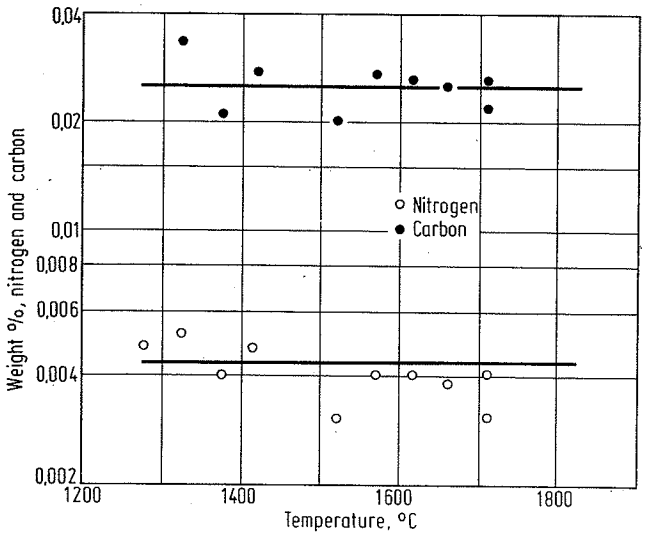


Fig. 7.47. Temperature dependence of carbon and nitrogen absorption of an Al_2O_3-CaO melt with 50 % CaO, 50 % Al_2O_3 (by weight) at p_{N_2} = 1.013 bar in molybdenum crucible after reaction period of 30 min [28]

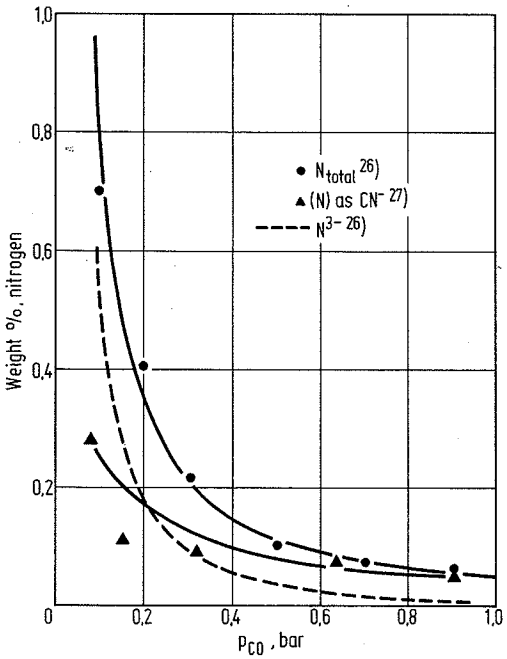


Fig. 7.49. Influence of CO partial pressure on total nitrogen contents as well as on the bonding forms of nitrogen and carbon in Al_2O_3-CaO melts with 50 % CaO, 50 % Al_2O_3 (by weight) in (CO + N_2) atmosphere (600 cm^3/min) at $p_{CO} + p_{N_2}$ = 1.013 bar [26]

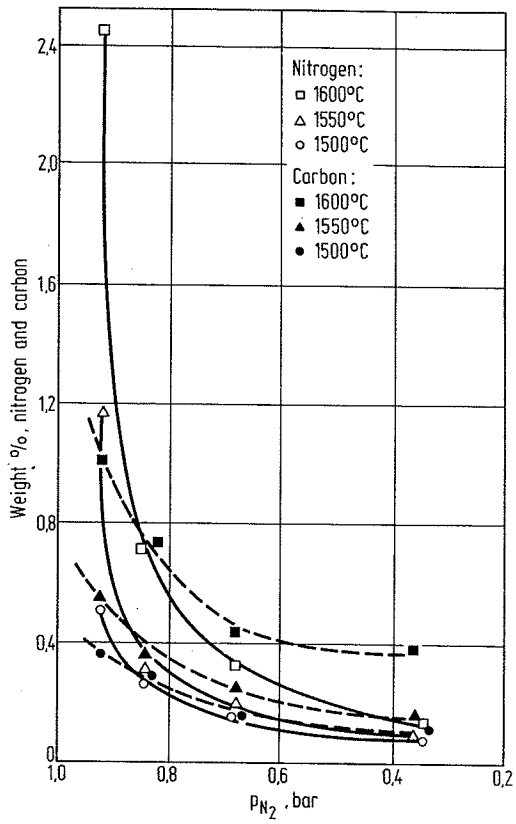


Fig. 7.50. Influence of nitrogen partial pressure on nitrogen and carbon content of an Al_2O_3-CaO melt with 50 % CaO, 50 % Al_2O_3 (by weight) in (CO + N_2) atmosphere at $p_{N_2} + p_{CO} = 1.013$ bar [25]

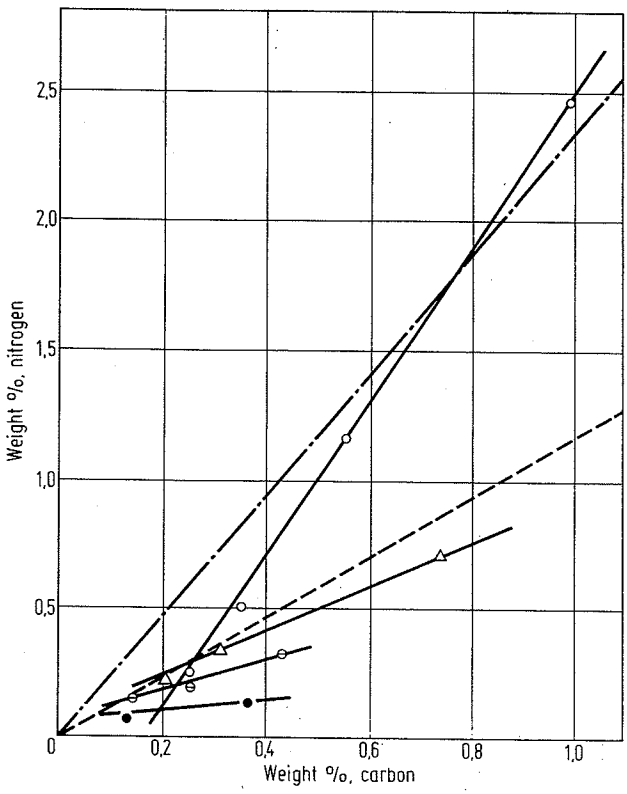


Fig. 7.52. Relationship between carbon and nitrogen content of CaO-Al_2O_3 melts at 1550 °C with 50 % CaO, 50 % Al_2O_3 (by weight) for different nitrogen partial pressures and $p_{CO} + p_{N_2} = 1.013$ bar [25]

○ $p_{N_2} = 0.93$ bar
△ $p_{N_2} = 0.85$ bar ····· CN_2^{2-}
⊖ $p_{N_2} = 0.69$ bar - - - - CN^-
● $p_{N_2} = 0.37$ bar

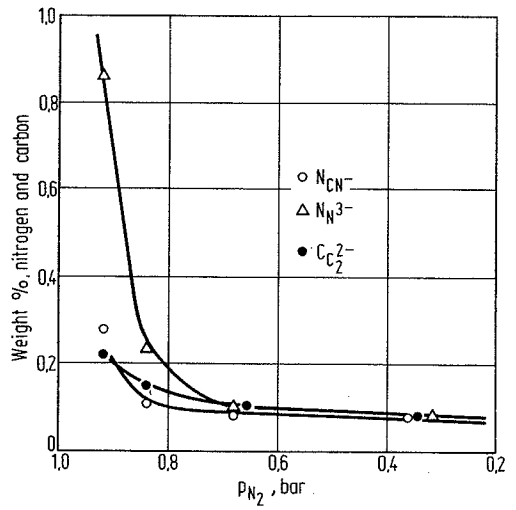


Fig. 7.51. Influence of the N_2 partial pressure on the binding types of nitrogen and carbon in an CaO-Al_2O_3 melt at 1550 °C with 50 % CaO, 50 % Al_2O_3 (by weight) in (CO + N_2) atmosphere at $p_{N_2} + p_{CO} = 1.013$ bar [27]

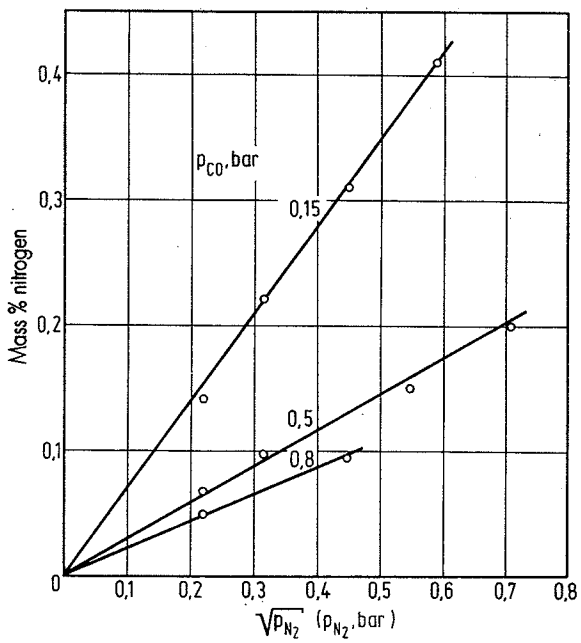


Fig. 7.53. Content of total nitrogen in relation to partial pressures of nitrogen and carbon monoxide at 1600 °C in an Al_2O_3-CaO melt with initial composition of 55 % CaO and 45 % Al_2O_3. (Straight lines were calculated with $K_{nitride} = 0.014$ % bar and $K_{cyanide} = 0.33$ %) [29]

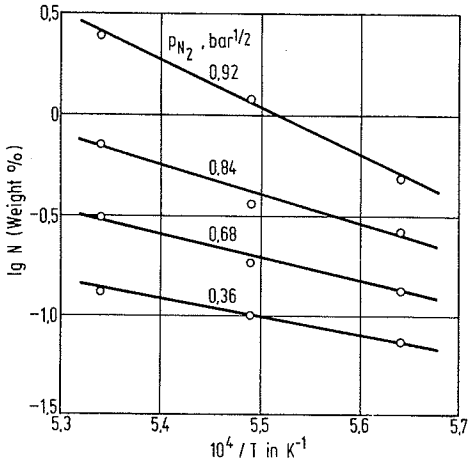


Fig. 7.54. Temperature dependence of total nitrogen content of Al_2O_3-CaO melts with 50 % CaO and 50 % Al_2O_3 in relation to nitrogen partial pressure for (p_{N_2} + p_{CO} = 1.013 bar) [27]. Further literature: [30, 31]

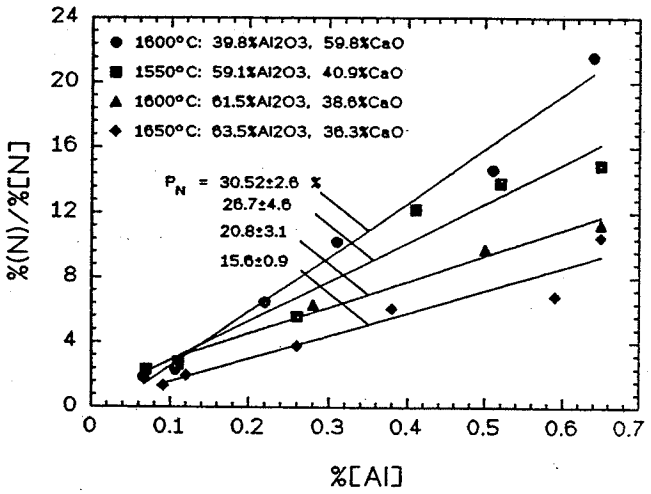


Fig. 7.55. Effect of the Al content of iron on nitrogen partition ratio in Al_2O_3-$CaO_{sat.}$ slags at P_{N_2} = 1 bar, P_N = % (N) / (% [N] % [Al]) [56]

CaF_2-CaO

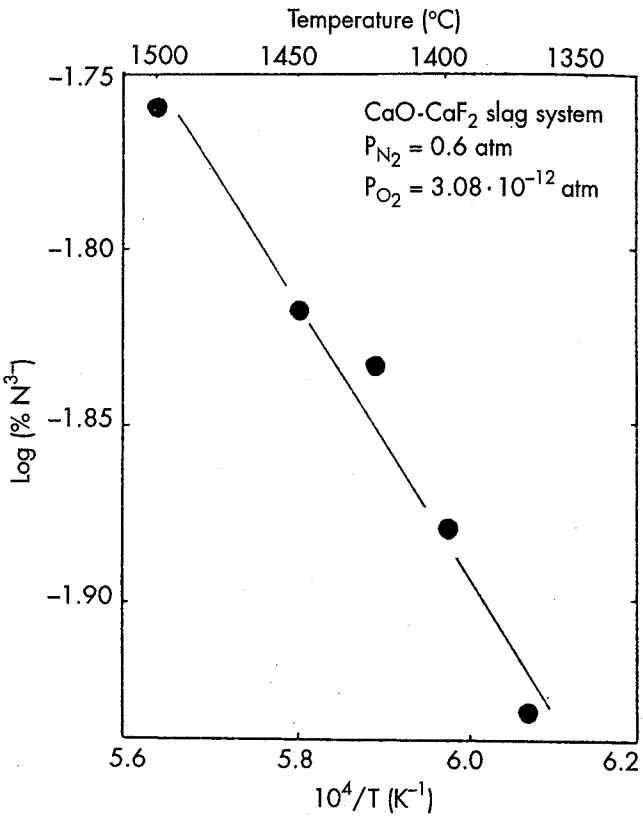


Fig. 7.56. Nitride content in CaF_2-CaO slags as a function of temperature [57]

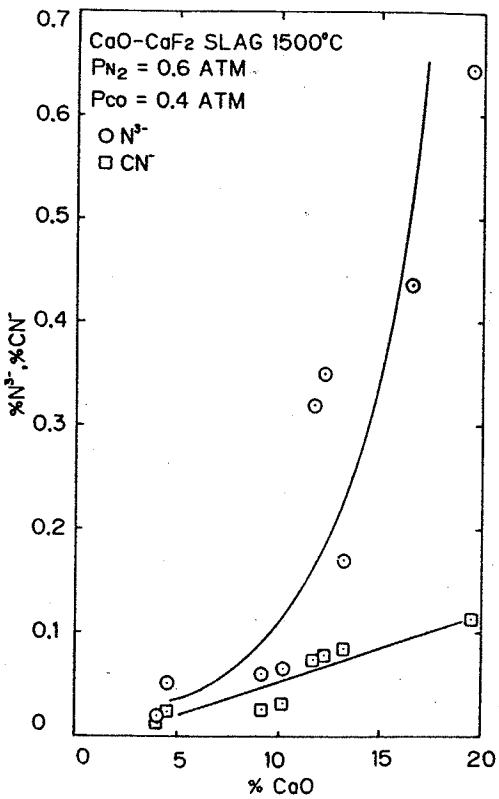


Fig. 7.57. Nitride and cyanide contents in CaF_2-CaO slags as a function of CaO content at 1500 °C [57]

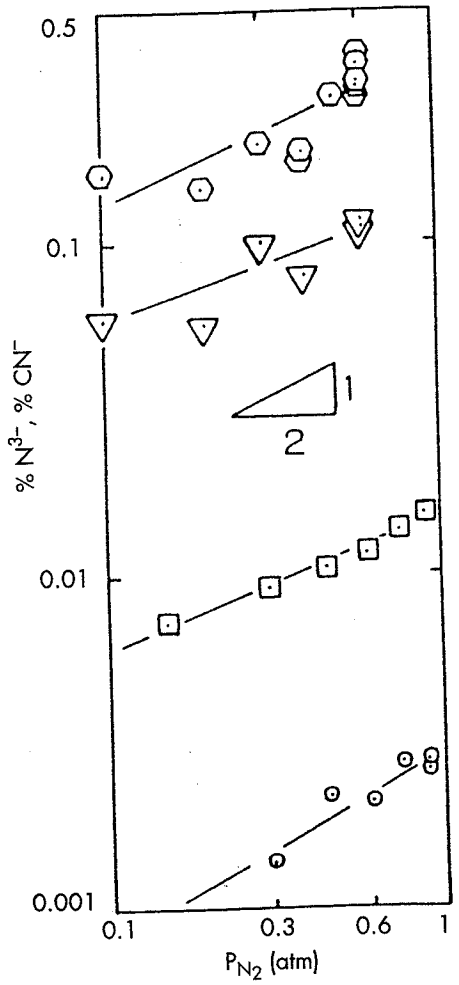


Fig. 7.58. Relationships between nitrogen partial pressure, nitride and cyanide contents in CaF_2-CaO slags at 1375 °C [57]
○ N^{3-}, $p_{O_2} = 4.95\ 10^{-9}$ atm.,
□ N^{3-}, $p_{O_2} = 3.08\ 10^{-12}$atm.,
⬡ N^{-3}, $p_{O_2} = 9.81\ 10^{-18}$atm.,
▽ CN^-, $p_{O_2} = 9.81\ 10^{-18}$atm.

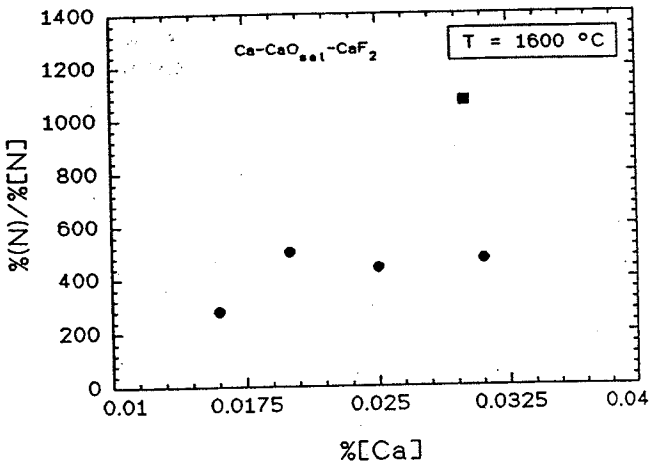


Fig. 7.59. Effect of the Ca content of iron on nitrogen partition ratio in CaF_2-$CaO_{sat.}$ slags at p_{N_2} = 1 bar. ● [58] ■ [59]

$CaO\text{-}SiO_2$

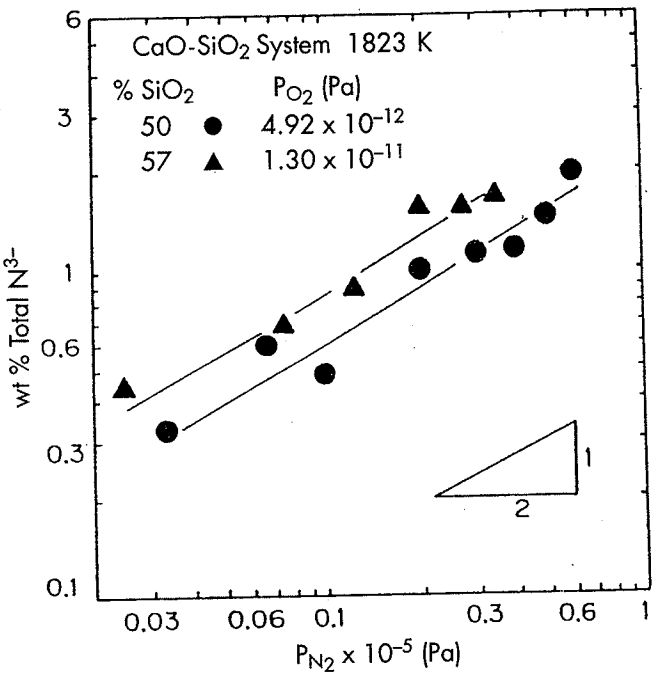


Fig. 7.60. Total nitrogen contents in $CaO\text{-}SiO_2$ slags as a function of nitrogen partial pressure with different oxygen partial pressure at 1823 K [60]

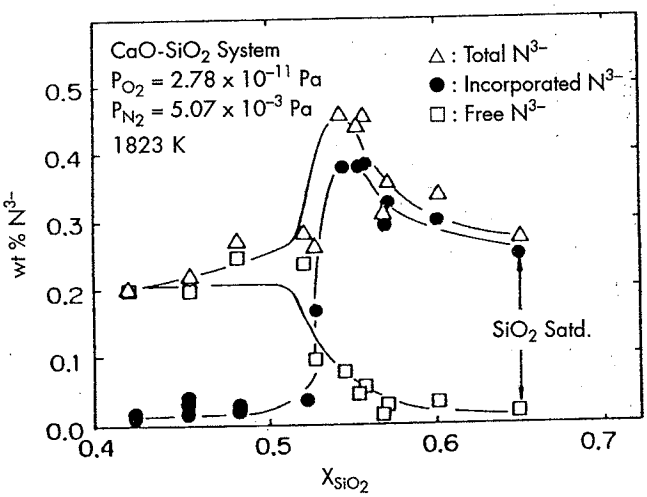


Fig. 7.61. Total, free and incorporated nitrogen contents in $CaO\text{-}SiO_2$ slags as a function of SiO_2 mole fraction [60]

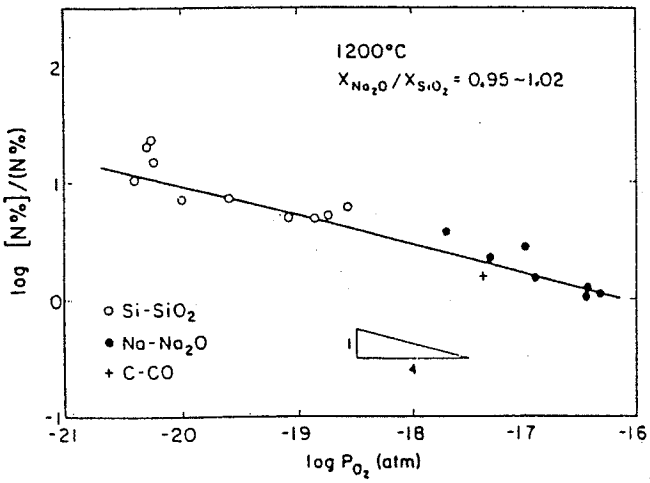


Fig. 7.62. Effect of oxygen partial pressure on nitrogen partition ratio in Na_2O-SiO_2 slag [61]

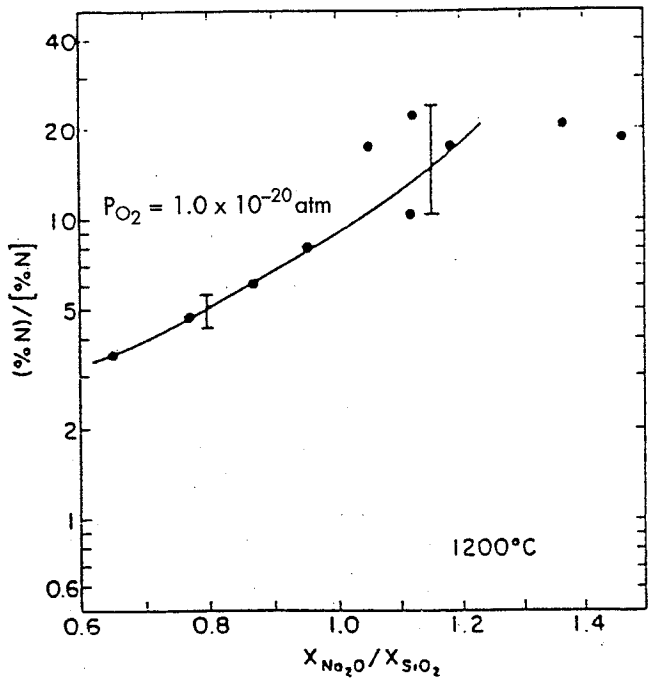


Fig. 7.63. Effect of basicity on nitrogen partition ratio in Na_2O-SiO_2 slag [61]

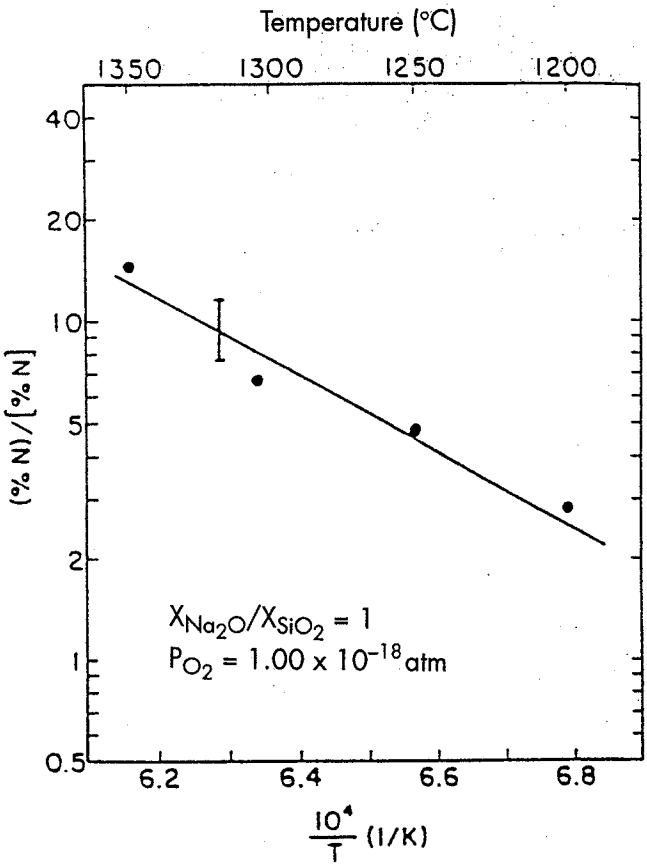


Fig. 7.64. Effect of temperature on nitrogen partition ratio in Na_2O-SiO_2 slag [61]

7.2.2 Ternary systems

Al_2O_3-CaF_2-CaO

Tab. 7.6. Solubilities in a melt with 32 % Al_2O_3, 36 % CaF_2 and 32 % CaO in a graphite crucible at 1600 °C and 1.013 bar [48]

p_{N_2}, Atm	p_{CO}, Atm	p_{Ar}, Atm	$(N)_{total}$, Wt Pct*	(CN), Wt Pct*	$(C)_{total}$, Wt Pct*	$K_{cyanide} = (CN)\sqrt{p_{CO}/p_{N_2}}$, Wt Pct
0.05	0.50	0.45	0.105	0.145	0.240	0.459
0.10	0.50	0.40	0.130	0.175	0.255	0.391
0.25	0.50	0.25	0.180	0.285	0.295	0.403
0.25	0.50	0.25	0.215	0.325	0.395	0.460
0.50	0.50	0	0.285	0.405	0.400	0.405
0.05	0.40	0.55	0.120	0.145	0.355	0.410
0.05	0.20	0.75	0.163	0.147	0.587	0.294
0.05	0.95	0	0.056	0.110	0.180	0.479
0.05	0.65	0.30	0.085	0.110	0.230	0.397
0.05	0.20	0.75	0.160	0.170	0.525	0.340
						Average: 0.404

*With the experiments conducted at $p_{CO} \leq 0.5$ atm there was a slight decrease (mostly less than 10 pct) of (CN) and $(C)_{total}$ contents, after maximum contents had been established (compare text). Average values for the time period from 22 h till the end of the experiment are listed in these columns.

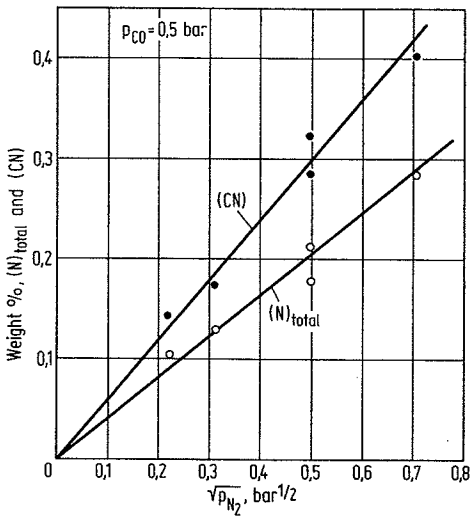


Fig. 7.65. Nitrogen and cyanid contents in relationship to nitrogen partial pressure at constant p_{CO} in a melt with a composition of 32 % Al_2O_3, 36 % CaF_2 and 32 % CaO at 1600 °C [48]

Al_2O_3-CaO-SiO_2

Tab. 7.7. Influence of slag composition on nitrogen solubility in Al_2O_3-CaO-SiO_2 melts in graphite crucibles at 1550 °C in (N_2 + CO + Ar) atmosphere at p_{N_2} = 0.51 bar, p_{CO} = 0.4 bar, p_{Ar} = 0.1 bar [32]

Composition of slag Mole fraction			Nitrogen contents		Number of heats
CaO	SiO_2	Al_2O_3	Mole fraction	Mass %	
0.551	0.310	0.120	0.0168 ± 0.0004	0.378 ± 0.009	6
0.520	0.337	0.124	0.0187 ± 0.0009	0.421 ± 0.020	7
0.496	0.359	0.121	0.0244 ± 0.0007	0.562 ± 0.016	4
0.471	0.379	0.121	0.0296 ± 0.0009	0.673 ± 0.020	8

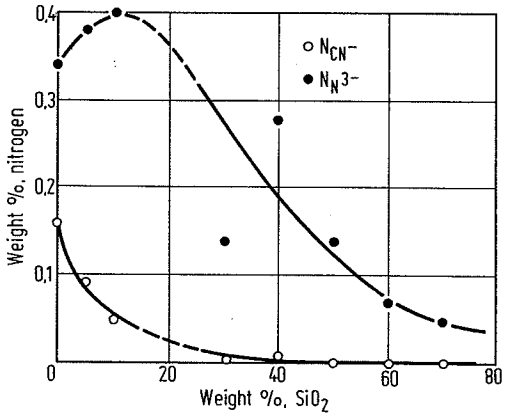


Fig. 7.66. Dependence of different bonding forms of nitrogen in Al_2O_3-CaO-SiO_2 melts on SiO_2 content at 1500 °C in (N_2 + CO) atmosphere, p_{CO} = 0.08 bar and CaO/Al_2O_3 = 1 [27]

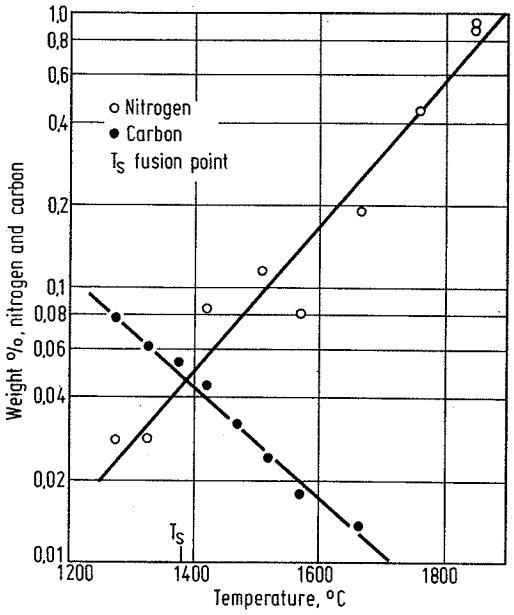


Fig. 7.67. Temperature dependence of carbon and nitrogen content of an Al_2O_3-CaO-SiO_2 melt at p_{N_2} = 1.013 bar for a composition (by weight) 40 % Al_2O_3, 40 % CaO, 20 % SiO_2 after a reaction time of 30 min in graphite crucible [28]

Tab. 7.8. Equilibrium nitrogen content of a melt with a composition of 48 % CaO, 40 % SiO_2 and 12 % Al_2O_3 at 1450 °C and 1.013 bar [49]

p_{N_2}	p_{CO}	$(N)_{total}$	(CN)	$(N)_{nitride}$*)	$\sqrt{p_{N_2}/p_{CO}^3}$	$\sqrt{p_{N_2}/p_{CO}}$
bar	bar	wt.%	wt.%	wt.%	bar^{-1}	bar^{-1}
0.05	0.95	0.033 ± 0.005	0.006 ± 0.002	0.030 ± 0.005	0.241	0.229
0.20	0.80	0.086 ± 0.008	0.012 ± 0.002	0.080 ± 0.008	0.625	0.50
0.50	0.50	0.27 ± 0.03	0.025 ± 0.003	0.257 ± 0.03	2.000	1.0

*) $(\%N)_{nitride} = (\%N)_{total} - \frac{14}{26}(\%CN)$

Tab. 7.9. Temperature dependence of nitrogen and carbon contents of an Al_2O_3-CaO-SiO_2 melt with 20 % Al_2O_3, 40 % CaO, 40 % SiO_2 in (N_2 + CO) atmosphere at p_{N_2} = 0.93 bar, p_{CO} = 0.08 bar in graphite crucible [27]

Temperature °C	Composition (mass %)				
	N (total)	N as CN^-	C (total)	C as C_2^{2-}	C as CN^-
1400	0.04	0.0034	0.06	0.06	0.0029
1450	0.15	0.0045	0.07	0.06	0.0039
1500	0.26	0.0062	0.08	0.08	0.0053
1550	2.01	0.0081	0.11	0.09	0.0069

Tab. 7.10. Influence of gas composition on nitrogen contents of Al_2O_3-CaO-SiO_2 melts in graphite crucible under (N_2 + CO + Ar) atmosphere at p_{total} = 1.013 bar [32]

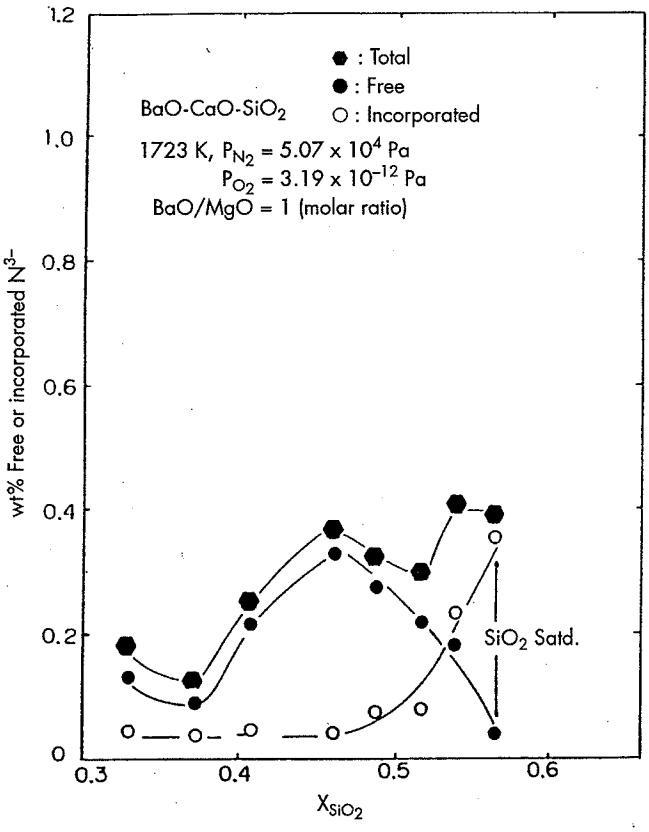
Temperature °C	Slag composition (mole %)			Gas composition			N contents		Number of heats
	% CaO	% SiO_2	% Al_2O_3	% N_2	% CO	% Ar	mole %	mass %	
				70	20	10	4.21 ± 0.31	0.975 ± 0.076	9
				55	25	20	3.101 ± 0.19	0.703 ± 0.03	8
				50	40	10	1.68 ± 0.04	0.378 ± 0.009	6
1550	55.1	30.95	12.0	20	40	40	1.10 ± 0.09	0.247 ± 0.021	8
				40	60	0	0.93 ± 0.08	0.211 ± 0.019	10
				20	60	20	0.784 ± 0.10	0.177 ± 0.02	9
				70	20	10			
				50	40	10	2.96 ± 0.09	0.673 ± 0.020	8
				20	40	40	1.90 ± 0.13	0.428 ± 0.030	13
1550	47.05	37.9	12.1	40	60	0	1.67 ± 0.07	0.379 ± 0.016	12
				20	60	20	1.19 ± 0.06	0.264 ± 0.012	5
				20	60	20	0.511 ± 0.03	0.116 ± 0.007	5
1500	47.05	37.9	12.1	20	40	40	1.819 ± 0.03	0.195 ± 0.01	8
				50	40	10	1.329 ± 0.10	0.303 ± 0.02	7
				20	60	20	1.19 ± 0.07	0.264 ± 0.02	7
1600	55.1	30.95	12.0	50	40	10	2.98 ± 0.16	0.674 ± 0.02	9
				55	25	20	6.021 ± 0.3	1.424 ± 0.07	6

Tab. 7.11. Temperature dependence of nitrogen and carbon content of an Al_2O_3-CaO-SiO_2 melt with 49 % CaO, 41 % SiO_2, 10 % Al_2O_3 (by weight) in equilibrium with a carbon saturated iron melt at p_{N_2} = 1.013 bar (experimental conditions: 60 g Fe and 30 g slag in graphite crucible, reaction duration 10 min) [28]

Temperature °C	1355	1400	1460	1505	1535	1580	1610	1620
% C	0.160	0.090	0.080	0.080	0.060	0.070	0.040	0.040
% N	0.0035	0.0040	0.0090	0.0110	0.0115	0.0145	0.0155	0.0220

Further literature references: [33, 34]

$BaO-MgO-SiO_2$



▶
Fig. 7.68. Total, free and incorporated nitrogen contents in $BaO-MgO-SiO_2$ slags as a function of SiO_2 mole fraction [60]

CaF_2-CaO-SiO_2

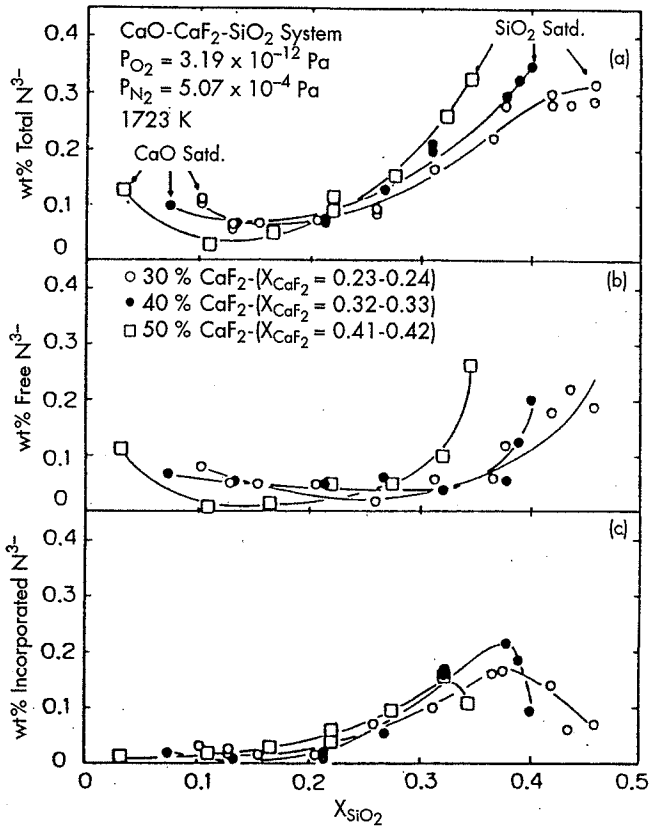


Fig. 7.69 a-c. Total, free and incorporated nitrogen contents in CaF_2-CaO-SiO_2 slags as a function of SiO_2 mole fraction [60]

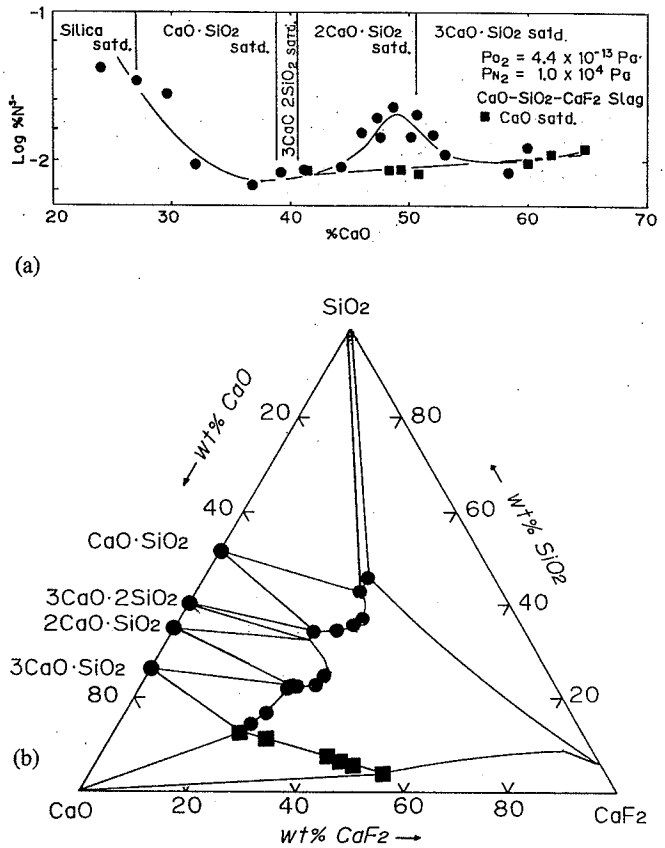


Fig. 7.70 a,b. Total nitrogen contents of CaF_2-CaO-SiO_2 melts along the 1573 K liquidus line as a function of CaO contents (a); the slag compositions are illustrated in (b) [62]

CaO-MgO-SiO_2

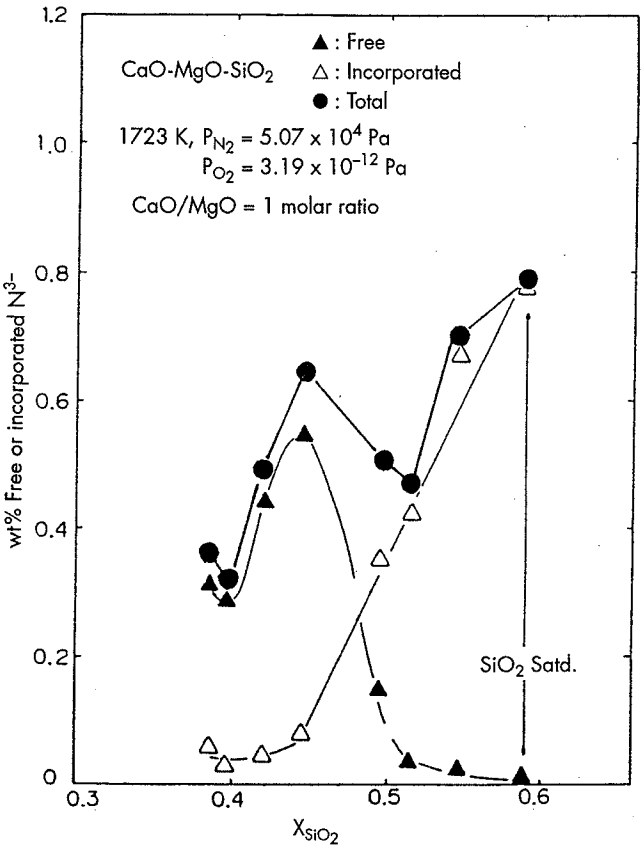


Fig. 7.71. Total, free and incorporated nitrogen contents in CaO-MgO-SiO_2 slags as a function of SiO_2 mole fraction [60]

7.2.3 Quaternary systems and systems with more components

Al_2O_3-CaO-MgO-SiO_2

Tab. 7.12. Influence of composition of Al_2O_3-CaO-MgO-SiO_2 melts on nitrogen solubility at 1550 °C in graphite crucible under (N_2 + CO + Ar) atmosphere with p_{N_2} = 0.51 bar, p_{CO} = 0.4 bar, p_{Ar} = 0.1 bar [32]

Slag composition mole %				N contents		Number of heats
CaO	SiO_2	Al_2O_3	MgO	mole %	Mass %	
46.7	31.5	12.5	7.5	1.80 ± 0.07	0.414 ± 0.015	6
41.4	36.2	12.4	7.45	2.49 ± 0.10	0.574 ± 0.024	10
39.8	37.8	12.1	7.3	3.04 ± 0.08	0.706 ± 0.018	20
47.0	24.7	12.4	14.8	1.04 ± 0.15	0.240 ± 0.035	12
43.4	28.2	12.3	14.8	1.29 ± 0.04	0.302 ± 0.009	6
40.3	31.0	12.3	14.7	1.68 ± 0.09	0.395 ± 0.021	16
35.15	35.6	12.2	14.7	2.34 ± 0.03	0.539 ± 0.007	4
32.55	37.9	12.15	14.55	2.87 ± 0.02	0.677 ± 0.005	5

Tab. 7.13. Nitrogen content of Al_2O_3-CaO-MgO-SiO_2 melts in equilibrium with carbon saturated silicon containing iron at 1450 to 1650 °C (experimental conditions: graphite crucible, stirred melt, air surface applied, reaction duration 60 min) [35]

Quantity g		Composition (weight %)							Composition in 10^{-1} % by weight		
		metal		slag					metal	slag	
metal	slag	[C]	[Si]	(Fe)	(CaO)	(SiO_2)	(Al_2O_3)	(MgO)	[N]	(N)	(CN)
Series I: slags alone molten 1550 °C, 60 min											
	36.1			0.032	24.9	54.4	10.2	9.9		770	6
	37.5			0.027	32.9	46.8	10.2	9.9		840	2
	36.7			0.027	39.3	40.4	10.1	9.9		950	13
	37.4			0.023	45.4	32.4	10.1	9.9		1120	80
Series II: slags as I, but at the end 2.0 g Wüstite added, 1550 °C, 60 min + 5 min											
0.37	38.8			2.21	24.2	52.7	9.9	9.6		250	4
0.23	38.8			1.66	32.2	45.6	9.9	9.7		190	4
0.93	40.1			1.69	38.4	39.4	9.9	9.7		25	4
0.74	38.7			0.92	44.9	33.9	10.0	9.8		15	5
Series III: slags as I, 6 g pig iron added, 1550 °C, 60 min											
6.06	36.0	3.68	5.00	0.054	25.4	53.7	10.4	10.1	< 10 (n.b.)	490	2
6.14	37.4	4.47	2.54	0.044	33.2	46.2	10.2	10.0	53 (67)	700	6
6.01	37.1	4.92	1.02	0.047	39.5	40.3	10.2	9.9	53 (75)	670	58
6.13	37.3	4.96	0.65	0.030	45.7	34.2	10.1	9.9	70 (62)	840	178
Series IV: as III, but after that added 2 g Wüstite, 1550 °C, 60 min + 5 min											
5.48	37.9	3.14	6.77	2.18	24.9	51.5	10.2	9.9	20 (22)	350	2
6.47	38.0	4.29	2.88	1.99	32.4	45.0	10.0	9.7	20 (25)	140	2
6.62	38.0	4.94	0.79	1.33	38.7	39.8	10.0	9.7	20 (30)	110	4
7.11	37.8	5.00	0.064	0.92	44.9	33.9	10.0	9.8	20 (24)	70	4
Series V: slags as I only, 2 g CaO_2 added at start, 1550 °C, 60 min											
	38.3			0.024	28.1	51.4	9.7	9.5		700	29
	36.9			0.028	36.0	43.5	9.8	9.5		1020	46
	36.1			0.038	41.9	38.2	9.7	9.4		930	5
	35.7			0.024	47.7	32.2	9.7	9.4		1260	7
Series VI: slags as V + 6 g pig iron, 1550 °C, 60 min											
6.16	37.2	3.04	7.61	0.045	28.9	50.5	10.0	9.7	35 (38)	770	10
6.17	39.5	4.14	3.78	0.054	36.2	43.4	9.8	9.6	35 (69)	1240	13
5.91	40.2	4.33	2.60	0.036	42.5	38.0	9.8	9.6	35 (58)	1070	19
6.33	41.8	4.15	3.53	0.036	48.3	31.7	9.8	9.5	35 (33)	1580	148
Series VII: slags as I, 1450 °C, 60 min											
	37.4			0.037	24.9	54.3	10.2	9.9		390	4
	37.4			0.025	32.9	48.5	10.2	9.9		350	3
	37.4			0.028	39.3	40.4	10.1	9.9		390	9
	37.4			0.021	45.4	34.1	10.1	9.9		530	39
Series VIII: slags as I, 1650 °C, 60 min											
	34.5			0.028	24.9	54.0	10.2	9.9		550	2
	35.7			0.021	32.9	46.5	10.2	9.9		950	2
	37.2			0.025	39.2	40.5	10.1	9.9		2220	14
	37.0			0.016	45.3	34.4	10.1	9.9		3150	22
Series IX: slags as I + 6 g pig iron, 1450 °C, 60 min											
6.07	37.9	4.21	2.32	0.103	24.9	54.2	10.2	10.0	< 10 (30)	510	7
5.99	38.1	4.63	0.94	0.067	32.9	46.5	10.2	9.9	70 (n.b)	460	11
5.94	37.8	4.84	0.48	0.051	39.3	40.4	10.1	9.9	70 (82)	390	44
6.04	37.7	4.84	0.38	0.030	45.6	34.4	10.1	9.9	53 (n.b.)	530	94
Series X: slags as I + 6 g pig iron, 1650 °C, 60 min											
7.25	32.1	0.88	18.51	0.027	28.1	50.5	11.0	10.7	53 (n.b.)	930	3
6.84	31.9	1.08	16.95	0.019	36.0	42.7	10.9	10.6	70 (n.b.)	930	3
6.22	37.0	4.47	3.29	0.043	39.7	39.9	10.2	10.0	70 (75)	1380	28
6.11	36.8	4.46	3.20	0.025	46.0	33.7	10.2	10.0	35 (44)	1840	116

n.b. = not determined

Al_2O_3-CaF_2-CaO-MgO-SiO_2

Tab. 7.14. Nitrogen content of Al_2O_3-CaF_2-CaO-MgO-SiO_2 melts in equilibrium with carbon saturated, silicon containing iron at 1550 °C (experimental conditions: graphite crucible, stirred melt, air surface applied, reaction duration 30 min, slag quantity 40 g) [35]

Iron g	$\frac{CaO + MgO}{SiO_2}$	Composition (weight %) % [Si]	% [C]	10^{-4} % [N]	10^{-4} % (N)	10^{-4} % (CN)	$\frac{(S)}{[S]}$	$\frac{[Mn]}{(Mn)}$
Series I: 10.0 g CaO and 20.0 g SiO_2								
3.2	0.71	8.6	2.84	16 (n.b.)	540	15	24	1.30
12.2	0.72	2.94	4.03	43 (83)	700	8	5.0	0.61
63.5	0.72	0.65	4.55	53 (69)	400	11	2.8	0.27
124.5	0.72	0.32	4.84	63 (58)	400	10	2.0	0.22
Series II: 11.25 g CaO and 18.75 g SiO_2								
3.2	0.82	7.1	3.22	12 (24)	630	14	27	1.61
12.3	0.83	2.20	4.28	49 (94)	720	11	9.9	0.70
63.3	0.83	0.46	4.80	61 (75)	400	13	3.8	0.31
124.4	0.82	0.17	4.97	62 (62)	370	12	2.8	0.26
Series III: 18.8 g CaO and 16.7 g SiO_2								
3.2	1.04	4.65	3.89	26 (37)	790	23	47	2.26
12.1	1.04	1.10	4.78	61 (n.b.)	630	37	20	1.00
63.3	1.03	0.20	5.03	72 (68)	300	24	6.3	0.42
124.5	1.03	0.11	5.12	69 (65)	260	20	4.5	0.35
Series IV: 15.0 g CaO and 15.0 g SiO_2								
3.2	1.23	1.90	4.70	56 (n.b.)	720	62	61	2.82
12.3	1.26	0.39	5.03	87 (84)	490	80	29	1.39
63.7	1.25	0.17	5.13	69 (62)	230	47	17	0.88
124.4	1.25	0.051	5.23	56 (64)	140	31	8.7	0.49
Series V: 16.35 g CaO and 13.65 g SiO_2								
3.1	1.47	1.20	5.02	56 (59)	700	171	97	4.45
12.1	1.48	0.26	n.b.	n.b.	230	81	70	2.50
12.2	1.47	0.20	5.28	66 (69)	470	129	73	2.46
63.6	1.47	0.093	5.19	63 (66)	140	108	22	0.85
63.3	1.47	0.049	5.20	60 (62)	230	59	25	0.91
124.1	1.46	0.019	5.20	66 (66)	230	34	14	0.54
Series VI: 17.5 g CaO and 12.5 g SiO_2								
3.1	1.70	0.98	4.89	n.b.	980	359	164	8.27
12.2	1.70	0.20	4.98	72 (68)	300	209	136	4.40
12.2	1.69	0.072	5.27	58 (73)	350	170	98	2.59
63.4	1.69	0.038	5.16	61 (64)	160	101	56	1.66
63.4	1.69	0.035	5.25	74 (73)	160	102	72	1.90
124.4	1.68	0.022	5.21	92 (57)	230	72	44	1.24
123.8	1.68	0.018	5.29	66 (70)	180	92	44	1.17

n.b. = not determined

Al_2O_3-CaO-Fe_3O_4-FeS-MgO-MnO-SiO_2

Tab. 7.15. Nitrogen contents of silicate-sulphide slags in graphite crucible in equilibrium with pig iron at 1550 °C (experimental conditions: graphite crucible, stirred melt, air surface applied, reaction period 6 h, constant sample weight: 60 g pig iron, 3.75 g MgO, 3.75 g Al_2O_3, 2.5 g FeS, 1.5 g MnO, 1.5 g Fe_3O_4) [36]. Further literature: [37-42]

time min	Composition (weight %)								(S) / [S]	[Mn] / (Mn)	CaO + MgO / SiO_2
	molten iron			slag							
	[C]	[Si]	[N] · 10^4	(N) · 10^4	(CN) · 10^4	(ΣC)	(C_R)	(ΔC)			
Series I: 9.3 g CaO, 20.7 g SiO_2											
0	3.75	0.042	70	50	6	0.025	0.024	0.001	0.05	0.04	0.619
5	4.85	0.068	60	110	6	0.033	0.036	< 0.001	0.39	0.03	0.622
15	4.80	0.24	70	230	6	0.034	0.033	0.001	0.97	0.13	0.624
30	4.92	0.48	40	350	9	0.034	0.025	0.009	1.53	0.20	0.645
60	4.78	1.00	80	480	12	0.047	0.027	0.020	3.0	0.30	0.659
120*	4.50	2.29	50	700	12	0.037	0.021	0.016	8.5	0.58	0.749
180	4.07	3.70	60	1300	22	0.064	0.046	0.018	15.2	0.91	0.839
270*	4.15	4.10	50	1400	19	0.084	0.050	0.034	20.3	1.17	0.901
360	3.60	5.48	30	1770	51	0.086	0.053	0.033	44	1.93	0.995
Series II: 12.3 g CaO, 17.7 g SiO_2											
0	4.16	0.013	60	40	3	0.029	0.020	0.009	0.11	0.04	0.891
5	5.05	0.014	40	50	2	0.034	0.030	0.004	0.66	0.09	0.905
15	5.04	0.025	50	110	4	0.040	0.025	0.015	1.14	0.12	0.910
30	5.06	0.125	50	250	8	0.069	0.050	0.019	2.82	0.23	0.926
60	4.98	0.50	80	490	17	0.065	0.048	0.017	6.45	0.47	0.968
120*	4.94	1.21	70	680	44	0.070	0.033	0.037	14.9	0.99	1.016
180	4.79	1.64	60	840	24	0.062	0.043	0.019	19	1.15	1.072
270*	4.53	2.46	65	1140	76	0.167	0.112	0.055	45	1.99	1.142
360	4.20	3.52	50	1350	68	0.131	0.087	0.044	88	3.56	1.296
Series III: 14.7 g CaO, 15.2 g SiO_2											
0	4.19	0.010	n.b.	20	5	0.027	0.020	0.007	0.22	0.04	1.196
5	5.05	0.0027	50	40	5	0.034	0.023	0.011	1.32	0.09	1.198
15	5.07	0.0048	50	50	7	0.034	0.031	0.003	2.51	0.13	1.197
30	5.13	0.034	70	180	19	0.049	0.030	0.019	6.9	0.31	1.198
60	5.11	0.143	80	280	33	0.049	0.025	0.024	13.1	0.66	1.210
120*	5.12	0.75	50	610	70	0.270	0.185	0.085	47	2.01	1.313
180	4.94	1.14	60	670	83	0.080	0.040	0.040	60	2.80	1.345
270*	4.63	2.25	50	1280	224	0.176	0.105	0.071	210	8.19	1.530
360	4.43	2.80	60	1750	169	0.188	0.138	0.050	389	13.2	1.575
Series IV: 17.0 g CaO, 10.0 g SiO_2											
0	4.12	< 0.001	40	20	4	0.029	0.010	0.019	1.40	0.07	1.584
5	4.92	0.0013	40	40	6	0.037	0.025	0.012	3.00	0.10	1.597
15	5.06	0.0044	60	90	24	0.052	0.030	0.022	10.9	0.35	1.583
30	5.03	0.021	80	250	47	0.054	0.035	0.019	32	1.04	1.608
60	5.03	0.13	75	420	126	0.090	0.055	0.035	72	2.7	1.627
120*	5.13	0.42	55	560	124	0.184	0.132	0.052	261	7.0	1.688
180	4.82	1.00	65	1120	130	0.202	1.175	0.027	334	11.5	1.791
270*	4.80	1.18	55	1260	132	0.343	0.189	0.154	301	17.3	1.845
360	4.71	1.55	55	1720	180	0.332	0.250	0.082	461	20.8	1.931

C_R: carbon in residue not soluble in acid; $\Delta C = (\Sigma C) - (C_R)$

n.b. = not determined

7.2.4 Technological slags

7.2.4.1 Blast furnace slags

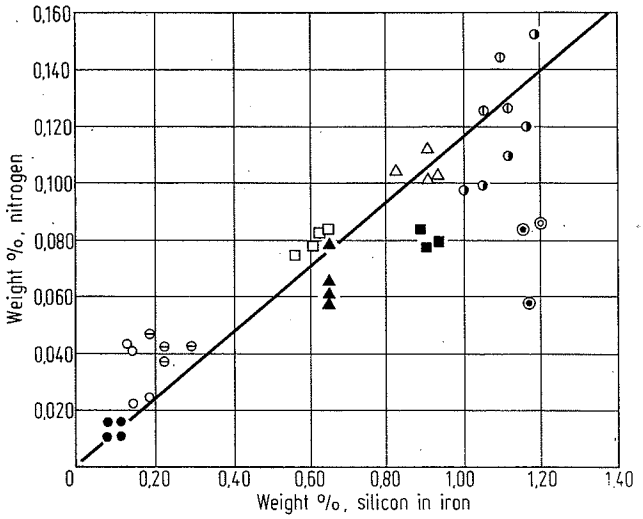


Fig. 7.72. Nitrogen content of blast furnace slag in relation to silicon content of pig iron at 1420 °C (experimental conditions: 75 g synthetic slag in contact with 600 g hot metal, p_{N_2} = 1.013 bar, slag stirred, reaction duration 90 min) [43]

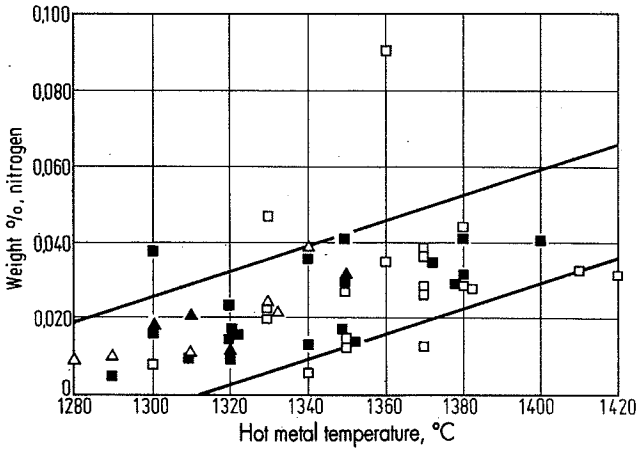


Fig. 7.73. Influence of hot metal temperature on nitrogen content of a blast furnace slag [43]
△, ▲: hot metal for LD process
□, ■: hot metal for basic Bessemer process

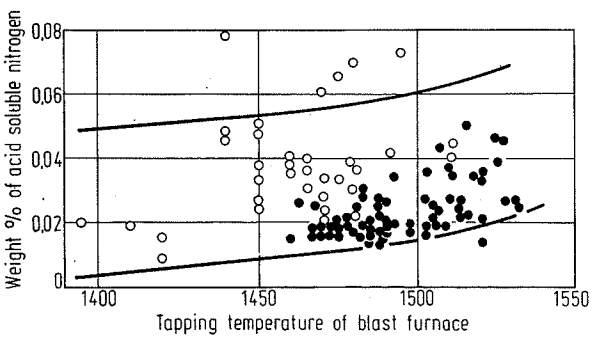


Fig. 7.74. Dependence of nitrogen content of a blast furnace slag on tapping temperature [44]. Further literature: [45]

7.2.4.2 Electric arc furnace slags

Tab. 7.16. Nitrogen content of an electric arc furnace slag with 58.4 % CaO, 27.3 % SiO_2, 6.3 % CaF_2, 0.1 % FeO at p_{N_2} = 1.013 bar [46]. Further literature: [49, 51]

Temperature °C	Reaction time min	Mass % nitrogen
1476	0	0.008
	47	0.008
	119	0.009
1565	50	0.007
	50	0.007
	95	0.007
1565	95	0.007

7.3 Carbon dioxide

7.3.1 Binary systems

Al_2O_3-CaO

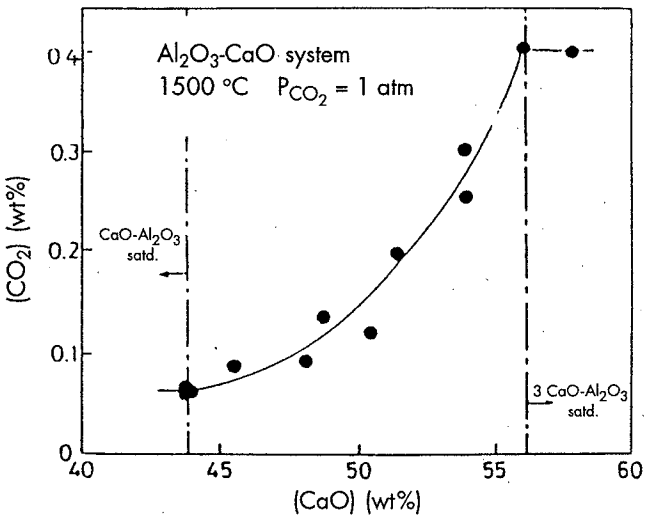


Fig. 7.75. CO_2 solubility in Al_2O_3-CaO slag as a function of CaO content [63]

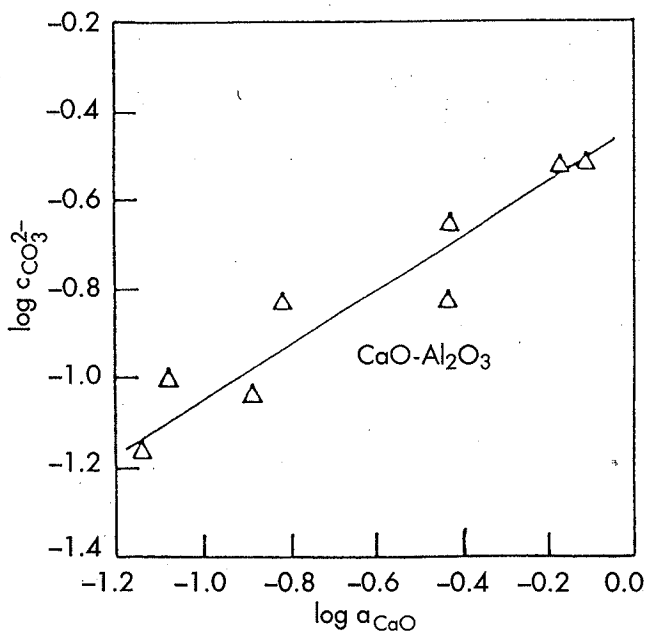


Fig. 7.76. Carbonate capacity of Al_2O_3-CaO slag as a function of CaO activity [63]
Carbonate capacity is defined as $C_{CO_3^{2-}} = \frac{\%\ (CO_3^{2-})}{P_{CO_2}}$

CaF_2-CaO

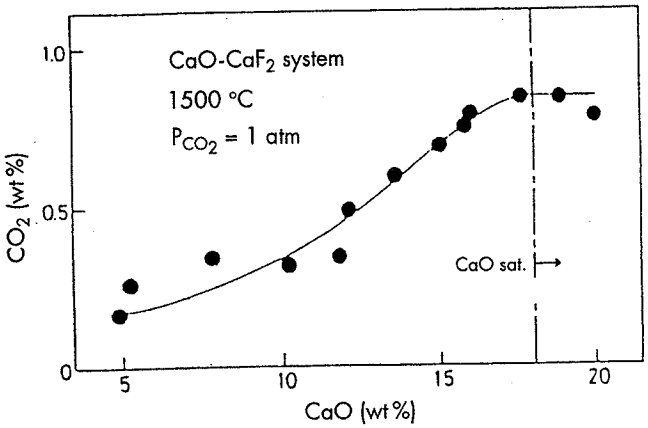


Fig. 7.77. CO_2 solubility in CaF_2-CaO slag as a function of CaO content [63]

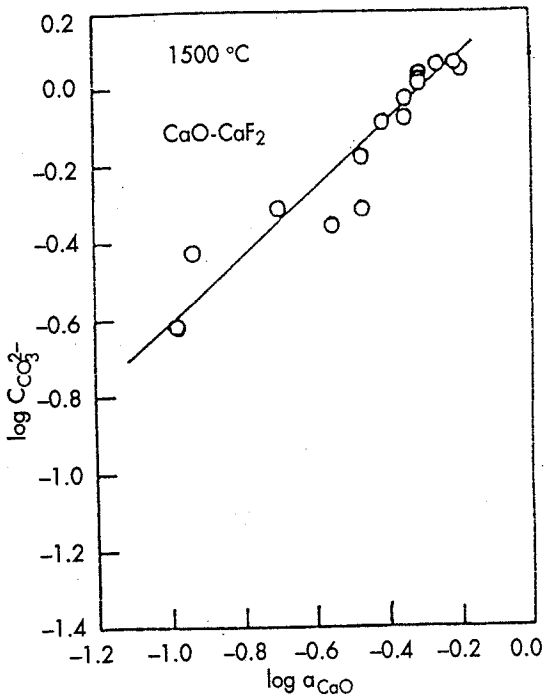


Fig. 7.78. Carbonate capacity (definition see Fig. 7.76) of CaF_2-CaO slag as a function of CaO activity [63]

CaO-Fe_2O_3

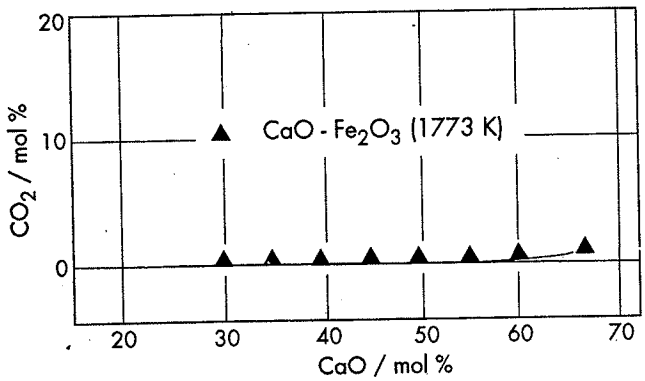


Fig. 7.79. CO_2 solubility in CaO-Fe_2O_3 slag as a function of CaO content [64]

Na_2O-P_2O_5

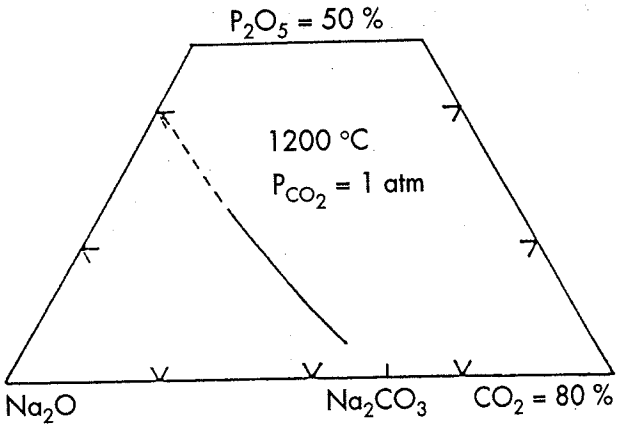


Fig. 7.80. CO_2 solubility line in Na_2O-P_2O_5 system [63]

Na_2O-SiO_2

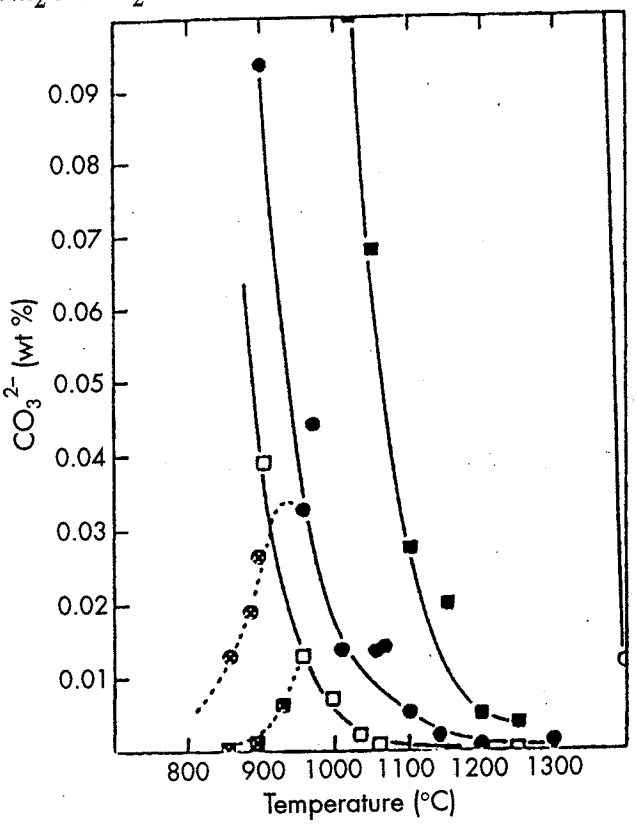


Fig. 7.81. Variation of the equilibrium carbonate content with temperature in Na_2O-SiO_2 slags [65]
p_{CO_2} = 1 bar
□ and ⊠ = 25 % Na_2O
● and ⊗ = 35 % Na_2O
■ = 43 % Na_2O
○ = 56 % Na_2O
See also [63]

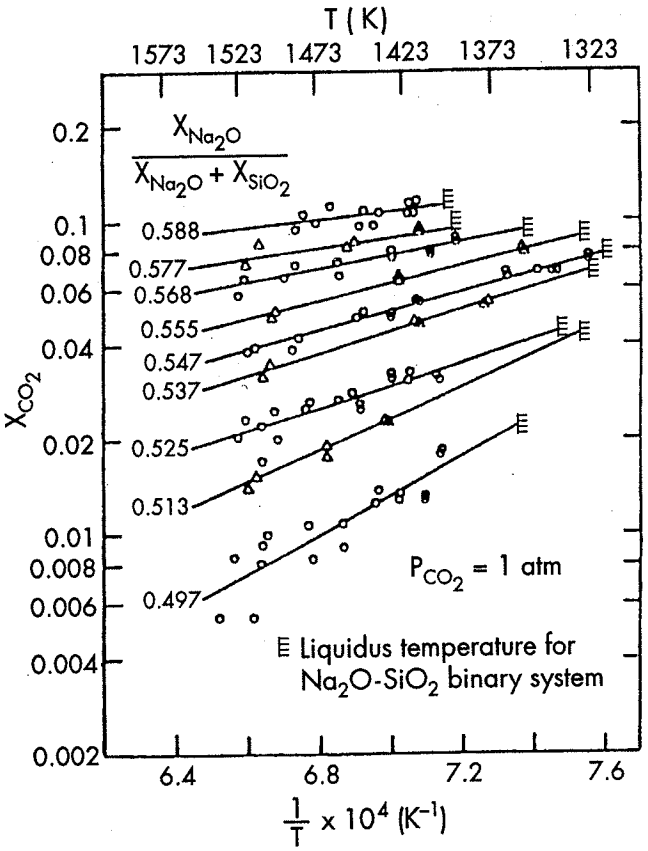


Fig. 7.82. CO_2 solubility in Na_2O-SiO_2 slag as a function of temperature and composition [66]

7.3.2 Ternary systems

$CaCl_2$-CaF_2-CaO

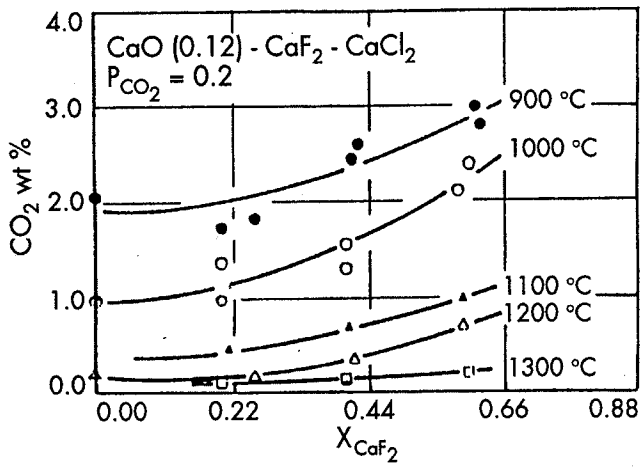
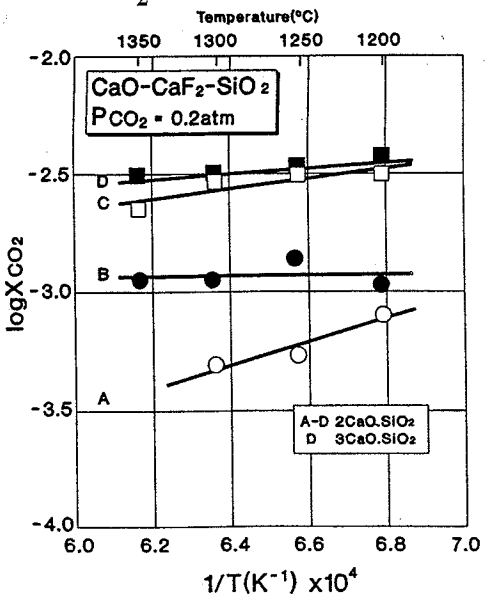
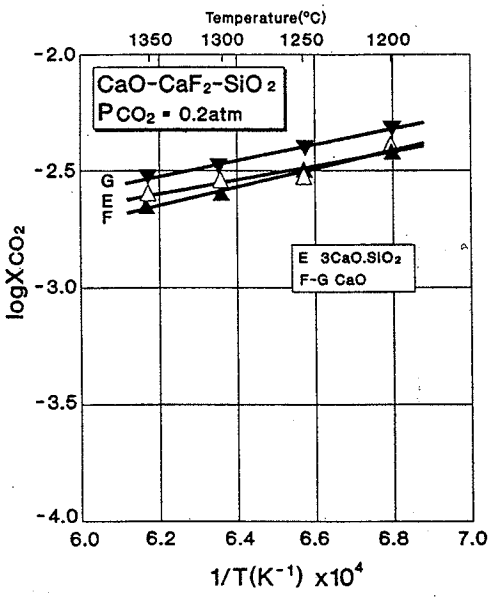


Fig. 7.83. CO_2 solubility in $CaCl_2$-CaF_2-CaO slag as a function of temperature and composition at a fixed X_{CaO} = 0.12 [67]

$CaCl_2$-CaO-SiO_2





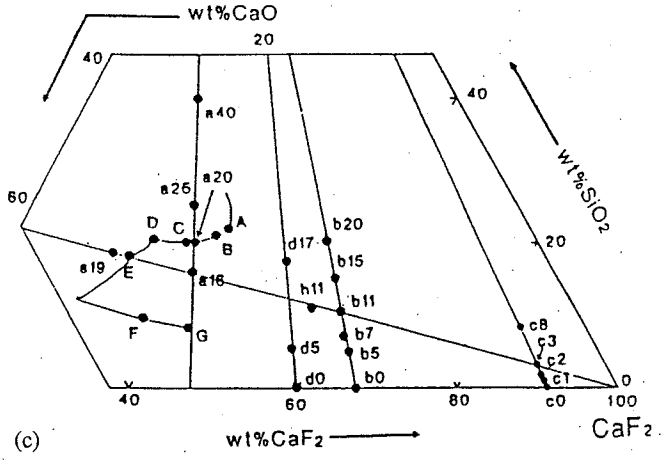


Fig. 7.84 a-c. Influence of temperature on the solubility of carbon dioxide in $CaCl_2$-CaO-SiO_2 slags at 1200 °C along the liquidus (c) for the compositions A, B, C, and D (a) and E, F, and G [68]

$CaO\text{-}Na_2O\text{-}SiO_2$

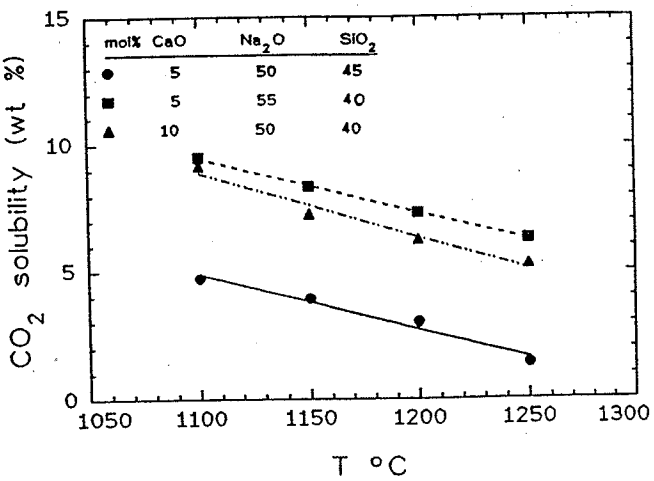


Fig. 7.85. CO_2 solubility in $CaO\text{-}Na_2O\text{-}SiO_2$ slags as a function of temperature and composition [69]

$Na_2O\text{-}P_2O_5\text{-}SiO_2$

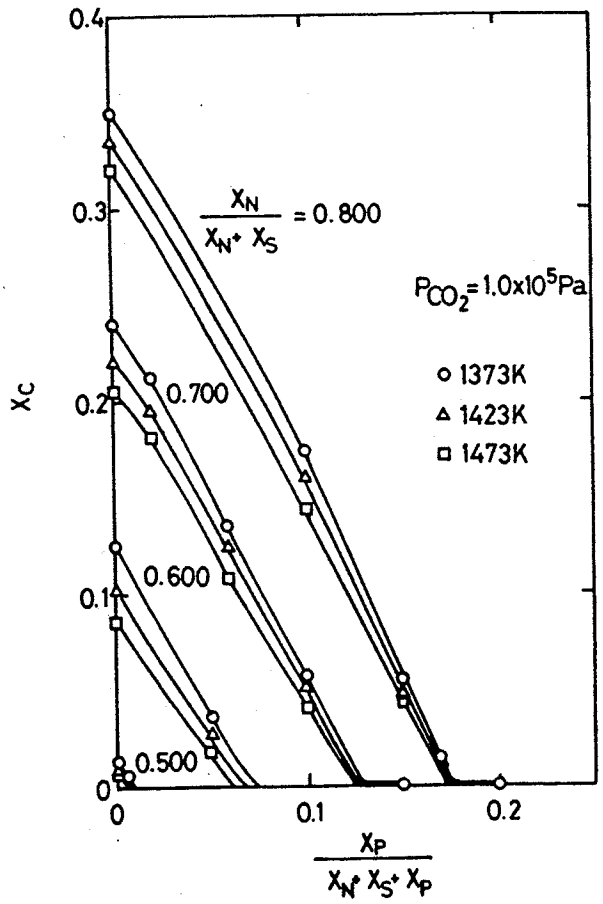


Fig. 7.86. Effect of P_2O_5 on the solubility of CO_2 at P_{CO_2} = 1.0 x 10^5 Pa at temperatures from 1373 to 1473 K for different mole ratios of $Na_2O/(Na_2O + SiO_2)$ [70]. See also the publication by Kawahara and coworkers, who deal with the solubility of CO_2 in basic fluxes as a measure of basicity [63]

7.4 References in Chapter 7

[1] Imai, M., H. Ovi, T. Emi: Tetsu-to-Hagane 50 (1964) 878 – 287.
[2] Sachdev, P. L.: Untersuchungen über die Wasserstofflöslichkeit von Schmelzen der Systeme $CaO\text{-}SiO_2$ und $CaO\text{-}SiO_2\text{-}Al_2O_3$. Aachen 1967 (Dr.-Ing.Thesis Techn. Hochsch. Aachen.).
[3] Fukushima, T., Y. Iguchi, S. Ban-Ya, T. Fuwa: Trans. Iron Steel Inst. Japan 6 (1966), 225 – 232.
[4] Wahlster, M., H.-H. Reichel: Arch. Eisenhüttenwes. 40 (1969), 19-25.
[5] Walsh, J. H., J. Chipman, T. B. King, N. J. Grant: J. Metals, Trans., 8 (1956), 1568-1576.
[6] Uys, J. M., T. B. King: Trans. Metallurg. Soc. AIME 227 (1963), 492 – 500.
[7] Iguchi, I., S. Ban-Ya, T. Fuwa: In: Chemical metallurgy of iron and steel. London 1973. (ISI publ. No. 146), 28 – 30.
[8] Imai, M., H. Ovi, T. Emi: Tetsu-to-Hagane 48 (1962) No. 2, 111 – 117.
[9] Iguchi, I., S. Ban-Ya, T. Fuwa: Trans. Iron Steel Inst. Japan 9 (1969), 189 – 195.
[10] Abe, U.: Tetsu-to-Hagane 47 (1961), 693 – 697.
[11] Imai, M., H. Ovi, T. Emi: Tetsu-to-Hagane 50 (1964), 465 – 467.
[12] Iguchi, Y., T. Fuwa: Trans. Iron Steel Inst. Japan 10 (1970), 29 – 35.
[13] Uys, J. M., T. B. King: Trans. Metallurg. Soc. AIME 227 (1963), 1457 – 1458.
[14] Ershov, G. S., I. A. Novokatskiy: Izvestiya Akademii Nauk SSSR, Metally, 1968, No. 2, 40-47; Russ. Metallurg. 1968, No. 2, 30 – 35.
[15] Wahlster, M., H.-H. Reichel, A. Hilpert: Rheinstahl-Technik 3 (1965), 291 – 299.
[16] Lüdemann, K.-F., H.-W. Fenzke: Freiberg. Forsch.-H., Reihe B, No. 98 (1964), 51 – 70.
[17] Dickens, P., P. König, K. Zimmermann: Stahl u. Eisen 86 (1966), 548 – 552.
[18] Herasymenko, P., P. Dombrowski: Arch. Eisenhüttenwes. 14 (1940), 109 – 115.
[19] Wentrup, H., H. Fucke, O. Reif: Stahl u. Eisen 69 (1949), 117 – 122.
[20] Russell, L. E.: J. Soc. Glass. Technol. 41 (1957), 304 – 317.
[21] Kurkjian, C. R., L. E. Russell: J. Soc. Glass. Technol. 42 (1958), 130 – 143.
[22] Tomlinson, J. W.: J. Soc. Glass Technol. 40 (1956), 25-31.
[23] Vinnicenko, E. V., L. B. Kosterev, V. J. Javoiskij: Izvestiya Vysshikh Uchebnykh Zavedenii, Chernaya Metallurgiya, 8 (1965) No. 3, 53 – 58.
[24] Nam, B. P., G. N. Ojks, V. A. Kudrus, J. M. Neckin: Izvestiya Vysshikh Uchebnykh Zavedenii, Chernaya Metallurgiya, 4 (1961) No. 9, 54 – 58.
[25] Shimoo, T., H. Kimura, M. Kawai: J. Japan Inst. Metals 35 (1971), 417 – 422.
[26] Choh, T., I. Hanaki, T. Kato, M. Inouye: Trans. Iron Steel Inst. Japan 13 (1973), 218 – 225.
[27] Shimoo, T., H. Kimura, M. Kawai: J. Japan Inst. Metals 36 (1972), 723 – 727.
[28] Pleschiutschnigg, F.-P.: Die Lösungsvorgänge des Stickstoffs in flüssigen $CaO\text{-}SiO_2\text{-}Al_2O_3$-Schlacken und die Thermodynamische Betrachtung der Stickstoffreaktionen zwischen Gas, Schlacke und Cges.-Eisen im Temperaturbereich von 1350 °C bis 1600 °C. Aachen 1972. (Dr.-Ing. Thesis Techn. Hochsch. Aachen.).
[29] Schwerdtfeger, K., H. G. Schubert: Arch. Eisenhüttenwes. 45 (1974), 649 – 655.
[30] Shimoo, T., T. Iida, H. Kimura, M. Kawai: J. Japan Inst. Metals 36 (1972), 728 – 733.
[31] Schenck, H., A. Majdič, W.-J. Ammerling: Aufstickung von Schlacken des Systems $CaO\text{-}SiO_2\text{-}Al_2O_3$. Köln/Opladen 1970. (Forschungsberichte des Landes Nordrhein-Westfalen No. 2046.).
[32] Davies, M. W., S. G. Meheralc: Metallurg. Trans. 2 (1971), 2729 – 2733.
[33] Chukmarev, S. K., O. A. Esin, V. M. Kamysov: Izvestiya Vysshikh Uchebnykh Zavedenii, Chernaya Metallurgiya, 8 (1965) No. 2, 5 – 9.
[34] Kamysov, V. M., O. A. Esin, S. K. Chukmarev: Izvestiya Vysshikh Uchebnykh Zavedenii, Chernaya Metallurgiya, 7 (1964) No. 7, 24 – 28.
[35] Oelsen, W., H. Keller, K.-H. Sauer: Arch. Eisenhüttenwes. 40 (1969), 911 – 923.
[36] Oelsen, W., K.-H. Sauer, H. Keller: Arch. Eisenhüttenwes. 40 (1969), 925 – 937.
[37] Oelsen, W., H. Keller, H. G. Schubert, H. Brockmann: Arch. Eisenhüttenwes. 40 (1969), 939 – 958.
[38] Oelsen, W., K.-H. Sauer, H. G. Schubert, R. Winzen: Arch. Eisenhüttenwes. 41 (1970), 829 – 834.
[39] Oelsen, W., H. G. Schubert: Arch. Eisenhüttenwes. 40 (1969), 809 – 812.
[40] Oelsen, W., H. G. Schubert, C. Bergianni: Arch. Eisenhüttenwes. 40 (1969), 901 – 909.
[41] Oelsen, W., K.-H. Sauer, K. Klein: Arch. Eisenhüttenwes. 41 (1970), 237 – 242.
[42] Oelsen, W.: Arch. Eisenhüttenwes. 41 (1970), 243 – 247.

43] Schürmann, E., F.-J. Hufnagel, A. Drevermann: Stahl u. Eisen 87 (1967), 645 – 654.
[44] Mahn, G., P. Ottmar, H. Voigt: Stahl u. Eisen 89 (1969), 262 – 273.
[45] Bosch, H., H.-P. Haastert, E. Köhler, E. Schürmann: Arch. Eisenhüttenwes. 40 (1969), 271 – 276.
[46] Schwerdtfeger, K., H. G. Schubert: Metallurg. Trans. 9 B (1978), 143 – 144.
[47] Schwerdtfeger, K., H. G. Schubert: Metallurg. Trans. 8 B (1977), 535 – 540.
[48] Schwerdtfeger, K., H. G. Schubert: Metallurg. Trans. 8 B (1977), 689 – 691.
[49] Schwerdtfeger, K., W. Fix, H. G. Schubert: Ironmaking and Steelmaking 5 (1978), 67 – 71.
[50] Lindeskog, B.: Jernkont. Ann. 150 (1966), 213 – 234.
[51] Ershov, G. S., Y. G. Orlov: Russ. Metallurg., Metally 1956, No. 6, 19 – 28.
[52] Mills, K.: Physical properties of slags. Final report of the ECSC Research Agreement 7210-CA/8/8066. National Physical Laboratory, Teddington, 1980.
[53] Mathis, P.: Beitrag zum Verhalten des Wasserstoffs beim ESU-Verfahren. Clausthal-Zellerfeld 1979. (Dr.-Ing. Thesis Techn. Univers. Clausthal).
[54] Iguchi, Y., et al.: Chemical Metallurgy of Iron and Steel, Int. Symp. on Metallurgical Chemistry – Applications in ferrous metallurgy, 19 – 21 July 1971, Sheffield, 561.
[55] Do, T. T.: Dr.-Ing. Thesis TH Aachen 1987.
[56] Wenz, H.: Dr.-Ing. Thesis, TU Clausthal, 1991.
[57] Martinez, E.; N. Sano: Steel Res. 58 (1987) 11, 485 – 490.
[58] Wenz, H.; D. Janke: Steel Res. 63 (1992), 47 – 59 and 105 – 111.
[59] Breitzmann, M.: Dr.-Ing. Thesis, TU Clausthal, 1987.
[60] Martinez, E.; N. Sano: Met. Trans. B. 21 B, Feb. 1990, 97 – 104.
[61] Tsukihashi, F.; R. J. Fruehan: Met. Trans. B. 17 B, Sept. 1986, 535.
[62] Martinez, E.; N. Sano: Met. Trans. B. 21 B, Feb. 1990, 105 – 109.
[63] Kawahara, T., et al.: 5th Int. Iron and Steel Congress, Proc. of the 6th Process Technology Conf. Vol. 6, AIME 1986, 691 – 703.
[64] Sumita, S., et al.: Tetsu-to-Hagane, 46, 1982, 369.
[65] Pearce, M. L.: J. Am. Cer. Soc., 47, July 1964, 342.
[66] Iwase, M., et al.: I & SM, Nov. 1987, 77.
[67] Maeda, M.; T. Ikeda: 3rd Int. Conf. on Molten Slags and Fluxes, Glasgow, 27 – 29 June 1988, 107.
[68] Ikeda, T., M. Maeda: The 6th Int. Iron and Steel Congress, Vol. 1, Nagoya, Oct. 21-26 1990, 272 – 278.
[69] Karvonen, P., et al.: Scand. J. Met., 17, 1988, 151 – 155.
[70] Yamato, N.; K. S. Goto: Nippon Kinzoku Gakkaishi 48 (1984), 983 – 989.

8

Densities of molten slags

B. J. Keene and K. C. Mills

8.1 Definitions

$$\text{Density } \rho = m/V \text{(mass density)} \tag{8.1}$$

where m: mass, g
V: volume, cm^3
Relative density $d = \rho/\rho_0$
where ρ_0: density of a reference material (e.g. water at 4 °C and 760 mm Hg)

When the temperature and pressure of the reference material are equal to those of the test material, the relative density is also known as the density ratio.

8.2 Methods

In general, the following methods and equipment are used to obtain density measurements.

8.2.1 Weighing method (pycnometry)

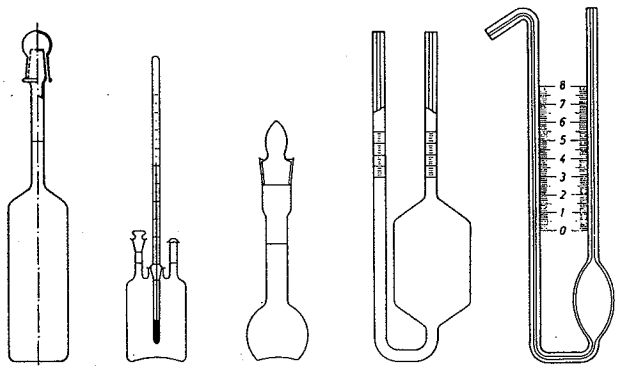


Fig. 8.1. Construction of pycnometers

The liquid under examination is poured into a vessel of known capacity up to a given mark. (For very accurate measurement, the effects of temperature on the vessel volume must be known.)

8.2.2 Buoyancy method (Archimedes Principle)

a) Direct method

$$\rho_{melt} = \frac{\Delta P}{V_{Bob}} \tag{8.2}$$

$\Delta P = (P_{Air} - P_{liq})$ is the difference between weights before and after immersion of the indicator into the molten material.

b) Indirect method

$$\rho_{melt} = \rho_{liq} \cdot \frac{m_{melt}}{\Delta P - \rho_{liq} \cdot V_{crucible}} \tag{8.3}$$

For special designs see White [124].
General note: – for pressure, upper case P is used in 8.2.2 whereas lower case P is used in 8.2.3 and 8.2.4.

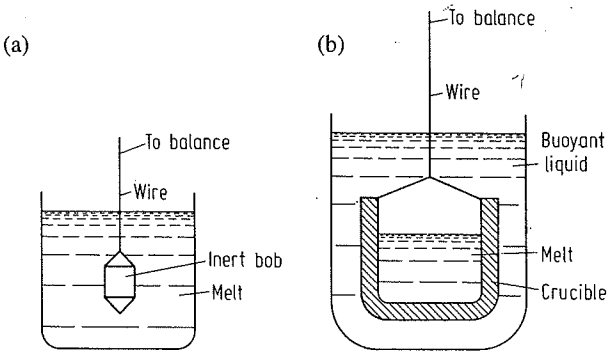


Fig. 8.2 a, b. Determination of density of molten materials using the Archimedes Principle

8.2.3 Volumetric method (dilatometer)

For the determination of volume of bodies or materials which must not come into contact with liquids, the known mass of the test material is placed in a known gas-filled volume V_1 at a pressure P_1 and then compressed to V_2 at p_2.

$$V_x = \frac{V_2 p_2 - V_1 p_1}{p_2 - p_1}. \tag{8.4}$$

For details of liquid dilatometers see White [124].

8.2.4 Pressure method

a) Manometer method:

$$\rho_{melt} = \rho_{manom} \cdot \frac{h}{H}. \tag{8.5}$$

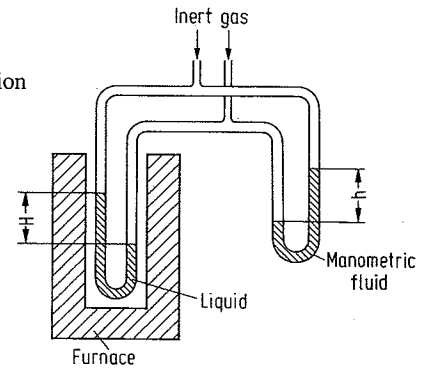


Fig. 8.3. Manometer method for determination of density of molten materials

b) Method of maximum bubble pressure:

$$\rho_{melt} = \frac{\Delta p}{\Delta h} = \frac{p_2 - p_1}{h_2 - h_1} \tag{8.6}$$

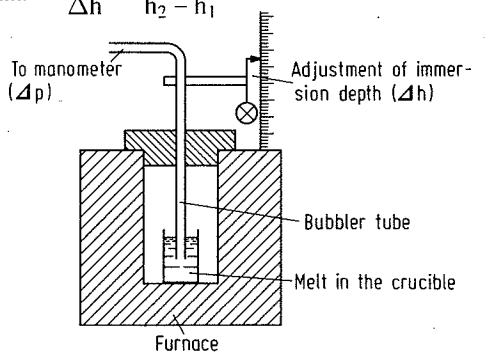


Fig. 8.4. Method of maximum bubble pressure for determination of density of molten materials

8.2.5 Droplet method

a) Droplet at rest (sessile droplet):

$$V = \frac{\pi \cdot b^2 \cdot (x')^2}{\beta} \cdot \frac{2}{b} - \frac{2\sin\Phi}{x'} + \frac{\beta(z')^2}{b^2}, \qquad (8.6)$$

$$\rho = \frac{m}{V}. \qquad (8.1)$$

Here, b, β: droplet constants
V: droplet volume, cm^3
Φ: phase boundary angle °
x': radius ($\overline{CE}$), cm
z': height ($\overline{DE}$), cm

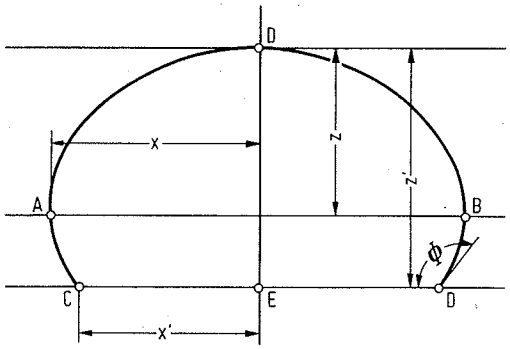


Fig. 8.5. Characteristic dimension of sessile droplet

b) Falling droplet method:

Liquid droplets of given volume fall through a liquid of lower density with a speed proportional to their density. If two equally sized spherical droplets ρ_1 and ρ_2 pass through a liquid of density ρ over a measured distance in t_1 and t_2 seconds, then:

$$\frac{t_1}{t_2} = \frac{\rho_2 - \rho}{\rho_1 - \rho} \qquad (8.7)$$

$$\rho_1 = \rho + \frac{t_2}{t_1}(\rho_2 - \rho) \qquad (8.8)$$

ρ_1 can be calculated if ρ of the liquid and ρ_2 of the droplet of reference material are known assumption: $V_1 = V_2$.

8.2.6 Suspension method

The material under investigation is placed in suspension in a non-reactive liquid. This is achieved by the mixing of two liquids, one heavier and the other lighter than the test material. The density of the mixture is then determined by the usual methods. (In modified form this is also known as the Schlieren method.)

8.3 Densities

8.3.1 Pure substances

CaF_2

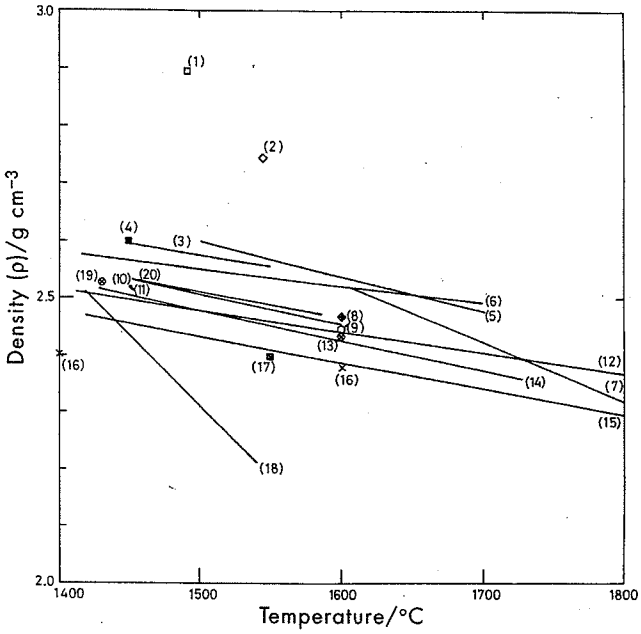


Fig. 8.6. Variation of the density of CaF_2 melts with temperature

Fe_xO

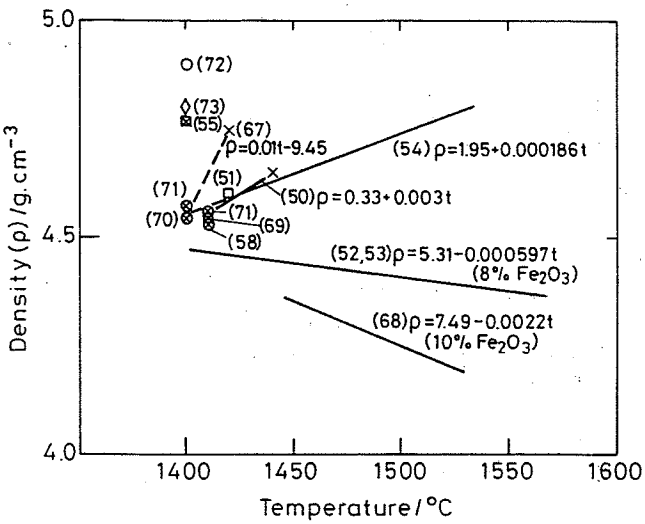


Fig. 8.7. Effect of temperature on the density of Fe_xO ($FeO + Fe_2O_3$)

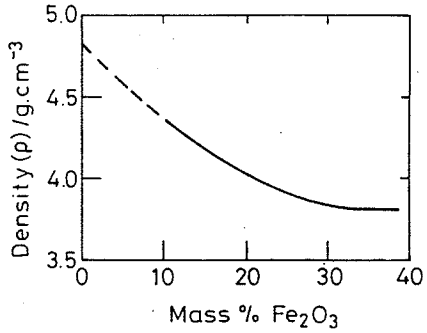


Fig. 8.8. Effect of Fe_2O_3 content in Fe_xO on the density at 1450 °C [Ref. 68]

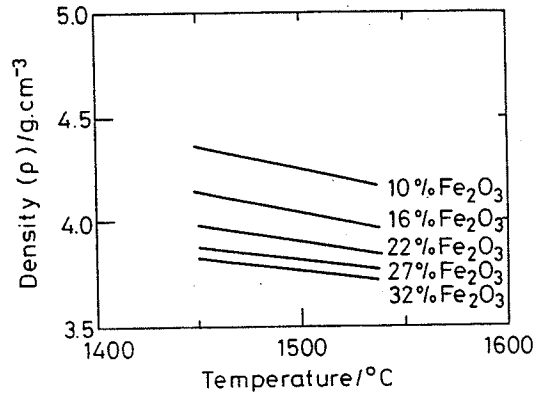


Fig. 8.9. Effect of temperature on the density of Fe_xO melts containing various levels of Fe_2O_3 [Ref. 68]

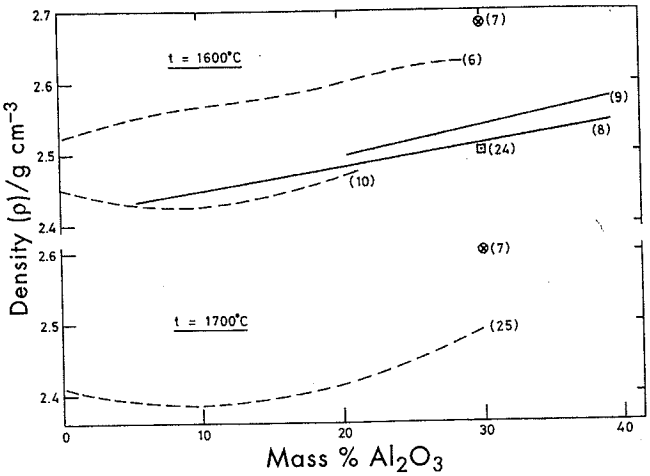


Fig. 8.11. Variation of the density of Al_2O_3 + CaF_2 melts with the Al_2O_3 concentration at 1600 °C and 1700 °C

8.3.2 Binary systems

Al_2O_3-CaF_2

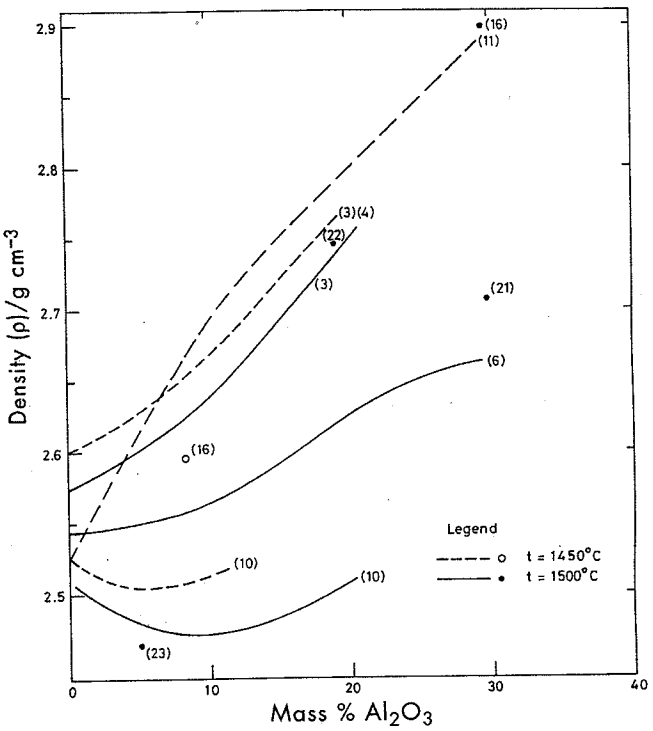


Fig. 8.10. Variation of the density of Al_2O_3 + CaF_2 melts with the Al_2O_3 concentration at 1450 °C and 1500 °C

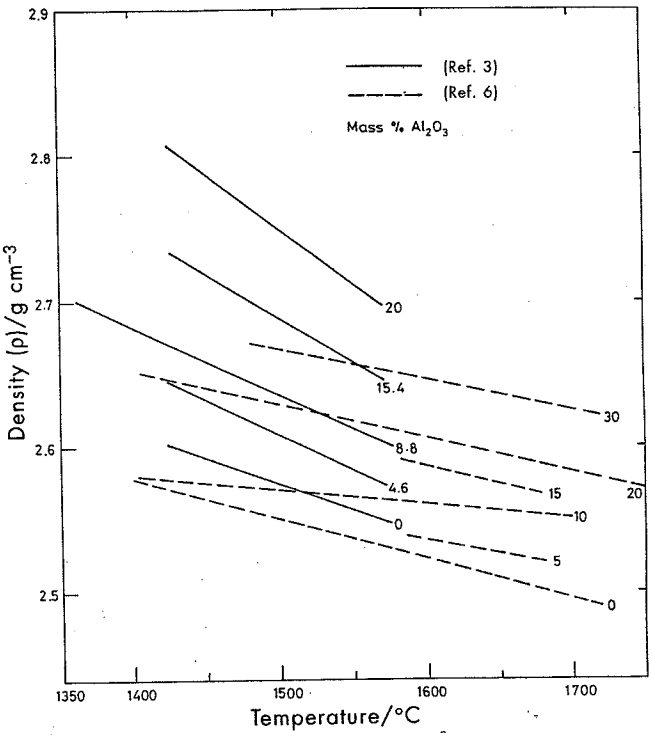


Fig. 8.12. Effect of temperature on the density of Al_2O_3 + CaF_2 melts containing various concentrations of Al_2O_3

Al_2O_3-CaO

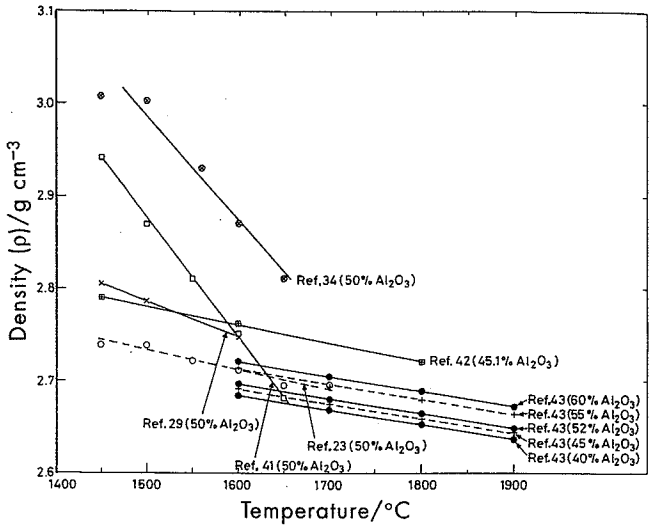


Fig. 8.13. Effect of temperature on the density of Al_2O_3 + CaO melts

Al_2O_3-Cr_2O_3

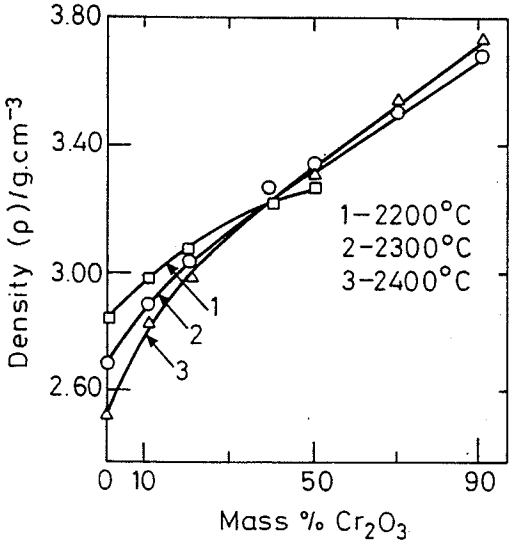


Fig. 8.15. Effect of Cr_2O_3 content on the density of Al_2O_3 + Cr_2O_3 melts at different temperatures [Ref. 46]

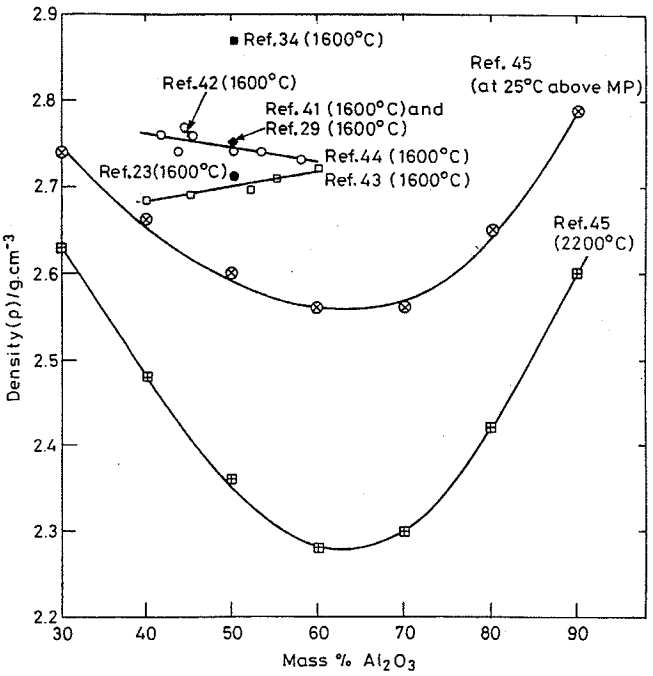


Fig. 8.14. Effect of Al_2O_3 content on the density of melts in the system Al_2O_3 + CaO

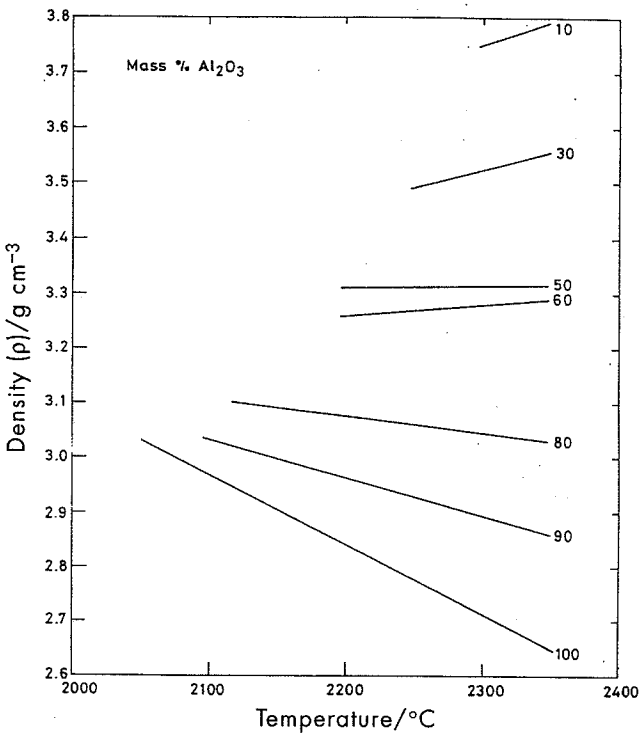


Fig. 8.16. Effect of temperature on the density of Al_2O_3 + Cr_2O_3 melts [Ref. 46]

Al_2O_3-MgO

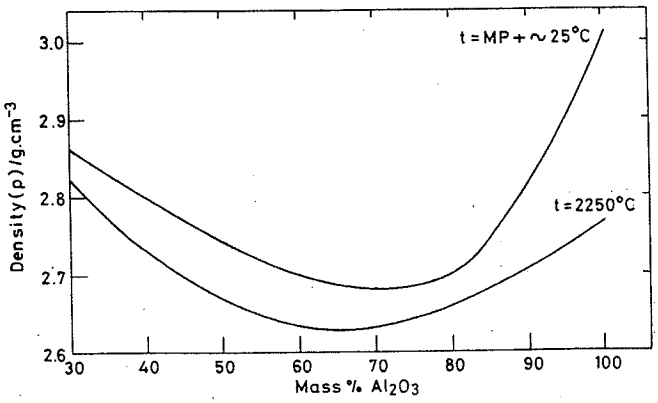


Fig. 8.17. Effect of Al_2O_3 on the density of melts in the system Al_2O_3 + MgO at 2250 °C and at temperature 25 °C above the melting point [Ref. 45]

Al_2O_3-SiO_2

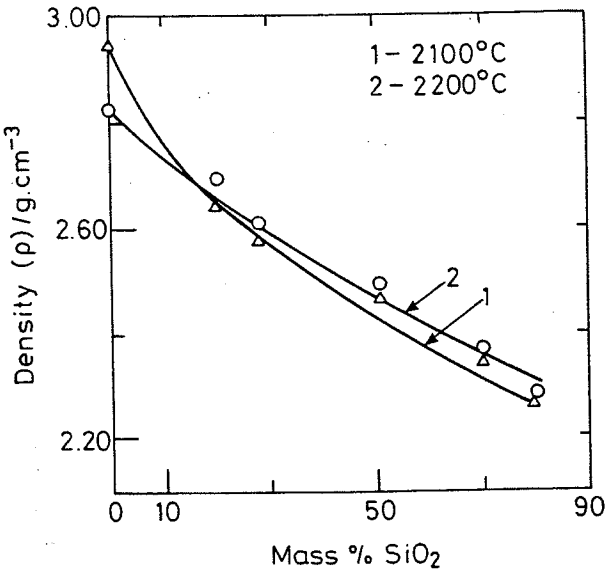


Fig. 8.18. Effect of SiO_2 concentration on the density of Al_2O_3 + SiO_2 melts at 2100 °C and at 2200 °C [Ref. 46]

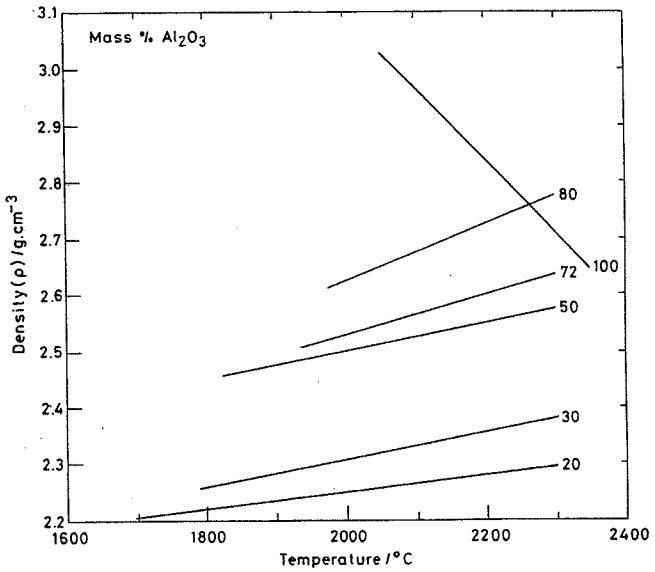


Fig. 8.19. Effect of temperature on the density of melts in the system Al_2O_3 + SiO_2 [Ref. 46]

B_2O_3-CaO

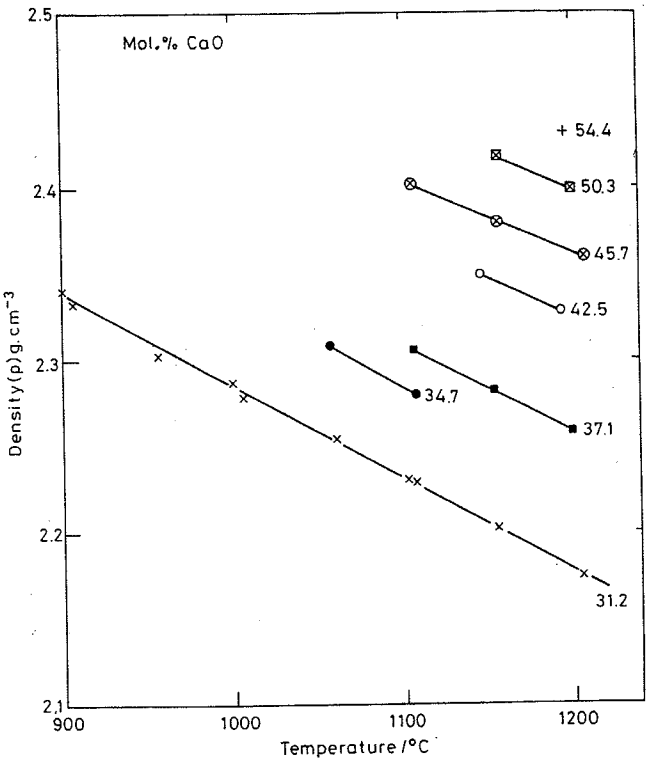


Fig. 8.20. Effect of temperature on the density of melts in the system B_2O_3 + CaO [Ref. 47]

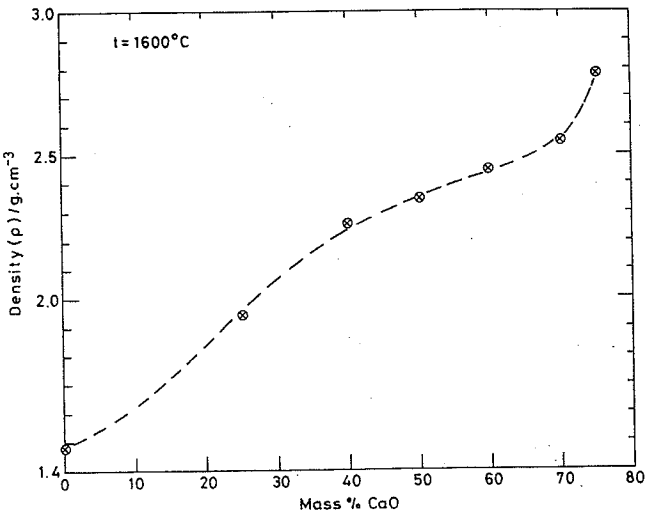


Fig. 8.21. Variation of the density of B_2O_3 + CaO melts with CaO content [Ref. 48]

CaF_2-CaO

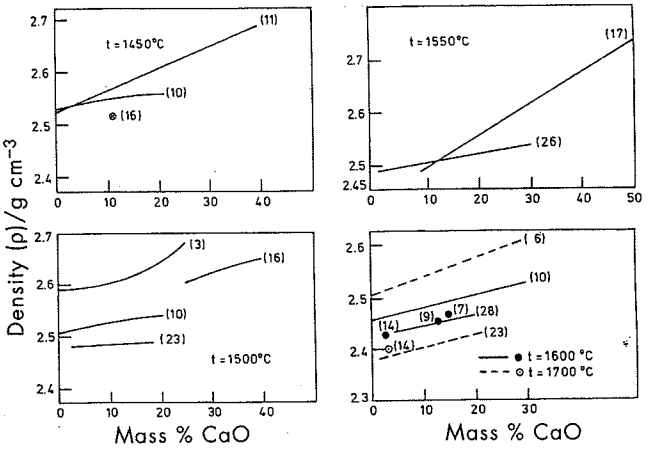


Fig. 8.22. Effect of CaO concentration in CaF_2 + CaO melts on the density at various temperatures

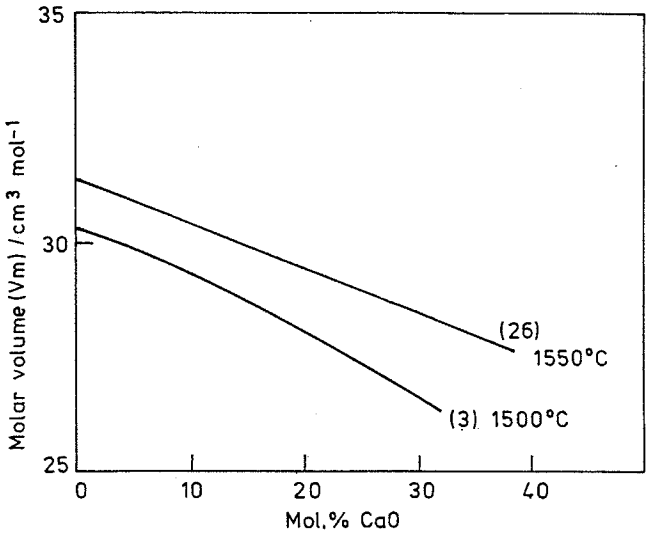


Fig. 8.23. Effect of CaO concentration on the molar volume of CaF_2 + CaO melts

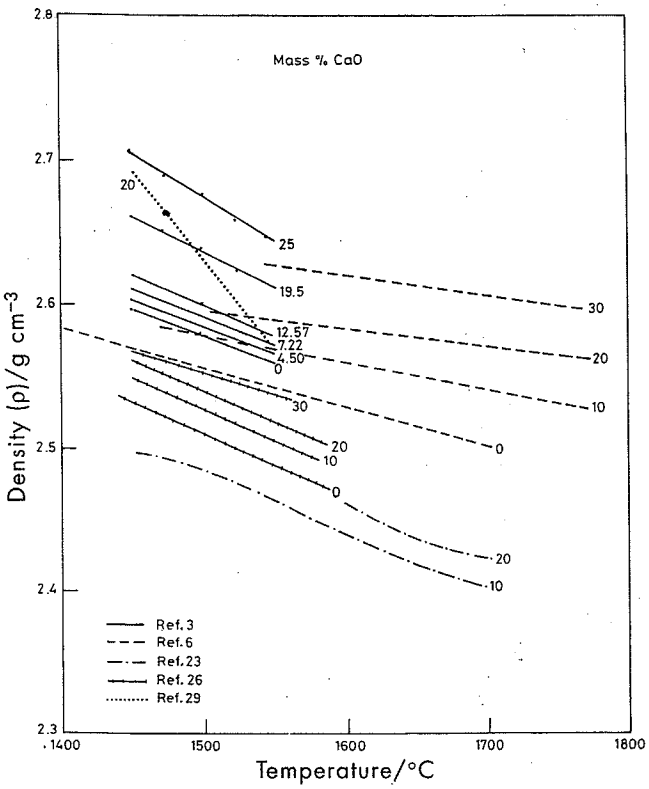


Fig. 8.24. Effect of temperature on the density of CaF_2 + CaO melts containing various amounts of CaO

CaF_2-Cr_2O_3

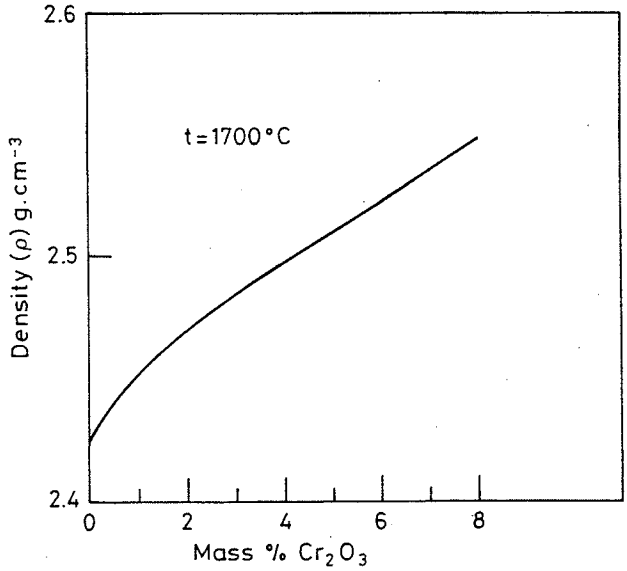


Fig. 8.25. Variation of density with Cr_2O_3 content of CaF_2 + Cr_2O_3 melts at 1700 °C [Ref. 27]

CaF_2-MgO

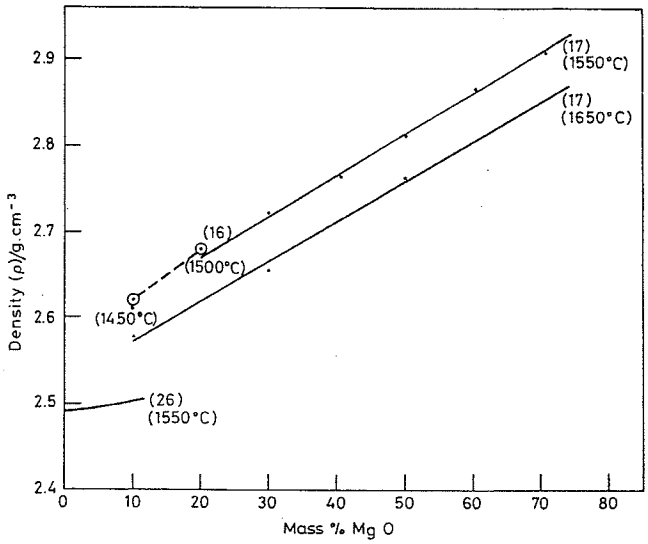


Fig. 8.26. Effect of MgO concentration on the density of CaF_2 + MgO melts at various temperatures

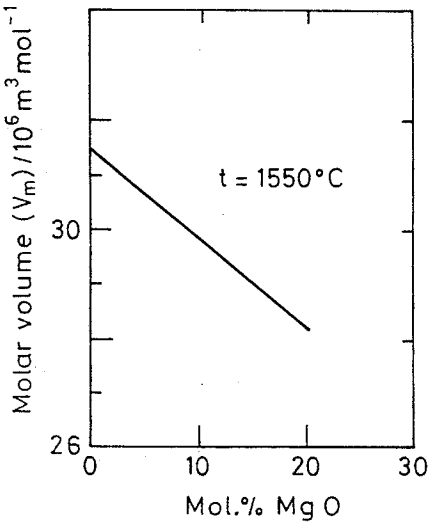


Fig. 8.27. Effect of MgO content in CaF_2 + MgO melts on the molar volume at 1550 °C [Ref. 26]

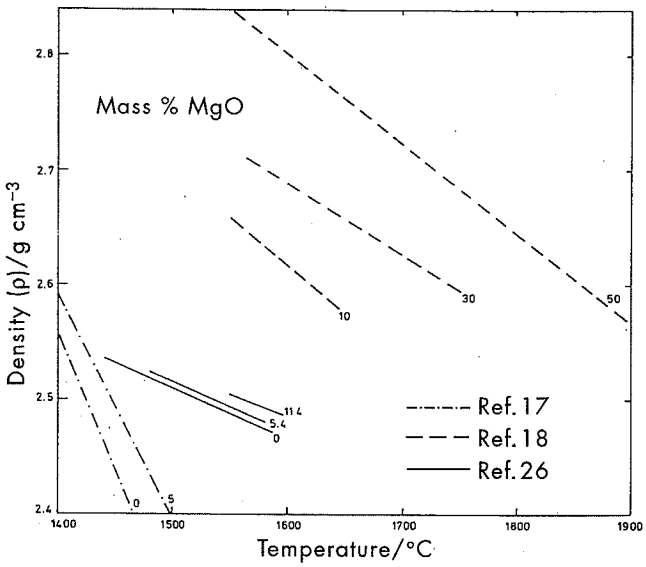


Fig. 8.28. Effect of temperature on the density of CaF_2 + MgO melts containing various concentrations of MgO

CaF_2-SiO_2

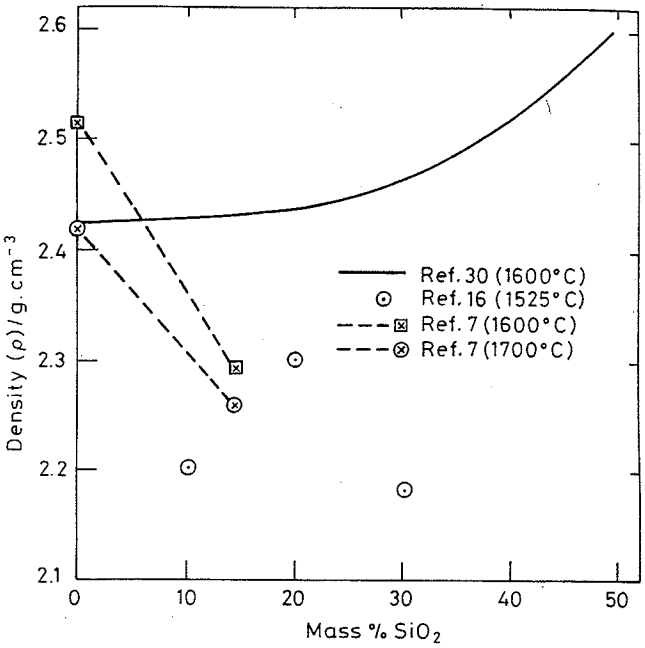


Fig. 8.29. Variation of density with the SiO_2 content of CaF_2 + SiO_2 slags

CaF_2-TiO_2

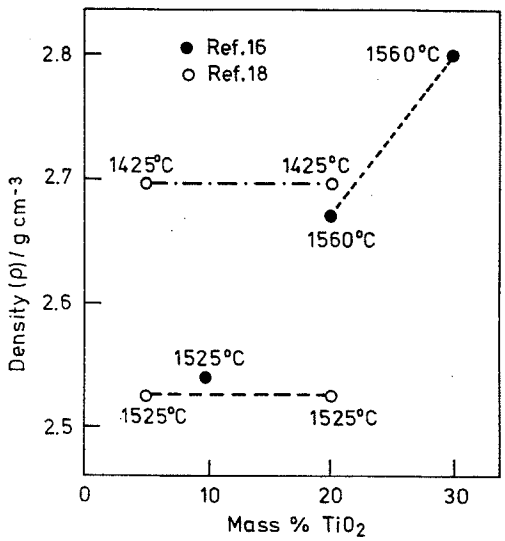


Fig. 8.30. Effect of the TiO_2 content on the density of CaF_2 + TiO_2 melts

CaF_2-V_2O_5

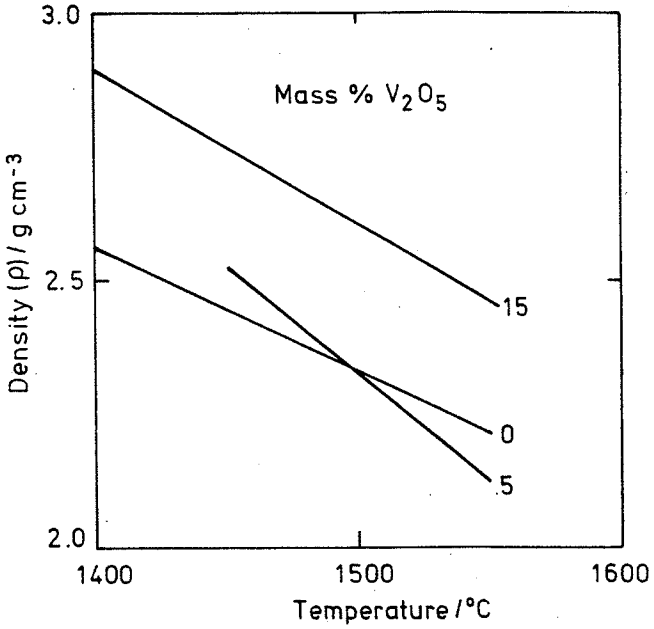


Fig. 8.31. Effect of temperature on the density of CaF_2 + V_2O_5 melts containing various levels of V_2O_5 [Ref. 18]

CaF_2-ZrO_2

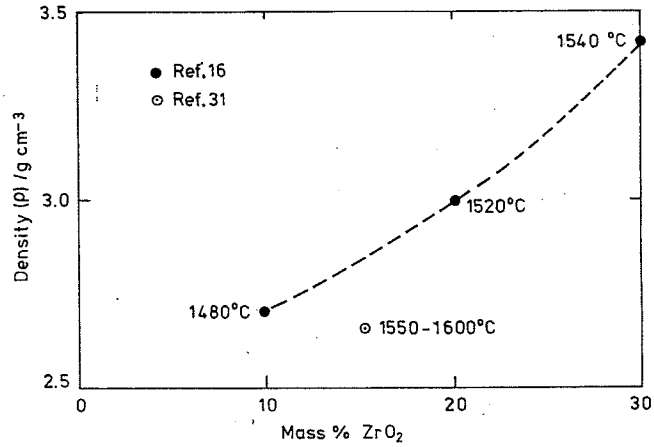


Fig. 8.32. Variation of density with ZrO_2 content of CaF_2 + ZrO_2 melts

CaO-Fe_xO

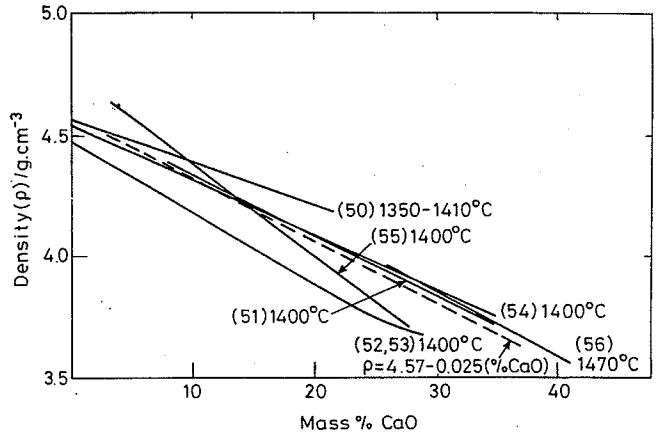


Fig. 8.33. Effect of CaO content on the density of CaO + Fe_xO melts (hatched line is mean, based on data given in figure)

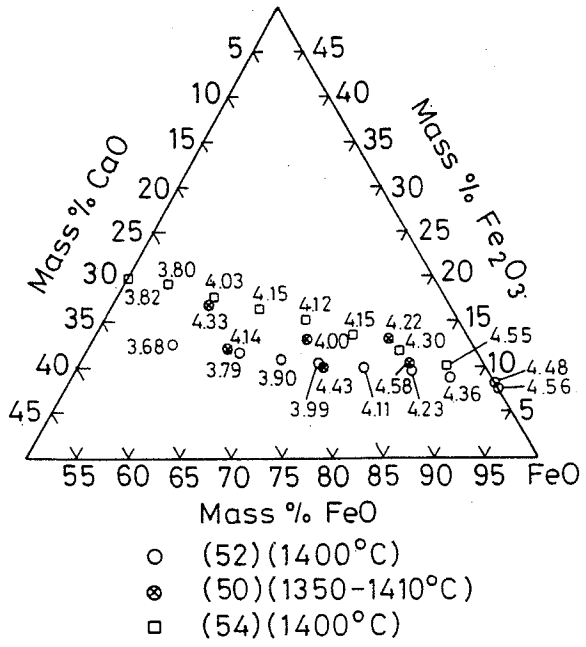
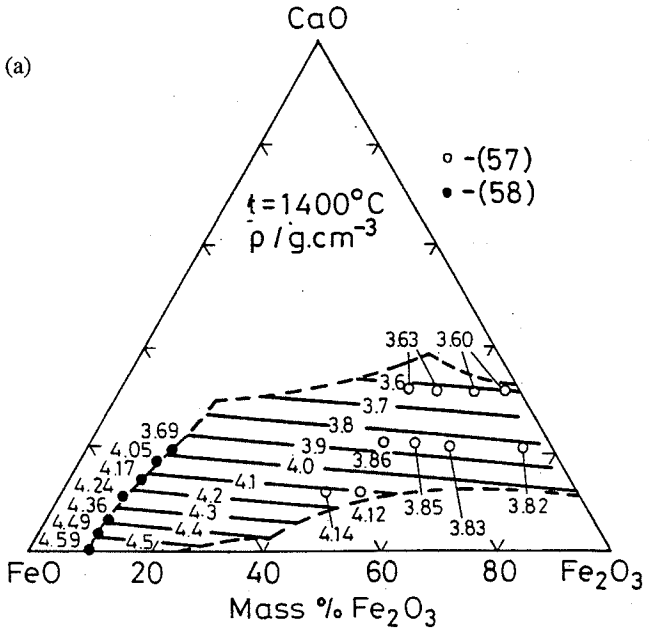


Fig. 8.34. Density of CaO + Fe_xO melts. (Fe_xO expressed as FeO + Fe_2O_3)



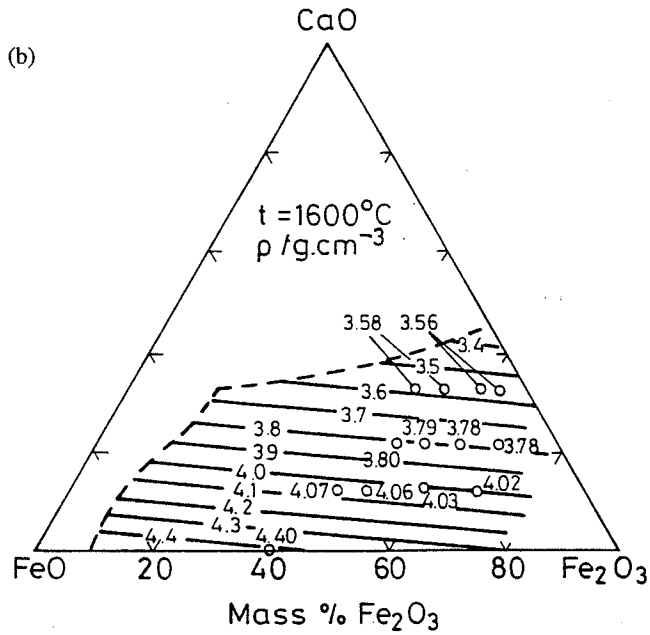
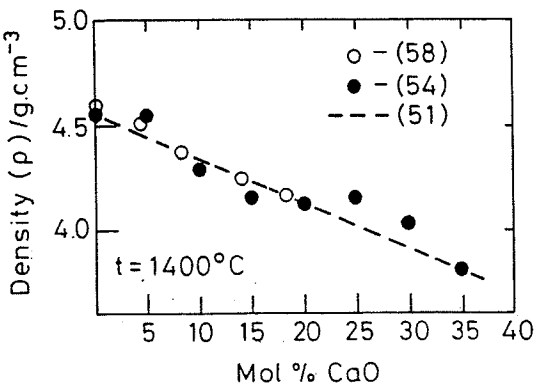
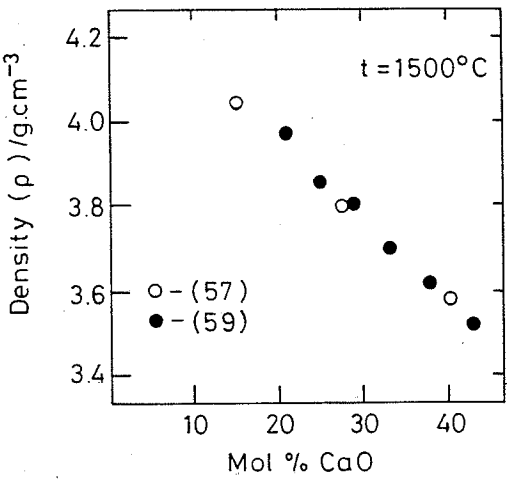


Fig. 8.35 a,b. Density of CaO + Fe_xO melts (a) at 1400 °C (b) at 1600 °C



(a)



(b)

Fig. 8.36 a,b. Effect of CaO content on the density of CaO + Fe_xO melts
(a) Equilibrium with solid Fe melts
(b) In air

Tab. 8.1. Composition and temperature (K) dependence of the density of melts in the CaO + Fe_xO system [Ref. 60]

Composition (mass %)			Density (ρ) = a - bT/g.cm^{-3}	
Fe_2O_3	FeO	CaO	a	b.10^3
79.46	9.97	10.37	6.713	1.422
80.49	3.47	15.84	6.102	1.163
73.37	7.28	18.98	6.297	1.310
73.50	1.29	24.96	6.727	1.635
69.16	5.27	30.02	6.232	1.380
67.19	2.57	30.00	5.788	1.177
63.97	1.03	34.70	5.654	1.147
59.76	2.12	37.77	6.099	1.436

CaO-P_2O_5

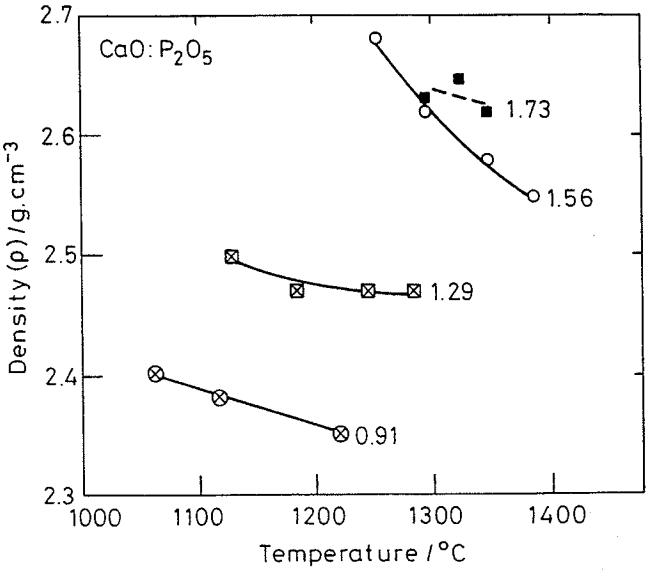


Fig. 8.37. Effect of temperature on the density of melts in the CaO + P_2O_5 system [Ref. 61]

CaO-SiO_2

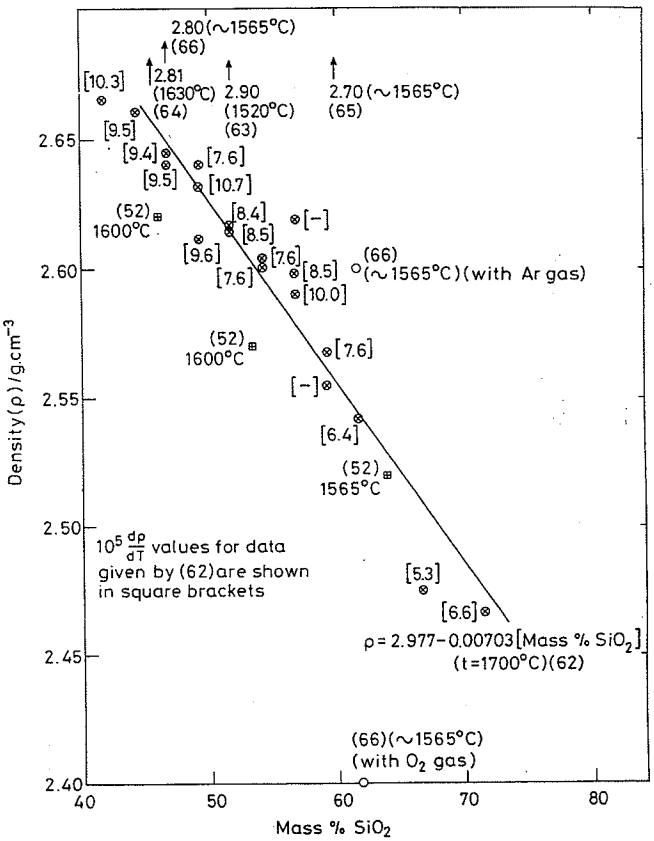


Fig. 8.38. Effect of SiO_2 content on the density of CaO + SiO_2 melts at various temperatures

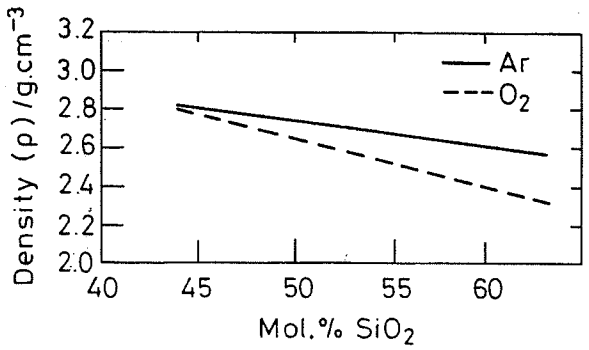


Fig. 8.39. Effect of bubbling gas used in the maximum bubble pressure technique to determine the density of CaO + SiO_2 melts [Ref. 66]

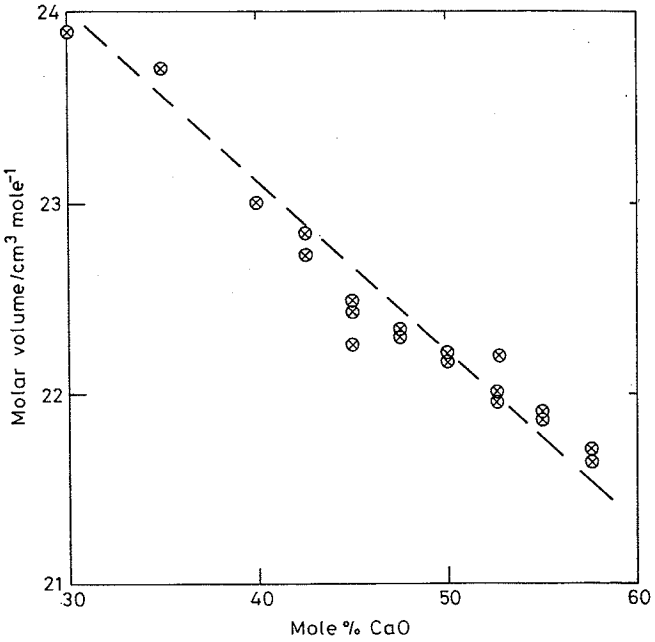


Fig. 8.40. Change in molar volume with CaO content of CaO + SiO_2 melts at 1700 °C [Ref. 62]

Fe_xO-SiO_2

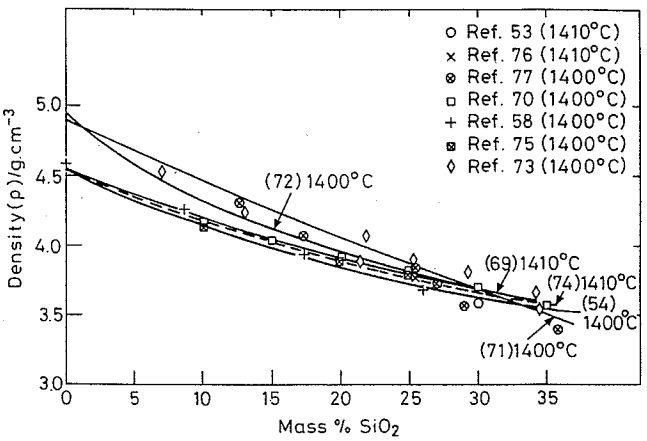


Fig. 8.41. Effect of SiO_2 content on the density of Fe_xO + SiO_2 melts at around 1400 °C

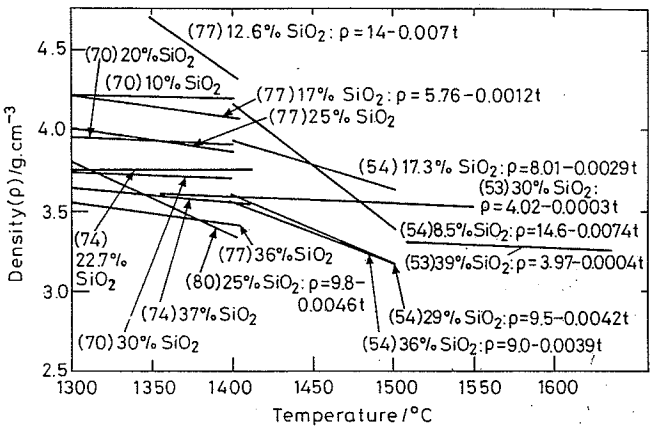


Fig. 8.42. Variation of density of Fe_xO + SiO_2 melts with temperature

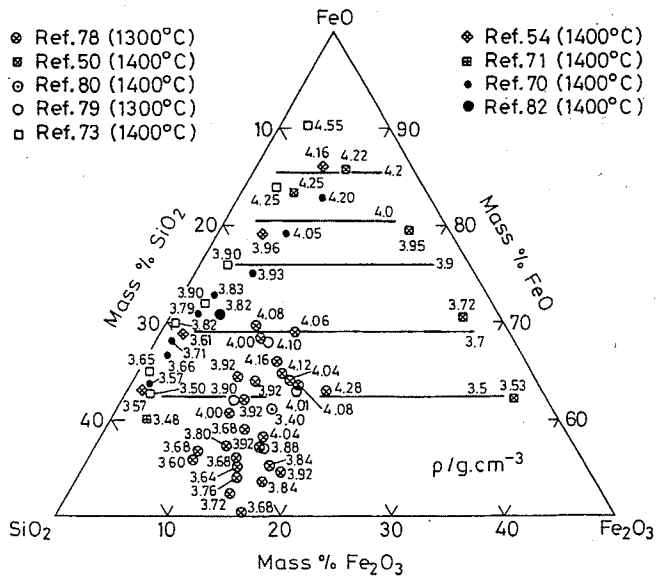


Fig. 8.43. Density of melts in the Fe_xO + SiO_2 system together with suggested isodensity lines at 1400 °C given in [Ref. 83]

$MgO\text{-}SiO_2$

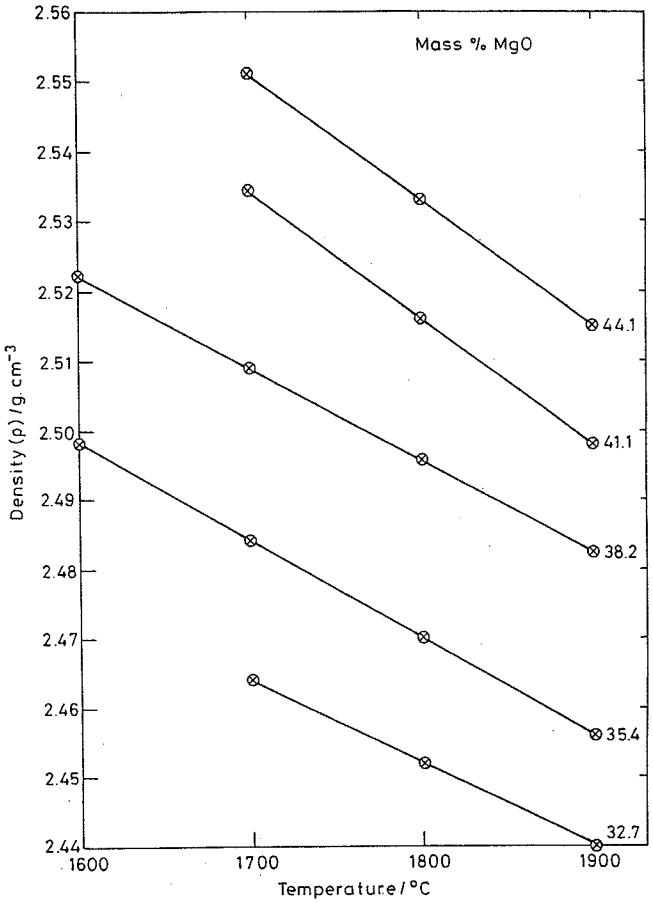


Fig. 8.44. Effect of temperature on the density of melts in the $MgO + SiO_2$ system [Ref. 62]

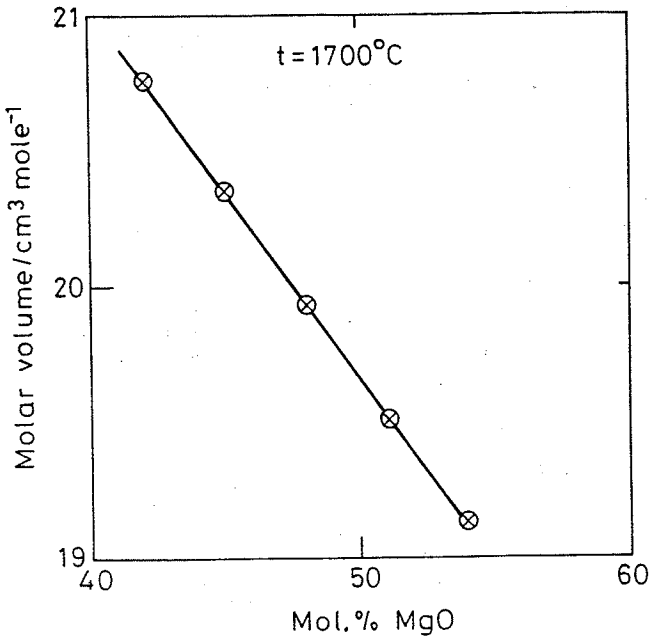


Fig. 8.45. Effect of MgO content on the molar volume of $MgO + SiO_2$ melts [Ref. 62]

$MnO\text{-}SiO_2$

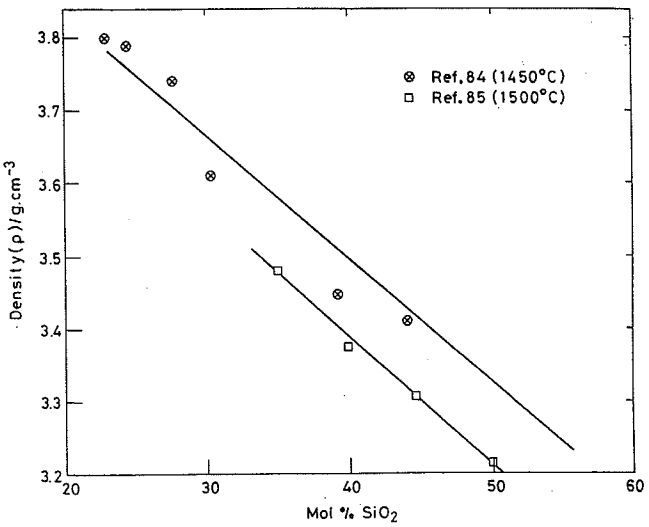


Fig. 8.46. Effect of SiO_2 concentration on the density of $MnO + SiO_2$ melts

$Na_2O\text{-}P_2O_5$

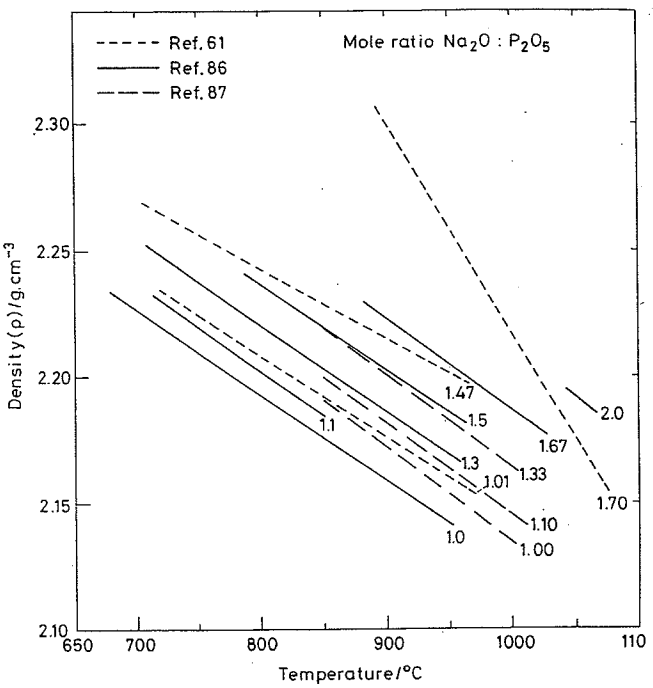


Fig. 8.47. Effect of temperature on the density of melts in the $Na_2O + P_2O_5$ system

Na_2O-SiO_2

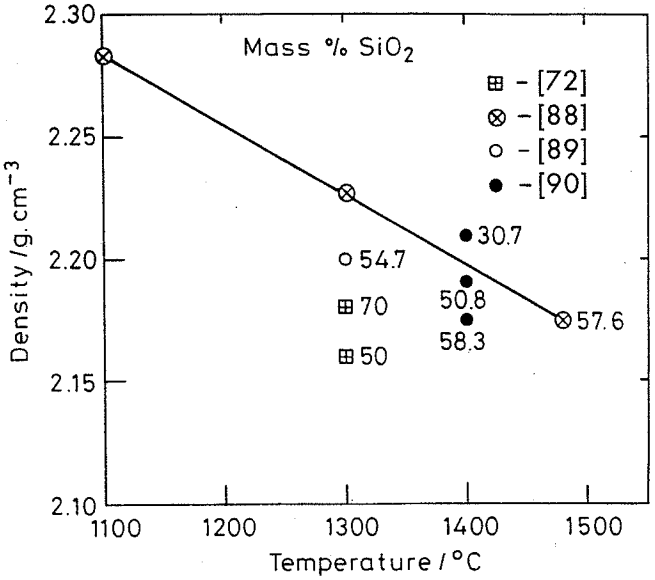


Fig. 8.48. Variation with temperature of the density of melts in the $Na_2O + SiO_2$ system

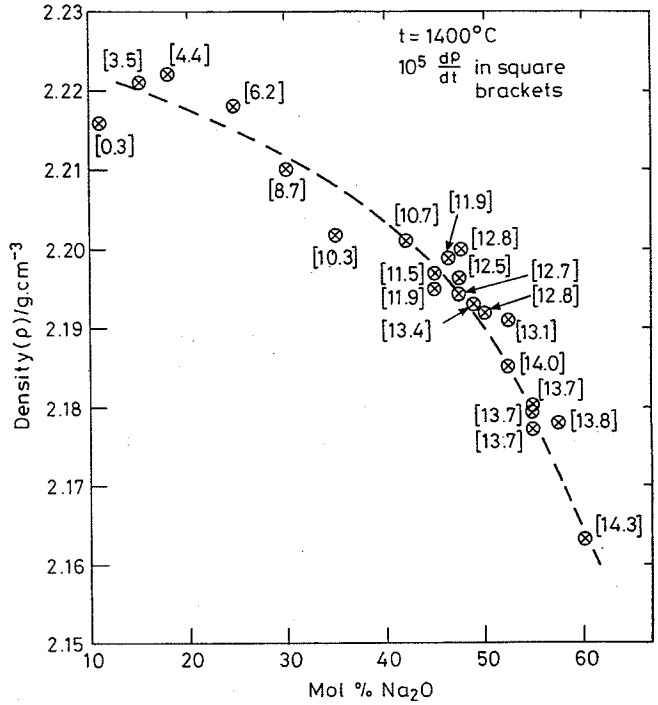


Fig. 8.49. Effect of Na_2O content on the density of $Na_2O + SiO_2$ melts [Ref. 90]

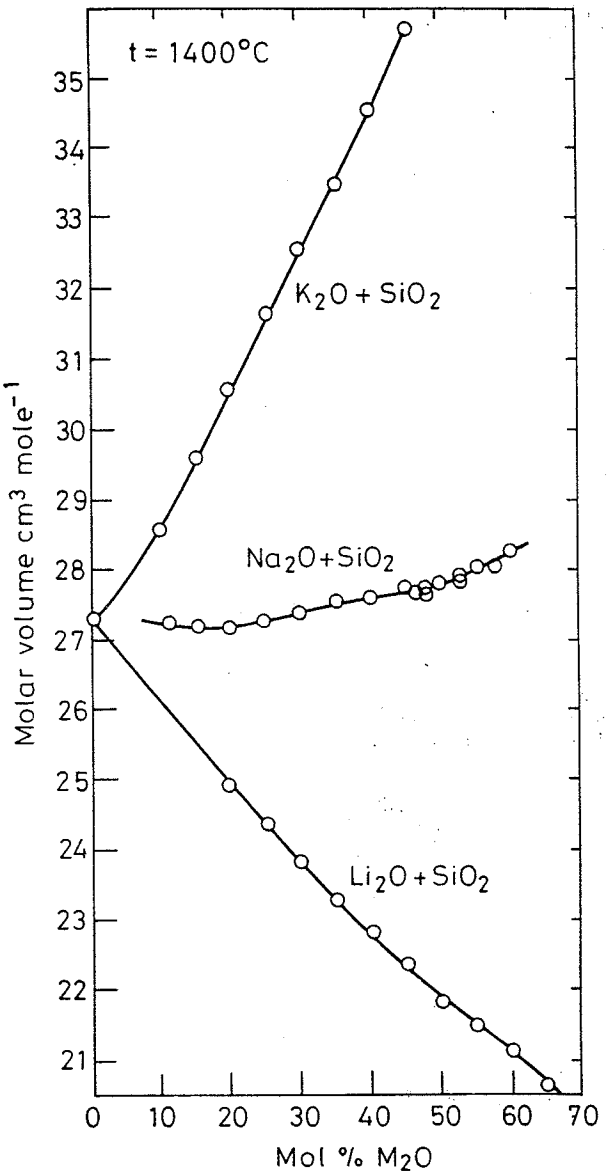


Fig. 8.50. Effect of Na_2O additions to SiO_2 on the molar volume of melts in comparison with the effects of other alkali metal oxides [Ref. 90]

8.3.3 Ternary systems

Al_2O_3-B_2O_3-CaF_2

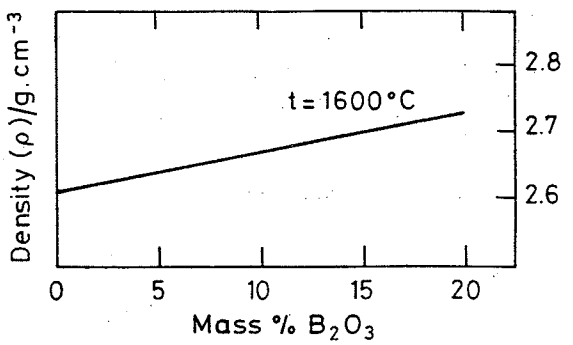


Fig. 8.51. Effect of B_2O_3 content on the density of melts based on the system (70 % CaF_2 + 30 % Al_2O_3) + B_2O_3 at 1600 °C [Ref. 24]

Al_2O_3-B_2O_3-CaO

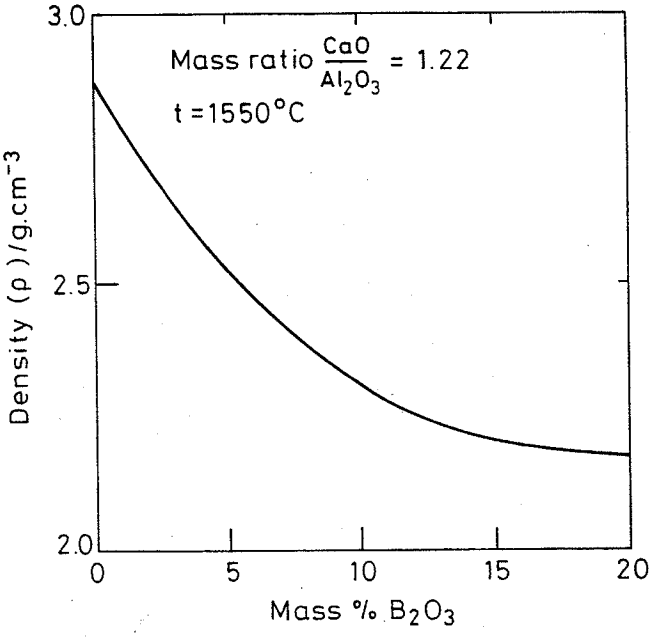


Fig. 8.52. Effect of B_2O_3 additions on the density of Al_2O_3 + CaO melts at 1550 °C [Ref. 91]

Al_2O_3-CaF_2-CaO

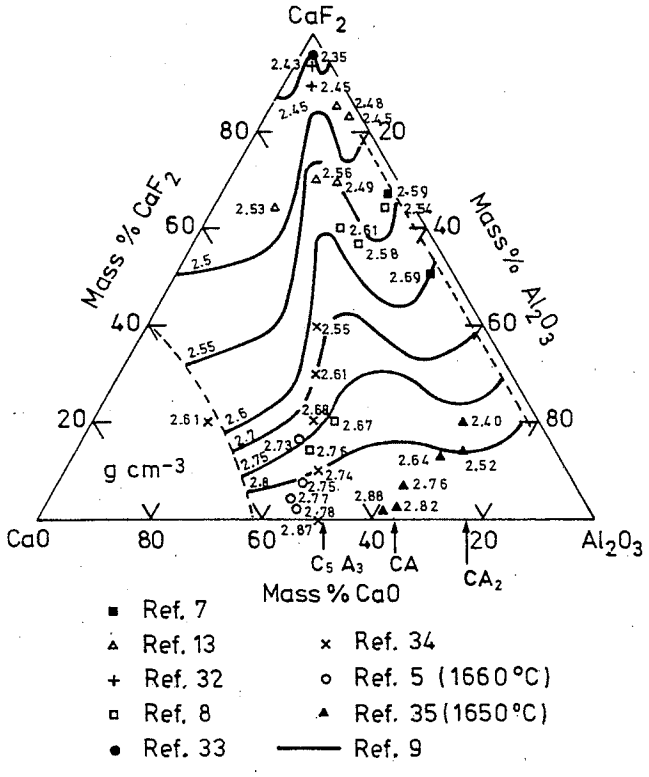


Fig. 8.53. Density of melts in the Al_2O_3 + CaF_2 + CaO system at 1600 °C

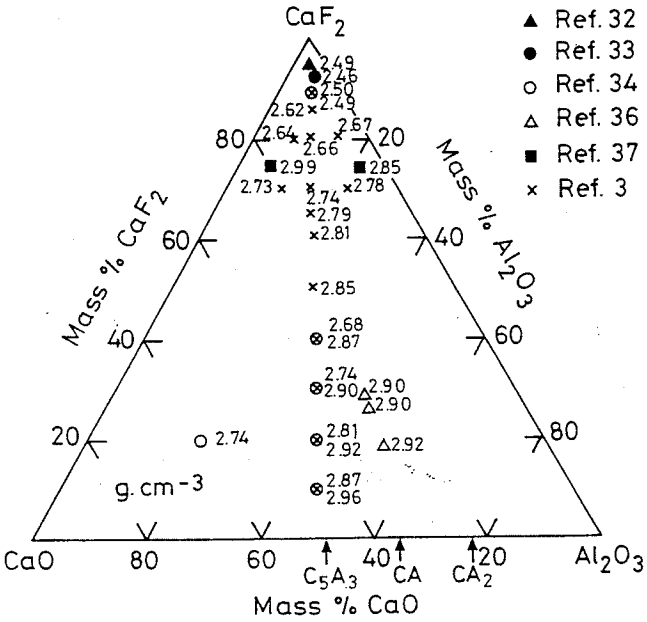


Fig. 8.54. Density of melts in the Al_2O_3 + CaF_2 + CaO system at 1500 °C

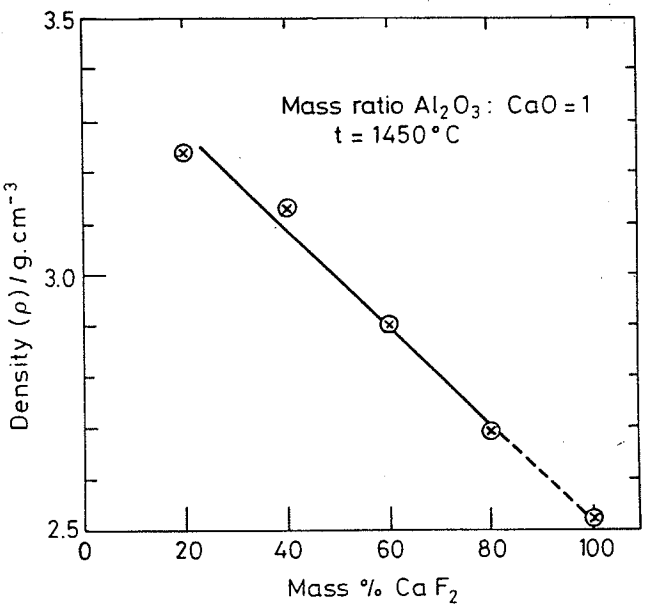


Fig. 8.55. Effect of CaF_2 content on the density of melts in the system (50 % Al_2O_3 + 50 % CaO) + CaF_2 at 1450 °C [Ref. 11]

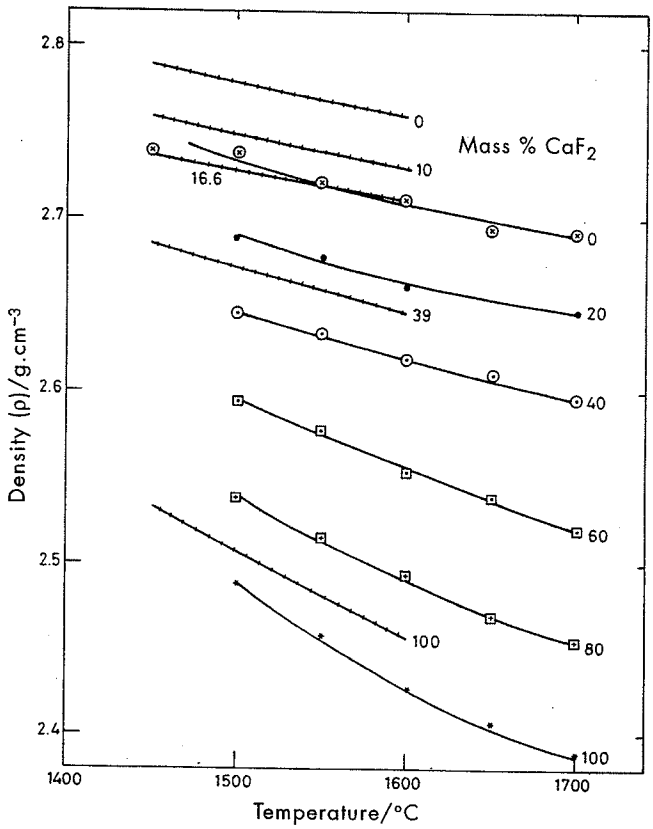


Fig. 8.56. Effect of temperature on the density of $Al_2O_3 + CaF_2 + CaO$ melts ($CaO:Al_2O_3=1$). Solid lines [Ref. 23]; crossed solid lines [Ref. 10]

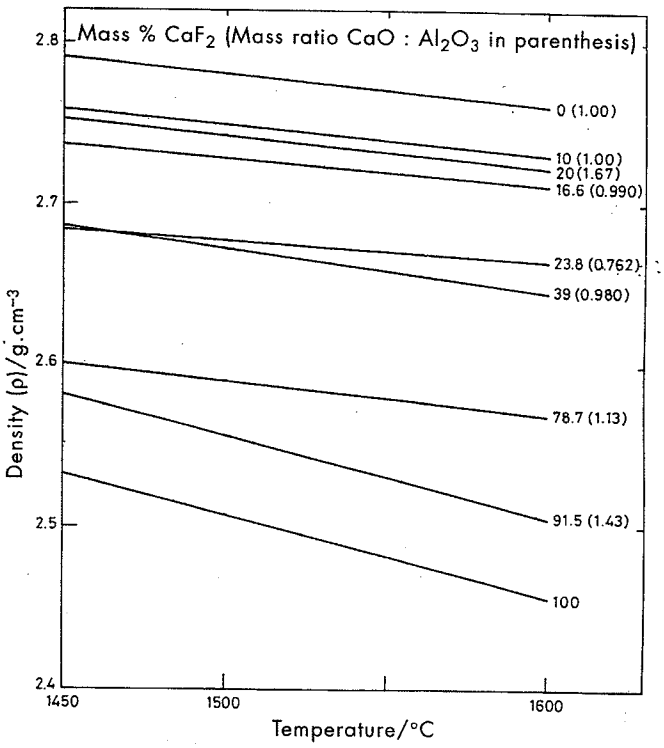


Fig. 8.57. Effect of temperature on the density of $Al_2O_3 + CaF_2 + CaO$ melts [Ref. 10]

Al_2O_3-CaF_2-MgO

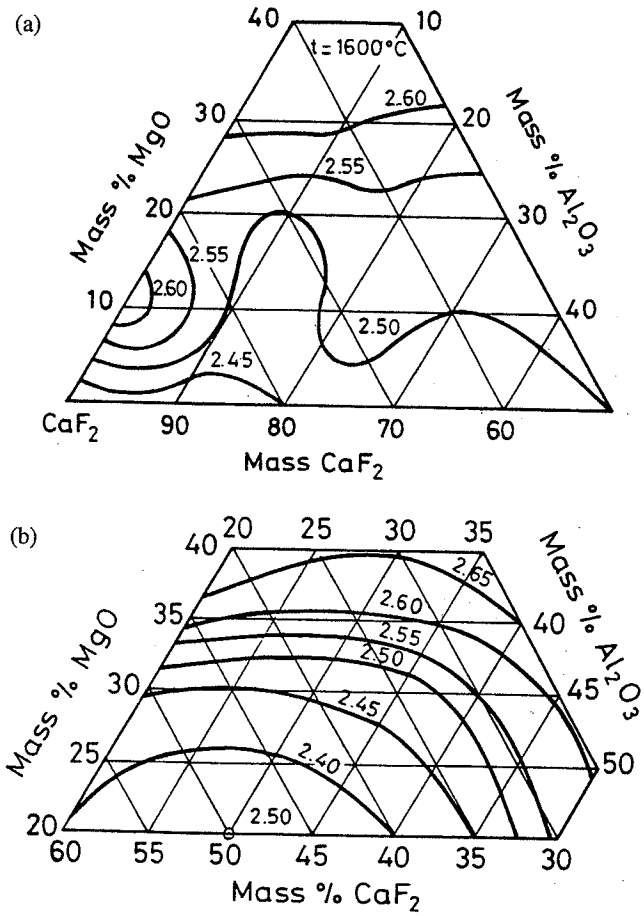


Fig. 8.58 a,b. Isodensity curves for the system $Al_2O_3 + CaF_2 + MgO$
(a) 1600 °C [Ref. 38]
(b) 1727 °C [Ref. 39]

Al_2O_3-CaF_2-Nb_2O_5

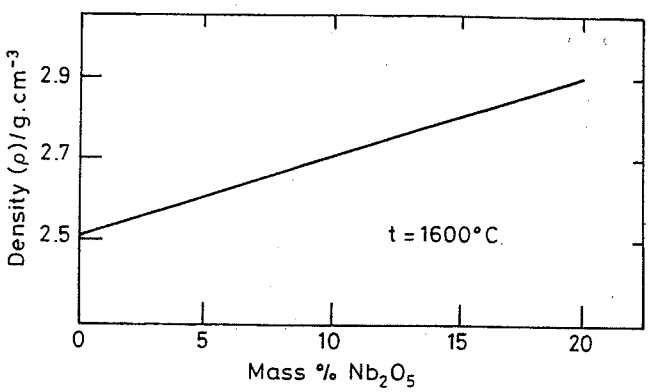


Fig. 8.59. Effect of Nb_2O_5 content on the density of (70 % CaF_2 + 30 % Al_2O_3) + Nb_2O_5 [Ref. 24]

Al_2O_3-CaF_2-TiO_2

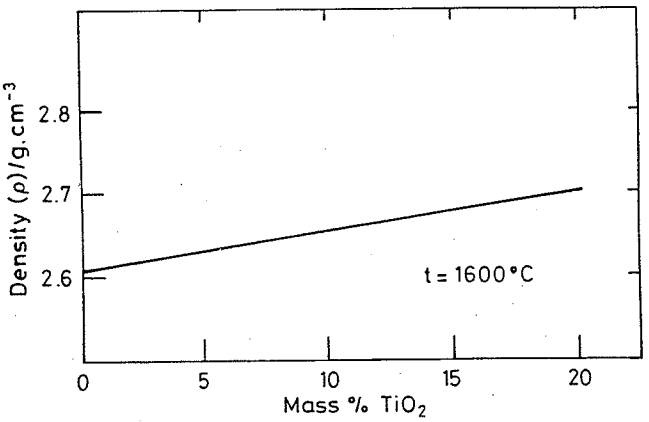


Fig. 8.60. Effect of TiO_2 content on the density of (70 % CaF_2 + 30 % Al_2O_3) + TiO_2 [Ref. 24]

Al_2O_3-CaF_2-V_2O_5

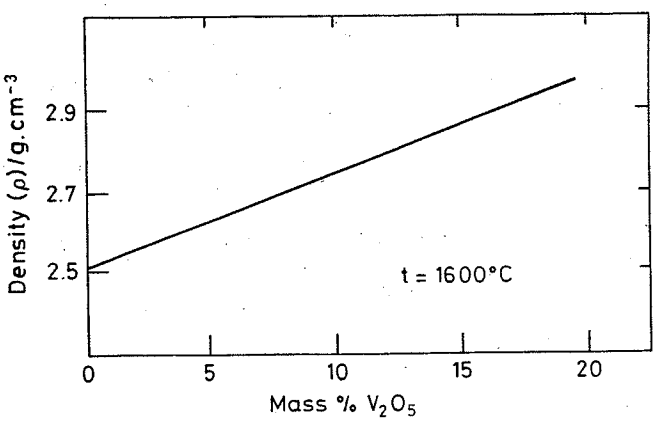


Fig. 8.61. Effect of V_2O_5 content on the density of (70 % CaF_2 + 30 % Al_2O_3) + V_2O_5 [Ref. 24]

Al_2O_3-CaO-Fe_2O_3

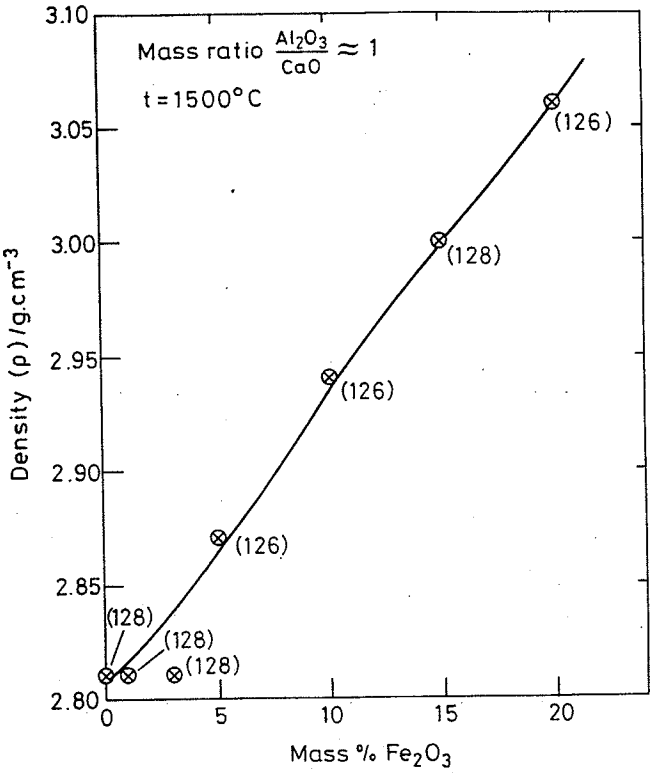


Fig. 8.62. Effect of Fe_2O_3 additions on the density of Al_2O_3 + CaO melts at 1500 °C. Respective temperature coefficients (x 10^5 / g.cm^{-3} K^{-1}) given in parenthesis [Ref. 41]

Al_2O_3-CaO-MgO

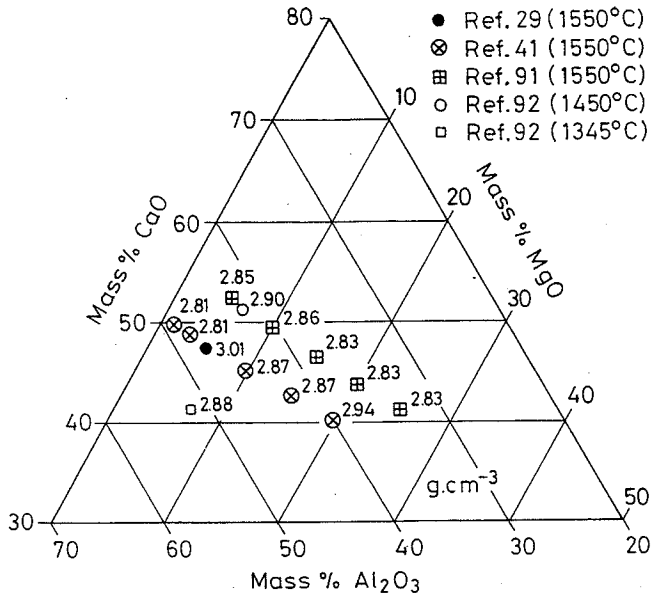


Fig. 8.63. Density of Al_2O_3 + CaO + MgO melts

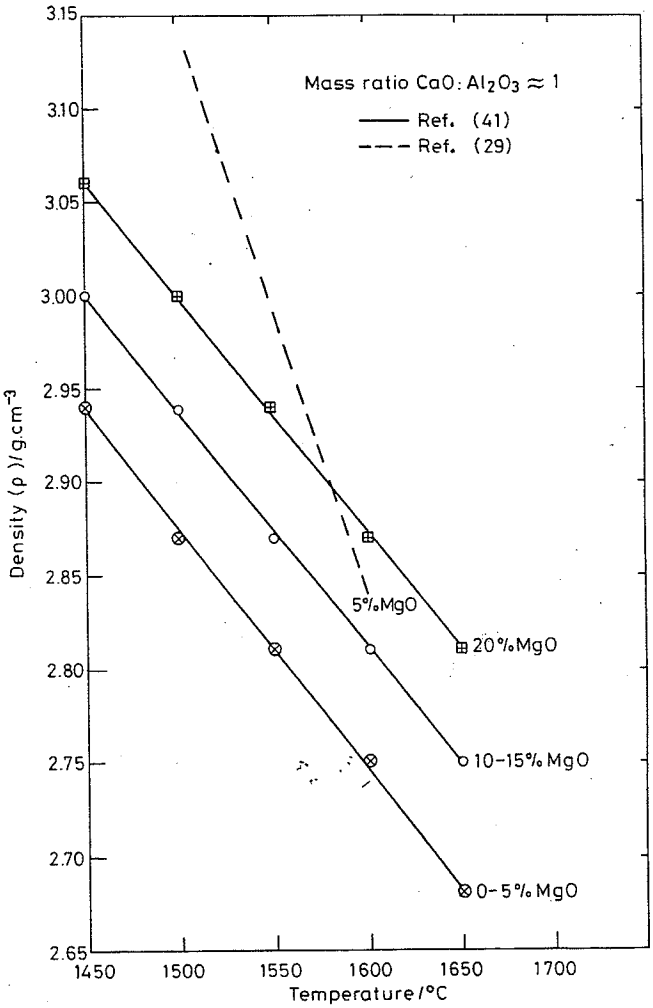


Fig. 8.64. Effect of temperature on the density of melts in the system Al_2O_3 + CaO + MgO

Al_2O_3-CaO-Na_2O

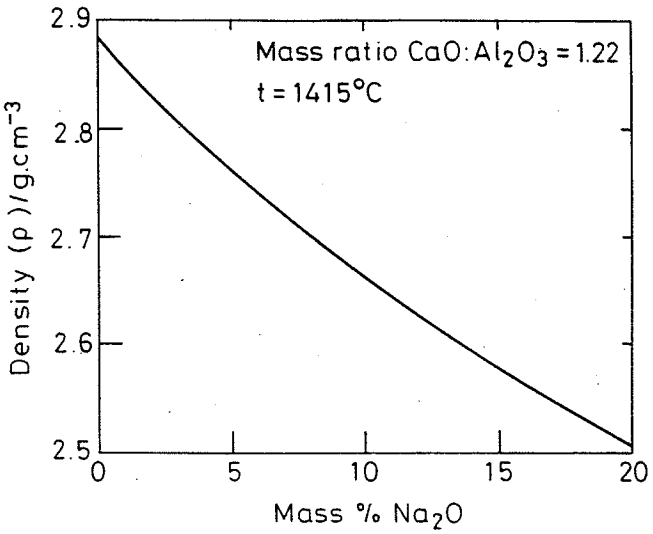


Fig. 8.65. Effect of Na_2O additions to Al_2O_3 + CaO on the density at 1415 °C [Ref. 91]

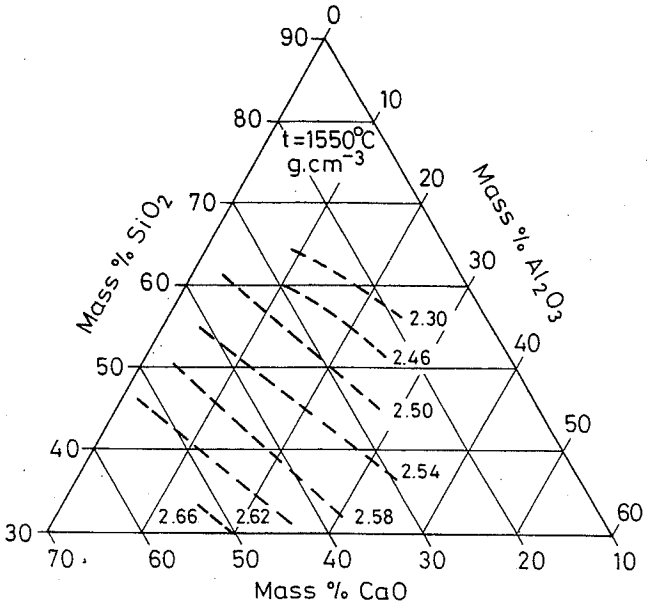


Fig. 8.67. Suggested isodensity lines [Ref. 93] for the system Al_2O_3 + CaO + SiO_2 based upon data given in [Refs. 93 and 96]

Al_2O_3-CaO-SiO_2

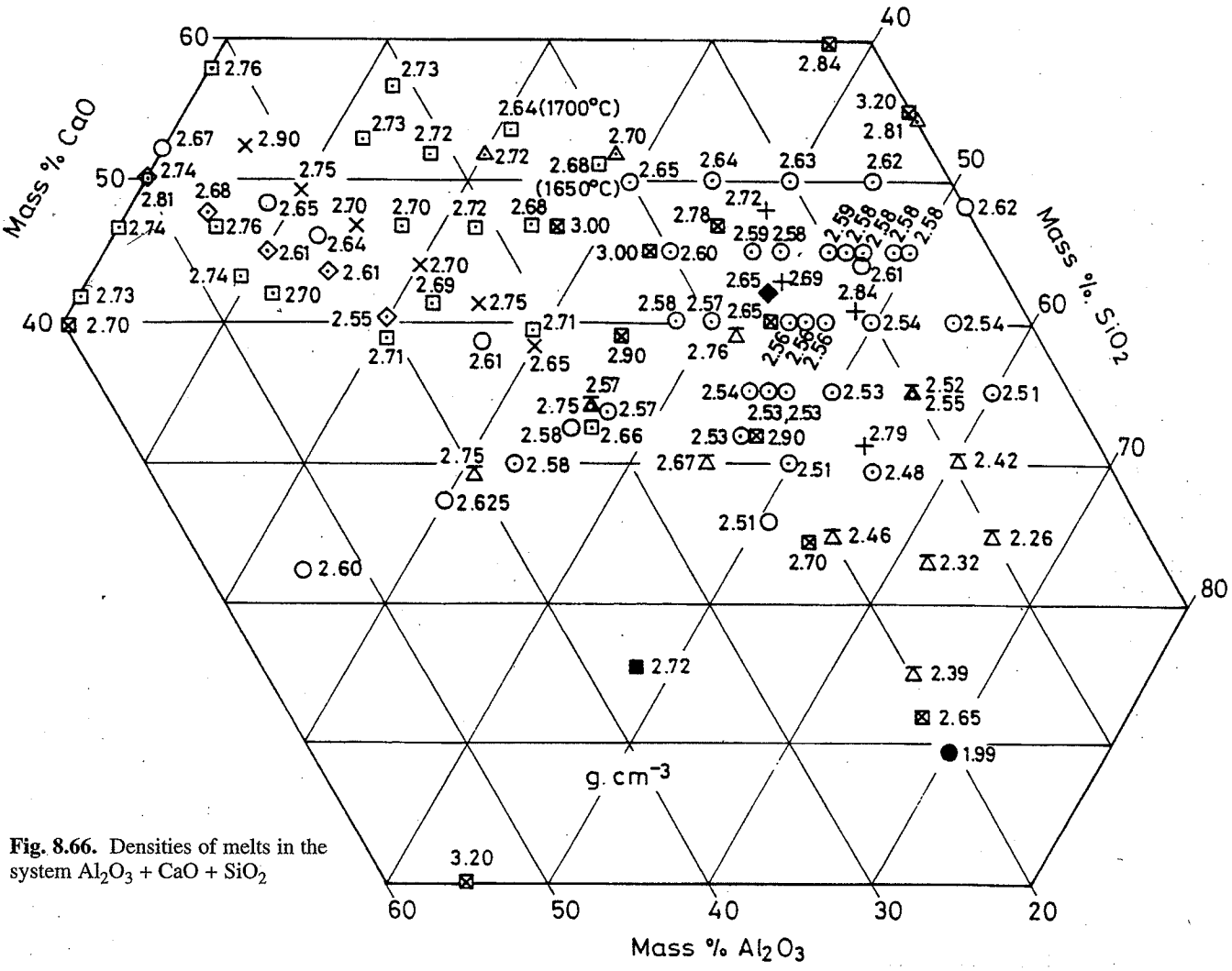


Fig. 8.66. Densities of melts in the system Al_2O_3 + CaO + SiO_2

◇ Ref.41 (1550°C)
□ Ref.44 (1600°C)
△ Ref.64 (1630°C)
⊠ Ref.65 (1565°C)
× Ref.91 (1480°C)
● Ref.92 (1345°C)
■ Ref.92 (1512°C)
⊙ Ref.93 (1550°C)
+ Ref.94 (1450°C)
○ Ref.95 (1727°C)
⧖ Ref.96 (1550°C)
◆ Ref.97 (1560°C)

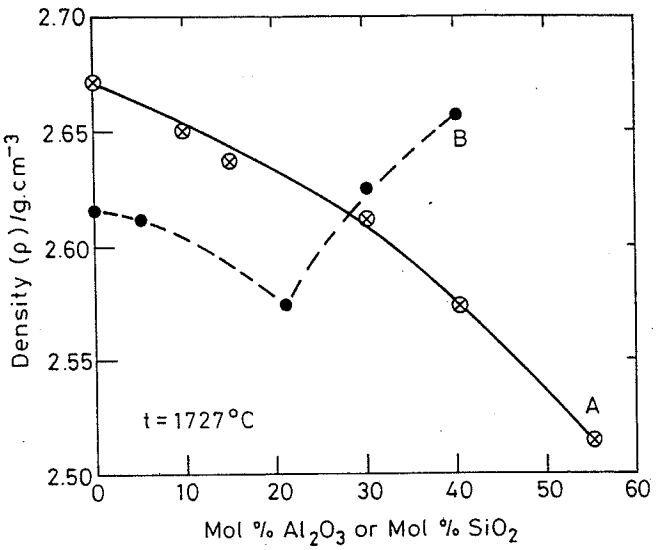


Fig. 8.68. Density of melts in the Al_2O_3 + CaO + SiO_2 system [Ref. 95]

Curve A: Effect of SiO_2 concentration with the mole ratio CaO:Al_2O_3 maintained at ≈ 2
Curve B: Effect of Al_2O_3 concentration with the mole ratio CaO:SiO_2 maintained at ≈ 1

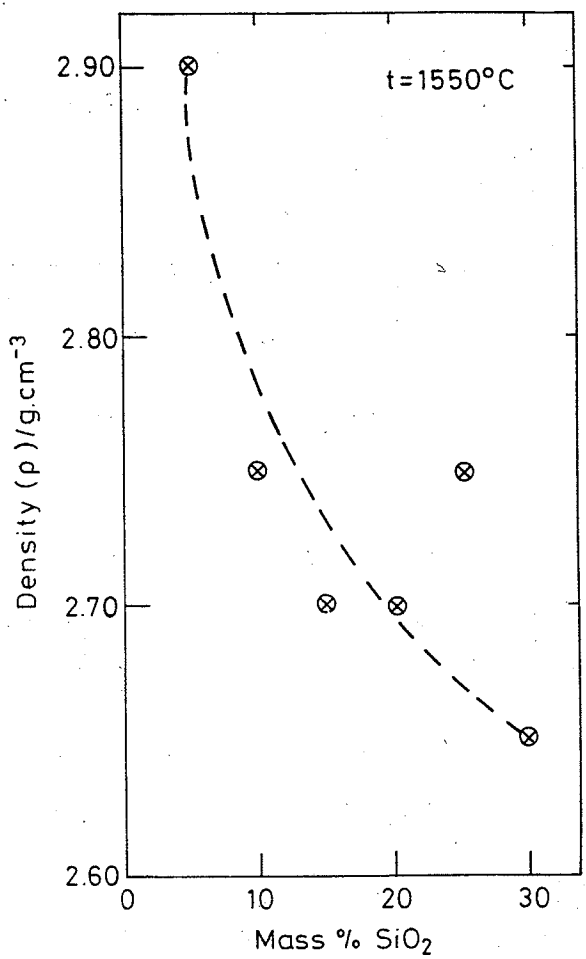
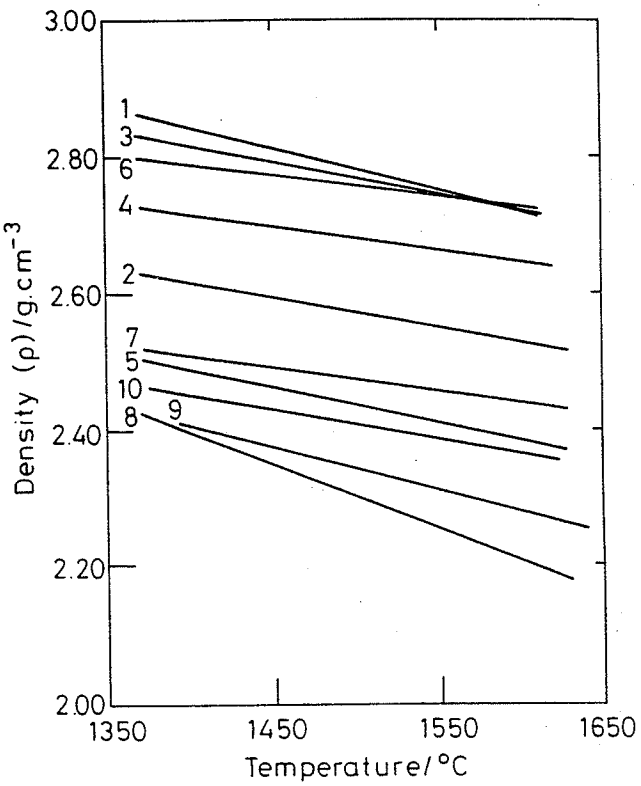


Fig. 8.69. Effect of SiO_2 additions to Al_2O_3 + CaO on the density at 1550 °C [Ref. 91]



No.	Al_2O_3	CaO	SiO_2
1	19	39	42
2	10	35	55
3	30	34	36
4	25	30	45
5	10	30	60
6	40	29	31
7	20	25	55
8	10	25	65
9	15	23	62
10	20	15	65

Fig. 8.70. Effect of temperature on the density of Al_2O_3 + CaO + SiO_2 melts [Ref. 96]

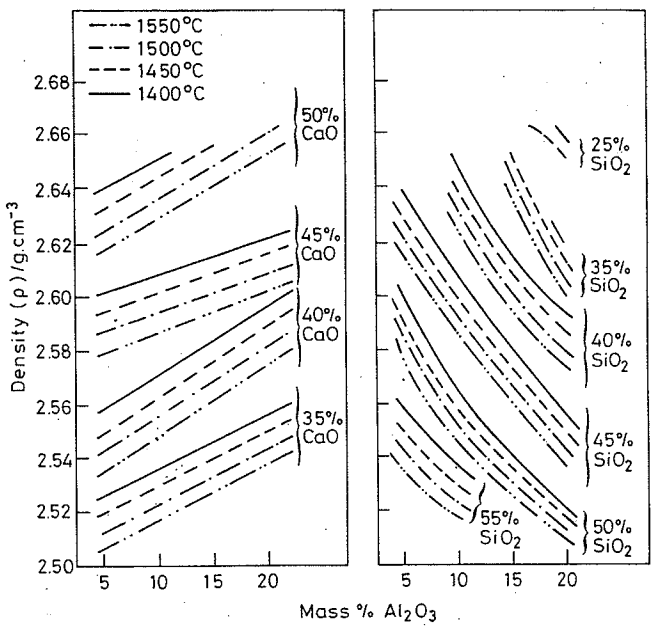


Fig. 8.71. Effects of Al_2O_3 content and of temperature on the density of Al_2O_3 + CaO + SiO_2 melts [Ref. 93]

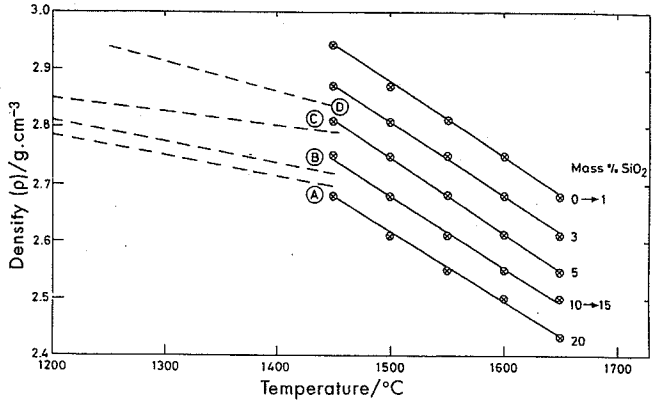


Fig. 8.72. Effect of temperature on the density of $Al_2O_3 + CaO + SiO_2$ melts
Solid lines: melts containing various amounts of SiO_2 with the mass ratio $CaO:Al_2O_3$ maintained at 1 [Ref. 41]
Hatched lines [Ref. 94]: compositions (mass %):
(A) 13.9 Al_2O_3 + 43.0 CaO + 43.1 SiO_2
(B) 12.7 Al_2O_3 + 47.8 CaO + 39.5 SiO_2
(C) 15.0 Al_2O_3 + 31.1 CaO + 33.9 SiO_2
(D) 10.6 Al_2O_3 + 40.9 CaO + 48.5 SiO_2

Al_2O_3-CaO-TiO_2

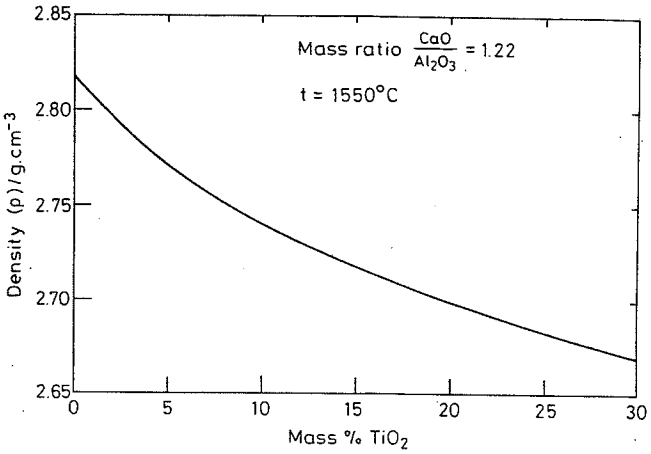


Fig. 8.73. Effect of TiO_2 content on the density of $Al_2O_3 + CaO + TiO_2$ melts (mass ratio $CaO:Al_2O_3 = 1.22$) [Ref. 91]

Al_2O_3-Fe_xO-SiO_2

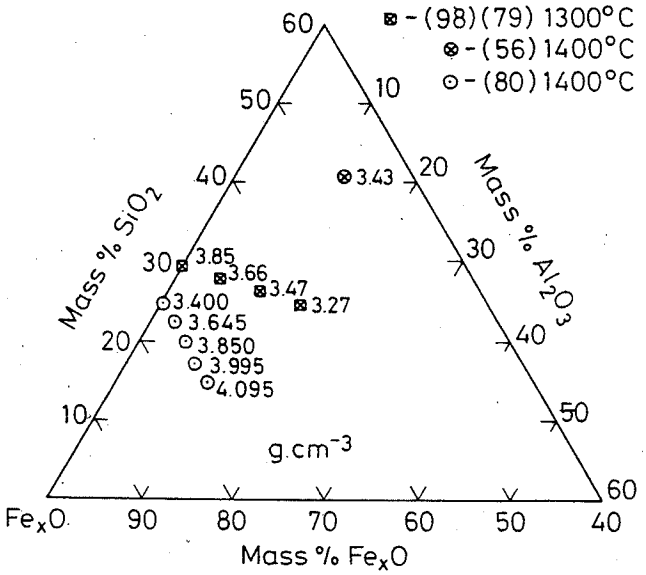


Fig. 8.74. Density of $Al_2O_3 + Fe_xO + SiO_2$ slags

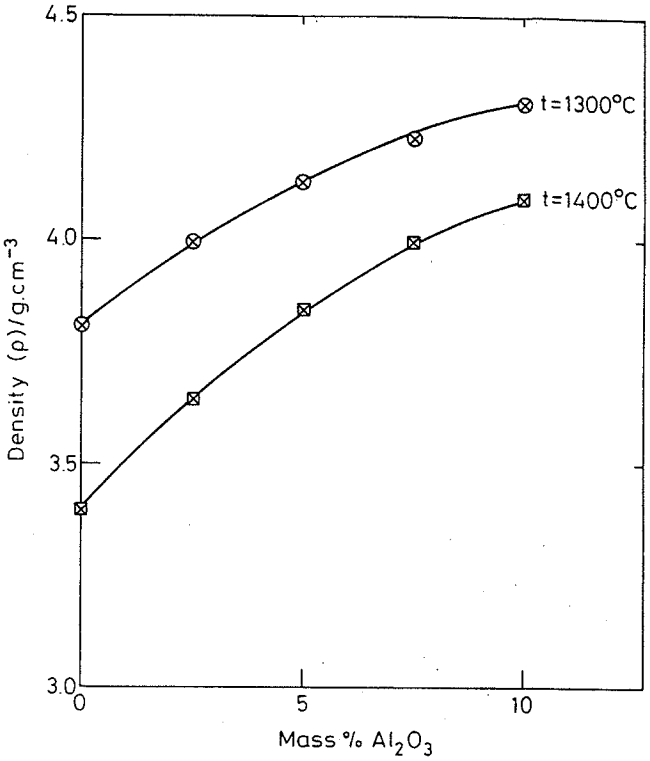
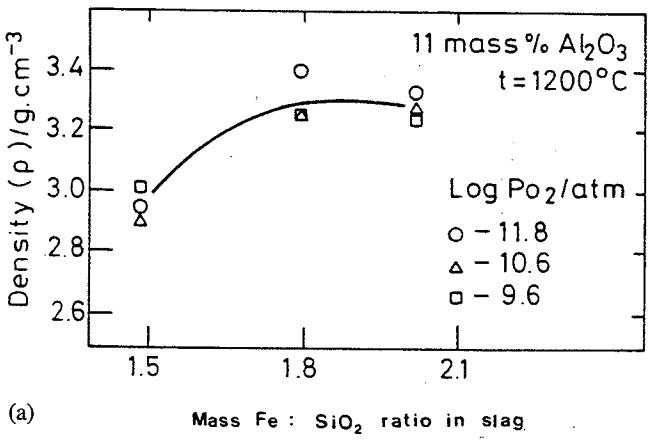
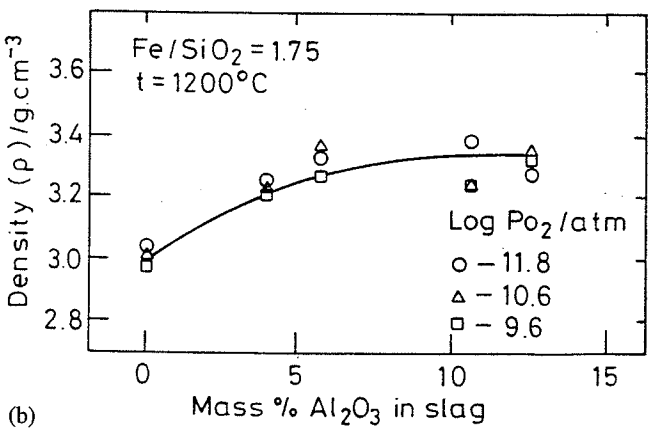


Fig. 8.75. Density of $Al_2O_3 + Fe_xO + SiO_2$ slags ($[Fe_xO] \approx 75$ %) [Ref. 80]



(a)



(b)

Fig. 8.76 a,b. Density of $Al_2O_3 + Fe_xO + SiO_2$ melts at 1200 °C [Ref. 99]
(a) Effect of Fe:SiO_2 ratio under various partial pressures of oxygen
(b) Effect of Al_2O_3 concentration under various partial pressures of oxygen

Al_2O_3-MgO-SiO_2

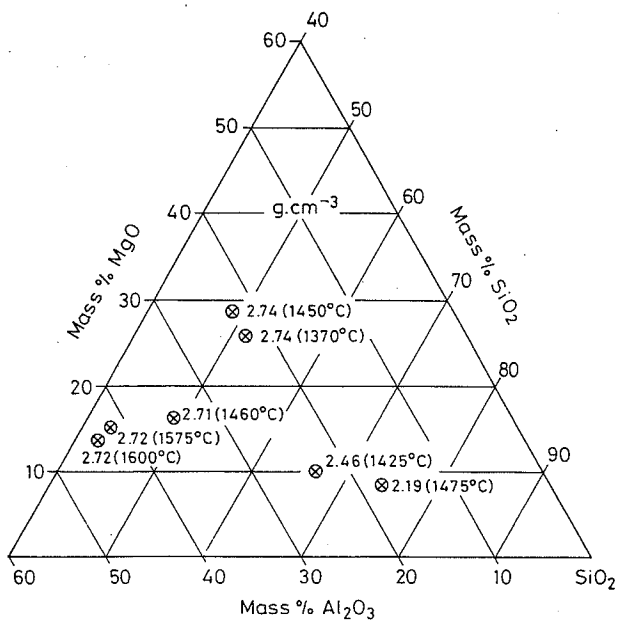
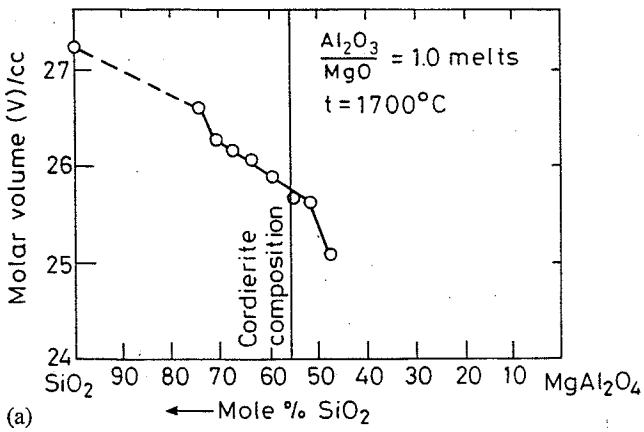


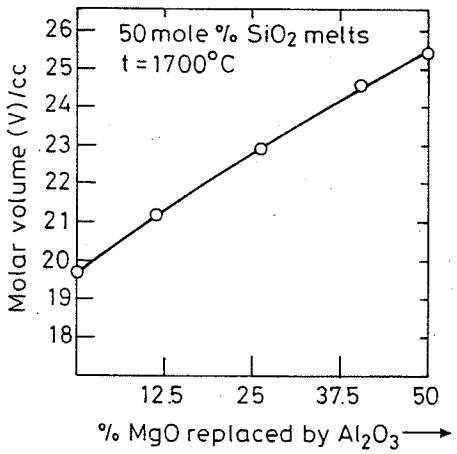
Fig. 8.77. Density of Al_2O_3 + MgO + SiO_2 at the liquidus temperatures of the melts (temperature shown in parenthesis) [Ref. 92]

Tab. 8.2. Density equations for Al_2O_3 + MgO + SiO_2 melts [Ref. 100] ($\rho = a - bT$)/g.cm^{-3} (with T/K)

Mole % Al_2O_3	Mole % SiO_2	a	b x 10^3
25.62	47.58	2.722	0.05599
23.49	51.98	2.669	0.06495
21.63	55.00	2.643	0.06531
19.49	59.55	2.576	0.05065
17.45	63.88	2.554	0.05549
15.10	67.83	2.410	–
13.90	70.94	2.397	–
11.92	74.59	2.221	–
19.98	49.81	2.692	0.07498
12.95	49.96	2.736	0.1016
6.09	50.24	2.742	0.1037



(a)



(b)

Fig. 8.78 a,b. Molar volumes of melts in the Al_2O_3 + MgO + SiO_2 system [Ref. 100]
(a) Effect of SiO_2 concentration in melts with mole ratio Al_2O_3:MgO = 1
(b) Effect of replacing MgO by Al_2O_3 in 50 mol. % SiO_2 melts

Al_2O_3-Na_2O-SiO_2

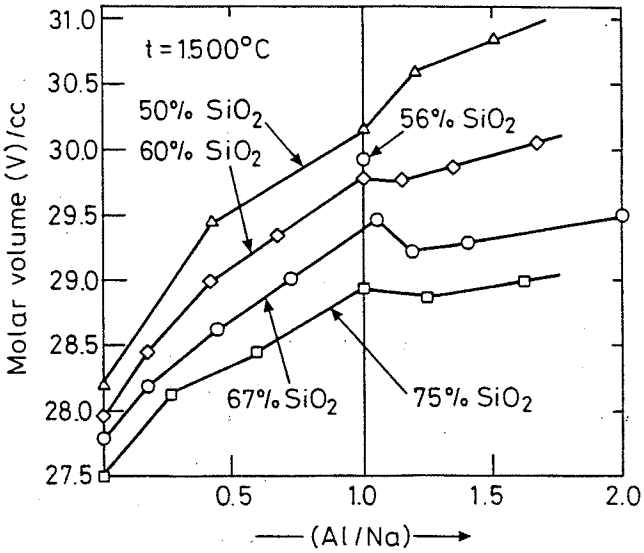


Fig. 8.79. Molar volume isotherms plotted as a function of the Al:Na ratio for constant SiO_2 content melts [Ref. 101]

Tab. 8.3 Density equations and discrete values for density of melts in the $Al_2O_3+Na_2O+SiO_2$ system, $(\rho = a - b \times 10^{-3} T)/g.cm^{-3}$ (with T/K)

Mole % Na_2O	Mole % SiO_2	a	b	$\rho(g/cm^{-3})$		Reference
				1500 °C	1700 °C	
27.9	67.2	2.462	0.1348	...	...	
22.9	66.8	2.355	0.05183	...	...	
18.9	67.3	2.301	0.01309	...	...	
16.3	66.5	...	...	2.290	2.290	
15.0	67.1	2.493	0.0973	...	...	
13.8	66.8	2.508	0.09664	...	...	
11.0	67.1	...	...	2.354	2.329	
33.9	60.1	2.524	0.1719	...	...	
28.1	60.0	2.511	0.1404	...	...	
24.1	59.6	2.420	0.06988	...	...	
20.1	60.0	...	...	2.31	2.29	
18.5	60.2	...	...	2.33	2.31	
17.0	60.1	2.597	0.1426	...	...	[101]
15.0	59.9	...	...	2.358	2.339	
35.1	50.0	2.537	0.1481	...	...	
23.0	49.4	2.567	0.1193	...	...	
20.1	49.8	...	...	2.368	2.360	
24.7	50.1	2.616	0.1457	...	...	
22.1	55.8	2.518	0.1049	...	...	
19.9	74.7	2.344	0.06478	...	...	
16.1	74.3	2.428	0.09212	...	...	
12.3	75.2	...	...	2.265	...	
11.1	74.9	...	...	2.290	...	
9.5	75.1	...	...	2.297	...	
42.0	53.1	–	–	2.37 (1300 °C)	–	[89]
39.9	50.5	–	–	2.45 (1300 °C)	–	

Al_2O_3-SiO_2-TiO_2

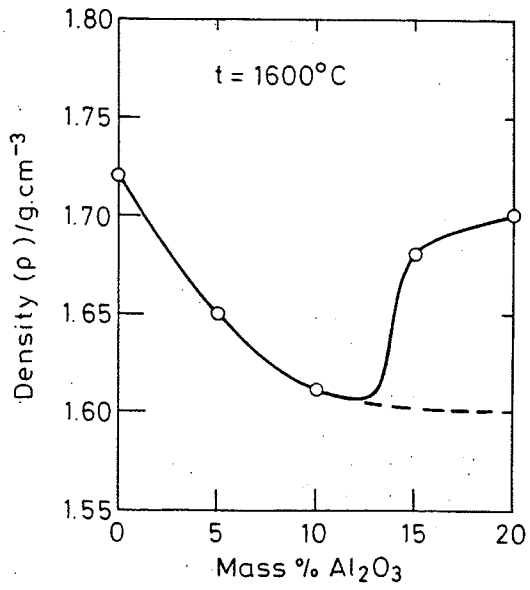


Fig. 8.80. Density of melts in the system Al_2O_3 + SiO_2 + TiO_2. The mass ratio SiO_2:TiO_2 is maintained at the eutectic composition ratio (89.5 mass % SiO_2 + 10.5 mass % TiO_2) [Ref. 102]

CaF_2-CaO-SiO_2

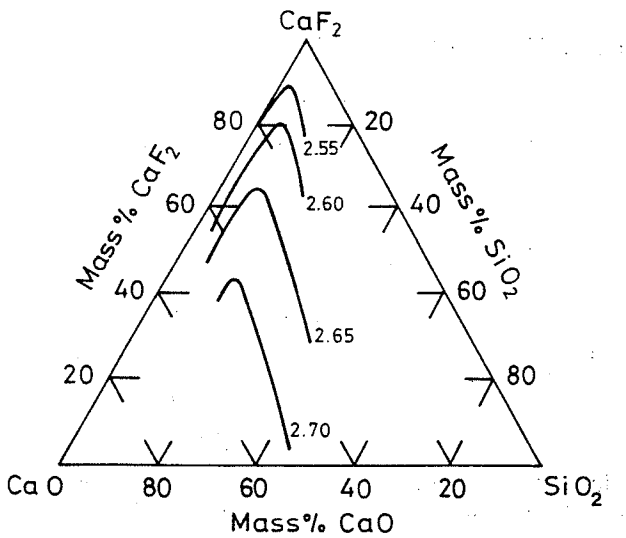


Fig. 8.81. Isodensity curves ($g.cm^{-3}$) for the CaF_2 + CaO + SiO_2 system at 1600 °C [Ref. 40]

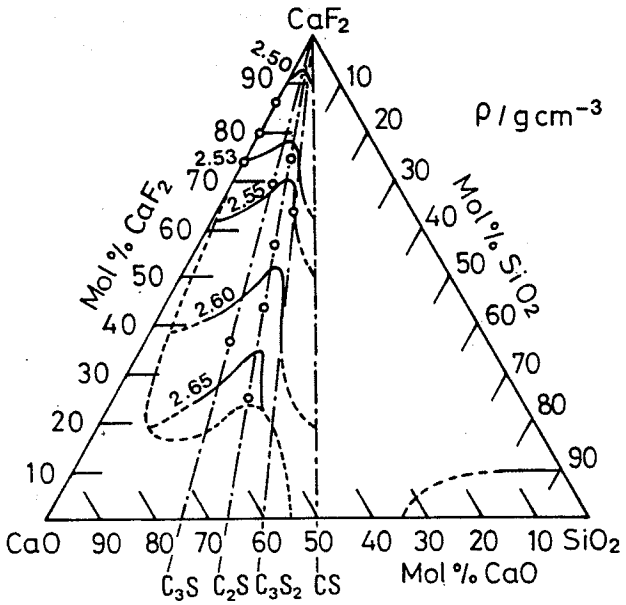


Fig. 8.82. Isodensity curves ($g.cm^{-3}$) for the CaF_2 + CaO + SiO_2 system at 1500 °C [Ref. 20]

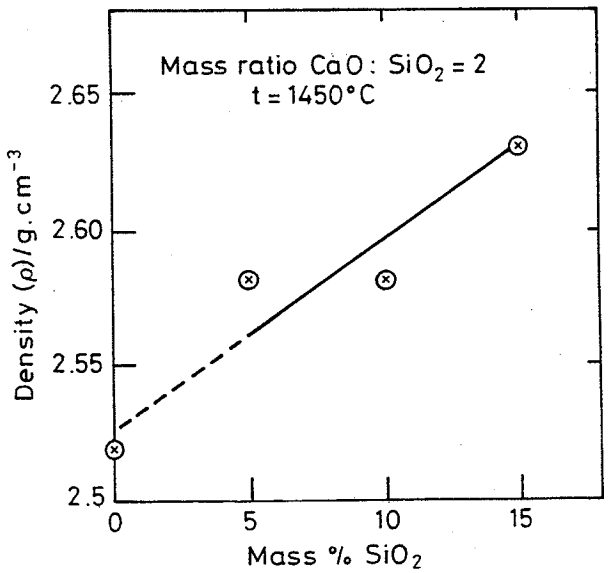


Fig. 8.83. Effect of SiO_2 content on the density of melts in the system CaF_2 + CaO + SiO_2 (CaO:SiO_2 = 2) [Ref. 11]

CaO-CaS-SiO_2

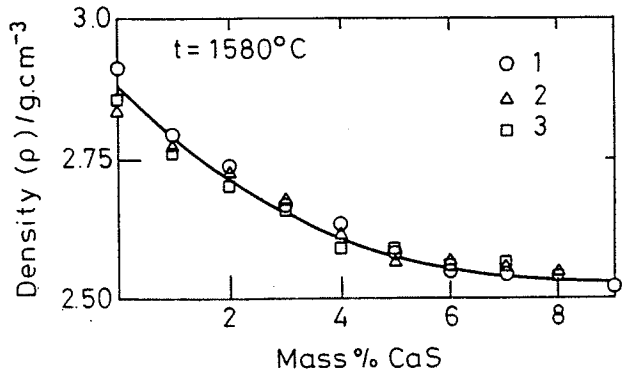


Fig. 8.84. Effect of CaS concentration on the density of CaO + CaS + SiO_2 melts with various basicities (B) [Ref. 103]
1 - B = 0.8 2 - B = 1.0 3 - B = 1.2

where $B = \frac{[CaO] + [CaS]}{SiO_2}$ (expressed as molar quantities)

CaO-Fe_xO-P_2O_5

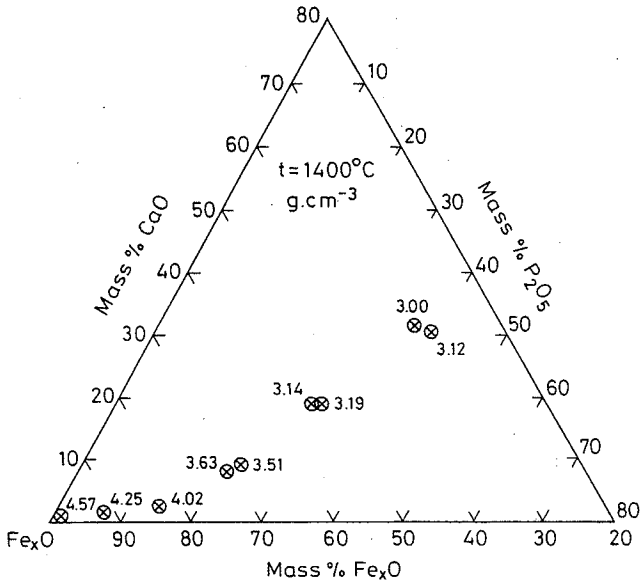


Fig. 8.85. Density of CaO + Fe_xO + P_2O_5 melts [Ref. 55]

CaO-Fe_xO-SiO_2

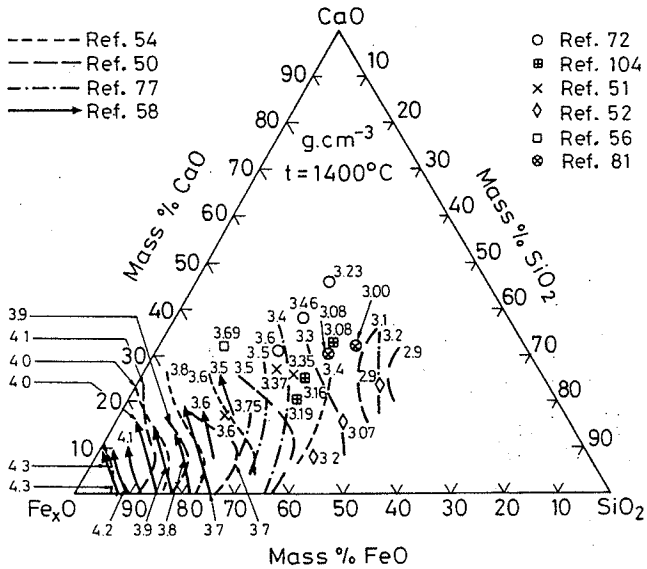


Fig. 8.86. Density of CaO + Fe_xO + SiO_2 melts from various sources [Ref. 83]

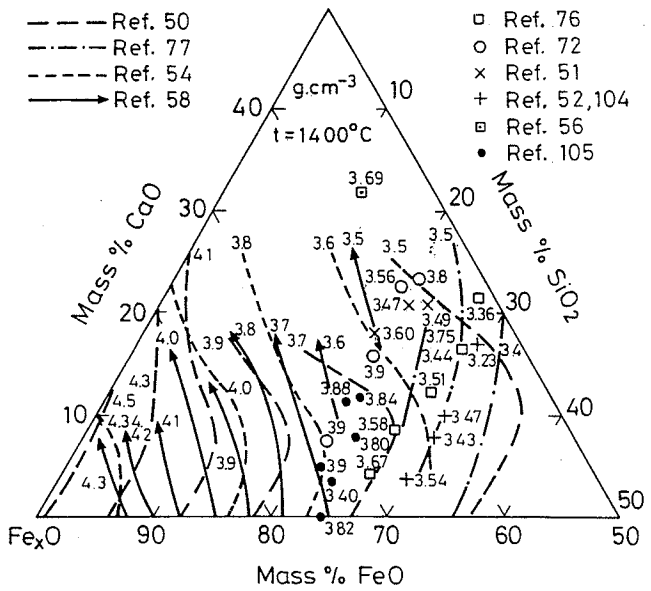


Fig. 8.87. Density of Fe_xO-rich melts of the CaO + Fe_xO + SiO_2 system given by various sources [Ref. 83]

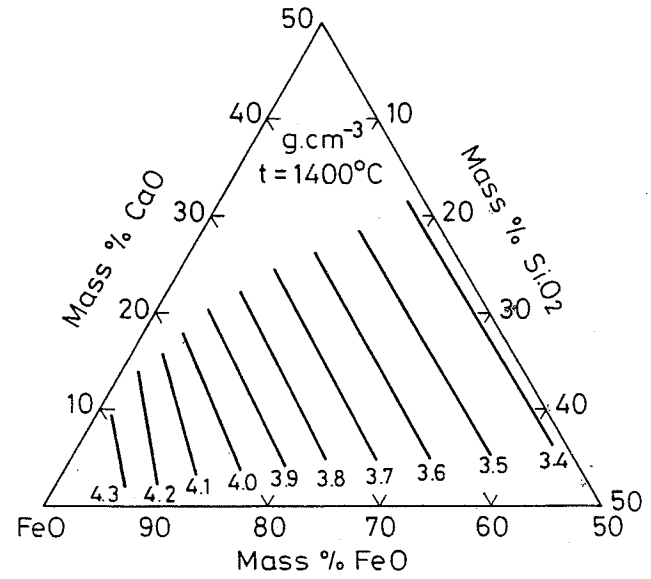
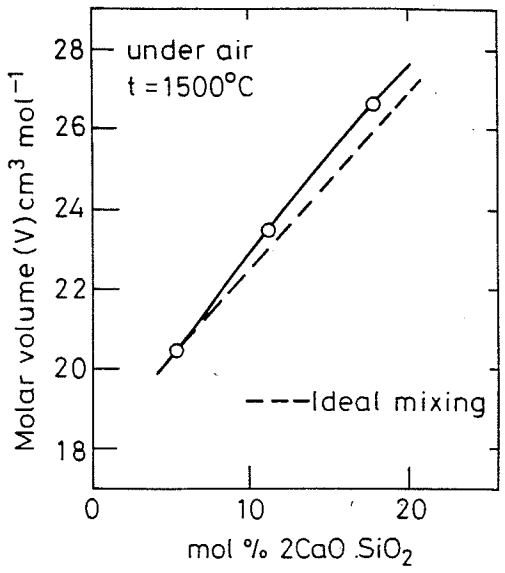
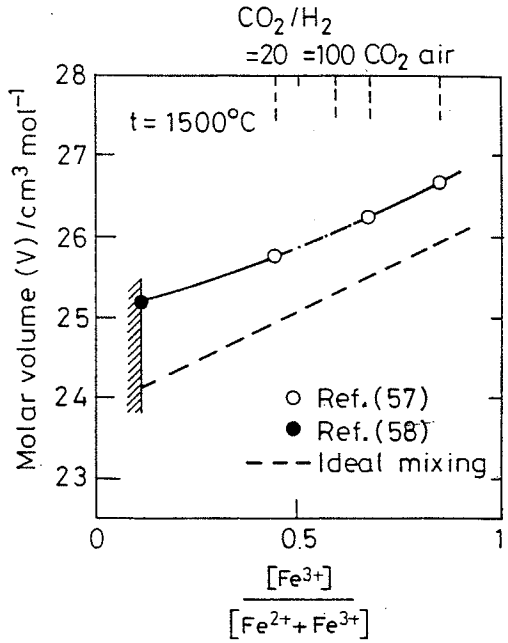


Fig. 8.88. Suggested isodensity lines for the system CaO + Fe_xO + SiO_2 at 1400 °C [Ref. 83]



(a)



(b)

Fig. 8.89 a,b. Molar volumes of CaO + Fe_xO + SiO_2 melts [Ref. 57]

(a) Molar volumes of Fe_xO + 2 $CaO.SiO_2$ under air

(b) Molar volumes of (17.7 mol. % 2 $CaO.SiO_2$) + Fe_xO melts under various oxidising conditions

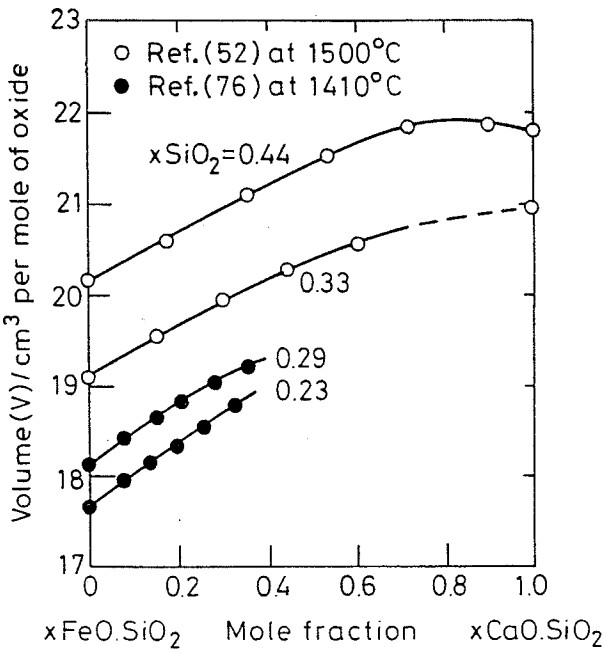


Fig. 8.90. Molar volumes of melts in the system $CaO + FeO + SiO_2$ [Ref. 106]

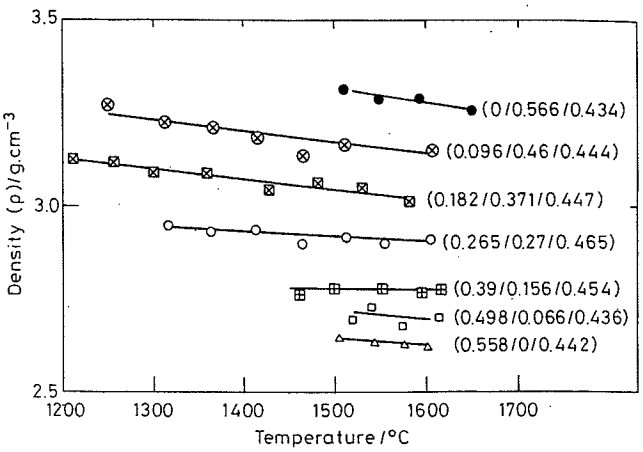


Fig. 8.92. Effect of temperature on the density of melts in the system ≈ 1.273 (FeO.CaO).SiO_2. (Numbers in parenthesis refer (from the left) to the respective mole fractions of CaO; FeO and SiO_2) [Ref. 52]

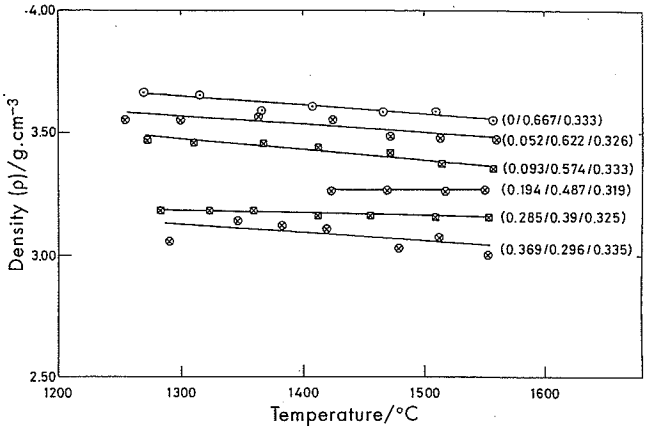


Fig. 8.91. Effect of temperature on the density of melts in the system ≈ 2 (FeO.CaO).SiO_2. (Numbers in parenthesis refer (from the left) to respective mole fractions of CaO; FeO and SiO_2) [Ref. 52]

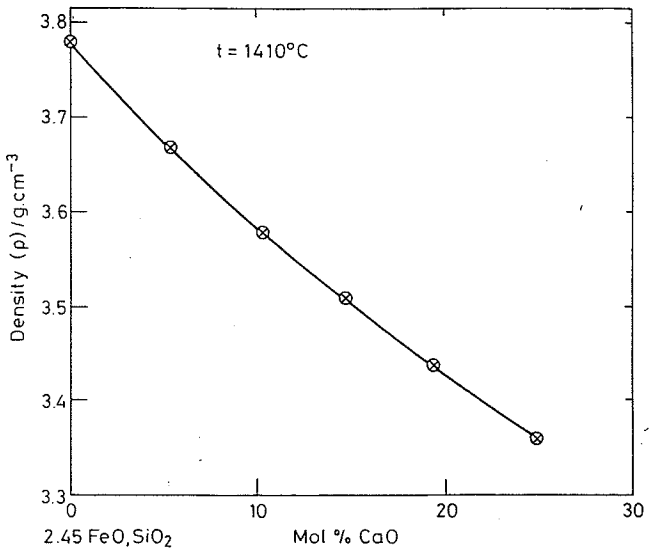


Fig. 8.93. Density of $CaO + Fe_xO + SiO_2$ melts - effect of CaO concentration of compositions along the $X_{SiO_2} = 0.29$ line. Melts in contact with solid Fe [Ref. 76]

Tab. 8.4. Temperature dependence of the density of melts in the system $CaO + Fe_xO + SiO_2$, described in the form $\rho = a + bT + cT^2$; (quadratic term is a consequence of the change in oxidation state of the iron with temperature/K) [Ref. 108]

Equilibrium composition at 1723 K. (mole fraction)				a/g.cm^{-3}	b.10^3/g.cm^{-3}.K^{-1}	c.10^7/g.cm^{-3}.K^{-2}
CaO	FeO	Fe_2O_3	SiO_2			
0.5	–	–	0.5	2.990	- 0.195	–
0.472	0.010	0.046	0.472	4.232	- 1.448	3.520
0.444	0.019	0.092	0.444	4.189	- 1.294	3.123
0.412	0.030	0.146	0.412	4.016	- 0.906	1.993
0.517	0.009	0.120	0.353	2.122	1.087	- 3.425
0.383	0.022	0.074	0.521	3.497	- 0.605	1.198
0.312	0.023	0.055	0.610	2.838	- 0.014	- 0.382

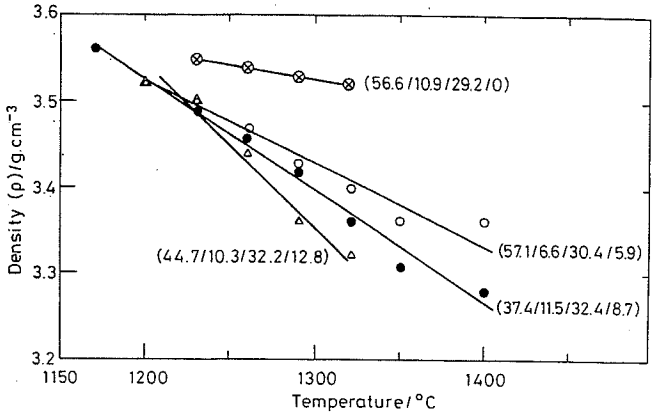


Fig. 8.94. Effect of temperature on the density of $CaO + Fe_xO + SiO_2$ melts, in which the concentration of CaO is progressively increased. (Numbers in parenthesis refer to mass % FeO; Fe_2O_3; SiO_2; CaO respectively) [Ref. 107]

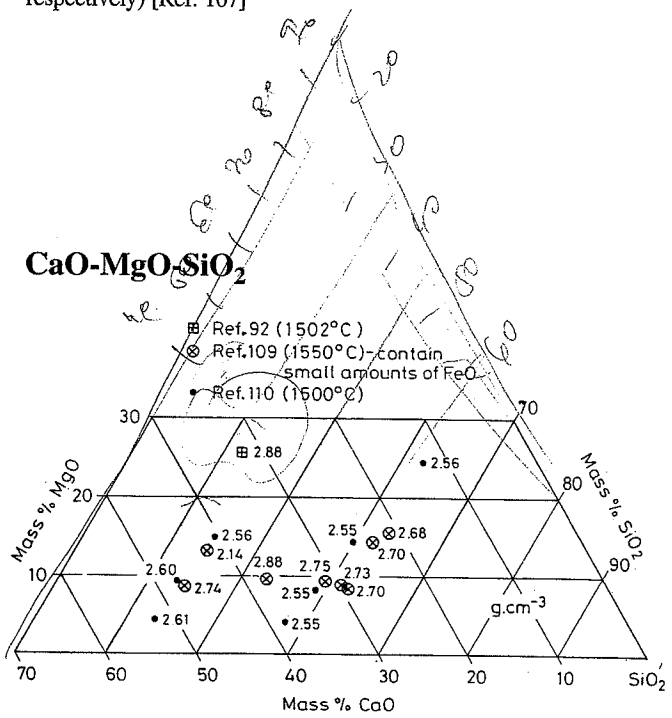


Fig. 8.95. Density of melts in the system $CaO + MgO + SiO_2$

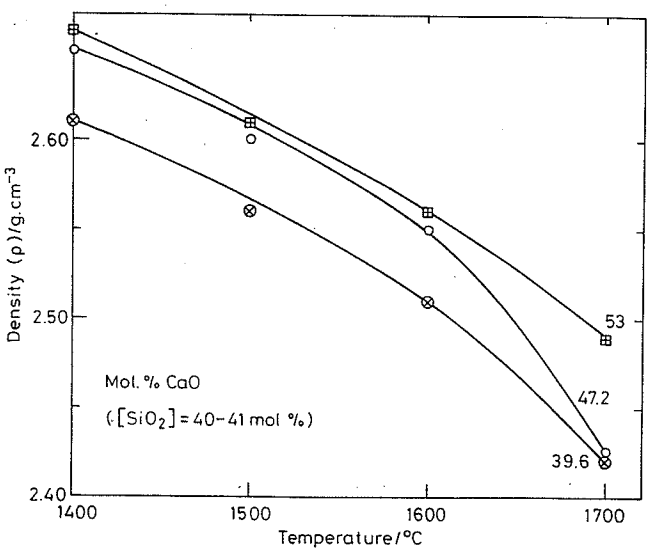


Fig. 8.96. Effect of temperature on the density of melts in the system $CaO + MgO + SiO_2$ [Ref. 110]

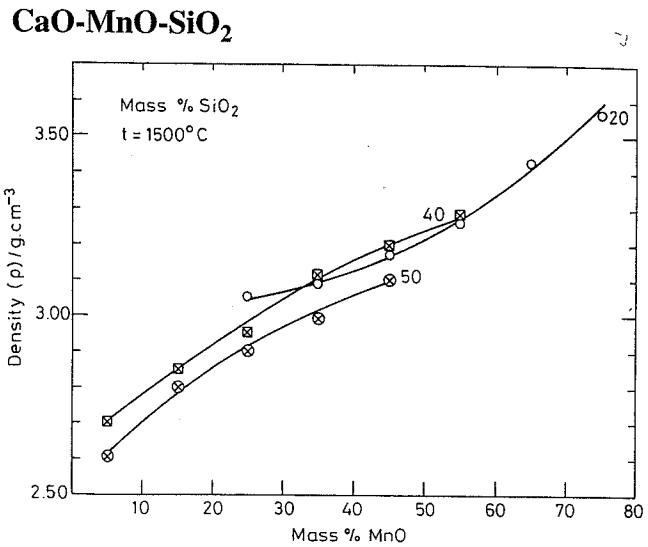


Fig. 8.97. Density of melts in the system $CaO + MnO + SiO_2$. Effect of MnO concentration in slags containing fixed amounts of SiO_2 [Ref. 111]

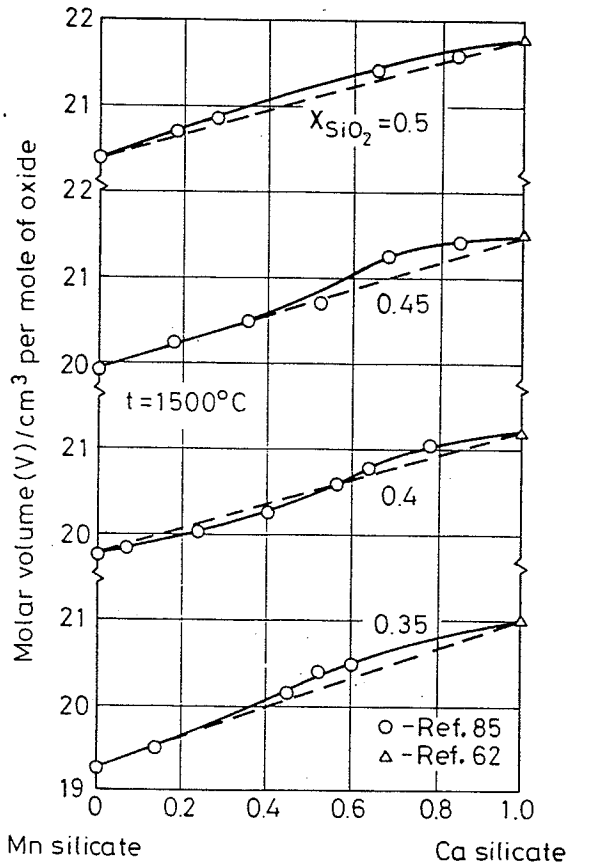


Fig. 8.98. Molar volume of melts in the system $CaO + MnO + SiO_2$ for various fixed mole fractions of SiO_2, showing the deviation from ideal behaviour [Ref. 85]

$CaO\text{-}Na_2O\text{-}SiO_2$

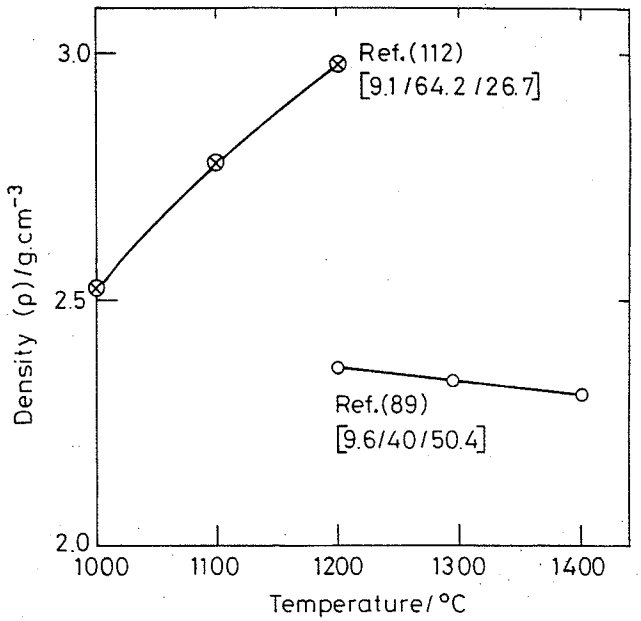


Fig. 8.99. Effect of temperature on two samples of $CaO + Na_2O + SiO_2$. (Numbers in brackets indicate (from the left), the negative mole % CaO; Na_2O; SiO_2)

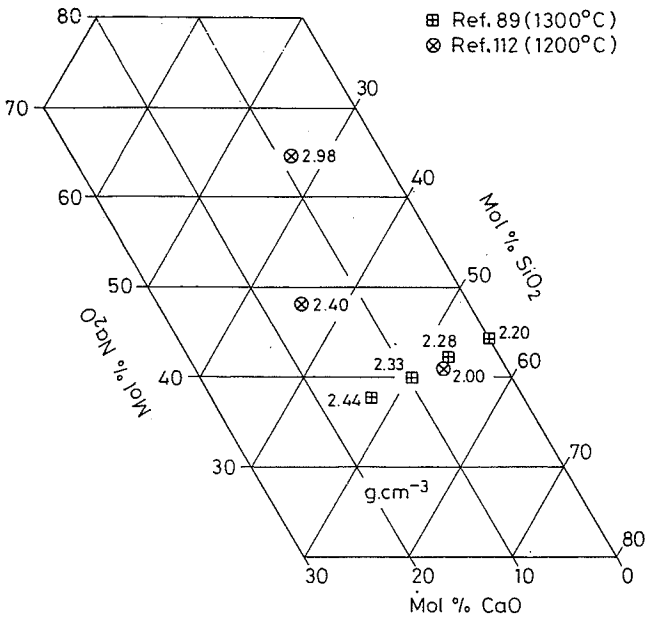


Fig. 8.100. Density of melts in the system $CaO + Na_2O + SiO_2$

$Fe_xO\text{-}MgO\text{-}SiO_2$

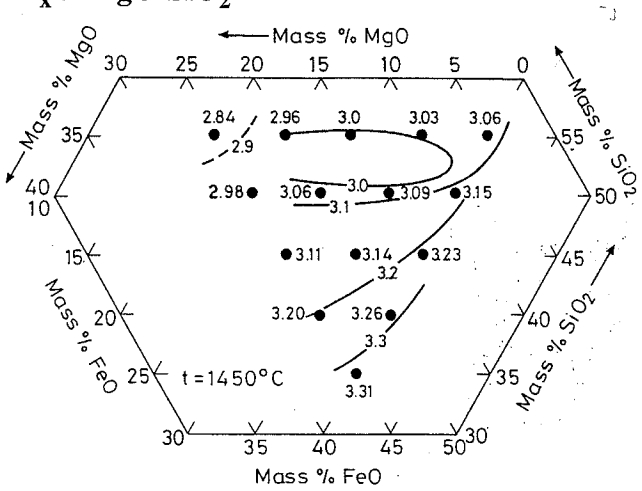


Fig. 8.101. Graph showing individual values derived for the densities of melts in the system $Fe_xO + MgO + SiO_2$, together with suggested isodensity lines based on these data [Ref. 113]

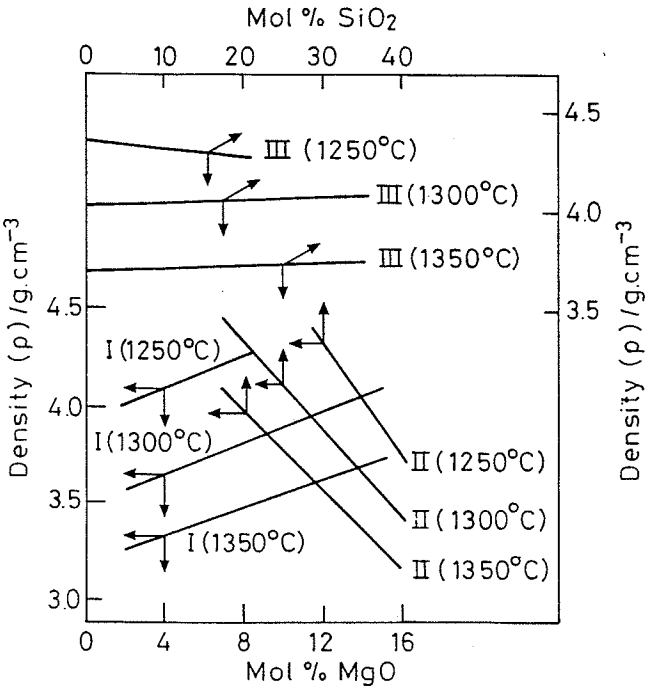


Fig. 8.102. Effects of variation in composition and of temperature on the density of melts in the system $Fe_xO + MgO + SiO_2$ [Ref. 114]

I: Effect of MgO concentration in melts containing ~ 60 mol. % Fe_xO
II: Effect of SiO_2 concentration in melts containing ~ 7.5 mol. % MgO
III: Effect of MgO concentration in melts containing ~ 25 mol. % SiO_2

Fe_xO-MnO-SiO_2

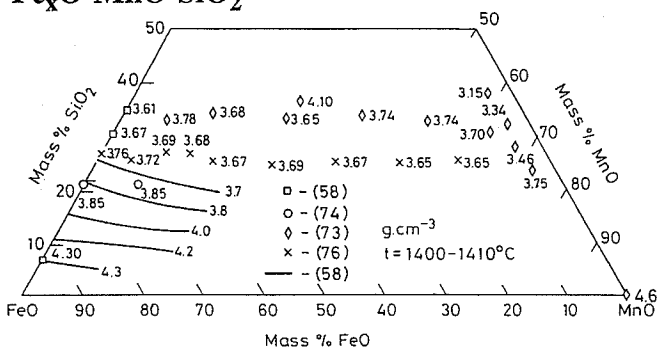


Fig. 8.103. Density of melts in the system Fe_xO + MnO + SiO_2

Fe_xO-Na_2O-SiO_2

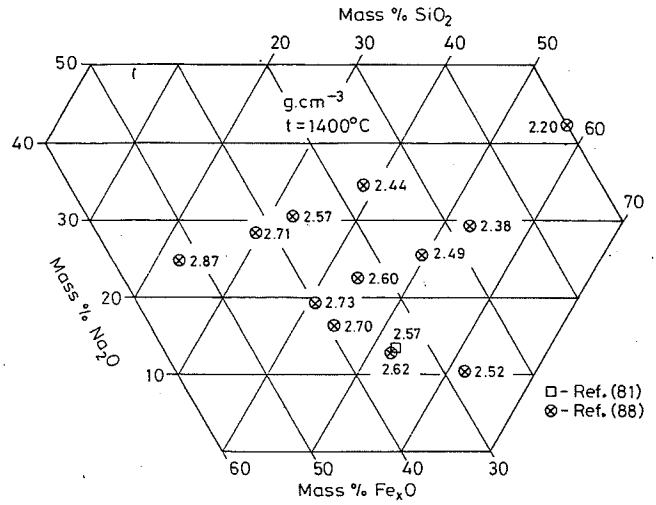


Fig. 8.104. Density of melts in the system Fe_xO + Na_2O + SiO_2

MgO-Na_2O-SiO_2

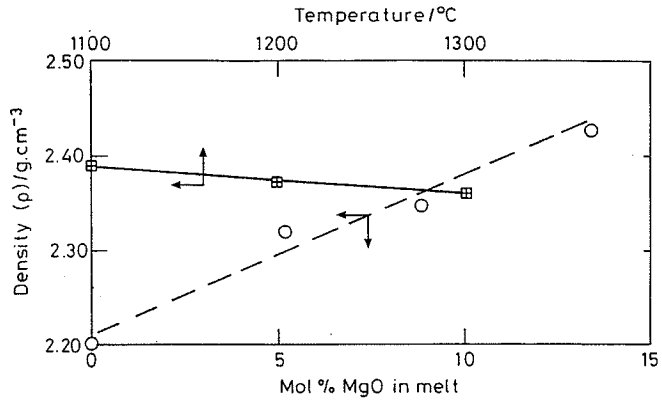


Fig. 8.105. Effect of MgO additions to Na_2O + SiO_2 (mole ratio = 1.25) on the density at 1300 °C. Effect of temperature on the density of the slag which contains 8.8 mol. % MgO [Ref. 89]

MnO-Na_2O-SiO_2

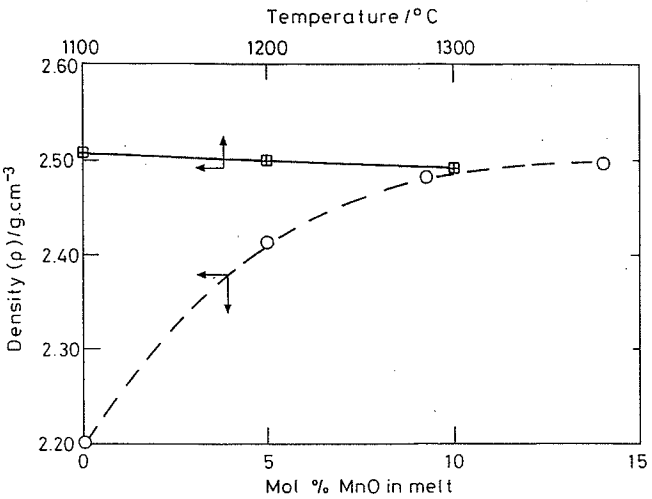


Fig. 8.106. Effect of MnO additions to Na_2O + SiO_2 (mole ratio = 1.25) on the density at 1300 °C. Effect of temperature on the density of the melt containing 9.2 mol. % MnO [Ref. 89]

MnO-P_2O_5-SiO_2

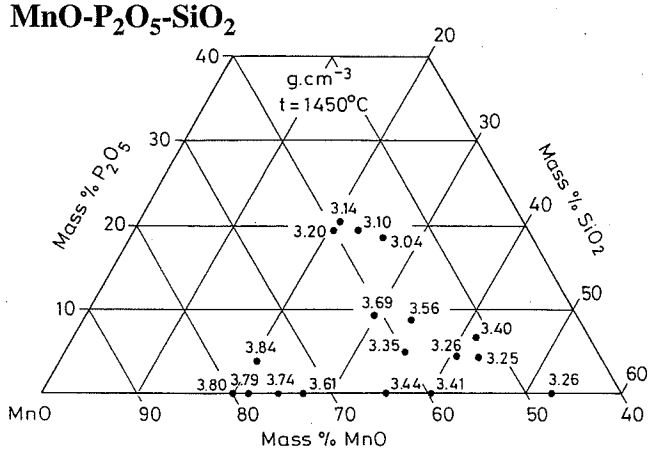


Fig. 8.107. Density of melts in the system MnO + P_2O_5 + SiO_2 [Ref. 115]

8.3.4 Quaternary systems

Al_2O_3-CaF_2-CaO-MgO

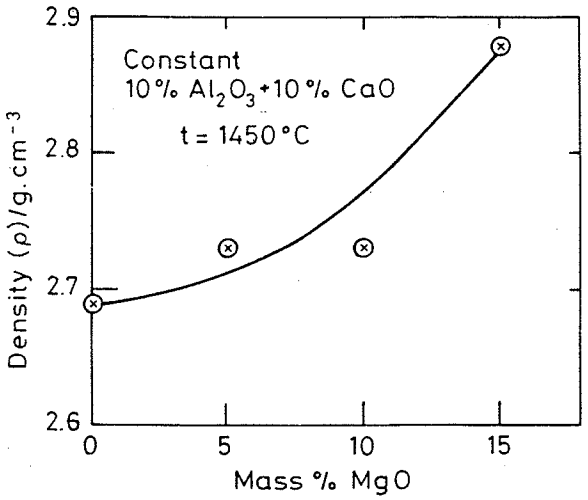


Fig. 8.108. Effect of MgO content on the density of melts in the Al_2O_3 + CaF_2 + CaO + MgO system, which contain 10 % Al_2O_3 and 10 % CaO [Ref. 11]

Al_2O_3-CaF_2-MgO-SiO_2

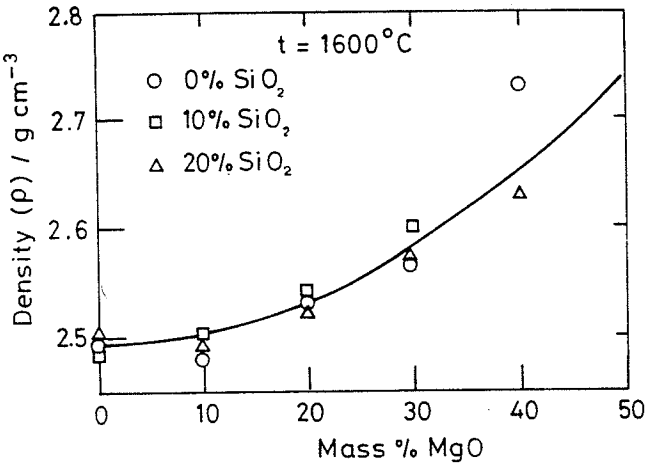
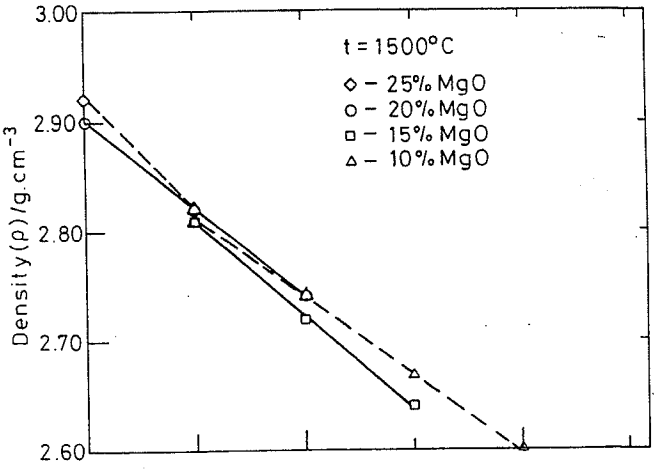
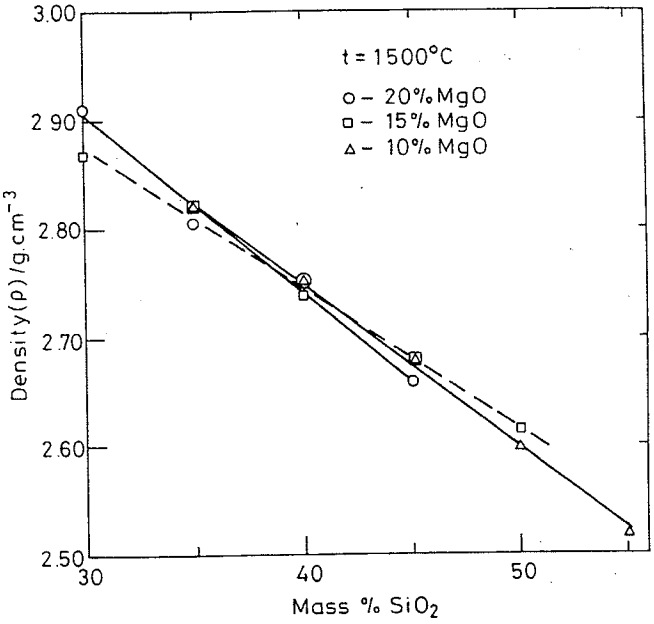


Fig. 8.109. Effect of MgO content on the density of melts in the system 50 % Al_2O_3 + CaF_2 + MgO + SiO_2, which contain 0 %, 10 % and 20 % SiO_2 [Ref. 38]

Al_2O_3-CaO-MgO-SiO_2



(a)



(b)

Fig. 8.110 a,b. Effect of SiO_2 concentration on the density of Al_2O_3 + CaO + MgO + SiO_2 [Ref. 118]
(a) 5 % Al_2O_3
(b) 10 % Al_2O_3

Al_2O_3-CaO-Fe_xO-SiO_2

Tab. 8.5. Density of Al_2O_3 + CaO + Fe_xO + SiO_2 systems

Mass % components				ρ/t °C relation	Reference
Al_2O_3	CaO	FeO + Fe_2O_3	SiO_2		
11.2	19.35	24.63 + 0.82	44.75	$\rho = 7.58 - 0.0037\ t/°C$ $\rho_{1350\ °C} = 2.59\ g.cm^{-3}$	[116]
11.15	14.8	29.26 + 0.24	44.5	$\rho = 7.68 - 0.0035\ t/°C$ $\rho_{1350\ °C} = 2.96\ g.cm^{-3}$	
10.45	5.45	43.4 + 0.81	39.76	$\rho = 3.92 - 0.00065\ t/°C$ $\rho_{1350\ °C} = 3.04\ g.cm^{-3}$	[117]
4.6	18.3	35.7 + 9.8	31.7	$\rho = 4.26 - 0.00067\ t/°C$ $\rho_{1350\ °C} = 3.36\ g.cm^{-3}$	[107]
9.1	17.4	33.9 + 9.3	30.8	$\rho = 4.23 - 0.00068\ t/°C$ $\rho_{1350\ °C} = 3.32\ g.cm^{-3}$	

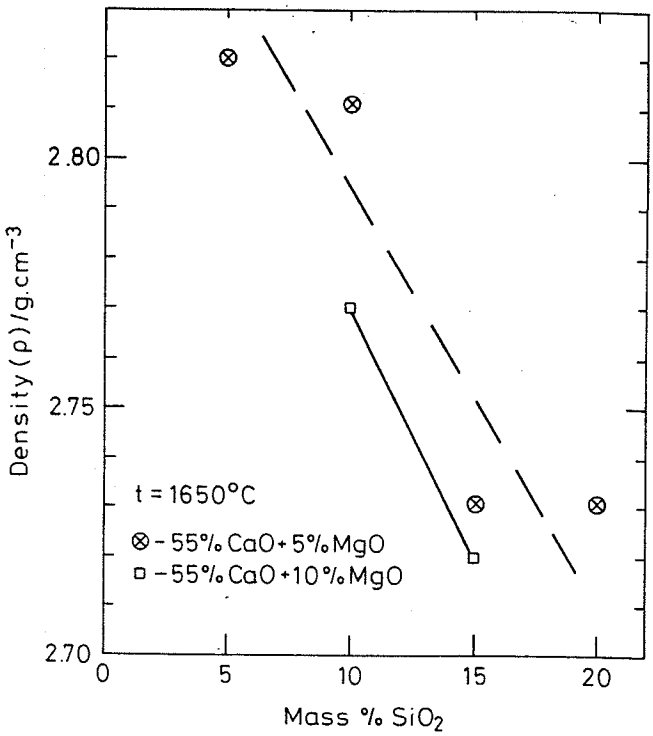


Fig. 8.111. Effect of SiO_2 concentration on the density of Al_2O_3 + CaO + MgO + SiO_2 melts [Ref. 119]

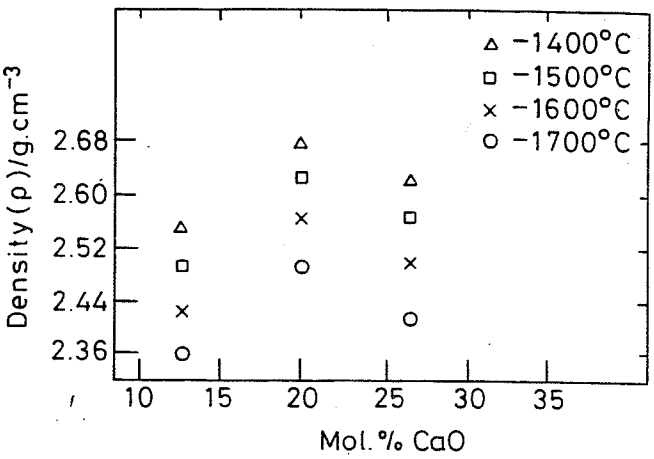
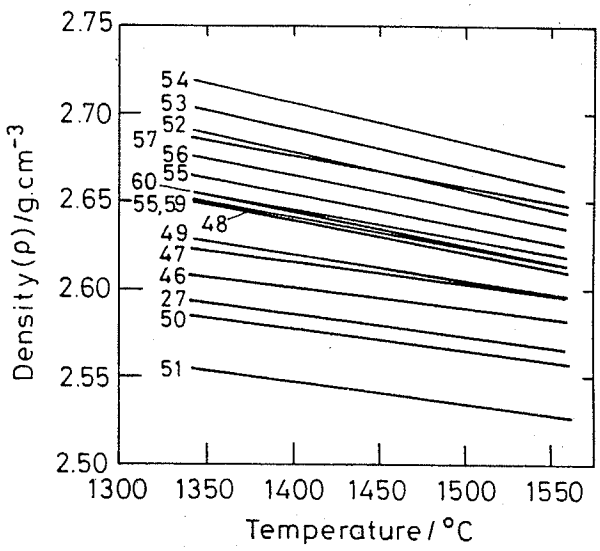


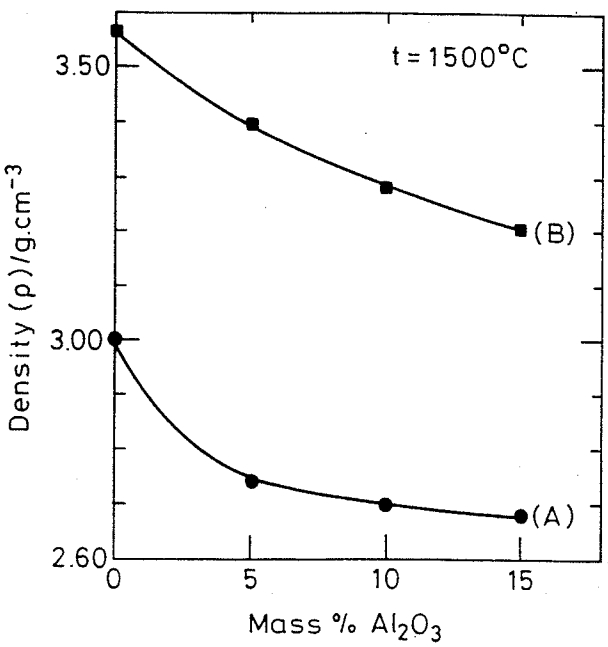
Fig. 8.112. Effect of replacing MgO by CaO on the density of Al_2O_3 + CaO + MgO + SiO_2 melts at various temperatures [Ref. 110]
[Al_2O_3] = 12-13 mol. %
[SiO_2] = 61.5 mol. %
[MgO] = 0-13 mol. %



Slag No.	CaO	MgO	Al_2O_3	SiO_2
27	38.0	-	20.0	42.0
46	35.8	5.7	18.9	39.6
47	33.9	10.7	17.9	37.5
48	35.0	10.0	5.0	50.0
49	31.7	9.0	4.5	54.8
50	28.3	8.1	4.0	59.6
51	25.0	7.4	3.5	64.1
52	38.4	9.5	4.7	47.4
53	41.6	9.0	4.5	44.9
54	45.8	8.3	4.2	41.7
55	33.7	13.4	4.8	48.1
56	32.3	16.9	4.6	46.2
57	30.7	21.1	4.4	43.8
58	33.0	9.5	10.4	47.1
59	31.3	8.9	15.0	44.8
60	29.5	8.4	20.0	42.1

Fig. 8.113. Variation of the density of Al_2O_3 + CaO + MgO + SiO_2 melts with temperature [Ref. 93]

Al_2O_3-CaO-MnO-SiO_2



▶
Fig. 8.114. Effect of Al_2O_3 additions on the density of CaO + MnO + SiO_2 melts [Ref. 111]
(A) Base slag 15 CaO + 35 MnO + 50 SiO_2
(B) Base slag 5 CaO + 75 MnO + 20 SiO_2

Al_2O_3-CaO-Na_2O-SiO_2

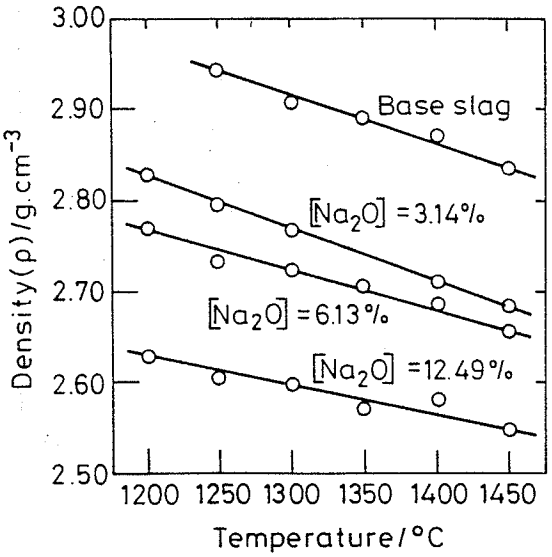


Fig. 8.115. Effect of temperature on the density of Al_2O_3 + CaO + Na_2O + SiO_2 melts [Ref. 94]. Composition of base slag (mass %) = 10.6 Al_2O_3 + 40.9 CaO + 48.5 SiO_2

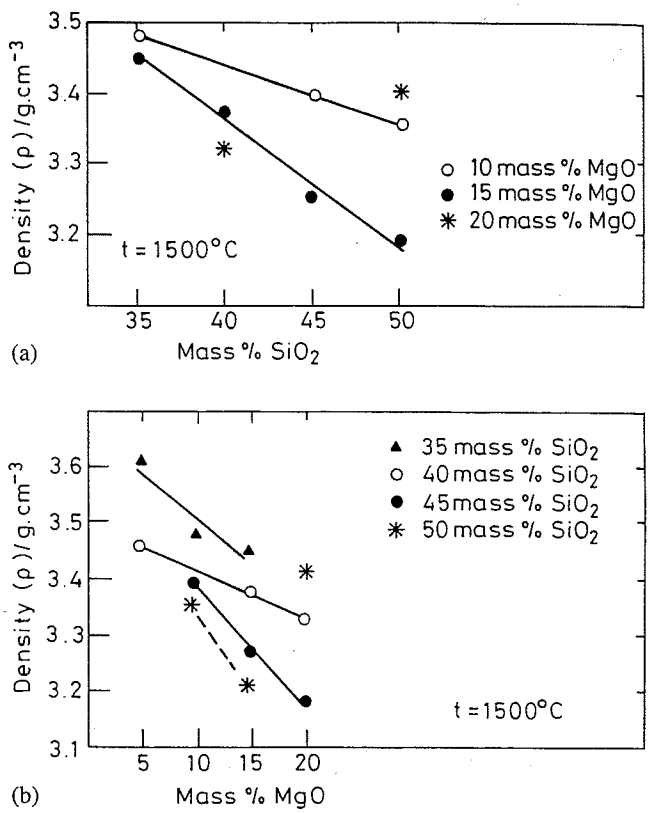


Fig. 8.117 a,b. Density of 5 % CaO + FeO + MgO + SiO_2 melts [Ref. 120]

(a) Effect of SiO_2 concentration on the density of melts which contain 10 %, 15 % or 20 % MgO respectively

(b) Effect of MgO concentration on the density of melts which contain 35 %, 40 %, 45 % or 50 % SiO_2 respectively

Al_2O_3-Fe_xO-MgO-SiO_2

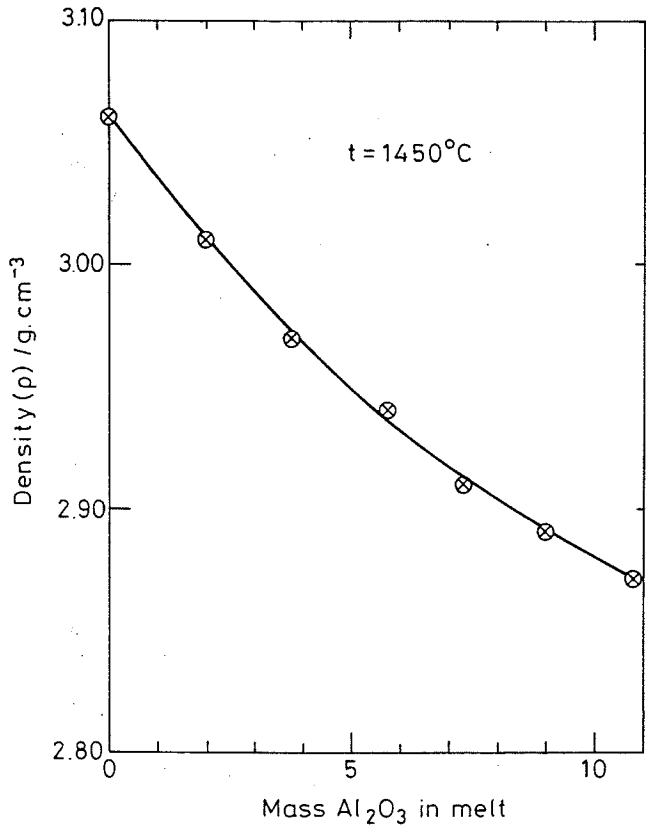


Fig. 8.116. Effect on the density of Al_2O_3 additions to a base melt containing approximately (mass %), 30 Fe_xO + 20 MgO + 50 SiO_2 [Ref. 113]

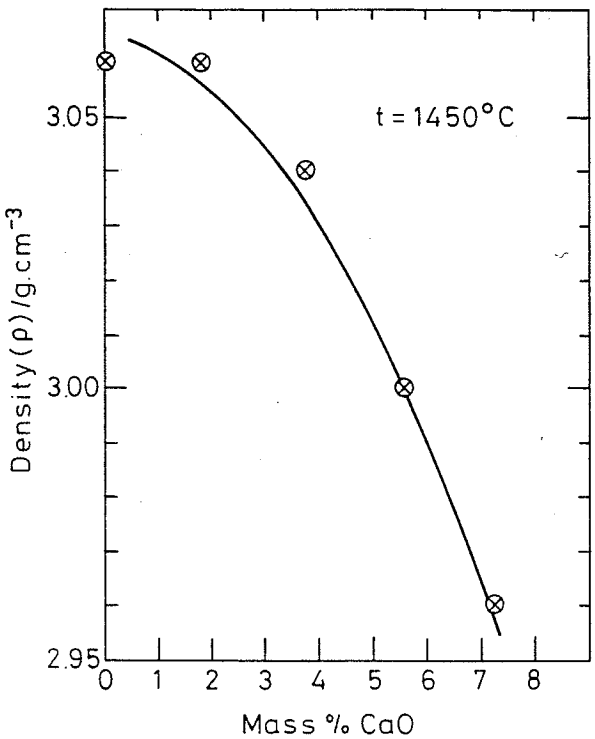


Fig. 8.118. Effect on the density of CaO additions to a base melt containing approximately (mass %), 30 Fe_xO + 20 MgO + 50 SiO_2 [Ref. 113]

$CaO\text{-}Fe_xO\text{-}MnO\text{-}SiO_2$

Tab. 8.6. Density of $CaO + Fe_xO + MnO + SiO_2$ melts at 1400 °C [Ref. 73]

Melt No.	Composition (Mass %)						Density $g.cm^{-3}$
	FeO	Fe_2O_3	$(FeO + Fe_2O_3)$	CaO	MnO	SiO_2	
1	16.3	2.06	18.4	33.4	10.0	38.2	3.40
2	11.5	0.97	12.5	34.3	15.2	37.0	3.50
3	5.85	0	5.9	35.5	19.8	38.4	3.40
4	30.2	3.90	34.1	11.6	17.2	35.6	3.54
5	33.2	2.26	35.5	12.1	16.4	34.6	3.50
6	32.7	2.00	34.7	15.7	12.1	36.2	3.60
7	35.0	2.00	37.0	20.3	5.6	35.8	3.40

$Fe_xO\text{-}MgO\text{-}Na_2O\text{-}SiO_2$

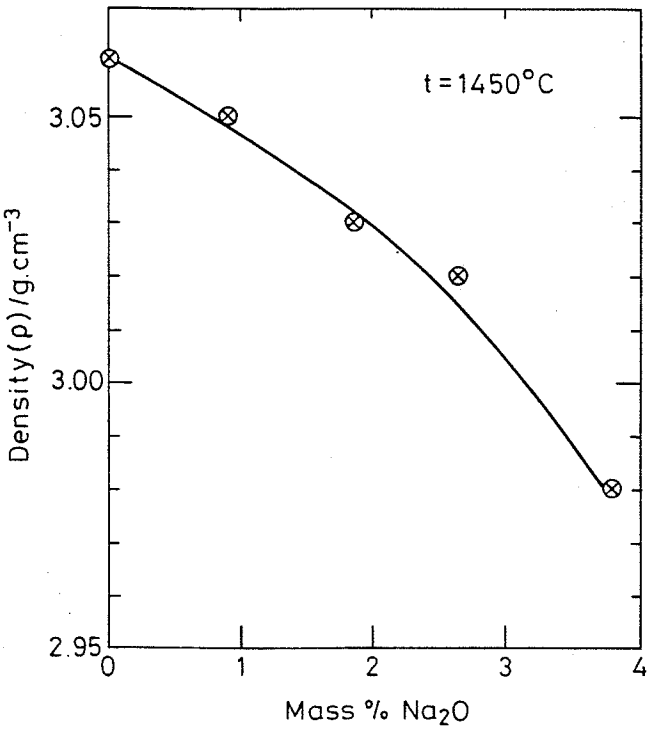


Fig. 8.119. Effect on the density of Na_2O additions to a base melt containing approximately (mass %), 30 Fe_xO + 20 MgO + 50 SiO_2 [Ref. 113]

8.3.5 Effect of Fe_xO concentration

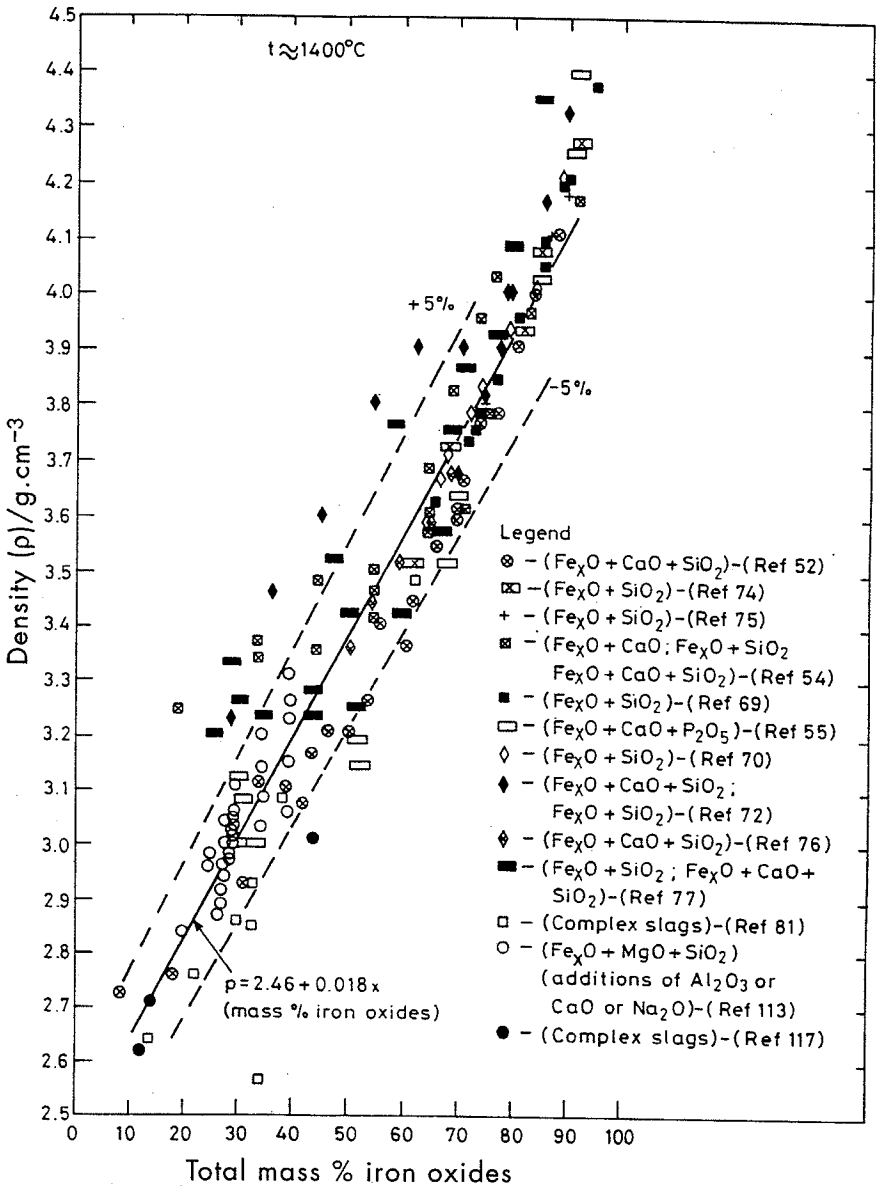


Fig. 8.120. Plot of density data for a wide range of oxide slags containing Fe_xO, showing the approximately linear increase in density with increase in Fe_xO concentration [Ref. 83]

8.4 Appendix [83]

8.4.1 Models to estimate some properties of slags

The use of models based on chemical composition is an attractive method for predicting the physical properties of slags, as chemical analyses of samples at different points in the slag path are readily available. The use of a reliable model to calculate physical properties of a slag would remove the difficulties encountered with interpolation on ternary graphs.

In developing reliable models for the calculation of physical properties, one severe restriction arises from the uncertainties with the experimental measurements. These vary according to the physical property being measured so that experimental uncertainties are about ± 2 % for density, about ± 10 % for surface tension, about 2 % for heat capacities, and about ± 25 % for viscosity measurements. It is unreasonable to expect any predictive model to produce data which are more accurate than those obtained experimentally, since the models use experimental results to derive values for the various partial molar parameters. Ideally, derivation of these parameters should be based upon proven reliable data, but for many slag systems experimental results are limited and consequently it is necessary to utilise data of greater uncertainty.

It should be noted that physical property measurements for slags containing iron oxides are complicated by the distribution of the iron between FeO, Fe_2O_3, and free iron. This creates difficulties with the models for density, viscosity, and particularly for surface tension.

8.4.2 Model for estimating the density ρ of slags

An additive method for the estimation of densities in alloys and slags has been widely used for some time. In this method, the molar volume V, can be obtained from equations (8.9) and (8.10) below where M, x, and $\overline{V}$ are the molecular weight, mole fraction, and the partial molar volume, respectively, and the subscripts 1, 2 and 3 denote the various oxide constituents of the slag

$$V = \frac{M_1x_1 + M_2x_2 + M_3x_3 + \ldots}{\rho} \qquad (8.9)$$

$$V = x_1\overline{V}_1 + x_2\overline{V}_2 + x_3\overline{V}_3 + \ldots \qquad (8.10)$$

The partial molar volume is usually assumed to be equal to the molar volume of the pure component V^0, but it has been pointed out by Lee and Gaskell [52] and Grau and Masson [121], that V of a slag is also related to its structure. Silicate slags contain a mixture of chains, rings and basic silicate units, which are dependent upon the silica concentration and the nature of the cations present. Thus the estimated densities of silicate slags, using a constant value for $\overline{V}_{SiO_2}$, will be subject to error as the arrangement of these silicate structures varies with silica concentration. Bottinga and Weill [122] produced a series of values of $\overline{V}$ for various oxides assuming a constant value for $\overline{V}_{SiO_2}$ and it was claimed that good estimations of the density could be obtained for compositions between 40 and 80 % SiO_2. However, the compositions of most BOS slags lie outside these compositional limits. Grau and Masson [121] pointed out that for the series MO, M_2SiO_3, $M_3Si_2O_7$ the partial molar volume of SiO_2 is not constant. They calculated a ΔV-term for the differences between any two members of the series and in this way calculated values were derived for $FeO\text{-}SiO_2$, $PbO\text{-}SiO_2$, $FeO\text{-}MnO\text{-}SiO_2$, and $CaO\text{-}FeO\text{-}SiO_2$ for compositions in the range $x_{SiO_2} = 0.5 - 1.0$. However, this method is not suitable for calculating densities of either multicomponent systems or of BOS slags.

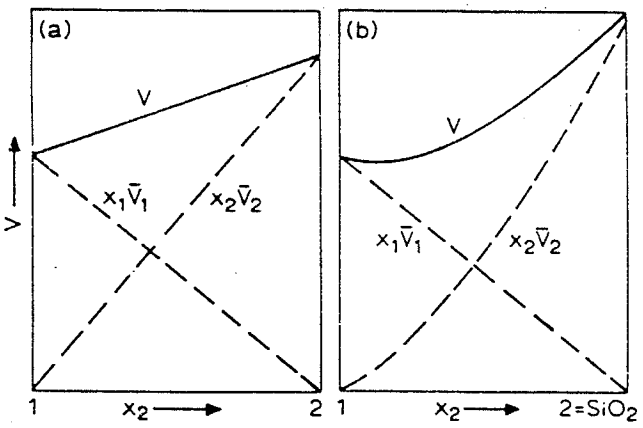


Fig. 8.121 a,b. Molar volume of binary slag system as a function of composition showing individual $x_i\overline{V}_i$ contributions
(a) System with molar volume and linear function of composition
(b) A binary silicate system

More recently, Bottinga et al. [123] have presented a model in which the partial molar volumes of alumina-silica liquids were considered to be composition dependent. However, the model is complicated and is applicable only to the compositional range 30-90 % SiO_2. Nevertheless, the authors claim the discrepancy between estimated and measured density values is of the order of 1 %. The present authors' experience suggests that density values calculated with this model are within ± 2-3 % of the measured values and this is the same magnitude as the experimental uncertainties for density measurements.

8.4.3 Alternative model for calculating the density of slags

Slags containing SiO_2, Al_2O_3 and P_2O_5 consist of chains, rings and complexes which are dependent upon the amount and nature of the cations present. Thus it is necessary to make the partial molar volumes dependent upon composition for oxides of this type. If, in a binary system, equation (8.10) were applicable and if $\overline{V}_i = V_i^o$, ie $\overline{V}$ is independent of composition, then the curve of V as a function of composition will be that shown by the solid line in **Fig. 8.121a** and the two $x_i\overline{V}_i$ contributions by the broken lines. In the case of a binary silicate system, the molar volume V would have the form shown as a solid line in **Fig. 8.121b.** It is reasonable to assume that $\overline{V}_{M_yO}$ is independent of composition and would have the form of $x_1\overline{V}_1$ in **Fig. 8.122.** The parameter $x_2\overline{V}_2$ can be derived for SiO_2 by use of equation (8.11) below:

$$x_2\overline{V}_2 = V - x_1\overline{V}_1 \qquad (8.11)$$

Thus $x_2\overline{V}_2$ will have the form of the curve shown in Fig. 8.122.

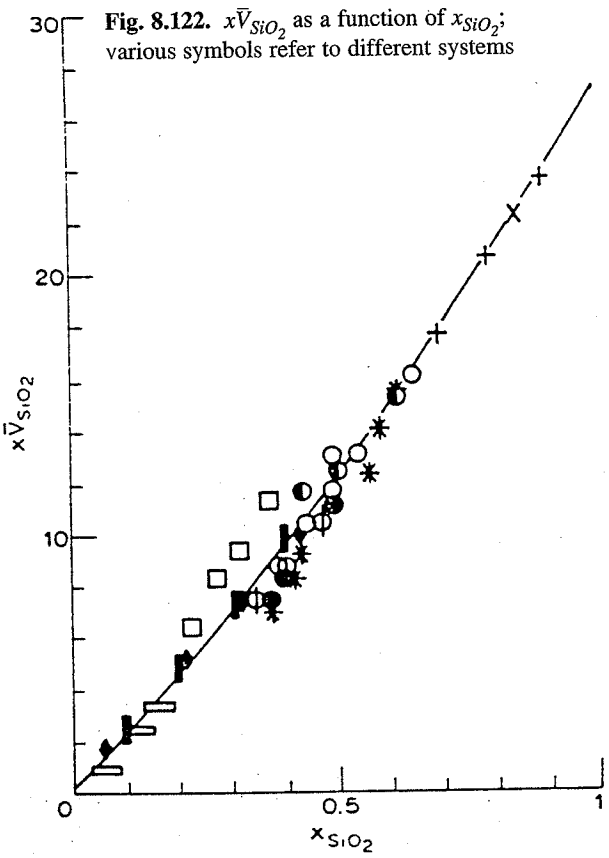


Fig. 8.122. $x\bar{V}_{SiO_2}$ as a function of x_{SiO_2}; various symbols refer to different systems

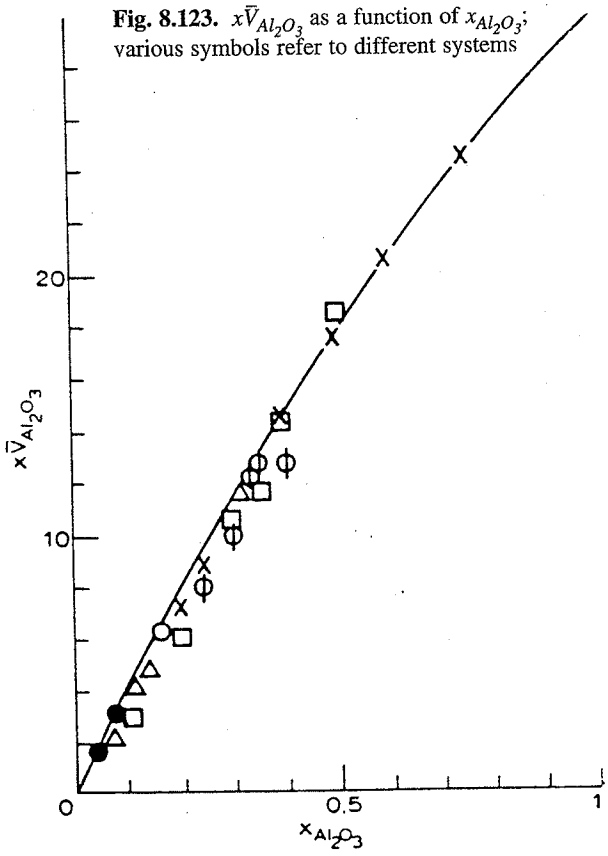


Fig. 8.123. $x\bar{V}_{Al_2O_3}$ as a function of $x_{Al_2O_3}$; various symbols refer to different systems

It is possible to derive $x\overline{V}$ for SiO_2 in ternary and quaternary slags by using equation (8.12)

$$x\overline{V}_{SiO_2} = V - x_1\overline{V}_1 - x_2\overline{V}_2 - x_3\overline{V}_3. \qquad (8.12)$$

Values for $x\overline{V}_{SiO_2}$ which have been derived from experimental density data for the systems, $FeO\text{-}SiO_2$, $CaO\text{-}SiO_2$, $MnO\text{-}SiO_2$, $Na_2O\text{-}SiO_2$, $K_2O\text{-}SiO_2$, and $CaO\text{-}FeO\text{-}SiO_2$, are plotted against x_{SiO_2} in Fig. 8.122. It can be seen from this figure that there is excellent agreement between values of $x\overline{V}_{SiO_2}$ calculated from different sources, with the exception of that for the $MnO\text{-}SiO_2$ system; however, the reliability of the experimental data for this system has been questioned previously. From this curve for $x\overline{V}_{SiO_2}$ the relation, $\overline{V}_{SiO_2} = 19.55 + 7.966x_{SiO_2}$ cm^3 mol^{-1} can be derived. The recommended values for $\overline{V}$ for the various oxides at 1500 °C are given in **Tab. 8.7.**

Values for $x\overline{V}_{Al_2O_3}$ were determined in a similar manner by using experimental density data for the systems; $Al_2O_3\text{-}CaO$, $Al_2O_3\text{-}CaF_2$, $Al_2O_3\text{-}SiO_2$, $Al_2O_3\text{-}CaO\text{-}MgO$, and $Al_2O_3\text{-}MnO\text{-}SiO_2$. The $x\overline{V}_{Al_2O_3}$ results are plotted in **Fig. 8.123** and the relation $\overline{V}_{Al_2O_3} = 28.31 + 32x_{Al_2O_3} - 31.45x^2_{Al_2O_3}$ was derived from this curve.

There are a few experimental data for the density of phosphate slags, $x\bar{V}_{P_2O_5}$ values were derived from data for the systems $CaO\text{-}FeO\text{-}P_2O_5$ and $Na_2O\text{-}P_2O_5$ and are plotted in **Fig. 8.124.** A constant value of $\overline{V} = 65.7$ cm^3 mol^{-1} was obtained from the selected linear relationship. In order to provide a temperature coefficient, the temperature dependencies of the molar volumes (dV/dT) of many slag systems were examined and a mean value of 0.01 % K^{-1} was adopted.

An analysis of the uncertainties associated with the estimation of densities with this model has not been completed yet. However, on the basis of those values obtained so far the standard deviation of the factor $(\rho_{est} - \rho_{exp})/\rho_{exp}$ is between 1 and 2 %. The experimental uncertainties associated with density measurements for slags is about ± 2 %.

[Note: "Slags" is an interactive software package for calculating physicochemical properties of slags. The program has been devised by K. C. Mills and is owned and licensed by the National Physical Laboratory, Teddington, Middlesex, UK (Tel. 0181-943 6592).]

Tab. 8.7. Recommended values for partial molar volume $\overline{V}$ of various slag constituents at 1500 °C

Constituent	$\overline{V}/cm^3\ mol^{-1}$
Al_2O_3	$[28.31 + 32x_{Al_2O_3} - 31.45\ x^2_{Al_2O_3}]$
CaF_2	31.3
CaO	20.7
FeO	15.8
Fe_2O_3	38.4
K_2O	51.8
MgO	16.1
MnO	15.6
Na_2O	33.0
P_2O_5	65.7
SiO_2	$[19.55 + 7.966x_{SiO_2}]$
TiO_2	24.0

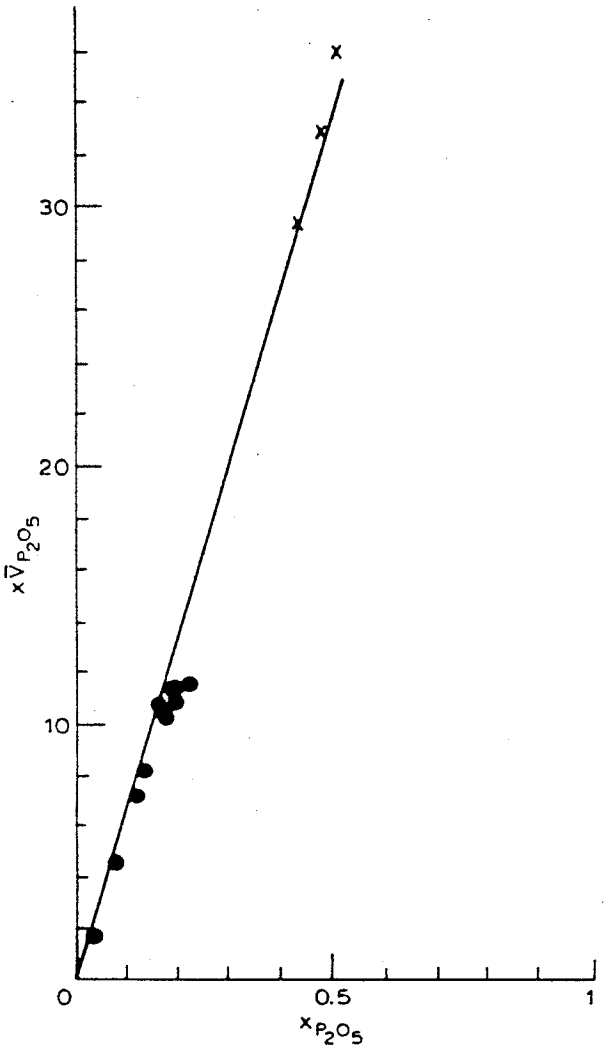


Fig. 8.124. $x\bar{V}_{P_2O_5}$ as a function of $x_{P_2O_5}$

8.5 References in Chapter 8

[1] Safonnikov, A. N.; Nikitin, Y. B.: Auto. Weld. 15 (9), (1962), 22
[2] Baak, T.: Acta. Chem. Scand. 9 (8), (1955), 1406
[3] Winterhager, H.; Kammel, R.; Gad, A.: Forschungsber. des Landes Nordrhein-Westfalen. Nr. 2115 (1970) Köln Opladen
[4] Kammel, R.; Winterhager, H.: Erzmetall. 9 (1968), 399
[5] Evseev, P. P.; Filippov, A. F.: Iz. Vuz. Chern. Metall. (3), (1965), 70
[6] Mitchell, A.; Joshi, S.: Metall Trans. 3 (1972), 2306
[7] Pupynina, S. M.; Volkov, S. E.; Bobkova, O. S.; Petukhov, V. S.: Sb. Tr. Tsent. Inst. Chern. Met. 70 (1967), 47
[8] Evseev, P. P.: Auto Weld. 20 (11), (1967), 42
[9] Voronov, V. A.; Nikitin, B. M.: Russ. Metall. (4), (1971), 76
[10] Ogino, K.; Hara, S.: Tetsu-to-Hagane. 63 (1977), 2141
[11] Stepanov, V. V.; Lopaev, B. E.: Auto. Weld. 20 (2), (1967), 46
[12] Kirshenbaum, A. D.; Cahill, J. A.; Stokes, C. S.: J. Inorg. Nucl. Chem. 15 (1960), 297
[13] Povolotskii, D. Ya.; Voronov, V. A.; Nikitin, B. M.: Steel in the USSR. 1 (12), (1971), 952
[14] Zhmoidin, G. I.: Russ. J. Phys. Chem. 49 (1975), 874
[15] Kulifeev, V. F.; Panchishni, V. I.; Stanolevich, G. P.: Iz. Vuz. Tsvetn. Metall (2), (1968), 116
[16] Yakobashvili, S. B.; Frumin, I. I.: Auto. Weld. 15 (10), (1962), 33
[17] Yakobashvili, S. B.; Tabidze, A. I.; Nebieridze, B. A.: Svar. Prot. Metall. (1), (1974), 104
[18] Goncharov, A. E.; Manakov, A. I.; Kovalev, P. K.: Tr. Inst. Met. AN. SSSR. Ural'sk. Nauk Tsentr. 27 (4), (1972), 159
[19] Patskevich, I. R.; Boiko, V. P.; Deev, G. F.; Krivinchuk, V. M.: Vestn. Kiev Politekh. Inst. 22, (1985), 81
[20] Hara, S. ; Shibaike, H.; Tarumoto, H.; Ogino, K.: Technol. 1st Int. Symp. Molten Salt Chem. Pub. Molten Salt Comm. Electrochem. Soc. Japan. Kyoto. (1983), 257-260
[21] Deryabin, A. A.; Popel, S. I.; Zupnik, A. E.: Russ. Metall. (2), (1968), 51
[22] El Gammal, T.; Hajouk, M.: Arch. Eisenhüttenw. 49 (1978), 235
[23] Zhmoidin, G. I.; Sokolov, L. N.; Podgornov, G. V.; Smirnov, G. S.: Teor. Met. Prots. (3), (1975), 150
[24] Isotomin, S. A.; Lepinskikh, B. M.; Manakov, A. I.; Pokrovskii, V. A.: VINITI (USSR). Rept. No. 2205-75 (1975)
[25] Ogino, K.; Hara, S.; Hashimoto, H.: Tetsu-to-Hagane. 64 (1978), 232
[26] Hara, S.; Ogino, K.: Nippon Kinzoku Gakkaishi 52 (11), (1988), 1098
[27] Lobzhandize, R. B.; Filippov, A. F.; Evseev, P. P.: Iz. VUZ. Chern. Metall. (7), (1970), 57
[28] Nikitin, Yu. P.; Safonnikov, A. N.: Sb. Nauchn. Tr. Uralsk. Politekh. Inst. 126 (1963), 68
[29] El Gammal, T.; Müllenberg, R.-D.: Arch. Eisenhüttenw. 51 (6), (1980), 221
[30] Gainullin, A. A.; Mal'kov, N. V.; Roschin, V. E.: Iz. VUZ. Chern. Metall. (2), (1985), 4
[31] Evseev, P. P.; Filippov, A. F.: Iz. VUZ. Chern. Metall. (3), (1965), 74
[32] Zhmoidin, G. I.; Baidov, V. V.: Ind. Lab. 39 (1973), 1427
[33] Yakobashvili, S. B.: Auto. Weld. 23 (6), (1970), 20
[34] Sikora, B.; Zielinski, M.: Hutnik 41 (9), (1974), 433
[35] Popel, S. I.; Deryabin, A. A.; Saburov, L. N.; Tarkanov, M. B.: Tr. Ural'sk. Nauchn. Issled Inst. Chern. Met. (12), (1971), 92
[36] Deryabin, A. A.; Popel, S. I.: Iz. VUZ. Chern. Metall. (8), (1964), 5
[37] Gogiberidze, Y. M.; Dzhincharadze, T. I.; Mikiashvili, Sh. M.: Soob AN. Gruz. SSR. (3), (1968), 695
[38] Povolotskii, D. Ya.: Iz. VUZ. Chern. Metall. (12), (1982) 1. (BISI 21861. Aug. 1983)
[39] Krichevets, M. I.; Grechishnyi, V. V.; Sherstobitov, M. A.; Pozdeev, N. P; Ostashov, S. S.; Voloshchuk, N. A.: Iz. AN. SSSR Metall. (5), (1984), 35
[40] Voronov, V. A.; Nikitin, B. M.: Fiz. Khim. Poverkh. Rasp. TBILISI. Izd. Metsniereba. (1977), 229-232.
[41] Zielinski, M.; Sikora, B.: Pr. Inst. Metall. Zelaza im St. Staszica. 29 (3-4), (1977), 157
[42] Evseev, P. P.; Filippov, A. F.: Iz. VUZ. Chern. Metall. (3), (1967), 55
[43] Dymov, V. V.; Baidov, V. V.: Sb. Tr. Tsent. Nauch-Issled Inst. Chern. Met. 61 (1968), 78
[44] Krinochkin, E. V.; Kurochin, K. T.; Umrikhin, P. V.: Fiz. Khim Poverkh. Yavlenii Rasp. Ed: V. N. Eremenko. Pub: Naukova Dumka. Kiev. (1971), 179-183
[45] Elyutin, V. P.; Mitin, B. S.; Anisimov, Yu. S.: Iz. VUZ. Tsvet. Metall. (4), (1974), 42

[46] Anisimov, Yu. S.; Grits, E. F.; Mitin, B. S.: Iz. AN. SSSR. Neorg. Mater. 13 (8), (1977), 1444
[47] Shartsis, L.; Shermer, H. F.: J. Am. Ceram. Soc. 37 (11), (1954), 544
[48] Sokolov, L. N.; Podgornov, G. V.; Okorokov, G. N.: Fiz. Khim. Osnovy. Metall. Prots. (1982), 47
[49] Ezikov, V. I.; Chuchmarev, S. K.: Visnyl'viv Politekh. Inst. 82 (1974) 43
[50] Henderson, J.: Trans. Metall. Soc. AIME. 230 (1964), 501
[51] Din-Fen, U.; Vishkarev, A. F.; Yavoiskii, V. I.: Iz. VUZ. Chern. Metall. 5 (9), (1962), 66
[52] Lee, Y. E.; Gaskell, D. R.: Metall. Trans. 5 (1974), 853
[53] Lee, Y. E.: Dissertation. - Univ. Pennsylvania. USA. (1972)
[54] Kawai, Y.; Mori, K.; Shiraishi, Y.; Yamada, N.: Tetsu-to-Hagane. 62 (1), (1976), 53
[55] Frohberg, M. G.; Brandi, H. H.: Arch. Eisenhüttenw. 34 (8), (1963), 591
[56] Abrodimov, A. S.; Gavrin, E. G.; Eremenchenkov, V. I.: Iz. VUZ. Chern. Metall. (8), (1975), 14 (English translation: BISI.13897. March 1976)
[57] Hara, S.; Irie, K.; Gaskell, D. R.; Ogino, K.: Trans. Jap. Inst. Met. 29 (12), (1988), 977
[58] Ogino, K.; Hirano, M.; Adachi, A.: Technol. Report. Osaka Univ. 24 (1974), 49
[59] Sumita, S.; Morinaga, K.; Yanagase, T.: Trans. Jap. Inst. Metals. 47 (2), (1983), 127
[60] Gulyaeva, R. I.; Shin, S. H.; Kuznetsov, P. A.; Okunev, A. I.: Melts. 4 (2), (1990), 80
[61] Boyer, A. J. G.; Fray, D. J.; Meadowcroft, T. R.: J. Phys. Chem. 71 (5), (1967), 1442
[62] Tomlinson, J. W.; Heynes, M. S. R.; Bockris, J. O'M.: Trans. Faraday Soc. 54 (1958), 1822
[63] Karakash, A. I.; Ternovoi, P. V.: Iz. VUZ. Chern. Metall. (10), (1977), 21
[64] Yakushev, A. M.; Romashin, V. M.; Ivanova, N. V.: Steel in the USSR. 15 (1985), 425
[65] Popel, S. I.: Sb. Nauchn. Tr. Ural'sk. Politekhn. Inst. (126), (1963), 5
[66] Ono, K.; Gunji, K.; Araki, T.: Nippon Kinzoku Gakhaishi 33 (3), (1969), 299
[67] Schenck, H.; Frohberg, M. G.; Hoffmann, K.: Arch. Eisenhüttenw. 33 (1962), 369
[68] Mori, K.; Suzuki, K.: Trans. ISIJ. 8 (1968), 382
[69] Gaskell, D. R.; Ward, R. G.: Trans. AIME. 239 (1967), 249
[70] Shiraishi, Y.; Ikeda, K.; Tamura, A.; Saito, T.: Trans. JIM. 19 (1978), 264
[71] Ward, R. G.; Sachdev, P. L.: Trans. AIME. 233 (1965), 1496
[72] Popel, S. I.; Esin, O. A.: J. Appl. Chem. USSR. 29 (1956), 707
[73] Sokolov, V. I.; Popel, S. I.; Esin, O. A.: Iz. VUZ. Chern. Metall. 13 (2), (1970), 10
[74] Henderson, J.; Hudson, R. G.; Ward, R. G.; Derge, D.: Trans. AIME. 221 (1961), 807
[75] Adachi, A.; Ogino, K.; Kawasaki, S.: Technol. Rept. Osaka Univ. 13 (580), (1963), 411
[76] Gaskell, D. R.; McLean, A.; Ward, R. G.: Trans. Faraday Soc. 65 (1969), 1498
[77] Adachi, A.; Ogino, K.: Technol. Rept. Osaka Univ. 12 (502), (1962), 147
[78] Holeczy, J.; Bodnar, L.; Tomasek, K.: Hutn. Listy. 27 (5), (1972), 364
[79] Bodnar, L.; Cempa, S.; Tomasek, K.; Bobok, L.: "Advances on Extractive Metallurgy". Pub. The Institution of Mining and Metallurgy, London (1977), 35-38
[80] Fadeev, O. N.; Khudyakov, I. F.; Kashcheev, I. D.; Kharitidi, G. P.: Iz. VUZ. Tsvet. Metall. (4), (1980), 17
[81] Mo, X.; Carmichael, I. S. E.; Rivers, M.; Stebbins, J.: Mineral Mag. 45 (1982), 237
[82] Popel, S. I.; Sokolov, V. I.: Poverkh. Yav. Rasp. Prots. Met. Akad. Nauk. SSR. Inst. Met. Spets. Splav. (1963), 364-369
[83] Mills, K. C.; Keene, B. J.: Int. Mater. Rev. 32 (1-2), (1987), 1
[84] Gogiberidze, Yu. M.; Kekelidze, M. A.; Mikiashvili, Sh. M.: Soob AN Gruz. SSR. 32 (1), (1963), 117
[85] Segers, L.; Fontana, A.; Winand, R.: Electrochem. Acta. 23 (1978), 1275
[86] Callis, C. F.; van Wazer, J. R.; Metcalf, J. S.: J. Am. Chem. Soc. 77 (1955), 1468
[87] Williams, D. J.; Bradbury, B. T.; Maddocks, W. R.: J. Soc. Glass. Technol. 43 (1959), 308
[88] Dingwell, D. B.; Brearley, M.; Dickinson, J. E.: Geochimica Cosmochim. Acta. 52 (1988), 2467
[89] Adachi, A.; Ogino, K.; Toritani, H.: Technol. Rept. Osaka Univ. 10 (1960), 149
[90] Bockris, J. O'M.; Tomlinson, J. W.; White, J. L.: Trans. Faraday Soc. 52 (1956), 299
[91] Bochorishvili, A. I.; Yakobashvili, S. B.: Svar. Proiz. (10), (1968), 13
[92] Ermolaeva, E. V.: Ogneupory. 20 (5), (1955), 221
[93] Winterhager, H.; Greiner, L.; Kammel, R.: Forschungsberichte des Landes Nordrhein-Westfalen. Nr. 1630. Pub.: Westdeutscher Verlag. (1966)
[94] Takayanagi, T.; Kato, M.; Minowa, S.: Imono. (J. Jap. Foundry Soc.) 48 (12), (1976), 779
[95] Sokolov, L. N.; Baidov, V. V.; Kunin, L. L.; Dymov, V. V.: Teor. Metall. Prots. (1971), 53
[96] Barrett, L. R.; Thomas, A. G.: J. Glass Technol. 43 (1959), 179s
[97] Sergienko, A. I.: Avt. Svarka. (6), (1965), 26
[98] Tomasek, K.; Bodnar, L.; Holeczy, J.: Hutn. Listy. 30 (2), (1975), 136
[99] Nakamura, T.; Noguchi, F.; Ueda, Y.; Nakajyo, S.: J. Min. Metall. Inst. Japan. 104 (1205), (1988), 463
[100] Riebling, E. F.: Canad. J. Chem. 42 (1964), 2811
[101] Riebling, E. F.: J. Chem. Phys. 44 (8), (1966), 2857
[102] Sugai, M.; Somiya, S.: J. Ceram. Soc. Japan. 90 (5), (1982), 262
[103] Panov, A. S.; Kulikov, I. S.; Tsylev, L. M.: Russ. J. Phys. Chem. 36 (6), (1962), 722
[104] Lee, Y. E.; Gaskell, D. R.: Trans. ISIJ. 11 (1971), 564
[105] Popel, S. I.; Sokolov, V. I.; Korpachev, V. G.: Sb. Nauchn. Tr. Ural'sk Politekhn. Inst. (126), (1963), 24
[106] Gaskell, D. R.: Adv. Phys. Geochem. 2 (1982), 153
[107] Murav'eva, E. L.; Kaplun, L. I.: Adgez. Rasp. Paika Mater. 12 (1984), 26
[108] Licko, T.; Danek, V.; Panek, Z.: Chem. Papers. 39 (5), (1985), 599
[109] Popel, S. I.; Deryabin, A. A.; Esin, O. A.: Iz. VUZ. Chern. Metall. (12), (1963), 5
[110] Staronka, A.; Piekarska, M.: Arch. Hutnict. 23 (1), (1978), 119
[111] Kekelidze, T. M.; Mikiashvili, Sh. M.; Dzhincharadze, T. I.; Khomeriki, R. V.: Izv. AN. GRUZ. SSR. 4 (3), (1978), 240
[112] Polyvyannyi, I. R.; Lata, V. A.; Adilova, A. A.; Ivakina, L. P.: VINITI (USSR). No. 3782-80. (1980)
[113] Bryantsev, B. A.: Zh. Prikl. Khim. 41 (10), (1968), 2156
[114] Vaisburd, S. E.; Yakovleva, N. A.: Pov. Yavleni Rasp. Prots. Poroshkovoi Met. A. N. Ukr. SSR. Inst. Metallokeram. Spets. Splav. (1963), 377-382
[115] Gogiberidze, Yu. M.; Kekelidze, M. A.; Mikiashvili, Sh. M.: Tr. Gruz. Inst. Met. 14 (1964), 97
[116] Ishchanov, T. K.; Sushkov, K. V.: Met. i. Metall. (3), (1974), 81
[117] Nelson, S. A.; Carmichael, I. S. E.: Contrib. Mineral Petrol. 71 (1979), 117
[118] Dzhincharadze, T. I.; Mikiashvili, Sh. M.; Khomeriki, R. V.: Pererabotna Zhelez. Margants. Rud. Zak. Pub. Metsniereba. Tbilisi. (1979), 141-148
[119] Komelkov, V. K.; Shirer, G. B.; Shalimov, A. G.; Voinov, S. G.: Teor. Met. Prots. 1 (1972), 50
[120] Yuan, Z.; Sun, M.; Chen, X.: Youse Jinshu. (Non-Ferrous Metals), 40 (1), (1988), 58
[121] Grau, A. E.; Masson, C. R.: Can. Metall. Quart. 15 (1976), 367
[122] Bottinga, Y.; Weill, D. F.: Am. J. Sci. 272 (1972), 438
[123] Bottinga, Y.; Weill, D. E.; Richet, P.: Geochim. Cosmochim. Acta. 46 (1982), 909
[124] Physicochemical measurements at high temperatures. Ed. by J. O'M. Bockris, J. L. White and J. D. Mackenzie. London (1959)
[125] Lucas, L. D.: In: Physicochemical measurements in metals research. Ed.: R. F. Bunshah. Vol. IV. Pt. 2, New York/London/Sidney/Toronto (1970), 219-292
[126] Kohlrausch, F.: Praktische Physik. Bd. 1, 22. Aufl., Stuttgart (1968), 303-310

9

Viscosities of molten slags

K. C. Mills

9.1 Introduction

Viscosity is a measure of the ability of one layer of molecules to move over an adjacent layer of molecules. Since liquid silicate melts contain various 3-dimensional structural units based on SiO_4^{4-} tetrahedra [1,2] the viscosity of the melt would be expected to be a function of the structure, ie the degree of polymerization of the melt.

9.1.1 Temperature dependence of viscosity

The temperature dependence of the viscosity (η) is usually expressed in one of the forms of the Arrhenius relationship shown in equations (9.1) to (9.3) where R is the gas constant, E the activation energy, and T the thermodynamic temperature (K).

$$\eta = A_A \exp(E_A/RT) \tag{9.1}$$

$$\log \eta = \log A_A + (E_A/RT) \tag{9.2}$$

$$\log \eta = \log A_A + (B_A/T). \tag{9.3}$$

Thus it is customary to present viscosity-temperature data in the form of log η as a function of reciprocal temperature (T^{-1}).

However, such plots for silicates usually display a slight curvature and improved fits can be obtained using the Weymann [3] and Brostow [4] relationships shown in equations (9.4) and (9.5) respectively.

$$\eta = A_W T \exp(E_W/RT) \tag{9.4}$$

$$\eta = \exp(A_B + B_B/T + C_B \log T) \tag{9.5}$$

9.2 Review of methods used to determine viscosities of slags [5, 6]

9.2.1 Capillary method

In this method the time required for a liquid to flow through a capillary tube (**Fig. 9.1**) is determined, the viscosity being calculated using the Poiseuille relationship (equation 9.6)

$$\eta = \frac{\pi r^4 p t}{8 v L} \tag{9.6}$$

where r = capillary radius, L = capillary length, p = constant pressure gradient between the ends of the capillary, v = volume of liquid discharged and t = time.

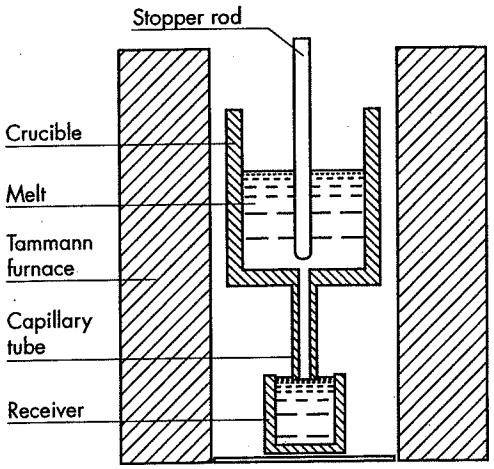


Fig. 9.1. Schematic drawing of capillary viscometer

Equation (9.6), however, does not account for, among other things, a certain amount of kinetic energy remaining in the liquid after it has left the capillary and which has not been expended in overcoming friction. This error can be compensated by the introduction of a correction factor H (Hagenbach):

$$\eta = \frac{r^4 \cdot p \cdot t}{8 \cdot v \cdot L} - H \tag{9.7}$$

$$H = \frac{v \cdot \rho}{8 \cdot \pi \cdot L \cdot t} \text{ (where } \rho = \text{liquid density).}$$

9.2.1.1 Applications

The capillary method has so far only found use in the medium temperature range. Above 1200 °C, complications arise in connection with the selection of a suitable crucible and capillary material in terms of dimensional stability and corrosion resistance (r^4!). However, the method has the following advantages: it permits, given suitable adjustment, absolute viscosity measurements to be made, ie the viscosity values can be calculated from the run-out vessel quantities and from the measurements obtained without the need for calibrating substances.

9.2.2 Falling body method

In this method the time for a body (usually a sphere) to fall due to gravity or to be dragged upwards through the melt is determined (**Fig. 9.2**). The viscosity is calculated using Stokes Law (equation 9.8)

$$\eta = \frac{2.g\, r^2(\rho_k - \rho_{liq})}{9S} \tag{9.8}$$

where g = gravitational constant, r is the radius of the sphere, ρ_k, ρ_{liq} are the densities of the ball and liquid and S is the velocity of descent or ascent of the sphere.

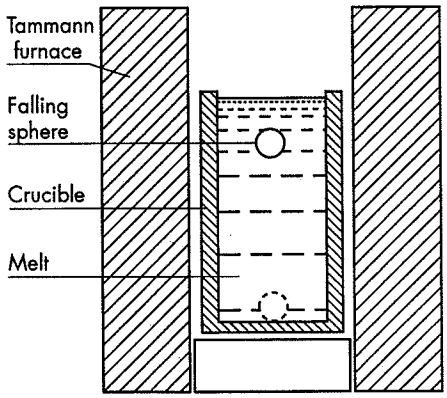


Fig. 9.2. Schematic drawing of the falling body method

The effect of thermal expansion of the liquid on the viscosity was accounted for by use of equation (9.9) due to Ladenberg [7] and is applicable [8] to systems where the diameter ratio, d (sphere/ D(crucible) is ≤ 0.1

$$\eta = \frac{2\, g\, r^2(\rho_k - \rho_{liq})}{9S\,(1 + 2.1\,(d/D))} \tag{9.9}$$

9.2.2.1 Applications

This method has been used for the measurement of the viscosity of glass and slag melts, the time taken to pull a ball out of the melt with constant force is measured [9,10]. The method does not permit absolute measurements, since an apparatus constant must be referred to which is derived from calibration curves using liquids of known viscosity.

9.2.3 Concentric cylinder (rotation) method

Viscometers of this type consist of two concentric cylinders ie a bob and a crucible and the viscosity is determined from measurements of the torque generated when one of the cylinders is rotated at a constant speed (**Fig. 9.3**).

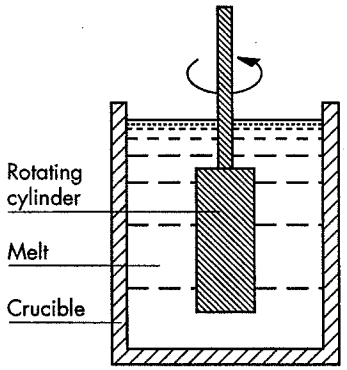


Fig. 9.3. Schematic drawing of the concentric cylinder method (rotating crucible method)

The viscosity is calculated by equation (9.10)

$$\eta \cdot = \frac{M}{8\pi^2 n h}\left(\frac{1}{r_i^2} - \frac{1}{r_o^2}\right) \tag{9.10}$$

where M is the torque, n the number of revolutions per sec, h and r_i the radius and height of the inner cylinder and r_o the radius of the outer cylinder. The above equation applies to infinitely long cylinders and it is normal practice to calibrate viscometers of these types with viscosity reference materials at both room and high temperatures. Viscosities are usually calculated by equation (9.11) where S is the scale deflection of the viscometer and G is the apparatus constant which is determined in the calibration experiments

$$\eta = G = S/n. \tag{9.11}$$

9.2.4 Oscillating methods

9.2.4.1 Oscillating cylinder or plate

In these methods the viscosity is measured by monitoring the logarithmic decrement of the swings of pendulum oscillating in the test liquid (**Fig. 9.4**).

Viscosities can be calculated [11] using equation (9.12) where ρ is the liquid density, τ = period of oscillation in empty system, θ = moment of inertia of oscillating system, λ = decrement due to damping effect of the liquid C (expressed in natural logarithm), R = radius of cylinder, d = thickness of cylinder.

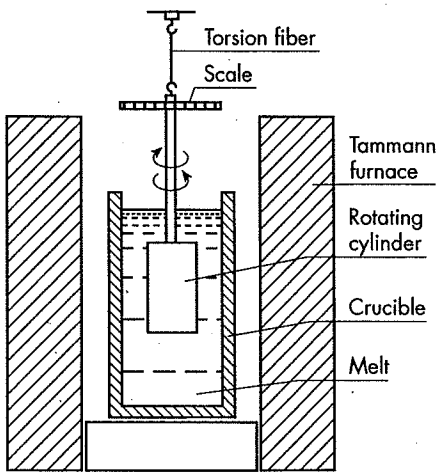


Fig. 9.4. Schematic drawing of oscillating cylinder method

$$\eta = \frac{2}{\pi \rho \tau}\left[\frac{2\theta\left(\frac{\lambda}{\pi}\right) + \left(\frac{\lambda}{\pi}\right)^2 + \ldots\ldots}{R^4 + R^3 d}\right] \tag{9.12}$$

The oscillating plate method [12] has been developed in recent years for slag viscosity measurements. Oscillating viscometers are usually used for determining relative values of viscosity and are calibrated with liquids of known viscosities. They have been used extensively in the determination of viscosities in the centipoise (mPa.S) range eg CaF_2 based slags, metals, etc.

9.2.4.2 Oscillating vessel method

An alternative method is to measure the logarithmic decrement of the oscillations of a pendulum consisting of a crucible containing the test liquid (**Fig. 9.5**).

The theory of damping of an oscillating crucible leads to equation (9.13),

$$\eta = \frac{1}{\rho \cdot \tau} \cdot \left[\frac{2 \cdot \theta \cdot \lambda}{R^4(\pi - \lambda)^{3/2} \cdot 2 \cdot L/2 + h \cdot R^3 \cdot L^*}\right] \tag{9.13}$$

$$L^* = \sum_n \left(\frac{4}{2n-1}\right)^2 \cdot \frac{(\pi^2 - 3\lambda \cdot s^2 \cdot T)W - \pi(2\lambda + s^2 \cdot T) \cdot V}{(V^2 + W^2)^3} \tag{9.14}$$

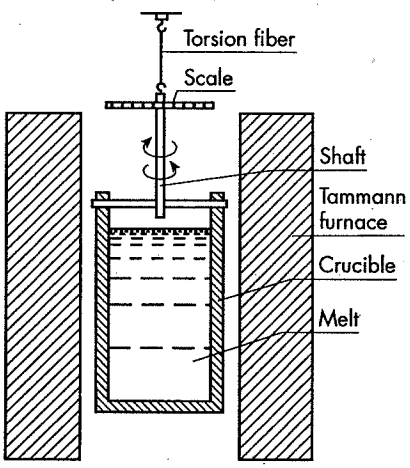


Fig. 9.5. Schematic drawing of oscillating vessel viscometer

It is usually assumed that λ is proportional to $\sqrt{\rho\eta}$ and relative values for the viscosity can be obtained by calibration of the apparatus using reference liquids with known viscosities, the viscosity being given by equation (9.15) where λ, λ_o are decrement (expressed as natural logarithm) for the full and empty crucibles, respectively and G is the apparatus constant

$$\eta = \frac{(\lambda - \lambda_o)^2}{G\rho}. \qquad (9.15)$$

Further details are given by Iida and Guthrie [13].

9.2.5 Industrial viscometers

Several simple viscometers have been developed for 'on plant' determinations of slag viscosities and for carrying out quality assurance testing.

9.2.6 Herty viscometer [14, 15]

Herty viscometers are shown in **Fig. 9.6 (a)** and **(b)**. The viscosities of the slags are determined from the length of the slag ribbon formed.

9.2.7 Krabiell immersion viscometer [16]

The vessel is attached to a rod and is heated for 7s in the furnace and is then immersed in the slag layer to the point where the mark coincides with the slag surface. The vessel is immersed for 5s and is then withdrawn and the relative viscosity is determined from the mass of slag which had entered the vessel through the nozzle.

9.2.8 Inclined plane method

In the inclined plane method molten slag is poured from a crucible (or from a sample spoon taken from the furnace) onto an inclined steel plane with V section. The viscosity can be related to the length of the slag ribbon obtained.

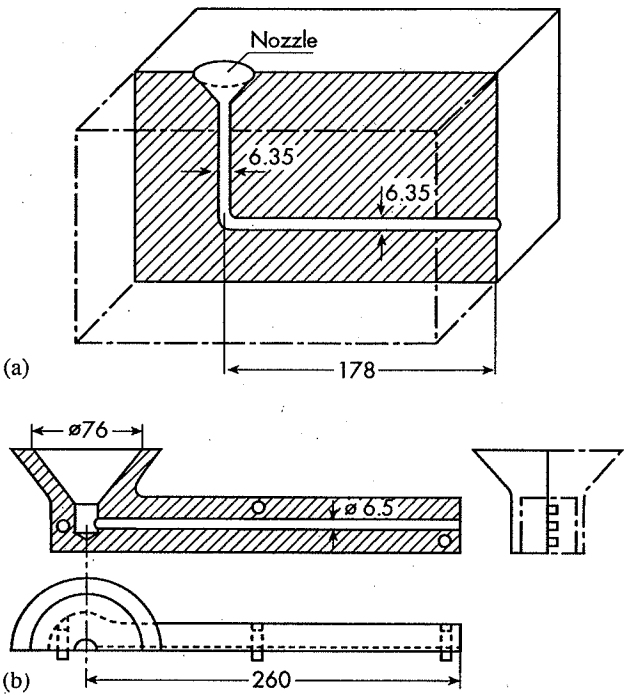


Fig. 9.6 a,b. Schematic drawing of (a) Herty industrial viscometer and (b) modified Herty viscometer [14, 15]

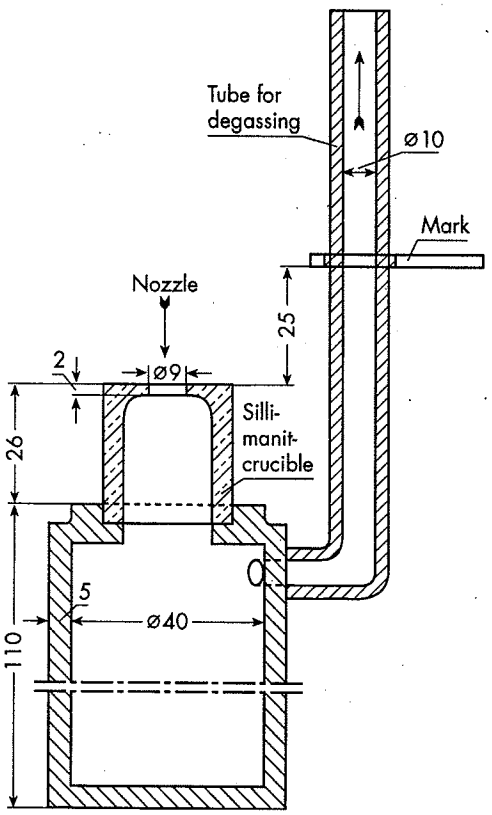


Fig. 9.7. Schematic drawing of Krabiell immersion viscometer [16]

9.3 Experimental uncertainties in viscosity measurements

Fig. 9.8 (a) shows a spread in the viscosities of a reference material reported by various laboratories, the scatter being $> \pm 50$ % around the mean. **Fig. 9.8 (b)** shows the agreement in viscosities ($\pm$ 10 %) between laboratories using viscometers with Mo components [17].

It was concluded that the prime sources of experimental uncertainties were (I) changes in the composition of the melt due to reaction between the melt and graphite and (II) to a lesser extent, errors in temperature measurements of the melt [17].

It was concluded that (I) most viscosity measurements were subject to experimental uncertainties of $\pm$ 25 %, (II) in some cases experimental uncertainties could be $> \pm 50$ % and (III) that experimental uncertainties of $\pm$ 10 % could be achieved by careful calibration of viscometers with high and low temperature reference materials.

9.4 Models for estimating the viscosities of multicomponent slags

Several models have been reported for the estimation of slag viscosities [18-20] but Riboud [21] and Urbain [22] models have been found to be the most effective since these make use of the Weymann equation for expressing the temperature dependence (equation 9.4).

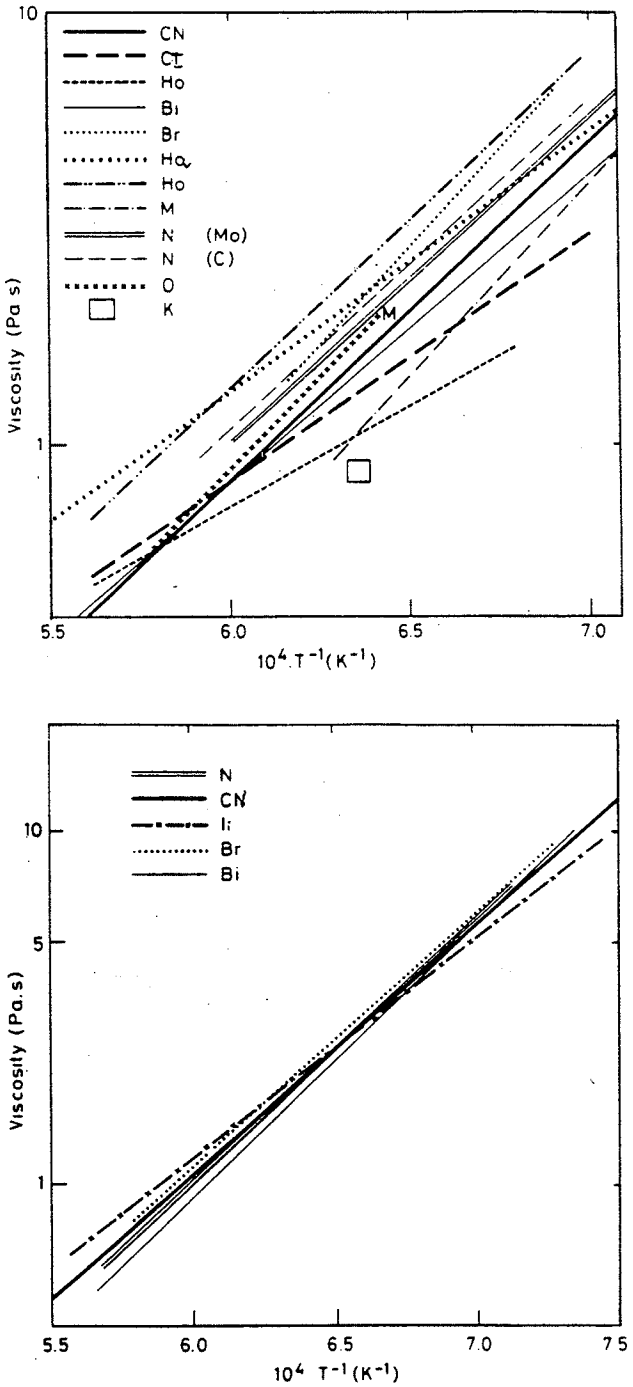


Fig. 9.8. Viscosities of a reference material reported by different laboratories as a function of reciprocal temperature (reference material: 15.5 % Al_2O_3, 21.2 % Li_2O, 63,3 % SiO_2 [17])

9.4.1 Model due to Riboud et al [21]

This model was developed to estimate the viscosities of mould powders but has been shown to have a wider applicability. The slag constituents are classified in five different categories in this model. The mole fractions for these categories being given by

(I) $X_{SiO_2} = X_{SiO_2} + X_{PO_{2.5}} + X_{TiO_2} + X_{ZrO_2}$

(II) $X_{CaO} = X_{CaO} + X_{MgO} + X_{FeO_{1.5}} + X_{MnO} + X_{BO_{1.5}}$

(III) $X_{Al_2O_3}$

(IV) X_{CaF_2}

(V) $X_{Na_2O} = X_{Na_2O} + X_{K_2O}$

The parameters A and B of equation (9.3) are calculated from the mole fraction of the five categories by using equations (9.16) and (9.17)

$$A = \exp(-17.51 + 1.73X_{CaO} + 5.82X_{CaF_2} + 7.02X_{Na_2O} - 33.76X_{Al_2O_3}) \quad (9.16)$$

$$B = +31140 - 23896X_{CaO} - 46356X_{CaF_2} - 39159X_{Na_2O} + 68833X_{Al_2O_3} \quad (9.17)$$

$$\eta = AT\exp(B/T).$$

9.4.2 Model due to Urbain et al [22]

This model is based on the CaO + Al_2O_3 + SiO_2 system. In this model the parameters A and B are calculated by dividing the slag constituents into three categories:

(I) 'glass formers', $X_G = X_{SiO_2} + X_{P_2O_5}$

(II) 'modifiers', $X_M = X_{CaO} + X_{MgO} + X_{Na_2O} + X_{K_2O} + 3X_{CaF_2} + X_{FeO} + X_{MnO} + 2X_{TiO_2} + 2X_{ZrO_2}$

(III) 'amphoterics', $X_A = X_{Al_2O_3} + X_{Fe_2O_3} + X_{B_2O_3}$.

Tab. 9.1. Equations for B-parameters in Urbain model for viscosity

B_0 =	13.8	+	39.9355 α	−	44.049 α^2
B_1 =	30.481	−	117.1505 α	+	139.9978 α^2
B_2 =	−40.9429	+	234.0486 α	−	300.04 α^2
B_3 =	60.7619	−	153.9276 α	+	211.1616 α^2

It has been pointed out [23] that in most metallurgical slags Fe_2O_3 has been classified as a modifier and in the calculations presented here $1.5X_{FeO_{1.5}}$ has been added to X_M and $X_{Fe_2O_3}$ deducted from X_A. 'Normalized" values X_G^*, X_M^*, and X_A^* are obtained by dividing the mole fractions, X_G, X_M, and X_A by the term $(1 + X_{CaF_2} + 0.5X_{FeO_{1.5}} + X_{TiO_2} + X_{ZrO_2})$. Urbain proposed that the parameter B was influenced both by the ratio $\alpha = X_M^*/(X_M^* + X_A^*)$ and by X_G^*. The parameter B can be expressed in the form of equation (9.18) where B_1, B_2, and B_3 can be obtained by equation (9.19).

$$B = B_0 + B_1X_G^* + B_2(X_G^*)^2 + B_3(X_G^*)^3 \quad (9.18)$$

$$B_i = \alpha_i + b_i\alpha + c_i\alpha^2. \quad (9.19)$$

B_0, B_1, B_2, and B_3 can be calculated from the equations listed in **Tab. 9.1** and these parameters are then introduced into equation (9.18) to calculate B. The parameter A can be

calculated from B by equation (9.20) and the viscosity of the slag (in poise) can then be determined by using equation (9.21)

$$-\ln A = 0.2693B + 11.6725 \qquad (9.20)$$

$$\eta = [ATexp(10^3B/T)]. \qquad (9.21)$$

Urbain [24] has recently modified the model to calculate separate B-values for different individual modifiers, CaO, MgO, and MnO. The global B-value for a slag containing all three oxides can be derived by equation (9.22).

$$B_{global} = \frac{X_{CaO}B_{CaO} + X_{MgO}B_{MgO} + X_{MnO}B_{MnO}}{X_{CaO} + X_{MgO} + X_{MnO}}. \qquad (9.22)$$

In calculations on the BOS slags the following relation was assumed

$$X(MnO) = X(FeO) + X(FeO_{1.5}) + X(MnO)$$

and used in equation (9.22), this was referred to as the Urbain III model.

9.5 Experimental data for viscosities

In the following collation of viscosity data for molten slags recommended values have been proposed by giving preference to those studies in which calibration of the apparatus was carried out with both room and high temperature reference materials.

9.5.1 Pure components

Al_2O_3

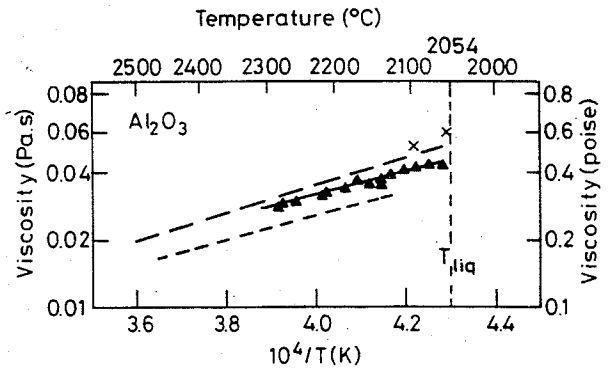


Fig. 9.9. Viscosity of molten Al_2O_3 as a function of temperature; -▲- recommended relationship due to Urbain [25]; - - , Elioutin [26]; X, Kozakevitch [33, 27] ..., Blomquist et al [28]. Recommended relationships where T is in K log η (poise) = log T + -7.16 +(5710/T); log η (Pa.s) = log T -8.16 +(5710/T)

B_2O_3

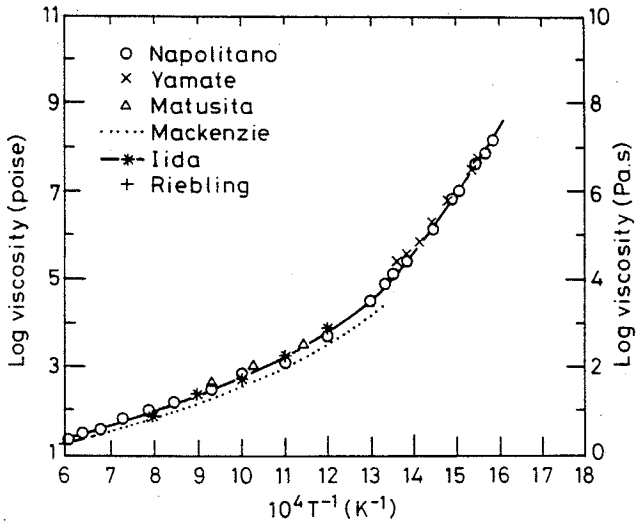


Fig. 9.10. Log viscosity for B_2O_3 as a function of reciprocal temperature; —, recommended curve based on [29-34]. Further Ref. [35-37]

CaF_2

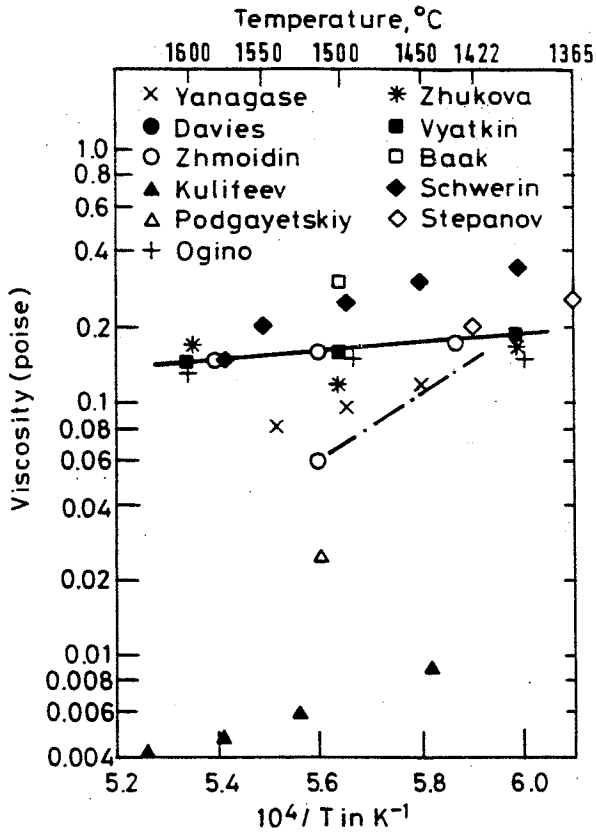


Fig. 9.11. Viscosity of CaF_2 as a function of reciprocal temperature [23, 38-49]; —, recommended relationship

CaO

Viscosity of molten CaO measured close to the liquidus temperature $\eta < 0.5$ poise = < 0.05 Pa.s [49].

FeO

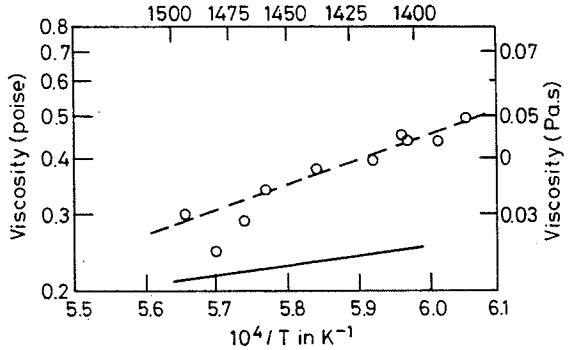


Fig. 9.12. Viscosity of FeO as a function of the reciprocal temperature; ___ recommended relationship [3]; log η (poise) = -5.427 +log T +(2649/T); log η (Pa.s) = -6.427 + log T + (2649/T); - - - [50]. Other Ref. [51-53]

P_2O_5

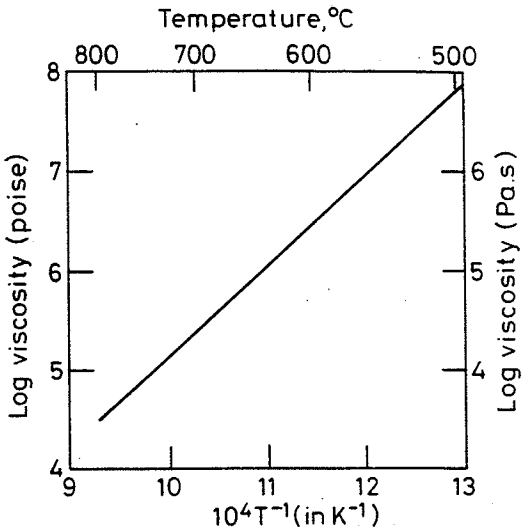


Fig. 9.13. Log viscosity of P_2O_5 as a function of reciprocal temperature [54]; log η (poise) = -4.073 +(9214/T); log η (Pa.s) = -5.073 +(9214/T)

SiO_2

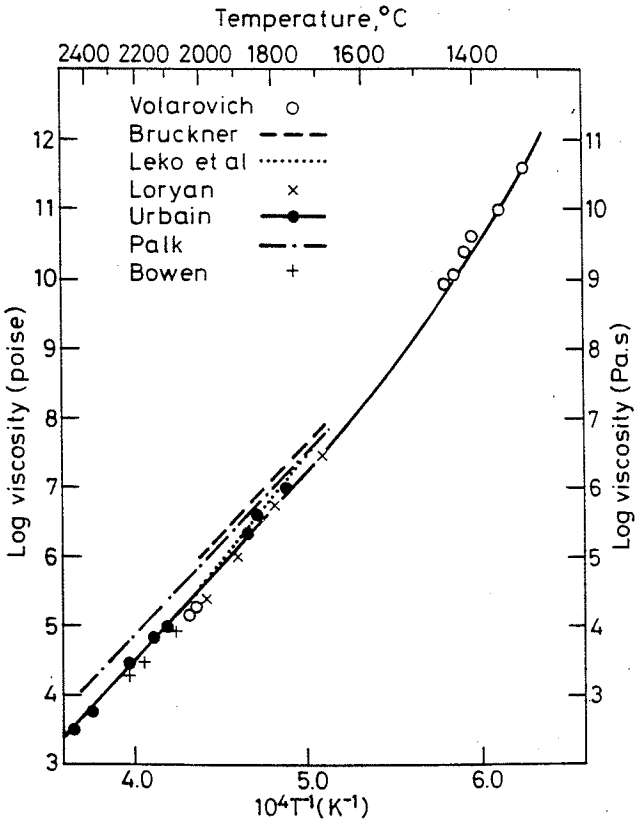


Fig. 9.14. The temperature dependence of the viscosity of SiO_2 [55-63]; for the molten region above 2000 K the recommended relation [1, 2 ,3] is log η (poise) = log T -10.32 +(28590/T) where T is in K; log η (Pa.s) = log T -11.32 +(28590/T). Further Ref. [64-66]

9.5.2 Binary systems

Al_2O_3-B_2O_3

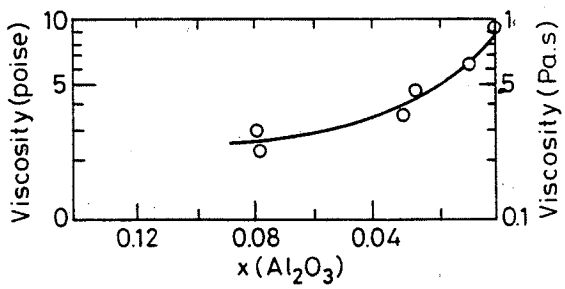


Fig. 9.15. Viscosities of Al_2O_3-B_2O_3 melts as a function of mole fraction Al_2O_3 [34]

Al_2O_3-CaF_2

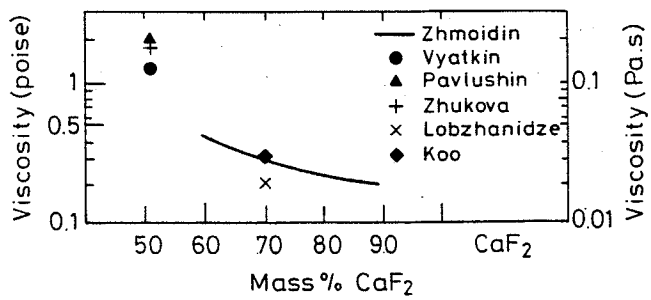
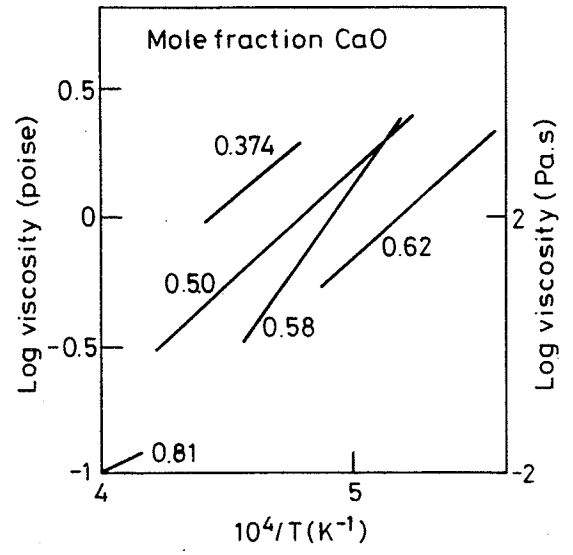
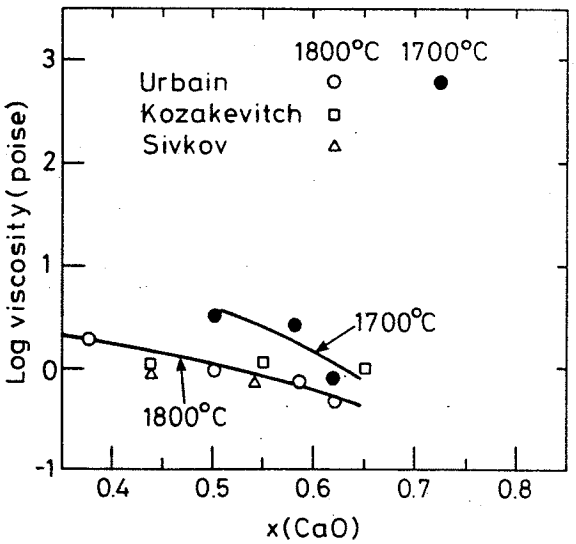


Fig. 9.16. Viscosities of Al_2O_3-CaF_2 melts at 1600 °C as a function of mole fraction of CaF_2 [67, 68, 40, 44, 46, 69, 70, 71,]; ___, recommended values. Note reported viscosities for 1500 °C refer to (solid+liquid) region. Further Ref. [42, 72-77]

Al_2O_3-CaO



(a)



(b)

Fig. 9.17 a,b. Viscosities of Al_2O_3-CaO melts as functions of (a) reciprocal temperature [78] and (b) mole fraction CaO [27, 78, 79,]; recommended curves, ___. Further Ref. [70, 77, 80-84]

Al_2O_3-FeO

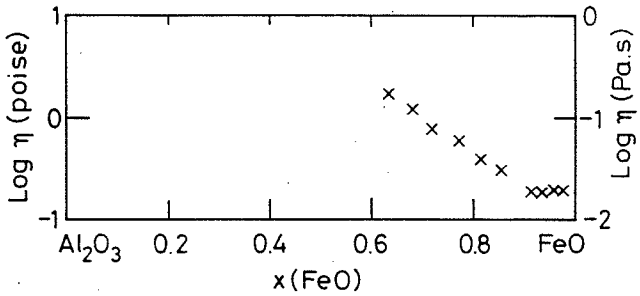


Fig. 9.18. Viscosities of Al_2O_3-FeO melts at 1700 °C [77]; values may be subject to error since values reported [77] for other systems diverge from recommended values. Further Ref. [53]

Al_2O_3-Gd_2O_3
Al_2O_3-La_2O_3
Al_2O_3-Nd_2O_3

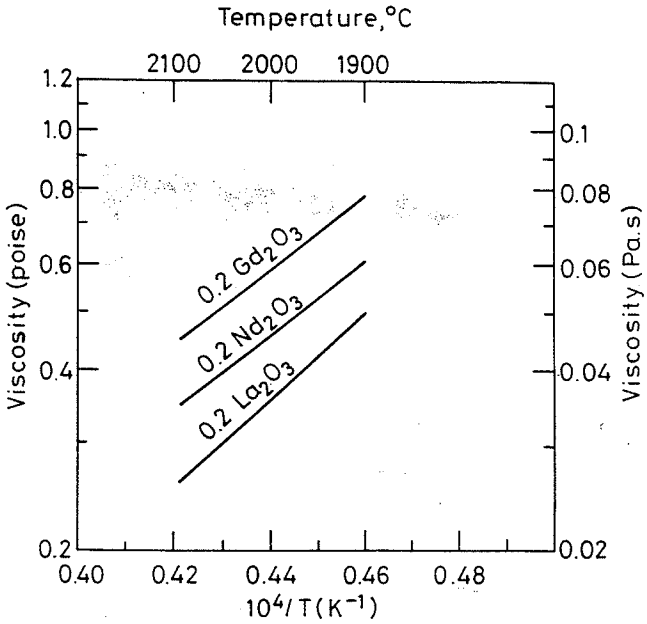


Fig. 9.19. Viscosities of melts with composition (0.8 Al_2O_3 + 0.2 M_2O_3) as a function of temperature [85] where M = Gd, Nd and La

Al_2O_3-SiO_2

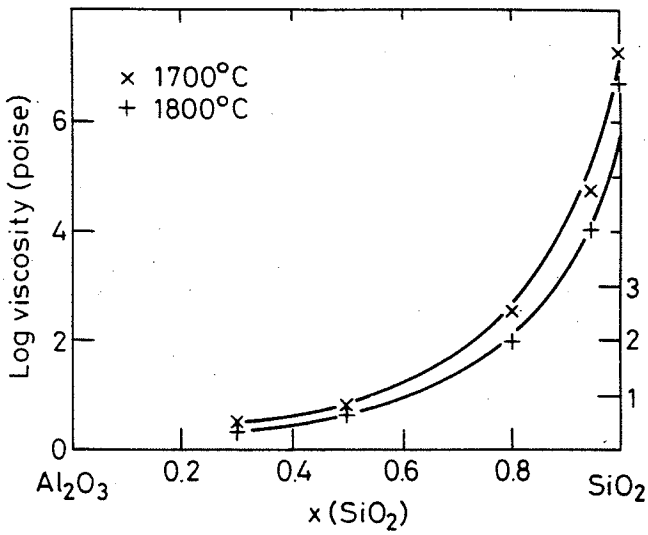
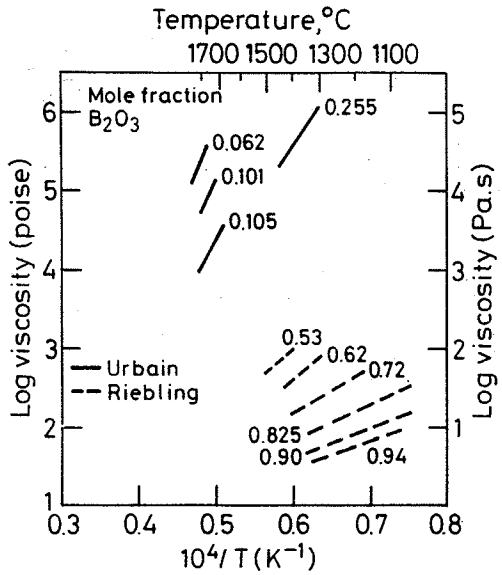
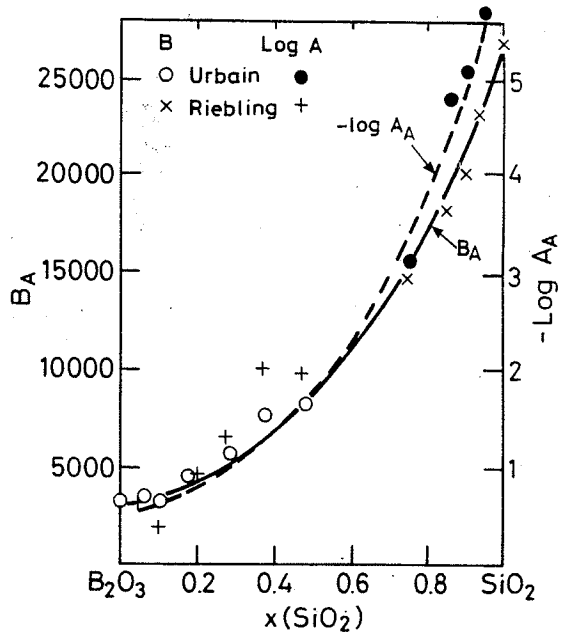


Fig. 9.20. Viscosity of Al_2O_3-SiO_2 melts at 1700 and 1800 °C as a function of mole fraction of SiO_2 [56]. Further Ref. [77]

B_2O_3-SiO_2



(a)



(b)

Fig. 9.21 a,b. Viscosities of B_2O_3-SiO_2 melts [57, 87-89] (a) as a function of temperature and (b) showing the parameters log A_A and B_A of the Arrhenius equation [87-89]

CaF_2-CaO

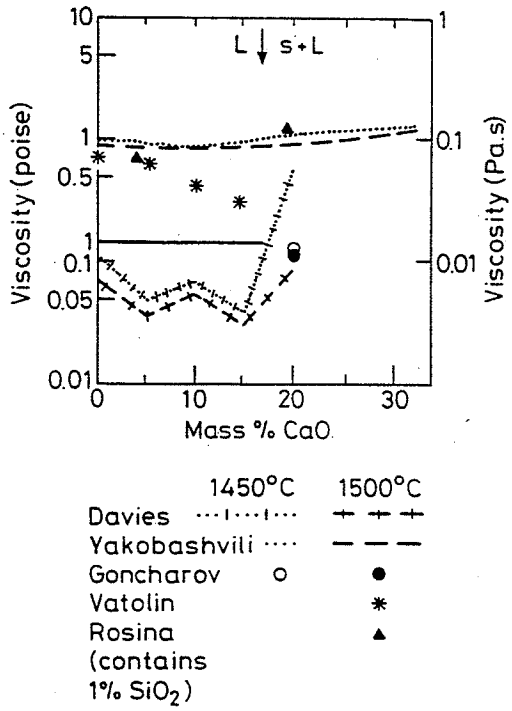


Fig. 9.22. Viscosities of CaF_2-CaO melts as a function of CaO content [67, 68, 42, 48, 72, 77, 92, 93]. (Given the scatter in the results, the solid line (based on the recommended values for CaF_2 at 1500 °C) is recommended

CaF_2-Cr_2O_3

Values of 0.1 and 0.5 poise, respectively have been reported for melts containing 3 and 5 mass % Cr_2O_3, respectively [10].

CaF_2-Li_2O

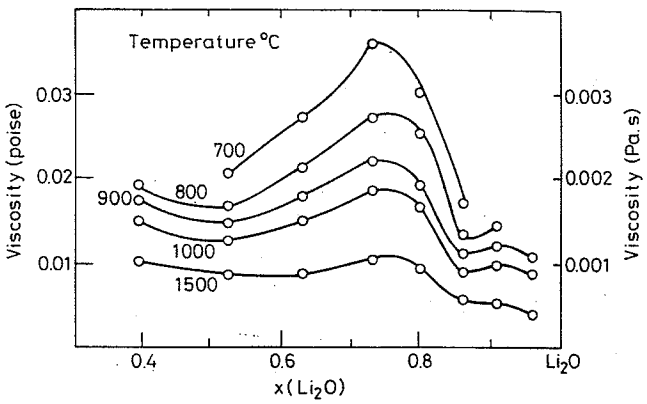


Fig. 9.23. Viscosities of CaF_2-Li_2O melts as a function of mole fraction Li_2O [94]; value of CaF_2 at 1500 °C is also shown

CaF_2-MgO

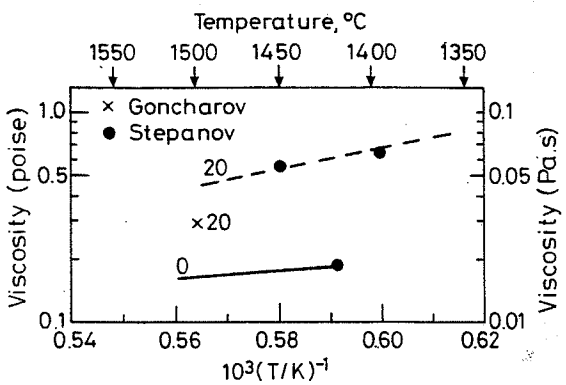


Fig. 9.24. Viscosities of CaF_2-MgO melts as a function of temperature [67, 78, 39, 92]; the experimental values due to Ref. [39] are preferred to those of Ref. [92]. The recommended values for CaF_2 are also shown

CaF_2-SiO_2

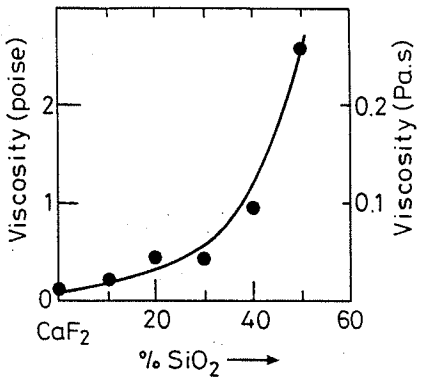


Fig. 9.25. Viscosities of CaF_2-SiO_2 melts at 1600 °C as a function of SiO_2 content [95]. Further Ref. [72]

CaF_2-TiO_2

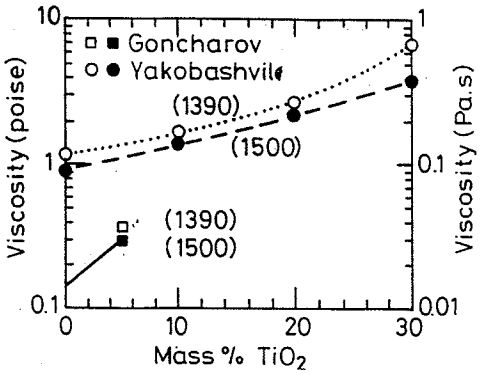


Fig. 9.26. Viscosities of CaF_2-TiO_2 melts as a function of TiO_2 content; —, preferred relation [92]. Further Ref. [72]

CaF_2-V_2O_5

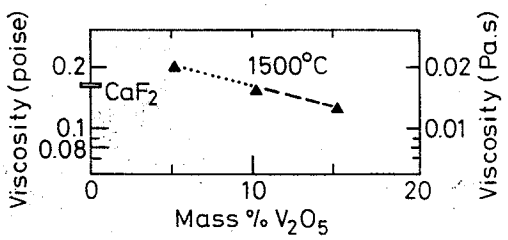
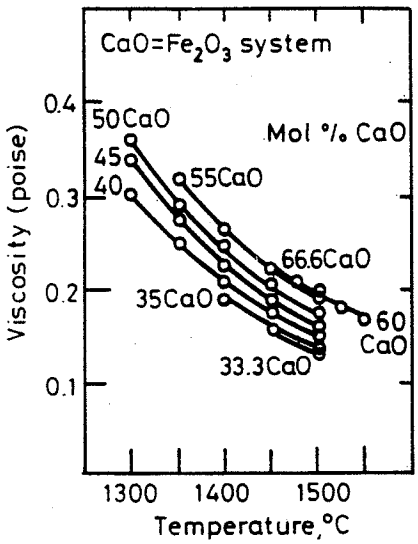
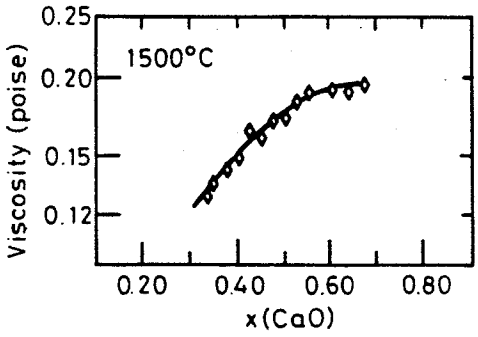


Fig. 9.27. Viscosities of CaF_2-V_2O_5 melts at 1500 °C as function of V_2O_5 content [67, 92]. Recommended value for CaF_2 is also shown

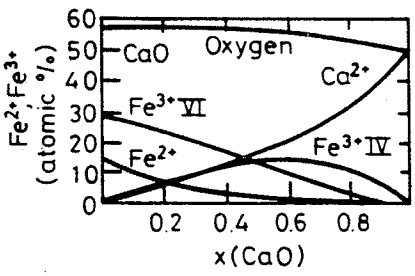
CaO-FeO_x



(a)



(b)



(c)

Fig. 9.28 a-c. Viscosities of CaO-Fe_2O_3 melts as a function of (a) temperature, (b) composition and (c) shows the distribution of Fe^{3+} (IV) Fe^{3+} (VI) and Fe^{2+} in the melts [90, 96]. Further Ref. [97, 98]

CaO-P_2O_5

Tab. 9.2. Temperature dependence of viscosity of CaO-P_2O_5 melts [99]

P_2O_5 wt %	Viscosity (poise) at												
	925 °C	950 °C	980 °C	1000 °C	1050 °C	1100 °C	1150 °C	1200 °C	1250 °C	1300 °C	1350 °C	1400 °C	1450 °C
43.4	–	–	–	–	–	–	–	–	–	1.0	0.6	0.5	0.4
51.2	–	–	–	–	–	–	–	–	1.0	0.95	0.8	0.7	0.5
55.9	–	–	–	–	–	–	–	–	–	1.0	0.8	0.7	0.7
57.4	–	–	–	–	–	–	–	1.2	1.1	1.0	1.0	0.8	0.7
68.9	–	–	14.0	11.1	6.7	4.4	3.1	2.8	1.8	1.4	1.1	1.0	–
75.2	57.0	48.5	26.5	21.5	13.5	9.0	–	–	–	–	–	–	–
76.8	65.0	48.5	33.5	26.0	15.0	9.5	–	–	–	–	–	–	–
77.2	66.0	50.5	35.0	27.0	16.5	10.5	–	–	–	–	–	–	–
78.6	76.0	56.0	39.0	31.0	17.0	10.5	–	–	–	–	–	–	–
83.1	–	76.0	51.5	41.0	21.0	11.0	11.5	–	–	–	–	–	–

$CaO\text{-}SiO_2$

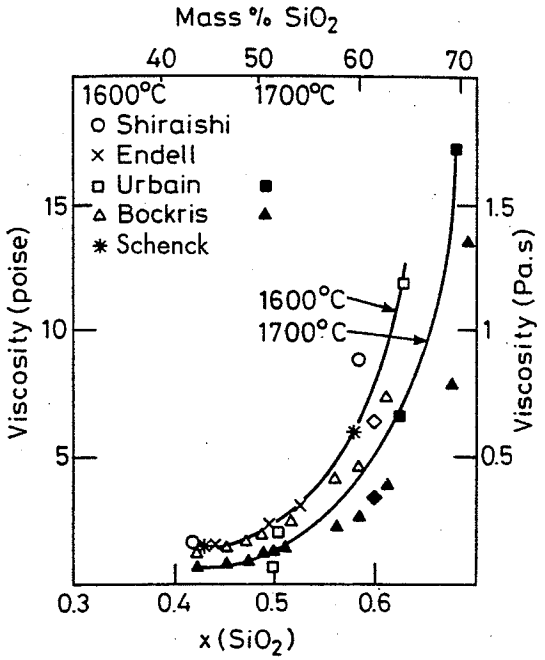


Fig. 9.29. Viscosities of $CaO\text{-}SiO_2$ melts at 1600 and 1700 °C [56, 98, 100-104], ___, recommended relations. Further Ref. [105-108]; experimental details [24]

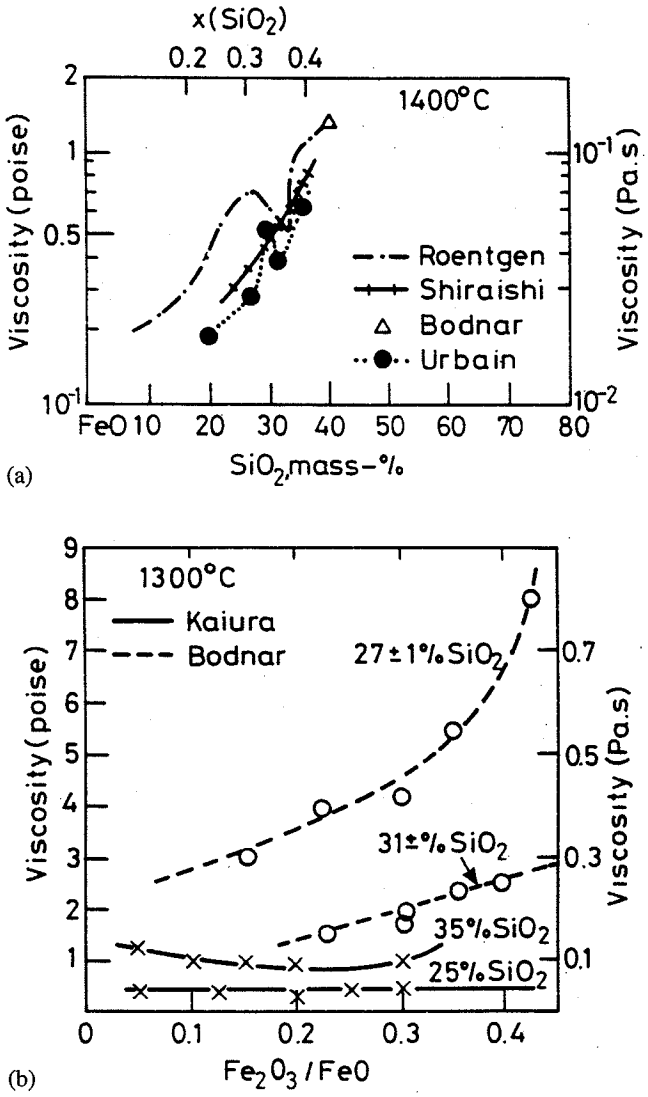


Fig. 9.31 a,b. Viscosities of $FeO_x\text{-}SiO_2$ melts (a) as a function of SiO_2 content in $FeO\text{-}SiO_2$ [56, 109, 111, 114] recommended values [56, 109] and (b) the effect of Fe_2O_3/FeO) ratio of $FeO\text{-}Fe_2O_3\text{-}SiO_2$ melts [11, 12]

$FeO_x\text{-}SiO_2$

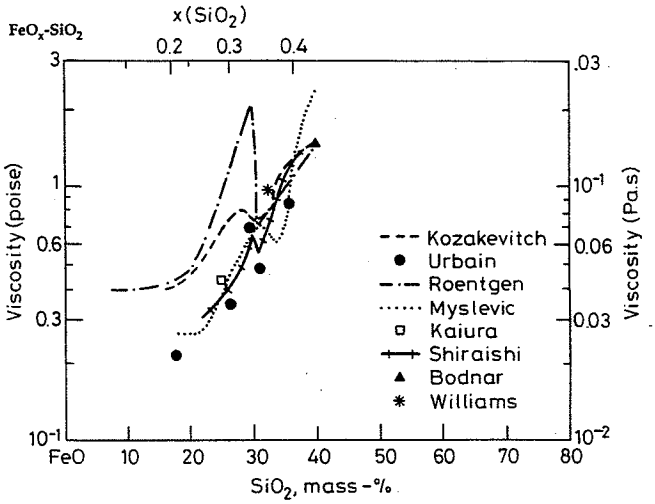


Fig. 9.30. Viscosities of $FeO_x\text{-}SiO_2$ melts at 1330 °C [56, 109-113] recommended values [56, 109] denoted ++, • , ... Further Ref. [114-116, 51], experimental details [24]

$FeO_x\text{-}TiO_2$

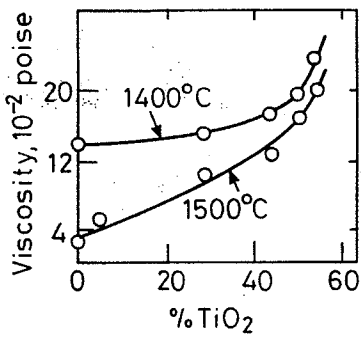


Fig. 9.32. Viscosities (in Pa.s = 10^{-2} poise) of $FeO_x\text{-}TiO_2$ melts as a function of TiO_2 content; (% FeO/% Fe_2O_3) ≃ 10 [53]

K_2O-SiO_2

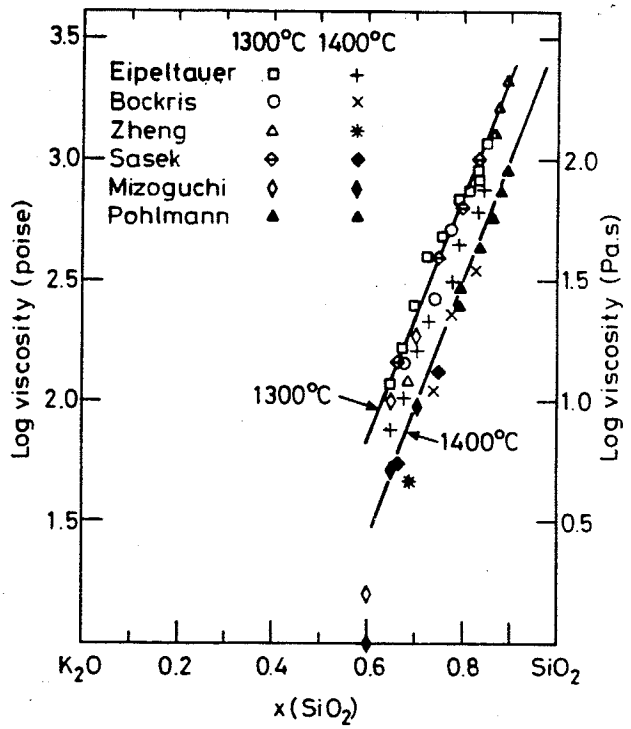


Fig. 9.33. Viscosities of K_2O-SiO_2 melts at 1300 and 1400 °C as a function of mole fraction SiO_2 [65, 91, 117-120]; —, recommended relationships

Li_2O-SiO_2

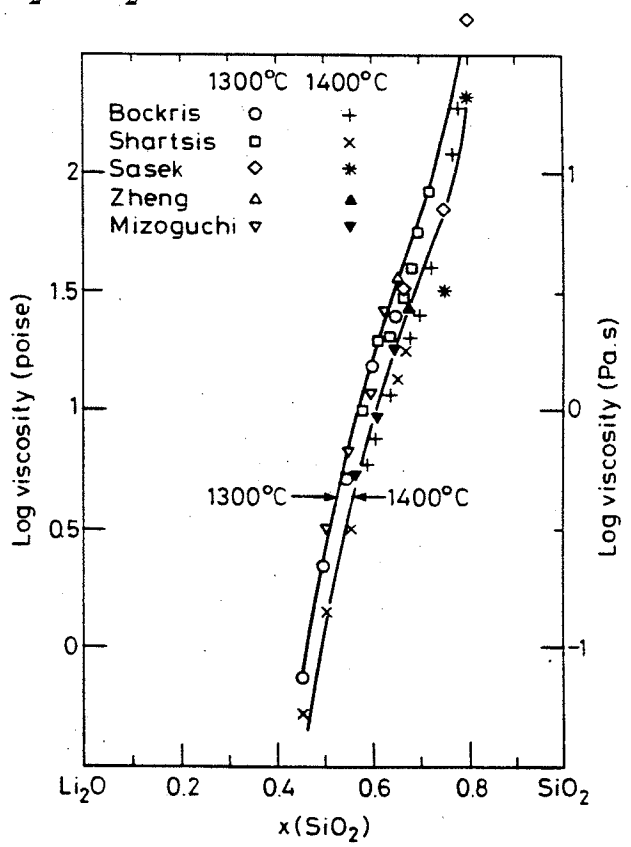


Fig. 9.34. Viscosities of Li_2O-SiO_2 melts at 1300 °C as a function of mole fraction SiO_2 [65, 91, 119-121]; —, recommended relationship

MgO-SiO_2

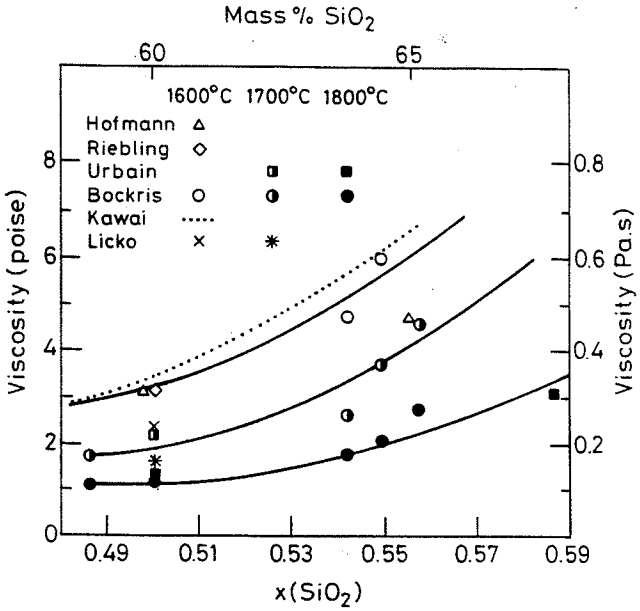


Fig. 9.35. Viscosities of MgO-SiO_2 melts as a function of SiO_2 content [56, 65, 107, 122, 123]; —, recommended relationship

MnO-SiO_2

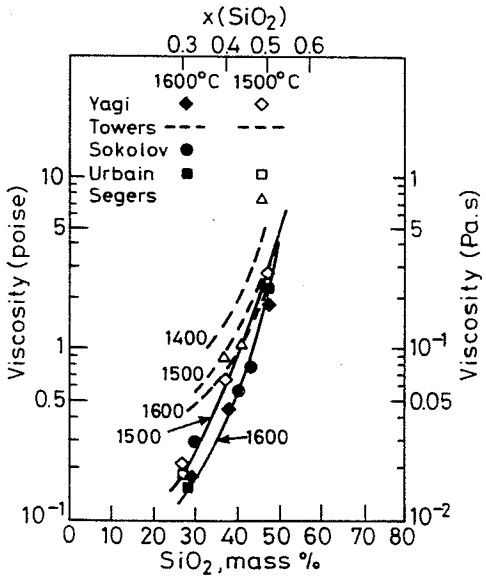


Fig. 9.36. Viscosities of MnO-SiO_2 melts as a function of SiO_2 content [56, 117, 124-126]

MnO-TiO_2

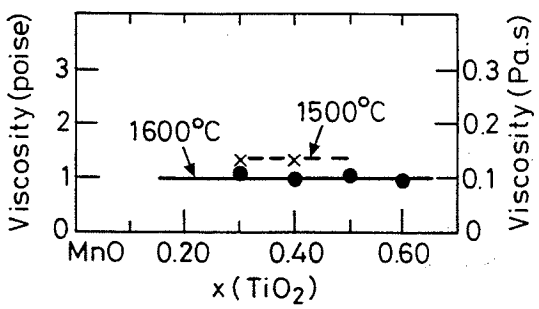


Fig. 9.37. Viscosities of FeO-TiO_2 melts as a function of mole fraction TiO_2 [126]

Na_2O-P_2O_5

Tab. 9.3. Viscosities of $Na_2O + P_2O_5$ melts [127]. Further Ref. [128]

Composition mol fraction		Viscosities (poise) at temperature (°C)						
Na_2O	P_2O_5	700	750	800	850	900	950	1000
0.5	0.5		4.7	3.2	2.3	1.7	1.3	1.0
0.519	0.481	4.8	3.3	2.3	1.7	1.3	1.0	0.3
0.563	0.437	2.0	1.5	1.1	0.9	0.7	0.6	0.5
0.6	0.4			0.8	0.6	0.5	0.4	0.4
0.636	0.364						0.4	0.3
0.667	0.333							0.3
0.682	0.318							0.3

Na_2O-SiO_2

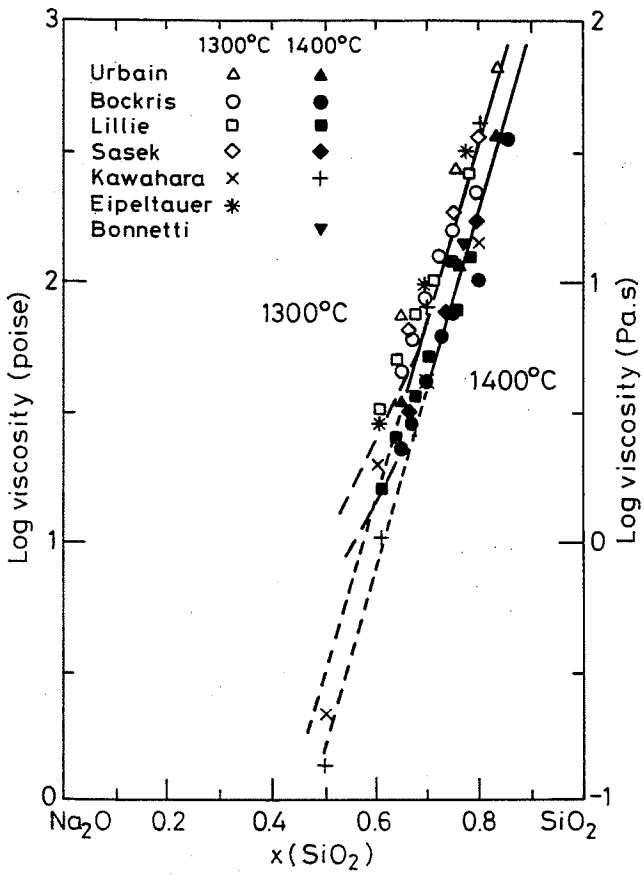
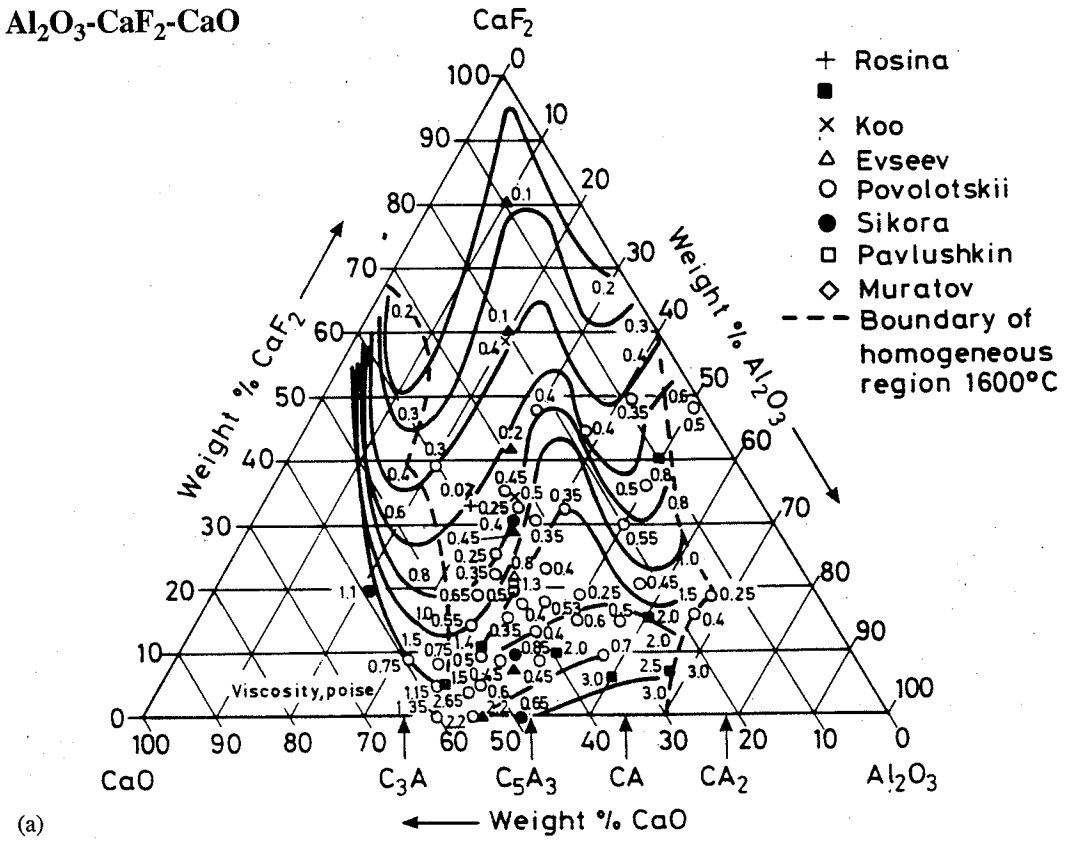
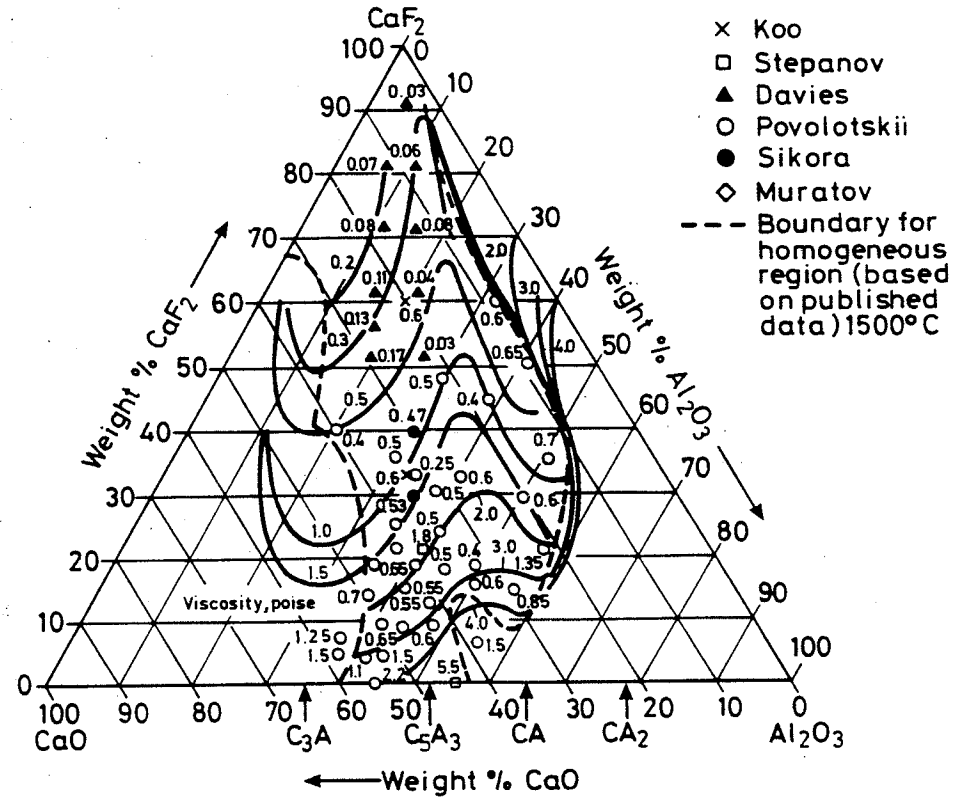


Fig. 9.38. Viscosities of $Na_2O + SiO_2$ melts at 1300 and 1400 °C as a function of mole fraction SiO_2; —, recommended relationship [129, 65, 118, 120, 130, 131]; — —, extrapolation based on majority of data; . . . ., extrapolation based on data for Na_2O-SiO_2 due to Kawahara et al. Further Ref. [121, 132]



(a)



(b)

Fig. 9.39 a,b. Viscosities (poise) for Al_2O_3-CaF_2-CaO melts at (a) 1500 °C, (b) 1600 °C [67, 69, 71, 74, 138-142]; —, preferred iso-viscosity contours [67, 138]. Further Ref. [42, 48, 93, 143, 144]; note iso-viscosity contours reported by Yanagase [148] are lower by a factor of 2 or 3 for compositions with CaF_2 > 50 %

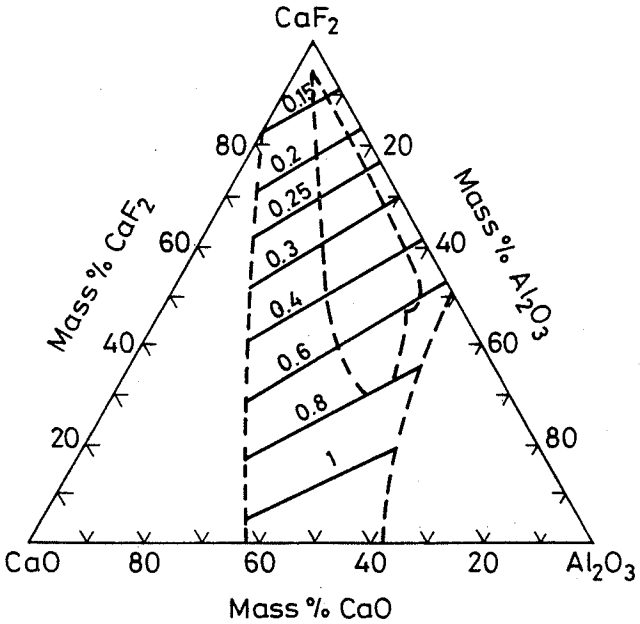


Fig. 9.40. Iso-viscosity contours for 1600 °C suggested by Mills [145] who attributed a complex shape of contours in Fig. 9.39 b to carrying out measurements in a two-liquid system

Al_2O_3-CaF_2-Nb_2O_5

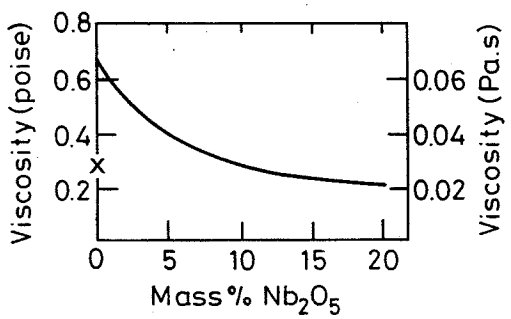


Fig. 9.41. The effect of additions of Nb_2O_5 on a melt of composition (70 % CaF_2 + 30 % Al_2O_3) on the viscosity at 1600 °C [73, 146]; X, recommended value for melt with 0 % Nb_2O_5 differs appreciably from measured values

Al_2O_3-CaF_2-SiO_2

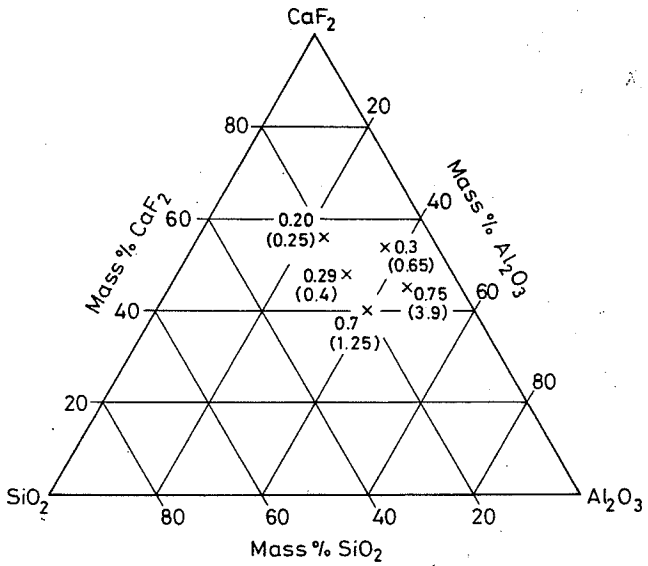


Fig. 9.42. Viscosities of Al_2O_3-CaF_2-SiO_2 melts at 1600 °C and (1500 °C) values for the latter are given in parenthesis [46]

Al_2O_3-CaF_2-TiO_2

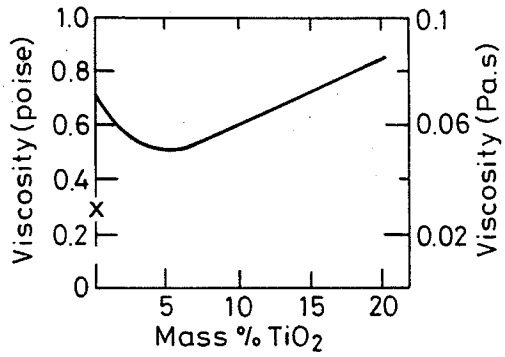


Fig. 9.43. The effect of TiO_2 additions on (70 % CaF_2 - 30 % Al_2O_3) melts at 1600 °C [73]; X, recommended value for melt with 0 % TiO_2 which is appreciably lower than value reported by Ref. [73]

Al_2O_3-CaF_2-V_2O_5

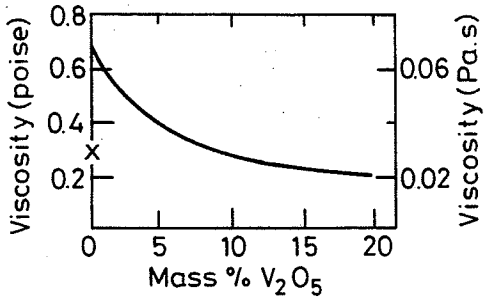


Fig. 9.44. The effects of V_2O_5 on the viscosities of (70 % CaF_2 - 30 % Al_2O_3) melts at 1600 °C [73, 146]; X, recommended value for melt with 0 % V_2O_5. A value of 4 poise at 1100 °C has been reported for 20 % Al_2O_3 - 20 % CaF_2 - 60 % V_2O_5 [147]

Al_2O_3-CaF_2-Y_2O_3

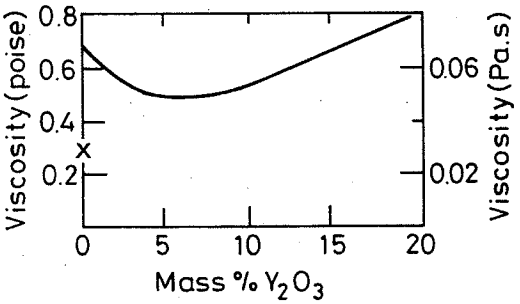


Fig. 9.45. The effects of Y_2O_3 on the viscosities of (70 % CaF_2- 30 % Al_2O_3) melts at 1600 °C [73, 146]; X, recommended value for melt with 0 % Y_2O_3: note difference from recommended values

Al_2O_3-CaO-MgO

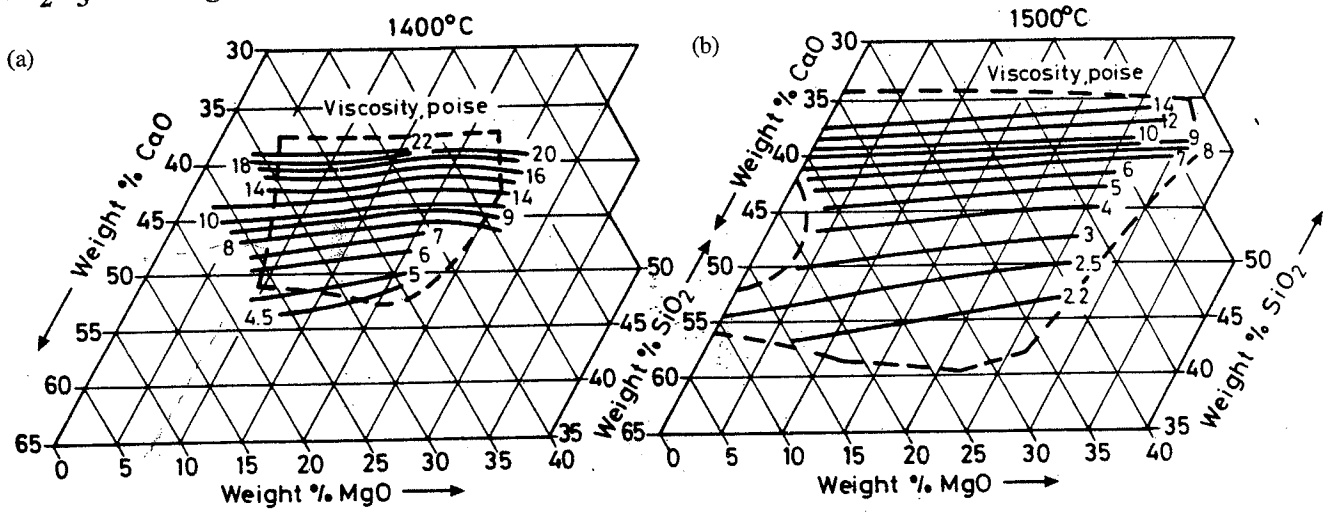


Fig. 9.46 a,b. Iso-viscosity (poise = 10^{-1} Pa.s) contours for Al_2O_3-CaO-MgO melts at (a) 1400 °C, (b) 1500 °C [148]. Further Ref. [149]

Al_2O_3-CaO-SiO_2

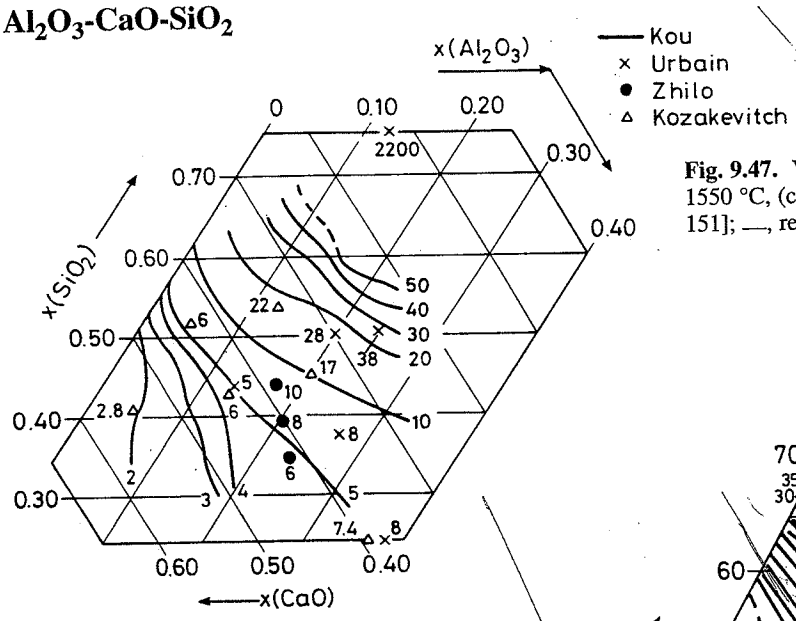


Fig. 9.47. Viscosities (poise) of Al_2O_3-CaO-SiO_2 melts at 1550 °C, (composition in mole fractions) [27, 56, 135, 150, 151]; —, recommended values

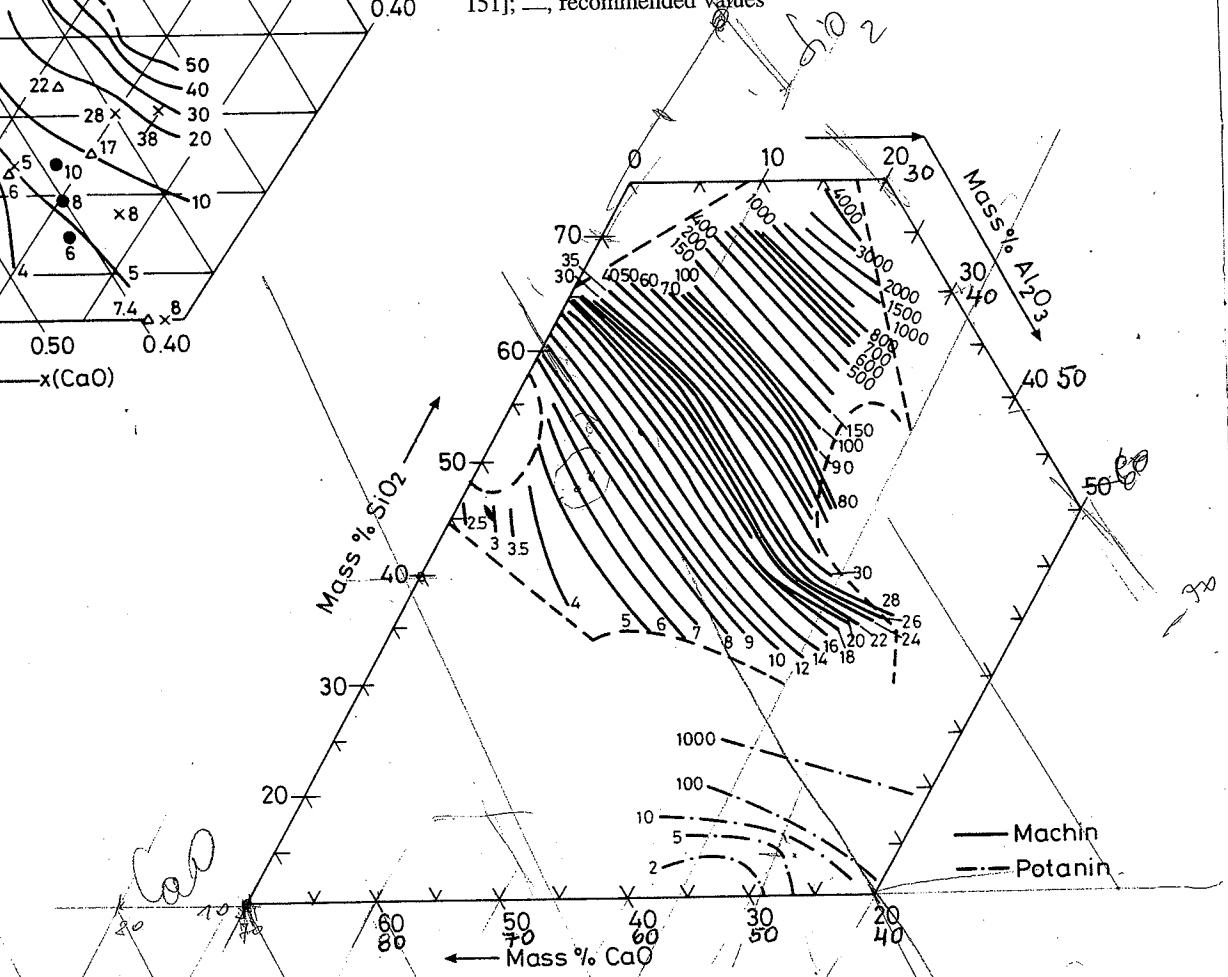


Fig. 9.48. Iso-viscosity (poise) contours of Al_2O_3-CaO-SiO_2 melts at 1500 °C [153, 154]; the preferred values due to [27, 56, 135] are ca. 20 % lower than contours shown [153]. Further values [152, 155-157]

Al_2O_3-CaO-TiO_2

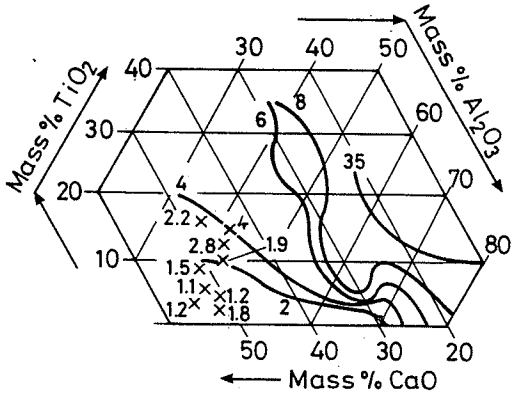


Fig. 9.49. Iso-viscosity (poise = 10^{-1} Pa.s) contours for Al_2O_3-CaO-TiO_2 melts at 1600 °C [79, 158]. Further Ref. [159]

Al_2O_3-FeO-SiO_2

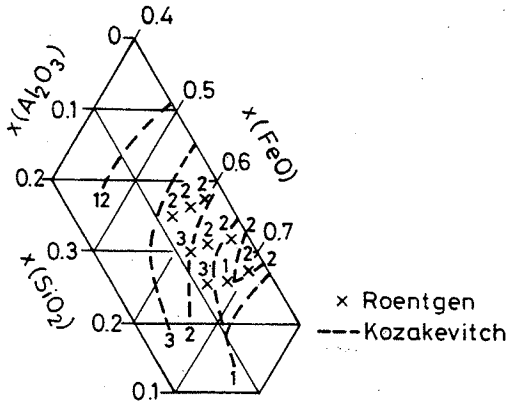
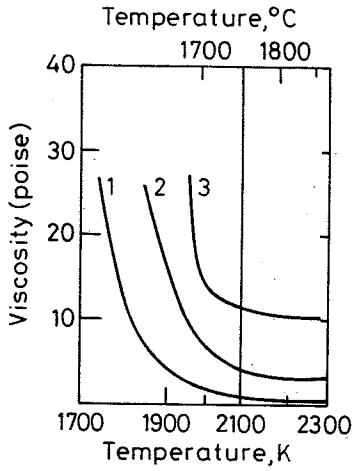


Fig. 9.51. Iso-viscosity (poise = 10^{-1} Pa.s) contours for Al_2O_3-FeO-SiO_2 melts at 1250 °C [161, 114]

Al_2O_3-CaO-ZrO_2



Slag	Composition, mass %		
	Al_2O_3	CaO	ZrO_2
1	60	30	10
2	50	25	25
3	40	20	40

Fig. 9.50. Temperature dependence of Al_2O_3-CaO-ZrO_2 slags [160]

Al_2O_3-K_2O-SiO_2

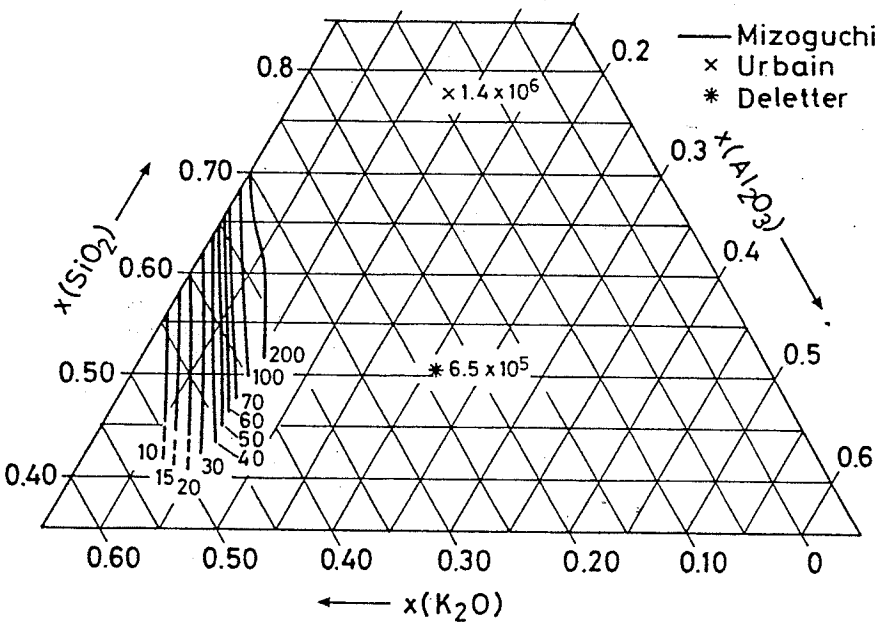


Fig. 9.52. Viscosities (poise = 10^{-1} Pa.s) of Al_2O_3-K_2O-SiO_2 melts at 1350 °C [91, 56, 164]

Al_2O_3-MgO-SiO_2

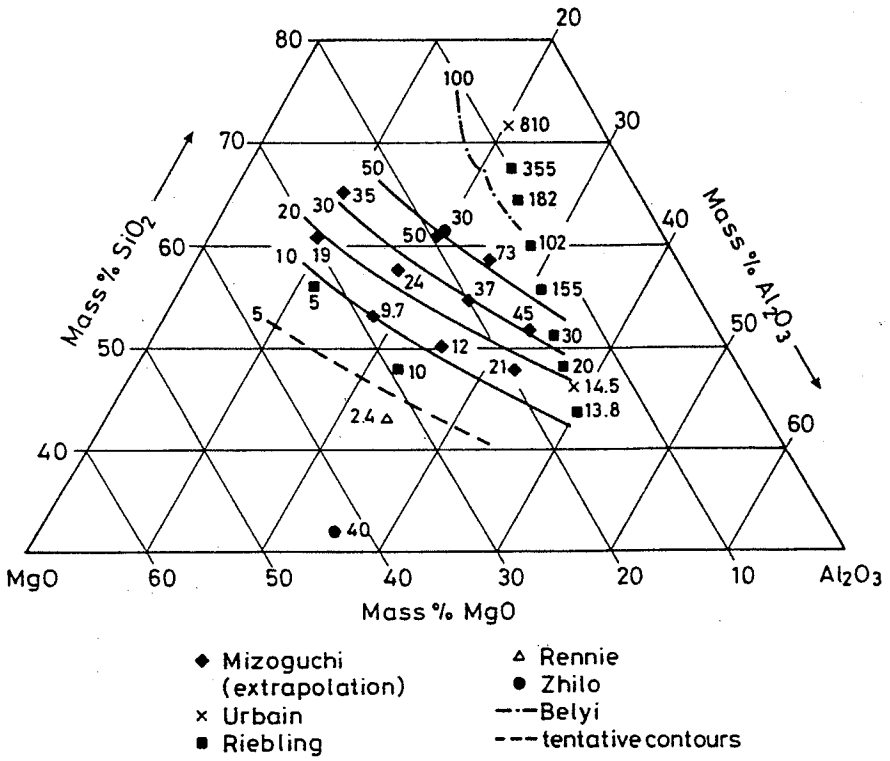


Fig. 9.53. Viscosities (poise = 10^{-1} Pa.s) of Al_2O_3-MgO-SiO_2 melts at 1600 °C [91, 56, 123, 167, 168]; recommended values, —, based on [91, 167]. Further Ref. [148, 169]

Al_2O_3-MnO-SiO_2

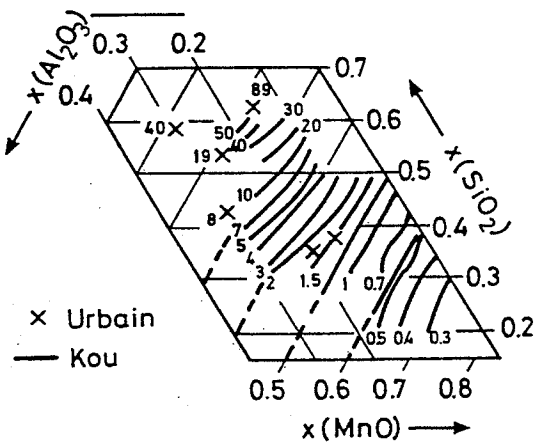


Fig. 9.54. Viscosities (poise = 10^{-1} Pa.s) for Al_2O_3-MnO-SiO_2 melts at 1550 °C [135, 56]. Further Ref. [124]

Al_2O_3-Na_2O-SiO_2

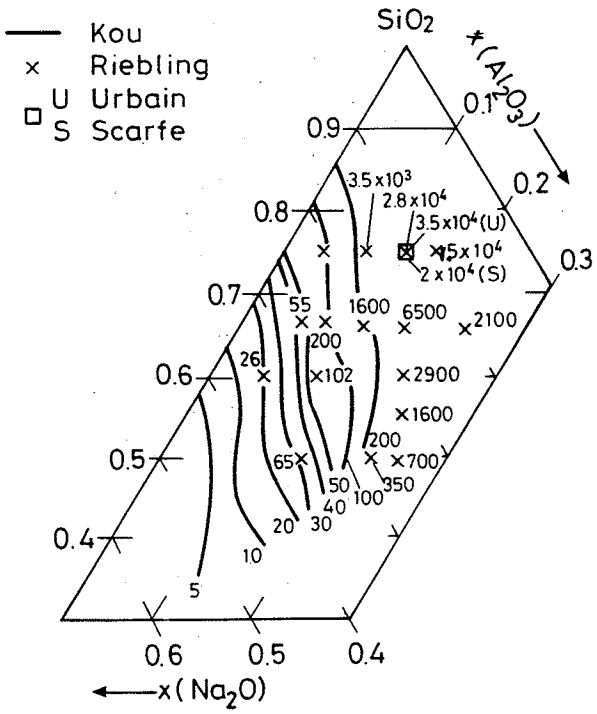


Fig. 9.55. Viscosities (poise = 10^{-1} Pa.s) for Al_2O_3-Na_2O-SiO_2 melts at 1500 °C [135, 56, 170-173]

Al_2O_3-SiO_2-TiO_2

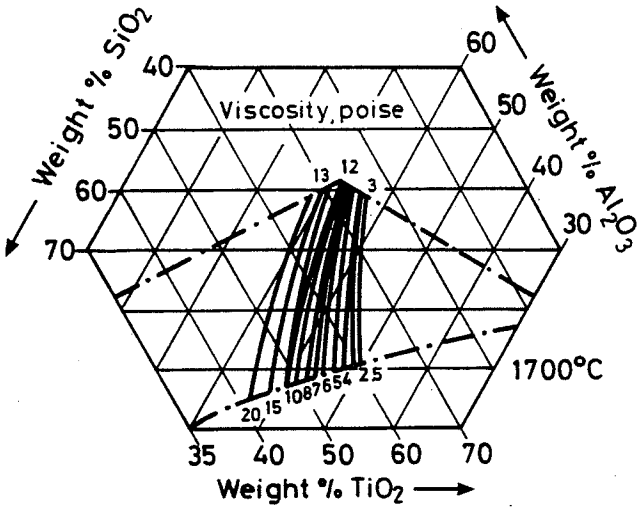


Fig. 9.56. Viscosities (poise = 10^{-1} Pa.s) of Al_2O_3-SiO_2-TiO_2 melts at 1700 °C [174]

Al_2O_3-SiO_2-ZnO

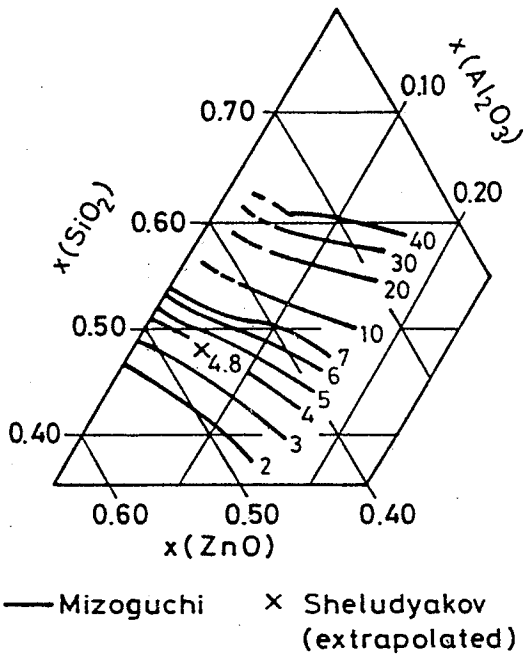


Fig. 9.57. Viscosities (poise = 10^{-1} Pa.s) of Al_2O_3-SiO_2-ZnO melts at 1550 °C [91, 175]

CaF_2-CaO-La_2O_3

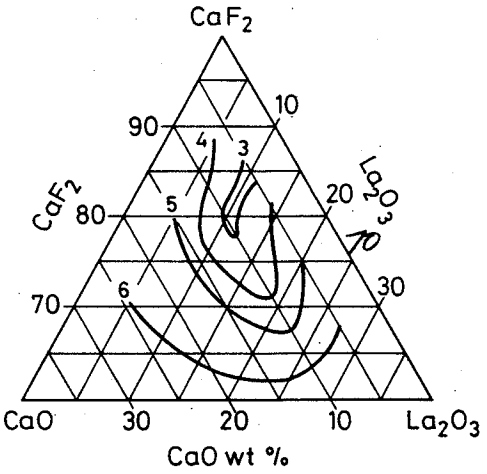


Fig. 9.58. Iso-viscosity contours (10^{-2} poise = mPa.s) of CaF_2-CaO-La_2O_3 melts at 1550 °C [179]

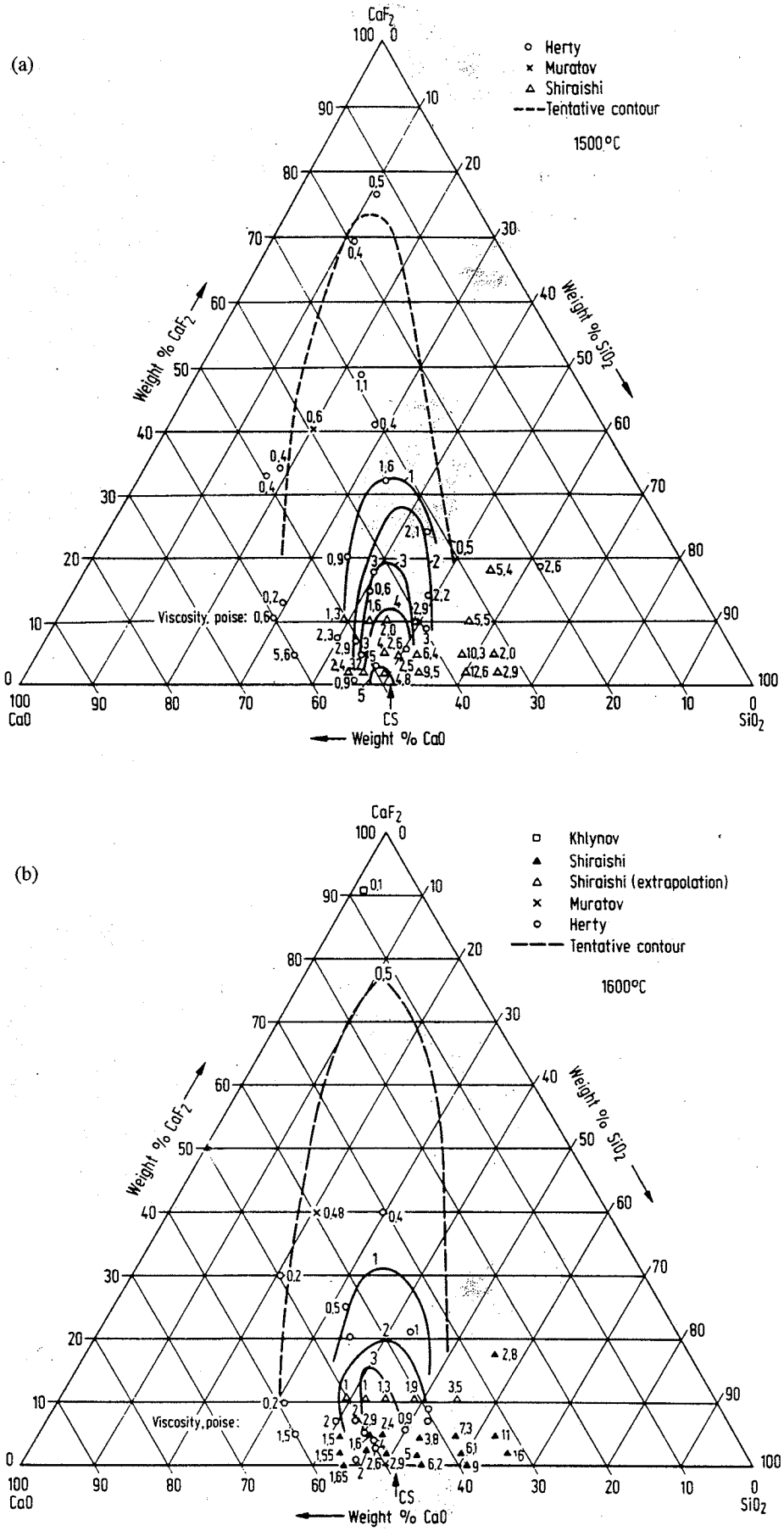


Fig. 9.59 a,b. Viscosities (poise = 10^{-1} Pa.s) of CaF_2-CaO-SiO_2 melts at (a) 1500 °C, (b) 1600 °C [139, 100, 104, 180]. Values for 1450 °C cited in [44]

CaF_2-SiO_2-$(RE)_2O_3$

$(RE)_2O_3$ = 50 % Ce_2O_3 + 20 % La_2O_3 + 9 % Nd_2O_3 + 16.5 % Pr_2O_3

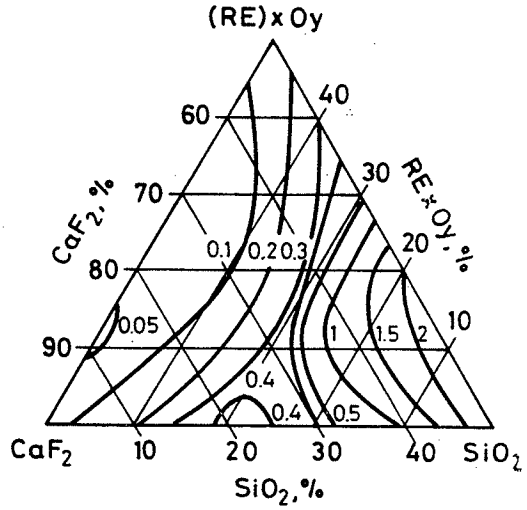


Fig. 9.60. Iso-viscosity (poise = 10^{-1} Pa.s) contours at 1600 °C for CaF_2-SiO_2-Rare Earth Oxide melts [95]

CaO-CoO-SiO_2

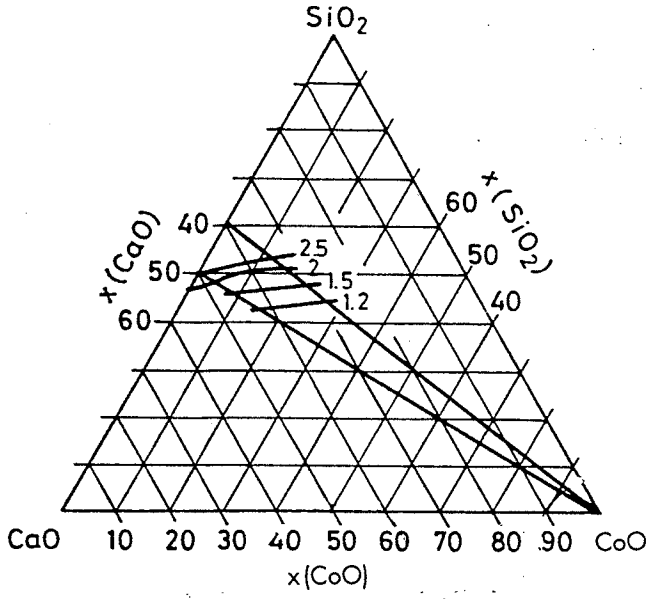
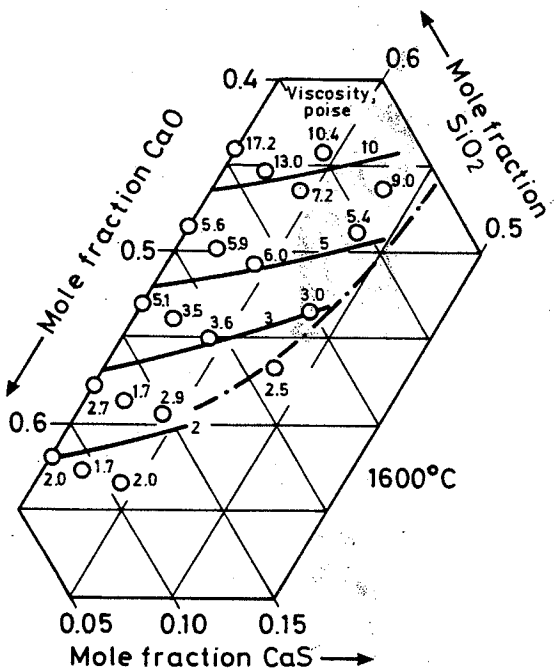
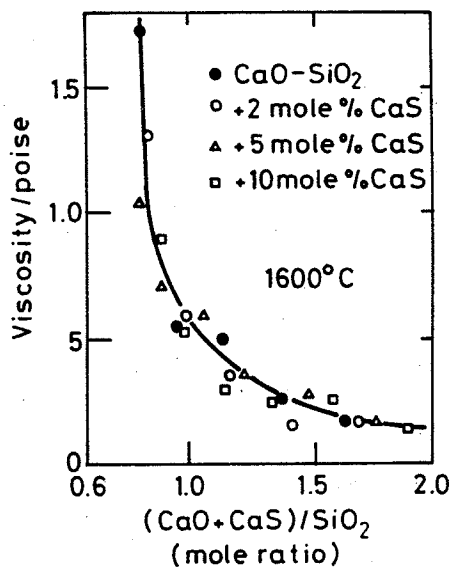


Fig. 9.62. Iso-viscosity (poise = 10^{-1} Pa.s) contours for CaO-CoO-SiO_2 melts at 1550 °C [183]

CaO-CaS-SiO_2



(a)



(b)

Fig. 9.61 a,b. Viscosities (poise = 10^{-1} Pa.s) of CaO-CaS-SiO_2 melts at 1600 °C plotted as (a) iso-viscosity contours [180], (b) as a function of [x(CaO) + x(CaS)/x(SiO_2)] ratio [181]. Further Ref. [182]

$CaO\text{-}Cr_2O_3\text{-}SiO_2$

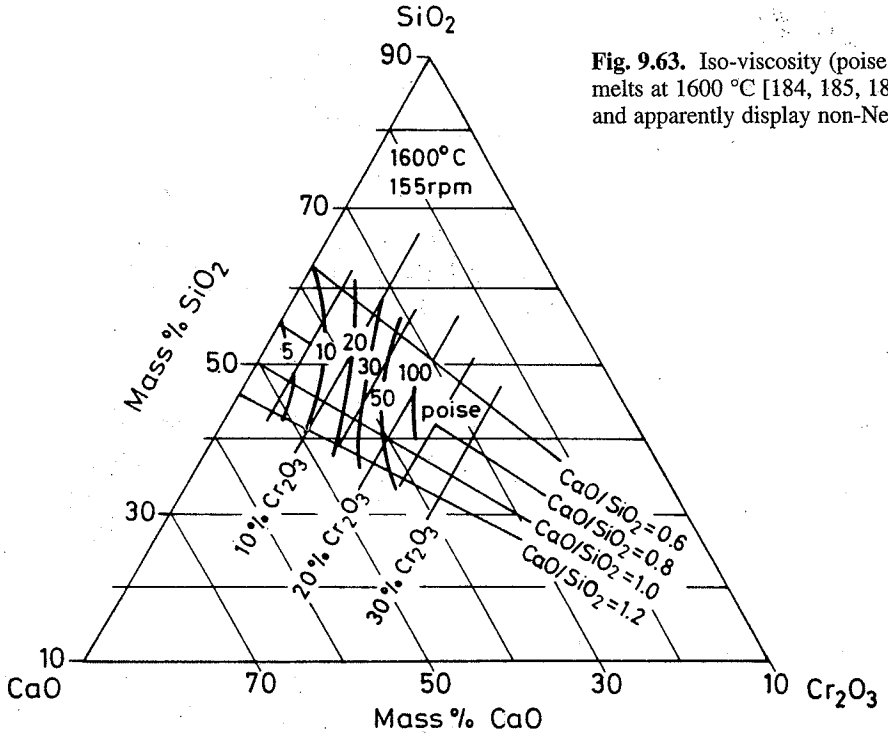


Fig. 9.63. Iso-viscosity (poise = 10^{-1} Pa.s) contours for $CaO\text{-}Cr_2O_3\text{-}SiO_2$ melts at 1600 °C [184, 185, 181]; the results refer to a two-liquid region and apparently display non-Newtonian behaviour

$CaO\text{-}Fe_xO\text{-}SiO_2$

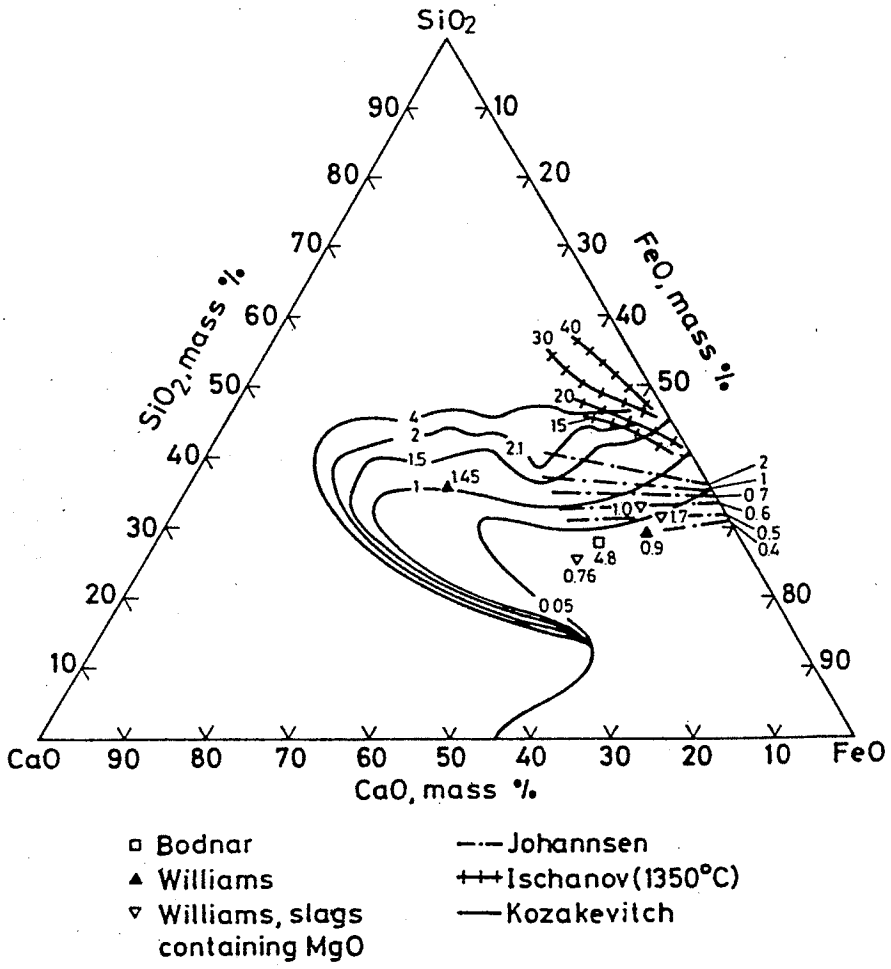


Fig. 9.64. Viscosities (poise = 10^{-1} Pa.s) of $CaO\text{-}FeO_x\text{-}SiO_2$ melts at 1400 °C [23, 52, 113, 187-189]. Recommended values, ——

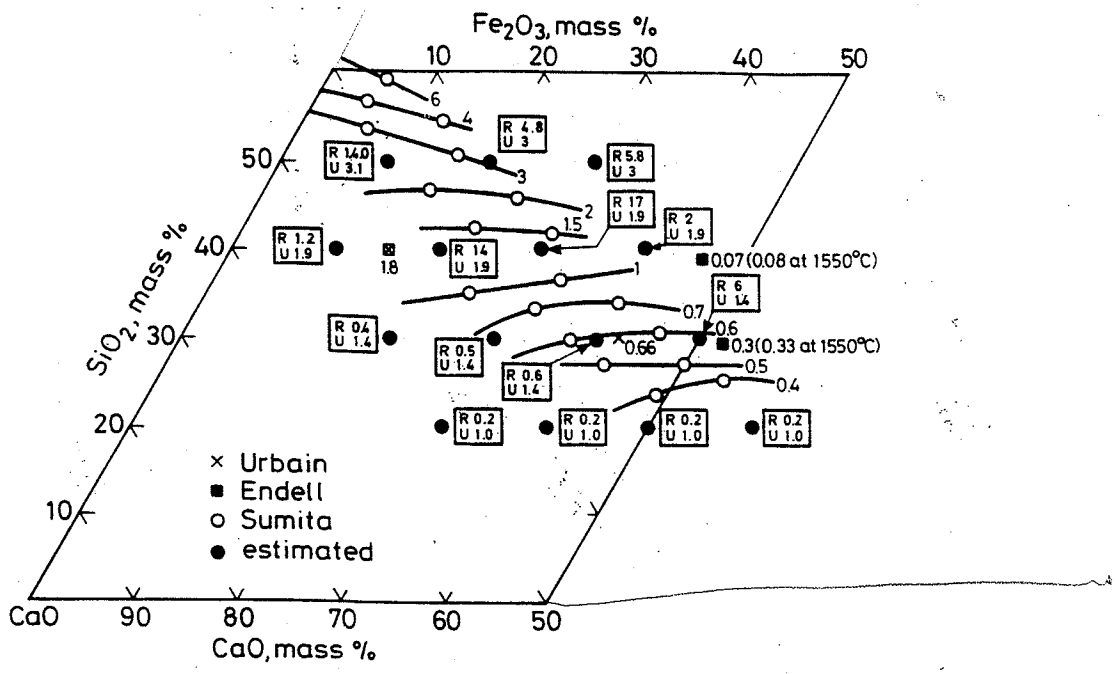


Fig. 9.65. Viscosities (poise = 10^{-1} Pa.s) of CaO-Fe_2O_3-SiO_2 melts at 1550 °C [56, 96, 98]; values in boxes are estimated by Riboud (R) [21] and Urbain II (U) [24] models. Recommended values, –o–; further Ref. [155]

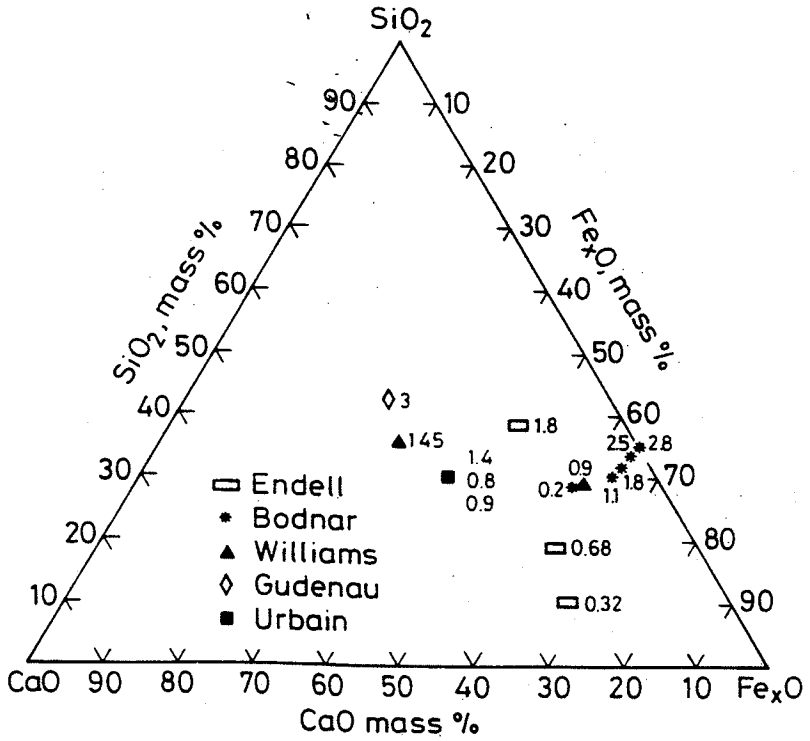


Fig. 9.66. Viscosities (poise = 10^{-1} Pa.s) of CaO-FeO-Fe_2O_3-SiO_2 melts at 1400 °C [23, 187, 113, 98, 190, 191]; values due to Urbain [56] are for x(FeO)/x(Fe_2O_3) ratios of 0.16 (1.4 poise), 1.13 (0.8 poise), 2.4 (0.9 poise)

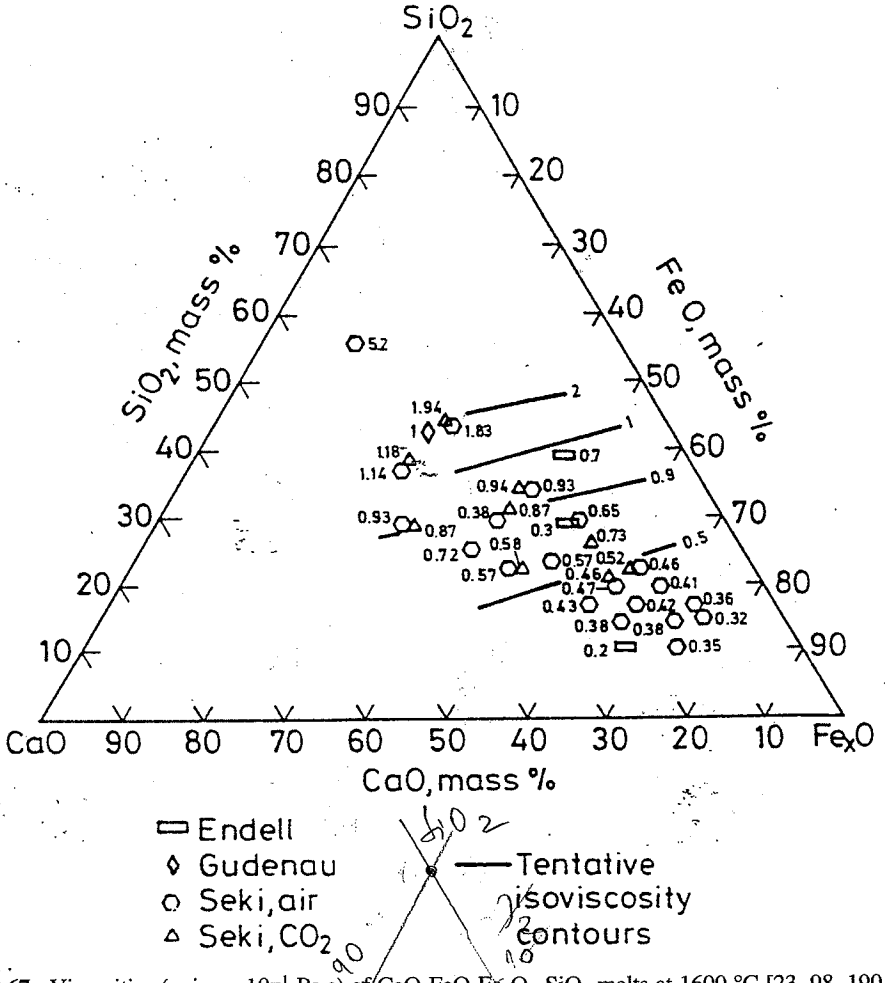


Fig. 9.67. Viscosities (poise = 10^{-1} Pa.s) of CaO-FeO-Fe_2O_3-SiO_2 melts at 1600 °C [23, 98, 190, 191]

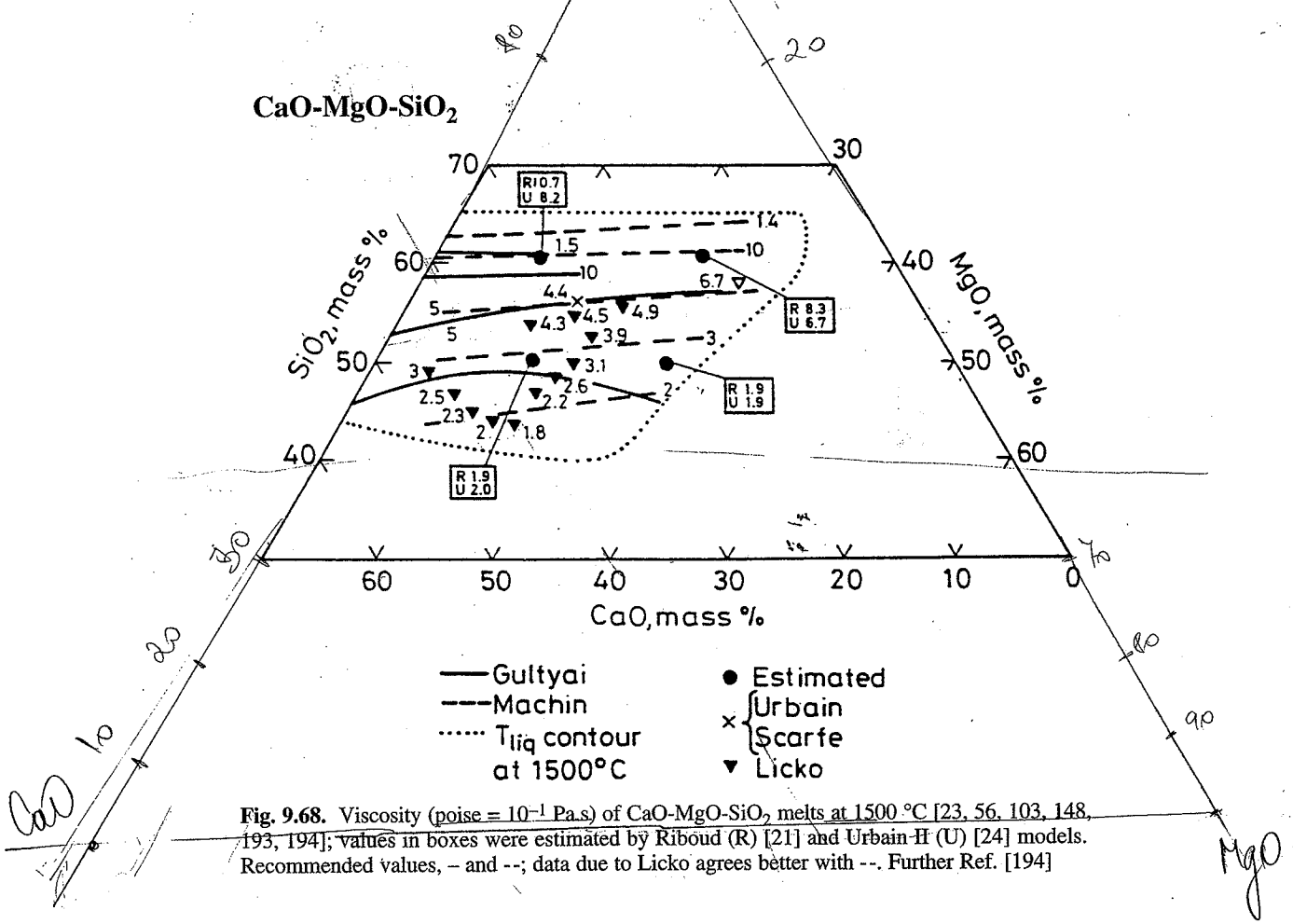


Fig. 9.68. Viscosity (poise = 10^{-1} Pa.s) of CaO-MgO-SiO_2 melts at 1500 °C [23, 56, 103, 148, 193, 194]; values in boxes were estimated by Riboud (R) [21] and Urbain-H (U) [24] models. Recommended values, – and --; data due to Licko agrees better with --. Further Ref. [194]

$CaO\text{-}MnO\text{-}SiO_2$

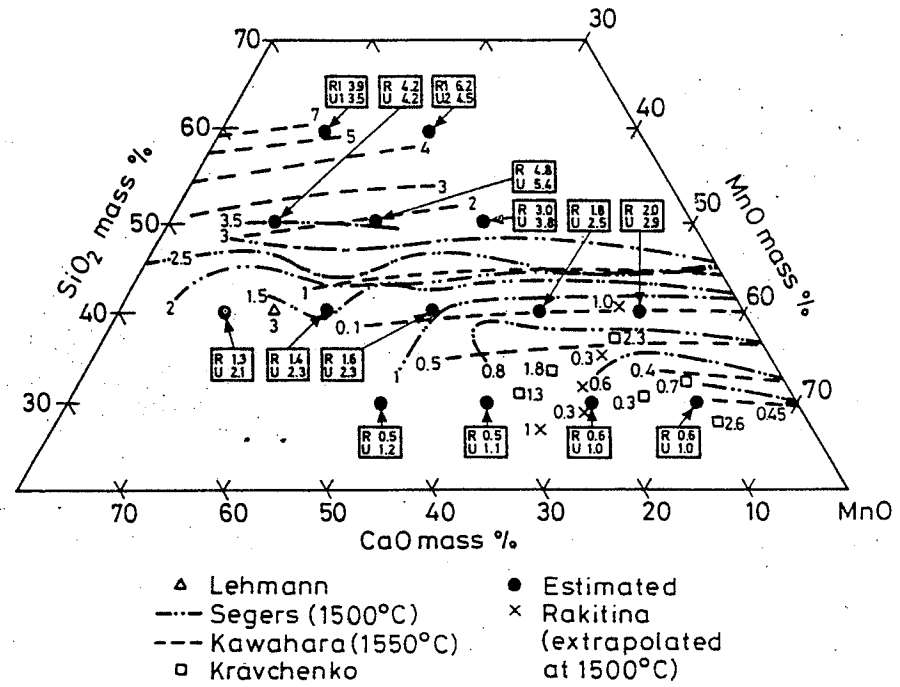


Fig. 9.69. Viscosities (poise = 10^{-1} Pa.s) of $CaO\text{-}MnO\text{-}SiO_2$ melts at 1500-1550 °C [23, 94-198]; values in boxes were estimated for 1527 °C using Riboud (R) [21] and Urbain III (U) [24] models. Recommended values, ---- , 1500 °C; --, 1550 °C

$CaO\text{-}Na_2O\text{-}SiO_2$

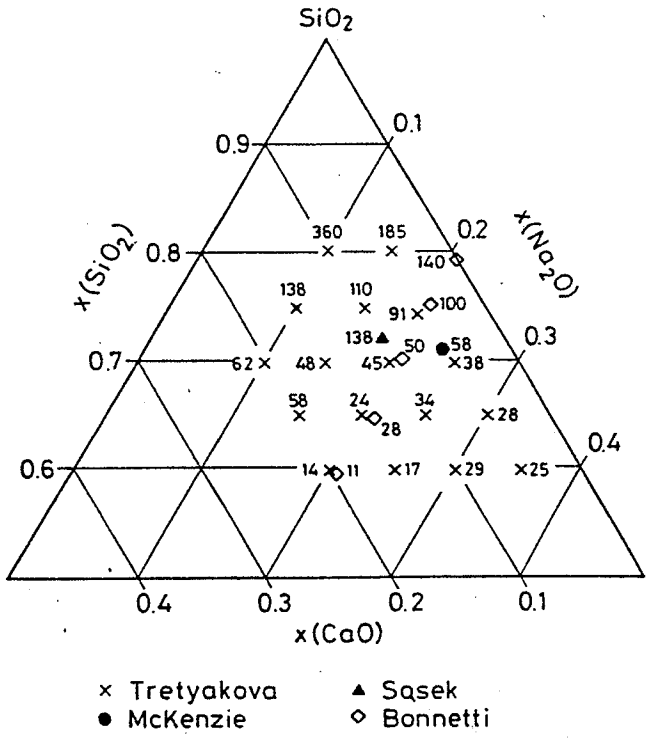


Fig. 9.70. Viscosities (poise = 10^{-1} Pa.s) of $CaO\text{-}Na_2O\text{-}SiO_2$ melts at 1400 °C [177, 199-201]

$CaO\text{-}NiO\text{-}SiO_2$

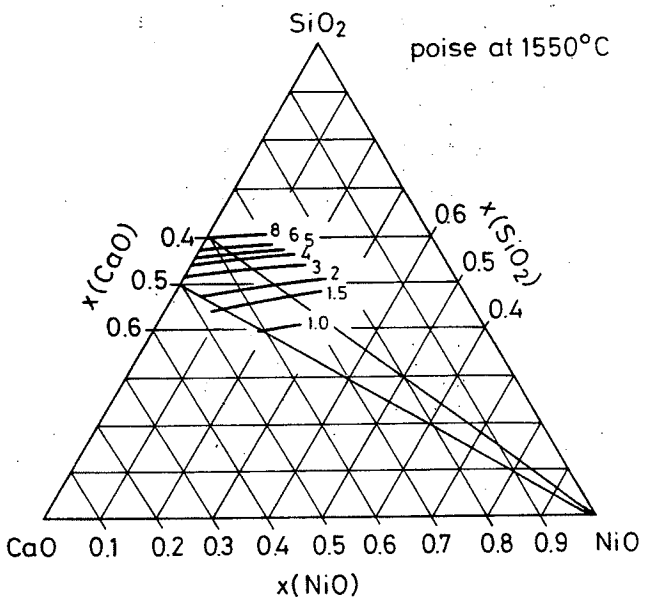


Fig. 9.71. Iso-viscosity (poise = 10^{-1} Pa.s) contours for $CaO\text{-}NiO\text{-}SiO_2$ melts at 1550 °C [202]

$CaO-P_2O_5-SiO_2$

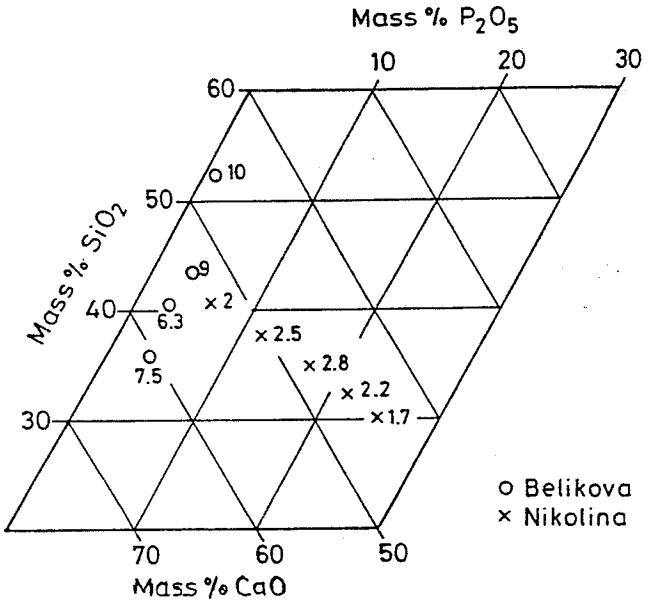


Fig. 9.72. Viscosities (poise = 10^{-1} Pa.s) reported for $CaO-P_2O_5-SiO_2$ melts at 1500 °C [203, 204]

$CaO-SiO_2-TiO_2$

Tab. 9.4. Viscosities of $CaO-SiO_2-TiO_2$ melts [178]

Composition, mole fraction			Viscosities (poise) at			
CaO	SiO_2	TiO_2	1400 °C	1450 °C	1500 °C	1550 °C
0,35	0,30	0,35	0,87	0,69	0,56	0,46

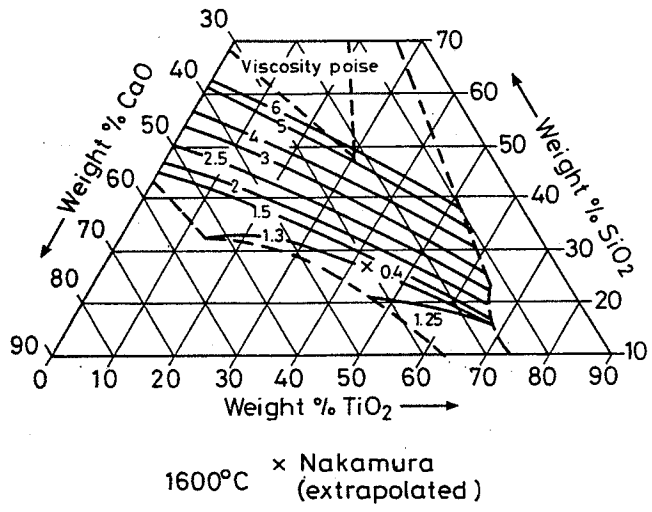


Fig. 9.73. Viscosities (poise = 10^{-1} Pa.s) of $CaO-SiO_2-TiO_2$ melts at 1600 °C [102, 178]; preferred value [178] is lower than contour. Further Ref. [205]

$CaO-SiO_2-ZnO$

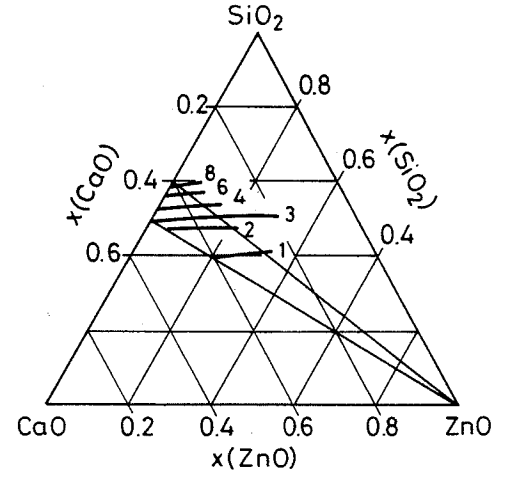


Fig. 9.74. Viscosities (poise = 10^{-1} Pa.s) of $CaO-SiO_2-ZnO$ melts at 1500 °C [206]

$CoO-Na_2O-SiO_2$

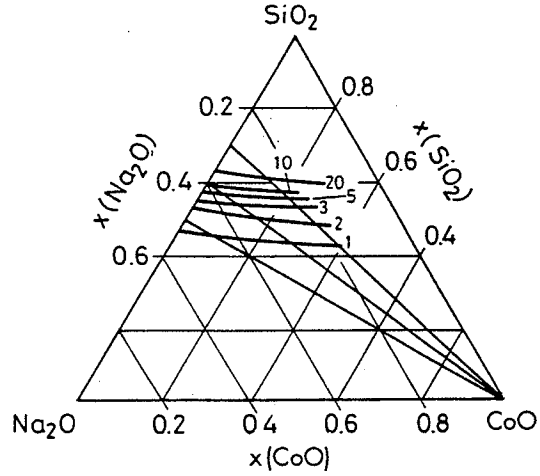


Fig. 9.75. Iso-viscosity (poise = 10^{-1} Pa.s) contours at 1400 °C for $CoO-Na_2O-SiO_2$ at 1400 °C [183]

$Fe_xO-MgO-SiO_2$

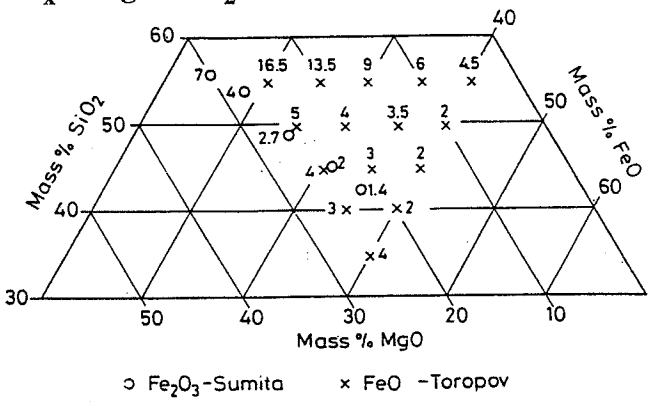


Fig. 9.76. Viscosities (poise = 10^{-1} Pa.s) of $Fe_xO-MgO-SiO_2$ melts at 1450 °C [96, 207]. Further Ref. [208]

Fe_xO-MnO-SiO_2

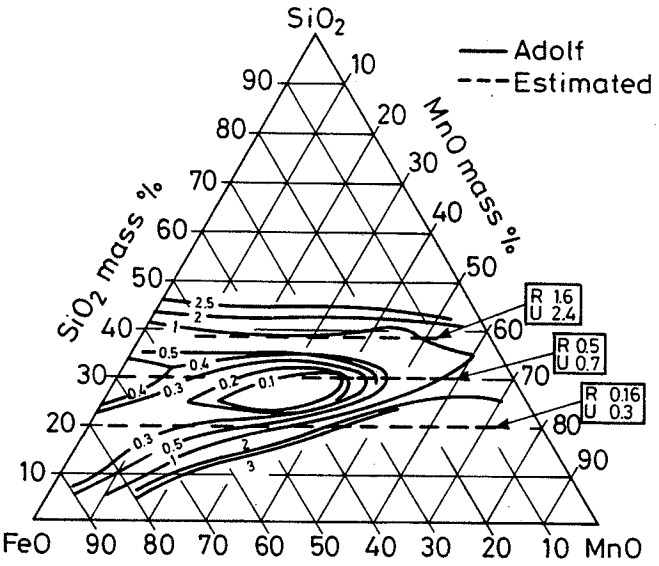


Fig. 9.77. Viscosities (poise) of FeO-MnO-SiO_2 melts at 1400 °C [209, 52, 116]; —, recommended values; estimated iso-viscosity contours calculated from Riboud (R) and Urbain II (U) models [21, 24]

Fe_xO-SiO_2-TiO_2

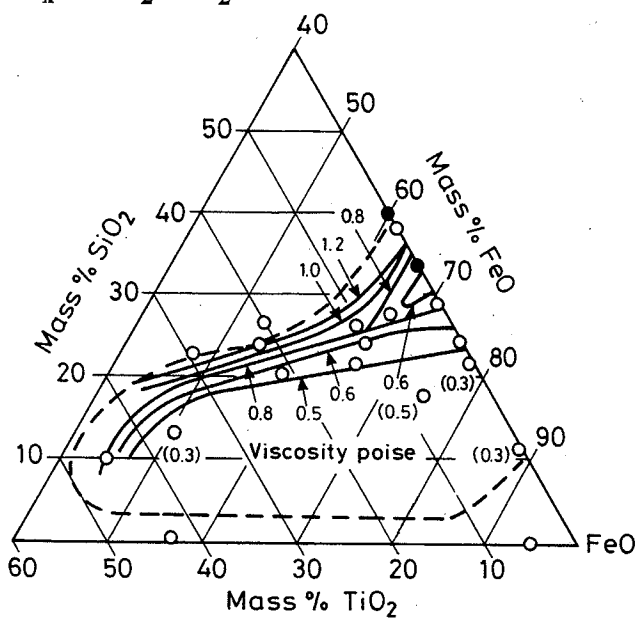
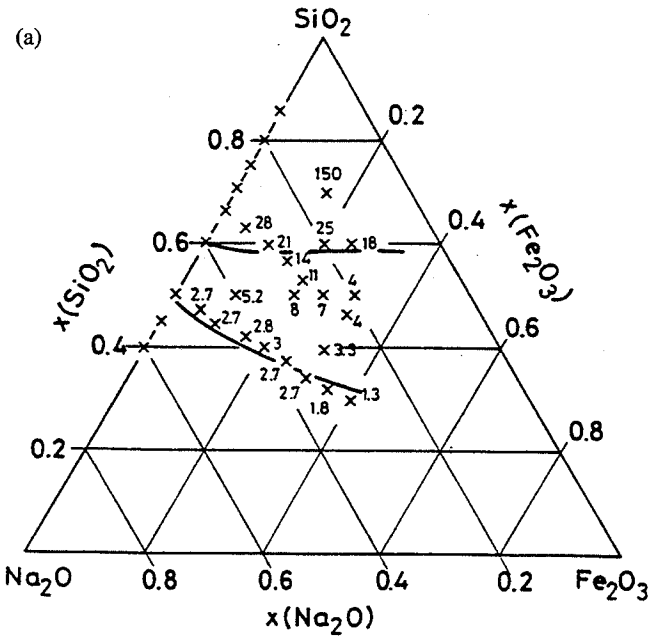


Fig. 9.79. Iso-viscosity (poise = 10^{-1} Pa.s) contours for FeO-SiO_2-TiO_2 melts at 1400 °C [52]

Fe_xO-Na_2O-SiO_2



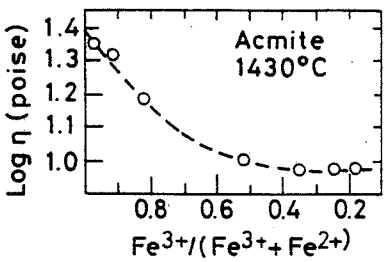


Fig. 9.78 a,b. (a) Viscosities (poise = 10^{-1} Pa.s) of Fe_2O_3-Na_2O-SiO_2 at 1300 °C [96] and (b) shows the effect of $Fe^{3+}/(Fe^{3+} + Fe^{2+})$ ratio on viscosity at 1430 °C of a melt, 35 % FeO_x + 14 % Na_2O + 51 % SiO_2 [210]

K_2O-SiO_2-TiO_2

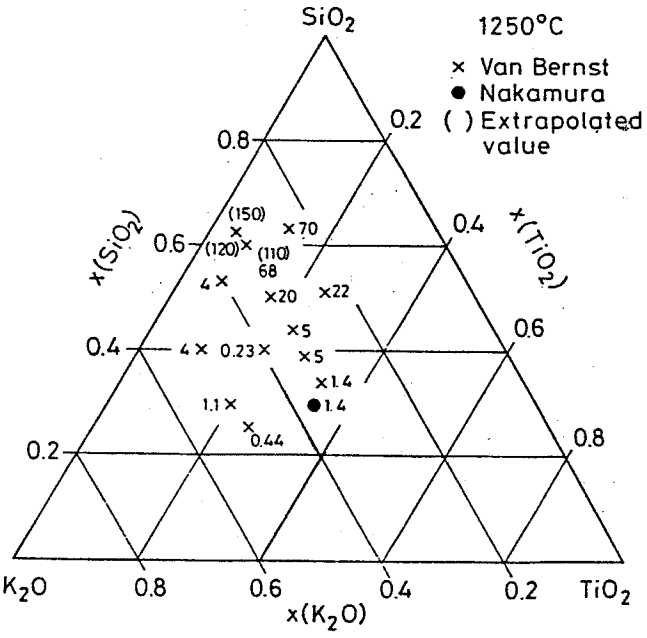


Fig. 9.80. Viscosities (poise = 10^{-1} Pa.s) for K_2O-SiO_2-TiO_2 melts at 1250 °C [178, 212]

Li_2O-SiO_2-TiO_2

Tab. 9.5. Viscosities of a Li_2O-SiO_2-TiO_2 melt [178]

Composition, mole fraction			Viscosity (poise) at			
LiO_2	SiO_2	TiO_2	1250 °C	1300 °C	1350 °C	1400 °C
0,35	0,30	0,35	0,45	0,40	0,35	0,31

$MgO\text{-}Na_2O\text{-}SiO_2$

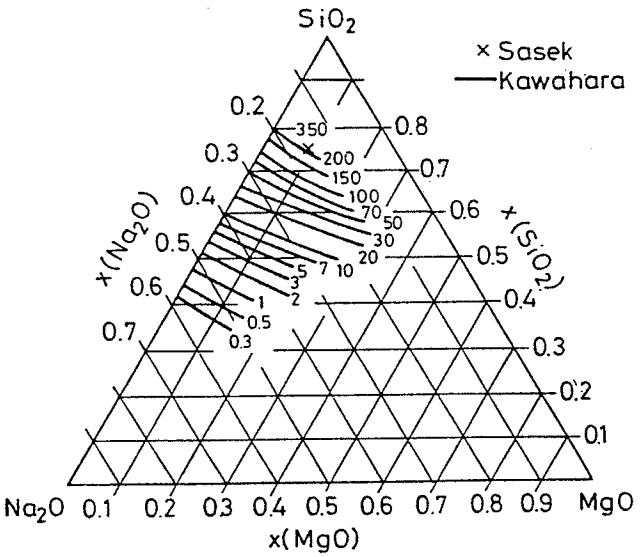


Fig. 9.81. Iso-viscosity (poise = 10^{-1} Pa.s) contours at 1350 °C for $MgO\text{-}Na_2O\text{-}SiO_2$ melts [131, 177]

$MgO\text{-}SiO_2\text{-}TiO_2$

Tab. 9.6. Viscosities of $MgO\text{-}SiO_2\text{-}TiO_2$ melt [178]

Composition, mole fraction			Viscosities (poise) at	
MgO	SiO_2	TiO_2	1500 °C	1550 °C
0.35	0.30	0.35	0.64	0.53

$MnO\text{-}Na_2O\text{-}SiO_2$

Tab. 9.7. Viscosities of $MnO\text{-}Na_2O\text{-}SiO_2$ melts [176]

Composition, mole fraction			Viscosity (poise) at		
MnO	Na_2O	SiO_2	1300 °C	1200 °C	1100 °C
0.1	0.2	0.7	57	138	377
0.2	0.2	0.6	39	100	294
0.1	0.3	0.6	3.7	23	145

$MnO\text{-}SiO_2\text{-}TiO_2$

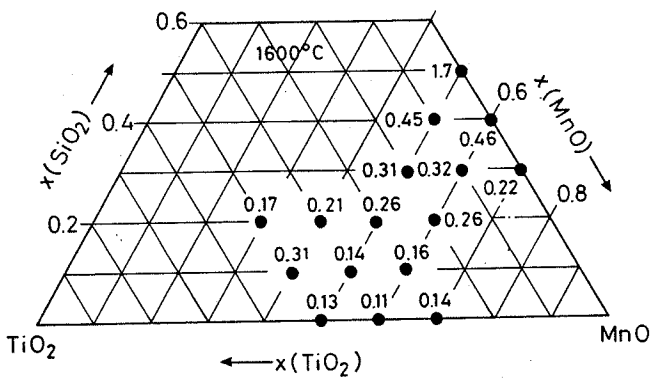


Fig. 9.82. Viscosities (poise = 10^{-1} Pa.s) of $MnO\text{-}SiO_2\text{-}TiO_2$ melts at 1600 °C [126]

$Na_2O\text{-}NiO\text{-}SiO_2$

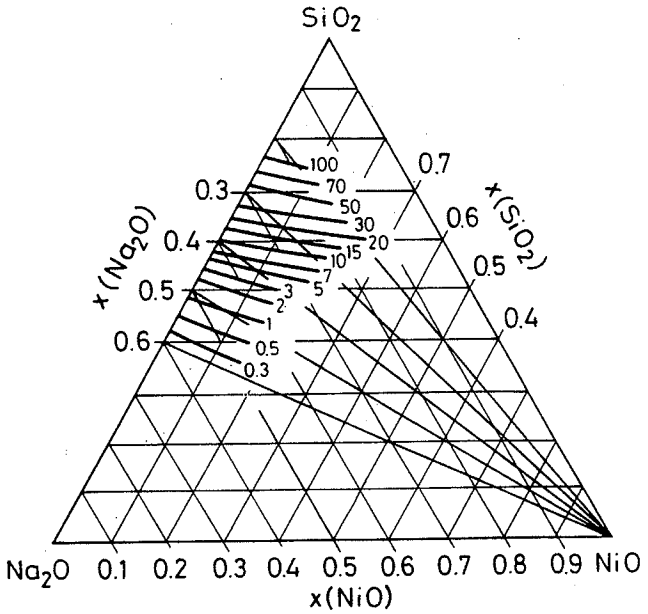


Fig. 9.83. Iso-viscosity (poise = 10^{-1} Pa.s) contours of $Na_2O\text{-}NiO\text{-}SiO_2$ melts at 1400 °C [202]

$Na_2O\text{-}SiO_2\text{-}SrO$

Tab. 9.8. Viscosities of $Na_2O\text{-}SiO_2\text{-}SrO$ melts [176, 177]

Composition, mole fraction			Viscosity (poise) at			Ref.
Na_2O	SiO_2	SrO	1300 °C	1200 °C	1100 °C	
0.2	0.7	0.1	100	252	730	[176]
0.2	0.6	0.2	33	92	300	[176]
0.3	0.6	0.1	29	66	170	[176]
0.18	0.72	0.10	245	600		[177]

$Na_2O\text{-}SiO_2\text{-}TiO_2$

Tab. 9.9. Viscosity of a $Na_2O\text{-}SiO_2\text{-}TiO_2$ melt [178]

Composition, mole fraction			Viscosity (poise) at			
Na_2O	SiO_2	TiO_2	1250 °C	1300 °C	1250 °C	1400 °C
0.35	0.30	0.35	0.65	0.57	0.49	0.43

$Na_2O\text{-}SiO_2\text{-}ZnO$

Tab. 9.10. Viscosities of $Na_2O\text{-}SiO_2\text{-}ZnO$ melts [176]

Composition, mole fraction			Viscosity (poise) at		
Na_2O	SiO_2	ZnO	1400 °C	1300 °C	1200 °C
0.2	0.70	0.10	80	200	520
0.2	0.60	0.10	29	70	193
0.2	0.60	0.10	15	35	90

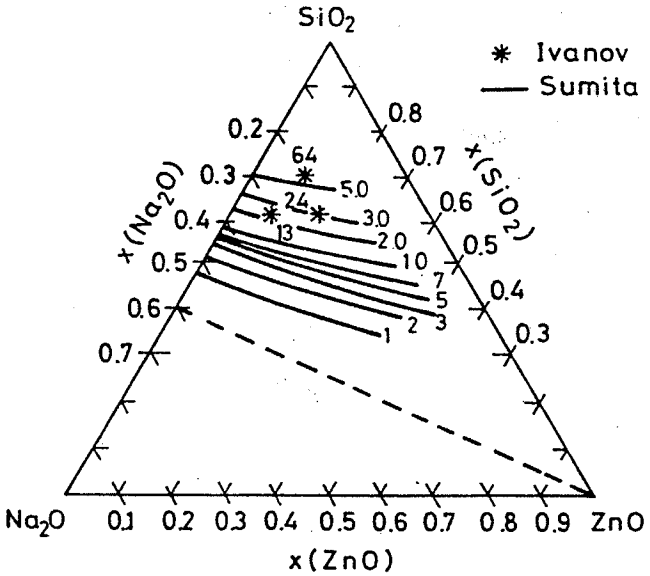


Fig. 9.84. Iso-viscosity (poise = 10^{-1} Pa.s) contours for Na_2O-SiO_2-ZnO melts at 1450 °C [206]

9.5.4 Quaternary systems

Al_2O_3-CaF_2-CaO-MgO

Tab. 9.11. Viscosities of Al_2O_3-CaF_2-CaO-MgO melts

Composition, mass %				Temp.	Viscosity	Ref.
Al_2O_3	CaF_2	CaO	MgO	°C	(poise)	
20.8	35.7	36.2	6.2	1400	0.7	[227]
20.2	32.8	34.1	12.1	1400	1.0	[227]
44	15.1	25.3	14.4	1600	0.4	[93]

Al_2O_3-CaF_2-CaO-MnO

Tab. 9.12. Viscosities of Al_2O_3-CaF_2-CaO-MnO melts

Composition, mass %				Temp.	Viscosity	Ref.
Al_2O_3	CaF_2	CaO	MnO	°C	(poise)	
28	32	40	0.2	1600	0.45-0.65	[138]
21.2	25.2	37	6.1	1400	1	[227]
18.8	30.3	31.6	17.9	1400	1.3	[227]

Al_2O_3-CaF_2-CaO-SiO_2

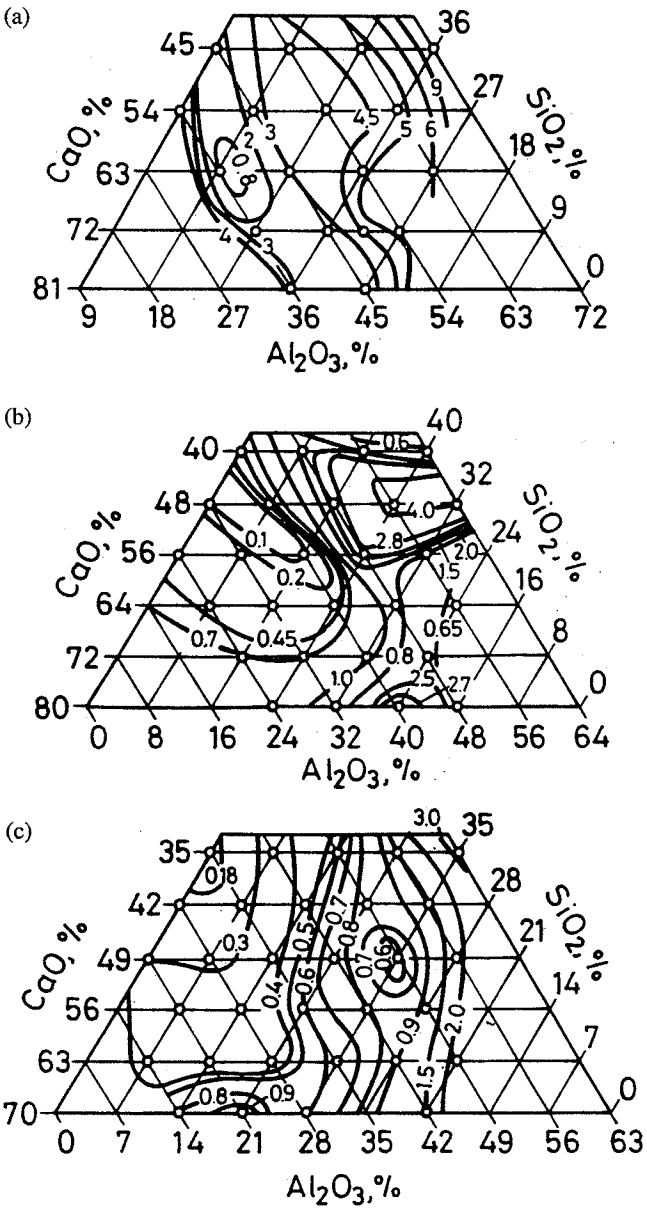


Fig. 9.85 a-c. Iso-viscosity (poise = 10^{-1} Pa.s) contours at 1600 °C for Al_2O_3-CaO-CaF_2-SiO_2 melts containing (a) 10 % CaF_2, (b) 20 % CaF_2, (c) 30 % CaF_2 [214]

Tab. 9.13. Viscosities reported for Al_2O_3-CaF_2-CaO-SiO_2 melts [23]. Further Ref. [155, 224-236]. Values estimated by Riboud (R) and Urbain (U) models

Ref.	Composition, %						Estimated η (poise)	
	Al_2O_3	CaF_2	CaO	SiO_2	T °C	η (poise)	R	U
Muratov [139]	15	40	40	5	1600	0.32		
	10	40	40	10	1600	0.35		
	5	40	40	15	1600	0.45	0.07	0.61
Toporishchev [216]	10.4	50.0	17.1	19.1	1550	0.32	0.01	1.0
	10.0	53.3	14.5	18.6	1550	0.29		
	13.6	50.3	6.7	25.0	1550	0.6		
	21.1	40.0	18.2	13.0	1550	0.45		
	14.4	36.8	10.8	34.4	1550	1.1	0.35	2.35
	13.2	46.3	18.2	20.5	1550	0.45		
	10.8	50.0	16.8	18.8	1550	0.35		
Kato [157]	20.5	7.9	34.6	37.0	1400	2.4	13	17.6
	18.5	16.7	31.3	33.5	1400	0.9		
	15.0	32.6	25.3	27.1	1400	0.17	0.35	4.2
Khlynov [217]	28.4	69	1.5	1.3	1600	0.15	–	0.65
Zhmoidin [138]	27.4	31.4	39.2	2	1600	0.5		
	26.7	30.5	38.1	5	1600	0.5		
	25.5	29.1	36.4	10	1600	0.5	0.04	1.3
	24.3	27.8	34.8	15	1600	0.75	0.07	1.6
Michel [218]	19.2	4.0	36.5	40.3	1300	23.9	56	59
	18.0	10.0	34.2	37.8	1300	9.5		
Yavoiskii [219]	28.0	69.0	1.4	1.0	1600	0.4	0.007	0.64
	40.6	26.2	30.6	3.2	1600	1.0		
	10	23	16	30	1600	0.6	0.47	2.0
	7	17	19	42	1550	3.1		
	40	15	10	24	1600	2.1	0.6	7.5
	41	7.5	49	2.5	1600	1.1	0.25	2.8
Evseev [220]	2.3	87.3	2.0	3.7	1500	0.14		
	25.3	60.4	10.5	2.7	1500	0.18	0.002	0.98
Vachugov [221]	28.7	62.8	4.0	1.8	1700	0.22		
	25.0	63.0	6.2	9.3	1700	0.23		
	25.0	60.9	6.6	5.8	1700	0.23		
	29.0	59	4.9	6.1	1700	0.24	0.003	0.64
Smirnov [222]	5.6	14.0	69.9	10.3	1600	0.32		
	3.0	11.2	67.8	17.8	1600	0.20		
	3.0	17.0	66.2	13.7	1600	0.19	0.04	0.80
Churkin [223]	15.1	45.0	34.5	5.4	1600	0.20		
	14.2	41.8	34.0	10.0	1600	0.25		
	12.8	38.1	34.0	15.1	1600	0.28		
	11.8	35.8	33.3	19.1	1600	0.32	0.015	0.88

Al_2O_3-CaF_2-CaO-TiO_2

Additions of up to 12 % TiO_2 to a (28 % Al_2O_3 - 32 % CaF_2 - 40 % CaO) had little effect on the viscosity at 1600 °C = 0.5 poise [138]

Al_2O_3-CaF_2-CaO-V_2O_5

Tab. 9.14. Viscosities of Al_2O_3-CaF_2-CaO-V_2O_5 melts [147]

Composition, mass %				Temp.	Viscosity
Al_2O_3	CaF_2	CaO	V_2O_5	°C	(poise)
20	5	15	60	1100	0.04
20	10	10	60	1100	0.05
20	5	35	40	1600	0.075
20	10	30	40	1500	0.12
20	15	25	40	1100	0.13

Al_2O_3-CaO-CaS-SiO_2

Tab. 9.15. Viscosity values for Al_2O_3-CaO-CaS-SiO_2 melts [52]

Chemical composition, mass %							Viscosity, (poise) at		
SiO_2	Al_2O_3	CaO	MgO	MnO	CaS	CaO/SiO_2	1500 °C	1450 °C	1400 °C
38.3	10.1	48.4	2.0	1.17	–	1.30	3.0	4.6	6.6
38.2	10.0	45.8	2.0	0.78	3.0	–	3.3	4.8	6.6
31.3	19.0	44.7	4.0	0.94	–	1.43	3.8	5.3	–
30.9	18.8	39.4	4.0	0.86	6.1	–	3.2	4.3	9.3
41.0	21.4	37.2	–	–	–	0.91	9.5	15.5	28.1
40.7	21.3	35.4	–	–	1.99	–	12.6	20.3	33.5

Al_2O_3-CaO-Cr_2O_3-SiO_2

Tab. 9.16. Viscosity values for Al_2O_3-CaO-Cr_2O_3-SiO_2 melts [157]

Composition, mass %				Viscosity, poise at	
Al_2O_3	CaO	Cr_2O_3	SiO_2	1400 °C	1500 °C
21.9	36.7	1.7	39.5	11	4.5
21.4	36.3	3.4	38.9		6.2
20.9	35.4	5.9	37.9		5.6

Al_2O_3-CaO-Fe_xO-SiO_2

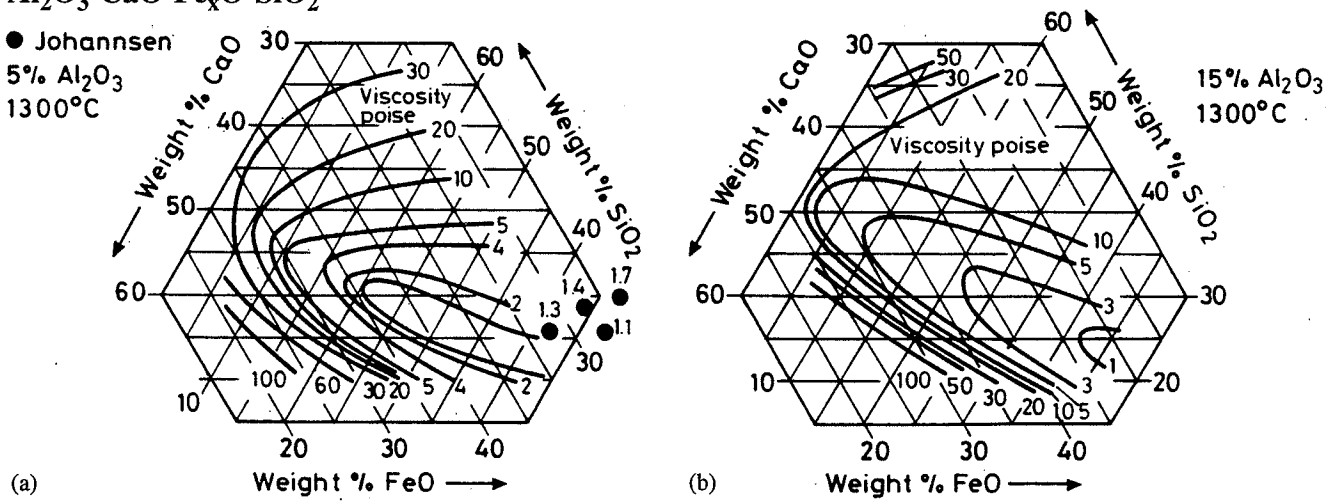


Fig. 9.86 a,b. Iso-viscosity (poise = 10^{-1} Pa.s) contours at 1300 °C for Al_2O_3-CaO-FeO-SiO_2 melts containing (a) 5 and (b) 15 mass % Al_2O_3 [228, 188]. Further Ref. [157]

Tab. 9.17. Viscosities reported for $Al_2O_3 + CaO + Fe_xO + SiO_2$ system

References	Composition, mass %				Viscosity (poise) at T °C Experimentally						Estimated
	Al_2O_3	CaO	Fe_xO	SiO_2	1250	1300	1400	1500	1600	1700	R , U
Kolesov [229]	7.3	22.4	19.2	38.1	12.7						
	3.7	5.4	65.4	20.3	1.1						
	5.5	9.2	51.1	31.5	1.9						8.7 , 10.8
	4.8	9.2	56.1	31.4	2.2						
	2.7	3.7	59.0	20.0	1.1						
	4.5	1.4	65.0	25.1	1.6	1.1					
	5.2	2.6	56.5	28.0	1.6	1.1					
	5.8	2.7	61.1	29.7	1.6	0.6					
	4.4	1.4	59.6	26.5	1.2	0.3					
	3.9	1.7	58.0	27.0	2.2	1.1					
	5.6	1.6	39.6	39.6	7.0	5.5					
	4.9	6.7	41.0	35.1	3.6	2.4					17 , 24
	7.0	17.4	44.6	26.6	2.0	1.7					
Izchanov [189]	10.2	1.9	47.8	39.7	10	4					
	10.5	5.8	44.6	40.3	19	8					(1300)
	10.4	9.9	40.2	39.8	40	17					34 , 39
	10.7	3.8	41.2	44.8	18	9					
	11.2	9.8	35.8	43.7	35	15					(1300)
	11.3	3.8	35.6	49.5	44	28					65 , 80
	11.0	9.9	30.4	50.9	88	45					
	11.1	3.9	31.3	54.8	60	40					(1300)
	11.4	10.2	25.0	54.7	190	115					143 , 232
Nurkeev [230]	26.6	14.6	4.6	52.2						60	(1700)
	26.1	16.5	4.5	51.1					140	48	58 , 74
	25.5	18.2	4.4	49.5					100	42	
	25.0	19.9	4.3	49.0					57		(1600)
	24.5	21.5	4.2	48.0					42		31 , 38
	23.9	23.6	4.1	46.8					22		(1600)
	23.3	25.5	4.0	45.6					18		19 , 24
Sheludyakov [175]	21.7	15.5	12.0	50.8			400				66 , 64
	18.5	13.2	25.0	43.3			45				
Kurochkin [231]	3.3	13.1	29.9	54.3		26					
	3.3	18.4	20.3	57.4		24					
	3.7	29.2	16.7	48.6		24					(1400)
	13.2	12.6	25.2	48.5			28	24			63 , 87
	12.6	17.1	19.9	50.6			41	32			(1400)
	11.6	20.6	14.8	52.6			32	29			68 , 100
	16.9	23.9	11.8	46.7			13	6			
	19.6	16.4	7.8	57.8			35	19			(1500)
	22.0	21.8	6.4	48.9			30	20			64 , 73
Johannsen [188]	4.6	4.5	54.7	34.2	2.8	2.0	1.2				(1400)
	4.1	8.1	50.6	35.2	3.3	2.5	1.3				4.1 , 5.4
	4.9	4.5	56.3	31.0	1.8	1.4	0.9				
	5.2	7.4	52.9	31.7	2.1	1.6	1.1				
	5.0	3.3	59.9	28.6	1.4	1.0	0.8				
	5.1	6.4	55.7	29.7	1.6	1.2	0.9				
	5.3	4.5	56.6	31.1	1.8	1.3	0.9				
	5.1	7.4	53.0	32.7	1.8	1.4	1.0				
	5.0	3.8	59.1	30.8	1.4	1.1	6.8				(1400)
	5.6	7.0	54.0	30.9	–	1.3	0.9				3 , 4

(a) R, U, Estimated by Riboud and Urbain methods respectively

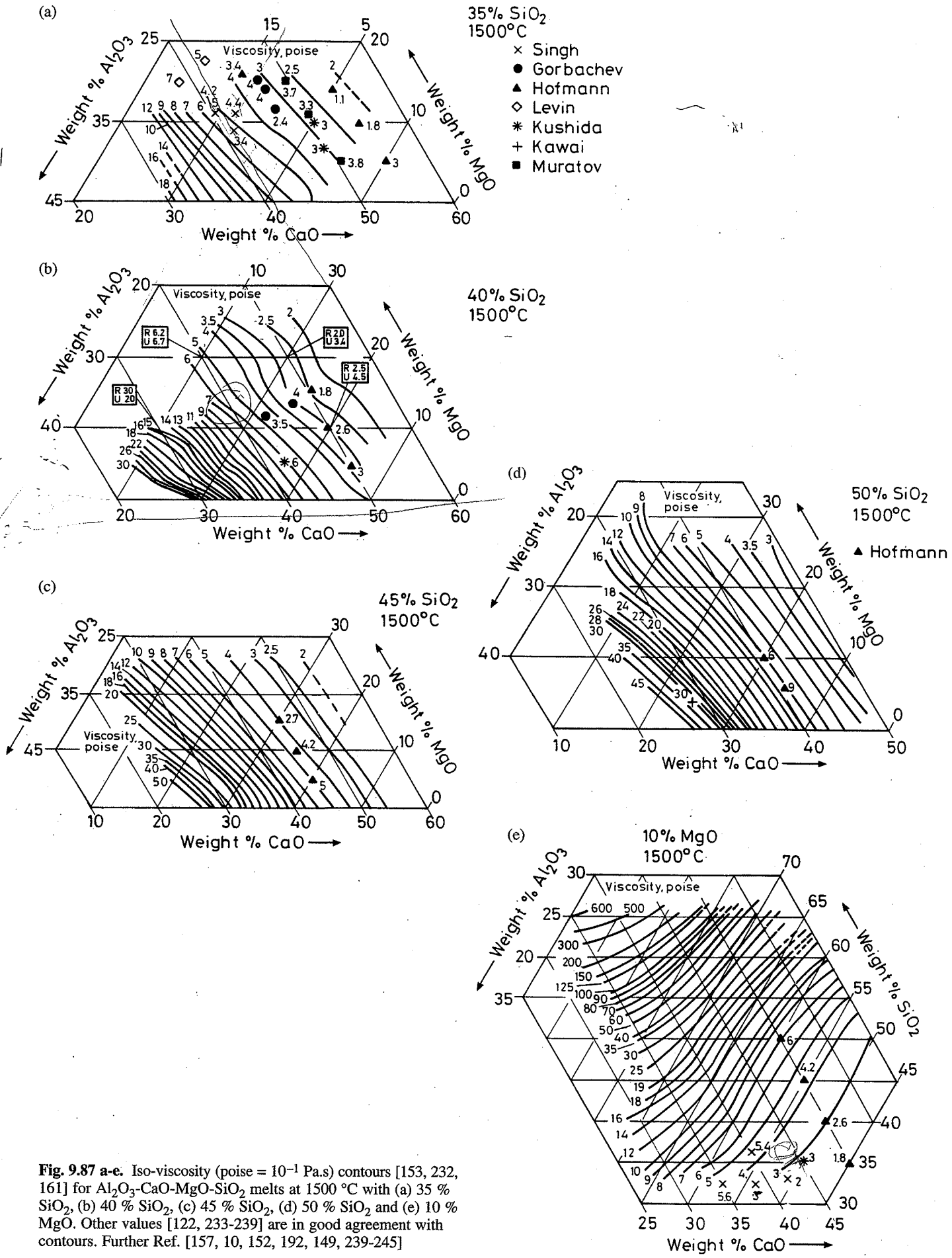


Fig. 9.87 a-e. Iso-viscosity (poise = 10^{-1} Pa.s) contours [153, 232, 161] for Al_2O_3-CaO-MgO-SiO_2 melts at 1500 °C with (a) 35 % SiO_2, (b) 40 % SiO_2, (c) 45 % SiO_2, (d) 50 % SiO_2 and (e) 10 % MgO. Other values [122, 233-239] are in good agreement with contours. Further Ref. [157, 10, 152, 192, 149, 239-245]

Al_2O_3-CaO-MnO-SiO_2

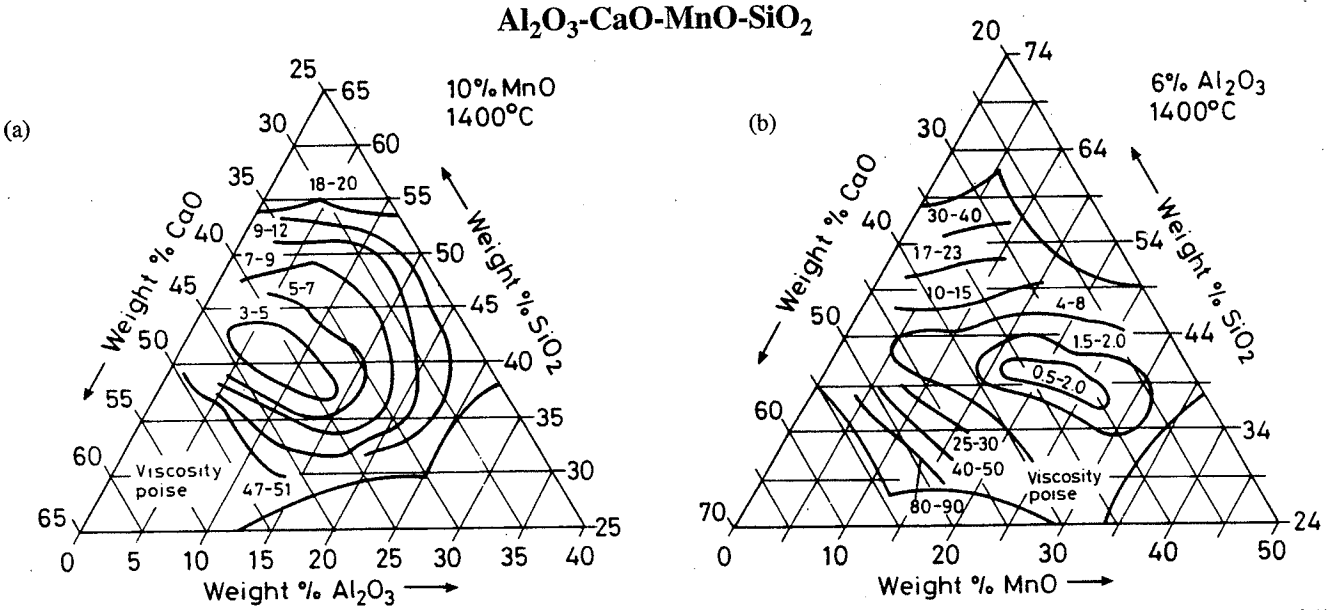


Fig. 9.88 a,b. Iso-viscosity (poise = 10^{-1} Pa.s) contours for Al_2O_3-CaO-MnO-SiO_2 melts at 1400 °C [246] with (a) 10 % MnO, (b) 6 % Al_2O_3. Further Ref. [156, 157, 184, 247, 248]

Al_2O_3-CaO-Na_2O-SiO_2

Tab. 9.18. Viscosities of Al_2O_3-CaO-Na_2O-SiO_2 melts [249, 250]

Composition, mass %				Viscosity (poise) at				Ref.
Al_2O_3	CaO	Na_2O	SiO_2	1500 °C	1600 °C	1650 °C	1700 °C	
21.6	3.8	9.1	65.5	8000	1500	–	–	[249]
27.0	10.0	5.4	57.6	900	250	–	–	[249]
31.2	15.2	2.8	50.8	300	100	–	–	[249]
28.6	10.0	7.3	54.1	980	340	195	–	[250]
28.6	10.8	5.5	55.1	1000	300	–	120	[250]

Al_2O_3-CaO-SiO_2-TiO_2

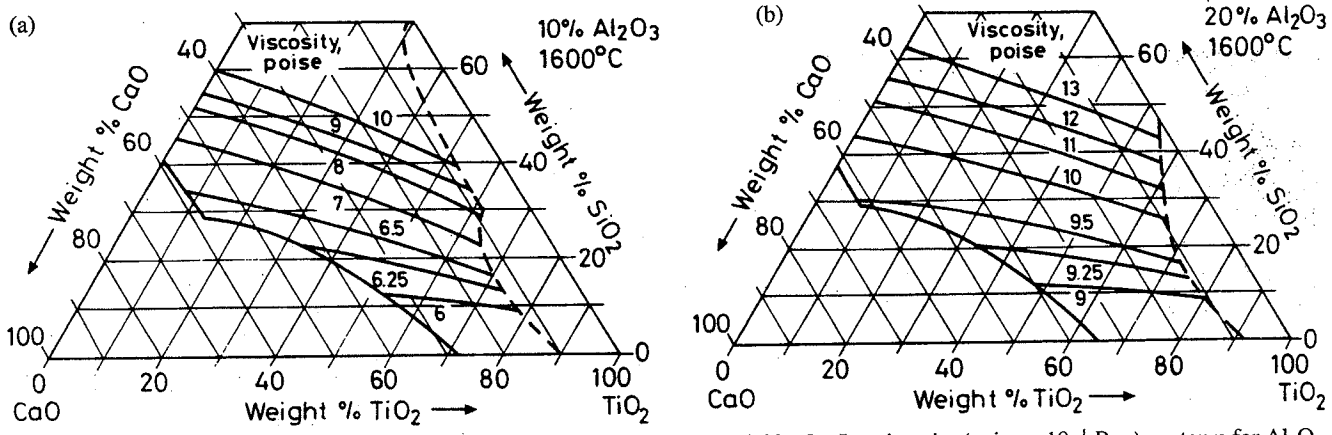


Fig. 9.89 a,b. Iso-viscosity (poise = 10^{-1} Pa.s) contours for Al_2O_3-CaO-SiO_2-TiO_2 melts [174] at 1600 °C for (a) 10 % Al_2O_3, (b) 20 % Al_2O_3. Further Ref. [152, 157]

Al_2O_3-Cr_2O_3-MgO-SiO_2

Tab. 9.19. Viscosities (poise = 10^{-1} Pa.s) of Al_2O_3-Cr_2O_3-MgO-SiO_2 melts [167]

Composition, mass %				Viscosity (poise) at		
Al_2O_3	Cr_2O_3	MgO	SiO_2	1650 °C	1700 °C	1800 °C
21.8	6.5	30.9	41.3	2.3	1.7	1.0
19.4	0.3	28.3	40.2	–	1.4	0.7

$CaO\text{-}Fe_xO\text{-}MgO\text{-}SiO_2$

Tab. 9.20. Viscosities of Al_2O_3-FeO_x-MgO-SiO_2 melts

Reference	Composition, mass %					Viscosity (poise) at		
	CaO	FeO	Fe_2O_3	MgO	SiO_2	1300 °C	1350 °C	1400 °C
Williams [113]	2.1	57.2	2.7	5.9	32.1	2.5	1.83	1.7
	2.1	54.5	2.6	7.5	32.9	3.6	1.40	1.05
	15.0	49.7	3.8	6.1	25.8	0.95	0.84	0.76
Bodnar [111 or 187]	9.3	50.1	13.1	3.0	24.6	2.5	–	–
	11.3	46.4	10.9	3.0	28.5	4.5	–	2.8
	10.9	45.1	10.6	5.7	27.7	9.5	–	4.8
	10.6	43.9	10.3	8.3	27.0	19	–	16
	11.8	42.1	7.4	2.8	35.9	1.3	–	–
	11.5	41.0	7.8	5.5	34.9	3.8	–	–
	11.2	39.9	7.0	8.0	34.0	8.0	–	–

$CaO\text{-}Fe_xO\text{-}MnO\text{-}SiO_2$

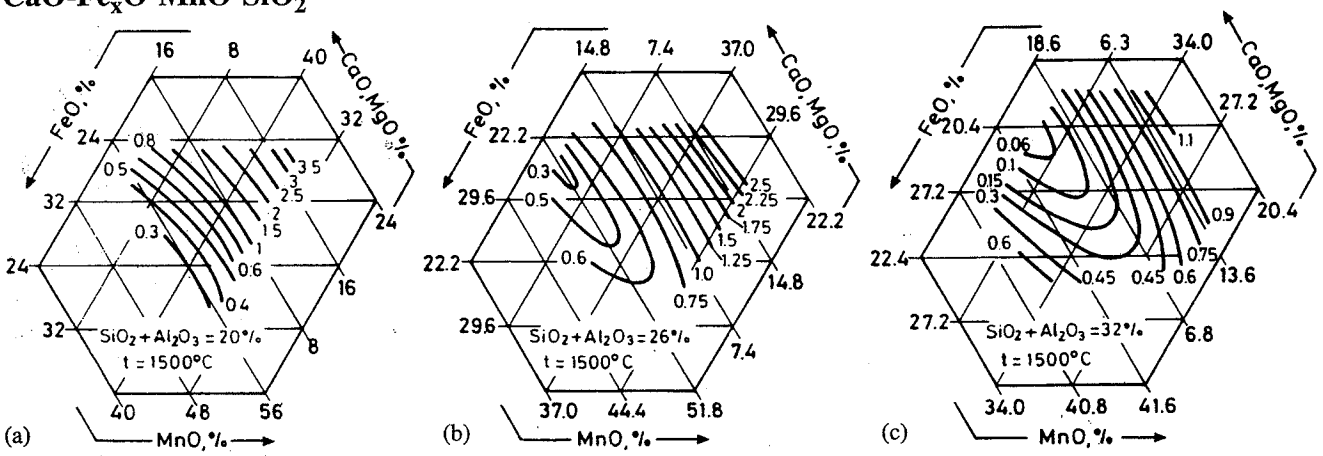


Fig. 9.90 a-c. Iso-viscosity (poise = 10^{-1} Pa.s) contours at 1500 °C for CaO-Fe_xO-MnO-SiO_2 melts containing 2 % Al_2O_3 for (SiO_2 + Al_2O_3) contents of (a) 20 %, (b) 25 %, (c) 32 % [251]. Further Ref. [16]

$CaO\text{-}MgO\text{-}MnO\text{-}SiO_2$

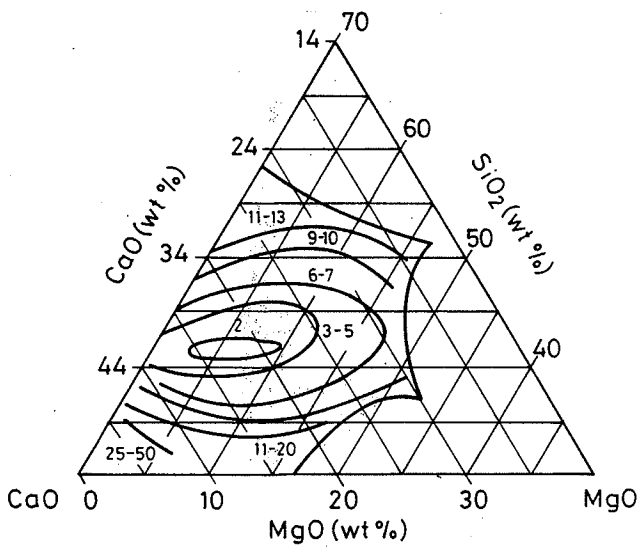


Fig. 9.91. Iso-viscosity (poise = 10^{-1} Pa.s) contours for CaO-MgO-MnO-SiO_2 melts with 10 % MnO at 1440 °C [246]

$CaO\text{-}MnO\text{-}P_2O_5\text{-}SiO_2$

Tab. 9.21. Viscosities of CaO-MnO-P_2O_5-SiO_2 [195]

Mass % (normalised)				Viscosity (poise) at		
CaO	MnO	P_2O_5	SiO_2	1300 °C	1400 °C	1500 °C
9.4	58.8	2.9	31.8	19.8	10.7	6.1
10.1	64.1	3.0	28.0	8.5	4.9	3.0
14.7	49.1	3.4	36.0	9.5	5.0	2.7
15.5	54.8	3.4	30.3	6.5	3.8	2.3
21.2	44.4	3.2	33.4	5.9	3.4	2.0
26.3	42.5	2.9	31.2	8.0	3.4	1.6

9.5.5 Systems with five and more components

Al_2O_3-CaF_2-CaO-MgO-SiO_2

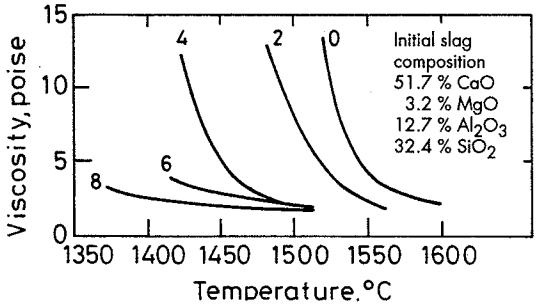


Fig. 9.92. Viscosities of Al_2O_3-CaF_2-CaO-MgO-SiO_2 melts with varying % CaF_2 as a function of temperature [161]. Further Ref. [68, 43, 217, 251]

Al_2O_3-CaO-FeO-MgO-SiO_2

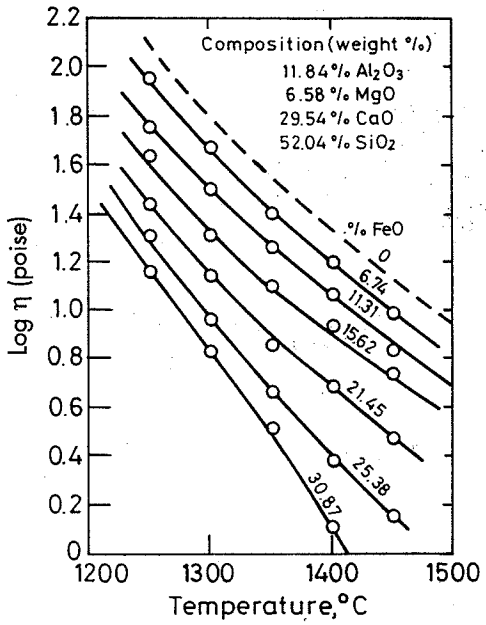


Fig. 9.93. Viscosities of Al_2O_3-CaO-FeO-MgO-SiO_2 melts with varying % FeO as a function of temperature [155]

Al_2O_3-CaO-CaS-MgO-MnO-SiO_2

Tab. 9.22. Viscosities in the system Al_2O_3-CaO-CaS-MgO-MnO-SiO_2 [243]

Chemical composition, mass %						Viscosity, (poise) at		
Al_2O_3	CaO	CaS	MgO	MnO	SiO_2	1500 °C	1450 °C	1400 °C
10.1	48.4	–	2.0	1.17	38.3	3.0	4.6	6.6
10.0	45.8	3.0	2.0	0.78	38.2	3.3	4.8	6.6
19.0	44.7	–	4.0	0.94	31.2	3.8	5.3	–
18.8	39.4	6.1	4.0	0.86	30.9	3.2	4.3	9.3
21.4	37.2	–	–	–	41.0	9.5	15.5	28.1
21.3	35.4	1.99	–	–	40.7	12.6	20.3	33.5

Al_2O_3-CaO-FeO-MgO-SiO_2

Tab. 9.23. Viscosities reported for the Al_2O_3-CaO-FeO-MgO-SiO_2 melts [252, 253]. Further Ref. [10, 161, 254, 255]

Composition, mass %					Viscosity (poise)				Ref.
Al_2O_3	CaO	FeO	MgO	SiO_2	1300 °C	1400 °C	1500 °C	1600 °C	
17.3	15.0	10.8	8.0	48.6	–	45	31	26	[252]
16.8	35.8	12.1	8.4	26.4	27.5	14.5	8.5	7	
10.4	30.2	10.3	8.9	50.8	–	54	33.5	25	
9.7	39.1	11.4	8.7	31.7	–	62.5	14.5	60	
18.9	19.8	4.4	8.2	48.3	49	29	21.5	17	
17.5	37.4	4.8	8.7	31.5	47.5	30.5	23	19	
9.7	28.8	4.2	9.1	47.7	40	25.5	18.5	15	
10.7	48.5	4.8	7.8	28.7	–	18.5	9.5	6	
16.3	27.3	7.1	8.3	41.2	–	5.8	29	20.5	
15.8	24.4	6.8	7.9	45.6	46.5	24.5	19.5	14	
14.9	19.9	7.1	7.1	50.3	–	–	51.5	37.5	
21.7	15.5	12.0	–	50.8	1350 °– 490	–			[253]
18.5	13.2	25.0	–	43.3	186	45			
22.5	16.1	2.8	6.0	52.6	–	255			
21.1	15.1	2.6	12.0	49.2	205	46			
20.4	14.5	2.5	15.0	47.6	122	31			
21.8	15.6	5.6	6.0	51.0	–	175			
20.4	14.6	5.2	12.0	47.8	110	33			
19.7	14.1	5.1	15.0	46.1	72	28			
22.2	15.9	6.9	1.0	52.0	–	166			
21.1	15.1	8.5	6.0	49.3	323	83			
19.1	13.6	7.7	15.0	44.6	58	22			

Al_2O_3-CaO-MgO-MnO-SiO_2

Tab. 9.24. Viscosities for blast furnace type slags from Al_2O_3-CaO-MgO-MnO-SiO_2 system [256, 257]; ( ) values estimated using Riboud and Urbain II model, respectively

	Composition, mass %					Viscosity (poise) at				Ref.
	Al_2O_3	CaO	MgO	MnO	SiO_2	1400 °C	1450 °C	1500 °C	1600 °C	
1	6.5	31.2	6.0	15.3	40.3	5.9 (4.5, 7.5)	4.6	4.1 (2.6, 4.2)		[256]
2	7.0	32.6	4.8	15.3	39.6	4.3	4.0	3.9		
3	6.4	31.2	5.0	25.3	32.1	4.6 (1.7, 3.9)	4.2	4.0 (1.0, 2.3)		
4	6.4	40.9	5.0	5.0	41.8	4.8 (4.8, 8.2)	4.2	4.0 (2.7, 4.5)		
5	6.0	36.4	5.1	15.5	36.8	4.8	4.3	4.0		
6	6.6	37.3	5.0	15.3	35.1	4.3	3.9	3.7		
7	6.2	37.8	5.1	15.5	35.0	4.1	3.9	3.8		
	10	30	5	10	45	5.0 (17)		2.1 (8.6)	1.4 (4.7)	[257]
	15	30	5	10	40	5.2		2.1	1.6	
	20	30	5	10	35	7.2		2.2	1.7	
	25	30	5	10	30	8.2 (16)		2.4 (8.4)	1.8 (4.6)	
	30	30	5	10	25	9.0		2.6	1.7	
	35	30	5	10	20	12.0 (15)		2.8 (7.6)	1.7 (4.2)	

Al_2O_3-CaO-MgO-SiO_2-TiO_2

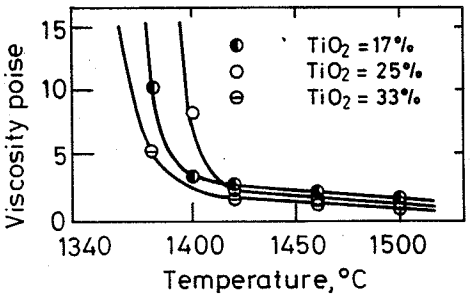


Fig. 9.94. Viscosities of Al_2O_3-CaO-MgO-SiO_2-TiO_2 melts with varying TiO_2 contents as a function of temperature [258]

Tab. 9.25. Viscosities reported for 'blast furnace' type slags of Al_2O_3+CaO-MgO-SiO_2-TiO_2 system [258, 259]. Further Ref. [260, 261]

Composition, mass %						Viscosity (poise) at				
Ref.	Al_2O_3	CaO	MgO	SiO_2	TiO_2	1300 °C	1400 °C	1460 °C	1500 °C	
[258]	15.5	30.8	8.9	27.9	17.0		3.6 (15)	2.2	1.9	(3.0)
	14.0	27.8	8.0	25.2	25.0		8.3 (3.8)	1.7	1.4	(2.3)
	12.5	24.8	7.2	22.5	33.0		–	1.4	1.1	(1.8)
	14.0	23.6	8.0	29.4	25.0	7.5	–	2.6	2.3	
	14.0	27.8	8.0	25.2	25.0		8.3	1.7	1.4	
	14.0	30.9	8.0	22.1	25.0		–	31.1	2.3	
	9.0	30.1	8.7	27.3	25.0		23	1.0	0.9	
	14.0	27.8	8.0	25.2	25.0		8.3	1.7	1.4	
	19.0	25.5	7.3	23.1	25.0		19.6	1.9	1.7	
	14.0	27.8	8.0	25.2	25.0		8.3	1.7	1.4	
	14.0	23.8	12.0	25.2	25.0	59.5		1.4	1.2	
	14.0	19.8	16.0	25.2	25.0	10.1		1.2	1.1	
	14.0	23.6	8.0	29.4	25.0	7.5		2.6	2.3	
	14.0	19.8	16.0	25.2	25.0	10.1		1.2	1.1	
	14.0	27.8	8.0	25.2	25.0		8.3	1.7	1.4	
	14.0	23.6	16.0	21.4	25.0		35.3	1.3	1.2	
[259]	11.2	18.7	18.7	26.7	24.8				0.9	(1.5)
	13.8	17.6	17.6	20.8	30.2				0.8	
	13.8	21.8	10.9	23.3	30.2				0.72	
	13.8	16.3	16.3	23.3	30.2				0.66	
	13.8	10.9	21.8	23.3	30.2				1.32	(1.2)
	13.8	12.5	12.5	31.1	30.2				1.8	
	16.8	12.4	13.4	19.2	37.2				0.8	(1.4)

( ) Estimated using Urbain III model; Riboud model gives high values

9.5.6 Iron and steelmaking slags

9.5.6.1 Blast furnace slags

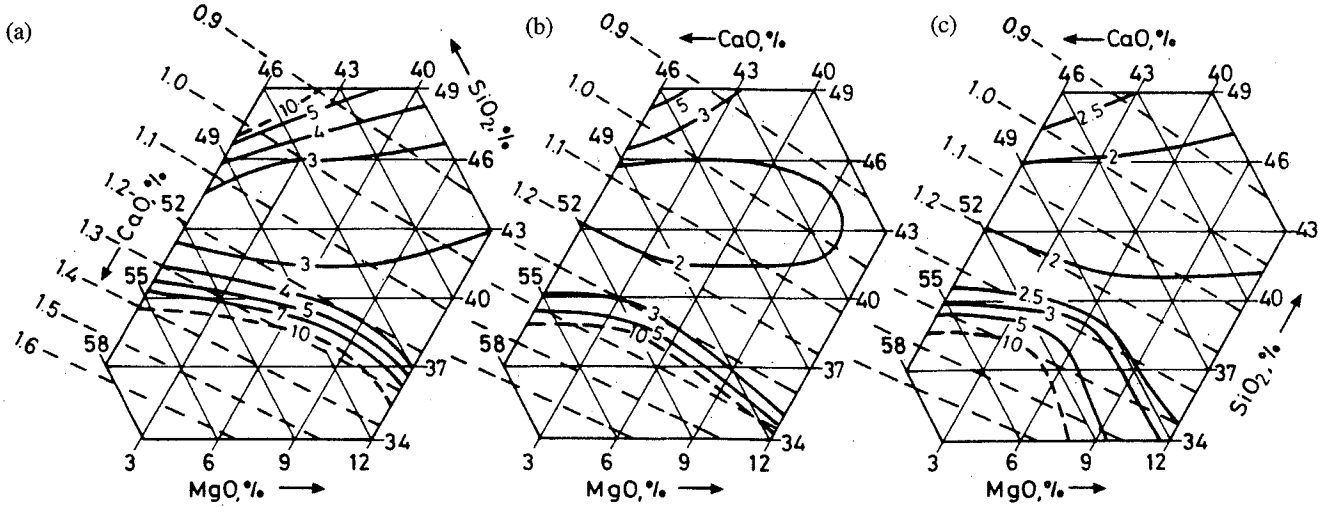


Fig. 9.95 a-c. Iso-viscosity (poise = 10^{-1} Pa.s) contours for blast furnace slags [262] CaO-MgO-SiO_2-5 % Al_2O_3-2% S-1 % MnO-0.5 % K_2O at (a) 1400, (b) 1450, (c) 1500 °C; - - -, ratio (% CaO / % SiO_2). Further Ref. [263]

Tab. 9.26. Viscosities of blast furnace type, synthetic slags containing various amounts of MgO and Al_2O_3 [264]

Slag No.		Slag composition, weight %				Viscosity (poise) at				
		CaO	SiO_2	MgO	Al_2O_3	1500 °C	1450 °C	1400 °C	1350 °C	1300 °C
I	30	44.05	48.95	3.0	4.0	5.6	7.7	9.7	12.4	–
	31	46.5	46.5	3.0	4.0	6.3 (3.3, 4.8)	7.5	9.6	12.0	–
	32	48.7	44.3	3.0	4.0	7.0	9.2	11.3	15.0	–
	33	50.7	42.3	3.0	4.0	5.9	8.1	10.0	15.2	32.9
	34	52.5	40.5	3.0	4.0	4.9 (1.6, 3.4)	9.1	16.9	29.0	–
II	1	37.8	47.2	9.5	5.5	6.8	9.1	10.9	13.7	18.5
	2	40.25	44.75	9.5	5.5	6.5	8.7	11.1	13.9	18.4
	3	42.5	42.5	9.5	5.5	7.5	9.1	10.9	13.4	16.3
	4	44.5	40.5	9.5	5.5	8.2	9.0	10.2	16.3	40.0
III	5	36.65	45.85	11.0	6.5	6.1 (3.4, 4.8)	7.6	9.7	12.7	17.2
	6	39.1	43.4	11.0	6.5	5.0	6.4	8.3	10.6	14.3
	7	41.25	41.25	11.0	6.5	5.6	6.8	8.6	10.5	13.4
	8	43.2	39.3	11.0	6.5	4.5 (1.6, 3.2)	5.1	6.3	14.0	–
IV	135	32.5	46.5	13.0	8.0	6.0	7.4	9.7	12.7	18.1
	9	35.1	43.9	13.0	8.0	5.6	7.2	10.6	12.7	19.0
	10	37.4	41.6	13.0	8.0	4.8	6.8	10.7	14.0	21.9
	11	39.5	39.5	13.0	8.0	5.2	6.9	8.7	11.0	–
	12	41.4	37.6	13.0	8.0	4.2	5.0	6.3	23.0	–
	13	43.1	35.9	13.0	8.0	3.1	4.3	11.4	33.9	–
V	142	28.0	48.0	15.0	9.0	6.4 (5.3, 6.4)	6.7	9.4	11.7	15.6
	14	33.8	42.2	15.0	9.0	5.0	6.0	7.2	9.7	4.1
	15	36.0	10.0	15.0	9.0	4.6	6.2	8.0	10.0	–
	16	38.0	38.0	15.0	9.0	4.4	4.7	5.9	9.1	26.3
	17	39.8	36.2	15.0	9.0	4.2	5.6	8.8	–	–
	18	41.5	34.5	15.0	9.0	4.7 (1.1, 2.8)	17.4	–	–	–
VI	140	26.5	44.5	18.0	11.0	4.2	6.4	12.7	16.8	24.1
	19	29.25	41.75	18.0	11.0	6.7	8.1	9.7	12.1	17.5
	137	31.5	32.5	18.0	11.0	4.6	6.3	8.5	10.7	14.6
	220	33.65	37.35	18.0	11.0	5.4	6.7	8.9	11.2	40
	121	35.5	35.5	18.0	11.0	4.1	5.1	6.7	8.0	41
	122	37.2	33.8	18.0	11.0	5.3	4.8	7.1	13.7	40.5
	123	40.15	30.05	18.0	11.0		7.6	32.0	–	–
VII	143	22.6	45.4	20.0	12.0	5.4 (4.8, 5.8)	7.5	9.9	14.7	29.6
	141	25.5	42.5	20.0	12.0	4.1	6.0	9.2	11.4	16.5
	24	28.0	40.0	20.0	12.0	4.5	5.9	6.3	8.3	12.1
	138	30.0	38.0	20.0	12.0	4.3	5.6	8.6	11.0	30.0
	25	32.2	35.8	20.0	12.0	6.0	7.5	10.3	20.5	–
	26	34.1	34.0	20.0	12.0	4.6	5.9	7.6	21.4	–
	128	37.1	30.9	20.0	12.0	4.4 (0.9, 2.5)	4.7	10.8	22.3	–
	129	38.4	29.6	20.0	12.0					

( ) = (Riboud, Urbain II) estimated values

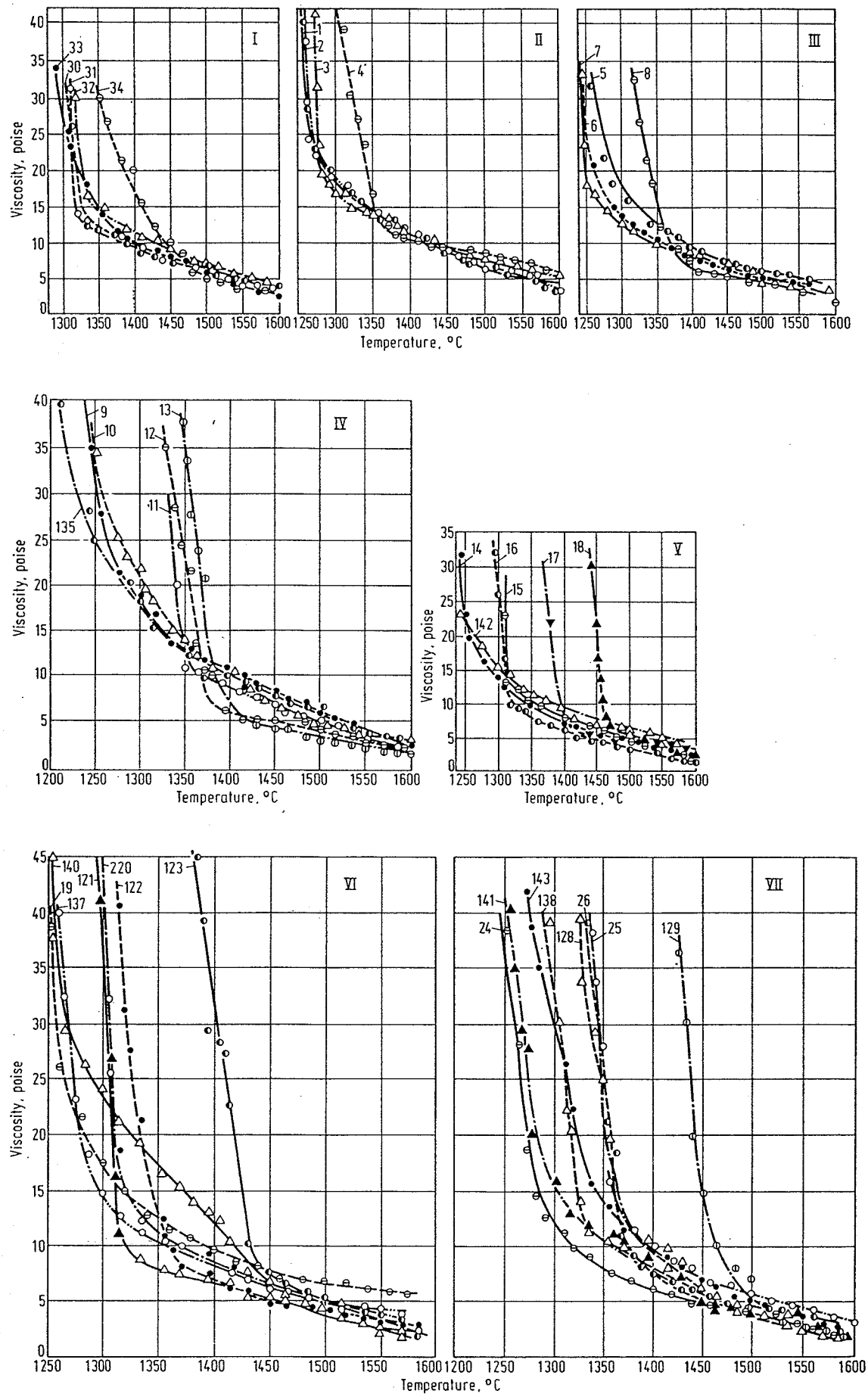


Fig. 9.96 (I-VII). Temperature dependence of viscosity of blast furnace type synthetic slags according to Tab. 9.26

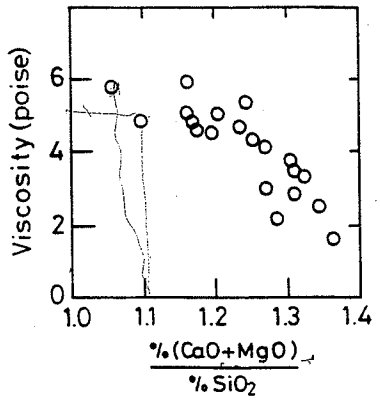
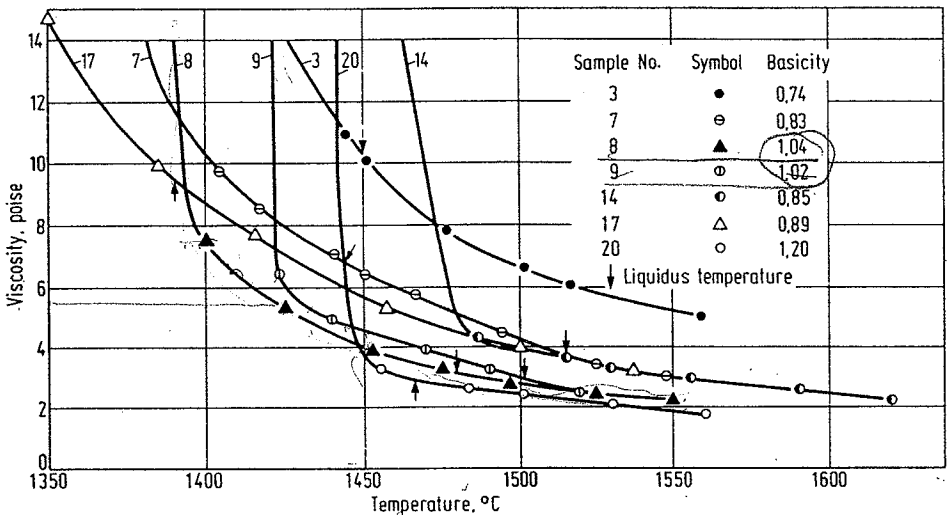


Fig. 9.97. The effect of [(% CaO + % MgO / % SiO_2] on viscosities of high Al_2O_3 blast furnace slags [233]. Further Ref. [265, 236]



Slag No.	Slag composition mass % Al_2O_3	CaO	MgO	FeO	MnO	SiO_2	S	$\frac{CaO + MgO}{SiO_2 + Al_2O_3}$	Liquidus Temp. °C
3	26.1	35.5	6.4	0.4	0.3	30.4	1.4	0.74	1450
7	18.7	40.6	3.4	0.7	-	31.1	0.97	0.83	1435
8	13.5	45.2	3.4	0.5	0.4	33.4		1.04	1480
9	15.2	45.1	3.5	0.8	1.3	32.2	-	1.02	1500
14	35.6	44.8	0.6	-	-	17.0	-	0.86	1515
17	15.2	38.5	5.1	1.0	0.7	36.0	0.79	0.89	1390
20	14.8	41.6	11.9	0.3	0.8	29.7	1.4	1.20	1460

Fig. 9.98. Viscosities of blast furnace slags as a function of temperature [236]

9.5.6.1.1 Effect of Al_2O_3 and MgO

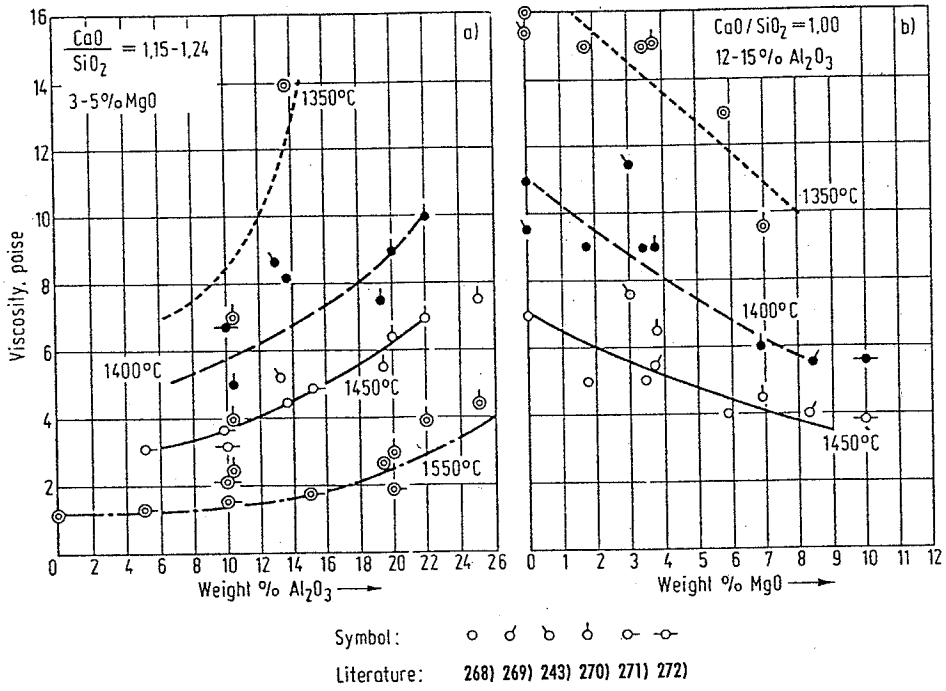


Fig. 9.99 a,b. Effect of Al_2O_3 and MgO on the viscosities of blast furnace slags [267]

9.5.6.1.2 Effect of Ti_2O_3 and TiO_2

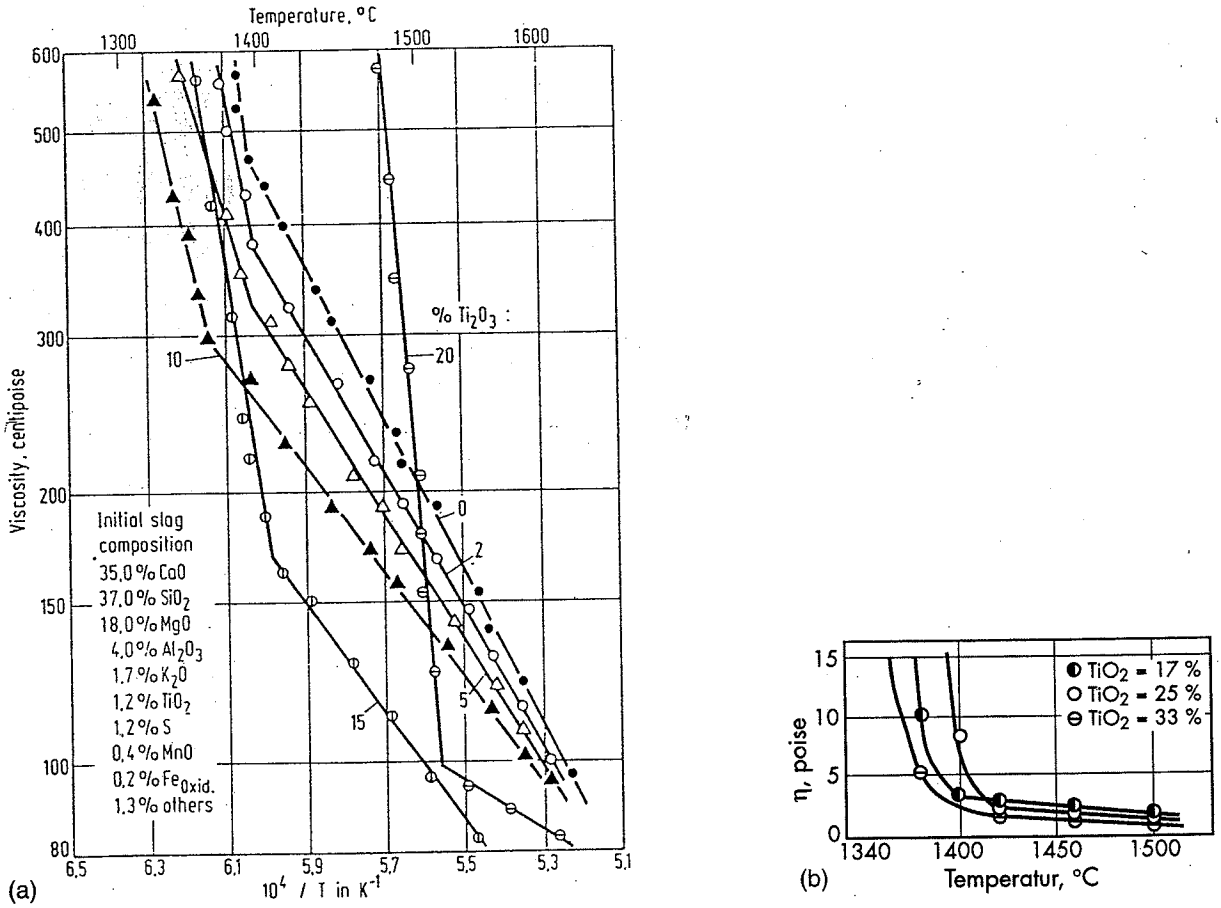


Fig. 9.100 a,b. Effect of (a) Ti_2O_3 [268] and (b) TiO_2 [258] contents on the viscosities of blast furnace slags

Tab. 9.27. Measured values for viscosities (poise = 10^{-1} Pa.s) of a selection of mould fluxes compared with values estimated by Riboud Model [21]. Further Ref. [281-284]

Ref.	Composition, mass %										Viscosity (poise) Expt [Estim]		
	SiO_2	Al_2O_3	CaO	MgO	Na_2O	K_2O	CaF_2 [F]	FeO	MnO	Others	1300 °C	1400 °C	1450 °C
	Continuous Casting Powders												
Lanyi[a]	38.8	9.0	34.8	0.9	4.6	1.2	[6.9]	2.6	0		3.9 [5.1]	2.2 [2.6]	
[275]	39.7	8.1	42.7	0.7	4.5	0.1	[1.5]	0.6	0		6.4 [8.4]	3.6 [4.2]	
	36.0	1.4	31.1	2.2	9.2	0.1	[4.8]	0.9	9.9		1.05[1.2]	0.75[0.8]	
	40.3	9.2	42.4	1.2	4.8	1.8	[1.8]	0.2	0		8.5 [8.2]	4.7 [4.1]	
McCau-	34.75	10.2	32.7	0.9	10.7	–	7.5	–			4.0 [3.5]	2.3 [1.8]	
ley	31.2	10.4	40.3	0.8	5.7	–	7.6	–			2.8 [2.6]	1.6 [1.4]	
[276]	48.0	10.6	28.6	0.8	6.5	–	3.3	–			28 [39]	13 [17]	
	30.6	10.0	36.2	1.0	10.3	–	7.0	–				1.7 [1.1]	
	39.1	10.4	32.6	0.9	11.3	–	1.7	–			14 [10.2]	7.2 [5.0]	
Mills[a]	40.8	8.7	40.3	1.2	4.4	0.2	[4.8]		–		4.5 [9.5]	2.0 [5.0]	
[277]	40.9	7.0	34.9	1.1	7.6	0.4	[7.2]				3.5 [6.0]	1.9 [3.0]	
	43.1	6.5	36.9	2.5	7.7	0.2	[2.0]				8.0 [10]	3.5 [5.3]	
	37.8	5.7	35.5	2.1	11.8	0.2	[7.0]				1.7 [2.5]	– –	
										Li_2O			
Chang	46.0	12.8	36.6	–	0.5	0.5	0.2	–	–	1.1	19.7		3.6
[278,	44.2	12.3	34.5		0.9	0.4	0.3	–	–	5.0	7.1		2.6
279]	42.4	11.9	35.0		0.7	0.6	5.5	–	–	1.1	7.3		2.8
	39.3	11.1	32.5		0.9	0.5	12.1	–	–	0.9	3.1		1.4
	44.0	12.0	34.8		0.6	4.2	0.3	–	–	1.0	20.1		4.4
	39.9	11.0	32.7		5.1	0.3	8.0	–	–	0.9	2.81		0.8
	Fluxes for Bottom Pouring											1400 °C	1500 °C
Nichols[a]	66.5	11.7	7.5	–	7.5	5.2	[0.1]	1.5	0.2			1910 [348]	789 [137]
[280]	51.0	22.0	12.2	0.5	4.1	4.2	[0.1]	4.4	0.1			598 [266]	139 [92]
	54.1	20.7	11.2	0.3	4.1	2.3	[2.0]	3.8	0.2			397 [285]	171 [100]
	40.5	25.9	3.9	0.8	6.6	4.4	[0.1]	16.5	0.2			220 [132]	76 [45]

[a] Post measurement analysis

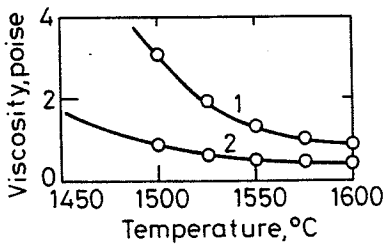


Fig. 9.101. Viscosities of open-hearth slags containing
(1) 3.7 % Al_2O_3 - 40.3 % CaO - 17 % Fe_2O_3 - 9.2 % MgO - 12.8 % MnO - 15.6 % SiO_2
(2) 2.8 % Al_2O_3 - 39.5 % CaO - 29.7 % Fe_2O_3 - 7.3 % MgO - 5.2 % MnO - 13.8 % SiO_2
as a function of temperature [197]. Further Ref. [98, 285]

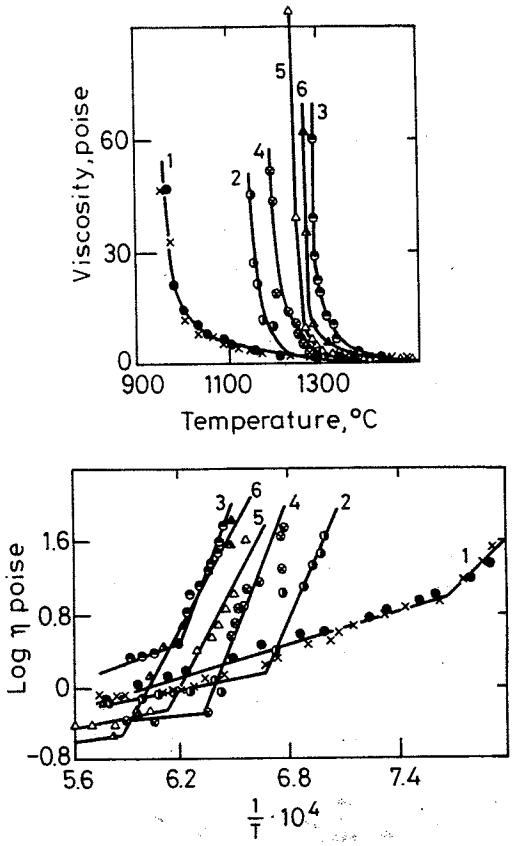
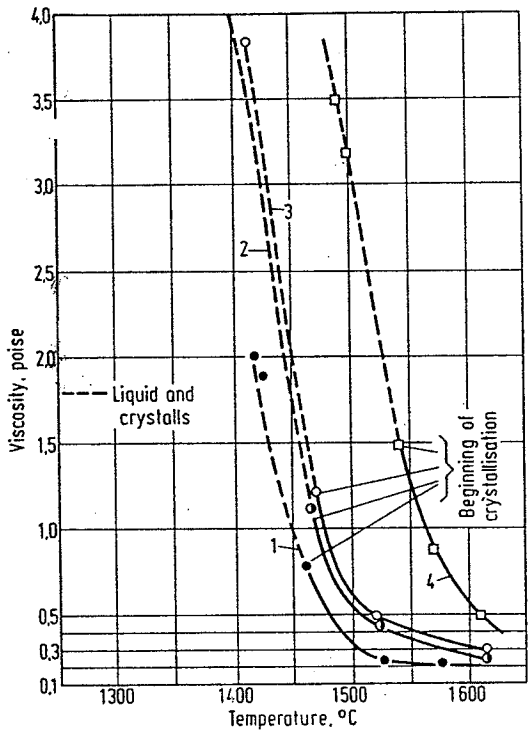


Fig. 9.102. The temperature dependence of viscosity of open-hearth slags



Slag No.	Slag composition, mass %									$\frac{CaO}{SiO_2}$	Viscosity at 1600 °C (poise)		
	FeO	Fe_2O_3	MnO	P_2O_5	Al_2O_3	CaO	MgO	SiO_3	S		Expt	R estimated	U estimated
1	9.8	6.8	8.6	3.2	1.5	49.9	6.5	9.6	0.2	5.2	0.2	0.05	0.4
2	5.7	3.1	9.3	1.4	1.6	47.4	8.3	20.6	0.1	2.3	0.26	0.13	0.69
3	6.1	3.1	13.9	2.2	1.4	46.1	5.6	19.0	0.3	2.4	0.32	0.12	0.64
4	12.7	4.1	10.3	1.8	1.5	41.5	9.8	14.3	0.3	2.9	0.55	0.07	0.47

R = Riboud Model [21]; U = Urbain Model [24]

Fig. 9.103. Viscosities of basic open-hearth slags as a function of temperature [98]

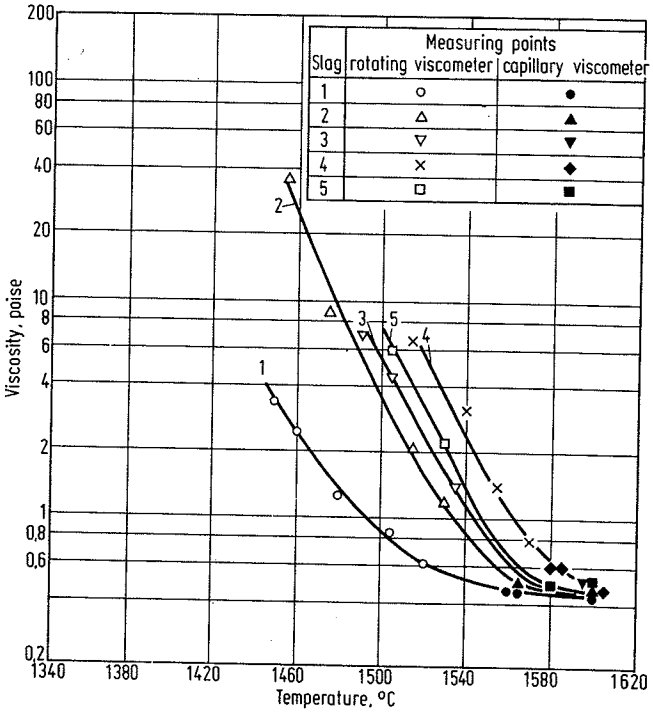


Fig. 9.104. Viscosities of basic open-hearth (finishing) slags as a function of temperature [285]

Slag No.	Slag composition, mass %								$\frac{CaO}{SiO_2}$	Viscosity at 1600 °C (poise)		
	FeO	Fe_2O_3	MnO	P_2O_5	Al_2O_3	CaO	MgO	SiO_2		Expt	R estimated	U estimated
1	16.3	4.8	8.2	3.1	4.6	43.4	6.7	11.9	3.65	0.45	0.08	0.53
2	12.6	3.8	8.4	3.5	4.3	45.7	9.7	11.8	4.71	0.47	0.07	0.52
3	11.5	4.0	7.9	3.5	4.0	47.1	9.4	11.8	3.99	0.48	0.07	0.53
4	9.9	3.4	8.7	3.7	4.5	49.4	6.8	12.7	3.89	0.5	0.08	0.60
5	10.5	2.8	7.6	3.4	5.0	48.9	6.1	15.1	3.24	0.52	0.11	0.7

R = Riboud Model [21]; U = Urbain Model [24]

9.5.6.4 Oxygen steelmaking slags

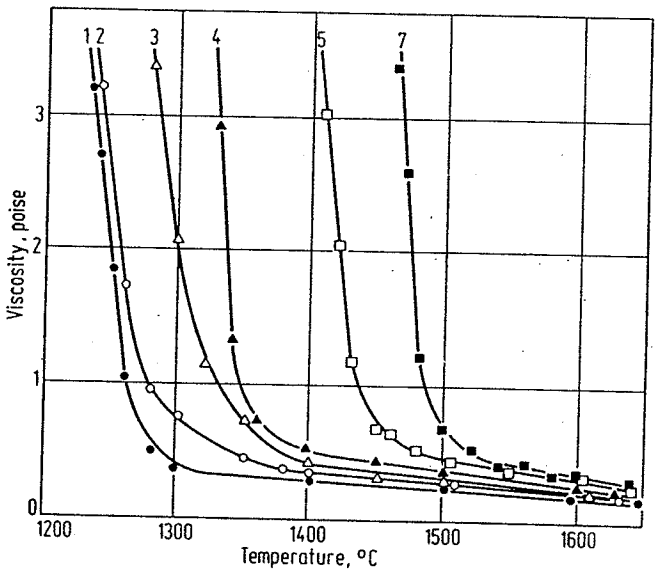


Fig. 9.105. Temperature dependence of the viscosity of LD slags at various stages in the process [287]

Time min	Slag No.	Slag composition, mass %									$\frac{CaO}{SiO_2}$
		FeO	Fe_2O_3	MnO	P	Al_2O_3	CaO	MgO	SiO_2	S	
3.00	1	7.1	1.1	24.5	0.71	0.69	32.85	1.8	31.05	0.2	1.06
5.92	2	6.83	2.42	20.68	0.94	0.82	35.33	2.2	30.61	0.72	1.15
8.97	3	6.52	2.34	7.84	1.78	0.98	39.75	2.34	29.25	0.19	1.36
11.87	4	8.20	3.80	15.20	1.21	1.00	40.50	2.80	26.63	0.16	1.52
14.82	5	7.65	4.94	12.58	1.27	0.84	46.10	3.32	23.25	0.15	1.98
19.02	7	15.06	2.41	18.67	0.92	1.37	29.81	2.31	29.21	0.24	1.02

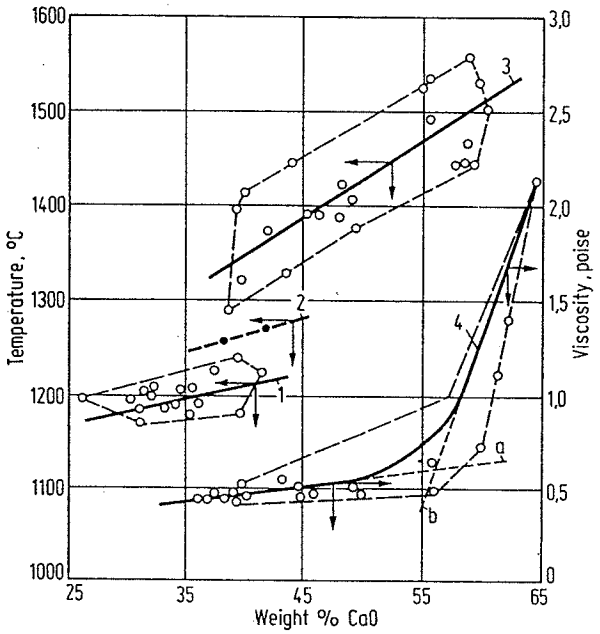


Fig. 9.106. Effect of CaO of the slag during the blowing process on the viscosity and liquidus temperature of LD slags [288]

(1) 10-17 % FeO and 13-18% Fe_{total}
(2) 14 % FeO and 11.5-18 % Fe_{total}
(3 and 4) 8.5 % FeO and 7-15 % Fe_{total} [197]

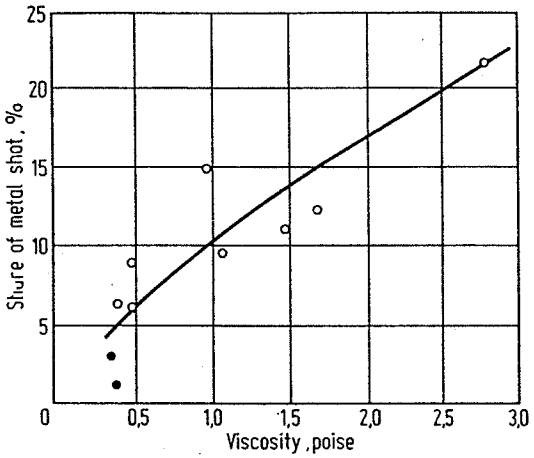


Fig. 9.108. Effect of granule content on the viscosity of LD slags [288]

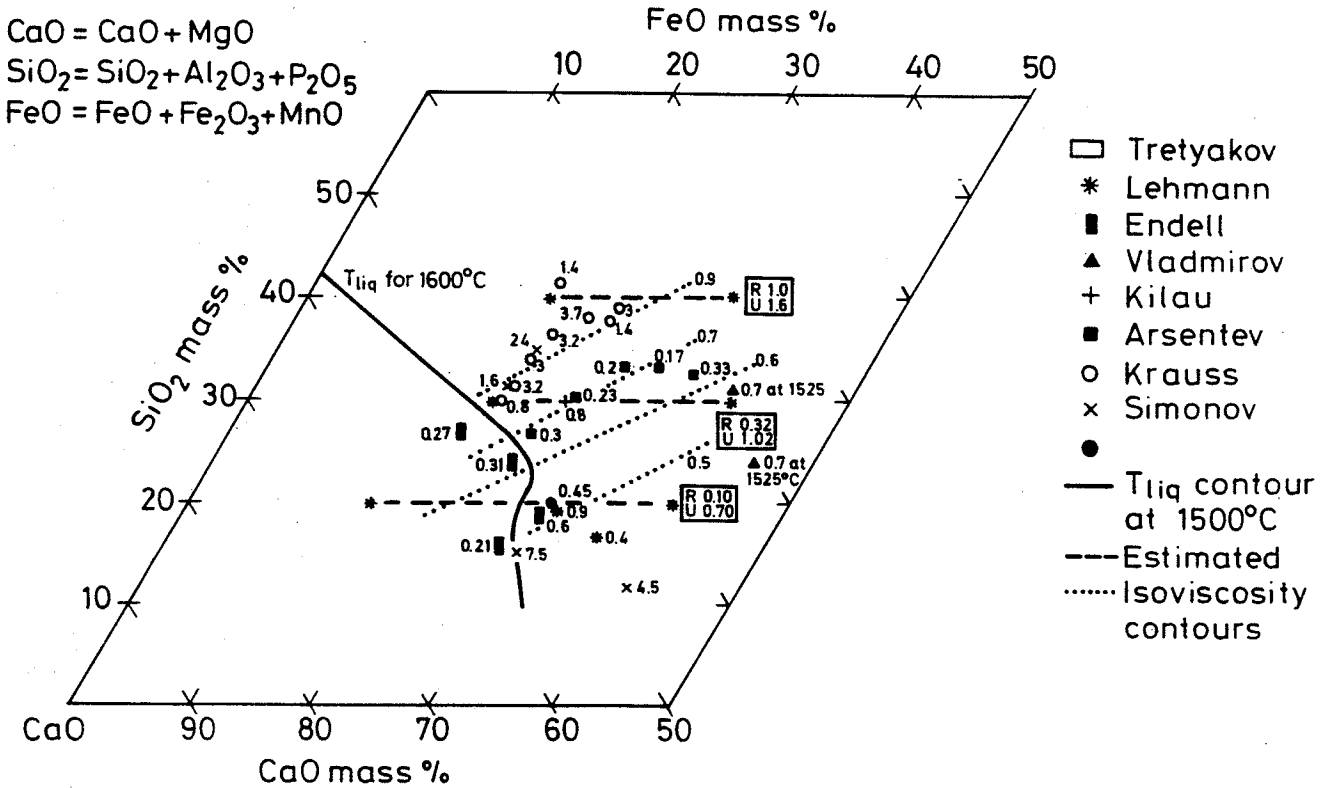
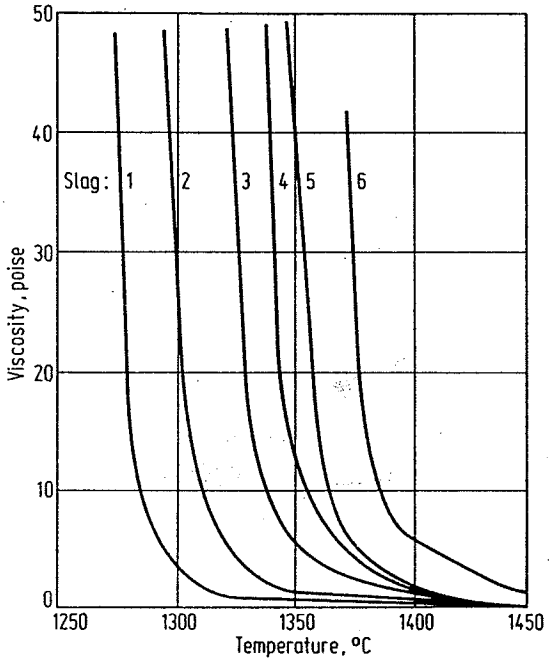
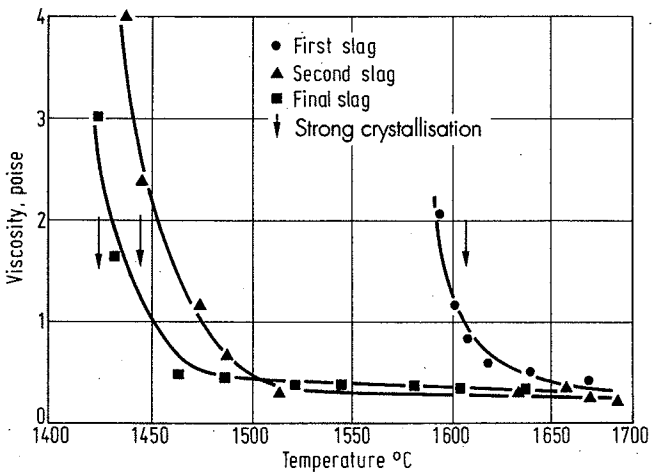


Fig. 9.107. Viscosities (poise = 10^{-1} Pa.s) reported for BOS slags at 1600 °C [98, 197, 289-293] compared with values estimated by Riboud [21] and Urbain II [24], -- , and by Urbain III model, ... [23]



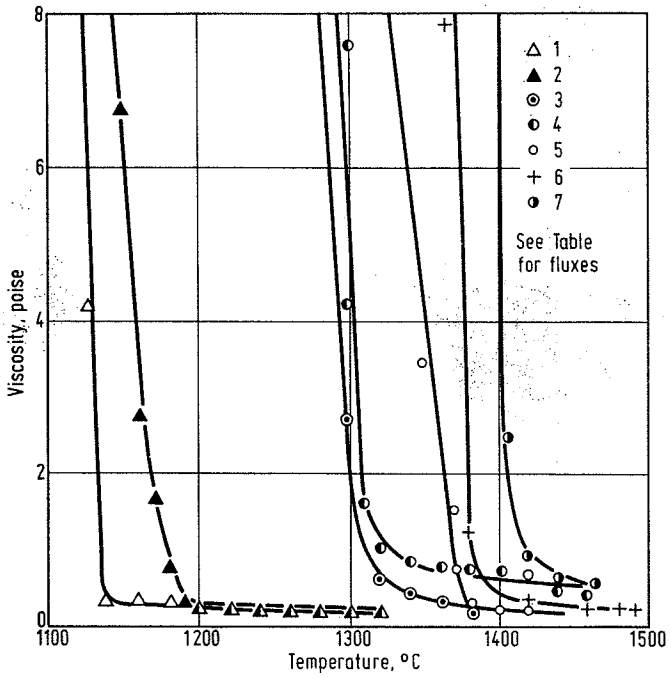
Slag No.	Slag composition, mass %									
	FeO	Fe_2O_3	MnO	P_2O_5	Al_2O_3	CaO	MgO	SiO_2	Cr_2O_3	S
1	38.53	1.66	10.74	11.03	1.03	22.51	2.89	10.80	0.58	0.18
2	19.35	5.89	14.01	16.95	1.50	27.65	7.08	6.45	-	0.09
3	24.80	9.90	7.05	11.48	1.42	39.02	1.52	2.80	0.30	0.20
4	12.62	7.15	9.26	25.61	1.29	32.05	7.95	3.04	-	0.08
5	13.00	10.54	8.01	15.29	1.63	44.65	1.67	3.36	0.74	0.09
6	7.18	7.53	7.45	23.49	1.54	43.84	1.48	3.92	0.62	0.16

Fig. 9.109. Viscosities of LDAC slags as a function of temperature [294]



Slag	Slag composition, mass %				
	FeO	P_2O_5	CaO	MnO	SiO_2
First slag	5.9	25.2	51.4	5.0	7.0
Second slag	15.5	16.2	52.0	6.6	4.7
Final slag	34.8	8.5	45.0	4.6	2.9

Fig. 9.110. Viscosities of LDAC slags as a function of temperature [99]



(a)

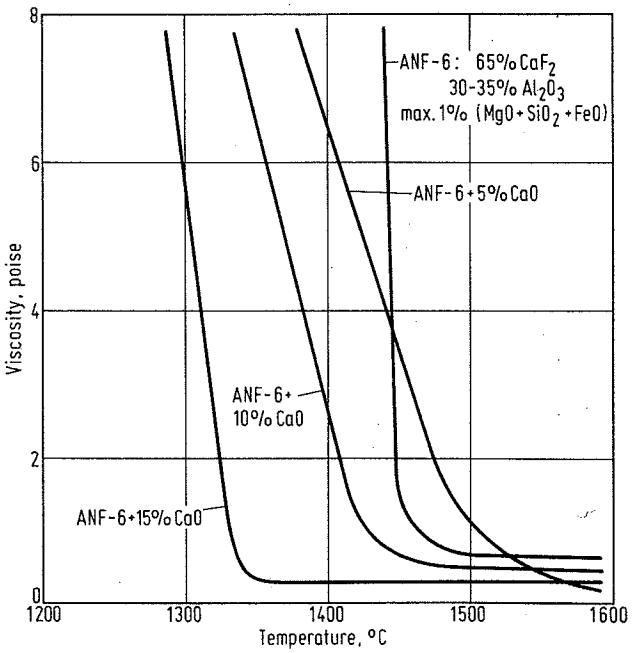
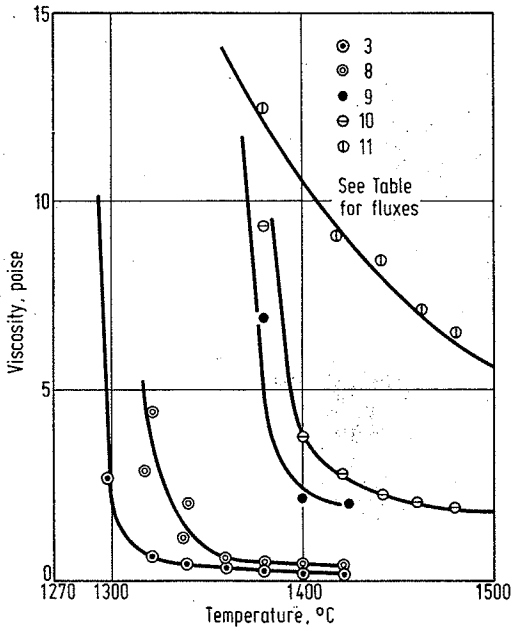


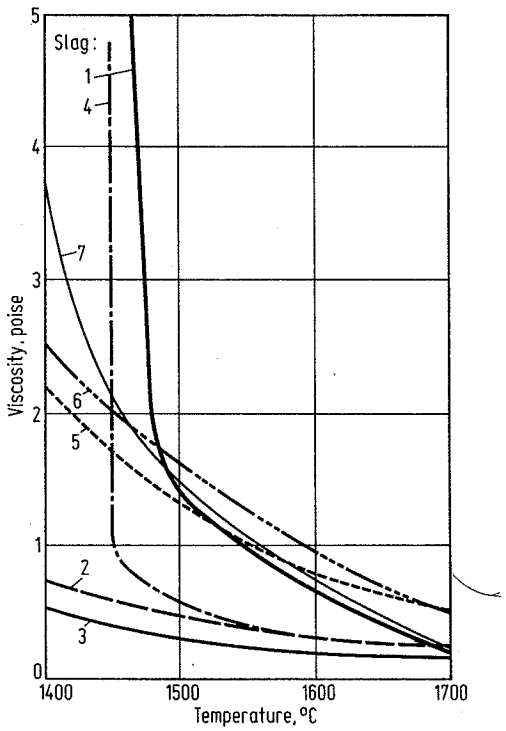
Fig. 9.112. Effect of CaO content on viscosity of an ESR slag (65 % CaF_2 - 35 % Al_2O_3) [273]



(b)

Slag No.	Slag composition, mass %					
	CaF_2	CaO	Al_2O_3	MgO	NaF	Na_3AlF_6
1	74.75	-	-	-	24.8	-
2	79.65	-	-	-	-	19.75
3	100	-	-	-	-	-
4	79.6	-	-	19.85	-	-
5	79.56	19.9	-	-	-	-
6	79.7	-	19.79	-	-	-
7	69.7	-	29.85	-	-	-
8	79.6	9.70	9.75	-	-	-
9	39.73	29.75	29.80	-	-	-
10	19.66	39.8	39.65	-	-	-
11	-	44.70	54.85	-	-	-

Fig. 9.111 a,b. Temperature dependence of viscosities of ESR slags [273]



Slag No.	Slag composition, mass %		
	CaF_2	Al_2O_3	CaO
1	70	30	-
2	50	10	40
3	60	20	20
4	50	30	20
5	40	30	30
6	30	30	40
7	40	40	20

Fig. 9.113. Temperature dependence of viscosities of various ESR slags [274]

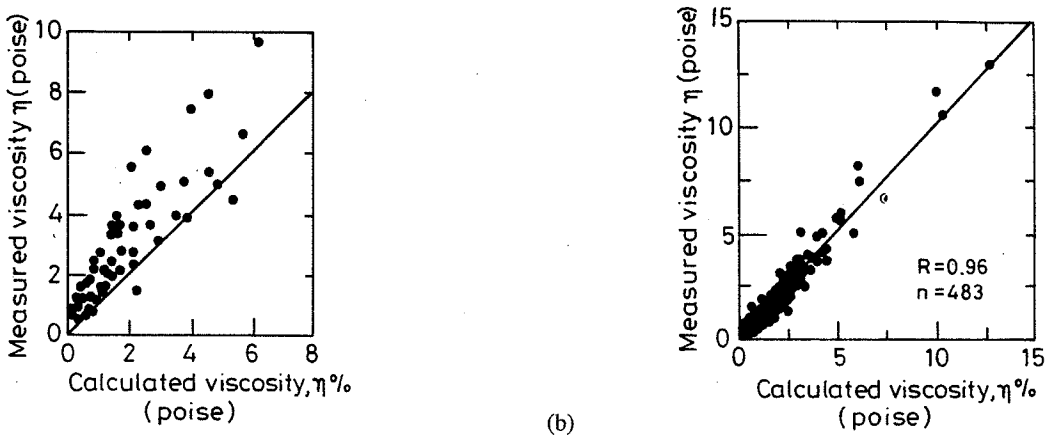


Fig. 9.114 a,b. Comparision of experimental viscosity (poise) values with those (a) predicted by the Riboud model [21] and (b) values predicted by relationship [284] $\ln \eta = (\ln A) + B/T$ where T in K and $\ln A = -0.242\ Al_2O_3 - 0.061\ CaO - 0.121\ MgO + 0.063\ CaF_2 - 0.19\ Na_2O - 4.816$ and $B = 92.59\ SiO_2 + 283.186\ Al_2O_3 - 165.635\ CaO - 413.646\ CaF_2 - 455.103\ Li_2O + 29012.564$ where oxides are in mol %. Further Ref. [283]

9.6 Performance of Riboud and Urbain models in predicting viscosities of industrial slags

It should be noted that experimental values of viscosities of industrial slags originating from different laboratories vary by ± 50 % (Fig. 9.8) thus divergences between experimental and estimated values of < ± 50 % can be considered to be acceptable.

Tab. 9.28. Summary of performance of Riboud and Urbain model in predicting viscosities of multicomponent industrial slags

Slag type	Comment
Blast furnace	Riboud and Urbain (II, III) models provide reasonable estimates, Urbain preferred.
ESR and CaF_2-based slags	Urbain model is preferred although tends to give values which are higher than experimental values by ca 250 %. Riboud model gives low values (700-1000 %). Other models such as that based on the viscosity-optical basicity relationship may be preferable.
Mould fluxes	Both models can be used but Riboud model is preferable and provides reasonable estimate.
Open hearth	Urbain model provides reasonable estimates; values predicted by Riboud model tend to be too low.
Oxygen steelmaking	Riboud and Urbain models provide reasonable estimates but do not reproduce complex shape of iso-viscosity contours.

9.7 References in Chapter 9

[1] Mysen, B. O.: Earth Science Rev. 27 (1990), 365
[2] Mills, K. C.: The structure of silicate melts, NPL Report DMM(A) 43 (1991)
[3] Urbain, G.; Boiret, M.: Ironmaking Steelmaking 17 (1990), 255-260
[4] McCauley, W. L.; Apelian, D.: Proc. of 2nd Int. Conf. on Metallurgical Slags and Fluxes. Ed. H. A. Fine and D. R. Gaskell, held Lake Tahoe, Nev. (1984). Publ. Met. Soc. AIME Warrendale, Pa, 925-947
[5] MacKenzie, J. D.: Physico-chemical measurements at high temperatures. Ed. J.O'M. Bockris; J. L. White; J. D. MacKenzie; publ. Butterworths, London (1959), Chap. 15
[6] Wittenberg, L.; Ofte, D.: Physico-chemical measurements. Ed. R. A. Rapp, Publ. Wiley, New York (1970), 193-217
[7] Ladenberg, R.: Ann. Phys. 22 (1907), 287
[8] Bacon, L R.: J. Franklin Inst. 221 (1936), 251-273
[9] Endell, K.; Tielsch, A.; Wens, C.: Metall u. Erz 31 (1934), 353-357
[10] Endell, K.; Kley, D.: Stahl u. Eisen 59 (1939), 677-685
[11] Meyer, O. E.: Poggendorfs Ann. 13 (1961), 55, 139, 383
[12] Morita, Z.: Iida, T.; Kawamoto, M.; Mori, A.: Tetsu-to-Hagane 170 (1984), 1242
[13] Iida, T.; Guthrie, R. I. L.: The physical properties of liquid metals. Clarendon Press, Oxford (1988)
[14] Herty, C. H.: Stahl u. Eisen 54 (1934), 610-612
[15] Herty, C. H.: Stahl u. Eisen 56 (1936), 165-170
[16] Krabiell, H. J.: Stahl u. Eisen 64 (1944), 399-404
[17] Mills, K. C.: Commission Report on Standard Reference Material (SRM) for high temperature viscosity measurements. NPL Report DMM(A) 30, Aug. 1991, available National Physical Laboratory, Teddington, UK
[18] Watt, J. D.; Fereday, F.: J. Inst. Fuel 338 (1969), 99
[19] Capps, W.; Kauffman, D.: Nat. Bur. Standards. Quart. Prog. Report to Office of Coal Research, US Dept. of Interior, 30.9.74
[20] McCauley, W. L.; Apelian, D.: Canad. Met. Quart. 20 (1981), 247
[21] Riboud, P. V.; Roux, Y.; Lucas, D.; Gaye, H.: Fachber. Hüttenprax. Metallweiterverarb. 19 (1981), 859
[22] Urbain, G.; Cambier, F.; Deletter, M.; Anseau, M. R.: Trans. Brit. Ceram. Soc. 80 (1981), 139
[23] Mills, K. C.; Keene, B. J.: Int. Materials Rev. 32 (1987), 1-120
[24] Urbain, G.: Steel Research 58 (1987), 111-115
[25] Urbain, G.: Rev. Int. Haut. Temp., Refract 19 (1982), 55-57
[26] Elioutin, V. P.; Mitin, B. C.; Nagibin, Y. A.: Fiz. Aerodispenik Sisk 7 (1972), 104-109
[27] Kozakevitch, P.: Rev. Metall. Paris 57 (1960), 149
[28] Blomquist, R. A.; Fink, J. K.; Leibowitz, L.: Ceram. Bull. 5 (1978), 522
[29] Napolitano, A.; Macedo, P. B.; Hawkins, E. G.: J. Amer. Ceram. Soc. 48 (1965), 613
[30] Yamate, T.; Kadogawa, Y.: Kenkyu Hokoku-Asahi Garasu Kogyo Gijutsu Shoreikai 44 (1984), 15-24
[31] Matusita, K.; Watanabe, T.; Kamiya, K.; Sakka, S.: Phys. Chem. Glasses 21 (1980), 78-84
[32] MacKenzie, J. D.: J. Phys. Chem. 63 (1959), 1875
[33] Iida, T.; Morita, Z.; Rokutanda, T.: Proc. of 3rd Int. Conf. on Molten Slags and Fluxes, held Univ. Strathclyde, Glasgow, (1988). Publ. Inst. of Metals, London, (1989), 195-198
[34] Riebling, E. F.: J. Amer. Ceram. Soc. 49 (1966), 19-23
[35] Dietzel, A.; Bruckner, R.: Glastech. Ber. 28 (1955), 455
[36] Boow, J.: Phys. Chem. Glasses 8 (1967), 45
[37] Eppler, R. A.: J. Amer. Ceram. Soc. 49 (1966), 679
[38] Podgayetski, V. V.: Avtomatičeskaja Svarka 9 No. 4 (1956), 30-49
[39] Stepanov, V. V.; Lopaev, B. E.; Stengelmeier, S. V.: Automat. Weld. 18 No. 11 (1965), 31
[40] Zhmoidin, G. I.: Russ. Metallurg., Metally, No. 6 (1969), 5-9
[41] Kulifeev, V. K.; Panchishni, V. I.; Stanolevich, G. P.: Izv. VUZ Chern. Met. No. 2 (1968), 116
[42] Davies, M. W.; Wright, F. A.: Chem. Ind. (1970), 359
[43] Schwerin, L.: Metals & Alloys, 5 (1934), 118-123
[44] Vyatkin, G. P.; Mischenko, V. Ya.; Gerasimov, V. K.: Metallurgia, Teoria Metallurgicheskikh Protsessov. Metallurgia (1974)
[45] Baak, T.: In the physical chemistry of steelmaking. Ed. by J. F. Elliott, New York/London, (1958), 84-86
[46] Zhukova, T. S.; Sheludyakov, L. N.: Tr. Inst. Khim. Nauk. Akad. Nauk. Kaz. SSR 40 (1975), 72-77
[47] Ogino, K.; Nishiwaki, J.; Onishi, H.: Nippon Tekko Kyokai (1979), 73
[48] Yanagase, T.; Morinaga, K.; Ohta, Y.; Aiura, T.: Proc. of 2nd Int. Conf. on Metall. Slags and Fluxes, held Lake Tahoe, Nev., 1984. Ed. H. A. Fine and D. R. Gaskell. Publ. Met. Soc. AIME, Warrendale, Pa., 995-1004
[49] Kozakevitch, P.: Private communication cited in Slag Atlas. Publ. Verlag Stahleisen, Düsseldorf (1981), 194
[50] Schenck, H.; Frohberg, M. G.; Rohde, W.: Archiv Eisenhüttenwes. 32 (1961), 521-523
[51] Kozakevitch, P.: Rev. Métallurg., Mém. 8 (1949), 505-516
[52] Kozakevitch, P.: Rev. Métallurg. 9 (1949), 572-582
[53] Lopatin, V. M.; Nikitin, Y. P.; Barmin, L. N.; Bobylev, I. B.: Fiz-Khim Issled Metall Protsessov (3) (1975), 63-66
[54] Cormia, R. L.; MacKenzie, J. D.; Turnbull, D.: J. Appl. Phys. 34 (1963), 2245
[55] Urbain, G.: Rev. Int. Haut. Temp. Refract. 26 (1990), 193-197
[56] Urbain, G.; Bottinga, Y.; Richet, P.: Geochim Cosmochin Acta 46 (1982), 1061-1072
[57] Hofmeir, G.; Urbain, G.: Sci. Ceram. 4 (1968), 25
[58] Volarovich, M. P.; Leontieva, A. A.: J. Soc. Glass Tech. 20 (1936), 141
[59] Brückner, R.: Glastech. Ber. 37 (1964), 413
[60] Leko, V. K.; Meshcheryakova, E. V.; Gusakova, N. K.; Lebedeva, R. B.: Opt. Mekh. Prom. (12) (1974), 42
[61] Loryan, S. G.; Kostanyan, K. A.; Saringyulyan, R. S.; Kafyrov, V. M.; Bogdasaryan, E. K.: Electron. Tekh. Ser. 6, Mater. (1976)
[62] Paek, U. C.; Schroeder, C. M.; Kurkjian, C. R.: Glass Technol. 29 (1988), 263
[63] Bowen, D. W.; Taylor, R. W.: Ceram. Bull. 57 (1978), 818-819
[64] Bacon, J. F.; Hasapis, A. A.; Wholley, J. W. Jr.: Phys. Chem. Glasses 1 (1960), 90-98
[65] Bochris, J. O'M.; MacKenzie, J. D.; Kitchener, J. A.: Trans. Faraday Soc. 51 (1955), 1734-1748
[66] Rosin, R.; Bersan, J.; Urbain, G.: Compt. Rendus 258 (1964), 562-564
[67] Mills, K. C.; Keene, B. J.: Int. Metals Review 21 (1981), 21-67
[68] Mills, K. C.: Review of viscosities of CaF_2 based slags. NPL Report Chem. '65 (1977). National Physical Laboratory, Teddington, UK
[69] Pavlushkin, N. M.; Petrova, S. V.; Egorova, L. S.: 'Shlaksital' 50, Moscow, Metallurgiya (1970)
[70] Lobzhanidze, R. B.; Filippov, A. F.; Evseev, P. P.: Izv. VUZ Chern. Met. (7) (1970), 57
[71] Koo, G. H.; Kou, H. S.: Chinese J. Mat. Sci. 20 (1988), (2) 51-57
[72] Yakobashvili, S. B.: Avtoreferat Kandidata Teckhn.; Nauk. Akad. Nauk. Ukr. SSR, Kiev, (1963)
[73] Isotomin, S. A.; Lepinskikh, B. M.; Manakov, A. I.; Krasikov, S. V.: Viscosity of fluoride-oxide melts containing variable valence oxides, Report No. 2202-75, Viniti, (1975)
[74] Stepanov, V. V.; Lopaev, B. E.: Autom. Weld. (USSR) 20 (1967), 46
[75] Kammel, R.; Winterhager, H.: Erzmetall 9 (1968), 399
[76] Joshi, S.; Mitchell, A.: Cited by A. Mitchell and B. Burel, in Met. Trans. 1 (1970), 2253
[77] Vatolin, N. A.; Vyatkin, G. P.; Zolatarevskii, B. M.; Izmailov, Y. G.; Ukhov, V. F.: Viniti, Tech. Report (1977) 4190-77
[78] Urbain, G.: Rev. Int. Haut. Temp. Refract. 20 (1983), 135-138
[79] Sivkov, S. I.; Suchilnikov, S. I.; Pavlov, B. A.: V. Sb. Proiz-vo Ferrosplavov (1975) (4), 45-52
[80] Zhmoidin, G. I.; Kulikov, I. S.: Izv. Akad. Nauk SSSR Metally (1965) (2), 42
[81] Evseev, P. P.; Sinyukova, L. I.; Filippov, A. F.: Izv. VUZ Chern. Met. (1966) (1), 74
[82] Shalimov, A. G.; Bobkiva, O. B.; Kuklev, V. G.; Sazonov, M. L.; Petrkhov, V. S.: Fiz-Khim Osnovy Proizv Stali Akad. Nauk SSSR, Inst. Met. To-6oi Konf., Moscow, (1961), publ. 1964, 176
[83] Chibulnilov, A.; Topotishchev, G. A.; Vachugov, G. A.; Mothir, E. D.; Vetysheva, V. V.: Izv. VUZ Chern. Met. (1973) (2), 5
[84] Povolotskii, D. Y.; Mischenko, V. Y.; Vyatkin, G. P.; Puzyrev, A. V.: Izv. VUZ Chern. Met. (1970), (12), 8
[85] Cures, J. P.; Benezech, G.; Antie-Fidanco, E.; Lemaitre-Blaise, M.: Rev. Phys. Appl. 12 (1977), 667 (cited in Ref. 86)
[86] Shiraishi, Y.: Handbook of Physico-Chemical properties at high temperatures. Ed. by Y. Kawai and Y. Shiraishi, Iron and Steel Inst., Japan. Special Issue No. 41, (1988), Chap. 4
[87] Urbain, G.; Millon F.; Cariset, S.: CR Hebd Séances, Acad. Sci., Ser. C, 290 (1980), 137-140
[88] Riebling, E.F.: J. Amer. Ceram. Soc. 47 (1964), 478
[89] Brückner, R.; Navarro, J. F.: Glastech. Ber. 39 (1966), 283
[90] Matano, T.; Sumita, S.; Morinaga, K.; Yanagase, T.: Nippon Kinzoku Gakkaishi 47 (1983), 25-30
[91] Mizoguchi, K.; Okamoto, K.; Suginohara, Y.: Nippon Kinzoku Gakkaishi 46 (1982), 1055-1060
[92] Goncharov, A. E.; Manakov, A. I.; Kovalev, P. K.: Tr. Inst. Met. Akad. Nauk, Uralsk Nauk Tsentr. 27 (1972) (4), 159
[93] Rosina, R.: Zelezarcki Zb. 15 (1981), 19-24
[94] Lepinskikh, B. M.; Ovcharenko, G. E.; Isotomin, S. A.; Bayur, S. D.: Tech. Report Viniti (1978), 1891-1978

[95] Malkov, N. V.; Roshchin, V. E.; Gainullin, A. I.: Izv. VUZ Chern. Met. (1986) (4), 31-34
[96] Sumita, S.; Mimori, T.; Morinaga, K.; Yanagase, T.: Nippon Konzoku Gakkai 44 (1980), 94-99
[97] Okunev, A. I.; Selivanov, E. N.; Shin, S. N.; Kuznetsov, P. A.: Russ. Metall. (1986) (5), 36-39
[98] Endell, K.; Heidtkamp, G.; Hax, L.: Arch. Eisenhüttenwes. 10 (1936), 85-96
[99] Kozakevitch, P.; Repetylo, O.; Thibault, J.: Rev. Metall. 62 (1965), 291-298
[100] Shiraishi, Y.; Saito, T.: Nippon Kinzoku Gakkai 29 (1965), 614-622
[101] Bockris, J. O'M.; Lowe, D. C.: Proc. Royal Soc. A226 (1954), 423
[102] Schenck, H.; Frohberg, M. G.: Arch. Eisenhüttenw. 33 (1962), 421
[103] Licko, T.; Danek, V.: Phys. Chem. Glasses 27 (1986), 22-26
[104] Herty, C. H.; Hartgren, F.; Frear, G.; Boyer, M.: US Bur. Mines Rept. RI 3232 (1934)
[105] McCaffery, R.: AIME Tech. Publ. No. 383 (1931)
[106] Rait, J.; Hay, R. J.: J. Roy. Tech. College, Glasgow, 4 (1938), 258 and 461
[107] Kawai, Y.: Nippon Kinzoku Gakkai Kaiho 18 (1979), 244
[108] Belikova, I. K.; Sultanova, I. G.; Nikiforova, G. N.; Faurnova, A. N.: Tr. Leningra N-i i Proekt In-Ta Osnovn Khim Prom sti (1975) (17), 26-29
[109] Shiraishi, Y.; Ikeda, K.; Tamura, A.; Saito, T.: Trans. Japan Inst. Met. 19 (1978), 264 (see also K. Ikeda et al. Tohoku Daigaku Senko Seiren Kenkyusho Iho 29 (1973) 24)
[110] Myslevic, T.; Wozniak, J.; Cerny, V.: Sb. Ved. Pr. Vys. Sk. Banaské Ostravé 20 (1974), 57
[111] Bodnar, L.; Tomasek, K.; Bobok, L.; Schmiedl, J.: Hutn. Listy 33 (1978) (7), 497
[112] Kaiura, G. H.; Toguri, J. M.; Marchant, G.: Canad. Metall. Q 16 (1977), 156
[113] Williams, P.; Sunderland, M.; Briggs, G.: Trans. Inst. Min. Metall. Eng. 92C (1983), 105
[114] Roentgen, P.; Winterhager, H.; Kammel, L.: Erzmetall 9 (1956), 207
[115] Urbain, G.; Hebd, C. R.: Séances Acad. Sci. II 232 (1951), 330
[116] Sokolov, V. I.; Popel, S. I.; Esin, O. A.: Izv. VUZ Chern. Met. (1970) (4), 40-45
[117] Pohlmann, H. J.: Glastechn. Ber. 49 (1976), 177-182
[118] Eipeltauer, E.; Jangg, G.: Kolloid Z 142 (1955), 77
[119] Zheng, Z.: Guisuanyan Xuebao 14 (1986) (3), 347-352
[120] Sasek, L.: Silikaty 21 (1977) (4), 291-305 (see also Sb Vys Sk Chem-Technol Praze, Chem. Technol. Silik. L6 (1975) 61-93)
[121] Shartsis, L.; Spinner, S.; Capps, W.: J. Amer. Ceram. Soc. 35 (1952), 155-160
[122] Hofmann, E. A.: Berg. Hüttenmänn. Monatsh. 106 (1959), 397
[123] Riebling, E. F.: Canad. J. Chem. 42 (1964), 2811
[124] Towers, H.; Gworek, J.: J. West Scot. Iron Steel Inst. (1943/44), 122
[125] Segers, L.; Fontana, A.; Winard, R.: Electrochim. Acta 24 (1979), 213-218
[126] Yagi, S.; Mizoguchi, K.; Suginohara, Y.: Kyushu Kogyo Daigaku Kenkyu, Hokoku, Kogaku (1980) (40), 33-38
[127] Callis, C. F.; van Wazer, J. R.; Metcalf, J. S.: J. Amer. Ceram. Soc. 77 (1955), 1468
[128] Hara, S.; Kitamura, M.; Ogino, K.: ISI Japan Int. 30 (1990), 714-721
[129] Urbain, G.: Rev. Int. Haut. Temp. Refract. 22 (1985), 39-45
[130] Lillie, H. R.: J. Amer. Ceram. Soc. 22 (1939), 367-374
[131] Kawahara, M.; Morinaga, K.; Yanagase, T.: Nippon Kinzoku Gakkaishi 41 (1977), 1047-1052
[132] Heidtkamp, G.: Glastechn. Ber. 14 (1936), 94
[133] Urbain, G.: Rev. Int. Haut. Temp. Refract. 21 (1984), 107-111
[134] Konavolov, A. S.; Evstropiev, K. S.: Zh. Fiz. Khim. 15 (1941), 109
[135] Kou, T.; Mizoguchi, K.; Suginohara, Y.: Nippon Kinzoku Gakkaishi 42 (1978), 775-781
[136] Ouchi, Y.; Kato, E.: Nippon Kinzoku Gakkaishi 43 (1979), 625-633
[137] Nemilov, S. V.; Ignatev, A. I.: Sov. J. Glass Phys. Chem. 16 (1990), 54-61
[138] Zhmoidin, G. I.; Moldavskiy, O. D.: Russ. Metall. (1970) (1), 42
[139] Muratov, A. M.: Russ. Metall. (1972) (3), 51
[140] Vachugov, G. A.; Toporischev, G. A.; Vetisheva, V. V.; Suburova, A. K.: Prob. Spets. Electrometall. (1975) (2), 52
[141] Gerasimenko, L. A.: Automat. Weld. (USSR) (1963) (5), 94
[142] Povolotskii, D. Y.; Voronov, V. M.; Nikitin, B. M.: Steel USSR 1 (1971) (12), 952
[143] Evseev, P. D.: Automat. Weld. (USSR) 20 (1967) (11), 42
[144] Sikorá, B.; Zielinski, M.: Hutnick 41 (1974), 433
[145] Mills, K. C.: Schlacken für das ESU. In: "Schlacken in der Metallurgie". Ed. K. Koch and D. Janke, Verlag Stahleisen, Düsseldorf (1984), 297-311
[146] Isotomin, S. A.; Lepinskikh, B. M.; Manakov, A. I.; Pokrovskii, V. A.: Viniti Tech. Report, 2205-75 (1975)
[147] Musikhin, V. I.; Chernyaev, V. G.; Ignatenko, G. F.; Pliner, U. L.; Rubinshteyon, E. A.: Sb. Tr. Klynchevsk Z-da Ferrosplavov 4 (1969), 32
[148] Machin, J. S.; Yee, T. B.: J. Amer. Ceram. Soc. 37 (1954), 177-186
[149] Shalimov, A. G.; Kuklev, V. G.: Isv. Akad. Nauk SSSR OTN Metallurgaga i Toplivo, (1962), (5), 43-53
[150] Scarfe, C. M.; Cronin, D. J.: Amer. Mineralogist 68 (1983), 1083-1088
[151] Zhilo, N. L.; Dosov, O. B.; Pershina, R. F.: Rasplavy 1 (1987), 69-73
[152] Johannsen, F.; Brunion, H.: Z. Erzbergbau u. Metallhüttenwes. 12 (1959), 211-279
[153] Machin, J. S.; Yee, T. B.; Hanna, D. C.: J. Amer. Ceram. Soc. 35 (1952), 322
[154] Potanin, V. N.; Shavin, S. V.; Panilov, M. I.: Russ. Metall. (1976) (2), 58-61
[155] Bills, P. M.: J. Iron Steel Inst. 201 (1963), 133-140
[156] Nowakowski, J.; Ptak, W.: Archiv Hutn. 30 (1985) (4), 435-442
[157] Kato, M.; Minowa, S.: Trans. ISI Japan 9 (1969), 31-38
[158] Breus, V. M.; Kosoi, L. F.; Ermolov, V. M.: Steel USSR 13 (1983), 451-452
[159] Slag Atlas. Verlag Stahleisen, Düsseldorf (1981), Fig. 30, 203
[160] Tregubenko, V. V.; Shushlebin, B. A.; Nemchinov, N. F.: Fiz-khim Osnovy Metallurg. Protsessov, M (1982), 44-47
[161] Kozakevitch, P.; Urbain, G.: Viscosite et structure des laitiers liquides. IRSID, Metz, (1954), (cited in Ref. 159)
[162] Shedudyakov, L. N.; Sarancha, E. T.; Vakhitov, A. A.: Tr. Inst. Khim. Nauk, Akad. Nauk. Kaz. SSR (1967), (15), 158
[163] Kolosov, A. G.; Stupin, V. A.; Fedorov, A. N.; Vanyukov, A. V.: Tsvet. Met. (1987) (3), 44-47
[164] Deletter, M.; Cambier, F.; N'Dala, I.; Urbain, G.: Br. Ceram. Trans. J. 83 (1984), 108-112
[165] Boiret, M.; Urbain, G.: CR Acad. Sci., Ser. 2, 305 (1987), 167-169
[166] Varshall, B. G.: J. Non-Cryst. Solids 123 (1990), 344-348
[167] Rennie, M. S.; Howat, D. D.; Jochens, P. R.: J. South Afr. Inst. Min. Metall. (1972), 1-9
[168] Belyi, Y. I.; Koleda, V. V.; Sardak, E. M.: Viniti Tech. Report. 2053-81, (1981)
[169] Zhilo, N. I.; Ostretsova, I. S.; Charushnikova, G. V.; Pershina, R. F.: Izv. VUZ Chern. Met. (1982), (4), 35-40
[170] Riebling, E. F.: J. Amer. Ceram. Soc. 51 (1968), 143
[171] Dingwell, D. B.: Geochim. Cosmochim. Acta 50 (1986), 1261-1265
[172] Scarfe, C. M.; Cronin, D. J.: Amer. Mineralogist 71 (1986), 767-771
[173] Brearley, M.; Dickinson, J. E., Jr.; Scarfe, C. M.: Geochim. Cosmochim. Acta 50 (1986), 2563-2570
[174] Frohberg, M. G.; Weber, R.: Arch. Eisenhüttenwes. 36 (1965), 477-480
[175] Sheludyakov, L. N.; Sarancha, E. T.; Vakhitov, A. A.: Tr. Inst. Khim. Nauk, Acad. Nauk Kaz. SSR 15 (1967), 158
[176] Ivanov, O. V.; Tretyakova, N. I.; Mazurin, O. V.: Steklo Keram. (1969) (7), 42 (cited by Ref. 86)
[177] Sasek, L.; Meissnerova, H.; Prochazka, J.: Sb. Yzs. Sb. Chem. Technol. Praze, Chem. Technol.; Silik, L6 (1976), 95, (cited by Ref. 86)
[178] Nakamura, T.; Morinaga, K.; Yanagase, T.: Nippon Konzoku Gakkaishi 41 (1977), 1300-1304
[179] Peng, Y.; Hong, Y.; Zhu, Y.: Jinshu Xuebao 18 (1982), 456-462
[180] Saito, T.: Sci. Rept. Inst. Mineral. Dressing, Tohoku Univ. 22 (1960), 7
[181] Shiraishi, Y.: Taehan Kumsok Hakhoechi 25 (1987), 824-834
[182] Panov, A. S.; Kulikov, I. S.; Selev, L. M.: Isv. Akad. Nauk SSSR, Otdel Teckn. Nauk, Metallurgia i Toplivo (1961) (3), 25-30
[183] Kuroda, K.; Kawahara, M.; Morinaga, K.; Yanagase, T.: Nippon Kinsoku Gakkaishi 46 (1982), 275-285
[184] Saito, T.; Saeki, K.: Gakushin Hokuku 19 Iinkai 7906 (1965)
[185] Saito, S.: Documentation of 19th "Kakushin" Committee 1965; see Tetsu-to-Hagane 51 (1965), 1851
[186] Selivanov, E. N.; Okunev, A. I.; Galimov, M. D.; Shin, S. N.: Russ. Metall (1986) (3), 49-53
[187] Bodnar, L.; Cempa, K.; Tomasek, K.; Bobok, L.: Chem. Zvesti 32 (1978), 798
[188] Johannsen, F.; Wieze, W.: Erzmetall 11 (1988), 1-15
[189] Izchanov, T. K.; Sishkov, K. V.: Nauk Tr. Kaz Politekh Inst. (1971), 446-455
[190] Gudenau, H. W.; Petry, J.: Fachber. Hüttenpraxis Metallweiterver. 19 (1981), 32
[191] Seki, K.; Oeters, F.: Trans. ISI Japan 24 (1984), 445
[192] Gultyai, I. I.: Izv. Akad. Nauk SSR Otdel Tekhn. Nauk, Metall Toplivo, (1962), 51-52
[193] Scarfe, C. M.; Cronin, D. S.; Wenzel, J. T.; Kaufman, D. A.: Amer. Mineralogist 68 (1963), 1083-1088

10

Surface tension of slag systems

B. J. Keene

10.1 Definitions

10.1.1 Surface and interfacial tension

The cohesive force (F) acting between adjacent molecules in a fluid, can be considered as the resultant between mutually opposing attraction and repulsion terms, both of which, vary inversely with a power of the molecular separation distance (d) in accord with the general equation

$$F = (\text{repulsion component}) + (\text{attraction component})$$

$$= \frac{A}{d^n} - \frac{B}{d^m} \left[\begin{array}{l}\text{where A and B are constants for the} \\ \text{particular system and } n > m\end{array}\right].$$

(By convention, repulsion forces are positive and attraction forces are negative). At the stable separation distance (d_o) the resultant force on the molecules is zero. When (d) < (d_o), the resultant force (F) is positive and there is a strong mutual repulsion between the molecules, and conversely, when (d) > (d_o), (F) is negative, and an attraction force prevails. As (d) increases beyond (d_o), the attraction force (F) goes through a maximum and then ultimately decreases to zero as the distance between the molecules becomes effectively infinite. Within the bulk of a fluid, every molecule (or particle) is surrounded by molecules possessing attraction force fields of similar strength and hence the overall field acting on each individual is balanced and uniform in all directions. At the free surface between a liquid and a gas the situation is different since the relative strengths of the attraction forces acting between molecules of liquid and gas are weak in comparison to the equivalent molecular forces present within the liquid bulk. In consequence, molecules of liquid at the free surface are subject to an asymmetric force field and the net resultant attraction force acting on each individual is directed normal to, and inward from, the surface. As a result of the imbalance between the intermolecular forces, the free surface of the fluid is in a state of tension and the whole surface layer behaves as if it were a thin elastic membrane. Surface tension (γ) of a fluid is a direct measure of the intermolecular forces acting at the surface and can be defined as the force acting normally across unit length in the free surface and has SI units of Newtons per metre ($N.m^{-1}$) (for direct numerical comparison with data given in terms of the obsolete CGS units (dyne cm^{-1}), it is customary to express surface tension in modified SI units viz $mN.m^{-1}$).

Although the terms "surface" and "interface" are mutually interchangeable, it is generally accepted practice to adopt "surface" when one of the two phases is a gas (or vapour), and "interface" when the phases are either two liquids or a solid and a liquid. Thus the tension acting at the boundary between two liquids (L_1 and L_2) is termed the interfacial tension ($\gamma_{L_1L_2}$), which has the same units as surface tension.

With interfacial tension data, it is essential to fully characterise the compositions of the two respective phases, since small differences in certain critical components can radically affect the value of the interfacial tension. It is also important to ensure that measurements are conducted when the system is at equilibrium, as any reaction or mass transfer across the interface will generally reduce the interfacial tension, which will continually vary until equilibrium is achieved (during periods of intense mass transfer, the interfacial tension can approach zero). With a liquid-gas surface, the change in surface tension with the composition of the gas will, in general, be negligible provided there is no interaction between the two phases (eg chemical reaction, change in oxidation state).

Data are sometimes expressed in terms of free surface or interfacial energy, which is the free energy per unit area of surface or interface and can be defined as the work necessary to increase the surface or interface by unit area. Surface and interfacial energy have SI units of Joules per metre squared (Jm^{-2}), and generally for liquids, they are numerically and dimensionally equal to the equivalent surface and interfacial tensions.

The two principal parameters affecting the magnitude of surface and interfacial tension, are the chemical composition of the phases and the temperature. As noted previously, the surface tension of any particular liquid depends upon the relative strengths of the intermolecular forces acting at the surface, which are governed by the chemical composition. The surface tension of any solvent can be markedly reduced by the presence of relatively low levels of certain solutes which are preferentially adsorbed at the surface. Such solutes are termed "surface-active" with respect to the solvent, and the magnitude of surface-activity (J) is defined as the change in surface tension per unit content of solute. The limiting or ultimate surface-activity (J_L) of a solute (x) is given by the slope of the $\gamma([x])$ curve in the region where [x] approaches zero ie

$$J_L = \left[\frac{d\gamma}{d[x]}\right]_{[x]\to 0}.$$

This factor is difficult to determine, particularly for highly surface-active solutes, since at the low concentrations, substantial errors can be incurred due to factors such as the steep slope of the $\gamma([x])$ curve and difficulty in achieving accurate chemical analysis for the material being measured. In practice, approximate values for (J) are derived by assuming a linear $\gamma([x])$ relation over a limited solute range from zero concentration. Values for (J) will generally be lower than (J_L).

Surface tension of liquids usually decrease with increasing temperature (ie the temperature coefficient ($d\gamma/dT$) is negative), the variation often following a linear relation over a limited temperature range viz

$$\gamma = \gamma_o + \left[\frac{d\gamma}{dT}\right] T.$$

Exceptionally, some liquids are found which exhibit positive values for ($d\gamma/dT$) over a limited range of temperature from the melting point. Examples of such systems are:

1) Slag melts containing high levels of SiO_2 in which large complex molecular structures are formed. As the temperature increases, these structures progressively dissociate, producing an increasing number of unsatisfied molecular bonds at the surface, with consequent increase in the free surface energy.

2) Groups VI elements in molten iron. In this instance, as the temperature increases, the surfactant (O, S, Se, Te) progressively desorbs from the surface layer and consequently the surface tension of the melt increases.

Surface tension cannot increase indefinitely with temperature, since it always tends to zero as the critical temperature is approached and it follows that for all systems which exhibit positive values for ($d\gamma/dT$) there must be a maximum in the $\gamma(T)$ curve.

When a surface tension gradient exists along the free surface of a liquid, there is a concomitant convective flow (Marangoni flow) induced at the surface. The relative strength of the flow is a function of both the surface tension gradient and the fluid viscosity. Surface tension varies with both temperature and concentration and it follows that Marangoni convection will always be generated when either a temperature or concentration gradient exists at the surface. Such Marangoni flows are known specifically as thermocapillary – and diffusocapillary flow respectively. Marangoni convection is always directed towards regions of higher surface tension and consequently the sign of the temperature and concentration coefficients of surface tension will control the direction of surface tension driven flow at the surface.

10.1.2 Contact angle, work of adhesion and spreading coefficient

Figs. 10.1 a and b show a sessile drop of liquid (L) resting in equilibrium on a flat horizontal solid surface (S) in a gaseous environment (G). The profile adopted by the liquid drop is the result of the balance between surface forces, which endeavour to minimise the free surface energy of the system by forming a sphere, and gravitational forces, which tend to flatten the drop. The contact angle (θ) (Figs. 10.1 a and b) can be defined as the angle included within the liquid phase, and which lies between the solid surface and the tangent to the liquid surface at point (A) (the point of three-phase contact). When $\theta > 90°$ (Fig. 10.1 a), the system is non-wetting. Wetting of the solid by the liquid occurs when $\theta < 90°$ (Fig. 10.1 b), complete wetting being achieved when $\theta = 0°$. At equilibrium, the respective tension forces at point (A) are related to the contact angle by the Young equation viz

$$\cos\theta = \frac{\gamma_{SG} - \gamma_{LS}}{\gamma_{LG}}. \qquad (10.1)$$

Fig. 10.1 c shows a drop of liquid (L_1) in a gaseous environment (G) at rest on the surface of another liquid (L_2) which is of sufficient extent to be effectively horizontal. At equilibrium, horizontal resolution of forces gives

$$\gamma_{L_2G}\cos\phi = \gamma_{L_1G}\cos\alpha + \gamma_{L_1L_2}\cos\beta.$$

This relation forms the basis of a technique to determine the liquid-liquid interfacial tension ($\gamma_{L_1L_2}$). In practice, (α) is the only angle which can be measured, and it is usually assumed that the angle (ϕ) is sufficiently small that $\cos\phi \approx 1$. Hence, calculations of contact angle ($\alpha + \beta$) and interfacial tension are based on the geometry shown in **Fig. 10.1 d.** Based on this geometry, the liquid-liquid contact angle can be determined by measurement of angle (α) and calculation of angle (β) by vertical resolution of forces viz

$$\gamma_{L_1G}\sin\alpha = \gamma_{L_1L_2}\sin\beta.$$

Consider a column of liquid (L_1) which has unit cross-sectional area and is surrounded by gas. The work necessary to section the column and produce two new surfaces of unit area is termed the work of cohesion (W_c) and since two liquid-gas surfaces are produced, it follows that,

$$W_c = 2\gamma_{L_1G}.$$

If the column of liquid (L_1) forms an interface with another liquid (L_2) or a solid (S), then on separation at this interface, two new surfaces of unit area are created (L_1G and L_2G or SG) and one interface of unit area is lost (L_1L_2 or L_1S). The work or change in interfacial energy, required to separate unit area of interface between two media is termed the work of adhesion (W_A) and, based on the gain and loss of interfaces;

$$W_A = \gamma_{L_1G} + \gamma_{L_2G} - \gamma_{L_1L_2}$$

or

$$\left[W_A = \gamma_{L_1G} + \gamma_{SG} - \gamma_{L_1S}\right]. \qquad (10.2)$$

From equations (10.1) and (10.2), it can be seen that the work of adhesion for a liquid-solid-gas system is given by the relation

$$W_A = \gamma_{LG}(1 + \cos\theta).$$

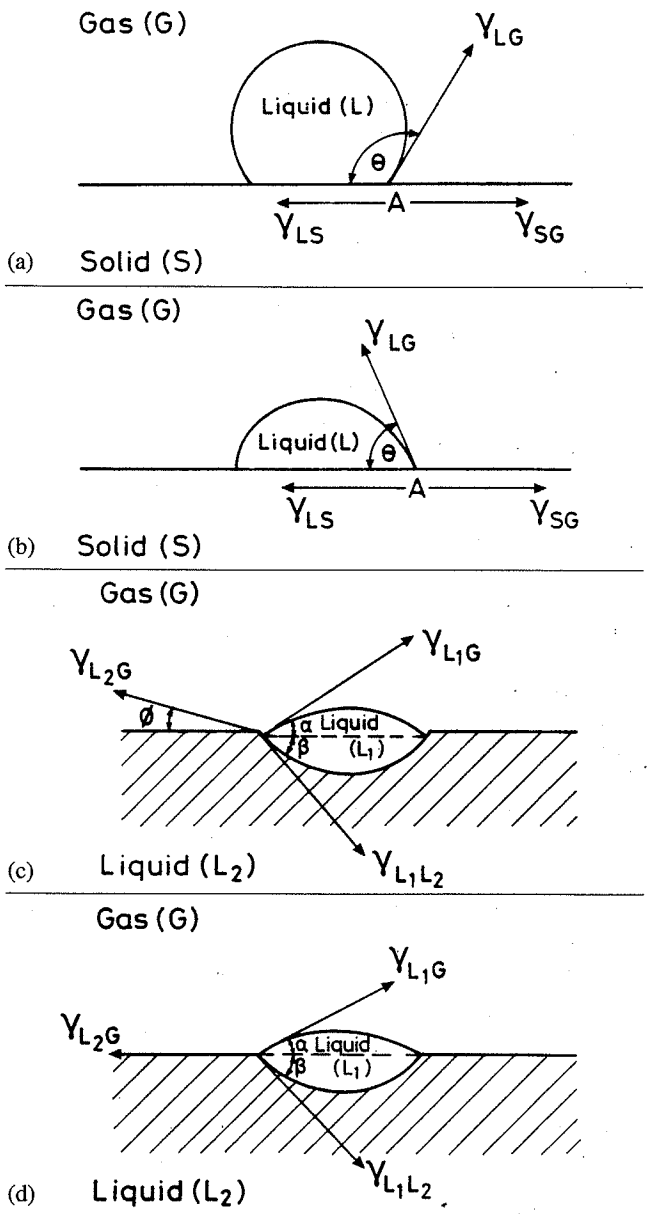


Fig. 10.1 a-d. Diagram showing the relation at equilibrium between the respective surface and interfacial tensions and the contact angle
(a) liquid on solid – (non-wetting condition)
(b) liquid on solid – (wetting condition)
(c) liquid on liquid
(d) liquid on liquid – (assuming angle $\Phi = 0$)

The difference between the work of adhesion and the work of cohesion of liquid (L_1) is termed the spreading coefficient (S_p) of liquid (L_1) on liquid (L_2) or solid (S) ie

$$S_p = W_A - W_c$$
$$= \gamma_{L_2G} - \gamma_{L_1G} - \gamma_{L_1L_2}$$

or

$$\left[S_p = \gamma_{SG} - \gamma_{L_1G} - \gamma_{L_1S}\right].$$

The spreading coefficient is a measure of the tendency for the liquid (L_1) to spread across (L_2) or (S); the more positive the value of (S_p), the greater the tendency to spread. In many metal refining processes, the value of (S_p) is an important measure of the tendency for the slag (or particle) to become entrapped in the metal during casting. Units of (W_c), (W_A) and (S_p) are as for surface energy viz (Jm^{-2}).

10.2 Methods to determine surface and interfacial tension at high temperatures

10.2.1 Introduction

When measuring the surface tension of liquids at high temperatures, it is vital to adopt a method which is appropriate to the experimental conditions. An important factor to consider is the wetting behaviour of the fluid in the system. For example, detachment techniques should ideally be used with systems which exhibit extremely good wetting behaviour ($\theta \approx 0°$). Consequently use of this technique with non-wetting systems would be entirely inappropriate, and a method which requires an obtuse contact angle, such as sessile drop, should be employed.

Reaction kinetics increase markedly at elevated temperatures, and one of the major problems encountered in the experimental determination of surface and interfacial tension under these conditions, is the need to ensure chemical compatibility between the melt and all material in contact with it. Any chemical reaction during the experiment would imply that the system was not at equilibrium and this could violate one of the basic criteria for some experimental methods. In addition, the chemical composition of the melt would alter and this could give rise to significant changes in the surface tension, particularly if the impurities introduced were surface-active.

Calculation of surface tension frequently entails a knowledge of the densities of the liquid at the relevant temperatures, and these are not always known accurately, so that, in addition to the normal experimental errors, a further uncertainty could be introduced. The situation with regard to these additional uncertainties is particularly acute with the measurement of interfacial tension, since, depending upon the particular technique used, the calculation requires values for either the densities or the surface tensions of both phases, all of which have been experimentally determined and are thus individually subject to errors, which will accumulate in the calculated value for the interfacial tension.

In this section, a description is given of the various techniques used at high temperature (> 1000 °C) to determine the surface tensions of slags and metals, and the interfacial tensions between slags and metals. More detailed descriptions are to be found in the literature [1 – 3].

Many of the methods to determine (γ) at high temperatures depend on solution of the Laplace equation, which relates the excess pressure (ΔP) at a curved surface or interface, with the principal radii of curvature (r_1 and r_2) at a point on the surface viz

$$(P_1 - P_2) = \Delta P = \gamma\left[\frac{1}{r_1} + \frac{1}{r_2}\right] \qquad (10.3)$$

(where P_1 and P_2 are respectively the pressure on the concave and the convex side of the meniscus).

This is the fundamental equation which describes the equilibrium shape of menisci such as drops and bubbles. Analysis of equation (10.3) shows that when the meniscus is spherical

$$(\text{ie } r_1 = r_2 = r),\ \Delta P = \frac{2\gamma}{r};$$

and when the surface is planar

$$(\text{ie } r_1 = r_2 = \infty),\ \Delta P = 0.$$

Equation (10.3) is applicable to both gas-liquid surfaces and to liquid-liquid interfaces (in the latter case, the γ term is the interfacial tension between the two fluids).

10.2.2 Maximum bubble pressure (MBP) and maximum drop pressure (MDP)

Both these techniques can be considered as quasi-dynamic methods since new surfaces are being produced throughout the experiment. **Fig. 10.2a** illustrates the principle behind a conventional (MBP) apparatus, in which a capillary tube of known radius (r) is immersed in the fluid to a known depth (h). A gas/liquid meniscus is produced at the capillary tip by progressively increasing the gas pressure in the tube until the applied pressure is sufficient for the meniscus to form an independent bubble which detaches from the orifice. The maximum pressure at this point is recorded by a suitable transducer system, and from this value, (γ) can be calculated. Considerably less attention has been paid to the (MDP) technique, which is similar in principle, except that the roles played by gas and fluid are interchanged, in that the pressure is applied to the fluid which is forced through a capillary into the gas phase.

If the capillary tube shown in Fig. 10.2a has a sufficiently small radius (r), the meniscus produced at the orifice will have a spherical contour. In this case, the two principal radii of curvature are equal and following from the Laplace relation equation (10.3) the pressure (P_γ) in the bubble at detachment is given by

$$P_\gamma = \frac{2\gamma}{r}.$$

If the tip of the capillary is immersed to a depth (h) in the fluid, then the total pressure (P_{max}) acting at the point of bubble detachment is given by

$$P_{max} = P_\gamma + \rho gh = \frac{2\gamma}{r} + \rho gh \qquad (10.4)$$

(where ρ = density difference between the fluid and gas).

In equation (10.4), (P_{max}) varies linearly with (h) and from a straight-line plot, (γ) can be determined by extrapolation to the intercept on the (P_{max}) axis, at which point (P_{max}) = (P_γ)

and hence

$$\gamma = \frac{r}{2}(P_{max})_{h=0}.$$

The density of the fluid can be derived from the slope (= ρg) of the line.

With conventional capillary tubes which have squared-off ends, the wall thickness is sufficient to give a significant difference between the internal and external radii at the tip, and the exact value of (r) to be substituted in equation (10.4) is dependent on the contact angle (θ). To overcome this uncertainty, special capillaries can be constructed. These capillaries have their ends chamfered and polished to produce smooth walls which taper to the orifice and effectively make the internal and external tube radii equal at this point. Tubes have been constructed with internal taper (Fig. 10.2a) and with external taper **(Fig. 10.2b)**. The latter design is easier to construct, but is less favoured on experimental grounds since there is a definite tendency for the bubble to move up the tapered wall before detachment.

Equation (10.4) pertains only to the limiting case of menisci which possess spherical contours, but in many practical situations the diameter of the tube is sufficiently large that the shape of the meniscus is modified by gravitational effects and it is necessary to account for the deviation from sphericity. The most widely used correction is the approximation derived by Schrödinger [4] viz

$$\gamma = \frac{P_\gamma \cdot r}{2}\left[1 - \frac{2}{3}\left[\frac{r\cdot\rho\cdot g}{P_\gamma}\right] - \frac{1}{6}\left[\frac{r\cdot\rho\cdot g}{P_\gamma}\right]^2\right]. \qquad (10.5)$$

The Schrödinger equation has proved to be accurate for systems in which

$$\left[\frac{r}{a}\right] < 0.2 \quad \left[\text{where } a = \left[\frac{2\gamma}{\rho g}\right]^{\frac{1}{2}}\right].$$

The rate of bubble formation in the (MBP) technique is very important, since high rates of production can lead to erroneous results. For liquids with high viscosity the pressure required to detach a bubble depends strongly on the bubble rate and for the best accuracy, rates of one bubble every one or two minutes are not uncommon. An experimental problem inherent to the single tube technique, is to accurately establish the depth (h) to which the capillary is immersed below the fluid surface. Corrections may also have to be introduced to account for (I) the liquid displacement (and hence change in (h)), due to insertion of the capillary and formation of the bubble and (II) changes in relevant dimensions due to thermal expansion.

A more rigorous treatment of the effects of non-sphericity of the meniscus is provided by the method proposed by Sugden [5]. Based on the tables produced by Bashforth and Adams [6], together with numerical calculations, Sugden developed a table of factors to determine (γ) which are valid for values of (r/a) ranging from 0 to 1.5. By a process of successive approximation the tables are used to obtain an accurate value for (a) and thus for (γ). Sugden's technique involves the use of two capillary tubes with known but different radii, which are both immersed to the same depth in the fluid. Using this procedure eliminates the need to obtain an exact value for the depth of immersion. There have been variations on the two-capillary method, eg two tubes of equal radii immersed at different depths and two tubes of

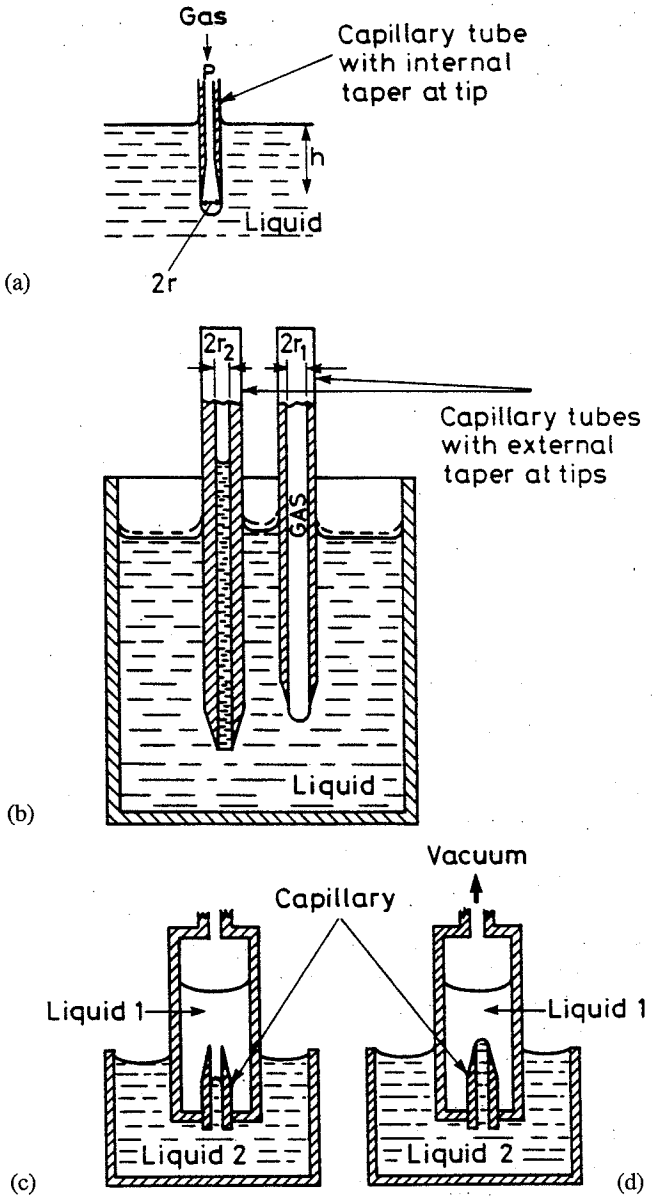


Fig. 10.2 a-d. Schematic diagrams of MBP and MDP techniques to determine surface and interfacial tensions respectively
(a) MBP – single capillary method
(b) MBP – two capillary method
(c) MBP – equal pressure on both fluid surfaces
(d) MBP – pressure differential between the two fluid surfaces

different radii immersed at different depths (Fig. 10.2b). It should be noted that for the majority of measurements at high temperatures the Schrödinger approximation (equation (10.5)) is usually considered to be sufficiently accurate and is preferred to the more complex Sugden technique.

The MDP method has been rarely used to determine (γ) but has found application in the determination of interfacial tension between liquid metals and slags [7]. **Fig. 10.2c** and **d** illustrate the principle. The apparatus consists of a vessel containing liquid 2, which is linked via a capillary to liquid 1 contained in a closed vessel. Fig. 10.2c shows the situation where the free surfaces of both liquids are at the same pressure. When a pressure differential is created eg by controlled evacuation of the closed vessel, the liquid 2 is constrained to rise up the capillary and form at the orifice, a meniscus (Fig. 10.2d), which ultimately detaches as a discrete drop. From the observed maximum pressure and the rele-

vant system dimensions, the interfacial tension can be determined, provided the difference between the densities of the respective liquids is known.

10.2.3 Sessile drop (SD)

Fig. 10.3 a shows the equilibrium profile of a sessile drop of liquid at rest on a horizontal solid surface. At any point (B) on the surface, the principal radii of curvature are (R_1) and (R_2) and the excess pressure due to surface curvature is given by the Laplace equation

$$P\gamma = \gamma\left[\frac{1}{R_1}+\frac{1}{R_2}\right] = \rho g Z + C \qquad (10.6)$$

(where Z = vertical distance of point (B) from the apex (0),
ρ = density difference between the two phases,
C = a constant).

If (ϕ) is the angle the normal at (B) makes with the axis of symmetry at (Q), then the two principal radii of curvature at (B) can be designated as R and (X/sinϕ) respectively. At the apex (0), the two principal radii of curvature are equal (= b) and the parameter (b), which depends upon the dimensions of the drop, is termed the "size factor". The constant C is given by the ratio 2γ/b. Equation (10.6) can be mathematically transformed into a non-dimensional form viz

$$\frac{1}{\left[\frac{R}{b}\right]}+\frac{\sin\phi}{\left[\frac{X}{b}\right]} = 2+\frac{\rho g b^2}{\gamma}\left[\frac{Z}{b}\right].$$

For convenience of operation, a parameter (β), called the "shape factor" of the drop, is defined by the relation:

$$\beta = \left[\frac{\rho g b^2}{\gamma}\right] \qquad (10.7)$$

and the non-dimensional equation becomes

$$\frac{1}{\left[\frac{R}{b}\right]}+\frac{\sin\phi}{\left[\frac{X}{b}\right]} = 2+\beta\left[\frac{Z}{b}\right]. \qquad (10.8)$$

Equation (10.8) mathematically describes the surface curvature of a meridional section of a sessile drop, and is a 2nd order/2nd degree differential equation relating X and Z, and can only be solved numerically by using approximation procedures such as Bashforth and Adams' tables [6]; or empirical relations [8, 9] or computer curve-fitting programs.

Bashforth and Adams obtained a series of numerical solutions to equation (10.8) using a method based on successive increments, and produced tables of (X/Z) and (β) for $\phi = 90°$ and of (X/b) and (Z/b) for various values of (β) and (ϕ). The simplest use of these tables is to measure the dimensions (X_{90}) and (Z_{90}) at $\phi = 90°$ (Fig. 10.3 a) and derive the equivalent values for (β) and (b). With these two factors the surface tension of the fluid can be calculated from equation (10.7).

The most accurate results for (γ) are obtained when the ratio (X_{90}/Z_{90}) lies between 1.5 and 2.0. As this ratio tends to unity, the profile of the sessile drop approaches sphericity and accuracy is considerably reduced. Accurate measurement of drop dimensions (particularly Z_{90}) is not easy and small differences can lead to significant errors in the calculated value for (γ). An alternative approach is to calculate (γ) from an empirical equation derived by Dorsey [8, 9].

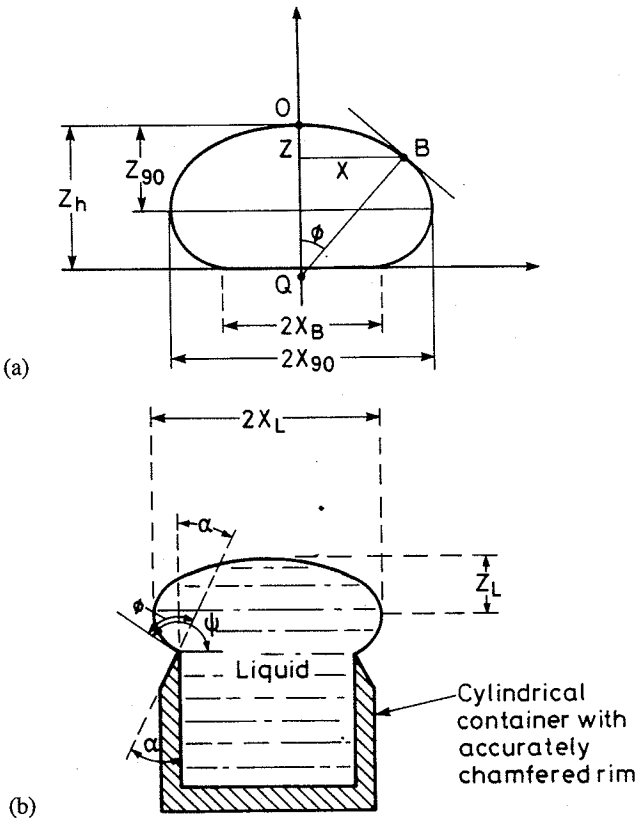


Fig. 10.3 a,b.
(a) The meridional section of a non-wetting sessile drop
(b) "Large drop" technique for producing a large symmetrical drop with both, wetting and non-wetting systems

Use of this equation avoids the need for precise location of the equatorial plane, but does demand careful geometrical construction of the tangent to the surface of the drop which intercepts the axis of symmetry at 45°. The distance (y′) between the intercept and the apex of the drop is measured and together with the value for (X_{90}), substituted in the Dorsey equation

$$\gamma = \rho g\,(X_{90})^2\left[\frac{0.052}{f}-0.1227+0.0481f\right]$$

where

$$f = \left[\frac{y'}{X_{90}}\right]-0.4142.$$

Measurements of sessile drop dimensions are usually obtained from photographic images. Recent developments have seen the use of computer curve-fitting techniques applied to the analysis of drop images obtained by high resolution video equipment. This technique offers advantages over the traditional manual method of image analysis, in that a large number of images can be quickly processed and, by elimination of human error, the accuracy of the data should be improved particularly since the coordinates of a considerable number of points along the drop perimeter can be accurately located.

If the overall drop height (Z_h) and the base diameter (X_B) (Fig. 10.3 a) are also determined, it is possible to use Bashforth and Adams' tables to compute both the contact angle (θ) and the drop volume (and hence the density of the liquid, if the mass is known).

Ideally, measurements should be made on the profiles of non-wetting sessile drops ($\theta > 90°$), since although it is possible to determine (γ) from drops for which $\theta < 90°$, the overall accuracy is reduced. Large sessile drops should be used for the best accuracy, but in practice, it is usually difficult to obtain large drops in isolation which are truly axisymmetric. To overcome problems of asymmetry, the "large drop" method [10] can be used. This modification of the sessile drop technique has two advantages, in that it produces a large axisymmetric meniscus and can be used with both wetting and non-wetting systems. A circular crucible or cup **(Fig. 10.3 b)** which has its upper circumferential edge chamfered to an acute angle (α), is overfilled with fluid so that an axisymmetric meniscus is produced which stands proud of the rim. The meniscus has a maximum diameter ($2X_L$) which exceeds the diameter of the crucible, and from measurements of ($2X_L$) and the distance (Z_L) together with relevant tables, which relate a factor (H) with the ratio (X_L/Z_L), the surface tension of the fluid can be calculated from the relation

$$\gamma = \frac{(2X_L)^2}{H} \cdot g \cdot \rho.$$

The necessary condition for the equator of the meniscus to exceed the internal diameter of the crucible is (ϕ) > (α). This condition is satisfied when the contact angle (θ) exceeds (α) and since the angle (α) at the rim can generally be made down to 20° – 30°, a wide range of wetting conditions can be accommodated. Best results [10] were obtained when the maximum diameter of the meniscus exceeded the rim diameter by about 5% and when the angle $\psi = 110 - 115°$.

The sessile drop technique is the method most often used to determine interfacial tension between liquid metals and slags at high temperatures. Two variants exist viz (A) a sessile drop of liquid metal submerged in slag and (B) a sessile drop of slag floating on the surface of liquid metal.

(I) Method (A)

The principle of this method is shown schematically in Fig. 10.1a, where (L) represents the liquid metal drop and the gas phase (G) is replaced by liquid slag. In practice, the metal drop rests on the flat horizontal base of a suitable container, which is filled with slag, and the interfacial tension is calculated in the usual manner from measurements of the sessile drop profile (account must be taken for the density of the slag). Since both the container and slag are opaque to visible radiation, images of the sessile drop have to be obtained by X-ray photography. This imposes certain practical problems, since in addition to the need for expensive equipment and extra safety precautions, it is not always easy to produce a sharply focussed image of the drop. To obtain an image of acceptable intensity it is often necessary to use relatively long exposure times (depending on system, ranging from seconds up to several minutes). In consequence there is a continual possibility of slight movement of the drop during the exposure period. Another difficulty inherent to this method, is the need to have a container which is reasonably transparent to X-rays and is chemically compatible with both the slag and metal. For calculation of the interfacial tension, it is necessary to know the density of both slag and metal.

(II) Method (B)

Fig. 10.1d shows the profile of a drop of liquid slag (L_1) floating on the horizontal surface of a liquid metal (L_2). If the spreading coefficient (S_p) is low, the slag drop will remain as a lens shape and will not spread across the surface. For equilibrium, resolution of forces gives

$$\gamma_{L_1G} \sin\alpha = \gamma_{L_1L_2} \sin\beta$$

and

$$\gamma_{L_2G} = \gamma_{L_1G} \cos\alpha + \gamma_{L_1L_2} \cos\beta.$$

Squaring both equations and adding to eliminate terms in (β), gives

$$\gamma^2_{L_1L_2} = \gamma^2_{L_1G} + \gamma^2_{L_2G} - 2\gamma_{L_1G}\,\gamma_{L_2G} \cos\alpha.$$

From measurement of the angle (α) and provided (γ_{L_1G}) and (γ_{L_2G}) are known, it is possible to compute ($\gamma_{L_1L_2}$).

This method is experimentally more simple than method (A), since the drop image can be obtained by optical means and compatibility problems are reduced to that between the metal and its container. One potential problem is that a relatively large surface area of liquid metal is required to ensure a good approximation to a horizontal surface. The metal surface is continually exposed to the environment and close control of gas or vacuum composition may be critical since the surface tensions of many metals are particularly sensitive to oxygen, even when present at very low levels. Variation in (γ_{L_2G}) will be reflected in the value obtained for ($\gamma_{L_1L_2}$), which will not pertain to the original system. The tip of a thin wire of inert metal can be inserted into the apex of the slag drop to restrain movement of the slag across the metal surface. The basic theory behind method (B) is less sound than that for method (A), since it is based on the assumption that angle (ϕ) (Fig. 10.1c) is effectively zero. Calculations have shown that for some systems eg slag on steel, this assumption would be valid. The magnitude of (ϕ) will be governed by (I) the values of the respective surface and interfacial tensions, (II) the density difference ($\Delta\rho$) between the two fluids ($\phi \uparrow$ as $\Delta\rho \downarrow$), and (III) the volume (V) of the drop ($\phi \uparrow$ as $V \uparrow$). The method is subject to accumulated errors arising from uncertainties in the respective values assumed for (γ_{L_1G}) and (γ_{L_2G}) and from difficulties in the accurate measurement of the angle (α).

10.2.4 Pendent drop (PD)

When a liquid drop hangs freely from an orifice of a capillary tube, it will adopt a shape which is generally similar to that shown in **Fig. 10.4**. The configuration of the pendent drop shape results from the balance between surface tension and gravitational forces acting in the system. A pendent drop, is in effect, an inverted sessile drop and is mathematically described by equation (10.6). In the case of the pendent drop, the origin is taken to be at the bottom of the drop and (following Bashforth and Adams' convention) [6], the sign of the shape factor (β) is negative. The Bashforth and Adams' mode of analysis for the sessile drop can also be applied to a pendent drop, but there are practical difficulties in obtaining an accurate determination of certain critical dimensions (eg (b) – the radius of curvature at the origin). To avoid this problem, the procedure developed by Andreas et al [11] is generally adopted. Andreas et al proposed a second shape factor (S), which is given by the ratio of the equatorial diameter (d_e) and the diameter (d_s) at a height (d_e) above the origin (Fig. 10.4) ie

$$S = \left[\frac{d_e}{d_s}\right].$$

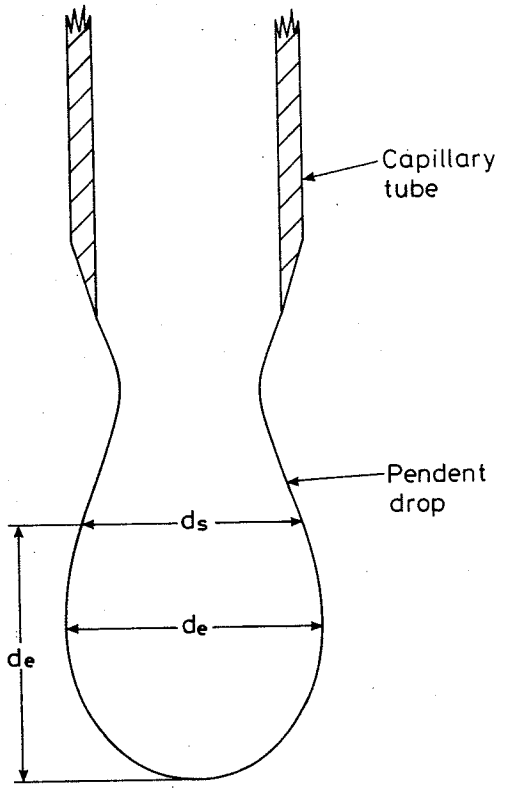


Fig. 10.4. Diagram of a pendent drop

A third shape factor (H) was also introduced, and is defined by

$$H = \beta \left[\frac{d_e}{b}\right]^2 = \frac{\rho g d_e^2}{\gamma} \qquad (10.9)$$

and a set of tables was produced, which relates S and (1/H). Having established the value for (S) from drop dimensions, the equivalent value for (H) is taken from the tables and substituted in equation (10.9) to give the ratio (ρ/γ) and hence (γ) if (ρ) is known accurately.

As with the sessile drop, computer curve-fitting techniques can be applied to images of the pendent drop. By using video-image analysis routines, Girault et al [12] have determined (γ) of organic liquids by location of the diameter at the point of inflexion on the surface contour. At this point, one of the principal radii of curvature is infinite and consequently, the mathematical treatment is somewhat simplified. The point of inflexion is difficult to locate manually, but from a video image, the relative locations of many points on the surface can be established, and the drop profile in the vicinity of the inflexion point can be equated to a best-fit polynomial.

In common with the sessile drop, the pendent drop method presents practical problems such as, chemical compatibility, accurate alignment of optics, careful measurement of relatively small dimensions. In addition, any instability induced during the experiment may lead to the drop becoming detached from the tube. The temperature range over which (γ) can be measured during a particular experiment is likely to be considerably less than that obtained with the sessile drop technique. One advantage that the pendent drop method offers, is the possibility of avoiding problems of chemical compatibility between the liquid and its container, by producing a drop at the end of a rod of the same material. This usually involves the use of a focussed heat source such as electron or laser beam which can introduce stability problems and difficulties in determining the temperature of the drop.

The pendent drop technique has been used to determine interfacial tension between organic liquids, but has found very little application at high temperatures, probably since it does not offer significant advantages over the well-established sessile drop methods.

10.2.5 Drop weight (DW)

The experimental basis of this technique, is to slowly produce at the end of a capillary tube, a liquid drop which increases in size until it ultimately detaches and is collected in a container. This procedure is repeated a number of times until sufficient material has accumulated to establish an accurate value for the mean weight per drop. Under ideal circumstances, the gravitational force acting on the drop at the point of detachment would be equal to the opposing surface tension force, in accord with Tate's Law

$$W_{ideal} = 2\,\pi r \cdot \gamma$$

(where r = radius of the tube).

In reality, the mechanism of drop formation and detachment is a complicated process and the actual weight of the drop is always less than the "ideal" weight. As the drop grows, the neck of liquid between it and the capillary tube continually elongates until ultimately, it is unable to support the mass of the growing drop. Premature detachment of the drop ensues and this is often accompanied by one or two very small satellite drops (Plateau Spherules), which originate from the region of the rupture neck. Some of the liquid from the neck remains attached to the capillary tube. Harkins and Brown [13] produced tables of empirically determined factors (f) which correct for the difference between the observed weight (W) and the "ideal" weight of a drop, as predicted by Tate's Law, ie

$$W = 2\,\pi r \gamma \cdot f.$$

In common with correction factors produced for some other techniques to determine (γ), values for (f) were derived by using low density liquids of known, but low surface tension (eg water, organic fluids) and it has not been fully established whether their application can be extended to measurements on liquids which have high density and surface tension (eg metals). The factor (f) is a function of the ratio $r/(V)^{1/3}$ (where V is the volume of the drop), and the usual procedure is to determine (V) from the drop weight (provided the density is known with sufficient accuracy), and establish the relevant value for (f) from tables [13] which relate (f) and $r/(V)^{1/3}$. The magnitude of the correction factor can be substantial, being up to 35 – 40% of the measured parameter. The tube dimensions for any experiment should ideally be selected such that the ratio $r/(V)^{1/3}$ lies between 0.6 and 1.2, since the variation in (f) is least over this range [2]. To minimise problems with wetting angle effects, tapered tubes can be used (as with the MBP and PD methods).

The DW technique is effectively a quasi-dynamic process and it is important that drops form slowly, particularly during the final stages before detachment. Controlled rate of drop formation is usually obtained by regulating the pres-

sure applied to the head of liquid above the capillary tube. For very high temperature, a variant of the established procedure is to produce drops by melting the tip of a rod of known radius. This avoids possible contamination by the container tubes, but introduces other problems eg special melting techniques are required to limit the molten zone to the tip of the rod; it is difficult to control the rate of drop formation; the temperature range is restricted to the vicinity of the melting point; the radius of the rod at the liquid/solid interface may change due to expansion and local vaporisation.

The interfacial tension between liquid metals and slags has been determined [14] by the DW technique. A thin rod of the metal, is held in a capillary tube, which is attached at one end to a balance. The other end is dipped into the molten slag, and the change in weight with each drop detachment is recorded. The usual relations can be applied provided allowance is made for the buoyancy effects acting on the drop, ie the density of both the slag and the metal need to be known. It is important to be aware of any mass transfer across the liquid/liquid interface as this will generate a dynamic state in which the interfacial tension continually varies and meaningless results would ensue until equilibrium is attained.

10.2.6 Detachment or maximum-pull methods

At high temperatures, these techniques have been mainly restricted to measurements on molten salts [15] and oxide systems such as slags, glasses, phosphates, borates [16] etc and they have been used rarely with metallic systems. Determination of (γ) by the detachment methods is based upon measurement of the maximum force exerted on a body as it is withdrawn from the surface of a liquid. The shape of the body used in the experiment can take a variety of forms, eg ring, thin plate, rod and hollow cylinder. When the body is slowly pulled from the surface of a fluid, then, providing the wetting conditions are appropriate, a meniscus of the liquid adheres to the base and continually extends as the body is withdrawn. The force acting is a resultant of the forces due to surface tension and mass. As the failure-point of the meniscus is approached, and force required to draw the body away from the surface goes through a maximum, and from measurement of this maximum force it is possible to calculate (γ).

The detachment method commonly used for slag melts at high temperatures is the maximum-pull on a hollow cylinder (MPC). A thin-walled cylindrical tube is attached by one end to a continuously recording balance and the rim of the opposite end is dipped just below the surface of the melt **(Fig. 10.5 a)**. The liquid level is slowly lowered and the meniscus attached to the rim of the cylinder gradually extends **(Fig. 10.5 b)** until it ultimately fails. If the maximum excess weight recorded by the balance is (W_{max}) then (γ) can be calculated from the relation

$$\gamma = \frac{(W_{max} \cdot g)}{4\pi r} \cdot F \qquad (10.10)$$

where r = mean radius of the cylinder,
F = a correction factor, which allows for the shape of the meniscus and the dimensions of the cylinder.

The factor (F) can be established by either calibration of the system with liquids of known (γ) or calculation using the somewhat cumbersome empirical equation derived by Verschaffelt [17]. Allowance has to be made for dimensional changes at high temperatures due to thermal expansion. The only criterion with regard to wetting of the cylinder by the melt, is that the adhesion at the liquid-solid interface must be sufficient to ensure that failure occurs within the meniscus [18]. When dealing with high viscosity liquids, it may be necessary to introduce an additional correction term in equation (10.1).

A variant of the (MPC) technique, which has often been used with molten salt systems, is the pin-detachment method developed by Janz and Lorenz [19]. The pin has a flat circular end-face (diameter = 1 mm) and is an integral part of a special bob **(Fig. 10.5 c)**, which is also used in the same experiment to determine the density of the melt by the Archimedean principle. The system is calibrated by using liquids of known (γ).

For completely wetting systems ($\theta = 0°$), a variation [3] on the detachment technique has been used, which entails measurement of the maximum force acting on a inverted cone as it is slowly withdrawn from a fluid. With the inverted cone configuration, the apex of the cone is still submerged below the liquid surface when the maximum force condition is attained, and consequently, it is unnecessary to completely withdraw the cone to break the meniscus (meniscus failure usually occurs when the apex is well clear of the surface). The cone method is claimed to possess a unique advantage over other maximum force (detachment) methods, in that the relation between surface tension and the

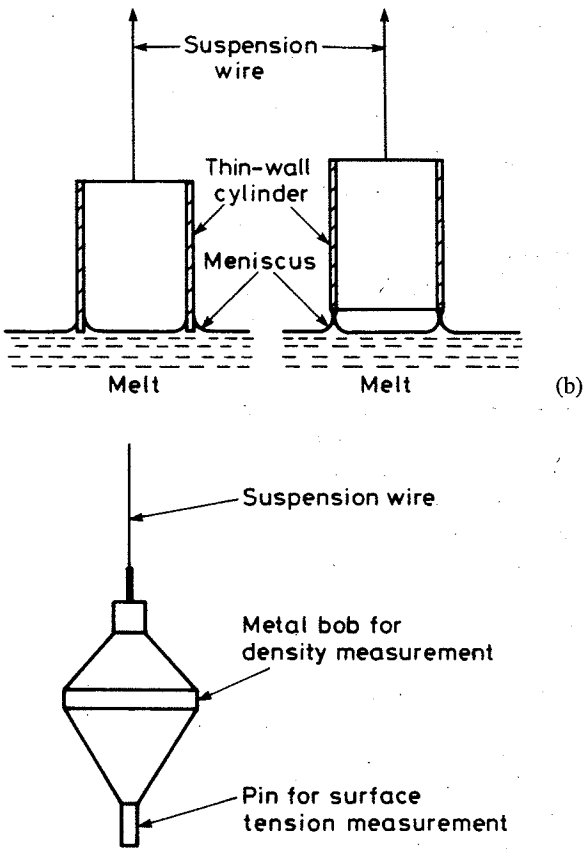
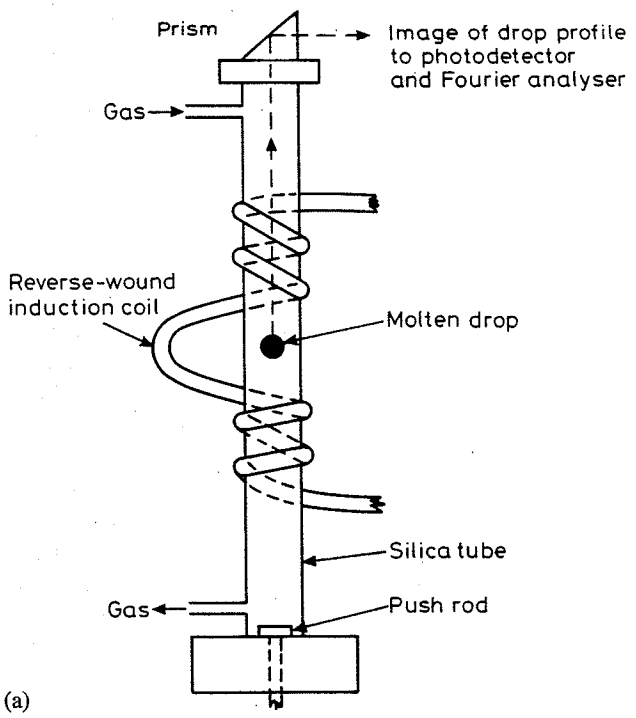
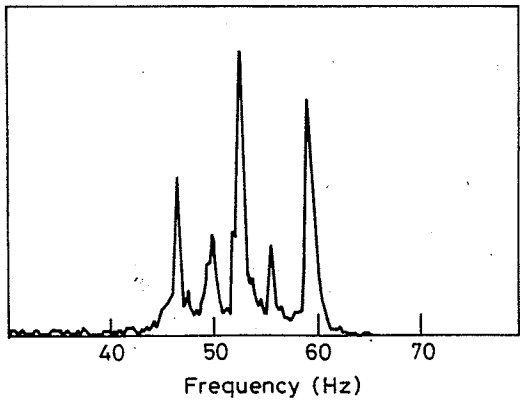


Fig. 10.5 a-c.
(a) Cylinder rim in contact with the surface of a melt
(b) Cylinder withdrawn from surface of the melt, showing the adherent meniscus just before failure
(c) Metal bob for method proposed by Janz and Lorenz [19], to measure surface tension and density of a melt in the same experiment



(a)



(b)

Fig. 10.6 a,b.
(a) Schematic diagram of levitating drop apparatus
(b) Typical frequency spectrum from a levitating drop

maximum excess force (expressed as maximum excess weight (W_{max})), is simple viz

$$\gamma = \rho \cdot g \cdot \left[\frac{W_{max}}{C}\right]^{2/3}$$

(where C is a cone constant, which depends upon the apex angle and is determined by calibration with liquids of known (γ)).

The maximum-pull technique has been used to determine interfacial tension at low temperatures, usually by pulling a ring or thin plate through the interface between the two liquids. The technique does not appear to have been used for slag/metal systems at high temperatures, possibly due to the difficulty in obtaining suitable materials which would be compatible with both fluids.

10.2.7 Levitating drop

This technique to measure (γ) is a relatively recent development and a schematic diagram of a typical apparatus is shown in **Fig. 10.6 a.** A sample of electrically conducting material (about 0.5 g) is introduced, via a push-rod, into the electromagnetic-field of an induction coil, where it levitates and melts. Small perturbations in the system cause the drop to continuously oscillate at its natural frequency (ω_n), which is related to the surface tension. To determine the oscillation frequency, an image of the drop is focussed on to a photodetector system, and the frequency content of the resultant electrical signal is displayed as a spectrum from a Fourier analyser. Provided the amplitude of the oscillations is small, the drop shape could be considered spherical, and for low viscosity fluids, the relation between (ω_n) and (γ) for a drop of mass (m) is given by the Rayleigh equation [20]

$$\gamma = \frac{3}{8} \cdot \pi \cdot m \cdot \omega_n^2.$$

In practice, the drops are aspherical and additional vibrational modes are present. **Fig. 10.6 b** is a record of a typical frequency spectrum (for molten iron) and shows five major peaks. The Rayleigh frequency (ω_n) is given by the centre peak which is flanked on either side by two satellite peaks resulting from other vibrational modes, possibly due to asphericity and rotation of the drop.

A unique advantage of this technique, is that there is no contact between the molten material and a solid medium and consequently, contamination is minimal. Determination of the sample temperature can be a problem, since only pyrometric methods can be used and consequently, either the emissivity of the material must be known or reliance has to be placed on measurements made with multi-colour pyrometers.

Because of the two basic requirements that the sample material is an electrical conductor and has low viscosity, applications of the levitating drop method at high temperatures have been confined to metallic systems. It is possible that with some systems, preheating of a slag may increase the electrical conductivity of the material sufficiently to allow the sample to couple with the electromagnetic field. A possible alternative to electromagnetic levitation, is the acoustic technique in which a liquid drop is levitated by a high intensity acoustic field generated by an ultrasonic transducer. In this case the sample does not need to be an electrical conductor. This method is capable of levitating drops of liquids with densities up to about 10 $g.cm^{-3}$, and has been successfully used to determine (γ) of water and organic liquids, but, to date, has not been developed for measurements at high temperature.

10.3 Surface tension data

10.3.1 Pure components

Tab. 10.1. Surface tension of some oxides at 1350 °C [Ref. 21]

Oxide	Surface tension/mN.m^{-1}
Al_2O_3 (s)	313
CaO (s)	310
CeO_2 (s)	315
Fe_2O_3 (s)	311
K_2O (l)	286
MgO (s)	314
Mn_2O_3 (s)	310
Na_2O (l)	298
SiO_2 (s)	303

Al_2O_3

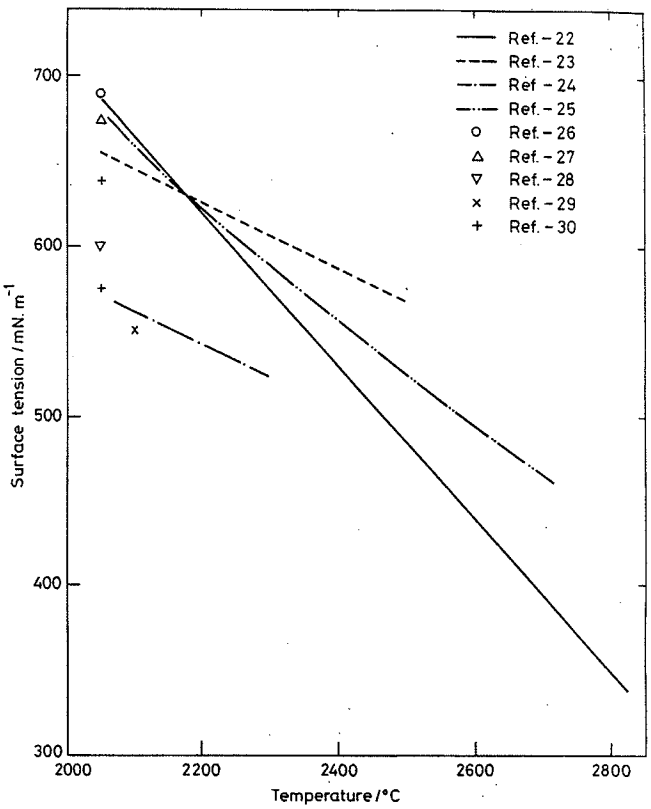


Fig. 10.7. Variation of the surface tension of Al_2O_3 with temperature

B_2O_3

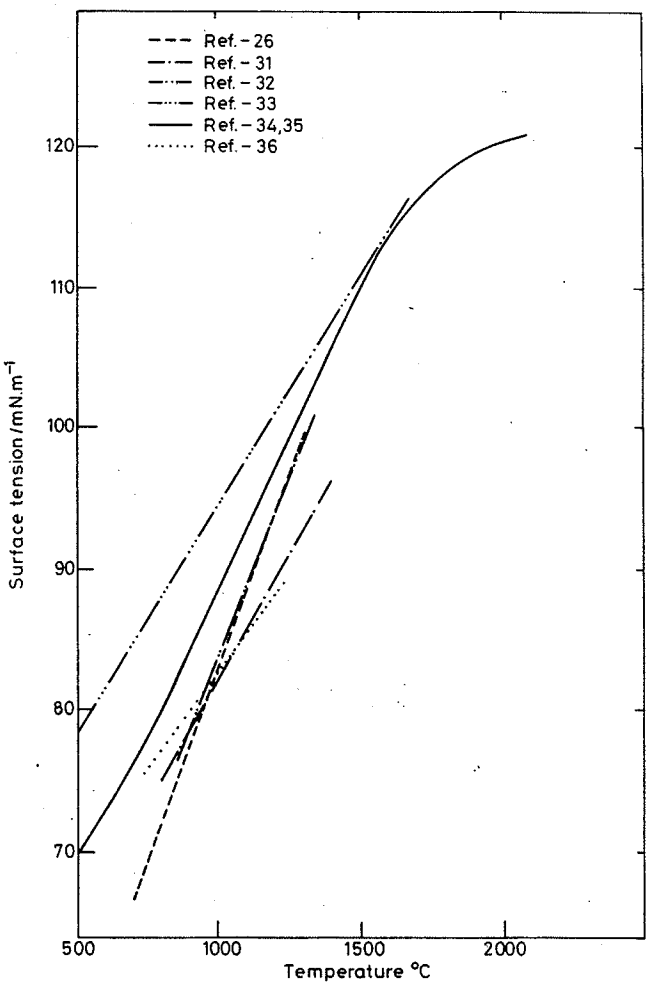


Fig. 10.8. Variation of the surface tension of B_2O_3 with temperature

CaF_2

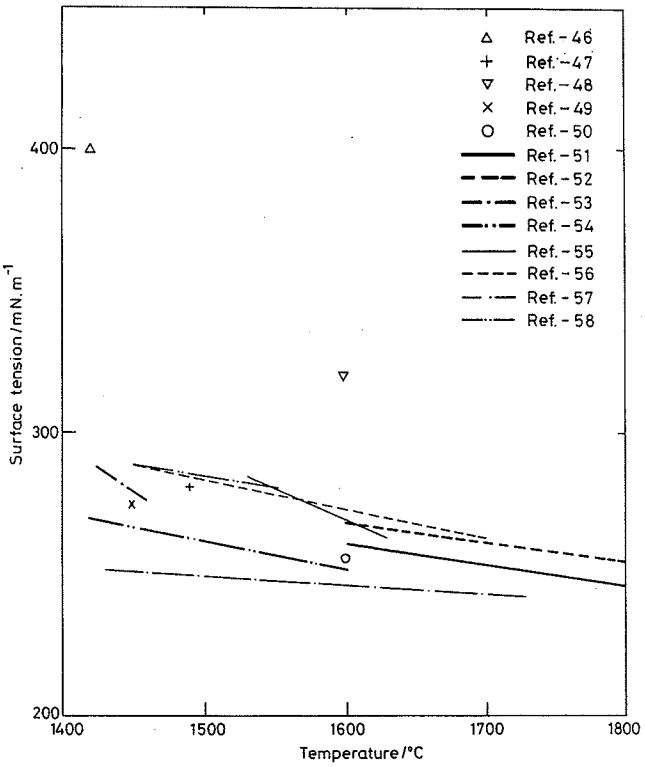


Fig. 10.9. Variation of the surface tension of CaF_2 with temperature

Cr_2O_3

Tab. 10.2. Surface tension of Cr_2O_3

Temperature / °C	Surface tension / mN.m^{-1}	Reference
MP (~ 2250 °)	812 ± 87	[37]

FeO, Fe_2O_3

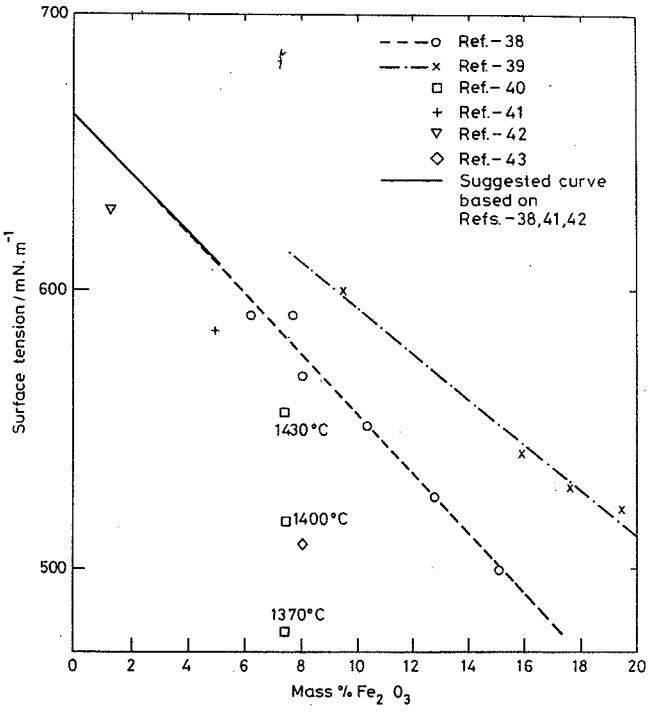


Fig. 10.10. The effect of Fe_2O_3 content on the surface tension of Fe_xO (FeO + Fe_2O_3) at about 1400 °C

FeS

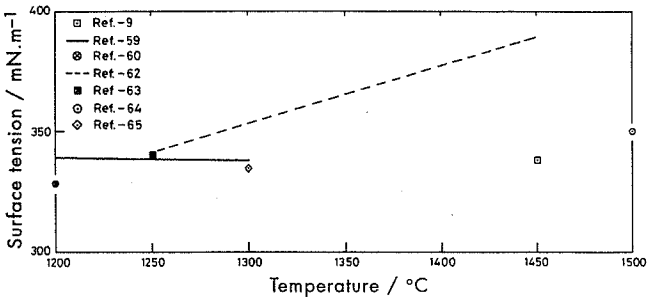


Fig. 10.11. Variation of the surface tension of FeS with temperature

MnO

Tab. 10.3. Surface tension of MnO

Temperature / °C	Surface tension/mN.m^{-1}	Reference
not quoted	595 (extrapolated)	[38]
1850 °	620	[42]

Na_3AlF_6

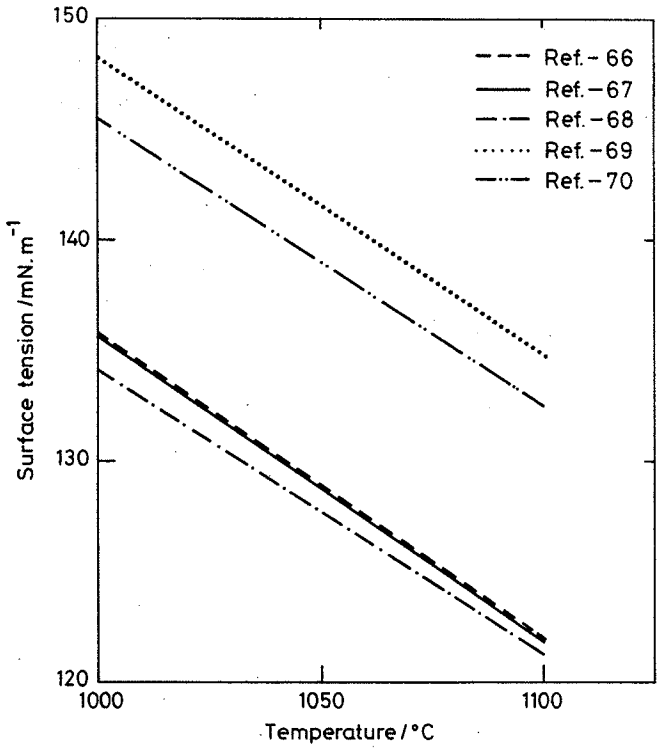


Fig. 10.12. Variation of the surface tension of Na_3AlF_6 with temperature

SiO_2

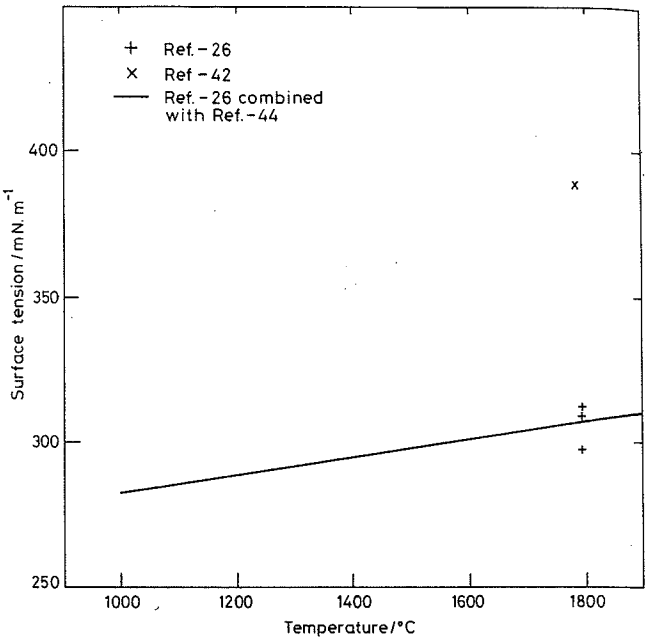


Fig. 10.13. Surface tension of SiO_2 at about the melting point and the suggested [Ref. 26] variation with temperature

TiO_2

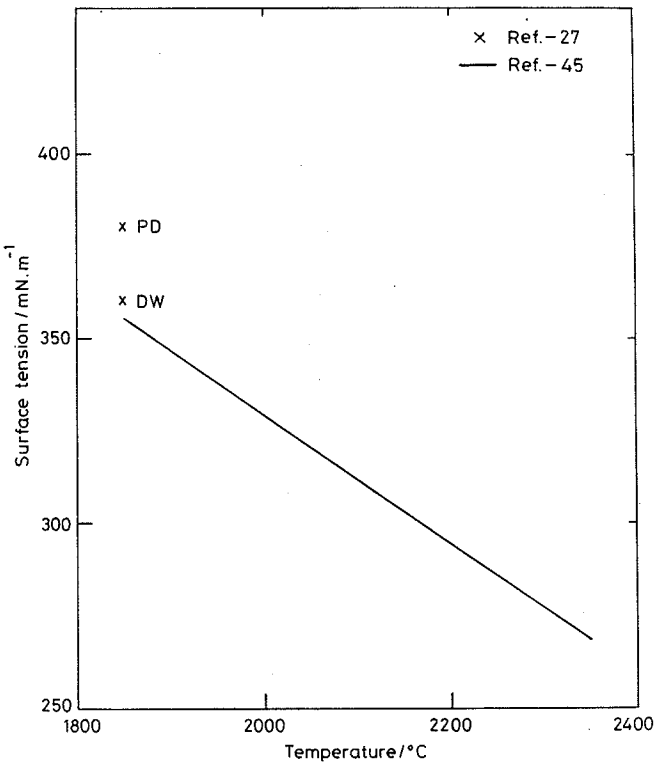


Fig. 10.14. Variation of the surface tension of TiO_2 with temperature

10.3.2 Binary systems

Al_2O_3-CaF_2

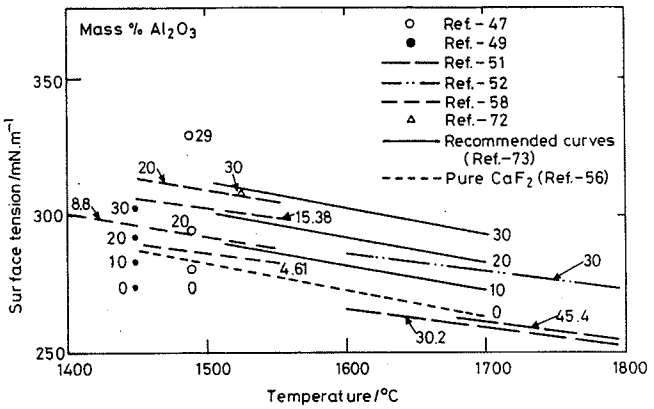


Fig. 10.15. Variation of the surface tension of Al_2O_3 + CaF_2 melts with temperature

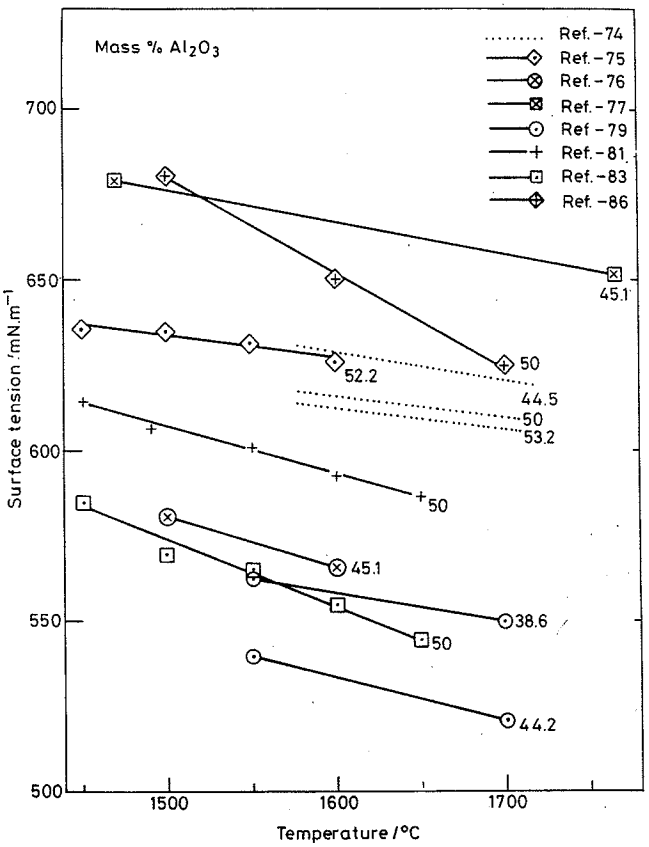


Fig. 10.17. Variation of the surface tension of the Al_2O_3 + CaO system with temperature

Al_2O_3-CaO

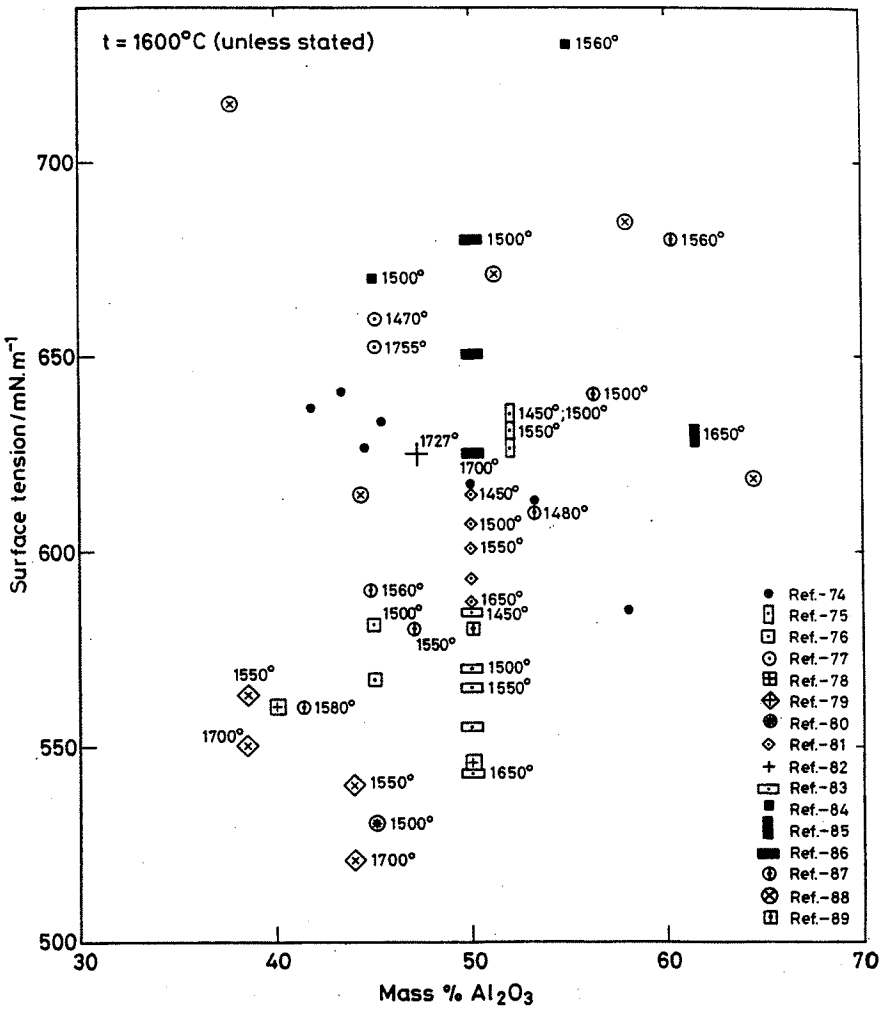


Fig. 10.16.
Surface tension of Al_2O_3 + CaO melts

Al_2O_3-Cr_2O_3

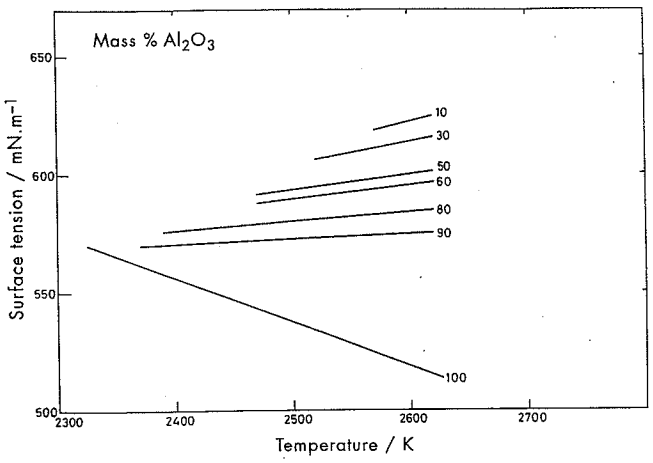


Fig. 10.18. Variation of the surface tension of Al_2O_3 + Cr_2O_3 melts with temperature [Ref. 90]

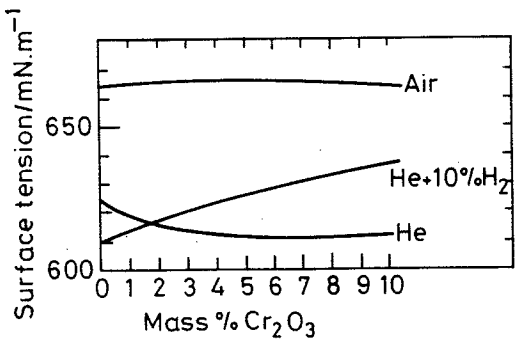


Fig. 10.19. Surface tension at the melting point of melts in the Al_2O_3 + Cr_2O_3 system under different atmospheres [Ref. 91]

Al_2O_3-MgO

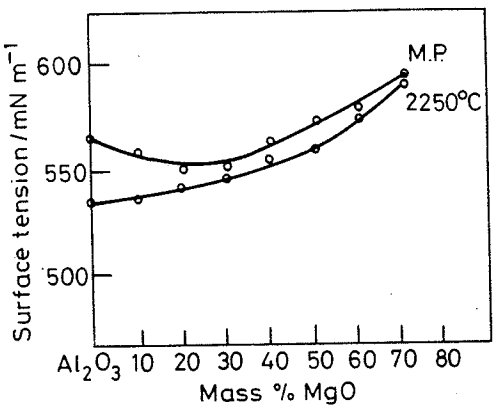


Fig. 10.20. Surface tension of Al_2O_3 + MgO melts at the melting point and at 2250 °C [Ref. 92]

Al_2O_3-SiO_2

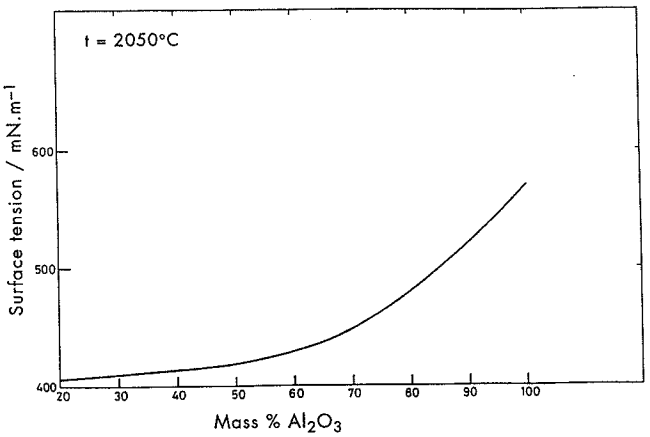


Fig. 10.21. Surface tension of Al_2O_3 + SiO_2 melts at 2050 °C [Ref. 90]

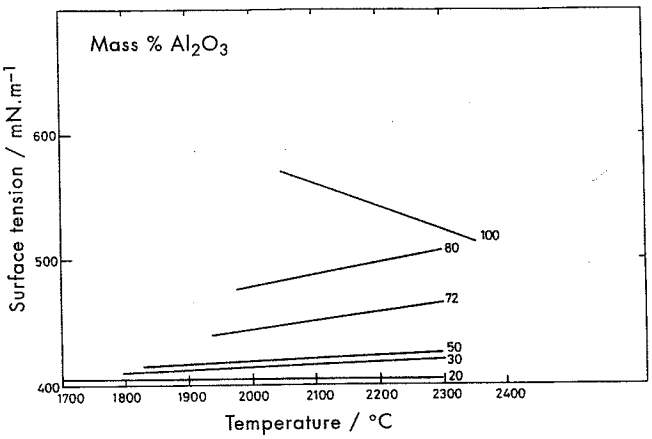


Fig. 10.22. Effect of temperature on the surface tension of Al_2O_3 + SiO_2 melts [Ref. 90]

Al_2O_3-TiO_2

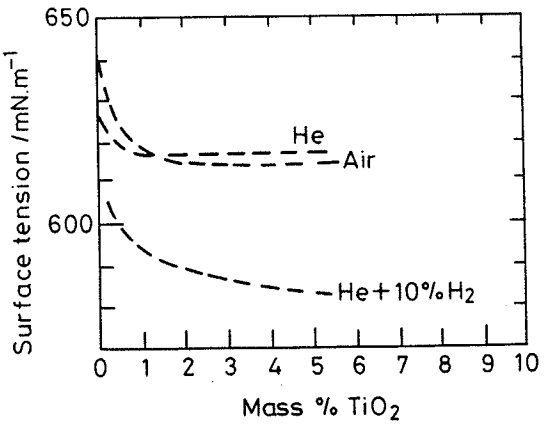


Fig. 10.23. Surface tension at the melting point of melts in the Al_2O_3 + TiO_2 system under different atmospheres [Ref. 91]

Al_2O_3-ZrO_2

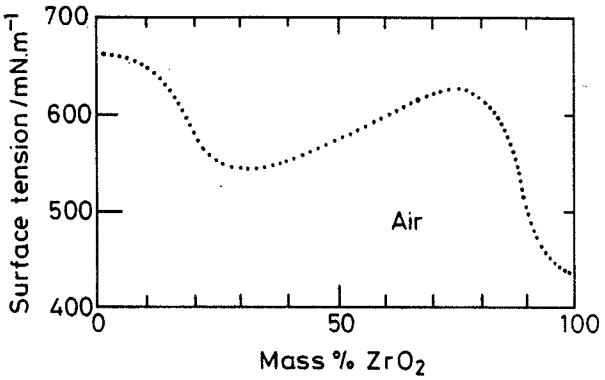


Fig. 10.24. Surface tension at the melting point of melts in the Al_2O_3 + ZrO_2 system [Ref. 91]

B_2O_3-CaO

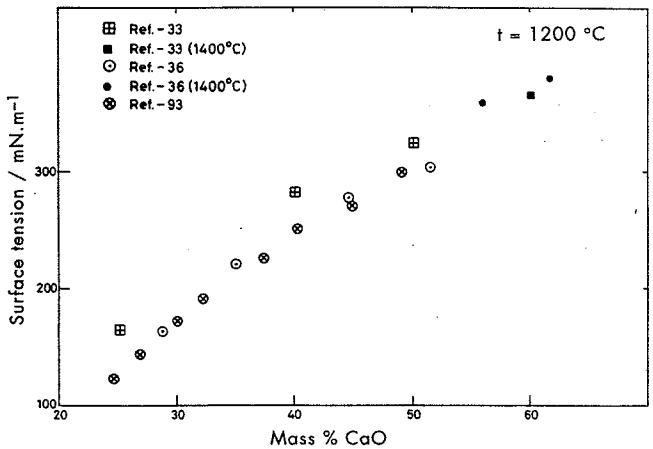


Fig. 10.25. Surface tension of B_2O_3 + CaO melts at 1200 °C

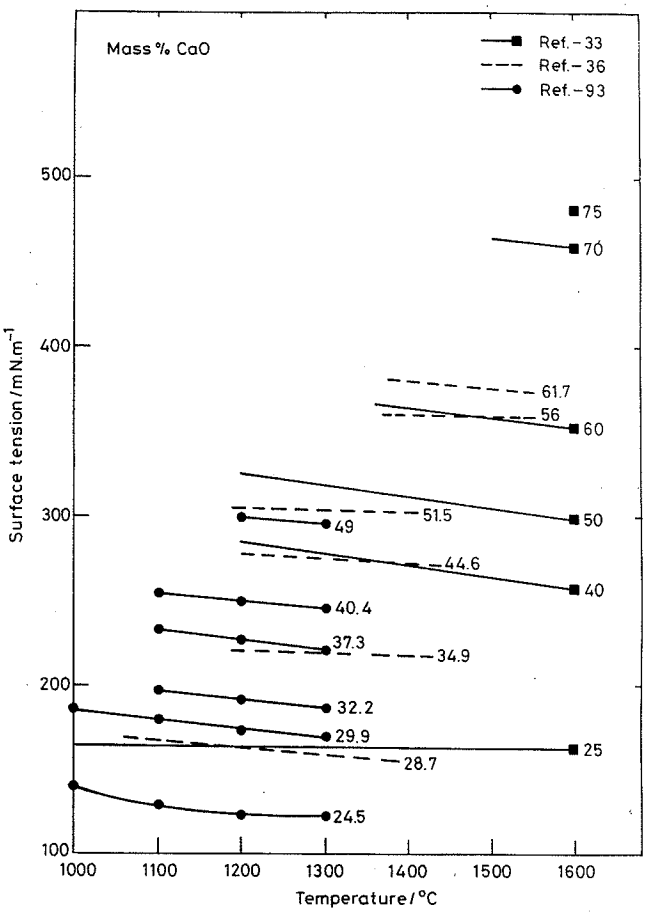


Fig. 10.26. Variation of the surface tension of B_2O_3 + CaO melts with temperature

CaF_2-CaO

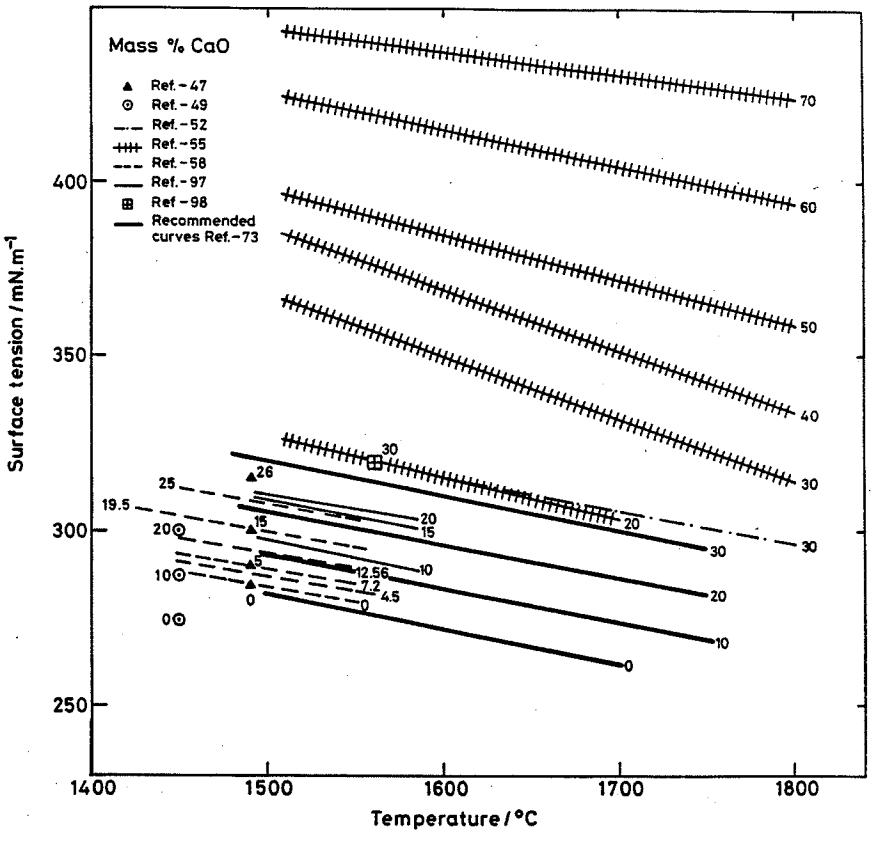


Fig. 10.27. Variation of the surface tension of CaF_2 + CaO melts with temperature

CaF_2-MgO

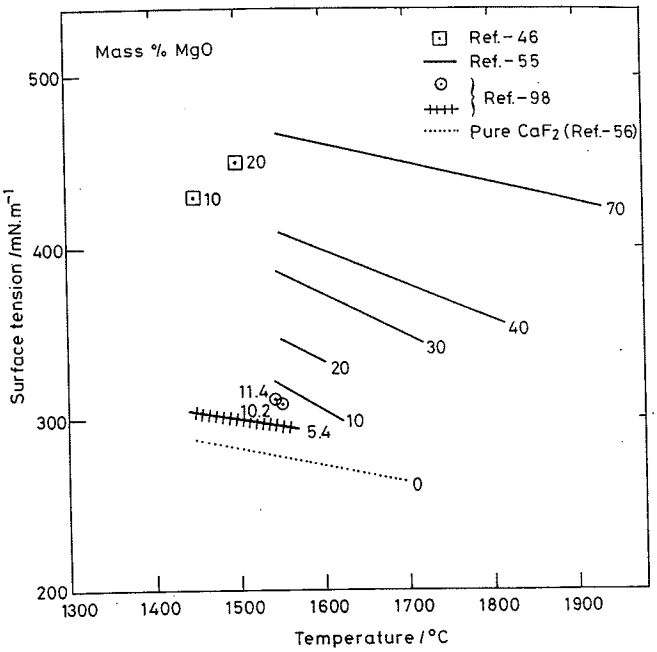


Fig. 10.28. Variation of the surface tension of CaF_2 + MgO melts with temperature

CaF_2-SiO_2

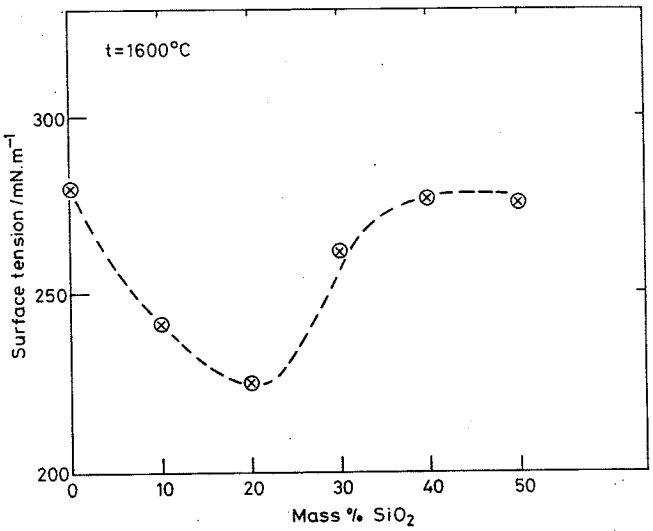


Fig. 10.29. Change in surface tension with composition of CaF_2 + SiO_2 melts at 1600 °C [Ref. 99]

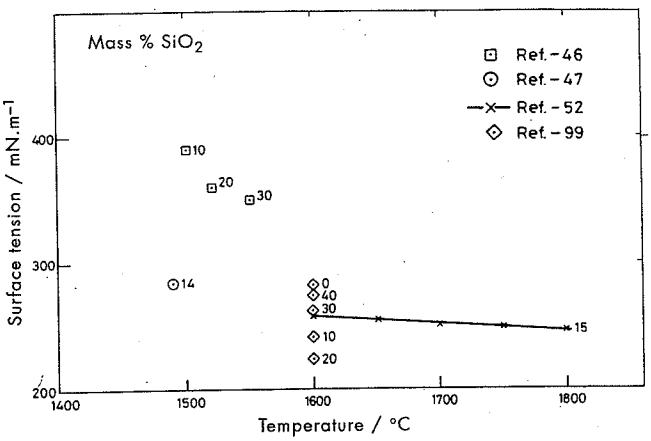


Fig. 10.30. Surface tension of CaF_2 + SiO_2 melts at various temperatures

CaF_2-TiO_2

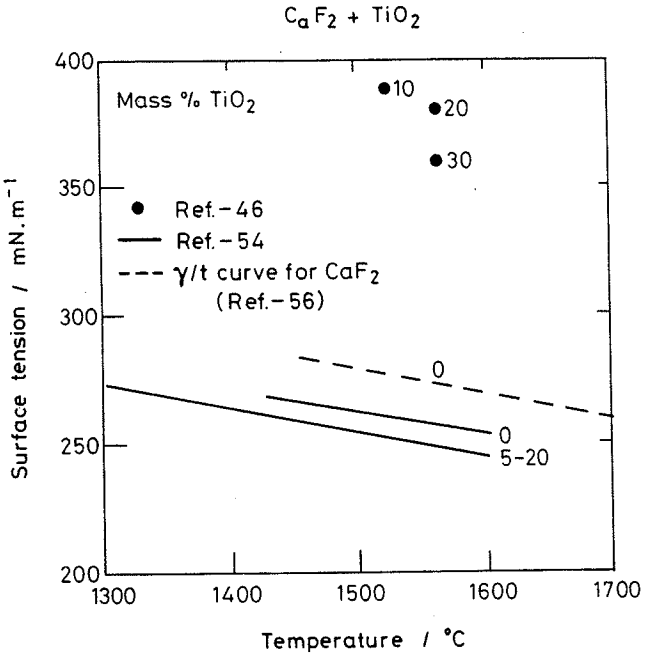


Fig. 10.31. Effect of temperature on the surface tension of some CaF_2 + TiO_2 melts

CaF_2-V_2O_5

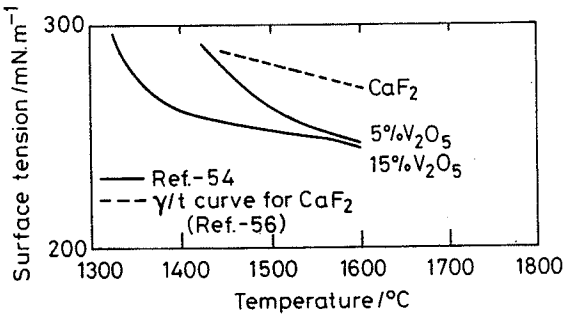


Fig. 10.32. Variation with temperature of the surface tension of CaF_2 + V_2O_5 melts containing 5 mass % and 15 mass % V_2O_5 respectively

CaO-Fe_xO

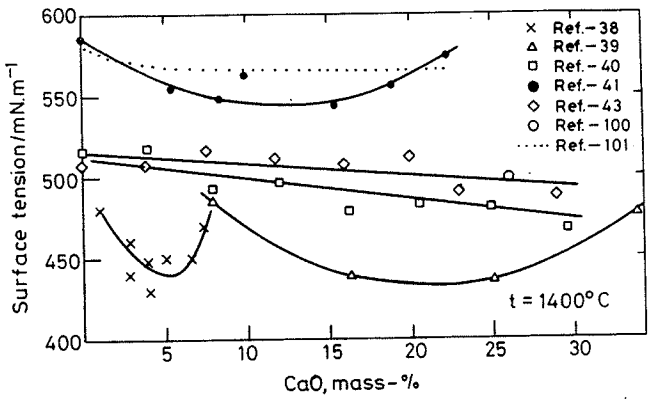


Fig. 10.33. Change in surface tension with composition of CaO + Fe_xO melts at 1400 °C

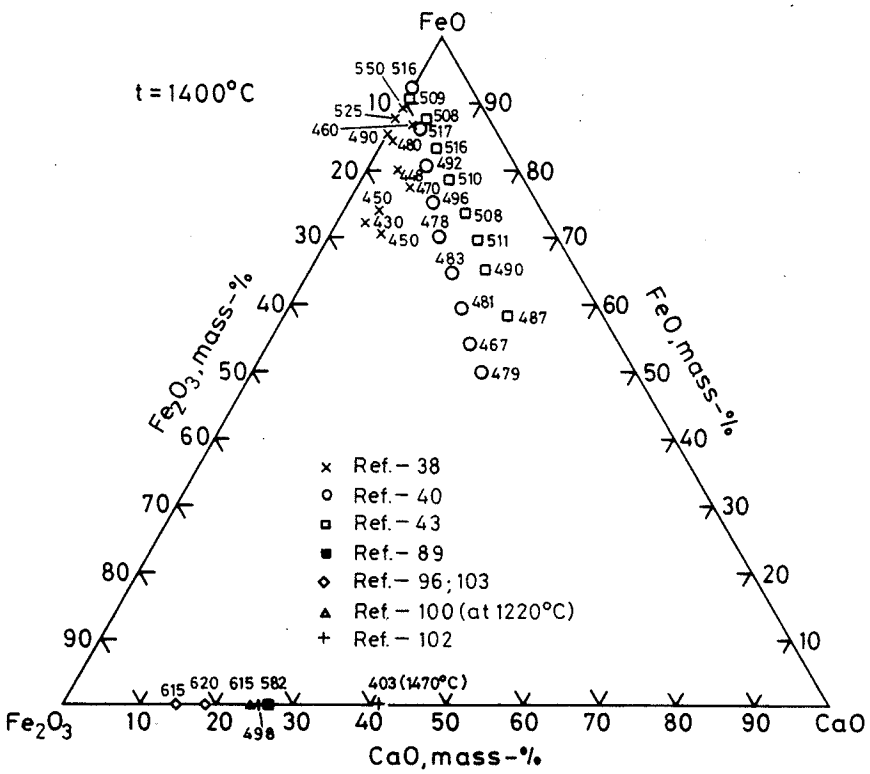


Fig. 10.34. Surface tension ($mN.m^{-1}$) of CaO + Fe_xO (expressed as CaO + FeO + Fe_2O_3) melts at 1400 °C

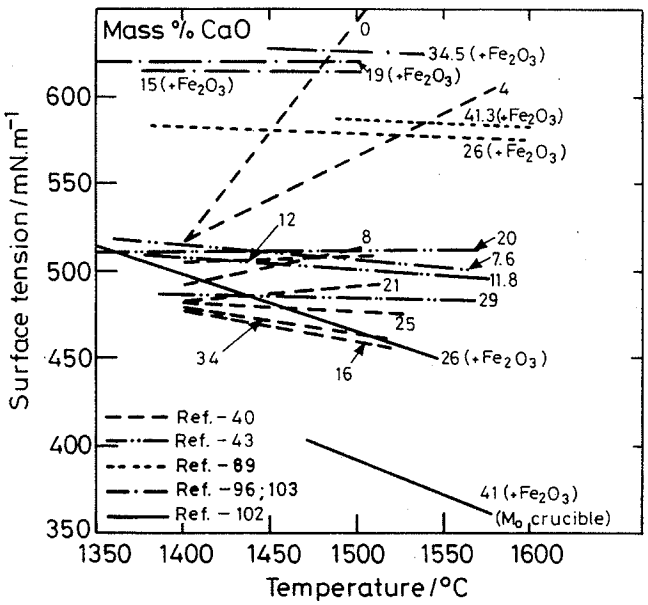


Fig. 10.35. Variation of the surface tension of CaO + Fe_xO melts and CaO + Fe_2O_3 melts (indicated by + Fe_2O_3 on diagram), with temperature

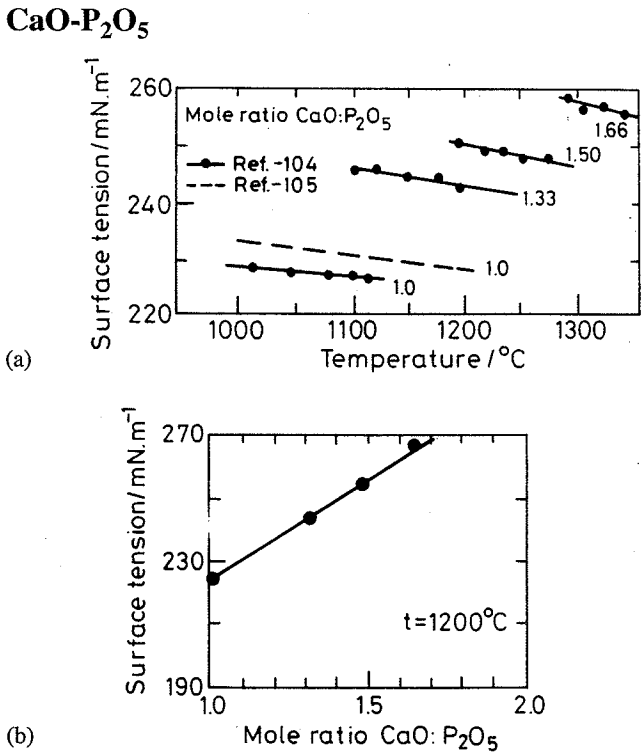


Fig. 10.36 a,b.
(a) Variation of the surface tension of CaO + P_2O_5 melts with temperature
(b) Change in surface tension with composition of CaO + P_2O_5 melts at 1200 °C [Ref. 104]

$CaO\text{-}SiO_2$

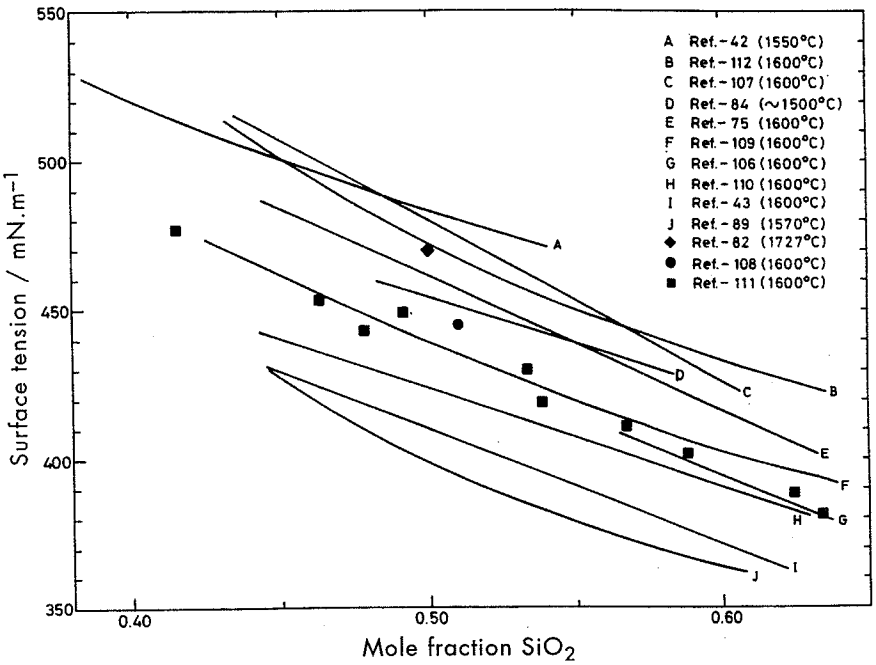


Fig. 10.37. Change in surface tension with composition of $CaO + SiO_2$ melts

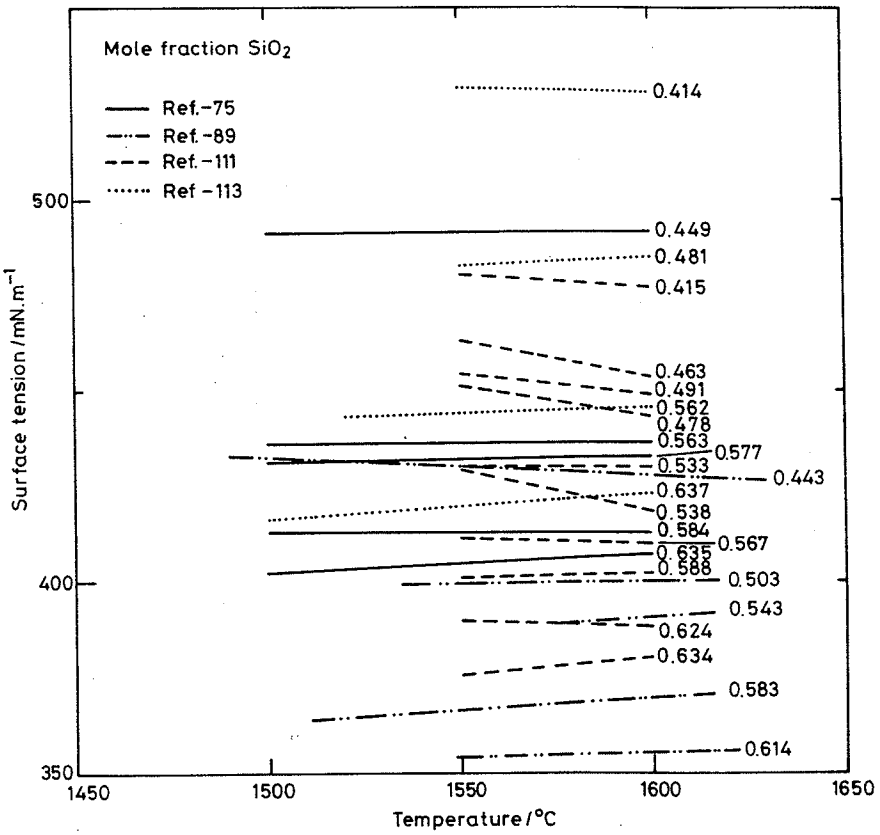


Fig. 10.38. Variation of the surface tension of $CaO + SiO_2$ melts with temperature

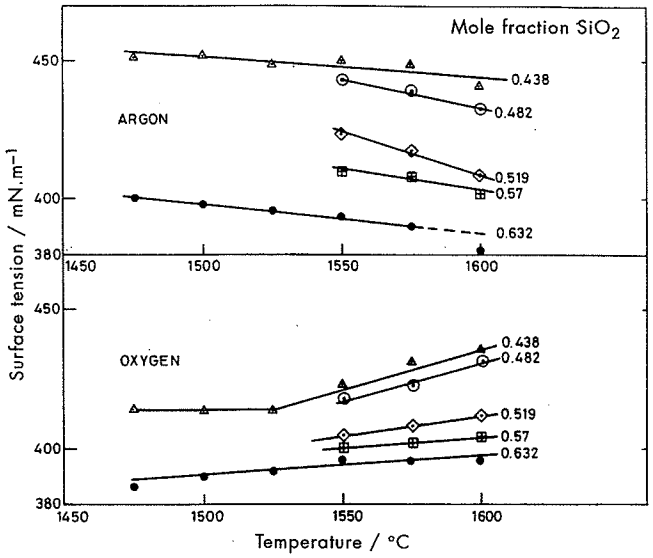


Fig. 10.39. Variation of the surface tension of CaO + SiO_2 melts with temperature, under argon and under oxygen [Ref. 110]

Fe_xO-MnO

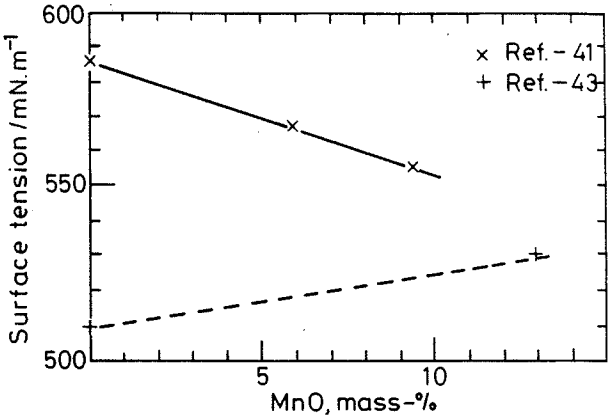


Fig. 10.41. Effect of composition on the surface tension of Fe_xO + MnO melts at 1414 °C [Ref. 41] and at 1460 °C [Ref. 43]

CaO-V_2O_5

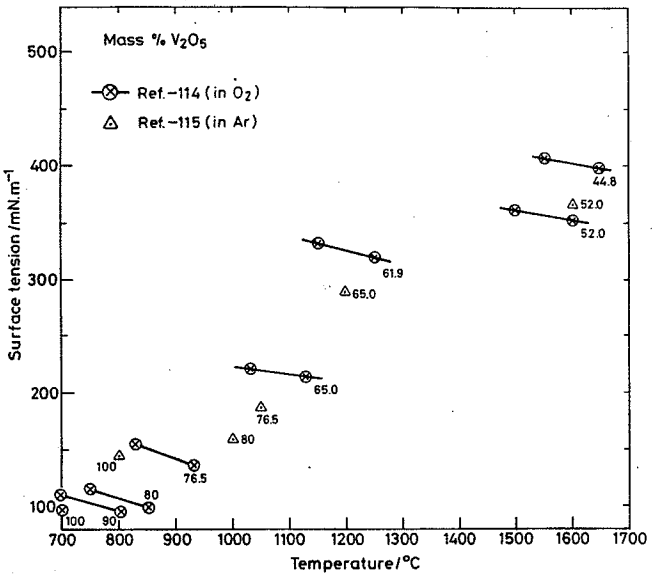


Fig. 10.40. Variation of the surface tension of CaO + V_2O_5 melts with temperature, under argon [Ref. 115] and under oxygen [Ref. 114]

Fe_xO-P_2O_5

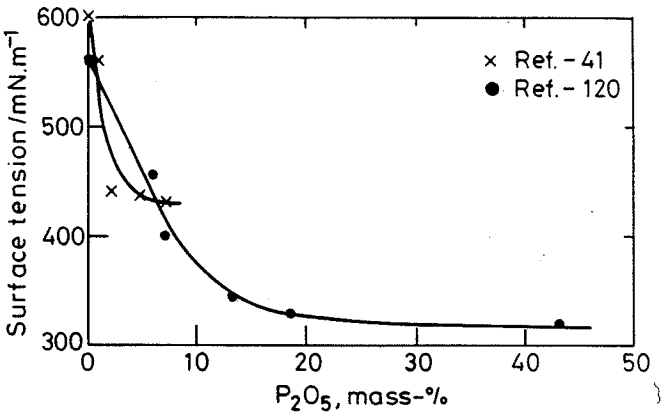


Fig. 10.42. Change in surface tension with composition of Fe_xO + P_2O_5 melts at 1480-1500 °C [Ref. 41] and at 1350-1400 °C [Ref. 120]

Fe_xO-SiO_2

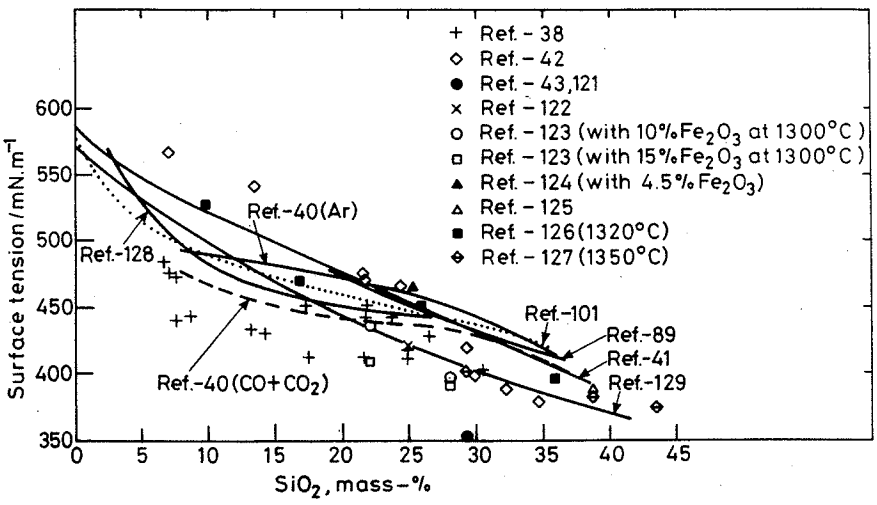


Fig. 10.43. Change in surface tension with composition of Fe_xO + SiO_2 melts at 1400 °C [Ref. 41] (or at temperature indicated on the legend)

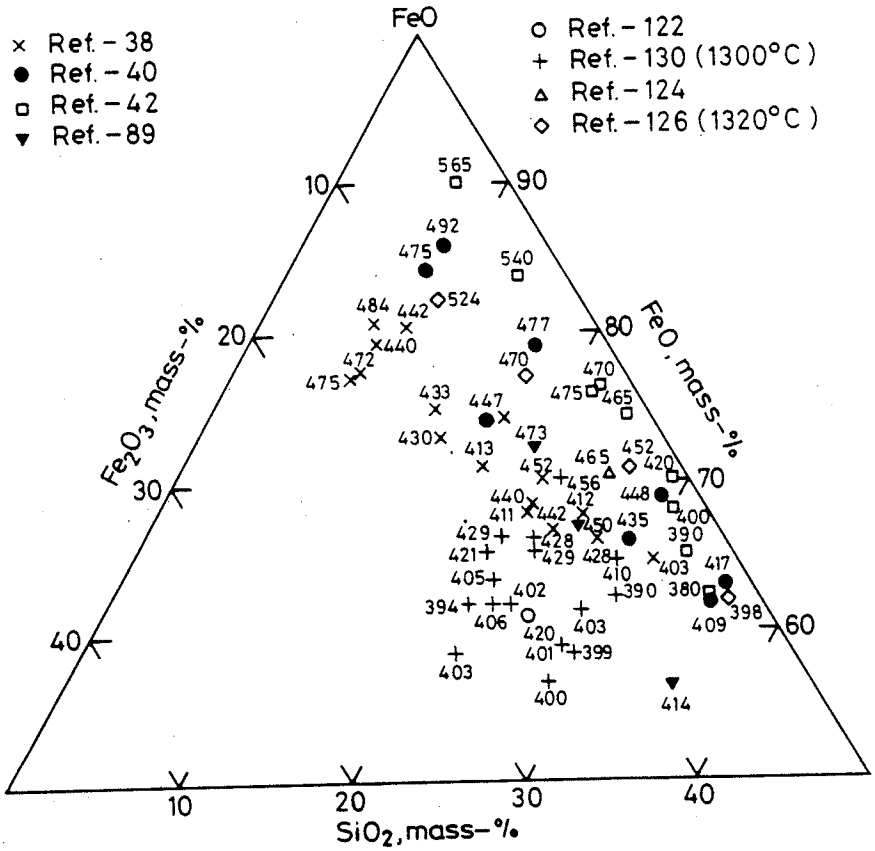


Fig. 10.44. Surface tension ($mN.m^{-1}$) of $Fe_xO + SiO_2$ (expressed as $FeO + Fe_2O_3 + SiO_2$) melts at 1400 °C (or at temperature indicated on the legend)

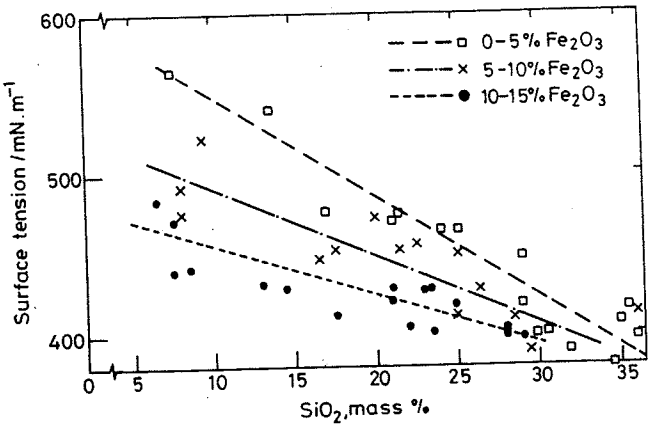


Fig. 10.45. Effect of SiO_2 concentration on the surface tension at 1400 °C, of $Fe_xO + SiO_2$ melts, for three ranges of Fe_2O_3 content [Ref. 131]

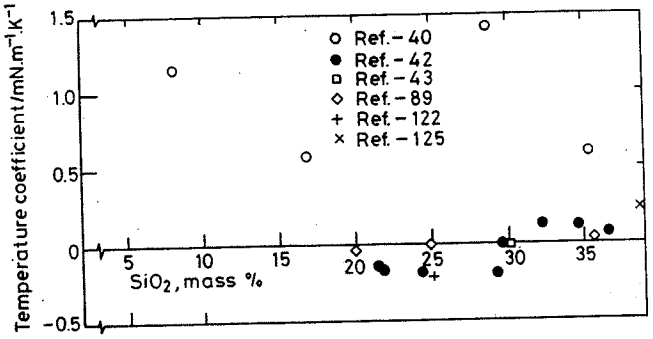


Fig. 10.46. Variation of the temperature coefficient of surface tension with composition of $Fe_xO + SiO_2$ melts

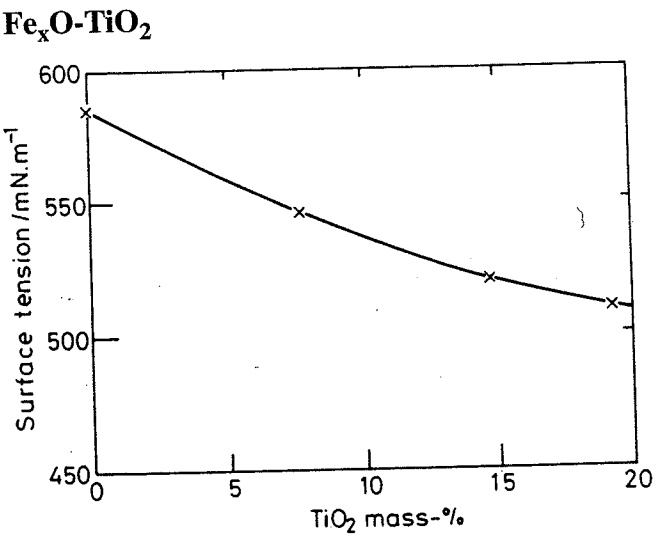


Fig. 10.47. Change in surface tension with composition of $Fe_xO + TiO_2$ melts at 1400 °C [Ref. 41]

K_2O-SiO_2

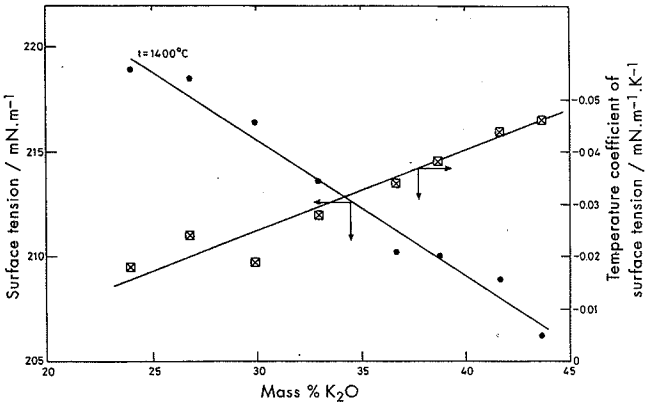


Fig. 10.48. Change in (I) the surface tension at 1400 °C, and (II) the temperature coefficient of surface tension, with composition of K_2O + SiO_2 melts [Ref. 132]

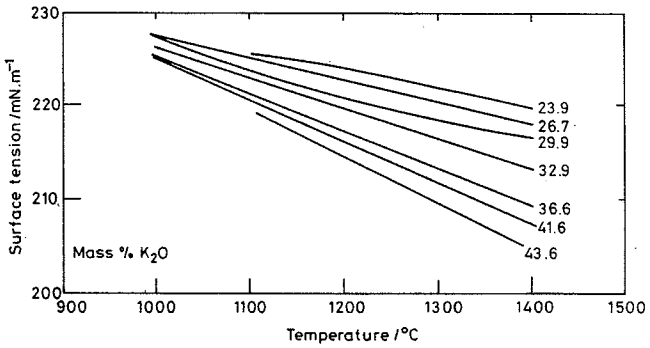


Fig. 10.49. Variation of the surface tension of K_2O + SiO_2 melts with temperature [Ref. 132]

Li_2O-SiO_2

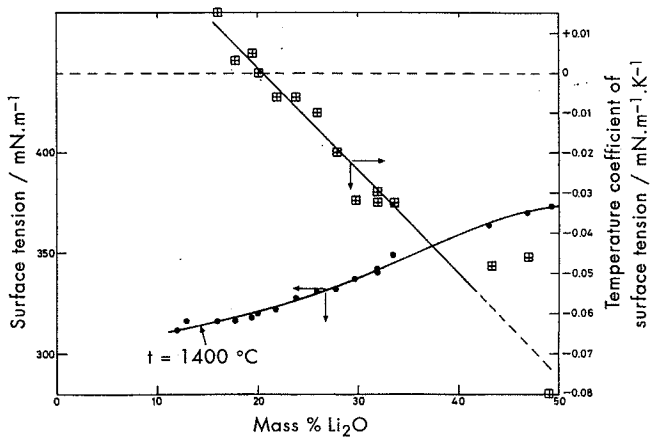


Fig. 10.50. Change in (I) the surface tension at 1400 °C, and (II) the temperature coefficient of surface tension, with composition of Li_2O + SiO_2 melts [Ref. 132]

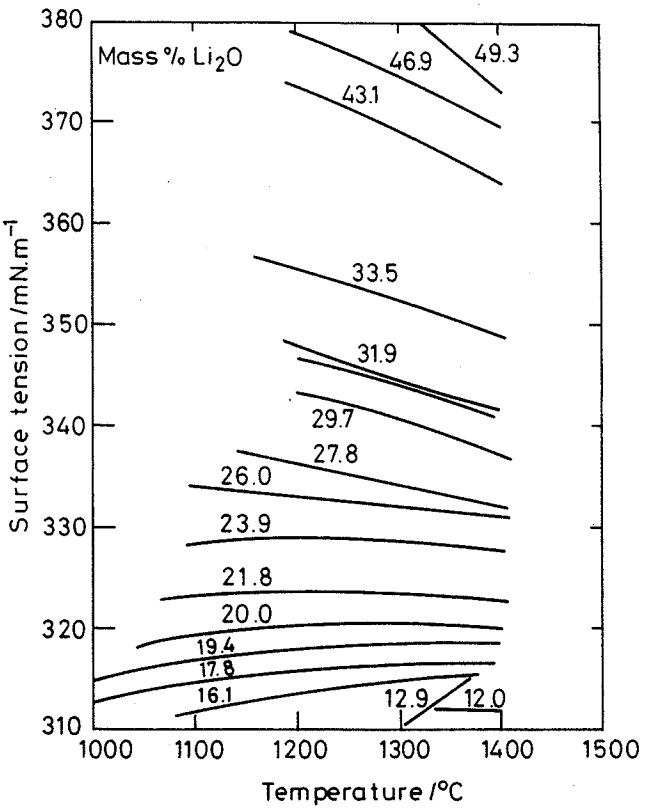


Fig. 10.51. Variation of the surface tension of Li_2O + SiO_2 melts with temperature [Ref. 132]

MgO-SiO_2

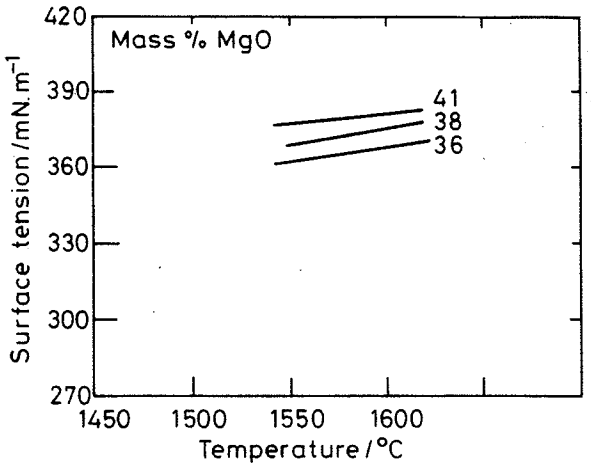


Fig. 10.52. Variation of the surface tension of MgO + SiO_2 melts with temperature [Ref. 89]

$MnO\text{-}SiO_2$

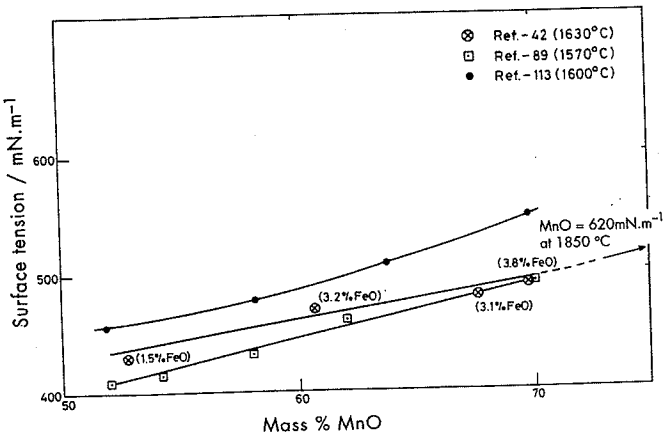


Fig. 10.53. Change in surface tension with composition of $MnO + SiO_2$ melts. (Melts studied by [Ref. 42] also contain small amounts of FeO.)

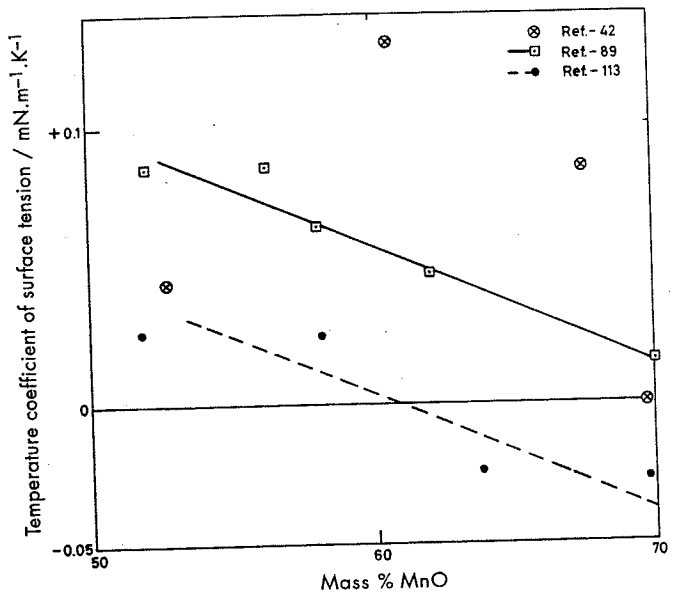


Fig. 10.54. Variation of the temperature coefficient of surface tension with the composition of $MnO + SiO_2$ melts

$Na_2O\text{-}SiO_2$

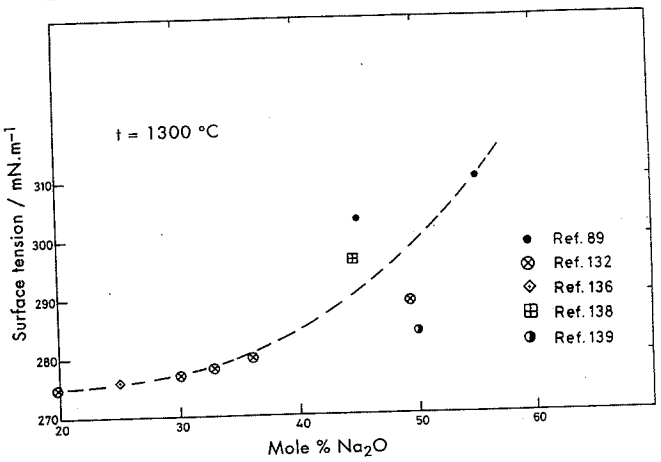


Fig. 10.55. Change in surface tension with composition of $Na_2O + SiO_2$ melts at 1300 °C

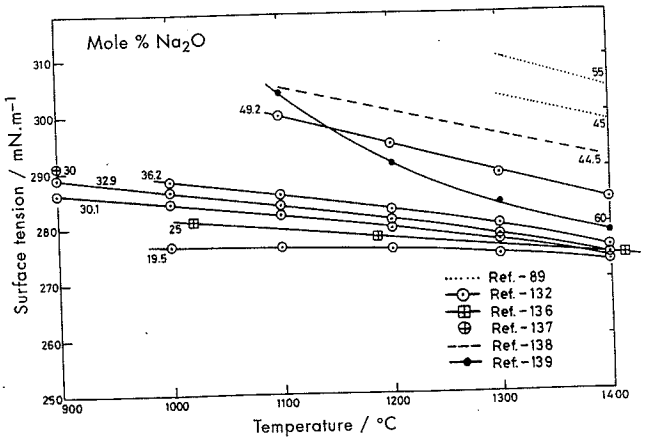
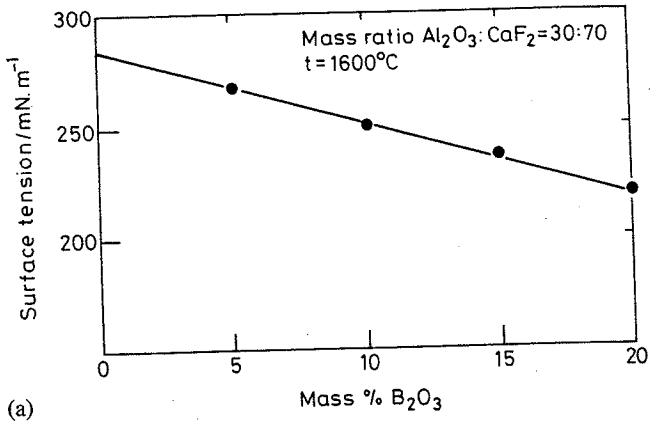


Fig. 10.56. Variation of the surface tension of $Na_2O + SiO_2$ melts with temperature

10.3.3 Ternary systems

$Al_2O_3\text{-}B_2O_3\text{-}CaF_2$



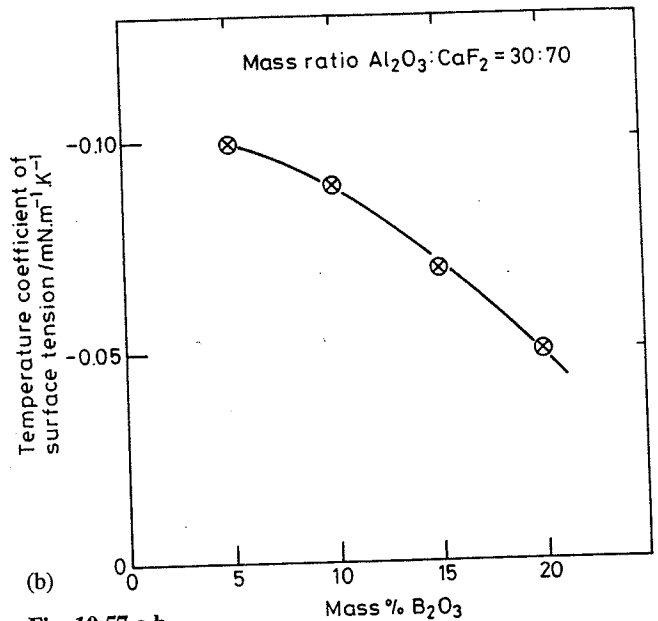


Fig. 10.57 a,b.
(a) Change in surface tension at 1600 °C with B_2O_3 content of $Al_2O_3 + B_2O_3 + CaF_2$ melts [Ref. 140]
(b) Variation of the temperature coefficient of surface tension with B_2O_3 content of $Al_2O_3 + CaF_2 + B_2O_3$ melts [Ref. 140]

Al_2O_3-B_2O_3-CaO

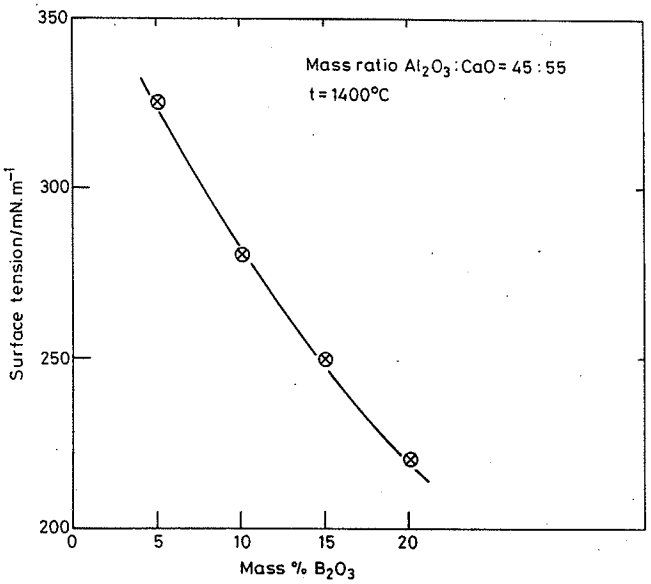


Fig. 10.58. Change in surface tension with B_2O_3 content of Al_2O_3 + B_2O_3 + CaO melts at 1400 °C [Ref. 141]

Al_2O_3-CaF_2-CaO

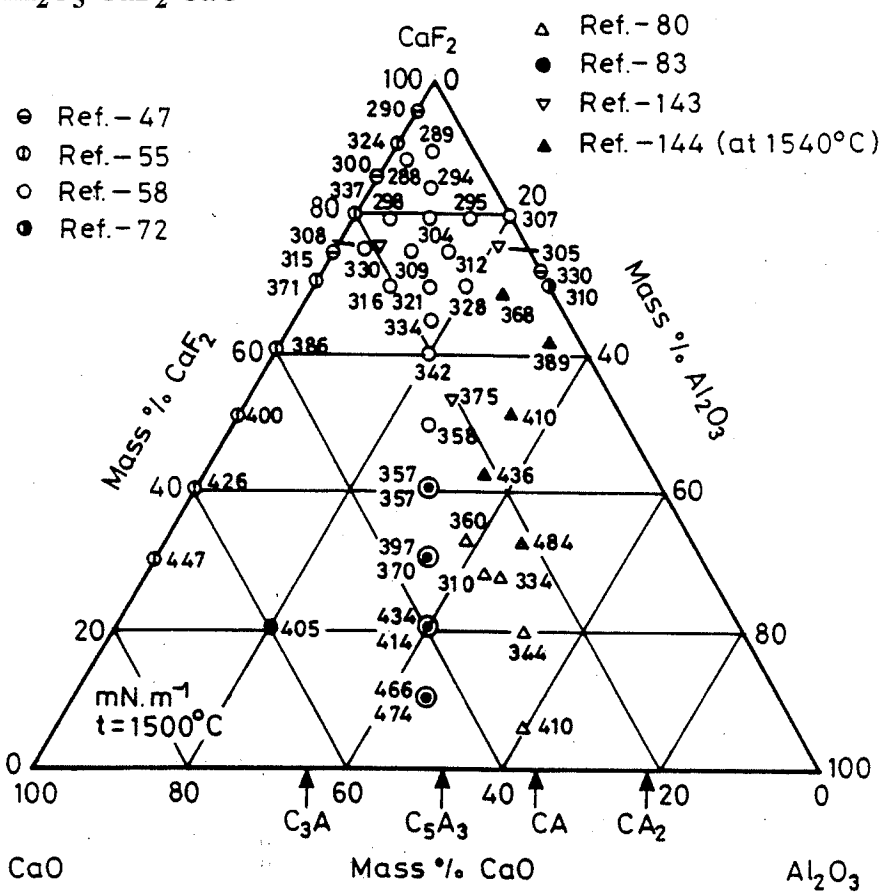


Fig. 10.59. Surface tension of Al_2O_3 + CaF_2 + CaO melts at 1500 °C

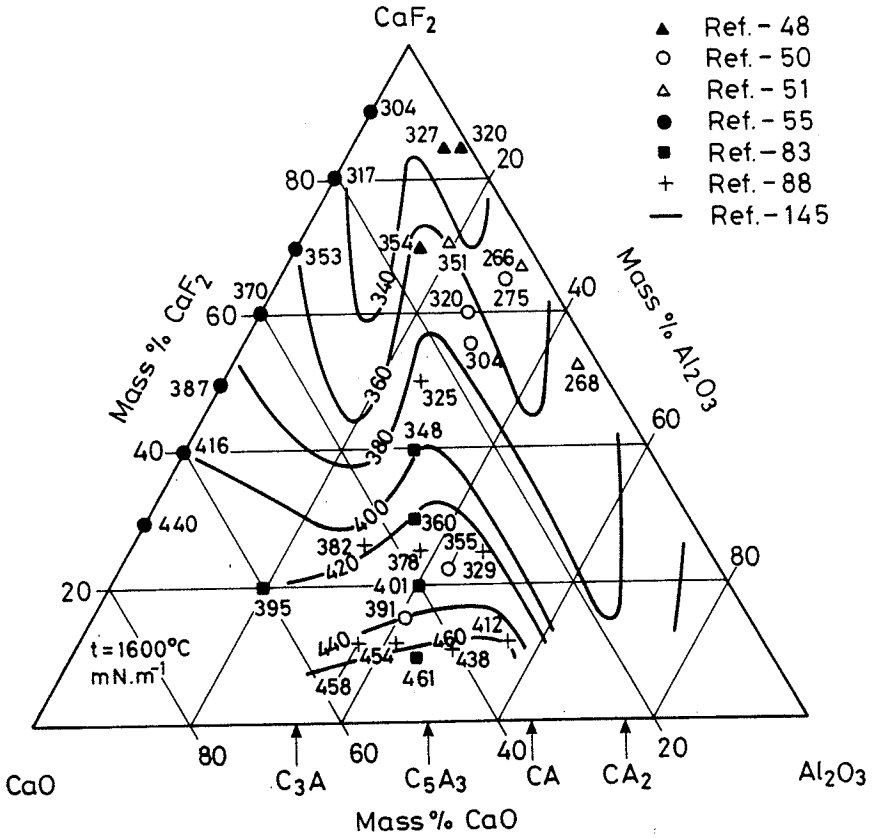
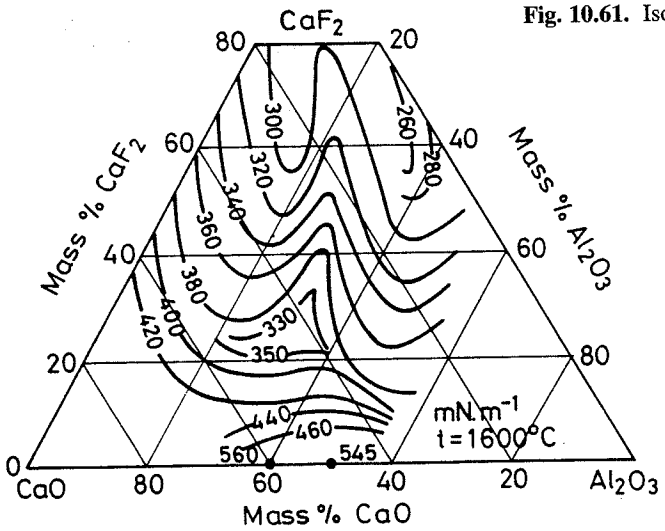


Fig. 10.60. Surface tension of Al_2O_3 + CaF_2 + CaO melts at 1600 °C

Fig. 10.61. Isotension lines for Al_2O_3 + CaF_2 + CaO melts at 1600 °C [Ref. 78]



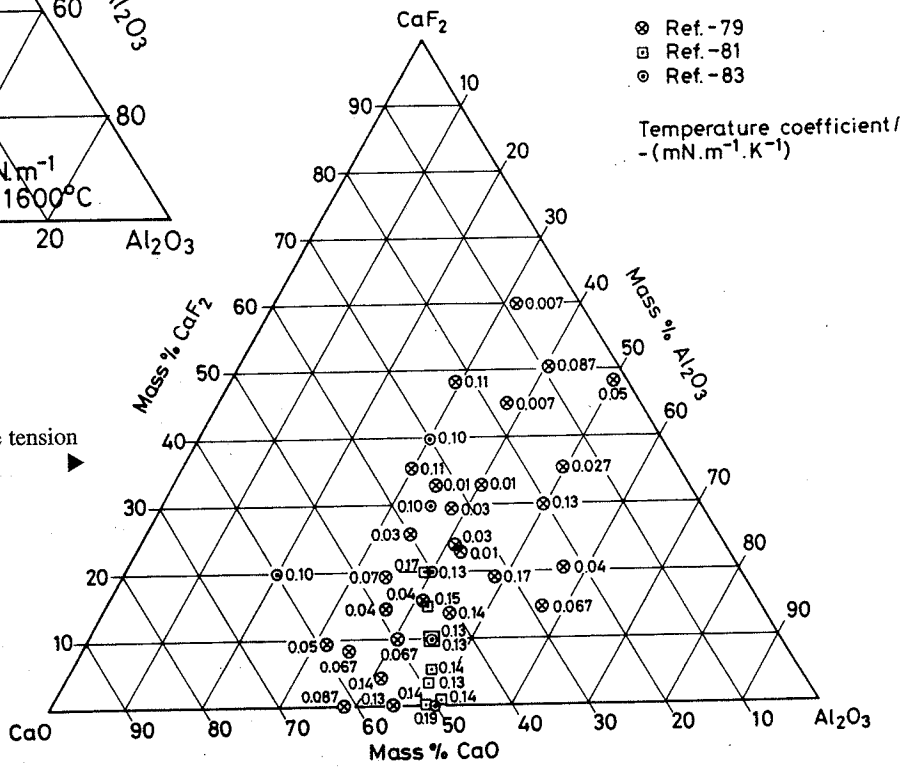


Fig. 10.62. Temperature coefficient of surface tension (all negative) for Al_2O_3 + CaF_2 + CaO melts ▶

Al_2O_3-CaF_2-MgO

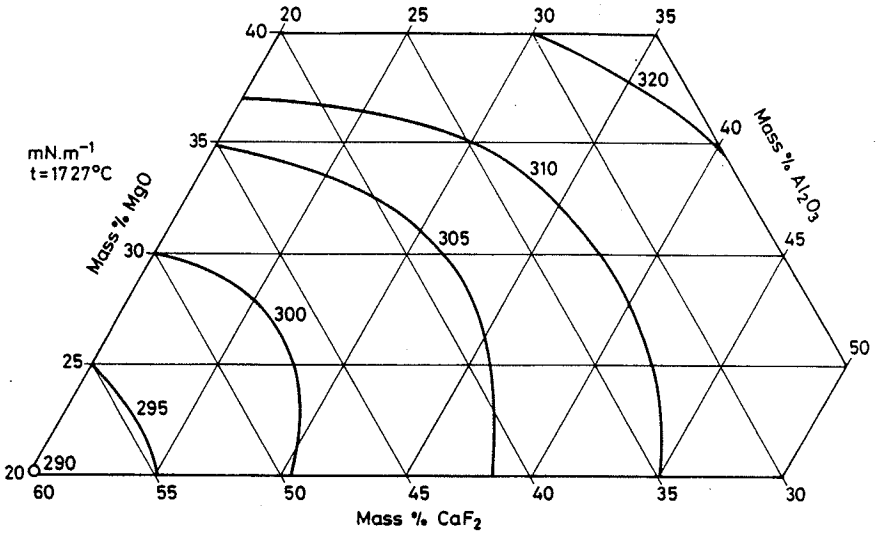


Fig. 10.63. Isotension lines for Al_2O_3 + CaF_2 + MgO melts at 1727 °C [Ref. 146]

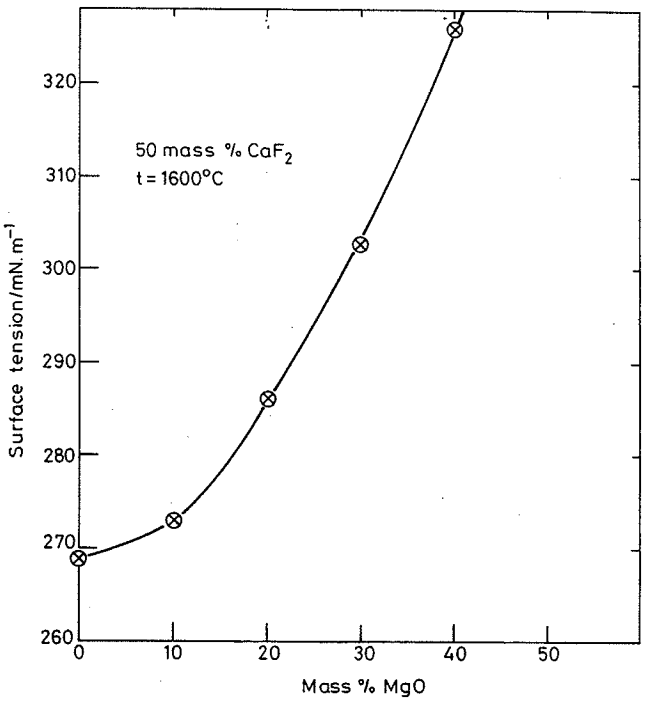


Fig. 10.64. Change in the surface tension with MgO content of Al_2O_3 + 50 % CaF_2 + MgO melts at 1600 °C [Ref. 147]

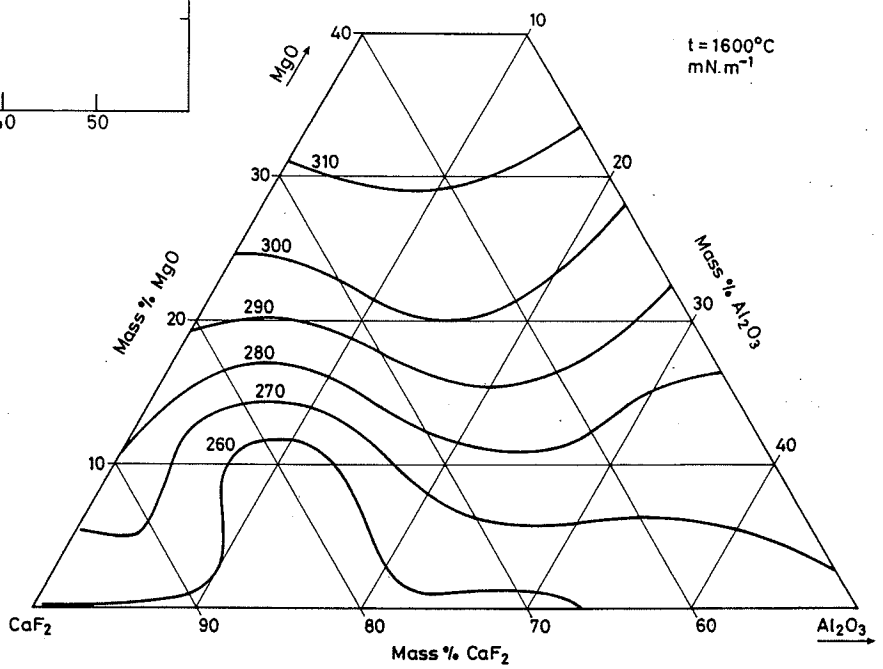


Fig. 10.65. Isotension lines for Al_2O_3 + CaF_2 + MgO melts at 1600 °C [Ref. 147]

Al_2O_3-CaF_2-TiO_2

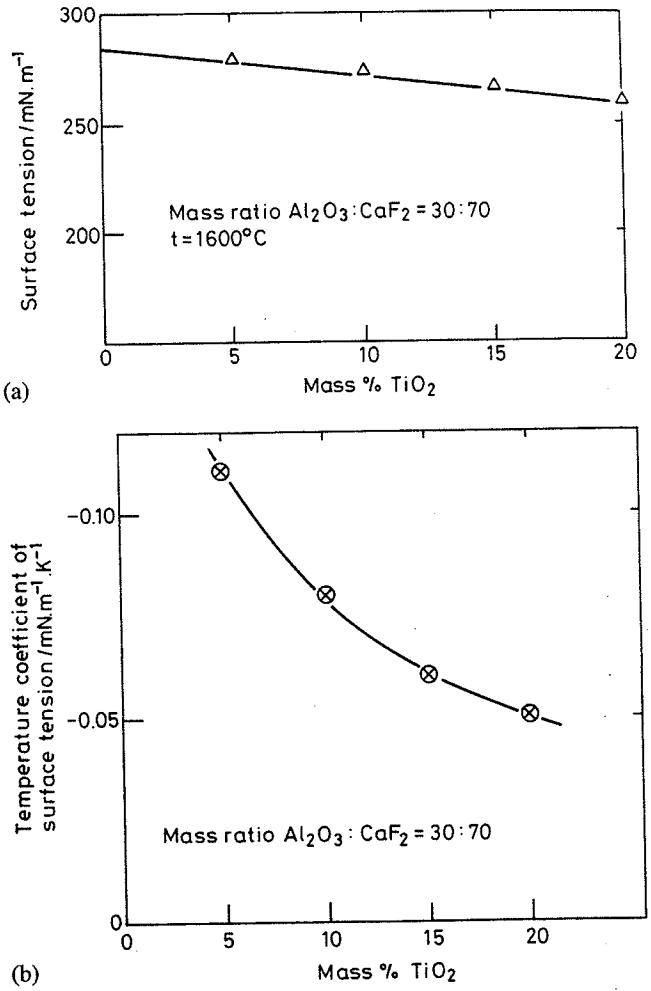


Fig. 10.66 a,b.
(a) Change in surface tension with TiO_2 content of Al_2O_3 + CaF_2 + TiO_2 melts at 1600 °C [Ref. 140]
(b) Variation of temperature coefficient of surface tension with TiO_2 content of Al_2O_3 + CaF_2 + TiO_2 melts [Ref. 140]

Al_2O_3-CaF_2-V_2O_5

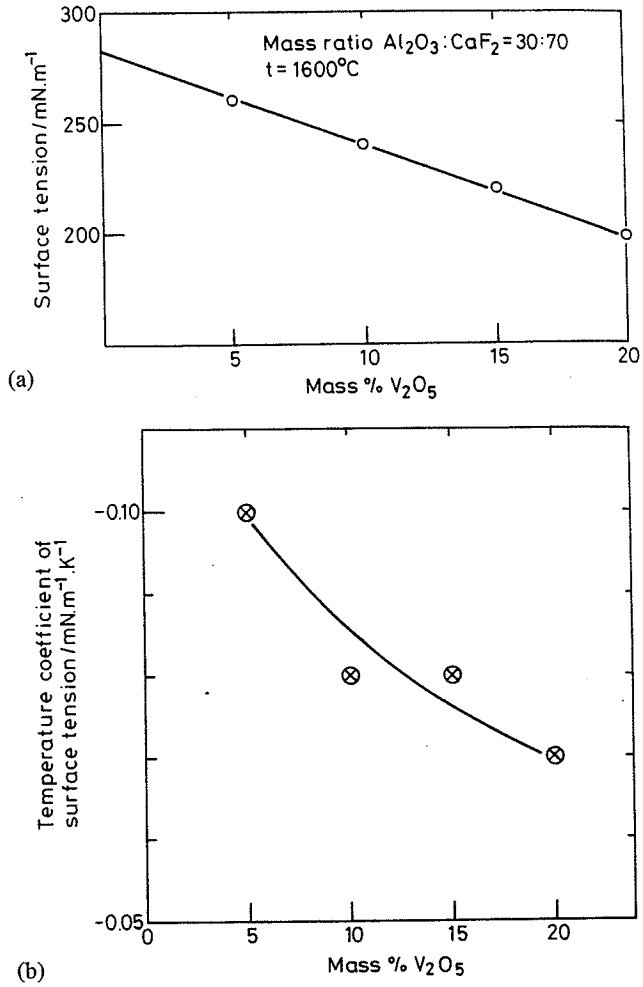


Fig. 10.67 a,b.
(a) Change in surface tension with V_2O_5 content of Al_2O_3 + CaF_2 + V_2O_5 melts at 1600 °C [Ref. 140]
(b) Variation of temperature coefficient of surface tension with V_2O_5 content of Al_2O_3 + CaF_2 + V_2O_5 melts [Ref. 140]

Al_2O_3-CaO-Cr_2O_3

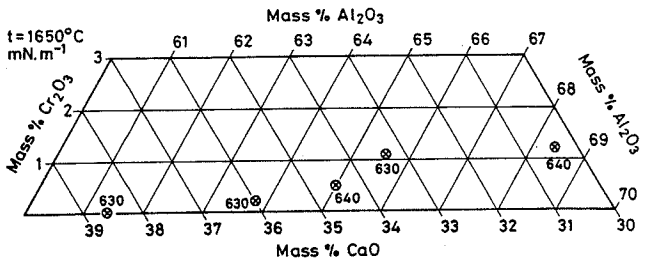


Fig. 10.68. Surface tension of Al_2O_3 + CaO + Cr_2O_3 melts at 1650 °C [Ref. 85]

Al_2O_3-CaO-Fe_2O_3

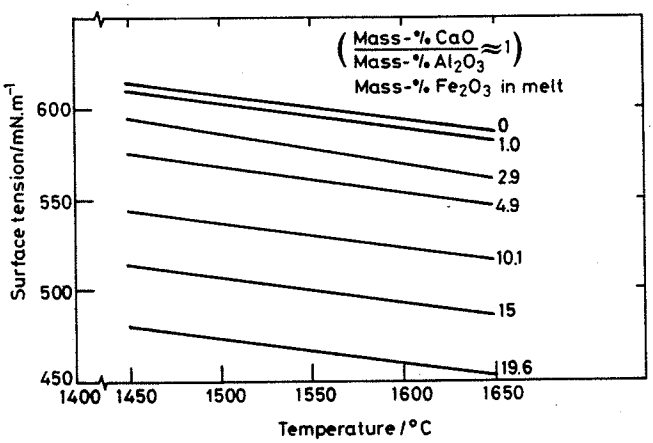


Fig. 10.69. Variation of surface tension of Al_2O_3 + CaO + Fe_2O_3 melts with temperature [Ref. 81]

Al_2O_3-CaO-K_2O

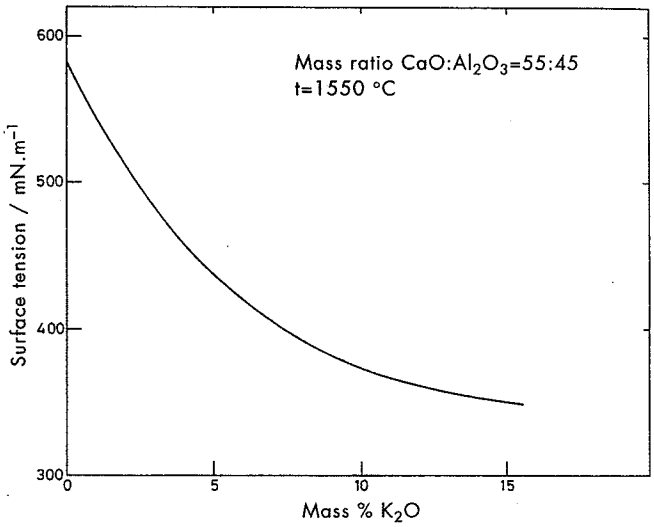


Fig. 10.70. Change in surface tension with K_2O content of Al_2O_3 + CaO + K_2O melts at 1550 °C [Ref. 141]

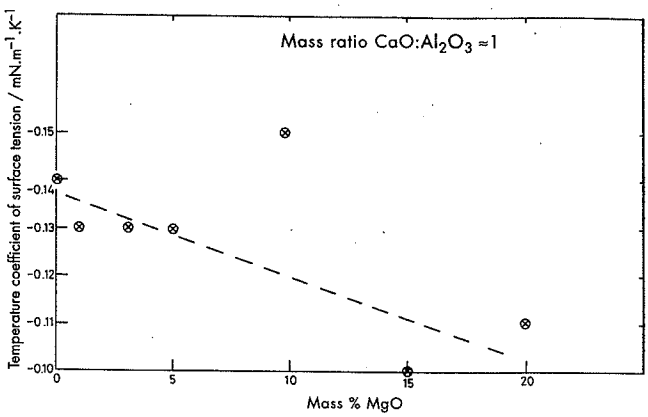


Fig. 10.73. Variation of the temperature coefficient of surface tension with MgO content of Al_2O_3 + CaO + MgO melts [Ref. 81]

Al_2O_3-CaO-Li_2O

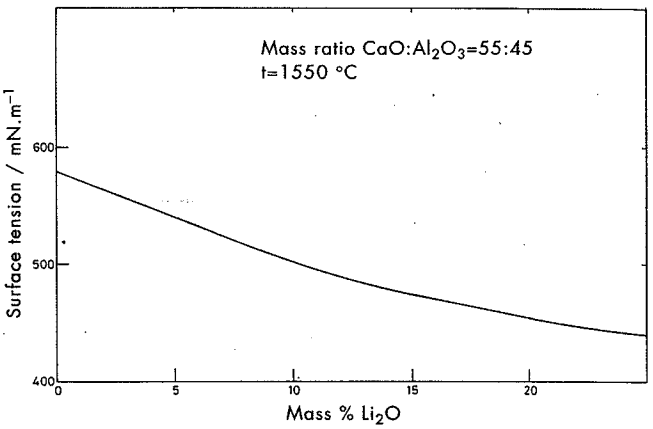


Fig. 10.71. Change in surface tension with Li_2O content of Al_2O_3 + CaO + Li_2O melts at 1550 °C [Ref. 141]

Al_2O_3-CaO-Na_2O

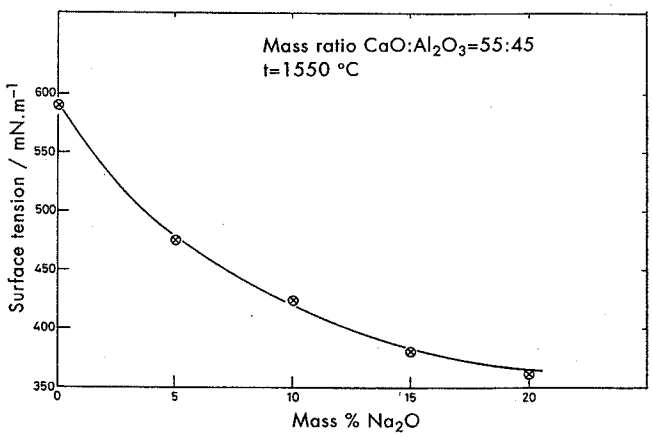


Fig. 10.74. Change in surface tension with Na_2O content of Al_2O_3 + CaO + Na_2O melts at 1550 °C [Ref. 141]

Al_2O_3-CaO-MgO

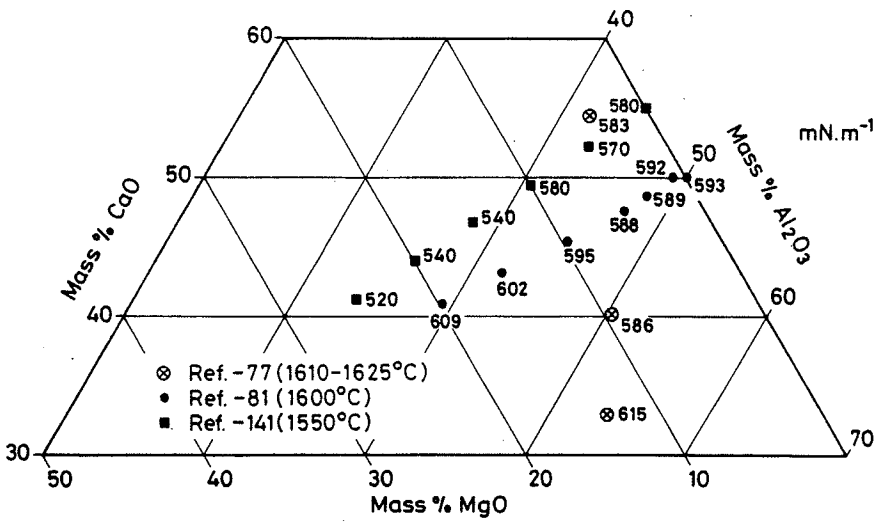


Fig. 10.72. Surface tension of Al_2O_3 + CaO + MgO melts

Al_2O_3-CaO-SiO_2

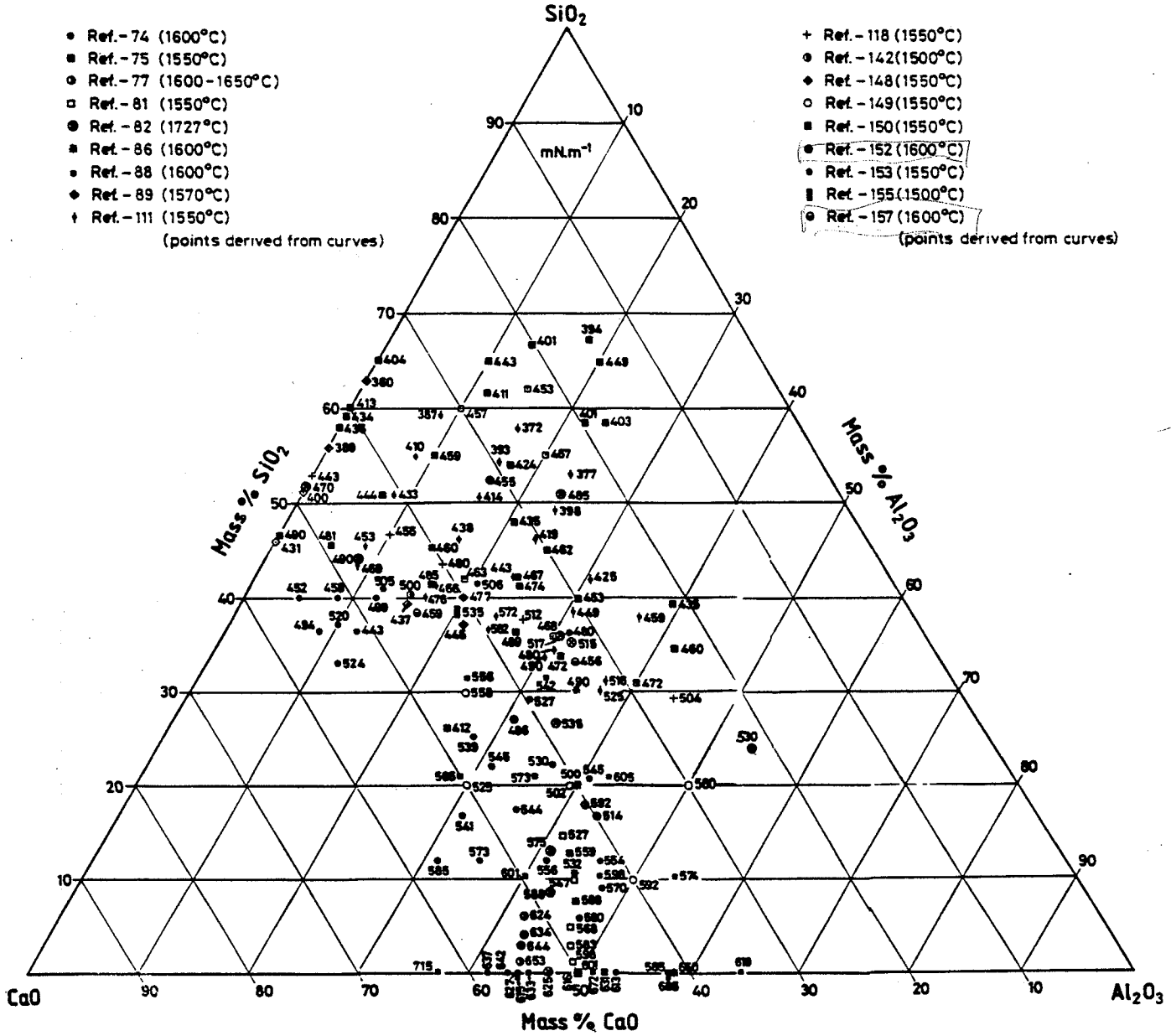


Fig. 10.75. Surface tension of Al_2O_3 + CaO + SiO_2 melts

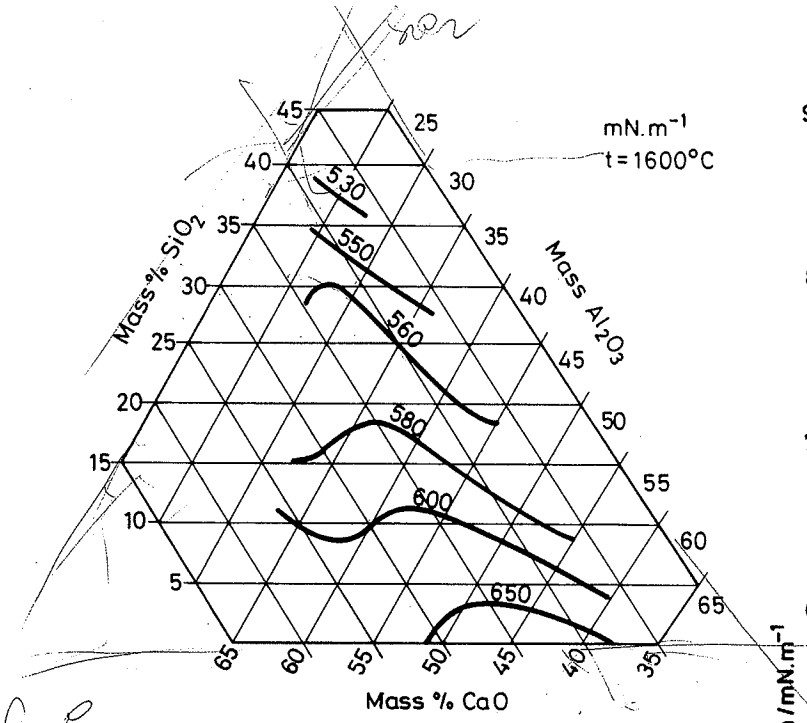
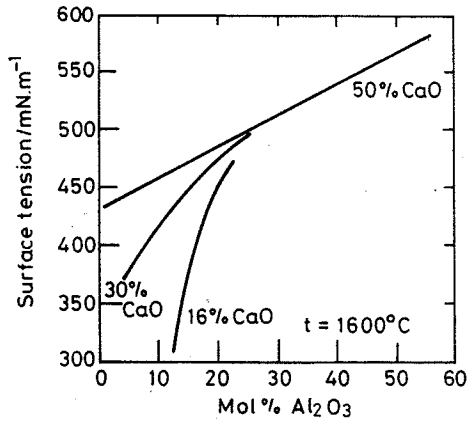
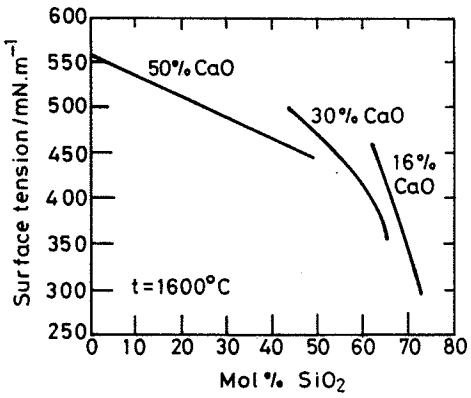


Fig. 10.76. Isotension lines for Al_2O_3 + CaO + SiO_2 melts at 1600 °C [Ref. 88]



(a)



(b)

Fig. 10.77 a,b. Change in surface tension with Al_2O_3 content and with SiO_2 content, of Al_2O_3 + CaO + SiO_2 melts at 1600 °C [Ref. 157]

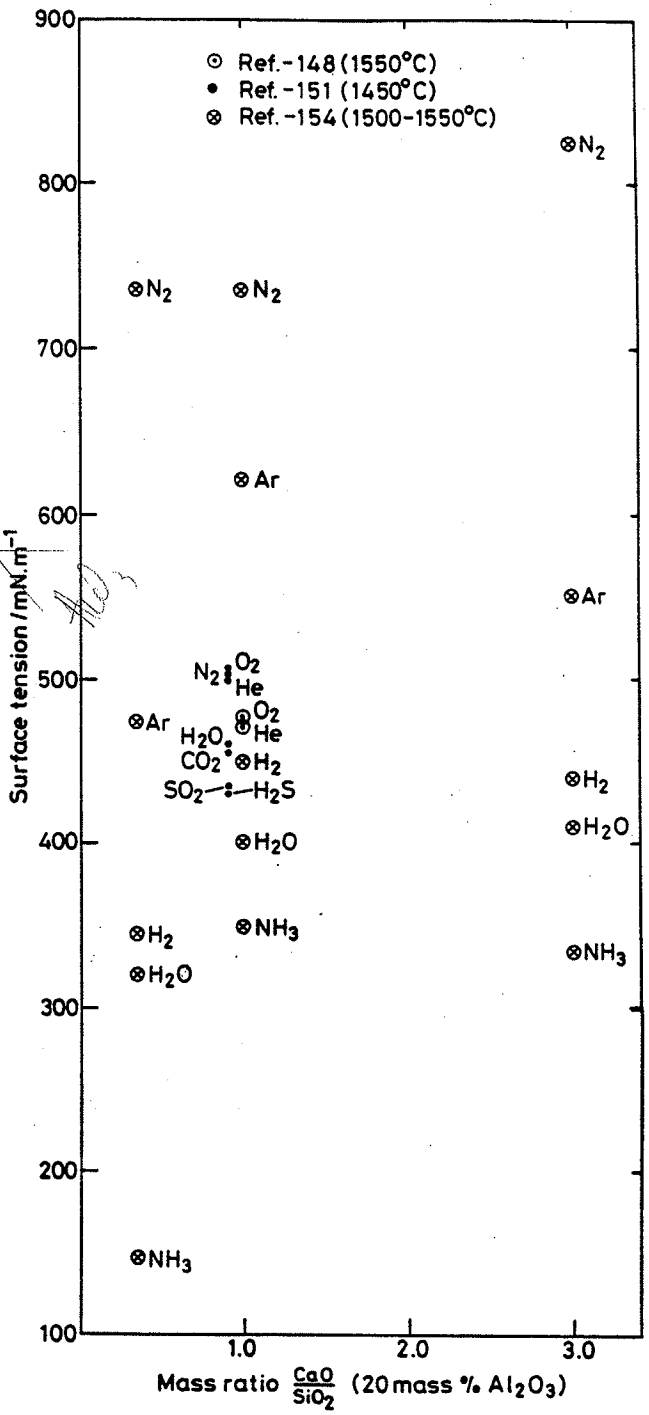
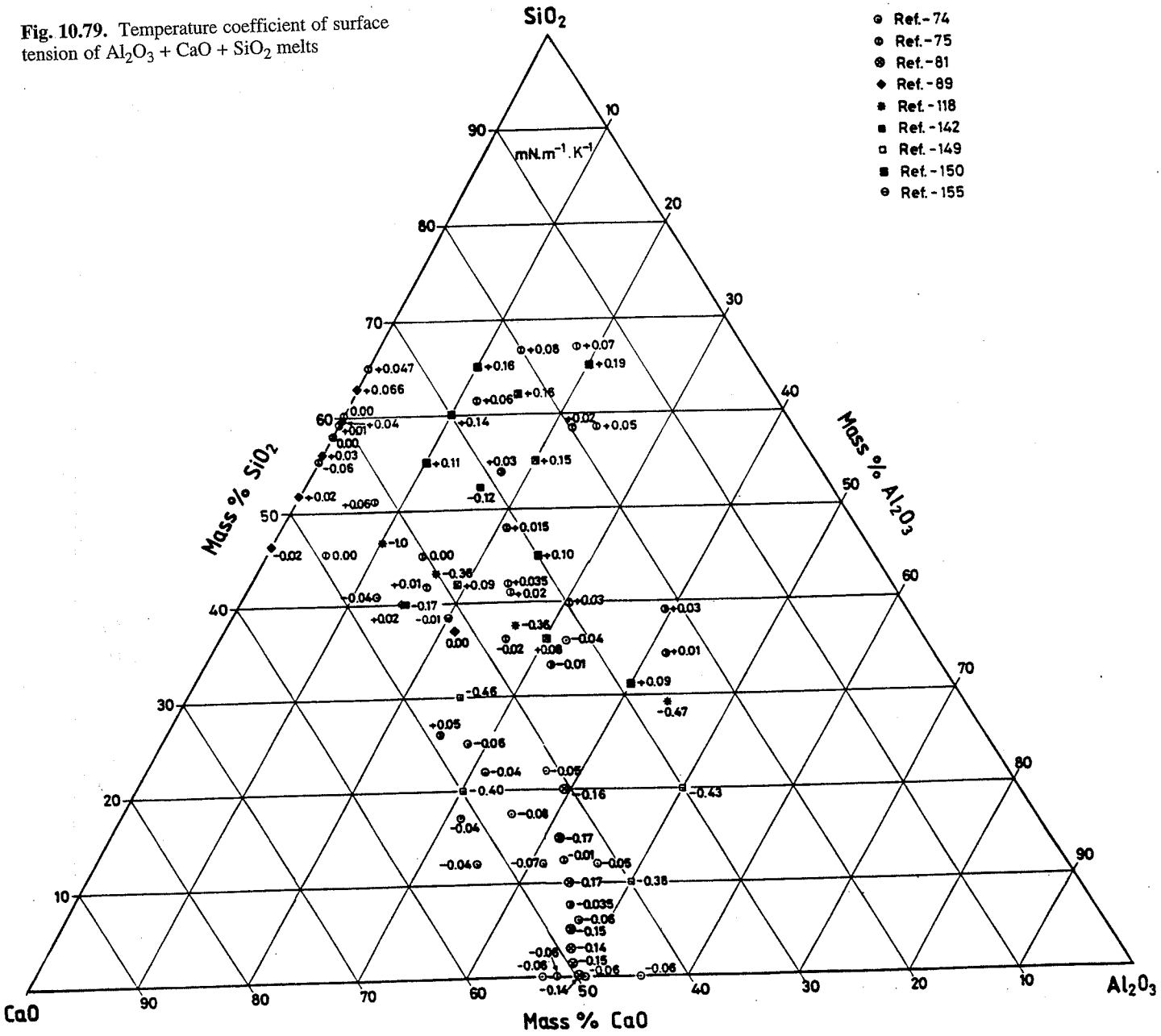


Fig. 10.78. Effect of various atmospheres on the surface tension of Al_2O_3 + CaO + SiO_2 melts

Fig. 10.79. Temperature coefficient of surface tension of $Al_2O_3 + CaO + SiO_2$ melts



Al_2O_3-CaO-TiO_2

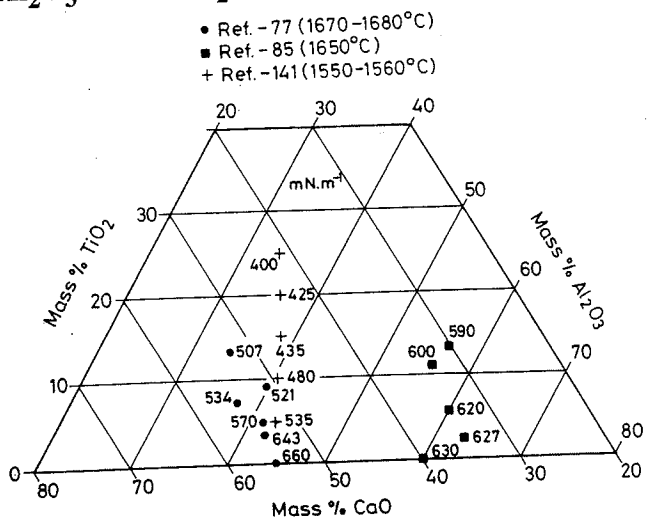


Fig. 10.80. Surface tension of $Al_2O_3 + CaO + TiO_2$ melts

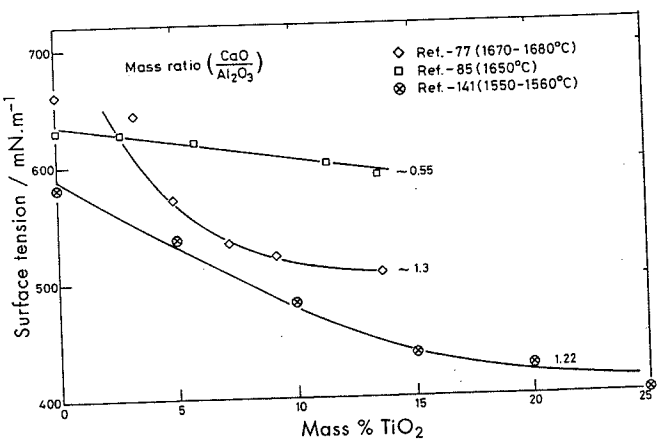


Fig. 10.81. Change in surface tension with TiO_2 content of $Al_2O_3 + CaO + TiO_2$ melts

Al_2O_3-CaO-V_2O_5

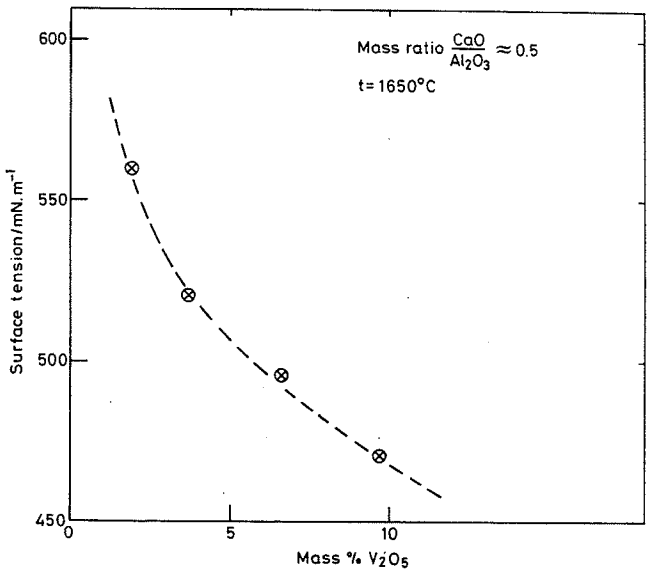


Fig. 10.82. Change in surface tension with V_2O_5 content of Al_2O_3 + CaO + V_2O_5 melts at 1650 °C [Ref. 85]

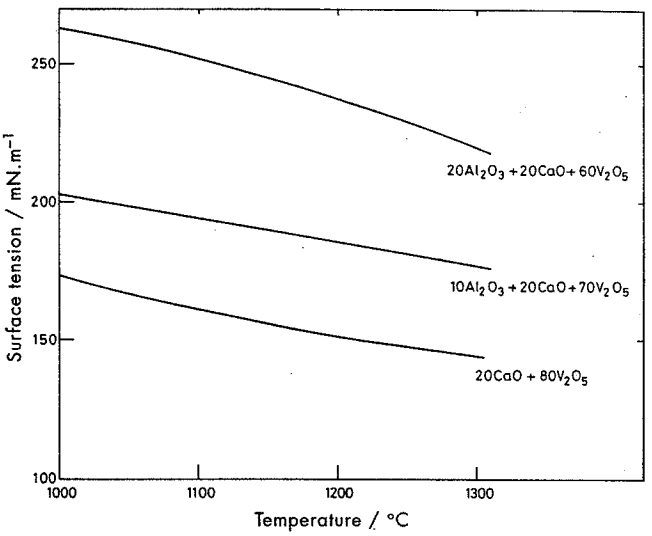


Fig. 10.83. Variation of surface tension of Al_2O_3 + CaO + V_2O_5 melts with temperature [Ref. 158]

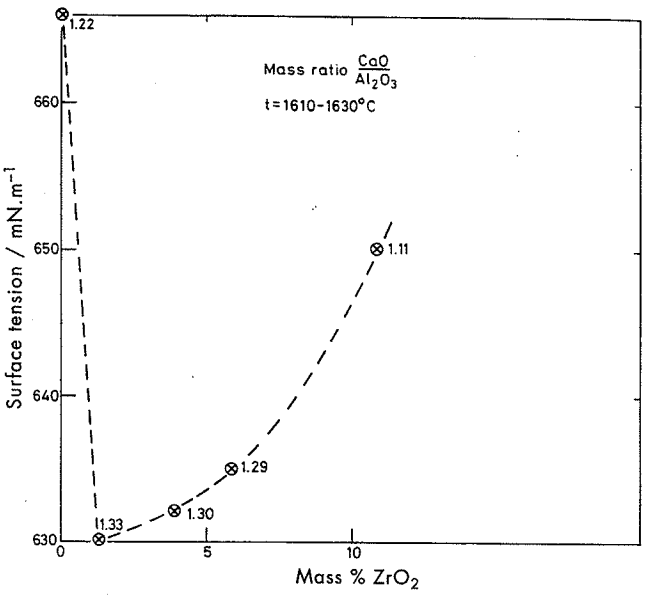


Fig. 10.84. Change in surface tension with ZrO_2 content of Al_2O_3 + CaO + ZrO_2 melts [Ref. 77]

Al_2O_3-Fe_xO-P_2O_5

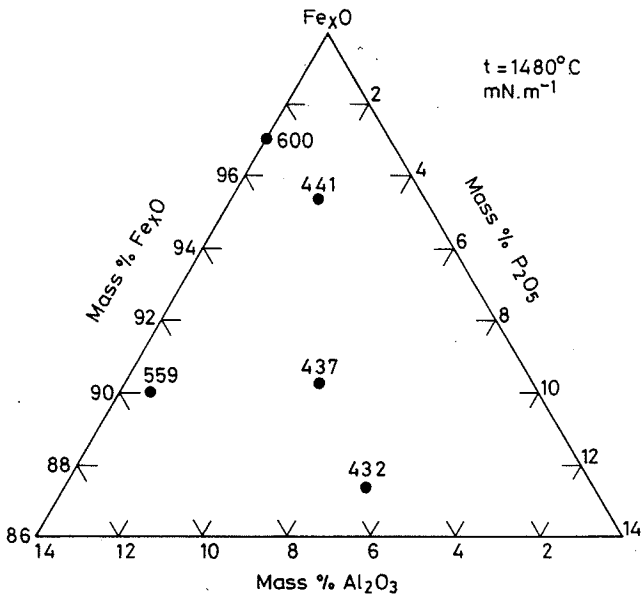


Fig. 10.85. Surface tension of Al_2O_3 + Fe_xO + P_2O_5 melts at 1480 °C [Ref. 159]

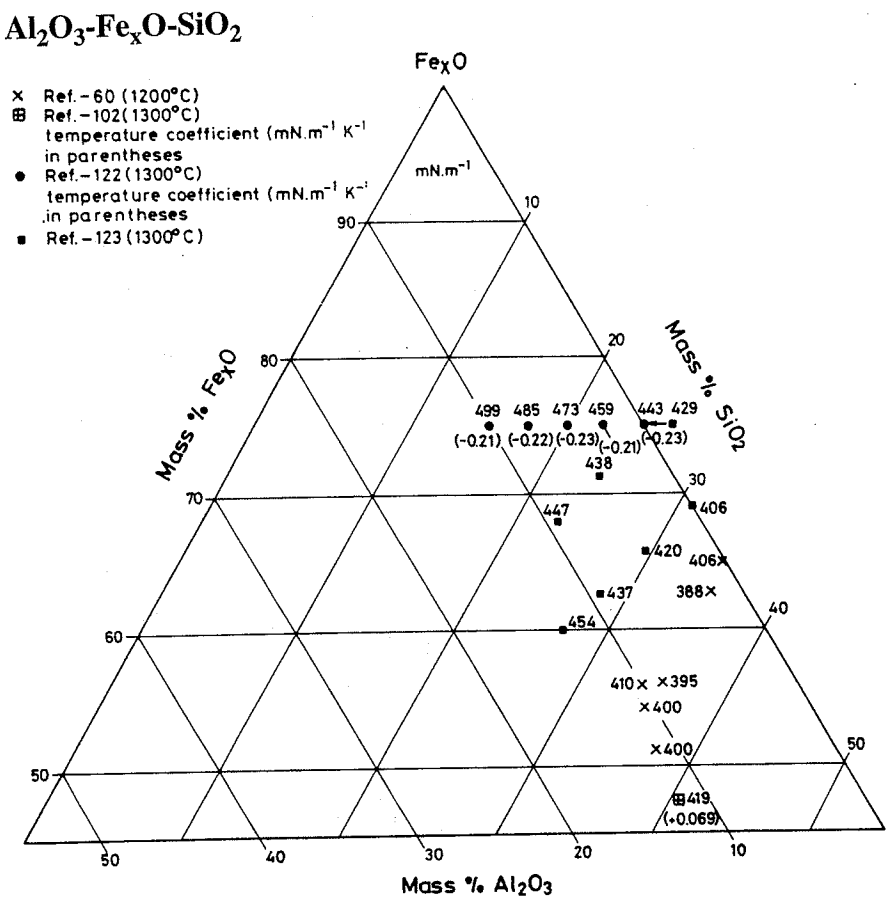


Fig. 10.86. Surface tension and temperature coefficient of surface tension, of $Al_2O_3 + Fe_xO + SiO_2$ melts

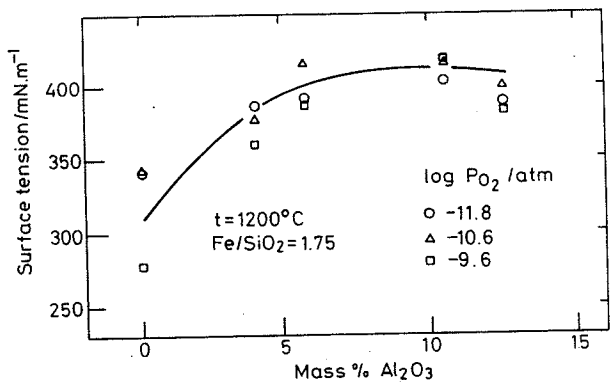


Fig. 10.87. Change in surface tension at 1200 °C with Al_2O_3 content of $Al_2O_3 + Fe_xO + SiO_2$ melts under various partial pressures of oxygen [Ref. 116]

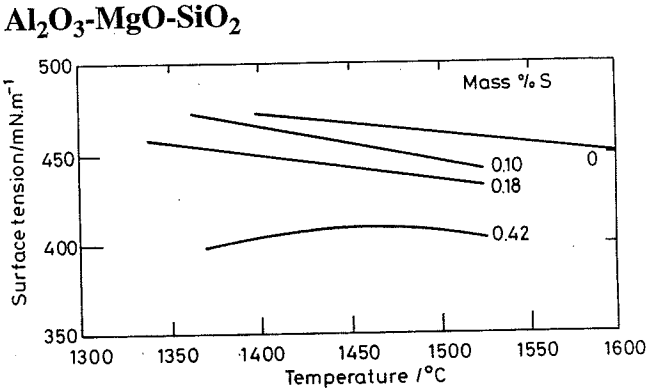


Fig. 10.88. Effect of temperature and of S additions, on the surface tension of a slag containing 16.4 mass % Al_2O_3 + 23.6 mass % MgO + 60 mass % SiO_2 [Ref. 142]

Al_2O_3-MnO-SiO_2

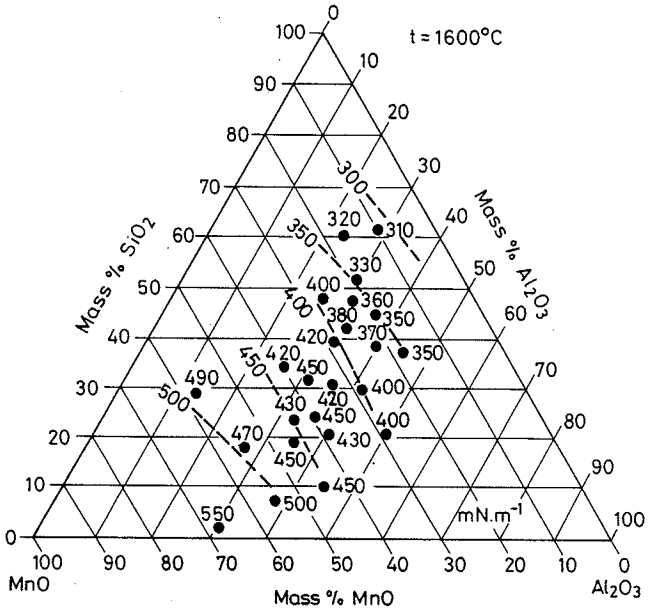


Fig. 10.89. Surface tension of Al_2O_3 + MnO + SiO_2 melts at 1600 °C [Ref. 161]

Al_2O_3-Na_2O-SiO_2

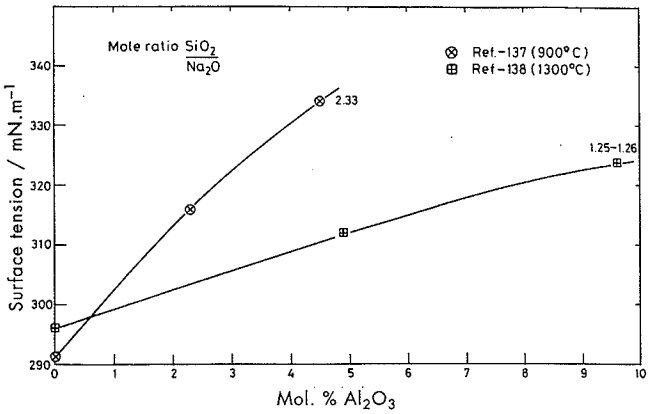


Fig. 10.91. Change in surface tension with Al_2O_3 content of Al_2O_3 + Na_2O + SiO_2 melts

Al_2O_3-SiO_2-TiO_2

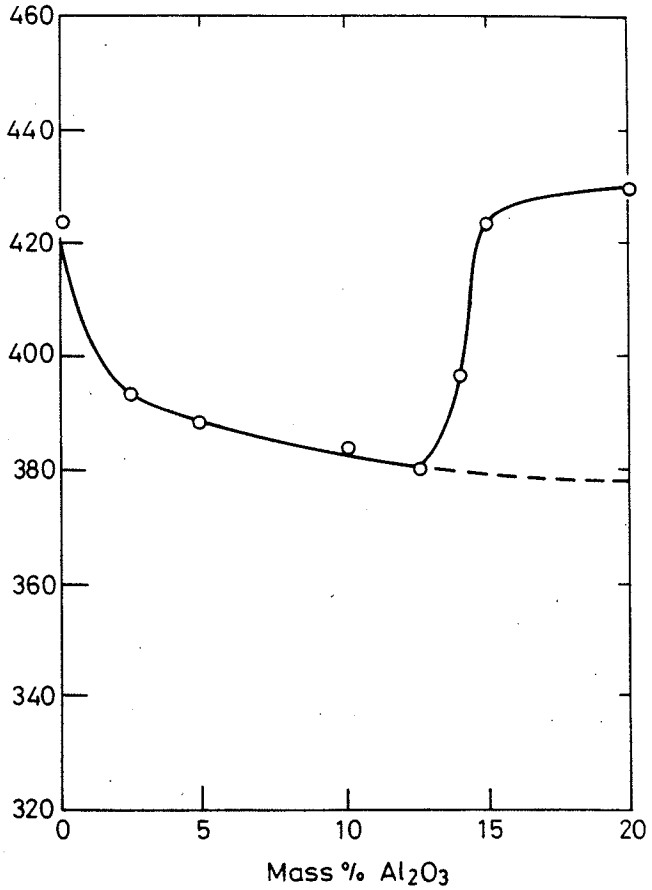


Fig. 10.92. Surface tension of Al_2O_3 + SiO_2 + TiO_2 melts at 1600 °C - effect of Al_2O_3 additions to the eutectic composition 89.5 mass % SiO_2 + 10.5 mass % TiO_2 [Ref. 162]. (Abrupt change in slope of curve at about 12.5 % Al_2O_3 was thought to be due to formation of mullite in the melt.)

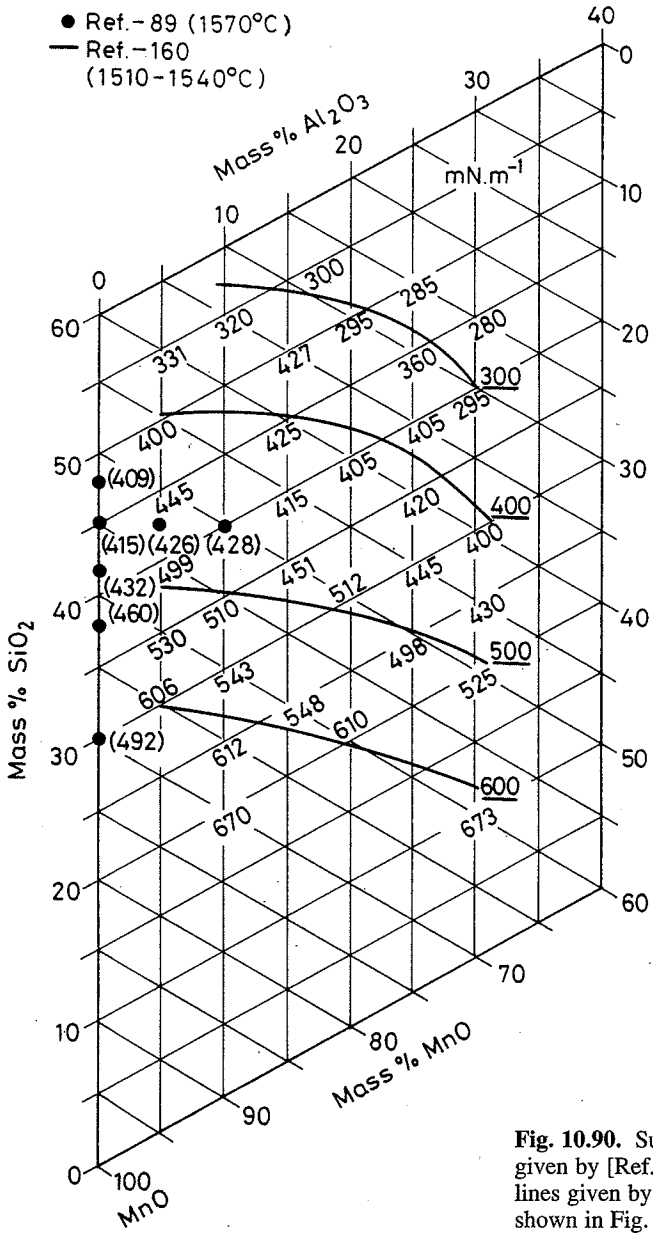
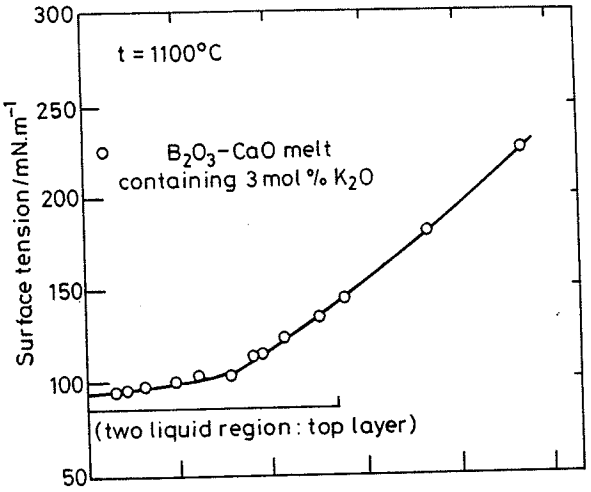


Fig. 10.90. Surface tension of Al_2O_3 + MnO + SiO_2 melts. (Data given by [Ref. 89] are shown in parentheses. The isotension lines given by [Ref. 160] were based upon the individual values shown in Fig. 10.90)

B_2O_3-CaO-K_2O



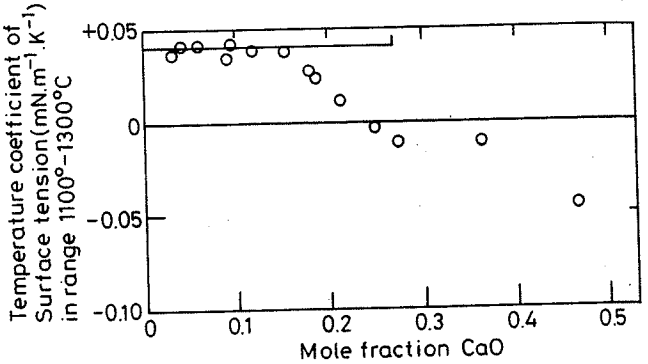


Fig. 10.93. Change in surface tension and in the temperature coefficient of surface tension, with CaO content of B_2O_3 + CaO + 3 mol % K_2O melts [Ref. 16]

B_2O_3-CaO-SiO_2

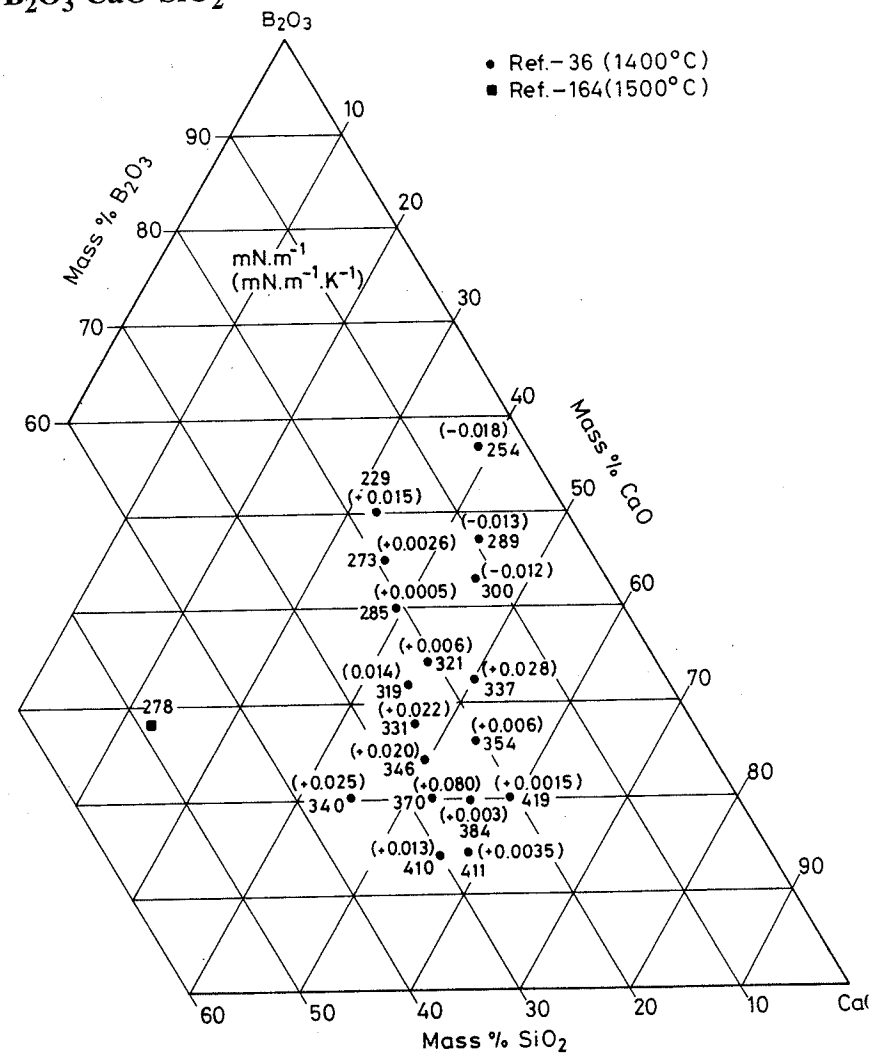


Fig. 10.94. Surface tension and temperature coefficient of surface tension (in parentheses) of B_2O_3 + CaO + SiO_2 melts

CaF_2-CaO-SiO_2

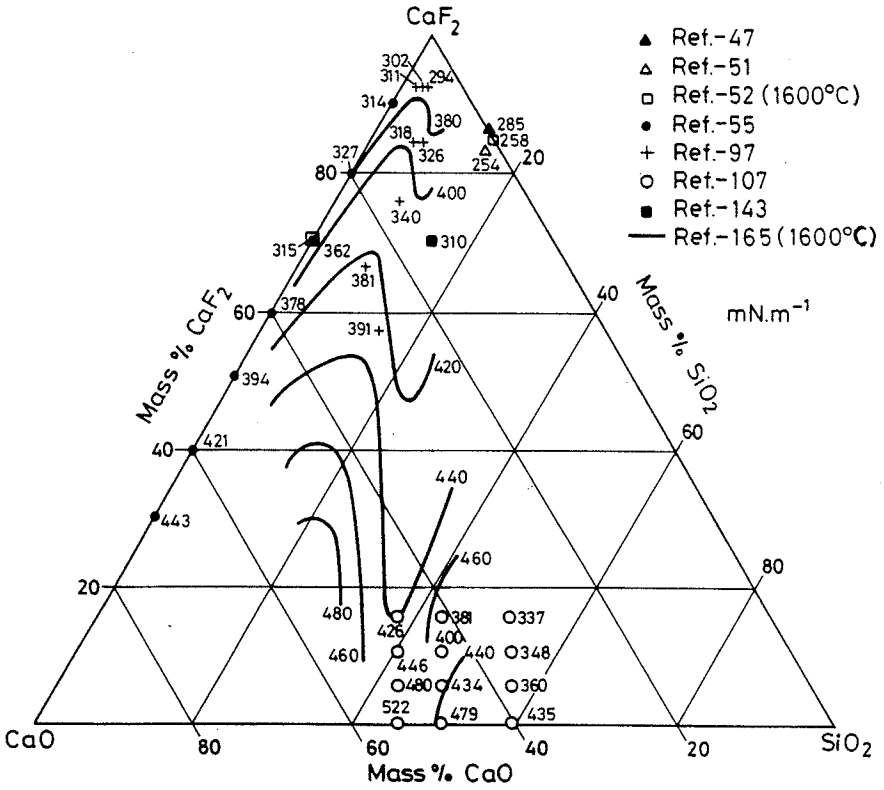


Fig. 10.95. Surface tension of CaF_2 + CaO + SiO_2 melts at 1500 °C and at 1600 °C

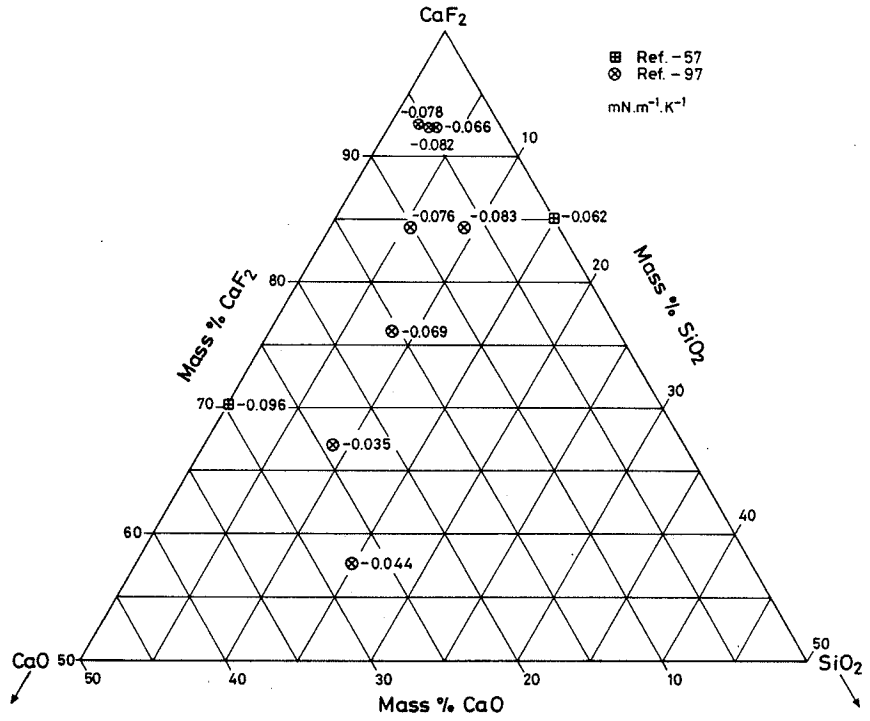


Fig. 10.96. Temperature coefficient of surface tension of CaF_2 + CaO + SiO_2 melts

CaO-CaS-SiO_2

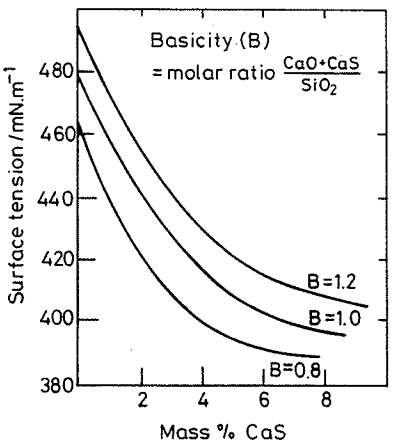


Fig. 10.97. Change in surface tension at 1580 °C, with CaS content of CaO + CaS + SiO_2 slags with different basicities [Ref. 166]

$CaO\text{-}Cr_2O_3\text{-}SiO_2$

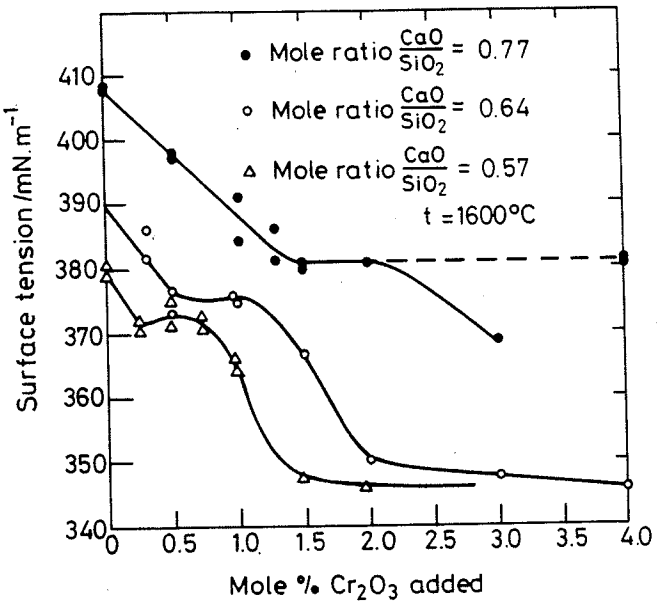


Fig. 10.98. Change in surface tension at 1600 °C, when Cr_2O_3 is added to $CaO + SiO_2$ melts [Ref. 106]

$CaO\text{-}Fe_xO\text{-}P_2O_5$

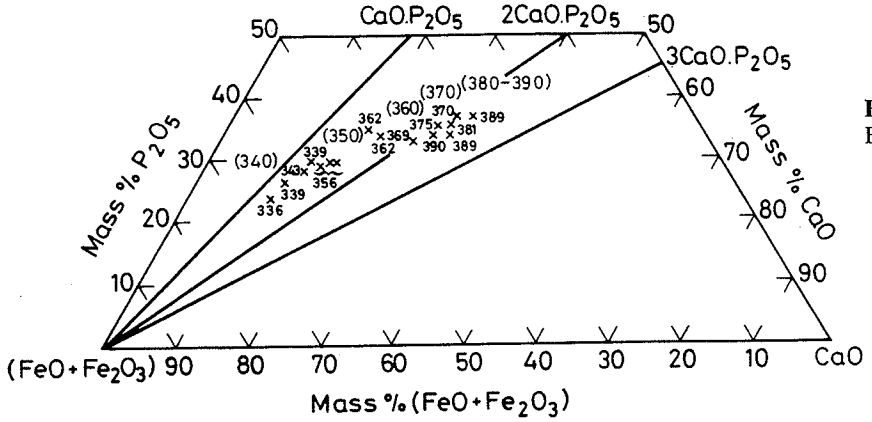


Fig. 10.99. Surface tension ($mN.m^{-1}$) of $CaO + Fe_xO + P_2O_5$ melts at 1350 °C [Ref. 120]

$(CaO\text{-}P_2O_5)\text{-}FeO\text{-}Fe_2O_3$

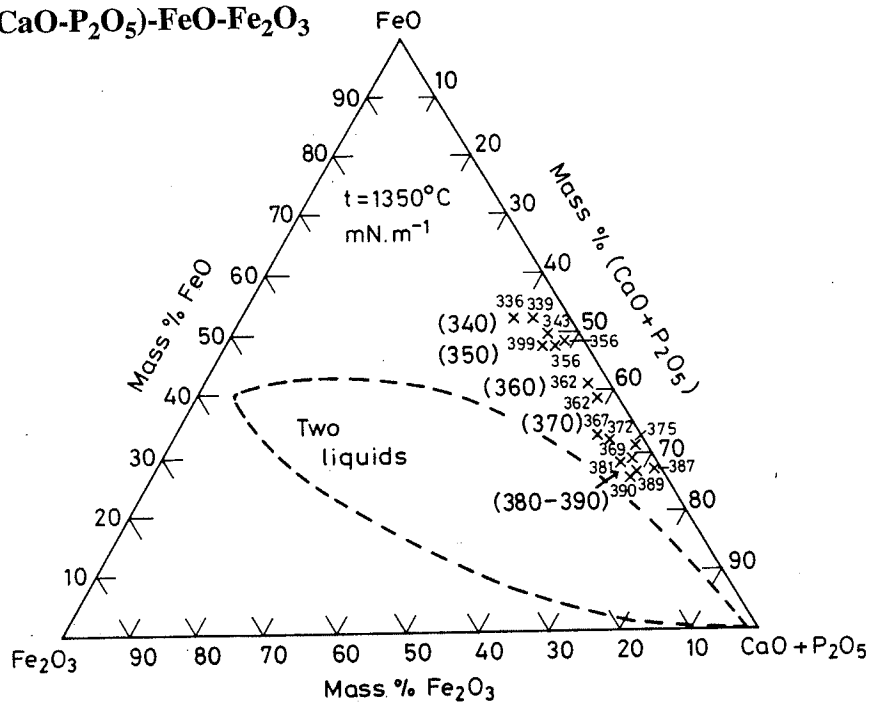


Fig. 10.100. Data from Fig. 10.99 expressed in terms of the pseudo-ternary system $(CaO + P_2O_5) + FeO + Fe_2O_3$ [Ref. 120]. (Figs. in parentheses give the approximate values of surface tension for the relevant compositional regions.)

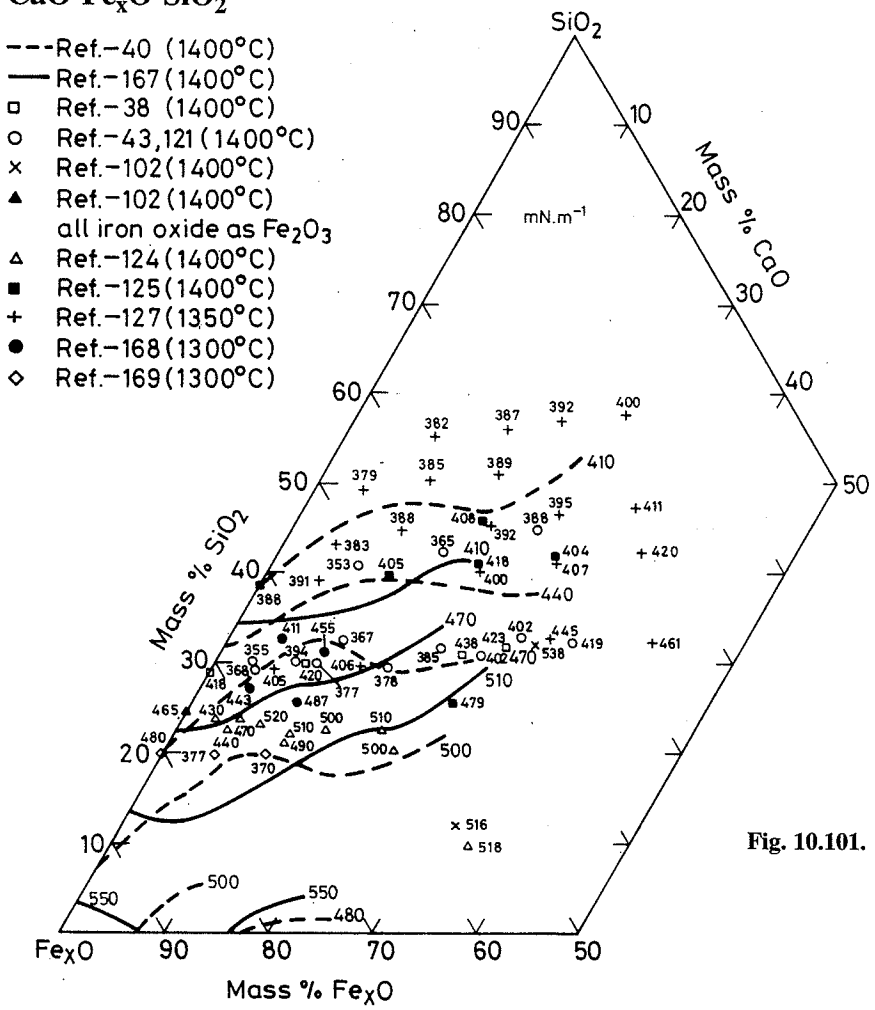


Fig. 10.101. Surface tension of $CaO + Fe_xO + SiO_2$ melts

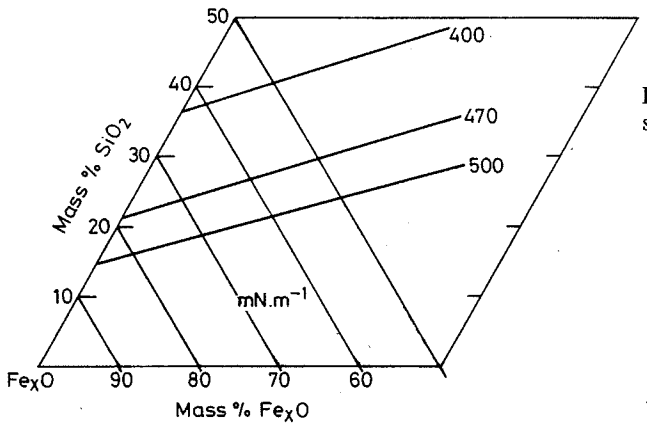


Fig. 10.102. Suggested isotension lines for the $CaO + Fe_xO + SiO_2$ system at 1400 °C [Ref. 131]

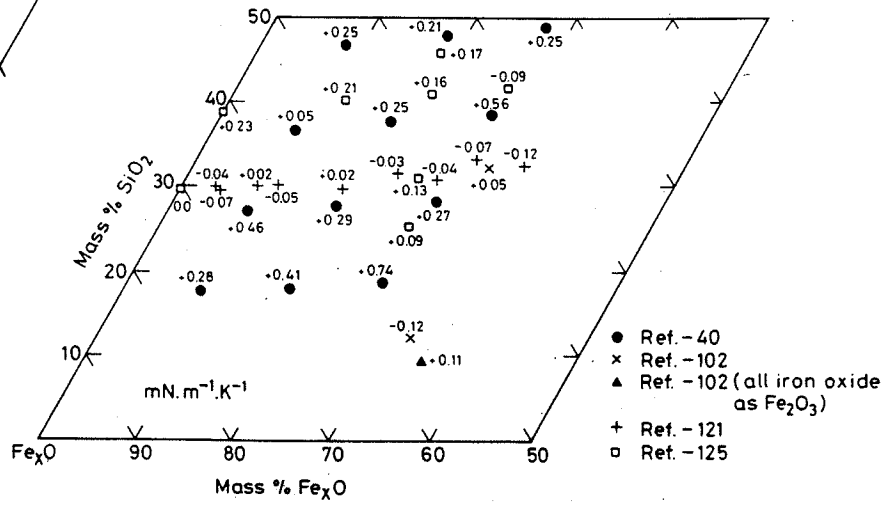


Fig. 10.103. Temperature coefficient of surface tension of $CaO + Fe_xO + SiO_2$ melts

$CaO\text{-}MgO\text{-}SiO_2$

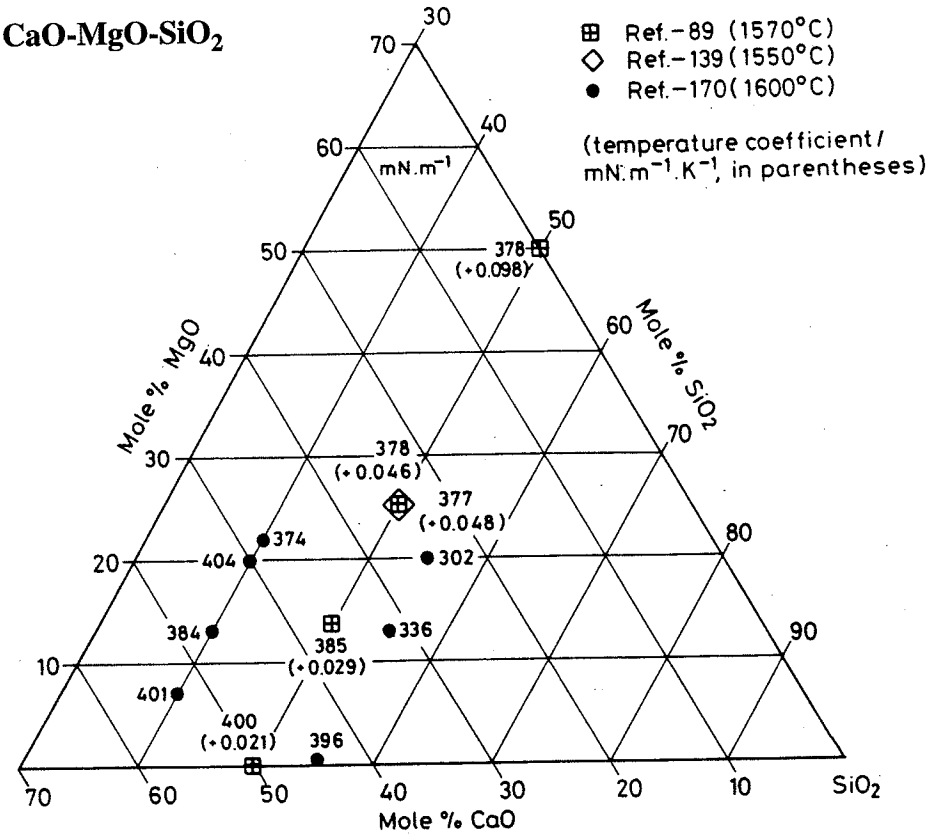


Fig. 10.104. Surface tension and the temperature coefficient of surface tension, of $CaO + MgO + SiO_2$ melts

$CaO\text{-}MnO\text{-}SiO_2$

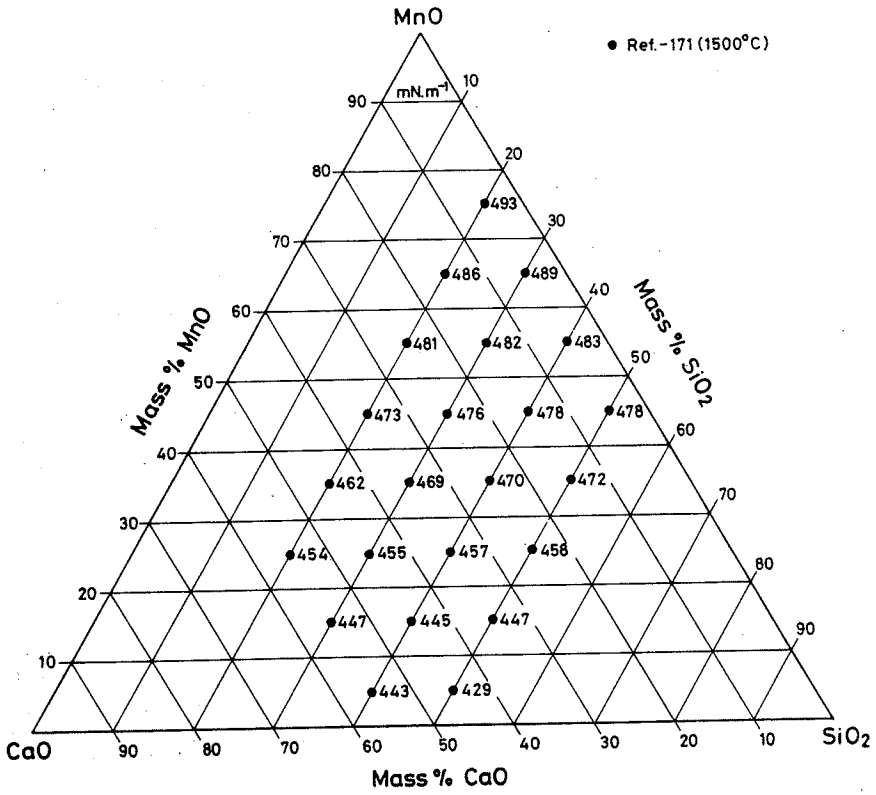
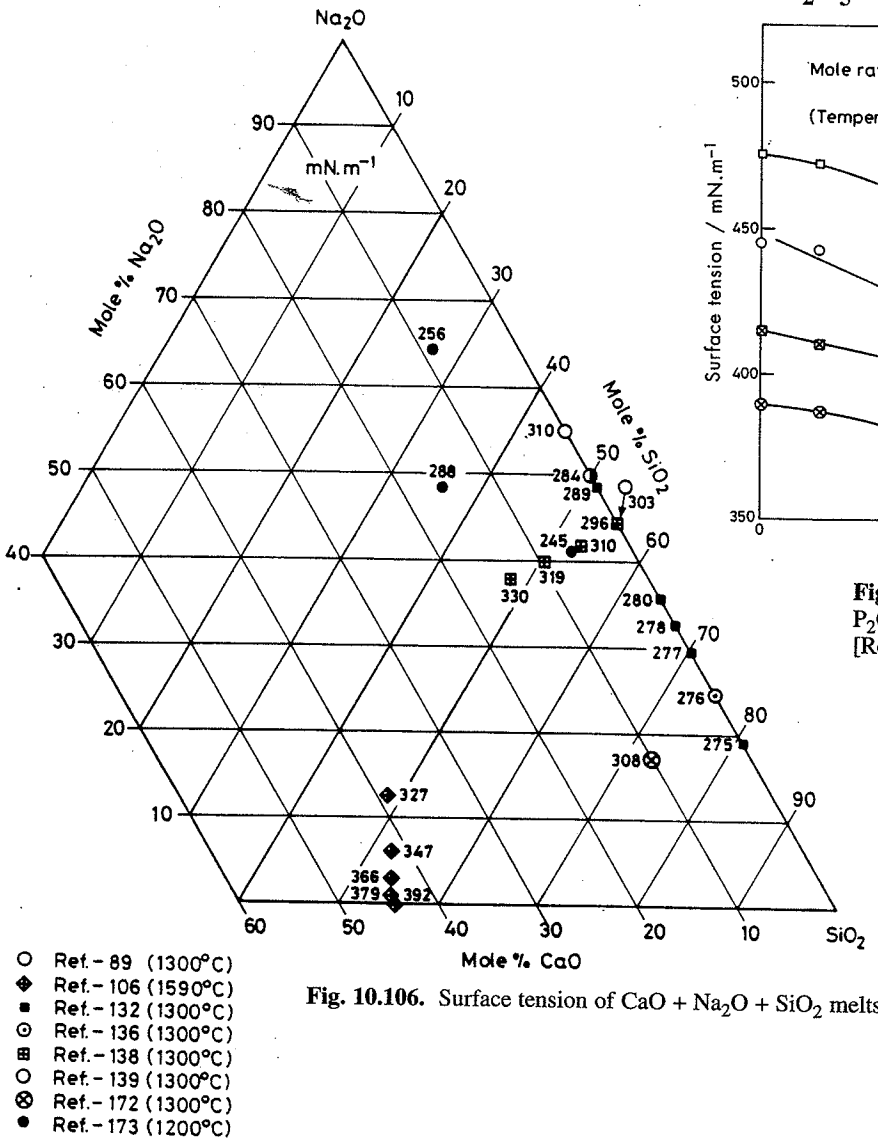


Fig. 10.105. Surface tension of $CaO + MnO + SiO_2$ melts at 1500 °C [Ref. 171]

$CaO\text{-}Na_2O\text{-}SiO_2$



- Ref. - 89 (1300°C)
- Ref. - 106 (1590°C)
- Ref. - 132 (1300°C)
- Ref. - 136 (1300°C)
- Ref. - 138 (1300°C)
- Ref. - 139 (1300°C)
- Ref. - 172 (1300°C)
- Ref. - 173 (1200°C)

Fig. 10.106. Surface tension of $CaO + Na_2O + SiO_2$ melts

$CaO\text{-}P_2O_5\text{-}SiO_2$

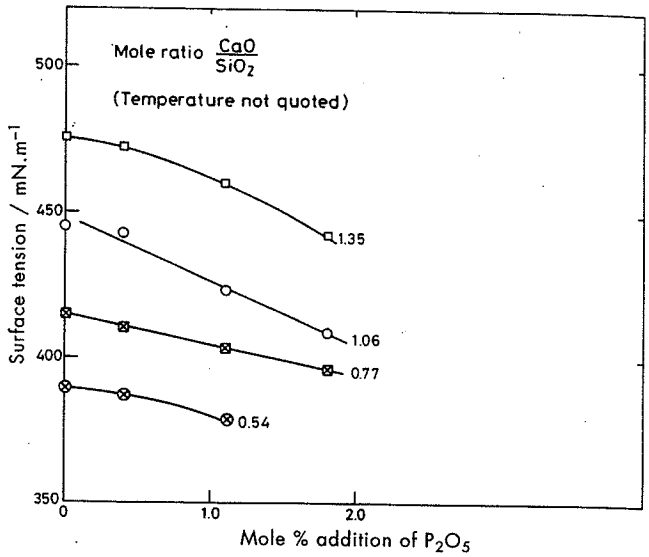


Fig. 10.108. Change in surface tension with P_2O_5 content of $CaO + P_2O_5 + SiO_2$ melts [Ref. 109]

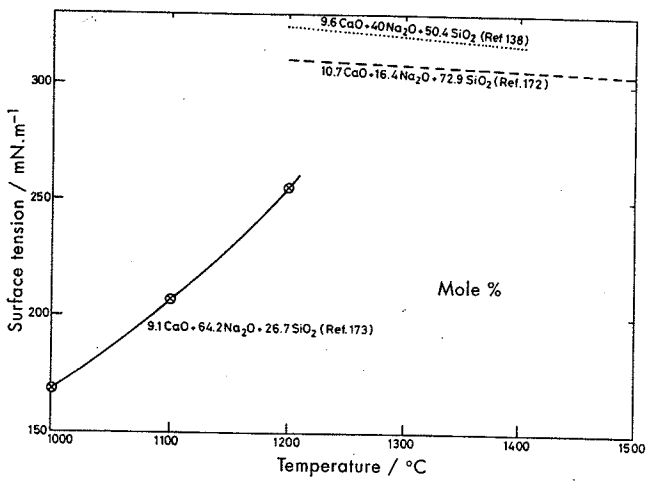


Fig. 10.107. Variation of surface tension with temperature of $CaO + Na_2O + SiO_2$ melts

$CaO\text{-}SiO_2\text{-}V_2O_5$

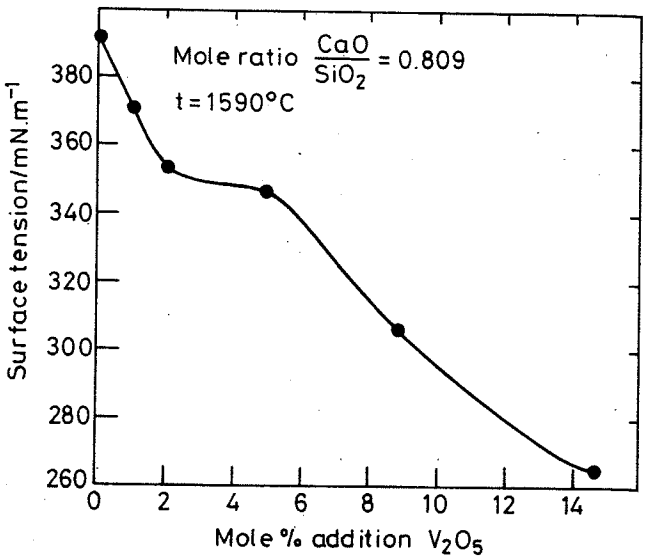


Fig. 10.109. Change in surface tension with V_2O_5 content of $CaO + SiO_2 + V_2O_5$ melts at 1590 °C [Ref. 106]

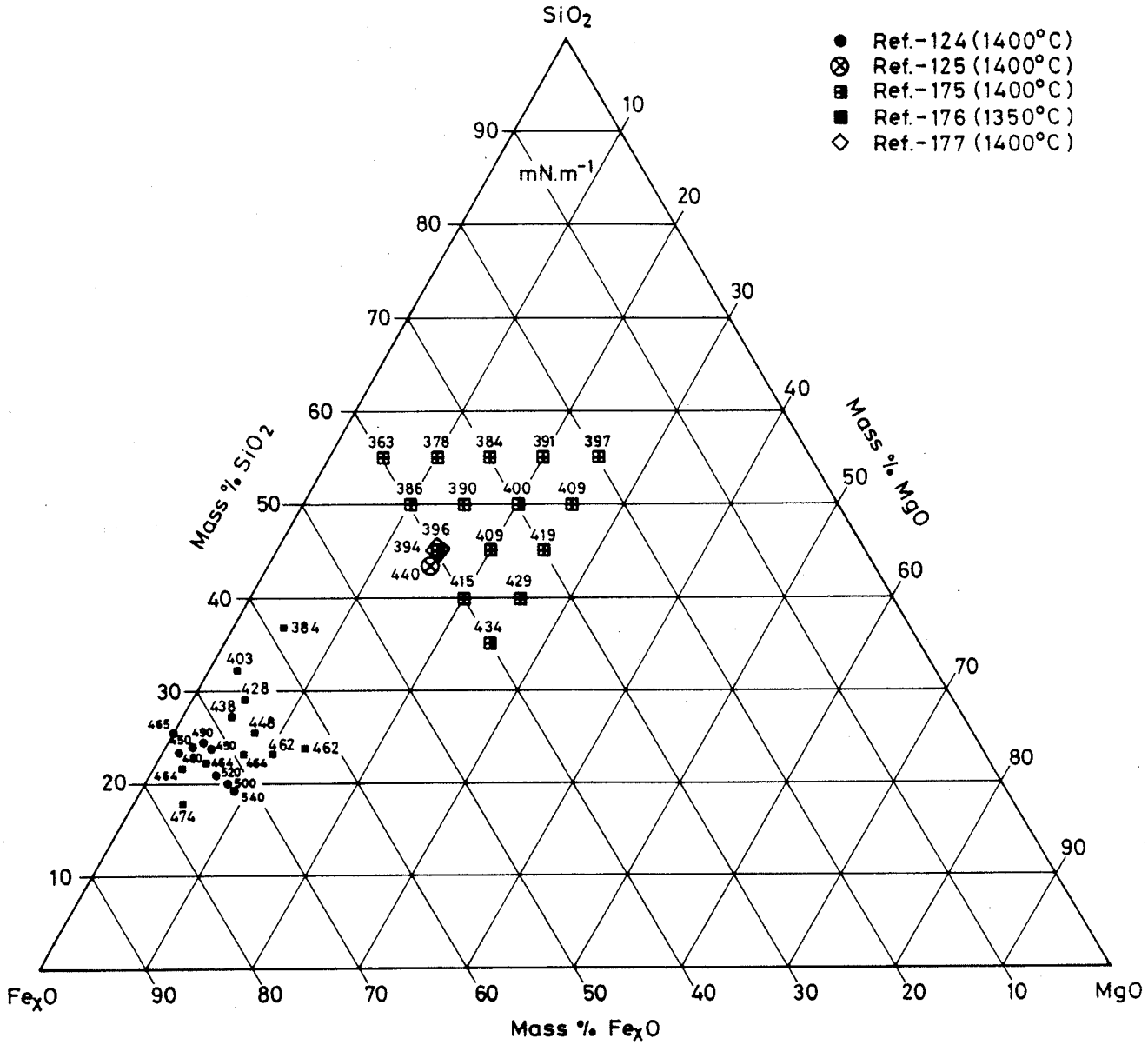


Fig. 10.110. Surface tension of Fe_xO + MgO + SiO_2 melts

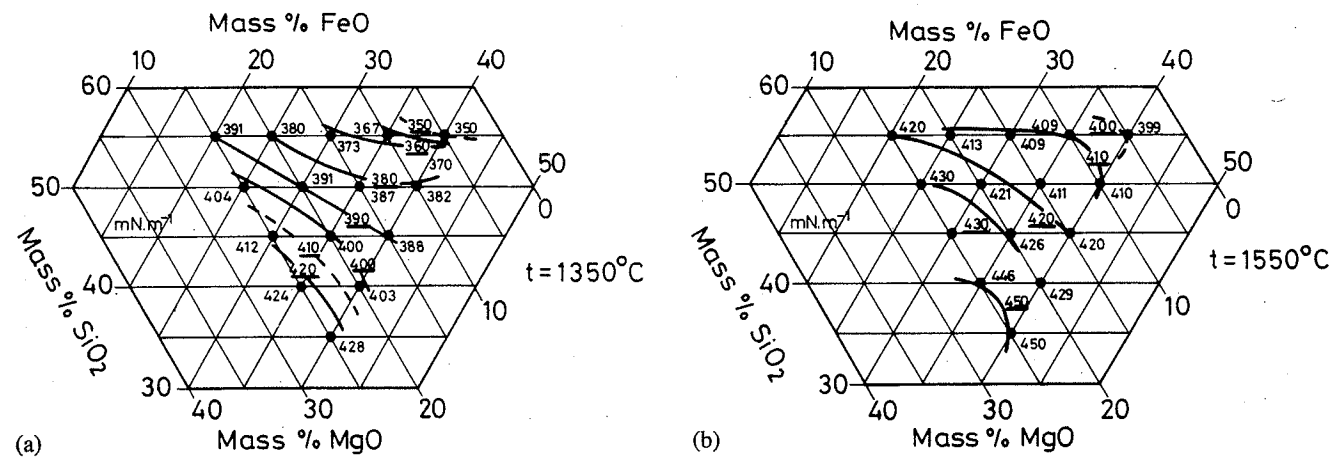


Fig. 10.111 a,b. Surface tension of Fe_xO + MgO + SiO_2 melts at 1350 °C and at 1550 °C [Ref. 175]

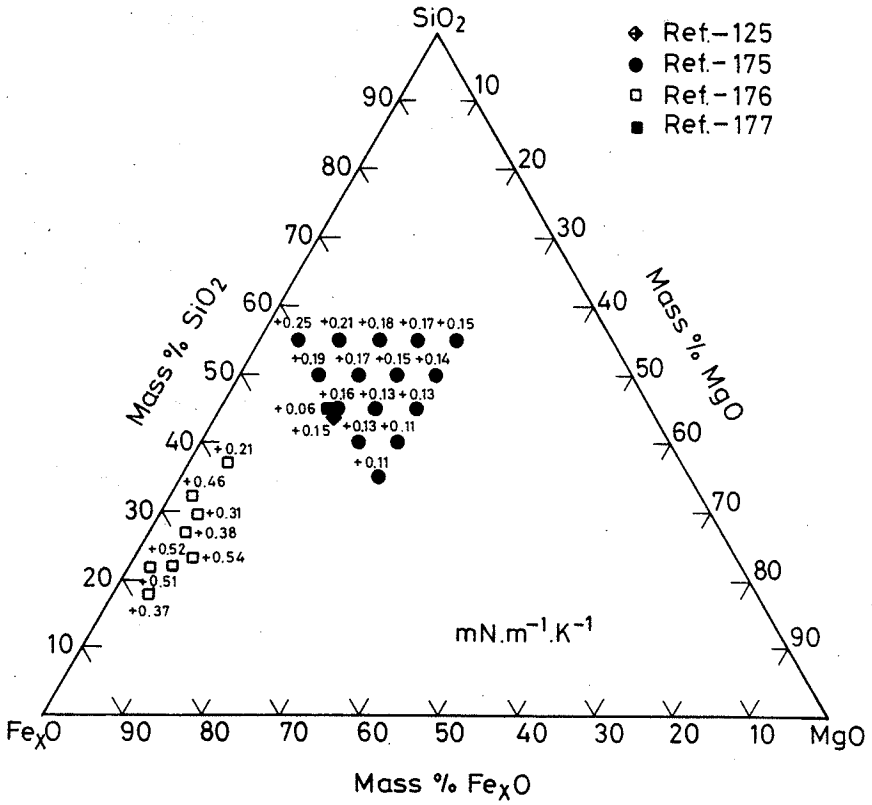


Fig. 10.112. Temperature coefficient of surface tension of $Fe_xO + MgO + SiO_2$ melts

Fe_xO-MnO-SiO_2

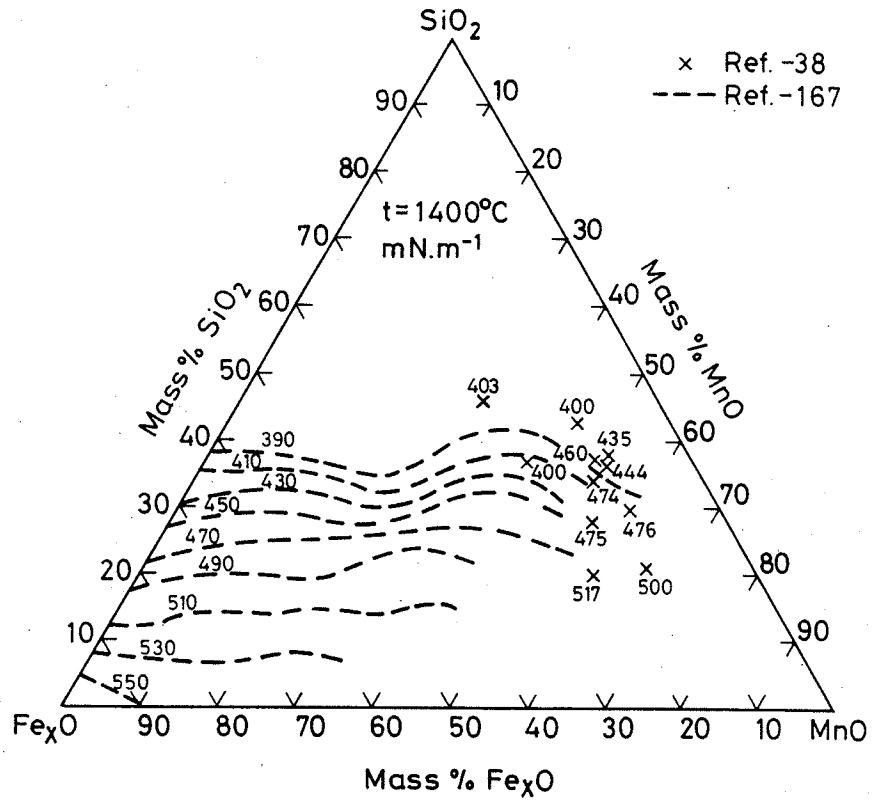


Fig. 10.113. Surface tension of $Fe_xO + MnO + SiO_2$ melts at 1400 °C

MgO-Na_2O-SiO_2

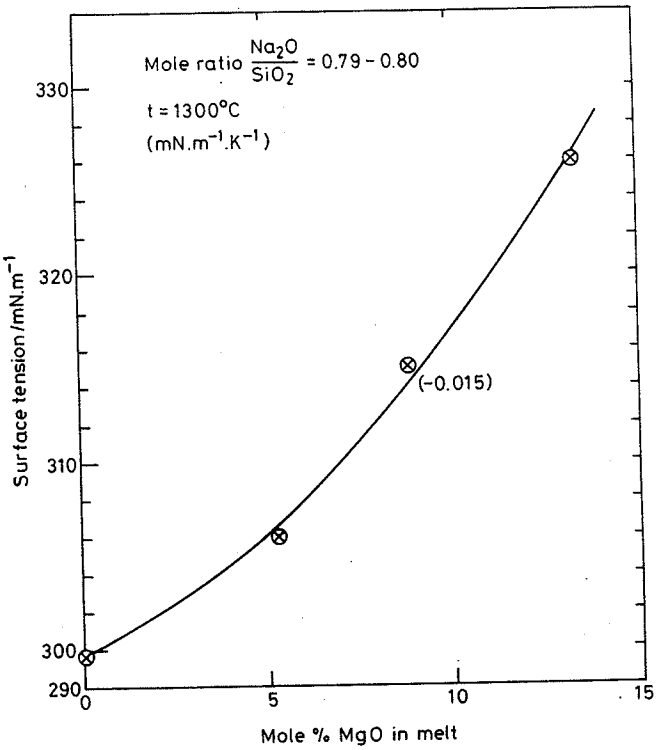


Fig. 10.114. Change in surface tension with MgO content of $MgO + Na_2O + SiO_2$ melts at 1300 °C and the temperature coefficient of surface tension for one melt [Ref. 138]

Al_2O_3-CaF_2-CaO-MgO

Tab. 10.4. Surface tension of $Al_2O_3 + CaF_2 + CaO + MgO$ melt at 1460 °C

Composition (mass %)				Surface tension/mN.m^{-1}	Reference
Al_2O_3	CaF_2	CaO	MgO		
40.4	17.6	26.3	15.7	430	[180]

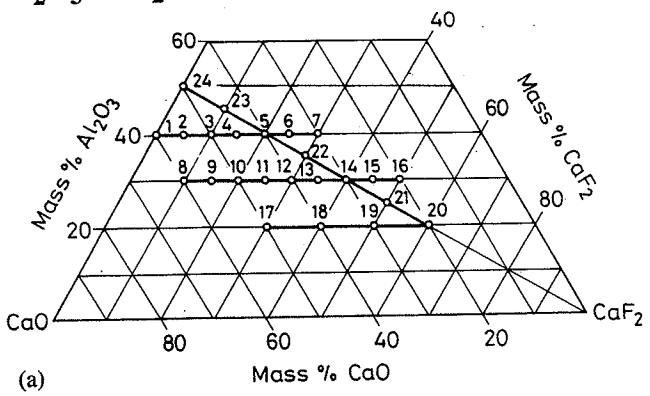
Al_2O_3-CaF_2-CaO-MnO

Tab. 10.5. Surface tension of $Al_2O_3 + CaF_2 + CaO + MnO$ melt at 1500-1550 °C

Composition (mass %)				Surface tension/mN.m^{-1}	Reference
Al_2O_3	CaF_2	CaO	MnO		
40	18	25	17	355	[72]

10.3.4 Quaternary systems

Al_2O_3-CaF_2-CaO-CaS



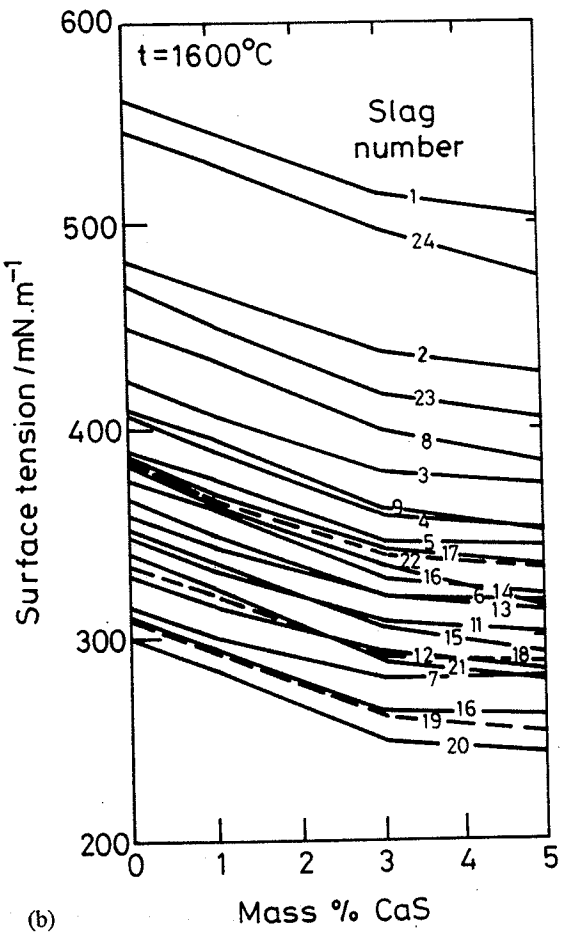


Fig. 10.115 a,b. Effect of CaS additions on the surface tension of $Al_2O_3 + CaF_2 + CaO$ melts at 1600 °C. Slag numbers refer to ternary compositions given in (a) [Ref. 181]

Al_2O_3-CaF_2-CaO-SiO_2

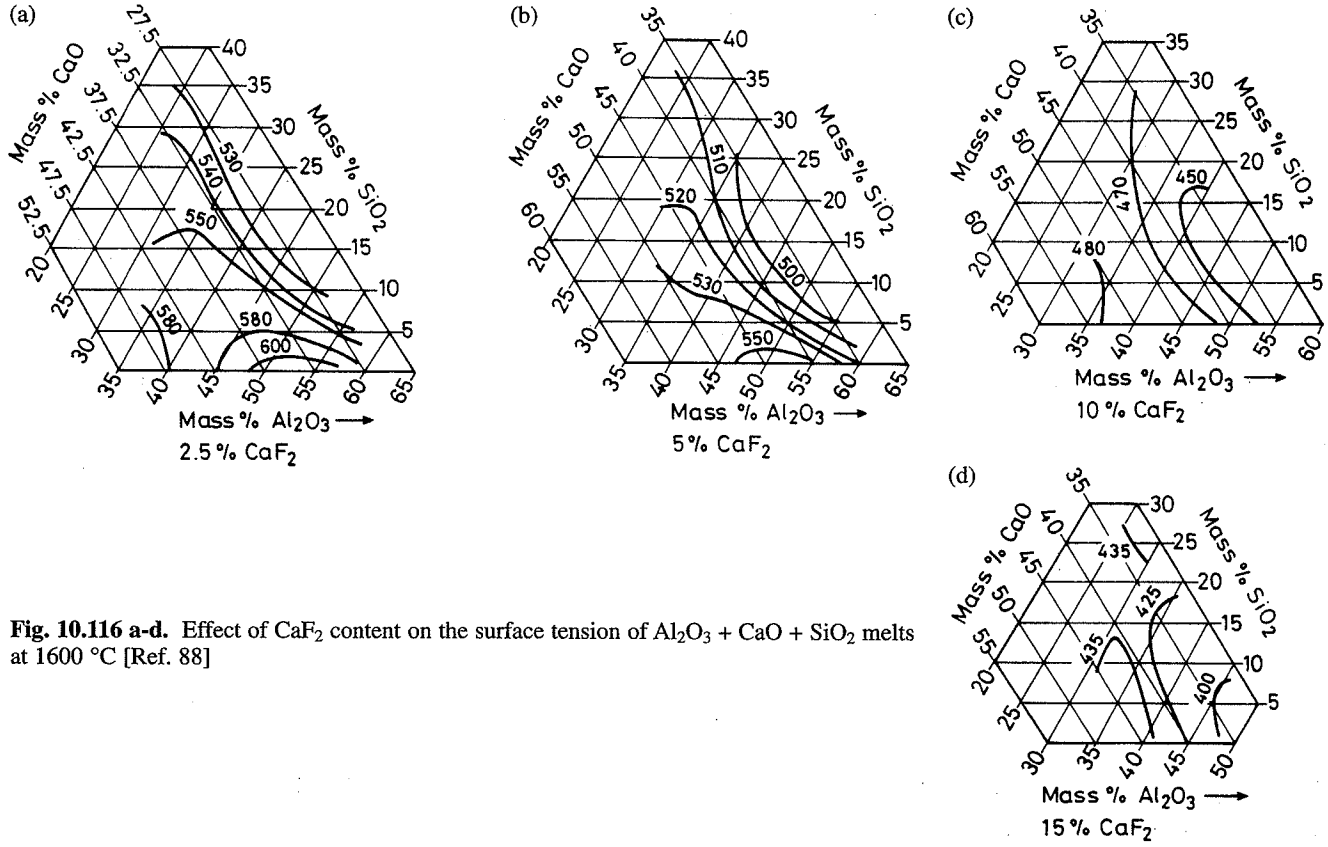


Fig. 10.116 a-d. Effect of CaF_2 content on the surface tension of Al_2O_3 + CaO + SiO_2 melts at 1600 °C [Ref. 88]

Tab. 10.6. Composition and surface tension-temperature data of slags in the system Al_2O_3 + CaF_2 + CaO + SiO_2

Reference	Slag No.	Slag Composition (mass) % CaF_2	% Al_2O_3	% CaO	% SiO_2	Surface tension (mN.m^{-1}) temp. (°C) relation and temp. range
Krusina [182]	1	5	20	45	30	γ = 835 – 0.2312 (t/°C): 1460° – 1535°
	2	10	20	42	28	735 – 0.2013 (t/°C): 1350° – 1498°
	3	15	10	45	30	624 – 0.1436 (t/°C): 1296° – 1548°
	4	20	5	45	30	604 – 0.1238 (t/°C): 1380° – 1490°
	5	5	25	50	20	917 – 0.3155 (t/°C): 1419° – 1512°
	6	10	20	50	20	672 – 0.1867 (t/°C): 1419° – 1507°
	7	15	15	50	20	623 – 0.1786 (t/°C): 1317° – 1479°
	8	20	10	50	20	536 – 0.1256 (t/°C): 1239° – 1423°
	9	5	45	40	10	1097 – 0.4348 (t/°C): 1427° – 1496°
	10	10	40	40	10	906 – 0.3292 (t/°C): 1440° – 1525°
	11	15	35	40	10	558 – 0.1085 (t/°C): 1365° – 1523°
	12	20	30	40	10	440 – 0.0470 (t/°C): 1357° – 1496°

(Continuation)

Tab. 10.6. Composition and surface tension-temperature data of slags in the system $Al_2O_3 + CaF_2 + CaO + SiO_2$

Reference	Slag No.	Slag Composition (mass) % CaF_2	% Al_2O_3	% CaO	% SiO_2	Surface tension ($mN.m^{-1}$) temp. (°C) relation and temp. range
Komelkov [183]	13	58.4	21.7	1.8	18.1	417 – 0.097 (t/°C): 1540° – 1650°
Goloshubov [184]	14	75	17	1.8	2	1037 – 0.442 (t/°C): 1440° – 1660°
	15	59	34	2.9	1	1057 – 0.438 (t/°C): 1480° – 1730°
Mazanek [144]		51.4	29.3	14.8	1.03	410 at 1520°C
		66.8	22.3	6.72	0.43	368 at 1510°C
		37.0	40.8	11.0	6.11	427 at 1530°C
		45.9	1.86	31.0	8.23	394 at 1500°C
		60.9	31.0	3.80	0.51	389 at 1500°C
		42.3	31.8	21.8	1.07	436 at 1520°C
		32.0	44.8	20.3	0.58	484 at 1540°C
		38.8	25.8	27.1	2.21	437 at 1540°C

NB The slags studied by Mazanek [144] also contain small amounts of FeO, Fe_2O_3 and MnO

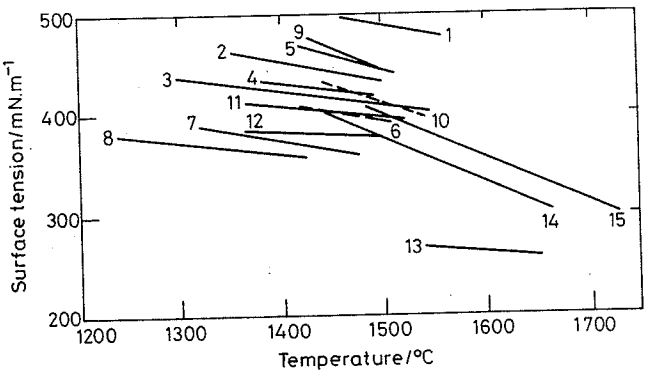


Fig. 10.117. Variation of the surface tension of $Al_2O_3 + CaF_2 + CaO + SiO_2$ melts with temperature. (Slag compositions are given in Tab. 10.6)

Al_2O_3-CaF_2-MgO-SiO_2

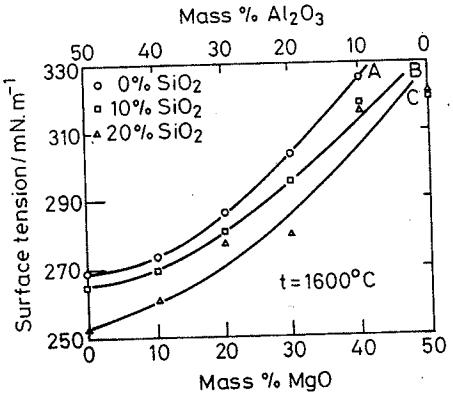


Fig. 10.119. Variation of the surface tension of Al_2O_3 + 50 mass % CaF_2 + MgO slag with MgO content (curve A) and effect of replacing CaF_2 by 10 % SiO_2 (curve B) and 20 % SiO_2 (curve C) [Ref. 147]

Al_2O_3-CaF_2-CaO-V_2O_5

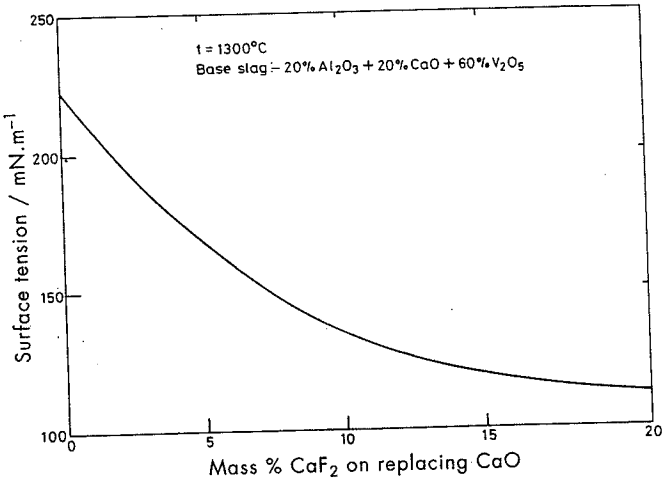


Fig. 10.118. Effect of replacing CaO by CaF_2 on the surface tension of $Al_2O_3 + CaO + V_2O_5$ slag at 1300 °C [Ref. 158]

Al_2O_3-CaO-Fe_xO-SiO_2

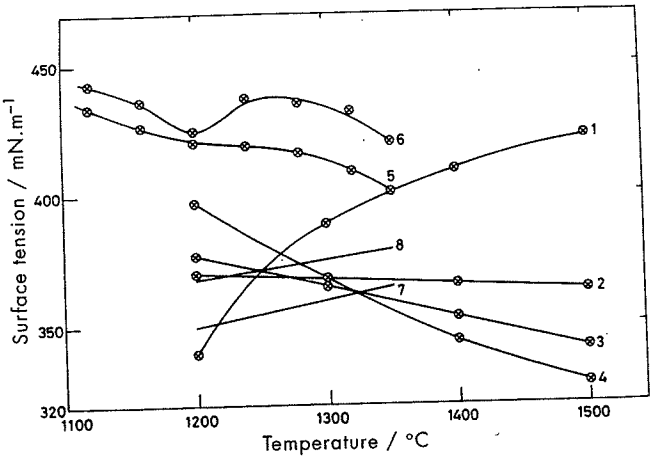


Fig. 10.120. Variation with temperature of the surface tension of $Al_2O_3 + CaO + Fe_xO + SiO_2$ slags. (Slag compositions are given in Tab. 10.7)

Tab. 10.7. Composition (mass %) and surface tension at 1200 °C of slags in the system $Al_2O_3 + CaO + Fe_xO + SiO_2$

Slag No. on diagram	Al_2O_3	Fe_xO	CaO	SiO_2	Surface tension $mN.m^{-1}$ at 1200 °C	Ref.
1	5.69	38.55 FeO	5.08	50.68	340	[119]
2	5.87	22.11 FeO	22.24	49.77	370	
3	5.57	14.19 FeO	28.84	51.21	377	
4	5.49	5.49 FeO	37.09	51.92	397	
5	4.6	35.7 FeO + 9.8 Fe_2O_3	18.3	31.7	421	[186]
6	9.1	33.9 FeO + 9.3 Fe_2O_3	17.4	30.8	424	
7	11.15	29.26 FeO + 0.24 Fe_2O_3	14.8	44.5	350	[185]
8	11.20	24.63 FeO + 0.32 Fe_2O_3	19.35	44.75	368	
–	8.58	56.66	2.88	33.15	426	[60]
–	9.96	50.28	3.92	32.30	416	
–	13.81	42.57	7.93	34.90	442	
–	9.88	46.04	7.99	32.94	417	
–	10.63	42.05	11.47	35.70	441	
–	10.00	53.00	3.00	34.00	419	
–	12.09	41.02	12.26	34.87	421	

Al_2O_3-CaO-MgO-SiO_2

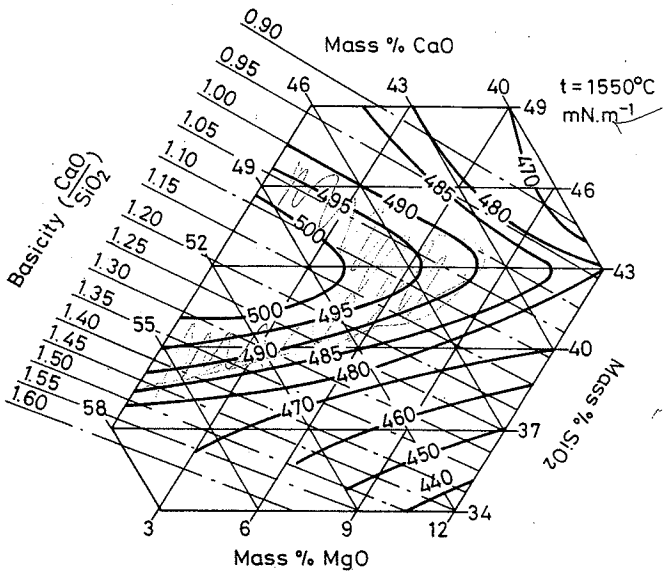
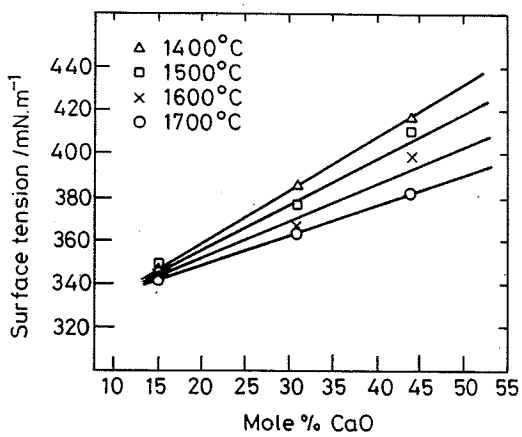
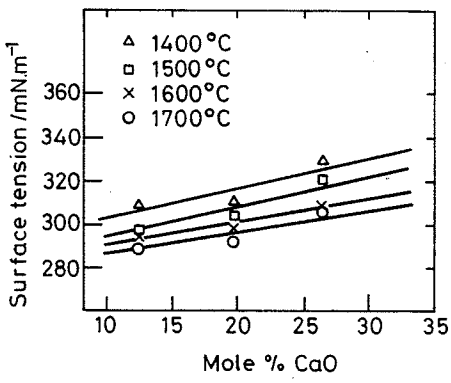


Fig. 10.121. Isotension lines for slags in the system 5 % Al_2O_3 + CaO + MgO + SiO_2 at 1550 °C [Ref. 188]



(a)



(b)

Fig. 10.122 a,b.
(a) Variation in surface tension with CaO content of Al_2O_3 + CaO + MgO + SiO_2 slags (12 mole % Al_2O_3 + 44 mole % SiO_2 + 0-29 mole % MgO) over a range of temperature [Ref. 170]
(b) Variation in surface tension with CaO content of Al_2O_3 + CaO + MgO + SiO_2 slags (12-13 mole % Al_2O_3 + 61.5 mole % SiO_2 + 0-13 mole % MgO) over a range of temperature [Ref. 170]

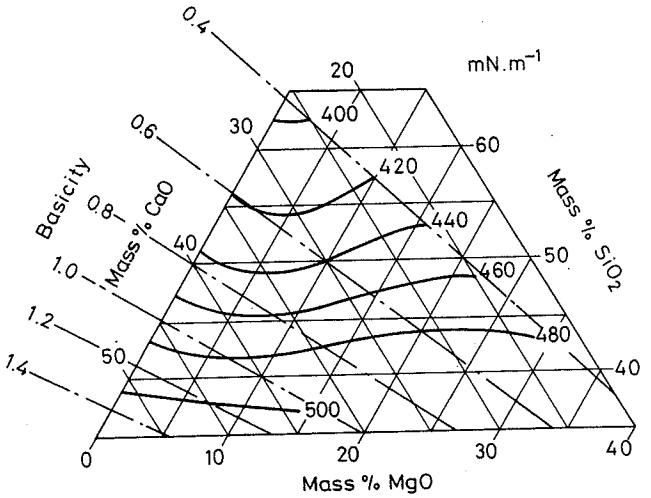
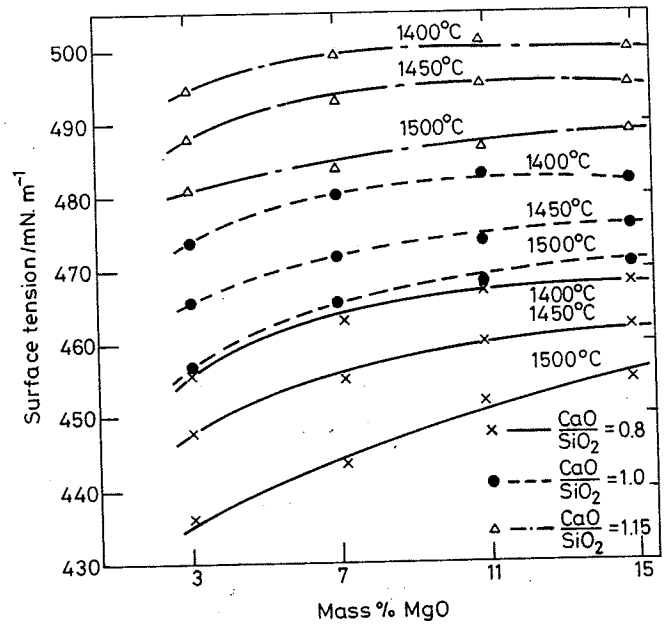


Fig. 10.123. Isotension lines for slags in the system 10 % Al_2O_3 + CaO + MgO + SiO_2 at 100 °C above the crystallisation temperature [Ref. 191]

Tab. 10.8. Surface tension and its temperature coefficient, of Al_2O_3 + CaO + MgO + SiO_2 melts

Composition (mass %)				Surface tension/ $mN.m^{-1}$ at 1450 °C	Temperature coefficient of surface tension/ $mN.m^{-1}.K^{-1}$	Ref.
Al_2O_3	CaO	MgO	SiO_2			
18.7	37.1	5.2	39.7	525	−0.059	[155]
16.8	37.9	7.9	38.0	507	−0.21	
16.4	39.7	7.1	37.1	524	−0.14	
15.2	39.3	10.6	35.1	537	−0.26	
13.4	42.3	6.8	38.4	528	−0.20	
17.2	42.3	3.8	38.3	543	−0.075	
15.2	43.5	4.9	37.1	548	−0.094	
10.0	35.0	10.0	45.0	455	–	[187]
24.86	34.96	6.17	34.02	460	−0.136	[189]



Al_2O_3	CaO	MgO	SiO_2	Basicity $\left[\frac{CaO}{SiO_2}\right]$
8.1	39.7	3.0	49.2	0.809
8.2	37.8	7.1	46.9	0.806
8.0	36.4	10.8	44.8	0.810
8.1	34.8	14.9	42.8	0.825
8.4	44.4	3.4	43.8	1.015
8.5	42.7	6.9	41.9	1.020
8.6	40.7	10.8	39.9	1.020
8.4	38.3	14.9	38.4	0.999
8.4	47.2	3.4	41.0	1.15
8.5	45.1	7.2	39.2	1.15
8.2	43.3	11.3	37.2	1.16
8.3	41.1	15.4	35.3	1.16

Fig. 10.124. Change in surface tension with MgO content and with temperature of Al_2O_3 + CaO + MgO + SiO_2 + slags [Ref. 190]

Al_2O_3-CaO-MnO-SiO_2

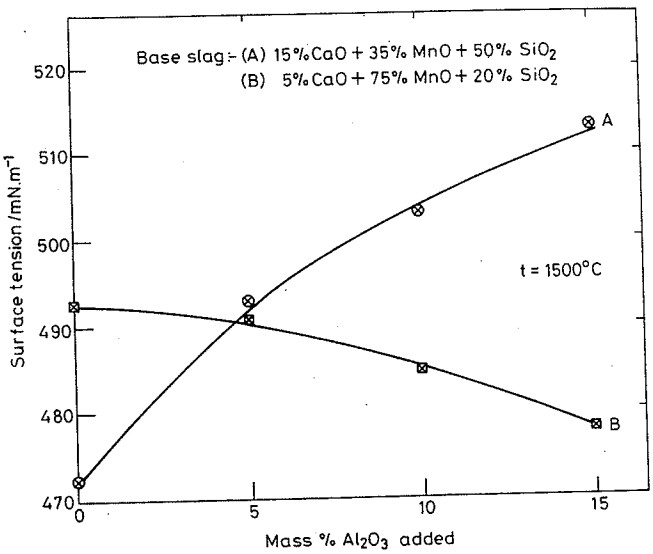
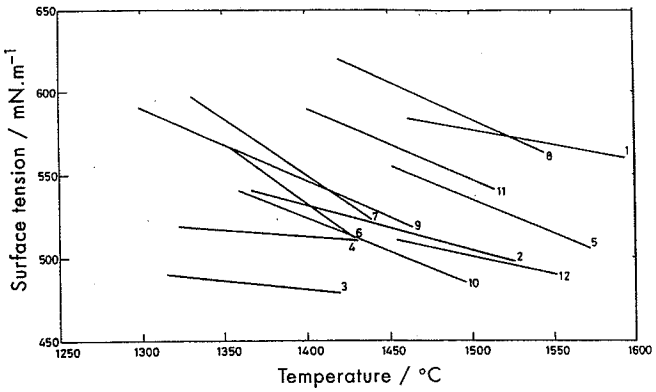


Fig. 10.125. Effect of Al_2O_3 additions on the surface tension of CaO + MnO + SiO_2 melts at 1500 °C [Ref. 171]



Slag No.	Composition (mass %) Initial (Final) content Al_2O_3	CaO	MgO	SiO_2	Temperature coefficient of surface tension $mN.m^{-1}.K^{-1}$
1	40 (43.28)	30 (27.12)	10 (10.55)	20 (18.86)	- 0.176
2	30 (30.0)	30 (32.40)	20 (18.19)	20 (18.72)	- 0.268
3	20 (21.08)	30 (31.04)	30 (28.33)	20 (19.32)	- 0.107
4	10 (9.86)	30 (30.12)	40 (39.6)	20 (19.85)	- 0.082
5	45 (46.08)	25 (25.48)	20 (17.3)	10 (11.0)	- 0.405
6	35 (33.84)	25 (24.8)	30 (31.3)	10 (9.6)	- 0.736
7	25 (28.08)	25 (27.24)	40 (34.6)	10 (10.8)	- 0.695
8	40 (41.34)	40 (42.6)	10 (5.95)	10 (10.04)	- 0.456
9	30 (31.76)	40 (43.0)	20 (15.46)	10 (9.52)	- 0.443
10	20 (23.02)	40 (43.02)	30 (23.6)	10 (10.26)	- 0.398
11	15 (15.52)	45 (45.28)	10 (8.83)	30 (29.84)	- 0.425
12	5 (4.64)	45 (46.08)	20 (18.67)	30 (30.0)	- 0.217

Fig. 10.126. Variation with temperature of the surface tension of melts in the system $Al_2O_3 + CaO + MnO + SiO_2$ [Ref. 192]

Al_2O_3-CaO-Na_2O-SiO_2

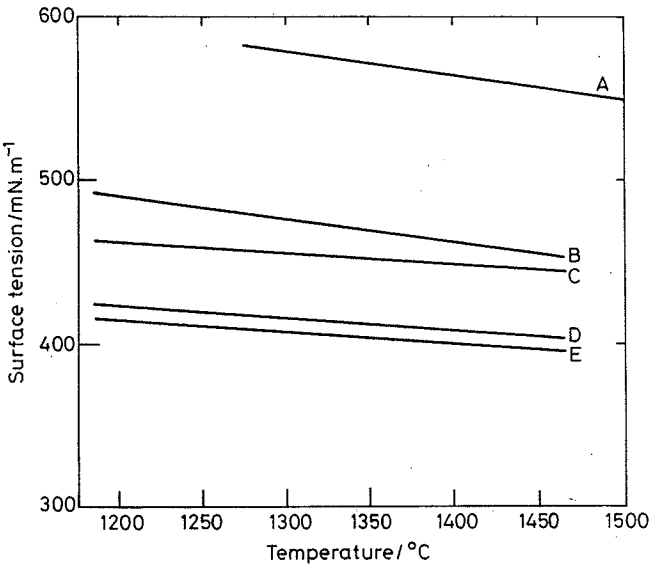


Fig. 10.127. Variation with temperature of slags in the system $Al_2O_3 + CaO + Na_2O + SiO_2$. Slag compositions (mass %):

Curve A - 10 % Al_2O_3 + 40 % CaO + 5 % Na_2O + 45 % SiO_2 [Ref. 194]
Curve B - 10.6 % Al_2O_3 + 40.9 % CaO + 48.5 % SiO_2 (Slag No. 1) [Ref. 193]
Curve C - Slag No. 1 + 3.14 % Na_2O [Ref. 193]
Curve D - Slag No. 1 + 6.13 % Na_2O [Ref. 193]
Curve E - Slag No. 1 + 12.49 % Na_2O [Ref. 193]

Al_2O_3-CaO-SiO_2-TiO_2

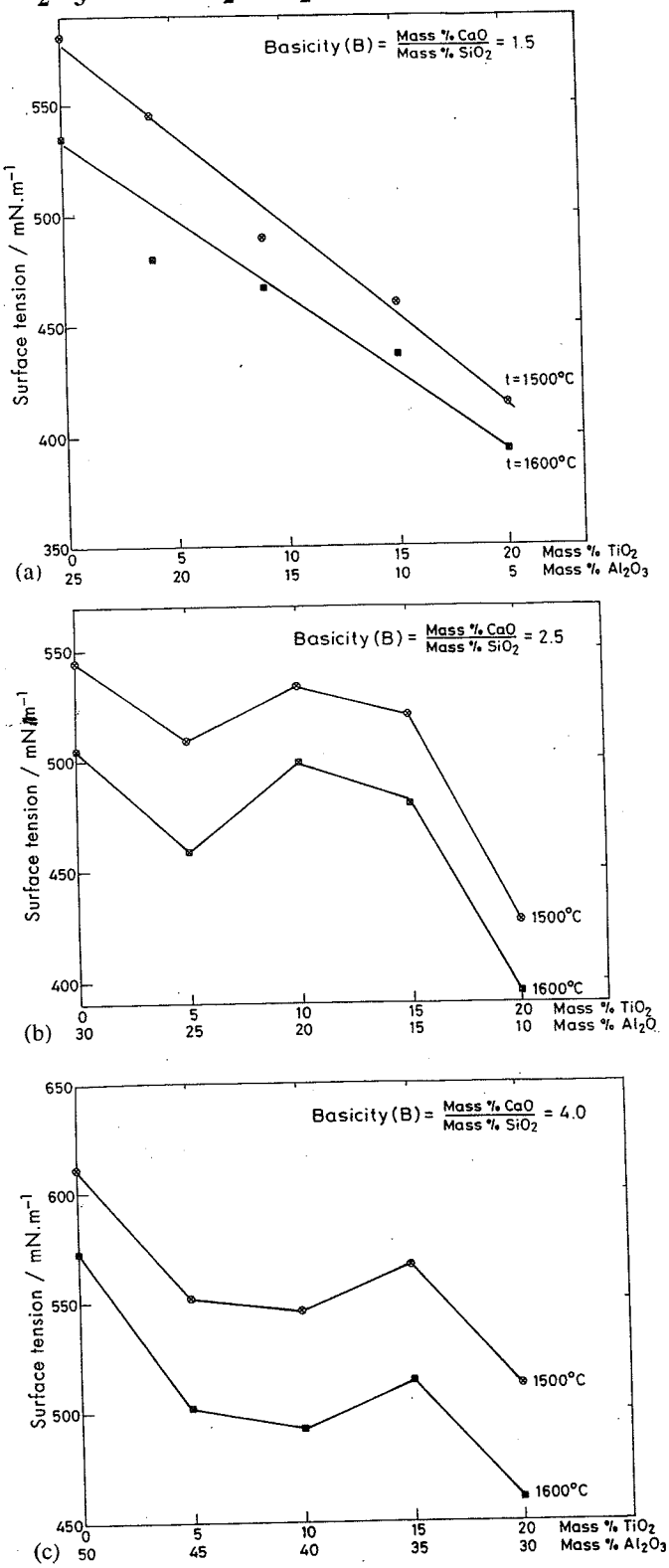
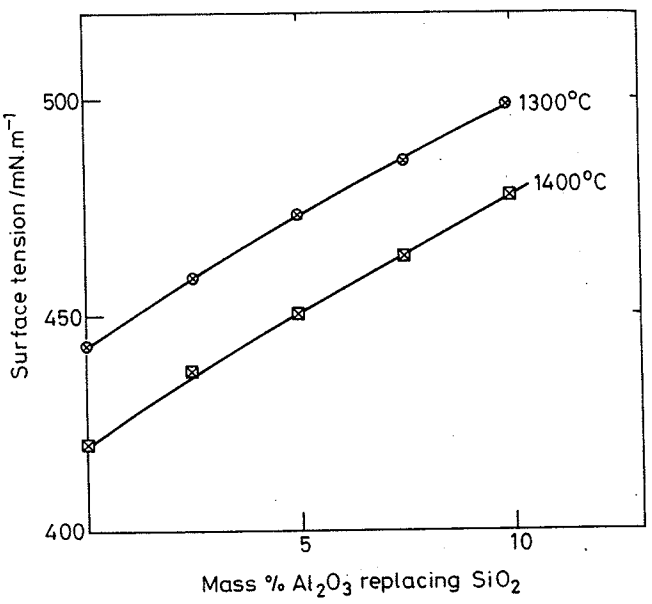


Fig. 10.128 a-c. Effect of replacing Al_2O_3 by TiO_2 on the surface tension of Al_2O_3 + CaO + SiO_2 + TiO_2 slags at 1500 °C and 1600 °C and various basicities [Ref. 195]

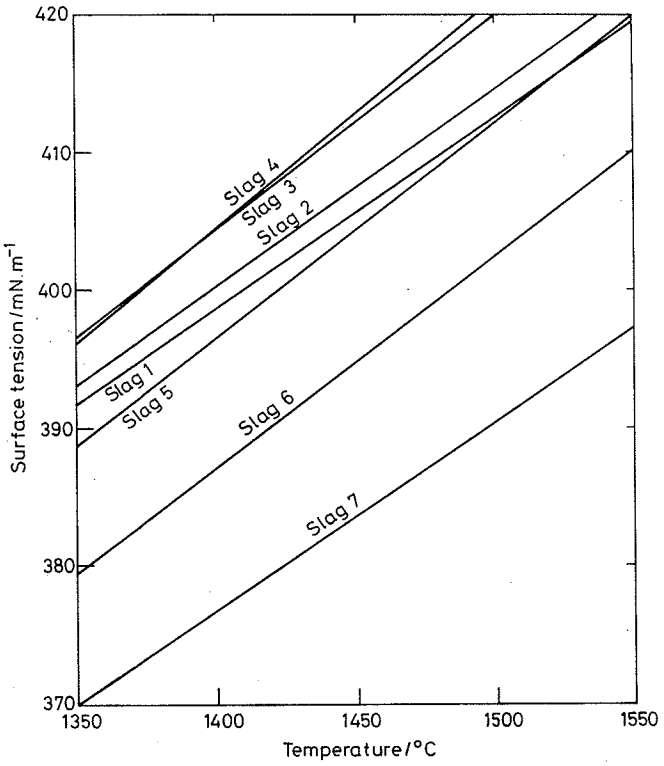
Al_2O_3-FeO-Fe_2O_3-SiO_2



Al_2O_3	FeO	Fe_2O_3	SiO_2
9.97	61.49	15.36	14.98
7.49	61.64	13.43	17.44
5.00	62.12	12.97	19.91
2.50	60.75	14.37	22.38
0	61.18	13.87	24.95

Fig. 10.129. Effect of replacing SiO_2 by Al_2O_3 on the surface tension of Al_2O_3 + FeO + Fe_2O_3 + SiO_2 (approximately 75 mass % Fe_xO) melts at 1300 °C and 1400 °C [Ref. 122]

Al_2O_3-Fe_xO-MgO-SiO_2



Slag No.	Slag composition, mass %					
	FeO	Fe_2O_3	Fe_{met}	Al_2O_3	MgO	SiO_2
1	28.83	0.69	0.56	–	20.69	49.29
2	28.29	0.69	0.59	1.93	14.41	49.09
3	27.97	0.52	0.64	3.72	19.18	47.97
4	26.89	0.78	0.70	5.69	18.73	47.21
5	26.95	0.51	0.43	7.30	18.44	46.37
6	26.64	0.42	0.36	8.98	18.10	45.50
7	26.15	0.34	0.41	10.77	17.71	44.62

Fig. 10.130. Variation of surface tension with temperature of melts in the Al_2O_3 + Fe_xO + MgO + SiO_2 system; showing the positive temperature coefficients [Ref. 196]

CaO-CaS-MgO-SiO_2

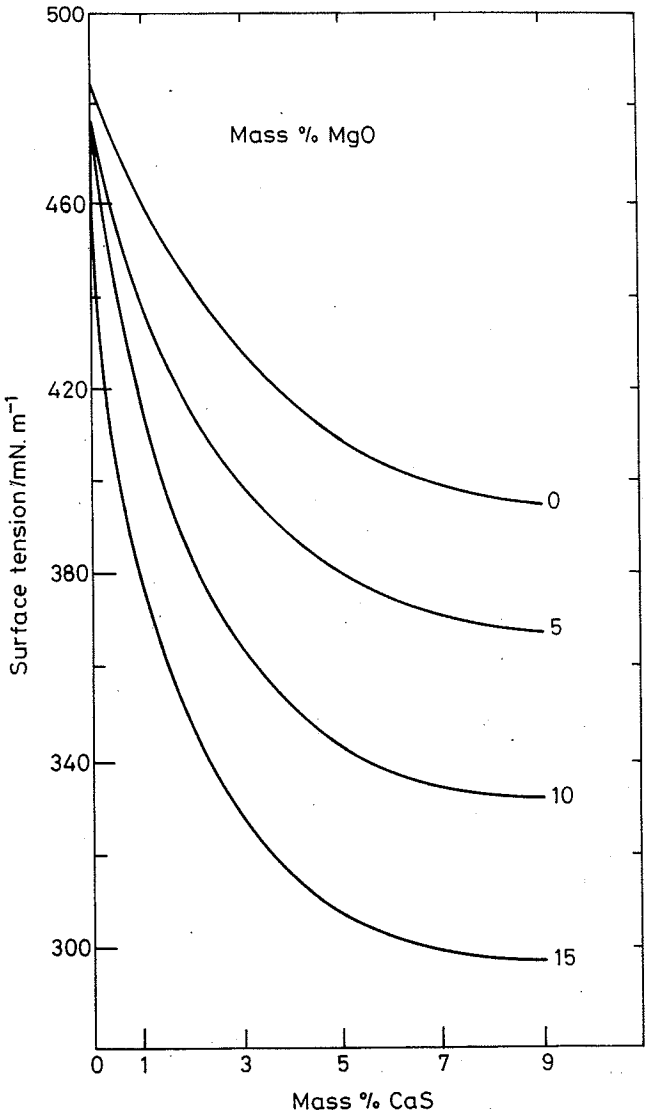
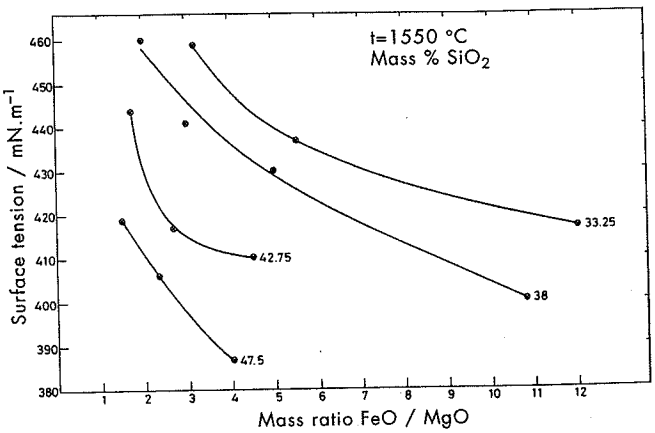


Fig. 10.131. Influence of CaS on the surface tension of CaO + CaS + MgO + SiO_2 melts at 1500 °C - 1600 °C [Ref. 197]

$$\left[\text{Basicity of melts} = \frac{\text{mass \% (CaO + CaS + MgO)}}{\text{mass \% } SiO_2} = 1.0\right]$$

$CaO\text{-}FeO\text{-}MgO\text{-}SiO_2$



Composition (mass %)						Surface tension/ $mN.m^{-1}$ at 1400 °C	Temp. coefficient of surface tension $mN.m^{-1}.K^{-1}$	Ref.
CaO	FeO	Fe_2O_3	Fe_{met}	MgO	SiO_2			
0	28.83	0.69	0.56	20.69	49.29	400	+ 0.15	[196]
1.8	28.3	0.65	0.57	19.5	49.18	407	+ 0.11	
3.73	27.59	0.74	0.61	19.31	48.02	412	+ 0.08	
5.59	27.1	0.81	0.43	18.94	47.13	419	+ 0.06	
7.25	26.74	0.83	0.39	18.39	46.4	424	+ 0.05	
16.0	51	13.3	–	0.8	19.1	405	–	[124]
14.7	49	14.3	–	1	20.8	415	–	
10.5	50.3	16.3	–	1.7	21.2	460	–	
5.7	53	13.8	–	2.1	26.4	480	–	
7.4	55.6	11.6	–	2.8	22.7	490	–	
1.4	58	12.3	–	4.6	23.6	475	–	
1.5	59.2	13.4	–	5.0	20.4	480	–	
5	28.5	–	–	19	47.5	419*	+ 0.04	[177]
5	33.25	–	–	14.25	47.5	400	+ 0.05	
5	38	–	–	9.5	47.5	387*	+ 0.10	
5	33.25	–	–	19	42.75	444*	+ 0.14	
5	38	–	–	14.25	42.75	414	+ 0.04	
5	42.75	–	–	9.5	42.75	402	+ 0.07	
5	38	–	–	19	38	460*	–	
5	42.75	–	–	14.25	38	423	+ 0.09	
5	47.5	–	–	9.5	38	427	+ 0.03	
5	52.52	–	–	4.75	38	393	+ 0.06	
5	47.5	–	–	14.75	33.25	459*	–	
5	52.52	–	–	9.5	33.25	435	+ 0.02	
5	57	–	–	4.75	33.25	413	+ 0.03	
0	40	–	–	15	45	394	+ 0.06	
10	36	–	–	13.5	40.5	424	+ 0.03	
5	33.25	–	–	14.25	47.5	401	+ 0.06	
5	33.25	–	–	14.25	47.5	430	0	
5	47.5	–	–	9.5	38	431	0	

* at 1500 °C

Fig. 10.132. Variation of the surface tension at 1500 °C of 5 mass % CaO + FeO + MgO + SiO_2 melts, with the mass ratio FeO/MgO and with the SiO_2 content [Ref. 177]

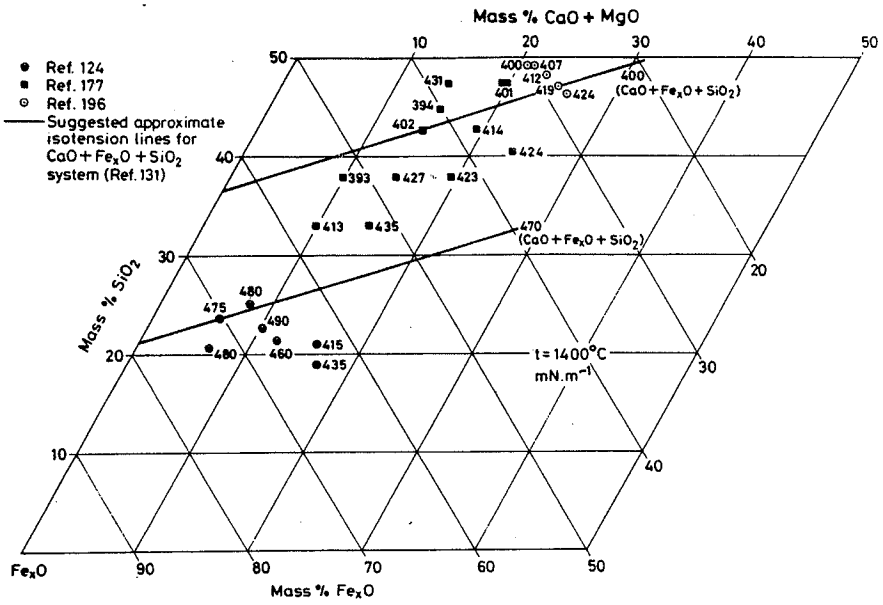


Fig. 10.133. Surface tension at 1400 °C of melts in the pseudo-ternary system (CaO + MgO) + Fe_xO + SiO_2. Also shown are the suggested isotension lines for CaO + Fe_xO + SiO_2 melts [Ref. 131], which would indicate that replacement of MgO by CaO or vice versa, in the pseudo-ternary melt, would have little effect on the surface tension

$CaO-MgO-Na_2O-SiO_2$

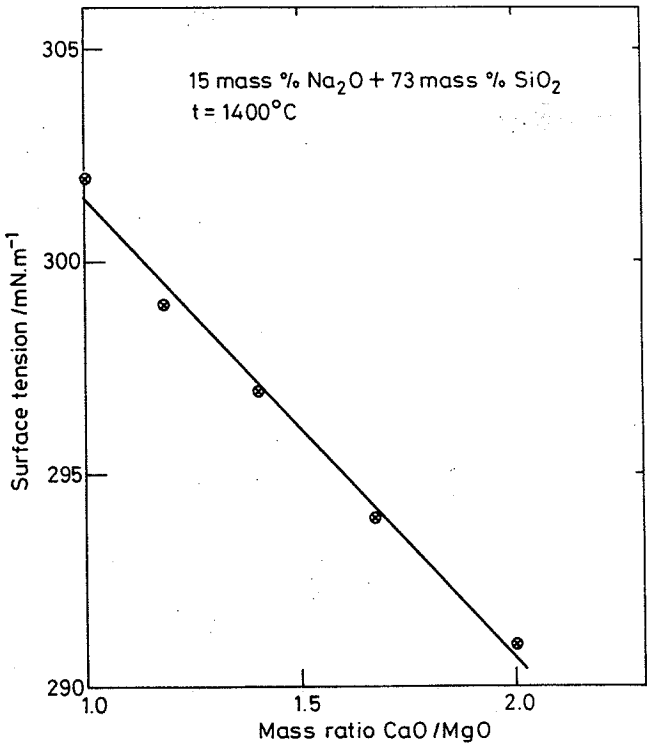


Fig. 10.134. Effect of the mass ratio CaO/MgO on the surface tension of CaO + MgO + 15 % Na_2O + 73 % SiO_2 melts at 1400 °C [Ref. 199]

Composition (mass %)				Surface tension/ $mN.m^{-1}$ at 1450 °C	Temperature coefficient of surface tension/ $mN.m^{-1}.K^{-1}$ (1050-1450 °C)
CaO	MgO	Na_2O	SiO_2		
8	4	15	73	287	- 0.45
9.2	4.6	17.2	69	292	- 0.44
8.6	4.3	16.1	71	290	- 0.50
8.3	4.15	15.55	72	289	- 0.46
7.7	3.85	14.45	74	291	- 0.56
7.4	3.7	13.9	75	296	- 0.62
7.11	3.56	13.33	76	296	- 0.65
6.81	3.41	12.78	77	301	- 0.64
6.52	3.26	12.22	78	305	- 0.74
7.5	4.5	15	73	288	- 0.63
7	5	15	73	290	- 0.60
6.5	5.5	15	73	291	- 0.67
6	6	15	73	296	- 0.66

FeO-Fe_2O_3-MgO-SiO_2

Tab. 10.9. Surface tension and its temperature coefficient of $FeO + Fe_2O_3 + MgO + SiO_2$ melts

Composition (mass %)				Surface tension/ $mN.m^{-1}$ at 1400 °C	Temperature coefficient of surface tension/ $mN.m^{-1}.K^{-1}$	Ref.
FeO	Fe_2O_3	MgO	SiO_2			
71.0	4.5	–	25.4	465	–	[124]
68.5	5.5	1.5	23.4	460	–	
65.5	9.4	1.6	23.6	440	–	
67.5	6.0	2.5	23.9	450	–	
60.3	11.6	3.6	24.6	490	–	
63.0	8.4	4.2	24.0	450	–	
59.8	11.3	5.7	23.2	520	–	
62.3	10.7	6.1	21.0	520	–	
60.3	11.9	7.8	20.0	500	–	
61.6	11.2	7.8	19.3	550	–	
62.0	10.4	8.6	19.5	540	–	
28.8	0.7	20.7	49.3	400	+ 0.15	[196]

Al_2O_3-CaF_2-CaO-MgO-SiO_2

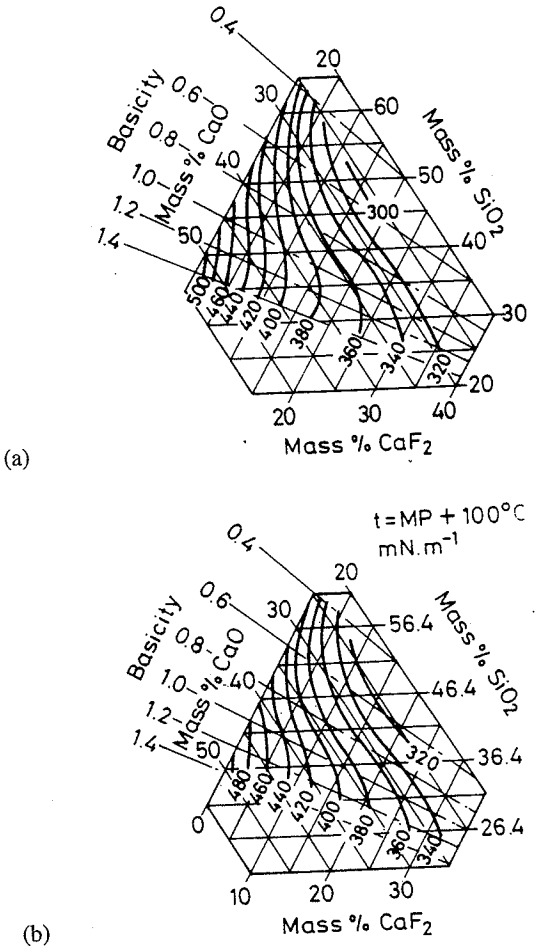


Fig. 10.136 a-d. Effect of MgO content on the surface tension of 10 mass % Al_2O_3 + CaF_2 + CaO + MgO + SiO_2 slags at a temperature 100 °C above the melting point [Ref. 191]
(a) 0 % MgO (b) 3.6 % MgO (c) 7.2 % MgO (d) 9 % MgO

10.3.5 Systems with five and more components

Al_2O_3-B_2O_3-CaO-MgO-SiO_2

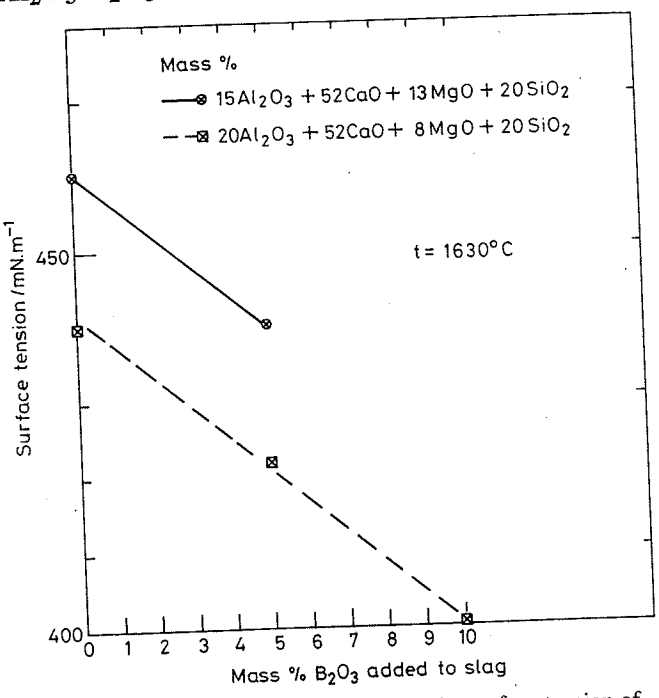
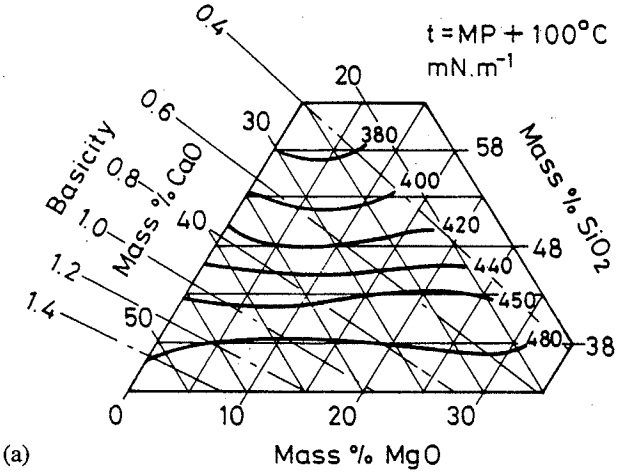
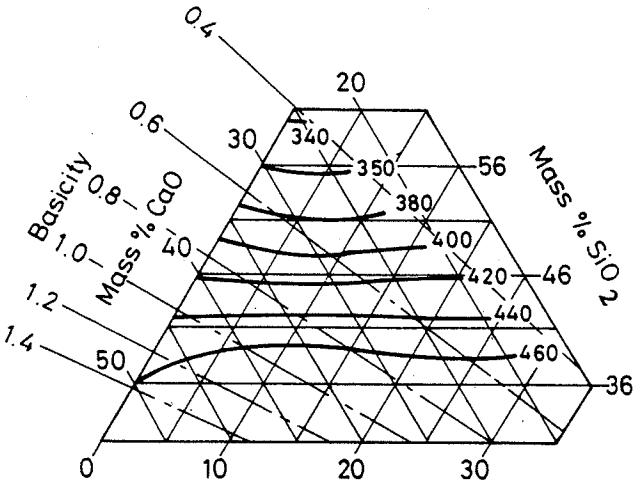


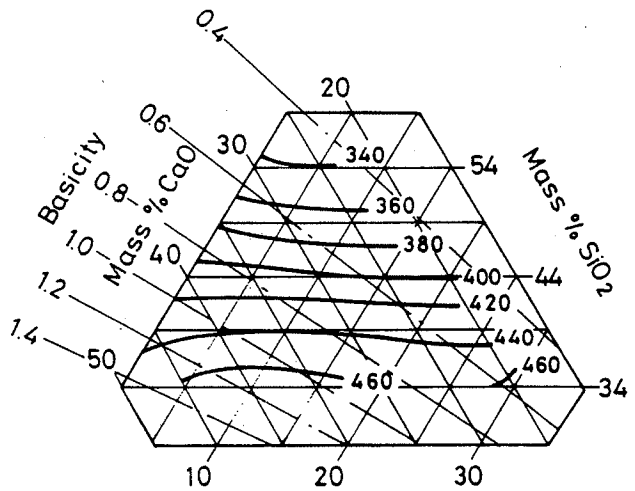
Fig. 10.135. Effect of B_2O_3 additions on the surface tension of Al_2O_3 + CaO + MgO + SiO_2 slags at 1630 °C [Ref. 200]



(a)



(b)



(c)

Fig. 10.137 a-c. Effect of CaF_2 content on the surface tension of 10 mass % Al_2O_3 + CaF_2 + CaO + MgO + SiO_2 slags at a temperature 100 °C above the melting point [Ref. 191]
(a) 2 % CaF_2 (b) 4 % CaF_2 (c) 6 % CaF_2

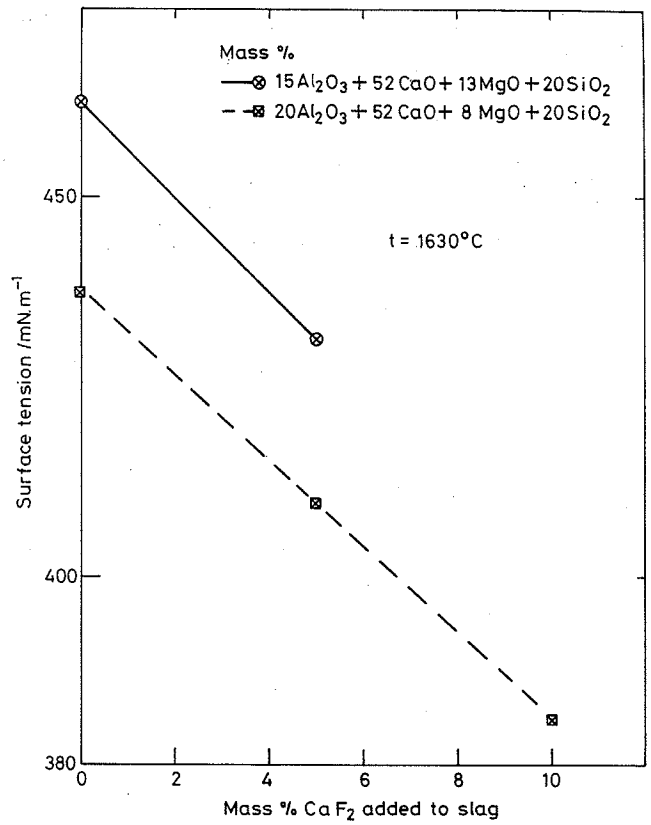
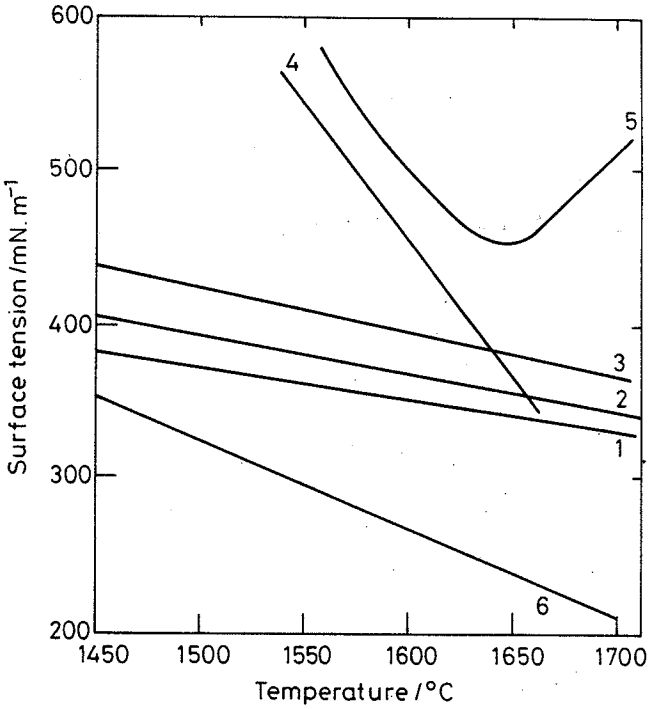


Fig. 10.138. Effect of CaF_2 additions on the surface tension of Al_2O_3 + CaO + MgO + SiO_2 slags at 1630 °C [Ref. 200]



Slag No.	Al_2O_3	CaF_2	CaO	MgO	SiO_2	(FeO)
1	3.3	9.1	57	5.9	24	0.6
2	4.2	16.8	46.4	18.7	13.5	0.4
3	4.1	8.2	49.9	14.6	22.2	0.7
4	4.0	7.7	46.9	19.5	21.2	0.5
5	3.2	6.7	45.8	23.5	20.3	0.4
6	10.5	9.6	49	7.3	23.6	–

▶
Fig. 10.139. Variation with temperature of slags in the system Al_2O_3 + CaF_2 + CaO + MgO + SiO_2 [Ref. 201]

Al_2O_3-CaF_2-CaO-Na_2O-SiO_2

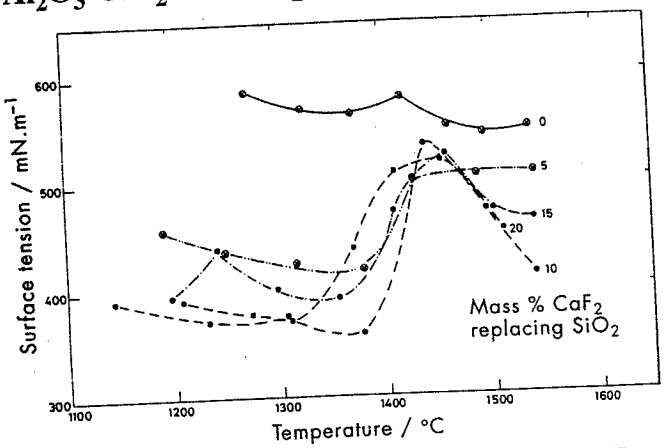


Fig. 10.140. Variation of the surface tension of Al_2O_3 + CaF_2 + CaO + Na_2O + SiO_2 slags with temperature and with replacement of SiO_2 by CaF_2. Composition of original slag (0 % CaF_2) is (mass %): 10 % Al_2O_3 + 40 % CaO + 5 % Na_2O + 45 % SiO_2 [Ref. 194]

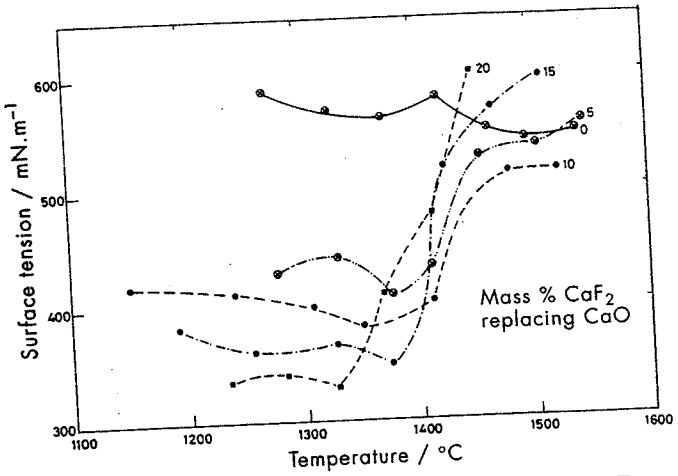
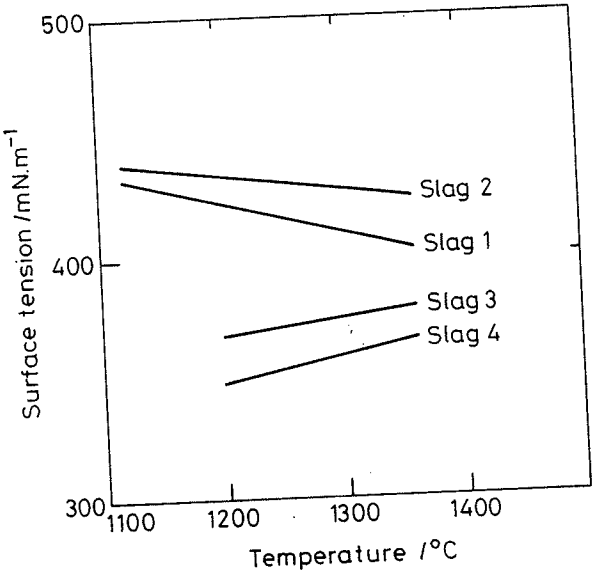


Fig. 10.141. Variation of the surface tension of Al_2O_3 + CaF_2 + CaO + Na_2O + SiO_2 slags with temperature and with replacement of CaO by CaF_2. Composition of original slag (0 % CaF_2) is (mass %): 10 % Al_2O_3 + 40 % CaO + 5 % Na_2O + 45 % SiO_2 [Ref. 194]

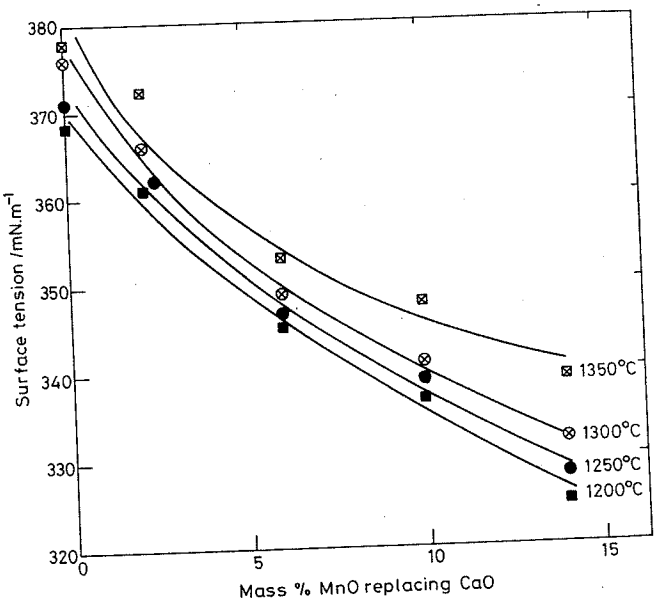
Al_2O_3-CaO-FeO-Fe_2O_3-SiO_2



Slag No.	Al_2O_3	CaO	FeO	Fe_2O_3	SiO_2	Ref.
1	4.6	18.3	35.7	9.8	31.7	[186]
2	9.1	17.4	33.9	9.3	30.8	
3	11.2	19.35	24.63	0.82	44.75	[185]
4	11.15	14.8	29.26	0.24	44.5	

Fig. 10.142. Variation with temperature of slags in the Al_2O_3 + CaO + FeO + Fe_2O_3 + SiO_2 system [Refs. 185; 186]

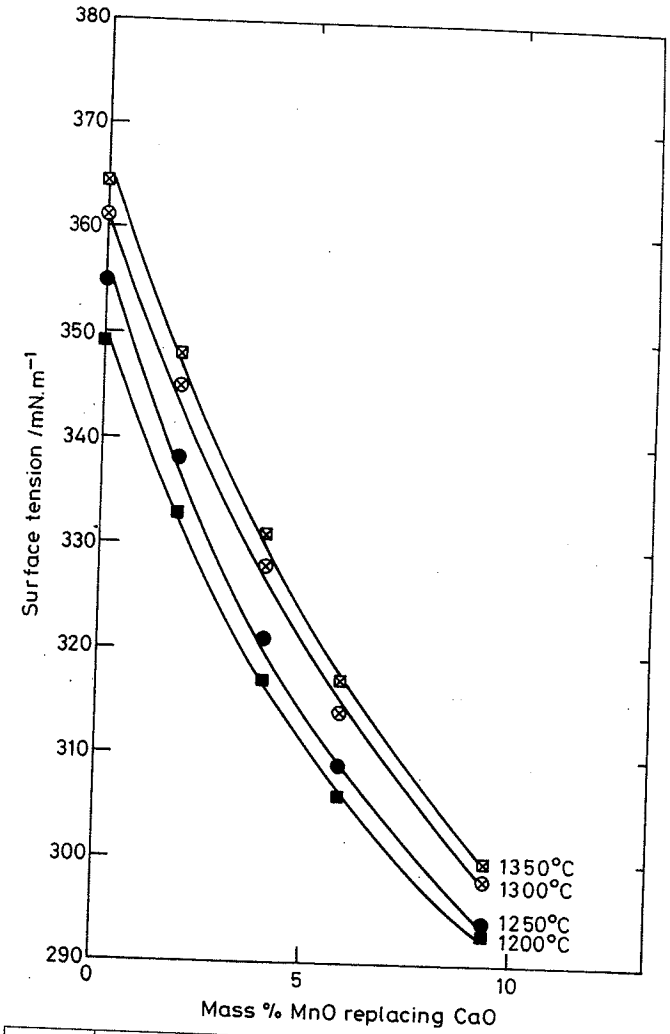
Al_2O_3-CaO-Fe_xO-MnO-SiO_2



Al_2O_3	CaO	FeO	Fe_2O_3	MnO	SiO_2	$\frac{d\gamma}{dT}$
11.2	19.35	24.63	0.82	0	44.75	+ 0.067
10.45	18.1	22.17	0.69	2.12	45.02	+ 0.073
10.35	13.7	23.17	0.88	6.0	44.47	+ 0.053
11.27	9.82	23.88	0.97	9.65	44.18	+ 0.075
11.52	5.63	24.15	0.46	13.9	44.27	+ 0.093

▶

Fig. 10.143. Effect of replacing CaO by MnO on the surface tension of Al_2O_3 + CaO + Fe_xO + (Fe_2O_3 < 1 %) + MnO +SiO_2 slags over the temperature range 1200 - 1350 °C. All slags contain ~ 11 % Al_2O_3; 23 - 25 % Fe_xO and ~ 45 % SiO_2 [Ref. 185]



Al_2O_3	CaO	FeO	Fe_2O_3	MnO	SiO_2	$\frac{d\gamma}{dT}$
11.15	14.8	29.26	0.24	0	44.5	+ 0.10
11.26	12.4	29.47	0.45	1.85	44.87	+ 0.10
10.67	10.76	29.18	0.67	4.02	45.15	+ 0.093
11.48	9.06	28.65	0.32	5.81	44.67	+ 0.073
10.17	4.97	28.46	0.94	9.35	44.87	+ 0.046

Fig. 10.144. Effect of replacing CaO by MnO on the surface tension of Al_2O_3 + CaO + Fe_xO (Fe_2O_3 < 1 %) + MnO + SiO_2 slags over the temperature range 1200 - 1350 °C. All slags contain ~ 11 % Al_2O_3; ~ 30 % Fe_xO and ~ 45 % SiO_2 [Ref. 185]

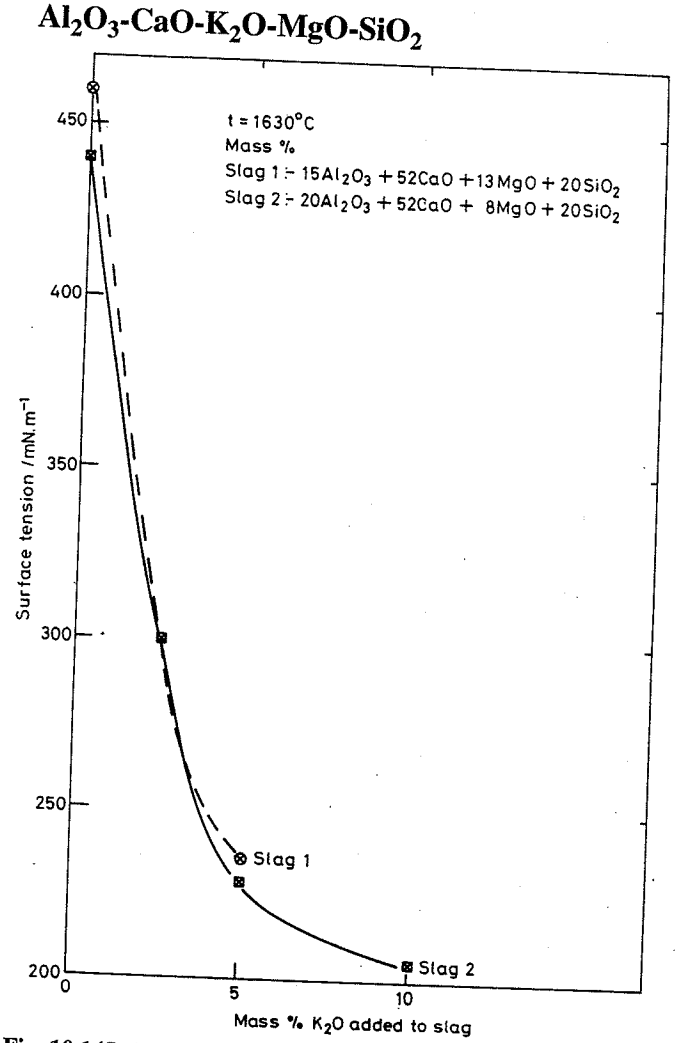


Fig. 10.145. Effect of K_2O additions on the surface tension of Al_2O_3 + CaO + MgO + SiO_2 slags at 1630 °C [Ref. 200]

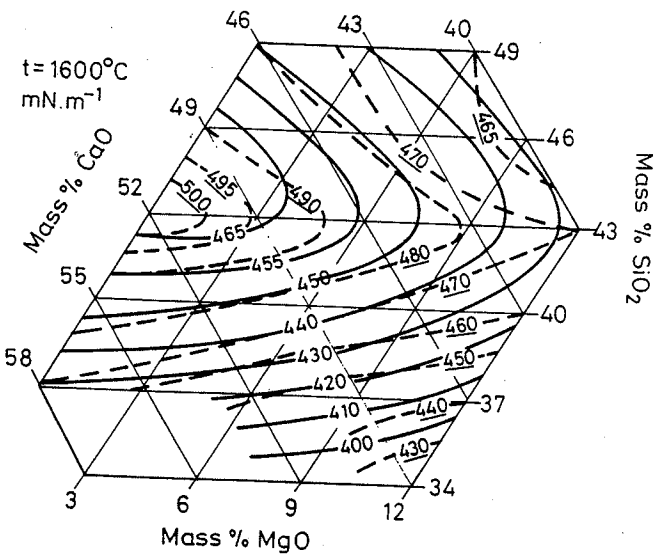


Fig. 10.146. Isotension lines for the slag system 5 % Al_2O_3 + CaO +MgO + SiO_2 (hatched lines) and for these slags containing 0.5 mass % addition of K_2O (solid lines) [Ref. 202]

Al_2O_3-CaO-MgO-Na_3AlF_6-SiO_2

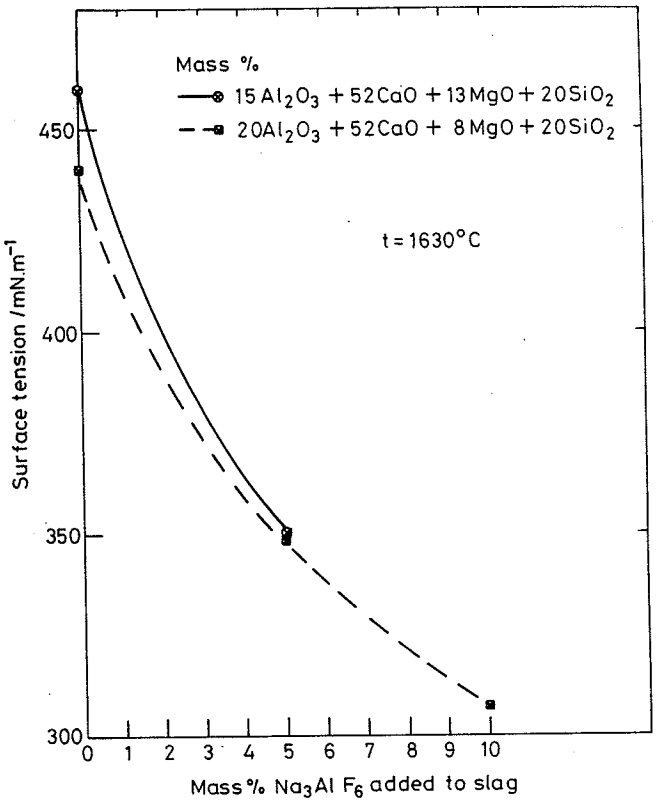


Fig. 10.147. Effect of Na_3AlF_6 additions on the surface tension of Al_2O_3 + CaO + MgO + SiO_2 slags at 1630 °C [Ref. 200]

Al_2O_3-CaO-MgO-Na_2O-SiO_2

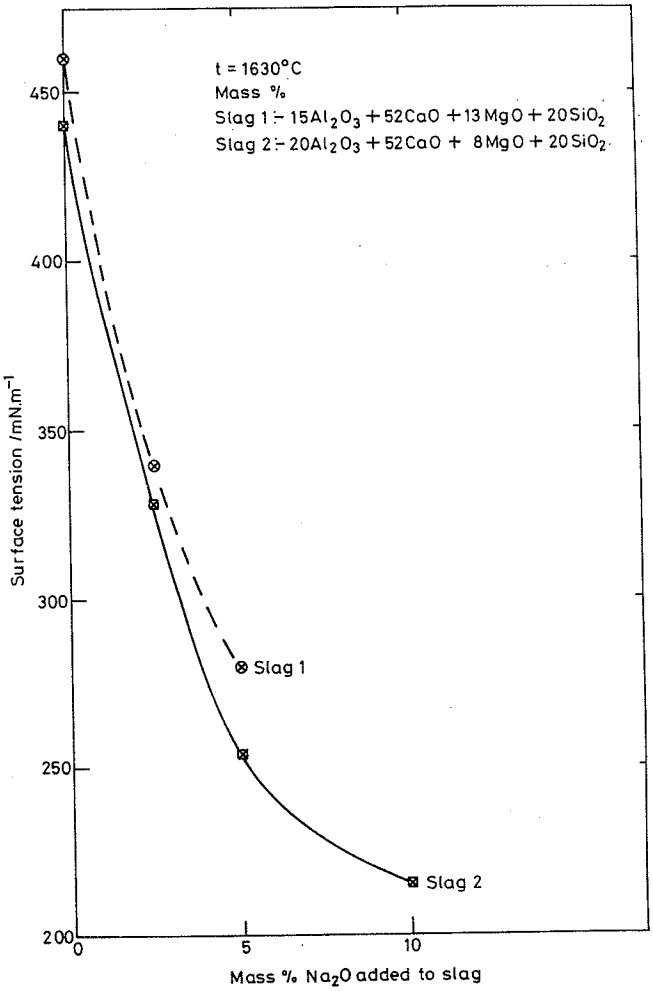
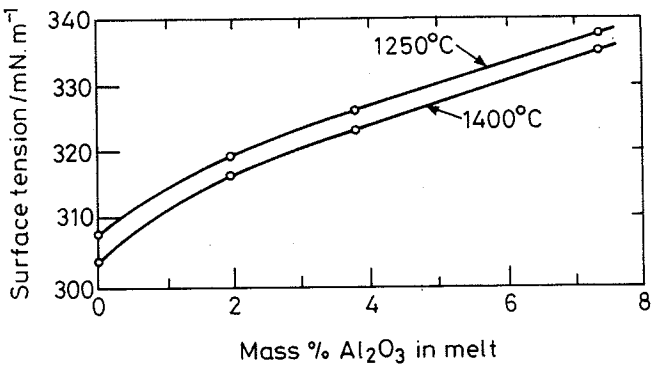


Fig. 10.148. Effect of Na_2O additions on the surface tension of Al_2O_3 + CaO + MgO + SiO_2 slags at 1630 °C [Ref. 200]



Al_2O_3	CaO	MgO	Na_2O	SiO_2	Surface tension at 1300 °C ($mN.m^{-1}$)	Temperature coefficient of surface tension ($mN.m^{-1}.K^{-1}$)
0	7.77	3.02	16.02	73.18	306	- 0.027
1.96	7.62	2.97	15.71	71.74	318	- 0.017
3.83	7.48	2.90	15.41	70.37	325	- 0.014
7.42	7.20	2.80	14.84	67.75	337	- 0.038

Fig. 10.149. Effect of Al_2O_3 additions on the surface tension of CaO + MgO + Na_2O + SiO_2 melts at 1250 °C and 1400 °C. Mass ratio CaO:MgO:Na_2O:SiO_2 maintained constant at 2.57:1:5.3:24.2 [Ref. 203]

Al_2O_3-CaO-MgO-S-SiO_2

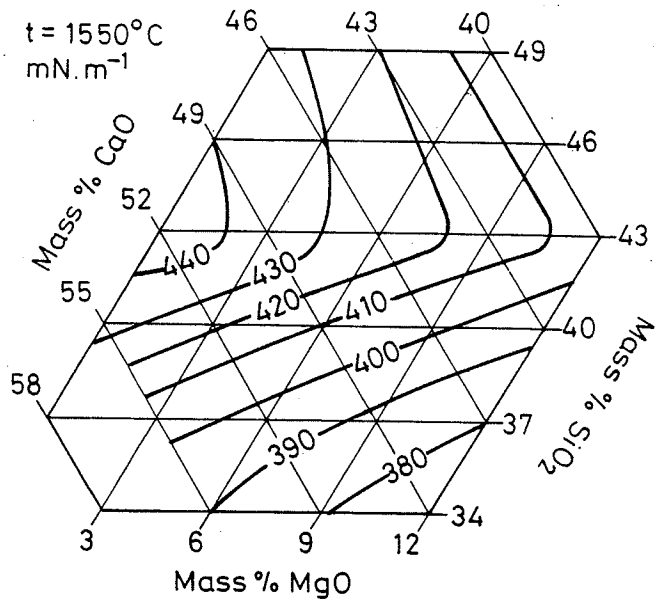


Fig. 10.150. Isotension lines at 1550 °C of slags in the system 5 mass % Al_2O_3 + CaO + MgO + SiO_2, to which have been added 2 mass % S [Ref. 188]

Al_2O_3-CaO-MgO-SiO_2-TiO_2

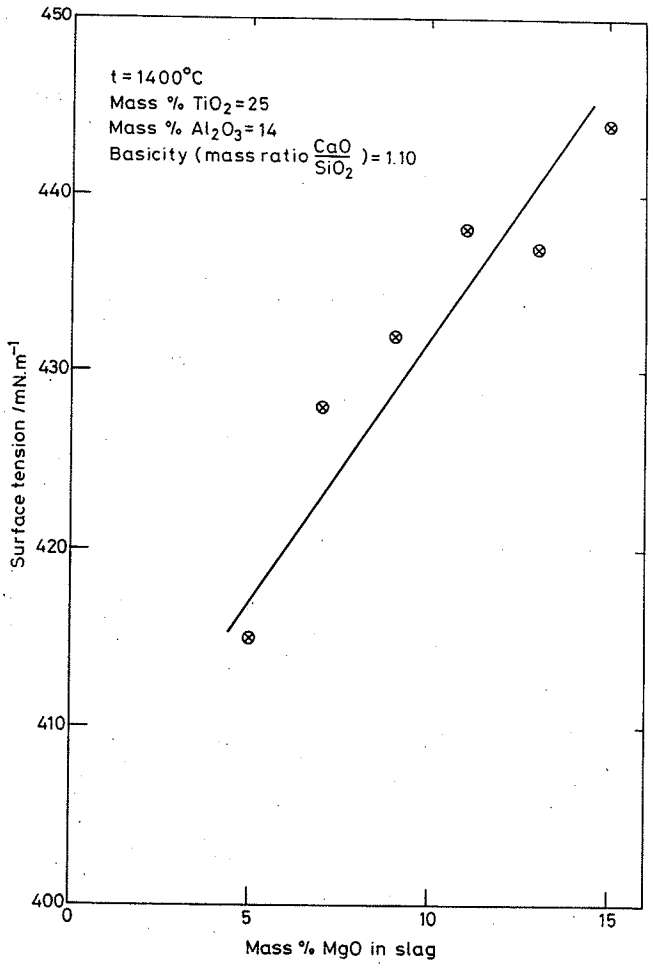


Fig. 10.151. Effect of the MgO concentration on the surface tension at 1400 °C, of slags in the Al_2O_3 + CaO + MgO + SiO_2 + TiO_2 system, which have constant Al_2O_3 and TiO_2 concentrations and a basicity of 1.1 [Ref. 204]

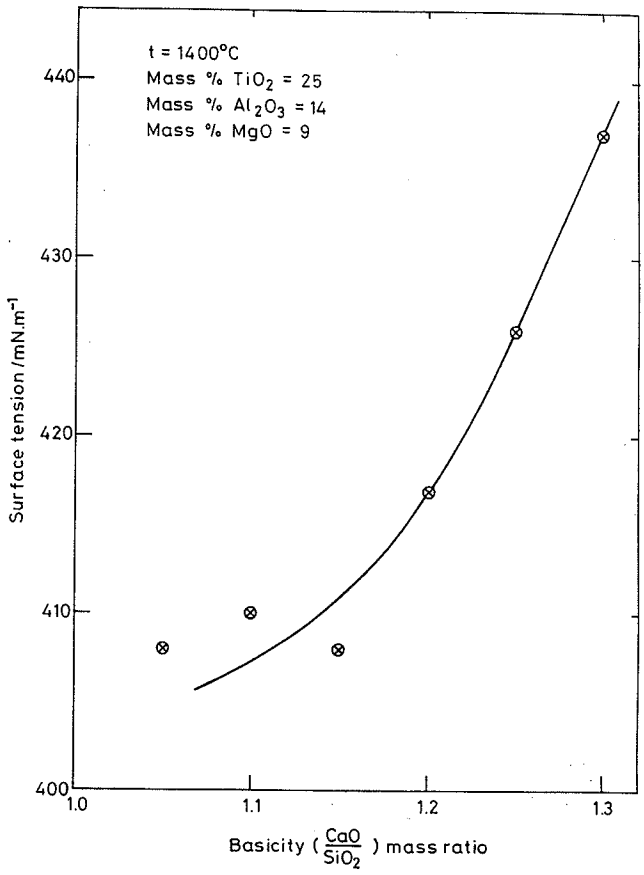


Fig. 10.152. Effect of the basicity on the surface tension at 1400 °C, of slags in the Al_2O_3 + CaO + MgO + SiO_2 + TiO_2 system, which have constant Al_2O_3, MgO and TiO_2 concentrations [Ref. 204]

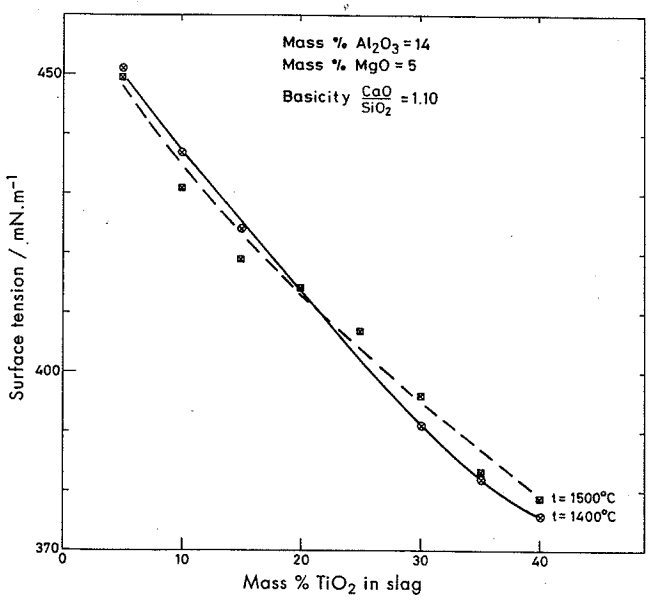
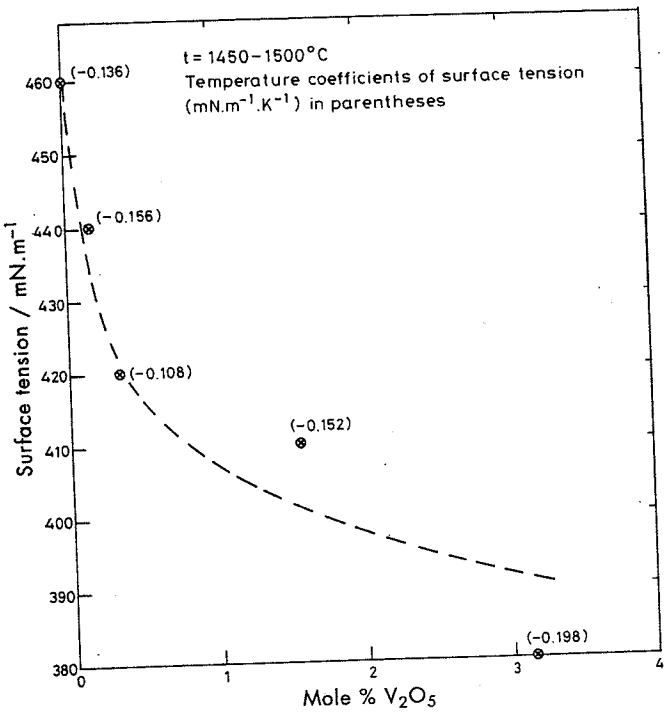


Fig. 10.153. Effect of the TiO_2 concentration on the surface tension at 1400 °C of slags in the Al_2O_3 + CaO + MgO + SiO_2 + TiO_2 system, which have constant Al_2O_3 and MgO concentrations and a basicity of 1.1 [Ref. 204]

Al_2O_3-CaO-MgO-SiO_2-V_2O_5



Al_2O_3	CaO	MgO	SiO_2	V_2O_5
15.37	39.3	9.65	35.7	0
15.34	39.25	9.64	35.6	0.162
15.31	39.2	9.63	35.5	0.34
15.1	38.8	9.5	35.1	1.56
14.85*	38.1	9.35	34.6	3.14

* quoted as 11.85 in [Ref. 189]

Fig. 10.154. Variation of surface tension with V_2O_5 content of Al_2O_3 + CaO + MgO + SiO_2 + V_2O_5 melts, together with the temperature coefficients of surface tension for the respective compositions. [Ref. 189]

10.4 References in Chapter 10

[1] Bikerman, J. J.: Physical Surfaces. Pub.: Academic Press (1970)
[2] Adamson, A. W.: Physical Chemistry of Surfaces. Pub.: John Wiley and Sons (1982)
[3] Jaycock, M. J.; Parfitt, G. D.: Chemistry of Interfaces. Pub.: Ellis Horwood (1981)
[4] Schrödinger, R.: Ann. Physik 46 (1915), 413
[5] Sugden, S.: J. Chem. Soc. 125 (1924), 27
[6] Bashforth, F.; Adams, J. C.: An Attempt to Test the Theory of Capillary Action. Pub.: Cambridge University Press (1883)
[7] Patrov, B. V.: Surf. Phenom. in Metall. Processes. Pub.: Consultants Bureau (1965), 129
[8] Dorsey, N. E.: J. Wash. Acad. Sci. 18 (1928), 505
[9] Kozakevitch, P.; Chatel, S.; Urbain, G.; Sage, S.: Rev. Metall. 52 (1955), 139
[10] Naidich, Yu. V.; Eremenko, V. N.: Fiz. Metal. Metall. 11 (6), (1961), 883
[11] Andreas, J. M.; Hauser, E. A.; Tucker, W. B.: J. Phys. Chem. 42 (1938), 1001
[12] Girault, H. H. J.; Schiffrin, D. J.; Smith, B. D. V.: J. Coll. Interface Sci. 101 (1), (1984), 257
[13] Harkins, W. D.; Brown, F. E.: J. Am. Chem. Soc. 41 (1919), 499
[14] Deryabin, A. A.; Saidulin, R. A.; Popel, S. I.: Zavod. Lab. 36 (3), (1970), 292
[15] Sternberg, S.; Terzi, M.: Rev. Roum. Chim. 20 (7), (1975), 1013
[16] Shartsis, L.; Shermer, H. F.; Bestul, A. B.: J. Am. Ceram. Soc. 42 (5), (1959), 242
[17] Verschaffelt, J. E.; Kamerlingh Onnes; H.: Commun. Phys. Lab., Univ. Leiden. Suppl. 42D, (1918)
[18] Kozakevitch, P.: Phys. Measurem. High Temp. Ed.: J. O'M Bockris et al. Pub.: Butterworth (1959), 208 – 224
[19] Janz, G. J.; Lorenz, M. R.: Rev. Sci. Instr. 31 (1), (1960), 18
[20] Lord Rayleigh. Proc. Roy. Soc. 29 (1879), 71
[21] Badger, A. E.; Parmelee, C. W.; Williams, A. E.: J. Am. Ceram. Soc. 20 (1937), 325
[22] Zubarev, Yu. V.; Kostikov, V. I.; Mitin, B. S.; Nagibin, Yu. A.; Nishcheta, V. V.: Inorg. Mater. 5 (9), (1969), 1325
[23] Elyutin, V. P.; Mitin, B. S.; Nagibin, Yu. A.: Ind. Lab. 37 (2), (1971), 246 and Fiz. Aerodispersnykl. Sist. (7), (1972), 104
[24] Elyutin, V. P.; Mitin, B. S.; Anisimov, Yu. S.: Inorg. Mater. 9 (9), (1973), 1408
[25] Shpil'rain, E. E.; Yakimovich, K. A.; Tsitsarkin, A. F.: High Temp. 11 (5), (1973), 894
[26] Kingery, W. D.: J. Am. Ceram. Soc. 42 (1), (1959), 6
[27] Maurakh, M. A.; Mitin, B. S.; Roitberg, M. B.: Ind. Lab. 33 (8), (1967), 1160
[28] McNally, R. N.; Yeh, H. C.; Balasubramanian, N.: J. Mater. Sci. 3 (2), (1968), 136
[29] Bartlett, R. W.; Hall, J. K.: Bull. Am. Ceram. Soc. 44 (5), (1965), 444
[30] Rasmussen, J. J.; Nelson R. P.: J. Am. Ceram. Soc. 54 (8), (1971), 398
[31] Shartsis, L.; Capps, W.: J. Am. Ceram. Soc. 35 (7), (1952), 169
[32] Li, P. C.; Ghose, A. C.; Su, C.-J.: Phys. Chem. Glasses 1 (6), (1960), 204
[33] Sokolov, L. N.; Podgornov, G. V.; Okorokov, G. N.: Fiz.-Khim. Osnovy. Metal. Prots. (1982), 47 – 49
[34] Shpil'rain, E. E.; Yakimovich, K. A.; Fromin, V. A.; Kagan, D. N.; Barkhatov, L. S.: Teplofiz. Svoistva. Zhidk. Mater. Vses. Teplofiz. Konf. 1971. Ed: Z. I. Gelle. Pub.: Nauka (1973), 27 – 33
[35] Shpil'rain, E. E.; Yakimovich, K. A.; Tsitsarkin, A. F.: High Temp. 12 (1), (1974), 68
[36] Walker, R. D.; Fray, T. A. T.: Int. Symp. – Advances in Extractive Metallurgy, London, 18 – 20 April 1977. Pub.: Inst. Mining. Metall. 13 – 19
[37] Rasmussen, J. J.: J. Am. Ceram. Soc. 55 (6), (1972), 326
[38] Popel, S. I.; Esin, O. A.: Zh. Fiz. Khim. 30 (6), (1956), 1193
[39] Din-Fen, U.; Vishkarev, A. F.; Yavoiskii, V. I.: Iz. Vuz. Chern. Metall. 6 (1), (1963), 27
[40] Kawai, Y.; Mori, K.; Shiraishi, Y.; Yamada, N.: Tetsu-to-Hagane 62 (1), (1976), 53
[41] Kozakevitch, P.: Rev. Metall. 46 (8), (1949), 505
[42] Popel, S. I.; Sokolov, V. I.; Esin, O. A.: Russ. J. Phys. Chem. 43 (12), (1969), 1782
[43] Lee, Y. E.: Dissertation, University of Pennsylvania, USA (1972)
[44] Parikh, N. M.: J. Am. Ceram. Soc. 41 (1), (1958), 18
[45] Mitin, B. S.; Nagibin, Yu. A.: Inorg. Mater. 7 (5), (1971), 709
[46] Yakobashvili, S. B.; Frumin, I. I.: Auto. Weld. (10), (1962), 33
[47] Nikitin, Yu. P.; Safonnikov, A. M.: Sb. Nauchn. Tr. Ural'sk, Politekhn. Inst. (126), (1963), 68
[48] Povolotskii, D. Ya.; Voronov, V. A.; Nikitin, B. M.: Steel in the USSR (12), (1971), 952
[49] Kammel, R.; Winterhager, H.: Z. Erzbergbau, Metallhüttenwesen, 21 (9), (1968), 399
[50] Evseev, P. P.: Auto. Weld. (11), (1967), 42
[51] Pupynina, S. M.; Volkov, S. E.; Bobkova, O. S.; Petukhov, V. S.: Sb. Tr. Tsentr. Inst. Chern. Met. (70), (1969), 47
[52] Pupynina, S. M.; Volkov, S. E.: Symp. – Teor. Metall. Prots. Pub.: Metallurgizdat. (1971), 156 – 161
[53] Kipov, I. G.; Zadumkin, S. N.: Russ. J. Phys. Chem. 46 (7), (1972), 1063
[54] Goncharov, A. E.; Manakov, A. I.; Kovalev, P. K.: Tr. Inst. Met. AN. SSSR. Ural. Nauk. Tsentr. 27 (4), (1972), 159
[55] Yakobashvili, S. B.; Tabidze, A. I.; Nebieridze, D. A.: Svar. Prot. v. Metall. (1), (1974), 104
[56] Zhmoidin, G. I.: Russ. J. Phys. Chem. 49 (6), (1975), 874
[57] Kulifeev, V. K.; Panchishnyi, V. I.; Rogozkin, B. D.; Sokolov, V. A.: Iz. VUZ. Tsvet. Metall. 12 (1), (1969), 80
[58] Winterhager, H.; Kammel, R.; Gad, A.: Forschungsberichte des Landes Nordrhein-Westfalen, Nr. 2115. Pub.: Westdeutscher Verlag, Köln und Opladen (1970)
[59] Tokumoto, S.; Kasama, A.; Fujioka, Y.: Technol. Rept. Osaka Univ. 22 (1064), (1972), 453
[60] Elliott, J. F.; Mounier, M.: Can. Metall. Quart. 21 (4), (1982), 415
[61] Johannsen, F.; Wiese, W.: Erzmetall. 11 (1), (1958), 1
[62] Vostryakov, A. A.; Lepinskikh, B. M.; Shibanova, L. N.: Russ. J. Phys. Chem. 60 (9), (1986), 1349
[63] Zaysev, V. Ya.; Vanyulov, A. V.; Kolossova, V. S.: Russ. Metall (5), (1968), 29
[64] Vaisburd, S. E.; Grigorev, G. N.: Fiz. Khim. Poverkh. Rasp. Tbilisi. Pub.: Metsniyereba (1977), 188

[65] Vaisburd, S. E.: Surface Phenomena in Metallurgical Processes. Ed.: A. I. Belyaev. Pub.: Consultants Bureau, New York, (1965), 138
[66] Bratland, D.; Ferro, C. M.; Ostvold, T.: Acta. Chem. Scand. A37 (1983), 487
[67] Fernandez, R.; Grjotheim, K.; Ostvold, T.: Light Metal. 2 (1986), 1025
[68] Bloom, H.; Burrows, B. H.: Proc. 1st Australian Conf. Electrochem. Pub.: Pergamon, Sydney, Hobart, Australia (1963), 882
[69] Vajna, A.: Alluminio 20 (1951), 29
[70] Kazantsev, G. E.; Lepinskikh, B. M.; Kozhevnikov, G. N.: Tr. Inst. Metall. AN. SSSR. Ural. Fil. 20, (1969), 63
[71] Anisimov, Yu. S.; Kozyreva, L. P.; Mitin, B. S.: Russ. J. Phys. Chem. 49 (4), (1975), 547
[72] Deryabin, A. A.; Popel, S. I.; Zupnik, A. E.: Russ. Metall. (2) (1968), 51
[73] Keene, B. J.; Mills, K. C.: NPL Report No. CHEM 60 (1976), National Physical Laboratory, Teddington, UK
[74] Krinochkin, E. V.; Kurochkin, K. T.; Umrikhin, P. V.: Fiz. Khim. Poverkh. Yav. Rasp. Ed.: V Eremenko. Pub.: Naukova Dumka, (1971), 179 – 182
[75] Mukai, K.; Ishikawa, T.: Nippon Kinzoku Gakkaishi 45 (2), (1981), 147
[76] Dragomir, I.; Rusu, E.: Metalurgia. 35 (4), (1983), 168
[77] Evseev, P. P.; Filippov, A. F.: Iz. VUZ. Chern. Metall. (3) (1967), 55
[78] Muu, B. van; Fenzke, H.-W.; Eckstein, H.-J.: Neue Hütte. 30 (9) (1985), 341
[79] Povolotskii, D. Ya.; Mishchenko, V. Ya.; Vyatkin, G. P.; Puzyrev, A. V.: Iz. VUZ. Chern. Metall. 13 (12), (1970), 8
[80] Deryabin, A. A.; Popel, S. I.: Iz. VUZ. Chern. Metall. (8), (1964), 5
[81] Zielinski, M.; Sikora, B.: Prace IMZ 29 (3 – 4), (1977), 157
[82] Sokolov, L. N.; Baidov, V. V.; Kunin, L. L.; Dymov, V. V.: Teor. Metall. Prots. (1971), 53 – 61
[83] Sikora, B.; Zielinski, M.: Hutnick. 41 (9) (1974), 433
[84] Popel, S. I.; Esin, O. A.: J. Inorg. Chem. USSR 2 (3), (1957), 252
[85] Popel, S. I.; Deryabin, A. A.; Saburov, L. N.; Tarkhanov, M. V.: Tr. Ural. Nauch. Issled. Inst. Chern. Met. (12), (1971), 92
[86] Ershov, G. S.; Popova, E. A.: Russ. J. Inorg. Chem. 9 (3), (1964), 361
[87] Yakobashvili, S. B.; Mudzhiri, T. G.; Skylyarov, A. V.: Auto. Weld. (8), (1965), 52
[88] Kim, A. S.; Akberdin, A. A.; Kulikov, I. S.: Viniti (USSR), Rept. No. 5508-81, (1981)
[89] King, T. B.: J. Soc. Glass Technol. 35 (1951), 241
[90] Anisimov, Yu. S.; Grits, E. F.; Mitin, B. S.: Inorgan. Mater. 13 (8), (1977), 1168
[91] Lihrmann, J. M.; Haggerty, J. S.: J. Am. Ceram. Soc. 68 (2), (1985), 81
[92] Elyutin, V. P.; Mitin, B. S.; Anisimov, Yu. S.: Iz. VUZ. Tsvet. Metall. (4), (1974), 42
[93] Shartsis, L.; Shermer, H. F.: J. Am. Ceram. Soc. 37 (1954), 544
[94] Partlow, D. P.; Smith, H. D.; Mattox, D. M.: Phys. Chem. Glasses, 21 (6), (1980), 221
[95] Sotnikov, A. I.; Petrov, V. V.; Kosenko, V. G.: Fiz. Khim. Stekla, 11 (3), (1985), 382
[96] Sumita, S.; Morinaga, K.; Yanagase, T.: Nippon Kinzoku Gakk. 47 (2), (1983), 127
[97] Hara, S.; Shibaike, H.; Tarumoto, H.; Ogino, K.: Proc. 1st Int. Symp. Molten Salt Chem. Technol. 20 – 22 April 1983. Kyoto, Japan
[98] Hara, S.; Ogino, K.: Nippon Kinzoku Gakkaishi, 52 (11), (1988), 1098
[99] Gainullin, A. A.; Mal'kov, N. V.; Roshchin, V. E.: Iz. VUZ. Chern. Metall. (2), (1985), 4
[100] Karakash, A. I.; Ternovoi, P. V.: Iz. VUZ, Chern. Metall. (10), (1977), 21. (Trans.: BISI 16876, Oct. 1978.)
[101] Kidd, M.; Gaskell, D. R.: Metall. Trans. B, 17B, (1986), 771
[102] Abrodimov, A. S.; Gavrin, E. G.; Eremeichenko, V. I.: Iz. VUZ. Chern. Metall (8) (1975), 14. (Trans: BISI 13897, March 1976.)
[103] Sumita, S.; Morinaga, K.; Yanagase, T.: Trans. JIM. 24 (1), (1983), 35
[104] Bradbury, B. T.; Maddocks, W. R.: J. Soc. Glass Technol. 43 (1959), 325
[105] Nijjar, R. S.; Williams, D. J.: Trans. Faraday Soc. 64 (1968), 1784
[106] Swisher, J. H.; McCabe, C. L.: Trans. Metall. Soc. AIME: 230 (1964), 1669
[107] Ejima, A.; Shimoji, M.: Trans. Faraday Soc. 66 (1), (1970), 99
[108] Bochnak, R.; Dobrovski, L.: Hutn. Listy 43 (5), (1988), 218
[109] Cooper, C. F.; Kitchener, J. A.: JISI. Sept. (1959), 48
[110] Ono, K.; Gunji, K.; Araki, T.: Nippon Kinzoku Gakkhai, 33 (3), (1969), 299
[111] Gunji, K.; Dan, T.: Trans. ISIJ. 14 (1974), 162
[112] Sharma, S. K.; Philbrook, W. O.: Scripta Metall. 4 (1970), 107
[113] Sharma, S. K.; Philbrook, W. O.: Proc. Int. Conf. Sci. Tech. Iron Steel, Tokyo, 7 – 11th Sept. 1970. Pub.: ISI, Japan (1971)
[114] Tarabrin, G. K.; Kozin, A. I.: Iz. VUZ. Chern. Metall. (5), (1972), 15
[115] Kozin, A. I.; Bobkova, O. S.: Iz. VUZ Chern. Metall. (11), (1975), 19
[116] Nakamura, T.; Noguchi, F.; Ueda, Y.; Nakajyo, S.: J. Min. Metall. Inst. Japan, 104 (1205), (1988), 463
[117] Kurochkin, A. F.; Onaev, I. A.; Kuzhamkulov, A. A.; Turisbekov, M.: Metall. Obogashch, 9 (1974), 70
[118] Mandira, M.; Dharwadkar, H. N.; Kumar, D.: Tans. Inst. Min. Metall. 96 (1987), C93
[119] Pavlov, A. V.; Kvyatkovskii, A. N.; Chentsov, B. P.; Vatolin, N. A.; Kurochkin, A. F.: Kompleksn. Ispol'z. Miner. Syr'ya (2) (1980), 39
[120] Din-Fen, U.; Vishkarev, A. F.; Yavoiskii, V. I.: Iz. VUZ. Chern. Metall (3) (1963), 40
[121] Lee, Y. E.; Gaskell, D. R.: Trans. ISIJ. 11 (1971), 564. (Suppl. Proc. ICSTIS 1970.)
[122] Fadeev, O. N.; Khudyakov, I. F.; Kashcheev, I. D.; Kharitidi, G. P.: Iz. VUZ. Tsvet. Metall (4), (1980), 17
[123] Bodnar, L.; Compa, S.; Tomasek, K.; Bobok, L.: Advances in Extractive Metallurgy, Inst. Min. Metal. London, (1977), 35 – 39
[124] Popel, S. I.; Sokolov, V. I.; Korpachev, V. G.; Sb. Nauch. Tr. Ural'sk, Politekhn, Inst. (126), (1963), 24
[125] Vanyukov, A. V.; Utkin, N. I.: Iz. VUZ. Tsvet. Metall (6), (1958), 43
[126] Montil'o, I. A.: Tr. Ural. Nauchn-Issled Proekt. Inst. Medn. Prom. (8), (1965), 401
[127] Vanyukov, A. V.; Utkin, N. I.: Nauk. Dokl. Vys. Shkoly. Met. (3), (1958), 22
[128] Kozakevitch, P.: J. Met. 21 (7) (1969), 57
[129] Zaimskikh, N. V.; Esin, O. A. Trudy Ural'sk, Politekhn. Inst. 49, (1954), 104
[130] Holeczy, J.; Bodnar, L.; Tomasek, K.: Hutn. Listy 27 (3), (1972), 201
[131] Mills, K. C.; Keene, B. J.: Int. Mat. Rev. 32 (1 – 2), (1987), 1
[132] Shartsis, L.; Spinner, S.: J. Res. NBS 46 (5), (1951), 385
[133] Kochergin, V. P.; Metal'nikov, B. I.: Fiz. Khim. Poverkh. Rasp. Pub.: Izd Metsniereba. Tbilisi, (1977), 241
[134] Callis, C. F.; Wazer, J. R. van; Metcalf, J. S.: J. Am. Chem. Soc. 77 (1955), 1468
[135] Boyer, A. J. G.; Fray, D. J.; Meadowcroft, T. R.: J. Phys. Chem. 71 (5), (1967), 1442
[136] Frischat, G. H.; Beier, W.: Glastechn. Ber. 52 (5), (1979), 116
[137] Perminov, A. A.; Popel, S. I.; Smirnov, N. S.: Zh. Prikl. Khim. 35 (2), (1962), 271
[138] Adachi, A.; Ogino, K.; Toritani, H.: Technol. Rept. Osaka Univ. 10 (379), (1960), 149
[139] Taniguchi, H.: Contrib. Mineral Petrol 100 (1988), 484
[140] Isotomin, S. A.; Lepinskikh, B. M.; Manakov, A. I.; Pokrovskii, V. A.: Viniti (USSR), Rept. No. 2205-75 (1975)
[141] Bochorishvili, A. I.; Yakobashvili, S. B.; Svar. Proiz. (10), (1968), 13
[142] Boni, R. E.; Derge, G.: Trans. AIME J. Metals, January (1956), 59
[143] Gogiberidze, Yu.; Dzhincharadze, T. I.; Mikiashvili, Sh. M.: Soob. Akad. Nauk. Gruz. SSR (3), (1968), 695
[144] Mazanek, C.; Szulc, M.: Hutnik 38 (3), (1971), 168
[145] Voronov, V. A.; Nikitin, B. M.: Russ. Metall. (4), (1971), 76
[146] Krichevets, M. I.; Grechishnyi, V. V.; Sherstobitov, M. A.; Pozdeev, N. P.: Russ. Metall. (5), (1984), 36
[147] Povolotskii, D., et al: BISI 21861, August 1983. Pub.: Bisits, The Metals Society. London, UK
[148] Agafonov, S. A.; Popova, E. A.; Lepinskikh, B. M.: Struktura i Fiz-Khim. Svoistva Met. i Oksio. Rasp. Sverdlovsk, (1986), 103 – 106
[149] Krusina, J.: Hutn. Listy. 26 (9), (1971), 625
[150] Barrett, L. R.; Thomas, A. G.: J. Soc. Glass Technol. 43 (1959), 179T
[151] Zavol'skii, V. A.; Lepinskikh, B. M.; Shkol'nik, Ya. Sh.: Zh. Prikl. Khim. 60 (1), (1987), 186
[152] Kozakevitch, P.; Lucas, L.-D.: Rev. Metall. 65 (9), (1968), 589
[153] Demidenko, T. V.; Chernov, N. N.; Safina, L. A.: Steel in the USSR (6), (1981), 322
[154] Kovalenko, A. M.; Novokhatskii, I. A.; Petrov, A. K.; Ershov, G. S.: Fiz-Khim. Poverkh. Yav. Rasp. Ed.: V. N. Eremenko, Pub.: Naukova Dumka, Kiev. (1971), 186 – 189
[155] Koshida, T.; Ogasawara, T.; Kishidaka, H.: Tetsu-to-Hagane 67 (9), (1981), 1491
[156] Kojima, Y.: Trans. ISIJ, 11 (1971), 349
[157] Fenzke, H.-W.: Neue Hütte 14 (9), (1969), 522
[158] Musikhin, V. I.; Chernyaev, V. G.; Ignatenko, G. F.; Pliner, Yu. L.; Rubinshtein, E. A.: Sbornik Turdov Klyuchevskogo Zavada Ferrosplavov 4 (1969), 32
[159] Kozakevitch, P.; Kononenko, A. F.: Zh. Fiz. Khim. 14 (1940), 1118
[160] Mikiashvili, Sh. M.; Samarin, A. M.; Cylev, L. M.: Physicochemical Fundamentals of Steel Production, Moscow (1957), 423 – 432
[161] Göhler, M.: Freiburger Forschungsh., B92 (1963), 41
[162] Sugai, M.; Somiya, S.: J. Ceram. Soc. Japan, 90 (5), (1982), 262
[163] Shermer, H. F.: J. Research NBS, 56 (3), (1956), 155
[164] Yakobashvili, S. B.; Zhukaev, V. I.: Fiz. Khim. Poverkh. Yavlenii Rasplav, Ed.: V. N. Eremenko. Pub.: Naukova Dumka, Kiev. (1971), 183 – 185

[165] Voronov, V. A.; Nikitin, B. M.: Fiz. Khim. Poverkh. Rasp. Pub.: Metsniereba. (1977) Tbilisi, 229 – 232
[166] Panov, A. S.; Kulikov, L. S.; Tsylev, L. M.: Russ. J. Phys. Chem. 36 (6), (1962), 722
[167] Kozakevitch, P.: Rev. Metall. 46 (9), (1949), 572
[168] Tomasek, K.; Bodnar, L.; Holeczy, J.: Hutn. Listy. 29 (12), (1974) 882
[169] Yamshchikova, E. A.; Butuzova, L. V.; Montil'O, I. A.: Tr. Ural'sk. Nauch-Issled. Proekt. Inst. Mednoi. Prom 12 (1969) 163
[170] Staronka, A.; Piekarska, M.: Arch. Hutn. 23 (1), (1978), 119
[171] Kekelidze, T. M.; Mikiashvili, Sh. M.; Dzhintsaradze, T. I.; Khomeriki, R. V.: Izv. AN. Gruz. SSR, Ser. Khim 4 (3), (1978), 240
[172] Danek, V.; Licko, T.: Silikaty, 25 (1981) 153
[173] Polyvyannyi, I. P.; Lata, V. A.; Adilova, A. A.; Ibakina, L. P.: Viniti (USSR), Rept. No. 3782-80 (1980)
[174] Kozakevitch, P.; Urbain, G.: Mem. Sci. Rev. Metall. 58 (7), (1961), 517
[175] Toropov, N. A.; Bryantsev, B. A.: Strukt. Prevrash. v. Stekla. Pri. Povyshen. Pub.: Nauka. Temp. (1965), 205 – 232
[176] Vaisburd, S. E.; Yakovleva, N. A.: Poverkh. Yav. Rasp. Prots. Porosh. Met. AN UKr. SSR. Inst. Metallokeram, Spets. Splav. (1963), 377 – 382
[177] Yuan, Z.; Sun, M.; Chen, X.: Youse Jinshu, 40 (1), (1988), 58
[178] Efimova, L. K.: Steklo. Emalirov. Met. (2), (1974), 80
[179] Efimov, V. N.; Popova, E. A.; Lepinskikh, B. M.; Chentsov, V. P.: Iz. VUZ. Tsvet. Metall. (2), (1982), 62
[180] Yakobashvili, S. B.: Auto. Weld. (11) (1965), 84
[181] Muu, B. van; Fenzke, H.-W.: Freiburger Forschungsh. B. B252 (1985), 40
[182] Krusina, J.: Hutn. Listy. 26 (1971), 783
[183] Komelkov, V. K.; Shirer, G. B.; Shalimov, A. G.; Voinov, S. G.: Teor. Met. Prots. Metallurgizdat, Moscow (1972), 50
[184] Goloshubov, V. I.: Auto. Weld. 25 (2), (1972), 61
[185] Ishchanov, T. K.; Sushkov, K. V.: Met. Metall. (3) (1974), 81
[186] Murav'eva, E. L.; Kaplun, L. I.: Adgez. Raps. Paika Mater. 12 (1984), 26
[187] Musikhin, V. I.; Lepinskikh, B. M.; Chernyaev, V. G.; Ishchuk, I. Ya.; Klibus, A. V.: Trudy Inst. Met. Sverd. (20), (1969), 75
[188] Nesterenko, S. V.: Russ. Metall (3), (1976), 45
[189] Shkol'nik, Ya. Sh.; Kochetov, N. N.: Tr. Ural. Nauch-Issled Inst. Chern. Metal. 8 (1968), 58
[190] Benesch, R.; Knihnicki, R.; Janowski, J.: Arch. Hutn. 21 (4), (1976), 591
[191] Kim, V. A.; Nikolai, E. I.; Akberdin, A. A.; Kim, A. S.: Iz. VUZ. Chern. Metall. (5), (1988), 1
[192] Krusina, J.: Hutn. Listy. 27 (9), (1972), 622
[193] Takayanagi, T.; Kato, M.; Minowa, S.: J. Jap. Foundry Soc. 48 (12), (1976), 779
[194] Krusina, J.; Myslivec, T.: Kovove Mater. 16 (4), (1978), 510
[195] Krusina, J.: Hutn. Listy. (1), (1974), 41
[196] Toropov, N. A.; Bryantsev, B. A.: Zhel-Magnez. Metall. Shlaki Kol'skogo Poluostrova, AN, SSR, Kol'skii. Fil. S M Kirova, Gornometall. Inst. Pub.: Nauka, Moscow, (1966), 10 – 22
[197] Panov, A. S.; Kulikov, I. S.; Tsylev, L. M.: Surface Phenom. in Metall. Processes, Pub.: Consultants Bur. Inc. (1965), 146 - 151
[198] Popel, S. I.: Metall. Shlkai Prim. ikh Stroit El'stve, Akad. Stroit i Arkhitekt, SSSR, Ural'sk Filial, 97 – 127
[199] Sasek, L.: Sb. Vys. Sk. Chem. Technol. Praze Chem. Technol. Silik. L9 (1982), 111
[200] Yakushev, A. M.; Romashin, V. M.; Ivanova, N. V.: Steel in the USSR, 15, (1985), 425
[201] Sokolov, G. A.; Sergeev, A. G.: Iz. VUZ, Chern. Metall. 13 (7), (1970), 22
[202] Nesterenko, S. V.; Khomenko, V. M.: Iz. An. SSSR. Metall. (2), (1985), 44
[203] Parmelee, C. W.; Harman, C. G.: J. Am. Ceram. Soc. 20 (1937), 224
[204] Yang, Z.; Wu, K.; Haung, Z.: Acta Metall. Sinica 24 (2), (1988), B142

11

Interfacial tension between ferrous melts and molten slags

B. J. Keene

11.1 Importance of interfacial tension in metallurgical processes

The magnitude of the interfacial tension acting between molten metal and either liquid slag or solid inclusion can have a marked effect on the efficiency of many metallurgical processes. Examples of circumstances in which surface and interfacial properties have an important influence are: 1. the refining of metals by mass transfer across the interface with a molten slag, 2. the transfer of solid and liquid inclusion from the metal bulk to the metal/slag interface, 3. the removal of many of the residual inclusions present in refined metal by filtration and 4. the electron beam button melting technique when used as a standard method to quantify the low levels of inclusions which remain in special alloys subsequent to the refining procedures.

11.1.1 Metal-slag refining processes

The principal purpose of the slag phase (S) in metallurgical refining processes, is to remove unwanted impurities from the molten metal (M), generally by mass transfer across the two-phase interface. During mass transfer, the kinetics of the chemical interactions will exert a strong influence on the magnitude of the interfacial tension (γ_{MS}). Under conditions of intense mass transfer, the interfacial tension will often decrease to very low values (of the order of zero in extreme cases), and will remain at this general level until the system approaches its chemical equilibrium, at which point the interfacial tension will gradually increase and ultimately attain an essentially constant (or equilibrium) value. By way of illustration [3], **Fig. 11.1 a** shows the change in (γ_{MS}) with time for a Fe + Al/oxide slag system, in which Al is being continually transferred across the two-phase interface (during which time, (γ_{MS}) is very low), until chemical equilibrium is attained **(Fig. 11.1 b)**. Extremely high rates of mass transport can lead to unstable interfacial tension gradients and the convective flow induced in the fluids (Marangoni effect) can be of sufficient intensity to generate interfacial turbulence and lead to metal/slag emulsification. Alternatively, the presence of a highly surface-active component in either of the liquids which is not transferred across the interfacial layer, can create a diffusion barrier at the interface and may impede mass transfer of other impurities.

The BOS process is characterised by rapid and efficient refining of the metal and, to a large extent, this is due to the initial low metal/slag interfacial tension which generates intense emulsification between the two liquids. During the refining operation, all the molten metal present in the system, passes through the slag phase in the form of fine droplets, with the consequence that an extremely high interfacial area per unit volume of metal makes direct contact with the slag. In many respects, dynamic values of (γ_{MS}) are most important in refining processes since they reflect the magnitude of the chemical kinetics associated with mass transfer. However dynamic values of (γ_{MS}) are difficult to determine experimentally and in addition, results showing the variation of (γ_{MS}) with time would be specific to the particular experimental conditions, e.g. quantity of metal and slag; shape and size of container. The bulk of interfacial tension data presented in the scientific literature pertain to equilibrium or quasi-equilibrium conditions.

The work of adhesion (W_A) between liquid metal and slag is a measure of the bond strength between the two media and is related to the respective surface and interfacial energies by the relation

$$W_A = \gamma_{MG} + \gamma_{SG} - \gamma_{MS}.$$

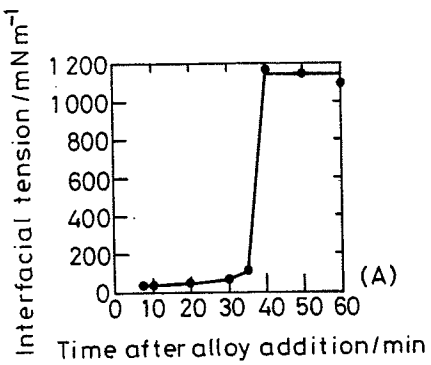
It follows that strong adhesion would be associated with low values of (γ_{MS}) i.e. the same condition which is favourable for good mass transfer. However, if (W_A) is very high (i.e. γ_{MS} very low), the bonding between the two phases would be very strong and physical separation of the metal and slag would be correspondingly more difficult to achieve. In addition, there would be an increased probability for slag droplets to become permanently entrapped as inclusions within the metal bulk during processing.

11.1.2 Removal of inclusions from molten metal

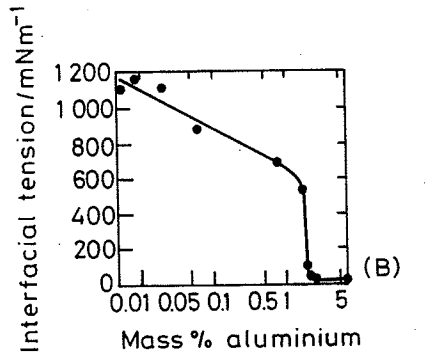
One factor which governs the ease of inclusion (I) removal from the bulk of a molten metal to a surface, is the magnitude of the energy at the metal/solid interface (γ_{MI}). Kozakevitch and Olette [4] studied the surface energy criteria necessary for emergence of a thin solid lamina at a metal/gas interface. Stable emergence could only occur when the resultant change in free surface energy (ΔG) is less than zero, and the more negative the value of (ΔG), the greater the probability for the inclusion to emerge and be retained at the interface. The energy condition for emergence is

$$\Delta G = \gamma_{GI} - \gamma_{MG} - \gamma_{MI} < 0. \qquad (11.1)$$

It follows that, (ignoring density and viscosity effects) emergence of an inclusion would be facilitated by high values for (γ_{MG}) and (γ_{MI}) relative to (γ_{GI}). The inequality (11.1) shows that irrespective of the value for (γ_{MI}), the condition for emergence would be satisfied when (γ_{GI}) < (γ_{MG}). Both sulphur and oxygen are highly surface-active in iron and steel, and the presence of even relatively low



(a)



(b)

Fig. 11.1 a,b. Interfacial tension between Fe + 4 % Al alloy and slag (20 % Al_2O_3 + 40 % CaO + 40 % SiO_2) at 1570 °C
a) Variation with time
b) Variation with aluminium content in iron [Ref. 3]

levels of these elements will lead to a marked diminution in the surface tension (γ_{MG}) and thus give rise to a lower probability for stable emergence of inclusions. Kozakevitch and Olette [4] extended their analysis to consider the surface energy criteria necessary for a solid lamina to emerge at a metal/slag interface. For this case it was established that the surface condition for emergence is given by

$$\Delta G = \gamma_{SI} - \gamma_{MS} - \gamma_{MI} < 0 \qquad (11.2)$$

i.e. emergence at a metal/slag interface would be most probable when $(\gamma_{MS} + \gamma_{MI}) \gg (\gamma_{SI})$. Since $(\gamma_{MI}) > 0$, it follows from inequality (11.2) that emergence could occur when $(\gamma_{SI}) < (\gamma_{MS})$ and this criterion is generally fulfilled with most molten iron or steel/slag/inclusion systems. If the lamina were liquid, then (γ_{SI}) would generally be extremely low and as a consequence, liquid inclusions would be expected to easily emerge at the interface where they would be rapidly absorbed into the slag.

For total emergence of a lamina into the main bulk of the slag phase, the necessary surface energy condition derived by Kozakevitch and Olette [4] is

$$\Delta G = \gamma_{SI} + \gamma_{MS} - \gamma_{MI} < 0.$$

11.1.3 Filtration of metals

In recent years, there has been an increasing demand for high quality special alloys (steels; super alloys), which contain the minimum of residual inclusions. To satisfy this requirement, supplementary refining techniques have been developed, which remove many of the residual inclusions from molten metal by filtration through a porous ceramic. During the filtration process removal of particles can be due to either 1. the size limit imposed by the physical dimensions of the filter pores or 2. retention at the ceramic wall by interfacial forces. The relative tendency for any particular type of inclusion to be trapped by surface forces will increase with increase in the work of adhesion between the particle and the filter material (F) [5], i.e. since

$$W_A = \gamma_{MG} + \gamma_{MI} - \gamma_{IF}$$

the surface energy conditions for removal of particles from the melt would be most favourable when

$$(\gamma_{MF} + \gamma_{MI}) \gg \gamma_{IF}.$$

For liquid inclusions in particular, (γ_{IF}) will normally be extremely low and once interfacial contact has been established, adhesion between the two phases is highly probable (possibly with subsequent chemical interaction). By comparison, (γ_{IF}) for solid particles will be relatively high and as a consequence, the likelihood of stable adhesion to the filter will be correspondingly reduced, unless the resultant interfacial energies are altered due to chemical interaction between the two phases. When adhesion between a solid inclusion and the filter is solely due to the relatively weak physical (or van der Waals) forces, there is a strong possibility that, as a consequence of the hydrodynamic forces, the particle could be detached from the ceramic wall and become re-entrained in the molten metal.

11.1.4 Assessment of the relative cleanness of refined alloys

The electron-beam button melting (EBBM) technique [6] is being considered as a possible standard procedure to monitor the low levels of inclusions retained in metal alloys after filtration. In the EBBM procedure, ingots of the filtered alloys are electron-beam melted and the molten drops which fall off, are collected in a water-cooled crucible. Melting of an ingot is continued until the crucible is full of metal, at which point the heat source is removed and a solid button of re-melted alloy is obtained. Throughout the melting process many metal droplets are formed which yield a large total surface area of metal available for emergence and retention of inclusions. As the volume of metal collected in the crucible increases, there is a concomitant increase in the quantity of inclusions floating on the molten surface of the button. By careful control of the final cooling procedure, all the inclusions floating on the metal surface can be concentrated as a 'raft' in the central region of the button prior to final solidification.

Analysis of the quantity, size and composition of the 'raft' contents is carried out to establish the relative cleanness of the particular melt. It follows, from the work of Kozakevitch and Olette [4], that, based on surface energy considerations, the probability of emergence for any particular type of inclusion would be high when the values of (γ_{MG}) and (γ_{MI}) are high. High values of (γ_{MG}) would be obtained with low surface-active impurity levels coupled with relatively low temperature of the melt. The values of (γ_{MI}) will vary with the composition of the respective inclusions, and knowledge of the respective values would be important in identifying those compositions for which the surface energy conditions would not be ideal for optimum emergence at the gas/liquid interface. Unfortunately, values of (γ_{MI}) with solid inclusions are not easy to determine directly and data quoted in the literature are generally calculated using the relation given for the balance of surface tension forces acting on a sessile drop (with contact angle θ) of the metal at equilibrium on a flat horizontal plane of the solid viz

$$\gamma_{MI} = \gamma_{IG} - \gamma_{MG}\cos\theta. \qquad (11.3)$$

Although (γ_{MG}) and (θ) can be easily measured, values for (γ_{IG}) are particularly difficult to determine, and as a consequence, literature data derived for (γ_{MI}) are generally restricted to simple oxides such as Al_2O_3; SiO_2 for which (γ_{IG}) has been calculated by separate experiments. Equation (11.3) shows that in order to calculate (ΔG) using equation (11.1), it is not necessary to have specific values for (γ_{MI}) and (γ_{IG}), since $(\gamma_{IG} - \gamma_{MI}) = \gamma_{MG}\cos\theta$ and equation (11.1) can be rewritten as

$$\Delta G = \gamma_{MG}(\cos\theta - 1).$$

11.2 Methods to determine interfacial tension (γ_{MS})

For high temperature liquid metal/slag systems three techniques have been used principally to determine (γ_{MS}) viz:

(a) measurement of the profile of a sessile drop of molten metal submerged in the slag,

(b) measurement of the profile of a lens of liquid slag floating on a flat horizontal surface of molten metal,

(c) determination of drop weight when the end of a metal rod is immersed in molten slag.

The basic principles of these three techniques have been outlined in a previous report [1].

11.3 Electrocapillary phenomena

When a molten metal is in equilibrium contact with an ionic solution, the metal surface will become electrically charged and acquire a potential difference with respect to the other liquid. Ions of opposite charge which are present in the solution, will migrate towards the metal surface and produce a surface excess at the interface. The charge density on the resultant electrical double-layer formed at the interfacial region will be related to the interfacial tension (γ_{MS}) between the two liquids. When a small external potential (which is of opposite polarity to that present at the metallic surface), is applied to the metal, the surface charge is reduced and (γ_{MS}) will increase. As the magnitude of the applied potential is progressively increased, the value of (γ_{MS}) will also increase until it ultimately attains a maximum value at which point the applied potential has totally nullified the original charge on the metal. Further increase in applied potential yields a reduction in (γ_{MS}) due to the formation of another electrical double-layer. Data obtained from electrocapillary experiments are generally presented in the form of electrocapillary curves which show the variation in (γ_{MS}) with both the polarity and the magnitude of the applied potential (E). Lippman [7] derived a general thermodynamic relation for 'ideal' (fully polarised system) electrocapillary curves viz

$$\left(\frac{\partial \gamma_{MS}}{\partial E}\right)_{T;P;\mu} = -q \qquad (11.4)$$

where q = charge density at the interface.

The differential capacity (C′) of the two-liquid interface is defined as $\left(\frac{\partial q}{\partial E}\right)_{T;P;\mu}$ and it follows from differentiation of equation (11.4) that:

$$\left(\frac{\partial^2 \gamma_{MS}}{\partial E^2}\right) = -C'.$$

This relation shows that, provided the capacity of the electric double-layer remains constant, electrocapillary curves should be parabolic [8], and some experimental curves do approximate to this condition. Equation (11.4) also shows that the maximum in the (γ_{MS})/(E) curve corresponds to the situation where the surface charge density (q) is zero. In general terms, the slope of the 'ideal' electrocapillary curve

Tab. 11.1. Composition of metals designated with 'M' numbers in captions

Metal No.	Composition (mass %)
M1	Fe: 0.001 - 0.002C; 0.002S; 0.002Ni
M2	Fe: 0.001C; 0.003Si; 0.002Mn; 0.001P; 0.001S; 0.006Cu; 0.001Ni; 0.001Cr; 0.005Ti; 0.001V; 0.002Al; 0.007Co; 0.002[N]
M3	Steel Kh14N14M2V2: 0.07C; 0.3Si; 0.26Mn; 0.009S; 0.007P; 13.43Cr; 14.05Ni; 2.07Mo; 1.85W; 0.0018[O]; 0.0001[H]; 0.027[N] Steel Kh15N28M4V2B: 0.10C; 0.24Si; 0.23Mn; 0.008S; 0.01P; 13.35Cr; 28.7Ni; 3.35Mo; 2.35W; 1.13Nb; 0.002[O]; 0.0002[H]; 0.062[N]
M4	Steel: 0.05C; 0.61Si; 9.25Mn; 4.75Ni; 18.2Cr
M5	Base Steel: 0.5Si; 0.8Cr; 0.4C
M6	Steel 100Cr6: 1.08C; 0.35Si; 0.34Mn; 0.02P; 0.004S; 1.41Cr; 0.22Cu; 0.03Mo; 0.01V; 0.03W; 0.09Ni; 0.01Co; 0.003[O]; 0.008[N] Steel x85WMoCo6.5.5: 0.87C; 0.18Si; 0.22Mn; 0.019P; 0.012S; 4.31Cr; 0.20Cu; 5.2Mo; 2.2V; 6.53W; 4.91Co; 0.15Ni; 0.0033[O]; 0.0119[N]
M7	Steel ShKh15: 1.0C; 0.34Mn; 0.26Si; 0.025P; 1.4Cr; 0.016S; 0.23Cu; 0.15Ni
M8	Steel H 52-3: 0.115C; 0.44Si; 1.32Mn; 0.22P; 0.035S; 0.0045[O]; 0.0115[N]
M9	Steel: 0.09C; 0.5Mn; 0.06Si; 0.029P; 0.026S
M10	Fe: 0.044C; 0.021Si; 0.22Mn; 0.0013P; 0.0011S; 0.0055Al; 0.0049[N]; 0.004[O]
M11	Carbonyl iron: 0.03C; 0.002-0.004S; 0.008P; 0.006Al; 0.006Si; 0.05Ni; 0.003Cu
M12	Steel: 1.0C; 0.34Mn; 0.26Si; 0.025P; 1.4Cr; 0.016S; 0.23Cu; 0.15Ni
M13	Steel EI.701: 0.7C; 0.3Si; 1.55Mn; 2.75Cr; 0.5V; 9.2W Steel Sv-08: 0.07C; 0.01Si; 0.55Mn; 0.021S; 0.031P Steel Sv-08KhGSMF: 0.1C; 1.5Si; 0.72Mn; 1.2Cr; 0.4V; 0.65Mo; 0.03S; 0.03P Steel Sv-08G2SA: 0.08C; 0.87Si; 1.59Mn; 0.03S; 0.03P Steel 10Kh 9: 0.12C; 0.08Si; 0.31Mn; 9.16Cr; 0.036S; 0.042P Steel 10F13: 0.13C; 0.06Si; 0.35Mn; 13.42V; 0.043S; 0.018P

Metal No.	Composition (mass %)
M14	Fe: 0.1Mn; 0.1Si; 0.03C; 0.009S
M15	Carbonyl iron: 0.03C; 0.002S; 0.009[O]
M16	Armco iron: 0.03C; 0.18Si; 0.15Mn; 0.14Ni; 0.028S; 0.009P
M17	Steel 0Kh13: 0.015C; 0.48Mn; 0.63Si; 0.014S; 0.034P; 11.76Cr Steel 1Kh13: 0.1C; 0.42Mn; 0.47Si; 0.01S; 0.027P; 12.8Cr Steel 2Kh13: 0.21C; 0.27Mn; 0.33Si; 0.01S; 0.018P; 12.86Cr; 0.0072[O] Steel 3Kh13: 0.32C; 0.33Mn; 0.37Si; 0.009S; 0.02P; 12.89Cr; 0.0054[O] Steel 4Kh13: 0.38C; 0.28Mn; 0.42Si; 0.005S; 0.025P; 13.08Cr; 0.0037[O] Steel Kh18N10T: 0.08C; 1.21Mn; 0.54Si; 0.009S; 0.032P; 17.78Cr; 0.0135[O]; 0.45Ti; 10.08Ni Steel 0Kh18N9: 0.015C; 1.16Mn; 0.38Si; 0.016S; 0.014P; 16.65Cr; 0.008[O]; 8.87Ni
M18	High carbon iron: 3.71C; 0.47Mn; 1.16Si; 0.43P; 0.037S Mild steel: 0.03C; 0.44Mn; 0.26Si; 0.02P; 0.021S
M19	Steel ShKh15: 1C; 0.34Mn; 0.26Si; 0.025P; 1.4Cr; 0.016S; 0.23Cu; 0.15Ni
M20	Steel: 0.44C; 0.38Mn; 0.2Ni; 14.37Cr
M21	Iron: 0.03Si; 0.007Mn; 0.006P; 0.007S; 0.001Cr; 0.006Ni
M22	Fe: carbonyl iron Chromium: 0.005C; 0.004Si; 0.005Ni; < 0.007Fe; 0.006Al; 0.001S; 0.003Cu; 0.005[O]; 0.006[N]
M23	Steel: 1.0C; 0.34Mn; 0.26Si; 0.025P; 1.4Cr; 0.016S; 0.23Cu; 0.15Ni
M24	Fe: 0.02C; 0.02Si; 0.007S; 0.005P; 0.002[O]
M25	SCh-21-40: 3.1C; 2.17Si; 0.66Mn; 0.32P; 0.01S
M26	Steel: 0.09C; 0.33Mn; 0.021S

at any point is equal to the quantity of electrical charge on the metal per unit area of interface. As would be anticipated, the application of an alternating potential to the metal [9] appears to have little effect on the magnitude of (γ_{MS}).

11.4 Data for interfacial tension and work of adhesion

This section gives the collated data for the interfacial tension and the work of adhesion between iron-based melts and either ceramic solids or molten slags. Data are presented under four broad headings, viz metal/solids; metal/CaF_2-containing slags; metal/oxide slags; electrocapillary curves. Presentation of data within each section is arranged in alphabetical order based on the composition of the slag or ceramic solid. Where appropriate, the symbol FeO_x has been used in the text, to represent the total concentration of iron oxides (FeO + Fe_2O_3) in a slag.
The metals given in this chapter are compiled in two tables. **Tab. 11.1** contains all metals with known compositions. Further steel grades with their average compositions or material numbers are listed in **Tab. 11.2.**

Tab. 11.2. Average compositions or material numbers (according to EN 10027-2)

Metal grade	Average composition (mass %)	Material number (EN 10027-2)	Typical composition (see Tab. 11.1)
OKh13		1.4000	M17
OKh18N9		1.4301	M17
1Kh13		1.4006	M17
2Kh13		1.4021	M17
3Kh13		1.4028	M17
4Kh13		1.4031	M17
10F13			M13
10Kh9			M13
12KhMFK	comp. unknown		
12Kh1MF	0.1C; 1.0Cr; 0.3Mo; 0.2V		
20K		1.0402	
45Kh		≈ 1.7035	
EI.701			M13
EI.847	16Cr; 15Ni; 3Mo; Nb		
Kh14N14M2V2			M3
Kh15N9Yu	15Cr; 9Ni; 1Al		
Kh15N28M4V2B			M3
Kh16N15M3B	16Cr; 15Ni; 3Mo; Nb		
Kh18N10T		1.4541	M17
SCh-21-40			M25
ShKh15		1.3505	M6, M7
ShKh15E	ball bearing steel (comp. unknown)		
ShKh15ESSh	ball bearing steel (comp. unknown)		
ShKh15SG		1.3520	
Sv-08			M13
Sv-08G2SA			M13
Sv-08KhGSMF			M13
U8A		1.1525	
X85WMoCo6.5.5		1.3243	M6

Fig. 11.3 a,b. Interfacial tension and work of adhesion between stainless steels and solid oxides under vacuum and argon at 1550 °C [Ref. 15]. Metal composition: M3
Curve 1 - Steel Kh14N14M2V2 (vacuum)
Curve 2 - Steel Kh15N28M4V2B (vacuum)
Curve 3 - Steel Kh14N14M2V2 (argon)
Curve 4 - Steel Kh15N28M4V2B (argon) ▶

11.4.1 Solid oxides

Various oxides

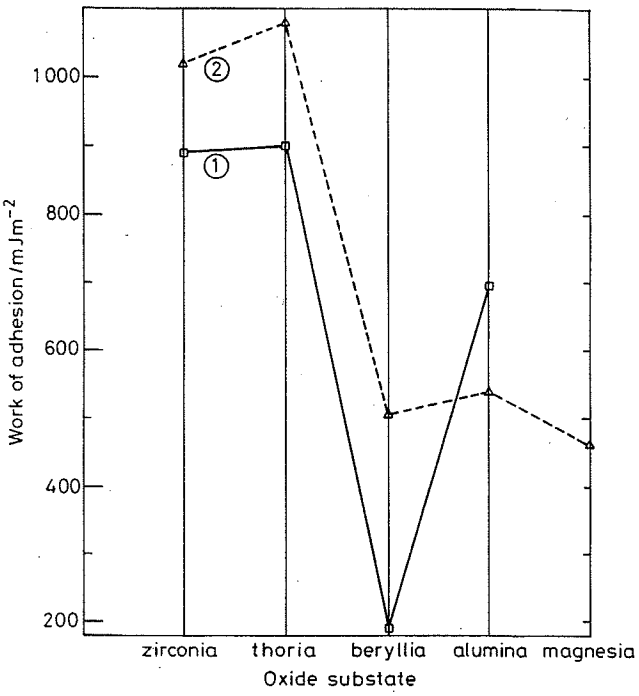
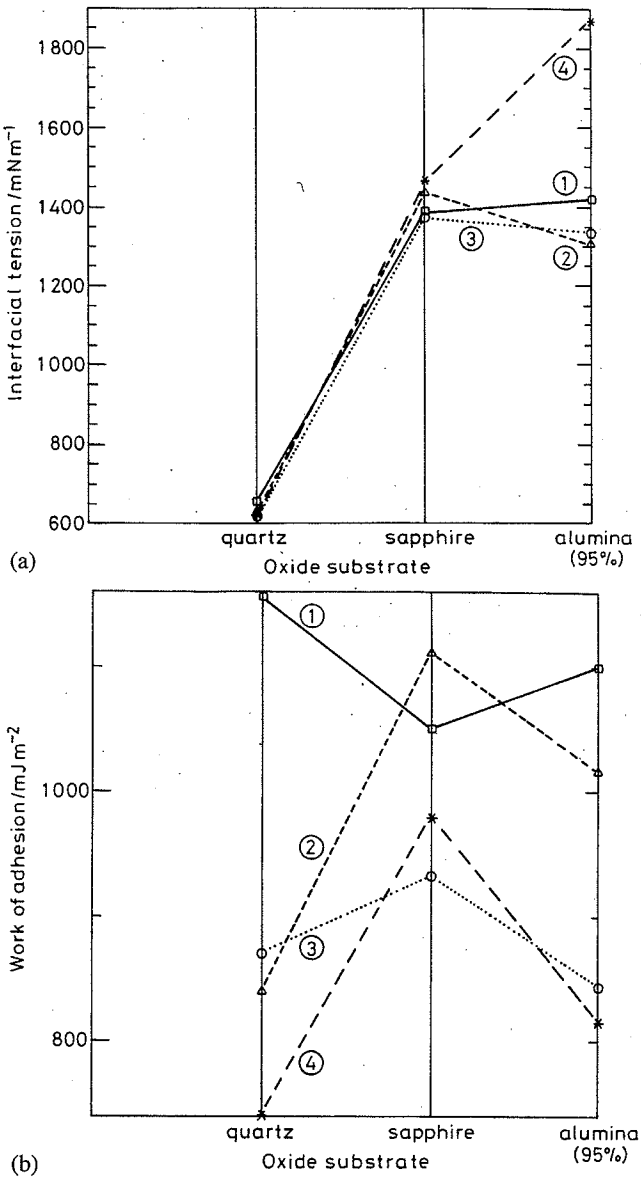
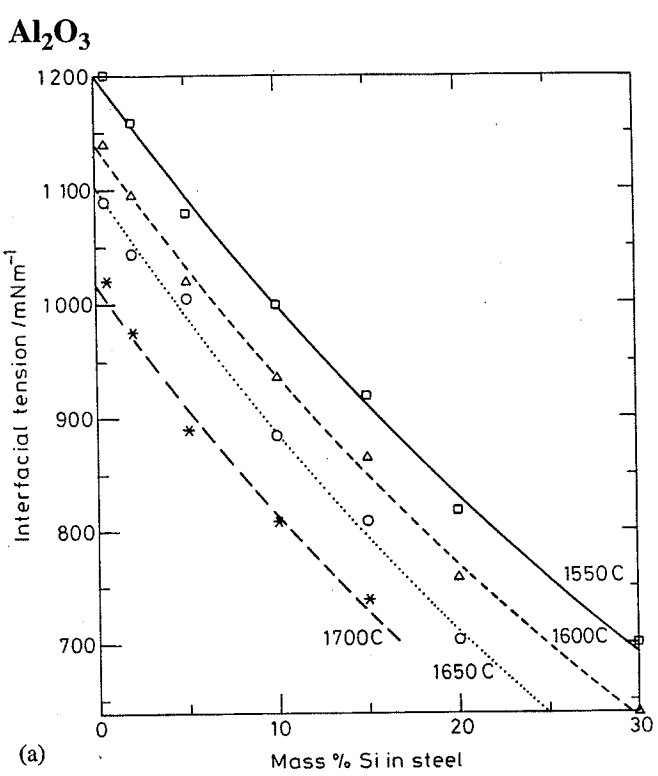


Fig. 11.2. Work of adhesion between Fe and various oxide substrates under H_2 or He at 1550 °C [Ref. 10]





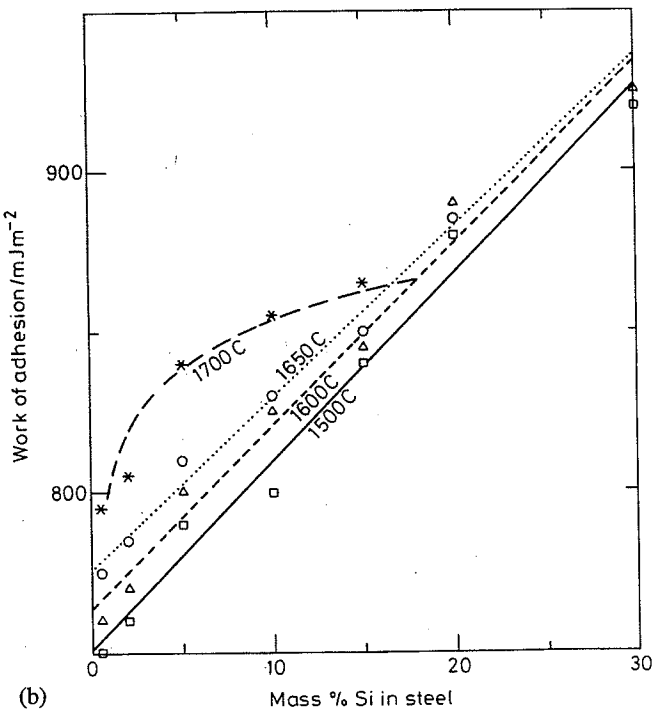


Fig. 11.4 a,b. Effect of Si content in steel on the interfacial tension and work of adhesion with Al_2O_3 at various temperatures [Ref. 17]. Metal composition: M5

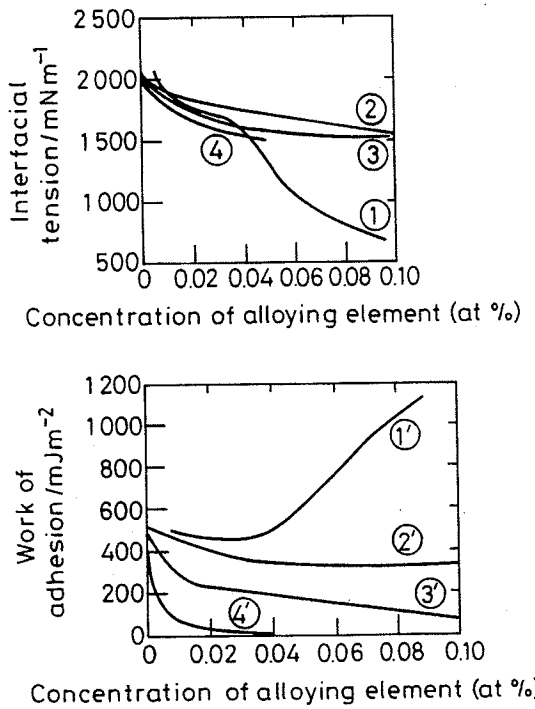


Fig. 11.5 a,b. Effect of concentration of alloying elements in Fe on the interfacial tension and work of adhesion with Al_2O_3 at 1600 °C [Ref. 14]

Curve 1, 1' - Fe + O
Curve 2, 2' - Fe + S
Curve 3, 3' - Fe + Se
Curve 4, 4' - Fe + Te

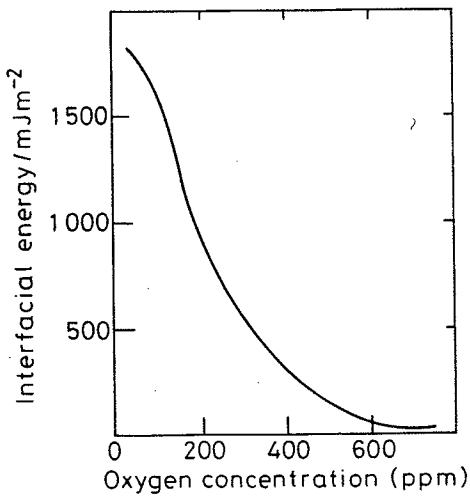


Fig. 11.6. Effect of oxygen content in Fe on the interfacial tension with Al_2O_3 at 1600 °C [Ref. 12]. Metal composition: M2

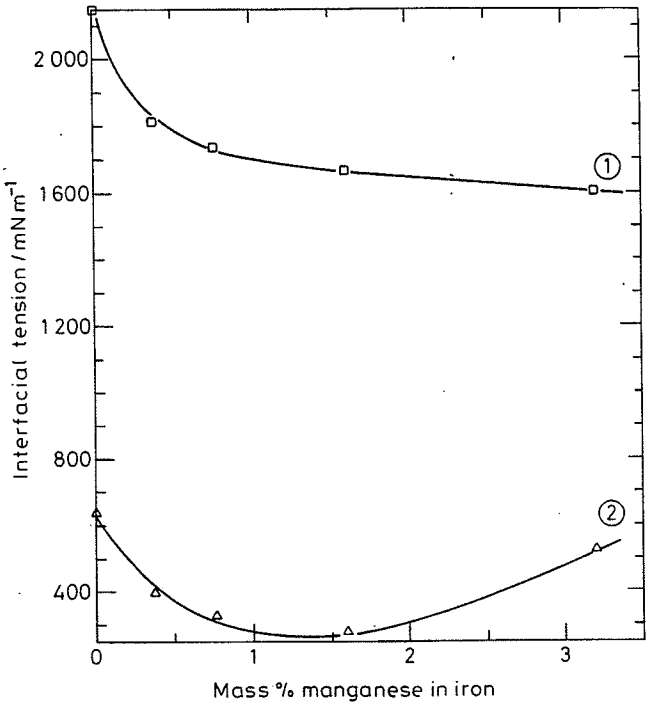


Fig. 11.7. Effect of Mn concentration in Fe on the interfacial tension with Al_2O_3 (curve 1) and SiO_2 (curve 2) at 1550 °C [Ref. 11]. Metal composition: M1

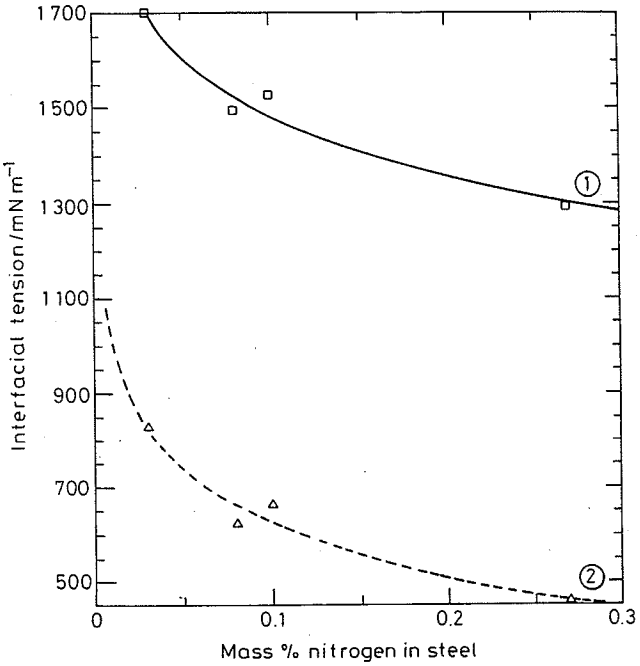


Fig. 11.9. Effect of nitrogen content in stainless steel on the interfacial tension with Al_2O_3 and SiO_2 at 1500 °C [Ref. 16]. Metal composition: M4

Curve 1 - Al_2O_3
Curve 2 - SiO_2

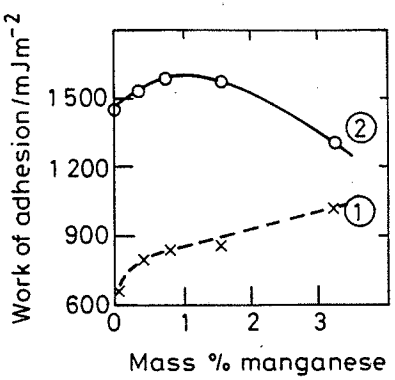


Fig. 11.8. Effect of Mn concentration in Fe on the work of adhesion with Al_2O_3 (curve 1) and SiO_2 (curve 2) at 1550 °C [Ref. 11]. Metal composition: M1

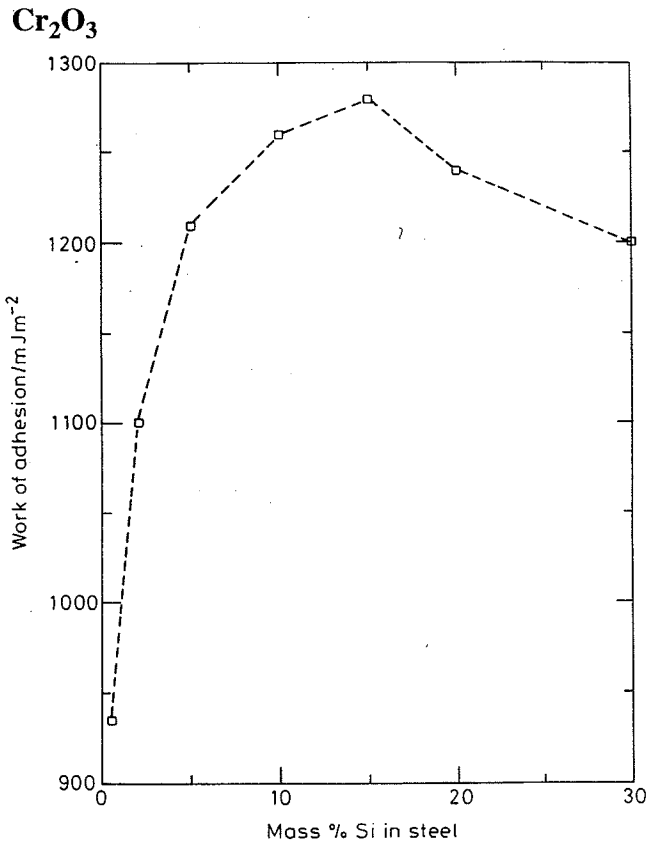


Fig. 11.10. Effect of Si content in steel on the work of adhesion with Cr_2O_3 at 1550 °C [Ref. 17]. Metal composition: M5

SiO_2

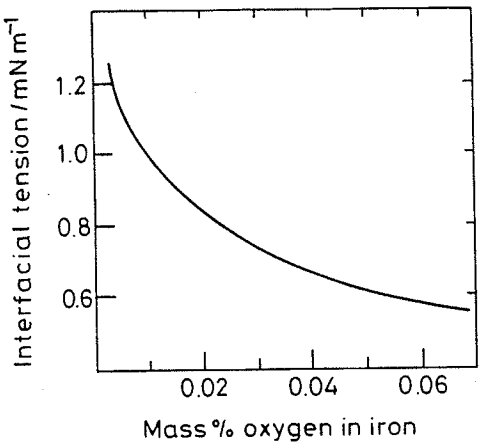


Fig. 11.11. Effect of oxygen content in Fe on the interfacial tension with SiO_2 at 1600 °C [Ref. 13]

11.4.2 Slags containing CaF_2

11.4.2.1 Pure CaF_2

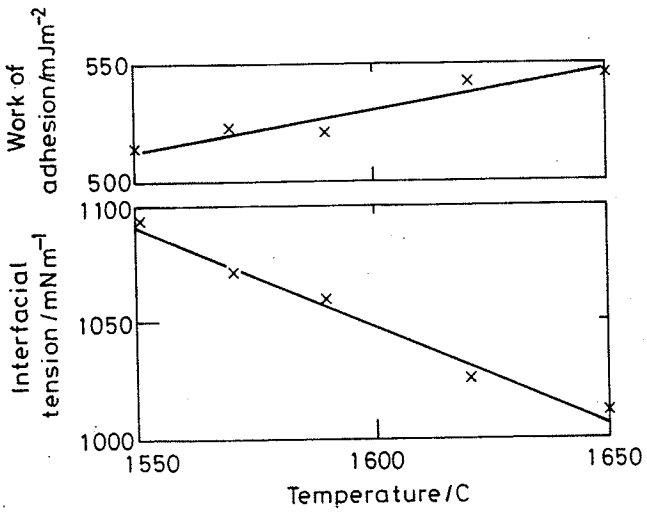


Fig. 11.12. Variation with temperature of the interfacial tension and work of adhesion between Armco iron and ANF-1 flux (CaF_2) [Ref. 18]

11.4.2.2 Binary systems (containing CaF_2)

Al_2O_3;CaO;MgO;NaF;SiO_2;TiO_2;ZrO_2

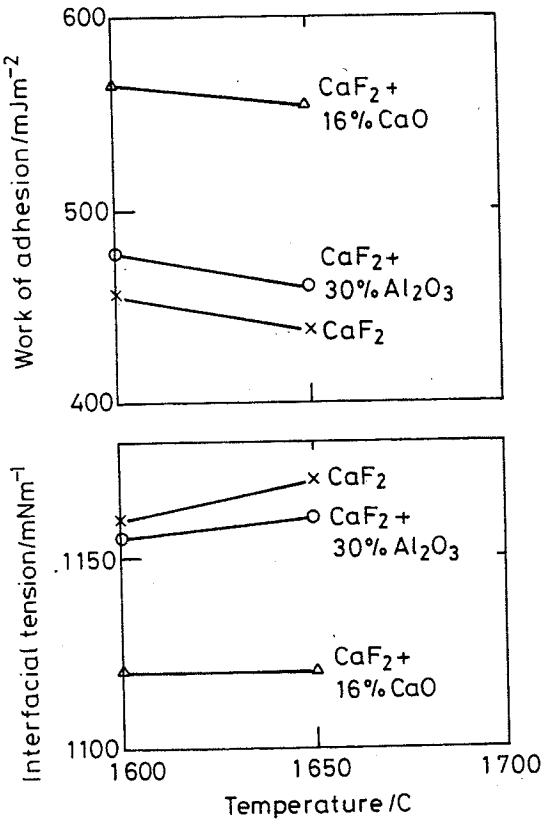


Fig. 11.13. Variation with temperature of the interfacial tension and work of adhesion between Armco iron and various CaF_2-based slags [Ref. 19]

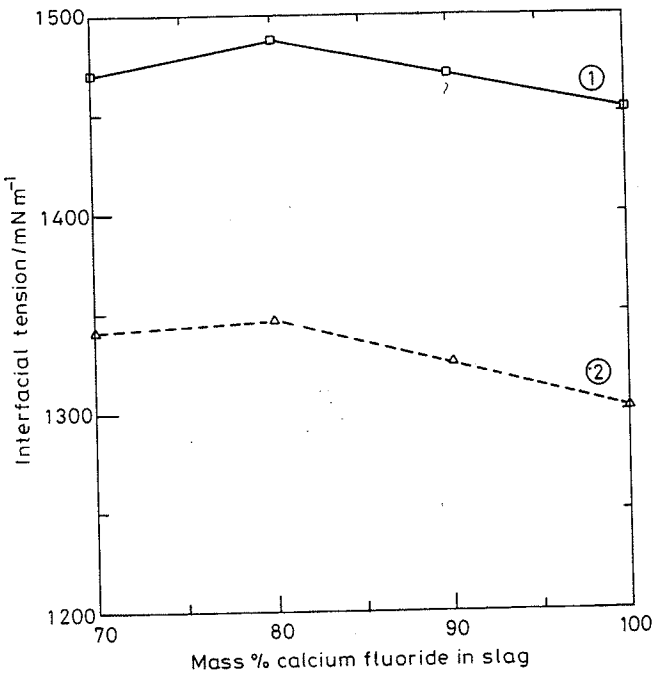


Fig. 11.14. Effect of CaF_2 content in CaF_2 + Al_2O_3 slags on the interfacial tension with steels 100Cr6 (curve 1) and X85WMoCo 6.5.5 (curve 2) at 1550 °C [Ref. 22]. Metal composition: M6

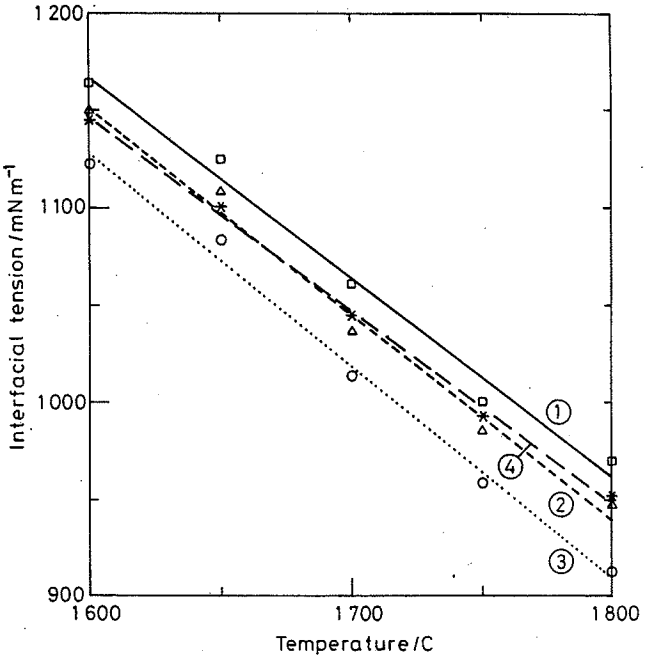


Fig. 11.15. Variation with temperature of the interfacial tension between steel Kh16N15M3B and various CaF_2-based slags [Ref. 20]

Curve 1 - CaF_2
Curve 2 - CaF_2 + 30 % Al_2O_3
Curve 3 - CaF_2 + 30 % CaO
Curve 3 - CaF_2 + 15 % SiO_2

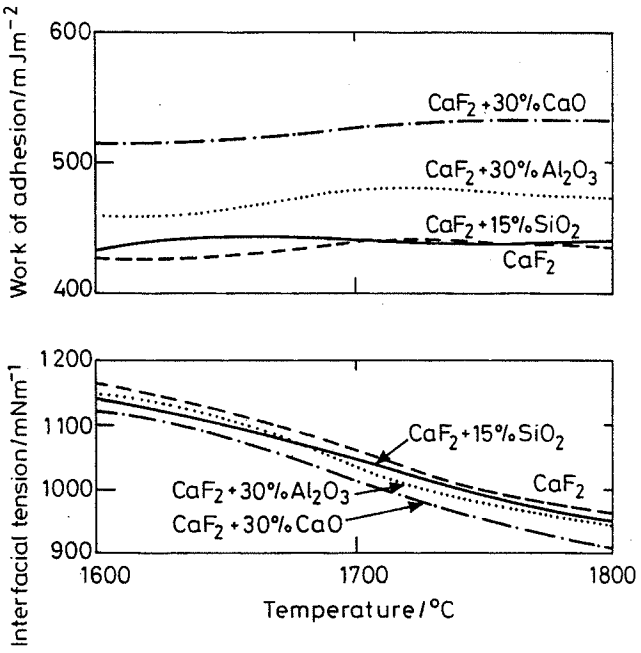


Fig. 11.16. Variation with temperature of the interfacial tension and work of adhesion between EI.847 steel and CaF_2-based slags [Ref. 20]

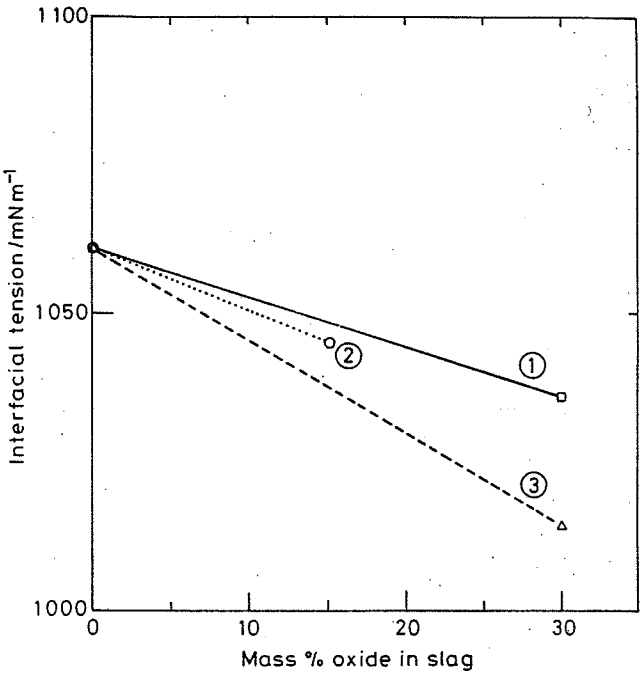
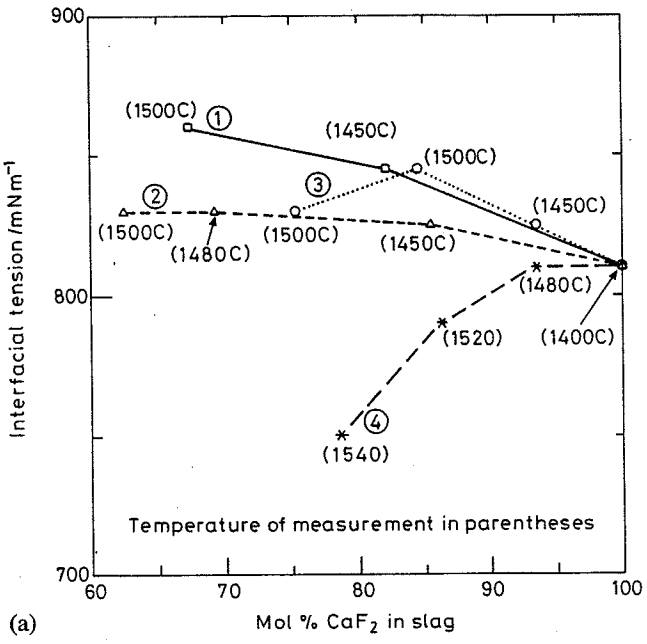


Fig. 11.17. Effect of oxide additions to CaF_2 on the interfacial tension with steel Kh16N15M3B at 1700 °C [Ref. 20]

Curve 1 - CaF_2 + Al_2O_3
Curve 2 - CaF_2 + SiO_2
Curve 3 - CaF_2 + CaO



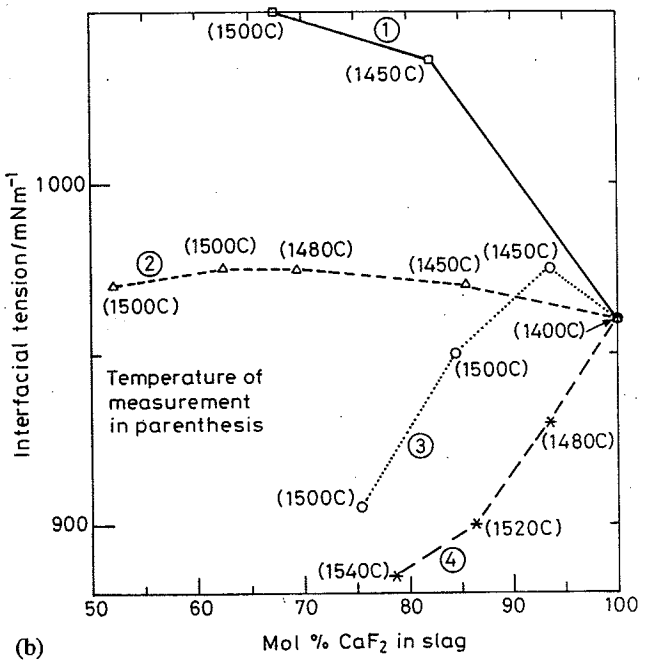
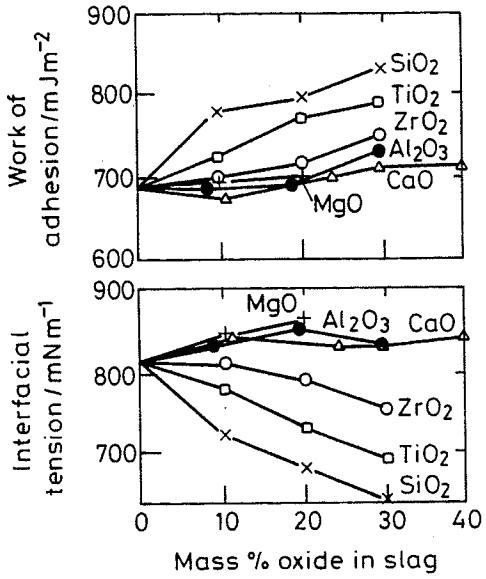


Fig. 11.18 a,b. Effect of CaF_2 content in binary slags on the interfacial tension with (a) steel Sv-08 and (b) steel EI.701 [Ref. 23]

Curve 1 - CaF_2 + MgO
Curve 2 - CaF_2 + CaO
Curve 3 - CaF_2 + Al_2O_3
Curve 4 - CaF_2 + ZrO_2



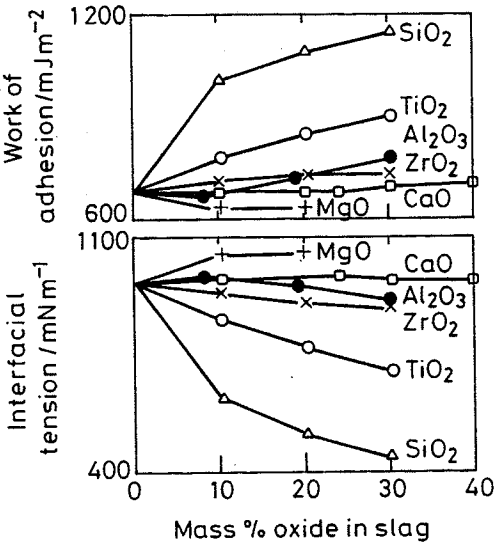


Fig. 11.19 a,b. Effect of oxide content in CaF_2 + oxide binary slags on the interfacial tension and work of adhesion with (a) Sv-08 weld steel and (b) steel EI.701 [Ref. 24]

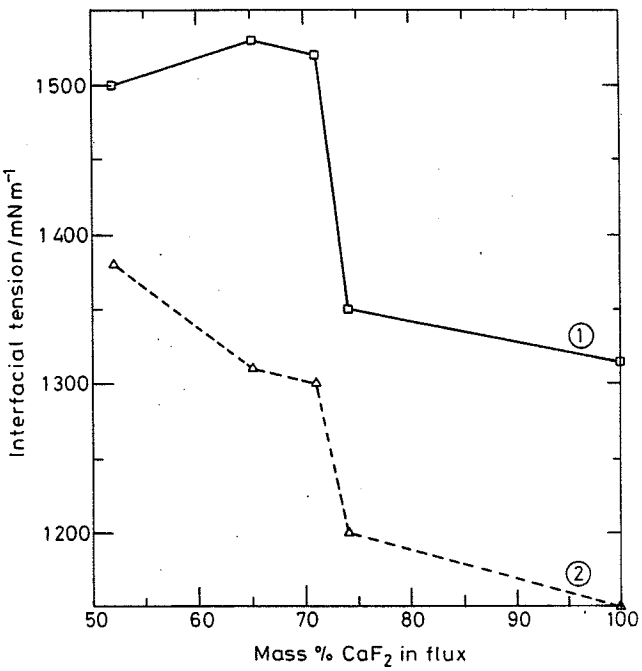


Fig. 11.20. Effect of CaF_2 content of fluxes on the interfacial tension with steels Kh15N9Yu (curve 1) and Kh18N10T (curve 2) at 1470 °C [Ref. 25]

Fluxes: ANF- 1 (100 % CaF_2)
ANF- 6 (71 % CaF_2 + 29 % Al_2O_3)
ANF- 7 (74 % CaF_2 + 26 % CaO)
ANF- 8 (52 % CaF_2 + 21 % CaO + 27 % Al_2O_3)
ANF-14 (65 % CaF_2 + 7 % CaO + 10 % Al_2O_3 + 12 % SiO_2 + 6 % MgO)

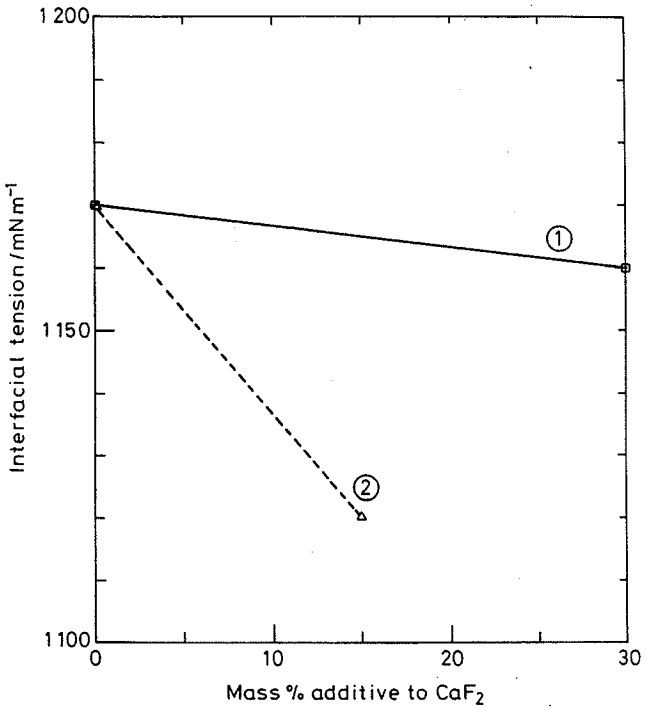


Fig. 11.21. Effect of Al_2O_3 (curve 1) and CaO (curve 2) additions to CaF_2 on the interfacial tension with Armco iron at 1650 °C [Ref. 19]

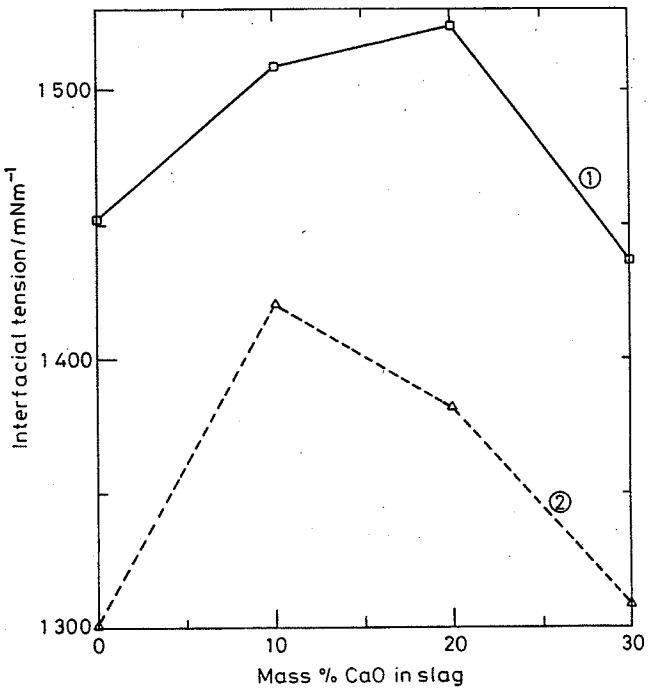
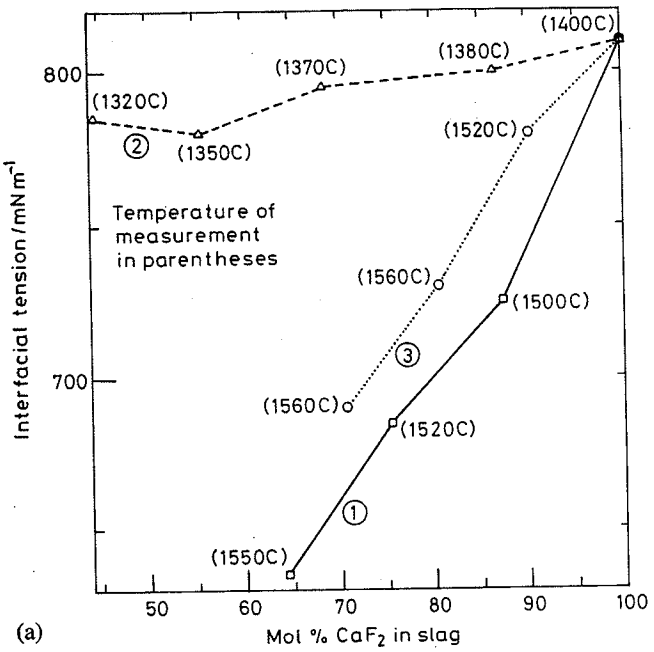
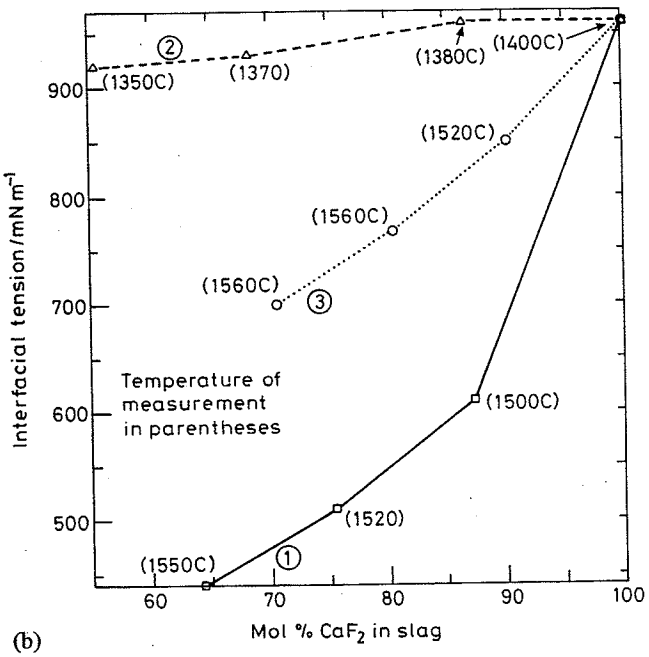


Fig. 11.22. Effect of CaO content in CaF_2 + CaO slags on the interfacial tension with steels 100Cr6 (curve 1) and X85WMoCo 6.5.5 (curve 2) at 1550 °C [Ref. 22]. Metal composition: M6



(a)



(b)

Fig. 11.23 a,b. Effect of CaF_2 content in binary CaF_2 + oxide and fluoride melts on the interfacial tension with (a) steel Sv-08 and (b) steel EI.701 [Ref. 23]

Curve 1 - $CaF_2 + SiO_2$
Curve 2 - $CaF_2 + NaF$
Curve 3 - $CaF_2 + TiO_2$

11.4.2.3 Ternary systems (containing CaF_2)

Al_2O_3-CaO

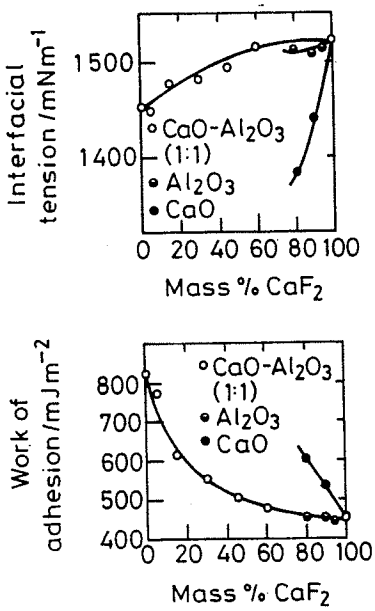


Fig. 11.24. Effect of CaF_2 content in slags on the interfacial tension and work of adhesion with low-carbon steel at 1600 °C [Ref. 21]

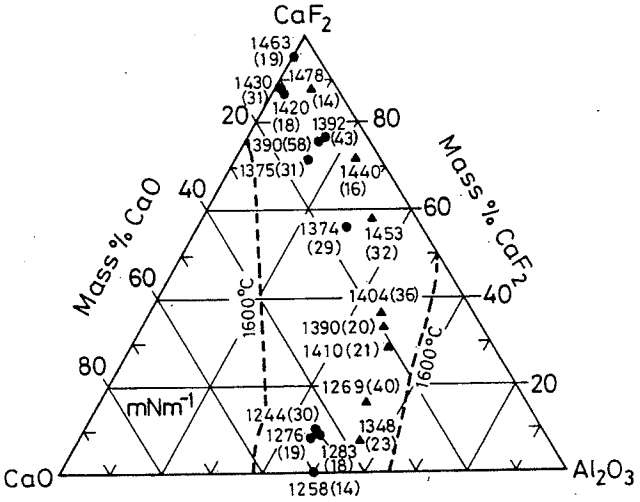
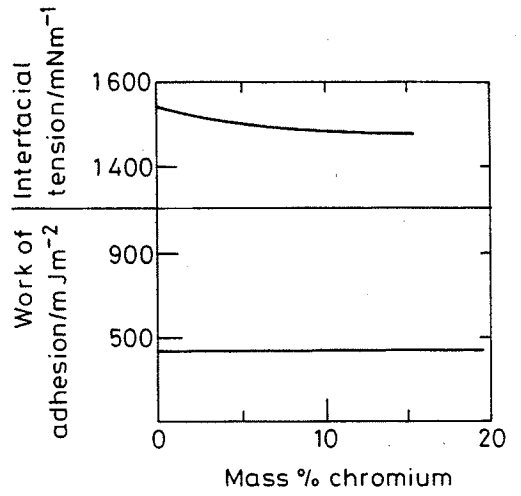
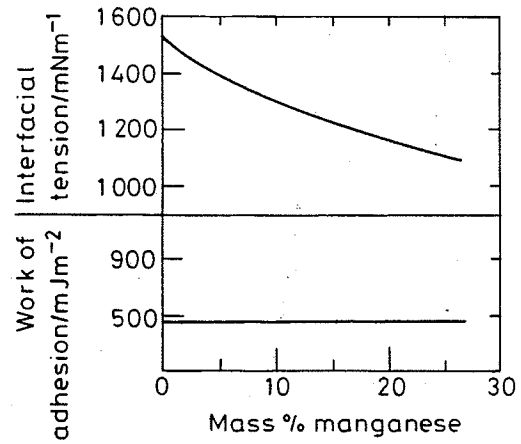


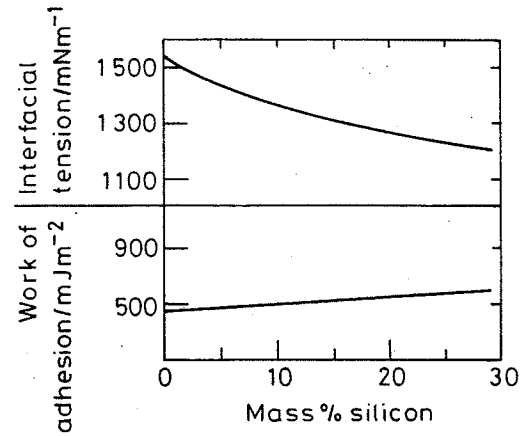
Fig. 11.25. Interfacial tension at 1600 °C between $CaF_2 + Al_2O_3$ + CaO slags and Fe + C + O alloys ([C] varies between 0 and 2 %). Oxygen activities are shown on the diagram in parentheses. Authors used two different techniques to determine interfacial tension viz profile of a slag droplet floating on the metal surface (data shown as circles), and profile of a sessile drop metal submerged in slag (data shown as triangles) [Ref. 26]



(a)



(b)



(c)

Fig. 11.26 a-c. Variation with (a) chromium, (b) manganese or (c) silicon content, of the interfacial tension and work of adhesion between (a) Fe + Cr, (b) Fe + Mn or (c) Fe + Si alloys and slag (60 % CaF_2 + 20 % Al_2O_3 + 20 % CaO) at 1600 °C [Ref. 21]

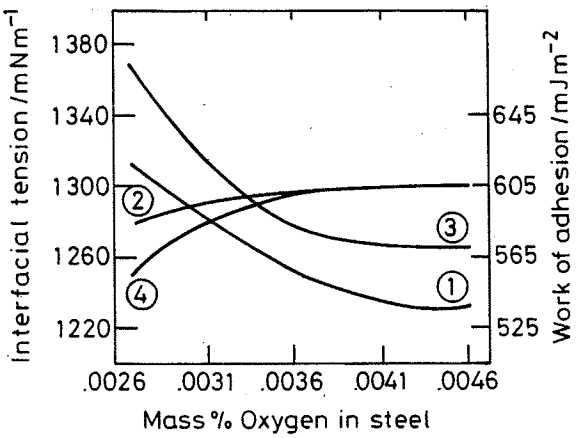


Fig. 11.27. Variation of interfacial tension (curves 1 and 3) and work of adhesion (curves 2 and 4) between steel ShKh15 and CaF_2-based slags, with the oxygen content of the steel at 1500 °C [Ref. 27]

Curves 1 and 2 - 75 % CaF_2 +21 % Al_2O_3 + 4 % CaO
Curves 3 and 4 - 75 % CaF_2 + 5 % Al_2O_3 +20 % CaO

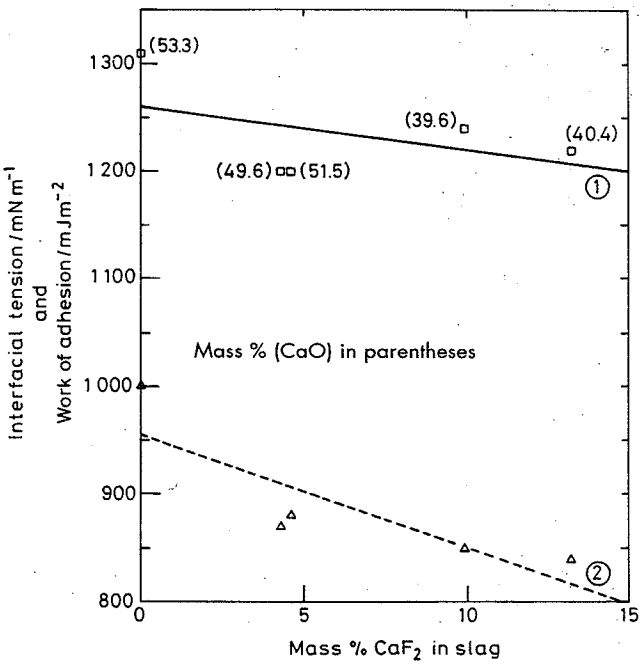
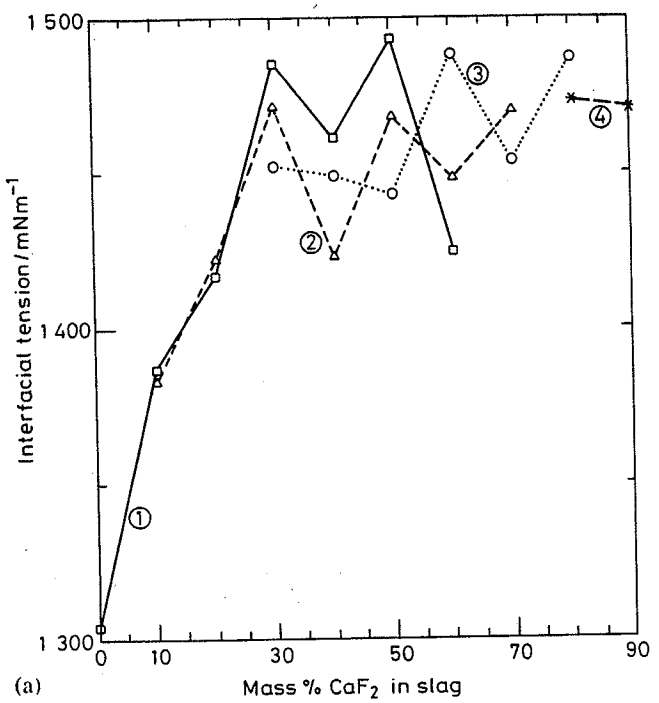
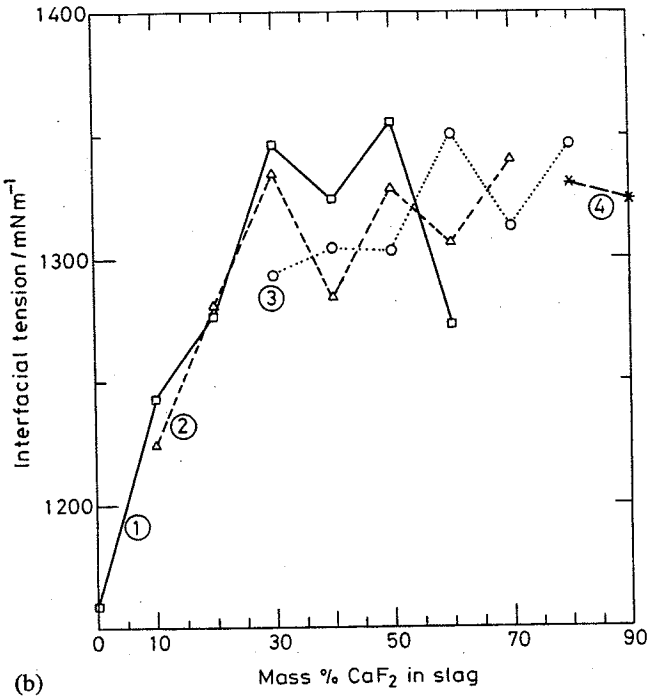


Fig. 11.28. Effect of CaF_2 content in CaF_2 + CaO + Al_2O_3 slags on the interfacial tension (curve 1) and the work of adhesion (curve 2) with steel ShKh15 at 1550 °C [Ref. 28].
Metal composition: M7



(a)



(b)

Fig. 11.29 a,b. Effect of CaF_2 content in $CaF_2 + Al_2O_3 + CaO$ slags on the interfacial tension with (a) steel 100Cr6 and (b) X85WMoCo 6.5.5 at 1550 °C [Ref. 22]. Metal composition: M6

Curve 1 - 40 % Al_2O_3
Curve 2 - 30 % Al_2O_3
Curve 3 - 20 % Al_2O_3
Curve 4 - 10 % Al_2O_3

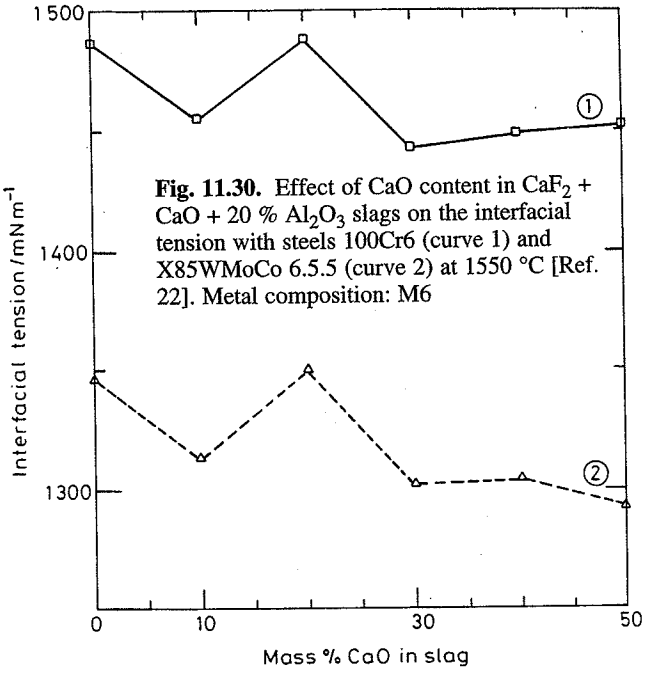
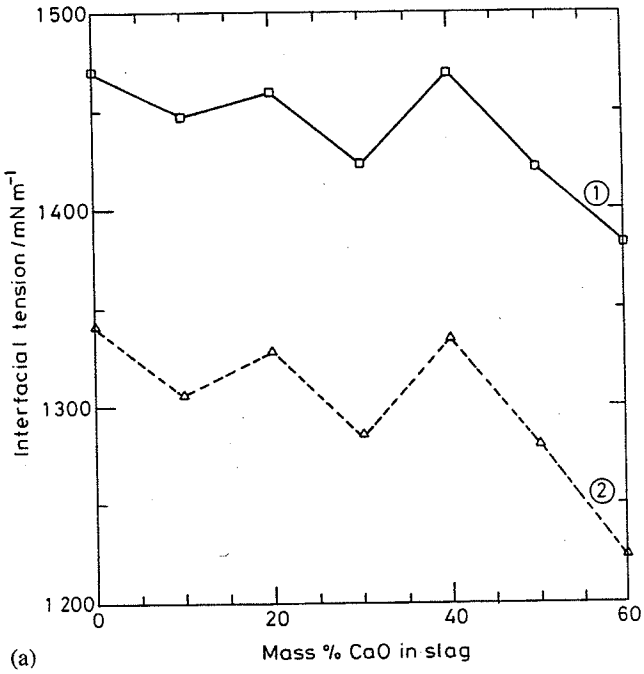
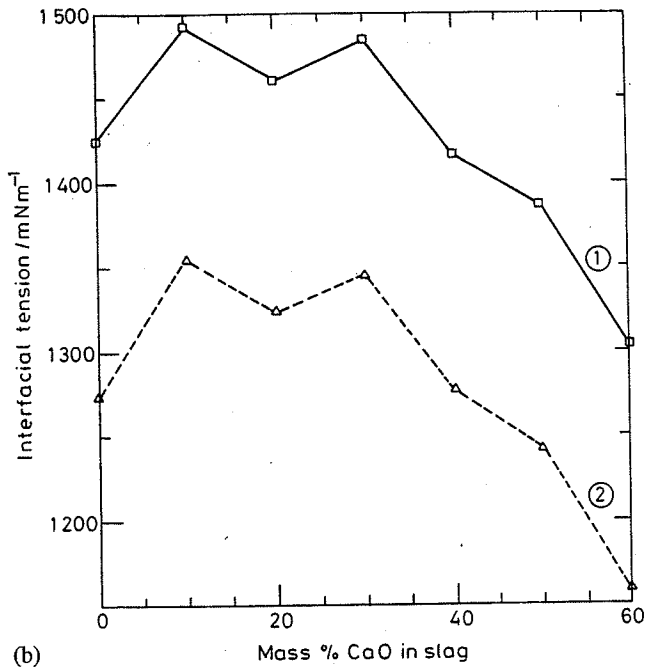


Fig. 11.30. Effect of CaO content in $CaF_2 + CaO + 20\ \% Al_2O_3$ slags on the interfacial tension with steels 100Cr6 (curve 1) and X85WMoCo 6.5.5 (curve 2) at 1550 °C [Ref. 22]. Metal composition: M6



(a)



(b)

▶

Fig. 11.31 a,b. Effect of CaO content (a) in $CaF_2 + CaO + 30\ \% Al_2O_3$ slags and (b) in $CaF_2 + CaO + 40\ \% Al_2O_3$ slags on the interfacial tension with steels 100Cr6 (curve 1) and X85WMoCo 6.5.5 (curve 2) at 1550 °C [Ref. 22]. Metal composition: M6

$CaO\text{-}SiO_2$

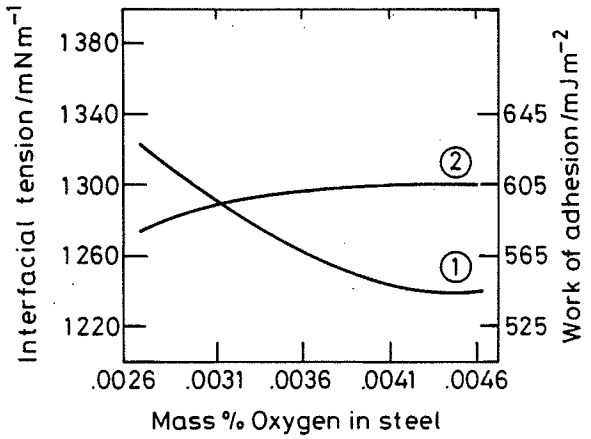
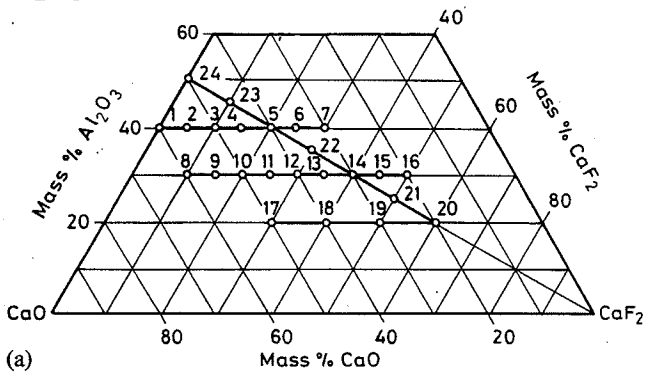
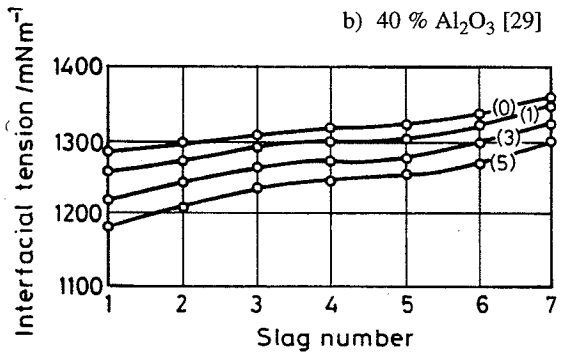


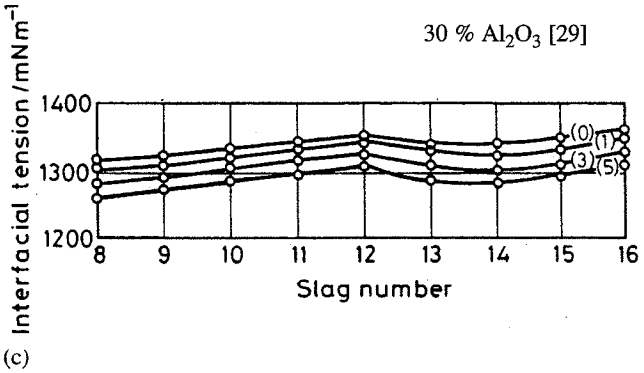
Fig. 11.32. Variation of interfacial tension (curve 1) and work of adhesion (curve 2) between steel ShKh15 and slag (70 % CaF_2 + 15 % CaO + 15 % SiO_2) with the oxygen content of the steel at 1500 °C [Ref. 27]

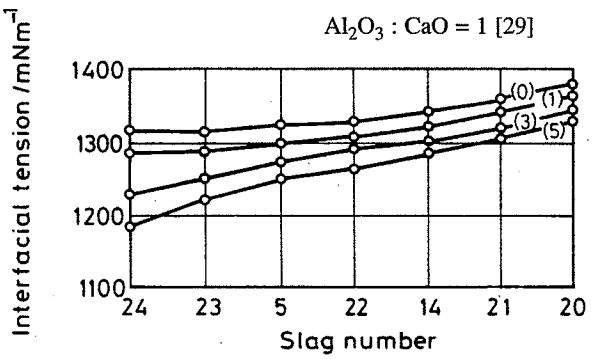
11.4.2.4 Quaternary systems (containing CaF_2)

$Al_2O_3\text{-}CaO\text{-}CaS$









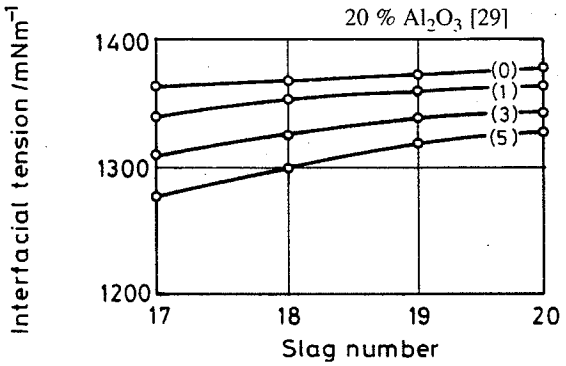
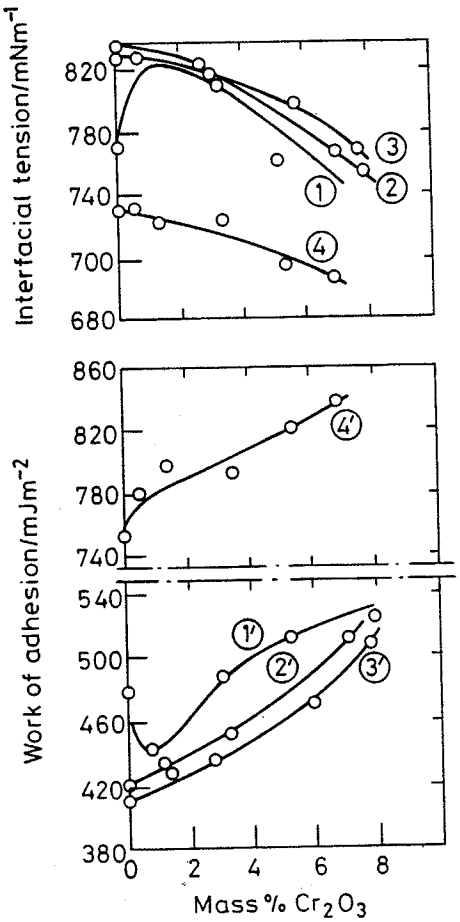


Fig. 11.33 a-e. Effect of CaS additions to CaF_2 + Al_2O_3 + CaO slags at 1600 °C on the interfacial tension with steel H52-3. Slag numbers refer to compositions shown in (a), the respective CaS contents (mass %) are given in parentheses in (b-e) [Ref. 29]

Al_2O_3-CaO-Cr_2O_3



Slag No.	Slag Composition (mass %)				
	CaF_2	CaO	Al_2O_3	BaO	Cr_2O_3
1	97.25	0.72	-	-	-
2	95.37	0.88	-	-	0.69
3	94.52	1.12	-	-	3.00
4	92.67	1.60	-	-	5.08
5	90.25	1.80	-	-	7.78
6	72.52	4.32	-	20.89	-
7	78.38	4.22	-	21.02	1.10
8	69.09	4.22	-	20.82	2.65
9	67.23	3.60	-	19.71	6.90
10	64.65	2.50	30.50	-	-
11	60.19	7.55	30.60	-	1.29
12	55.64	7.98	30.70	-	3.26
13	50.96	10.30	31.54	-	5.82
14	49.54	11.42	30.26	-	7.58
15	4.25	41.98	53.25	-	-
16	4.05	41.67	53.08	-	0.52
17	4.10	41.36	52.56	-	1.41
18	3.89	41.05	51.39	-	3.40
19	3.80	40.75	50.06	-	5.21
20	3.60	38.48	50.84	-	6.68

Fig. 11.34. Effect of Cr_2O_3 additions to CaF_2-containing slags on the interfacial tension and work of adhesion with ferrochrome (~71 % Cr) at 1700 °C [Ref. 30]

Curve 1, 1' - CaF_2 + CaO + Cr_2O_3 (slags 1-5)
Curve 2, 2' - CaF_2 + BaO + CaO + Cr_2O_3 (slags 6-9)
Curve 3, 3' - CaF_2 + Al_2O_3 + CaO + Cr_2O_3 (slags 10-14)
Curve 4, 4' - CaF_2 + Al_2O_3 + CaO + Cr_2O_3 ([CaF_2] ≈ 4 %) (slags 15-20)

Al_2O_3-CaO-SiO_2

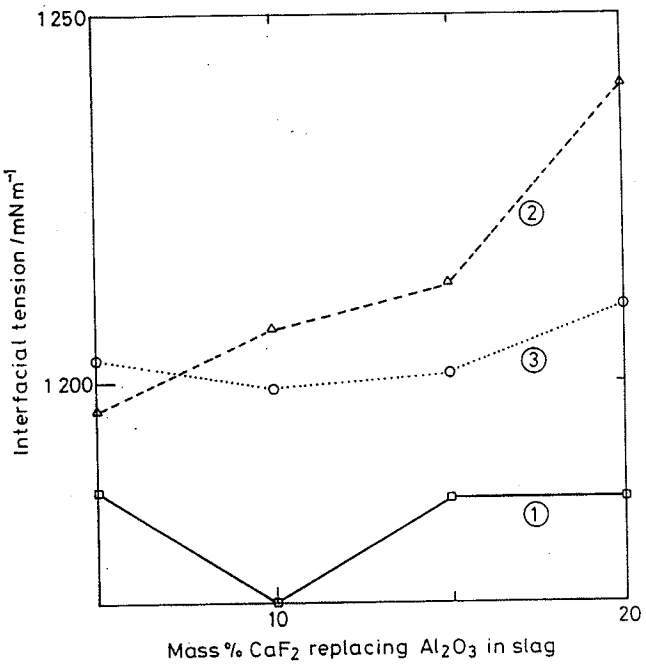


Fig. 11.35. Effect of replacing Al_2O_3 by CaF_2 in Al_2O_3 + CaO + SiO_2 slags, on the interfacial tension with steel at 1550 °C [Ref. 31]. Metal composition: M9

Curve 1 - initial [Al_2O_3] = 25 %; basicity = 1.5
Curve 2 - initial [Al_2O_3] = 30 %; basicity = 2.5
Curve 3 - initial [Al_2O_3] = 50 %; basicity = 4.0

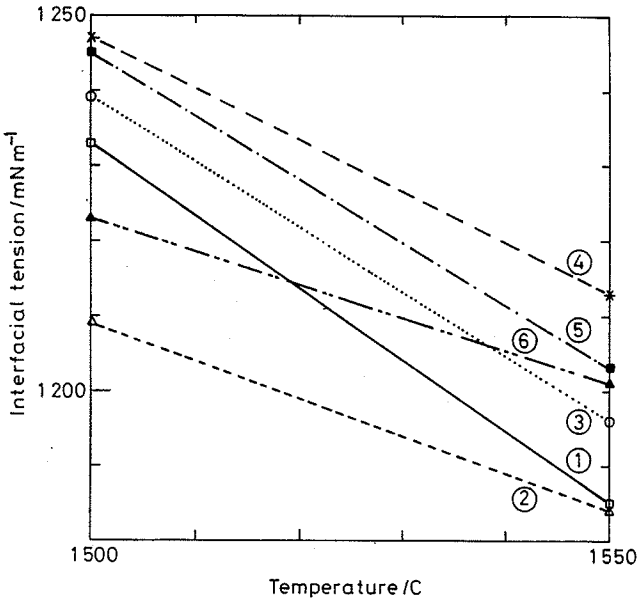


Fig. 11.36. Effect of temperature on the interfacial tension between CaF_2 + Al_2O_3 + CaO + SiO_2 slags and steel [Ref. 31]. Metal composition: M9

Curve 1 - 5 % CaF_2; basicity = 1.5 (45 % CaO)
Curve 2 - 5 % CaF_2; basicity = 2.5 (50 % CaO)
Curve 3 - 5 % CaF_2; basicity = 4.0 (40 % CaO)
Curve 4 - 15 % CaF_2; basicity = 1.5 (45 % CaO)
Curve 5 - 15 % CaF_2; basicity = 2.5 (50 % CaO)
Curve 6 - 15 % CaF_2; basicity = 4.0 (40 % CaO)

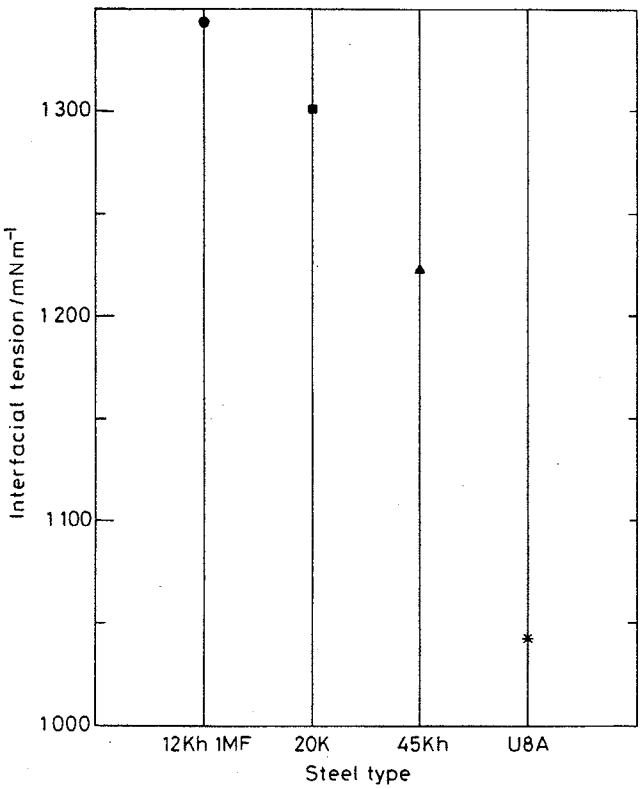


Fig. 11.37. The interfacial tension between various steels and a CaF_2-based slag at 1600 °C [Ref. 32]. (Slag composition: 58.4 % CaF_2 + 21.7 % Al_2O_3 + 1.8 % CaO + 18.1 % SiO_2)

11.4.2.5 Systems with five and more components (containing CaF_2)

Al_2O_3-B_2O_3-CaO-MgO-Na_3AlF_6-SiO_2

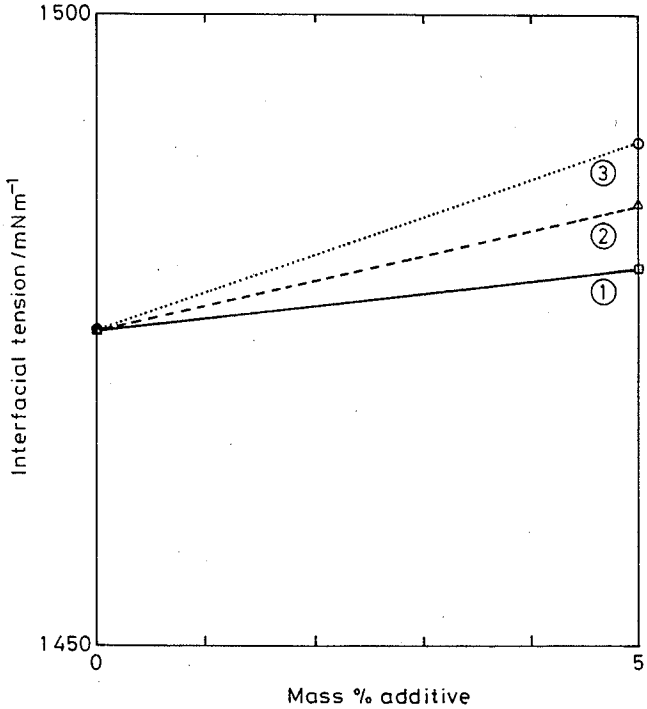
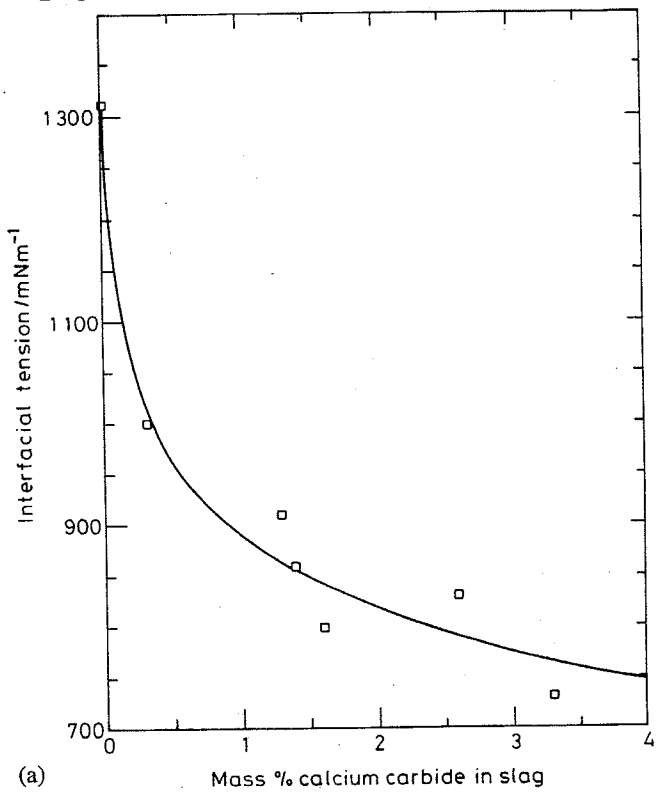


Fig. 11.38. Effect of B_2O_3; CaF_2 and Na_3AlF_6 additions to slag (15% Al_2O_3 + 52 % CaO + 13 % MgO + 20 % SiO_2) on the interfacial tension with iron at 1630 °C [Ref. 33]

Curve 1 - B_2O_3
Curve 2 - CaF_2
Curve 3 - Na_3AlF_6

Al_2O_3-CaC_2-CaO-MgO-SiO_2



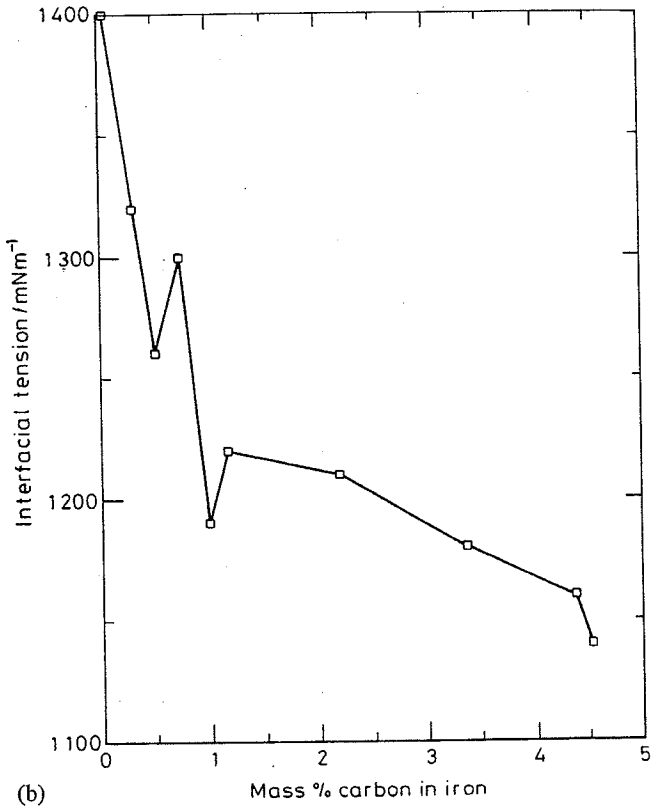
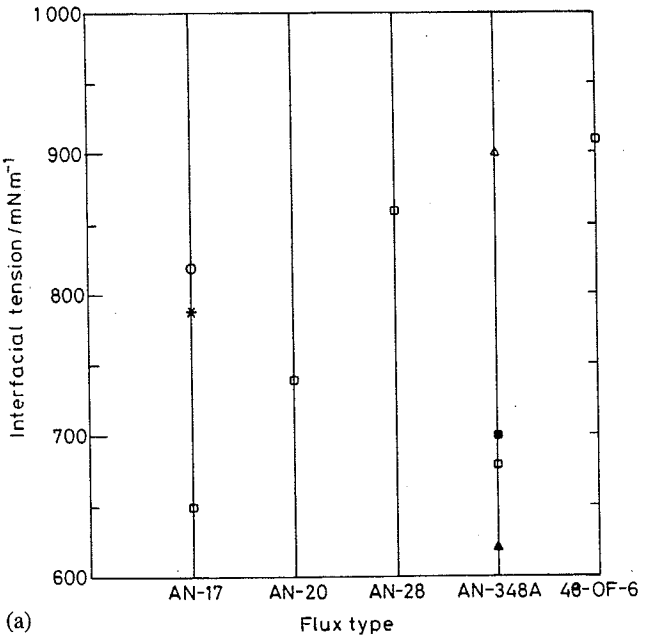
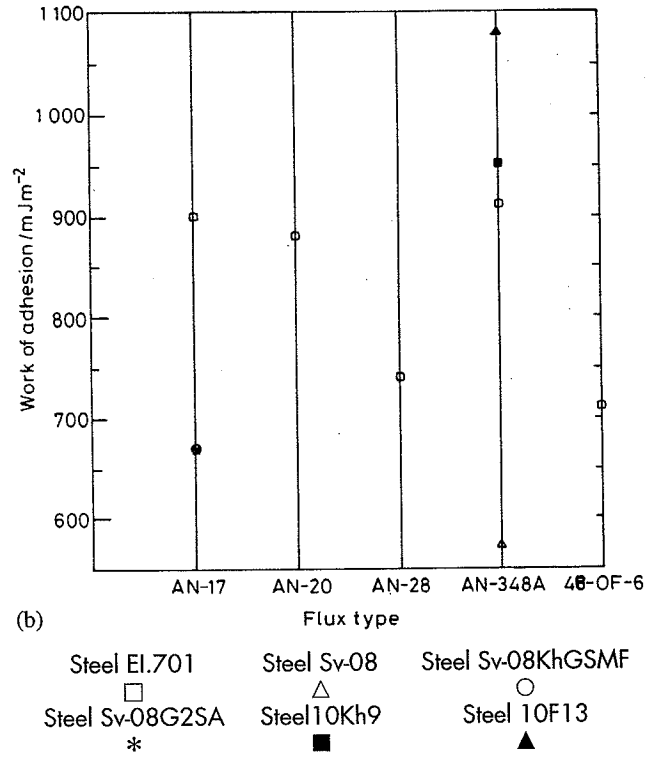


Fig. 11.39 a,b. Effect of CaC_2 (a) in slag and (b) of carbon content in iron on the interfacial tension (a) with pure iron and (b) with slag at 1560 °C [Ref. 35]. Metal composition: M11. Slag composition (mass %): 16.7 CaF_2, 3.7 Al_2O_3, 50 CaO, 10 MgO, 20 SiO_2

Al_2O_3-CaO-FeO-K_2O-MgO-MnO-SiO_2



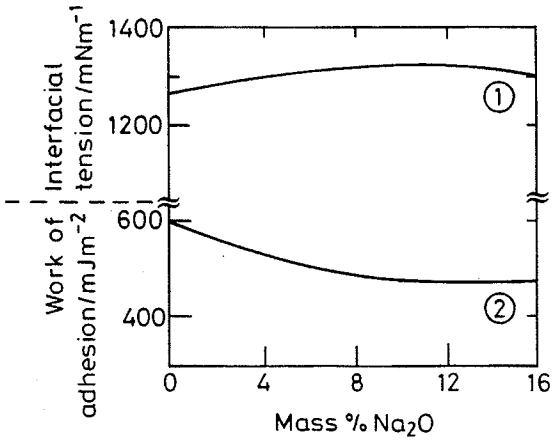


Flux	Mass % CaF_2	Al_2O_3	CaO	MgO	SiO_2	MnO	K_2O	FeO
48-0F-6	52.2	24	19.6	3	2	-	-	-
AN-20	29.8	30	6	10	21	-	2	-
AN-28	14	39	36.8	-	8	-	2.4	-
An-358A	4.4	2.6	4.7	7.7	41	37	-	2
(AN-17)*	19.3	25	15	9.8	18	4.4	-	8

* Analysis of AN-17 is not quoted in Ref. 38 and the above composition is taken from Ref. 23

Fig. 11.40 a,b. The interfacial tension (a) and the work of adhesion (b) between alloy steels and various welding fluxes [Ref. 38]. Metal composition: M13

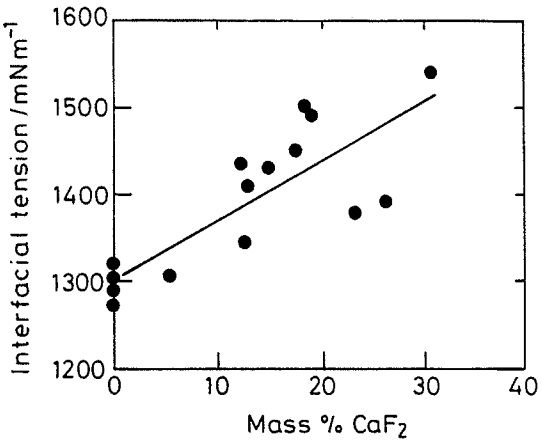
Al_2O_3-CaO-MgO-Na_2O-SiO_2



Slag Composition (mass %)					
CaO	SiO_2	Al_2O_3	MgO	CaF_2	Na_2O
18.4	20.5	32.3	5.5	23.3	-
17.7	19.7	30.6	5.4	22.4	4.2
16.6	18.3	28.6	5.1	21.6	10.4
15.6	17.2	27.2	4.5	19.5	16.0

Fig. 11.41. Effect of Na_2O content in oxide slags (containing 20 - 30 % CaF_2) on the interfacial tension (curve 1) and the work of adhesion (curve 2) with steel 12KhMFK at 1600 °C [Ref. 37]

Al_2O_3-CaO-MgO-SiO_2



Composition of slags (mass %)						γ/mN.m^{-1}
CaO	SiO_2	Al_2O_3	CaF_2	MgO	FeO	
31.4	39.1	5.8	-	20.4	-	1320
31.1	38.5	6.2	-	21.1	0.43	1304
32.3	39.7	6.0	-	16.9	0.50	1271
32.3	48.3	11.1	-	-	0.54	1290
29.1	35.7	5.2	5.2	19.5	0.36	1306
26.3	27.8	28.0	12.2	-	0.17	1424
28.3	32.1	4.9	12.5	18.0	0.26	1346
26.1	29.0	27.3	12.7	-	0.17	1407
26.8	27.3	4.8	14.7	20.2	0.25	1430
27.2	23.7	4.0	17.3	18.3	0.30	1449
18.6	27.2	3.6	18.2	28.2	0.28	1499
17.6	28.4	3.6	18.8	27.0	0.36	1490
31.3	28.1	5.3	23.0	bal	-	1378
27.1	28.9	9.9	26.0	-	0.18	1392
27.6	31.1	5.3	30.4	bal	0.15	1540

Fig. 11.42. Effect of CaF_2 additions to Al_2O_3 + CaO + MgO + SiO_2 slags, on the interfacial tension with pure iron at 1600 °C [Ref. 34]. Metal composition: M10

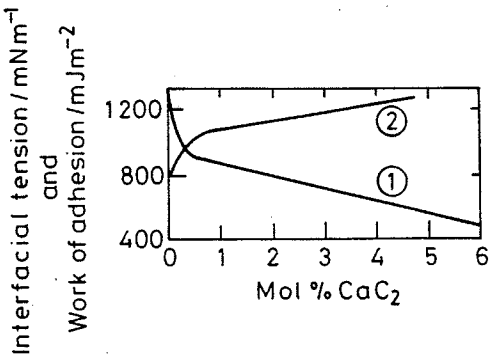


Fig. 11.43. Effect of CaC_2 in slag on the interfacial tension (curve 1) and the work of adhesion (curve 2) with steel at 1550 °C [Ref. 36]. (Slag composition (mass %): 20 CaF_2 + 3 Al_2O_3 + 47 CaO + 10 MgO + 20 SiO_2)

11.4.3.1 Binary systems

Al_2O_3-CaO

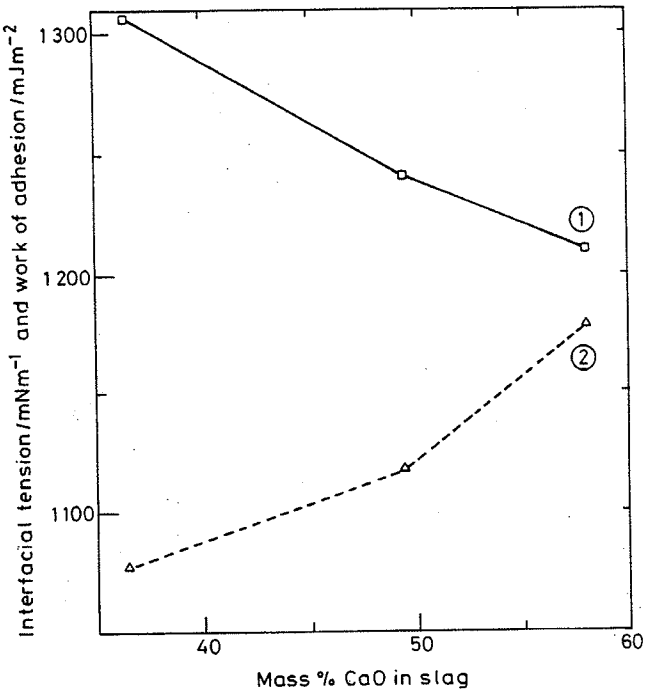


Fig. 11.44. Effect of CaO content in Al_2O_3 + CaO slags on the interfacial tension (curve 1) and work of adhesion (curve 2) with pure iron at 1600 °C [Ref. 39]

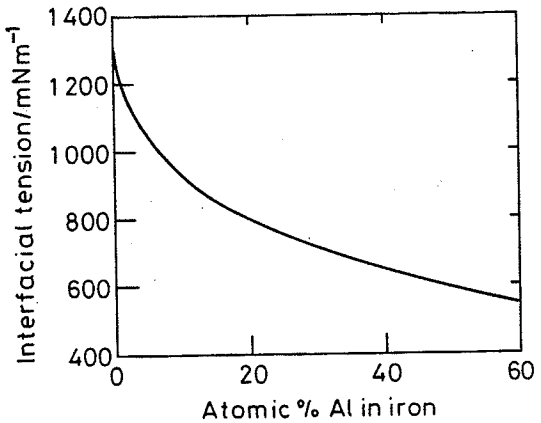
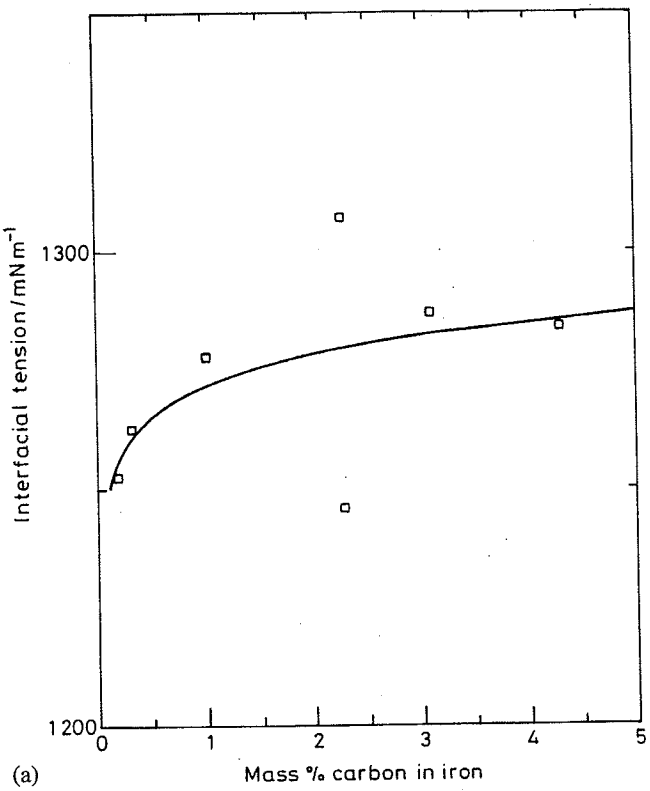


Fig. 11.45. Variation of the interfacial tension between Fe + Al alloys and slag (60 % Al_2O_3 + 40 % CaO), with the aluminium content of the alloy at 1650 °C [Ref. 40]



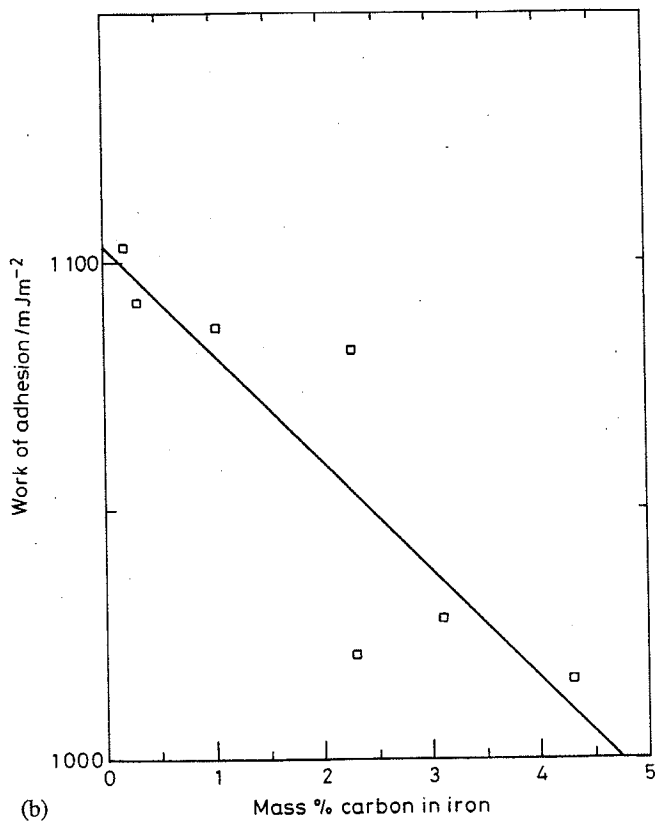


Fig. 11.46 a,b. Effect of carbon content of iron (a) on the interfacial tension and (b) on the work of adhesion with slag (50 % Al_2O_3 + 50 % CaO) at 1600 °C [Ref. 41]

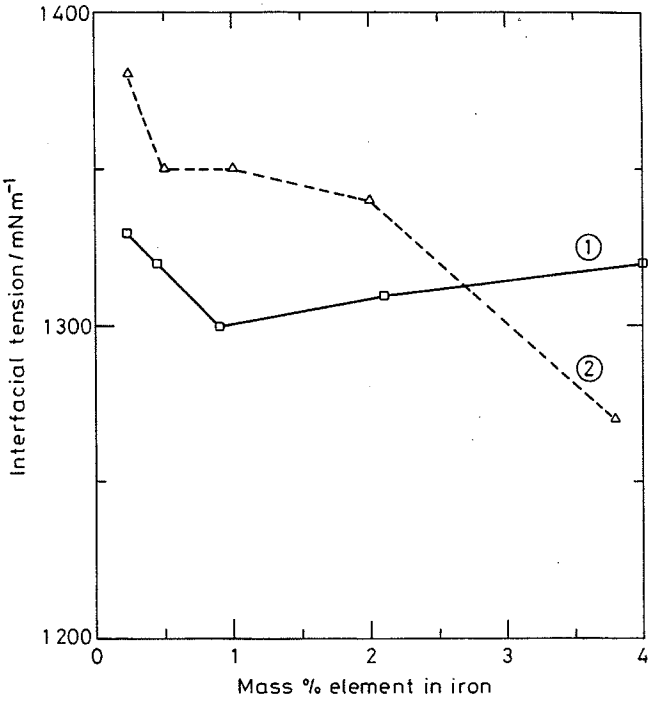


Fig. 11.47. Effect of silicon (curve 1) and carbon (curve 2) in iron on the interfacial tension with slag (53.2 % Al_2O_3 + 46.8 % CaO) under hydrogen at 1550-1600 °C [Ref. 42]

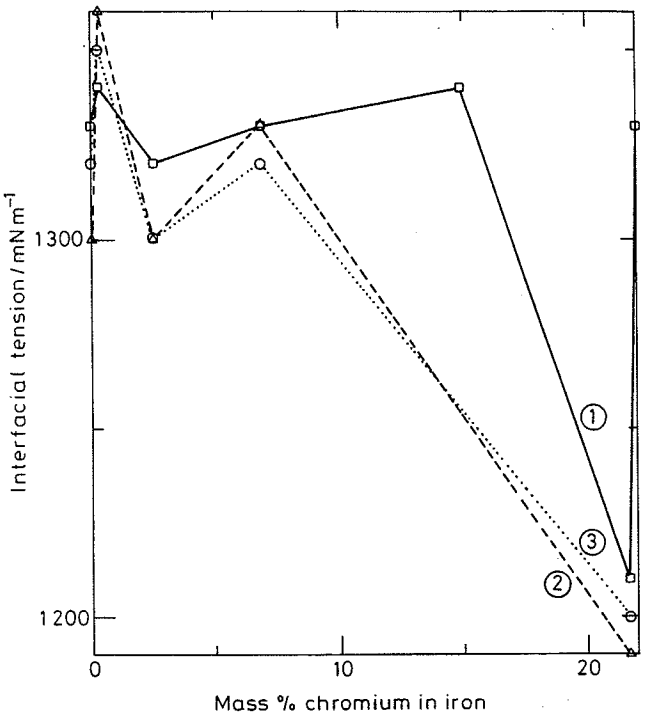


Fig. 11.50. Effect of chromium content in iron on the interfacial tension with slag (53.2 % Al_2O_3 + 46.8 % CaO) at 1550-1600 °C under hydrogen (curve 1), vacuum (curve 2) and nitrogen (curve 3) [Ref. 42]

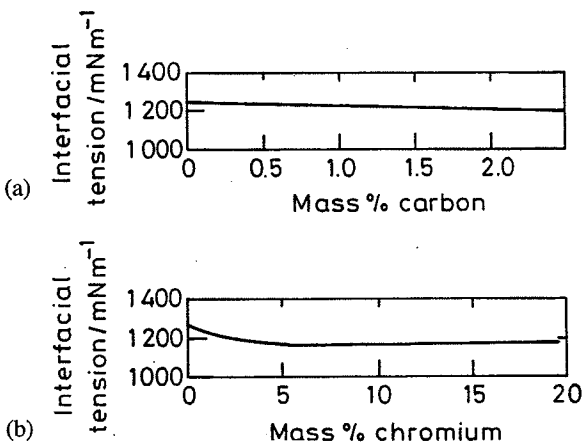


Fig. 11.48 a,b. Effect of (a) carbon and (b) chromium content in iron on the interfacial tension with slag (50 % Al_2O_3 + 50 % CaO) at 1570 °C. Measurements made within 0.5 seconds of the contact between the two liquids [Ref. 43]

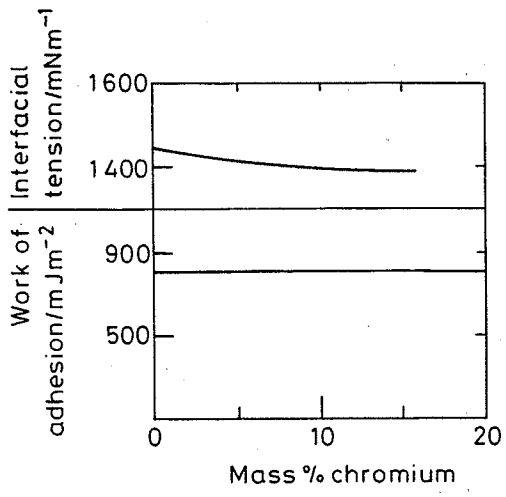


Fig. 11.51. Effect of chromium concentration in iron on the interfacial tension and work of adhesion with slag (50 % Al_2O_3 + 50 % CaO) at 1600 °C [Ref. 21]

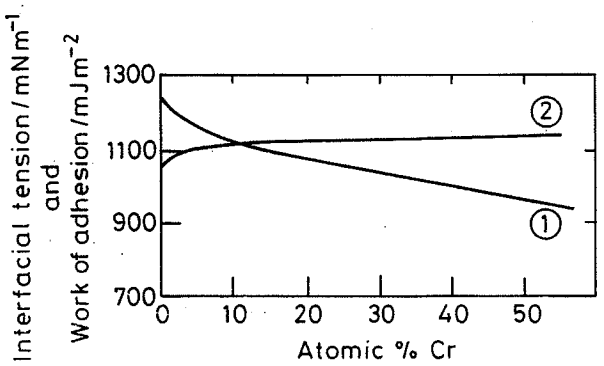


Fig. 11.49. Effect of chromium concentration in iron on the interfacial tension (curve 1) and work of adhesion (curve 2) with slag (60 % Al_2O_3 + 40 % CaO) at 1650 °C [Ref. 44]

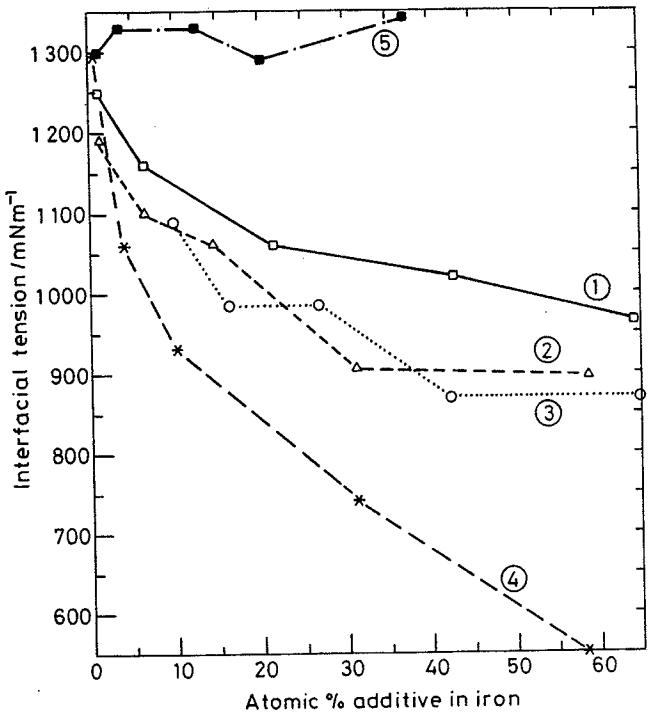


Fig. 11.52. Effect of the composition of some iron binary alloys on the interfacial tension with slag (60 % Al_2O_3 + 40 % CaO) at 1650 °C [Ref. 45]

Curve 1 - Fe + Cr
Curve 3 - Fe + V
Curve 5 - Fe + Mo
Curve 4 - Fe + Al
Curve 2 - Fe + Nb

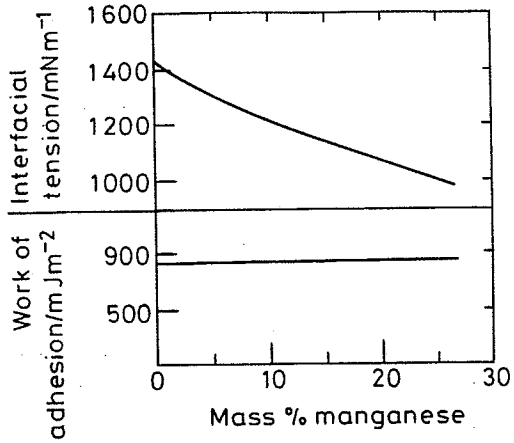


Fig. 11.53. Interfacial tension and work of adhesion between Fe + Mn alloys and slag (50 % Al_2O_3 + 50 % CaO) at 1600 °C [Ref. 21]

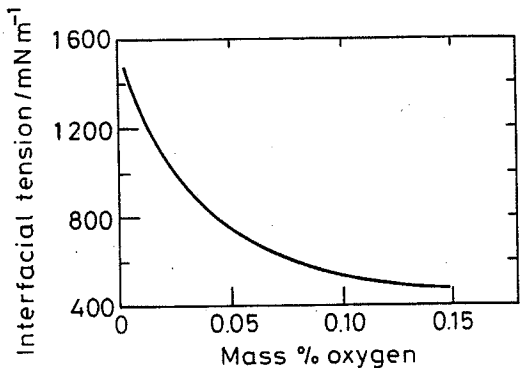


Fig. 11.54. Variation of the interfacial tension between iron and slag (50 % Al_2O_3 + 50 % CaO) with the oxygen content of the metal at 1570 °C [Ref. 43]

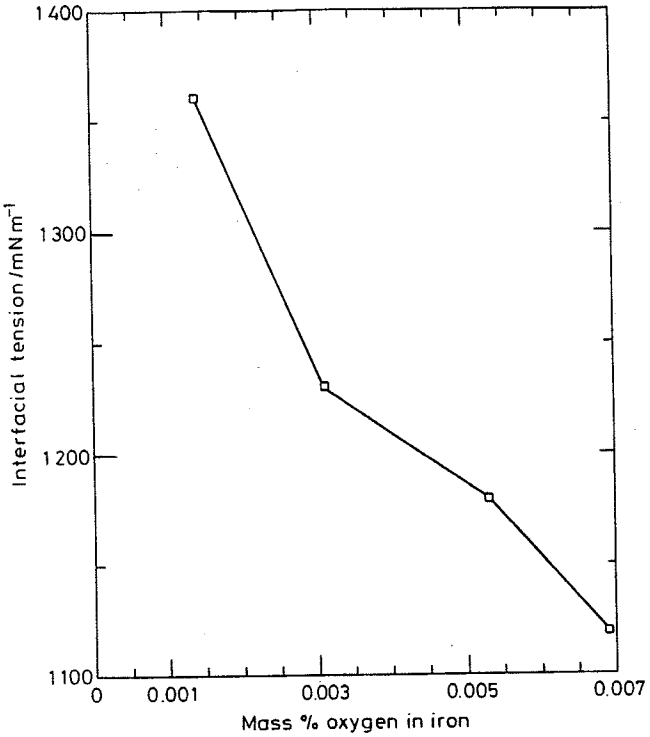


Fig. 11.55. Effect of oxygen in iron on the interfacial tension with slag (53.2 % Al_2O_3 + 46.8 % CaO) at 1550-1660 °C under hydrogen [Ref. 42]

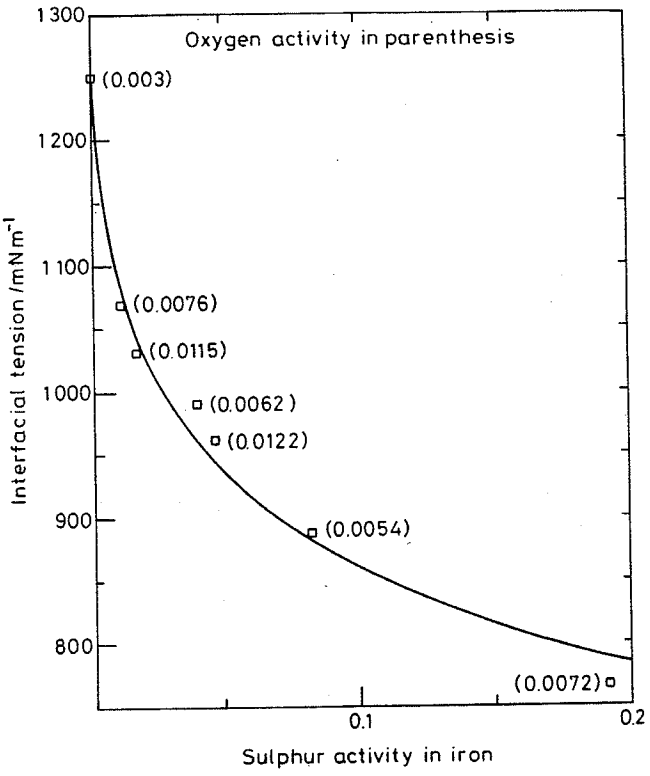


Fig. 11.56. Effect of sulphur activity in molten iron on the interfacial tension with slag (approximately 50 % Al_2O_3 + 50 % CaO) at 1660 °C [Ref. 26]

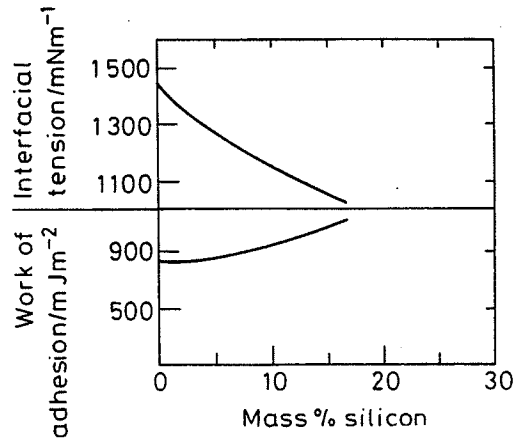


Fig. 11.57. Interfacial tension and work of adhesion between Fe + Si alloys and slag (50 % Al_2O_3 + 50 % CaO) at 1600 °C [Ref. 21]

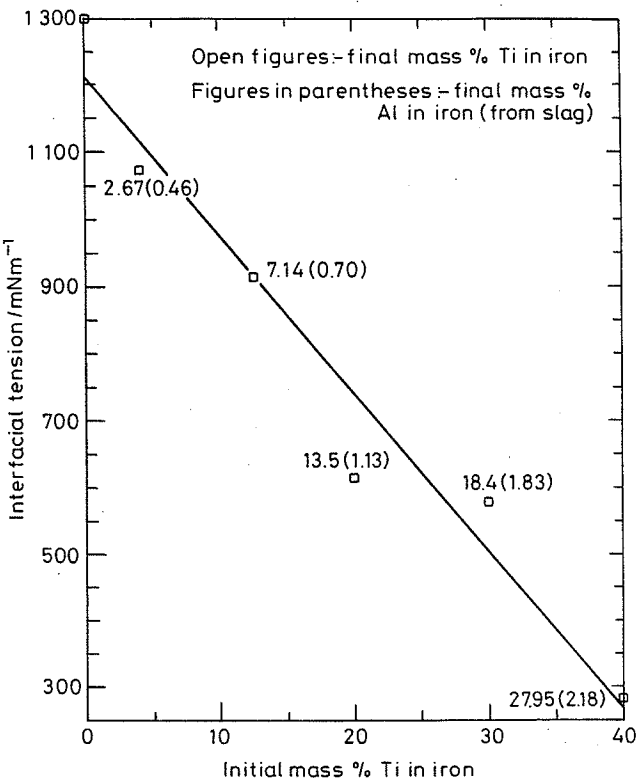


Fig. 11.58. Effect of titanium content in iron on the equilibrium interfacial tension with slag (60 % Al_2O_3 + 40 % CaO) at 1650 °C [Ref. 40]

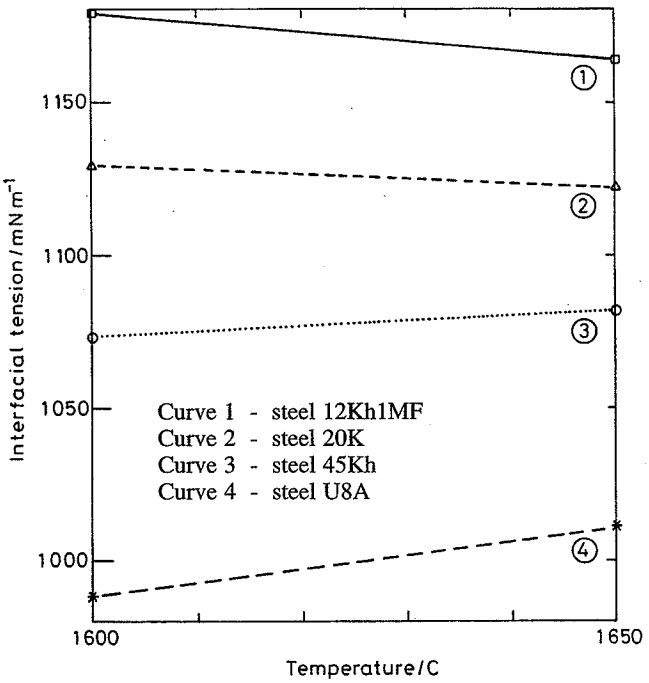


Fig. 11.59. Effect of temperature on the interfacial tension between steels and slag (43 % Al_2O_3 + 57 % CaO) [Ref. 32]

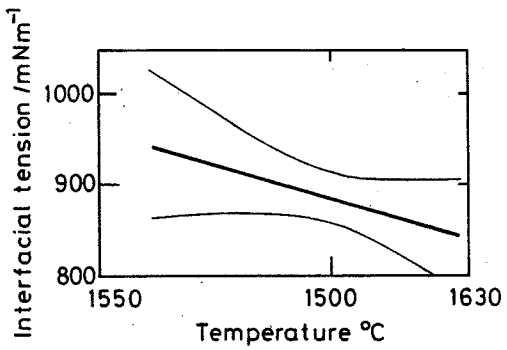


Fig. 11.61. Variation with temperature of the interfacial tension between carbon-saturated iron and slag (60 % Al_2O_3 + 40 % CaO). Faint lines show 95 % confidence range [Ref. 46]

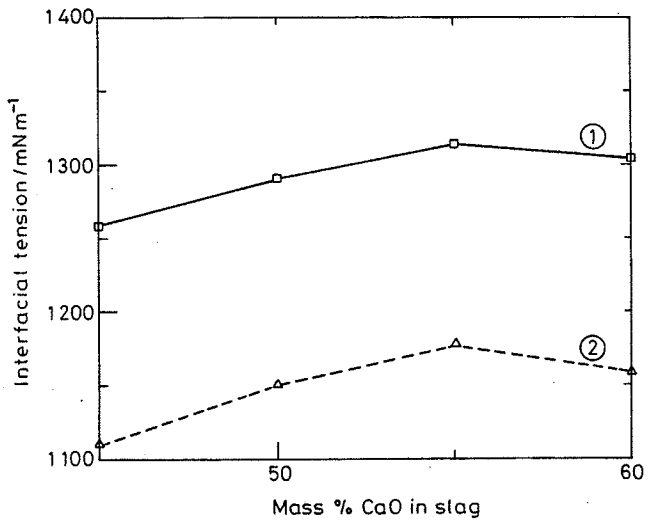


Fig. 11.60. Effect of CaO content in Al_2O_3 + CaO slag on the interfacial tension with steels 100Cr6 (curve 1) and X85WMoCo6.5.5 (curve 2) at 1550 °C [Ref. 22]. Metal composition: M6

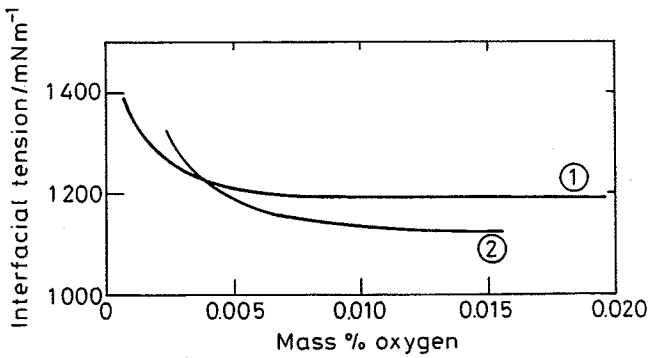


Fig. 11.62. Relation between the initial oxygen content of liquid iron and the interfacial tension with slag (55 % CaO + 45 % Al_2O_3). Interfacial tension measured within 0.5 seconds after contact between the liquids. Curve 1 - 1550 °C; curve 2 - 1600 °C [Ref. 47]

$CaO\text{-}SiO_2$

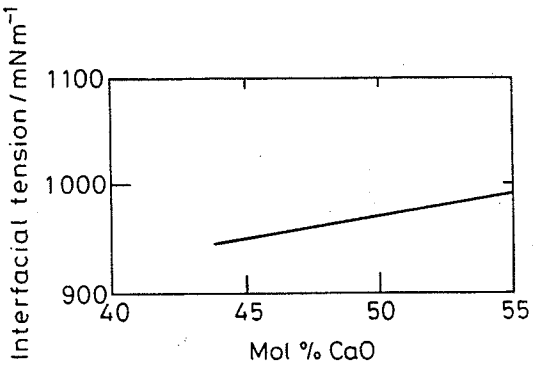


Fig. 11.63. Effect of CaO content in CaO + SiO_2 slags on the interfacial tension with Fe + 4.3 % C alloy at 1570 °C [Ref. 48]

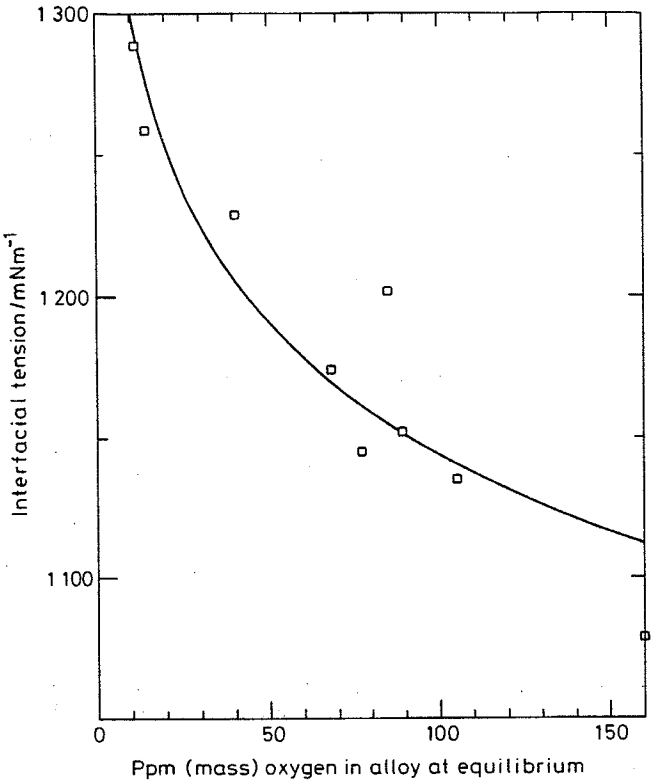


Fig. 11.64. Effect of the equilibrium oxygen content of dilute Fe + Si + O alloys on the equilibrium interfacial tension with slag (% CaO : % SiO_2 ~ 1.0) at 1550 °C [Ref. 47]

$Fe_xO\text{-}MnO$

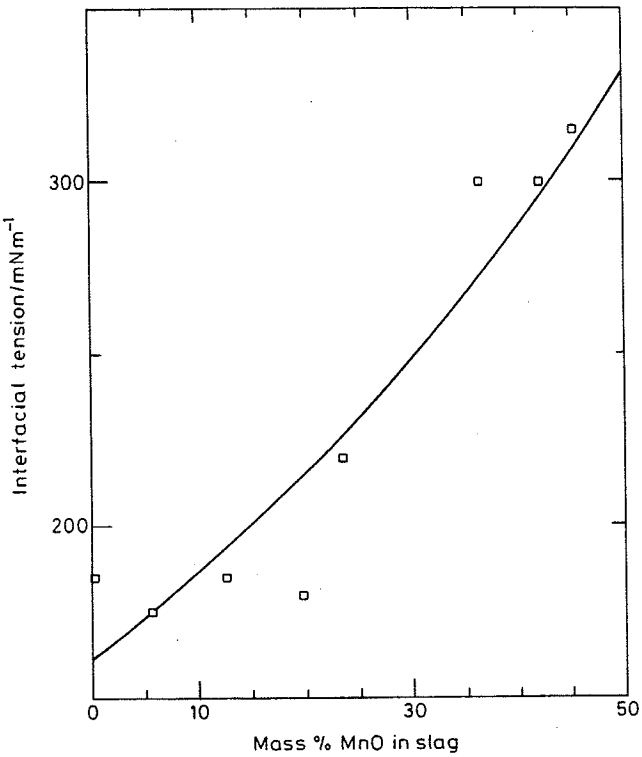


Fig. 11.65. The effect of replacing (FeO + Fe_2O_3) by MnO in slags (which contain small amounts of CaO + MgO + SiO_2) on the interfacial tension with iron at 1550 °C [Ref. 49]. Metal composition: M14

$MnO\text{-}SiO_2$

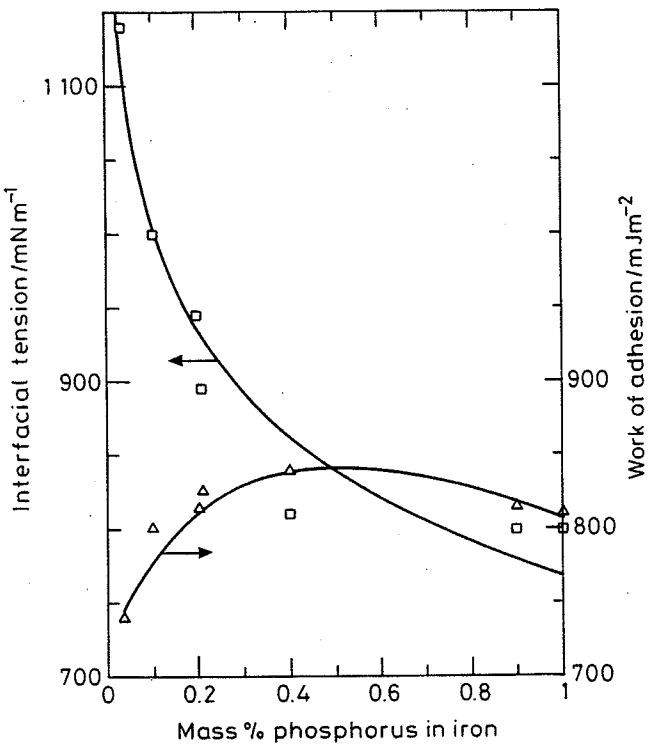


Fig. 11.66. Effect of phosphorous content in iron on the interfacial tension and work of adhesion with slag (64.4 % MnO + 35.4 % SiO_2) at 1500 °C [Ref. 50]. Metal composition: M15

11.4.3.2 Ternary systems

Al_2O_3-CaO-FeO

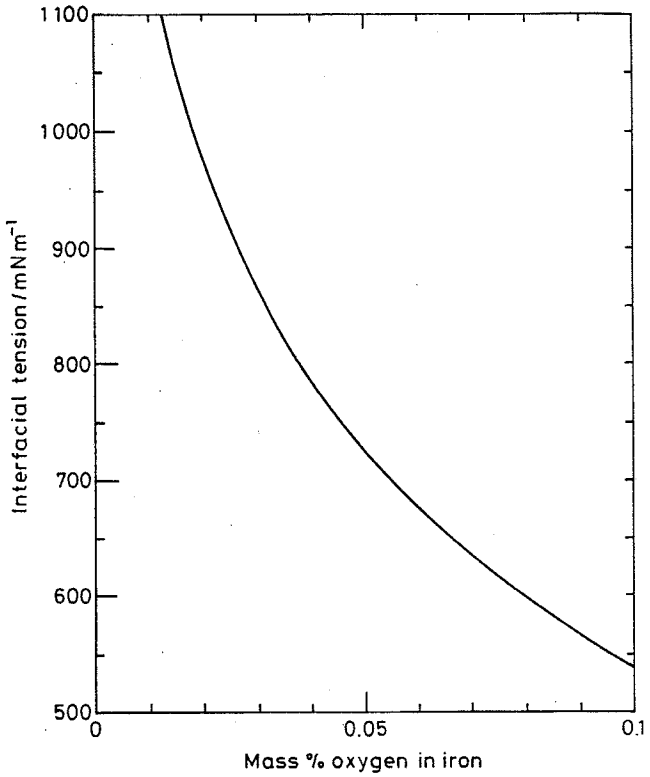


Fig. 11.67. Effect of oxygen content in liquid iron on the interfacial tension with slag (46.5 % Al_2O_3 + 46.5 % CaO + 7 % FeO) at 1580 °C [Ref. 52]

Al_2O_3-CaO-SiO_2

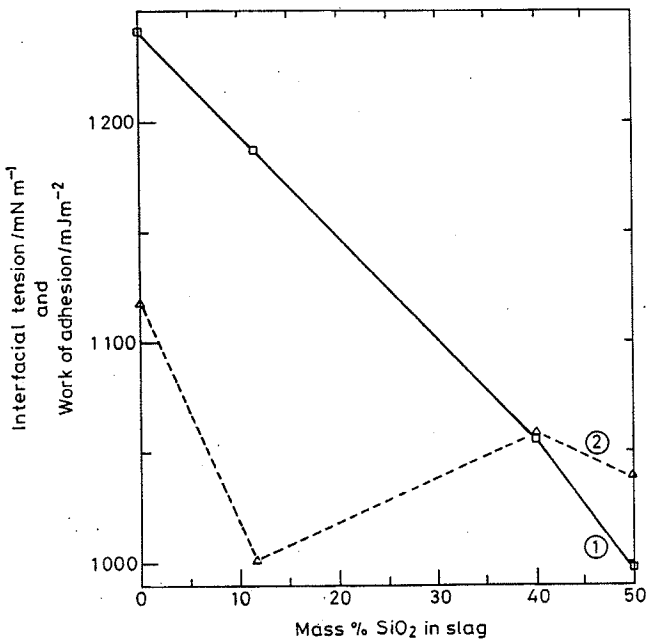


Fig. 11.68. Effect of SiO_2 content in Al_2O_3 + CaO + SiO_2 slags (approximately 50 % CaO) on the interfacial tension (curve 1) and work of adhesion (curve 2) with pure iron at 1600 °C [Ref. 39]

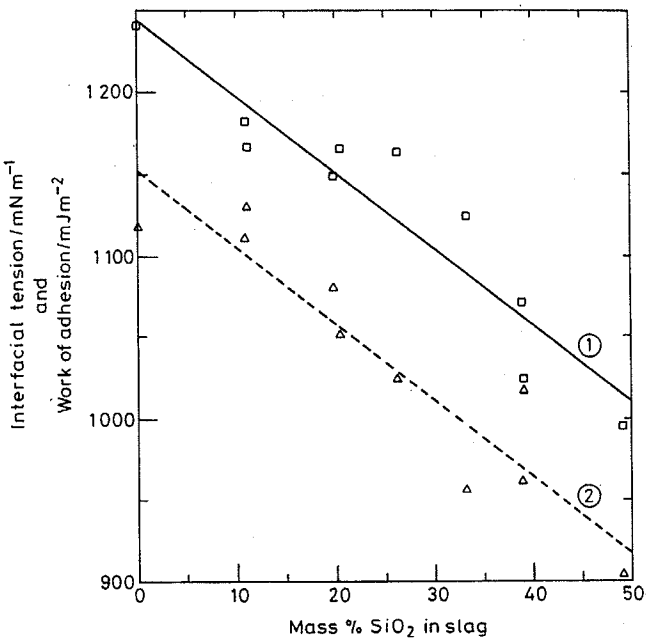


Fig. 11.69. Effect of SiO_2 level in Al_2O_3 + CaO + SiO_2 slags (mass ratio Al_2O_3 : CaO = 1) on the interfacial tension (curve 1) and the work of adhesion (curve 2) with pure iron at 1600 °C [Ref. 53]

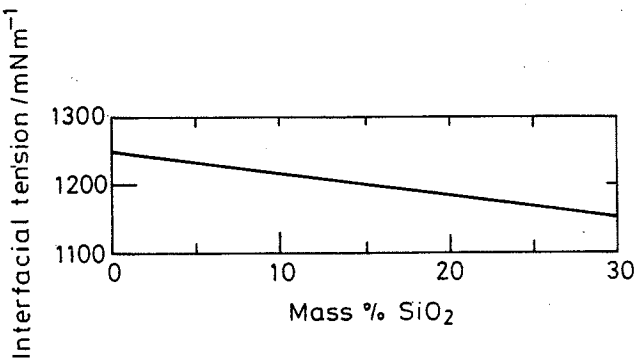


Fig. 11.70. Effect of SiO_2 in Al_2O_3 + CaO + SiO_2 slags (Al_2O_3 : CaO = 1) on the interfacial tension with iron at 1570 °C. Interfacial tension determined within 0.5 seconds after mutual contact [Ref. 43]

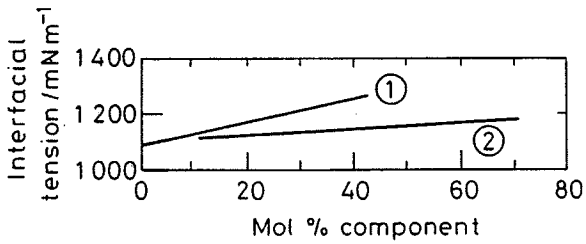


Fig. 11.71. Effect of Al_2O_3 levels in Al_2O_3 + 40 mol % CaO + SiO_2 (curve 1), and of CaO levels in 13 mol % Al_2O_3 + CaO + SiO_2 (curve 2), on the interfacial tension with iron at 1580 °C [Ref. 54]

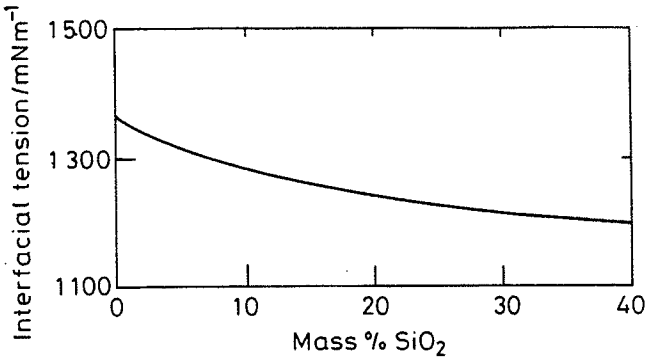


Fig. 11.72. Effect of SiO_2 content in Al_2O_3 + 46.8 mass % CaO + SiO_2 slags on the interfacial tension with iron at 1550-1600 °C [Ref. 42]

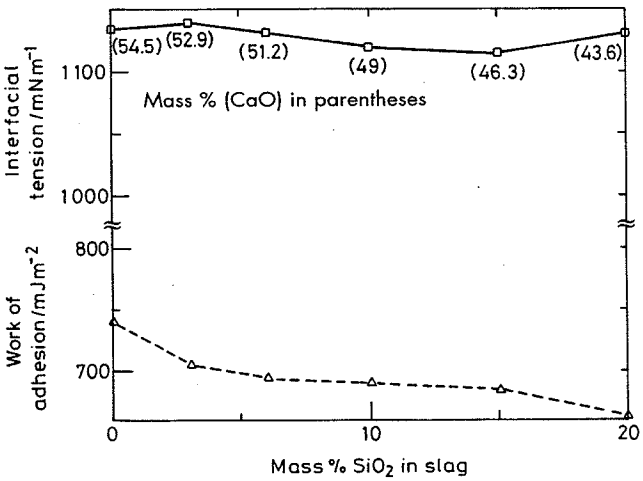


Fig. 11.73. Effect of SiO_2 content in Al_2O_3 +CaO + SiO_2 slags on the interfacial tension and the work of adhesion (dashed line) with Armco iron at 1600 °C [Ref. 55]. Metal composition: M16

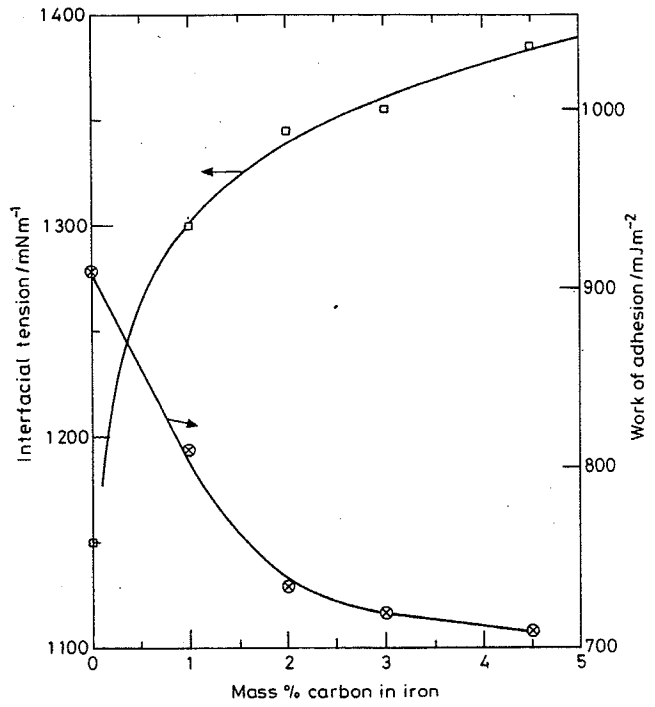


Fig. 11.74. Interfacial tension and work of adhesion between Fe + C alloys and slag containing 20 % Al_2O_3 + 40 % CaO + 40 % SiO_2 at 1350-1500 °C [Ref. 56]

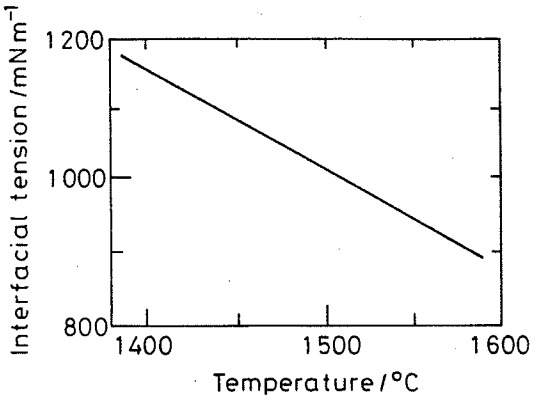


Fig. 11.75. Effect of temperature on the interfacial tension between Fe + 4.3 mass % C alloys and slag (15 mol % Al_2O_3 + 45 mol % CaO + 40 mol % SiO_2) [Ref. 48]

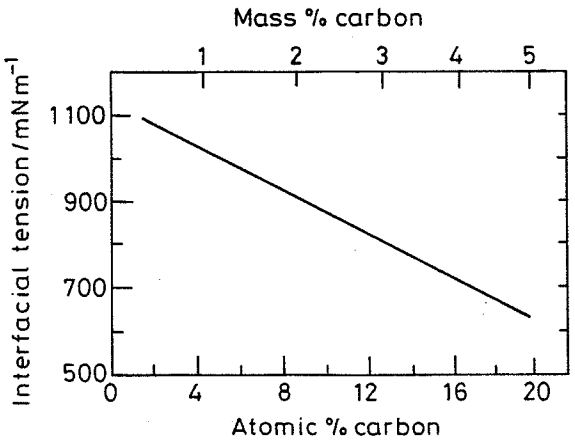


Fig. 11.76. Effect of carbon in iron on the interfacial tension with slag (26 % Al_2O_3 + 39 % CaO + 36 % SiO_2) at 1450-1500 °C [Ref. 57]

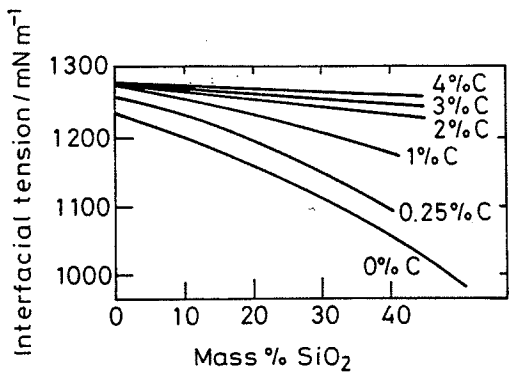


Fig. 11.77. Effect of SiO_2 in Al_2O_3 + CaO + SiO_2 slags (Al_2O_3 : CaO = 1) on the interfacial tension with Fe + C alloys at 1600 °C [Ref. 41]

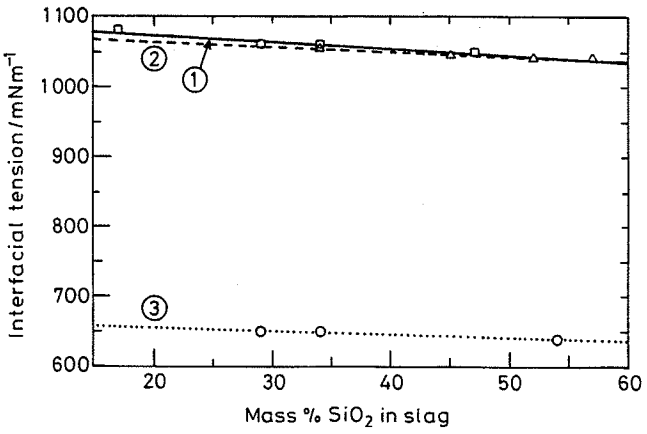


Fig. 11.78. Effect of SiO_2 content in Al_2O_3 + CaO + SiO_2 slags on the interfacial tension with Fe + C alloys [Ref. 58]

Curve 1 - 21 % Al_2O_3/0.6 % C at 1570-1620 °C
Curve 2 - 16 % Al_2O_3/0.6 % C at 1580-1600 °C
Curve 3 - 21 % Al_2O_3/4.4 % C at 1520-1540 °C

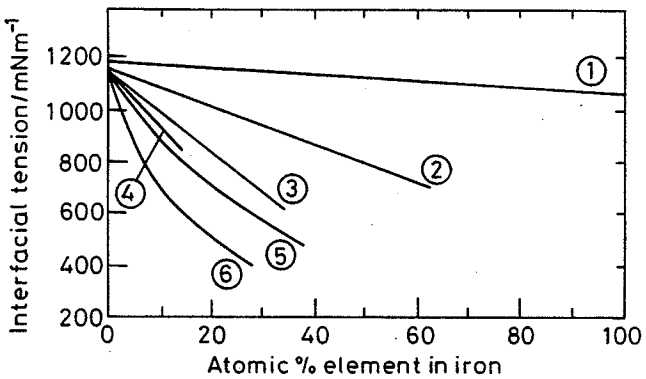


Fig. 11.79. Effect of additives to iron on the interfacial tension with Al_2O_3 + CaO + SiO_2 slags at 1560 °C [Ref. 59]

Curve 1 - Fe + Mn/12 % Al_2O_3 + 25 % CaO + 65 % SiO_2
Curve 2 - Fe + Si/18 % Al_2O_3 + 46 % CaO + 36 % SiO_2
Curve 3 - Fe + P/26 % Al_2O_3 + 39 % CaO + 35 % SiO_2
Curve 4 - Fe + C/26 % Al_2O_3 + 39 % CaO + 35 % SiO_2
Curve 5 - Fe + V/18 % Al_2O_3 + 46 % CaO + 36 % SiO_2
Curve 6 - Fe + Ti/18 % Al_2O_3 + 46 % CaO + 36 % SiO_2

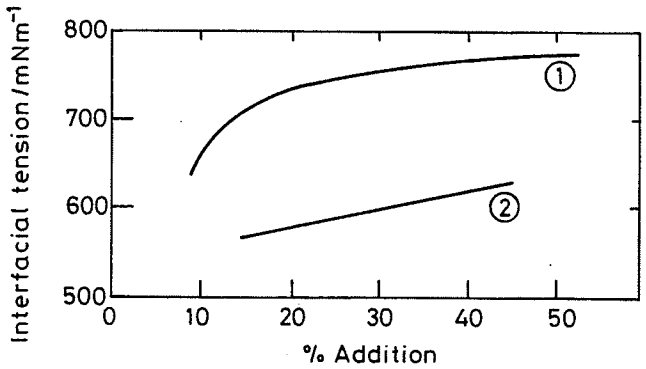


Fig. 11.80. Variation of the interfacial tension between Al_2O_3 + CaO + SiO_2 slags and pig iron [Ref. 60]

Curve 1 - Effect of Al_2O_3 content in slag (CaO = 47 %) on interfacial tension with industrial pig iron (3.45 % C; 2.2 % Si; 0.64 % Mn; 0.26 % P) at 1420 °C

Curve 2 - Effect of CaO content in slag (Al_2O_3 = 26 %) on interfacial tension with synthetic pig iron (4.6 % C; 0.4 % Si) at 1500 °C (Al_2O_3 + CaO + SiO_2 = 100 %)

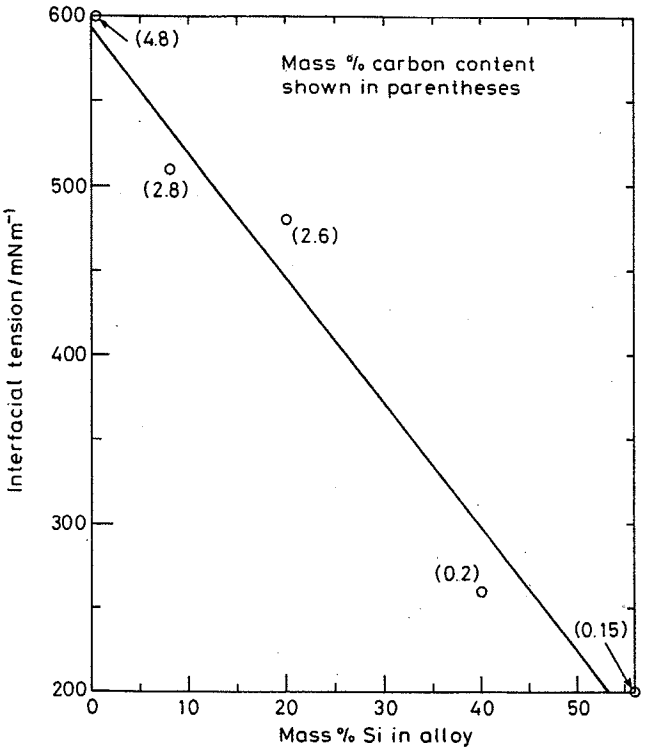


Fig. 11.81. Effect of silicon content in Fe + C + Si alloys on the interfacial tension with slag (26 % Al_2O_3 + 26 % CaO + 48 % SiO_2) at about 1450 °C [Ref. 60]

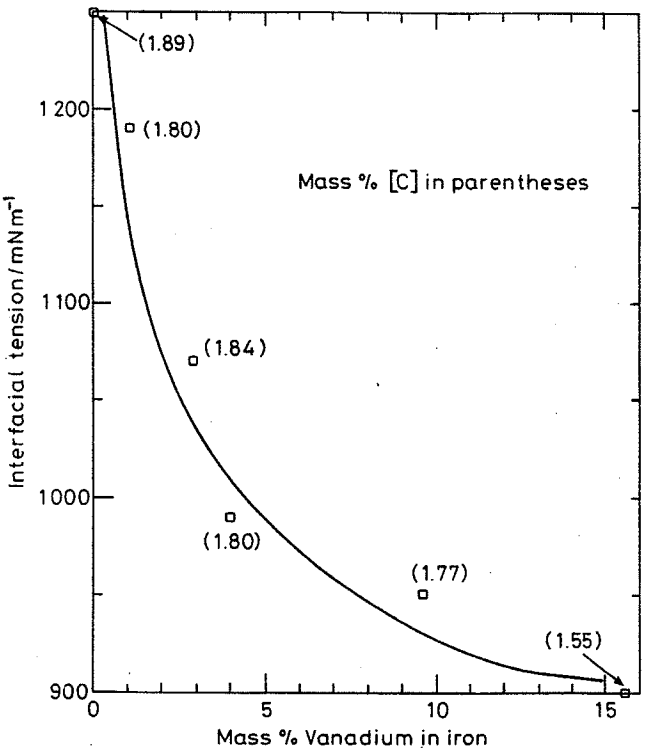


Fig. 11.82. Effect of vanadium content in Fe + C + V alloys on the interfacial tension with slag (20 % Al_2O_3 + 40 % CaO + 40 % SiO_2) at about 1450 °C [Ref. 61]

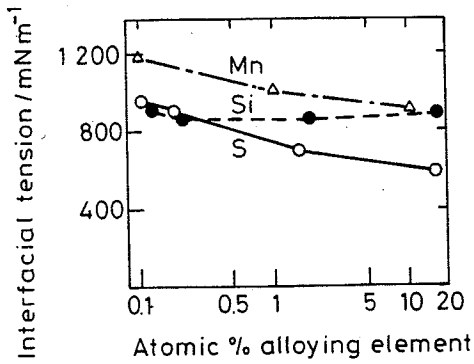


Fig. 11.83. Effect of manganese, sulphur and silicon in iron on the interfacial tension with slag (20 % Al_2O_3 + 40 % CaO + 40 % SiO_2) at about 1570 °C [Ref. 3]

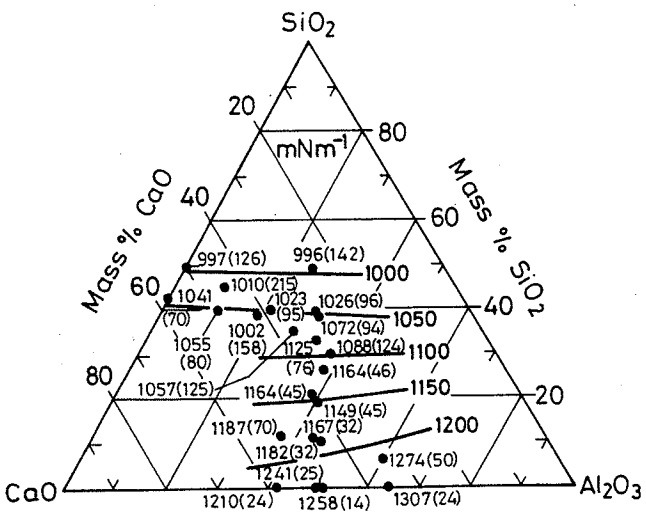


Fig. 11.84. Interfacial tension between Fe + O + Si alloys and Al_2O_3 + CaO + SiO_2 slags (containing some Fe_xO due to equilibration) at 1600 °C. Oxygen activities for respective points are shown in parentheses [Ref. 26]

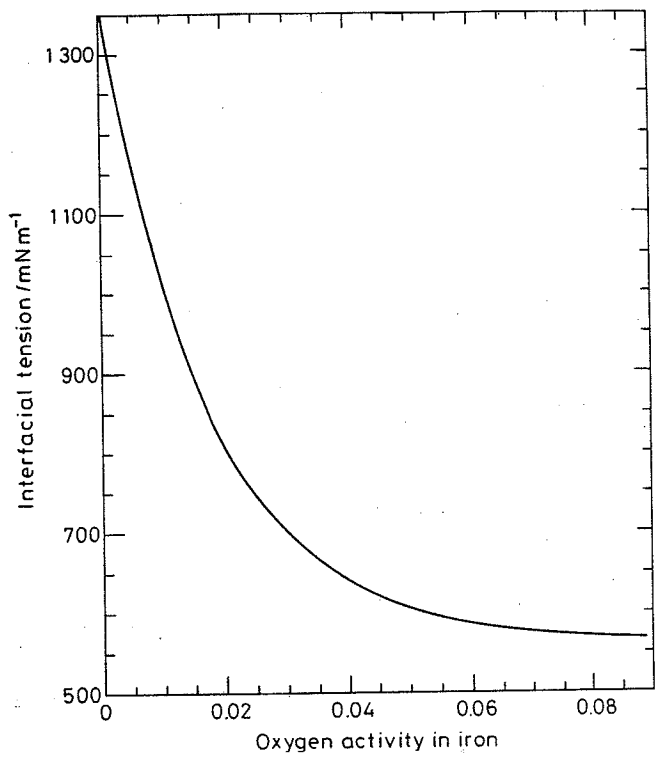


Fig. 11.85. Curve showing the general effect of oxygen activity in iron on the interfacial tension with various slags containing Al_2O_3 + CaO + SiO_2 at 1600 °C [Ref. 26]

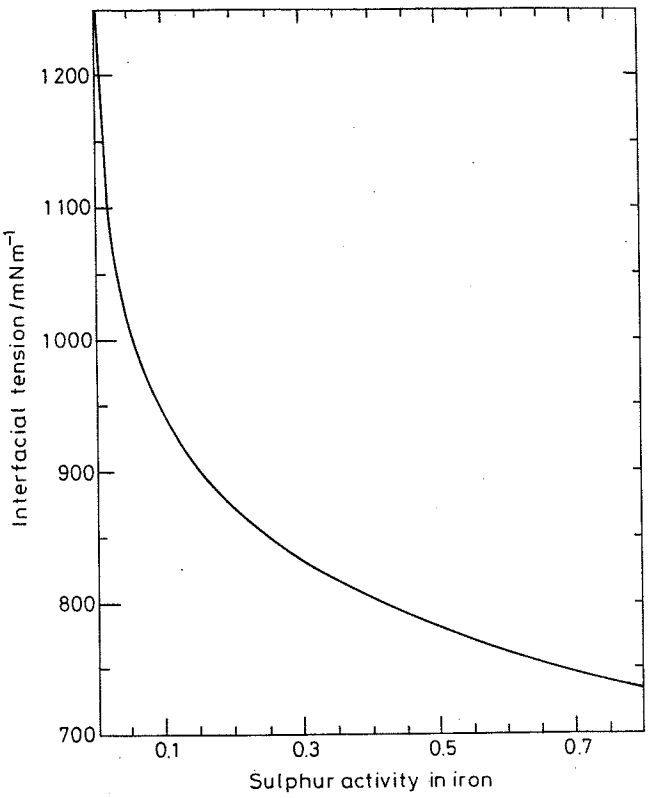
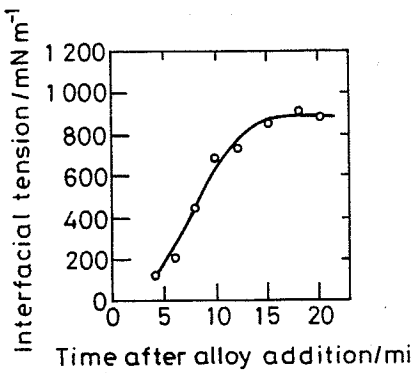
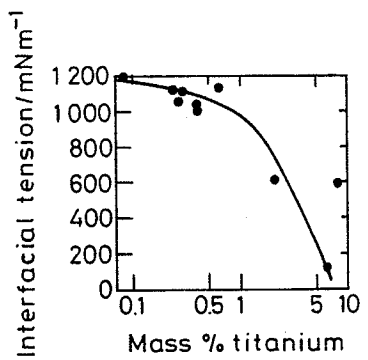


Fig. 11.86. Curve showing the general effect of sulphur activity in iron on the interfacial tension with various slags containing Al_2O_3 + CaO + SiO_2 (19-54 % SiO_2) at 1600 °C [Ref. 26]



(a)



(b)

Fig. 11.87 a,b. Variation of the interfacial tension between Fe + Ti alloys and slag (20 % Al_2O_3 + 40 % CaO + 40 % SiO_2) at 1570 °C [Ref. 3]

a) - Variation with time for Fe + 7.4 % Ti alloy

b) - Variation with Ti concentration in alloy

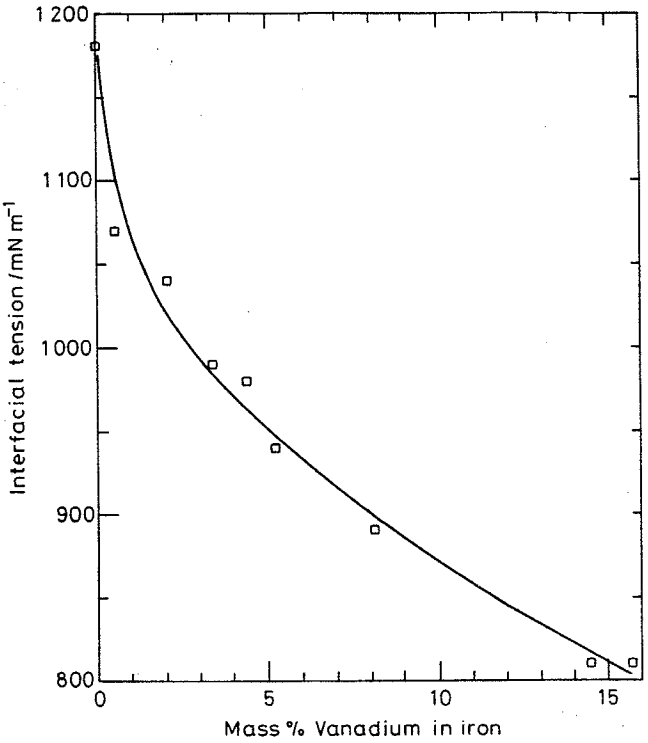
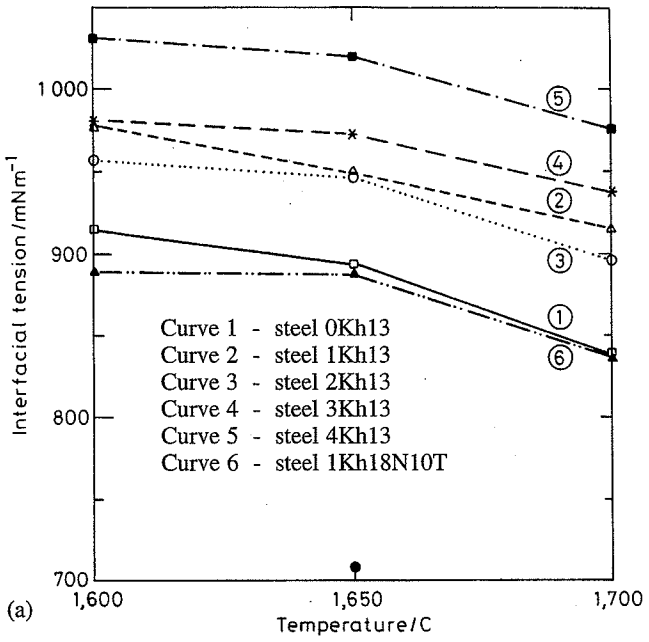
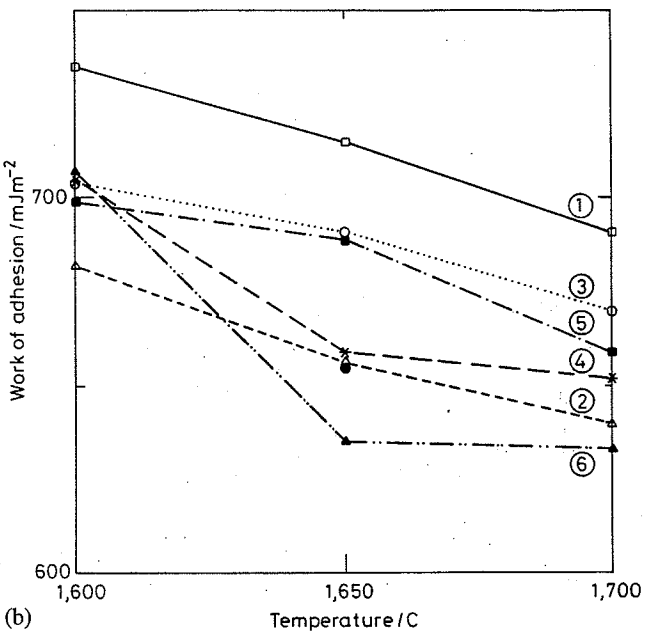


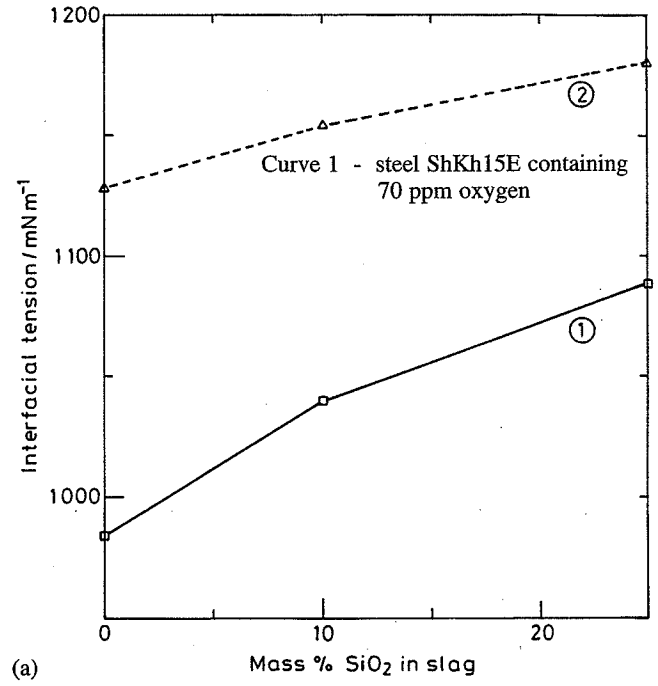
Fig. 11.88. Effect of vanadium content of Fe + V alloys on the interfacial tension with slag (20 % Al_2O_3 + 40 % CaO + 40 % SiO_2) at 1550 °C [Ref. 61]





▶

Fig. 11.90 a,b. Variation with temperature of (a) the interfacial tension and (b) the work of adhesion between various steels and oxide slag (44 % Al_2O_3 + 49.8 % CaO + 3 % SiO_2 + 2 % MgO + 0.5 % FeO) [Ref. 63]. Metal composition: M17



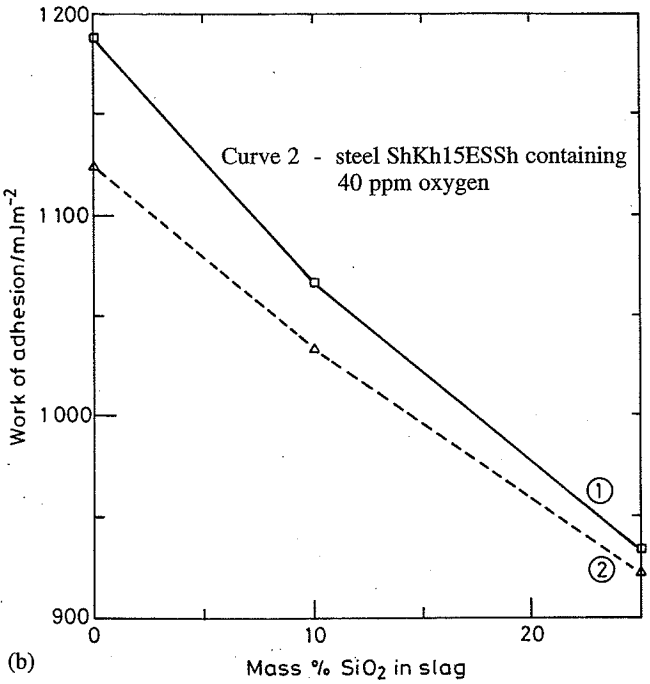


Fig. 11.89 a,b. Effect of replacing Al_2O_3 by SiO_2 in slag (45 % Al_2O_3 + 55 % CaO) (a) on the interfacial tension and (b) the work of adhesion with steel [Ref. 62]

Al_2O_3-MgO-SiO_2

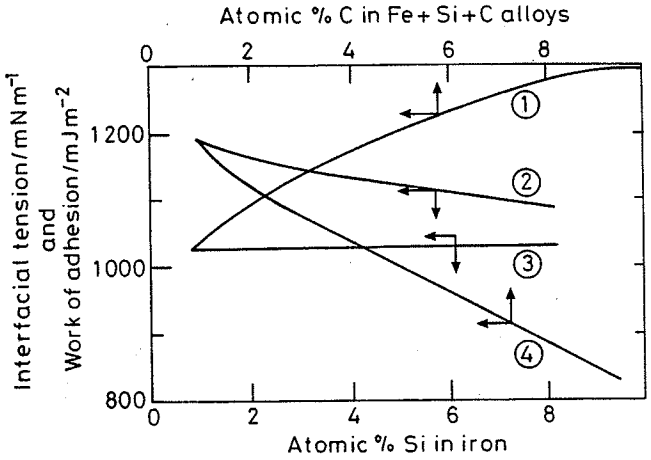


Fig. 11.91. Effect of variations in carbon and silicon levels in iron-based melts on the interfacial tension and work of adhesion with slag (35 % Al_2O_3 + 20 % MgO + 45 % SiO_2 (mass %)) at 1500-1550 °C [Ref. 64]

Curve 1 - γ_{ms} for C in Fe + Si + C alloys
Curve 2 - γ_{ms} for Si in Fe + Si alloys
Curve 3 - W_A for Si in Fe + Si alloys
Curve 4 - W_A for C in Fe + Si + C alloys

Al_2O_3-MnO-SiO_2

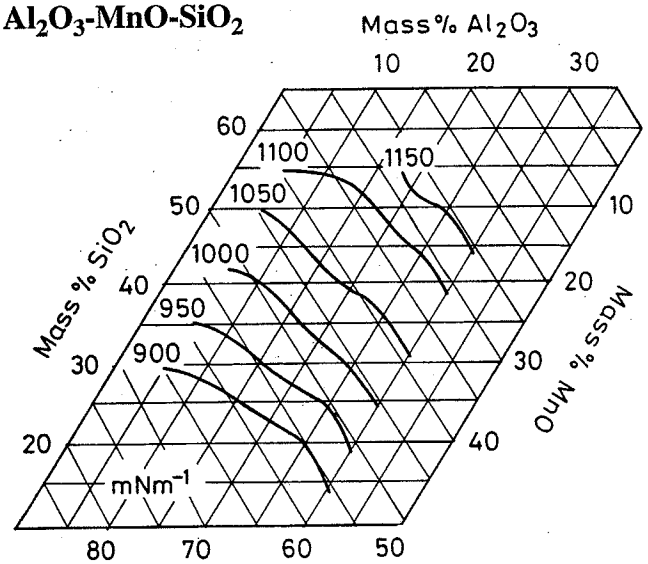


Fig. 11.92. Interfacial tension between iron and Al_2O_3 + MnO + SiO_2 slag at 1560 °C [Ref. 59]

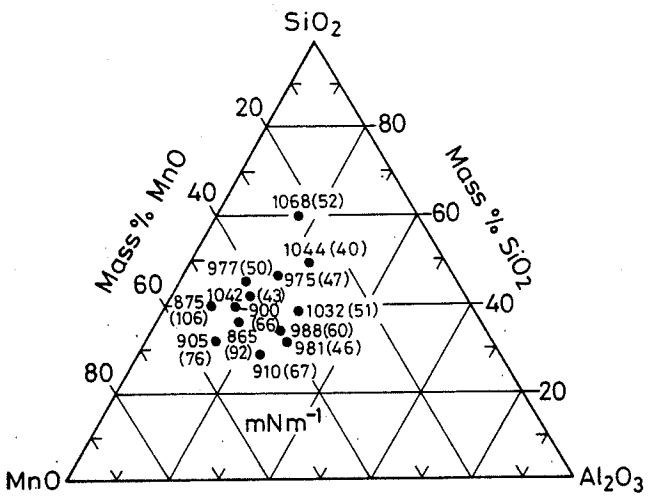


Fig. 11.93. Interfacial tension data for the system Fe + Mn + O + Si/Al_2O_3 + MnO + SiO_2 at 1600 °C. (Figures in parentheses refer to the metal oxygen activity in ppm.) [Ref. 26]

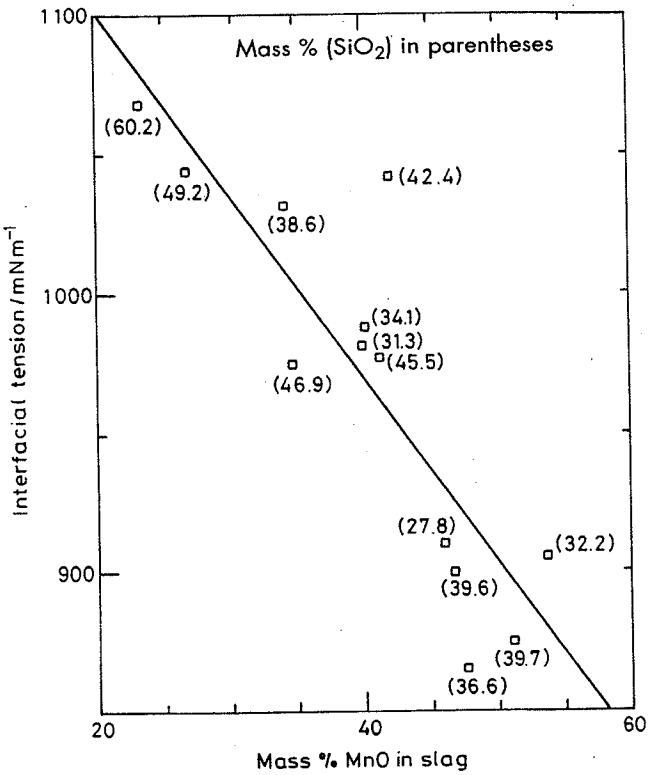


Fig. 11.94. Effect of MnO content in Al_2O_3 + MnO + SiO_2 slags on the interfacial tension with molten Fe + Mn (up to 1.76 % Mn), at 1600 °C [Ref. 26]

Al_2O_3-MnO-TiO_2

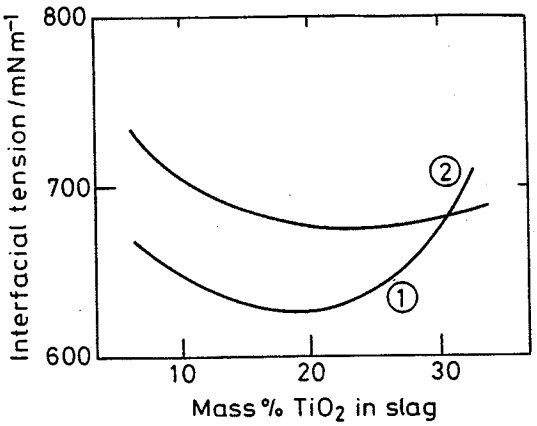


Fig. 11.95. Effect of TiO_2 content in Al_2O_3 + MnO + TiO_2 slags on the interfacial tension with high carbon (3.71 %) iron at 1460 °C [Ref. 66]. Metal composition: M18

Curve 1 - 50 % MnO
Curve 2 - 60 % MnO

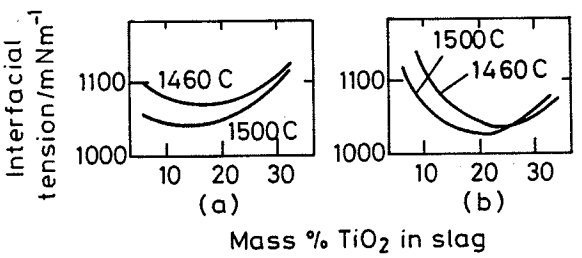


Fig. 11.96 a,b. Variation with temperature and slag composition of the interfacial tension between Al_2O_3 + MnO + TiO_2 slags and mild steel [Ref. 66]. Metal composition: M18

(a) - slag containing 50 % MnO
(b) - slag containing 60 % MnO

$CaO\text{-}FeO\text{-}SiO_2$

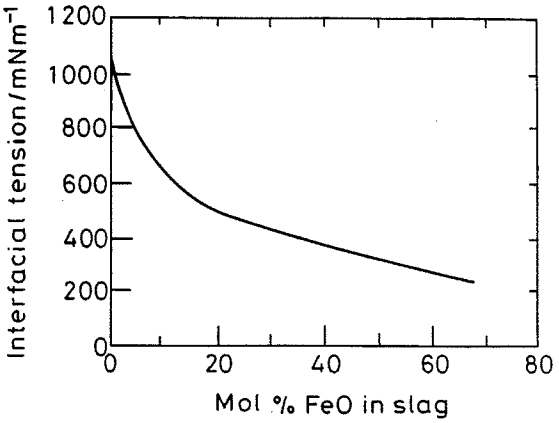


Fig. 11.97. Effect of FeO in CaO + FeO + SiO_2 slags (all slags contain ~ 30 mol % SiO_2) on the interfacial tension with iron at 1580 °C [Ref. 54]

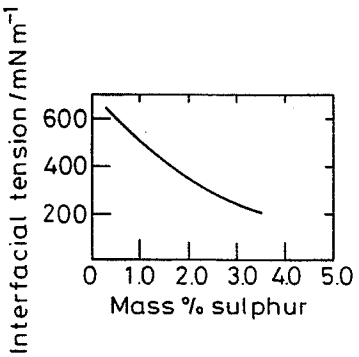


Fig. 11.98. Effect of sulphur content in iron on the interfacial tension with slag (35 % CaO + 27 % FeO + 27 % SiO_2) at 1560 °C [Ref. 59]

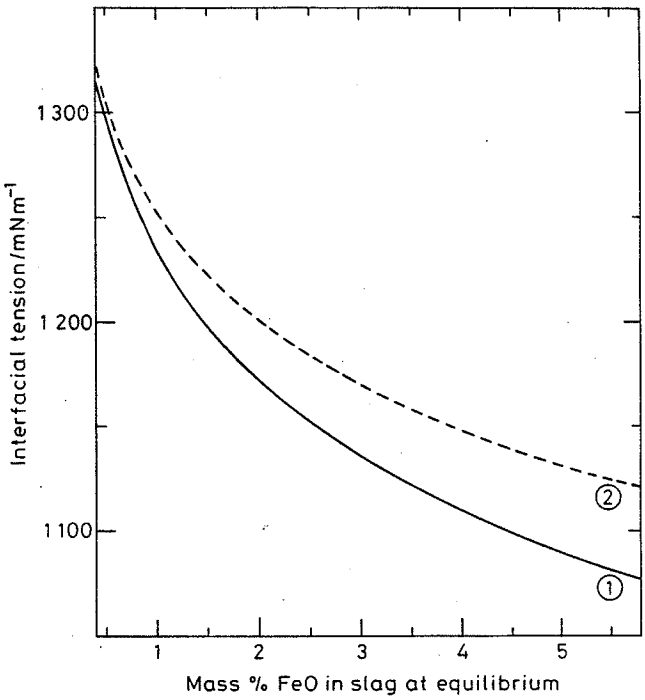


Fig. 11.99. Variation of the interfacial tension between dilute Fe + O + Si alloys with the equilibrium level of FeO in CaO + FeO + SiO_2 [Ref. 47]
Curve 1 - % CaO : % SiO_2 = 1.1 at 1600 °C
Curve 2 - % CaO : % SiO_2 = 1.0 at 1550 °C

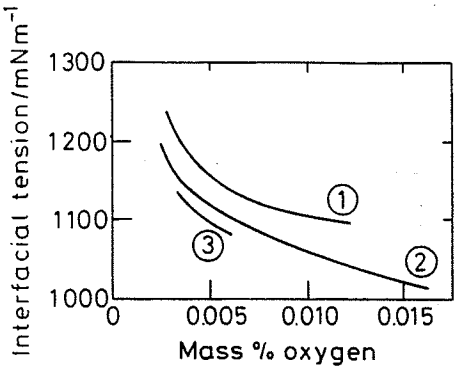


Fig. 11.100. Relation between the initial interfacial tension and the initial oxygen level in the metal for the system Fe/CaO + FeO + SiO_2 at 1600 °C [Ref. 47]
Mass % CaO : Mass % SiO_2 = 1.2
Curve 1 - 3 % FeO
Curve 2 - 5 % FeO
Curve 3 - 8 % FeO

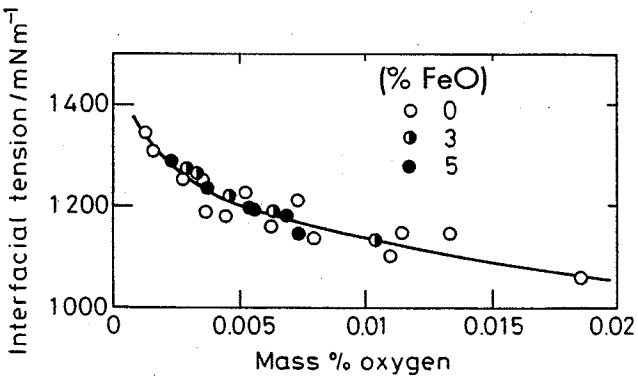


Fig. 11.101. Relation between the equilibrium interfacial tension and the equilibrium oxygen level in the metal for the system Fe/CaO + FeO + SiO_2 at 1600 °C.
Original mass % CaO : mass % SiO_2 = 1.2 [Ref. 47]

$CaO\text{-}MgO\text{-}SiO_2$

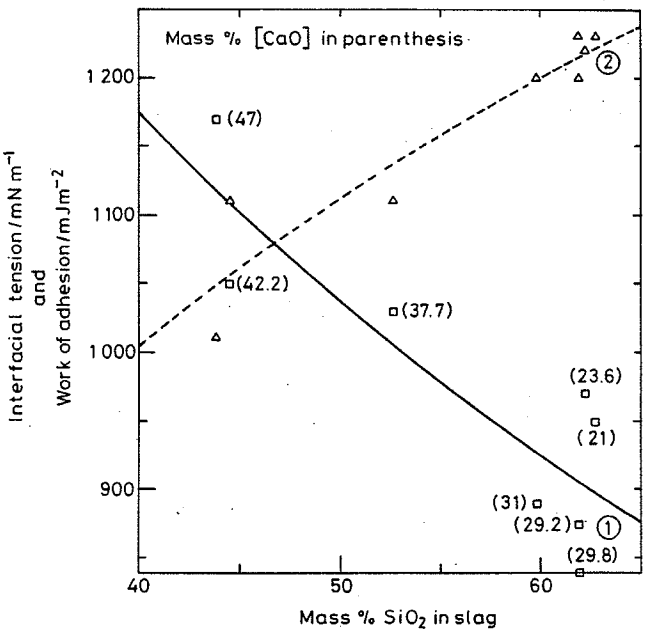


Fig. 11.102. Effect of SiO_2 content in CaO + MgO + SiO_2 slags on the interfacial tension (curve 1) and work of adhesion (curve 2) with steel ShKh15 at 1550 °C [Ref. 68]. Metal composition: M19

$CaO-MnO-SiO_2$

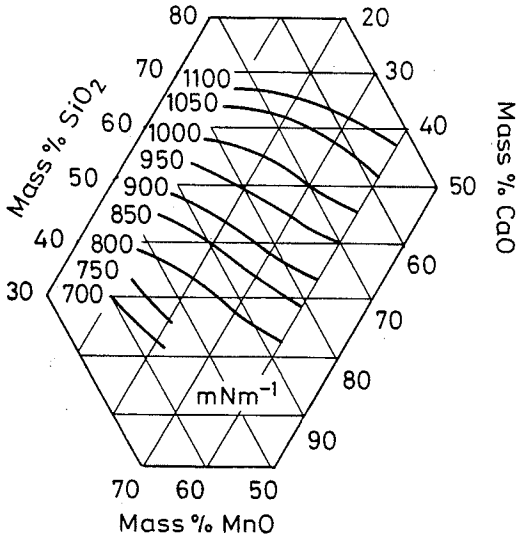
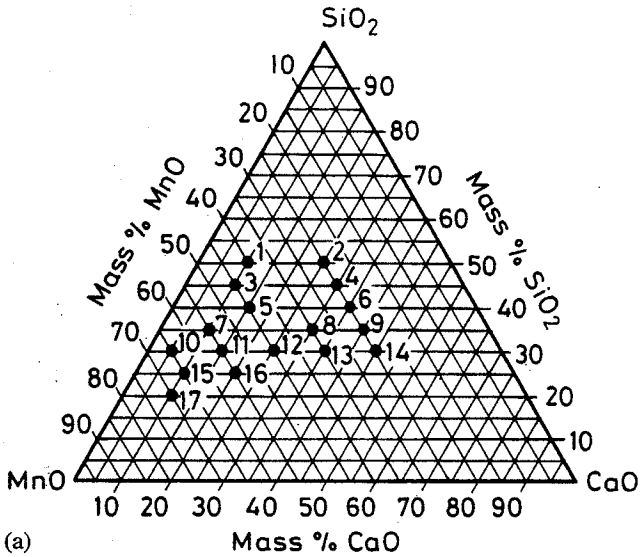
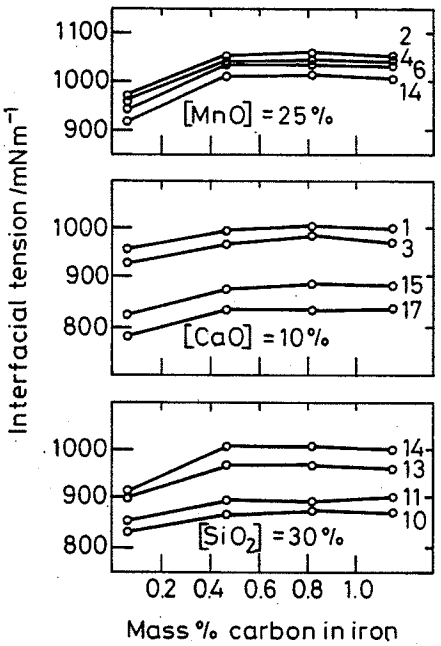


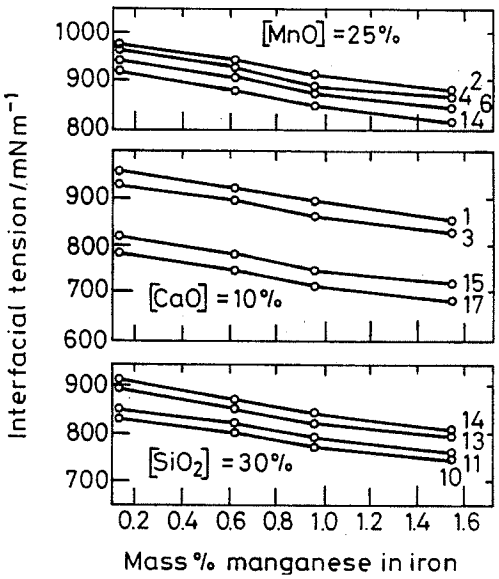
Fig. 11.103. Interfacial tension between iron and CaO + MnO + SiO_2 slags at 1560 °C [Ref. 59]



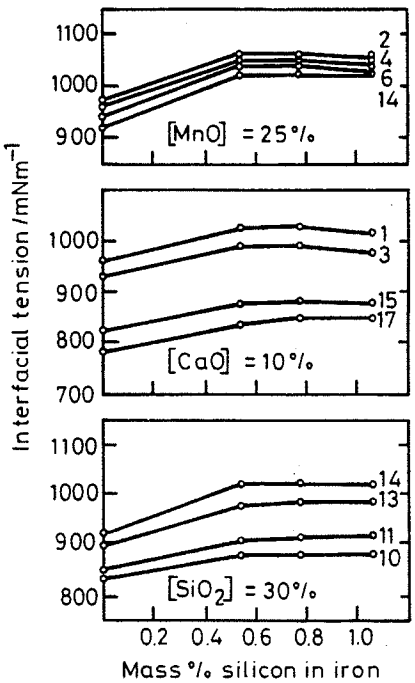
(a)



(b)



(c)



(d)

Fig. 11.104 a-d. Effect of (b) carbon, (c) manganese and (d) silicon in Armco iron on the interfacial tension with CaO + MnO + SiO_2 slags at 1550-1570 °C [Ref. 69]. Slag compositions are shown in (a).

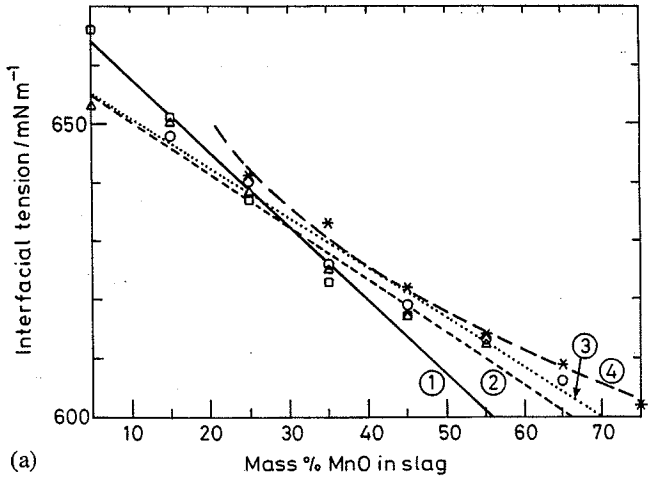


Fig. 11.105 a,b. Effect of MnO content in CaO + MnO + SiO_2 slags (a) on the interfacial tension and (b) on the work of adhesion with Fe + Mn alloy (78.35 % Mn) at 1500 °C [Ref. 70]

Curve 1 - 50 % SiO_2
Curve 2 - 40 % SiO_2
Curve 3 - 30 % SiO_2
Curve 4 - 20 % SiO_2

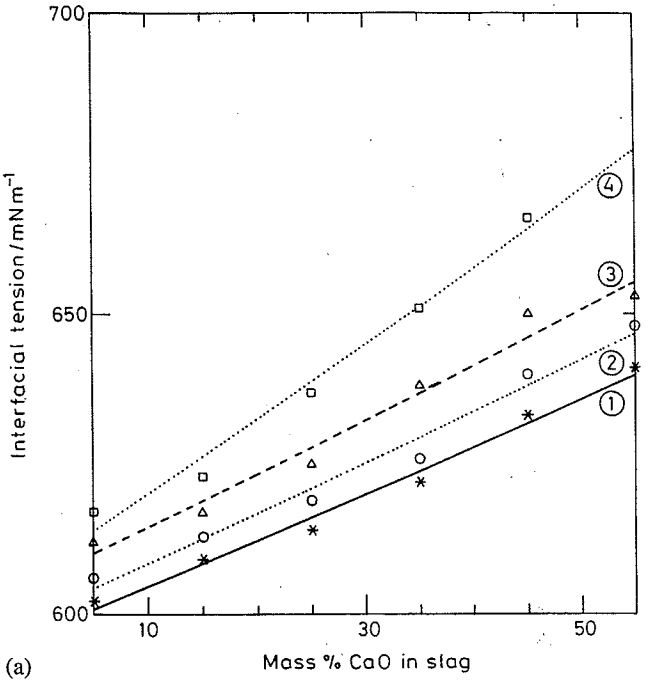


Fig. 11.106 a,b. Effect of CaO content in CaO + MnO + SiO_2 slags (a) on the interfacial tension and (b) on the work of adhesion with Fe + Mn alloy (78.3 % Mn) at 1500 °C [Ref. 70]

Curve 1 - 20 % SiO_2
Curve 2 - 30 % SiO_2
Curve 3 - 40 % SiO_2
Curve 4 - 50 % SiO_2

$FeO\text{-}MnO\text{-}SiO_2$

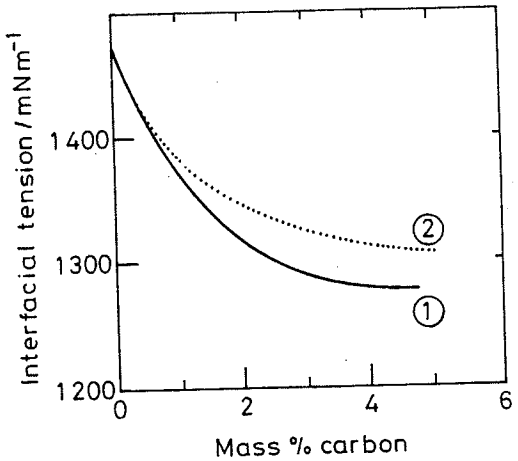


Fig. 11.107. Effect of carbon content of iron on the interfacial tension with FeO + MnO + SiO_2 slags [Ref. 71].
Major components of slags
Curve 1 - 5 % FeO + 59 % MnO + 28.2 % SiO_2
Curve 2 - 29 % FeO + 35 % MnO + 29 % SiO_2

$MnO\text{-}P_2O_5\text{-}SiO_2$

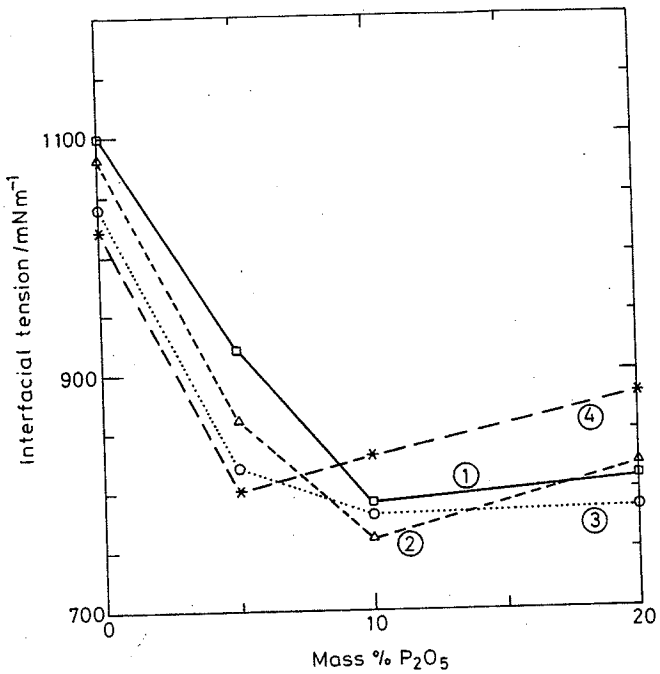


Fig. 11.108. Effect of P_2O_5 content in MnO + P_2O_5 + SiO_2 slags on the interfacial tension with Fe + P alloy (0.035 % P) at 1450 °C [Ref. 72]
Curve 1 - SiO_2 : MnO = 1.5
Curve 2 - SiO_2 : MnO = 2
Curve 3 - SiO_2 : MnO = 2.5
Curve 4 - SiO_2 : MnO = 3

$MnO\text{-}SiO_2\text{-}TiO_2$

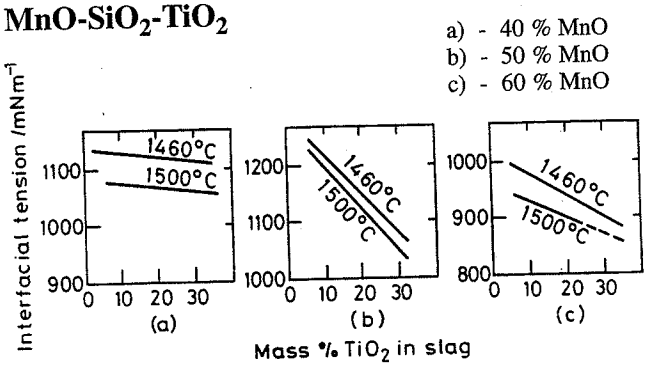


Fig. 11.109 a-c. Effect of TiO_2 content in MnO + SiO_2 + TiO_2 slags on the interfacial tension with mild steel at 1460 °C and 1500 °C [Ref. 66]. Metal composition: M18

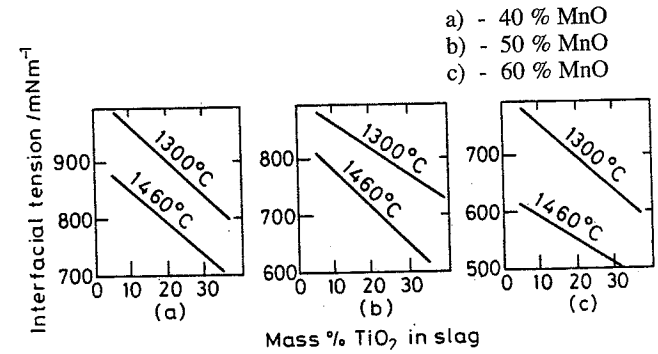


Fig. 11.110 a-c. Effect of TiO_2 content in MnO + SiO_2 + TiO_2 slags on the interfacial tension with high carbon iron (3.7 % C) at 1300 °C and 1460 °C [Ref. 66]. Metal composition: M18

$MnO\text{-}SiO_2\text{-}ZrO_2$

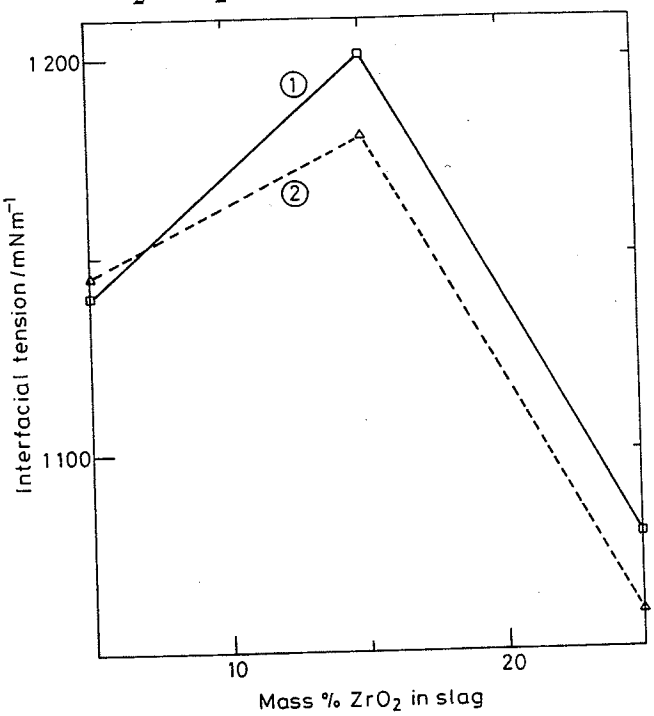


Fig. 11.111. Effect of ZrO_2 content in MnO + SiO_2 + ZrO_2 slags on the interfacial tension with chromium steel (14.4 % Cr) at 1500 °C (curve 1) and at 1525 °C (curve 2) [Ref. 73].
Metal composition: M20

$MnO\text{-}SiO_2$-(various oxides)

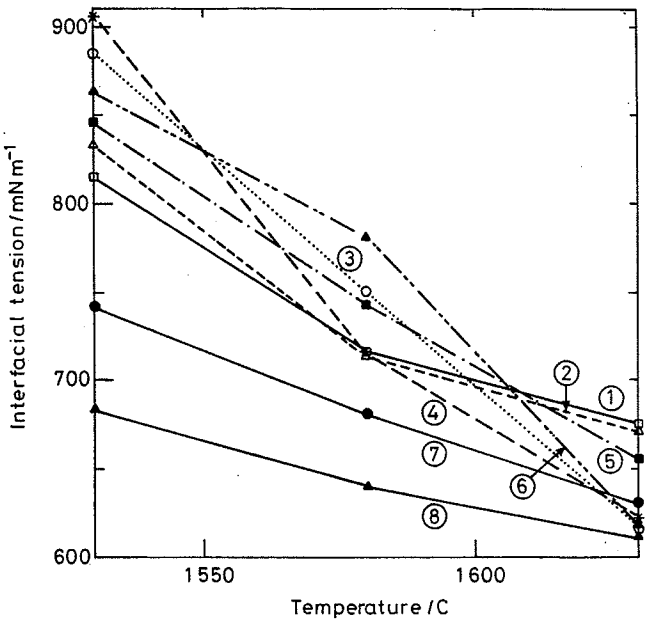


Fig. 11.112. Variation with temperature of the interfacial tension between steel Sv-08 and slags containing MnO + SiO_2 + oxide. (All slags contain 40 % MnO). [Ref. 65]

Curve 1 - 5 % Al_2O_3
Curve 2 - 10 % Al_2O_3
Curve 3 - 5 % MgO
Curve 4 - 10 % MgO
Curve 5 - 5 % CaO
Curve 6 - 10 % CaO
Curve 7 - 5 % FeO
Curve 8 - 10 % FeO

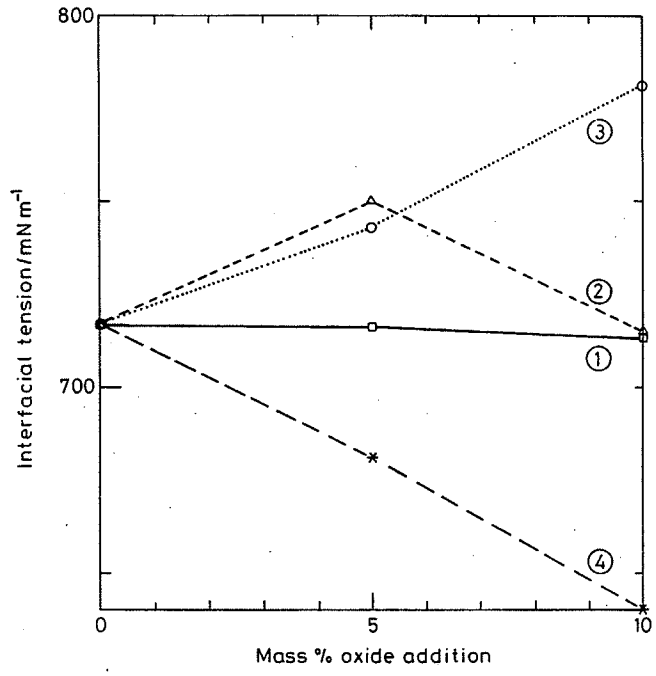


Fig. 11.113. Effect of various oxides in MnO + SiO_2 slags on the interfacial tension with steel Sv-08 at 1580 °C. (All slags contain 40 % MnO). [Ref. 65]

Curve 1 - Al_2O_3
Curve 2 - MgO
Curve 3 - CaO
Curve 4 - FeO

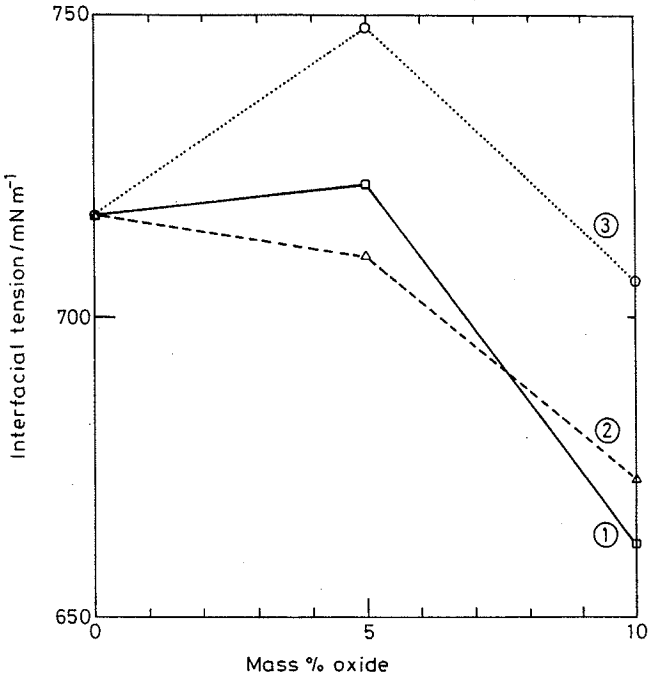


Fig. 11.114. Effect of various oxides in MnO + SiO_2 slags on the interfacial tension with steel Sv-08 at 1580 °C. (All slags contain 40 % MnO). [Ref. 65]

Curve 1 - Na_2O
Curve 2 - K_2O
Curve 3 - TiO_2

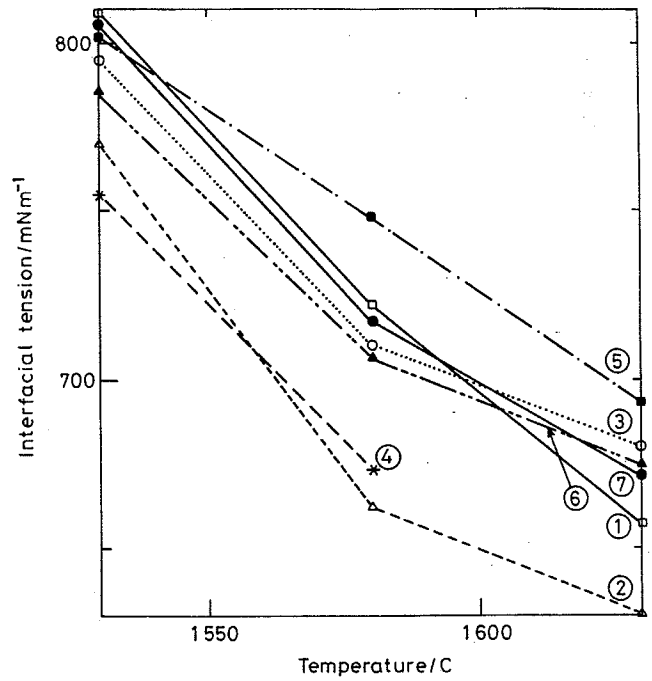


Fig. 11.115. Variation with temperature of the interfacial tension between steel Sv-08 and slags containing MnO + SiO_2 + an additional oxide. (All slags contain 40 mass % MnO). [Ref. 65]

Curve 1 - 5 % Na_2O
Curve 2 - 10 % Na_2O
Curve 3 - 5 % K_2O
Curve 4 - 10 % K_2O
Curve 5 - 5 % TiO_2
Curve 6 - 10 % TiO_2
Curve 7 - Base slag 40 % MnO + 60 % SiO_2

11.4.3.3 Quaternary systems

Al_2O_3-CaO-FeO-SiO_2

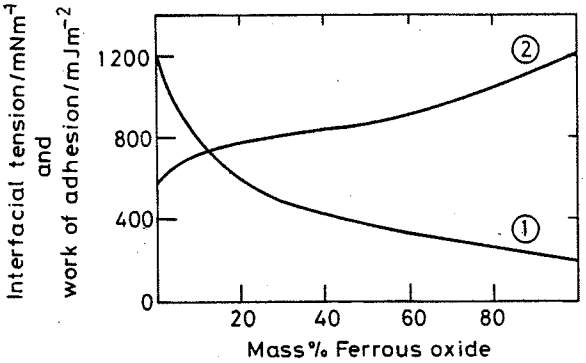


Fig. 11.116. Effect of variation in FeO content of slag (original slag - 20 % Al_2O_3 + 40 % CaO + 60 % SiO_2) on the interfacial tension (curve 1) and work of adhesion (curve 2) with iron at 1520-1550 °C [Ref. 74]. Metal composition: M21

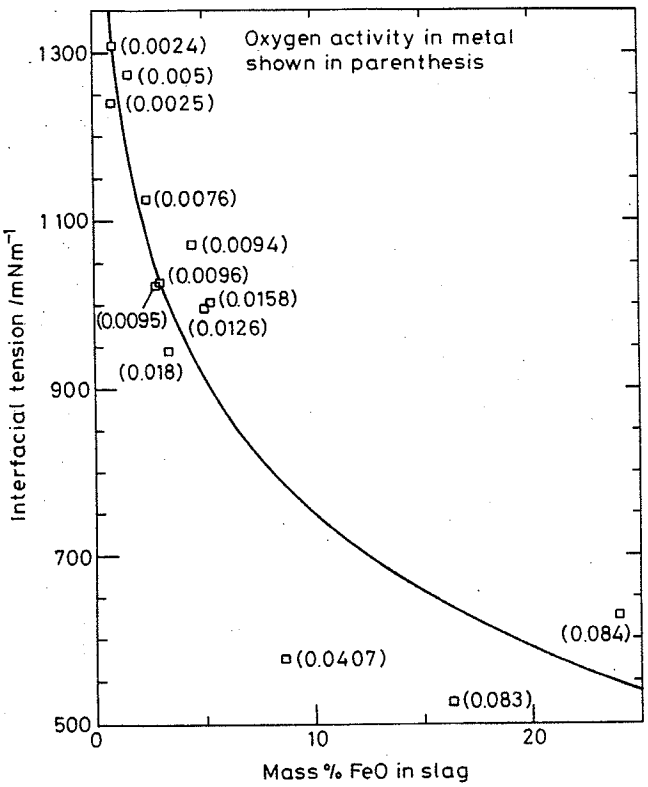


Fig. 11.117. General effect of variation in FeO content of various Al_2O_3 + CaO + SiO_2 slags on the interfacial tension with iron at 1600 °C [Ref. 26]

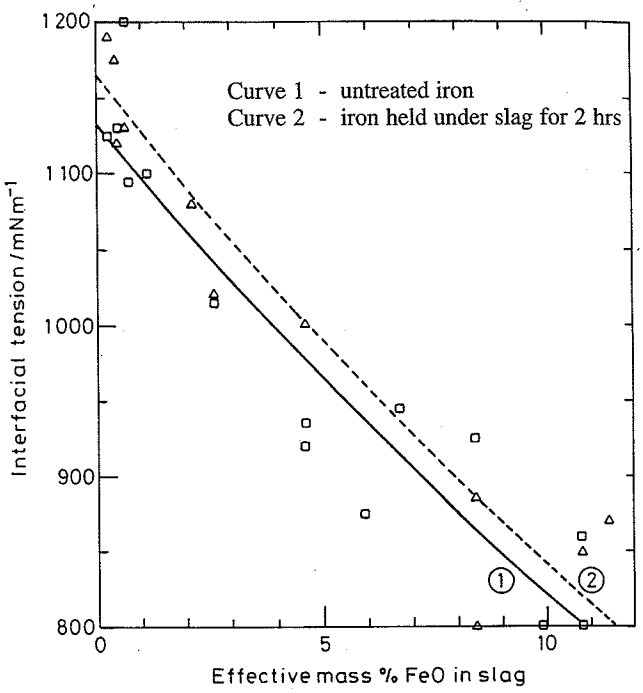


Fig. 11.118. Effect of FeO content in slag (20 % Al_2O_3 + 40 % CaO + 40 % SiO_2) on the interfacial tension with iron at 1530 °C [Ref. 75]

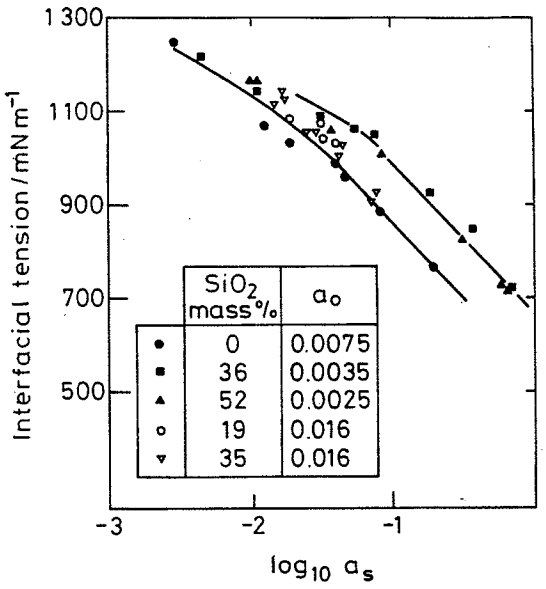
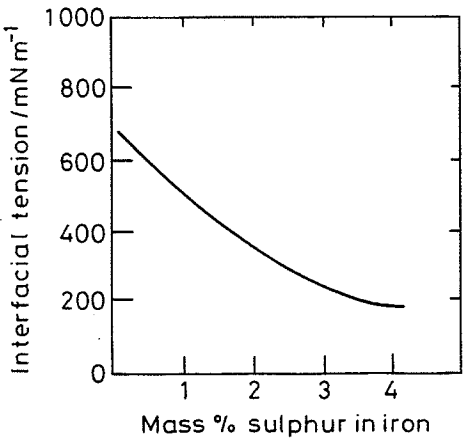


Fig. 11.119. Influence of sulphur activity on the interfacial tension between Fe-S-O-Si alloys and various slags in the system Al_2O_3 + CaO + Fe_xO + SiO_2 at 1600 °C [Ref. 26]



▶

Fig. 11.120. Effect of sulphur in iron on the interfacial tension with slag (23 % Al_2O_3 + 47 % CaO + 1 % FeO + 27 % SiO_2) [Ref. 76]

Al_2O_3-CaO-MgO-SiO_2

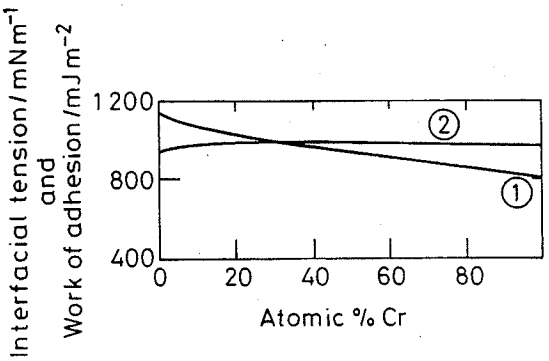


Fig. 11.121. Effect of chromium content in Fe + Cr alloys on the interfacial tension (curve 1) and the work of adhesion (curve 2) with slag (20 % Al_2O_3 + 10 % CaO + 30 % MgO + 40 % SiO_2) at 1730 °C (1830 °C for pure Cr) [Ref. 77]. Metal composition: M22

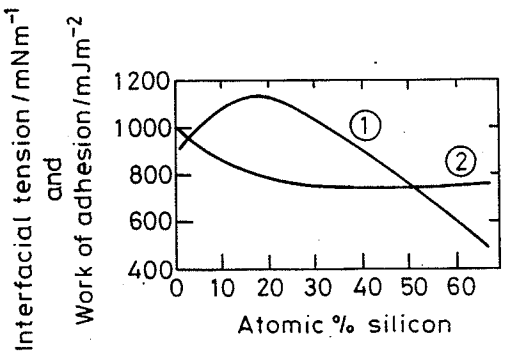


Fig. 11.122. Effect of silicon concentration in Fe + Cr + Si alloys (Cr:Fe = 2.3:1 (atomic)), on the interfacial tension (curve 1) and the work of adhesion (curve 2) with slag (9 mol % Al_2O_3 + 46 mol % CaO + 13 mol % MgO + 32 mol % SiO_2) at 1700 °C [Ref. 78]

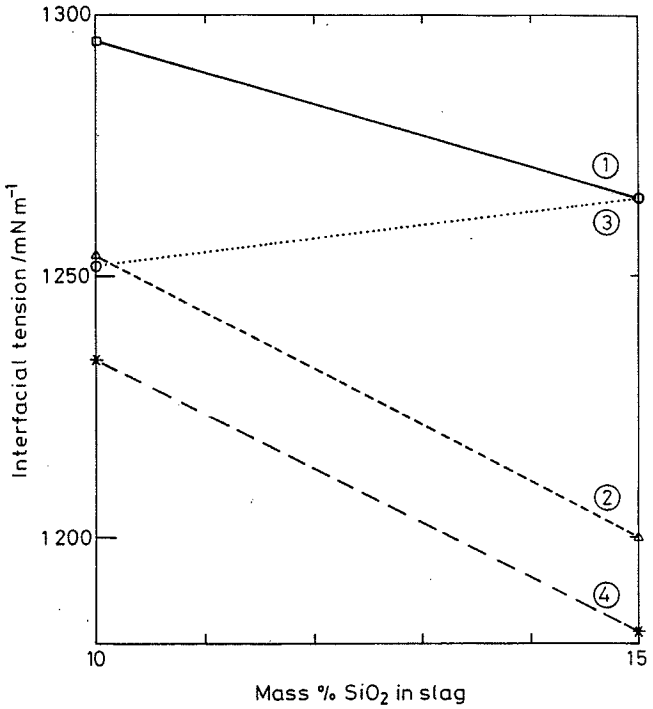


Fig. 11.123. Effect of replacing some Al_2O_3 by SiO_2 in Al_2O_3 + CaO + MgO + SiO_2 slags on the interfacial tension with various steels. (CaO and MgO concentrations fixed at 55 % and 5 % respectively) [Ref. 32]
Curve 1 - steel 12Kh1MF at 1600 °C
Curve 2 - steel 20K at 1600 °C
Curve 3 - steel 12Kh1MF at 1650 °C
Curve 4 - steel 20K at 1650 °C

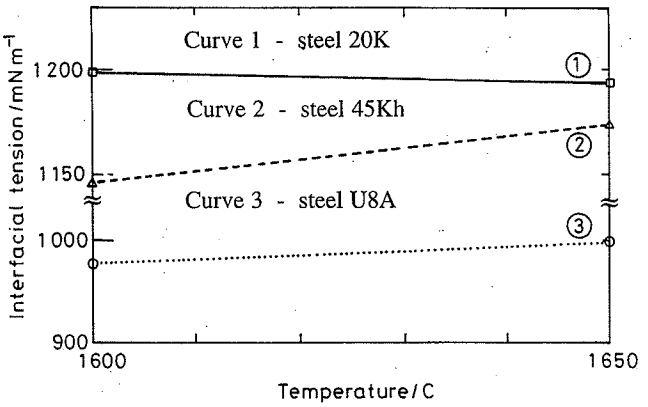


Fig. 11.124. Effect of temperature on the interfacial tension between slag (20 % Al_2O_3 + 55 % CaO + 10 % MgO + 15 % SiO_2) and steels [Ref. 32]

Al_2O_3-CaO-MnO-SiO_2

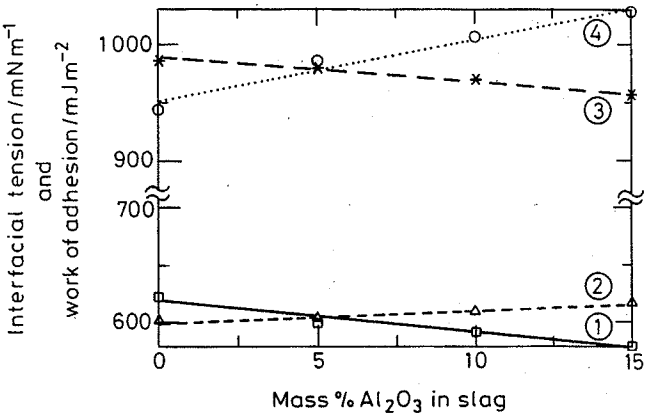


Fig. 11.125. Effect of Al_2O_3 content in CaO + MnO + SiO_2 slags on the interfacial tension (curves 1 and 2) and the work of adhesion (curves 3 and 4) with ferro-manganese (78.35 % Mn) at 1500 °C [Ref. 79]
Curves 1 and 4 - Original slag 15 % CaO + 35 % MnO + 50 % SiO_2
Curves 2 and 3 - Original slag 5 % CaO + 75 % MnO + 20 % SiO_2

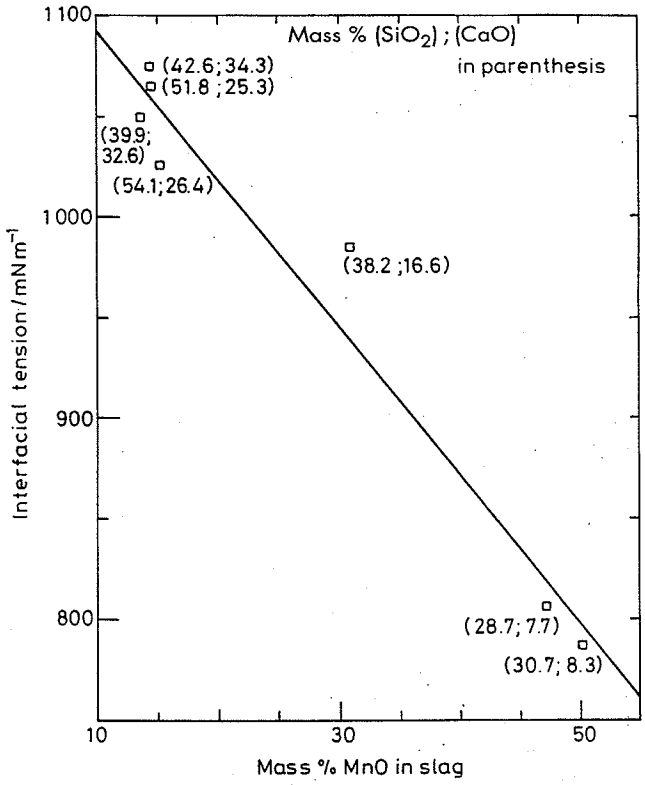


Fig. 11.126. General effect of MnO content in various Al_2O_3 + CaO + MnO + SiO_2 slags on the interfacial tension with dilute Fe + Mn alloys (Mn level up to 1.56 %) at 1600 °C [Ref. 26]

Al_2O_3-CaO-Na_2O-SiO_2

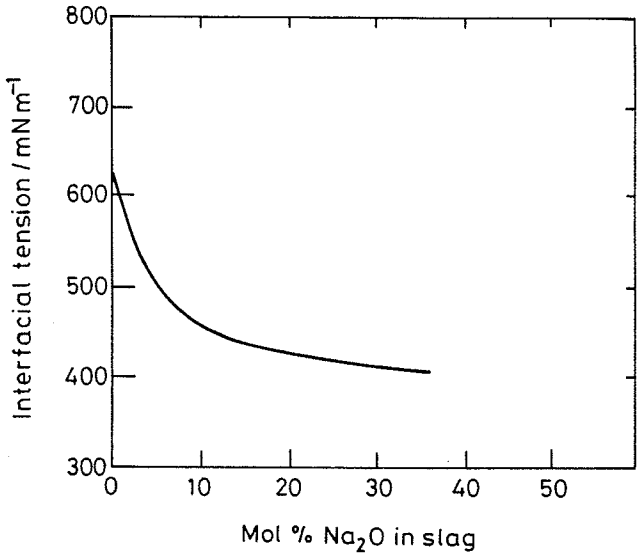


Fig. 11.127. Effect of Na_2O content (mol %) in Al_2O_3 + CaO + Na_2O + SiO_2 slags on the interfacial tension with synthetic pig iron (4.6 % C; 0.4 % Si) at 1450 °C [Ref. 60]
Al_2O_3 = 26 mass %; SiO_2 = 35 mass %
(Al_2O_3 + CaO + Na_2O + SiO_2 = 100 %)

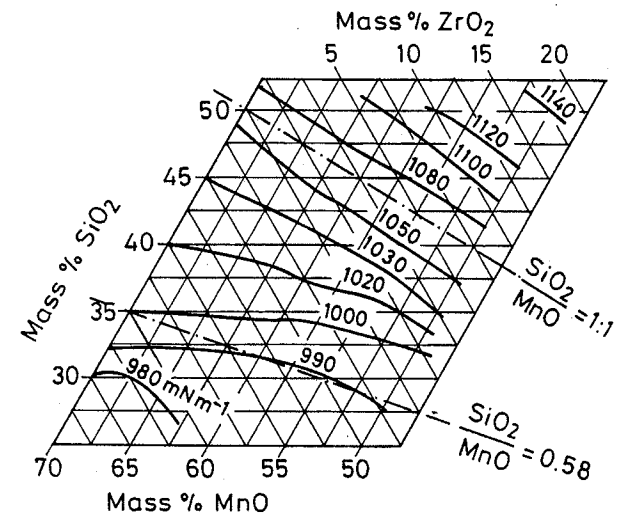


Fig. 11.129. Interfacial tension between 5 % Al_2O_3 + MnO + SiO_2 + ZrO_2 slags and molten iron at 1550 °C [Ref. 81]. Metal composition: M24

Al_2O_3-MnO-SiO_2-ZrO_2

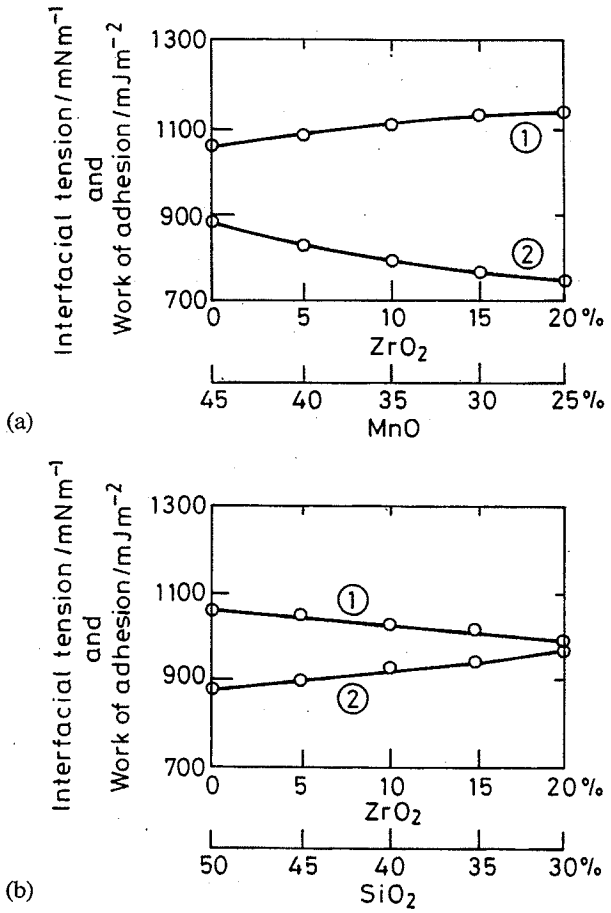


Fig. 11.128 a,b. Effect of replacing (a) MnO and (b) SiO_2 by ZrO_2 in 5 % Al_2O_3 + MnO + SiO_2 + ZrO_2 slags on the interfacial tension (curve 1) and the work of adhesion (curve 2) with iron at 1550 °C [Ref. 81]. Metal composition: M24

CaO-CaS-MnO-SiO_2

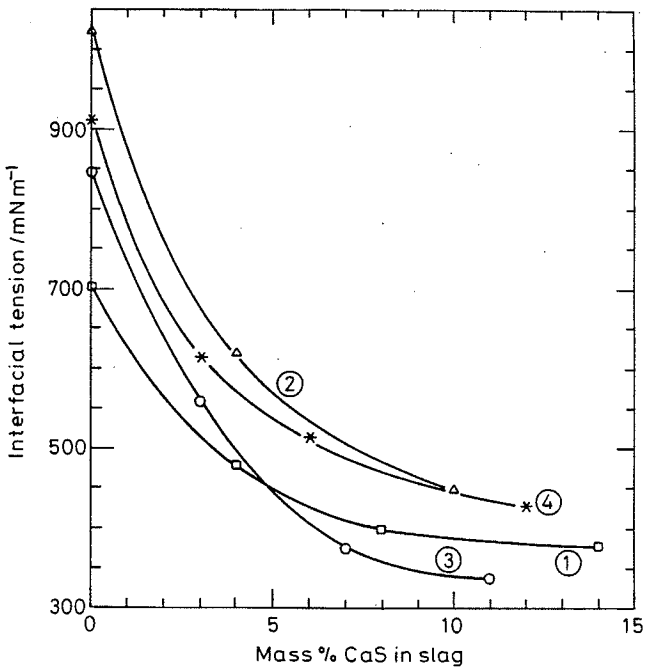


Fig. 11.130. Effect of CaS in CaO + MnO + SiO_2 slags on the interfacial tension with molten mild steel [Ref. 82]
Curve 1 - 10 % CaO + 60 % MnO + 30 % SiO_2
Curve 2 - 10 % CaO + 30 % MnO + 60 % SiO_2
Curve 3 - 20 % CaO + 40 % MnO + 40 % SiO_2
Curve 4 - 30 % CaO + 40 % MnO + 30 % SiO_2

$CaO-MgO-MnO-SiO_2$

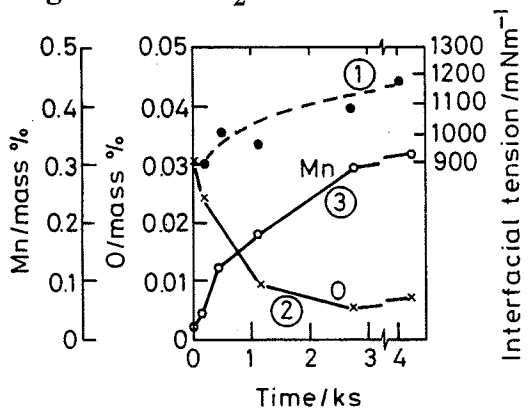


Fig. 11.131. Effect of decreasing oxygen content of liquid iron on the interfacial tension (curve 1) with slag (initial composition 40.4 % CaO + 16.6 % MgO + 2 % MnO + 40.4 % SiO_2 + (0.6 % FeO)) at 1600 °C [Ref. 83]

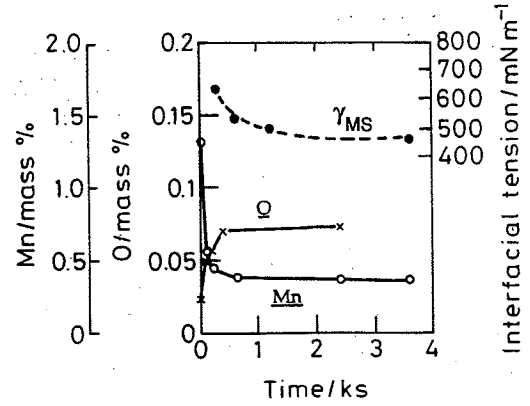


Fig. 11.132. Effect with time of the increasing oxygen content in iron on the interfacial tension with slag at 1600 °C [Ref. 83]. Initial slag composition: 40.4 % CaO + 2 % MnO + 16.6 % MgO + 40.4 % SiO_2 + (0.6 % FeO)

$CaO-MnO-MnS-SiO_2$

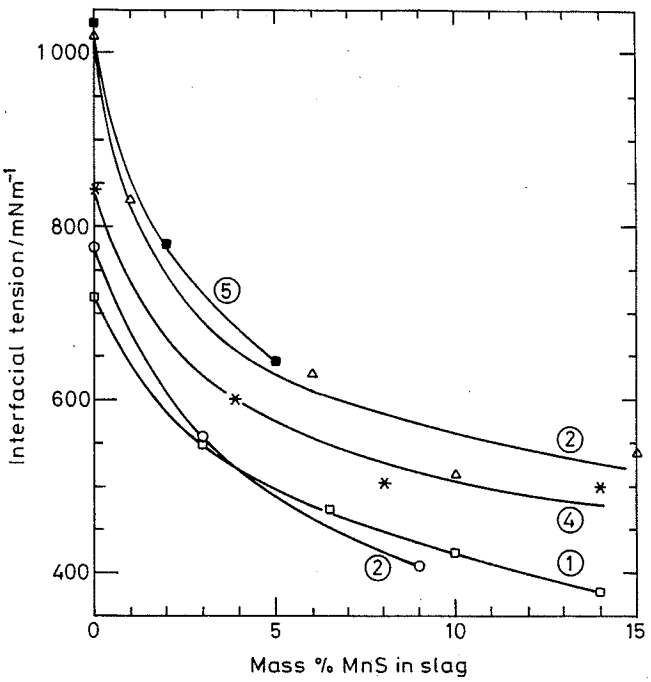


Fig. 11.133. Effect of MnS addition to CaO + MnO + SiO_2 slags on the interfacial tension with mild steel [Ref. 82]

Curve 1 - 10 % CaO + 60 % MnO + 30 % SiO_2
Curve 2 - 10 % CaO + 30 % MnO + 60 % SiO_2
Curve 3 - 20 % CaO + 50 % MnO + 30 % SiO_2
Curve 4 - 20 % CaO + 40 % MnO + 40 % SiO_2
Curve 5 - 20 % CaO + 20 % MnO + 60 % SiO_2

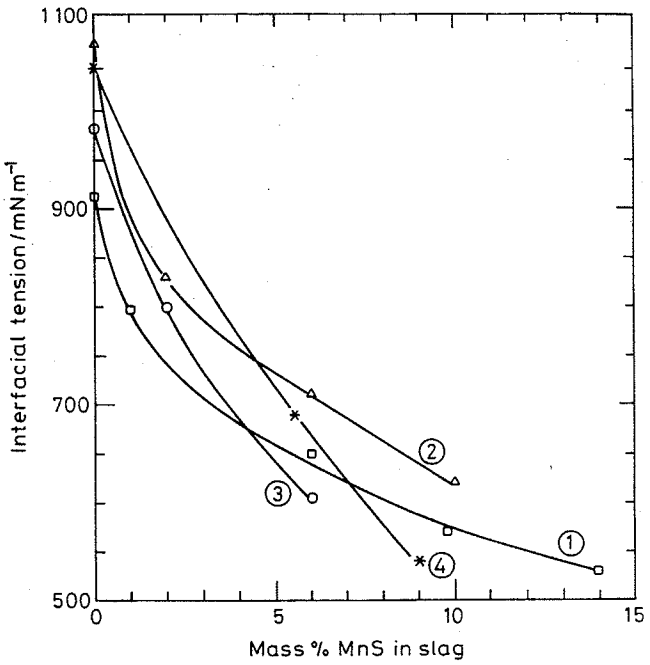
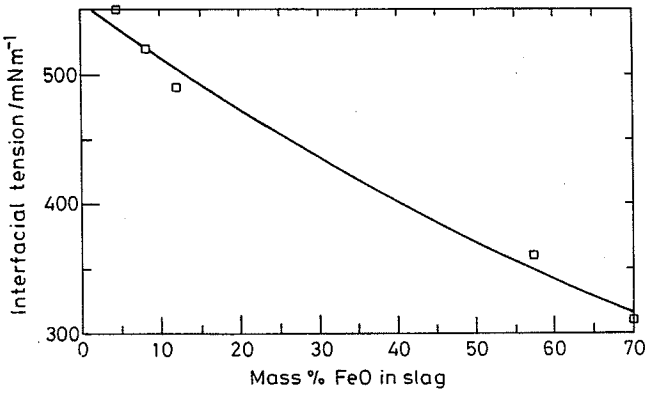


Fig. 11.134. Effect of MnS addition to CaO + MnO + SiO_2 slags on the interfacial tension with mild steel [Ref. 82]

Curve 1 - 30 % CaO + 40 % MnO + 30 % SiO_2
Curve 2 - 30 % CaO + 10 % MnO + 60 % SiO_2
Curve 3 - 40 % CaO + 20 % MnO + 40 % SiO_2
Curve 4 - 40 % CaO + 10 % MnO + 50 % SiO_2

11.4.3.4 Systems with five and more components

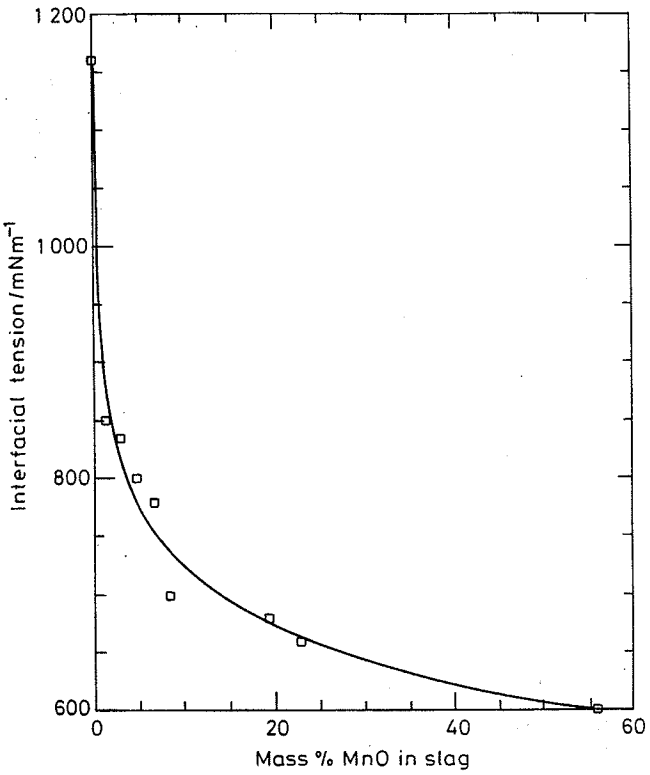
Al_2O_3-CaO-Fe_xO-MgO-MnO-P_2O_5-SiO_2

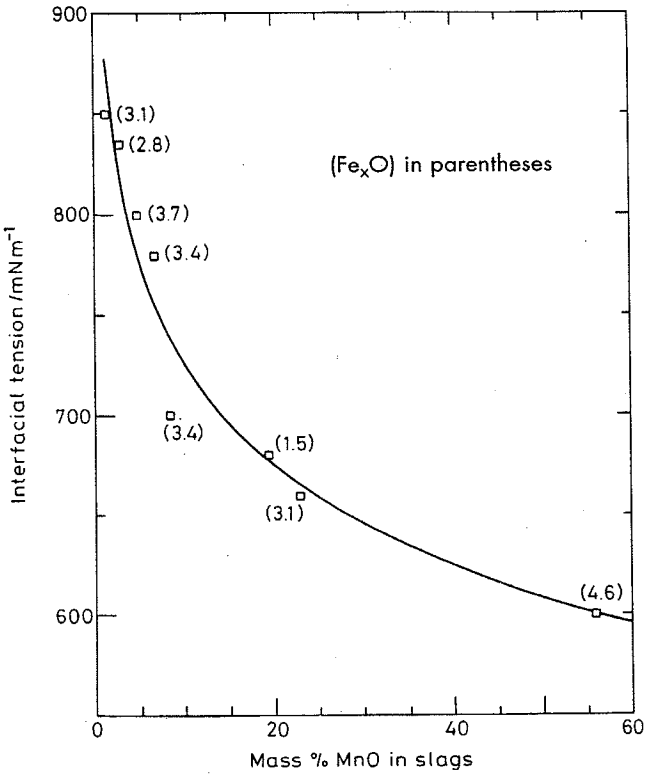


Mass %							
FeO	SiO_2	CaO	MgO	Al_2O_3	MnO	Fe_2O_3	P_2O_5
70.0	8.4	21.6	-	-	-	-	-
57.3	4.8	37.9	-	-	-	-	-
12.0	3.3	22.1	33.5	4.8	5.6	15.8	1.4
8.3	1.0	25.2	30.5	5.9	6.3	19.6	0.5
4.6	2.4	26.5	23.3	5.5	6.1	18.0	0.3

Fig. 11.135. Effect of FeO content in oxide slags on the interfacial tension with iron (0.04 % C) at 1560 °C [Ref. 58]

Al_2O_3-CaO-Fe_xO-MgO-MnO-SiO_2





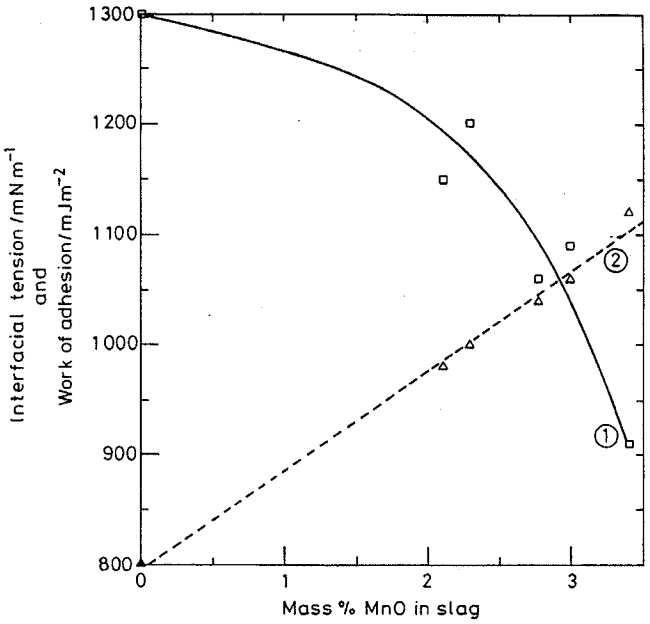
Mass %						
MnO	CaO	SiO_2	Al_2O_3	MgO	FeO	Fe_2O_3
1.3	26.4	30.7	34.9	2.8	1.3	1.8
2.8	24.3	30.2	35.8	4.1	1.9	0.9
4.7	18.5	30.8	34.8	8.2	2.8	0.9
6.6	15.9	31.5	34.3	7.8	2.2	1.2
8.3	12.2	30.0	35.3	10.7	2.3	1.1
19.4	1.8	36.0	28.2	12.6	1.0	0.5
22.8	2.2	31.4	26.2	12.4	2.4	0.7
55.9	2.6	23.8	2.6	9.9	3.3	1.3

Fig. 11.137. Effect of MnO content in slags on the interfacial tension with iron at 1560 °C [Ref. 59]

◀

Mass %						
MnO	CaO	Al_2O_3	SiO_2	MgO	FeO	Fe_2O_3
-	39.0	26.0	35.0	-	~ 0.5	-
1.3	26.4	34.9	30.7	2.8	1.3	1.8
2.8	24.3	35.8	30.2	4.1	1.9	0.9
4.7	18.5	34.8	30.8	8.2	2.8	0.9
6.6	15.9	34.3	31.5	7.8	2.2	1.2
8.3	12.2	35.3	30.0	10.7	2.3	1.1
19.3	1.8	28.2	36.0	12.6	1.0	0.5
22.8	2.2	26.2	31.4	12.4	2.4	0.7
55.9	2.6	2.6	23.8	9.9	3.3	1.3

Fig. 11.136. Effect of increasing MnO content in slags on the interfacial tension with iron at 1550 °C [Ref. 49]. Metal composition: M14



Mass %					
MnO	FeO	SiO_2	CaO	Al_2O_3	MgO
0	0.70	33.4	19.3	41.0	5.6
2.11	1.40	56.9	15.4	19.2	5.0
2.29	0.45	56.16	13.5	22.6	5.0
2.77	0.63	59.4	23.0	7.2	7.0
2.99	0.77	56.7	2.6	28.0	8.93
3.40	0.70	59.4	22.3	7.1	7.1

Fig. 11.138. Effect of MnO content in oxide slags on the interfacial tension (curve 1) and the work of adhesion (curve 2) with steel ShKh15 at 1550 °C [Ref. 68]. Metal composition: M19

Al_2O_3-CaO-Fe_xO-MgO-SiO_2

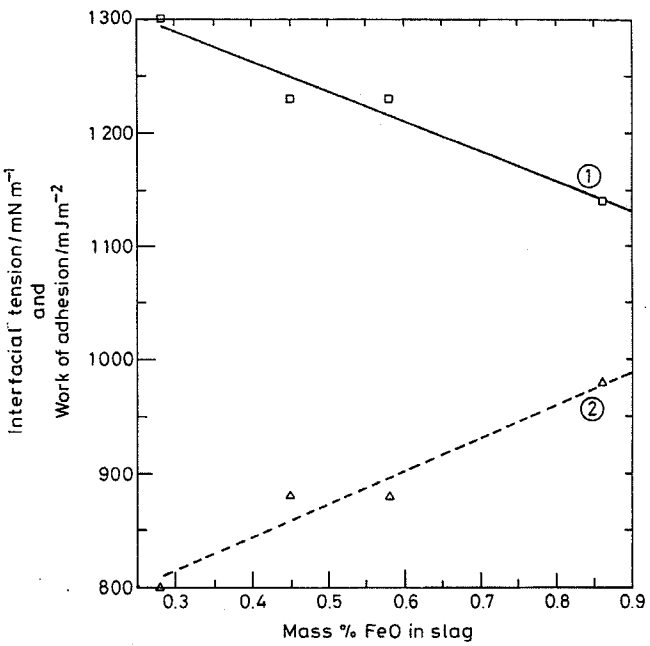
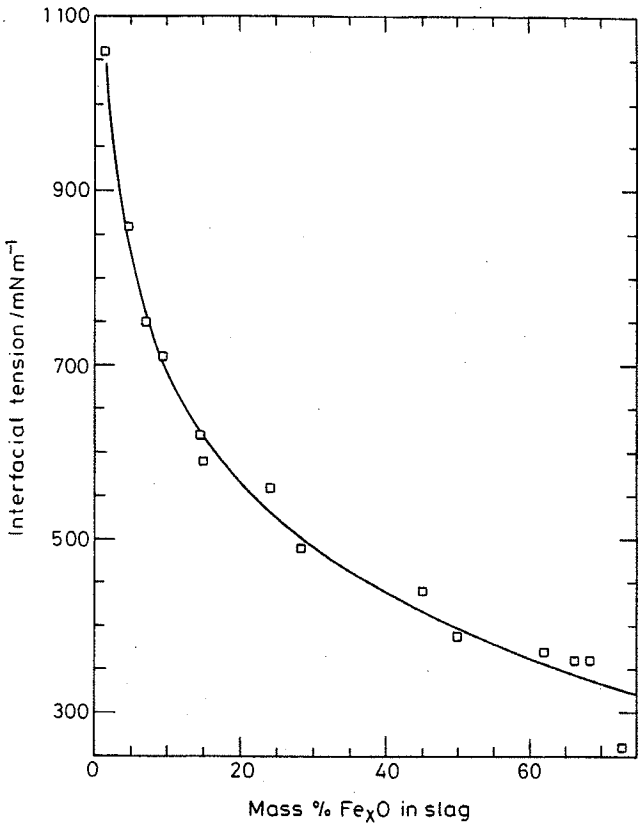
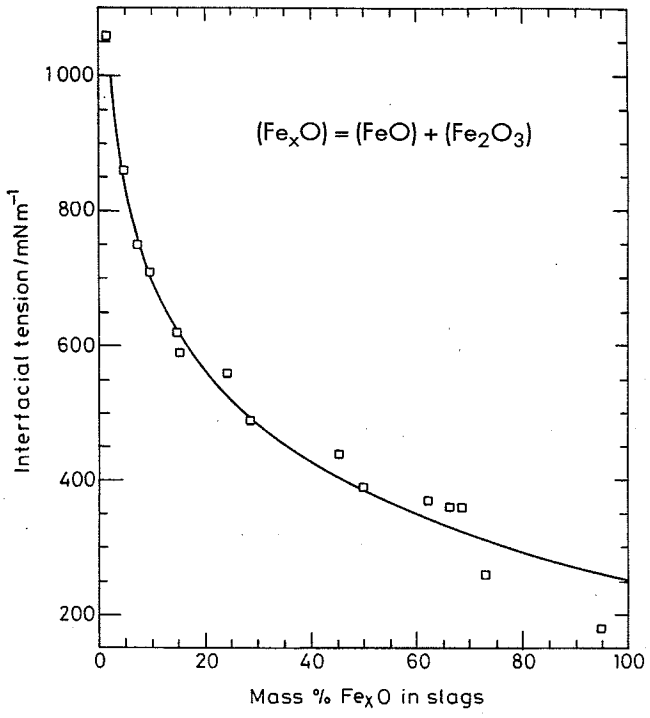


Fig. 11.139. Effect of FeO content in Al_2O_3 + CaO + MgO + SiO_2 slags on the interfacial tension (curve 1) and the work of adhesion (curve 2) with steel ShKh15 at 1550 °C [Ref. 80]. Composition of original slag - 46.9 % Al_2O_3 + 0.28 % FeO + 18.2 % MgO + 34.6 % SiO_2. Metal composition: M23



Mass %						
FeO	Fe_2O_3	Fe_xO	CaO	SiO_2	MgO	Al_2O_3
1.3	0.03	1.33	58.5	29.2	5.9	2.5
4.2	0.4	4.6	52.3	28.6	6.3	2.5
6.2	0.9	7.1	52.4	30.1	7.4	2.5
7.9	1.6	9.5	43.2	28.1	8.6	6.0
12.5	2.1	14.6	40.9	28.8	12.4	2.5
13.1	2.0	15.1	42.6	28.9	9.4	2.0
20.8	3.3	24.1	32.0	26.5	13.0	2.5
24.0	4.4	28.4	29.5	29.4	11.5	1.1
37.2	8.0	45.2	12.0	21.3	17.3	3.2
47.5	2.4	49.9	1.5	18.0	21.5	2.0
56.1	6.0	62.1	1.0	16.9	18.3	1.4
59.2	7.1	66.3	0.9	15.5	14.4	1.8
62.9	5.6	68.5	2.1	12.4	12.5	1.2
68.6	4.3	72.9	-	17.9	9.2	-
85.6	7.0	92.6	-	-	7.4	-

Fig. 11.140. Effect of Fe_xO content in Al_2O_3 + CaO + Fe_xO + MgO + SiO_2 slags on the interfacial tension with iron at 1550-1580 °C [Ref. 54]



Mass %						
FeO	Fe_2O_3	Fe_xO	CaO	SiO_2	MgO	Al_2O_3
1.3	0.03	1.33	58.5	29.2	5.9	2.5
4.2	0.4	4.6	52.3	28.6	6.3	2.5
6.2	0.9	7.1	52.4	30.1	7.4	2.5
7.9	1.6	9.5	43.2	28.1	8.6	6.0
12.5	2.1	14.6	40.9	28.8	12.4	2.5
13.1	2.0	15.1	42.6	28.9	9.4	2.0
20.8	3.3	24.1	32.0	26.5	13.0	2.5
24.0	4.4	28.4	29.5	29.4	11.5	1.1
37.2	8.0	45.2	12.0	21.3	17.3	3.2
47.5	2.4	49.9	1.5	18.0	21.5	2.0
56.1	6.0	62.1	1.0	16.9	18.3	1.4
59.2	7.1	66.3	0.9	15.5	14.4	1.8
62.9	5.6	68.5	2.1	12.4	12.5	1.2
68.6	4.3	72.9	-	17.9	9.2	-
85.5	9.2	94.7	2.3	0.5	3.4	-

Fig. 11.141. Effect of Fe_xO content in oxide slags on the interfacial tension with iron at 1560 °C [Ref. 59]

Al_2O_3-CaO-Fe_2O_3-MgO-SiO_2

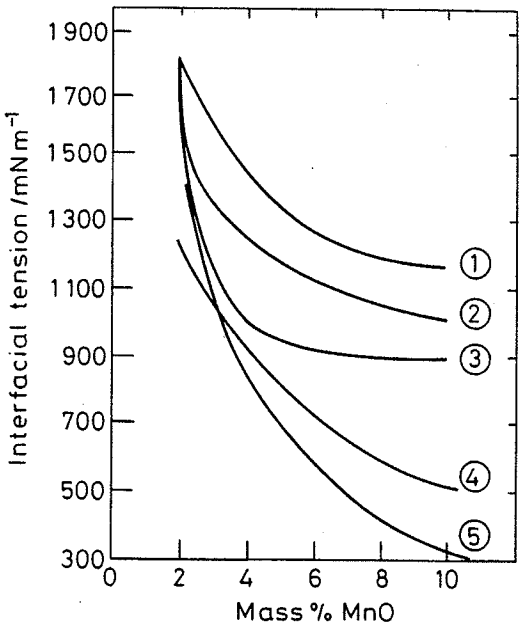


Fig. 11.142. Effect of MnO in slags on the interfacial tension with cast iron SCh-21-40 at 1350 °C [Ref. 88]. All slags contain 6 % Al_2O_3; 5 % MgO and 3 % Fe_2O_3.

Basicity (B) of slag defined as $\frac{[CaO] + [MgO]}{[SiO_2]}$.

Metal composition: M25

Curve 1 - B = 0.4
Curve 2 - B = 0.8
Curve 3 - B = 0.6
Curve 4 - B = 1.4
Curve 5 - B = 1.1

Al_2O_3-CaO-FeO-MnO-SiO_2

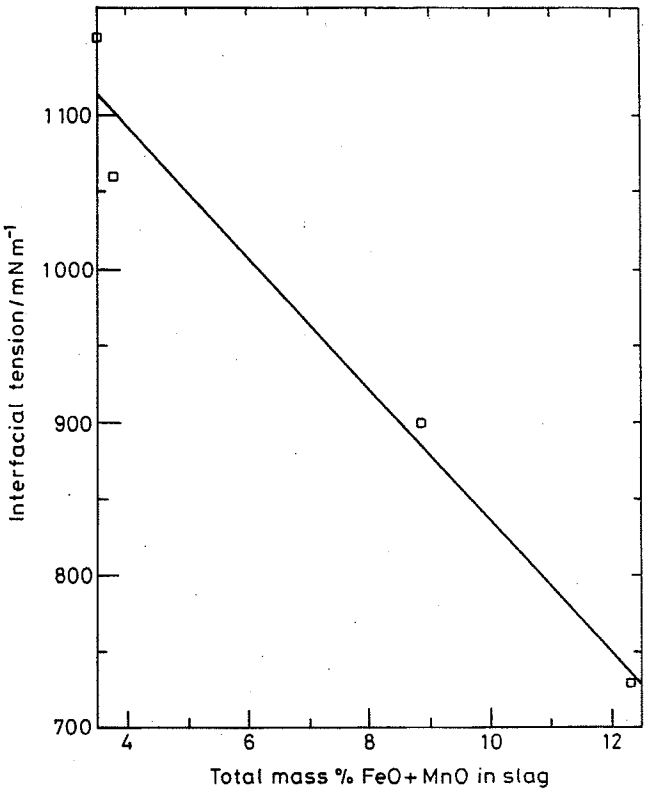
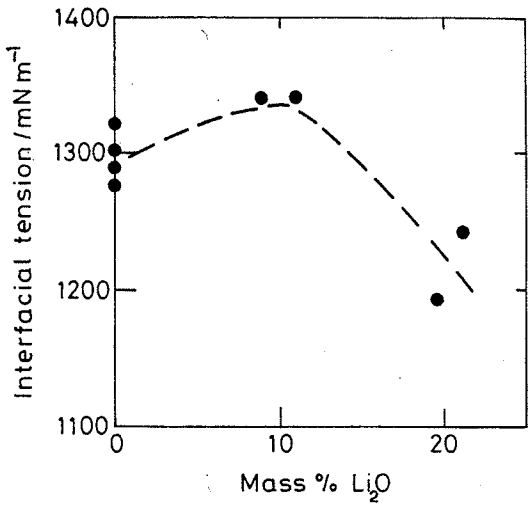


Fig. 11.143. Variation at 1550 °C of the interfacial tension between steel ShKh15 and slag, with the total content of FeO + MnO in the slag. (Base slag contains 30 % Al_2O_3 + 10 % CaO + 60 % SiO_2). [Ref. 84]

Respective points are shown for:
a) 1.4 % FeO + 2.11 % MnO
b) 0.77 % FeO + 2.99 % MnO
c) 4.05 % FeO + 4.79 % MnO
d) 6.51 % FeO + 5.8 % MnO

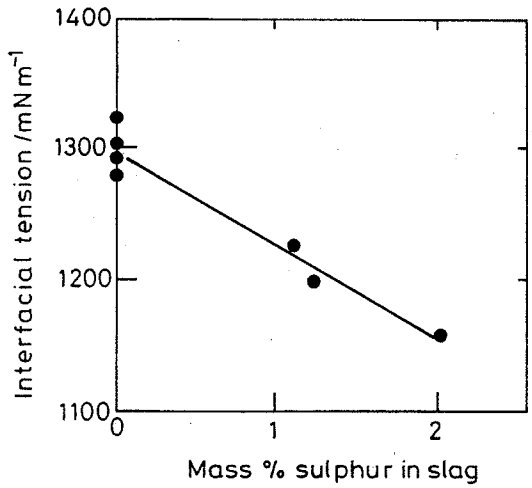
Al_2O_3-CaO-Li_2O-MgO-SiO_2



Mass %						
Al_2O_3	CaO	Li_2O	MgO	SiO_2	FeO	γ_{ms}/mN.m^{-1}
5.9	22.5	8.8	11.8	39.5	0.36	1341
6.1	29.7	10.8	11.5	37.7	0.28	1342
5.6	28.0	19.5	9.5	33.5	0.55	1192
4.9	26.2	21.0	10.6	33.8	0.73	1242
5.8	31.4	-	20.4	39.1	-	1320
6.2	31.1	-	21.1	38.5	0.43	1304
6.0	32.3	-	16.9	39.7	0.50	1271
11.1	32.3	-	-	48.3	0.54	1290

Fig. 11.144. Effect of Li_2O in slag on the interfacial tension with iron at 1600 °C [Ref. 34]. Metal composition: M10

Al_2O_3-CaO-MgO-S-SiO_2

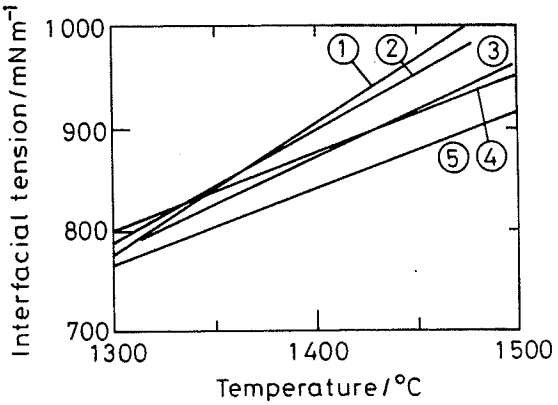


Mass %						
Al_2O_3	CaO	MgO	S	SiO_2	FeO	γ_{ms}/mN.m^{-1}
6.2	32.3	17.9	1.1	38.1	0.43	1224
6.5	34.9	15.7	1.2	40.1	0.46	1198
6.7	31.8	16.9	2.1	38.3	0.69	1156
5.8	31.4	20.4	-	39.1	-	1320
6.2	31.1	21.1	-	38.5	0.43	1304
6.0	32.3	16.9	-	39.7	0.50	1271
11.1	32.3	-	-	48.3	0.54	1290

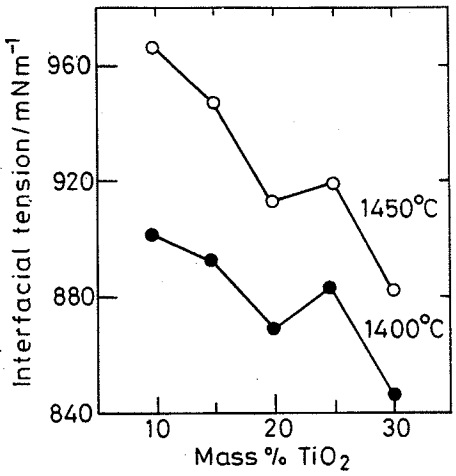
▶

Fig. 11.145. Effect of sulphur (in the form of Na_2S addition) in slag on the interfacial tension with iron at 1600 °C [Ref. 34]. Metal composition: M10

Al_2O_3-CaO-MgO-SiO_2-TiO_2



(a)

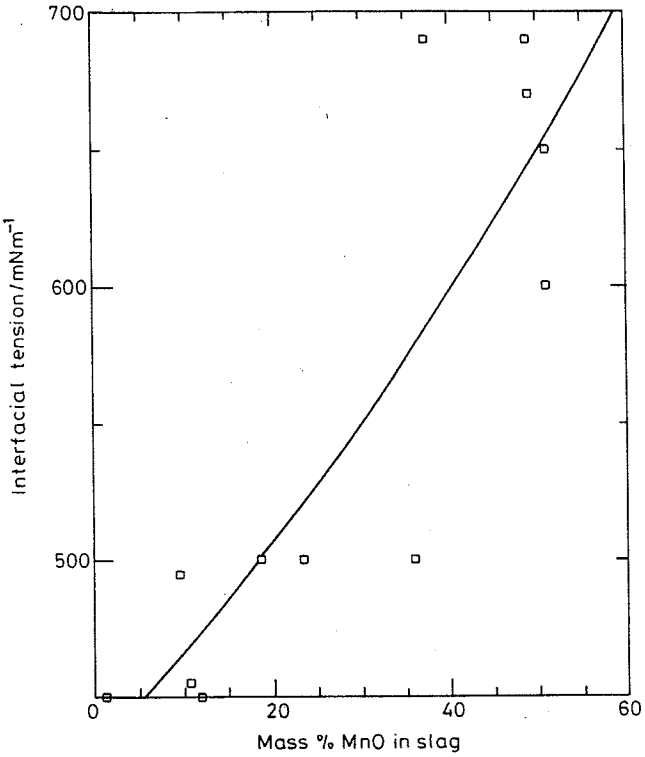


(b)

Slag No.	Mass %				
	Al_2O_3	CaO	MgO	SiO_2	TiO_2
1	14	37.2	5	33.8	10
2	14	34.6	5	31.4	15
3	14	32.0	5	29.0	20
4	14	29.3	5	26.7	25
5	14	26.7	5	24.3	30

Fig. 11.146 a,b. Effect (a) of temperature and (b) of TiO_2 content in slags on the interfacial tension between TiO_2-containing slags and iron alloy (0.13 % Si, 0.14 % Ti, 0.066 % S) [Ref. 86]

Al_2O_3-Fe_xO-MgO-MnO-SiO_2



Mass %					
FeO	Fe_2O_3	MnO	SiO_2	MgO	Al_2O_3
44.4	3.7	1.2	31.0	18.0	1.8
39.1	5.1	9.5	29.2	15.8	1.0
37.7	5.5	10.7	21.0	21.5	2.1
35.0	5.1	11.7	21.9	21.2	2.2
24.8	4.5	18.6	23.3	24.3	1.8
20.3	4.1	23.4	24.8	22.8	1.4
11.7	4.5	36.0	24.0	19.7	2.0
7.7	1.9	37.5	25.5	17.9	2.7
6.4	1.9	51.0	15.2	14.7	1.2
3.9	1.2	49.2	25.2	2.0	1.5
3.5	1.5	51.1	25.7	15.7	2.4
1.5	-	49.0	27.4	20.2	1.8

Fig. 11.147. Effect of replacing Fe_xO in slags by MnO on the interfacial tension with iron at 1550 °C [Ref. 49].
Metal composition: M14

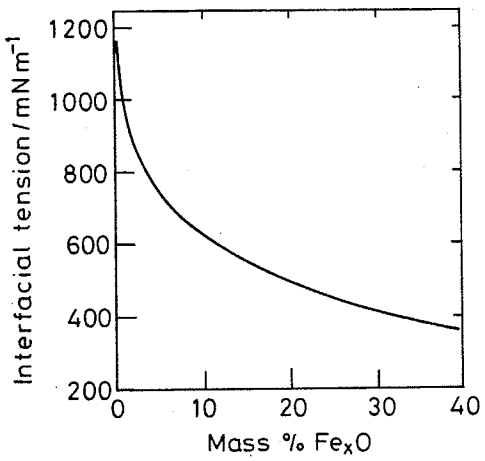


Fig. 11.148. Effect of the Fe_xO content in CaO + Fe_xO + MgO + MnO + SiO_2 slags of various compositions, on the interfacial tension with iron at 1600 °C [Ref. 87]

11.4.3.5 Various complex slags

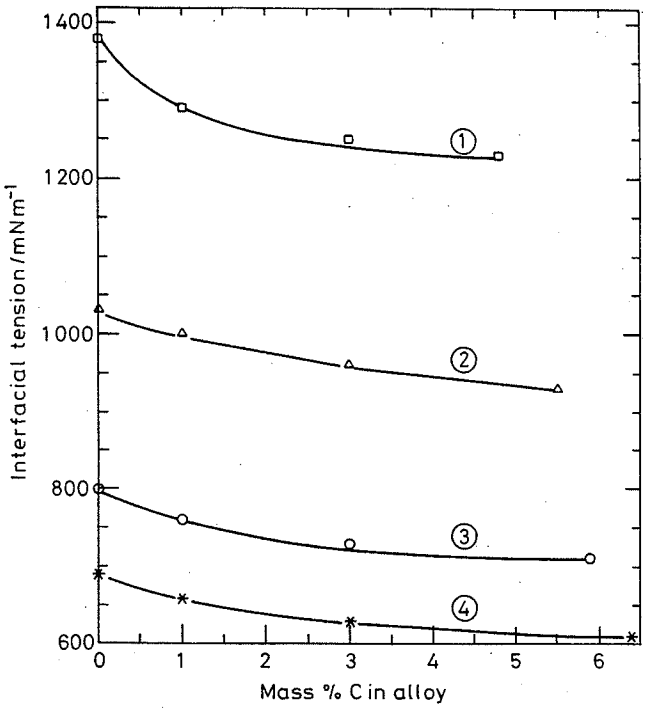


Fig. 11.149. Effect of carbon content in iron and in Fe + Mn alloys on the interfacial tension with a complex basic oxide slag at 1550 °C [Ref. 71]
Slag composition (mass %): 30.1 MnO; 26.5 FeO; 18.8 SiO_2; 17.9 CaO; 1.3 BaO; 3.3 (K_2O; + Na_2O); 1.3 Al_2O_3; 0.9 MgO; 0.85 P_2O_5
Curve 1 - Fe
Curve 2 - Fe : Mn = 4
Curve 3 - Fe : Mn = 1.5
Curve 4 - Fe : Mn = 0.66

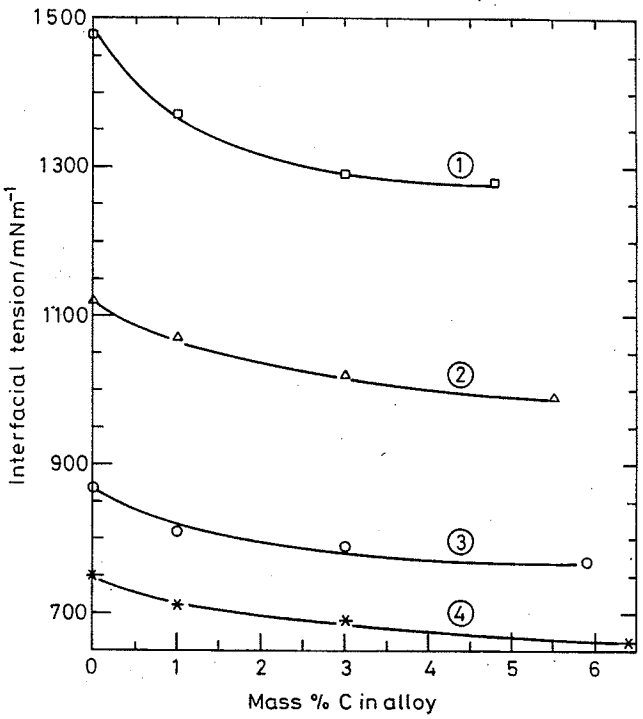


Fig. 11.151. Effect of carbon content in iron and in Fe + Mn alloys on the interfacial tension with complex acidic slag at 1550 °C [Ref. 71]
Slag composition (mass %): 59.4 MnO; 5.1 FeO; 28 SiO_2; 3.2 (K_2O + Na_2O); 1.4 Al_2O_3; 1.4 BaO; 0.9 MgO; 0.9 P_2O_5
Curve 1 - Fe
Curve 2 - Fe : Mn = 4
Curve 3 - Fe : Mn = 1.5
Curve 4 - Fe : Mn = 0.66

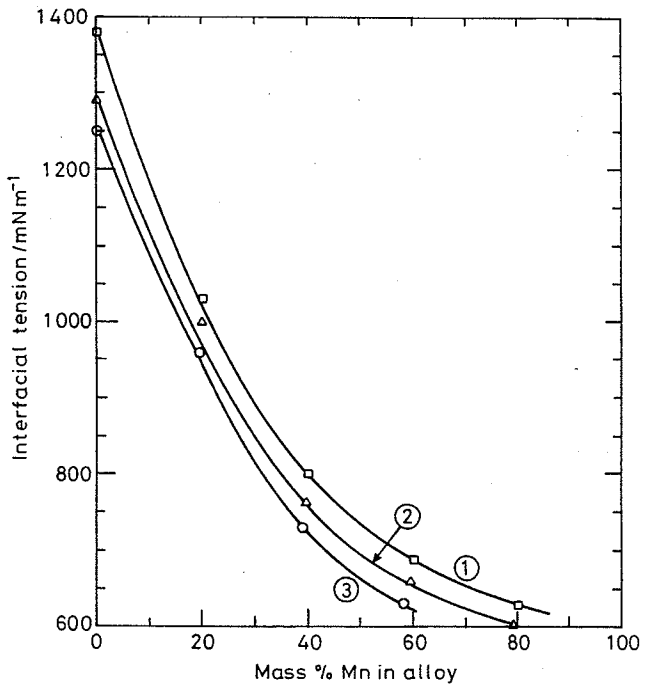


Fig. 11.150. Effect of manganese content in Fe + Mn and in Fe + Mn + C alloys on the interfacial tension with a complex basic slag at 1550 °C [Ref. 71]
Slag composition as given for Fig. 11.149.
Curve 1 - 0 % C in alloy
Curve 2 - 1 % C in alloy
Curve 3 - 3 % C in alloy

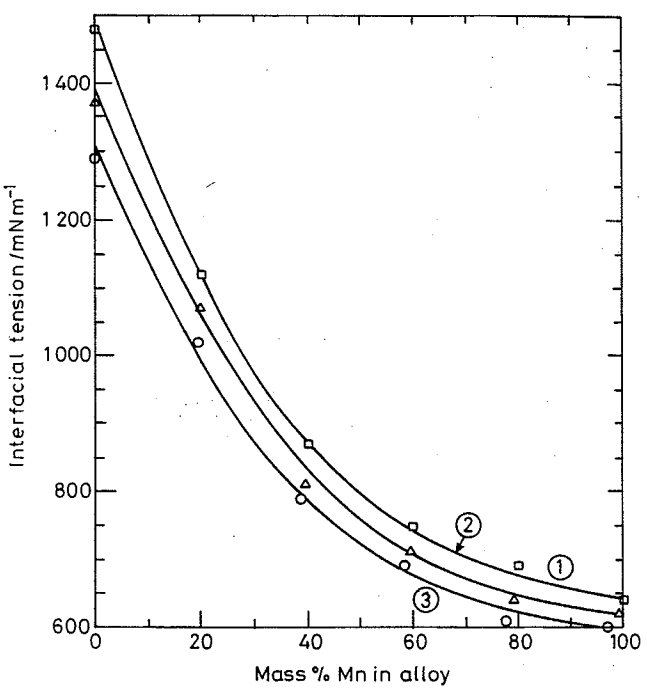


Fig. 11.152. Effect of manganese content in Fe + Mn and in Fe + Mn + C alloys on the interfacial tension with a complex acidic slag at 1550 °C [Ref. 71]
Slag composition as given for Fig. 11. 151.
Curve 1 - 0 % C in alloy
Curve 2 - 1 % C in alloy
Curve 3 - 3 % C in alloy

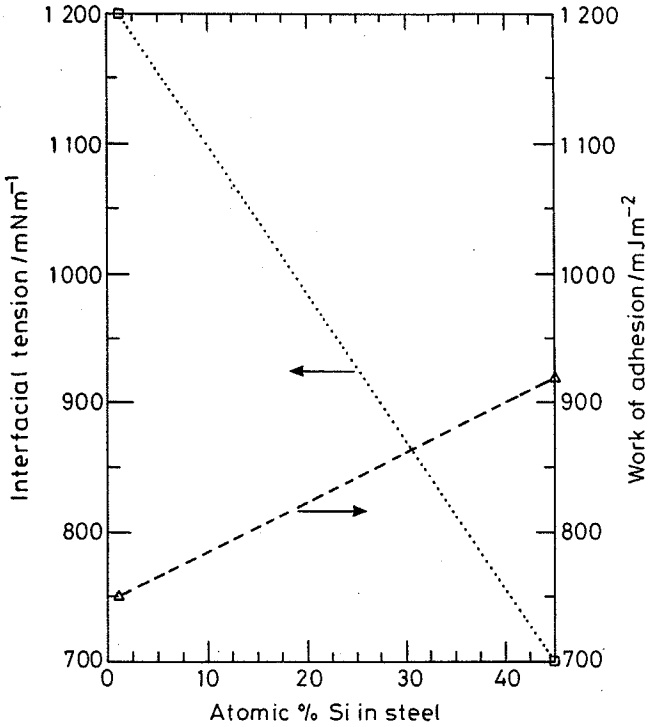


Fig. 11.153. Effect of silicon content in low alloy steel on the interfacial tension and work of adhesion with a complex acidic slag at 1550 °C [Ref. 89]
Slag composition (mass %): 10 Al_2O_3 + 28.9 CaO + 24.2 MgO + 3.4 MnO + 2 FeO + 1.4 Cr_2O_3 + 0.3 V_2O_5 + 0.3 P_2O_5 + 29.1 SiO_2

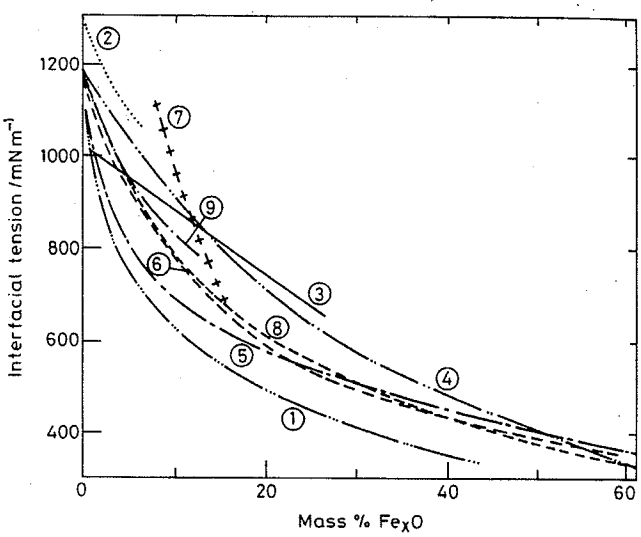


Fig. 11.155. Compilation of literature data, illustrating the general trend for the interfacial tension γ_{MS} between iron and slag to decrease with increase in the Fe_xO content of the slag [Ref. 91]

Curve 1 - [Ref. 87]
Curve 2 - [Ref. 48]
Curve 3 - [Ref. 92]
Curve 4 - [Ref. 49]
Curve 6 - [Ref. 93]
Curve 7 - [Ref. 94]
Curve 8 - [Ref. 74]
Curve 9 - [Ref. 75]

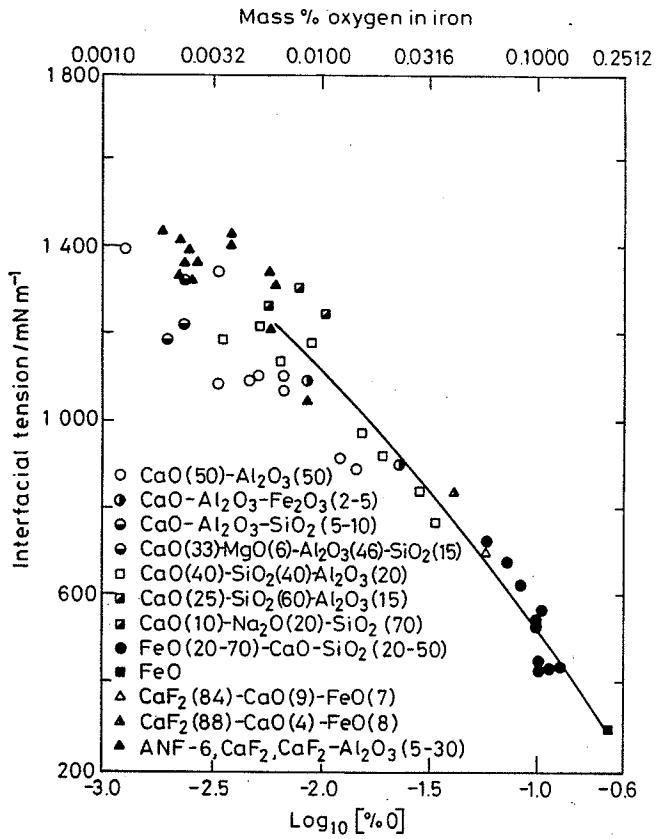


Fig. 11.154. General relation between the oxygen content of iron and the interfacial tension between the metal and various slag systems at 1580 °C [Ref. 90]

11.5 Electrocapillary data

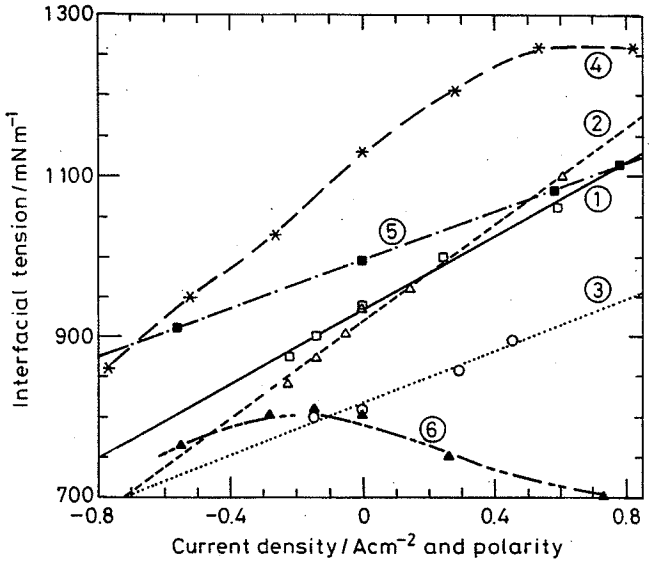


Fig. 11.156. Electrocapillary curves for the systems low carbon steel/SiO_2-based binary slags [Ref. 95]. Metal composition: M26
Curve 1 - 17 % Na_2O at 1530 °C
Curve 2 - 17 % K_2O at 1530 °C
Curve 3 - 17 % K_2O at 1630 °C
Curve 4 - 50 % CaO at 1530 °C
Curve 5 - 50 % CaO at 1580 °C
Curve 6 - 40 % MnO at 1530 °C

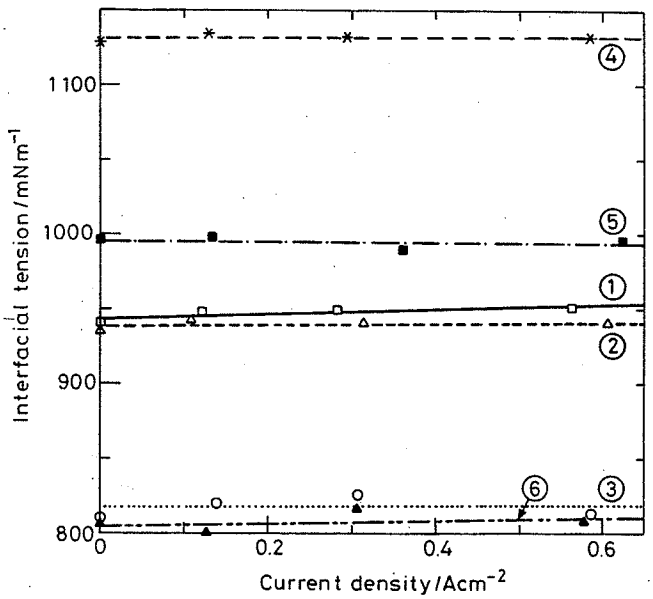


Fig. 11.157. Effect of alternating current (Hz not quoted) on the interfacial tension between low carbon steel and SiO_2-based binary slags [Ref. 9]. (Curve numbers correspond to those given for Fig. 11.156

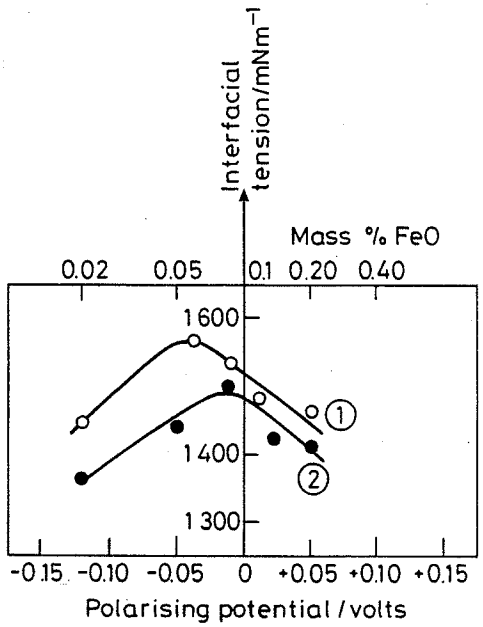


Fig. 11.158. Electrocapillary curves for the system Al_2O_3 + CaO + SiO_2/carbon saturated iron, at 1450 °C [Ref. 96]
Curve 1 - 15 % Al_2O_3 + 45 % CaO + 40 % SiO_2
Curve 2 - 15 % Al_2O_3 + 35 % CaO + 50 % SiO_2

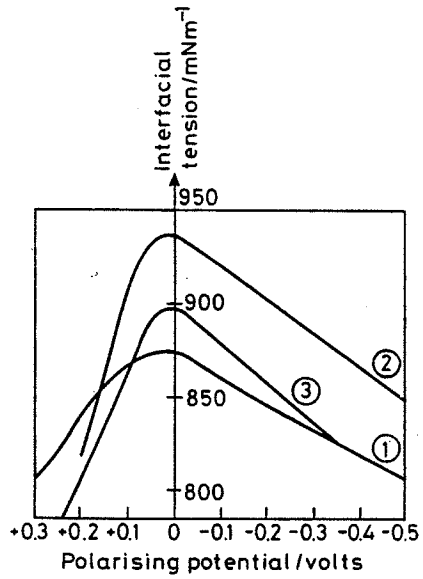


Fig. 11.159. Electrocapillary curves for the systems Fe + 13 atomic % C/oxide slags at 1450-1480 °C [Ref. 97]
Curve 1 - 5.2 % Al_2O_3 + 48.4 % CaO + 46.2 % SiO_2
Curve 2 - 11.1 % Al_2O_3 + 50.3 % CaO + 38.6 % SiO_2
Curve 2 - 7.2 % Al_2O_3 + 49.2 % CaO + 43.5 % SiO_2

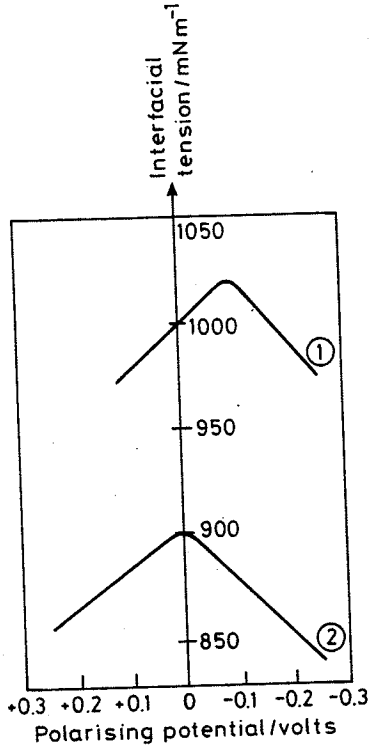


Fig. 11.160. Electrocapillary curves showing the effect of Si in the metal, for the systems Fe + C/slag (mol %: 11.1 Al_2O_3 + 41.6 CaO + 47.3 SiO_2) at 1450-1480 °C [Ref. 97]

Curve 1 - Fe containing (atomic %); 14 C + 0.9 Si + 2.0 Mn + 0.06 S
Curve 2 - Fe containing (atomic %); 13 C + 3.5 Si + 2.1 Mn + 0.06 S

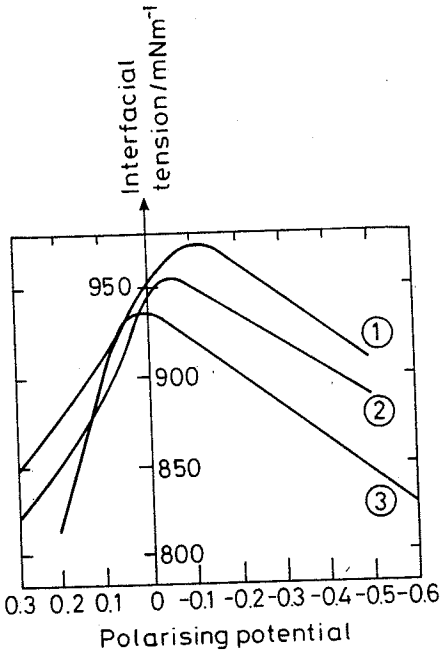


Fig. 11.162. Electrocapillary curves showing the effect of slag composition on the interfacial tension with Fe containing (atomic %; 13 C + 3.5 Si + 0.6 Mn + 0.06 S + 0.6 P, at 1450-1480 °C [Ref. 97]

Slag compositions (mol %):
Curve 1 - 11.1 Al_2O_3 + 41.6 CaO + 47.3 SiO_2
Curve 2 - 11.1 Al_2O_3 + 43.8 CaO + 45.1 SiO_2
Curve 3 - 11.1 Al_2O_3 + 50.3 CaO + 38.6 SiO_2

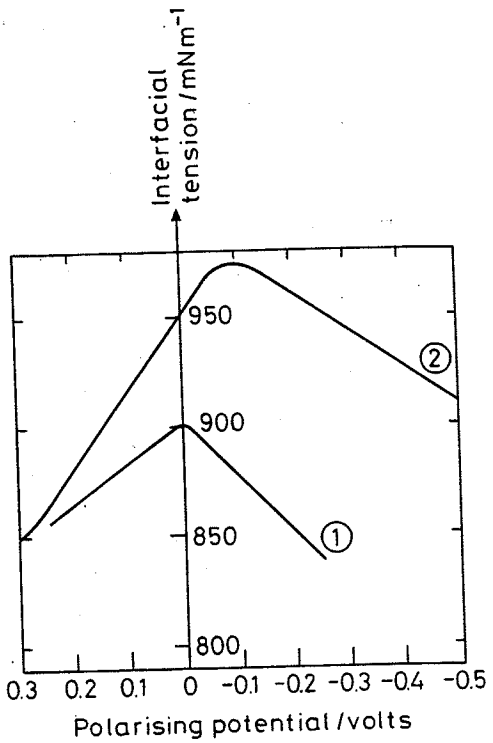


Fig. 11.161. Electrocapillary curves showing the effect of Mn in the metal for the systems Fe + C/slag (mol %: 11.1 Al_2O_3 + 41.6 CaO + 47.3 SiO_2) at 1450-1480 °C [Ref. 97]

Curve 1 - Fe containing (atomic %); 13 C + 3.2 Si + 2.1 Mn + 0.06 S
Curve 2 - Fe containing (atomic %); 13 C + 3.5 Si + 0.6 Mn + 0.06 S

11.6 References in Chapter 11

[1] Keene, B.J.: "Surface tension of slag systems". ECSC Research Contract 7210-CF/107 – NPL Report DMM(D)32, dated May 1990
[2] Keene, B.J.: "Contact angle and work of adhesion between ferrous melts and non-metallic solids". ECSR Research Contract 7210-CF/107 – NPL Report DMM(D)65, dated January 1991
[3] Ooi, H.; Nozaki, T.; Yoshii, Y.: Tetsu-to-Hagane 58 (7), 1972, 830
[4] Kozakevitch, P.; Lucas, L.D.: Rev. Metall. 65 (9), 1968, 589
[5] Mills, K.C.: "A literature review of inclusion removal by filtration and flotation". NPL Report DMM(A)13, dated March 1991
[6] Keene, B.J.: "Contact angle and work of adhesion between Ni-based melts and non-metallic solids". NPL Report DMM(A)23, dated March 1991
[7] Lippman, G.: Ann. Chim. Phys. 5 (5), 1875, 494
[8] Davies, J.T.; Rideal, E.K.: Interfacial Phenomena. Pub. Academic Press, 1961
[9] Deev, G.D.; Patskevich, I.R.: Avt. Svarka (5), 1980, 67
[10] Humenik Jr., M.; Kingery, W.D.: J. Am. Ceram. Soc. 37 (1), 1954, 18
[11] Volkov, S.E.; Mchedlishvili, V.A.; Samarin, A.M.: Dokl, Akad. Nauk. 149 (5), 1963, 1131
[12] Ogino, K.; Nogi, K.; Koshida, Y.: Tetsu-to-Hagane, 59 (10), 1973, 1380
[13] Kishimoto, M.; Izumi, H.; Mori, K.; Kawai, Y.: J. JIM. 44 (9), 1980, 1053
[14] Ogino, K.; Nogi, K.; Yamase, O.: Tetsu-to-Hagane, 66 (2), 1980, 179
[15] Ageev, P.Ya.; Grebenkin, V.I.; Kalmykov, V.A.; Sveshkov, Yu.V.: Fiz. Khim. Obra. Mater. (6), 1968, 120
[16] Cosma, D.: Metalurgia. 23 (12), 1971, 804
[17] Vatolin, N.A.; Ukhov, V.F.; Pokrovskii, V.A.: Trud. Inst. Met. Sverdlovsk, (20), 1969, 55
[18] Yakobashvili, S.B.: Avt. Svarka. (6), 1970, 22
[19] Pupynina, S.M.; Volkov, S.E.; Bobkova, O.S.; Petukhov, V.S.: Sb. Trudy Tsentr. Inst. Chem. Met. (70), 1969, 47

[20] Pupynina, S.M.; Volkov, S.E.: Teor. Metall. Prots. 1971, 156
[21] Ogino, K.; Hara, S.: Tetsu-to-Hagane, 63, 1977, 2141
[22] van Muu, B.; Krauss, S.; Burghardt, H.: Neue Hütte, 21 (6), 1976, 335
[23] Yakobashvili, S.B.: AN Ukr SSR - Ordena Trud. Kras. Znameni. Inst. Elektrosvarka im Akad. E O PATONA - Kiev (1963)
[24] Yakobashvili, S.B.; Frumin, I.I.: Avt. Svarka. (10), 1962, 41
[25] Safonnikov, A.F.; Nikitin, Yu.P.: Avt. Svarka. (9), 1962, 27
[26] Gaye, H.; Lucas, L.D.; Olette, M.; Riboud, P.V.: Canad. Metall. Quart. 23 (2), 1984, 179
[27] Gogiberidze, Yu.M.; Dzhincharadze, T.I.; Mikiashvili, Sh.M.: Soob. AN Gruz. SSR (3), 1968, 695
[28] Deryabin, A.A.; Popel, S.I.: Iz. VUZ Chern. Metall. (8), 1964, 5
[29] van Muu, B.; Fenzke, H.W.: Freiburg. Forschungs-B. B252, 1985, 40
[30] Lobzhanidze, R.B.; Filippov, A.F.; Evseev, P.P.: Iz. VUZ Chern. Metall. (7), 1969, 56
[31] Krusina, J.; Myslivec, T.: Kovove Mater. 16 (1), 1978, 98
[32] Komelkov, V.K.; Shirer, G.B.; Shalimov, A.G.; Voinov, S.G.: Teor. Met. Prots. 1, 1972, 50
[33] Yakushev, A.M.; Romashin, V.M.; Ivanova, N.V.: Steel in the USSR, 15 (9), 1985, 425
[34] Shinozaki, N.; Fujiike, K.; Mori, K.; Kawai, Y.: Technol. Rept. Kyushu Univ. 62 (5), 1989, 573
[35] Popel, S.I.; Esin, O.A.; Dzhemilev, N.K.: Iz. VUZ Chern. Metall. (6), 1963, 5
[36] Popel, S.I.; Deryabin, A.A.: Iz. VUZ Chern. Metall. (9), 1963, 16
[37] Padalka, V.G.; Yavoiskii, V.I.; Nechkin, Yu.M.; Einkovskii, I.V. Ovchinnikov, N.A.: v Sb Razlivka Stali v Slitki i Ikh. Kachestvo. (4), 1975, 61
[38] Yakobashvili, S.B.: Auto. Weld. (9), 1962, 31
[39] Bretonnet, J.L.; Lucas, L.D.; Olette, M.: Circ. Inf. Techn. Cent. Doc. Sider. 33 (1), 1976, 105
[40] Saburov, L.N.; Popel, S.I.; Deryabin, A.A.: Steel in the USSR, (8), 1971, 658
[41] Bretonnet, J.L.; Lucas, L.D.; Olette, M.: C R Acad. Sci. Paris, 285 (Ser C), July 1977, 45
[42] Krinochkin, E.V.; Kurochkin, K.T.; Umrikhin, P.V.: Nauchn. Trudy Mosk. Inst. Stali Splav, (79), 1973, 31
[43] Mukai, K.; Kato, T.; Sakao, H.: Tetsu-to-Hagane, 59 (1), 1973, 55
[44] Deryabin, A.A.; Popel, S.I.; Saydulin, R.A.; Tarkhanov, M.V.: Fiz. Khim. Poverkh. Yav. Rasp. 1971, 261. Ed.: V.N. Eremenko. Pub.: Naukova Dumka Kiev
[45] Saburov, L.N.; Popel, S.I.; Deryabin, A.A.: Russ. Metall. (3), 1973, 44
[46] El Gammal, T.; Müllenberg, R.-D.: Arch. Eisenhüttenw., 51 (6), 1980, 221
[47] Mukai, K.; Furukawa, H.; Tsuchikawa, T.: Tetsu-to-Hagane, 63 (9), 1977, 1484
[48] Adachi, A.; Ogino, K.; Suetaki, T.: Tetsu-to-Hagane, 50, 1964, 1838
[49] Popel, S.I.; Konovalov, G.F.: Iz. VUZ Chern. Metall. 2 (8), 1959, 3
[50] Gogiberidze, Yu.M.; Kekelidze, M.A.; Mikiashvili, Sh.M.: Soob. AN Gruz. SSR, 32 (1), 1963, 117
[51] Mori, K.; Fadsimura, M.: JISI Japan, 40, 1954, 274
[52] Ogino, K.; Hara, S.; Miwa, T.; Kimoto, S.: Tetsu-to-Hagane, 65 (14), 1979, 2012
[53] Bretonnet, J.L.; Lucas, L.-D.; Olette, M.: CR Acad. Sci. Paris, 280 (Ser. C), 1975, 1169
[54] Popel, S.I.: Zh. Fiz. Khim. 32 (10), 1958, 2398
[55] Smolyarenko, V.D.; Yakushev, A.M.; Edneral, F.P.: Iz. VUZ Chern. Metall. (3), 1965, 36
[56] Baryshnikov, V.G.; Deryabin, A.A.; Popel, S.I.; Panfilov, A.M.: Russ. J. Phys. Chem. 46 (7), 1972, 1057
[57] Popel, S.I.; Esin, O.A.; Nikitin, Yu.P.: DAN SSSR 83 (2), 1952, 253
[58] Popel, S.I.: Iz. VUZ Chern. Metall. (8), 1962, 9
[59] Popel, S.I.: Sb. Nauchn. Tr. Ural'sk Polit. (126), 1963, 5
[60] Popel, S.I.; Esin, O.A.; Gel'd, P.V.: Dokl. AN SSSR, 75 (2), 1950, 227
[61] Deryabin, A.A.; Smirnov, L.A.; Popel, S.I.: Iz. VUZ Chern. Metall. (2), 1982, 157
[62] Evtyukhina, I.A.; Kozin, A.I.; Kunin, L.L.: Teor. Metall. Prots. 2, 1974, 137
[63] Gavrilenko, Yu.V.; Chernyakov, V.A.; Voinov, S.G.: Iz. VUZ Chern. Metall. (10), 1973, 57
[64] Deryabin, A.A.; Popel, S.I.; Eupnik, A.E.: Iz. AN SSSR Metall. (2), 1968, 78
[65] Deev, G.F.; Patskevich, I.R.: Avt. Svarka. (2), 1971, 5
[66] Pham, G.K.; Krusina, J.; Myslivec, T.: Kovove Mater. 16 (1), 1978, 81
[67] Perminov, A.A.; Popel, S.I.; Poltarak, A.M.: Zashchita Metallov. 6 (1), 1970, 97
[68] Popel, S.I.; Deryabin, A.A.: Fiz. Khim. Rasp. Shlakov. 1970, 121-129
[69] Mazanek, T.: Arch. Hutnictwa 8 (2), 1963, 119
[70] Kekelidze, T.M.; Mikiashvili, Sh.M.; Khomeriki, R.V.: Pererot. Zhelez. Margant. Rud. Zakav. Pub: Metsniereba. TBILISI, 1979, 133
[71] Rudenko, V.A.; Tolstoguzov, N.V.: Iz. VUZ Chern. Metall. (12), 1968, 64
[72] Gogiberidze, Yu.M.; Kekelidze, M.A.; Mikiashvili, Sh.M.: Trudy. Gruz. Inst. Met. 14, 1964, 97
[73] Linzer, E.; Myslivec, T.: Kovove Mater. 16 (3), 1978, 312
[74] Saydulin, R.A.; Deryabin, A.A.; Popel, S.I.: Iz. AN SSSR Metall. (5), 1971, 79
[75] Deryabin, A.A.; Saydulin, R.A.; Popel, S.I.: Zavod. Lab. 36 (3), 1970, 292
[76] Popel, S.I.; Esin, O.A.; Konovalov, G.F.; Smirnov, N.S.: Proc. Acad. Sci. USSR (Phys. Chem.), 112, 1957, 27
[77] Saydulin, R.A.; Deryabin, A.A.; Popel, S.I.; Kozhurkov, V.N.: Iz. AN SSSR Metall. (1), 1973, 63
[78] Bairamov, B.I.; Popel, S.I.; Deryabin, A.A.: Iz. VUZ Chern. Metall. (1), 1979, 5
[79] Kekelidze, T.M.; Mikiashvili, Sh.M.; Dzhincharadze, T.I.; Khomeriki, R.B.: Iz. AN Gruz. SSR (Khim.) 4 (4), 1978, 327
[80] Popel, S.I.; Deryabin, A.A.; Esin, O.A.: Iz. VUZ Chern. Metall. (12), 1965, 5
[81] Samarin, A.M.; Mikiashvili, Sh.M.; Dzhincharadze, T.I.; Gogiberidze, Yu.M.: Fiz. Khim. Osn. Proiz. Stal. Mater. Simp. Met. Metall. 1968, Pub.: 1971. 248-51
[82] Mikiashvili, Sh.M.: Tr. Gruz. Inst. Met. 14, 1964, 91
[83] Shinozaki, N.; Kurashige, T.; Mori, K.; Kawai, Y.: J. JIM 46 (1), 1982, 60
[84] Popel, S.I.; Deryabin, A.A.; Esin, O.A.: Iz. VUZ Chern. Metall. (12), 1963, 5
[85] Yakushev, A.M.; Romashin, V.M.; Ivanova, N.V.: Steel in the USSR 15 (9), 1985, 425
[86] Mao Yuwen; Luo Weizhong; Lu Furong; Zhu Yuankai: Gangtie 22 (4), 1987, 11
[87] Kawai, Y.; Shinozaki, N.; Mori, K.: Canad. Metall. Quart. 21 (4), 1982, 385
[88] Boton, M.; Valchev, I.: Metallurgia (Sofia) 29 (2-3), 1974, 5
[89] Vatolin, N.A.; Ukhov, V.G.: Smach. Poverkh. Svoista Rasp. Tverd. Tel. 1972, 186-189
[90] Ogino, K.; Hara, S.; Miwa, T.; Kimoto, S.: Trans. ISIJ 24, 1984, 522
[91] Mills, K.C.; Keene, B.J.: Int. Mater. Rev. 32 (1-2), 1987, 1
[92] Popel, S.I.; Esin, O.A.; Knovalov, G.F.; Smirnov, N.S.: Dokl. AN SSSR 112 (1), 1957, 104
[93] Popel, S.I.: Iz. VUZ Chern. Metall. (8), 1962, 9
[94] Povolotskii, D.Ya.; Stroganov, A.I.; Puzyrev, A.V.: Steel in the USSR 1 (6), 1971, 428
[95] Deev, G.F.; Patskevich, I.R.: Avt. Svarka. (1), 1973, 12
[96] Ogino, K.; Hara, S.; Adachi, A.; Kuwata, H.: Tetsu-to-Hagane 59 (1), 1973, 28
[97] Patrov, B.V.: Surface Phenomena in Metallurgical Processes 1963. Pub.: Consultants Bureau, New York. 129-133

12

Contact angle and work of adhesion between ferrous melts and non-metallic solids

B. J. Keene

12.1 Introduction

The wetting behaviour and the adhesion between molten metals and solid ceramics are important factors which can radically affect the efficiency of some metallurgical processes. Examples of situations in which these phenomena can play an important role are:

1) Removal of solid inclusions from the melt, either by flotation or filtration;
2) Electron beam button melting techniques to assess the cleanness of metals;
3) Metal casting and moulding processes;
4) Production of metal-matrix/ceramic reinforced composite materials;
5) Production of cermets;
6) Clogging of ceramic nozzles in steelmaking procedures;
7) Erosion of refractory containers and linings.

Practical determination of the wetting and adhesional properties of liquid-solid systems at high temperature are generally carried out by either sessile drop or tensiometric techniques.

12.2 Contact angle (θ) and work of adhesion (W_A)

The profile adopted by a liquid drop resting in equilibrium on a flat horizontal surface, is governed by the balance between surface and gravitational forces **(Fig. 12.1)**. The relation between the contact angle and the respective interfacial tensions (γ_{LG}; γ_{LS}; γ_{SG}) acting at the point of three-phase contact (A in Fig. 12.1), is given by the Young equation viz

$$(\gamma_{SG} - \gamma_{LS}) = \gamma_{LG} \cdot \cos\theta. \qquad (12.1)$$

When (θ) = 180°, the liquid is wholly non-wetting with respect to the particular solid, and conversely, for systems in which (θ) = 0°, the solid is completely wetted by the liquid. (θ) = 90° is the transition angle and systems having values of (θ)>90° or <90° are described respectively as non-wetting **(Fig. 12.1 a)** and wetting **(Fig. 12.1 b)**.

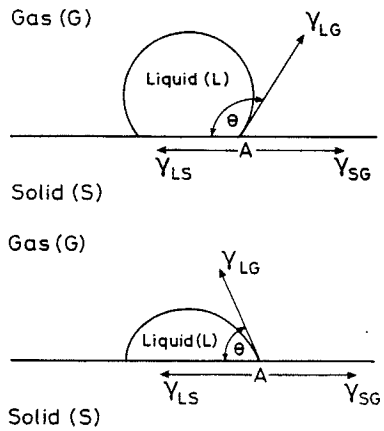


Fig. 12.1 a,b. The relation at equilibrium between the respective surface- and interfacial-tensions and the contact angle (θ)
a) Liquid on solid (non-wetting condition)
b) Liquid on solid (wetting condition)

Work of adhesion is a measure of the energy change (per unit area of contact) on separating the two media at a liquid/solid interface, and is defined by the Dupre relation:

$$W_A = \gamma^e_{LG} + \gamma^e_{SG} - \gamma^e_{LS} \qquad (12.2)$$

(where γ^e_{LG}, γ^e_{SG} and γ^e_{LS} are the surface energies per unit area of the respective interfaces). The Dupre relation shows that the lower the liquid/solid interfacial energy relative to the sum of the other two interfacial energies the greater the work of adhesion (i.e. bond strength) between the two media.

The interfacial tension and interfacial energy are generally numerically equal for liquids. From equations (12.1) and (12.2) and using the numerical equivalence between γ_{LG} and γ^e_{LG}, we obtain

$$W_A = |\gamma_{LG}| \, (1 + \cos\theta). \qquad (12.3)$$

Under certain conditions, molecules of the liquid vapour can be adsorbed on to the free surface of the solid with the consequence that the effective interfacial energy of the solid will be reduced and equation (12.3) has to be modified to account for this:

$$W_A = \gamma^e_{LG} (1 + \cos\theta) + \pi \text{ where } \pi \text{ (the surface pressure)}$$

= reduction in the surface energy of the solid/gas interface ($\Delta\gamma^e_{SG}$).

It follows from equation (12.3) that over the measureable range of θ:

$$2\gamma^e_{LG} \geq W_A \geq 0$$

and that for the wetting condition (θ < 90°):

$$W_A > \gamma^e_{LG}.$$

The relation given in equation (12.1) is indeterminate when θ = 0° and to obviate this problem, Bortell and Osterhof [2] proposed an alternative expression:

$$\gamma_{SG} - \gamma_{SL} = K.\gamma_{LG}$$

(where K is termed the "adhesion constant" and equals cos θ when θ > 0°, but can have values in excess of unity when θ = 0°). Introduction of the adhesion constant removes the limitation implicit in equation (12.3) that the maximum value for $W_A = 2\gamma^e_{LG}$.

Individually, γ_{SG} and γ_{SL} are difficult to measure, but provided θ > 0°, their difference (= γ_{LG} cos θ), can be experimentally determined by the sessile drop method. The product (γ_{LG}. cos θ) is termed the "adhesion tension (A)" or the "wetting energy". A high value of (A) correlates with good bonding at the solid/liquid interface i.e. with a low value of γ^e_{SL}. Dokhov [3] has derived an equation with which γ^e_{SL} can be calculated from a knowledge of γ^e_{LG} and θ viz:

$$\gamma^e_{SL} = \gamma^e_{LG} \left(\frac{2 - 3\cos\theta + \cos^3\theta}{4} \right)^{1/3}.$$

This relation has been used [4] to calculate γ^e_{SL} for various liquid metal/solid oxide systems, and with the Young equation (12.1), values for γ^e_{SG} were also derived. Accurate values of γ^e_{LG} and the associated equilibrium contact angle are necessary and ideally both should be determined in the same experiment. Dokhov [4] observed that, in practice the solid-vapour interfacial energy could be significantly reduced by adsorption of liquid vapour at the surface, which may account for the relatively low values obtained.

The spreading coefficient (S) is a relative measure of the tendency for a non-reacting liquid to spread across the surface of a given solid. (S) is defined as the difference between the work of adhesion at the solid/liquid interface and the work of cohesion of the liquid ($= 2\gamma^e_{LG}$) i.e.

$$S = W_A - W_c$$

$$= W_A - 2\gamma^e_{LG} \qquad (12.4)$$

From equations (12.1), (12.2) and (12.4):

$$S = \gamma^e_{SG} - \gamma^e_{LS} - \gamma^e_{LG} \qquad (12.5)$$

$$= |\gamma_{LG}| \ (\cos\theta - 1). \qquad (12.6)$$

The more positive the value of (S), the greater the tendency for a liquid to spread across the solid i.e. from (12.5), (γ^e_{SG}) would be high relative to $(\gamma^e_{LS} + \gamma^e_{LG})$. It follows from equation (12.6), that over the measurable range of (θ):

$$0 \geq S \geq -2\gamma^e_{LG}.$$

The value of the spreading coefficient is a measure of the relative tendency for particles of a particular material to become entrapped within the metal during casting processes. The more negative the value of (S), i.e. the change in free energy, the greater the probability of emergence of a particle at the metal/gas or metal/slag interface.

In production of metal-matrix composites, good infiltration of uncoated ceramic fibres by the molten metal is facilitated by high values of (S). Additions of surfactants to the metal can improve infiltration (by lowering (γ_{LG}) and hence increasing (S)), but it is important to ensure that improvement in spreadability of the liquid does not also arise as a result of chemical reaction with the fibres which could lead to a reduction in the integrity and strength of the reinforcing medium.

12.3 Factors affecting wettability and adhesion

12.3.1 Intermolecular bonding

The strength of the bond between a liquid metal and a ceramic is principally governed by the action of two distinct types of intermolecular force viz (a) physical or dispersion forces of the London – van der Waals' type and (b) chemical forces due to adsorption or reactions between components of the system.

12.3.2 Dispersion forces

These are weak attraction forces acting between atoms or molecules and their effect is represented by the (a) term in the van der Waals' equation of state. In contrast to chemical forces, these forces are characterised by a relatively weak dependence on temperature. In simplistic terms, dispersion forces are generated by the transient dipoles induced by continual fluctuations in the electron configurations of the respective molecules and their strength varies inversely as the seventh power of the intermolecular distance (the energy of attraction between two atoms varies inversely as the sixth power of the distance). These forces are a dominant factor controlling the bond strength between liquid metals and solid ceramics when no chemical interactions occur. Calculations have been made as to the magnitude of the expected contribution of dispersion forces to the work of adhesion in metal-ceramic systems and the maximum value derived was found to be about 600 $mJ.m^{-2}$. Surface energies of many liquid metals are in excess of this value and since the condition for wetting is $W_A > \gamma^e_{LG}$, it follows that for many metal/ceramic systems it is probable that the strength of the physical forces alone would be insufficient to give rise to a wetting condition. Wetting would only occur when additional forces due to chemical interactions were present to supplement the dispersion forces.

12.3.3 Chemical forces

If chemical action occurs when contact is made between the liquid and solid, then initially the system will be in a non-equilibrium state. The metal will spread across the solid and there will be a progressive change with time in the magnitudes of γ^e_{SL}, θ, W_A and possibly γ^e_{LG} until equilibrium is attained i.e. the chemical potentials of the respective components at the interface and in each phase, are equal.

If the nature of the chemical action in the system is solely adsorption, then immediately after contact, surface-active species migrate to, (but do not traverse), the two-phase interface. The time to attain equilibrium will be controlled by the rates of diffusion of the respective species and these will be dependent on temperature. Systems in which only chemical adsorption occurs, are characterised by a monotonic decrease in γ^e_{SL} with time [5]. The driving force (F_D) for spreading which acts at the three phase boundary can be expressed as [6]:

$$F_D = \gamma_{LG} (\cos\theta_o - \cos\theta_t)$$

where θ_o = equilibrium contact angle
θ_t = contact angle at time (t).

It follows that $F_D = 0$ when $\theta_t = \theta_o$.

Throughout the period of spreading, measurements of (θ) would yield non-equilibrium values and use of equation (12.1) to calculate variations in (γ_{SL}) would not be strictly valid. However, Naidich [6] proposed that, provided the change in (γ_{SL}) is sufficiently slow and the viscosity of the liquid is low, the drop would be able to deform sufficiently quickly to acquire a quasi-equilibrium shape. In these circumstances it would be acceptable to use equation (12.1) to calculate instantaneous values of (γ_{SL}) from successive images of the drop profile during the spreading process. (Note that if chemical reactions occur, (γ_{LG}) is also likely to vary throughout the non-equilibrium state).

Chemical reactions between the liquid and solid are accompanied by mass transfer across the two-phase interface to produce new solutions and/or compounds. With strong reactions it has been found [5] that the variation of (γ_{SL}) with time goes through a minimum before recovering to the final equilibrium value. The time taken to achieve equilibrium depends upon the reaction kinetics and is thus strongly dependent upon the temperature of the system. Obviously in these cases, the final equilibrium contact angle and adhesion pertain to the ultimate composition of the metal which could be substantially different from that of the start material.

Efforts have been made to relate experimentally determined values of (θ) and (W_A) to chemical properties of the respective systems. **Fig. 12.2** shows linear relations derived by

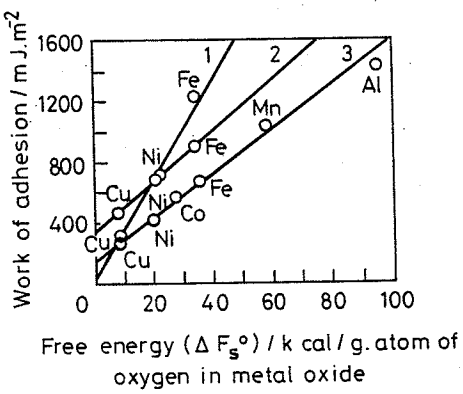


Fig. 12.2. Relation between the work of adhesion in metal-oxide systems and the free energy of formation of the oxide of the liquid metal [Ref. 7]
Curve 1 - SiO_2 Curve 2 - Y_2O_3 Curve 3 - Al_2O_3

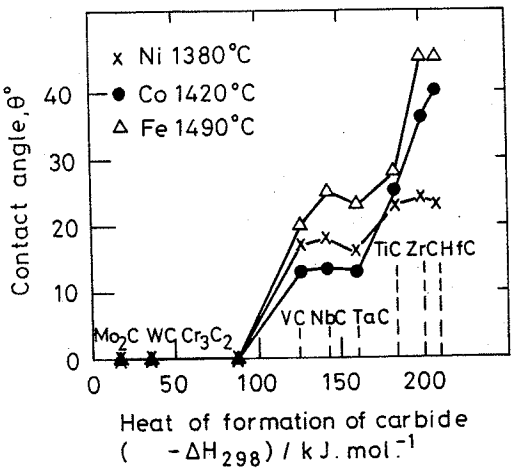


Fig. 12.3. Relation between heat of formation of carbide substrates and their contact angles with molten iron-group metals [Ref. 8]. Metal composition: M1

Sheshkov et al [7] for the variation of (W_A) in metal/oxide system with the change in free energy of formation (ΔF_s^0) of the oxide of the metal. A general equation for the three individual lines was given as:

$$W_A = W_o + A(\Delta F_s^0). \qquad (12.7)$$

The (W_o) term represents the contribution to bonding by dispersion forces and is related to the dielectric constant of the oxide support. The second term in equation (12.7) ($A(\Delta F_s^0)$) represents the energy due to chemical interaction between the molten metal and the oxygen anions present at the surface of the oxide. It was suggested that the slope of the lines (A) could depend upon the screening action of the cations on the respective oxide surfaces.

Ramqvist [8] measured the contact angles between molten Fe, Co and Ni on various carbide substrates and plotted them against the heat of formation of the substrate material **(Fig. 12.3)**. The curves show that (θ) increases as the heat of formation increases, i.e. the less stable the carbide the more readily it is wet by the three transition metals.

Kamyshov et al [9] plotted the contact angles obtained between iron-base melts and transition metal nitrides, against the acceptor capacity (k) of the metal component of

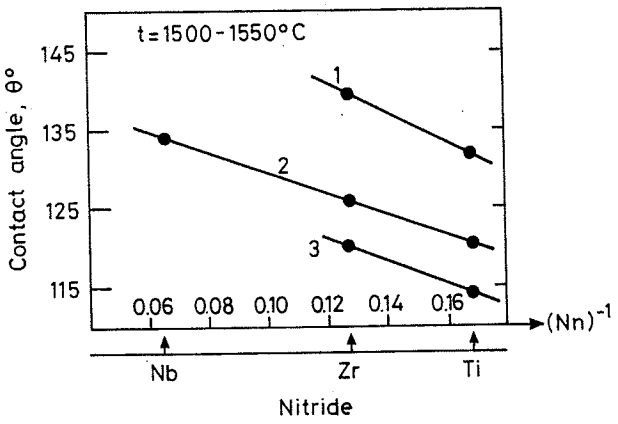


Fig. 12.4. Dependence upon the acceptor capacity $(Nn)^{-1}$ of the wetting angle between solid nitrides of transition elements and molten Fe (curve 1), Fe + 0.5 % C (curve 2), steel ShKh15 (curve 3), under NH_3 [Ref. 9]. Steel composition: M2

the nitrides. **(Fig. 12.4)** (k) is an approximate measure of the incompleteness of the d-electron shell of the transition metals and is given by the relation:

$$k = (nN)^{-1}$$

where n = number of electrons in the d-shell,
N = principal quantum number at this level.

Fig. 12.4 shows that, (in contrast to borides and carbides) [9], the contact angles decrease with increase in (k). To account for this, Kamyshov et al proposed that as (k) increased, both γ^e_{SG} and γ^e_{SL} would increase, but in the case for nitrides, γ^e_{SG} increased relatively more than γ^e_{SL} and hence (from 12.1), cos θ would be more positive.

12.4 Surface topography

Derivation of the Young equation was based on the assumption that the surface of the solid in contact with the liquid was perfectly smooth, and to emulate this condition, the surfaces of substrates used in sessile-drop experiments are usually highly polished. In many practical situations however, the surface cannot be considered smooth and consequently the true area (α_T) of contact between the liquid and solid interfaces will differ from the apparent contact area (α_A) based on the assumption of a smooth surface. In general, provided there is no gas trapped in the interstices at the interface, $\alpha_T > \alpha_A$. From consideration of the effect of changes in surface energy (due to differences in surface roughness) on the adhesion tension between a sessile-drop and a solid substrate, Wenzel [10] derived a simple relation for the observed or apparent contact angle (θ_R) on a rough surface and the angle (θ_s) found with a perfectly smooth surface of the same solid viz:

$$\cos\theta_R = R.\cos\theta_s.$$

Where R (the surface roughness factor) ≥ 1 and is defined, as the ratio of the true surface area to the geometric area based on the assumption of a smooth surface.

The Wenzel equation predicts that the observed contact angle for wetting (non-wetting) systems will decrease (increase) with increase in (R).

Huh and Mason [11] used a mechanistic model to study the effect of the random nature of surface roughness on (θ). They considered an idealised situation in which various degrees of surface roughness were simulated by series of regular grooves cut in the surface. The random nature of the roughness was produced by grooves with different cross-sections and orientations. Huh and Mason found that, provided the height profile of the surface features followed a Gaussian distribution, the Wenzel equation should be valid when the drop size was large compared to the dimensions of the surface roughness.

Verification of the Wenzel relation has been provided by the experimental work of Ogino [12], whose data are reproduced in **Fig. 12.5** and show an increase in the observed contact angle with increase in the surface roughness for the non-wetting molten iron/solid alumina system.

The porosity of the solid medium is another factor which can affect the contact angle between liquid metal and ceramic, particularly with good wetting systems. Samsonov et al [13] carried out wetting experiments on substrates of ZrC which had various levels of porosity. With non-wetting metals e.g. Cu, it was found that the porosity of the substrates (up to 35 % porosity) had no significant effect on the contact angle. In contrast, with a good wetting metal (molten Ni), there was a marked decrease in (θ) with increase in porosity (**Fig. 12.6**). Humenik and Kingery [14] studied the wettability between molten Fe and solid BeO and also found that substrate porosity (up to 10 %) had little effect on (θ) in non-wetting systems.

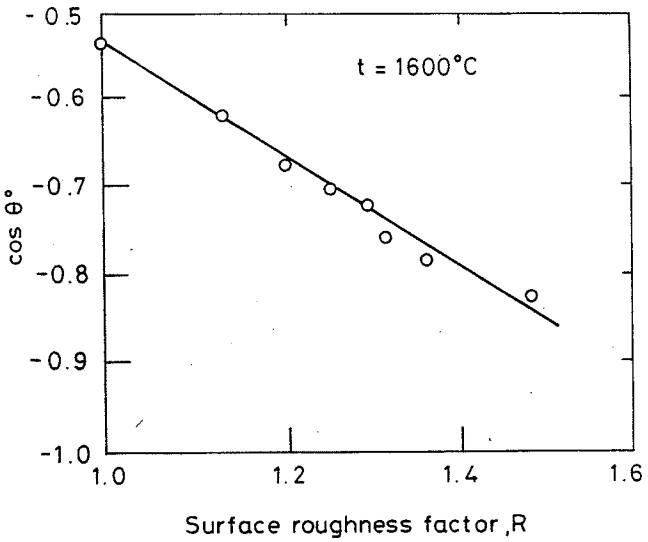


Fig. 12.5. Experimental data verifying Wenzel's relation between observed wettability (Cos *θ)* and the surface roughness factor (R) of the plaque for the Fe-Al_2O_3 system [Ref. 12]

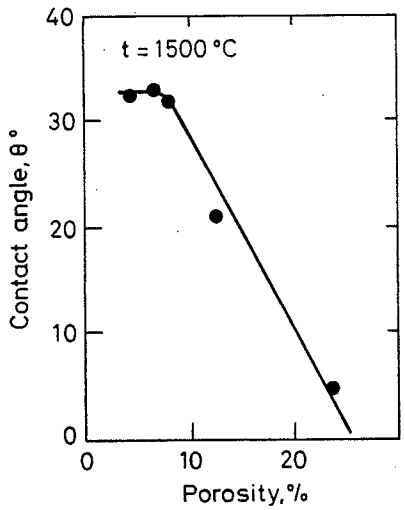


Fig. 12.6. Variation of contact angle with substrate porosity for molten Ni-ZrC systems (holding time 15 minutes) [Ref. 13]

12.5 Temperature

In general, increase in temperature will increase both the work of adhesion (W_A) and the wettability (cos θ), the magnitude of the changes being dependent to a large extent on whether chemical reactions take place at the interface. Systems, in which chemical reactions occur, are often characterised by a wetting threshold temperature, above which both wettability and adhesion rapidly increase.

12.6 Data

This section gives the collated data for contact angle and work of adhesion between Fe-based melts and ceramic solids, the presentation being based upon the composition of the solid. Data for the respective systems are given in alphabetical order (based on chemical formulae) relevant to the chemical composition of the solids.

It would have been beyond the scope of this chapter to give the full data available. Therefore, section **12.6.1 – 12.6.5** represent only an extract. The omitted data are, however, given in form of a list in section **12.6.6.** For further information users are asked to refer to the original publications.

Where available, the metal compositions are given in section **12.7** and are referred to in this section under the relevant 'M' numbers.

12.6.1 Carbides and graphite

Graphite

Tab. 12.1. Contact angle and work of adhesion between molten Fe (including a Fe+C alloy) on substrate of graphite

Metal	Temp. °C	Contact Angle θ°	Atmosphere	Work of Adhesion mJm^{-2}	Reference
Fe	1550	37	H_2	2600	[14]
Fe	1550	51	He	2100	[14]
Fe	1550	0	Vac	–	[14]
Fe	1550	37	Vac	3300	[17]
Fe	1550	50	Vac	3040	[18]
Fe+3.77 % C	1550	107	Vac	1830	[18]

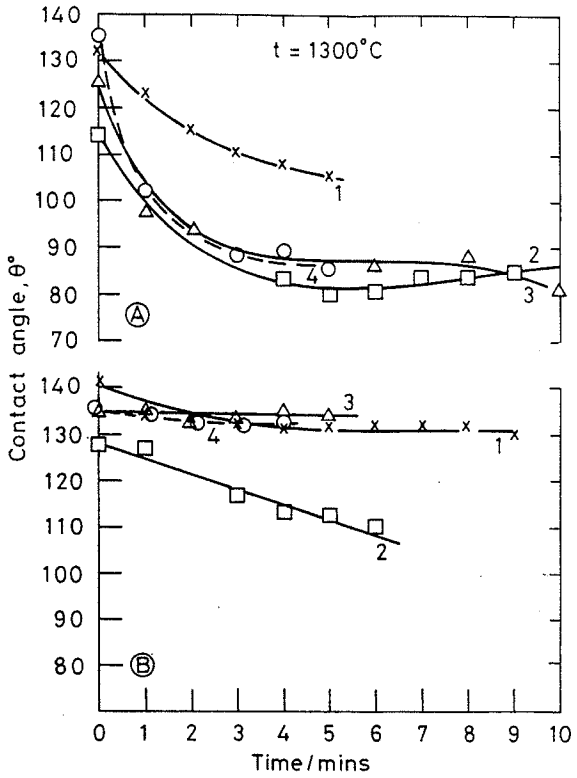


Fig. 12.7. Variation with time of the contact angle between cast irons and various forms of graphite under Ar [Ref. 20]
A - Normal flake graphite cast iron with composition (mass %): 3.88 [C]; 1.58 [Si]; 1.22 [Mn]; 0.028 [P]; 0.015 [S]; 0.002 [Mg].
B - (Ni-Mg) treated nodular cast iron with composition (mass %): 3.35 [C]; 3.09 [Si]; 0.6 [Mn]; 0.023 [P]; 0.012 [S]; 0.049 [Mg].
Curve 1 - unpolished, unorientated graphite
Curve 2 - polished, random orientated graphite
Curve 3 - unpolished pyrolytic graphite with surface parallel to base plane
Curve 4 - polished pyrolytic graphite with surface parallel to base plane

SiC

Tab. 12.2. Contact angle and work of adhesion between molten Fe/Fe alloys and substrate of SiC

Type of SiC	Metal	Temp. °C	Contact Angle θ°	Atmosphere	Work of Adhesion mJm^{-2}	Reference	Metal Composition
s.c. (n-type)	Fe	1600	82	Ar	–	[22]	–
s.c. (p-type)	Fe	1600	72	Ar	–	[22]	–
poly	Fe	1600	84	Ar	–	[22]	–
HP	Fe	1600	24+	Ar	2334	[24]	M4
RB	Fe	1600	29++	Ar	2278	[24]	M4
s.c.	Fe_2Al_5	1300	58	Vac	–	[25]	–
s.c.	FeSi	1420	<40	Vac	–	[25]	–
s.c.	Fe_2Si_5	1350	<40	Vac	–	[25]	–
Impure	Steel35	1300	55*	Ar	–	[26]	–

s.c. – single crystal; poly – polycrystal; Impure – (84.1 SiC + 4.3 SiO_2 + 1.8 Al_2O_3), porosity = 30 %; HP – hot-pressed; RB – reaction-bonded
\+ –46 at % Si in melt at equilibrium
++ –48 at % Si in melt at equilibrium
* – After 70 minutes at temperature

TiC

Tab. 12.3. Contact angle and work of adhesion between molten Fe alloys and substrate of TiC

Metal	Temp. °C	Contact Angle θ°	Atmosphere	Work of Adhesion mJm^{-2}	Reference
Steel 35L	1550	60	Vac	1800	[16]
Cast iron	1550	82	Vac	1230	[16]
Fe + 2.24 Ni + 0.07 C	1490	38	Vac	–	[28]
Fe + 3.56 Ni + 0.07 C	1490	37	Vac	–	[28]
Fe + 9.27 Ni + 0.09 C	1490	43	Vac	–	[28]
Fe + 12.3 Ni + 0.10 C	1490	54	Vac	–	[28]
Fe + 20.1 Ni + 0.09 C	1490	30	Vac	–	[28]
Fe + 30 Ni + 0.09 C	1490	11	Vac	–	[28]
Fe + 7.85 Cr + 0.06 C	1490	30	Vac	–	[28]
Fe + 11 Cr + 0.07 C	1490	34	Vac	–	[28]
Fe + 16 Cr + 0.005 C	1490	52*	Vac	–	[28]
Fe + 25.8 Cr + 0.06 C	1490	36	Vac	–	[28]
Fe + 1.23 Si + 0.19 C	1490	36	Vac	–	[28]
Fe + 2.29 Si + 0.18 C	1490	18	Vac	–	[28]
Fe + 3.3 Si + 0.16 C	1490	22	Vac	–	[28]
Fe + 5.4 Si + 0.16 C	1490	0	Vac	–	[28]

*Drops solidified owing to the formation of reaction products, which have a melting point in excess of 1490 °C

TiC + WC

Tab. 12.4. Contact angle and work of adhesion between molten Fe/Fe alloys and substrate of TiC + WC (1:1) [Ref. 30]. Base iron composition: M6

Metal	Temp. °C	Contact Angle θ°	Atmos-phere	Work of Adhesion mJm^{-2}
Fe	1420	38	Vac	3414*
Fe	1380	40	Vac	3442*
Fe + 12 ppm O	1480	32^+	Vac	–
Fe + 12 ppm O	1550	29^+	Vac	–
Fe + 12 ppm O	1520	22^+	Vac	–
Fe + 12 ppm O	1550	13^+	Vac	–
Fe + 70 % Co	1420	27^+	Vac	3612*
Fe + 30 % Co	1420	34^+	Vac	–
Fe + 36 % Co	1420	29^+	Vac	–
Fe + 80 % Ni	1380	26^+	Vac	–
Fe + 60 % Ni	1380	30^+	Vac	3405*
Fe + 63 % Ni	1380	26^+	Vac	–
Fe + 50 % Ni	1380	26^+	Vac	–

+ – after 10 minutes at temperature
* – calculated using surface tension data from another source

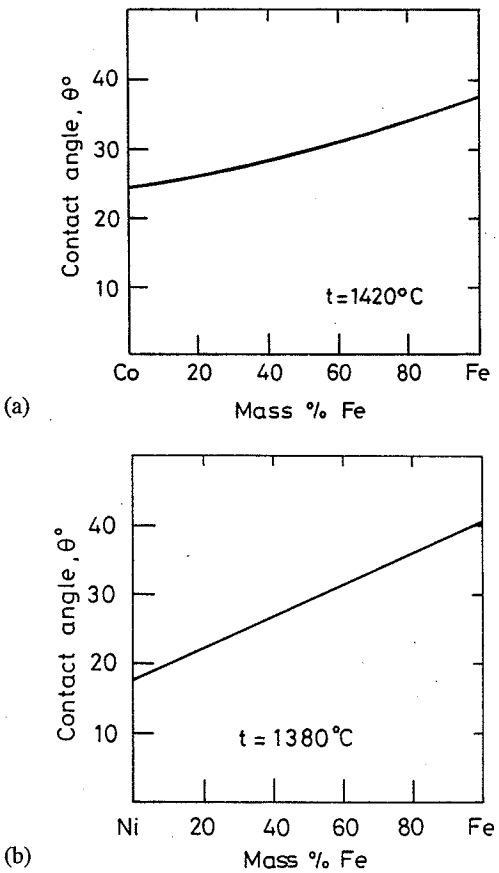


Fig. 12.8 a,b. Effect of Fe content (a) in Fe + Co and (b) in Fe + Ni alloys on the contact angle with the mixed carbide 50 mass % WC + 50 mass % TiC under vacuum. (Contact angle after 10 minutes at temperature) [Ref. 30]. Base iron composition: M6

12.6.2 Nitrides

AlN

Tab. 12.5. Contact angle and work of adhesion between molten Fe/steels and AlN substrate [Ref. 31]. Alloy compositions: M7

Metal	Temp. °C	Contact Angle θ°	Atmos-phere	Work of Adhesion mJm^{-2}
Fe	1600	130	NH_3	624
2Kh13	1600	118	NH_3	861
Kh17N2	1600	120	NH_3	763
1Kh18N9	1600	123	NH_3	643
20Kh16N3MA	1600	118	NH_3	659
12Kh5MA	1600	126	NH_3	624
20Kh3MF	1600	115	NH_3	814
12Kh2MF	1600	124	NH_3	741
12Kh1MF	1600	118	NH_3	727
4Kh15G14ST	1600	147	NH_3	170
30KhGSA	1600	123	NH_3	780
30KhMA	1600	122	NH_3	707
St40	1600	121	NH_3	678
39KhVFYu	1600	111	NH_3	426
12Kh2N4A	1600	111	NH_3	993
18Kh2N4VA	1600	128	NH_3	657
45G17Yu3	1600	132	NH_3	440
Kh25T	1600	131	NH_3	309
ShKh15	1600	110	NH_3	960
K25T	1600	131	NH_3	309

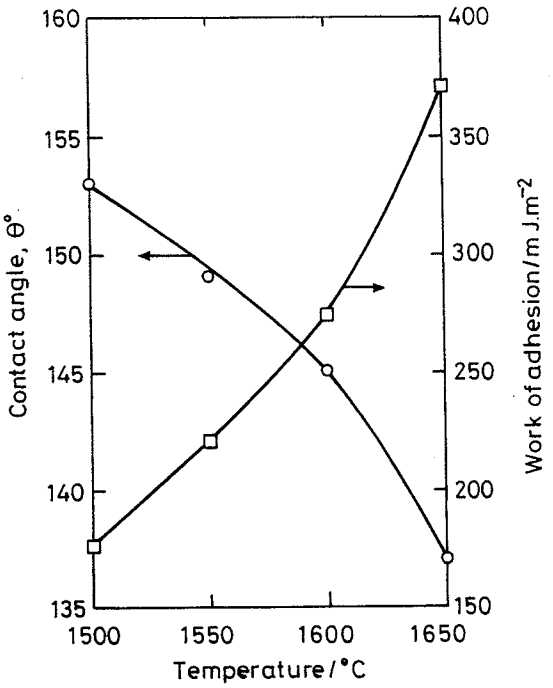


Fig. 12.9. Variation of contact angle and work of adhesion with temperature for the system molten steel EI.844B and AlN [Ref. 32]. Steel composition: M8

BN

Tab. 12.6. Contact angle and work of adhesion between Fe/Fe alloys/steels and substrate of BN

Metal	Temp. °C	Contact Angle θ°	Atmosphere	Work of Adhesion mJm^{-2}	Reference	Metal Composition
Fe	1535	112	Ar	–	[15]	–
Fe	1535	150	NH_3	200	[33]	M9
Fe_2Al_5	1300	45*	Vac	–	[25]	–
FeSi	1550	66*	Vac	–	[25]	–
Fe_2Si_5	1500	82*	Vac	–	[25]	–
Fe + 0.5 % C	1535	147	NH_3	260	[33]	M9
ShKh15	1535	153	NH_3	150	[33]	M9
ShKh15	1600	114	NH_3	875	[31]	–
Kh25T	1600	146	NH_3	170	[31]	–
45G17Yu3	1600	132	NH_3	413	[31]	–
12Kh2MF	1600	126	NH_3	624	[31]	–

* Pyrolytic BN

Si_3N_4

Tab. 12.7. Contact angle and work of adhesion between Fe/Fe alloys/steels and substrate of Si_3N_4

Metal	Temp. °C	Contact Angle θ°	Atmosphere	Work of Adhesion mJm^{-2}	Reference	Metal Composition
Fe	1535	95	NH_3	1500	[33]	M9
Fe	1530	90*	Ar	–	[15]	–
Fe_2Al_5	1300	66	Vac	–	[25]	–
FeSi	1500	76	Vac	–	[25]	–
Fe_2Si_5	1450	66	Vac	–	[25]	–
Fe + 0.5 % C	1535	133	NH_3	520	[33]	M9
ShKh15	1535	90	NH_3	1400	[33]	M9

* Nitrogen evolved due to reaction between metal and substrate

TiN

Tab. 12.8. Contact angle and work of adhesion between Fe/Fe alloys/steels and substrate of TiN

Metal	Temp. °C	Contact Angle θ°	Atmosphere	Work of Adhesion mJm^{-2}	Reference	Metal Composition
Fe	1550	93	Vac	1649	[16]	–
Fe	1550	132	NH_3	500	[33]	M9
Fe + 0.5 % C	1550	120	NH_3	820	[33]	M9
Cast iron	1550	115	Vac	622	[16]	–
35L	1550	98	Vac	1032	[16]	–
ShKh15	1550	115	NH_3	800	[33]	M9
ShKh15	1600	110	NH_3	1007	[31]	M7
Kh25T	1600	129	NH_3	705	[31]	M7
45G17Yu3	1600	123	NH_3	780	[31]	M7
12Kh2MF	1600	117	NH_3	842	[31]	M7

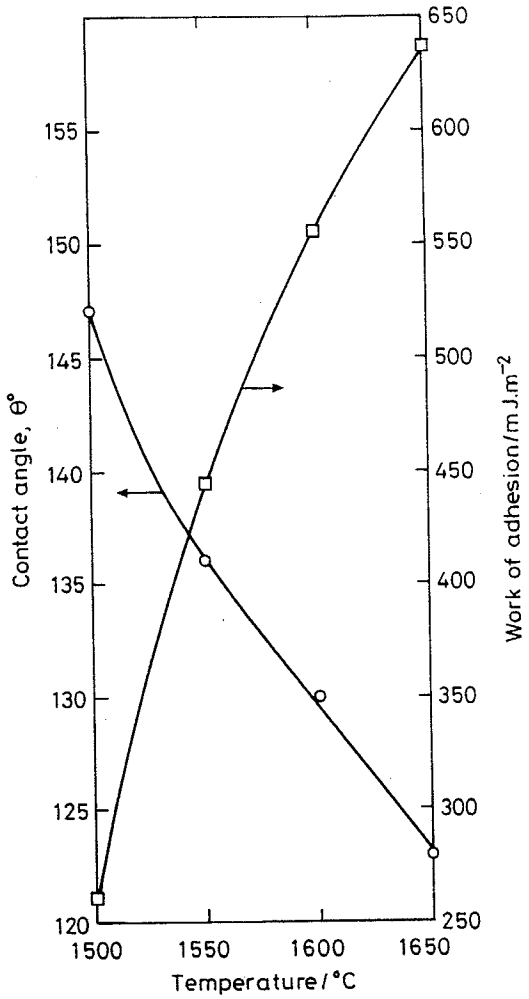


Fig. 12.10. Variation of contact angle and work of adhesion with temperature for the system molten steel EI.844B and solid TiN [Ref. 32]. Steel composition: M8

12.6.3 Oxides

12.6.3.1 Pure oxides

Al_2O_3

Tab. 12.9. Contact angle and work of adhesion between molten Fe and Al_2O_3 substrate

Type of Al_2O_3	Metal	Temp. °C	Contact Angle θ°	Atmosphere	Work of Adhesion mJm^{-2}	Reference	Metal Composition
	ARMCO	1550	141	Vac	–	[14]	–
	Electrolytic	1550	121	H_2	695	[14]	–
	Electrolytic	1550	129	He	540	[14]	–
	–	1575	111	–	–	[34]	–
	–	1600	137	H_2	~500	[35]	M10
	–	1600	122	Ar	–	[36]	–
s.c.	–	1600	118	Ar	–	[36]	–
98.8 %	–	1600	118	H_2	840	[37]	M11
	–	1550	138	Ar	–	[38]	–
	–	1530	134	Ar	504	[39]	M12
s.c.	–	1600	92*	Ar	1309	[40]	–
s.c. (ruby)**	–	1570	93*	Ar	1375	[40]	–
	–	1550	128	He	661	[41]	M13
	–	1600	132	He	–	[42]	–
	–	1600	128	H_2	–	[43]	M14
	–	1600	124	–	–	[44]	M15
	–	1600	140	Ar	–	[45]	–
	–	1550	140	Ar	402	[46]	–
	–	1550	141	H_2	386	[47]	–
	–	1600	137	Ar	–	[48]	–

s.c. – single crystal
* Composition of iron not given, but low value quoted for the surface tension (viz 1440 $mN.m^{-1}$), suggests the presence of significant impurity levels (possibly O_2), which may account for the rather low values of θ
** Cr content of ruby not specified

Tab. 12.10. Contact angle and work of adhesion between molten Fe alloys/steels and Al_2O_3 substrate

Type of Al_2O_3	Alloy or Steel	Temp. °C	Contact Angle θ°	Atmosphere	Work of Adhesion mJm^{-2}	Reference	Metal Composition
s.c.	Fe_2Al_5	1400	67	Vac	–	[25]	–
	Fe + 3.9 % C	1570	105	He	1289	[41]	M13
	Fe + Cr (Ferrochrome ~ 70 % Cr)	1700	90	Ar	1000	[63]	M20
s.c.	FeSi	1500	85	Vac	–	[25]	–
s.c.	Fe_2Si_5	1450	90	Vac	–	[25]	–
	Fe + 0.043 % Y	1550	151	Vac	–	[64]	–
	Fe + 0.15 % Y	1550	150	Vac	–	[64]	–
	A-12	1560	113	He	760	[65]	M21
	G13L	1560	120	Ar	635	[66]	M22
	H52-3	1600	128	–	599	[44]	M15
	Kh14N14M2V2	1550	126	Ar	555	[67]	–
s.c.	"	1550	107	Vac	1050	[68]	M23
s.c.	"	1550	108	Ar	932	[68]	M23
95 % (3 % SiO_2 + 2 % CaO)	"	1550	108	Vac	110	[68]	M23
"	"	1550	109	Ar	843	[68]	M23
s.c.	"	1550	108	Ar	970	[69]	–
s.c.	"	1550	108	Ar	932	[69]	–
s.c.	"	1600	108	Ar	928	[69]	–
	Kh15N28M4V2B	1550	125	Ar	636	[67]	–
s.c.	"	1550	107	Vac	1110	[68]	M23
s.c.	"	1550	110	Ar	980	[68]	M23
95 % (3 % SiO_2 + 2 % CaO)	"	1550	106	Vac	1015	[68]	M23
"	"	1550	123	Ar	815	[68]	M23
s.c.	"	1500	113	Ar	913	[69]	–
s.c.	"	1550	110	Ar	980	[69]	–
s.c.	"	1600	110	Ar	975	[69]	–
	Kh18N9T	1560	124	Ar	570	[66]	M22
	ShKh15	1600	124	Ar (impure)	570	[70]	M24
	"	1600	143	Ar (pure)	285	[70]	M24
	"	1535	115	–	840	[71]	M25
	"	1560	114	Ar	931	[72]	–
	St50	1560	120	He	640	[65]	M21
	St60	1560	117	He	710	[65]	M21
	Vst. 3sp	1560	120	He	800	[65]	M21
	X6CrNiMn17-4-8	MP	115	Ar	745	[39]	M12
	"	MP	119	Ar	701	[39]	M12
	X15CrNiSi25-20-2	MP	125	Ar	633	[39]	M12
98.5 % (Porosity = 25 %)	08kp	1550	70+	Ar	–	[26]	M5
98.5 % (Porosity) = 0.04 %)	08kp	1550	70+	Ar	–	[26]	M5
	08Yu	1560	125	He	585	[65]	M21
	10KhSD	1560	118	He	730	[65]	M21
	10SpN	1560	120	He	666	[65]	M21
	11YuA	1550	107	Ar	1040	[72]	–
	12Kh2N4A	1570	107	Ar	1090	[72]	–
	12KhMF	1550	119	Ar	726	[72]	–
	15GYuT	1560	118	He	800	[65]	M21
	18KhGT	1570	100	Ar	1075	[72]	–
	18YuA	1560	127	He	606	[65]	M21
	20	1550	123	Ar	572	[46]	–
	20K	1560	115	Ar	790	[72]	–
	20K	1560	118	He	840	[65]	M21
	30KhGSA	1560	110	Ar	962	[72]	–
98.5 % (Porosity = 0.04 %)	35	1500	112/104*	Ar	917	[26]	M5

Tab. 12.10. (continuation)

Type of Al_2O_3	Alloy or Steel	Temp. °C	Contact Angle θ°	Atmosphere	Work of Adhesion mJm^{-2}	Reference	Metal Composition
98.5 % (Porosity = 25 %)	35	1550	105+	Ar	–	[26]	M5
"	35	1550	74+	Ar++	–	[26]	M5
	35L	1560	130	Ar	540	[66]	M22
	38KhMYuA	1535	105	–	1060	[71]	–
	40Kh	1535	122	–	700	[71]	–
	45	1535	105	–	950	[71]	–
	55S2	1535	117	–	740	[71]	–
	Steel	1530	109*	He	965	[73]	M26
	Steel	1530	100**	He	1130	[73]	M26
	Steel	1550	136	–	410	[74]	M27

s.c. – single crystal
MP – melting point
* First value – initial contact angle at 1500 °C
Second value – contact angle after 40 minutes soak at 1550 °C
\+ After 40 minutes soak at 1550 °C
++ Atmosphere slightly oxidising
. Deoxidised with Ca + Si
.. Deoxidised with Al

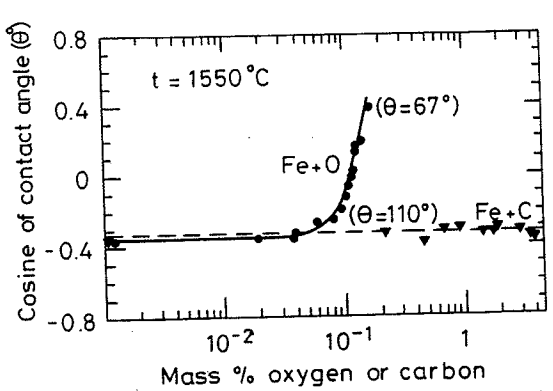
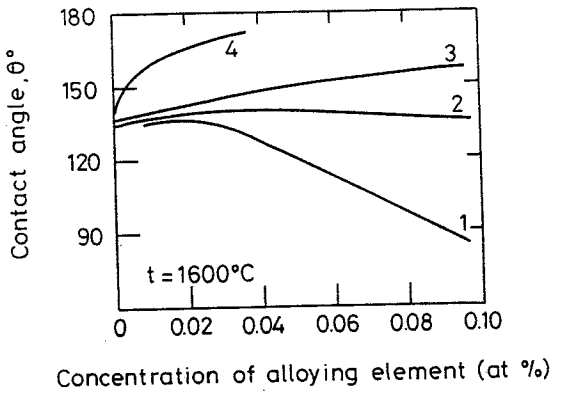


Fig. 12.11. Variation of the wettability (Cos θ) of Al_2O_3 by Fe + O and Fe + C alloys as a function of the respective oxygen and carbon contents [Ref. 34]



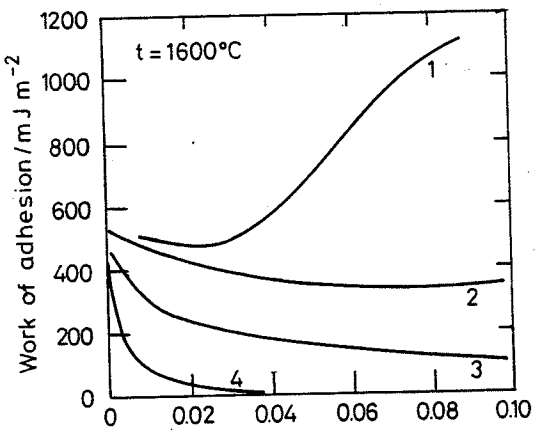


Fig. 12.12 a,b. Effect of low levels of Group VI elements in Fe (a) on the contact angle and (b) work of adhesion with Al_2O_3 [Ref. 50]. Base Iron composition: M17
Curve 1 - Fe + O under $H_2 + H_2O$
Curve 2 - Fe + S under $H_2 + H_2S$
Curve 3 - Fe + Se under H_2
Curve 4 - Fe + Te under H_2

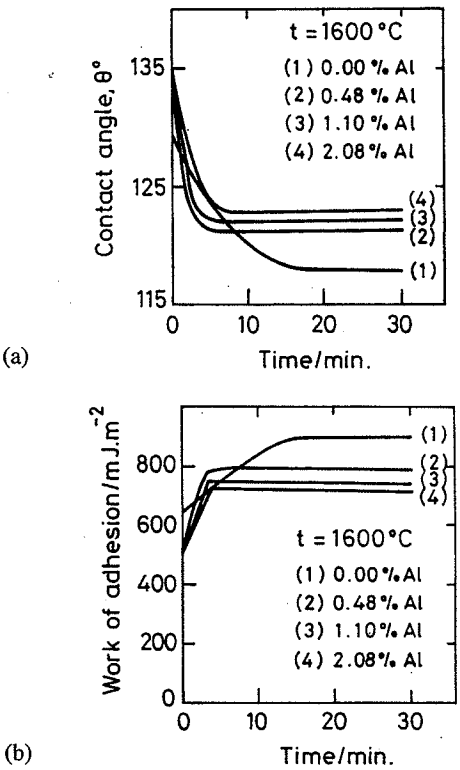


Fig. 12.13 a,b. Variation with time (a) of the contact angle and (b) work of adhesion between Al_2O_3 and molten Fe and Fe + Al alloys under H_2 [Ref. 43]. Base iron composition: M14

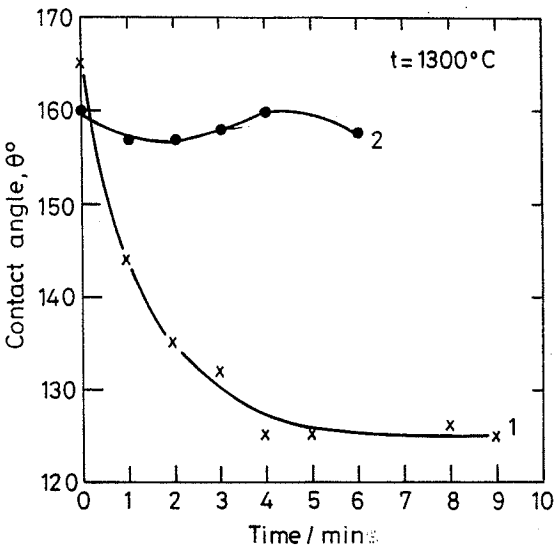


Fig. 12.15. Variation with time of the contact angle between cast irons and Al_2O_3 under Ar [Ref. 20]
Curve 1 - normal flake graphite cast iron (analysis as given with Fig. 12.7)
Curve 2 - (Ni-Mg) treated nodular cast iron (analysis as given with Fig. 12.7)

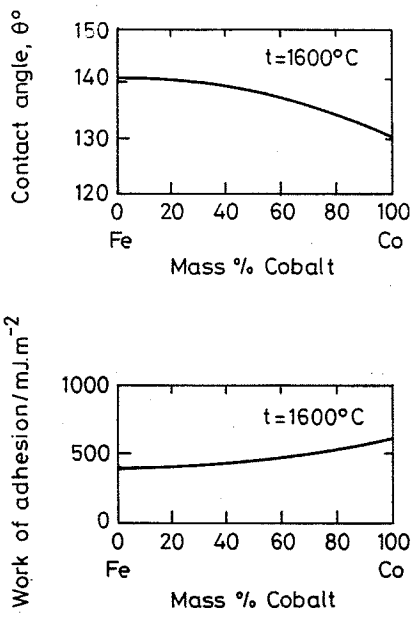


Fig. 12.16 a,b. Effect of Co content in Fe + Co alloys (a) on the contact angle and (b) work of adhesion with Al_2O_3 under H_2 [Ref. 52]

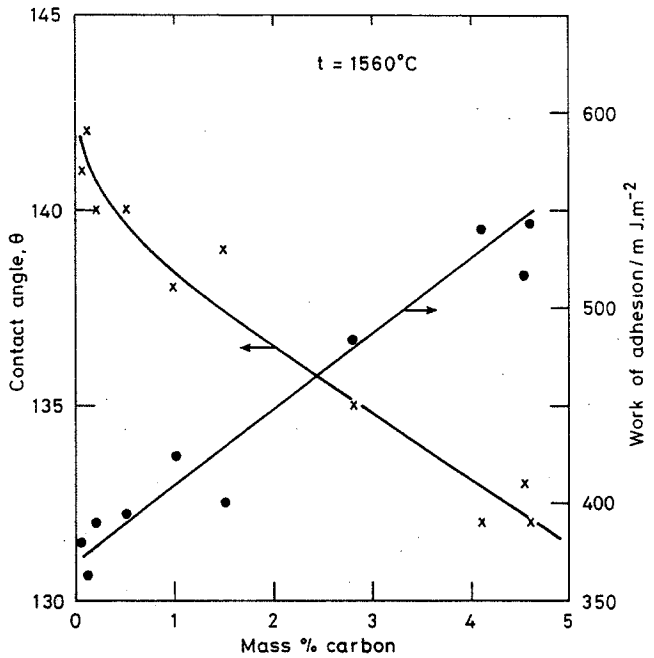


Fig. 12.14. Effect of carbon content on the contact angle and work of adhesion between Fe + C alloys and Al_2O_3 under Ar [Ref. 51]. Base iron composition: M18

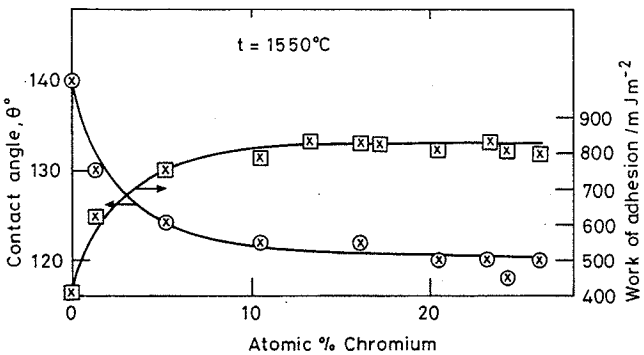


Fig. 12.17. Effect of Cr content on the contact angle and work of adhesion between molten Fe + Cr alloys and Al_2O_3 under Ar [Ref. 53]

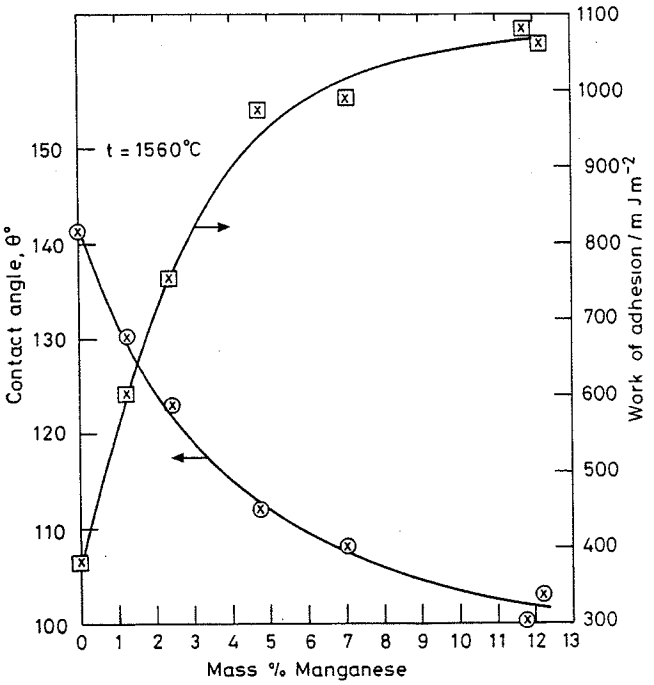


Fig. 12.18. Effect of Mn content on the contact angle between Fe + Mn alloys and Al_2O_3 under Ar [Ref. 55]

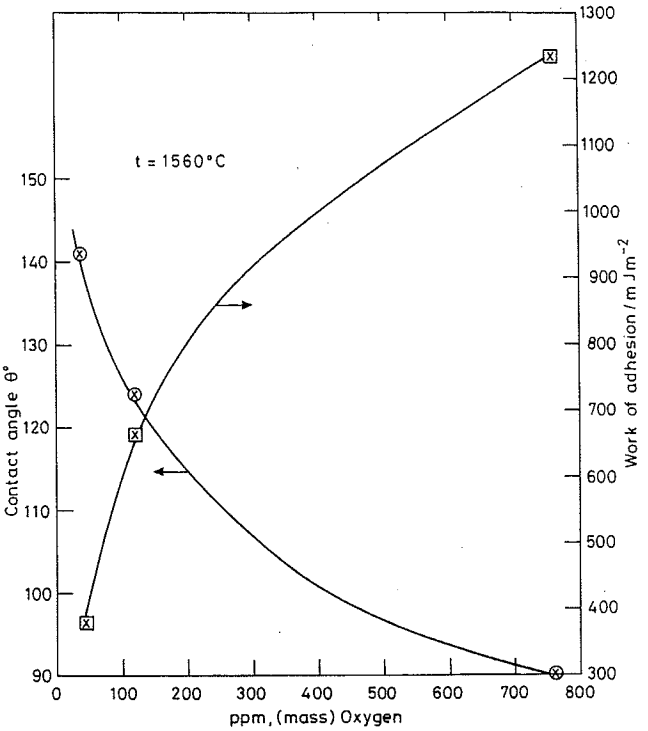


Fig. 12.21. Effect of oxygen content in molten Fe on the contact angle and work of adhesion with Al_2O_3 under Ar [Ref. 55]

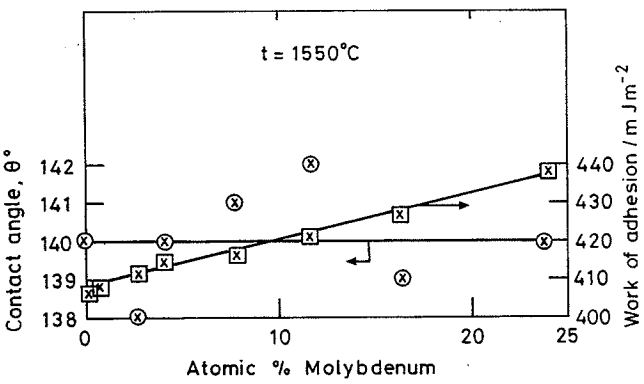


Fig. 12.19. Effect of Mo content on the contact angle and work of adhesion between molten Fe + Mo alloys and Al_2O_3 under Ar [Ref. 53]

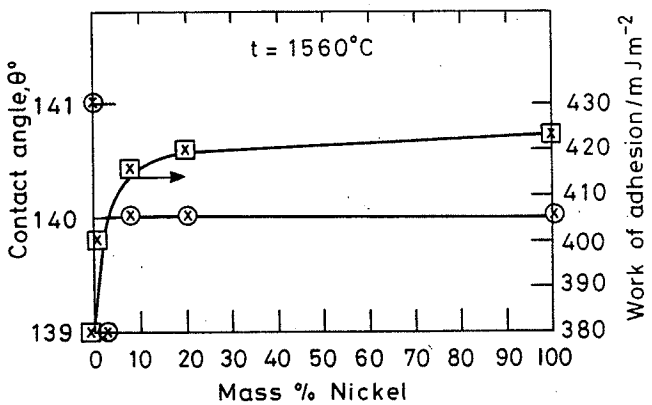


Fig. 12.20. Effect of Ni content on the contact angle and work of adhesion between Fe + Ni alloys and Al_2O_3 under Ar [Ref. 55]

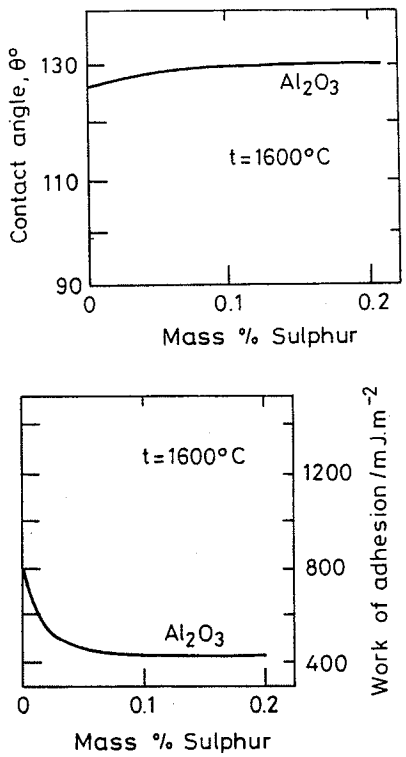


Fig. 12.22 a,b. Effect of S content in molten Fe (a) on the contact angle and (b) work of adhesion with Al_2O_3 under Ar and Ar + 5 % H_2 [Ref. 59]

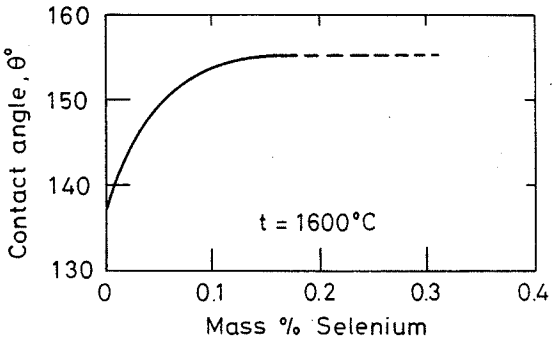


Fig. 12.23. Effect of Se content in molten Fe on the contact angle with Al_2O_3 (98.8 %) under Ar + Se [Ref. 35]. Composition of base iron: M10

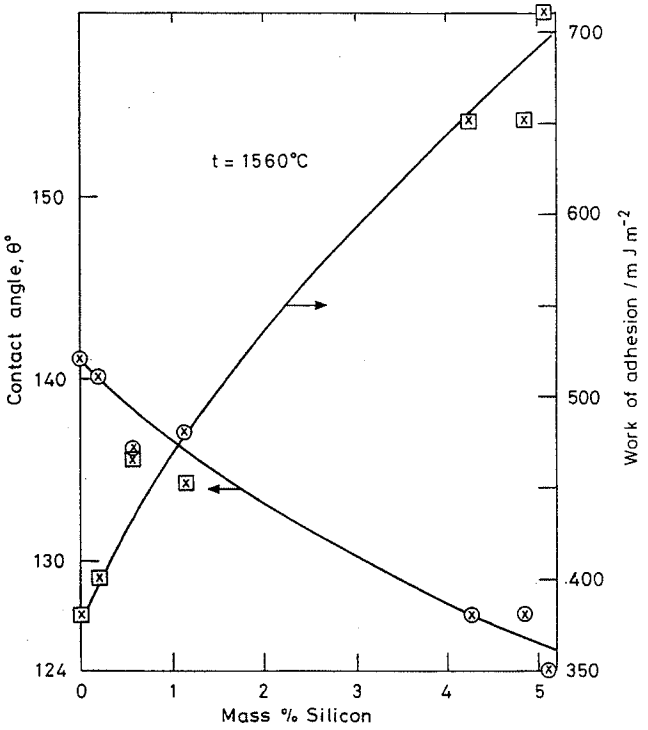


Fig. 12.24. Effect of Si content on the contact angle and work of adhesion between molten Fe + Si alloys and Al_2O_3 under Ar [Ref. 55]

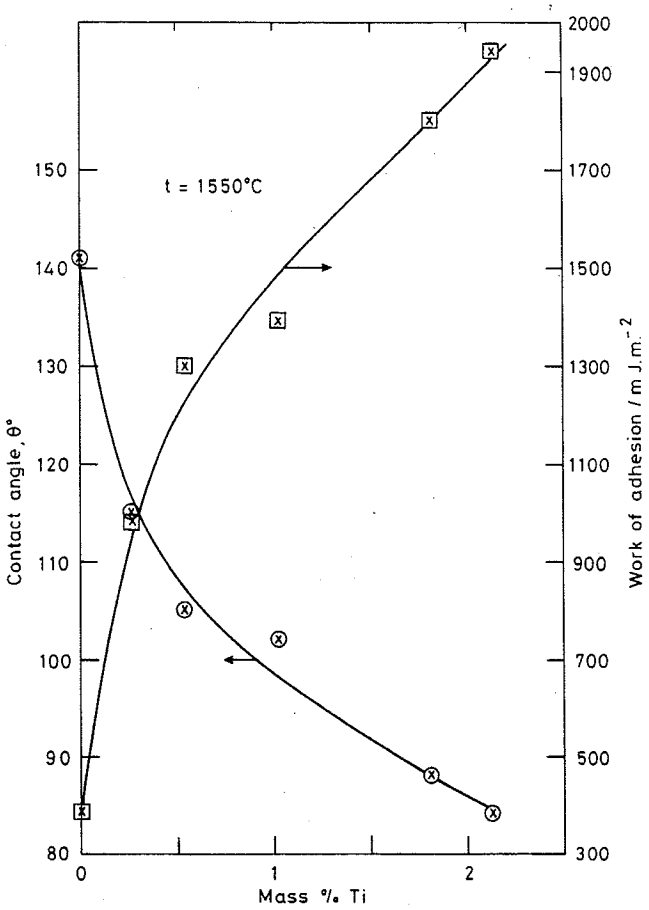


Fig. 12.25. Effect of Ti content in molten Fe + Ti alloys on the contact angle and work of adhesion with Al_2O_3 under H_2 [Ref. 62]

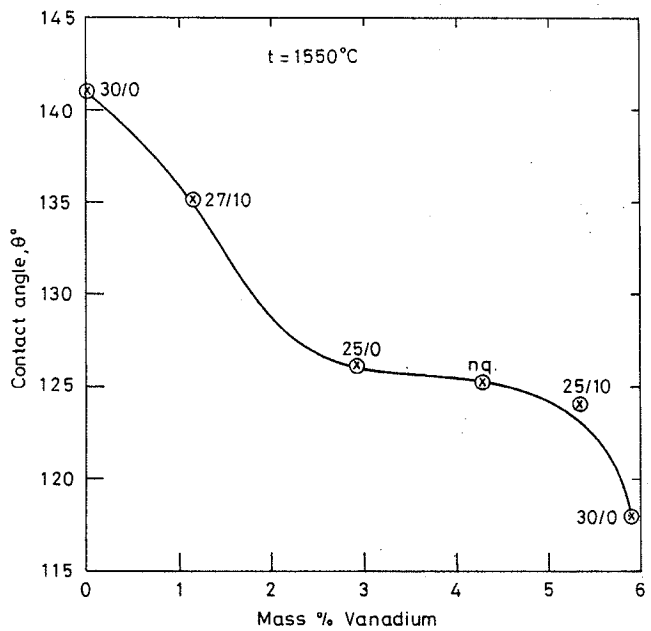


Fig. 12.26. Effect of V content on the contact angle between molten Fe + V alloys and Al_2O_3 under H_2. (Values next to individual points indicate oxygen/nitrogen levels in ppm mass; n.q. - not quoted). [Ref. 47]

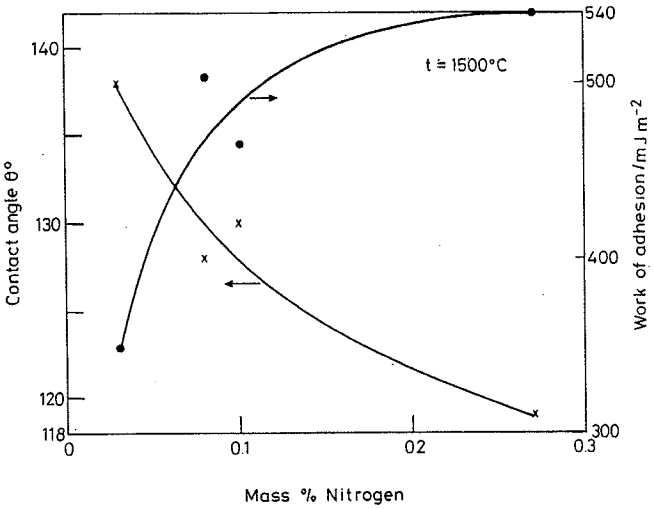


Fig. 12.27. Effect of N in austenitic stainless steel on the contact angle and work of adhesion with Al_2O_3 under Ar [Ref. 78]. Steel composition: M29

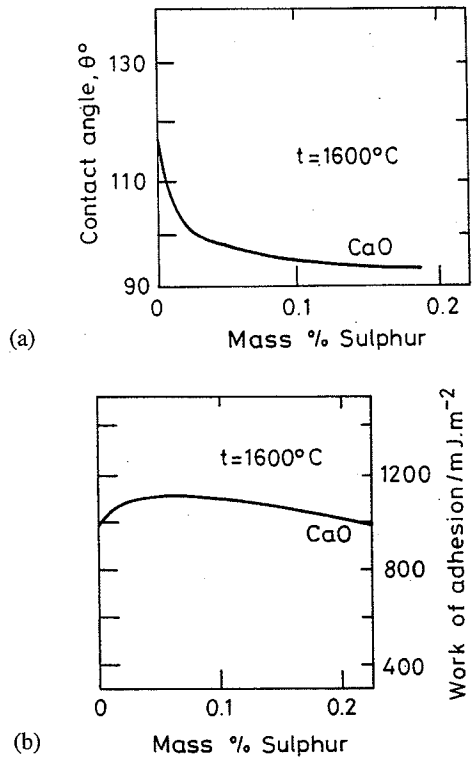


Fig. 12.29 a,b. Effect of S content in molten Fe (a) on the contact angle and (b) work of adhesion with CaO under Ar and Ar + 5 % H_2 [Ref. 59]

CaO

Tab. 12.11. Contact angle and work of adhesion between molten Fe/steel and CaO substrate

Metal	Temp. °C	Contact Angle θ°	Atmosphere	Work of Adhesion mJm^{-2}	Reference	Metal Composition
Fe	1600	104	Ar	–	[36]	–
Fe	1600	–	H_2	1106	[37]	M11
Fe	1550	120	Ar	–	[38]	–
Fe	1550	132	–	–	[38]	–
Fe	1530	121	Ar	805	[39]	M12
Fe	1600	105	H_2	–	[43]	M14
Fe	1600	116	–	814	[44]	M16
30KhGSNA	1600	108	Ar	925	[79]	–
X15CrNiSi25-20-2	MP	112	Ar	907	[39]	M12
X6CrNiMn17-4-8	MP	103	Ar	981	[39]	M12
(after argon refining)	MP	108	Ar	945	[39]	M12
H52-3	1600	121	–	757	[44]	M15

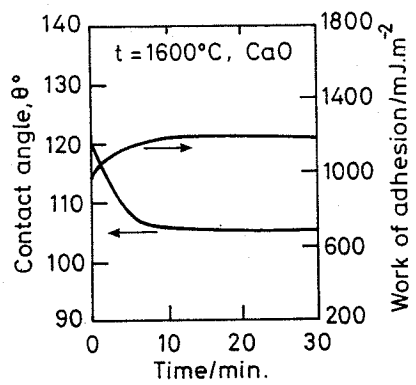


Fig. 12.28. Variation with time of the contact angle and work of adhesion between molten Fe and CaO under H_2 [Ref. 43]. Iron composition: M14

Cr_2O_3

Tab. 12.12. Contact angle and work of adhesion between molten Fe/steel and substrate of Cr_2O_3

Metal	Temp. °C	Contact Angle θ°	Atmosphere	Work of Adhesion mJm^{-2}	Reference	Metal Composition
Fe	1550	100	–	–	[38]	–
Fe	1600	97	–	1273	[44]	M15
Fe	1535	88	Ar	–	[81]	–
Steel H52-3	1600	103	–	1209	[44]	M15
Steel	1550	110	–	935	[74]	M27

HfO_2

Tab. 12.13. Contact angle between molten Fe and substrate of HfO_2 [Ref. 38]

Temp. °C	Contact Angle θ°	Atmosphere
1550	110	Ar

MgO

Tab. 12.14. Contact angle and work of adhesion between molten Fe and substrate of MgO

Temp. °C	Contact Angle θ°	Atmosphere	Work of Adhesion mJm^{-2}	Reference	Metal Composition
1600	96	H_2	–	[43]	M14
1600	120	–	725	[44]	M15
1600	127	H_2	–	[48]	–
1550	130	He	462	[14]	–
1550	123	Vac	–	[14]	–
1600	96	Ar	–	[36]	–
1600	–	H_2	1490	[37]	M11
1550	127	Ar	–	[38]	–
1530	128	Ar	637	[39]	M12

Tab. 12.15. Contact angle and work of adhesion between molten Fe alloys and substrate of MgO

Metal Alloy or Steel	Temp. °C	Contact Angle θ°	Atmosphere	Work of Adhesion mJm^{-2}	Reference	Metal Composition
Fe + Cr (Ferro-chrome ~ 70 % Cr)	1700	125	Ar	425	[63]	M20
Fe + 80 % Ni	1490	141	Ar	–	[82]	–
08kp*	1550	86+	Ar	–	[26]	M5
30KhGSNA	1600	118	Ar	722	[79]	–
35*	1550	87+	Ar	–	[26]	M5
35L	1560	121	Ar	660	[66]	M22
35L**	1560	115	Ar	780	[66]	M22
G13L	1560	114	Ar	700	[66]	M22
G13L**	1560	112	Ar	750	[66]	M22
H52-3	1600	125	–	665	[44]	M15
Kh18N9T	1560	123	Ar	580	[66]	M22
Kh18N9T**	1560	114	Ar	720	[66]	M22
X6CrNiMn17-4-8	MP	109	Ar	834	[39]	M12
X6CrNiMn17-4-8 (after argon refining)	MP	114	Ar	782	[39]	M12
X15CrNiSi25-20-2	MP	128	Ar	738	[39]	M12
Steel	1530	108•	He	940	[73]	M26
Steel	1530	108••	He	975	[73]	M26

MP – melting point
* On magnesite (96.7 MgO + 1.4 SiO_2; porosity 0.9 %)
** On magnesite
\+ After 40 minutes at temperature
. deoxidised with Ca + Si
.. deoxidised with Al

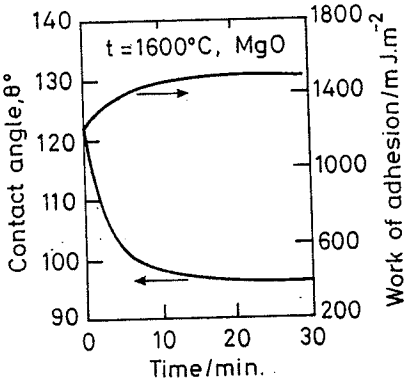


Fig. 12.30. Variation with time of the contact angle and the work of adhesion between molten Fe and MgO under H_2 [Ref. 43]. Iron composition: M14

Rare-earth oxides

Tab. 12.16. Contact angle between molten Fe and substrates of rare-earth oxides (REO)

REO	Temp. °C	Contact Angle θ°	Atmos-phere	Reference
Ce_2O_3	1550	105	Ar	[38]
Dy_2O_3	1550	102	Ar	[38]
La_2O_3	1550	110	Ar	[38]
La_2O_3	1600	117	–	[34]
Lu_2O_3	1550	106	Ar	[38]
Nd_2O_3	1550	108	Ar	[38]
Tb_2O_3	1550	102	Ar	[38]
Yb_2O_3	1550	100	Ar	[38]

SiO_2

Tab. 12.17. Contact angle and work of adhesion between molten Fe and substrate of SiO_2

Temp. °C	Contact Angle θ°	Atmosphere	Work of Adhesion mJm^{-2}	Reference	Metal Composition
1600	116	Ar	–	[36]	–
1600	–	H_2	860	[37]	M11
1550	120	Ar	–	[38]	–
1530	110	Ar	1097	[39]	M12
1575	91*	Ar	1420	[40]	–
1600	127	H_2	–	[43]	M14
1600	109	–	978	[44]	M15
1535	112	Ar	–	[83]	–
1535	115	N_2	–	[84]	–
1550	106	Ar	1250	[46]	–

* Analysis for Fe not given, but low value quoted for surface tension (viz. 1446 mNm^{-1}) suggests significant levels of impurities (possibly oxygen), which may account for the relatively low value of θ

Tab. 12.18. Contact angle and work of adhesion between molten Fe alloys/steels and SiO_2 substrate

Alloy or Steel	Temp. °C	Contact Angle θ°	Atmosphere	Work of Adhesion mJm^{-2}	Reference	Metal Composition
Fe + Cr (Ferro-chrome ~70 % Cr)	1700	73	Ar	1293	[63]	M20
08Yu	1560	116	He	780	[65]	M21
10KhSD	1560	115	He	800	[65]	M21
10SpN	1560	112	He	870	[65]	M21
11YuA	1550	106	Ar	1055	[72]	–
12Kh2N4A	1600	103	Ar	1220	[72]	–
12KhMF	1550	103	Ar	1090	[72]	–
15GYuT	1560	113	He	880	[65]	M21
18KhGT	1570	90	Ar	1300	[72]	–
18YuA	1560	112	He	820	[65]	M21
20	1550	81	Ar	1505	[46]	–
20K	1560	110	Ar	902	[72]	–
"	1560	114	He	850	[65]	M21
30KhGSA	1560	97	Ar	1289	[72]	–
"	1600	115	Ar	753	[79]	–
35L	1560	124	Ar	630	[66]	M22
A-12	1560	108	He	860	[65]	M21
H52-3	1600	114	–	925	[44]	M15
Kh14N14M2V2	1550	105	Vac	1156	[68]	M23
"	1550	107	Ar	870	[68]	M23
Kh15N28M4V2B	1550	108	Vac	840	[68]	M23
"	1550	109	Ar	742	[68]	M23
Kh18N9T	1560	120	Ar	635	[66]	M22
ShKh15	1560	105	Ar	1163	[72]	–
"	1600	101	Ar (impure)	1040	[70]	M24
"	1600	121	Ar (pure)	680	[70]	M24
St50	1560	111	He	830	[65]	M21
St60	1560	112	He	815	[65]	M21
Vst-3sp	1560	115	He	847	[65]	M21
X6CrNiMn17-4-8 (")	MP	93	Ar	1171	[39]	M12
(after argon refining)	MP	97	Ar	1162	[39]	M12
X15CrNiSi25-20-2	MP	99	Ar	1224	[39]	M12
Steel	1530	104*	He	995	[73]	M26

MP – melting point
* Deoxidised with Si

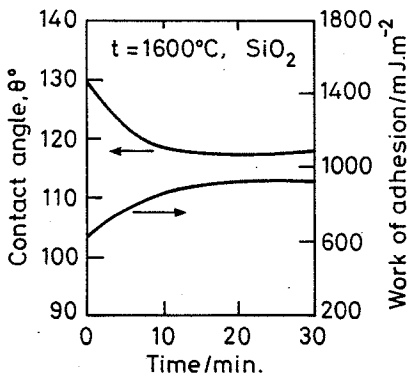


Fig. 12.31. Variation with time of the contact angle and the work of adhesion between molten Fe and SiO_2 under H_2 [Ref. 43]. Iron composition: M14

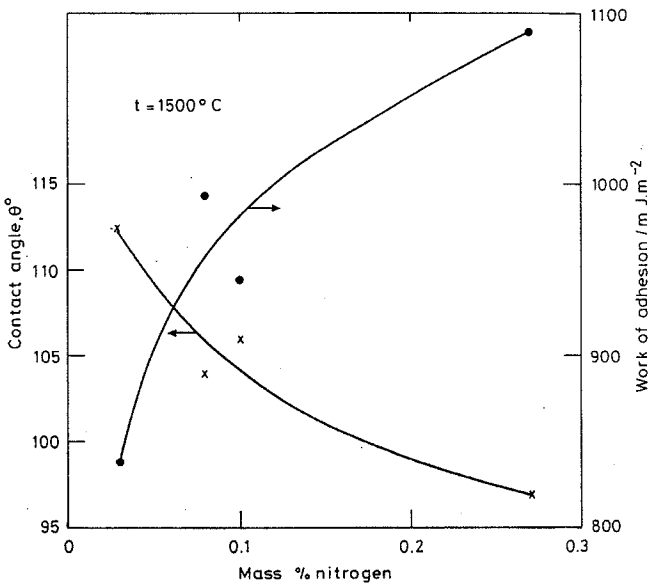


Fig. 12.32. Effect of N content in austenitic stainless steel on the contact angle and work of adhesion with SiO_2 under Ar [Ref. 78]. Steel composition: M29

ThO_2

Tab. 12.19. Contact angle and work of adhesion between molten Fe and ThO_2 substrate

Temp. °C	Contact Angle θ°	Atmos-phere	Work of Adhesion mJm^{-2}	Reference
1545	113	–	–	[34]
1550	112	H_2	900	[14]
1550	100	He	1080	[14]
1550	111	Ar	–	[38]
1550	101	He	–	[85]

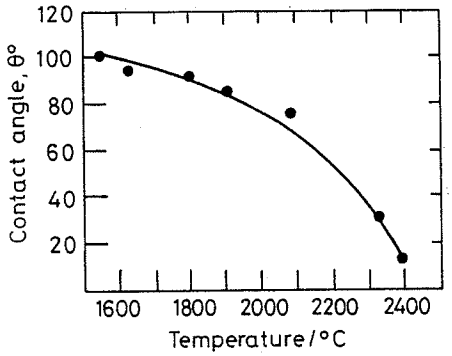


Fig. 12.33. Variation with temperature of the contact angle between Fe and ThO_2 under He [Ref. 85]

TiO_2

Tab. 12.20. Contact angle and work of adhesion between molten Fe/steel and TiO_2 substrate

Metal	Temp. °C	Contact Angle θ°	Atmosphere	Work of Adhesion mJm^{-2}	Reference	Metal Composition
Fe	1550	84	H_2	900	[14]	–
Fe	1550	0	He	–	[14]	–
Fe	1550	72	Vac	–	[14]	–
Fe	1600	81	–	1676	[44]	M15
Steel H52-3	1600	88	–	1614	[44]	M15

ZrO_2

Tab. 12.21. Contact angle and work of adhesion between molten Fe an ZrO_2 substrate

Temp. °C	Contact Angle θ°	Atmosphere	Work of Adhesion mJm^{-2}	Reference	Metal Composition
1600	115	–	–	[34]	–
1550	111	H_2	890	[14]	–
1550	102	He	1020	[14]	–
1550	92	Vac	–	[14]	–
1600	–	H_2	1140*	[37]	M11
1530	119	Ar	847	[39]	M12
1600	105	H_2	–	[43]	M14
1600	124	H_2	–	[48]	–
1535	120	Ar	–	[83]	–

* Substrate: 94 % ZrO_2 + 4 % CaO

Tab. 12.22. Contact angle and work of adhesion between molten Fe alloy/steels and ZrO_2 substrate

Alloy or Steel	Temp. °C	Contact Angle θ°	Atmosphere	Work of Adhesion mJm^{-2}	Reference	Metal Composition
Fe + 80 % Ni	1490	147	Ar	–	[82]	–
X6CrNiMn17-4-8	MP	97	Ar	1116	[39]	M12
(after argon refining)	MP	105	Ar	1004	[39]	M12
X15CrNiSi 25-20-2	MP	109	Ar	974	[39]	M12
35	1500	110/92*	Ar	1019	[26]	M5

MP – melting point
* Substrate: 95.7 % ZrO_2 + 1.5 % TiO_2 + 1.2 % CaO (porosity 0.5 %). First value for θ is the initial contact angle at 1500 °C; second value is angle after 40 minutes at 1550 °C

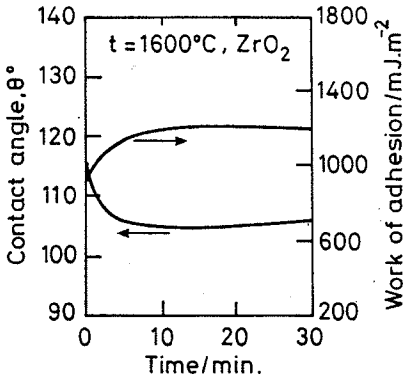


Fig. 12.34. Variation with time, of the contact angle and the work of adhesion between molten Fe and ZrO_2 under H_2 [Ref. 43]. Iron composition: M14

12.6.3.2 Mixed oxides

Tab. 12.23. Contact angle and work of adhesion between molten Fe/Fe alloys/steels and substrates of mixed oxides

Substrate Material	Metal, Alloy or Steel	Temp. °C	Contact Angle θ°	Atmosphere	Work of Adhesion mJm^{-2}	Reference	Metal Composition
$3Al_2O_3.2SiO_2$	Fe	1600	131	H_2	–	[48]	–
Fireclay	Fe	1600	91	–	1425	[44]	M15
Chrome magnesite	"	"	100	–	1198	[44]	"
Silica	"	"	102	–	1148	[44]	"
Magnesite chrome	"	"	103	–	1124	[44]	"
Sintered dolomite	"	"	106	–	1050	[44]	"
Magnesite	"	"	111	–	930	[44]	"
Mullite	"	"	113	–	883	[44]	"
MgO + 5 % Nd_2O_3	Fe + 80 % Ni	1490	145	Ar	–	[82]	–
MgO + 15 % Nd_2O_3	"	"	149	"	–	[82]	–
MgO + 5 % CeO_2	"	"	142	"	–	[82]	–
MgO + 15 % CeO_2	"	"	144	"	–	[82]	–
ZrO_2 + 10 % Ta_2O_5	"	"	126	"	–	[82]	–
ZrO_2 + 10 % Y_2O_3	"	"	122	"	–	[82]	–
ZrO_2 + 10 % CeO_2	"	"	119	"	–	[82]	–
90 Al_2O_3 + 10 SiO_2	Steel 20	1550	112	Ar	812	[46]	–
75 Al_2O_3 + 25 SiO_2	"	"	94	"	1210	[46]	–
Al_2O_3 - SiO_2 - SiC	Steel 35	1550	126/126*	Ar	574	[26]	M5
Zircon	"	"	127/115*	"	528	[26]	"
High alumina	"	"	115/107*	"	804	[26]	"
Periclase-spinel	"	"	110/103*	"	1019	[26]	"
Zircon	Steel 08 kp	"	93$^+$	"	–	[26]	"
High alumina	"	"	109$^+$	"	–	[26]	"
Periclase-spinel	"	"	94$^+$	"	–	[26]	"
Fireclay	Steel H52-3	1600	98	–	1343	[44]	M15
Chrome magnesite	"	"	106	–	1130	[44]	"
Silica	"	"	108	–	1078	[44]	"
Magnesite chrome	"	"	110	–	1026	[44]	"
Sintered dolomite	"	"	112	–	976	[44]	"
Magnesite	"	"	116	–	876	[44]	"
Mullite	"	"	117	–	851	[44]	"

* First value – initial contact angle at 1500 °C; second value – angle after 40 minutes at 1550 °C
$^+$ After 40 minutes at 1550 °C

Al_2O_3 – SiO_2 – SiC	– 41 Al_2O_3 + 27.9 SiO_2 + 25.2 SiC (21 % porosity)
Zircon	– 58.7 ZrO_2 + 36.3 SiO_2 (21 % porosity)
High alumina	– 74.6 Al_2O_3 + 20.9 SiO_2 (10 % porosity)
Periclass-spinel	– 71.6 MgO + 9.1 Cr_2O_3 + 6.9 Fe_2O_3 + 4.8 Al_2O_3 + 4.8 SiO_2 + 2.3 CaO (12 % porosity)
Fireclay	– 52.3 SiO_2 + 38.2 Al_2O_3 + 2.5 Fe_2O_3 + 1.3 CaO + 1.8 Alkali (25 % porosity)
Chrome magnesite	– 10.7 SiO_2 + 8.4 Al_2O_3 + 10.7 Fe_2O_3 + 0.8 CaO + 39.1 MgO + 30.1 Cr_2O_3 (23 % porosity)
Silica	– 95.6 SiO_2 + 0.7 Al_2O_3 + 1.0 Fe_2O_3 + 2.4 CaO (24 % porosity)
Magnesite chrome	– 5.8 SiO_2 + 5.2 Al_2O_3 + 5.6 Fe_2O_3 + 1.7 CaO + 68.5 MgO + 13 Cr_2O_3 (23 % porosity)
Sintered dolomite	– 6.7 SiO_2 + 0.4 Al_2O_3 + 2.3 Fe_2O_3 + 53.6 CaO + 37 MgO
Magnesite	– 2.8 SiO_2 + 0.8 Al_2O_3 + 4.2 Fe_2O_3 + 1.9 CaO + 86 MgO
Mullite	– 29 SiO_2; ≥ 70 Al_2O_3; ≤ 1 Fe_2O_3

Tab. 12.24. Effect of gaseous environment and variation in temperature on the contact angle between iron-based melts and various refractory oxides [Ref. 87]. Alloy compositions: M30

t, °C	Alloy No.	Contact Angle, θ°											
		Al_2O_3				MgO				MgO + 6 % FeO			
		Ar	N_2	H_2	CO	Ar	N_2	H_2	CO	Ar	N_2	H_2	CO
1530	1	130	126	128	125	129	125	128	126	116	110	115	131
1580		128	122	127	122	126	121	124	121	114	108	112	109
1630		124	120	125	121	123	119	120	119	109	105	110	107
1530	2	126	123	127	122	128	126	126	124	112	110	110	110
1580		123	121	124	118	124	120	121	120	106	106	107	107
1630		119	118	119	117	121	119	118	117	102	102	103	103
1530	3	120	121	123	118	120	121	122	120	108	110	110	107
1580		117	119	119	116	118	116	118	117	104	107	107	103
1630		110	114	115	110	115	114	114	113	100	102	103	100
1530	4	116	109	115	108	116	110	113	110	101	101	102	101
1580		114	106	112	106	112	106	110	107	98	99	100	100
1630		112	105	110	104	110	104	107	103	95	97	98	94
1530	5	124	123	122	123	124	124	123	123	110	109	107	106
1580		119	118	119	120	118	120	120	119	102	100	101	103
1630		115	116	117	116	117	118	116	116	100	97	99	100

12.6.4 Sulphides

Tab. 12.25. Contact angle and work of adhesion between Fe/steels and substrate of CaS [Ref. 39]. Metal composition: M12

Metal	Temp. °C	Contact Angle θ°	Atmos-phere	Work of Adhesion mJm^{-2}
Fe	1530	87	Ar	1745
XCrNiSi 25-20-2	MP	86	Ar	1557
X6CrNiMn 17-4-8	MP	82	Ar	1430
(after argon refining)	MP	85	Ar	1468

MP – Melting point

12.6.5 Silicides

Tab. 12.26. Contact angle between molten Fe and substrate of $MoSi_2$ [Ref. 15]

Temp. °C	Contact Angle θ°	Atmosphere
1530	0	Ar

12.6.6 Additional data to section 12.6

Tab. 12.27. Borides, carbides and nitrides as substrates

Substrate	Metal	Reference
CrB_2	Molten iron	[15]
TiB_2	Iron, cast iron, steel 35L (1.0501)	[15, 16]
ZrB_2	Iron, cast iron, steel 35L (1.0501)	[15, 16]
Graphite	Iron with increasing C content	[19]
Graphite	Iron with increasing C content and various Mn contents	[21]
B_4C	Molten iron	[22, 23]
Cr_3C_2	Iron, e.g. iron M1 [Ref. 8]	[8, 13, 15]
HfC	Iron, e.g. iron M1 [Ref. 8]	[8, 13]
Mo_2C	Iron, e.g. iron M1 [Ref. 8]	[8, 13]
NbC	Iron, e.g. iron M1 [Ref. 8]	[8, 13]

Tab. 12.27. (continuation)

Substrate	Metal	Reference
TaC	Iron, e.g. iron M1 [Ref. 8]	[8, 13]
TiC	Iron, e.g. iron M1 [Ref. 8]	[8, 13, 15, 16, 27]
TiC	Iron with increasing C content	[16]
TiC	Iron with various Cr contents	[29]
TiC	Iron with various Ni contents	[28]
TiC	Iron with various Si contents	[29]
VC	Iron, iron M1 [Ref. 8]	[8, 13]
WC	Iron, cast iron, steel 35L (1.0501)	[8, 13, 15, 16]
WC	Iron with increasing C content	[16]
ZrC	Iron (e.g. M1, [Ref. 8], cast iron, steel 35L (1.0501)	[8, 13, 15, 16]
ZrC	Iron with increasing C content	[16]
AlN	Steel ShKh15 (1.3505)	[31]
NbN	Iron-carbon alloy	[33]
NbN	Steel EI.844B (M8)	[32]
VN	Steel EI.844B (M8)	[32]
ZrN	Steel EI.844B (M8)	[32]
ZrN	Fe, Fe + 0,5 % C, ShKh15SG (1.3520) M9	[33]

Tab. 12.28. Pure oxides as substrates

Substrate	Metal	Atmosphere	Reference
Al_2O_3	Iron M14	H_2	[43]
Al_2O_3	Pure iron M16	vacuum	[49]
Al_2O_3	Fe-Mn alloys (up to 3 %)	He	[54]
Al_2O_3	Fe-Ni alloys (up to 100 %)	H_2	[52]
Al_2O_3	Ni + 20 % Fe	Ar	[56]
Al_2O_3	Iron with 0.143 % O	diff. p_{O_2}	[57]
Al_2O_3	Iron with oxygene (up to 750 ppm)	not quoted	[58]
Al_2O_3	Fe-Pd alloys (up to 100 % Pd)	not quoted	[42]
Al_2O_3	Fe-Si alloys (up to 10 % Si)	not quoted	[60]
Al_2O_3	Fe-Si alloys (up to 76 % Si)	He	[61]
Al_2O_3	Fe-Te alloys (up to 0.09 % Te)	H_2	[48]
Al_2O_3	Fe-V alloys (up to 6 % V)	H_2	[62]
Al_2O_3	Fe + % C + Ti (up to 2.4 % Ti)	H_2	[75]
Al_2O_3	Different steel (M 28)	Ar	[76]
Al_2O_3 s.c.	Two stainless steels (M 23)	Ar	[77]
Al_2O_3	Steel 30KhGSNA (0.3 C, 1 Si, 1 Mn, 1 Cr, 1.5 Ni)	Ar	[79]
Al_2O_3	Steel M 27 with incr. Si cont.	He	[74, 80]
BaO	Molten iron	Ar	[36]
BeO	Iron, iron with 0.01 and 0.06 % Y	H_2, He, Ar, Vac	[14, 37, 38, 43, 64]
CaO	Steel 30 KhGSNA (0.3 C, 1 Si, 1 Mn, 1 Cr, 1.5 Ni)	Ar	[79]
Cr_2O_3	Steel M 27 with incr. Si cont.	He [Ref. 80]	[74, 80]
MgO	Iron with C content up to 4 %	Ar	[51]
MgO	Ni with 20 % Fe	Ar	[56]
MgO	Steel 30KhGSNA (0.3 C, 1 Si, 1 Mn, 1 Cr, 1.5 Ni)	Ar	[79]
MgO	Iron with Te (up to 0.06 %)	H_2	[48]
MnO	Iron, steels X6CrNiMn 17-4-8 and X15CrNiSi 25-20 (M12)	Ar	[39]
NiO	Molten iron	not quoted	[38]
SiO_2	Fe with 2 % Si	diff. p_{O_2}	[57]
SiO_2	Iron with Mn (up to 3.2 %)	He	[54]
SiO_2	Steel 30KhGSNA (0.3 C, 1 Si, 1 Mn, 1 Cr, 1.5 Ni)	Ar	[79]
SiO_2	Iron with Si (up to 2 %)	H_2	[43]
UO_2	Molten iron	not quoted	[86]
Y_2O_3	Iron with Y (up to 0.8 %)	vacuum	[64]
Y_2O_3	Fe – C alloys with Y (up to 0.9 %)	vacuum	[64]
ZrO_2	Fe – Ni alloys (up to 100 % Ni)	H_2	[14]
ZrO_2	Iron with Te (up to 0.09 %)	H_2	[48]

Tab. 12.29. Mixed oxides as substrates

Substrate		Metal	Atmosphere	Reference
$Al_2O_3 + CaO + SiO_2$	Al_2O_3 incr. from 60 to 95 %	M 15	not quoted	[44]
$Al_2O_3 + CaO + SiO_2$	SiO incr. from 5 to 35 %	X15CrNiSi 25-20 (M12)	not quoted	[88]
$Al_2O_3 + Cr_2O_3$	Cr_2O_3 from 0 to 100 %	Iron	Ar	[89, 90]
Al_2O_3 with various additions of Cr_2O_3, ZrO_2 and $ZrSiO_4$		Steel 10KP (1.0301)	not quoted	[91]
Al_2O_3 with various additions of ZrO_2 and/or $MgAl_2O_4$		Armco-iron	Ar	[92]
$Al_2O_3 + SiO_2$	SiO_2 from 0 to 100 %	Fe + 0.023 % O	Ar	[46]
$3Al_2O_3 \cdot 2SiO_2$		Fe + Te	H_2	[48]
$Al_2O_3 + SiO_2$	Al_2O_3 from 72 to 100 %	Steel 10KP (1.0301) and steel 00Kh18N10 (1.4306)	vacuum	[91]
$Al_2O_3 + SiO_3$	SiO_2 from 5 to 35 %	Steels Kh14N14M2V2, Kh15N28M4V2B (M 23)	Ar	[69]
$Al_2O_3 + SiO_2$	with low additions of MgO	Steel 10KP (1.0301)	vacuum	[91]
CaO + MgO	CaO from 0 to 75 %	M 31		[93]
CaO + MgO + SiO_2	CaO from 45 to 65 %	Armco-iron and steel H52-3 (M15)	not quoted	[44]
CaO + MgO + SiO_2	CaO from 50 to 65 % different grain diameters of substrate	Steel X15CrNiSi 25-20 (M 12)	not quoted	[88]

12.7 Composition of ferrous melts

Tab. 12.30.

No.	Ref.	Composition
M1	[8]	Iron (ppm): 3 [Si]; 3 [Mg]; 1 [Ag]; 2 [Cu]; 2 [Ni]; 2 [Mn]; 300 [C]; 100 [O]; 100 [N]
M2	[9]	Steel ShKh15SG: 1 % C; 1.4 % Mn; 1.4 % Cr
M3	[21]	Iron (ppm): 40 [C], 30 [P]; 10 [S]; 20 [O]; 20 [N]; 10 [Si]
M4	[24]	Iron (ppm): 18 [O] (initial); 4 [O] (final)
M5	[26]	Steel 35: 0.33 % C; 0.29 % Si; 0.7 % Mn; 0.026 % P; 0.025 % S; 0.09 % Cr; 0.29 % Ni; 0.22 % Cu Steel 08kp: 0.08 % C; 0.0043 % Si; 0.38 % Mn; 0.015 % P; 0.021 % S; 0.02 % Cr; 0.02 % Ni; 0.03 % Cu
M6	[30]	Base iron (ppm): 3 [Mn]; 2 [Mg]; 4 [Si]; 12 [O]
M7	[31]	

Mass %

Steel	C	Mn	Si	P	S	Cr	Ni	Cu	Ti	W	Mo	V	Others
2Kh13	0.19	0.22	0.27	0.014	0.012	12.5	0.15	0.10	0.03	–	–	–	–
30KhMa	0.29	0.53	0.30	0.013	0.01	0.96	0.07	0.07	0.03	–	0.15	–	–
20Kh3MVF	0.2	0.44	0.37	0.018	0.01	3.07	0.20	0.10	–	0.5	0.46	0.76	–
30KhGSA	0.32	1.06	1.05	0.013	0.008	0.94	0.08	0.12	0.03	–	–	–	–
1Kh17N2	0.16	0.38	0.39	0.012	0.011	17.95	1.81	0.06	0.02	–	–	–	–
18Kh2N4VA	0.16	0.38	0.27	0.017	0.018	1.47	4.2	0.11	0.03	0.55	0.14	–	–
12Kh2N4A	0.13	0.40	0.21	0.016	0.008	1.28	3.36	0.09	–	–	–	–	–
38KhVFYu	0.40	0.37	0.23	0.014	0.008	1.71	0.07	0.08	0.02	0.32	–	0.17	0.49Al
12Kh1MF	0.11	0.49	0.34	0.012	0.012	1.04	0.12	0.16	–	–	0.28	0.22	–
12Kh5MA	0.14	0.27	0.36	0.019	0.007	4.65	0.16	0.14	0.02	–	0.52	–	–
St40	0.42	0.64	0.25	0.01	0.008	0.07	0.08	0.08	–	–	–	–	–
12Kh2MF	0.11	0.56	0.60	0.012	0.004	1.78	0.08	0.08	–	–	0.61	0.29	0.003B
45G17Yu3	0.47	16.95	0.32	0.032	0.008	0.35	0.09	–	–	–	–	–	3Al
Kh25T	0.07	0.34	0.62	0.026	0.008	25.0	0.35	0.14	0.72	–	–	–	–
4Kh15G14ST	0.35	14.4	1.46	0.047	0.008	14.6	0.24	0.15	0.54	–	–	–	–

M8	[32]	Steel EI.844B: 0.03 % C; 0.56 % Mn; 0.38 % Si; 0.15 % V; 0.015 % P; 0.005 % S; 16.8 % Cr; 15.4 % Ni; 0.4 % Nb; 0.25 % Ti; 0.029 % N; 0.004 % O
M9	[33]	Iron (ppm): 300 [C]; 20 [S]; 80 [P]; 60 [Al]; 60 [Si]; 500 [Ni]; 30 [Cu] Steel ShKh15SG: 1 % C; 1.4 % Mn; 0.26 % Si; 1.4 % Cr; 0.15 % Ni; 0.23 % Cu; 0.025 % P; 0.016 % S
M10	[35]	Iron (Base material): 0.05 % C; 0.0018 % O
M11	[37]	Iron (ppm): 10 [C]; 30 [Si]; 20 [Mn]; 10 [P]; 10 [S]; 60 [Cu]; 10 [Ni]; 10 [Cr]; 20 [Al]; 70 [Co]; 20 [N]
M12	[39]	Iron (ppm): 130 [C]; 600 [Mn]; 50 [Si]; 80 [P]; 100 [S]; 3200 [Ni]; 420 [Cu]; 50 [Mo]; 40 [Al] Steel X15CrNiSi 25-20-2: 0.15 % C; 0.78 % Mn; 2.78 % Si; 0.035 % P; 0.02 % S; 19.5 % Ni; 24.7 % Cr; 0.11 % Cu; 0.12 % Mo; 0.3 % W Steel X6CrNiMn 17-4-8: 0.06 % C; 8.3 % Mn; 0.46 % Si; 0.03 % P; 0.014 % S; 5.12 % Ni; 16.6 % Cr; 0.19 % Cu; 0.35 % Mo
M13	[41]	Iron (ppm): 500 [Ni]; 20 [Al]; 100 [Mo]; 100 [Cu]; 400 [Si]; 50 [C]; 20 [P]; 100 [O]; 50 [S]; 9 [N]
M14	[43]	Iron (ppm): 100 [C]; 30 [Si]; 20 [Mn]; 10 [P]; 10 [S]; 60 [Cu]; 10 [Ni]; 10 [Cr]; 50 [Ti]; 10 [V]; 20 [Al]; 70 [Co]; 20 [N]
M15	[44]	ARMCO Iron (ppm): 180 [C]; 100 [Si]; 1600 [Mn]; 60 [P]; 250 [S]; 550 [O]; 36 [N] Steel H52-3: 0.11 % C; 0.44 % Si; 1.32 % Mn; 0.022 % P; 0.035 % S; 0.0045 % O; 0.011 % N
M16	[49]	Pure iron: 0.01 % C; 0.044 % O Fe+C alloys: (i) 0.22 % C; 0.0049 % O (ii) 0.25 % C; 0.0042 % O (iii) 0.76 % C; 0.0029 % O (iv) 1.14 % C; 0.002 % O Fe + Al + C alloys: 0.26 % C; 1.85 % Al; 0.0031 % O
M17	[50]	Iron (ppm): 10 [C]; 30 [Si]; 20 [Mn]; 10 [P]; 60 [Cu]; 10 [Ni]; 10 [S]; 10 [Cr]; 50 [Ti]; 10 [V]; 20 [Al]; 70 [Co]; 20 [N]; 80 [O]
M18	[51]	Pure iron (ppm): 350 – 700 [C]; 40 [S]; 60 [P]; 10 [Cr]; 40 [O]; Commercial Iron (ppm): 900 [C]; 900 [Mn]; 260 [S]; 250 [P]; 140 [O]

Tab. 12.30. (continuation)

No.	Ref.	Composition
M19	[58]	Iron (ppm): 10 [C]; 30 [Si]; 20 [Mn]; 10 [P]; 10 [S]; 60 [Cu]; 10 [Ni], 10 [Cr]; 50 [Ti]; 10 [V]; 20 [Al]; 70 [Co]; 20 [N]
M20	[63]	Ferrochrome alloy: 71 % Cr; 0.1 % Si; 0.06 % C; 0.05 % P; 0.02 % S; 0.34 % O; 0.05 % Al
M21	[65]	Composition (mass %) after experiment

Steel	C	Si	Mn	S	P	Ti	Al	O
08Yu	0.06	0.01	0.3	0.02	0.003	–	0.04	0.009
10spN	0.07	0.17	0.35	0.026	0.009	–	0.006	nd
10KhSD	0.09	0.9	0.52	0.02	0.024	0.027	nd	0.0088
A-12	0.12	0.26	0.78	0.123	0.114	–	0.007	0.008
15GYuT	0.13	0.25	0.11	0.023	0.018	0.051	0.048	0.0077
Vst3sp	0.16	0.22	0.59	0.03	0.012	–	0.022	0.0039
18YuA	0.18	0.07	0.3	0.02	0.007	–	0.06	0.009
20K	0.19	0.3	0.65	0.03	0.016	0.02	0.025	0.0075
St50	0.5	0.08	0.25	0.026	0.009	–	0.005	0.0023
St60	0.63	0.3	0.56	0.025	0.008	–	0.008	0.0021

nd – not determined

No.	Ref.	Composition
M22	[66]	Steel 35L: 0.38 % C; 0.42 % Si; 0.56 % Mn; 0.04 % P; 0.03 % S Steel Kh18N9T: 0.18 % C; 0.67 % Si; 0.52 % Mn; 0.04 % P; 0.02 % S; 18.7 % Cr; 8.7 % Ni; 0.4 % Ti Steel G13L: 1.1 % C; 0.3 % Si; 12.6 % Mn; 0.06 % P; 0.01 % S
M23	[68]	Steel Kh14N14M2V2: 0.07 % C; 0.3 % Si; 0.26 % Mn; 0.009 % S; 0.007 % P; 13.4 % Cr; 14 % Ni; 2.07 % Mo; 1.85 % W; 0.0018 % O; 0.0001 % H; 0.027 % N Steel Kh15N28M4V2B: 0.1 % C; 0.24 % Si; 0.23 % Mn; 0.008 % S; 0.01 % P; 13.4 % Cr; 28.7 % Ni; 3.34 % Mo; 2.35 % W; 1.13 % Nb; 0.002 % O; 0.0002 % H; 0.062 % N
M24	[70]	Steel ShKh15: 1.02 % C; 0.28 % Mn; 0.31 % Si; 0.002 % S; 0.011 % P; 1.39 % Cr; 0.15 % Ni; 0.0025 % O
M25	[71]	Steel ShKh15: 1.0 % C; 0.34 % Mn; 0.25 % Si; 1.4 % Cr; 0.016 % S; 0.025 % P; 0.23 % Cu; 0.13 % Ni
M26	[73]	Steel: 0.61 % C; 0.67 % Mn; 0.27 % Si; 0.016 % P; 0.25 % S; 0.12 % Cu; 0.03 % Cr; 0.04 % Ni
M27	[74]	Steel: 0.5 % Si; 0.8 % Cr; 0.4 % C made from carbonyl iron (20 ppm S; 20 ppm O; 2 ppm Si)
M28	[76]	Composition (mass %)

Steel	C	Mn	Si	S	P	Cr	Ni	W	Mo	Ti	V
18KhNVA	0.16	0.37	0.23	0.006	0.006	1.42	4.21	0.95	0.07	0.3	–
30KhSGA	0.29	0.97	1.01	0.009	0.015	0.95	0.10	–	–	0.3	–
SP28	0.28	0.68	0.98	0.006	0.009	2.85	1.08	0.86	0.42	–	0.12
ShKh15SG	1.02	1.08	0.6	0.006	0.018	1.48	0.09	–	–	–	–
1Kh18N10T	0.08	1.37	0.41	0.007	0.03	17.35	10.4	–	–	0.44	–

No.	Ref.	Composition
M29	[78]	Steel: 0.05 % C; 0.61 % Si; 9.25 % Mn; 4.75 % Ni; 18.2 % Cr
M30	[87]	Alloy 1: 0.05 % C; 0.07 % Mn; 0.018 % S Alloy 2: 0.09 % C; 0.33 % Mn; 0.021 % S Alloy 3: 0.08 % C; 1.67 % Mn; 0.82 % Si; 0.03 % S Alloy 4: 0.13 % C; 6.1 % Mn; 0.4 % Si; 9.64 % Ni; 18.6 % Cr Alloy 5: 0.83 % C; 0.21 % Mn; 0.28 % Si; 0.01 % S
M31	[93]	Iron: 0.01 % C; 0.0043 % O

12.8 References in Chapter 12

[1] Keene, B. J.; NPL Report. DMM(D)32, dated May 1990, „Surface tension of slag systems" - ECSC Research Contract 7210-CF/107
[2] Bartell, F. E.; Osterhof, H. J.: Ind. Eng. Chem. 19 (11) 1927; 1277
[3] Dokhov, M. P.: Zh Fiz Khim 55 (5) 1981, 1324
[4] Dokhov, M. P.: Iz AN SSSR Metall (3) 1985, 66
[5] Askay, I. A.; Hoge, C. E.; Pask, J. A.: J. Phys. Chem. 78 1974, 1178
[6] Naidich, Yu. V.: Russ. J. Phys. Chem. 42 (8) 1968, 1023
[7] Sveshkov, Yu. V.; Mogilenskii, V. I.; Polonskii, Yu. A.; Val'Man, O. A.: Zh. Prikl. Khim. 49 (12) 1976, 2629
[8] Ramqvist, L.: Int. J. Powder Metall. 1 (4) 1965, 2
[9] Kamyshov, V. M.; Esin, O. A.; Chuchmarev, S. K.: Russ. J. Phys. Chem. 40 (1) 1966, 142
[10] Wenzel, R. N.: Ind. Eng. Chem. 28 1936, 988
[11] Huh, C.; Mason, S. G.: J. Coll. Interface Sci. 60 1977, 11
[12] Ogino, K.: Taikabutsu Overseas 2 (2), (undated) 80–84
[13] Samsonov, G. V.; Panasyuk, A. D.; Kozina, G. K.: Porosh. Metall. 11 (71) 1968, 42

[14] Humenik, M.; Kingery, W. D.: J. Am. Ceram. Soc. 37 (1) 1954, 18
[15] Yasinskaya, G. A.: Porosh. Metall. (7) (43) 1966, 53
[16] Terskov, Yu I.; Babkin, V. G.: Adgez. Rasp. Paika Mater. (4) 1979, 58
[17] Naidich, Yu V.; Kolesnichenko, G. A.: Porosh. Metall. (6) 1961, 55
[18] Naidich, Yu V.; Kolesnichenko, G. A.: Surface Phenomena in Metallurgical Processes. Ed.: A. I. Belyaev. Pub.: Consultants Bureau, N.Y. 1965, 218–223
[19] Naidich, Yu V.; Perevertailo, V. M.; Loginova, O. B.: Russ. Metall (4) 1979, 33
[20] Paul, G.: Giessereiforschung (in English) 23 (1) 1971, 13
[21] Rudenko, V. A.; Tolstoguzov, N. V.: Iz. Vuz Chern. Metall. (12) 1968, 64
[22] Samsonov, G. V.; Danasyuk, A. D.; Kozin, G. K.: Dop. AN. Ukr. RSR A. (5) 1969, 468
[23] Panasyuk, A. D.; Oreshkin, V. D.; Maslennikova, V. R.: Porosh Metall. (7) (199) 1979, 79
[24] Nogi, K.; Ogino, K.: Advanced Structural Materials – Montreal, Canada. 28–31 Aug. 1988. Pub.: Pergamon
[25] Champion, J. A.; Keene, B. J.; Allen, S.: J. Mater. Sci 8 1973, 423
[26] Prokof'eva, E. A.: Ogneupory (II) 1969, 51
[27] Humenik, M.; Parikh, N. M.: J. Am Ceram. Soc. 39 (2) 1956, 60
[28] Panasyuk, A. D.; Kyubarsepp, Ya. P.; Dzykovich, I. Ya.; Val'dma, L. E.: Porosh. Metall. (4) (220) 1981, 66
[29] Kyubarsepp, Ya. P.; Dzykovich, I. Ya.: Adgez. Rasp. Paika Mater. (13) 1984, 66
[30] Warren, R.: Int. J. Powder Metall. 4 (1) 1968, 51
[31] Ershov, G. S.; Kovalenko, A. M.: Russ. Metall. (1) 1968, 47
[32] Ershov, G. S.; Bychev, V. M.: Iz. Vuz. Chern. Metall. (4) 1975, 72
[33] Chuchmarov, S. K.; Esin, O. A.; Kamyshchov, V. M.: Iz. Vuz. Chern. Metall (1) 1967, 16
[34] Eustathopoulos, N.; Passerone, A.: Phys. – Chim. Sider. C-R Congr. 1978, 61–65 Pub.: Soc. Fr. Metall. Paris. (Reference to unpublished work by L. D. Lucas.)
[35] Ogino, K.; Nogi, K.; Yamase, O.: Trans. ISIJ 23 1983, 234
[36] Ogino, K.: Denki-Sheiko 52 1981, 262
[37] Ogino, K.; Adachi, A.; Nogi, K.: Tetsu-to-Hagane. 59 (9) 1973, 1237
[38] Chernov, B. G.: Iz. Vuz. Chern. Metall (6) 1983, 4
[39] Staronka, A; Gotas, W.: Arch. Eisenhüttenw. 50 (6) 1979, 237
[40] Kalmykov, V. A.; Sveshkov, Yu. V.; Elezov, S. A.: Fiz. Khim. Obrab. Mater. (8) 1976, 64
[41] Allen, B. C.; Kingery, W. D.: Trans. Met. Soc. AIME. 215 1959, 30
[42] Vatolin, N. A.; Ukhov, V. F.; Esin, O. A.; Dubinin, E. L.: Trudy Inst. Metal. Sverdlovsk (20) 1969, 42
[43] Ogino, K.; Nogi, K.: Technol. Rept. Osaka Univ. 20 (No. 946) 1970, 509
[44] van Muu, B.; Fenzke, H.-W.; Neuhof, G.: Neue Hütte 29 (4) 1984, 128
[45] Kozakevitch, P.; Lucas, L.-D.: Rev. Metall 65 (9) 1968, 589
[46] Mchedlishvili, V. A.; Mikiashvili, Sh. M.; Samarin, A. M.: Pov. Yav. Rasp. Voz. Tverd Faz. 1965, Pub.: Nal'chik, 389–399
[47] Popel, S. I.; Smirnov, L. A.; Tsarevskii, B. V.; Dzhemilev, N. K.; Pastukhov, A. I.: Russ. Metall. (1) 1965, 46
[48] Nogi, K.; Ogino, K.: Can. Metall. Quart. 22 (1) 1983, 19
[49] Ogino, K.; Nishiwaki, A.; Nogi, K.; Kurachi, T.: Proc. Int. Conf. Vac. Metall. (4th). 1973 Pub.: ISIJ Tokyo, 47–51
[50] Ogino, K.; Nishiwaki, A.; Nogi, K.: Phys. Chem. Metall. Proc. – Spec. Rept. ISIJ. 25 (Jpn-USSR), Symp 1977, 1–11
[51] Tsarevskii, B. V.; Popel, S. I.: Iz. Vuz. Chern. Metall. (8) 1960, 15
[52] Ogino, K.; Taimatsu, H.; Nakatani, F.: Nippon Kinzoku Gakkaishi. 46 (11) 1982, 1049
[53] Tsarevskii, B. V.; Popel, S. I.; Domozhirov, B. F.: Pov. Yav. Rasp. Voz. Tverd. Faz 1965 Pub.: Nal'chik, 316
[54] Volkov, S. E.; Mchedlishvili, V. A.; Samarin, A. M.: Dokl. AN. SSSR 149 (5) 1963, 1131
[55] Tsarevskii, B. V.; Popel, S. I.: Iz. Vuz Chern. Metall. (12) 1960, 12
[56] Karasev, V. P.; Turozhuman Gazi; Kalmykov, V. A.; Frolov, Yu. L.; Egorov, A. V.: Adgez. Rasp. Paika Mater. (12) 1984, 55
[57] Kishimoto, M.; Izumi, H.; Mori, K.; Kawai, Y.: Nippon Kinzoku Gakkaishi 44 (9) 1980, 1053
[58] Ogino, K.; Nogi, K.; Koshida, Y.: Tetsu-to-Hagane 59 (10) 1973, 1380
[59] Nogi, K.; Ogino, K.: J. High Temp. Soc. Japan. 16 (1) 1990, 20
[60] Nogi, K.; Ogino, K.: J. High Temp. Soc. Japan. 15 (5) 1989, 204
[61] Pavars, I. A.; Baum, B. A.; Ryss, M. A.: Tr. Ural. Politekhn. Inst. 167 1968, 145
[62] Smirnov, L. A.; Popel, S. I.; Tsarevskii, B. V.: Pov. Yav. Rasp. Voz. Tverd. Faz. 1965 Pub.: Nal'chik, 320–326
[63] Lobzhanidze, R. B.; Filippov, A. F.; Evseev, I. I.: Iz. Vuz. Chern. Metall (7) 1969, 56
[64] Mrdjenovich, R.; Kaufman, S. M.; Whalen, T. J.; Corey, C. L.: Metall. Trans. 1 1970, 2175
[65] Antipin, V. G.; Chebotarev, V. I.; Korotkikh, V. F.; Bakhscheyev, L. Yu: Russ. Metall. (1) 1978, 55
[66] Tsareskii, B. V.; Popel, S. I.: Iz. Vuz. Chern Metall. (12) 1963, 9
[67] Sveshkov, Yu. V.; Kalmykov, V. A.: Iz. Vuz. Chern. Metall. (5) 1973, 43
[68] Ageev, P. Ya.; Grebenkin, V. I.; Kalmykov, V. A.; Sveshkov, Yu. V.: Fiz. Khim. Obra. Mater. (6) 1968, 120
[69] Sveshkov, Yu. V.; Kalmukov, V. A.: Opt. Met. Prots. 6 1972, 40
[70] Voronov, V. A.; Nikitin, B. M.; Strigachev, E. M.: Smach. Rast. Adgez. Akad. Nauk. Ukr. SSR. 1977, 77–83
[71] Deryabin, A. A.; Popel, S. I.; Zupnik, A. E.: Iz. AN. SSSR. Metall. (2) 1968, 78
[72] Efimov, V. A.; Ishchuk, N. Ya; Cheburko, V. V.; Klibus, A. V.; Lepinskikh, B. M.: Russ. Metall. (5) 1971, 10
[73] Popel, S. I.; Deryabin, A. A.; Saburov, L. N.; Isaev, N. I.; Vasilenko, G. N.: Iz. Vuz. Chern. Metall 12 (8) 1969, 5
[74] Vatolin, N. A.; Ukhov, V. F.: Smach. Poverkh. Svoist. Rasp. Tverd Tel. Naukova Dumka. Kiev, 1972, 186
[75] Smirnov, L. A.; Popel, S. I.; Tsarevskii, B. V.: Iz. Vuz. Chern. Metall. (3) 1965, 10
[76] Malinovskii, E. I.; Voronov, V. A.: Proiz. Issled Stalei. Splavov. 4 1970, 42
[77] Sveshkov, Yu. V.; Kalmykov, V. A.: Optimiz. Met. Prots. 6 1972, 40
[78] Cosma, D.: Metallurgia (Bucharest) 23 (12) 1972, 804
[79] Malinovskii, E. I.; Voronov, V. A.: Russ. Metall. (2) 1969, 24
[80] Vatolin, N. A.; Ukhov, V. F.; Pokrovskii, V. A.: Trudy Inst. Met. Sverdlovsk (20) 1969, 55
[81] Eremenko, V. N.; Naidich, Yu V.: Wetting Refractory Oxides with Rare Metals. Acad. Sci. Ukr., 1958
[82] Kalmykov, V. A.; Frolov, Yu. L.; Kondrat'ev, A. S.; Ikonnikov, V. I.: Adgez. Rasp. Paika Mater. (12) 1984, 51
[83] Tsarevski, B. V.; Popel, S. I.: Chern. Met. 8 1960, 15
[84] Levin, A. M.: Reference in „Methods to Improve the Casting of Steel", 1963, 151, Efimov, V. A.; Ossipov, V. P.; Grebeniouk, V. P.
[85] Manning, C. R.; Stoops, R. F.: J. Am. Ceram. Soc. 51 (8) 1968, 415
[86] Eustathopoulos, N.; Passerone, A.: Phys. – Chim. Sider. C-R Congr. Pub.: Soc. Fr. Metall, Paris. 1978, 61–65
[87] Patskevich, I. R.; Deev, G. F.: Avtom. Svarka. (12) 1979, 40
[88] Staronka, A.; Gotas, W.: Arch. Eisenhüttenw. 51 (10) 1980, 403
[89] Eremenko, V. N.; Naidich, Yu. V.: Zh. Fiz. Khim. 33 1959, 1238
[90] Aratani, K.; Tamai, Y.: Yogyo-Kyokai-Shi. 89 (9) 1981, 480
[91] Usatikov, I. F.; Kalita, G. E.; Gal'chenko, T. G.: Ogneupory. (4) 1978, 53
[92] Kozlova, O. B.; Suvorov, S. A.: Ogneupory. (12) 1976, 41
[93] Sveshkov, Yu. V.; Borisov, V. G.; Val'dman, O. A.; Kalmykov, V. A.: Russ. Metall. (4) 1977, 74

13

Diffusion coefficients in molten slags

K. C. Mills

13.1 Introduction

Diffusion is the movement of the constituent species of the melt from point to point within the melt. There are the following forms of diffusion:

(I) *Self diffusion* which involves the movement of various species present in the melt by random motions; for self-diffusion there is no nett flux of any species and there are no chemical potential gradients within the melt.

(II) *Tracer diffusion* is essentially the same process as self diffusion except that a fraction of one (or more) of the species is radioactive in order to monitor its movement. Consequently in tracer diffusion there are nett fluxes and chemical potential gradients but these only occur for the tracer species. In solids, tracer diffusion results from the successive jumps of tracer atoms and is related to the random movement of vacancies thus tracer diffusivities are less than self diffusivities. In liquids the tracer diffusivity is considered to be equivalent to the self diffusivity. It is also customary to quote self diffusivity values for impurity elements in the melt, although strictly this is chemical diffusion since a concentration gradient exists.

(III) *Chemical diffusion* is the movement of a species in the melt in response to the establishment of a chemical potential gradient resulting from either concentration or temperature gradients in the melt. Chemical diffusion occurs in a direction such that there is a reduction in the concentration gradient causing the diffusion. Chemical diffusion resulting from a temperature gradient is referred to as *Soret diffusion*. Diffusion involving local changes in the redox state is considered to be chemical diffusion.

(IV) *Interdiffusivity*. When chemical diffusion involves the movement two (or more) species, say a cation and an anion, if the cation is more mobile than the anion an electrical field is established which reduces the cation flux and increases the anion flux to prevent a space charge being established.

13.2 Theory

13.2.1 Single component diffusion

Single component diffusion is usually associated with self diffusion but could apply to chemical diffusion where only one species is involved eg oxygen. For an isotropic medium, diffusion is determined according to Ficks First and Second Laws given in equations (13.1) and (13.2), where J is the flux across a plane, (dC/dy) is the concentration gradient normal to the plane, D is the diffusion coefficient and t is time.

$$J = -D(dC/dy) \quad (13.1)$$

$$(dC/dt) = D(d^2C/dy^2) \quad (13.2)$$

There have been three approaches taken to relate the self diffusion coefficient [1] to other parameters, these are outlined below.

13.2.1.1 Mean free path or statistical approach

The diffusing particle can be considered as moving in a series of jumps, the start and finish of each jump being determined by its interaction with other particles in the system. Equation (13.3) was derived for self diffusion, where λ and τ are the mean free path and mean time per jump, respectively.

$$D = n\lambda^2/2\tau \quad (13.3)$$

13.2.1.2 Friction coefficient approach

In this approach the friction coefficient (β) of the diffusing species is calculated and results in equation (13.4) where k is the Boltzmann constant; T the thermodynamic temperature, m the mass of the diffusing species

$$D = kT/m\beta \quad (13.4)$$

The Stokes-Einstein relation can be derived from equation (13.4), (see Section 13.5).

13.2.1.3 Absolute rate theory approach

When the absolute rate theory is applied to an isotropic medium it yields equation (13.5) where η is the viscosity of the melt

$$D = kT/\eta\lambda \quad (13.5)$$

13.2.2 Multi-component diffusion [2]

Multi-component diffusion is treated through the Onsager extension of Fick's First Law and results in equation (13.6) where i and j are the diffusing components and Dij is the diffusion coefficient of i in response to a concentration gradient for j, ie (dC_j/dy)

$$J_i = \Sigma_j D_{ij} (dC_j/dy) \quad (13.6)$$

Several solutions have been proposed [3 – 6]. Okongawu et al [6] obtained equations (13.7) and (13.8) which could be reduced to equation (13.9) by assuming that there was no build-up in space charge and that there was uniform anion concentration ie $(dC_k/dy) = O$.

$$J_1 = -D_{ij} (dC_i/dy) - D_{ij} (dC_j/dy) \quad (13.7)$$

$$J_2 = -D_{ij} (dC_i/dy) - D_{ij} (dC_j/dy) \quad (13.8)$$

$$J_i = -D(dC_i/dy) \text{ and } J_j = -D (dC_j/dy) \quad (13.9)$$

13.3 Experimental methods

The principal methods used in measuring diffusion coefficients in melts are outlined below, comprehensive reviews of the methods have been given elsewhere [7, 8].

13.3.1 Instantaneous plane source (IPS)

A tracer (usually radioactive) is deposited as a thin layer at one end of a long column, which can be considered to be infinitely long (**Fig. 13.1**) and the diffusion coefficient can be derived by use of equation (13.10) where m is the mass of tracer deposited.

$$C(x,t) = m/(\pi Dt)^{0.5} \exp(y^2/4Dt) \quad (13.10)$$

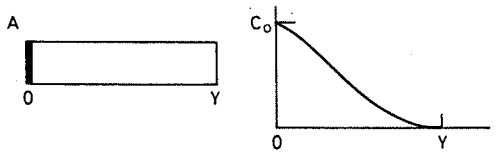


Fig. 13.1. Schematic representation of the instantaneous plane source method and the form of the concentration gradient established after some time

13.3.2 Capillary reservoir (CR) or Immersion method

In this method the diffusing species is held in a capillary which is immersed in the melt and diffusion occurs between the contents of the capillary and the liquid. The capillary is removed after a set time and the distribution of the species determined.

13.3.3 Diffusion couple (DC) method

The diffusion couple consists of two melts of identical composition except that one contains the tracer element (**Fig. 13.2.**). The diffusion coefficient can be derived by linear regression of concentration versus distance (y) plots, the slope being equal to $0.5(Dt)^{-0.5}$.

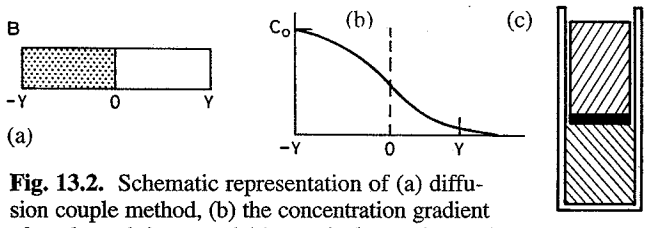


Fig. 13.2. Schematic representation of (a) diffusion couple method, (b) the concentration gradient after elapsed time t and (c) a typical experimental arrangement

13.3.4 Electrochemical method

An electrochemical cell is established which contains a metal electrode containing the diffusing species and the molten slag composition of interest and electrolysis is carried out at uniform current (I). If the electrode reaction is controlled by diffusion equation (13.11) can be used to derive the diffusion coefficient where z ist the valence of the diffusing species and F is the Faraday constant.

$$I = zFD(dC/dy)_{y=0} \qquad (13.11)$$

13.3.5 Molecular dynamics (MD) calculations

Diffusion coefficients derived by molecular dynamics calculations have been found to be in good agreement with values derived experimentally.

13.3.6 Experimental errors

The experimental uncertainties associated with many of the diffusion coefficient and activation energy values cited in the literature are large; Turkdogan [2] has pointed out that, in general, the values obtained in more recent determinations are to be preferred since there have been significant improvements in experimental techniques in recent years.

13.4 Factors affecting diffusion coefficients

13.4.1 Temperature

The diffusion coefficient increases with increasing temperature and the temperature dependence is satisfactorily ex-

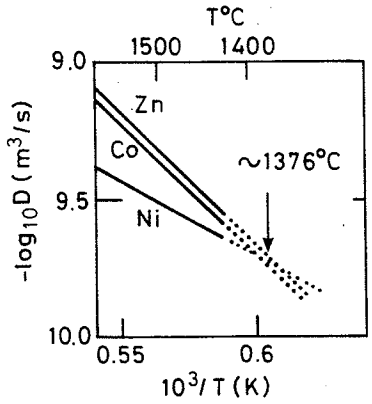


Fig. 13.3. Impurity coefficients of Co, Ni and Zn in $CaO.MgO.2SiO_2$[12]

pressed by the Arrhenius relation (equation 13.12 where D_o is the frequency factor, E_D the activation energy for diffusion, R the gas constant and T the thermodynamic temperature (K)).

$$D = D_o \exp(-E_D/RT) \qquad (13.12)$$

This can be expressed in the form of equation (13.13) where E_D is in kJ mol^{-1}.

$$\log D = \log D_o (-E_D/19.14\,T) \qquad (13.13)$$

It has been observed that the diffusion coefficients for various diffusing species have identical values at a specific ("crossover") temperature around 1400 °C; this can be seen from **Fig. 13.3.** This "compensation effect" [1, 9 – 12] results from the inverse relationship between log D_o and E_D **(Fig. 13.4)** given in equation (13.14) due to Hofmann [11]

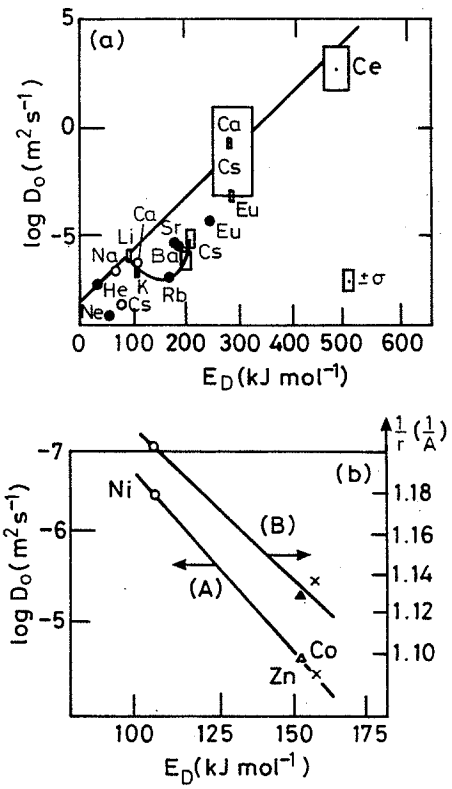


Fig. 13.4 a,b. Relationship between log D_o and the activation energy (E_o) ('compensation effect') (a) for various impurity species in solid obsidian (73 % SiO_2, 13 % Al_2O_3, 5 % Na_2O, 4 % K_2O) [13] and (b) for Co^{2+}, Ni^{2+} and Zn^{2+} in liquid $CaO.MgO.2SiO_2$ (curve A); curve B shows the relationship between log D_o and the ionic radius (r) of the diffusing species [12]

where E_D is in kJ mol^{-1} and D, D_o in m^2s^{-1}.

$$\log D = 0.45\, E_D - 9.50 \qquad (13.14)$$

13.4.2 Pressure

The effect of pressure (p) on the diffusion coefficients for molten silicates can usually be expressed in the form of equation (13.15) where B is the activation volume [1].

$$\log D = \log D_o\, (E_D/19.14T) - (Bp/19.14T) \qquad (13.15)$$

13.4.3 Slag composition

13.4.3.1 SiO_2 content

It can be seen from **Fig. 13.5 a** and **13.5 b** that tracer and impurity diffusion coefficients decrease with increasing SiO_2 content and this also applies to chemical diffusion. This implies that the structure (ie the degree of depolymerisation expressed by the (NBO/T) ratio) of the slag effects the diffusion process and the ratio is also shown in these figures. The calculation of (NBO/T) is outlined in Appendix 1 (see 13.7.1).

13.4.3.2 Moisture content

The addition of water to melts has been found to produce a dramatic increase in chemical diffusion coefficients (**Fig. 13.6.**) and a decrease in the activation energy. Enhancement in D of 6 to 50 fold and decreases in E_D of 4 fold have been recorded with H_2O additions of ca. 5 % [17 – 19].

13.4.4 Radius and valency of diffusing species

13.4.4.1 Cations

It can be seen from **Figs.** 13.4.b, **13.7** and **13.8** that the diffusion coefficients of cations decrease as the valency (z) increases and the radius increases eg D(Li) > D(Na). The effect of valence on the diffusion coefficient can be clearly seen in Fig. 13.7. where the diffusing species all have similar radii and the effect of ionic radius can be seen in Figs. 13.4 b and 13.8.

13.4.4.2 Anions

As can be seen from Fig. 13.5 b the diffusion coefficients of Si and O are much smaller than those of cations such as Ca. The similarity in the D values for Si and O has led to the suggestion that the movements of the two atoms are linked [16]. However, it can be seen from **Fig. 13.9** that there is a large discrepancy in the diffusion coefficients for O reported by several workers. Dunn [1] commenting on the differences between the D(O) values reported [20, 21] for CaO, MgO, $2SiO_2$ suggested that the higher D(O) value referred primarily to the diffusion of molecular oxygen whereas the lower D(O) values referred to both the diffusion of oxygen bound in silicate ions and molecular oxygen, the latter being much larger. These mechanisms can be expressed [22] by equations (13.16) and (13.17) where $\oplus$ represents a positive hole.

$$O_2 \text{ (gas phase)} = O_2 \text{ (molten slag)} \qquad (13.16)$$

$$O_2 \text{ (gas phase)} = 2O^{2-} \text{ (molten slag)} + 4 \oplus \qquad (13.17)$$

Sasabe and Asamura [22] observed that FeO, MnO and NiO increased the transport rate of O and suggested that oxygen

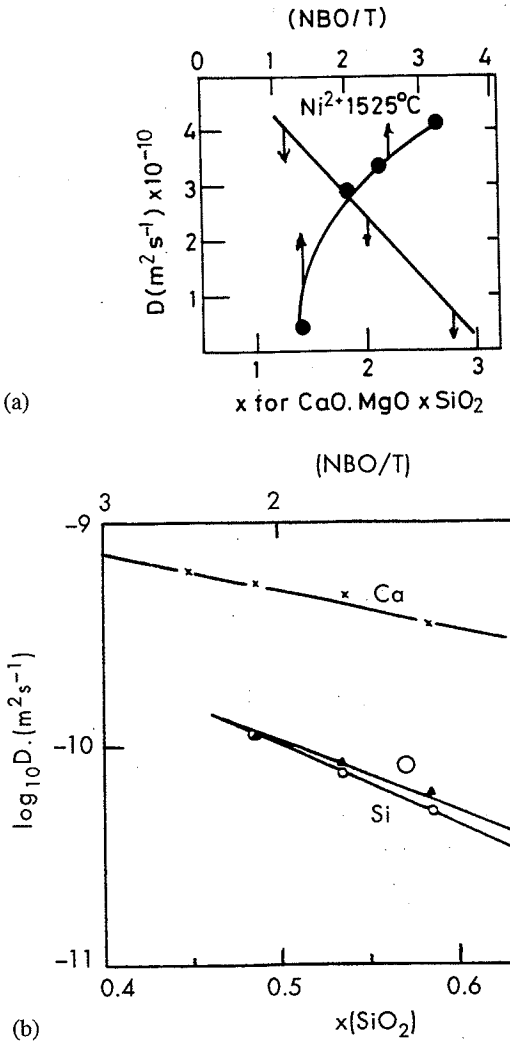


Fig. 13.5 a,b. The effect of SiO_2 content and (NBO/T) ratio on (a) the impurity diffusion coefficient of Ni^{2+} at 1525 °C on CaO-MaO-SiO_2 melts [12] and (b) the self (tracer) diffusion coefficients of Ca, O, an Si in CaO-SiO_2 melts at 1600 °C [14-16]

diffusion occurred primarily by the mechanism shown in equation (13.17) in systems containing transition metal oxides and by equation (13.16) where the melt contained no transition metal oxide.

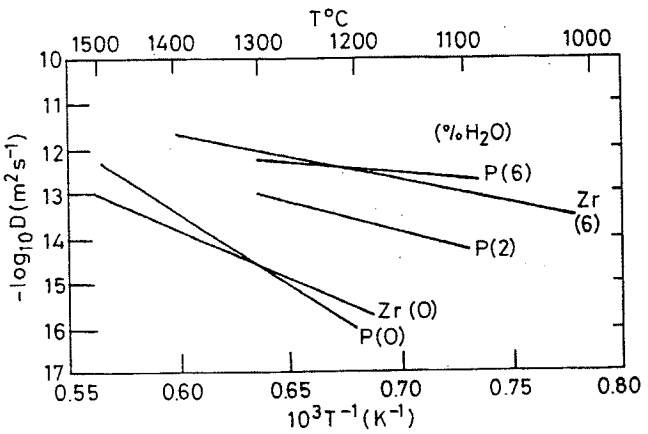


Fig. 13.6. The effect of additions of 2 and 6 % H_2O on the chemical diffusion coefficients of Zr and P in granitic melts [18]; values given in parenthesis denote % H_2O

13.5 Relationship of diffusivity with other properties

13.5.1 Viscosity (η)

a) Stokes-Einstein relationship

$$D = kT/6\pi\eta r \qquad (13.18)$$

where k = Boltzmann constant, r = radius of diffusing species.

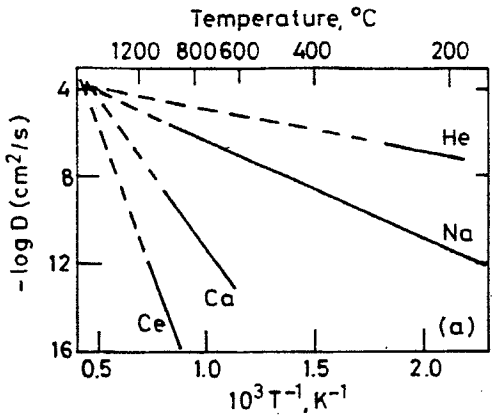
The Stokes-Einstein relationship does not work for slags, principally because it assumes that the diffusing species is large whereas in practice the cations are small compared with the silicate anions.

b) Eyring relationship

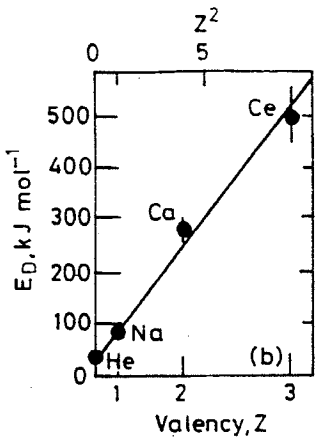
$$D = kT/\eta\lambda \qquad (13.19)$$

where λ = is mean interatomic difference (2r).

This equation has been used successfully by several workers but values of λ slightly greater than 2r were needed to obtain good agreement with experimental data [1, 23].



(a)



(b)

Fig. 13.7 a,b. The effect of valency on (a) diffusion coefficients and (b) activation energies for various ions with similar ionic radii in solid granites (SiO_2 73 %, Al_2O_3 12 %, Na_2O 5 %, K_2O 4 %)[13]

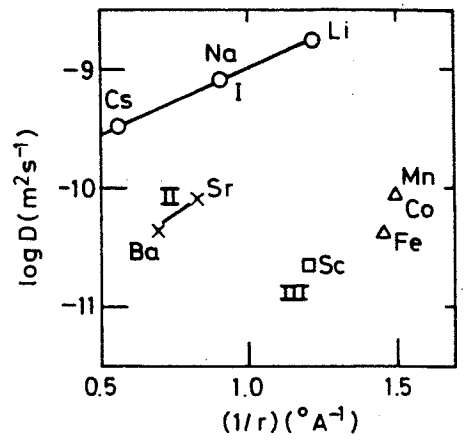
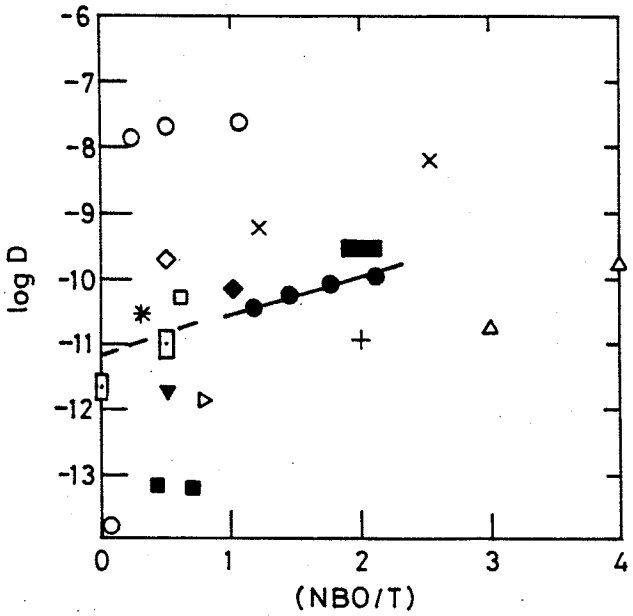


Fig. 13.8. Diffusion coefficients at 1400 °C in basalt melts for various ions under oxidising conditions, as a function of reciprocal ionic radii showing the effects of both ionic radius and valence



- ● Keller C-S
- × Shiraishi C-S
- ◇ Koros A-C-S
- ◆ Oishi A-C-S
- O Sasabe A-C-S
- ▯ Dunn A-C-M-S
- \+ Dunn C-M-S
- ▬ Semkow C-M-S
- ■ May K-O
- ▷ May C-N-S
- ▼ Oishi N-S
- △ Schmalzriedt P-S
- ✳ Wendlandt Andesite
- □ Basalt

where $A=Al_2O_3$, $C=CaO$
$K=K_2O$, $M=MgO$
$N=Na_2O$, $P=PbO$, $S=SiO_2$

Fig. 13.9. Diffusion coefficients for oxygen, at temperatures close to the liquidus temperatures as a function of the ratio, (NBO/T). Note the much higher values (denoted O) due to Sasabe and Asamura [22] for the Al_2O_3-CaO-SiO_2 system which suggests that diffusion occurs by a different mechanism to those in other experiments

13.5.2 Electrical conductivity (κ)

Nernst-Einstein relationship

$$\kappa = z^2F^2DC/RT \qquad (13.20)$$

where z is the valence of the diffusing species, F the Faraday constant and C the concentration.

Values of D calculated from this equation tend to be higher than calculated values [24].

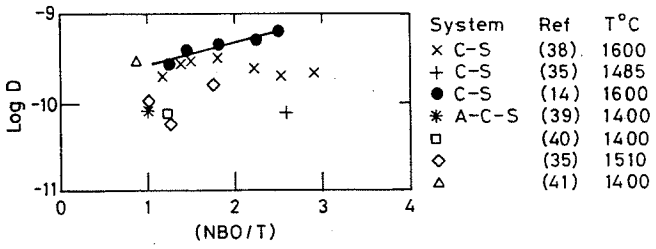


Fig. 13.10. Self (tracer) diffusion coefficient of Ca at temperatures close to the liquidus temperature as a function of the ratio of (NBO/T)

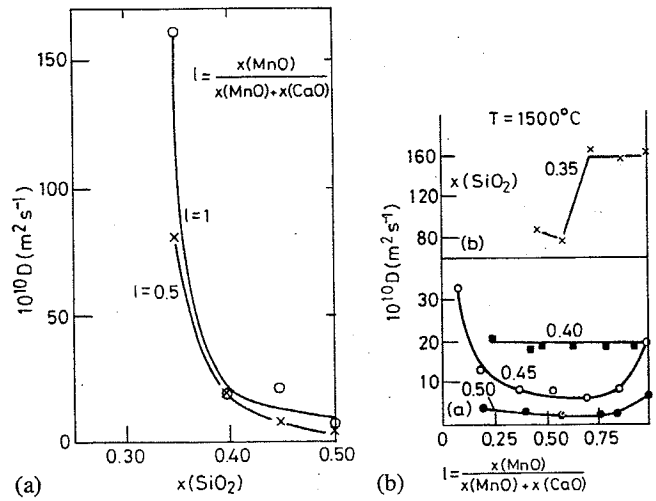


Fig. 13.11 a,b. Self diffusion coefficients of Mn in CaO-MnO-SiO_2 melts at 1500 °C as a function of (a) mole fraction SiO_2 and (b) the ratio x (MnO)/[x(MnO) + x(CaO)] [50]

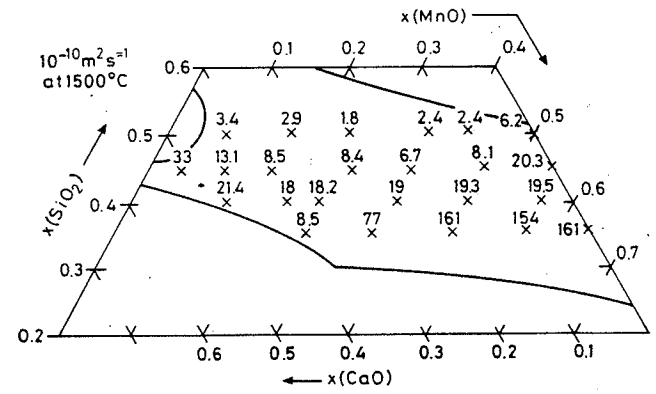


Fig. 13.12. Iso-diffusivity contours (10^{-10} m^2s^{-1}) for Mn at 1500 °C in CaO-MnO-SiO_2 melts [50]; the solid lines represent the liquidus contours for 1500 °C

13.6 Experimental data

The experimental results reported in the literature for diffusion coefficients in molten slags are given below in **Tabs. 13.1 – 13.4.** These data were collated from reviews [2, 11, 25 – 28] and recent publications. No diffusion coefficient values are given in this report for solid glasses and slags, data on these systems are available in other reviews [28, 25, 26].

Data are given in the form of equation 13.13 viz

$$\log_{10}D = \log_{10}D_o - (E_D/19.14T)$$

where D and D^o are in m^2s^{-1} and E_D in kJ mol^{-1}. Compositions are cited as either mass % (eg 36.7) or mole fraction (eg (0.367)) and typical compositions for materials are given in Appendix 2 (see 13.7.2).

13.6.1 Self diffusion coefficients in pure oxides

Tab. 13.1. Self diffusion coefficients for pure oxides

Species	Melt	log D_o	E_D	Tκ	– log D °C	Temp Range,	Method	Ref.	Comment
Al^{26}	Al_2O_3	– 6.64	88.7			2050 – 2300	IPS	[29]	
O^{18}	B_2O_3	–	137			350 – 650	GE	[30]	p_{O_2} = 0.13 bar
O	Fe_xO			1823	– 8.30	1550	O + R	[31]	
		– 6.18	44.8	1823	– 7.46	1420 – 1550	O + R	[32]	Fe^{3+}/Fe^{2+} + Fe^{3+} = 0.12
		– 5.79	69.5	1823	– 7.78	1510 – 1550			= 0.33
O	PbO	– 3.08	96	1373	– 6.73	1000 – 1200	O_2-P	[33]	

13.6.2 Self diffusion coefficients in molten slags

Tab. 13.2. Self (tracer) diffusion coefficients in molten slags; mole fractions

Species	Slag composition				log D_o	E_D	Tκ	– log D	Temp Range, °C	Method	Ref.	Comment
Al^{26}	Al_2O_3	CaO	SiO_2									
	10.1	43.5	46.5	–	+ 0.63	356	1700	10.37	1440 – 1520	CR	[34]	
	20	39	41		– 3.27	251	1700	10.98	1398 – 1487		[34]	
Ca^{45}	Al_2O_3	CaO	SiO_2									
	51.3	48.7			– 2.64	251	1758	10.10	1693 – 1788	DC	[35]	
	50.0	50.0			– 4.15	150.6	1773	8.58	1450 – 1500	CR	[36]	D_{Ca} is higher
	49.9	50.1			– 4.68	133.5	1773	8.61	1400 – 1600	O_2P	[37]	than in silicate
		(.376)	(.624)				1873	9.7	1600 – 1700	CR	[38]	See Fig. 13.10
		(.406)	(.594)				1873	9.55	1600 – 1700			
		(.426)	(.574)				1873	9.5	1600 – 1700			
		(.467)	(.533)				1873	9.45	1600 – 1700			
		(.497)	(.503)				1873	9.5	1600 – 1700			
		(.528)	(.472)				1873	9.6	1600 – 1700			
		(.557)	(.443)				1873	9.7	1600 – 1700			
		(.587)	(.413)				1873	9.7	1600 – 1700			
		(.569)	(.439)		– 3.94	209	1758	10.15	1758 – 1803	DC	[35]	Fig. 13.10
		(.366)	(.634)		– 5.43	146	1873	9.54	1500 – 1650	DC	[14]	Recommended
		(.413)	(.587)		– 6.04	125	1873	9.44	1560 – 1650		[14]	see Figs. 13.5 b, 13.10
		(.47)	(.53)		– 5.62	142	1873	9.33	1550 – 1700		[14]	13.5 b, 13.10
		(.512)	(.488)		– 5.34	142	1873	9.27	1550 – 1650		[14]	13.5 b, 13.10
		(.552)	(.448)		– 5.70	121	1873	9.21	1500 – 1700		[14]	13.5 b, 13.10
	20	40	40		– 1.203	287	1723	9.90	1350 – 1540		[39]	
Ca^{45}	18	43	39		– 6.24	126			1350 – 1450	CR	[40]	Fig. 13.10
	20	38	42		– 5.538	128	1723	9.32	1300 – 1600	IPS	[41]	
	20	40	40		– 1.0	293			1350 – 1540	CR	[42]	
	19.0	39.8	41.2				1713	10.0	1350 – 1440	DC	[35]	Fig. 13.10
	20.2	43.0	37.2				1783	9.72	1440 – 1510	DC	[35]	
	11.7	48.9	39.4				1783	9.77	1440 – 1510	DC	[35]	
	18.6	45.2	36.3				1783	10.07	1510 – 1530	DC	[35]	
	20.5	45.6	34.1		– 3.10	239	1783	10.08	1440 – 1575	DC	[35]	
	20.3	48.4	31.3				1813	10.26	1540 – 1565	DC	[35]	
	CaO	Na_2O	SiO_2									
	12	16	72		– 4.20	181	1473	10.60	1000 – 1400	IPS	[43]	
	(.167)	(.167)	(.666)		– 0.88	239	1473	9.35	850 – 1210	IPS	[44]	
	Al_2O_3	CaO	MgO	SiO_2								
	19.5	43.4	5.4	31.8			1783	10.01	1485 – 1530	DC	[35]	
Co^{57}	CoO	SiO_2										
	(.635)	(.365)			– 1.69	217			1427 – 1572	CR	[45]	
Fe^{59}	FeO	SiO_2										
	56	43			– 2.80	155	1600	[7.86]	1250 – 1304	CR	[46]	in Air
	67	33			– 6.74	72.9	1600	[9.10]	1362 – 1540	CR	[47]	
	Fe_2O_3	SiO_2										
	70.5	29.5			– 5.19	72.8			1250 – 1450	IPS	[37]	
Fe^{59}	CaO	Fe_2O_3	SiO_2									
	33	40	27		– 4.70	109	+log $P_{O_2}^{1/85}$		1360 – 1460	IPS	[48]	
Fe^{59}	CaO	FeO	SiO_2				1523	9.51				
							1873	8.84	1250 – 1600	CR	[47]	

Tab. 13.2. (continuation)

Species	Slag composition				log D_o	E_D	Tκ	– log D	Temp Range, °C	Method	Ref.	Comment
K^{42}	K_2O (.125)	Na_2O (.125)	SiO_2 (0.75)		– 6.20	75.3			850 – 1050	CR	[49]	
Mn	MnO (0.50)	SiO_2 (0.50)			– 7.38	61.6	1773	9.20	1400 – 1550	CHRP	[50]	Fig. 13.11
	(0.55)	(0.45)			– 3.92	161.8	1773	8.69				
	(0.60)	(0.40)			– 6.69	68.2	1773	8.70				
	(0.65)	(0.35)			– 2.06	194.5	1773	7.79				
	CaO	MnO	SiO						1500			See Figs. 13.12, 13.11
Na^{22}	Na_2O (0.25)	SiO_2 (0.75)			– 6.33	67.4			850 – 1500	CR	[51]	
					– 6.50	59.0			750 – 1150	CR	[49]	
Na^{24}	(0.333)	(0.667)			– 6.64	52.0			850 – 1500	CR	[51]	
	(0.333)	(0.667)			– 6.70	51.5			900 – 1150	CR	[49]	
	(0.333)	(0.667)			– 7.24	29.5			1027 – 1420	CR	[52]	
	(0.333)	(0.667)			– 6.74	50			850 – 1210	IPS	[53]	
	CaO	Na_2O	SiO_2									
Na^{22}	12	16	72		– 4.21	181	1473	9.28	1000 – 1400	IPS	[43]	
Na^{24}	14.4	17.3	67.1		– 5.92	83.3	1473	8.87	850 – 1210	IPS	[37]	
Na^{24}	MgO (.167)	Na_2O (.167)	SiO_2 (.666)		– 5.80	85.8			850 – 1210	IPS	[53]	
Na^{24}	SrO (.167)	Na_2O (.167)	SiO_2 (.666)		– 4.96	110			1123 – 1483	IPS	[53]	
Na^{24}	Na_2O 36	P_2O_5 3.8	SiO_2 60.2		– 6.56	48.1	1573	8.16	1097 – 1362	CR	[52]	
	37.8	7.2	55.0		– 6.81	40.2	1573	8.15	1067 – 1257	CR	[52]	
	39.5	10.4	50.1		– 6.87	37.9	1573	8.13	1097 – 1402	CR	[52]	
	41.1	13.4	45.5		– 6.66	47.3	1573	8.23	1107 – 1402	CR	[52]	
O^{18}	CaO (0.366)	SiO_2 (.634)					1873	10.46	1520 – 1650	CR	[16]	Recommended (Fig. 13.5 b) See Fig. 13.9
	(0.417)	(.583)					1873	10.22				
	(0.467)	(.533)					1873	10.08				
	(0.517)	(.483)					1873	9.96				
O^{18}	(0.56)	(0.44)			+ 2.82	408	1873	8.2	1550 – 1650	CR	[54]	
	(0.38)	(0.62)			+ 0.09	365	1873	9.2		CR		
	(0.4)	(0.6)					1873	10.1	1600	MD	[55]	
	(0.5)	(0.5)					1873	9.75		MD		
	(0.6)	(0.4)					1873	9.5		MD		
O^{18}	K_2O (.264)	SiO_2 (.736)			– 4.62	192	1173	13.17	700 – 1000	GE	[56]	$P_{o_2} < 0.13$ bar
	(.175)	(.825)			– 2.40	258	1173	13.19	750 – 1000	GE		
	37.2	62.2			– 2.77	250	1173	13.9	820 – 902	GE	[57]	
O^{18}	Na_2O (0.20)	SiO_2 (0.80)			– 5.10	186	1473	11.70	1100 – 1400	GE	[58, 3]	
O^{18}	PbO (0.9)	SiO_2 (0.1)					1123	– 8.85		PF	[59]	
	(0.8)	(0.2)					1123	– 9.25				
	(0.7)	(0.3)					1123	– 9.80				
	(0.6)	(0.4)					1123	– 10.80				
	(0.9)	(0.1)			– 3.08	100	1123	[7.73]	1000 – 1450	O_2P	[33,23]	
	(0.8)	(0.2)			– 3.08	105	1123	[7.96]	1000 – 1450			
	(0.7)	(0.3)			– 3.08	109	1123	[8.15]	1000 – 1450]			

Tab. 13.2. (continuation)

Species	Slag composition				$\log D_o$	E_D	T_K	$-\log D$	Temp Range, °C	Method	Ref.	Comment
O^{17}	Al_2O_3	CaO	SiO_2									
	20	40	40		+ 1.57	356	1673	9.54	1372 – 1535	CR	[60]	
O^{18}	20	40	40		+ 1.67	356	1673	9.44	1372 – 1535	CR	[60]	
O^{18}	19.7	39.8	41.1		– 2.74	227	1673	9.84	1320 – 1540	GE	[58, 3]	
O	15	45	40		0.78	142	1673	7.65	1335 – 1427	O_2-P	[33, 22]	
O	20	40	40		1.11	155	1673	7.7	1330 – 1440	O_2-P	[33, 22]	
O	10	25	65		1.07	167	1673	7.85	1314 – 1420	O_2-P	[33, 22]	
O	Al_2O_3	Na_2O	SiO_2									p = 15 kbar
	(0.1)	(0.1)	(0.8)				1723	12.7	1400 – 1600		[23]	
O	CaO	MgO	SiO_2				1673	11.0	1400 – 1460		[1]	
	(0.25)	(0.25)	(0.5)				1723	10.75	1400 – 1460			
	(0.25)	(0.25)	(0.5)		+ 0.73	335	1723	9.35	1450	CyV	[21]	
O	CaO	Na_2O	SiO_2									
	12	16	72		– 5.35	162	1273	12.0	800 – 1450	GE	[61]	
O	K_2O	SrO	SiO_2									
	20	20	60		– 5.07	219			680 – 1121		[62]	
O	Na_2O	P_2O_5	SiO_2									
	(0.50)	(0.45)	(0.05)				1403	4.96	893 – 1130	CR	[63]	
	(0.50)	(0.47)	(0.03)				1403	4.38	893 – 1130			
	(0.50)	(0.48)	(0.02)				1403	4.30	1000 – 1130			
O	Al_2O_3	CaO	MgO	SiO_2			1673	11.0		Fe	[20]	
	(.105)	(.25)	(.145)	(.50)			1723	10.8		reduction		
	(.15)	(.25)	(.10)	(.50)			1673	11.6		in		
							1723	11.45		spheres		
O^{18}	CaO	MgO	Na_2O	SiO^2	5.20	208			700 – 1083		[62]	
	8.8	4.2	13.8	72.6								
P^{32}	Na_2O	P_2O_5	SiO_2									
	36	3.8	60.2		– 6.37	66.3			1097 – 1362	CR	[52]	
	37.8	7.2	55.0		– 5.27	93.7			1067 – 1257			
	39.5	10.4	50.1		– 7.28	35.1			1097 – 1402			
	41.1	13.4	45.5		– 6.03	77.6			1107 – 1402			
Pb^{210}	PbO	SiO_2										
	0.9	0.1					1123	9.15		PF	[59]	
	0.8	0.2					1123	9.30				
	0.7	0.3					1123	9.70				
	0.6	0.4					1123	10.10				
	0.5	0.5					1123	10.7				
	0.4	0.6					1123	10.4				
Si	CaO	SiO_2										
	(.376)	(.624)					1873	10.0	1600 – 1700	CR	[38]	
	(.406)	(.594)					1873	9.75				
	(.426)	(.574)					1873	9.5				
	(.467)	(.533)					1873	9.5				
	(.497)	(.503)					1873	9.6				
	(.528)	(.472)					1873	9.6				
	(.557)	(.443)					1873	9.6				
	(.587)	(.413)					1873	9.45				
Si^{31}	(.366)	(.634)					1873	10.49	1600	DC	[15]	Recommended
	(.417)	(.583)					1873	10.29				Fig. 13.5 b
	(.466)	(.534)					1873	10.12				
	(.516)	(.484)					1873	9.95				
Si^{28}	CoO	SiO_2										
	(0.635)	(0.365)			+ 13.2	766	1833	8.16	1427 – 1572	CR	[45]	
Si^{30}	PbO	SiO_2										
	(0.9)	(0.1)					1123	9.20	850	PF	[59]	
	(0.8)	(0.2)					1123	9.50	850			
	(0.7)	(0.3)					1123	9.85	850			
	(0.6)	(0.4)					1123	10.4	850			
	(0.5)	(0.5)					1123	11.25	850			
Si^{31}	Al_2O_3	CaO	SiO_2									
	21	39	40		– 2.02	293	1703	10.98	1363 – 1460	CR	[64]	

13.6.3 Impurity diffusion coefficients in molten slags

Tab. 13.3. Impurity diffusion coefficients in molten slags

Species	Slag composition				$\log D_o$	E_D	T_K	$-\log D$	Temp Range, °C	Method	Ref.	Comment
Ba^{140}	K_2O	Na_2O	SiO_2									
	(0.25)		(0.75)		−5.80	134			850 – 1200		[65]	
		(0.25)	(0.75)		−5.89	117			850 – 1200			
	Andesite				−4.36	210	1573	11.35	1300 – 1400	CR	[66]	Figs. 13.8, 13.13
	Basalt				+5.0	172	1573	10.70	1300 – 1400	CR	[66]	Figs. 13.8, 13.13
							1573	10.70		TS	[11]	Figs. 13.8, 13.13
	Obsidian						1573	11.40		CR	[67]	Figs. 13.8, 13.13
	Pantellerite						1573	11.45		CR	[67]	Figs. 13.8, 13.13
Ca^{45}	K_2O	Na_2O	SiO_2									
	(0.25)		(0.75)		−4.30	188				RA	[65]	
		(0.25)	(0.75)		−4.80	151						
	Basalt						1573	10.40		TS	[11]	
Co^{2+}	CaO	MgO	Na_2O	SiO_2								
							1873	8.59		Electro-	[68]	
			0.333	0.667	−5.11	150				chem	[69]	
	(0.25)	(0.25)		(0.50)	−4.61	163	1723	9.54	1350 – 1500	CyV	[12]	Figs. 13.8, 13.13
	Andesite				−1.80	280	1573	11.10	1300 – 1400	RA	[66]	
	Basalt				−3.83	201	1573	10.50	1300 – 1400	RA	[64]	
							1573	10.2	1300 – 1400	TS	[11]	
	Obsidian						1573	11.6	1300 – 1400	RA	[1]	
Cs	Andesite				−3.31	251			1300 – 1400	RA	[66]	Figs. 13.8, 13.13
	Basalt				−2.0	272			1300 – 1400	RA	[66]	
	Obsidian						1573	11.9	1300 – 1400	RA	[67]	
	Pantellerite						1573	11.2	1300 – 1400	RA	[67]	
F	Al_2O_3	CaO	SiO_2		−6.10	83.7			1450 – 1500	CR	[36]	
	20	38	42									
Fe^{2+}	Al_2O_3	CaO	SiO_2									
	46	54					1873	7.8	1600	Oxidation	[70]	
							1873	8.89	–	–	[68]	
	20	40	40		−0.15	279			1350 – 1450	DC	[71]	
	20	38	42		−5.18	127			1300 – 1600	IPS	[41]	
	CaO	Na_2O	SiO_2									
Fe^{3+}	12	16	72		−5.12	156			1250 – 1400	CHRP	[72]	
	Andesite				−2.5	272			1300 – 1400	RA	[66]	
	Basalt				−2.2	264			1300 – 1400	RA	[66]	
	Obsidian						1573	12.10	1300 – 1400	RA	[67]	
	Pantellerite						1573	12.35	1300 – 1400	RA	[67]	Figs. 13.8, 13.13
H	Al_2O_3	CaO	SiO_2									
	16.3	27.3	56.4				1683	9.0	1410	Removal	[73]	
	28.4	49.3	22.3				1873	8.60	1600	rate of		
										H_2O		
K^{42}	Na_2O		SiO_2									
	(0.25)		(0.75)		−6.50	71.1			850 – 1050	CR	[49]	
	K^2O	PbO										
	14.4	19.1	66.4		−5.40	105	1273	9.70	730 – 1000	RA	[74]	
	7.4	14.7	77.6		−4.95	135	1273	10.50	780 – 1160	RA	[74]	
	5.9	20.5	73.3		−4.75	140	1273	10.50	780 – 1160	RA	[74]	
	2.9	35.0	61.6		−4.20	143	1273	10.06	720 – 1000	RA	[74]	
Li	Basalt						1573	8.95	1300 – 1400	RA	[66]	Figs. 13.8, 13.13
							1673	8.75			[66]	
Mg	Al_2O_3	CaO	SiO_2									
	20	40	40		−5.48	97.1			1300 – 1450	DC	[71]	in air
	CaO	Fe_2O_3	SiO_2									
	30	25	45		−5.67	96.2			1350 – 1450	DC	[71]	
Mn	Al_2O_3	CaO	SiO_2									
	20	40	40		−1.77	238			1350 – 1450	DC	[71]	
	CaO	Fe_2O_3										
	30	25	45		−4.62	142			1350 – 1450	DC	[71]	
	Andesite				−3.0	243	1573	11.07	1300 – 1400	RA	[66]	Figs. 13.8, 13.13
	Basalt				−3.80	200	1573	10.44	1300 – 1400	RA	[66]	
							1573	10.40	1300	TS	[11]	
	Obsidian						1573	11.6	1300 – 1400	RA	[67]	

Tab. 13.3. (continuation)

Species	Slag composition				log D_o	E_D	Tκ	– log D	Temp Range, °C	Method	Ref.	Comment
N	Al_2O_3	CaO	SiO_2									
	50	50					1873	9.28	1600	N_2	[75]	
	19.6	50.1	30.3				1773	10.30	1500	Removal	[76]	
	18.6	36.5	44.6				1773	9.30	1500	rate	[76]	
	20.1	47.2	32.7				1773	10.02	1500		[76]	
Na^{22}	(0.25)	(0.75)			– 6.36	71.5			800 – 1150	CR	[49]	Figs. 13.8, 13.13
	Andesite				– 6.0	100	1573	9.32	1300 – 1400	RA	[66]	
	Basalt				– 4.02	163	1573	9.43	1300 – 1400	RA	[66]	
							1573	9.60	1300 – 1400	TS	[11]	
	Obsidian						1573	9.20	1300 – 1400	RA	[67]	
	Pantellerite						1573	8.9	1300 – 1400	RA	[67]	
Ni^{2+}	Na_2O	SiO_2										
	(0.333)	(0.667)			– 5.71	135			1150 – 1350	CHRP	[72]	
	CaO	Fe_2O_3	SiO_2									
Ni	30	25	45		– 2.55	213			1350 – 1450	DC	[71]	
	CaO	MgO	SiO_2									
	(0.25)	(0.25)	(0.5)		– 6.40	108	1800	9.53	1440 – 1520	CyV	[12]	
	(0.375)	(0.375)	(0.25)				1800	9.40	1520			
	(0.27)	(0.27)	(0.46)				1800	9.50	1520			
	(020)	(0.20)	(0.60)				1800	10.52	1520			
Ni^{2+}	CaO	Na_2O	SiO_2									
	12	16	72		– 6.50	131			1250 – 1400	CHRP	[72]	
P	CaO	Fe_2O_3	SiO_2									
	30	25	45		– 2.53	243			1350 – 1450	DC	[71]	
S^{35}	Al_2O_3	CaO	SiO_2									
	10.4	50.3	39.3		– 3.85	205			1445 – 1580	DC	[27]	
	9.6	42.5	47.9				1713	10.09	1440		[77]	
Pb^{2+}	Na_2O		SiO_2									
	(0.333)		(0.667)		– 8.39	52.3			900 – 1150	CHRP	[78]	
O	Basalt						1573	11.40		TS	[11]	
							1623	11.0				
Sc^{3+}	Andesite				– 5.8	184	1573	11.91	1300 – 1400	CR	[66]	
	Basalt				– 4.55	197	1573	11.09	1300 – 1400	CR	[66]	
Sn^{123}	K_2O	PbO	SiO_2									
	14.4	19.1	66.4		+ 0.9	293	1273	11.11	800 – 1000	RA	[74]	
	7.4	14.7	77.6		– 3.9	213	1273	12.64	900 – 1200	RA	[74]	
	6.4	10.4	74.0		– 4.9	181	1273	12.33	900 – 1200	RA	[74]	
	5.9	20.5	73.3		– 5.5	160	1273	12.06	900 – 1200	RA	[74]	
	2.9	35.0	61.6		+ 0.8	270	1273	10.28	730 – 950	RA	[74]	
Sr	K_2O	Na_2O	SiO_2									
	(0.25)	–	(0.75)		– 6.10	138			810 – 1180	Integral	[65]	
		(0.25)	(0.75)		– 6.10	117			790 – 1140	activity	[65]	
	Andesite				– 6.3	138	1573	10.85	1300 – 1400	CR	[66]	
	Basalt				– 3.46	213	1573	10.55	1300 – 1400	CR	[66]	
							1573	10.60			[11]	
Ti	Al_2O_3	CaO	SiO_2									
	20	40	40		– 6.64	245			1350 – 1450	DC	[71]	
	CaO	Fe_2O	SiO_2									
	30	25	45		+ 0.20	335			1350 – 1450	DC	[71]	
V	Basalt						1573	11.30	1300	TS	[11]	
Zn^{2+}	CaO	Na_2O	SiO_2									
	–	(0.333)	(0.667)		– 5.15	157			1150 – 1350	CHRP	[72]	
	12	16	78		– 7.48	105			1250 – 1400	CHRP	[72]	
	CaO	MgO	SiO_2									
	(0.25)	(0.25)	(0.5)		– 4.48	169	1723	9.60	1420 – 1520	CyV	[12]	
							1800	9.39				
Zr^{95}	K_2O	PbO	SiO_2									
	14.4	19.1	66.4		– 2.4	220	1273	11.43	780 – 1000	RA	[74]	
	7.4	14.7	77.6		– 4.1	203	1273	12.43	800 – 1200	RA	[74]	
	6.4	10.4	74.0		– 3.8	205	1273	12.21	800 – 1200	RA	[74]	
	2.9	35.0	61.6		– 3.7	170	1273	10.68	720 – 1000	RA	[74]	

13.6.4 Chemical diffusion coefficients in molten slags

Tab. 13.4. Oxygen chemical diffusion coefficients

Species	Slag composition				$\log D_o$	E_D	T_K	$-\log D$	Temp Range, °C	Method	Ref.	Comment
O	CaO 21	Fe_2O_3 40	SiO_2 39		−6.08	55.6	1723	7.76	1350 – 1550	O_2-TGA	[79]	See Figs. 13.9, 13.14
	29	40	31		−5.77	57.3	1723	7.50	1350 – 1550			
	36	40	24		−5.92	48.5	1723	7.39	1350 – 1550	O_2-TGA		
	24.5	30	45.5		−4.70	106.7	1723	7.94	1350 – 1550			
	34	30	36		−6.22	46.0	1723	7.61	1350 – 1500			
	39	20	41				1723	7.73	1450			
	33	62.5	4.5				1723	6.98	1350 – 1500			
O	(0.30)	(0.10)	(0.60)		−2.0	197	1723	7.97	1350 – 1600	O_2-P	[80, 22]	See. Figs. 13.9, 13.14
	(0.283)	(0.15)	(0.567)		−1.92	197	1723	7.89	1350 – 1600			
	(0.20)	(0.40)	(0.40)		−2.42	197	1723	8.39	1350 – 1600			
	(0.475	(0.05)	(0.475)		−1.93	197	1723	7.90	1350 – 1600			
	(0.425)	(0.15)	(0.425)		−1.81	197	1723	7.78	1350 – 1600			
	(0.30)	(0.40)	(0.30)		−2.32	197	1723	8.29	1350 – 1600			
	(0.34)	(0.15)	(0.51)		−1.74	197	1723	7.70	1350 – 1600			
	(0.36)	(0.24)	(0.24)		−2.25	197	1723	8.22	1350 – 1600			
O	Al_2O_3 9.8	CaO 39.6	Fe_2O_3 1.0	SiO_2 39.6			1723	6.72	1350	O_2-P	[81]	See Figs. 13.9, 13.14
	Andesite						1623	10.35	1260 – 1380	O_2-TGA	[82]	
							1573	10.60				
	Basalt						1623	9.55	1180 – 1360	O_2-TGA	[82]	
							1573	9.75				
							1473	10.25				

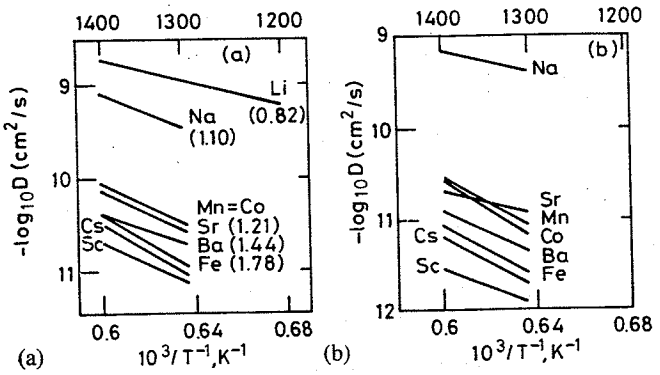


Fig. 13.13 a,b. Tracer impurity diffusivities for (a) basaltic and (b) andesitic melts [66]

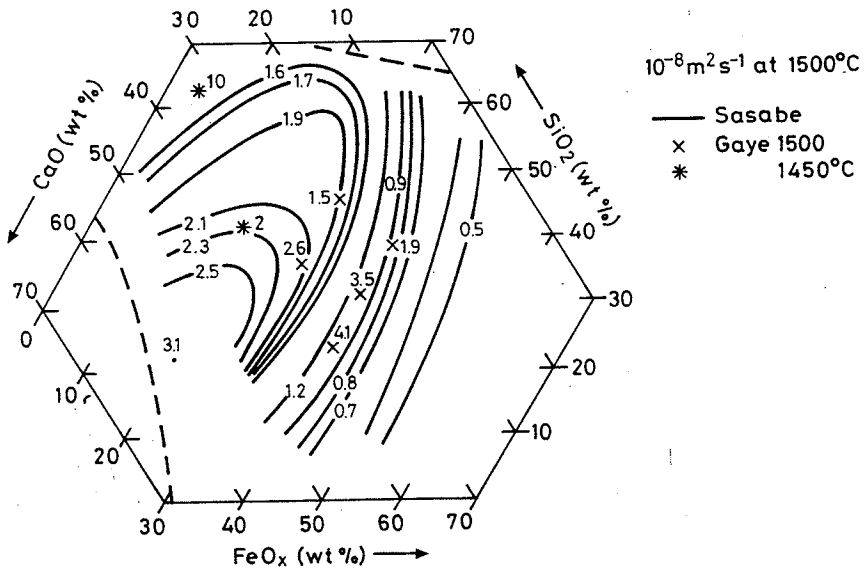


Fig. 13.14. Oxygen self diffusion coefficient for $CaO\text{-}FeO_x\text{-}SiO_2$ melts at 1500 °C

Tab. 13.5. Interdiffusivities for chemical diffusion in molten slags

Species	Slag composition				log D_o	E_D	T_K	– log D	Temp Range, °C	Method	Ref.	Comment
Quasi Al_2O_3-FeO	FeO	(100%)					1723	8.52		Dissolution of Al_2O_3	[83,84]	
Quasi Al_2O_3 -SiO_2	Al_2O_3	SiO_2										
	4.3	95.7			+ 19.54	1287			1650 – 1800	CR	[85]	
	6.0	94.0			+ 17.39	1197						
	7.6	92.4			+ 15.21	1108						
	9.2	90.8			+ 13.33	1025						
	12.4	87.6			+ 9	851						
	16.4	83.6			+ 3.80	636						
	20	80			– 1.47	418						
	22.3	77.7			– 5.72	245						
Quasi CaO-CoO	CaO	CoO	SiO_2									
	30.4	3.3	66.3				1873	8.50	1600	Galvanostatic	[86]	
	24.2	9.0	66.8				1873	9.08	1600			
Quasi CaO-FeO	CaO	FeO	SiO_2									
	32.9	30.2	35.6		– 4.24	183			1400 – 1480	CHRP	[87]	
	33.3	27.5	39.3		– 4.73	174						
	26.3	30.0	43.8		– 5.05	232						
	31.0	2.0	67.0				1873	– 7.82	1600	Galvanostatic	[86]	
	30.1	4.0	65.9				1873	– 8.77		Galvanostatic	[86]	
	29	5.5	65.5				1873	– 8.55		Galvanostatic	[86]	
	25	11.6	63.4				1873	– 9.52		Galvanostatic	[86]	
	20	20	60				1873	– 9.10		Galvanostatic	[86]	
Quasi CaO-NiO	CaO	NiO	SiO_2									
	30.5	2.5	67				1873	7.80	1600	Galvanostatic	[86]	
	29	4	67				1873	7.72	1600	Galvanostatic	[86]	
	26	9	65				1873	7.66	1600	Galvanostatic	[86]	
Quasi CaO-SiO_2	Al_2O_3	CaO	SiO_2									
	10.5	37.5	52		– 5.35	121			1450 – 1500	DC	[88]	
	10.5	32.5	57		– 6.41	88			1450 – 1560	DC	[88]	
	10.5	27.5	62		– 6.00	117			1380 – 1560	DC	[88]	
	20	40	40		– 0.35	328			1337 – 1367	CHRP	[89]	
	16.5	27.8	55.7		+ 1.46	377			1500 – 1600	DC	[90]	
	16.5	37.1	46.4		+ 1.20	367			1500 – 1600	DC	[90]	
	21.0	26.3	52.7		+ 1.11	367			1500 – 1600	DC	[90]	
	21.0	35.1	43.9		– 1.82	259			1500 – 1600	DC	[90]	
	27.0	32.4	64.9		– 2.72	220			1500 – 1600	DC	[90]	
F-O	Albite				– 8.74	121	1578	– 12.84	1200 – 1400	Volatilisation of F	[91]	
	Jadeite				– 6.50	144	1573	– 11.24	1200 – 1400			
	Peraluminous				– 6.09	180	1573	– 11.98	1200 – 1400			
Quasi FeO-MnO	FeO	MnO	SiO_2		– 3.61	170.5			1267 – 1400	CHRP	[92]	
	39.8	18.2	42.0									
Quasi FeO-SiO_2	Fe_2O_3	Na_2O	SiO_2									
	Y	(0.5)	(1)				1473	– 9.49Y + 13.4	1200	DC	[93]	Y = 0.05 – 0.15
	Y	(0.4)	(1)					– 11.5Y + 14.9	1200			
	Y	(0.3)	(1)					– 14.4Y + 16.6	1200			
Quasi FeO-ZrO_2	FeO											
	100				– 1.11	174			1400 – 1500	Dissolution of ZrO_2	[94]	
K_2O SiO_2	K_2O	SiO_2										
	43	57					1473	11.65	1200	Dissolution of SiO_2	[95]	
	26.7	73.3					1273	12.44	1000 – 1200			
							1473	11.99				
	34.6	65.4					1473	11.97	1000			
	30	70			– 5.72	163			600 – 1400		[96]	

Tab. 13.5. (continuation)

Species	Slag composition				log D_o	E_D	Tκ	– log D	Temp Range, °C	Method	Ref.	Comment
Li_2O-SiO_2	Li_2O 20 30	SiO_2 80 70			– 6.14 – 6.52	138 121			1100 – 1350 1200 – 1350	CHRP	[97]	
Na_2O SiO_2	Na_2O (0.25) (0.333) 51-33 40 50.8	SiO_2 (0.75) (0.667) 49-77 60 49.2			– 1.54 – 7.00 + 1.59	292 121 142	 1473 1223 1443 1523 1633	 7.32 11.36 10.03 9.60 9.42	1200 – 1500 1050 – 1250 – 0.0557 (% SiO_2)	Dissolution of SiO_2	[98] [99] [100] [95, 99] [100] [102] [102] [102]	
PbO SiO_2	PbO (090) (0.80) (0.70) (060)	SiO_2 (0.10) (0.20) (0.30) (0.40)					1223 1223 1223 1223	9.89 10.32 11.0 11.89	DC DC DC DC	PF	[59]	

Tab. 13.6. Chemical diffusion – coefficients for inter-diffusivity matrix of molten ternary slags [24]

Further details [2]

System XO-YO-ZO

$$J_x = D_{xx}^{zo}\left(\frac{dC_{xo}}{dx}\right) - D_{xy}^{zo}\left(\frac{dC_{yo}}{dx}\right)$$

$$J_y = D_{xy}^{zo}\left(\frac{dC_{xo}}{dx}\right) - D_{yy}\left(\frac{dC_{yo}}{dx}\right)$$

where J = flux of ion: (dC/dx) = concentration gradient

$J_x + J_y + J_z = 0.$

Species	Slag composition			log D_o	E_D	Tκ	– log D	Temp Range, °C	Method	Ref.
	Al_2O_3 20	CaO 40	SiO_2 40							
D_{CaCa}^{SiO}				8.9×10^{-11}	254			1450 – 1550	DC	[103]
D_{CaAl}^{SiO}				-2.5×10^{-11}	194					
D_{AlCa}^{SiO}				-4.0×10^{-11}	178					
D_{AlAl}^{SiO}				6.12×10^{-11}	318					
	CaO 35	Fe_2O_3 25	SiO_2 45							
D_{CaCa}^{SiO}				11.5×10^{-4}	235			1420 – 15400	DC	[104]
D_{CaFe}^{SiO}				-8.30×10^{-4}	236				DC	[104]
D_{FeCa}^{SiO}				-11.1×10^{-4}	230				DC	[104]
D_{FeFe}^{SiO}				-3.27×10^{-4}	209				DC	[104]

13.7 Appendix

13.7.1 Appendix 1

Calculation of NBO/T

$$Y_{NB} = \Sigma 2\,[x(CaO) + x(MgO) + x(FeO) + x(MnO) + x(Na_2O) + x(K_2O)] + 6(1 - f)\,x(Fe_2O_3) - 2x(Al_2O_3) - 2fx(Fe_2O_3)$$

$$x_T = \Sigma\, x(SiO_2) + 2x(Al_2O_3) + 2fx(Fe_2O_3) + x(TiO_2) + 2x(P_2O_5)$$

$$(NBO/T) = (Y_{NB}/x_T)$$

where x = mole fraction, $f = FE^{3+}(IV)/(Fe^{3+}(IV) + Fe^{3+}(VI)$, ie fraction of Fe^{3+} with IV coordination.

13.7.2 Appendix 2

Tab. 13.7. Some typical compositions for minerals

	Composition, mass %									NBO/T
	Al_2O_3	CaO	FeO	Fe_2O_3	K_2O	MgO	Na_2O	SiO_2	TiO_2	
Albite	18						12	70		0
Andesite	16.8	5.1	5.2	–	1.7	3.3	5.0	62	0.7	0.3
Basalt	16.6	9.6	3.2	9.7	1.7	6.3	3.7	46	3.7	0.6
Jadeite	25						15.6	59.4		0
Obsidian	12.4	0.4	1	1	4.5	0.5	4.7	75	0.1	0.1
Peraluminous	21.3						8.6	70.1		0

13.8 References in Chapter 13

[1] Dunn, T.: Diffusion in Silicate melts in Short Course in silicate melts. Edit CM Scarfe. Publ. Mineralogical Soc., Canada, Ottawa, Ont. (1986), Chapter 3, 57 – 92
[2] Turkdogen, E. T.: Physico-chemical properties of molten slags and glasses. Publ. Metals Society, London (1983), 28 – 51
[3] Oishi, Y.: J. Chem. Phys. 43 (1965), 1611
[4] Cooper, A. R.: Phys Chem Glasses 6 (1965), 55
[5] Cooper, A. R.; Heasley, J. H.: J. Amer. Ceram. Soc. 49 (1966), 280
[6] Okongawu, D. A.; Lu, W.-K.; Hamielec, A. E.; Kircaldy, J. S.: J. Chem. Phys. 58 (1973), 777
[7] Le Claire, A. E.: Diffusion and mass transport measurements in the characterisation of high temperature materials: Physical and elastic characteristics. Edited by M. McLean. Publ. Inst. of Metals, London (1989), Chapter 5, 139 – 176
[8] Walls, H. A. (Chapter 9C); Lundy, T. S. (Chapter 9A): Diffusion Measurements in Physicochemical Measurements in Metals Research. Edited by R. A. Rapp. Publ. Interscience, New York (1970)
[9] Winchell, P; Norman, J. H.: A study of diffusion of radioactive nuclei-ides in molten silicates at high temperatures in High Temperature Technology. Proc. 3rd Intl. Symp. Asilomar 1967, 479 – 492
[10] Winchell, P.: High Temp. Sci. 1 (1969), 200 – 215
[11] Hofmann, A. W.: Diffusion in natural silicate melts in Physics of Magmatic Processes. Edited by R. B. Hargreaves. Publ. Princeton Univ. Press, Princeton, NJ (1980), 385 – 417
[12] Semkow, K. W.; Rizzo, R. A.; Haskin, L. A.; Lindstrom, D. J.: Geochim Cosmochim Acta 46 (1982), 1879 – 1889
[13] Jambon, A.: J. Geophys. Res. 87 (1982), 10797 – 10810
[14] Keller, H.; Schwerdtfeger, K.; Hennesen, K.: Metall Trans. 10B (1979), 67 – 70
[15] Keller, H.; Schwerdtfeger, K.: Metall. Trans. 10B (1979), 551 – 554
[16] Keller, H.; Schwerdtfeger, K.; Petri, H.; Holzle, R.; Hennesen, K.: Metall Trans. 13B (1982), 237 – 240
[17] Fujii, T.: Trans. Amer. Geophys. Union. EOS, 62 (1981), 428
[18] Harrison, T. M.; Watson, E. B.: Contrib. Mineral Petrol. 84 (1983), 66 – 72
[19] Rapp, R. P.; Watson, E. B.: Trans. Amer. Geophys. Union EOS. 66 (1985), 416
[20] Dunn, T.: Geochim Cosmochim Acta 46 (1982), 2293 – 2299
[21] Semkow, K. W.; Haskin, L. A.: Geochim Cosmochim Acta 49 (1985), 1897 – 1908
[22] Sasabe, M.; Asamura, A.: Proc. of 2nd Intl. Symp. on Metall Slags and Fluxes, held Lake Tahoe, Nev., Nov. 1984. Edited H. A. Fine and D. R. Gaskell. Publ. Metall. Soc. AIME, Warrendale, Pa, 651 – 667
[23] Shimizu, N.; Kushiro, K.: Geochim Cosmochim Acta 48 (1984), 1295 – 1303
[24] Goto, K. S.: Proc. 2nd Intl. Conf. on Metallurgical Slags and Fluxes, held Lake Tahoe, Nev., Nov. 1984. Edited H. A. Fine and D. R. Gaskell. Publ. Metall. Soc. AIME, Warrendale, Pa (1984), 847
[25] Iwamoto, N.: Trans. Jap. Weld. Res. Inst., Osaka Univ., 6 (1977) (1), 145 – 157
[26] Kubaschewski, O.; von Goldbeck, O.: Diffusionsgeschwindigkeiten in festen u. flüssigen Oxiden sowie in flüssigen Schlacken. VDEh-Rept. Nr. 0.015, March (1983), Düsseldorf
[27] Nagata, K.; Ono, Y.; Ejima, T.; Yamamura, T.: Diffusion in Handbook of Physico-chemical Properties. Edited Y. Kawai and Y. Shiraishi. Special Issue No. 41. Publ. Iron Steel Inst. Japan (1988), Chapter 7, 194 – 204
[28] Freer, R.: Contrib. Mineral Petrol. 76 (1981), 440 – 454
[29] Anisimov, Y. S.; Mitin, B. S.: Izv. Akad Nauk SSSR, Neorg. Mater. 13 (1977), 1442
[30] Tokuda, T.; Ito, T.; Yamaguchi, T.: Z. Naturforsch. 26A (1971), 2058
[31] Grieveson, P.; Turkdogan, E. T.: Trans AIME 230 (1964), 1609
[32] Mori, K.; Suzuki, K.: Tetsu-to-Hagane 54 (1968), 1199
[33] Sasabe, M.; Goto, K. S.; Someno, M.: Tetsu-to-Hagane 59 (1973), 715
[34] Henderson, J.; Yang, L.; Derge, G.: Trans AIME 221 (1961), 56
[35] Saito, T.; Maruya, K.: Sci. Rep. Res. Inst. Tohoku Univ. A 10 (1958), 306

[36] Taylor, J.: Proc. of Intl. Symp. "Chemical Metallurgy of Iron and Steel", held Univ. of Sheffield (1971)
[37] Nagata, K.; Sata, N.; Goto, K.: Tetsu-to-Hagane 68 (1982), 1694
[38] Majdic, A.; Hennig, H.: Ber. Deut. Keram. Ges. 47 (1970), 53 – 59
[39] Kawai, Y.: Kotai Butsuri B 1 (1976), 63
[40] Niwa, K.: Nippon Kinzoku Gakkaishi 21 (1957), 304
[41] Johnston, R. F.; Stark, R. A.; Taylor, J.: Ironmaking and Steelmaking 4 (1974), 220
[42] Towers, H.; Paris, M.; Chipman, J.: J. Metals 5 (1957), 769
[43] Wakabayashi, H.: J. Non-Cryst. Solids 24 (1977), 427
[44] Malkin, V. I.; Khoklov, S. P.; Shvartsman, L. A.: Radioisotopes in Physical Sciences and Industry. Intl. Atomic Energy Agency, Vienna (1962), 169
[45] Kiefer, J.; Borchardt, G.; Scherrer, S.; Weber, S.: Mater. Sci. Forum, 7 (1986), 243
[46] Yang, L.; Chien, C.; Derge, G.: J. Chem. Phys. 30 (1959), 1627
[47] Agarwal, D. P.; Gaskell, D. R.: Metall Trans. B 6B (1975), 263
[48] Goto, K. S.; Kurahashi, T.; Sasabe, M.: Metall Trans B, 8B (1977), 523
[49] Negodaev, G. D.; Ivanov, I. A.; Evstopev, K. K.: Elektrokhimya, 8 (1972), 234
[50] Fontana, A.; Segers, L.; Winand, R.: Proc. of 1st Intl. Conf. on Metall. Slags and Fluxes, held Halifax, NS, 1980
[51] Gupta, Y. P.; King, T. B.: Trans AIME 239 (1967), 1701
[52] Perron, P. O.; Bell, H. B.: Trans. Brit. Ceram. Soc. 66 (1967), 347
[53] Malkin. V. I.; Mogutnov, B. M.: Akad Nauk SSSR, Dokl. 141 (1961), 1127
[54] Shiraishi, Y.; Nagahama, H.; Ohta, H.: Proc. of 1st Intl. Conf. on Metall. Slags and Fluxes, held Halifax, NS, (1980)
[55] Matsumiya, T.; Nogami, A.; Fukuda, Y.: Proc. 4th Intl. Conf. Molten Slags and Fluxes, held Sendai, Japan, June 1992. Publ. ISI Japan
[56] May, H. B.; Lauder, I.; Wollast, R.: J. Amer. Ceram. Soc. 57 (1974), 197
[57] DeBerg, K. C.; Lauder, I.: Phys. Chem. Glasses 21 (1980), 106
[58] Oishi, Y.; Terai, R.; Ueda, H.: Mass Transport Phenomena in Ceramics. Edited by A. R. Cooper and A. H. Heuer. Publ. Plenum, NY (1975), 297
[59] Schmalzried, H.; Takada, Y.; Langanke, B.: Z. Phys. Chem. NF. 128 (1981), 205
[60] Koros, P.; King, T. B.: Trans. AIME 224 (1962), 299
[61] Terai, R.; Oishi, Y.: Glastech. Ber. 50 (1977), 68
[62] Yinnon, H.; Cooper, A. R.: Phys. Chem. Glasses 21 (1980), 204
[63] Cleland, J. H.; Fray, D. J.: Metall. Trans B, 9B (1978), 539
[64] Towers, H.; Chipman, J.: J. Metals 9 (1957), 304
[65] Ivanov, I. A.; Pavlov, A. B.: Elektrokhhimiya 11 (1975), 1362
[66] Lowry, R. K.; Henderson, P.; Nolan, J.: Contrib. Mineral Petrol 80 (1982), 254 – 262
[67] Henderson, P.; Nolan, J.; Cunningham, G. C.; Lowry, R. K.: Contrib. Mineral Petrol 89 (1985), 262 – 272
[68] Nowack, N.; Schwerdtfeger, K.: Metal-slag-gas-reactions. Edited by Z. A. Foroulis and W. W. Smeltzer (1975), Princeton. Publ. Electrochem Soc., 98
[69] Takahashi, K.; Miura, Y.: Proc. of 12th Intl. Congress on Glass, (1980), 527
[70] Seshardri, V.; Schwerdtfeger, K.: Ironmaking Steelmaking 1 (1975), 56
[71] Ukyo, Y.; Goto, K. S.: Testu-to-Hagane 68 (1982), 1981
[72] Takahashi, K.; Maiura, Y.: Proc. of 12th Intl. Conf. on Glass (1980), 527
[73] Novokhatskii, I. A.; Esin, O. A.; Chuchmarev, S. K.: Izv. VUZ Chern. Met. (1961) (4), 5
[74] Ivanov, I. A.; Shatkov, V. M.; Shaskin, V. S.: Sov. J. Glass Phys. Chem. 14 (1988), 46 – 49
[75] Ershov, G. S.: Izv. VUZ Chern. Met. (1967) (8), 11
[76] Kamyshov, V. M.; Esin, O. A.; Chuchmarev, S. K.: Izv. Akad Nauk SSSR Metally, (1967) (8), 11
[77] Elliott, J. F.; Gleiser, M.; Ramakrishma, V.: Thermochemistry for Steelmaking. Publ. Pergamon Press (1963)
[78] Strzelbicka, B.; Bocacz, A.: Electrochimica Acta 30 (1985), 865
[79] Gaye, H.; Riboud, P. V.: CR Acad. Sci. Paris, Ser. C 280 (1975), 1165 – 1167
[80] Sasabe, M.; Jibiki, M.: Tetsu-to-Hagane, 68 (1982), 767
[81] Sasabe, M.; Kinoshita, Y.: Tetsu-to-Hagane, 65 (1979), 1727
[82] Wendlandt, R. F.: Trans Amer. Geophys. Union EOS 61 (1980), 1142
[83] Olsson, R. G.; Perzak, T. F.; Koump, V.: Trans AIME 242 (1968), 776
[84] Kobayashi, H.; Oyama, T.: Yogyo Kyokaishi 83 (1975), 97
[85] Davis, R. F.; Pask, J. A.: J. Amer. Ceram. Soc. 55 (1972), 525
[86] Nowack, N.: Arch. Eisenhüttenwes. 53 (1982), 253
[87] Kishimoto, M.; Fujii, S.; Mori, K.; Kawai, Y.: Nippon Kinzoku Gakkaishi 25 (1984), 197
[88] McCallum, N.; Barrett, L. R.: Trans. Brit. Ceram. Soc. 51 (1952), 523
[89] Nagata, K.; Goto, K. S.: Ironmaking Steelmaking 1 (1977), 23
[90] Majdic, A.; Wagner, H.: Arch. Eisenhüttenwes. 41 (1970), 529
[91] Dingwell, D. B.; Scarfe, C. M.: Earth Planet Sci. Letters 73 (1985), 377 – 384
[92] Kishimoto, M.; Mishima, S.; Mori, K.; Kawai, Y.: Nippon Kinzoku Gakkaishi 48 (1984), 79
[93] Pearce, M. L.; Beisler, J. F.: J. Amer. Ceram. Soc. 49 (1966), 547
[94] Kobayashi, H.; Oyama, T.: Yogyo Kyokaishi 82 (1974), 546
[95] Schwerdtfeger, K.: J. Phys. Chem. 70 (1966), 2131
[96] May, H. B.; Wollast, R.: J. Amer. Ceram. Soc. 57 (1976), 30
[97] Kawakami, M.; Nagata, K.; Goto, K. S.: J. Electrochem. Soc. 125 (1978), 395
[98] Barklage-Hilgefort, H. S.; Frischat, G. H.: Phys. Chem. Glasses 21 (1980), 212
[99] Truhlarova, M.; Veprek, O.: Glastechn. Ber. 40 (1967), 257
[100] Hlavac, J.; Nademlynska, H.: Glass Techn. 10 (1969), 54
[101] Kreider, K. G.; Cooper, A. R.: Glass Techn. 8 (1967), 71
[102] Shurygin, P. M.; Barmin, L. N.; Esin, O. A.: Izv. VUZ Chern Met. (1962) (5), 5
[103] Sugawara, H.; Nagata, K.; Goto, K. S.: Metall Trans. 8B, (1977), 605
[104] Ukyo, Y.; Goto, K. S.: Metall Trans B, 12B (1981), 449

14

Electrical conductivities of molten slags

K. C. Mills

14.1 Introduction

The specific electrical conductivity (κ) is the conductivity of a cube of solution of side one metre and is defined by equation (14.1) where c is the concentration, z and u, the charge and mobility of ionic species and F the Faraday constant.

$$\kappa = F \sum c_i z_i u_i \qquad (14.1)$$

14.1.1 Temperature dependence of electrical conductivity

The temperature dependence of the specific electrical conductivity is usually expressed by the Arrhenius relationship shown in equations (14.2) and (14.3).

$$\kappa = A_\kappa \exp(-E_\kappa/RT) \qquad (14.2)$$

$$\log \kappa = \log A_\kappa - (E_\kappa/RT) \qquad (14.3)$$

where A_κ is the constant, E_κ the activation energy, R the gas constant and T the thermodynamic temperature.

14.1.2 Effects of double layer and of polarisation resistance on conductivity

When a metallic electrode is immersed in an electrolyte there is a potential difference across the interface. One phase acquires a net positive charge and the other a net negative charge. In the Helmholtz model there is a layer of charge at the electrode surface, to which the irons of the opposite charge are rigidly held in the electrolyte as shown in **Fig. 14.1 a.** The Helmholtz double layer is equivalent to a simple parallel plate capacitor. The Stern model of the double layer is more satisfactory as it allows for the thermal motion of the ions, as shown in **Figs. 14.1 b** and **c.** In this model the charges are adsorbed on the electrode and are rigidly fixed there by the presence of an immobile layer of oppositely charged ions in the electrolyte. Further into the electrolyte there is a diffuse layer of charge which may have a sign either the same or opposite to that of the absorbed layer. Only the diffuse layer is free to move under the influence of an applied potential.

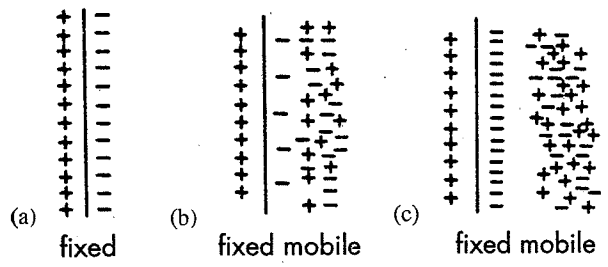


Fig. 14.1 a-c. Schematic representations of models of the double layer (a Helmholtz; b, c Stern)

Polarisation arises from concentration gradients within the electrolyte of the cell which manifests itself as a back EMF opposing the applied voltage and is usually referred to as the electrode reaction. This can be represented as an additional resistance. The combined effect of the double layer and polarisation can be represented by a resistance and a capacitance in parallel, the resistance representing the resistance of the electrolyte to the processes of reaction and diffusion.

14.1.3 Experimental methods used to measure electrical conductivity

14.1.3.1 Capillary methods

Capillary cells have been widely used for the determination of electrical conductivity of molten salts. The melt is held in long thin capillaries of an electrically insulating tube. The dimensions of the capillary are arranged such that the resistance R measured is fairly large; as $R = G/\kappa$, where G is the cell constant and is dependent upon the dimensions of the capillary, $G = l/a$ where l and a are the length and area of cross-section of the capillary, respectively. The resistance is usually measured by an ac bridge. This method is not very well suited to work with slags, which react with all known insulating materials.

14.1.3.2 Crucible cells

In this technique the slag is held in a crucible and the resistance is measured between two electrodes immersed in the slag. The major disadvantage is that the cell constant and hence the resistance of the melt is much smaller than that observed in capillary cells and thus the measured resistance is more prone to errors caused by polarisation and other effects. Another disadvantage is that the cell constant is dependent upon the depth of immersion of the electrodes in the slag. The various types of cell are described below. The resistance measurements can be made by ac bridges, by potentiometric techniques, and by other less-conventional techniques; these also are described below.

14.1.3.3 Central electrode cell

In this method [1] the electrode is placed centrally and the crucible serves as the other electrode as is shown in **Fig. 14.2 a.** The major advantage of this arrangement is that the areas of the electrodes are large. The disadvantages are that the electrode must be positioned accurately and the measured resistance is small.

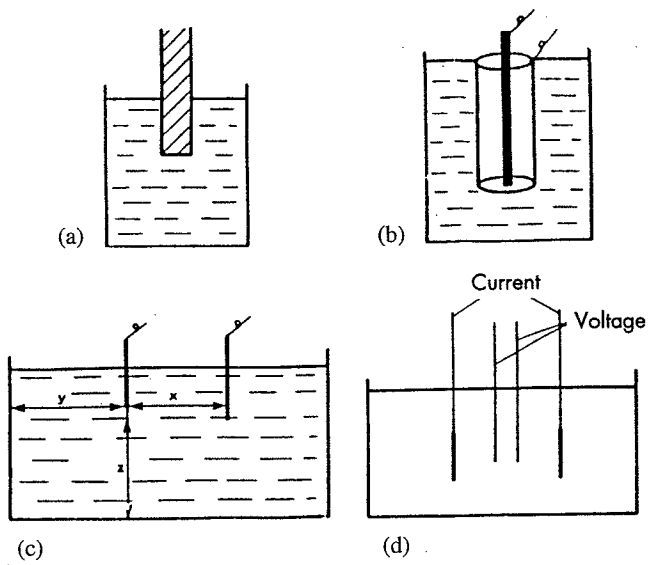


Fig. 14.2 a-d. Schematic representations of (a) central electrode, (b) two-electrode, (c) ring-electrode and (d) four-electrode cells

14.1.3.4 Two-electrode cell

In this cell arrangement [2] the two electrodes are immersed in the electrolyte as shown in **Fig. 14.2 b.** It is necessary to avoid electrical leakage and for this reason it is arranged that $y > x$ and $z > x$. The advantage of this method is that the

electrodes have the same area. The disadvantage of this arrangement lies in the fact that the area of the electrodes is very small and hence polarisation can become an important factor.

14.1.3.5 Ring electrode cell

This is a variation of the two-electrode arrangement described above, in which the two electrodes are two concentric cylinders, [3] as shown in **Fig. 14.2 c.** The major advantages of this cell arrangement are (1.) that stray electrical paths and leakages are largely eliminated and (2.) that the area of the electrodes is large. The major problem with this cell configuration is that the areas of the two electrodes are different.

14.1.3.6 Four-electrode system

This cell was designed to be used in conjunction with potentiometric methods of measuring resistance, see the section 'Potentiometric techniques' below. In this arrangement four electrodes are immersed in the cell as shown in **Fig. 14.2 d,** two of the electrodes carry the current and the other two monitor the potential. In this way the effects of polarisation at the current-carrying electrodes can be largely eliminated [4, 5] and the effect of alternative paths is reduced.

14.1.3.7 Measurement of resistance by ac bridges

Various ac bridges have been employed for the measurement of the resistance of molten salts; these have been reviewed by Solomons [6] and by Robbins [7]. Wheatstone bridges are not suitable, as the resistances of crucible cells are quite low, and the Kelvin (or Thomson) bridge shown in **Fig. 14.3** is usually employed for the measurement of these small values. The Kelvin bridge measures only the active resistance of the cell.

14.1.3.8 Potentiometric techniques

This technique has been the most popular method of measuring the resistance of slags. The resistance is determined by measuring the potential and current from an ac source and applying Ohm's law. The major problem with this technique is that the passage of current gives rise to polarisation effects. The use of a 4-terminal system helps to minimise these effects. However, it is also necessary to use a small current and as low a potential as possible to avoid the distortions in the waveform which lead to the effects generally referred to as polarisation.

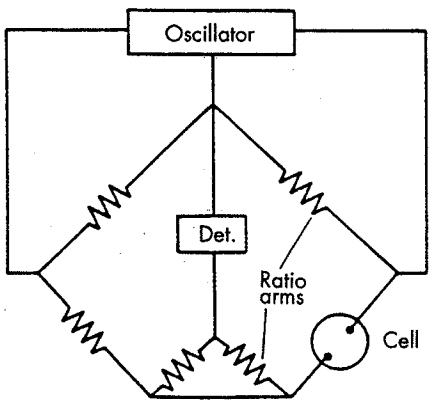


Fig. 14.3. Schematic diagram of AC bridge arrangement

14.1.3.9 Use of phase-shift devices

Phase-sensitive instruments such as oscilloscopes and phase-sensitive bridges have been used to obtain the resonance frequency [1, 8, 9] ie the frequency at which the inductive impedance of the cell and circuit are assumed to compensate the capacitive impedance of the electrode/slag interface. However, it is possible that experimentally the resonance point is rather broad and that this could lead to errors.

14.1.3.10 Other techniques of resistance measurement

Solomons [6] has reviewed the more unconventional techniques which could be used in the measurement of the conductivity of molten salt systems. These are (1.) galvanostatic transient techniques, (2.) square wave methods, and (3.) electrodeless methods.

14.1.4 Frequency dependency of conductivity and analysis of results

The total resistance measured in an experiment is made up of several terms, additional to the resistance of the slag, namely, the impedance associated with the electrode/slag interface, the resistance of the leads, etc. Failure to subtract these terms from the measured resistance would lead to a value for the slag resistance which is too high, ie a falsely low value for the electrical conductivity is derived.

14.1.4.1 Circuits used for the representation of the measuring cell

Several equivalent circuits have been reported for the representation of the measurement cell such as that shown in **Fig. 14.4.** Mills and Keene [10] have reviewed the complex equivalent circuits adopted by various investigators [1, 7, 11–13].

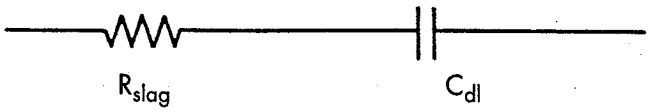


Fig. 14.4. Equivalent circuit of measuring cell for low applied potential [7]

14.1.4.2 Relationship between conductivity and frequency

There is some doubt as to the exact relationship between frequency (f) and the measured conductivity, the various relationships proposed have been reviewed [7, 10]. Several investigators [1, 11] have assumed the impedance of the electrode/slag region was a function f^{-1}. Ueda at al [14] reported that κ increased with increasing frequency in small crucibles but was independent of frequency in large crucibles.

14.2 Experimental date for specific electrical conductivity

Details of the experimental conditions used by various investigators can be derived from reviews [10, 15–19] and the original papers.

14.2.1 Single components

Al_2O_3

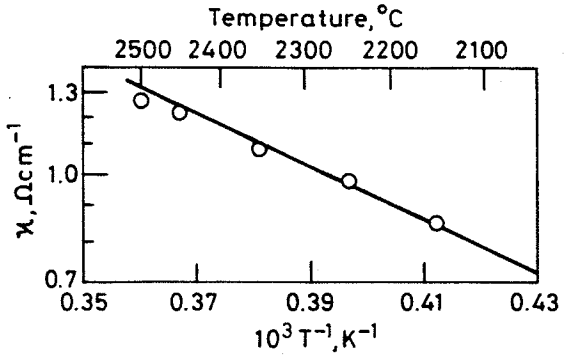


Fig. 14.5. Specific electrical conductivity of molten Al_2O_3 as a function of reciprocal temperature [20]. Further Ref. [21]

FeO

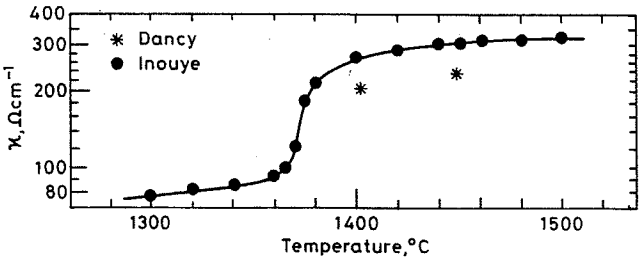


Fig. 14.7. Specific electrical conductivity of FeO as a function of temperature [37, 38]. Further Refs. [39, 40]

Fe_2O_3

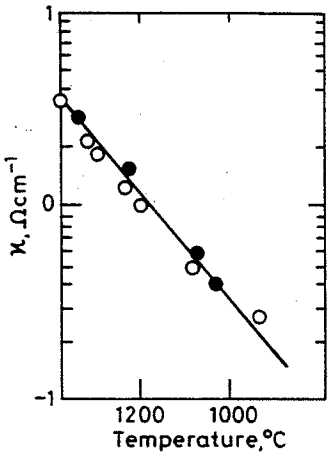
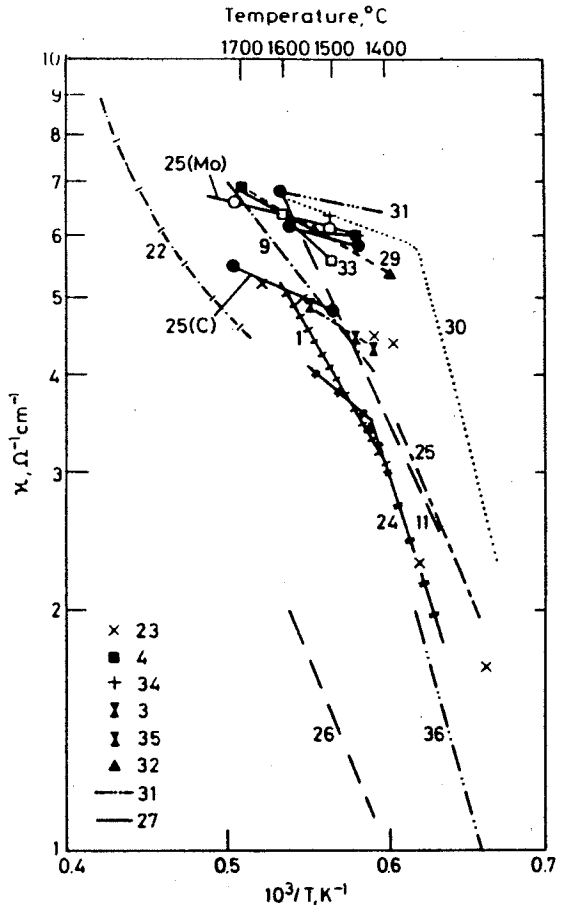
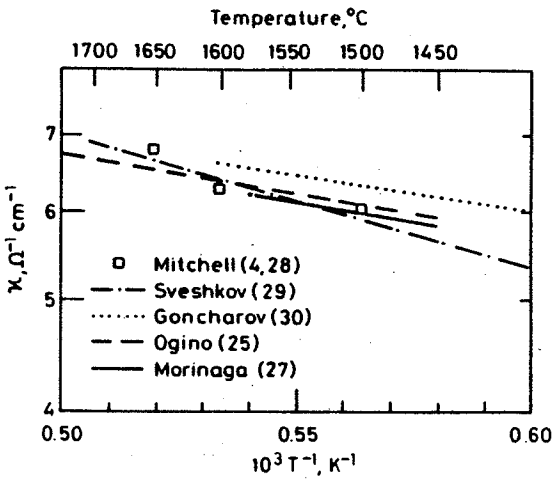


Fig. 14.8. Specific electrical conductivity of Fe_2O_3 as a function of temperature [41]

CaF_2



(a)



(b)

Fig. 14.6 a,b. Specific electrical conductivity of CaF_2 as a function of reciprocal temperature [1-4, 9, 11, 12, 16-19, 22-36] (a), (b); it can be seen from (a) that values reported by Ogino [25] using graphite crucibles lie below those obtained in Mo crucibles; thus results in C crucibles [2, 24, 26] are probably suspect. The results due to Ogino [25] and Morinaga [27] are recommended. Experimental details [see Refs. 16-18]

SiO_2

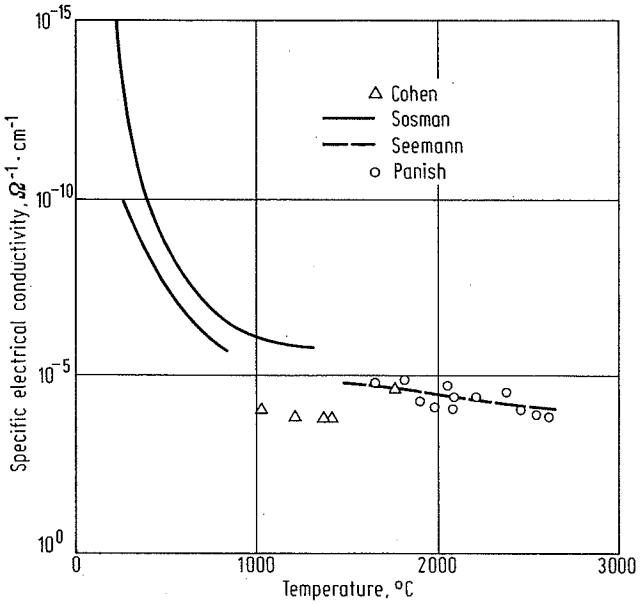


Fig. 14.9. Electrical conductivity of SiO_2 after several authors. Measuring methods: Wheatstone brigde, 10 kHz, W electrodes [42]; current-voltage measurement, direct current, Pt electrodes, vacuum [43]; current-voltage measurement, Cu electrodes [44]. Further Ref. [45]

Al_2O_3-CaO

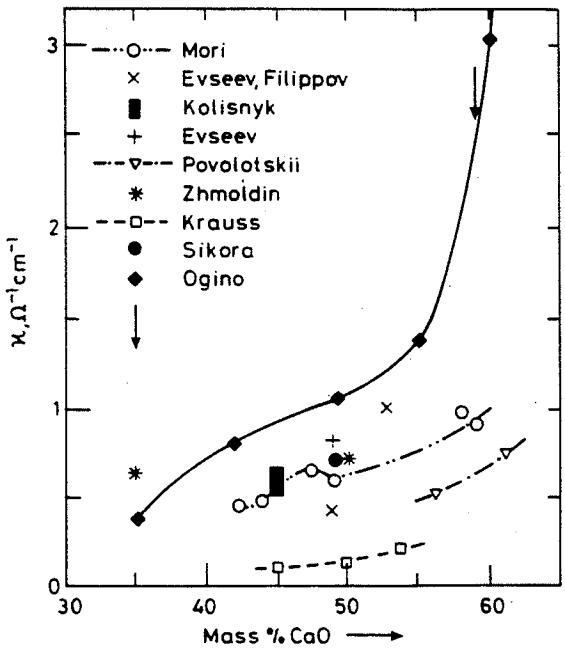


Fig. 14.11. Specific electrical conductivity of Al_2O_3-CaO melts at 1600 °C as a function of composition [8, 22, 23, 50-55]; the data shown as a solid line are tentatively recommended; ↓ denotes compositional range which is liquid at 1600 °C. Further Ref. [56]

14.2.2 Binary systems

Al_2O_3-CaF_2

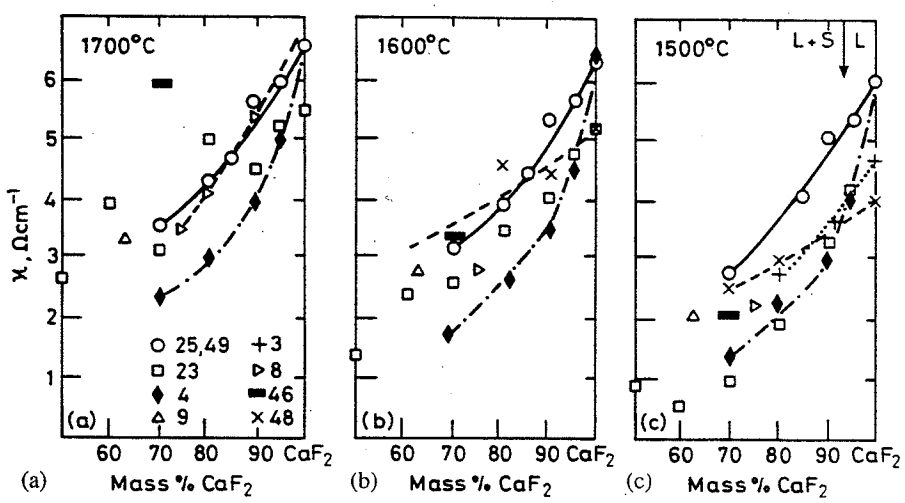


Fig. 14.10 a-c. Specific electrical conductivity of Al_2O_3-CaF_2 slags as a function of composition [1-4, 8, 9, 16-18, 23, 25, 35, 46-49]. The discrepancies in the data are probably due to the formation of variable amounts of CaO due to reactions of CaF_2 with Al_2O_3 and HF [17, 18]. The higher values shown as a solid line are recommended [25, 49, 17, 18]

Al_2O_3-FeO

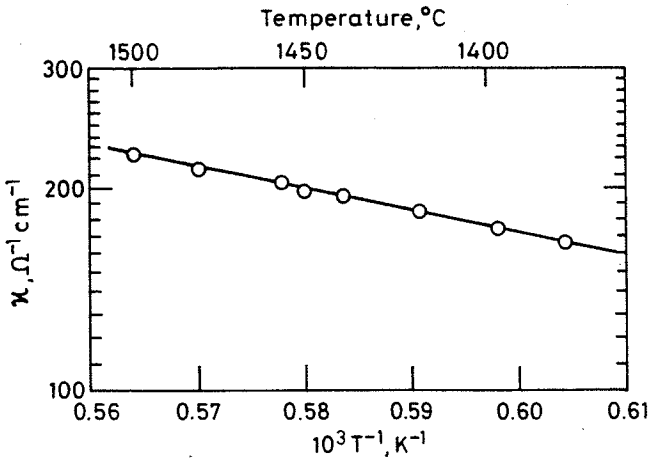


Fig. 14.12. Specific electrical conductivity of slag with composition 3.6 % Al_2O_3 - 96.4 % FeO as a function of reciprocal temperature [38]

Al_2O_3-SiO_2

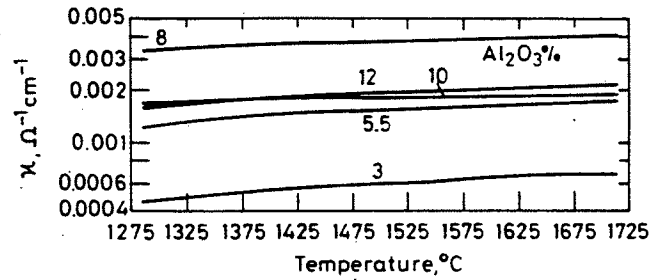


Fig. 14.13. Specific electrical conductivity of Al_2O_3-SiO_2 slags containing up to 12 % Al_2O_3 as a function of temperature [57]

B_2O_3-CaF_2

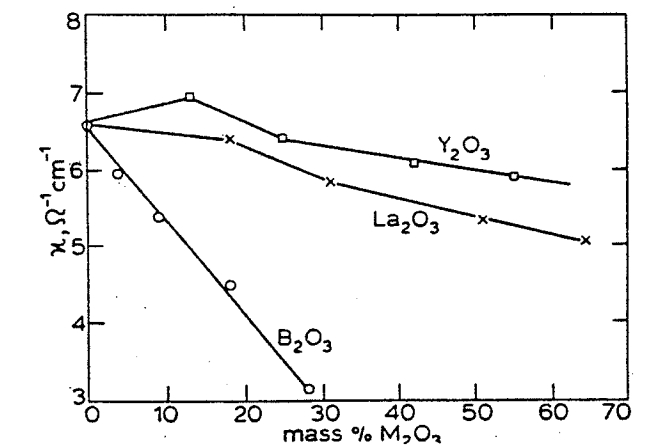


Fig. 14.14. Specific electrical conductivity of B_2O_3-CaF_2 and CaF_2-La_2O_3 and CaF_2-Y_2O_3 as a function of composition [29]

CaF_2-CaO

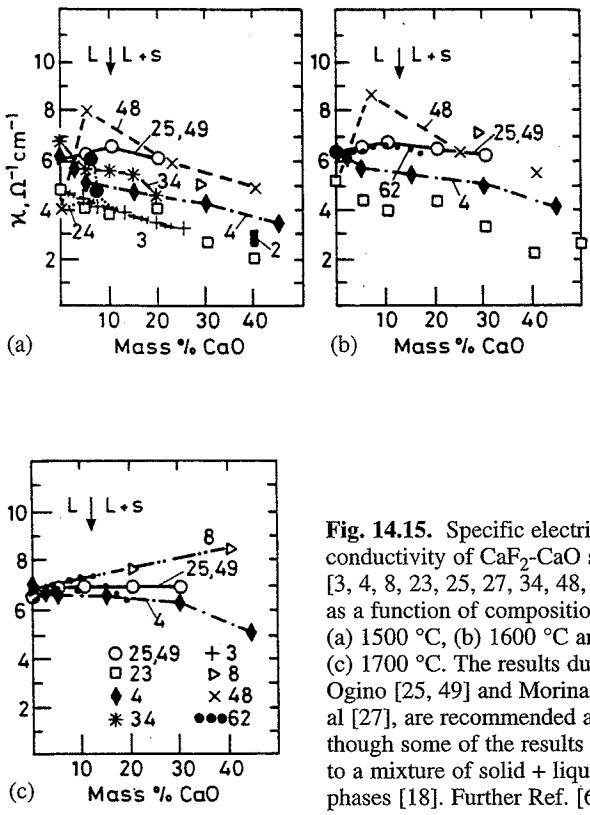


Fig. 14.15. Specific electrical conductivity of CaF_2-CaO slags [3, 4, 8, 23, 25, 27, 34, 48, 49] as a function of composition at (a) 1500 °C, (b) 1600 °C and (c) 1700 °C. The results due to Ogino [25, 49] and Morinaga et al [27], are recommended although some of the results refer to a mixture of solid + liquid phases [18]. Further Ref. [61]

CaF_2-FeO

Tab. 14.1. Temperature dependence of electrical conductivity of CaF_2-CaO melts with weight proportions of 94.1 % CaF_2, 5.13 % FeO and 0.77 % Fe_2O_3 [40]. According to the phase diagram these results would refer to the solid phase exept at 1400 °C where 2 liquids co-exist [18]. Further Ref. [39]

Temperature °C	1000	1100	1200	1300	1400
κ, Ω^{-1} cm^{-1}	0.09	0.43	1.30	2.72	3.6

CaF_2-La_2O_3

Specific electrical conductivities of CaF_2-La_2O_3 melts [29] at 1600 °C are given in Fig. 14.14.

CaF_2-MgO

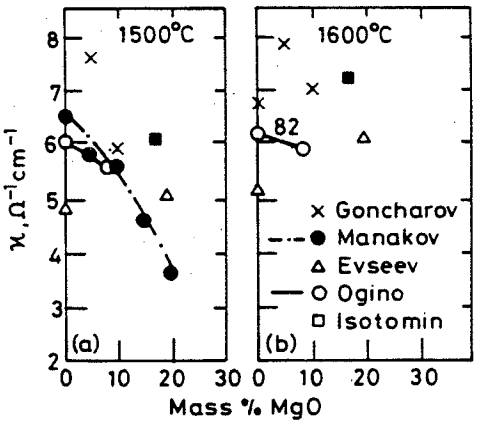


Fig. 14.16 a,b. Specific electrical conductivity of CaF_2-MgO melts at (a) 1500 °C and (b) 1600 °C as a function of composition [8, 30, 31, 34, 49]

CaF_2-SiO_2

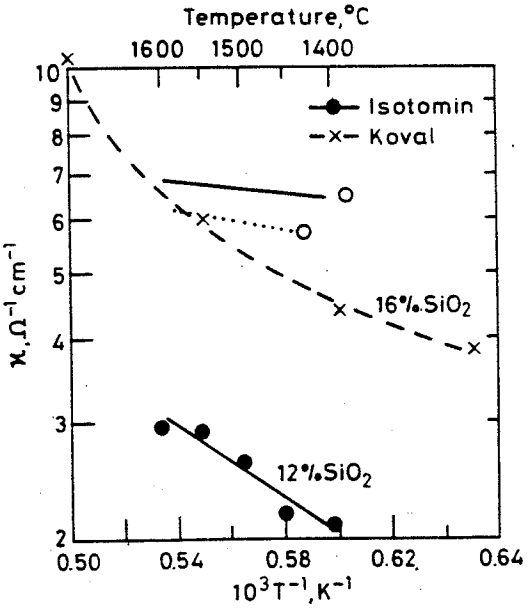


Fig. 14.17. Specific electrical conductivity of CaF_2-SiO_2 melts as a function of reciprocal temperature [46, 31]; ..., recommended value for CaF_2. These melts probably contain CaO as a result of reactions of SiO_2 and H_2O with CaF_2. The data due to Isotomin et al [31] are preferred

CaF_2-TiO_2

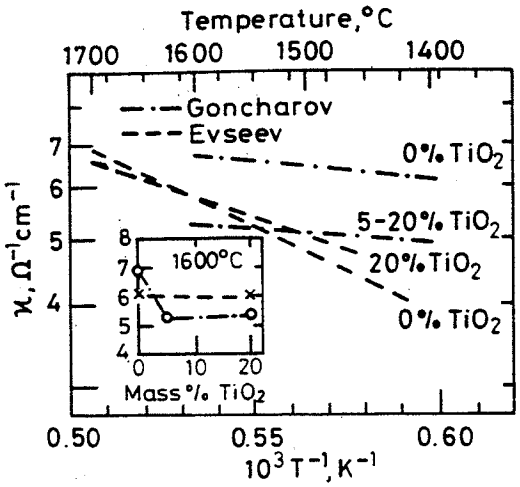


Fig. 14.18. Specific electrical conductivity of CaF_2-TiO_2 melts as a function of reciprocal temperature [8, 30]; the melts probably contained CaO formed by reactions of TiO_2 and H_2O with CaF_2 [18]

CaF_2-Y_2O_3

Specific electrical conductivities of CaF_2-Y_2O_3 melts [29] at 1600 °C are given in Fig. 14.14.

CaF_2-ZrO_2

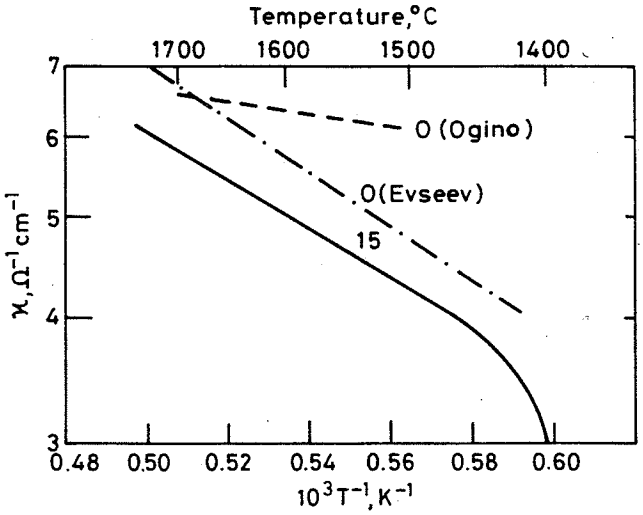


Fig. 14.19. Specific electrical conductivity of CaF_2-ZrO_2 melts [8, 62] as a function of temperature

CaO-FeO

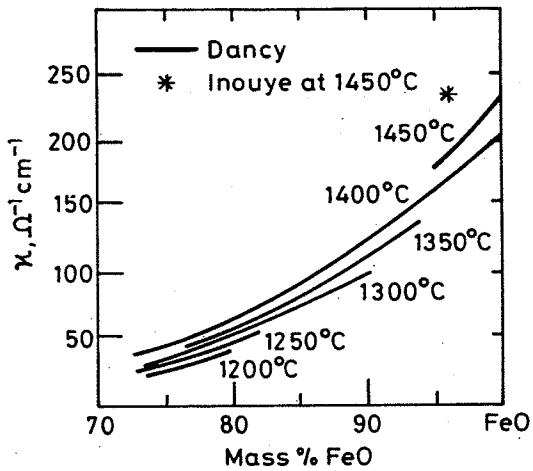


Fig. 14.20. Specific electrical conductivity of CaO-FeO melts [37, 38] as a function of FeO content

CaO-Fe_2O_3

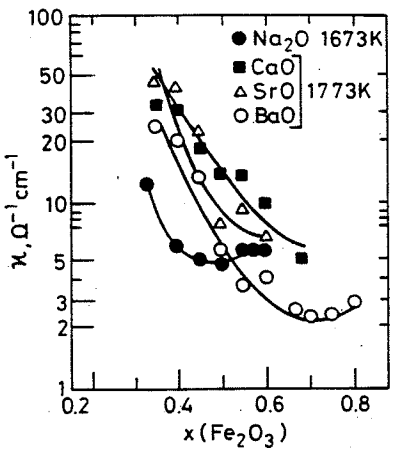


Fig. 14.21. Specific electrical conductivity of CaO-Fe_2O_3 melts at 1500 °C as a function of mole fraction Fe_2O_3 [58]. Further Refs. [63, 64]

$CaO\text{-}SiO_2$

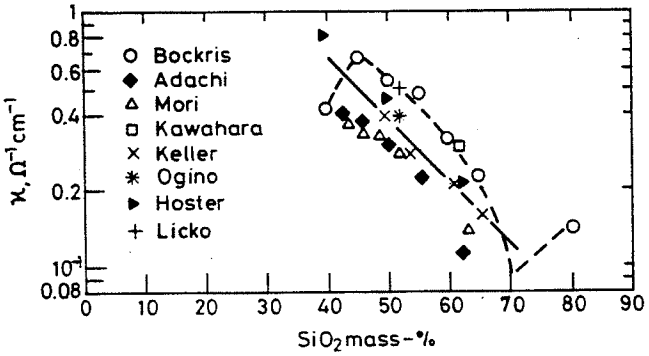


Fig. 14.22. Specific electrical conductivity of $CaO\text{-}SiO_2$ melts at 1600 °C as a function of composition [32, 57, 59, 63, 65-74]. The data denoted by x and * are recommended. Experimental details [10]

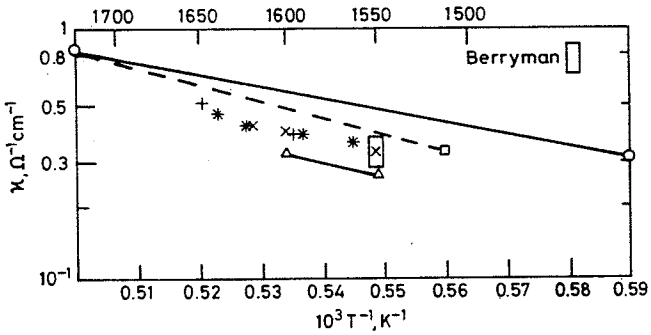


Fig. 14.23. The temperature dependence of the electrical conductivity of 48 %CaO - 52 % SiO_2 melt [57, 66, 74]. Symbols as in Fig. 14.22.

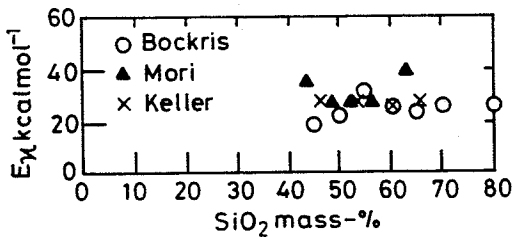


Fig. 14.24. Activation energy of electrical conductivity of $CaO\text{-}SiO_2$ melts as a function of composition [57, 65, 66]

FeO-MnO

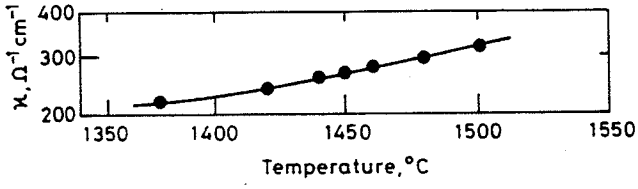


Fig. 14.25. Specific electrical resistance of 95 % FeO - 5 % MnO as a function of temperature [38]

$Fe_2O_3\text{-}Na_2O$

The specific electrical conductivities of $Fe_2O_3\text{-}Na_2O$ melts at 1400 °C are given in Fig. 14.21.

$FeO_x\text{-}SiO_2$

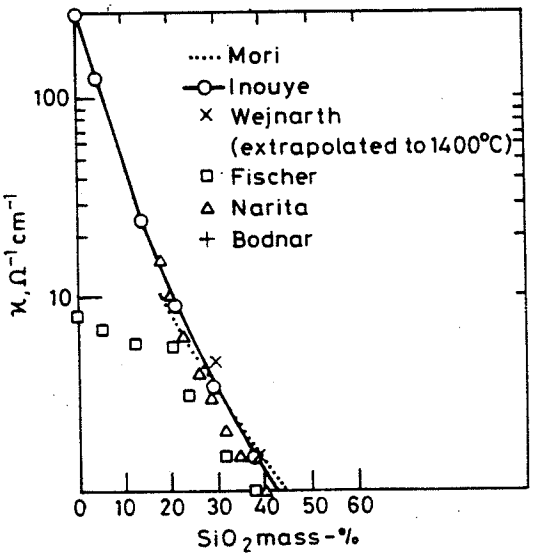


Fig. 14.26. Specific electrical conductivity of $FeO\text{-}SiO_2$ melts at 1400 °C as a function of composition [38-40, 75-78]. Further Refs. [79, 80, 73]. The solid line is recommended

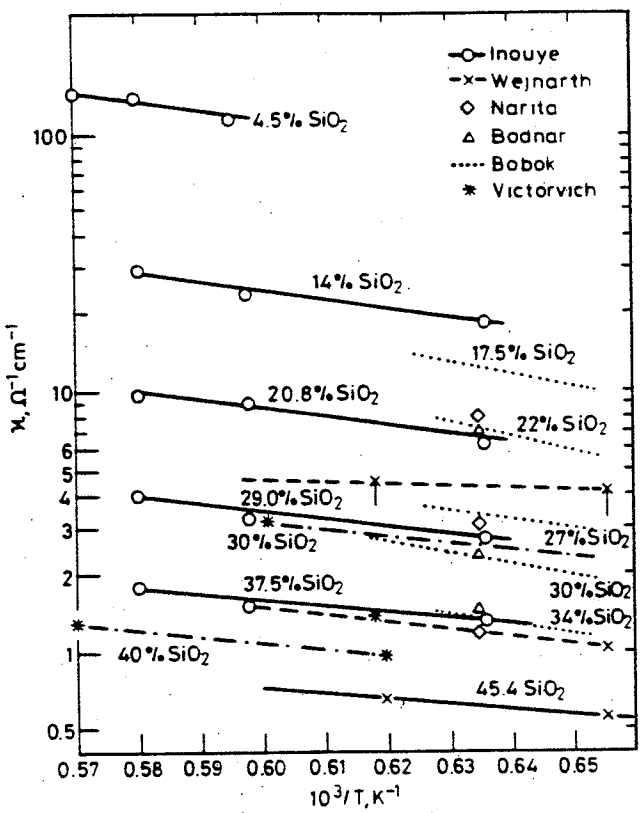


Fig. 14.27. The temperature dependence of electrical conductivities of $FeO_x\text{-}SiO_2$ melts [38,76-79, 81]

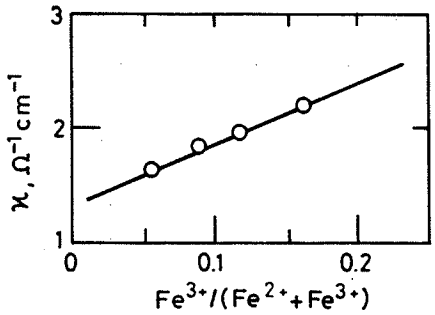


Fig. 14.28. Specific electrical conductivity of FeO_x-SiO_2 melts [80] at 1200 °C as a function of Fe_2O_3 content, expressed as $[Fe^{3+}/(Fe^{2+} + Fe^{3+})]$

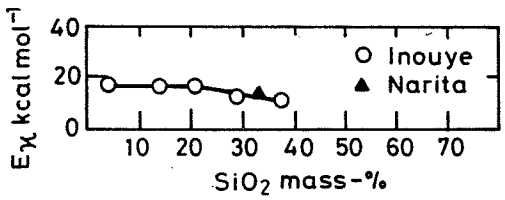
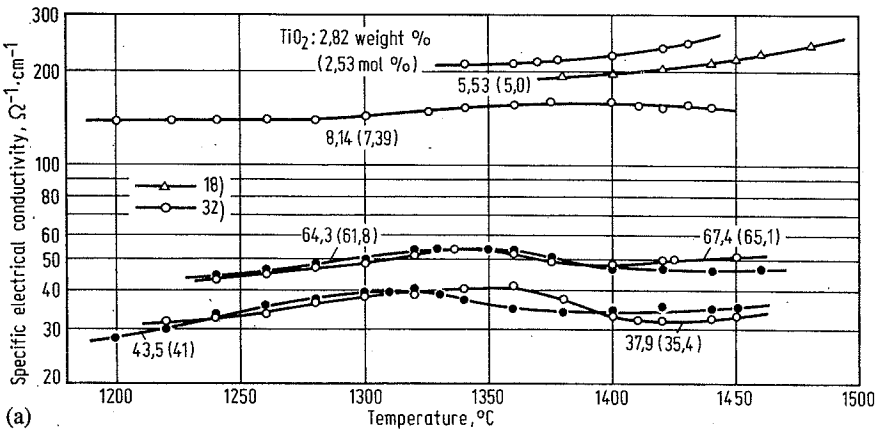


Fig. 14.29. Activation energies of FeO_x-SiO_2 melts as a function of SiO_2 content [38, 77]

Fe_2O_3-SrO_2

Specific electrical conductivities of Fe_2O_3-SrO_2 melts at 1500 °C are given in Fig. 14.21.

FeO_x-TiO_2



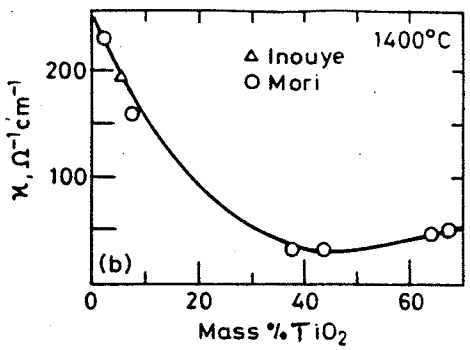


Fig. 14.30 a,b. Specific electrical conductivities of FeO-TiO_2 melts [38, 82] as functions of (a) temperature and (b) TiO_2 content for system containing small amounts of Fe_2O_3. Further Refs. [83, 84]

K_2O-SiO_2

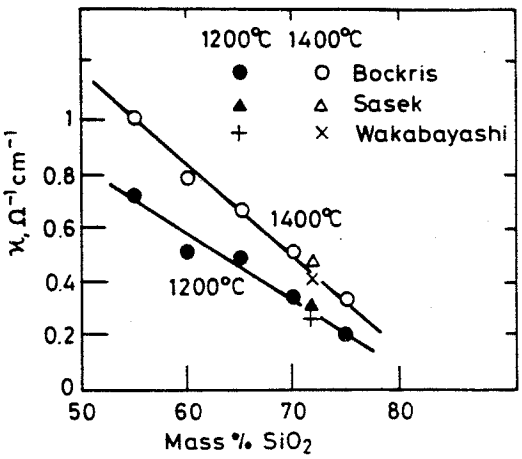


Fig. 14.31. Specific electrical conductivities of K_2O-SiO_2 melts at 1200 and 1400 °C as a function of composition [59, 85, 86]

Li_2O-SiO_2

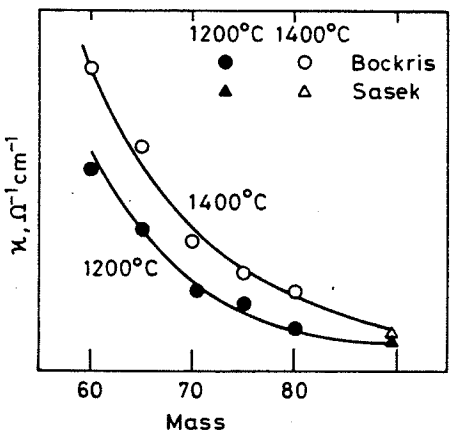


Fig. 14.32. Specific electrical conductivities of Li_2O-SiO_2 melts at 1200 and 1400 °C as a function of composition [59, 85]

$MgO\text{-}SiO_2$

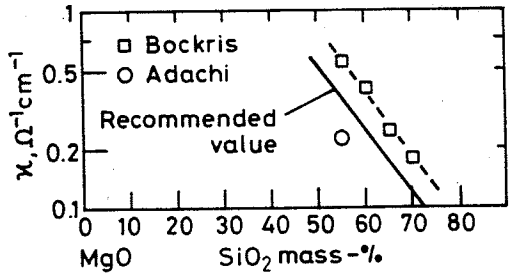
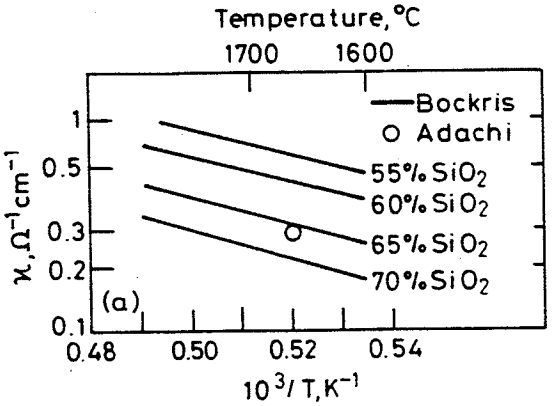
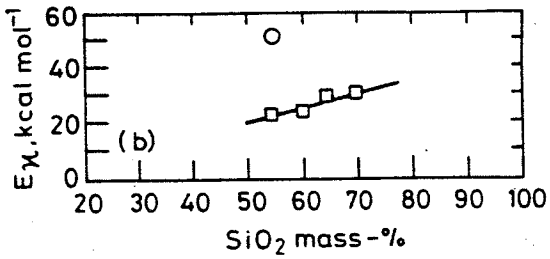


Fig. 14.33. Specific electrical conductivities of $MgO\text{-}SiO_2$ melts at 1600 °C [59, 87] as a function of composition; a recommended curve based on the mean of these studies is shown [10]



(a)



(b)

Fig. 14.34 a,b. Temperature dependence (a) and activation energy (b) for specific electrical conductivity of $MgO\text{-}SiO_2$ melts [59, 87]

$MnO\text{-}SiO_2$

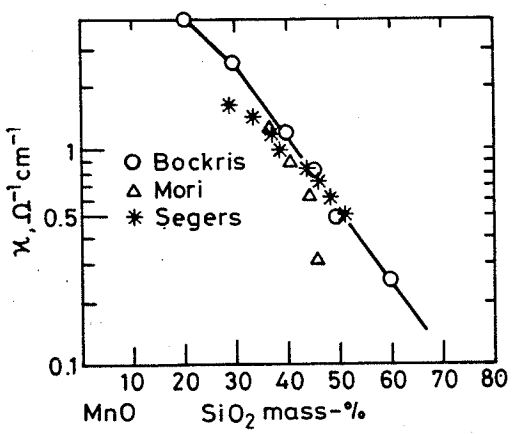
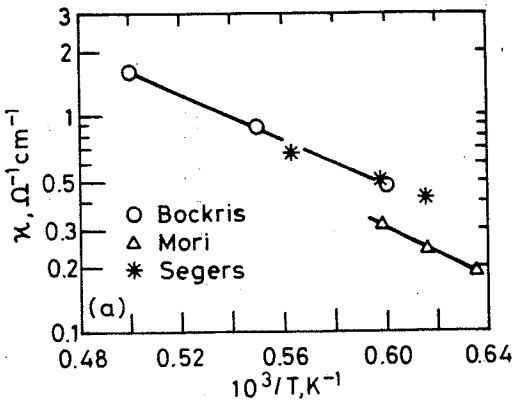
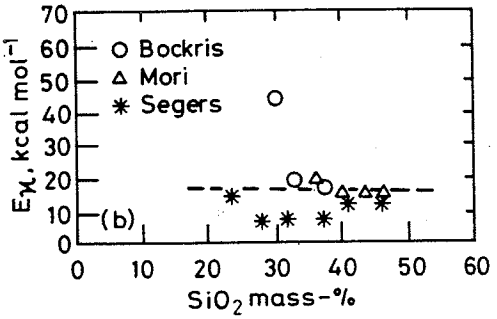


Fig. 14.35. Specific electrical conductivities of $MnO\text{-}SiO_2$ melts at 1400 °C as a function of composition [59, 65, 88-90]



(a)



(b)

Fig. 14.36 a,b. Temperature dependence (a) and activation energies (b) of specific electrical conductivities of $MnO\text{-}SiO_2$ melts [59, 65, 88-90]

$MnO\text{-}TiO_2$

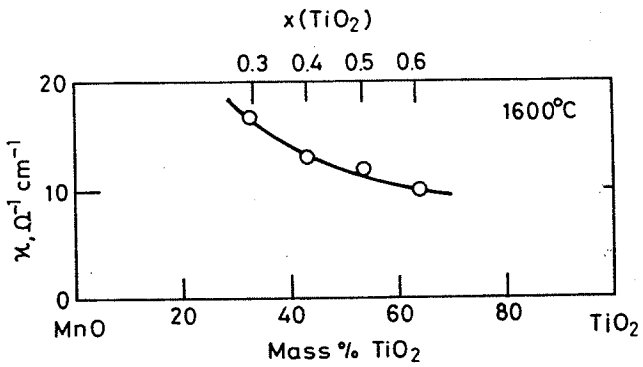


Fig. 14.37. Specific electrical conductivity of $MnO\text{-}TiO_2$ melts at 1600 °C as a function of composition [91]

Na_2O-SiO_2

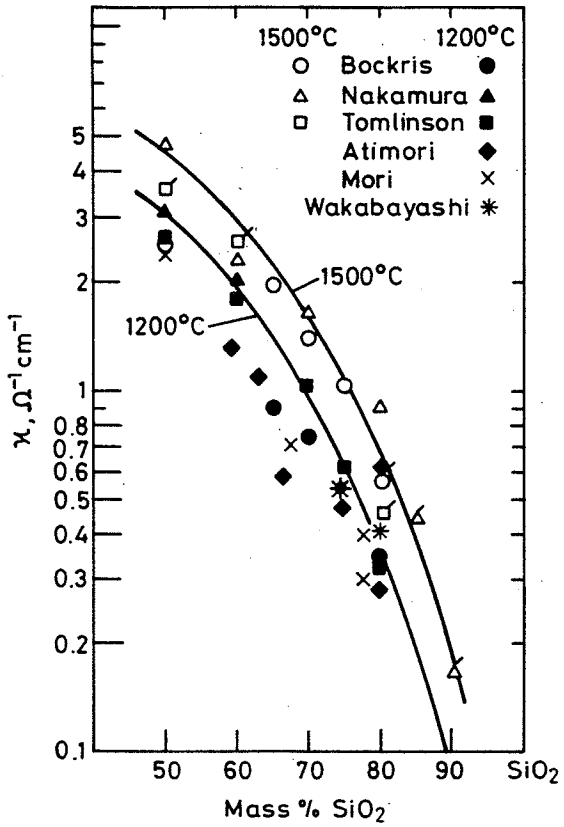


Fig. 14.38. Specific electrical conductivities of Na_2O-SiO_2 melts at 1200 and 1500 °C as a function of chemical composition [59, 65, 82, 92-94] Δ indicates extrapolated value. Solid lines are recommended curves. Further Ref. [95]

SiO_2-SrO

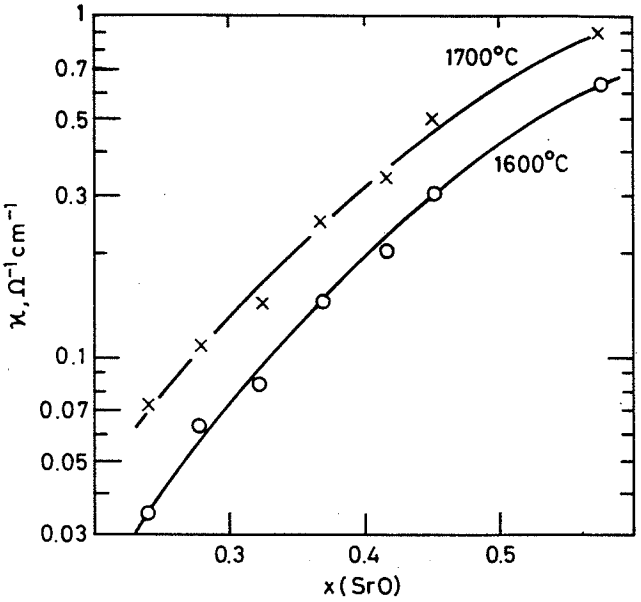


Fig. 14.39. Specific electrical conductivity of SiO_2-SrO melts at 1600 and 1700 °C as a function of mole fraction of SrO [59]

14.2.3 Ternary systems

Al_2O_3-CaF_2-CaO

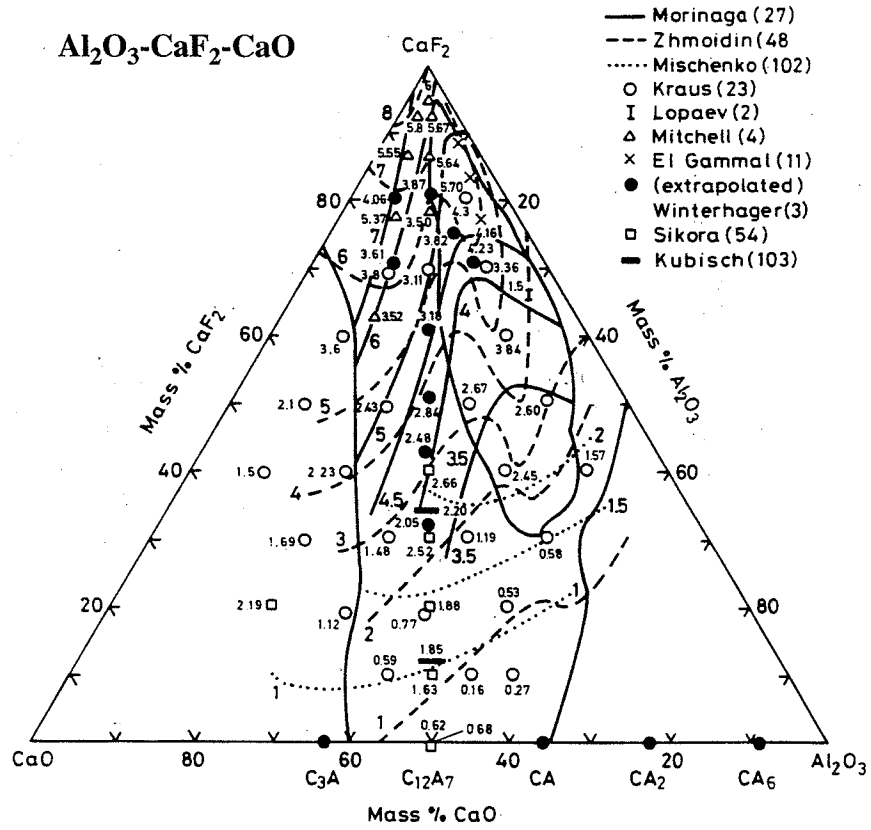


Fig. 14.40. Specific electrical conductivities of Al_2O_3-CaF_2-CaO melts at 1600 °C [2-4, 11, 23, 27, 48, 54, 102, 103]. The solid lines due to Moringa et al [27] are recommended; the dashed lines due to Zhemoidin [48] are in resonable agreement with these data

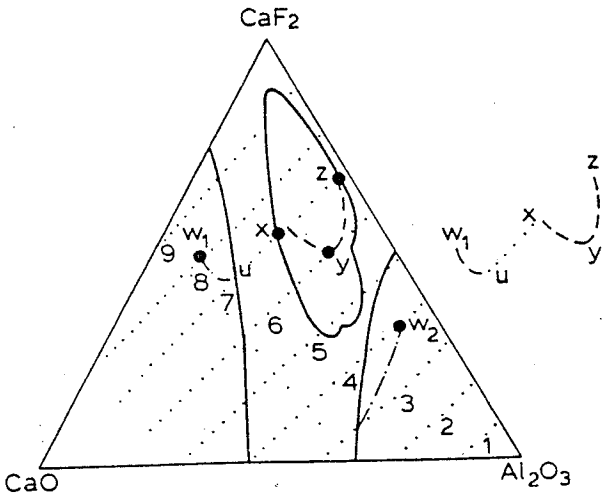


Fig. 14.41. Iso-conductivity contours for Al_2O_3-CaF_2-CaO melts at 1600 °C, [17, 18] who attributed the shape (wuxyz) of the contours to the difficulties of making measurements in 2-liquid region and recommended the dotted lines as the true contours

Al_2O_3-CaO-SiO_2

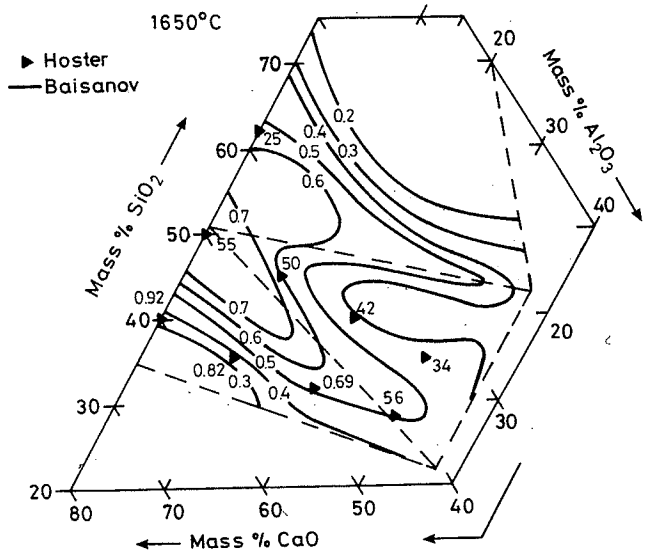
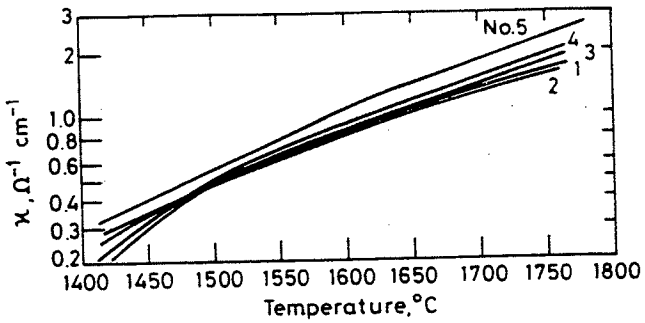


Fig. 14.43. Iso-conductivity (Ω^{-1} cm^{-1}) contours at 1650 °C for Al_2O_3-CaO-SiO_2 melts [34, 104]

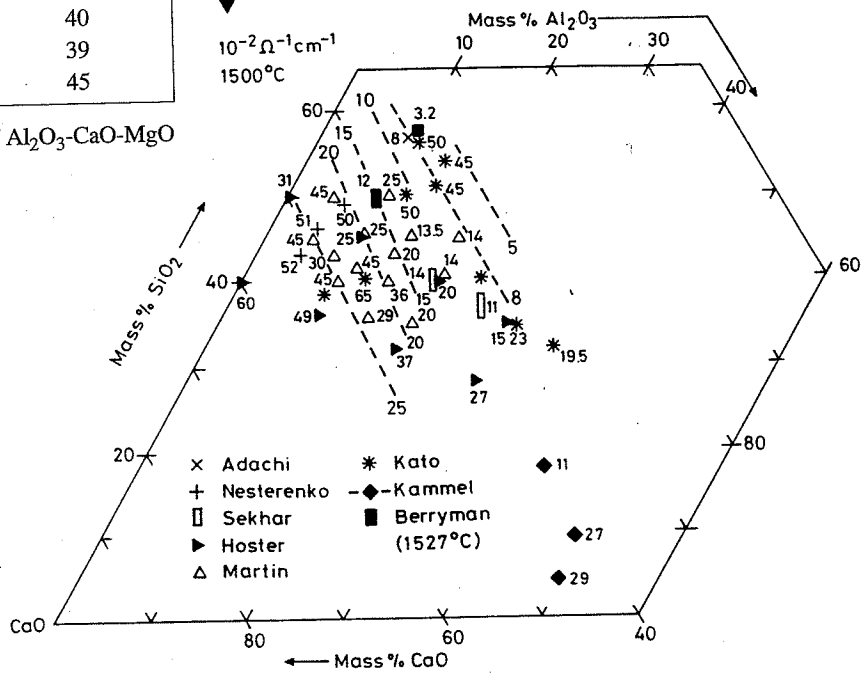
Al_2O_3-CaO-MgO



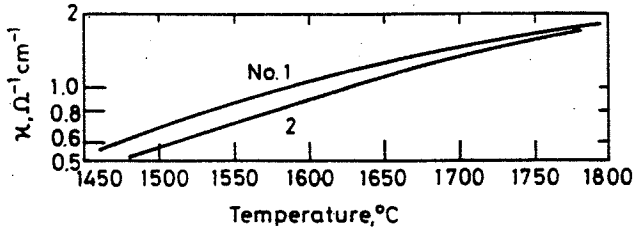
No.	Mass % CaO	Al_2O_3	MgO	Activation energy (kcal/mol)
1	49.05	51.20	-	36
2	52.20	41.70	3.70	38
3	40.20	50.20	9.50	40
4	35.80	53.80	13.50	39
5	44.60	39.20	17.20	45

Fig. 14.42. Specific electrical conductivities of Al_2O_3-CaO-MgO melts as a function of temperature [51]

Fig. 14.44. Specific electrical conductivity (10^{-2} Ω^{-1} cm^{-1}) values reported for Al_2O_3-CaO-SiO_2 melts at 1500 °C [32, 63, 74, 104-110]. Further Ref. [111]



Al_2O_3-CaO-TiO_2



No.	Mass %			Activation energy (kcal/mol)
	CaO	Al_2O_3	TiO_2	
1	38.2	39.5	21.2	27
2	51.0	39.2	9.8	34

Fig. 14.45. Specific electrical conductivity of Al_2O_3-CaO-TiO_2 slags as a function of temperature [51]. Further Ref. [56]

Al_2O_3-CaO-ZrO_2

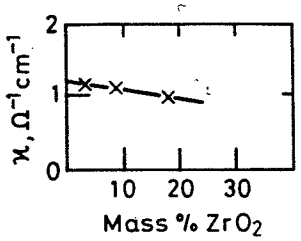
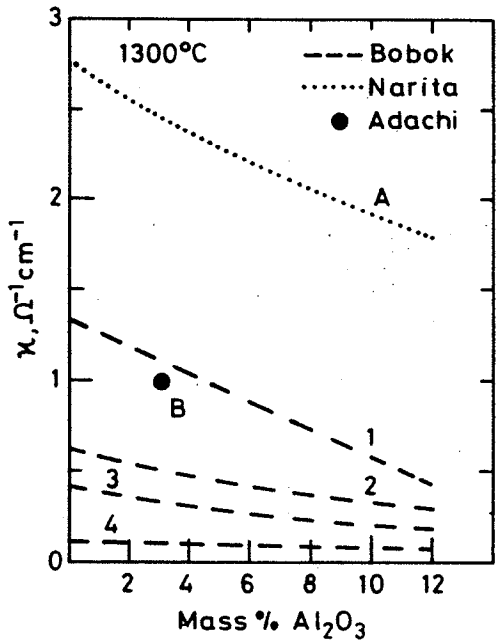


Fig. 14.46. The effect of ZrO_2 additions on the specific electrical conductivity of 47 % Al_2O_3 - 53 % CaO melts at 1700 °C [51, 56]

Al_2O_3-FeO_x-SiO_2



Slag	FeO	Fe_2O_3	SiO_2
1	75.5	7.0	17.5
2	67.7	8.5	23.8
3	69.4	4.2	26.4
4	63.8	2.6	33.7
5	67.5	-	32.5
6	73.3	-	25.7

Fig. 14.47. The effect of Al_2O_3 additions on the specific electrical conductivity of FeO_x-SiO_2 melts at 1300 °C [63, 79, 77]; note in case of slag A the Al_2O_3 replaced SiO_2 only, FeO_x was maintained constant

Al_2O_3-MgO-SiO_2

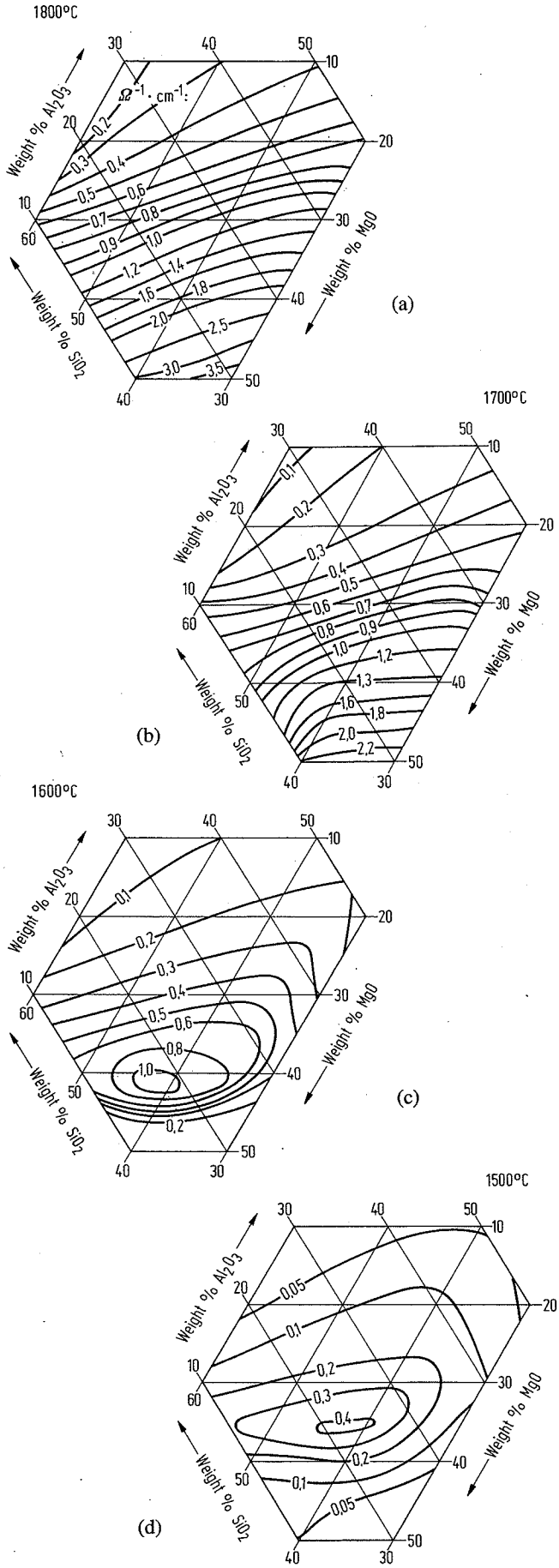


Fig. 14.48 a-d. Iso-conductivity contours of Al_2O_3-MgO-SiO_2 melts [114] and are compared with other reported values [87, 111-113] at 1600 °C [111, 112] and 1700 °C [113]

Al_2O_3-MnO-SiO_2

Tab. 14.2. Specific electrical conductivities, activation energies and in A values for Al_2O_3-MnO-SiO_2 melts [105]

Mass %			κ, Ω^{-1} cm^{-1} at 1500 °C	ln A_κ	E_κ kJ mol^{-1}
Al_2O_3	MnO	SiO_2			
0	73.4	26.6	3.29	10.919	75.5
10.8	70.1	19.1	3.22	11.214	80.2
19.7	67.1	12.2	3.17	12.978	106.4
29.8	64.4	5.8	3.95	15.478	144.3

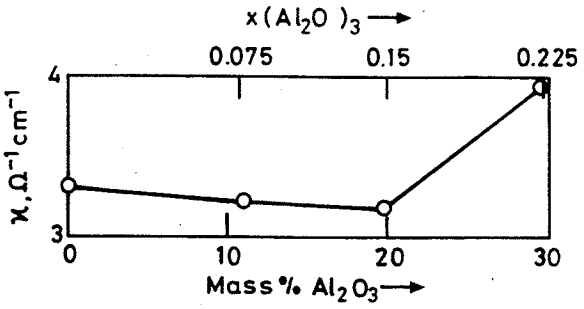


Fig. 14.49. Effect of substituting Al_2O_3 for SiO_2 on specific electrical conductivity of 0.70 % MnO - 0.30 % SiO_2 melts at 1500 °C [90]

Al_2O_3-Na_2O-SiO_2

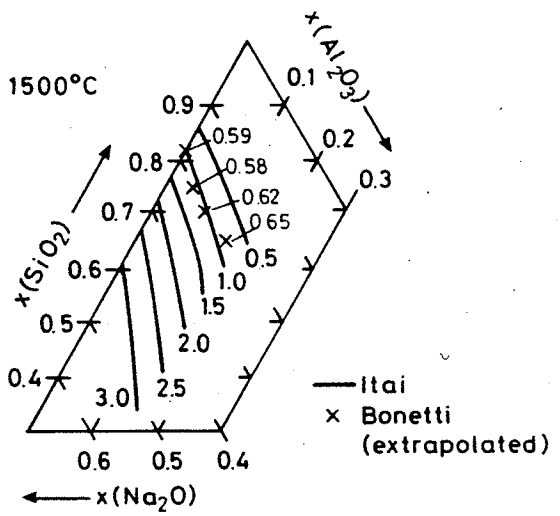
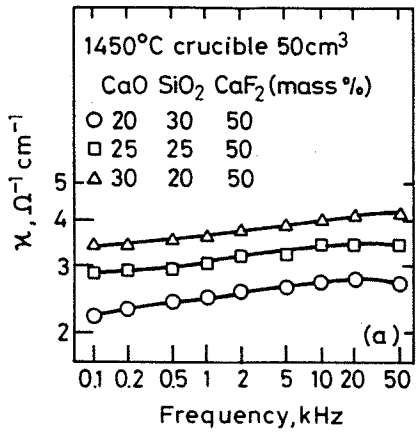
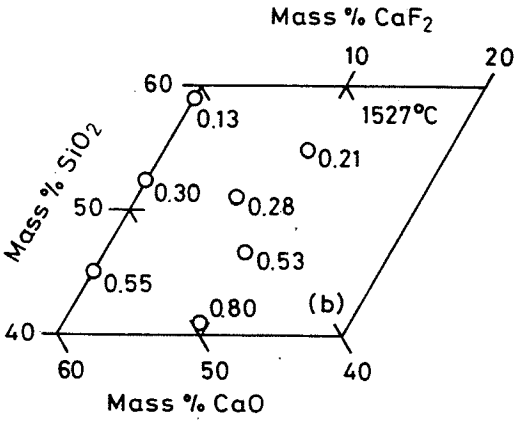


Fig. 14.50. Iso-conductivity contours (Ω^{-1} cm^{-1}) for Al_2O_3-Na_2O-SiO_2 melts at 1500 °C [101, 95]

CaF_2-CaO-SiO_2



(a)



(b)

Fig. 14.51 a,b. Specific electrical conductivity (Ω^{-1} cm^{-1}) of CaF_2-CaO-SiO_2 melts (a) at 1450 °C as a function of frequency; the effect of frequency was much diminished in larger crucibles (100 ml) [114], (b) at 1527 °C [74]. It should be noted that changes in melt composition will occur by reactions of CaF_2 with SiO_2 + H_2O [18]. Further work CaF_2 - 18.8 % CaO - 1.5 % SiO_2 [25]

CaF_2-CaO-TiO_2

Ogino et al [49] have reported specific electrical conductivities for a single composition 77 % CaF_2 - 7.5 % CaO - 15.5 % TiO_2; TiO_2 additions apparently reduced the electrical conductivity. It should be noted that the melt composition will change due to the reaction of CaF_2 with TiO_2 and H_2O (g) [18]

CaF_2-CaO-ZrO_2

Ogino et al [49] have reported a value of k = 4.2Ω^{-1} cm^{-1} at 1600 °C for a melt with the composition 69 % CaF_2 -7 % CaO - 24 % ZrO_2

CaF_2-FeO-SiO_2

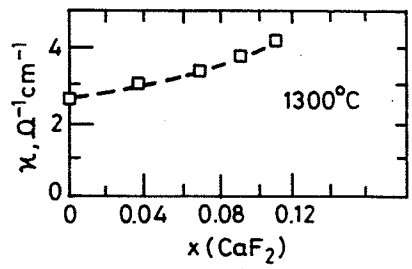


Fig. 14.52. The effect of CaF_2 additions on the specific conductivity of 2FeO·SiO_2 (fayalite) slag at 1300 °C [77]

CaF_2-MgO-SiO_2

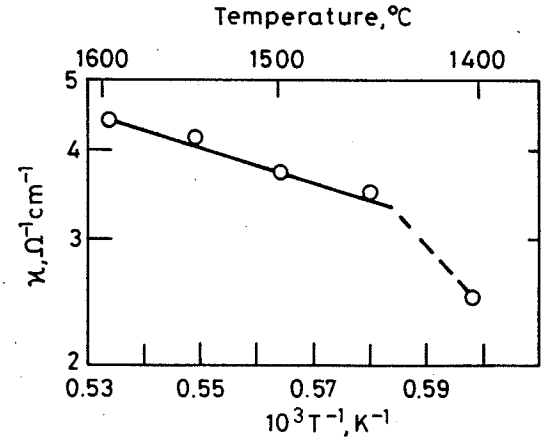


Fig. 14.53. Specific electrical conductivity of 72 % CaF_2 - 16 % MgO - 12 % SiO_2 as a function of reciprocal temperature [31]

CaO-Cr_2O_3-SiO_2

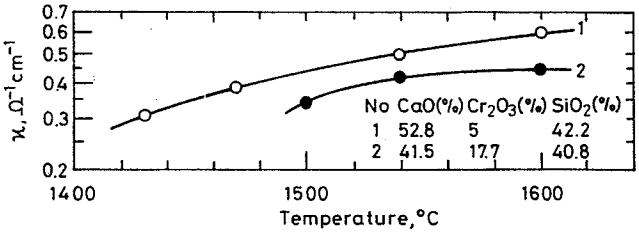


Fig. 14.54. Specific electrical conductivity of two CaO-Cr_2O_3-SiO_2 melts as a function of temperature [111]

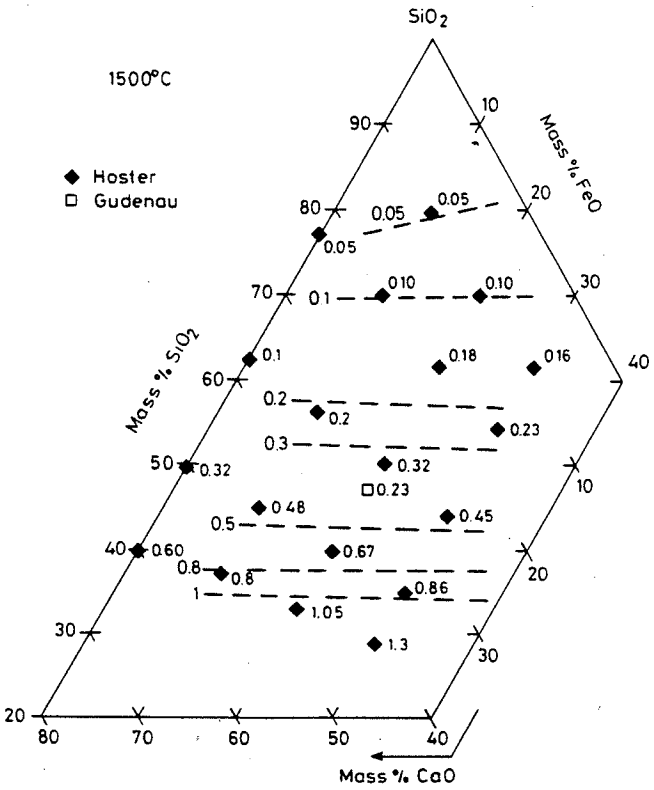


Fig. 14.56. Iso-electrical conductivity (Ω^{-1} cm^{-1}) contours at 1500 °C for the CaO-FeO-SiO_2 system [117, 32]. Further Ref. [71]

CaO-FeO_x-SiO_2

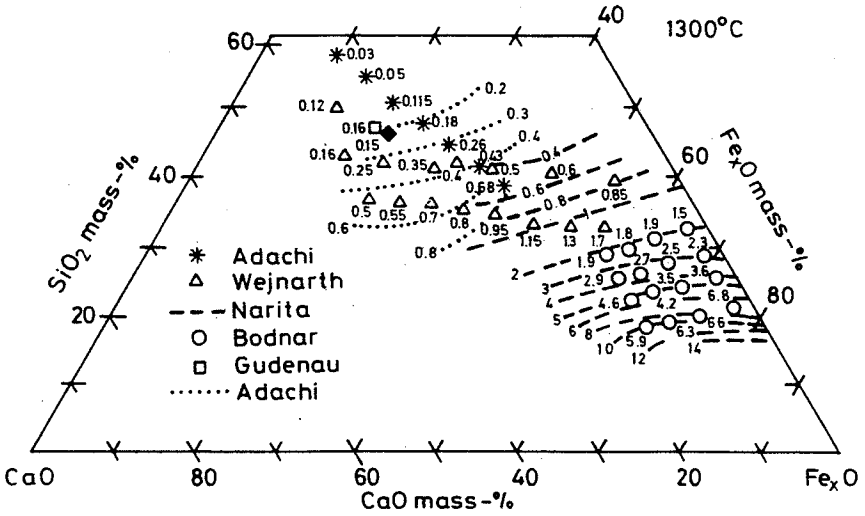


Fig. 14.55. Iso-electrical conductivity (Ω^{-1} cm^{-1}) contours at 1300 °C for the CaO-FeO-SiO_2 system [63, 76-78, 117]. Further Refs. [39, 40]

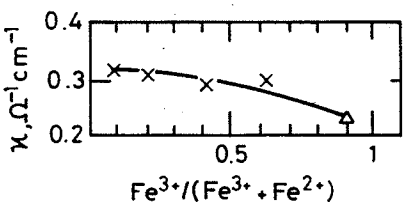


Fig. 14.57. The effect of (Fe^{3+}/Fe^{2+}) ratio on the specific electrical conductivity of a slag with composition 33 % CaO + 20 % FeO_x + 47 % SiO_2 [117]

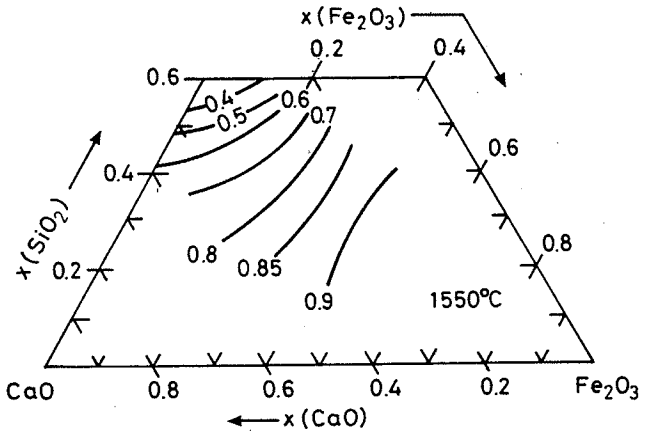


Fig. 14.58. Iso-electrical conductivity (Ω^{-1} cm^{-1}) contours for $CaO + Fe_2O_3 + SiO_2$ melts at 1550 °C [68]. Further Ref. for lower temperatures [63]

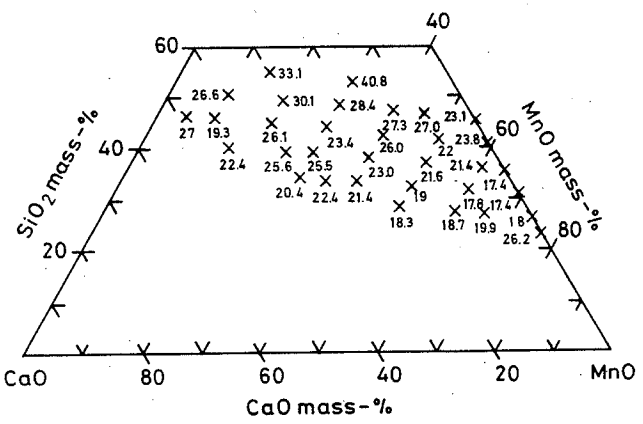


Fig. 14.61. Activation energies (kcal mol^{-1}) for CaO-MnO-SiO_2 melts [88, 89]

$CaO-MgO-SiO_2$

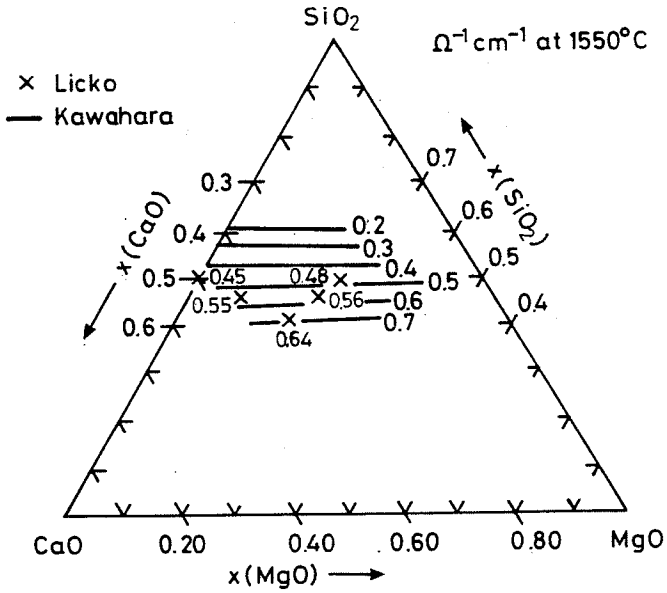


Fig. 14.59. Iso-electrical conductivity (Ω^{-1} cm^{-1}) contours for CaO-MgO-SiO_2 melts at 1550 °C [69, 72]. Further Ref. [118]

$CaO-Na_2O-SiO_2$

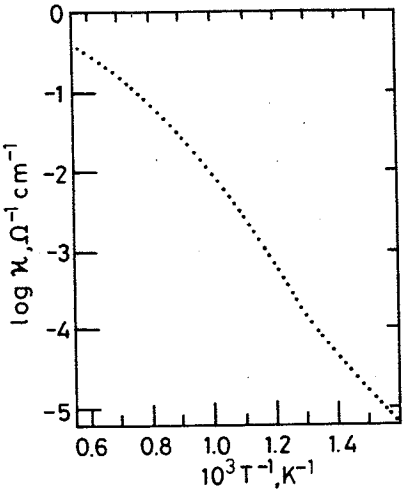


Fig. 14.62. Specific electrical conductivity for 12 % CaO - 16 % Na_2O - 72 % SiO_2 as a function of reciprocal temperature [86] .

$CaO-MnO-SiO_2$

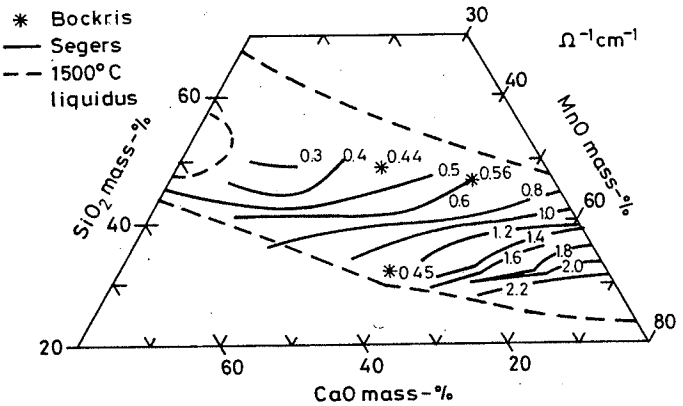


Fig. 14.60. Iso-electrical contours (Ω^{-1} cm^{-1}) for CaO-MnO-SiO_2 melts at 1500 °C [59, 88, 89]

$CaO-P_2O_5-SiO_2$

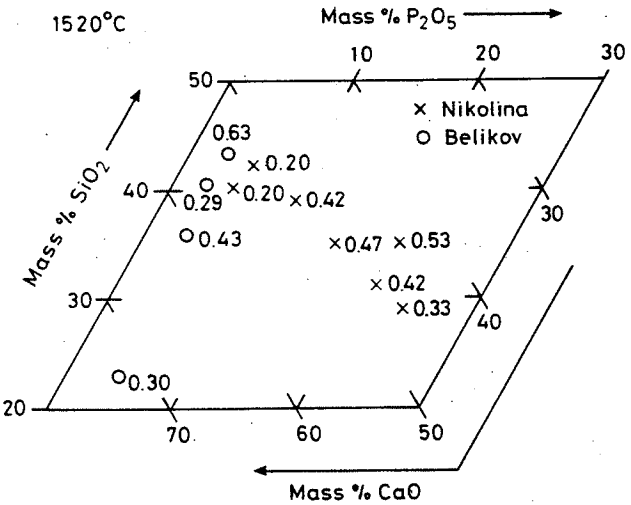


Fig. 14.63. Specific electrical conductivity (Ω^{-1} cm^{-1}) of CaO-P_2O_5-SiO_2 melts at 1520 ° C [120, 121]

$CaO\text{-}SiO_2\text{-}TiO_2$

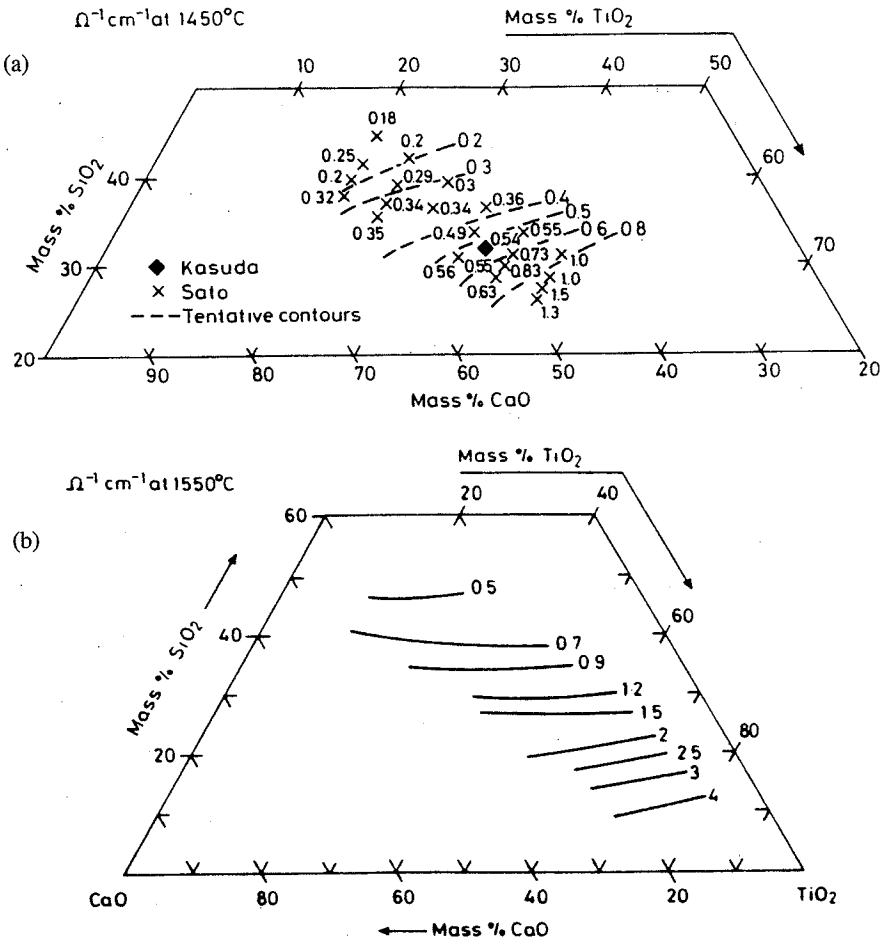


Fig. 14.64 a,b. Iso-electrical conductivity (Ω^{-1} cm^{-1}) contours for $CaO\text{-}SiO_2\text{-}TiO_2$ [123, 124] melts (a) at 1450 °C [115, 122, 123] and (b) at 1550 °C [123]. Values reported by Mori shown in Fig. 14.65 are considerably higher

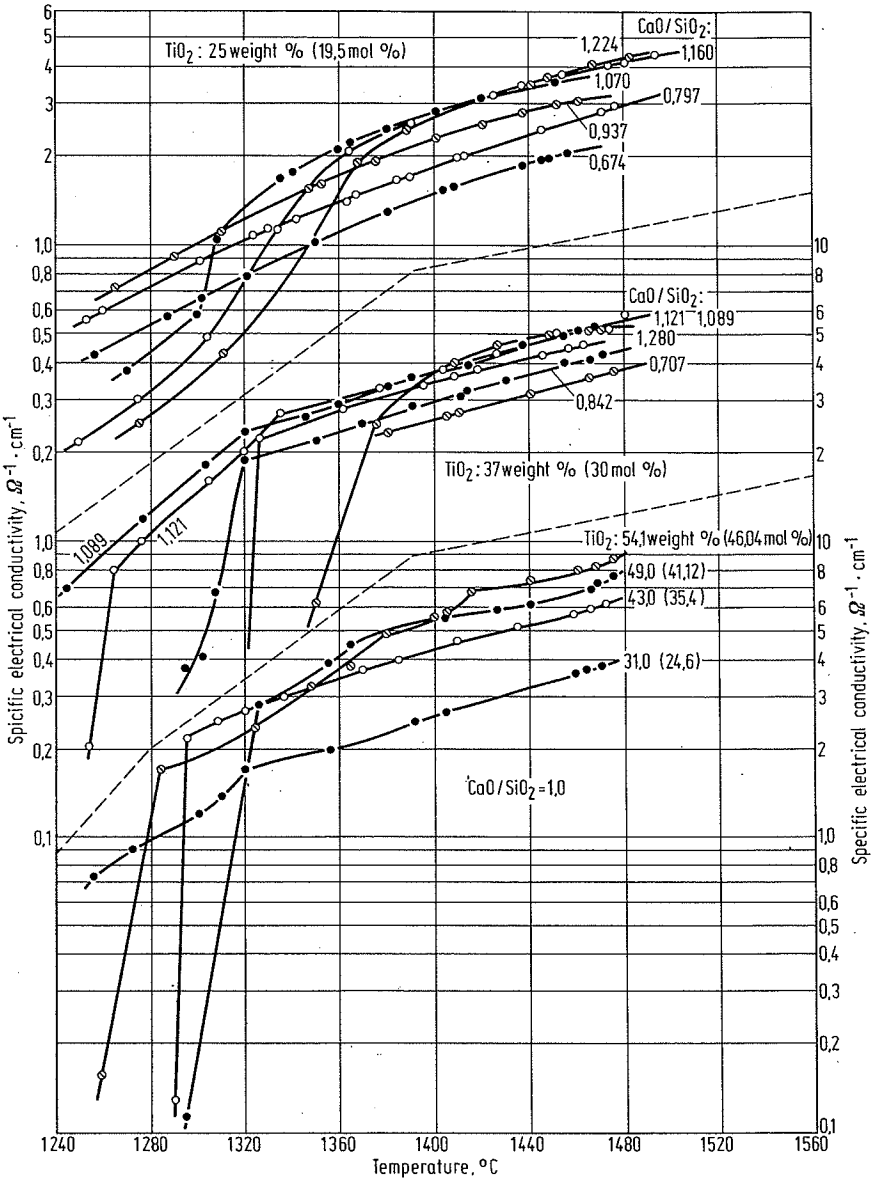


Fig. 14.65. Specific electrical conductivities of $CaO\text{-}SiO_2\text{-}TiO_2$ melts as a function of temperature [123, 124] as given in [15]

$CaO\text{-}SiO_2\text{-}ZnO$

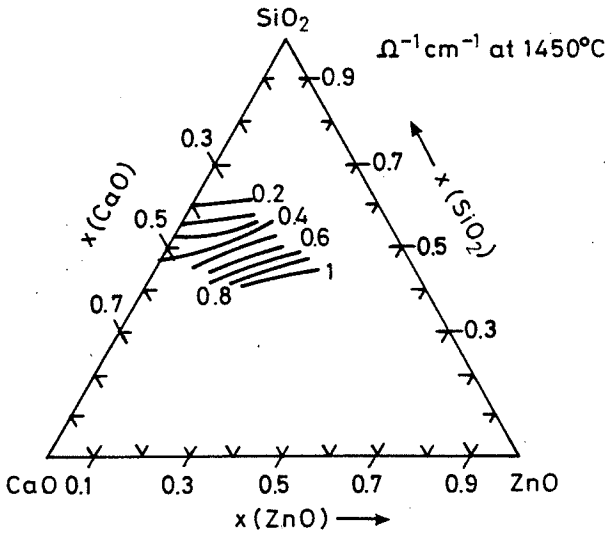
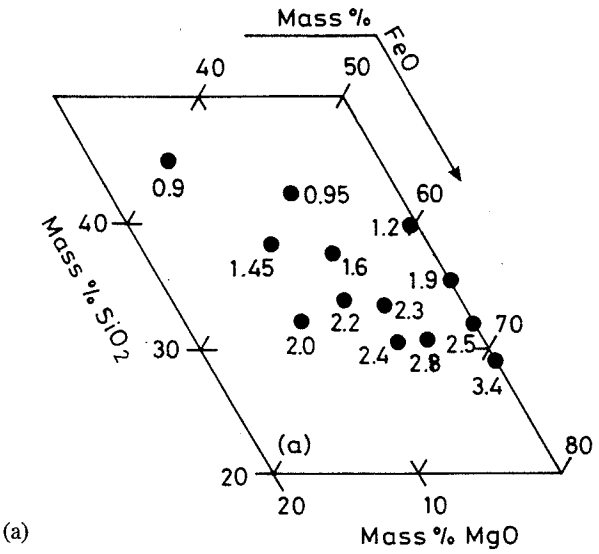
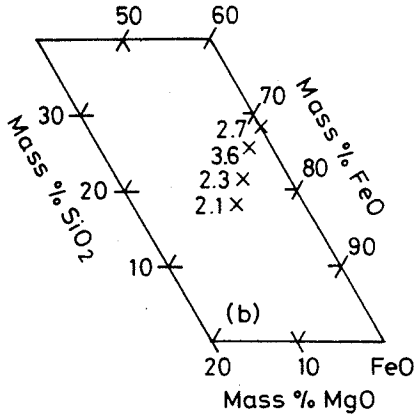


Fig. 14.66. Iso-electrical conductivity (Ω^{-1} cm^{-1}) contours at 1450 °C for the $CaO\text{-}SiO_2\text{-}ZnO$ system [125]

$FeO\text{-}MgO\text{-}SiO_2$



(a)



(b)

Fig. 14.67 a,b. Specific electrical conductivity (Ω^{-1} cm^{-1}) of $FeO\text{-}MgO\text{-}SiO_2$ melts (a) at 1400 °C [81], (b) high MgO melts at 1300 °C [77]. Further Ref. [77]

$FeO\text{-}MnO\text{-}SiO_2$

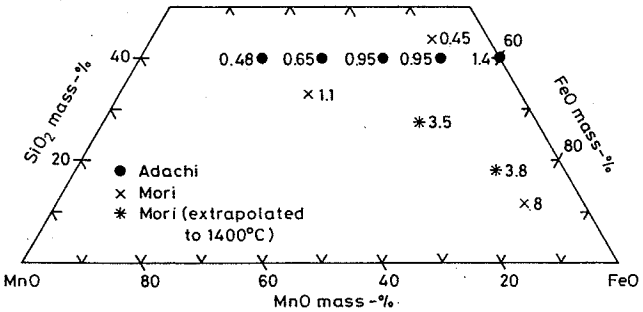
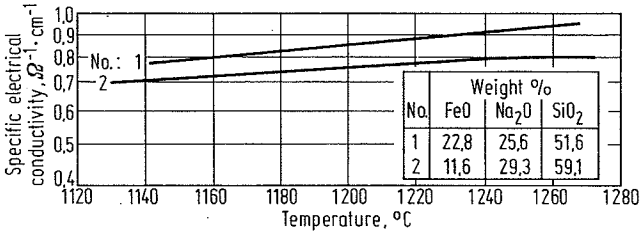


Fig. 14.68. Specific electrical conductivity (Ω^{-1} cm^{-1}) of $FeO\text{-}MnO\text{-}SiO_2$ melts at 1400 °C [103, 127]

$FeO_x\text{-}Na_2O\text{-}SiO_2$



No.	Weight % FeO	Na_2O	SiO_2
1	22,8	25,6	51,6
2	11,6	29,3	59,1

Fig. 14.70. Specific electrical conductivity of $FeO\text{-}Na_2O\text{-}SiO_2$ melts as a function of temperature [128]

$FeO\text{-}MnO\text{-}TiO_2$

No.	Weight % (mol %) MnO	TiO_2	FeO
1	55,8 (58,5)	43,3 (40,4)	1,0 (1,1)
2	51,2 (53,6)	46,9 (43,5)	2,9 (2,9)
3	45,6 (48,6)	53,5 (50,5)	0,9 (0,9)
4	40,5 (43,1)	59,1 (56,0)	0,5 (0,5)
5	34,9 (38,4)	63,8 (60,1)	1,3 (1,4)
6	30,5 (33,0)	68,5 (66,0)	1,0 (1,1)

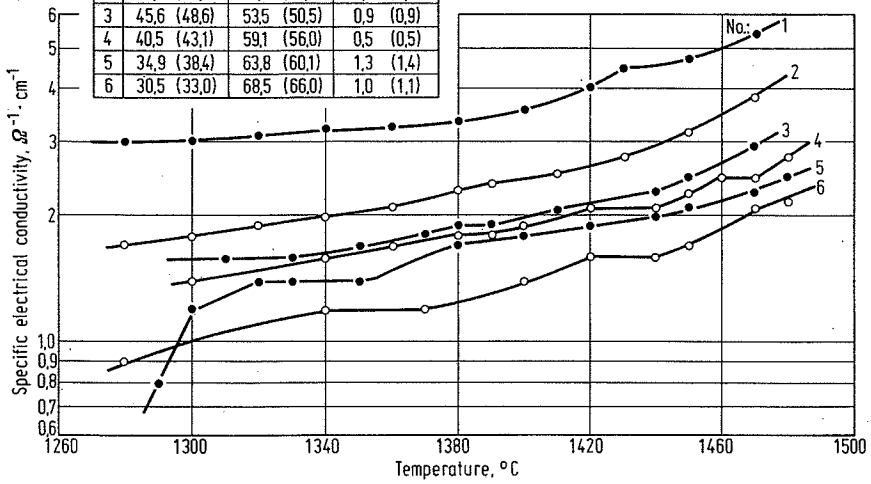


Fig. 14.69. Specific electrical conductivity of $FeO\text{-}MnO\text{-}TiO_2$ melts as a function of temperature [84]

Fe_2O_3-Na_2O-SiO_2

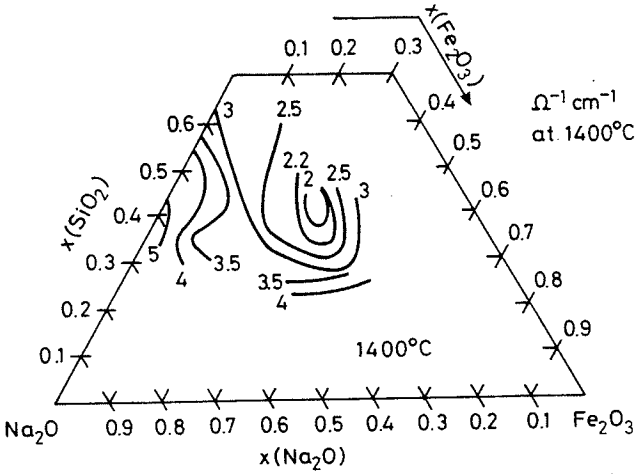


Fig. 14.71. Iso-electrical conductivity (Ω^{-1} cm^{-1}) contours for Fe_2O_3-Na_2O-SiO_2 melts at 1400 °C [68]. Further Ref. [129]

FeO-SiO_2-TiO_2

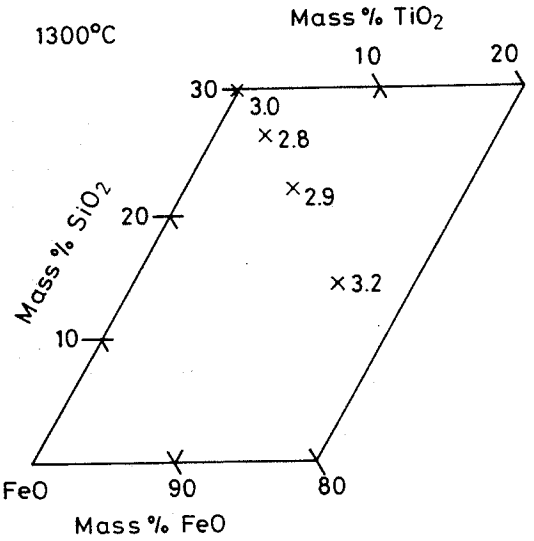


Fig. 14.72. Specific electrical conductivity (Ω^{-1} cm^{-1}) of FeO-SiO_2-TiO_2 melts at 1300 °C [77]

K_2O-MgO-SiO_2

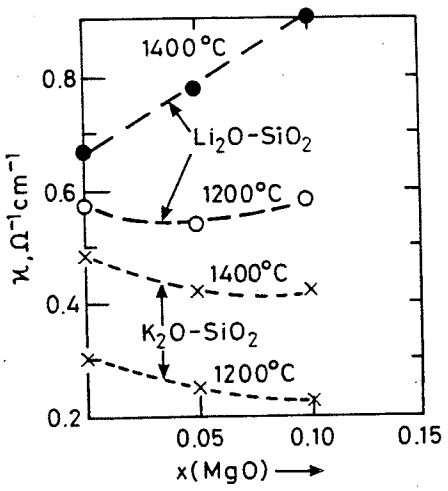


Fig. 14.73. Specific electrical conductivity of 0.2 K_2O-xMgO-(0.8-x) SiO_2 and Li_2O-xMgO-(0.8-x) SiO_2 melts at 1200 and 1400 °C [85]

K_2O-SiO_2-TiO_2

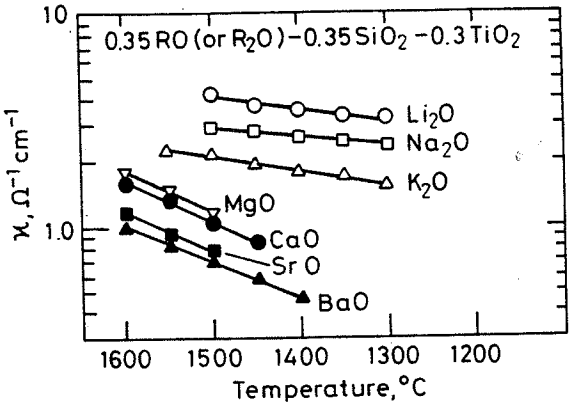


Fig. 14.74. Specific electrical conductivity of 0.35 M_2O - 0.35 SiO_2 - 0.3 TiO_2 and 0.35 MO - 0.35 SiO_2 - 0.3 TiO_2 melts as a function of temperature [19]

Li_2O-MgO-SiO_2

Specific electrical conductivities of two compositions are given in Fig. 14.73.

Li_2O-SiO_2-TiO_2

The specific electrical conductivity of a single composition in this system is given in Fig. 14.74.

MgO-MnO-SiO_2

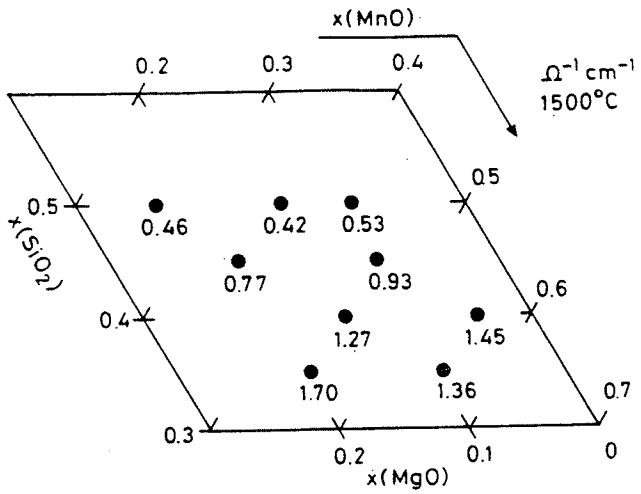


Fig. 14.75. Specific electrical conductivity of MgO-MnO-SiO_2 melts at 1500 °C [90]

$MgO\text{-}Na_2O\text{-}SiO_2$

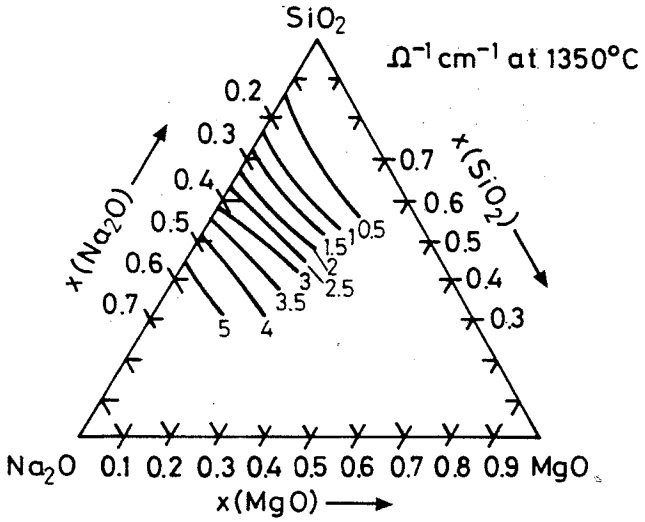


Fig. 14.76. Iso-electrical conductivity (Ω^{-1} cm^{-1}) contours for $MgO\text{-}Na_2O\text{-}SiO_2$ melts at 1350 °C [69]

$MgO\text{-}SiO_2\text{-}TiO_2$

The specific electrical conductivity of a single composition of this system is given in Fig. 14.74 [19].

$MnO\text{-}SiO_2\text{-}TiO_2$

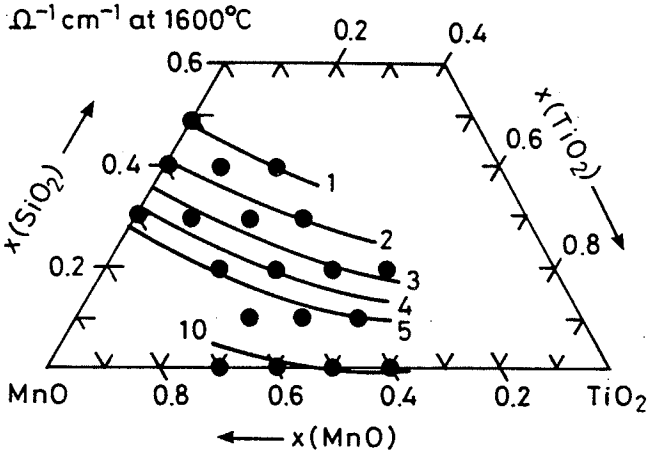


Fig. 14.77. Iso-electrical conductivity (Ω^{-1} cm^{-1}) contours for the $MnO\text{-}SiO_2\text{-}TiO_2$ system at 1600 °C [91]

$Na_2O\text{-}SiO_2\text{-}TiO_2$

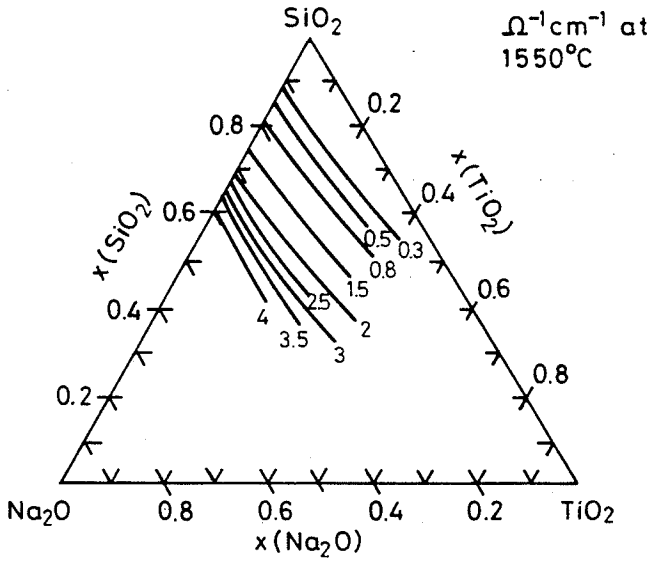


Fig. 14.78. Iso-electrical conductivity (Ω^{-1} cm^{-1}) contours of $Na_2O\text{-}SiO_2\text{-}TiO_2$ melts at 1550 °C [94]

$Na_2O\text{-}SiO_2\text{-}ZnO$

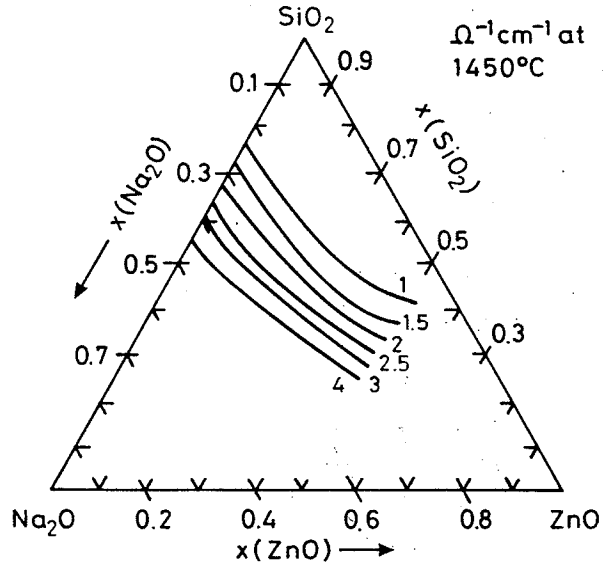
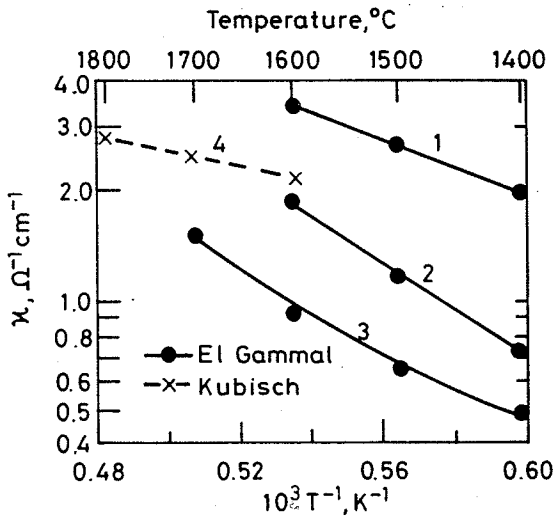


Fig. 14.79. Iso-electrical conductivity contours at 1450 °C for the $Na_2O\text{-}SiO_2\text{-}ZnO$ system [125]

14.2.4 Quaternary systems

Al_2O_3-CaF_2-CaO-MgO



Slag No.	Mass % Al_2O_3	CaF_2	CaO	MgO
1	27.1	47.6	23.4	2.0
2	40.1	33.0	21.9	4.0
3	32.7	14.0	52.4	1.3
4	30	30	20	20

Fig. 14.80. Specific electrical conductivity of Al_2O_3-CaF_2-CaO-MgO melts dependent on reciprocal temperature [11, 103]

Al_2O_3-CaF_2-CaO-SiO_2

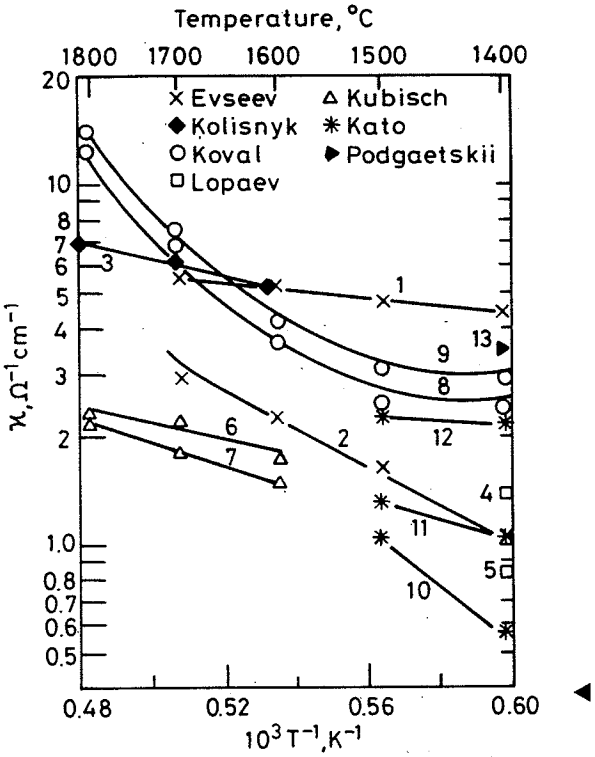
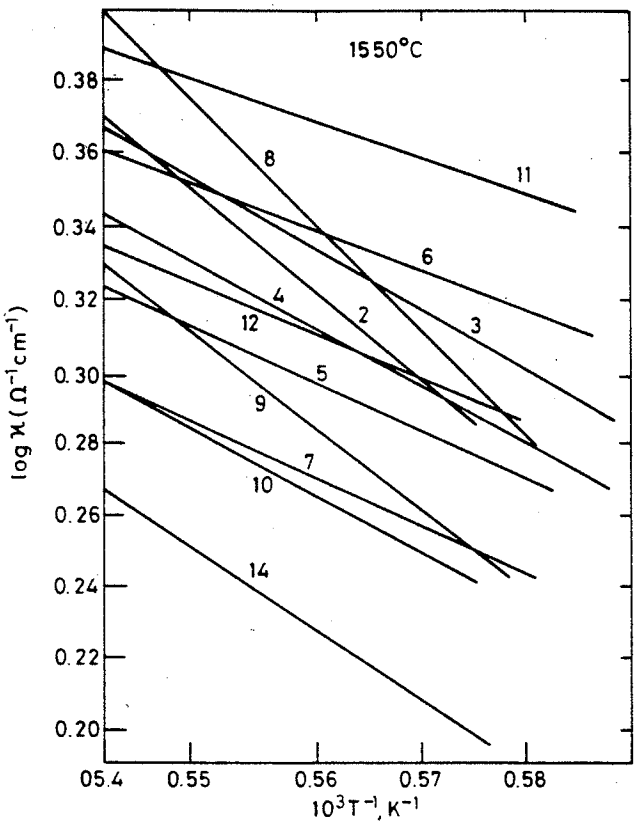


Fig. 14.81. Specific electrical conductivities of Al_2O_3-CaF_2-CaO-SiO_2 melts as a function of reciprocal temperature [2, 9, 22, 46, 103, 105, 131]. Further Ref. [47]



Slag No.	Mole fraction, x Al_2O_3	CaF_2	CaO	SiO_2
1	0.230	0.680	0.074	0.016
2	0.193	0.573	0.218	0.016
3	0.175	0.523	0.286	0.016
4	0.162	0.477	0.346	0.015
5	0.143	0.436	0.406	0.015
6	0.179	0.545	0.219	0.057
7	0.168	0.511	0.217	0.104
8	0.172	0.489	0.284	0.055
9	0.155	0.464	0.280	0.101
10	0.145	0.423	0.275	0.152
11	0.151	0.450	0.345	0.054
12	0.142	0.418	0.340	0.100
13	0.128	0.381	0.340	0.151
14	0.118	0.358	0.333	0.191

Fig. 14.82. Specific electrical conductivities of Al_2O_3-CaF_2-CaO-SiO_2 melts as function of reciprocal temperature [132]

Slag No.	Mass % Al_2O_3	CaF_2	CaO	SiO_2
1	2.3	87.3	2.0	3.7
2	25.3	60.4	10.5	2.7
3	26.6	52.3	19.1	1.8
4	20	65	5	10
5	15	10	50	25
6	42	12	42	4
7	30	30	20	20
8	23.9	65.1	5.1	2.8
9	20.2	63.3	9.5	4.2
10	12.8	8.2	39.5	39.5
11	11.4	9.0	34.8	34.8
12	8.7	37.7	26.8	26.8
13	32.6	63.2	1.0	1.0

Al_2O_3-CaF_2-CaO-TiO_2

Koval et al [46] have reported specific electrical conductivity values of 2.8, 3.0, 4.1, 7.1 and 13.2 Ω^{-1} cm^{-1} at 1400, 1500, 1600, 1700 and 1800 °C, respectively, for a slag 17.3 % Al_2O_3 - 66.9 % CaF_2 - 3 % CaO - 6.8 % (TiO_2 + Ti_2O_3)

Al_2O_3-CaF_2-MgO-SiO_2

Kubisch et al [103] have reported specific electrical conductivity values of 0.95, 1.2, 1.4, 1.7 (Ω^{-1} cm^{-1}) for 1600, 1700, 1800 and 1900 °C, respectively, for 40 % Al_2O_3 - 40 % CaF_2 - 5 % MgO - 15 % SiO_2

Al_2O_3-CaO-Cr_2O_3-SiO_2

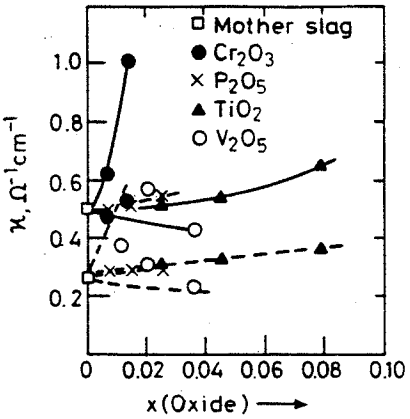


Fig. 14.83. The effect of additions of Cr_2O_3, P_2O_5, TiO_2 and V_2O_5 on specific electrical conductivity of 0.14 Al_2O_3 - 0.43 CaO - 0.43 SiO_2 [105] at 1400 and 1500 °C

Al_2O_3-CaO-FeO_x-SiO_2

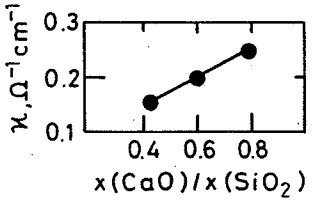


Fig. 14.84. The effect of basicity on specific electrical conductivity of 2.6 % Al_2O_3-CaO - 33.7 % FeO-SiO_2 melts at 1300 °C [77]

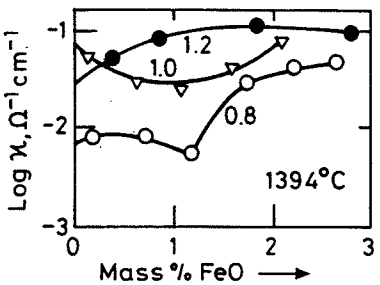
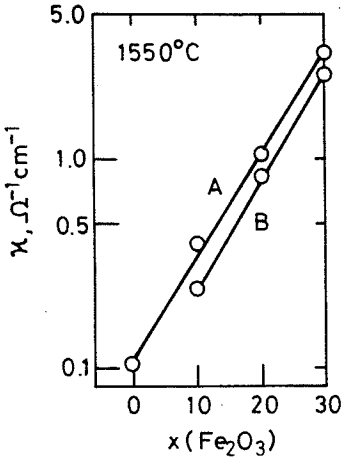


Fig. 14.85. The effect of FeO additions and basicity, B = (% CaO/% SiO_2) on the specific electrical conductivity of 11.5 % Al_2O_3-CaO-FeO-SiO_2 melts at 1394 °C [134]



A = Al_2O_3 - 0.35 CaO-Fe_2O_3 - 0.35 SiO_2
B = Al_2O_3 - 0.233 CaO-Fe_2O_3 - 0.467 SiO_2

Fig. 14.86. Specific electrical conductivities of melts from the system, (0.3-x) Al_2O_3-CaO-xFe_2O_3-SiO_2 containing x (CaO + SiO_2) = 0.70 [135]

Al_2O_3-CaO-MgO-SiO_2

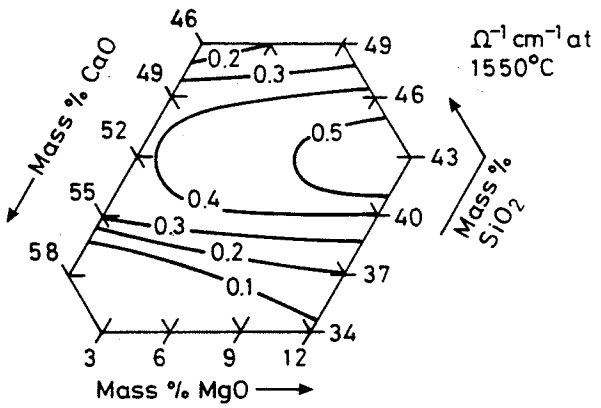
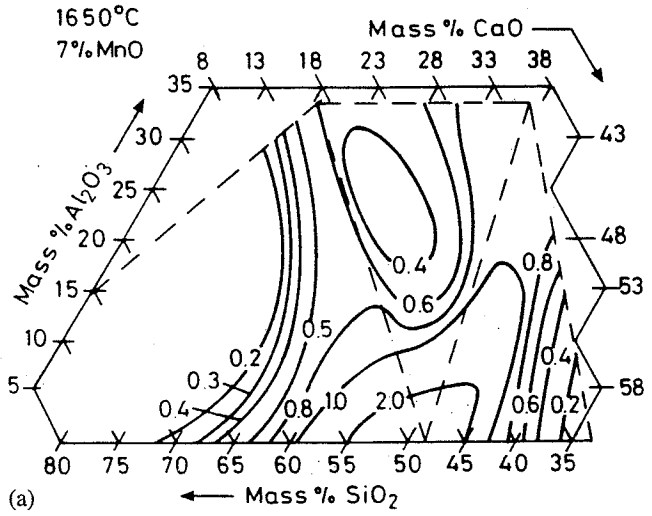


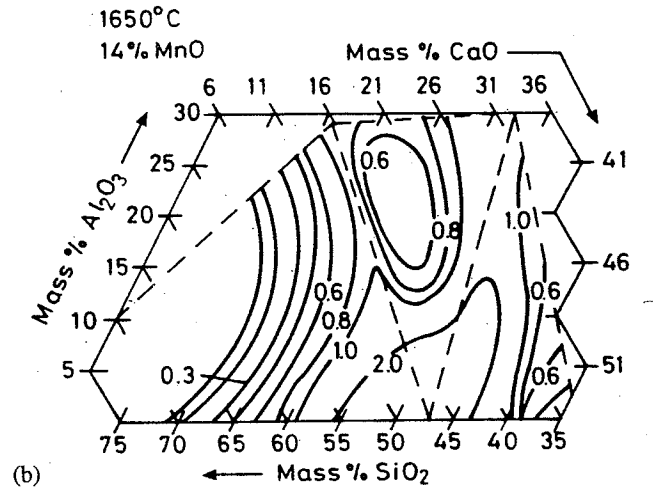
Fig. 14.87. Iso-electrical conductivity (Ω^{-1} cm^{-1}) contours for 5 % Al_2O_3-CaO-MgO-SiO_2 melts at 1550 °C [108]

Tab. 14.3. Experimental values reported for the specific electrical conductivity of Al_2O_3-CaO-MgO-SiO_2 slags [87, 105 – 108, 136]. Further Ref. [137]

						κ (Ω^{-1} cm^{-1})					
Reference	Slag No.	Al_2O_3	CaO	MgO	SiO_2	1350 °C	1400 °C	1450 °C	1500 °C	1550 °C	1600 °C
Winterhager [133]	1	18.9	35.8	5.7	39.6	0.048	0.071	0.103	0.147	0.205	
	2	17.9	33.9	10.7	37.5	0.060	0.097	0.140	0.199	0.274	
	3	5.0	35.0	10.0	50.0	0.083	0.116	0.159	0.216	0.287	
	4	4.5	31.7	9.0	54.8	0.052	0.076	0.107	0.147	0.199	
	5	4.0	28.3	8.1	59.6	0.034	0.050	0.072	0.101	0.139	
	6	3.5	25.0	7.4	64.1	0.022	0.032	0.046	0.065	0.091	
	7	4.7	38.4	9.5	47.4	0.091	0.135	0.186	0.254	0.341	
	8	4.5	41.6	9.0	44.9	0.110	0.159	0.215	0.292	0.385	
	9	4.2	45.8	8.3	41.7	0.197	0.266	0.355	0.461	–	
	10	4.8	33.7	13.4	48.1	0.097	0.141	0.192	0.257	0.335	
	11	4.6	32.3	16.9	46.2	0.122	0.160	0.224	0.299	0.389	
	12	4.4	30.7	21.1	43.8	0.075	0.191	0.263	0.354	0.460	
	13	10.4	33.0	9.5	47.1	0.060	0.091	0.129	0.175	0.234	
	14	15.0	31.3	8.9	44.8	0.052	0.079	0.110	0.151	0.104	
	15	20.0	29.5	8.4	42.1	0.043	0.068	0.091	0.137	0.284	
Nesterenko [108]		5	43	3	49				0.180	0.191	0.230
		5	40	6	49				0.212	0.239	0.258
		5	46	3	46				0.307	0.359	0.420
		5	43	6	46				0.331	0.412	0.450
		5	40	9	46				0.350	0.438	0.462
		5	49	3	43				0.364	0.438	0.502
		5	46	6	43				0.387	0.472	0.535
		5	43	9	43				0.412	0.496	0.557
		5	40	12	43				0.440	0.506	0.591
		5	52	3	40				0.198	0.350	0.438
		5	49	6	40				0.220	0.410	0.475
		5	46	9	40				0.248	0.435	0.482
		5	43	12	40				0.269	0.451	0.500
		5	55	3	37				0.034	0.050	0.230
		5	52	6	37				0.060	0.110	0.268
		5	49	9	37				0.095	0.160	0.306
		5	46	12	37				0.128	0.213	0.310
		5	55	3	34				0.057	0.090	0.110
		5	49	9	34				0.054	0.110	0.190
Rennie [112]	A6	22.3	6.0	29.0	41.4				0.260	0.319	0.388
	B6	31.3	5.6	22.4	41.4				0.142	0.192	0.244
Sarkar [106, 107]		20	38	4	38				0.190	0.246	0.282
		20	36	8	36				0.234	0.280	0.344
		26	35	4	35				0.150	0.212	0.270
		26	33	8	33				0.190	0.270	0.315
Kato [105]		21.9	36.7	1.5	39.6		0.33		0.58		
		21.6	36.4	3.0	39.0		0.36		0.62		
		21.1	35.6	5.2	38.2		0.38		0.63		
Adachi [87]	1	20	5	25	50		.056	.075	.105	.155	.190
	2	25	5	20	50		.018	.026	.053	.065	.090
	3	30	5	15	50		.011	.017	.030	.046	.070
	4	20	5	20	55		.013	.020	.032	.046	.078
	5	25	5	15	55		.0095	.015	.023	.038	–
	6	15	5	20	60		.008	.013	.021	.032	.054
	7	20	5	15	60		.0033	.007	.012	.020	.031
	8	25	5	10	60		.0022	.0043	.008	.015	–
	9	30	10	20	60		.021	.032	.054	.082	.11

Al_2O_3-CaO-MnO-SiO_2





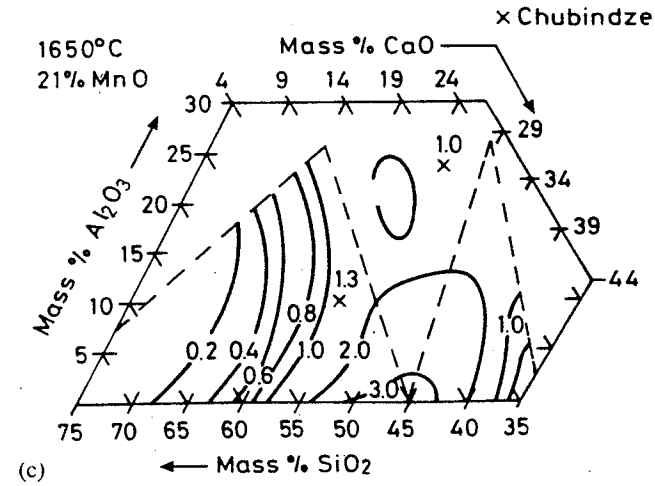


Fig. 14.88 a-c. Iso-electrical conductivity (Ω^{-1} cm^{-1}) of Al_2O_3-CaO-MnO-SiO_2 melts at 1650 °C with (a) 7 % MnO, (b) 14 % MnO and (c) 21 % MnO [104, 138]. Further Ref. [105]

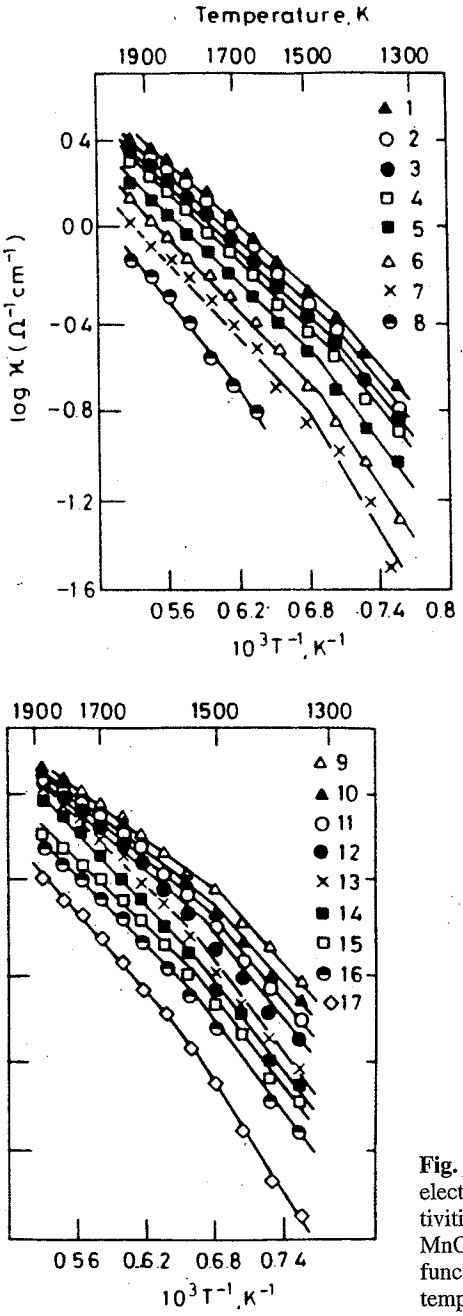


Fig. 14.89. Specific electrical conductivities of Al_2O_3-CaO-MnO-SiO_2 melts as a function of reciprocal temperature [138]

Slag No.	Mass %			
	Al_2O_3	CaO	MnO	SiO_2
1	11.5	11.5	45	32
2	12	12	43	33
3	13	13	40	34
4	15	15	37	33
5	16.5	16.5	34	33
6	20.5	20.5	29	30
7	23	24	23	30
8	30	32	10	27
9	4	10	48	38
10	4.3	10.7	46	39
11	4.5	11.5	43	41
12	5	12	41	42
13	5.5	13.5	38	43
14	6	14.5	35.5	44
15	7	16.5	32	44.5
16	8	19.5	27.5	45
17	10	24	20	46

Al_2O_3-CaO-P_2O_5-SiO_2

The effect of additions of P_2O_5 on specific electrical conductivity of 0.14 Al_2O_3 - 0.43 CaO - 0.43 SiO_2 slag at 1400 and 1500 °C is shown in Fig 14.83 [105].

Al_2O_3-CaO-SiO_2-TiO_2

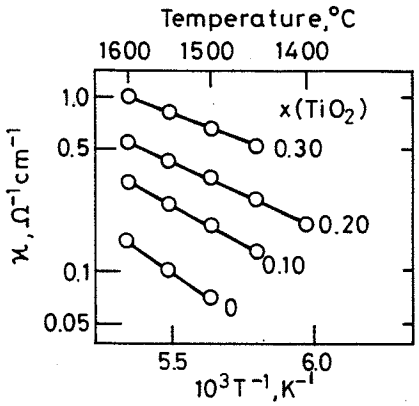


Fig. 14.90. Specific electrical conductivities (0.3 - x) Al_2O_3 - 0.35 CaO - 0.35 SiO_2 - xTiO_2 melts as a function of reciprocal temperature [132], see Fig. 14.83. Further Ref. [105].

Al_2O_3-CaO-SiO_2-V_2O_5

The effect of additions of V_2O_5 on the specific electrical conductivity of 0.14 Al_2O_3 - 0.43 CaO - 0.43 SiO_2 at 1400 and 1500 °C is shown in Fig. 14.83 [105].

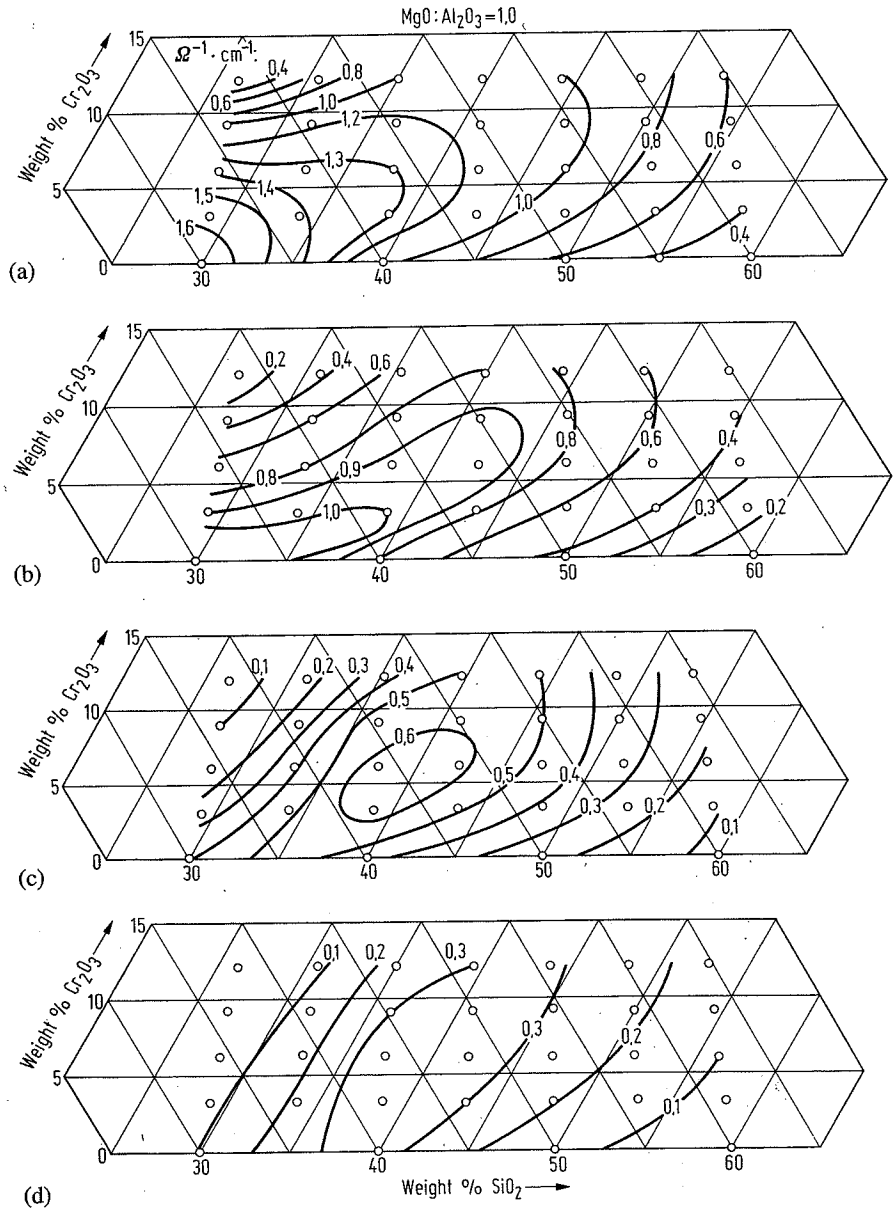


Fig. 14.91 a-d. Iso-electrical conductivity (Ω^{-1} cm^{-1}) of Al_2O_3-Cr_2O_3-MgO-SiO_2 melts with (% MgO/% Al_2O_3) = 1 at (a) 1800, (b) 1700, (c) 1600 and (d) 1500 °C [139]. Further Ref. [112]

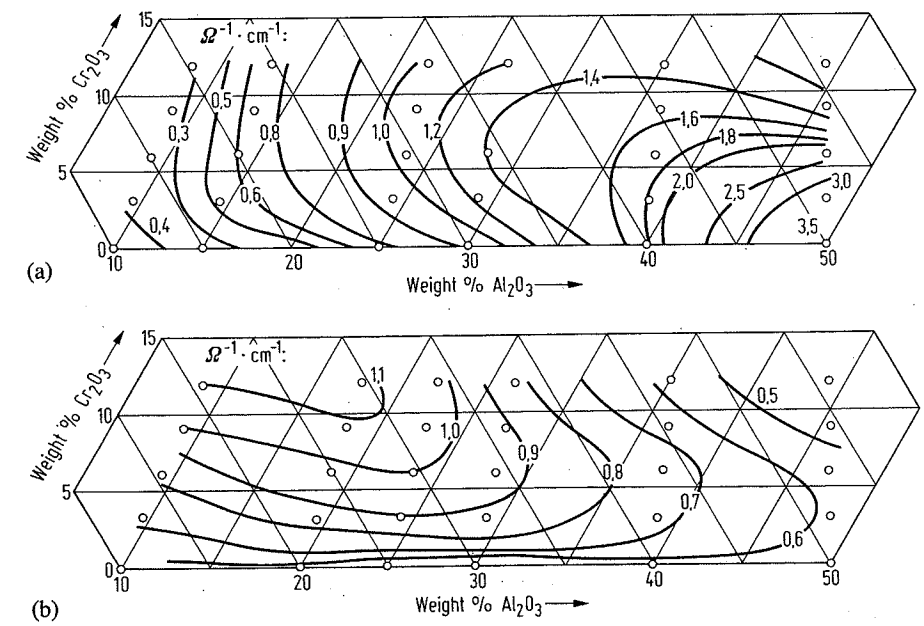
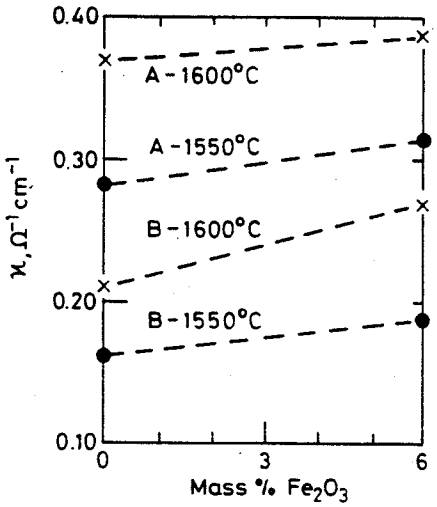


Fig. 14.92 a,b. Iso-electrical conductivity (Ω^{-1} cm^{-1}) contours of Al_2O_3-Cr_2O_3-MgO-SiO_2 melts at 1800 °C with (a) (% Al_2O_3/% SiO_2) = 0.5 and (b) (% MgO/% SiO_2) = 0.5 [136]. Further Ref. [112]

Al_2O_3-Fe_2O_3-MgO-SiO_2



Slag	% Al_2O_3	% MgO	% SiO_2
A	24.0	31.6	43.2
B	32.5	23.0	43.8

Fig. 14.93. The effect of additions of Fe_2O_3 on the specific electrical conductivity of Al_2O_3-FeO-MgO-SiO_2 melts [112]

Al_2O_3-Fe_2O_3-Na_2O-SiO_2

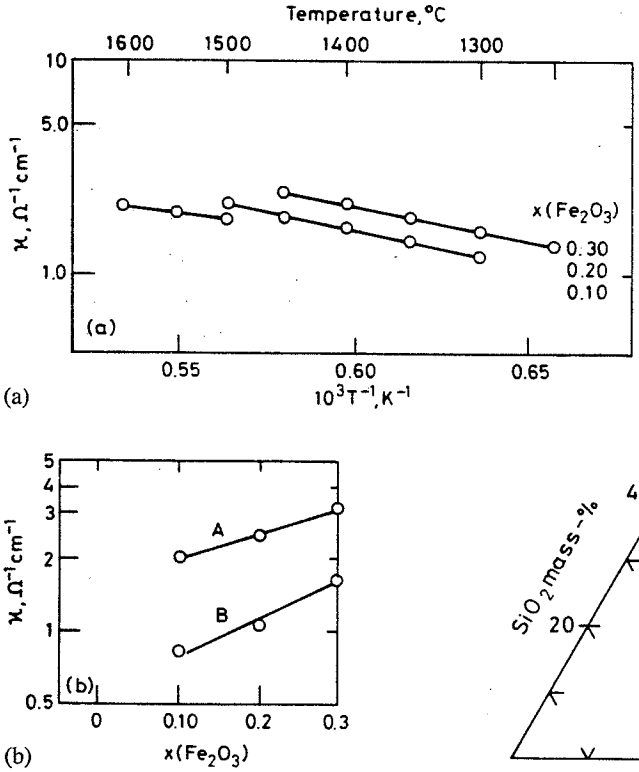


Fig. 14.94 a,b. Specific electrical conductivities of (a) slag A [(0.3-x) Al_2O_3-x Fe_2O_3 - 0.35 Na_2O - 0.35 SiO_2] as a function of reciprocal temperature and (b) slags A and B [(0.3-x) Al_2O_3-x Fe_2O_3 - 0.21 Na_2O - 0.49 SiO_2] melts as a function of mole fraction, x, Fe_2O_3 content [135]

Al_2O_3-Na_2O-SiO_2-TiO_2

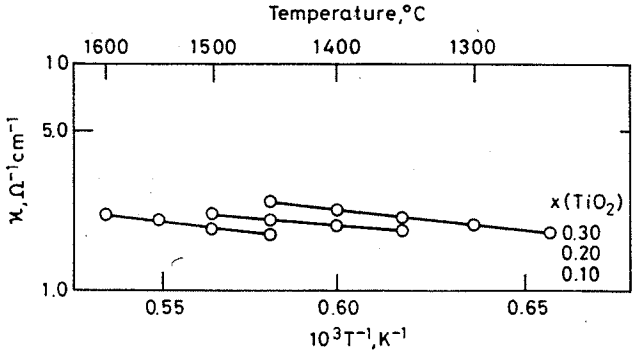


Fig. 14.95. Specific electrical conductivities of (0.3-x) Al_2O_3-0.35 Na_2O-0.35 SiO_2-xTiO_2 melts as a function of reciprocal temperature [135]

CaF_2-CaO-MgO-SiO_2

Koval et al [46] have reported specific electrical conductivities of 4.7, 6.2, 8.8 and 11.7 (Ω^{-1} cm^{-1}), respectively, for temperatures of 1400, 1500, 1600 and 1700 °C for 86 % CaF_2 + 10 % CaO + 1% MgO + 3 % SiO_2.

CaO-FeO-MgO-SiO_2

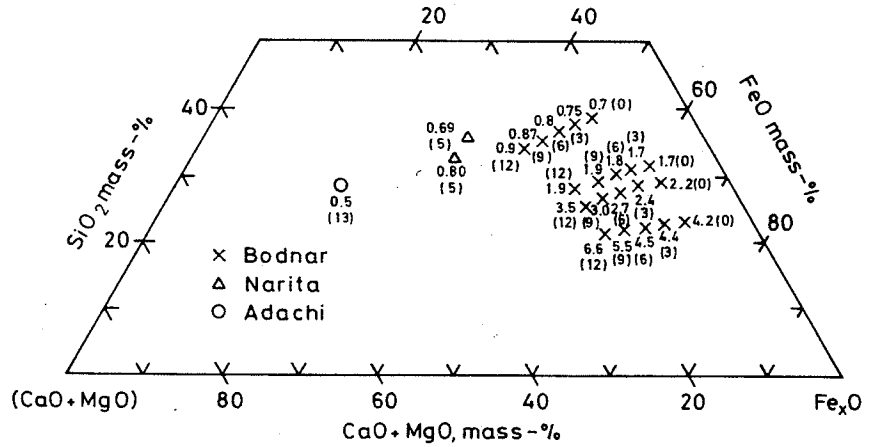
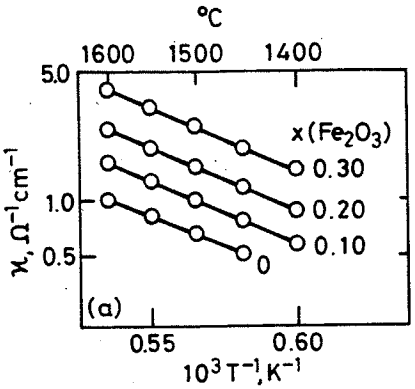


Fig. 14.96. Specific electrical conductivities (Ω^{-1} cm^{-1}) at 1300 °C plotted as a pseudoternary (CaO + MgO) - Fe_xO-SiO_2, the values in parenthesis refer to mass % MgO in slag [63, 77, 78]

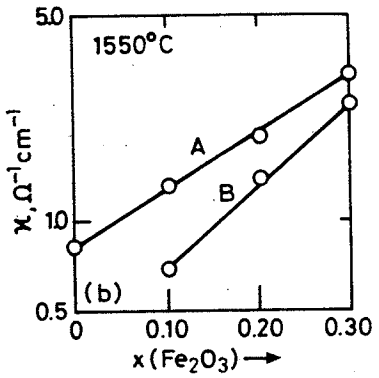
Jiao and Themelis [140] have reported that specific electrical conductivities at 1500 °C and 1400 °C, can be calculated using equations (14.4) and (14.5) respectively for slags within the following composition range: x(Al_2O_3) 0 - 0.03; x(CaO) 0 - 0.47; x(FeO) 0.1 - 0.83; x(MgO) 0 - 0.25; x(SiO_2) 0.17 - 0.49

1500 °C: ln κ (Ω^{-1} cm^{-1}) = –4.45 + 9.15 x(FeO) + 5.34 (x(CaO) + x(MgO)) (14.4)
1400 °C: ln κ (Ω^{-1} cm^{-1}) = –5.21 + 9.92 x(FeO) + 5.94 (x(CaO) + x(MgO)) (14.5)

$CaO-Fe_2O_3-SiO_2-TiO_2$



(a)



(b)

Fig. 14.97 a,b. Specific electrical conductivities of (a) slag A = (0.35 CaO - x(Fe_2O_3) - 0.35 SiO_2 - (0.3-x) TiO_2) as a function of reciprocal temperature and (b) slags A and B (0.233 CaO-x Fe_2O_3 - 0.35 SiO_2 - (0.467-x) TiO_2) as a function of mole fraction (x) Fe_2O_3 [135]

$CaO-MgO-MnO-SiO_2$

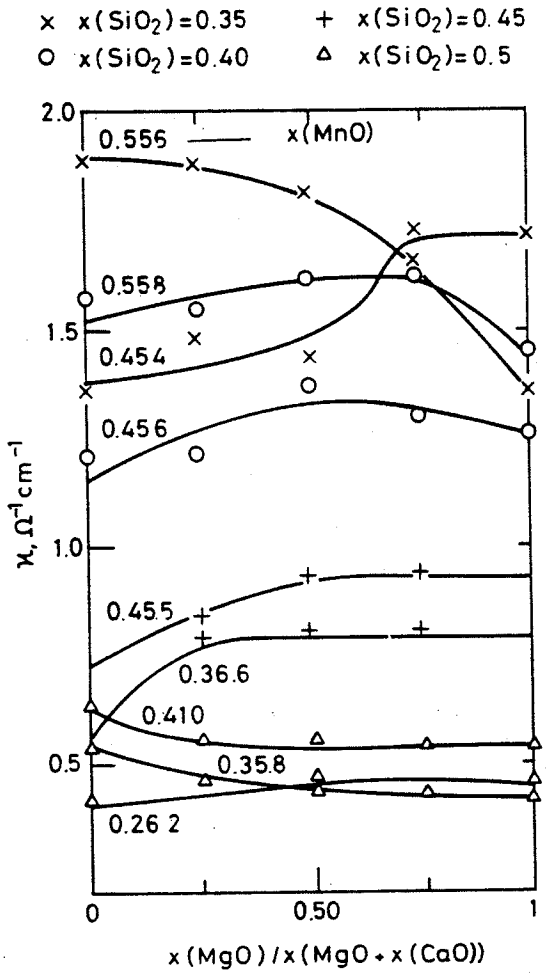


Fig. 14.98. Specific electrical conductivity of CaO-MgO-MnO-SiO_2 melts at 1500 °C as a function of (x(MgO)/(x(MgO) + x(CaO)) [90]

Jiao and Themelis [140] reported that specific electrical conductivities at 1500 °C and the activation energies of CaO-MgO-MnO-SiO_2 melts can be calculated by equations (14.6) and (14.7) respectively

$$\kappa\ (\Omega^{-1}\,cm^{-1}) = -3.34 + 6.41\ x(CaO) + 6.75\ x(MgO) + 8.06\ x(MnO) \quad (14.6)$$

$$E_\kappa\ (kJ\ mol^{-1}) = 24.44 - 28.2\ x(CaO) - 34.1\ x(MgO) - 28.8\ x(MnO) \quad (14.7)$$

$Fe_2O_3-Na_2O-SiO_2-TiO_2$

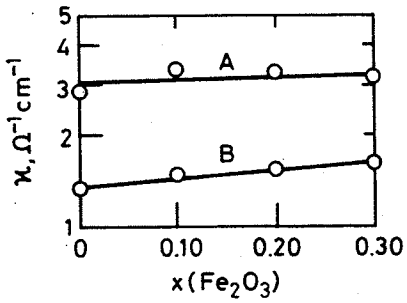
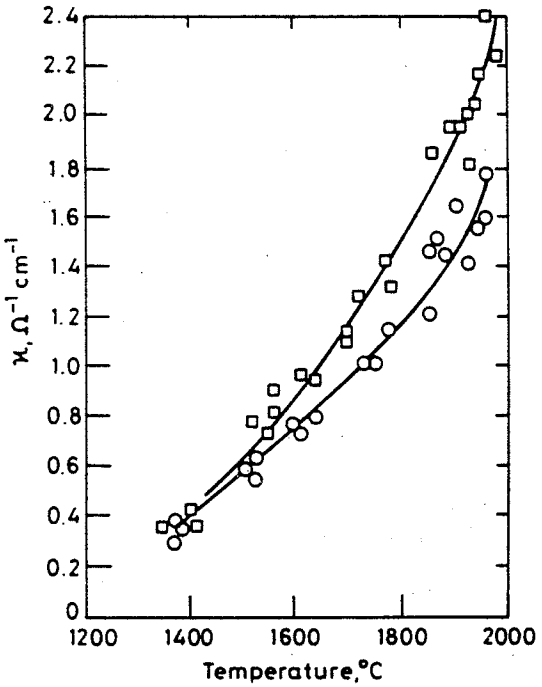


Fig. 14.99. Specific electrical conductivities of slag A (x Fe_2O_3 - 0.21 Na_2O - 0.49 SiO_2 - (0.3-x) TiO_2 and slag B (x Fe_2O_3 - 0.35 Na_2O - 0.35 SiO_2 - (0.3 x) TiO_2 at 1550 °C as a function of mole fraction x (Fe_2O_3) [135]

14.2.5 Systems with five and more components

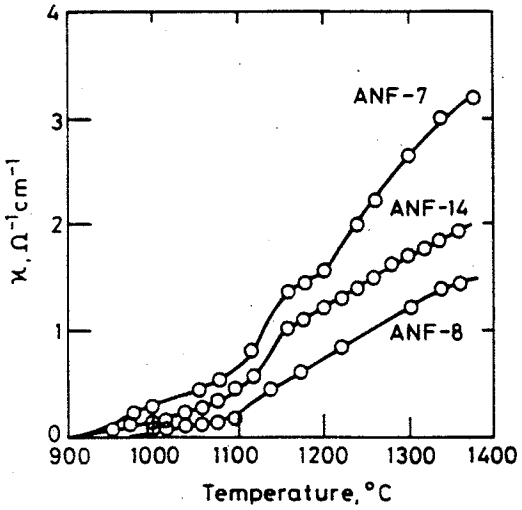
Al_2O_3-CaF_2-CaO-FeO-MgO-MnO-SiO_2



	Mass %								
	SiO_2	Al_2O_3	CaO	MgO	MnO	CaF_2	FeO	S	P
○	33.8	16.8	6.6	5.2	23.4	13.3	13.3	.007	.073
□	29.9	15.0	8.0	3.8	28.0	11.9	3.7	-	-

Fig. 14.100. Specific electrical conductivity of Al_2O_3-CaF_2-CaO-FeO-MgO-MnO-SiO_2 melts as a function of temperature [22]

Al_2O_3-CaF_2-CaO-Fe_2O_3-MgO-SiO_2



Slag	Mass %					
	CaF_2	CaO	Al_2O_3	MgO	SiO_2	Fe_2O_3
ANF - 7	63.2	1.0	32.6	-	1.7	1.5
ANF - 8	51.8	20.5	24.0	-	-	3.5
ANF -14	33.8	11.8	9.4	11.3	12.6	2.3

Fig. 14.101. Specific electrical conductivities of Al_2O_3-CaF_2-CaO-Fe_2O_3-MgO-SiO_2 melts as a function of temperature [51]

Al_2O_3-CaF_2-CaO-MgO-SiO_2

Tab. 14.4. Specific electrical conductivities reported for Al_2O_3-CaF_2-CaO-MgO-SiO_2 system

Reference	Composition/mass %						κ/Ω^{-1} cm^{-1}					
	Al_2O_3	CaF_2	CaO	MgO	SiO_2	Impurities	1400 °C	1500 °C	1600 °C	1700 °C	1800 °C	1900 °C
Nikitin [26]	3.6	6.9	56.0	9.7	22.4			0.09	0.25	0.56		
	3.6	26.2	48.0	5.4	16.2			0.59	0.84	1.17		
	3.9	10.9	45.5	20.0	20.0			0.25	0.30	0.71		
Evseev	33.2	19.2	31.5	11.3	1.9	Σ Fe = 0.5	0.62	0.87	1.23	2.2		
Filippov [9]	40.5	20.4	27.8	7.3	2.5	Σ Fe = 0.7	0.43	0.74	1.39	2.0		
	54.2	3.8	36.3	3.7	1.2	Σ Fe = 0.5	0.10	0.22	0.47	1.0		
Kubisch [103]	30	35	10	15	10				1.4	1.7	2.0	2.2
	35	25	20	5	15				1.45	1.8	2.2	2.5
	30	30	20	15	5				2.2	2.5	2.8	2.85
	35	25	20	10	10				1.4	1.8	2.2	2.5
Lopaev [2]	14	80	3	1	2		1.7					
	30	14	40	10	6		1.1					
Koval [46]	38.3	17.2	28.0	12.3	2.1	FeO = 0.5	1.35	1.65	2.32	4.65	10.0	
	34.3	14.3	31.1	11.4	5.2	FeO = 0.5	1.52	1.86	2.62	4.94	10.6	
Podgaetskii [131]	9.4	53.8	11.8	11.9	12.6	Fe_2O_3 = 2.3	2.0					
Gerasimenko [141]	2.4	31.4	14.1	1.2	7.9	Fe_2O_3 = 4.2 TiO_2 = 38.4	1.75					

Al_2O_3-CaO-Cr_2O_3-MgO-SiO_2

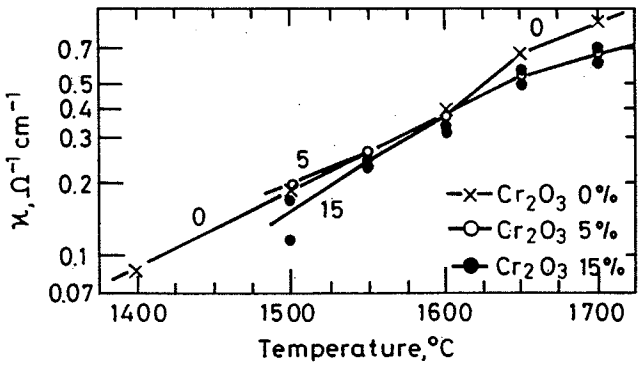


Fig. 14.102. The effect of Cr_2O_3 additions on the temperature dependencies of specific electrical conductivities of 30 % Al_2O_3 - 20 % CaO - 30 % MgO - 20 % SiO_2 slag [111]

Al_2O_3-CaO-FeO-MgO-SiO_2

Tab. 14.5. Specific electrical conductivities of Al_2O_3-CaO-FeO-MgO-SiO_2 slags [143]

Slag	Mass %					IC (Kl.Kappa), $\Omega^{-1}cm^{-1}$		
	Al_2O_3	CaO	FeO	MgO	SiO_2	1400 °C	1500 °C	1600 °C
1	10.7	20.8	7.4	8.2	61.2	0.024	0.047	0.070
2	10.1	25.0	6.7	7.4	49.5	0.032	0.056	0.073
3	9.3	30.8	5.9	6.5	47.3	0.036	0.060	0.067
4	8.5	35.1	5.2	5.7	45.6	0.053	0.094	0.100
5	7.1	40.4	4.4	6.0	44.1	0.100	0.176	0.220
6	5.9	46.2	3.6	4.3	41.5	0.064	0.218	0.244

Al_2O_3-CaO-MgO-MnO-SiO_2

Tab. 14.6. Specific electrical conductivities, activation energies and in A for Al_2O_3-CaO-MgO-MnO-SiO_2 melts [90]?

Mole fraction, x					κ at 1500 °C Ω^{-1} cm^{-1}	$\ln A_\kappa$	Eκ kJ mol^{-1}
Al_2O_3	CaO	MgO	MnO	SiO_2			
0.125	0.179	0.059	0.262	0.375	0.38	11.754	119.8
0.25	0.179	0.059	0.262	0.25	0.33	15.509	177.1
0.30	0.179	0.059	0.262	0.20	0.22	18.837	232
0.125	0.105	0.035	0.36	0.375	0.52	11.680	114
0.25	0.105	0.035	0.36	0.25	0.46	15.227	168
0.30	0.105	0.035	0.36	0.20	0.30	17.193	203
0.112	0.146	0.048	0.356	0.338	0.63	11.286	105
0.225	0.146	0.048	0.356	0.225	0.52	12.054	119
0.27	0.146	0.048	0.356	0.180	0.38	15.477	175
0.10	0.225	0.075	0.30	0.30	0.29	11.45	104.3
0.20	0.225	0.075	0.30	0.20	0.67	12.11	116.6
0.24	0.225	0.075	0.30	0.16	0.58	15.29	165.5
0.30	0.225	0.075	0.30	0.10	0.40	17.0	196.1
0.10	0.109	0.036	0.445	0.30	1.10	10.26	82
0.20	0.109	0.036	0.445	0.20	1.03	12.0	108.6
0.24	0.109	0.036	0.445	0.16	0.86	12.77	122.5
0.30	0.109	0.036	0.445	0.10	0.69	16.37	178.8
0.087	0.070	0.024	0.556	0.263	1.77	11.15	88.1
0.175	0.070	0.024	0.556	0.175	1.60	10.52	80.3
0.262	0.070	0.024	0.556	0.088	1.34	11.37	95.4
0.35	0.070	0.024	0.556	0	0.98	13.18	126.6
0.087	0.047	0.047	0.556	0.263	1.69	12.39	107
0.175	0.047	0.047	0.556	0.175	1.48	12.31	107.8
0.21	0.047	0.047	0.556	0.14	1.41	13.05	119.4
0.262	0.047	0.047	0.556	0.088	1.23	14.63	144.7

Al_2O_3-CaO-MgO-SiO_2-TiO_2

Specific electrical resistivity values of 1.25, 1.79 and 2.22 Ω^{-1} cm^{-1} have been reported for 1400, 1500 and 1550 °C, respectively for a slag containing 13.8 % Al_2O_3 - 16.3 % CaO - 16.3 % MgO - 23,3 % SiO_2 - 30.2 % TiO_2 [144]

14.2.6 Blast furnace slags

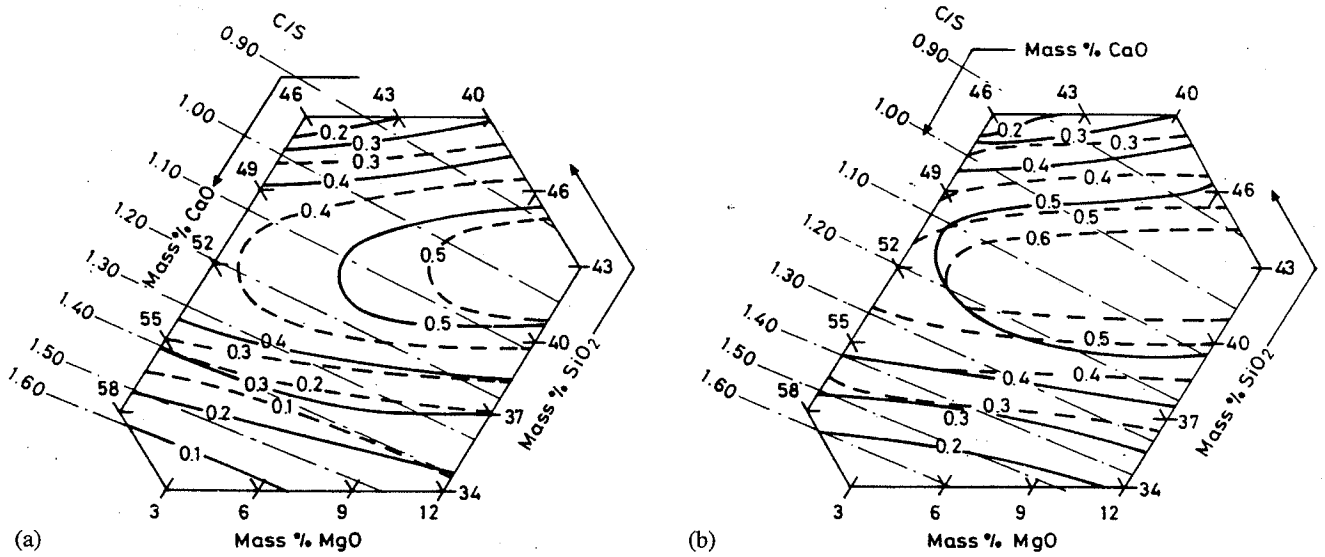


Fig. 14.103 a,b. The effect of 0.5 % K_2O on the specific electrical conductivities (Ω^{-1} cm^{-1}) of 5 % Al_2O_3-CaO-MgO-SiO_2 (blast furnace type slags) at (a) 1550, (b) 1600 °C; — . 0 % K_2O; – –, 0.5 % K_2O — . — (% CaO/% SiO_2) ratio [108]. Synthetic blast furnace slags see Tab. 14.2.

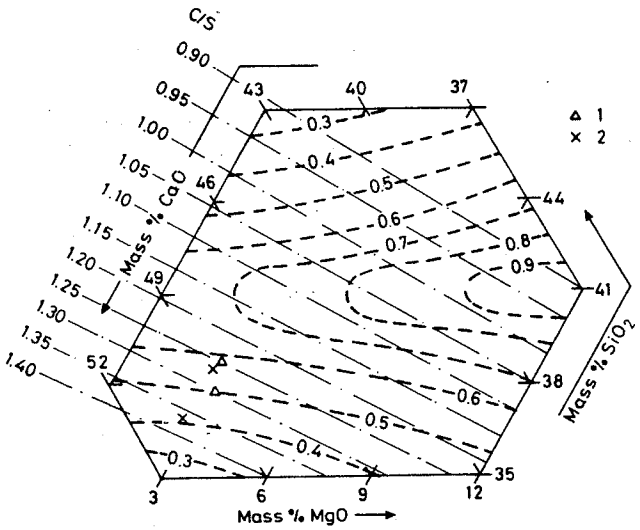


Fig. 14.104. Specific electrical conductivities (Ω^{-1} cm^{-1}) for blast furnace slags containing constant contents of Al_2O_3 (10 %) MnO (1%) K_2O (0.5 %) and S (1 %) [145] at 1500 °C. Further Ref. [137]

14.2.7 BOS slags

It has been suggested [10] that the value [63] shown as a circle in Fig. 14.96 lies closest to BOS compositions.

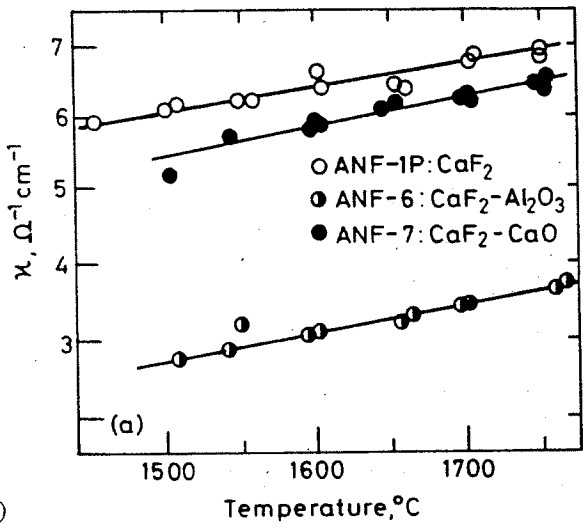
14.2.8 Coal slags

Bates [146] proposed the empirical relationship shown in equation (14.8) for coal slags with both high and low FeO_x contents.

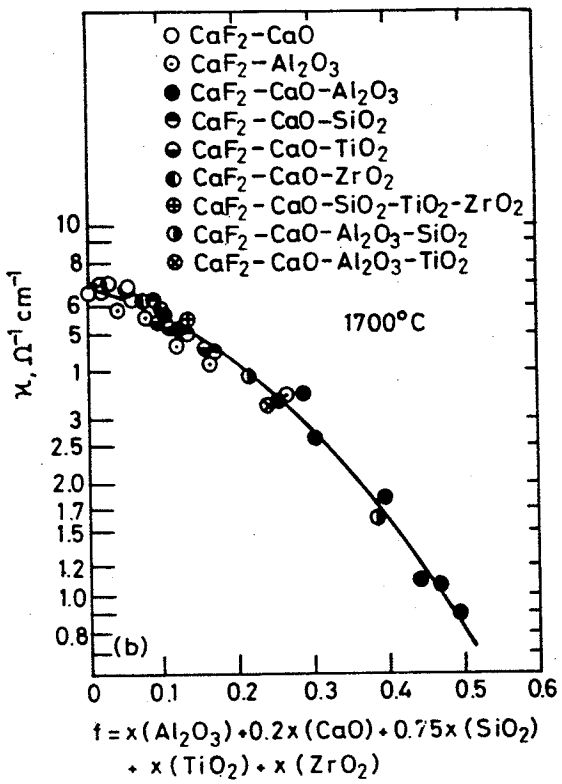
$$\log \kappa = 0.697 - 2.86\ F \text{ where } F = \%\ SiO_2/(\%\ CaO + \%\ Fe_2O_3 + \%\ MgO + SiO_2) \quad (14.8)$$

Further Refs. [157-159]

14.2.9 ESR slags



(a)



(b)

Fig. 14.105 a,b. Specific electrical conductivities of ESR slags as (a) a function of temperature [25] and (b) at 1700 °C as a function of the compositional parameter, f [62]

Ogino [62] has reported equation (14.9) for the specific electrical conductivities of ESR slags for the compositional range;
$x(Al_2O_3)$ 0-0.38; $x(SiO_2)$ 0-0.17; $x(TiO_2)$ = 0-0.18; $x(ZrO_2)$ 0-0.15; x(CaO) 0-0.65 and for temperatures between 1550 - 1780 °C;

$$\kappa\ (\Omega^{-1}\ cm^{-1}) = \exp(1.911 - 1.38\ F - 5.69\ F^2) + 0.39 \times 10^{-2}\ (T - 1700) \quad (14.9)$$

where $F = x(Al_2O_3) + 0.2 \times (CaO) + 0.75 \times (SiO_2 + 0.5\ (x(TiO_2) + x(ZrO_2))$ and T = °C

14.3 References in Chapter 14

[1] Zhmoidin, G. I.: Ind. Lab. 35 (1969), 668
[2] Lopaev, B. E.: Plyshevskii; A. A., Stepanov, V. U.: Automat. Weld. (USSR) (1966) (1), 31 – 34
[3] Winterhager, H.; Kammel, R.; Gad, A.: Forschungsber. des Landes Nordrhein-Westfalen, Westdeutscher Verlag, Köln, Opladen (1970), 2115
[4] Mitchell, A.; Cameron, J.: Metall. Trans. 2 (1971), 3361
[5] Ogino, K.; Hashimoto, H.; Hara, S.: Tetsu-to-Hagane 64 (1978), (2), 41
[6] Solomons, C.: Physico-chemical measurements in metals research (Ed. R. A. Rapp), Vol. 2, Publ. Wiley, New York, (1970), 35
[7] Robbins, G. D.: J. Electrochem. Soc. 116 (1969), 813
[8] Evseev, P. P.: Automat. Weld. (USSR) (1967), (11), 42
[9] Evseev, P. P.; Filippov, A. F.: Izv VUZ Chern. Met. (1965) (3), 74 – 76
[10] Mills, K. C.; Keene, B. J.: Intl. Materials Rev. 32 (1987), 1 – 120
[11] El Gammal, T.; Hajduk, M.: Arch. Eisenhüttenwes. 49 (1978), 235
[12] Gerischer, H.: Z. Elektrochem. 58 (1954), 9
[13] Warburg, E.: Ann. Phys. 6 (1901), 125
[14] Ueda, K.; Doi, S.; Kondo, A.: Nippon Kinzoku Gakkaishi 47 (1983), 17 – 20
[15] Handbook of properties of liquid iron and slag. Publ. Iron and Steel Inst. Japan, Tokyo (1972), 244 – 286
[16] Ogino, K.; Hara, S.: Properties of Electroslag Remelting slags. Publ. Iron and Steel Inst. Japan, Tokyo (1972), 63 – 74
[17] Mills, K. C.; Powell, J. S.: The physico-chemical properties of slags. Part VI. Review of electrical conductivity data for CaF_2-based slags. NPL Chem Rept. 103 (1979). Publ. National Physical Laboratory, Teddington, UK
[18] Mills, K. C.; Keene, B. J.: Intl. Metals Review 26 (1981), 21 – 69
[19] Kozuka, Z.; Morinaga, K.: Handbook of physico-chemical properties at high temperatures. Ed. Y. Kawai and Y. Shiraishi. Publ. Iron and Steel Inst. Japan (1988), Chapter 8, 216 – 243
[20] Elyutin, V. P.; Mitin, B. S.; Nagabin, A.: Inorganic Mater. 8 (1972), 416 – 418
[21] Fay, H.: J. Phys. Chem. 70 (1966), 890
[22] Kolisnyk, V. N.: Autom. Weld. (USSR), 1964, (4), 9 – 13
[23] Kraus, S.; Neuhof, G.: Dr.-Ing. Thesis, Bergakad. Freiberg, 1973
[24] Baak, T.: Acta Chem. Scand 9 (1955), 8
[25] Ogino, K.; Hashimoto, H.; Hara, S.: Tetsu-to-Hagane 64 (1978) (2), 225
[26] Nikitin, B. M.; Chuilo, N. M.: Izr. VUZ Chern Met. 1963, (8), 60 – 67
[27] Morinaga, K.; Ohta, Y.; Yanagase, T.: Nippon Kinzoku Gakkaishi 50 (1986), 907 – 914
[28] Bacon, G.; Mitchell, A.; Nishizaki, R. M.: Metall. Trans. 3 (1972), 631
[29] Sveshkov, Yu. V.; Kalmykov, V. A.; Kamenetskii, M. V.; Nasredinov, V. Kh.: Inorg. Mater. 13 (1977), 850
[30] Goncharov, A. E.; Manakov, A. I.; Kovalev, P. K.: Tr. Inst. Met. Akad. Nauk SSSR Uralsk. Nauk Tsentr. 27 (1972) (4), 159
[31] Isotomin, A. A.; Lepinskikh, K. B.; Kokarev, S. N.; Drozdov, I. V.: Russ. Metall. 1980 (3), 60 – 63
[32] Hoster, T.; Pötschke, J.: Arch. Eisenhüttenwes. 54 (1983), 389 – 394
[33] Stepanov, V. V.; Lopaev, B. E.: Automat. Weld (USSR) 20 (1967) (2), 46
[34] Manakov, A. I.; Lepinskikh, B. M.; Bukmoyarov, O. I.; Goncharov, A. E., Solovev, G. I.: Izv. VUZ Chern met. (1975), (12) 14
[35] Kammel, R.; Winterhager, H.: Erzmetall, 9, (1968), 399
[36] Podgayetskiy, V. V.: Avtom. Svarka 9, (1956), (4), 30
[37] Dancy, E.; Derge, D. G.: Trans. Metall. Soc. AIME 236 (1966), 1642 – 1648
[38] Inouye, H.; Tomlinson, J.; Chipman, J.: Trans. Farad. Soc. 49 (1953), 796-801
[39] Fischer, W. A.; vom Ende, H.: Arch. Eisenhüttenwes. 21 (1950), 217 – 224
[40] Fischer, W. A.; vom Ende, H.: Arch. Eisenhüttenwes. 22 (1951), 417 – 423
[41] Mizoguchi, S.: Phys. Stat. Solid. 41 (1977), 591
[42] Panish, M. B.: J. Phys. Chem. 63 (1959), 1337 – 1338
[43] Cohen, J.: J. Appl. Phys. 28 (1957), 795
[44] Seemann, H. E.: Phys. Rev. 31 (1928), 119
[45] Sosman, R.: Properties of silica. Washington (Amer. Chem. Soc. Monograph), 1927, 528
[46] Koval, A. E.; Chuiko, N. M.; Degtyarev, V. S.; Denison, S. L.; Nikitin, B. M.: Izv. VUZ Chern Met. 13, (1970) (12), 71 – 74
[47] Chmelar, L.: Sb. VSB Ostrave Rada. Hutnicka. 13, (1967), 75 – 85
[48] Zhmoidin, G. I.: Russ. Metall (1970) (3), 48
[49] Ogino, K.; Hara, S.; Hashimoto, H.: Tetsu-to-Hagane 64, (1978), 232
[50] Mori, K.; Matsushita, Y.: Tetsu-to-Hagane 38 (1952), 531
[51] Evseev, P. P.; Filippov, A. F.: Izv. VUZ Chern. Met (1967) (1), 55 – 60
[52] Povolotskii, D.; Mischenko, V. Y., Vyatkin, G. P.; Puzylev, A. V.: Izv VUZ Chern. Met. (1970) (12), 8
[53] Zhmoidin, G. I.: Izv. Akad Nauk SSSR Metally (1970), 69
[54] Sikora, B.; Zielinski, M.: Hutnik 41 (1974), 433
[55] Ogino, K.; Nishiwaki, A.: cited in ref. 16, 72
[56] Sivkov, S. L.; Suchilnikov, S. I.; Pavlov, V. A.: V. Sb. Proiz-vo Ferrosplavov, M (1975) (4), 45 – 52
[57] Bockris, J. O'M.; Kitchener, J. A.; Ignatowicz, S.; Tomlinson, J. W.: Disc. Farad. Soc. 4 (1948), 265 – 281
[58] Sumita, S.; Morinaga, K.; Yanagase, T.: Nippon Kinzoku Gakkaishi, 24 (1983), 35
[59] Bockris, J. O'M; Kitchener, J. A.; Ignatowicz, S.; Tomlinson, J. W.: Trans. Farad. Soc. 48 (1952) 75 – 91
[60] Baak, T.: Acta Chem. Scand. 8 (1954), 75 – 91
[61] Starkova, N. K.; Starkov, L. N.; Sryvalin, I. T.: Russ. J. Phys. Chem. 46, (1972), 901
[62] Ogino, K.; Hara, S.; Nagai, S.: Trans ISI Jap. 20 (1980), B16
[63] Adachi, A.; Ogino, K.: Yoyuen (Fused Salts) 1 (1961), 151
[64] Adachi, A.; Ogino, K.: Nippon Kinzoku Gakkaishi 22 (1958), 661
[65] Mori, K.; Matsushita, Y.: Tetsu-to-Hagane 38 (1952), 283 – 288
[66] Keller, H.; Schwerdtfeger, K.; Hennesen, K.: Metall. Trans 10B (1979), 67
[67] Ogino, K.; Nishiwaki, A.: results cited in ref. 66
[68] Morinaga, K.; Suginohara, Y.; Yanagase, T.: Nippon Kinzoku Gakkaishi, 39 (1975), 1312
[69] Kawahara, M.; Ozima, Y.; Morinaga, K.; Yanagase, T.: Nippon Kinzoku Gakkaishi 48 (1978), 618 – 623
[70] Belikova, I.; Sultanova, I. G.; Nikiforova, G. N.; Faurnova, A. N.: Tr. Leningr. N-i. Proekt. In-ta Osnovn. Khim Prom-sti 17 (1975), 26 – 29
[71] Alyabin, V. I.; Ershov, V. A.; Kuznetsova, V. L.; Reutovich, L. N.; Sultanova, L. G.: Protsessy i Apparaty v Khim Elektrotermii i v Prve Fosfor Solei, L. (1984), 17 – 22
[72] Licko, T.; Danek, V.: Silicaty 27 (1983) (1), 55 – 62
[73] Baak, T.: Acta Chem. Scand. 8 (1954), 1727
[74] Berryman, R. A.; Sommerville, I. D.: Proc. of 3rd Intl Conf. on Metall. Slags and Fluxes, held in Glasgow, June 1988. Publ. Inst of Metals, London, 202 – 206
[75] Mori, K.: Tetsu-to-Hagane 42 (1956), 8
[76] Weijnarth, A.: Trans. Electrochem. Soc. 65 (1934), 177
[77] Narita, K.; Onoye, T.; Ishii, T.; Uemara, K.: Tetsu-to-Hagane 61 (1975), 2943 – 2951
[78] Bodnar, L.; Bobok, L.; Schmiedl, J.: Proc. 3rd Intl. Conf. on „Molten Salt Chemistry", Wydawn University, Wroclaw, 1979, 7 – 13
[79] Bobok, L.; Bodnar, L., Schmiedl, J.: Hutn Listy 37 (1982), 419 – 424
[80] Fuwa, A.; Bessho, M.: Nippon Kogyo Kaishi 104 (1988), 37 – 41
[81] Victorovich, G. S.; Diaz, C.; Vallbacka, D. K.: Proc. of 2nd Intl. Symp. Metall. Slags and Fluxes, held in Lake Tahoe Nev. 1984. Edited H. A. Fine, D. R. Gaskell. Publ. Metall Soc. AIME, Warrendale, PA, 907 – 924
[82] Mori, K.; Matsushita, Y.: Tetsu-to-Hagane 42 (1956), 1024 – 1029
[83] Nikitin, Y.; Lopatin, V. M.; Barmin, L. N.: Izv VUZ Chern. Met. (1973) (2), 17 – 18
[84] Lepinskikh, B. M.; Esin, O. A.; Shaurin, S. B.: Zhur. Priklad Khim, 21 (1956), 1813 – 1821
[85] Sasek, L.; Meissnerova, H.; Persin, J.: Sb vys Sk Chem-Technol Praze, Chem. Technol. Silik, L4 (1973), 87 – 138
[86] Wakabayashi, H.; Terai, R.: 91 (1983), 335 – 338
[87] Adachi, A.; Ogino, K.: Yoguen (Fused Salts) 7 (1964), 370
[88] Segers, L.; Fontana, A.; Winard, R.: Trans. Inst. Min Metall Engrs. 88C (1979), 53
[89] Segers, L.; Fontana, A.; Winard, R.: Electrochim, Acta 23 (1978), 1281
[90] Segers, L.; Fontana, A.; Winard, R.: Can. Metall. Q. 22 (1983), 429 – 435
[91] Shinozaki, N.; Mizoguchi, K.; Suginohara, Y.: Nippon Kinzoku Gakkaishi 42 (1978), 162 – 168
[92] Arimori, T.; Ihara, M.; Yamamoto, T.: Yoyuen (Fused Salts) 5 (1962), 785
[93] Tomlinson, J. W.: The Physical Chemistry of Melts (1953), 22
[94] Nakamura, T.; Suginohara, Y., Yanagase, T.: Nippon Kinzoku Gakkaishi. 39 (1975), 48-52
[95] Bonetti, G.: Riv. Stn. Sper. Vetro (Murano, Italy) 6 (1976) (6), 241 – 250
[96] Ito, H.; Yanagase, T.: Trans. Jap. Inst Metals 1 (1960), 115 – 120
[97] Saito, H.; Goto, K.; Someno, M.: Tetsu-to-Hagane 55 (1969), 539 – 549
[98] Bockris, J. O'M; Mellors, G. W.: J. Phys. Chem, 60 (1956), 1321 – 1327
[99] Ejima, T.; Watanabe, Y.; Kameda, M.: Nippon Kinzoku Gakkaishi 32 (1968), 1250 – 1256
[100] Pal, U.; Debroy, T.; Simkovich, G.: Can Metall. Q 23 (1984), 295 – 302
[101] Itai, Y.; Masuda, G.; Mizoguchi, K.; Suginohara, Y.: Kyushu Kogyo Daigaku Kenkyu Hokoku, Kogaku, No. 41 (1980), 95 – 101
[102] Mischenko, V. Ya.; Vyatkin, G. P.; Krichevets, M. I.; Rusakov, L. N.: Sb. Nauch. Tr. Chelyabinsk. Politekhn. Inst. 1971, (93), 35

[103] Kubisch, C.; Jäger, H.; Hars, G.: Paper presented at Conf. 'ESR-material for the future?' University of Strathclyde, Glasgow, 1979, The Metals Society
[104] Baisanov, S. O.; Takenov, T. D.; Gabdullin, T. G.; Buketov, E. A.: VINITI Tech Report 1770 – 81 (1981)
[105] Kato, M.; Minowa, S.: Trans ISI Jap. 9 (1969), 39 – 46
[106] Sarkar, S. B.: Trans. ISI Jap. 29 (1989), 348 – 351
[107] Sarkar, S. B.; Sen, P. K.: Trans Ind. Inst. Met. 31 (1978), 276 – 278
[108] Nesterenko, S.; Khomenko, V. M.: Russ. Metall. (1985) (2), 42 – 45
[109] Martin, A. E.; Derge, G.: Trans AIME 154 (1943), 104
[110] Kammel, R.; Winterhager, H.: Erzmetall. 18 (1965), 9
[111] Downing, J. H.; Urban, L.: J Metals (1966), 337 – 344
[112] Rennie, M. S.; Howat, D. D.; Jochens, P. R.: J. South Afr. Inst. Min. Metall. (1972), 1 – 9
[113] Zhilo, N. L.; Ostretsova, I. S.; Charushnikova, G. V.; Pershina, R. F.: Izv VUZ Chern Met. (1982) (4), 35 – 40
[114] Lyutikov, R. A.; Tsylev, L. M.: Izv. Akad Nauk SSR, Otd Tekh. Nauk Met i Gorn Delo (1963) (1), 41
[115] Kusuda, Y.; Nakamura, T.; Yanagase, T.: Nippon Kinzoku Gakkaishi 41 (1977), 160 – 164
[116] Kuroda, K.; Kawahara, M.; Morinaga, K.; Yanagase, T.: Nippon Kinzoku Gakkaishi 46 (1982), 275 – 280
[117] Gudenau, H. W.; Petry, J.: Fachber. Hüttenprax. Metallweiterverarb. 19 (1981), 32
[118] Nesterenko, C. V.; Andronov, V. N.: Izv VUZ Chern. Met. (1974) (2), 40
[119] Kawahara, M.; Morinaga, K.; Yanagase, T.: Nippon Kinzoku Gakkaishi 43 (1979), 55 – 60
[120] Nikolina, E. S.; Aziev, R. G.; Karyazin, I. A.; Morozov, A. A.: Khim. Prom-st. (1982) (4), 222 – 224
[121] Belikova, I. K.; Sultanova, I. G.; Nikiforova, G. N.: Tr Leningr. Gos. Nauchno-Issled Proektn Inst Osnovn. Khim Prom. -sti. 13 (1975), 18 – 22
[122] Sato, H.; Sakao, H.: Electrochem. 26 (1958), 569 (as cited in ref. 15)
[123] Morinaga, K.; Suginohara, Y.; Yanagase, T.: Nippon Kinzoku Gakkaishi 38 (1974), 658 – 662
[124] Mori, K.: Tetsu-to-Hagane 46 (1960), 134 – 140 and 143, (1957) 379 – 380 (cited in ref. 15, 272)
[125] Sumita, S.; Takano, H.; Morinaga, K.; Yanagase, T.: Nippon Kinzoku Gakkaishi 46 (1982), 280 – 285
[126] Li, X.; Jeanloz, R.: Geophys Res Lett. 14 (1987), 1075 – 1078
[127] Mori, K.; Matsushita, Y.: Tetsu-to-Hagane 38 (1952), 365
[128] Mori, K.; Matsushita, Y.: Tetsu-to-Hagane 38 (1952), 444 – 448
[129] Bogacz, A.; Gospos, J.; Bozena, Z.: Pr. Nauk Inst. Chem. Nieorg. Metal. Pierwiastkow Rzadkich Politech. Wroclaw. 27 (1975), 43 – 55
[130] Kawahara, M.; Morinaga, K.; Yanagase, T.: Nippon Kinzoku Gakkaishi 43 (1979), 309 – 315
[131] Podgaetskii, V. V.; Gerasimenko, L. A.: Automat. Weld. 1960 (11), 84 – 86
[132] Churkin, A. S.; Tsikarev, Y. M.; Toporishchev, G. A.; Lazarev, V. I.; Khasin, G. A.: Fiz-khim Issled metallurg. Protsessov (Sverdlovsk) (1979), (7), 40 – 47
[133] Sokolov, A. E.; Deev, V. I.; Tikhonov, A. I.: Nauch Tr Perm. Politekn. Inst. 135 (1973), 118 – 123
[134] Hofmann, H. B.; Marincek, B.: Archiv Eisenhüttenwes. 25 (1954), 523 – 526
[135] Kusuda, Y.; Nakamura, T.; Morinaga, K.; Yanagase, T.: Kyushu Daigaku Kogaku Shuho. 50 (1977), 133 – 138
[136] Winterhager, H.; Greiner, L.; Kammel, R.: Untersuchungen über die Dichte und die elektrische Leitfähigkeit von Schmelzen der Systeme CaO-Al_2O_3-SiO_2, ·Köln/Opladen (1966). (Forschungsber. des Landes Nordrhein-Westfalen 1630)
[137] Dobovisek, B.: Rud. Metal Zb 29 (1982) (1), 33 – 38
[138] Chubinidze, T. A.; Maisuradze, G. D., Baider, V. D.: Fiziokhim Metall Margantsa 1983, 20/3 (available B. N. Laskorin 50 HXA. Publ. Izd. Nauka, Moskow)
[139] Schlackenatlas. Publ. Verlag Stahleisen mbH, Düsseldorf (1981), 280
[140] Jiao, Q.; Themelis, N. J.: Met. Trans 19B (1988), 133 – 140
[141] Podgaetskii, V. V.; Gerasimenko, L. A.: Automat. Weld. (1960) (11), 84 – 86
[142] Turkeev, M. E.; Nikiforov, Y. A.; Sabitov, M. S.: Metallurgiya i Obogashch (Alma-Alta) (1978) (13), 48-58
[143] Luganov, V. A.; Turkeev, M. E.; Ishchanov, T. K.: Metallurgia i Obogashch (1977) (12), 75 – 83
[144] van der Colf, D.; Howat, D.: J. South Afr. Inst. Min. Metall. 79 (1979), 327 – 332
[145] Nesterenko, S. V.: Russ. Metall 1981 (4), 21 – 24
[146] Bates, J. L.: Electrical conductivity of molten slag – potassium seed relating to open-cycle MHD. Publ. Argone Nat. Lab. Report ANL-77 – 21, (1977), 196
[147] Pollina, R.; Larsen, R.: Eng. Aspects Magnetohydrodyn. 17 (1978), C 6.1-6.6
[148] Cumming, J. W.: J. Inst. Energy 53 (1980), 153 – 154
[149] White, G. S.; Hosler, W. R.; Castallano, T. J.: J. Am. Ceram. Soc. 64 (1981), 649 – 652

15

Thermal conductivities of slags

K. C. Mills and M. Susa

15.1 Introduction

It is customary to measure thermal conductivities (k) from measurements of either heat flux (Q) or thermal diffusivity (a) using the relationships given in equations (15.1) and (15.2), respectively.

$$Q = -k_{eff}\,(dT/dx) = \frac{-k_{eff} \cdot \Delta T}{d} \qquad (15.1)$$

where k_{eff} is the effective thermal conductivity, ΔT the temperature gradient over the distance, d.

$$k_{eff} = a_{eff} \cdot C_p \cdot \rho \qquad (15.2)$$

where C_p and ρ are the heat capacity and density, respectively. The term "effective" is used since the thermal conductivity and diffusivity can contain contributions from various heat transfer mechanisms, viz, the lattice ("phonon") thermal conductivity, k_L, the radiation ("photon") conductivity, k_R, and the electronic thermal conductivity, k_{el}. Under "optically thick" conditions k_{eff} can be derived [1, 2] from equation (15.3).

$$k_{eff} = k_L + k_R + k_{el} \qquad (15.3)$$

15.1.1 Thermal conduction mechanisms

15.1.1.1 Lattice or "phonon" thermal conductivity (k_L)

Heat is transferred through a medium by phonons, which are quanta of energy associated with each mode of vibration in the sample. This mode of conduction is thus referred to as thermal, phonon or lattice conduction. Scattering of the phonons causes a decrease in the thermal conductivity which is therefore sensitive to the structure of the sample. Scattering of the phonons can occur by collisions of the phonons with one another, or by impact with grain boundaries or crystal imperfections, such as pores. Thus a low-density, highly-porous material will have a low thermal conductivity. In glassy, non-crystalline materials it has been suggested [3] that thermal conductivity decreases as the disordering of the silicate network increases.

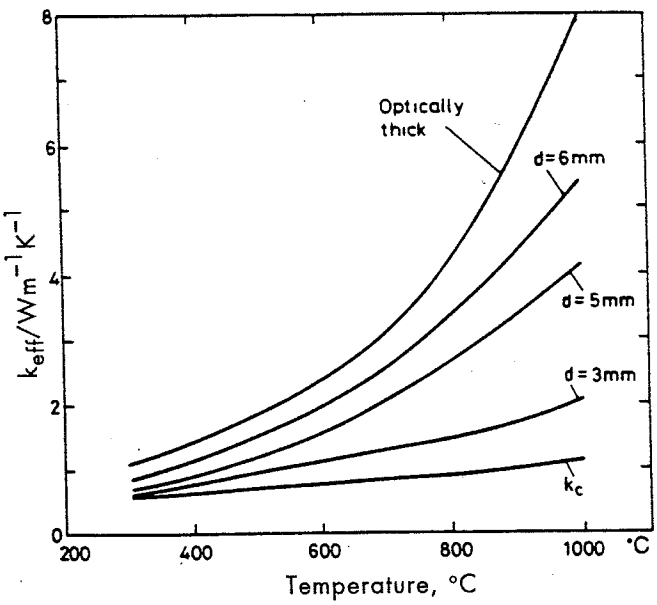


Fig. 15.1. The dependence of the effective thermal conductivity upon the thickness of the specimen

15.1.1.2 Radiation conductivity (k_R)

Measurements of the thermal conductivity of glasses were found to be dependent upon the thickness of the specimens used, **(Fig. 15.1.)**. This behaviour was ascribed to the contribution from radiation conductivity, k_R, which can occur in semi-transparent media like slags. Radiation conductivity occurs by a mechanism involving absorption and emittance of radiant energy by various sections through the medium [1, 2]. Consider a thin section in the slag, radiant energy absorbed by the section will cause it to increase in temperature and consequently radiant heat will be emitted to cooler sections. This process can occur continuously through the medium and it is obvious that the energy transferred in this way will increase with increasing number of sections (ie increasing thickness) until the point is reached where k_R attains a constant value. At this point the slag is said to be "optically thick", and this is usually considered to occur when $\alpha d > 3.5$, where α and d are the absorption coefficient and thickness of the slag sample, respectively.

At high temperature, radiation conduction is frequently the dominant mode of heat transfer, eg in glassmaking more than 90 % of the thermal transfer occurs by radiation conduction. The radiation conductivity can be calculated for an optically-thick sample if steady-state conditions apply and if it is assumed that the absorption coefficient of the medium, α, is independent of wavelength, λ, ie grey-body conditions obtain. For these conditions k_R can be calculated by use of equation (15.4), where σ and n are the Stefan-Boltzmann constant and refractive index, respectively.

$$k_R = \frac{16\,\sigma\,n^2\,T^3}{3\,\alpha} \qquad (15.4)$$

The above equation can not be applied to "optically thin" conditions (ie $\alpha d < 3.5$); for these conditions, equations (15.5) and (15.6) may be used [4, 5] in conjunction with tabulated data for the reflection coefficient, R (= 1 – ϵ) of the boundary and where ϵ is the emissivity and τ is the optical density

$$k_R = 8n^2\sigma\,T^3 \left\{ \frac{(1-R)}{2(1+R)} - \frac{\tau(1-4R+R^2)}{(1+R)^2} \right\} \qquad (15.5)$$

$$k_R = \frac{16n^2\,\sigma\,T^3}{3}\,\gamma\,(\epsilon, \tau) \qquad (15.6)$$

15.1.1.3 Electronic conductivity (k_{el})

It has been suggested that slags containing high concentrations of Fe^{2+} ions could behave like semiconductors in that heat could be transferred by conduction electrons, holes, etc. However, on the basis of electrical conductivity data [6] it can be concluded that electronic conduction only becomes significant when the FeO content of the slag is > 70 %.

15.2 Experimental methods [7 – 9]

The techniques for the determination of thermal conductivity can be divided into three classes: (I) steady-state methods, (II) non-steady state methods, and (III) transient methods. The steady-state methods usually yield k_{eff} values and the non-steady state techniques usually produce thermal diffusivity (a_{eff}) values, which can be converted to thermal conductivity values by use of equation 15.2.

15.2.1 Steady state techniques

15.2.1.1 Linear heat flow method

In this method two disc-shaped specimens are placed on either side of an electrically-heated plate and the temperature profiles across the samples are monitored by thermocouples sited on both faces of the specimen. The apparatus is well insulated to minimise heat losses. In some versions of this method, the total heat flux passing through the samples is determined by calorimeters in contact with the specimens. When high-temperature measurements are required, this technique is usually operated as a comparative method [10].

15.2.1.2 Radial heat flow (RHF) method

In this method the specimen is in the shape of a hollow cylinder **(Fig. 15.2.)** which is positioned in the annulus between two coaxial cylinders with the internal cylinder acting as a radial heat source [11, 12]. The temperature profile across the specimen is determined by thermocouples placed on the inside walls of the two cylinders. This method requires a large isothermal zone in the furnace, which is difficult to achieve at high temperatures. The results contain contributions from radiation conduction and when this technique is used for measurements on liquids, errors can occur from convective heat transfer.

15.2.2 Non-steady state methods

15.2.2.1 Radial wave (RW) method

In this method the slag is placed in a cylindrical crucible situated in the isothermal zone of a furnace, and thermocouples are located on the walls and along the geometric axis of the crucible (the slag). The outside wall of the crucible is then subjected to a variation of temperature and the variation in temperature of the central thermocouple is monitored. There is a phase shift between the input and output which is related to the thermal diffusivity of the slag. In the modification of this apparatus used by Elliott and co-workers [13, 14] the periodic variation in temperature is produced in a wire running along the central axis of the cylindrical crucible, and the phase shift is measured by thermocouples located on the walls of the crucible. The thermal diffusivity values obtained with this method may be vulnerable to errors arising from convective and radiative heat transfer.

15.2.2.2 Modulated beam technique

In this method the specimen is in the form of a disc, which is maintained at a constant temperature, whilst the front face is subjected to a laser beam which produces a periodic variation in temperature of constant frequency. The phase shift between this input and the signal from a temperature sensor in contact with the back face is determined. By carrying out measurements at two or more frequencies, Schatz and Simmons [15] were able to derive values of both a_{eff} and the extinction coefficient. If this method were applied to measurements for liquids, it too would be prone to errors caused by convection.

15.2.3 Transient methods

In these experiments the transient of the temperature-time curve produced by an input of energy is monitored during the short duration of the experiment (10 seconds or less).

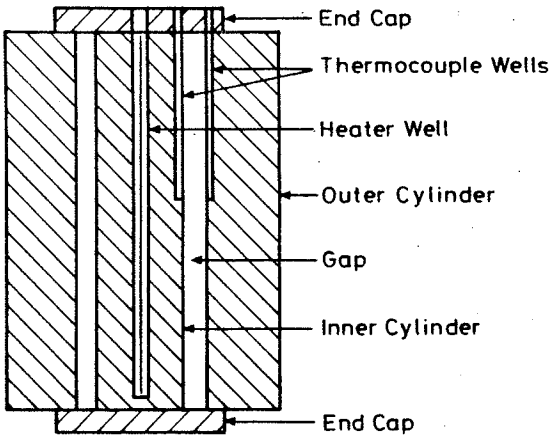


Fig. 15.2. Schematic representation of radial heat flow (or concentric cylinder) apparatus

15.2.3.1 Laser pulse (LP) method

The sample used in this technique is usually a disc of 10 – 15 mm diam x 1 – 2 mm **(Fig. 15.3a)** which may be coated with metallic coatings on both planar surfaces [16, 17]. A laser pulse is directed onto the front face of the specimen and the temperature of the back face is monitored continuously. The temperature transient **(Fig. 15.3b)** exhibits a maximum (ΔT_{max}) and the thermal diffusivity (a) can be calculated from equation (15.7) where $t_{0.5}$ is the time to reach 0.5 ΔT_{max} and d is thickness of the specimen. Corrections are usually made to account for radiation losses.

$$a_{eff} = \frac{1.37\ d^2}{\pi^2\ t_{0.5}} \qquad (15.7)$$

For measurements on liquid slags [18, 19] a laser pulse of short duration is directed onto platinum disc on the surface of the slag **(Fig. 15.4a)** and the temperature transient of this disc is monitored continuously **(Fig. 15.4b)**. Numerical

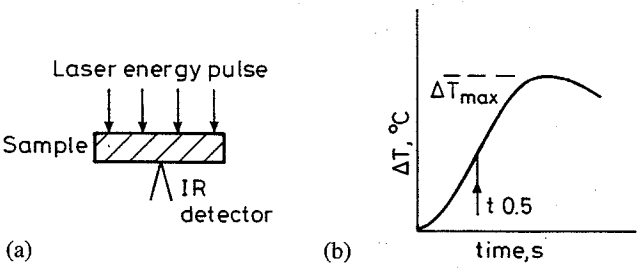


Fig. 15.3 a,b. The laser pulse (LP) method used for determination of the thermal diffusivities of solids showing (a) the specimen assembly and (b) the temperature transient

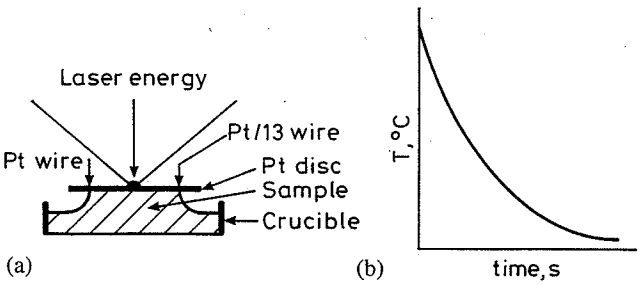


Fig. 15.4 a,b. The laser pulse method used for determinations of the thermal diffusivities of liquids showing (a) the cell assembly used and (b) the temperature transient

analysis have been used to separate k_R and k_L contributions in these experiments [18, 19].

15.2.3.2 Line source (LS) method

In this method [20, 21] current is applied for a short period ca. ls to a long thin wire which is immersed in a cylinder of molten or solid slag (**Fig. 15.5 a**). The wire acts as both heating element and resistance thermometer and the temperature of the wire is monitored continuously during the application of current. The thermal conductivity can be calculated from equation (15.8) but in practice it is usually derived from the slope ($\equiv$ 1/k) of the plot of ΔT as a function of ln time (**Fig. 15.5 b**).

$$\Delta T = \frac{q}{4\pi k} \ln \frac{4at}{r^2 C} \qquad (15.8)$$

where q is the heat input per unit length or wire, r is the radius of the wire and C = exp.γ where γ is Eulers Constant. More recently Nagata and co-workers [22] have used a thin Pt strip in place of a hot wire. The principal advantages of the line source technique are (I) that any convection occurring results in a departure from linearity (Fig. 15.5 b) and (II) k_R is thought to be low in these experiments [23].

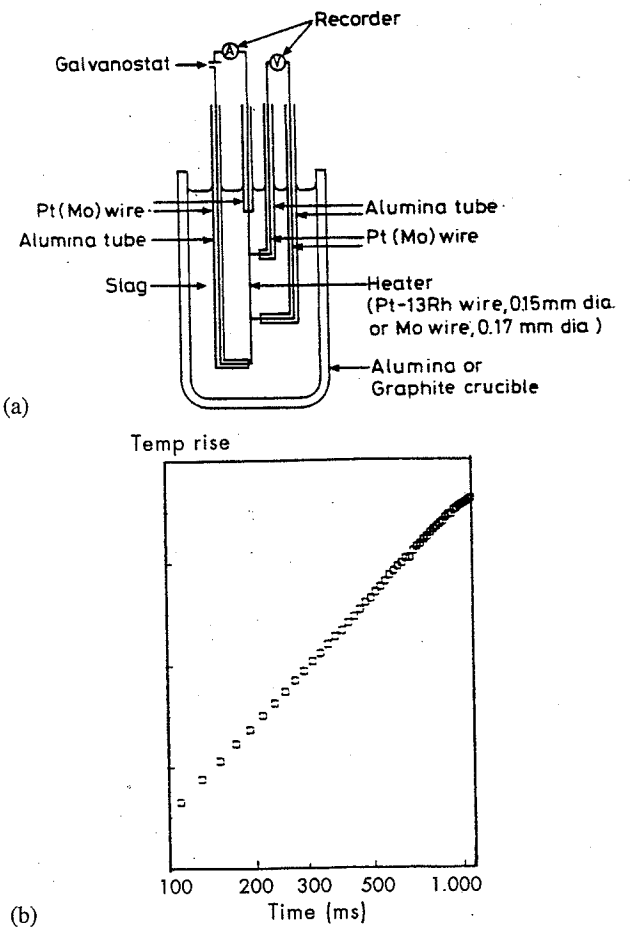


Fig. 15.5 a,b. The line source method (a) schematic drawing of the probe [21] and (b) temperature transient

15.3 Factors affecting thermal conductivity

15.3.1 Solids

15.3.1.1 Crystallinity of sample

The thermal conductivities of crystalline phases tend to be higher than those for glassy phases. Thus the thermal conductivity (or diffusivity) of a slag tends to be dependent upon its thermal history.

15.3.1.2 Porosity of sample

The thermal conductivites of crystalline materials are reduced by the presence of flaws in the lattice such as pores, microcracks. Several equations have been proposed for calculating the effective thermal conductivites, of sintered and powder samples from the thermal conductivity of the theoretically dense solid and the porosity of the sample [24, 25].

15.3.1.3 Glass transition temperature (Tg)

The thermal conductivity of glassy slags goes through a maximum at the glass transition temperature, Tg which is associated with the large increase in thermal expansion coefficient (ie "free volume") which occurs above Tg [26] (see **Fig. 15.6**).

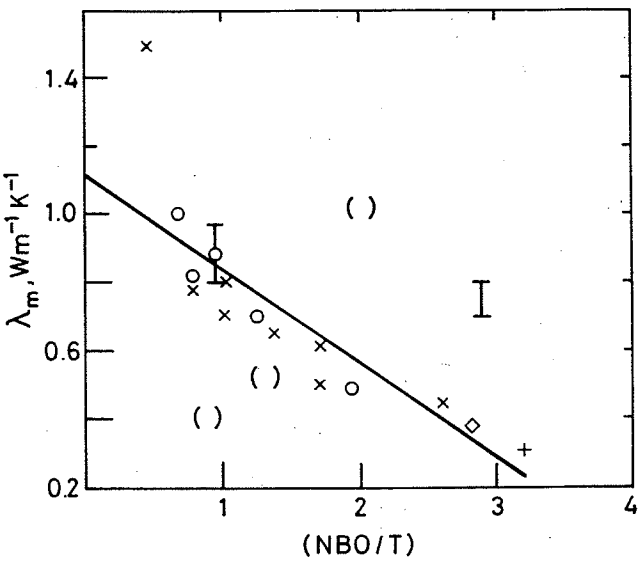


Fig. 15.6. The thermal conductivity at the liquidus temperature, k_m as function of (NBO/T) ratio, ie the number of non-bridging oxygens per tetrahedrally-co-ordinated atom

15.3.2 Liquids

15.3.2.1 Degree of polymerisation of the sample

The thermal conductivity of a liquid at the liquidus temperature, k_m, increases with increasing SiO_2 content, ie increasing degree of polymerisation [26]. The (NBO/T), ie the number of non-bridging oxygens per tetrahedrally-co-ordinated atom (eg Si, Al) is a measure of the degree of depolymerisation. It can be seen from Fig. 15.6 that k_m decreases as (NBO/T) increases.

15.3.2.2 Relation to velocity of sound

The relationship between the velocity of sound (phonons) in the slag (v) and the thermal conductivity (k_L) is given in equation (15.9) where L is the mean free path of the phonons. Values of L derived from k_m values and velocity of sound data were found to approximate to the Si-O interatomic distance [26].

$$k_L = \tfrac{1}{3} (C_p.v.L) \qquad (15.9)$$

15.4 Thermal conductivity data

15.4.1 Pure substances

CaF_2

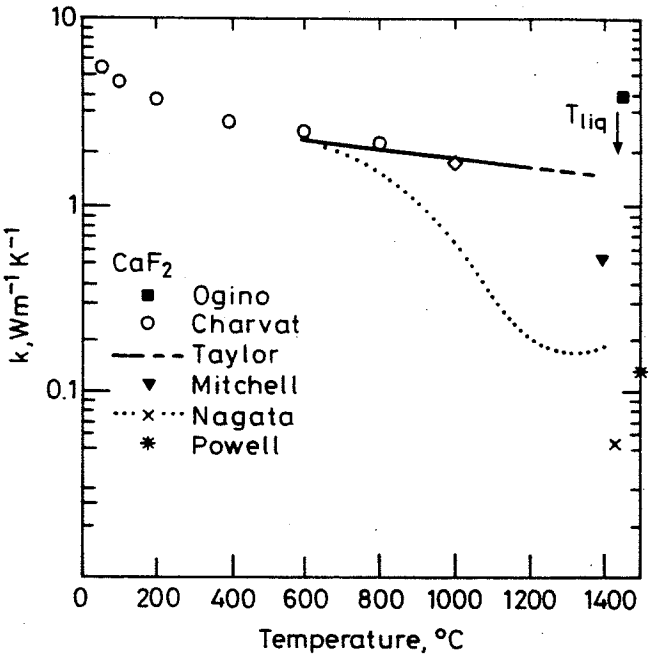


Fig. 15.7. The thermal conductivity of CaF_2 as a function of temperature [11, 17, 27-30] the value reported by Ogino [11] for the liquid probably contains significant contributions from radiation conductivity [30]

SiO_2

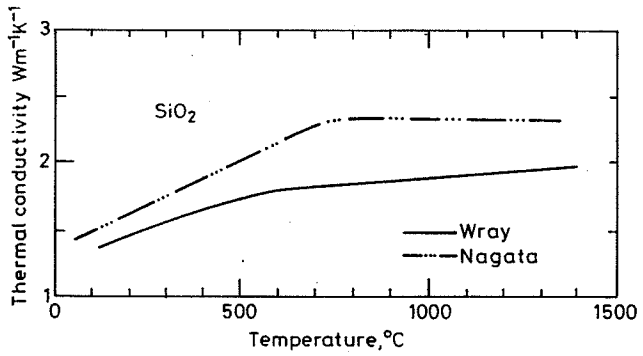


Fig. 15.8. Thermal conductivity of SiO_2 as a function of temperature [20, 31]

15.4.2 Binary systems

Al_2O_3-CaO

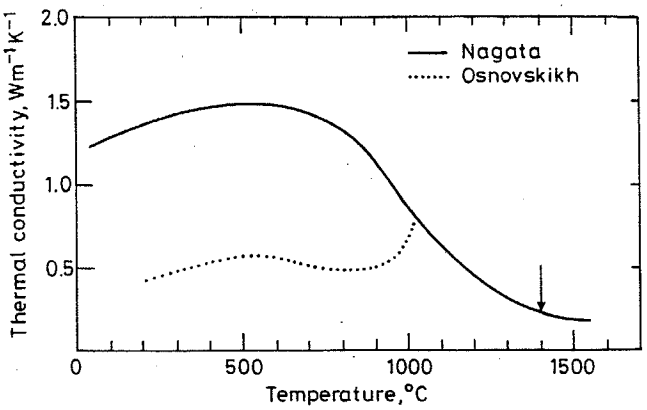


Fig. 15.9. Thermal conductivity of slags containing 50 % Al_2O_3 - 50 % CaO as a function of temperature [20, 32]

Al_2O_3-MgO

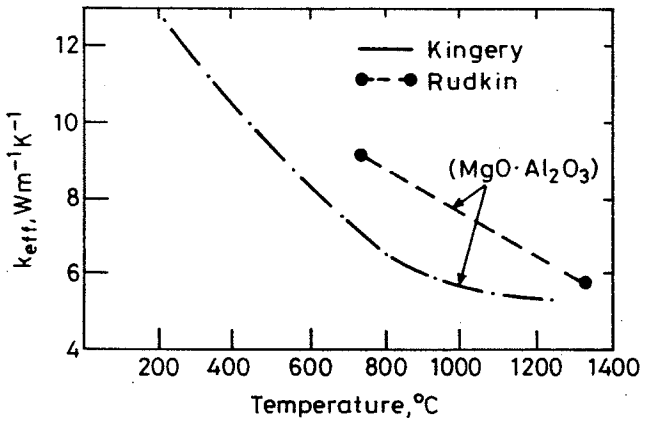


Fig. 15.10. Thermal conductivity as a function of temperature for spinel ($MgO.Al_2O_3$) [10], and values derived [30] from thermal diffusivity measurements [33]

Al_2O_3-SiO_2

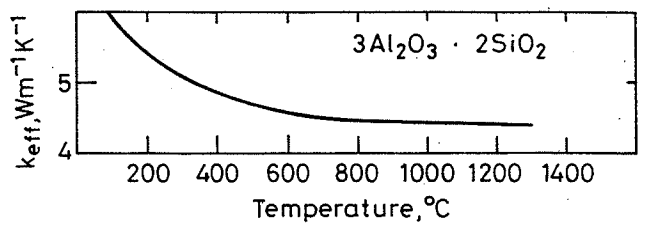
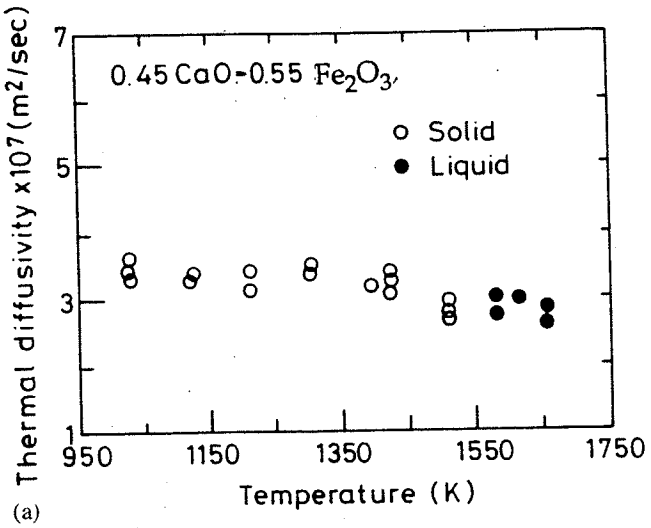
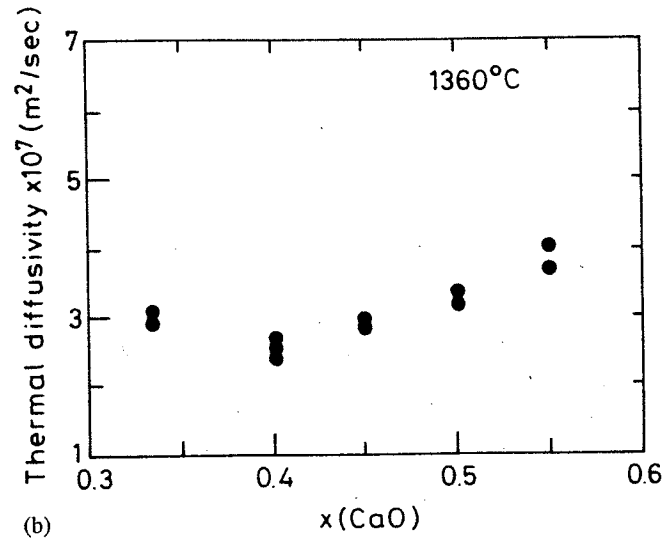


Fig. 15.11. Thermal conductivity of sintered mullite ($3Al_2O_3.SiO_2$) as a function of temperature [10]

$CaO\text{-}Fe_2O_3$



(a)



(b)

Fig. 15.12 a,b. Thermal diffusivity of $CaO\text{-}Fe_2O_3$ slags as a function of (a) temperature (b) CaO content [34]

$CaO\text{-}SiO_2$

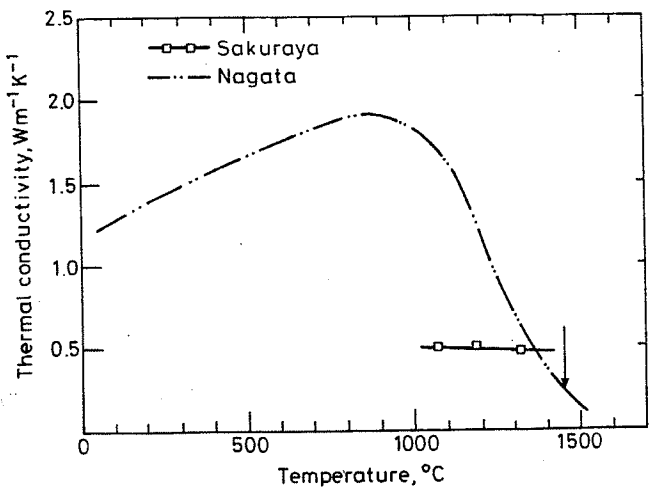


Fig. 15.13. Thermal conductivity of slags with composition 55 % CaO - 45 % SiO_2 as a function of temperature [20, 35]

$K_2O\text{-}SiO_2$

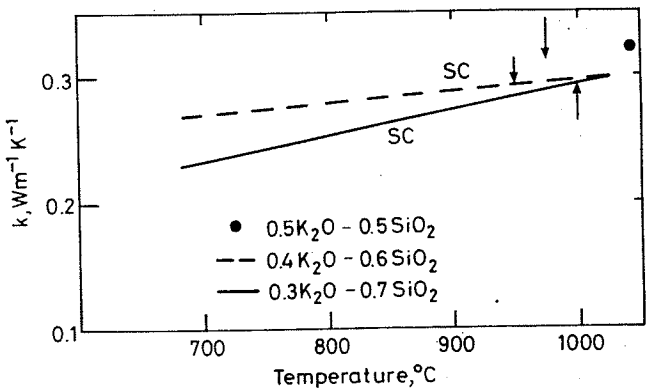


Fig. 15.14. Thermal conductivity of $K_2O\text{-}SiO_2$ melts as a function of temperature [18]; arrows indicate liquidus temperatures and sc the supercooled liquid state

$MgO\text{-}SiO_2$

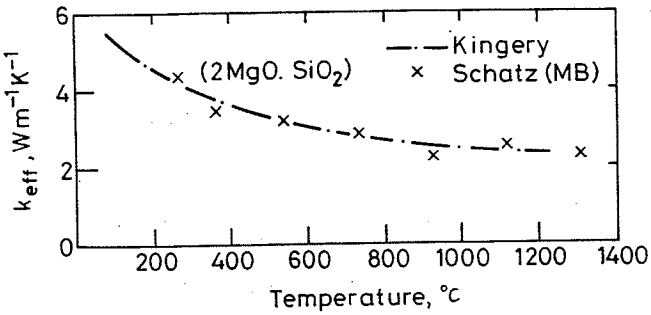


Fig. 15.15. Thermal conductivity of forsterite ($2MgO.SiO_2$) as a function of temperature [10, 15]

$Na_2O\text{-}SiO_2$

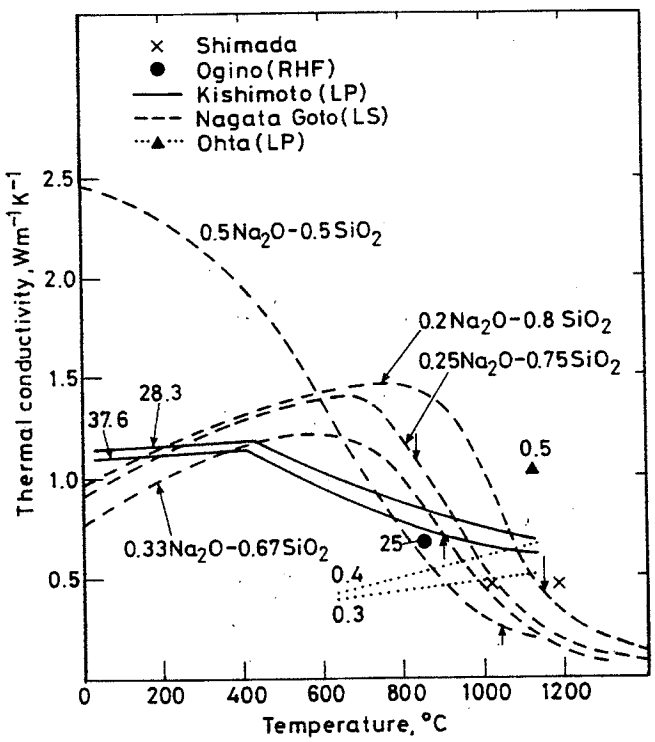


Fig. 15.16. Thermal conductivity of $Na_2O\text{-}SiO_2$ slags as a function of temperature [11, 18, 19, 20, 36]; compositions expressed in mole fractions and mass %

15.4.3 Ternary systems

Al_2O_3-CaO-SiO_2

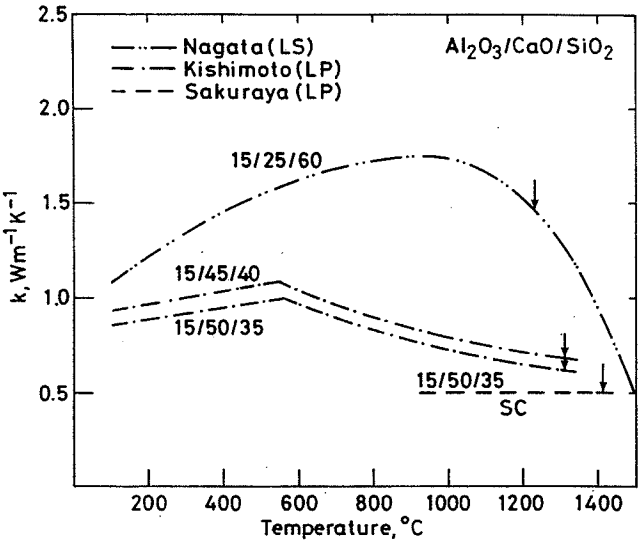


Fig. 15.17. Thermal conductivity values for other compositions in the Al_2O_3-CaO-SiO_2 system as a function of temperature obtained using transient techniques [19, 20, 35]; sc denotes supercooled liquid state

CaO-Fe_2O_3-SiO_2

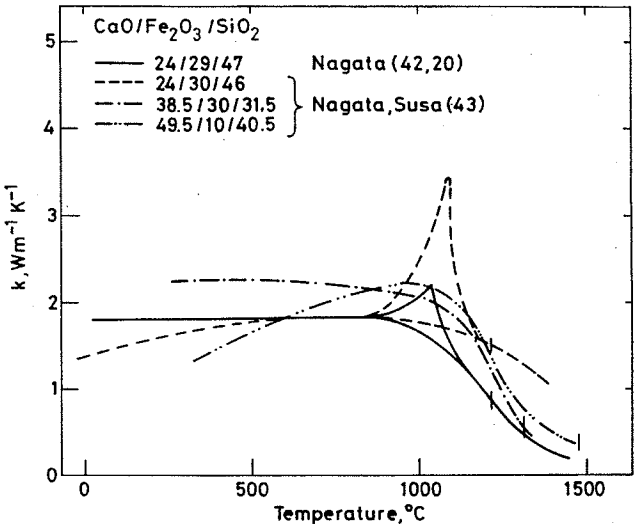
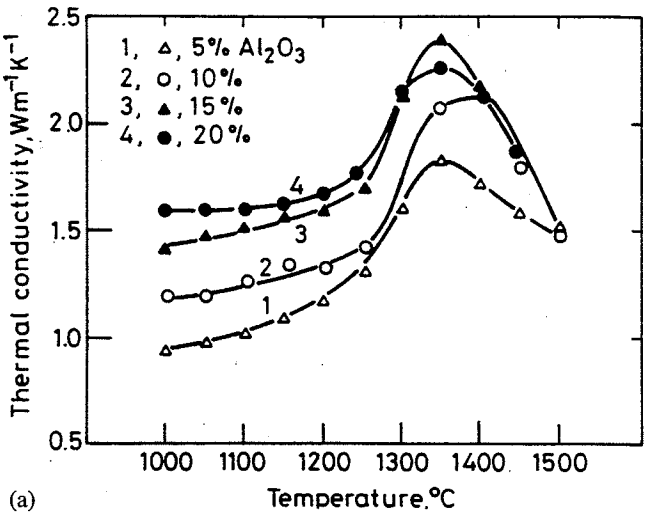
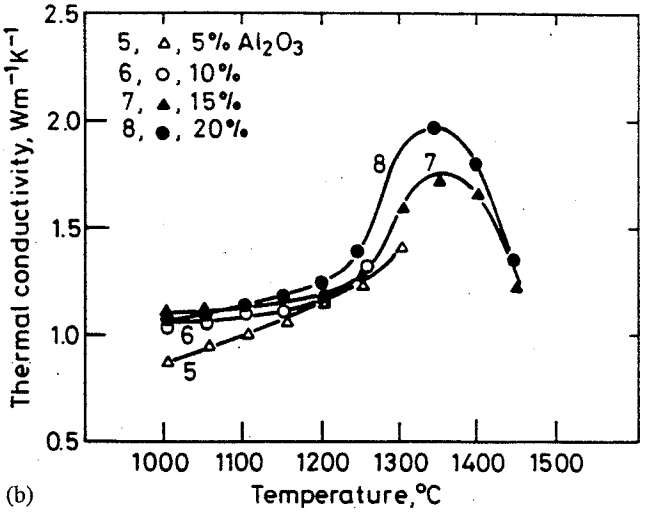


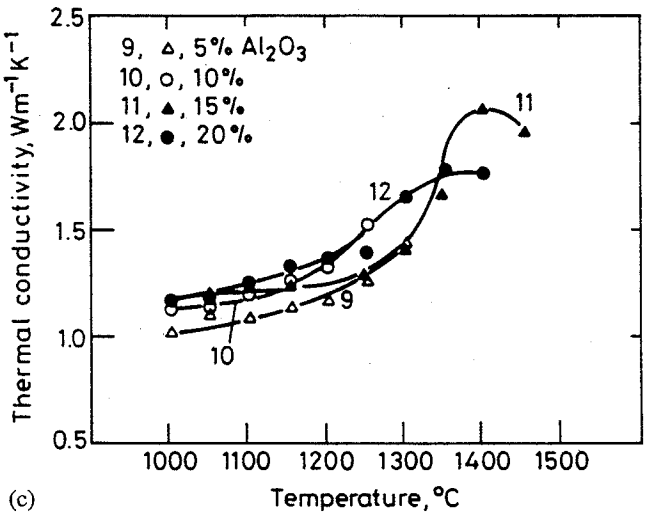
Fig. 15.19. Thermal conductivity of CaO-Fe_2O_3-SiO_2 slags as a function of temperature (20, 42, 43); the (Fe^{2+}/Fe^{3+}) ratio was ca (0.2-0.3) in these slags [43]. See also Ref. [13, 14 and 41]



(a)



(b)



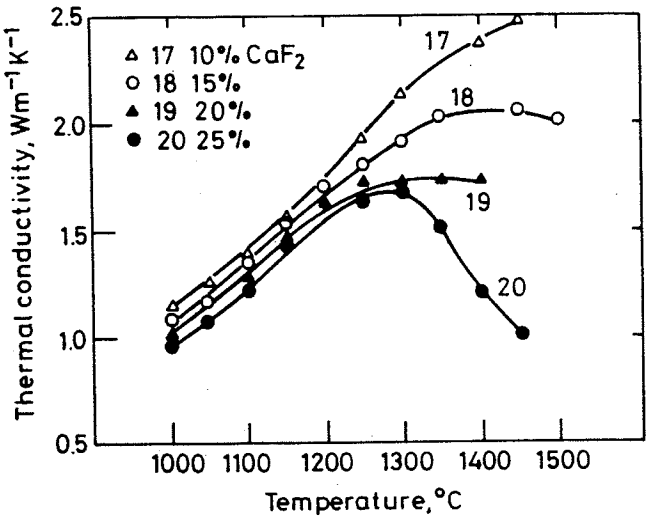
(c)

No.	Al_2O_3 (%)	CaO (%)	SiO_2 (%)	T_{liq} (°C)	T_{sol} (°C)
1	5.00	42.75	52.25	1485	1170
2	10.00	40.50	49.50	1420	1307
3	15.00	38.25	46.75	1355	1265
4	20.00	36.00	44.00	1300	1265
5	5.00	47.50	47.50	1480	1310
6	10.00	45.00	45.00	1405	1265
7	15.00	42.50	42.50	1325	1265
8	20.00	40.00	40.00	1340	1265
9	5.00	52.25	42.75	1400	1310
10	10.00	49.50	40.50	1340	1310
11	15.00	46.75	38.25	1395	1310
12	20.00	44.00	36.00	1465	1318

Fig. 15.18 a-c. Thermal conductivity (k_{eff}) as a function of Al_2O_3-CaO-SiO_2 slags obtained using (RHF) steady state techniques [12]; these values probably contain significant contributions from radiation conduction

15.4.4 Quaternary systems

Al_2O_3-CaF_2-CaO-SiO_2



Mass %				
Slag No.	Al_2O_3	$CaFe_2$	CaO	SiO_2
17	13.5	10	34.4	42.1
18	12.8	15	32.5	39.7
19	12.0	20	30.6	37.4
20	11.3	25	28.7	35.1

Fig. 15.20. Thermal conductivity of Al_2O_3-CaF_2-CaO-SiO_2 slags as a function of temperature obtained using radial heat flow method [12]; these results probably contain a contribution from radiation conduction

Al_2O_3-CaO-SiO_2-TiO_2

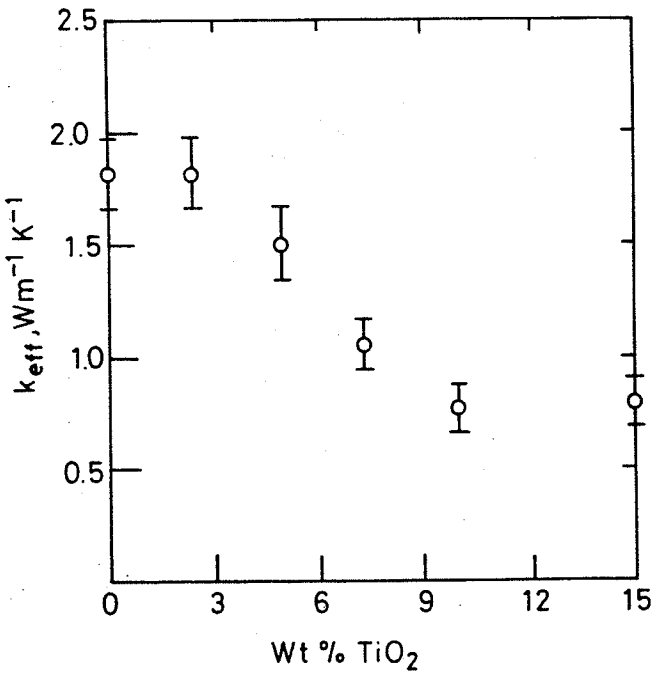


Fig. 15.21. The effect of TiO_2 additions on the thermal conductivity of a slag containing 20 % Al_2O_3 - 40 % CaO - 40 % SiO_2 [40]; the decrease in k_{eff} was attributed to a decrease in k_R with increasing TiO_2 [40]

15.4.5 Continuous casting powders and slags

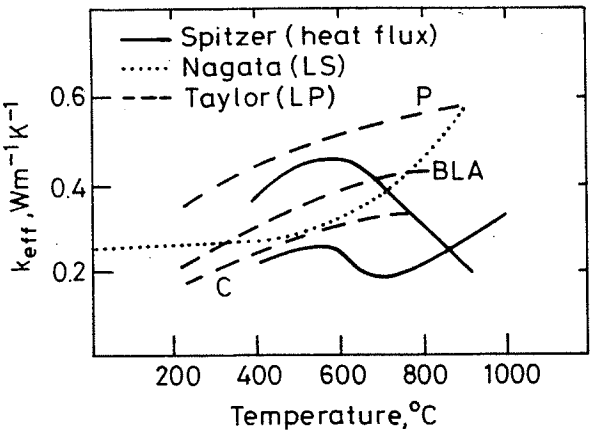


Fig. 15.22. Thermal conductivity of powder form of continuous casting fluxes as a function of temperature [20, 51, 52]; powder P [52] was in granulated form, all others were in the powder form

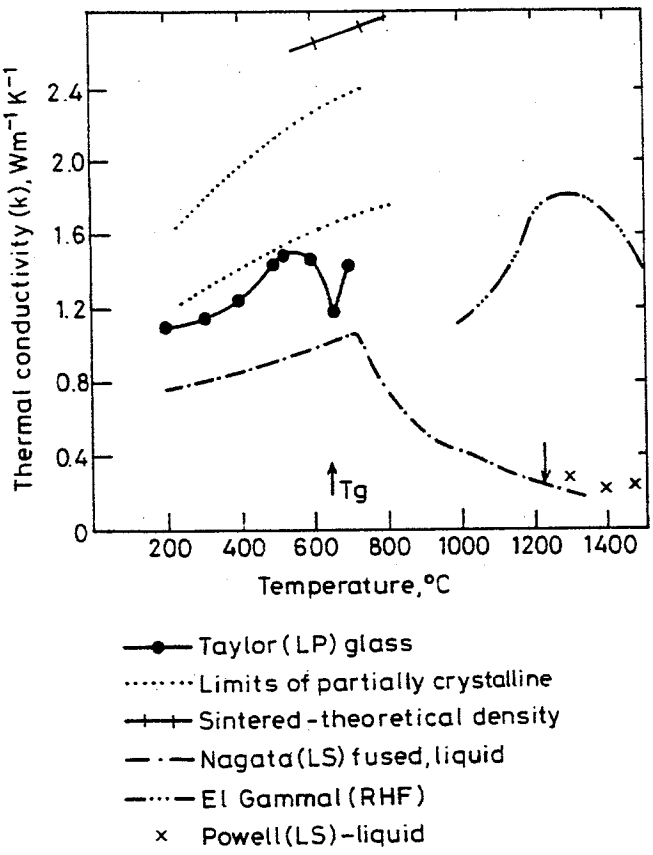


Fig. 15.23. Thermal conductivities of continuous casting slags in the glassy and crystalline states as a function of temperature [12, 20, 52, 53]; the values reported by El Gammal [12] probably include contributions from radiation conduction

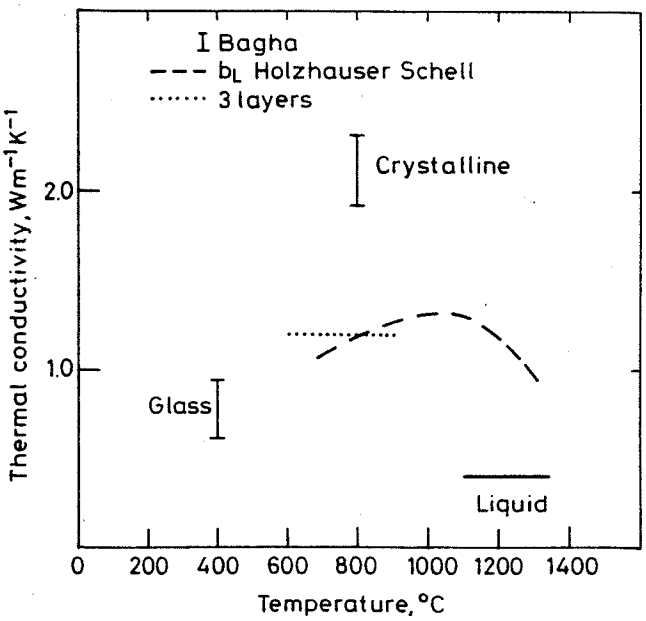


Fig. 15.24. Thermal conductivity of continuous casting slags as a function of temperature as determined by analysis of heat flux measurements obtainend in simulation tests [54-57]; the results are in agreement with results shown in Fig. 15.22. Further reference [58]

15.4.6 ESR slags

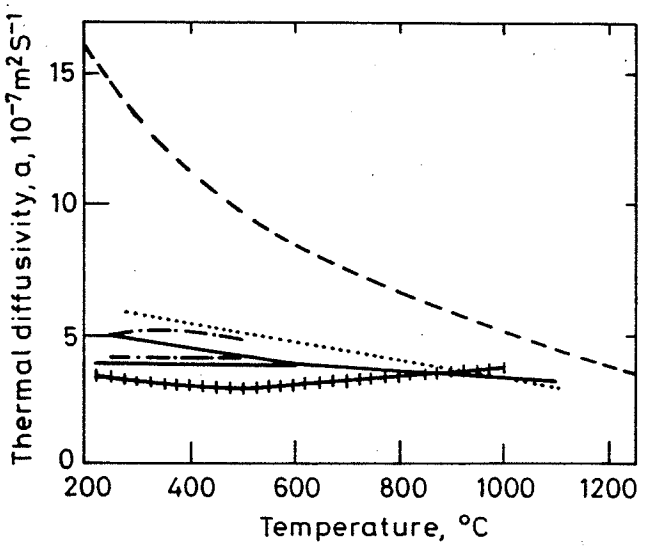
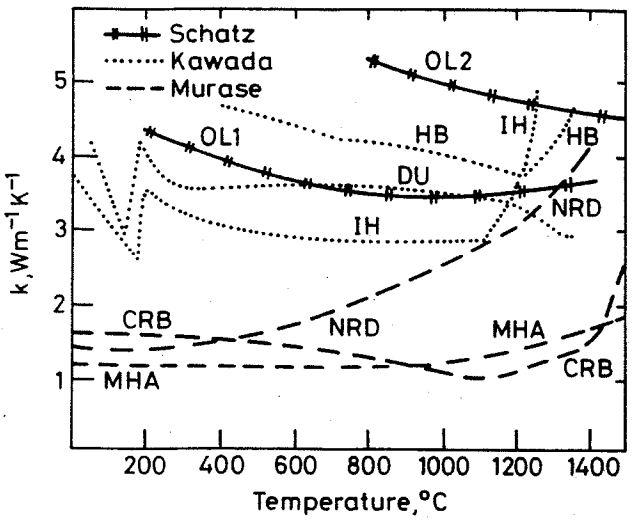


Fig. 15.25. Thermal diffusivities of various (sintered) CaF_2-based slags in Ar as a function of temperature [59, 17]; a value for the thermal conductivity k of 0.4 $Wm^{-1}K^{-1}$ has been reported for liquid CaF_2 - 15 % Al_2O_3 - 15 % CaO [28]

15.4.7 Rocks, Minerals



Ref.	No.	Composition, mass %				
		SiO_2	MgO	CaO	FeO	Al_2O_3
[59]	HB	49.0	45.0	-	6.0	-
	I	45.0	46.0	0.5	7.0	1.5
	IH	45.0	42.0	4.0	5.0	4.0
	DU	43.5	38.5	-	13.0	(5 % Cr_2O_3)
[60] (RHF)	NRD	74.0	0.5	1.5	2.4	14.0 (+8 % Na_2O+ K_2O)
	LRB MHA	60-75	-	Low	-	15-25
				-	-	-
[15] (MB)	01	40.8	49.3	-	9.9	-
	02	41.6	52.7	-	5.7	-
	DU	44.3	53.9	-	1.8	-

Fig. 15.26. Thermal conductivities of rocks and minerals as a function of temperature [15, 59, 60]

15.5 References in Chapter 15

[1] Gardon, R.: Proc. 2nd Intl. Thermal Conductivity Conference, held Ottawa, (1962), 167

[2] Gardon, R.: J. Amer. Ceram. Soc., 44 (1961), 305 – 312

[3] Ammar, M. M.; Gharib, S.; Halawa, N. M.; El Badry, K.; Ghoneim, N. A.; Batal, N. A.; Batal, H. A.: J. Non-Cryst. Solids, 53 (1982), 165

[4] Filippov, L. P.: Investigation of the thermal conductivity of liquids. Publ. Moscow State University (1970)

[5] Sergeev, O. A.; Men, A. A.: Thermophysical properties of translucent materials. Publ. Standartov, Moscow (1970)

[6] Chuchmarev, S. K.; Esin, O. A.; Pastukhov, E. A.: Fiz Khim Elektrokhim Rasplov Solei Shlakov Tr Vsesoyz Sov. 3rd Edition, 1966, publ. (1968), 143

[7] Tye, R. P.: Thermal conductivity. Vol. 1 & 2. Publ. Academic Press, New York, 1969

[8] Gardon, R.: Review of thermal conductivity data in glass. Part I: Thermal conductivity at low and moderate temperatures; and Blazek, A.; Endrys, J.: Part 2. Thermal conductivity at high temperatures. Publ. Intl. Commission on Glas (1983)

[9] Mardulcar, U. V.; Nieto de Castro, C. A.: Measurement of high temperature thermal conductivity of liquids. Final Report on Contract 3314/1/0/154/89/8 to BCR, Brussels. Publ. Inst. de Cienia Aplicada e Tecnologia, Lisbon, 1990
[10] Kingery, W. D.; Francl, J.; Coble, R. L.; Vasilos, T.: J. Amer. Ceram. Soc., 37 (1954), 107
[11] Ogino, K.; Nishiwaki, A.; Yamamoto, K.; Hara, S.: Paper presented at Intl. Symposium Phys. Chem. Steelmaking, Toronto, (1982) III – 33. Metall Soc. Canad. Inst. Min. Metall; see also Tetsu-to-Hagane, 65 (1979), S683
[12] El Gammal, T.; Jofre, S. J.; Sanchez de Loria: Steel Research, 57 (1986), 620 – 625
[13] Fine, H. A.; Engh, T.; Elliott, J. F.: Metall Trans B, 7B (1976), 277 – 285
[14] Nauman, J.; Foo, G.; Elliott, J. F.: Extractive Metallurgy of Copper, Chapter 12, 237
[15] Schatz, J. F.; Simons, G.: J. Geophys. Res., 77 (1972), 6966
[16] Gibby, R. L.; Bates, J. L.: Proc. 10th Thermal Conductivity Conf., held Newton, Mass., Sept. 1970, IV – 7, 8
[17] Taylor, R.; Mills, K. C.: Archiv f. Eisenhüttenwes., 53 (1982), 55
[18] Ohta, H.; Shiraishi, Y.: Proc. of 2nd Intl. Symp. on Metallurgical Slags and Fluxes, held Lake Tahoe, Nev., Nov. 1984. Publ. Metall Soc. AIME, Warrendale, Pa, 863 – 873
[19] Kishimoto, M.; Maeda, M.; Mori, K.; Kawai, Y.: ibid 891 – 905
[20] Nagata, K.; Goto, K. S.: ibid 875 – 889
[21] Powell, J. S.: Measurement Sci. Technol., 2 (1991), 111 – 117
[22] Susa, M.; Nagata, K.; Goto, K. S.: Trans JIM, 29 (1988), 133 – 142
[23] Nieto de Castro, C. A.; Li, S. F.; Maitland, G. C.; Wakeham, W. A.: Intl. J. Thermophys., 4 (1983), 311
[24] Crane, R. A.; Vachon, R. I.; Khadar, M. S.: Proc. of 7th ASME Symp. Thermophys. Properties, held Gaithersburg, Md, May 1977. Publ. ASME New York, 109 – 123
[25] Lin, F.; Ford, J. D.: Canad. J. Chem. Eng., 62 (1984), 125 – 134
[26] Mills, K. C.: Proc. of 3rd Intl. Conf. Metall. Slags and Fluxes, held Strathclyde University, Glasgow, 1988. Publ. Inst. of Metals London (1989), 229 – 232
[27] Charvat, F. R.; Kingery, W. D.: J. Amer. Ceram. Soc., 40 (1957), 306
[28] Mitchell, A.; Wadier, J. F.: Canad. Metall Q, 20 (1981), 373
[29] Powell, J. S.: Unpublished data. National Physical Laboratory
[30] Mills, K. C.; Keene, B. J.: Intl. Materials Rev., 32 (1987), 1 – 120
[31] Wray, K. L.; Connolly, T. J.: J. Appl. Phys., 30 (1959), 1702
[32] Osnovskikh, L. I.; Kochetov, N. N.; Bratchikov, S. G.: Trudy Ural, Nauchno-issled Chern Met., 1968 (8), 71
[33] Rudkin, R. I.: Tech. Doc. Ref. ASD-TDR, 62-24 (Part II). US Air Force Systems Command, Aeron Systems Div., 1963
[34] Ohta, H.; In-Kook, Suh; Waseda, Y.: Proc. of 3rd Intl. Conf. on Molten Slags and Fluxes, held Strathclyde University, Glasgow, 1988. Publ. Inst. of Metals, London, (1989), 223 – 225
[35] Sakuraya, T.; Emi, T.; Ohta, H.; Waseda, Y.: Nippon Kinzoku Gakkaishi, 46 (1982), 1131 – 1138
[36] Shimada, M.; Scarfe, C. M.; Schloessin, H. H.: Phys. Earth Planet, Interiors, 37 (1985), 206 – 213
[37] Ishikuro, S.; Nagata, K.; Goto, K. S.: Trans ISI Jap., 21 (1981) (1), B13
[38] Susa, M.: MSc Thesis. Tokyo Inst. Technology, (1982)
[39] Li, F.; Susa, M.; Nagata, K.: Nippon Kinzoku Gakkaishi, 55 (1991) (2), 194 – 203
[40] Mikrovas, A. C.; Argyropoulos, S. A.; Sommerville, I. D.: Iron and Steelmaker, (1991), 51 – 61
[41] Mills, K. C.: Proc. of Intl. Seminar on Heat Transfer and Heat Recovery in Iron and Steel, held Tokyo Inst. Technol., Mar 1985
[42] Nagata, K.; Susa, M.; Goto, K. S.: Tetsu to Hagane, 69 (1983), 1417 – 1424
[43] Nagata, K.; Susa, M.: Private Communication. Tokyo Inst. Technol., April 1992 – recalculated data from results reported in DSc Thesis of F. Li, Tokyo Inst. Technol. (1991)
[44] Rafalovich, I. M.; Denisova, I. A.: Fiz Khim Rasplav, Schlakov, (1970), 181
[45] Vargaflik, N. B.; Oleshchuk, O. N.: Teploenergetika, 4 (1955), 13
[46] Ischenko, K. D.: Metall Kokosokhim, (1970) (21), 82
[47] Rhines, J. M.; Putland, F. H.; Mills, K. C.: High Temp – High Pressure, 17 (1985), 173
[48] Mills, K. G.; Rhine, J. M.: Fuel, 68 (1989), 904 – 910
[49] Chesnovskoi, V. Y.; Ulashchik, A. N.: Teplofiz Vsokikh Temp, 25 (1987), 924 – 928
[50] Gibby, R. L.; Bates, J. L.: Proc. of 10th Thermal Conductivity Conf., held Newton, Mass., Sept. 1970, IV-7,8 through W. Capps, Eng. Aspects Magnetohydrodyn, 16 (1977), VIII-3.21
[51] Spitzer, K. H.; Holzhauser, J. F.; Bruckner, F. U.; Siera, B.; Grethe, H. J.; Schwerdtfeger, K.: Stahl u. Eisen, 108 (1988) (9), 441 – 450
[52] Taylor, R.; Mills, K. C.: Ironmaking and Steelmaking, 15 (1988), 187 – 194
[53] Powell, J. S.: Unpublished results. National Physical Laboratory, Teddington
[54] Bagha, S.; Machingawujta, N.; Grieveson, P.: Proc. 3rd Intl. Conf. on Molten Slags and Fluxes, held Strathclyde Univ. Glasgow, 1988. Publ. Inst. of Metals, London, 1989, 235 – 240
[55] Holzhauser, J. F.; Spitzer, K. H.; Schwerdtfeger, K.: Influence of casting aids on heat transfer in the mould surface quality and incidence of breakout on continuous casting of steel. Final Report, ECSC Contract – 7210 – CA/139, Dec (1988)
[56] Scheel, R.; Rüttiger, K.: Influence of powder composition on the physical properties of continuous casting powders. Report EUR 106 62 Vol. II DE Report on Contract 7210 – CA/135, (1987)
[57] Scheel, R.; Korte, W.: Metall. Plant and Technol., 1987 (6), 22 – 33
[58] Ohmiya, S.; Tacke, K. H.; Schwerdtfeger, K.: Ironmaking and Steelmaking, 10 (1983), 24 – 30
[59] Kawada, K.: Bull Earthquake Res. Inst., 44 (1966), 1071
[60] Murase, T.; McBirney, A. R.: Science, 170 (1970), 165

16

Optical properties of slags: Data for refractive indices and absorption coefficients

M. Susa and K. C. Mills

16.1 Introduction

Heat transfer through semi-transparent media such as slags and glasses is very complex since heat can be transported by three mechanisms, viz lattice (or "phonon") conduction, radiation (or "photon") conduction, and electronic conduction [1]. At high temperatures radiation conduction can be the predominant mode of heat transfer and for "optically thick" conditions the radiation conductivity (k_R) is given by equation (16.1)

$$k_R = 16\,\sigma n^2 T^3 / 3\alpha \qquad (16.1)$$

where σ is the Stefan-Boltzmann constant, T is the thermodynamic temperature and n and α the refractive index and absorption coefficient of slags, respectively. Thus for the development of mathematical models of iron and steelmaking processes, data are needed for the refractive indices and absorption coefficients and these are given below.

16.2 Refractive indices of slags

16.2.1 Introduction

When light is obliquely incident on an interface separating two media the direction of the beam is altered **(Fig. 16.1).** The refraction of the light is caused by the differences in the velocity of light in the different media.

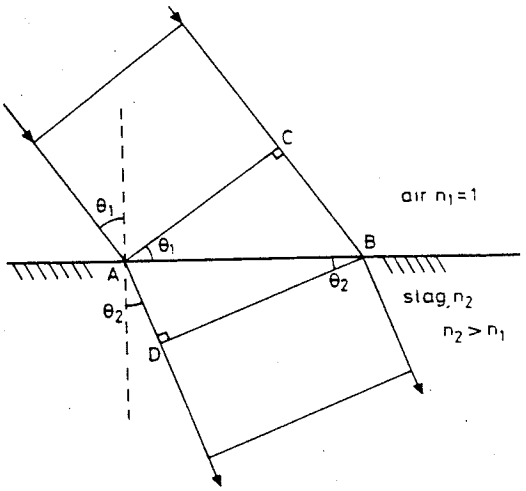


Fig. 16.1. Schematic drawing illustrating the refraction of light

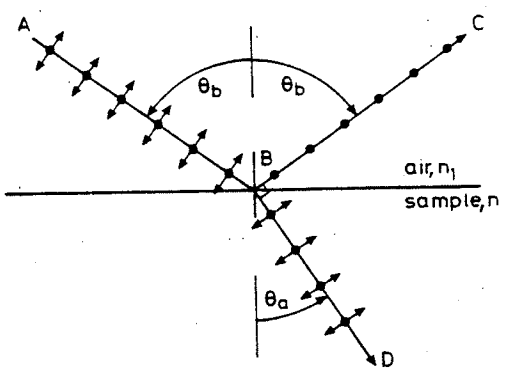


Fig. 16.2. Schematic drawing showing the Brewster angle

If the velocity of light in vacuo is taken as a standard, the refractive index (n) of a medium can be defined by equation (16.2)

$$n = \frac{\text{velocity in "vacuo"}}{\text{velocity in medium}} \qquad (16.2)$$

Since the refractive index for air has a value close to unity, (1.0003), in practice, air is frequently used as the reference medium. Thus the refractive index of a slag represents the refractive index of this material relative to that of air. It can be seen from Fig. 16.1. that the relationships shown in equations (16.3) and (16.4) obtain:

$$AB = BC/\sin\theta_1 = AD/\sin\theta_2 \qquad (16.3)$$

$$\sin\theta_1/\sin\theta_2 = BC/AD. \qquad (16.4)$$

Since the lengths of BC and AD correspond to the velocities of light in air and slag, respectively, the refractive index is given by equation (16.5) where 1 and 2 represent air and the slag respectively, this is often known as Snell's Law.

$$\sin\theta_1/\sin\theta_2 = n_{21} = n_2/n_1 \qquad (16.5)$$

The refractive index is dependent upon the wavelength of light (section 16.2.3.3) and consequently the refractive index (n_D) is often measured for the wavelength associated with the D line of sodium (λ = 589 nm).

16.2.2 Experimental methods

The principal methods used to determine refractive index are outlined below.

16.2.2.1 Immersion method (IM) [2-5]

A powdered sample is placed in a liquid of known refractive index and examined under a microscope when using parallel light. If n(sample) < n(liquid) the system acts a diverging lens and on raising the objective above the focus a bright border will pass from the sample to the liquid and on lowering the objective the border will appear to enter the sample. If n(sample) > n(liquid) the reverse phenomena occur. By using liquids with known refractive indices, n(sample) can be rapidly determined to ± 0.002.

16.2.2.2 Brewster angle method (BR) [6]

In this method the Brewster angle (denoted θ_b in **Fig. 16.2**) is measured using unpolarized light; θ_b occurs when the angle between the refracted and reflected beams is at 90°. The refractive index can be calculated from equation (16.6).

$$n(\text{sample})/n_1(\text{air}) = \tan\theta_b \qquad (16.6)$$

16.2.2.3 Pulfrich refractometer (PR) [7, 8]

The sample is placed on a thin liquid layer covering a prism; both the liquid and prism have higher refractive indices than the sample. When a convergent beam of monochromatic light is incident on the sample **(Fig. 16.3)** some of the light will enter the prism and emerge from another surface of the prism. The only light entering the prism is that contained within the critical angle (θ_c) which can be determined by the "light and shade" image appearing at the position of the

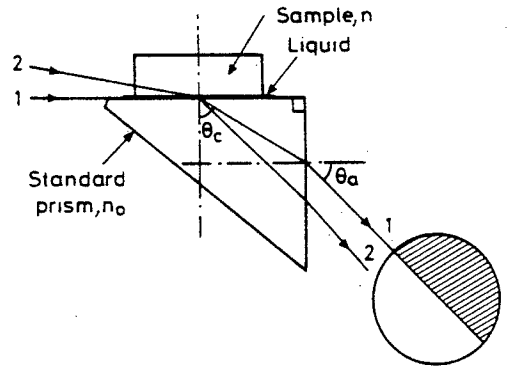


Fig. 16.3. Schematic diagram illustrating the principle of the Pulfrich refractometer

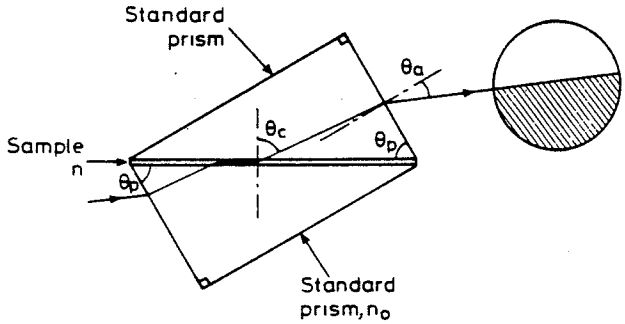
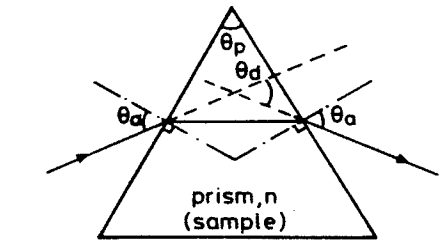
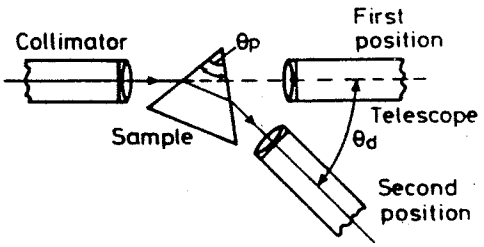


Fig. 16.4. Schematic drawing showing the arrangement used in the Abbé refractometer



(a)



(b)

Fig. 16.5 a,b. Schematic drawings showing arrangements used in the minimum deviation method

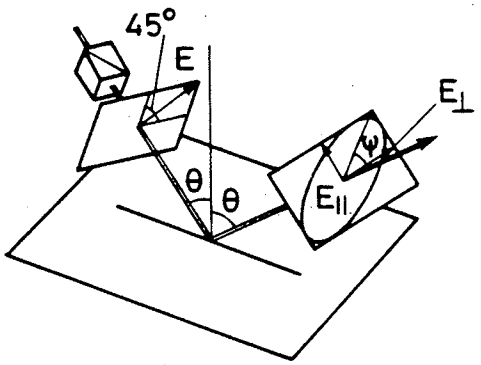


Fig. 16.6. Schematic diagram showing the principle of ellipsometry

emergent angle (θ_a). Thus the refractive index can be determined by equation (16.7) where n_o is the refractive index of the prism

$$n = (n_o^2 - \sin^2 \theta_a)^{0,5.} \qquad (16.7)$$

16.2.2.4 Abbé refractometer (AR) [9-11]

This method is based on the same principles as that for the Pulfrich refractometer. The arrangement shown in **Fig. 16.4** is used to determine the critical angle (θ_c) which can be recognised by the "light and shade" image appearing at the emergent angle (θ_a) in the telescope. The refractive index can be calculated from equation (16.8) where θ_p and θ_a are shown in Fig. 16.4.

$$n = \cos \theta_p \cdot \sin \theta_a \pm \sin \theta_p \, (n_o^2 - \sin^2 \theta_a)^{0.5.} \qquad (16.8)$$

16.2.2.5 Minimum deviation method (MD) [12-16]

In this method the sample is made into a prism with a refracting angle of ca. 60°. When the prism is arranged **(Fig. 16.5 a)** so that a beam of light will pass through the prism symmetrically, the prism is said to be in a position of minimum deviation and θ_d is the angle of minimum deviation. Measurements of θ_d are made using the procedure outlined in **Fig. 16.5 b** and the refractive index is measured using equation (16.9) where θ_p is the refracting angle of the prism

$$n = \frac{\sin [(\theta_p + \theta_d)/2]}{\sin (\theta_p/2)}. \qquad (16.9)$$

16.2.2.6 Ellipsometry (EL) [17, 18]

The principles involved in ellipsometry are shown in **Fig. 16.6.** Linearly polarised monochromatic light with a direction of vibration at 45° to the plane of incidence is directed onto the sample. Measurements are made of (I) the angle of incidence (θ) (II) the ratio of the electric vectors of the amplitudes of the elliptically-polarised light parallel ($E\|$) and perpendicular ($E\perp$) to the plane of incidence and (III) the phase difference (Δ) between them. Values of n and the extinction coefficient K can be derived from equations (16.10) and (16.11) where $\tan\psi = (E\|/E\perp)$.

$$\frac{n^2 - K^2 = \tan^2 \theta \sin^2 \theta \, (\cos^2 \psi - \sin^2 2\psi \sin^2 \Delta)}{(1 + \sin 2\psi \cos \Delta)^2 + \sin^2 \theta} \qquad (16.10)$$

$$2nK = \tan^2 \theta \sin^2 \theta \sin 4\psi \sin \Delta / (1 + \sin 2\psi \cos \Delta)^2 \qquad (16.11)$$

16.2.3 Factors affecting refractive indices

The principal factors affecting the refractive index are outlined below.

16.2.3.1 Density (ρ)

The refractive index is related to the density via equation (16.12) where R ist the molar refractivity and M the molecular mass and slags with higher densities tend to have higher refractive indices

$$\frac{(n^2 - 1)}{(n^2 + 2)} = \frac{\rho R}{M}$$

16.2.3.2 Composition

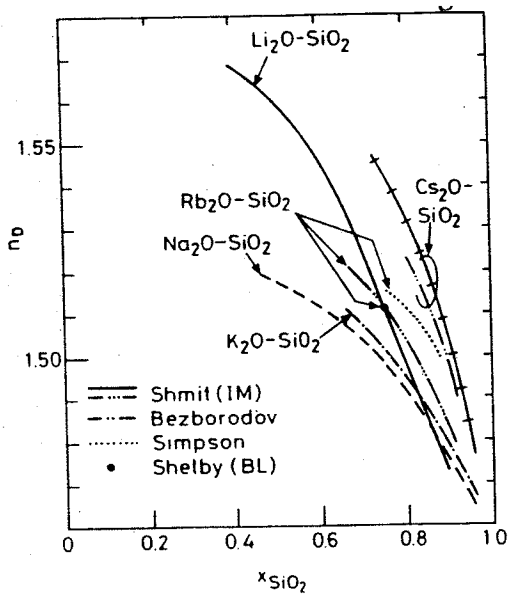
The above equation can also be expressed in the form of equation (16.13) where N is the number of ions per unit volume, β the electron polarisability of the ions and 1, 2, 3, etc represent the different ions

$$\frac{(n^2-1)}{(n^2+2)} = \frac{4\pi}{3}(N_1\beta_1 + N_2\beta_2 + N_3\beta_3 + \ldots) \qquad (16.13)$$

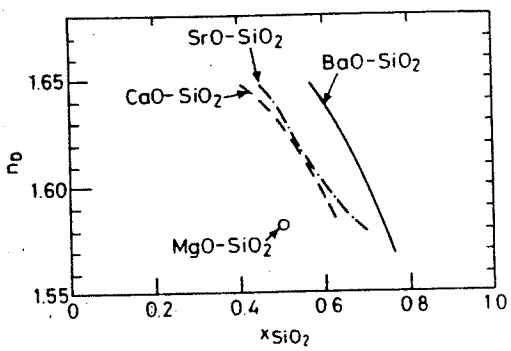
Thus slags containing ions with high electron polarisabilities will tend to have high refractive indices. Ions which have electrons firmly bound to the nuclei have low electron polarisabilities and consequently the latter increase with increasing atomic number (**Fig. 16.7**) and tend to be higher for anions than cations. It has been observed that the refractive indices of basic slags are high, this can be attributed to the increased concentrations of non-bridging (O^-) and free oxygen (O^{2-}) ions in the glass or melt.

16.2.3.3 Wavelength

The refractive index is dependent upon wavelength, it can be seen from **Fig. 16.8** that the refractive indices of SiO_2 (and other silicates) tend to decrease with increasing wavelength [20].



(a)



(b)

Fig. 16.7 a,b. Refractive index as function of mole fraction metal oxide for binary (a) M_2O-SiO_2 glass and (b) MO-SiO_2 glass at 25 °C both showing the tendency of increased refractive index with increasing atomic number

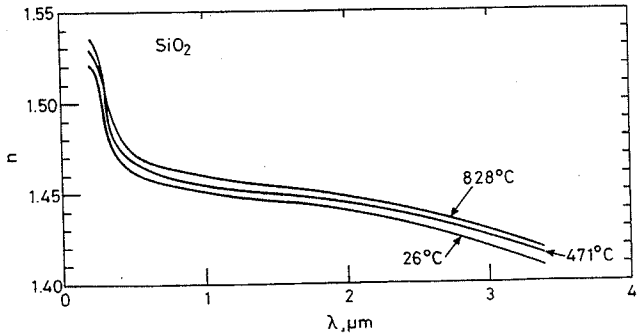


Fig. 16.8. The refractive index of SiO_2 as a function of wavelength

16.2.3.4 Temperature

It can be seen from **Fig. 16.9** that increasing temperature results in a small increase in the refractive index of SiO_2.

16.3 Refractive index data

16.3.1 Pure substances

Al_2O_3

A value n = 1.744 at λ = 0.633 μm has been reported for liquid Al_2O_3 [19].

SiO_2

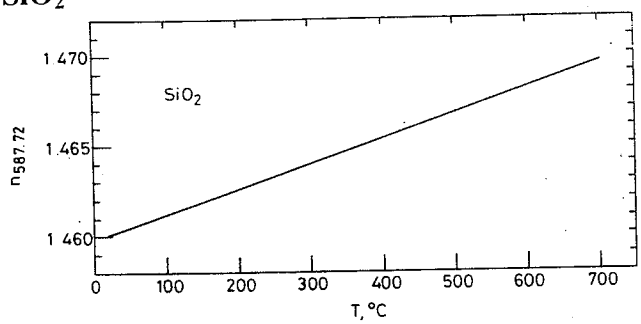


Fig. 16.9. The refractive index (n_D) of SiO_2 as a function of temperature [20, 21]

16.3.2 Binary systems

Al_2O_3-SiO_2

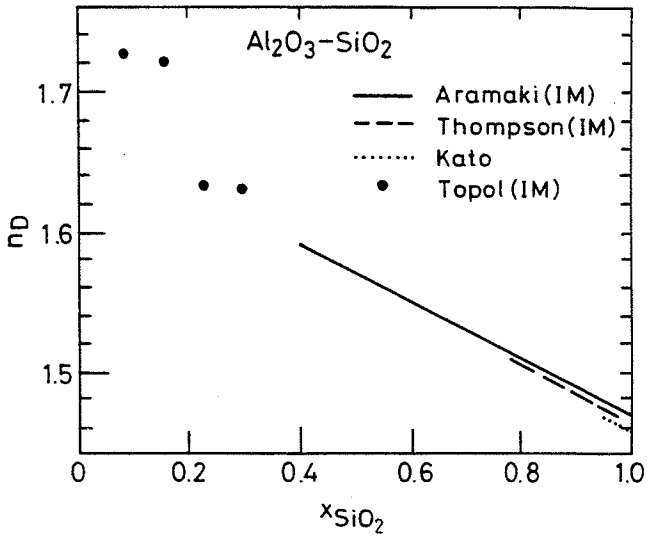


Fig. 16.10. The refractive indices (n_D) of Al_2O_3-SiO_2 glasses at 25 °C [22-25]

B_2O_3-SiO_2

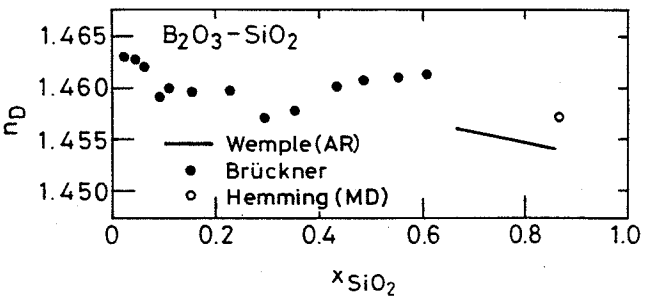


Fig. 16.11. The refractive index (n_D) of B_2O_3-SiO_2 glasses at 25 °C as a function of mole fraction B_2O_3 [26-28]

BaO-SiO_2
CaO-SiO_2

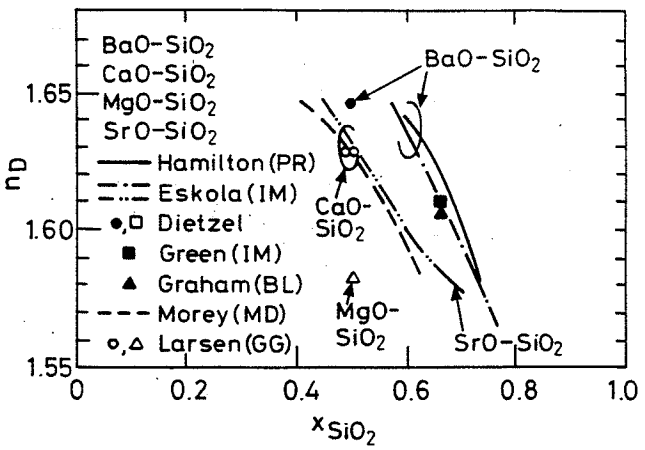


Fig. 16.12. Refractive indices (n_D) for BaO-SiO_2, CaO-SiO_2, MgO-SiO_2, SrO-SiO_2 systems at 25 °C as a function of mole fraction silica [29-35]

Cs_2O-SiO_2

Values [36, 37] are given in Fig. 16.7 a.

GeO_2-SiO_2

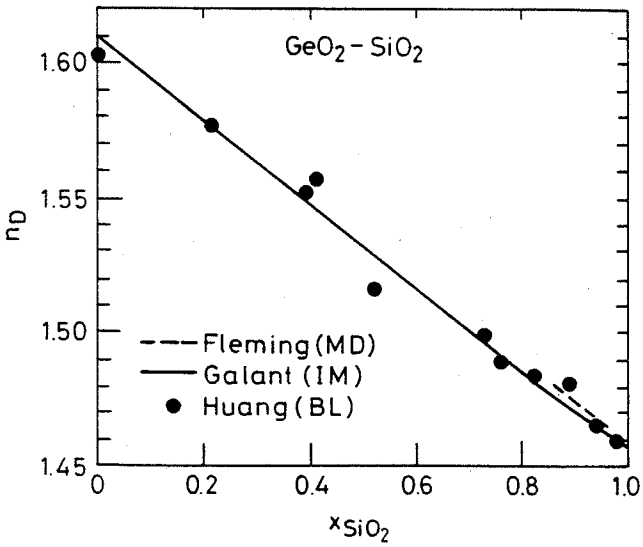


Fig. 16.13. Refractive indices (n_D) for GeO_2-SiO_2 glasses [28, 38, 39] at 25 °C as a function of mole fraction SiO_2

K_2O-SiO_2

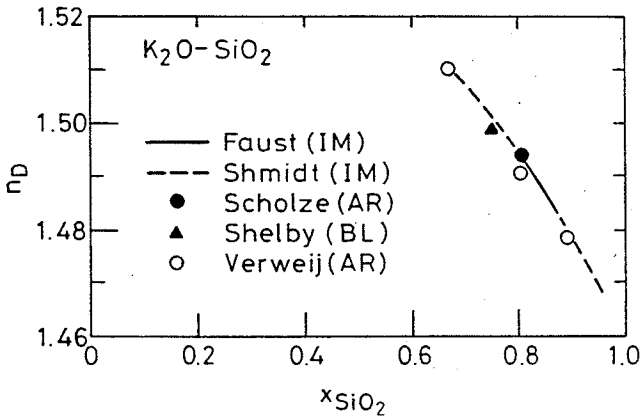


Fig. 16.14. Refractive indices of K_2O-SiO_2 glasses at 25 °C as functions of silica content [46-51]

Li_2O-SiO_2

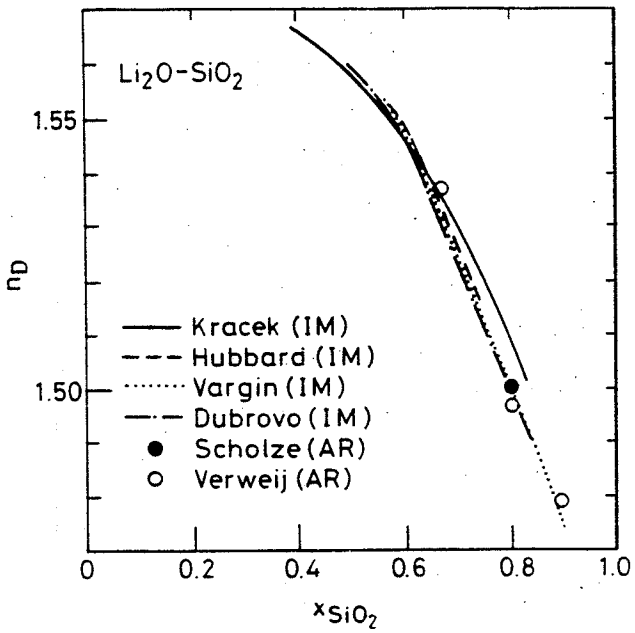


Fig. 16.15. Refractive indices of Li_2O-SiO_2 glasses at 25 °C as functions of silica contents [40-45]

PbO-SiO_2

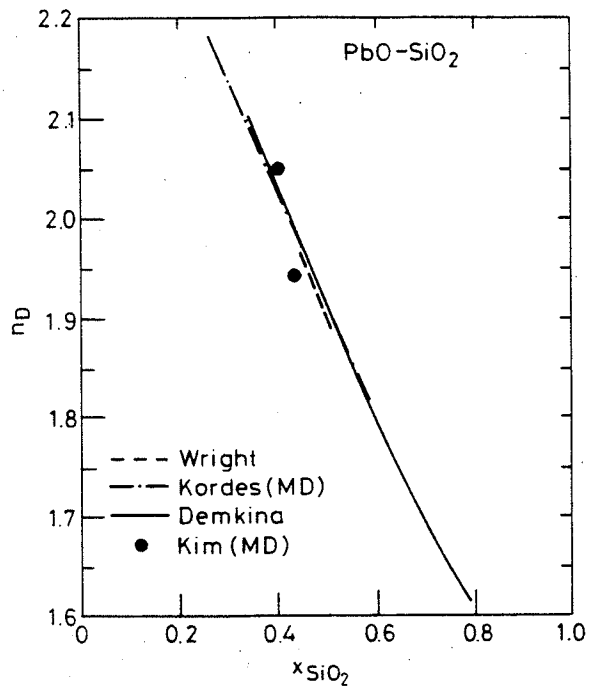


Fig. 16.17. Refractive indices of PbO-SiO_2 glasses at 25 °C as a function of SiO_2 content [52-55]

MgO-SiO_2

A value of $n_D = 1.58$ has been reported [35] for MgO-SiO_2 (Fig. 16.7 b).

Na_2O-SiO_2

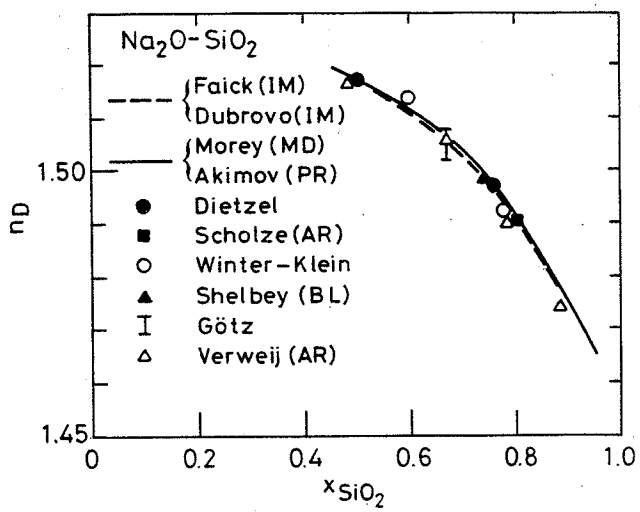


Fig. 16.16. Refractive indices (n_D) for the Na_2O-SiO_2 glasses at 25 °C as a function of SiO_2 content [30, 32, 43, 44, 45, 47, 48]

P_2O_5-SiO_2

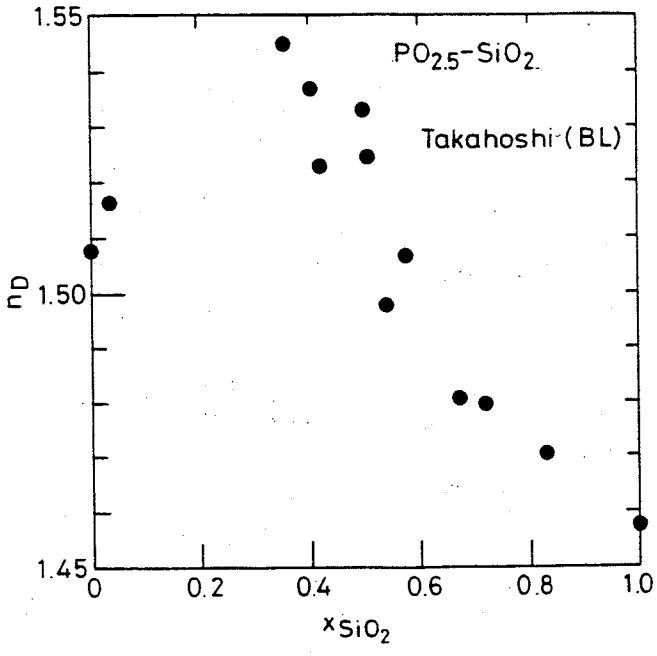


Fig. 16.18. Refractive indices (n_D) of $PO_{2.5}$-SiO_2 system at 25 °C as a function of mole fraction silica [56]

Rb_2O-SiO_2

Reported values [36, 47, 57] are given in Fig. 16.7 a.

SrO-SiO_2

Reported values [29] are given in Fig. 16.7 b.

SiO_2-TiO_2

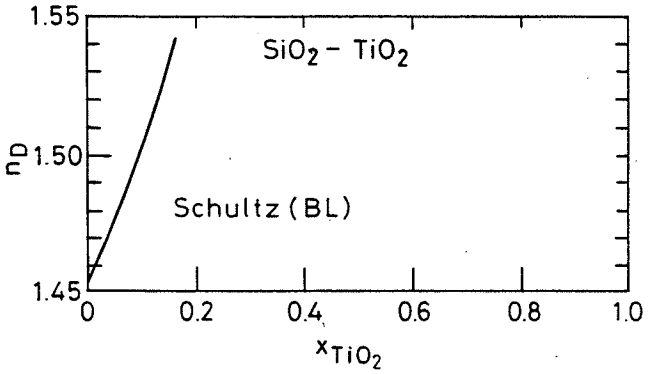


Fig. 16.19. Refractive indices (n_D) of SiO_2-TiO_2 glasses at 25 °C [58] as a function of mole fraction TiO_2

Al_2O_3-K_2O-SiO_2

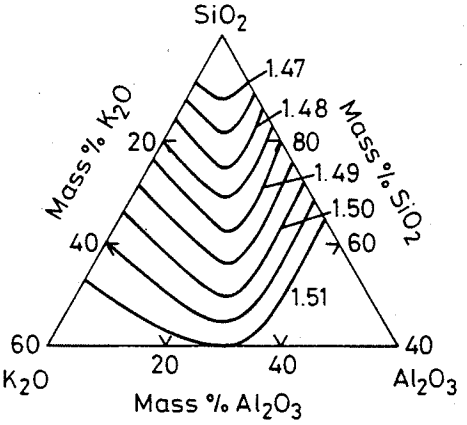


Fig. 16.22. Refractive indices of Al_2O_3-K_2O-SiO_2 glasses at 25 °C [63]

16.3.3 Ternary systems

Al_2O_3-CaO-SiO_2

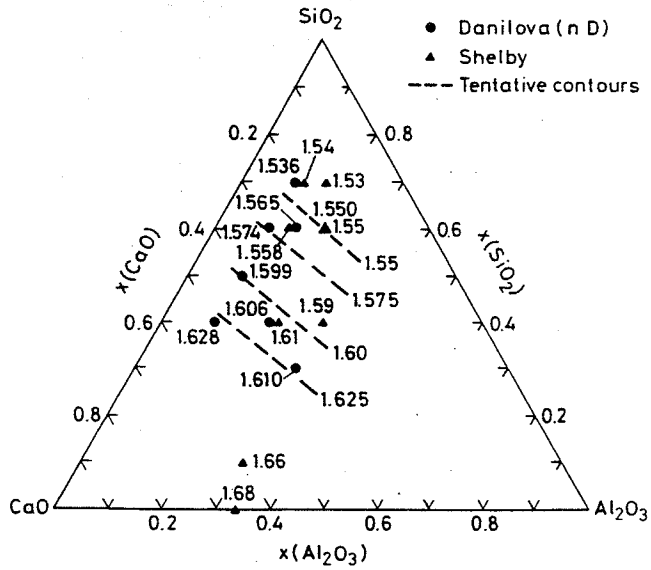


Fig. 16.20. Refractive indices (n_D) of Al_2O_3-CaO-SiO_2 glasses at 25 °C [59, 60]

Al_2O_3-FeO-SiO_2

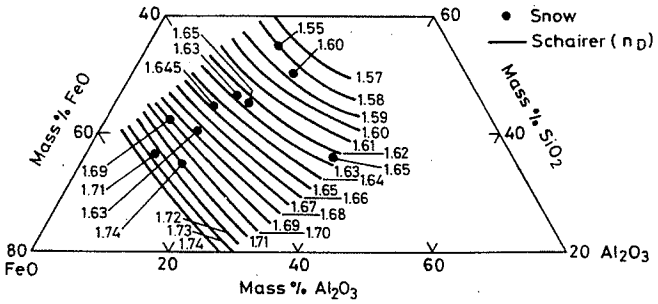


Fig. 16.21. Refractive indices of Al_2O_3-FeO-SiO_2 glasses at 25 °C [61, 62]

Al_2O_3-MnO-SiO_2

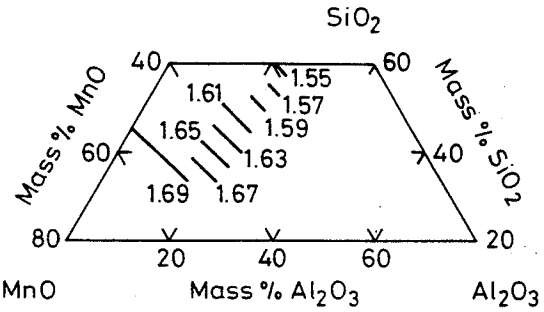


Fig. 16.23. Refractive indices of Al_2O_3-MnO-SiO_2 glasses at 25 °C [64]

Al_2O_3-Na_2O-SiO_2

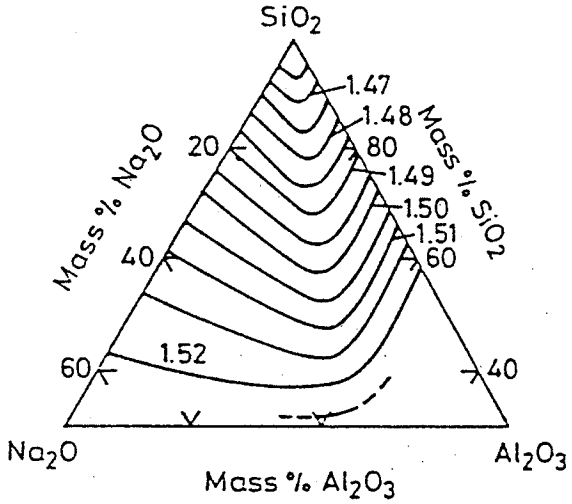


Fig. 16.24. Refractive indices of Al_2O_3-Na_2O-SiO_2 glasses at 25 °C [65]

$CaO\text{-}FeO\text{-}SiO_2$

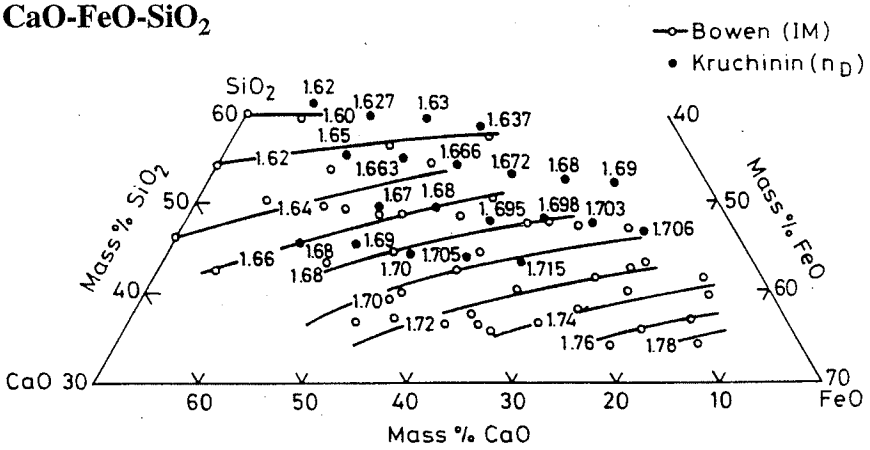


Fig. 16.25. Refractive indices of $CaO\text{-}FeO\text{-}SiO_2$ glasses at 25 °C [66, 67]

$CaO\text{-}MgO\text{-}SiO_2$

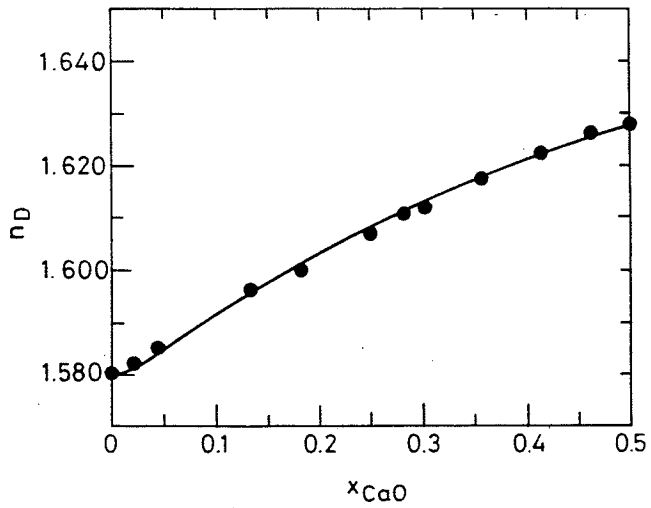


Fig. 16.26. The effect of replacing MgO with CaO on the refractive index at 25 °C in $CaO\text{-}MgO\text{-}SiO_2$ glasses with constant silica content ($x(SiO_2) = 0.5$) [35]

$CaO\text{-}Na_2O\text{-}SiO_2$

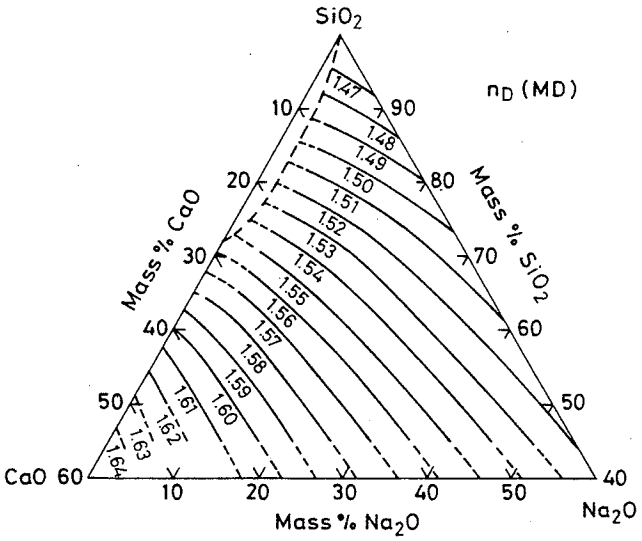
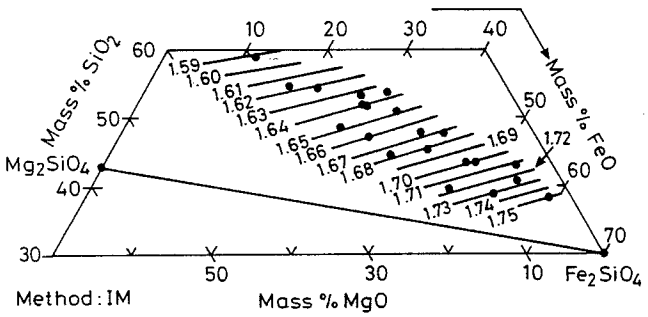


Fig. 16.27. Refractive indices (n_D) of $CaO\text{-}Na_2O\text{-}SiO_2$ glasses at 25 °C [30]

$FeO\text{-}MgO\text{-}SiO_2$



16.28. Refractive indices of $FeO\text{-}MgO\text{-}SiO_2$ glasses at 25 °C [68]

$Fe_2O_3\text{-}K_2O\text{-}SiO_2$

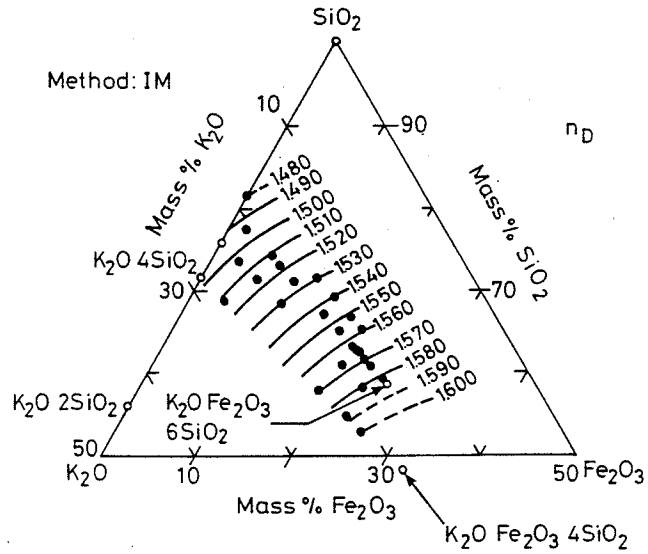


Fig. 16.29. The refractive indices (n_D) of $Fe_2O_3\text{-}K_2O\text{-}SiO_2$ glasses at 25 °C [46]

Fe_2O_3-Na_2O-SiO_2

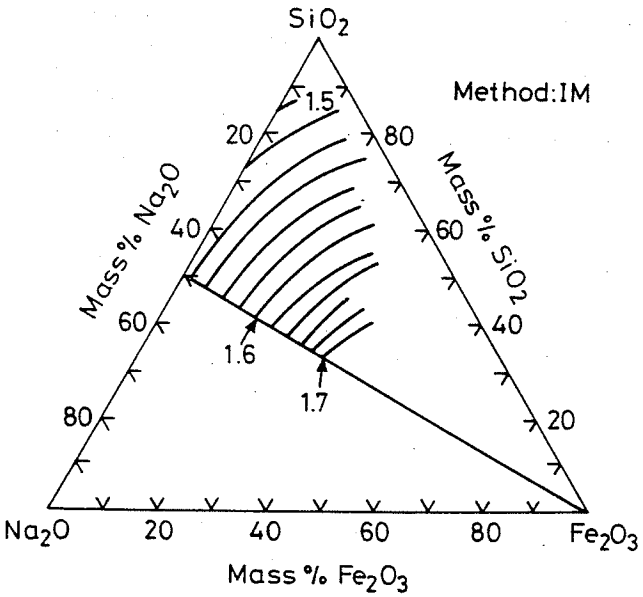


Fig. 16.30. Iso-fracts for Fe_2O_3-Na_2O-SiO_2 glasses at 25 °C [69]

MnO-Na_2O-SiO_2

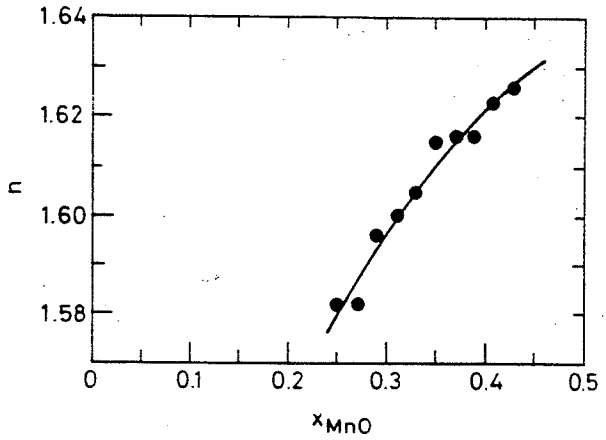


Fig. 16.31. The effect of replacing SiO_2 by MnO on the refractive index at 25 °C of MnO-Na_2O-SiO_2 glasses containing a constant Na_2O content ($x(Na_2O) = 0.15$) [70]

16.3.4 Quaternary systems

Al_2O_3-CaO-Fe_2O_3-SiO_2

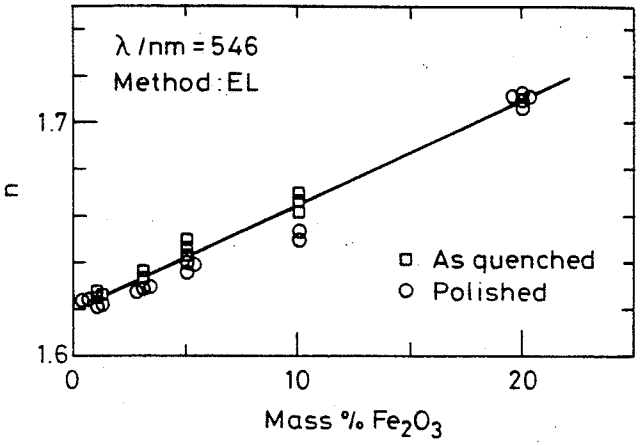


Fig. 16.32. The effect of Fe_2O_3 additions on the refractive index at 546 nm of 20 % Al_2O_3 - 40 % CaO – 40 % SiO_2 [18]

Al_2O_3-CaO-Na_2O-SiO_2

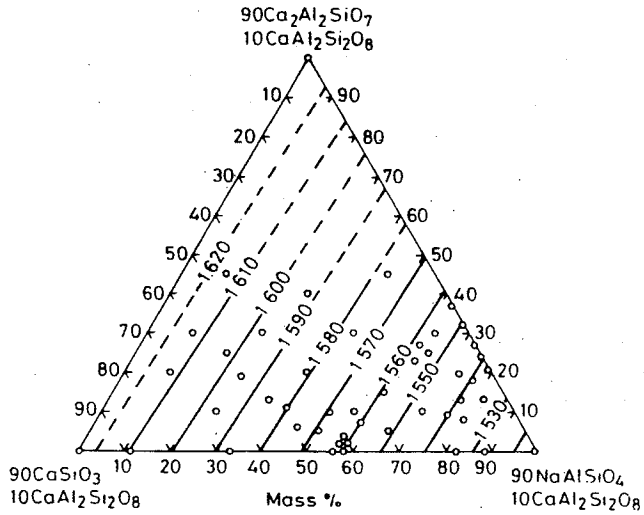


Fig. 16.33. Refractive indices at 25 °C for Al_2O_3-CaO-Na_2O-SiO_2 glasses containing 10 mass % $CaO.Al_2O_3.2SiO_2$ (anorthite) [71]

16.3.5 Continuous casting slags

Refractive index data is given in Tab. 16.1.

Tab. 16.1. Refractive index data for continuous casting slags

Reference	Slag composition, mass %									n_D
	CaO	SiO_2	Al_2O_3	MgO	Na_2O*	FeO	MnO	F	C	
[72]	34.8	35.6	7.3	4.4	8.4	0.65	3.1	6.2	0.45	1.588
[73]	44.1	39.0	7.0	1.0	5.5	0.7	0.1	4.8	0.15	1.60
*Na_2O + K_2O										

16.4 Absorption coefficients of slags

16.4.1 Introduction

The intensity of light passing through a medium (other than vacuum) is reduced due to absorption, scattering and reflection of the photons. Absorption results from (I) rotation and vibration of molecules, (II) electron transitions and (III) interactions between electrons and phonons. Scattering occurs at grain boundaries and defects and reflection at the surface and interfaces of the sample.

The absorption coefficient (α) is given by equation [16.14] where I_o and I denote the original and transmitted intensities respectively, and d the thickness of the sample.

$$I = I_o \exp(-\alpha d). \tag{16.14}$$

In solids it is necessary to use the extinction coefficient (E) since the transmission of the sample is affected by both the absorption and scattering of photons; the extinction coefficient is defined by equation (16.15) where s is the scattering coeffient.

$$E = \alpha + s. \tag{16.15}$$

16.4.2 Experimental methods

16.4.2.1 Transmission methods [74 – 77, 18]

Absorption and extinction coefficients are usually measured by determining the transmittance of the sample using an arrangement such as that shown in Fig. **16.34**, in which the intensities of the incident (I_o) and emergent (I) beams are measured using a spectrophotometer. Values of α or E can then be derived by using equation (16.14).

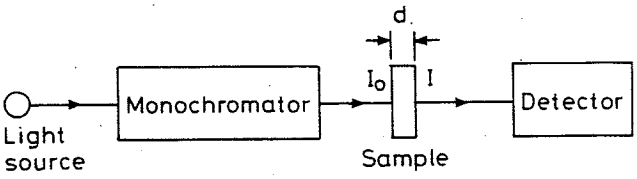


Fig. 16.34. Schematic diagram of the apparatus used in transmission experiments

16.4.2.2 Reflectance measurements [76]

Measurements of both the transmittance (t) and reflectance (r) have been used to determine absorption coefficient of slags using equations (16.16) and (16.17), where t_a is the apparent transmittance and r_a the apparent reflectance of the sample **(Fig. 16.35).** Alternatively, absorption coefficients can be derived solely from equation (16.16) by using samples with different thicknesses (d).

$$t_a = \left(I_t/I_o\right) = \frac{(1-r)^2 \exp^{-\alpha d}}{1 - r^2 \exp^{-2\alpha d}} \tag{16.16}$$

$$r_a = \left(I_t/I_o\right) = r\left\{1 + \frac{(1-r)^2 \exp^{-2\alpha d}}{1 - r^2 \exp^{-2\alpha d}}\right\} \tag{16.17}$$

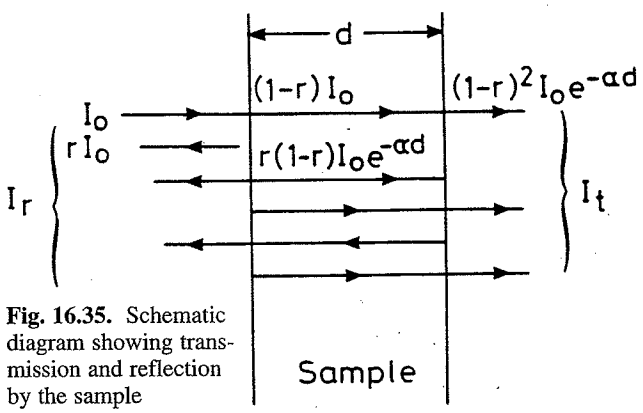


Fig. 16.35. Schematic diagram showing transmission and reflection by the sample

16.4.3 Factors affecting absorption coefficients

The principal factors affecting absorption and extinction coefficients are outlined below.

16.4.3.1 Wavelength

The effect of wavelength on the absorption coefficient can be clearly seen in **Figs. 16.36 a** and **b.** The strong absorption peak above 4.5 μm is due to the vibrations of the SiO_2 structure and Fe^{2+} absorbs strongly around 1.1 μm.

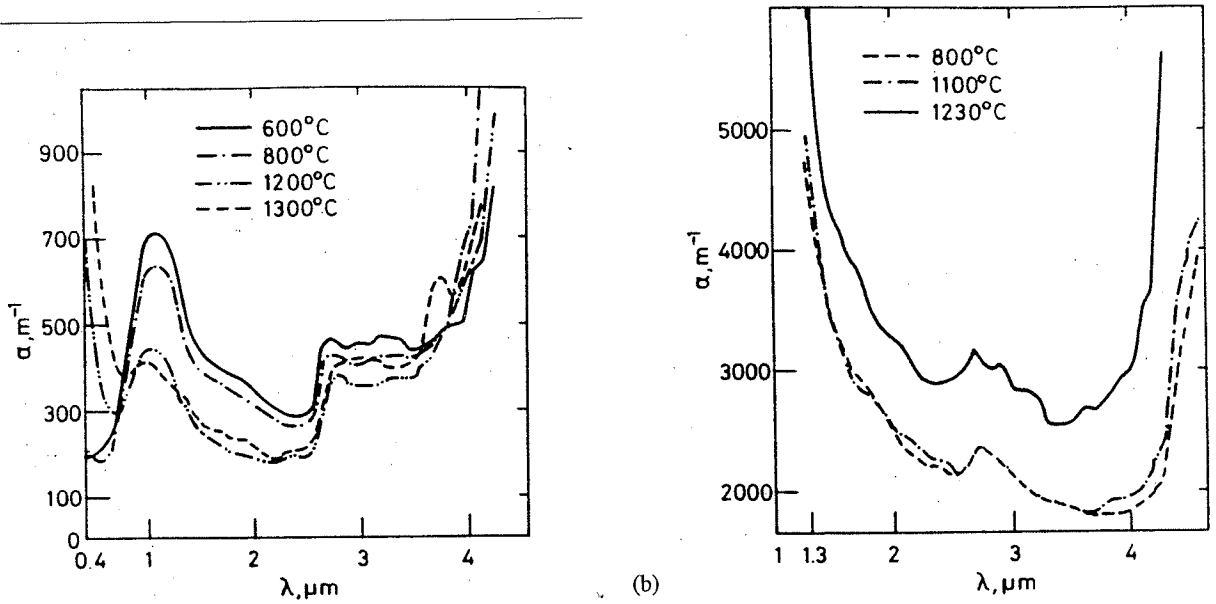


Fig. 16.36 a,b. Absorption coefficient [78] as a function of wavelength and temperature for (a) a glass with a low FeO content (0.34 %) [78] and (b) a glass with composition 67 % SiO_2 + 16 % Na_2O + 9 % (FeO + Fe_2O_3)

16.4.3.2 Temperature

It can be seen from Fig. 16.36. that the absorption coefficient is dependent upon temperature, however the effect is difficult to predict since the absorption coefficients increase with decreasing temperature in Fig. 16.36a and increasing temperature in Fig. 16.36b [78].

The temperature also affects the wavelength distribution used to derive the global value of the absorption coefficient **(Fig. 16.37)** where the fraction of the total energy emitted in the 1-4.4 μm "window" constitutes 61.1, 79.5 and 81.9 % of the total energy at 1073, 1573 and 1773 K, respectively [79].

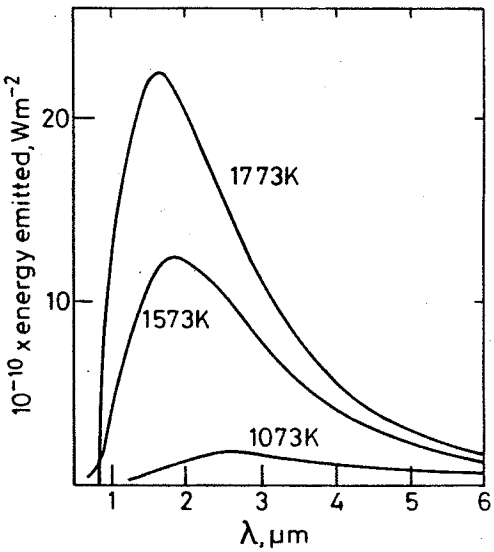


Fig. 16.37. Wavelength distribution of the source energy emission of a black body [79]

16.4.3.3 Transition metal oxides

Absorption coefficients are very dependent upon the concentrations of transition metal oxide eg (FeO, MnO) but are less affected by Fe_2O_3 as can be seen by **Fig. 16.38.** A rule for estimating [79] the average absorption coefficient (equation 16.18) was derived from transmission data and predicted values are in reasonable agreement with the measured values [80] shown in Fig. 16.38.

$$\alpha(m^{-1}) = 1100\ (\%\ FeO). \qquad (16.18)$$

Increases in the partial pressures of oxygen and sulphur above MnO-SiO_2 melts were both found [81] to increase the absorption coefficients **(Fig. 16.39).**

16.4.3.4 Crystallinity

In solid samples the extinction coefficient will be greatly influenced by the crystallinity of the specimen since increased crystallinity will cause more scattering of the photons and result in an increase in the scattering coefficient (equation 16.15). Thus extinction coefficients will be dependent upon the thermal histories of the samples.

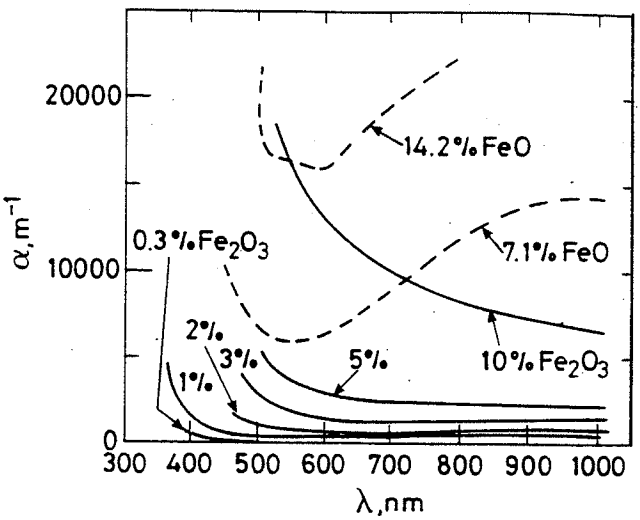
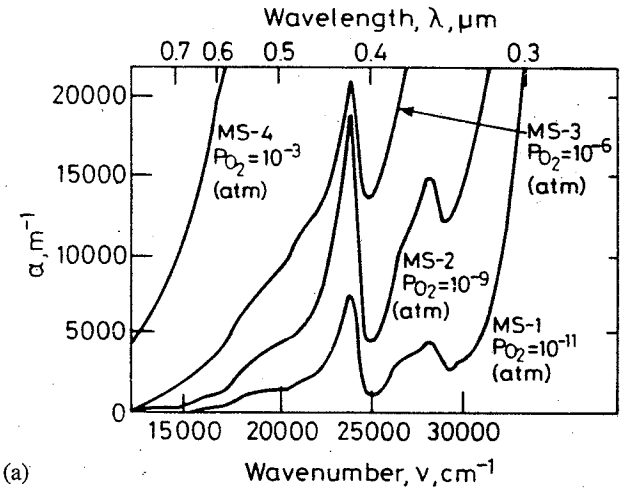
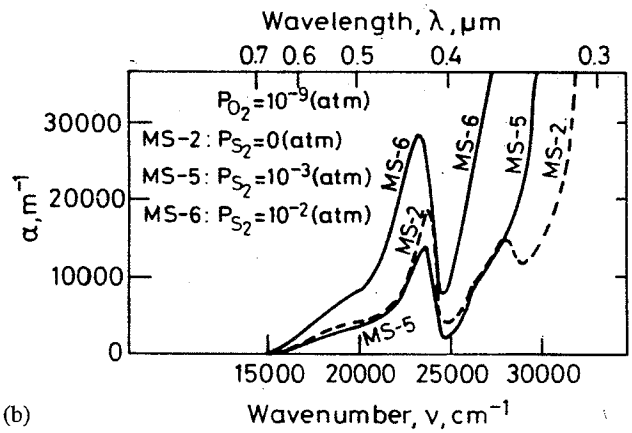


Fig. 16.38. The effect of FeO and Fe_2O_3 contents on the absorption coefficients (at 25 °C) of slags containing 20 % Al_2O_3 – 46 % CaO – 40 % SiO_2, – and 14.6 % Al_2O_3 – 36.6 % CaO – 12.2 % MgO – 36.6 % SiO_2, - - - [18]



(a)



(b)

Fig. 16.39 a,b. The effects of (a) P_{O_2} and (b) P_{S_2} in the gas phase above 59 % MnO – 41% SiO_2 melts at 1350 °C [81] on the absorption coefficients (at 25 °C) of the quenched glasses

16.5 Absorption coefficient data

The absorption coefficients of metallurgical slags are primarily controlled by the concentrations of transition metal oxides and these slags always contain FeO, MnO, etc. Consequently, the main focus of this review has been directed at the effects of transition metal concentrations and not the "background" absorption due to the silicate lattice.

16.5.1 Pure substances

CaF_2

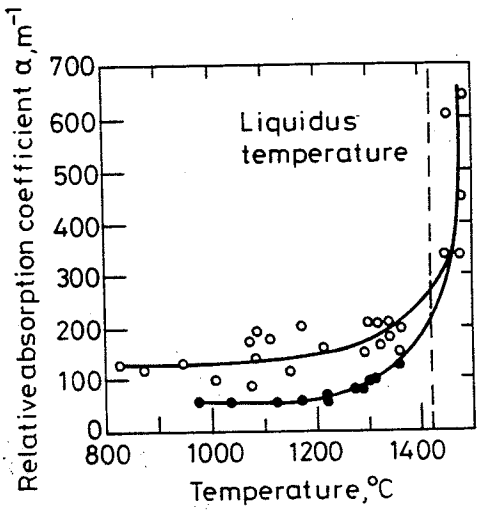


Fig. 16.40. Absorption coefficients reported for CaF_2 as a function of temperature [82]; O, experimental results for melt and solidified melt; ●, polished CaF_2 plate

SiO_2

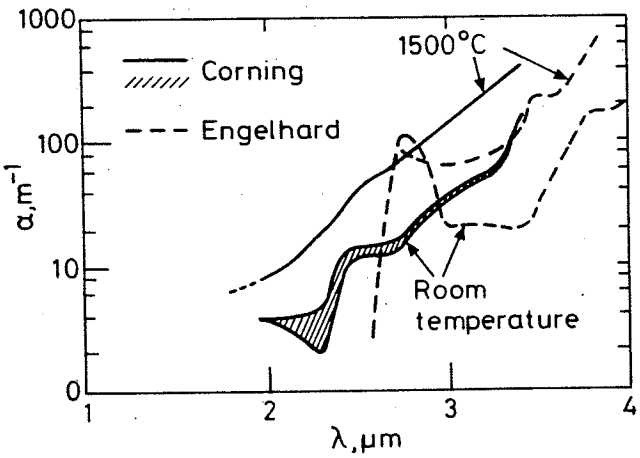


Fig. 16.41. Extinction coefficients of SiO_2 as a function of wavelength; Corning, IR glass; Englehard – UV glass [83]

16.5.2 Binary systems

K_2O-SiO_2
Li_2O-SiO_2

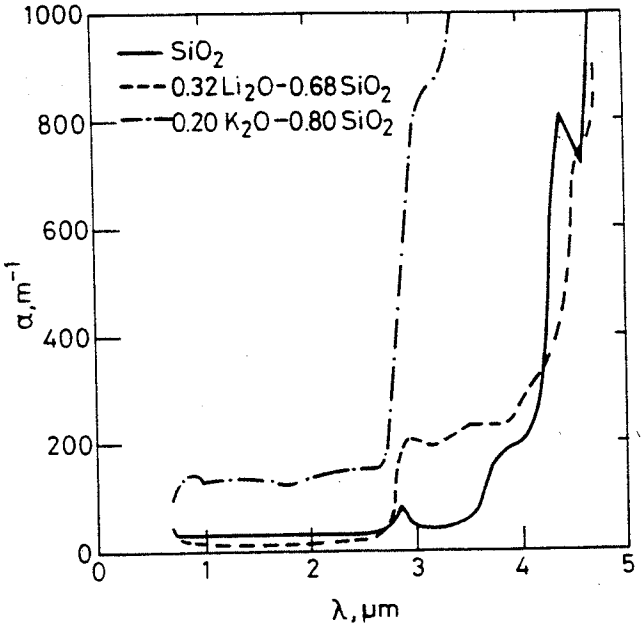


Fig. 16.42. Absorption coefficients (calculated from transmission data [84]) as a function of wavelength

MgO-SiO_2

Schatz and Simmons [85] have reported values for the extinction coefficient of $MgO.SiO_2$ from a "best fit" analysis of experimental thermal flux data.

MnO-SiO_2

Extinction coefficients at 25 °C of MnO-SiO_2 slags have been determined by Goto et al [81] and are shown in Fig. 16.39.

Na_2O-SiO_2

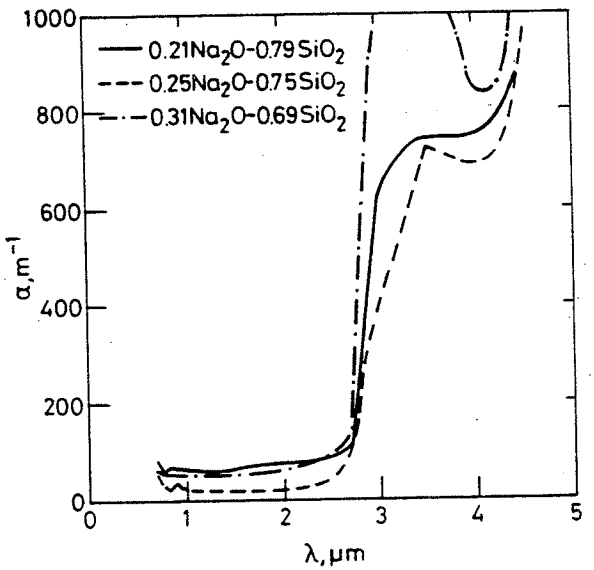


Fig. 16.43. Absorption coefficients (calculated from transmission data [84]) of Na_2O-SiO_2 glasses as a function of wavelength

$PbO\text{-}SiO_2$

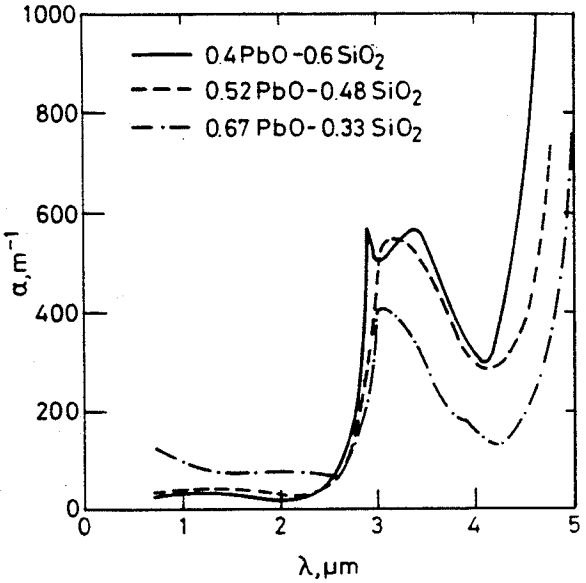


Fig. 16.44. Absorption coefficients (calculated from transmission data [84]) for $PbO\text{-}SiO_2$ glasses as a function of wavelength

16.5.3 Ternary systems

$Al_2O_3\text{-}CaF_2\text{-}CaO$

Mitchell and Wadier [86] have reported a value of $\alpha = 130\ m^{-1}$ for molten 15 % Al_2O_3 - 70 % CaF_2 - 15 % CaO slags.

$Al_2O_3\text{-}CaO\text{-}SiO_2$

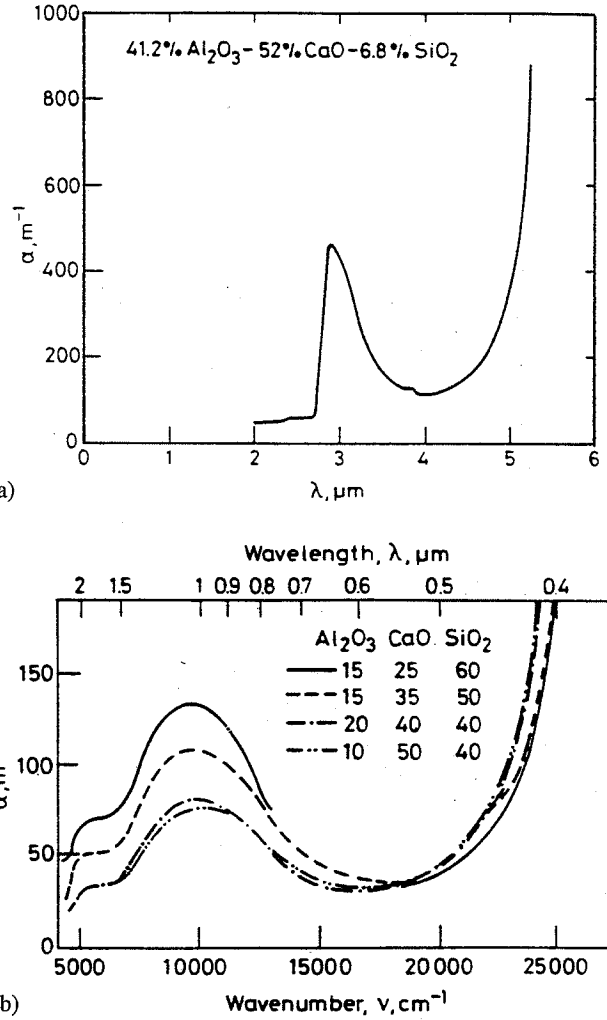


Fig. 16.45 a,b. The extinction (at 25 °C) of $Al_2O_3\text{-}CaO\text{-}SiO_2$ slags (a) containing 41.2 % Al_2O_3 - 52 % CaO - 6.8 % SiO_2 [87] and (b) four compositions containing 0.3 % Fe_2O_3 as a function of wavenumber (reciprocal wavelength) [75]

Fe_2O_3-Na_2O-SiO_2

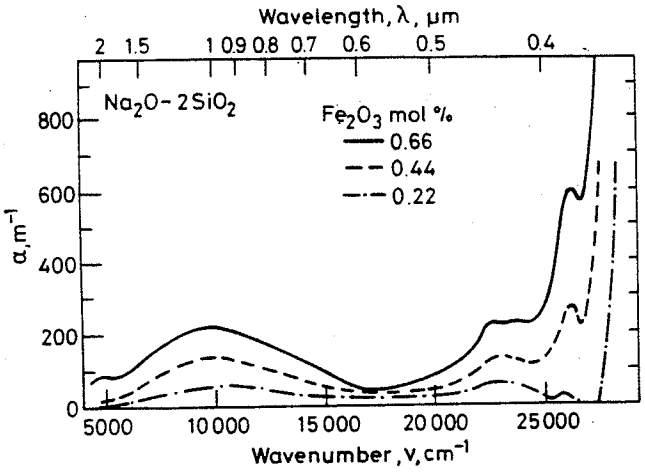


Fig. 16.46. The effect of Fe_2O_3 content on the extinction coefficients (at 25 °C) of $Na_2O.2SiO_2$ [75] as a function of wavenumber (reciprocal wavelength)

16.5.4 Quaternary systems

Al_2O_3-CaO-FeO_x-SiO_2
Al_2O_3-CaO-FeO_x-MgO-SiO_2

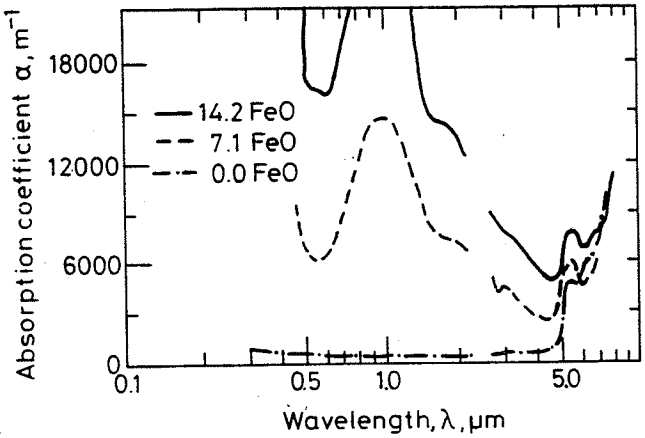
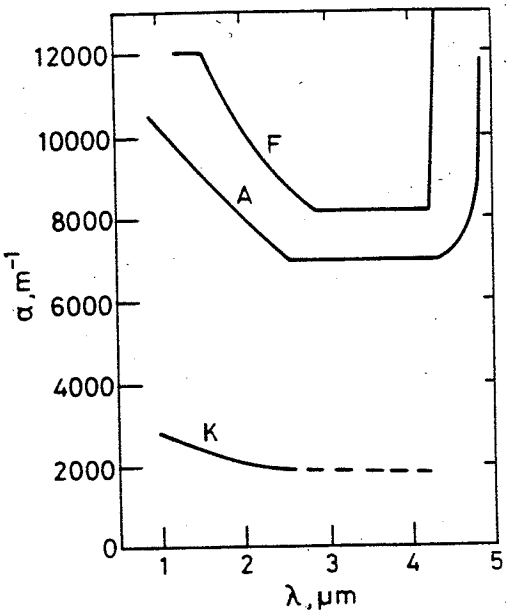


Fig. 16.47. The effect of additions of 7.1 and 14.2 % FeO on the extinction coefficients at 25 °C of 14.6 % Al_2O_3 - 36.6 % CaO - 12.2 % MgO - 36.6 % SiO_2 slags [77]. See also Fig. 16.38.

16.5.5 Coal slags

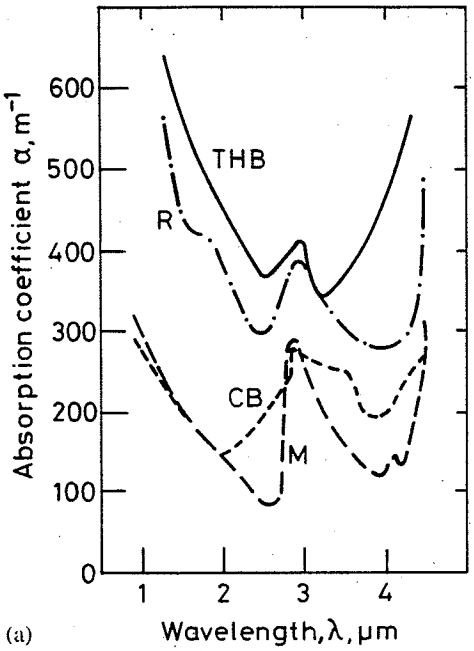


	Mass %				
	CaO*	SiO_2	Al_2O_3	Na_2O^+	FeO
A	24.8	36.4	22.2	2.9	5.3
F	18	33	26.7	4.3	3.3
K	29.3	36.3	28.0	2.6	0.5

*CaO + MgO $^+Na_2O + K_2O$

Fig. 16.48. Extinction coefficients of coal slags at 25 °C as a function of wavelength [88]

16.5.6 Continuous casting slags

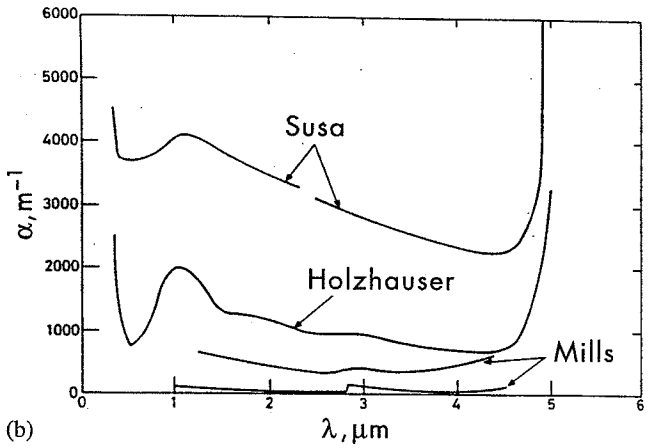


(a)

Slag/[Ref.]	Mass %								
	CaO	SiO_2	Al_2O_3	MgO	Na_2O*	FeO	MnO	F	C
THB+ [87]	32.3	25.5	7.8	0.7	11.5	2.3	5.7	6	-
R [87]	31.0	32.0	8.5	1.3	4.1	0.2	0.1	4	-
CB [87]	33.5	31.5	6.5	-	4.5	0.5	-	5.3	-
M [87]	34	34	5.5	-	4.0	0.2	-	5.3	-
ST1 [73]	44.1	39.0	7.0	1.0	5.5	0.7	0.1	4.8	0.15
Mould Slag [72]	34.8	35.6	7.3	4.4	8.4	0.65	3.1	6.2	0.45

*$Na_2O + K_2O$ +Powder analysis

Fig. 16.49 a,b.
(a) Extinction coefficients of glassy continuous casting slags at 25 °C as a function of wavelength [89]
(b) Extinction coefficients at 25 °C of continuous casting slags for (a) glassy [73, 89] samples and a slag taken from the mould [72]. Average values of 1300 and 2300 m^{-1} have also been reported [90] for glass, crystalline and liquid of a slag



(b)

16.5.7 Glasses

Absorption coefficients for typical glasses are shown in Fig. 16.36., other examples are given in references [74, 78, 79].

16.5.8 Minerals, Rocks

Values for the absorption coefficients of rocks and minerals have been reported by several investigators [76, 85, 92, 93]. It was reported that the absorption coefficient of peridot increased from 50 m^{-1} at 25 °C to 430 m^{-1} at 1240 °C [76].

16.6 References in Chapter 16

[1] Mills, K. C.; Susa, M.: NPL Report. DMM (A) 68 (1992)
[2] Hartschorne, N. H.; Stuart, A.: "Crystals and the Polarising Microscope". E. Arnold and Co., London, (1950)
[3] Aramaki, Sh.; Roy, R.: J. Am. Ceram. Soc., 45 (1962), 229
[4] Williamson, J.; Glasser, F. P.: Phys. Chem., Glasses, 5 (1964) 52
[5] Arndt, J.; Stoffler, D.: Phys. Chem. Glasses, 10 (1969), 117
[6] Pfund, A. H.: J. Opt. Soc., Amer., 31 (1941), 679
[7] Akimov, V. V.: Zh. Prikl. Khim., 33 (1960), 2190
[8] Hamilton, E. H.; Cleek, G. W.; Grauer, O. H.: J. Am. Ceram. Soc., 41 (1958) 209
[9] Scholze, H.; Franz, H.; Merker, L.: Glastech. Ber., 32 (1959), 421
[10] Schroeder, J.; Mohr, R.; Macedo, P. B.; Montrose, C. J.: J. Am. Ceram. Soc., 56 (1973) 510
[11] Verweij, H.; Buster, J. H. J. M.; Remmers, G. F.: J. Mater. Sci., 14 (1979), 931
[12] Wray, J. H.; Neu, J. T.: J. Opt. Soc., Am., 59 (1969), 774
[13] Fleming, J. W.: J. Am. Ceram. Soc., 59 (1976), 503
[14] Takahashi, S.; Shibata, S.: J. Non-Crystall. Solids, 30 (1979), 359
[15] Kim, B. H.; Yamane, M.: J. Ceram. Soc., Jpn., 88 (1980), 191
[16] Freeman, M. H.: Optics, 10th ed, Butterworths, (1990), 360
[17] Vasicek, A.: J. Opt. Soc., Amer., 37 (1947), 145 and 979
[18] Susa, M.; Li, F.; Nagata, K.: Metall. Trans. B, 23B (1992), 331 – 337
[19] Krishnan, S.; Weber, J. K. R.; Schiffman, R. A.; Nordine, P. C.; Reed, R. A.: J. Amer. Ceram. Soc., 74 (1991), 881 – 883
[20] Wray, J. H.; Neu, J. T.: J. Opt. Soc. Am., 59 (1969), 774 – 776
[21] Austin, J. B.; Pierce, R. H. H.: Physics, 6 (1935), 43 – 46
[22] Aramaki, Sh.; Roy, R.: J. Amer. Ceram. Soc., 45 (1962), 229 – 242
[23] Topol, L. E.; Hengstenberg, D. H.; Blander, M.; Happe, R. A.; Richardson, N. L.; Nelson, L. S.: J. Non-Crystall. Solids, 12 (1973), 377 – 390
[24] Kato, D.: J. Appl. Phys., 47 (1976), 5344 – 5348
[25] Thompson, C. L.; Parmelee, C. W.: J. Am. Ceram. Soc., 20 (1937), 305 – 308
[26] Bruckner, R.; Navaro, J. M. F.: Glastech. Ber., 39 (1966), 283 – 293
[27] Wemple, S. H.; Pinnow, D. A.; Rich, T. C.; Jaeger, R. E.; van Uitevt, L. G.: J. Appl. Phys., 44 (1973), 5432 – 5437
[28] Flemming, J. W.: J. Am. Ceram. Soc., 59 (1976), 503 – 507
[29] Eskola, P.: Am. J. Sci., 4 (1922), 331 – 375
[30] Morey, G. W.; Merwin, H: E.: J. Opt. Soc., Amer., 22 (1932), 632 – 662
[31] Green, K. T.; Morgan, W. R.: J. Amer. Ceram. Soc., 24 (1941), 111 – 116
[32] Dietzel, A.; Florke, O. W.: Glastech. Ber., 28 (1955), 423 – 426
[33] Hamilton, E. H.; Cleek, G. W.; Grauer, O. H.: J. Amer. Ceram. Soc. 41 (1 958), 209 – 215
[34] Graham, P. W. L.; Rindone, C. E.: Phys. Chem., Glasses, 8 (1967), 160 – 163
[35] Larsen, E. S.: Am. J. Sci., Ser IV, 28 (1909), 263 – 274
[36] Shmidt, Yu. A.; Alekseeva, Z. D.: Zh. Prikl. Khim., 37 (1964), 2299 – 2303
[37] Bezborodov, M. A.; Bobkova, N. M.: Dokl. Akad. Nauk. SSSR, 116 (1957), 652 – 655, Influence of Cesium on some properties of silicate and Borate glasses. Minsk, (1958) 42, (in Russian), and Silikattechnik, 10 (1959) 584/586. Bobkova, N.M.: Tr. Beloruss. Politekh. Inst., (1958), 16 – 26

[38] Galant, E. I.: Fiz. Khim. Stekla, 6 (1980), 121 – 124
[39] Huang, Y. Y.; Sarkav, A.; Schultz, P. C.: J. Non-Crystall. Solids, 27 (1978), 29 – 37
[40] Kracek, F. C.: J. Phys. Chem., 34 (1930), 2641 – 2650
[41] Hubbard, D.; Cleek, G. W.: J. Res. Nat. Bur. Stand., 49 (1952), 267 – 272
[42] Vargin, V. V.; Zasolotskaya, M. V.; Kind, N. E.; Kondratiev, Yu. N.; Milyukov, E. M.; Tudorovskaya, N. A.: Catalysed Regulated Crystallisation of Glasses of Li_2O-Al_2O_3-SiO_2 System. Leningrad pt. 2, (1971), 200 (in Russian)
[43] Dubrovo, S. K.; Shmidt, Yu. A.: Zh. Prikl. Khim., 32 (1959), 742 – 749
[44] Scholze, H.; Franz, H.; Merker, L.: Glastech. Ber., 32 (1959), 421 – 426
[45] Verweij, H.; Buster, J. H. J. M.; Remmers, G. F.: J. Mater. Sci., 14 (1979), 931 – 940
[46] Faust, G. T.; Peck, A. B.: J. Am. Ceram. Soc., 21 (1938), 320 – 324
[47] Shelby, J. E.; Day, D. E.: J. Am. Ceram. Soc:, 52 (1969), 169 – 177
[48] Faick, C. A.; Finn, A. N.: J. Res. Nat. Bur. Stand., 6 (1031), 993 – 1002 and J. Am. Ceram. Soc., 14 (1931), 518 – 528
[49] Winter-Klein, A.: Verres Refr., 13 (1959), 125 – 130
[50] Akimov, V. V.: Zh. Prikl. Khim., 33 (1960), 2190 – 2197
[51] Götz, W.; Sönnichsen, P.; Berner, W.; Schwabe, K. D.: Silikat-Technik, 28 (1977), 175 – 177
[52] Wright, F. E.: J. Am. Ceram. Soc., 3 (1920), 783 – 832
[53] Kordes, E.: Z. Anorg. Allg. Chem., 241 (1939), 1 – 38
[54] Demkina, L. I.: Dependence of Properties of Glasses on their Compositions. Leningrad, (1958), 237 (in Russian)
[55] Kim, B. H.; Yamane, M.: J. Ceram. Soc., Jpn., 88 (1980), 191 – 196
[56] Takahashi, K.; Mochida, N.; Matsui, H.; Takeuchi, S.; Gohshi, Y.: J. Ceram. Soc., Jpn., 84 (1976), 482 – 490
[57] Simpson, H. E.: Glass Ind., 42 (1961), 189 – 193 and 222 – 223
[58] Schultz, P. C.: J. Am. Ceram. Soc., 59 (1976), 214 – 219
[59] Danilova, N. P.; Dubrovo, S. K.: Zh. Prikl. Khim., 40 (1967), 992 – 998
[60] Shelby, J. E.: J. Am. Ceram. Soc., 68 (1985), 155 – 158
[61] Snow, R. B.; McCaughey, W. J.: J. Am. Ceram. Soc., 25 (1942), 151 – 160
[62] Schairer, J. F.; Yagi, K.: Am. J. Sci., Bowen vol. pt.2, (1952), 471 – 512
[63] Schairer, J. F.; Bowen, N. L.: Am. J. Sci., 253 (1955), 681 – 746
[64] Snow, R. B.: J. Am. Ceram. Soc., 26 (1943), 11 – 20
[65] Schairer, J. F.; Bowen, N. L.: Am. J. Sci., 254 (1956), 129 – 195
[66] Bowen, N. L.; Schairer, J. F.; Posnjak, E.: Am. J. Sci., 20 (1933), 193 – 284
[67] Kruchinin, Yu. D.; Kuleshov, E. A.: Fiz. Khim. Stekla, 5 (1979), 392 – 397
[68] Bowen, N. L.; Schairer, J. F.: Am. J. Sci., 29 (1935), 151 – 217
[69] Bowen, N. L.; Schairer, J. F.; Willems, H. W. V.: Am. J. Sci., 20 (1930), 405 – 455
[70] Shcheglova, M. D.; Sadomskaya, T. A.: Vopr. Khim Tekhnol. Kharkov, 73 (1983), 6 – 8
[71] Yoder, H.S.: J. Geol., 60 (1952), 586
[72] Susa, M.: Unpublished results
[73] Holzhauser, J. F.; Spitzer, K. H.; Schwerdtfeger, K.: Final report ECSC Contract 7210-CA/139
[74] Grove, F. J.; Jellyman, P. E.: J. Soc., Glass Technol., 39 (1955), 3 – 15T
[75] Ito, T.; Goto, K. S.: Tetsu-to-Hagane, 60 (1974), 184 – 191
[76] Aronson, J. R.; Bellotti, L. H.; Eckroad, S. W.; Emslie, A. G.; McConnell, R. K.; von Thuna, P. C.: J. Geophys. Res., 75 (1910), 3443 – 3456
[77] Fine, H. A.; Engh, T.; Elliott, J. F.: Metall. Trans. B, 7B (1976), 277 – 285
[78] Blazek, A.; Endrys, J.: Review of Thermal Conductivity data on glass. Part II: Thermal conductivity at high temperatures. Publ. Intl. Comm. on Glass, (A5) (1983), 34 – 100
[79] Mills, K. C.: Mineral Matter and Ash in Coal. Edit K. S. Vorres, ACS Symp. Ser. 301 (1986), 256 – 276
[80] Steele, F. N.; Douglas, R. W.: Phys. Chem., Glasses, 6 (1965), 246 – 252
[81] Goto, K.; Lodde, J.; Pluschkell, W.: Metall. Trans., 2 (1971), 2633 – 2636
[82] Keene, B. J.; Mills, K. C.: Arch. of Eisenhüttenwes., 52 (1981), 313
[83] Beder, E. C.; Bass, C. D.; Shackleford, W. L.: Appl. Optics, 10 (1971), 2263 – 2268
[84] Florence, J. M.; Glaze, F. W.; Hahner, C. H.; Stair, R.: J. Res. NBS, 41 (1948), 623 – 626
[85] Schatz, J. H.; Simmons, G.: J. Geophys. Res., 77 (1972), 6966 – 6983
[86] Mitchell, A.; Wadier, J. F.: Can. Metall. Q, 20 (1981), 373
[87] Glaze, F. W.: Ceram. Bulletin, 34 (1955), 291 – 294
[88] Mills, K. C.; Rhine, J. M.: Fuel, 68 (1989) 904 – 910
[89] Mills, K. C.; Olusanya, A.; Brooks, R.; Morrell, R.; Bagha, S.: Ironmaking and Steelmaking, 15 (1988), 257 – 264
[90] Ohmiya, S.; Tacke, K. H.; Schwerdtfeger, K.: Ironmaking and Steelmaking, 10 (1983), 24
[91] Coenen, M.: Glastech. Ber., 41 (1968), 1 – 10
[92] Clarke Jr., S. P.: Amer. Mineralog., 42 (1957), 732
[93] Fukao, Y.; Mitzutani, H.; Uyeda, S.: Phys. Earth Planet. Interiors, 1 (1968), 57